

AD-A286 738



# II-VI COMPOUNDS 1993

DTIC  
SELECTED  
EC 2 8 1994  
F

This document has been approved  
for public release and sale; its  
distribution is unlimited.

95 3 31 006

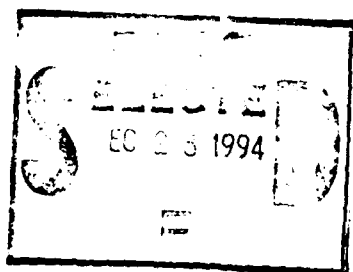
95-01109



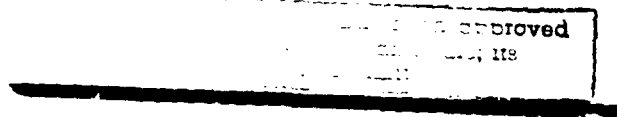
North-Holland

# II-VI COMPOUNDS 1993

Proceedings of the Sixth International  
Conference on II-VI Compounds and  
Related Optoelectronic Materials  
Newport, RI, USA, 13-17 September 1993



Edited by:  
R.N. Bhargava  
R.P. Ruth  
T. Yao  
A.V. Nurmikko



19941223 106

North-Holland



# II-VI COMPOUNDS 1991

PROCEEDINGS OF THE SIXTH INTERNATIONAL  
CONFERENCE ON II-VI COMPOUNDS AND  
RELATED OPTOELECTRONIC MATERIALS  
NEWPORT, RI, USA, 13-17 SEPTEMBER 1993

EDITED BY

**R.N BHARGAVA**

*Nanocrystals Technology, Briarcliff Manor, NY, USA*

**R.P. RUTH**

*Santa Barbara Research Center, Goleta, CA, USA*

**T. YAO**

*Hiroshima University, Higashi-Hiroshima, Japan*

**A.V. NURMIKKO**

*Brown University, Providence, RI, USA*

*Cosponsored by*

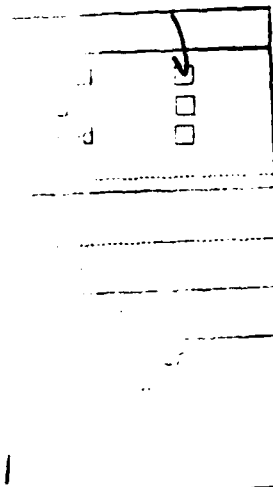
Brown University - Center for Advanced Materials Research  
US Office of Naval Research  
US Advanced Research Projects Agency  
Hughes Research Laboratories  
Santa Barbara Research Center



ELSEVIER

AMSTERDAM-LONDON-NEW YORK-TOKYO

DTIC QUALITY INSPECTED 1



© 1994 Elsevier Science B.V. All rights reserved

*No part of this publication may be reproduced, stored in a retrieval system or transmitted in any form or by any means, electronic, mechanical, photocopying, recording or otherwise, without the written permission of the publisher, Elsevier Science B.V., Copyright and Permissions Department, P.O. Box 521, 1000 AM Amsterdam, The Netherlands*

*Special regulations for readers in the USA: This publication has been registered with the Copyright Clearance Center Inc. (CCC), Salem, Massachusetts. Information can be obtained from the CCC about conditions under which photocopies of parts of this publication may be made in the USA.*

*All other copyright questions, including photocopying outside of the USA, should be referred to the Publisher.*

*No responsibility is assumed by the Publisher for any injury and / or damage to persons or property as a matter of products liability, negligence or otherwise, or from any use or operation of any methods, products, instructions or ideas contained in the material herein. Although all advertising material is expected to conform to ethical standards, inclusion in this publication does not constitute a guarantee or endorsement of the quality or value of such product or of the claims made of it by its manufacturer.*

*This volume is printed on acid-free paper.*

Reprinted from:  
JOURNAL OF CRYSTAL GROWTH 138 (1994) Nos. 1-4

The Manuscripts of the Proceedings were  
received by the Publisher: September 1993 / January 1994

*Printed in The Netherlands*

SIXTH INTERNATIONAL CONFERENCE ON II-VI COMPOUNDS AND  
RELATED OPTOELECTRONICS MATERIALS

II-VI Compounds 1993

Newport, RI, USA, 13-17 September 1993

*Conference Chair*

R.N. Bhargava

*Program Chair*

A.V. Nurmikko

*International Advisory Committee*

I. Broser (Germany)  
B. Cavenett (UK)  
R.L. Gunshor (USA)  
J. Kossut (Poland)  
H. Kukimoto (Japan)  
Y. Marfaing (France)  
T. McGill (USA)  
Y.S. Park (USA)  
H. Ruda (Canada)  
S. Shionoya (Japan)

*Program Committee*

G. Bauer (Austria)  
L.L. Chang (USA)  
J.M. DePuydt (USA)  
S. Fujita (Japan)  
J.F. Furdyna (USA)  
R.R. Galazka (Poland)  
E. Gobel (Germany)  
O. Goede<sup>†</sup> (Germany)  
H. Kobayashi (Japan)  
L. Kolodziejski (USA)  
H. Mariette (France)  
T. Mitsuyu (Japan)  
N. Taskar (USA)  
C. van de Walle (USA)

<sup>†</sup> Deceased 1993

## Acknowledgments

The editors would like to acknowledge the diligent and prompt effort of many anonymous referees and the support of session Chairpersons without whom the preparation of these proceedings would have not been possible. Special thanks are due to Françoise Y. Verploegh Chassé, Technical Editor of the *Journal of Crystal Growth*, whose relentless eighteen-hour days at the conference and expertise in compiling the manuscripts afterwards made this special issue possible.

We also want to thank for their generous financial support the US Office of Naval Research, US Advanced Research Projects Agency, Hughes Research Laboratories, Santa Barbara Research Center, and Brown University Center for Advanced Materials Research.

The excellent organizational skills and support provided by the staff of the Center for Advanced Materials Research Center at Brown University made this conference possible. Special thanks to Sue C. Masoian (financial officer and conference coordinator) and staff members Toni Barbosa, Marn-Yee Lee, and Susan E. Whitney, along with several graduate students, who all contributed to its success.

## Editors' preface

The Sixth International Conference on II-VI Compounds and Related Optoelectronic Materials was held at the Doubletree Hotel in Newport, Rhode Island, USA, from 13 to 17 September 1993. This special volume of the Journal of Crystal Growth is devoted to a collection of papers presented at the above conference. This meeting was the sixth in a series of international conferences on II-VI compounds first held at Durham, UK (1982), Aussois, France (1985), Monterey, USA (1987), Berlin, Germany (1989) and Tamano, Japan (1991). The location of this conference also marked the 26th anniversary of the first ever organized international conference on II-VI semiconducting compounds held on 6 to 8 September 1967 at Brown University, Providence, Rhode Island, USA. The site at Newport, Rhode Island, provided the scenic ocean view and grandeur among its famous mansions and yachts.

The conference differed significantly from earlier conferences. In previous conferences, the feasibility of achieving injection devices based particularly on the wide bandgap II-VI semiconductors was considered to be somewhat of a long range event. The initial breakthrough results of blue-green lasers were first reported at the last conference in Tamano. At this conference, we felt increased enthusiasm, vigor and eagerness to achieve practical optoelectronic devices as early as possible. As a measure of the rapid progress, work on advanced ZnSe-based quantum well heterostructures has led to the demonstration of room temperature continuous-wave diode lasers, even if short-lived for now. This accomplishment is a striking example of the benefit that basic research has endowed to the field. To further vitalize the conference, an effort was made to incorporate invited talks on III-V semiconductor lasers, in order to learn the material and device issues from this mature technology. We believe that this overlap will speed up the commercialization of the shorter wavelength lasers.

The conference was well attended and attracted over 250 participants from 20 countries. The invited and contributed oral papers were presented in a single session format and were accompanied by several poster sessions. The quantity of the presentations and enthusiasm among the participants was evident in the excellent audience attendance during the entire conference.

To mark the event of the first international II-VI meeting held at Brown University in 1967, a special retrospective evening session ("A Quarter Century of II-VI Semiconductor Research: Was it worth it?") was organized. The talks were given by Professor Shigeo Shionoya, Professor Immanuel Broser, and Dr. Manuel Aven, and summarized the trials and tribulations of the II-VI semiconductor research from 1950 to 1975. Their combined pioneering effort represents over one hundred years of active research in the field of wide bandgap II-VI semiconductors. We were fortunate to have several of these eminent scientists among us who "believed" in the field and encouraged younger generations not to give up.

With the recent device breakthroughs, we look forward in the future to acceptance of the potential optoelectronic applications of II-VI semiconductors by the broader scientific community. The recent improvements in heterostructure materials design and device performance have attracted new blood to our research community. This is clearly evident by the number of invited talks on II-VI semiconductors presented in other recent prestigious meetings. At the same time, the advances on the device front have,

if anything, showed the need to pursue basic research in the II-VI semiconductors with full vigor. Among the current critical issues are doping and defects as well as heterojunction physics. Progress in these and other problems connected with the efficiency and lifetime of light emitting diodes and lasers is a pre-requisite for technologically viable devices.

The next (seventh) conference will be held in 1995 at Heriot Watt University, Edinburgh, UK, and we convey our best wishes to the organizers for a successful conference.

During the preparation for this conference in Newport, we were saddened to learn of the loss of a valuable colleague and member of our program committee, Professor Otfried Goede of the Humboldt University, Berlin. Professor Goede made many important contributions to the understanding of electronic structures of wide gap II-VI compounds, especially for isoelectronic centers in solid solutions. We wish to dedicate this volume to his memory.

Ramesh Bhargava  
Ralph Ruth  
Takafumi Yao  
Arto Nurmikko

# Contents

Editors' preface	ix
SECTION I. EPITAXIAL AND HETEROSTRUCTURE GROWTH AND CHARACTERIZATION	
(In,Ga)P buffer layers for ZnSe-based visible emitters K. Lu, J.L. House, P.A. Fisher, C.A. Coronado, E. Ho, G.S. Petrich and L.A. Kolodziejski	1
Epitaxial overgrowth of II-VI compounds on patterned substrates D. Schikora, H. Hausleitner, S. Einfeldt, C.R. Becker, Th. Widmer, C. Giftge, K. Lübke, K. Lischka, M. von Ortenberg and G. Landwehr	8
Migration enhancement on ZnSe surface in photoassisted molecular beam epitaxy and long duration time of the effects S. Ichikawa, N. Matsumura, K. Yamawaki, K. Senga and J. Saraie	14
Metalorganic molecular beam epitaxial growth kinetics and doping studies of (001) ZnSe D. Rajavel, J.J. Zinck and J.E. Jensen	19
Growth of ZnS and ZnCdSse alloys on GaP using an elemental sulfur source by molecular beam epitaxy K. Ichino, T. Onishi, Y. Kawakami, Sz. Fujita and Sg. Fujita	28
Optimization of strained short-period ZnSse/ZnSe superlattices grown by metalorganic vapour phase epitaxy J. Söllner, M. Scholl, A. Schneider, M. Heuken and J. Woitok	35
Use of germanium interfacial layer for the hetero-epitaxial growth of CdTe on Si substrates W.-S. Wang and I. Bhat	43
Molecular beam epitaxial growth mechanism of ZnSe epilayers on (100) GaAs as determined by reflection high-energy electron diffraction, transmission electron microscopy and X-ray diffraction P. Ruppert, D. Hommel, T. Behr, H. Heinke, A. Waag and G. Landwehr	48
Surface engineering during molecular beam epitaxial growth of wide-gap II-VI structures J. Griesche, N. Hoffmann and K. Jacobs	55
On the mechanism of reflection high-energy electron diffraction oscillations studied by phase-locked epitaxy of ZnSe J. Griesche, N. Hoffmann and K. Jacobs	59
Atomic layer epitaxy of CdSe/ZnSe short period superlattices T. Matsumoto, T. Iwashita, K. Sasamoto and T. Kato	63
Critical thickness in heteroepitaxial growth of zinc-blende semiconductor compounds G. Cohen-Solal, F. Bailly and M. Barbé	68
Influence of growth non-stoichiometry on optical properties of doped and non-doped ZnSe grown by chemical vapour deposition E. Krause, H. Hartmann, J. Menninger, A. Hoffmann, Ch. Fricke, R. Heitz, B. Lummer, V. Kutzer and I. Broser	75
Structural properties of perfect ZnTe epilayers on (001) GaAs substrates M. Lang, D. Schikora, T. Widmer, C. Giftge, A. Forstner, V. Holy, J. Humenberger, K. Lischka, G. Brunthaler, H. Sitter and M. von Ortenberg	81
Growth and characterization of electrodeposited films of cadmium telluride on silicon J.M. Fisher, L.E.A. Berlouis, L.J.M. Sawers, S.M. MacDonald, S. Affrossman, D.J. Diskett and M.G. Astles	86
Compensation processes in molecular beam epitaxially grown zinc selenide doped with nitrogen K.A. Prior, B. Murdin, C.R. Pidgeon, S.Y. Wang, I. Hauksson, J.T. Mullins, G. Horsburgh and B.C. Cavenett	94

\* Invited paper.

Observation of preferential donor-acceptor pairing in ZnSe:Na	99
L. Radomsky, G.-J. Yi and G.E. Neumark	
Organometallic vapor phase epitaxial growth of p-type ZnSe using phenylhydrazine as the dopant source	105
S. Akram and I. Bhat	
Auto-doping of Ga in ZnSe-GaAs layers grown at low temperatures by post-heated molecular beam epitaxy	110
M. Yoneta, H. Saito and M. Ohishi	
Low pressure growth and nitrogen doping in metalorganic vapor phase epitaxy of ZnSe	114
K. Nishimura, Y. Nagao and K. Sakai	
Contamination effects from tellurium in ZnS-ZnSe superlattices	121
D. Bouchara, A. Abounadi, M. Di Blasio, N. Briot, T. Cloitre, O. Briot, B. Gil, J. Calas, M. Averous and R.L. Aulombard	
Atomic layer epitaxial growth studies of ZnSe using dimethylzinc and hydrogen selenide	127
I. Bhat and S. Akram	
Growth of CdTe-CdZnTe strained-layer single quantum wells by modified hot-wall epitaxy method and their properties	131
J.-S. Hwang, B.J. Koo, I.H. Chang, H.L. Park and C.H. Chung	
Thickness dependent properties of ZnSe on (100) GaAs grown by atomic layer epitaxy	136
C.D. Lee, B.K. Kim, J.W. Kim, H.L. Park, C.H. Chung, S.K. Chang, J.I. Lee and S.K. Noh	
The metalorganic chemical vapour deposition and photoluminescence of tellurium-doped ZnS, CdS:Te strained layer superlattices	140
K.A. Dhese, J.E. Nicholls, W.E. Hagston, P.J. Wright, B. Cockayne and J.J. Davies	
Epitaxial growth of ZnS on GaP by molecular beam deposition	145
H. Kanie, H. Araki, K. Ishizaka, H. Ohta and S. Murakami	
Strain relief and growth modes in wurtzite type epitaxial layers of CdSe and CdS and in CdSe-CdS superlattices	150
M. Grün, M. Hetterich, C. Klingshirn, A. Rosenauer, J. Zweck and W. Gebhardt	

## SECTION II. BULK GROWTH AND CHARACTERIZATION

Wide gap Cd <sub>1-x</sub> Mg <sub>x</sub> Te: molecular beam epitaxial growth and characterization	155
A. Waag, F. Fischer, Th. Litz, B. Kuhn-Heinrich, U. Zehnder, W. Ossau, W. Spahn, H. Heinke and G. Landwehr	
CdTe and CdTe <sub>1-x</sub> Se <sub>x</sub> crystals grown by the travelling heater method using a rotating magnetic field	161
M. Salk, M. Fiederle, K.W. Benz, A.S. Senchenkov, A.V. Egorov and D.G. Matioukhin	
Growth of large, high purity, low cost, uniform CdZnTe crystals by the "cold travelling heater method"	168
A.H. Mokri, R. Triboulet, A. Lussou, A. Tromson-Carli and G. Didier	
On the nature of the excitonic luminescence in narrow-gap Hg <sub>1-x</sub> Cd <sub>x</sub> Te ( $x \approx 0.3$ )	175
J.W. Lomm, K.H. Herrmann, W. Hoerstel, M. Lindstaedt, H. Kissel and F. Fuchs	
Study of electronic structure in strained ZnSe-GaAs thin films by nonlinear optical and Brewster-angle reflection spectroscopies	182
K. Inoue, I. Kuroda, F. Minami, K. Yoshida, M. Hayashi	
Nonlinear refraction and optical limiting in bulk ZnTe crystal	187
W. Ji, A.K. Kukawadia, Z.C. Feng, S.H. Tang and P. Becla	
Influence of the screening of piezo-fields on the carrier dynamics in CdS-CdSe superlattices	191
W. Langbein, H. Kalt, M. Hetterich, M. Grün and C. Klingshirn	
Resonant Brillouin scattering in biaxially strained ZnSe	195
H. Mayer, U. Rössler, S. Permogorov, H. Stolz, H. Vogelsang and W. von der Osten	
Alloy broadening in photoluminescence spectra of Cd <sub>1-x</sub> Zn <sub>x</sub> Te crystals grown from Te solution	199
K. Suzuki, N. Akita, K. Inagaki, A. Nishihata, N. Takojima and S. Dairaku	
Polarized photoluminescence in vacancy-ordered Ga <sub>2</sub> Se <sub>3</sub>	204
I. Okamoto, A. Yamada, M. Konagai and K. Takahashi	
Temperature dependence of luminescence in ZnSe and role of excitation transfer	208
G. J. Yi, L. Radomsky and G.E. Neumark	
Nonlinear optical switching fronts in CdS	213
R. Schmolke, F. Scholl, M. Nägele and J. Gutowski	
Photoluminescence of vapor and solution grown ZnTe single crystals	219
Y. Biao, M. Azoulay, M.A. George, A. Burger, W.E. Collins, E. Silberman, C.-H. Su, M.E. Volz, F.R. Szofran and D.C. Gillies	
Optical properties of "pure" CdS and metal-insulator-semiconductor structures on CdS at electrical operation	225
M.A. Jakobson, V.D. Kagan, R.P. Seisyan and E.V. Goncharova	



Measurement of optical nonlinear susceptibility of CdS single crystal using a single beam	
Z. Li, G. Xiong, Z. Zhao and X. Fan	231
First realization of bistable light emitting devices	
B. Ullrich, A. Kazlauskas, S. Zerlauth and T. Kobayashi	234
Raman, infrared, photoluminescence and theoretical studies of the II–VI–VI ternary CdSeTe	
Z.C. Feng, P. Becla, L.S. Kim, S. Perkowitz, Y.P. Feng, H.C. Poon, K.P. Williams and G.D. Pitt	239
Optical and thermal spectroscopy of vanadium-doped CdTe and related photorefractive effect	
E. Rzepka, A. Aoudia, M. Cuniot, A. Lussan, Y. Marfaing, R. Triboulet, G. Brémond, G. Marrakchi, K. Cherkaoui, M.C. Busch, J.M. Koebel, M. Hage-Ali, P. Siffert, J.Y. Moisan, P. Gravey, N. Wolffer and O. Moine	244
Systematic steps towards exactly stoichiometric and uncompensated CdTe Bridgman crystals	
P. Rudolph, U. Rinas and K. Jacobs	249
Iodine doping in ZnSe films grown by vapor phase epitaxy	
T. Muranoi, S. Onizawa and M. Sasaki	255
ZnSe single crystal growth by the method of dissociative sublimation	
H. Hartmann and D. Siche	261
Characterization of impurities in II–VI semiconductors by time-resolved lineshape analysis of donor–acceptor pair spectra	
P. Bäume, E. Kubaeki and J. Gutowski	266
Studies on the diffusion of zinc in cadmium telluride at 800 °C	
E.D. Jones, J.C. Clark, J.B. Mullin and A.W. Brinkman	274
Incorporation of iodine into CdTe by diffusion	
E.D. Jones, J. Malzbender, J.B. Mullin and N. Shaw	279
Complex formation in In- and Ag/Cu-doped CdTe	
M. Rüb, N. Achtziger, J. Meier, U. Reislöhner, P. Rudolph, M. Wienecke and W. Witthuhn	285

### SECTION III. DOPING

#### III.A. Modeling

Lattice location of N atoms in heavily N-doped ZnSe studied with ion beam analysis and its implication on deep level defects	
T. Yao, T. Matsumoto, S. Sasaki, C.K. Chung, Z. Zhu and F. Nishiyama	290
Acceptor and donor states of impurities in wide band gap II–VI semiconductors	
D.J. Chadi	295
Interaction between N <sub>2</sub> and stabilized ZnSe surface	
T. Uenoyama, T. Nakao and M. Suzuki	301
Limits of acceptor impurity doping in wide band gap II–VI semiconductors	
Y. Marfaing	305
Systematic investigation of shallow acceptor levels in ZnSe	
Y. Zhang, W. Liu, B.J. Skromme, H. Cheng, S.M. Shibli and M.C. Tamargo	310
Acceptor state instabilities in ZnSe under hydrostatic pressure	
D.J. Strachan, M.M. Li, M.C. Tamargo and B.A. Weinstein	318
Comparison between gallium-implanted layers of ZnSe and ZnS <sub>0.5</sub> Se <sub>0.5</sub> by optical, electrical and electron beam characterization methods	
G. Giletsmann, N. Ammann, J. Hermans, A. Schneider, J. Geurts, P. Karduck and M. Heuken	324
Correlation between electrical and structural properties of chlorine doped ZnSe epilayers grown by molecular beam epitaxy	
D. Hommel, B. Jobst, T. Behr, G. Bilger, V. Beyersdorfer, E. Kurtz and G. Landwehr	331
Effects of C incorporation on the luminescence properties of ZnSe grown by metalorganic chemical vapor deposition	
B.J. Skromme, W. Liu, K.E. Jensen and K.P. Giapis	338
Defect-induced emission band in CdTe	
S. Seto, A. Tanaka, F. Takeda and K. Matsuura	346

#### III.B. Characterization

p-Type ZnSe:N grown by molecular beam epitaxy: evidence of non-radiative recombination centers in moderately to heavily doped material *	
L.C. Calhoun, C.M. Rouleau, M.H. Jeon and R.M. Park	352

Laser induced doping profiles in molecular beam epitaxy grown ZnSe doped with iodine J.T. Mullins, G. Horsburgh, J. Simpson, P. Thompson, M.R. Taghizadeh, I. Hauksson, S.Y. Wang, K.A. Prior, B.C. Cavenett, G.M. Williams and A.G. Cullis	357
Optical study of interdiffusion in CdTe and ZnSe based quantum wells D. Tönnies, G. Bacher, A. Forchel, A. Waag, Th. Litz, D. Hommel, Ch. Becker, G. Landwehr, M. Heuken and M. Scholl	362
Phase separation in $\text{ZnSe}_{1-x}\text{S}_x$ and $\text{Zn}_{1-x}\text{Mg}_x\text{Se}_{1-x}\text{S}_x$ layers grown by molecular beam epitaxy G.C. Hua, N. Otsuka, D.C. Grillo, J. Han, L. He and R.L. Gunshor	367
In-situ monitoring by spectroscopic ellipsometry in ZnSe crystal growth by molecular beam epitaxy K. Kato, F. Akinaga, T. Kamai and M. Wada	373
Incorporation of nitrogen in ZnSe grown by metalorganic vapour phase epitaxy A. Hoffmann, R. Heitz, B. Lummer, Ch. Fricke, V. Kutzer, I. Broser, W. Taudt, G. Gleitsmann and M. Heuken	379
Shallow impurity- and defect-related complexes in undoped ZnSe crystals U.W. Pohl, G.H. Kudlek, A. Klimakow and A. Hoffmann	385

### III.C. Implementation

Blue-green light-emitting diodes with p-ZnSSe highly doped with nitrogen grown by metalorganic molecular beam epitaxy and molecular beam epitaxy * M. Migita, A. Taike, M. Momose and J. Gotoh	391
Molecular beam epitaxy of ZnSe doped with nitrogen on vicinal (100)-oriented and (211)-oriented GaAs substrates Z. Zhu, T. Ebisutani, K. Takebayashi, K. Tanaka and T. Yao	397
p-Type doping of ZnSe with a novel nitrogen exciter T. Matsumoto, T. Inaba, Y. Yoda, K. Egashira, T. Kato and T. Akitsu	403
Nitrogen doping into ZnSe by the catalysis of transition metal H. Tojima, T. Okamoto, A. Yamada, M. Konagai and K. Takahashi	408
Growth and doping of ZnTe and ZnSe epilayers with metalorganic vapour phase epitaxy K. Wolf, H. Stanzl, A. Naumov, H.P. Wagner, W. Kuhn, B. Hahn and W. Gebhardt	412
Low temperature growth and plasma enhanced nitrogen doping of ZnSe by metalorganic vapour phase epitaxy W. Taudt, A. Schneider, M. Heuken, Ch. Fricke and A. Hoffmann	418
Metalorganic molecular beam epitaxy doping of II-VI compound semiconductors R.N. Bicknell-Tassius, W.M. Theis, T. Cole, K.T. Higa and T.J. Groshens	425
Atomic nitrogen production in nitrogen-plasma sources used for the growth of ZnSe:N and related alloys by molecular-beam epitaxy R.P. Vaudo, J.W. Cook, Jr. and J.F. Schetzina	430
Halogen doping of II-VI semiconductors during molecular beam epitaxy A. Waag, Th. Litz, F. Fischer, H. Heinke, S. Scholl, D. Hommel, G. Landwehr and G. Bilger	437
Nitrogen doping of molecular beam epitaxially grown CdTe with a radio-frequency plasma source K.A. Dhesi, D.E. Ashenford, J.E. Nicholls, P. Devine, B. Lunn, C.G. Scott and J. Jaroszyński	443
Investigation of hydrogen, carbon and further impurities in the metalorganic vapour phase epitaxy of ZnSe with ditertiary-butylselenide and methylallylselenide W.S. Kuhn, R. Driad, H. Stanzl, A. Lussan, K. Wolf, B. Qu'Hen, H. Sabin, L. Svob, C. Grattepain, X. Quesada, W. Gebhardt and O. Gorochov	448

### SECTION IV. TRANSPORT AND CONTACTS

Integrated heterostructure devices composed of II-VI materials with Hg-based contact layers * J. Ren, D.B. Eason, L.E. Churchill, Z. Yu, C. Boney, J.W. Cook, Jr., J.F. Schetzina and N.A. El-Masry	455
Ohmic contacts and transport properties in ZnSe-based heterostructures * J. Han, Y. Fan, M.D. Ringle, L. He, D.C. Grillo, R.L. Gunshor, G.C. Hua and N. Otsuka	464
The growth of HgSe by molecular beam epitaxy for ohmic contacts to p-ZnSe S. Einfeldt, H. Heinke, M. Behringer, C.R. Becker, E. Kurtz, D. Hommel and G. Landwehr	471
The hole diffusion length in epitaxial zinc selenide J. Zheng and J.W. Allen	477
Mesoscopic phenomena in a dilute magnetic semiconductor $\text{Hg}_{1-x}\text{Cd}_x\text{Mn}_x\text{Te}$ G. Grabecki, T. Dietl, W. Plesiewicz, A. Lenard, T. Skośkiewicz, E. Kamińska and A. Piotrowska	481

A prediction of the electron mobility in medium gap HgCdTe and HgZnTe solid solutions R. Granger and C.M. Pelletier	486
Low temperature variable range hopping conductivity in doped CdTe crystals N.V. Agrinskaya	493

## SECTION V. ELECTRONIC STRUCTURE OF BULK AND HETEROSTRUCTURES

<i>Ab initio</i> calculation of electronic structure and structural properties of $\text{ZnSe}_{1-x}\text{Te}_x$ B. Freytag and U. Rössler	499
Photoionization of a deep centre in zinc selenide giving information about the conduction band structure J. Zheng and J.W. Allen	504
Measurement of the $\text{MgSe}/\text{Cd}_{0.54}\text{Zn}_{0.46}\text{Se}$ valence band offset by X-ray photoelectron spectroscopy M.W. Wang, J.F. Swenberg, R.J. Miles, M.C. Phillips, E.T. Yu, J.O. McCaldin, R.W. Grant and T.C. McGill	508
Superlattice effects on phonons in strained ZnTe–ZnSe structures J. Frandon, M.A. Renucci, N. Briot, O. Briot and R.L. Aulombard	513
Interface morphology studies of liquid phase epitaxy grown HgCdTe films by atomic force microscopy M. Azoulay, M.A. George, A. Burger, W.E. Collins and E. Silberman	517
Investigation of crystal quality and surface morphology of ZnTe:N epilayers grown on ZnTe and GaSb substrates R.J. Miles, J.F. Swenberg, M.W. Wang, M.C. Phillips and T.C. McGill	523
Comparison of CdTe, $\text{Cd}_{0.9}\text{Zn}_{0.1}\text{Te}$ and $\text{CdTe}_{0.9}\text{Se}_{0.1}$ crystals: application for $\gamma$ - and X-ray detectors M. Fiederle, D. Ebling, C. Eiche, D.M. Hofmann, M. Salk, W. Stadler, K.W. Benz and B.K. Meyer	529
The study of lattice strain and high-resolution transmission electron microscopy in ZnSe/ZnS strained-layer superlattices Z.P. Guan, S.H. Song, G.H. Fan, X.W. Fan, Y.G. Peng and Y.K. Wu	534
Transmission electron microscopy investigations of II–VI/GaAs heterostructures P.D. Brown, Y.Y. Loginov, J.T. Mullins, K. Durose, A.W. Brinkman and C.J. Humphreys	538
Scanning tunneling microscopy of CdSe single crystal cleaved and “real” surface J. Vaitkus, R. Baubinas, V. Kazlauskienė, D. Kuciauskas, J. Miskinis, U. Karlsson, M. Hammar, M. Göthelid, M. Björqvist and E. Lindberg	545

## SECTION VI. OPTICAL PROPERTIES OF QUANTUM WELLS AND SUPERLATTICES

ZnTe fractional monolayers and dots in a CdTe matrix * N. Magnea	550
Deep blue and UV photoluminescence from ZnS/CdS superlattices and quantum wells G. Brunthaler, M. Lang, A. Forstner, C. Gittge, D. Schikora, S. Ferreira, H. Sitter and K. Lischka	559
Optical confinement in ZnSe-based quantum well structure using impurity induced disordering T. Yokogawa, P.D. Floyd, J.L. Merz, H. Luo and J.K. Furdyna	564
Ultraviolet lasing and excitonic gain in $\text{Cd}_{1-x}\text{Zn}_x\text{S}/\text{ZnS}$ strained-layer multiple quantum wells Y. Yamada, Y. Masumoto and T. Taguchi	570
Exciton dynamics and high density effects in ZnSe/ZnMnSe quantum structures grown by molecular beam epitaxy A. Schulzgen, F. Kreller, F. Henneberger, M. Lowisch and J. Puls	575
Confined and propagating phonons in atomic layer epitaxy grown $(\text{CdTe})_n(\text{ZnTe})_m$ superlattices T. Fromherz, E. Oh, A.K. Ramdas, E. Köppensteiner, G. Bauer, W. Faschinger and H. Sitter	580
Temperature dependence of optical gain in CdTe/CdMnTe heterostructures R. Legras, I.S. Dang, C. Bodin, J. Cibert, F. Marceat, G. Feuillet, J.L. Pautrat, D. Herve and E. Moly	585
Photoluminescence of CdTe/ZnTe semiconductor wires and dots C. Gourgon, B. Eriksson, I.S. Dang, H. Mariette and C. Vieu	590
Exciton recombination in $\text{ZnSe}_{1-x}\text{Te}_x/\text{ZnTe}$ QWs and $\text{ZnSe}_{1-x}\text{Te}_x$ epilayers grown by metalorganic vapour phase epitaxy A. Naumov, H. Stanzl, K. Wolt, A. Rosenauer, S. Lankes and W. Gebhardt	595
Ramaneto-optical study of ZnSe/(Zn,Mn)Se and ZnSe/(Zn,Cd,Mn)Se quantum well structures and superlattices W. Hembrodt, O. Goede, V. Weinhold, M. Happ, R. Knoch, K. Hieke, N. Hoffmann, J. Griesche, K. Jacobs, F. Neugebauer, D. Suisky and J. Rösler	601
Electron-gas screening of the piezoelectric fields in indium-doped (211) CdTe/ $\text{Cd}_{1-x}\text{Zn}_x\text{Te}$ quantum wells F. Bassani, K. Kheng, M. Mamor, R.E. Cox, N. Magnea, K. Saminadayar and S. Tatarenko	607
Optical and X-ray analysis of $\text{ZnS}_{1-x}\text{Se}_x/\text{ZnSe}$ superlattices grown on GaAs by metalorganic vapour phase epitaxy I. Hermans, J. Woutok, W. Schiffrers, J. Geurts, A. Schneider, M. Scholl, J. Söllner and M. Heuken	612

Characterization of alloy formation at the ZnSe/CdSe quantum-well interface by photoluminescence spectroscopy Z. Zhu, H. Yoshihara, K. Takebayashi and T. Yao	619
Light interference effect in optical bistability of multiple quantum well etalons D.Z. Shen, X.W. Fan and B.J. Yang	625
Growth and optical bistability of $\text{Zn}_{0.78}\text{Cd}_{0.22}\text{Se}$ -ZnSe multiple quantum wells by metalorganic chemical vapor deposition B.J. Yang, L.C. Chen, X.W. Fan, J.Y. Zhang, Z.H. Zheng, Y.M. Lu, Z.P. Guan, A.H. Yang and S.M. Wang	629
Photoluminescence of ultrathin ZnSe-ZnTe superlattices N. Takojima, F. Iida, K. Imai and K. Kumazaki	633
Fabrication and optical characterization of wet chemically etched CdTe/CdMgTe wires M. Illing, G. Bacher, A. Forchel, A. Waag, T. Litz and G. Landwehr	638
Structural characteristics and higher-order zone-folded phonon modes in ZnSe-ZnS strained-layer superlattices A. Yamamoto, Y. Kanemitsu and Y. Masumoto	643
A ZnSe/ZnCdSe quantum well symmetric self-electro-optic effect device operating in the blue-green region S.Y. Wang, P. Thompson, G. Horsburgh, J.T. Mullins, I. Hauksson, K.A. Prior and B.C. Cavenett	647
Polar magneto-optic Kerr effect in (Cd,Mn)Te/CdTe superlattices B. Buda, M. Dahl, N. von Truchsess and A. Waag	652
Spin-flip Raman scattering by electrons bound to donors in CdTe/Cd <sub>1-x</sub> Mn <sub>x</sub> Te multiple quantum well structures as a function of barrier composition D. Wolverson, J.J. Davies, S.V. Railson, M.P. Halsall, D.E. Ashenford and B. Lunn	656
Optical studies of quantum wells induced by magnetic fields in Cd <sub>1-x</sub> Mn <sub>x</sub> Te/Cd <sub>1-x</sub> Zn <sub>x</sub> Te epitaxial structures J.J. Davies, R.T. Cox and G. Feuillet	661

## SECTION VII. BLUE-GREEN DIODE LASERS AND LIGHT EMITTING DIODES

### VII.A. Device engineering and concepts

Room temperature II-VI lasers with 2.5 mA threshold * J.M. DePuydt, M.A. Haase, S. Guha, J. Qiu, H. Cheng, B.J. Wu, G.E. Höfler, G. Meis-Haugen, M.S. Hagedorn and P.F. Baude	667
Advances in blue laser diodes * A. Ishibashi and Y. Mori	677
Improvement in lasing characteristics of II-VI blue-green lasers using quaternary and ternary alloys to produce pseudomorphic heterostructures * J. Petruzzello, R. Drenten and J.M. Gaines	686
Advances in the development of graded injector visible light emitters J.F. Swenberg, M.W. Wang, R.J. Miles, M.C. Phillips, A.T. Hunter, J.O. McCaldin and T.C. McGill	692
Electrical and optical modeling of II-VI semiconductor diode lasers P.M. Mensz	697
Quaternary II-VI alloys for blue and green light emitting diode applications D.B. Eason, Z. Yu, C. Boney, J. Ren, L.E. Churchill, J.W. Cook, Jr., J.F. Schetzina and N.A. El-Masry	703
Optical modulators using quantum confined Stark effect in ZnSe based multiple quantum well structures F. Jain, W. Huang, R. LaComb, C. Chung and G. Drake	709
Quantitative study of mechanism responsible for high operating voltage in II-VI laser diodes I. Suemune	714

### VII.B. Device physics and materials science

Gain and dynamics in ZnSe-based quantum wells * J. Ding, M. Hagerott, P. Kelkar, A.V. Nurmikko, D.C. Grillo, L. He, J. Han and R.L. Gunshor	719
Comparison of GaN- and ZnSe-based materials for light emitters * T. Matsuoka, A. Ohki, T. Ohno and Y. Kawaguchi	727
Photo-assisted metalorganic vapor-phase epitaxy for nitrogen doping and fabrication of blue-green emitting devices of ZnSe-based semiconductors * Sz. Fujita, T. Asano, K. Machara, T. Tojyo and Sg. Fujita	737
Helium gas mixing in nitrogen plasma for the control of the acceptor concentration in p-ZnSe M. Kobayashi, H. Tosaka, T. Nagatake, T. Yoshida and A. Yoshikawa	745

Improvement of electrical and optical properties of ZnSse p-n heterostructure diodes with optimization in metalorganic vapor phase epitaxy I. Suemune, Y. Fujii and M. Fujimoto	750
Metalorganic vapor phase epitaxy growth of p-type ZnSse and its application for blue-green lasers K. Yanashima, D. Yamasaki, S. Watabe, K. Hara, J. Yoshino and H. Kukimoto	755
Photoluminescence excitation spectroscopy of the lasing transition in ZnSe-(Zn,Cd)Se quantum wells Y. Kawakami, I. Hauksson, J. Simpson, H. Stewart, I. Galbraith, K.A. Prior and B.C. Cavenett	759
Dependence of device characteristics on quantum well thickness in ZnSe/ZnCdSe multi-quantum well blue-green laser diodes Y. Tomomura, S. Hirata, T. Okumura, M. Kitagawa, A. Suzuki and H. Takiguchi	764

## SECTION VIII. III-V LIGHT EMITTERS

InGaAlP visible light laser diodes and light-emitting diodes * K. Itaya, H. Sugawara and G. Hatakoshi	768
Recent progress in III-V quantum optoelectronic devices * C. Weisbuch	776

## SECTION IX. NONLINEAR OPTICS AND EXCITATION KINETICS

Stimulated emission of II-VI epitaxial layers C. Klingshirn, H. Kalt, M. Umlauff, W. Petri, F.A. Majumder, S.V. Bogdanov, W. Langbein, M. Grün, M. Hetterich, K.P. Geyzers, M. Heuken, A. Naumov, H. Stanzl and W. Gebhardt	786
Dephasing excitons in a CdTe/Cd <sub>0.96</sub> Mn <sub>0.04</sub> Te multiple quantum well R. Hellmann, M. Koch, J. Feldmann, S.T. Cundiff, E.O. Göbel, D.R. Yakovlev, A. Waag and G. Landwehr	791
Two-photon spectroscopy in ZnSe/ZnS quantum wells F. Minami, K. Yoshida, K. Inoue and H. Fujiyasu	796
Nonlinear quantum beat spectroscopy of bound biexcitons in II-VI semiconductors J. Erland, B.S. Razbirin, V.G. Lyssenko, K.-H. Pantke and J.M. Hvam	800
Free induction decay and quantum beat of excitons in ZnSe T. Saiki, K. Takeuchi, K. Ema, M. Kuwata-Gonokami, K. Ohkawa and T. Mitsuyu	805
Degenerate four-wave mixing at bound excitons in II-VI semiconductors I. Broser, B. Lummer, R. Heitz and A. Hoffmann	809
Time-resolved donor-acceptor pair recombination luminescence in highly n- and p-doped II-VI semiconductors Ch. Fricke, R. Heitz, B. Lummer, V. Kutzer, A. Hoffmann, I. Broser, W. Taudt and M. Heuken	815
Energy transfer processes via the interface of ZnSe/GaAs epilayers N. Presser, Ch. Fricke, G. Kudlek, R. Heitz, A. Hoffmann and I. Broser	820
Polarization dependent dephasing measurements in Cd <sub>1-x</sub> Zn <sub>x</sub> Te/ZnTe multiple quantum well structures J.P. Doran, R.P. Stanley, J. Hegarty, R.D. Feldman and R.F. Austin	826
Exciton transfer dynamics in CdTe/(Cd,Zn)Te asymmetric double quantum well structures S. Haacke, N.T. Pelekanos, H. Mariette, A.P. Heberle, W.W. Rühle and M. Zigone	831
Excitonic emission in ZnCdSe-ZnSe multiple quantum wells J.-Y. Zhang, X.W. Fan, B.J. Yang, Z.P. Guan, Y.M. Lu and D.Z. Shen	838
Nonlinear transmission dynamics of ZnS <sub>1-x</sub> Se <sub>x</sub> /ZnSe and ZnS <sub>1-x</sub> Se <sub>x</sub> /ZnS <sub>1-y</sub> Se <sub>y</sub> (x > y) waveguide structures M. Nägele, W. Ebeling, J. Gutowski, K.P. Geyzers and M. Heuken	842
Exciton relaxation dynamics in ultrathin CdSe/ZnSe single quantum wells U. Neukirch, D. Weckendrup, W. Faschinger, P. Juza and H. Sitter	849
Many body effects in transient luminescence spectra of a homogeneous electron-hole plasma in CdTe/CdMnTe quantum wells G. Bacher, F. Daiminger, A. Forchel, A. Waag, Th. Litz and G. Landwehr	856
Dynamical properties of excitons in Zn <sub>1-x</sub> Cd <sub>x</sub> Se/ZnSe quantum wells and Zn <sub>1-x</sub> Cd <sub>x</sub> Se epilayers grown by molecular beam epitaxy U. Neukirch, D. Weckendrup, J. Gutowski, D. Hommel and G. Landwehr	861
Photo-induced screening of the excitonic interaction in ZnSe-ZnTe type II strained-layer superlattices B. Gil, T. Cloutre, N. Briot, O. Briot, P. Boring and R.L. Aulombard	868

Exciton and Raman processes of ZnS under tunable picosecond light pulse excitations H. Uchiki, H. Kinto, T. Moriyama, S. Hata, N. Tsuboi, J. Wang and S. Iida	873
--	-----

## SECTION X. DILUTED MAGNETIC SEMICONDUCTORS

Antiferromagnetic spin ordering and interlayer magnetic correlations in MnTe/CdTe superlattices * T.M. Giebultowicz, W. Faschinger, V. Nunez, P. Klosowski, G. Bauer, H. Sitter and J.K. Furdyna	877
Photoluminescence in a ZnSe/(Zn,Mn)Se heterostructure: magnetic-field induced transition from light to heavy excitons E. Deleporte, T. Lebiheb, P. Roussignol, B. Ohnesorge, C. Delalande, S. Guha and H. Muneke	884
Magnetic field dependence of the exciton transfer in semimagnetic double quantum well structures Th. Pier, K. Hieke, B. Henninger, W. Heimbrodt, O. Goede, H.-E. Gumlich, J.E. Nicholls, M. O'Neill, S.J. Weston and B. Lunn	889
Orbital exchange in diluted magnetic semiconductors A.K. Bhattacharjee	895
Magnetic properties of $\text{Cd}_{1-x}\text{Mn}_x\text{Te}$ grown by molecular beam epitaxy M. Sawicki, M.A. Brummell, P.A.J. de Groot, G.J. Tomka, D.E. Ashenford and B. Lunn	900
The influence of exchange interaction on the composition dependence of interband transitions in $\text{Zn}_{1-x}\text{Mn}_x\text{Se}$ Ch. Jung, H.-Ch. Mertins, S. Katholy and H.-E. Gumlich	905
Magnetic or nonmagnetic behavior of isolated scandium ions in II–VI compounds D. Schumann, H.-E. Mahnke, B. Spellmeyer, G. Sulzer, H. Waldmann, W.-D. Zeitz, U.W. Pohl and H.-E. Gumlich	910
Nature of the absorption bands in $\text{Zn}_{1-x}\text{Co}_x\text{S}$ L. Martinez, S.A. Lopez-Rivera, W. Giriat and F. Medina	913

## SECTION XI. NARROW GAP SEMICONDUCTORS

Electron beam induced current assessment of doped and diffused junctions in epitaxial $\text{Cd}_{1-x}\text{Hg}_x\text{Te}$ M.P. Hastings, C.D. Maxey, B.E. Matthews, N.E. Metcalfe, P. Capper, C.L. Jones and I.G. Gale	917
Characterization of intrinsic and impurity deep levels in ZnSe and ZnO crystals by nonlinear spectroscopy V. Gavryushin, G. Račiukaitis, D. Juodžbalis, A. Kazlauskas and V. Kubertavičius	924
Angle resolved X-ray photoelectron spectroscopy of the surface of $\text{Hg}_{0.85}\text{Zn}_{0.15}\text{Te}$ and after passivation processes A. Quemerais, K.H. Khelladi, D. Lemoine, R. Granger and R. Triboulet	934
Ultrafast diffusion of Hg in $\text{Hg}_{1-x}\text{Cd}_x\text{Te}$ ( $x \approx 0.21$ ) E. Belas, P. Höschl, R. Grill, J. Franc, P. Moravec, K. Lischka, H. Sitter and A. Toth	940
Indium doped $\text{Hg}_{0.7}\text{Cd}_{0.3}\text{Te}$ /undoped $\text{Hg}_{0.8}\text{Cd}_{0.2}\text{Te}$ /CdTe heterojunction grown by Te-rich liquid phase epitaxy S.W. Moon, S.H. Suh and C.S. Choi	944
$\text{Hg}_{0.8}\text{Cd}_{0.2}\text{Te}$ grown by liquid phase epitaxy using $\text{Cd}_{0.94}\text{Zn}_{0.06}\text{Te}$ buffer layer N.J. Kwak, I.H. Choi, S.W. Lim and S.H. Suh	950
Bridgman growth of $\text{Hg}_{1-x}\text{Cd}_x\text{Te}$ from melt of constant composition P. Höschl, R. Grill, J. Svoboda, P. Hlídek, P. Moravec, J. Franc and E. Belas	956
HgTe and $\text{Hg}_{1-x}\text{Cd}_x\text{Te}$ vapor phase epitaxial growth under controlled Hg pressure H. Kuwabara, H. Tatsuoka, Y. Nakanishi, A. Ichida, H. Fujiyasu, M. Nakayama and T. Yamanari	964

## SECTION XII. NANOCCLUSERS AND QUANTUM SIZE STRUCTURES

Doped zinc sulfide nanocrystals precipitated within a poly(ethylene oxide) matrix – processing and optical characteristics * D. Gallagher, W.E. Heady, J.M. Racz and R.N. Bhargava	970
Electric field induced absorption modulation of CdS quantum dots in an organic matrix U. Woggon, S.V. Bogdanov, O. Wind and V. Sperling	976
Photoluminescence study of HgTe– $\text{Hg}_{0.9}\text{Cd}_{0.1}\text{Te}$ superlattices J.R. Meyer, A.R. Reisinger, K.A. Harris, R.W. Yanka, L.M. Mohnkern and L.R. Ram-Mohan	981
CdS quantum dots in the weak confinement U. Woggon, M. Saleh, A. Uhrig, M. Portuné and C. Klingshirn	988
CdS quantum dots in colloids and polymer matrices: electronic structure and photochemical properties V.S. Gurin and M.V. Artemyev	993

Absorption properties of CdS nanocrystals in glasses: evidence of both weak and strong confinement regimes J. All��gre, G. Arnaud, H. Mathieu, P. Lefebvre, W. Granier and L. Boudes	998
Carrier dynamics in CdS quantum dots embedded in glass J. Puls, V. Jungnickel, F. Henneberger and A. Sch��lzen	1004

### SECTION XIII. ELECTROLUMINESCENCE AND CORE EXCITATIONS

SrS-ZnS electroluminescence materials *	
H. Kobayashi	1010
Trailing edge phenomena in SrS:CeCl <sub>3</sub> thin film electroluminescent devices U. Troppenz, B. H��ttl, K.O. Velthaus and R.H. Mauch	1017
Space charge and excitation efficiency in ZnS thin film electroluminescent devices A. Zeinert, P. Benalloul, J. Benoit, C. Barthou and H.-E. Gumlich	1023
Mn-3d derived partial density of states at the interface of epitaxially grown zinc-blende MnTe on CdTe(100) P.R. Bressler and H.-E. Gumlich	1028
Peculiarities of transport properties in semiconductors with resonant impurities: HgSe:Fe versus PbTe:Cr E. Grodzicka, W. Dobrowolski, J. Kossut, T. Story and B. Witkowska	1034
The thermodynamics of indium-vacancy pairs in Hg <sub>0.70</sub> Cd <sub>0.21</sub> Te Wm.C. Hughes, J.C. Austin and M.L. Swanson	1040
Electroluminescence spectra of rare-earth-doped ZnS <sub>1-x</sub> Se <sub>x</sub> thin films N. Miura, K. Ogawa, S. Kobayashi, H. Matsumoto and R. Nakano	1046
Formation and optical properties of homogeneous solid solutions of Ca <sub>1-x</sub> Sr <sub>x</sub> S:Ce B.W. Arterton, J.W. Brightwell, B. Ray and I.V.F. Viney	1051
Electrical and optical stimulation of luminescence in Ca <sub>1-x</sub> Cd <sub>x</sub> S I.V.F. Viney, B.W. Arterton, B. Ray and J.W. Brightwell	1055
Growth and characterization of SrS/ZnS multilayered electroluminescent thin films grown by hot wall technique K. Ohmi, Y. Yamano, S.T. Lee, T. Ueda, S. Tanaka and H. Kobayashi	1061
The influence of crystal structure on the Zn 3d states in Zn <sub>1-x</sub> Mn <sub>x</sub> S Ch. Jung, H.-Ch. Mertins and H.-E. Gumlich	1066

### SECTION XIV. LATE NEWS PAPERS

The nitrogen-hydrogen complex in ZnSe J.A. Wolk, J.W. Ager III, K.J. Duxstad, W. Walukiewicz, E.E. Haller, N.R. Taskar, D.R. Dorman and D.J. Olego	1071
The influence of nitrogen on the p-conductivity in ZnSe epilayers grown by molecular beam epitaxy A. Hoffmann, B. Lummer, L. Eckey, V. Kutzer, Ch. Fricke, R. Heitz, I. Broser, E. Kurtz, B. Jobst and D. Hommel	1073
SrS single crystals grown by physical vapor transport R. Helbing and R.S. Feigelson	1075
Studies of blue-green laser structures with asymmetric and pseudomorphic ZnSe wave guides D. Hommel, E. Kurtz, T. Behr, A. Jakobs, B. Jobst, S. Scholl, K. Sch��ll, V. Beyersd��rfer, G. Landwehr and H. Cerva	1076
Ridge waveguide, separate confinement green-blue heterostructure lasers A. Salokatve, H. Jeon, M. Hovinen, P. Kelkar, A.V. Nurmikko, D.C. Grillo, L. He, J. Han, Y. Fan and R.L. Gunshor	1077
Reduction of the Au/p-ZnSe(100) Schottky barrier height using a thin Se interlayer W. Chen, J. Gaines, C. Ponzoni, D. Olego, P.S. Mangat, P. Soukiasian and A. Kahn	1078
Growth of MgTe and Zn <sub>1-x</sub> Mg <sub>x</sub> Te thin films by metalorganic vapour phase epitaxy B. Qu'Hen, X. Quesada, W.S. Kuhn, J.E. Bour��e, L. Svob, A. Lussan and O. Gorochov	1079
Author index	1081
Subject index	1097



ELSEVIER

Journal of Crystal Growth 138 (1994) 1-7

JOURNAL OF **CRYSTAL  
GROWTH**

## (In,Ga)P buffer layers for ZnSe-based visible emitters

K. Lu <sup>a</sup>, J.L. House <sup>a</sup>, P.A. Fisher <sup>a</sup>, C.A. Coronado <sup>b</sup>, E. Ho <sup>a</sup>,  
G.S. Petrich <sup>a</sup>, L.A. Kolodziejski <sup>\*a</sup>

<sup>a</sup> *Research Laboratory of Electronics, Department of Electrical Engineering and Computer Science,  
Massachusetts Institute of Technology, Cambridge, Massachusetts 02139, USA*

<sup>b</sup> *Department of Materials Science and Engineering, Research Laboratory of Electronics,  
Massachusetts Institute of Technology, Cambridge, Massachusetts 02139, USA*

### Abstract

The growth of ZnSe on pseudomorphic and partially relaxed (In,Ga)P epitaxial buffer layers has been investigated. The (In,Ga)P and ZnSe layers were grown in separate gas source molecular beam epitaxy systems using elemental sources for the cation species and cracked PH<sub>3</sub> and H<sub>2</sub>Se for the anion species. Surface morphology studies using scanning electron microscopy showed that the ZnSe layers were featureless at a magnification of  $1.2 \times 10^4$ . Four crystal (400) X-ray rocking curves indicated that the ZnSe full width at half maximum (FWHM) was  $130''$ , while the pseudomorphic (In,Ga)P buffer layer FWHM was  $18''$ . The (511) reflections of X-ray rocking curves were used to measure the residual strain as well as the composition in the (In,Ga)P buffer layers. The low temperature photoluminescence spectra from the ZnSe films grown on partially relaxed (In,Ga)P exhibited intensities of the donor-bound and free exciton transitions of nearly equal magnitude, as well as transitions due to extended defects, suggesting highly pure material. The luminescence from the (In,Ga)P buffer layers was also detected.

### 1. Introduction

The wide range of direct energy bandgaps available in the ZnSe-based material system, including (Zn,Mg)(S,Se) quaternaries and (Zn,Cd)Se ternaries, offers the potential to obtain light emitters functioning at any wavelength throughout the visible or shallow UV spectrum. A significant obstacle to achieving long-lived device performance, however, is the lack of large area bulk II-VI substrates. Recent progress [1] in bulk ZnSe crystal growth and related surface preparation

techniques by the Eagle-Pitcher Company has provided high quality, highly resistive substrates, whereas conducting material has not yet been achieved. Since n- and p-type conducting bulk substrates are unavailable, the II-VI device structures must be grown on III-V substrates, such as GaAs, either as pseudomorphic layers that are completely strained, or as relaxed, and thus dislocated, layers. Laser devices fabricated to date have almost exclusively utilized the former approach, and thus are severely constrained in the choice of material compositions available to achieve a particular optical source operating at a specified wavelength [2-8]. Removing the requirement that the structure be pseudomorphic

\* Corresponding author.



would permit far greater flexibility in selecting a material composition, but the resultant lattice-mismatch between the III-V substrate and the II-VI epitaxial layer causes the formation of strain-related defects and dislocations. For example, the 0.27% lattice-mismatch between ZnSe and GaAs gives rise to a large number ( $> 10^6 \text{ cm}^{-2}$ ) of misfit, and thus threading, dislocations and defects which severely degrade the optical and electronic properties of ZnSe. These strain-related defects have been shown to propagate throughout the ZnSe-based light emitting diode structures during device operation which reduces the lifetime by the creation of dark line defects [9].

(In,Ga)P epitaxial buffer layers (grown on GaAs substrates) provide an "alternative substrate" for the subsequent growth of the II-VI compound family. By varying the In mole fraction, the lattice constant of the buffer layer can be varied from GaP, which is nearly lattice-matched to ZnS, to InP, which is lattice-matched to  $\text{Zn}_{0.52}\text{Cd}_{0.48}\text{Se}$ . By using a specific (In,Ga)P buffer layer, designed to be lattice-matched to a particular II-VI device structure, the strain-induced misfit dislocations can be confined to remain primarily near the (In,Ga)P/GaAs interface via the insertion of dislocation blocking strained-layer superlattice structures. The strain in the II-VI layer is thus minimized even during the heteroepitaxial nucleation of the II-VI device layer. Elimination of the problems due to lattice-mismatch would require the use of bulk crystals having the appropriate lattice constant. Additional benefits are anticipated due to the larger (In,Ga)P energy bandgap enabling a grading of the valence band discontinuity present between the GaAs and the ZnSe; such bandgap engineering is anticipated to improve the transport properties of the laser and light emitting diode devices. Chemical differences between the ZnSe and (In,Ga)P, as compared to GaAs, may also enhance future device processing technologies due to the capability of using various new selective etches.

In this investigation, ZnSe epilayers were grown on a range of  $\text{In}_x\text{Ga}_{1-x}\text{P}$  buffer layers, having various In mole fractions ( $0.46 < x < 0.55$ ),

on GaAs substrates; both II-VI and III-V semiconductors were deposited by gas source molecular beam epitaxy (GSMBE). During the various growths and while the II-VI layer was nucleated on the III-V surface, the films were analyzed in situ by reflection high-energy electron diffraction (RHEED). The surface morphology and the structural properties were characterized by scanning electron microscopy (SEM), high resolution X-ray diffraction, and cross-sectional transmission electron microscopy, whereas the optical properties were investigated by photoluminescence spectroscopy (PL).

## 2. Experimental procedure

The III-V buffer layers were grown in a dedicated GSMBE reactor utilizing cracked arsine ( $\text{AsH}_3$ ) and phosphine ( $\text{PH}_3$ ) as the anion species, and elemental In and Ga as the cation species. Thermal pyrolysis of the hydrides was carried out in a single gas cracker at  $900^\circ\text{C}$ . The procedure for GaAs (100) substrate preparation has been described previously [10]. Prior to growth of the (In,Ga)P buffer layers, a  $0.5 \mu\text{m}$  epitaxial layer of undoped GaAs was grown on the GaAs substrate, at a temperature of  $600^\circ\text{C}$ , in order to achieve an epitaxially smooth surface. The substrate temperature was calibrated using an optical pyrometer to observe the eutectic phase transition of  $500 \text{ \AA}$  of Au on Ge ( $356^\circ\text{C}$ ) and the melting point of InSb ( $525^\circ\text{C}$ ). The  $\text{AsH}_3$  flow rate was 1.5 SCCM. Upon completing the growth of the GaAs epilayer, a diffraction pattern showing a sharp ( $2 \times 4$ ) reconstruction was observed with RHEED. The substrate temperature was then reduced to  $450^\circ\text{C}$ , where a  $c(4 \times 4)$  RHEED pattern appeared prior to initiating the growth of (In,Ga)P.

At the beginning of each (In,Ga)P layer growth, a sharp ( $2 \times 1$ ) surface reconstruction pattern was routinely obtained by RHEED, complete with the observation of strong RHEED intensity oscillations which persisted for many minutes. Information derived from these RHEED intensity oscillations was used to estimate the growth rate and alloy composition. The precise alloy composition

was determined by (400) and (511) X-ray diffraction rocking curves. The phosphine flow rate was 1.8 SCCM. For both the GaAs and (In,Ga)P layers, the group V to group III ratio was approximately 2:1 as determined by both group III-limited and group V-limited measurements of RHEED intensity oscillations. For the aforementioned gas flows, the chamber pressure was typically  $(1-2) \times 10^{-5}$  Torr. The (In,Ga)P buffer layers were grown to a thickness of approximately 1  $\mu\text{m}$  or 4  $\mu\text{m}$ . Upon completion of the III-V buffer layer structure, amorphous As was used to passivate the (In,Ga)P in situ by exposing the (In,Ga)P surface to a cracked arsine flux for 30 min once the substrate temperature had cooled to below 100°C. Transfer to the II-VI dedicated growth chamber was then carried out ex situ through air.

The ZnSe layers were grown using elemental Zn and hydrogen selenide ( $\text{H}_2\text{Se}$ ) as source materials. An optical pyrometer observing the Au/Ge eutectic phase transition (356°C) was used to calibrate the substrate temperature. (The Au/Ge eutectic sample was mounted with a liquid In/Ga solder when the sample was transferred ex situ from the III-V GSMBE to the II-VI GSMBE.) A majority of the ZnSe films were grown at a substrate temperature of 275°C with the surface stoichiometry maintained slightly Zn-rich, as determined by the surface reconstruction pattern obtained during growth. The Zn flux, measured by a water-cooled crystal oscillator placed at the position of the substrate, was approximately 0.7 Å/s. The cracker temperature and the flow rate of the  $\text{H}_2\text{Se}$  were 1000°C and 1.5 SCCM, respectively. Additional information regarding the growth and material quality of the ZnSe has been described in ref. [11]. The passivating layer of amorphous arsenic was desorbed in the II-VI growth chamber at approximately 270°C until recovery of the  $(2 \times 1)$  reconstruction pattern characteristic of the (In,Ga)P surface was observed. A streaky RHEED pattern appeared immediately upon the nucleation of ZnSe, and persisted throughout the entire growth on (In,Ga)P films having lattice constants near that of ZnSe [12].

### 3. Results and analysis

The quality of the (In,Ga)P surface was crucial for the subsequent nucleation of ZnSe. After the growth of the (In,Ga)P layers, in situ RHEED observations showed a sharp  $(2 \times 1)$  reconstruction pattern, indicating good surface quality. During the ex situ transfer step, one of the two (In,Ga)P samples was removed for surface analysis. The surface of the films were featureless when viewed by SEM at a magnification of  $1.2 \times 10^4$ ; cross-hatching at the surface was not observed for a variety of (In,Ga)P films grown at 450°C. At lower magnifications, oval defects and particulates were observed. Under the same SEM magnification of  $1.2 \times 10^4$ , the ZnSe surface was also found to be featureless [12]. In contrast, (In,Ga)As buffer layers, that are lattice-matched to ZnSe, have been found to exhibit a cross-hatched surface [13]. However, cross hatching was observed for high temperature (above 500°C) growth of partially relaxed  $\text{In}_x\text{Ga}_{1-x}\text{P}$  layers having compositions with  $x \sim 0.45$ , which results in the layers existing under tension.

To obtain ZnSe layers free from misfit dislocations using a GaAs substrate, one possible method is to grow an  $\text{In}_{0.52}\text{Ga}_{0.48}\text{P}$  buffer layer, which would provide a lattice-match to ZnSe when relaxed with respect to the GaAs substrate. For lattice-mismatched epitaxial layers, it is well known that below a certain critical thickness,  $h_c$ , the misfit strain between the epilayer and substrate will be accommodated by elastic deformation. Under such pseudomorphic conditions, the in-plane lattice constant of the epilayer,  $a_{\parallel}$ , will be equal to that of the underlying substrate. Based on the force balance model of Matthews and Blakeslee [14], the critical thickness of  $\text{In}_{0.52}\text{Ga}_{0.48}\text{P}$  on GaAs is predicted to be approximately 0.047  $\mu\text{m}$ . Using double crystal X-ray diffraction rocking curve techniques, measurements of the (511) peaks, for  $\text{In}_{0.52}\text{Ga}_{0.48}\text{P}$  epilayers of approximately 1  $\mu\text{m}$  in thickness, indicated that  $a_{\parallel}$  of the epilayer was equal to the lattice constant of the GaAs substrate. The X-ray analysis indicated that the  $\text{In}_{0.52}\text{Ga}_{0.48}\text{P}$  films are still pseudomorphic for thicknesses much greater than

the critical thickness predicted by the force balancing model.

Ozasa et al. [15] have reported that the energy balancing model is more appropriate to describe the lattice relaxation mechanism of (In,Ga)P. From this model,  $h_c$  is given by:

$$h_c = \frac{1}{16\pi\sqrt{2}} \frac{1-\nu}{1+\nu} \left( \cos^2\theta + \frac{\sin^2\theta}{1-\nu} \right) \times \frac{b^2}{a} \frac{1}{f^2} \ln\left(\frac{h_c}{b}\right),$$

where  $a$  is the relaxed lattice constant of the film,  $b$  is the length of the Burgers vector of the dislocation line (equal to  $a/\sqrt{2}$ ),  $\nu$  is the Poisson ratio,  $\theta$  is the angle between the dislocation line and its Burgers vector ( $60^\circ$  for (In,Ga)P),  $\alpha$  is  $60^\circ$ , and  $f$  is the absolute value of the misfit strain between the (In,Ga)P epilayer and GaAs substrate [16]. From the formula, the critical thickness calculated for an  $\text{In}_{0.52}\text{Ga}_{0.48}\text{P}$  epilayer on bulk GaAs is  $3.4 \mu\text{m}$  and is significantly larger

than the  $h_c$  calculated from the force balancing model. Using the prediction of a critical thickness of  $3.4 \mu\text{m}$ , the  $\text{In}_{0.52}\text{Ga}_{0.48}\text{P}$  layers were grown to dimensions of approximately  $4 \mu\text{m}$ . Subsequent measurements of the (511) X-ray peaks, obtained using double crystal X-ray diffraction rocking curve techniques, indicated a 0.11% lattice-mismatch to still remain between the  $\text{In}_{0.52}\text{Ga}_{0.48}\text{P}$  and the ZnSe, indicating that the buffer layer was only partially relaxed.

X-ray diffraction rocking curve techniques offer one method of determining the crystalline quality of a multilayered structure; the breadth of the features is indicative of the amount of scattering of the X-rays by dislocations and defects. Four crystal X-ray diffraction rocking curves obtained on the  $1.15 \mu\text{m}$  (In,Ga)P epilayer showed a FWHM of 18 arc sec, which was comparable to the FWHM of the GaAs substrate ( $14''$ ). (For the measurement, the ZnSe was selectively etched away from the (In,Ga)P.) The extremely narrow (400) peak suggested that the  $1.15 \mu\text{m}$  (In,Ga)P

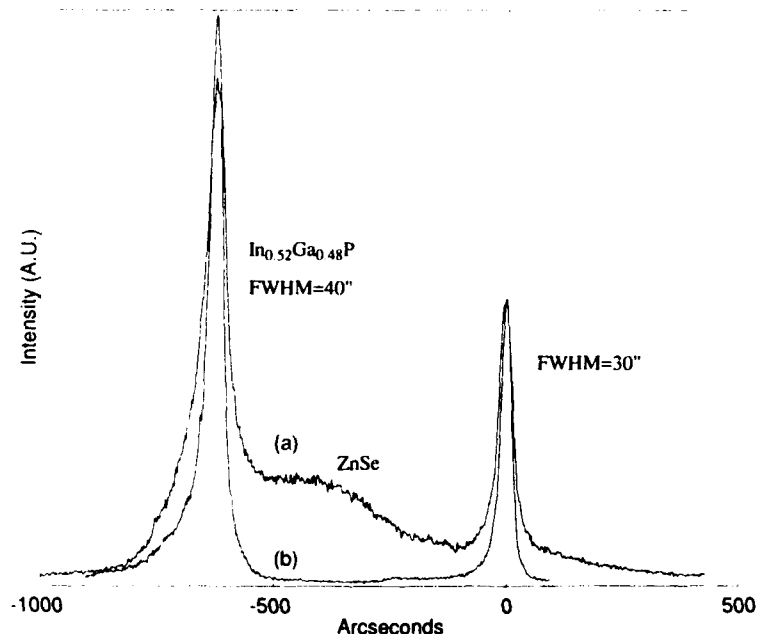


Fig. 1. (a) (400) X-ray rocking curve obtained from a  $1.1 \mu\text{m}$  ZnSe film grown on  $4.3 \mu\text{m}$  (In,Ga)P. The residual strain between the GaAs substrate and the (In,Ga)P buffer layer is  $\Delta a/a = 0.15\%$ . (b) (In,Ga)P film X-ray rocking curve obtained after the ZnSe had been selectively etched away. The peak of the GaAs substrate feature has been shifted to  $0''$  for clarity.

layer was pseudomorphic to the GaAs substrate and was subsequently confirmed by cross-sectional transmission electron micrographs. Fig. 1 shows the double crystal X-ray rocking curve obtained from the structure containing the  $4.3 \mu\text{m}$   $\text{In}_{0.52}\text{Ga}_{0.48}\text{P}$  buffer layer. The (400) reflections for structures with and without the ZnSe epilayer are shown. The FWHM for each of the peaks from the III-V layers are  $30''$  for GaAs and  $40''$  for the (In,Ga)P. For mole fractions of In and Ga of approximately 50:50, Masselink et al. [17] have observed the tendency for ordering of (In,Ga)P grown by GSMBE. The presence of ordering appears as a shoulder on the (400) X-ray reflection on the side away from the GaAs. As can be seen in Fig. 1, the (In,Ga)P peak does not contain a shoulder of significant intensity. However, for thinner ( $\sim 1 \mu\text{m}$ ) (In,Ga)P pseudomorphic layers, the shoulder was observed in the X-ray spectra [11]. The increasing width of the feature originating from (In,Ga)P is due to the partial relax-

ation of the epilayer; (511) reflections indicate that the (In,Ga)P is still mismatched (0.11%) to the ZnSe layer. For the  $1.8 \mu\text{m}$  fully relaxed ZnSe film, grown on the  $1.15 \mu\text{m}$  (In,Ga)P buffer layer, the FWHM of the (400) X-ray rocking curve is approximately  $130''$ , while a larger FWHM is observed for the ZnSe films grown on the  $4.3 \mu\text{m}$  (In,Ga)P layers (as seen in Fig. 1). Although it is expected that the FWHM for the ZnSe should be narrower for a smaller degree of mismatch, additional difficulties in the arsenic evaporation and subsequent nucleation of the ZnSe layer on these particular partially relaxed (In,Ga)P surfaces is believed to be contributing to the broader rocking curve for the ZnSe growth on the  $4.3 \mu\text{m}$  (In,Ga)P layers. ZnSe grown on a GaAs substrate exhibited FWHMs in the range of  $180''$  to  $230''$ .

The optical properties of the ZnSe films were examined by low temperature (10 K) photoluminescence spectroscopy. As shown in Fig. 2, the

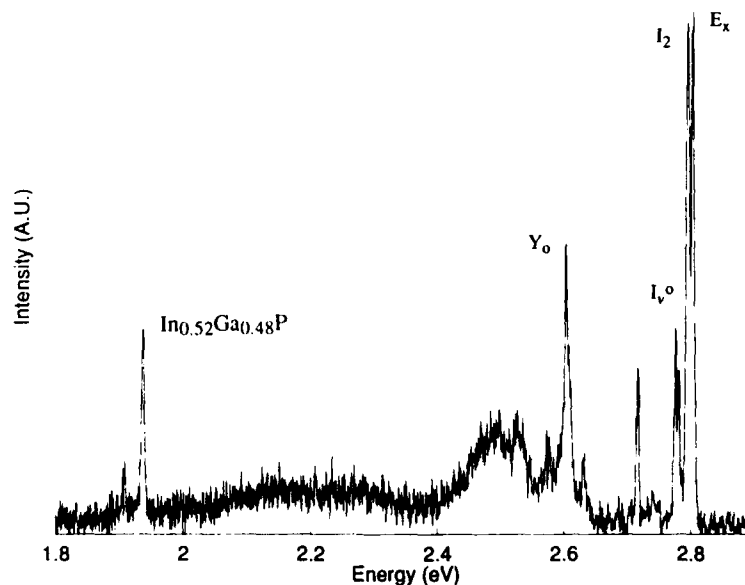


Fig. 2. 10 K photoluminescence spectrum of the  $1.1 \mu\text{m}$  ZnSe film grown on partially relaxed  $4.3 \mu\text{m}$  (In,Ga)P film. The feature at  $1.938 \text{ eV}$  is attributed to the photoluminescence from the (In,Ga)P buffer layer. Features at  $2.803$ ,  $2.795$ ,  $2.776$  and  $2.603$  are identified as  $E_x$ ,  $I_2$ ,  $I_0'$ , and  $Y_0$ , respectively. The origin of the feature at  $2.717$  is unknown and is under investigation. (The feature at  $1.907 \text{ eV}$  is the second harmonic of the  $3250 \text{ \AA}$  line from the HeCd laser.)

donor-bound exciton ( $I_2$ ) and free exciton ( $E_x$ ) transitions were of nearly equal intensity for the 1.1  $\mu\text{m}$  ZnSe layer grown on the 4.3  $\mu\text{m}$   $\text{In}_{0.52}\text{Ga}_{0.48}\text{P}$  buffer layer, indicating that the ZnSe epilayer had a low donor concentration and high crystalline purity. The  $Y_0$  transition at 2.602 eV and the  $I_V^0$  transition at 2.775 eV have been attributed to extended defects and are typically observed in high purity ZnSe epilayers [18-22]. The wider FWHM of the X-ray rocking curves, and the presence of the  $Y_0$  and the  $I_V^0$  transitions, suggest that the ZnSe layer still contains a number of dislocations, and requires confirmation by transmission electron microscopy. The transition at 1.938 eV is due to photoluminescence originating from the (In,Ga)P buffer layer.

#### 4. Summary

High quality ZnSe epilayers have been grown on (In,Ga)P buffer layers by GSMBE. The critical thickness of the (In,Ga)P epilayers greatly exceeded the value predicted by the Matthews and Blakeslee force balancing model, as well as by a model which uses an assumption of energy balance. SEM investigations of the (In,Ga)P layers showed that the surfaces were featureless, and did not exhibit any evidence of cross-hatching on partially relaxed (In,Ga)P buffer layers. ZnSe layers grown on the pseudomorphic (In,Ga)P buffer layers had a FWHM of approximately  $130''$ , as determined by (400) X-ray rocking curves indicating good structural quality. Photoluminescence spectra of ZnSe on partially relaxed  $\text{In}_{0.52}\text{Ga}_{0.48}\text{P}$  also suggests that the films were of high purity. In conclusion, (In,Ga)P is a promising substrate material for the realization of devices based on ZnSe and its related II-VI compounds.

#### 5. Acknowledgments

The authors would like to thank J.N. Damask of MIT for many valuable discussions and for performing the SEM investigation. They also acknowledge Dr. G.C. Hua and Professor N. Otsuka of Purdue University for the TEM analysis,

and D. Grillo of Purdue University for performing the four crystal X-ray diffraction rocking curve measurements. This research project was sponsored by the National Center for Integrated Photonic Technology (Contract No. 542-381), the Advanced Research Projects Agency/Office of Naval Research University Research Initiative (Grant # 284-25041), and the National Science Foundation (Grant # DMR-92-02957).

#### 6. References

- [1] J. Ren, D.B. Eason, L.E. Churchill, Z. Yu, C. Boney, J.W. Cook, Jr., J.F. Schetzina and N.A. El-Masry, *J. Crystal Growth* 138 (1994) 455.
- [2] M. Haase, J. Qiu, J. DePuydt and H. Cheng, *Appl. Phys. Lett.* 59 (1991) 1272.
- [3] H. Jeon, J. Ding, W. Patterson, A.V. Nurmikko, W. Xie, D. Grillo, M. Kobayashi, R. L. Gunshor, C.G. Hua and N. Otsuka, *Appl. Phys. Lett.* 59 (1991) 3619.
- [4] H. Jeon, J. Ding, A.V. Nurmikko, W. Xie, D. Grillo, M. Kobayashi and R.L. Gunshor, *Appl. Phys. Lett.* 60 (1992) 2045.
- [5] S.Y. Wang, J. Simpson, H. Stewart, S.J.A. Adams, I. Hauksson, Y. Kawakami, M.R. Taghizadeh, K.A. Prior and B.C. Cavenett, *Physica B* 185 (1993) 508.
- [6] H. Okuyama, T. Miyajima, Y. Morigana, F. Hiei, M. Ozawa and K. Akimoto, *Electron. Lett.* 28 (1992) 1798.
- [7] J.M. Gaines, R.R. Denten, K.W. Haberen, T. Marshall, P. Mensz and J. Petruzello, *Appl. Phys. Lett.* 62 (1993) 2462.
- [8] Also, see for example, this Proc. 6th Intern. Conf. on II-VI Compounds and other Related Optoelectronic Materials, Newport, RI, 1993, *J. Crystal Growth* 138 (1994).
- [9] J.M. DePuydt, M.A. Haase, S. Guha, J. Qiu, H. Cheng, B.J. Wu, G.E. Höfler, G. Meis-Haugen, M.S. Hagedorn and P.F. Baude, *J. Crystal Growth* 138 (1994) 667.
- [10] C.A. Coronado, E. Ho, L.A. Kolodziejki and C.A. Huber, *Appl. Phys. Lett.* 61, (1992) 534.
- [11] C.A. Coronado, E. Ho, P.A. Fisher, J.L. House, K. Lu, G.S. Petrich and L.A. Kolodziejki, *J. Electron. Mater.*, in press.
- [12] If the temperature of the (In,Ga)P buffer layer was increased to temperatures above 350°C prior to the nucleation of ZnSe, the initial ZnSe RHEED pattern was indicative of a bulk diffraction pattern suggestive of three-dimensional nucleation. The surface of the ZnSe layer following growth was also very rough as determined by SEM micrographs. We speculate that excess phosphorus evaporation may occur at high temperatures giving rise to a consequent roughening of the (In,Ga)P surface and thus the ZnSe surface.
- [13] R.L. Gunshor, Purdue University, private communication.

- [14] J.W. Matthews and A.E. Blakeslee, *J. Crystal Growth* 27 (1974) 118.
- [15] K. Ozasa, M. Yuri, S. Tanaka and H. Matsunami, *J. Appl. Phys.* 68 (1990) 1.
- [16] R. People and J.C. Bean, *Appl. Phys. Lett.* 47 (1985) 322.
- [17] W.T. Masselink, M. Zachau, T.W. Hickmott and K. Hendrickson, *J. Vac. Sci. Technol. B* 10 (1992) 966.
- [18] S. Satoh and K. Igaki, *Jap. J. Appl. Phys.* 22 (1983) 68.
- [19] S. Myhajlenko, J.L. Batstone, H.J. Hutchinson and J.W. Steeds, *J. Phys. C* 17 (1984) 6477.
- [20] J. Saraie, N. Matsumura, M. Tsubokura, K. Miyagawa and N. Nakamura, *Jap. J. Appl. Phys.* 28 (1989) L108.
- [21] K. Shahzad, J. Petruzzello, D.J. Olego, D.A. Cammack and J.M. Gaines, *Appl. Phys. Lett.* 57 (1990) 2452.
- [22] K. Shahzad and D.A. Cammack, *Appl. Phys. Lett.* 56 (1990) 180.



ELSEVIER

Journal of Crystal Growth 138 (1994) 8–13

JOURNAL OF  
**CRYSTAL  
GROWTH**

## Epitaxial overgrowth of II–VI compounds on patterned substrates

D. Schikora <sup>\*,a</sup>, H. Hausleitner <sup>b</sup>, S. Einfeldt <sup>c</sup>, C.R. Becker <sup>c</sup>, Th. Widmer <sup>a</sup>,  
C. Giftge <sup>a</sup>, K. Lübke <sup>b</sup>, K. Lischka <sup>b</sup>, M. von Ortenberg <sup>d</sup>, G. Landwehr <sup>c</sup>

<sup>a</sup> *Institut für Halbleiterphysik und Optik, Technische Universität Braunschweig, Mendelssohnstrasse 3, D-38106 Braunschweig, Germany*

<sup>b</sup> *Forschungsinstitut für Optoelektronik, Universität Linz, A-4040 Linz, Austria*

<sup>c</sup> *Physikalisches Institut, Universität Würzburg, Am Hubland, D-97074 Würzburg, Germany*

<sup>d</sup> *Fachbereich Physik, Lehrstuhl für Magnetotransport, Humboldt-Universität Berlin, Invalidenstrasse 110, D-10115 Berlin, Germany*

### Abstract

The selected area epitaxial overgrowth of narrow gap HgTe as well as wide gap CdTe and ZnTe on CdTe/GaAs substrates which had been structured by dry etching techniques, has been investigated. A plasma etching process using a barrel reactor with  $\text{CH}_4\text{--H}_2$  gases has been employed to prepare stripes with a width of about  $1\ \mu\text{m}$  with anisotropic as well as isotropic etching profiles. It has been found, that the selected area HgTe overgrowth takes place with a high local selectivity to the low index planes of the patterned surface. In contrast, the selected area overgrowth of the wide gap CdTe and ZnTe is controlled by anisotropic growth kinetics provided that the substrate temperature is not lower than  $220^\circ\text{C}$  and the starting surface consists of well developed low index crystallographic planes.

### 1. Introduction

The epitaxial overgrowth on patterned substrates has been studied in the last decade to our knowledge entirely for III–V compounds. It is of technological importance for the fabrication of index of refraction guided injection lasers [1] as well as for the synthesis of low dimensional structures [2] which could form the basis for novel device applications. The basic idea of a “true” selected area epitaxy (SAE) is (i) to adjust the pattern dimensions of the substrate surface to correspond to the diffusion length of the adatoms

and (ii) to exploit the anisotropy of the growth kinetics. If the dimensions of the structures in the pattern are of the order of the surface diffusion length of the adatoms, then the adatoms can migrate to planes with lower surface energies and condense there. Therefore a peculiar feature of growth on patterned substrates is a position dependent growth rate across the surface which provides the possibility to induce localized condensation and thereby to generate laterally defined structures. The MBE growth kinetics of II–VI compounds is not uniform. The sticking coefficients of cations and anions of wide gap II–VI compounds are comparable over a wide temperature range and therefore the minority flux determines the growth rate [3]. But growth

\* Corresponding author.

regimes are known, where a self-regulation behaviour takes place, e.g. the chalcogen atom sticks only in the presence of a metal atom, similar to the III–V semiconductors [4]. On the other hand, the sticking coefficients of the narrow gap II–VI compounds containing Hg differ by at least two orders of magnitude and show an unusually strong dependence on the growth direction [5]. The purpose of the present work is to study the SAE growth mechanism of wide gap as well as narrow gap II–VI compounds on structured surfaces in general and to determine the possibility of direct preparation of as-grown nanometer structures on micrometer scaled surface structures.

## 2. Experimental setup

The CdTe/GaAs substrates used in the following SAE experiments consist of approximately 30  $\mu\text{m}$  of CdTe grown on (100) GaAs by hot-wall epitaxy [6]. These CdTe/GaAs substrates are referred to as CdTe substrates in the following. The CdTe layers were etched using a  $\text{CH}_4$ - $\text{H}_2$  plasma in a barrel reactor. Details of this process are described elsewhere [7]. Both the anisotropic and isotropic etch regimes, were used to generate periodically corrugated CdTe surfaces as shown in Figs. 1a and 1b, which are scanning electron microscopy (SEM) images of cross sections of an

isotropically etched and an anisotropically etched stripe pattern, respectively. Characteristic dimensions of the investigated patterns are a stripe width of 1  $\mu\text{m}$ , a stripe height of 0.8–1.5  $\mu\text{m}$  and a stripe to stripe distance of 10–100  $\mu\text{m}$ . All stripes were oriented parallel to [110] directions with a {100} surface plane. Electrical measurements were conducted on contact areas of about  $300 \times 500 \mu\text{m}$ , which were placed on both ends of the stripes.

The epitaxial overgrowth of HgTe and CdTe was carried out in a Riber 2300 MBE system, which was adapted to the special requirements of Hg as described elsewhere [8]. The patterned CdTe/GaAs substrates were cleaned with standard solvents and etched with HCl in order to remove oxygen from the surface. The substrates were then mounted on a molybdenum holder with a graphite solution. All substrates were thermally cleaned in vacuum at 350°C for 2 min. Before overgrowth a homoepitaxial buffer layer of 500 Å was grown to ensure the reproducibility of the nucleation process. The HgTe layers were grown at a temperature of 180°C and the CdTe layers at 230°C. Some of the experiments, in particular the ZnTe overgrowth, were carried out in a hot wall beam epitaxy (HWBE) system. The principle of the HWBE has been described elsewhere [9]. The ZnTe growth rate was varied between 0.4 and 2.7  $\mu\text{m}/\text{h}$  in order to investigate

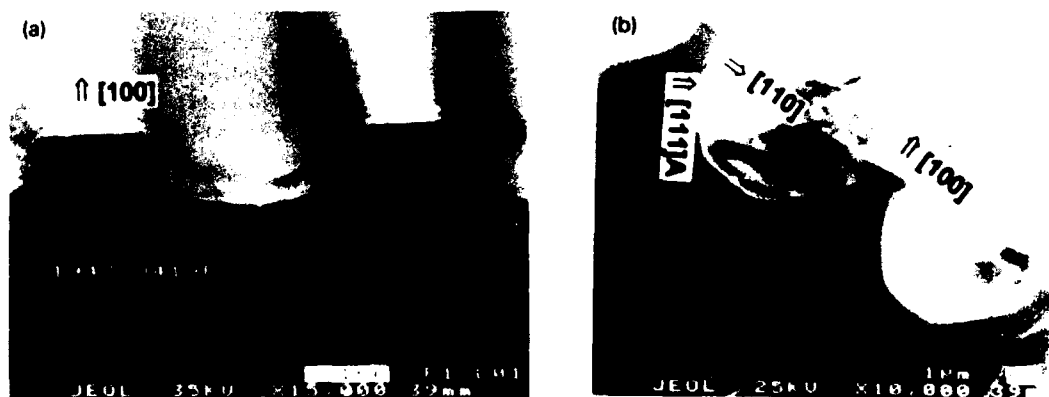


Fig. 1. (a) SEM image of the cross section profile of an isotropic etched CdTe stripe pattern. (b) SEM image of the cross section profile of an anisotropic etched CdTe stripe pattern.



the influence of the growth rate as well as the growth temperature on the selected area growth mechanism.

### 3. Results and discussion

The epitaxial HgTe overgrowth was carried out on patterned CdTe/GaAs in order to investigate the influence of the crystal orientation on the HgTe growth rate. A scanning electron microscopy image of a (100) surface, which was overgrown with a 0.2  $\mu\text{m}$  thick epilayer of HgTe, is shown in Fig. 2. The image was made in the Hg-sensitive compositional-contrast mode and shows the lateral distribution of HgTe after the growth process. It can be seen, that HgTe has grown only on the (100) oriented surface plane, i.e. on top of the smooth surface of the stripes as well as on the rough surface between the stripes, as indicated by the uniform gray color. No growth was observed on the {111} planes on both sides of the stripes or on the {110} oriented sides of the stripes, which is indicated by the darker color. It has been experimentally shown that the HgTe growth rate and hence the Hg sticking coefficient  $S$  is orientation dependent according to the following relationship [7]:

$$S(111)B > S(100) > S(111)A > S(110).$$

Apparently overgrowth has been performed in a

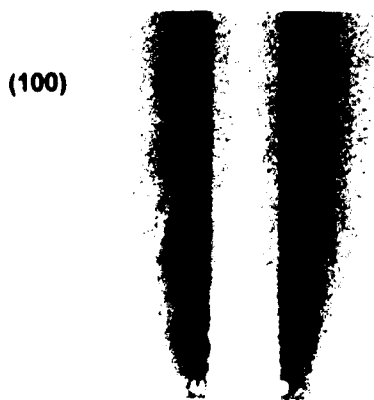


Fig. 2. SEM compositional contrast image of HgTe selected area epitaxy.

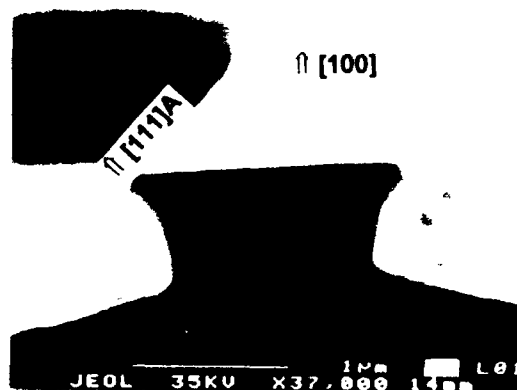


Fig. 3. Cleaved cross section of a single CdTe stripe overgrown with HgTe.

regime where the basic condition for epitaxial growth.

$$K_{\text{HgTe}}(T_{\text{substrate}}) > p_{\text{Hg}}\{hkl\}p_{\text{Te}}^{1/2}.$$

was fulfilled only for the {100} planes. Here  $K_{\text{HgTe}}(T_{\text{substrate}})$  is the temperature dependent equilibrium coefficient of condensation,  $p_{\text{Hg}}\{hkl\}$  is the Hg partial pressure (concentration of physisorbed Hg) and  $p_{\text{Te}}$  is the partial pressure of tellurium (concentration of physisorbed Te). The orientation dependence of the Hg sticking coefficient implies that the concentration of physisorbed Hg is also dependent on the orientation of the growth surface. The substrate temperature and flux intensities chosen for this experiment, have enabled hetero-nucleation of HgTe for the {100} oriented surfaces but not for the other surface orientations of the patterned substrate, which we assume are {111} A surfaces. This result confirms qualitatively the orientation dependence of the Hg sticking coefficient and demonstrates that it should be possible to use this behavior for local selectivity of epitaxial overgrowth. High resolution X-ray diffraction has shown for all experiments that the full width at half maximum of the corresponding rocking curves was significantly smaller after the epitaxial overgrowth with typical values of about 200 arc sec. Fig. 3 shows a cleaved {110} cross section SEM image of a single CdTe stripe after HgTe overgrowth. It can be seen, that on top of the stripe a faceted structure has formed

with two {111} side surfaces and a {100} top surface. This indicates, that the growth rate  $R$  of HgTe for the {111} surfaces must be smaller than for the {100} surface. Tellurium determines the growth rate in the MBE growth of HgTe, which took place at a very low substrate temperature (180°C), and therefore, the migration anisotropy of the rate determining species should be rather low. The growth rates on {100} and {111} in this case are mainly influenced by the ratio of effective incident fluxes  $F$ :

$$F\{111\}A = F\{100\} \cos(54.7^\circ).$$

This results in the formation of a truncated pyramid on top of the stripes. The measured growth rate ratio  $Q(\text{HgTe}) = R\{111\}A/R\{100\}$  is shown in Table 1 and confirms that this growth rate relationship is reproducible; therefore it seems possible to reduce the width of the top {100} HgTe surface from 1  $\mu\text{m}$  down to a few tens of nanometers, and thus to fabricate quantum wires which are in an as-grown state. The principal advantage of the selected area overgrowth on top of a mesa-type pattern, demonstrated in this work, is that epitaxy takes place on surfaces which are almost in an as-grown state and not damaged by the plasma. In order to determine the electrical properties of the 200 nm thick HgTe overgrowth stripes, Shubnikov–De Haas (SdH) measurements were performed. The contact areas were bonded with gold/indium contacts and the transverse magneto-resistance was measured. From the positions of the oscillations a donor concentration of  $6 \times 10^{15} \text{ cm}^{-3}$  and a mobility of  $3.2 \times 10^4 \text{ cm}^2 \text{ V}^{-1} \text{ s}^{-1}$  at 4.2 K were determined. This is

comparable with data of good quality MBE grown HgTe layers as reported in the literature [10] and clearly demonstrates the possibility of growing epitaxial HgTe layers of sufficient quality on top of CdTe stripes.

The overgrowth behavior of wide gap II–VI compounds was investigated with a series of growth experiments with CdTe and ZnTe. The starting surface was the same as that used in MBE overgrowth of HgTe, i.e. CdTe/GaAs was dry etched to generate mesa shaped stripes along the [110] direction. The overgrowth of CdTe was carried out after the surface was thermally cleaned and the buffer layer was grown as described above. The substrate temperature was decreased to 230°C and the CdTe overlayers were grown using an additional Cd source, in order to maintain a more stoichiometric growth. In some cases, HgTe layers were overgrown on top of the CdTe overgrowth, which reproduces the features discussed above. Fig. 4a shows a SEM image of a cleaved cross section of such a structure. The starting surface profile was isotropically etched as shown in Fig. 1a. It is easily recognized, that the CdTe overgrowth on the stripe starts also with the formation of two {111} facets on both sides of the stripe but obviously now with {111}B polarity. Because of the incident flux relationships, the growth rate of these two {111} facets is smaller than that of the {100} growth plane. The stripe width becomes larger as the overgrowth proceeds which implies the {111}B polarity of the surface. When the HgTe overgrowth is started, the cross section profile changes immediately; the HgTe forms {111} facets with the opposite polarity and the stripe width becomes smaller as discussed above. The mechanism behind the formation of the opposite type {111} facets is not fully understood at the present. If we consider the surface profile between the stripes, we observe the formation of “lips” near the stripes. The measurement of the overlayer thickness between the stripes results in a constant value of 1.5  $\mu\text{m}$ , which indicates that in the case of an isotropically etched substrate profile the surface diffusion is less efficient and the selectivity of the growth rate is suppressed. The formation of “lips” is therefore caused by a shadow effect from the stripes

Table 1  
Growth rate ratio  $Q = R\{111\}/R\{100\}$  for overgrown layers

Sample No.	Overgrown layer	Growth rate along [100] ( $\mu\text{m}/\text{h}$ )	$Q(\text{HgTe})$	$Q$
Q419a	HgTe/CdTe	0.65	0.52	0.26
Q419b	HgTe/CdTe	0.65	0.58	0.51
Q419c	CdTe	0.45	–	0.34
1866-4	HgTe/CdTe	0.35	0.64	0.38
1866-6	HgTe/CdTe	0.35	0.63	0.38
1866-8	ZnTe	0.45	–	0.27
1866-10	ZnTe	2.75	–	0.61

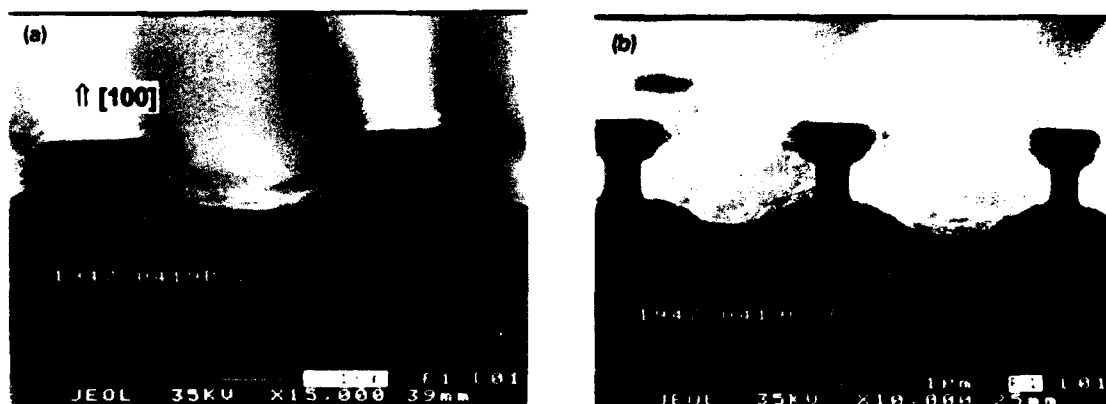


Fig. 4. (a) Selected area growth of HgTe/CdTe on isotropically etched stripe pattern. (b) Selected area epitaxy of CdTe on anisotropically etched stripe pattern.

and not influenced by surface kinetics. The same surface profiles were obtained for low growth rates of about  $0.5 \mu\text{m}$  and high growth rates of  $2.5 \mu\text{m}$ . For comparison, CdTe overlayers were grown on anisotropically etched surfaces which are shown in Fig. 1b. Fig 4b shows the resulting cross section surface profile after deposition of  $0.9 \mu\text{m}$  of CdTe with the same growth parameters as described above. One can see that a completely different profile of the surface between the stripes results without the presence of "lips". In analyzing this behavior, we have measured the thickness distribution, considering that the Cd and Te flux densities arriving at the {111} and {100} planes is different from geometrical reasons. Without sufficient surface migration we would expect a relationship for the growth rates on {100} and {111}, analogous to the situation for the low temperature HgTe growth, i.e.  $R\{111\} = R\{100\}\cos(54.7^\circ)$ . Hence, if the measured ratio  $Q = R\{111\}/R\{100\}$  is significantly greater or smaller than 0.57, the surface kinetics and in particular the migration of adatoms influences the growth velocity of the adjacent planes. The measured ratio in the experiment discussed here is

$$Q = R\{111\}/R\{100\} \\ = 0.15 \mu\text{m/h}/0.45 \mu\text{m/h} = 0.34.$$

This means that the growth velocity of the {111} facets is reduced due to a net flow of the rate determining species from the {111} facet to the adjacent {100} plane. Such a net flow can only occur if the mobility of the adatoms on the {111} facets is sufficiently high and exceeds the mobility at the {100} plane. In this context, one can explain the absence of "lips" in all experiments with anisotropically etched surfaces. The large surface diffusion compensates local inhomogeneities in the incident fluxes, i.e. shadows. Table 1 summarizes the measured growth rate ratio  $Q$  for HgTe as well as CdTe and ZnTe overgrowth on anisotropically etched starting surfaces.

#### 4. Summary and conclusions

Selected area epitaxial overgrowth of narrow gap HgTe and wide gap CdTe and ZnTe on dry etched CdTe/GaAs substrates has been investigated. A plasma etch process using a barrel reactor with  $\text{CH}_4\text{-H}_2$  gases has been employed to prepare stripes with dimensions of about  $1 \mu\text{m}$  and with anisotropic as well as isotropic etched profiles. It has been found, that HgTe grow with a reduced growth rate anisotropy because of the low mobility of the rate determining Te adatoms at substrate temperatures of  $180^\circ\text{C}$ . A significant

anisotropic behavior of the growth rate is influenced only by the geometry of the facets and planes which form the initial surface. On the other hand, the selectivity of the epitaxial overgrowth of Hg compounds is rather high, due to the strong orientation dependence of the Hg sticking coefficient. The initial width of the substrate stripes can be reduced by HgTe selected area overgrowth and opens the possibility of directly preparing low dimensional structures during the epitaxial growth process. It can be expected that the crystalline perfection of such quantum wires is sufficiently high, because of the non-damaged starting surface on top of the CdTe stripes. In comparison, the selected area overgrowth of wide gap compounds, as demonstrated here for the examples of CdTe and ZnTe overgrowth, can be carried out with kinetically determined growth rate anisotropy, provided that the substrate temperature is not lower than 220°C, the starting substrate surface consists of anisotropically etched low index planes and the growth rate in the [100] direction does not exceed 0.6  $\mu\text{m}/\text{h}$ . It has been found that the epitaxial overgrowth of HgTe and CdTe starts with the formation of {111} facets of different polarity. The reasons are unknown at the present; however, experimental investigations using transmission electron microscopy have been started.

## 5. Acknowledgments

This work was supported from the Deutsche Forschungsgemeinschaft, the Bundesministerium für Forschung und Technologie (contract number TK 0369) and the Fonds zur Förderung der wissenschaftlichen Forschung in Österreich.

## 6. References

- [1] J.S. Smith P.L. Derry, S. Margalit and A. Yariv, *Appl. Phys. Lett.* 47 (1985) 712.
- [2] Y. Nakamura, S. Koshiya, M. Tsuchiya, H. Kano and H. Sakaki, *Appl. Phys. Lett.* 59 (1991) 6.
- [3] T. Yao and Y. Miyoshi, *Jap. J. Appl. Phys.* 16 (1977) 369.
- [4] W. Faschinger, P. Juza, S. Ferreira, H. Zajicek, A. Pesek, H. Sitter and K. Lischka, *Thin Solid Films* 225 (1993) 270.
- [5] J.P. Faurie, *J. Crystal Growth* 81 (1987) 483.
- [6] D. Schikora, H. Sitter, J. Humenberger and K. Lischka, *Appl. Phys. Lett.* 48 (1986) 1276.
- [7] M. Neswal, K.H. Gresslehner, K. Lischka, P. Bauer, A. Brandstätter and K. Lübke, *Mater. Sci. Eng. B* 16 (1993) 108.
- [8] C.R. Becker, L. He, M.M. Regnet, M.M. Kraus, Y.S. Wu, G. Landwehr, X.F. Zhang and H. Zhang, *J. Appl. Phys.* 74, (1993) 2486.
- [9] J. Humenberger, K.H. Gresslehner, W. Schirz, K. Lischka and H. Sitter, *Mater. Res. Soc. Symp. Proc.* 216 (1991) 53.
- [10] R.J. Justice, D.G. Seiler and W. Zawadzki, *Appl. Phys. Lett.* 52, (1988) 1332.

## Migration enhancement on ZnSe surface in photoassisted molecular beam epitaxy and long duration time of the effects

S. Ichikawa, N. Matsumura \*, K. Yamawaki, K. Senga, J. Saraie

*Department of Electronics and Information Science, Faculty of Engineering and Design, Kyoto Institute of Technology, Matsugasaki, Kyoto 606, Japan*

### Abstract

With He–Cd laser irradiation during MBE growth of ZnSe at 250°C, the density of hillocks of epilayers was reduced from  $10^6$  to  $10^4$  cm<sup>-2</sup>. The critical thickness was extended and the intensities of free-exciton emissions were remarkably increased. These results can be explained by the migration of surface adatoms being enhanced by the irradiation. Chopped irradiation was used during growth and it was revealed that the effects persisted at least 5 ms after the light was turned off, which suggests that the change in the charge state of the surface which causes the change of the behavior of the adatoms during irradiation endures for a long time after the light is turned off.

### 1. Introduction

We have studied photoassisted molecular beam epitaxial (MBE) growth of ZnS<sub>x</sub>Se<sub>1-x</sub> [1–5]. Crystalline quality improvement [1] and low-temperature epitaxial growth at 150°C [2] in ZnSe are already established by this method. The desorption of adsorbed atoms in photoassisted MBE of ZnSe was reported by several researchers [6,7]. These effects are attributed to weak adsorption forces due to the excess carriers photogenerated in the epilayer [3]. In these previous studies, continuous illumination was used and the thicknesses of the epilayers were about 2 μm. In this study, the change in the crystallinity of ZnSe epilayers was investigated when the epilayer

thickness or the chopping frequency of the irradiation light was varied, which can give information on the behavior of surface adatoms and the duration time of the light-irradiation effects.

### 2. Experimental procedure

ZnSe epilayers were grown on GaAs(100) substrates by photoassisted MBE. 6N Zn and 6N Se were used as source materials. The molecular beam intensity ratio of the group VI element to the group II element ( $J_{\text{VI}}/J_{\text{II}}$  ratio) was usually 2. In the study of  $J_{\text{VI}}/J_{\text{II}}$  ratio dependence, the ratio was changed from unity to 2. The substrate temperature was 250°C and the growth rate was about 0.5 μm/h. The epilayer thicknesses were varied by the growth time. A He–Cd laser (441.6 nm, ~250 mW/cm<sup>2</sup>) was used as an irradiation source. Both irradiated and unirradiated epilay-

\* Corresponding author.

ers were obtained in a single growth run because the laser beam, with a diameter of 5 mm, irradiated only part of the substrate. Continuous irradiation was used in the experiments of the epilayer–thickness dependence. The chopping frequencies with a duty cycle ratio of 50% were varied from 1 Hz to 20 kHz by using an optical chopper (Scitec Instruments, 300CD).

The lattice constants normal to the epilayer surface were determined by X-ray diffraction, and the lattice deformation and relaxation were examined. The epilayers were characterized by photoluminescence at 11 K. The exciting light was a 365 nm line from an ultrahigh-pressure Hg lamp.

### 3. Results and discussion

#### 3.1. Thickness dependence of the irradiation effects

Fig. 1 shows the surface morphologies of unirradiated (Fig. 1a) and irradiated (Fig. 1b) epilayers with thicknesses of about 2  $\mu\text{m}$ . Many pyramidal hillocks with a basal planes with  $\langle 011 \rangle$  oriented sides are observed in the unirradiated epilayers. The density is of the order of  $10^6 \text{ cm}^{-2}$ . The density increased with increasing the epilayer thickness. With laser irradiation, the density is remarkably decreased to the order of  $10^4 \text{ cm}^{-2}$ . It is considered that the hillocks are the result of three-dimensional nucleation caused by the insufficient migration of adatoms, because the substrate temperature of 250°C is close to a critical temperature for epitaxial growth without

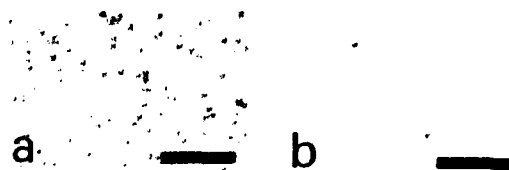


Fig. 1. Surface morphologies of unirradiated (a) and irradiated (b) epilayers grown at 250°C with thicknesses of about 2  $\mu\text{m}$ . Marker represents 20  $\mu\text{m}$ .

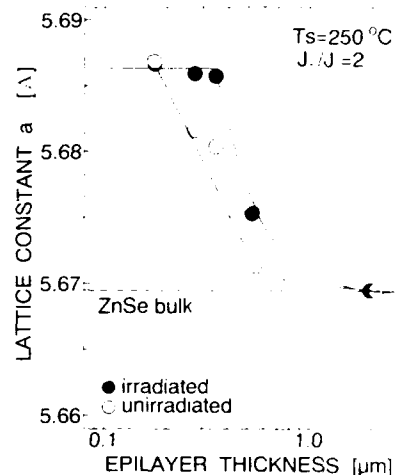


Fig. 2. Thickness dependence of the lattice constants normal to the epilayer surface ( $a_{\perp}$ ).

irradiation [4]. The reason why the density decreases with irradiation is that the enhancement of the migration of the surface adatoms by the irradiation leads to the enhancement of two-dimensional growth.

Fig. 2 shows the thickness dependence of the lattice constants normal to the epilayer surface ( $a_{\perp}$ ). The critical thickness of the unirradiated epilayer is about 0.2  $\mu\text{m}$ . With laser irradiation, the critical thickness is extended to about 0.35  $\mu\text{m}$ . The lattice relaxation may be enhanced in the unirradiated part by a coexistence of inhomogeneous tensile and compressive strain which is induced by three-dimensional growth. With laser irradiation, as mentioned above, two-dimensional growth is enhanced, and as a result, the critical thickness is extended. The critical thickness is large compared to the generally accepted value ( $\sim 0.15 \mu\text{m}$ ). The reason is not clear at this stage. But we consider that the growth condition of  $J_{\text{VI}}/J_{\text{II}}$  ratio of 2 and a low growth temperature of 250°C may be responsible.

Fig. 3 shows the thickness dependence of the intensities of the free exciton emissions in the photoluminescence spectra. In the unirradiated epilayers, the intensities increase with increasing the thickness and saturate at 0.6  $\mu\text{m}$ . It is consid-

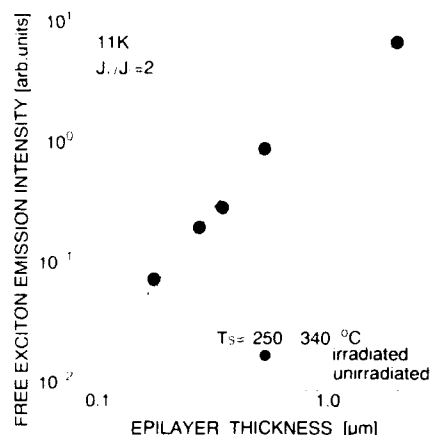


Fig. 3. Thickness dependence of the intensities of the free-exciton emissions in photoluminescence spectra.

ered that the saturation is related to the crystallinity remaining constant beyond the thickness of  $0.6 \mu\text{m}$  and the small penetration depth of the exciting light ( $365 \text{ nm}$ ), that is, the thickness of ZnSe which gives photoluminescence is considered to be smaller than  $0.6 \mu\text{m}$ . Intensities in the irradiated epilayers are larger than those in unirradiated epilayers and this effect becomes remarkably large with increasing the epilayer thickness. The intensities are as strong as those in unirradiated epilayers grown under an optimum growth temperature of  $340^\circ\text{C}$ . The increase due to the irradiation is attributed to the improvement of the crystallinity of the epilayers, that is, reduction in the density of non-radiative recombination centers. The intensities do not saturate at a thickness above  $0.6 \mu\text{m}$  but increase almost linearly with increasing the thickness up to about  $2 \mu\text{m}$ . This indicates that the quality of the surface region of the epilayer is improving more and more with increasing the thickness. Such improvement is attributed to the enhanced migration which is similar to that at a substrate temperature of  $340^\circ\text{C}$  and to the increase in the total number of the photogenerated carriers with increasing thickness. The penetration depth of the irradiating light is larger than that of the exciting light in photoluminescence measurements be-

cause the photon energy ( $2.807 \text{ eV}$ ) of a He-Cd laser is close to the bandgap energy of ZnSe.

In our previous study, we clarified that physisorbed atoms desorb by light irradiation and that the effective  $J_{\text{VI}}/J_{\text{II}}$  ratio decreases with the irradiation [4]; for example, the ratio becomes 1.6 in the irradiated part when the beam with a  $J_{\text{VI}}/J_{\text{II}}$  ratio of 2 is supplied at a substrate temperature of  $250^\circ\text{C}$ . Therefore, samples with various  $J_{\text{VI}}/J_{\text{II}}$  ratios were grown in order to investigate whether the change in the effective  $J_{\text{VI}}/J_{\text{II}}$  ratio by the irradiation is the origin or not of the improvement of the crystalline quality and of the reduction in the density of hillocks. As a result, the intensity of free-exciton emission became a maximum at a  $J_{\text{VI}}/J_{\text{II}}$  ratio around 1.5 in the unirradiated epilayers. However, with laser irradiation the intensities were larger than that in the unirradiated epilayers at every  $J_{\text{VI}}/J_{\text{II}}$  ratio studied, especially at a  $J_{\text{VI}}/J_{\text{II}}$  ratio around unity where the intensity of the unirradiated epilayer drastically decreased, the intensity increased by several orders of magnitude with irradiation in spite of the less favorable (Zn-rich)  $J_{\text{VI}}/J_{\text{II}}$  ratio. The density of hillocks on the unirradiated epilayers is reduced to the order of  $10^5 \text{ cm}^{-2}$  by setting the  $J_{\text{VI}}/J_{\text{II}}$  ratio to 1.6. But the densities can be reduced further to the order of  $10^4 \text{ cm}^{-2}$  by the irradiation at all  $J_{\text{VI}}/J_{\text{II}}$  ratios studied. These results indicate that the quality improvement by the irradiation in Figs. 1 and 3 cannot be explained by the decrease in the effective  $J_{\text{VI}}/J_{\text{II}}$  ratio. The migration enhancement of surface adatoms is really caused by the irradiation.

### 3.2. Chopping-frequency dependence of the irradiation effects

Fig. 4 shows the chopping-frequency dependence of lattice constants ( $a_{\perp}$ ). The epilayer thicknesses in this study were about  $0.3 \mu\text{m}$ . As shown in Fig. 2, the epilayer with continuous irradiation grows coherently and the epilayer without irradiation partially relaxes ( $a_{\perp} = 5.68 \text{ \AA}$ ) at this thickness. The  $a_{\perp}$  value of the epilayer with a chopping frequency of  $1 \text{ Hz}$  is the same as the unirradiated epilayer, that is, no irradiation effect is observed at this frequency. At a chop-

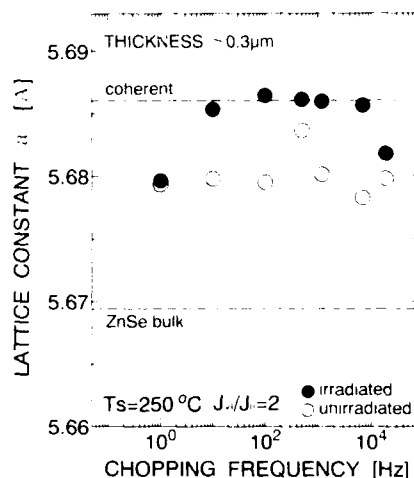


Fig. 4. Chopping-frequency dependence of the lattice constants normal to the epilayer surface ( $a_{\perp}$ ).

ping frequency above 10 Hz, the epilayers grow coherently, that is, the irradiation effect appears clearly. At a frequency of  $10^4$  Hz the epilayer partially relaxes. This is not clear at this stage. However, we do not consider that the irradiation effects on the epilayer is weak, because, as is shown in Fig. 5, the intensity ratio of free exciton

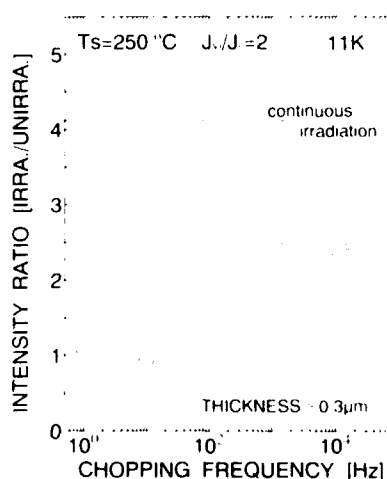


Fig. 5. Chopping-frequency dependence of the intensity ratios of the free-exciton emissions of the irradiated and the unirradiated epilayer.

emission is similar to the values of the other epilayers at a frequency above  $10^2$  Hz.

Fig. 5 shows the chopping-frequency dependence of the intensity ratios of the free-exciton emissions of the irradiated and the unirradiated epilayer. The ratio is unity at a chopping frequency of 1 and 10 Hz. At a frequency above 100 Hz, the ratios are about 2.5, that is, the irradiation effect is observed though the ratios do not reach the value with the continuous irradiation (about 4.1). The difference in the critical frequency in Figs. 4 and 5 shows that the photoluminescence is a more sensitive measure than the lattice constant for characterizing crystalline quality. We can say that the light-irradiation effects last at least 5 ms after the light is turned off.

We previously clarified that photons with energies larger than the bandgap of the epilayers and both photogenerated electrons and holes are responsible for the light-irradiation effects [3,5], and proposed a selective charge-transfer model of photogenerated carriers to the chemisorbed atoms [5]. Now we discuss this long duration time of the effects based on the model. The lifetime of photogenerated carriers in the ZnSe bulk is reported to be 85 ps [8], which is much shorter than this duration time. Therefore, the bulk carrier lifetime does not determine the long duration time. We have to consider the behavior of carriers at the surface region of the epilayers. A (100) growing surface consists of both Zn and Se exposed atoms. If photogenerated electrons transfer selectively to the uppermost chemisorbed Zn atoms, and holes to the uppermost chemisorbed Se atoms, electrons and holes separate spatially. In this situation, the modified charge state of the surface atoms may last for a long time after the light is turned off because of the difficulty in recombination of those carriers. The modified charge state may reduce the adsorption forces of physisorbed atoms, which enhances the desorption and migration of the adatoms.

#### 4. Conclusion

The surface morphologies of the epilayers were improved and the critical thickness was increased



by the light irradiation. The crystallinity of the growing surface was improved by continuous irradiation with increasing epilayer thickness, judging from the fact that the free exciton-emission intensities were increased. It was shown that these improvements due to the irradiation cannot be explained by the decrease in the effective  $J_{V1}/J_H$  ratio, but can be explained by the migration enhancement of the surface adatoms by the irradiation. It was shown by chopped-light irradiation that the light-irradiation effects last at least 5 ms after the light is turned off. This long duration of the effects suggests that the change in the charge state of the surface due to the selective transfer of photogenerated carriers endures for a long time after the light is turned off.

## 5. References

- [1] N. Matsumura, T. Fukada and J. Saraie, *J. Crystal Growth* 101 (1990) 61.
- [2] T. Fukada, N. Matsumura, Y. Fukushima and J. Saraie, *Jap. J. Appl. Phys.* 29 (1990) L1585.
- [3] N. Matsumura, M. Tsubokura, K. Miyagawa, N. Nakamura, Y. Miyanagi, T. Fukada and J. Saraie, *Jap. J. Appl. Phys.* 29 (1990) L723.
- [4] N. Matsumura, T. Fukada, K. Senga, Y. Fukushima and J. Saraie, *J. Crystal Growth* 111 (1991) 787.
- [5] N. Matsumura, K. Senga, J. Kakuta, T. Fukada and J. Saraie, *J. Crystal Growth* 115 (1991) 279.
- [6] M. Ohishi, H. Saito, H. Torihara, Y. Fujisaki and K. Ohmori, *J. Crystal Growth* 111 (1991) 792.
- [7] J. Simpson, S.J.A. Adams, S.Y. Wang, J.M. Wallace, K.A. Prior and B.C. Cavenett, *J. Crystal Growth* 117 (1992) 134.
- [8] J.A. Bolger, I. Galbraith, A.K. Kar, J. Simpson, S.Y. Wang, K.A. Prior, B.C. Cavenett and B.S. Wherrett, *Appl. Phys. Lett.* 63 (1993) 709.

## Metalorganic molecular beam epitaxial growth kinetics and doping studies of (001) ZnSe

D. Rajavel \*, J.J. Zinck, J.E. Jensen

*Hughes Research Laboratories, Malibu, California 90265, USA*

### Abstract

Thermally pre-cracked diethylzinc and diethylselenide were used for the metalorganic molecular beam epitaxial growth of (001) ZnSe films on (001) GaAs substrates. The growth kinetics of (001) ZnSe was studied by measuring the growth rate as a function of the substrate temperature and the II/VI flux ratio. Arrhenius plot of the Se-limited growth rate indicated an activation energy of 0.08 eV for the desorption of the Se species using Se and Se<sub>2</sub> species for ZnSe growth. Triallylamine, allylamine, tertiary-butylamine and ammonia were evaluated as sources for the N doping of ZnSe. Secondary ion mass spectrometry measurements were used to determine the impurity concentrations. When the amines were pre-cracked in the cracker cell, N concentrations in excess of  $1 \times 10^{19} \text{ cm}^{-3}$  were incorporated in films grown at  $\leq 225^\circ\text{C}$ . The N concentration decreased sharply with increased substrate temperature. Large concentrations of C and H were measured in films doped using the amines, and correlated with N concentrations; with ammonia, high H concentrations were observed and also correlated with the N concentration.

### 1. Introduction

The successful p-type doping of ZnSe has resulted in the development of light emitters operating in the blue region of the visible spectrum. This advancement has been possible due to the incorporation of electrically active nitrogen atoms in the ZnSe lattice using a nitrogen plasma source during molecular beam epitaxy (MBE) [1–5]. Other vapor phase epitaxial growth techniques such as metalorganic chemical vapor deposition (MOCVD) and metalorganic molecular beam epitaxy (MOMBE) have also been used to investigate p-type doping of ZnSe and related wide band-gap materials [6,7]. The MOMBE growth

kinetics of (001) ZnSe, determined by measuring the growth rate as a function of the growth parameters such as the II/VI flux ratio and the substrate temperature, is reported here. Information obtained from the growth kinetics was used to identify the optimal growth conditions for (001) ZnSe and to determine the desorption activation energy of the Se species. In MOMBE, the gas phase source materials are directed through thermal cracker cells before they are incident on the growth surface. The source materials can be either allowed to decompose on the growth surface, or pre-cracked in the cracker cell before incidence on the substrate surface. This provides an additional degree of flexibility for the decomposition of the dopant source material for the incorporation of the dopant impurities in the host lattice. Both pre-cracked and surface-cracked modes were utilized to investigate four different

\* Corresponding author.

nitrogen compounds, triallylamine, allylamine, tertiary-butylamine and ammonia for N doping of ZnSe layers. The concentrations of nitrogen and other potential contaminants incorporated in ZnSe, and their dependence on the dopant cracker cell temperature and the substrate temperature is reported.

## 2. Experimental procedure

The experiments were conducted in a custom Vacuum Generators MOMBE system [8] equipped with separate cracker cells for the group II, VI and the nitrogen dopant source. The flow rates of the source materials were controlled by regulating the pressure on the upstream side of an orifice attached to the inlet port of each cracker cell. Diethylzinc (DEZn) and diethylselenide (DESe) were pre-cracked at 800 and 900°C, respectively, and the ZnSe films were deposited on (001) GaAs substrates. The system was equipped with a quadrupole mass spectrometer (QMS) that could be moved via a translation stage to the substrate position. In this line-of-site geometry, the QMS could sample the flux directly incident on the substrate, prior to any collision or recombination at the surrounding liquid-nitrogen cooled panels. QMS measurements determined that DEZn decomposed at 800°C in the group II cracker cell to produce Zn and hydrocarbon fragments, and DESe decomposed in the group VI cracked cell to produce Se, Se<sub>2</sub> and hydrocarbon fragments. There was no detectable polyatomic selenium species, Se<sub>n</sub> ( $n > 2$ ) even when the QMS mass resolution was reduced to maximize sensitivity, for ionization energies between 10 and 70 eV. Furthermore, monomer Se was detected when the ionization energy of the QMS was reduced to 10 eV, which was less than the energy required to fragment Se<sub>2</sub>. Thus the Se-species consisted exclusively of Se and Se<sub>2</sub> which is in contrast to the Se<sub>n</sub> ( $n = 2, 3, 5, 6, 7, 8$ ) species produced during thermal evaporation of elemental Se from a conventional MBE effusion cell [9]. Details of the dependence of the Se<sup>+</sup> QMS signal on the ionization energy will be reported elsewhere [10]. The dopant cracker cell was operated over a

range of temperatures in order to study the effect of pre-cracking the nitrogen compounds on the incorporation of nitrogen in the ZnSe films.

## 3. Results and discussion

### 3.1. MOMBE growth kinetics of (001) ZnSe

It has been shown that the II/VI flux ratio of the growth species has a profound influence on the structural and optical properties of the deposited films [11]. Studies of the growth kinetics can provide information about the stoichiometry of the growth surface, as well as the sticking coefficient and desorption activation energies of the constituent elements. Thus information obtained from the growth kinetics can be utilized to optimize the growth conditions to obtain high quality material. The MOMBE growth kinetics of ZnSe were determined by measuring the growth rate of the film as a function of the substrate temperature and the II/VI flux ratio. Growth rates were determined in situ from RHEED intensity oscillations. The electron gun was operated at an acceleration potential of 10 keV and a filament current of 2 A, producing an emission current of 2 mA. It has been reported that the electron beam used for RHEED analysis can stimulate the desorption of Se species from ZnSe via a thermally activated process [12,13]. To evaluate the extent of the electron stimulated desorption, ZnSe growth rates were also determined from in-situ time resolved reflectivity (TRR) measurements using a HeNe laser ( $\lambda = 632.8$  nm), and compared with values obtained from RHEED oscillation measurements. In TRR measurements the interference of the laser beam reflected from the substrate–film and the film–vacuum interfaces results in the temporal variation of the reflected intensity, with a peak-to-peak separation corresponding to a film thickness of  $\lambda/2n$  (for normal incidence), where  $n$  is the refractive index of ZnSe at the growth temperature [14]. The uncertainty in the growth rates determined by either of these techniques is  $< \pm 5\%$ . Growth rates determined by TRR measurements were 5–10% higher than those evaluated from RHEED

intensity oscillation measurements. This corresponded to a reduction of the growth rate due to electron beam stimulated desorption of  $< 0.07 \mu\text{m/h}$ . Farrell et al. had reported that a static Se stabilized  $(2 \times 1)$  surface reconstruction reverts to the unreconstructed surface, and this transition is accelerated in portions of the sample exposed to the electron beam [12]. However, we could not observe the same enhancement of the transition upon reposition the electron beam on different parts of the sample. Furthermore, the maximum growth rate reduction of  $0.07 \mu\text{m/h}$  observed here is far smaller than the  $0.4 \mu\text{m/h}$  reduction observed during MBE growth by Farrell et al. [12]. Thus for the operating conditions of the electron gun, and for the Se and  $\text{Se}_2$  group VI species employed in our experiments, we find that the electron stimulated desorption was minimal. Thus growth rates determined from the RHEED intensity oscillations were used to study the growth kinetics, which provides semi-quantitative and qualitative information regarding the dependence of the surface stoichiometry on the

II/VI flux ratio. However, for the calculations of the desorption activation energy, where the absolute values of the growth rates are required, supporting TRR measurements were also used.

The growth rate of (001) ZnSe was measured as a function of the II/VI flux ratio by keeping the upstream pressure of DESe ( $P_{\text{DESe}}$ ) fixed, and varying  $P_{\text{DEZn}}$ . The growth rate measurements were performed for substrate temperatures between 275 and 375°C, and the results are illustrated in Fig. 1. RHEED intensity oscillations measurements were performed after the growth of  $\approx 2 \mu\text{m}$  of ZnSe on the (001) GaAs substrate, and were observed over a wide range of growth conditions. The symbols represent growth rates determined from RHEED oscillations and the solid lines serve to guide the eye. For a fixed  $P_{\text{DESe}}$ , the growth rate increased monotonically with increasing  $P_{\text{DEZn}}$ , and saturated at a maximum value. The saturated maximum growth rate decreased systematically with increasing substrate temperature. In the Se-limited (Zn-saturated) regime the maximum growth rate is determined

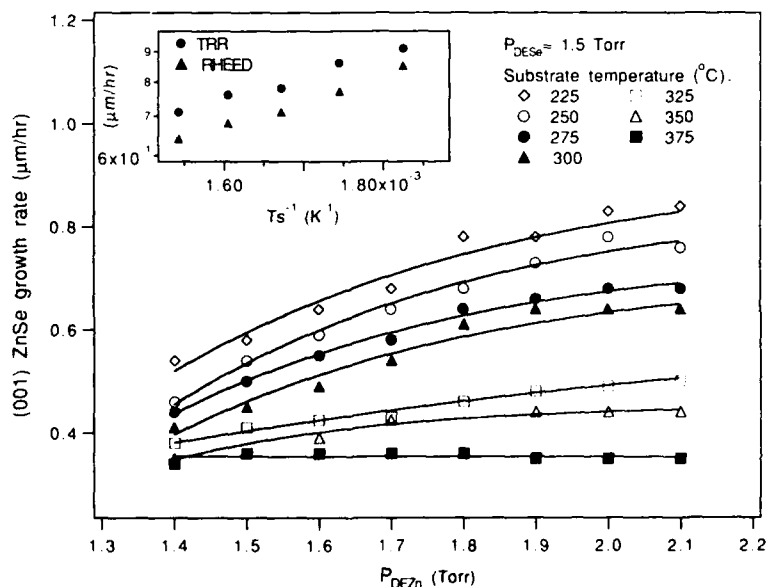


Fig. 1. The growth rate of (001) ZnSe as a function of the DEZn upstream pressure and the substrate temperature. The points represent growth rates determined from RHEED oscillation measurements, and the lines serve to guide the eye. The inset shows the Arrhenius plots of the growth rates determined from RHEED and TRR measurements under Se-limited growth conditions. The slopes indicate an average activation energy of 0.08 eV for desorption of the Se species.

by the re-evaporation rate of the Se-species. Thus the temperature dependence of the Se-limited growth rates are indicative of the desorption kinetics of the growth rate limiting Se species.

(001) ZnSe growth rates in the Se-limited (Zn-saturated) regime were measured for substrate temperatures between 275 and 375°C, using  $P_{\text{DEZn}}$  higher than that shown in Fig. 1, to ensure saturation of the growth rate. Arrhenius plots of these growth rates determined from RHEED and TRR measurements are shown in the inset of Fig. 1. The slopes of the best-fit straight lines are approximately the same and yield an average activation energy of 0.08 eV. This value is more than a factor of 10 lower than that reported for the desorption of Se from a static ZnSe surface by Cornelissen et al. [15] (1.2 eV) and Ohishi et al. [13] ( $\leq 1.23$  eV), and values measured for desorption from the surface during growth by Zhu et al. (0.90) eV [16]. However, these values reported in the literature are for the MBE process employing the polyatomic  $\text{Se}_n$  ( $n \geq 2$ ) species. It appears that the low desorption activation energy measured in this study is related to the Se species, which in this case, consisted exclusively of Se and  $\text{Se}_2$ . It should be noted that measurements on a static surface correspond to the desorption of Se species from a ZnSe surface initially stabilized with Se, as indicated by the  $(2 \times 1)$  surface reconstruction. However, the values reported here are those measured during film growth, corresponding to the desorption of Se species from a Zn-stabilized surface as inferred from the  $c(2 \times 2)$  surface reconstruction, and the growth rate curves which indicated Se-limited growth. However, in a recent study of the desorption of Te from the CdTe surface during MOMBE growth, Benz et al. measured activation energies more than a factor of 10 lower than that measured for a static CdTe surface, a result attributed to low binding energy precursor states of the Te species [17].

In general, the crystalline quality of an epitaxial layer is best when growth is performed under near-stoichiometric conditions that require minimal re-evaporation of the excess species incident on the surface. Achieving this condition requires the optimization of the II/VI flux ratio at a given

growth temperature. As shown in Fig. 1, for a fixed  $P_{\text{DESe}}$ , the growth rate increased with increasing  $P_{\text{DEZn}}$ , and saturated with a further increase in  $P_{\text{DEZn}}$  corresponding to near-stoichiometric growth conditions. The near stoichiometric growth conditions were chosen as the initial growth parameters. Films deposited under Se-stabilized growth conditions which exhibited the  $(2 \times 1)$  Se reconstruction had the best x-ray rocking curves. Films of 2–3  $\mu\text{m}$  thickness deposited on GaAs substrates at temperatures between 325 and 225°C exhibited X-ray full widths at half the intensity maximum (FWHM) of 170–220 arc sec, which compared favorably with values reported in the literature. Single crystalline films were deposited at temperatures as low as 150°C, results similar to that obtained by using a Se cracker cell in MBE growth [9,18].

### 3.2. Nitrogen doping of (001) ZnSe

Nitrogen doping of ZnSe using a plasma nitrogen source has been the most successful means of realizing low resistivity p-type ZnSe. Doping in MOMBE using gas sources such as ammonia and t-butylamine has also showed promise [19,20]. Here we present the first studies on N doping using triallylamine ( $(\text{H}_2\text{C}=\text{CHCH}_2)_3\text{N}$ , BP = 150°C) allylamine ( $\text{H}_2\text{C}=\text{CHCH}_2\text{NH}_2$ , BP = 53°C), as well as t-butylamine ( $(\text{CH}_3)_3\text{C}-\text{NH}_2$ , BP = 46°C) and ammonia ( $\text{NH}_3$ ). Hoke et al. have reported that delocalization of the electronic charge in a parent molecule enhances the formation of stable decomposition products thereby reducing the energy required for decomposition [21]. The delocalization effect is significant in compounds with one or more carbon-carbon double bonds. Thus as the allyl radical is relatively stable, triallylamine and allylamine were anticipated to decompose at lower temperatures than that required to decompose  $\text{NH}_3$ . Nitrogen incorporation in ZnSe was investigated by utilizing thermally pre-cracked dopant sources and also by allowing decomposition on the growth surface. Nitrogen incorporation was studied as a function of the dopant cracker cell temperature and the substrate temperature. A detailed quadrupole mass spectrometric study of the py-

pyrolysis process will be reported elsewhere [22]. Secondary ion mass spectrometric (SIMS) measurements were performed to determine the concentrations of potential contaminants in the films. The detection limit of H, C, O and N in the films is  $\approx 5 \times 10^{17} \text{ cm}^{-3}$ , and is limited by the presence of these elements in the SIMS ambient. The absolute concentration of N in the films was referenced to a N implanted sample. It has been reported that the presence of high levels of C that can be incorporated in ZnSe films grown by MOCVD affect the structural, optical and electrical properties of the films [23]. However, SIMS evaluation of undoped ZnSe films grown by MOMBE indicated that the concentrations of C and O were below the detection limit. The variation of N, H, C and O concentrations in the doped films with the growth conditions is discussed.

### 3.2.1. Nitrogen doping using triallylamine ( $\text{H}_2\text{C}=\text{CHCH}_2)_3\text{N}$

Quadrupole mass spectrometry studies were undertaken to study the cracker cell temperature

dependence of the pyrolysis products. Triallylamine decomposed in the cracker cell at temperatures in excess of  $700^\circ\text{C}$ . Due to the large hydrocarbon background in the MOMBE chamber it was not possible to determine all the pyrolysis products, but no N or  $\text{N}_2$  fragments were detected. The use of triallylamine as a dopant source for N doping of ZnSe was investigated at substrate temperatures of  $225^\circ\text{C}$  and  $325^\circ\text{C}$ , and for dopant cracker cell temperatures of  $250^\circ\text{C}$  (without pre-cracking the dopant source),  $700^\circ\text{C}$ ,  $800^\circ\text{C}$  and  $900^\circ\text{C}$ . The SIMS depth profile of a doped ZnSe film grown at  $225^\circ\text{C}$  for cracker cell temperatures of  $700^\circ\text{C}$ ,  $800^\circ\text{C}$  and  $900^\circ\text{C}$  is shown in Fig. 2. The concentration of N in the doped portions of the sample was  $\approx 1 \times 10^{18} \text{ cm}^{-3}$ , and was constant when the cracker cell was operated above  $700^\circ\text{C}$ . In addition, the concentrations of H and C were  $3 \times 10^{19}$  and  $1 \times 10^{15} \text{ cm}^{-3}$ , respectively, in the doped region. For the same dopant flow rate, and cracker cell temperature, films grown at  $325^\circ\text{C}$  have N, H and C, levels, over a factor of ten lower than that measured at the lower growth temperature. In contrast, when tri-

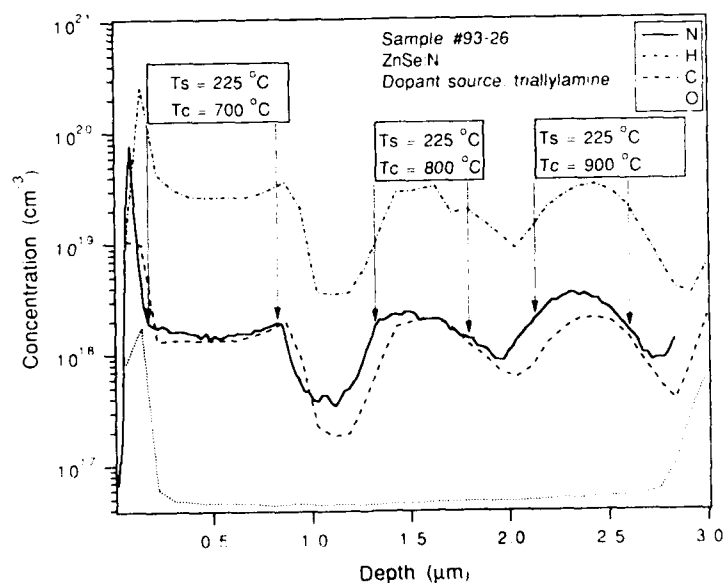


Fig. 2. The concentration profiles of N, H, C and O in a doped ZnSe film using triallylamine as the dopant source material. The growth conditions at each region of the sample represented by arrows are given in the adjoining box. The substrate and dopant cracker cell temperatures are represented by  $T_s$  and  $T_c$ , respectively.

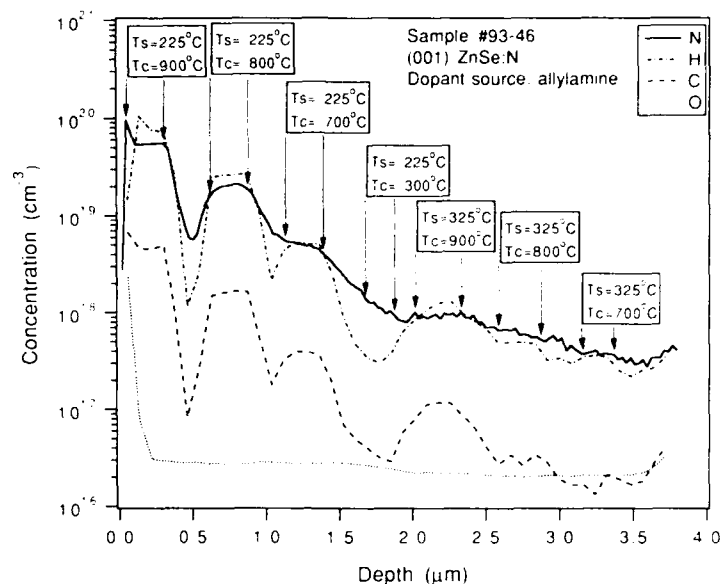


Fig. 3. The concentration profiles of N, H, C and O in a doped ZnSe film using allylamine as the dopant source material.

allylamine was directly incident on the growth surface without being pre-cracked (cracker cell temperature = 250°C), the measured concentra-

tion of N in the films was  $< 1 \times 10^{-17} \text{ cm}^{-3}$ , over the 225–325°C substrate temperature range investigated. Thus, although triallylamine was com-

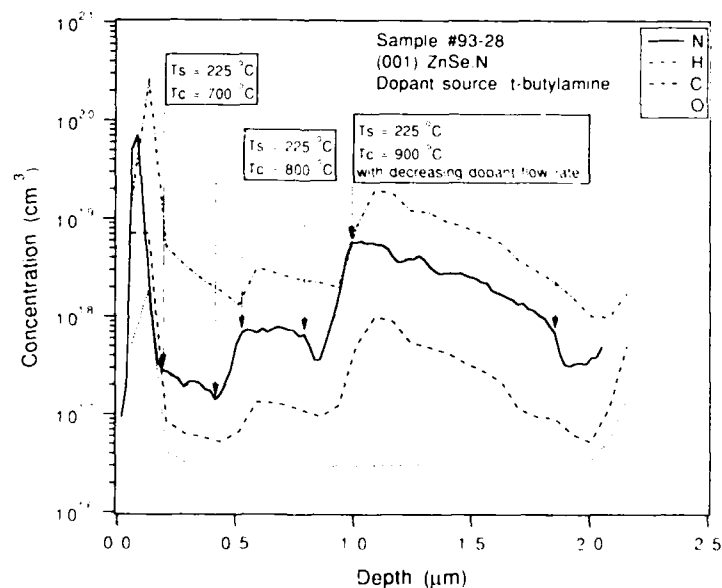


Fig. 4. The concentration profiles of N, H, C and O in a doped ZnSe film using t-butylamine as the dopant source material.

pletely decomposed at 700°C, a temperature significantly lower than that required to decompose ammonia. Its direct incidence on the growth surface (without pre-cracking) did not result in the incorporation of N in ZnSe.

### 3.2.2. Nitrogen doping with allylamine ( $H_2C=CH-CH_2NH_2$ )

Doping studies were performed over a range of cracker cell temperatures and substrate temperatures. The flow rate of allylamine was approximately a factor of four higher than that of DESe. Quadrupole mass spectrometric studies indicated that allylamine undergoes nearly complete decomposition at a cracker cell temperature of 900°C.  $NH$  and  $NH_3$  species were produced upon pyrolysis. The impurity profiles of a ZnSe sample doped with allylamine for cracker cell temperatures of 300 (without pre-cracking the dopant source), 700, 800 and 900°C at substrate temperatures of 225 and 325°C is shown in Fig. 3. The highest concentration of N ( $5 \times 10^{19} \text{ cm}^{-3}$ ) was obtained at a growth temperature of 225°C with the cracker cell operating at 900°C. The concentration of H in the film was approximately

the same as that of N, while the concentration of C was lower by an order of magnitude. The concentrations of N, H and C dropped dramatically with a decrease in the cracker cell temperature or an increase in the growth temperature, as shown in Fig. 3.

### 3.2.3. Nitrogen doping using *t*-butylamine ( $(CH_3)_3C-NH_2$ )

The use of *t*-butylamine as a dopant source for N doping of ZnSe was investigated over a substrate temperature range of 175–325°C, and at dopant cracker cell temperatures of 250°C (without pre-cracking the dopant source), 700, 800 and 900°C. There was no detectable N in the ZnSe films when *t*-butylamine was not pre-cracked for all substrate temperatures investigated. However, when thermally pre-cracked *t*-butylamine was supplied to the growth surface, N concentration in the film increased with the cracker cell temperature, attaining a N concentration of  $3 \times 10^{19} \text{ cm}^{-3}$  (at  $T_s = 175^\circ\text{C}$ ), the highest level observed for this dopant source. Similar to the trend observed with the other amines, significant levels of C and H were present in the

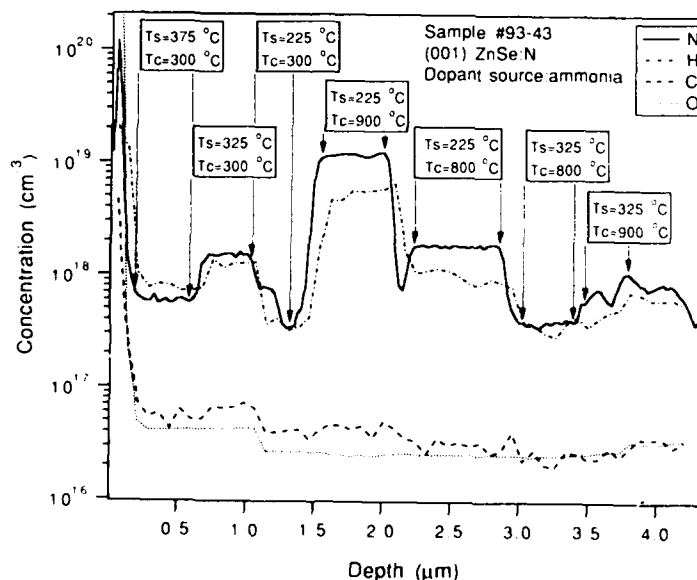


Fig. 5. The concentration profiles of N, H, C and O in a doped ZnSe film using ammonia as the dopant source material.



films. A SIMS profile of the impurities as a function of the cracker cell temperature is shown in Fig. 4. The maximum N concentration measured at the growth temperature of 225°C was  $7 \times 10^{18} \text{ cm}^{-3}$ . These results are similar to that reported by Zhang and Kobayashi [19] when t-butylamine was employed for N doping by migration enhanced epitaxy. A five-fold decrease in the dopant flow rate in steps of  $\approx 0.2 \text{ SCCM}$ , from the maximum of  $\approx 1 \text{ SCCM}$ , also resulted in a decrease in the impurity concentrations by the same degree. The dependence of the impurity concentrations on the dopant flow rates is indicated by the SIMS profiles at a depth between 1.0 and 2.0  $\mu\text{m}$  from the surface.

#### 3.2.4. Nitrogen doping using ammonia

Migita et al. have demonstrated electroluminescence in ZnSe diodes which were doped p-type using ammonia as the dopant source material by MOMBE, although only about 4% of the nitrogen atoms were electrically active [20]. In those experiments ammonia was allowed to dissociate at growth surface, with the highest concentration of N obtained at a growth temperature of 350°C. Here we examine the effect of pre-cracking ammonia on N incorporation, and examine the dependence of N and H incorporation on the cracker cell and substrate temperatures. The pressure of ammonia was controlled at 10.0 Torr on the upstream side of the cracker cell orifice. Under these conditions, the ammonia flow rate was one order of magnitude higher than that of DESe, and the pressure in the MOMBE chamber during growth was  $2 \times 10^{-4} \text{ Torr}$ . Quadrupole mass spectrometric analysis indicated that at the maximum investigate cracker cell temperature of 900°C, decomposition of  $\text{NH}_3$  was not complete. The products on the partial pyrolysis of  $\text{NH}_3$  were  $\text{N}_2$  and  $\text{H}_2$ . The SIMS profile of an ammonia-doped ZnSe film is shown in Fig. 5. With the cracker cell at 300°C, pulse-doped profiles were grown at substrate temperatures of 225, 325 and 375°C. The highest concentration of N of  $1.5 \times 10^{18} \text{ cm}^{-3}$  was measured for a substrate temperature of 325°C. At the growth temperatures of 375 and 225°C, the nitrogen incorporation levels were significantly lower, similar to that reported by

Migita et al. [20]. On operating the cracker cell at 900°C, the concentration of N in the films increased by a order of magnitude, with a maximum concentration of  $1 \times 10^{19} \text{ cm}^{-3}$  measured at a growth temperature of 225°C. The concentration of H is approximately the same as that of N on surface cracking  $\text{NH}_3$ , and about a factor of two lower than the nitrogen levels when  $\text{NH}_3$  was thermally pre-cracked at 900°C. It appears that the low electrical activity observed by Migita et al. can be attributed to the presence of H in the films. However, based on this information, it is not clear if H is present as  $\text{H}$ ,  $\text{H}_2$ ,  $\text{NH}$  or a combination of these. Despite the presence of H in the films, the 5K PL spectrum was dominated by the acceptor-bound excitonic emission at 2.792 eV [20].

#### 4. Summary

Thermally pre-cracked DESe and DEZn were used to grow (001) ZnSe films on (001) GaAs substrates. Analysis of the pyrolysis products of the DESe cracker cell operating at 900°C indicated that the selenium species consisted exclusively of Se and  $\text{Se}_2$ . The growth kinetics of (001) ZnSe was studied by measuring the dependence of the growth rate on the substrate temperature and the II/VI flux ratio. For a fixed DESe flow rate, the growth rate of ZnSe increased linearly with DEZn flow rate and saturated to a maximum value, corresponding to Se-limited growth conditions. High quality (001) ZnSe films were deposited on GaAs substrates under Se-stabilized growth conditions. An Arrhenius plot of the growth rates measured by RHEED and TRR measurements under Se-limited growth conditions indicates an activation energy of 0.08 eV for the desorption of the Se species during growth. The Se growth species produced upon pyrolysis of DESe, which consisted exclusively of Se and  $\text{Se}_2$ , appear to account for the small desorption activation energy.

Nitrogen doping of ZnSe was studied using triallylamine, allylamine t-butylamine, and ammonia as the dopant source material. The dependence of the impurity concentration on growth

parameters such as cracker cell and substrate temperatures were studied. The concentrations of N as well as H, C and O were measured by SIMS. N concentration in excess of  $1 \times 10^{19} \text{ cm}^{-3}$  were incorporated in the films when the sources were pre-cracked in the cracker cell, for substrate temperatures  $< 225^\circ\text{C}$ . However, large amounts of C and H were also detected in the films doped using the amines. Nitrogen incorporation from ammonia was highest when the dopant source was thermally pre-cracked in the cracker cell. Significant amounts of H were also incorporated in the films. The PL spectrum of ammonia doped ZnSe films exhibited the nitrogen acceptor bound excitonic emission. The concentrations of C and H in the undoped ZnSe films were below the SIMS detection limit, but correlated with the concentration of N in films doped with the amines. It appears that hydrocarbon species per se were not incorporated in the ZnSe films during MOMBE growth, as demonstrated by SIMS data. It is reasonable to postulate that the C and H observed in the films doped with the amines result from incorporation of N-containing hydrocarbon products that are present due to incomplete fragmentation upon pyrolysis of the amines. A further evaluation of novel precursors will be required to overcome the C and H contamination problem encountered with the amines investigated here.

## 5. Acknowledgments

The authors thank Drs. A.T. Hunter and R.G. Wilson for the assistance with the PL and SIMS analyses, respectively. The expert technical assistance of C. LeBeau and the support of L. Warren and C. Haussler in characterizing the films is thankfully acknowledged.

## 6. References

- [1] J. Qui, J.M. DePuydt, H. Cheng and M.A. Haase, *Appl. Phys. Lett.* 59 (1991) 2992.
- [2] R.M. Park, *J. Vac. Sci. Technol. A* 10 (1992) 701.
- [3] W. Xie, D.C. Grillo, R.L. Gunshor, M. Kobayashi, G.C. Hua, N. Otsuka, H. Jeon, J. Ding and A.V. Nurmikko, *Appl. Phys. Lett.* 60 (1992) 463.
- [4] J. Ren, K.A. Bowers, B. Sneed, F.E. Reed, J.W. Cook and J.F. Schetzina, *J. Crystal Growth* 111 (1991) 829.
- [5] K. Ohkawa, A. Ueno and T. Missuyu, *Jap. J. Appl. Phys.* 30 (1991) 3873.
- [6] A. Ohki, N. Shibata, K. Ando and A. Katsui, *J. Crystal Growth* 93 (1988) 692.
- [7] M. Konogai, *J. Crystal Growth* 120 (1992) 261.
- [8] D. Rajavel and J.J. Zinck, *Appl. Phys. Lett.* 63 (1993) 322.
- [9] H. Cheng, J.M. DePuydt, M.A. Haase and J.E. Potts, *J. Vac. Sci. Technol. B* 8 (1990) 181.
- [10] J.J. Zinck and D. Rajavel, *Appl. Phys. Lett.*, to be submitted.
- [11] J.M. DePuydt, H. Cheng, J.E. Potts, T.L. Smith and S.K. Mohapatra, *J. Appl. Phys.* 62 (1987) 4756.
- [12] H.H. Farrell, J.L. deMiguel and M.C. Tamargo, *J. Appl. Phys.* 65 (1989) 4084.
- [13] M. Ohishi, H. Saito, H. Torihara, Y. Fujisaki and K. Ohmori, *Jap. J. Appl. Phys.* 30 (1991) 1647.
- [14] G. Olson and J.A. Roth, *Mater. Sci. Rept.* 3 (1988) 1.
- [15] H.J. Cornelissen, D.A. Cammack and R.J. Dalby, *J. Vac. Sci. Technol. B* 6 (1988) 769.
- [16] Z. Zhu, T. Nomura, M. Miyao and M. Hagino, *J. Crystal Growth* 95 (1989) 529.
- [17] R.G. Benz, B.K. Wagner, A. Conte and C.J. Summers, *J. Electron. Mater.* 22 (1993) 815.
- [18] D.A. Cammack, K. Shahzad and T. Marshall, *Appl. Phys. Lett.* 56 (1990) 845.
- [19] S. Zhang and N. Kobayashi, *Jap. J. Appl. Phys.* 31 (1992) L666.
- [20] M. Migita, A. Taike and H. Yamamoto, *J. Crystal Growth* 111 (1991) 776.
- [21] W.E. Hoke, P.J. Lemonias and R. Korenstein, *J. Mater. Res.* 3 (1988) 329.
- [22] J.J. Zinck and D. Rajavel, *J. Crystal Growth*, to be submitted.
- [23] K.P. Giapis, K.F. Jensen, J.E. Potts and S.J. Pachuta, *J. Electron. Mater.* 19 (1990) 453.



ELSEVIER

Journal of Crystal Growth 138 (1994) 28–34

JOURNAL OF **CRYSTAL  
GROWTH**

## Growth of ZnS and ZnCdSSe alloys on GaP using an elemental sulfur source by molecular beam epitaxy

Kunio Ichino <sup>\*,1</sup>, Toshikazu Onishi, Yoichi Kawakami, Shizuo Fujita, Shigeo Fujita

*Department of Electrical Engineering, Kyoto University, Kyoto 606-01, Japan*

### Abstract

MBE growth of ZnS and ZnS-based alloys using an elemental sulfur source is reported. The initial growth process has been investigated by reflection high-energy electron diffraction, and crystalline quality is evaluated by X-ray rocking curve measurement. It is shown that crystalline quality is greatly improved by using ZnS buffer grown at a high substrate temperature. However, the quality of ZnSSe with nearly lattice-matched composition is still not perfect. The results are discussed in terms of relationship between growth process and crystalline quality.

### 1. Introduction

Since the first operation of ZnSe-based laser diodes (LDs) have been reported [1,2], remarkable progress has been made in the development of blue and blue-green light-emitting devices.

On the other hand, ultraviolet (UV) and/or near-UV light-emitting devices are attractive as next targets because large readout density in optical recording will be achieved by the use of shorter wavelength light [3]. So far, several groups have reported UV-light-emitting devices using ZnCdS/ZnS multiple quantum wells (MQWs) on GaAs substrates [4] and GaN system [5].

We have previously proposed ZnCdSSe/ZnSSe (ZnCdS) quantum well (QW) system grown on GaP substrates for UV and/or near-UV light-emitting devices and obtained preliminary results for fabrication of multi-layered structure

[6]. The advantages of the structures are as follows: (1) ZnCdSSe/ZnSSe(ZnCdS) QW structures in which bandgap energies of the wells correspond to the near-UV spectral region can be grown coherently on GaP substrates, and (2) large band offsets for conduction and valence bands can be expected as a result of composition differences in both group II and group VI elements between wells and barriers.

Mitsuishi et al. have reported metalorganic vapor phase epitaxy of ZnSSe on GaP and improvement of the crystalline quality by lattice-matching [7]. However, for construction of QW structures, it is important to control layer thickness precisely as well as to make smooth and abrupt interfaces. For such purposes, molecular beam epitaxy (MBE) is a more suitable growth technique. As a sulfur source in MBE, ZnS has commonly been used for the growth of alloys with small sulfur content such as ZnSSe nearly lattice-matched to GaAs. However, it is impossible to control the flux ratio of sulfur to zinc by this method. And this would result in the diffi-

\* Corresponding author.

<sup>1</sup> A member of Fellowships of the Japan Society for the Promotion of Science for Japanese Junior Scientists.

culty for the control of electrical properties of alloys with large sulfur content.

In this paper, we report the growth of ZnS and

ZnS-based alloys on GaP substrates by MBE using an elemental sulfur source. Although MBE of ZnS has been reported by several groups [8–18], the relationship between growth process and film quality is unknown. Therefore, we mainly investigate the effects of the initial stage of the growth and the misorientation of the substrate on the quality of the epitaxial layers.

## 2. Experimental procedure

The samples were grown using a MBE system. Source materials are elemental zinc, cadmium, sulfur and selenium (6N purity each). As for the n-type doping,  $\text{ZnCl}_2$  (5N purity) was used. Conventional Knudsen cells were used except for sulfur. Owing to low operating temperature resulting from very high vapor pressure of sulfur, accurate control of beam flux can not be easily achieved. This makes it difficult to grow alloys such as  $\text{ZnSSe}$  and  $\text{ZnCdSSe}$  with sufficient uniformity of sulfur composition. In this study, we used a cracking cell specially designed for the use of sulfur (made by ULVAC Japan Ltd.).

The temperature of a sulfur-source effuser was kept constant using oil flowing from a constant-temperature oil bath. Stabilities of the temperature and flux intensity measured by a nude ion gauge were in the range of  $\pm 0.1^\circ\text{C}$  and  $\pm 5\%$ , respectively. The temperature of the cracker is kept at  $200^\circ\text{C}$ , thus sulfur molecules probably are not cracked to smaller species such as  $\text{S}_2$ .

Two types of GaP substrates, whose orientations are just (100) (just substrate) and misoriented  $6^\circ$  toward  $[01\bar{1}]$  (misoriented substrate) were used. Before the growth, the substrates were degreased and etched, followed by  $(\text{NH}_4)_2\text{S}_8$  treatment [19,20].

## 3. Results and discussion

### 3.1. RHEED observation

Fig. 1 shows reflection high-energy electron diffraction (RHEED) patterns observed when ZnS was grown directly on the misoriented sub-

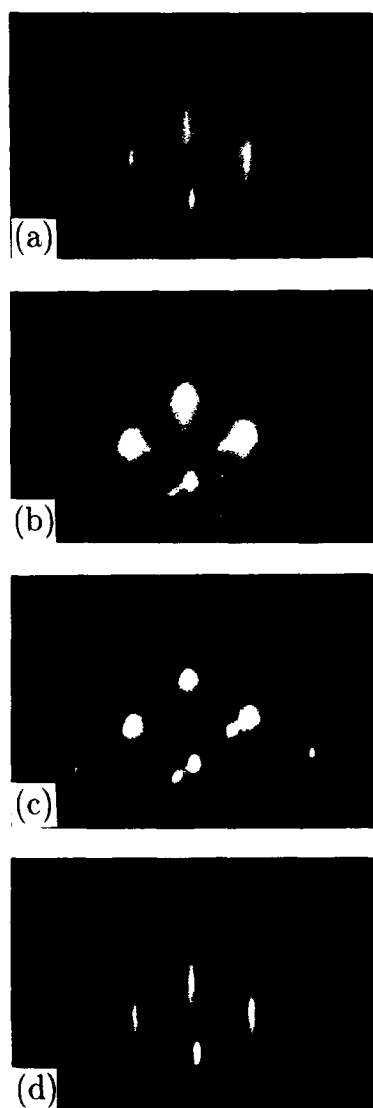
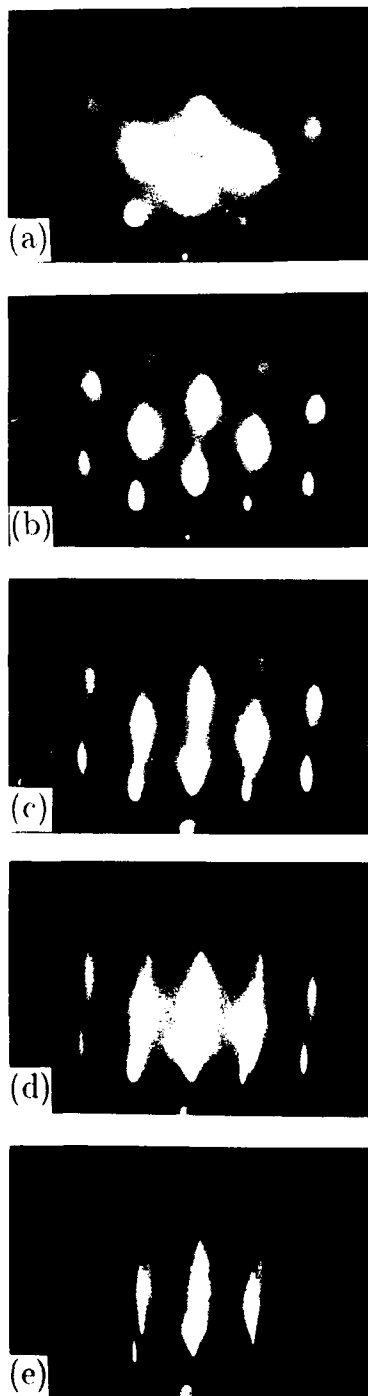


Fig. 1. RHEED patterns along  $[011]$  direction for ZnS grown directly on GaP substrate at several thickness: (a) 270 Å; (b) 480 Å; (c) 780 Å; (d) 2300 Å. Twin spots were observed at the thickness of around 480 Å. Orientation of the substrate is (100) misoriented  $6^\circ$  toward  $[01\bar{1}]$ . Thicknesses are estimated assuming that the growth rate in the early stage of nucleation is the same as that in the growth of thick layer.



strate at the substrate temperature ( $T_{\text{sub}}$ ) of 330°C. In this case, RHEED pattern changes as follows: (1) diffuse spots, (2) lattice pattern, (3) spotty pattern with twin spots, (4) streak pattern. Twin spots are due to crystals rotated on the (11 $\bar{1}$ ) plane. They were observed under wide range of growth condition, such as substrate temperature and flux intensity of group II and VI sources, on either the just or the misoriented substrates. Moreover, they were also seen during the growth of ZnS-based alloys such as ZnSSe and ZnCdS.

Appearance of such twins shows that a large number of defects are produced at the initial stage of the growth. Therefore, it is desirable that epitaxial growth is carried out without twin formation.

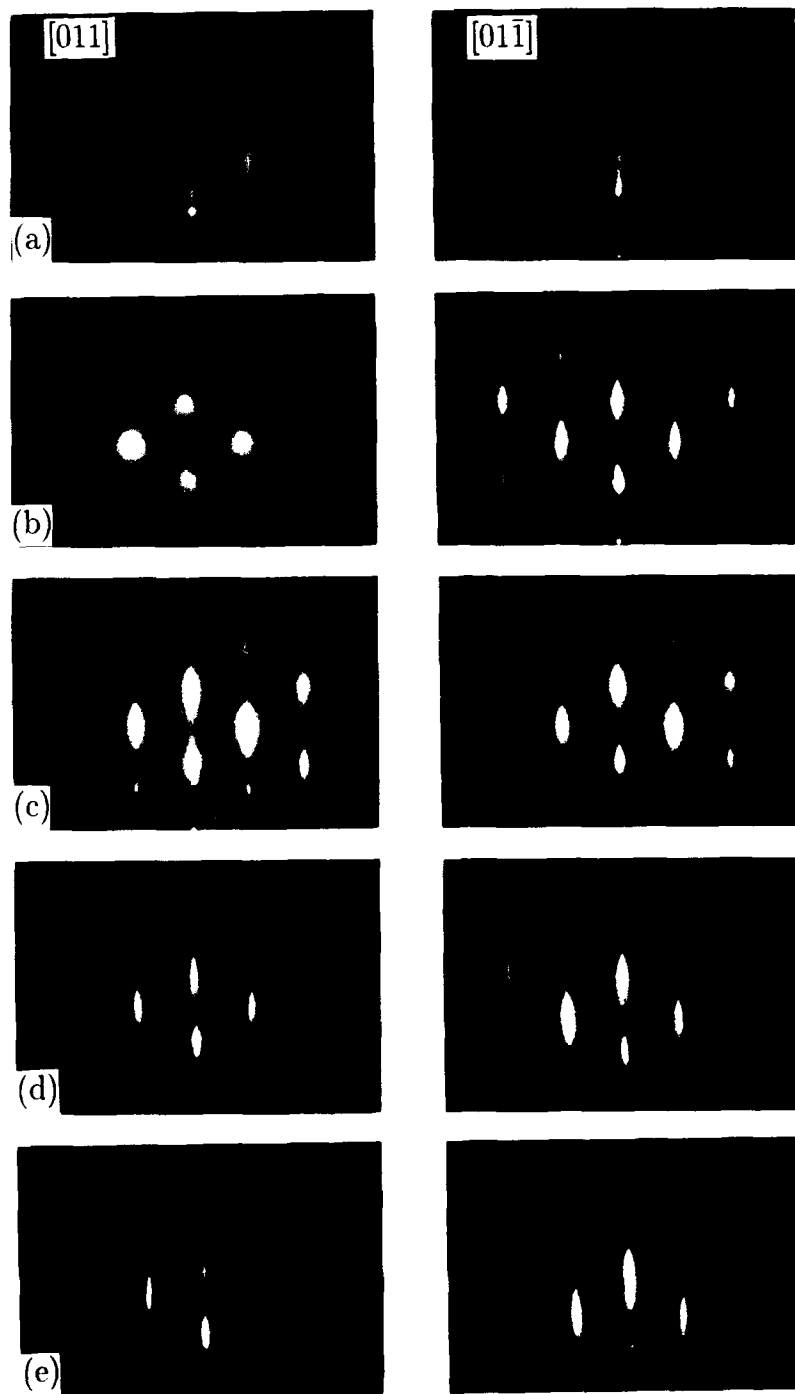
We found that twin spots are not observed during the growth of thin ZnS buffer layer up to the thickness ( $t$ ) of about 200 Å at  $T_{\text{sub}} = 490^\circ\text{C}$ , and following ZnS growth at  $T_{\text{sub}} = 330^\circ\text{C}$ , as shown in Fig. 2. As will be shown later, this insertion of ZnS buffer layer improves the crystalline quality effectively.

Fig. 3 shows RHEED patterns observed during the growth of ZnS with the buffer layer on the just substrate. Narrow v-shape streaks were observed along [011] direction at  $t = 400$  Å and  $t = 1600$  Å, while such patterns were not observed for the growth on the misoriented substrate (see Fig. 2). This indicates that facets with small misorientation from (100) plane are formed rather than (100) plane on the just substrate, whereas only one type of surface is formed on the misoriented substrate.

### 3.2. X-ray rocking curve measurement

Dependence of full width at half-maximum (FWHM) of X-ray rocking curve (XRC) of (400) diffraction on sulfur composition was investigated. Fig. 4 shows the dependence of FWHM on

Fig. 2. RHEED pattern observed during the growth of ZnS buffer at 490°C. (a)–(c), and following ZnS growth at 330°C. (d) and (e), on the misoriented substrate: (a) 50 Å; (b) 150 Å; (c) 200 Å; (d) 410 Å; (e) 4300 Å. Twin spots were not observed during the whole stage of the growth.



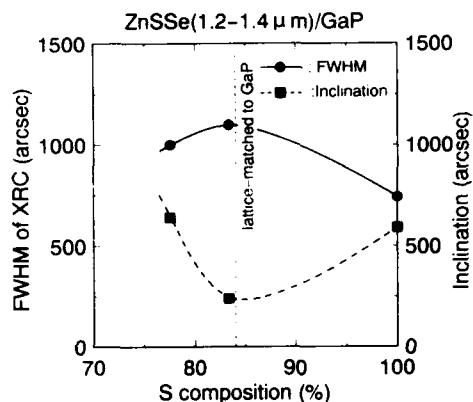


Fig. 4. FWHM of XRC and inclination of ZnSSe layers grown directly on the substrate as functions of S composition.

sulfur composition for ZnSSe grown directly on the substrates (solid line). The dashed line in Fig. 4 shows the inclination of the crystal axis of the epitaxial layers with respect to the substrates.

FWHM values are rather large in the whole sulfur composition range and do not show the effect of lattice-matching condition to GaP. On the other hand, inclination is reduced around lattice-matching composition.

Fig. 5 shows FWHM and inclination dependence for the layers grown on the ZnS buffer layers. Compared to Fig. 4, FWHM values are drastically reduced. This is most likely caused by the improved process in which twins are not produced. However, narrowing of XRC peaks by lattice-matching is still not observed and reduction of inclination is observed again.

To investigate the reason for which lattice-matching effects on FWHM of XRC are not observed, thickness dependence of FWHM were assessed. Two samples, nearly lattice-matched  $\text{ZnS}_{0.87}\text{Se}_{0.13}$  and ZnS, both of which were grown on the ZnS buffer, were chemically etched in  $\text{H}_2\text{SO}_4$  and  $\text{K}_2\text{Cr}_2\text{O}_7$  solution.

For as-grown layers ( $t \sim 1.1 \mu\text{m}$ ), the FWHMs for ZnS and ZnSSe are similar values of around

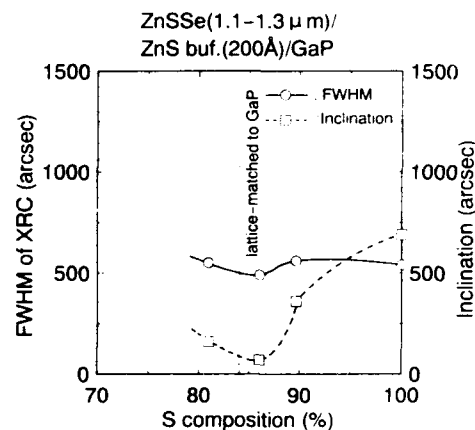


Fig. 5. FWHM of XRC and inclination of ZnSSe layers grown on the buffer as functions of S composition.

500–600 arc sec. However, when the layers were thinned to the thickness of 1900 Å, the FWHM values for the ZnS increases to 1500 arc sec, while the value for ZnSSe shows only a slight increase to about 800 arc sec. From this result, we see that the lattice-matching effect on FWHM of XRC can be observed for thin layers, while the effect is screened by another cause for thick ( $t \geq 1 \mu\text{m}$ ) layers.

### 3.3. Discussion

By means of RHEED observation at the initial stage of growth, it is suggested that three-dimensional (3D) nucleation occurs at any substrate temperature. It is also suggested that twins are readily formed on the (111) facet at a typical substrate temperature of 330°C. However, since twin spots become weak and disappear as the growth proceeds, it is likely that such twins are not formed on the flat surface, i.e., the (100) plane.

On the other hand, during the growth of ZnS buffer layer at the high substrate temperature of 490°C, twins are not formed owing to the en-

Fig. 3. RHEED pattern along [011] and [01 $\bar{1}$ ] direction for ZnS buffer (a)–(c), and ZnS, (d) and (e), on just (100)-oriented GaP substrate: (a) 20 Å; (b) 100 Å; (c) 200 Å; (d) 400 Å; (e) 6200 Å. V-shape streaks, which were not seen on the misoriented substrate, were observed along [011] direction during upper ZnS growth ((d), (e)).

hancement of migration of the source species, although the nucleation is still 3D mode.

Once the surface becomes relatively flat as a result of the high temperature growth of the ZnS buffer, it is likely that the following ZnS or ZnSse growth proceeds without twin formation even at  $T_{\text{sub}} = 330^\circ\text{C}$ .

Thus, we can speculate that a rough surface causes the formation of twins and related defects. This is coincident with the effect of the misoriented substrate. As stated previously, the smoother surface is formed on the misoriented substrate rather than on the just substrate. In addition, the FWHM values of XRC for the ZnS or ZnSse layers on the misoriented substrates (500–600 arc sec) are better than those on the just substrates (700–800 arc sec). Therefore, we can conclude that crystalline quality is related to surface smoothness during the growth, and that the surface should be kept flat to obtain high quality crystals.

Next, the reason why lattice-matching effect is not observed for ZnSse is discussed.

If the unexpectedly large FWHM value of 500 arc sec for ZnSse layers grown under lattice-matching condition is due to the composition fluctuation during growth, it corresponds to more than 7% of fluctuation in solid composition. This fluctuation is too large to be explained by the variation of the beam flux. In fact, the position of the X-ray diffraction peak does not vary with thickness, which was ascertained by etching experiments. Thus the fluctuation in composition is not the main cause.

On the other hand, the FWHM values of the ZnS films are reduced to about 300 arc sec with increasing thickness to about 2.5  $\mu\text{m}$ . Thus, if the ZnSse layers are grown coherently on the substrate, the FWHM values are supposed to be at least less than 300 arc sec, whereas the values remain about 500 arc sec. Therefore, we can estimate that the quality of the ZnS(Se)/ZnS-buffer/GaP interface is still rather poor and this causes the relatively large FWHM values.

As for ZnSe/GaAs, it has been reported that the formation of  $\text{Ga}_2\text{Se}_3$  interfacial layers results in good nucleation [21]. However, the nature of chemical bonding and its effect on the interfacial

properties have not been assessed yet for the ZnS(Se)/GaP system. We expect that further modification of the GaP surface and/or utilization of some refined growth techniques such as cracking of a sulfur source [15,18] would be effective for the two-dimensional nucleation and also for the improvement of crystalline quality of ZnS-based alloy layers.

Although the qualities of ZnS and ZnS-based alloys are still to be improved, we have fabricated ZnCdSSe/ZnSse metal-insulator-semiconductor LEDs to evaluate the potential of this material system at the present stage. We obtained strong near-UV emission at 77 K, which suggests a high potential of the material system. Details are reported elsewhere [22]. This fact indicates that high performance will be achieved using this material system if the crystalline quality of the ZnSse/GaP system is further improved.

#### 4. Summary

The influence of the growth process on the crystalline quality has been investigated. We have shown that the crystalline quality of ZnS and ZnSse is greatly improved by using a ZnS buffer grown at a high substrate temperature. However, the crystalline quality is still not perfect, even for lattice-matched composition. It is likely that this is mainly due to the defects generated at the ZnS(Se)/ZnS-buffer/GaP interface.

#### 5. Acknowledgements

We would like to thank Mitsubishi Kasei Corporation for supplying the GaP substrates. This work was supported in part by a Grant-in-Aid for Scientific Research from the Ministry of Education, Science and Culture.

#### 6. References

- [1] M.A. Haase, J. Qiu, J.M. DePuydt and H. Cheng, Appl. Phys. Lett. 59 (1991) 1272.



- [2] H. Jeon, J. Ding, W. Patterson, A.V. Nurmikko, W. Xie, D.C. Grillo, M. Kobayashi and R.L. Gunshor, *Appl. Phys. Lett.* 59 (1991) 3619.
- [3] G.E. Thomas, *Philips Tech. Rev.* 44 (1988) 51.
- [4] Y. Yamada, Y. Masumoto, J.T. Mullins and T. Taguchi, *Appl. Phys. Lett.* 61 (1992) 2190.
- [5] I. Akasaki, H. Amano, M. Kito and K. Hiramatsu, *J. Luminescence* 48/49 (1991) 666.
- [6] K. Ichino, K. Iwami, Y. Kawakami, Sz. Fujita and Sg. Fujita, *J. Electron. Mater.* 22 (1993) 445.
- [7] I. Mitsuishi, H. Mitsuhashi and H. Kukimoto, *Jap. J. Appl. Phys.* 28 (1993) L275.
- [8] T. Yao and S. Maekawa, *J. Crystal Growth* 53 (1981) 423.
- [9] K. Yoneda, T. Toda, Y. Hishida and T. Niina, *J. Crystal Growth* 67 (1984) 125.
- [10] S. Kaneda, S. Sato, T. Setoyama, S. Motoyama, M. Yokoyama and N. Ota, *J. Crystal Growth* 76 (1986) 440.
- [11] M. Yokoyama, K. Kashiwa and S. Ohta, *J. Crystal Growth* 81 (1987) 73.
- [12] O. Kanehisa, M. Shiiki, M. Migita and H. Yamamoto, *J. Crystal Growth* 86 (1988) 367.
- [13] A. Yoshikawa, H. Oniyama and H. Kasai, *J. Crystal Growth* 95 (1989) 572–579.
- [14] Y.-H. Wu, T. Toyoda, Y. Kawakami, Sz. Fujita and Sg. Fujita, *Jap. J. Appl. Phys.* 29 (1990) L144.
- [15] Y. Tomomura, M. Kitagawa, A. Suzuki and S. Nakajima, *J. Crystal Growth* 99 (1990) 451.
- [16] M. Kitagawa, Y. Tomomura, K. Nakanishi, A. Suzuki and S. Nakajima, *J. Crystal Growth* 101 (1990) 52.
- [17] J.W. Cook, Jr., D.B. Eason, R.P. Vaudo and J.F. Schetzina, *J. Vac. Sci. Technol.* B10 (1992) 901.
- [18] M. Yoneta, M. Ohishi, H. Saito and T. Hamasaki, *J. Crystal Growth* 127, (1993) 314.
- [19] H. Oigawa, J. Fan, Y. Nannichi, H. Sugahara and M. Oshima, *Jap. J. Appl. Phys.* 30 (1991) L322.
- [20] A. Wakahara, X.L. Wang and A. Sasaki, *J. Crystal Growth* 124 (1992) 118.
- [21] J. Qiu, D.R. Menke, M. Kobayashi, R.L. Gunshor, D. Li, Y. Nakamura and N. Otsuka, *Appl. Phys. Lett.* 58 (1991) 2788.
- [22] K. Ichino, T. Onishi, Y. Kawakami, Sz. Fujita and Sg. Fujita, *Jap. J. Appl. Phys.* 32 (1993) L1200.



ELSEVIER

Journal of Crystal Growth 138 (1994) 35–42

CRYSTAL  
GROWTH

## Optimization of strained short-period ZnSSe/ZnSe superlattices grown by metalorganic vapour phase epitaxy

J. Söllner<sup>a</sup>, M. Scholl<sup>a</sup>, A. Schneider<sup>a</sup>, M. Heuken<sup>\*a</sup>, J. Woitok<sup>b</sup>

<sup>a</sup> Institut für Halbleitertechnik, RWTH Aachen, Templergraben 55, D-52056 Aachen, Germany

<sup>b</sup> I. Physikalisches Institut, RWTH Aachen, Templergraben 55, D-52056 Aachen, Germany

### Abstract

Series of ZnSe/ZnS<sub>1-x</sub>Se<sub>x</sub> strained-layer superlattices with  $x = 0.1$ – $0.14$  grown by MOVPE using either diethylsulphide (DES) or hydrogen sulphide (H<sub>2</sub>S) as the sulphur source have been studied with X-ray double-crystal diffractometry and photoluminescence. The effects of period thickness, number of periods, growth interruption and stabilization of the ZnSSe-to-ZnSe interface as well as buffer layers on the structural and optical properties were determined. These data serve as basis for optimization of the growth parameters. High quality material was obtained as indicated by narrow peak widths and numerous satellite peaks in the X-ray diffraction profiles for optimized samples grown with DES (120 periods, without stabilization, without buffer). Highly efficient blue luminescence at 2.7 eV observed at room temperature confirms the excellent properties of the heterostructures. Because of the high resolution of the double-crystal X-ray diffraction we were enabled to detect very small variations of layer thickness and composition in the superlattice systems.

### 1. Introduction

III–V semiconductors operate very successful in optoelectronic devices in the red spectral region (e.g. lasers, modulators and waveguides) but to reach the shorter wavelength range there is a strong interest in wide bandgap II–VI compounds. In 1991 the first blue-green laser diode was reported [1] and by now room temperature pulsed blue-green injection lasers operating at 2.45 eV were achieved [2]. Even a real blue (2.67 and 2.64 eV at 300 K) photopumped laser was developed using ZnSSe/ZnMgSSe and ZnSe/ZnSSe heterostructures [3,4], respectively, but a

deep blue laser diode operating at room temperature has not been demonstrated to date.

In particular, the ternary ZnS<sub>1-x</sub>Se<sub>x</sub> ( $0 \leq x \leq 1$ ) is very promising material to obtain a blue laser at 300 K because the bandgap can be varied from 2.7 to 3.6 eV (blue to ultraviolet) at room temperature. Especially superlattice structures of this material are potential candidates to achieve this object, because the carrier confinement in the optically active region or even localized states should reduce the laser threshold [4,5]. In addition, the luminescence is tunable from blue to ultraviolet due to the quantum size effect (QSE). It has already been shown in the AlGaAs/GaAs material system that superlattice structures used as buffer can strongly improve the crystalline and optical properties of the layers on top [6]. Het-

\* Corresponding author.

erostructures consisting of ZnSSe are under compressive strain caused by their lattice mismatch to the GaAs substrate and their different thermal expansion coefficients. To avoid crystalline defects in these structures which degrade the optical properties, very thin pseudomorphic layers with an adequate composition and layer thickness are necessary to ensure an average lattice constant for the heterostructure stack which is nearly lattice matched to the substrate. Also the properties of the heterointerfaces show great influence on the crystalline and optical properties of the superlattice structures. In this work the optimization of strained short period superlattice structures consisting of ZnSSe is discussed. The MOVPE growth parameters, the well and barrier thickness, the number of periods, a stabilization method and the sulphur sources were varied to study the effects on strain and interface quality which were monitored by photoluminescence and X-ray diffractometry.

## 2. Experimental setup

The growth was carried out in a horizontal metalorganic vapour phase epitaxy (MOVPE) system. This computer-controlled system works at atmospheric pressure and uses a rotating susceptor to improve the homogeneity of the epilayers [7]. The samples were grown on epi-ready (100) GaAs misoriented 2° off, which leads to a lattice mismatch of 0.27% for ZnSe and –4.32% for ZnS, respectively ( $a_{\text{GaAs}} = 5.6535 \text{ \AA}$ ,  $a_{\text{ZnSe}} = 5.6686 \text{ \AA}$ ,  $a_{\text{ZnS}} = 5.4093 \text{ \AA}$ ) [8]. The growth temperature was set to 480°C and the total gas flow achieved the value of about 4–5 l/min with a gas velocity of about 15 cm/s. Palladium-purified hydrogen was used as a carrier gas, as precursors the metalorganic sources diethylzinc (DEZn), diethylselenide (DESe) and diethylsulphide (DES) were used, and as second sulphur source the hydride hydrogen sulphide ( $\text{H}_2\text{S}$ ) were in use. The samples were characterized by photoluminescence (PL) and by X-ray double-crystal diffractometry. Symmetrical (004) reflections were measured using a diffractometer with (004) Si first crystal and  $\text{Cu K}\alpha_1$  radiation. Quantitative

structural informations were obtained by comparing the experimental data with simulations based on the dynamical theory [9]. The PL investigations were performed using a He–Cd laser with a laser line at 325 nm. Therewith the emission of the upper 100 nm of the ZnSSe heterostructure could be detected from low temperatures (10 K) up to room temperature. On the other hand, the X-ray technique samples the entire structure including the underlying substrate. A comparison of the results of these characterization methods was done by taking the difference of the penetration depth into account.

## 3. Growth procedure

In this paper we report the result of several series of samples grown with  $\text{H}_2\text{S}$  ( $x = 14\%$ ) or with DES ( $x = 10\%$ ) as sulphur source. The varied parameters for the  $\text{H}_2\text{S}$  grown structures are the following: well and barrier thickness (2.5 or 5 nm), with and without stabilization during the interruption time, without or with a buffer consisting either of ZnSe or of ZnSSe, and the numbers of periods (30, 60 and 120). For the superlattices grown with DES, the layer thicknesses, the stabilization procedure, the buffer and the number of periods also were varied as enumerated for the samples produced with  $\text{H}_2\text{S}$ . It is known that the hydrides react in the gas phase with the MO sources even at room temperature, which results in an unintentional coating and powder in the reactor. The resulting sulphur depletion in the gas phase leads to inhomogeneities in the layer thickness and composition. Using DES, a less pronounced gas phase reaction could be observed, but to achieve sufficient growth rates and high sulphur content in the ternary layers, we were forced to use a high gas flow of  $\text{H}_2$  through the DES bubbler, because the decomposition rate at a temperature of 480°C is much lower compared to the other MO sources [10].

After each layer growth it is useful to interrupt the growth for several seconds ( $t_p = 5\text{--}20 \text{ s}$ ) to achieve smoother interfaces caused by migration and to suppress a carry-over of sulphur. However, we have recently shown that sulphur desorbs from

the surface of the ternary layer if there is no suitable stabilization [11]. With the hydrogen flow only, broadened wells with graded interfaces were obtained. To avoid the sulphur desorption, a stabilization with  $H_2S$  or DES and DESe was developed. To flush the sulphur and the selenium reactants out of the reactor to avoid an interference with the growth of the next layer, a purge for 4 s only with hydrogen and DESe is compulsory.

#### 4. Characterization of superlattices grown with $H_2S$

In this section the heterostructures grown with  $H_2S$  as sulphur source are discussed. To investigate the stabilization effect on the ZnSSe-to-ZnSe interface, samples have been grown under similar conditions, but with different growth interruptions. From the measured growth rates and sulphur concentrations of thick ZnSe and ZnSSe reference layers, the thicknesses and sulphur content of the superlattice structures were calculated; these are the “nominal” values. In Fig. 1, the near-bandedge PL at 11 K of two sets of superlattice structures with 60 periods and nominally  $x = 14\%$  in the barrier, but with different barrier and well thicknesses, are shown. Reflectivity spectra show that the peak at higher energies is the free exciton heavy hole transition peak (FE); the lower energy peak is supposed to be correlated to a bound exciton transition (BE). This result is in accordance with the literature [12]. The structures (a) and (b) were grown with the same parameters, giving a nominal well and barrier thickness of 5 nm (period thickness 10 nm), but sample (b) is with and sample (a) is without stabilization. The same applies to the sample pair (c) and (d), but with a nominal well and barrier thickness of 2.5 nm (period thickness 5 nm). From the X-ray data, the period thickness were evaluated to be for sample (a)  $13.2 \pm 0.3$  nm, for sample (b)  $16.6 \pm 0.3$  nm, for sample (c)  $7.0 \pm 0.3$  nm and for sample (d)  $5.8 \pm 0.3$  nm. Obviously, these values differ from the nominal ones. Comparing the PL peak positions of sample (a) and (b), also (c) and (d), it is obvious that a

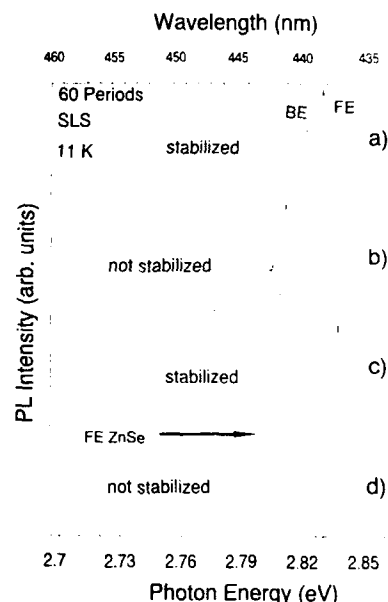


Fig. 1. 11 K PL spectra of ZnSSe/ZnSe superlattice structures with different period thicknesses and stabilizations. The period thickness for sample (a) is  $13.2 \pm 0.3$  nm, for sample (b)  $16.6 \pm 0.3$  nm, for sample (c)  $7.0 \pm 0.3$  nm and for sample (d)  $5.8 \pm 0.3$  nm.

blue shift occurs for sulphur-stabilized samples. Therefore we suggest that stabilized structures consist of more sulphur in the barrier or more abrupt interfaces compared to unstabilized samples. If we compare the stabilized samples (a) and (c) and also the unstabilized samples (b) and (d), it can be seen clearly that the PL peaks of the thinner wells show an enhanced blue shift.

The interpretation of the enhanced sulphur content in the stabilized samples is confirmed by X-ray diffraction measurements. The two rocking curves shown in Fig. 2 are taken from the same samples as shown in Figs. 1a and 1b. For both samples, several orders of intense, well-defined satellite peaks could be detected, indicating the homogeneous periodicity and the high quality of the structures. The superlattice period was evaluated from the angular spacing. As shown in Fig. 2, all satellites are broad as compared to the substrate peak. This suggests that both superlattices are not free from dislocations. In addition,

variations in the period thickness may broaden the satellite peaks. The unstabilized sample shows on the left-hand side of the GaAs reflection a pronounced feature which does not correspond to the diffraction profile of the periodic structure and which may be attributed to a highly disordered part of the superlattice close to the substrate. Although our simulation model assumes perfectly coherent films free of disorder, we tentatively compared the X-ray data with theory. The simulated spectra using a two-layer model fit quite well the intensity ratios of the superlattice reflections when the following parameters are used for simulation: sample (a) 11.3 nm well and 5.3 nm barrier thickness with  $x = 18.5\%$ , and sample (b) 5.7 nm well and 7.5 nm barrier thickness with  $x = 28.2\%$ , respectively. Obviously, the stabilized superlattice structure contains in total more sulphur compared to the unstabilized heterostructure in accordance with the PL measurements in Fig. 1.

To study the effect of lattice strain, different kind of buffer layers were investigated. Without

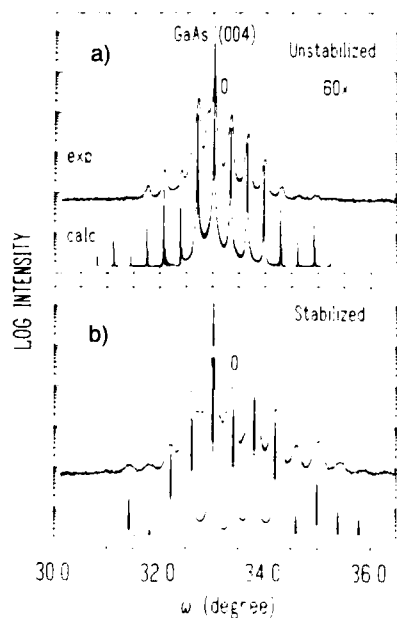


Fig. 2. X-ray diffraction pattern and corresponding simulations of stabilized and unstabilized superlattice structures.

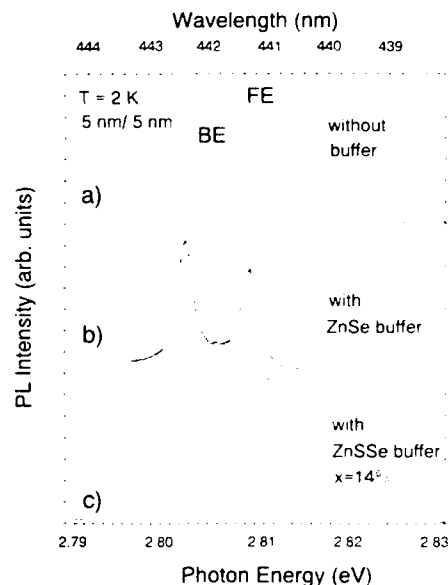


Fig. 3. 2 K PL spectra of superlattices with different buffer material: sample (a) without, sample (b) with ZnSe and sample (c) with ZnSSe ( $x = 14\%$ ) buffer.

any buffer, both the barrier and the well are strained in opposite direction and only the entire superlattice stack is nearly lattice matched to the substrate. With a relaxed ZnSe buffer the well should be unstrained, but the ternary barrier is under strain, with a ZnSSe buffer ( $x = 14\%$ ) the situation is reversed. In Fig. 3 the near-band-edge PL spectra of three superlattice structures (well and barrier thickness nominal 5 nm/5 nm,  $x = 14\%$ , 60 periods, 20 s interruption time without stabilization), sample (a) without buffer, sample (b) with a 1  $\mu\text{m}$  thick ZnSe buffer and sample (c) with a 1  $\mu\text{m}$  thick ZnSSe buffer ( $x = 14\%$ ), are shown. The ratio of the free exciton (FE) to the bound exciton (BE) indicates the quality of the layers. By comparing sample (a) without buffer and sample (c) with ZnSSe buffer (FE/BE = 1.9 and 2.1, respectively), it is evident that the ZnSSe buffer does not improve the superlattice heterostructure, because both spectra have nearly the same lineshape. The free-to-bound-exciton ratio of sample (b) is much smaller (FE/BE = 0.8) as compared to the FE/BE = 1.9 ratio of sample (a), where the free exciton is dominating. This

can be explained by the fact that the relaxed ZnSe buffer shows structural defects – caused by the relaxation process – which continue into the upper superlattice.

To examine the dependence of optical properties on the number of superlattice periods, room temperature PL was chosen because optoelectronic devices should operate at 300 K. A large near-bandedge to deep centre emission ratio is a strong hint on good structural properties, whereas enhanced deep level emissions indicate crystalline defects. In Fig. 4 the room temperature PL spectra of three different samples are shown. These are structures with well and barrier thicknesses of nominal 5 nm/5 nm without stabilization, but with different numbers of periods: 30, 60 and 120, respectively. The upper two spectra in Fig. 4 with 60 and 120 periods show strong blue luminescence (2.7 eV) at room temperature with nearly negligible deep traps, but the sample with only 30 periods shows dominating deep center emissions at about 2.1 eV in the spectrum. With increasing number of periods in the superlattice structure grown under these conditions, the ratio

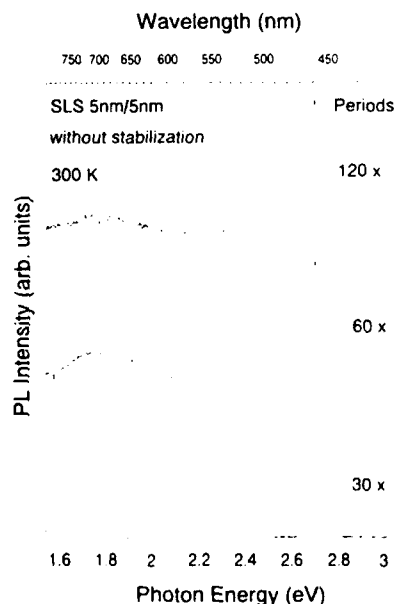


Fig. 4. 300 K PL spectra of SL structures with different numbers of periods.

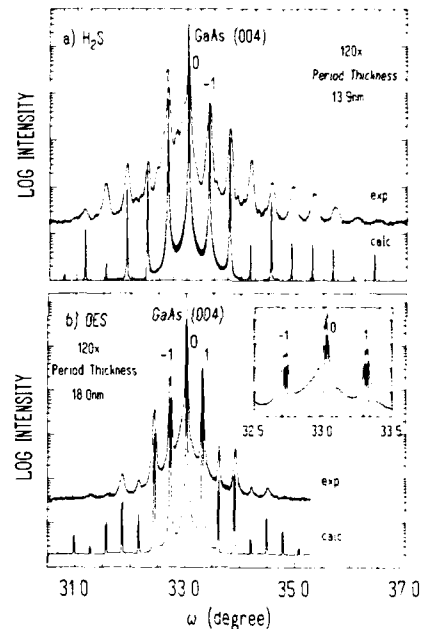


Fig. 5. Comparison of X-ray diffraction pattern of 120 period samples grown with different sulphur precursors: (a)  $\text{H}_2\text{S}$  (simulation spectra with 8.0 nm ZnSe well and 6.0 nm ZnSSe barrier  $x = 14\%$ ); (b) DES

of near-bandedge to deep-centre emission also increases and at least 60 periods are needed to achieve good optical properties, but PL only monitors the upper layers of the structure (penetration depth approximately 100 nm). From binary quantum well structures it is known that the layers close to the substrate are very wavy and many crystalline defects are observable by scanning transmission electron microscopy (STEM) [13]. Going to the top of the structure, the layers are getting smoother and the defects are reduced. In the ternary material investigated here it is similar [14], so that the layers close to the substrate act as a buffer region to reduce defects as previously investigated in III–V heterostructures [6].

The X-ray diffraction pattern shown in Fig. 5a of the 120-period sample of Fig. 4 exhibits a large number of satellite peaks indicating smooth interfaces with well-defined modulated structures. However, the satellite peak intensities are clearly

asymmetric about the zero-order peak, which closely matches to the substrate peak, because of the lattice matching of the superlattice structure to the substrate. In addition to the substrate peak and to the superlattice satellite peaks, sets of weaker peaks can be resolved in the tails between the satellites. These peaks have nearly the same spacing as the other, but correspond to a different average lattice constant. This superlattice is believed to consist of a number of different superlattices with nearly constant period thickness but compositional variation. Using a two-layer model, no reasonable combination of layer thickness and sulphur content could be found to produce an adequate fit to the experimental data (Fig. 5a). Although the peak positions fit very well the calculated intensities of the satellite peaks are clearly larger than the measured ones. Additionally, the relative peak intensities of the  $-4$  and  $+3$  order peak differ remarkably as compared to the experimental curve.

Room-temperature PL from stabilized SL structures with 120 periods showed no significant luminescence. From the observed cross-hatch pattern on the surface we conclude that this stabilized superlattice with 120 periods exceeds the critical thickness, because of the enhanced sulphur content in the barriers. For that reason crystalline defects are produced on top of the structure, which destroy optical transitions in the upper layers.

##### 5. Characterization of ZnSSe/ZnSe superlattices grown with DES

In this section, samples grown with DES as sulphur source are analysed. In Fig. 6, the near-bandedge emissions of a superlattice structure (7.3 nm/10.7 nm, 120 periods, without stabilization and  $x = 10\%$ ) with different excitation intensities  $I_{ex}$  are shown (1 and 31 mW/cm<sup>2</sup>). The peaks were identified experimentally from their intensity dependence and from reflectivity spectra. The dominant peak is the free exciton light hole transition which increases linearly with increasing excitation intensity. The second peak, labelled BE, is very likely a bound exciton which

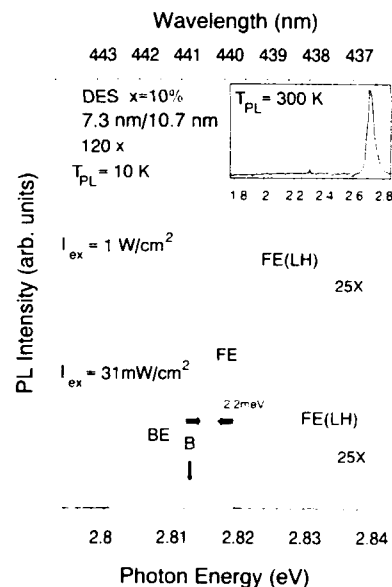


Fig. 6. 10 K PL spectra of a superlattice structure grown with DES measured with different excitation intensities. The inset shows the room temperature PL of this sample.

saturates with increasing  $I_{ex}$  as the theory demands for bound excitons in accordance with the nomenclature used in Fig. 1. An additional peak can be observed, denoted B [15], which is only 3 meV below the free exciton. This peak increases superlinearly with the excitation intensity, but the origin is still under discussion. The very low halfwidth of the free exciton peak with 2.2 meV and the large FE-to-BE ratio (FE/BE = 5 for  $I_{ex} = 1$  W/cm<sup>2</sup> and FE/BE = 2.7 for  $I_{ex} = 31$  mW/cm<sup>2</sup>) indicate very good optical properties of the samples grown with DES. Additionally, the free exciton light hole transition peak in both spectra could be observed 15 meV above the FE peak. This peak was labelled FE(LH) in accordance with the literature [15]. Also, the inset of Fig. 6 with the room temperature luminescence of this sample shows the excellent properties. The very intense excitonic emission without deep levels shows the improved luminescence properties as compared to the sample grown with H<sub>2</sub>S and 120 periods shown in Fig. 4, where deep traps can still be recognized.

For comparison, the X-ray diffraction patterns of both samples just discussed are shown in Fig. 5. Several orders of intense satellites could be detected; their widths increase progressively with the satellite order. This effect is usually interpreted as a drift of period thickness. Whereas for the sample grown with  $H_2S$  even the first order reflections are symmetrically broadened (Fig. 5a), the central reflections  $(-1, 0, 1)$  in Fig. 5b are clearly splitted into separate narrow peaks (inset Fig. 5b). This situation is difficult to observe very close to the substrate peak where one zero-order peak at the higher angular side could not be well resolved. Nevertheless, the occurrence of two zero-order peaks indicates that the structure consists of at least two superlattices whose average lattice constants are slightly different. The separation of the corresponding higher-order peaks leads to nearly the same period of  $18.0 \pm 0.2$  nm. The simulated diffraction profile was calculated from a model with periods 1–60 of 7.3 nm ZnSe/10.7 nm  $ZnS_{0.095}Se_{0.905}$  and periods 61–120 of 7.3 nm ZnSe/10.7 nm  $ZnS_{0.10}Se_{0.90}$ . The agreement of simulation and experimental data is very satisfactory in both the relative positions and the relative intensities of the corresponding peaks. The presence of more than one superlattice was also observed in other samples. From the splitting of the higher order satellites, differences in periodicity of the superlattices of approximately 0.7 nm were calculated, corresponding to two monolayers [16].

Also, the effects of buffer layers on the X-ray diffraction pattern have been investigated. For superlattices grown on a 1  $\mu$ m thick ZnSe buffer layer, we observed a large increase of the peak widths as compared to a ternary buffer ( $x = 10\%$ ) of equal thickness. Nevertheless, samples grown without any intentional buffer show so far the best structural properties.

## 6. Conclusion

In this work the optimization of optical and crystalline properties of strained short-period ZnSSe/ZnSe superlattice structures were presented. It was shown that a stabilization with the

sulphur and selenium sources during the interruption time – between the growth of the ZnSSe and ZnSe layer – can be used to prevent the sulphur desorption from the interface region and the broadening of the wells. Therefore we get sharper heterointerfaces with less graded composition of the layers, and an enhanced blue shift of the PL emission peaks results. X-ray measurements also proved the lower sulphur content in the entire unstabilized superlattice stack caused by the desorption from the surface region. A ternary buffer could not increase the PL efficiency as compared to a SL structure without buffer; on the other hand, ZnSe as buffer material even decreases the luminescence caused by the larger strain from buffer to the superlattice stack. Due to this fact, structural defects disturb the optical transitions. The photoluminescence at room temperature showed the excellent quality of the SL structures and the need of at least 60 periods to obtain PL spectra with low deep centre emissions. The underlying layers act as buffer and improve the crystalline quality of the upper layers, which are monitored by PL measurements. Structures with 120 periods show a very strong excitonic emission with negligible deep traps. It was shown that DES is a more suited sulphur source compared to  $H_2S$ , which shows a tendency for prereaction in the gas phase.

## 7. Acknowledgements

The authors would like to thank Prof. Dr. K. Heime for fruitful discussions. The 2 K PL measurements were kindly provided by the group of Prof. Dr. J. Gutowski, University of Bremen. Financial support for this work was given by Volkswagen-Stiftung and technical support by Aixtron Semiconductor Technologies, Aachen.

## 8. References

- [1] M.A. Haase, J. Qiu, J.M. DePuydt and H. Cheng, Appl. Phys. Lett. 59 (1991) 1272.
- [2] H. Jeon, M. Hagerott, J. Ding, A.V. Nurmikko, D.C. Grillo, W. Xie, M. Kobayashi and R.L. Gunshor, Opt. Letters 18 (1993) 125.



- [3] Y. Morinaga, H. Okuyama and K. Akimoto, *Jap. J. Appl. Phys.* 32 (1993) 678.
- [4] K. Nakanishi, I. Suemune, Y. Fujii, Y. Kuroda and M. Yamanishi, *Appl. Phys. Lett.* 59 (1991) 1401.
- [5] Y. Kuroda, I. Suemune, Y. Fujii and M. Fujimoto, *Appl. Phys. Lett.* 61 (1992) 1182.
- [6] H. Lakner, B. Bollig, E. Kubalek, M. Heuken, K. Heime, F. Scheffer and F.E.G. Guimarães, *J. Crystal Growth* 107 (1991) 452.
- [7] J. Söllner, M. Heuken and K. Heime, *Proc. SPIE* 1361 (1991) 963.
- [8] K. Shazad, D.J. Olego and C.G. Van de Walle, *Phys. Rev. B* 38 (1988) 1417.
- [9] W.J. Bartels, J. Hornstra and D.J. Lobeck, *Acta Cryst. A* 42 (1986) 539.
- [10] M. Heuken, K.-P. Geysers, J. Söllner, A. Schneider, F.E.G. Guimarães and K. Heime, *J. Crystal Growth* 124 (1992) 633.
- [11] A. Schneider, K.-P. Geysers, J. Söllner and M. Heuken, *J. Appl. Phys.* 74 (1993) 7181.
- [12] K. Mohammed, D.J. Olego, P. Newbury, D.A. Cammack, R. Dalby and H. Cornelissen, *Appl. Phys. Lett.* 50 (1987) 1820.
- [13] B. Bollig, P. Thorhauer, E. Kubalek, J. Söllner, F.E.G. Guimarães, M. Heuken and K. Heime, *J. Crystal Growth* 124 (1992) 639.
- [14] B. Bollig, K.-P. Geysers and M. Heuken, *Adv. Mater. Opt. Electron.*, in press.
- [15] Y. Kuroda, I. Suemune, M. Fujimoto, Y. Fujii, N. Otsuka and Y. Nakamura, *J. Appl. Phys.* 72 (1992) 3029.
- [16] J. Hermans, J. Woitok, W. Schiffrers, J. Geurts, A. Schneider, M. Scholl, J. Söllner and M. Heuken, *J. Crystal Growth* 138 (1994) 612.

## Use of germanium interfacial layer for the hetero-epitaxial growth of CdTe on Si substrates

Wen-Sheng Wang, Ishwara Bhat \*

*Electrical, Computer, and Systems Engineering, Rensselaer Polytechnic Institute, Troy, New York 12180, USA*

### Abstract

Epitaxial (100) CdTe layers have been grown by atmospheric pressure organometallic vapor phase epitaxy (OMVPE) on Si(100) substrates misoriented 9° towards the (110) direction. A thin Ge buffer layer grown at low temperature followed by an interfacial layer of ZnTe was used to get high quality (100) CdTe. The layers were characterized by X-ray diffraction and optical microscopy. X-ray rocking curve with FWHM of about 260 arc sec has been obtained for a 4  $\mu\text{m}$  thick CdTe layer. The results presented demonstrate a novel technique to grow high quality CdTe on Si in a single OMVPE reactor.

### 1. Introduction

HgCdTe is an important semiconductor material for the fabrication of infrared focal plane arrays. Epitaxial growth of this material is carried out on CdTe substrates, since they are nearly lattice matched and chemically compatible. However, in recent years, there has been a considerable interest in using CdTe epitaxial layers grown on alternate substrates, since bulk CdTe is not available in large area wafer form. GaAs substrates have been studied extensively for this purpose and high quality CdTe and HgCdTe layers were grown on them. However, the Si substrate is preferable for CdTe and HgCdTe growth, since it will reduce the thermal mismatch problems encountered when a Si wafer with signal processing electronics is bonded to detector arrays. In addition, Si is available in larger area than GaAs.

There are two approaches to achieve CdTe growth on Si. One approach in OMVPE is the use of commercially available GaAs/Si substrates [1,2]. Since considerable effort has gone into developing the "CdTe on GaAs" technology, use of a commercially available GaAs/Si substrate is an excellent alternative. However, it is better to avoid GaAs since Ga and As are both dopant impurities in II–VI compounds and hence any high temperature heat treatment may cause significant out-diffusion of Ga and As to the active layer. In addition, the complete structure (HgCdTe/CdTe/GaAs/Si) cannot be grown in a single reactor, adding considerable amount to the starting wafer cost.

The best alternative, then, will be direct growth of CdTe on Si. This has been attempted by the molecular beam epitaxy (MBE) method [3,4] during the last few years, and by hot wall epitaxy [5]. A few studies were reported by OMVPE [6] as well, but detailed structural characterization was

\* Corresponding author.

not available. Most of these studies have concentrated on (111) oriented CdTe on (100) silicon. Vapor phase epitaxy of (111) oriented CdTe is frequently subject to twin defect formation, which does not seem to be the case in (100) oriented epitaxy. Hence, it is important to study the growth of (100) oriented CdTe on (100) Si for the subsequent growth of HgCdTe. Even though (100) oriented epitaxy historically had hillock problems, control of their density to within  $50 \text{ cm}^{-2}$  is possible using careful control of initial growth conditions [1].

The main difficulty for growing high quality CdTe directly on Si arises from the presence of a strong native oxide on Si. This native oxide can be removed by baking the wafer at low temperature to remove the adsorbed moisture, followed by a deoxidation step at high temperature, generally in the range 800–900°C. However, the high temperature heat treatment is not preferred in the OMVPE of CdTe/Si because Te is known to react with the Si surface [7]. Unless the reactor is previously cleaned or baked at high temperature, this deoxidation step can result in pitted surfaces caused by Te from previous growth runs. Therefore, it is better to avoid the high temperature step before CdTe growth. In this paper, we will describe, for the first time, a novel method to grow (100) CdTe on Si substrate using Ge and ZnTe interfacial layers, without subjecting Si to high temperature deoxidation step.

## 2. Experimental details

For all the studies reported here, (100) oriented Si substrates which are misoriented 9° towards (110) were used. The cleaning process is very similar to that outlined in ref. [8]. Before the substrates were loaded into the reactor, the native oxide was removed in HF:methanol (1:5 by volume) solution [9]. Ge growth on Si was carried out by the decomposition of  $\text{GeH}_4$  [10] in a 2 inch diameter horizontal reactor operated at atmospheric pressure. No load lock or glove box was present and therefore the reactor was exposed to air and moisture during sample loading. Pd-purified  $\text{H}_2$  was used as the carrier gas and

the growth temperature was varied from 420 to 700°C. CdTe and ZnTe films were grown in the same reactor on Ge/Si substrates using dimethylcadmium (DMCd), dimethylzinc (DMZn) and diethyltellurium (DETe) as the precursors. The CdTe growth temperature was 360°C and that of ZnTe was 420°C. The thickness of the Ge layer was measured using a Tecon  $\alpha$ -step profiler by selectively etching the Ge layer.

## 3. Results and discussions

### 3.1. Ge growth

We initially investigated the heteroepitaxy of Ge on Si at various temperatures from 420 to 700°C. Layers grown at higher temperatures had rough surface morphology, whereas those grown at lower temperature had smooth surface. However, the growth rate at lower temperature was not high enough to grow thick layers. The rough surface morphology we found at higher temperature may be caused by surface contamination of the starting Si substrate during heat up. When Si is heated to higher temperature for growth, Si oxidation is very likely caused by desorbed  $\text{O}_2$  and moisture from the reactor walls, and any residual contaminations from the  $\text{H}_2$  gas. Growth on such a substrate will result in poor quality films. In addition, Ge growth on Si is known to occur by the formation of three-dimensional islands at higher temperatures [11], which finally coalesce to form a continuous film. This also will give rise to rough surface as shown in Fig. 1.

We developed a two-step growth process to obtain perfectly specular Ge on Si substrates. First, a 300 Å thick layer of Ge was grown at 420–450°C range, followed by a thicker layer at 650°C. This growth process resulted in Ge layers with specular surfaces and good crystal quality. The results are shown in Fig. 2. For example, for a 1  $\mu\text{m}$  thick Ge grown with the two-step process, the X-ray FWHM of (004) reflection was only 140 arc sec, whereas 1  $\mu\text{m}$  thick Ge grown directly at 650°C had FWHM of 350 arc sec. As shown in Fig. 1, the surface morphology was excellent for Ge grown with the two-step process. The better

crystal quality and the surface morphology can be explained as follows. Ge growth at low temperature results in two-dimensional nucleation, as demonstrated by Cunningham et al. [11] in UHV CVD growth studies. In addition, the low temperature grown Ge layer protects the reactive Si surface from the contaminants ( $O_2$ ,  $CO_2$  or moisture) in the reactor. Since  $GeO$  is unstable at high temperature, any  $GeO$  will desorb at the higher growth temperature.

### 3.2. CdTe growth

After the Ge growth, CdTe layers were grown in the temperature range of 360 to 450°C. It is

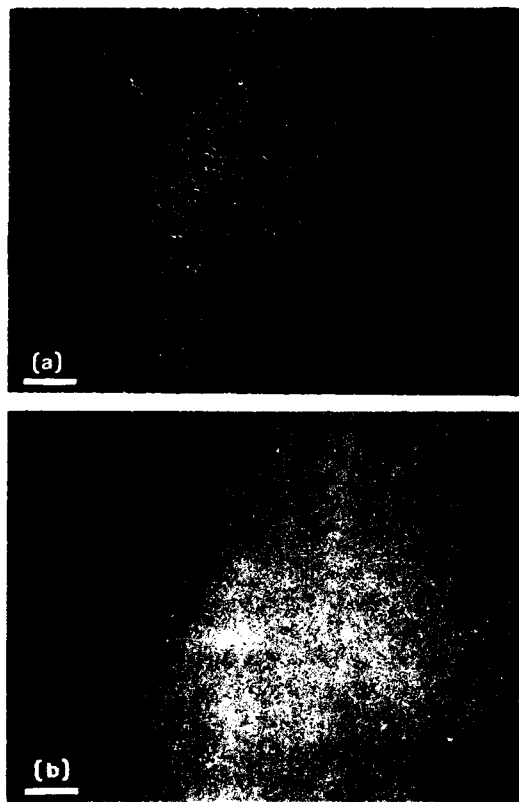


Fig. 1. Surface morphology of 1  $\mu m$  thick Ge layer grown on (100)Si. (a) 1  $\mu m$  thick Ge grown directly at 650°C. (b) 1  $\mu m$  thick Ge layer grown using the two-step process: a 300 Å thick Ge at 450°C followed by 1  $\mu m$  thick Ge at 650°C. The marker represents 25  $\mu m$ .

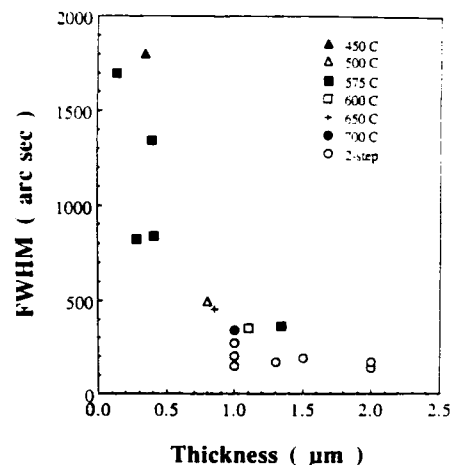


Fig. 2. Double-crystal X-ray FWHM of Ge layers grown on Si substrates.

well known that direct growth of CdTe on Si or GaAs can result in both (100) and (111) oriented layers, depending on the initial nucleation conditions. Hence, it is very likely that a (100) oriented wafers may have small percentage of (111) phase as well. This may be the cause for the pyramidal hillocks generally observed on the surface when direct growth of CdTe is carried out on GaAs [7]. However, ZnTe on the above substrate always resulted in (100) oriented layers with significant improvement in surface morphology and crystal quality as well. Hence, prior to CdTe growth a thin layer of ZnTe was grown on Ge to force (100) CdTe nucleation. All the CdTe growths we report here are with the ZnTe nucleation layer.

Fig. 3 shows the X-ray FWHM of (004) reflection of CdTe as a function of thickness, grown with ZnTe/Ge interfacial layers. These results represent the highest crystalline quality ever obtained for CdTe on Si substrates grown in a single OMVPE reactor. Similar results were only obtained earlier by using GaAs/Si commercial wafers [1]. The results are comparable in quality to the recent results on CdTe, grown on ZnTe/Si substrates using MBE [12]. Fig. 4 shows the Nomarski contrast micrograph of a 4  $\mu m$  thick CdTe layer grown on Si, indicating the excellent surface morphology. Such smooth surfaces were obtained

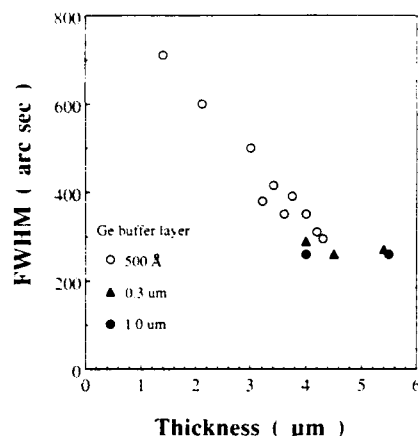


Fig. 3. Double-crystal X-ray FWHM of CdTe layers grown on ZnTe/Ge/Si as a function of CdTe thickness.

only on 9° misoriented (100) wafers. Growth on non-misoriented (100) wafers resulted in rough surface, with antiphase domains.

In order to understand the role of Ge interfacial layer, we carried out some direct growth of CdTe on Si. The CdTe films directly grown on Si substrates were always (111) oriented polycrystals when the growth temperatures were in the range 300 to 450°C [7]. The absence of epitaxial growth

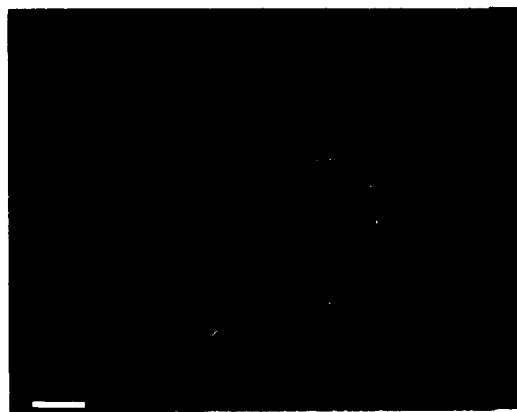


Fig. 4. Surface morphology of 4 μm thick CdTe layer grown on (100)Si, misoriented 9° towards (110). The marker represents 25 μm.

may be caused by two reasons. First, the Si surface may be covered with sub-monolayer native oxide even after the HF etch. There are many reports in the literature which show that HF etched Si is passivated with hydrogen [13], and oxide-free surface can be obtained if loaded quickly into an UHV chamber. However, presence of sub-monolayer oxide cannot be completely ruled out due to variations in the processing conditions. For example, we used an atmospheric pressure reactor without a load-lock, so that Si surface oxidation during heat-up is very likely from the adsorbed O<sub>2</sub> and moisture on the reactor wall.

A second reason for the polycrystalline CdTe growth can be the presence of strong Si-H bonds which are stable up to about 520°C. Epitaxial Si growth has been demonstrated on hydrogen passivated Si in MBE at 370°C [14], much below the hydrogen desorption temperature. However, in another study [15], the authors have shown that introduction of  $\sim 10^{-5}$  Torr of hydrogen during MBE growth could suppress (100) Si epitaxy and this was attributed to hydrogen segregation up to the monolayer level on Si surface. Even though these results cannot be directly extended to CdTe growth, we postulate that hydrogen coverage of Si is partially responsible for non-epitaxial CdTe growth. If H<sub>2</sub> coverage is not perfect, there will be nucleation sites for polycrystalline CdTe growth. Otherwise, a perfect H<sub>2</sub> coverage may result in amorphous CdTe, provided the growth temperature is low. On recrystallization, this amorphous CdTe may give rise to (111) CdTe, since (111) is the natural growth plane for CdTe. A systematic study in a MBE system with and without H<sub>2</sub> passivation should be carried out to confirm this.

As mentioned above, a high temperature treatment to desorb native oxides cannot be used in our system. Even when a "clean" surface is obtained, the presence of H<sub>2</sub> may hinder the growth of epitaxial (100) CdTe on (100)Si. When we used germane gas, it reduces SiO<sub>2</sub> to Si forming GeO [16,17] which is volatile and desorbs. Since the Ge-H bond is weaker than the Si-H bond, the presence of hydrogen does not affect the CdTe growth on Ge.

#### 4. Conclusion

We have shown that high quality CdTe can be grown on Si substrates in a single atmospheric pressure OMVPE reactor without using commercially available GaAs/Si wafers. The growths were carried out in a simple horizontal reactor without any load lock system. Prior to CdTe growth, a thin Ge layer was grown using germane, which facilitated desorption of Si native oxide at low temperature. A 4  $\mu\text{m}$  thick CdTe on Si had an X-ray FWHM of 260 arc sec, demonstrating the excellent quality of the layers. A complete HgCdTe/CdTe/Si structure can now be grown in a single OMVPE reactor for the fabrication of infrared focal plane arrays.

#### 5. Acknowledgements

The authors would like to thank J. Barthel for technical assistance and P. Magilligan for manuscript preparation. Partial support was provided by grants from the Raytheon Corporation and Texas Instruments. This support is gratefully acknowledged.

#### 6. References

- [1] S.M. Johnson, J.A. Vigil, J.B. James, C.A. Cockrum, W.H. Konkel, M.H. Kalisher, R.E. Risser, T. Tung, W.J. Hamilton, W.L. Ahlgren and J.M. Myrosznyk, *J. Electron. Mater.* 22 (1993) 835.
- [2] P.D. Edwall, J. Bajaj and E.R. Gertner, *J. Vac. Sci. Technol. A* 8 (1990) 1045.
- [3] R. Sporken, S. Sivananthan, K.K. Mahavadi, G. Monfrou, M. Boukerche and J.P. Faurie, *Appl. Phys. Lett.* 55 (1989) 1879.
- [4] R. Sporken, Y.P. Chen, S. Sivananthan, M.D. Lange and J.P. Faurie, *J. Vac. Sci. Technol. B* 10 (1992) 1405.
- [5] R. Korenstein, P. Madisan and P. Hallock, *J. Vac. Sci. Technol. B* 10 (1992) 1370.
- [6] R.L. Chou, M.S. Lin and K.S. Chou, *J. Crystal Growth* 94 (1989) 551.
- [7] W.S. Wang, H. Ehsani and I. Bhat, *J. Electron. Mater.* 22 (1993) 873.
- [8] A. Ishizaka and Y. Shiraki, *J. Electrochem. Soc.* 133 (1986) 666.
- [9] P.J. Grunthaner, F.J. Grunthaner, R.W. Fathauer, T.L. Lin, M.H. Hecht, L.D. Bell, W.J. Kaiser, F.D. Schowengerdt and J.H. Mazur, *Thin Solid Films* 183 (1989) 197.
- [10] T.F. Kuech, M. Maenpaa and S.S. Lau, *Appl. Phys. Lett.* 39 (1981) 245.
- [11] B. Cunningham, J. Chu and S. Akbar, *Appl. Phys. Lett.* 59 (1991) 3574.
- [12] T.J. de Lyon, J.A. Roth, O.K. Wu, S.M. Johnson and C.A. Cockrum, *Appl. Phys. Lett.* 63 (1993) 818.
- [13] B.S. Meyerson, F.J. Himpel and K.J. Uram, *Appl. Phys. Lett.* 57 (1990) 1034.
- [14] D.J. Eaglesham, G.S. Higashi and M. Cerullo, *Appl. Phys. Lett.* 685 (1991) 59.
- [15] S.H. Wolff, S. Wagner, J.C. Bean, R. Hull and J.M. Gibson, *Appl. Phys. Lett.* 55 (1989) 2017.
- [16] Y. Takahashi, H. Ishii and K. Fujinaga, *Appl. Phys. Lett.* 57 (1990) 599.
- [17] J.E. Morar, B.S. Meyerson, U.O. Karlsson, F.J. Himpel, F.R. McFeely, D. Rieger, A. Taleb-Ibrahimi and J.A. Yarmoff, *Appl. Phys. Lett.* 50 (1987) 463.



ELSEVIER

Journal of Crystal Growth 138 (1994) 48–54

JOURNAL OF  
**CRYSTAL  
GROWTH**

## Molecular beam epitaxial growth mechanism of ZnSe epilayers on (100) GaAs as determined by reflection high-energy electron diffraction, transmission electron microscopy and X-ray diffraction

P. Ruppert, D. Hommel<sup>\*</sup>, T. Behr, H. Heinke, A. Waag, G. Landwehr

*Physikalisches Institut, Universität Würzburg, D-97074 Würzburg, Germany*

### Abstract

The properties of molecular beam epitaxial growth of ZnSe epilayers deposited directly on a GaAs substrate are compared to those grown on a GaAs buffer layer. The superior quality of the latter is confirmed by RHEED, TEM and X-ray diffraction. Based on RHEED oscillation studies, a model explaining the dependence of the ZnSe growth rate on Zn and Se fluxes and the substrate temperature is developed taking into account physi- and chemisorbed states. For partially relaxed epilayers, the correlation between the relaxation state and the crystalline mosaicity, as found by high resolution X-ray diffraction, is discussed.

### 1. Introduction

The growth of ZnSe layers on GaAs substrates is of high practical importance due to the application in blue-green emitting laser structures [1,2]. Recently even room temperature CW lasing has been reported [3]. To obtain long term stable lasing, the growth conditions have to be optimized in order to improve the interface quality and to reduce the dislocation density. Reflection high-energy electron diffraction (RHEED), as a surface sensitive method, is a powerful tool for studying the growth conditions in situ. Observing the changes of RHEED patterns, a phase dia-

gram of the surface growth conditions was obtained [4]. Diffusion lengths of Zn and Se have been determined by RHEED oscillation studies during ZnSe growth on slightly misoriented GaAs substrates [5]. The quality of ZnSe/GaAs interfaces has been proved by transmission electron microscopy (TEM) [6], but only recently were systematic studies of the initial growth conditions performed [7,8].

Despite the problem of lattice mismatch between ZnSe and GaAs, an important question is how a GaAs buffer layer deposited prior to II–VI growth influences the crystalline quality. To answer this, high-resolution X-ray diffraction measurements of epilayer and quantum well structures have been performed and results correlated to cross-sectional TEM images. Further on, a

<sup>\*</sup> Corresponding author.

ZnSe growth model has been developed based on in situ RHEED oscillation studies. It will be shown further on that X-ray diffraction is a powerful tool for studying partly relaxed epilayers and that by this non-destructive method a correlation between the relaxation state of the epilayer and its mosaicity can be obtained.

## 2. Sample preparation and experimental results

All studied epilayers and quantum well structures have been grown by molecular beam epitaxy (MBE) in a 6-chamber Riber 2300 system. A GaAs chamber has been adapted recently to the three II–VI growth chambers. They all are connected via an UHV module track to an analytical (XPS, AES) and a metallization chamber. Elemental Se, Zn and Cd have been used as source materials (Asahi Osaka). Lattice matched  $\text{ZnS}_{1-x}\text{Se}_x$  has been grown using a compound  $\text{ZnS}$  source. The Se:Zn flux ratio has been varied between 1:1 (Zn-rich growth with  $c(2 \times 2)$  RHEED reconstruction) and 2:1 (Se-rich,  $(2 \times 1)$ ). Better growth has been achieved in the latter case, and thus results reported here have been obtained under Se-rich conditions. The substrate temperature was usually kept at 300°C. The growth rate was typically 0.35  $\mu\text{m}/\text{h}$ .

The studied RHEED patterns generated by a 35 keV electron gun were monitored by a CCD camera and stored by a video recorder. A 6-crystal diffractometer consisting of a four-reflection Bartels monochromator ( $4 \times \text{Ge } 220$ ), an analyser crystal (Si 111) and the sample itself were used for high-resolution X-ray diffraction. Details about the TEM imaging used can be found elsewhere [9].

## 3. ZnSe growth on GaAs substrates and GaAs buffer layers

Studies of the RHEED pattern, especially in the first 10–15 min after the growth started, allow a qualitatively good prediction of the interface and crystalline quality. The problem with the growth directly on a GaAs substrate is connected

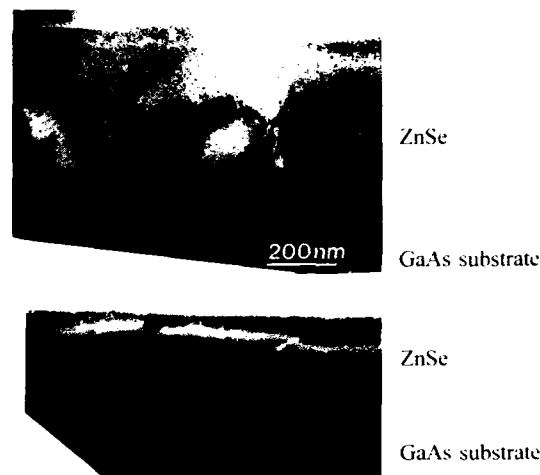


Fig. 1. High density of dislocations in the first 100 nm of a ZnSe epilayer grown directly on a (100) GaAs substrate (top). Even under optimized growth conditions the interface region is far from being dislocation free (bottom).

with a sufficient oxygen desorption prior to growth. As long as this cannot be done under As partial pressure, which is not possible in a II–VI chamber due to cross-contamination, the substrate surface either becomes Ga-rich or still contains some oxygen, as found by XPS studies [10]. Under such conditions, fully reproducible and reliable sample preparation is not possible. Typical cross-sectional TEM images are seen in Fig. 1. In the first 300 nm from the ZnSe/GaAs interface, the density of dislocations is very high (Fig. 1, top), but there are only a few dislocations reaching the epilayer surface. This is in line with the RHEED observation that after 5–10 min the surfaces recover and two-dimensional patterns are observed again. Even for the best ZnSe epilayers grown directly on the GaAs substrate, the interface region is still characterized by many dislocations (Fig. 1, bottom).

The dependence of the full width at half maximum (FWHM) of the (004) reflection in X-ray diffraction as a function of epilayer thickness is given in Fig. 2. A thin, completely strained, pseudomorphic layer (150 nm) has the same FWHM (109 arc sec) as a 5  $\mu\text{m}$  thick, fully relaxed layer



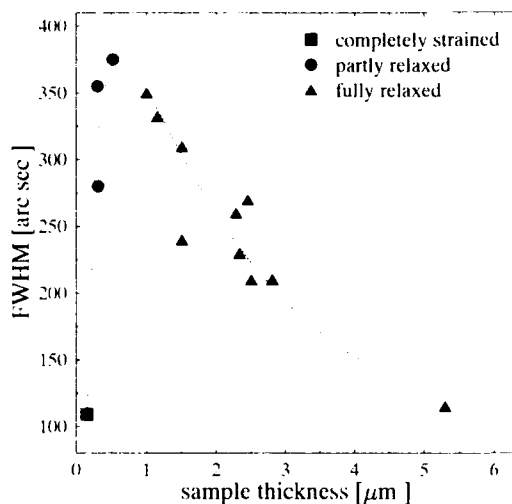


Fig. 2. Dependence of the rocking curve FWHM on the epilayer thickness. For thin pseudomorphic (150 nm) and thick, fully relaxed (5.2  $\mu\text{m}$ ) epilayers, the same values are obtained due to neglectable misfit dislocations.

(115 arc sec). In both cases misfit dislocations either do not exist or can be neglected.

A completely different situation takes place when the substrate is covered by a GaAs buffer layer. A much better quality of the interfaces can be obtained. This is confirmed by TEM and X-ray diffraction where the FWHM of a 1  $\mu\text{m}$  thick ZnSe epilayer could be improved from about 350 to 220 arc sec, a value far below the curve given in Fig. 2. Also, nearly lattice matched ternary  $\text{ZnS}_{1-x}\text{Se}_x$  epilayers (850 nm) with  $x = 4.8\%$  and a 004 FWHM as narrow as 32 arc sec have been grown on a GaAs buffer (Fig. 3). The best value we obtained without buffer was 110 arc sec.

#### 4. RHEED model of ZnSe growth

The following investigations were made in order to determine the dependence of ZnSe growth rate from the three parameters Zn flux, Se flux and substrate temperature. A model was used in which scattering processes of atoms during diffusion in the precursor state can be taken into account. It will be shown that the observations agree well with model calculations. In this model the following processes (as shown in Fig. 4 for

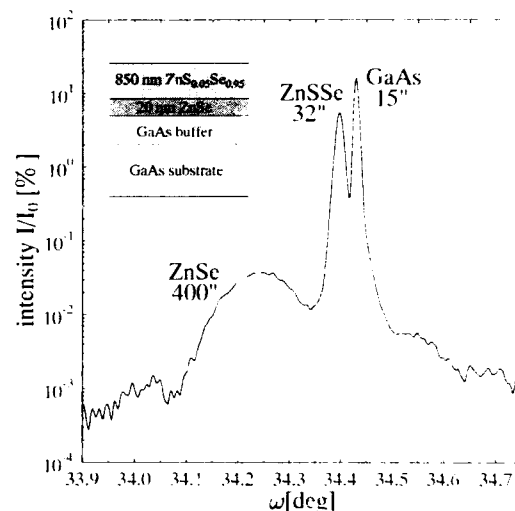


Fig. 3. For a nearly lattice-matched  $\text{ZnS}_{0.95}\text{Se}_{0.05}$  layer grown on a GaAs buffer, a rocking curve half-width as narrow as 32 arc sec has been obtained.

one of the two species, Zn or Se) with the described probabilities are included:

- entering the precursor state (with the probability 1);
- diffusion in the precursor state ( $p_m$  and  $p'_m$ );
- scattering in the precursor state, causing chemisorption ( $p_a$ ) or desorption from the precursor state ( $p'_a$ );
- desorption of localized adatoms from the chemisorbed state ( $p_{d, ch}$ ).

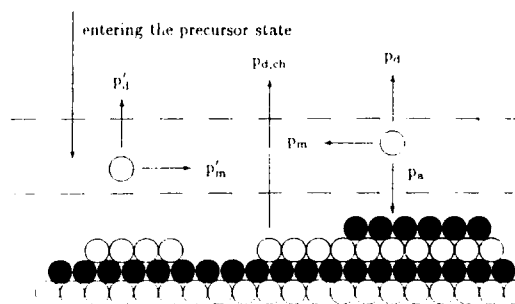


Fig. 4. Model for the MBE growth process. For one kind of species the probabilities for adsorption, desorption and diffusion at a scattering event are shown. Scattering of this atom on a surface covered with the other species is labelled with  $p$ , and on a surface covered with the same kind of species with  $p'$ .

For the following calculations, the desorption from chemisorbed states was neglected. The probability of an impinging atom (species  $i$ ) to be chemisorbed is expressed by

$$p_i = \frac{p_{a,i}}{p_{a,i} + p_{d,i}} \frac{1 - \theta_i}{1 - \theta_i \left(1 - \frac{p'_{d,i}}{p_{a,i} - p_{a,i}}\right)} \quad (1)$$

with  $i = 1, 2$ .

The equations for the growth rate  $R$  and surface coverage  $\theta$ , using the abbreviations ( $F_i$  = particle flux in A/s)

$$S_i = p_{a,i} / (p_{a,i} + p_{d,i}), \quad (2)$$

$$k_i = 1 - p'_{d,i} / (p_{a,i} + p_{d,i}), \quad (3)$$

$$\theta_1 + \theta_2 = 1, \quad (4)$$

are

$$R = F_i p_i = F_i S_i \frac{1 - \theta_i}{1 - \theta_i k_i}, \quad (5)$$

$$n\dot{\theta}_1 = F_1 S_1 \frac{1 - \theta_1}{1 - \theta_1 k_1} - F_2 S_2 \frac{1 - \theta_2}{1 - \theta_2 k_2}, \quad (6)$$

$$n\dot{\theta}_2 = F_2 S_2 \frac{1 - \theta_2}{1 - \theta_2 k_2} - F_1 S_1 \frac{1 - \theta_1}{1 - \theta_1 k_1}, \quad (7)$$

where  $n$  is the surface concentration of atoms on the ZnSe (100) surface.  $S_i$  represents the maximum for the function  $p_i(\theta_i)$ , and  $k_i$  describes the influence of surface diffusion on the growth rate and surface coverage. For the steady state  $\dot{\theta}_i = 0$  the growth rate is given by:

$$R = 2F_1 S_1 \left\{ 1 + \frac{F_1 S_1}{F_2 S_2} + \left[ \left( 1 - \frac{F_1 S_1}{F_2 S_2} \right)^2 + 4 \frac{F_1 S_1}{F_2 S_2} \alpha \right]^{1/2} \right\}^{-1}, \quad (8)$$

with

$$\alpha = (1 - k_1)(1 - k_2). \quad (9)$$

$\alpha$  can be determined explicitly from fitting the model to measured growth rates alone (Eqs. (8) and (9)), but the individual  $k_i$  cannot. The coefficients

$k_i$  need additional observations of the ZnSe specular spot intensity [11].

The probabilities are taken to get an Arrhenius form. Fitting the model to measured ZnSe growth rates (taken from RHEED oscillations) leads to the functions

$$S_{\text{Se}}(T_S) = \frac{1}{1 + \exp(3.7 - 0.27 \text{ eV}/kT_S)} \quad S_{\text{Zn}} = 1, \quad (10)$$

$$\alpha(T_S) = \exp(11.8 - 0.75 \text{ eV}/kT_S) S_{\text{Se}}(T_S). \quad (11)$$

and the growth rate of ZnSe can be written as follows:

$$R(F_{\text{Zn}}, F_{\text{Se}}, T_S) = 2F_{\text{Se}} S_{\text{Se}}(T_S) \left\{ 1 + \frac{F_{\text{Se}} S_{\text{Se}}(T_S)}{F_{\text{Zn}}} + \left[ \left( 1 - \frac{F_{\text{Se}} S_{\text{Se}}(T_S)}{F_{\text{Zn}}} \right)^2 + 4 \frac{F_{\text{Se}} S_{\text{Se}}(T_S)}{F_{\text{Zn}}} \alpha(T_S) \right]^{1/2} \right\}^{-1}. \quad (12)$$

The measured and calculated growth rates for a constant Se flux are shown in Fig. 5. Including the desorption of Se (which cannot be neglected above  $T_S \approx 390^\circ\text{C}$ ) from the chemisorbed states in

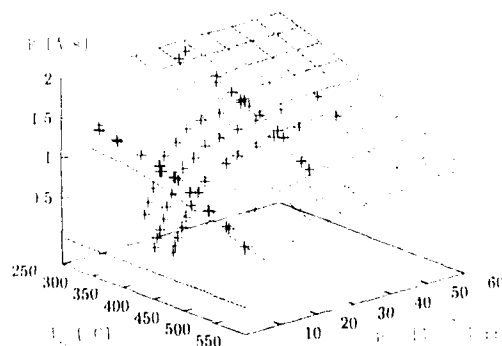


Fig. 5. Calculated growth rates compared to experimental results taken from RHEED oscillations. The Se flux was kept constant.

the calculations will cause changes for the function  $\alpha(T_S)$  above  $T_S = 390^\circ\text{C}$ . The shown dependence of growth rate on the flux and substrate temperature will not be affected by these considerations [11].

### 5. ZnSe/GaAs relaxation process studied by high-resolution X-ray diffraction

The relaxation process of ZnSe layers grown directly on GaAs substrates has been investigated by X-ray diffraction. Fig. 6 shows the (004) reciprocal space map of a 310 nm thick epilayer. In the contour plot, the logarithm of the intensity as a function of the coordinates in reciprocal space is expressed in terms of the non-integer Miller indices  $h$  and  $l$ .

The triangular shape of the reciprocal lattice point (RLP) of the layer was found to be characteristic for partially relaxed layers. The coexistence of different strain states in the epilayer causes a broadening of the RLP parallel to the surface normal [001]. In addition, the distortion observed perpendicular to the [001] direction can be related to mosaicity. A mosaic crystal is an ensemble of perfect crystal blocks whose lattice planes are tilted with respect to each other and whose block sizes vary around a mean value. Here the mosaic block size is in the range of tenths of  $\mu\text{m}$ , and the maximum tilt angle is 200

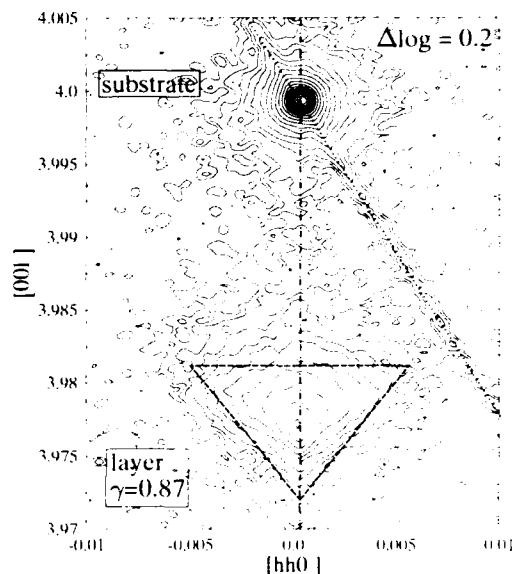


Fig. 6. Reciprocal space map of the (004) reflection. The contour plot on a logarithmic scale shows the scattered intensity as a function of the real Miller indices  $h$  and  $l$ , according to the azimuth reference [110] and the surface normal [001]. (---) Subsidiary line along surface normal; (.....) Ewald sphere; (—) relaxation-mosaicity triangle.

arc sec. The corresponding broadening enhances with increasing  $l$ -values, or equivalently, with progressive relaxation. Such a direct relation between the relaxation state and structural imperfection (mosaicity) has been predicted theoret-

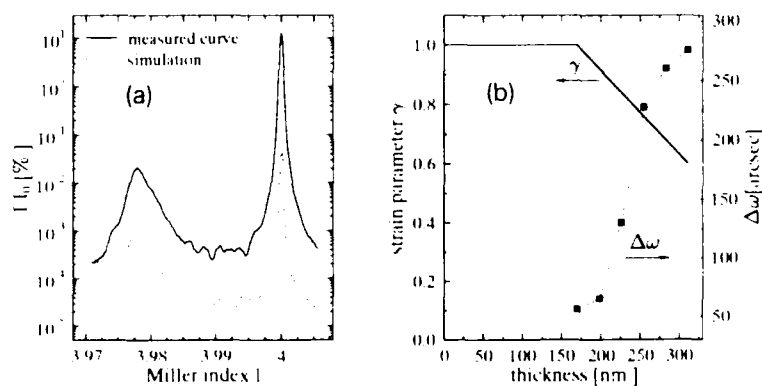


Fig. 7. Measured and simulated curves for a scan along the surface normal through the (004) reciprocal lattice point (a), and depth dependence of the mosaicity obtained for this strain profile (b).

cally [12], but not confirmed experimentally by studies of a single layer. This non-destructive method of reciprocal space mapping allows such a direct correlation to be established.

Laterally, the studied partially relaxed layer was found to be homogeneous. Thus the coexistence of different strain states is caused by a depth profile of the strain. This profile can be determined quantitatively by comparing a measured diffraction profile to a dynamic simulation. Fig. 7a shows a measured and a simulated curve for a scan along the surface normal through the (004) RPL. The dynamic simulation was carried out using the formalism developed by Bartels et al. [13]. The influence of the apparatus, both polarization states and the background was taken into account. (For details, see ref. [14].) The asymmetry of the layer peak is caused by the depth profile of the strain. To obtain good agreement between the measured and simulated curves, a full lattice match has been assumed until at a layer thickness of 170 nm the relaxation process starts. This value of the critical thickness for ZnSe growth on GaAs is in good agreement with other published data [15,16].

Knowing the strain gradient and the correlation between strain and mosaicity, it is possible to derive a depth profile of mosaicity. For this,  $\omega$ -scans perpendicular to the scattering vector have been performed. Their FWHM is a measure of the mean tilt angle between the various mosaic blocks. Therefore, mosaicity can be related also quantitatively to the strain state (determined from the intersection of the corresponding  $\omega$ -scans with the surface normal). Using the strain gradient discussed above, the depth dependence of the mosaicity has been obtained (Fig. 7b). For the ZnSe epilayer studied the increase of mosaicity starts at the critical thickness and saturates at a strain parameter of  $\gamma = 0.6$ . This agrees well with the minimum strain state at the layer top derived from the simulation.

## 6. Conclusions

The quality of ZnSe and  $\text{ZnS}_{1-x}\text{Se}_x$  epilayers grown directly on GaAs substrates has been anal-

ysed versus those grown on a GaAs buffer layer. Based on RHEED, TEM and X-ray diffraction studies, a significantly higher ZnSe/GaAs interface quality can be obtained in the latter case. Based on RHEED oscillation studies, a model for the growth rate dependences of ZnSe has been developed. Using high-resolution X-ray diffraction, a correlation between the relaxation state and the mosaicity was found for partially relaxed ZnSe layers. The depth profile of the strain can be studied by this non-destructive method of reciprocal space mapping.

## 7. Acknowledgements

This work has been supported by the Bundesministerium für Forschung und Technologie and partly by the Deutsche Forschungsgemeinschaft (H. Heinke). The authors would like to thank Mrs. P. Wolf and Mr. Th. Schuhmann for assistance in sample preparation, Mr. F. Gosenhofer for thickness measurements, and Messrs. A. Schönteich and R. Brauner for keeping the whole MBE system running.

## 8. References

- [1] M.A. Haase, J. Oiu, J.M. DePuydt and H. Cheng, *Appl. Phys. Lett.* 59 (1991) 1272.
- [2] H. Jeon, J. Ding, W. Patterson, A.V. Nurmikko, W. Xie, D.C. Grillo, M. Kobayashi and R.N. Gunshor, *Appl. Phys. Lett.* 59 (1991) 3619.
- [3] N. Nakayama, S. Itoh, T. Ohata, K. Nakano, H. Okuyama, M. Ozawa, A. Ishibashi, I. Ikeda and Y. Mori, *Electron. Lett.* 29 (1993) 1488.
- [4] K. Menda, I. Takayasu, T. Minato and M. Kawashima, *Jap. J. Appl. Phys.* 26 (1987) L1326.
- [5] J.M. Gaines and C.A. Ponzoni, *J. Vac. Sci. Technol.* 10 (1992) 918.
- [6] J. Petruzzello, B.L. Greenberg, D.A. Cammack and R. Dalby, *J. Appl. Phys.* 63 (1988) 2299.
- [7] S. Guha, H. Munkata, F.K. LeGoues and L.L. Chang, *Appl. Phys. Lett.* 60 (1992) 3220.
- [8] S. Guha, H. Munkata and L.L. Chang, *J. Appl. Phys.* 73 (1993) 2294.
- [9] H. Cerva and H. Oppolzer, *Progr. Crystal Growth Characterization* 20 (1990) 231.
- [10] R. Schmiedel and D. Hommel, unpublished.

- [11] P. Ruppert, D. Hommel, A. Waag and G. Landwehr, J. Appl. Phys., to be published.
- [12] K. Durose, A. Turnbull and P. Brown, Mater. Sci. Eng. B 16 (1993) 96.
- [13] W.J. Bartels, J. Hornstra and D.J. Lobeck, Acta Cryst. A 42 (1986) 539.
- [14] H. Heinke, M.O. Möller, D. Hommel and G. Landwehr, J. Crystal Growth 135 (1994) 41.
- [15] K. Mohammed, D.A. Cammack, R. Dalby, P. Newbury, B.L. Greenberg, J. Petruzzello and R.N. Bhargava, Appl. Phys. Lett. 50 (1987) 37.
- [16] T. Yao, Y. Okada, S. Matsui, K. Ishia and I. Fushimoto, J. Crystal Growth 81 (1987) 518.



ELSEVIER

Journal of Crystal Growth 138 (1994) 55–58

JOURNAL OF  
**CRYSTAL  
GROWTH**

## Surface engineering during molecular beam epitaxial growth of wide-gap II–VI structures

J. Griesche, N. Hoffmann, K. Jacobs \*

*MBE-Labor, Fachbereich Physik, Humboldt-Universität zu Berlin, Invalidenstrasse 110, D-10115 Berlin, Germany*

### Abstract

Systematic investigations have been carried out in order to control the surface morphology of ZnSe and related compounds. Rough surfaces can be smoothed by means of growth interruptions. The smoothing of the surface is reflected in the halfwidth of the intensity distribution along the 00 rod of the reflection high-energy electron diffraction (RHEED) pattern. Reduction of the halfwidth is observed to occur within times of less than a minute; a fast process removes short range disturbances of the surface morphology. A more detailed analysis of the intensity distribution reveals a fine structure. From this, it can be derived that the distance of surface terraces is made uniform during the growth interruption, but this takes several minutes; a slow process removes long range disturbances. Degree and time dependence of surface smoothing are influenced by the beam equivalent pressure ratio during layer growth.

### 1. Introduction

Molecular beam epitaxy (MBE) grown wide-gap II–VI materials are promising candidates for blue light emitting devices [1–3]. Advanced device structures require ultrathin layers of well defined dimensions with sharp interfaces. Flat surfaces are a pre-requisite to produce sharp interfaces. Furthermore, starting the growth on a flat surface, RHEED oscillations occur and can be taken to control layer thicknesses. Growing a thick layer, however, the surface becomes rough due to growth fluctuations. The surface must therefore be smoothed. Rough surfaces can be smoothed by means of growth interruptions. In the case of ZnSe, the basic wide-gap II–VI com-

pound, growth interruptions turned out to be most efficient if the Zn source is closed while the Se source is kept open [4]. What is going on during growth interruptions can be investigated by means of RHEED reflection profile analysis [5,6]. Here, the intensity distribution along the 00 rod is measured. Smoothing the surface yields a reduction of the halfwidth of the intensity distribution. Furthermore, the fine structure revealed within the intensity distribution can be exploited to estimate the average distance of surface terraces [7].

### 2. Experiments

ZnSe layers have been grown on almost exactly (001) oriented GaAs epi-ready substrates in a DCA 350 MBE system. The growth conditions

\* Corresponding author.

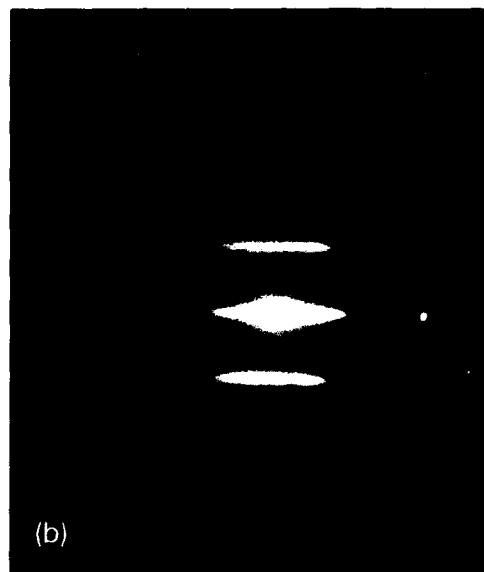
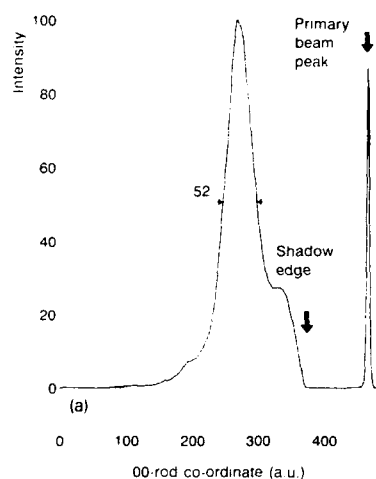


Fig. 1. ZnSe growth on stoichiometric conditions: (a) RHEED intensity distribution; (b) RHEED pattern.

have been changed between stoichiometric and Se-rich. Se-rich conditions mean that a well-developed  $(1 \times 2)$  reconstruction of the RHEED pattern is solely seen. The term stoichiometric refers to conditions where a  $c(2 \times 2)$  reconstruc-

tion as well as a weaker  $(1 \times 2)$  reconstruction are seen simultaneously [4].

Fig. 1a shows the intensity distribution along the 00 rod of the RHEED pattern (Fig. 1b). This pattern has been taken during the growth of

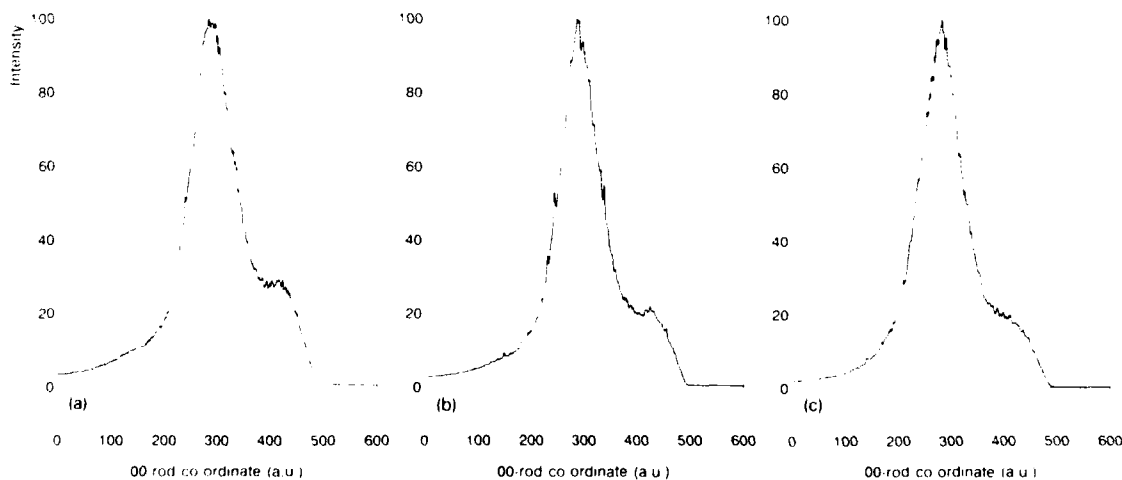


Fig. 2. RHEED intensity distribution (higher resolution), stoichiometric growth conditions: (a) ZnSe growth; (b) growth interruption 1 min; (c) growth interruption 16 min.

Table 1  
Halfwidth (a.u.) of the intensity distribution along the 00 rod

	Growth conditions	
	Stoichiometric	Se-rich
ZnSe growth	52	47
Interruption 1 min	47	43
Interruption 16 min	48	43

ZnSe under stoichiometric conditions. The acceleration voltage is 15 kV and the azimuth is [110]. Besides the reflection itself, the shadow edge and the peak of the primary electron beam are clearly seen. Herefrom, the angle of incidence has been derived to be  $1.5^\circ$ . A background correction has been applied.

Table 1 summarizes the halfwidths of the intensity distribution during growth, after a growth interruption of 1 min duration, and after a growth interruption of 16 min duration. The samples have been grown under stoichiometric and Se-rich conditions, respectively.

The halfwidth reduces during the first minute of the growth interruption, but it remains unchanged during the next 15 min of interruption. The process that is reflected in the reduction of the halfwidth is completed after 1 min. The

smoothing process is thought to consist of the re-evaporation of isolated ad-atoms and of the diffusion of atoms along the edges of terraces, which smoothes the edges. In general, it is a fast process, removing short range disturbances of the surface morphology. With respect to this process, no difference between stoichiometric and Se-rich growth conditions has been observed.

Figs. 2 and 3 show the intensity distribution during growth and after a growth interruption of 1 min and 16 min duration for stoichiometric and Se-rich growth conditions, respectively. The resolution of the reciprocal space axis is higher than in Fig. 1a, thus making it possible to reveal a fine structure. The occurrence of a fine structure would indicate the presence of surface terraces of regular distances. Here, there is a difference between stoichiometric and Se-rich growth conditions. The case of stoichiometric conditions will be discussed first (Fig. 2).

During growth (Fig. 2a), there is only a weak indication of a fine structure. This means that the terraces occurring and disappearing during growth show a relatively wide distribution in size. After 1 min interruption (Fig. 2b), a fine structure is clearly seen. It is, however, not developed in a regular manner. The terraces have become

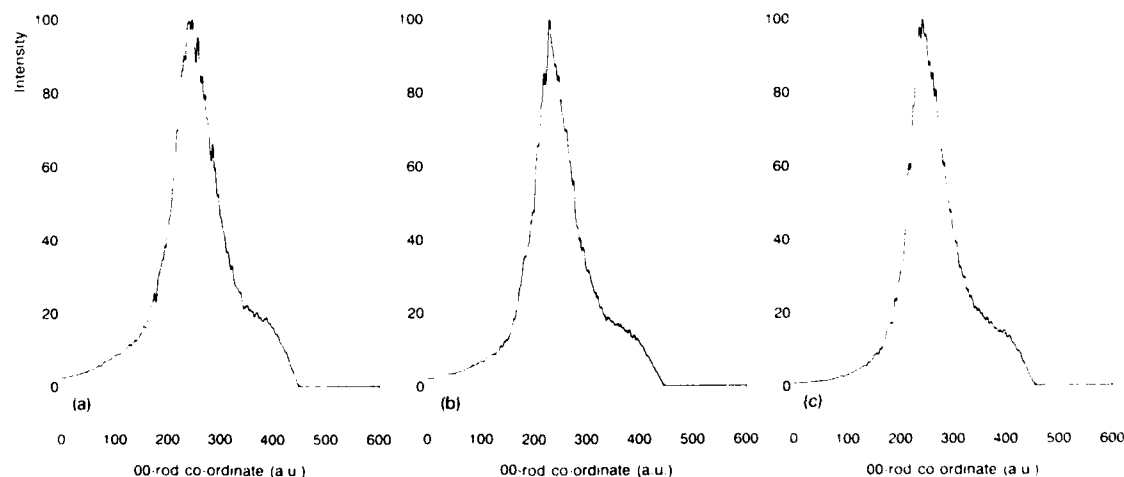


Fig. 3. RHEED intensity distribution (higher resolution). Se-rich growth conditions: (a) ZnSe growth; (b) growth interruption 1 min; (c) growth interruption 16 min.



more uniform, but several diffraction processes are still super-imposed. Only after 16 min growth interruption (Fig. 2c) is a regular fine structure found, which indicates the terraces to have been made uniform. The distance of the peaks that form the fine structure shows that the distance of terraces is in the order of 100 nm. In addition to the fast process mentioned above, there is a slow process. It is thought to consist of the re-evaporation of whole terraces of small size and of the diffusion of atoms between terraces to make their distances more uniform. In general, the slow process removes long range disturbances of the surface morphology [8].

The matter seems to be more sophisticated in the case of Se-rich growth conditions (Fig. 3). A fine structure is seen during growth (Fig. 3a), but it is totally irregular. In principle, it is the same as in the case of stoichiometric growth conditions: terraces show a relatively wide distribution in size during growth. A regular fine structure is found after 1 min interruption (Fig. 3b). This again indicates the terraces to have been made uniform. Their distance is also in the same order of magnitude like above, but it has taken less time to get this surface morphology. There is no distinction between a fast process and a slow process. After 16 min interruption (Fig. 3c), the fine structure seems to be more irregular again. This indicates the surface morphology to have become worse in too long a growth interruption. The process that makes the morphology worse is not yet understood.

### 3. Conclusions

RHEED reflection profile analysis is a useful tool to get detailed information on the surface morphology during growth and during growth interruptions. What is going on during a growth interruption with a ZnSe sample grown under stoichiometric conditions can be explained in terms of a fast process and a slow process that

remove short range disturbances and long range disturbances of the surface morphology, respectively. The matter is less clearly understood in the case of Se-rich growth conditions. However, too long a growth interruption seems to make the surface more rough again.

The results obtained by means of RHEED reflection profile analysis agree with experience obtained from the occurrence of RHEED oscillations. In order to get RHEED oscillations, growth must start with two-dimensional nucleation. In other words, nucleation sites that compete with two-dimensional nucleation should be removed. This is fulfilled after a long growth interruption in the case of stoichiometric growth conditions. A set of uniform terraces supplies a minimal number of nucleation sites; only the ledges compete with two-dimensional nucleation. The best developed RHEED oscillations have actually been seen under these conditions.

Further investigations that interpret the intensity distributions by statistical means are in progress.

### 4. References

- [1] M.A. Haase, J. Qiu, J.M. DePuydt and H. Cheng, *Appl. Phys. Lett.* 59 (1991) 1272.
- [2] H. Jeon, J. Ding, W. Patterson, A.V. Nurmikko, W. Xie, D.C. Grillo, M. Kobayashi and R.L. Gunshor, *Appl. Phys. Lett.* 59 (1991) 3619.
- [3] H. Jeon, J. Ding, A.V. Nurmikko, W. Xie, D.C. Grillo, M. Kobayashi, R.L. Gunshor, G.C. Hua and N. Otsuka, *Appl. Phys. Lett.* 60 (1992) 2045.
- [4] J. Reichow, J. Griesche, N. Hoffmann, C. Muggelberg, H. Rossmann, L. Wilde, F. Henneberger and K. Jacobs, *J. Crystal Growth* 131 (1993) 277.
- [5] M.G. Lagally, in: *Methods of Experimental Physics*, Vol. 22, *Solid State Physics – Surfaces*, Eds. R.L. Park and M. Lagally (Academic Press, New York, 1985).
- [6] P.I. Cohen, P.R. Pukite, J.M. Van Hove and L.S. Lent, *J. Vac. Sci. Technol. A* 4 (1986) 1251.
- [7] L. Däweritz, J. Griesche, R. Hey and J. Herzog, *J. Crystal Growth* 111 (1991) 65.
- [8] J. Griesche, N. Hoffmann, M. Rabe and K. Jacobs, *Appl. Surf. Sci.*, in press.



ELSEVIER

Journal of Crystal Growth 138 (1994) 59–62

JOURNAL OF **CRYSTAL  
GROWTH**

## On the mechanism of reflection high-energy electron diffraction oscillations studied by phase-locked epitaxy of ZnSe

J. Griesche, N. Hoffmann, K. Jacobs \*

*MBE-Labor, Fachbereich Physik, Humboldt-Universität zu Berlin, Invalidenstrasse 110, D-10115 Berlin, Germany*

### Abstract

Molecular beam epitaxy (MBE) is one of the most promising methods for growth of sophisticated device structures. Starting the growth on a flat surface, reflection high-energy electron diffraction (RHEED) oscillations occur. The question which phase of the oscillations corresponds to lattice plane completion and the most flat surface morphology is not yet fully resolved. There is hardly a direct access to the answer. Phase-locked epitaxy (PLE), however, appears to be a tool for studying this phase problem. PLE permits the growth of layers without losing RHEED oscillations due to damping the thickness of which is great enough to become measurable by common techniques. This enables to compare the directly determined layer thickness with that obtained by counting the number of RHEED oscillation periods. Results are presented that show the phase relation between RHEED oscillations and lattice plane completion.

### 1. Introduction

One of the most important advantages of MBE is that the technique works in ultra-high vacuum, permitting simultaneous performance of electron diffraction experiments. Most popular is RHEED. RHEED oscillations are frequently used to monitor layer thicknesses. However, the question which phase of the oscillations corresponds to lattice plane completion and the most flat surface morphology is not yet fully resolved, neither in the field of III–V semiconductor compounds nor in the field of II–VI compounds [1]. Furthermore, only a limited number of oscillations can be seen due to damping. This means that the growth of

thicker layers cannot be monitored by means of RHEED oscillations.

PLE [2,3] helps to give an answer to the phase problem and overcomes the damping of RHEED oscillations. In PLE mode, only a few lattice planes are grown. Then, the surface is given time to smooth during a growth interruption, and so on. Growth and growth interruption make a cycle. The shutter operation is locked onto the phase of the oscillations observed. During growth interruptions, the Zn source is closed while the Se source is kept open.

### 2. Experiments

ZnSe layers have been grown on almost exactly (001) oriented GaAs epi-ready substrates in a

\* Corresponding author.

DCA 350 MBE system [4]. Buffer layers of several 100 nm thickness were grown in conventional MBE mode first. After a growth interruption to smooth the surface of the buffer layer, growth was continued in PLE mode.

Fig. 1 shows the specular beam intensity of a sample that has been grown using 40 cycles, each consisting of 3 oscillation periods and 10 s interruption. The sample has been grown closing the shutter 180° after the 3rd maximum. Even the 120th period is well seen. Starting growth, the intensity increases in contrast to what seems to be common for III–V materials. The lattice planes are therefore thought to become complete at the oscillation minimum rather than at the maximum.

Although only 3 oscillation periods are seen per cycle, 4 lattice planes are grown. This has been found by means of an experiment where the thickness of a layer was determined by IR interferometry and compared with the number of cycles counted [5]. The growth of the first lattice plane is indicated by a shoulder, see arrows in the

figure. The figure demonstrates that the growth of a layer of 45 nm thickness can be monitored by means of RHEED oscillations.

To answer the question which phase of RHEED oscillations actually corresponds to lattice plane completion, a sample has been grown that is drawn schematically in Fig. 2. ZnSe layers have been grown in PLE mode closing the shutter 90°, 180°, 270° and 360° after the 3rd oscillation maximum, respectively. Fig. 3 illustrates what these angles refer to. In addition, one layer has been grown in the conventional MBE mode for testing; it is not involved in the current discussion. The ZnSe layers are separated by (Zn<sub>0.82</sub>Cd<sub>0.18</sub>)Se layers of about 10 nm thickness. The thicknesses of the ZnSe layers have been measured by means of scanning electron microscopy using a cleavage plane. The results are summarized in Table 1. The phase question can now easily be answered. If the shutter is closed when the growth of a lattice plane is completed, an integer number of lattice planes will be grown

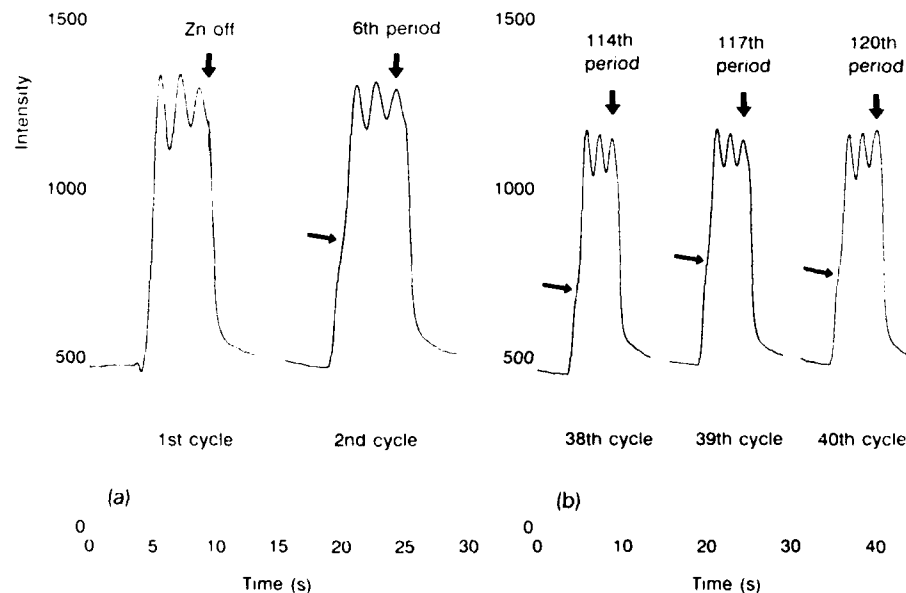


Fig. 1. Specular beam intensity during PLE: (a) cycles 1 and 2; (b) cycles 38, 39 and 40. The arrows mark a shoulder, see text.

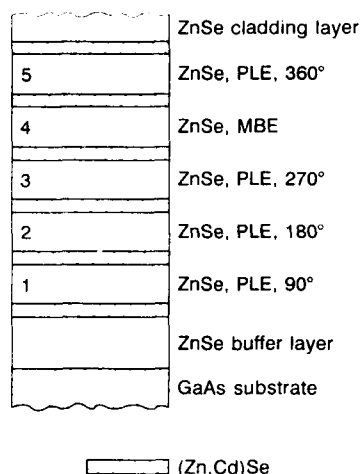


Fig. 2. Schematic drawing of the sample grown to answer the phase question.

in each cycle. Otherwise, the number of lattice planes that is grown per cycle is fractional. Obviously, it is

$$n = 2d/ma, \quad (1)$$

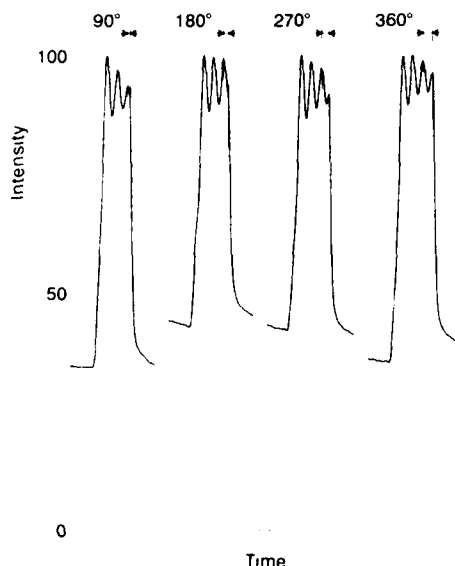


Fig. 3. Different phases of shutter operation.

Table 1  
Layer thicknesses

Layer	Mode	$d$ (nm)	$n$
1	PLE, 90°	$125 \pm 4$	$3.7 \pm 0.1$
2	PLE, 180°	$139 \pm 7$	$4.1 \pm 0.2$
3	PLE, 270°	$137 \pm 4$	$4.0 \pm 0.1$
4	Conventional MBE <sup>a</sup>	$103 \pm 4$	–
5	PLE, 360°	$143 \pm 7$	$4.2 \pm 0.2$

<sup>a</sup> Growth rate and time have been aimed to get a thickness of 100 nm.

where  $n$  is the number of lattice planes grown per cycle,  $d$  the thickness of the layer,  $m$  the number of cycles and  $a$  the lattice constant. The number of cycles has been chosen to be 120 and the ZnSe lattice constant is 566.8 pm.

In the case of layer 1 (see Table 1),  $n$  has a fractional part that exceeds the error range. The shutter has not been closed at lattice plane completion. It has been closed before completion of the 4th plane. In the case of layer 5,  $n$  has also a remarkable fractional part. The shutter has been closed after completion of the 4th plane. The 5th plane has already begun to grow. In the case of layers 2 and 3, the fractional part of  $n$  is small in comparison with the error range. The shutter has been closed near completion of the 4th plane. At the diffraction conditions applied, a phase of 180°–270° corresponds to lattice plane completion.

### 3. Conclusions

PLE turned out to be a good technique to overcome the damping of RHEED oscillations. In this mode, also the growth of thicker layers can be monitored by means of RHEED oscillations. Layers can be grown in PLE mode with RHEED monitoring, the thickness of which is great enough to become measurable by means of IR interferometry or scanning electron microscopy on cleavage edges. This gives the possibility to answer the question which phase of the RHEED oscillations corresponds to lattice plane completion. Investigating the number of lattice planes grown per cycle, a phase between 180° and 270° has been found to correspond to lattice

plane completion. With this, the phase problem is solved, at least for the diffraction conditions applied here.

Further investigations with narrower phase angle step width and elucidation of the diffraction conditions are in progress.

#### 4. Acknowledgement

We would like to thank G. Neubert for thickness measurements by scanning electron microscopy.

#### 5. References

- [1] L.-M. Peng and M.J. Whelan, *Proc. Roy. Soc. (London) A* 435 (1991) 257.
- [2] T. Sakamoto, H. Funabashi, K. Ohta, T. Nakagawa, N.J. Kasai, T. Kojima and Y. Bando, *Superlattices Microstruct.* 1 (1985) 347.
- [3] T. Sakamoto, H. Funabashi, K. Ohta, T. Nakagawa, N.J. Kasai and T. Kojima, *Jap. J. Appl. Phys.* 23 (1984) 657.
- [4] J. Reichow, J. Griesche, N. Hoffmann, C. Muggelberg, H. Rossmann, L. Wilde, F. Henneberger and K. Jacobs, *J. Crystal Growth* 131 (1993) 277.
- [5] J. Griesche, N. Hoffmann, M. Rabe and K. Jacobs, *Appl. Surf. Sci.*, in press.

## Atomic layer epitaxy of CdSe/ZnSe short period superlattices

Takashi Matsumoto \*, Taizo Iwashita, Kenji Sasamoto, Takamasa Kato

*Department of Electronic Engineering, Yamanashi University, Takeda 4, Kofu 400, Japan*

### Abstract

Short period superlattices with structures of  $\{(\text{CdSe})_n(\text{ZnSe})_{10}\}_m$  with  $n = 1-4$  and  $m = 1-30$  were grown on GaAs(100) substrates using an atomic layer epitaxy (ALE) method by alternately supplying Zn, Cd and Se source beams in a molecular beam epitaxy (MBE) system. The influence of source flux density, shutter opening duration, buffer layer thickness and substrate temperature has been studied. Satellite peaks due to the superlattice structures and subpeaks between the satellite peaks according to the Laue functions of the superlattices were observed in X-ray diffraction patterns. Photoluminescence (PL) due to the transitions in the CdSe quantum wells was observed. The well-width dependence of the PL peak energy is explained by the Kronig-Penney model.

### 1. Introduction

Wide-gap II–VI compound superlattices of CdSe/ZnSe show strong exciton emissions in the blue-green region of the spectrum [1], and are important materials for the active layers of short wavelength laser diodes. A point which should be noted is the lattice mismatch between the two materials of as large as 7%. The large mismatch induces uniaxial strain and reduces the degeneracy of the valence band top. The large mismatch also brings lattice relaxation of a strained layer to an unstrained layer by introducing misfit dislocations when a layer thickness exceeds the critical thickness. The critical thickness of quantum wells in the CdSe/ZnSe strained layer system was reported to be of order 4 monolayers [2]. In this paper, we describe atomic layer epitaxy (ALE) of CdSe/ZnSe short period superlattices. Atomic

configurations at the heterointerface are expected to be controlled at an atomic level by ALE technique. The influence of source flux density, shutter opening duration, buffer layer thickness and substrate temperature will be described. X-ray diffraction and photoluminescence (PL) properties of superlattices with different thicknesses of the quantum wells and different numbers of superlattice periods are discussed.

### 2. Experiments

ZnSe and CdSe layers were grown with ALE method by supplying source beams alternately in an MBE system. One monolayer per cycle growth of ZnSe was obtained in the range of substrate temperatures of 280–360°C on GaAs(100) substrates. The source-cell shutter opening sequence for one monolayer growth was as follows: Zn opened for 4 s/all shutters closed for 1 s/Se opened for 4 s/all shutters closed for 1 s. The

\* Corresponding author.

growth rate was confirmed to be independent of source beam intensities in the range of  $(2\text{--}4) \times 10^{15}$  atoms  $\text{cm}^{-2} \text{s}^{-1}$  with VI/II ratio of about unity for a substrate temperature of 280°C. Growth conditions of CdSe ALE will be described in the next section.

Short period superlattices with structures of  $\{(\text{CdSe})_n(\text{ZnSe})_{10}\}_m$  with  $n = 1\text{--}4$  and  $m = 1\text{--}30$  were grown on GaAs(100) substrates at 310°C. ZnSe buffer layers of different thickness were inserted between the superlattice and the substrate. The effects of the Cd beam intensity, shutter opening duration and buffer layer thickness on the quality of the superlattices were studied.

### 3. Results and discussion

The optimum value of Cd beam intensity was determined by monitoring X-ray diffraction patterns and PL spectra of samples prepared with a shutter opening sequence for the growth of superlattices with a structure of  $\{(\text{CdSe})_2(\text{ZnSe})_{10}\}_{30}$ . The buffer layer was 30-monolayer ZnSe. The intensities of the Zn and Se beams were  $3.4 \times 10^{15}$   $\text{cm}^{-2} \text{s}^{-1}$ , and the shutter opening sequence for the ALE growth of ZnSe layers was as described in the last section. The shutter sequence for one monolayer growth of CdSe was as follows: Cd opened for 4 s/all shutters closed for 1 s/Se opened for 8 s/all shutters closed for 1 s. We have found that the sticking coefficient of Se atoms on the Cd surface of CdSe is smaller than that of Se atoms on the Zn surface of ZnSe by in situ observation of the specular beam intensity of reflection high-energy electron diffraction (RHEED). The details will be reported elsewhere. Therefore, we doubled the Se shutter opening time for the ALE of CdSe. The thickness of one cycle of the superlattice was estimated from the positions of satellite peaks of X-ray diffraction patterns. Fig. 1 shows the one-cycle thicknesses of the superlattices prepared with different Cd beam intensities. We can see that the thickness of one cycle of the superlattices is about 36.5 Å and is almost independent of the Cd beam intensity over the range of  $3 \times 10^{13}$  to  $1 \times$

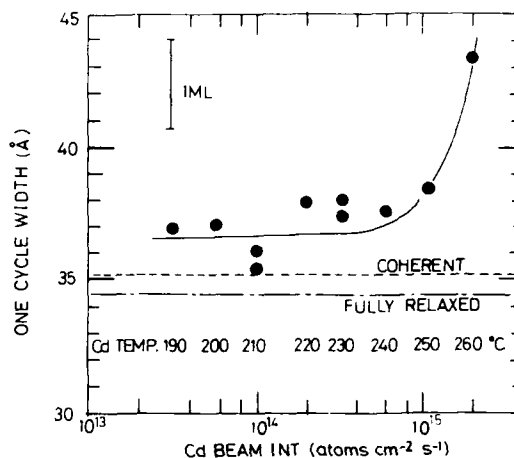


Fig. 1. One cycle width of  $\{(\text{CdSe})_2(\text{ZnSe})_{10}\}_{30}$  superlattices prepared with different Cd beam intensities. The dashed and dot-dashed lines show the expected values for superlattices coherently grown on GaAs(100) and fully relaxed, respectively. The vertical bar in the figure indicates one-monolayer thickness.

$10^{15}$   $\text{cm}^{-2} \text{s}^{-1}$ . The period of the superlattice coherently grown on GaAs(100) substrate is calculated to be 35.10 Å by using the lattice constants and elastic constants given in Table 1, and that of a fully relaxed superlattice is calculated to be 34.34 Å. The measured value is in good agreement with the calculated one. The growth rate of the CdSe layers was independent of the shutter-opening durations of Cd and Se over the range of 2–30 s and 8–30 s, respectively.

Table 1  
Physical parameters of ZnSe and CdSe used for the calculations

Parameter (unit)	ZnSe	CdSe
Lattice constant (Å)	5.6684	6.077 [3]
Energy gap (eV)	2.821 (9 K) [4]	1.765 (9 K) [4]
Dielectric constant, $\epsilon_0$	9.1	10.2
Electron effective mass ( $m_0$ )	0.16	0.13 [4]
Hole effective mass ( $m_0$ )	0.6	0.45 [4]
Elastic constant $C_{11}$ ( $10^{10} \text{ N m}^{-2}$ )	8.10 [5]	6.67 [6]
Elastic constant $C_{12}$ ( $10^{10} \text{ N m}^{-2}$ )	4.88 [5]	4.63 [6]
Deformation potential $a$ (eV)	−4.17 [7]	−3.664 [4]
Deformation potential $b$ (eV)	−1.2 [7]	−0.8 [4]
Valence-band discontinuity	0.23 [4]	0.23 [4]

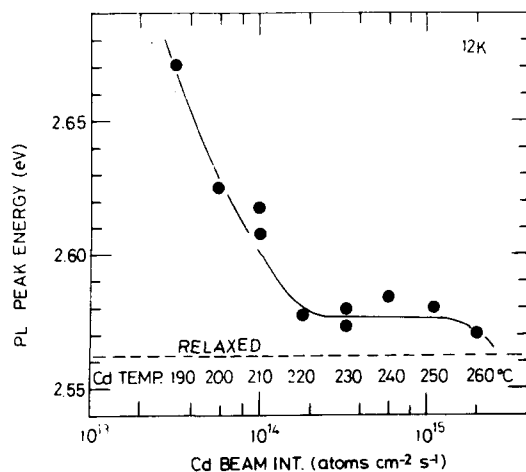


Fig. 2. Peak energies of PL from  $(\text{CdSe})_n(\text{ZnSe})_{10}$  superlattices prepared with different Cd beam intensities. The dashed line indicates a peak energy expected for a square quantum well with a thickness of 2 monolayers CdSe.

Fig. 2 shows PL peak energies observed from superlattices prepared with different Cd beam intensities. When the Cd beam intensity is in the range of  $1.8 \times 10^{14}$  to  $1.2 \times 10^{15} \text{ cm}^{-2} \text{ s}^{-1}$ , the peak energy is around 2.57 eV and is independent of the Cd beam intensity. The value of the peak energy is in agreement with the value calculated for a square quantum well with a width corresponding to two monolayers of CdSe, as described later. The energy change induced by a deviation of the well thickness by one monolayer is calculated to be 0.14 eV, as can be seen later in Fig. 4. This result indicates that one monolayer growth of CdSe per cycle of the shutter sequence of "Cd = 4 s/pause = 1 s/Se = 8 s/pause = 1 s" was realized with the Cd beam intensities. When the Cd beam intensity departed from the optimum range to the lower side, the PL peak energy became higher than the expected value. This means that the effective width of the quantum well becomes narrower with decreasing Cd beam intensity. The thickness of one cycle of the superlattice, however, did not change, as can be seen in Fig. 1. The discrepancy between the data of X-ray diffraction and PL measurement can be explained as follows: When the Cd beam intensity decreases, the quantum well of CdSe is deficient

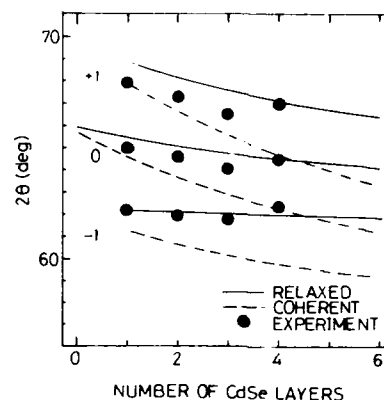


Fig. 3. X-ray diffraction angles  $2\theta$  of satellite peaks of  $(\text{CdSe})_n(\text{ZnSe})_{10}$  superlattices on GaAs(100) substrates as a function of the numbers of CdSe layers. The solid and dashed lines indicate the calculated reflection angles for the relaxed- and coherent-growth cases.

of Cd atoms at the heterointerface and the effective width of the well is reduced, but the period of the superlattice does not change. The PL from the quantum well was the highest in intensity when the Cd beam intensity was  $3.3 \times 10^{14} \text{ cm}^{-2} \text{ s}^{-1}$ . The intensity of satellite peaks in X-ray diffraction showed a maximum at the same Cd beam intensity. Therefore, we adopted the value

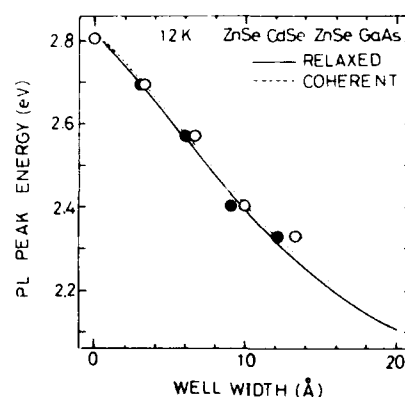


Fig. 4. PL peak energies of  $(\text{CdSe})_n(\text{ZnSe})_{10}$  superlattices for  $n = 1, 2, 3$  and 4. The data at zero well-width are the free exciton energy observed in a thin ZnSe layer coherently grown on GaAs(100). Solid and dashed lines show calculated peak energies of exciton emission in CdSe quantum wells for the relaxed- and coherent-growth cases, respectively.



of the Cd beam intensity for the preparation of superlattices described below.

X-ray diffraction spectra of a series of short period superlattices of  $\{(\text{CdSe})_n(\text{ZnSe})_{10}\}_{30}$  with  $n = 1, 2, 3$  and 4 were studied around the symmetric (400) reflection. Besides the substrate reflection, the peaks of zeroth-order satellite and first-order satellites of the superlattices were clearly observed. Fig. 3 shows X-ray diffraction angles  $2\theta$  of the satellite peaks as a function of the number of CdSe layers. The solid and dashed lines indicate the calculated angles for the cases of fully-relaxed and coherent growth, respectively. The experimental diffraction angles are in agreement with the calculated ones of the coherent case for  $n = 1$  and with the relaxed case for  $n = 4$ . The intensity of each satellite peak was observed to become smaller with increasing number of CdSe layers in a well layer. The zeroth-order satellite decreased in intensity more rapidly than the first-order satellites. The zeroth-order satellite reflects the average properties of the superlattice, whereas the first order satellites come from the periodic stacking of the CdSe layers. The critical thickness of the coherent growth of CdSe on ZnSe coherently grown on GaAs(100) substrates is calculated to be a few to 15 Å [8–10], and the lattice coherency is expected to be broken when the number of CdSe layers exceeds 2 or 3. The break of the coherency results in the degradation of the average properties of the superlattice, and brings a rapid decrease of the intensity of the zeroth-order satellite. The first-order satellites reflecting the periodic stacking of CdSe layers in the superlattices are relatively insensitive to the lattice relaxation.

Fig. 4 shows PL peak energies from the superlattices of  $\{(\text{CdSe})_n(\text{ZnSe})_{10}\}_{30}$  with  $n = 1, 2, 3$  and 4 as a function of the thickness of CdSe well layers. The closed and open circles show experimental data. The well width was estimated on the basis of the number of CdSe layers for the two cases, i.e., the superlattice is coherently grown on GaAs substrates (open circles) and it is fully relaxed (solid circles). The solid and dashed lines show the energies of exciton emissions in the CdSe quantum wells calculated by the Kronig-Penney model for the relaxed- and coherent-

growth cases, respectively. The parameters used for the calculation are given in Table 1. The good agreement between the observed and calculated variation of PL peak energy with the well width confirms that the observed PL emissions originate from transitions between the electronic states in the conduction and the valence band in the quantum wells. The intensity of PL from the  $n = 1$  superlattice was smaller than that of  $n = 2$ , partly due to the spill-over effect of excited carriers from the quantum well. When the number of CdSe layers was increased to 4, the PL intensity was reduced strongly, and was weaker than that of  $n = 2$  and  $n = 3$  superlattices by two orders of magnitude. This degradation is due to the relaxation of the lattice mismatch by introducing misfit dislocations, which act as nonradiative recombination centers. The FWHM of the PL line from the  $n = 2$  sample was 25 meV at 12 K. It was reduced to 15 meV by increasing the buffer layer thickness up to 400–800 monolayers of ZnSe.

Finally, we describe the properties of  $\{(\text{CdSe})_n(\text{ZnSe})_{10}\}_m$  superlattices with smaller numbers of superlattice cycles. Subpeaks according to the Laue function of the superlattice were clearly observed between the zeroth-order and the first-order satellite peaks. The subpeaks were observed from the samples with  $m$  values down to 3. This observation confirms that the short period superlattices prepared by the ALM method are of high quality. PL peaks due to the quantum-well transitions were also observed from the superlattices with small  $m$  values.

#### 4. Conclusions

Short period superlattices with structures of  $\{(\text{CdSe})_n(\text{ZnSe})_{10}\}_m$  with  $n = 1, 2, 3$  and 4 and  $m = 1$ –30 were grown on GaAs(100) substrates with buffer layers of 30–800 monolayers of ZnSe. Source beam intensities and source-cell shutter opening sequences for one monolayer growth of ZnSe and CdSe were described. Growth temperature was 310°C. Satellite peaks originating from the superlattice structure and subpeaks according to the Laue functions of the superlattice were clearly observed in the X-ray diffraction patterns.

The observation confirmed the high quality of the short period superlattice grown by the ALE technique. PL peaks due to transitions between the quantum states in the CdSe well layers sandwiched by ZnSe barrier layers were observed from superlattices with well widths of 1, 2, 3 and 4 monolayers of CdSe. The peak energy variations with the well-layer width were explained by the Kronig-Penney model.

### 5. Acknowledgements

This work was partly supported by a Grant-in-Aid for Scientific Research on Priority Areas, New Functional Materials – Design, Preparation and Control from Ministry of Education, Science and Culture, Japan.

### 6. References

- [1] K.P. O'Donnell, P.J. Parbrook, B. Henderson, C. Trager-Cowan, X. Chen, F. Yang, M.P. Halsall, P.J. Wright and B. Cockayne, *J. Crystal Growth* 101 (1990) 554.
- [2] P.J. Parbrook, B. Henderson, K.P. O'Donnell, P.J. Wright and B. Cockayne, *J. Crystal Growth* 117 (1992) 492.
- [3] N. Samarth, H. Luo, J.K. Furdyna, S.B. Qadri, Y.R. Lee, A.K. Ramdas and N. Otsuka, *Appl. Phys. Lett.* 54 (1989) 2680.
- [4] H.J. Lozykowski and V.K. Shastri, *J. Appl. Phys.* 69 (1991) 3235.
- [5] D. Berlincourt, H. Jaffe and L.R. Shiozawa, *Phys. Rev.* 129 (1963) 1009.
- [6] R.M. Martin, *Phys. Rev. B* 6 (1972) 4546.
- [7] D.W. Langer, R.N. Euwema, K. Era and T. Koda, *Phys. Rev. B* 2 (1970) 4005.
- [8] J.W. Matthews and A.E. Blakeslee, *J. Crystal Growth* 27 (1974) 118.
- [9] R. People and C.J. Bean, *Appl. Phys. Lett.* 47 (1985) 322, 49 (1986) 229.
- [10] D.C. Houghton, D.D. Perovic, J.M. Baribeau and G.C. Weatherly, *J. Appl. Phys.* 67 (1990) 1850.



ELSEVIER

Journal of Crystal Growth 138 (1994) 68–74

JOURNAL OF  
**CRYSTAL  
GROWTH**

## Critical thickness in heteroepitaxial growth of zinc-blende semiconductor compounds

G. Cohen-Solal <sup>\*</sup>, F. Bailly, M. Barbé

*Laboratoire de Physique des Solides de Bellevue, CNRS, 1 Place A. Briand, F-92195 Meudon Cedex, France*

### Abstract

It is assumed that the critical layer thicknesses (CLT) in strained heteroepitaxial layers of zinc-blende semiconductor compounds depend on an energy balance relation between the strain energy and the deformation energy induced by the misfit dislocations. The first energy is evaluated by theoretical means and confirmed by calculation. In order to calculate the latter energy, we have developed an interfacial misfit dislocation model in association with a computer simulation method based on Keating's valence force field approximation. In this way the energy of the relaxed grown layer is obtained in the case of a complete network of two-dimensional misfit dislocations. The computer simulation results are compared with published experimental data. The predicted values are in excellent agreement with the experimental CLT measurements for CdTe on CdZnTe substrates as well as for GeSi on Si substrates, over the entire alloy compositional range. It is shown that the CLT depends in fact only on lattice mismatch  $\eta$ . The  $\eta^{-3/2}$  law of variation of the CLT found in this way may thus be considered as quite general and is extended to GaInAs/GaAs, GaSbAs/GaAs and GaInAs/InP systems.

### 1. Introduction

Most of the calculations of the critical thicknesses are based on assumptions concerning the mechanisms for misfit dislocation generation [1–4]. Recent studies assumed either the force balance model proposed by Matthews and Blakeslee [5,6] on the basis of energy considerations, or the minimum strain energy density required to nucleate dislocations [7–9]. A kinetic model of misfit accommodation was developed recently by Dodson and Tsao [10]. A model based on energy minimization was proposed by Jesser and Van der Merwe [11]. However, it is to be noted that

agreement between the model calculations of critical thicknesses in various systems and the experimental published data is often rather poor, with discrepancies as high as an order of magnitude [11–13].

In the present paper a simplified model is proposed to determine the equilibrium critical thicknesses of semiconductor layers grown by heteroepitaxy. The misfit associated with the interface between the two different crystals is assumed to be accommodated by misfit strain (coherent case) or by both misfit strain and misfit dislocations (relaxed case). A valence force field (VFF) approximation, considered from the point of view of energy minimization criterion, is used for the calculations. In the foregoing it is assumed that the two crystals have the same thermal expansion coefficient.

<sup>\*</sup> Corresponding author.

## 2. Computational procedure

### 2.1. Relaxation procedure

A numerical procedure is used to relax both bond-length and bond-angle distortions [14] of each atom  $k$  in tetrahedrally coordinated structures by minimizing the Keating elastic energy expression [15]

$$V_k = \sum_{p=1}^4 \frac{3\alpha}{16r_0^2} (r_{kp}^2 - r_0^2)^2 + \sum_{p,q>p}^4 \frac{3\beta}{8r_0^2} \left( \mathbf{r}_{kp} \cdot \mathbf{r}_{kq} + \frac{1}{3}r_0^2 \right)^2, \quad (1)$$

valid for small displacements, where  $\alpha$  and  $\beta$  are bond-stretching and bond-bending force constants, respectively [16,17], and where  $r_0$  is the normal bond-length and  $\arccos(-1/3)$  the normal cubic angle. The sums in the expression are on the four nearest neighbours, specified by  $p$ , with a separation  $\mathbf{r}_{kp}$ .

Starting from the approximate equilibrium coordinates before relaxation, the program moves each atom in the entire volume to the equilibrium position defined as zero-force point under the Keating potential. The used potential leads to 22 force components: with 4 central ( $\alpha$ ), and 18 non-central ones ( $\beta$ ), and where 6 forces are related to the nearest neighbours and 12 to the second neighbours. The total strain energy is then calculated. The motion of each atom is repeated over many cycles (100 to 20000) until the total strain energy converges to a definite minimum.

### 2.2. Computational reference volume

Throughout the strain energy determinations we consider a very simple heterostructure model containing a bi-crystal with an interface perpendicular to the  $\langle 001 \rangle$  axis (Fig. 1). The misfit is defined as  $\eta = (b - a)/a$ , where  $a$  and  $b$  are the normal atomic spacings of the substrate and the epilayer, respectively. The computational reference volume consists of a parallelepiped with a square basis (of  $\eta^{-2}$  atoms at the interface) and variable height. Two-dimensional periodic bound-

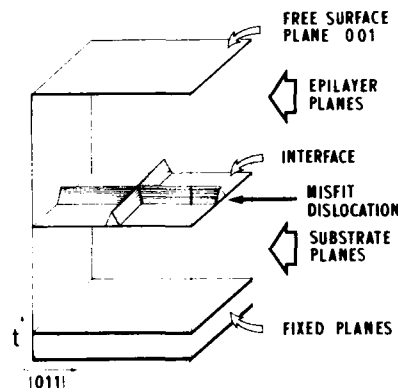


Fig. 1. Schematic drawing of computational reference volume. The cell consists of two regions: the region of epilayer planes with a free surface and the substrate region with fixed planes at the bottom. A crossing of misfit dislocations is located at the  $\langle 001 \rangle$  interface, and the basic surface is  $\eta^{-1} \times \eta^{-1}$  times  $b^2/2$ .

ary conditions, with regard to the forces acting on the atoms, are used in the  $\langle 110 \rangle$  directions.

A set of misfit dislocations of Lomer type are located at the  $\langle 001 \rangle$  interface along the  $\langle 110 \rangle$  and  $\langle \bar{1}10 \rangle$  axes. During the relaxation procedure, all the atoms are permitted to move except those of the bottom plane of the substrate, which are held fixed in their original lattice sites.

## 3. Principles for the calculation of critical thickness

The central idea is based on the comparison, at given misfit, between the elastic energy due to coherency stresses,  $E_{\text{coh}}$ , and the total energy of a completely relaxed structure,  $E_{\text{rel}}$ , as a function of the thickness, expressed in atomic layers. For the sake of simplicity, the calculations are made throughout the computational reference volume. The critical thickness  $t_c$  is then obtained when

$$E_{\text{coh}}(t_c) = E_{\text{rel}}(t_c). \quad (2)$$

As it will be shown later, at the critical thicknesses, a small part of the misfit-induced strain is used to build the dislocations. The major part of the elastic strain is redistributed between substrate and layer, as proposed by Junqua and

Grilhé [18], in a ratio depending on the elastic constants of the two materials. The main effect of this process is to reduce significantly the residual strain energy in the epilayer. In the foregoing it is assumed that the misfit is entirely accommodated by both misfit strain and a complete square array of interfacial misfit dislocations. That is to say that neither the exact mechanism by which misfit dislocations are nucleated nor the kinetics of strain relief are taken under consideration. Another assumption is that no intermixing of the elements occurs across the interface which is in other respects supposed to be geometrically flat and perfect.

### 3.1. Elastic energy calculation

Suppose that the stress in the epilayer, on a thick (essentially rigid) substrate, arises only from homogeneous isotropic elastic misfit strain. In this case the simplest approximation is to consider that the energy per atom is proportional to the square of the misfit,  $e = B\eta^2$ , through a parameter,  $B$ , which depends solely on the elastic constants of the deposited material.

The calculations are made using the Keating potential and the values of  $\alpha$  and  $\beta$  tabulated by Martin [17]. The results shown in Fig. 2 are obtained using arbitrary values. It can be seen

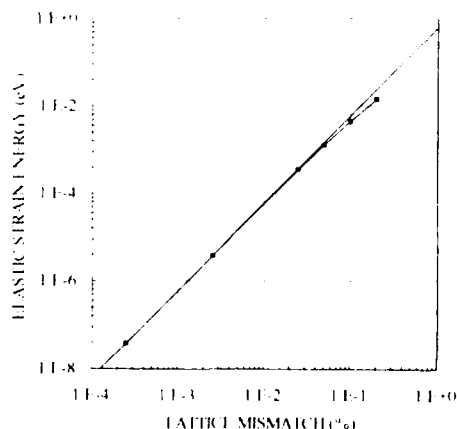


Fig. 2. Elastic strain energy versus lattice mismatch. Calculation is made using arbitrary  $\alpha$  and  $\beta$  elastic constants. The slope of the straight line is 2.

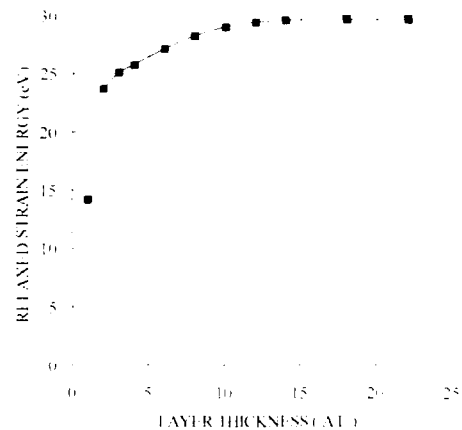


Fig. 3. Dependence of strain energy of totally relaxed structure on number of atomic layer plane for CdTe on (001) GaAs. Calculation is made using Keating's potential where elastic constants  $\alpha$  and  $\beta$  are of Martin [17].

that the computed values of the elastic strain energy as a function of  $\eta$  fall close to a straight line with slope 2. The deviation for increasing values of the misfit ( $\eta > 10\%$ ) indicates that the chosen harmonic potential is rather inaccurate in that case.

Thus the energy in the computational reference volume  $\eta^{-2}t$ , where  $t$  is the thickness, is

$$E_{\text{coh}}(\eta, t) = Bt. \quad (3)$$

It is to be noted (i) that the energy of a given area of  $\eta^{-2}$  (times  $b^2/2$ ) is *no more dependent on the misfit* and (ii) that the parameter  $B$  can be interpreted as the plane energy in a fictive coherent unit cell.

### 3.2. Energy of relaxed structure

Consider a completely relaxed layer and remember that the strain is then distributed between substrate and layer. The calculations are carried out, under the conditions previously listed (see Fig. 1), first for a two-plane layer, then for a three-plane layer, and so on. The dependence of  $E_{\text{rel}}$  on the number of planes,  $t$ , is illustrated in Fig. 3.

The fact that the energy of the outer plane is always found to be about half of the energy of the

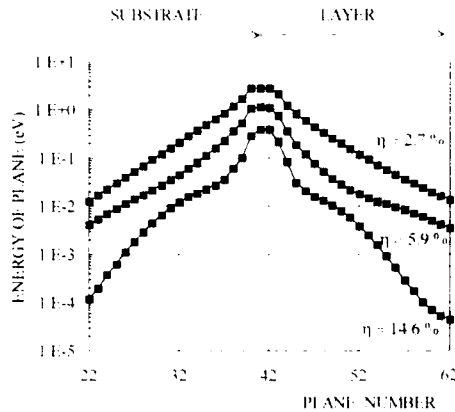


Fig. 4. Energy of atomic planes versus plane number, for three given values of misfit  $\eta = 2.7\%$ ,  $5.9\%$  and  $14.6\%$ . Calculation is made using the same arbitrary elastic constants for the substrate (from plane number 1 to plane 42) and the layer (number 43 up to 84). In the model, the theoretical "interface" is located at plane number 41.

underlying plane is not very surprising and can be understood as an effect due to the superficial dangling bonds. What is interesting to note is that the energy of each other plane *does not depend* on the total number of planes, used in the calculation, but only on its own height in the layer. Furthermore, it is seen that, beyond a given thickness, the total energy remains almost constant, indicating that the normal atomic spacing in the layer is then more or less recovered.

The share-out of the energy between substrate and layer depends on the elastic constants of the two materials. The choice of equal elastic values leads to an equipartition of the energy, symmetrical with respect to the interface, as shown in Fig. 4 for three given values of misfit. Now, as suggested by the above observations, the energy of a plane can be approximately given by the expression

$$e_p = A\eta^{-3/2}L_s(t), \quad (4)$$

with

$$L_s(t) = \frac{1}{\pi} \frac{\epsilon(\eta)}{\epsilon^2(\eta) + t^2}, \quad (5)$$

and where  $\epsilon$  is a constant versus  $t$ .

Integrating expression (4), the total energy can be written, for given misfit  $\eta$ , by

$$E_{\text{rel}}(t) = \int_x^t e_p(z) dz \\ = A\eta^{-3/2} \left[ \frac{1}{2} + \frac{1}{\pi} \arctan \frac{t}{\epsilon(\eta)} \right]. \quad (6)$$

Comparison of the computed values of  $E_{\text{rel}}$  from Keating's equation (1) with the results calculated from expression (6) shows a very reasonable agreement.

Note that even for low values of  $t$ , the plateau of the curve  $E_{\text{rel}}(t)$  may be rapidly attained if  $\epsilon$  is small enough, which is generally the case.

#### 4. Critical layer thickness

Now the critical thickness is obtained through the implicit equation

$$Bt_c = E_{\text{rel}}(t_c), \quad (7)$$

which can be easily solved graphically by intersecting, for the same given misfit, the straight line  $E_{\text{coh}}(t)$  with the curve  $E_{\text{rel}}(t)$ . It is clear that for thicknesses which are not too small (or for relatively small  $\eta$ ), the intersection of the two curves will be located in the plateau, where  $E_{\text{rel}}$  is roughly constant, so that the critical thickness is now simply

$$t_c = E_{\text{rel}}(\eta, \infty)/B. \quad (8)$$

Let us deal with the problem of the critical thickness-misfit dependence. Consider a given height  $t$ , corresponding to the flat part of the energy curve  $E_{\text{rel}}(t) \sim E_{\text{rel}}(\infty)$ , as shown in Fig. 3 (although the approximation will be reasonably valid for smaller  $t$ ). The variation with  $\eta$  can be expressed as

$$E_{\text{rel}}(\infty) = A\eta^{-3/2}, \quad (9)$$

which yields for the critical thickness

$$t_c = A\eta^{-3/2}/B. \quad (10)$$

Note that as  $A$  and  $B$  are basically dependent on the same deformation potential with regard to the elastic constants, one may speculate that their ratio  $A/B = A^*$  does not vary too much, at least

Table 1  
Calculated critical thicknesses in atomic layers (AL) for various heterostructures; the  $A^*$  values are obtained using  $\alpha$  and  $\beta$  elastic constants tabulated by Martin [17]

	Mismatch $\eta$ (%)	Constant $A^*$ (AL)	Critical thickness $t_c$ (AL)
CdTe/CdZnTe	1–2.7	0.14–0.15	130–33
GeSi/Si	1–4	0.12–0.15	120–19
GaAs/Si	4	0.14	18
GaSb/GaAs	~8	0.15	~7
ZnTe/GaAs	8	0.19	~9
CdTe/GaAs	14.3	0.3	5–6

as long as the model is valid. That leads us to suggest that the critical thickness varies more or less *only with lattice mismatch* for all zinc-blende semiconductor systems. This belief is strengthened by the values calculated via Eq.(10) for various heterostructures and is shown in Table 1. A good approximation seems to get the value  $A^* \sim 0.15$  in the majority of examples, except for CdTe/GaAs. Two arguments can be invoked to explain the relatively high value  $A^* = 0.30$  found in that case: (i) the misuse of the Keating potential which is less valid for large misfit and (ii) a too small critical thickness which requires, for

better accuracy, to be calculated using the implicit equation (7).

Another remark has to be made on the fact that the self-energy of the dislocations has been neglected in the evaluation of the total energy of relaxed layer  $E_{rel}$ . Suppose that  $e_d$  is the self-energy per unit length (expressed in interatomic spacing times  $\sqrt{2}/2$ ) of a misfit dislocation between an epilayer and a thick substrate. As the total dislocation length per unit cell is  $2\eta^{-1}$ , the approximate value of the energy per unit area will be

$$E_d = 2e_d\eta^{-1}. \quad (11)$$

On the one hand the evaluated values of  $e_d$  are fairly small and on the other hand the  $-1$  power law variation, for small enough misfit, is overcome by the  $-3/2$  power law variation found for  $E_{rel}(\infty)$  so that the including of  $E_d$  in the expression of the total energy will have no significant effect on critical thickness determination.

## 5. Comparison with experimental results

Experimental data on critical thicknesses in II–VI compounds are of Tatarenko et al. [19,20]. Measurements on samples grown by molecular

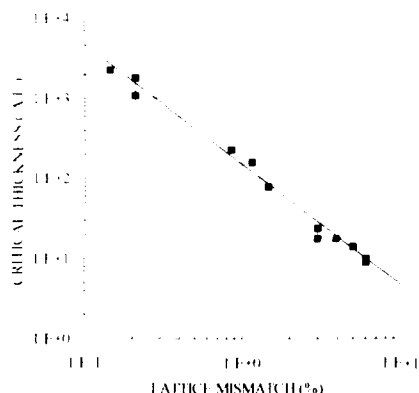


Fig. 5. Calculated critical layer thicknesses as a function of lattice mismatch for CdTe on (001) CdZnTe alloys, compared with experimental data of Tatarenko et al. [19,20]. Calculation is made using elastic constants  $\alpha$  and  $\beta$  tabulated by Martin [17].

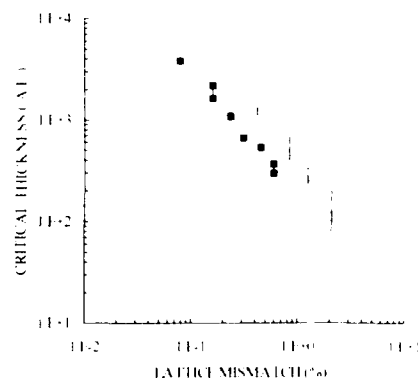


Fig. 6. A plot of critical layer thicknesses against lattice mismatch for SiGe alloys on (001)Si (■) data of Kasper et al. [21,22], (○) data of Kohama et al. [24,25], and (×) data of Bevk et al. [23]. The fit is obtained with  $A^* = 0.15$  for the first data set and  $A^* = 0.36$  for the others.

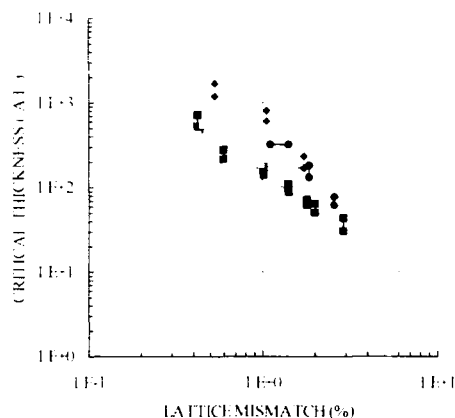


Fig. 7. Critical thicknesses versus misfit for III-V heteroepitaxial systems: ( $\diamond$ ) InGaAs/GaAs data of Laidig et al. [26], ( $\circ$ ) data of Gourley et al. [27], ( $\blacklozenge$ ) data of Orders and Usher [28] and ( $\blacksquare$ ) data of Weng [29]; ( $\bullet$ ) InGaAs/InP data of Takano et al. [30] and ( $\square$ ) GaSbAs/GaAs data of Hobson et al. [31]. The predicted straight lines are calculated using eq. (10) where  $A^* = 0.15$  (lower one), 0.35 (middle) and 0.50 (upper one).

beam epitaxy (MBE) of CdTe on (001) CdZnTe were made using either RHEED or photoluminescence on single quantum wells. As shown in Fig. 5, the agreement between experiment and prediction is surprisingly good considering the simplicity of the model.

Good agreement is again found for the SiGe/Si structures shown in Fig. 6, where we have plotted the data reported by Kasper et al. [21,22], Bevk et al. [23] and Kohama et al. [24,25]. Note that the data of Kohama et al. and Bevk et al. can be fitted to Eq. (10) if a value  $A^* = 0.36$  is taken. In Fig. 7, the experimental data for critical thickness in GaInAs/GaAs reported by Laidig et al. [26], Gourley et al. [27], Orders and Usher [28] and Weng [29], together with those in GaInAs/InP given by Takano et al. [30] and those in GaSbAs/GaAs reported by Hobson et al. [31], are plotted as a function of the misfit. Solid lines are predictions calculated using Eq. (10) where  $A^* = 0.15, 0.35$  and 0.50.

## 6. Discussion

The model describes well the variation of  $t_c$  with the misfit at least for the  $-3/2$  power law,

except for a part of the curve reported by Hobson et al. which presents a change in the slope in the high misfit region. However the fact that  $A^*$  values greater than 0.15 have to be used sometimes to fit the data is believed to result from two types of factors:

- Firstly, as suggested by Van de Leur et al. [32], those related to the experimental conditions of the layer deposition (i.e. growth technique, temperature and deposition rate) and their correlation with strain relief. Also the effect of relaxation kinetics in the determination of limiting thickness as emphasized by Fritz [13] and Freund [12]. Furthermore Dodson and Tsao [10] have reported that the misfit of an initially strained layer can be accommodated by both misfit dislocations and a thickness-dependent elastic strain retained in the overlayer, explaining by this way the results of People and Bean [33] on thermodynamically unstable SiGe films, as clearly demonstrated by Van de Leur et al. One other source of discrepancy may be found in the epitaxial growth mode, in particular for the island-type 3D growth, where the strain relaxation is often partial and occurs locally, so that the status of the coherent-relaxed transition is no more defined.

- Secondly, the experimental conditions of critical thickness measurement have to be taken into account, particularly when comparing direct or derived thicknesses obtained by numerous techniques of observation such as: reflection high energy electron diffraction [19,20,23], ion backscattering and X-ray diffraction [26,28,31], photoluminescence [20,27,29], electron beam induced current [24,25], optical interference contrast [29,31] and transmission electron microscopy [20,21]. In fact, some of these techniques provide apparent critical thicknesses generally thicker than the expected equilibrium values calculated using Eq. (10).

All the above considerations suggest that an empirical appropriate  $A^*$  value for fitting to theoretical prediction has to depend not only on the elastic constants (although in a rather complicated way), but also has to take into account actual growth conditions and measurement techniques. However, the fact remains that for obtaining a rough estimation of critical thicknesses it is



enough to choose a value  $A^* = 0.15$  in Eq. (10). However, if need be (for example in the case of variable misfit systems), a more precise determination may be obtained by using the  $\eta^{-3/2}$  variation law together with a specific value of  $A^*$  which can be obtained by means of just one experimental measurement at a given misfit

## 7. Conclusion

We have proposed an energy balance model for calculating critical layer thicknesses in heteroepitaxial growth of semiconductor compounds. The energies to be compared are the classical strain energy (without any change of the substrate nor misfit dislocation formation) and the deformation energy due to a full system of interfacial misfit dislocations. Both energies have been calculated by means of a computer simulation method based on Keating's valence force field approximation. The method yields a very simple  $\eta^{-3/2}$  law where critical thicknesses depend mainly on lattice mismatch  $\eta$ . This law may thus be considered as quite general and has been extended to various systems. The predicted values have been compared with published experimental data, revealing an excellent agreement as well for II–VI and IV–IV compounds as for III–V compounds.

## 8. Acknowledgement

This work has been partly supported by CNRS PIRMAT/DRED/DRET.

## 9. References

- [1] J.W. Matthews, in: *Dislocations in Solids*, Ed. F.R.N. Nabarro (North-Holland, Amsterdam, 1979).
- [2] B.A. Fox and W. Jesser, *J. Crystal Growth* 109 (1991) 252.
- [3] Y. Fukuda, Y. Kohama and Y. Ohmachi, *Jap. J. Appl. Phys.* 29 (1990) 1, 20.
- [4] P.M. Maree, J.C. Barbour and J.E. van der Veen, *J. Appl. Phys.* 62 (1987) 4413.
- [5] J.W. Matthews and A.E. Blakeslee, *J. Crystal Growth* 27 (1974) 118.
- [6] J.W. Matthews, *J. Vac. Sci. Technol.* 12 (1975) 126.
- [7] J.H. van der Merwe, *Surf. Sci.* 31 (1972) 198.
- [8] J.H. van der Merwe and C.A. Ball, in: *Epitaxial Growth*, Part B, Ed. J.W. Matthews (Academic Press, New York, 1975) ch. 6.
- [9] J.C. Bean, L.C. Feldman, A.T. Fiori, S. Takahara and I.K. Robinson, *J. Vac. Sci. Technol. A* 2 (1984) 436.
- [10] B.W. Dodson and J.Y. Tsao, *Appl. Phys. Lett.* 51 (1987) 1325.
- [11] W.A. Jesser and J.H. van der Merwe, in: *Dislocations in Solids*, Ed. F.R.N. Nabarro (North-Holland, Amsterdam, 1980) p. 421.
- [12] L.B. Freund, *J. Appl. Phys.* 68 (1990) 2073.
- [13] I.J. Fritz, *Appl. Phys. Lett.* 51 (1987) 1080.
- [14] P. Steinhardt, R. Alben and D. Weaire, *J. Non-Crystalline Solids* 15 (1974) 199.
- [15] P.N. Keating, *Phys. Rev.* 145 (1966) 637.
- [16] J.P. Musgrave and J.A. Pople, *Proc. Roy. Soc. (London)* A 268 (1962) 474.
- [17] R.M. Martin, *Phys. Rev. B* 1 (1970) 4005.
- [18] N. Junqua and J. Grilhé, *Phys. Status Solidi (b)* 169 (1992) 73.
- [19] S. Tatarenko, I. Cibert, G. Feuillet, K. Saminadayer, Le Si Dang and A. Nahmani, 1st Conf. on Epitaxial Growth, EPI-I, Budapest 1990.
- [20] I. Cibert, Y. Gobil, Le Si Dang, S. Tatarenko, G. Feuillet, P.H. Jouneau and K. Saminadayer, *Appl. Phys. Lett.* 56 (1990) 292.
- [21] E. Kasper, H.J. Herzog and H. Kibbel, *Appl. Phys. S.* (1975) 199.
- [22] E. Kasper and H.J. Herzog, *Thin Solid Films* 44 (1977) 357.
- [23] J. Bevk, J.P. Mannaerts, L.C. Feldman, B.A. Davisson and A. Ourmazd, *Appl. Phys. Lett.* 49 (1986) 286.
- [24] Y. Kohama, Y. Fukuda and M. Seki, *Appl. Phys. Lett.* 52 (1988) 380.
- [25] Y. Fukuda, Y. Kohama, M. Seki and Y. Ohmachi, *Jap. J. Appl. Phys.* 28 (1989) 119.
- [26] W.D. Laidig, C.K. Peng and Y. Lin, *J. Vac. Sci. Technol. B* 2 (1984) 181.
- [27] P.L. Gourley, I.J. Fritz and R.L. Dawson, *Appl. Phys. Lett.* 52 (1988) 377.
- [28] P.J. Orders and B.E. Usher, *Appl. Phys. Lett.* 50 (1987) 980.
- [29] S.L. Weng, *J. Appl. Phys.* 66 (1989) 2217.
- [30] M. Takano, Y. Sugiyama and Y. Takeuchi, *Appl. Phys. Lett.* 58 (1991) 2420.
- [31] G.L. Hobson, B. Khamsehpoor, K.E. Singer and W.S. Truscott, *J. Crystal Growth* 95 (1989) 220.
- [32] R.H.M. van de Leur, A.G.J. Schellingerhout, F. Tumstra and J.E. Mooy, *J. Appl. Phys.* 64 (1988) 3043.
- [33] R. People and J.C. Bean, *Appl. Phys. Lett.* 49 (1985) 322.



ELSEVIER

Journal of Crystal Growth 138 (1994) 75–80

JOURNAL OF  
**CRYSTAL  
GROWTH**

## Influence of growth non-stoichiometry on optical properties of doped and non-doped ZnSe grown by chemical vapour deposition

E. Krause <sup>a,\*</sup>, H. Hartmann <sup>a</sup>, J. Menninger <sup>b</sup>, A. Hoffmann <sup>c</sup>, Ch. Fricke <sup>c</sup>, R. Heitz <sup>c</sup>,  
B. Lummer <sup>c</sup>, V. Kutzer <sup>c</sup>, I. Broser <sup>c</sup>

<sup>a</sup> Institut für Kristallzüchtung, Berlin, Rudower Chaussee 6, D-12489 Berlin, Germany

<sup>b</sup> Paul-Drude-Institut für Festkörperphysik, Berlin, Hausvogteiplatz 5–7, D-10117 Berlin, Germany

<sup>c</sup> Institut für Festkörperphysik, Technische Universität Berlin, Hardenbergstrasse 36, D-10623 Berlin, Germany

### Abstract

Thick poly-ZnSe layers used for optical components in infrared laser systems show strongly varying laser damage thresholds. This is due to difference in kind and concentration of carrier trapping defects in the material grown under various Se/Zn partial pressure ratios. The VI/II ratio determines a non-stoichiometric growth and determine an upper limit for the concentration of native defects. The optical properties of poly-ZnSe are studied by means of time-integrated and time-resolved photoluminescence (PL) as well as spatially resolved cathodoluminescence (CL). It is shown that samples grown in Se excess are of good quality and have the lowest defect concentrations. The changing of properties of non-stoichiometric grown samples by doping with Li and In in a post-grown diffusion process was also studied.

### 1. Introduction

There is some evidence that the problems of carrier type and conductivity control in wide gap II–VI compounds are strongly related to native defects generated by non-stoichiometric composition during growth or additional thermal treatment, causing the phenomena of self-compensation [1–4].

ZnSe is the most promising II–VI material for the fabrication of pn-junction devices (blue laser diode) and has been intensively studied during recent years. It is also very important for optical

components in infrared laser applications. There is, however, a very strong difference in the desired optical and electrical properties between both applications. For the infrared devices the carrier concentrations (free carriers, in shallow traps, in deep levels) must be as low as possible, asking for extremely low impurity contents and stoichiometry control. Therefore, we grow polycrystalline ZnSe sheets by a special chemical vapour deposition method (CVD), and investigate the interrelation between growth conditions, defect generation, and optical properties. The deposition temperature and the Zn/Se ratio in the gas phase are the main parameters governing the formation of stoichiometry-related defects. In this work we report on investigations on ZnSe

\* Corresponding author.

platelets grown under different VI/II ratios at constant deposition temperature. We used low temperature photoluminescence (PL) and cathodoluminescence (CL) in connection with colour imaging to characterize our samples with respect to impurities and intrinsic defects.

## 2. Experimental procedure

ZnSe layers of comparable thickness (400–500  $\mu\text{m}$ ) were deposited on glassy carbon sheets in a CVD process using the reaction of the elemental vapours Zn and Se ( $\text{Se}_2$  mainly) in argon ambient. In this work we report mainly on a “stoichiometry row” deposited at the optimum growth temperature of 675°C (optimal with respect to measured laser induced damage threshold at 10.6  $\mu\text{m}$ ) and a Se/Zn ratio between 0.3 and 2.4, i.e., between 70% excess of Zn and up to 140% excess of Se over the stoichiometric quantities. Growth rates were found to be 30–50  $\mu\text{m}/\text{h}$ , depending on component concentration in the gas phase. The diffusion doping experiments were carried out in sealed quartz ampoules at 420°C for 48 h. Dopant source was stoichiometric ZnSe powder containing  $10^{-4}$  g/g ZnSe of Li or In metal, respectively.

For the PL spectra the ZnSe layers are excited above the band gap by the 364 nm line of an Ar-ion laser (spectra physics), for time-resolved measurements by a dye laser synchronously pumped by an actively mode-locked Nd:YAG laser (coherent) with a frequency-tripling BBO crystal. Luminescence transients are detected by a micro-channel-plate photomultiplier tube in conjunction with the time correlated single-photon-counting technique. The transients are fitted by convolution of the apparatus response with two exponential functions, one for the luminescence rise ( $\tau_r$ ) and one for the luminescence decay ( $\tau_d$ ). CL measurements and colour imaging were made using a scanning electron microscope (JEOL-U3) at carefully controlled excitation conditions of 25 keV and 30 nA at about 77 K. The excitation depth was estimated to be 2–3  $\mu\text{m}$ . Spectra were recorded with a mirror spectrometer and conventional lock-in technique. Details of

the optical arrangement were published by Menninger et al. [5]. In the case of In doping, phase-angle correlated (PAC)  $\gamma$ -ray spectroscopy was performed for testing the incorporation of In on Zn lattice sites.

## 3. Experimental results

### 3.1. Cathodoluminescence studies

Typical CL spectra show a series of deep-level transitions beside the known exciton lines. It is possible to distinguish between defects by studying the dependence of optical properties on the Se/Zn ratio. Fig. 1 shows the result of such an experiment for the “optimum” temperature 675°C and a VI/II ratio of 1.13. In addition to the exciton line, the donor–acceptor pair luminescence, the Y-band, the so-called Cu-green emission and the luminescence of the self-activated (SA) centre can be seen.

By colour imaging we are able to compare different wavelength images in regard to the localization of different deep level emissions (seen in Fig. 1). It is clearly seen that the Y-band is localized at large crystallographic defects like grain boundaries, twins, or dislocation networks. The Cu-green luminescence is observed in the same crystal areas as the Y-band. The distribution is homogeneous in the neighbourhood of the defects. The SA luminescence is typically observed in point defect clouds, whereas the excitonic luminescence is only seen in those crystal regions with low crystallographic defect concentration. That means that electron–hole pairs are trapped by deep defects suppressing the excitonic luminescence.

The doping experiments add some interesting results. Comparing the Li-doped to non-doped sample pieces treated in the same run, a noticeable change is observed for near stoichiometric material where the deep levels disappear. In the Se excess layers the Y-band is strongly diminished. It is concluded that Li is bound to extended lattice defects, in this way changing the self-trapped exciton centre (Y-band). No specific feature could be found in colour imaging. It is

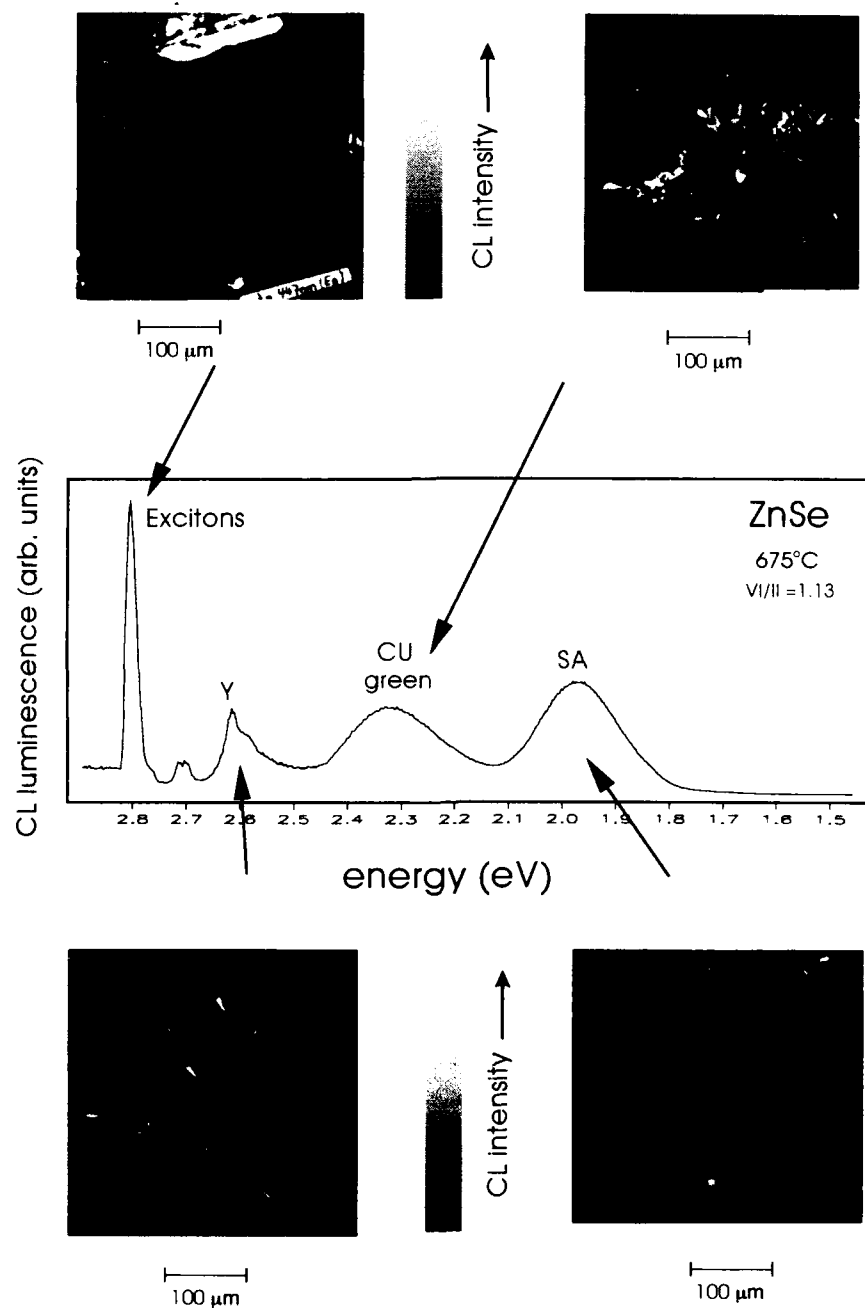


Fig. 1. 90 K cathodoluminescence spectrum of polycrystalline ZnSe grown with Se excess. Colour imaging of the exciton, the Y-band, the Cu-green and the SA luminescence, representing an area of approximately  $300\ \mu\text{m} \times 300\ \mu\text{m}$  with a spatial resolution of about  $1\ \mu\text{m}$ .

consistent with the results to assume Li incorporation on interstitial sites.

In the case of In-doping only Se excess layers show remarkable changes, increasing with Se excess. This can be interpreted in terms of defect chemistry very simply with the need of Zn vacancies for In substitution on Zn lattice sites and the also likely formation of these under Se excess. High donor and acceptor concentrations and an increasing amount of deep levels (yellow-green, SA) are measured. Our results correspond with those of Shirakawa and Kukimoto [6]. The puzzling result comes from PAC measurements where 7% of In at maximum are found on lattice sites. That means that at a diffusion temperature of 420°C, practically no In atoms substitute Zn lattice atoms. Therefore, the mechanism of In impact on optical properties should be considered to involve other possibilities as interstitial positions of In or complex formation. Also no specific In-related defect could be found in the spectra and in colour images.

### 3.2. Photoluminescence studies

Further information on the defect concentration and the quality of the ZnSe crystals was obtained using time-integrated and time-resolved PL investigations at helium temperatures. Typical PL spectra of ZnSe with varied Se/Zn ratios at one fixed growth temperature are seen in Fig. 2. In the excitonic region (right-hand side of Fig. 2), the luminescence of the free exciton (FE), the donor bound exciton ( $I_2$ ), the acceptor bound exciton ( $I_1$ ), and of an exciton bound to a deep acceptor is observed ( $I_{1c}$ ). With increasing Se/Zn mol ratio the line is boosted, demonstrating that this deeply bound exciton line is correlated with Zn vacancies. Decreasing the Se/Zn ratio, the intensity of the shallow bound exciton lines  $I_1$  and  $I_2$  is enhanced in comparison to  $I_{1c}$ .

The halfwidths of the bound and free exciton lines are comparable to those in single-crystalline ZnSe. This shows that the extension of the single crystalline regions is relatively large, i.e., for the exciton grain boundaries can be neglected. The appearance of the Y-band and the self-activated band at 2.0 eV (left-hand side of Fig. 3) is con-

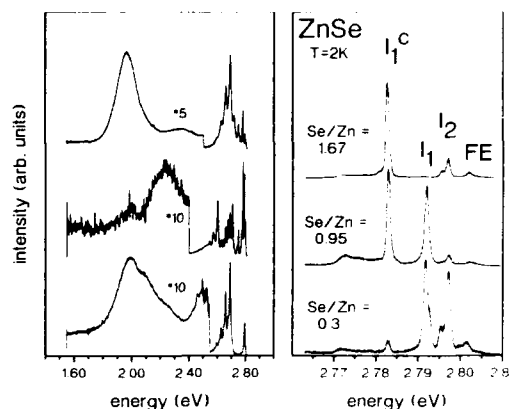


Fig. 2. Typical luminescence spectra of poly-ZnSe at 1.6 K varying the Se/Zn mol ratio.

needed with the growth condition under Se excess, indicating an association with Zn vacancies, whereas the donor–acceptor pair luminescence and the emission bands at 1.95 eV as well as at 1.85 eV are enhanced in crystals grown under Zn excess.

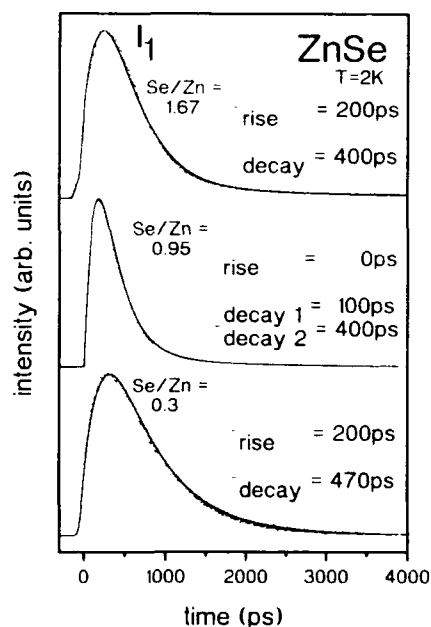


Fig. 3. Transients of the  $I_1$  bound exciton emission varying the Se/Zn mol ratio.

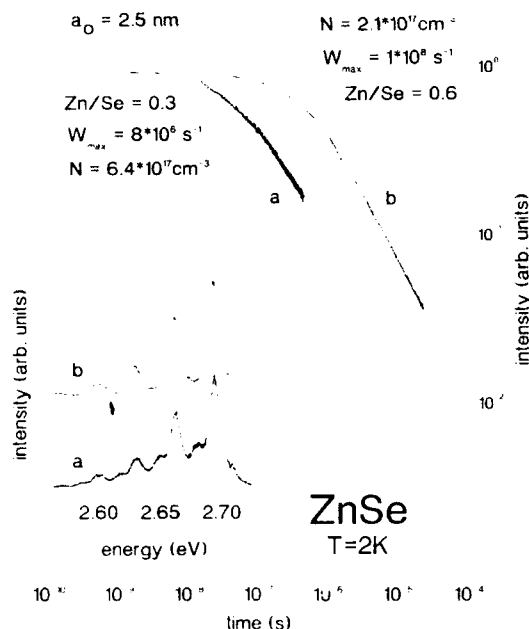


Fig. 4. Transients of the donor-acceptor pair luminescence varying the Se/Zn mol ratio. In the inset the corresponding DAP luminescence spectra are given.

Time-resolved PL measurements (Fig. 3) of samples grown with a large Se or Zn excess demonstrate that the lifetimes of the different exciton lines are relatively long and comparable with those in MBE ZnSe epilayers [8] or single crystals of good quality [9]. Obviously there is only relatively little non-radiative decay of electron-hole pairs via deep centres. We found the free exciton life times to range between 100 and 200 ps, whereas the life time of the acceptor bound exciton  $I_1$  amounts to 400 ps in samples grown with Se excess. This demonstrates that the defect concentration in these samples is small. In crystals grown with a Se/Zn mol ratio near 1, the exciton lifetimes are drastically reduced, revealing competitive non-radiative processes introduced by a degraded crystal quality.

The inset of Fig. 4 depicts the donor-acceptor pair (DAP) luminescence band at 2 K of the same

samples grown under varying Se/Zn ratio. This ratio critically determines the concentration of deep native defects generated during growth at 675°C. Using a model proposed by Thomas et al. [10], we evaluate from DAP luminescence transients the shallow donor concentration  $N_D$  of samples grown in Se excess (seen in Fig. 4), and  $W_{\text{max}}$ , a factor proportional to the recombination probability in that model. A detailed description of the fitting procedure is given elsewhere [11]. The DAP luminescence grown with a Se/Zn mol ratio of 0.3 decays considerably faster than that of the sample with a Se/Zn mol ratio of 0.6, suggesting a much higher native defect concentration. This is obvious from the large increase of  $W_{\text{max}}$ . However, there is no corresponding significant change in the impurity concentration, as determined from the DAP transients. So we find an increased defect generation with larger deviation from stoichiometric growth conditions.

#### 4. Conclusion

The analysis of time-integrated and time-resolved PL as well as CL investigations yields a fast and reliable access to investigation of the influence of impurity concentrations and compensation effects on the optical properties in semiconductors. In this paper a strong influence of the stoichiometry on defect generation in poly-ZnSe is established. Assuming a constant, low impurity level, we conclude that the effects found are related to native defects in the Zn or Se sublattice. Material grown under Se excess has the lowest defect concentrations as compared to samples grown with Zn excess and with a near stoichiometric Se/Zn ratio. With respect to the doping experiments, it is noteworthy that no specific dopant-related defect emission was found, but large differences in the kind and the concentrations of defects generated in dependence on non-stoichiometric growth. Therefore, it seems possible that complexes of intrinsic defects are only modified by introducing impurities. The role of large crystallographic defects (twins, dislocations) as source or drain of optically active point defects should be studied more intensively.

## 5. References

- [1] G.F. Neumark, *J. Appl. Phys.* 51 (1980) 3383.
- [2] W. Ray and F.A. Kröger, *J. Electrochem. Soc.* 125 (1978) 1348.
- [3] R.W. Jansen and O.F. Sankey, *Solid State Commun.* 64 (1987) 197.
- [4] M. Karai, K. Kido, H. Naito, K. Kurosawa, M. Okuda, T. Fujino and M. Kitagawa, *Phys. Status Solidi (a)* 117 (1990) 15.
- [5] H. Menninger, H. Zscheile and H. Raidt, *Exptl. Tech. Physik* 23 (1975) 91.
- [6] Y. Shirakawa and H. Kukimoto, *J. Appl. Phys.* 51 (1980) 2014.
- [7] P.J. Dean and J.L. Merz, *Phys. Rev.* 178 (1969) 1310.
- [8] G. Kudlek, C.H. Fricke, N. Presser, R. Heitz, A. Hoffmann, J. Gutowski and I. Broser, in: *Proc. 21st Int. Conf. on Physics of Semiconductors*, Beijing, 1992 (World Scientific, Singapore, 1992) p. 1168.
- [9] R. Heitz, C.H. Fricke, A. Hoffmann and I. Broser, *Mater. Sci. Forum* 83–87 (1992) 1241.
- [10] G. Thomas, J.J. Hopfield and W.M. Augustyniak, *Phys. Rev.* 140 (1965) A202.
- [11] Ch. Fricke, R. Heitz, B. Lummer, V. Kutzer, A. Hoffmann, I. Broser, W. Taudt and M. Heuken, *J. Crystal Growth* 138 (1994) 815.

## Structural properties of perfect ZnTe epilayers on (001) GaAs substrates

M. Lang <sup>a</sup>, D. Schikora <sup>b</sup>, T. Widmer <sup>b</sup>, C. Giftge <sup>b</sup>, A. Forstner <sup>c</sup>, V. Holy <sup>d</sup>,  
J. Humenberger <sup>a</sup>, K. Lischka <sup>\*a</sup>, G. Brunthaler <sup>c</sup>, H. Sitter <sup>a</sup>, M. von Ortenberg <sup>b</sup>

<sup>a</sup> Forschungsinstitut für Optoelektronik, Universität Linz, A-4040 Linz, Austria

<sup>b</sup> Institut für Halbleiterphysik, TU Braunschweig, D-38106 Braunschweig, Germany

<sup>c</sup> Institut für Halbleiterphysik, Universität Linz, A-4040 Linz, Austria

<sup>d</sup> Department of Solid State Physics, Masaryk University, 602 00 Brno, Czech Republic

### Abstract

We report on molecular beam epitaxy and hot-wall beam epitaxy growth of ZnTe epilayers on (001) GaAs substrates. The surface reconstruction of (001) ZnTe is measured by reflection high-energy electron diffraction (RHEED). The RHEED pattern as a function of the beam equivalent pressure ratio  $p_{\text{Te}}/p_{\text{Zn}}$  and substrate temperature is studied. Mosaic structures of the ZnTe epilayers grown under optimized conditions are investigated quantitatively by high resolution X-ray diffraction and photoluminescence. These data, which are related to the three-dimensional perfection of epilayers, are contrasted to RHEED measurements of the surface morphology.

### 1. Introduction

The interest in epitaxial growth of ZnTe has recently been stimulated by the fact that graded bandgap Zn(Se,Te) ohmic contact can improve the characteristic of p-type contacts for blue-green and blue emitting ZnSe based lasers [1]. High-quality ZnTe epilayers may also be used as substrate material for the growth of HgSe/(Hg,Fe)Se semimagnetic semiconductor heterostructures and superlattices. These structures are expected to have interesting physical properties [2].

The epitaxial growth of ZnTe layers by molecular beam epitaxy (MBE) has been reported first

in the middle of the seventies [3]. Later, ZnTe has been grown also by metalorganic chemical vapor deposition (MOCVD) [4–6], atomic layer epitaxy (ALE) [7] and hot-wall epitaxy (HWE) [8,9] on GaAs. The main problem of heteroepitaxial growth of ZnTe on GaAs results from different lattice constants of ZnTe ( $a_{\text{ZnTe}} = 6.104$  Å) and GaAs ( $a_{\text{GaAs}} = 5.654$  Å). The mismatch of 7.6% influences the nucleation behavior in the initial growth stage [10] by formation of dislocations.

In this paper, we report on the growth of ZnTe/GaAs epilayers with optimal structural properties, the quantitative measurements of the mosaic structure in these layers by high resolution X-ray diffraction (HRXD) and photoluminescence and the investigation of the surface morphology by RHEED.

\* Corresponding author.



## 2. Experimental setup

Growth of our ZnTe epilayers was performed in an MBE and a hot-wall beam epitaxy (HWBE) system both designed and constructed at Linz University. Each system consists of a load-locked substrate preparation chamber coupled to the main growth chamber. The principle of HWBE has been described elsewhere [11]. All epilayers were grown on epi-ready (001) GaAs substrates which were  $2^\circ$  misoriented towards the next [110] direction. The epi-ready GaAs were preheated prior to growth in order to remove the oxid layer. The temperature of the substrate holder in both systems was calibrated allowing one to compare the results of both growth methods. The MBE growth was carried out using elemental Zn and Te evaporation sources with 6N and 7N purity purchased from Nippon Mining. The ZnTe source material for HWBE was prepared by closed zone melting from Zn with 6N purity and Te with 7N purity. This granular compound consisted of large stoichiometric monocrystalline grains. The MBE growth chamber was equipped with a 35 kV RHEED system. Intensity profiles and the full width at half maximum (FWHM) of the RHEED reflections were obtained from digitized high resolution photographic pictures taken from the RHEED screen during growth. The epilayers were characterized by high-resolution X-ray diffraction. Rocking curves of the (002) and (004) Bragg reflection were measured using a 5-crystal diffractometer. The X-ray wavelength was 1.5406 Å. 4.2 K photoluminescence (PL) spectra were measured using a standard set-up and argon ion laser excitation at 458 nm.

## 3. Results and discussion

In a series of RHEED experiments, the relation between the substrate temperature, the beam equivalent pressure (BEP) ratio  $p_{\text{Te}}/p_{\text{Zn}}$  and the surface reconstruction has been investigated. Fig. 1 shows the results of these experiments. The surface reconstruction diagram can be divided into 5 regions. Regular two-dimensional (2D) growth is obtained in regions I, II and III. In

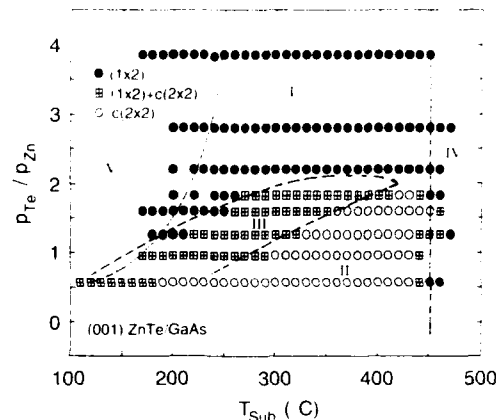


Fig. 1. The surface reconstruction of MBE-grown (001) ZnTe/GaAs epilayers as a function of growth temperature and the equivalent beam pressure ratio  $p_{\text{Te}}/p_{\text{Zn}}$ . The RHEED pattern in region I shows a  $(1 \times 2)$  reconstruction and in region II a  $c(2 \times 2)$  reconstruction is observed. A mixture of both reconstructions can be observed in region III indicating a stoichiometric surface. Region IV is the condensation boundary and in region V three-dimensional growth occurs.

these regions, two different reconstructions of the (001) ZnTe surface are observed. A streaky  $(1 \times 2)$  half-order reconstruction along the  $[110]$  azimuth is observed in region I. In this region, the BEP of the Te beam is high and we believe that this region represents a Te-rich surface composition. In region II which, on the other hand, is assumed to represent a Zn-rich surface, a streaky two-fold  $c(2 \times 2)$  reconstruction along the  $[100]$  azimuth is observed by RHEED. Both types of reconstruction,  $c(2 \times 2)$  and  $(1 \times 2)$ , are observed simultaneously in region III. Our established surface phase diagram for (001) ZnTe is similar to that of (001) ZnSe [12], where two regions of  $c(2 \times 2)$  and  $(1 \times 2)$  surface reconstructions have been clearly identified. However, an extended region of coexistence of both surface reconstructions was not observed. The existence of only two different reconstructions on the (001) ZnTe surface agrees with measurements and tight-binding calculations of the total energy of the (001) ZnSe surface [13].

It has been shown that the coexistence of both reconstructions indicates a nearly stoichiometric surface condition [14], yielding optimum condi-

tions for the growth of high quality ZnTe epilayers. This has been proofed by measuring the width of the X-ray rocking curves of epilayers which were all grown at the same BEP ratio but with different substrate temperatures. The minimum of the rocking curve full width at half maximum (FWHM) was observed for those samples which are found clearly within region III in the surface phase diagram.

For substrate temperatures above 450°C, the growth rate decreases rapidly because of enhanced re-evaporation of adatoms (region IV). At substrate temperatures below about 200°C (region V), a transition to a three-dimensional (3D) growth mode and facetting due to the reduced mobility of the surface atoms is observed.

The growth optimization in the HWBE has been carried out by measuring the half-width of X-ray rocking curves as a function of the substrate temperature. The layer thickness was held in the range of 3.2–4.5  $\mu\text{m}$  for these experiments. Because of the use of a binary compound source, the vapor composition is rather stable with a Zn-to-Te ratio of about 1. This vapor ratio provides a Te-rich surface at lower substrate temperatures at 300–330°C and a Zn-rich surface at higher substrate temperatures at 400°C, as it has been measured. It is not possible to determine a surface reconstruction diagram for HWBE growth optimization because of the constant flux ratio which is supplied by the ZnTe source.

The best values of the half-width of the X-ray rocking curves were  $\text{FWHM} \leq 150$  arc sec for 3  $\mu\text{m}$  layer thickness. This high crystalline quality of the ZnTe films was achieved for a substrate temperature of 370°C.

After we had obtained the optimal conditions for MBE and HWBE growth, a set of epilayers with a thickness between 0.2 and 6  $\mu\text{m}$  were grown. For MBE, a BEP ratio of about 1.5 was used and the substrate temperature was 330°C; for HWBE, it was 370°C. The FWHM of the (002) reflection rocking curves of these epilayers was about 1500 arc sec for the thinnest layers and it decreased to 140 arc sec for the 5.6  $\mu\text{m}$  thick HWBE-grown layer. We find for equally thick epilayers that the FWHM of HWBE films is about 30% smaller than that of the MBE-grown

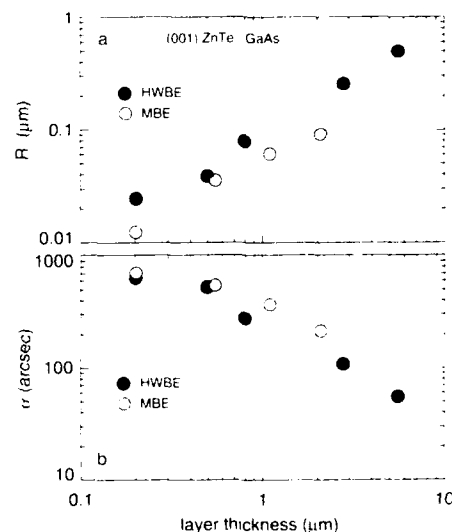


Fig. 2. The radius of mosaic blocks  $R$  (a) and their average misorientation  $\alpha$  (b) from MBE- and HWBE-grown (001) ZnTe/GaAs epilayers versus thickness of the epilayers.

epilayers, indicating that the density of extended defects in HWBE-grown epilayers is smaller than in MBE-grown ones. If we compare our HRND results with published data [4,9,15], we find that for a given layer thickness our HWBE-grown films have excellent structural properties. To our knowledge the FWHM value of 140 arc sec for a 5.6  $\mu\text{m}$  thick ZnTe epilayer is among the best values reported so far.

Recently we have shown that the size and average misorientation of mosaic blocks in epilayers can be obtained from an analysis of the form of the rocking curves [16]. This theoretical model of X-ray scattering in non-perfect crystals, which is described in detail in ref. [16], has been used to calculate the radius and the misorientation of mosaic blocks in our epilayers. Results are shown in Fig. 2. The mosaic block size is approximately linearly increasing with the layer thickness. The penetration depth of the X-ray beams is about 2  $\mu\text{m}$  for the (002) Bragg reflection. Therefore the obtained mosaic block parameters are an average over this depth range. This is important especially for thin layers where the mosaic size is strongly varying with thickness.

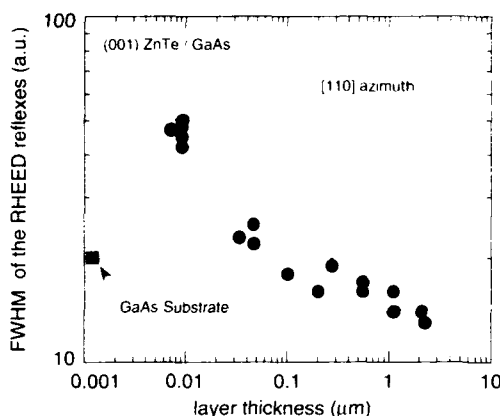


Fig. 3. The FWHM of the (01) RHEED reflection measured in the [110] azimuth from MBE-grown (001) ZnTe epilayers versus layer thickness and from the GaAs substrate as measured before growth was started.

The block size in HWBE epilayers is about twice that in MBE-grown epilayers. Since this relation holds for the whole range of layer thicknesses, we suppose that the mosaic size is influenced by the nucleation rate during the growth of the first atomic layers (initial growth). In the quasi-closed space HWBE system, a quasi-thermodynamic equilibrium between source and substrate is established. We assume that the formation of islands with minimum orientation disorder is more likely in HWBE than in MBE, due to the more intensive exchange between the solid and the gas phase during the nucleation process.

It has been shown by computer simulation [17] that the intensity profile (e.g. the FWHM) of RHEED reflections is sensitive to the surface morphology. Fig. 3 shows the FWHM of the (01) RHEED reflex measured parallel to the shadow edge and recorded during the growth of our MBE samples. Also shown in Fig. 3 is the FWHM of the RHEED reflection from the GaAs surface as measured immediately before growth was started. The FWHM of the RHEED reflection from the layer is decreasing with layer thickness from a value which is significantly larger than that from the GaAs surface to values which are smaller than the substrate value when the layer thickness exceeds about 0.2  $\mu\text{m}$ . These data

demonstrate that the surface morphology of ZnTe epilayers (thickness  $> 0.2 \mu\text{m}$ ) is superior to that of the GaAs before growth.

The 4.2 K PL emission from a 5.6  $\mu\text{m}$  thick HWBE-grown ZnTe epilayer is plotted in Fig. 4. The spectrum is dominated by bound exciton emission lines ( $A^0X$ ). The weaker emission lines are due to donor bound exciton ( $D^0X$ ) and free exciton (FE) recombination. We find that the near-band-edge emission in thin layers is significantly reduced. In order to compare PL data from epilayers with different thickness we have related the intensity of the 2.369 eV bound exciton line,  $I_{\text{exciton}}$ , to the total PL emission between 1.8 and 2.4 eV,  $I_{\text{total}}$ . The value of  $I_{\text{exciton}}/I_{\text{total}}$  is plotted versus mosaic radius in the inset of Fig. 4. Only for those epilayers where the mosaic radius is significantly larger than the radius of bound excitons, which is about 50 Å in ZnTe, is a pronounced near-band-edge emission observed. In those layers where the mosaic block size and the exciton radius are of comparable size, the radiative recombination of excitons is suppressed due to enhanced non-radiative recombination at the grain boundaries.

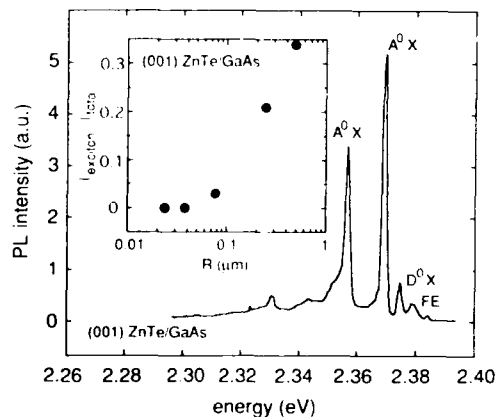


Fig. 4. The 4.2 K near-band-edge PL emission from a 5.6  $\mu\text{m}$  thick (001) ZnTe layer grown by HWBE on (001) GaAs. The lines are due to acceptor ( $A^0X$ ) and donor ( $D^0X$ ) bound excitons, as well as to free exciton (FE) recombination. The insert shows the normalized excitonic PL intensity versus mosaic block radius of the ZnTe layer.  $I_{\text{exciton}}$  is the intensity of the 2.368 eV ( $A^0X$ ) line and  $I_{\text{total}}$  is the integrated intensity between 1.8 and 2.4 eV.

#### 4. Summary and conclusions

We have established a surface reconstruction diagram of ZnTe which has been used to optimize the growth conditions of (001) ZnTe epilayers on (001) GaAs substrates. The structural properties of MBE- and HWBE-grown epilayers were investigated by HRXD yielding the size and misalignment of mosaic blocks. The block size is linearly increasing with the layer thickness. The FWHMs of the HRXD rocking curves of our HWBE epilayers indicate their superior quality. The FWHM of the (01) RHEED reflection, which is directly related to the surface morphology, is decreasing with layer thickness. It has a smaller value than that from the GaAs surface when the ZnTe layer thickness exceeds about  $0.2\ \mu\text{m}$ , revealing the good surface morphology of the epilayers. The PL spectra of thick ZnTe layers which have a mosaic block size significantly larger than the excitonic radius are dominated by bound exciton emission.

#### 5. Acknowledgments

This work is partially supported by the "Fonds zur Förderung der wissenschaftlichen Forschung" P8358-PHY and P8833-PHY, and the "Jubiläumsfonds der Österreichischen Nationalbank", No. 4442.

#### 6. References

- [1] Y. Fan, J. Han, L. He, J. Saraie, R.L. Gunshor, M. Hagerott, H. Jeon, A.V. Nurmikko, G.C. Hua and N. Otsuka, *Appl. Phys. Lett.* 61 (1992) 3160.
- [2] M. von Ortenberg, *Adv. Solid State Phys.* 31 (1991) 261.
- [3] D.L. Smith and V.Y. Pickhardt, *J. Appl. Phys.* 41 (1975) 2366.
- [4] H. Shtrikman, A. Raizman, M. Oron and D. Eger, *J. Crystal Growth* 88 (1988) 522.
- [5] H. Ogawa, M. Nishio, M. Ikejiri and H. Tuboi, *Appl. Phys. Lett.* 58 (1991) 2384.
- [6] H.P. Wagner, W. Kuhn and W. Gebhardt, *J. Crystal Growth* 101 (1990) 199.
- [7] T. Yao and T. Takeda, *Appl. Phys. Lett.* 48 (1986) 160.
- [8] A. Lopez-Otero, *Thin Solid Films* 49 (1978) 3.
- [9] E. Abramof, K. Hingerl, A. Pesek and H. Sitter, *Semicond. Sci. Technol.* 6 (1991) A80.
- [10] S. Tatarenko, J. Cibert, K. Saminadayar, P.H. Jouneau, V.H. Etgens, M. Sauvage-Simkin and R. Pinchaux, *J. Crystal Growth* 127 (1993) 339.
- [11] J. Humenberger, H. Sitter, K. Lischka, A. Pesek and H. Pascher, in: *Proc. 20th Int. Conf. on Physics of Semiconductors*, Thessaloniki, 1990 (World Scientific, Singapore, 1990) p. 312.
- [12] K. Menda, I. Takayasu, T. Minato and M. Kawashima, *Jap. J. Appl. Phys.* 26 (1987) L1376.
- [13] D. Schikora, A. Josiek, R. Enderlein, in: *Proc. European MBE Workshop*, Tampere, 1991, p. 83.
- [14] S.M. Newstead, R.A.A. Kubiak and E.H.C. Parker, *J. Crystal Growth* 81 (1987) 49.
- [15] J.T. Mullins, P.A. Clifton, P.D. Brown, A.W. Brinkman and J. Woods, *J. Crystal Growth* 101 (1990) 100.
- [16] V. Holy, J. Kubena, E. Abramof, K. Lischka, A. Pesek and E. Köppensteiner, *J. Appl. Phys.*, to be published.
- [17] C. Gifftge and D. Schikora, to be published.



ELSEVIER

Journal of Crystal Growth 138 (1994) 86–93

JOURNAL OF  
**CRYSTAL  
GROWTH**

## Growth and characterization of electrodeposited films of cadmium telluride on silicon

J.M. Fisher <sup>a</sup>, L.E.A. Berlouis <sup>\*a</sup>, L.J.M. Sawers <sup>a</sup>, S.M. MacDonald <sup>a</sup>,  
S. Affrossman <sup>a</sup>, D.J. Diskett <sup>b</sup>, M.G. Astles <sup>c</sup>

<sup>a</sup> Department of Pure and Applied Chemistry, University of Strathclyde, Glasgow G1 1XL, UK

<sup>b</sup> Applied Physics and Electro-Optics Group, Royal Military College of Science, Shrivenham, Swindon SN6 8LA, UK

<sup>c</sup> Defence Research Agency, St. Andrews Road, Great Malvern, Worcestershire WR14 3PS, UK

### Abstract

This work describes the growth and characterization of electrodeposited films of the II–VI semiconductor CdTe directly on to p- and n-type silicon. In-situ ellipsometry has revealed the presence of a spontaneously deposited Te layer on illuminated p-type Si and on n-type Si. The growth of the spontaneous layer has been verified by the other techniques used to characterize the electrodeposited films, such as differential scanning calorimetry, X-ray photoelectron spectroscopy, energy dispersive analysis by X-rays, Rutherford backscattering and X-ray diffraction. The subsequent growth of the CdTe layer on top of this is close to stoichiometric composition but the film does not appear to form a coherent layer.

### 1. Introduction

CdTe is of current interest in the field of infrared detector technology as it provides a near ideal substrate for the epitaxial growth of Cd<sub>1</sub>Hg<sub>1</sub>Te (CMT). The direct growth of CdTe on silicon therefore forms a key component in the development of monolithic detectors based on CMT for infrared focal plane array applications [1–3]. Another important area for the CdTe/Si heterojunction is in X-ray imaging sensors [4–6] as well as in solar energy applications [4]. The CdTe/Si heteroepitaxial growth has been achieved by molecular beam epitaxy (MBE) [7–9],

metalorganic vapour phase epitaxy (MOVPE) [10–12] and also by closed hot wall epitaxy (CHWE) [13]. Although a large lattice mismatch (19%) ostensibly exists between the CdTe and Si, the epitaxial relationship is CdTe{111} on Si{100} which results in a lattice mismatch of only 3.4% along the CdTe[211] direction [9]. The electrodeposition method for CdTe was first established by Panicker and co-workers [14] in 1978 and offered an alternative low-cost pathway, in comparison to the above growth methods, for the attainment of good quality CdTe layers on a variety of conductive substrates. Since that time, the electrochemical route has been the subject of considerable study, in particular for the development of solar cells based on the CdTe/CdS heterojunction [15–26]. Although various electrochemical mechanisms have been proposed [14,15,17,23,25] for

<sup>\*</sup> Corresponding author.

the deposition of CdTe as the alloy rather than metallic Cd and Te, the essential step has been the shift in the Cd deposition potential towards that of tellurium, assisted partly by the free energy of formation of the alloy and also by the ca. 2550:1 concentration ratio in the solution of cadmium to tellurium [14]. The substrates employed for deposition have ranged from In or Sb doped tin oxide coated glass [14,18,20] to titanium [16,19,27] and CMT [27]. The temperature range for the deposition is usually 70 to 90°C, with increase in crystallinity reported for the higher temperature deposits and also after annealing of the electrodeposited films [14,19]. Circulation of the electrolyte in the deposition cell is also carried out to increase the mass transport of the limiting reactant, viz.  $\text{HTeO}_3^-$  to the substrate so that more uniform growth can be achieved.

## 2. Experimental procedure

The electrodepositions were carried out on {100} p-type Si (B-doped) and {111} n-type (Sb-doped), obtained from Wacker-Chemitronic GMBH. The cell employed for electrodeposition was the in-situ ellipsometry cell described in a previous work on CdTe electrodeposition on CMT [27]. The Si wafers (10 cm diameter) were first cleaved into samples of around 1 cm<sup>2</sup>. The back of the sample was then either etched in 2M  $\text{NH}_4\text{F}$  (pH 4.5) for 15 min in the way described by Kautek and co-workers [28] or alternatively, it was roughened with 1200 grade emery paper before electrical contact was established between the Si sample and the cell baseplate, using gallium–indium eutectic. The sample was then sealed in place using silicone rubber sealant and the surface cleaned with 1,1,1 trichloroethylene prior to etching with either 10% HF or the  $\text{NH}_4\text{F}$  solution described above. Etching using the 10% HF solution was carried out under a nitrogen blanket so that the surface of the silicon was not exposed to oxygen before deoxygenated deposition solution was added to the cell. This consisted of an aqueous solution of 0.5M  $\text{CdSO}_4$  and 25 ppm Te (as  $\text{HTeO}_3^-$ ) at pH 1.8. The electrodeposition temperature was in the range of 55 to 70°C,

although the temperature control for each deposition run was to within  $\pm 1^\circ\text{C}$ . The solution in the cell was maintained at the growth temperature by constant circulation from a thermostatted reservoir. The solution was circulated from the reservoir and the cell by a peristaltic pump. The lower temperature limits employed here were necessary due to the distortion at higher temperatures of the in-situ cell which was constructed from perspex. Quartz windows were fixed to the cell such that the laser struck the window surfaces at normal incidence and penetrated through forming an angle of incidence of  $70^\circ$  with the substrate. A platinum flag or a graphite rod was employed as the secondary electrode. The reference electrode used was the saturated (KCl) calomel electrode (SCE) which has a potential of 0.242 V versus NHE (the normal hydrogen electrode). All potentials were measured and are reported in this paper with respect to this reference electrode. In-situ ellipsometry was performed throughout the electrodeposition, using a Gaertner L116B Auto Gain Ellipsometer with a He–Ne laser ( $\lambda = 632.8 \text{ nm}$  / 1 mW). The electrodeposited films were then further characterised in their “as-grown” state or after annealing in air at 400°C for 10 min. Several techniques were employed for ex-situ analysis of the electrodeposited films. Of particular importance were X-ray diffraction (XRD) and X-ray photoelectron spectroscopy (XPS). The XPS data here were obtained with a VSW 100 mm hemispherical analyser and X-ray source with an aluminium anode.

## 3. Results and discussions

The electrodeposition of CdTe on both n- and p-type Si was carried out by linearly decreasing the potential from the equilibrium value of ca.  $-0.2 \text{ V}$  to the final growth potential between  $-0.5$  to  $-0.8 \text{ V}$  and maintaining that potential until the desired film thickness was obtained. A typical cyclic voltammogram is shown in Fig. 1 in which the potential was swept between the limits of  $-0.2$  and  $-1.0 \text{ V}$ . The oscillations produced in the “plateau” current are due to the flow

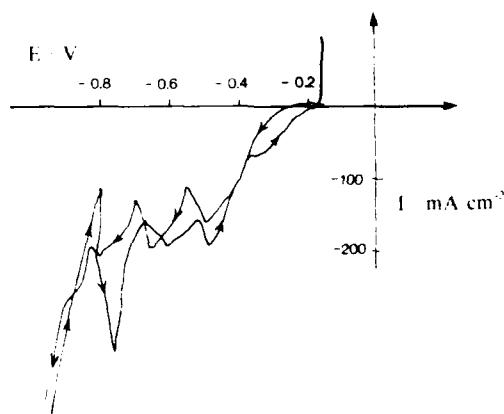


Fig. 1. Cyclic voltammogram recorded on *n*-type Si in a solution containing 0.5M CdSO<sub>4</sub> and 25 ppm HTeO<sub>3</sub> at pH 1.8, *T* = 60 °C (sweep rate = 5 mV s<sup>-1</sup>).

conditions from the peristaltic pump since the reaction in this region is occurring under mass transport control. The large increase in current at the end of the plateau is due to the electrodeposition of metallic cadmium. The thermodynamic potential for the reduction of Cd<sup>2+</sup> ions to Cd under the conditions here is -0.664 V. The potential observed here for the deposition of Cd is obviously more negative, and we attribute this in part to the increase in resistance of the substrate due to the deposited CdTe. Furthermore, at this potential ( $\approx -0.85$  V), Cd would be electrodepositing on CdTe. Thus, as the mechanism leading to an effective underpotential deposition of Cd (to form CdTe) does not apply here, an overpotential for the Cd deposition is found.

It was apparent from the analysis of the ellipsometry data that the optical constants measured for the "bare" silicon substrate in contact with the deposition solution did not correspond to that of Si. To investigate this anomaly, ellipsometry experiments were carried out where the silicon surface was monitored from the moment of contact with solutions containing the various components of the deposition solution. Thus, in a 25 ppm Te solution at pH 1.8 and 55 °C, there was no detectable change in the optical constants observed over a period of 2 h. In a 0.5M CdSO<sub>4</sub> solution at the same pH and temperature, there

was a reaction but only in the area of laser impingement for *p*-type Si, causing the formation of a cream coloured film. No deposit was found on the areas of silicon untouched by the laser and this was confirmed by ex-situ measurements. Thus the reaction taking place in the CdSO<sub>4</sub> solution is catalysed by intense light, and not by normal laboratory illumination. This is not unexpected since both visible and UV laser-induced deposition on semiconductor substrates including silicon is already well documented [29–31]. When the deposition solution was used, a film spontaneously formed and was visible to the naked eye over the whole of the Si surface although it was strongest at the point where the laser beam impinged the surface. This reaction is therefore catalysed even by normal laboratory illumination and it is worth noting that no deposition occurred when a *p*-type sample was placed in contact with the deposition solution in the dark, even after 12 h. A typical ellipsometry trace monitored for the spontaneous deposition of the film on illuminated *p*-type silicon is shown in Fig. 2.

The optical constants obtained, refractive index  $n = 1.52$  and extinction coefficient  $k = 0.135$  for the first part of this curve are consistent with those previously measured in this laboratory for thin electrodeposited films of tellurium on various substrates [27]. Thus it would appear that an electrodeless plating mechanism for Te operates

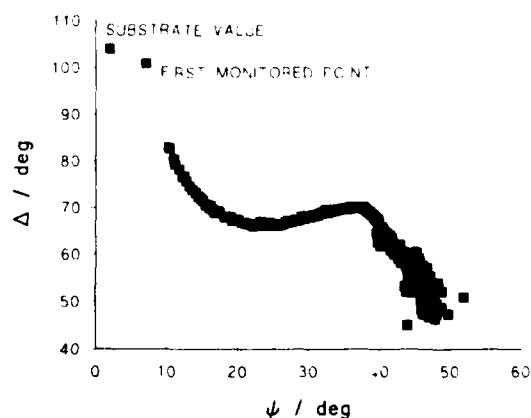


Fig. 2. Experimental  $\Delta$ - $\Psi$  plot for the growth of a spontaneous Te layer on illuminated *p*-type Si.

when silicon is in contact with a solution containing both Cd and Te ions. The shift in Te deposition potential when Cd is present in the solution is of course fundamental to the simultaneous deposition reaction to form CdTe [14]. Electron (or hole) injection into the conduction (or valence) band of the Si substrate will occur if the band edges are in close proximity to reduced (or oxidised) states respectively of the redox species in the solution. This situation becomes somewhat more complex if surface states are present on the silicon. For bare Si, the conduction and valence band edges in aqueous solutions have been reported as  $-1.79$  and  $-0.69$  V, respectively [28]. Under the conditions of our experiments, the  $\text{Cd}/\text{Cd}^{2+}$  redox species lies at  $-0.654$  V and that of the  $\text{Te}/\text{HTeO}_2^-$  at  $0.156$  V. Hence, Cd and not Te would be expected to undergo a deposition reaction by hole injection into the Si valence band. The fact that it is tellurium which is deposited would suggest that under the acidic conditions here, cadmium must subsequently undergo a dissolution reaction (essentially a corrosion reaction). This would provide the necessary electrons for the tellurium deposition which would be in competition with the hydrogen evolution reaction as the corresponding cathodic corrosion process.

XPS measurements (Fig. 3) were carried out on a p-type Si sample which was left standing in a solution containing 3000 ppm  $\text{Cd}^{2+}$  and 30 ppm  $\text{HTeO}_2^-$  at pH 1.6 and  $T = 56^\circ\text{C}$ . The measurements indicated that no cadmium was to be found

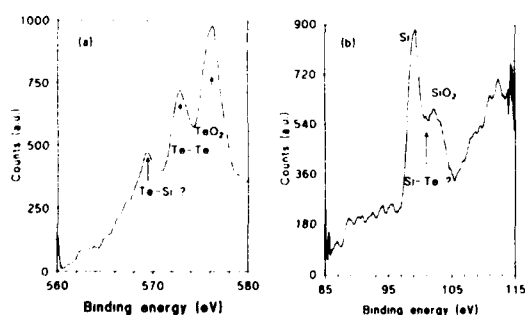


Fig. 3. XPS spectra of (a) Te 3d<sub>5/2</sub> and (b) Si 2p measured for the Te layer on Si.

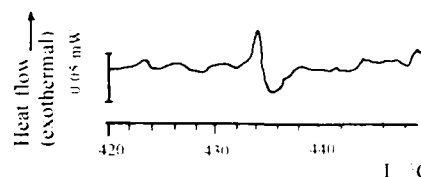


Fig. 4. DSC trace recorded for the Te layer on Si (heating rate  $10\text{ K min}^{-1}$ ).

in the sample. However, values of 576.1, 572.9 and 569.46 eV for the Te 3d<sub>5/2</sub> binding energies were recorded. The first two correspond to  $\text{TeO}_2$  and Te, respectively [32]. The third peak can tentatively be assigned to Te associated with a more electropositive element and this is most likely to be Si. No data are currently available which relate this value to that of a tellurium silicide. However, examination of the corresponding Si 2p spectrum shows the Si-Si peak at 99.4 eV and a peak around 103.4 eV corresponding to  $\text{SiO}_2$ . The latter peak is broad and we note that an Si-Te bond would appear in this region. It should also be noted that in certain electroless depositions involving visible radiation, silicide layers have been known to form on silicon substrates [31,33]. Further evidence for this tellurium layer comes from analysis of the layer by DSC. Fig. 4 shows the trace obtained and an endothermic transition is observed at  $435^\circ\text{C}$ , which has been attributed to the melting of thin films of tellurium metal [27,34]. No other peaks were observed over the temperature range studied, up to  $1000^\circ\text{C}$ .

From the above discussion, it would therefore appear that the subsequent electrodeposition reaction for CdTe occurs not on the silicon surface but on a tellurium layer as once the Si surface is covered by the metal film, the substrate behaves like the metal electrode with respect to redox species in the solution. Thus, the mechanism proposed by Panicker and co-workers [14] for the electrodeposition of CdTe using the above solution is equally valid here and the shift to more positive values in the deposition potentials of both Te and Cd will occur. Indeed, the single deposition wave shown in Fig. 1 indicates that the alloy CdTe is formed rather than the separate depositions.



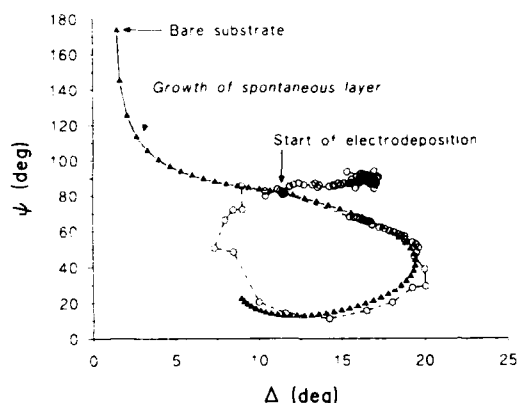


Fig. 5. Experimental  $\Delta$ - $\Psi$  plot (○) for the growth of CdTe on n-type Si. The model (△) shows the first layer due to spontaneous Te growth ( $n = 1.66$ ,  $k = 0.08$  and thickness 320 Å) and the second layer of electrodeposited CdTe ( $n = 2.65$ ,  $k = 0.512$ ).

A typical ellipsometry  $\Delta$ - $\Psi$  plot monitored during electrodeposition of CdTe on n-type Si is shown in Fig. 5. This clearly shows the change in the  $\Delta$ - $\Psi$  values which occurs due to the formation of the spontaneous layer on the silicon surface, prior to the start of the electrodeposition reaction. The difference between the bare Si substrate value and that at the start of the electrodeposition reaction can be accounted for by the spontaneous deposition of a 320 Å thick film having  $n = 1.66$  and  $k = 0.08$ . These values are in close agreement to experimentally determined optical constants for thin, electrodeposited layers of tellurium [27]. The second layer which grows on top of this corresponds to CdTe with optical constants of  $n = 2.65$  and  $k = 0.512$  [35]. The model provides a close match to the experimental data up to a CdTe thickness of 900 Å after which, there is a quite substantial divergence. This might not be too surprising since over the time scale of deposition here, the composition of the solution would be altered as the tellurium concentration becomes depleted, which in turn further affects the stoichiometric composition of the deposit as has been discussed in a previous paper [27].

The XRD spectrum of a film electrodeposited on n-type Si at  $-0.8$  V is shown in Fig. 6.

Although the spectrum is quite noisy, there are two distinct peaks at  $2\theta = 23.9^\circ$  and  $39.5^\circ$ , corresponding to  $d$ -spacings of 3.72 and 2.28 Å along the {111} and {220} orientations of CdTe, respectively. These are in close agreement with XRD data for CdTe [36]. After annealing in air at  $400^\circ\text{C}$  for 10 min, these peaks become sharper and there is also an increase in intensity (Fig. 6). Two new peaks at  $27.7^\circ$  and  $46.8^\circ$  are also brought into prominence. These correspond to the  $d$ -spacing of 3.22 Å in  $\text{CdO}\cdot\text{TeO}_2$  and to the CdTe  $d$ -spacings of 1.94 Å along the {311} direction respectively. These are again in excellent agreement with literature values [36]. Annealing produces an increase in the crystallinity of the film, as might be expected, and also a slight preferred orientation along the {111} axis. This orientation of CdTe is the one most commonly found for electrodeposited films [23].

A CdTe film was also prepared by the electrodeposition method on p-type Si. DSC analysis on this film did not reveal the presence of either free tellurium or cadmium in the unannealed film. Rutherford Backscattering (RBS) carried out on this sample using 2 MeV  $^4\text{He}$  ions is shown in Fig. 7. This shows the sample to be non-uniform in the area analysed by the beam (ca.  $0.2\text{ mm}^2$ ) as evidenced by the sloping back edge of the Cd/Te signal and the sloping front edge of the Si signal.

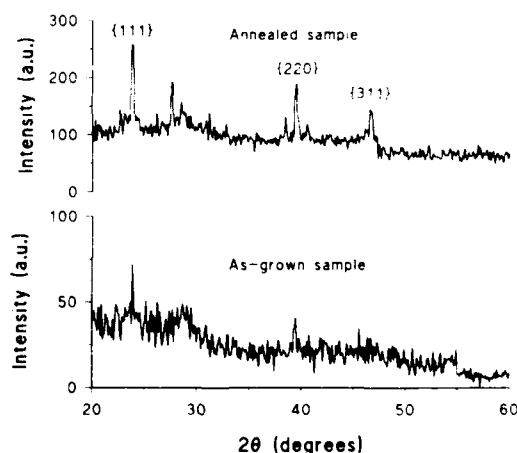


Fig. 6. XRD spectra for the electrodeposited CdTe on n-type Si, before and after a 10 min anneal in air at  $400^\circ\text{C}$ .

The small signal corresponding to silicon at the surface suggests that there is either pinholing or a small amount of Si incorporation into the layer. The presence of an oxygen signal indicates that this element is to be found throughout the layer. A careful examination of the Cd/Te signal gives a Cd:Te ratio of 0.8:1. This excess of Te was also evident from EDAX analysis of this layer which gave a ca. 0.3:1 Cd:Te ratio in the film. The lower ratio seen by the EDAX analysis stems from the fact that the depth probed by the analysis (17 keV electron beam) will be much greater than that of the RBS and will certainly be picking up the tellurium layer initially formed on the Si surface. The fact that DSC analysis did not show this Te excess might be because this is present as the silicide, as implied by the in-situ ellipsometry data and by the XPS results of the spontaneous deposit or that it has been transformed to the dioxide prior to DSC analysis.

A 4700 Å film was electrodeposited at  $-0.8$  V on n-type Si and annealed. The film appeared dull grey prior to annealing and metallic looking subsequently. XPS analysis showed the presence of a strong  $\text{SiO}_2$  signal which is surprising since the substrate should be buried under the relatively thick deposit. This would indicate that the electrodeposited film must be non-uniform, allowing access of the beam to the silicon. It should

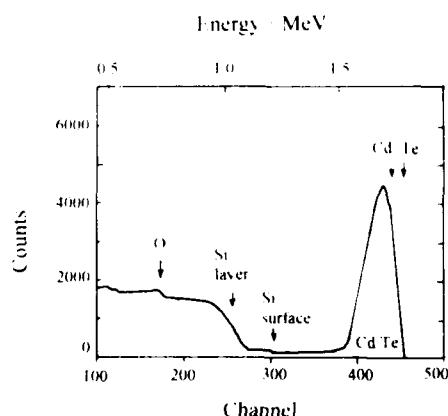


Fig. 7. 2 MeV  $^4\text{He}$  RBS spectrum of electrodeposited CdTe on p-type Si.

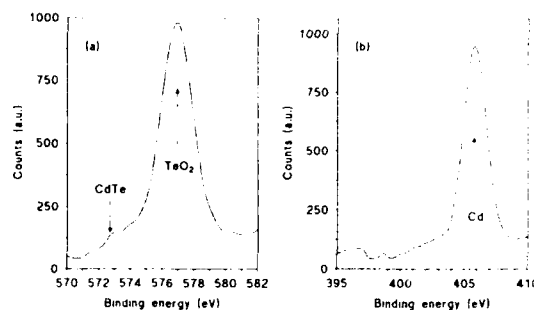


Fig. 8. XPS spectra of (a) Te  $3d_{5/2}$  and (b) Cd  $3d_{5/2}$  for the annealed electrodeposited CdTe layer on n-type Si.

be noted that a similar conclusion as to the nature of the film on p-type Si was reached after analysis of the RBS data of Fig. 7. The XPS spectra for Cd and Te in this film are given in Fig. 8 and indicate that the majority of Te is present as  $\text{TeO}_2$  ( $E_B = 576.1$  eV). There is, however, a small shoulder at ca. 572.7 eV that could correspond to either Te-Te or CdTe, as these compounds have binding energies that are very close together, 572.9 and 572.7 eV, respectively [32]. The calculation for the Cd:Te ratio in the film is made more difficult here by the fact that the Te at the surface is present as  $\text{TeO}_2$  and as noted above, the film is also discontinuous. However, if we assume that the CdTe film is homogeneous and thick in those regions of the substrate on which it grows, the value calculated, corrected for sensitivity and inelastic escape depth differences, is Cd:Te 0.8:1. Kohiki and co-workers [37] have reported a surface ratio for Cd:Te of 0.5:1 for CdTe oxidized in ambient atmosphere over a period of ten days. They suggested that the incorporation of oxygen caused the breaking of the Cd-Te bonds and the formation of Te-O and Cd-O bonds at the surface. Subsequently, the CdO, which is less stable than  $\text{TeO}_2$ , vaporizes, leaving the oxide layer rich in Te.

#### 4. Conclusions

The electrodeposition of CdTe from aqueous solution containing  $\text{HTeO}_2^+$  and  $\text{Cd}^{2+}$  ions at pH

1.8 and temperature range 55 to 70°C has been carried out on p-type {100} and n-type {111} silicon substrates. There is strong evidence to suggest that on both surfaces, a spontaneous layer of tellurium is deposited prior to any electrochemical reaction. This is most likely to be initiated by hole injection into the valence band of Si. Growth of the CdTe occurs on this layer and a single wave is observed for the electrodeposition indicating that alloy formation occurs rather than individual deposition of the two components. Annealing at 400°C for 10 min increases the crystallinity of the layer, although the surface layer appears to become heavily oxidized, with the majority of surface Te species present as TeO<sub>2</sub>. The CdTe films do not appear to form a coherent layer on the silicon surface. Further studies on the growth mechanism of the spontaneous Te layer and on the role of the photon in the process are currently in progress.

## 5. Acknowledgements

The authors wish to thank Mr. Mark Hartshorne for carrying out some of the XPS analysis on the samples and also Dr. P J Hall for the DSC experiments. This work has been supported by the Defence Research Agency, Malvern, United Kingdom.

## 6. References

- [1] I.M. Baker and R.A. Ballingall, in: Proc. SPIE 28th Int. Tech. Symp. San Diego, CA, 1984.
- [2] S.M. Jackson, M.H. Kalisher, W.L. Ahlgren, J.B. James and C.A. Cockrum, *Appl. Phys. Lett.* 56 (1990) 946.
- [3] S.M. Johnson, J.A. Vigil, J.B. James, C.A. Cockrum, W.H. Konkel, M.H. Kalisher, R.F. Risser, T. Tung, W.J. Hamilton, W.L. Ahlgren and J.M. Myrosznyk, *J. Electron. Mater.* 22 (1993) 835.
- [4] H. Mimura, S. Kajiyama, M. Nogami and Y. Hatanaka, *Jap. J. Appl. Phys.* 24 (1985) L717.
- [5] Y. Hatanaka, Y. Tomita, H. Mimura and M. Nogami, *Jap. J. Appl. Phys.* 25 (1986) L909.
- [6] S.G. Meikle and Y. Hatanaka, *Jap. J. Appl. Phys.* 26 (1987) L1812.
- [7] Y. Lo, R.N. Bicknell, T.H. Myers, J.F. Schetzina and H. Stadelmeier, *J. Appl. Phys.* 54 (1983) 4238.
- [8] R. Sporken, M.D. Lange, C. Masset and J.P. Faurie, *Appl. Phys. Lett.* 57 (1990) 1449.
- [9] J.P. Faurie, R. Sporken, Y.P. Chen, M.D. Lange and S. Sivananthan, *Mater. Sci. Eng. B* 16 (1993) 51.
- [10] R.L. Chou, M.S. Lin and K.S. Chou, *Appl. Phys. Lett.* 48 (1986) 523.
- [11] A. Nouhi, G. Radhakrishnan, J. Katz and K. Kolwad, *Appl. Phys. Lett.* 52 (1988) 2028.
- [12] H. Ebe and H. Takigawa, *Mater. Sci. Eng. B* 16 (1993) 57.
- [13] T.C. Kuo, Y.T. Chi, P.K. Ghosh, P.G. Kornreich and J. Beasock, *Thin Solid Films* 197 (1991) 107.
- [14] M.P.R. Panicker, M. Knaster and F.A. Kröger, *J. Electrochem. Soc.* 125 (1978) 566.
- [15] F.A. Kröger, *J. Electrochem. Soc.* 125 (1978) 2028.
- [16] R.N. Bhattacharya and K. Rajeshwar, *J. Electrochem. Soc.* 131 (1984) 2032.
- [17] W.J. Danaher and L.E. Evans, *Australian J. Chem.* 37 (1984) 689.
- [18] B.M. Basol, O.M. Stafsudd and A. Bindal, *Solar Cells* 15 (1985) 279.
- [19] A. Darkowski and M. Cocivera, *J. Electrochem. Soc.* 132 (1985) 2768.
- [20] C. Sella, P. Boncorps and J. Vedel, *J. Electrochem. Soc.* 133 (1986) 2043.
- [21] B.M. Basol and E.S. Tseng, *Appl. Phys. Lett.* 48 (1986) 946.
- [22] D. Ham, K.K. Mishra, A. Weiss and K. Rajeshwar, *Chem. Mater.* 1 (1989) 619.
- [23] P. Cowache, D. Lincot and J. Vedel, *J. Electrochem. Soc.* 136 (1989) 1646.
- [24] E. Mori and K. Rajeshwar, *J. Electroanal. Chem.* 258 (1989) 415.
- [25] G.C. Morris and S.K. Das, *Solar Energy Mater. Solar Cells* 30 (1993) 223.
- [26] L. Ndiaye, P. Cowache, M. Cadene, D. Lincot and J. Vedel, *Thin Solid Films* 224 (1993) 227.
- [27] J.M. Fisher, L.E.A. Berlouis, B.N. Rospendowski, P.J. Hall and M.G. Astles, *Semicond. Sci. Technol.* 8 (1993) 1459.
- [28] W. Kautek, N. Sorg and W. Paatsch, *Electrochim. Acta* 36 (1991) 1803.
- [29] S. Tamir and J. Zahavi, *J. Vac. Sci. Technol. A* 3 (1985) 2312.
- [30] A. Aydinli and A.D. Compaan, *Adv. Mater. Opt. Electron.* 2 (1993) 79.
- [31] J. Zahavi, S. Tamir and M. Halliwell, in: *Materials Issues in Silicon Integrated Circuit Processing*, Mater. Res. Soc. Symp. Proc., Vol. 71 (Mater. Res. Soc., Pittsburgh, PA, 1986) p. 173.
- [32] D. Briggs and M.P. Seah, Eds., *Practical Surface Analysis by Auger and X-Ray Photoelectron Spectroscopy* (Wiley, Chichester, 1983).
- [33] Y.C. Kiang, J.R. Moulic and J. Zahavi, *IBM Tech. Disclosure Bull.* 26 (1983) 327.

- [34] W.Y. Lin, K.K. Mishra, E. Mori and K. Rajeshwar, *Anal. Chem.* 62 (1990) 821.
- [35] E.D. Palik, (Ed.), *Handbook of Optical Constants of Solids* (Academic Press, New York, 1985) p. 146.
- [36] L.G. Barry, Ed., *Inorganic Index to the Powder Diffraction File* (Joint Committee on Powder Diffraction Standards, Philadelphia, 1970) p. 750.
- [37] S. Kohiki, K. Nishikura, T. Wada and T. Hirao, *Appl. Surf. Sci.* 59 (1992) 39.



ELSEVIER

Journal of Crystal Growth 138 (1994) 94–98

CRYSTAL  
GROWTH

## Compensation processes in molecular beam epitaxially grown zinc selenide doped with nitrogen

K.A. Prior <sup>\*</sup>, B. Murdin, C.R. Pidgeon, S.Y. Wang, I. Hauksson, J.T. Mullins,  
G. Horsburgh, B.C. Cavenett,

*Department of Physics, Heriot-Watt University, Edinburgh EH14 4AS, UK*

### Abstract

Recent work has shown that nitrogen produced in a plasma source is a p-type dopant in MBE grown ZnSe with  $N_a - N_d$  to  $1 \times 10^{18} \text{ cm}^{-3}$ , but at these concentrations the material is highly compensated. In a previous study, we have examined the PL spectra of nitrogen doped material grown in our laboratory and have shown that there are two sets of donor–acceptor pair (DAP) peaks which can be explained by a simple model involving a nitrogen acceptor and two donors. The first donor is a native shallow donor and the second is a nitrogen related compensating donor thought to be a complex of the form  $V_{\text{Se}}\text{--Zn--N}_{\text{Se}}$ . Optically detected magnetic resonance results on samples showing both shallow and deep DAP luminescence show signals due to the shallow isotropic donors and deep anisotropic donors consistent with our proposed model. Calculations of the vacancy concentrations and degree of compensation that should be expected in nitrogen doped ZnSe show that at all temperatures and under all growth conditions the material is highly undersaturated with vacancies. The barriers operating to prevent the compensation are discussed.

### 1. Introduction

The behaviour of the group V element nitrogen in ZnSe is currently of great interest as at present it is the only reliable p-type dopant available which can be used in the molecular beam epitaxial growth of ZnSe. Nitrogen can only be incorporated into the ZnSe epilayers by being activated in an RF discharge as first shown by Ohkawa [1] and Park [2]. Qiu et al. [3] showed that doping levels of  $1 \times 10^{18} \text{ cm}^{-3}$  could be obtained with substrate temperatures during growth of 250–300°C and that this upper limit

was relatively insensitive to total nitrogen flux. Higher doping levels of  $2 \times 10^{18} \text{ cm}^{-3}$  were obtained by these authors with a reduction in the growth temperature to 150°C [4].

ZnSe doped with nitrogen shows weak acceptor bound exciton emission and prominent donor–acceptor pair (DAP) emission at 4 K. We have previously shown that there are two sets of DAP transitions involving nitrogen acceptors and two different donors, these being native residual donors and deeper donors situated approximately 44 meV below the conduction band edge [5–7]. The deep donor concentration increases with the incorporation of nitrogen and we have suggested that this deep donor is actually a complex consisting of a nitrogen acceptor and a doubly charged

<sup>\*</sup> Corresponding author.

selenium vacancy donor on next nearest neighbour sites ( $N_{Se}-Zn-V_{Se}^{2+}$ ). The complexing of nitrogen atoms with vacancies results in the auto-compensation of the material and leads to a lowering of  $N_A - N_D$ . Subsequently, the presence of large numbers of vacancies within ZnSe:N has also been suggested by Petruzzello et al. [8] as an explanation for the anomalous relaxation of the lattice parameter of heavily doped ZnSe:N as observed by double crystal rocking curves. Our proposals are also consistent with these authors' TEM and Raman measurements.

In this paper, we present recent results obtained by optically detected magnetic resonance (ODMR) which are also in accord with the model developed in ref. [7]. Also, as vacancies are a mobile species within the semiconductor lattice, the dynamic properties of vacancies and any complex involving them are of interest. We have previously shown that the complexing process can continue after growth even at room temperature consistent with the diffusion of vacancies from the surface [6,7]. In order to understand the behaviour of this material, we have modelled the vacancy concentrations as a function of temperature and selenium and zinc overpressures. We have found that the material is always undersaturated with vacancies and that there is a substantial concentration gradient leading to the subsequent indiffusion of vacancies.

## 2. Experimental procedure

The samples were grown in a Vacuum Generators 288 MBE system on GaAs(100) substrates at a growth temperature of 280°C. Solid Knudsen sources of zinc and selenium were used and the selenium was not cracked. Nitrogen doping was obtained by using an Oxford Applied Instruments plasma source.

ODMR on these samples was carried out at 9.32 GHz with a 2.5 T superconducting magnet. The luminescence was excited with 350 nm from a coherent krypton ion laser and microwave induced changes in the emission were detected using an S20 photomultiplier and a lock-in detector. The microwaves were modulated at 300 Hz.

Details of the technique can be found in Cavenett [9].

## 3. ODMR results

Fig. 1 shows the emission spectra at 2 K for two ZnSe:N samples. The shallow DAP recombination transitions are shown in (a) for a sample with  $N_A - N_D = 9 \times 10^{16} \text{ cm}^{-3}$ . A weak deep DAP recombination can be seen between the main transitions which are separated by the LO phonon energy. In (b) the deep DAP emission dominates the spectrum for a sample with  $N_A - N_D = 4 \times 10^{17} \text{ cm}^{-3}$ .

Fig. 2 shows the ODMR signals for the two samples shown in Fig. 1 where the maximum microwave induced change in the luminescence was 0.5%. Fig. 2a shows the results for the sample with lower nitrogen doping with the emission spectrum given in Fig. 1a and the three signals which are increases in emission correspond to  $g$  values of  $1.11 \pm 0.02$ ,  $1.38 \pm 0.03$  and  $2.00 \pm 0.02$ , as indicated. The resonance at  $g = 1.11$  is well known as the shallow donor resonance and has been reported previously by Dunstan et al. [10]. The  $g = 2$  resonance is typical of deep acceptors in ZnSe [11], whereas the  $g = 1.38$  resonance has not been observed before. In the case of the

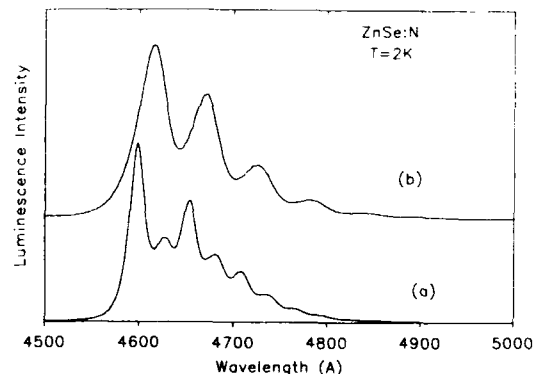


Fig. 1. Photoluminescence spectra of the samples used. (a) Low nitrogen concentration sample ( $N_A - N_D = 9 \times 10^{16} \text{ cm}^{-3}$ ) showing deep and shallow DAP recombination. (b) High nitrogen concentration sample ( $N_A - N_D = 4 \times 10^{17} \text{ cm}^{-3}$ ) showing deep DAP recombination only.

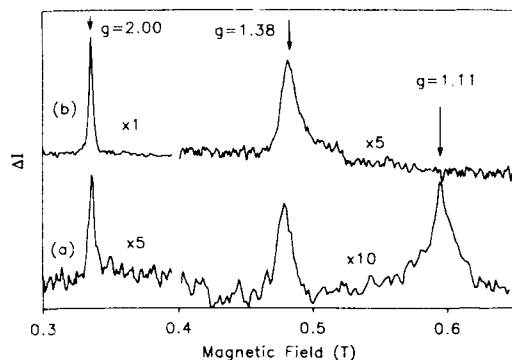


Fig. 2. ODMR signals: (a) from the sample shown in Fig. 1a; (b) from the sample shown in Fig. 1b. The scale factors are relative to the largest signal, which was a change in luminescence of 0.5%. Note that the signals in (b) were actually negative, see text.

sample shown in Fig. 1b where the emission is from deep DAP recombination, only two resonances are observed, and these are decreases in the emission corresponding to the case where there is a decrease in the radiative DAP transitions because of competing non-radiative recombination processes. The absence of the shallow donor signal is consistent with the fact that the shallow DAP transitions have been largely suppressed at the higher nitrogen concentrations.

The recombination model proposed by Hauksun et al. [7] involves two recombination paths, namely, shallow donor to nitrogen acceptor and deep donor to nitrogen acceptor. We assign the  $g = 1.11$  resonance to the 25 meV shallow donors, the  $g = 1.38$  signal to the 44 meV deep donor and the  $g = 2.00$  resonance to the 110 meV deep nitrogen acceptor.

#### 4. Selenium vacancies in ZnSe

The proposed role of  $V_{Se}$  centres in the compensation process in p-type ZnSe was supported by the observation [7] that over a period of four months the carrier concentration as measured by C-V profiling, changed from a uniformly doped layer to one showing a surface depletion region and a decrease in  $N_A - N_D$  characteristic of de-

fects diffusing from the surface. A similar change can also be seen in the photoluminescence as shown in Fig. (3). Curve (a) shows the initial PL data characteristic of a p-type sample with  $N_A - N_D \approx 5 \times 10^{16} \text{ cm}^{-3}$ , that is, showing principally shallow DAP transitions. After six months, curve (b) the deep DAP transitions are very much stronger, implying that the compensation process has proceeded at room temperature.

The compensation of semiconductors by charged vacancies has been studied by a number of authors since Mandel [12] showed that almost complete compensation could occur in II–VI semiconductors via the singly and doubly charged vacancies. Recently, the behaviour of vacancies in ZnSe has been investigated with a view to finding conditions which could limit the compensation by these charged species [13–15]. Ichimura et al. [13] have examined the concentrations of vacancies which occur under conditions of thermal equilibrium and photoirradiation and find that a substantial reduction in concentrations may occur with weak levels of above bandgap irradiation. Using the equations and free energy terms given in ref. [13], we have examined the concentrations of vacancies which should occur as a function of temperature and growth conditions. The complete set of equations used is given in ref. [13] and only those equations showing the formation

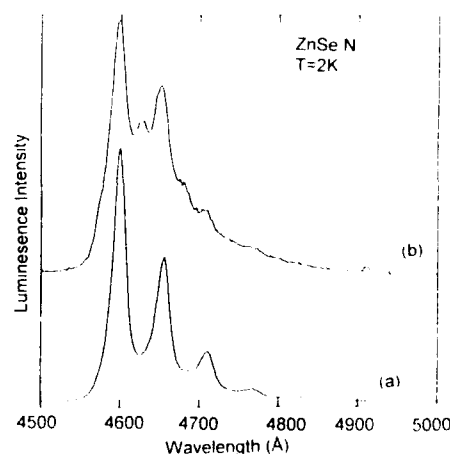


Fig. 3. PL spectra of sample taken: (a) immediately after growth; (b) after six months.

of selenium vacancies are given here to illustrate the main points.

The concentration of neutral and charged selenium vacancies can be obtained from the following equilibria:

$$\text{Zn}_g = \text{Zn}_{\text{Zn}} + \text{V}_{\text{Se}}^0, \quad (1)$$

$$\text{V}_{\text{Se}}^0 + \text{V}_{\text{Se}}^+ + e^-, \quad (2)$$

$$\text{V}_{\text{Se}}^+ = \text{V}_{\text{Se}}^{2+} + e^-. \quad (3)$$

Similar equations can be written for the zinc vacancy species. Eq. (1) involves only neutral species, and gives a value for the concentration of the neutral selenium vacancy which is independent of any dopants present within the material. Thus, we can determine the concentration of neutral selenium vacancies:

$$K_1 = [\text{V}_{\text{Se}}^0] / p_{\text{Zn}}, \quad (4)$$

Here, quantities in square brackets refer to molar concentrations and  $p_{\text{Zn}}$  is the zinc partial pressure above the ZnSe surface. Eqs. (2) and (3) involve charged species, however, and thus depend upon the concentrations of electrons present within the material. The equations for the two charged selenium vacancies are:

$$K_2 = (n/N_c) [\text{V}_{\text{Se}}^+] / [\text{V}_{\text{Se}}^0], \quad (5)$$

$$K_3 = (n/N_c) [\text{V}_{\text{Se}}^{2+}] / [\text{V}_{\text{Se}}^+]. \quad (6)$$

Here  $n$  is the electron concentration and  $N_c$  is the density of states in the conduction band. Eqs. (4)–(6) may be then combined to give  $[\text{V}_{\text{Se}}^{2+}]$  in terms of  $p_{\text{Zn}}$  and  $n$ :

$$[\text{V}_{\text{Se}}^{2+}] = K_1 K_2 K_3 N_c^2 p_{\text{Zn}} / n^2. \quad (7)$$

Alternatively, the concentrations of the charged vacancy species can be expressed as functions of the Fermi level position:

$$[\text{V}_{\text{Se}}^{2+}] = K_1 K_2 K_3 p_{\text{Zn}} \exp[2(E_c - E_F) / k_B T]. \quad (8)$$

The concentrations of all charged species are not independent, but are related by the electroneutrality relationship

$$\begin{aligned} n + N_1 ([\text{V}_{\text{Zn}}] + 2[\text{V}_{\text{Zn}}^{2+}]) + N_A \\ = p + N_1 ([\text{V}_{\text{Se}}] + 2[\text{V}_{\text{Se}}^{2+}]) + N_D, \end{aligned} \quad (9)$$

where  $N_1$  is the number of lattice sites, and  $N_A$  and  $N_D$  are the shallow acceptor and donor concentrations. Given these equations, and those describing the concentrations of the charged zinc vacancies, the concentrations of all charged species can be determined at different temperatures and zinc and selenium pressures. We have obtained values for the charged and neutral vacancy concentrations for a wide variety of initial conditions covering the temperature range 25–300°C. The pressures of zinc and selenium used correspond either to those found above ZnSe under free evaporation (with no applied pressures of zinc and selenium and  $p_{\text{Zn}} = 2p_{\text{Se}}$ ) or to a range of overpressures corresponding to those used in MBE at normal growth rates. Under normal p-type doping conditions *at equilibrium* it can easily be shown that the doubly charged selenium vacancy is, by several orders of magnitude, by far the most common species and changes remarkably little in concentration over many orders of magnitude pressure change and several hundred degree change in substrate temperature. These results are similar to those published, using the same thermodynamic data, by Ichimura et al. [13] for higher substrate temperatures and larger overpressures.

The result of this high degree of compensation is that the maximum possible hole concentrations are predicted to be several orders of magnitude smaller than those observed in practice and are typically in the range  $10^{14}$ – $10^{15}$  cm<sup>-3</sup>. This suggests that there may be a kinetic barrier or process which prevents the formation of  $\text{V}_{\text{Se}}^{2+}$  at the surface of the growing semiconductor, leaving the epitaxial layer undersaturated with vacancies. The slow compensation process, shown in our samples, is therefore a natural adjustment of the vacancy levels towards their equilibrium values, and it is the low levels of compensation obtained by nitrogen doping which must be explained.

One solution, suggested by Woodall et al. [15] is that band bending at the surface leads to an increase in the Fermi level at the surface with a corresponding reduction in  $[\text{V}_{\text{Se}}^{2+}]$ . This is shown in Eq. (8), where for a constant zinc pressure and a fixed temperature of, for example, 550 K a change in the Fermi level by only 0.5 eV will



decrease  $[V_{\text{Se}}^{\cdot\cdot}]$  at equilibrium by  $\times 10^{19}$ . The neutral vacancy will then become the dominant defect, and after the growth front has passed, the Fermi level will move towards its bulk value with the simultaneous ionization of the selenium vacancies. A lower limit to the compensation level will be given by the concentration of neutrals which incorporate at the surface. As the selenium vacancies ionise, there exists a large concentration gradient of neutral vacancies in the subsurface region.

Woodall et al. have estimated the rate of indiffusion of vacancies under MBE growth conditions, and obtain a value of  $10^{-12} \text{ cm}^2 \text{ s}^{-1}$ , which is considerably in excess of the measured value for diffusion constants at the growth temperature. At room temperature, the vacancies are seen to move distances of the order of  $0.1 \mu\text{m}$  over times of the order of months, implying diffusion constants in the region of  $10^{-17} \text{ cm}^2 \text{ s}^{-1}$ . This is still rather fast, and suggests that the diffusion over these timescales may involve other mechanisms. In addition to neutral vacancy migration, the charged vacancies will also migrate in the electric field in the depletion region of the semiconductor. With the addition of an applied field, we have seen enhancements in the rates of diffusion, however these are still not large enough to account for the extremely fast movement seen in our samples. One further possibility is that the large number of threading dislocations can act as fast routes for vacancy transport. Further study using lattice matched samples with low dislocation densities is therefore needed to separate these mechanisms.

## 6. Conclusion

We present ODMR data which show the presence of the selenium vacancy-nitrogen deep donor in agreement with our previous analysis. Our

calculations show that p-type ZnSe is undersaturated with vacancies at the growth temperature and at room temperature. We suggest that the band bending at the surface presents a barrier to the formation of the charged vacancies in agreement with the model proposed by Woodall et al. [15].

## 7. Acknowledgements

We are grateful to the SERC for funding of this work and for financial contributions from VG Semicon and BT Research.

## 8. References

- [1] K. Ohkawa, T. Karasawa and T. Mitsuoka, *J. Crystal Growth* 111 (1991) 797.
- [2] R.M. Park, M.B. Troffer, C.M. Rouleau, J.M. DePuydt and M.A. Haase, *Appl. Phys. Lett.* 57 (1990) 2127.
- [3] J. Qiu, J.M. DePuydt, H. Cheng and M.A. Haase, *Appl. Phys. Lett.* 59 (1991) 2992.
- [4] J. Qiu, H. Cheng, J.M. DePuydt and M.A. Haase, *J. Crystal Growth* 127 (1993) 279.
- [5] J. Simpson, I. Hauksson, S.Y. Wang, H. Stewart, K.A. Prior and B.C. Cavenett, *Physica B* 185 (1993) 164.
- [6] J. Simpson, S.Y. Wang, H. Stewart, J. Wallace, S.J.A. Adams, I. Hauksson, K.A. Prior and B.C. Cavenett, *J. Electron. Mater.* 22 (1993) 431.
- [7] I. Hauksson, J. Simpson, S.Y. Wang, K.A. Prior and B.C. Cavenett, *Appl. Phys. Lett.* 61 (1992) 2208.
- [8] J. Petruzzello, J. Gaines, P. van der Sluis, D. Olego and C. Ponzoni, *Appl. Phys. Lett.* 62 (1993) 1496.
- [9] B.C. Cavenett, *Adv. Phys.* 30 (1981) 475.
- [10] D.J. Dunstan, B.C. Cavenett, R.F. Brunwin and J.F. Nicholls, *J. Phys. C* 10 (1977) L361.
- [11] D.J. Dunstan, J.F. Nicholls, B.C. Cavenett and J.J. Davies, *J. Phys. C* 13 (1980) 6409.
- [12] G. Mandel, *Phys. Rev.* 134 (1964) A1073.
- [13] M. Ichimura, T. Wada, Sz. Fujita and Sg. Fujita, *Jap. J. Appl. Phys.* 30 (1991) 3475.
- [14] J.F. Wager, *Phil. Mag. A* 67 (1993) 897.
- [15] J.M. Woodall, R.T. Hodgson and R.L. Gunshor, *Appl. Phys. Lett.* 58 (1991) 379.



ELSEVIER

Journal of Crystal Growth 138 (1994) 99–104

JOURNAL OF  
CRYSTAL  
GROWTH

## Observation of preferential donor–acceptor pairing in ZnSe:Na

L. Radomsky\*, G.-J. Yi, G.F. Neumark

*Department of Chemical Engineering, Materials Science and Mining Engineering, Columbia University, New York, New York 10027, USA*

### Abstract

Donor–acceptor preferential pairing can occur in compensated semiconductors due to the Coulomb attraction between ionized donors and acceptors. However, extensive preferential pairing requires high ion mobilities at relatively low temperatures, and has been very difficult to establish conclusively. We here report identification of such preferential pairing, from donor–acceptor pair luminescence in two samples of Na-doped ZnSe. We observed essentially identical close pair lines (both in location and in relative intensity) in both samples, but the associated distant pair peak was observed at a higher energy in one sample than in the other. We explain this by assuming that there is strong preferential pairing in the first sample and weaker pairing in the second sample. Our observation of preferential pairing also shows that one can have high ion mobilities in ZnSe.

### 1. Introduction

It has been postulated in a number of instances that in compensated semiconductors one can have preferential (versus random) donor–acceptor pairing, due to the Coulomb attraction between ionized donors and acceptors. However, any preferential pairing that is sufficiently extensive to be observed requires high ion mobilities, and has been difficult to prove. A good tool for such studies is donor–acceptor pair (DAP) photoluminescence (PL), which in general is a useful tool for the studies of impurity properties [1,2]. By our observation of preferential pairing, we here show that one *can* have such high ion mobilities in ZnSe.

Before proceeding to describe random and preferential pairing, it is important to first review

DAP theory. Specifically, DAP luminescence can be divided into two ranges, one involving (sharp) lines due to close pairs and the other involving a broad peak (and its phonon replicas) due to the distant pairs (e.g., refs. [1,2]). This behavior can best be understood by consideration of the underlying equations. The emission energy from any given DAP,  $h\nu$ , can be well approximated (neglecting the quantum overlap term, which is significant only at fairly small  $R$ ) as a function of the pair separation,  $R$ , by:

$$h\nu = h\nu' + e^2/\epsilon R, \quad (1)$$

$$h\nu' = E_g - (E_D + E_A), \quad (2)$$

where  $h\nu'$  is the emitted energy at infinite pair separation, the  $e^2/\epsilon R$  term results from the Coulomb interaction between the ionized donor and acceptor,  $\epsilon$  is the dielectric constant,  $e$  is the electron charge ( $3.847 \times 10^{-4}$  eV cm),  $E_g$  is the band gap energy, and  $E_D$  ( $E_A$ ) is the donor

\* Corresponding author.

(acceptor) ionization energy. Discrete lines often result from close pairs due to a large emission energy spread between the lines (small  $R$ !). The intensity distribution of these lines is determined by the number of sites available for each shell (where a set of lattice positions at a given  $R$  is called a shell). For distant pairs, using  $I(h\nu) = I(R) dR/dh\nu$  [1–3],

$$I(h\nu) = N_{\text{maj}}(\epsilon/e^2)R^2P(R)W(R)f(R), \quad (3)$$

$$P(R)$$

$$= 4\pi N_{\text{maj}}R^2 \exp(\alpha/R) \exp(-4\pi N_{\text{maj}}R^3/3), \quad (4)$$

$$W(R) = W_0 \exp(-2R/a_B), \quad (5)$$

$$f(R) = [1 + W(R)/g\sigma(R)]^{-1}, \quad (6)$$

$$\sigma(R) = AR^2, \quad (7)$$

$$\alpha = e^2/\epsilon kT, \quad (8)$$

where  $I(h\nu)$  is the emission intensity,  $P(R)$  the distribution of pairs [3],  $W(R)$  the radiative transition probability,  $a_B$  the Bohr radius of the shallower member of the pair,  $f(R)$  the fraction of excited pairs,  $N_{\text{maj(min)}}$  the concentration of the neutral majority (minority) dopant,  $\alpha$  the temperature dependent Coulomb term [3],  $k$  the Boltzmann constant,  $T$  the temperature at which ion mobility ceases,  $g$  the continuous excitation intensity,  $\sigma(R)$  the capture cross section, and  $A$  and  $W_0$  are constants. For distant pairs, the pair lines overlap, leading to a broad peak in intensity versus energy. This “distant pair” peak occurs because the luminescence intensity first increases with increasing  $R$  as more sites become available for the second member of the pair. However, the radiative transition probability,  $W(R)$ , decreases exponentially with increasing  $R$ , and the intensity eventually decreases because the most distant pairs hardly contribute to the luminescence.

The degree of preferential pairing is given by the temperature dependent Coulomb term (8):  $\alpha = 0$  ( $T \rightarrow \infty$ ) for random pairing, and  $\alpha > 0$  for preferential pairing. From (8), it can be seen that any preferential pairing that is sufficiently extensive to be observed requires ions to be mobile to relatively low temperatures. Moreover, in prac-

tice, it is generally very difficult to determine whether such pairing is indeed present, since data can usually be fitted either by this pairing or by adjusting other parameters of the theory, such as the impurity radius, where the latter is usually poorly known.

It can be noted that in preferential pairing, due to the Coulomb attraction, the average pair separation is smaller than the one in random pairing. Thus, from (1), it can be seen qualitatively that a preferential pairing peak will appear at a higher energy (smaller  $R$ ) than a random pairing peak. The same can be shown quantitatively. Eqs. (1)–(8) lead to a maximum in  $I(h\nu)$  versus  $h\nu$ . In the notation of ref. [2], the value of  $R$  at the maximum,  $R_m$ , can be expressed as [3]:

$$2\pi N_{\text{maj}}R_m^3 + f_m R_m/a_B + \alpha/2 R_m + f_m - 3 = 0, \quad (9)$$

where  $f_m$  is the value of  $f(R)$  at separation  $R_m$ . This result also gives the corresponding Coulomb energy,  $E_m$  [2]:

$$E_m = e^2/\epsilon R_m. \quad (10)$$

Therefore, from (9), it can be seen that the distant pair peak due to preferential pairing will be found at a higher energy than the one due to random pairing.

The distant DAP peak position also depends on excitation intensity. In ref. [4], it is shown that distant pair peaks shift to higher energies as the excitation intensity,  $g$ , is increased. We have also calculated the excitation intensity dependence of the DAP peak position as a function of  $\alpha$  by substituting (6) and (8) into (9) and solving for the normalized excitation intensity ( $gA/W_0$ ), using  $N_{\text{maj}} = 10^{16} \text{ cm}^{-3}$  and  $a_B = 3.6 \times 10^{-7} \text{ cm}$  [5]. The plot of the normalized excitation intensity versus the Coulomb energy is shown in Fig. 1 for random pairing ( $\alpha = 0 \text{ cm}$ ) and for preferential pairing ( $\alpha = 6.5 \times 10^{-7} \text{ cm}$ ), where we assume the ion mobility to cease at  $T = 400 \text{ K}$ . It can be seen that at high excitation intensity, the Coulomb shift is larger for preferential pairing than for random pairing, 5 meV in this example. We further note (eq. (9) and e.g. ref. [6]) that the rate of shift also depends on  $a_B$  and  $N_{\text{maj}}$ , although the

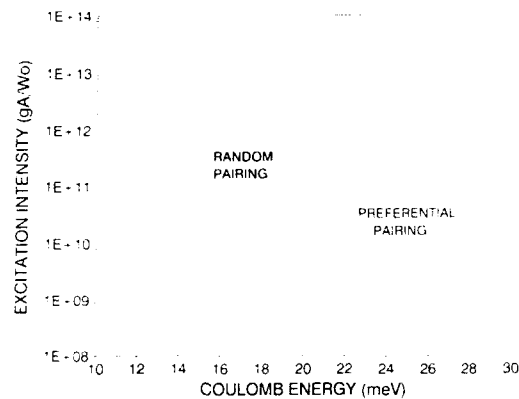


Fig. 1. Plot of normalized excitation intensity,  $gA/W_0$ , versus the Coulomb energy,  $E_m$ , for random and preferential pairing, using  $T = 400$  K,  $a_B = 36$  Å and  $N_{\text{maj}} = 10^{16}$  cm $^{-3}$ .

effect of the latter is relatively minor. Thus, if  $a_B$  is poorly known,  $\alpha$  cannot be determined from the shift of the peak with intensity.

## 2. Experimental procedure

The two specific samples on which we report here were Na doped ZnSe. The spectra of one (A) has been reported and discussed previously [6,7]. This sample was grown by adding Na<sub>2</sub>Se and Se to a Bi melt, and heating ZnSe crystalline wafers in contact with this melt. The procedure is similar to that used for liquid phase epitaxy (LPE) layers in ZnSe, except that Zn was omitted from the melt. This was done to encourage the Na to be incorporated on the substitutional Zn sites. The other sample (B) was grown via the vertical zone method [8] from 50 g ingots at 1574°C. The dopant was Na<sub>2</sub>Se (Cerac), 99.9% pure, introduced to the top of the charge. The crystals contained less than 20 ppm of all impurities, with sulfur being the major impurity [8].

The low temperature PL measurements of these samples were made at 9 K using a Janis Closed Cycle Refrigeration System. The excitation source was a HeCd CW laser emitting in the UV (325 nm; a UG-11 filter was used to eliminate the low power emission at 442 nm). The spectra were processed by a Jarrell–Ash 0.75m

Czerny–Turner Spectrometer (model 78-496) and detected by a cooled Hamamatsu R329-02 photomultiplier tube. The PMT signal was recorded by an SR400 Gated Photon Counter, whose output was plotted on a computer.

## 3. Results and discussion

The spectrum of sample A is shown in Fig. 2 (the spectrum was retaken here, for better comparison to B). As shown previously [6,7], there are close pair lines from 2.78 eV down to 2.73 eV, a pronounced DAP peak at 2.685 eV (with phonon replicas at lower energies), and a shoulder at 2.704 eV. One can also note bound exciton lines: two  $I_1$  lines (at 2.7942 and 2.7936 eV, due to Na<sub>Zn</sub>), an  $I_2$  line (at 2.7979 eV, due to donors), and a phonon replica of the  $I_1$  lines (the notation is standard [1,6,7]). The pair line intensity distri-

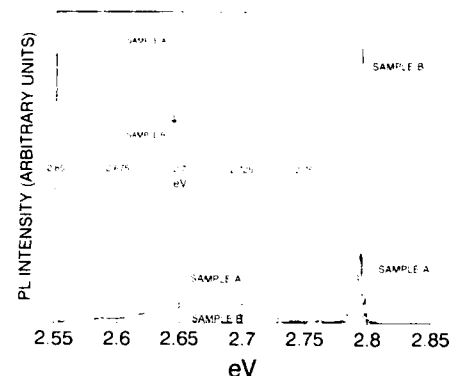


Fig. 2. Photoluminescence of samples A and B at 9 K. The insert shows a close up of the DAP peaks and lines from close pairs of both samples. In sample A, there are close pair lines from 2.78 eV down to 2.73 eV, a pronounced DAP peak at 2.685 eV (with phonon replicas at lower energies), a shoulder at 2.704 eV, two  $I_1$  lines (at 2.7942 and 2.7936 eV, due to Na<sub>Zn</sub>), an  $I_2$  line (at 2.7979 eV, due to donors), and a phonon replica of the  $I_1$  lines. In sample B, there are close pair lines between 2.73 and 2.78 eV (where for this sample the spectrum in this region must be magnified for this observation), a pronounced DAP peak at 2.683 eV (with phonon replicas at lower energies), a shoulder at 2.695 eV (arrow), an  $I_1$  line (at 2.7943 eV, corresponding to the position for Na, with the second Na line not resolved), an  $I_2$  line (at 2.7980 eV, due to donors), an  $I_1^{\text{deep}}$  line (at 2.7828 eV) and a phonon replica of the  $I_1$  line.

bution is different for donors and acceptors on the same type of lattice site (type I) than for donors and acceptors on different lattice sites (type II). The pair lines in sample A were identified as type II [7] by successfully matching them with similar type II lines in GaP and with theoretical predictions for type II spectra. Attempts to superimpose the pair line spectra on known type I spectra in ZnSe with Li acceptors were unsuccessful. It was determined that in view of Na doping and the observation of Na exciton lines that the acceptor species must be Na on the Zn site ( $\text{Na}_{\text{Zn}}$ ). This means that the donor in the peak associated with the type II pairs must be on a site other than Zn, and it was attributed to an interstitial Na donor ( $\text{Na}_i$ ) [6,7]. Also, using reasonable values for pump intensity and doping density, it was determined that only one assignment results in a correct value of the Coulomb shift,  $E_m$ : the close pairs are associated with the shoulder at 2.704 eV, which is due to  $\text{Na}_{\text{Zn}}$  acceptor and  $\text{Na}_i$  donor, and the peak at 2.685 eV is then attributed to  $\text{Na}_{\text{Zn}}$  acceptor and a group III metal on a Zn site as donor, making it the so-called "P" peak [9].

The luminescence spectrum of sample B is also shown in Fig. 2. As in sample A, one can note close pair lines between 2.73 and 2.78 eV (where for this sample the spectrum in this region must be magnified for this observation), and the "P" peak at 2.683 eV; however, there now is a

shoulder at 2.695 eV rather than at the previously observed 2.704 eV. An  $I_1$  line (at 2.7943 eV; corresponding to the position for Na, with the second Na line not resolved), an  $I_2$  line (at 2.7980 eV), an  $I_1^{\text{Deep}}$  line (at 2.7828 eV) and a phonon replica of the  $I_1$  line are also visible.

The close pair lines from samples A and B are shown in Fig. 3. The relative intensities of pair lines of both samples are just about identical [10]. The line energies of specific shells of both samples are also very similar (sample B exhibits more substructure, which could be due to better resolution of shell substructure, but the overall similarity is still very striking) [11]. Therefore, the DAP species must be the same in both cases, and thus the lines in B also cannot be associated with the "P" peak at 2.683 eV, but must be associated with the shoulder at 2.695 eV. Thus two shoulders (i.e. minor peaks), one at 2.704 eV (A) and the other at 2.695 (B) eV are associated with identical DAP species. This requires stronger preferential pairing in one case (A) than in the other (B). We still note in this connection that a peak at  $\approx 2.69$  eV could be associated with  $\text{Li}_{\text{Zn}}$  as acceptor instead of  $\text{Na}_{\text{Zn}}$ . However, no lithium acceptor bound exciton (expected at 2.7921 eV e.g. ref. [12]) was observed, and this rules out that the shoulder is this peak. Another peak observed at  $\approx 2.69$  eV, the free-to-bound (conduction band to  $\text{Na}_{\text{Zn}}$  transition) peak, can also be ruled out because free-to-bound peaks do not shift with

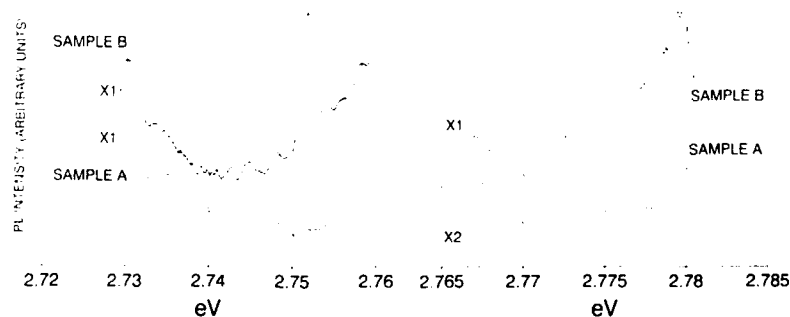


Fig. 3. Lines from close pairs of sample A (bottom) and sample B (top) at 9 K. The  $I_1^{\text{LO}}$  peaks of both samples (2.759–2.764 eV) are omitted. There is a change of scale for sample A from 1X to 2X as indicated. Note that the large peak at 2.7513 eV in sample B is the phonon replica of the  $I_1^{\text{Deep}}$ .

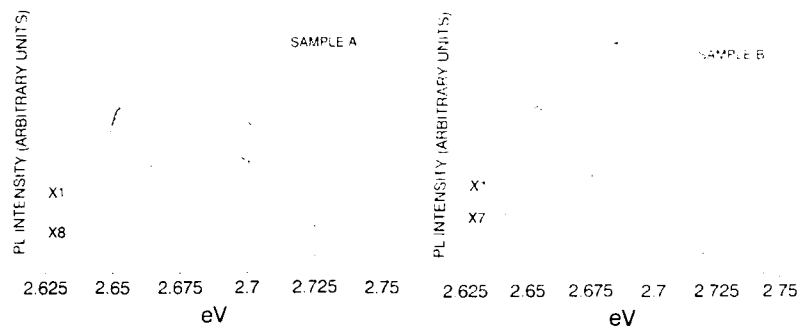


Fig. 4. Excitation intensity dependence of DAP peaks and shoulders of sample A (left) and sample B (right). The excitation intensity is 10 times higher for the spectra at the top than for the spectra at the bottom. There is a change of scale as indicated.

excitation intensity [1], while as shown in Fig. 4 the shoulder shifted with excitation intensity [13]. Thus, as stated above, we conclude that the shoulder at 2.695 eV in sample B *must also* be due to  $\text{Na}_1\text{--Na}_{\text{Zn}}$  pairs, but with weaker pairing than in sample A.

Our conclusion regarding preferential pairing is supported by the excitation intensity dependence of the spectra, shown in Fig. 4. The shoulders in both samples shift to higher energy with increasing excitation intensity faster than the “P” peaks. However, because  $\text{Na}_1$  donors in the shoulders have a lower binding energy than group III donors in the “P” peaks [2], we expect  $\text{Na}_1$  donors to have a larger Bohr radius [5] than group III donors. It is to be noted that, in absence of preferential pairing, a larger Bohr radius leads to a smaller Coulomb shift [6]. Thus, the observed larger shift of the shoulders must be attributed to preferential pairing (however, as argued above, sample B has weaker preferential pairing than sample A).

In conclusion, based on association of two different peaks in sample A and sample B with the same species and on the shift with excitation intensity of these peaks we have shown the existence of preferential pairing in  $\text{ZnSe}:\text{Na}$ . Also, from the peak location in the two samples, we conclude that there is stronger pairing in one sample (A) than in another (B). We also note that we believe this is the first time that different

DAP peaks have been associated with the same close pair lines.

#### 4. Acknowledgments

The samples were supplied by Philips Laboratories. We would like to thank Dr. M. Shone and Dr. B.J. Fitzpatrick for them. This work was supported by NSF grant DMR 91-21302.

#### 5. References

- [1] P.J. Dean, in: *Progress in Solid State Chemistry*, Vol. 8, Eds. J.O. McCaldin and J. Somorjai (Pergamon, Oxford, 1973) p. 1.
- [2] G.F. Neumark, *J. Electrochem. Soc.* 136 (1989) 3135.
- [3] W.E. Hagston, *J. Luminescence* 3 (1971) 253.
- [4] D.G. Thomas, M. Gershenson and F.A. Trumbore, *Phys. Rev.* 133 (1964) A269.
- [5] G.-J. Yi and G.F. Neumark, *Phys. Rev. B*, in press. (Note that we consider the Bohr radius of 36 Å given here as more reliable than an earlier value of 24 Å – e.g. ref. [2].)
- [6] G.F. Neumark, S.P. Herko and B.J. Fitzpatrick, *J. Electron. Mater.* 14 (1985) 1205. (Note that there is a misprint in Eq. (3) of this paper: the term  $(e^2/\epsilon_0)$  should have been  $(\epsilon_0/e^2)$ .)
- [7] G.F. Neumark, S.P. Herko, T.F. McGee III and B.J. Fitzpatrick, *Phys. Rev. Lett.* 53 (1984) 604.
- [8] M. Shone, B. Greenberg and M. Kaczinski, *J. Crystal Growth* 86 (1988) 132.
- [9] R.N. Bhargava, R.J. Seymour, B.J. Fitzpatrick and S.P. Herko, *Phys. Rev. B* 20 (1979) 2407.

- [10] Note that the intensities of the  $I_1$  line and its first phonon replica are higher in sample B than in sample A. Thus the relative intensity of the pair lines corresponding to shells No. 23–26 next to  $I_1^O$  (not shown in Fig. 3) is higher in B than in A due to peak overlap.
- [11] The position of comparable close pair lines in samples A and B differ by less than 1 meV. This is well within the experimental error.
- [12] P.J. Dean, D.C. Herbert, C.J. Werkhoven, B.J. Fitzpatrick and R.N. Bhargava, *Phys. Rev. B* 23 (1981) 4888.
- [13] As can be seen in Fig. 4, the shoulder in sample B is apparent only at high excitation intensity. This observation shows that it shifts to higher energy with increasing excitation intensity faster than the “P” peak.



ELSEVIER

Journal of Crystal Growth 138 (1994) 105–109

JOURNAL OF  
**CRYSTAL  
GROWTH**

## Organometallic vapor phase epitaxial growth of p-type ZnSe using phenylhydrazine as the dopant source

Salman Akram, Ishwara Bhat \*

*Electrical, Computer and Systems Engineering Department, Rensselaer Polytechnic Institute, Troy, New York 12180, USA*

### Abstract

The growth and nitrogen doping of ZnSe by photo-assisted organometallic vapor phase epitaxy (OMVPE) have been investigated using phenylhydrazine (PhHz) as the dopant source. The layers were characterized using photoluminescence (PL), secondary ion mass spectroscopy (SIMS) and capacitance–voltage ( $C-V$ ) measurements. A high incorporation of nitrogen was observed over the growth temperature range between 350 and 400°C, even when extremely low dopant partial pressure of  $10^{-8}$  atm was used. Typical layers had active acceptor concentrations of  $(1-2) \times 10^{17} \text{ cm}^{-3}$ . Low temperature growth kinetics with the above dopant source were investigated and a possible model for the nitrogen incorporation is presented.

### 1. Introduction

During the past two years, we have seen progress being made in achieving heavily doped, low resistivity p-type ZnSe [1]. This resulted in the demonstration of blue-green laser diodes at low temperatures [2], making the quest for efficient blue emission from ZnSe-related structures a reality. However, this success has been restricted to the use of molecular beam epitaxially (MBE) grown ZnSe, doped by active nitrogen. The demonstration of highly doped, low resistivity ZnSe:N material has remained elusive in an OMVPE environment, in spite of the fact that incorporation of nitrogen as a shallow acceptor was first demonstrated by OMVPE [3]. Earlier

studies on the use of ammonia ( $\text{NH}_3$ ) [4] as a dopant source for n-doped ZnSe by OMVPE did not result in low resistivity material. Recently, rapid thermal annealing (RTA) at 700–800°C of n-doped ZnSe doped by  $\text{NH}_3$  has yielded layers with a carrier concentration in the range of  $(1-3) \times 10^{16} \text{ cm}^{-3}$  [5]. Nitrogen from ammonia is believed to incorporate as  $\text{NH}$  or  $\text{NH}_2$ , thereby being electrically inactive. RTA may break some of these incorporated  $\text{NH}$  molecules, resulting in electrical activity. Therefore, alternate nitrogen precursors such as hydrazines and alkylamines must be explored which are thermally less stable than ammonia, and preferably deliver atomic nitrogen at the growth surface.

Hydrazine ( $\text{N}_2\text{H}_4$ ) is an undesirable dopant source because of its explosive nature, but phenylhydrazine, on the other hand, is less reactive and hence can easily be handled and purified. One advantage of the hydrazines over amines

\* Corresponding author.



Table 1  
Bond strength of hydrazine sources [6]

Source	Bonding	Bond strength <i>D</i> (kcal/mol)
Ammonia (NH <sub>3</sub> )	H–NH <sub>2</sub>	107.4
Hydrazine (N <sub>2</sub> H <sub>4</sub> )	H <sub>2</sub> N–NH <sub>2</sub>	65.8
Methylhydrazine (CH <sub>3</sub> HN <sub>2</sub> H <sub>3</sub> )	CH <sub>3</sub> HN–NH <sub>2</sub>	64.1
Dimethylhydrazine [(CH <sub>3</sub> ) <sub>2</sub> N <sub>2</sub> H <sub>2</sub> ]	(CH <sub>3</sub> ) <sub>2</sub> N–NH <sub>2</sub>	59
Phenylhydrazine [(C <sub>6</sub> H <sub>5</sub> )HN <sub>2</sub> H <sub>2</sub> ]	C <sub>6</sub> H <sub>5</sub> HN–NH <sub>2</sub>	52.3

is that the bonding configuration which includes a single nitrogen–nitrogen bond (N–N) is expected to have a lower bond strength than the single carbon–nitrogen (C–N) bond in the amine group of similar structural configuration. In Table 1, the bond strength of ammonia and some possible hydrazine source materials for nitrogen are listed [6]. Phenylhydrazine is seen to be thermally less stable as compared to other hydrazines. This should enable a much higher incorporation of nitrogen with low dopant flux and at low growth temperatures. Another advantage of phenylhydrazine is that its decomposition results in two nitrogen-containing radicals. The first radical, NH<sub>2</sub>·, is similar to that liberated in the decomposition of ammonia and the alkyl amines such as tertiarybutylamine ((CH<sub>3</sub>)<sub>3</sub>CNH<sub>2</sub>) and is a source of nitrogen. A significant ratio of these nitrogen radicals may incorporate directly as NH<sub>2</sub> or NH instead of N, which are likely to be electrically inactive.

Nitrogen liberated from the second radical (C<sub>6</sub>H<sub>5</sub>)HN could incorporate as atomic nitrogen at the growth surface, liberating benzene. Carbon contamination in the doped layers is expected to be low because the strong bonding configuration of carbon in the phenyl group may prevent cleavage of carbon from the ring at low growth temperatures. These advantages make PhHz a highly desirable source for n-doping of ZnSe by photo-assisted OMVPE.

We have explored the use of phenylhydrazine (C<sub>6</sub>H<sub>5</sub>HN–NH<sub>2</sub>) and obtained a typical acceptor concentration ( $N_A - N_D$ ) of  $1 \times 10^{18} \text{ cm}^{-3}$ . In addition, low temperature growth kinetics using

this new precursor were investigated, and a possible model for dopant incorporation is presented here.

## 2. Experimental procedure

The growth of ZnSe on GaAs substrates was carried out in a horizontal reactor using dimethylzinc (DMZn), dimethylselenide (DMSe) and phenylhydrazine (PhHz) as the reactants. Semi-insulating (100)GaAs, misoriented 2° towards (110), was used as a substrate. Growth was carried out at a reactor pressure of 300 Torr and a susceptor temperature in the range of 350–400°C using photo-assisted OMVPE [7]. Near bandgap photoexcitation at 50 mW/cm<sup>2</sup> level from a mercury arc lamp was used to irradiate the growth surface to enhance the growth rate. A 0.5 μm thick undoped buffer layer was first grown at 525°C, without using UV excitation, followed by a doped 2–3 μm active layer at 350–400°C range. Typical partial pressures used for DMZn and DMSe were  $2 \times 10^{-4}$  atm and  $8 \times 10^{-4}$  atm, respectively. Partial pressures of PhHz were in the range  $(1-10) \times 10^{-5}$  atm.

The grown layers were characterized by secondary ion mass spectroscopy (SIMS), capacitance–voltage (C–V) measurements and photoluminescence (PL). PL spectra were measured at 10 K using a 10 mW argon ion laser.

## 3. Results and discussions

First, we have carried out growth at high temperatures (500–525°C) and found that incorporation of nitrogen is negligible [8]. Growth at lower temperature, with UV excitation, resulted in significant incorporation of nitrogen. Typical spectra of doped ZnSe are shown in Fig. 1. The partial pressure of PhHz was  $8 \times 10^{-5}$  atm and the ratio of PhHz/DMSe was  $1 \times 10^{-1}$  for Fig. 1a. The PL spectra shown in Fig. 1a are dominated by a strong donor–acceptor pair (DAP) emission, at about 2.70 eV accompanied by phonon replicas and the near bandedge emission is dominated by an acceptor–bound exciton peak (I<sub>1</sub>) at 2.791 eV.

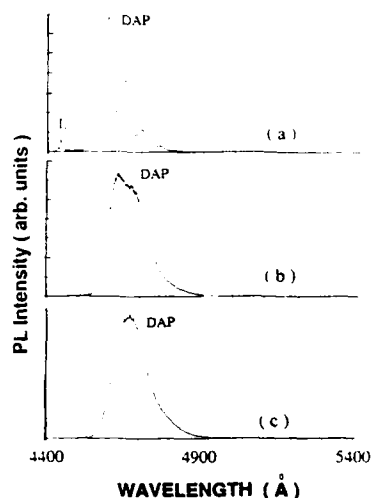


Fig. 1. PL spectra of doped layers: (a)  $\text{PhHz} = 8 \times 10^{-8}$  atm, temperature =  $380^\circ\text{C}$ ; (b)  $\text{PhHz} = 8 \times 10^{-8}$  atm, temperature =  $350^\circ\text{C}$ ; (c)  $\text{PhHz} = 1.6 \times 10^{-7}$  atm, temperature =  $350^\circ\text{C}$ .

The free exciton emission line ( $E_x$ ) and the donor-bound exciton peak ( $I_2$ ) are also observed, but with significantly lower intensities. Also shown in Fig. 1 are the PL spectra for  $\text{ZnSe:N}$  films grown under different conditions. Fig. 1b shows the PL spectrum for a sample grown with identical partial pressure as Fig. 1a, but at a lower growth temperature of  $350^\circ\text{C}$ . Fig. 1c is a PL spectrum from a sample grown at  $350^\circ\text{C}$ , but with a higher partial pressure of  $\text{PhHz}$  ( $1.6 \times 10^{-7}$  atm). Figs. 1b and 1c are dominated by a broadband DAP emission shifted to longer wavelengths, indicating significant acceptor compensation compared to sample of Fig. 1a. No emissions were observed in the excitonic region for these heavily doped layers.

The nitrogen concentration (N) in the  $\text{ZnSe:N}$  layer shown in Fig. 1a was determined to be  $2.5 \times 10^{18} \text{ cm}^{-3}$ . The SIMS profile for this film is shown in Fig. 2. The net acceptor concentration ( $N_A - N_D$ ) in  $\text{ZnSe:N}$  layers was estimated using conventional  $C-V$  profiling at 1 MHz. Two coplanar Schottky diodes were used for  $C-V$  measurements [8]. The actual capacitance measured needs to be corrected for large series resistance effects [9] when using high frequencies. Our

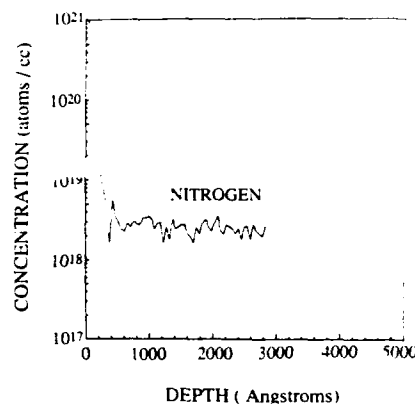


Fig. 2. SIMS profile of the nitrogen doped  $\text{ZnSe}$  shown in Fig. 1a.

structure has a series resistance of  $\sim 16 \text{ k}\Omega$  and the necessary corrections were made to the measured capacitance to obtain the junction capacitance. Fig. 3 shows  $1/C^2$  versus  $V$  plot of a layer which had a nitrogen concentration of  $2.5 \times 10^{18} \text{ cm}^{-3}$  measured by SIMS. The carrier concentration measured by  $C-V$  is approximately  $1 \times 10^{18} \text{ cm}^{-3}$ .  $C-V$  measurements on layers with broadband donor-acceptor (D-A) emissions showed them to be fully depleted, and therefore highly compensated.

Fig. 4 shows the growth rate at  $350^\circ\text{C}$  of  $\text{ZnSe:N}$  epilayers as a function of the dopant flow. A decrease in the growth rate is observed with an increase in  $\text{PhHz}$  flow. Fig. 5 shows the variation in growth rate with temperature for undoped  $\text{ZnSe}$  (A) and doped  $\text{ZnSe}$  (B) for a dopant partial pressure of  $3.0 \times 10^{-8}$  atm. A re-

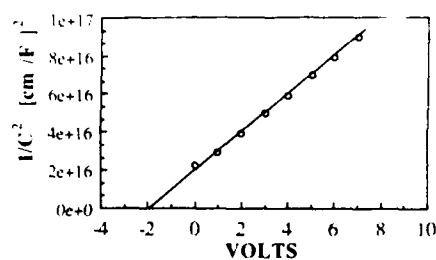


Fig. 3.  $C-V$  plot of  $\text{Au/ZnSe}$  Schottky barrier. Layer thickness is  $\sim 3.2 \mu\text{m}$ .

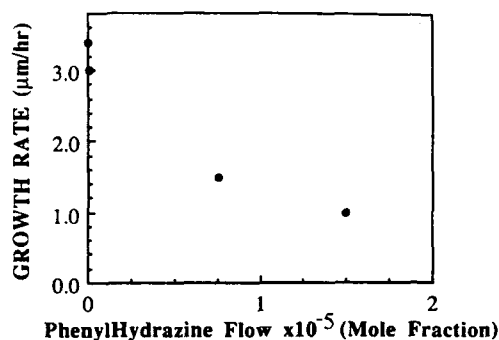


Fig. 4. Growth rate 350°C ( $\mu\text{m/h}$ ) as a function of PhHz flow rate.

duction in growth rate is observed for ZnSe:N layers. However, this reduction is seen to reduce with increased growth temperature. This clearly indicates that the decomposition products of phenylhydrazine being heavy molecules take longer to desorb from the growth surface at low temperatures (350°C), thereby blocking sites for incorporation of Zn and Se on the growth surface. At higher temperatures (380°C), the desorption of benzene is enhanced, thereby increasing nucleation sites for Zn and Se atoms on the surface. The flow of PhHz is low (PhHz/DMSe  $\approx 1 \times 10^{-4}$ ), so depletion of source molecules by parasitic gas phase reaction or adduct formation can be discounted. Based on these observations,

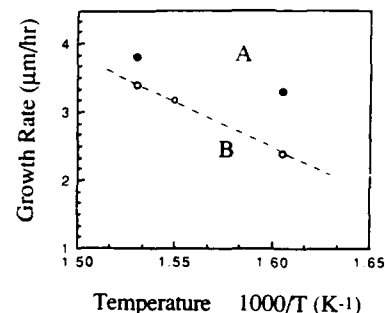


Fig. 5. Temperature dependence of growth rate for doped ZnSe (A) with a PhHz partial pressure of  $3.0 \times 10^{-5}$  atm and for undoped ZnSe (B).

we present a growth model for the incorporation of N into the ZnSe epilayers, as shown in Fig. 6. The phenylhydrazine molecule on arrival at the growth surface decomposes into two radicals ( $\text{C}_6\text{H}_5\text{HN}$  and  $\text{NH}_x$ ,  $\text{NH}_x$  ( $x \leq 2$ )) can incorporate as electrically inactive nitrogen. The second radical ( $\text{C}_6\text{H}_5\text{HN}$ ) may decompose into atomic nitrogen on the surface and benzene. If the growth rate is fast, this atomic nitrogen can incorporate before recombining with other nitrogen or hydrogen. However, the possibility of hydrogen from other sources to complete the benzene ring cannot be ruled out, thereby leaving  $\text{NH}$  on the growth surface as opposed to atomic nitrogen. The use of He as a carrier gas instead of  $\text{H}_2$

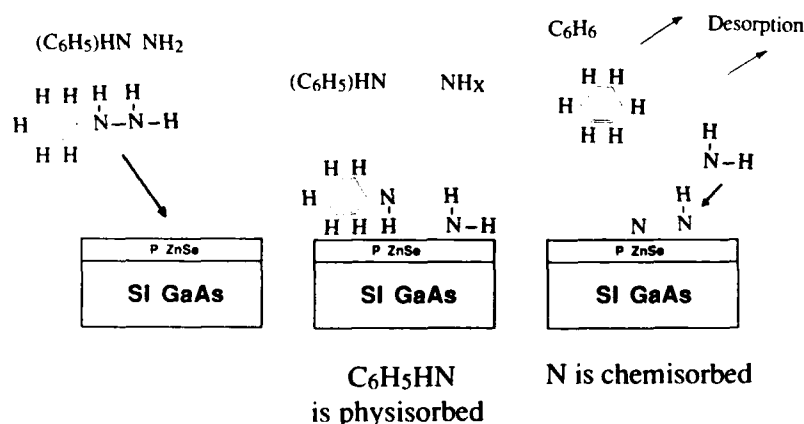


Fig. 6. A possible growth model for the incorporation of nitrogen using PhHz as the dopant source.

could reduce such an effect. Based on the electrical activity of our doped layers, we believe both atomic nitrogen and  $\text{NH}_x$  radicals get incorporated. A higher growth rate and a lower pressure with He carrier gas may enhance the incorporation of atomic nitrogen, based on the above model. Preliminary studies with layers grown at  $380^\circ\text{C}$  (Fig. 5) which exhibited a higher growth rate revealed more electrically active nitrogen as expected.

#### 4. Conclusion

Photo-assisted OMVPE growth of nitrogen-doped ZnSe was investigated using phenylhydrazine. SIMS measurement show that nitrogen incorporation of  $2.5 \times 10^{18} \text{ cm}^{-3}$  is possible with very low dopant partial pressures, typically in the  $10^{-8}$  atm range. The incorporation efficiency of nitrogen from PhHz is 3–4 orders of magnitude higher than from ammonia or alkylamines. PL measurements on ZnSe:N layers confirmed the incorporation of nitrogen as a shallow acceptor.  $\text{C}-1^+$  measurements of the ZnSe:N layers indicated p-type conductivity with net acceptor ( $N_A - N_D$ ) concentration typically in the  $(1-2) \times 10^{15} \text{ cm}^{-3}$  range. The growth kinetics of the doped layers was also investigated and a possible incorporation model was presented based on these experimental observations. These initial results show that phenylhydrazine is a promising dopant

source, and the use of optimized growth technique and RTA anneals may further increase the active concentration.

#### 5. Acknowledgements

We would like to thank J. Barthel for technical assistance and P. Magilligan for manuscript preparation. We are grateful to Andreas Melas for providing the new nitrogen source and Steve Novak of Evans East for SIMS measurements. Partial support was provided by N.A. Philips Laboratories in the form of a student fellowship to S.A. and is gratefully appreciated.

#### 6. References

- [1] R.M. Park, M.B. Trotter, C.M. Rouleau, J.M. DePuydt and M.A. Haase, *Appl. Phys. Lett.* 57 (1990) 2127.
- [2] M.A. Haase, J. Qiu, J.M. DePuydt and H. Cheng, *Appl. Phys. Lett.* 59 (1991) 1272.
- [3] W. Stutius, *Appl. Phys. Lett.* 40 (1982) 246.
- [4] A. Yoshikawa, S. Muto, S. Yamaga and H. Kosai, *Jap. J. Appl. Phys.* 27 (1988) 992.
- [5] N.R. Taskar, B.A. Khan, D.R. Dorman and K. Shahzad, *Appl. Phys. Lett.* 62 (1993) 270.
- [6] CRC Handbook of Physics and Chemistry 10th ed., Ed. R.C. Weast (CRC Press, 1990).
- [7] Sz. Fujita and Sg. Fujita, *J. Crystal Growth* 117 (1992) 67.
- [8] S. Akram and I.B. Bhat, *J. Electron. Mater.*, in press.
- [9] B. Hu, G. Karczewski, H. Luo, N. Samarth and J. Furdyna, *Appl. Phys. Lett.* 64 (1993) 358.



ELSEVIER

Journal of Crystal Growth 138 (1994) 110–113

JOURNAL OF  
**CRYSTAL  
GROWTH**

## Auto-doping of Ga in ZnSe/GaAs layers grown at low temperatures by post-heated molecular beam epitaxy

Minoru Yoneta, Hiroshi Saito \*, Masakazu Ohishi

*Department of Applied Physics, Okayama University of Science, Ridai-cho 1-1, Okayama 700, Japan*

### Abstract

The donor species in Li acceptor-doped ZnSe epilayers grown on GaAs substrate are determined by means of the secondary ion mass spectroscopy (SIMS). The compositional depth profile by the SIMS points out that a large amount of Ga atoms are incorporated into the ZnSe epilayer regardless of doping. In doped epilayers, the Ga atoms are concentrated at the region where the Li atoms are doped. We conclude that Ga atoms originating from the droplets due to the thermal cleaning of the substrate are most likely the major donor species.

### 1. Introduction

A new technique for doping nitrogen in molecular beam epitaxy has enabled us to grow low resistive p-type ZnSe epilayers [1]. What hinders us to grow low resistive p-type ZnSe using other acceptor species such as Li, P, etc.? Does the problem exist only in the doping techniques? For epilayers doped with these acceptor species, low temperature photoluminescence (PL) spectra show without exception emission lines due to the recombination of donor–acceptor pairs, the so-called Q-DAP band, even if no donor species are intentionally doped [2]. This is usually ascribed to the occurrence of shallow donors in conjunction with the doping process. Nevertheless, no new bound exciton line associated with the induced donor could be observed. Furthermore, it is be-

yond our understanding that the reduction of resistivity for highly N-doped ZnSe is closely related to the appearance of another DAP band in the low energy side of the Q-DAP band, indicating that other deeper donors are induced [3].

The present studies are intended to make sure which kinds of species are responsible to the donors, i.e. induced donors or external donors. Li-doped ZnSe epilayers were grown by using the post-heated molecular beams. Low temperature PL and secondary ion mass spectroscopy (SIMS) have clarified that Ga atoms originating from Ga droplets on the substrate are major donors.

### 2. Experimental procedures

Semi-insulating Cr- and O-doped GaAs with surface orientation of (001) are used as substrates. After chemical etching using the conventional  $\text{H}_2\text{SO}_4$  and  $\text{H}_2\text{O}_2$  solution, two types of surface cleaning were employed in the high vac-

\* Corresponding author.

uum growth chamber prior to the molecular beam epitaxial (MBE) growth: (1) The substrate is only thermally cleaned at the typical temperature of 580°C, showing the  $(4 \times 1)$  reflection high-energy electron diffraction (RHEED) reconstruction pattern. It is well known that Ga droplets are formed by the thermal cleaning at high temperatures [4]. Process (2) is aimed at obtaining Ga droplet-free substrate surface. That is, just after the RHEED streaky pattern appears, which indicates the achievement of the thermal cleaning, the substrate is exposed to an As beam cracked at 600°C with a beam pressure of  $P(\text{As}) \sim 3 \times 10^{-6}$  Torr until the substrate is cooled down to 400–250°C. RHEED showed the  $(2 \times 1)$  reconstruction pattern, which however was different from the  $c(2 \times 2)$  pattern usually observed for the As-stabilized surface. In this paper we refer mainly to the results obtained using process (2).

ZnSe/GaAs epilayers were grown by using hot Zn and Se molecular beams (PH-MBE) at growth temperatures of  $T_g = 250^\circ\text{C}$  [5]. Both the Zn and the Se beams were post-heated at 600°C with flux pressures of  $P(\text{Zn}) \sim 3 \times 10^{-7}$  Torr and  $P(\text{Se}) \sim 1 \times 10^{-6}$  Torr, respectively, measured by means of an ion gauge, corresponding to VI/II  $\sim 1$  in terms of the number of atoms [6]. As the p-type doping material we used Li. The doping levels were varied by changing the Li effuser temperature,  $T(\text{Li})$ . In order to study the extent of the diffusion of doped-Li atoms, we have grown epilayers with a structure consisting of three layers, i.e., Li-doped ZnSe is sandwiched by non-doped ZnSe layers. Each layer was grown for 1 h and has nearly the same thickness of about 0.4  $\mu\text{m}$ .

Grown layers were characterized by low temperature photoluminescence (PL), and double crystal X-ray diffraction measurements. The compositional depth profile was measured by SIMS using  $\text{Ar}^+$  ions with the energy of 11–17 keV as the primary ion beam.

### 3. Experimental results and discussion

Fig. 1 shows PL spectra measured at 4 K for Li-doped epilayers grown on substrates prepared

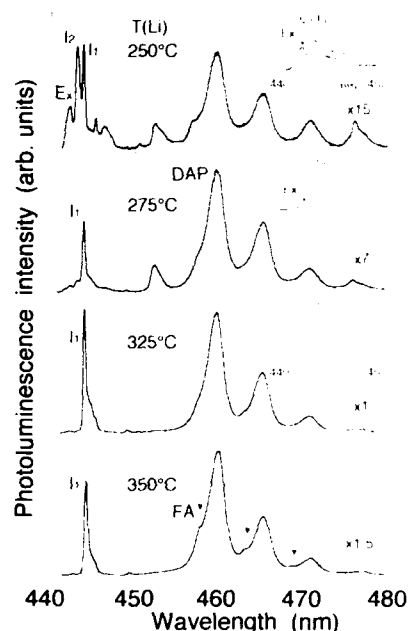


Fig. 1. Photoluminescence spectra measured at 4 K for epilayers grown at 250°C under different Li doping levels on substrates prepared by process (2).

by process (2), where the As-treatment was performed at 580°C for 10 min. At the lowest doping level the spectra consist of two sharp lines denoted as  $I_2$  and  $I_1$  and equally spaced 3 to 4 broader lines denoted as DAP. With increasing doping level, both  $I_1$  and the DAP become stronger, whereas the  $I_2$  line intensity remains nearly constant. At higher doping levels the intensity of these luminescence lines decreases, and instead another equally spaced line denoted as FA appears at the high-energy side of the DAP. In addition to these results, measurements of temperature dependence and excitation intensity dependence of PL spectra have clarified that the  $I_1$  line is ascribed to the bound exciton recombination associated with the Li acceptor, the DAP band to the recombination between unknown donor and Li acceptor, corresponding to the so-called Q-DAP band, and FA is the free carrier-to-Li acceptor recombination. The energetic position of these lines and bands yields the binding energy of the Li acceptor of about 110 meV and

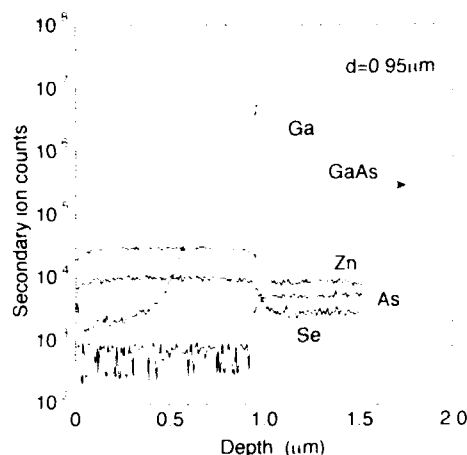


Fig. 2. Compositional depth profile measured by SIMS for non-doped sample grown at 250 °C on substrate prepared by process (2).

that of the unknown donor of about 28 meV, assuming the Coulomb energy associated with the donor-acceptor recombination to be 14 meV [7]. This value of the binding energy for the unknown donor is very close to that for a typical donor in ZnSe such as Cl and Ga [8]. It is pointed out that epilayers grown on the substrate prepared by process (1) show almost the same PL spectra as those shown in Fig. 1.

Full widths at half maximum (FWHMs) of the rocking curves measured by the double-crystal X-ray diffraction method are about  $\theta = 250$  arc sec for epilayers grown below  $T(\text{Li}) < 200^\circ\text{C}$  and are narrower than that for non-doped samples. For  $T(\text{Li}) > 200^\circ\text{C}$  the value of FWHM increases and at  $T_e = 275^\circ\text{C}$  it amounts to about  $\theta = 700$  arc sec. The results suggest the degradation of crystal quality for highly doped epilayers, in accordance with the decrease in PL intensity.

In order to determine which kinds of donor species are responsible for the DAP band, we analyzed epilayers by means of the SIMS. Fig. 2 shows a typical result of the compositional depth profile analysis in a non-doped sample grown at  $T_e = 250^\circ\text{C}$  on a substrate prepared by process (2), where the As-treatment was continued down to  $300^\circ\text{C}$ . No correction of the sensitivity of the apparatus for each ion was made. The steep

decrease of the Ga concentration near 1 μm depth from the surface corresponds to the interface between the GaAs substrate and the ZnSe epilayer. The shoulder following the steep decrease points out the existence of Ga atoms inside the ZnSe layer. The Ga concentration decreases with increasing distance from the interface, and then increases suddenly on the surface. The secondary ion count of Ga in the GaAs substrate is of nearly the saturation level of the apparatus, and therefore does not show the actual Ga concentration. We did not observe either the As distribution inside ZnSe or the Zn and Se distributions inside GaAs, indicating that the Ga distribution inside ZnSe is not caused by the mutual diffusion across the heterointerface. The Ga atoms are considered to be incorporated from the droplets on the growing surface into the epilayer.

Actually the Ga concentration in epilayers grown on the substrates prepared by process (2), e.g., Fig. 2, is found to be lower than in those grown on the substrate prepared by process (1). The results shown in Figs. 1 and 2 indicate that there exist still a large amount of Ga atoms even on the As-treated substrate surface.

Fig. 3 depicts an example of the SIMS analysis for a Li-doped epilayer grown on the substrate

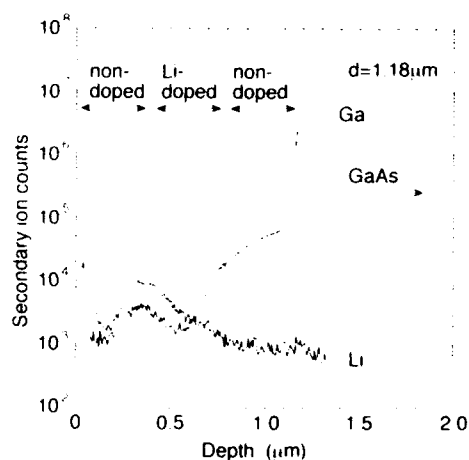


Fig. 3. Compositional depth profile measured by SIMS for Li-doped sample grown at 250 °C on substrate prepared by process (2).

prepared by process (2), where the As-treatment was continued down to 300°C. In Fig. 3 are shown the depth profiles only of Ga and Li to see clearly the relation between them. Remarkable difference compared with the non-doped sample shown in Fig. 2 is that the Ga distribution has a peak just at the position where Li shows a peak, although the peak is located not at the center of the Li-doped layer, but at the boundary of Li-doped and non-doped ZnSe. Similar depth profiles of Li and Ga are observed for epilayers grown under different As-treatment conditions. We cannot mention at present why the Ga atoms are concentrated in the Li-doped region and also whether a similar depth profile occurs even if other acceptor dopants, such as N, are used.

The SIMS analyses show no other III-group elements such as Al and In. Although the SIMS apparatus has almost no sensitivity for VII-group elements such as Cl and Br, which are also the donor species, we believe that no halogens are supplied from the source materials such as Li and Se. If any halogens are supplied from the Li dopant, the  $I_2$  intensity should increase with increasing doping level. If any halogens are supplied from the Se source, the  $I_2$  intensity should decrease with increasing doping level, because some portion of halogen atoms should take part in the DAP recombination. Experimentally the  $I_2$  line intensity remains nearly constant, independent of the Li-doping level. The SIMS results lead us to the conclusion that the Ga atoms are most likely the donor species contributing to the DAP band. The conclusion is in accordance with the observed binding energy for the unknown donor of about 28 meV. We need not to take any induced donors in conjunction with the Li-doping such as the interstitial Li atoms into consideration.

The SIMS result that the maximum of the Li distribution exists at the boundary of Li-doped and non-doped ZnSe epilayers cannot be ascribed to the thermal diffusion of Li atoms. The

probability of incorporation of Li atoms into ZnSe epilayers is considered to be in proportion to the Li density on the growing surface. We assume that the Li atoms are accumulated on the growing surface because the vapor pressure of Li is low enough compared with Zn and Se. This makes the maximum of the Li concentration to shift toward the direction of the epilayer surface.

Summarizing the results, Li-doped ZnSe layers grown by PH-MBE show the  $I_1$  neutral acceptor bound exciton line and the so-called Q-DAP band in low temperature photoluminescence spectra. SIMS analyses have clarified that a large amount of Ga atoms are incorporated into ZnSe epilayer whether Li is doped or not. Furthermore, the Ga atoms are concentrated in the region where the Li atoms are doped. These results lead us to the conclusion that the Ga atoms which may originate from the droplets owing to the thermal cleaning of the substrate are most likely the donor species contributing to the DAP band. The preparation of Ga-droplet-free substrate surfaces is an urgent problem to settle if thus incorporated Ga atoms are major donors in ZnSe.

#### 4. References

- [1] K. Ohkawa, T. Karasawa and T. Mitsuyu, *J. Crystal Growth* 111 (1991) 797.
- [2] Z. Zhu, H. Mori, M. Kawashima and T. Yao, *J. Crystal Growth* 117 (1992) 400.
- [3] L.S. Hauksson, J. Simpson, S.Y. Wang, K.A. Prior and B.C. Cavenett, *Appl. Phys. Lett.* 61 (1992) 2208.
- [4] B.A. Joyce, in: *Molecular Beam Epitaxy and Heterostructures*, Eds. L.L. Chang and K. Ploog (Nijhoff, Dordrecht, 1985) ch. 2, p. 37.
- [5] M. Yoneta, T. Hamasaki, M. Ohishi and H. Saito, *J. Vac. Sci. Technol. B* 11 (1993) 878.
- [6] M. Yoneta, M. Ohishi, H. Saito and T. Hamasaki, *Jap. J. Appl. Phys.* 32 (1993) L1106.
- [7] P.J. Dean, W. Stutius, G.F. Neumark, B.J. Fitzpatrick and R.N. Bhargava, *Phys. Rev. B* 27 (1983) 2419.
- [8] P.J. Dean, D.C. Herbert, C.J. Werkhoven, B.J. Fitzpatrick and R.N. Bhargava, *Phys. Rev. B* 25 (1981) 4888.





ELSEVIER

Journal of Crystal Growth 138 (1994) 114–120

JOURNAL OF  
**CRYSTAL  
GROWTH**

## Low pressure growth and nitrogen doping in metalorganic vapor phase epitaxy of ZnSe

Kohsuke Nishimura \*, Yasuyuki Nagao, Kazuo Sakai

*KDD R&D Laboratories, 2-1-15 Ohara, Kamifukuoka-shi, Saitama 356, Japan*

### Abstract

Low pressure (0.1–1.0 Torr) metalorganic vapor phase epitaxy (MOVPE) of ZnSe, using tertiarybutylselenol (t-BuSeH) as a selenium source precursor, was studied. Although several growth properties at such a low pressure were different from those at a higher reactor pressure, the quality of the layers grown at 1.0 Torr was as good as that of the layers grown at 300 Torr. Nitrogen doping into ZnSe was carried out at 1.0 Torr using nitrogen plasma excited by 2.45 GHz microwave. Nitrogen concentrations [N] of the doped layers ranged from  $2 \times 10^{17}$  to  $8 \times 10^{18} \text{ cm}^{-3}$ , measured by secondary ion mass spectrometry (SIMS), and photoluminescence spectra measured at 4.2 K of such layers were dominated by donor–acceptor pair emissions. However, all the as-doped layers were highly resistive n-type. It was found that hydrogen was incorporated into the doped layers, and its concentration was about 1.7 times more than [N] as established by SIMS measurement. Therefore it is probable that hydrogen passivates nitrogen acceptors in the doped layers. Several doped layers were annealed at 550–700°C in atmospheric  $\text{N}_2$  after deposition of  $\text{SiO}_2$  cap layers. The carrier types of part of the annealed samples were inverted to p-type, and their net acceptor concentrations were  $(3\text{--}7) \times 10^{15} \text{ cm}^{-3}$ .

### 1. Introduction

Nitrogen doping using plasma cell has been established as a doping technique for p-type ZnSe in molecular beam epitaxy (MBE) [1–3]. However, this technique was not studied much in metalorganic vapor phase epitaxy (MOVPE) growth of ZnSe. There are two major requirements for applying nitrogen plasma doping to MOVPE. One requirement is to lower the reactor pressure ( $P_r$ ), since the nitrogen radicals excited in plasma would be inactivated by colliding with the carrier gas molecules before reaching

the epilayer surface. The other requirement is to lower the growth temperature ( $T_g$ ) in order to enhance the sticking probability of nitrogen radicals onto the layer surface. As for lowering  $T_g$ , the authors have reported on MOVPE of ZnSe and ZnSSe at temperatures as low as 280°C, without premature reaction, using tertiarybutylselenol (t-BuSeH) as a selenium source precursor [4,5].

In this paper, we examined low pressure growth of non-doped ZnSe at 0.1–1.0 Torr. The quality of the epilayers grown at low pressure was as good as that of epilayers grown at atmospheric pressure. We also examined nitrogen plasma doping at 1.0 Torr. The nitrogen concentrations of the doped layers were as high as  $10^{17}\text{--}10^{18} \text{ cm}^{-3}$ .

\* Corresponding author.

However, all the as-doped samples were highly resistive n-type. Annealing these doped samples, their carrier types were inverted to p-type with net acceptor concentrations of  $(3\text{--}7) \times 10^{15} \text{ cm}^{-3}$ .

## 2. Experiments

Fig. 1 shows a schematic illustration of the MOVPE reactor. It consists of a horizontal reactor and a plasma cell, which are separated by a stainless orifice of 0.3 mm diameter located 80 mm apart from an RF heated carbon susceptor. A stainless shutter is also equipped in the vicinity of the orifice, so as to achieve a sharp interface of nitrogen-doped and non-doped (or n-doped) layers. The matrix source precursors are mixed in the tubings just before being introduced into the reactor, and blow against the substrate through a quartz nozzle. The reactor pressure,  $P_r$ , is controlled in the range 0.1–10 Torr by a variable conductance valve. Dopant gas, pure nitrogen ( $\text{N}_2$ , > 99.9999%), is introduced into the plasma cell through a microdust filter and a mass flow controller. The plasma cell pressure ( $P_p$ ) is determined by the  $\text{N}_2$  flow rate ( $[N_2]$ ) and  $P_r$ . The

microwave is fed from a 2.45 GHz magnetron oscillator, of which the output power ( $P_m$ ) is variable in the range 0–1 kW, to the plasma cell.

Semi-insulating (100) GaAs was used as a substrate. Matrix source precursors, diethylzinc (DEZn) and t-BuSeH, were transported by hydrogen ( $\text{H}_2$ ) carrier gas employing conventional bubbling method. The molar flow rate of DEZn ( $[DEZn]$ ) was constant at  $5 \mu\text{mol/min}$ , while  $[t\text{-BuSeH}]$  (or  $[VI]/[III]$  ratio) was varied in the range  $5\text{--}100 \mu\text{mol/min}$  ( $[VI]/[III] = 1\text{--}20$ ).  $T_s$  and  $P_r$  were varied in the range  $300\text{--}350^\circ\text{C}$  and  $0.1\text{--}1.0$  Torr, respectively.  $[\text{H}_2]$  and  $[\text{N}_2]$  were also varied in the range  $30\text{--}1000$  SCCM and  $2\text{--}20$  SCCM, respectively.

The grown layers were characterized by photoluminescence (PL) measured at room temperature (RT) or 4.2 K using the 325 nm line of a He–Cd laser as the excitation light. Double-crystal X-ray rocking curves were measured using  $\text{Cu K}\alpha_1$  radiation and (400) reflection. Secondary ion mass spectrometry (SIMS) measurement and capacitance–voltage ( $C\text{--}V$ ) measurement were also done for several doped samples.  $C\text{--}V$  measurements were performed at 10 kHz with the double-Schottky barrier configuration. After

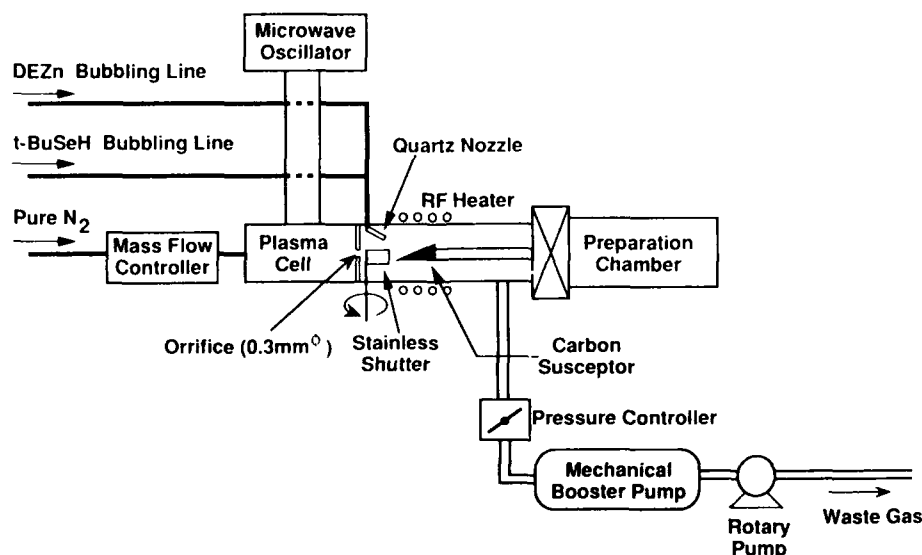


Fig. 1. Schematic illustration of the low pressure MOVPE reactor with a plasma cell.

evaporating gold on the epilayer surface as a Schottky electrode, the rings of 5  $\mu\text{m}$  in width and 500  $\mu\text{m}$  in diameter were removed by photolithography technique. The area ratio (or capacitance ratio) of smaller to larger electrode was typically 0.01.

### 3. Results and discussion

#### 3.1. Non-doped layers

Fig. 2 shows the growth rate dependence on the ratio of total flow rate (TFR) introduced into the reactor to  $P_r$ , which indicates the gas flow velocity. The growth rate decreased almost exponentially with increasing the velocity, except when the TFR/ $P_r$  ratio was more than several thousands. It suggests that the source precursors diffuse through the boundary layer in the vicinity of the substrate surface when the TFR/ $P_r$  ratio is less than 1000. As evidence, the in-plane deviation of thickness was relatively small ( $\pm 1$ –5%), even though the gaseous sources blew against the substrate through the nozzle.

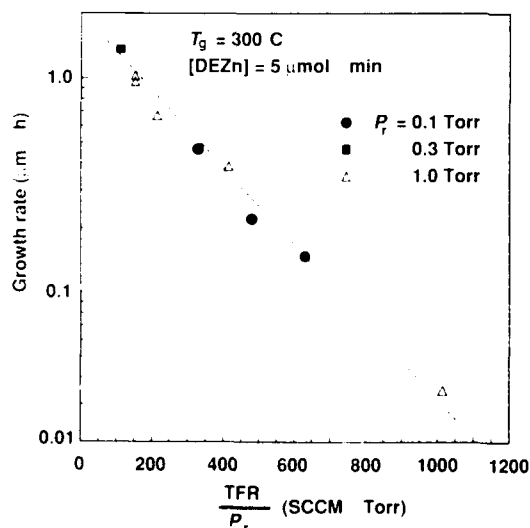


Fig. 2. Growth rate dependence on the ratio of the total flow rate (TFR) to the reactor pressure ( $P_r$ ).

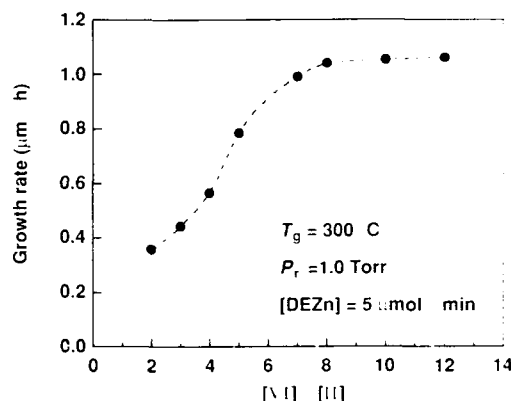


Fig. 3. Growth rate dependence on [VI]/[II] ratio.

Fig. 3 shows the growth rate at  $T_g = 300^\circ\text{C}$  and  $P_r = 1.0$  Torr as a function of [VI]/[II] ratio. As seen from the figure, the growth rate at 1.0 Torr did not saturate in the range [VI]/[II]  $\leq 8$ , while that at 300 Torr saturated in the range [VI]/[II]  $\geq 1$  [5]. It is presumable that the reduction of the partial pressure of t-BuSeH resulted in a higher desorption ratio of Se from the epilayer surface. This also implies that the [VI]/[II] ratio in order to achieve ZnSe of good quality is higher at 1.0 Torr than that at 300 Torr. Therefore the [VI]/[II] ratio was set at 10 for the growths discussed hereafter.

All the layers exhibited almost deep-free PL spectra at RT. We also measured PL spectra at 4.2 K for non-doped layers. A typical spectrum is shown in Fig. 4. The spectrum is dominated by near-band-edge (NBE) emissions together with several emissions denoted by Y and S, which are generally attributed to the extended-defect related emissions [6]. The deep-center emissions denoted by SA, which are generally attributed to the donor zinc-vacancy complex emissions [7], were relatively weak. The NBE emissions consist of free-exciton emissions ( $E_x$ ) and neutral-donor-bound exciton emissions ( $I_2$ ), of which the superscripts lh and hh stand for light- and heavy-hole transitions [8]. The peak intensity of  $E_x$  is larger than that of  $I_2$ , and it is proof of the high purity of these non-doped layers. We have found previously that the donor impurities, which form

$I_2$  emission centers, originated from t-BuSeH, and the major residual impurity might be chlorine [5,6]. The auto-doping of donor impurity is an unfavorable phenomenon in terms of carrier compensation of nitrogen acceptor, which is discussed in the next section. However, all these non-doped samples were n-type but highly resistive, and we could not evaluate the free electron concentration by Hall measurement. Therefore the background donor concentration is expected to be low enough not to spoil the p-type doping.

The full width at half maximum of the X-ray rocking curve for the layer of 1.1  $\mu\text{m}$  thickness grown at 300°C, 1.0 Torr and 200 SCCM was 300 arc sec. It is as small as those for the layers grown at 300 Torr [6].

### 3.2. Nitrogen doped layers

The nitrogen doping was carried out with nitrogen plasma flow and with the shutter open. The typical growth rate was 1.1  $\mu\text{m}/\text{h}$ , and typical thickness of the doped layer was 3.3  $\mu\text{m}$ .

Fig. 5 shows the 4.2 K PL spectra of the doped layers with various nitrogen concentrations. The donor-to-acceptor pair (DAP) emission, which was weak in the non-doped layer spectra, is dominant and its phonon replicas are clearly observed. The zero-phonon lines for relatively light-doped layers stand at 2.70 eV, while those for heavy-doped layers shift to the lower energy side. Such behavior of DAP emission is similar to that reported for MBE grown N-doped layers. The FWHMs of X-ray rocking curves of doped layers were 10–20% larger than those of non-doped layers.

Fig. 6 shows the nitrogen concentration [N] measured by SIMS versus  $P_p$  when  $P_m = 200$  W and  $P_r = 1.0$  Torr. [N] increases from  $7 \times 10^{17}$  to  $8 \times 10^{18} \text{ cm}^{-3}$  as  $P_p$  increases from 6 to 13 Torr. It saturates at  $[N] \approx 8 \times 10^{18} \text{ cm}^{-3}$  in the range  $13 \leq P_p \leq 21$  Torr, and [N] drops again in the range  $P_p \geq 21$  Torr. Fig. 7 shows the  $P_m$  dependence of [N] when  $P_r = 1.0$  Torr and  $P_p = 6.0$  Torr. [N] gradually increases as  $P_m$  increases, but the varying range is not so wide as the varying range with  $P_p$ .

In spite of the existence of nitrogen acceptors,

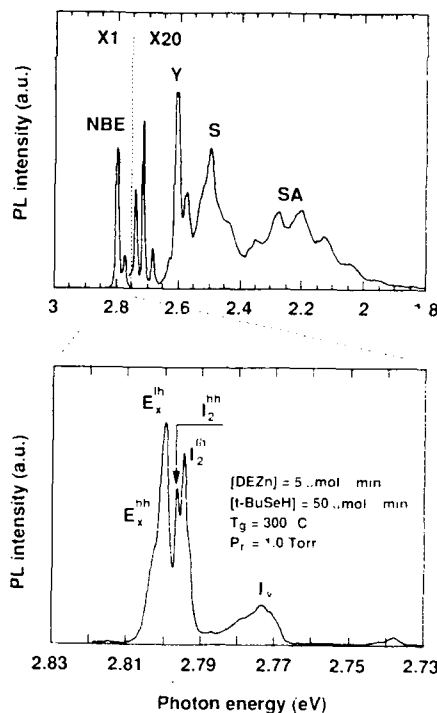


Fig. 4. Typical photoluminescence spectrum measured at 4.2 K for non-doped ZnSe layer grown at 1.0 Torr.

all these as-doped layers were highly resistive n-type, as found by  $C-V$  measurement. Fig. 8 shows the hydrogen concentration [H] of these layers as a function of [N]. There can be seen a linear relation between [N] and [H], and  $[H]/[N] \approx 1.7$ . Since the hydrogen concentrations of non-doped layers are below detection level, doping of nitrogen radicals induces hydrogen incorporation. Therefore it is supposed that the hydrogen-related centers passivate the nitrogen acceptors. Kamata et al. reported similar results for atmospheric pressure MOVPE of ZnSe using ammonia ( $\text{NH}_3$ ) as a dopant [9]. They also found hydrogen incorporation in nitrogen-doped layers, and concluded that the hydrogen was one of the most probable inactivation centers of the nitrogen acceptor.

In order to clarify the origin of hydrogen in nitrogen-doped layers, several growths in  $\text{N}_2$  carrier gas were carried out. Both [N] and [H] in the

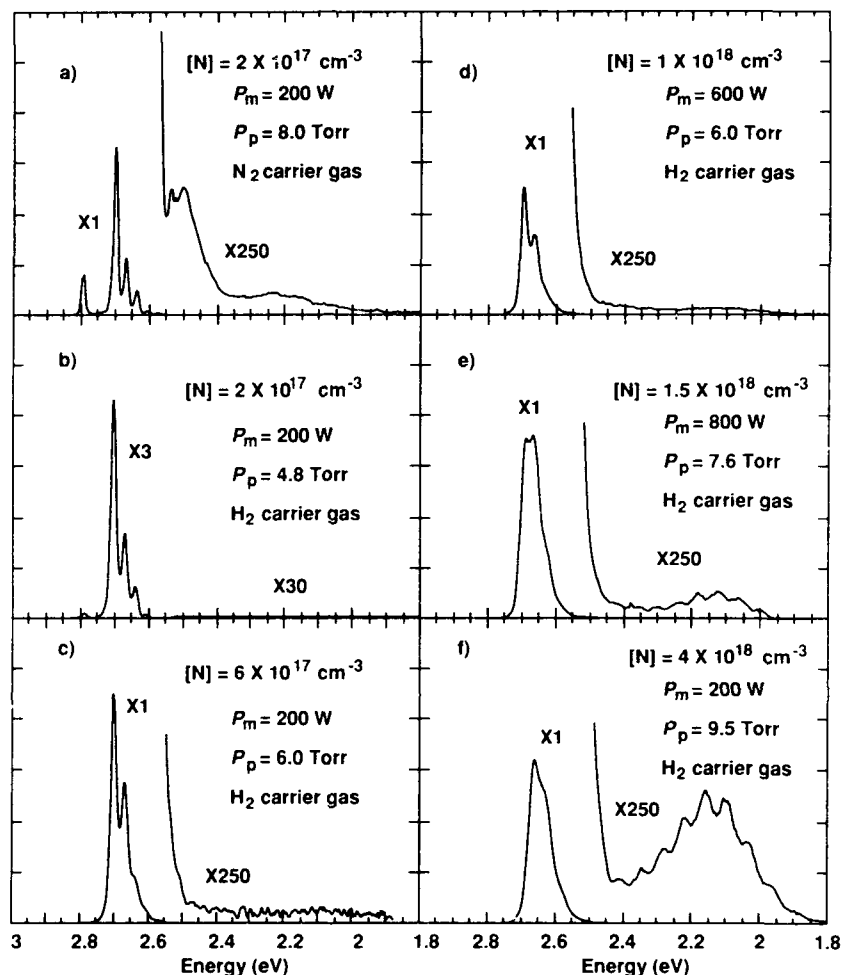


Fig. 5. 4.2 K photoluminescence spectra for nitrogen doped layers with various nitrogen concentrations. The growth conditions for each layer are shown in the figure.

layers grown in  $N_2$  were about 1/10 of those in the layers grown in  $H_2$  with identical growth parameters, but the  $[H]/[N]$  ratio did not change. Since the hydrogen in the doped layers grown in  $N_2$  cannot be from the carrier gas, it must come from the source precursors. From this result, we can say that most of the nitrogen radicals react with carrier  $H_2$ . In addition, they also react with hydrogen involved in the organic source precursors, although their rate is less than that of the  $H_2$  carrier gas. These reactions between nitrogen

radicals and hydrogen probably produce  $NH$  or  $NH_2$  radicals, which has high chemical reactivity.

We tried to anneal several samples after depositing  $SiO_2$  cap layers by plasma-assisted chemical vapor deposition. They were annealed at 550–700°C in atmospheric nitrogen varying the annealing temperature ( $T_a$ ) and duration time ( $t_a$ ). It was found that the conductivity type of part of these samples was inverted to p-type. However, the dependence of carrier type inversion on  $T_a$  or  $t_a$  was not definitely confirmed.

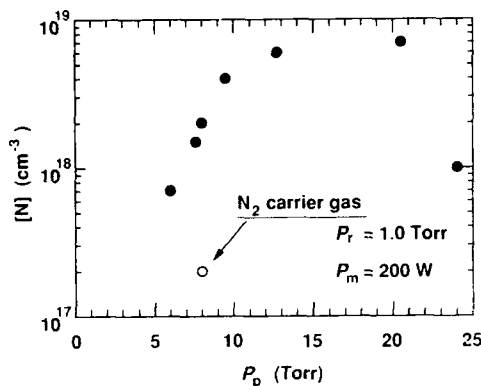


Fig. 6. Nitrogen concentration ( $[N]$ ) as a function of plasma cell pressure ( $P_p$ ): (●)  $[N]$  in the layers grown in  $H_2$  carrier gas, (○)  $[N]$  in the layer grown in  $N_2$  carrier gas.

The net acceptor concentrations,  $N_a - N_d$ , of annealed layers ranged from  $3 \times 10^{15}$  to  $7 \times 10^{15} \text{ cm}^{-3}$ . The rate of activation,  $(N_a - N_d)/[N]$ , was still less than 1% after annealing. It suggests that most of the nitrogen acceptors were still compensated.

SIMS measurements of doped and annealed samples were carried out. There was no distinct difference in both  $[H]$  and  $[N]$  between as-doped samples and annealed samples. Therefore rearrangement of either hydrogen or nitrogen atoms probably yields free acceptors. Taskar et al. also reported on the annealing effect of MOVPE-grown nitrogen-doped layers using  $NH_3$  [10]. They

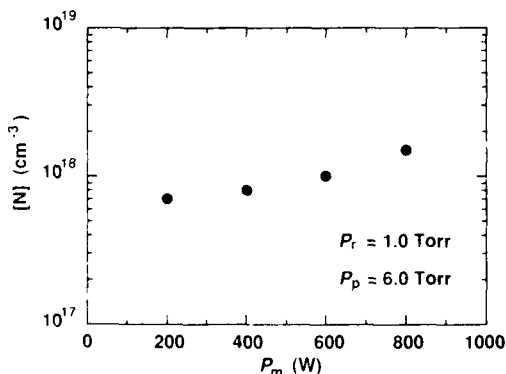


Fig. 7. Nitrogen concentration ( $[N]$ ) as a function of microwave power ( $P_m$ ).

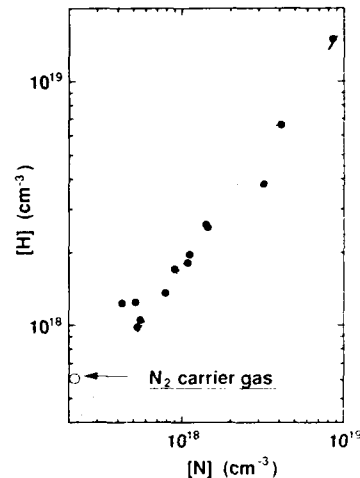


Fig. 8. Hydrogen concentration ( $[H]$ ) versus nitrogen concentration ( $[N]$ ) for nitrogen doped layers: (●) plots for the layers grown in  $H_2$  carrier gas, (○) plot for the layer grown in  $N_2$  carrier gas.

reported that annealing N-doped samples, which were also highly resistive when as-grown, at temperatures higher than  $700^\circ\text{C}$  in atmospheric nitrogen resulted in the inversion of carrier type from n- to p-type. The p-type conversion for our samples occurred at a lower temperature than that for their samples, and it is probably due to the fact that our samples were grown at lower temperature than their samples.

#### 4. Conclusion

Low pressure MOVPE growth of ZnSe using t-BuSeH as a selenium precursor was studied. Although several growth properties such as growth rates were different from those for atmospheric pressure growth, the quality of the layers grown at low pressure was as high as that of the layers grown at atmospheric pressure.

Nitrogen radical doping using plasma cell was examined, and doped layers incorporated nitrogen at concentrations as high as  $2 \times 10^{17}$  to  $8 \times 10^{18} \text{ cm}^{-3}$ . However, these as-doped samples were all highly resistive n-type. From SIMS results, the most probable species that compensates nitrogen

acceptor is hydrogen, which has originated mainly from  $H_2$  carrier gas.

Doped samples were annealed at 550–700°C in atmospheric  $N_2$  with  $SiO_2$  cap layers. The carrier types of doped and annealed samples were inverted, and net acceptor concentrations were  $N_A - N_D = (3-7) \times 10^{15} \text{ cm}^{-3}$ .

### 5. Acknowledgments

The authors would like to thank Drs. Y. Urano and Y. Takahashi for their continuous encouragement. They are also grateful to Drs. Y. Mimura and Y. Matsushima for fruitful discussions, and to Mr. N. Ishihara of the Electro-Communication University for assistance in measurement.

### 6. References

- [1] R.M. Park, M.B. Trotter, C.M. Rouleau, J.M. DePuydt and M.A. Haase, *Appl. Phys. Lett.* 57 (1990) 2127.
- [2] K. Ohkawa, T. Karasawa and T. Mitsuyu, *Jap. J. Appl. Phys.* 30 (1991) L152.
- [3] J. Ou, J.M. DePuydt, H. Cheng and M.A. Haase, *Appl. Phys. Lett.* 59 (1991) 2992.
- [4] K. Nishimura, Y. Nagao and K. Sakai, *Jap. J. Appl. Phys.* 32 (1993) L428.
- [5] K. Nishimura, Y. Nagao and K. Sakai, *J. Crystal Growth* 134 (1993) 293.
- [6] S. Myhalenko, J.L. Batstone, H.J. Hutchinson and J.W. Steeds, *J. Phys. C* 17 (1984) 6177.
- [7] J.C. Bouley, P. Blanconnet, A. Herman, P. Ged, P. Henoc and J.P. Noblanc, *J. Appl. Phys.* 46 (1976) 3539.
- [8] K. Shahzad, *Phys. Rev. B* 38 (1988) 8309.
- [9] A. Kamata, H. Fujita and H. Mitsuhashi, in: *Extended Abstracts 53rd Autumn Meeting of the Japan Society of Applied Physics*, Suita, 1992, p. 226.
- [10] N.R. Laskar, B.A. Khan, D.R. Dorman and K. Shahzad, *Appl. Phys. Lett.* 62 (1993) 270.



ELSEVIER

Journal of Crystal Growth 138 (1994) 121–126

CRYSTAL  
GROWTH

## Contamination effects from tellurium in ZnS–ZnSe superlattices

D. Bouchara, A. Abounadi, M. Di Blasio, N. Briot, T. Cloitre, O. Briot, B. Gil <sup>\*</sup>,  
J. Calas, M. Averous, R.L. Aulombard

*Groupe d'Etudes des Semiconducteurs, Université de Montpellier II, Case Courrier 074, F-34095 Montpellier Cedex 5, France*

### Abstract

We have studied the temperature dependence of the photoluminescence of tellurium-doped ZnS–ZnSe superlattices. By comparing the reflectivity and photoluminescence data, we were able to identify both free exciton recombination and self-trapped exciton band energy split by 90 meV. The behaviour of the photoluminescence with temperature results from trapping versus detrapping effects which are ruled by an activation energy of 80 meV. This behaviour is analysed in the context of a configuration coordinate diagram.

### 1. Introduction

There is a currently increasing interest in ZnS–ZnSe superlattices due to their potential utilization for realization of advanced visible light emitters. Various substrates have been tested in the literature, including GaAs [1–5], Si [6], ZnS [7], CaF<sub>2</sub> [8,9], etc. Presently, it seems that GaAs is established as the best candidate, due to combined reasons that are linked to its lower cost and high crystalline quality when compared to other polar substrates. The growth of ZnS–ZnSe directly onto GaAs may lead to contamination by diffusion from the substrate. It is thus essential to employ a good quality II–VI buffer layer between the substrate and the superlattice in order to optimize the electronic properties of the structure. In this context, we expect a very low defect density if growth of the II–VI superlattice occurs

after a ZnS<sub>0.6</sub>Te<sub>0.4</sub> buffer layer, lattice-matched to GaAs, has been deposited. However, earlier spectroscopic studies have widely demonstrated that alloying ZnX (X = S, Se) with Te leads to exciton self-trapping, causing a strong Stokes shift between luminescence and reflectivity features, even at very low tellurium concentration [10–13]. Moreover, the photoluminescence of samples where exciton self-trapping occurs is several orders of magnitude more intense than in the absence of this effect. Such a phenomenon should be encountered in ZnS–ZnSe superlattices if contaminated by tellurium. It is therefore important to determine how large could be the consequences of tellurium incorporation for the optical properties of such superlattices.

This work reports on the influence of the introduction of tellurium at doping level (assuming that a ZnS–ZnSe superlattice and a ZnSTe buffer were grown in the same growth chamber, during the same run) on the optical properties of a ZnS–ZnSe superlattice. A series of reflectivity and photoluminescence data revealed a small

<sup>\*</sup> Corresponding author.



Stokes shift (10 meV) between the two experiments. The 2 K photoluminescence spectrum exhibits a strong photoluminescence band about 90 meV below the free exciton band. This low energy band disappears when the temperature increases, and the photoluminescence is dominated by free-exciton contribution at high temperature. We interpret this in terms of exciton self-trapping at tellurium centers and analyse our data in the context of the configuration coordinates approach in order to obtain the activation energies which rule the effect.

## 2. Sample growth

The ZnS–ZnSe superlattice was grown using an ASM OMR 12 MOVPE equipment. The sample was deposited onto a (100) epi-ready GaAs wafer. Prior to the growth, the surface oxide was thermally desorbed from the substrate for 10 min at 550°C under a hydrogen flow. We have employed the triethyl amine dimethyl zinc adduct ( $\text{Me}_2\text{ZnNEt}_3$ ) as a zinc precursor in order to minimize the premature reactions with the hydrides [14].  $\text{H}_2\text{Se}$  and  $\text{H}_2\text{S}$  were used as selenium and sulfur precursors, respectively. The carrier gas was palladium-purified hydrogen and the  $\text{H}_2$  flow through the reactor was 3.3 SLM (standard litres per minute) during the growth experiment. The VI/II molar flow ratio was set to 5 during both ZnSe and ZnS layer growth. The precursor flows were set as follows:  $\text{Me}_2\text{ZnNEt}_3 = 30 \mu\text{mol/min}$ ,  $\text{H}_2\text{S} = 150 \mu\text{mol/min}$  and  $\text{H}_2\text{Se} = 150 \mu\text{mol/min}$ . The deposited structure consists of 45 periods of 37 nm ZnSe and 33 nm thick ZnS layers deposited onto a 0.3  $\mu\text{m}$  thick ZnSe buffer layer. These thicknesses were deduced from the growth rates, and were confirmed by X-ray experiments. Growth interruptions were introduced between each layer deposition in order to optimize the interface abruptness since such a procedure is of crucial importance, as previously demonstrated for ZnSe–ZnTe superlattices [15]. In order to simulate the effect of residual tellurium contamination originating from a ZnSTe buffer layer, we have grown the superlattice immediately after the growth of a ZnTe

layer had been performed in the same growth chamber. No particular reactor cleaning was performed between these two growth runs. We believe that this procedure is particularly useful to evaluate separately the effect of cross contamination between a tellurium-containing buffer layer and the ZnS–ZnSe superlattice.

## 3. Experimental data

Fig. 1 illustrates the reflectivity and high-energy photoluminescence features at 2 K. The transitions related to the buffer layer are detected at 2.8 eV and those related to the superlattice at 2.95 and 3.05 eV. A small Stokes shift is observed between the free exciton photoluminescence peak and the low-energy reflectance structure of the superlattice. The 2.95 eV structure is more pronounced than its higher energy (3.05 eV) companion, as expected when these two transitions are identified as the heavy-hole excitons and the light-hole excitons [16]. In fact, an intensity ratio of 3:1 is given by standard group theory for the band-to-band process in zinc-blende crystals [17]. The high-energy (3.23 eV) reflectance structure corresponds to the spin-orbit split-off exciton freely propagating in the ZnSe buffer layer. This transition is the analogue of the 2.8 eV structure corresponding to  $\Gamma_8$ -related heavy-hole and light-hole transitions in this ZnSe buffer layer.

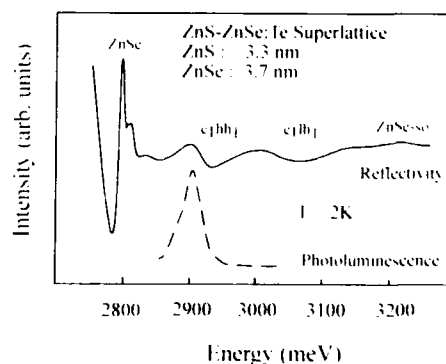


Fig. 1. 2 K reflectivity (upper curve) and near-band-edge photoluminescence (lower curve) for a 3.3 nm–3.7 nm ZnS–ZnSe superlattice.

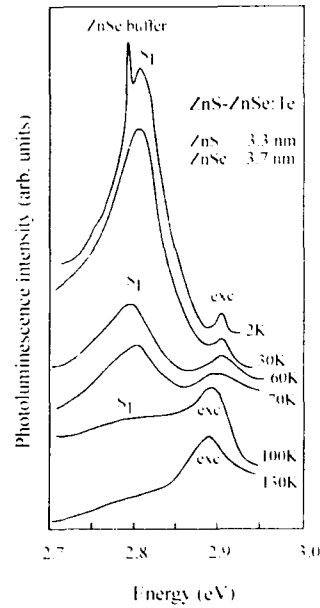


Fig. 2. Temperature dependence of the photoluminescence in ZnS-ZnSe:Te superlattice. Note the exchange of amplitude between free exciton (exc) and self-trapped exciton (S1) bands. Also note the photoluminescence signal of the ZnSe buffer (needle on the 2 K spectrum).

Following is a discussion on the photoluminescence data. Fig. 2 shows the evolution of the photoluminescence spectrum as the sample temperature increases. The 2 K photoluminescence spectrum exhibits a strong band (hereafter denoted S1) peaking at around 90 meV below the free exciton emission. When increasing the temperature, this S1 band collapses from 30 K, and disappears completely above 100 K, while the exciton transitions grows. This behaviour is similar to that previously reported for ZnSeTe alloys, where tellurium acts as an isoelectronic centre [10–13]. This strongly suggests that tellurium incorporation occurred in the sample during the growth. By analogy to data reported for ZnSeTe alloys, we interpret the photoluminescence behaviour in terms of thermally activated detrapping of excitons localized at Te-related centres [11,12].

#### 4. Data analysis

To quantify more completely the mechanisms involved in the evolution of the photoluminescence spectra with temperature, we employed a model to evaluate the electronic population of various levels resulting in these spectra. This model is based on arguments linked to a detailed balance principle similar to the model developed by Leroux-Hugon and Mariette [18] for studying the temperature dependence of exciton transfer between isoelectronic centres in GaP. Therefore,

$$\frac{dn_{Te}}{dt} = G_{Te} - R_{Te} = \phi_{ehp \rightarrow Te} + \phi_{exc \rightarrow Te} + \phi_{nr \rightarrow Te} - \phi_{ehp \leftarrow Te} - \phi_{exc \leftarrow Te} - \phi_{nr \leftarrow Te} - \frac{n_{Te}}{\tau_{Te}} \quad (1)$$

$$\frac{dn_{exc}}{dt} = G_{exc} - R_{exc} = \phi_{ehp \rightarrow exc} + \phi_{exc \rightarrow Te} + \phi_{exc \rightarrow nr} - \phi_{ehp \leftarrow exc} - \phi_{exc \leftarrow Te} - \phi_{exc \leftarrow nr} - \frac{n_{exc}}{\tau_{exc}} \quad (2)$$

The levels included in our model are: (i) the free electron-hole pair (ehp); (ii) free exciton (exc); (iii) tellurium self-trapped exciton (Te) and (iv) a certain number of non-radiative levels (nr). Here,  $n_i/\tau_i$  is the decay rate,  $\phi_{\alpha \rightarrow \beta}$  is the trapping rate from state  $\alpha$  to state  $\beta$ , and  $\phi_{\alpha \leftarrow \beta}$  is the detrapping rate from  $\beta$  to  $\alpha$ . We next assume that the generation rate  $G_{Te}$ , essentially  $\phi_{ehp \rightarrow Te}$ , is constant within the range of temperature of the experiments [12]. The temperature dependence of  $n_{Te}$  will therefore be essentially controlled by detrapping mechanisms via free exciton states and non-radiative centres. Taking into account two non-radiative centres, this can be written as:

$$\frac{dn_{Te}}{dt} = 0 = G_{Te} - \frac{n_{Te}}{\tau_{Te}} - n_{Te} \left[ \alpha_{Te \rightarrow exc} \exp\left(\frac{E_{Te} - E_{exc}}{k_B T}\right) + \alpha_{Te \rightarrow nr1} \exp\left(\frac{E_{Te} - E_{nr1}}{k_B T}\right) + \alpha_{Te \rightarrow nr2} \exp\left(\frac{E_{Te} - E_{nr2}}{k_B T}\right) \right] \quad (3)$$

$$\frac{dn_{exc}}{dt} = 0 = -\frac{n_{exc}}{\tau_{exc}} - n_{exc}\alpha_{exc \rightarrow chp} \times \exp\left(\frac{E_{exc} - E_{chp}}{k_B T}\right) + n_{Te}\alpha_{Te \rightarrow exc} \exp\left(\frac{E_{Te} - E_{exc}}{k_B T}\right). \quad (4)$$

Concerning Eq. (2), we assume the outcome rate from the free exciton level to non-radiative levels to be negligible. This is justified as follows: the non-radiative centres must probably lay in the vicinity of tellurium centres. For the trapped exciton, the mean free path is severely impeded by the high value of its effective mass [11]. On the other hand, as tellurium atoms must cause some disturbance in the lattice because of their size, one can think that they are associated with extended defects such as dislocations. Moreover, II–VI semiconductors generally exhibit a larger density of such defects than III–V compounds. Using these arguments, it can be understood that the coupling between trapped exciton and non-radiative centres is significant, while the coupling between the free exciton and these same non-radiative centres is negligible.

Rather than the capture cross section  $\alpha_{Te \rightarrow exc}$ , fitting of Eqs. (3) and (4) gives the product  $\tau_{Te}\alpha_{Te \rightarrow exc}$  together with 4 activation energies. Among these 4 activation energies, one ( $E_{chp} - E_{exc}$ ) can be taken from previous studies of electron to heavy-hole binding energies in ZnS–ZnSe superlattices. Since non-radiative levels do not appear directly in photoluminescence spectra, their presence in the sample is deduced from the irregular behaviour of the photoluminescence features.

Fig. 3 displays the behaviour of the S1-like and exciton luminescence features versus temperature. We did not succeed in fitting the experimental data without including non-radiative centres. In such a case, the filled S1 peak height remains unaltered at low temperature [12], while we clearly observe a decrease in the experimental data. We need to include two non-radiative levels in our calculations in order to correctly fit the experimental curve. The activation energies deduced from the fit are:  $E_{nr1} - E_{Te} = 2$  meV and

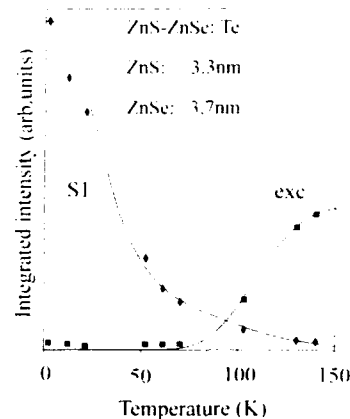


Fig. 3. Evolution of the integrated intensity of the photoluminescence bands in the ZnS–ZnSe:Te superlattice. Squares and diamonds are used to represent the experimental data for free exciton band and self-trapped exciton band respectively. The curves represent the fit to the data.

$E_{nr2} - E_{Te} = 12$  meV, with  $E_{exc} - E_{Te} = 80$  meV and  $E_{chp} - E_{exc} = 40$  meV. The series of  $\alpha\tau$  coefficients used in the fit is:

$$\tau_{Te}\alpha_{Te \rightarrow nr1} = 0.8, \quad \tau_{Te}\alpha_{Te \rightarrow nr2} = 37, \\ \tau_{Te}\alpha_{Te \rightarrow exc} = 28000, \quad \tau_{exc}\alpha_{exc \rightarrow chp} = 10.$$

Taking  $\tau_{exc} = 100$  ps [19] gives  $\alpha_{exc \rightarrow chp} \sim 10^{11}/s$ .

In the context of a configuration coordinate diagram, this gives the scheme reported in Fig. 4. The barrier potential is 16 meV for the exciton-to-tellurium path, while we fit 80 meV for the reverse process (tellurium to free exciton thermal detrapping). Including a temperature dependence for the generation rate  $G_{Te}$  would have intro-

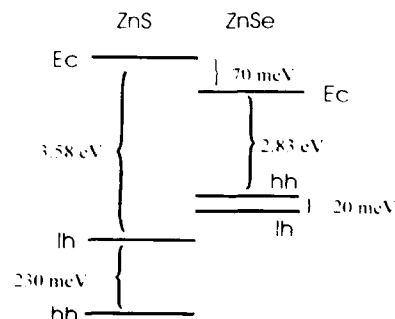


Fig. 4. Band line-ups in the ZnS–ZnSe superlattice.

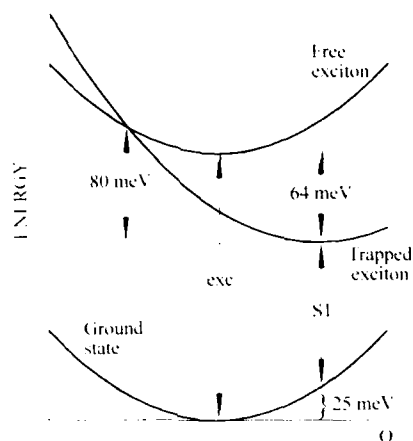


Fig. 5. Configuration coordinate diagram deduced from the fit to the data (see text for details).

duced additional parameters in the fitting procedure, but would not have significantly modified the conclusions, since trapping and detrapping mechanisms occur via barrier potential in a ratio 1:5! This *a posteriori* confirms the validity of this approximation. The binding energy of the electron-hole pair, say  $E_{\text{chp}} - E_{\text{exc}}$ , used in the fitting procedure is 40 meV. There is a significant increase in the binding energy in the sample compared to the bulk ZnSe value ( $\sim 17$  meV) [20]. This large value is related to the exciton confinement and is close to the one reported by Minami et al. [21] who found 41 meV from two-photon absorption spectroscopy for 20–20 Å ZnS–ZnSe free-standing superlattices, and is consistent with a type I configuration for the electron to heavy-hole transition.

The optical data have also been fitted in the context of the envelope function approach in the free standing hypothesis. The light-hole to heavy-hole splitting is 20 meV in the ZnSe layers and around 230 meV in the ZnS layer. In case of lattice matching to ZnSe buffer, we would have a larger splitting in the ZnS layers. The sensitivity of envelope function calculations is not sufficient enough (due to large dispersion of data in the literature for ZnS and ZnSe bulk parameters) to allow an accurate determination of the valence band offset in such samples when optical transi-

tions are broad. So, we preferred to use the values previously reported in the article. The observed experimental energies are nicely reproduced by using the conduction valence band profiles reported in Fig. 5 after Minami et al. [21]. We note that the confining potential is small in the conduction band and large in the valence band; it is also in good agreement with the theoretical predictions of Van de Walle [22] and Bertho and Jouanin [23].

## 5. Conclusion

We have studied the photoluminescence of tellurium-doped ZnS–ZnSe superlattices. The photoluminescence displays a complex temperature dependence. Both free exciton and self-trapped exciton photoluminescence lines are detected with energy differences of 90 meV. At liquid-helium temperature, the photoluminescence is dominated by contribution of self-trapped excitons. Increasing the temperature, the free exciton emission dominates the spectrum, and a quenching of the self-trapped exciton band is produced. The temperature dependence of the photoluminescence for the exciton and self-trapped exciton bands is interpreted in the context of a configuration coordinate diagram and is ruled by an activation energy of 80 meV. The Rydberg energy fit from the experiment is 40 meV, in agreement with values of the literature.

## 6. Acknowledgments

This work was supported by the Commission of the European Communities under contract Esprit III Basic Research number 6675 and by the "Région Languedoc-Roussillon".

## 7. References

- [1] H. Oniyama, S. Yamaga and A. Yoshikawa, Jap. J. Appl. Phys. 28 (1989) L2137.
- [2] P.J. Wright, B. Cockayne and P.J. Parbrook, J. Crystal Growth 104 (1990) 601.

- [3] J. Hermans, V. Wagner, J. Geurts, J. Woitok, J. Sölner, M. Heuken and K. Heime, *J. Vac. Sci. Technol. B* 10 (1992) 2062.
- [4] J. Cui, H. Wang and F. Gan, *J. Crystal Growth* 117 (1992) 505.
- [5] Y. Kawakami, T. Taguchi and A. Hiraki, *Technol. Rept. Osaka Univ.* 38 (1988) 109.
- [6] T. Yokogawa, H. Sato and M. Ogura, *J. Appl. Phys.* 64 (1988) 5101.
- [7] Y. Yamada and T. Taguchi, *J. Crystal Growth* 101 (1990) 661.
- [8] S. Denzhen, F. Xiwu and F. Guanghan, *Chin. J. Semicond.* 12 (1991) 758.
- [9] T. Yokogawa, T. Saitoh and T. Narusawa, *Appl. Phys. Lett.* 58 (1991) 1754.
- [10] S. Permogorov, A. Retznitskii, S. Verbin, G.O. Müller, P. Flögel and M. Nikitorova, *Phys. Status Solidi (b)* 113 (1982) 589, and references therein.
- [11] D. Lee, A. Mysyrowicz, A.V. Nurmikko and B.J. Fitzpatrick, *Phys. Rev. Lett.* 58 (1987) 1475.
- [12] C.D. Lee, H.L. Park, C.H. Chung and S.K. Chang, *Phys. Rev. B* 45 (1992) 4491; S.K. Chang, C.D. Lee, H.L. Park and C.H. Chung, *J. Crystal Growth* 117 (1992) 793.
- [13] K. Dhese, J. Goodwin, W.E. Hagston, J.E. Nicholls, J.J. Davies, B. Cockayne and P.J. Wright, *Semicond. Sci. Technol.* 7 (1992) 1210.
- [14] P.J. Wright, B. Cockayne, P.J. Parbrook, P.E. Oliver and A.C. Jones, *J. Crystal Growth* 108 (1991) 525.
- [15] N. Briot, T. Cloitre, O. Briot, B. Gil, D. Bertho, C. Jouanin, R.L. Aulombard, J.P. Hirtz and A. Huber, *J. Electron. Mater.* 22 (1993) 537.
- [16] B. Gil, Y.El Khalifi, H. Mathieu, C. de Paris, J. Massies, G. Neu, T. Fukunaga and H. Nakashima, *Phys. Rev. B* 41 (1990) 2885.
- [17] G. Bastard, *Wave Mechanics Applied to Semiconductor Heterostructures* (Editions de Physique, Paris, 1988).
- [18] P. Leroux-Hugon and H. Mariette, *Phys. Rev. B* 30 (1984) 1622.
- [19] Jie-Cui, Hai-Long Wang, Fu-Xi Gan, Xu-Guang Huang, Zhi-Gang Cai, Qing-Xing Li and Zhen-Xin Yu, *Appl. Phys. Lett.* 61 (1992) 1540.
- [20] H.W. Hölscher, A. Nöthe and Ch. Uhlem, *Phys. Rev. B* 31 (1985) 2379.
- [21] F. Minami, K. Yoshida, J. Gregus and K. Inoue, in: *Optics of Excitons in Confined Systems*, *Inst. Phys. Conf. Ser.* 123, Eds. A. D'Andrea, R. Del Sole, R. Girlanda and A. Quattropani (Inst. Phys., Bristol, 1992) p. 249.
- [22] C.G. Van de Walle, *Phys. Rev. B* 39 (1989) 1871.
- [23] D. Bertho and C. Jouanin, *Phys. Rev. B* 47 (1993) 2184.



ELSEVIER

Journal of Crystal Growth 138 (1994) 127–130

CRYSTAL  
GROWTH

## Atomic layer epitaxial growth studies of ZnSe using dimethylzinc and hydrogen selenide

Ishwara Bhat \*, Salman Akram

*Electrical, Computer, and Systems Engineering Department, Rensselaer Polytechnic Institute, Troy, New York 12180, USA*

### Abstract

Atomic layer epitaxial (ALE) growth studies of ZnSe were carried out in a low pressure horizontal metalorganic vapor phase epitaxial (MOVPE) reactor. Growth was carried out by alternately exposing the GaAs substrate to hydrogen selenide ( $H_2Se$ ) and dimethylzinc (DMZn) using flow modulation epitaxy (FME). It was found that at a susceptor temperature of 200°C and above, the adsorption of either of the reactants is extremely small and hence self-limiting monolayer growth does not take place. Significant deposition of ZnSe took place on the reactor wall in front of the susceptor as well. A hot wall reactor with colder susceptor configuration was used to prevent deposition on the reactor walls and also to confirm the growth model proposed.

### 1. Introduction

ALE is an attractive growth technique suitable for the deposition of thin, uniform layers with monolayer abruptness. The technique has been used for the growth of various II–VI semiconductors [1–6], using molecular beam epitaxy (MBE) and MOVPE. In MBE, constituent elements are deposited alternately on the substrate followed by a growth interruption. When more than a monolayer (ML) of material is deposited, the first ML is chemisorbed, and anything beyond are only physisorbed. Hence, during the growth interruption which is generally of the order of a few seconds, all the physisorbed elements are desorbed thus leaving 1 ML. The desorption of this chemisorbed ML element takes longer time and

the deposition of next layer occur before that happens.

In MOVPE, however, gaseous sources of the constituent elements are used. ALE growth is accomplished by the sequential flow of each reactant over the substrate followed by a flushing period. This is also termed as flow modulation epitaxy. If the gaseous sources decompose partially on the surface, then chemisorption of these constituents up to a ML is possible. This happens in the case of CdTe [5] where dimethylcadmium (DMCd) and diethyltelluride (DETe) are used as constituent precursors. During DMCd cycle, it decomposes on the surface in to Cd (or some intermediate) and covers the surface up to a monolayer level. During the DETe cycle, DETe reacts with fully adsorbed Cd to form a ML of CdTe. On the other hand, if gaseous sources do not decompose even partially, only physisorption of source molecules occurs. In this case, true ALE growth may or may not be possible depend-

\* Corresponding author.

ing on the desorption times of the adsorbed molecules. If the desorption time required is large in comparison to the gas flushing time, then self-limiting growth up to a ML may be possible.

Growth of ZnSe by ALE technique has been reported by many workers in a metalorganic molecular beam epitaxy (MOMBE) system [7,8]. Since Zn and Se source gases were cracked in MOMBE, the growth kinetics are similar to that of MBE. Koukita et al. [9] reported atmospheric pressure ALE growth of ZnSe using elemental zinc and hydrogen selenide. The GaAs substrate was alternately exposed to elemental Zn and  $H_2Se$  vapors by moving the substrates using a mechanical arm. ALE growth was obtained over the temperature range of 350 to 500°C, for various  $H_2Se$  and Zn pressures. In all the above cases, chemisorption of Zn takes place on ZnSe surface, and hence self-limiting ALE growth was observed.

Shibata and Katsui have used diethylzinc (DEZn) and  $H_2Se$  for the growth of ZnSe in an atmospheric pressure vapor phase epitaxial reactor using flow modulation technique [10]. Their system is potentially superior to the one using elemental Zn because of the ease of handling alkyl sources, and hence commercially viable. They have carried out the growth by the sequential introduction of DEZn and  $H_2Se$ , without any flushing period between them. They obtained a growth rate of more than 1 ML/cycle, indicating significant intermixing of gases caused by the absence of flushing period. Hence, the results were not conclusive whether ALE growth was achieved.

In this work, we have undertaken a careful study of ALE growth of ZnSe using dimethylzinc (DMZn) and  $H_2Se$  in a horizontal low pressure reactor. Our objective here is to investigate whether ALE growth of ZnSe using the above two precursors is a practical method to grow device quality ZnSe.

## 2. Experimental details

ALE growth experiments were conducted in a horizontal, 50 mm diameter reactor operated un-

der low pressure. The reactor pressure was kept at 100 Torr. Dimethylzinc (DMZn) and hydrogen selenide ( $H_2Se$ ) were used as the reactants. The flow velocity of the total gas through the reactor was over 13 cm/s so that it took less than a second to flush out the reactants from the front of the susceptor. To avoid any gaseous intermixing, we kept the flush period at 3 s. A typical ALE cycle consisted of 2 s of DMZn flow, 3 s of hydrogen flush period, 2 s of  $H_2Se$  flow and 3 s of  $H_2$  flush period, which will be designated as 2:3:2:3. These are typical numbers, but were varied to find out their effects on the growth rate. The reactor was equipped with a fast switching manifold.

## 3. Results and discussion

Fig. 1 shows the growth rate as a function of susceptor temperature. For this set of experiments, DMZn and  $H_2Se$  partial pressures were  $3 \times 10^{-5}$  and  $2 \times 10^{-4}$  atm, respectively, and flow sequence was 2:3:2:3. As the temperature was increased, there is a steady decrease in the growth rate and at 250°C and above, negligible growth rate was observed. In addition, the growth rate was not very uniform over the whole wafer, but gradually decreased along the flow direction. This is contrary to what is expected if the growth were true ALE type. Since  $H_2Se$  and DMZn react even at room temperature, significant deposition

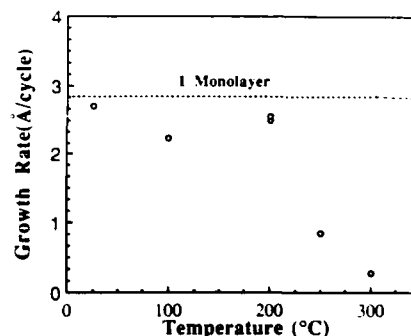


Fig. 1. Growth rate of ZnSe as a function of growth temperature.

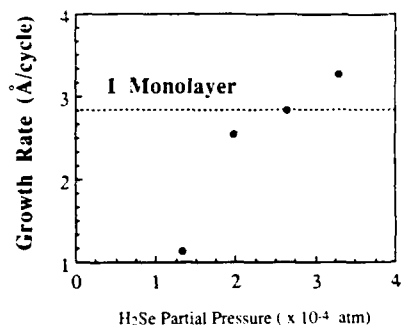


Fig. 2. Growth rate of ZnSe as a function of H<sub>2</sub>Se partial pressure. Growth temperature = 200°C. DMZn partial pressure =  $3 \times 10^{-5}$  atm.

was observed in the reactor tube in front of the susceptor as well.

To determine whether the supply of H<sub>2</sub>Se is limiting the ALE growth rate at 200°C, we increased the H<sub>2</sub>Se partial pressure keeping all other parameters constant. The results are shown in Fig. 2. As H<sub>2</sub>Se was increased, the growth rate continuously increased, but no clear saturation in the growth rate was observed. The growth rate increased beyond 1 ML/cycle, indicating that there is some intermixing of gases, even though we used sufficient time to flush out all the gases from the previous cycle. Therefore, effect of flushing period on the ZnSe growth rate was studied.

Fig. 3 shows the growth rate as a function of

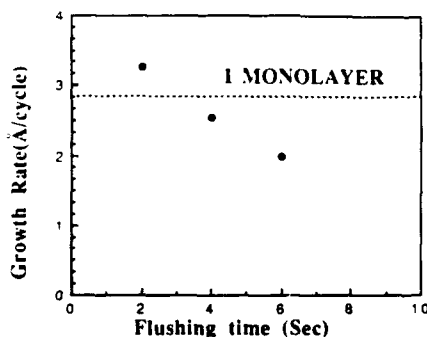


Fig. 3. Growth rate of ZnSe as a function of flushing period. Growth temperature = 200°C.

the flushing period of hydrogen. No self-limiting growth window was obtained under the conditions studied. Since, the growth rate decreased when the flushing period was increased, we believe the adsorption of either precursors is too weak for ALE growth to occur. Once again, the growth rates were not uniform over the whole sample on the susceptor, indicating that self-limiting growth windows were not obtained.

A more exhaustive investigation was undertaken in order to explain the above results. Based on our studies, we can explain the growth mechanism as follows. During DMZn part of ALE cycle, the reactant will get adsorbed on all colder part of the reactor and to a lesser extent on the heated sample as well. Since, DMZn does not decompose at the temperature studied, it will only be physisorbed. During the flushing cycle, all the reactants from the gas phase will be flushed out from the reactor as expected based on the flow rates used for the carrier gas. However, the desorption of DMZn from the reactor walls is a continuous process and will continue during the H<sub>2</sub>Se cycle as well. Hence, these desorbed DMZn will react with H<sub>2</sub>Se in the gas phase and this will result in growth of ZnSe on samples in the susceptor. H<sub>2</sub>Se will also react with the remaining DMZn on the reactor walls to form a continuous film on the wall.

In order to confirm the above model, a mass spectrometer should be installed to sample the exhaust gas. If the model is true, the DMZn (or H<sub>2</sub>Se) peak would steadily decay instead of abruptly dropping to the background level during the flush period. Since the mass spectrometer was not available, we tested the hypothesis by carrying out ALE growth experiments by heating the front end of the reactor tube. This will reduce the adsorption of DMZn (or H<sub>2</sub>Se) on the wall in front of the susceptor. Since ALE growth rate is close to zero at a growth temperature of 300°C, we kept the wall temperature at 300°C to prevent any growth at the walls, and kept the susceptor at 200°C. This arrangement should prevent any adsorption of the species on the wall, thus eliminating any depletion of the reactants, if any. Based on the decomposition study of Yoshikawa et al. [11], neither of the above reactants should de-



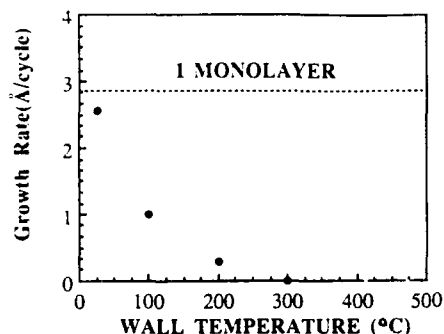


Fig. 4. Growth rate of ZnSe as a function of wall temperature. The susceptor was kept at 200°C.

compose due to the heated wall. No growth was observed either on the wall or on the samples. The results of repeating the experiments under various wall temperatures are plotted in Fig. 4. Note that negligible growth was observed even when the wall was heated to only 200°C. This indicates that the growths which occurred in our earlier experiments are due to the desorbed DMZn (or  $H_2Se$ ) from the reactor wall rather than from the adsorbed reactants on the substrates. This is our key result. The results were the same even when ZnSe coated reactor tubes were used. Hence, the adsorption of DMZn (or  $H_2Se$ ) is extremely low at growth temperatures of 200°C and above. When the wall temperature is 200°C or above, no adsorption of DMZn takes place on the wall and therefore no source of precursors for ZnSe growth during  $H_2Se$  growth cycle. Since the growth model suggests that it is not true ALE, the layers are not very uniform. Our studies indicate that the adsorption of DMZn or  $H_2Se$  is extremely small at the conditions studied, and much higher flows or flow times may be needed for monolayer adsorption. Yoshikawa et al. [7] also observed negligible adsorption of  $H_2Se$  on the substrates when growth was carried out in MOMBE system. Pre-cracking of DMZn source gas may be necessary to achieve device quality ALE layers.

#### 4. Summary

We have investigated the ALE growth of ZnSe in a low pressure MOVPE system using  $H_2Se$  and DMZn as the reactants. Growth was carried out using flow modulation epitaxy. Reactor conditions were varied in order to identify ALE growth window for ZnSe. We have found that true ALE of ZnSe using the above two sources may not be possible because the adsorption of the reactants on the substrate is very weak. Significant adsorption and subsequent desorption of the precursors take place on the reactor wall in front of the susceptor.

#### 5. Acknowledgement

We would like to thank J. Barthel for technical assistance. S.A. was partially supported by a fellowship grant from Philips Laboratories, and is gratefully appreciated.

#### 6. References

- [1] J. Lilja, J. Keskinen, H. Asonen and M. Pessa, *J. Crystal Growth* 95 (1989) 522.
- [2] S. Dosho, Y. Takemura, M. Konagai and K. Takahashi, *J. Appl. Phys.* 66 (1989) 2597.
- [3] C.H.L. Goodman and M.V. Pessa, *J. Appl. Phys.* 60 (1986) R65.
- [4] S. Yamaga and A. Yoshikawa, *J. Crystal Growth* 117 (1992) 152.
- [5] W.S. Wang, H. Ehsani and I.B. Bhat, *J. Crystal Growth* 124 (1992) 670.
- [6] Y. Wu, T. Toyoda, Y. Kawakami, S. Fujita and S. Fujita, *Jap. J. Appl. Phys.* 29 (1990) 1727.
- [7] A. Yoshikawa, T. Okamoto, H. Yasuda, S. Yamaga and H. Kasai, *J. Crystal Growth* 101 (1990) 86.
- [8] Y. Kawakami, T. Toyoda, Y. Wu, S. Fujita and S. Fujita, *Jap. J. Appl. Phys.* 29 (1990) 2440.
- [9] A. Koukitu, A. Saegusa, M. Kitho, H. Ikeda and H. Seki, *Jap. J. Appl. Phys.* 29 (1990) L2165.
- [10] N. Shibata and A. Katsui, *J. Crystal Growth* 101 (1990) 91.
- [11] A. Yoshikawa, H. Oniyama, S. Yamaga and H. Kasai, *J. Crystal Growth* 95 (1989) 572.



ELSEVIER

Journal of Crystal Growth 138 (1994) 131–135

JOURNAL OF  
CRYSTAL  
GROWTH

## Growth of CdTe/CdZnTe strained-layer single quantum wells by modified hot-wall epitaxy method and their properties

J.-S. Hwang <sup>\*</sup>, B.J. Koo <sup>1</sup>, I.H. Chung <sup>2</sup>, H.L. Park, C.H. Chung

*Department of Physics, Yonsei University, Seoul 120-749, South Korea*

### Abstract

Several CdTe/CdZnTe strained-layer single quantum well (SLSQW) structures, with CdTe well width ranging from 15 to 240 Å, were grown on GaAs(100) substrates, by modified hot-wall epitaxy (HWE) method for the first time. Our HWE system is equipped with a gold tube radiation shield which is more effective in heat confinement and temperature stability than conventional metal tubes. Photoluminescence (PL) measurements of SLSQW showed that the sharp  $e_1h_1$  excitonic transition peaks in the range of 1.597 to 1.624 eV shifted to the higher energy with decreasing well width. From the PL excitation (PLE) measurements of SLSQW, we obtained the  $n = 1, 2, 3$  and  $n = 1, 2$  excitonic transition peaks for the 240 and 120 Å CdTe well width SLSQW structures, respectively. The excitonic transition energies were calculated considering strain effects and this results were agreed well with experimental ones considering the exciton binding energy. Moreover, the FWHMs of excitonic transition peaks obtained from PL and PLE measurements were about 2 meV and Stokes shifts between PL and PLE spectra were about 1 meV. It indicates that the SLSQWs grown by HWE in this study have a high quality comparable to MBE-grown ones.

### 1. Introduction

Strained-layer structures in semiconductors have a great interest recently because of their device applications including high speed devices, laser diodes and infrared detectors [1,2]. Strained-layers modify the energy band gaps, heterojunction band offsets and band structures. Moreover, II–VI-based structures grown on the GaAs

substrate are increasingly studied and their strain effects are more important because of their large lattice mismatch. Strain can also inhibit the defect propagation. Sugiyama et al. [3] used the CdTe/CdZnTe strained-layer superlattices as a buffer layer to reduce the dislocation for fabricating HgCdTe epilayers on GaAs substrates.

Strained-layer structures are fabricated by various crystal growth techniques such as molecular beam epitaxy (MBE), metalorganic chemical vapor deposition (MOCVD) and hot-wall epitaxy (HWE). Among these techniques, HWE is a simple and inexpensive method compared to MBE or MOCVD, however, many studies report that HWE grown epilayers have a high quality, as good as MBE or MOCVD [4,5]. Therefore, HWE

<sup>\*</sup> Corresponding author.

<sup>1</sup> Present address: GoldStar Cable Co. Ltd., Anyang, South Korea.

<sup>2</sup> Present address: Samsung Electro-Mechanics Co. Ltd., Suwon, South Korea.

can be a promising epilayer growth technique for the production of strained-layer structures which can be used as a devices.

In this paper, we report the growth of CdTe/CdZnTe strained-layer single quantum wells (SLSQWs) on GaAs substrates for the first time by modified HWE method. The epilayer quality and the strain effect in CdTe/CdZnTe SLSQWs were examined by low temperature photoluminescence (PL) and PL excitation (PLE) spectroscopy. The results were compared with the calculated values considering strain effects and exciton binding energy.

## 2. Experiments

CdTe/CdZnTe SLSQWs were grown by the modified HWE system. Our system used a gold coated quartz tube as a radiation shield because it enhances the thermal properties (i.e., heat confinement and temperature stability) by its good infrared reflecting property. The detailed system modification and experimental results were reported elsewhere [6].

For the CdTe/CdZnTe SLSQW growth, (100)-oriented Cr-doped semi-insulating GaAs was used as a substrate. Sample preparation and growth procedure were described in ref. [7]. The structures of CdTe/CdZnTe SLSQWs consist of a CdTe well (width from 15 to 240 Å) sandwiched between 3 μm thick buffer and 1000 Å thick top CdZnTe barrier layers in which Zn composition is 6.4%. Low temperature PL was measured using a He-Ne laser (632.8 nm), a SPEX 1702 monochromator, a RCA-4832 photomultiplier tube and a conventional lock-in system at 18 K. The PLE measurement was the same as the PL measurement, except for the use of a Ti-sapphire laser which was tunable between 690 and 825 nm and excited by a 5 W Ar<sup>+</sup> laser.

## 3. Results and discussion

### 3.1. PL measurements

Fig. 1 shows the PL emission spectra of five CdTe/CdZnTe SLSQWs. The main peaks in the

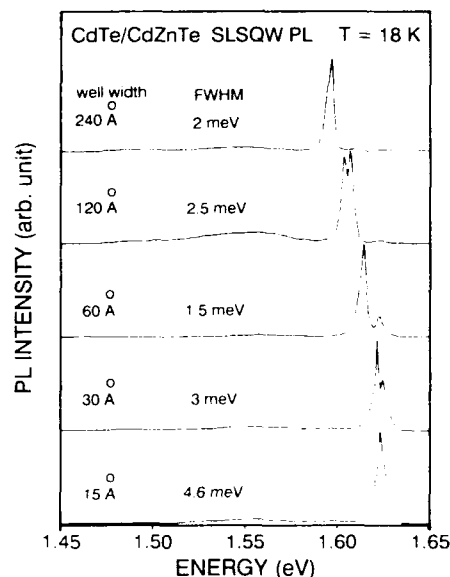


Fig. 1. Photoluminescence emission spectra at 20 K of CdTe/CdZnTe single quantum wells with different CdTe well widths (15, 30, 60, 120, and 240 Å).

energy range of 1.5967 to 1.6240 eV in the PL spectra were identified as  $e_1h_1$  excitonic transition peaks and shifted to the higher energy (blue shift) with decreasing CdTe well width as expected. From Fig. 1, the full width at half maxima (FWHMs) of  $e_1h_1$  excitonic transition peaks were about 2 meV in the well width of over 60 Å at 18 K, whose value is comparable to the MBE-grown ones, and it indicates that the HWE-grown SLSQWs have high quality structures. For 30 and 15 Å well width, due to the thickness fluctuation, PL spectra show slightly larger FWHM values, 3 and 4.6 meV, respectively. Because our HWE system does not use a shutter, which is used in MBE, the thickness fluctuation in a very thin epilayer (about 10 Å) is inevitable. In a SLSQW with 120 Å CdTe well, two main peaks were observed. The peak at 1.6069 eV was due to the  $e_1h_1$  excitonic transition peak and the peak at 1.6039 eV, 3 meV below the  $e_1h_1$  excitonic transition peak, was reported as a result of excitons trapped on impurities or interface defects [8]. Also, a broad defect band can be observed around 1.55 eV. The defect band intensity of 120 Å well

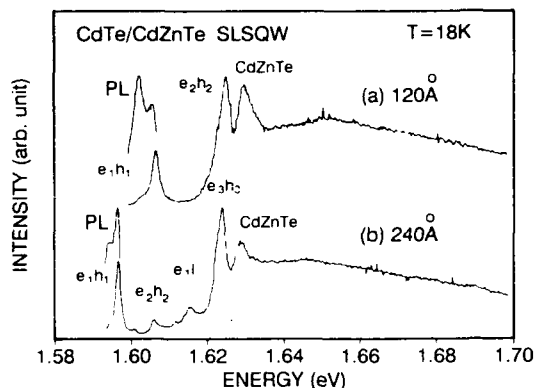


Fig. 2. Photoluminescence excitation spectra of CdTe/CdZnTe single quantum well with a CdTe well width of 240 Å (a) and 120 Å (b). The  $e_1h_1$  excitonic transition peak obtained from photoluminescence is inserted.

width was markedly intense in comparison with the others, and it is consistent with the appearance of the impurity related peak at 1.6039 eV. We obtained a peak at 1.6250 eV which is considered as an impurity bound exciton peak of CdZnTe barriers from five SLSQWs (in 15 Å well width; this peak is embedded in the main peak). This peak intensity, relatively smaller compared to the  $e_1h_1$  intensity at the width of 240 Å, was

increased with decreasing CdTe well width and was clearly observable for the thinner well width below 60 Å. It is believed that the excitonic emission intensity of relatively thinner well width is small due to the influence of thickness fluctuation.

### 3.2. PLE measurements

To obtain transition energies higher than the  $e_1h_1$  transition peak, we measured the PLE spectrum. In Fig. 2a, six peaks were observed. According to the quantized energy state calculation of 240 Å well width, it can have  $n = 1, 2$  and 3 states and therefore, the peaks at 1.597, 1.606 and 1.624 eV were considered as  $n = 1, 2$  and 3 excitonic transitions, respectively. The small peak at 1.601 eV was the first excited state of  $n = 1$  exciton and the peak at 1.629 eV has originated from the acceptor bound exciton of the CdZnTe buffer. We also obtained a small peak at 1.616 eV, which is considered to be the transition between the ground state electron and the light hole.

The PLE spectrum of 120 Å well width is shown in Fig. 2b. The peaks at 1.606 and 1.625 eV were  $n = 1$  and 2 excitonic transitions, respectively, and the peak at 1.630 eV has originated

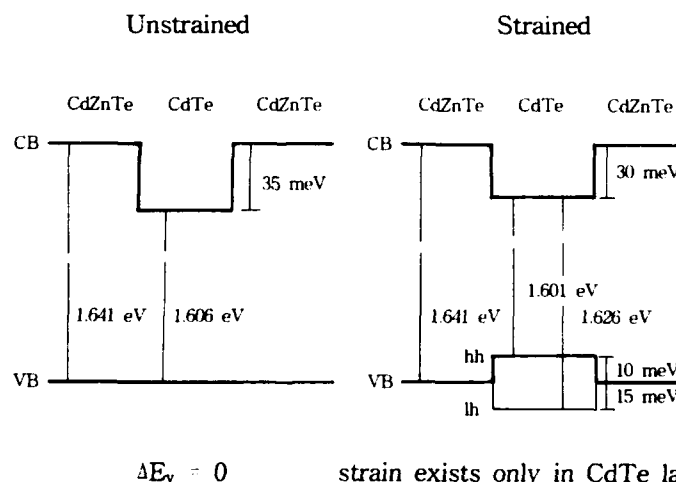


Fig. 3. Sketch of the CdTe/CdZnTe single quantum well conduction and valence band profiles: (a) unstrained and (b) strained. The thick and thin lines represent the heavy and light hole, respectively. Zn composition was 6.4%.

from the CdZnTe buffer layer, the same as the case of the 240 Å well width. Bastard et al. [9] explained that the Stokes shift between the absorption and the luminescence spectra was induced from the impurities or the excitons bound to the interface defect. Generally, the Stokes shift in III-V compounds was about 5 meV. For the case of 240 Å well width, an  $n = 1$  transition energy of 1.5964 and 1.5969 eV was obtained from PL and PLE, respectively. In the case of 120 Å well width, these energies were 1.6053 and 1.6064 eV obtained from PL and PLE, respectively. Thus, the Stokes shifts have small values of 0.5 and 1.1 meV in this experiment and such small values imply that the HWE-grown SLSQWs have a good interface.

### 3.3. Strain effect in CdTe/CdZnTe SLSQWs

In semiconductor heterostructures, the interfaces are strained due to lattice mismatch. The residual strain changes the band configuration and splits the degenerate valence band into heavy and light hole bands [10,11].

In Fig. 3, we depicted our result. In our calculations, we took the parameters from ref. [11]. The strain effect was considered only for a CdTe layer for two reasons: first due to the critical thickness, the 3  $\mu\text{m}$  thick CdZnTe buffer layer grown on a GaAs substrate was fully strain relaxed [12]; second, the CdTe layer is thin enough compared to the CdZnTe layers and so it does not affect the CdZnTe top layer. Therefore, we assume that the CdZnTe barriers have no strain. A calculation of quantized electron and hole sub-band energies was performed for each CdTe layer thickness by the finite potential well problem familiar from quantum theory. The valence band offset was assumed to be zero, and  $m_e^* = 0.099m_0$  and  $m_{hh}^* = 0.513m_0$  [13] were used. Fig. 4 shows the calculated  $e_1h_1$  excitonic transition energies (solid line) and the experimental ones obtained from PL and PLE measurements (open squares and filled triangles, respectively) as a function of the confined CdTe well widths. The experimental values showed a similar trend as the calculated values, but several meV below the calculated values. This difference is due to the heavy hole

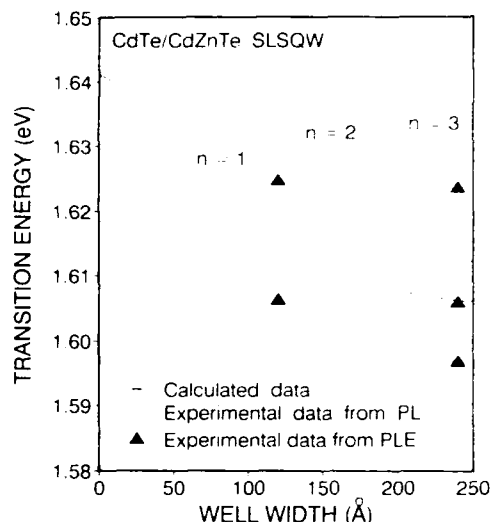


Fig. 4. The  $e_1h_1$  excitonic transition energies of different CdTe well width in a CdTe/CdZnTe single quantum well. Solid lines are calculated data considering the strain effects. Open squares and filled triangles are experimental data obtained from photoluminescence and photoluminescence excitation measurements, respectively.

exciton binding energy. From Fig. 4, we found that the exciton binding energy was about 10 meV for above 60 Å well width and 13 and 15 meV for 30 and 15 Å well width, respectively. As we know, the exciton binding energy increases as the well widths decrease. However, the reported value of exciton binding energy are around 14 meV for the range of 100 to 300 Å well width CdTe/CdZnTe SLSQW [14], and we consider that this difference has originated from the low CdZnTe barrier height and the thickness fluctuation in SLSQW.

### 4. Conclusion

In summary, high quality CdTe/CdZnTe SLSQWs were grown by modified HWE method. From the PL measurements of each SLSQW, the  $e_1h_1$  excitonic transition was obtained and its energy increased with decreasing CdTe layer thickness. We obtained the quantized excitonic transitions from the PLE spectra. Quantized sub-

band energies of the SLSQWs were calculated taking into account strain effects and the calculated  $e_1h_1$  transition energy agreed well with the experimental values. The obtained PL and PLE spectra indicate that the SLSQWs grown by HWE in this study have a high quality comparable to MBE grown ones. Thus, we conclude that HWE is a versatile method for the growth of high quality II–VI quantum wells.

### 5. Acknowledgements

We are indebted to Professor J.C. Woo, Seoul National University, for the PLE measurements and helpful discussions. This work was supported in part by the Korea Science and Engineering Foundation (KOSEF) through the SPRC of the Jeonbuk National University.

### 6. References

- [1] R. Hull and J.C. Bean, in: *Principles and Concepts of Strained-Layer Epitaxy in Semiconductors and Semimetals*, Vol. 33, Ed. R.K. Willardson and A.C. Beer (Academic Press, New York, 1991) ch. 1.
- [2] R.N. Bhargava, *J. Crystal Growth* 117 (1992) 894.
- [3] I. Sugiyama, A. Hobbs, T. Saito, O. Ueda, K. Shinohara and H. Takikawa, *J. Crystal Growth* 117 (1992) 161.
- [4] D. Schikora, H. Sitter, J. Humenberger and K. Fischka, *Appl. Phys. Lett* 48 (1986) 1276.
- [5] A. Ishida, K. Muramatsu, H. Takashida and H. Fujiyasu, *Appl. Phys. Lett* 55 (1989) 430.
- [6] J.-S. Hwang, B.J. Koo, I.H. Chung, H.L. Park and C.H. Chung, *J. Crystal Growth* 130 (1993) 617.
- [7] J.-S. Hwang, I.H. Chung, B.J. Koo, S.K. Chang, H.L. Park and C.H. Chung, *J. Korean Phys. Soc.* 26 (1993) 150.
- [8] Y. Merle D'Aubigné, H. Mariette, N. Magnea, H. Tuffigo, R.T. Cox, G. Lentz, Le Si Dang, J.-L. Pautrat and A. Wasiela, *J. Crystal Growth* 101 (1990) 650.
- [9] G. Bastard, C. Delalande, M.H. Meynadier, P.M. Emlink and M. Voos, *Phys. Rev. B* 29 (1984) 7042.
- [10] J. Allegre, J. Chlatayud, B. Gil, H. Mathieu, H. Tuffigo, G. Lentz, N. Magnea and H. Mariette, *Phys. Rev. B* 41 (1990) 8195.
- [11] H. Mathieu, J. Allegre, A. Chatt, P. Letebvre and J.P. Faurie, *Phys. Rev. B* 38 (1988) 7740.
- [12] H. Tatsuoka, H. Kuwabara, Y. Nakanishi and H. Fujiyasu, *J. Appl. Phys.* 67 (1990) 6860.
- [13] Ch. Neumann, A. Nöthe and N.O. Lipari, *Phys. Rev. B* 37 (1988) 922.
- [14] H. Tuffigo, N. Magnea, H. Mariette, A. Wasiela and Y. Merle D'Aubigné, *Phys. Rev. B* 43 (1991) 14629.

## Thickness dependent properties of ZnSe on (100) GaAs grown by atomic layer epitaxy

C.D. Lee <sup>a</sup>, B.K. Kim <sup>a</sup>, J.W. Kim <sup>a</sup>, H.L. Park <sup>a</sup>, C.H. Chung <sup>a</sup>, S.K. Chang <sup>\*a</sup>,  
J.I. Lee <sup>b</sup>, S.K. Noh <sup>b</sup>

<sup>a</sup> Department of Physics, Yonsei University, Seoul 120-749, South Korea

<sup>b</sup> Vacuum and Surface Science Laboratory, Korea Research Institute of Standards and Science, Taejeon 305-600, South Korea

### Abstract

ZnSe epilayers were grown on semi-insulating GaAs (100) substrates by ALE (atomic layer epitaxy) modified from CVD (chemical vapor deposition). The optical properties of ZnSe films depending on thickness were studied through micro-Raman and PL (photoluminescence) spectroscopy. The critical thickness was determined to be about 0.1  $\mu\text{m}$  by analyzing the change in the peak shift of LO-phonon modes of ZnSe films. This is confirmed from the increase of the intensities of the deep center band in the PL spectra when the thickness exceeds 0.1  $\mu\text{m}$ .

### 1. Introduction

The ZnSe/GaAs (100) system has attracted considerable attention due to the success of blue-green laser diodes at 77 K in 1991 [1]. Until now, since high-quality ZnSe bulk material as a substrate is difficult to obtain, most ZnSe based materials are grown on GaAs substrates. Because of the lattice mismatch between the two materials (0.27%), ZnSe films grown on GaAs substrates are under biaxial compressive stress in the direction parallel to the heterointerface. In this case, the strain is formed in the lattice structure. While for very thin films, elastic strain is accommodated, films with thicker thickness start formation of dislocations. Such a strain has much effect on the electronic structures, optical properties, and

other physical properties such as the degradation phenomena of ZnSe-based devices due to the misfit dislocations [2]. The effects of the strain for ZnSe/GaAs heterointerfaces have been studied through X-ray diffraction [3], TEM (transmission electron microscopy) [4], and the optical measurements [5].

Atomic layer epitaxy (ALE), which is well known as a method to control to the monolayer by supplying the source materials alternatively, has been applied to the various kinds of the compound semiconductors since the original development by Suntola and Anston [6] in 1974. ALE includes the important characteristics of the self-limiting mechanism; the growth becomes saturated automatically, independent of the main growth parameters. Therefore, ALE is useful to grow thin films, superlattice structures, the active layers in semiconductor devices, and all the processes in which more accurate thickness control is

<sup>\*</sup> Corresponding author.

required. Furthermore, ALE is known [7] to be a useful method in studying the growth mechanism, because the growth is performed in a two-dimensional layer-by-layer mode.

In this paper, ZnSe films were grown with  $\text{ZnCl}_2$  and  $\text{H}_2\text{Se}$  source gases by using the ALE technique modified from CVD (chemical vapor deposition). For ZnSe films with various thicknesses, optical properties were studied through micro-Raman and photoluminescence spectroscopy. The experimental results are discussed with the focus of the thickness-dependent properties of ZnSe films on GaAs substrates.

## 2. Experimental procedure

The (100) GaAs substrate was degreased in organic solvents, etched chemically in a  $\text{H}_2\text{SO}_4:\text{H}_2\text{O}_2:\text{H}_2\text{O}$  (4:1:1) solvent for 90 s, rinsed with deionized water, and loaded into the reactor. Before growth, the substrate was heated at  $600^\circ\text{C}$  for 10 min in  $\text{H}_2$  gas flow for initial oxide desorption. After lowering the temperature down to the growth temperature ( $450^\circ\text{C}$ ),  $\text{ZnCl}_2$  and  $\text{H}_2\text{Se}$  reactant gases were supplied alternatively by rotating the substrate. To get a series of ZnSe films with different thicknesses, we kept all the growth parameters the same and varied only the operating cycles. This is based on the “self-limiting mechanism”, one of the important properties of ALE, which has been reported in detail [8].

Optical properties of ZnSe/GaAs films were studied through micro-Raman and photoluminescence (PL) spectroscopy. Micro-Raman spectra were taken under excitation of the 476.5 nm line from an Ar-ion laser at room temperature, in the back scattering geometry. Raman spectra were analyzed using a double monochromator (SPEX 1403,  $f = 0.85$  m). Photoluminescence spectra were measured in a He cycling refrigerator. The excitation source for the luminescence was the 365 nm line of a Hg lamp.

## 3. Results and discussion

The lattice constant of ZnSe ( $a_{\text{ZnSe}} = 5.669$  Å) is slightly larger than that of GaAs ( $a_{\text{GaAs}} = 5.6533$

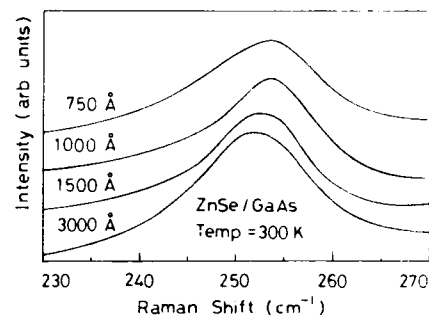


Fig. 1. Raman spectra of ZnSe films with various thicknesses.

Å). Hence, the epitaxial growth of ZnSe on (100) GaAs substrate produces a strain in the lattice structure due to a biaxial compression along the directions parallel to the interface. When the atoms have slightly deviated from the original positions, a coherent interface is formed between the substrate and the film due to elastic deformation. However, when the stress is relatively large, at equilibrium, the crystal energy becomes minimum with the proper combination of residual elastic deformation and formation of misfit dislocation [9]. Therefore, when the film is very thin, only elastic deformation takes place without formation of misfit dislocations. With an increase of the thickness of the film, the density of the misfit dislocations increases [10].

Fig. 1 shows Raman spectra due to the zone center ( $\Gamma$ ) LO phonons of ZnSe films with thicknesses of 750, 1000, 1500, and 3000 Å. The LO phonon frequency  $\omega$  of the ZnSe thicker than 3000 Å is  $252.5$   $\text{cm}^{-1}$ , which is consistent with that of bulk ZnSe. On the other hand, for films with thickness less than 1000 Å, a blue shift of  $1$   $\text{cm}^{-1}$  was observed with respect to that of the bulk, and  $\omega$  of a 1500 Å thick ZnSe film is between that of 1000 and 3000 Å. The shifts of LO phonon frequency are summarized in Fig. 2.

To explain the observed changes of phonon frequency, we discuss the effect of the deformation on the lattice vibration depending on the film thickness. Generally, since the GaAs substrate is much thicker ( $\sim 600$   $\mu\text{m}$ ) than the ZnSe film, the lattice constant of ZnSe parallel to the heterointerface is considered to be the same as



that of GaAs in complete deformation. In this case, the strain  $\epsilon$  is  $-0.0027$ , and LO phonon frequency  $\omega$  depends on  $\epsilon$  with the expression [11]

$$\omega = \omega_{\text{LO}} + 2 \Delta\Omega_{\text{II}} - \frac{2}{3} \Delta\Omega, \quad (1)$$

where  $\omega_{\text{LO}}$  is the phonon frequency of bulk ZnSe, and  $\Delta\Omega_{\text{II}}$  and  $\Delta\Omega$  are

$$\Delta\Omega_{\text{II}} = - \frac{p + 2q}{6\omega_{\text{LO}}^2} \frac{S_{11} + 2S_{12}}{S_{11} + S_{12}} \omega_{\text{LO}} \epsilon, \quad (2)$$

$$\Delta\Omega = \frac{p - q}{2\omega_{\text{LO}}^2} \frac{S_{11} - S_{12}}{S_{11} + S_{12}} \omega_{\text{LO}} \epsilon. \quad (3)$$

In the case of ZnSe, the deformation potentials,  $-(p + 2q)/6\omega_{\text{LO}}^2$  and  $(p - q)/2\omega_{\text{LO}}^2$ , are known to be 1.15 and 0.62, respectively [12]. Here, substituting  $S_{11} + S_{12} = 0.0145$ ,  $S_{11} + 2S_{12} = 0.006$ , and  $S_{11} - S_{12} = 0.0315$  [11], the shift of the LO phonon frequency  $\delta\omega_{\text{LO}}$  becomes

$$\delta\omega_{\text{LO}} = -385.04\epsilon \text{ (cm}^{-1}\text{)}. \quad (4)$$

Substituting  $\epsilon = -0.0027$ , the blue shift of  $1 \text{ cm}^{-1}$  is obtained.

As shown in Fig. 2, LO phonon peaks of ZnSe are blue-shifted for ZnSe films with a thickness of less than  $1000 \text{ \AA}$  in comparison with that of bulk ZnSe, which is indicated by the solid line. This value corresponds to that of completely strained ZnSe films. As the thickness becomes larger, the LO phonon frequency comes closer to that of bulk ZnSe. Such experimental results indicate that if the film thickness is larger than  $1000 \text{ \AA}$ , relaxation starts to occur due to formation of

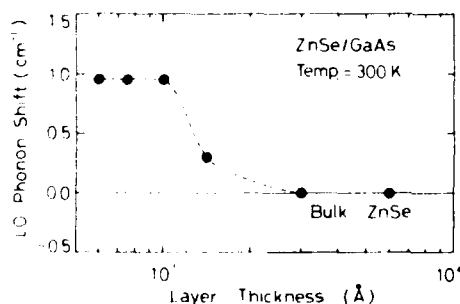


Fig. 2. Energy shift of LO phonon depending on the film thickness.

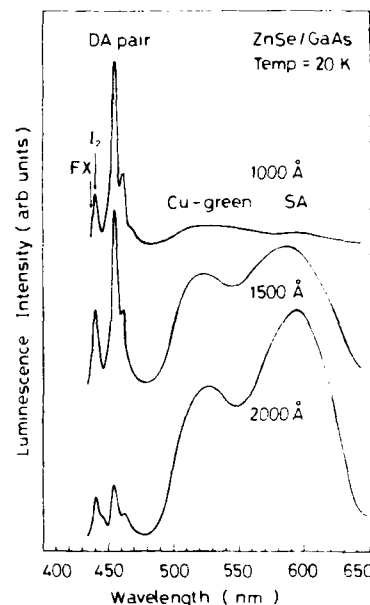


Fig. 3. Photoluminescence spectra of ZnSe films with various thicknesses.

misfit dislocation. The critical thickness  $h_c$ , the maximum thickness before the formation of misfit dislocation, is estimated to be  $1000 \text{ \AA}$ .

For further understanding of relaxation of strain for ZnSe films grown thicker than the critical thickness on GaAs substrates, the photoluminescence spectrum was studied. Fig. 3 shows PL spectra of ZnSe films of  $1000$ ,  $1500$ , and  $2000 \text{ \AA}$ . The PL spectra consist of the  $I_2$  line ( $2.797 \text{ eV}$ ), DA (donor-acceptor) pair ( $2.783 \text{ eV}$ ), SA (self-activated) band ( $2.07 \text{ eV}$ ), Cu-green band ( $2.34 \text{ eV}$ ), and free exciton peak ( $2.802 \text{ eV}$ ) which is overlapped with the  $I_2$  line. Here, the  $I_2$  line is the peak due to the exciton bound to the neutral Cl, which appears because of the source material  $\text{ZnCl}_2$ . The PL spectra show that the intensity of the deep center band increases with an increase of the film thickness above  $1000 \text{ \AA}$  in comparison with intensities of  $I_2$  line and DA pair. Relative intensities of  $I_2$  line peak with respect to deep center band ( $I_2/\text{SA}$ ) are plotted in Fig. 4. The ratio of intensity,  $I_2/\text{SA}$ , increases up to  $1000 \text{ \AA}$ , and above that thickness, it starts decreasing. This is explained by the fact that the relaxations

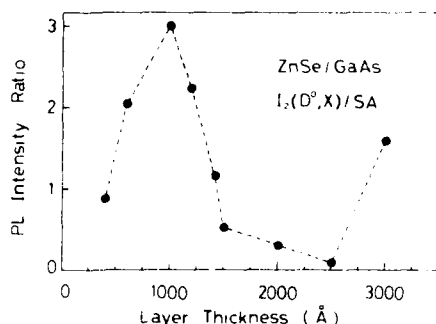


Fig. 4. Intensity ratio of photoluminescence spectra ( $I_2/SA$ ) depending on the film thickness.

of strain bring the change in the quality of films; that is, as the film grows thicker than the critical thickness, impurities such as Cu, Cl and Zn-vacancies are collected around dislocations. Also, visual observation of film surface gives the similar results; while films with thickness of less than or equal to 1000 Å show a homogeneous mirror surface, films with thickness above 3000 Å show rough a surface. This indicates that the increase of dislocations results in formation of crystal defects.

On the basis of results of micro-Raman and Photoluminescence spectra, we conclude that the critical thickness of ZnSe films on GaAs substrates grown by ALE is 1000 Å. This value is considered quite reasonable compared with the theoretical value of 750 Å [13] and other experimental values [14].

#### 4. Summary

ZnSe films with various thicknesses were grown on GaAs (100) substrates using atomic layer epitaxy modified from CVD. The thicknesses of epilayers were controlled by the operating cycle using the principal advantage of ALE, self-limiting mechanism. To investigate the effect of the strain due to the lattice mismatch between substrates and films, micro-Raman spectroscopy was performed, which resulted in the observation of blue shifts in the LO phonon peak with a decrease of the thickness. With thickness above 1000 Å, as

the strain was being relaxed, the LO phonon peak was shifted to the LO phonon frequency of bulk ZnSe. From this result, the critical thickness – which is the maximum thickness of growing good films without formation of dislocations – was determined to be 1000 Å. Furthermore, the PL spectra showing free exciton peak,  $I_2$  peak, DA pair and SA center confirm the critical thickness of 1000 Å through an analysis of the change of intensity ratio of the exciton peak to the deep center band ( $I_2/SA$ ).

#### 5. Acknowledgements

The authors are indebted to Mr. J.S. Kim of ISRC for his help in the micro-Raman measurements. This work was supported in part by the KOSEF through KRIS in 1993 and in part by the ministry of Education of Korea through ISRC in 1992.

#### 6. References

- [1] M.A. Haase, J. Qiu, J.M. DePuydt and H. Cheng, Appl. Phys. Lett. 59 (1991) 1272.
- [2] K. Shahzad, Phys. Rev. B 38 (1988) 8309.
- [3] H. Mitsuhashi, I. Mitsuishi, M. Mizuta and H. Kukimoto, Jap. J. Appl. Phys. 24 (1985) 1578.
- [4] D.J. Olego, J. Vac. Sci. Technol. B 6 (1988) 1193.
- [5] K. Shahzad, D. Olego, C.G. Van de Walle and D.A. Cammack, J. Luminance 46 (1990) 109.
- [6] T. Suntola and J. Anston, Finish Patent No. 52359 (1974).
- [7] Y. Mochizuki, E. Takada and A. Usui, Jap. J. Appl. Phys. 32 (1993) 1197.
- [8] C.D. Lee, B.H. Lim, H.I. Park, C.H. Chung and S.K. Chang, J. Crystal Growth 117 (1992) 148.
- [9] K. Henry and J.K. Butler, Semiconductor Lasers and Hetero-Junction LED's (Academic Press, New York, 1977) p. 298.
- [10] J. Petruzzello and B.L. Greenberg, J. Appl. Phys. 63 (1988) 2299.
- [11] E. Cerderia, C.J. Buchenauer, F.H. Pollak and M. Cardona, Phys. Rev. B 5 (1972) 580.
- [12] D.J. Olego, K. Shahzad, J. Petruzzello and D. Cammack, Phys. Rev. B 36 (1987) 7674.
- [13] J.H. van der Merwe, Single Crystal Films (Pergamon, Oxford, 1964) p. 139.
- [14] T. Yao, Y. Okada, S. Matsui, K. Ishida and I. Fujimoto, J. Crystal Growth 81 (1987) 518.



ELSEVIER

Journal of Crystal Growth 138 (1994) 140–144

JOURNAL OF  
**CRYSTAL  
GROWTH**

## The metalorganic chemical vapour deposition and photoluminescence of tellurium-doped ZnS/CdS:Te strained layer superlattices

K.A. Dhese <sup>a,\*</sup>, J.E. Nicholls <sup>a</sup>, W.E. Hagston <sup>a</sup>, P.J. Wright <sup>b</sup>, B. Cockayne <sup>b</sup>,  
J.J. Davies <sup>c</sup>

<sup>a</sup> Department of Applied Physics, The University of Hull, Hull HU6 7RX, UK

<sup>b</sup> Defence Research Agency, St. Andrews Road, Great Malvern WR14 3PS, UK

<sup>c</sup> School of Physics, The University of East Anglia, Norwich NR4 7TJ, UK

### Abstract

Tellurium (Te) exciton traps have been doped into the wells of ZnS/CdS:Te superlattices to investigate the potential for achieving enhanced blue emission intensities at room temperature. Exciton trapping and corresponding blue emission was confirmed from photoluminescence studies, however, the emission was found to quench above about 200 K, which is probably attributable to dislocation formation in highly strained layers when large ions such as Te are incorporated. Comparison of the emission linewidths with that of bulk CdS:Te show that the nature of electron–phonon coupling to the Te centres changes in the superlattice structures compared to bulk material.

### 1. Introduction

Rapid advances in epitaxial growth, electrical doping and structural quality of wide bandgap II–VI compounds in recent years has led to continuing development of blue light emitting and laser diodes, for which a fundamental problem concerns the radiative quantum efficiency. Low-dimensional structures are known to exhibit increased radiative efficiency as well as optical tunability. However, an alternative way of increasing the radiative efficiency may be possible by incorporation of isoelectronic impurities which are

known, in certain II–VI compounds, to lead to intense bound exciton luminescence. In addition, since such impurities are electrically neutral, this should not significantly alter the electrical behaviour. Isoelectronic traps occur when atoms from the same group of the periodic table as that of the host atom substitute isovalently. The resulting short range potential leads to tight localization of one carrier type followed by coulombic attraction of the other carrier, thereby creating a bound exciton.

Isolated tellurium (Te) isoelectronic ions are known to produce deep exciton traps in CdS leading to intense orange luminescence at 2.05 eV [1]. In addition, the bandgap of ZnS (3.84 eV, 4 K) is approximately 1.3 eV larger than that of

\* Corresponding author.

CdS. Consequently, the aim of this work was to confine Te trapped excitons in thin ( $\leq 25$  Å) CdS wells of ZnS/CdS superlattices to obtain intense luminescence in the blue region (2.6–2.8 eV). In this paper, we report on the initial attempts at achieving such emission from Te doped ZnS/CdS superlattices grown by metalorganic chemical vapour deposition (MOCVD).

## 2. Growth

Growth was carried out in a horizontal flow atmospheric pressure MOCVD reactor essentially similar to that described previously [2]. The ZnS/CdS and ZnS/CdS:Te superlattice structures were deposited onto (001) GaAs substrates after first growing an  $\sim 3000$  Å ZnS buffer layer which was expected to be fully relaxed [3]. The substrates were cleaned in boiling propan-2-ol and then chemically etched in a 5:1:1 solution of  $\text{H}_2\text{SO}_4:\text{H}_2\text{O}:\text{H}_2\text{O}_2$  at  $40^\circ\text{C}$  for 10 min. Substrates were loaded into the reactor on a SiC coated graphite susceptor. The reactor was flushed with purified  $\text{H}_2$  before heating the susceptor to  $600^\circ\text{C}$  for 10 min under  $\text{H}_2$  flow.

Dimethylzinc–triethylamine [ $\text{Me}_2\text{Zn}(\text{NEt}_3)$ ], dimethylcadmium [DMCd], and hydrogen sulphide [ $\text{H}_2\text{S}$ ] were used as the zinc, cadmium and sulphur sources, respectively. For Te-doped structures diethyltelluride (DETe), with a partial vapour pressure of  $\sim 8$  Torr at room temperature, was used. The low levels of Te incorporation required in the CdS layers were achieved using the diffusion cell doping technique described previously [4]. Essentially, a single diffusion channel leading from the Te source cell is fed into a fast flowing bypass line, which leads to the reactor vessel. For a fixed diffusion channel length and diameter, the concentration diffusing into the bypass line is proportional to the partial vapour pressure of the precursor. In this way levels of Te below  $10^{19} \text{ cm}^{-3}$  were achieved, as determined from the photoluminescence of corresponding CdS:Te epilayers. The growth conditions used are summarized in Table 1.

The lattice mismatch between cubic ZnS ( $a_{\text{ZnS}} = 5.4093$  Å) and CdS ( $a_{\text{CdS}} = 5.8320$  Å) is  $\sim$

Table 1

Parameters used during growth of ZnS/CdS and ZnS/CdS:Te superlattices in this work

Growth temperature	300 °C
$\text{H}_2\text{S}$ (5% in $\text{H}_2$ ) flow rate	50 $\text{cm}^3/\text{min}$
$\text{Me}_2\text{Zn}(\text{NEt}_3)$ bubbler (17.5 °C) flow rate	20–30 $\text{cm}^3/\text{min}$
DMCd bubbler (RT) flow rate	2–3 $\text{cm}^3/\text{min}$
Total reactor flow ( $\text{H}_2$ + reactants)	8 l/min
Reactor (1 litre volume) flush-out time	20 s
DETe diffusion channel length	35 cm
DETe diffusion channel diameter	4 mm
Diffusion channel bypass flow	250 $\text{cm}^3/\text{min}$

7.25%, making the corresponding superlattice system highly strained. Consequently, the majority of superlattices were grown with 50–60 short periods ( $< 50$  Å) and narrow CdS layers ( $< 25$  Å), in order to maintain pseudomorphic growth to the relaxed ZnS buffer. In this instance, the CdS layers are expected to be fully strained.

## 3. Photoluminescence

Low temperature (1.8 K) PL spectra obtained from a typical Te doped and an undoped superlattice are shown in Fig. 1. The superlattice layer thicknesses were obtained by a TEM. Fig. 1 also shows the PL spectrum of a Te doped CdS:Te epilayer grown onto (001) GaAs (Fig. 1c). The epilayer was  $\sim 1$   $\mu\text{m}$  thick and is assumed to have relaxed to the wurtzite phase [5]. The wurtzite bandgap of CdS is marked on Fig. 1. The PL spectrum of the CdS:Te epilayer is dominated by an intense broad (FWHM  $\sim 215$  meV) band peaking at 2.05 eV. This band has previously been attributed to exciton trapping at isolated Te centres, with a trapping depth of 260 meV [6]. The smooth broad lineshape is the result of strong electron–phonon coupling associated with the tightly localized hole.

The PL spectra from the undoped ZnS/CdS structure (Fig. 1a) shows a superlattice emission peak at 2.924 eV, in the violet region. This emission has previously been attributed to quantum confined free exciton recombination (e.g., refs. [7,8]). The large blue shift with respect to the CdS bandgap is expected for such a narrow well struc-

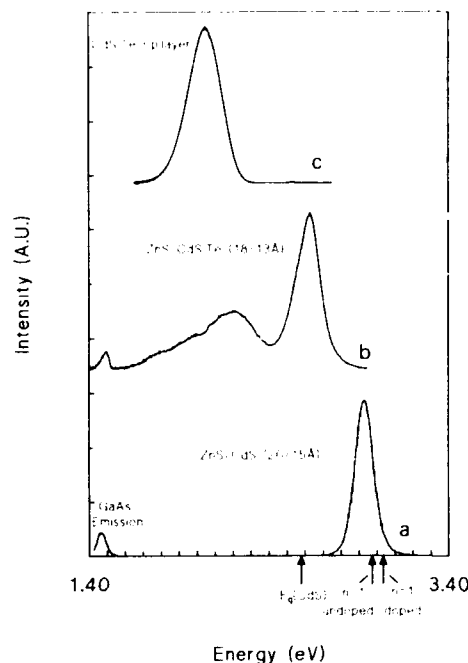


Fig. 1. Low temperature (1.8 K) photoluminescence spectra from a ZnS/CdS (a) and a ZnS/CdS:Te (b) superlattice, and from a CdS:Te epilayer (c). All samples were excited using 351.1 nm radiation at  $1 \text{ W cm}^{-2}$  intensity. Well and barrier thicknesses obtained by TEM are indicated.

ture having a large band offset. Intense superlattice emission in the violet/UV region (up to 3.3 eV) with little or no deep centre emission was observed from the range of undoped superlattices grown with the narrowest CdS wells, typically  $< 20 \text{ \AA}$ . In wider well samples, reduced superlattice emission intensities (implying increased non-radiative recombination) and relative increases in deep centre emission were observed, both of which can be attributed to relaxation of the strained cubic CdS well layers with the consequent introduction of misfit dislocations and phase instabilities.

The PL from the doped structure (Fig. 1b) shows a superlattice emission peaking in the blue (2.627 eV) as well as significant deep centre emission. In addition, the superlattice emission intensity was approximately an order of magnitude lower compared with Fig. 1a. Indeed, most of the

Te doped structures grown were found to exhibit a reduced superlattice emission intensity and deep centre emission. In many cases, no superlattice emission was observed at all, with only deep centre emission present. These findings probably result from substitution of large Te impurities into the very thin and highly strained CdS layers. It is possible that such large ions enhance the onset of dislocation production and the subsequent relaxation of the layers. Temperature dependence measurements on the superlattice emission intensities further reveal the consequences of deep radiative and non-radiative centres. The superlattice emission of undoped structures could be observed up to room temperature, whereas for doped structures, the emission attenuated more rapidly and was quenched above 200 K.

The superlattice emissions of the doped structures were mainly observed to occur close to the CdS bandgap (e.g., Fig. 1b) giving blue emissions. Clearly, the large quantum confined blue shifts observed in undoped structures are absent in the doped structures, and to illustrate this further, an estimate of the electron-heavy hole  $n = 1$  transition energy was made using an envelope function approximation [9]. An arbitrary valence band offset of 300 meV was used leaving most of the band offset in the conduction band, in agreement with the common anion rule. Since data are scarce concerning the low temperature cubic bandgap of CdS, the wurtzite band was used, which is a reasonable approximation in view of the same room temperature bandgap (2.50 eV) quoted for both wurtzite and zincblende phases [10]. The predicted  $n = 1$  transition energies for both the doped and the undoped superlattice of Fig. 1 are indicated. The higher calculated energy for the doped structure simply reflects the slightly thinner well width. It is clear from Fig. 1 that the superlattice emission is significantly red-shifted with respect to the corresponding  $n = 1$  transition for the doped structure ( $\sim 400 \text{ meV}$ ) compared with the undoped structure ( $\sim 50 \text{ meV}$ ). Similar large red-shifts were observed for the range of Te doped superlattices grown. This is a clear indication that trapping of excitons at Te centres occurs in the doped wells. Further, it is

noted that the extra red-shift for the doped superlattice of Fig. 1b ( $\sim 350$  meV) compared to the undoped structure is larger than the bulk CdS:Te exciton trapping depth of 260 meV. It is thus possible that the Te trapping depth has increased in the CdS superlattice layers, caused by a perturbation of the highly localized Te bound hole by the confining ZnS barriers. We have calculated, from application of a hole capture theory previously developed for Te isoelectronic traps in ZnSe [11], that the effective diameter (assuming a spherical potential) of the trapping potential for isolated Te traps in CdS is  $\sim 16$  Å. The well widths of the doped structures grown here were comparable with or smaller than this diameter, and would support the idea that the Te impurity potential may be modified by the ZnS barriers.

Finally, it is noted that the linewidths of superlattice emission from doped and undoped structures are comparable (e.g., Fig. 1), and are found to lie in the range 100–150 meV. Such large linewidths are attributed to interface roughness, the effects of which are pronounced in large band offset systems such as ZnS/CdS. In view of the

tight localization of holes expected at Te centres, the linewidths from doped structures might be expected to be larger than those from undoped structures, and closer to those of epilayers (Fig. 1c). This was not found and thus it appears that the strong electron–phonon coupling associated with Te ions in bulk CdS does not occur in thin quantum confined CdS layers. This is further highlighted by the variation of FWHM with temperature for CdS:Te epilayer emission and the superlattice emissions from doped and undoped superlattices, as shown for typical samples in Fig. 2. The rapid broadening of the epilayer emission with increasing temperature is a classic characteristic of a strongly coupled centre [1], whereas the two superlattice emissions behave in a similar, less dramatic way. It is possible therefore, that the confining ZnS barriers not only alter the Te centre trapping depth, but also the nature of the electron–phonon coupling to such centres.

#### 4. Conclusions

ZnS/CdS and ZnS/CdS:Te strained layer superlattices were grown to investigate the potential of using deep isoelectronic Te traps to enhance the radiative efficiency of superlattice emission at the technologically important blue wavelengths. Exciton trapping was confirmed at the Te centres in the CdS superlattice layers resulting in blue emission, although the emission was less persistent with increasing temperature than that for undoped superlattices. This is attributed mainly to the problems of doping large impurity ions, such as Te, into the thin, highly strained CdS layers. Future progress may depend on the growth of II–VI superlattices with ternary compounds such as ZnS/ZnCdS to reduce the interlayer strain whilst still allowing quantum emission in the blue/violet region. In addition, Te isoelectronic traps are known to produce deep efficient luminescent traps throughout the  $\text{Zn}_{1-x}\text{Cd}_x\text{S}$  composition range [12].

#### 5. Acknowledgments

We wish to thank the Science and Engineering Research Council of the UK for financial sup-

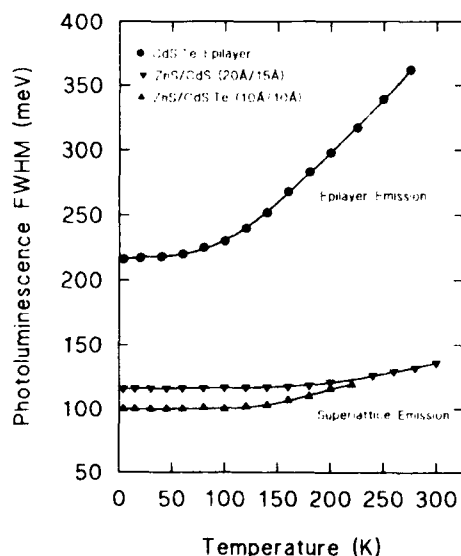


Fig. 2. Variation of photoluminescence linewidth (FWHM) as a function of temperature for a ZnS/CdS and ZnS/CdS:Te superlattice, and for a CdS:Te epilayer.

port. The investigation has been carried out with the support of the Procurement Executive, Ministry of Defence.

## 6. References

- [1] D.M. Roessler, *J. Appl. Phys.* 41 (1970) 4589.
- [2] P.J. Wright and B. Cockayne, *J. Crystal Growth* 59 (1982) 148.
- [3] I. Mitsuishi, H. Mitsuhashi and H. Kukimoto, *Jap. J. Appl. Phys.* 27 (1988) L15.
- [4] K.A. Dhese, J.E. Nicholls, P.J. Wright, B. Cockayne and J.J. Davies, *J. Crystal Growth* 126 (1993) 179.
- [5] A.G. Cullis, P.W. Smith, P.J. Parbrook, B. Cockayne, P.J. Wright and G.M. Williams, *Appl. Phys. Lett.* 55 (1989) 2081.
- [6] O. Goede, W. Heimbrodt and R. Müller, *Phys. Status Solidi (b)* 105 (1981) 543.
- [7] S. Ohta, S. Kobayashi, F. Kaneko and K. Kashiro, *J. Crystal Growth* 106 (1990) 166.
- [8] P.J. Parbrook, P.J. Wright, B. Cockayne, A.G. Cullis, B. Henderson and K.P. O'Donnell, *J. Crystal Growth* 106 (1990) 503.
- [9] G. Bastard, *Phys. Rev. B* 24 (1981) 5693.
- [10] Landolt-Börnstein, Vol. III, 17b, Semiconductors: Physics of II-VI and I-VII Compounds, Semimagnetic Semiconductors (Springer, Berlin, 1982) pp. 166, 176.
- [11] K. Dhese, J. Goodwin, W.E. Hagston, J.E. Nicholls, J.J. Davies, B. Cockayne and P.J. Wright, *Semicond. Sci. Technol.* 7 (1992) 1210.
- [12] G.W. Iseler and A.J. Strauss, *J. Luminescence* 3 (1970) 1.

## Epitaxial growth of ZnS on GaP by molecular beam deposition

H. Kanie <sup>\*</sup>, H. Araki, K. Ishizaka, H. Ohta, S. Murakami

*Department of Applied Electronics, Science University of Tokyo, Noda 278, Japan*

### Abstract

Nearly coherent growth of ZnS on GaP by using a ZnS compound as a source material of Zn and S was achieved. The strains in the epilayers were determined by both X-ray diffraction and the measurement of reflection and Raman spectra. The measured value of strain in the 200 nm thick layers grown at a substrate temperature of 240 °C shows that the epilayer lattice in the plane of the interface matches the substrate lattice. In the epilayer of 200 nm to 1000 nm thickness grown at  $T_{\text{sub}} = 160^\circ\text{C}$  the lattice strain is fully relaxed. It was observed that the thickness of the epilayers grown at  $T_{\text{sub}} = 240^\circ\text{C}$  was limited to 200 nm.

### 1. Introduction

Zinc sulphide is a promising material for an optoelectronic device in the violet and blue region because of its wide band gap. Intensive study has been done to produce ZnS thin films for light emitting diodes, laser diodes and light modulators. To obtain a ZnS layer of high quality for optoelectronic devices, techniques for epitaxial growth, such as molecular beam epitaxy (MBE) [1], metalorganic molecular beam epitaxy (MOMBE) [2], metalorganic chemical vapor deposition (MOCVD) [3], and atomic layer epitaxy (ALE) [4], have been developed.

In MBE or MOCVD growth, GaAs, GaP and Si are used as substrates. The lattice mismatch between ZnS and GaP is 0.7%, which is larger than that between ZnSe and GaAs at 0.3%. The general growth process of lattice-mismatched systems has been well documented. In the early

stages of growth, the epitaxial layer grows coherently to the substrate with the elastic strain energy density increasing with thickness. When the thickness reaches a critical thickness, the formation of misfit dislocation begins to lower the total energy of the system. The critical thickness is an important parameter in the design process of the devices.

For MBE growth of ZnS it has been difficult to control the S vapor pressure when solid sulphur was used as a source material, because of its high vapor pressure even at temperatures of about 200°C. If a ZnS compound is used as a source of S and also Zn, it is easy to control the S vapor pressure. Yoneda et al. [5] reported on the epitaxial growth of ZnS on GaP using a ZnS source in an MBE chamber, but they did not achieve a coherent growth of ZnS.

We report the demonstration of the coherent growth of ZnS on (001) GaP at a substrate temperature of 240°C in an MBE system using a ZnS compound source. We find that the thickness of layers grown at the substrate temperature is 200

<sup>\*</sup> Corresponding author.



nm independent of the growth time. The techniques of X-ray diffraction and the measurement of reflectance and Raman spectrum were employed to evaluate the lattice strain in the grown layers.

## 2. Experimental procedure

Zinc sulphide is grown in an MBE system (Nissin Mini Bee) equipped with diffusion pump. The MBE growth chamber was baked at 200°C for 24 h before growth. The sulphur-doped GaP (001) substrate was etched in  $\text{HCl}:\text{HNO}_3:\text{H}_2\text{O} = 1:1:1$  at room temperature for 30 min, and then thermally cleaned at 650°C for 30 min in the growth chamber at  $5 \times 10^{-10}$  Torr.

A beam flux intensity of ZnS was maintained at  $5 \times 10^{-7}$  Torr by controlling the ZnS K-cell temperature around 750°C. A background pressure during the growth was  $5 \times 10^{-10}$  Torr. Samples were grown at substrate temperatures of 160, 200 and 240°C and growth times from 1.5 to 12 h. The RHEED patterns were observed during the growth. The thickness of the grown ZnS layers was measured by ellipsometry. A reflectance spectrum and a Raman spectrum at 77 K were measured with a grating monochromator (Jobin-Yvon HR640). A light source for the reflectance measurement was a Xe lamp and for photoluminescence a He–Cd (325 nm) laser. The lattice constant perpendicular to the growth surface was measured with a diffractometer (Rigaku Rad-C).

## 3. Results and discussion

The morphology and RHEED patterns of epitaxially grown ZnS did not change with the substrate temperature, but the growth rate and the thickness of the layer did change. Grown surfaces were flat and mirror-like smooth. The RHEED patterns of the epilayers grown at substrate temperatures in the range of 160 to 240°C were streaky. It was observed in a preliminary experiment that twin spots or ring patterns appeared when the substrate temperature was lower than 160°C or higher than 300°C. The measured thicknesses of the epilayers and their growth conditions are shown in table 1. The thickness of the layers grown at  $T_{\text{sub}} = 160^\circ\text{C}$  increases proportionally with growth time. The growth rate is 1.2 nm/min. This is rather slower than that reported in ref. [5], even though the layers were grown at higher substrate temperatures. The thickness of the layers grown at  $T_{\text{sub}} = 240^\circ\text{C}$  was constant and independent of the growth time. The growth rate at  $T_{\text{sub}} = 240^\circ\text{C}$  within 1.5 h of the beginning of growth is supposed to be the same as that at  $T_{\text{sub}} = 160^\circ\text{C}$ . When the substrate temperature was 300°C, the grown-out layer was very thin and we were not able to measure the thickness.

The relaxation of the lattice mismatch in the layers has been determined by X-ray diffraction (XRD) in conjunction with the low-temperature reflectance spectrum. For thin layers one expects ZnS, with a smaller equilibrium lattice constant, to experience a tetragonal distortion under biax-

Table 1

Summary of the growth conditions and the experimental values for the ZnS epilayers as a function of thickness,  $d$ , from XRD and reflectance results

No.	Condition	$d$ (nm)	$a_{\text{c}}$ (Å)	$E_{\text{ex}}$ at 77 K (eV)	$\epsilon^{\text{XRD}}$ ( $\times 10^{-3}$ )	$\epsilon^{\text{opt}}$ at 77 K ( $\times 10^{-3}$ )	$\Delta E(2) - \Delta E(1)$ (meV)
27	240°C: 8 h	206	5.365	3.783	−6.4	−6.5	−16
28	240°C: 4 h	204	5.364	3.783	−6.6	−6.5	−16
29	240°C: 6 h	207	5.368	3.784	−6.0	−5.9	−14
31	200°C: 8 h	325	5.393	3.795	−2.4	0	0
32	160°C: 8 h	575	5.404	3.794	−0.8	−0.5	−1
33	160°C: 4 h	367	5.404	3.793	−0.8	−1.1	−3
37	160°C: 6 h	591	5.407	3.796	−0.3	0.5	1
38	160°C: 12 h	1014	5.406	3.795	−0.5	0	0
41	160°C: 1.5 h	170	5.393	3.795	−2.4	0	0

ial tensile stress parallel to the interface. This results in a decrease of  $a_{\perp}$ , the lattice constant normal to the interface. The value of  $a_{\perp}$  is given by [6]

$$a_{\perp} = a_0 [1 - (2c_{12}/c_{11})\epsilon], \quad (1)$$

where  $a_0$  is the equilibrium lattice constant of ZnS.  $c_{12}$  and  $c_{11}$  are elastic stiffness constants and  $\epsilon$  is the strain component in the plane of the interface.

The XRD measurement of  $a_{\perp}$  in the 1014 nm thick epilayer yields 5.406 Å. This agrees fairly well with the value of the equilibrium ZnS lattice constant. It indicates an almost complete relaxation of the misfit strain in the thick layer.

The value of  $a_{\perp}$  for samples of the same thickness of 200 nm is dependent on the substrate temperature. The lattice constant  $a_{\perp}$  of the 200 nm layers grown at  $T_{\text{sub}} = 160^{\circ}\text{C}$  is almost the same as that of the 1014 nm layers. The 200 nm epilayer grown at  $T_{\text{sub}} = 240^{\circ}\text{C}$  yields 5.365 Å. This value is 0.8% less than that of the layers at  $T_{\text{sub}} = 160^{\circ}\text{C}$  with the same thickness.

The value of  $\epsilon$ , the strain component in the plane of the interface, is calculated using expression (1) and the values of  $c_{11} = 9.81 \times 10^{10} \text{ N/m}^2$  and  $c_{12} = 6.27 \times 10^{10} \text{ N/m}^2$  [7]. The values of  $a_{\perp}$  and  $\epsilon^{\text{XRD}}$ , the calculated value of  $\epsilon$ , are shown in table 1. The value of  $\epsilon^{\text{XRD}}$  is approximately 0.6% for the 200 nm thick epilayers grown at  $T_{\text{sub}} = 240^{\circ}\text{C}$ ; it is 79% of the lattice mismatch of this system. This indicates that nearly coherent growth can be achieved in the layers grown at  $T_{\text{sub}} = 240^{\circ}\text{C}$ .

Fig. 1 shows the changes in the reflection spectra of the epilayers grown at three different substrate temperatures. The position of the dip in the reflectance spectrum shifts toward higher energy as  $T_{\text{sub}}$  lowers. The position of the dip becomes vague for the layer grown at  $T_{\text{sub}} = 240^{\circ}\text{C}$ . The energy of the dip position corresponds to  $E_{\text{ex}}$ , the energy of the absorption band of a free exciton.

For a zincblende-type crystal the valence band at  $k = 0$  consists of a fourfold  $P_{3/2}$  multiplet and a twofold  $P_{1/2}$  multiplet [8]. Under biaxial stress the  $P_{3/2}$  multiplet band splits into two valence bands, a heavy hole valence band noted as  $\nu_1 (J =$

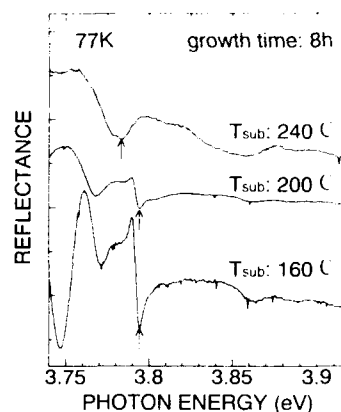


Fig. 1. Reflection spectra of the ZnS epilayers for different substrate temperatures. The dip position shifts toward lower energy as the substrate temperature rises.

$3/2, m_j = \pm 3/2)$  and a light hole valence band  $\nu_2 (J = 3/2, m_j = \pm 1/2)$  [8]. The numerical relationship of the shifts in the bandgap energies between a conduction band and the two valence bands and  $\epsilon$ , the strain component in the interface plane, is obtained using the expressions in ref. [8]. To make the calculation, we set the hydrostatic deformation potential  $a = -4.25 \text{ eV}$  and the shear deformation potential  $b = -0.53 \text{ eV}$  [9]. The value of  $a$  is calculated using the relationship in ref. [8] taking the hydrostatic coefficient of the energy gap  $\partial E/\partial P = 5.7 \times 10^{-6} \text{ eV/Pa}$  [9]. The numerical relations are obtained as:

$$\Delta E(1) = 1.857\epsilon, \quad (2)$$

$$\Delta E(2) = 4.272\epsilon. \quad (3)$$

Since this study is concerned with the amount of change in the bandgap energy, we take  $\Delta E(1)$ , the difference from the energy of the reflection dip of the thickest epilayer, which is 3.795 eV. The value of  $\Delta E(1)$  for the epilayer is shown in table 1 in terms of  $\epsilon^{\text{opt}}$ , the calculated value using eq. (2).

The value of  $\epsilon^{\text{opt}}$  is almost the same as that of  $\epsilon^{\text{XRD}}$  in the layers grown at  $T_{\text{sub}} = 240^{\circ}\text{C}$ . The X-ray diffraction patterns and reflectivity spectra

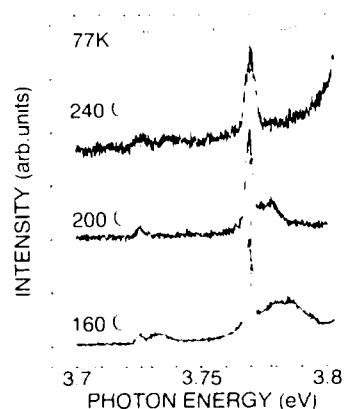


Fig. 2. Raman spectra of ZnS epilayers for different substrate temperatures. Incident light is the 325 nm (3.815 eV) lasing line from a He–Cd laser. The three labels, RTO, RLO and RLO represent a Raman line due to one TO phonon, one LO phonon and two LO phonons, respectively [11,12]. The peak position of the RLO line shifts toward higher energy as the substrate temperature rises.

show that the lattice of the epilayers grown at  $T_{\text{sub}} = 240^\circ\text{C}$  is distorted to match the substrate lattice and those at 160 and 200 °C are fully or partly relaxed.

The energy difference in the split bands is shown in the last column of table 1. This difference is 16 meV for the layers grown at  $T_{\text{sub}} = 240^\circ\text{C}$ . The split of the bands may cause the shape of the dip to broaden in fig. 2.

The value of  $\epsilon^{\text{epi}}$  is slightly less than that of  $\epsilon^{\text{NRD}}$ . As the X-ray diffraction is measured at room temperature and the reflectance spectrum is measured at 77 K, the difference between the thermal expansion coefficient of the epilayer and the substrate was tried to be taken into account. The thermal expansion coefficient of ZnS is larger than that of GaP. When the system is heated from 77 to 300 K, the tensile strain in the ZnS epilayer should decrease by an amount of  $3.0 \times 10^{-3}$ . So, we conclude that this is not the case.

The reflected lights will sample a very thin layer only at a skin depth from the top surface. On the other hand, the X-rays sample the entire thickness of the epilayer. So, the fact that the

value of  $\epsilon^{\text{epi}}$  is less than  $\epsilon^{\text{NRD}}$  may indicate the relaxation of the lattice constant towards its equilibrium value near the top surface [10].

Fig. 2 shows the Raman spectrum at 77 K in the region near the band gap. Three peaks at 3.778, 3.770, and 3.726 eV are Raman scattered lines of the 325 nm lasing line of a He–Cd laser [11,12]. The 3.770 eV peak is assigned to a line scattered by a longitudinal optical phonon of ZnS. The peak position shifts towards higher energy as  $T_{\text{sub}}$  rises. The shift of LO phonon frequency is explained in terms of the frequency dependence on the lattice strain [10]. The relation predicts the red shift in the frequency for tensile strain.

Finally we discuss the reduction in the growth rate of the epilayers grown at  $T_{\text{sub}} = 240^\circ\text{C}$ . In order to realize coherent growth, it is necessary for the molecule to have adequate thermal energy to migrate on the top surface, locate at a quasisustainable site and then make a bond there. With increasing substrate temperatures, the life time of the impinging molecule becomes shorter and the sticking coefficient of a molecule in the incident beam becomes smaller. The rate of re-evaporation and sticking of ZnS balances to result in a reduction of the growth rate to zero with a rise of the substrate temperature. At the top surface of the substrate, an exothermic reaction for the growth of ZnS from the vapor occurs. As the thermal conductivity of ZnS is three times less than that of GaP, the temperature at the top surface of the grown layer rises higher than that at the start of growth with an increase in the ZnS layer thickness. We think that when the thickness reaches 200 nm, the temperature rises to the critical value and the growth rate reduces to zero.

## 5. Conclusions

It was demonstrated that ZnS layers grow epitaxially on GaP (001) substrate by using ZnS compound as a source material for Zn and S. We show that the ZnS epilayer lattice in the plane of the interface is deformed to match the substrate lattice when the layer is grown at a substrate

temperature of 240°C. The results were studied by X-ray diffraction and the measurement of reflection spectra and Raman shift.

The critical thickness of ZnS layers was observed to vary with the substrate temperature. It is thinner than 200 nm for layers grown at  $T_{\text{sub}} = 240^\circ\text{C}$  and much thinner than 200 nm for layers grown at  $T_{\text{sub}} = 160^\circ\text{C}$ . It was also observed that the thickness of the layers grown at 240°C is limited to 200 nm. Additional experimental and theoretical work is needed in determining the limitation of thickness.

## 6. Acknowledgments

The authors wish to thank Professor T. Watanabe, Science University of Tokyo, for the use of the diffractometer.

## 7. References

- [1] T. Yao and S. Maekawa, *J. Crystal Growth* 53 (1981) 423.
- [2] H. Ando, A. Taike, M. Konagai and K. Takahashi, *J. Appl. Phys.* 62 (1987) 1251.
- [3] P.J. Dean, A.D. Pitt, M.S. Skolnick, P.J. Wright and B. Cockayne, *J. Crystal Growth* 59 (1982) 301.
- [4] A. Koukitu, T. Miyazawa, H. Ikeda and H. Seki, *J. Crystal Growth* 123 (1992) 95.
- [5] K. Yoneda, T. Toda, Y. Nishida and T. Niina, *J. Crystal Growth* 67 (1984) 125.
- [6] J. Petruzzello, B.L. Greenberg, D.A. Cammack and R. Dalby, *J. Appl. Phys.* 63 (1988) 2299.
- [7] Y.K. Vekilov and A.P. Rusakov, *Soviet Phys. Solid State* 13 (1972) 956.
- [8] H. Asai and K. Oe, *J. Appl. Phys.* 54 (1983) 2052.
- [9] A. Gavini and M. Cardona, *Phys. Rev. B* 1 (1970) 672.
- [10] D.J. Olego, K. Shahzad, J. Petruzzello and D. Cammack, *Phys. Rev. B* 36 (1987) 7674.
- [11] J.F. Scott, T.C. Damen, W.T. Silfvast, R.C.C. Leite and L.E. Cheesman, *Opt. Commun.* 1 (1970) 397.
- [12] H. Kanie, M. Nagano and M. Aoki, *Jap. J. Appl. Phys.* 30 (1991) 1360.



ELSEVIER

Journal of Crystal Growth 138 (1994) 150–154

JOURNAL OF  
**CRYSTAL  
GROWTH**

## Strain relief and growth modes in wurtzite type epitaxial layers of CdSe and CdS and in CdSe/CdS superlattices

M. Grün <sup>a,\*</sup>, M. Hetterich <sup>a</sup>, C. Klingshirn <sup>a</sup>, A. Rosenauer <sup>b</sup>, J. Zweck <sup>b</sup>,  
W. Gebhardt <sup>b</sup>

<sup>a</sup> Department of Physics, University of Kaiserslautern, D-67653 Kaiserslautern, Germany

<sup>b</sup> Department of Physics, University of Regensburg, D-93053 Regensburg, Germany

### Abstract

The relaxation of the mismatch-induced strain in (0001) wurtzite type epilayers of CdSe and CdS and of related superlattices on GaAs(111) is discussed. For CdSe/GaAs(111), high-resolution electron microscopy shows that the misfit dislocations are 60° dislocations, the glide of which is limited to the plane parallel to the interface. The epilayers are therefore free of in-grown threading arms. The thickness of that region in the layer, which is significantly strained, is found to be larger in case of a two-dimensional growth mode than in case of a three-dimensional one.

### 1. Introduction

In this article the relief of mismatch-induced strain in II–VI epitaxial layers with the wurtzite type crystal structure is studied. The orientation of the primary glide planes relative to the interface is found to have significant influence on the dislocation structure induced by lattice mismatch. In (001) zinc-blende type epilayers, which are commonly used, the four {111} glide planes allow misfit segment formation by glide of existing dislocations or surface nucleated half loops. The line ends of the half loops extend into the growing layer and form the well-known network of threading arms [1], which degrade the electrical

and optical epilayer properties. The dislocation density in the active layer of ZnCdSe/ZnSe based GRINSCH single quantum well laser diodes, for instance, can exceed  $1 \times 10^7 \text{ cm}^{-2}$  because of these in-grown threading arms [2]. They originate in these devices mainly from misfit dislocations at the barrier-cladding interface.

Here we report a study of (0001) wurtzite type II–VI epitaxial layers by high-resolution electron microscopy (HREM) and by reflective high-energy electron diffraction (RHEED). The only primary glide plane in these structures is situated parallel to the interface. We show that the formation of threading arms is then eliminated completely. The structures studied are CdSe and CdS layers and CdSe/CdS superlattices grown on GaAs(111), which are highly mismatched. The (111) substrate orientation provides the required (0001) layer orientation.

\* Corresponding author.

## 2. Experiment

The wurtzite type epitaxial layers were grown by hot-wall epitaxy and hot-wall beam epitaxy on  $(\bar{1}\bar{1}\bar{1})$ B GaAs [3]. The substrates were etched in the standard manner and deoxidized in a hydrogen atmosphere. CdSe and CdS were evaporated from two parallel effusion cells and the substrate was moved to each of the desired cells. CdSe layers were grown at 470°C without a spacing between the substrate and the effusion cell, which is the usual hot-wall epitaxy (HWE). CdS layers and CdSe/CdS superlattices were grown at 430°C with a spacing of 10 mm, which is called hot-wall beam epitaxy (HWBE) [4]. In-situ RHEED was carried out at the CdS growth position in the HWBE mode. The CdSe/CdS strained layer superlattices (SLSs) were grown on thick CdS buffer layers and consist of 30 symmetric periods capped with thin CdS layers. Growth of CdSe/CdS SLSs by metalorganic chemical vapour deposition has already been reported by Halsall et al. [5].

HREM was performed using a Philips CM 30 microscope operated at 300 kV. The point resolution was 0.23 nm. Cross-sectional samples were prepared in a conventional manner using a two-side argon ion milling process at liquid nitrogen temperature for final thinning.

## 3. Results

### 3.1. HREM

An example of single-beam bright field imaging of the CdSe/GaAs(111) interface is shown in Fig. 1. The photograph reveals only a few planar defects, but no further dislocations in the layer. The selected area diffraction pattern shows a nearly unstrained wurtzite type epilayer. Multi-beam lattice images show a few stacking faults within the wurtzite type layer (Fig. 2a). Misfit dislocations were recognized by Fourier filtering of selected atomic netplanes in the high-resolution image (Fig. 2b). Dislocations are found within the first few CdSe bilayers at an averaged distance of  $5.27 \pm 0.13$  nm in the  $\langle 11\bar{2} \rangle_{\text{GaAs}}$  direction. The observed dislocation distance corre-

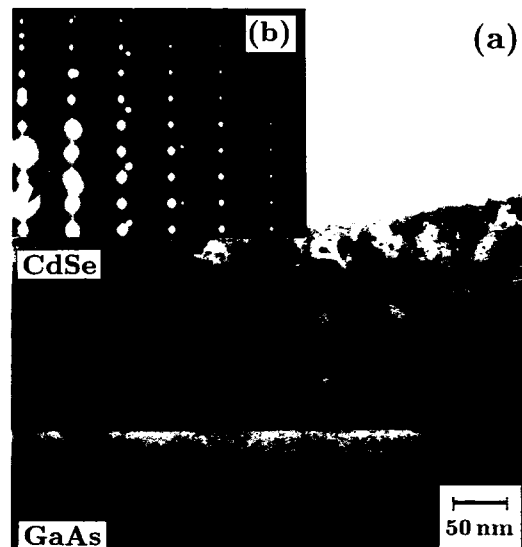


Fig. 1. (a) Cross-sectional single-beam bright field TEM micrograph of a CdSe/GaAs(111) interface. Horizontal lines in the undamaged layer region are attributed to planar defects. (b)  $\langle 11\bar{2} \rangle_{\text{CdSe}} \parallel \langle 1\bar{1}0 \rangle_{\text{GaAs}}$  selected area diffraction pattern with the (000) reflection marked.

sponds to a relief of  $95 \pm 2\%$  of the strain, which is induced by the mismatch of  $-6.9\%$  at the growth temperature. The Burgers vectors of the misfit dislocations were determined from Burgers circuits. Fig. 3 shows a circuit around a dislocation. The Burgers vector is parallel to the interface plane with magnitude  $\frac{1}{2}a_{\text{GaAs}}\langle 1\bar{1}0 \rangle$ . It belongs to a full or possibly dissociated  $60^\circ$  dislocation, the glide of which is limited to the (0001) plane. This limitation of the glide motion parallel to the interface rules out the formation of threading arms, which produces a CdSe epilayer nearly free from in-grown dislocations.

For CdS epilayers unfortunately low resolution single-beam images were not taken, but the absence of threading arms is similarly probable in this system. Multi-beam lattice images of the CdS/GaAs(111) interface show an interface region of about 8 nm width with a high stacking fault density. Misfit dislocations are spread within

this region. A measurement of the amount of strain relief using the Fourier filtering technique failed. From these observations we suppose a significantly more sluggish strain relief in CdS/GaAs(111) than in CdSe/GaAs(111).

### 3.2. RHEED

The HWBE grown CdS layers always show streaky RHEED patterns. The associated quasi-

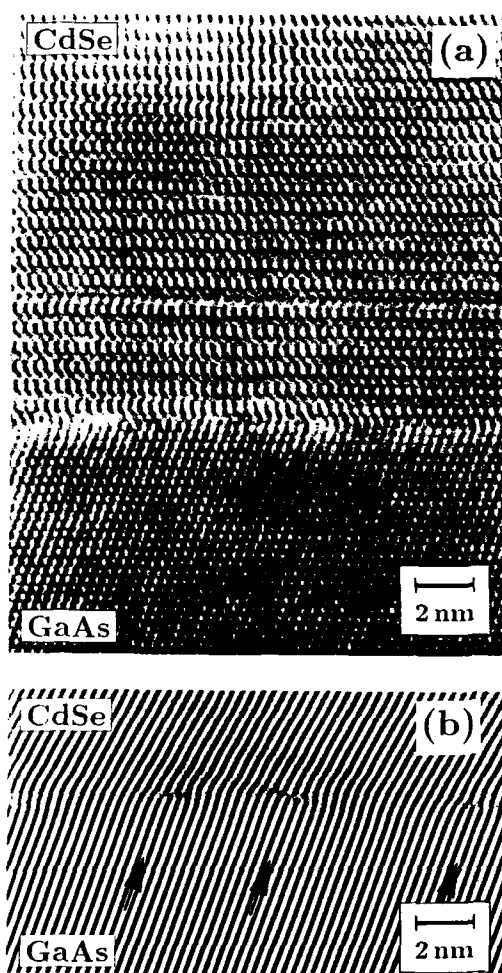


Fig. 2. (a) HREM image of a CdSe/GaAs(111) interface in  $[110]_{\text{GaAs}}$  projection. (b) Interface region after Fourier filtering; the black arrows indicate terminating {111} substrate planes.

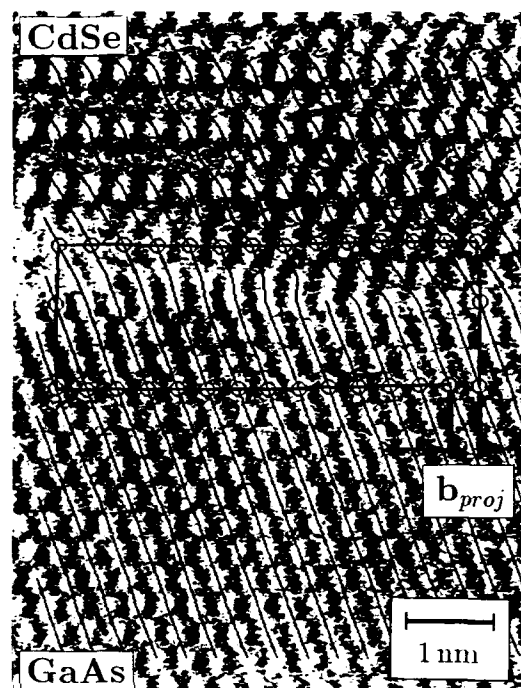


Fig. 3. Burgers circuit around an interfacial misfit dislocation from an enlarged section of Fig. 2a. The black lines are guides to the eye in order to recognize more easily the dislocation site.

two-dimensional (2D) growth mode is obtained throughout the whole growth cycle. Unfavourable growth conditions induce spotty RHEED patterns, which give some evidence for cubic twinning during the initial growth stage. The HWE grown CdSe layers either on GaAs or on CdS buffer layers show a spotty RHEED pattern, i.e. a three-dimensional (3D) growth mode. Possibly, this finding is due to the limited range of growth conditions available in our epitaxy apparatus or to the different lattice mismatches. Cubic twinning is not observed for CdSe.

The RHEED patterns of the CdSe/CdS SLSs show a transition from streaky patterns to spotty ones. Fig. 4 is a series of patterns obtained during growth of a superlattice with a period length of 8 nm. The streaky pattern is preserved up to about the 7th period corresponding to approximately 50 nm total SLS thickness (Figs. 4b and 4c). Then it

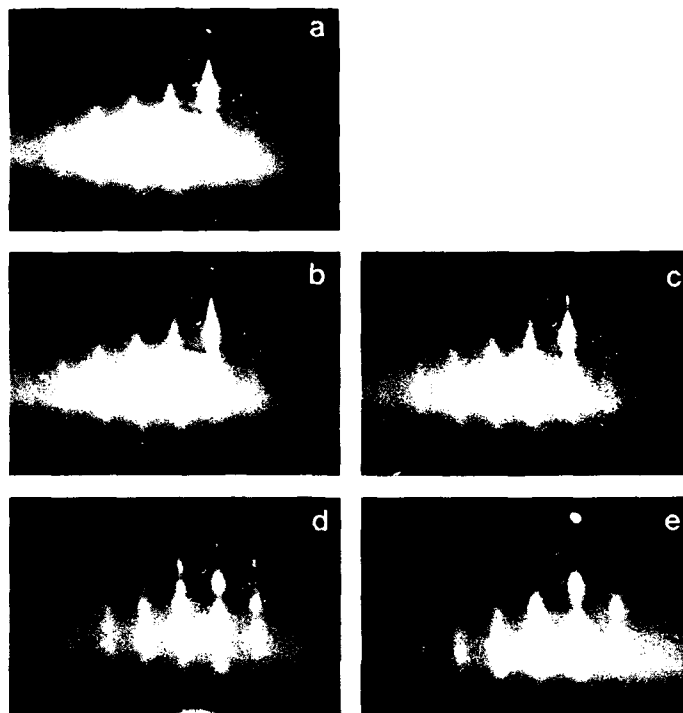


Fig. 4. Set of RHEED patterns during growth of a 4×4 nm CdSe/CdS superlattice on a 700 nm CdS buffer layer on GaAs(111): (a) CdS buffer layer; (b) 4th SLS period; (c) 7th SLS period; (d) 15th SLS period; (e) 20th SLS period.

gradually changes into a spotty pattern within the next 10 periods (Figs. 4d and 4e). The spotty pattern then remains unchanged during growth of the remaining SLS. It reveals some cubic twinning. During cap layer growth the streaky pattern is restored. The growth mode transition from quasi-2D to 3D is related to the relaxation of the initially pseudomorphic SLS.

#### 4. Discussion

The stacking fault region at the CdS/GaAs (111) interface observed in HREM and RHEED is ascribed to the presence of compressive strain. Compressive strain larger than about 1% should cause a loss of stability of the bulk-stable phase in layer growth via an increase of the actual bond length ratio of vertical to in-plane bonds over the

corresponding ratio of the metastable phase [6]. The observed stacking faults are assumed to be due to this effect or possibly due to stacking fault bands of strain relieving Shockley partials. This assumption allows a consistent interpretation of our HREM and RHEED results: the mismatch-induced strain in (0001) wurtzite type layers is relieved by full or dissociated 60° dislocations, the nucleation of which does not take place via a half-loop mechanism and is hampered by a 2D growth mode and facilitated by a 3D growth mode.

The 3D growth of CdSe/GaAs(111) results in an efficient strain relief near the interface and subsequent growth with low stacking fault density. The 2D growth of CdS/GaAs(111) and the SLSs causes strained layer regions of noticeable thickness. The observed "critical thickness" referring here to the thickness of a significantly



strained region is about 8 nm for CdS/GaAs(111) with  $-3.1\%$  mismatch as deduced from HREM. For the CdSe/CdS SLS the onset of a 3D growth mode above 50 nm total superlattice thickness allows formation of misfit dislocations, which shifts the SLS in-plane lattice constant from that of the buffer layer to that of the free-standing SLS [7]. The RHEED deduced value of 50 nm represents therefore roughly a "critical thickness" of the SLS as a whole, which has a  $-1.9\%$  mismatch to the CdS buffer layer. Possibly, the free-standing part is relaxed to a certain extent due to its 3D growth mode and only the pseudomorphic part is coherent. The cubic twinning in the SLS most likely originates from the compressively strained CdSe layers.

From photoluminescence measurements, a "critical thickness" value of about 5 nm for the individual CdSe and CdS layers within the SLS is estimated ( $-3.8\%$  mismatch in the pseudomorphic case). A detailed discussion of this result is beyond this article. We state here only that the energy of the luminescent electron-hole transition in the coherently strained SLSs depends linearly on the period length due to strain-induced piezo-electric fields [3, 5]. Strain relaxation is thus indicated by a deviation from this linear period length dependence.

The observed "critical thickness" values are a factor of 2 to 5 above the Matthews–Blakeslee critical thickness calculated for a (111) oriented zinc-blende type epilayer and  $60^\circ$  dislocations [1]. We believe that the delayed strain relaxation is caused mainly by the loss of the half-loop nucleation mechanism in the (0001) wurtzite structure. Nucleation of the observed  $60^\circ$  dislocations most probably requires at least a bilayer surface step, the density of which is low on smooth 2D surfaces.

The details of the nucleation mechanism are still an open question. In case of 3D growth, the base edges of small islands are likely to serve as nucleation sites, as considered by Snyder et al. [8] for InGaAs/GaAs(001) and by Horn-von Hoegen et al. [9] for Ge/Si(111). The latter authors reported also misfit dislocations with Burgers vectors parallel to the interface. Rosenauer et al. [10] recently found strain relief by only this type

of dislocations in cubic ZnTe grown on GaAs(111). These two results show that the suppression of threading arm formation in mismatched epitaxy is also possible in zincblende type epilayers, provided that a (111) interface is used and that only misfit dislocations are generated with glide planes parallel to the interface.

## 5. Conclusions

Wurtzite type epilayers of CdSe and CdS in (0001) orientation show no extension of mismatch-induced dislocations into the epilayer volume. The misfit dislocations in CdSe/GaAs(111) are full or dissociated  $60^\circ$  dislocations, the glide motion of which is limited to the interfacial (0001) plane. Threading arms are therefore not formed. RHEED data of CdSe and CdS layers and of CdSe/CdS superlattices give evidence that the strain relief is speeded up by a 3D growth mode.

## 6. References

- [1] See, e.g., R. Hull, *Crit. Rev. Solid State Mater. Sci.* 17 (1992) 507.
- [2] C.T. Walker, J.M. DePuydt, M.A. Haase, J. Qiu and H. Cheng, *Physica B* 185 (1993) 27.
- [3] M. Grün, M. Hetterich, U. Becker, Th. Gilsdorf, H. Giessen, H. Zangerle, M. Müller, J. Loidolt, F. Zhou and C. Klingshirn, in: *The Physics of Semiconductors*, Vol. 1, Proc. 21st Int. Conf. on Physics of Semiconductors, Beijing, August 1992, Eds. P. Jiang and H.-Z. Zheng (World Scientific, Singapore 1992) p. 574.
- [4] M.A. Herman and H. Sitter, *Molecular Beam Epitaxy* (Springer, Berlin, 1989) p. 108.
- [5] M.P. Halsall, J.E. Nicholls, J.J. Davies, B. Cockayne and P.J. Wright, *J. Appl. Phys.* 71 (1992) 907.
- [6] For a relation between the wurtzite parameter and the phase stability see, e.g., P. Lawaetz, *Phys. Rev. B* 5 (1972) 507.
- [7] E. Kasper in: *Physics and Applications of Quantum Wells and Superlattices*, Eds. E.E. Mendez and K. von Klitzing (Plenum, New York, 1987) p. 101.
- [8] C.W. Snyder, B.G. Orr, D. Kessler and L.M. Sander, *Phys. Rev. Lett.* 66 (1991) 3032.
- [9] M. Horn-von Hoegen, M. Pook, A. Al Fakou, B.H. Müller and M. Henzler, *Surf. Sci.* 284 (1993) 53.
- [10] A. Rosenauer, H. Stanzl, K. Wolf, S. Bauer, M. Kastner, M. Grün and W. Gebhardt, in: *Proc. 17th Int. Conf. on Defects in Semiconductors*, Gmunden, July 1993 (Trans Tech, Zürich, in press).

## Wide gap $\text{Cd}_{1-x}\text{Mg}_x\text{Te}$ : molecular beam epitaxial growth and characterization

A. Waag<sup>\*</sup>, F. Fischer, Th. Litz, B. Kuhn-Heinrich, U. Zehnder, W. Ossau, W. Spahn, H. Heinke, G. Landwehr

*Physikalisches Institut der Universität Würzburg, Am Hubland, D-97074 Würzburg, Germany*

### Abstract

We have grown the ternary alloy  $\text{Cd}_{1-x}\text{Mg}_x\text{Te}$  as well as  $\text{Cd}_{1-x}\text{Mg}_x\text{Te}/\text{CdTe}$  quantum well structures by molecular beam epitaxy – to our knowledge for the first time.  $\text{Cd}_{1-x}\text{Mg}_x\text{Te}$  exhibits some very interesting features: The band gap has been determined as a function of Mg concentration, and a band gap of 3.0 eV was found for zincblende  $\text{MgTe}$  at room temperature.  $\text{Cd}_{1-x}\text{Mg}_x\text{Te}$  thin films with Mg concentrations of up to 0.75 were fabricated, which corresponds to a band gap of 2.8 eV at low temperatures. Therefore, the whole visible band gap range (at room temperature) can be covered with Mg concentrations between 0.30 (red) and 0.75 (blue). Bulk  $\text{MgTe}$  crystallizes in the wurtzite structure, but zincblende  $\text{MgTe}$  could be grown on (100) oriented  $\text{CdTe}$  substrates up to a layer thickness of approximately 500 nm. The lattice mismatch between zincblende  $\text{MgTe}$  and  $\text{CdTe}$  was found to be as small as 1.0%. The growth of cubic  $\text{MgTe}$  could be followed by reflection high energy electron diffraction (RHEED) oscillations. In general, excellent structural quality could be reached, which is demonstrated by the FWHM of 22 arc sec for a  $\text{Cd}_{1-x}\text{Mg}_x\text{Te}$  thin film with 0.44 Mg concentration on a  $\text{Cd}_{1-x}\text{Zn}_x\text{Te}$  nearly lattice matched substrate. The Poisson number of  $\text{Cd}_{1-x}\text{Mg}_x\text{Te}$  has been determined by X-ray diffraction as a function of Mg concentration.  $\text{Cd}_{1-x}\text{Mg}_x\text{Te}/\text{CdTe}$  single quantum well structures have been fabricated with a large confinement energy of up to 0.8 eV. The photoluminescence spectra show exciton lines with very narrow linewidths. We are able to observe excited exciton states, and from the energetic difference between 1s and 2s heavy hole exciton lines we deduce exciton binding energies. Very bright luminescence could be seen even at room temperature, which is an indication of a large exciton binding energy and an effective radiative recombination.

### 1. Introduction

$\text{CdTe}$  itself exhibits a lot of interesting features: a band gap in the middle of the solar spectrum, a high atomic weight for X-ray detection, and an electro-optic coefficient, which is a

factor of 4 higher than in  $\text{GaAs}$ . In addition,  $\text{CdTe}$  is the base material for the related ternary alloys  $\text{HgCdTe}$  and  $\text{Cd}_{1-x}\text{Mn}_x\text{Te}$ .  $\text{HgCdTe}$  is an important infrared detector material, and  $\text{Cd}_{1-x}\text{Mn}_x\text{Te}$  as a dilute semiconductor exhibits unique features like, e.g., a giant Faraday rotation and magnetic polaron formation.

$\text{Cd}_{1-x}\text{Mn}_x\text{Te}$  as well as  $\text{Cd}_{1-x}\text{Zn}_x\text{Te}$  have been intensively studied in the past as barrier materials for  $\text{CdTe}$  based quantum well struc-

<sup>\*</sup> Corresponding author.

tures [1,2]. In principle,  $\text{Cd}_{1-x}\text{Mn}_x\text{Te}$  is suited for light emitting devices in the whole visible region: MnTe is a wide gap semiconductor with a band gap of 3.2 eV, and recently an electron pumped  $\text{Cd}_{1-x}\text{Mn}_x\text{Te}/\text{CdTe}$  quantum well laser emitting in the red was fabricated [3]. However, on the one hand the intra-3d transition of the Mn ions limits the recombination energy in bulk  $\text{Cd}_{1-x}\text{Mn}_x\text{Te}$ . On the other hand, the lattice mismatch to CdTe is relatively high (2.3%), leading to a small critical layer thickness or a high dislocation density. This is especially relevant for higher manganese contents. The band gap of ZnTe is only 2.3 eV at room temperature, and therefore it is not possible to reach the entire visible range with this material. In addition, a large lattice mismatch of 5.5% occurs between CdTe and ZnTe. Therefore we have searched for an alternative material with a better lattice matching to CdTe, which in a ternary alloy with CdTe would cover the entire visible region of the spectrum.

$\text{Cd}_{1-x}\text{Mg}_x\text{Te}$  is such an alternative ternary alloy. Recently, we have demonstrated the first  $\text{Cd}_{1-x}\text{Mg}_x\text{Te}$  thin film growth by molecular beam epitaxy (MBE) [4]. In this contribution we report on the optical and structural properties of  $\text{Cd}_{1-x}\text{Mg}_x\text{Te}$  thin films as well as on  $\text{Cd}_{1-x}\text{Mg}_x\text{Te}/\text{CdTe}$  quantum well structures. This is to our knowledge the first time that  $\text{Cd}_{1-x}\text{Mg}_x\text{Te}/\text{CdTe}$  quantum well structures have been grown by any thin film technique.

## 2. Experimental procedure

The MBE growth procedure has been described in detail elsewhere [4]. The thin films were grown on (100)CdTe and (100) $\text{Cd}_{1-x}\text{Zn}_x\text{Te}$  substrates. The  $\text{Cd}_{1-x}\text{Mg}_x\text{Te}$  structures were grown at a substrate temperature of 250°C. Reflection high energy electron diffraction (RHEED) was used to monitor the MBE growth in situ. The lattice constant as well as the strain in the layers was determined using a five/six crystal X-ray diffractometer. The optical properties of the structures were investigated using photoluminescence (PL) and photoluminescence ex-

citation (PLE) spectroscopy at temperatures ranging from 1.7 K up to room temperature. An argon ion laser (476 nm or 514 nm) or a dye laser (DCM, Pyridin) was used for the PL and PLE measurements, respectively.

## 3. Results and discussion

The bulk properties of the ternary alloys  $\text{Cd}_{1-x}\text{Mg}_x\text{Te}$  and  $\text{Zn}_{1-x}\text{Mg}_x\text{Te}$  have been studied in the past by different groups [5–15].

There have been some discrepancies in the literature concerning the band gap and lattice constant of  $\text{Cd}_{1-x}\text{Mg}_x\text{Te}$ . We therefore determined both band gap and lattice constant as a function of Mg concentration. For this the Mg concentration has been calibrated via X-ray photoelectron spectroscopy (XPS), and the band gap and lattice constant have been determined by PL and X-ray diffraction (XRD). The PL excitonic recombination energies were directly used for the band gap determination, no correction for excitonic localization energies has been applied. The errors inferred with this are small compared to the error of the determination of the Mg concentrations via XPS, which is estimated to be about 10%–20%. The XPS measurements were performed in a surface analysis chamber which was directly connected to the MBE growth chamber by a UHV transfer tunnel. Therefore any surface contamination could be minimized. Mg 1s and Cd 3d<sub>5/2</sub> peaks with sensitivity factors of 3.65 and 2.55, respectively, have been used for the analysis [17].

The results of such measurements are shown in Fig. 1, where the energy of the band gap is plotted versus the lattice constant for the ternary alloy  $\text{Cd}_{1-x}\text{Mg}_x\text{Te}$ . We find a room temperature band gap for the zincblende MgTe of 3.0 eV, and a lattice constant which is only 1.0% smaller than that of CdTe ( $a_{\text{MgTe}}(\text{cubic}) = 6.417 \text{ \AA}$ ).

These results could be very interesting in terms of visible light emitting devices based on  $\text{Cd}_{1-x}\text{Mg}_x\text{Te}$ . The band gap of  $\text{Cd}_{1-x}\text{Mg}_x\text{Te}$  can be tuned through the whole visible range by varying the Mg concentration from 30% up to 75%. In the same range the lattice constant changes by

only 0.45%. If a suitable substrate is used, which is lattice matched to  $\text{Cd}_{1-x}\text{Mg}_x\text{Te}$  with a Mg concentration of about 0.50, then a lattice mismatch to the substrate of only 0.25% occurs if the band gap is tuned through the whole visible range.  $\text{Cd}_{1-x}\text{Zn}_x\text{Te}$  substrates with a Zn content of about 0.09 would fulfil these requirements, and in addition such substrates are commercially available.

The high structural quality of  $\text{Cd}_{1-x}\text{Mg}_x\text{Te}$  thin films grown on nearly lattice matched  $\text{Cd}_{1-x}\text{Zn}_x\text{Te}$  substrates is demonstrated in Fig. 2. Here rocking curves of the (004) reflection are plotted for  $\text{Cd}_{1-x}\text{Mg}_x\text{Te}$  thin films with three different Mg concentrations:  $x_{\text{Mg}} = 0.10$  corresponds to a band gap of 1.65 eV,  $x_{\text{Mg}} = 0.40$  corresponds to a band gap of 2.1 eV, and  $x_{\text{Mg}} = 0.63$  corresponds to a band gap of 2.45 eV. The film thickness was only 500 nm, and therefore the intensity of the layer peak is relatively small. The lattice constant of the thin film with the lowest Mg concentration of  $x_{\text{Mg}} = 0.10$  is larger than

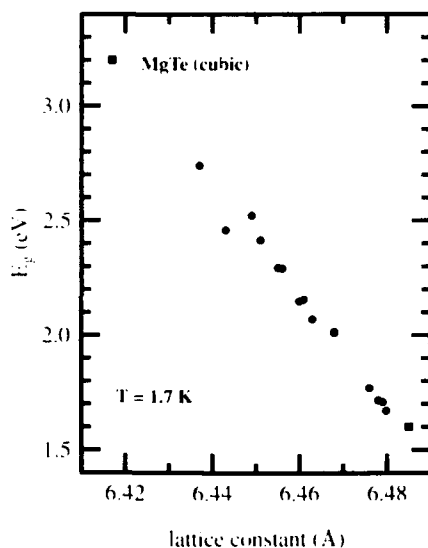


Fig. 1. Band gap of cubic  $\text{Cd}_{1-x}\text{Mg}_x\text{Te}$  as a function of its lattice constant. The  $x$ -values for some of the thin films were calibrated by X-ray photoelectron spectroscopy. The band gap can be tuned through the whole visible range with Mg concentrations varying from 0.30 to 0.75. In this range the lattice constant changes by only 0.45%.

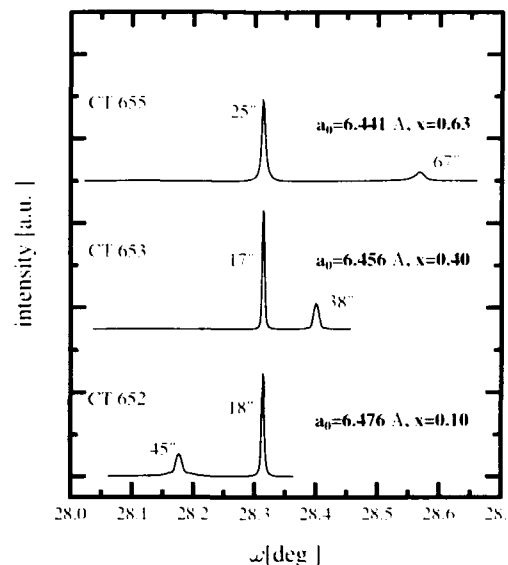


Fig. 2. Rocking curves from X-ray diffraction for three  $\text{Cd}_{1-x}\text{Mg}_x\text{Te}$  layers with varying Mg concentration on  $\text{Cd}_{1-x}\text{Zn}_x\text{Te}$  substrates. The band gap is varied through the whole visible range, and the lattice mismatch to the substrate still stays small. The FWHM of the substrate reflection is around 20 arc sec, whereas the FWHM of the  $\text{Cd}_{1-x}\text{Mg}_x\text{Te}$  layer depends on the lattice mismatch to the substrate. For small Mg concentrations the lattice constant of the layer is larger than the one of the substrate. For higher Mg concentrations the situation is vice versa.

that of the substrate, whereas the lattice constant of the thin film with the highest Mg concentration of  $x_{\text{Mg}} = 0.63$  is smaller than that of the substrate. For all Mg concentrations shown the structural quality is very good, which is indicated by the small full width at half maximum (FWHM) of the layer peaks. Rocking curves with a FWHM of the (004) reflection of as low as 22 arc sec for a  $\text{Cd}_{1-x}\text{Mg}_x\text{Te}$  layer with a Mg concentration of 0.44 on a  $\text{Cd}_{1-x}\text{Zn}_x\text{Te}$  substrate could be obtained.

The strain in the layers has been investigated by reciprocal space mapping of asymmetric X-ray reflections. From this a strain parameter  $\gamma$  was deduced, which reflects the degree of relaxation of the layers.  $\gamma = 1$  corresponds to a fully strained layer, whereas  $\gamma = 0$  corresponds to a fully relaxed layer [4]. For the three layers of Fig. 1,  $\gamma$

Table 1

Poisson number of  $\text{Cd}_{1-x}\text{Mg}_x\text{Te}$  as a function of Mg concentration: the value for CdTe is taken from ref. [11];  $a_0$  is the lattice constant for the relaxed material

$x_{\text{Mg}}$	$2C_{12}/C_{11} = P$	$a_0$ (Å)
0	1.3758	6.4825
0.10	1.364	6.4758
0.40	1.33	6.4560

turned out to be one. Nevertheless, a better lattice matching results in a smaller FWHM of the rocking curve, as can be seen from the figure.

From the XRD determination of the lateral and perpendicular lattice spacings of strained  $\text{Cd}_{1-x}\text{Mg}_x\text{Te}$  layers, the Poisson number could be derived. For this, layers on CdTe and  $\text{Cd}_{1-x}\text{Zn}_x\text{Te}$  substrates with varying degree of relaxation were investigated. In Table 1 the Poisson numbers derived are given for  $\text{Cd}_{1-x}\text{Mg}_x\text{Te}$  thin films with different Mg concentration. As can be seen from the table, the Poisson number is only very slightly decreasing with increasing Mg concentration. This result is important for the determination of  $\text{Cd}_{1-x}\text{Mg}_x\text{Te}$  lattice constants via XRD, because the Poisson number of CdTe had been used for the calculation of the relaxed lattice constant. Table 1 shows that this simplification made for the data points shown in Fig. 1 introduces a negligible error.

In bulk  $\text{Cd}_{1-x}\text{Mg}_x\text{Te}$ , a zincblende-to-wurtzite transition occurs for Mg concentrations above 0.50 [12]. We did not find such a behaviour for  $\text{Cd}_{1-x}\text{Mg}_x\text{Te}$  thin films grown on zincblende CdTe or  $\text{Cd}_{1-x}\text{Zn}_x\text{Te}$  substrates, with film thicknesses ranging up to 2  $\mu\text{m}$  and Mg concentration below 0.75. In addition, for Mg concentrations above 0.50, bulk  $\text{Cd}_{1-x}\text{Mg}_x\text{Te}$  gets very hygroscopic [9]. Chemical reaction with water produces  $\text{MgO}$  and  $\text{H}_2\text{Te}$ , which decomposes immediately, leading to a black Te deposit. In contrast to this, we were able to produce  $\text{Cd}_{1-x}\text{Mg}_x\text{Te}$  thin films with Mg concentrations of up to 0.75, which did not show a visible deterioration of the surface, as is the case for pure MgTe. MgTe immediately reacts in air, the thin film is destroyed, and a black residue is easily visible. No surface passivation was used in our case. The Mg concentration

of 0.75 corresponds to a band gap of 2.63 eV at room temperature and a wavelength of 472 nm, which is high enough for the emission of blue light. Therefore the instability of highly Mg rich bulk  $\text{Cd}_{1-x}\text{Mg}_x\text{Te}$  ternary alloys does not seem to be a limiting factor for the tunability of the band gap through the whole visible region of the spectrum in  $\text{Cd}_{1-x}\text{Mg}_x\text{Te}$  thin films.

If one wants to fabricate CdTe-based quantum well structures, the small lattice mismatch between CdTe and MgTe (1.0%) is advantageous compared to (CdZn)Te and (CdMn)Te, which are in general used as barrier materials. We have grown – to our knowledge for the first time –  $\text{Cd}_{1-x}\text{Mg}_x\text{Te}/\text{CdTe}$  quantum well structures. A typical sample consists of a  $\text{Cd}_{1-x}\text{Mg}_x\text{Te}$  buffer on a (100)  $\text{Cd}_{1-x}\text{Zn}_x\text{Te}$  substrate, followed by a series of quantum wells, which are separated by 50 nm thick  $\text{Cd}_{1-x}\text{Mg}_x\text{Te}$  barriers.

An efficient electron-hole confinement is important for a possible usage of  $\text{Cd}_{1-x}\text{Mg}_x\text{Te}/\text{CdTe}$  quantum well structures in optoelectronic devices. We have investigated confinement effects in such quantum well structures, and from the heavy hole–light hole splittings for different quantum well widths, a valence band offset of 0.30 of the band gap difference between  $\text{Cd}_{1-x}\text{Mg}_x\text{Te}$  and CdTe could be derived [18]. In combination with a large difference in the band gaps obtainable, this ensures a good electron as well as hole confinement.

Fig. 3 shows a PL spectrum for a set of quantum wells with a well thickness between 2.1 and 11 nm, at a temperature of 1.7 K. At this temperature sharp excitonic transitions can be observed. The FWHM of thin quantum wells at low temperature originate from monolayer fluctuations of the well widths. In our case, the FWHM is in general smaller than what one would expect from one monolayer fluctuation (3.2 Å for CdTe). This is an indication that the interfaces are rough with lateral islands on the order of the exciton Bohr radius [19]. For smaller quantum well widths, the FWHM increases as expected, because then the well width fluctuations have a larger effect on the subband energies.

The same quantum well structure as in Fig. 3 shows efficient PL even at room temperature; the

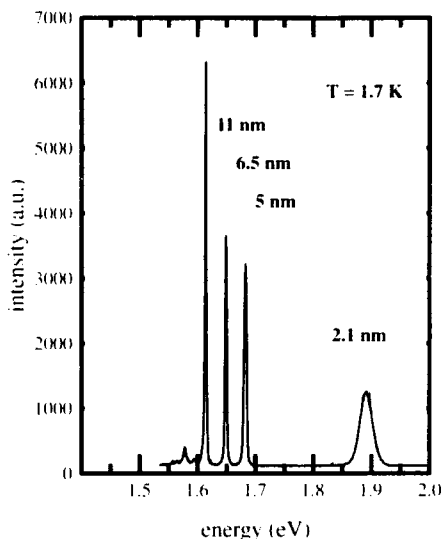


Fig. 3. Photoluminescence spectrum of a series of  $\text{Cd}_{1-x}\text{Mg}_x\text{Te}/\text{CdTe}$  quantum wells at a temperature of 1.7 K.

spectrum is plotted in Fig. 4. All quantum wells involved can be identified in the room temperature spectrum – despite the strong coupling to longitudinal optical (LO) phonons in CdTe which

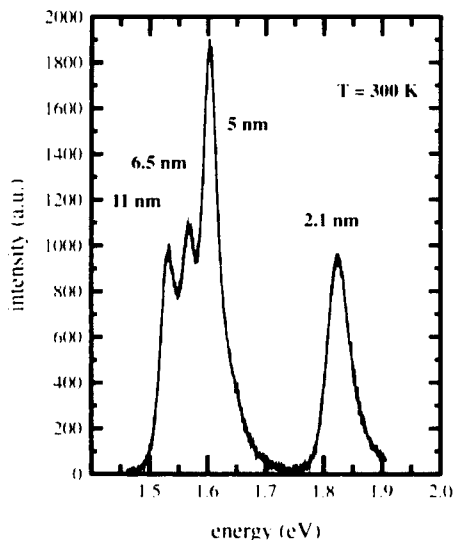


Fig. 4. Photoluminescence spectrum of the same structure as in Fig. 3, but at room temperature.

destroys the PL efficiency in bulk CdTe. Similar results have been observed in  $(\text{ZnCd})\text{Se}/\text{ZnSe}$  and  $(\text{CdZn})\text{Te}/\text{CdTe}$  quantum well structures [20,21]. The reason for this behaviour is the fact that the exciton binding energy gets enhanced in two-dimensional systems, and can become larger than the LO phonon energy  $\hbar\omega_{\text{LO}}$ . As a result the phase space available for the LO scattering processes is reduced.

For some of the  $\text{Cd}_{1-x}\text{Mg}_x\text{Te}$  quantum wells, the 2s heavy hole exciton could be directly observed in addition to the 1s heavy hole transition. From this a lower limit for the exciton binding energy of 28 meV was derived for the 5 nm well, and a binding energy of 23 meV for the 6.5 nm well, which is much higher compared to 10 meV for bulk CdTe. These values of the exciton binding energy are higher than the LO phonon energy of 21 meV in bulk CdTe, which is obviously the reason for the efficient room temperature radiative recombination observed in  $\text{Cd}_{1-x}\text{Mg}_x\text{Te}/\text{CdTe}$  quantum wells. It is interesting to note that the intensity of the 11 nm well is smaller than the intensity of the 5 nm well at room temperature – which is in contrast to the low temperature case (see Fig. 3). This is expected, because the exciton binding energy is smaller for larger quantum well widths.

In Fig. 5 the integrated PL intensity is plotted as a function of temperature for a 5 nm quantum well as well as for a  $\text{Cd}_{1-x}\text{Mg}_x\text{Te}$  layer. The intensity of the  $\text{Cd}_{1-x}\text{Mg}_x\text{Te}$  layer decreases drastically with increasing temperature, whereas the intensity of the 5 nm  $\text{Cd}_{1-x}\text{Mg}_x\text{Te}/\text{CdTe}$  quantum well decreases by less than one order of magnitude. This again demonstrates the stability of the confined excitons at room temperature.

The efficient radiative recombination in  $\text{Cd}_{1-x}\text{Mg}_x\text{Te}/\text{CdTe}$  quantum well structures even at room temperature is a key point for the efficiency of optoelectronic light emitting devices.

#### 4. Summary

In summary, we have investigated the structural as well as the optical properties of  $\text{Cd}_{1-x}\text{Mg}_x\text{Te}$  layers and  $\text{Cd}_{1-x}\text{Mg}_x\text{Te}/\text{CdTe}$  sin-

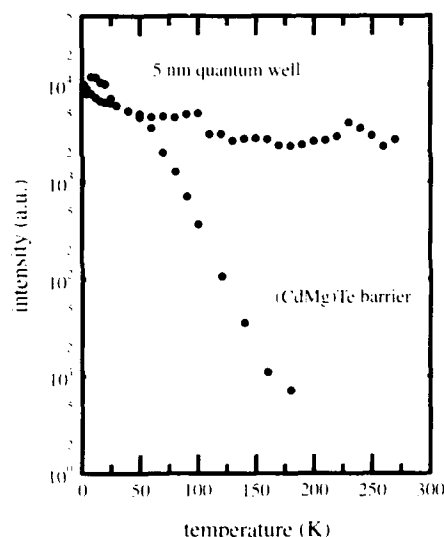


Fig. 5. Photoluminescence intensity as a function of temperature for a 5 nm  $\text{Cd}_{1-x}\text{Mg}_x\text{Te}/\text{CdTe}$  quantum well and a  $\text{Cd}_{1-x}\text{Mg}_x\text{Te}$  layer. The room temperature intensity of the quantum well is only about one order of magnitude smaller than compared to the low temperature case. This is in contrast to the  $\text{Cd}_{1-x}\text{Mg}_x\text{Te}$  layer, where the intensity decreases by more than three orders of magnitude. For a better comparison, relative intensities are given.

gle quantum well structures grown by MBE.  $\text{Cd}_{1-x}\text{Mg}_x\text{Te}$  shows some very interesting properties: the band gap can be tuned through the whole visible range by varying the Mg concentration from 0.30 to 0.75. In this range the lattice constant changes by only 0.45%. In addition, a large confinement of excitons can be reached in  $\text{Cd}_{1-x}\text{Mg}_x\text{Te}/\text{CdTe}$  quantum wells, leading to a high exciton binding energy and therefore to a high efficiency for radiative recombination even at room temperature. These properties could make the  $\text{Cd}_{1-x}\text{Mg}_x\text{Te}$  ternary alloy very interesting for optoelectronic applications.

## 5. Acknowledgements

We want to thank M. Bruder (AEG Heilbronn) for supplying us with CdTe source material, as well as P. Wolf and Th. Schuhmann for the substrate preparation. This project was partly supported by the Bundesminister für Forschung

und Technologie as well as the Deutsche Forschungsgemeinschaft.

## 6. References

- [1] D.R. Yakovlev, I.N. Ural'tsev, W. Ossau, G. Landwehr, R.N. Bicknell-Tassius, A. Waag and S. Schmeusser, *Surf. Sci.* 263 (1992) 485.
- [2] J. Cibert, R. André, C. Deshayes, Le Si Dang, H. Okumura, S. Tatarenko, G. Feuillet, P.H. Jouneau, R. Mallard and K. Saminadayar, *J. Crystal Growth* 117 (1992) 424.
- [3] J. Cibert, C. Bodin, Le Si Dang, G. Feuillet, P.H. Jouneau, E. Molva, R. Accomo and G. Labrunie, *Mater. Sci. Eng. B* 16 (1993) 279.
- [4] A. Waag, H. Heinke, S. Scholl, C.R. Becker and G. Landwehr, *J. Crystal Growth* 131 (1993) 607.
- [5] G.A. Saum and E. Hensley, *Phys. Rev.* 113 (1959) 1019.
- [6] R. Yamamoto, M. Inoue, K. Itoh and T. Shitaya, *Jap. J. Appl. Phys.* 6 (1967) 537.
- [7] R. Yamamoto and K. Itoh, *Jap. J. Appl. Phys.* 8 (1969) 341.
- [8] S.G. Parker, A.R. Reinberg, J.E. Pinnell and W.C. Holton, *J. Electrochem. Soc. (Solid State Sci.)* 118 (1971) 979.
- [9] A. Kuhn, A. Chevy and M.-J. Naud, *J. Crystal Growth* 9 (1971) 263.
- [10] S. Nakashima, T. Fukumoto, A. Mitsuishi and K. Itoh, *J. Phys. Soc. Japan* 32 (1972) 1438.
- [11] Landolt-Börnstein, *Zahlenwerte und Funktionen aus Naturwissenschaft und Technik*, Vol. 17b, Eds. K.H. Hellwege and O. Madelung (Springer, Berlin, 1982).
- [12] S. Nakashima, T. Fukumoto, A. Mitsuishi and K. Itoh, *J. Phys. Soc. Japan* 35 (1973) 1437.
- [13] D. Barbier and A. Laugier, *Solid State Commun.* 23 (1977) 435.
- [14] D. Boulanger and M.-S. Martin, *Phys. Status Solidi (b)* 85 (1978) 597.
- [15] B. Montegu, A. Laugier and D. Barbier, *Phys. Rev. B* 19 (1979) 1920.
- [16] D.T.F. Marple, *J. Appl. Phys.* 35 (1964) 539.
- [17] C.D. Wagner, W.M. Riggs, L.E. Davies, J.F. Moulder and G.E. Muilenberg, Eds., *Handbook of X-Ray Photoelectron Spectroscopy* (Perkin-Elmer, Eden Prairie, MN, 1978).
- [18] B. Kuhn-Heinrich, W. Ossau, H. Heinke, F. Fischer, Th. Litz, A. Waag and G. Landwehr, *Appl. Phys. Lett.*, in press.
- [19] A. Waag, S. Schmeusser, R.N. Bicknell-Tassius, D.R. Yakovlev, W. Ossau, G. Landwehr and I.N. Ural'tsev, *Appl. Phys. Lett.* 59 (1991) 2992.
- [20] N.T. Pelekanos, J. Ding, M. Hagerott, A.V. Nurmikko, H. Luo, N. Samarth and J.K. Furdyna, *Phys. Rev. B* 45 (1992) 6037.
- [21] N.T. Pelekanos, H. Haas, N. Magnea and A. Wasieleski, *Appl. Phys. Lett.* 61 (1992) 3154.



ELSEVIER

Journal of Crystal Growth 138 (1994) 161–167

JOURNAL OF  
**CRYSTAL  
GROWTH**

## CdTe and CdTe<sub>0.9</sub>Se<sub>0.1</sub> crystals grown by the travelling heater method using a rotating magnetic field

M. Salk <sup>a,\*</sup>, M. Fiederle <sup>a</sup>, K.W. Benz <sup>a</sup>, A.S. Senchenkov <sup>b</sup>, A.V. Egorov <sup>b</sup>,  
D.G. Matioukhin <sup>c</sup>

<sup>a</sup> Kristallographisches Institut, Universität Freiburg, D-79104 Freiburg, Germany

<sup>b</sup> SPLAV Technical Center, 107497 Moscow, Russian Federation

<sup>c</sup> Riga Scientific Research Institute for Radioisotope Apparatus, Riga, Latvia

### Abstract

CdTe and CdTe<sub>0.9</sub>Se<sub>0.1</sub> crystals were grown by the travelling heater method under different material transport regimes. The different transport regimes in the liquid zone were either caused by diffusion (and residual convection), or by 1g convection, or by forced convection. The forced convection was produced by a  $B = 2$  mT rotating magnetic field (400 Hz) under  $\mu g$  conditions. The equations for describing the model of the rotating magnetic field are derived, showing that the magnetic force term in the Navier–Stokes equation can be calculated separately in the case of  $\mu g$  conditions and small magnetic field. The rotating magnetic field generates a stable steady flow in the solution zone, which improves the radial and axial distribution of  $\mu\tau$  products.

### 1. Introduction and experimental conditions

A homogeneous distribution of defects and dopants is desirable for certain semiconductor applications. Both defects and dopants are influenced by the material transport in the liquid zone during crystal growth using the travelling heater method. The scientific objectives are to study the influence of different material transport mechanisms in the liquid zone and the resulting crystal properties. Experiments were carried out for different material transport regimes, which were either caused by diffusion (and residual convection under  $\mu g$ ), or by 1g convection, or by forced

convection under  $\mu g$  conditions by a rotating magnetic field.

CdTe and CdTe<sub>0.9</sub>Se<sub>0.1</sub> crystal growth experiments were successfully performed during the unmanned PHOTON 7 and PHOTON 8 missions in October 1991 and 1992, respectively. The crystals were grown in the furnace ZONA 4 by the travelling heater method. All experiments were accompanied by theoretical modelling of temperature profiles, phase boundaries and flow patterns in the Te zone.

The mission support of the PHOTON 7 mission and first results as well as the ampoule design are described in refs. [1–3]. The seed crystals CdTe and the feed materials CdTe:Cl were used during the PHOTON 7 mission and CdTe<sub>0.9</sub>Se<sub>0.1</sub>:Cl during the PHOTON 8 mission.

\* Corresponding author.



A rotating magnetic field with a magnetic induction of 2 mT and a frequency of 400 Hz was chosen for the experiments. The magnetic field rotates perpendicularly to the ampoule axis. Compared with the experiment without a magnetic field, these values ensure an appreciable change of mass transfer and Cd distribution in the solution zone. Their values simultaneously cause a stable steady flow at the crystallization front [4,5].

The timeline of the PHOTON 7 experiment within the rotating magnetic field is described in ref. [3]. The timeline is subdivided into 5 phases. At first the heater was switched on and the Te zone was heated up to 750°C. After a homogenization time of 2 h, the ampoule was moved with a pulling rate of 0.27 mm/h for 100 h. For the first 50 h, the crystal was grown within the rotating magnetic field, then the magnetic field was switched off.

In the following section, fluid dynamic calculations have been performed in order to show the theoretical influence of a rotating magnetic field on the flow pattern in the THM solution zone. Experimental results will be given for  $\mu g$  experiments.

## 2. Theoretical examination

### 2.1. Fluid-dynamical modelling

This model is used for the description of travelling heater crystal growth experiments within and without a rotating magnetic field. The scientific objectives of the calculations are to determine the phase boundaries, the local growth rates and the segregation. The following hydrodynamical equations, given in the nondimensional form, are needed: Navier–Stokes equations (1), continuity equation in the Boussinesq approximation (2), convective diffusion equation for each species (3), and convective heat transfer equation (4):

$$\begin{aligned} (\mathbf{V}^* \cdot \nabla) \mathbf{V}^* &= \frac{1}{\text{Re}} \Delta \mathbf{V}^* \\ &+ \frac{\text{Ha}^2 \text{Re}_D^M}{\text{Re} \text{Re}^M} (\mathbf{j}^* \times \mathbf{B}^*), \end{aligned} \quad (1)$$

$$\nabla \cdot \mathbf{V}^* = 0, \quad (2)$$

$$\frac{\partial c_i^*}{\partial t} + \mathbf{V}^* \cdot \nabla c_i^* = \frac{1}{\text{Pe}_D} \Delta c_i^*, \quad (3)$$

$$\frac{\partial T^*}{\partial t} + \mathbf{V}^* \cdot \nabla T^* = \frac{1}{\text{Pe}} \Delta T^*. \quad (4)$$

The description of the rotating magnetic field requires the Maxwell equations in the hydrodynamic approximation (5)–(8) and Ohm's law in the generalized form (9):

$$\nabla \cdot \mathbf{j}^* = 0, \quad (5)$$

$$\nabla \cdot \mathbf{B}^* = 0, \quad (6)$$

$$\nabla \times \mathbf{B}^* = \text{Re}_M^M \mathbf{j}^*, \quad (7)$$

$$\nabla \times \mathbf{E}^* = -\partial \mathbf{B}^* / \partial t, \quad (8)$$

$$\mathbf{j}^* = \sigma [\mathbf{E}^* + (\mathbf{V}^* \times \mathbf{B}^*)]. \quad (9)$$

Ohm's law in the nondimensionalized form (10) can be obtained from Eq. (9) by using the characteristic values  $\tilde{V}$ ,  $\tilde{L}$ ,  $\tilde{E}$  and  $\tilde{B}$ :

$$\mathbf{j}^* = \mathbf{E}^* + \frac{\text{Re}^M}{\text{Re}_D^M} (\mathbf{V}^* \times \mathbf{B}^*). \quad (10)$$

The following assumptions and simplifications are made:

- The flow is laminar and quasistationary.
- Buoyancy and solutal convection are neglected under microgravity conditions.
- Local thermodynamical equilibrium at the interfaces.
- In order to use 2D calculations, the flow is assumed to be axi-symmetrical.
- According to the regular associated solution model of Jaugier [6], the following species have to be regarded in the Te zone: CdTe, CdSe and Se (the diffusion coefficients are assumed to be equal).
- Fused silica ampoule and the crystals are electrical insulators.
- Crystallization heat is neglected.

The boundary conditions are the following:

- Axial symmetry:

$$\partial y_i / \partial r|_{r=0} = 0, \quad (11)$$

with  $y_i = V_i, U_i, T, B_r, B_z, B_\phi, E_r, E_z, E_\phi, c_i$ .

- At the phase boundaries and the ampoule walls the velocities are zero.

- The heat transfer between heater and ampoule wall occurs by radiation; Eq. (12) can be obtained from the Stefan–Boltzmann law for radiation, the Fourier law of heat conduction and the continuity equation for energy:

$$\partial T^*/\partial r^*|_{r=R} = Sk (T^{*4} - T^{*4}). \quad (12)$$

- The mass flux through the ampoule wall:

$$\partial c_i^*/\partial r^*|_{r=R} = 0. \quad (13)$$

- The mass transport at the phase boundaries is caused only by diffusion. The concentration of the species are taken according to Laugier [6]:

$$Pe_D U^* (c_i^* - c_i^{l*}) = \partial c_i^*/\partial n, \quad (14)$$

- The ampoule and the crystals are electrical insulators:

$$j_r^*(r=R) = 0, \quad (15)$$

$$j_n^* = 0, \quad (16)$$

where  $j_n^*$  is the current normal to the phase boundary.

- The magnetic field is continuous at all boundaries, because the relative magnetic permeability of the crystal, Te zone and ampoule is nearly 1.

## 2.2. Theoretical modelling of the rotating magnetic field

The current density in the Te zone is described in Eq. (10):

$$j^* = E^* + \frac{Re^M}{Re_\Omega^M} (V^* \times B^*). \quad (10)$$

In this nondimensional form  $E^*$  and  $(V^* \times B^*)$  are of the order of 1. According to experimental data [7,8], the ratio  $Re^M/Re_\Omega^M = U^*/R^*\omega$  is small ( $\sim 0.01$ ) for small Hartmann numbers (here:  $Ha \approx 0.5$ ). Therefore Eq. (10) can be simplified to

$$j^* = E^*. \quad (17)$$

With this approximation, the Maxwell equations are separated from the Navier–Stokes equations and can be treated independently. This separation can only be done for small Hartmann numbers under microgravity conditions. Under earth conditions, the Hartmann number has to be chosen large enough to dominate the buoyancy con-

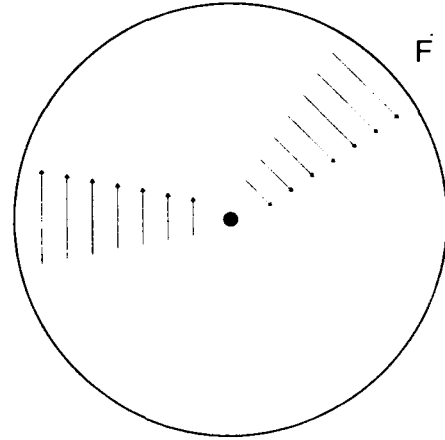


Fig. 1. The electromagnetic force causing azimuthal motion in the Te zone.

vection term and we have to use the full set of coupled equations. Now we combine Eq. (17) with Eq. (7) and calculate the curl:

$$\nabla \times (\nabla \times B^*) = \nabla \times (Re_\Omega^M E^*), \quad (18)$$

with

$$\nabla \times (\nabla \times B^*) = -\Delta B^* + \nabla(\nabla \cdot B^*) = -\Delta B^* \quad (19)$$

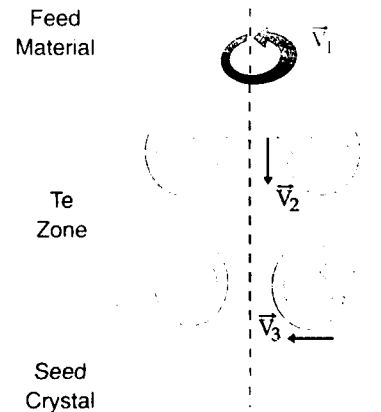


Fig. 2. Velocities of volume parts in the Te zone in the rotating magnetic field under  $\mu g$  conditions ( $V_1$ : azimuthal velocity;  $V_2$ : axial velocity;  $V_3$ : radial velocity).

Table 1  
Influence of the rotating field on the different velocities in the Te zone

Magnetic induction (mT)	Maximal velocity (cm/s)		
	Aximuthal	Axial	Radial
0	0	$1.58 \times 10^{-3}$	$7.12 \times 10^{-4}$
1	$2.11 \times 10^{-2}$	$2.43 \times 10^{-3}$	$1.75 \times 10^{-3}$
2	$7.23 \times 10^{-2}$	$1.22 \times 10^{-2}$	$1.19 \times 10^{-2}$
4	$2.01 \times 10^{-1}$	$3.71 \times 10^{-2}$	$4.15 \times 10^{-2}$

and Eq. (8), we obtain

$$\Delta B^* = \text{Re} \frac{M}{\Omega} \partial B^* / \partial t, \quad (20)$$

$$\nabla \cdot B^* = 0. \quad (21)$$

The magnetic field is separated from the electric field. After the calculation of the magnetic field, the electrical field is obtained by Eq. (8). The electromagnetic force term in (1) combined with (17) is given by

$$F^* = \frac{Ha^2 \text{Re} \frac{M}{\Omega}}{\text{Re} \text{Re}^M} (E^* \times B^*). \quad (22)$$

The difference between a rotating magnetic field and a static magnetic field should be emphasized.

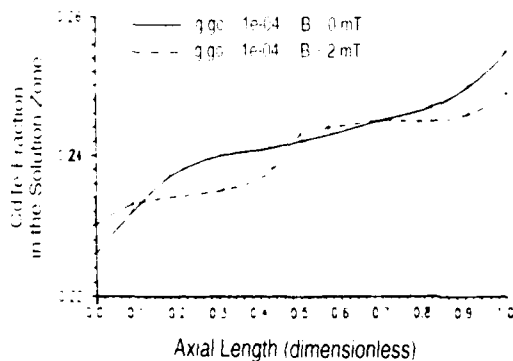
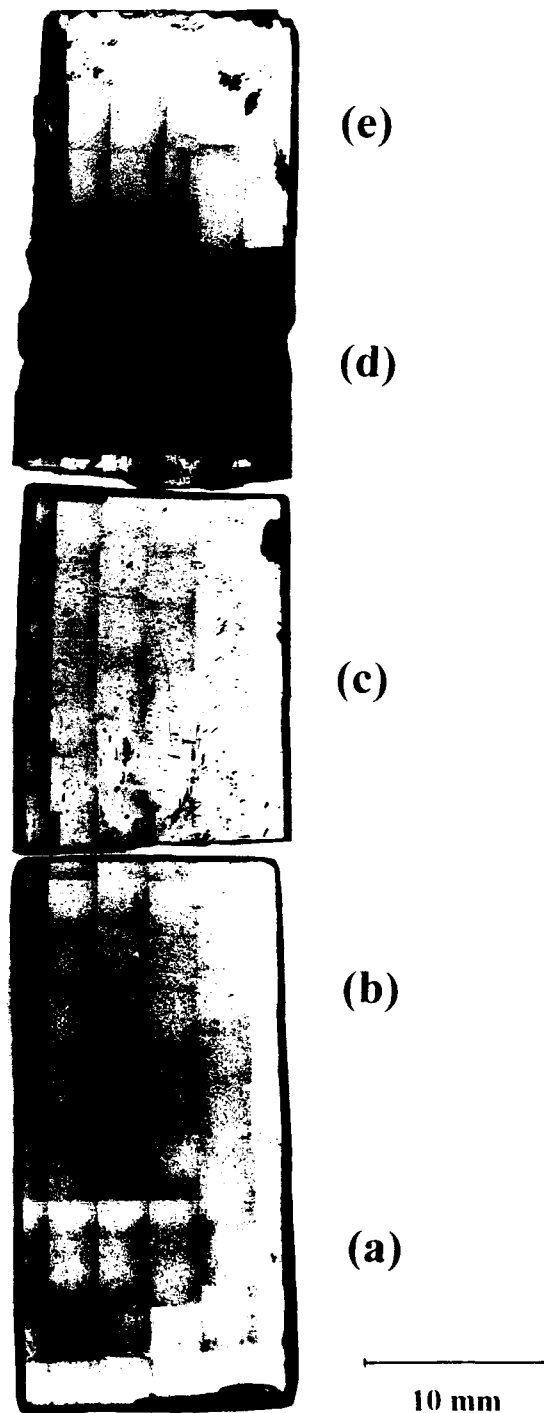


Fig. 3. Influence of the rotating magnetic field on the Cd/Te concentration distribution along the solution zone axis under  $\mu g$  conditions.

Fig. 4. Infrared image of an axial crystal slice of 2 mm (Te inclusions are black). (a) seed crystal; (b) grown crystal within the rotating magnetic field; (c) grown crystal without the magnetic field; (d) Te zone; (e) feed material.



In a constant magnetic field, the current is produced by the motion of the fluid in the magnetic field. The Lorentz force which acts upon this current, results in a damping of the velocity normal to the magnetic field. In a rotating magnetic field under microgravity conditions the motion of the fluid can be neglected. The current is produced by induction, and the resulting force generates a forced convection.

### 2.3. Theoretical results

Fig. 1 shows the electromagnetic force in the centre of the Te zone. The force only has an azimuthal component. Near the phase boundaries both radial and axial components are present. This force produces an azimuthal primary flow.

The velocity at the phase boundary is zero, and therefore the viscous forces produce a secondary flow, consisting of two toroidal convection rolls. The resulting flow pattern with the different velocities are depicted in Fig. 2. At 1g the rotating magnetic field has no influence on the flow pattern and the material transport, due to the weakness of the magnetic field. Table 1 shows the calculated velocities depending on the magnetic induction for the frequency of 400 Hz under  $\mu g$  conditions. The theoretical calculations of the

exact flow patterns and the corresponding axial cuts of the crystals are given in refs. [3,4].

In spite of an increase of velocity in the solution zone, the temperature field inside the ampoule is insignificantly deformed. The secondary flow accelerated appreciably the mass transfer through the zone. The influence of the rotating magnetic field on the concentration distribution along the solution zone axis is shown in Fig. 3. The solid line shows the CdTe concentration distribution in the Te solution without the magnetic field, and the dashed line the distribution with the rotating magnetic field. The dashed line resembles two plateaus, which are produced by the mixing of the convection tori in the solution zone. For the rotating magnetic field we stress the fact that the CdTe fraction in the solution zone is significantly larger on the seed crystal side.

### 3. Growth results

The description of the axial cuts of the grown CdTe crystals is given in refs. [3,4]. This article summarizes the rotating magnetic field experiment under  $\mu g$  conditions. Fig. 4 shows the infrared image of an axial crystal slice with a thick-

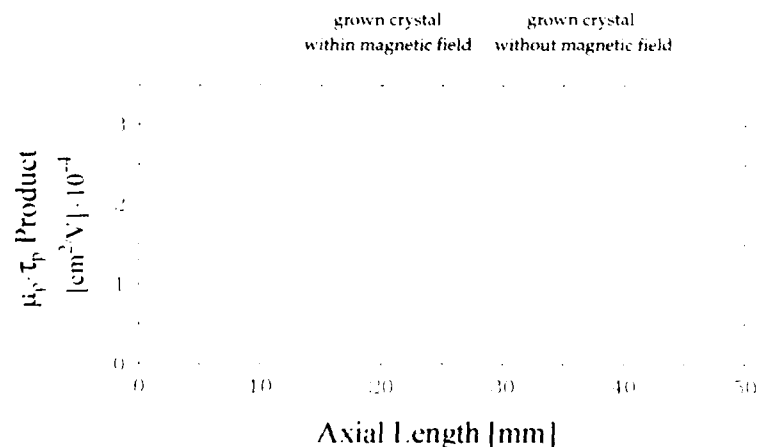


Fig. 5. Axial distribution of the  $\mu_0 \tau_p$  products. The first part is grown within a rotating magnetic field, the last part without the magnetic field.

ness of 2 mm. The picture shows two sections of the grown crystal: one with the rotating magnetic field and one without. The magnetic field was switched off after half of the crystal growth time had elapsed. This produced a change in the flow pattern and the solution zone supersaturated nearby the crystallization front (Fig. 3). A temporally high growth rate [4,5] results and creates a thick heavily disturbed region of about 1 mm. This region is full of Te inclusions, where the grown crystal broke during the cooling process.

The part of the crystal which was grown within the rotating magnetic field shows the most homogeneous  $\mu\tau$  products (Fig. 5) and resistivity distribution [3]. All other experiments without the magnetic field at 1g and  $\mu g$  conditions reveal a wide distribution of  $\mu\tau$  products.

#### 4. Conclusions

The equations for describing the rotating magnetic field were derived for  $\mu g$  conditions and small Hartmann numbers. The rotating magnetic field generates a stable steady flow in the Te-zone, improving the radial and axial distribution of the Te inclusions and the  $\mu\tau$  products.

#### 5. Acknowledgments

We would like to thank I. Koch, L. Rees and M. Kranz for their technical assistance and S. Huggle for fruitful discussions. Financial support was granted by the Federal Minister of Research and Technology (BMFT) under project management by the German Space Agency (DARA).

##### 5.1. Nomenclature

$B = \tilde{B}B^*$	Dimensionalized magnetic field strength
$c_i = \tilde{c}_i c_i^*$	Dimensionalized concentration of component $i$
$c_i^l$	Liquidus concentration of component $i$
$c_i^s$	Solidus concentration of component $i$

$\tilde{E} = \omega \tilde{B} \tilde{R}$	Characteristic electric field
$E = \tilde{E} E^*$	Dimensionalized electric field
$j = \tilde{j} j^*$	Dimensionalized current density
$j = \sigma \omega \tilde{B} \tilde{R}$	Characteristic current density
$n$	Normal vector
$r, \varphi, z$	Radial, azimuthal and axial components
$\tilde{R}$	Ampoule radius
$t = 1/\omega$	Characteristic time
$T = \tilde{T} T^*$	Dimensionalized temperature
$T_f = \tilde{T}_f T_f^*$	Dimensionalized furnace temperature
$U^*$	Dimensionless local growth rate
$V = \tilde{V} V^*$	Velocity
$y_r, y_\varphi, y_z$	Radial, azimuthal and axial components of vector $y$
$y^*, \tilde{y}$	Dimensionless and characteristic quantities of $y$
$\zeta$	Stefan-Boltzmann radiation constant
$\mu_0$	Magnetic permeability
$\omega$	Frequency of the rotating magnetic field

##### 5.2. Material parameters

$D_i$	Diffusion coefficient
$\epsilon$	Emissivity
$\kappa$	Thermal diffusivity
$\lambda$	Thermal conductivity
$\nu$	Kinematic viscosity
$\rho$	Density of the melt
$\sigma$	Electric conductivity of the melt

##### 5.3. Dimensionless numbers

$Ha = \tilde{B} \tilde{R} \sqrt{\frac{\sigma}{\nu \rho}}$	Hartmann number
$Pe = \frac{\tilde{V} \tilde{R}}{D}$	Peclet number
$Pe_p = \frac{\tilde{V} \tilde{R}}{D}$	Solutal Peclet number
$Re = \frac{\tilde{V} \tilde{R}}{\nu}$	Reynolds number
$Re^M = \tilde{V} \tilde{R} \mu_0 \sigma$	Magnetic Reynolds number
$Re_\Omega^M = \tilde{R}^2 \omega \mu_0 \sigma$	Rotational magnetic Reynolds number
$Sk = \frac{\zeta \tilde{T}^3 \tilde{R}}{\lambda}$	Stark number

## 6. References

- [1] P. Sickinger, P. Hofmann, K. Kemmerle, E. Wulf, R. Klett, A.S. Senchenkov, A.V. Egorov, I.V. Barmin, D.G. Matioukhin, M. Salk and K.W. Benz, in: Proc. 8th Europ. Symp. on Material and Fluid Sciences in Microgravity, Brussels, 1992.
- [2] P. Hofmann, K. Kemmerle, R. Klett, P. Sickinger, J. Winter, I.V. Barmin, I.G. Filatov, A.V. Egorov, A.S. Senchenkov and K.W. Benz, *Microgravity Sci. Technol.* 4 (1991) 273.
- [3] M. Salk, B. Lexow, K.W. Benz, D.G. Matioukhin, Y.M. Gelfgat, M.Z. Sorkin, A.S. Senchenkov, A.V. Egorov, I.V. Barmin, P. Sickinger, P. Hofmann and R. Klett, *Microgravity Sci. Technol.* 6 (1993) 88.
- [4] I.V. Barmin, A.V. Egorov, I.G. Filatov, A.S. Senchenkov, K.W. Benz, B. Lexow, M. Salk, P. Hofmann, P. Sickinger, Y. Gelfgat, M.Z. Sorkin and D.G. Matioukhin, in: Proc. 8th Europ. Symp. on Material and Fluid Sciences in Microgravity, Brussels, 1992.
- [5] A.S. Senchenkov, I.V. Fryazinov and M.P. Zabelina, in: Proc. Int. Symp. on Heat and Mass Transfer, Perm, Moscow, 1991.
- [6] A. Laugier, *Rev. Physique Appl.* 8 (1973) 259.
- [7] T. Robinson and K. Larsson, *J. Fluid Mech.* 60 (1973) 641.
- [8] V.I. Doronin, V.V. Driemov and A.B. Kapusta, *Magneto-hydrodynamics* 3 (1973) 138.



ELSEVIER

Journal of Crystal Growth 138 (1994) 168–174

CRYSTAL  
GROWTH

## Growth of large, high purity, low cost, uniform CdZnTe crystals by the “cold travelling heater method”

A. El Mokri, R. Triboulet \*, A. Lusson, A. Tromson-Carli, G. Didier

*Laboratoire de Physique des Solides de Bellevue, CNRS, 1 Place A. Brizard, F-92195 Meudon Cédex, France*

### Abstract

The cold travelling heater method (CTHM) has been used to grow CdZnTe crystals ( $x_{Zn} = 0.04$  and  $0.20$ ) of 2 inch diameter, which is the largest diameter ever used in THM. A simple model confirms that convection is the dominant mechanism of matter transport in THM, justifying the use of the accelerated crucible rotation technique (ACRT), in which is imposed a forced convection regime, to enlarge the size of the crystals and increase the growth rate. In order to obtain single crystals, solid state recrystallization (SSR) has been applied for the first time to CdTe. Ingots of excellent axial and radial uniformity have been obtained by CTHM, as well as crystals purer than the Bridgman grown ones, from 5N elements as source material at ten times lower price than the 6N ones classically used for Bridgman growth. SSR crystals have been found also of lower purity than the CTHM ones. It follows that contamination in CdTe growth is expected to occur not only from the starting elements but particularly from the high temperatures used. The main agents of high temperature contamination are shown to be Li and Cu. Some mosaic structure of the crystals comes from the off-stoichiometric THM growth conditions and could be avoided by SSR annealing under Cd vapour pressure.

### 1. Introduction

The use of lattice-matched CdZnTe substrates for the epitaxial growth of HgCdTe is recognized as a key for making high performance IR detectors [1,2].

Commercially available CdZnTe substrates are produced from vertical and horizontal Bridgman growth by the major world suppliers. These techniques present nevertheless some limitations concerning uniformity (difficult control of Zn segre-

gation, for instance), purity (need of high purity starting material, for a disappointing final purity) and cost (complex set-up and process) of the substrates.

The cold travelling heater method (CTHM) has been shown as an attractive, simple and inexpensive technique to produce such compounds as CdTe and ZnTe [3]. In this technique, a composite source material, constituted of a Cd (or Zn) rod surrounded by Te pieces and powder, is used. The compound never reaches its melting point during the whole process (from which the name of “cold”). It has been adapted to the growth of CdZnTe ingots of diameter as large as 2 inch, which is the largest diameter ever used in THM.

\* Corresponding author.

In order to obtain large single crystals, three approaches have been followed:

- optimization of the main growth parameters;
- accelerated crucible rotation technique (ACRT);
- solid state recrystallization (SSR) used for the first time, to our knowledge, for CdTe.

The assessment of the crystals has been achieved using IR microscopy, scanning electron microscopy, X-ray topography, X-ray double diffraction, photoluminescence, Hall effect, electrical conductivity and chemical analysis.

## 2. Experimental procedure

The crystals have been grown by CTHM according to the experimental process described in ref. [3]. In order to grow 2 inch diameter CdZnTe ingots, both Cd and Zn rods, of appropriate diameter to obtain the desired composition, surrounded by Te pieces and powder, have been used as source material. Let us recall that synthesis, growth and purification are achieved at low temperature, at the same time, in a simple and inexpensive furnace, in contrast to other processes. The very principle of this technique allows the growth of large diameter ingots, because there is no need to prepare a pre-synthesized source material. The material never reaching its melting point during the whole process, which limits drastically any contamination from the surroundings, and the efficient purification of solution zone refining allows the use of 5N elements, as starting materials, at ten times lower price than the 6N ones for a better final purity of the crystals, provided that very pure 6N Te is used as the solvent. The growth temperature was 780°C for  $x_{Zn} = 0.04$  and 850°C for  $x_{Zn} = 0.20$ . Because of the lack of compactness of the composite source material, limiting the definition of the growth interface position, a second THM pass was achieved to obtain large single crystals.

### 2.1. Optimization of the growth parameters

Optimum growth conditions for a given diameter cannot be easily extrapolated to larger sizes,

because several parameters change drastically with diameter, like temperature gradients, supercooling amount, etc. On the other hand, the composite nature of the CTHM source material makes it difficult to perfectly control the growth interface position.

The optimization has concerned essentially the initial amount of tellurium, which conditions the height of the solvent zone and thus the position and shape of the growth interface in the furnace, and the growth rate which was varied between 2 and 3.6 mm/day. In order to check the significance of the growth parameters experimentally determined, a simple model has been used.

Following the work of Cherepanova [4], we have adapted to our configuration a quasi-diffusive one-dimensional model (diffusion of CdZnTe in a CdZnTe + Te mixture) in which the matter transport can be described by the equation:

$$D_s \frac{\partial^2 C}{\partial z^2} + V \frac{\partial C}{\partial z} = 0, \quad (1)$$

with the boundary conditions:

$$-D_s \left( \frac{\partial C}{\partial z} \right)_{z_1} = V (C_1^0 - C_s),$$

where  $V$  is the travelling rate of the ampoule,  $D_s$  the solutal diffusion coefficient and  $C$  the concentration in CdZnTe, with  $C_1^0$  and  $C_2^0$  the concentrations at the growth ( $z = z_1$ ) and dissolution ( $z = z_2$ ) interfaces, respectively.

According to the diagram of Fig. 1,  $L_0$  is the initial zone length,  $Y_1$  and  $Y_2$  are the slopes  $\partial T / \partial z$ ,  $C_m$  is the initial concentration of CdZnTe in the liquid zone,  $T_1$  is the dissolution temperature and  $T_0$  is the maximum temperature.

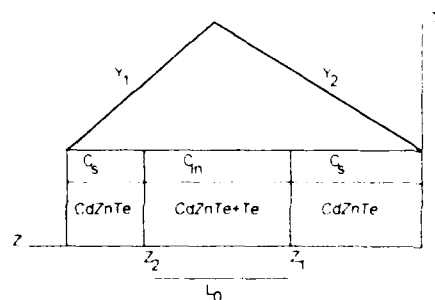


Fig. 1. Diagram of the distribution of temperature and concentration versus distance near the THM solvent zone.



The parameters used for the growth of  $\text{Cd}_{0.8}\text{Zn}_{0.2}\text{Te}$  were  $C_\infty = 1$ ,  $C_m = 0.184$ ,  $T_0 = 850^\circ\text{C}$ ,  $L_0 = 50$  mm,  $V = 3.6$  mm/day,  $R = 25$  mm,  $Y_1 = 37^\circ\text{C/cm}$ ,  $Y_2 = 47^\circ\text{C/cm}$  and  $D_\infty = 5 \times 10^{-9}$   $\text{m}^2/\text{s}$  (for CdTe).

Solving Eq. (1) under its dimensionless form gives the concentration and temperature difference between dissolution and crystallization interface,  $\Delta C = C_2^0 - C_1^0 = 0.08$  and  $\Delta T = T_2^0 - T_1^0 = 73^\circ\text{C}$ , respectively, and the final zone length  $L_1 = 58$  mm. Introducing these values into the expressions of the dimensionless numbers gives:

- thermal Rayleigh number,  $Ra^t = \alpha g R^3 \Delta T / (D_1 \nu) = 2.5 \times 10^6$ ;
- solutal Rayleigh number,  $Ra^s = \beta g R^3 \Delta C / (D_\infty \nu) = 9.3 \times 10^6$ ;
- Lewis number,  $Le = D_1 / D_\infty = 780$ ;
- Prandtl number,  $Pr = \nu / D_1 = 0.04$ .

Here  $\alpha$  and  $\beta$  are the thermal and solutal expansion coefficients, respectively,  $D_1$  and  $D_\infty$  are the thermal and solutal diffusion coefficients, respectively, and  $\nu$  is the kinematic viscosity.

A slight increase of the solvent zone length ( $L_1/L_0 = 1.2$ ) is observed: the growth and dissolution interfaces have not suffered an important distortion during growth, as confirmed by the large size of the crystals obtained. The solutal Rayleigh number is larger than the thermal one confirming, as shown experimentally by Schwenkenbecher and Rudolph [5], that solutal convection is the dominant mechanism in THM growth. This justifies the use of ACRT to enlarge the size of the crystals and increase the growth rate.

## 2.2. Accelerated crucible rotation technique

The accelerated crucible rotation technique has been developed initially by Scheel and co-workers [6] for the solution growth of garnets at high temperatures, and has been modelled by Schulz-Dubois [7]. An improvement of the size of the crystals by a factor of 1000 over growth without ACRT was obtained by the authors.

Natural convection being the most effective and dominant mechanism of matter transport in CdTe THM growth makes ACRT very promising for creating a forced convection regime that is reproducible and amenable to control, contrary

to natural convection, as already proposed by Wald and Bell [8]. One can expect ACRT to be particularly efficient in the case of large diameters where the "supercooling amount" is quite large [9] and should impose excessively low growth rates.

Different flows have been shown to occur in rotating systems [7]: the Ekman-layer flow has been stated to be the most prominent under spin-up and spin-down, especially in containers that are not very tall compared to their diameter [11] as in the THM case (5 cm diameter,  $\sim 3$  cm long for the solvent zone in our case). It is a radial flow that occurs in a narrow horizontal layer just above the boundary layer through which only diffusion must take place, ensuring a supply of material near the growing interface. Under spin-up, an Ekman layer forms at the bottom of the ampoule. Inside this layer, the liquid is submitted to a fast radial movement and is rejected toward the top near the walls in spiral arms. The expressions of the time during which the flow decreases,  $T_1$ , the Ekman layer thickness,  $d$ , the radial velocity within this layer,  $V$ , the vertical velocity in the container,  $W$ , and the Ekman constant,  $E$ , are given in ref. [7].

Spiral shearing distortion describes a laminar and two-dimensional flow of liquid under spin-up and spin-down in a tube long enough for the influence of the bottom to be neglected. It is therefore a secondary mechanism in THM under ACRT conditions. It is caused by fluid at the walls changing velocity faster than in the bulk. The width of the arms of the "spiral shearing distortion",  $\Delta r$ , the number of spiral arms,  $N$ , and the time after which the rotation rate at the centre of the liquid is reduced to about  $\Omega_0/2$ ,  $T_2$ , are also given in ref. [7].

In two experiments, respectively noted A and B, for  $\text{Cd}_{0.8}\text{Zn}_{0.2}\text{Te}$ , the maximum rotation rate was  $\Omega_0 = 80$  rpm with the ACRT cycle displayed in Fig. 2.

The following parameters can be calculated:  $E = 3 \times 10^{-5}$ ,  $T_1 = 22$  s,  $T_2 = 401$  s,  $d = 1.37 \times 10^{-2}$  cm,  $V = 21$  cm/s,  $W = 0.11$  cm/s,  $\Delta r = 3.7 \times 10^{-3}$  cm and  $N = 667$ .

For a diffusion coefficient of CdTe in liquid Te of  $\sim 10^{-5}$   $\text{cm}^2 \text{ s}^{-1}$  ( $\sim 800^\circ\text{C}$ ), the homoge-

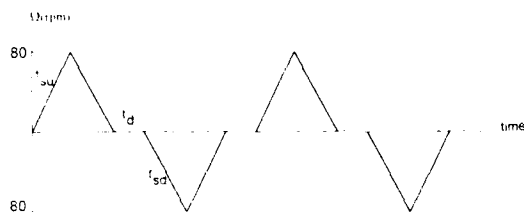


Fig. 2. ACRT cycle used (rotation rate versus time).

nization will occur within about 1 s for a distance between spiral arms of  $3.7 \times 10^{-3}$  cm. The high radial velocity of 21 cm/s ensures a fast supply of the material near the growing interface. Growth, geometrical and ACRT parameters for experiments A and B are given in Table 1.

Crystal A consisted of small grains, with a regular structure. In crystal B, the grains have grown considerably, due to the modification of the ACRT parameters. Spin-up and spin-down times (25 s) for A are higher than the Ekman time  $T_1$  (22 s). The stop-time is rather large (11 s). By comparison, spin-up and spin-down times for B (14 s) are lower than the Ekman time and the stop-time as well. This allows a faster transport of matter to the interface, as was also observed by Capper and co-workers [10] for the growth of CdTe and CdZnTe by Bridgman method using ACRT.

In spite of a very significant improvement in the grain size of the crystals grown using ACRT and a substantial increase in the growth rate, the optimization needs further experiments. Solid state recrystallization has been tried in order to obtain larger crystals.

Table 1  
Growth, geometrical and ACRT parameters for two experiments noted A and B

Parameter	A	B
Ingot length (mm)	110	100
Ingot diameter (mm)	50	50
Initial amount of Te (g)	397	312
Growth rate (mm/day)	7.2	6
Spin-up time, $t_{su}$ (s)	25	14
Spin-down time, $t_{sd}$ (s)	25	14
Stop time, $t_d$ (s)	11	6

### 2.3. Solid state recrystallization

Solid state recrystallization (SSR), essentially used for metals, has been proposed by Kruse and Schmit [11], according to a "quench-anneal" process, for the growth of HgCdTe single crystals. To our knowledge, it has never been used before for CdTe. Energetically, this process is favoured by the multi-grain state of the material, which is



Fig. 3. Cross-sectional views of a CdTe CTHM ingot: (a) fine grain structure resulting from an intentional maladjustment of the growth parameters; (b) same ingot after solid state recrystallization.

thermodynamically unstable. Energy accumulates in the grain boundaries which are the most unstable zones. Their disappearance by minimization of energy is the driving force of recrystallization. In isothermal recrystallization, a first step is to heat slowly the multi-grain charge to a temperature  $T_c$  lower than the melting point by about a hundred degrees, allowing the formation of nuclei, and to keep this temperature during a time  $t$  chosen according to the growth rate of the nuclei. The growth of a grain happens at the expense of its neighbours.

We have found that a significant asset of THM is the possibility of obtaining, with parameters intentionally maladjusted for the CdTe growth, a regular fine grain size structure, as shown in Fig. 3a, all the more adapted to recrystallization because the high temperature gradient at the liquid–solid interface brings about some quenching effect. Such ingots have been used for SSR experiments and heated up under vacuum to the recrystallization temperature  $T_c$  at about 4°C/h, in order to avoid the thermal strains due to an abrupt thermal change. In a first experiment, where  $T_c = 1060^\circ\text{C}$ , very close to the melting point, a significant increase in the grain size was obtained, but the crystals presented many gas bubbles. In a second experiment,  $T_c$  has been reduced to  $990^\circ\text{C}$  and kept two months at this value. A cross-section of this ingot shows a grain occupying more than half the section, demon-

Table 2  
Electrical characteristics of typical CTHM, SSR and Bridgman samples

Parameters	Annealed CTHM sample	Annealed SSR sample	As-grown Bridgman sample
Name	CTHM9	CTRE	C4
Purity of the elements used	5N Cd, 5N Te 6N QZR Te solvent	5N Cd, 5N Te 6N QZR solvent	6N DZR Cd 6N DZR Te
Growth temp. (°C)	780	990	1100
$N_A$ (cm <sup>-3</sup> )	$1.5 \times 10^{13}$	$2.2 \times 10^{13}$	$3.5 \times 10^{13}$
$N_D$ (cm <sup>-3</sup> )	$3.4 \times 10^{14}$	$7.6 \times 10^{14}$	$1.47 \times 10^{15}$
$\mu_{\text{room}}$ (cm <sup>2</sup> /V·s)	840	780	750
$\mu_{\text{min}}$ (cm <sup>2</sup> /V·s)	41380 (28 K)	9000 (22 K)	13000 (40 K)
$E_D$ (meV)	15	11.2	15
$N_A/N_D$ (%)	4.4	3	22

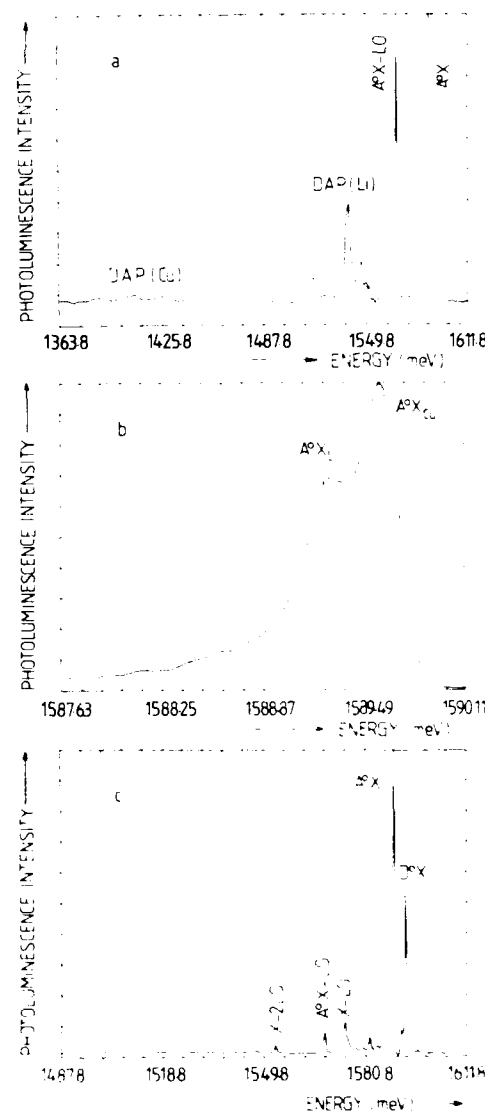


Fig. 4. Low temperature photoluminescence spectra: (a) SSR sample; (b) A'X of the (a) spectrum at higher magnification; (c) CTHM sample.

strating the efficiency of the process (Fig. 3b). New experiments are in progress in order to obtain only one crystal over the whole volume, after optimization of the parameters (initial structure, heating time, SSR temperature and time, and vapour pressure).

### 3. Material assessment

#### 3.1. Purity

Electrical characteristics of typical Cold THM, SSR and Bridgman samples are displayed in Table 2. By comparison with the Bridgman sample,  $N_A$  and  $N_D$  are about ten times lower for the THM sample, with higher low and room temperature mobilities, indicating a higher purity level. Moreover, the THM sample had to be annealed to convert its conductivity type from p, resulting from the Te rich growth conditions, to n, suitable for electrical measurements. As a matter of fact, for a significant comparison, the as-grown Bridgman sample has to be brought in the same state, because residual impurities, segregated into Te precipitates, out-diffuse during annealing [12]. The best low temperature mobilities measured among many annealed CdZnTe samples coming from various suppliers never exceeded  $5 \times 10^5 \text{ cm}^2/\text{V} \cdot \text{s}$ . This demonstrates not only the benefit of CTHM to reach a high purity level at low price, but also the fact that contamination in Bridgman growth comes not only from the initial purity of the starting elements, but also from the high temperatures used.

The low temperature photoluminescence spectrum of a typical SSR crystal (Fig. 4a), is dominated by the classical  $A^0X$  emission, showing two components at 1.5895 and 1.5892 eV (Fig. 4b) attributed to Cu and Li, respectively [13], with its two phonon replicas. By comparison with the PL spectrum of a cold THM sample, with only the classical X,  $D^0X$  and  $A^0X$  lines and their phonon replicas (Fig. 4a), the SSR sample shows two additional DAP transitions at 1.550 eV and  $\sim 1.42$  eV (Fig. 4b), corresponding to Li and Cu respectively. Chemical analysis confirms the presence of Li and Cu (0.5 and 1 ppm, respectively) in the SSR samples. It stems from these optical features as well as from the electrical characteristics displayed in Table 2 that the purity of the SSR samples, although higher than the annealed Bridgman ones, is lower than that of the CTHM ones. Some contamination occurs from impurities, mainly Li and Cu, diffusing into the ingots from their environment during the high tempera-

ture processes. This confirms the significance of growth temperature with regard to contamination.

#### 3.2. Uniformity

The longitudinal composition profile, measured by electron microprobe analysis (EMA), of a  $\text{Cd}_{0.8}\text{Zn}_{0.2}\text{Te}$  ingot prepared by CTHM is shown in Fig. 5a. A stationary state is reached right from the beginning of the growth leading to a large uniform fraction of the ingot. The average composition is  $20\% \pm 1.5\%$ , which is quite acceptable. The radial homogeneity (Fig. 5b) is found to be better than  $\pm 0.1\%$  over a 2 inch diameter slice. Such results have been found repeatable.

#### 3.3. Crystallographic properties

The presence of a sub-grain boundary structure, typical of CdTe crystals grown under off-stoichiometric conditions, is revealed by X-ray topography (contrasts indicating a misorientation between sub-grains in the crystal), X-ray double diffraction (multipeak rocking curves) and electron microscopy in cathodoluminescence mode

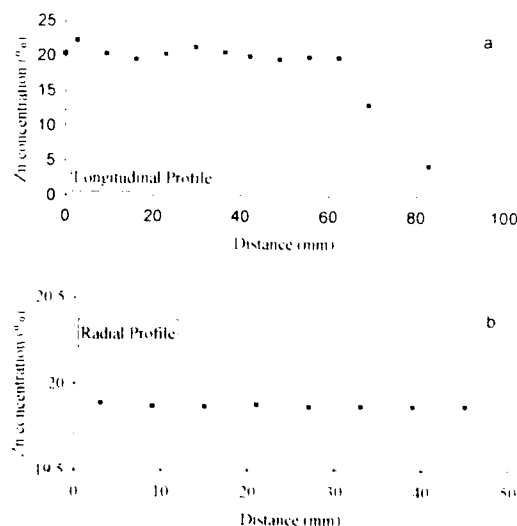


Fig. 5. Longitudinal (a) and radial (b) composition profiles of a CTHM ingot.

(direct observation of a sub-grain lattice). In order to avoid this kind of detrimental structure, experiments of SSR under Cd vapour pressure are in progress.

#### 4. Conclusions

Cold THM has been tried to grow CdZnTe crystals ( $x_{Zn} = 0, 0.04$  and  $0.20$ ) of 2 inch diameter which is the largest diameter ever used in THM. A simple model confirms that convection is the dominant mechanism of matter transport in THM. This has justified the use of the accelerated crucible rotation technique, in which a forced convection regime is imposed, to enlarge the size of the crystals and increase the growth rate. In order to obtain larger single crystals, solid state recrystallization (SSR) has been applied for the first time to CdTe.

The ingots grown by CTHM have been found of excellent axial and radial uniformity. Crystals purer than those grown by Bridgman, as shown from electrical and optical measurements, have been obtained by CTHM, using only 5N elements as source material, at ten times lower price than those regularly used for Bridgman growth. SSR crystals have been found also of lower purity than the CTHM ones because of contamination occurring during the high temperature process. It follows that contamination comes not only from the starting elements but particularly from the high

temperatures used. The main agents of contamination have been shown to be Li and Cu. The SSR crystals, as the CTHM ones, show a mosaic structure as a result of the initial off-stoichiometric THM growth conditions. Experiments with a saturated Cd vapour pressure during the SSR process are in progress to overcome this drawback.

#### 5. References

- [1] R. Triboulet, A. Tromson-Carli, D. Lorans and T. Nguyen-Duy, *J. Electron. Mater.* 22 (1993) 827.
- [2] R.E. DeWames, J.M. Arias, J.G. Pasko, S.H. Shin, M. Zandian and G.M. Williams, 1992 US Workshop on Physics and Chemistry of Mercury Cadmium Telluride and Other IR Materials.
- [3] R. Triboulet, Khoan Pham Van and G. Didier, *J. Crystal Growth* 101 (1990) 216.
- [4] T.A. Cherepanova, *Crystal Res. Technol.* 17 (1982) 735.
- [5] K. Schwenkenbecher and P. Rudolph, *Crystal Res. Technol.* 20 (1985) 1609.
- [6] H.J. Scheel, *J. Crystal Growth* 13–14 (1972) 560.
- [7] E.O. Schulz-Dubois, *J. Crystal Growth* 12 (1972) 81.
- [8] F.V. Wald and R.O. Bell, *J. Crystal Growth* 12 (1975) 29.
- [9] R.U. Bloedner and P. Gille, *J. Crystal Growth* 130 (1993) 181.
- [10] P. Capper, J.E. Harris, E. O'Keefe, C.L. Jones, C.K. Ard, P. Mackett and P. Dutton, *Mater. Sci. Eng. B* 16 (1993) 29.
- [11] P.W. Kruse and J.L. Schmit, US Patent 3,723,190 (1973).
- [12] J.L. Pautrat, J.M. Francou, N. Magnea, E. Molya and K. Saminadayar, *J. Crystal Growth* 72 (1985) 194.
- [13] E. Molya, J.P. Chamonat and J.L. Pautrat, *Phys. Status Solidi (b)* 109 (1982) 635.

## On the nature of the excitonic luminescence in narrow-gap $\text{Hg}_{1-x}\text{Cd}_x\text{Te}$ ( $x \cong 0.3$ )

J.W. Tomm <sup>a,\*</sup>, K.H. Herrmann <sup>a</sup>, W. Hoerstel <sup>a</sup>, M. Lindstaedt <sup>a</sup>, H. Kissel <sup>a</sup>,  
F. Fuchs <sup>b</sup>

<sup>a</sup> FB Physik, Humboldt-Universität zu Berlin, Unter den Linden 6, D-10099 Berlin, Germany

<sup>b</sup> Fraunhofer-Institut für Angewandte Festkörperphysik, Tullastrasse 72, D-79108 Freiburg i. Brsg., Germany

### Abstract

Exciton luminescence is studied in a series of annealed narrow-gap  $\text{Hg}_{1-x}\text{Cd}_x\text{Te}$  ( $0.3 < x < 0.4$ ) crystals grown by the travelling heater method (THM). A number of techniques – photoluminescence (PL), PL excitation, magnetoluminescence – was applied to get insight in the action of many-body effects (band gap renormalization, free excitons and their localization) in this narrow-gap material.

### 1. Introduction

This infrared luminescence study of  $\text{Hg}_{0.7}\text{Cd}_{0.3}\text{Te}$  is motivated mainly by two reasons: Firstly there exist general questions after the action of excitons in narrow-gap semiconductors because oscillator strength as well as binding energy decrease with decreasing gap ( $E_g$ ).  $\text{Hg}_{1-x}\text{Cd}_x\text{Te}$  is the best known semiconductor where the energy gap scales down from the wide-gap region ( $E_g(\text{CdTe}) \cong 1.6$  eV) to zero and therefore seems to be a good model substance. The second motivation arises from the optical properties of the mixed crystal itself. As outlined below, there appear changes in the luminescence behaviour in even the composition range which was studied. Further motivation comes from the diode lasers as well as the need to develop mag-

neto-luminescence as a method for sample characterization.

In recent years much work was done to clear up the nature of the excitonic luminescence in  $\text{Hg}_{1-x}\text{Cd}_x\text{Te}$  ( $0.4 < x < 1$ ) with comparatively large gaps between 0.4 and 1.6 eV [1,2]. If these “broader gap” samples have a sufficiently small carrier concentration and if they were grown near the thermodynamic equilibrium by the travelling heater method (THM) or the liquid phase epitaxy (LPE), the photoluminescence (PL) in the  $0.4 < x < 0.85$  mole fraction range is dominated by localized intrinsic excitons trapped in potential wells generated by alloy disorder. This is proved by the fact that the thermal delocalization energy for samples of this kind is proportional to the disorder function  $x(1-x)$  [2]. The typical luminescence line shape is a symmetric line followed by 1–3 replicas separated by the CdTe phonon energy as shown in the inset of Fig. 1 for  $\text{Hg}_{0.268}\text{Cd}_{0.732}\text{Te}$ . Fig. 1 shows the separation between the dominant line and the next transition

\* Corresponding author.

at lower quantum energies. For  $x > 0.4$  the distance is equal to the LO phonon energy (full line) obtained by Raman scattering [3]. The data in Fig. 1 were obtained from PL spectra of p-type samples with comparable electrical and optical properties.

Doped samples (or samples with larger concentrations of native defects) exhibit *additional* lines identified as transitions involving hydrogen-like acceptors, Hg-vacancy-related deeper acceptors, deep levels, donor-acceptor pair transitions and band-to-band transitions (see, e.g., ref. [4–6]).

Samples grown by methods where the growth process is realized farther from the thermodynamic equilibrium as molecular beam epitaxy (MBE) exhibit as a rule only one broad line caused by localized carriers (see, e.g., ref. [7]).

Because of the changes visible in Fig. 1, it seems to be interesting to discuss the nature of the optical transitions producing the luminescence in the left region of Fig. 1 ( $x < 0.4$ ). A typical PL spectrum of a  $\text{Hg}_{0.64}\text{Cd}_{0.353}\text{Te}$  sample ( $p_0 = 7 \times 10^{15} \text{ cm}^{-3}$ , at  $T = 77 \text{ K}$  and  $4.2 \text{ K}$ ) exhibiting PL in that spectral region is plotted at the top of Fig. 2. The question concerning the nature of the main line can partially be answered with the help of the spectrum at the bottom of this figure: With Fourier transform techniques [10] it has been possible to obtain the photolumi-

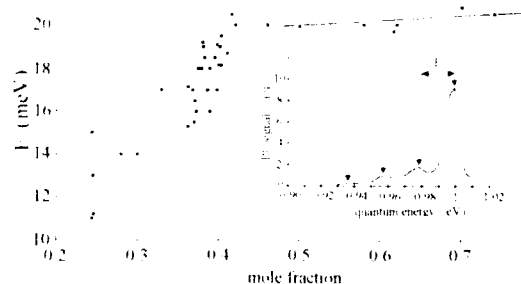


Fig. 1. Energetic distance between the peak positions of the first and second PL line versus mole fraction for high quality THM-grown samples with a carrier concentration of about  $p_0 = 10^{15} \text{ cm}^{-3}$  at  $T = 77 \text{ K}$ . The full line represents the LO phonon energy in CdTe-rich  $\text{Hg}_{1-x}\text{Cd}_x\text{Te}$  obtained in ref. [3]. The inset shows a PL spectrum from a  $\text{Hg}_{0.268}\text{Cd}_{0.732}\text{Te}$  sample at  $T = 5 \text{ K}$  and  $I_0 = 1 \text{ W cm}^{-2}$ . The arrows mark line positions.

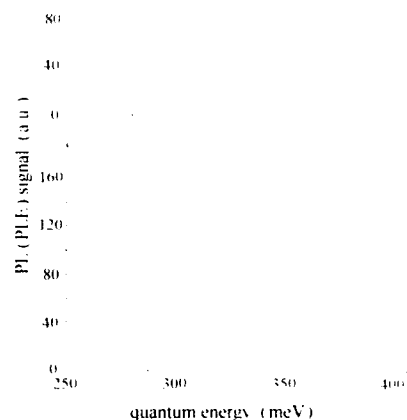


Fig. 2. PL spectrum (top) and PLE spectrum (bottom) of  $\text{Hg}_{0.64}\text{Cd}_{0.353}\text{Te}$  at  $T = 13 \text{ K}$  ( $E_g = 317 \text{ meV}$ ). The transition at lower energy separated by  $15.6 \text{ meV}$  from the dominant PL line was used for detection during the PLE measurement.

nescence excitation (PLE) spectrum shown in the lower part of this figure. The lower energy line of the PLE spectrum at  $300 \text{ meV}$  is an artefact and gives the spectral position of the monitored wavelength of the PL in this type of experiment. It is interesting to observe in the PLE spectrum a strong enhancement of the oscillator strength at  $310 \text{ meV}$  where the band-to-band contribution sets in. Recombination of an electron-hole plasma cannot explain such an enhancement. This is only possible by inclusion of excitonic contributions. (Note that the critical screening density is somewhat lower than the  $p_0$  value mentioned above.)

This study is devoted to the *excitonic* luminescence in  $\text{Hg}_{1-x}\text{Cd}_x\text{Te}$  ( $x < 0.4$ ) in a composition range where the spectrum looks very different as compared with the better investigated broader gap region (compare inset in Fig. 1 and Fig. 2).

## 2. Experimental details

The  $\text{Hg}_{1-x}\text{Cd}_x\text{Te}$  ( $x \leq 0.4$ ) samples investigated in this study were grown by the travelling heater method (THM) according to Gille et al. [8]. The starting point was a set of samples with carrier concentrations between  $p_0 = 10^{13} \text{ cm}^{-3}$

and up to  $p_0 = 5 \times 10^{16} \text{ cm}^{-3}$  (at  $T = 77 \text{ K}$ ). For reaching the low concentration range, a special annealing procedure in Hg-rich atmosphere was carried out. Typical mobilities were 320–380 and  $470 \text{ cm}^2 (\text{V} \cdot \text{s})^{-1}$  for annealed samples (at  $T = 77 \text{ K}$ ).

In section 3.2, mainly the results obtained from two samples are discussed:

- Sample (a):  $x = 0.300 \pm 0.003$ , has a carrier concentration of  $p_0 = 1.1 \times 10^{16} \text{ cm}^{-3}$  (at  $T = 77 \text{ K}$ ) and a hole mobility of  $320 \text{ cm}^2 (\text{V} \cdot \text{s})^{-1}$ . The slope  $d(\hbar\omega_{\text{max}})/dI_0$  (see section 3.1) is positive and has a value of about 2 meV per decade.
- Sample (b):  $x = 0.367 \pm 0.004$ , has a carrier concentration of  $p_0 = 2 \times 10^{15} \text{ cm}^{-3}$  (at  $T = 77 \text{ K}$ ) and a hole mobility of  $380 \text{ cm}^2 (\text{V} \cdot \text{s})^{-1}$ . The slope  $d(\hbar\omega_{\text{max}})/dI_0$  is negative and comes to  $-0.7 \text{ meV}$  per decade (see Fig. 3c).

The PL was excited by a CW Nd:YAG laser (by choice of pulsed operation equipped with a Q-switch,  $\tau_{\text{FWHM}} \approx 70 \text{ ns}$ ). We applied excitation densities in the  $10 \text{ mW cm}^{-2}$  range for continuous (CW) and in the  $10 \text{ W cm}^{-2}$  to  $100 \text{ kW cm}^{-2}$  range for pulsed operation (PW). Detection was performed by various  $\text{Hg}_{1-x}\text{Cd}_x\text{Te}$  and InSb detectors. The samples were mounted in an Oxford Spectromag 4000 system which allows measurements in magnetic fields up to 7 T. A more detailed description of the experimental setup is given in ref. [9].

### 3. Results and discussion

#### 3.1. Characterization of the samples by PL

The excitation ( $I_0$ ) dependence of the luminescence line position ( $\hbar\omega_{\text{max}}$ ) is determined by several mechanisms delivering contributions with opposite signs. For our experiments the relevant mechanisms are:

(i) *Many particle effects (band gap renormalization)*. The experimental estimation of the static band gap renormalization due to a given equilibrium carrier concentration is difficult to be determined because the “real” gap of a given mixed crystal is not known exactly. This is one of the possible reasons why the variety of  $E_g(x, T)$

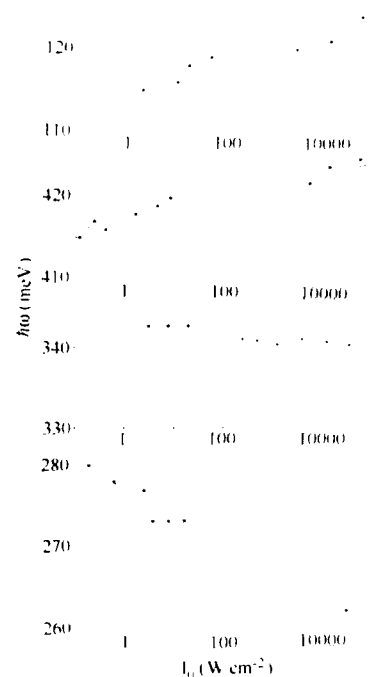


Fig. 3. PL line shift versus excitation density for  $\text{Hg}_{1-x}\text{Cd}_x\text{Te}$  ( $0.23 < x < 0.41$ ,  $T = 6 \text{ K}$ ) with various equilibrium carrier concentrations  $p_0$  (from top to bottom):  
(a)  $p_0 = 9.2 \times 10^{15} \text{ cm}^{-3}$ ,  $x = 0.230 \pm 0.002$ ,  
(b)  $p_0 = 5 \times 10^{16} \text{ cm}^{-3}$ ,  $x = 0.415 \pm 0.005$ ,  
(c)  $p_0 = 2 \times 10^{15} \text{ cm}^{-3}$ ,  $x = 0.367 \pm 0.004$ ,  
(d)  $p_0 = 10^{13} \text{ cm}^{-3}$ ,  $x = 0.334 \pm 0.003$ .

relations for  $\text{Hg}_{1-x}\text{Cd}_x\text{Te}$  in the literature do not correspond to each other better than a few meV. For samples with small carrier concentrations (as compared with the non-equilibrium carrier concentration  $\delta n = \delta p$ ), a dynamic effect should be observable. An estimation for this effect can be made in the framework of the theory by Vashishta et al. [11,12] or by Röpke et al. [13], and gives an infrared (IR) shift of  $\Delta E \approx -3 \text{ meV}$  for  $\delta p = 10^{17} \text{ cm}^{-3}$  at the present material parameters for our samples ( $\text{Hg}_{0.65}\text{Cd}_{0.35}\text{Te}$ ,  $R_s \approx 1.3 \text{ meV}$  and  $a_s \approx 300a_0$ ).

(ii) *Burstein–Moss effect*. The static Burstein–Moss effect does not contribute because our samples are p-type (Degenerated samples are not investigated in this study.) The dynamic Burstein–Moss effect (band filling) can be calcu-



lated according to ref. [7] and reaches positive values of a few meV.

(iii) *Thermal effect* via effective carrier temperature ( $T_c$ ) or statistics, respectively. This effect gives a positive contribution of about  $\Delta E = \frac{1}{2}kT_c$  for the plasma (see ref [7]). If localized excitons are considered, the increase of  $T_c$  causes thermal delocalization. For our samples, thermal delocalization energies ( $\Delta E_T$ ) amount to 5–8 meV and produce a positive contribution (blue shift).

(iv) *Thermal effects* via lattice temperature and change at  $E_g(T)$ . Effects of this type are ruled out in the experiments discussed here because of the use of PW PL for higher excitation densities. Due to the positive sign of  $dE_g(T)/dT$  for  $x < 0.5$ , this effect should produce a shift towards higher energies.

The sum of all these contributions can be either positive or negative. Typical dependencies of the PL peak position on excitation density are plotted in Fig. 3. As the energy scales indicate, the behaviour is mainly dependent on  $p_0$  and not on the mole fraction ( $x$ ). However, for samples with nearly the same value of  $p_0$  we found a composition dependence of the slope  $d(\hbar\omega_{\max})/dI_0$  caused by the decreasing combined density of states for decreasing  $x$  (cf. Fig. 3a).

The positive slope in Figs. 3a and 3b indicates mainly band filling, whereas the negative slope in Figs. 3c and 3d essentially can be explained with “dynamic” band gap renormalization. This is shown for the sample with the smallest  $p_0$  in Fig. 3d. The dotted line is calculated following ref. [12] using the relevant material parameters. This description cannot be extended towards higher densities (see experimental data) because of increasing  $T_c$  (see ref. [13]) and the use of Boltzmann statistics in ref. [12]. The dramatic infrared shift with increasing densities is caused by contributions of stimulated emission of exciton, as already discussed in refs. [5,14].

The “usual” behaviour of stimulated emission (line narrowing, pronounced bend in the PL output versus excitation curve as well as geometry effects) by electron–hole plasma transitions was observed for a  $\text{Hg}_{0.65}\text{Cd}_{0.35}\text{Te}$  sample with  $p_0 > 10^{16} \text{ cm}^{-3}$ . Furthermore, temperature dependencies of the CW PL of various samples were mea-

sured to estimate thermal delocalization energies using relation (1):

$$\Delta E_T = [\hbar\omega_{\max}(50 \text{ K}) - \hbar\omega_{\max}(4.2 \text{ K})] - [E_g(50 \text{ K}) - E_g(4.2 \text{ K})], \quad (1)$$

which is valid for trapped intrinsic excitons. These values range (in agreement with ref. [2]) around 5–8 meV without any systematic dependence on the carrier concentration.

### 3.2. Magnetic field behavior of the luminescence

Magneto-optics in  $\text{Hg}_{1-x}\text{Cd}_x\text{Te}$  is a field where a lot of experimental work has been performed in the 1960s and 1970s [15,16]. Magnetotransmission experiments allow an exact determination of the near-to-edge band structure above  $E_g$ . Knowledge of precise parameters determined in this way is an advantage for our further discussion of the elementary excitations measured by luminescence in the near-to-edge region below  $E_g$ .

In the present work the magnetoluminescence of a number of samples was measured. Here we discuss only the data of two samples, called (a) and (b) which were chosen because the  $\hbar\omega_{\max}(I_0)$  dependencies show opposite signs (Fig. 3c displays data from sample (b)). Sample parameters are listed in section 2.

(i) For low excitation densities (CW PL, about  $1\text{--}10 \text{ W cm}^{-2}$ ) all samples show only one single symmetric line exhibiting a decreasing full width at half maximum (FWHM) with increasing magnetic field  $B$ . The  $B$ -dependent spectral position for sample (a) is displayed in Fig. 4a (full circles). The insert illustrates the decreasing FWHM. A plot for adequate data of sample (b) is given in Fig. 4b (full circles). The lines are calculated and will be discussed below.

(ii) For high excitation densities (PW PL, about  $100 \text{ kW cm}^{-2}$ ) the typical magnetic field behaviour of the PL for the same samples differs significantly: For sample (b), besides the band gap renormalization (IR shift), the magnetic field dependence looks very similar as compared to (i) (see empty triangles in Fig. 4b). The lineshape does not change significantly with increasing magnetic field. Sample (a) and only other highly

doped samples exhibit a *distinct line splitting* as demonstrated in Figs. 5a and 5b.

For the quantitative interpretation of the experimental results, we adapted the calculations given by Guldner et al. [15] using material parameters collected by Dornhaus and Nimtz [16]. Magnetic-field-dependent free exciton binding energies were used following Ekardt [17]. Taking into account the selection rules  $\Delta N = 0$  and  $\Delta m_x = 0$  (Voigt geometry) and  $\Delta m_x = \pm 1$  (Faraday geom-

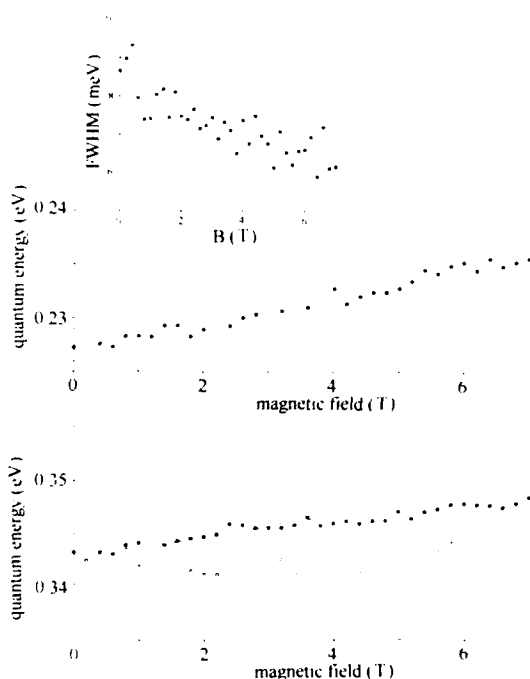


Fig. 4. (a)  $\hbar\omega_{\max}(B)$  dependence for sample (a) (full circles) at  $T = 6$  K for  $I_0 = 10$  W cm $^{-2}$  in Faraday configuration. The inset shows the decrease of the FWHM with increasing magnetic field. The lines are calculated as described in the text (dotted line: lowest allowed interband transition; dashed line: lowest allowed interband transition inclusively corrections due to free exciton contributions). The absolute position on the energy scale for the calculation was chosen according to Fig. 5b. (b)  $\hbar\omega_{\max}(B)$  dependence for sample (b) (full circles) at  $T = 6$  K for  $I_0 = 10$  W cm $^{-2}$  (full circles) and for  $I_0 = 100$  kW cm $^{-2}$  (triangles) in Faraday configuration. The lines are calculated as described in the text (dotted line: lowest allowed interband transition; dashed line: lowest allowed interband transition including corrections due to free exciton contributions; full line: estimation of the influence of localization; see text).

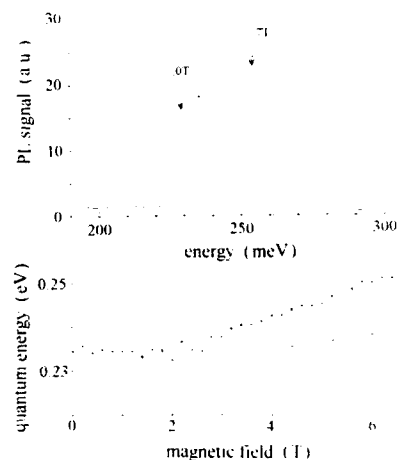


Fig. 5. (a) PL spectra for sample (a) at zero and  $B = 7$  T at  $T = 6$  K and  $I_0 = 100$  kW cm $^{-2}$  in Faraday configuration. (b)  $\hbar\omega_{\max}(B)$  dependence for sample (a) according to (a). The curves (full lines) represent the positions for the lowest allowed transitions.

etry), we were able to calculate fan charts for interband transitions and free exciton transitions (subtracting the exciton binding energy  $R_x(B)$ ). A detailed description of the calculations will be given elsewhere [18].

The curve calculated for the lowest allowed interband transition in Faraday geometry is plotted in Figs. 4a and 4b (dotted line), whereas the dashed line takes into account the excitonic corrections. For  $B = 0$  the difference between the curves is equal to  $R_x$ . For Fig. 5b, the two lowest transitions including excitonic corrections are plotted. All calculated curves are computed *without* any free parameters except  $E_g$ , which can be “shifted” by several meV (within the limits given by the error of the chemical mole fraction determination). This possible “shift” does not change the material parameters significantly and consequently the magnetic field dependencies ( $d(\hbar\omega_{\max})/dB$ ) are calculated without any adjustable parameters. Therefore, the displayed results imply the following:

(1) Obviously, for all samples the  $\hbar\omega_{\max}(B)$  dependencies require excitonic corrections (free exciton).

(2) A complete fit in the framework of free exciton transitions is only possible for “strongly” doped samples in magnetic fields above 4 T (for sample (a)  $\gamma$  (4 T) =  $\hbar\omega_c/R_\infty \approx 13$ ), especially for higher excitation densities.

(3) For fields below 3 T ( $\gamma < 10$ ), deviations become evident, especially for lower doped samples, where excitonic effects are more pronounced.

(4) The observed splitting (Fig. 5) can be quantitatively explained with transitions between the spin-split conduction band and the heavy hole band.

The latter statement was proved with additional measurements in Voigt geometry. As expected, the splitting was smaller ( $\approx 10\%$ ). For the 4–7 T range we calculated  $d(\hbar\omega_{\max})/dB = 1.706 \pm 0.004$  meV/T for the Faraday and  $1.560 \pm 0.004$  meV/T for the Voigt geometry. The corresponding experimental values are  $2.21 \pm 0.07$  and  $1.88 \pm 0.11$  meV/T. The consideration of linear shifts applies very well because the bowing caused by magnetic-field-enhanced  $R_\infty$  compensates the inverse bowing caused by non-parabolicity. The difference between both corresponds to twice the splitting of the parabolic heavy hole band.

Nevertheless, there are still open questions with respect to weaker magnetic fields ( $\gamma < 10$ ) where additional magnetic field dependent localization must be assumed to fit the experimental data. A simple estimation for magnetic-field-dependent localization is plotted in Fig. 4b as a full line. For the calculation we assumed that this contribution is inversely proportional to the volume reduction of the free exciton in the magnetic field.

#### 4. Summary

A study of the excitonic luminescence in  $\text{Hg}_{1-x}\text{Cd}_x\text{Te}$  ( $0.23 < x < 0.41$ ) applying PL, PLE and magnetoluminescence spectroscopy is presented.

The samples for this investigation were chosen mainly with respect to the excitonic contribution to the luminescence. Band gap renormalization – first reported in this paper for narrow-gap

$\text{Hg}_{1-x}\text{Cd}_x\text{Te}$  – was used as a measure to estimate contributions of electron–electron (–hole) interaction.

In addition, magnetic-field-dependent PL spectra are discussed. For all samples, magnetic field dependencies of PL spectra can be fitted with excitonic corrections (free excitons) better than neglecting them. The splittings of the PL lines in Faraday and Voigt geometry are *quantitatively* interpreted as spin splittings of both conduction and heavy hole band.

Samples with comparable thermal delocalization energies of the localized intrinsic excitons trapped in disorder-induced potential wells exhibit very different magnetic-field-dependent localization. The solution of this question will improve the knowledge about alloy disorder in ternary compounds.

#### 5. Acknowledgements

The authors wish to thank P. Gille for providing the samples and K.-P. Möllmann for helpful discussions. Technical assistance by Ch. Mrosek is acknowledged. This work was supported in part by the DFG.

#### 6. References

- [1] R. Legros and R. Triboulet, *J. Crystal Growth* 72 (1985) 264.
- [2] A. Lusson, F. Fuchs and Y. Marfaing, *J. Crystal Growth* 101 (1990) 673.
- [3] A. Lusson and J. Wagner, *Phys. Rev. B* 38 (1988) 10064.
- [4] B.L. Gelmont, V.I. Ivanov-Omskii, V.A. Maltseva and V.A. Smirnov, *Fiz. Tekh. Poluprov.* 15 (1981) 1109.
- [5] L. Werner, J.W. Tomm and K.H. Herrmann, *Infrared Phys.* 31 (1991) 49.
- [6] K.H. Herrmann, V. Hoerstel, K.-P. Möllmann, U. Sassenberg and J.W. Tomm, *Semicond. Sci. Technol.* 7 (1992) 578.
- [7] K.H. Herrmann, M. Happ, H. Kissel, K.-P. Möllmann, J.W. Tomm, C.R. Becker, M.M. Kraus, S. Yuan and G. Landwehr, *J. Appl. Phys.* 73 (1993) 3486.
- [8] P. Gille, F.M. Kiessling and M. Burkert, *J. Crystal Growth* 111 (1991) 77.
- [9] J.W. Tomm, H. Schmidt, L. Werner and K.H. Herrmann, *Crystal Res. Technol.* 25 (1990) 1069.

- [10] F. Fuchs, K. Kheng, K. Schwarz and P. Koidl, *Semicond. Sci. Technol.* 8 (1993) S75.
- [11] P. Vashishta, P. Bhattacharyya and K.S. Singwi, *Phys. Rev. B* 10 (1974) 5108.
- [12] P. Vashishta and R.K. Kalia, *Phys. Rev. B* 25 (1982) 6492.
- [13] G. Röpke, T. Seifert, H. Stolz and R. Zimmermann, *Phys. Status Solidi (b)* 100 (1980) 215.
- [14] V.I. Ivanov-Omskii, K.R. Kurbanov, R.B. Rustamov, V.A. Smirnov and Sh.U. Yuldashev, *Fiz. Tekh. Poluprov.* 18 (1984) 1509.
- [15] Y. Guldner, C. Rigaux, A. Mycielski and Y. Couder, *Phys. Status Solidi (b)* 81 (1977) 615; *Phys. Status Solidi (b)* 82 (1977) 149.
- [16] A review is given in: R. Dornhaus and G. Nimtz, The properties and applications of the  $\text{Hg}_{1-x}\text{Cd}_x\text{Te}$  alloy system, in: *Springer Tracts in Modern Physics*, Vol. 98, Narrow-Gap Semiconductors (Springer, Berlin, 1983) p. 119.
- [17] W. Ekardt, *Solid State Commun.* 16 (1975) 233.
- [18] J.W. Tomm and H. Kissel, to be published.



ELSEVIER

Journal of Crystal Growth 138 (1994) 182–186

JOURNAL OF  
**CRYSTAL  
GROWTH**

## Study of electronic structure in strained ZnSe/GaAs thin films by nonlinear optical- and Brewster-angle reflection spectroscopies

Kuon Inoue <sup>\*a</sup>, Takashi Kuroda <sup>a</sup>, Fujio Minami <sup>b</sup>, Kouji Yoshida <sup>a</sup>, Masaki Hayashi <sup>a</sup>

<sup>a</sup> *Research Institute for Electronic Science, Hokkaido University, Sapporo 060, Japan*

<sup>b</sup> *Department of Applied Physics, Tokyo Institute of Technology, Meguro-ku, Tokyo 152, Japan*

### Abstract

Two kinds of novel spectroscopic methods of two-photon resonant second-harmonic generation (SHG) and Brewster-angle reflection were investigated for exploring the electronic structure in strained ZnSe/GaAs thin films. A line splitting into two, which is caused by in-plane tensile strain, in the excitation spectrum of the normally forbidden SHG signal was observed in resonance with the 2P exciton, whereas three lines in resonance were observed with the 1S exciton polaritons. In the Brewster-angle reflection spectrum, on the other hand, only one broad line with the width presumably broadened inhomogeneously, was observed in the 1S exciton region. Next, Brewster-angle reflection spectroscopy was also investigated in a few samples of ZnSe/ZnS quantum wells. For those, two split lines were distinctly observed in the 1S exciton region, as it should be. Comparison between those spectral lines and the one-photon excitation spectrum of luminescence indicates that they are consistent. Thus, it is concluded that both methods should serve as a simple and novel tool for characterizing II–VI thin films.

### 1. Introduction

In the last decade, a variety of II–VI thin films have been fabricated, mostly on a GaAs substrate, by state-of-the-art epitaxial growth methods. Those samples are expected to be used for potential applications to diode lasers and optoelectronic devices, operating in the blue-to-green region. The quality of those heteroepitaxial samples is different from one to another, which causes great influence on the physical properties such as the band-structural, electronic, and optical properties; an extent as well as a distribution of both

fluctuations at the interface and strains inevitably involved, the latter being due to the lattice mismatch, are always problems. In order to establish the best way of fabricating a sample of good quality, simple and powerful methods of characterizing a sample are unquestionably necessary. This is also true for exploring the electronic structure in those samples, particularly that in quantum wells. Up until now, several methods have already been introduced such as X-ray, TEM, Raman scattering and photoluminescence excitation (PLE) spectroscopy [1]. However, those complementary methods do not necessarily suffice to work, depending on the case. In view of the above situation, we have tried to develop two novel methods, resonant second-harmonic gener-

<sup>\*</sup> Corresponding author.

ation (RSHG) and Brewster-angle reflection (BAR), both of which have the advantage of making measurements without removing the substrate. In this paper, we have adopted two kinds of strained thin films, i.e., ZnSe thin film and ZnSe/ZnS quantum well, both grown on a GaAs substrate.

## 2. Experimental procedure

A home-made repetitively-pulsed titanium-sapphire laser (Ti-S laser) was employed for an experiment of RSHG. This wavelength-tunable laser had the representative characteristics of 0.5 kW peak power, 0.3 meV spectral width and 3 kHz repetition rate. A focused beam from the laser was made incident on the substrate and propagated perpendicularly to the film layer ( $z$ -axis). A SHG signal emerging in the forward direction was collected by a lens, fed to a single-grating monochromator, and then detected by a cooled optical multichannel detector of diode-array type. The incident polarization was set in parallel to the  $x$ - or  $y$ -axis. The resonant SHG signal was observed with twice the incident photon energy,  $2\hbar\omega_i$ , swept through the exciton region. It should be noted that no absorption of incident beam due to a GaAs substrate took place.

For reflection measurement, a conventional halogen lamp, a standard monochromator and a photomultiplier were used. An incident-beam divergence of less than  $3^\circ$  was utilized. As the Brewster angle, a value calculated from the refractive index far below the direct-band-gap frequency was adopted at the first setting, and then by changing the incident angle around this value, the angle for getting the best signal was experimentally searched. For comparison, the PLE spectrum was also observed in each sample by making use of the SHG light of Ti-S laser.

For the ZnSe/GaAs film, two samples with thicknesses of 4.8 and 2.1  $\mu\text{m}$  were adopted, which were fabricated by a MOCVD technique. For the ZnSe/ZnS quantum well, a few samples fabricated by a hot-wall epitaxy method with ZnSe well thicknesses from 50 to 10  $\text{\AA}$  against 50  $\text{\AA}$

thick ZnS (barrier) on GaAs without buffer and cap layers were utilized. All measurements were performed at 4.2 or 2 K.

## 3. Results and discussion

### 3.1. Resonant SHG spectroscopy

In Fig. 1, examples of the SHG signal appearing as a result of two-photon resonance in the exciton region are shown for a 4.8  $\mu\text{m}$  thick ZnSe/GaAs sample, where the polarization of the incident beam was set parallel to the  $y$ -axis. Variation of the SHG intensity as a function of  $2\hbar\omega_i$ , or the excitation spectrum of SHG, is also shown in Fig. 1. It can be seen that three and two peaks emerge in the 1S and 2P exciton regions, respectively. The SHG signal in the present configuration is normally forbidden in the electric-dipole approximation, since only off-diagonal SHG tensors such as  $d_{xyz}$  are nonvanishing in the relevant tetragonal  $\bar{4}2m$  symmetry considering the involvement of in-plane strain. This is a first observation of a two-photon resonant forbidden

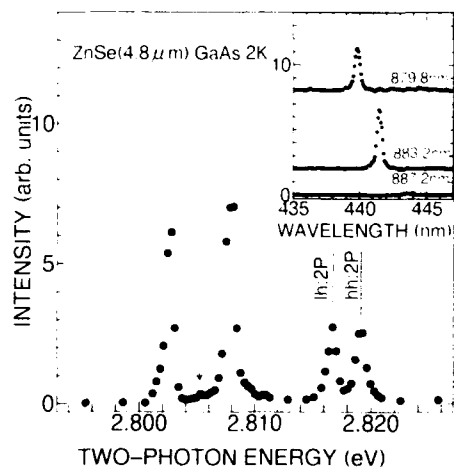


Fig. 1. The two-photon excitation spectrum of the forbidden SHG in the exciton region for a ZnSe/GaAs film, where three lines other than the two marked (2P exciton) lie in the 1S exciton region. In the inset, examples of the SHG signal are shown with the excitation wavelength.

SHG phenomenon in this configuration [2,3]. The present configuration is much easier in measurement than or superior to the previous one [3,4], where incident light was made propagating parallel to a very thin layer. In the case of the 2P exciton, the polariton effect may be ignored owing to the small oscillator strength of the one-photon transition. Consequently, the two observed lines can be assigned as arising respectively from light-hole (l-h) and heavy-hole (h-h) related 2P excitons split due to the in-plane (biaxial) tensile strain caused by the lattice mismatch already described. From the value of energy separation, the magnitude of the strain can be estimated to be  $\sim 5 \times 10^{-4}$  [4,6]. The spectral width is presumably dominated by the inhomogeneity, rather than by the phase matching, unlike the allowed SHG case [2]. In contrast, three lines manifest themselves in the 1S exciton region with the two definite lines and a very weak one in between. The energy splitting between the two definite lines does not coincide with that for the 2P exciton, obviously indicating that the splitting is not solely caused by strain. Instead, the splitting may be reasonably interpreted as reflecting the exciton-polariton effect [7], the relevant transverse-longitudinal splitting being 1.5 meV, and the energy splitting due to the strain as well. The highest and lowest energy lines should arise from the uppermost and the middle polariton branches, respectively. Although the energy location observed for the former is reasonable, that for the latter is somewhat lower compared to the PLE. The reason for this is not clear at present. The weak middle line is very likely to correspond to the highest longitudinal exciton, judging from the observed energy position. Since SHG due to the longitudinal exciton is absolutely forbidden, this line might be observed due to a large collecting angle for the signal. This speculation may be supported by the fact that the signal in question becomes larger when the sample is slightly tilted relative to the incident beam direction. The spectral widths of the excitation spectrum of RSHG are seen to differ from those in the PLE spectrum (Fig. 2). It is speculated that the contribution of inhomogeneity to the width is different between the linear and nonlinear spectra. Fur-

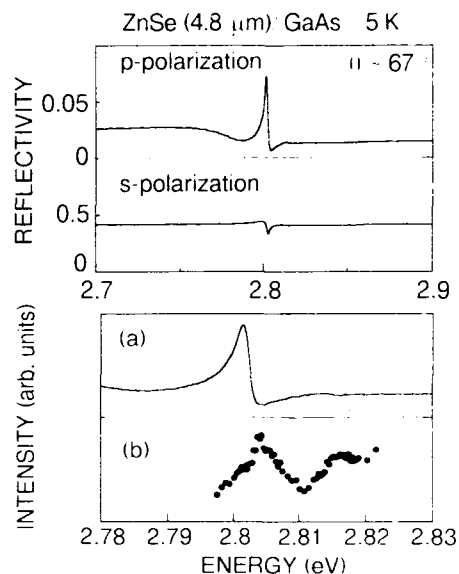


Fig. 2. An example of the BAR spectra observed for p- and s-polarization in a ZnSe/GaAs film (upper). A comparison between the BAR (a) and PLE (b) spectra is also presented (lower).

ther, the latter is influenced also by the phase mismatch.

Thus, we propose that the present RSHG spectroscopy should provide a useful tool for characterizing a thin film such as ZnSe/GaAs through the energy splitting and the inhomogeneous broadening of the relevant excitonic structure. In addition, the present method is capable of examining easily the position-dependent characteristics over the plane of a sample.

### 3.2. Brewster-angle reflection spectroscopy

An example of the raw BAR spectrum for a 4.8  $\mu\text{m}$  thick ZnSe/GaAs sample is shown in Fig. 2, together with PLE. A similar spectrum was also observed in a 2.1  $\mu\text{m}$  thick sample. A salient structure can be seen in the 1S exciton region. It was observed that the magnitude of the nonresonant background reflection for the p-polarization was reduced by more than one order of magnitude, compared to the normal incidence case. It is likely that, in BAR, the background in the

lower energy region below the 1S excitonic transition is dominated by the reflection from the GaAs substrate. As a result, a clear-cut but broad reflection peak shows up for the p-polarization. In the PLE, however, as shown in Fig. 2, which was observed with almost normal incidence concerning the incident beam, two peaks are seen to exist, with a weak one on the shoulder of the major one. This intensity ratio observed is considered to reflect the relative spin multiplicity. It is noted that for the h-h exciton, one-photon absorption is not allowed for  $e_i \parallel z$ , with  $e_i$  being the unit polarization of incident photon, while for the l-h exciton, it is allowed both for  $e_i \parallel z$  and for  $e_i \perp z$ . Taking this selection rules into account, two peaks should be observed with almost similar relative strength in BAR. However, a computer simulation indicates that the shape of the spectrum depends crucially on the incident angle as well as on the relevant inhomogeneous broadening, and that the center frequency can also deviate to some extent from that of PLE. This may be the reason that one broad spectrum has been observed rather than that with a two-split structure. The details of the analysis based on a polariton picture will be presented elsewhere.

### 3.3. Brewster-angle reflection spectroscopy in ZnSe/ZnS quantum wells

In Fig. 3, an example of the BAR spectrum in a 30 Å ZnSe/50 Å ZnS sample is shown, together with the PLE spectrum. In the case of a

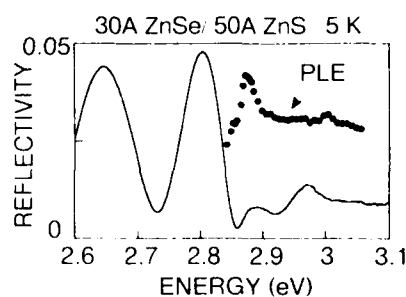


Fig. 3. An example of the BAR spectrum observed in a ZnSe/ZnS quantum well. The PLE spectrum is shown for comparison.

quantum well, the interpretation of both results by two methods is rather straightforward, since an analysis not taking into account the polariton effect may be justified. It is found that two distinct reflection peaks can be observed. The signals in this case are less clear than for thin films, due to the larger inhomogeneous broadening. This is the first Brewster-angle reflection measurement, to our best knowledge, on a II-VI quantum well [8]. It is noted that this structure disappears in the normal incidence reflection spectrum. The respective peak energies are found to be consistent with those in the PLE spectrum, the former being somewhat lower than the latter, which can be explained on the basis of computer simulation, as already described. The existence of two peaks can undoubtedly be attributed to the splitting of the degenerate 1S exciton into the l-h and h-h related ones due to the superlattice potential in addition to the strain [1,9]. It is remarked that their spectral width should be caused by an inhomogeneous broadening in the present case.

The BAR spectroscopy, which allows the elimination of strong background and Fabry-Perot interference, may be very useful for characterizing the electronic structure in II-VI thin film samples including quantum wells. If the inhomogeneous broadening is small enough, the weak electronic details could be observed, examples of which will be presented in a separate paper. It should be noted that the measurement is very easy to carry out with a substrate kept unremoved. This method may be an alternative way to direct one-photon absorption, and also is superior to PLE spectroscopy, since a valuable wavelength tunable laser is not needed. Furthermore, the present one can be applied to even such a sample as not emitting luminescence.

### 4. Acknowledgments

The authors are grateful to Professor H. Kukimoto and Professor H. Fujiyasu for supplying them samples. The work was supported by a Grant-in-Aid for Scientific Research from the Ministry of Education, Science and Culture.



## 5. References

- [1] See, for example, K. Shahzad, D.J. Olego, C.G. Van de Walle and D.A. Cammack, *J. Luminescence* 46 (1990) 109.
- [2] As for the allowed configuration, a 1S resonant SHG phenomenon was already reported in bulk samples of solids: D.C. Haukeisen and H. Mahr, *Phys. Rev. B* 8 (1973) 734.
- [3] For thin films, a similar measurement (allowed) to ref. [2] was also made only in the 1S exciton region: B.F. Levine, R.C. Miller and W.A. Norland, Jr., *Phys. Rev. B* 12 (1975) 4512.
- [4] F. Minami, K. Inoue, Y. Kato, K. Yoshida and K. Era, *Phys. Rev. Lett.* 67 (1991) 3708.
- [5] K. Inoue, F. Minami, Y. Kato, K. Yoshida and K. Era, *J. Crystal Growth* 117 (1992) 738.
- [6] F. Minami, Y. Kato, K. Yoshida, K. Inoue and K. Era, *Appl. Phys. Lett.* 59 (1991) 712; *J. Crystal Growth* 117 (1992) 565.
- [7] D. Bogett and R. Loudon, *Phys. Rev. Lett.* 28 (1972) 1051; *J. Phys. C (Solid State Phys.)* 6 (1973) 1763.
- [8] A pioneering Brewster-angle reflection measurement was successfully done in GaAs/AlAs superlattices: I.N. Uraltsev, E.L. Ivchenko, P.S. Kopev, V.P. Kochereshko and D.R. Yakovlev, *Phys. Status Solidi (b)* 150 (1988) 673.
- [9] F. Minami, K. Yoshida, J. Gregus, K. Inoue and H. Fujiyasu, in: *Optics of Excitons in Confined Systems*, Eds. A. D'Andrea et al. (Inst. Phys., Bristol, 1992) p. 249.



ELSEVIER

Journal of Crystal Growth 138 (1994) 187–190

JOURNAL OF  
CRYSTAL  
GROWTH

## Nonlinear refraction and optical limiting in bulk ZnTe crystal

W. Ji <sup>\*a</sup>, A.K. Kukaswadia <sup>a</sup>, Z.C. Feng <sup>a</sup>, S.H. Tang <sup>a</sup>, P. Becla <sup>b</sup>

<sup>a</sup> Department of Physics, National University of Singapore, Lower Kent Ridge Road, Singapore 0511, Singapore

<sup>b</sup> Francis Bitter Magnet Laboratory, Massachusetts Institute of Technology, Cambridge, Massachusetts 02139, USA

### Abstract

We report the observation of a refractive nonlinearity ( $\sim 3 \times 10^{-21} \text{ cm}^3$ ) in bulk ZnTe crystal at wavelengths just below the band edge, using nanosecond laser pulses. A comparison with band-filling theory indicates that the dynamic Burstein–Moss shift should be the mechanism responsible for the observed nonlinearity. Optical limiting has also been demonstrated with the use of this refractive nonlinearity.

### 1. Introduction

In the last decade, semiconductors exhibiting strong optical nonlinear refractive behaviour have been under intensive investigation [1]. The interest in these semiconductors has been stimulated by their potential in optical device applications for optical switching and optical limiting. The semiconductor ZnTe with a direct band-gap energy of  $\sim 2.26 \text{ eV}$  ( $\sim 550 \text{ nm}$ ) at room temperature represents a promising candidate for such applications in the visible region. The thermal and electro-optical refractive nonlinearities in ZnTe have been studied by Schmidt et al. [2]. These nonlinearities have been employed to demonstrate optical bistability [2]. The bound electronic and free-carrier refractive nonlinearity at a photon energy considerably below the band-gap energy have also been reported by Said et al.

[3]. By using the Z-scan technique with picosecond pulses of  $1.06 \mu\text{m}$  wavelength laser light, they have experimentally found the bound electronic nonlinearity to be  $8.3 \times 10^{-10} \text{ esu}$  and the free-carrier nonlinearity to be  $-7.5 \times 10^{-22} \text{ cm}^3$ .

In this paper, we report both the measurement of free-carrier nonlinearity and the observation of optical limiting in ZnTe at wavelengths just below the band edge. The nonlinear refraction in a bulk ZnTe crystal was determined with the use of the method of beam profile distortion due to self-defocusing. By illuminating nanosecond laser pulses onto the ZnTe sample, the spatial profiles of the transmitted pulses were measured. By fitting a self-defocusing model to the experimental results, we obtained a nonlinear refractive cross-section which is defined as the change in the refractive index per pair of photo-generated carriers in unit volume. The mechanism responsible for the observed free-carrier nonlinearity was discussed. Based on this nonlinear refraction, we also demonstrated optical limiting of nanosecond laser pulses in ZnTe.

\* Corresponding author.

## 2. Nonlinear refraction

### 2.1. Experiment

The experimental ZnTe sample used in this investigation was grown by Bridgman technique. The bulk crystal after growth was cut into 1.0 mm thick pieces and polished mechanically and chemically on both sides. The sample was examined by Raman scattering and absorption spectra. The Raman study [4] showed very sharp and narrow Raman lines, and up to the 8th order longitudinal optical (LO) phonon modes under excitations from an argon ion laser, which offered the evidence for the high crystalline perfection of our experimental sample. The absorption spectrum was obtained from using a Hitachi U-3410 spectrophotometer. It was confirmed that at room temperature the band-gap energy of the ZnTe crystal was 2.25 eV, which agrees with the published result [5].

The experimental layout for refractive nonlinearity measurements is similar to the system described previously [6] except that a frequency-doubled Nd:YAG pumped dye laser was used to generate optical pulses of duration 6 ns. The spatial profile of the pulses was of nearly Gaussian form after employing a spatial filter. The pulses were then focused onto the ZnTe sample by a focusing mirror ( $f = 100$  cm). The sample was placed at the minimum beam waist where the spot size  $r_0$  was 100  $\mu\text{m}$  (half width at  $e^{-2}$  of the maximum). The transmitted spatial profiles were recorded by scanning the energy detector (Laser Precision, RjP-765 probe) across the beam with a 15  $\mu\text{m}$  diameter pinhole mounted in the front. The peak irradiance of the incident pulses was set at the same value during each scanning. In order to determine the sign of the refractive nonlinearity responsible for the observed effect, the spatial profiles of the transmitted fluence were measured in the near field ( $z = 6$  cm behind the exit plane of the sample).

As the wavelength of the laser pulses was tuned towards the band edge, the irradiance-dependent spatial profiles of the transmitted pulses were observed. Fig. 1 shows a typical experimental measurement at a wavelength of 563 nm. The

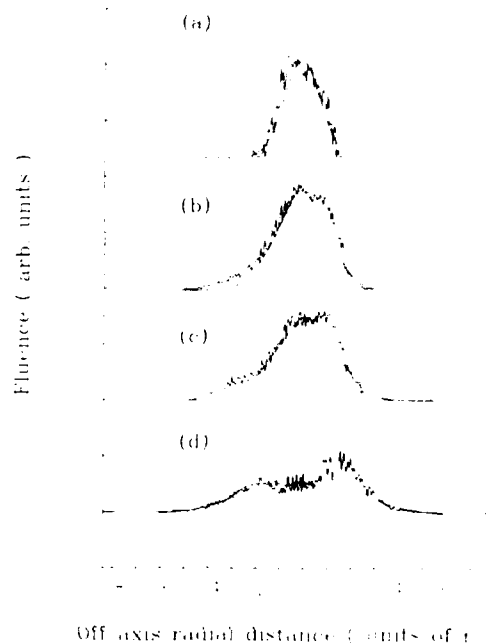


Fig. 1. Near-field transmitted beam profiles at peak incident irradiances: (a) 0.13  $\text{MW}/\text{cm}^2$ ; (b) 1.3  $\text{MW}/\text{cm}^2$ ; (c) 2.6  $\text{MW}/\text{cm}^2$ ; (d) 4.1  $\text{MW}/\text{cm}^2$ . The smooth curves are the theoretical fits described in the text.

spatial profiles of the transmitted pulses begin to broaden when the incident irradiance is increased to about 1  $\text{MW}/\text{cm}^2$ , and break up as the incident irradiance arises to above 4  $\text{MW}/\text{cm}^2$ . Similar results were obtained for wavelengths ranging from 561 to 565 nm. These experimental data clearly indicate that the observed nonlinear optical effect is self-defocusing and has a negative sign for the refractive nonlinearity.

### 2.2. Determination of free-carrier nonlinearity

In Fig. 1, we also present the theoretical curves calculated with the following model. Free carriers, generated as a result of single-photon absorption on the tail of the band edge, modify the absorption spectrum and, hence, change the re-

fractive index. The change in refractive index may be written as

$$\Delta n = \sigma \Delta N, \quad (1)$$

where  $\sigma$  is the nonlinear refractive cross-section and  $\Delta N$  is the density of photo-generated free carriers. Since the duration of our pulses is much shorter than the carrier recombination time [7] (and ignoring the carrier diffusion),  $\Delta N$  is given by

$$\Delta N = \frac{\alpha I_0}{\hbar \omega} \int_{-\infty}^t f(t') dt', \quad (2)$$

where  $\alpha$  is the single-photon absorption coefficient,  $\omega$  is the angular frequency of incident light,  $\hbar$  is Planck's constant and  $I_0$  is the peak irradiance inside the sample. By using the Huygens–Fresnel propagation formalism [8] with the presence of the nonlinear refractive index governed by Eqs. (1) and (2), we calculate numerically the spatial profiles of the transmitted pulses at 7 cm away from the sample for various incident irradiances. The best fits between the model and the experimental measurements give a  $\sigma$  value of  $-(2.8 \pm 0.4) \times 10^{-21} \text{ cm}^3$ . It is interesting to note that this nonlinearity is higher than that found in ZnSe [3] by a factor of about 2.

### 2.3. Band-filling theory

We attribute the observed effect to the nonlinear refraction caused by a band-filling mechanism. This mechanism is based on the fact that free carriers photo-excited into the conduction band partially block interband transitions above the fundamental absorption edge (dynamic Burstein–Moss shift), and, hence, alter the refractive index at the incident wavelength. The theoretical treatment of the band-filling mechanism has been described in detail [9]. Under the two-band approximation, using the Kramers–Kronig relations and the Boltzmann statistics, the nonlinear refractive cross-section can be derived as

$$\sigma = -\frac{2\pi e^2}{m_c n_0 \omega^2} \left[ 1 + Z \frac{m_{ch}}{m} J_{hc} + \frac{m_c}{m_h} \left( 1 + Z \frac{m_{ch}}{m} J_{hh} \right) \right], \quad (3)$$

with

$$J_{ij} = \int_0^\infty \frac{x^2 e^{-x^2}}{x^2 + a_{ij}} dx, \quad (4)$$

$$a_{ij} = \frac{\hbar \omega - E_g}{kT} \frac{m_{ci}}{m_j}, \quad (5)$$

where  $e$  is the electric charge of the electron,  $n_0$  is the linear refractive index,  $m$  is the electron mass,  $m_{ch}$  is the reduced mass ( $m_{ch} = m_c m_h / (m_c + m_h)$ ),  $m_c$  and  $m_h$  are the effective masses for the conduction and heavy-hole valence bands, respectively).

$$Z = \frac{4}{3\sqrt{\pi}} \frac{mP^2}{\hbar^2} \frac{1}{kT},$$

$P$  is the momentum matrix element ( $mP^2/\hbar^2$  is approximately 11 eV for zinc-blende semiconductors),  $k$  is Boltzmann's constant, and  $T$  is the temperature in kelvins.  $J_{hc}$  and  $J_{hh}$  include the effect of resonance between the operating frequency ( $\omega$ ) and the band-gap energy.

Using the published data for  $m_c = 0.12m$  [5],  $m_h = 0.60m$  [5],  $E_g = 2.26 \text{ eV}$  [5],  $n_0 = 3.18$  [10], and our experimental condition for  $T = 295 \text{ K}$ ,  $\hbar \omega \sim 2.2 \text{ eV}$ , we calculate the nonlinear refractive cross-sections to be  $-3 \times 10^{-21} \text{ cm}^3$ , which is in good agreement with our measured results.

### 3. Optical limiting

The geometry we used for optical limiting was a one-to-one inverting telescope formed by two focusing mirrors ( $f = 100 \text{ cm}$ ). The same ZnTe crystal was placed at the focus of the first focusing mirror. The pulsed laser radiation was provided by the same laser system. As the input pulse irradiance was varied from 0.1 to 10 MW/cm<sup>2</sup>, both input and output light energy were simultaneously monitored by using a calibrated beam splitter and two Laser Precision energy probes. A limiting behaviour was observed due to interband absorption and subsequent photogenerated free-carrier defocusing. The optical limiting capabilities are very much dependent on the operating wavelength. At 562 nm, the absorp-

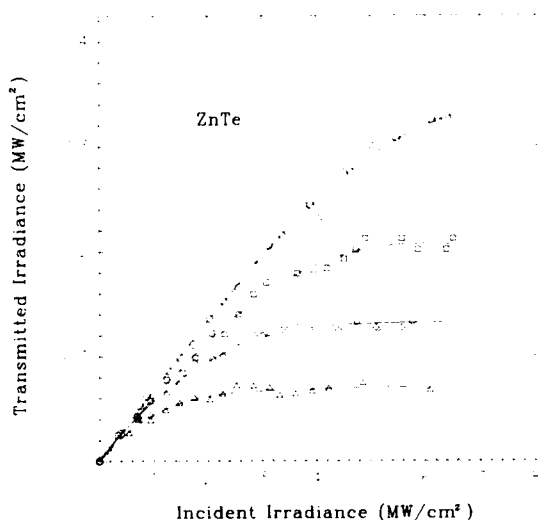


Fig. 2. The transmitted irradiance as a function of the incident irradiance of the pulses at wavelengths of: ( $\Delta$ ) 562 nm; ( $\diamond$ ) 563 nm; ( $\square$ ) 564 nm; ( $\circ$ ) 565 nm. The curves are guides to the eye.

tion coefficient is high, a large density of free carriers is thereby created, resulting in a strong self-defocusing effect. Thus a lower limiting threshold ( $\sim 1.5 \text{ MW/cm}^2$ ) is observed, as shown in Fig. 2. When the input irradiance is above  $1.5 \text{ MW/cm}^2$ , the output irradiance is effectively saturated at  $60 \text{ kW/cm}^2$ . The ZnTe crystal continued to regulate the output irradiance until a permanent melting damage occurred on the surface of the crystal. The single-shot damage threshold was found to range from 8 to  $10 \text{ MW/cm}^2$ . As the wavelength of laser pulses was tuned away from the band edge, the absorption process became less efficient, and hence the limiting behaviour was less pronounced, which is consistent with our observation of the wavelength-dependent limiting performance shown in Fig. 2.

#### 4. Conclusion

We have observed and quantified a relatively large, room-temperature refractive nonlinearity of electronic origin in ZnTe at wavelengths just below the band-gap energy. The refractive nonlinearity is found to be in agreement with a band-filling model. Based on the observed nonlinear refraction, the optical limiting of nanosecond laser pulses in ZnTe has been demonstrated.

#### 5. Acknowledgment

We gratefully acknowledge the financial support of the National University of Singapore (research project reference number: RP910687).

#### 6. References

- [1] H. Haug, Ed., *Optical Nonlinearities and Instabilities in Semiconductors* (Academic Press, New York, 1988).
- [2] A. Schmidt, M. Kunz, I. Laciš, A. Daunois and C. Klingshirn, *Z. Physik B - Condensed Matter* 86 (1992) 337.
- [3] A.A. Said, M. Sheik-Bahae, D.J. Hagan, T.H. Wei, J. Wang, J. Young and E.W. Van Stryland, *J. Opt. Soc. Am. B* 9 (1992) 405.
- [4] Z.C. Feng, S. Perkowitz and P. Becla, *Solid State Commun.* 78 (1991) 1011.
- [5] Landolt-Börnstein, *Numerical Data and Functional Relationships in Science and Technology*, Vol. 17b, Semiconductors, Ed. K.-H. Hellwege (Springer, Berlin, 1982).
- [6] W. Ji, S.H. Tang and A.K. Kukawadia, *J. Appl. Phys.* 73 (1993) 8455.
- [7] M. Nagabhooshanam, *Crystal Res. Technol.* 23 (1988) 1385.
- [8] J.R. Milward, W. Ji, A.K. Kar, C.R. Pidgeon and B.S. Wherrett, *J. Appl. Phys.* 69 (1991) 7351.
- [9] B.S. Wherrett, A.C. Walker and F.A.P. Tooley, Nonlinear refraction for cw optical bistability, in: *Optical Nonlinearities and Instabilities in Semiconductors*, Ed. H. Haug (Academic Press, New York, 1988) p. 239.
- [10] K. Sato and A. Adachi, *J. Appl. Phys.* 73 (1993) 926.

## Influence of the screening of piezo-fields on the carrier dynamics in CdS/CdSe superlattices

W. Langbein, H. Kalt, M. Hetterich, M. Grün, C. Klingshirn \*

*Fachbereich Physik, Universität Kaiserslautern, E.-Schrödinger-Strasse, D-67663 Kaiserslautern, Germany*

### Abstract

The internal piezofields in strained layer CdS/CdSe superlattices lead to a strong deformation of the bandstructure due to a large lattice mismatch. A screening of these piezo-fields by increasing carrier densities leads to a blue shift of the emission by 400 meV. The experiments and the calculation of the eigenstates clearly show this effect, leading to a shift of the spectral emission maximum with the logarithm of delay time after ps excitation. First CW pump-and-probe beam experiments reveal the blue shift of higher subbands.

### 1. Introduction

Compound semiconductors with, e.g., zincblende type ( $T_d$ ) or wurtzite type ( $C_{6v}$ ) symmetries show the piezo-effect under applied stress. The same holds for strained layer superlattices prepared from such materials. The situation for cubic II–IV materials has been reviewed recently [1]. We concentrate here on the band structure and the optical properties of hexagonal CdS/CdSe superlattices under the coupled influences of piezo-fields and optically excited electron–hole pairs. We vary the concentration of carrier pairs from close to zero ( $\leq 10^9 \text{ cm}^{-2}$ ) up to the onset of stimulated emission ( $\geq 10^{13} \text{ cm}^{-2}$ ). First results for this system have been published already in refs. [2,3].

### 2. Results and discussion

In contrast to the MOVPE technique used in ref. [2], the samples presented here have been grown by hot-wall-beam epitaxy on GaAs (111) substrates with CdS buffer and cladding layers. The SL contain typically 30 periods of CdS/CdSe layers of nominally equal thicknesses around 5 nm. Details are given in refs. [3,4]. In Fig. 1 we show self-consistently calculated band structures and envelope wavefunctions of electrons and holes for the first two minibands at the zone-centre  $k_z = 0$  at two different carrier densities. Details of this calculations are given elsewhere [5]. For  $n_e = n_h = 1.2 \times 10^9 \text{ cm}^{-2}$ , the carrier influence on the bandstructure is almost negligible. One can nicely see the alternating tilt of the band bottoms which results, similarly to the quantum-confined Stark effect (QCSE) [6], in a red shift of the transition energies compared to the flat-band situation. The internal piezo-fields are in the

\* Corresponding author.

order of  $10^8$  V/m compared to values around  $10^7$  V/m in the cubic II–IV superlattices [1] and in QCSE devices [6]. For increasing carrier densities, the band structure approaches this flat band situation due to the screening of the piezo-fields by the carriers. Simultaneously, the transition energies shift to the blue by about 0.4 eV, and the spatial overlap of the wavefunctions increases. In Fig. 2 we show emission spectra of a CdS/CdSe SL under CW and ns pulsed excitation. The emission for a sample with a total period length of 8 nm starts under CW Hg lamp excitation (not shown here) at 1.43 eV, shifts under CW He–Ne laser excitation at  $I_{\text{exc}} = 10$  W/cm<sup>2</sup> to 1.58 eV and continues under pulsed ns excitation up to 1.8 eV in agreement with the calculations in Fig. 1. At the highest pump powers stimulated emission sets in. This topic is treated in more detail in ref. [7].

The temporal evolution of the emission maximum of a sample with a period length of 12 nm has been investigated after excitation with 70 ps pulses from a quenched cavity dye laser at 2.47 eV. The emission which has been recorded by a streak camera shifts with time from about 1.71

eV down to 1.56 eV at the detection threshold, as shown in the inset of Fig. 3. The remarkable point is that this energy shift follows a logarithmic law over several decades of time delay. This behaviour is derived also from theory. It is a consequence of the decreasing overlap of the electron and hole wave functions with decreasing electron–hole pair density. Details of the calculations are again given in [5].

In Fig. 4 we show first results of CW pump-and-probe beam experiments using a He–Ne laser as excitation source. A sample has been glued on a sapphire chip and the GaAs substrate has been removed by selective etching. We see in Fig. 4 Fabry–Perot modes in the transparent part of the spectrum below 1.7 eV and the onset of the absorption of the CdS buffer and cladding layers around 2.5 eV. The onset of the absorption of the CdS/CdSe SL starting around 1.7 eV is rather weak. This is due to the low total thickness of CdSe of  $30 \times 6$  nm only. Also the weak overlap of the electron and hole wave functions (see Fig. 1) reduces the absorption of the lower minibands. Under CW excitation of 0.5 W/cm<sup>2</sup> with a He–Ne laser, we get a clear signal in the differential

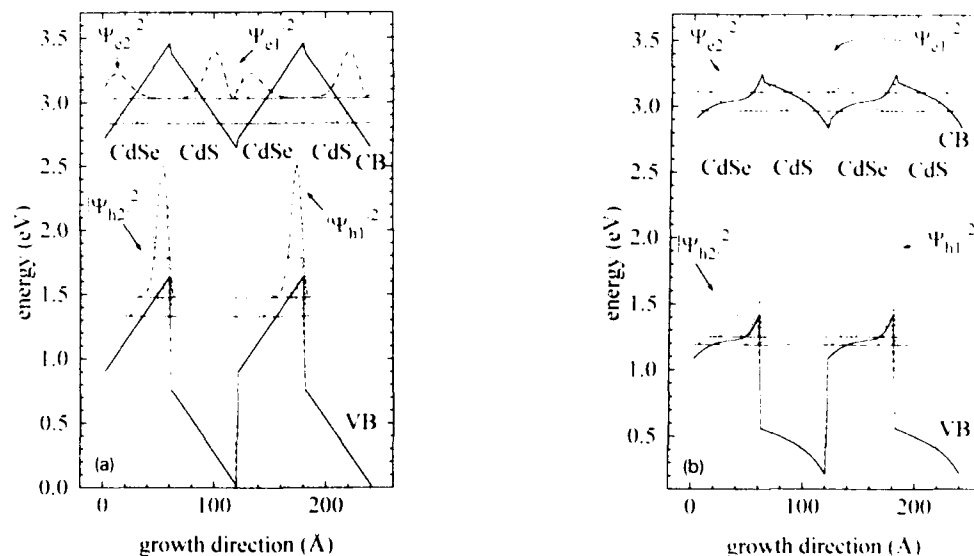


Fig. 1. Calculated band structure and squared wavefunctions of the lowest two minibands in a CdS/CdSe SL for low excitation of  $1.2 \times 10^9$  cm<sup>-2</sup> (a) and high excitation of  $1.2 \times 10^{13}$  cm<sup>-2</sup> (b).

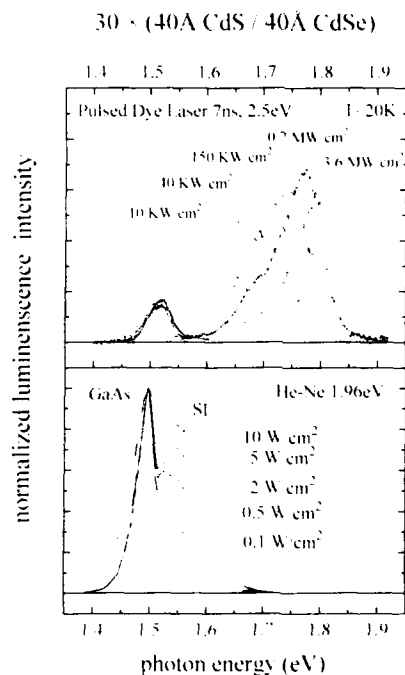


Fig. 2. Emission spectra of a CdS/CdSe SL (30 × 6 nm CdS / 6 nm CdSe) under increasing CW excitation with a He-Ne laser and under pulsed ns excitation at 20 K.

transmission spectra (DTS) (Fig. 4), which is caused by a blue shift of the minibands in analogy to the behaviour of the emission in Fig. 2. We resolve three different minibands. An extension of these measurements to higher pump powers and an exact identification of the structures are under way.

### 3. Conclusion and outlook

It has been shown that CdS/CdSe SL show promising linear and nonlinear optical properties in the red part of the spectrum, complementing thus the ZnSe-based structures for the blue-green spectral range. The growth and the emission wavelength of these structures are both compatible with standard AlGaAs MQW structures. The shift of the emission due to screening of the internal piezo-fields is 0.4 eV, more than an

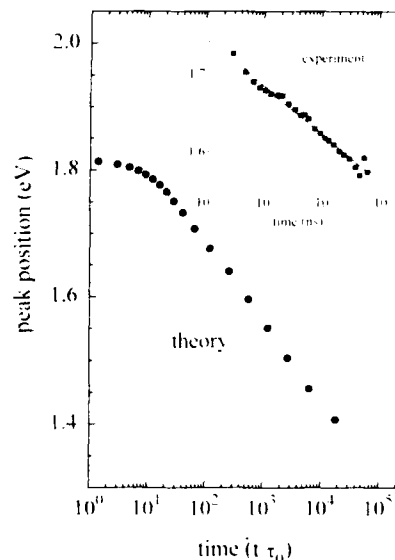


Fig. 3. Calculated and measured shift of the emission maximum as function of time after ps pulsed excitation.

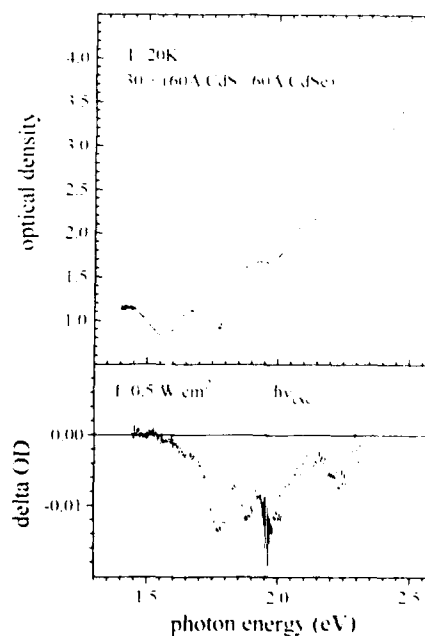


Fig. 4. Absorption spectrum and DTS spectrum of a CdS/CdSe SL at 20 K.



order of magnitude larger than the one obtained with external fields in SEED devices based on the QCSE. Consequently, interesting aspects of application may emerge for this system in the future.

#### 4. Acknowledgement

This work has been supported by the Deutsche Forschungsgemeinschaft.

#### 5. References

- [1] J. Cibert, R. André, C. Bodin, G. Feuillet, P.H. Jouneau and Le Si Dang, in: Europhysics Conf. Abstracts 17A, SC XVII (Phys. Scripta, to be published).
- [2] X. Chen, P.J. Parbrook, C. Treager-Cowan, B. Henderson, K.P. O'Donnell, M.P. Halsall, J.J. Davies, J.E. Nichols, P.J. Wright and B. Cockayne, *Semicond. Sci. Technol.* 5 (1990) 997.
- [3] M.P. Halsall, J.E. Nicholls, J.J. Davies, B. Cockayne and P.J. Wright, *J. Appl. Phys.* 71 (1992) 907.
- [4] D. Wolverson, M.P. Halsall and J.J. Davies, *Semicond. Sci. Technol.* 6 (1991) A123.
- [5] M. Grün, U. Becker, Th. Gilsdorf, M. Hetterich, H. Giessen, H. Zangerle, M. Müller, J. Loidolt, F. Zhou and C. Klingshirn, in: *Proc. 21st Int. Conf. on Physics of Semiconductors*, Beijing, 1992, Eds. Ping Jiang and Hou-Zhi Zeng (World Scientific, Singapore, 1992).
- [6] M. Grün, M. Hetterich, C. Klingshirn, A. Rosenauer, J. Zweck and W. Gebhardt, *J. Crystal Growth* 138 (1994) 150.
- [7] W. Langbein, H. Kalt, M. Hetterich, M. Grün and C. Klingshirn, *Appl. Phys. Lett.*, submitted.
- [8] DAB Miller, D.S. Chemla and S. Schmitt-Rink, *Phys. Rev. B* 33 (1986) 6976, and references therein.
- [9] C. Klingshirn, H. Kalt, M. Umlauff, W. Petri, F.A. Majumder, S.V. Bogdanov, W. Langbein, M. Grün, M. Hetterich, K.P. Geysers, M. Heuken, A. Naumov, H. Stanzl and W. Gebhardt, *J. Crystal Growth* 138 (1994) 786.

## Resonant Brillouin scattering in biaxially strained ZnSe

H. Mayer <sup>a</sup>, U. Rössler <sup>\*a</sup>, S. Permogorov <sup>b,1</sup>, H. Stolz <sup>b</sup>, H. Vogelsang <sup>b</sup>,  
W. von der Osten <sup>b</sup>

<sup>a</sup> *Institut für Theoretische Physik, Universität Regensburg, D-93040 Regensburg, Germany*

<sup>b</sup> *Fachbereich Physik, Universität-GHS Paderborn, D-33098 Paderborn, Germany*

### Abstract

Resonant Brillouin scattering experiments have been performed in the 1S exciton region of ZnSe layers grown on GaAs substrate. Information about the biaxial strain in the ZnSe epilayer, the exchange splitting  $\delta$ , and the longitudinal-transverse splitting  $\Delta_{\text{LT}}$  can be obtained by comparing the experimental Stokes shifts with those calculated from the dispersion of the 1S exciton-polariton in the strained crystal. For these calculations we used a Hamiltonian which contains the kinetic energy of the exciton center-of-mass motion, the electron-hole exchange interaction and the strain-induced effects. The polariton dispersion is calculated using a multi-component oscillator model. We find a quantitative agreement between the calculated and experimental Stokes shifts for a biaxial strain of  $+0.03\%$  and exchange parameters  $\delta = 0.4$  meV and  $\Delta_{\text{LT}} = 1.2$  meV.

### 1. Introduction

Resonant Brillouin scattering (RBS) of exciton-polaritons is a very useful tool for investigating the polariton dispersion in the spectral region of the exciton resonance [1]. For a given energy of the incident photon, the scattered light spectra show various lines with lower (Stokes) or higher (anti-Stokes) energy, due to polariton scattering by emission or absorption of an acoustic phonon. Sweeping the photon frequency through the excitonic resonance yields a whole system of observed shifts, from which the polariton dispersion can be deduced.

About one decade ago, resonant Brillouin scattering experiments in ZnSe bulk material have

been used to determine a complete set of parameters for this material [2]. Recently, RBS could be observed in a ZnSe epitaxial layer grown on GaAs [3]. In the present paper we report the detailed analysis of these experiments.

Lattice mismatch and different thermal expansion coefficients of the GaAs substrate and ZnSe cause a biaxial strain in the epilayer upon cooling down the sample from the growth temperature of 340°C down to 2 K. In addition to an overall shift of the 1S exciton resonance, the strain also modifies the internal structure of the resonance. A theoretical model which describes the dispersion of the 1S exciton-polariton [4] will be applied to explain the experimentally observed Stokes shifts.

### 2. Experiment

The epitaxial ZnSe layers (thickness 10  $\mu\text{m}$ ) were grown by conventional metalorganic vapor

<sup>\*</sup> Corresponding author.

<sup>1</sup> Permanent address: A.F. Ioffe Physico-Technical Institute, 194021 St. Petersburg, Russian Federation.

phase epitaxy (MOVPE) technique on (100) oriented GaAs substrates at  $T = 340^\circ\text{C}$  using extremely pure source materials. The optical measurements at  $T = 2\text{ K}$  were performed in a  $90^\circ$  scattering geometry with the light entering the epilayer under Brewster's angle ( $\alpha_B \sim 70^\circ$ ). Due to the large refractive index of ZnSe ( $n \approx 2.85$ ), this geometry corresponds to nearly  $180^\circ$  backscattering with the propagation directions of incident and scattered light oriented under angles of  $20^\circ$  and  $7^\circ$  to the surface normal [3].

For excitation we used a pulsed dye laser (pulsewidth 33 ps, average excitation power  $10\text{ W/cm}^2$ ) synchronously pumped at 76 MHz by the third harmonics of a mode-locked Nd-YLF laser. The emission of the sample was dispersed by a double grating monochromator and detected by a microchannel plate photomultiplier operating in single photon counting mode (time resolution 50 ps). Compared to the usual method of Brillouin spectroscopy, by sampling the intensity only during the laser pulse our technique allows to efficiently discriminate the fast scattering lines from the longer lived luminescence background that has plagued previous investigations [2].

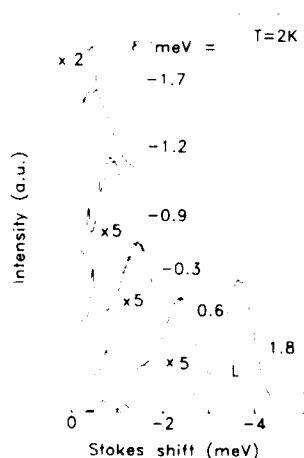


Fig. 1. Brillouin scattering spectra under resonant excitation of the 1S exciton transition. The scattered intensity at energy  $E_s$  is plotted against the Stokes shift  $E_s - E_i$  with the excitation photon energy  $E_i$  given as  $\epsilon = E_i - 2802\text{ meV}$ . The Brillouin lines are indicated by vertical bars.

For above-bandgap excitation the emission spectra of our samples contain strong free but comparatively weak bound exciton luminescence, implying a high purity of the samples. Tuning the excitation laser frequency into resonance with the free exciton transitions leads to the appearance of additional strong narrow lines with pronounced resonance behaviour (Fig. 1). Their shift with respect to the exciting laser line depends on the laser energy resulting in a strong dispersive behaviour (see Fig. 3). This allows one to interpret these lines as due to RBS of exciton-polaritons.

The clear occurrence of Brillouin scattering indicates the very high quality of our samples. It means that inelastic scattering by acoustic phonons constitutes the most important mechanism of exciton relaxation and that elastic scattering in  $k$ -space by impurities or defects does not blur this process significantly.

### 3. Theory

For a quantitative analysis of the experiment a detailed description of the dispersion of the polariton states is needed. We use the Hamiltonian given in ref. [4] to describe the 1S exciton states, including the effects of electron-hole exchange interaction (or fine-structure splitting), the effect of biaxial strain and the influence of a finite centre-of-mass wave vector.

The electron-hole exchange Hamiltonian is written as

$$H_{\text{exch}} = \delta_0 + \frac{1}{8}\delta(3 - 4\sigma \cdot J) + H_{\text{L-T}}, \quad (1)$$

where  $\delta$  is the exchange energy and  $H_{\text{L-T}}$  gives the longitudinal-transverse splitting  $\Delta_{\text{L-T}}$ .

For biaxial strain  $\epsilon_{\text{biax}}$  along a [001] crystal axis, the strain tensor components are given by  $\epsilon_{xx} = \epsilon_{yy} = \epsilon_{\text{biax}}$  and  $\epsilon_{zz} = 2\epsilon_{\text{biax}}s_{12}/(s_{11} + s_{12})$ , with the compliance constants  $s_{11}$  and  $s_{12}$ .

Diagonalization of the  $8 \times 8$  Hamiltonian matrix yields the exciton energies  $\omega_{\text{exc},i}(\mathbf{k})$  and the corresponding eigenvectors for given  $\mathbf{k}$  and  $\epsilon_{\text{biax}}$ , from which the oscillator strengths  $\beta_i(\mathbf{k})$  can be calculated [4]. The polariton energies  $\omega_{\text{pol},n}(\mathbf{k})$

result from a multi-component polariton expression [5]:

$$\epsilon(\mathbf{k}, \omega) = \frac{k^2 c^2}{\omega^2} + \epsilon_b + \sum_{i=1}^8 \frac{4\pi\beta_i(\mathbf{k})\omega_{\text{exc},i}^2(\mathbf{k})}{\omega_{\text{exc},i}^2(\mathbf{k}) - \omega^2}, \quad (2)$$

where  $\epsilon_b$  is the background dielectric constant.

Once the polariton dispersion is obtained, it is straightforward to deduce the resulting Stokes shifts for emission of acoustic phonons. For the phonon wave vectors involved in RBS experiments the phonon frequency is linear in the wave vector and determined by the sound velocity  $v_s$ . For the quasi-backscattering geometry used in the experiment the wave vectors of incident and scattered photon are approximately  $\mathbf{k}_i = (0, 0, k_i)$  and  $\mathbf{k}_s = (0, 0, -k_s)$ . The conservation laws for momentum and energy for scattering from polariton branch  $m$  to polariton branch  $n$  for the Stokes process thus read:

$$k_i + k_s = q, \quad (3)$$

$$\omega_{\text{pol},n}(-k_s) - \omega_{\text{pol},m}(k_i) = -v_s q. \quad (4)$$

Solving these conditions for given energy  $E = \hbar\omega_{\text{pol},m}$  of the incident photon yields the desired Stokes shifts

$$S_{m,n}(E) = \omega_{\text{pol},n}(k_s) - \omega_{\text{pol},m}(k_i). \quad (5)$$

For the experimental setup described above there are two dipole-active exciton components, which give three polariton branches, usually labelled as U (upper), I (intermediate) and L (lower). Scattering may occur between any of these, thus leading to at most nine Stokes or anti-Stokes lines.

#### 4. Results

A parameter set for unstrained ZnSe has been determined by Sermage and Fishman ( $\delta = -0.08$  meV,  $\Delta_{1,1} = 1.45$  meV) [2]. Reflection data obtained from the strained crystal, however, indicate that a significantly different value has to be used for the exchange parameter  $\delta$  [3]. Moreover,

the exchange parameter  $\delta$  as determined by fitting to experimental data in ref. [2] was found to be negative in contrast to general considerations according to which  $\delta$  has to be positive.

The biaxial strain in the ZnSe layer is due to two effects: (1) Due to lattice mismatch between the GaAs substrate and the ZnSe epilayer of  $-0.25\%$  there is a compressive strain, which in the growth process is relaxed up to an unknown extent  $\epsilon_{340^\circ\text{C}}$ . (2) Upon cooling down the sample from the growth temperature ( $340^\circ\text{C}$ ) to 2 K, an additional tensile strain  $\epsilon_{\text{therm}} = +0.09$  results from the different thermal expansion coefficients:

$$\epsilon_{\text{therm}} = \int_{340^\circ\text{C}}^{2\text{K}} [\alpha_{\text{GaAs}}(T) - \alpha_{\text{ZnSe}}(T)] dT. \quad (6)$$

The biaxial strain in the epilayer is the net effect of both strains:

$$\epsilon_{\text{biax}} = \epsilon_{340^\circ\text{C}} + \epsilon_{\text{therm}}. \quad (7)$$

The value of  $\epsilon_{\text{biax}} = +0.03\%$  was determined by fitting the calculated Stokes shifts to the experimental values using the parameter set of ref.

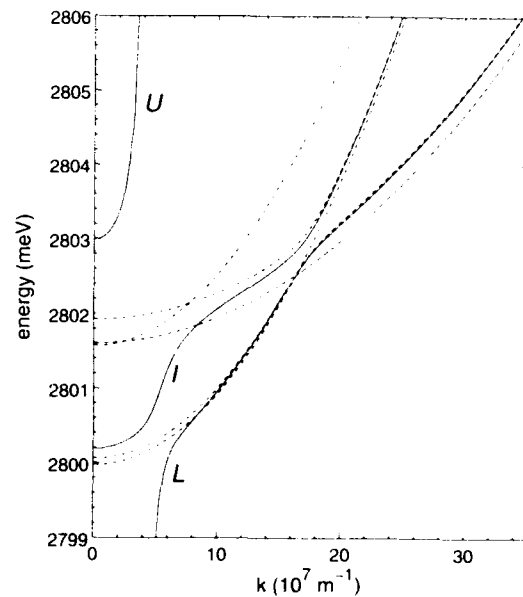


Fig. 2. Calculated 1S exciton (dashed lines) and polariton (solid lines) branches for  $\mathbf{k} \parallel [001]$  and  $[001]$  biaxial strain  $\epsilon_{\text{biax}} = +0.03\%$ .

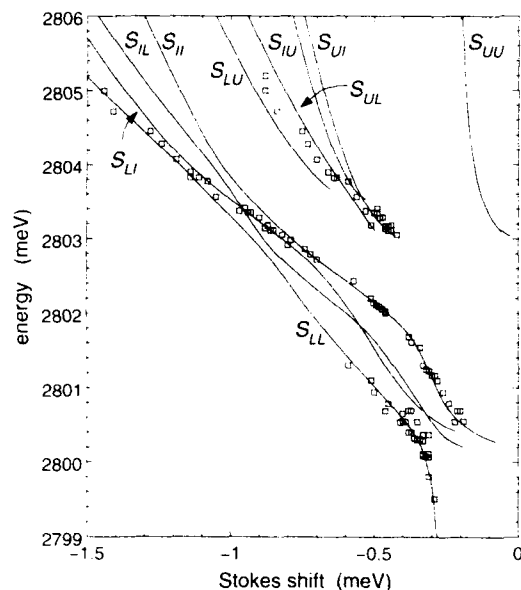


Fig. 3. Experimental Stokes shifts and calculated shifts for  $\epsilon_{\text{biax}} = +0.03\%$ .

[2] and the deformation potentials and compliance constants from the Landolt-Börnstein tables [6]. This value of  $\epsilon_{\text{biax}}$  means that the compressive strain at growth temperature was  $\epsilon_{340^\circ\text{C}} = -0.06\%$  and is overcompensated by the thermal effect to give a tensile strain at 2 K. This fit was then improved by variation of  $\delta$  and  $\Delta_{\text{LT}}$ . We found best agreement for  $\delta = 0.4$  meV and  $\Delta_{\text{LT}} = 1.2$  meV.

The resulting polariton dispersion and the Stokes shifts for  $\epsilon_{\text{biax}} = +0.03\%$  and our parameters are displayed in Figs. 2 and 3. For photon energies below 2800.6 meV, only a single Stokes line is observed, which can be ascribed to scattering between the lower polariton branch ( $S_{\text{LI}}$ ). With increasing photon energies, a second line

appears which is detected up to photon energies of 2805 meV. For energies below 2802.6 meV, this line is associated with scattering from and to the low-energy intermediate branch. For energies between 2802.6 and 2803.6 meV, it might be due to scattering from the high-energy lower branch to the low-energy intermediate branch. Finally, for energies above 2803.6 meV, this line is assigned to scattering from and to the high-energy lower branch. For energies above 2803 meV, an additional line shows up in the experiment, which is detected up to a photon energy of 2805.2 meV. This line is ascribed to scattering from the upper to the high-energy lower polariton branch. No scattering between the upper polariton branch ( $S_{\text{LU}}$ ) is observed, which is due to the stray light from the surface.

## 5. Acknowledgements

We acknowledge partial support of this work by the Deutsche Forschungsgemeinschaft and the Bayerische Forschungsförderung (FOROPTO).

## 6. References

- [1] C. Weisbuch and R.G. Ulbrich, in: *Light Scattering in Solids III*, Eds. M. Cardona and G. Güntherodt (Springer, Berlin, 1982).
- [2] B. Sermage and G. Fishman, *Phys. Rev. B* 23 (1981) 5107.
- [3] S. Permogorov, H. Stolz, H. Vogelsang, Th. Weber, W. von der Osten and A. Lebedev, *Solid State Commun.*, to be published.
- [4] D. Fröhlich, F. Kubacki, M. Schlierkamp, H. Mayer and U. Rössler, *Phys. Status Solidi (b)* 177 (1993) 379.
- [5] G.D. Mahan and J.J. Hopfield, *Phys. Rev.* 135 (1964) A428.
- [6] Landolt-Börnstein New Series, Vol. III/22a, *Semiconductors*, Eds. O. Madelung and M. Schulz (Springer, Berlin, 1987).



ELSEVIER

Journal of Crystal Growth 138 (1994) 199–203

JOURNAL OF  
**CRYSTAL  
GROWTH**

## Alloy broadening in photoluminescence spectra of $\text{Cd}_{1-x}\text{Zn}_x\text{Te}$ crystals grown from Te solution

K. Suzuki <sup>\*a</sup>, N. Akita <sup>a</sup>, K. Inagaki <sup>a</sup>, A. Nishihata <sup>a</sup>, N. Takojima <sup>a</sup>, S. Dairaku <sup>b</sup>

<sup>a</sup> Hokkaido Institute of Technology, Sapporo, Hokkaido 006, Japan

<sup>b</sup> Sumitomo Metal Mining Co., Ltd., Ohme, Tokyo 198, Japan

### Abstract

The excitonic line broadening of both donor and acceptor bound excitons in bulk  $\text{Cd}_{1-x}\text{Zn}_x\text{Te}$  crystal grown from Te solution has been investigated. The maximum linewidth of 3 meV for the neutral donor bound exciton ( $\text{D}^0\text{X}$ ) emission is for the first time determined and is in excellent agreement with the existing theory. On the other hand, the linewidth of 10 meV for the acceptor bound exciton ( $\text{A}^0\text{X}$ ) in a highly alloyed sample seems to be incompatible with the theory. With an increase in measurement temperature, the  $\text{A}^0\text{X}$  emission quenches much faster with larger red shift than the  $\text{D}^0\text{X}$  emission. This observation indicates that the binding energy of the exciton to the acceptor itself is distributed. In addition to the generally accepted alloy broadening mechanism (microscopic compositional fluctuation), this distribution is probably the cause of the  $\text{A}^0\text{X}$  line broadening.

### 1. Introduction

The excitonic line broadening due to microscopic compositional fluctuation in  $\text{Cd}_{1-x}\text{Zn}_x\text{Te}$  crystals is reported for MBE grown thin films [1] and THM grown bulk crystals [2]. The linewidth of 10 meV for neutral copper bound exciton emission in highly alloyed samples [2], however, seems to be much larger than the value expected from the recent theoretical work of Zimmermann [3]. According to the theory, a maximum linewidth of as much as 3 meV is expected for bound exciton emission in  $\text{Cd}_{1-x}\text{Zn}_x\text{Te}$  crystal. Oettinger et al. [2] proposed a “pseudo-donor” model in order to account for this large discrepancy.

Cohen et al. [4] investigated the alloy broadening for very limited compositions ( $x = 0.03$  and  $0.1$ ) in their literature on the damping processes of excitons in  $\text{Cd}_{1-x}\text{Zn}_x\text{Te}$ . However, no systematic investigations on the broadening of donor bound exciton emission ( $\text{D}^0\text{X}$ ) line width of this material have been reported. We therefore measured the composition dependent broadening of both donor and acceptor bound exciton lines in donor doped  $\text{Cd}_{1-x}\text{Zn}_x\text{Te}$  crystals grown from Te solution.

### 2. Experimental procedure

The samples used for the measurements were grown from Te solution. The growth temperature was about 200°C lower than the melting point

\* Corresponding author.

because of the starting composition in excess of Te ((Cd,Zn):Te = 3:7). Indium-doped CdTe crystal ( $1 \times 10^{16} \text{ cm}^{-3}$ ) grown by conventional gradient freeze method and purchased ZnTe polycrystal (6N) were used as starting materials. The growth ampoule was set in a 3-zone furnace whose temperature was electrically controlled to realize the relative translation motion between the ampoule and the furnace. In order to cover the complete  $x$  range, several ingots with different Zn/Cd ratio were grown. Since Vegard's law is valid in this alloy system [5], the composition of the crystals was determined from the change in the lattice constant by using X-ray diffraction measurements. The composition of some of the samples was also measured by proton induced X-ray emission (PIXE) method. Good agreement was obtained between those two methods. Details of the growth and the crystalline quality of the solution grown  $\text{Cd}_{1-x}\text{Zn}_x\text{Te}$  crystals will be reported separately.

The grown samples were sliced, polished and etched with 3% Br in methanol solution. Some of the samples were sliced parallel to the (111) face and their etch pit densities were measured by using Nakagawa etchant [6]. A dislocation density of as low as  $2 \times 10^4 \text{ cm}^{-2}$  was obtained for all samples, irrespective of the composition  $x$ . Electrical properties were investigated by Hall measurements with the Van der Pauw configuration. All the grown crystals ( $0 < x \leq 1$ ) show p-type conduction with a residual carrier concentration of about  $10^{14}$  to mid- $10^{15} \text{ cm}^{-3}$ .

The temperature dependence of the photoluminescence (PL) was measured by using the 488 nm line of an  $\text{Ar}^+$  ion laser as an excitation source. The samples were set in a variable-temperature Dewar and were immersed in cold He gas. The temperature was stabilized in  $\pm 0.2 \text{ K}$  over 9.3–70 K. The PL light was analyzed by a 1 m Jobin–Yvon double monochromator and processed with a photon-counting system. Another equipment was used for the measurements of the excitation intensity dependence of PL. The measurements were performed at 4.2 K by a conventional lock-in technique. The samples were freely suspended in liquid He. The 514.5 nm line of an  $\text{Ar}^+$  ion laser was used as the excitation source.

The range of excitation intensity was controlled over nearly three orders of magnitude by using neutral density filters. The PL signal was detected by a photomultiplier with a cooled GaAs cathode through a 1.5 m Jobin–Yvon single monochromator.

### 3. Results and discussion

Fig. 1 shows an example ( $x = 0.74$ ) of the PL spectrum at 9.3 K. Except for its energy position, the spectral line shape itself is qualitatively similar to those reported by Cohen et al. [4] for  $x = 0.03$ . Furthermore, it is almost unchanged for a wide range of composition ( $0 < x < 1$ ). The spectral components are therefore deduced to be the lines due to free excitons, neutral donor bound excitons ( $\text{D}^0\text{X}$ ) and neutral acceptor bound excitons ( $\text{A}^0\text{X}$ ), as labeled in the figure. In addition,

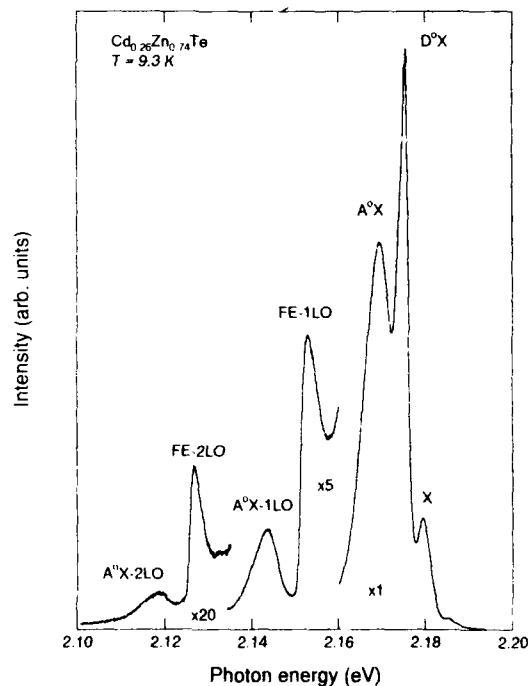


Fig. 1. Typical photoluminescence spectrum of bulk  $\text{Cd}_{1-x}\text{Zn}_x\text{Te}$  crystal grown from Te solution measured at 9.3 K for  $x = 0.74$ .

the LO-phonon sidebands of the free exciton and the  $A^0X$  are clearly seen in the lower energy side of the principal bound exciton region. On the other hand, no phonon sidebands for  $D^0X$  emission are detected, indicating that the phonon coupling is much stronger in the  $A^0X$  transition than in that of the  $D^0X$ , as is usually the case in binary CdTe crystal.

Fig. 2 shows the logarithm of the integrated emission intensity ( $I$ ) of near-band-edge lines plotted versus the logarithm of the excitation intensity ( $I_e$ ) for the sample with  $x = 0.12$ . As it is seen from the figure, both lines show roughly (though not completely) linear  $\log(I) - \log(I_e)$  dependence ( $I \sim I_e^k$ ) at the lower excitation region with a slope  $k$  of about 1.2. The super-linear ( $k > 1$ ) dependence is a characteristic feature of bound exciton recombination [7]. Identifications of these lines as due to  $A^0X$  and  $D^0X$  recombination are thus confirmed. Since In was introduced in the starting material CdTe, it is natural to conclude the origin of the donor to be In on Cd site. On the other hand, since no acceptor impurity was intentionally introduced during growth, residual Cu is the most probable candidate.

The broadening widths of both  $D^0X$  and  $A^0X$  are plotted against  $x$  in Fig. 3, where the contri-

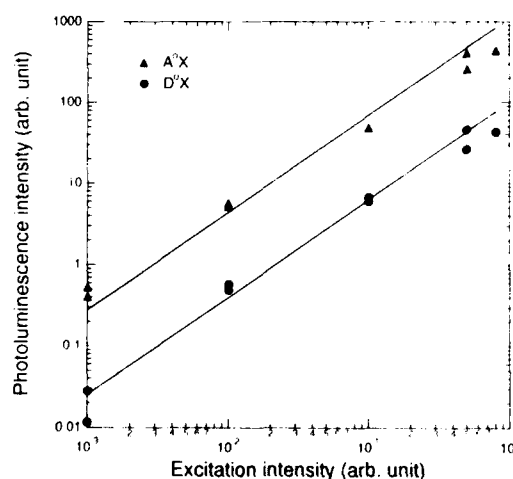


Fig. 2. Dependence of the luminescence intensity on excitation intensity for near-band-edge emission lines. The solid line indicates the  $I \sim I_e^k$  law with  $k = 1.2$ .

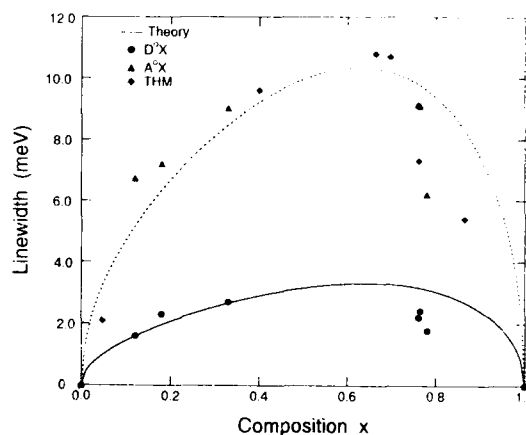


Fig. 3. Alloy broadening of  $A^0X$  and  $D^0X$  as a function of composition  $x$ . The solid line is based on Eq. (1) with the parameters described in the text. The dashed line is to guide the eye. Data labeled as THM are taken from ref. [2].

bution of the binary compounds is subtracted. Although they show characteristic alloy broadening features, the linewidth of  $A^0X$  is much larger than that of  $D^0X$ . The resultant maximum linewidth of as large as 10 meV for  $A^0X$  is in good agreement with the values previously reported [1,2]. On the other hand, the maximum linewidth of 3 meV for  $D^0X$  is measured for the first time. This large discrepancy in the broadening width of  $A^0X$  and  $D^0X$  was previously pointed out by Cohen et al. [4]. In the literature, the phenomenon was explained by the difference in the effective mass Bohr radii of neutral donor and acceptor. We believe, however, that the exciton radius itself has a decisive role in determining the broadening width.

In binary alloy CdTe, the corresponding linewidths are 0.4 and 0.3 meV for  $D^0X$  and  $A^0X$ , respectively, and in ZnTe only the  $A^0X$  line is observed with its FWHM of 0.6 meV. This small difference of  $A^0X$  and  $D^0X$  linewidths in the binary alloy cannot account for the large difference in the ternary. The calculated linewidth based on the theory [3] is also drawn in the figure. The dependence of the Gaussian linewidth on composition  $x$  is

$$\sigma^2(x) = \left( \frac{dE(x)}{dx} \right)^2 x(1-x) \frac{V_0(x)}{V_1(x)}. \quad (1)$$



where  $V_0$  is a quarter of the volume of the unit cell, because there are four cations in the unit cell of the zinc-blende structure.  $dE(x)/dx$  is the slope of the bound exciton transition energy with respect to  $x$ . Since the dependence of  $E(x)$  on  $x$  is in quite good agreement with the result reported by Olego et al. [1], we employ Eq. (2) of ref. [1] as  $dE/dx$  in our calculation.  $V_1$  is the volume probed by the exciton recombination transition and is given by [3]

$$V_1 = 8\pi a_b^3, \quad (2)$$

where  $a_b$  is the exciton radius. The linear interpolation between  $a_{b,\text{CdTe}}$  (64.9 nm) and  $a_{b,\text{ZnTe}}$  (53.5 nm) is used for the calculation. As is seen from the figure, the broadening width of the  $D^0X$  emission is in excellent agreement with the value expected theoretically; on the other hand, it is clear that the linewidth of the  $A^0X$  is incompatible with the theory. In order to elucidate this large discrepancy between the  $A^0X$  linewidth and the theoretical one, the temperature dependence of the luminescence has been investigated.

Fig. 4 shows the logarithm of the integrated emission intensities of two excitonic transitions versus inverse temperature for  $x = 0.74$ . In the lower temperature region, the  $A^0X$  reduces its intensity rather rapidly as compared with  $D^0X$ , while in the higher temperature region both lines have almost the same quenching rate against temperature. The thermal quenching of both  $A^0X$  and  $D^0X$  can be fitted with well-known two-step dissociation processes [8] expressed as

$$\frac{I_t}{I_0} = \left[ 1 + C_1 \exp\left(-\frac{E_1}{kT}\right) + C_2 \exp\left(-\frac{E_2}{kT}\right) \right]^{-1}, \quad (3)$$

where  $C_1$  and  $C_2$  are the pre-exponential factors for each dissociation step. For the  $D^0X$  transition,  $E_1$  is 4.4 meV and  $E_2$  is 14 meV, while for the  $A^0X$  transition,  $E_1$  is 1.7 meV and  $E_2$  is 14.5 meV. The binding energies of  $A^0X$  and  $D^0X$  are estimated by measuring the energy separation from free exciton emission to be 10 and 4.0 meV, respectively, in this sample. The good agreement between the value of  $E_1$  and the binding energy of  $D^0X$  indicates that the first dissociation pro-

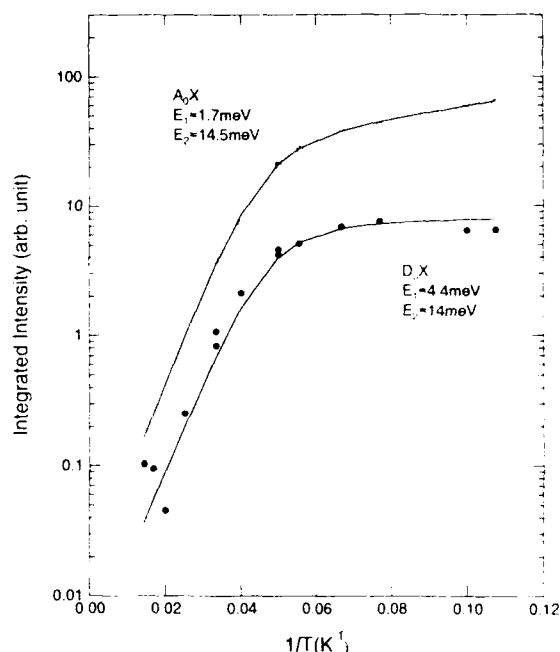


Fig. 4. Temperature dependence of the integrated luminescence intensity of the  $A^0X$  and  $D^0X$  bands for  $x = 0.74$ .

cess in the  $D^0X$  emission is the thermalization of bound exciton into free (extended) state. On the other hand, for  $A^0X$  emission,  $E_1$  is much smaller than the binding energy. In III–V semiconductors, ionization of neutral  $A^0X$  to  $A^-X$  is proposed as the first dissociation process [8]. However, in II–VI alloys, because of the large effective mass ratio ( $m_h \gg m_e$ ), such a process is ruled out [9]. Fig. 5 shows the temperature dependence of the peak positions of both  $A^0X$  and  $D^0X$  lines. With increasing temperature, the peak position of the  $A^0X$  emission shifts to much lower energy than that of  $D^0X$  emission. This larger red shift and the smaller  $E_1$  energy of the  $A^0X$  emission can be explained as follows: Assuming that the binding energy of the exciton to the neutral acceptor is not unique but spread in energy, then with an increase in temperature, the shallower part of the distribution will thermalize first, leaving a combination between much deeper states and resulting in a lower energy of the luminescence. This is the reason for such a distribution in the

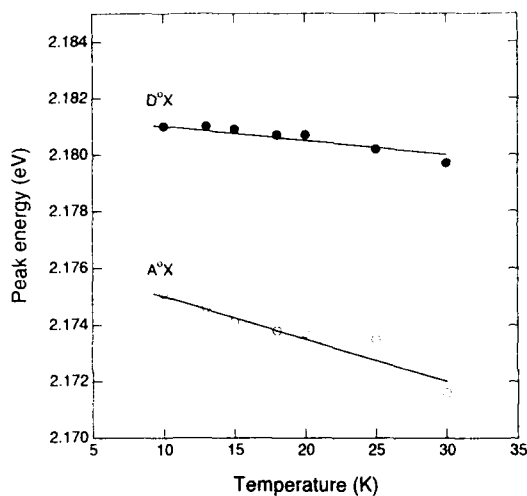


Fig. 5. Temperature dependence of the peak energy of the A<sup>0</sup>X and D<sup>0</sup>X lines for  $x = 0.74$ .

binding energy is not clear at the moment; however, since the acceptor state has originated mainly from the p orbitals, its energy location will be very much affected if the bond length and/or the bond angle fluctuate by alloying. As is well known, a highly distorted anion sublattice was predicted in EXAFS measurement [5]. Almost no effect on the broadening width of D<sup>0</sup>X is consistent with the s character of the donor state.

#### 4. Conclusion

The alloy broadening of donor and acceptor bound exciton has been investigated on Cd<sub>1-x</sub>Zn<sub>x</sub>Te crystals grown from Te solution. Special attention is paid to the different broadening width of A<sup>0</sup>X and D<sup>0</sup>X emission lines. In

addition, the broadening of the D<sup>0</sup>X in Cd<sub>1-x</sub>Zn<sub>x</sub>Te crystal is for the first time investigated systematically. The obtained maximum linewidth of 3 meV for the D<sup>0</sup>X emission is in excellent agreement with the theory. From the temperature dependence of PL measurement, evidence of the distribution in the exciton binding energy to neutral acceptor is found. In addition to the generally accepted broadening mechanism, it seems that this distribution has a decisive role for the alloy broadening of A<sup>0</sup>X emission.

#### 5. Acknowledgments

We would like to thank T. Haga of the Hokkaido University for PIXE measurements and S. Seto of the Ishikawa College of Technology for fruitful discussions.

#### 6. References

- [1] D.J. Olego, J.P. Faurie, S. Sivanathan and P.M. Raccach, *Appl. Phys. Lett.* 47 (1985) 1172.
- [2] K. Oettinger, D.M. Hofmann, A.L. Efros, B.K. Meyer, M. Salk and K.W. Benz, *J. Appl. Phys.* 71 (1992) 4523.
- [3] R. Zimmermann, *J. Crystal Growth* 101 (1990) 346.
- [4] E. Cohen, R.A. Street and A. Muranevich, *Phys. Rev. B* 28 (1983) 7115.
- [5] N. Motta, A. Balzarotti, P. Letradi, A. Kisiel, M.T. Czyzyk, M. Zinnal-Stamawaska and M. Podgorny, *Solid State Commun.* 53 (1985) 509.
- [6] K. Nakagawa, K. Maeda and S. Takeuchi, *Appl. Phys. Lett.* 34 (1979) 574.
- [7] T. Schmidt, G. Daniel and K. Lischka, *J. Crystal Growth* 117 (1992) 748.
- [8] D. Bimberg, M. Sondergeld and E. Grobe, *Phys. Rev. B* 4 (1971) 3451.
- [9] R.E. Halsted, in: *Physics and Chemistry of II-VI Compounds*, Eds. M. Aven and J.S. Prener (North-Holland, Amsterdam, 1967) p. 394.



ELSEVIER

Journal of Crystal Growth 138 (1994) 204–207

JOURNAL OF  
**CRYSTAL  
GROWTH**

## Polarized photoluminescence in vacancy-ordered $\text{Ga}_2\text{Se}_3$

Tamotsu Okamoto <sup>a</sup>, Akira Yamada <sup>b</sup>, Makoto Konagai <sup>\*a</sup>, Kiyoshi Takahashi <sup>b</sup>

<sup>a</sup> Department of Electrical and Electronic Engineering, Tokyo Institute of Technology, 2-12-1, O-okayama, Meguro-ku, Tokyo 152, Japan

<sup>b</sup> Department of Physical Electronics, Tokyo Institute of Technology, 2-12-1, O-okayama, Meguro-ku, Tokyo 152, Japan

### Abstract

Optical properties of  $\text{Ga}_2\text{Se}_3$  films grown on (100)GaAs by molecular beam epitaxy (MBE) have been investigated by photoluminescence (PL) measurement at low temperature. In the vacancy-ordered  $\text{Ga}_2\text{Se}_3$  grown with a high VI/III ratio, a broad emission peak centered at around 610 nm was observed. Furthermore, the intensity of [01 $\bar{1}$ ] polarization component was much stronger than that of [011] polarization in the vacancy-ordered  $\text{Ga}_2\text{Se}_3$ . On the other hand, in the disordered  $\text{Ga}_2\text{Se}_3$  grown with a low VI/III ratio, PL intensity was extremely weak, and deep level emissions centered at around 750 and 900 nm were dominant.

### 1. Introduction

The III–VI compound semiconductor such as  $\text{Ga}_2\text{Se}_3$  is a promising material for new optoelectronic devices;  $\text{Ga}_2\text{Se}_3$  has a defect zincblende structure, in which 1/3 of the Ga sites are vacant, and has a relatively wide bandgap (around 2.1 eV at room temperature) [1,2]. Up until now, we investigated the molecular beam epitaxy (MBE) growth of  $\text{Ga}_2\text{Se}_3$  films on (100)GaP and (100)GaAs substrates, and it has been found that a superstructure, which has a periodicity three times as large as that for a zincblende structure in the [011] direction, was formed by spontaneous ordering of Ga vacancies under Se-rich growth conditions [3–7]. Furthermore, we have observed very large absorption anisotropy ( $\Delta\alpha > 10^4 \text{ cm}^{-1}$ ) in vacancy-ordered  $\text{Ga}_2\text{Se}_3$ ; the absorption coefficient for [01 $\bar{1}$ ] polarization is larger than that for

[011] polarization [5,6]. In this paper, we carried out polarized photoluminescence (PL) measurements of  $\text{Ga}_2\text{Se}_3$  films grown by MBE for further investigation of the optical properties of the  $\text{Ga}_2\text{Se}_3$ . There was no report on the PL of  $\text{Ga}_2\text{Se}_3$ , except the report on the deep level emission centered at 900 nm of bulk  $\text{Ga}_2\text{Se}_3$  [1]. This is the first report on the PL of  $\text{Ga}_2\text{Se}_3$  epitaxial thin films.

### 2. Experimental procedure

$\text{Ga}_2\text{Se}_3$  films were grown on SI (100)GaAs by MBE technique. The growth temperature was 500°C, and the VI/III ratio was varied in the range of 150 to 800. The growth rate was around 200 nm/h, and film thickness was around 800 nm. The [011] and [01 $\bar{1}$ ] directions of the substrates were determined by anisotropic etching. GaAs substrates were etched in a 3:1:1  $\text{H}_2\text{SO}_4:\text{H}_2\text{O}_2:\text{H}_2\text{O}$  solution at 60°C for 1.5 min.

\* Corresponding author.

followed by etching in a  $\text{Br}_2\text{-CH}_3\text{OH}$  solution for 2 min. After chemical etching, the substrates were introduced into the growth chamber. Thermal etching at high temperature was not carried out because it is difficult to control the vacancy ordering direction by the effect of As desorption from GaAs substrate. The evaluation of vacancy ordering was performed by electron diffraction and Raman spectroscopy.  $\text{Ar}^+$  laser (514.5 nm, 50 mW) was used for Raman spectroscopy.

PL measurements were carried out on the  $\text{Ga}_2\text{Se}_3$  films at 4.2–60 K. The 488.0 nm emission line of an  $\text{Ar}^+$  laser (NEC GLS3300) polarized along  $[01\bar{1}]$  was used as the excitation light. The excitation intensity was 200 mW if not specified. The spectra were analyzed with a Jobin-Yvon THR1000 monochromator and a Hamamatsu photonics 7102 photomultiplier tube.  $[01\bar{1}]$  and  $[011]$  polarization components of PL were measured by polarizer. Depolarizer was used for eliminating the polarization dependence of monochromator and photomultiplier.

### 3. Results and discussion

First of all, we investigated the PL of the vacancy-ordered  $\text{Ga}_2\text{Se}_3$ . As previously reported, the vacancy ordering occurs under Se-rich conditions [3–6]. Fig. 1a shows the polarized Raman spectra of the  $\text{Ga}_2\text{Se}_3$  grown at a high VI/III ratio (VI/III = 800). Raman spectra were mea-

sured for two configurations of  $Z[YY]\bar{Z}$  and  $Z[XX]\bar{Z}$ ; X, Y and Z denote  $[01\bar{1}]$ ,  $[011]$  and  $[100]$  direction, respectively. In Fig. 1a, a sharp peak located at  $155\text{ cm}^{-1}$ , which has originated in the zone-folding by vacancy ordering [7,8], was observed. Furthermore, the intensity of the peak in the  $Z[YY]\bar{Z}$  spectrum is much stronger than that in the  $Z[XX]\bar{Z}$ . These results indicate that long-range ordering of Ga vacancies toward  $[011]$  direction is highly developed. We confirmed that the vacancy-ordered superstructure was formed in  $[011]$  direction by transmission electron diffraction (TED). Fig. 1b shows the polarized PL spectra of the vacancy-ordered  $\text{Ga}_2\text{Se}_3$  films. The solid line and the dashed line denote  $[01\bar{1}]$  and  $[011]$  polarization component of PL spectra, respectively. A broad emission peak centered at around 610 nm was observed. The PL intensity increases at a wavelength of around 540 nm, and the energy corresponding to this wavelength is close to the reported bandgap of bulk  $\text{Ga}_2\text{Se}_3$  at 4.2 K, which is about 2.3 eV [1]. Furthermore, the PL spectra show an anisotropic feature; the intensity of the  $[01\bar{1}]$  polarization component is much stronger than that of  $[011]$  polarization. We confirmed that the anisotropy in emission was independent of the polarization of the excitation light. These results indicate that the electron transition probability for  $[01\bar{1}]$  polarization is larger than that for  $[011]$  polarization in vacancy-ordered  $\text{Ga}_2\text{Se}_3$ , and corresponds to the large absorption coefficient for  $[01\bar{1}]$  polarization [5,6].

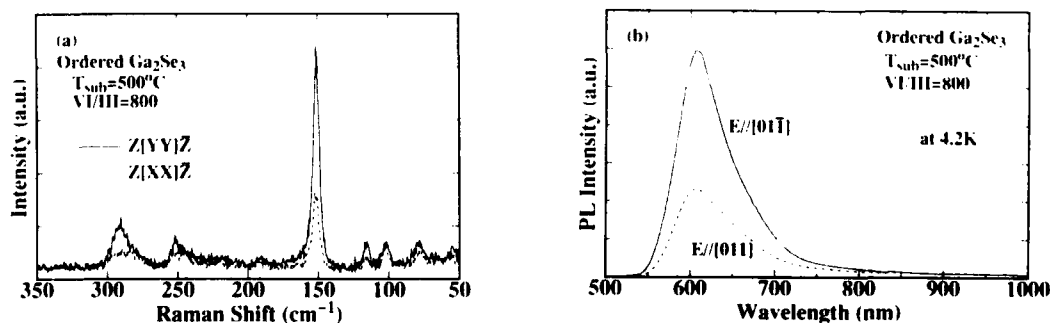


Fig. 1. (a) Polarized Raman spectra and (b) polarized photoluminescence spectra of the vacancy-ordered  $\text{Ga}_2\text{Se}_3$  grown with a high VI/III ratio (VI/III=800).

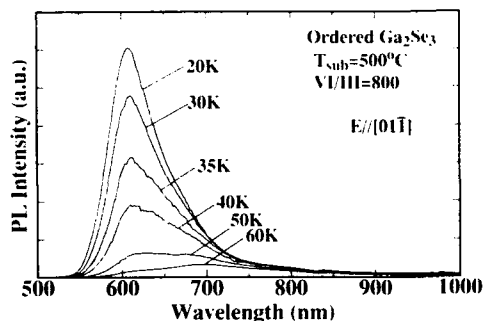


Fig. 2. Temperature dependence of PL spectra of the vacancy-ordered  $\text{Ga}_2\text{Se}_3$ .

However, the anisotropic feature in the PL peak energy, which was observed in the PL of the ordered  $\text{Ga}_{0.5}\text{In}_{0.5}\text{P}$  [9–11], was not observed.

Furthermore, we measured the temperature dependence of the PL in the vacancy-ordered  $\text{Ga}_2\text{Se}_3$ . Fig. 2 shows the temperature dependence of PL spectra of the vacancy-ordered  $\text{Ga}_2\text{Se}_3$  film shown in Fig. 1. The  $[01\bar{1}]$  polarization component of the PL was measured in Fig. 2. PL spectra were almost invariant below 20 K. However, a steep decrease of the intensity of the emission peak centered at around 610 nm was observed with temperature increasing above 20 K, and deep level emission at around 700 nm was dominant at 60 K. Furthermore, at a temperature of 40 K, the other emission peak at around 630 nm appears, which suggests that the broad emission peak at 610 nm is a mixture of many emission peaks. In addition, we measured the PL spectra at different excitation intensities. The ex-

citation intensity was varied in a range of 2 to 200 mW. The shift of emission peak with increasing excitation intensity was not observed, which indicates that the emission centered at 610 nm is no donor–acceptor pair emission.

For a comparison with the PL in the vacancy-ordered  $\text{Ga}_2\text{Se}_3$ , we investigated the PL of the disordered  $\text{Ga}_2\text{Se}_3$ . The disordered  $\text{Ga}_2\text{Se}_3$  was grown at a relatively low VI/III ratio (VI/III = 150) [3–6]. Fig. 3a shows the polarized Raman spectra of the  $\text{Ga}_2\text{Se}_3$  grown at a VI/III ratio of 150. The intensity of the peak located at  $155\text{ cm}^{-1}$ , which is associated with vacancy ordering, is very weak as compared with Fig. 1a. This indicates that the Ga vacancies are almost randomly distributed in this film [7,8]. Fig. 3b shows the polarized PL spectra of the disordered  $\text{Ga}_2\text{Se}_3$  films. As indicated in Fig. 3b, there is a remarkable difference in the PL spectra between the vacancy-ordered and the disordered  $\text{Ga}_2\text{Se}_3$ ; the intensity of PL at 610 nm is extremely weak, and deep level emissions centered at around 750 and 900 nm are dominant for the disordered  $\text{Ga}_2\text{Se}_3$ . The RHEED pattern of the disordered  $\text{Ga}_2\text{Se}_3$  was spotty, which indicates the epitaxial growth of  $\text{Ga}_2\text{Se}_3$ . Furthermore, in X-ray diffraction measurements, no differences of the intensities and FWHM of  $(400)\text{Ga}_2\text{Se}_3$  peak between the vacancy-ordered and the disordered  $\text{Ga}_2\text{Se}_3$  were observed, although the peak position shift was observed [4]. From these results, we speculated that the difference of PL spectra between the vacancy-ordered and the disordered  $\text{Ga}_2\text{Se}_3$  is not due to the poor crystallinity of the disordered

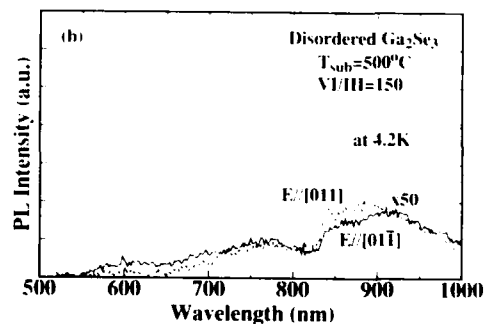
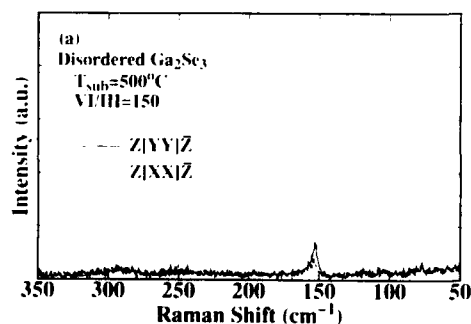


Fig. 3. (a) Polarized Raman spectra and (b) polarized photoluminescence spectra of the disordered  $\text{Ga}_2\text{Se}_3$  grown with a low VI/III ratio (VI/III = 150).

$\text{Ga}_2\text{Se}_3$  and that the PL emission centered at 610 nm might have originated in the vacancy ordering of  $\text{Ga}_2\text{Se}_3$ .

#### 4. Conclusions

We investigated the optical properties of  $\text{Ga}_2\text{Se}_3$  films grown on (100)GaAs by MBE by photoluminescence (PL) measurement at low temperature, and the following results have been obtained:

- (1) In the vacancy-ordered  $\text{Ga}_2\text{Se}_3$  grown with a high VI/III ratio, a broad emission peak centered at around 610 nm was observed.
- (2) The intensity of the  $[0\bar{1}\bar{1}]$  polarization component was much stronger than that of  $[011]$  polarization in the vacancy-ordered  $\text{Ga}_2\text{Se}_3$ .
- (3) In the disordered  $\text{Ga}_2\text{Se}_3$  grown with a low VI/III ratio, PL intensity was extremely weak, and deep level emissions centered at around 750 and 900 nm were dominant.

#### 5. Acknowledgement

This work was partially supported by a Grant-in-Aid for General Scientific Research, of the

Ministry of Education, Science and Culture, No. 04452088.

#### 6. References

- [1] M. Springford, Proc. Phys. Soc. (London) 82 (1963) 1020.
- [2] G. Guzzetti and F. Meloni, Nuovo Cimento 1D (1982) 503.
- [3] N. Teraguchi, F. Kato, M. Konagai, K. Takahashi, Y. Nakamura and N. Otsuka, Appl. Phys. Lett. 59 (1991) 567.
- [4] N. Teraguchi, M. Konagai, F. Kato and K. Takahashi, J. Crystal Growth 115 (1992) L143.
- [5] T. Okamoto, N. Kojima, A. Yamada, M. Konagai, K. Takahashi, Y. Nakamura and K. Takahashi, Jap. J. Appl. Phys. 31 (1992) L143.
- [6] T. Okamoto, M. Konagai, N. Kojima, A. Yamada, K. Takahashi, Y. Nakamura and O. Nittono, J. Electron. Mater. 22 (1993) 229.
- [7] A. Yamada, N. Kojima, K. Takahashi, T. Okamoto and M. Konagai, Jap. J. Appl. Phys. 31 (1992) L186.
- [8] E. Finkman, J. Tauc, R. Kershaw and A. Wold, Phys. Rev. B 11 (1975) 3785.
- [9] A. Mascarenhas, S. Kurtz, A. Kibbler and J.M. Olson, Phys. Rev. Lett. 63 (1989) 2108.
- [10] T. Kanata, M. Nishimoto, H. Nakayama and T. Nishino, Phys. Rev. B 45 (1992) 6637.
- [11] G.W. 't Hooft, C.J.B. Riviere, M.P.C.M. Krijn, C.T.H.F. Liedtbaum and A. Valster, Appl. Phys. Lett. 61 (1992) 3169.



ELSEVIER

Journal of Crystal Growth 138 (1994) 208–212

JOURNAL OF  
**CRYSTAL  
GROWTH**

## Temperature dependence of luminescence in ZnSe and role of excitation transfer

G.-J. Yi, L. Radomsky \*, G.F. Neumark

*Department of Chemical Engineering, Materials Science and Mining Engineering, Columbia University, New York, New York 10027, USA*

### Abstract

Excitation transfer among localized states has often been neglected for semiconductor luminescence. We have recently shown that such transfer is far more prevalent in the low temperature luminescence in ZnSe than had been realized. In this work, we studied the temperature dependence of the luminescence, and observed the phonon-assisted transfer between two bound excitons at relatively high temperature. This observation correlates with the result of a theoretical model consisting of a two-level system. Our results also show that excitation transfer may well be playing a role in the origin of the blue room temperature luminescence in ZnSe.

In view of the interest in ZnSe for visible light emission, which culminated in the recent demonstration of the blue-green laser diode [1], the blue room temperature photoluminescence (PL) of this material has been studied in a number of investigations [2–6]. However, so far there has been no conclusive answer as to its origin. A recent overview [2] of the literature has stated that almost every conceivable emission has been suggested as being responsible for the blue PL at room temperature. In this paper, we will present evidence of phonon-assisted (“upward”) excitation transfer between two localized excitonic states as a function of temperature, and show that such a mechanism must be considered in connection with the origin of this blue PL. Our experimental results are also supported by a theoretical analysis of a two-level system which in-

cludes an interstate transfer term between these two excitons.

In characterizing the origin of room temperature blue luminescence in ZnSe [2–6], the usual approach is to study the temperature dependence of the PL spectra. Thus, the low temperature lines are quite well understood, and consequently, if one follows the low temperature luminescence lines to high temperature, one should be able to identify the origin of the blue luminescence. However, this simple scheme is complicated by the broadening of spectral lines with increasing temperature. In prior studies [2–5], the samples used were mostly n-type material because of the difficulties of preparing p-type ZnSe (e.g., good p-type has become available only recently, via a free radical nitrogen plasma source during molecular beam epitaxial growth [7]). At low temperature, the typical PL spectra of these n-type samples has a strong donor bound exciton (DBE) line, often together with weaker free exci-

\* Corresponding author.

ton (FE) lines on the higher energy side, and an acceptor bound exciton (ABE) line on the lower energy side. There are often also relatively strong (depending on the compensation in the material) donor–acceptor pair (DAP) peaks below the exciton range, but these will here be discussed only minimally because of their much lower energy position, which cannot account for the room temperature blue luminescence [8]. In connection with the prior [2–5] investigations, it is of interest to note that the ABE, when present, quenches appreciably faster than the DBE. This is surprising, since the ABE is deeper. Indeed, we do not see how this can be compatible with carrier transfer through the bands. We have recently investigated the recombination processes in Na doped ZnSe by time-decay measurements [9], and concluded that the excitation transfer among localized states is far more prevalent in semiconductor luminescence than had previously been realized. However, our previous experiments were primarily carried out in the low temperature ( $< 10$  K) regime, where carriers can only transfer to lower (or equal) energy states. We felt that, as temperature increases, there might also be an “upward” or phonon-assisted transfer from lower to higher energy states, which could explain the puzzling observation of the fast quench of ABE in n-type material. For this reason, we have chosen p-type compensated material, which, at low temperature, has a very strong ABE while still also showing the DBE. We have extended our temperature range in studying the PL spectra. The results not only support our previous conclusion about excitation transfer, but also show that it may well play a role in the blue room temperature PL in ZnSe.

The samples used here were grown by the zone melting technique, and were doped with Na [10]. We have measured the conductivity of these samples by the potential profiling technique [11], showing that they are p-type but highly resistive. The PL measurements are carried out in a closed-cycle refrigeration system (Janis) with a Lake Shore 805 temperature controller. The excitation source is a HeCd laser (Liconix 33101) with a lasing frequency of 325 nm and an output power of  $\sim 10$  mW. The actual power used for PL measurements is much less than the maximum

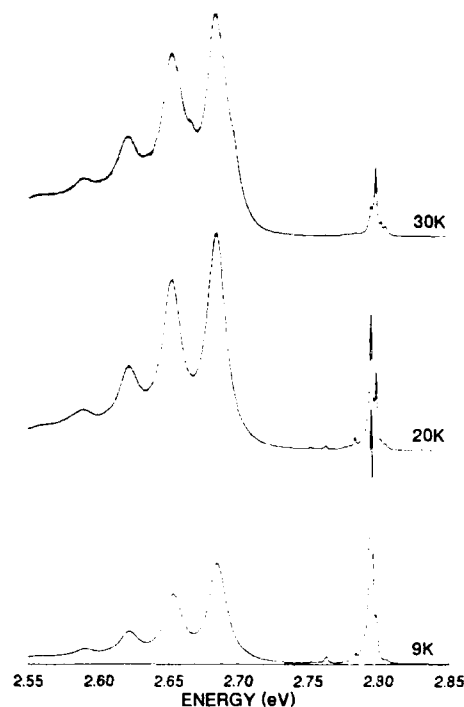


Fig. 1. Temperature dependence of the PL up to 30 K. The spectrum includes both the exciton range (2.78–2.81 eV) and the DAP luminescence, with a zero-phonon peak at 2.685 eV.

output in order to avoid heating of the samples. The luminescence is collected and directed into a 3/4 meter spectrometer (Jarrell–Ash) with 0.83 nm/mm spectral resolution, and recorded by a photon counting system (Stanford SR400).

A typical example of the PL spectra in the low temperature range (10–30 K) is shown in Fig. 1. At the lowest temperature ( $< 10$  K), the excitons dominate the spectrum; the DAP (with its phonon replicas) is clearly seen in the lower energy range, indicating the samples are compensated. The excitons quench rapidly with increasing temperature. By 20 K, the intensity of excitons is below the intensity of the DAP. At 30 K, a shoulder is seen on the high energy side of the DAP. This emission is called free-to-bound (FB) because the electron bound to the donor is thermalized into the conduction band, and results in the free-electron-to-bound-hole transition. At higher temper-



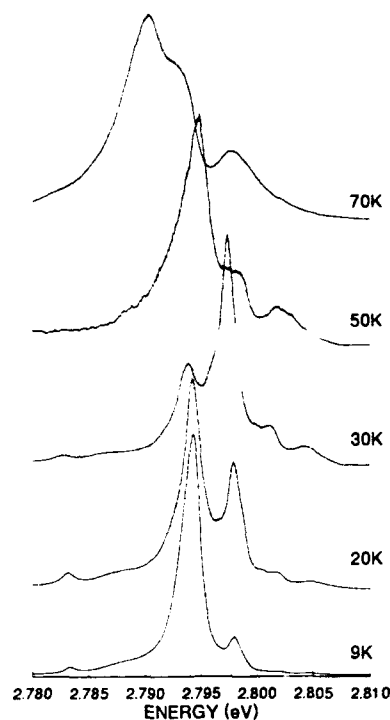


Fig. 2. Temperature dependence of the exciton luminescence up to 70 K. The spectrum at 9 K includes a main peak at 2.7943 eV which is the ABE due to Na acceptor, a DBE peak at 2.7980 eV, and two free excitons at 2.8019 and 2.8047 eV (lower and upper polaritons). Peak shifts are due to band gap changes with temperature.

ature ( $> 50$  K), all electrons are freed from the donors, and the DAP is replaced by the FB. The details of the exciton region (2.78–2.81 eV) as a function of temperature are shown in Fig. 2. At the lowest temperature (9 K), the ABE (Na) at 2.7943 eV is clearly the strongest luminescence line, with a weaker, and shallower, DBE at 2.7980 eV, and a pair of free excitons, FE(U) and FE(L), at 2.8047 and 2.8019 eV, respectively. The pair of FEs is due to the exciton–photon interaction [3], which is often referred to as polaritons, and correspond to the upper and lower branch of the polariton. The same type of emission has also been observed in other compound semiconductors [12,13]. As the temperature increases, first, we notice that the ABE quenches at a much faster rate than the DBE. By 30 K, the DBE is

clearly the main peak in the exciton range, and by 50 K the ABE is almost invisible. An additional trend is that the two FEs increase, although relatively slowly, with respect to the DBE. One can also note that the energy separation between the FE(L) and the FE(U) increases somewhat, with the FE(L) moving closer to the DBE. As a consequence of the increase in, and shift of, the FE(L), this peak merges with the DBE, and by 100 K (not shown) only a single broad peak remains. We have compared the peak positions of the DBE and FEs with the values of n-type ZnSe [2,3], and found that they are the same within experimental error.

The reason that the intensities of both FEs increase with respect to the BEs with increasing temperature may well be due to the thermal dissociation of the excitons bound to the impurities, since the binding energies of exciton to donor ( $\sim 6$  meV) and acceptor ( $\sim 10$  meV) are much smaller than the binding energy of the free exciton itself, which is about 20 meV. However, the relative intensity of ABE versus DBE in Fig. 2 cannot be explained by assuming thermal dissociation of excitons, since the DBE has a smaller binding energy than the ABE. This observation is also consistent with many other reports on the temperature dependence of excitons [2,3,13,14]. To explain this phenomenon, we propose that there must be a phonon-assisted (upward) excitation transfer from the lower ABE to the higher DBE energy states. The same conclusion has also been reached previously for CdTe [14].

To check our conclusion from the temperature dependence data, a theoretical model consisting of a two-level system has been analyzed by one of us [15]. Basically, the results indicate that, with a fast transfer rate between these two levels and with a relatively low excitation intensity, the main recombination path can change from a lower energy level to a higher one with increasing temperature. This conclusion corresponds to what we observed between the DBE and the ABE in Fig. 2. Furthermore, the time-resolved photoluminescence by Kudlek et al. [16] has shown indisputable evidence of energy transfer from DBE to ABE at low temperature (“downward” transfer), which is exactly the reverse process from our

phonon-assisted transfer at high temperature. With the support of the theoretical analysis [15] and the time-resolved data [9,16], we feel confident to say that the fact that the DBE dominates at relatively high temperature is the result of an upward transfer process. Further, such a transfer process may well also be affecting the FEs, but details of this aspect remain to be investigated.

It remains to discuss the relevance of our results for the blue room temperature PL. There is little doubt that up to about 50 K it is the DBE which dominates. Beyond this, as mentioned, the FE(L) gradually increases with respect to the DBE, and gradually decreases in peak energy, so that by 100 K it overlaps with the DBE. There now is one broad line, and the DBE and FE(L) can no longer be distinguished; however, projecting the gradual intensity increase of the FE(L), one would conjecture that it is this FE(L) which will now dominate. Nevertheless, this conjecture must be viewed with caution; thus our data indicates an energy shift of the FE(L) with respect to the FE(U), but past results [2,3] have claimed that the energy separation between the broad line and the FE(U) remains *constant*. This point remains to be investigated. It is still to be noted that at this time we cannot exclude the possibility that this apparent discrepancy is merely the result of different processes dominating in different samples.

There are also other explanations for the blue room temperature PL in the literature. One explanation is by Shirakawa and Kukimoto (SK) [3], who suggested a free hole to bound donor transition. They base this assignment on the observation of a "new" line (their A' line) on the low-energy side of the DBE. We note that this line is not observed by either Newbury [2,17] or ourselves. This may of course result from a sample dependence; alternative possibilities are either (1) that the A' line in Newbury's and our samples comes in at higher temperatures, where it can no longer be distinguished from the high-temperature single broad line, or (2) since the A' line is only a shoulder on the DBE line, with the consequence that it is difficult to obtain accurate line energies, it may be, instead, the ABE line. In any case SK argued against the DBE since they felt

the activation energy of the blue PL (27 meV) was too high to be consistent with the DBE. However, this argument is not valid in the presence of excitation transfer, since this can drastically change the thermalization of the DBE line. We also noted that the FE(L) line of ours and that of SK is about 20–29 meV below the bandgap, which is not inconsistent with the activation energy reported by SK. Zheng and Allen (ZA) [5], in support of the conclusion of SK, suggest that although the DBE line is in the right energy position, the binding energy of the DBE is too low for it to exist at room temperature. However, we have pointed out examples of shallower bound excitons enduring at higher temperature than the deeper ones. Certainly, with increasing temperature, the excitons do dissociate more readily, and the excitonic intensity does decrease with increasing temperature, as can be seen in Fig. 1. However, if other recombination paths are not very efficient, and the transfer to the excitons is fast, which seems to be the case [16], there can still be substantial PL via bound excitons. Similar to the result of SK, the energy position given by ZA for the blue luminescence is not inconsistent with the energy position of either the DBE or the FE(L).

In summary, the temperature dependence of the donor and acceptor bound excitons gives direct evidence of excitation transfer, in support of our previous conclusion derived from a different experimental approach. This observation is also consistent with a theoretical model of excitation transfer in a two-exciton system [15]. The origin of the room temperature blue luminescence, based on our data, appears to be either the DBE or the FE(L), or due to the combination of these two; nevertheless, we cannot exclude SKs bound-electron to free-hole suggestion, nor that the mechanism is sample dependent. Further investigations of this aspect are required.

This work was supported by the National Science Foundation grant DMR 91-21302. The samples were grown at Philips Laboratories, and we would like to thank Dr. M. Shone and Dr. B.J. Fitzpatrick for providing them.

## 1. References

- [1] M.A. Haase, J. Qiu, J.M. DePuydt and H. Cheng, *Appl. Phys. Lett.* 59 (1991) 1272.
- [2] P.R. Newbury, PhD Thesis, Columbia University (1990).
- [3] Y. Shirakawa and H. Kukimoto, *J. Appl. Phys.* 51 (1980) 2014.
- [4] J.C. Boulay, P. Blanconnier, A. Herman, Ph. Ged, P. Henoc and J.P. Noblanc, *J. Appl. Phys.* 46 (1975) 3549.
- [5] J. Zheng and J.W. Allen, *J. Appl. Phys.* 67 (1990) 2060.
- [6] S. Fujita, H. Mimoto and T. Noguchi, *J. Appl. Phys.* 50 (1979) 1079.
- [7] R.M. Park, M.B. Troffer, C.M. Rouleau, J.M. DePuydt and M.A. Haase, *Appl. Phys. Lett.* 57 (1990) 2127.
- [8] However, we do not exclude the possibility of their playing a role in affecting the intensity of excitons at high temperature due to a transfer process between excitons and DAP.
- [9] G.-J. Yi, J.A. Tuchman and G.F. Neumark, *Appl. Phys. Lett.* 58 (1991) 520;  
G.-J. Yi and G.F. Neumark, *J. Luminescence* 52 (1992) 243.
- [10] M. Shone, B. Greenberg and M. Kaczinski, *J. Crystal Growth* 86 (1988) 132;  
B.J. Fitzpatrick, T.F. McGee III and P.M. Harnack, *J. Crystal Growth* 78 (1986) 242.
- [11] G.F. Neumark, B.J. Fitzpatrick, P.M. Harnack, S.P. Herko, K. Kosai and R.N. Bhargava, *J. Electrochem. Soc.* 127 (1980) 983.
- [12] D.D. Sell, S.E. Stokowski, R. Dingle and J.V. DiLorenzo, *Phys. Rev. B* 7 (1973) 4568.
- [13] C. Uzan, H. Mariette and A. Muranevich, *Phys. Rev. B* 34 (1986) 8728.
- [14] H. Zimmermann, R. Boyn, C. Michel and P. Rudolph, *J. Crystal Growth* 101 (1990) 691.
- [15] G.F. Neumark, *Mater. Sci. Forum.* to be published.
- [16] G. Kudlek, A. Hoffman, R. Heitz, C. Fricke, J. Gutowski, G.F. Neumark and R.N. Bhargava, *J. Luminescence* 48& 49 (1991) 138.
- [17] Newbury's [2] explanation for the origin of the broad line is that it is due to a new emission line on the *high* energy side of the DBE. However, based on a closer examination of the data, we suggest that the so called "new" line is actually the lower branch of the polariton FE(L).



ELSEVIER

Journal of Crystal Growth 138 (1994) 213–218

JOURNAL OF  
**CRYSTAL  
GROWTH**

## Nonlinear optical switching fronts in CdS

R. Schmolke <sup>\*,a</sup>, E. Schöll <sup>a</sup>, M. Nägele <sup>b</sup>, J. Gutowski <sup>b</sup><sup>a</sup> *Institute of Theoretical Physics, Technical University of Berlin, Hardenbergstrasse 36, D-10623 Berlin, Germany*<sup>b</sup> *Institute of Experimental Physics, University of Bremen, P.O. Box 330440, D-28334 Bremen, Germany*

### Abstract

Nonlinear impurity-related optical switching at low temperatures was found in CdS at moderate illumination intensities. A theoretical analysis of this effect based on the bleaching of ionized acceptor states is performed with the help of generation-recombination kinetics and travelling field equations. We demonstrate by numerical simulation that the optical switching process involves a switching front that propagates from the front facet where the exciting laser light enters the crystal to the far end of the crystal. Experimental evidence for our theoretical prediction is presented. The experimental results were obtained with the help of a pump-and-probe experiment where the probe was perpendicular to the pump and placed at various positions along the crystal. The results show a clear dependence of the onset of the transmitted pulse with regard to the onset of the pump pulse on the position of the probe along the crystal. Problems associated with the experiment, i.e. that the results could only be obtained for a narrow regime of (temporal) mean pump intensities, are discussed.

### 1. Introduction

In previous experiments the transmissivity of not intentionally or lightly In-doped CdS crystals under moderate laser excitation with photon energies just below the fundamental absorption edge was studied [1,2]. The crystals were kept in superfluid helium and the laser light was pulsed as to avoid heating effects. A switching of the crystals from a state of low transmissivity into a state of high transmissivity was found. It was conjectured that the switching might be due to a transmissive optical bistability [1]. To find out if the crystals indeed perform such an optical bistability, we put forward a spatially homogeneous three-level

model containing the acceptor states, the donor states and the conduction band [3]. Similar to a proof for a particular two-level model [5], we showed that this spatially homogeneous three-level model does not exhibit transmissive optical bistability if the reflectivity of the crystal surfaces is below 33% [6]. This is the same condition for the occurrence of transmissive optical bistability as deduced for the particular two-level model. Since the natural surface reflectivity of CdS in the spectral range studied is only 25%, we excluded transmissive optical bistability as the underlying mechanism of the observed switching into a state of high transmissivity. However, within the framework of the spatially homogeneous three-level model, we showed that the switching reported in ref. [1] is due to the temporal form of the excitation [3].

\* Corresponding author.

Since the above result and further investigation [6] showed that the essential physics is also contained in a two-level model obtained by neglecting the donors, we have analysed the nonlinear spatio-temporal solutions that arise if one simulates an excitation as in the experiment with the help of a two-level model. Here we will review and extend our theoretical predictions already reported in ref. [7] and add an experimental result that supports the theory.

## 2. The two-level model

In contrast to our previous three-level model, where we considered the recombination of electrons in the conduction band as well as the recombination of electrons at neutral donor sites into neutral acceptor sites [3], we will now consider the recombination of electrons in the conduction band only. This can be interpreted as merging the two recombination channels contained in the previous model into an effective recombination channel. For the spatially homogeneous case our previous model then reduces to the following equations:

(i) The rate equation for the spatially homogeneous ionized acceptor density  $n_A(t)$  becomes

$$\frac{d}{dt}n_A(t) = -W_A N_{ph}(t) n_A(t) + T_A^* [N_A - n_A(t)] n(t). \quad (1)$$

Here  $W_A$  is the transition coefficient for the photoexcitation of electrons from ionized acceptor sites into the conduction band,  $T_A^*$  is the transition coefficient for the recombination of electrons in the conduction band into neutral acceptor states,  $N_A$  is the density of acceptor states and  $N_{ph}$  is the density of photons in the crystal.

(ii) The local charge neutrality condition, which yields the spatially homogeneous density  $n(t)$  of carriers in the conduction band, becomes

$$n(t) = N_A - n_A(t). \quad (2)$$

(iii) The equations for the travelling field amplitudes  $E^\pm(z, t)$  propagating in the  $\pm z$  direction remain

$$\begin{aligned} \frac{\partial}{\partial t}E^\pm(z, t) \pm v_g \frac{\partial}{\partial z}E^\pm(z, t) \\ = -\frac{\Gamma W_A}{2}n_A(t)E^\pm(z, t). \end{aligned} \quad (3)$$

The travelling field amplitudes are normalized, e.g., to  $\text{cm}^{3/2}$ .  $\Gamma$  is the confinement factor and  $v_g$  is the velocity of the laser light in the crystal.

(iv) The boundary conditions for the travelling field amplitudes remain

$$\begin{aligned} E^+(0, t) &= \sqrt{1-r^2}E_{in}(t) - \sqrt{r^2}E^-(0, t), \\ E^-(d, t) &= -\sqrt{r^2}E^+(d, t), \\ E_{out}(t) &= \sqrt{1-r^2}E^+(d, t). \end{aligned} \quad (4)$$

Here,  $r^2$  is the reflectivity of the CdS surface in the spectral range studied.  $E_{in}(t)$  and  $E_{out}(t)$  are the travelling field amplitudes of the incident and transmitted laser light, respectively, and  $d$  is the thickness of the crystal in  $z$  direction.

(v) The spatially averaged photon density  $N_{ph}(t)$  is still given by

$$\begin{aligned} N_{ph} = \frac{1}{d} \int_0^d dz \left[ \left| E^+ \left( z, t - \frac{d-z}{v_g} \right) \right|^2 \right. \\ \left. + \left| E^- \left( z, t + \frac{d-z}{v_g} \right) \right|^2 \right]. \end{aligned} \quad (5)$$

When extending the above equations to the spatially inhomogeneous situation in the direction of the light propagation ( $z$  direction), one has to discuss in which way the standing wave pattern created by the light beams propagating in the  $+z$  and  $-z$  directions has to be taken into account, since effects due to the standing wave pattern can lead to transmissive optical bistability for surface reflectivities below 33% [8]. For the case we are considering, this leads to the question in how far the distribution of the acceptors allows for a spatial modulation of a  $z$ -dependent ionized acceptor density  $n_A(z, t)$  on the scale set by the standing wave pattern. This can be answered by calculating the mean distance between two neigh-

bouring acceptors,  $\langle \Delta z \rangle = N_A^{-1/3}$ . With  $N_A \approx 10^{16} \text{ cm}^{-3}$  we find  $\langle \Delta z \rangle \approx 5 \times 10^{-6} \text{ cm}$ . The scale set by the standing wave pattern of the light in the crystal is  $S_{\text{char}} \approx \lambda_L / (2\epsilon_x)$  with  $\lambda_L \approx 480 \text{ nm}$  [1] being the vacuum wavelength of the light and  $\epsilon_x \approx 5.5$  [9] being the dynamic dielectric function at infinite frequency. From this we find  $S_{\text{char}} \approx 10^{-5} \text{ cm}$ . So we find that the mean distance between two acceptors corresponds to the distance between two nodes of the standing wave pattern. Thus the standing wave pattern does not have to be taken into account when extending the above model to the spatially inhomogeneous situation in the longitudinal direction.

Secondly, one has to discuss the influence of drift and diffusion processes associated with the electrons in the conduction band. To do this, one has to consider the length and time scales associated with the drift-diffusion process and those either set by the experimental set-up or given by the slowly-varying amplitude approximation which was made to derive Eq. (3). To be consistent with the slowly-varying amplitude approximation, we have to restrict ourselves to length scales ( $\lambda_{\text{char}}$ ) much larger than the wavelength of the exciting laser light in the crystal and to time scales ( $\gamma_{\text{char}}$ ) much longer than the inverse laser light frequency. This restriction is in accordance with the experimentally used spatial and temporal resolution. The length scale  $\lambda$  and the time scale  $\gamma$  associated with the drift-diffusion problem are the effective Debye length and the effective Maxwell dielectric relaxation time, respectively. For parameters which are typical for CdS at low temperatures, we have outlined that  $\lambda/\lambda_{\text{char}}, \gamma/\gamma_{\text{char}} \ll 1$  [7]. Thus drift-diffusion can be treated in a perturbative way similar to the singular perturbation theory, which in leading order yields the model equations:

$$\begin{aligned} \frac{\partial}{\partial t} n_A(z, t) = & -W_A N_{\text{ph}}(z, t) n_A(z, t) \\ & + T_A^* [N_A - n_A(z, t)] n(z, t), \end{aligned} \quad (6)$$

$$n(z, t) = N_A - n_A(z, t), \quad (7)$$

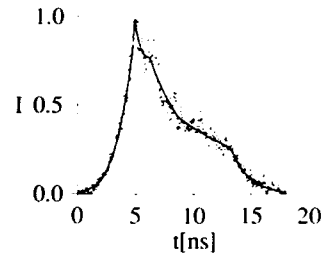


Fig. 1. Fit (line) to an experimental incident laser light pulse (dots). The intensity is normalized to unity.

$$\begin{aligned} \frac{\partial}{\partial t} E^+(z, t) \pm v_g \frac{\partial}{\partial z} E^+(z, t) \\ = - \frac{\Gamma W_A}{2} n_A(t) E^+(z, t), \end{aligned} \quad (8)$$

$$N_{\text{ph}}(z, t) = |E^+(z, t)|^2 + |E^-(z, t)|^2, \quad (9)$$

for the spatially inhomogeneous situation in the direction of the light propagation. The boundary conditions for  $E^+(z, t)$  are still given by (4).

In the next section we will analyse the spatio-temporal dynamics associated with an excitation of a CdS crystal as applied in ref. [1].

### 3. Front-like solutions

To simulate an excitation as used in ref. [1], we fitted an experimentally obtained excitation pulse as shown in Fig. 1. Using the fit and scaling it in a way that its temporal mean incident intensity corresponded to  $100 \text{ kW/cm}^2$ , we obtained the results illustrated in Figs. 2 and 3 for a system of 2 mm thickness and a surface reflectivity of 25%.

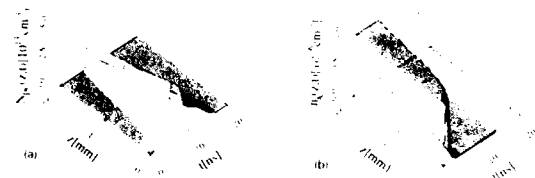


Fig. 2. Spatio-temporal evolution (a) of the photon density and (b) of the ionized acceptor density while an incident laser light pulse with a shape as shown in Fig. 1 was applied. The temporal mean incident intensity of the pulse was  $100 \text{ kW/cm}^2$ ,  $r^2$  was 25% and  $d$  was 2 mm.

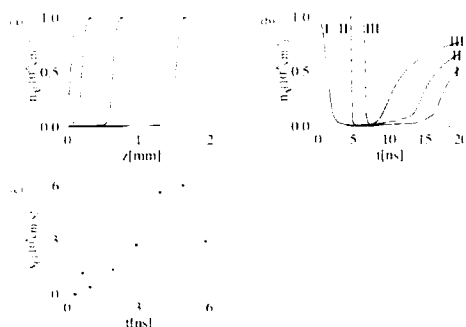


Fig. 3. Results of the simulation for a crystal with  $d = 2$  mm and  $r^2 = 25\%$ . The temporal mean incident intensity  $\bar{I}_p$  of the pulse was  $100 \text{ kW/cm}^2$ . (a) Ionized acceptor density as a function of the spatial position  $z$  for different  $t = 1.3$  ns, 2.6 ns, 3.9 ns, 5.2 ns (from left to right). (b) Ionized acceptor density as a function of time  $t$  for three different positions along  $z$ , i.e. for  $z = 0$  (I),  $z = 1$  mm (II) and  $z = 2$  mm (III). (c) Front velocity  $v_f$  as a function of time.

The latter value corresponds to the natural surface reflectivity of CdS in the spectral range studied.

Figs. 2a and 2b depict the spatio-temporal photon and ionized acceptor density, respectively. Clearly front-like structures emerge that traverse the crystal and do not reoccur while the incident intensity decreases. Note that  $N_{ph}(0, t)$  is given by the square of the sum composed of

$$(1 - r^2)I_0(t)/(h\omega r_g) \quad \text{and} \quad rE^-(0, t),$$

with  $I_0(t)$  being illustrated in Fig. 1 and  $\omega$  being the frequency of the exciting laser light.

Fig. 3a shows the ionized acceptor density as a function of  $z$  for  $t = 1.3$  ns, 2.6 ns, 3.9 ns and 5.2 ns. As is obvious, the front moves at a nonuniform velocity  $v_f$ . By analysing the time evolution of the deflection point of  $n_A(z, t)$  one can get an estimate of  $v_f$  as a function of time (Fig. 3c). The maximum  $v_f$  is about  $6 \times 10^8 \text{ cm/s}$ . It can be intuitively understood that the shape of  $v_f(t)$  follows the shape of  $I_0(t)$  (Fig. 1) within the time period during which the front-like structure exists in the crystal in the following way: Neglecting recombination, the characteristic time which the front needs to bleach a characteristic penetration depth – given by the absorption length

$v_g/(FW_A N_A)$  – is determined by  $\tau = 1/(W_A N_{ph}(z_f, t))$  (see Eq. (6)).  $N_{ph}(z_f, t)$  represents the photon density at time  $t$  at the position  $z_f$  of the front. As long as the front is not too close to the far end of the crystal  $E^-(z, t)$  will be negligible compared to  $E^+(z, t)$  at the front position. Finally, the regions passed by the front can be considered as entirely bleached (Fig. 3a), so that  $\tau$  can be approximated by  $1/[W_A(1 - r^2)|E_m|^2(t)]$ . Since  $I_0(t) = h\omega r_g |E_m|^2(t)$ , we find for this particular simulation

$$v_f \approx (1 - r^2)I_0(t)/(FN_A h\omega). \quad (10)$$

Finally Fig. 3b illustrates the ionized acceptor density as a function of time for three different positions along the crystal (front (I), centre (II) and back (III)). Since  $n_A(z, t)$  is proportional to the absorption coefficient, this figure illustrates that the transmissivity switches up (i.e.,  $n_A$  switches down) at different times for the different positions along the crystal.

#### 4. Experiment

With reference to Fig. 3b we tried to gain experimental evidence of the switching front by using the experimental set-up shown in Fig. 4: A pump pulse of intensity  $I_p$  is directed onto a CdS crystal of 2 mm thickness. The temporal mean incident intensity  $\bar{I}_p$  was  $100 \text{ kW/cm}^2$ . Perpendicular to the pump a probe beam with temporal mean intensity  $\bar{I}_0 = 1 \text{ kW/cm}^2$  was applied at different positions along the crystal (front, centre and back corresponding to A, B and C in Fig. 4.

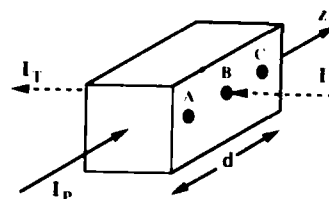


Fig. 4. Sketch of the experimental set-up used to observe the switching front.  $I_p$ , pump laser intensity, and  $I_0$  and  $I_1$  incident and transmitted probe laser intensity. A, B and C are positions of the incident probe laser beam.

respectively). There was no delay between the pump and the probe pulse. The intensity  $I_T$  of the probe pulse transmitted by the crystal was measured and compared with its intensity before traversing the sample (Fig. 5). Fig. 5a shows the transmitted ( $\alpha$ ) and incident ( $\beta$ ) probe pulses as a function of time for the three different positions along the crystal, and Fig. 5b depicts  $I_T/I_0$  over time. In Fig. 5a, the pulses were normalized so that the incident and the transmitted intensities as a function of time coincide at the beginning of the excitation for each of the positions along the crystal. Note that consequently curves ( $\alpha$ ) and ( $\beta$ ) are normalized by different units. The closer the probe laser is to the front facet where the pump laser enters the crystal, the sooner occurs the switch-up of the induced transmissivity with regard to the pump pulse. The induced transmissivity shows up as an increased intensity in ( $\alpha$ ) relative to the incident intensity

( $\beta$ ). This can be interpreted as a bleaching front of the pump pulse which travels through the crystal in  $z$  direction, and behind which the bleached region leads to a high induced transmissivity for the probe pulse (see also Fig. 3b).

With the help of Fig. 5b we can estimate the velocity  $v_F$  of the switching front: At the far side the up-switch occurs about 1 ns later than at the near side. Since the crystal has a thickness of about 2 mm, we get an order of magnitude  $v_F \approx 2 \times 10^8$  cm/s. This is about 3 times smaller than the peak velocity of  $v_F$  predicted theoretically for the same situation as in the experiment.

## 5. Discussion

According to our investigations, the switching observed in ref. [1] is associated with a switching front which moves through the crystal. The

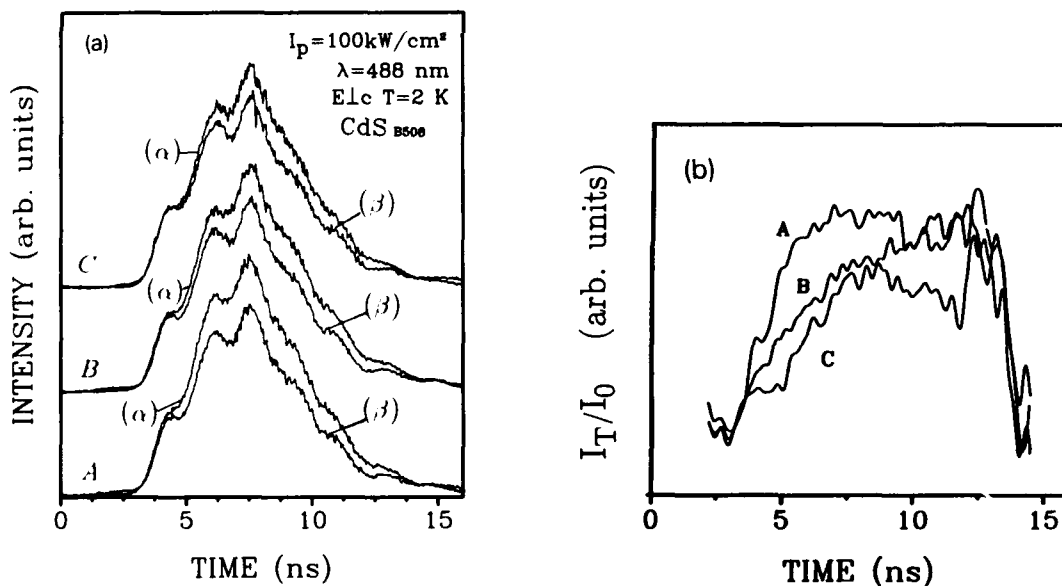


Fig. 5. (a) Measured intensity of the transmitted ( $\alpha$ ) and the incident ( $\beta$ ) probe pulse as a function of time for various positions of the probe laser along the crystal (A, B and C). (b) Measured transmissivity  $I_T/I_0$  as a function of time for the various positions along the crystal.  $I_T$  denotes the transmitted and  $I_0$  the incident intensity both of the probe pulse. The crystal was kept at 2 K. The wavelength  $\lambda$  emitted by the pump laser as well as by the probe laser was 488 nm and the transversal electric field  $E$  emitted by each of the lasers was perpendicular to the  $c$  axis of the crystal. The temporal mean incident intensity  $I_p$  of the pump pulse was  $100 \text{ kW/cm}^2$  and that of the probe pulse ( $I_0$ ) was  $1 \text{ kW/cm}^2$ . The thickness of the crystal was 2 mm.



switching front separates the bleached spatial region from the unbleached one. It moves at a velocity not constant in time. We have presented for the first time a theoretical estimate of the peak velocity dependent on the temporal mean incident intensity applied (see (10)).

Experimental evidence has been given for our theoretical result. The problem related with the experiment, however, is that we could find the results depicted in Fig. 5 only in a narrow regime of temporal mean pump intensities. We conjecture that this is due to the following two facts:

- (i) If  $\bar{I}_p$  is chosen too low, the data become too noisy, making an analysis with regard to the switching front impossible.
- (ii) If  $\bar{I}_p$  is chosen too high, then  $v_F$  will be too fast to be detectable by nanosecond experiments.

## 6. Acknowledgements

The financial support of the Deutsche Forschungsgemeinschaft (DFG) is gratefully ac-

knowledged. M.N. and J.G. thank R. and I. Broser for supplying the CdS crystal.

## 7. References

- [1] T. Hönig and J. Gutowski, *Phys. Status Solidi (b)* 150 (1988) 833.
- [2] T. Hönig and J. Gutowski, *Phys. Status Solidi (b)* 159 (1990) 363.
- [3] R. Schmolke, E. Schöll and J. Gutowski, *J. Crystal Growth* 117 (1992) 650.
- [4] P.N. Butcher and D. Cotter, *The Elements of Nonlinear Optics* (Cambridge University Press, Cambridge, 1990).
- [5] B.S. Ryvkin, *Soviet Phys. Semicond.* 19 (1985) 1.
- [6] R. Schmolke, PhD Thesis, Technical University of Berlin (Köster, Berlin, 1993).
- [7] R. Schmolke, E. Schöll, M. Nägele and J. Gutowski, *Adv. Mater. Opt. Electron.*, in press.
- [8] F. Henneberger, *Phys. Status Solidi (b)* 137 (1986) 371.
- [9] I. Broser, R. Broser and I. Rosenzweig, in: *Landolt-Börnstein*, Vol. III/17b, Eds. K.-H. Hellwege and O. Madelung (Springer, Berlin, 1982).



ELSEVIER

Journal of Crystal Growth 138 (1994) 219–224

JOURNAL OF  
**CRYSTAL  
GROWTH**

## Photoluminescence of vapor and solution grown ZnTe single crystals

Y. Biao <sup>a</sup>, M. Azoulay <sup>a</sup>, M.A. George <sup>a</sup>, A. Burger <sup>\*a</sup>, W.E. Collins <sup>a</sup>, E. Silberman <sup>a</sup>,  
C.-H. Su <sup>b</sup>, M.E. Volz <sup>b</sup>, F.R. Szofran <sup>b</sup>, D.C. Gillies <sup>b</sup>

<sup>a</sup> Center for Photonic Materials and Devices, Department of Physics, Fisk University, Nashville, Tennessee 37208, USA

<sup>b</sup> Space Science Lab, Marshall Space Flight Center, Huntsville, Alabama 35812, USA

### Abstract

ZnTe single crystals grown by horizontal physical vapor transport (PVT) and by vertical traveling heater method (THM) from a Te solution were characterized by photoluminescence (PL) at 10.6 K and by atomic force microscopy (AFM). Copper was identified by PL as a major impurity existing in both crystals, forming a substitutional acceptor,  $\text{Cu}_{\text{Zn}}$ . The THM ZnTe crystals were found to contain more Cu impurity than the PVT ZnTe crystals. The formation of  $\text{Cu}_{\text{Zn}}\text{-V}_{\text{Te}}$  complexes and the effects of annealing, oxygen contamination and intentional Cu doping were also studied. Finally, the surface morphology analyzed by AFM was correlated to the PL results.

### 1. Introduction

High purity and good quality single crystals of ZnTe have been grown by various techniques over the years for their potential application as visible light emitting devices. Most of them were grown at temperatures below the melting point (1290°C) of ZnTe, which improved the crystalline perfection and reduced the possibility of contamination from or through crucibles. However, relatively high levels of unintentional dopants, particularly Cu, have been usually found in the grown crystals [1,2]. Similar to other direct-gap semiconductors, the low temperature PL spectrum of ZnTe crystals consists of three regions: (A) shallow-level free or bound excitons (2.25–2.39 eV); (B) donor–acceptor pair (DAP) recombination

(2.10–2.25 eV); and (C) deep-level defects, such as vacancy complexes (1.60–2.10 eV). The free-exciton recombinations were identified at 2.381 eV for  $(\text{X})_{n-1}$ , 2.391 eV for  $(\text{X})_{n-2}$  and 2.392 eV for  $(\text{X})_{n-3}$ , and a direct energy gap ( $E_g$ ) of 2.3941 eV was estimated by photoluminescence at 1.6 K [3]. A center is considered simple when an impurity or a vacancy occupies a Zn or the Te lattice site, such as  $\text{Cu}_{\text{Zn}}$  and  $\text{V}_{\text{Te}}$ , and contributes a single additional charge carrier; its energy levels are analogous to that of hydrogen. Consequently, the activation energy of the single carrier bound to the substitutional impurity is close to that calculated from the hydrogen model. The typical emission of  $\text{A}_1^{\text{Cu}}$ , a Cu acceptor substituting for Zn atoms, has been found at 2.3746 eV in the 1.6–4.0 K temperature range, although its emission peak is sometimes observed to broaden and shift towards lower energy as the temperature and Cu concentration increase [4,5]. In high qual-

\* Corresponding author.

ity ZnTe crystals, the two-hole transition, having an energy difference  $A_2^{\text{Cu}} - A_1^{\text{Cu}}$  of 125 meV, may be used as evidence for Cu impurity.

Deep level emissions were sometimes observed in the PL spectra of PVT grown ZnTe crystals. These levels are very broad and have too high a binding energy to be hydrogenic centers, so they are referred to as complex centers. Besides Zn vacancy and Te vacancy complexes, deep levels associated with O, Cu, Mn, Pb, Sn, and some other transition metals could become part of these complexes. As the binding energy of an electron or a hole bound to a single substitutional impurity increases, the interaction of the electron with the lattice vibrations or the electron–phonon coupling gets stronger. In this particular case the longitudinal optical (LO) phonon coupling is by far the strongest because of the polarization field associated with it. The phonon energies of LO( $\Gamma$ ), LO(X), LA, TO( $\Gamma$ ) and TA were measured to be 26.1, 23.6, 13.6, 22.5 and 5.7 meV, respectively [3]. In this work we have performed low temperature PL measurements of ZnTe crystals grown by PVT and THM in order to identify the presence of impurities and native defects associated with these growth techniques. The morphology of the crystal surfaces were analyzed by AFM and correlations to the PL spectra were obtained.

## 2. Experimental procedure

Single crystals of ZnTe were grown without any intentional doping by two different techniques: horizontal physical vapor transport (PVT ZnTe) and vertical traveling heater method from tellurium solution (THM ZnTe). In order to confirm the nature of the impurities in both the PVT and THM grown crystals, Cu was diffused into the PVT ZnTe crystals by depositing a thin film of Cu onto its wafers, annealing them for 1 h at 250°C, and then removing the remaining Cu film by etching. As a reference, another as-grown PVT crystal went through the same annealing procedure, but without Cu deposition. Previous chemical analysis data and low temperature IR transmission measurements indicated that the PVT ZnTe single crystals had a better overall purity

than the THM ZnTe crystals [2]. Both of them and PVT ZnTe:Cu crystals were further aged at ambient for about 6 months, and then annealed under vacuum at 600°C for 1 h. The samples were either cleaved or polished and etched, with a 5% bromine in methanol solution, for PL and AFM measurements.

Low temperature PL measurements were performed on crystal samples which were cooled down to 10.6 K by a APD Cryogenic Inc system equipped with dual HC-4MK1 helium compressors. The 488.0 nm line, with power of 15 mW/mm<sup>2</sup>, from an ILT 5500A air-cooled argon ion laser was selected for excitation. The PL spectra were recorded using a Spex 1877D Triplemate Spectrophotometer and a liquid nitrogen cooled CCD detector. In the spectrograph stage of the spectrometer, a 30  $\mu$ m slit and a 300 grooves/mm grating were employed.

The surface morphology of the single crystals was studied by atomic force microscopy (AFM), using a Digital Instruments Nanoscope II, equipped with piezoelectric tube scanners allowing imaging of cleaved or polished crystals from atomic resolution up to 130  $\mu$ m maximal scans. The cantilevers were commercial nanoprobe, made of gold coated silicon nitride with a force constant of 0.06 N/m.

## 3. Results and discussion

Fig. 1 shows the full range photoluminescence spectra of PVT ZnTe crystals at 10.6 K: annealed at 250°C (Fig. 1a), aged for about 6 months (Fig. 1b), and annealed under vacuum at 600°C for 1 h (Fig. 1c). In the spectrum shown in Fig. 1a, the principal bound exciton (PBE) at 2.3746 eV (FWHM = 1.0 meV) has been attributed to the exciton bound to Cu acceptor,  $A_1^{\text{Cu}}$ . The interval on the lines above the spectra represent the successive LO-phonon replicas. The LO-phonon replica peaks and two-hole transition ( $A_2^{\text{Cu}}$ ) at 2.2495 eV are relatively sharp and strong to be identified together with  $A_1^{\text{Cu}}$ . The energy difference between  $A_1^{\text{Cu}}$  and  $A_2^{\text{Cu}}$ , known as  $E_{\text{Cu}}(1s) - E_{\text{Cu}}(2s)$  for a hydrogenic model, is the same as that found in the literature [3,5]. The lines la-

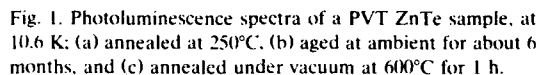
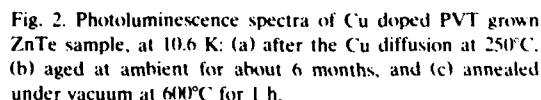


Fig. 1c. The free exciton recombination is resolved from the PBE line, while the LO-phonon replicas of  $A_1^{\text{Cu}}$  have almost vanished. Cu has a very high diffusion coefficient in ZnTe and consequently has a very high degree of association with other point defects (including other copper atoms) present in the crystal, as indicated by the peaks of the  $C_n$  series which are intense enough to overlap the occurrences of the DAP, the FB and the  $A_2^{\text{Cu}}$  transitions.

Fig. 2 shows the PL spectra of PVT ZnTe:Cu crystals: (a) after the Cu diffusion at 250°C, (b) after aging, and (c) after annealing under vacuum at 600°C for 1 h. Spectrum 2a shows features which are very different from the spectra found in the literature and those obtained by us on samples which were highly contaminated by Cu during growth. The line at 2.3827 eV and a small shoulder at 2.3895 eV are attributed to  $D_1^0$  and the free exciton (x), respectively. A new set of [DAP]<sub>i</sub> at 2.3215 eV and associated phonon replicas may be attributed to interstitial Cu. The occurrence of  $C_{10}$  line and its phonon coupling are due to copper diffusion. The spectrum in Fig. 2b is similar to that in Fig. 1b, which indicates that the Cu impurity has completely diffused into the crystal lattice to occupy  $V_{Zn}$  and form more  $Cu_{Zn}$  centers. The vanishing of the [DAP]<sub>i</sub> makes DAP



and FB well resolved. The Cu diffusion also produced more defects associated with the broad band at 1.78 eV (probably  $\text{Cu}_{\text{Zn}}-\text{V}_{\text{Te}}$  centers), the sharp line  $\text{C}_0$  and its two successive LO-phonon replicas. After annealing the crystal, it can be observed in the spectrum shown in Fig. 2c that  $\text{A}_1^{\text{Cu}}$  is broadened and decreased in intensity, and that the structure of the  $\text{C}_n$  series is clearly resolved. The broad band at 1.78 eV and the triple lines have almost vanished. New peaks at 1.97 eV were produced during the annealing process. These are thought to be due to in the form of oxygen centers ( $\text{O}_{\text{Te}}$ ), without the fine structure of the Zn–O axial centers.

The larger intensity ratio of PBE to  $\text{C}_2$  in Fig. 1c, as compared to Fig. 2c, indicates that the undoped crystals contain less total Cu impurity, and the PL structure of 1a is comparable to that of the crystals having Cu atoms of about  $10^{17} \text{ cm}^{-3}$  [5]. Earlier studies on the PVT ZnTe crystals with chemical analysis showed that an unintentional Cu concentration of 50 ppba ( $3 \times 10^{16} \text{ cm}^{-3}$ ) from atomic absorption ( $< 3000$  ppba from spark source mass spectrography), while no IR absorption was observed [2].

The full range photoluminescence spectra of a THM grown ZnTe crystal are shown in Fig. 3: (a) as-grown crystal; (b) aged crystal for about 6

months; and (c) re-annealed at  $600^\circ\text{C}$  for 1 h. The broad band of deep level with the center of 1.9 eV has the typical triplet fine structure of a LO phonon replica, and its zero-phonon lines at 1.9874, 1.9798 and 1.9724 eV can be explained by the associated donor–acceptor pair (Zn–O) model, assuming axial symmetry [7,8]. In the THM sample the presence of oxygen impurity caused the donor-bound-exciton line,  $\text{D}_1$ , at 2.3825 eV to be well resolved. The oxygen atom might act as a donor and affect the position and the shape of the DAP peak and its replica. The intensity ratios for PBE/DAP and PBE/Zn–O center are equal to 15 and 5, respectively. The  $\text{A}_1^{\text{Cu}}$  line still appears as a typical PBE, together with the  $\text{D}_1$  line. The PL spectrum of the aged crystal, as shown in Fig. 3b, shows the occurrence of the successive phonon coupling of  $\text{A}_1^{\text{Cu}}$ . In Fig. 3c the PL spectrum of the THM ZnTe sample after annealing at  $600^\circ\text{C}$  for 1 h is shown: when compared to the unannealed sample and the annealed PVT ZnTe crystals different features are evident: (i) the strongest emission line is  $\text{C}_3$  instead of  $\text{A}_1^{\text{Cu}}$ , (ii) the triplet structure, together with LO-phonon, in the deep-level region has vanished, which means the decomposition of Zn–O center. The DAP recombination may contribute some energy of several LO-phonons to the Zn–O center. The spectrum of Fig. 3c provides evidence that the  $\text{C}_n$  line series originate from complex centers, distinguished from  $\text{A}_1^{\text{Cu}}$ , and that these complexes are associated with Cu and O atoms.

Fig. 4 shows AFM images of (110) crystallographic planes cleaved from different crystals. The structure of the cleavage steps appear to be affected by the crystal growth method or by post growth treatments, a phenomenon recently observed on the cleaved surfaces of as-grown and annealed CdZnTe crystals [9]. The steps of the THM ZnTe crystal surface, shown in Fig. 4a, are not as straight as those of the PVT as presented in Fig. 4b. The post-growth doping of the PVT grown crystal with Cu at  $250^\circ\text{C}$  caused a modification of the microstructure, apparently, as a result of the stress induced during the diffusion process. This effect is illustrated in the image of Fig. 4c, where the shape of cleavage steps has been deformed and presumably Cu inclusions are

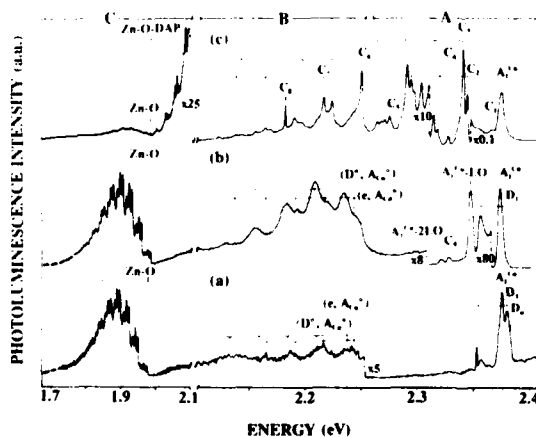


Fig. 3. Photoluminescence spectra, at 10.6 K, of a ZnTe crystal grown by THM: (a) as-grown crystal, (b) aged crystal for about 6 months, and (c) annealed at  $600^\circ\text{C}$ , in vacuum for 1 h.

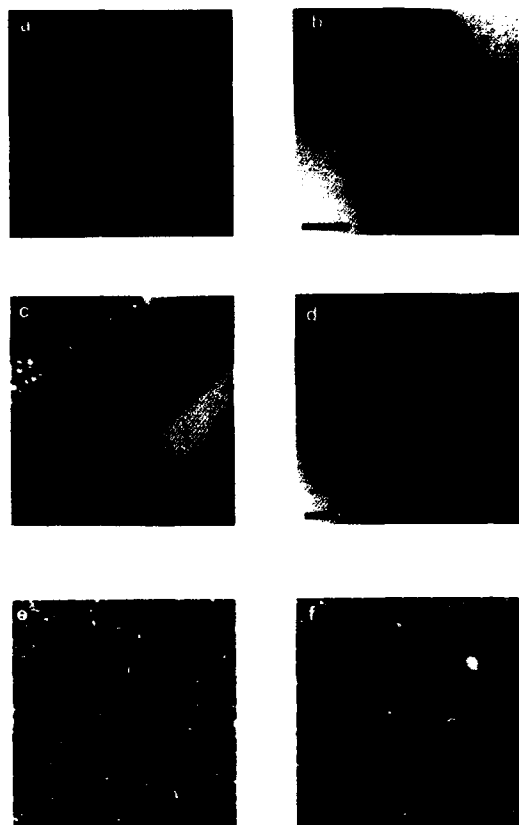


Fig. 4. Crystal surfaces at ambient, as imaged by atomic force microscopy, with the marker representing 1  $\mu\text{m}$ : (a) as-cleaved THM ZnTe, (b) as-cleaved PVT ZnTe, (c) as-cleaved PVT ZnTe Cu doped, (d) PVT ZnTe Cu doped, as-cleaved after the annealing treatment at 600°C, (e) THM ZnTe sample after polishing and etching in Br-methanol solution, and (f) PVT ZnTe sample after polishing and etching in Br-methanol solution.

present. The induced stress has been relieved by the annealing treatment at 600°C, and Fig. 4d shows that the step shape has recovered its original shape of the as-grown crystal presented in Fig. 4b. The polished and etched surfaces of the THM and PVT crystals were also imaged and are shown in Figs. 4e and 4f, respectively. The size and the density of the residues, as well as the surface roughness, vary significantly.

The surface morphology of the samples qualitatively correlates to the PL spectra. Table 1

summarizes the full width at half maximum ( $F = \text{FWHM}$ ) of  $A_1^{\text{Cu}}$  and the intensity ratio  $I = A_1^{\text{Cu}}/C$ , where  $C$  is the intensity of the deep level broad band of region C (1.60–2.10 eV). It is commonly accepted that lower  $F$  values indicate a higher crystalline quality, while lower  $I$  value is associated with higher defect density [10]. Considering the crystal growth techniques, and comparing the PVT grown to the THM grown crystals, it is clear that the PVT crystal exhibits, both higher crystalline perfection and lower impurity content. These quantitative results are well correlated to the morphological images shown in Figs. 4a, 4b, 4e and 4f, indicating that both the as-cleaved and the etched surfaces of the THM grown surfaces are rougher and exhibit higher density of residues, as compared to those of the PVT grown crystal. Further, the intentional doping of the PVT grown crystal increased the  $F$  value and decreased the  $I$  value, indicating the deterioration in the crystalline quality and the increasing content of various types of impurities and defects. The effects of these post growth processes on the morphology the cleaved surfaces are demonstrated in Figs. 4c and 4d. Considering the PL data together with the AFM analysis, we may conclude that the doping process not only produced the diffusion of Cu, but also introduced high density of defects, which are clearly visible in Fig. 4c, where the structure of cleavage steps has been modified and a region of highly concentrated inclusions (clus-

Table 1  
Summary of the  $F$  and  $I$  values as calculated from the PL spectra

Type of sample, treatment	FWHM (meV)	$I$
PVT, polished and etched	1	3200
PVT, cleaved	3	2000
PVT, aged	4.5	1800
PVT, annealed	8	300
THM, polished and etched	8	5
THM, aged	6	640
THM, annealed	6	130
PVT, Cu doped, etched	8	0.2
PVT, Cu doped, aged	4	660
PVT, Cu doped, annealed	6	800

ters) was produced. After annealing, the stress has been relieved, and the shape of the cleavage steps was restored to that of the as-cleaved crystal. To some extent, the surface preparation methods were found to affect the PL spectra; the cleaved surface exhibited slightly broader emission peaks, as well as slightly lower  $I$  value as compared to the polished etched surfaces. In spite of the fact that the cleaved surface is smoother than the etched one, it appears that the cleaving process introduces surface defects which have not been observed by AFM, but contribute to a deterioration of the PL spectrum. Apparently, the etching process clears away some of the surface defects which are introduced during the mechanical polishing procedure, providing the band sharpening of the PL spectrum.

In conclusion, PVT ZnTe crystals have been confirmed, by low temperature photoluminescence and atomic force microscopy, to have a better purity and quality than THM ZnTe crystals. The as-grown crystals contain different levels of Cu impurity and the THM ZnTe crystals also contain isoelectronic oxygen substituting for Te atoms. After doping Cu into the PVT ZnTe crystals by diffusion, new interstitial Cu acceptor centers and more vacancies of Te are formed. Additionally, the process of annealing at 600°C causes the vanishing of the Zn–O center in THM

ZnTe crystals and reduces the vacancies of PVT ZnTe.

#### 4. Acknowledgement

This work was supported by NASA Grant number NAGW-2025.

#### 5. References

- [1] R. Triboulet, G. Neu and B. Fotouhi, *J. Crystal Growth* 65 (1983) 262.
- [2] C.-H. Su, M.P. Volz, D.C. Gillies, E.R. Szofran, S.L. Lehoczky, M. Dudley, G.-D. Yao and W. Zhou, *J. Crystal Growth* 128 (1993) 627.
- [3] H. Venghaus and P.J. Dean, *Phys. Rev. B* 21, (1980) 1596.
- [4] L. Svob and Y. Marfaing, *Solid State Commun.* 58 (1986) 343.
- [5] N. Magnea, D. Bensahel, J.L. Pautrat, K. Saminadayar and J.C. Pfister, *Solid State Commun.* 30 (1979) 259.
- [6] B. Monemar, P.O. Holtz, H.P. Gilason, N. Magnea, Ch. Uihlein and P.L. Liu, *J. Luminescence* 31/32 (1984) 476.
- [7] J.L. Merz, *Phys. Rev. B* 176 (1968) 961.
- [8] V. Slusarenko, Y. Burki, W. Czaja and H. Berger, *Phys. Status Solidi (b)* 161 (1990) 897.
- [9] M. Azoulay, M.A. George, A. Burger, W.E. Collins and E. Silberman, *J. Vac. Sci. Technol. B* 11 (1993) 148.
- [10] N.C. Giles-Taylor, R.N. Bicknell, D.K. Blanks, T.H. Myers and J.F. Schetzina, *J. Vac. Sci. Technol. A* 3 (1988) 391.



ELSEVIER

Journal of Crystal Growth 138 (1994) 225–230

JOURNAL OF  
**CRYSTAL  
GROWTH**

## Optical properties of “pure” CdS and metal–insulator–semiconductor structures on CdS at electrical operation

M.A. Jakobson \*, V.D. Kagan, R.P. Seisyan, E.V. Goncharova

*A.F. Ioffe Physical-Technical Institute, Politeknicheskaja 26, 194021 St. Petersburg, Russian Federation*

### Abstract

The quadratic Stark effect on the  $A_F$ ,  $A_I$  and  $I_3$  exciton lines was observed at 1.8 K in the absorption spectra for MIS structures with CdS. Impact ionization of free and bound excitons by free carriers in an electric field in CdS crystals with ohmic contact were investigated in the spectrum of luminescence. A theoretical analysis of the results has made it possible to identify the mechanisms of relaxation of high-energy electrons predominating in CdS at low temperatures.

### 1. Introduction

This paper discusses electrical field effects on free and bound excitons observed in absorption and luminescence spectra in the exciton region.

The absence of published data on the Stark effect in the ground state of  $A_{n-1}$  excitons is in all likelihood due to the fact that field intensities (up to  $10^5$  V/cm) required are difficult to obtain in structures with ohmic contacts because of thermal breakdown of crystals. Our experiment was carried out employing a metal–insulator–semiconductor (MIS) structure (Au– $Al_2O_3$ –CdS–In) subjected to a reverse bias. The current then is limited by the insulator layer. In case of the ground state of the 1s type, which includes  $A_{n-1}$ , we can expect only a weak quadratic Stark effect

manifested by a small long-wavelength line shift ( $\Delta\epsilon < 0.1R$ , where  $R$  is the binding energy of an exciton).

The impact ionization of free excitons and delocalization of excitons bound to impurities for cadmium sulfide was also investigated. The investigation was carried out by optical methods involving observation of quenching of the exciton photoluminescence spectra in an electric field and a theoretical analysis of the experimental results obtained in this way.

Structures for the Stark effect investigations were fabricated from single crystals grown by the Frerichs method [1]. The thickness of the crystals was 10–30  $\mu\text{m}$ . In–CdS– $Al_2O_3$ –Au structures were formed by evaporation technique.

For investigation of the luminescence line quenching, the ohmic contacts were used. The contacts were in the form of longitudinal In strips with a gap of 1 mm.

\* Corresponding author.



## 2. Experimental results

The  $A_{n=1}$  exciton absorption line was investigated by employing mainly the  $E \parallel c$  polarization, forbidden for this line, so that even a small unbalance angle was sufficient to record the  $A_L$  and  $A_F$  absorption lines clearly. This enabled us to consider the field-induced shift of these lines without invoking polariton effects.

The absorption spectra were recorded simultaneously with the current–voltage and capacitance–voltage characteristics. This permitted estimation of the thickness of the space charge layer, which at the working temperature ( $T = 4.2$  K) was comparable with or greater than the thickness of the crystal. Hence, we concluded that the voltage drop, across the semiconductor subjected to a negative bias, was distributed uniformly over the whole single crystal.

Fig. 1 depicts the experimental absorption spectra of a crystal, No. 2714, at zero and maxi-

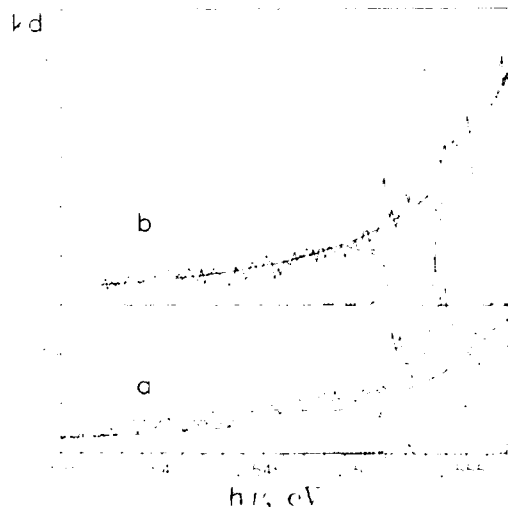


Fig. 1. Experimental absorption spectra of an Au- $\text{Al}_2\text{O}_3$ -CdS structure (No. 2714) and their components obtained as a result of decomposition: (1) background due to the B exciton line ( $h\nu = 2.5686$  eV); (2)  $A_1$  absorption line ( $h\nu = 2.5554$  eV); (3)  $A_2$  absorption line ( $h\nu = 2.5524$  eV).  $T = 4.2$  K and  $E \parallel c$ . Reverse voltage  $U_r$  (V): (a) 0; (b) 230. The origin of the ordinates of the curves in (b) is shifted upwards in  $kd$  for clarity ( $kd$  optical density).

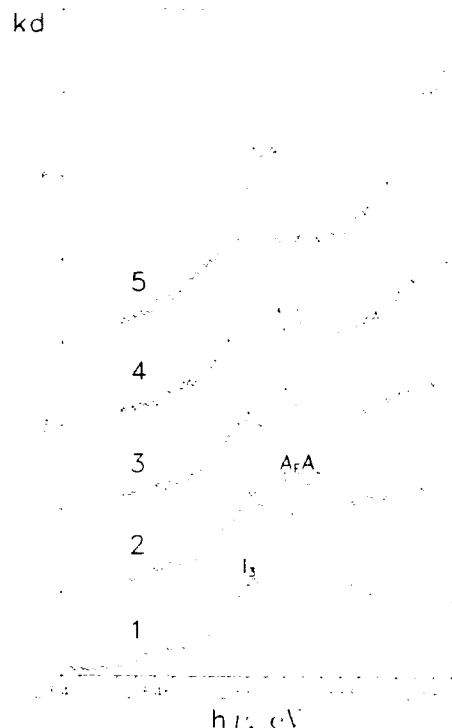


Fig. 2. Profile of the  $A_1$  ( $h\nu = 2.5545$  eV),  $A_2$  ( $h\nu = 2.5524$  eV), and  $I_3$  ( $h\nu = 2.5499$  eV) absorption lines of structure No. 2195 on increase in the reverse bias voltage  $U_r$  (V): (1) 0; (2) 55; (3) 65; (4) 75; (5) 90.  $T = 4.2$  K. Unpolarized light. The origin of the ordinates of curves 2–5 is shifted upwards in  $kd$  for clarity.

mum ( $U = 230$  V) external bias voltages, as well as their individual components.

The effect of an electric field on the exciton complex  $I_3$  ( $h\nu = 2.5499$  eV,  $\lambda = 4861.7$  Å), allowed only in the  $E \perp c$  polarization, was studied by recording the absorption of unpolarized light. This exciton complex gave rise to the strongest absorption exhibited by our crystals. Fig. 2 shows the absorption spectra of unpolarized light obtained for a crystal, No. 2195, using different values of the applied voltage ranging from zero to  $-90$  V. This series of spectra also illustrates the rates of the  $A_1$ ,  $A_2$  and  $I_3$  lines decreasing in amplitude under an external electric field. (Fig. 5a shows it more distinctly.)

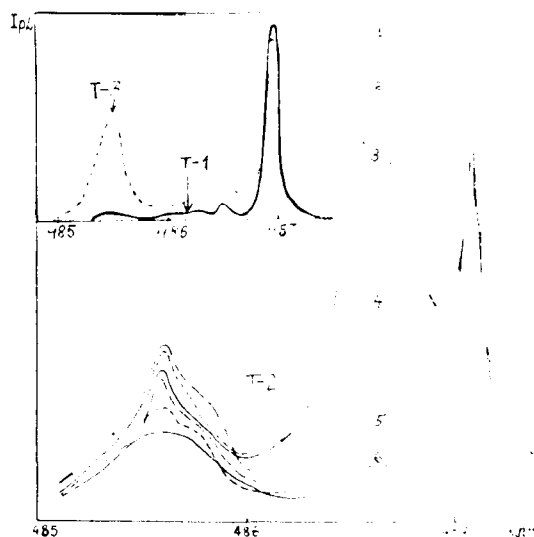


Fig. 3. Exciton luminescence spectra of CdS samples recorded at 1.8 K: (a) T-1 and T-3 samples in zero electric field, and (b) T-2 samples in different electric fields  $E$  (V/cm): (1) 0; (2) 300; (3) 350; (4) 450; (5) 650; (6) 800.

With respect to exciton luminescence spectra, the "pure" CdS crystals available to us could be divided into three types: (1) T-1 crystals exhibiting a strong bound-exciton line and weak free-exciton line  $A_{n-1}$ ; (2) T-2 crystals with a group of strong bound-exciton lines  $I_2$  and  $I_2'$  and a moderately strong free-exciton line  $A_{n-1}$ ; (3) T-3 crystals with a strong  $A_{n-1}$  line and  $I_3$  line of a comparable intensity. Fig. 3 shows the spectra of these types and the dependence of T-2 spectrum on the electric field applied to an In-CdS structure. It is clear from this figure that the order in which the lines are quenched is determined by the binding energies of the excitons  $I_2'$  ( $\lambda = 486.6$  nm),  $I_2$  ( $\lambda = 487.2$  nm) and  $A_{n-1}$  ( $\lambda = 485.3$  nm). The last to be quenched was the  $A_{n-1}$  line, the binding energy of free excitons being the highest (28 meV) among the observed luminescence lines. In sufficiently large fields (800 V/cm) all the luminescence lines were largely quenched.

Our measurements of the Stark effect (absorption spectrum) and of the impact ionization effects (luminescence spectrum) were carried out

under DC conditions. As such, one of the greatest problems to avoid was thermal effects. Our estimation of the Joule heat indicated that the critical power leading to an increase of temperature as a result of unbalance between the sample and liquid helium [2] was not reached.

### 3. Discussion

#### 3.1. The Stark effect

The Stark shift of the energy position of the ground state of an exciton in the case of simple bands considered in the hydrogen-like approximation is described by the expression

$$\Delta\epsilon(E) = h\nu_0 - h\nu(E) = 9\phi^2 R/8, \quad (1)$$

where  $\phi = E/E^*$ ,  $E^* = R/ae$  is the ionization field,  $e$  is the electron charge,  $a$  is the exciton radius,  $R$  is the effective Rydberg constant, and  $E$  is the external electric field.

The experimentally observed dependence was steeper than quadratic. We can assume that such a steep rise of  $\Delta\epsilon$ , on increase in the potential difference, is due to a change in the distribution of the external electric field between the insulator and semiconductor layer as the voltage is increased.

We determined experimentally the voltage drop across the semiconductor and found the effective voltage,  $U_{\text{eff}}$ , of the bulk of material using the same CdS single crystal for both an MIS structure (No. 2795), and a metal-semiconductor structure (inset in Fig. 4). We corrected the results for the voltage drop across the insulator. The results shown in Fig. 4 depict dependence of the shift of the exciton absorption bands on the effective field (this figure includes the theoretical dependence, represented by the solid line). One can see that the experimental dependence is close to the theoretical predictions. The clearest result was obtained for the  $A_1$  absorption line, which is the strongest in the spectrum.

Analysis of shifts of the  $A_1$  and  $I_3$  absorption lines in the same crystal on the applied voltage (Fig. 2) indicates that the log dependences,  $\Delta\epsilon(U)$ , are equivalent, and consequently the Stark

shift coefficient of the free- and bound-exciton lines is also equivalent:

$$K_{St}^{theor} = 9e^2a^2/8R. \quad (2)$$

We can therefore conclude that the effective radius of an exciton bound to an ionized donor is equal to the radius of a free exciton under the conditions of interaction with an external electric field.

Fig. 5 demonstrates the difference between (a) electric field effects and (b) effect of impact ionization. In the case of electric field effects, the decreasing amplitude of the exciton lines is due to the exciton ionization and is determined by the bound energy of the exciton. The amplitude reduction for free  $A_{n-1}$  and bound  $I_3$  excitons is the same. In the case of impact ionization, the decay of the free exciton is determined by the

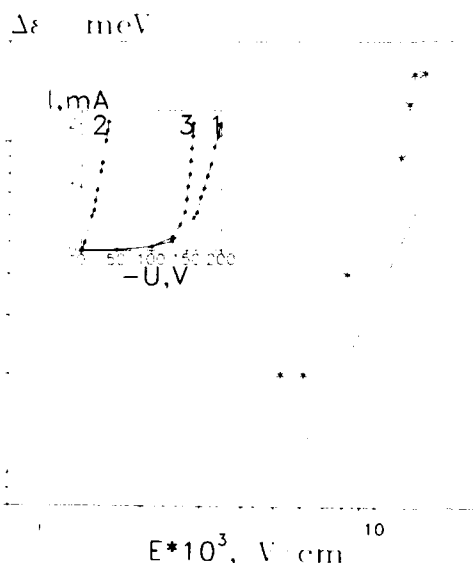


Fig. 4. Shifts of the exciton absorption lines with the effective voltage applied to sample No. 2795. The continuous straight line represents theoretical data. The insert shows the current-voltage characteristics of MIS (1) and metal-semiconductor (2) structures made of a CdS single crystal (No. 2795), as well as the calculated current-voltage characteristics of the insulator layer (3). The characteristics were obtained under the same conditions as in recording the absorption spectra.

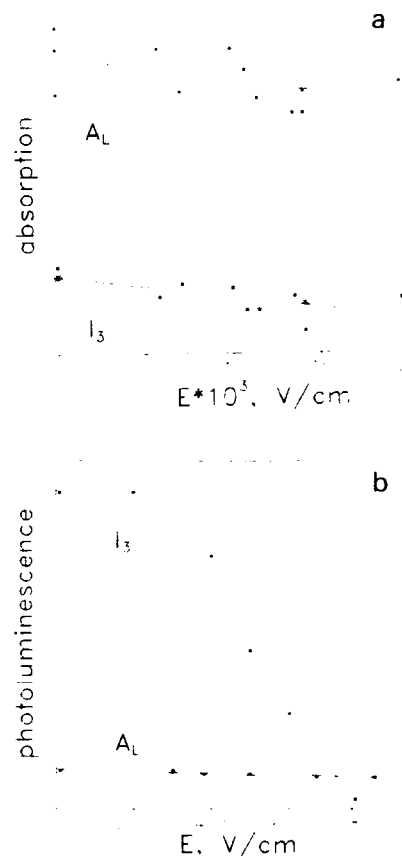


Fig. 5. Different mechanisms of the excitonic line intensity reduction: (a) field ionization; (b) impact ionization.

exciton bound energy, whereas the decay of the bound exciton is determined by the binding energy of exciton to the centre, which is much smaller. The quenching of  $I_3$  is quicker than that of  $A_{n-1}$ .

In summary, the use of an MIS structure enabled us to record for the first time the Stark shift of the absorption lines of the free  $A_{n-1}$  and bound  $I_3$  excitons. Determination of the effective voltage acting on the bulk of the semiconductor made it possible to describe satisfactorily the results obtained by the quadratic Stark dependence.

### 3.2. Impact ionization

Under steady-state conditions, the simple equation for the number of excitons results in the following dependence of the luminescence intensity  $I$  on the applied electric field:

$$I/I_0 = (1 + W_E/W_0)^{-1}. \quad (3)$$

Here  $I_0$  is the luminescence intensity in the absence of an electric field,  $W_0$  the probability of ionization of a free exciton (or delocalization of a bound exciton) in the absence of an electric field and  $W_E$  the probability of impact ionization in the presence of an electric field. The latter is described by different asymptotes:

$$\begin{aligned} W_E &= W_1 \exp(-E_{01}/E), \\ W_E &= W_2 \exp(-E_{02}/E^2), \end{aligned} \quad (4)$$

the Townsend–Shockley and Davydov–Wolf laws. Conditions of validity of the Townsend–Shockley impact ionization law in semiconductors have been considered by Kagan [3]. The explicit expressions of parameters  $E_{01}$  and  $E_{02}$  are in terms of kinetic characteristics of crystals. These asymptotic dependences (4) work only provided the probability of impact ionization is small, i.e. the modulus of the exponent is large.

To compare the experimental data with the dependences of Eqs. (4), we have plotted, in Fig. 6,  $\ln[I/(I_0 - I)]$  versus  $E^{-1}$  (curve a) and versus  $E^{-2}$  (curve b) for luminescence line  $I_2$ . In fields

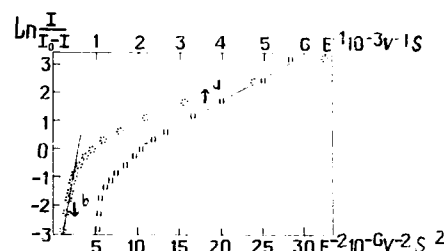


Fig. 6. Dependence of the intensity of the bound-exciton luminescence ( $\epsilon_1 \approx 4$  meV) on the electric field applied to a sample of the T-2 type. The experimental points are plotted as dependences of  $\ln[I/(I_0 - I)]$  on  $E^{-1}$  (a) and  $E^{-2}$  (b).

less than or of the order of 450 V/cm, curve (a) becomes linear, i.e. obeys the Townsend–Shockley law, while in sufficiently strong fields (650 V/cm), curve (b) becomes linear, indicating that the Davydov–Wolf asymptote is applicable. The slopes of the asymptotes yield the constants  $E_{01}$  and  $E_{02}$  listed in Table 1 for different types of samples and different luminescence lines (the values given in parentheses in this table are the fields in which the relevant dependence was observed). It is clear from Table 1 that the lines for higher binding energies correspond to larger values of the constants  $E_{01}$  and  $E_{02}$ . An analysis of these experimental results, on the basis of the theory presented in ref. [2], gives valuable information on the mean free paths of high-energy electrons.

Table 1

Parameters  $E_{01}$  and  $E_{02}$  and ranges of validity of the corresponding dependences (in parentheses) listed in units of volts per centimeter for three types of samples and three different photoluminescence lines (the binding energy is given in parentheses)

Type of sample	$I_2^1$ (4 meV)		$I_2$ (7 meV)		$A_{n-1}$ (28 meV)	
	$E_{01}$	$E_{02}$	$E_{01}$	$E_{02}$	$E_{01}$	$E_{02}$
T-1	1000 (400–700)	1050 (800–1400)	1400 (400–90)	3000 (1060–1100)	–	–
T-2	800 (175–500)	1400 (500–800)	1200 (300–1000)	3500 (1000–1700)	5000 <sup>a</sup> (775–950)	1500 <sup>a</sup> (775–950)
T-3	90 (50–250)	440 (300–650)	130 (50–250)	180 (300–650)	180 (100–200)	750 (300–400)

<sup>a</sup> In the case of T-2 crystals, the intensity of the  $A_{n-1}$  line was insufficient to distinguish reliably between  $E^{-1}$  and  $E^{-2}$  dependences.

The mean free path of 4 meV electrons in moderate fields is  $10^{-4}$  cm in the “pure” samples and  $5 \times 10^{-6}$  cm in the remaining samples [4].

To the best of our knowledge, to date, there have been no attempts to analyse the experimentally observed influence of an electric field on the exciton luminescence spectra using a theory leading to a dependence of a Townsend–Shockley type. We have demonstrated the value of such an approach. In essence, it permits quenching by the electric field of the low temperature exciton lumi-

nescence in cadmium sulfide as a tool for measuring the mean free paths of high-energy electrons.

#### 4. References

- [1] B. Frerichs, *Naturwissenschaften* 33 (1946) 384.
- [2] Zavaritskaya, *Elec. Opt. Svoistva Poluprovodn.* 77 (1966) 41.
- [3] V.D. Kagan, *Zh. Eksper. Teor. Fiz.* 94 (1988) 258.
- [4] M.A. Jakobson, V.D. Kagan, R. Katilus and G.O. Müller, *Phys. Status solidi (b)* 161 (1990) 395.



ELSEVIER

Journal of Crystal Growth 138 (1994) 231–233

JOURNAL OF  
**CRYSTAL  
GROWTH**

## Measurement of optical nonlinear susceptibility of CdS single crystal using a single beam <sup>\*</sup>

Zhengang Li <sup>1</sup>, Guangnan Xiong <sup>\*</sup>, Zhihong Zhao, Xiwu Fan <sup>2</sup>

*Tianjin Institute of Technology, Tianjin 300191, People's Republic of China*

### Abstract

We report a measurement of optical nonlinear susceptibility of CdS using the Z-scan method. The input laser light irradiating on the CdS single crystal had a wavelength of 514.5 nm and a flux density of 16 kW/cm<sup>2</sup>. We estimate a nonlinear susceptibility of  $\chi^{(3)} = 3.5 \times 10^{-9}$  (esu) being in agreement with an anharmonic oscillator model based on excitons. We also found that when a DC electric field was added on the sample of CdS, the nonlinear absorption increased as the applied DC electric field was increased.

### 1. Introduction

We have reported [1] that nonlinearity occurs in CdS when the irradiated power by 514.5 nm laser beam is more than 15.2 kW/cm<sup>2</sup>. We found that there were slow and fast processes of nonlinear absorption. The slow process is due to thermal effect and the fast process originates from the exciton–electron scattering. Here we report a measurement of optical nonlinear susceptibility of CdS using a single Gaussian laser beam of 514.5 nm.

Recently, the technique of the Z-scan method has become an attractive method for estimating both the magnitude and the sign of the third-order nonlinear susceptibility because of its simplicity as well as its high sensitivity, especially for the intense nonlinear absorptive samples. The theories have been discussed extensively in the literature [2–5]. Using the Z-scan method with the same input light wavelength and power, we have measured the optical nonlinear refractive index of a CdS single crystal.

### 2. Experiments

The experiments in CdS were performed with a frequency of A<sup>3+</sup> laser with photon energy just below the exciton transition energy in CdS. The experimental setup is shown in Fig. 1.

The output pulses from a mode-locked A<sup>3+</sup> laser were focused with a spot diameter of 25 μm on a 200 μm thick CdS sample. The temporal

<sup>\*</sup> Corresponding author.

<sup>\*</sup> Work supported by the National Science Foundation of China.

<sup>1</sup> Present address: Department of Physics, Tianjin Normal University, Tianjin 300074, People's Republic of China.

<sup>2</sup> Present address: Changchun Institute of Physics, Chinese Academy of Sciences, Changchun 130021, People's Republic of China.

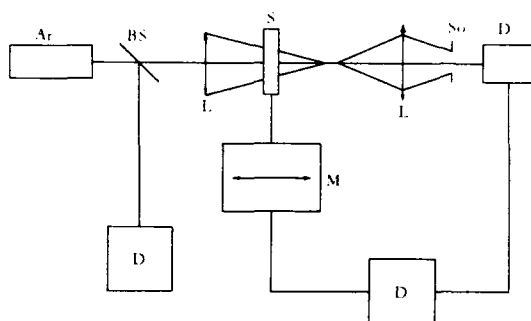


Fig. 1. Experimental setup of Z-scan for measuring the non-linear refractive index. S, sample;  $L_1$  and  $L_2$ , focusing lenses;  $D_1$  and  $D_2$ , detectors;  $S_0$ , pinhole; M, Z-scan; D, x-y recorder.

width of the laser pulses was 100 ps (FWHM), the repetition rate was  $82 \times 10^6$  Hz and the wave vector was perpendicular to the optic axis of the crystal. An undoped CdS single crystal was used.

Using the Gaussian laser beam in a tight focus geometry, we measured the transmittance of CdS through a finite aperture in the far field as a function of the sample position  $z$  relative to the focal plane. The experimental results are shown in Fig. 2 with an aperture diameter of 3 mm and in Fig. 3 with an aperture diameter of 0.45 mm. The results with the normalized transmittance in Fig. 3 being divided by the normalized transmittance in Fig. 2 is shown in Fig. 4. From Fig. 4, we obtain that the difference between the normalized transmittance peak and valley  $\Delta T_{p-v}$  is 0.176.

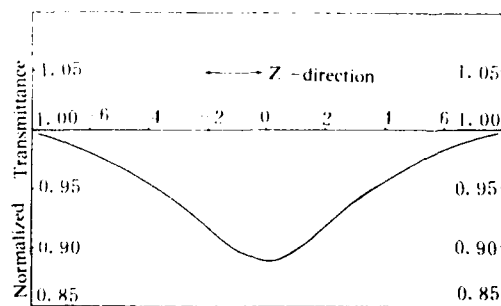


Fig. 2. Transmittance measured as a function of the position relative to the focal point in the CdS single crystal sample, with a 3 mm pinhole.

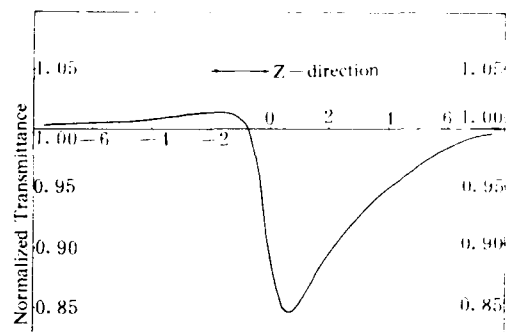


Fig. 3. Transmittance measured as a function of the position relative to the focal point in the CdS single crystal sample, with a 0.45 mm pinhole.

The formula [4] we used is

$$\text{Re}(\chi^{(3)}) = \frac{n_0 \Delta T}{12\pi \times 0.406(1-s)^{0.25} k I_0 L_{\text{eff}}} \quad (1)$$

where  $I_0$  is the instantaneous input power (on the sample),  $s = 1 - \exp(-2r_a^2/w_a^2)$  is the aperture linear transmittance with denoting the beam radius at the aperture in the linear regime,  $L_{\text{eff}} = (1 - e^{-\alpha L})/\alpha$  (with  $L$  the sample thickness and  $\alpha$  the linear absorption coefficient) and  $k = 2\pi/\lambda$ . In our experiments,  $r_a = 0.23$  mm,  $w_a = 0.33$  mm,  $\alpha = 25 \text{ cm}^{-1}$ ,  $\lambda = 5.145 \times 10^{-5}$  cm, and the single pulse power was 1  $\mu\text{J}$ . So we had a third-order susceptibility of  $\chi^{(3)} = 3.5 \times 10^{-9}$  esu.

Generally, when the flux density is low, the third-order susceptibility in CdS is about  $10^{-12}$  esu.

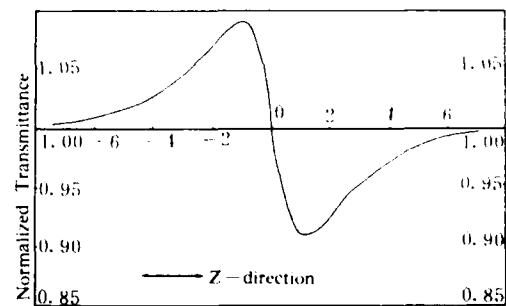


Fig. 4. A curve obtained from the curve in Fig. 3 being divided by the curve in Fig. 2. The difference in transmittance between the peak and valley is 0.176.

We have reported [1] that excitons played an important role in optical nonlinear absorption in CdS single crystal when the input light wavelength was 514.5 nm and the flux density was higher than 15.2 kW/cm<sup>2</sup>. Its mechanism is electron–exciton scattering and the exciton lifetime is about 100 ps. The exciton is composed of a electron and a hole. Its radius is about 10<sup>−6</sup> cm in CdS and its behavior is similar to a harmonic oscillator. Its contribution to the third-order susceptibility is from its anharmonicity.

If we assume that the nonlinearity is due to generation of an exciton that can be treated as an anharmonic oscillator; the third-order susceptibility is given by [6]

$$\chi^{(3)} = \frac{N_0 e^3}{m^*{}^2 (\omega_0^2 - \omega^2)^2 a}, \quad (2)$$

where  $m^*$  is the reduced effective mass of the electron–hole pair,  $N_0$  the number of excitons per cm<sup>3</sup>,  $\omega_0$  the resonance frequency of the anharmonic oscillator, and  $a$  the exciton radius.

Inserting  $\omega_0 = 3.74 \times 10^{15} \text{ s}^{-1}$ ,  $m^* = 0.5m_e$ ,  $a = 10^{-6} \text{ cm}$ , and  $N_0 = 4.1 \times 10^{16} \text{ cm}^{-3}$  in Eq. (2), we obtained a theoretical value of  $\chi^{(3)} = 11 \times 10^{-9} \text{ esu}$ , which was of the same order of magnitude as the experimental value  $\chi^{(3)} = 3.5 \times 10^{-9} \text{ esu}$ .

The rise time of a thermal lens in a solid is determined by the acoustic transit time across the light beam,  $\tau = w_0/v_s$ , where  $v_s$  is the velocity of sound in the solid. For CdS, with  $v_s = 0.3 \times 10^6 \text{ cm/s}$  and  $w_0 = 25 \mu\text{m}$ , we obtained a rise time of  $\tau = 8.17 \text{ ns}$ , which was almost two orders of magnitude longer than the input laser pulsewidth. Therefore, we can neglect the thermal effect.

We also observed an optical nonlinear absorption in CdS under an external DC electric field at room temperature. The nonlinear absorption increased with the increase of the applied voltage, while the incident light intensity needed for the appearance of nonlinear absorption decreased with the increase of the applied voltage.

### 3. References

- [1] F. Yang, G. Xiong and X. Xu, *Phys. Status Solidi (b)* 150 (1988) 765.
- [2] J. Qi, G. Xiong and X. Xu, *J. Luminescence* 45 (1990) 292.
- [3] A.A. Said et al., *J. Opt. Soc. Am. B* 9 (1992) 405.
- [4] A.A. Said et al., *IEEE J. Quantum Electron.* QE-26 (1990) 760.
- [5] S.C. Yang et al., *Acta Opt. Sinica* 12 (1992) 223.
- [6] M. Sheik-Bahae et al., *Opt. Lett.* 14 (1989) 955.
- [7] N. Bloembergen, *Nonlinear Optics* (Benjamin, New York, 1977) p. 5.





ELSEVIER

JOURNAL OF  
**CRYSTAL  
GROWTH**

Journal of Crystal Growth 138 (1994) 234–238

## First realization of bistable light emitting devices

B. Ullrich <sup>a,\*</sup>, A. Kazlauskas <sup>b</sup>, S. Zerlauth <sup>c</sup>, T. Kobayashi <sup>a</sup>

<sup>a</sup> Department of Physics, University of Tokyo, 7-3-1 Hongo, Bunkyo-ku, Tokyo 113, Japan

<sup>b</sup> Department of Nonlinear Spectroscopy, Vilnius University, Naugarduko 24, 2006 Vilnius, Lithuania

<sup>c</sup> Technische Universität Graz, Institut für Festkörperphysik, Petersgasse 16, A-8010 Graz, Austria

### Abstract

A newly observed effect is presented: intrinsic bistability in luminescence. In particular, the bistable properties in reflection of thin (10  $\mu\text{m}$ ) CdS:Cu films were investigated with the 514.5 nm Ar<sup>+</sup> laser line at 80 K. The reflected beam exhibits only poorly contrasted (7%) bistable loops. However, if we put cut-off filters which are transparent in the red region of the spectrum (e.g. RG 780) in the reflected beam, very well contrasted ( $\geq 70\%$ ) bistable loops were observed. Hence, the bistable switch of the infra-red luminescent light was observed. Bistability in luminescence was also achieved in hybrid modes, i.e., the film was illuminated with a constant power and a variable voltage was applied to the sample. At a certain threshold of the voltage the luminescence intensity of the sample exhibits bistability. Finally, some applications of bistabilities in luminescence are discussed.

### 1. Introduction

Information carried by light, i.e., photonic data processing, will extend or even replace common electronics in part because of the rapidly growing importance of lightwave systems. The next century is expected to become an *Optopia* where extensive developments in photonics will be attained [1]. In the last decade [2,3] strong research efforts have started including semiconductors as well as organics in various forms (bulk, thin films, microcrystallites and multiple-quantum wells), in order to find best suited materials and concepts for all-optical bistability (all-OB), i.e., optical bistability without external feedbacks. Laser in-

duced optical devices (LIODs) [4,5] which consist of polycrystalline thin ( $\leq 10 \mu\text{m}$ ) CdS films on Pyrex<sup>®</sup> exhibit well contrasted all-OB in transmission [6–10] and reflection [11]. The driving physical principle of a LIOD is known as all-OB due to increasing absorption by photo-irradiation [12–17]. It is worthwhile to stress at this point that the reflection properties of thin CdS films show peculiar properties. Firstly, the bistable switch of transmission and reflection occurs – against the prediction of the conventional rate equation [18] of thermo-optical effects – non-coincidentally if the temperature dependence of the reflection exhibits larger dynamics than that of the transmission in the temperature range where the thermo-optical bistability occurs [11]. Secondly, at a suitable temperature, a non-bistable increase of the reflected signal takes place during the bistable switch-down of the transmis-

\* Corresponding author.

sion if the reflection depends in a much less pronounced way on temperature than the transmission [19]. Beyond that, an all-optical photonic reflection oscillator has been primarily realized with thin CdS films [20]. In general, the reflection of thin CdS films exhibits highly unexpected and surprising properties and already linear features cannot be described with standard theories in contrast to the transmission [19].

Hoffmann et al. have reported bistability in luminescence of CdS:Cu crystals [21]. However, the origin of the bistability was the formation of a thin He gas film on the surface of the crystal. In other words, the bistability in luminescence was not induced by an intrinsic feature of the crystal, whereas the observed phenomenon reported in the present paper underlies intrinsic properties of thin CdS:Cu films. Hence, according to our knowledge, we present in the present publication the first observation of both intrinsic all-optical and hybrid bistabilities (HB) in luminescence.

## 2. Sample preparation and experiment

The samples were prepared by reactive spray deposition on a Pyrex<sup>®</sup> substrate [8,22] with  $10^{-2}$  M Cu<sub>2</sub> in the solvent. The optical excitation of the thin (10  $\mu$ m) film was performed by the 514.5 nm line of an argon laser with a spot diameter of 300–400  $\mu$ m. In order to measure reflection, the sample was mounted obliquely (30°–45° with respect to the incident beam) in a tunable (80–380 K) cold-finger nitrogen cryostat keeping the sample in vacuum ( $1 \times 10^{-4}$  mbar). The modulation of the intensity of the incident laser beam was performed by two polarizers, a fixed and a rotating one. The intensities of the incident beam, reflection and luminescence were measured with Si photodiodes. For further details of the experimental setup, see ref. [10]. The HB was investigated with the use of electrical contacts which consisted of two evaporated In stripes, 0.5 mm wide and 5 mm long, separated by a 1 mm gap.

Fig. 1 shows schematically the performed experiments. In the upper part (a) the standard experiment of reflection is shown. Only very poor

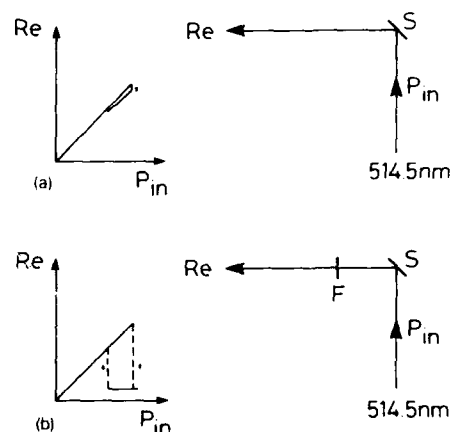


Fig. 1. Schematic sketches of the experimental arrangements. The upper figure (a) shows the result of a common reflection measurement. Only a poorly contrasted bistable loop is observable. The lower figure (b) shows that the contrast of the loop increases considerably if one puts a cut-off filter, which is transparent in the red part of the spectrum (e.g. RG 780) in the reflected beam.  $P_{in}$  is the power of the incident 514.5 nm line, S the sample and Re the measured reflected light intensity.

contrasted (7%) bistable loops were observed. However, if cut-off filters which are transparent in the red region of the spectrum (e.g. Schott RG 715, RG 780 and RG 1000) are put in the reflected beam as shown in Fig. 1b, very well contrasted ( $\geq 70\%$ ) bistable loops were observed.

## 3. All-optical and hybrid bistabilities in luminescence of LIODs

The experimental results obtained with the configurations of Figs. 1a and 1b are shown in Figs. 2 and 3, respectively. The poorly contrasted loop in reflection (Fig. 2) can be drastically enlarged by simply introducing a cut-off filter (RG 780) in the reflected beam (Fig. 3). The poor loop of Fig. 2 is reasonable, since the reflection depends only extremely weakly on temperature, as shown in Fig. 4. It was pointed out [19] that the contrast of the bistable reflection loop (7%, see Fig. 2) is in agreement with the decrease in the reflected light intensity by 7% between 270 and 286 K where the bistability switches. This means

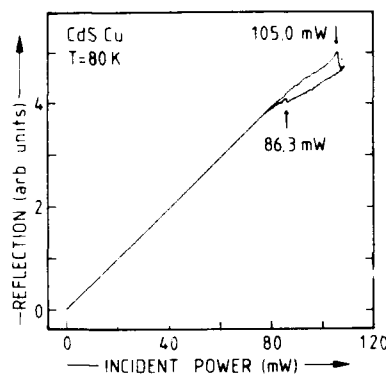


Fig. 2. Reflected light intensity of the 514.5 nm line as a function of the incident power at 80 K. The observed contrast of the bistable loop is only about 7% since the reflected light intensity depends only weakly on temperature, as will be shown in Fig. 4.

that the loop contrast observed in Fig. 2 is already the maximum which can be expected for the thermo-optical bistability in reflection. Hence, the results shown in Fig. 3 cannot be attributed to common reflection properties of the sample but correspond to bistability in luminescence which is measured in reflection geometry. Therefore, we stay in the present paper with the indication reflection and note the cut-off filter used. We want to point out that the observation of bistability in luminescence cannot be concluded straight-

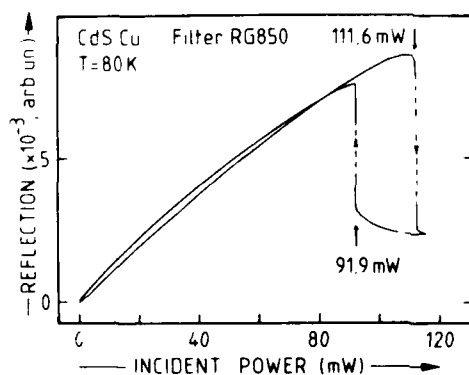


Fig. 3. Repetition of the measurement of Fig. 2, putting the cut-off filter RG 780 into the reflected beam. A completely different behavior with a considerably larger loop contrast (63%) is measured.

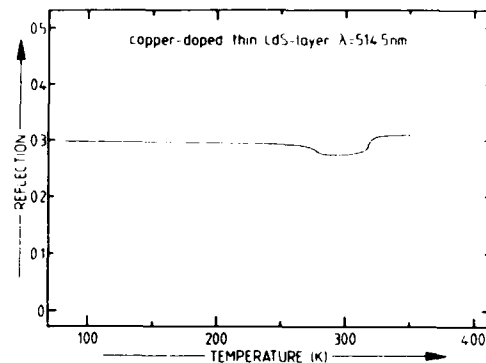


Fig. 4. Dependence of the reflected light intensity on temperature of a thin CdS:Cu film. The decrease (7%) of the reflected light intensity around 300 K is in agreement with the loop contrast of Fig. 2. The measurement is performed under the same conditions as the experiment of Fig. 2. However, low intensity ( $\leq 15 \mu\text{W}/\text{cm}^2$ ) monochromatic light (514.5 nm) was used in order to measure the dependence of the reflection on the ambient temperature without an additional optical warm-up.

forwardly from common interpretations of thermo-optical bistabilities [4,12–17], since the thermo-optical shift of Urbach's tail around 2.4 eV does not necessarily influence transitions around 1.55 eV ( $= 780 \text{ nm}$ ) in such drastic ways as shown in Fig. 3. It is worthwhile to stress at this point that clearly contrasted (50%) bistable reflection loops in CdS platelets have been observed [23]. However, one must bear in mind that thin films are not heated uniformly by the incident laser beam as platelets due to the substrate which acts as an effective heat sink [24]. Furthermore, as already mentioned above, the reflection properties of thin films exhibit peculiar features which were never reported for platelets. Hence, a comparison of results achieved with thin films and platelets must be treated carefully.

Fig. 5 shows the hybrid bistability in luminescence. The bistable switch is induced by the applied voltage. The power of the incident laser beam (optical bias) is constant (100 mW). We want to point out that the observation of Fig. 5 opens possibilities for realizations of a new class of hybrid elements, i.e., *bistable light emitting devices*. The output of an electronic logic can be converted into photonic pulses. Typical values for

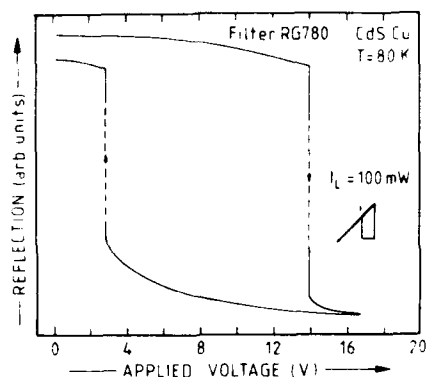


Fig. 5. First observation of intrinsic hybrid bistability in luminescence measured in reflection geometry using the cut-off filter RG 780. The experiment was performed at 80 K with a constant incident power of 100 mW of 514.5 nm line. The observed contrast of the bistable loop was nearly 70%. The inset shows the position of the optical bias ( $I_L$ ) with respect to the bistability loop of luminescence in the specific case.

the high level in common electronics are around 5 V, but 14 V are necessary for the bistable switch-down in Fig. 5. However, the real criterion for an application is the dynamic range of the applied voltage, i.e., the difference of the applied voltages where bistable switches down and up take place, 14 and 3 V respectively, in Fig. 5. This means that a logic level of 11 V would be necessary to drive the device. However, the width of the loop can be reduced considerably by reducing the power of the optical bias. If the optical bias is 79 mW, the bistable switch-down takes place at 18.0 V and the switch-up at 15.3 V. Therefore, the output of a common TTL logic in addition to a constant electrical bias of 14 V is highly sufficient to drive the device.

#### 4. Discussion and further proposals for future applications

The discovered new effect – *intrinsic bistability in luminescence* – inaugurates new possibilities to devise new concepts for the application of thin films in optical material characterizations. The switch-down contrasts of the loops depend strongly on the filter used: OG 590 13%, RG 630

15%, RG 715 49%, RG 780 63% (see Fig. 3) and RG 1000 73%. Obviously, the most contrasted loops are in the vicinity of the gap of GaAs (880 nm at 300 K). Hence, besides the above-mentioned creation of a bistable light emitting device, it is conceivable to develop a new method to measure optically the electronic properties (e.g. doping concentrations) of GaAs wafers on the basis of the presented results.

Among other things, the switching speed of bistabilities in luminescence is currently under investigation in order to understand the mechanism which underlies the discovered effect. It is the question whether the effect is only thermally induced or whether also some electronic contributions take place, since the luminescence features depend strongly on the lifetime of the excited carriers. The optical transitions which underlie the luminescent process arise from deep impurities and disturbed stoichiometry. In fact, spray-deposited thin CdS films exhibit a strong luminescence in the red ( $> 600$  nm) region of the spectrum [25]. We have observed that doping with copper increases the sensitivity of the luminescence to temperature. The luminescence intensity in the range 600–1000 nm decreases more strongly in thin CdS:Cu films than in undoped CdS films if the sample is heated from 80 to 350 K. Therefore, bistable loop contrasts in luminescence observed in CdS:Cu films are larger (70%) than in undoped CdS films (50%). A detailed comparison of the bistable features of CdS and CdS:Cu thin films will be published in a forthcoming paper which includes also encouraging results concerning the above-discussed method to investigate optically the electrical properties of GaAs wafers. Epitaxial CdS layers produced by closed-space vapor transport (CSVT) [8] probable do not exhibit bistability in luminescence because of the well-established stoichiometry. However, studies of bistability in luminescence were performed up to now only with spray-deposited layers, since CSVT layers created already serious problems by the observation of all-OB in transmission [6–8].

In conclusion, the results presented open new horizons for both basic research and new applications in photonics and measuring techniques.

confirming the importance of further research on nonlinear and bistable properties, respectively of thin semiconducting films.

### 5. Acknowledgement

We are grateful to H. Nguyen Cong and Professor P. Chartier for the excellent sample preparation. B.U. and A.K. acknowledge financial support of the Japan Society for the Promotion of Science and of Mittel für ausländische Gäste der Technischen Universität Graz, respectively.

### 6. References

- [1] T. Kobayashi, IEICE Trans. Fundamentals E75-A (1992) 38.
- [2] H.M. Gibbs, Optical Bistability: Controlling Light with Light (Academic Press, London, 1985) p. 86.
- [3] T. Kobayashi, Ed., Nonlinear Optics of Organics and Semiconductors (Springer, Berlin, 1989) Part II, p. 38; Part V, p. 126.
- [4] B. Ullrich, C. Bouchenaki and S. Roth, Appl. Phys. A 53 (1991) 539.
- [5] B. Ullrich, C. Bouchenaki, S. Roth and G. Leising, J. Crystal Growth 117 (1992) 925.
- [6] C. Bouchenaki, J.Y. Bigot, A. Daunois, J.P. Zielinger, J.L. Loison, H. Nguyen Cong and P. Chartier, Proc. Soc. Photo-Opt. Instr. Eng. 1127 (1989) 21.
- [7] C. Bouchenaki, B. Ullrich, J.P. Zielinger, H. Nguyen Cong and P. Chartier, J. Crystal Growth 101 (1990) 797.
- [8] C. Bouchenaki, B. Ullrich, J.P. Zielinger, H. Nguyen Cong and P. Chartier, J. Opt. Soc. Am. B 8 (1991) 691.
- [9] B. Ullrich, C. Bouchenaki, J.P. Zielinger, H. Nguyen Cong and P. Chartier, J. Appl. Phys. 69 (1991) 7357.
- [10] B. Ullrich and C. Bouchenaki, Jap. J. Appl. Phys. 30 (1991) L1285.
- [11] B. Ullrich and S. Zerlauth, Nonlinear Opt., in press.
- [12] J. Hajtő and I. Jánossy, Phil. Mag. B 47 (1983) 347.
- [13] F. Henneberger and H. Rossmann, Phys. Status Solidi (b) 121 (1984) 685.
- [14] D.A.B. Miller, A.C. Gossard and W. Wiegmann, Opt. Lett. 9 (1984) 162.
- [15] M. Dagenais and W.F. Sharfin, Appl. Phys. Lett. 45 (1984) 210.
- [16] I. Jánossy, M.R. Taghizadeh, J.G.H. Mathew and S.D. Smith, IEEE J. Quantum Electron. QE-21 (1985) 1447.
- [17] M. Lambsdorff, C. Dörfeld and C. Klingshirn, Z. Physik B 64 (1986) 409.
- [18] I. Haddad, M. Kretschmar, H. Rossmann and F. Henneberger, Phys. Status Solidi (b) 138 (1986) 235.
- [19] B. Ullrich, A. Kazlauskas, S. Zerlauth, H. Nguyen Cong and P. Chartier, in: Extended Abstracts 1993 Int. Conf. on Solid State Devices and Materials, Chiba, Japan, 1993, p. 669.
- [20] B. Ullrich, Jap. J. Appl. Phys. 32 (1993) L411.
- [21] A. Hoffmann, I. Broser, P. Thürian and R. Hertz, J. Crystal Growth 101 (1990) 532.
- [22] P. Chartier, B. Ba, J. Ebothe, N. Alonso Vante and H. Nguyen Cong, J. Electroanal. Chem. 138 (1982) 381.
- [23] J. Gutowski, J. Hollandt and I. Broser, Z. Physik B 76 (1989) 547.
- [24] B. Ullrich, Nonlinear Opt. 4 (1993) 63.
- [25] C. Bouchenaki, B. Ullrich and J.P. Zielinger, J. Luminescence 48&49 (1991) 649.



ELSEVIER

Journal of Crystal Growth 138 (1994) 239–243

JOURNAL OF  
CRYSTAL  
GROWTH

## Raman, infrared, photoluminescence and theoretical studies of the II–VI–VI ternary CdSeTe

Z.C. Feng <sup>a,\*</sup>, P. Becla <sup>b</sup>, L.S. Kim <sup>c</sup>, S. Perkowitz <sup>c</sup>, Y.P. Feng <sup>a</sup>, H.C. Poon <sup>a</sup>,  
K.P. Williams <sup>d</sup>, G.D. Pitt <sup>d</sup>

<sup>a</sup> Department of Physics, National University of Singapore, Singapore S0511, Singapore

<sup>b</sup> Room 13-4111, Massachusetts Institute of Technology, Cambridge, Massachusetts 02139, USA

<sup>c</sup> Department of Physics, Emory University, Atlanta, Georgia 30322, USA

<sup>d</sup> Renishaw, Old Town, Wotton-under-edge, Gloucestershire GL12 7DH, UK

### Abstract

We have examined Bridgman-grown zincblende CdSe<sub>1-x</sub>Te<sub>x</sub> ( $x < 0.36$ ) by Raman scattering, Fourier transform infrared reflectivity, photoluminescence and theoretical analysis. The Raman data showed evidence of surface structural improvement by long-term room temperature annealing. The combined Raman and infrared data confirmed the interpretation that a third infrared mode besides the CdTe- and CdSe-like transverse optical phonon modes, arose from non-random atomic clustering. Room temperature photoluminescence spectra were obtained and compared with pseudopotential calculations.

### 1. Introduction

Cadmium telluride, cadmium selenide and their pseudobinary compounds are very suitable for various optoelectronic devices, such as photoconductors, photovoltaic detectors, photoelectrochemical and solar energy cells, and as substrates for growth of quantum wells and epitaxial layers of HgCdTe, HgZnTe and HgMnTe (refs. [1,2] and references therein). The II–VI–VI ternary semiconductor CdSe<sub>1-x</sub>Te<sub>x</sub> possesses the zincblende structure for  $x < 0.36$ . Its energy bandgap  $E_g$  decreases as  $x$  increases in this range. Beyond  $x \approx 0.4$ , it exhibits the hexagonal structure with its

energy bandgap increasing until it reaches the value for pure CdSe [3]. Several studies of absorption [4] and reflectance [3,5] reveal that  $E_g$  versus Se composition  $x$  displays a large bowing effect, with the minimum value of  $E_g$  occurring for  $x$  between 0.36 and 0.5. There is considerable variation among data from different authors. Nakhory et al. [6] have recently given expressions for the band gaps of the quaternary ZnCdSeTe and its boundary ternary alloys, including CdSe<sub>1-x</sub>Te<sub>x</sub>, as functions of composition at 4 and 300 K. These results motivate further study of the band gap.

Earlier investigations of infrared (IR) reflectance [7,8] and Raman scattering [9] from CdSe<sub>1-x</sub>Te<sub>x</sub> have shown the typical two-mode behavior of the long wavelength optical phonons. However, Perkowitz et al. [10] recently reported a

\* Corresponding author.

third mode which was attributed to substantial non-random clustering of the anions around the cations.

In this paper, we present a combined Raman, infrared, photoluminescence (PL) and theoretical study of five zincblende  $\text{CdSe}_x\text{Te}_{1-x}$  crystals with  $x = 0$  (i.e. pure CdTe), 0.05, 0.15, 0.25 and 0.35. The Raman data show a possibility of surface structural improvement by long term room temperature annealing, and show that the previously observed third mode seen in infrared spectra is a bulk effect. Using a new type of optical spectrometer, we have successfully obtained room temperature photoluminescence spectra of these alloys, which were not detectable previously using an old type of scanning spectrometer. These data are compared to empirical and to first principles pseudopotential calculations.

## 2. Experiment

The samples were prepared by the Bridgman technique at Massachusetts Institute of Technology.  $\text{CdSe}_x\text{Te}_{1-x}$  alloys were prepared by reacting the 99.9999% pure elemental constituents at  $\sim 1150^\circ\text{C}$  in evacuated, sealed quartz tubes. These were regrown by directional solidification at rates of 0.8–1 mm/h in a Bridgman–Stockbarger-type furnace. The resultant boules were cut into slices, 1–2 mm thick, and perpendicular to the growth axis. These were annealed at  $650^\circ\text{C}$  in a Se atmosphere, to improve the crystalline perfection. Consequently they were lapped, polished, and etched in a bromine–methanol solution. The alloy compositions were set by the ratio of constituents before growth, and confirmed by X-ray diffraction and transmission measurements after preparation. These samples were found to be single-crystal with the zincblende structure.

Raman scattering and Fourier transform infrared (FTIR) reflectivity measurements were made using facilities at Emory University described elsewhere [11]. The room temperature (RT) PL measurements were performed in Singapore using a new Renishaw model 2000 Raman and PL spectrometer with a single grating, notch filter, microprobe capability and CCD detection.

## 3. Results and discussion

### 3.1. Raman scattering

Fig. 1 displays the Raman spectra of the four  $\text{CdSe}_x\text{Te}_{1-x}$  crystals, measured at 80 K and excited by the 501.7 nm line from an  $\text{Ar}^+$  laser. CdTe-like and CdSe-like transverse optical (TO) and longitudinal optical (LO) phonons, labeled as  $\text{TO}_1$ ,  $\text{TO}_2$ ,  $\text{LO}_1$  and  $\text{LO}_2$ , respectively, are seen between 140 and  $200\text{ cm}^{-1}$ . Their frequencies versus  $x$  are shown in Fig. 2, which also shows the results for pure CdTe and pure CdSe as given in the literature [12]. The solid lines in the figure are guides to the eye.  $\text{LO}_2$  increases and  $\text{LO}_1$  decreases in wavenumber markedly, while  $\text{TO}_2$  decreases and  $\text{TO}_1$  increases only slightly, as  $x$  increases from 0 to 0.35.

The features between 300 and  $400\text{ cm}^{-1}$  in Fig. 1 are due to second order LO phonons, i.e. combinations of  $\text{LO}_1$  and  $\text{LO}_2$ ,  $2\text{LO}_1$ ,  $\text{LO}_1 + \text{LO}_2$  and  $2\text{LO}_2$ . The strength and sharpness of high order phonons in semiconductors are generally sensitive to the degree of the crystalline perfection. As  $x$  increases, the intensities of the second order LO peaks relative to the first order peaks decrease, indicating the increased disorder. The broad feature near  $250\text{ cm}^{-1}$  is perhaps due to defects, whose origin is unknown.

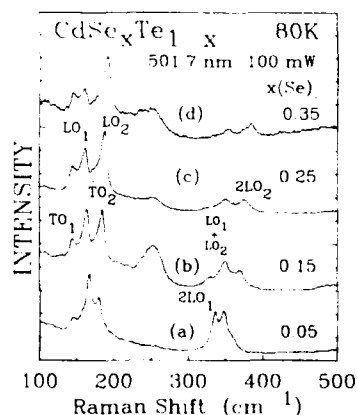


Fig. 1. Raman spectra of Bridgman-grown bulk  $\text{CdSe}_x\text{Te}_{1-x}$  at 80 K, excited by 501.7 nm, with values of  $x$  being (a) 0.05, (b) 0.15, (c) 0.25, and (d) 0.35.

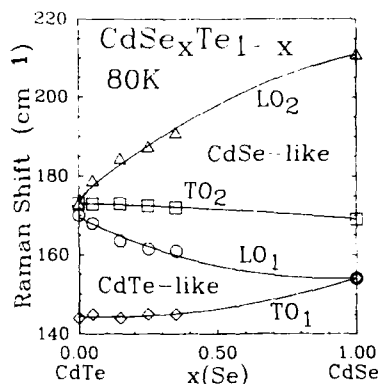


Fig. 2. Raman peak position at 80 K versus  $x$  for  $\text{CdSe}_x\text{Te}_{1-x}$ .

Fig. 3 exhibits the Raman spectra of these four samples, excited at 488.0 nm and taken over a year ago, but with all other experimental conditions similar to those used for Fig. 1. This comparison, and comparisons between old and new data all obtained at 488.0 nm, show that the new Raman spectra are substantially improved over the earlier data, with better separation among the first order lines and clearer second order lines. This improvement after a year's time suggests that long term room-temperature annealing may have some effects on the crystalline quality of the samples, especially near the surface.

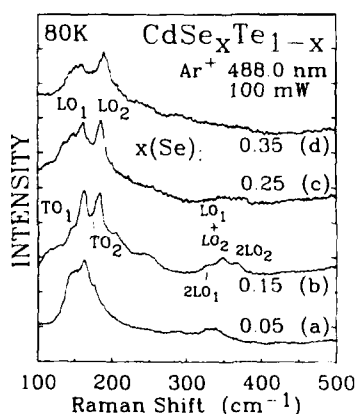


Fig. 3. Raman spectra of Bridgman-grown bulk  $\text{CdSe}_x\text{Te}_{1-x}$  at 80 K, excited by 488.0 nm, with values of  $x$  being (a) 0.05, (b) 0.15, (c) 0.25, and (d) 0.35. These spectra were measured more than year earlier than those in Fig. 1.

The earlier Raman study of  $\text{CdSe}_x\text{Te}_{1-x}$  [9] was excited at 1.06  $\mu\text{m}$  by a YAG:Nd laser, and was carried out at room temperature only. Our new study at 80 K and visible wavelengths (501.7 and 488.0 nm) reduces the laser penetration into the sample to less than a few hundred ångströms, to probe the near surface region, and can have sensitivity to surface segregation due to room-temperature annealing.

The observed variation of Raman spectra over a long period cannot be caused by the surface oxidation. The oxides are generally transparent to the visible laser beam. The naturally oxidized surface layer is extremely thin and it is not possible to cause important effects on the Raman spectra of  $\text{CdSeTe}$  alloy. In fact, we also did not find any features from Raman and FTIR spectra, which could be related to the surface oxides. Even if the surface oxidation occurred and the oxide layer would become thicker after a long period, its effects, if any, would make the Raman spectrum from the crystal beneath worse than before, which is opposite to the observed results. Further investigation on the surface variations of  $\text{CdSe}_x\text{Te}_{1-x}$  by surface science analytical techniques may shed light on this problem.

### 3.2. Fourier transform infrared reflectivity

Figs. 4 and 5 display the FTIR reflectivity spectra of the four  $\text{CdSe}_x\text{Te}_{1-x}$  samples at 300 and 82 K, respectively [10]. Below 170  $\text{cm}^{-1}$ , the regular reststrahlen band characteristic of the CdTe-like TO phonon is seen in all the samples at 300 and 82 K. Beyond 170  $\text{cm}^{-1}$ , there is a

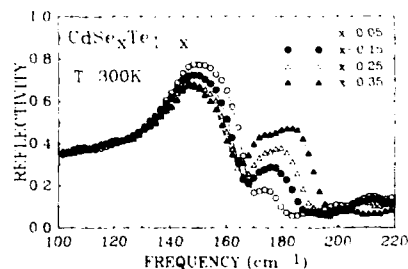


Fig. 4. FTIR reflectivity of bulk  $\text{CdSe}_x\text{Te}_{1-x}$  at 300 K, with  $x = 0.05, 0.15, 0.25$ , and  $0.35$ .



CdSe-like TO band which grows with  $x$  and splits into two bands. The splitting is more apparent in the sharper peaks at 82 K, but cannot be clearly resolved at 300 K. There is, however, no evidence of this splitting in the low temperature Raman data shown in Fig. 1. This indicates that the third peak comes from the bulk, not from the surface, because infrared excitation penetrates into the sample more deeply than the visible excitation used in the Raman measurements. A bulk origin for the third peak strengthens the earlier interpretation that it comes from non-random cluster effects [10].

### 3.3. Room temperature photoluminescence

Fig. 6 shows RT PL spectra of  $\text{CdSe}_x\text{Te}_{1-x}$ , including pure CdTe, using the Renishaw model 2000 spectrometer. The excitation was He–Ne 633 nm with approximate 1 mW at the sample over a spot of about 1  $\mu\text{m}$  diameter. In earlier measurements, using a standard double spectrometer–photomultiplier–photon counting system, or a triple spectrometer–Si array optical multichannel analyzer detection system, we obtained PL spectra of these same samples below 150 K, but could not obtain RT PL spectra. Fig. 6 shows that the PL band shifts down in energy as  $x$  increases from 0 to 0.35, indicating a decrease in the energy band gap. We also made absorption measurements on these samples (not shown here) and the same result was obtained. More work on PL of  $\text{CdSe}_x\text{Te}_{1-x}$  and their variations with temperature and time is in process and will be published later.

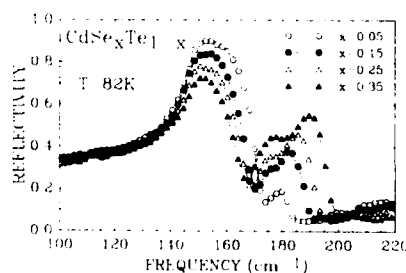


Fig. 5. FTIR reflectivity of four bulk  $\text{CdSe}_x\text{Te}_{1-x}$ , with  $x = 0.05, 0.15, 0.25$ , and  $0.35$ , taken at 82 K.

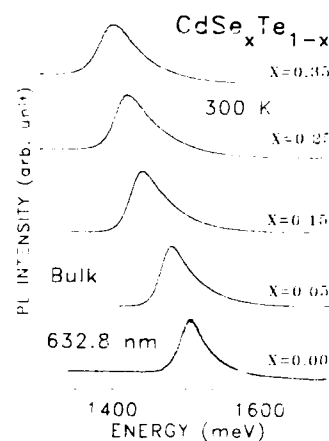


Fig. 6. Room temperature photoluminescence of bulk  $\text{CdSe}_x\text{Te}_{1-x}$  with  $x = 0, 0.05, 0.15, 0.25$ , and  $0.35$ , respectively.

### 3.4. Theoretical calculation of $E_g$ – $x$ relation

To better understand its optical properties, we performed band structure calculations for the  $\text{CdSe}_x\text{Te}_{1-x}$  ternary alloy using both empirical, and self-consistent, pseudopotential methods [13,14]. The energy gap obtained from the empirical pseudopotential method is shown in Fig. 7a as a function of  $x$  with RT PL results from Fig. 6 (filled circles) and the curve given by Nahory et al. (dashed line) [5]. The virtual crystal approximation (VCA) was used in our empirical pseudopotential calculation. For the pure binary compounds CdSe and CdTe, we used the form factors given by Cohen and Bergstresser [13]. The form factor of the ternary alloy is assumed to be a quadratic function of  $x$ , with a bowing factor which is about 10% of the average of the form factors of CdTe and CdSe. The zincblende crystal structure was assumed in this calculation, with the lattice constant varying linearly with  $x$ .

The first principles pseudopotential calculation on the bowing effect of the energy band gap of  $\text{CdSe}_x\text{Te}_{1-x}$  is presented in Fig. 7b. The relativistic norm-conserving pseudopotentials of the ion cores were constructed using a method due to Bachelet et al. [15]. The valence charge density and crystal pseudopotential were calculated self-

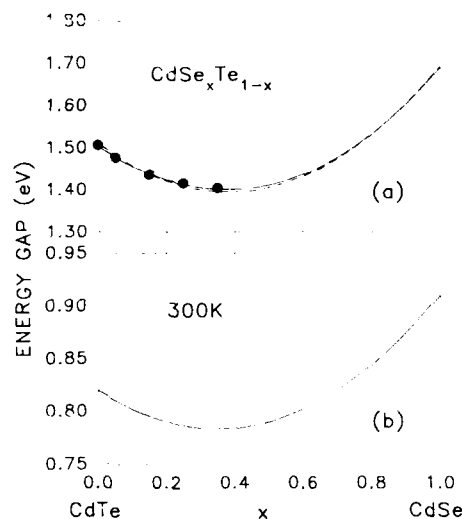


Fig. 7. Energy gap versus  $x$  of  $\text{CdSe}_x\text{Te}_{1-x}$ . For (a), the solid line shows our calculated results by the empirical pseudopotential method, the dashed line is from Nahory et al. [6], and the filled circles represent our experimental results from Fig. 6. The first principles calculation for the bowing effect is sketched in (b).

consistently by the local density functional approximation. The band structure was evaluated from this self-consistent potential. The VCA, and a linear dependence of lattice constant on composition, were assumed as in the semi-empirical calculation.

It is well known that the absolute value of the gap is underestimated because these calculations neglect certain many body effects, which makes the bandgap values in Fig. 7b quite different from those in Fig. 7a. However, the overall trend agrees well with experiments. The two types of theoretical calculations also compare well with each other, showing a similar bowed shape and similar positions for the minimum in  $E_g$ . More details of the theoretical analysis and comparison with other II–VI ternary compounds will be given in a future publication.

#### 4. Conclusion

A multi-technique study using Raman scattering, FTIR reflectance, photoluminescence, and

pseudopotential calculations has been made on Bridgman-grown bulk  $\text{CdSe}_x\text{Te}_{1-x}$  with zincblende structure ( $x < 0.36$ ). The noteworthy changes in Raman spectra taken more than a year apart suggest that long-term room temperature annealing may improve sample quality, especially near the surface. The Raman spectra are also consistent with an earlier interpretation of infrared data, where a third mode is ascribed to non-random clustering. RT PL spectra from  $\text{CdSe}_x\text{Te}_{1-x}$  alloys are obtained, for the first time, to our knowledge. Theoretical calculations, based upon empirical and first principles pseudopotential methods, have been performed, and compared well the experimental results.

#### 5. References

- [1] S.M. Babu, T. Rajalakshmi, R. Dhanasekaran and P. Bamasamy, *J. Crystal Growth* 110 (1991) 423.
- [2] M. Bouroushian, Z. Loizos, N. Spyrellis and G. Maurin, *Thin Solid Films* 229 (1993) 101.
- [3] M.S. Brodin, N.I. Vitrikhovich, A.A. Kipen and I.B. Mizetskaya, *Sov. Phys.-Semicond.* 6 (1972) 601.
- [4] L.V. Prytkina, V.V. Volkov, A.N. Mentser, A.V. Vanyukov and P.S. Kireev, *Sov. Phys.-Semicond.* 2 (1968) 509.
- [5] H. Tai, S. Nakashima and S. Hori, *Phys. Status Solidi (a)* 30 (1975) K115.
- [6] M.J. Nahory, S.P. Brasel and M. Tamargo, in: *Semiconductor Interfaces and Microstructures*, Ed. Z.C. Feng (World Scientific, Singapore, 1992) p. 238.
- [7] M. Gorska and W. Nazarewicz, *Phys. Status Solidi (b)* 57 (1973) K65; 65 (1974) 193.
- [8] E.A. Vinogradov, L.K. Vodopyanov and G.S. Oleinik, *Sov. Phys.-Solid State* 15 (1973) 322.
- [9] V.G. Plotnichenko, L.V. Golubev and L.K. Vodopyanov, *Sov. Phys.-Solid State* 19 (1977) 1582.
- [10] S. Perkowitz, L.S. Kim and P. Becla, *Phys. Rev. B* 43 (1991) 6598.
- [11] M. Macler, Z.C. Feng, S. Perkowitz, R. Rousina and J. Webb, *Phys. Rev. B* 46 (1992) 6902.
- [12] Landolt-Börnstein Numerical Data and Function Relations in Science and Technology, Vol. 17b, Ed. O. Madelung (Springer, Berlin 1982) pp. 213, 227.
- [13] M.L. Cohen and T.K. Bergstresser, *Phys. Rev.* 141 (1966) 789.
- [14] J. Ihm, A. Zunger and M.L. Cohen, *J. Phys. C* 12 (1979) 4409.
- [15] G.B. Bachelet, D.R. Hamann and M. Schluter, *Phys. Rev. B* 26 (1982) 4199.



ELSEVIER

Journal of Crystal Growth 138 (1994) 244–248

CRYSTAL  
GROWTH

## Optical and thermal spectroscopy of vanadium-doped CdTe and related photorefractive effect

E. Rzepka <sup>a,\*</sup>, A. Aoudia <sup>a</sup>, M. Cuniot <sup>a</sup>, A. Lusson <sup>a</sup>, Y. Marfaing <sup>a</sup>, R. Triboulet <sup>a</sup>,  
G. Brémond <sup>b</sup>, G. Marrakchi <sup>b</sup>, K. Cherkaoui <sup>b</sup>, M.C. Busch <sup>c</sup>, J.M. Koebel <sup>c</sup>,  
M. Hage-Ali <sup>c</sup>, P. Siffert <sup>c</sup>, J.Y. Moisan <sup>d</sup>, P. Gravey <sup>d</sup>, N. Wolffer <sup>d</sup>, O. Moine <sup>d</sup>

<sup>a</sup> Laboratoire de Physique des Solides de Bellevue, CNRS, 1 Place A. Briand, F-92195 Meudon Cedex, France

<sup>b</sup> Physique de la Matière, INSA, F-69621 Villeurbanne Cedex, France

<sup>c</sup> PHASE, CNRS, BP 20, F-67037 Strasbourg Cedex, France

<sup>d</sup> Département TAC, CNET, BP 40, F-22301 Lannion, France

### Abstract

The energy level diagram of substitutional vanadium in CdTe (and also Cd<sub>0.96</sub>Zn<sub>0.04</sub>Te) has been investigated by using a variety of optical and thermal spectroscopy techniques: optical absorption, photoconductivity, photoluminescence, deep level optical spectroscopy, DLTS and thermally stimulated current (PICTS). This study has led to set the V<sup>2+</sup>/V<sup>3+</sup> level at 0.95 eV below the conduction band with an optical photoionization threshold at 1.03 eV. Two-wave mixing experiments were used to evaluate the photorefractive properties. Gain coefficients in excess of 10 cm<sup>-1</sup> have been measured at  $\lambda = 1.32 \mu\text{m}$  with applying a 40 Hz AC electric field.

### 1. Introduction

CdTe is a promising semiconductor material for application of photorefractivity to information optical processing. The large electrooptic coefficient leads to a figure of merit 3–4 times higher than in the III–V semiconductors GaAs and InP [1,2]. Furthermore, several types of deep centres exist, allowing one to obtain a photoresponse in the wavelength ranges of interest [3,4].

Vanadium doping has been used most extensively in the current studies of the photorefractivity effect in CdTe. Amplification gain in two-wave mixing experiments has been observed at several

wavelengths from 1.06 to 1.52  $\mu\text{m}$  [1,2,5–7]. However, there has been no detailed investigation of the energy level structure of V within the CdTe bandgap, since the work of Slodowy and Baranowski [8].

In the present paper we report on a spectroscopic study of vanadium in CdTe using a combination of several experimental techniques: optical absorption, photoconductivity, photoluminescence, thermally and optically stimulated capacitance (DLTS, DIOS) and thermally stimulated current (PICTS). All these results will allow us to propose a configuration coordinate diagram for the transitions due to V in CdTe. In addition, we present recent wave-mixing experiments which demonstrate the possibilities of the photorefractive effect at various wavelengths.

\* Corresponding author.

## 2. Crystal growth

Two kinds of crystals were used. Most of the samples reported on here were cut from CdTe and  $\text{Cd}_{0.96}\text{Zn}_{0.04}\text{Te}$  crystals grown by the vertical Bridgman method with vanadium added in the melt at a nominal concentration of  $10^{19}$  atoms  $\text{cm}^{-3}$ . The vanadium concentration in the crystals, deduced from calibrated SIMS measurements, is in the range  $10^{16}$ – $10^{18}$  atoms  $\text{cm}^{-3}$ . A strong segregation of vanadium towards the tail of the ingots is observed, which indicates a distribution coefficient far below unity. The electrical resistivity of the as-grown crystals is  $10^9$ – $10^{10}$   $\Omega$  cm.

Some CdTe crystals were grown by travelling heater method (THM) using Te as the solvent. Vanadium was introduced in the Te zone (at  $10^{19}$  atoms  $\text{cm}^{-3}$ ). The concentration in the crystals measured by atomic absorption is in the range  $10^{16}$ – $10^{17}$  atoms  $\text{cm}^{-3}$ . The electrical resistivity is around  $10^8$   $\Omega$  cm.

Some  $\text{Cd}_{0.96}\text{Zn}_{0.04}\text{Te}$  samples were annealed at 700°C under saturated Cd vapour pressure in order to convert them to n-type conductivity. The measured room temperature electron concentration was about  $5 \times 10^{15}$   $\text{cm}^{-3}$ . These samples were used to perform space-charge capacitance spectroscopies (DLTS, DLOS).

## 3. Optical spectroscopy of as-grown crystals

An optical absorption spectrum at 6 K of a Bridgman grown CdTe:V sample was published earlier [3]. Three intra-atomic transition bands at 0.47, 0.82 and 1.2 eV were observed corresponding to transitions from the configuration  $^4T_1(^4F)$  to  $^4T_2(^4F)$ ,  $^4A_1(^4F)$  and  $^4T_1(^4P)$ , respectively, in the  $\text{V}^{2+}$  state. The last transition is partially structured into three bands (1.08, 1.15 and 1.23 eV). We have never observed the transition at 0.9 eV reported in ref. [8] and associated by these authors to the state  $^2E(^2F)$ . However, in most  $\text{Cd}_{0.96}\text{Zn}_{0.04}\text{Te}:\text{V}$  crystals an additional transition consistently appears around 0.94 eV. We have no definite explanation for this band.

Photoconductivity spectra were measured on a

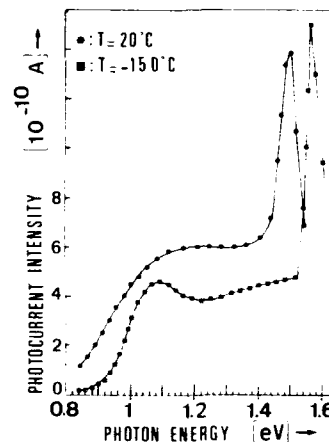


Fig. 1. Photoconductivity spectra of a CdTe:V crystal at two temperatures.

Bridgman grown CdTe:V crystal at room temperature and below ( $-150^\circ\text{C}$ ) (Fig. 1). The low-temperature spectrum shows a steep rise from a threshold around 0.9 eV and a maximum near 1.1 eV. This structure seems to correspond to photoionization transitions of the  $\text{V}^{2+}$  centres via the first excited state  $^4T_1(^4P)$  referred to above. This structure is broadened at room temperature due to increased phonon contribution. Intrinsic absorption leads to the high photoconductivity peaks observed at higher energy.

Photoluminescence spectra were recorded on a series of Bridgman-grown and THM-grown V-doped crystals. Two broad bands are seen at low temperature, with emission maximum at 0.8 and 1.1 eV. They are not detected in the absence of vanadium. After annealing of the crystals under Cd vapour, the photoluminescence intensity is strongly reduced.

## 4. Space-charge spectroscopy and thermally stimulated current

Space-charge spectroscopy was carried out on Schottky diodes realized by gold deposition on n-type vanadium doped  $\text{Cd}_{0.96}\text{Zn}_{0.04}\text{Te}$  samples.

First DLTS spectra were recorded which reveal five electron traps (Fig. 2). The trap param-

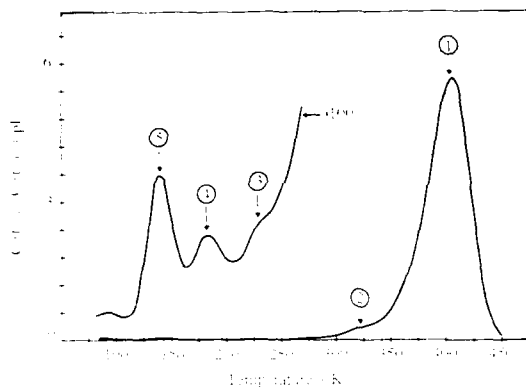


Fig. 2. DLTS spectrum of an n-type vanadium-doped  $\text{Cd}_{0.96}\text{Zn}_{0.04}\text{Te}$  crystal.

ters are collected in Table 1. The dominant centre has the highest activation energy (0.95 eV). Its concentration is in the range of the effective trap density deduced from the photorefractivity effect. Hence we assign this deep centre to substitutional vanadium. The other traps have concentrations at least 10 times smaller. They cannot be identified for the moment.

**Deep level optical spectroscopy (DLOS)** relies on capacitance transients associated with optical excitation [9,10]. This technique was used to determine the photoionization cross-section of centre 1 for transitions to the conduction band  $\sigma_n^0$ . For this experiment the temperature was set at 312 K, where all the traps except centre 1 are ionized under reverse bias in the dark. A fit to this spectral variations of  $\sigma_n^0$  has been made using a theoretical expression given by Martinez

Table 1  
Parameters of the traps detected by DLTS on an n-type vanadium-doped  $\text{Cd}_{0.96}\text{Zn}_{0.04}\text{Te}$  crystal

Trap	Activation energy (eV)	Apparent capture cross section ( $\text{cm}^2$ )	Concentration ( $\text{cm}^{-3}$ )
1	0.95	$5 \times 10^{-15}$	$1.5 \times 10^{15}$
2	0.78	$9 \times 10^{-15}$	$8 \times 10^{13}$
3	0.44	$1 \times 10^{-16}$	$8 \times 10^{12}$
4	0.26	$1 \times 10^{-15}$	$3 \times 10^{12}$
5	0.20	$2 \times 10^{-16}$	$(3-5) \times 10^{12}$

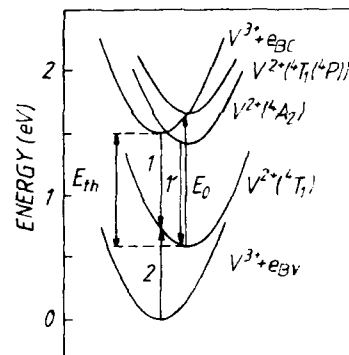


Fig. 3. Configuration coordinate diagram of the  $\text{V}^{3+} - \text{V}^{4+}$  state in CdTe.

et al. [11] which accounts for transitions between vibronic levels.

$$\sigma_n^0 = \frac{A}{h\nu} \exp(-x^2) \frac{(\beta + x)^{1/2}}{[h\nu + \Gamma_b x + E_0(\alpha_c - 1)]^2}$$

$E_0$  is the optical threshold energy,  $h\nu$  is the photon energy,  $\Gamma_b$  is the broadening parameter,  $\beta = (h\nu - E_0)/\Gamma_b$  and  $\alpha_c = m/m_c^*$ ,  $m$  and  $m_c^*$  being the free electron mass and the conduction band mass. From this fit the following values are deduced:  $E_0 = 1.03$  eV and  $\Gamma_b = 0.1$  eV.

**Photo-induced current transient spectroscopy (PICTS)** is a thermally stimulated current technique. It was applied to as-grown semi-insulating CdTe:V samples grown by THM. A trap with an activation energy of 0.65 eV is detected.

## 5. Configuration coordinate diagram for V in CdTe

The above spectroscopy results leads to the coordinate configuration diagram shown in Fig. 3. It is essentially built from the optical threshold energy  $E_0$  (1.03 eV) determined by DLOS and the thermal activation energy  $E_{th}$  (0.95 eV) obtained from DLTS.

This diagram allows us to interpret the other spectroscopy experiments. The low temperature photoconductivity response gives evidence of a particular resonance between the excited  $^4\text{T}_1(^4\text{P})$

state at 1.08 eV and the conduction band. As a matter of fact, the minimum of the configuration curve associated with this excited state is nearly coincident with the conduction electron configuration curve (Fig. 3). This induces a highly efficient electron transfer from this excited state to the conduction bands and explains the photoconductivity peak observed at  $-150^{\circ}\text{C}$  near 1.1 eV. Electron transfer from the higher excited states is less probable at low temperature, despite the larger absorption coefficient.

The photoluminescence bands observed in the as-grown crystals seem to involve a configuration change from  $\text{V}^{3+}$  to  $\text{V}^{2+}$ . The lower emission band, around 0.8 eV, would be due to a combination of free electron radiative capture by the empty donor states ( $\text{V}^{3+}$ ) and transitions from the  $^3\text{A}_2$  excited state to the ground state (processes 1 and 1' in Fig. 3). The higher emission band, around 1.1 eV, is explainable in terms of electron capture on the  $^4\text{T}_1(^4\text{P})$  excited states and transitions to the ground state. Optical excitation at energy higher than the band gap makes possible this type of electron capture. In the annealed crystals, all the  $\text{V}^{3+}$  centres are converted to the  $\text{V}^{2+}$  equilibrium configuration. Thus the occurrence of the above transitions is less probable because they first require the capture of holes. This agrees with the observed reduction in photoluminescence intensity.

At last, the trap energy at 0.65 eV deduced from PICTS experiments could correspond to hole emission from the  $\text{V}^{3+}$  state to the valence band (process 2 in Fig 3).

## 6. Photorefractive properties

Bridgman-grown vanadium-doped  $\text{Cd}_{0.96}\text{Zn}_{0.04}\text{Te}$  crystals have been used for photorefractive measurements in a two-wave mixing configuration. Fitting the dependence of gain coefficient on incident intensity  $I$  at wavelengths of 1.32 and  $1.535\text{ }\mu\text{m}$  (no external electric field, room temperature) to the theoretical expression,

$$I' = I_0 / (1 + I_0/I),$$

allows one to determine the saturated gain coefficient

Table 2

Photorefractivity properties at two wavelengths of two vanadium-doped  $\text{Cd}_{0.96}\text{Zn}_{0.04}\text{Te}$  crystals

Crystal	Wave-length ( $\mu\text{m}$ )	$I_0$ ( $\mu\text{W}/\text{cm}^2$ )	$I_0'$ ( $\text{cm}^{-1}$ )	$\xi$	$N_A$ ( $10^{14}\text{ cm}^{-3}$ )
DAV 30	1.32	75	0.24		
DAV 30	1.535	155	0.26	0.71	8.4
DAV 31	1.32			0.68	13.7
DAV 31	1.535			0.87	17.4

coefficient  $I_0'$  and the equivalent dark irradiance  $I_0$ . These values are collected in Table 2. They indicate a good photosensitivity of the material at

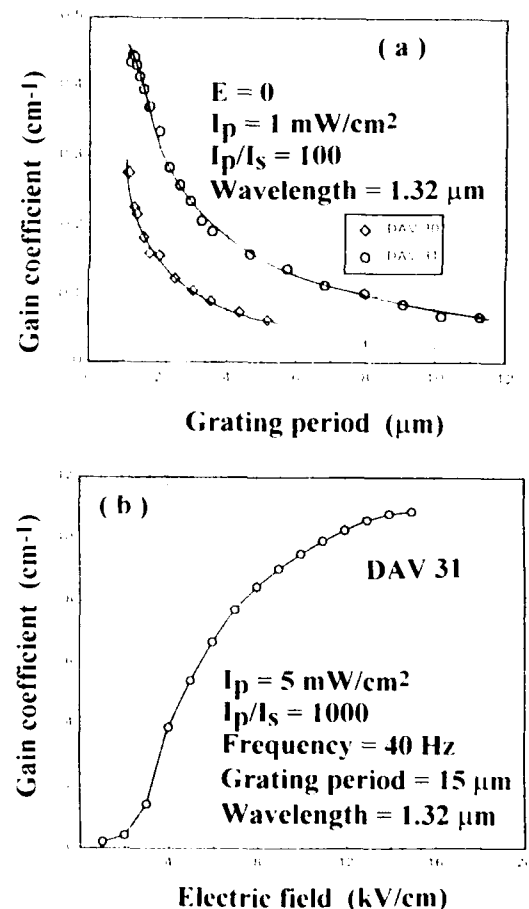


Fig. 4. TWM gain coefficient versus (a) grating period in two vanadium-doped  $\text{Cd}_{0.96}\text{Zn}_{0.04}\text{Te}$  crystals and (b) AC electric field amplitude.

these two wavelengths of interest for optical telecommunication. The variations of beam-coupling gain coefficient at  $1.32\ \mu\text{m}$  as a function of grating period are shown in Fig. 4a for two different crystals. DAV 31 contains about twice more vanadium (about  $10^{17}\ \text{cm}^{-3}$ ) than DAV 30. The theoretical fit to these curves, using a single level model, gives values of the electron–hole competition factor  $\xi$  and of the effective trap density  $N_A$  (Table 2). Approximately equal  $N_A$  values are evaluated at  $1.32$  and  $1.535\ \mu\text{m}$ , which suggests that the same level is involved in both cases. On the other hand, other experiments have shown that the majority of the photoexcited carriers at these two wavelengths are holes. The higher magnitude of  $\xi$  at  $1.525\ \mu\text{m}$  indicates a larger contribution of holes at this wavelength.

By application of an AC electric field, the gain coefficient can be enhanced. This is exemplified in Fig. 4b for a 40 Hz field frequency. Gain coefficients in excess of  $10\ \text{cm}^{-1}$  are readily measured.

## 7. Conclusions

Optical and thermal spectroscopy techniques have been used to determine the energy level diagram of the vanadium deep donor in CdTe (or CdZnTe). The  $V^{2+}/V^{3+}$  level is located in the lower half of the band gap at 0.95 eV below the conduction band. A group of  $V^{2+}$  excited states is resonant with the conduction band states which affects the photoionization and the photoluminescence spectra. The optical excitation threshold to the conduction band is set at 1.03 eV, which points out the existence of a relatively small Franck–Condon shift (0.08 eV). Photosensitivity at wavelengths longer than  $1.3\ \mu\text{m}$  is mainly due to hole transitions between the  $V^{3+}$  state and the valence band, in accordance with the photorefractivity experiments which show a majority hole contribution at  $\lambda = 1.32\ \mu\text{m}$  and  $1.535\ \mu\text{m}$ . The effective trap density of about  $8 \times 10^{14}\ \text{cm}^{-3}$  evalu-

ated in crystal DAV 30 may be compared to the 0.95 eV deep centre concentration of  $(0.9\text{--}1.5) \times 10^{15}\ \text{cm}^{-3}$  measured by DLTS on a similar crystal. Compatibility between these two values would imply approximate equality between the filled and empty trap concentrations. Further work is necessary to give a better determination of the trap occupation ratio. More generally, the transitions with the valence band have to be studied in detail. It is well known that a number of deep levels exist in the lower half of the band gap, in particular those associated with the cadmium vacancy–donor impurity pairs. This raises the question of the eventual contribution of such deep centres to the observed photosensitivity at long wavelengths. Better knowledge of the transitions in play and of the material parameters will allow one to fully exploit the capability of the CdTe:V system.

## 8. References

- [1] R.B. Bylisma, P.M. Bridenbaugh, D.M. Olson and A.M. Glass, *Appl. Phys. Lett.* 51 (1987) 889.
- [2] J.Y. Moisan, P. Gravey, G. Picoli, N. Wolffler and V. Vieux, *Mater. Sci. Eng. B* 16 (1993) 257.
- [3] E. Rzepka, Y. Marfaing, M. Cuniot and R. Triboulet, *Mater. Sci. Eng. B* 16 (1993) 262.
- [4] P. Moravec, M. Hage-Ali, I. Chibani and P. Siffert, *Mater. Sci. Eng. B* 16 (1993) 223.
- [5] A. Partovi, J. Millerd, E.M. Garmire, M. Ziari, W.H. Steier, S.B. Trivedi and M.B. Klein, *Appl. Phys. Lett.* 57 (1990) 846.
- [6] M. Ziari, W.H. Steier, P.M. Ranon, M.B. Klein and S. Trivedi, *J. Opt. Soc. Am. B* 9 (1992) 1461.
- [7] J.C. Launay, V. Mazoyer, M. Tapiero, J.P. Zielinger, Z. Gnelli, Ph. Delaye and G. Roosen, *Appl. Phys. A* 55 (1992) 33.
- [8] P.A. Slodowy and J.M. Baranowski, *Phys. Status Solidi* (b) 49 (1972) 499.
- [9] A. Chantre, G. Vincent and D. Bois, *Phys. Rev. B* 23 (1981) 5355.
- [10] G. Brémond, G. Guillot and A. Nouailhat, *Rev. Physique Appl.* 22 (1987) 873.
- [11] G. Martinez, A.M. Hennel, W. Szuszkiewicz, M. Balkanski and B. Clerjaud, *Phys. Rev. B* 23 (1981) 3920.



ELSEVIER

Journal of Crystal Growth 138 (1994) 249–254

JOURNAL OF  
**CRYSTAL  
GROWTH**

## Systematic steps towards exactly stoichiometric and uncompensated CdTe Bridgman crystals

P. Rudolph, U. Rinas, K. Jacobs \*

*Institut für Kristallographie und Materialforschung, Fachbereich Physik, Humboldt-Universität zu Berlin, Invalidenstrasse 110, D-10115 Berlin, Germany*

### Abstract

A modified vertical Bridgman arrangement with Cd extra source and variable CdTe melt surface temperature is used to find out conditions for the growth of near stoichiometric CdTe crystals. Growth experiments were carried out with different temperature courses according to predictions for the optimum temperature program obtained from thermodynamic calculations. The transition point from p- to n-type conductivity for inclusion-free crystals was observed at a CdTe melt surface temperature of 1118°C and a Cd source temperature of 850°C. The incorporation of shallow acceptors (Ag, Cu) as a function of the deviation from stoichiometry during the growth was analysed by photoluminescence, mass spectroscopy and atomic absorption spectrophotometry. The incorporation coefficients of atoms substituting Cd were deduced in dependence on their total concentration in the melt and the Te excess. The maintenance of nearly stoichiometric growth conditions drastically reduces the substitutional impurity fraction, acting as shallow acceptors, and therefore the carrier concentration.

### 1. Introduction

There are increasing efforts to produce highly perfect semi-insulating CdTe crystals for applications in X- and  $\gamma$ -ray detectors, electro-optical modulators and IR devices. Well known is the method of compensative doping (by chlorine or indium, for example) leading to samples with high resistivities [1,2]. However, the growth of crystals homogeneously doped along the whole as-grown ingot is complicated by segregation effects, formation of point defect complexes and dopant clustering [3,4]. Growth of undoped nearly stoi-

chiometric CdTe Bridgman crystals with free carrier concentrations below  $10^{14} \text{ cm}^{-3}$  and high electrical resistivities  $\rho$  up to  $10^7$ – $10^8 \Omega \text{ cm}$  at 300 K has been sporadically successful [5–9]. The highest values of  $\rho$  in undoped CdTe ( $3 \times 10^9 \Omega \text{ cm}$ ) and  $\text{Cd}_{0.8}\text{Zn}_{0.2}\text{Te}$  ( $10^{11} \Omega \text{ cm}$ ) were reported by Butler et al. [10]. In essence, these authors attribute their results to the maintenance of nearly stoichiometric crystal composition and cleanliness during the entire growth process. Despite such excellent empirical results, systematic theoretical and practical investigations are missing in the literature.

In the present work, the influence of a well-defined Cd overpressure, adjusted by a separate Cd source, on the electrical properties of crystals grown by a modified vertical Bridgman technique

\* Corresponding author.



has been studied. The necessary temperature of the Cd extra source is estimated from thermodynamic calculations, taking into account the temperature decrease of the free melt surface during the ampoule movement. The experiments show a very sensitive dependence of the type and concentration of free carriers on the temperature–time program of the Cd source.

In connection with this, the influence of residual impurities is quite important. With increasing Cd pressure, a considerable reduction of the content of shallow acceptors in substitutional positions has already been obtained [11,12]. In the present paper, the coefficients of incorporation of silver and copper atoms in dependence on the concentration of the excess component (Te) will be presented.

## 2. Thermodynamic relationships

### 2.1. The $T$ – $y$ phase projection

The uncertainties of the solidus and liquidus line shapes in the  $T$ – $y$  phase projection near the congruent melting point  $T_{\text{mp}}$  (1092°C) turn out to be one of the difficulties to determine the conditions for the growth of an exactly stoichiometric CdTe crystal [13]. Assuming the fully drawn liquidus line (Fig. 1) to be valid, an Cd excess in the melt of about  $\delta y_{\text{Cd}} \approx 1.5 \times 10^{-4}$  ( $\approx 5 \times 10^{18} \text{ cm}^{-3}$ ) is necessary to obtain a stoichiometric solid. According to the  $P$ – $y$  phase projection [14] such a melt composition requires a Cd equilibrium pressure of about 2.0 atm at the corresponding liquidus point. Despite the low equilibrium segregation coefficient  $k_0^{\text{Cd}}$  of about  $3 \times 10^{-2}$ , the enrichment of Cd excess at the crystallization front can be neglected because of the small growth rates (between 0.5 and 1 mm h<sup>-1</sup>) and the action of buoyancy driven convection [13].

### 2.2. Calculation of the temperature of the Cd extra source

For a first crude approximation in the following calculations, thermodynamic equilibrium within the growth ampoule and ideal behaviour

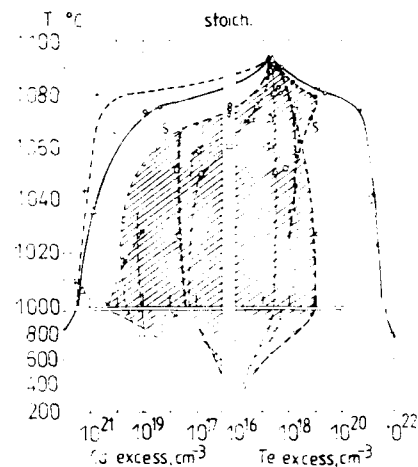


Fig. 1. The  $T$ – $y$  phase projection of CdTe. The data points are taken from various authors completely referred to in ref. [13,14]: (●) Yu.M. Ivanov, Moscow, 1993 (private communication).

of the mixtures are assumed. Supposing the validity of Raoult's law, the equilibrium distribution of Cd between melt and vapour is given by the Rayleigh equation [15]:

$$\frac{x_v}{1-x_v} = \frac{P_{\text{Cd}}^*}{P_{\text{Te}}^*} \frac{x_l}{1-x_l}, \quad (1)$$

or, rearranged,

$$x_v = \frac{\alpha x_l}{1 + (\alpha - 1)x_l}, \quad (2)$$

$x_v$  and  $x_l$  are the mole fractions of Cd in vapour and melt, respectively,  $\alpha$  is the relative volatility ( $P_{\text{Cd}}^*/P_{\text{Te}}^*$ ), and  $P_{\text{Cd}}^*$  and  $P_{\text{Te}}^*$  are the pressures of the pure elements Cd and Te, respectively. The partial pressure of Cd in an ideal gas mixture is given by

$$p_{\text{Cd}} = P_{\text{CdTe}} x_v, \quad (3)$$

where  $P_{\text{CdTe}}$  is the total pressure over the Cd/Te melt. Substituting Eq. (2) into (3) yields

$$p_{\text{Cd}} = P_{\text{CdTe}} \frac{\alpha x_l}{1 + (\alpha - 1)x_l}. \quad (4)$$

After Hultgren et al. [16], the Cd and  $\text{Te}_2$  pressures as a function of temperature are given by

$$\log P_{\text{Cd}}(\text{atm}) = -5317/T + 5.119, \quad (5)$$

$$\log P_{\text{Te}_2}(\text{atm}) = -5960/T + 4.7191. \quad (6)$$

Combining Eq. (4) with Eq. (5) leads to

$$T_{\text{Cd}} = \frac{5317}{5.119 - \log\left(\frac{\alpha}{1/X_{\text{L}} + (\alpha - 1)} P_{\text{CdTe}}\right)}. \quad (7)$$

$P_{\text{CdTe}}$  depends on the temperature  $T_{\text{b}}$  at the melt/vapour boundary. It can be estimated from the Clausius–Clapeyron equation as

$$P_{\text{CdTe}} = P_{\text{CdTe}}^{\text{m}} \exp\left[-\frac{\Delta H_{\text{VL}}}{R} \left(\frac{1}{T_{\text{b}}} - \frac{1}{T_{\text{m}}}\right)\right], \quad (8)$$

where  $P_{\text{CdTe}}^{\text{m}}$  is the total pressure at the melting point  $T_{\text{m}}$ ,  $\Delta H_{\text{VL}}$  is the heat of evaporation at the melt temperature and  $R$  is the universal gas constant.

Due to the shift of the growth ampoule with respect to the temperature profile,  $T_{\text{b}}$  changes and the required synchronous  $T_{\text{Cd}}$  change is calculated from Eq. (8) for the temperature range of 1100 to 1200°C, using the parameters  $\Delta H_{\text{VL}} = 198.45 \text{ kJ mol}^{-1}$  [17],  $P_{\text{CdTe}}^{\text{m}} = 2.0 \text{ atm}$  [14] and  $x_{\text{L}} = 0.50015$ , and the vapour pressures from Eqs. (5) and (6) (curve 1 in Fig. 3a).

### 3. Experimental procedure

#### 3.1. Crystal growth

A diagram of the modified vertical Bridgman apparatus and its axial temperature distribution is shown in Fig. 2. Similar growth arrangements are well known for other semiconductor compounds like ZnSe [18] and the III–V compounds [19]. The starting materials Te and Cd were repeatedly purified up to 6N quality by procedures described in ref. [20]. A constant motion of the melting point isotherm through the melt was established by a furnace travel rate of  $v = 0.6 \text{ mm h}^{-1}$ . The starting temperatures of the Cd extra source,  $T_{\text{Cd}}^2 = 855^\circ\text{C}$  (point 2, Fig. 2, and curve 2,

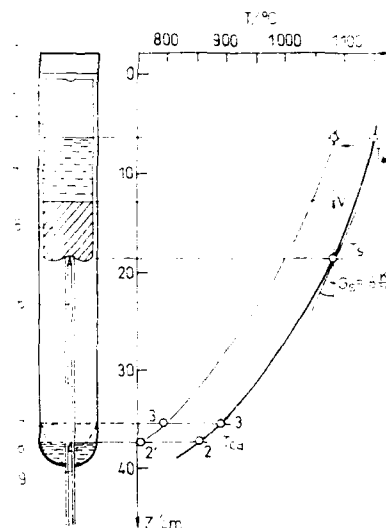


Fig. 2. Vertical Bridgman growth arrangement for CdTe: (1) plug, (2) outer silica container, (3) inner silica growth ampoule, (4) CdTe melt, (5) solidified fraction of CdTe, (6) capillary with thermocouple, (7) position of Cd source according to curve 3 in Fig. 3a, (8) position of Cd source according to curve 2 in Fig. 3a, (9) thermocouple;  $G_z$ , temperature gradient at the interface;  $T_{\text{b}}$ , temperature at the CdTe melt surface.

Fig. 3a) and  $T_{\text{Cd}}^3 = 895^\circ\text{C}$  (point 3, Fig. 2, and curve 3, Fig. 3a), were adjusted by varying the distances between outer and inner ampoule bottom (Fig. 2). The cooling rates  $v(dT/dz)$  of the Cd source and the melt surface were almost identical, i.e. the traces  $T_{\text{Cd}}^2$ –2' and  $T_{\text{Cd}}^3$ –3' respectively, follow  $T_{\text{b}}$  (Fig. 2).

#### 3.2. Assessment of the crystals

The free carrier concentration and electrical resistivity of the as-grown crystals were measured by the Van der Pauw method as well as by IR extinction analysis at 300 K, as described in ref. [21]. The energy dependence of the scattering coefficient obtained by the IR transmission spectroscopy was used to determine the excess Te content in the as-grown crystals [21].

The total concentration of residual impurities has been determined by spark source mass spectroscopy (SSMS), atomic absorption spectrophotometry (AAS) and photoluminescence (PL) [3].

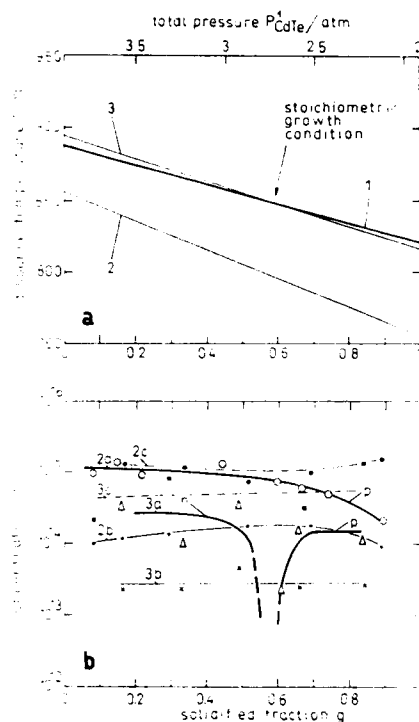


Fig. 3. The time programs of Cd source (a) and corresponding free carrier and substitutional impurity distributions (b) as a function of solidified fraction. (1) Calculated curve of stoichiometric growth conditions in an arrangement shown in fig. 2; (2, 3) measured courses at different source positions with starting temperatures  $855^\circ\text{C}$  (2) and  $895^\circ\text{C}$  (3); (2a, 3a) free carrier concentrations according to curves 2, 3 in (a); (2b, 3b and 2c, 3c) substitutional Ag and Cu concentrations in Cd positions, according to curves 2 and 3 in (a), respectively.

PL enabled the determination of substitutional impurity concentrations with an accuracy of about  $10^{12} \text{ cm}^{-3}$  [22]. Twelve undoped and two silver-doped CdTe Bridgman crystals grown with different deviations from stoichiometry have been involved in the evaluation program. Additionally, crystals grown by the horizontal Bridgman technique have been investigated for comparison.

#### 4. Results and discussion

Curve 1 in Fig. 3a shows the calculated temperature of the Cd extra source,  $T_{Cd}$ , that is

necessary in order to maintain conditions for constant stoichiometric solid phase crystallization in the vertical Bridgman arrangement, shown in Fig. 2, as a function of the solidified part of the melt. Of course, the lower the melt surface temperature  $T_b$ , the lower is the necessary value of  $T_{Cd}$ . Two measured temperature courses of differently positioned Cd sources with various starting values of  $T_{Cd} = 855^\circ\text{C}$  (curve 2) and  $895^\circ\text{C}$  (curve 3) are added. Whereas curve 2 is below curve 1 during the whole crystallization process (corresponding to the growth of a slightly tellurium-rich crystal), curve 3 intersects the calculated curve 1 at a solidified fraction  $g = 0.6$ . Hence, a change from Cd- to Te-rich composition could occur around this point.

As can be seen from Fig. 3b, the experimentally determined axial free carrier distributions in the two corresponding as-grown CdTe crystals (curves 2a and 3a) show quite good conformity with Fig. 3a. While the ingot 2 shows only p-type conductivity, curve 3a suffers a change from p- to n-type just at  $g \approx 0.6$ . This point is characterized by  $T_{Cd} = 850^\circ\text{C}$ ,  $T_b = 1118^\circ\text{C}$  and  $P_{CdTe}^1 = 2.77 \text{ atm}$ . This is, somewhat surprisingly, due to the crude approximations for the calculations, just in accordance with the calculated changeover point.

Undoped vertical Bridgman crystals grown at lower constant  $T_b \approx 1110^\circ\text{C}$  and a corresponding lower invariable  $T_{Cd} = 840^\circ\text{C}$  show the same results. Lowest carrier concentrations and electrical resistivities obtained were about  $10^{12} - 10^{13} \text{ cm}^{-3}$  and up to  $10^5 \Omega \text{ cm}$ , respectively. These data are constant along the crystal axis, as already demonstrated in refs. [3] and [23]. Moreover, such crystals were free of inclusions with diameters  $\geq 1 \mu\text{m}$ , in accordance with the present sample 3 (Fig. 3a).

In crystals grown by the horizontal boat technique ( $p \approx 10^{11} \text{ cm}^{-3}$ ,  $\rho \approx 10^6 \Omega \text{ cm}$ ), lower transition temperatures of  $T_{Cd} = 800^\circ\text{C}$  at  $T_b = 1100^\circ\text{C}$  than predicted by Eq. (8) ( $T_{Cd,calc} = 827^\circ\text{C}$ ) have been found. This is in good agreement with results of Medvedev et al. [5] ( $T_b = 1100^\circ\text{C}$ ,  $T_{Cd} = 800^\circ\text{C}$ ,  $\rho = 10^8 \Omega \text{ cm}$ ) and Chevart et al. [9] ( $T_b = 1100^\circ\text{C}$ ,  $T_{Cd} = 800^\circ\text{C}$ ,  $\rho = 10^7 \Omega \text{ cm}$ ). Obviously, the direct contact between the Cd vapour and the as-grown free crystal surface closer to the

melting point leads to a change of stoichiometry in the solid phase, despite the presence of a slightly Te-rich melt.

Curves 2b, 2c and 3b, 3c in Fig. 3b show the substitutional concentrations of silver (b) and copper (c), respectively, on Cd sites, as determined by PL. It can be seen that the content of both dopants, acting as shallow acceptors, decreases with closer approach to growth conditions leading to exact 1:1 stoichiometry. This is in agreement with the decrease in the concentration of Cd vacancies  $[V_{Cd}]$  [3,12]. The low free carrier concentration in crystals grown under nearly stoichiometric growth conditions shows that the reduced supply of  $V_{Cd}$  will favour the interstitial incorporation of Ag and Cu atoms, probably acting as deep donors in such positions.

Furthermore, the substitutional incorporation coefficient  $k_{Cd}^i = c_{Cd}^i / c_i^i$  of Ag and Cu, respectively, has been determined for a large number of crystals grown either vertically or horizontally by the Bridgman technique at various Te excess concentrations (Figs. 4a and 4b).  $c_{Cd}^i$  is the concentration of a substitutional impurity  $i$  on Cd positions;  $c_i^i$  is the total starting concentration of  $i$  in the melt. Whereas the total content of impurities (dopants) in the solid phase  $c_i^s$  is determined by segregation coefficients which are close to unity (Fig. 4a, curves 1 and 2,  $k_0^{Ag} = c_{Cd}^{Ag} / c_i^{Ag} = 0.3$  and  $k_0^{Cu} = c_{Cd}^{Cu} / c_i^{Cu} = 0.2$ ), the substitutional concentrations  $c_{Cd}^{Ag}$  and  $c_{Cd}^{Cu}$  are much lower. They depend sensitively on the tellurium excess (curves 3, 4 and 5–7, Fig. 4, for Cu and Ag, respectively).

Without Cd extra source, at a common residual impurity level of  $c_i \approx 10^{16} \text{ cm}^{-3}$  [20] and a Te excess in the solid phase of  $\approx 5 \times 10^{17} \text{ cm}^{-3}$  ( $\delta y^{Te} \approx 2 \times 10^{-5}$ ), about  $2 \times 10^{14} \text{ cm}^{-3}$  Ag atoms (curve 5) and about  $2 \times 10^{15} \text{ cm}^{-3}$  Cu atoms (curve 3) will occupy the Cd sites at the growth temperature. In the case of nearly stoichiometric composition, only  $2 \times 10^{13} \text{ cm}^{-3}$  Ag atoms (curve 7) and  $8 \times 10^{14} \text{ cm}^{-3}$  Cu atoms (curve 5) are contained in Cd positions.

Fig. 4b shows the dependence of the incorporation coefficients  $k_{Cd}^{Ag}$  (curves 5–7) and  $k_{Cd}^{Cu}$  (curves 3 and 4) on the total starting concentration  $c_i$  and the Te excess content in comparison to the segregation coefficients (curves 1 and 2)

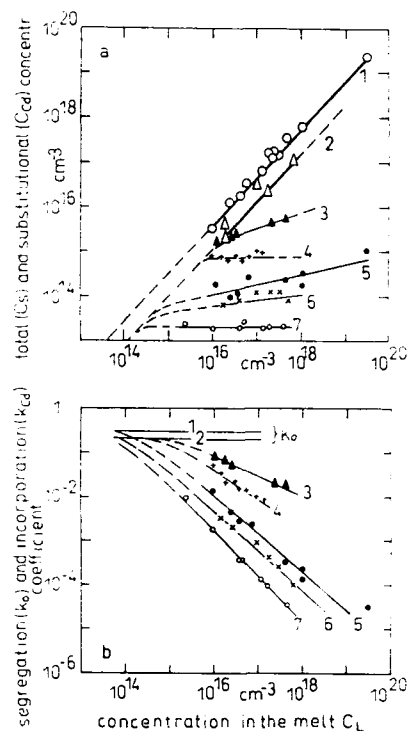


Fig. 4. The incorporation concentrations (a) and the incorporation coefficients (b) of Ag and Cu in CdTe crystals grown at various Te excesses in dependence on the starting concentrations in the melt. (1, 2) total concentration in the solid (a) and segregation coefficients (b) of Ag (1) and Cu (2), substitutional concentration of Cu in Cd positions at Te excess of  $5 \times 10^{17} \text{ cm}^{-3}$  (3) and stoichiometry (4), substitutional concentration of Ag in Cd positions at Te excess of  $5 \times 10^{17} \text{ cm}^{-3}$  (5),  $\approx 10^{16} \text{ cm}^{-3}$  (6) and stoichiometry (7).

for silver and copper, respectively. It can be seen that nearly stoichiometric solid phase crystallization conditions drastically reduce the substitutional incorporation of Ag and Cu. This is important in order to obtain crystals with low carrier concentrations and high electrical resistivities. For most other substitutional atoms (Au, Na and K on Cd sites, and P, As and Sb on Te sites), a similar behaviour is to be expected.

## 5. Acknowledgements

The authors are indebted to A.K. Bluhm for material synthesis, to K. Peters and A. Wenzel (Crystal GmbH Berlin) for horizontal Bridgman growth, and to M. Wienecke, H. Zimmermann, G. Müller-Vogt (University of Karlsruhe) and G. Liebig (IFW Dresden) for crystal characterization by Hall measurements, PL, AAS and SSMS, respectively. The investigations were supported by the Deutsche Forschungsgemeinschaft under contract No. Ru 505/3-1.

## 6. References

- [1] K. Zanio, in: *Semiconductors and Semimetals*, Vol. 13, Eds. R.K. Willardson and A.C. Beer (Academic Press, New York, 1978).
- [2] CdTe and Related Cd-Rich Alloys, Proc. Symp. F of 1992 E-MRS Spring Conference, Strasbourg, June 1992, Eds. R. Triboulet, W.R. Wilcox and O. Oda (North-Holland, Amsterdam, 1993).
- [3] H. Zimmermann, R. Boyn, P. Rudolph, C. Albers, K.W. Benz, D. Sinerius, C. Eiche, B.K. Meyer and D.M. Hoffmann, *J. Crystal Growth* 128 (1993) 593.
- [4] K. Yokata, H. Nakai, K. Satoh and S. Katayama, *J. Crystal Growth* 112 (1991) 723.
- [5] S.A. Medvedev, S.N. Maksimovskij, Yu.V. Klevkov and P.V. Schapkin, in: *Tellurid Kadmiya* (Nauka, Moscow, 1968) p. 7.
- [6] Song Wen-Bin, Yu Mei-Yun and Wu Wen-Hai, *J. Crystal Growth* 86 (1988) 127.
- [7] A.A. Kahn, W.P. Allred, B. Dean, S. Hooper, J.E. Hawkey and C.J. Johnson, *J. Electron. Mater.* 15 (1986) 181.
- [8] K. Yokata, T. Yoshikawa, S. Inano and S. Katayama, *Jap. J. Appl. Phys.* 28 (1989) 1556.
- [9] P. Cheuvart, U. El-Hanani, D. Schneider and R. Triboulet, *J. Crystal Growth* 101 (1990) 270.
- [10] J.K. Butler, F. Doty, B. Apotovsky, J. Lajzerowicz and L. Verger, *Mater. Sci. Eng. B* 16 (1993) 291.
- [11] E. Weigel, G. Müller-Vogt, B. Steinbach, W. Wendl, W. Stadler, D.M. Hoffmann and B.K. Meyer, *Mater. Sci. Eng. B* 16 (1993) 17.
- [12] P. Rudolph, H. Schröter, U. Rinas, H. Zimmermann and R. Boyn, *Advan. Mater. Opt. Electron.*, to be published.
- [13] P. Rudolph, in: *Progress in Crystal Growth and Characterization of Materials*, Ed. J.B. Mullin (Pergamon, Oxford, to be published).
- [14] K. Peters, A. Wenzel and P. Rudolph, *Crystal Res. Technol.* 25 (1990) 1107.
- [15] *Chimica – Ein Wissensspeicher*, Band II (VEB Deutscher Verlag für Grundstoffindustrie, Leipzig, 1972) p. 195.
- [16] K. Hultgren, F.R. Desai and A. Kelley, *Selected Values of the Thermodynamic Properties of the Elements* (Am. Soc. for Metals, Metals Park, OH, 1973).
- [17] P. Höschl and Č. Koňák, *Phys. Status Solidi* 9 (1965) 167.
- [18] I. Kikuma, A. Kikuchi, M. Yageta, M. Sekine and M. Fukukoshi, *J. Crystal Growth* 98 (1989) 302.
- [19] W.A. Gault, E.M. Monberg and J.E. Clemans, *J. Crystal Growth* 74 (1986) 491; E.M. Monberg, W.A. Gault, F. Simcheck and F. Dominguez, *J. Crystal Growth* 83 (1987) 174.
- [20] P. Rudolph, M. Mühlberg, M. Neubert, T. Boeck, P. Möck, L. Parthier, K. Jacobs and E. Kropp, *J. Crystal Growth* 118 (1992) 204.
- [21] U. Becker, P. Rudolph, R. Boyn, M. Wienecke and I. Utke, *Phys. Status Solidi (a)* 120 (1990) 653.
- [22] H. Zimmermann, R. Boyn, C. Michel and P. Rudolph, *Phys. Status Solidi (a)* 118 (1990) 225.
- [23] P. Rudolph and M. Mühlberg, *Mater. Sci. Eng. B* 16 (1993) 8.



ELSEVIER

Journal of Crystal Growth 138 (1994) 255–259

JOURNAL OF  
**CRYSTAL  
GROWTH**

## Iodine doping in ZnSe films grown by vapor phase epitaxy

Tetsuo Muranoi \*, Susumu Onizawa, Masataka Sasaki

*Department of Electrical and Electronics Engineering, Faculty of Engineering, Ibaraki University, Hitachi-shi, 316, Japan*

### Abstract

Properties of ZnSe films doped with iodine impurities were investigated. The ZnSe films in most cases were grown at 350°C by using metallic zinc and selenium as the source materials; their vapors were transported separately by  $H_2$  gas under atmospheric pressure.  $CH_3I$  (9.4 ppm, diluted in helium) was used as a dopant source. Epitaxial growth occurred when the flow rate of  $CH_3I$  was below 0.025  $\mu\text{mol}/\text{min}$ . The electron concentration could be controlled in the range  $5 \times 10^{16}$ – $7 \times 10^{17} \text{ cm}^{-3}$ , which was proportional to the dopant flow rate between 0.0021 and 0.016  $\mu\text{mol}/\text{min}$ . In a film grown at 300°C, the electron concentration reached  $4.4 \times 10^{18} \text{ cm}^{-3}$ . A high quality PL property was observed for the film grown with the minimum flow rate of  $CH_3I$ . When the  $[\text{Se}]$  to  $[\text{Zn}]$  flow rate ratio was varied from 0.69 to 3.53 at a constant  $CH_3I$  flow rate of 0.0042  $\mu\text{mol}/\text{min}$ , the deep-level emission almost disappeared above  $[\text{Se}]/[\text{Zn}] = 2.2$ . The value of full width at half maximum of the (600)  $\text{Cu K}\alpha$  X-ray diffraction peaks showed its minimum at the same flow rate ratio. Two-step doping of iodine was also attempted to obtain the optically and electrically desirable ZnSe film as a blue-emission layer. SIMS analysis confirmed that the ZnSe film with a two-step iodine concentration was indeed grown.

### 1. Introduction

Zinc selenide (ZnSe) is a suitable material for efficient blue-light emitting diodes (LEDs) and lasers. We have investigated the epitaxial growth of ZnSe by conventional vapor phase epitaxy (VPE) [1–3], and succeeded in growing p-type layers with hole concentration  $6 \times 10^{18} \text{ cm}^{-3}$  [2]. Following this result, in order to fabricate blue LEDs by VPE, the conductivity of n-type layers must be controlled.

The n-type ZnSe films of high quality have been grown by doping chlorine in molecular beam

epitaxy (MBE) [4] or iodine in metalorganic vapor phase epitaxy (MOVPE) [5,6]. As for VPE, sufficient control of the n-type conductivity has not been achieved yet [7].

This paper describes the characteristics of iodine doping in VPE ZnSe films, as determined by electrical measurements, photoluminescence (PL), X-ray diffraction, and secondary ion mass spectrometry (SIMS) analyses.

### 2. Experimental procedure

The experimental procedure was the same as in previous papers [1–3,7], i.e. ZnSe films were grown by atmospheric pressure VPE using metallic zinc and selenium as source materials. Their

\* Corresponding author.

vapors were transported separately to the vicinity of the substrates through thin quartz tubes. The carrier gas was  $H_2$  of 7-nine purity. The flow rates of Zn and Se were varied from 1.6 to 5.6  $\mu\text{mol/min}$  and from 2.7 to 13.3  $\mu\text{mol/min}$ , respectively. Highly conductive p-type (100)GaAs was used for the substrates ( $4 \times 4$  mm). The substrates were chemically etched with  $H_2SO_4:H_2O_2:H_2O$  (5:1:1). Thermal cleaning of the substrates was carried out at 600°C for 5 min in an  $H_2$  flow before film growth, in most cases at 350°C. Methyl iodide ( $CH_3I$ ) diluted to 9.4 ppm in helium was used as a dopant source. The purity of helium gas was 6 nines. Hall effect measurements by the Van der Pauw method were carried out to determine the electrical properties. The films were 1–3  $\mu\text{m}$  in thickness.

### 3. Results and discussion

Epitaxial growth occurred when the flow rate of  $CH_3I$  ( $FR_{\text{iodine}}$ ) was below 0.025  $\mu\text{mol/min}$ . Fig. 1 shows the electron concentration as a function of flow rate of  $CH_3I$  when  $T_{Zn} = 540^\circ\text{C}$  and  $T_{Se} = 390^\circ\text{C}$ . The concentration was nearly proportional to the flow rate of  $CH_3I$  between 0.0021 and 0.0147  $\mu\text{mol/min}$ . Hall effect measurements could not be made for the film grown at  $FR_{\text{iodine}}$

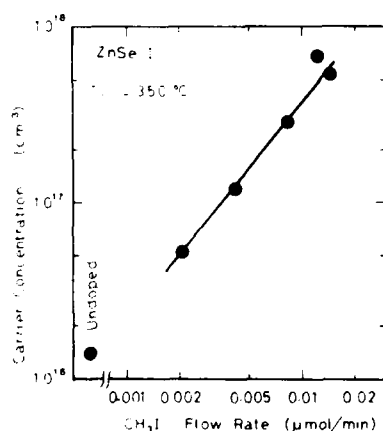


Fig. 1. Carrier concentration in an iodine-doped ZnSe film as a function of the flow rate of  $CH_3I$ .

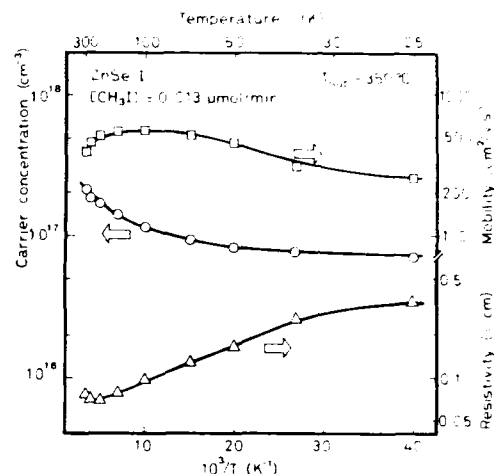


Fig. 2. Temperature dependence of electrical properties in an iodine-doped ZnSe film grown at  $T_{\text{sub}} = 350^\circ\text{C}$ ,  $T_{Zn} = 540^\circ\text{C}$ ,  $T_{Se} = 390^\circ\text{C}$  and  $FR_{\text{iodine}} = 0.013 \mu\text{mol/min}$ .

$= 0.016 \mu\text{mol/min}$  since the film was poorly conductive. It is considered that the crystallinity of this film was poor. Yoshikawa et al. [6] have reported that iodine-doped ZnSe films with a

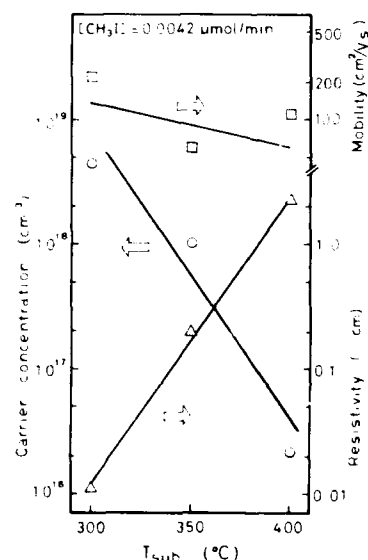


Fig. 3. Dependence of the electrical properties of iodine-doped ZnSe films on the growth temperature.  $T_{Zn} = 525^\circ\text{C}$ ,  $T_{Se} = 370^\circ\text{C}$ , and  $FR_{\text{iodine}} = 0.0042 \mu\text{mol/min}$ .

carrier concentration between  $10^{15}$  and  $10^{19}$   $\text{cm}^{-3}$  were grown by low-pressure MOVPE, using ethyl iodide ( $\text{C}_2\text{H}_5\text{I}$ ) as a dopant source with a flow rate that was varied from 0.0034 to 3.1  $\mu\text{mol}/\text{min}$ . In the present investigation, it is believed that too much iodine was taken in for an epitaxial film to be grown even at  $\text{FR}_{\text{iodine}} = 0.025$   $\mu\text{mol}/\text{min}$ . The iodine concentration should be measured to confirm this result.

Fig. 2 shows the temperature dependence of the Hall effect in a film grown at  $\text{FR}_{\text{iodine}} = 0.013$   $\mu\text{mol}/\text{min}$ . The curve for electron concentrations in this figure was drawn to fit the observed values to the equation

$$\frac{n(n + N_a)}{N_d - N_a - n} = \frac{N_c}{2} \exp\left(-\frac{E_d}{kT}\right), \quad (1)$$

which was derived using nondegenerate statistics.  $N_d$ ,  $N_a$  and  $E_d$  denote the effective donor concentration, the effective acceptor concentration and the donor level, respectively, and  $N_c = 2(2\pi m^* kT/h^2)^{3/2}$ . The parameters obtained by the curve fitting were  $N_d = 5.3 \times 10^{17}$   $\text{cm}^{-3}$ ,  $N_a =$

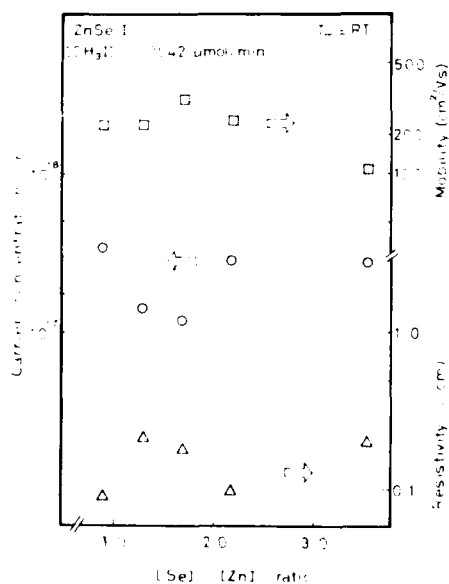


Fig. 4. Dependence of the electrical properties iodine-doped ZnSe films on the source flow rate ratio  $[\text{Se}]/[\text{Zn}]$ .  $T_{\text{sub}} = 350$   $^{\circ}\text{C}$  and  $\text{FR}_{\text{iodine}} = 0.0042$   $\mu\text{mol}/\text{min}$ .

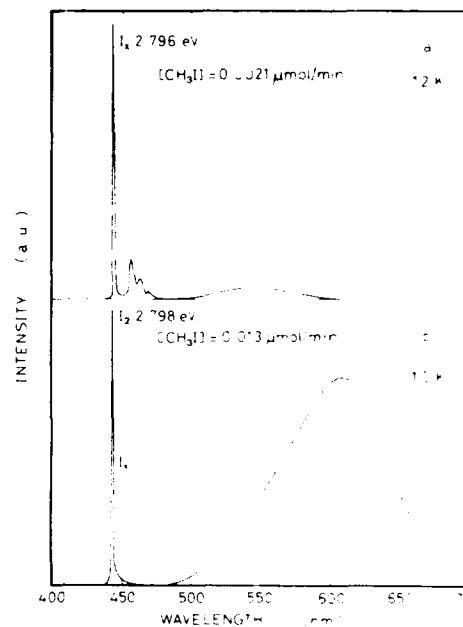


Fig. 5. Low temperature PL properties on iodine-doped ZnSe films when  $\text{FR}_{\text{iodine}}$  was varied.  $\text{FR}_{\text{iodine}}$ : (a) 0.0021  $\mu\text{mol}/\text{min}$  and (b) 0.013  $\mu\text{mol}/\text{min}$ .  $T_{\text{sub}} = 350$   $^{\circ}\text{C}$ ,  $T_{\text{PL}} = 540$   $^{\circ}\text{C}$ , and  $T_{\text{L}} = 390$   $^{\circ}\text{C}$ .

$2.4 \times 10^{17}$   $\text{cm}^{-3}$  and  $E_d = 0.012$  eV. Therefore, the compensation ratio  $N_a/N_d$  was 0.46.

Fig. 3 shows the growth temperature dependence on the electrical properties when  $\text{FR}_{\text{iodine}}$  was kept constant (0.0042  $\mu\text{mol}/\text{min}$ ). An electron concentration of  $4.4 \times 10^{18}$   $\text{cm}^{-3}$  was obtained at 300  $^{\circ}\text{C}$ , and it decreased sharply with increasing growth temperature. Fig. 4 shows the dependence of the electrical properties at room temperature on the flow rate ratio of the sources when  $\text{FR}_{\text{iodine}} = 0.0042$   $\mu\text{mol}/\text{min}$ . Carrier concentration and resistivity were scattered, probably because of larger measurement error when the film was thin (the film thickness ranged from 1 to 3  $\mu\text{m}$ ), but may be constant below  $[\text{Se}]/[\text{Zn}] \approx 3$ . Mobilities, on the other hand, were significant since it was unnecessary to take the thickness into account in their measurements. It is not clear at present if the mobility decreased at  $[\text{Se}]/[\text{Zn}] > 3$ .

A high quality PL property was observed for a film grown under the minimum flow rate of  $\text{CH}_3\text{I}$ .



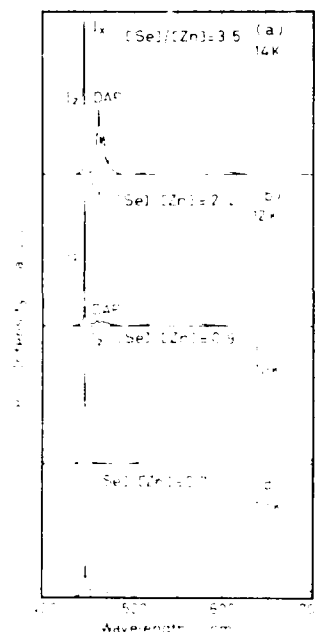


Fig. 6. Low temperature PL properties on iodine-doped ZnSe films when the source flow rate ratio  $[Se]/[Zn]$  was varied.  $[Se]/[Zn]$ : (a) 3.5, (b) 2.2, (c) 0.9, and (d) 0.7.  $T_{\text{exc}} = 350^\circ\text{C}$  and  $FR_{\text{iodine}} = 0.0042 \mu\text{mol/min}$ .

while deep-level emission increased with  $\text{CH}_3\text{I}$ , as shown in Fig. 5. Fig. 6 shows the low temperature PL properties when the flow rate ratio was varied. The deep-level emission almost disappeared above  $[Se]/[Zn] = 2.2$ . The (600)  $\text{Cu K}\alpha$  X-ray diffraction peaks for the sample shown in Fig. 6b appear in Fig. 7. The value of full width at half maximum (FWHM) of the (600) diffraction peaks for the ZnSe layer was nearly the same as that the  $\text{K}\alpha_1$  diffraction peak for the GaAs substrate. Fig. 8 shows the FWHM of the  $\text{Cu K}\alpha_1$  diffraction peaks for ZnSe epilayers versus the  $[Se]/[Zn]$  flow rate ratio. The film thickness increased in the range between 0.9 and  $3.5 \mu\text{m}$  with increasing  $[Se]/[Zn]$  ratio. The poor crystallinity at low  $[Se]/[Zn]$  ratio was attributed to higher incorporation of iodine atoms, since iodine could substitute into Se lattice sites, although the carrier concentration was almost constant. At high  $[Se]/[Zn]$  ratio, poor crystallinity was probably due to increased numbers of unknown impurities

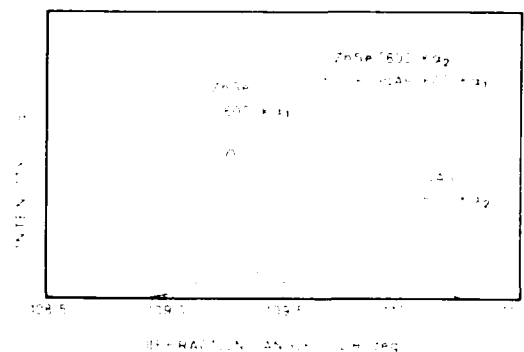


Fig. 7. X-ray diffraction pattern for the same sample as in Fig. 5b.

incorporated in Zn lattice sites, judging from the increase of D–A pair emission intensity.

When the n-type ZnSe film grown by VPE is used as an active layer in blue LEDs, as mentioned above, the optical properties are poor when the  $FR_{\text{iodine}}$  is high, while the carrier concentration is not enough when the  $FR_{\text{iodine}}$  is low; hence series resistance loss becomes high. Then, step doping of iodine was attempted to obtain the optically and electrically desirable ZnSe films as a blue-emission layer. SIMS profiles in such a film are shown in Fig. 9. This film was grown as

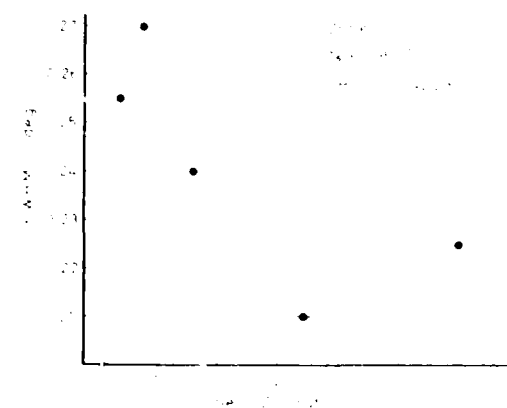


Fig. 8. The FWHM values of (600)  $\text{Cu K}\alpha$  X-ray diffraction peaks for ZnSe films grown on (100) GaAs as a function of the source flow rate ratio  $[Se]/[Zn]$ . The film thickness increased in the range between 0.9 and  $3.5 \mu\text{m}$  with increasing  $[Se]/[Zn]$  ratio.

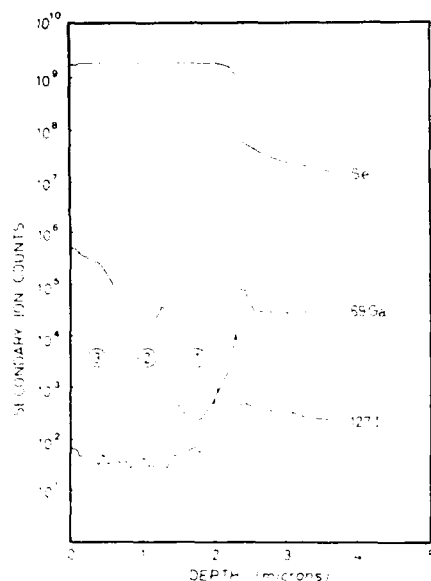


Fig. 9. SIMS profiles of impurities in the ZnSe film with a two-step iodine doping: (1) undoped layer, (2) iodine-doped layer at  $FR_{\text{iodine}} = 0.0042 \mu\text{mol/min}$ , and (3) iodine-doped layer at  $FR_{\text{iodine}} = 0.013 \mu\text{mol/min}$ . Each layer was successively grown for 2 h.

follows: an undoped layer was grown at first for 2 h (1),  $\text{CH}_3\text{I}$  was supplied at  $FR_{\text{iodine}} = 0.0042 \mu\text{mol/min}$  for the next 2 h (2), and  $\text{CH}_3\text{I}$  was supplied at  $FR_{\text{iodine}} = 0.013 \mu\text{mol/min}$  for the last 2 h (3). This figure shows that the ZnSe film with a two-step iodine concentration was indeed grown.

#### 4. Conclusion

Properties of VPE ZnSe films doped with iodine impurities were investigated. The carrier concentration was controlled between  $5 \times 10^{16}$  and  $7 \times 10^{17} \text{ cm}^{-3}$  at  $T_{\text{sub}} = 350^\circ\text{C}$ . The electron concentration reached  $4.4 \times 10^{18} \text{ cm}^{-3}$  on a film

grown at  $300^\circ\text{C}$ .  $FR_{\text{iodine}}$  was very low in order to get epitaxial growth in an atmospheric pressure system. A high quality PL property was observed for film grown under the minimum flow rate of  $\text{CH}_3\text{I}$ . When the  $[\text{Se}]/[\text{Zn}]$  ratio was varied at a constant  $\text{CH}_3\text{I}$  flow rate, there was an optimum  $[\text{Se}]/[\text{Zn}]$  ratio for crystallinity. Two-step doping of iodine was attempted to obtain the electrically and optically desirable ZnSe film as a blue-emission layer. SIMS analysis confirmed that the ZnSe film with a two-step iodine concentration was indeed grown.

#### 5. Acknowledgments

This work was supported in part by a Grant-in Aid for Scientific Research on Priority Areas, New Functionality Materials – Design, Preparation and Control, from The Ministry of Education, Science and Culture of Japan. Nippon Mining Company Ltd. and Hitachi Cable Ltd. are acknowledged for supplying “super-high-purity” selenium and GaAs substrates, respectively. The SIMS analysis was carried out by the Foundation for Promotion of Materials Science and Technology of Japan, at the authors’ request.

#### 6. References

- [1] T. Muranoi, K. Kurosawa, K. Yamamoto, T. Miyokawa, M. Shimizu and M. Furukoshi, *Jap. J. Appl. Phys.*, 29 (1990) 2820.
- [2] T. Muranoi, Y. Fujita, T. Watanabe, N. Ishii, Y. Moto and M. Furukoshi, *Jap. J. Appl. Phys.*, 29 (1990) L1959.
- [3] T. Muranoi, *J. Crystal Growth* 115 (1992) 679.
- [4] K. Ohkawa, T. Mitsuyu and O. Yamazaki, *J. Appl. Phys.* 62 (1987) 3216.
- [5] N. Shibata, H. Nomura and S. Zembutsu, *Jap. J. Appl. Phys.*, 27 (1988) L251.
- [6] A. Yoshikawa, H. Nomura, S. Yamaga and H. Kasu, *Jap. J. Appl. Phys.*, 27 (1988) L251.
- [7] T. Muranoi, M. Hirose, M. Razip, T. Akasaka and K. Ohno, *J. Electron. Mater.* 22 (1993) 505.

## ZnSe single crystal growth by the method of dissociative sublimation

H. Hartmann \*, D. Siche

*Institut für Kristallzüchtung im Forschungserbund Berlin e.V., Rudower Chaussee 6, D-12489 Berlin, Germany*

### Abstract

ZnSe single crystals of good quality have been grown from the vapour phase by dissociative sublimation in sealed ampoules. Under  $p_{\text{min}}$  conditions, maximum transport rates have been measured. The grown crystals had convex growth faces. However, the majority of runs in this category yielded relatively poor quality boules. As the vapour approaches conditions for depositing nearly stoichiometric solid ZnSe, at decreasing growth rates, large strain-free single crystals without twinning and morphological instability were successfully grown. Additional critical parameters which contribute to this behaviour are growth temperature, temperature gradient and temperature difference between source and crystal.

### 1. Introduction

In recent years, there have been several reports on epitaxial growth of ZnSe on GaAs substrates by metalorganic chemical vapour deposition (MOCVD) and molecular beam epitaxy (MBE), resulting in the development of the first blue-green laser diodes [1,2]. However, in the epitaxial system ZnSe–GaAs significant biaxial strain is introduced because of the lattice mismatch and different thermal expansion coefficients. TEM studies have shown that a highly defective Ga<sub>2</sub>Se<sub>3</sub> layer is formed at the interface [3].

To overcome these difficulties, homoepitaxy has to be applied using ZnSe substrates. In com-

parison with ZnSe melt growth under pressure, gas phase methods have the advantage of requiring lower temperatures. Twin free substrate-quality crystals with reduced defect density and controlled (non)-stoichiometry were grown. The search for optimum doping conditions is closely connected with investigations to control native point defects, and native disorder, in turn, correlates with deviations from stoichiometric composition. This paper presents results of studies on transport and growth effect dependence upon (non)-stoichiometry in the vapour phase. This will be done with regard to other authors [4,7,11,13].

### 2. Mass transport and non-stoichiometry

In general, maximum transport of material in closed ampoules from the source to the growth zone was obtained for a stoichiometric vapour

\* Corresponding author.

under  $p_{\min}$  conditions. Equilibrium constant  $K_p$  and  $p_{\min}$  are given by:

$$K_p = p_{\text{Zn}} p_{\text{Se}_2} \quad (1)$$

$$p_{\min} = \frac{1}{2} (2K_p)^{1/3}, \quad p_{\min, \text{Zn}} = (2K_p)^{1/3}, \quad p_{\min, \text{Se}_2} = \frac{1}{2} (2K_p)^{1/3} \quad (2)$$

The net fluxes of Zn and Se components being transported through unit cross-sectional area of the tube per second can be expressed, based upon some idealizing assumptions, as:

$$J_{\text{Zn}} = v p_{\text{Zn}} / RT - D_{\text{Zn}} / RT \, dp_{\text{Zn}} / dx, \quad (3)$$

$$J_{\text{Se}} = 2v p_{\text{Se}_2} / RT - 2D_{\text{Se}_2} / RT \, dp_{\text{Se}_2} / dx. \quad (4)$$

In these equations,  $v$  is the flow velocity,  $D$  the diffusion coefficient,  $x$  the axial coordinate, and  $p_{\text{Zn}}$  and  $p_{\text{Se}_2}$  are the partial pressures of components. Eqs. (3) and (4) indicate that there are two components of  $J$ , namely diffusion flux and mean drift velocity of molecules (Stefan flow) [11].

Calculations of partial pressures have been related to the  $p_{\text{Zn}}-T$  diagram (Fig. 1). Actually, the solidus range of ZnSe is slightly asymmetric, and congruent points at minimum pressure do not exactly coincide with stoichiometric points. If  $p_{\text{Zn}} / \sum p_{\text{Se}_2}$  in the vapour at the growing surface is not equal to the stoichiometric composition of the solid, a build-up of one component with growth time will occur, leading to increasing boundary layer effects. It is seen from the diagram (Fig. 1) that for ZnSe deposition the composition of the vapour and the solid differs in any case. Therefore, this effect contributes to the flux by initiating diffusion processes.

### 3. Experimental conditions

The growth method has been described in previous papers [5,6]. ZnSe crystals studied in this work were prepared in closed tube systems under nearly stationary conditions without seeding (Fig. 2). Table 1 shows the experimental parameters which have been applied in our studies. The growth optimization has been performed in two ways:

– Starting material was crystalline ZnSe powder

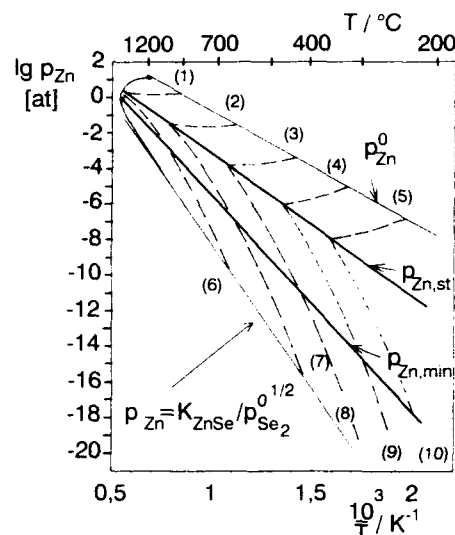


Fig. 1. Homogeneity range of ZnSe in  $p-T$  coordinates. Dashed lines indicate equal composition and refer to the following net vacancy concentrations ( $\text{cm}^{-3}$ ):  $[V_{\text{Se}}] - [V_{\text{Zn}}] = 10^{16}$  (1);  $10^{14}$  (2);  $10^{12}$  (3);  $10^{10}$  (4);  $10^8$  (5);  $[V_{\text{Zn}}] - [V_{\text{Se}}] = 10^{16}$  (6);  $10^{14}$  (7);  $10^{12}$  (8);  $10^{10}$  (9);  $10^8$  (10).  $p_{\text{Zn}, \text{st}}$  is the zinc partial pressure over the stoichiometric compound [6].

of 5N purity. In general, it contains a substantial portion (up to 0.2 wt%) of unreacted Zn or Se. To remove these components and volatile impurities, the source powders were sublimed at temperatures around 1000°C under dynamic vacuum. ZnSe with definite (non)-stoichiometric composition was equilibrated by long-time annealing un-

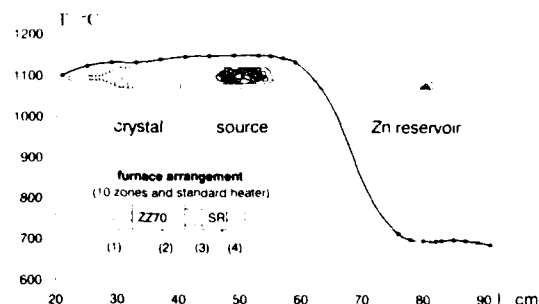


Fig. 2. Furnace temperature profile and growth capsule. Inset: (1) ceramic pipe, (2) 10-zone furnace, (3) isolation and (4) reservoir furnace.

Table 1  
Parameters for ZnSe crystal growth by dissociative sublimation

Tube geometry	
Diameter	6–25 mm
Length	50–250 mm
Source temperature $T_s$	1100–1250 °C
Growth temperature $T_g$	1050–1230 °C
Apparent undercooling $\Delta T$	5–50 °C
Temperature gradient at interface $dT/dx$	0.5–10 °C/cm
Vacuum	$8 \times 10^{-4}$ Pa (or, at RT, $p_{\text{At}} = 5 \times 10^{-4}$ – $1.4 \times 10^{-3}$ Pa)
Growth time $t$	2–21 days
Growth rate $J$	$1 \times 10^{-9}$ – $4 \times 10^{-7}$ mol/cm <sup>2</sup> ·s

der controlled partial pressures of Zn with regard to growth temperatures.

– A reservoir containing metallic Zn was sealed to the growth tube and communicated via a narrow orifice. By controlling the temperature of the reservoir during the growth process, some measure of control over the vapour composition in the capsule was obtained [7]. Here untreated source material can be used.

Furthermore, attempts have been made to match the gas phase stoichiometry in a self-adjusting system analogous to Factor et al. [11] and Lauck et al. [12]. A hole of 100  $\mu\text{m}$  diameter was drilled in the capsule near the source end. The ampoule was suspended in vacuum. However, our experimental results indicate that there was some uncertainty in the effect of the leak hole. The effluxes of species depend in a complicated manner on the individual source excess and hole diameter. Moreover, the leak efficiency varies with growth time and decreasing interface distance from the leak hole.

In the growth zone, various temperature gradients up to 10 °C/cm have been realized. Source and reservoir are placed in temperature plateaus ( $\Delta T < \pm 0.5^\circ\text{C}$ ). A capillary-tipped cavity (cold finger) is connected to the end of the ampoule in the growth section and provides a channel for volatile impurities and excess components [6,8,10].

#### 4. Results

For experiments performed under  $p_{\text{min}}$  conditions, maximum mass transport up to  $4 \times 10^{-7}$  mol cm<sup>2</sup> s<sup>−1</sup> from source to growth zone has been found by weighing the transported mass. This behaviour indicates that for evaporation and condensation processes quasi-equilibrium is dominant. When the Zn partial pressure was changed, the resulting deviation from stoichiometry in the gas phase caused a sharp decrease of measured transport rates (Fig. 3a). Otherwise, source material with definite Zn excess, resulting in values  $p_{\text{Zn,st}}$  (Fig. 1) in the vapour, have the effect of favouring the deposition of solid ZnSe in stoi-

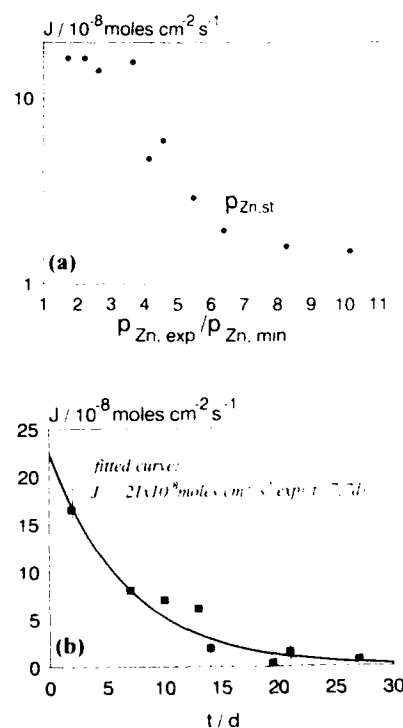


Fig. 3. (a) Variation of sublimation growth rate  $J$  of ZnSe as a function of  $p_{\text{Zn}}$  in the ampoule.  $T_g = 1280^\circ\text{C}$ ;  $\Delta T = 10^\circ\text{C}$ ;  $l = 120$  mm; diameter = 6 mm;  $p_{\text{Zn,min}} = 3.95 \times 10^{-3}$  MPa;  $p_{\text{Se,min}} = 1.97 \times 10^{-3}$  MPa;  $p_{\text{Zn,st}} = 2.5 \times 10^{-2}$  MPa;  $p_i = p_{\text{Zn}} + p_{\text{Se}}$ ;  $p_{\text{min}} = 5.92 \times 10^{-3}$  MPa (experimental values). (b) Transport rates  $J$  versus sublimation time  $t$  ( $\Delta T = 15^\circ\text{C}$ ;  $dT/dx = 1.5^\circ\text{C/cm}$  in growth zone).

chiometric composition. A striking feature of mass transport analysis is the dramatic variation of rates with the degree of non-stoichiometry in the gas phase. The material transport will be reduced significantly and can become under these circumstances the process limiting step. Moreover, in closed systems with non-stoichiometric gas phase, a continuous decrease of transport and growth rates with experimental time was found (Fig. 3b). It is reasonable to expect that the growth mechanism is controlled by enrichment of the majority component near the interface. Experimental results indicate in this case the dominance of the boundary layer resistance with overlapping surface kinetics.

Crystallographic perfection and morphological stability of ZnSe single crystals are strongly related to the composition of the vapour phase with regard to growth rates. In most cases, for boules which were grown with maximum growth rates under  $p_{\text{min}}$  conditions, the habitus is dominated by rounded convex faces (Fig. 4). This is usually interpreted as an indication of mainly diffusion-limited growth. Multiple nucleation on the ampoule wall occurred and a heavily twinned polycrystalline cone with many grains was produced. The surfaces of the boules follow the general contour of the ampoule. Growth over the full tube diameter has been observed. The dislocation etch pit density (EPD) on (110) was  $(1.0 \pm 0.2) \times 10^5 \text{ cm}^{-2}$ . Step generation on growth faces may



Fig. 4. ZnSe crystal grown under  $p_{\text{min}}$  condition (scale paper background).



Fig. 5. ZnSe single crystal of nearly stoichiometric composition grown at  $T_g = 1135^\circ\text{C}$  under non-stoichiometry with  $p_{\text{Zn,Se}}$  in the gas phase (scale paper background).

be attributable to adsorption effects of the majority component Zn. Zn segregation was detected by EDAX analysis.

Slower growing crystals of near-stoichiometric composition were often faceted, and did not reach the full possible size. Typically, growth rates of about  $2 \times 10^{-8} \text{ mol cm}^{-2} \text{ s}^{-1}$  have been evaluated from weight analysis of mass transport (from this value 0.5 mm/day could be estimated). Growth conditions for the deposition of stoichiometric ZnSe favour the formation of a single nucleus at the tip of the ampoule without requiring seeds. Under optimized conditions (source material composition, adequate supersaturation and centre-piece of ampoule tip with regard to the growth isotherm), multiple nucleation on the ampoule wall has been avoided. Free-growing ZnSe single crystals with a volume of about  $2 \text{ cm}^3$ , without grains and twinning, frequently have been observed (Fig. 5). No strain was found by polarisation microscopy. The crystals became very clear and pale yellow in colour. They showed morphological stability with dominant (110) and small (111) faces. The EPD (NaOH etchant) on (110) was  $10^4 \text{ cm}^{-2}$  with dislocation-free regions of 100–120  $\mu\text{m}$  in diameter. X-ray transmission topographs revealed also heterogeneous dislocation distributions. X-ray diffraction rocking curves showed FWHMs of about 5 arc sec (Fig. 6). The IR absorption at  $10.6 \mu\text{m}$  was 0.2%. Photoluminescence spectra exhibited more gap-near emis-

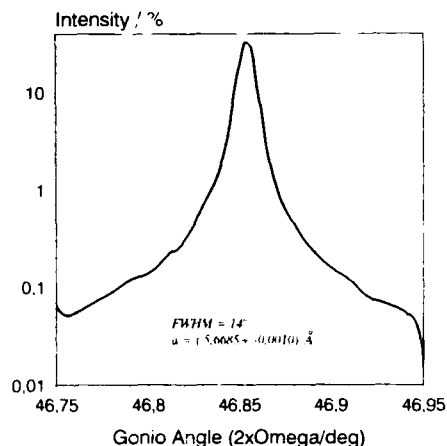


Fig. 6. Double-crystal X-ray diffraction rocking curve for a nearly stoichiometric ZnSe single crystal [ $\text{CuK}\alpha_1$ , Ge (220)].

sion than deep-level emission under focussed  $\text{N}_2$ -laser excitation.

All as-grown ZnSe crystals had high resistivities in the range of  $10^{11}$  up to  $10^{12} \Omega \text{ cm}$ . The most important method to purify the probes from compensating contaminants is the extraction technique in liquid Zn [6,14]. This technique consists of annealing the crystals in contact with the Zn melt for 50 to 300 h at  $1000^\circ\text{C}$ . By this treatment the resistivities were reduced to several  $10^{-1} \Omega \text{ cm}$  with electron mobilities of 500 to 600  $\text{cm}^2 \text{ V}^{-1} \text{ s}^{-1}$ . Since equilibration with the liquid component metal brings the crystal to a state on the metal-rich boundary of the homogeneity range, the highest possible room temperature electron concentration (about  $5 \times 10^{17} \text{ cm}^{-3}$ ) should be expected. For doping experiments, substantial quantities of dopant elements (for instance Al, Ga) were mixed into the Zn melt.

## 5. Conclusions

Optimization experiments for ZnSe crystal growth by dissociative sublimation, especially with regard to high crystallographic perfection, have been successful under the following prerequisites:

- sufficiently high growth temperature level ( $T_g$

$> 1100^\circ\text{C}$ ) to restrict condensation and source evaporation limitations;

- relatively low undercooling  $\Delta T < 30^\circ\text{C}$ : faster growth rates induced by a higher  $\Delta T$  result in  $da/dx > 0$  ( $a$  is activity) and due to constitutional supercooling the interface is no longer stable;

- temperature gradients  $dT/dx < 5^\circ\text{C}/\text{cm}$  in front of the growing crystal result in a decrease of supersaturation and growth rates: imposing  $dT/dx > \Delta T/l$  ( $l$  is ampoule length) will produce morphological stability in accordance with Factor et al. [11];

- partial pressures in the gas phase appropriate to deposition of solid ZnSe in stoichiometric composition;

- mainly diffusion-controlled mass transport.

On this basis, growth conditions were established for the deposition of stoichiometric ZnSe and the formation of free-growing single crystals without morphological instabilities. Under  $p_{\text{min}}$  conditions we achieved maximum transport rates, but the majority of runs in this category yielded relatively poor-quality boules. Furthermore, growth experiments were strongly affected by purity and composition of source material.

## 6. Acknowledgements

We are indebted to Mr. R. Krupka from the Institut für Strahlwerkzeuge at Stuttgart University for measuring the IR absorption and to Dr. E. Hommel from the Institute of Physics of the Würzburg University for the X-ray topographs. This work is supported by the Deutsche Forschungsgemeinschaft.

## 7. References

- [1] J.M. DePuydt, M.A. Haase, J. Qiu and H. Cheng, *J. Crystal Growth* 117 (1992) 1078.
- [2] J. Ren, K.A. Bowers, R.V. Vaudo, J.W. Cook, J.E. Schetzina, J. Ding, H. Jeon and A.V. Nurmikko, *J. Crystal Growth* 117 (1992) 510.
- [3] J.O. Williams, A.C. Wright and H.M. Yates, *J. Crystal Growth* 17 (1972) 441.

- [4] G. Cantwell, W.C. Harsch, H.L. Cotal, B.G. Markey, S.W.S. McKeever and J.E. Thomas, *J. Appl. Phys.* 71 (1992) 2931.
- [5] H. Hartmann, *J. Crystal Growth* 42 (1977) 144.
- [6] H. Hartmann, R. Mach and B. Selle, Wide gap II–VI compounds as electronic materials, in: *Current Topics in Materials Science*, Vol. 9, Ed. E. Kaldis (North-Holland, Amsterdam, 1982).
- [7] J.R. Cutter and J. Woods, *J. Crystal Growth* 47 (1979) 405.
- [8] P. Blanconnier and P. Henoc, *J. Crystal Growth* 17 (1972) 218.
- [9] K.F. Burr and J. Woods, *J. Crystal Growth* 9 (1971) 183.
- [10] W.M. de Meis and A.E. Fisher, *Mater. Res. Bull.* 2 (1967) 465.
- [11] M.M. Faktor, R. Heckingbottom and J. Garrett, *J. Crystal Growth* 9 (1971) 3.
- [12] R. Lauck, G. Müller-Voigt and G. Wendl, *J. Crystal Growth* 74 (1986) 570.
- [13] D.W. Ballentyne, S. Wetwatana and E.A.D. White, *J. Crystal Growth* 7 (1970) 79.
- [14] M. Aven and H.H. Woodbury, *Appl. Phys. Lett.* 1 (1962) 53.



## Characterization of impurities in II–VI semiconductors by time-resolved lineshape analysis of donor–acceptor pair spectra

P. Bäume, F. Kubacki \*, J. Gutowski

*Institut für Experimentelle Physik, Universität Bremen, P.O. Box 330 440, D-28334 Bremen, Germany*

---

### Abstract

Strength and energy position of donor–acceptor pair (DAP) luminescence bands are often used for a crude estimate of impurity incorporation and nature in II–VI epilayer structures. We demonstrate that analysis of DAP emission has to be performed more carefully to get reliable information of that kind. A thorough lineshape analysis allows one to determine the acceptor binding energy quite exactly if the donor energy is known, and beyond this the phonon-coupling parameters. A missing or reduced line narrowing of the DAP bands in thin epilayers for decreasing excitation densities is due to inhomogeneous impurity distribution within the strain-profiled layers. In ns time-resolved analysis, DAP decay is shown to depend sensitively on detection energy within the band but is, at all energies, perfectly described by biexponential fits. Fit parameters involve impurity binding energies and, thus, are an independent tool of verifying data obtained from lineshape analysis. Spectrally unresolved double bands can be identified and distinguished by this method.

---

### 1. Introduction

Reliable p-doping of II–VI semiconductors like ZnSe is still one of the major problems in crystal growth and epitaxy [1–3]. Difficulties arise even in estimating the dopant concentration and in characterizing intentional and unintentional impurities by determining their binding energies. Energies of bound excitons are often close together, and their two-electron satellites yielding precise impurity energies are hardly observable already at moderately enlarged dopant concentrations. Any fine structure (discrete pair lines) of donor–acceptor pair emission (DAP) or transi-

tions from and into excited states of impurities as accurate measures for dopant studies are rarely seen in the samples [4]. Other methods like secondary ion mass spectrometry (SIMS) are only applicable in the heavy-doping limit. Therefore, very rough estimates of dopant concentrations are based on the determination of intensity ratios of donor–acceptor pair bands to the excitonic luminescence.

Although the DAP luminescence is well understood in principle since more than two decades, little effort has been made to use the full theory in characterization of semiconductors. By combining both intensity-dependent and time-dependent spectroscopy of DAP luminescence, we present a powerful tool to determine the acceptor binding energy and the phonon coupling parameters.

\* Corresponding author.

For this purpose, we use an advanced theory based on the model proposals of Thomas and Hopfield [5]. It was expanded by Colbow and Yuen [6] who gave a lineshape analysis of the intensity-dependent DAP. We have included the phonon coupling [7,8] and give additional remarks on the distant-neighbour recombinations. Furthermore, the recombination rate of excited pairs as calculated by Bindemann and Unger [9] is included.

Measurements of DAP bands in ZnSe bulk crystals are compared with the theory outlined above. Further, we investigated DAP emission in strained ZnSe/GaAs epilayers as being important for devices with regard to the peculiarities of the bands in inhomogeneously strained systems.

## 2. Experimental setup

The epilayers used in this study were grown either by MBE (Purdue University) or by metal-organic vapour phase-epitaxy (MOVPE) on GaAs substrates (Inst. für Halbleitertechnik, RWTH, Aachen). The bulk material was grown out of a solution and was doped with Li.

Photoluminescence was measured at 1.6 K using the 325 and 441.6 nm emission lines of a He–Cd laser (Omnichrome). The excitation power density is varied from 1 mW/cm<sup>2</sup> to 500 W/cm<sup>2</sup>. The spectra were analysed by using a 1 m Spex monochromator (resolution 0.07 meV) and a bi-alkali photomultiplier.

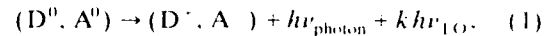
An excimer-laser pumped dye laser served as light source (12 ns pulses) for the time-resolved measurements. The excitation wavelength was chosen in the spectral regime of the free exciton (441.6 nm). The time-resolved spectra of the DAP signal were recorded with a gated optical multi-channel analyser (OMA) system. The gate widths were 10 and 20 ns for time delays to the exciting pulse below and beyond 200 ns, respectively.

## 3. Theory of donor–acceptor pairs

### 3.1. Lineshape in case of steady-state excitation

Standard treatments [5,6] analyse the LO-phonon assisted DAP recombination process, Eq. (1),

by taking into account a next-neighbour recombination exclusively:



$$E_{\text{photon}} = E_{\text{gap}} - E_A - E_D - k E_{\text{LO}} + E_c, \quad (2)$$

$$E_c = e^2 / 4\pi\epsilon_0\epsilon(0)r, \quad (3)$$

with  $E_A$  and  $E_D$  the acceptor and donor ionization energy, respectively,  $r$  the acceptor–donor pair distance,  $E_c$  the Coulomb binding energy of the  $(D^+, A^-)$  pair, and  $k$  an integer to give the number of emitted LO phonons.

The lineshape of the DAP emission has to be analysed with regard to the following considerations:

- For a given acceptor A the probability  $g(r)dr$  of finding the next-neighbour donor D at distance  $r$  can be calculated as (if  $N_D \gg N_A$  [6],  $N_D$ ,  $N_A$  donor/acceptor concentration)

$$g(r) dr = 4\pi N_D r^2 dr \exp(-\frac{4}{3}\pi N_D r^3), \quad (4)$$

- For the recombination rate  $W(r)$  of the process  $(D^0, A^0) \rightarrow (D^+, A^-) + h\nu_{\text{photon}}$ , we prefer the calculation of Bindemann and Unger [9] yielding a more precise description of  $W(r)$  than the simple exponential law used in refs. [10,11]:

$$W(r) = W_0 \frac{8(AB)^{3/2}}{(A^2 - B^2)^{3/2} r} \times \left\{ [4AB + (A^2 - B^2)Br] \exp(-Ar) - [4AB - (A^2 - B^2)Ar] \exp(-Br) \right\}, \quad (5)$$

where  $A$  and  $B$  denote the reciprocal Bohr radii of the donor and the acceptor, respectively.  $W_0$  is an unknown constant giving the recombination rate at the pair distance  $r = 0$ .

- The steady-state fraction  $f_e(r)$  of excited pairs with a pair separation  $r$  is calculated by using a simple steady-state rate equation. Excitation of a pair from the ground state  $(D^+, A^-)$  into the state  $(D^0, A^0)$  possesses a capture cross-section  $\sigma(r)$ . For thermal equilibrium in the conduction band,  $\sigma \sim r^2$  [12]. By assuming a photogeneration rate  $g$  of free carriers, one obtains

$$f_e(r) = [1 + W(r)/g\sigma(r)]^{-1}. \quad (6)$$

• Based on the adiabatic approximation [7], the probability  $W_k$  for the creation of  $k$  phonons at DAP recombination (Eq. (1)) is included as being Poisson distributed

$$W_k(r) = \exp[-S(r)] S^k(r)/k!. \quad (7)$$

The phonon coupling function  $S(r)$  covers the details of lattice and impurity interaction, and gives a different value for each pair separation  $r$ . The coupling function derived in ref. [8] contains two free parameters  $S'$  and  $S''$

$$S(r) = S' \left\{ 2 - \frac{32}{5\delta} \left[ 1 - e^{-\delta} \left( 1 + \frac{11}{16}\delta + \frac{3}{16}\delta^2 + \frac{1}{48}\delta^3 \right) \right] \right\} + S'' \delta^{-4} \left[ 1 - e^{-\delta} \left( 1 + \delta + \frac{1}{2}\delta^2 \right) \right]^2, \quad (8)$$

where  $\delta$  denotes the dimensionless number  $2r/a_D$ , with the donor Bohr radius  $a_D$ . Combining these terms, the lineshape of the  $k$ th phonon replica reads:

$$I_k(E_c) \sim r^2 g(r) f_c(r) W(r) W_k(r) = r^2 g(r) f_c(r) W(r) \times \frac{S^k(r)}{k!} \exp[-S(r)], \quad (9)$$

The theoretical lineshape applied in this paper is the sum of the zero-phonon band and three phonon replicas (replicas with  $k > 3$  are known to hardly contribute to the spectra):

$$I(E) dE \sim \sum_{k=0}^3 \theta(E_c + k\hbar\omega_{LO}) I_k(E_c + k\hbar\omega_{LO}), \quad (10)$$

where the Heavyside function  $\theta(E_c + k\hbar\omega_{LO})$  cancels out contributions with negative Coulomb energies. Eq. (3) provides  $E_c(r)$ , and  $I(r) dr \sim r^2 I(r) dE_c$  is used.

$dI_k/dE_c = 0$ , with  $I_k$  according to Eq. (9), yields a relation of excitation intensity to zero-phonon peak position. For sufficiently high concentrations  $N_D \gg N_A$  a neutral acceptor may interact not only with the nearest donor but also

with distant donors. In our model each next-neighbour DAP is embedded in a background distribution of neutral donors. The altered steady-state fraction  $f_c^*$  of excited pairs takes into account the additional recombination rates. A numerical integration about distant-pair recombinations is performed as

$$I_k(E_c) \sim r^2 W(r) \frac{S^k(r)}{k!} \exp[-S(r)] \times \left[ g(r) f_c^*(r) + 4\pi N_D r^2 \left( \int_a^r g(R) f_c^*(R) dR \right) \right]. \quad (11)$$

### 3.2. Transient behaviour of DAP bands

After generation of  $N_c^0(E_c)$  pairs with separation  $r$  by a single laser pulse, the intensity of radiative recombination at energy  $E = E_{gap} - (E_D + E_A) + E_c$  is given by

$$I(E, t) = N_c^0(E_c) \exp[-S(E_c)] \times W(E_c) \exp[-W(E_c)t] + N_c^0(E_c + \hbar\omega_{LO}) \times \exp[-S(E_c + \hbar\omega_{LO})] S(E_c + \hbar\omega_{LO}) \times W(E_c + \hbar\omega_{LO}) \times \exp[-W(E_c + \hbar\omega_{LO})t]. \quad (12)$$

Only the zero- and one-phonon replicas are taken into account for the analysis at energies on the zero-phonon band where  $k$ -LO replicas with  $k > 1$  hardly contribute. Distant-neighbour recombination becomes negligible at low dopant concentrations of  $N_D < 1.0 \times 10^{17} \text{ cm}^{-3}$ . The constant effective recombination rate  $W(E_c)$  after Eq. (5) yields an exponential decay for each pair distance  $r$ , being observable on all phonon replica. Eq. (12) is a two-exponential law and can, for fit purposes, be replaced by

$$I(E, t) = I_0^0 \exp(-t/\tau_0) + I_0^1 \exp(-t/\tau_1) \quad (13)$$

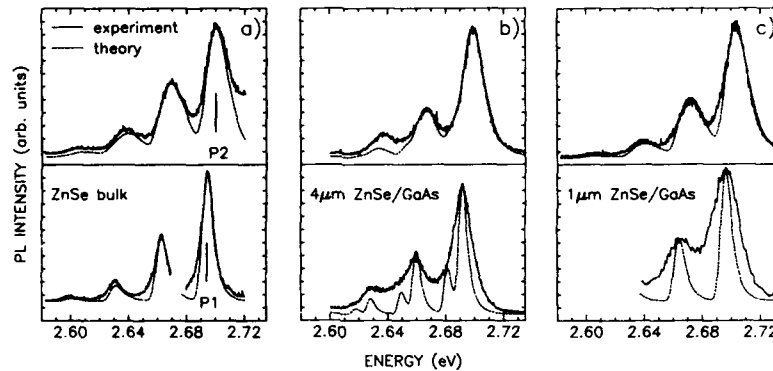


Fig. 1. Photoluminescence spectra of DAP for three different samples for representative high ( $500 \text{ W/cm}^2$ , upper curves) and low excitation densities ( $20 \text{ mW/cm}^2$ , lower curves). Solid lines refer to the experiment and dashed lines show theoretical curves.

#### 4. Experimental results

##### 4.1. Lineshape fits

Excitation-density dependent luminescence spectra for both ZnSe bulk crystals and epilayers are depicted in Fig. 1. All samples show a shift of the DAP bands to lower energies as the excitation densities decrease. The bulk sample exhibits a distinct line narrowing for low excitation densities (Fig. 1a), as is expected from Eq. (10). The  $4 \mu\text{m}$  ZnSe:Ga/GaAs layer shows a much weaker line narrowing (Fig. 1b). Additionally, it is proven by time-resolved analysis that the spectra are

composed by two DAP bands involving two different acceptors in this sample. The thin ZnSe/GaAs layer ( $1.0 \mu\text{m}$ ) being N-doped shows no line narrowing at all, as generally observable for thin epilayers.

For a least-squares fit of Eq. (10) to each of the high-excitation shapes,  $E_D$  as a known constant and four fit parameters were used: The energy difference between acceptor and donor level  $E_{AD}$ ,  $N_D$ , and the two phonon coupling parameters  $S'$  and  $S''$  (Eq. (8)). Furthermore,  $E_{\text{gap}} = 2.82014 \text{ eV}$  [13]. From this, we calculated  $E_A = E_{\text{gap}} - E_D - E_{AD}$ . The fit is very sensitive to the parameter  $E_{AD}$ , the fitting error  $\Delta E_{AD}$  is less

Table 1  
Least-squares fit parameters from lineshapes analysis

Figure	Sample	Fixed $E_D^a$ (meV)	$E_A$ (meV)	Acceptor identification	$N_D$ ( $10^{16} \text{ cm}^{-3}$ )	$S'$ (1)	$S''$ (1)
Fig. 1a and curve A of fig. 3 Curve B of Fig. 3 Fig. 2 all curves	ZnSe bulk	30	113	Li	2.4	0.37	214
	Li-doped	30	104 <sup>b</sup>		2.4	0.37	214
		30	113	Li	40	0.35	214
Fig. 1b	ZnSe/GaAs	27.9	115	Li	4.4	0.4	40
	$4 \mu\text{m}$ ZnSe/GaAs Ga implantation	27.9	125	Na	4.4	0.4	40
Fig. 1c	ZnSe/GaAs $1 \mu\text{m}$ , N-doped	30	111	N	3.0	0.40	110

<sup>a</sup> The donor binding energies  $E_D$  are not fitting parameters, but fixed constants during the least squares fit.

<sup>b</sup> Concerning difficulties in determining  $E_A$  in this case, see text.

than 1 meV. For the Li-doped bulk material (Fig. 1a) we found  $E_A = 113$  meV, being close to the reported values of  $E_A^{(1)} = 114$ –118 meV [2] and  $E_A^{(1)} = 114.4 \pm 0.4$  meV [4]. For the N-doped layer (Fig. 1c) we determined  $E_A = 111$  meV. Reported values are  $E_A^N = 109$ –112 meV if some clear outliers in previous work are ignored [2]. For the Ga-implanted layer (Fig. 1b), the known donor binding energy  $E_D^{(0)} = 27.9$  meV [2] results in two acceptors with binding energies  $E_A^{(1)} = 115$  meV and  $E_A^{(2)} = 125$  meV. Here,  $E_A^{(2)}$  belongs to the second acceptor giving rise to the weaker luminescence. The ratio of intensities  $\text{DAP}^{(2)}/\text{DAP}^{(1)} = 0.32$  as determined from the lineshape fit directly measures the ratio of concentrations; hence,  $N_A^{(2)}/N_A^{(1)} = 0.32$ . Na as a common acceptor in ZnSe is reported to possess  $E_A^N = 125$ –130 meV when disregarding a number of outliers [2]. Thus, we identify the two acceptors in our Ga-doped samples as Li and Na and believe our value for Li to be closer than 1 meV to the true value (if the reported binding energy for Ga is true).

The values for the concentrations of the major impurity given in Table 1 should be treated with caution. The lineshape including distant neighbour recombinations (Eq. (11), which we regard to be a better one than Eq. (9) including next-neighbour-recombinations exclusively), is presented in Fig. 2 where the next-neighbour and distant-neighbour contributions are given sepa-

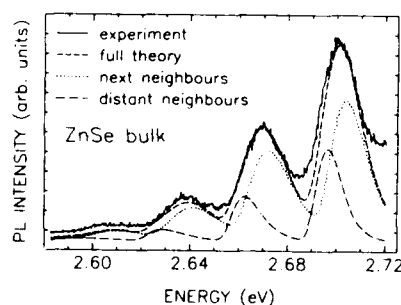


Fig. 2. The theoretical DAP lineshape including distant-neighbour recombinations (Eq. (11), labelled "full theory") in comparison with the bulk luminescence (solid line). The label "next neighbours" belongs to the next-neighbour part of Eq. (11), while the label "distant neighbours" belongs to the distant-neighbour part of Eq. (11) exclusively.

ately and are combined. However, a fit based on Eq. (11) becomes ambiguous. If we assume a low concentration  $N_D$  the influence of distant-neighbour recombinations can be neglected and a satisfying linefit can be achieved with  $N_D = 3.0 \times 10^{16} \text{ cm}^{-3}$  (Fig. 1a). Assuming a high concentration  $N_D$  we have to perform the full theory (Eq. (11)) yielding the result of a similarly satisfying linefit at  $N_D = 4.0 \times 10^{17} \text{ cm}^{-3}$  (Fig. 2 and Table 1).

In most samples, we found that the adiabatic approximation (Eq. (7)) for the phonon coupling is valid. However, for the  $4 \mu\text{m}$  sample the phonon coupling is obviously not poisson distributed. Here, the intensities of the two- and three-phonon-replica are underestimated in general. This may be due to lattice distortion by ion implantation. The given values for the phonon coupling parameters  $S'$  and  $S''$  (Table 1) are hard to judge on because no other work on phonon coupling in ZnSe using the theory of Röpke et al. [8] had come to our knowledge.

As a further test on our theory, the parameters determined from the high-excitation spectra were used to plot theoretical low-excitation spectra (see Figs. 1a–1c, lower curves). In order to do this we calculated an effective rate  $g$  that transports the DAP curve to the experimentally determined peak position. The results indicate good agreement for the bulk sample, less satisfying agreement for the  $4 \mu\text{m}$  layer, and poor agreement for the thin layer. This indicates that the strong broadening of the DAP bands in the latter cases is indeed caused by the extreme inhomogeneity of the strain within the first  $1 \mu\text{m}$  layer upon the interface.

#### 4.2. Zero-phonon-peak position

In a second step, we derive the dependence of zero-phonon-peak position on excitation density  $I^{ex}$  by connecting Eq. (9) to the photogeneration rate  $g$  of free carriers (Eq. (6)) by setting

$$g = \chi I^{ex}, \quad (14)$$

$\chi$  being the quantum efficiency. Fig. 3, curve A, shows the predicted peak position when using the lineshape-determined parameters. The contradic-

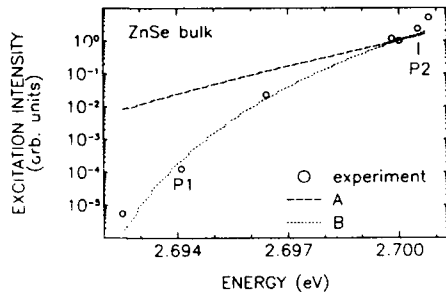


Fig. 3. Zero-phonon peak position versus excitation density for the bulk sample. Open circles belong to experimental peak positions, and dashed curve A and dotted curve B refer to theory. The labels P1 and P2 refer to the low- and high-excitation spectra shown in Fig. 1a, respectively.

tion to the experiment is clearly seen. It should be noted that the theoretical curves were normalized and fixed at an arbitrary point of the experimental data due to the unknown quantity  $\chi$ . Fig. 3, curve B, matches the experimental points and is a result of least-squares fitting (see Table 1). However,  $E_{\lambda} = 104$  meV being derived disagrees with the value obtained from lineshape analysis (113–115 meV). The reversed calculation of a lineshape with  $E_{\lambda} = 104$  meV leads to a rather poor matching to the experimental lineshapes. This contradiction is found in both bulk material and layers. We believe that the simple connection  $g \sim I^{\chi}$  is not valid. Due to the high absorption coefficient for a band-to-band excitation, only

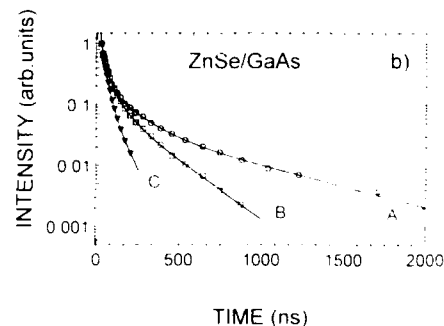
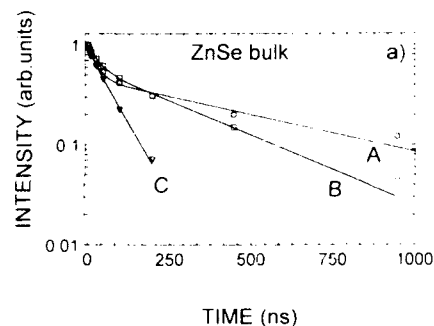


Fig. 4. (a) Time-dependent luminescence intensity  $I(t)$  of the DAP zero-phonon band for the bulk sample at three different spectral positions A, B and C. The labels A–C refer to Fig. 5a. The solid lines represent the biexponential fitting curves. (b) Time-dependent luminescence intensity  $I(t)$  of the DAP zero-phonon band for the Ga-doped layer at three different spectral position. The solid lines represent the four-exponential fitting curves.

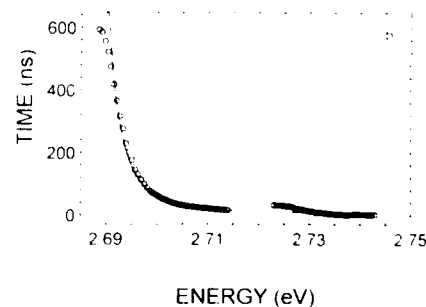
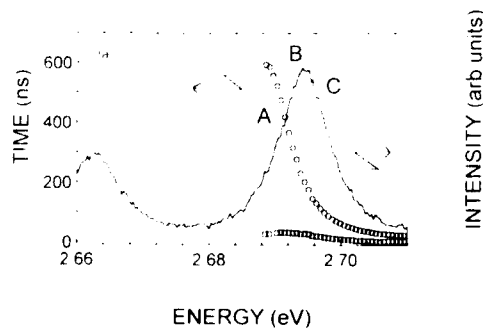


Fig. 5. (a) Fitted lifetimes versus spectral position for the bulk sample in a biexponential model. The luminescence spectrum serves as a guide to identification of detection energies within the bands. (b) Fit of the theoretical lifetime function  $1/(B(I))$  (solid line, Eq. (5)) to the lifetimes in the bulk sample (open circles, see Fig. 4a).

Table 2  
Least-squares fit parameters from decay analysis

Figure	Sample	Model	Fixed $E_D^a$ (meV)	$E_A$ (meV)	Acceptor identification	$W_0$ ( $10^8 \text{ s}^{-1}$ )
Fig. 5b	ZnSe bulk Li-doped	Biexponential decay law	30	117	Li	13
No picture	ZnSe/GaAs	Four-exponential decay law	27.9	117	Li	7.9
	4 $\mu\text{m}$ Ga implantation		27.9	123	Na	10.0

<sup>a</sup> The donor binding energies  $E_D$  are not fitting parameters, but fixed constants during the least-squares fit.

carrier transport by diffusion should feed the DA pairs in the volume of the crystal. Additionally, there is low reabsorption of DAP light. Hence, all parts of the inhomogeneously excited crystal contribute to the detected light. This effect should be strongest in the case of bulk material, where red-shifted luminescence contributes from a large volume out of the deep of the crystal. Indeed, the deviation of the predicted zero-phonon-peak position to the experiment is strongest in bulk samples.

#### 4.3. Time-resolved spectra

The decay model described in section 3 being fitted to the time-resolved luminescence intensity  $I(t)$  at different fixed spectral positions  $E$  (see Fig. 4a for the transients at energies A, B and C as marked in Fig. 5a) provides an independent check of  $E_A$  and  $E_D$  obtained so far. For the bulk sample, we fitted by using the biexponential model described above (Eq. (13)). The resulting lifetimes  $\tau_1(E)$  and  $\tau_2(E)$  are shown in Fig. 5a. The origin of the shorter lifetime  $\tau_2(E)$  is due to the contribution of photons from the DAP-1LO process. Hence,

$$\tau_2(E) = \tau_1(E + \hbar\omega_{1LO}). \quad (15)$$

Thus, one may shift the experimentally determined values  $\tau_2$  to higher energies by  $\hbar\omega_{1LO} = 31.5 \text{ meV}$  (Fig. 5b). A least-squares fit of Eq. (5) to these lifetimes by using the relation between rates and lifetimes,  $W(E) = 1/\tau(E)$ , yields  $E_A = 117 \text{ meV}$ , deviating by 4 meV from the value obtained from the lineshape analysis. For the Ga-doped layer containing two acceptor species,

we use a four-exponential decay law (Fig. 4b).  $E_A^{(1)} = 117 \text{ meV}$  and  $E_A^{(2)} = 123 \text{ meV}$  thus obtained (see Table 2), exhibit good agreement with the values from the lineshape analysis (cf. Table 1).

We repeated the fitting procedure in the region of the 1-LO-phonon band and found the same decay characteristic as in the region of the zero-phonon band at just the  $E - \hbar\omega_{1LO}$  energy, respectively (not depicted). Identical lifetimes in the four-exponential model were found at an energy spacing of one LO phonon. This strongly verifies our model, as it is expected that in the region of the one-phonon band the luminescence is dominated by a superposition of the one- and two-phonon replica (Eq. (10)).

In conclusion, our results show that DAP analysis is a useful means of impurity identification if performed carefully with sophisticated model descriptions but should be looked sceptically upon if used for crude estimations only due to its sensitivity on intensity, strain and superposition of different DAP luminescence series.

#### 5. Acknowledgements

We would like to thank Professor R.L. Gunshor (Purdue University West Lafayette, IN, USA) and Dr. M. Heuken (Rheinisch Westfälische Technische Hochschule, Aachen, Germany) for providing the MBE and MOVPE samples, respectively, and Dr. R.N. Bhargava (Philips Lab., Briarcliff Manor, NY, USA) for providing the ZnSe bulk crystals.

## 6. References

- [1] P.J. Dean, D.C. Herbert, C.J. Werkhoven, B.J. Fitzpatrick and R.N. Bhargava, *Phys. Rev. B* 23 (1981) 4888.
- [2] J. Gutowski, N. Presser and G. Kudlek, *Phys. Status Solidi (a)* 120 (1990) 11.
- [3] K. Shahzad, D.J. Olego and J. Petruzello, *J. Luminescence* 52 (1992) 17.
- [4] Y. Zhang and B.J. Skromme, *Phys. Rev. B* 47 (1993) 2107.
- [5] D.G. Thomas, J.J. Hopfield and W.M. Augustyniak, *Phys. Rev.* 140 (1965) A202.
- [6] K. Colbow and K. Yuen, *Can. J. Phys.* 50 (1972) 1518.
- [7] H.L. Malm and R.R. Haering, *Can. J. Phys.* 49 (1971) 2970.
- [8] G. Roepke, A. Zehe, N. Januzzi and A. Juarez, *Solid State Commun.* 43 (1982) 495.
- [9] R. Bindemann and K. Unger, *Phys. Status Solidi (b)* 66 (1974) 133.
- [10] G.F. Neumark, *J. Electrochem. Soc.* 136 (1989) 3135.
- [11] G.J. Yi, J.A. Tuchman and G.F. Neumark, *Appl. Phys. Lett.* 58 (1991) 520.
- [12] A. Zehe, G. Roepke and A. Juarez, *Solid State Commun.* 50 (1984) 203.
- [13] Landolt-Börnstein, Vol. III: 17b, *Semiconductors: Physics of II–VI and I–VII Compounds, Semimagnetic Semiconductors*, Ed. K.H. Hellwege (Springer, Berlin, 1982).





ELSEVIER

Journal of Crystal Growth 138 (1994) 274–278

JOURNAL OF  
**CRYSTAL  
GROWTH**

## Studies on the diffusion of zinc in cadmium telluride at 800°C

E.D. Jones <sup>\*a</sup>, J.C. Clark <sup>a</sup>, J.B. Mullin <sup>b</sup>, A.W. Brinkman <sup>c</sup><sup>a</sup> School of Natural and Environmental Sciences, Coventry University, Coventry CV1 5FB, UK<sup>b</sup> Electronic Materials Consultant, The Hoo, Brockhill Road, West Malvern, Worcester WR14 3PS, UK<sup>c</sup> Applied Physics Group, University of Durham, Durham DH1 3LE, UK

### Abstract

The diffusion of zinc into bulk grown cadmium telluride has been studied at 800°C as a function of anneal time and mass of the diffusion source. The diffusions were carried out in evacuated silica ampoules and the diffusion profiles were measured using a radiotracer sectioning technique, although some measurements were obtained using scanning electron microscopy with an EDAX attachment. When the mass of zinc placed in the ampoule exceeded 2 mg, a ternary compound of  $\text{Zn}_x\text{Cd}_{1-x}\text{Te}$ , with  $x = 0.8$ , was formed on the surface of the slice early on in the diffusion and the diffusion profiles consisted of two components. Two values of the diffusivity were obtained,  $D_{\text{slow}} \rightarrow 2 \times 10^{-11} \text{ cm}^2 \text{ s}^{-1}$  and  $D_{\text{fast}} \rightarrow 2 \times 10^{-10} \text{ cm}^2 \text{ s}^{-1}$ , for anneal times exceeding 6 h and a mass of zinc of 8 mg placed in the ampoule. This contrasted with the results when the mass of zinc was less than 2 mg when no effective surface layer of the ternary compound was formed and diffusion profiles consisting of a single component were obtained. It is proposed that two diffusion mechanisms are operating, one due to zinc atoms diffusing from the vapour into the  $\text{Zn}_x\text{Cd}_{1-x}\text{Te}$  layer and the second an interdiffusion between the ternary compound in the surface of the slice and the CdTe in the bulk.

### 1. Introduction

The II–VI semiconductor CdTe has a wide variety of applications including  $\gamma$ -ray detectors, solar cells and electro-optical modulators, but the most common use is as a substrate, a barrier layer or a capping layer in the production of  $\text{Hg}_x\text{Cd}_{1-x}\text{Te}$  (MCT) infra-red detectors.

One of the greatest problems in manufacturing MCT devices is the difficulty in obtaining bulk grown CdTe substrates of high quality. Bulk grown CdTe contains defects such as twins, sub-grain boundaries and tellurium precipitates, and some

of these defects will propagate up into the growing MCT epitaxial layer, producing inferior quality devices. In addition, there is poor lattice matching between the CdTe substrate and the MCT epilayer and because of this, alternative fabrication routes have been investigated. One of the most successful is the use of  $\text{Zn}_x\text{Cd}_{1-x}\text{Te}$  (ZCT) crystals as substrates on which to grow the MCT devices directly. This material possesses similar crystal imperfections to CdTe, but when  $x = 0.05$ , the ZCT substrate and MCT epilayer are lattice matched and hence far fewer defects will propagate from the interface into the epilayer. It is therefore important to know the rate of diffusion of zinc in CdTe, and to study the Zn–Cd–Te system in detail.

\* Corresponding author.

There has been very little work done on diffusion in the Zn–Cd–Te system, the most important being that of Aslam et al. [1]. Studies on self-diffusion in ZnTe [2] and on self-diffusion in CdTe [3,4] have been reported extensively. In this paper, the diffusion of zinc in bulk CdTe at 800°C is reported, and the effects of varying the duration of the diffusion anneal and the mass of the diffusion source are examined. Extensive optical microscopy studies have been carried out on the CdTe slices used, both before and after diffusion, and the conclusions will be discussed in this paper.

## 2. Experimental procedure

Bulk-grown CdTe slices of approximate size 8 mm × 8 mm and thickness 0.8 mm were used in this study. The surfaces of the slices used for diffusion were prepared by mechanical polishing with successively finer grades of diamond paste (6 μm, 1 μm, 1/4 μm) followed by a chemical polish with 1% bromine in methanol for 10 min. The material removed in this procedure (200 μm by mechanical polishing, 100 μm by etching) was sufficient to remove all surface damage caused by sawing the slices from the boule. A CdTe slice was then sealed in an evacuated silica ampoule with a known mass of radioactive <sup>65</sup>Zn foil.

After annealing for a known time in a horizontal tube furnace at 800°C, the concentration of radioactive zinc atoms in the slice was measured by sectioning with a chemical etch of 1% bromine in methanol [5]. The majority of the diffusion profiles obtained possessed two distinct components and were fitted using a computer fitting programme [6] comprising either the sum of two gaussian functions or two complementary error functions. The former function gave the best fit when the mass of zinc in the diffusion source was not sufficient to maintain a saturated vapour pressure over the slice throughout the diffusion (limited source conditions), whereas the latter function was used when saturated vapour conditions were maintained (infinite source conditions where the mass of zinc was greater than 20 mg). In certain instances where the mass of zinc used

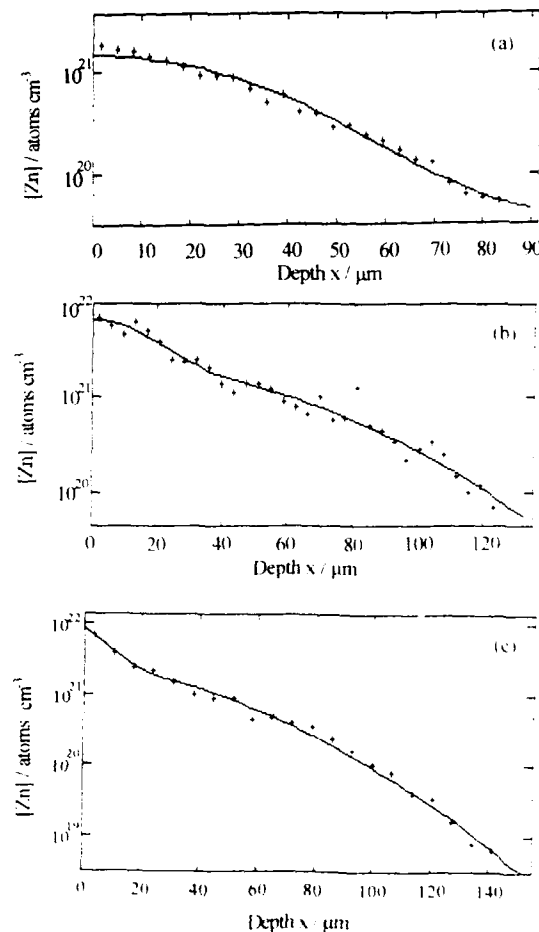


Fig. 1. Typical concentration profiles for the diffusion of zinc in CdTe at 800°C. (a) Single component profile showing the gaussian fit:  $m = 1.762$  mg,  $t = 48$  h,  $D = 4.640 \times 10^{-11}$  cm<sup>2</sup> s<sup>-1</sup>. (b) Double profile fitted by the sum of two gaussian functions:  $m = 8.2$  mg,  $t = 1.3$  h,  $D_{\text{slow}} = 5.264 \times 10^{-10}$  cm<sup>2</sup> s<sup>-1</sup>,  $D_{\text{fast}} = 1.497 \times 10^{-9}$  cm<sup>2</sup> s<sup>-1</sup>. (c) Double profile fitted by the sum of two complementary error functions:  $m = 31.6$  mg,  $t = 24$  h,  $D_{\text{slow}} = 4.815 \times 10^{-12}$  cm<sup>2</sup> s<sup>-1</sup>,  $D_{\text{fast}} = 1.219 \times 10^{-10}$  cm<sup>2</sup> s<sup>-1</sup>.

was low (< 2 mg), a single gaussian function gave the best fit to the experimental data. Typical diffusion profiles are shown in Fig. 1. The variation of  $D$  with the duration of the anneal and with the mass of zinc in the diffusion source is shown in Figs. 2 and 3, respectively.

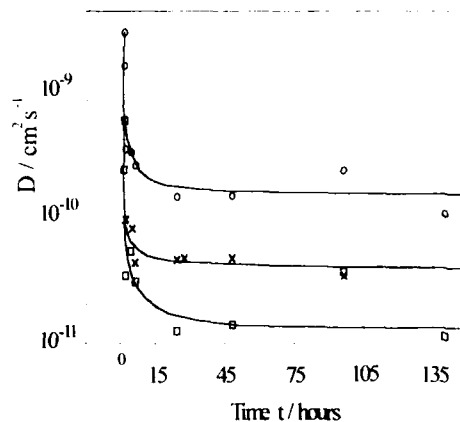


Fig. 2. Graph showing the variation of  $D$  with the duration of the anneal: (○)  $D_{\text{fast}}$  for  $m = 8$  mg; (□)  $D_{\text{slow}}$  for  $m = 8$  mg; (×)  $D$  for  $m = 1.8$  mg.

### 3. Surface effects of diffusion anneal

On many occasions after the anneal, the surface of the CdTe slice was covered with cracks in a regular "lattice" pattern, as shown in Fig. 4, which were still present when the surface of the slice was sectioned in the measurement of the diffusion profile. The cracks became more apparent and penetrated deeper into the slice when

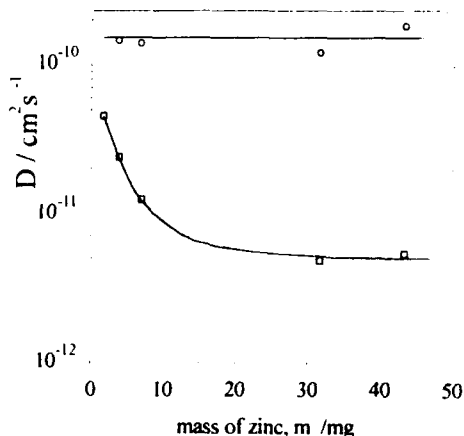


Fig. 3. Graph showing the variation of  $D$  with mass of zinc in the diffusion source for anneal times of 24 h at 800°C: (○)  $D_{\text{fast}}$ ; (□)  $D_{\text{slow}}$ .



Fig. 4. Photograph showing the surface cracking effects after diffusion with zinc (8 mg) at 800°C for 1 h. Magnification is  $\times 115$ .

the mass of zinc in the diffusion source was increased. In addition, as the sectioning continued, the action of the etch caused the cracks to open up and become more prominent, although at the end of sectioning fewer cracks remained. This compares with the slices which had been diffused with a low mass of zinc ( $< 2$  mg) and where a single diffusion component was measured, where far less cracking, if any, was observed.

It is known [1] that when zinc diffuses into CdTe, a continuous solid solution of  $\text{Zn}_{1-x}\text{Cd}_x\text{Te}$  is formed for all values of  $x$ . During these diffusions, the surface of the slice became a ternary alloy with  $x$  approaching 0.8. This was confirmed using non-radioactive zinc as a source and investigating the surface of the slice using a scanning electron microscope (SEM) with energy dispersive analysis of X-rays (EDAX) attachment. The resulting ZCT surface layer has properties more akin to ZnTe, with a reduced lattice parameter of 610 nm compared to CdTe whose lattice spacing is 648 nm, and also a different coefficient of thermal expansion. These factors could be responsible for the surface cracking effects, due to the creation of regions of high stress within the lattice, between the ZCT surface layer and the remainder of the CdTe slice. Aslam et al. [1] reported surface cracking effects at temperatures between 550 and 700°C with a pure zinc diffusion source of mass approximately 30 mg, but did not

observe these effects outside this temperature range or when Cd or Te was added to the diffusion source at all temperatures.

It is thought that the surface cracking occurs when the ampoule is removed from the furnace and cooled to room temperature. This conclusion was reached after examination of the diffusion profiles such as those in Fig. 1. If the cracks appeared near the start of the diffusion, the zinc would be expected to diffuse via these short circuit paths and penetrate deep into the slice very quickly. This would be shown on the resulting profile as a long diffusion “tail”, extending deep into the slice with a corresponding high value of  $D_{\text{fast}}$ , much higher than those measured. The absence of these tails in the profiles suggests that the cracks have no significant effect on the diffusion.

#### 4. Quality of the slices used

The quality of the material, with respect to defect density, was investigated using the defect etch Inoue E-Agl [7]. This produced etch pits on the surface which were investigated using an optical microscope with either differential interference contrast or Nomarski attachments, the



Fig. 5. Photograph showing the sub-grain structure of a typical CdTe slice used in the diffusion experiments. It illustrates the variation in etch pit density across the slice, along with the different shaped etch pits, indicating different orientations. Magnification is  $\times 320$ .

shape of the pits being dependent on the orientation of the surface [8]. A typical slice is shown in Fig. 5 after being etched for 1 min. This slice is typical of those used as it possesses sub-grains of different orientations, it contains twins and sub-grains which are shown up by the etch as triangular pits of different shape and orientation. The defect density of the slice on the left-hand side of the photograph was measured as  $2.1 \times 10^5$  pits  $\text{cm}^{-2}$ ; however, the density on the right-hand side is too large to measure accurately but is  $> 10^7$  pits  $\text{cm}^{-2}$ , the pits are clustered together too closely to differentiate them individually. The band of less dense etch pits at the right of the photograph is a twin band and this marks the interface between the two sub-grains.

#### 5. Discussion and conclusions

The values of the diffusivities at  $800^\circ\text{C}$  presented in this paper are in good agreement with those presented by Aslam et al. [1] ( $D_{\text{slow}} = 5 \times 10^{-11}$   $\text{cm}^2 \text{ s}^{-1}$  as against  $D_{\text{slow}} = 2 \times 10^{-11}$   $\text{cm}^2 \text{ s}^{-1}$ , for this work for anneal times  $> 6$  h and a high mass of zinc) who obtained profiles of both one and two components, depending on the sectioning method used.

Results on the variation of  $D$  with time  $t$  for mass  $m = 8$  mg shown in Fig. 2 indicate that each profile consists of two components and that the corresponding values of  $D$  decrease rapidly with increasing  $t$  for  $t < 6$  h, and then become independent of  $t$ . In the corresponding results for  $m = 1.8$  mg, only a single value of  $D$  could be resolved from the profiles, but the same variation between  $D$  and  $t$  was observed; however, the decrease in  $D$  for  $t < 6$  h was much less in this case. These results indicate that a non-equilibrium situation exists for  $t < 6$  h, whereas the diffusion becomes independent of  $t$  for  $t > 6$  h.

Results on the variation of  $D$  with mass for  $t = 24$  h show that two-component profiles were obtained except for the profile obtained with the smallest mass of zinc as the diffusion source ( $m = 1.8$  mg), where only one value of  $D$  could be resolved in the computer fitting. It can be seen that  $D_{\text{fast}}$  is virtually independent of mass,

whereas  $D_{\text{slow}}$  decreases with mass to become independent of mass for  $m > 20$  mg.

The results reported here indicate that the types of diffusion profiles obtained are very dependent on the mass of the zinc placed in the capsule. The rapid variation of  $D$  with  $t$  for  $t < 6$  h is due to the formation of the ternary compound  $\text{Zn}_x\text{Cd}_{1-x}\text{Te}$  with  $x = 0.8$  on the surface of the CdTe slice, and the thickness of this layer is related to the amount of zinc placed in the capsule at the start of the diffusion. For  $t > 6$  h, three distinct differences can be seen:

- (a) For  $m < 2$  mg, the thickness of the ternary layer is so thin that it does not affect the diffusion in any way or possibly no layer is formed. Diffusion is due to zinc atoms diffusing from the vapour phase directly into the CdTe giving a one component profile possessing a gaussian shape, indicating that "limited source" conditions apply.
- (b) For  $2 < m < 20$  mg, two component profiles are obtained which are fitted best by the sum of two gaussian functions indicating that the diffusion is still "source limited", and where the value of  $x$  will decrease during the diffusion. The majority of the diffusion measurements were made in this region and it is suggested that diffusion is occurring via two different mechanisms: one from the vapour phase ( $D_{\text{slow}}$ ) as described in (a), which is dependent on  $m$ , and a second which is an interdiffusion between the ZCT layer and the CdTe slice ( $D_{\text{fast}}$ ), which is independent of  $m$ .
- (c) For  $m > 20$  mg, again two component profiles are seen, and a function composed of the sum of two complementary error functions gives the best fit to the data indicating that "infinite source" conditions apply, with negligible source dilution occurring during the diffusion. Here again the two diffusion mechanisms described in (b) are operating.

The suggestion given above, that  $D_{\text{slow}}$  is a measure of the rate of diffusion of zinc atoms from the vapour into the ZCT ternary layer on the surface of the slice, is borne out by other published data on diffusion at 800°C. When  $m \rightarrow 0$ ,  $D_{\text{slow}} \rightarrow 1 \times 10^{-10} \text{ cm}^2 \text{ s}^{-1}$  which is the rate of diffusion of zinc in CdTe in a negligible concentration gradient, and this compares favourably with the value for the self-diffusion of Cd in CdTe [3]. At the other end of the scale, when  $m \rightarrow 30$  mg,  $D_{\text{slow}} \rightarrow 4 \times 10^{-12} \text{ cm}^2 \text{ s}^{-1}$ , which is a measure of the rate of diffusion of zinc in  $\text{Zn}_{0.8}\text{Cd}_{0.2}\text{Te}$  in the absence of a concentration gradient, which again compares favourably with the value of  $3 \times 10^{-12} \text{ cm}^2 \text{ s}^{-1}$  published by Reynolds and Stevenson [2] for the self-diffusion of zinc in ZnTe at 800°C.

## 6. Acknowledgements

The authors wish to thank Dr. E. O'Keefe of GEC-Marconi Infra-Red, Southampton, for providing the CdTe slices used in this work.

## 7. References

- [1] N. Aslam, E.D. Jones, T.C.Q. Noakes, J.B. Mullin and A.F.W. Willoughby, *J. Crystal Growth* 117 (1992) 249.
- [2] R. Reynolds and D.A. Stevenson, *J. Phys. Chem. Solids* 30 (1969) 139.
- [3] E.D. Jones, N.M. Stewart and J.B. Mullin, *J. Crystal Growth* 130 (1993) 6.
- [4] D. Shaw, *J. Crystal Growth* 86 (1988) 778.
- [5] N.A. Archer, H.D. Palfrey and A.F.W. Willoughby, *J. Crystal Growth* 117 (1992) 177.
- [6] N.M. Stewart, PhD Thesis, Coventry University (1990).
- [7] M. Inoue, I. Teramoto and S. Takayanagi, *Appl. Phys. Lett.* 34 (9) (1979) 574.
- [8] K. Durose, PhD Thesis, University of Durham (1985).



ELSEVIER

Journal of Crystal Growth 138 (1994) 279–284

JOURNAL OF  
**CRYSTAL  
GROWTH**

## Incorporation of iodine into CdTe by diffusion

E.D. Jones <sup>a,\*</sup>, J. Malzbender <sup>a</sup>, J.B. Mullin <sup>b</sup>, N. Shaw <sup>c</sup>

<sup>a</sup> School of Natural and Environmental Sciences, Coventry University, Coventry CV1 5FB, UK

<sup>b</sup> Electronic Materials Consultant, The Hoo, Brockhill Road, West Malvern, Worcester WR14 4DL, UK

<sup>c</sup> DRA Electronics Division, RSRE, St Andrews Road, Great Malvern, Worcester WR14 3PS, UK

### Abstract

Initial studies on the diffusion of iodine into CdTe are described. Diffusion anneals were carried out at selected temperatures in the range between 20 and 270°C in evacuated silica ampoules using a diffusion source of either elemental iodine or CdI<sub>2</sub>, both under saturated vapour pressure conditions. The concentration profiles were measured using either a radiotracer sectioning technique or secondary ion mass spectrometry (SIMS). The profiles were found to be composed of four parts to which a computer package consisting of the sum of four complementary error functions (erfc) gave satisfactory fits to the data. The fastest diffusing component gave values of the diffusivity, which agreed with previously published data. Proposals explaining how this type of diffusion may occur are given, but the results indicate that iodine diffused into CdTe from the vapour is not suitable as a long term stable dopant in devices where sharp junctions are required.

### 1. Introduction

The II–VI group of semiconducting compounds has been recognised as being important since they offer a range of materials whose energy gaps span the entire visible spectrum [1], and whose optical conversion efficiencies are very high [2]. Although the II–VI compounds have been investigated extensively for many years, their considerable potential has not been fully realized because of difficulties involved in their growth.

The ability to prepare doped p–n epitaxial structures, such as in the fabrication of (Hg<sub>1-x</sub>Cd<sub>x</sub>)Te devices, is an essential requirement if some of the new developments in infrared photo-

voltic detectors are to be realised in practice. The location of the doped region must be well defined within the structure and the concentration of the active impurities has to be controlled accurately. Despite advances in material technology, it remains a difficult task to control the conductivity and to maintain a stable junction in the device. The criteria required for such dopants have been discussed by Easton et al. [3]. Consequently it is vital that the rates of diffusion of these dopants through the host material are known so that the most suitable one can be selected for a particular device. Very often diffusion rates are measured using radioactive tracer sectioning techniques [4].

Currently indium is the most widely used n-type dopant in CdTe and (Hg<sub>1-x</sub>Cd<sub>x</sub>)Te, but it is a fairly fast diffusant ( $117 \exp(-2.21 \text{ eV}/kT) \text{ cm}^2 \text{ s}^{-1}$  at  $p_{\text{Cd}}(\text{sat})$  [5]). In contrast to indium, the

\* Corresponding author.

halogens are expected to reside on anion sites. As iodine is the largest of the group of elements comprising the halogens, it is expected to be the least susceptible to diffusion [6]. Further it is the least reactive of the halogens and consequently the least likely to form compounds with Cd. Very little is known about the rates of diffusion of iodine in CdTe and associated ternary compounds. Gorodetskii et al. [7] measured the rates of diffusion of iodine and indium in CdTe by investigating the changes in electrical conductivity of the slices which had been doped by ion bombardment and calculated the diffusion parameters for iodine at a temperature of 200°C, which gave the following Arrhenius relationship:

$$D = 10^{-8} \exp[-(0.4 \pm 0.1 \text{ eV})/kT] \text{ cm}^2 \text{ s}^{-1}.$$

Measurement of the concentration profile provides information on the shape of the diffusion profiles, and in particular, about the fast diffusion components which are common in II–VI semiconductors and may affect the electrical performance of the semiconductor devices in a detrimental manner.

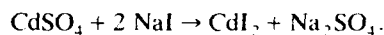
## 2. Experimental techniques

Bulk grown CdTe wafers and epitaxial layers, thickness 10–15  $\mu\text{m}$ , which had been grown on CdTe substrates by liquid phase epitaxy, were used in this investigation. Single crystal slices (about 8 mm  $\times$  8 mm  $\times$  0.08 mm) were cleaved out of polycrystalline wafers and polished to minimize the effect of surface damage on the diffusion. This was done using either mechanical polishing with fine-grade diamond (1/10  $\mu\text{m}$ ) or bromine etching (1% bromine in methanol) and in this process a total thickness of between 100 and 200  $\mu\text{m}$  was removed from the surface of each slice.

Four diffusion anneals were carried out at selected temperatures in the range 20 to 270°C in evacuated silica capsules under saturated vapour pressure conditions using either elemental iodine or  $\text{CdI}_2$  as the diffusion source. The diffusions were carried out under isothermal conditions in an electric furnace. It has been reported [8] that

it is not possible to use elemental iodine as a diffusion source at temperatures above 100°C as the iodine reacts with the CdTe in the surface of the slice even when elemental Cd is placed in the capsule along with the iodine, subsequently  $\text{CdI}_2$  was used as diffusion source.

For the radiotracer diffusions the radioactive isotope  $^{125}\text{I}$ , which is a fission product with a half-life of 60 days [9], was obtained in NaOH solution.  $\text{CdI}_2$  was produced directly using the reaction [10]:



The iodine concentration profiles were measured using either radiotracer sectioning at Coventry University when radioactive iodine was used as a diffusion source, or using secondary ion mass spectrometry (SIMS) at DRA, Malvern, when non-radioactive iodine was used. In the case of the radiotracer sectioning, a combination of anodic oxidation (section thickness: 0.006–0.2  $\mu\text{m}$  to a depth of 2  $\mu\text{m}$ ) and bromine etching (section thickness: 0.3–5  $\mu\text{m}$  to a depth of 30  $\mu\text{m}$ ) was used on CdTe slices possessing a mesa structure [11]. The iodine concentration was measured directly using a liquid scintillation counter.

## 3. Results and discussion

The details of four diffusion anneals reported here are given in Table 1 along with the relevant diffusion parameters, which were obtained from the diffusion profiles. Two diffusions were carried out at elevated temperatures (run B, shown in Fig. 2 at 270°C and run D at 85°C) and two at ambient temperatures (run A, shown in Fig. 1 and run C, both at 20°C). The shape of each of the profiles can be divided up into four distinct regions and each profile can be described mathematically by a function consisting of the sum of four complementary error functions (erfc) giving four values for the diffusivity, one for each part of the profile. The four parts to each profile can be clearly distinguished in Figs. 1 and 2.

The corresponding values of the diffusivities for the four diffusion measurements have been plotted on an Arrhenius graph in Fig. 3 along

Table 1  
Diffusion details and diffusion parameters (cf. Fig. 3)

Run No.	Temp. (°C)	Duration (s)	Source	CdTe	Polishing	Profile measurement	Diffusion parameters	
							$D$ (cm <sup>2</sup> s <sup>-1</sup> )	$C$ (cm <sup>-3</sup> )
A (Δ)	20	$1.47 \times 10^7$	Iodine	Bulk	Mechanical	SIMS	$D_1 = 3 \times 10^{-17}$	$C_{01} = 4.4 \times 10^{20}$
							$D_2 = 1 \times 10^{-16}$	$C_{02} = 9 \times 10^{19}$
							$D_3 = 2.5 \times 10^{-15}$	$C_{03} = 5 \times 10^{18}$
							$D_4 = 3 \times 10^{-14}$	$C_{04} = 1.4 \times 10^{17}$
B (□)	270	$0.79 \times 10^7$	CdI <sub>2</sub>	Bulk	Bromine	RTS	$D_1 = 2 \times 10^{-18}$	$C_{01} = 9 \times 10^{21}$
							$D_2 = 3 \times 10^{-17}$	$C_{02} = 1 \times 10^{22}$
							$D_3 = 4 \times 10^{-15}$	$C_{03} = 1 \times 10^{20}$
							$D_4 = 3 \times 10^{-12}$	$C_{04} = 1 \times 10^{19}$
C (▽)	20	$5.18 \times 10^7$	CdI <sub>2</sub>	Bulk	Mechanical	RTS	$D_1 = 2 \times 10^{-20}$	$C_{01} = 4 \times 10^{21}$
							$D_2 = 6 \times 10^{-19}$	$C_{02} = 3 \times 10^{20}$
							$D_3 = 3 \times 10^{-17}$	$C_{03} = 7 \times 10^{19}$
							$D_4 = 2 \times 10^{-14}$	$C_{04} = 2 \times 10^{18}$
D (○)	85	$0.3 \times 10^7$	CdI <sub>2</sub>	Epitaxial	—	RTS	$D_1 = 5 \times 10^{-20}$	$C_{01} = 9 \times 10^{20}$
							$D_2 = 4 \times 10^{-18}$	$C_{02} = 1 \times 10^{20}$
							$D_3 = 3 \times 10^{-16}$	$C_{03} = 3 \times 10^{19}$
							$D_4 = 9 \times 10^{-14}$	$C_{04} = 5 \times 10^{18}$

with the Arrhenius expression reported by Gorodetskii et al. [7], which has been extrapolated down to 20°C. It can be seen that the diffusivities reported here for each of the fastest components  $D_4$  agree closely with the results of Gorodetskii et al. [7], who reported an activation energy of  $0.4 \pm 0.1$  eV. In addition, it can be seen that an activation energy of this value for the  $D_4$  component along with a diffusivity value of  $10^{-14}$

cm<sup>2</sup> s<sup>-1</sup> at 20°C indicate that when iodine is diffused into CdTe from the vapour, it is not suitable as a long term stable dopant in devices where sharp junctions are required.

When comparing the diffusivities  $D_1$ ,  $D_2$  and  $D_3$  for the four profiles, it can be seen in Fig. 3 that the results obtained from the diffusions carried out using a CdI<sub>2</sub> diffusion source (runs B, C and D) are reasonably consistent, giving activa-

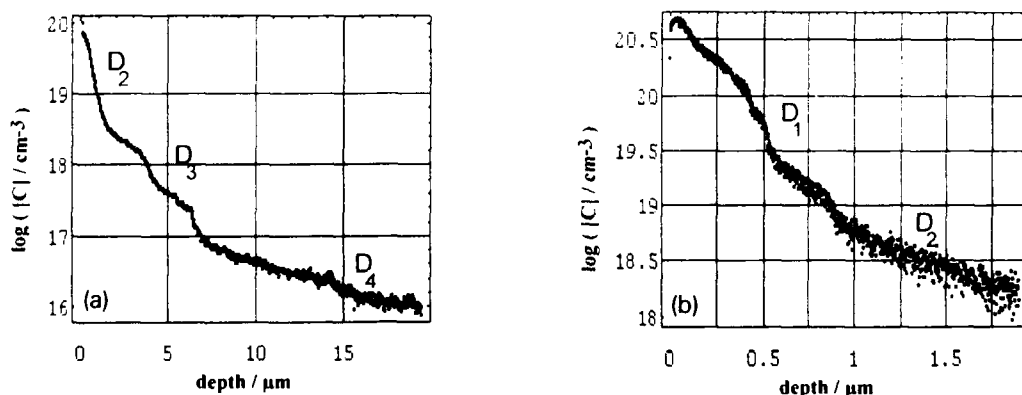


Fig. 1. A typical concentration profile for the diffusion of iodine into CdTe (run A) which has been diffused under saturated vapour pressure conditions using elemental iodine at ambient temperature (20°C). The profile was measured using SIMS. The three deeper components are shown in (a) and the first two components are shown under increased resolution in (b).



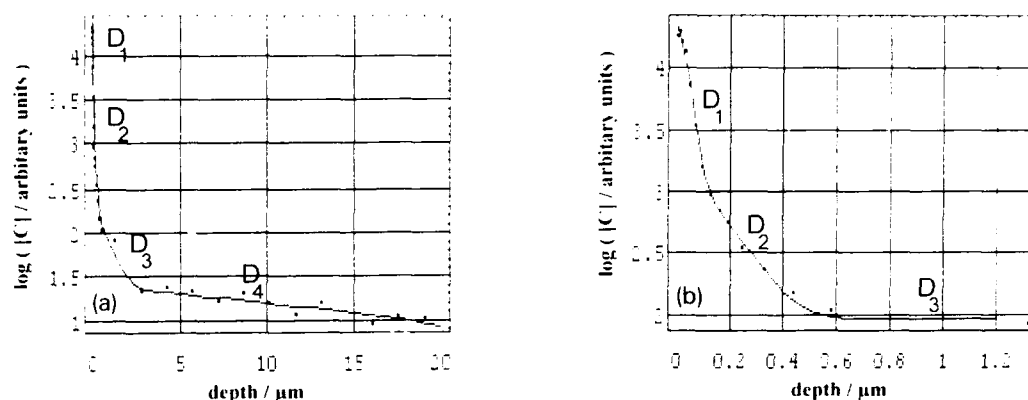


Fig. 2. A typical concentration profile for the diffusion of iodine into CdTe (run B) which has been diffused under saturated vapour pressure conditions using  $\text{CdI}_2$  as the diffusion source. The profile was measured using RTS sectioning. The four components are shown in (a) and the first two components are shown with increased resolution in (b).

tion energies which are close to the value of 0.4 eV reported by Gorodetskii et al. [7]. This contrasts with the two diffusions carried out at 20°C in which the diffusivities from run A, where an elemental iodine source was used, are consistently higher than the diffusivities from run C where a  $\text{CdI}_2$  source was used.

Whereas the diffusivities gave reasonably consistent results, there is a much wider spread in

the values of  $C_0$ , which was possibly due to uncertainties in the experimental calibration of the two measuring techniques, radiotracer sectioning (RTS) and SIMS, or to variations in the quality of the CdTe used for the diffusions. It is important to point out that the  $C_{01}$  values are exceedingly high ( $10^{21}$ – $10^{22} \text{ cm}^{-3}$ ) in all runs, which could possibly be due to a layer of  $\text{CdI}_2$  forming on the surface of the CdTe during the diffusion.

Values of the diffusivities and the surface concentrations can be compared directly in runs B, C and D where  $\text{CdI}_2$  was used as the diffusion source in all three cases and all the profiles were obtained using the RTS technique. The use of epitaxially grown material in run D gave values of the diffusivity which were consistent with those in runs B and C, where bulk material was used, but the value of the surface concentration in run D was much lower than for corresponding values in runs B and C. In addition, the value of  $D_1$  in runs B and C, where the slices were prepared using bromine etching and mechanical polishing, respectively, gave values which were in agreement with run D, where an epitaxially grown slice was used. This implies that the method used in the prediffusion preparation had no significant effect on the diffusion profile.

The occurrence of two component diffusion profiles, particularly in II–VI semiconductors, is

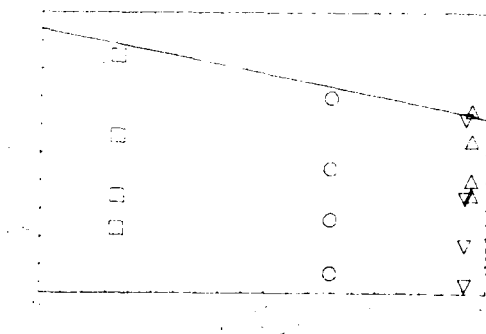


Fig. 3. An Arrhenius graph showing a comparison between the values of the diffusivities obtained in this investigation with the results obtained by Gorodetskii et al. [7]: ( $\Delta$ ) run A; ( $\square$ ) run B; ( $\nabla$ ) run C; ( $\circ$ ) run D. The diffusion details and parameters obtained from the profiles are presented in Table 1.

common and several explanations have been proposed including the following. They have been ascribed to interstitial–substitutional mechanisms in impurity diffusion [12], whereas in isoconcentration and self-diffusion the second, faster component is due to short circuit paths (e.g., dislocations or subgrain boundaries) [13] or chemical disequilibrium. The occurrence of four component diffusion profiles is a new phenomena and could be caused by one or several of the following factors:

(a) A feature of the experimental technique. In the experiments described here, where the iodine diffusion at low temperatures was fast, the iodine is diffused into the slice directly from the vapour, whereas when iodine is used in device fabrication and is thought to be a relatively slow diffuser [14], the iodine is deposited directly into lattice sites during epitaxial growth.

(b) Pipe diffusion along line defects such as dislocations forming localised regions of high iodine concentrations. It is possible that the iodine atoms diffuse along these pipes and collect at centres, which act as sinks, then the iodine may rediffuse radially out from these centres through the lattice. These centres could be impurity atoms that segregate out during crystal growth, precipitates or regions of high strain. Shcherbak et al. [15] observed the occurrence of amorphous inclusions in CdTe which were possibly associated with lattice strain and the formation of dislocations.

(c) A surface layer of a different identity. The profiles indicate that the surface of the diffused slices contained high concentrations of iodine. In spite of the fact that it was not possible to observe such layers visually after the diffusion anneal, such a layer which might have been a separate compound or complex, may have formed during the diffusion. This would have possibly resulted in two separate diffusion processes, one from the vapour and the second from the surface layer, each contributing to a double profile.

#### 4. Conclusions

Diffusion measurements are still being undertaken on this project, but the following conclusions

can be drawn from the work completed to date:

(a) When iodine diffuses into CdTe, four component profiles are produced and a function composed of the sum of four complementary error functions gives satisfactory fits to the experimental data.

(b) Iodine diffuses into CdTe at 20°C.

(c) During the diffusion, the concentration of iodine in the surface of the CdTe slice approaches that of Cd or Te in CdTe.

(d) The results indicate that iodine diffused into CdTe from the vapour is not suitable as a long-term stable dopant in devices where sharp junctions are required.

#### 5. Acknowledgements

The authors wish to thank Dr. E. O'Keefe, GEC Marconi Infrared, Southampton, for supplying the CdTe slices, Dr. M.G. Astles, DRA Electronic Division, Malvern, who suggested the project and supplied the epitaxially grown slices, Mr. G. Blackmore, DRA Electronic Division, Malvern, for carrying out the SIMS measurements and Mr. J.W. Brightwell, Coventry University, for advising on the chemistry aspects of the work.

#### 6. References

- [1] K. Zanio, in: *Semiconductors and Semimetals*, Vol. 13, Cadmium Telluride, Eds. R.K. Willardson and A.C. Beer (Academic Press, New York, 1978).
- [2] A.J. Strauss, *Appl. Phys. Rev.* 12 (1977) 166.
- [3] B.C. Easton, C.D. Maxey, P.A.C. Whiffin, J.A. Roberts, I.G. Gales, F. Grainger and P. Capper, *J. Vac. Sci. Technol. B* 3 (1991) 1682.
- [4] E.D. Jones, J.B. Mullin and V. Thambipillai, *J. Crystal Growth* 118 (1992) 1.
- [5] E. Watson and D. Shaw, *J. Phys. C* 16 (1983) 515.
- [6] D. Rajavel, B.K. Wagner, R.G. Benz II, A. Conte, K. Maruyama, C.L. Summers and J.D. Benson, *J. Vac. Sci. Technol. B* 10 (1992) 1432.
- [7] E.A. Gorodetskii, G.A. Kachurin and C.S. Smirnov, *Dif. fuz. Poluprov.* (1967) 72.
- [8] J. Malzbender, E.D. Jones, J.B. Mullin and N. Shaw, *J. Crystal Growth*, submitted.
- [9] C.M. Lederer, J.M. Hollander and I. Perlman, *Table of Isotopes* (Wiley, New York, 1967) p. 69.

- [10] A. Vogel, *Jahresber. Fortschr. Chem.* (1864) 242.
- [11] N.M. Stewart, E.D. Jones and J.B. Mullin, *J. Mater. Sci.* 3 (1992) 211.
- [12] E.D. Jones and N.M. Stewart, *J. Crystal Growth* 84 (1987) 289.
- [13] D. Shaw, *Semicond. Sci. Technol.* 7 (1992) 1230.
- [14] C.D. Maxey, P.A.C. Whiffin and B.C. Easton, *Semicond. Sci. Technol.* 6 (1991) C26.
- [15] L.P. Shcherbak, I.M. Fodchuk and O.M. Tikhonova, *Sov. Phys.-Cryst.* 36 (1991) 862.



ELSEVIER

Journal of Crystal Growth 138 (1994) 285–289

JOURNAL OF  
**CRYSTAL  
GROWTH**

## Complex formation in In- and Ag/Cu-doped CdTe

M. Rüb<sup>a</sup>, N. Achtziger<sup>a</sup>, J. Meier<sup>a</sup>, U. Reislöhner<sup>a</sup>, P. Rudolph<sup>b</sup>,  
M. Wienecke<sup>b</sup>, W. Witthuhn<sup>\*,a</sup>

<sup>a</sup> *Physikalisches Institut, Universität Erlangen–Nürnberg, D-91058 Erlangen, Germany*

<sup>b</sup> *Fachbereich Physik, Humboldt-Universität Berlin, D-10099 Berlin, Germany*

### Abstract

Interactions between In donors and Ag, Cu and acceptor-like native defects have been studied in p- and n-type CdTe single crystals by perturbed angular correlation (PAC) spectroscopy on <sup>111</sup>In probe atoms. Silver diffusion into the p-type samples at room temperature results in the formation of a distinct complex characterized by an interaction frequency  $eQV_{zz}/h = 60.1$  MHz and an asymmetry parameter  $\eta = 0.15$ . At room temperature the relative fraction of this complex increases within a few hours and decreases with a significantly longer time constant. After copper doping, a similar complex with 57.5 MHz and  $\eta = 0.16$  was observed which, however, did not show any decrease. The observed behaviour is explained by fast diffusion of Ag (or Cu) via an interstitial mechanism and the interaction with cation vacancies. Finally, In–Ag (or In–Cu) complexes are formed.

### 1. Introduction

The II–VI semiconductor CdTe has recently received increasing attention because of promising applications in optoelectronic devices, as radiation detectors and as material for solar cells. It can be obtained with either n- or p-type conductivity. The controlled doping, however, depends strongly on deviations from stoichiometry during growth, as well as on the nature and concentration of residual impurities. Highly resistive semi-insulating samples can be produced by doping p-type grown crystals with n-type impurities. Despite the intensive research, details of this self-

compensation mechanism, as well as of impurity interactions in general, are still unknown or are discussed controversially.

In the present paper we have studied the interaction of indium donors and native acceptors like  $V_{Cd}$ . Main emphasis was put on the influence of additional Ag and Cu impurities, which interact strongly with the cation vacancies [1,2].

The complex formation has been studied by perturbed angular correlation (PAC) spectroscopy. By this nuclear technique, formation, local atomic and electronic structure, as well as thermal stability of complexes are studied directly on an atomic scale. Previous PAC studies on CdTe were reported on ion-implanted samples [3], on n-type materials [4] and on  $In_{Cd}-V_{Cd}$  pairs in p-type crystals [5,6].

\* Corresponding author.

## 2. Experimental details

The PAC method is based on the observation of the defect specific electric charge distribution in the neighbourhood of the radioactive probe atom characterized by the traceless tensor  $V$  of the electric field gradient (EFG). The components  $V_{ij}$  are deduced from the recorded PAC time spectra  $R(t)$ . The largest component  $V_{zz}$  is usually expressed by the quadrupole coupling constant  $\nu_Q = eQV_{zz}/h$ , where  $Q$  is the nuclear quadrupole moment. The other components are combined to the asymmetry parameter  $\eta = (V_{xx} - V_{yy})/V_{zz}$  with  $1 \geq \eta \geq 0$ . For an axially symmetric EFG (i.e.  $\eta = 0$ ) and nuclear spin  $I = 5/2$ ,  $\nu_Q$  is related to the basic modulation frequency  $\omega_0$  by  $\nu_Q = (10/3\pi)\omega_0$ . The relative fraction  $f(i)$  of probe atoms decorated with a specific defect complex (i) and the orientation of the associated EFG(i) can be extracted directly from the modulation patterns. Furthermore, a damping of the time spectra gives information on remote defects or dynamic processes [7,8]. A general description of the PAC method is given in ref. [9], and details especially for applications to semiconductors can be found in refs. [10,11].

In the present experiment, the PAC measurements were performed at the isomeric  $5/2^+$  level of  $^{111}\text{Cd}$ , which is populated by the EC decay of  $^{111}\text{In}$  with a half-life of 2.8 days. Therefore the trapping and detrapping of impurities or defects is governed by the electronic properties of indium donors, whereas the EFG is measured at cadmium atoms, which are no longer impurities.

The samples of CdTe single crystals were doped with  $^{111}\text{In}$  probe atoms by diffusion between 700 and 800°C. After the PAC experiments, the indium profile was measured by the sequential etching of the original samples: in the p-type crystals (diffusion depth around 100  $\mu\text{m}$ ) the concentrations were  $10^{14} \text{ In/cm}^3$ , and in the n-type sample  $2 \times 10^{13} \text{ In/cm}^3$ .

The non-stoichiometry of the p-type samples was controlled by performing the In diffusion in tellurium-rich vapour maintained by an additional CdTe:Te source according to the three-phase equilibrium at the respective temperature. An overall hole concentration in the order of  $10^{16} \text{ cm}^{-3}$  was achieved, which was checked by conductivity measurements. The n-type sample was pre-annealed for several days with a cadmium-rich additional CdTe: Cd source. After the heat treatment, all samples were quenched to room temperature within a few seconds.

The doping with silver was performed at room temperature by dipping the samples into a 1% aqueous solution of  $\text{AgNO}_3$  for 30 s followed by rinsing in distilled water. For the copper-doping an analogous process was used (10% aqueous solution of  $\text{CuSO}_4$  for 80 s at 370 K). The characteristic data of the samples are listed in Table 1.

## 3. Results and discussion

The results of the present PAC measurements depend strongly on the type of the sample and on the annealing conditions; an influence of the crys-

Table 1

Characteristic data of the samples used in the present investigation; sample L was doped with Cu, all other samples were doped with Ag after the indium diffusion

Sample	Diffusion time (h)	Additional source material	Dopant	Observed complex	Crystal orientation
F	24	CdTe:Te	Ag	$f(1)$	$\langle 111 \rangle$
G	30	CdTe:Te	Ag	$f(1)$	$\langle 111 \rangle$
H	42	CdTe:Te	Ag	$f(3) \Rightarrow f(1)$	$\langle 111 \rangle$
I	26	CdTe:Te	Ag	$f(1)$	$\langle 100 \rangle$
K	45	CdTe: Cd	Ag	No complexes	$\langle 111 \rangle$
L	49	CdTe:Te	Cu	$f(2)$	$\langle 111 \rangle$
M	24 + 48	CdTe:Te CdTe:Te	Ag	No complexes $f(1)$ and $f(3) \Rightarrow f(1)$	$\langle 100 \rangle$

tal orientation has not been observed. After the diffusion process, the  $^{111}\text{In}$  atoms are expected to occupy substitutional Cd sites. Without additional defects, the cubic zincblende structure is characterized by a vanishing EFG at this lattice site, resulting in unmodulated PAC spectra. Indeed, this has been observed for samples F, G, I, K and L (see Table 1). Samples H and M exhibit a strong modulation directly after the diffusion process, indicating the formation of a complex involving indium atoms. This difference may be caused by the different annealing times (summarized in Table 1). Shorter annealing times could result in incomplete Te saturation and a lower Cd-vacancy concentration in these samples. Since native vacancies are very mobile at higher temperatures, a further reason for the observed results may be due to slightly different conditions

of the quenching process. In all p-type crystals, the following doping with silver or copper significantly changed the observed modulation patterns.

### 3.1. n-Type material (sample K)

Here the PAC spectra did not show any modulation either before or after silver doping, or after different annealing conditions. This result indicates that no defect or impurity was trapped at the indium donor. It can be explained in a straightforward manner if one assumes the cation vacancy  $V_{\text{Cd}}$  – they are believed not to be present in n-type material – to be the necessary condition for a complex formation with the In atoms. Our result agrees with the data reported by Wolf et al. [5] who did not observe complexes in samples annealed under Cd overpressure either.

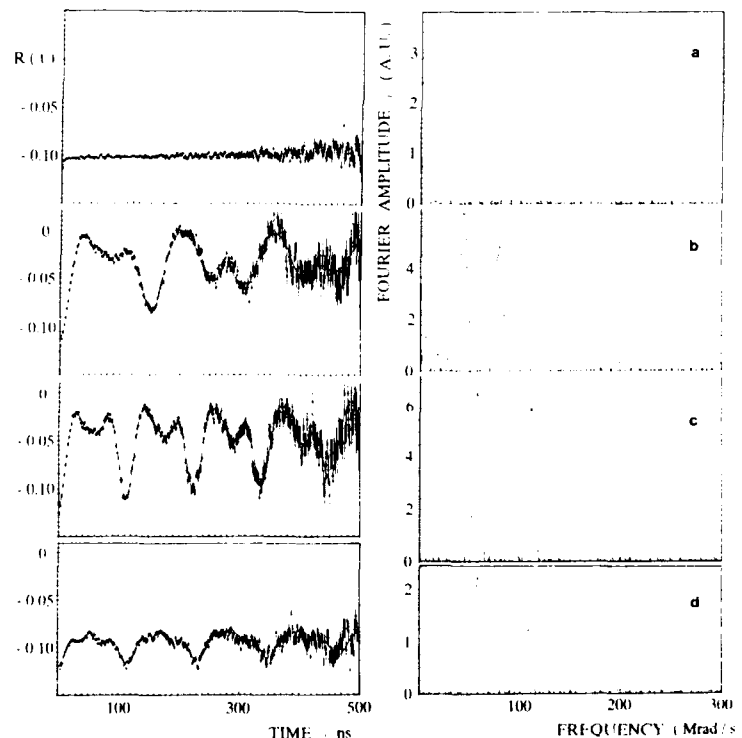


Fig. 1. PAC time spectra (left side) and the corresponding Fourier transforms of  $^{111}\text{In}$  in CdTe single crystals at room temperature: (a) after indium diffusion (samples F, G, I, K and L); (b) before and (c) 2 h after Ag doping of sample H; (d) after doping with Cu (sample L).

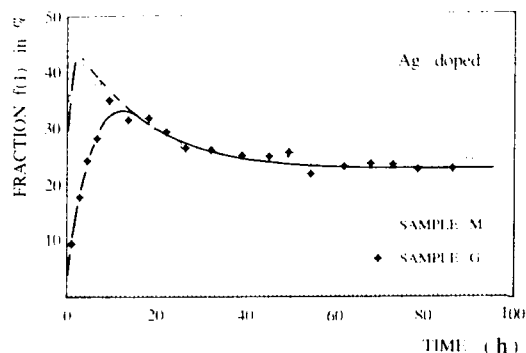


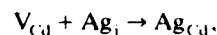
Fig. 2. Time dependence of the concentration of complex  $f(1)$ . The data of sample M have been normalized to the fraction of sample G (at long annealing times).

### 3.2. *p*-Type material (samples F, G, I and L)

Here, after the In diffusion, the EFG at all indium atoms is zero (see Fig. 1a), as expected for an  $\text{In}_{\text{Cd}}$  lattice site with unperturbed surroundings. After silver doping at room temperature, a distinct complex  $f(1)$  is formed (Fig. 1c) characterized by the coupling constant  $\nu_{\text{Q}1} = 60.1(3)$  MHz and the asymmetry parameter  $\eta_1 = 0.15(4)$  (at  $T = 295$  K). The fraction  $f(1)$  of this complex increases with a time-constant of  $\tau_1 = 2$  h and then decreases with a significant longer time constant  $\tau_d = 20$  h, as shown in Fig. 2 (sample G).

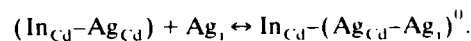
These trapping and “detrapping” processes can be frozen in by storing the sample at 77 K: sample I was stored alternatively at room temperature and at 77 K. The dependence of  $f(1)$  on time agrees exactly with that observed for the other samples if the storage time at 77 K is ignored.

Combining these data, the formation of complex  $f(1)$  obviously requires the presence of  $\text{V}_{\text{Cd}}$  and Ag impurities. The important first step is certainly the defect reaction



which had been identified by the enhancement of the ( $\text{A}^0$ , X) line in PL spectra [2]. We propose the observed complex  $f(1)$  – with  $\nu_{\text{Q}} = 60.1$  MHz and  $\eta = 0.15$  – to be due to the trapping of  $\text{Ag}_{\text{Cd}}$  acceptors by the indium donors resulting in an  $\text{In}_{\text{Cd}}-\text{Ag}_{\text{Cd}}$  configuration. Within this picture the

observed slow decrease of  $f(1)$  can be explained by the trapping of a second silver atom (at about 1/3 of the  $\text{In}_{\text{Cd}}-\text{Ag}_{\text{Cd}}$  pairs):



As the  $\text{Ag}_{\text{Cd}}-\text{Ag}_i$  pair close to the  $\text{In}_{\text{Cd}}$  donor is expected to be neutral and lattice relaxations are expected to be small, the EFG at the  $\text{In}_{\text{Cd}}$  site is expected to be negligibly small and below the detection limit of the PAC spectroscopy. Thus, the trapping of the second Ag atom does not result in a new modulation of the PAC spectra, in agreement with the experiment. The trapping of this additional Ag atom proceeds slowly ( $\tau_d$ ) and seems to saturate after decorating about 1/3 of the  $\text{In}_{\text{Cd}}-\text{Ag}_{\text{Cd}}$  pairs. The binding energy should be small, since the fraction  $f(1)$  of the  $\text{In}_{\text{Cd}}-\text{Ag}_{\text{Cd}}$  pairs can be increased again by a moderate annealing at only 373 K, i.e. the bound  $\text{Ag}_i$  atom is split off easily.

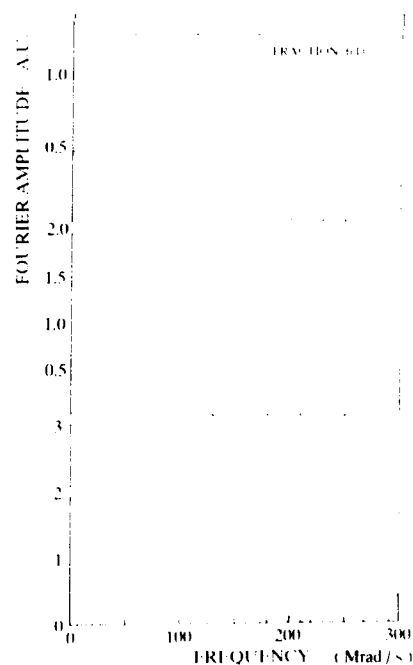


Fig. 3. Conversion of fractions  $f(1)$  and  $f(3)$  observed at sample M; before (upper part), 0.8 h (middle) and 2.3 h (lower part) after Ag doping.

After copper-doping (sample L, see Fig. 1d) a similar complex  $f(2)$  was formed, characterized by  $\nu_{Q2} = 57.5$  MHz and  $\eta_2 = 0.16$ , whose fraction increases slowly with time at room temperature. The essentially identical hyperfine parameters indicate an analogous  $\text{In}_{\text{Cd}}\text{-Cu}_{\text{Cd}}$  complex. The missing decrease of the fraction  $f(2)$  at longer times may be due to a significantly lower concentration of copper impurities or a negligibly small binding energy of  $\text{Cu}_i$  to the  $\text{In}_{\text{Cd}}\text{-Cu}_{\text{Cd}}$  complex.

### 3.3. *p-Type material (samples H and M)*

Here the indium diffusion was performed for longer times and with excess source material. Subsequently they showed a distinct modulation  $f(3)$  in the PAC spectra with significantly different EFG parameters:  $\nu_{Q3} = 40.5$  MHz and  $\eta_3 = 0.32$  (see Fig. 1b). After Ag-doping, this complex converts within a few hours into the known  $f(1)$  complex, as demonstrated clearly in Fig. 3. The most straightforward interpretation is the assignment of the 40.5 MHz configuration to an  $\text{In}_{\text{Cd}}\text{-V}_{\text{Cd}}$  complex, the well-known A-centre [12].

## 4. Conclusion

The formation of complexes between substitutional  $\text{In}_{\text{Cd}}$  donors and acceptor-like defects as  $\text{V}_{\text{Cd}}$ ,  $\text{Ag}_{\text{Cd}}$  and  $\text{Cu}_{\text{Cd}}$  has been observed in p-type CdTe. The present experiment reveals details of the trapping process of silver atoms: a first “fast” step results in the formation of  $\text{In}_{\text{Cd}}\text{-Ag}_{\text{Cd}}$  pairs.

The second “slow” step involves an additional  $\text{Ag}_i$  atom forming a neutral  $(\text{Ag}_{\text{Cd}}\text{-Ag}_i)^0$  complex, still bound to the  $\text{In}_{\text{Cd}}$  donor.

## 5. Acknowledgement

This work has been financially supported by the Bundesminister für Forschung und Technologie under the contract No. CHR2ERL.

## 6. References

- [1] B. Monemar, E. Molva and Le Si Dang, Phys. Rev. B 33 (1986) 1134.
- [2] H. Zimmermann, R. Boyn, P. Rudolph, J. Bollmann and A. Klimakow, Mater. Sci. Eng. B 16 (1993) 139.
- [3] R. Kalish, M. Deicher and G. Schatz, J. Appl. Phys. 53 (1992) 4793.
- [4] D. Wegner and E.A. Meyer, J. Phys. Condens. Matter 1 (1989) 5403.
- [5] H. Wolf, T. Krings, U. Ott, U. Hornauer and T. Wichert, Mater. Sci. Forum 83–87 (1992) 1259.
- [6] T. Wichert, T. Krings and H. Wolf, Physica B 185 (1993) 297.
- [7] W. Witthuhn, Nucl. Instr. Methods B 63 (1992) 209.
- [8] N. Achtziger and W. Witthuhn, Phys. Rev. B 47 (1993) 6990.
- [9] H. Frauenfelder and R.M. Steffen, in: Alpha-, Beta-, Gamma-Ray Spectroscopy, Ed. K. Siegbahn (North-Holland, Amsterdam, 1965) Vol. 2, p. 997.
- [10] W. Witthuhn, Hyperfine Interactions 24–26 (1985) 547.
- [11] T. Wichert, N. Achtziger, H. Metzner and R. Sielemann, in: Hyperfine Interaction of Defects in Semiconductors, Ed. G. Langouche (Elsevier, Amsterdam, 1992) ch. 2, p. 79.
- [12] F.F. Morehead and G. Mandel, Phys. Rev. 137 (1965) A924.



## Lattice location of N atoms in heavily N-doped ZnSe studied with ion beam analysis and its implication on deep level defects

T. Yao <sup>\*</sup>, T. Matsumoto, S. Sasaki, C.K. Chung <sup>1</sup>, Z. Zhu, F. Nishiyama

*Department of Electrical Engineering, Hiroshima University, Higashi-Hiroshima 724, Japan*

### Abstract

Molecular beam epitaxially grown ZnSe doped with <sup>15</sup>N as high as  $1.5 \times 10^{20} \text{ cm}^{-3}$  is characterized by means of ion beam analysis technique. Resonant nuclear reaction of <sup>15</sup>N(p,  $\alpha\gamma$ )<sup>12</sup>C is utilized to detect <sup>15</sup>N, while particle induced X-ray emission (PIXE) is detected to get insight into the effect of N-doping on the lattice location of Zn and Se atoms. It is demonstrated that the incorporated N atoms are located at the substitutional sites and that both Zn and Se atoms are located at the substitutional sites. The results suggest that the carrier compensation in heavily N-doped ZnSe is not caused by such donors as N<sub>int</sub> or N<sub>Se</sub>–Zn<sub>int</sub>, but by complex defects which include donor-type complexes such as N<sub>Se</sub>–Zn–V<sub>Se</sub> and/or N<sub>Zn</sub>–N<sub>Se</sub>. It is also suggested that a cluster of N<sub>Se</sub> such as (N<sub>Se</sub>)<sub>n</sub>–Zn may play a role as a deep acceptor.

### 1. Introduction

A plasma source is frequently used for nitrogen doping of ZnSe by molecular beam epitaxy (MBE). To date the highest net acceptor concentration ( $N_A - N_D$ ) using nitrogen, is about  $1 \times 10^{18} \text{ cm}^{-3}$  [1]. A comparison of the net acceptor concentration measured by *C*–*V* with the nitrogen concentration [N] as determined by secondary ion mass spectroscopy (SIMS) shows that typically  $N_A - N_D$  reaches a value of  $\sim 5 \times 10^{17} \text{ cm}^{-3}$  in proportion to [N], but then saturates at around  $\sim 1 \times 10^{18} \text{ cm}^{-3}$  and eventually de-

creases. In attempts to understand the dopant saturation and improve the performance of laser diodes, the electronic and optical properties of N-doped ZnSe have been characterized [2,3]. Typical PL properties of N-doped ZnSe are as follows: when ZnSe is lightly doped with N which gives rise to a net acceptor concentration of less than  $\sim 1 \times 10^{17} \text{ cm}^{-3}$ , a shallow donor-to-acceptor pair (DAP) emission with zero-phonon energy of  $\sim 2.696 \text{ eV}$  appears; in the case of intermediate doping concentration with the value around  $1 \times 10^{17} \text{ cm}^{-3}$ , a new DAP emission with zero-phonon energy of  $\sim 2.678 \text{ eV}$  appears in addition to the shallow DAP emission; for heavily N-doped ZnSe, the lower energy DAP transitions dominate the spectrum. The lower energy DAP emission has been assigned to a transition between an N-associated deep donor and an N-acceptor level

<sup>\*</sup> Corresponding author.

<sup>1</sup> On leave from Department of Physics, Dongguk University, Seoul 100715, South Korea.

[4,6]. It has been speculated that the N-associated deep donor plays an important role in the carrier compensation mechanism. Hauksson et al. proposed that the compensating donor is a complex involving a native defect such as  $V_{Se}-Zn-N_{Se}$  which acts as a single donor [4]. On the other hand, Petruzzello et al. reported that the ZnSe lattice constant decreases as the N concentration increases [5]. The reduction of the lattice constant is greater than can be explained by the shorter Zn–N bond distribution of model prediction. They attributed the excess lattice contraction to the generation of point defects accompanying N doping. They reported that the Raman spectra display a broadening of the linewidth as the N concentration increases, which supports the notion of point defect creation with N doping. However, less attention has been paid to the structural properties of these layers from a microscopic point of view, although they give some insight into the understanding of compensation mechanism.

In this paper, we will present the results of ion beam analysis of ZnSe:N utilizing the nuclear reaction of  $^{15}N(p, \alpha\gamma)^{12}C$  and particle induced X-ray emission (PIXE). It is clearly indicated that most of the N atoms are situated at Se substitutional sites, and that Zn and Se are situated at their substitutional sites, but with somewhat displaced positions. The present results suggest that N forms either an  $N_{Se}-V_{Se}$  complex,  $N_{Zn}-N_{Se}$ , and/or  $(N_{Se})_n-Zn$  clusters in heavily N-doped ZnSe.

## 2. Experimental procedure

A heavily N-doped ZnSe was grown on GaAs(100) by MBE, in which  $^{15}N$  was used as doping species. The N concentration was estimated to be  $1.5 \times 10^{20} \text{ cm}^{-3}$  by the nuclear reaction analysis. The layer thickness was 3000 Å. Fig. 1 shows the depth profile of  $^{15}N$  obtained from the nuclear reaction analysis. Resonant nuclear reaction analyses were performed using 0.878 MeV proton beams as a primary ion beam generated by Van de Graaff accelerator. The primary beam causes resonant nuclear reaction of

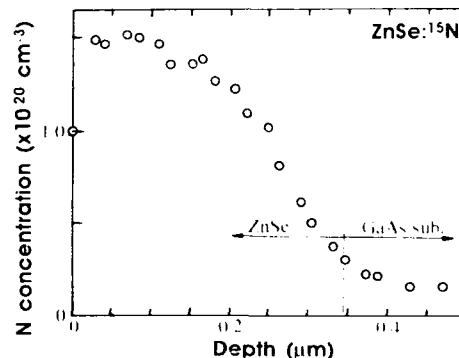


Fig. 1. The depth profile of nitrogen in the ZnSe epilayer obtained from the resonant nuclear reaction analysis.

$^{15}N(p, \alpha\gamma)^{12}C$  and the generated  $\gamma$ -ray was detected. We measured PIXE using  $\alpha$  particles accelerated at 2.0 MeV as a primary beam and the generated X-ray was detected with a Si–Li solid state detector. Rutherford backscattering (RBS) measurements were also performed using either  $\alpha$  particles or proton beams. We measured photoluminescence spectra at 12 K using the 3250 Å line of a He–Cd laser as an excitation source.

## 3. Ion beam analysis

The optical properties of N-doped ZnSe with N concentration of  $1.5 \times 10^{20} \text{ cm}^{-3}$  were investigated by photoluminescence spectroscopy. The ZnSe:N exhibits strong and broad emission at 2.48 eV at 12 K, as shown in Fig. 2. The emission energy shifts to the high energy side as the excitation intensity increases, indicating DAP emission. In highly N-doped ZnSe with  $[N]$  larger than  $1 \times 10^{18} \text{ cm}^{-3}$ , the DAP emission appears typically at 2.682 eV [6], in which a pair of an N-associated deep donor with ionization energy of 55 meV and a shallow N acceptor (110 meV) participates in the transition. We have observed a shift of DAP emission energy to the low energy side as the N concentration increased [6]. For this particular sample with N concentration of  $1.5 \times 10^{20} \text{ cm}^{-3}$ , the concentration-dependent shift is estimated to be around  $\sim 200$  meV, suggesting

the formation of an N-associated deep donor with an ionization energy of  $\sim 255$  meV or the formation of an N-associated deep acceptor level with  $\sim 310$  meV. The broad linewidth is due to merging of phonon replicas.

The high N-doping results in the formation of defects which limit the attainable net acceptor concentration. Ion beam analysis is used to investigate the lattice location of N and the displacements of Zn and Se atoms from the regular lattice sites. Fig. 3 shows the channeling angular distributions for X-ray emitting from Zn (open circles) and Se (closed circles) for both (a)  $^{15}\text{N}$ -doped and (b) undoped ZnSe. Measurements are for the  $\langle 110 \rangle$  axis at 300 K. Although it is hard to observe apparent narrowing in the channeling dip and increase in the minimum yield, we observe a considerable enhancement in the yield at around  $1^\circ$  off the arrangement direction for N-doped ZnSe compared to undoped ZnSe. These facts indicate that Zn and Se are situated at the substitutional sites although slightly displaced and that there are no detectable interstitial Zn and Se atoms in N-doped ZnSe. The observed displacements of Zn and Se are possibly induced by the presence of substitutional N atoms, since the bond lengths of N–Se and N–Zn are smaller than that of Zn–Se.

The angular distributions of  $\gamma$ -rays (closed circles) emitted from  $^{15}\text{N}$  clearly show dips for the (a)  $\langle 110 \rangle$  and (b)  $\langle 100 \rangle$  channeling, as shown in Fig. 4, where the angular distribution of proton

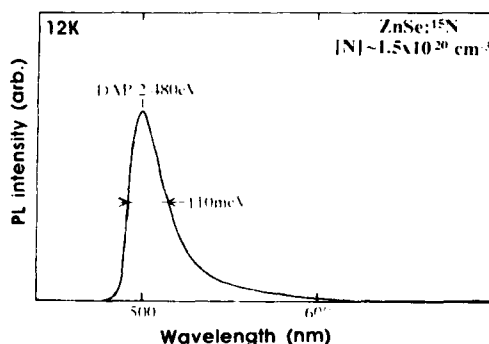


Fig. 2. Photoluminescence spectrum of ZnSe:N with  $[\text{N}] = 1.5 \times 10^{20} \text{ cm}^{-3}$  at 12 K.

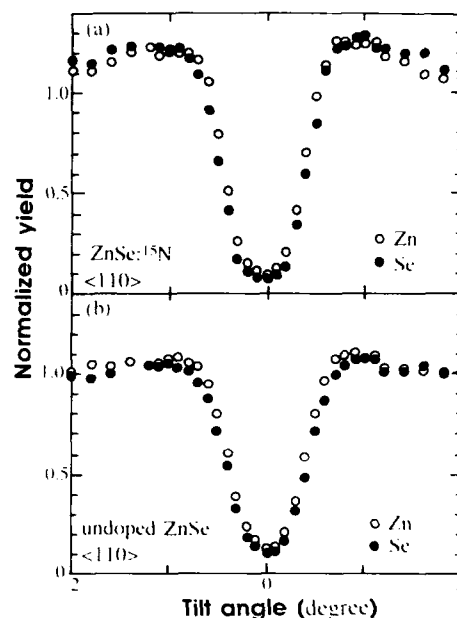


Fig. 3. Angular distribution of X-ray emitting from Zn (○) and Se (●) for (a) N-doped ZnSe and (b) undoped ZnSe. Measurements are for the  $\langle 110 \rangle$  axis at 300 K.

(open circles) scattered from ZnSe is also shown. The angular distribution is simulated on the basis of the formalism developed by Picraux et al. [7]. The dashed curve shows a calculated angular distribution, where all of the N atoms incorporated into ZnSe are assumed to be at the substitutional sites, while the dotted curve is for the displacement of N atoms by  $0.4 \text{ \AA}$  from the substitutional site. These facts indicate that most of the incorporated N is situated at the substitutional sites, although slightly displaced, and that there are no detectable interstitial N atoms in heavily-N doped ZnSe.

#### 4. Deep levels in N-doped ZnSe

We have measured deep level transient spectroscopy (DLTS) and isothermal capacitance transient spectroscopy (ICTS) for N-doped ZnSe at various N concentrations. We observed two hole traps with activation energies around 0.28

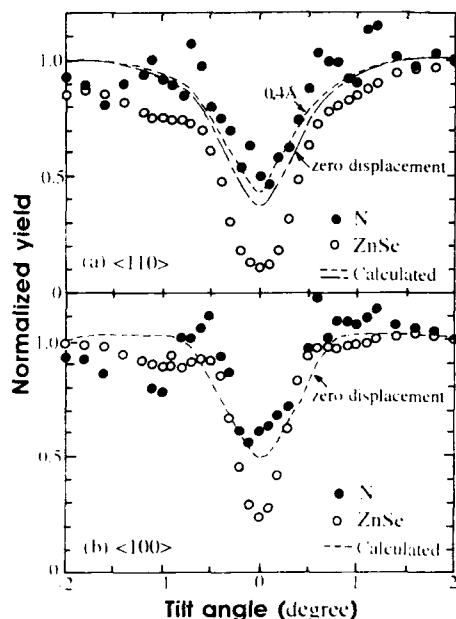


Fig. 4. Angular distribution of  $\gamma$ -rays ( $\bullet$ ) emitted from  $^{15}\text{N}$  doped in ZnSe for the (a)  $\langle 110 \rangle$  and (b)  $\langle 100 \rangle$  axes. The angular distribution of protons ( $\circ$ ) scattered from ZnSe for N-doped ZnSe is also shown. The dashed and dotted curves are calculated angular distributions for the displacements of 0 and 0.4 Å, respectively.

and 0.52 eV. The capture cross sections for the two trap levels were  $5 \times 10^{-17}$  and  $6 \times 10^{-21} \text{ cm}^2$ , respectively. The concentrations of the deep levels were, for instance,  $1 \times 10^{15}$  and  $8 \times 10^{14} \text{ cm}^{-3}$ , respectively, for the sample of  $N_{\text{A}} - N_{\text{D}} = 5 \times 10^{16} \text{ cm}^{-3}$ .

## 5. Discussion

Based on the above findings, we will discuss possible N-associated complex defects which are responsible for the carrier compensation in heavily N-doped ZnSe. Recently, theoretical studies have suggested the formation of deep donor defects associated with N at an interstitial site [8,9].

However, the present results clearly demonstrate that N atoms are situated at the substitutional sites. It is speculated that  $\text{Zn}_{\text{int}}$  and a complex defect consisting of an  $\text{N}_{\text{Se}}$ -acceptor and an interstitial Zn atom may act as a compensating donor. However, these defects should not be responsible for the carrier compensation, since no detectable interstitial Zn atom is found in the present ion beam analysis.

The complex defects consisting of an  $\text{N}_{\text{Se}}$ -acceptor and Se vacancy ( $\text{N}_{\text{Se}} - \text{Zn} - \text{V}_{\text{Se}}$ ) were proposed through the studies on PL and electrical measurements [4]. It is obvious that this model is consistent with the present experimental results. In fact, in the model, N atoms are situated at the Se substitutional sites and the displacement of N atoms may be induced by adjacent Zn atoms which are slightly displaced because of the presence of adjacent Se vacancy. The recent XRD study shows anomalous contraction of lattice parameter in N-doped ZnSe [5]. Although the correlation of the anomalous lattice contraction with native point defects is not clear yet, it should be noted that anomalous contraction of lattice parameter was observed in B-doped GaAs and that the excess contraction is interpreted in terms of the formation of As-vacancy associated complex defects [10].

Other complex defects which may be suggested based on the present experimental results are deep acceptors consisting of N clusters such as  $(\text{N}_{\text{Se}})_n - \text{Zn}$  and donor-type complex defects which consist of an N pair consisting of a substituting N at an Se site and an N atom being situated at an adjacent Zn site ( $\text{N}_{\text{Se}} - \text{N}_{\text{Zn}}$ ). These defects are shown schematically in Fig. 5. The cluster-type complex defect may act as deep acceptors and the most probable cluster would be  $(\text{N}_{\text{Se}})_2 - \text{Zn}$ , where two of four Se atoms surrounding a Zn atom are substituted by N atoms. We have found deep hole trap levels at 0.28 and 0.58 eV above the valence band in DLTS and isothermal capacitance transient spectroscopy measurements of N-doped ZnSe layers. The deep level with 0.28 eV agrees fairly well with the acceptor level ( $\sim 0.31 \text{ eV}$ ) estimated from the PL study mentioned above. It is likely that the hole trap of 0.28 eV is related with  $\text{N}_{\text{Se}} - \text{Zn} - \text{N}_{\text{Se}}$  clusters.

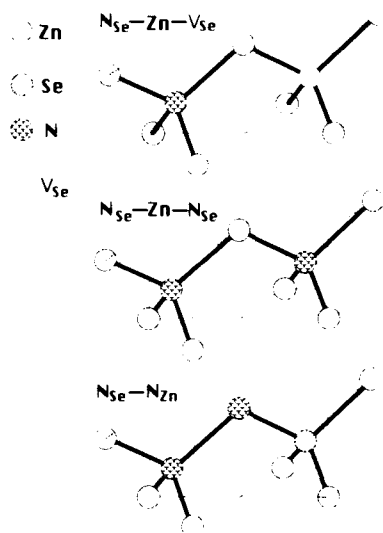


Fig. 5. Schematic representation of the proposed complex defects which may be responsible for carrier compensation in heavily N-doped ZnSe: (a) deep single donor of  $N_{Se}-Zn-V_{Se}$ ; (b) deep acceptor of  $N_{Se}-Zn-N_{Se}$ ; (c) N pair of  $N_{Se}-N_{Zn}$ .

## 6. Conclusion

We have investigated the lattice location of N atoms in a heavily N-doped ZnSe epilayer with N concentration of  $1.5 \times 10^{20} \text{ cm}^{-3}$ . Neither interstitial N atoms nor the deep donor associated with interstitial Zn atoms are detected in the N-doped ZnSe epilayer. The present results suggest three kinds of complex defects associated with N in heavily doped ZnSe, which are respon-

sible for carrier compensation: a deep single donor consisting of an N-acceptor and Se vacancy ( $N_{Se}-Zn-V_{Se}$ ); deep acceptors consisting of an N cluster such as  $N_{Se}-Zn-N_{Se}$ ; an N pair consisting of a substituting N at an Se site and an N atom being situated at an adjacent Zn site ( $N_{Se}-N_{Zn}$ ).

## 7. Acknowledgements

The authors are grateful to K. Ohkawa and T. Mitsuyu of Matsushita Electric Company for supplying the N-doped ZnSe sample and to T. Uenoyama of Matsushita Electric Company for valuable discussion.

## 8. References

- [1] J. Oiu, J.M. DePuydt, H. Cheng and M.A. Haase, *Appl. Phys. Lett.* 59 (1991) 2993.
- [2] K. Ohkawa and T. Mitsuyu, *J. Appl. Phys.* 70 (1991) 439.
- [3] A. Ohki, Y. Kawaguchi, K. Ando and A. Katui, *Appl. Phys. Lett.* 59 (1991) 671.
- [4] I.S. Hauksson, J. Simpson, S.Y. Wang, K.A. Prior and B.C. Cavenett, *Appl. Phys. Lett.* 61 (1992) 2208.
- [5] J. Petruzzello, J. Gaines, P. van der Sluis, D. Olego and C.A. Ponzoni, *Appl. Phys. Lett.* 62 (1993) 1496.
- [6] Z. Zhu, K. Takebayashi, K. Tanaka, T. Ebisutani, J. Kawamata and T. Yao, *Appl. Phys. Lett.*, to be published.
- [7] S.T. Pieraux, W.L. Brown and W.M. Gibson, *Phys. Rev. B* 6 (1972) 1382.
- [8] J. Chadi and N. Troullier, *Physica B* 185 (1993) 128.
- [9] M. Suzuki, T. Uenoyama and A. Yanase, in: *Extended Abstracts 1993 Int. Conf. on Solid State Devices and Materials*, 1993, pp. 74-76.
- [10] Y. Okada and F. Orito, *Appl. Phys. Lett.* 52 (1988) 582.

## Acceptor and donor states of impurities in wide band gap II–VI semiconductors

D.J. Chadi

NEC Research Institute, 4 Independence Way, Princeton, New Jersey 08540-6634, USA

### Abstract

The stability of substitutional versus displaced atomic configurations for N, Al, Ga, Cl, and isoelectronic O impurities in ZnSe, ZnTe, MgSe, and MgTe wide band gap semiconductors were examined via first-principles pseudopotential calculations. Negatively charged DX centers with very large lattice relaxations are found to be the stable states of Al and Ga donor impurities in ZnTe and MgTe but to be high energy metastable states in ZnSe and MgSe. The acceptor state of O in ZnSe is identified with a strongly bonded configuration in which a Zn–O bond replaces a Zn–Se bond. The idea of a *beneficial* defect-mediated doping mechanism is proposed and applied to an explanation of the properties of N impurities in ZnSe.

### 1. Introduction

Difficulties in finding suitable impurities for doping large band gap II–VI semiconductors both p- and n-type led to a decrease in interest and research on these semiconductors in the early 1970's. The recent success [1–3] in doping ZnSe p-type by using a pure nitrogen source has revived interest in II–VI and other wide band gap materials and has greatly stimulated new experimental and theoretical investigations.

The microscopic nature of the difficulties in doping most II–VI semiconductors remain only partially understood [4–11]. There are many possible explanations for why it is difficult, for example, to dope ZnTe n-type, but they generally fail when applied to ZnSe or most other II–VI selenides and sulfides which can be easily n-doped. The sharp difference in the doping properties of ZnSe and ZnTe is sometimes explained qualitatively by noting that, on an absolute energy scale,

the valence-band maximum (VBM) of ZnTe is about 1 eV higher than ZnSe and similarly the conduction-band minimum (CBM) of ZnTe is about 0.6 eV higher than in ZnSe. It can be argued that the high energy of the CBM in ZnTe is the main reason for the difficulties in n-type doping as this increases the likelihood of formation of localized defect states with lower energy. This argument, although useful, does not provide any information on the microscopic nature and properties of defect states which interfere with doping.

In this paper we report the results of first-principles calculations on the properties of acceptor, donor, and isoelectronic impurities in several II–VI semiconductors. The goal of this study is to determine the *intrinsic* electronic properties of impurities, i.e., to find whether in the absence of compensating defects such as vacancies, these impurities are electrically active or not. The idea of self-compensation by native defects is re-ex-

aminated in section 2. The acceptor-like states of isoelectronic O impurities and the results of new calculations for N impurities in ZnSe and MgSe are discussed in section 3. Donor impurities are examined in section 3, where it is proposed that n-type doping in II–VI tellurides is complicated by the formation of DX centers even in the absence of compensating defects.

The ab initio total energy calculations were done on three-dimensionally periodic unit cells containing 18 atoms per cell using a 340 eV cutoff energy for the plane wave expansions. The possibility of atomic displacements away from substitutional positions were considered in every case and the relative stabilities of various bonding configurations were determined.

## 2. Compensation by native defects

Despite recent success in achieving high hole concentrations in ZnSe with N as a dopant, the microscopic origin of the difficulties in the p-type doping of II–VI selenides and sulfides and n-type doping in the tellurides remains unclear. Even for N in ZnSe, it is not known what limits the maximum achievable hole concentration to a value of about  $10^{18} \text{ cm}^{-3}$ . The most widely held idea is that doping induces the formation of native defects [4], for example, vacancies on Se sites, or Zn interstitials, which compensate the acceptors. The introduction of acceptor impurities greatly enhances the probability of such defects because impurity compensation lowers the formation energy by an amount approximately the size of the band gap for a single donor or twice as much for a double donor. When the band gap is large, as in ZnSe where  $E_{\text{gap}} = 2.8 \text{ eV}$ , the decrease in defect formation energy is very significant. Recently, Laks et al. [9,10] have suggested on the basis of first-principles calculations that self-compensation by native defects is not important in *perfectly stoichiometric* ZnSe. However, tiny deviations away from perfect stoichiometry can lead to the formation of a large compensating background of defects. Laks et al. argued that if self-compensation by native defects were important, then it would be impossible to dope ZnSe either n- or

p-type, and this would be contrary to experimental results where no problem with n-type doping is encountered. On this basis, it was concluded that self-compensation via defect formation cannot be the primary reason for doping difficulties in II–VI semiconductors. In the following we suggest that native defect formation in response to doping is, in fact, an important process, and that successful doping can be achieved in spite of defect formation and may even, in some cases, benefit from the presence of such defects.

Let us consider the p-type doping of ZnSe with N and take the situation where the incorporation of acceptor-like substitutional N impurities at the growth surface leads to the formation of donor-like vacancies on Se sites. It might be expected that under this condition no doping can be achieved. However, this conclusion ignores other important processes which can affect the doping. Most importantly, *interstitial* N, with a structure similar to that of interstitial O in Si, is an acceptor [12] and it is expected to be as mobile as O in Si where the energy barrier for diffusion is around 2 eV. The diffusing acceptor-like N is attracted by the donor-like Se vacancy. The recombination of the two is an energetically favorable reaction and leads to the formation of a substitutional N atom on a Se site which is a desired reaction for p-type doping. Under appropriate growth conditions and an efficient recombination regime, a high initial density of Se site vacancies may not only be ineffective in leading to self-compensation but could in fact lead to a high doping level. This would suggest that p-type doping should be possible even under a *Zn-rich* growth condition which favors the formation of Se vacancies. Doping under this condition has been demonstrated experimentally [13]. The defect mediated doping mechanism has other consequences. If there are  $10^{18} \text{ cm}^{-3}$  Se vacancies in the system at a particular growth temperature, the filling of the vacancies by diffusing N interstitials will initially result in an increase in the hole concentration and the doping efficiency will be close to 1. However, at some point, the probability that a diffusing N atom meets a Se vacancy becomes equal to that for encountering a substitutional N atom. If captured by the vacancy, an

additional hole is created, but as discussed below, the formation of a N–N split-interstitial complex at a substitutional site leads to a *neutralization* of a hole. In this regime, the doping efficiency drops to zero. In the final state where most of the Se vacancies in the bulk have been filled by N atoms, the presence of additional diffusing N atoms can only lead to N–N complex formation and the doping efficiency becomes *negative*, i.e., the hole concentration actually drops. This sequence of a doping efficiency changing from unity to zero and then negative is observed experimentally [14,15]. For the success of this argument it is necessary to assume that the formation of additional Se vacancies in the bulk in response to substitutional N acceptors is suppressed by the much larger energy needed for creating a vacancy-interstitial pair defect (as compared to a simple vacancy near the surface).

The same type of mechanism can be operative for the case of n-type doping of ZnSe. Let us consider the case where Ga donor impurities are being used for the doping and assume, as before, that at the growth front the incorporation of a Ga atom leads to the creation of a compensating acceptor-like defect, in this case a vacancy on a Zn site. If interstitial Ga atoms are donor-like, then they would be attracted by the acceptor-like vacancies and recombination of the two would give a Ga on a Zn site which is a donor and is a desired reaction. Interstitial Ga, in various bonding configurations, is in fact a donor [12] so the situation for n-type doping is similar to that for p-type doping and the fact that compensating native defects form does not necessarily lead to problems with doping.

Is there experimental support for an increase in the concentration of vacancies or other compensating centers with doping? Miyajima et al. [16] have shown via positron annihilation studies that the concentration of negatively charged Zn vacancies (which attract positrons) increases in ZnSe with Ga-doping. If the material is doped with N or O (which is found to have an acceptor state in ZnSe), no increase in the density of negatively charged defects is seen; the expected increase in positively charged defects cannot be seen by the method. Similar results were found

by Tanigawa et al. [17] in a III–V semiconductor: Si-doped GaAs. In this case the incorporation of Si at concentrations near and above  $10^{18} \text{ cm}^{-3}$  led to a significant increase in the density of compensating Ga vacancies, in agreement with theoretical expectations [18].

We have also previously examined the possibility of a shallow–deep transition of P and As induced acceptor states in ZnSe caused by a large lattice relaxation [7]. In these cases a low doping level occurs independently of the presence or absence of compensating defects. Another possibility opened by the above discussion is that P doping is not as effective as N doping because interstitial P diffusion and recombination with vacancies on Se sites is not as effective as for N.

### 3. p-Type doping

#### 3.1. Acceptor states of oxygen in ZnSe

Oxygen is an isoelectronic impurity in II–VI semiconductors and is not expected to be electrically active when on a substitutional site. This was confirmed by our tight-binding calculations for O based on matrix elements obtained from crystalline ZnSe and ZnO. There are a number of reports [19–21], however, that O gives rise to effective-mass type acceptor states in ZnSe and a number of other II–VI semiconductors (in concentrations of about  $10^{16} \text{ cm}^{-3}$ ) and the p-type doping has been ascribed to interstitial O. We have examined the properties of O interstitial impurities in ZnSe via an *ab initio* pseudopotential approach using “hard” pseudopotentials for Zn for greater accuracy. The “hard” potential treats the core d-electrons of Zn on an equal footing with the other valence electrons. This increases the complexity of the calculation but leads to more reliable bond lengths. The results of the calculations indicate that interstitial O forms a strong Zn–O bond by attacking and breaking a Zn–Se bond from an antibonding (111) direction of a Zn atom. The resulting *onefold* coordinated O atom is a shallow acceptor in this configuration and is negatively charged. Other interstitial geometries were also examined. In



particular, a twofold coordinated bridge position in which O forms bonds to both Zn and Se atoms is electrically inactive as might be expected.

The onefold coordinated geometry was also examined for F impurities in ZnSe and it was found that this configuration also leads to an acceptor state even though substitutional F is a donor. It would be quite interesting to see if interstitial doping of ZnSe via F can be achieved experimentally.

### 3.2. Nitrogen

Calculations were carried out for substitutional N in ZnSe and zincblende MgSe. The latter compound has a band gap of nearly 3.6 eV [22] and a lattice constant of 5.89 Å as compared to 2.8 eV and 5.66 Å for ZnSe. In both materials N is found to be strongly fourfold coordinated despite the large inward pulling of neighboring Zn or Mg atoms caused by the small covalent radius of N. Nitrogen is found to give a delocalized acceptor state with small binding energy typical of an effective-mass state for ZnSe. In MgSe, a localized state with a binding energy of 0.2 eV with respect to the VBM is found. Off-center displacements of N were found to increase the total-energy in agreement with the recent results of Kwak et al. [11].

The small 0.7 Å covalent bonding radius of N suggests that an interstitial configuration with a structure similar to that of twofold coordinated interstitial O in Si is also likely to occur for N in ZnSe. Such interstitials may be very important in understanding the doping properties of N. Experimentally [13,14], it is found that the hole concentration in N doped ZnSe saturates at a value of about  $10^{18} \text{ cm}^{-3}$  and then goes down rapidly as the N concentration exceeds a value of about  $10^{19} \text{ cm}^{-3}$ . At high N concentrations, the possibility that diffusing N interstitials come into contact with other interstitials and substitutional N atoms to form  $\text{N}_2$  complexes has to be considered. A reaction of an interstitial N with a substitutional N to form a split-interstitial  $\text{N}_2$  complex can be shown on the basis of filling of all available bonding states to a neutralization of the electrical activities of both N atoms [23]. The formation of

such a complex will tend to counterbalance the compressive strain introduced into the lattice by other isolated substitutional N atoms and it is also aided by the greater strength of the N–N bond as compared to all other bonds in the system and by the small size of N. It should be possible to experimentally detect the presence of such  $\text{N}_2$  complexes through vibrational spectroscopy of the N–N bond. The barrier for diffusion inhibits the motion of N interstitial atoms at low temperatures and this should prevent the formation of complexes. This is consistent with the experimentally observed result that higher acceptor concentrations can be obtained at lower growth temperatures (up to the point where the reduction in the diffusion length of atoms at the surface results in the formation of other defects).

## 4. Donor impurities

### 4.1. Al and Ga

The electronic properties of Al and Ga donor impurities were examined in ZnSe, ZnTe, MgSe and MgTe. The main result of the calculations is that these impurities lead to localized donor states in the tellurides but not in the selenides. The localized donor states in ZnTe and MgTe are very similar to those arising from DX centers in AlGaAs alloys [24], i.e., they are *negatively* charged and result from a large lattice relaxation at the impurities. The formation of DX centers is described by



in which half the donor atoms in the system become positively charged and the other half negatively charged. The notation  $d$  is used to denote a substitutional tetrahedrally coordinated donor atom. The symmetry of the negatively charged DX center is trigonal and the donor atom is displaced by close to 1.85 Å along an antibonding (111) direction. The large displacement leads to the breaking of a donor–anion bond. The formation of DX centers results in a significant increase of the thermal binding energy of electrons, particularly in ZnTe where the reaction in Eq. (1) is exothermic by 0.5 eV for Ga

and 0.20 eV for Al impurities. The reaction is endothermic in ZnSe by 0.5 eV for Ga and 0.95 eV for Al and DX centers are a relatively high energy metastable state. As in the case of DX centers in AlGaAs, there is a large Stokes shift between the optical and thermal excitation energies of DX centers. For ZnTe, the optical ionization energy of a Ga-induced DX center is calculated to be 0.34 eV *higher* than the 2.39 eV band gap; for Al, this energy is 0.37 eV smaller than the gap. Analysis of the results for ZnSe and ZnTe, together with experimental data on the variation of the valence and conduction band edges with alloying suggests [25] that an alloy with composition near  $\text{ZnSe}_{0.7}\text{Te}_{0.3}$  (with a band gap of nearly 2.4 eV) should be superior to ZnSe for both n- and p-type doping properties.

#### 4.2. Cl

In AlGaAs alloys donor impurities on both the cation and anion sites of the lattice are found to give rise to DX centers [24]. This is not found to be the case for II–VI semiconductors. Substitutional Cl in ZnSe and ZnTe does not lead to a large lattice relaxation similar to that of S in AlGaAs. Nevertheless, the impurity appears to lead to a much more localized state in ZnTe than in ZnSe.

#### 4.3. Experiments

There is strong experimental evidence for the presence of DX centers in a number of II–VI semiconductors. Such centers have been detected in In [26] and Ga-doped [27]  $\text{Zn}_{1-x}\text{Cd}_x\text{Te}$ , In-doped  $\text{Cd}_{1-x}\text{Mn}_x\text{Te}$  [28], and in CdTe under pressure [29]. The addition of Zn or Mn to CdTe, or the application of pressure to CdTe itself, has the effect of raising the CBM and bringing the DX state into the band gap. The absence of an EPR signal [26] in  $\text{Zn}_{1-x}\text{Cd}_x\text{Te}$  is consistent with the negative- $U$  reaction given by Eq. (1).

#### 5. Summary

In conclusion, the results of our *ab initio* total-energy calculations indicate that formation

of DX centers in column III n-doped II–VI semiconductors is likely in ZnTe and MgTe, but not in ZnSe and MgSe. A defect mediated doping mechanism was proposed and applied to an explanation of the observed saturation of acceptor levels in N doped ZnSe. The acceptor state of O in ZnSe is identified with a strongly bonded Zn–O state of interstitial O.

#### 6. Acknowledgment

I would like to thank Dr. N. Troullier for his help in the choice of pseudopotentials and for the use of efficient computational schemes employed in this study.

#### 7. References

- [1] R.M. Park, M.B. Trofer, C.M. Rouleau, J.M. DePuydt and M.A. Haase, *Appl. Phys. Lett.* 57 (1990) 2127.
- [2] M.A. Haase, J. Qiu, J.M. DePuydt and H. Cheng, *Appl. Phys. Lett.* 59 (1991) 1272.
- [3] H. Jeon, J. Ding, W. Patterson, A. Nurmikko, W. Xie, D. Grillo, M. Kobayashi and R.L. Gunshor, *Appl. Phys. Lett.* 59 (1991) 3619.
- [4] G. Mandel, *Phys. Rev.* 134, (1964) A 1073; G. Mandel, F.F. Morehead and P.R. Wagner, *Phys. Rev.* 136 (1964) A826.
- [5] S.Y. Ren, J.D. Dow and J. Shen, *Phys. Rev. B* 38 (1988) 10677; J.D. Dow, R.D. Hong, S. Klemm, S.Y. Ren, M.H. Tsai, O.F. Sankey and R.V. Kasowski, *Phys. Rev. B* 43 (1991) 4396.
- [6] R.W. Jansen and O.F. Sankey, *Phys. Rev. B* 39 (1989) 3192.
- [7] D.J. Chadi and K.J. Chang, *Appl. Phys. Lett.* 55 (1989) 575; D.J. Chadi, *Appl. Phys. Lett.* 59 (1991) 3589.
- [8] T. Sasaki, T. Oguchi and H. Katayama-Yoshida, *Phys. Rev. B* 43 (1991) 9362.
- [9] D.B. Laks, C.G. Van de Walle, G.F. Neumark and S.T. Pantelides, *Phys. Rev. Lett.* 66 (1991) 648; *Appl. Phys. Lett.*, to be published.
- [10] D.B. Laks, C.G. Van de Walle, G.F. Neumark, P.E. Blochl and S.T. Pantelides, *Phys. Rev. B* 45 (1992) 10965.
- [11] K.W. Kwak, R.D. King-Smith and D. Vanderbilt, to be published.
- [12] D.J. Chadi, *Phys. Rev. B* 46 (1992) 9400; D.J. Chadi and N. Troullier, *Physica B* 185 (1993) 128.
- [13] A. Taïke, M. Migita and H. Yamamoto, *Appl. Phys. Lett.* 56 (1990) 1989.

- [14] J. Qiu, J.M. DePuydt, H. Cheng and M.A. Haase, *Appl. Phys. Lett.* 59 (1991) 2992.
- [15] S. Ito, M. Ikeda and K. Akimoto, *Jap. J. Appl. Phys.* 31 (1992) L1316.
- [16] T. Miyajima, H. Okuyama, K. Akimoto, Y. Mori, L. Wei and S. Tanigawa, *Appl. Phys. Lett.* 59 (1991) 1482.
- [17] S. Tanigawa, J.L. Lee, L. Wei, M. Kawabe, T. Miyajima, H. Okuyama, K. Akimoto and Y. Mori, in: *Materials Research Soc. Symp. Proc.*, Vol. 262, Eds. S. Ashok, J. Chevalier, K. Sumino and E. Weber (Materials Research Society, Pittsburgh, PA, 1992) p. 597.
- [18] S.B. Zhang and J.E. Northrup, *Phys. Rev. Lett.* 67 (1991) 2339.
- [19] K. Akimoto, T. Miyajima and Y. Mori, *Phys. Rev. B* 39 (1989) 3138.
- [20] M.P. Kulakov and V.D. Negriy, *J. Crystal Growth* 101 (1990) 525.
- [21] K. Shahzad, K.S. Jones, P.D. Lowen and R.M. Park, *Phys. Rev. B* 43 (1991) 9247.
- [22] H. Okuyama, K. Nakano, T. Miyajima and K. Akimoto, *J. Crystal Growth* 117 (1992) 139.
- [23] The split-interstitial consists of two N atoms on a Se vacancy. Each N atom forms two bonds with nearest-neighbor Zn atoms and one N–N bond. The two N atoms bring 10 valence electrons to the vacancy. Six of these electrons are used in the bonds with the 4 neighboring Zn atoms, 2 are used in the  $pp\sigma$  bond between the N atoms and 2 are in a  $pp\pi$  bond. The lowest unoccupied state of the complex corresponds to an antibonding  $pp\pi$  state of the N atoms.
- [24] D.J. Chadi and K.J. Chang, *Phys. Rev. Lett.* 61 (1988) 873; *Phys. Rev. B* 39 (1989) 10063; S.B. Zhang and D.J. Chadi, *Phys. Rev. B* 42 (1990) 7174.
- [25] D.J. Chadi, *Phys. Rev. Lett.* 72 (1994), in press.
- [26] K. Khachatryan, K. Kaminska, E.R. Weber, P. Becla and R.A. Street, *Phys. Rev. B* 40 (1989) 6304.
- [27] B.C. Burkey, R.P. Khosla, J.R. Fischer and D.L. Losee, *J. Appl. Phys.* 47 (1976) 1095.
- [28] I. Terry, T. Penney, S. von Molnar, J.M. Rigotty and P. Becla, *Solid State Commun.* 84 (1992) 235.
- [29] G.W. Iseler, J.A. Kafkas, A.J. Strauss, H.F. MacMillan and R.H. Bube, *Solid State Commun.* 10 (1972) 619.



ELSEVIER

JOURNAL OF **CRYSTAL  
GROWTH**

Journal of Crystal Growth 138 (1994) 301–304

## Interaction between $N_2$ and stabilized ZnSe surface

T. Uenoyama \*, T. Nakao, M. Suzuki

*Central Research Laboratories, Matsushita Electric Industrial Co., Ltd., Moriguchi, Osaka 570, Japan*

### Abstract

The interaction between excited  $N_2$  molecules and dimers at stabilized ZnSe (100) surface has been studied theoretically. The dimerization at the surface is treated as a one-dimensional lattice distortion, the so-called Peierls transition, and the stability of the dimerization is evaluated within the mean field approximation. When the orbital energy in the  $N_2$  molecule gets close to the energy band of the one-dimensional electron gas, the dimerization is not a preferable state, and this result is consistent with the  $N_2$  adsorption and dissociation mechanism on a ZnSe surface we had proposed using the cluster model in ref. [3].

### 1. Introduction

The nitrogen plasma doping method [1] has successfully realized reliable low-resistivity p-type ZnSe and it has led to blue-green laser oscillation at room temperature [2]. However, the net hole concentration is not high enough to carry out adequate ohmic contact at the electrodes of devices and it is important to clarify the doping mechanism of nitrogen into ZnSe. We have theoretically analyzed the adsorption and dissociation mechanism of  $N_2$  on ZnSe surface for the first time [3] and shown that surface atoms of this kind give rise to a significantly different reaction between  $N_2$  molecule and the surface. This mechanism could explain why the nitrogen atoms reside selectively at Se sites in molecular beam epitaxy

growth. Recently, the dependence of doping efficiency on the surface termination on ZnSe (100) has been investigated using the planar-doping technique [4] and it shows that a higher hole concentration is obtained by the planar doping at the Zn-stabilized surface. In our previous analysis [3], a simple cluster model was adopted to describe the ZnSe surface, and the surface reconstruction effect was ignored. The dimerization has taken place at the stabilized ZnSe (100) surface where  $(2 \times 1)$  or  $c(2 \times 2)$  Zn or Se surface is reconstructed [5].

In this paper, we have studied the interaction between excited  $N_2$  molecules and the stabilized ZnSe surface theoretically. As the ZnSe(100) stabilized surface, the dimerization line is taken into account and the each line is assumed to be independent since the second layer atoms are bonded in the direction perpendicular to the dimerization line. We have treated the dimerization as a one-dimensional lattice distortion, the so-called

\* Corresponding author.

Peierls transition [6], and included the interaction with the  $N_2$  molecule. To investigate the stability of this system, the gap equation is derived in terms of the finite-temperature Green function formalism. Then, we have discussed the stability using the results of the cluster model calculation and have shown that the  $N_2$  molecule tends to be adsorbed and dissociated even at the Zn-stabilized ZnSe surface. This result is consistent with the planar-doping experiment [4].

## 2. Dimerization model

Fig. 1 shows the surface atoms along  $\langle 110 \rangle$  direction schematically. The solid-line circles indicate surface atoms at the ideal sites and the dashed-line circles indicate the stabilized surface atoms. Since the surface atoms are bonded to the second layer atoms in the  $\langle 1\bar{1}0 \rangle$  direction, the lattice displacement should be considered only in the  $\langle 110 \rangle$  direction. On the other hand, ZnSe has such a strong ionicity that the two electrons in the valence 4s orbital of the Zn atom are almost all transferred into Se sites in bulk ZnSe, according to the pseudo-potential energy band calculation [7]. Then, we expect that there is a single free electron (hole) at the surface Zn (Se) site. Hereafter, we proceed to the case of the Zn surface and will discuss the case of the Se surface later. Thus, since each Zn site at the surface has a single electron and can move only in the  $\langle 110 \rangle$  direction, the dimerization in this direction corresponds to the Peierls transition of a one-dimensional system. Therefore, we shall focus on the interaction between a  $N_2$  molecule and a one-dimensional dimerization line as the stabilized surface. The Hamiltonian which describes such a

one-dimensional system with the  $N_2$  molecule is given by

$$H = \sum_k \epsilon_k c_k^\dagger c_k + \sum_q \omega_q b_q^\dagger b_q + f \sum_{k,q} (b_{-q}^\dagger + b_q) c_{k+q}^\dagger c_k + \epsilon_0 a^\dagger a + T \sum_k a^\dagger c_k + T^* \sum_k c_k^\dagger a, \quad (1)$$

where  $c_k^\dagger$  ( $c_k$ ) and  $a^\dagger$  ( $a$ ) are the electron creation (annihilation) operators of the one-dimensional electron gas and the orbital state in the  $N_2$  molecule, respectively.  $b_q^\dagger$  ( $b_q$ ) are the phonon creation (annihilation) operators of the one-dimensional lattice vibration and the third term expresses the Fröhlich type electron–phonon interaction [8].  $\epsilon_0$  is the orbital energy in the  $N_2$  molecule and  $T$  is the tunneling matrix element between the  $N_2$  molecule and the one-dimensional electron gas. Here, we ignore the spin indices of the electron operators, since the Peierls transition is not dependent on the spin density, but on the charge density. We introduce the following correlation functions to investigate the stability of the system:

$$\begin{aligned} \mathcal{G}_{n,m}(k, \tau - \tau') &= -\langle T c_{k+nQ, 2}(\tau) c_{k+mQ, 2}^\dagger(\tau') \rangle, \\ \mathcal{F}_m(k, \tau - \tau') &= -\langle T a(\tau) c_{k+mQ, 2}^\dagger(\tau') \rangle, \end{aligned}$$

where  $Q$  is twice the Fermi wave vector  $k_F$ .  $\mathcal{G}_{n,n}$  are the usual Green functions and  $\mathcal{G}_{-1,1}$  is related to the order parameter of the phase transition.  $\mathcal{F}_m$  expresses the electron transfer between the  $N_2$  molecule and the one-dimensional electron gas. From the finite temperature equation of motion, the above correlation functions are coupled as

$$\begin{aligned} (i\omega_n - \epsilon_{k+Q, 2}) \mathcal{G}_{1,1}(k, i\omega_n) - f \Delta^* \mathcal{G}_{-1,1}(k, i\omega_n) \\ - T^* \mathcal{F}_1(k, i\omega_n) &= 1, \\ (i\omega_n - \epsilon_{k-Q, 2}) \mathcal{G}_{-1,1}(k, i\omega_n) - f \Delta \mathcal{G}_{1,1}(k, i\omega_n) \\ - T^* \mathcal{F}_1(k, i\omega_n) &= 0, \\ (i\omega_n - \epsilon_0) \mathcal{F}_1(k, i\omega_n) - T (\mathcal{G}_{1,1}(k, i\omega_n) \\ + \mathcal{G}_{-1,1}(k, i\omega_n)) &= 0. \end{aligned} \quad (2)$$

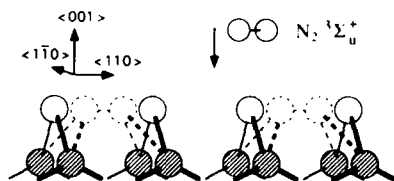


Fig. 1. Surface atoms along the  $\langle 110 \rangle$  direction.

Here, we kept only terms with  $q = Q$  or  $-Q$  and made a mean field approximation for mixed Green functions, proportional to  $\langle Tb_q c_k c_k^\dagger \rangle$ , etc.  $\Delta$  is the mean value of the lattice displacement and corresponds to the order parameter in the Peierls transition. When the lattice is distorted,  $\Delta$  is finite and time-independent. From the equation of motion of the phonon operator,  $\Delta$  is related to the charge density as

$$\Delta = \langle b_Q^\dagger + b_{-Q} \rangle$$

$$= -\frac{f}{\omega_Q \beta} \sum_k \sum_{i\omega_n} \mathcal{G}_{1,1}(k, i\omega_n), \quad (3)$$

where  $\beta$  is inverse temperature. After summing over the Matsubara frequency  $\omega_n = (2n+1)\pi/\beta$ , the gap equation is given by

$$1 = \frac{f^2}{\omega_Q} \frac{L}{2\pi} \int dk \frac{\epsilon_0 - |T|^2/f\Delta - \alpha}{(\beta - \alpha)(\gamma - \alpha)}. \quad (4)$$

Here, we consider the limiting case, such as zero temperature.  $\alpha$ ,  $\beta$  and  $\gamma$  ( $\alpha \leq \beta \leq \gamma$ ) are roots of the equation for  $z$ , given by

$$(z - \epsilon_0) \left[ (z - \epsilon_{k+Q/2})(z - \epsilon_{k-Q/2}) - f^2|\Delta|^2 \right] - [2z - \epsilon_{k+Q/2} - \epsilon_{k-Q/2} + 2f\Re(\Delta)] = 0. \quad (5)$$

When  $\epsilon_0$  is larger than  $\epsilon_k$ ,  $\alpha$ ,  $\beta$  and  $\gamma$  can be expressed approximately within the order of  $|T|^2$ :

$$\alpha = E_- + \frac{|T|^2 [2E_- - \epsilon_{k+Q/2} - \epsilon_{k-Q/2} + 2f\Re(\Delta)]}{(\epsilon_0 - E_-)(E_- - E_+)} \quad (6)$$

$$\beta = E_+ - \frac{|T|^2 [2E_+ - \epsilon_{k+Q/2} - \epsilon_{k-Q/2} + 2f\Re(\Delta)]}{(\epsilon_0 - E_+)(E_+ - E_-)} \quad (7)$$

$$\gamma = \epsilon_0 + \frac{|T|^2 [2\epsilon_0 - \epsilon_{k+Q/2} - \epsilon_{k-Q/2} + 2f\Re(\Delta)]}{(\epsilon_0 - E_-)(\epsilon_0 - E_+)} \quad (8)$$

where

$$E_\pm = \frac{1}{2}(\epsilon_{k+Q/2} + \epsilon_{k-Q/2} \pm \sqrt{(\epsilon_{k+Q/2} - \epsilon_{k-Q/2})^2 + 4f^2|\Delta|^2}). \quad (9)$$

If the gap equation has the real value solution of  $\Delta$ , the Peierls instability occurs and the dimers are reconstructed at the surface. However, the numerator of the integral in Eq. (4) changes the sign at

$$|T|^2 = (\epsilon_0 - \alpha)f\Delta. \quad (10)$$

If the right-hand side of Eq. (4) becomes negative, the real solution of  $\Delta$  does not exist and the Peierls transition does not occur. Thus, Eq. (10) shows the criterion of the dimer stability and it indicates that even small  $|T|$  can cause the dimer to be unstable if  $\epsilon_0$  is close to  $\alpha$ , which is roughly  $E_-$ .

### 3. Discussion

Fig. 2 shows the orbital energies of an excited  $N_2$  molecule and two clusters,  $ZnSe_2H_6$  and  $SeZn_2H_6$ , corresponding to Zn and Se surface, respectively. The orbital energies are calculated within the Hartree-Fock approximation. The size of the basis and other detailed conditions in the

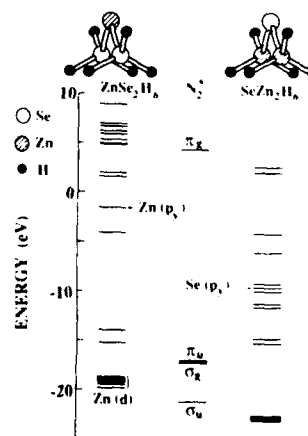


Fig. 2. Orbital energies of excited nitrogen molecule and ZnSe cluster models.

calculation are discussed in ref. [3]. According to the cluster model calculation, the Zn valence p orbital perpendicular to the Se–Zn–Se plane in  $\text{ZnSe}_2\text{H}_6$  does not contribute to the bonding with the second layer atoms and the phase of the wave function matches the nitrogen  $\pi_g$  antibonding orbital. Thus, it is assumed that the single free electron at the Zn surface atom belongs to the p orbital and the matrix element  $T$  describes the transition between the p orbital of the Zn atom and the nitrogen antibonding orbital. Then,  $\epsilon_0$  and the band energy,  $\epsilon_k$  in the dimer model correspond to the  $\pi_g$  antibonding orbital energy and the p orbital energy of the surface atom, respectively. Since the energy difference between the Zn valence p orbital and antibonding  $\pi_g$  is 5.71 eV, which is much smaller than the case of the Se valence p orbital (14.15 eV) in Fig. 2, it is expected that the Peierls instability condition is more easily broken at the Zn surface than at the Se surface; in other words, Zn dimers become easily destructed as the excited  $\text{N}_2$  molecule approaches the ZnSe surface. After the bonds of the Zn dimers are broken down, they may be treated as Zn atoms. Then, the assumption of the cluster model becomes reasonable and we can explain that nitrogen atoms are selectively doped into Se sites in molecular beam epitaxy growth, even if the ZnSe surface is stabilized. In the case of the Se surface, the energy difference between the Se valence p orbital and antibond  $\pi_g$  is large and it needs a large  $T$  to satisfy Eq. (10). Thus, the Se dimers are stable and moreover, the Se surface atom tends to withdraw the electron from the  $\text{N}_2$  molecule. This property is not preferable for the dissociation of the  $\text{N}_2$  molecule.

In summary, we have studied the interaction between  $\text{N}_2$  molecule and stabilized ZnSe surface theoretically. The dimerization on a ZnSe (100) surface is considered as the stabilized surface and

is treated as a one-dimensional lattice distortion (Peierls transition). Then, we have evaluated the stability of the one-dimensional lattice, interacting with the excited  $\text{N}_2$  molecule within the mean field approximation. We have made it clear that the Zn dimer at the surface tends to be unstable when the excited nitrogen molecule approaches the dimer. Then, our cluster model analysis of the interaction between  $\text{N}_2$  molecules and ZnSe surface can be used, even if the surface is stabilized.

#### 4. Acknowledgements

The authors would like to express their gratitude to Dr. T. Mitsuyu and Dr. K. Ohkawa for helpful discussions and to Dr. S. Hatta and Dr. S. Yamashita for their encouragement. One of the authors (T.U.) wishes to acknowledge Dr. D. Coffey at the State University of New York at Buffalo for his useful comments.

#### 5. References

- [1] K. Ohkawa, T. Karasawa and T. Mitsuyu, *J. Crystal Growth* 111 (1991) 797.
- [2] M.A. Haase, J. Qiu, J.M. DePuydt and H. Cheng, *Appl. Phys. Lett.* 59 (1991) 1272; S. Hayashi, A. Tsujimura, S. Yoshii, K. Ohkawa and T. Mitsuyu, *Jap. J. Appl. Phys.* 30 (1992) L1478.
- [3] T. Nakao and T. Uenoyama, *Jap. J. Appl. Phys.* 32 (1993) 660.
- [4] S. Matsumoto, H. Tosaka, T. Yoshida, M. Kobayashi and A. Yoshikawa, *Jap. J. Appl. Phys.* 32 (1993) L229.
- [5] H.H. Farrell, M.C. Tamargo and J.L. de Miguel, *J. Vac. Sci. Technol. B* 6 (1988) 767.
- [6] R.E. Peierls, *Quantum Theory of Solids* (Oxford University Press, Oxford, 1955) ch. 5.
- [7] M.L. Cohen, *Science* 179 (1973) 1189.
- [8] F. Fröhlich, H. Pelzer and S. Zienau, *Phil. Mag.* 41 (1950) 221.



ELSEVIER

Journal of Crystal Growth 138 (1994) 305–309

JOURNAL OF **CRYSTAL  
GROWTH**

## Limits of acceptor impurity doping in wide band gap II–VI semiconductors

Y. Marfaing

*Laboratoire de Physique des Solides de Bellevue CNRS, 1 Place A. Briand, F-92195 Meudon Cedex, France*

### Abstract

The limits of acceptor doping in wide band gap semiconductors are examined by considering the case of nitrogen-doped ZnSe. Starting from experimental observations on defect generation associated with N doping, it is shown how self-compensation due to impurity-defect pairs leads to a saturation of the free carrier concentration, in agreement with published electrical measurements. At high doping level, the statistical fluctuations in local impurity and compensating centre concentrations produce a random distribution of potential wells and hills in the semiconductor. An expression of the effective free carrier concentration above the mobility edge is obtained which predicts a sharp drop of the electrical conductivity with increasing impurity content.

### 1. Introduction

Efficient doping of ZnSe with the nitrogen acceptor has recently been realized [1–3] and has allowed the fabrication of devices based on bipolar electrical injection, light emitting diodes (LED) and lasers [4–8]. This achievement points out limited material purity as the main reason explaining the previous unsuccessful attempts on acceptor doping. However, electrical and optical measurements performed on N-doped ZnSe show that the semiconductor becomes increasingly compensated with increasing nitrogen concentration [8,9,16]. Hence the maximum hole concentration is limited to about  $10^{18} \text{ cm}^{-3}$ . Furthermore, the carrier concentration tends to decrease at high acceptor concentration. ZnSe thus appears as the prototype material for analysis of acceptor doping in wide band gap semiconductors.

In this paper we discuss the above results from

the point of view of self-compensation. We show that the formation of native defect–impurity pairs can actually be the cause of doping limitation. On the other hand, the rapid decrease of free carrier concentration at high doping is accounted for by considering the potential fluctuations occurring in the compensated state.

### 2. Self-compensation in nitrogen doped ZnSe

Several facts suggest the existence of self-compensation in N-doped ZnSe. Analysis of donor–acceptor pair luminescence transitions allowed Hauksson et al. [9] to conclude that a deep compensating donor with a binding energy of 44 meV exists in more heavily doped material. A deep donor at about 50 meV was also reported by Ohkawa et al. [8]. A reduction in lattice constant with increasing N concentration was attributed to



the generation of point defects (vacancies) accompanying N doping [10]. Supportive evidence for the generation of point defects was obtained in the latter work from the observation of wave vector non-conservative Raman scattering.

On the theoretical side, a first-principle calculation of the formation energy of native point defects has recently appeared [11,12]. The authors have concluded that the dominant native defect in p-type ZnSe is the interstitial  $\text{Zn}_i^{2+}$ , the concentration of which amounts to  $10^{17}$ – $10^{18} \text{ cm}^{-3}$  in material grown under minimum Se chemical potential. They said that other native defects have concentrations four orders of magnitude smaller than the Zn interstitial. Although the reduction in lattice constant observed in ref. [10] is more in agreement with the formation of vacancy-type defects, the above theoretical work confirms the fact that native defects are generated in nitrogen-doped ZnSe.

We intend to show that these defects can induce significant self-compensation, not by themselves, but through the formation of defect-impurity complexes. This aspect was not examined in ref. [12]. To be specific, we consider the case of pairing between Se vacancy donors ( $\text{V}_\text{Se}^{2+}$ ) and N acceptors ( $\text{A}_\text{N}$ ). Replacement of Se vacancies by Zn interstitials would formally lead to similar results.

The pairing reaction and the associated mass-action relation can be written as



$$[(\text{V}_\text{Se}\text{A}_\text{N})^-] / [\text{A}_\text{N}] = K_p [\text{V}_\text{Se}^{2+}]. \quad (2)$$

The pairing constant  $K_p$  is of the form  $K_p = K_p \exp(-\Delta H_p/kT)$  where the enthalpy  $\Delta H_p$  represents the electrostatic interaction between the charged species and is negative. Thus  $K_p$  increases with decreasing temperature. Due to this fact, the compensation ratio (2) may reach significant values for relatively small concentrations of isolated ionized vacancies. On the same foot, the neutrality equation simply reads

$$p = [\text{A}_\text{N}] - [(\text{V}_\text{Se}\text{A}_\text{N})^-], \quad (3)$$

where  $p$  is the hole carrier concentration. Now the incorporation of acceptor on anion sites from

the gaseous phase and the generation of vacancies can be expressed in the usual mass-action formalism:

$$p[\text{A}_\text{N}^-] = K_1 [\text{A}_\text{g}] [\text{V}_\text{Se}^0], \quad (4)$$

$$[\text{V}_\text{Se}^{2+}] = K_{D_1} K_{D_2} [\text{V}_\text{Se}^0] p^2 / n_i^4, \quad (5)$$

where  $[\text{A}_\text{g}]$  represents the activity of the acceptors in the external phase,  $\text{V}_\text{Se}^0$  is the neutral vacancy state,  $K_1$  is the incorporation constant of acceptors in the ionized state,  $K_{D_1}$  and  $K_{D_2}$  are the ionization constants of the vacancy and  $n_i$  is the intrinsic carrier concentration. Finally, the hole carrier concentration is obtained from (3), by using (2), (4) and (5):

$$p = \left( \frac{K_1 [\text{A}_\text{g}] [\text{V}_\text{Se}^0]}{1 + K_1 K_p K_{D_1} K_{D_2} [\text{V}_\text{Se}^0]^2 [\text{A}_\text{g}] / n_i^4} \right)^{1/2}. \quad (6)$$

This expression causes the appearance of a maximum carrier concentration at high doping level given by

$$p_m = n_i^2 / (K_p K_{D_1} K_{D_2} [\text{V}_\text{Se}^0])^{1/2}. \quad (7)$$

A plot of the relationship (6) cannot be made directly, because the various reaction constants  $K$  are largely unknown. The concentration  $[\text{V}_\text{Se}^0]$  is related to the activity of X in the external phase (vapour pressure) and does not depend on impurity content, but its accurate evaluation is difficult. However, it is possible to illustrate the behaviour considered here by introducing the total impurity concentration in the solid:

$$N_1 = [\text{A}_\text{N}] + [(\text{V}_\text{Se}\text{A}_\text{N})^-]. \quad (8)$$

Then, using  $p_m$  from Eq. (7) as a parameter, an expression equivalent to (6) can be obtained under the implicit form

$$p(1 + p^2/p_m^2) = N_1(1 - p^2/p_m^2). \quad (9)$$

This relation is plotted in Fig. 1 as  $p = f(N_1)$  by taking  $p_m = 10^{18} \text{ cm}^{-3}$ , the maximum doping value of ZnSe:N most often quoted in the literature.

The doping limitation expressed in Eq. (7) has previously been invoked [13] to account for the maximum free carrier concentration observed in a number of semiconductors and related to a

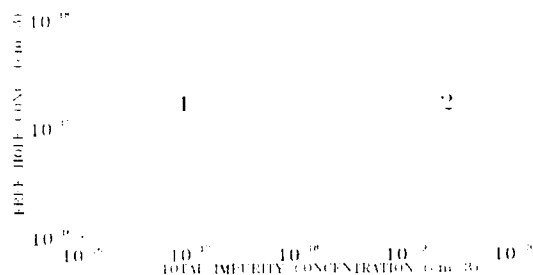


Fig. 1. Theoretical variations of free carrier concentration versus total impurity concentration in acceptor doped ZnSe.

Fermi stabilization energy [14]. In the specific case of II–VI compounds, saturation of free carrier concentration has been reported several times. Thus Khun [15] observed that the hole concentration in As-doped ZnTe grown by Metalorganic vapour phase epitaxy (MOVPE) levelled off at approximately  $10^{18} \text{ cm}^{-3}$  as the partial pressure of tertiarybutylarsenic increases by a factor of five. Qiu et al. also noted that in N-doped ZnSe the net acceptor concentration becomes nearly independent of nitrogen density above some concentration value [3]. Detailed electrical measurements on p-type N-doped ZnSe films have been reported by Yang et al. [16]. Analysis of the data has allowed the authors to determine separately the concentration of acceptors  $N_A$  and compensating donors  $N_D$ . These results are replotted in Fig. 2 in the form of the net acceptor concentration  $N_A - N_D$  as a function of  $N_A + N_D$ .

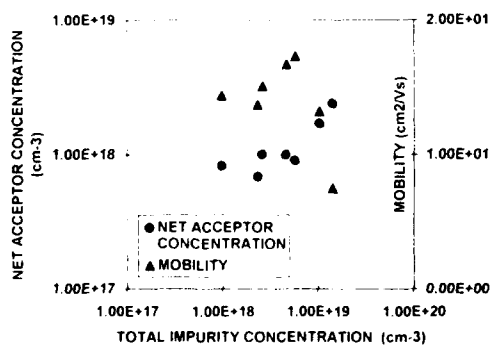


Fig. 2. Experimental variations of net acceptor concentration and hole mobility versus total charged centre concentration (from [16]).

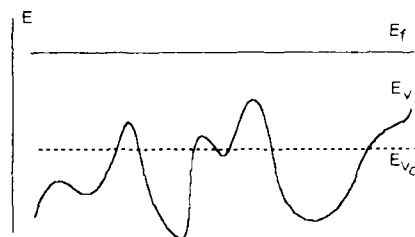


Fig. 3. Scheme of valence band affected by potential fluctuations in a compensated semiconductor.

In the spirit of the above analysis, we assume that  $N_D$  is the concentration of defect–impurity pairs, so that  $N_A + N_D$  represents the total nitrogen concentration in the films. It is seen that  $N_A - N_D$  remains nearly constant as  $N_A + N_D$  increases by a factor of five. Beyond this plateau,  $N_A - N_D$  seems to increase again, but this part corresponds to a different conduction regime evidenced by the sharp drop in hole mobility, suggesting impurity band conduction. The specific case of high doping will be considered in the next section.

### 3. Behaviour at high doping

In compensated semiconductors, statistical fluctuations in local impurity concentrations lead to a random distribution of potential wells and potential hills in the material (Fig. 3). Free carrier accumulate in the wells, which reduces the electrical conduction above the mobility edge. The theory of potential fluctuations in compensated semiconductors has been developed by Shklovskii and Efros [17]. In a Gaussian approximation, the potential distribution is given by

$$P(E_v - E_{v0}) = \frac{1}{\gamma\sqrt{\pi}} \exp\left(-\frac{(E_v - E_{v0})^2}{\gamma^2}\right). \quad (10)$$

The mean fluctuation of the impurity number in a volume  $R^3$  is  $[(N_A + N_D)R^3]^{1/2}$ , so that the associated potential fluctuation is

$$\Delta E_v = \frac{q^2}{4\pi\epsilon\epsilon_0 R} [(N_A + N_D)R^3]^{1/2}. \quad (11)$$

where  $q$  is the electronic charge and  $\epsilon\epsilon_0$  is the material permittivity. It is expected that long range fluctuations are screened by free carriers, which allows one to define a screening radius  $R_c$  by equating  $p$  to the mean excess impurity concentration in volume  $R_c^3$ :

$$p = [(N_A + N_D)R_c^3]^{1/2}/R_c^3. \quad (12)$$

Now the standard deviation  $\gamma$  is taken equal to the potential fluctuation  $\Delta E_v$  (Eq. (11)) associated with the screening radius  $R_c$  (Eq. (12)). This allows us to express  $\gamma$  as a function of  $p$  and  $N_A + N_D$

$$\gamma \propto (N_A + N_D)^{2/3}/p^{1/3}. \quad (13)$$

The potential distribution function (10) can be used to compute two characteristic average carrier concentrations in the system. First the total carrier concentration is given by

$$p = N_v \int_{-\infty}^{+\infty} \mathcal{F}_{1/2} \left( \frac{E_f - E_v}{kT} \right) \frac{1}{\gamma \sqrt{\pi}} \times \exp \left( - \frac{(E_v - E_{v_0})^2}{\gamma^2} \right) dE_v, \quad (14)$$

where  $N_v$  is the valence band density of states and  $\mathcal{F}_{1/2}$  is the usual Fermi function. Taking  $p$  as given, equal to the concentration limit  $p_m$  (Eq. (7)), expression (14) gives a relation between  $\gamma$  and the Fermi level position  $E_f - E_{v_0}$ . Such a relation is presented in Fig. 4 in the case of ZnSe at 300 K for  $p_m = 10^{18} \text{ cm}^{-3}$ . It is seen that the Fermi level rises in the band gap as  $\gamma$ , related to  $N_A + N_D$  by (13), increases.

The measured free carrier concentration is defined as the population of the valence band around and below the mobility edge taken at  $E_{v_0}$  [18]:

$$p_e = N_v \int_{-\infty}^{E_{v_0} + kT} \exp \left( - \frac{E_f - E_v}{kT} \right) \frac{1}{\gamma \sqrt{\pi}} \times \exp \left( - \frac{(E_v - E_{v_0})^2}{\gamma^2} \right) dE_v. \quad (15)$$

Using the above relation between  $E_f - E_{v_0}$  and  $\gamma$ , the effective carrier concentration  $p_e$  is computed as a function of  $\gamma$ , i.e. as a function of the

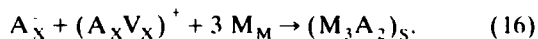


Fig. 4. Fermi level position versus mean potential fluctuation in compensated acceptor-doped ZnSe with total carrier concentration of  $10^{18} \text{ cm}^{-3}$ .

total charged centre concentration  $N_A + N_D$  (Eq. (13)). The result of this calculation is given by curve 2 in Fig. 1, which shows a sharp drop of the carrier concentration. The assembling of the two curves in Fig. 1 provides the general relationship between carrier concentration and doping level as deduced from our analysis.

#### 4. Conclusions

The limits of doping efficiency in ZnSe:N have been examined. Several observations indicate that defects, more probably of the vacancy-type, are generated along with N incorporation. Starting from this fact, a model of acceptor self-compensation has been presented which predicts a saturation of the free carrier concentration, in agreement with experimental results. On the other hand, the impurity–vacancy pairs, assumed to be the self-compensating centres, may be viewed as precursors of precipitation, according to



In this way the nitrogen solubility limit would be associated with the formation of the second phase  $Zn_3N_2$ . This bound was theoretically considered in ref. [12] and evaluated to near  $10^{20} \text{ cm}^{-3}$ . Thus the solubility limit does not appear to

fix the maximum doping which, in our analysis, is accounted for by a self-compensation mechanism.

At high doping levels, more complex phenomena come into play. Potential fluctuations related to the random distribution of donor and acceptor charged species lead to a redistribution of free carriers in the energy bands of the semiconductor. A strong decrease of electrical conductivity can then occur, as analysed in this paper. Confirmation of this behaviour has been given [19]. Furthermore the predicted rise of Fermi level (Fig. 4) could lead to partial deionization of the nitrogen acceptor level. This aspect has not been examined here, but it could give rise to significant conduction through the acceptor states. This is probably the case for the highest doped samples studied in ref. [16]. As suggested above, impurity band conduction could explain the simultaneous occurrence of a strong mobility decrease and a slight concentration increase (Fig. 2).

## 5. References

- [1] R.M. Park, M.B. Trofer, C.M. Rouleau, J.M. DePuydt and M.A. Haase, *Appl. Phys. Lett.* 57 (1990) 2127.
- [2] K. Ohkawa, T. Karasawa and T. Mitsuyu, *J. Crystal Growth* 111 (1991) 797.
- [3] J. Qiu, J.M. DePuydt, H. Cheng and M.A. Haase, *Appl. Phys. Lett.* 59 (1991) 2992.
- [4] M.A. Haase, J. Qiu, J.M. DePuydt and H. Cheng, *Appl. Phys. Lett.* 59 (1991) 1272.
- [5] H. Jeon, J. Ding, W. Patterson, A.V. Nurmikko, W. Xie, D.C. Grillo, M. Kobayashi and R.L. Gunshor, *Appl. Phys. Lett.* 59 (1991) 3619.
- [6] Z. Yu, J. Ren, B. Sneed, K.A. Bowers, K.J. Gossett, C. Boney, Y. Lansari, J.W. Cook, Jr., J.F. Schetzina, G.C. Hua and N. Otsuka, *Appl. Phys. Lett.* 61 (1992) 1266.
- [7] S.Y. Wang, J. Simpson, H. Stewart, S.J.A. Adams, I. Hauksson, Y. Kawakami, M.R. Taghizadeh, K.A. Prior and B.C. Cavenett, in: *Wide-Band-Gap Semiconductors, Proc. 7th Trieste ICTP-IUPAP Semiconductor Symp.*, Ed. C.G. Van de Walle (North-Holland, Amsterdam, 1993) p. 508.
- [8] K. Ohkawa, A. Tsujimura, S. Hayashi, S. Yoshii and T. Mitsuyu, in: *Wide-Band-Gap Semiconductors, Proc. 7th Trieste ICTP-IUPAP Semiconductor Symp.*, Ed. C.G. Van de Walle (North-Holland, Amsterdam, 1993) p. 112.
- [9] I.S. Hauksson, J. Simpson, S.Y. Wang, K.A. Prior and B.C. Cavenett, *Appl. Phys. Lett.* 61 (1992) 2208.
- [10] J. Petruzello, J. Gaines, P. van der Sluis, D. Olego and C. Ponzoni, *Appl. Phys. Lett.* 62 (1993) 1496.
- [11] D.B. Laks, C.G. Van de Walle, G.F. Neumark, F.E. Blöchl and S.T. Pantelides, *Phys. Rev. B* 45 (1992) 10965.
- [12] C.G. Van de Walle, D.B. Laks, G.F. Neumark and S.T. Pantelides, *Phys. Rev. B* 47 (1993) 9425.
- [13] Y. Marfaing, *J. Vac. Sci. Technol. B* 10 (1992) 1444.
- [14] E. Tokumitsu, *Jap. J. Appl. Phys.* 26 (1990) L698.
- [15] W. Kuhn, private communication.
- [16] Z. Yang, K.A. Bowers, J. Ren, Y. Lansari, J.W. Cook, Jr. and J.F. Schetzina, *Appl. Phys. Lett.* 61 (1992) 2671.
- [17] B.I. Shklovskii and A.L. Efros, *Sov. Phys.-JETP* 34 (1972) 435.
- [18] B. Pistoulet, J.L. Robert, J.M. Dusseau and L. Ensueque, *J. Non-Crystalline Solids* 29 (1978) 29.
- [19] C.T. Walker, J.M. DePuydt, M.A. Haase, J. Qiu and H. Cheng, in: *Wide-Band-Gap Semiconductors, Proc. 7th Trieste ICTP-IUPAP Semiconductor Symp.*, Ed. C.G. Van de Walle (North-Holland, Amsterdam, 1993) p. 27.



ELSEVIER

Journal of Crystal Growth 138 (1994) 310–317

JOURNAL OF  
**CRYSTAL  
GROWTH**

## Systematic investigation of shallow acceptor levels in ZnSe

Y. Zhang <sup>a</sup>, W. Liu <sup>a</sup>, B.J. Skromme <sup>\*a</sup>, H. Cheng <sup>b</sup>, S.M. Shibli <sup>c,1</sup>, M.C. Tamargo <sup>c,2</sup><sup>a</sup> Department of Electrical Engineering and Center for Solid State Electronics Research, Arizona State University, Tempe, Arizona 85287-5706, USA<sup>b</sup> 3M Company, 201-1N-35, 3M Center, St. Paul, Minnesota 55144, USA<sup>c</sup> Bellcore, 331 Newman Springs Road, Red Bank, New Jersey 07701, USA

### Abstract

A systematic investigation of shallow acceptor levels in ZnSe grown by molecular beam epitaxy (MBE) has been performed using low temperature photoluminescence (PL) measurements as a function of excitation level, temperature, strain, and laser energy (i.e., selectively excited donor–acceptor pair luminescence or SPL). Five of the levels are due to N, Li, As, P, and O, while the chemical origins of two levels, denoted A<sub>1</sub> and A<sub>2</sub>, have not yet been determined. The A<sub>1</sub> level is observed in undoped material after annealing using diamond-like C (DLC) caps, while the A<sub>2</sub> level is observed in nominally Na-doped material. The ionization energies of these levels are accurately determined from the temperature dependence of the band-to-acceptor (e–A<sup>0</sup>) peak positions, accounting for strain. Those energies are  $114.3 \pm 0.5$ ,  $114.2 \pm 0.3$ ,  $111.3 \pm 0.5$ ,  $106.1 \pm 0.6$ ,  $95.0 \pm 0.4$ ,  $88.4 \pm 0.5$ , and  $83 \pm 3$  meV, respectively, for As, Li, N, A<sub>1</sub>, A<sub>2</sub>, P, and O in unstrained material. Several excited states have been observed in SPL measurements for As, A<sub>2</sub>, O, and P for the first time. The excited states of As, O, and A<sub>2</sub> fit well to effective mass theory, while those for P do not. A model for the strain splitting of shallow acceptor-bound excitons has been developed and confirmed using measurements on samples whose substrates have been removed. Haynes's Rule is shown to be inapplicable to shallow acceptors in ZnSe. A strain splitting of the (e–A<sup>0</sup>) peak for As or Li acceptors in annealed material is clearly resolved and modeled.

### 1. Introduction

Remarkable progress has been made in the last few years in the p-type doping of ZnSe and related materials, particularly with regard to the use of N plasma doping sources during MBE growth [1,2]. However, a fundamental under-

standing of the past difficulties in doping this material, and a detailed knowledge of the behavior of various acceptor dopants has not yet been achieved. Moreover, p-type doping levels need to be further improved in both metalorganic chemical vapor deposition (MOCVD) and molecular beam epitaxy (MBE) material. In the following, we discuss some progress in these directions, based on a study of MBE material doped with a total of seven different acceptor species. A highly accurate and reliable method of determining acceptor binding energies in ZnSe is described, and then applied wherever possible to these levels. The problems with prior measurement tech-

<sup>\*</sup> Corresponding author.

<sup>1</sup> Present address: Instituto de Física Gleb Wataghin, UNICAMP 13081, Campinas/SP, Brazil.

<sup>2</sup> Present address: Department of Chemistry, City College of the CUNY, New York, New York 10031, USA.

niques are briefly discussed for comparison; in particular, we emphasize the lack of validity of Haynes's Rule type of relationships for shallow acceptors in ZnSe. Two as-yet unidentified acceptor levels are observed and characterized; at least one of these may have significant future potential as a dopant. The excited states of several of these levels are determined and compared to effective mass theory. The effects of strain are carefully examined and shown to have important effects on both acceptor-bound excitons and band-to-acceptor transitions.

## 2. Results and discussion

The growth and doping of the N-, Li-, As-, P-, O-, and Na-doped MBE-grown ZnSe/GaAs samples used in this study is described in refs. [2–7], respectively; the capping and annealing procedures used to introduce the “ $A_1$ ” acceptor discussed below are described in ref. [8]. The PL system used in this work is described in ref. [9].

### 2.1. Accurate determination of acceptor binding energies in ZnSe

Our method of determining acceptor ground state binding energies is similar to that which has been used in many III–V materials, and is based on the measurement of conduction band-to-acceptor ( $e-A^0$ ) peak positions in low temperature PL spectra at various temperatures. This method has rarely been applied in ZnSe, perhaps because of concerns voiced in ref. [10] concerning the influence of acoustic phonon coupling on the ( $e-A^0$ ) lineshape, or simply because the ( $e-A^0$ ) peaks have never been detected at liquid He temperatures in bulk or homoepitaxial ZnSe, which is usually n-type. A further complication in heteroepitaxial material is the necessity to account for the effects of strain, which we show how to do in the following. Our study of the ( $e-A^0$ ) peaks as a function of temperature, e.g. in Li-doped MBE material [9], has shown that these peaks are in fact frequently observable at low temperature in p-doped MBE samples, even though they have not always been identified as

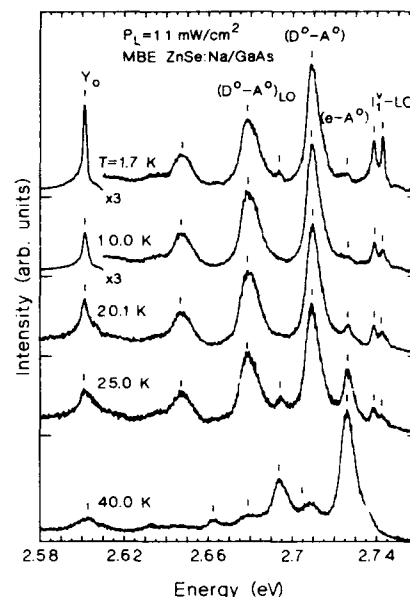


Fig. 1. PL spectra under low excitation as a function of temperature for a high resistivity Na-doped ZnSe/GaAs layer (see ref. [7]) grown at 260 °C with a Se/Zn beam equivalent pressure ratio of four and a Na Knudsen cell temperature of 125 °C. The elemental Na source was 99.95% pure, and the Na concentration in the sample is  $3.0 \times 10^{17} \text{ cm}^{-3}$ . Instrumental resolution is 0.5 meV.

such in the past. We have also shown that the widths of these peaks agree reasonably well up to about 45 K with the theoretical  $1.8k_B T$  dependence ( $k_B$  is Boltzmann's constant and  $T$  the absolute temperature) expected from Eagles' theory of ( $e-A^0$ ) lineshapes, even though this theory ignores phonon coupling [11].

To illustrate the method, we show a set of PL data as a function of temperature in Fig. 1 for an MBE sample which was doped with Na [7]. The possible origin of this level (which might not involve Na) is discussed below in section 2.3. In Fig. 1, we clearly observe *both* the ( $D^0-A^0$ ) and the ( $e-A^0$ ) peaks associated with this level at  $2.7086 \pm 0.0004$  (1.7 K) and  $2.7262 \pm 0.0004$  eV (20.1 K), respectively. The quenching of the ( $D^0-A^0$ ) peak involves the thermal ionization of the shallow donor levels into the conduction band, while the broadening of the ( $e-A^0$ ) peak at high  $T$  is due to the kinetic energy distribution of

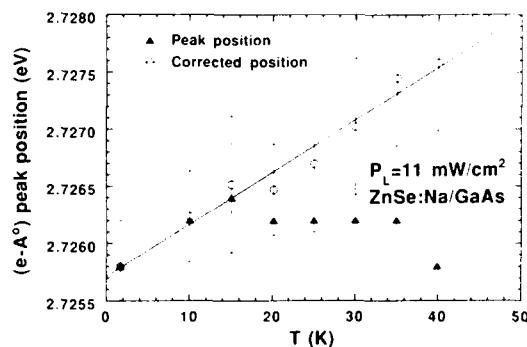


Fig. 2. Position of the  $(e-A^0)$  peak in the sample of Fig. 1 as a function of temperature. The filled triangles are the raw values, and the open circles are corrected for the temperature dependence of the band gap. The solid line is a least squares fit to the corrected data. The error bars (shown only on the corrected data for clarity) are "worst case"; the scatter in the data and results of various fitting procedures used to determine peak positions suggest that the true errors are significantly less than those indicated.

electrons in the conduction band. We note that a trace of the  $(e-A^0)$  peak is detectable even at 1.7 K, similar to the previously discussed case of ZnSe:Li [9]. The initial anomalous quenching of this peak from 1.7–10 K is similar to that we observed for ZnSe:Li, and can be explained in terms of temperature-dependent non-radiative recombination rates [9]. The identification of the  $(e-A^0)$  peak in this sample has been confirmed using intensity-dependent measurements, and also with magnetospectroscopy in the similar case of ZnSe:Li [9].

The position of the  $(e-A^0)$  peak is plotted as a function of lattice temperature (which we assume to equal the electron temperature for the low excitation conditions used in this work) is plotted in Fig. 2 for the data of Fig. 1. Both the raw data and those corrected for the temperature dependence of the band gap determined from the bound exciton peak positions as discussed in ref. [9] are shown. The solid line is a linear fit to the corrected data, which has an intercept of 2.7257 eV and a slope of 0.045 meV/K, in good agreement with the theoretical value [11] of  $0.5k_B = 0.043$  meV/K. The use of this linear fitting procedure reduces the random error associated with the

effects of noise on peak position determination by a factor of  $N^{1/2}$  for the final intercept, where  $N$  is the number of data points ( $N = 9$  in Fig. 2), yielding a conservatively estimated uncertainty of less than  $\pm 0.00017$  eV in the intercept. The uncertainty in  $E_g(T)$  introduces some additional error (about  $\pm 0.0002$  eV, based on  $E_g(T)$  data for 24 samples), but this error is systematic rather than random and therefore affects the slope more than the intercept, which varies by no more than  $\pm 0.0001$  eV for various  $E_g(T)$  fits. The intercept is just  $E_g(T=0) - E_A$ , where  $E_g = 2.8218$  eV at  $T=0$  is the band gap of unstrained ZnSe, and  $E_A$  is the ground state acceptor binding energy. Uncertainty in  $E_g(T=0)$  (probably  $\pm 0.0005$  eV) affects the  $E_A$  values obtained from our analysis, but does so equally for all acceptors and does not influence the overall precision, which is about  $\pm 0.0002$  eV.

The above analysis would apply directly to homoepitaxial or unstrained bulk material. However, it does not account for the effects of thermal expansion mismatch strain on this relaxed, heteroepitaxial material. The biaxial tensile strain in this type of sample has the well-known effects of reducing the gap and of splitting the valence band into separate light and heavy hole bands, which is reflected for example in the splitting of the free exciton peak [12]. This shift and splitting are easily resolved and accounted for in the excitonic PL and reflectance spectra of this sample (not shown). In addition, the acceptor level itself is expected to split into light and heavy hole components, which can be estimated in the framework of perturbation theory [13]. Since this expected splitting is not resolved in the data of Fig. 1, it is necessary to determine whether the observed peak positions correspond to the light hole level, the heavy hole level, or an average of the two. We argued in the case of Li [9] and As [14] acceptors that the heavy hole component is usually dominant, especially at about 10 K and above. This is so because the splitting is relatively small, so that the effects of thermalization into the light hole state are generally outweighed by the three times larger oscillator strength of transitions involving the heavy hole ( $|m_j| = 3/2$ ) states. A splitting similar to the expected strain

Table 1  
PL peak positions, binding energies, and ground state-to-excited state energy separations for acceptors in ZnSe

Acceptor	References ( $E_A$ )	$E_A$ ( $1s_{1/2}$ )	Energy separations <sup>a</sup> (meV)							
			$1s_{1/2}-2p_{1/2}$	$1s_{1/2}-2s_{1/2}$	$1s_{3/2}-2p_{3/2}$ ( $I_8$ )	$1s_{3/2}-2p_{5/2}$ ( $I_7$ )	$1s_{3/2}-3s_{3/2}$	$1s_{3/2}-2p_{1/2}$	$1s_{3/2}-4s_{3/2}$	
S <sup>2-</sup>	[26]	~56	37.4	40.2						
O	Present work	83 ± 3	47.8	56.7		63.9	67.3			
P	Present work	88.4 ± 0.5		69.3 <sup>b</sup>	72.6 <sup>b</sup>	73.9 <sup>b</sup>	75.6 <sup>b</sup>			
A <sup>2-</sup>	Present work	95.0 ± 0.4								
A <sub>1</sub>	Present work	106.1 ± 0.6		75.4	79.4	84.2				
N	Present work	111.3 ± 0.5	67.8	79.9	82.6	89.8	92.8	98.5	102.2	
Li	Present work	114.2 ± 0.3	72.9	82.6	85.8	93.0	97.8	100.0	102.5	
As	Present work	114.3 ± 0.5	73.6	83.9		93.5	98.4			
Na	[23,28]	~124–128	83.1	97.6	100.4	106.8	110.5	113.0	114.7	
Ag	[29]	~431		393.5			412.5		419.3	
Au	[29]	~550								

<sup>a</sup> Typical accuracies are ±0.1–0.2 meV.

<sup>b</sup> Note: Assignment of these levels is arbitrary because they do not conform to effective mass theory.



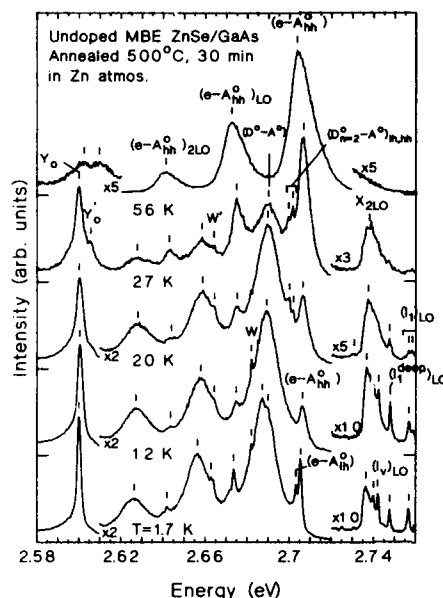


Fig. 3. PL spectra under  $28 \text{ mW/cm}^2$  UV excitation for a  $4.4 \mu\text{m}$  thick undoped MBE ZnSe layer, annealed in a Zn-rich atmosphere after growth. Instrumental resolution is  $0.3 \text{ meV}$ .

splitting has even been resolved in the case of the  $(e-A^0)$  peak involving P acceptors [15]. However, the possibly axial symmetry of the rather unusual (see below) P-related center makes the origin of the splitting a little ambiguous in that case.

Fig. 3 provides data that validate our assumption unambiguously. This figure displays PL spectra as a function of temperature for an undoped MBE layer that was annealed under a Zn overpressure for 30 min at  $500^\circ\text{C}$  in a "leaky tube" diffusion system designed for Zn diffusion into III-V materials [16]. An unintentional result of this particular anneal was the introduction of an acceptor level due to Li or possibly As (which have virtually indistinguishable binding energies, as discussed below). A second effect of the anneal was an increase over the normal amount of thermal tensile strain in the material, due to relaxation of the increased thermally-induced mismatch at the annealing temperature. The increased strain produces a larger than "normal" splitting in the  $(e-A^0)$  peak, which is clearly resolved in the  $1.7 \text{ K}$  PL spectrum. The observed

splitting is  $2.0 \pm 0.4 \text{ meV}$ . Given the observed free exciton splitting of  $3.8 \pm 0.15 \text{ meV}$  in this sample, the ratio of the experimental splittings yields the shear deformation potential of the acceptor-bound hole as  $b' = -0.56 \pm 0.11 \text{ eV}$ . This value is in fair agreement with the theoretical value of  $b' = -0.81 \text{ eV}$ , calculated using the theory of ref. [13] and the parameters in ref. [9]. Even at  $1.7 \text{ K}$ , the higher energy heavy hole component is dominant (which should be even more true in cases with smaller, unresolved strain splittings). The peak that grows to dominance at high  $T$  can be definitely traced to the heavy hole rather than to the light hole component at low  $T$ . To our knowledge, this is the first directly resolved observation of the strain splitting of an acceptor level in the PL spectrum of any compound semiconductor. We also note the observation of a lower energy doublet (e.g. at  $2.7000$  and  $2.7020 \pm 0.0004 \text{ eV}$  at  $20 \text{ K}$ ), which we tentatively attribute to recombination between donors in their first excited state and holes on the light and heavy hole acceptor levels. This excited-state donor-to-acceptor recombination mechanism has been previously reported in GaAs and InP [17].

Based on the above experimentally determined shear deformation potential, we can return for example to the data of Fig. 1 and estimate a  $1.6 \pm 0.3 \text{ meV}$  splitting of the acceptor level from the observed  $2.8 \text{ meV}$   $X_{hh}/X_{lh}$  splitting in that sample. The  $X_{lh}$  peak position in this sample is shifted  $3.2 \text{ meV}$  to lower energy than the bulk value, implying a light hole band gap  $E_g^{lh} = 2.8186 \text{ eV}$ . The intercept observed above then implies that  $(E_g^{lh} - E_A^{hh}) = 92.9 \pm 0.2 \text{ meV}$ , which is added to the  $1.5 \text{ meV}$   $(E_A^{hh} - E_A^{lh})$  splitting to yield the binding energy of the light hole acceptor level in the strained material as  $94.4 \pm 0.4 \text{ meV}$ . Finally, the binding energy in unstrained material can be calculated following ref. [9], using the experimental  $b'$  value given above, to yield  $95.0 \pm 0.4 \text{ meV}$ . The latter value is the one we quote as characteristic of the level, since the strain varies in different types of material. Using the same procedures, we have determined the binding energies of six different levels, which are listed in Table 1. (The value for O is based on data at only two temperatures, which were fit

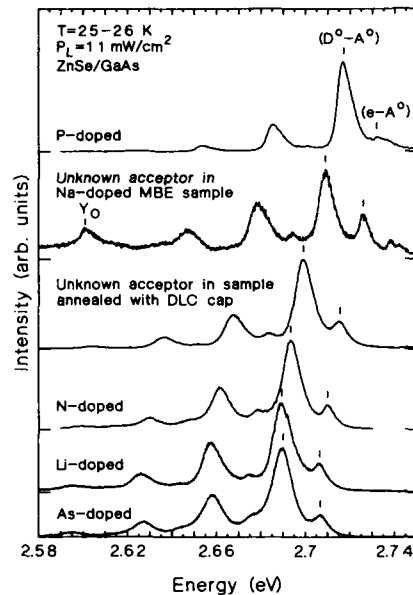


Fig. 4. Representative PL spectra at  $\sim 25$  K under low level UV excitation for a series of MBE ZnSe/GaAs samples doped with different acceptors (five samples) or annealed after growth (one sample). Both  $(D^0-A^0)$  and  $(e-A^0)$  peaks and their phonon replicas are visible in each case.

with a fixed slope equal to the theoretical value. A different value of  $b'/b = 0.84$  was used for the P acceptor, based on the directly resolved splitting of this level.) Where reliable previous estimates are available for a given level, they are generally in good agreement with these values, and where we obtained good quality data for the same acceptor in several samples, the spread among values obtained from them is within the quoted error limits. To further illustrate the type of data on which these values are based, we show PL spectra in Fig. 4 for samples doped with each of those six levels at a fixed temperature of 25–26 K, where both the  $(D^0-A^0)$  and  $(e-A^0)$  peaks are visible in every case. Full temperature-dependent data, however, were always used in the determination of  $E_A$ .

Previous determinations of acceptor binding energies in ZnSe have generally been based on other techniques, such as: (1) estimates based on  $(D^0-A^0)$  peak positions at some fixed excitation

level, arbitrarily assuming a value for  $E_D$  and the Coulomb term, (2) estimates based on the localization energy of the neutral acceptor-bound exciton ( $I_1$ ) peak using "Haynes's Rule" [18], (3) fits to the positions of discrete donor-acceptor pair lines in bulk or homoepitaxial material, with assumed values of the dielectric constant, or (4) estimates based on measurements of the ground-state-excited state separation energies, in conjunction with effective mass theory. The first method is subject to considerable uncertainty in the value of the Coulomb term, which generally depends on the excitation level, the doping level, and the non-radiative recombination rates; the particular donor ionization energy to use in a given sample is also usually unknown. The second method is completely unreliable to distinguish between different shallow acceptors in ZnSe, as we have pointed out previously [9]. The reason is that the exciton localization energy is *not* a linear function of acceptor binding energy in this (or most other direct gap) materials, contrary to the very early claim by Halsted and Aven [19].

The third method can yield reasonable results in bulk material if the appropriate dielectric constant is well known and a good quality fit to well-resolved data can be obtained. However, the quality of discrete pair line spectra is rarely adequate in modern heteroepitaxial material, and our method is more reliable in that it does not depend on the dielectric constant. The fourth method is subject to several problems, including uncertainties in the valence band parameters, the question of how to incorporate  $q$ -dependent screening and central cell "corrections" into effective mass theory, and the accuracy of the theory in general. We conclude that the present method is the best available one to determine binding energies in an accurate and reproducible way. Uncertainties in  $E_g$  do affect the results, but do so equally for all acceptors.

## 2.2. Excited states of shallow acceptor levels in ZnSe

We have determined the energy separations between the ground state and several excited states for several acceptors, including four that

have not been studied in this way previously. The experimental method is selectively-excited donor-acceptor pair luminescence (SPL) [20]. The experimental data will be presented elsewhere (see ref. [14] for the As case). The results are summarized in Table 1. Strain splittings are generally expected in the data and some splittings were experimentally resolved, but the values in Table 1 are not corrected for strain and represent average values in strained material. The identifications of particular states are based on comparisons with effective mass theory, and on the theoretical expectation that transitions involving even parity states should be the strongest ones in the spectrum.

Calculations using effective mass theory [21], with the Luttinger parameters of ref. [22] and an empirically adjusted dielectric constant, were performed to compare to the data; details will be presented elsewhere. The 1s central cell correction of one acceptor was taken as an adjustable parameter, and the correction was assumed to be zero for the p-states and scaled according to the probability density at the origin for the higher s wave functions. However, it was not possible to achieve a good fit to all of the acceptors simultaneously, even by adjusting the Luttinger parameters. Separate adjustment of the dielectric constant and central cell parameter for each acceptor was however quite successful, except in the case of P. The excited states we observed for this acceptor do not seem to follow effective mass theory at all, due perhaps to the possibility that this level may involve a complex.

### 2.3. Observation of new shallow acceptor levels

The "A<sub>2</sub>" acceptor level observed in the Na-doped MBE sample of Figs. 1 and 2 is *not* the ~124 meV level usually assigned to Na in bulk material [23], although it may be the same as the one observed in ref. [24] and speculatively attributed there to a Na<sub>Zn</sub>-V<sub>Se</sub> complex. Since only a donor-to-acceptor (D<sup>0</sup>-A<sup>0</sup>) peak was observed in ref. [24], whose position can vary considerably with excitation and doping levels, we cannot be certain if it is the same level. Previous studies of Na-doped MBE material [7,25] also reported a

(D<sup>0</sup>-A<sup>0</sup>) peak similar to the one observed here and in ref. [24], but did not observe the (e-A<sup>0</sup>) peak that allows us to evaluate its binding energy accurately. Other alkali metals such as K are common contaminants in Na [25], and could be the origin of this level. Further work is in progress to determine if the level in fact involves Na, K, some other impurity, or a complex.

The A<sub>1</sub> acceptor level described in Table 1 was originally observed in ref. [8], although it was mistakenly identified there (on the basis of the I<sub>1</sub> peak position) as Li. The insensitivity of I<sub>1</sub> localization energy with respect to E<sub>A</sub> makes the I<sub>1</sub> peak position an unreliable means of identifying acceptors, especially in strained material. This level is observed only in samples that have been subject to a rapid thermal anneal after encapsulation with a diamond-like C film, as described in ref. [8]. Otherwise identical anneals using other capping materials such as SiO<sub>2</sub> and SiN<sub>x</sub> never produced this level, and it has not been previously reported in the literature, to our knowledge. A 5 s anneal at 500°C produced relatively weak PL features related to this acceptor, while 5 s anneals at 550 and 600°C produced stronger peaks. These results imply that the impurity in question diffuses reasonably rapidly into ZnSe, but not so rapidly at low temperature that it is likely to be unstable (like Li) as a dopant. The properties of this impurity suggest that it might be very useful as a new p-type dopant in ZnSe and related materials, once it has been chemically identified. Work is currently in progress toward this objective.

### 2.4. Strain splitting of the neutral acceptor-bound exciton emission in ZnSe

Since we discussed the strain splitting of the (e-A<sup>0</sup>) peak above, we mention here that we have developed a detailed model of the strain splitting of the I<sub>1</sub> peaks in ZnSe, including the effects of hole-hole exchange interaction and crystal field splitting (the effects of the electron-hole exchange interaction are assumed to be negligible) [9,14]. The model has been confirmed using samples whose substrates have been selectively removed to release the thermal strain [15].

A more detailed discussion will be given elsewhere.

### 3. Conclusions

Using variable temperature PL measurements and the SPL technique, we have been able to show the existence of seven distinct shallow acceptor levels in ZnSe, not counting the previously investigated  $\sim 124$  meV Na level [23] and the  $\sim 56$  meV "S" level [26]. The binding energies have been accurately determined for all of these levels using temperature-dependent conduction band-to-acceptor PL peak positions. The investigation of the excited states using SPL has shown that As, Li, N, and the "A<sub>2</sub>" level are all effective mass-like, while the more unusual shallow P-related acceptor is not. Further work is needed to understand the fundamental reasons why As and P have not yet produced p-type conductivity in spite of their shallow levels, and to determine the way in which O incorporates to produce a shallow acceptor level. It is also important to identify the chemical origin of the A<sub>1</sub> and A<sub>2</sub> levels. In particular, there seems to be a significant probability that the A<sub>2</sub> level might be a useful new p-type dopant. Finally, the effects of strain on the acceptor-related PL features in heteroepitaxial material have been observed and successfully modeled.

### 4. Acknowledgments

The ASU portion of this work was supported by the National Science Foundation under Grant No. DMR-9106359. We thank R. Roedel for the use of his leaky-tube diffusion system for the conventional furnace anneals.

### 5. References

- [1] R.M. Park, M.B. Troffer, C.M. Rouleau, J.M. DePuydt and M.A. Haase, *Appl. Phys. Lett.* 57 (1990) 2127.
- [2] J. Qiu, J.M. DePuydt, H. Cheng and M.A. Haase, *Appl. Phys. Lett.* 59 (1991) 2992.
- [3] H. Cheng, J.M. DePuydt, J.E. Potts and T.L. Smith, *Appl. Phys. Lett.* 52 (1988) 147.
- [4] S.M. Shibli, M.C. Tamargo, B.J. Skromme, S.A. Schwarz, C.L. Schwartz, R.E. Nahory and R.J. Martin, *J. Vac. Sci. Technol. B* 8 (1990) 187.
- [5] J.M. DePuydt, T.L. Smith, J.E. Potts, H. Cheng and S.K. Mohapatra, *J. Crystal Growth* 86 (1988) 318.
- [6] K. Akimoto, T. Miyajima and Y. Mori, *Phys. Rev. B* 39 (1989) 3138.
- [7] J.E. Potts, H. Cheng, J.M. DePuydt and M.A. Haase, *J. Crystal Growth* 101 (1990) 425.
- [8] B.J. Skromme, N.G. Stoffel, A.S. Gozdz, M.C. Tamargo and S.M. Shibli, in: *Advances in Materials, Processing, and Devices for III-V Compound Semiconductors*, Eds. D.K. Sadana, L.E. Eastman and R. Dupuis (Mater. Res. Soc., Pittsburgh, PA, 1989) p. 391.
- [9] Y. Zhang, B.J. Skromme and H. Cheng, *Phys. Rev. B* 47 (1993) 2107.
- [10] P.J. Dean and J.L. Merz, *Phys. Rev.* 178 (1969) 1310.
- [11] D.M. Eagles, *J. Phys. Chem. Solids* 16 (1960) 76.
- [12] T. Yao, Y. Okada, S. Matsui, K. Ishida and J. Fujimoto, *J. Crystal Growth* 81 (1987) 518.
- [13] M. Schmidt, *Phys. Status Solidi (b)* 79 (1977) 533.
- [14] Y. Zhang, B.J. Skromme, S.M. Shibli and M.C. Tamargo, *Phys. Rev. B* 48 (1993) 10885.
- [15] Y. Zhang, B.J. Skromme and H. Cheng, in: *Semiconductor Heterostructures for Photonic and Electronic Applications*, Mater. Res. Soc. Symp. Proc. 281, Eds. D.C. Houghton, C.W. Tu and R.T. Tung (Mater. Res. Soc., Pittsburgh, PA, 1993) p. 567.
- [16] R.J. Roedel, J.L. Edwards, A. Richter, P.M. Holm and H.H. Erkaya, *J. Electrochem. Soc.* 131 (1984) 1726.
- [17] B.J. Skromme and G.E. Stillman, *Phys. Rev. B* 29 (1984) 1982.
- [18] J.R. Haynes, *Phys. Rev. Lett.* 4 (1960) 361.
- [19] R.E. Halsted and M. Aven, *Phys. Rev. Lett.* 14 (1965) 64.
- [20] H. Tews and H. Venghaus, *Solid State Commun.* 30 (1979) 219.
- [21] N.O. Lipari, *Phys. Lett. A* 81 (1981) 75.
- [22] H. Venghaus, *Phys. Rev. B* 19 (1979) 3071.
- [23] R.N. Bhargava, R.J. Seymour, B.J. Fitzpatrick and S.P. Herko, *Phys. Rev. B* 20 (1979) 2407.
- [24] V. Swaminathan and L.C. Greene, *Phys. Rev. B* 14 (1976) 5351.
- [25] J.M. DePuydt, T.L. Smith, J.E. Potts, H. Cheng and S.K. Mohapatra, *J. Crystal Growth* 86 (1988) 318.
- [26] P. Blanconnier, J.F. Hogrel, A.M. Jean-Louis and B. Sermage, *J. Appl. Phys.* 52 (1981) 6895.
- [27] K. Shahzad, B.A. Khan, D.J. Olego and D.A. Cammack, *Phys. Rev. B* 42 (1990) 11240.
- [28] H. Tews, H. Venghaus and P.J. Dean, *Phys. Rev. B* 19 (1979) 5178.
- [29] P.J. Dean, B.J. Fitzpatrick and R.N. Bhargava, *Phys. Rev. B* 26 (1982) 2016.



ELSEVIER

Journal of Crystal Growth 138 (1994) 318–323

JOURNAL OF  
**CRYSTAL  
GROWTH**

## Acceptor state instabilities in ZnSe under hydrostatic pressure

D.J. Strachan <sup>a</sup>, M. Ming Li <sup>a</sup>, M.C. Tamargo <sup>b</sup>, B.A. Weinstein <sup>\*a</sup>

<sup>a</sup> Department of Physics, 239 Fronczak Hall, SUNY, Buffalo, New York 14260, USA

<sup>b</sup> Department of Chemistry, City College of CUNY, New York, New York 10031, USA

### Abstract

Photoluminescence experiments on ZnSe doped with P and As have been conducted at high pressure and low temperature. We find evidence that deep states arising from these impurities become unstable between 15 and 25 kbar. Although our results are not yet definitive, some interesting implications for current models are discussed.

The study of impurities in semiconductors has benefited from high pressure experiments, which often allow band-edge assignment of shallow levels, and can reveal deep levels that are resonant with the electronic continuum at 1 atm. Although this is well established for donors in group IV and III–V materials (a prime example being the shallow-to-deep transition of the DX center in GaAs), there are few pressure studies of acceptors, especially in II–VI compounds. For acceptors it is possible, depending on the valence band deformation potential, to have deep-to-shallow transitions, i.e., the converse of the DX center. This possibility is quite intriguing, given the interest in realizing high conductivity p-type ZnSe for photonics, and the suggestion that DX-like traps may inhibit this [1].

Previous photoluminescence (PL) studies on the pressure dependence of electronic states in ZnSe have concentrated on the absorption edge and near band-edge PL energy regions [2,3]. The prominent spectral features – direct edge, shal-

low exciton PL lines and donor–acceptor pair (DAP) PL lines – exhibit pressure coefficients in the 6–7.3 meV/kbar range. Pressure experiments on deep levels in ZnSe have been limited to a preliminary study by the authors, and recent work on some transition metal impurities [4–6].

In the set of experiments reported here we examine the effect of hydrostatic pressure on P and As impurities in ZnSe. We are looking primarily for evidence of a deep-to-shallow transition which might be associated with instability in the impurity bonding configuration. Although our results are not yet definitive, some interesting implications for current models are discussed.

Melt-grown ZnSe:P and modulation doped epitaxial ZnSe:As films, both with as-grown atomic impurity levels of  $\sim 10^{18}$ – $10^{19}$  cm<sup>-3</sup>, were measured. The former was supplied by R.K. Watts and is some of the same material used in his original 1 atm PL and electron spin resonance (ESR) studies [7,8]. The ZnSe:As film was grown on (001) GaAs by MBE to a thickness of 1.5  $\mu$ m; this has been described elsewhere [9].

The PL measurements were performed in a hydraulically-driven diamond-anvil cell (DAC)

\* Corresponding author.

placed within a He-gas circulation cryostat operating at temperatures of 7–300 K [10]; the pressure was determined by using the ruby fluorescence method. The pressure transmitting medium was a 4:1 methanol:ethanol mixture. Strain gradients in this medium were minimized by frequently annealing at 180 K. Typically, pressure changes of less than 10 kbar at 7 K could be accomplished with little non-hydrostatic broadening in the sharp exciton lines. PL excitation was by  $\sim 0.1$ – $10$  mW 368 nm  $\text{Kr}^+$  CW laser light focused into a  $60\text{ }\mu\text{m}$  spot.

The PL spectrum for the  $\text{ZnSe:P}$  sample at 1 atm (7 K) consists mainly of two classes of DAP transitions; band 1 at 2.7 eV arises from shallow states, and band 2, the “red band” near 1.9 eV, involves most likely (see discussion below) unintentional shallow donors and deep acceptors. In Fig. 1 the shift of both bands to higher energy under increasing pressure is clear. A most interesting feature is their separation, which decreases with increasing pressure. This indicates that the energy position of the “red band” is increasing faster than the direct band gap. The situation is made complicated by the appearance of a third peak (band 3) that appears between the other two. As the pressure increases, this band grows in intensity at the expense of the original “red band” which cannot be resolved above 25 kbar. A fur-

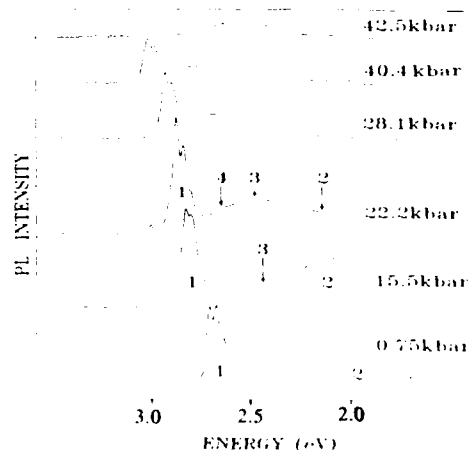


Fig. 1. Measured PL spectra of  $\text{ZnSe:P}$  at 7 K and various pressures between 0.75 and 40.4 kbar.

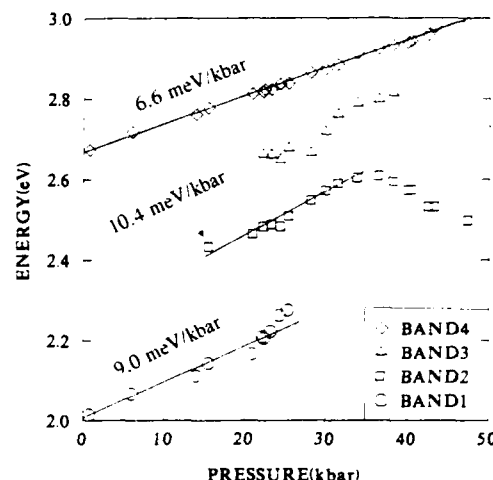


Fig. 2. The pressure dependence of the PL band maxima in P-doped  $\text{ZnSe}$  at 7 K.

ther complication appears in the range 25–35 kbar, when a fourth peak (band 4) becomes evident. The sequence of the above events are best illustrated in Fig. 2, where all energy positions have been determined by fitting the bands/lines to Gaussian profiles. Least squares pressure coefficients (accurate to  $\pm 15\%$ ) are given in the figure. These pressure-induced changes in the PL spectrum of  $\text{ZnSe:P}$  are reversible until 55 kbar, when all the PL features seem to undergo a nonreversible decrease in intensity.

In the case of  $\text{ZnSe:As}$ , both a red and a green band are already present at 1 atm. As with the  $\text{ZnSe:P}$  data, the gradual transfer of oscillator strength from the red to the green band with increasing pressure (up to 20 kbar) is evident. In Fig. 3, three representative spectra are plotted at different pressures. This exchange of oscillator strength from red to green PL emission was easily seen by eye in  $\text{ZnSe:As}$  upon excitation of the sample by the  $\text{Kr}^+$  laser. The red band, although diminishing in intensity, did not disappear as happened with  $\text{ZnSe:P}$ . Fig. 4 shows the energy shift with pressure of the bands in  $\text{ZnSe:As}$ .

Above 20 kbar in  $\text{ZnSe:As}$ , there is a precipitous drop in the intensity of the acceptor bound exciton. At the same time the near edge DAP band originating from shallow levels narrows to a

single line (labeled “new band”), losing all of its phonon structure. The absolute intensity of this band is not altered significantly by this process. In this pressure regime the deeper green band disappears, leaving the red band as the sole remaining source of deep broad-band PL. On reducing the pressure from 30 kbar, all of the spectral features in the ZnSe:As sample return within the same pressure ranges, but at reduced intensities. This indicates only partial reversal.

We have also measured the temperature dependence of the PL intensity ( $I_{PL}$ ) of the 1.9 eV band in the ZnSe:P sample at high pressure. Fig. 5 gives the observed behavior plotted in a  $\log(I_{PL})$  versus  $1/T$  format for this deep red band at 1 atm and 22.4 kbar. The thermal quenching activation energy (obtained by fitting to the standard

formula [11]) decreases from  $0.27 \pm 0.07$  eV at 1 atm to  $0.13 \pm 0.07$  eV at 22.4 kbar. The 1 atm result agrees with the 0.3 eV value given in refs. [7] and [8]. The pressure variation of about  $-6$  meV/kbar for the deep acceptor ground state implied from these thermal data compares favorably with the more rapid pressure shift measured for the red PL band, assuming that the excited state giving rise to this red emission follows the conduction band edge.

Watts et al. [7,8] found direct evidence from ESR results that P substitutes at Se sites, and attributed the origin of the red band luminescence to internal transitions of the  $P_{Se}$  acceptors. According to this picture, the highly localized acceptor ground state is expected to be insensitive to pressure, while the excited state should be

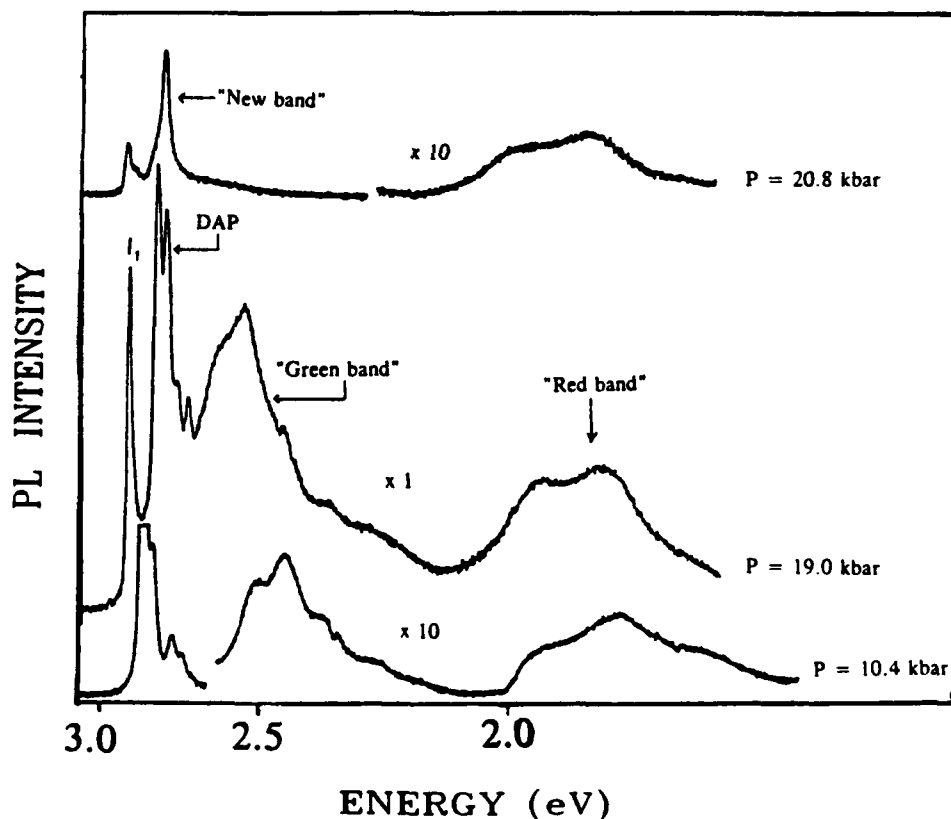


Fig. 3. Measured PL spectra of ZnSe:As at 7 K and various pressures between 10.4 and 20.8 kbar.

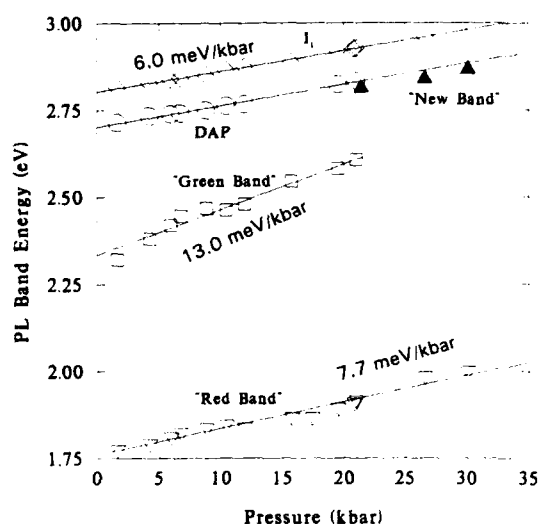


Fig. 4. The pressure dependence of the PL band maxima in As-doped ZnSe at 7 K.

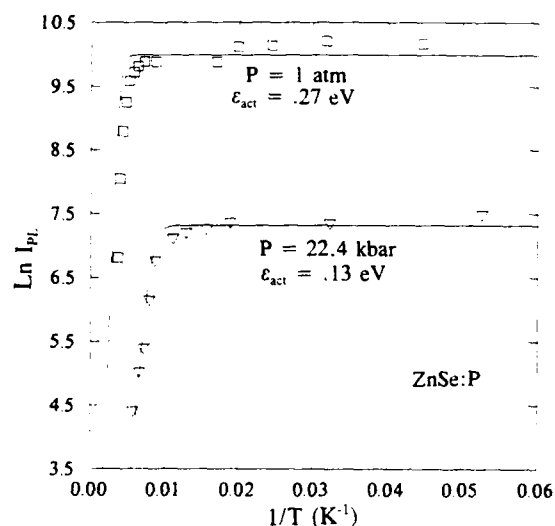


Fig. 5. The temperature dependence of the PL intensity of the 1.9 eV red band in ZnSe:P at pressures of 1 atm and 22.4 kbar.

conduction-band-like and correspond to a normal tetrahedral substitutional site. The present results are fully consistent with this picture.

A more recent study on ZnSe doped with P and Ga by Davies and Nicholls [12] have used an alternative model for the origin of the deep red

band luminescence. In this model a DAP transition between a shallow  $\text{Ga}_{\text{Zn}}$  donor and a localized acceptor level,  $\sim 0.6$  eV above the valence band, is responsible for the 1.9 eV emission. The

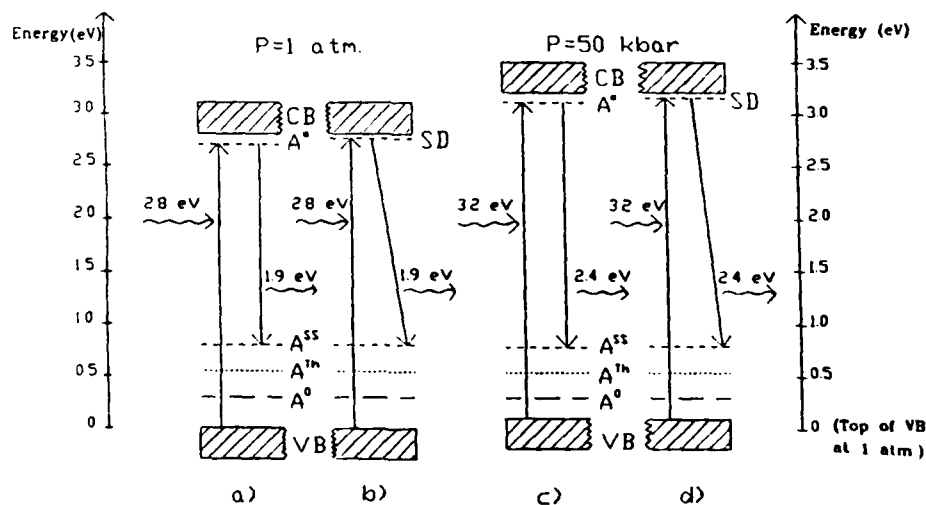


Fig. 6. Energy-level diagram showing two models for the pressure dependence of the deep "red" PL peak in ZnSe:P relative to the band edges.  $A^0$  and  $A^*$  denote ground and excited acceptor levels at trigonal sites;  $A^{\text{Th}}$  and  $A^{\text{SS}}$  denote tetrahedral ground acceptor levels accessible thermally (Th), or via the Stokes shifted (SS) PL; SD is an unintentional shallow-donor level. (a), (c) and (b), (d) depict the models of refs. [7] and [12], respectively.



present bulk ZnSe:P samples are likely to contain unintentional donors, and for this reason we believe the Davies and Nicholls model is more appropriate for these bulk specimens. In the ZnSe:As samples the likelihood of Ga diffusion from the GaAs substrate also leads us to favor this alternate picture.

In Fig. 6, the energy level diagrams for the Watts et al. model are shown in (a) and (c) scaled to represent pressures of 1 atm and 50, kbar respectively. The internal transition of the deep  $P_{sc}$  center between the excited state ( $A^*$ ) and the Stokes shifted ground state ( $A^{ss}$ ) that results in the 1.9 eV emission is represented by the downward vertical arrow. Also, the energy level diagrams for the Davies and Nicholls model are shown in (b) and (d) for the same pressures. Here, the donor–acceptor pair recombination between a residual shallow donor (SD) and the Stokes shifted ground state of the deep acceptor center  $A^{ss}$  level is represented by the slanted arrow. In both models, the energy of the deep acceptor ground state is assumed to be relatively insensitive to hydrostatic pressure, while the excited state follows the band edge.

For ZnSe:P and ZnSe:As our results indicate that the deep acceptor ground-state level and the valence band edge approach each other at the approximate rates of  $-1.5 \pm 0.5$  and  $-2.5 \pm 0.5$  meV/kbar, respectively. These values have the same sign as the pressure derivative of the acceptor thermal ionization energy obtained in ZnSe:P, but are two to four times lower in magnitude. Based on these results, a deep-to-shallow transition is not anticipated by a simple level crossing mechanism in the present experiments.

The above results for the red band pressure coefficient imply a value of  $-1.2 \pm 0.3$  eV for the absolute deformation potential ( $dE_V/d \ln V$ ) of the valence band in ZnSe. This is comparable, within uncertainty, to the  $-1.4 \pm 0.2$  eV result obtained by Wasik et al. [6]. Some questions still remain, however, about the validity of using transition-metal states (or other deep states) as immobile reference levels. These questions arise mainly because of the substantially different results produced by doping with heavy, as opposed to with light transition metals [6].

In conclusion: The results presented in this paper do not indicate a high pressure deep-to-shallow transition for P and As acceptors in ZnSe. The disappearance and/or changes in intensity of the red and green bands in ZnSe:P and ZnSe:As, and the sudden appearance of the “new band” in ZnSe:As at the expense of the green band, can be explained straightforwardly by instabilities that relax the bonding configuration at the deep acceptor sites. Another possible explanation, however, is changes arising from plastic flow in the ZnSe lattice [13]. We believe that this has been minimized by frequent annealing of strain gradients in the DAC pressure medium. Furthermore, changes due to plastic flow, such as creation of stacking faults, should not be reversible, even partially. This is in conflict with our pressure cycling results. Indeed, a comparison of the  $LO(\Gamma)$  Raman peaks in ZnSe:As before and after the pressure PL experiments reveals no increase in disorder.

The energy separation between the deep acceptor ground state responsible for the red PL band and the valence band-edge is found to decrease by about  $-2.0 \pm 0.5$  meV/kbar for both P and As acceptors. This corresponds to an absolute deformation potential of  $-1.2 \pm 0.3$  eV for the valence band of ZnSe, a result which agrees well with the recent value of  $-1.4 \pm 0.2$  eV reported by Wasik et al. [6].

We thank D.J. Chadi for initially suggesting this problem, and R.K. Watts for supplying the ZnSe:P samples. This work was supported by ONR contract No. N00014-89-J-1797.

## 1. References

- [1] D. Chadi, Appl. Phys. Lett. 59 (1991) 3589.
- [2] W. Shan, J. Hays, X. Yang, J. Song, E. Cantwell and J. Aldridge, Appl. Phys. Lett. 60 (1992) 736.
- [3] S. Ves, K. Strossner, N. Christensen, C.K. Kim and M. Cardona, Solid State Commun. 56 (1985) 479.
- [4] M.M. Li, D.J. Strachan, M. Tamargo and B.A. Weinstein, in: Proc. 14th AIRAPT Conf., Colorado, 1993.
- [5] U.D. Venkateswaran, C. Mak, J. Bak, R. Sooryakumar and B. Jonker, in: Proc. 14th AIRAPT Conf., Colorado, 1993.

- [6] D. Wasik, Z. Liro and M. Baj, *J. Crystal Growth* 101 (1990) 466.
- [7] A.R. Reinberg, W.C. Holton and M. de Wit and R.K. Watts, *Phys. Rev. B* 3 (1971) 410.
- [8] R.K. Watts, W.C. Holton and M. de Wit, *Phys. Rev. B* 3 (1971) 404.
- [9] S. Shibli, M. Tamargo, B. Skromme, S. Schwarz, C. Schwarz, R. Nabory and R. Martin, *J. Vac. Sci. Technol. B* 8 (1990) 187.
- [10] B.A. Weinstein, *Phil. Mag.* B 50 (1984) 709.
- [11] H. Bebb and E. Williams, in: *Semiconductors and Semimetals*, Vol. 8, Transport and Optical Phenomena, Eds. R.K. Willardson and A.C. Beer (Academic Press, New York, 1972) ch. 4.
- [12] J.J. Davies and J.E. Nicholls, *J. Luminescence* 18/19 (1979) 322.
- [13] T. Suzuki, S. Takeuchi and H. Yoshinaga, in: *Dislocation Dynamics and Plasticity*, Springer Series in Materials Science, Vol. 12, Ed. U. Gonser (Springer, Berlin, 1991) p. 114.



ELSEVIER

Journal of Crystal Growth 138 (1994) 324–330

JOURNAL OF **CRYSTAL  
GROWTH**

## Comparison between gallium-implanted layers of ZnSe and $\text{ZnS}_x\text{Se}_{1-x}$ by optical, electrical and electron beam characterization methods

G. Gleitsmann <sup>a</sup>, N. Ammann <sup>b</sup>, J. Hermans <sup>c</sup>, A. Schneider <sup>a</sup>, J. Geurts <sup>c</sup>,  
P. Karduck <sup>b</sup>, M. Heuken <sup>\*a</sup>

<sup>a</sup> Institut für Halbleitertechnik, RWTH Aachen, Templergraben 55, D-52056 Aachen, Germany

<sup>b</sup> Gemeinschaftslabor für Elektronenmikroskopie, RWTH Aachen, Templergraben 55, D-52056 Aachen, Germany

<sup>c</sup> Physikalisches Institut, RWTH Aachen, Templergraben 55, D-52056 Aachen, Germany

### Abstract

Optoelectronic devices in the blue spectral region require doped  $\text{ZnS}_x\text{Se}_{1-x}$  layers for electrical confinement and optical waveguiding. Since ion implantation is often used to realize heavy doping in thin layers, we implanted gallium ions with different doses and energies into ZnSe and  $\text{ZnS}_x\text{Se}_{1-x}$  ( $x \leq 0.4$ ) layers, grown by metalorganic vapor phase epitaxy (MOVPE) on GaAs. Rapid thermal annealing was performed after  $\text{SiO}_2$  capping. For characterization, we used electron probe micro-analysis (EPMA), photoluminescence (PL) at 11 K, Raman spectroscopy, far infrared reflectivity (FIR) and Hall measurements. In ZnSe, the Ga depth profiles remain nearly gaussian after annealing, indicating weak diffusion. PL shows that both the overall intensity and the ratio of excitonic to deep centre emissions are maximum for annealing at 850°C (30 s), implying optimum crystalline quality and maximum carrier concentration. In addition, the conductivity is maximum ( $10 \Omega^{-1} \text{cm}^{-1}$ ). However, FIR reveals a heavily doped layer at the GaAs interface, which is assigned to the annealing-induced Zn diffusion into the substrate. Furthermore, the PL spectra show donor-acceptor pair (DAP) transitions which can be attributed to shallow acceptors due to complexes of Ga and intrinsic defects. With increasing ion dose the free carrier concentration saturates at  $4 \times 10^{17} \text{cm}^{-3}$  probably due to self-compensation caused by zinc vacancies ( $V_{\text{Zn}}$ ). For  $\text{ZnS}_{0.3}\text{Se}_{0.7}$ , EPMA measurements show a diffusion of the Ga towards the surface, while S- and Ga-rich surface defects appear during annealing. After implantation the PL spectra show deep level emissions at 2.08 and 2.35 eV, which were assigned to  $[\text{Ga}_{\text{Zn}}-V_{\text{Zn}}]$  complexes and to  $\text{Zn}_{\text{Se}}$ . Optimum annealing seems to occur at 850°C for 30 s, resulting in a maximum PL intensity with strong DAP and excitonic contributions. Similar behaviour was observed for  $\text{ZnS}_{0.4}\text{Se}_{0.6}$ . Up to now, due to the diffusion and compensation, the implanted and annealed ternary layers remain semi-insulating.

### 1. Introduction

There has been much effort in investigating ZnSSe, because it is a promising material for

opto-electronic devices (e.g. lasers and light emitting diodes) working in the blue region of the visible spectrum [1,2]. The future usefulness of this material system depends on the ability to achieve low resistivities and ohmic contacts. Since in silicon technology ion implantation is a standard method, it may also be a potential technology

\* Corresponding author.

to achieve highly doped ZnSSe, although a higher implantation-induced damage might be expected. Efficient shaping of carrier concentration in heterostructures requires knowledge about implantation profiles and their diffusion behaviour. Besides the implantation energy, the annealing parameters play an important role. Yodo et al. have reported that optimum annealing depends mainly on the type of dopants [3]. For Li and Na implantation in ZnSe, they found that optimum annealing conditions are 1 min at 757°C and 5 min at 557°C. However, for doses beyond  $10^{15} \text{ cm}^{-2}$ , the radiation damage cannot be removed completely.

In this work, ion implantation of Ga into ZnSSe was used for the first time to investigate the dependence of electrical properties on ion dose. We have chosen gallium in order to compare our results with those of other groups [4,5]. We used EPMA to get information about the sulphur homogeneity and the Ga profiles before and after annealing. PL spectroscopy was performed to get information about the crystalline quality, the stoichiometry of ternary layers and transition energies of impurity levels in the band gap. Raman measurements were used to investigate the crystalline quality of the layers and to estimate the carrier concentration optically. Hall-effect measurements yielded details about the dependence of electrical properties on implantation and annealing parameters.

## 2. Experimental procedure

The layers were grown on semi-insulating GaAs:Cr substrates ( $2^\circ$  off (100)) by atmospheric pressure MOVPE under optimized growth conditions (480°C, VI/II = 1 for ZnSe and VI/II  $\geq$  21 for ZnSSe) using diethylzinc, diethylselenide and hydrogen sulphide as precursors [6]. To achieve highly homogeneous layers, a rotating susceptor was used [7]. We investigated nominal sulphur contents  $x$  of 0%, 15%, 30% and 40%. The optically determined layer thickness was 4  $\mu\text{m}$  for ZnSe and up to 2  $\mu\text{m}$  for ternary material. The critical thicknesses  $d_c$  are about 150 nm for ZnSe and 90 nm for  $\text{ZnS}_{0.15}\text{Se}_{0.85}$ . At sulphur contents beyond 30%,  $d_c$  is below 20 nm [8,9]. Thus the layers considered in the present work are fully

relaxed. After growth, the layers were implanted with  $^{71}\text{Ga}$  ions of energies between 120 and 340 keV in a low-current implanter. In order to avoid channeling during implantation, the layers were tilted  $7^\circ$  off. Subsequently, rapid thermal annealing (RTA) at temperatures about 850°C was performed. To avoid desorption during annealing, the layers were capped with 150 nm  $\text{SiO}_2$  which was removed by 40% HF afterwards. The EPMA measurements were carried out using a Cameca SX50 microprobe at electron beam currents of about 100 nA, energies of 2–30 keV and a beam cross section of a few  $\mu\text{m}^2$ . The samples were excited at normal or tilted ( $60^\circ$ ) incidence. The total power was about 1 mW, and consequently the maximum temperature of the specimen could not exceed 100°C [10]. By varying the beam energy and the tilt angle, definite but changing sections of the dopant depth profiles are excited and emit characteristic X-rays [11]. The sheet dopant concentration and the first two statistical moments of the profiles have been determined from the Ga  $L\alpha$  intensities by means of theoretical calculations based upon Monte Carlo (MC) simulated electron densities [12]. In contrast to SIMS, EPMA does not require a priori information on the implantation dose [12]. PL measurements have been performed at 11 K using a HeCd laser of 325 nm (3.81 eV) wavelength and a SPEX 1704 monochromator of 1 m focal length, giving a spectral resolution better than 0.03 nm. The excitation density was about 0.1  $\text{W}/\text{cm}^2$ . For the Raman analysis we used an Ar-ion laser. In order to vary penetration depth and scattering efficiency, the laser lines were varied between 514 and 457 nm. Spectra were taken in backscattering configuration 100(010;001) $\bar{1}$ 00 at 295 and 77 K. The input power was 35 mW, while the focus diameter was about 0.1 mm. The scattered light was analysed with a SPEX 1402 double monochromator, using a RCA 14034A-02 GaAs photomultiplier and an optical multichannel analyser (OMA) for the detection. The spectral accuracy was  $\pm 0.15 \text{ cm}^{-1}$ . Ohmic contacts to the layers have been realized by alloying indium dots at 300°C under HCl atmosphere. Hall measurements in Van der Pauw configuration were performed at 77 and 295 K.

### 3. Results and discussion

#### 3.1. Depth profiles and stoichiometry

To get more information on the diffusion behaviour of Ga in ZnSe, we investigated samples which were uniformly implanted with  $7 \times 10^{15} \text{ cm}^{-2}$  Ga at 300 keV and annealed for 30 to 80 s at temperatures between 700 and 900°C. The sheet Ga concentrations measured by EPMA after annealing are listed in Table 1. Obviously, the implanted Ga is partly out-diffused during the annealing process. This effect depends strongly on annealing temperature, but only weakly on annealing time. From this we conclude that the main part of the out-diffusion takes place in the early stage of the anneal, which can be explained by diffusion of Ga through the  $\text{SiO}_2$  cap. Additionally, the EPMA measurements revealed an increased Ga surface concentration after the anneals. Depending on annealing temperature, this increase corresponds to a segregated surface coverage of up to  $1.2 \times 10^{14} \text{ cm}^{-2}$ . Apart from the surface concentration the Ga profiles remain localized with a diffusion length of about 50 nm for the anneal at 900°C for 60 s, for instance. We reported recently [13] that implantation profiles of Ga in ZnSe are approximately gaussian since the third moment ratio is sufficiently low.

For  $x \geq 0.3$ , annealing-induced diffusion of Ga towards the surface is the predominant effect. The Ga profile is now located at the surface [13]. Additionally, the surface quality is degraded. Scanning electron microscopy (SEM) scans show clearly droplets with a diameter of about 0.5  $\mu\text{m}$ . XPS and AES measurements revealed that these droplets are Ga- and S-rich.

Table 1

Ga concentration (in  $\text{cm}^{-2}$ ) of ZnSe:Ga versus annealing parameters; the layers were uniformly implanted with  $7 \times 10^{15} \text{ cm}^{-2}$  at 300 keV

Annealing time (s)	Annealing temperature (°C)		
	700	800	900
30	$6.7 \times 10^{15}$	$5.5 \times 10^{15}$	$4.9 \times 10^{15}$
60	$6.3 \times 10^{15}$	$5.1 \times 10^{15}$	$4.3 \times 10^{15}$
80	$6.1 \times 10^{15}$	$5.0 \times 10^{15}$	$4.3 \times 10^{15}$

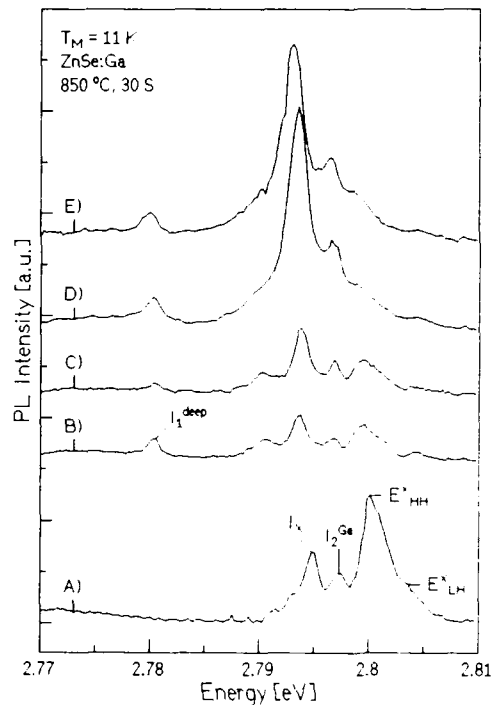


Fig. 1. Excitonic emissions of ZnSe:Ga, implanted with an ion energy of 120 keV and annealed at 850°C for 30 s. (A) as-grown; (B) not implanted, annealed; (C) like (B), with indium contact; (D) Ga-implanted and annealed; (E) like (D), with indium contact.

EPMA analysis of the Se  $L\alpha$  and S  $K\alpha$  intensities in ternary layers before annealing yields a sulphur content of 33% and 37% for the layers denoted as  $\text{ZnS}_{0.33}\text{Se}_{0.67}$  and  $\text{ZnS}_{0.37}\text{Se}_{0.63}$ , respectively. According to SIMS measurements, the Zn, S and Se concentrations are homogeneous in the growth direction. However, the measurements indicate a slightly reduced S content after annealing.

#### 3.2. Crystalline quality and transition energies of impurities

Fig. 1 shows the excitonic spectra of ZnSe:Ga. All samples annealed for 30 s at 850°C exhibit a peak called  $I_1^{\text{deep}}$  at 2.780 eV, which can be assigned to excitons bound to  $V_{\text{Zn}}$  [14]. For non-implanted layers, this effect could probably be ex-

plained by a thermally induced increase of  $[V_{Zn}]$  [15] due to annealing. The spectra of Ga-implanted samples show a more intense  $I_1^{deep}$  emission. This is correlated with the enhanced formation of zinc vacancies in presence of Ga donors, which is well known from MBE-grown and in-situ doped layers [5]. The intensities of the transitions denoted  $I_2$  and  $I_3$  are maximum for Ga-implanted layers and the ratio  $I_2/I_3$  is constant. Non-implanted annealed layers (B, C) show no significant change in  $I_2$  and  $I_3$  intensities, merely the free excitonic transitions weakened. Apart from a further decrease of the free excitonic intensity, samples with alloyed indium contacts (C, E) exhibit the same spectra. From the spectra in Fig. 1, the behaviour of the  $I_3$  emission implies its correlation to Ga donors. Besides the peaks in Fig. 1, there are in Ga-implanted ZnSe four transitions at 2.666, 2.697, 2.714 and 2.746 eV. Since donor to valence band transitions ( $D^0-h$ ) are suppressed [16], only donor to acceptor ( $D^0-A^0$ ) or conduction band to acceptor ( $e-A^0$ ) transitions can be observed. Since the peaks at 2.666 and 2.714 eV have an energy distance of 31 meV to the two other peaks, they seem to be LO phonon replica. The transitions at 2.697 and 2.746 eV can be assigned to acceptor levels having ionization energies of 72 and 122 meV, respectively. Since they do not occur in undoped and in nitrogen-implanted ZnSe [17], they are clearly Ga-related. Since  $V_{Zn}$  are known to be mobile above 400 K [15], they can form complexes with Ga on Zn lattice sites, namely  $[Ga_{Zn}-V_{Zn}]$ , with an ionization energy of 68 meV [4]. Comparing the peak PL intensities and considering  $[V_{Zn}] \gg [Zn_{Se}]$  over a large range of temperatures [15], we can assign the ( $e-A^0$ ) transition at 2.746 eV ( $E_A = 72$  meV) to the  $[Ga_{Zn}-V_{Zn}]$  complex, whereas  $E_A = 122$  meV (2.697 eV) is most probably due to  $[Ga_{Zn}-Zn_{Se}]$ .

Fig. 2 shows the PL spectra of  $ZnS_{0.3}Se_{0.7}:Ga$  ( $E_{ion} = 120$  keV). Due to a rotational symmetric variation of the S concentration for ternary ZnSSe grown in our reactor [18], the band edge luminescence in Fig. 2 varies between 2.96 ( $x = 0.27$ ) and 2.99 eV ( $x = 0.31$ ). The mole fraction  $x$  was calculated by  $E_g = E_g^{ZnS}x + E_g^{ZnSe}(1-x) - b(1-x)x$ ,  $b = 0.67$  eV [19]. Besides, deep emission

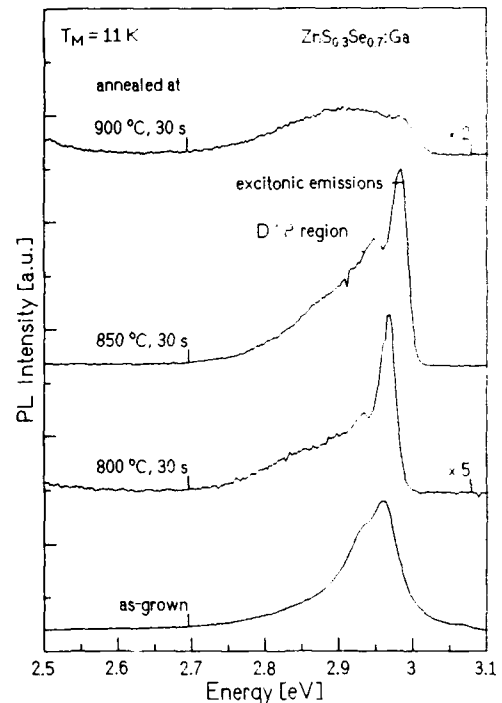


Fig. 2. PL spectra of  $ZnS_{0.3}Se_{0.7}:Ga$  implanted with  $1.5 \times 10^{13} \text{ cm}^{-2}$  at 120 keV and annealed under different conditions.

peaks at 2.08 and 2.35 eV occur. Similar to ZnSe [4], they are tentatively assigned to  $V_{Zn}$  and  $Zn_{Se}$ , respectively. Comparison of overall intensity and shape of the PL spectra shows that the ratios of excitonic to DAP and excitonic to deep emissions are minimum at 900°C, i.e. the crystalline quality is heavily degraded. The overall intensity of the sample annealed at 850°C is 5 times higher than that of the sample annealed at 800°C. Therefore, optimum annealing seems to take place at 850°C. In the case of  $ZnS_{0.4}Se_{0.6}:Ga$  ( $E_{ion} = 120$  keV), we observe similar behaviour.

Fig. 3 compares typical Raman spectra of  $ZnS_{0.15}Se_{0.85}$  samples measured at 77 K. Besides the LO phonon at  $296 \text{ cm}^{-1}$  and the symmetry-forbidden TO phonon at  $272 \text{ cm}^{-1}$  of the GaAs substrate, the as-grown sample shows three other spectral features which originate from the mixed crystal  $ZnS_{0.15}Se_{0.85}$ : the Zn-Se TO vibration at  $210 \text{ cm}^{-1}$  and the LO vibrations Zn-Se ( $252.3$

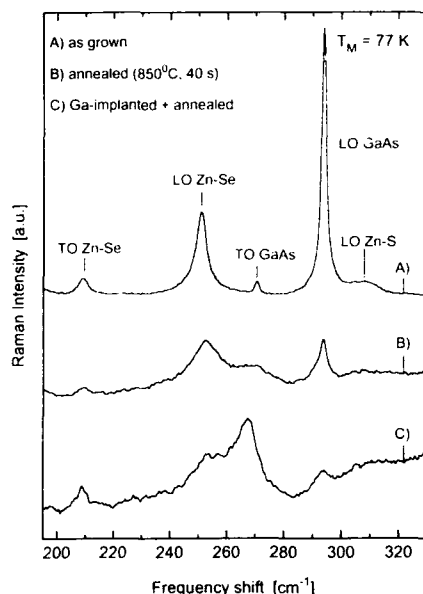


Fig. 3. Raman spectra of  $\text{ZnS}_{0.15}\text{Se}_{0.85}$  implanted with  $1.5 \times 10^{13} \text{ cm}^{-2}$  gallium at 120 keV, taken at 77 K.

$\text{cm}^{-1}$ ) and Zn-S ( $308.5 \text{ cm}^{-1}$ ). The broadening of the ternary LO vibration modes and the higher TO/LO intensity ratio, compared to GaAs, result from the intrinsic disorder in the mixed crystal. Already the annealing induces an intense background originating from deep centre luminescence. The superimposed LO phonon of the Zn-Se mode shows a strong defect-induced broadening, which considerably exceeds the annealing-induced broadening in ZnSe [17]. After implantation and annealing, an even stronger increase of the phonon half-width and the TO/LO intensity ratio is observed, which leads to the conclusion that the implantation-induced defects do not reconstruct completely. The best crystalline quality was obtained for the annealing temperature of  $850^\circ\text{C}$ .

### 3.3. Electrical properties

As shown in the Raman spectra of Fig. 3, already after annealing the LO phonon of the GaAs substrate is strongly reduced and a broad

structure occurs at about the TO phonon frequency. From its resonance behaviour and its temperature-independent frequency, we conclude that this spectral feature emanates from a LO-phonon-plasmon mode in the upper GaAs substrate region as a result of Zn diffusion across the interface. A similar effect was observed for the heterostructure ZnSe/GaAs with FIR spectroscopy [17]. Since the ZnSe layers in this work are n-type even when non-implanted (see below), a hetero p-n junction occurs at the interface. Therefore, in Van der Pauw experiments, contributions from currents through the p-type GaAs region can be neglected since the p-n junction acts as two diodes, one of them reversely biased.

To judge the electrical properties of Ga-implanted layers, it is necessary to investigate non-implanted material which was also annealed for 30 s at  $850^\circ\text{C}$ . Electrical measurements at 295 K yielded a conductivity of  $6.5 \times 10^{-2} \Omega^{-1} \text{ cm}^{-1}$  and an electron concentration of  $2.5 \times 10^{15} \text{ cm}^{-3}$ . To optimize the annealing parameters, the electrical properties of ZnSe layers implanted with  $1.5 \times 10^{13} \text{ cm}^{-2}$  Ga and annealed under different conditions were studied. Acceptable electrical and optical properties were obtained for annealing temperatures between 830 and  $860^\circ\text{C}$  and annealing times between 20 and 40 s. Annealing at  $850^\circ\text{C}$  for 30 s results in a maximum conductivity of about  $10 \Omega^{-1} \text{ cm}^{-1}$ . To investigate upper limitations of carrier activation and the dependence of the Hall ratio  $r_{\text{H}} = \mu_{\text{H}}/\mu$  ( $\mu_{\text{H}}$  is the measured and  $\mu$  the actual parameter) on ion dose, Hall measurements for various ion doses between  $3.5 \times 10^{12}$  and  $7.5 \times 10^{14} \text{ cm}^{-2}$  were performed. The implantation energies were 120 or 240 keV. Fig. 4 shows the dependence of the sheet Hall carrier concentration  $n_{\text{H}}$  of ZnSe on ion dose  $N_0$  for two  $E_{\text{ion}}$ , measured at 77 and 295 K. For  $N_0 < 1.5 \times 10^{13} \text{ cm}^{-2}$ ,  $n_{\text{H}}$  increases with increasing  $N_0$ . In the range  $1.5 \times 10^{13} \leq N_0 \leq 3.75 \times 10^{14} \text{ cm}^{-2}$ ,  $n_{\text{H}}$  remains nearly constant at about  $(5-6) \times 10^{12} \text{ cm}^{-2}$  at 295 K. In order to derive the corresponding volume concentrations, we approximate the gaussian dopant profile by a rectangular profile having a width of  $2\sqrt{3} \Delta R_p$  and a dopant concentration of  $N_0/2\sqrt{3} \Delta R_p$ . Both projected range ( $R_p$ ) and projected range standard

deviation ( $\Delta R_p$ ) depend approximately linearly on  $E_{\text{ion}}$  [20]. From EPMA we obtained that for  $E_{\text{ion}} = 240$  keV,  $R_p$  and  $\Delta R_p$  are 108 and 52 nm, respectively. At 120 keV these values are lower by a factor of about two. Using this approximation,  $n_{\text{H}}$  follows to be  $(2.8\text{--}3.3) \times 10^{17} \text{ cm}^{-3}$  for  $E_{\text{ion}} = 240$  keV and  $(5.6\text{--}6.6) \times 10^{17} \text{ cm}^{-3}$  for  $E_{\text{ion}} = 120$  keV. The measured mobilities can be used to determine the compensation ratio  $\theta$  and the Hall ratio. Briot et al. have calculated  $\mu_{\text{H}}$  and  $r_{\text{H}}$  as functions of the Hall constant  $R_{\text{H}}$  which is the direct experimental parameter [21]. Table 2 shows  $\theta$  and  $r_{\text{H}}$  versus ion dose. The compensation ratio is about 0.5 at low ion doses and saturates at 0.9 at ion doses beyond  $7.5 \times 10^{13} \text{ cm}^{-2}$ .

For  $\text{ZnS}_{0.3}\text{Se}_{0.7}$  and  $\text{ZnS}_{0.4}\text{Se}_{0.6}$ , Hall measurements yielded conductivities below  $10^{-8} \Omega^{-1} \text{ cm}^{-1}$ , i.e. the layers are semi-insulating. This may

Table 2

Comparison of  $\mu_{\text{H}}$ ,  $R_{\text{H}}$ ,  $\theta$  and  $r_{\text{H}}$  at different ion doses; the measurements were performed at 295 K

$N_0$ ( $10^{13} \text{ cm}^{-2}$ )	$R_{\text{H}}$ ( $\text{cm}^3/\text{As}$ )	$\mu_{\text{H}}$ ( $\text{cm}^2/\text{V}\cdot\text{s}$ )	$\theta$	$r_{\text{H}}$
0.35	68	380	0.5	1.1
0.75	38	290	0.7	1.1
1.5	34	270	0.8	1.2
7.5	32	180	0.85	1.2
35	31	120	0.9	1.3
75	28	130	0.9	1.3

be explained by the degraded crystalline quality of the layers as observed from the Raman spectra in Fig. 3. Besides, the effective dopant concentration is diminished by the Ga segregation, which was observed by EPMA.

#### 4. Conclusions

We have shown that Ga implantation profiles in ZnSe do not broaden evidently, even during annealing at 850°C. With increasing ion dose the free electron concentration saturates and the compensation ratio increases to 0.9. This can be explained by the formation of  $[\text{V}_{\text{Zn}}\text{--Ga}_{\text{Zn}}]$  complexes, as observed from a DAP peak in PL. In the case of  $\text{ZnS}_{1-x}\text{Se}_x$  ( $0 < x \leq 0.4$ ), anomalous diffusion during annealing leads to post-implantation profiles which are located at the surface within a depth below 40 nm. Best crystalline properties were observed after annealing for 30 s at 850°C. Besides an optically observed high hole concentration at the unintentionally doped interface region, from Hall measurements performed at ZnSe layers we derived an upper limit for the electron concentration of about  $6.5 \times 10^{17} \text{ cm}^{-3}$ , which is quite low with a view to electronic applications.

#### 5. Acknowledgements

The authors would like to thank Prof. Dr. K. Heime for the fruitful discussions and M. Scholl and K.P. Geyzers for supporting this work by growing the epitaxial layers. We are indebted to

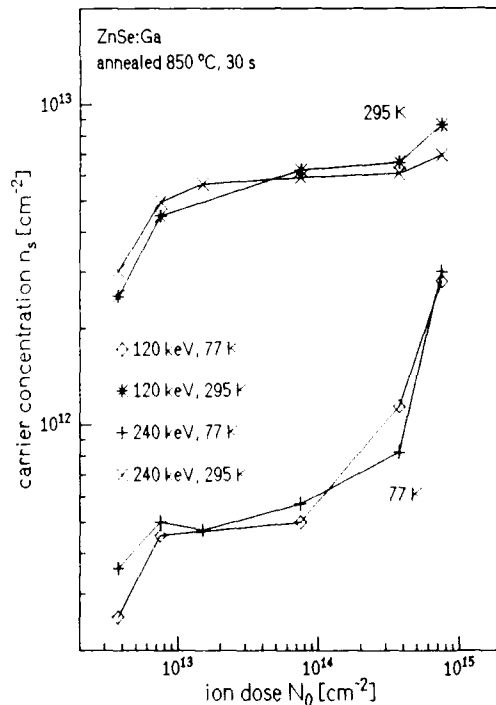


Fig. 4. Sheet carrier concentrations versus ion doses for different implantation energies annealed at 850°C for 30 s.



the "Deutsche Forschungsgemeinschaft" for financial support.

## 6. References

- [1] M. Nägele, D. Weckendrup, U. Neukirch and J. Gutowski, *Adv. Mater. Opt. Electron.*, in press.
- [2] M. Umlauff, H. Kalt, W. Langhein, O. Wind, K.P. Geysers and M. Heuken, *Adv. Mater. Opt. Electron.*, in press.
- [3] T. Yodo, K. Ueda, K. Morio, K. Yamashita and S. Tanaka, *J. Appl. Phys.* 68 (1990) 3212.
- [4] B.J. Skromme, S.M. Shibli, J.L. de Miguel and M.C. Tamargo, *J. Appl. Phys.* 65 (1989) 3999.
- [5] T. Miyajima, H. Okuyama, K. Akimoto, Y. Mori, L. Wei and S. Tanaka, *Appl. Phys. Lett.* 59 (1991) 1482.
- [6] M. Heuken, K.P. Geysers, J. Söllner, A. Schneider, F.E.G. Guimarães and K. Heime, *J. Crystal Growth* 124 (1992) 633.
- [7] J. Söllner, M. Heuken and K. Heime, in: *Physical Concepts of Materials for Novel Optoelectronic Device Applications I: Materials Growth and Characterization*, Proc. SPIE 1361, Ed. M. Razeghi (1991) p. 963.
- [8] T. Kanda, J. Suemune, K. Yamada, Y. Kan and M. Yamanishi, *J. Crystal Growth* 93 (1988) 662.
- [9] J.W. Matthews and A.E. Blakeslee, *J. Crystal Growth* 27 (1974) 118.
- [10] S.J.B. Reed, *Electron Microprobe Analysis* (Cambridge University Press, Cambridge 1975).
- [11] L. Reimer, *Scanning Electron Microscopy*, Springer Series in Optical Sciences, Vol. 45 (Springer, Berlin, 1985).
- [12] N. Ammann and P. Karduck, in: *Microbeam Analysis 1990* (San Francisco Press, San Francisco, 1990) p. 150.
- [13] N. Ammann, G. Gleitsmann, M. Heuken, K. Heime and P. Karduck, *Microchim. Acta*, in press.
- [14] J. Gutowski, N. Presser and G. Kudlek, *Phys. Status Solidi (a)* 120 (1990) 11.
- [15] D.B. Laks, C.G. Van de Walle, G.F. Neumark, P.E. Blüchl and S.T. Pantelides, *Phys. Rev. B* 45 (1992) 10965.
- [16] J.I. Pankove, *Optical Processes in Semiconductors* (Dover, New York, 1975).
- [17] J. Geurts, J. Hermans, G. Gleitsmann, K.P. Geysers, A. Schneider, M. Heuken and K. Heime, *Physica B* 185 (1993) 174.
- [18] A. Schneider, K.P. Geysers, F.E.G. Guimarães and M. Heuken, *Adv. Mater. Opt. Electron.*, in press.
- [19] P.R. Newbury, K. Shahzad, J. Petruzzello and D.A. Cammack, *J. Appl. Phys.* 66 (1989) 4950.
- [20] J. Lindhard, M. Scharff and H.E. Schiott, *Kgl. Danske Videnskab. Selskab., Mat.-Fys. Medd.* 33 (1963) No. 14.
- [21] O. Briot, N. Briot, T. Cloitre, R. Sauvezon and R.L. Aulombard, *Semicond. Sci. Technol.* 6 (1991) A24.



ELSEVIER

Journal of Crystal Growth 138 (1994) 331–337

JOURNAL OF  
**CRYSTAL  
GROWTH**

## Correlation between electrical and structural properties of chlorine doped ZnSe epilayers grown by molecular beam epitaxy

D. Hommel <sup>\*a</sup>, B. Jobst <sup>a</sup>, T. Behr <sup>a</sup>, G. Bilger <sup>b</sup>, V. Beyersdorfer <sup>a</sup>, E. Kurtz <sup>a</sup>,  
G. Landwehr <sup>a</sup>

<sup>a</sup> *Physikalisches Institut, Universität Würzburg, D-97074 Würzburg, Germany*

<sup>b</sup> *Zentrum für Sonnenenergie und Wasserstoffforschung, D-70569 Stuttgart, Germany*

### Abstract

ZnSe epilayers have been studied by Van der Pauw measurements, *C–V* profiling, SIMS, TEM and X-ray diffraction in order to correlate electrical and structural properties. At least up to  $10^{19} \text{ cm}^{-3}$ , SIMS and electrical data are in good agreement, indicating a high efficiency of the chlorine incorporation at optimum growth conditions. Homogeneously and planar doped epilayers have been grown either directly on the (100) GaAs substrate or on an undoped, relaxed ZnSe buffer layer. For a given SIMS concentration of chlorine atoms, the free carrier concentration can be enhanced up to one order of magnitude for planar doped samples. The influence of a relaxed buffer layer on dopant activation and depth profile is discussed and correlated to dislocation distribution determined by TEM.

### 1. Introduction

The superiority of group VII elements as donor dopants in ZnSe has been early established [1]. In metalorganic chemical vapour deposition (MOCVD), iodine is widely used [2], whereas for n-type doping of ZnSe epilayers grown by molecular beam epitaxy (MBE),  $\text{ZnCl}_2$  is taken as source material [3,4]. Free electron concentrations of up to  $10^{19} \text{ cm}^{-3}$  can be obtained reproducibly. In contrast to  $\text{CdTe:Cl}$  layers, where the free carrier concentration reaches a maximum at  $2 \times 10^{18} \text{ cm}^{-3}$  and decreases with further increase of the  $\text{ZnCl}_2$  cell temperature [5], no such

strong compensation was found for  $\text{ZnSe:Cl}$ . From XPS studies on  $\text{ZnCl}_2$ -doped CdTe follows further that Cl is incorporated as a single impurity. The Zn:Cl ratio was 1:2, but no chemical shifts due to Zn–Cl bonds were found [6]. Besides Hall and Van der Pauw measurements, a powerful tool is electrochemical *C–V* profiling [7]. A new approach to n-type doping was introduced by Zhu et al. [8]. They found that planar doped  $\text{ZnSe:Cl}$  layers are superior to uniformly doped ones, especially for high Cl doping. Homoepitaxial growth on ZnSe substrates has been compared to  $\text{ZnSe/GaAs}$  heteroepitaxy for n-type  $\text{ZnSe:Cl}$  layers by Ohkawa et al. [9]. They found a higher peak mobility for Cl-doped homoepitaxial layers.

Detailed studies of the correlation between electrical and structural properties are still of current interest due to application in ZnSe-based

<sup>\*</sup> Corresponding author.

blue-green laser diodes [10,11]. Serious efforts are made to study degradation mechanisms, which are closely related to crystalline perfection and dislocation behaviour. Therefore, a better understanding and optimization of doping conditions will be very helpful.

## 2. Sample preparation and experiment

All ZnSe:Cl epilayers were grown on (100) GaAs substrates in a 6-chamber Riber 2300 MBE system using elemental sources for Zn and Se from Asahi Osaka and  $\text{ZnCl}_2$  for doping. For the ternary  $\text{ZnS}_{1-x}\text{Se}_x$  epilayers, ZnS has been used as a source material to obtain lattice matching to the GaAs substrate. The substrate temperature was 300°C. The Se:Zn beam pressure ratio was varied from 1:1 (Zn-rich,  $(2 \times 2)$  reconstruction) to 2:1 (Se-rich growth,  $(2 \times 1)$  RHEED pattern). Typical thicknesses of homogeneously doped ZnSe:Cl epilayers and of undoped ZnSe buffer layers were 1  $\mu\text{m}$  and 600 nm, respectively. For planar doping, a sequence of 2 nm ZnSe:Cl and 8 nm undoped ZnSe has been repeated 50 times, resulting in a total thickness of 500 nm.

Recently a new growth chamber for GaAs has been connected to the three II–VI growth chambers. This allows a careful oxide desorption under As partial pressure and the growth of n-type GaAs:Si buffer layers. The substrate is then transferred directly to the ZnSe growth chamber. The first promising results are discussed in the last section.

Electrical measurements have been performed either in the Van der Pauw configuration getting Hall mobilities and average carrier concentrations, or by electrochemical  $C-V$  profiling giving information about the net doping profile as a function of grown layer thickness. For the latter case a  $C-V$  profiler 4800 from BIO-RAD has been used successfully. Sulphur composition and full width at half maximum (FWHM) of X-ray rocking curves ( $(400)$  reflection) have been measured by a high-resolution X-ray diffractometer, consisting of a four-reflection Bartels monochromator and a single analyser crystal. In order to determine the total amount of Cl atoms incorpo-

rated, secondary ion mass spectroscopy (SIMS) measurements were performed. Using positive ion SIMS, the matrix elements Zn and Se can be measured, whereas negative ion SIMS allows us to detect Se and Cl. The ratio of the Se/Cl counts is then calibrated to the Cl concentration measured for highly doped samples ( $10^{20} \text{ cm}^{-3}$ ) by X-ray photoemission spectroscopy (XPS). Using the XPS calibration, the absolute Cl content can then be determined by SIMS for lower doped samples, too. Cross-sectional transmission electron microscopy (TEM) was used to get information about the depth dependence of the dislocations in the doped epilayers. Details concerning the TEM method can be found elsewhere [12].

## 3. Experimental results

### 3.1. Homogeneous doping

While for the first grown ZnSe:Cl epilayers with high free carrier concentration ( $8 \times 10^{18} \text{ cm}^{-3}$ ) the FWHM of the  $(400)$  reflection was as high as 620 arc sec, this value could be reduced later on for the same electron concentration to 220 arc sec, which corresponds to the best results ever reported [3]. The improved structural quality of the epilayers is connected with the fact that, for fixed Se and Zn fluxes during MBE growth, a significantly lower Cl-cell temperature (e.g. lower Cl flux) was used. In that case less Cl is incorporated into the ZnSe host lattice. In line with this, the electrical efficiency of the Cl incorporation could be enhanced drastically comparing SIMS and Van der Pauw data. In the former case, less than 10% of the incorporated Cl atoms contributed to the free carrier concentration; in the latter case, a total amount of  $1 \times 10^{19} \text{ cm}^{-3}$  resulted in a free electron concentration of  $n = 8 \times 10^{18} \text{ cm}^{-3}$ . Electrically inefficient Cl incorporation means that the Cl atoms, which do not act as donors (Cl on Se lattice site), create deep compensating complexes, providing a decrease of the crystalline quality.

For low doping levels with a net donor concentration of less than  $10^{17} \text{ cm}^{-3}$ , a freeze-out of electrons is observed with decreasing tempera-

Table 1

Comparison between samples grown by planar doping (pl) with buffer (bu) and uniform doping (uni) method: concentration values and effective  $\text{ZnCl}_2$  cell temperature are averaged in case of planar doping

Sample	$T_{\text{Cl,eff}}$ (°C)	$N_{\text{Cl}}$ ( $\text{cm}^{-3}$ )	$n$ ( $\text{cm}^{-3}$ )	$\mu_n$ ( $\text{cm}^2/\text{V}\cdot\text{s}$ )
ZS-n 26 pl + bu	157	$1.8 \times 10^{20}$	$1.0 \times 10^{19}$	$1.2 \times 10^2$
ZS-n 8 uni	160	$9.6 \times 10^{19}$	$2.9 \times 10^{18}$	$0.5 \times 10^2$
ZS-n 27 pl + bu	137	$1.4 \times 10^{19}$	$4.0 \times 10^{18}$	$1.2 \times 10^2$
ZS-n 9 uni	140	$9.0 \times 10^{18}$	$3.1 \times 10^{17}$	$0.5 \times 10^2$

ture. From Van der Pauw data, plotted versus inverse temperature, the donor activation energy, measured for different samples, can be estimated to be 22 meV. Hall mobilities for an epilayer with  $n = 1 \times 10^{17} \text{ cm}^{-3}$  are  $400 \text{ cm}^2/\text{V}\cdot\text{s}$  at 300 K and  $1000 \text{ cm}^2/\text{V}\cdot\text{s}$  at 85 K (Fig. 1). This value is close to that reported for homoepitaxy [9]. The temperature dependence can be fitted for higher temperatures to  $T^{-3/2}$ , indicating a dominant scattering by optical phonons, and for lower temperatures to  $T^{-3/2}$ , as expected for ionized impurity scattering. Results given below are compared for samples grown under similar growth conditions and are therefore comparable to each other.

### 3.2. Planar doping and influence of buffer layers

Measuring planar doped  $\text{ZnSe}:\text{Cl}$  layers by the Van der Pauw method, an average carrier concentration is obtained. Also, with  $C$ - $V$  profiling measurements such thin layer structures (2 nm doped, 8 nm undoped) cannot be resolved. From SIMS results of Zhu et al. [8] can be concluded that no significant diffusion of Cl atoms takes place. Knowing the dependence of the measured Cl fluxes on the  $\text{ZnCl}_2$  cell temperatures

and relating it to the other parameters like Zn and Se fluxes during epilayer growth, a so-called effective Cl-cell temperature can be provided. This allows us to compare the averaged electrical properties of planar doped structures (Table 1) and the doped regions themselves (Table 2) to uniform doping. In both cases, the absolute SIMS concentrations are similar, although the planar doped epilayers have significantly higher free carrier concentrations.

To separate the contribution from planar doping and undoped buffer layers, uniform (Table 3) and planar (Table 4) doped  $\text{ZnSe}:\text{Cl}$  samples, grown directly on the GaAs substrate or a relaxed undoped ZnSe buffer are compared. While the growth on a buffer enhances the free carrier concentration by a factor of five for uniformly doped layers, no such dependence could be found for planar doped layers. The FWHM value of the X-ray diffraction, being a measure of crystalline quality, is in the case of uniform doping much smaller when growing on a relaxed buffer. This effect is less pronounced in the case of planar doping. To make these results more reliable, a pair of uniform and planar doped epilayers of the same total thickness have been grown on un-

Table 2

Comparison as in table 1; here concentration values and effective  $\text{ZnCl}_2$  cell temperature refer to doped regions in case of planar doping

Sample	$T_{\text{Cl,eff}}$ (°C)	$N_{\text{Cl}}$ ( $\text{cm}^{-3}$ )	$n$ ( $\text{cm}^{-3}$ )	$\mu_n$ ( $\text{cm}^2/\text{V}\cdot\text{s}$ )
ZS-n 26 pl + bu	190	$9.0 \times 10^{20}$	$5.0 \times 10^{19}$	$1.2 \times 10^2$
ZS-n 5 uni	190	No result	$1.3 \times 10^{18}$	$0.5 \times 10^2$
ZS-n 27 pl + bu	170	$7.0 \times 10^{19}$	$2.0 \times 10^{19}$	$1.2 \times 10^2$
ZS-n 6 uni	170	$5.0 \times 10^{19}$	$4.6 \times 10^{18}$	$0.7 \times 10^2$

Table 3

Comparison between uniform doping with and without buffer; both samples were grown at  $T_{\text{Cl,eff}} = 158^\circ\text{C}$ 

Sample	$n$ ( $\text{cm}^{-3}$ )	$N_{\text{Cl}}$ ( $\text{cm}^{-3}$ )	$\mu_{\text{h}}$ ( $\text{cm}^2/\text{V}\cdot\text{s}$ )	$\rho$ ( $\Omega\text{ cm}$ )	FWHM (arc sec)	Thickness ( $\mu\text{m}$ )
ZS-n 29 uni + bu	$1.5 \times 10^{19}$	$1.4 \times 10^{20}$	$1.3 \times 10^2$	$3.1 \times 10^{-1}$	375	1.3 ± 1.3
ZS-n 30 uni	$3.0 \times 10^{18}$	$1.2 \times 10^{20}$	$0.9 \times 10^2$	2.2	650	1.2

Table 4

Comparison between planar doping with and without buffer; both samples were grown at  $T_{\text{Cl,eff}} = 127^\circ\text{C}$ 

Sample	$n$ ( $\text{cm}^{-3}$ )	$\mu_{\text{h}}$ ( $\text{cm}^2/\text{V}\cdot\text{s}$ )	$\rho$ ( $\Omega\text{ cm}$ )	FWHM (arc sec)	Thickness ( $\mu\text{m}$ )
ZS-n 38 pl + bu	$3.8 \times 10^{18}$	$1.8 \times 10^2$	$9.0 \times 10^{-1}$	308	0.43 ± 0.65
ZS-n 37 pl	$3.1 \times 10^{18}$	$2.2 \times 10^2$	$9.4 \times 10^{-1}$	435	0.43

Table 5

Comparison between samples with buffer grown by planar doping and by uniform doping, both at  $T_{\text{Cl,eff}} = 170^\circ\text{C}$ 

Sample	$n$ ( $\text{cm}^{-3}$ )	$N_{\text{Cl}}$ ( $\text{cm}^{-3}$ )	$\mu_{\text{h}}$ ( $\text{cm}^2/\text{V}\cdot\text{s}$ )	$\rho$ ( $\Omega\text{ cm}$ )	FWHM (arc sec)	Thickness ( $\mu\text{m}$ )
ZS-n 27 pl + bu	$2.0 \times 10^{19}$	$7.0 \times 10^{19}$	$1.2 \times 10^2$	$2.6 \times 10^{-1}$	1370	0.5 ± 0.6
ZS-n 28 uni + bu	$1.0 \times 10^{19}$	$6.0 \times 10^{19}$	$1.1 \times 10^2$	4.4	1790	0.5 ± 0.6

doped relaxed buffer layers. Results given in Table 5 indicate that the doping efficiency is still higher by a factor of two for planar doping.

### 3.3. Correlation between structural and electrical properties

According to the results given in Table 3, a lower free carrier concentration is found for the direct deposition of ZnSe:Cl onto a GaAs substrate. To find out the reasons for this,  $C$ – $V$  profiles have been measured and compared to TEM cross-sectional images taken from the same samples. As can be seen in Fig. 2a, the doping level is uniform when a thick (relaxed) undoped ZnSe buffer layer has been deposited prior to the ZnSe:Cl growth. In contrast, the depth profile shows a lower electron concentration near the ZnSe:Cl/GaAs interface with a minimum at about 600 nm, followed by an increase to the level obtained for the growth on a buffer (Fig. 2b). This depth dependence is the reason for the lower average free carrier concentration obtained by Van der Pauw measurements.

This behaviour corresponds qualitatively to the TEM results (Fig. 3). Inside the first 600 nm of a ZnSe:Cl epilayer grown directly on GaAs, a high density of dislocations is observed. Therefore, the observed lower free carrier concentration might be connected with impurity gettering at such dislocations. For undoped ZnSe epilayers grown under the same conditions, similar intermediate layers with high dislocation density do not exceed 300 nm. Thus, most of the dislocations formed near the interface disappear within an undoped buffer layer. TEM pictures also confirm that no additional dislocations are formed at the ZnSe:Cl/ZnSe interface. This leads to the observed homogeneous doping profile.

### 4. Discussion

From these results it is evident that the doping efficiency depends strongly on the growth conditions and the defect and dislocation density. The lattice constant misfit between GaAs and ZnSe at room temperature is 0.26%. Exceeding the criti-

cal thickness of about 150 nm, the ZnSe epilayer starts to relax and to reduce its elastic strain by the formation of misfit dislocations. All of our ZnSe:Cl epilayers show a high density of dislocations below a thickness of 600 nm when grown directly on a GaAs substrate. This leads to a lower doping efficiency, because at least part of the incorporated Cl atoms are not on a Se lattice site, thus not acting as donors. Unrelated acceptor defects due to complexes caused by the mentioned lattice imperfections may also contribute to the observed decrease in free carrier concentration. From luminescence measurements, no evidence for significant concentrations of other single impurities acting as compensating acceptors could be found. Therefore, the growth on an undoped ZnSe buffer has two advantages. Most of the dislocations occur at a thickness well below 300 nm and no additional dislocations are formed

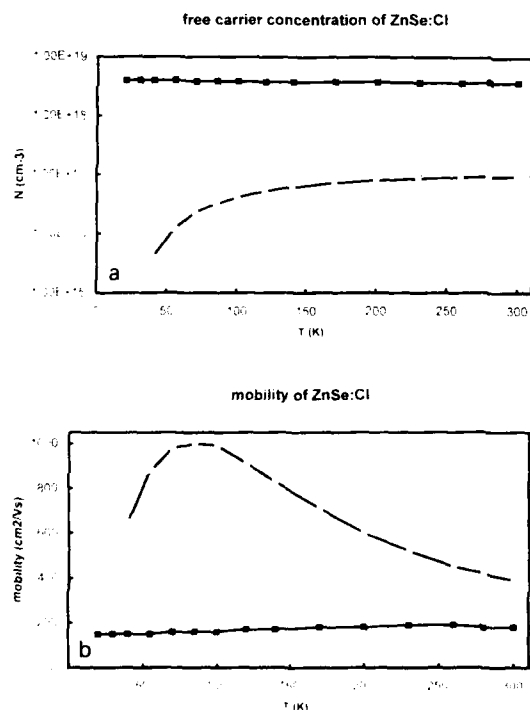


Fig. 1. Temperature dependence of the free carrier concentration and mobility measured by the Van der Pauw method for a lightly and a degenerately doped ZnSe:Cl epilayer.

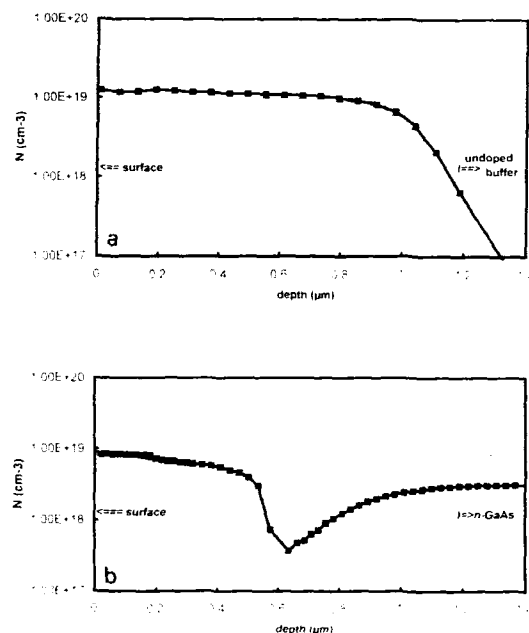


Fig. 2. Free carrier concentration profile determined by electrochemical  $C-V$  profiling for uniformly doped layers grown on a relaxed undoped ZnSe buffer (a) and directly on the GaAs substrate (b).

at the interface ZnSe:Cl/ZnSe. Both findings have been confirmed by cross-sectional TEM. For device application such an undoped buffer is not helpful. Other methods of improving the ZnSe/GaAs interface quality are therefore needed.

The growth of GaAs buffer layers leads to superior interface qualities. The FWHM of a 1 μm ZnSe epilayer could be reduced from typically 350 to 220 arc sec, indicating a much lower dislocation and defect density near the interface ZnSe/GaAs(buffer). Nearly lattice matched  $\text{ZnS}_{0.05}\text{Se}_{0.95}$  has been grown on a GaAs buffer with a half-width as narrow as 32 arc sec. Without a GaAs buffer such ternary layers had at best a FWHM of 110 arc sec. An n-type doped ternary layer with  $6 \times 10^{17}$  cm⁻³ carrier concentration had a room temperature mobility of 300 cm²/V·s, which is a good value for this doping level. Peak mobilities are not as high as for binary ZnSe:Cl epilayers, indicating additional scatter-

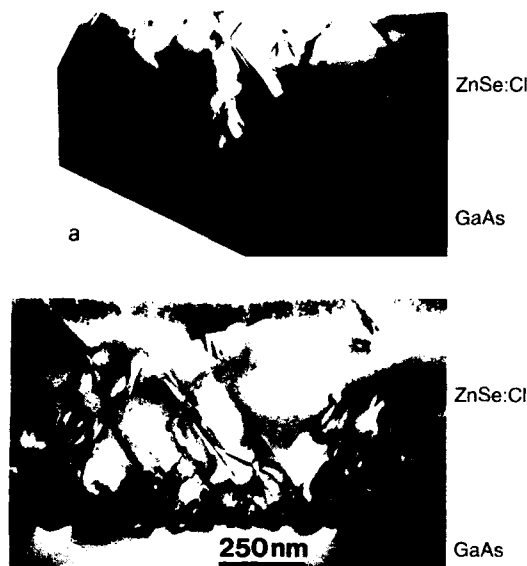


Fig. 3. Cross-sectional TEM image of a chlorine doped ZnSe epilayer grown on a GaAs substrate. Inside the first 600 nm a high density of dislocations is observed, which corresponds well to the observed decrease in free carrier concentration.

ing processes at low temperatures due to alloy fluctuations. Further detailed studies are needed to get a more quantitative understanding of the doping behaviour of ternary layers. There seems to be a competition between the incorporation of chlorine and sulphur, too, because higher ZnS cell temperatures (higher fluxes) have to be used in order to obtain the same composition compared to undoped  $\text{ZnS}_{1-x}\text{Se}_x$ . Although further detailed investigations are needed, one can predict that more uniform doping and higher mobilities due to better crystallinity can be achieved when growing on GaAs buffer layer.

The thin planar layers have an at least one order of magnitude higher free electron concentration compared to uniform doping without a buffer layer. This effect is even more pronounced for higher doping levels. Based on luminescence spectra (ratio of the excitonic emission to the deep-level emission) and RHEED observations, Zhu et al. [13] argued that a better crystallinity is responsible for that. This can be confirmed by

our X-ray diffraction measurements, too. Assuming that the ZnSe lattice recovers during the undoped parts or such a planar doping period, one should doubt whether the doping level can be easily controlled by changing the period of the Cl doping, as stated in ref. [13].

Even when the growth occurs on relaxed undoped buffer layers, higher free carrier concentrations can be obtained by the planar doping method. On the other hand, it has been demonstrated by us (Table 4) that such a buffer layer has a negligible influence in the case of planar doping. This is in accordance with the  $C-V$  profile measurements, where the part disturbed by high density of dislocations near the interface is much smaller and does not exceed 100 nm, a thickness much below that for uniform doping (about 600 nm). It indicates that the periodically changed growth conditions during planar doping hamper the propagation of dislocations into the bulk. Detailed TEM studies are under way.

It should be mentioned here that our studies on p-type doping with nitrogen using an Oxford plasma source yield the astonishing result that, besides p-type conduction in the high  $10^{17} \text{ cm}^{-3}$  also stable n-type conductivity up to  $2 \times 10^{17} \text{ cm}^{-3}$  can be obtained by changing the ZnSe growth regime and the plasma source parameters. This can be taken as an indication that nitrogen doping, giving an acceptor on the Se-site, cannot only provide compensating defects, but can also create efficiently complex donor-like centres in ZnSe. Detailed investigations are under way and should give a better understanding of the defect chemistry in ZnSe related compounds under heavy doping. Results will be published soon [14].

## 5. Conclusion

It has been shown that the higher free carrier concentration obtained by planar doping and the improved electrical properties can be correlated to the dislocation density found in cross-sectional TEM studies when growing on a relaxed buffer layer.  $C-V$  measurements of a uniformly doped ZnSe:Cl epilayer grown directly on the GaAs substrate show a depth profile with a reduced

carrier density in the first 600 nm. This explains the lower average electron concentration compared to doped epilayers grown on ZnSe buffers as found by Van der Pauw measurements. First results indicate that the growth on GaAs buffer layers may significantly improve this situation.

## 6. Acknowledgments

This work is supported by the Bundesministerium für Forschung und Technologie, Bonn and partly by the Deutsche Forschungsgemeinschaft (E. Kurtz). The authors would like to thank Mrs. P. Wolf and Mr. Th. Schuhmann for assistance in sample preparation, Mr. F. Goschenhofer for thickness measurements and Mr. A. Schönteich for keeping the whole MBE system running.

## 7. References

- [1] A. Kamata, T. Uemoto, M. Okajima, K. Hirahara, M. Kawachi and T. Beppu, *J. Crystal Growth* 86 (1988) 285.
- [2] A. Yoshikawa, H. Nomura, S. Yamaga and H. Kasai, *J. Appl. Phys.* 65 (1989) 1223.
- [3] K. Ohkawa, T. Mitsuyu and O. Yamazaki, *J. Appl. Phys.* 62 (1964) 3216.
- [4] H. Cheng, J.M. DePuydt, J.E. Potts and M.A. Haase, *J. Crystal Growth* 95 (1989) 512.
- [5] D. Hommel, A. Waag, S. Scholl and G. Landwehr, *Appl. Phys. Lett.* 61 (1992) 1546.
- [6] D. Hommel, S. Scholl, T.A. Kuhn, W. Ossau, A. Waag and G. Landwehr, *Mater. Sci. Technol.* B 16 (1993) 178.
- [7] S.Y. Wang, J. Simpson, K.A. Prior and B.C. Cavenett, *J. Appl. Phys.* 72 (1992) 5311.
- [8] Z. Zhu, H. Mori and T. Yao, *Appl. Phys. Lett.* 61 (1992) 2811.
- [9] K. Ohkawa, A. Ueno and T. Mitsuyu, *J. Crystal Growth* 117 (1992) 375.
- [10] M.A. Haase, J. Qiu, J.M. DePuydt and H. Cheng, *Appl. Phys. Lett.* 59 (1991) 1272.
- [11] H. Jeon, J. Ding, W. Patterson, A.V. Nurmikko, W. Xie, D.C. Grillo, M. Kobayashi and R.N. Gunshor, *Appl. Phys. Lett.* 59 (1991) 3619.
- [12] H. Cerva and H. Oppolzer, *Progr. Crystal Growth Characterization* 20 (1990) 231.
- [13] Z. Zhu, K. Takebayashi and T. Yao, *Jap. J. Appl. Phys.* 32 (1993) 654.
- [14] E. Kurtz et al., to be published.



## Effects of C incorporation on the luminescence properties of ZnSe grown by metalorganic chemical vapor deposition

B.J. Skromme <sup>\*a</sup>, W. Liu <sup>a</sup>, K.F. Jensen <sup>b</sup>, K.P. Giapis <sup>c</sup>

<sup>a</sup> Department of Electrical Engineering and Center for Solid State Electronics Research, Arizona State University, Tempe, Arizona 85287–5706, USA

<sup>b</sup> Department of Chemical Engineering, Massachusetts Institute of Technology, Cambridge, Massachusetts 02139, USA

<sup>c</sup> Division of Chemistry and Chemical Engineering, California Institute of Technology, Pasadena, California 91125, USA

### Abstract

The effects of C incorporation in heteroepitaxial ZnSe grown on GaAs by metalorganic chemical vapor deposition (MOCVD) with methylallylselenide (MASE), diethylselenide (DESe), and hydrogen selenide (H<sub>2</sub>Se) selenium precursors together with dimethylzinc (DMZn) are investigated. The effects of growth temperature and VI/II ratio are determined. In material grown at 480°C and above, all of the low temperature photoluminescence (PL) peaks are generally shifted several meV lower in energy than in material grown in the 300–425°C range. In particular, the light hole component of the neutral donor-bound exciton shifts down to around 2.792 eV, where it was incorrectly identified in previous work as an exciton bound to a complex involving C. Detailed PL and reflectance measurements give conclusive evidence for this interpretation. The peak shifts are attributed to increased thermal mismatch strain resulting from the higher growth temperature used with MASE and DESe. However, the VI/II ratio strongly affects the strain in samples grown at 500°C using DESe, suggesting that heavy C incorporation at the ZnSe/GaAs interface may stimulate the thermal relaxation. The mechanism might involve the formation of C-related microprecipitates near the interface, which then nucleate misfit dislocations. We conclude that C from the growth precursors does not produce any new PL peaks above 1.4 eV in MOCVD ZnSe. Moreover, the room temperature PL efficiency is not degraded in C-contaminated material, suggesting that C is not an important non-radiative recombination center in ZnSe. The incorporation of moderate C levels is found to have little effect on the optoelectronic properties of MOCVD ZnSe.

### 1. Introduction

A fundamental concern in the MOCVD growth of any electronic material is the possibility of unintentional incorporation of C from the organic component of the growth precursors. In III–V

materials this problem is well known, particularly in the case of Al-containing compounds, where strong Al–C bonds exist. In most III–V compounds such as GaAs, C incorporates solely on the column V site as a shallow acceptor, both as a common residual impurity and in recent years as a well-behaved p-type dopant [1]. In some In-containing materials such as InGaAs and InP it is believed to be amphoteric and may substitute on

<sup>\*</sup> Corresponding author.

the cation site as a shallow donor [2], and in MBE (and occasionally MOCVD) GaAs and AlGaAs it is suspected of being involved in a complicated series of acceptor complexes that is frequently observed in PL measurements [3]. Its behavior in II–VI materials, as well as that of other column IV impurities, is much less well known at present, although it might be expected to form a double donor on a Zn site or a double acceptor on a Se site. Other column IV impurities have been observed to substitute on the Zn site in ZnSe by electron paramagnetic resonance [4], but no such information is available for C. A determination of its behavior is important in assessing the future prospects of MOCVD growth of ZnSe and related materials for optoelectronic applications, once the p-type doping problem has been solved in this growth technique.

Previous work by Giapis et al. [5–7] has shown conclusively using calibrated SIMS measurements that high levels of C incorporate in ZnSe layers grown on GaAs using MAs<sub>2</sub> and DMZn, particularly near the ZnSe/GaAs interface. The C concentration increased dramatically with VI/II ratio up to  $10^{21}$  cm<sup>-3</sup> or higher, which caused polycrystalline growth. The use of this growth precursor also caused a peculiar surface morphology and rather low electron mobilities [6]. All of these effects were absent using H<sub>2</sub>Se and DMZn at lower growth temperatures (300–325°C). These workers also observed a bound exciton peak at around 2.792 eV in low temperature PL spectra of samples grown using MAs<sub>2</sub> + DMZn at 480°C and above and DESe + DMZn at 500°C. They denoted this peak I<sup>c</sup> and attributed it to excitons bound to a C-containing complex, whose electronic nature was not determined. The occurrence of this peak was interpreted as a signature of C incorporation, and previous literature results were re-interpreted on this basis.

In the present study, we re-examine the optical properties of MOCVD material grown using MAs<sub>2</sub>, DESe, and H<sub>2</sub>Se, using detailed low temperature PL and reflectance studies. We present a new, carefully supported interpretation which demonstrates that neither the “I<sup>c</sup>” peak nor any other PL feature above 1.4 eV can be directly attributed to C incorporation, although the C

does apparently affect the relaxation of thermal strain in the material in a dramatic way. The I<sup>c</sup> peak is identified as the light hole component of the ordinary neutral donor-bound exciton, shifted by strain. We also show that C incorporation from the growth precursors in MOCVD ZnSe does not cause significant non-radiative recombination, as long as the material remains single crystal.

## 2. Experimental procedure

The growth of the not intentionally doped MOCVD samples in this study is described in ref. [6], as well as the results of the SIMS and SEM characterization of the material. The luminescence measurements in the present study were performed using a 1.0 m double spectrometer under excitation from a UV Ar<sup>+</sup> or blue dye laser, with the samples mounted strain-free in flowing superfluid or gaseous He. Reflectance was performed using a tungsten-halogen lamp. The data are corrected for the spectral response of the PL system where necessary. Room temperature PL measurements were performed with the samples in air, without any chemical etching. Undoped heteroepitaxial ZnSe/GaAs material grown by MBE and annealed using SiN<sub>4</sub> caps in a rapid thermal annealer for 5 s at various temperatures [8,9] is used to illustrate the effects of thermal relaxation on the PL spectrum for comparison to the MOCVD case. Further details of the PL apparatus are given elsewhere [10].

## 3. Results and discussion

Low temperature excitonic PL spectra are shown in Fig. 1 for three different ZnSe/GaAs samples grown using MAs<sub>2</sub> under the indicated conditions, and one reference sample grown using H<sub>2</sub>Se. A single reflectance spectrum is also shown as an example, corresponding to the uppermost PL spectrum. We interpret the dominant PL peak in each spectrum as the light hole component of the neutral donor-bound exciton in-

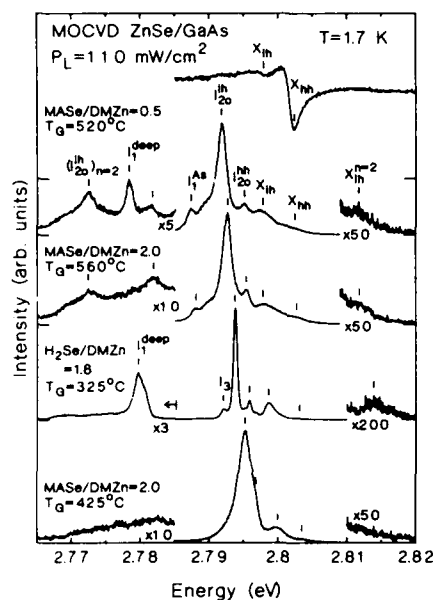


Fig. 1. Low temperature excitonic PL spectra for four MOCVD ZnSe/GaAs samples grown under the indicated conditions. The uppermost spectrum is a reflectance spectrum corresponding to the top PL spectrum. The layer thicknesses are 2.4, 1.8, 8.0, and 1.8  $\mu\text{m}$ , respectively, from top to bottom in this figure. Instrumental resolution is 0.07 meV or better in each case.

volving ordinary shallow donors,  $I_{20}^{1h}$ , which is split from the heavy hole component ( $I_{20}^{hh}$ ) by the biaxial tensile strain in the material resulting from the thermal expansion mismatch between ZnSe and GaAs [9,11]. The biaxial compressive lattice mismatch strain at the growth temperature is mostly relaxed in layers of these thicknesses [11]. The  $I_{20}^{1h}$  peak position ranges from 2.7954 to 2.7918 eV in Fig. 1. The thermal strain splits the free exciton to a larger degree into corresponding light and heavy hole components ( $X_{1h}$  and  $X_{hh}$ , respectively). The assignment of the free exciton peaks in each spectrum has been confirmed using reflectance spectra, as shown for the uppermost PL spectrum in Fig. 1. The  $X_{1h}$  and  $X_{hh}$  PL peaks precisely match the energies of the reflectance dips in this case, as they did in the other samples (not shown). The shift in the  $n=2$  free exciton PL peaks ( $X_{1h}^{n=2}$ ), which remain about 14.6 meV

above the ground state, further confirms our interpretation.

All of the samples we have examined that exhibit a peak near 2.792 eV also show correspondingly increased free exciton splittings and shifts. In particular, the *average* of the  $I_{20}^{1h}$  and  $I_{20}^{hh}$  peak positions, and the *average* of the  $X_{1h}$  and  $X_{hh}$  positions, both of which should reflect only the *hydrostatic* strain, are separated by about 5.6–6.2 meV from each other in all of the samples with various strains, in reasonable agreement with the known 4.9–5.7 meV (depending on the donor) localization energies of neutral donor-bound excitons in unstrained ZnSe [12]. The absence of reflectance or other similar measurements in refs. [5–7] was probably responsible for the failure there to recognize the increased strain and free exciton splitting in the MASE samples grown at 480°C and above, and for the incorrect assignment of the PL peaks in those studies (the  $I_{20}^{1h}$  peak was associated with C ("I"), while the  $I_{20}^{hh}$  peak was misidentified as  $I_{20}^{1h}$  in the MASE samples.)

Each of the samples in Fig. 1 is seen to have a different degree of strain, which correlates loosely with the growth temperature as would be expected. To measure the strains we use the observed light hole free exciton position, which is generally easier to measure than the heavy hole position and more sensitive to strain. With deformation potentials  $a = -4.35$  and  $b = -1.06$  eV obtained from our recent study of strain splitting in pseudomorphic ZnSe/InGaAs [13], and elastic coefficients  $c_{11} = 88.3$  and  $c_{12} = 53.1$  GPa from an average of the results quoted in ref. [14], we determine the tensile strain to be approximately  $1.01, 0.88, 0.78$ , and  $0.59 \times 10^{-3}$  for the top through bottom samples in Fig. 1, respectively. However, the dependence is not monotonic, since the 325°C sample grown with  $\text{H}_2\text{Se}$  has more net strain than the MASE sample grown at 425°C, and the 560°C sample is less strained than the 520°C sample. Clearly, then, the relaxation of thermal mismatch strain at the growth temperature, which is frozen in upon cooling down, depends on factors other than just the growth temperature. These factors are probably related to the kinetic limitations on the nucleation and mul-

tiplication of misfit dislocations near the interface [15]. This point will be further amplified in connection with Fig. 3. However, the growth temperature obviously places an upper limit on the amount of this strain that can occur. Calculations based on the thermal expansion of ZnSe and GaAs as a function of temperature as given in ref. [16] yield maximum expected strains of 0.88, 1.20, 1.58, and  $1.75 \times 10^{-3}$  for growth temperatures of 325, 425, 520, and 560°C, respectively, all of which exceed the corresponding experimental values quoted above.

Further support for the varying amounts of strain in the samples of Fig. 1 is obtained by noting that the ionized donor-bound exciton ( $I_1$ ), neutral As (or Li) acceptor-bound exciton  $I_1^A$  [10,17], and deep Cu acceptor bound exciton ( $I_1^{\text{deep}}$ ) [18] peaks all shift to lower energies along with the  $I_2$  and free exciton peaks. For example, the  $I_1^{\text{deep}}$  peak shifts from 2.7797 to 2.7784 eV in the 325°C and 520°C samples, and the lower energy  $I_1^A$  component (the only one visible at 1.7 K) shifts from 2.7879 to 2.7873 eV in the 560 and 520°C samples. A good quantitative modeling of the latter data can be achieved using calculations based on the theory given in refs. [10] and [17], if the strains are estimated from the observed  $X_{1h}$  positions. To achieve a good fit to data taken on these and other samples over a wide range of strains, we use a shear deformation potential for the acceptor-bound hole of  $b = -0.55$  eV, derived from our recent independent measurement of strain-induced splittings in the band-to-acceptor peak, and we assume that the zero-strain peaks lie in the range 2.7919–2.7923 eV [12]. This procedure predicts  $I_1^A$  positions of 2.7880 and 2.7874 eV for the 560 and 520°C samples, respectively, in excellent agreement with experiment.

A further confirmation of the excitonic peak assignments comes from the observation of a two electron replica 19.5–20.0 meV below the  $I_{20}^h$  peak in the 520 and 560°C samples. In contrast to the statements in refs. [5–7], selective excitation of  $I_{20}^h$  using a tunable dye laser does yield clear resonant enhancement of this two-electron replica, proving the nature of the  $I_{20}^h$  peak. In addition, the LO phonon coupling strength of the  $I_{20}^h$  peak (not shown in Fig. 1) is characteristic of

the  $I_{20}$  peaks in ZnSe, and should be substantially larger if the peak were due to an acceptor or isoelectronic trap-bound exciton.

We have examined the thermalization and excitation intensity-dependent behavior of several of the excitonic spectra of samples in Fig. 1 (and in Fig. 3 below) with both larger and smaller thermal strains. We find similar behavior independent of strain, including the previously established thermalization between  $I_{20}^h$  and  $I_{20}^b$  and between  $X_{1h}$  and  $X_{hh}$  [19], and the thermal ionization of the  $I_{20}$  peaks in favor of the free excitons at high  $T$  [19]. The  $I_{20}$  peaks also show the expected saturation in favor of the free exciton peaks at high excitation levels. All of these observations provide strong evidence for our interpretation of the excitonic spectra.

Strong support for the effects of thermal strain on the PL spectrum of the MOCVD material is provided by a comparison to excitonic spectra of MBE samples annealed at various temperatures, as shown in Fig. 2. The most notable effect of annealing is the introduction of a dominant  $I_1^{\text{deep}}$  peak, resulting from the generation of Zn vacancies during the anneal and their occupation by Cu impurities, as discussed previously [8]. However, we also observe a shift to lower energy and increased splitting of both the  $I_{20}$  and  $X$  components, similar to that we reported earlier [9]. The peaks in the sample shown here, however, are much sharper than those in the earlier case, due to use of purer source materials in the MBE growth. The splittings are thus even clearer in the present case. The splitting of  $I_{20}$  is less than that of  $X$ , which is just due to the reduced shear deformation potential of the hole in the bound exciton complex [19]. The main point to be made in comparing Figs. 1 and 2 is that the 700°C anneal produces peak positions that closely match those in the MASE sample grown at 560°C, even though the annealed samples contain negligible carbon. (The positions in the unannealed sample match those in the sample grown at 425°C, while the upper 500°C annealed sample matches the 325°C MOCVD sample.) The higher annealing temperature necessary to achieve thermal relaxation in the MBE material similar to that for MOCVD growth at much lower temperatures is

evidence of the kinetic limitations to relaxation and the influence of interfacial C (to be discussed below), although the sample temperature during the rapid thermal anneal is a little uncertain due to the nature of the annealing system. Moreover, anneals at nominally the same temperature with, e.g., different caps typically produced varying amounts of strain (see Fig. 2).

As an indication of the vastly different thermal strains that can occur at a given temperature, we show excitonic PL and reflectance spectra in Fig. 3 for two samples grown using DESe and DMZn at 500°C, where the only difference in growth conditions is the VI/II ratio. The reflectance spectra, as well as the  $n=2$  free exciton and two-electron replica peaks in the PL spectra confirm the difference in strain (0.67 versus  $1.06 \times$

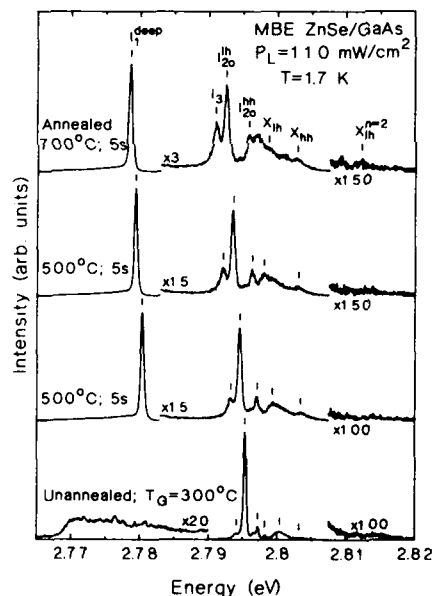


Fig. 2. Low temperature excitonic PL spectra for a virgin undoped  $8.4 \mu\text{m}$  thick MBE ZnSe/GaAs layer grown at 300°C (bottom spectrum), and for the same layer after annealing at each of the indicated temperatures. Resolution is 0.03 meV. The two samples annealed at 500°C differed only in the system used to deposit the  $\text{SiN}_x$  cap prior to annealing; the difference between these two samples illustrates that, as in the MOCVD material, the dependence on temperature is not one-to-one. The peak positions should be compared to those in Fig. 1.

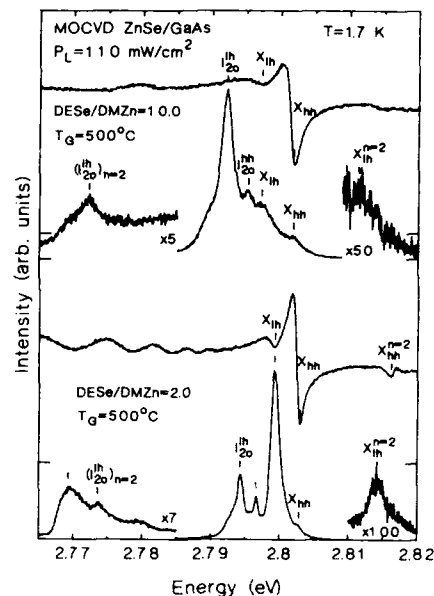


Fig. 3. Low temperature reflectance and PL spectra for two samples grown at different VI/II ratios using DESe (each reflectance spectrum is directly above the corresponding PL spectrum). The layer thicknesses are 2.7 and  $5.7 \mu\text{m}$  for the VI/II = 10.0 and 2.0 samples, respectively. Resolution is 0.07 meV in each case.

$10^{-3}$ , based on the  $X_{1h}$  positions). This difference was not recognized in the earlier work, which led to the erroneous conclusion that the 2.792 eV peak in the upper PL spectrum was a new, C-related peak. Since the  $I_2$  peaks are much stronger relative to the free excitons at high VI/II ratio, we conclude that this condition strongly favors the incorporation of residual donors (possibly halogens). Moreover, these conditions are chemically expected to produce increased C incorporation at the ZnSe/GaAs interface, similarly to the MASE case [5–7]. Since donor doping has never been observed to enhance strain relaxation in ZnSe, to our knowledge, and since all samples grown with DESe showed the characteristic behavior shown in Fig. 3, we attribute the enhanced relaxation in the DESe samples grown at high VI/II ratios and in the MASE samples grown at 480°C or above to the interfacial C present at high VI/II ratios.

The effects of C on structural properties of the

films are made plausible by a comparison to the case of heavy doping with N, a similarly small atom, which has been found to alter the configuration of misfit dislocations at the ZnSe/GaAs interface in a drastic way [20,21]. However, the N doping reportedly reduced the amount of strain relaxation in layers of a given thickness [20], whereas we find an increase in the case of C. Also, the large and consequently not very soluble Na atom has been found to generate dislocations in MBE ZnSe/GaAs when used as a dopant [22]. We speculate that in the case of C (and possibly in the Na case as well), microprecipitates may be formed near the interface, which act as nucleation sites for misfit dislocations. The precise mechanism by which these dopants affect the structural properties remains to be established by further experimental work, but is an important consideration relevant to the reliability of light-emitting devices based on this material.

No new donor-to-acceptor ( $D^0-A^0$ ) or band-to-acceptor ( $e-A^0$ ) peaks were observed in any of the MASE or DESe samples having high C concentrations, indicating that C does not form any shallow acceptor level in this MOCVD material. The As or Li (which have virtually indistinguishable binding energies [10,17]) acceptor-related ( $D^0-A^0$ ) and ( $e-A^0$ ) peaks were, however, observed to shift to lower energy by the expected amount in the DESe sample having higher strain (i.e. grown at VI/II = 10.0), which further proves our interpretation of the excitonic PL spectra. In fact, a clear strain splitting of the ( $e-A^0$ ) peak at 1.7 K into light and heavy hole components was observed in some of the more highly strained samples. The deep level PL peaks were typically stronger in samples that have higher C content, but these samples also have higher residual donor concentrations, and the deep level peaks we observe (aside from the usual Y and S bands) are generally those around 2.0 and 2.2 eV attributed to donor-Zn vacancy complexes [23], and are unlikely to be directly C-related.

To test for the presence of C-related non-radiative recombination centers, we measured the strength of the integrated room temperature PL signal (in arbitrary units), which is proportional to the internal quantum efficiency, for a number of

samples grown under high C-producing (MASE, and DESe growth at VI/II = 10.0) and low C-producing conditions (H<sub>2</sub>Se, and DESe growth at VI/II = 2.0). The results are plotted in Fig. 4 (note the logarithmic scale). The integrated total, deep level, and band edge intensities are each indicated.

The internal PL quantum efficiency is given by  $\tau_{nr}/(\tau_{rad} + \tau_{nr})$ , where  $\tau_{rad}$  and  $\tau_{nr}$  are the radiative and non-radiative minority carrier lifetimes, respectively. The radiative lifetime in the case of pure band-to-band recombination is given by  $\tau_{rad}^{-1} = Bn_0$ , where  $B$  is the radiative recombination coefficient of ZnSe and  $n_0$  is the majority carrier concentration (assuming low level injection). Since the MASE, and DESe (VI/II = 10.0) samples have higher donor impurity contents, based on the low temperature excitonic spectra, their quantum efficiency should be higher (assuming constant  $\tau_{nr}$ ). Electrical measurements were not possible in most cases [6], probably due to compensation and/or deep levels. Moreover, the importance of deep radiative levels modifies the analysis in ways that are not easy to determine without a knowledge of the deep level parameters and concentrations, so that quantitative estimates of the reduction in  $\tau_{rad}$  are not feasible. We conclude, however, that if C produced effective non-radiative recombination centers in this mate-

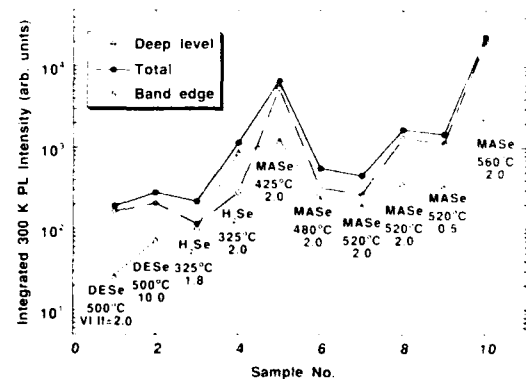


Fig. 4. Absolute integrated 300 K PL intensities for a series of MOCVD samples grown using various precursors and growth conditions. The Zn precursor was DMZn in all cases. Layer thicknesses vary from 1.8 to 9.0  $\mu\text{m}$ . The total, band edge, and deep level intensities are shown separately in each case.

rial,  $\tau_{nr} \propto [C]^{-1}$  (neglecting surface recombination) would be drastically reduced, and the PL efficiency would be degraded in the high [C] samples. Since this effect is not evident in Fig. 4, in spite of very high [C] in some cases (compare, e.g., the MAsE and  $H_2Se$  samples), we conclude that C does not form any major non-radiative defects in MOCVD ZnSe. On the other hand, the centers that do cause the several orders of magnitude variations of PL efficiency among the various samples in Fig. 4 should be identified and eliminated if the quality of the material is to be optimized.

#### 4. Conclusions

We have shown that, contrary to previous claims, C does not introduce any new bound excitons or other radiative centers in the PL spectrum of MOCVD ZnSe above 1.4 eV (the limit of the detector used in this study), and does not introduce substantial non-radiative recombination. We have not determined whether the C has any electrical activity in the material, since such effects (if any) may have been masked by incorporation of other impurities from the precursors. The presence of high interfacial C levels does apparently have a profound influence on the structural properties of the material, in particular the extent to which thermal mismatch strain relaxes at the growth temperature. While very high interfacial C levels can degrade crystallinity, morphology, and stimulate lattice relaxation, and precursors yielding these high levels should be avoided in future work, our overall conclusion is that moderate C incorporation from the precursors used in MOCVD growth has negligible effect on the optoelectronic properties of ZnSe. This conclusion implies that MOCVD should be a highly promising technique for the large-scale production of blue light-emitting devices, once the p-type doping problem in this growth technique has been solved and the structural and deep level properties of the material are fully under control.

#### 5. Acknowledgments

The ASU portion of this work was supported by the National Science Foundation under Grant No. DMR-9106359. We thank M.C. Tamargo for providing the undoped MBE sample used for comparison.

#### 6. References

- [1] See, e.g., B.T. Cunningham, M.A. Haase, M.J. McCollum, J.E. Baker and G.E. Stillman, *Appl. Phys. Lett.* 54 (1989) 1905; T.F. Kuech, M.A. Tischler, P.-J. Wang, G. Scilla, R. Potemski and F. Cardone, *Appl. Phys. Lett.* 53 (1988) 1317.
- [2] See, e.g., H. Ito and T. Ishibashi, *Jap. J. Appl. Phys.* 30 (1991) L944.
- [3] See, e.g., K. Akimoto, M. Dohsen, M. Arai and N. Watanabe, *Appl. Phys. Lett.* 45 (1984) 922, and references therein.
- [4] See R.K. Watts, *Point Defects in Crystals* (Wiley, New York, 1977) p. 255, and references therein.
- [5] K.P. Giapis and K.F. Jensen, *Appl. Phys. Lett.* 55 (1989) 463.
- [6] K.P. Giapis, K.F. Jensen, J.E. Potts and S.J. Pachuta, *J. Electron. Mater.* 19 (1990) 453.
- [7] K.P. Giapis and K.F. Jensen, *J. Crystal Growth* 101 (1990) 111.
- [8] B.J. Skromme, N.G. Stoffel, A.S. Gozdz, M.C. Tamargo and S.M. Shibli, in: *Advances in Materials, Processing, and Devices for III-V Compound Semiconductors*, Eds. D.K. Sadana, L.E. Eastman and R. Dupuis (Materials Research Society, Pittsburgh, PA, 1989) p. 391.
- [9] B.J. Skromme, M.C. Tamargo, F.S. Turco, S.M. Shibli, W.A. Bonner and R.E. Nahory, in: *GaAs and Related Compounds*, Atlanta, 1988, *Inst. Phys. Conf. Ser.* 96, Ed. J.S. Harris (Inst. Phys., Bristol, 1989) p. 205.
- [10] Y. Zhang, B.J. Skromme, S.M. Shibli and M.C. Tamargo, *Phys. Rev. B* 48 (1993) 10885.
- [11] T. Yao, Y. Okada, S. Matsui, K. Ishida and I. Fujimoto, *J. Crystal Growth* 81 (1987) 518.
- [12] P.J. Dean, D.C. Herbert, C.J. Werkhoven, B.J. Fitzpatrick and R.N. Bhargava, *Phys. Rev. B* 23 (1981) 4888. Note that the localization energy of  $I_{2,0}^1$  is apparently quoted incorrectly in this reference (the observed peak position implies a value of 5.65 meV).
- [13] B.J. Skromme, Y. Zhang, M.C. Tamargo and W.A. Bonner, presented at 5th Int. Conf. on III-VI Compounds, Tamano, Japan, 1991, unpublished.
- [14] S. Lee, B. Hillebrands, G.I. Stegeman, H. Cheng, J.E. Potts and F. Nizzoli, *J. Appl. Phys.* 63 (1988) 1914. The values in Table I of this reference were averaged, with

- the exception of the early ones by Berlincourt et al., which were excluded.
- [15] See, e.g., B.W. Dodson and J.Y. Tsao, *Appl. Phys. Lett.* 51 (1987) 1325.
- [16] Y.S. Touloukian, R.K. Kirby, R.E. Taylor and T.Y.R. Lee, Thermal expansion – nonmetallic solids, in: *Thermophysical Properties of Matter*, Vol. 13 (IFI/Plenum, New York, 1970).
- [17] Y. Zhang, B.J. Skromme and H. Cheng, *Phys. Rev. B* 47 (1993) 2107.
- [18] D.J. Robbins, P.J. Dean, P.E. Simmonds and H. Tews, in: *Deep Centers in Semiconductors*, Ed. S. Pantelides (Gordon and Breach, New York, 1986) p. 717.
- [19] B.J. Skromme, M.C. Tamargo, J.L. de Miguel and R.E. Nahory, in: *Epitaxy of Semiconductor Layered Structures*, Eds. R.T. Tung, L.R. Dawson and R.L. Gunshor (Materials Research Society, Pittsburgh, PA, 1988) p. 577.
- [20] J. Petruzzello, J. Gaines, P. van der Sluis, D. Olego, T. Marshall and C. Ponzoni, *J. Electron. Mater.* 22 (1993) 453.
- [21] L.H. Kuo, L. Salamanca-Riba, J.M. DePuydt, H. Cheng and J. Qiu, in: *Semiconductor Heterostructures for Photonic and Electronic Applications*, Mater. Res. Soc. Symp. Proc., Vol. 281, Eds. D.C. Houghton, C.W. Tu and R.T. Tung (Materials Research Society, Pittsburgh, PA, 1993) p. 561.
- [22] J.E. Potts, H. Cheng, J.M. DePuydt and M.A. Haase, *J. Crystal Growth* 101 (1990) 425.
- [23] See, e.g., B.J. Skromme, S.M. Shibli, J.L. de Miguel and M.C. Tamargo, *J. Appl. Phys.* 65 (1989) 3999, and references therein.





ELSEVIER

Journal of Crystal Growth 138 (1994) 346–351

JOURNAL OF  
**CRYSTAL  
GROWTH**

## Defect-induced emission band in CdTe

S. Seto <sup>a,\*</sup>, A. Tanaka <sup>b</sup>, F. Takeda <sup>c</sup>, K. Matsuura <sup>c</sup>

<sup>a</sup> *Isikawa National College of Technology, Tsubata, Kahoku, Ishikawa 929-03, Japan*

<sup>b</sup> *Sumitomo Metal Mining Co., Ltd. Suehiro, Ohme, Tokyo 198, Japan*

<sup>c</sup> *Department of Electrical and Electronic Engineering, Tottori University, Koyama, Tottori 680, Japan*

### Abstract

We report on a distinct correlation between the 1.47 eV emission band and the dislocation density in bulk CdTe. The 1.47 eV band intensifies around the high-dislocation area (lineage structure) and at the position just on dislocation bundle. On the other hand, the 1.47 eV band was hardly observed in the low-dislocation area (etch pit density less than  $2 \times 10^4 \text{ cm}^{-2}$ ) or at the position away from the dislocation bundle. Furthermore, the 1.47 eV band was intensified by  $\gamma$ -ray irradiation of  $1.7 \times 10^7 \text{ Gy}$ , which produced a great number of Frenkel defects. It was shown that the 1.47 eV band is related not only to an extended defect such as a dislocation, but also to a point defect such as a Frenkel defect. These results suggest that the strain field induced in the vicinity of the defects is responsible for the recombination center of the 1.47 eV band.

### 1. Introduction

Recently, CdTe films on various substrates, such as sapphire, GaAs and InSb, have been grown by molecular beam epitaxy (MBE), hot wall epitaxy (HWE) or metalorganic chemical vapor deposition (MOCVD). However, because of the large lattice mismatches between CdTe and these substrates, a high-density dislocation is generated into such heteroepitaxial CdTe layers.

For evaluating the CdTe films, the photoluminescence (PL) is a useful nondestructive technique because of its high sensitivity on the crystal quality such as residual impurities and structural defects. For example, the peak intensity ratio of

the 1.3–1.5 eV emission band to the principal bound-exciton line has been used as a measure for the crystal quality of CdTe films [1,2]. The emissions in the energy region of 1.3–1.5 eV are composed of many peaks originating from the different emission centers [3–8]. It is therefore necessary to discriminate and identify these emission bands. Among these bands, a relatively strong and unidentified emission band has often been observed around 1.47 eV (8400 Å) in CdTe crystals, especially in heteroepitaxial films. Dean et al. labeled this emission band as  $Y_0$  line [9], since the band in CdTe looks notably similar to the  $Y_0$  band in ZnSe [10]. Several authors including Dean et al. reported on the nature of the 1.47 eV band and discussed the origin of the band [9,11–13]. Dean et al. expected that the band results from electron–hole recombination at extended defects and has a characteristic of bound-exciton. Also,

\* Corresponding author.

Onodera and Taguchi have pointed out that the band behaves like a bound exciton trapped at an extended defect from the temperature dependence and time-resolved spectra of this band [12]. However, a direct comparison between the intensity of the 1.47 eV band and dislocation to confirm their interpretations for the recombination center of the band has not been reported previously.

In order to confirm directly their interpretation for the recombination center of the 1.47 eV band, we have compared the intensities of the band in the several samples with different etch pit patterns and investigated the influence of  $\gamma$ -ray irradiation on the band in bulk CdTe. On the basis of these experimental results, we discuss the origin of the 1.47 eV band.

## 2. Experimental procedure

CdTe crystals were grown by the vertical gradient freeze technique and traveling heater method (THM) from a high-purity source of 6N grade. All samples used in this study are p-type. The samples for evaluating the etch pit density (EPD) were cut parallel to {111} from the crystal ingot. After polishing, the surfaces were chemically etched to remove the surface damage due to the polishing. To evaluate the dislocation density, the etch pit patterns were revealed on {111}<sub>Cd</sub> faces by the Nakagawa etchant [14]. Irradiation was with  $^{60}\text{Co}$   $\gamma$ -rays of  $1.7 \times 10^{-7}$  Gy to investigate the influence of point defects on the 1.47 eV band.

The PL spectra were measured at 4.2 K by a conventional lock-in technique. To see the correspondence between the EPD and the PL spectrum, especially the EPD and the intensity of the 1.47 eV band, the samples were chemically etched to reveal the etch pit patterns before being loaded into a liquid-He dewar. In particular, we have paid attention to the correspondence between the position of the exciting laser beam for PL and the etch-pit pattern on that position. The PL was excited using the 5145 Å line from an Ar-ion laser. The PL signals were detected by a photo-

multiplier with a cooled GaAs cathode through a 1.5 m Jobin–Yvon single monochromator.

## 3. Results and discussion

Fig. 1 shows the PL spectra obtained from the different dislocation density areas on the same sample: Figs. 1a and 1b are the spectrum taken from the low- and high-dislocation density areas, respectively. The corresponding etch pit patterns in the vicinity of the positions measured for the spectra of Figs. 1a and 1b are shown in Figs. 2a and 2b, respectively. The EPD pictured in Fig. 2a is  $2 \times 10^5 \text{ cm}^{-2}$ . It should be noted that the high-dislocation area in Fig. 2b exhibits a lineage structure. The spectrum (Fig. 1a) taken from the low-dislocation area demonstrates that the area measured is of high quality, because: (i) a sharp acceptor bound exciton ( $A^0X$ ) line together with its LO-phonon replicas ( $A^0X\text{-LO}$ ,  $A^0X\text{-2LO}$ ,  $A^0X\text{-3LO}$ ) and the LO-phonon replicas of free excitons, FE-LO, FE-2LO, are clearly observed; (ii) no donor–acceptor pair (DAP) emissions in the 1.3–1.5 eV region, except for the weak 1.47 eV (8400 Å) band, were observed. On the other hand, the 1.47 eV band in the spectrum (Fig. 1b) taken from the high-density area intensifies and

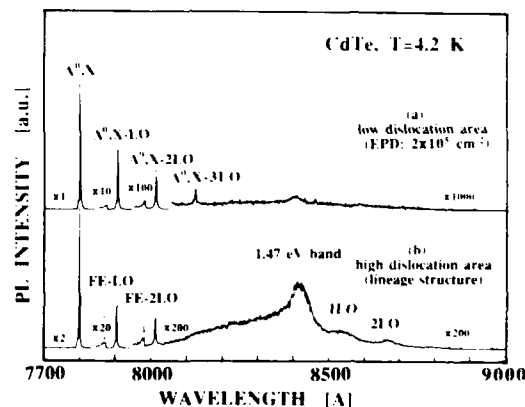


Fig. 1. PL spectra of CdTe with different dislocation density: (a) spectrum taken from low-dislocation area; (b) spectrum taken from the position with lineage structure. The corresponding etch pit patterns are shown in Fig. 2.

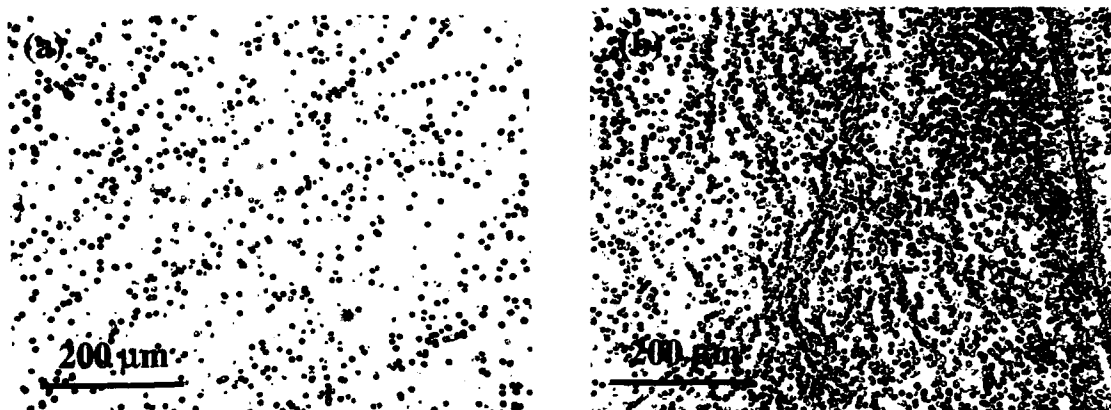


Fig. 2. Etch pit patterns in the vicinity of the laser beam positions measured for Figs. 1a and 1b, respectively. The EPD in (a) is  $2 \times 10^5 \text{ cm}^{-2}$ .

slightly shifts in energy position relative to that in Fig. 1a: the precise peak energies of the 1.47 eV bands in Figs. 1a and 1b are 1.475 eV (8403 Å) and 1.473 eV (8416 Å), respectively. The other PL peaks such as the  $A^0X$  line and the LO-phonon replicas of free excitons were not notably different in intensity or lineshape. It is shown that the increase in the intensity of the 1.47 eV band has evidently been caused by the increase of dislocations. As reported by Dean et al. and Onodera and Taguchi, the 1.47 band observed in Fig. 1 is accompanied by its weak LO-phonon replicas, which is a unique feature characterizing the 1.47 eV band [9,12]. Therefore, the 1.47 eV band observed in Fig. 2b is identical with the defect band discussed by these authors.

Another example of the correlation between the 1.47 eV band and the dislocation patterns is shown in Figs. 3 and 4. Figs. 3a and 3b show the PL spectra taken from the low-dislocation area, which is the position away from the dislocation bundle, and at the position on the dislocation bundle. In particular, the spectrum in Fig. 3b was taken when the excited laser beam was focused just on the dislocation bundle seen in Fig. 4b. The corresponding etch pit patterns for the above two spectra (Figs. 3a and 3b) are shown in Figs. 4a and 4b, respectively. The EPD pictured in Fig. 4a is  $1 \times 10^5 \text{ cm}^{-2}$ . It should be pointed out here that the peak energy and lineshape of the 1.47 eV

band observed in Fig. 3b are slightly different from those in Fig. 1b. The precise peak energy of the 1.47 eV band observed in Fig. 1b is 1.475 eV (8403 Å), which value is almost the same as those reported by other researchers, while that in Fig. 3b is 1.476 eV (8399 Å), which value is at a slightly higher energy position than those reported by other researchers. A similar peak energy difference was also observed between the

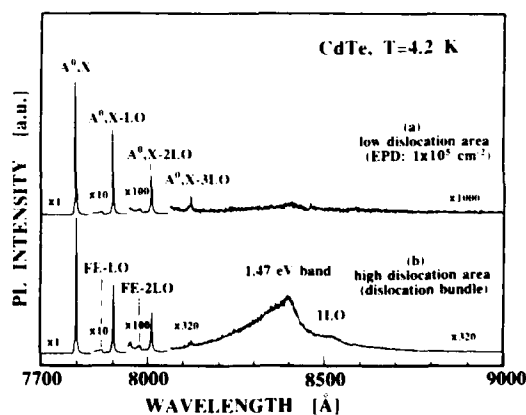


Fig. 3. PL spectra of CdTe with different dislocation structure: (a) spectrum taken from low-dislocation area where is the position away from the dislocation bundle; (b) spectrum taken from the position just on a dislocation bundle, as can be seen in Fig. 4b.

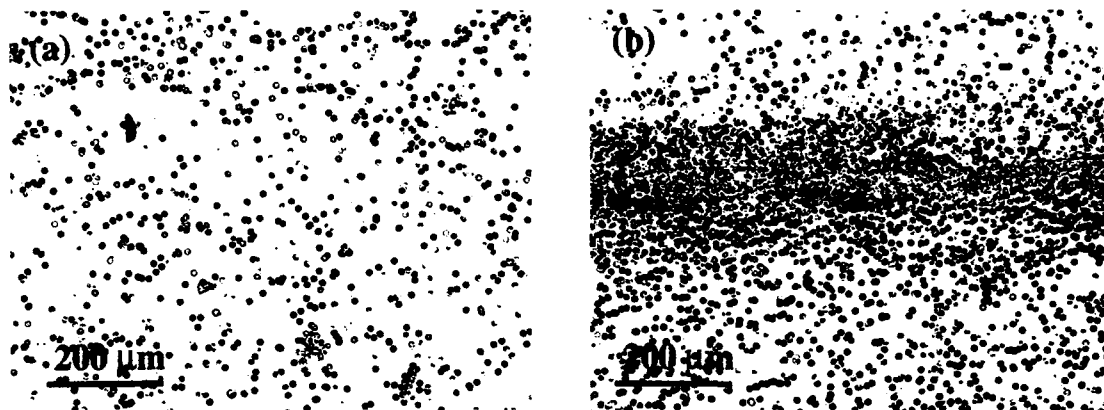


Fig. 4. Etch pit patterns in the vicinity of the laser beam positions measured for Figs. 3a and 3b, respectively. The EPD in (a) is  $1 \times 10^5 \text{ cm}^{-2}$ .

spectra in Figs. 1a and 1b. Furthermore, the high-energy tail of the band is stronger in Fig. 3b than in Fig. 1b. In spite of these differences, the 1.47 eV band observed in Fig. 3b is also followed by its weak LO-phonon replicas, which is an important feature for characterizing this band, so that the origin of the band in Fig. 3b is considered to be same as that in Fig. 1b. It seems likely that the peak energy variation of the 1.47 eV band is related to the difference of the binding potentials around the dislocations measured, as discussed by Dean et al. [9]. These differences associated with the 1.47 eV bands are not discussed any more in this paper. Anyway, it was also shown that the intensity of the 1.47 eV band is used as a measure to evaluate nondestructively the misfit dislocations in heteroepitaxial films.

In order to investigate the influence of point defects on the 1.47 eV band, the intensities of the 1.47 eV band before and after  $\gamma$ -ray irradiation were compared.

The  $^{60}\text{Co}$   $\gamma$ -rays of  $1.7 \times 10^7 \text{ Gy}$  can produce a great number of Frenkel defects, since Compton scattering is a dominant process in that energy region and the energy transferred from  $\gamma$ -ray to crystal is sufficient to displace host atoms in CdTe. Although the effects of  $\gamma$ -ray irradiation on PL spectrum in the energy region above 1.5

eV have been reported by Taguchi and Inuishi, they have not discussed the 1.47 eV band [15].

Fig. 5 shows a comparison of the PL spectra before and after  $\gamma$ -ray irradiation. Fig. 6 shows the expanded spectra in the excitonic region of Fig. 5. As can be seen in Fig. 5, the intensity of the 1.47 eV band after  $\gamma$ -ray irradiation increases by a factor of 10. On the other hand, the intensity of the excitonic PL lines such as  $A^0X$  and  $D^0X$  decreases by a factor of 1/3 after  $\gamma$ -ray irradiation.

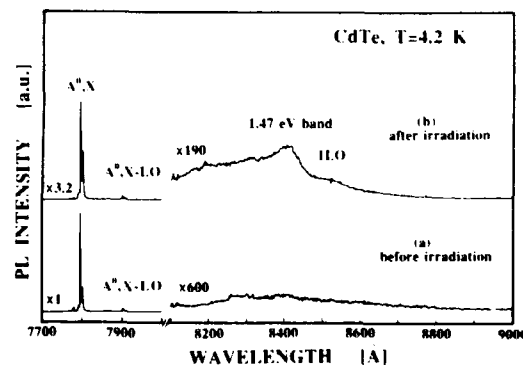


Fig. 5. PL spectra before and after  $\gamma$ -ray irradiation of  $1.7 \times 10^7 \text{ Gy}$ .

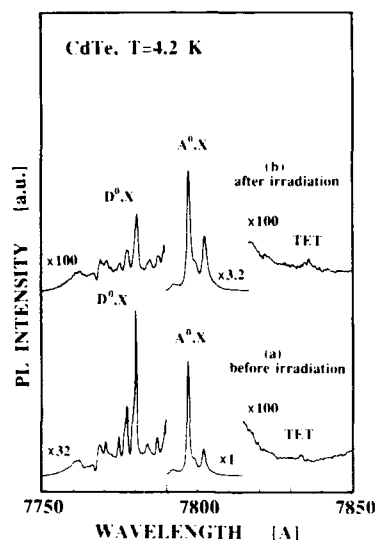


Fig. 6. Expanded PL spectra in excitonic region of Fig. 5.

tion. This decrease in the intensity of the excitonic lines is considered to be due to the increase in the strength of another nonradiative recombination process by  $\gamma$ -ray irradiation. This result demonstrates that the 1.47 eV bands are induced not only by extended defects like dislocations, but also by point defects like Frenkel defects. However, there is another possibility that could explain the above  $\gamma$ -ray irradiation effect on the 1.47 eV band. That is due to secondary defects such as dislocation loops, and not due to point defects. This is because the interstitial atoms generated by  $\gamma$ -ray irradiation can move and then interact with one another during room temperature storage. Anyway, these experimental results including the comparisons between the PL spectra for high- and low-dislocation positions shown in Figs. 1 and 2 strongly suggest that the existence of the strain field is important for the appearance of the 1.47 eV band. The variation of the peak positions of the bands, which is considered to be due to the variation of the strength of binding potentials from sample to sample, supports this interpretation, as pointed out by Dean et al. [9]. Also, the recent preliminary result of the uniaxial

stress effect on the 1.47 eV band, namely that the band is intensified by a uniaxial stress, supports the above interpretation [16]. Considering these results as well as the results by Dean et al. and Onodera and Taguchi, it is strongly suggested that the 1.47 eV band is due to the emission from excitons trapped at the strain field induced around the defects such as dislocations.

In summary, we have demonstrated that there is a distinct correlation between the 1.47 eV band and the dislocation density. The bands increase in intensity on the high-dislocation density positions, such as around lineage structure and just on dislocation bundle. It shows a possibility that the intensity of the 1.47 eV band can be used as a measure to evaluate the dislocation density. Furthermore, the 1.47 eV band was intensified by  $\gamma$ -ray irradiation. These results indicate that the strain field in the vicinity of the defects is responsible for the recombination center of the 1.47 eV band.

#### 4. Acknowledgements

This work was partially supported by the Shibuya Juridical Foundation of Education, Art, Culture and Sport Promotion, and a Grant-in-Aid from the Ministry of Education, Science and Culture in Japan. We thank Dr. K. Chino for encouragement throughout this study.

#### 5. References

- [1] Z.C. Feng, M.J. Bevan, W.J. Choyke and S.V. Krishnaswamy, *J. Appl. Phys.* 64 (1988) 2959.
- [2] D. Schikora, H. Sitter, J. Humenberger and K.L. Lischka, *Appl. Phys. Lett.* 48 (1986) 1276.
- [3] C.E. Barnes and K. Zanio, *J. Appl. Phys.* 45 (1975) 3959.
- [4] J.P. Chamonal, E. Molva and J.L. Pautrat, *Solid State Commun.* 43 (1982) 801.
- [5] J.M. Wrobel, J.J. Dubouski and P. Becla, *J. Vac. Sci. Technol. A* 7 (1989) 338.
- [6] S. Seto, A. Tanaka, K. Suzuki and M. Kawashima, *J. Crystal Growth* 101 (1990) 430.
- [7] S. Seto, A. Tanaka, Y. Masa and M. Kawashima, *J. Crystal Growth* 117 (1992) 271.

- [8] D.M. Hofmann, P. Omling, H.G. Grimmeiss, B.K. Meyer, K.W. Benz and D. Sinerius, *Phys. Rev. B* 45 (1992) 6247.
- [9] P.J. Dean, G.M. Williams and G.B. Blackmore, *J. Phys. D (Appl. Phys.)* 17 (1984) 2291.
- [10] P.J. Dean, A.D. Pitt, P.J. Wright, M.L. Young and B. Cockayne, *Physica B* 116 (1983) 508.
- [11] T. Taguchi and M. Suita, *Jap. J. Appl. Phys.* 34 (1989) L1889.
- [12] C. Onodera and T. Taguchi, *J. Crystal Growth* 101 (1990) 502.
- [13] T.A. Kuhn, W. Ossau, A. Waag, R.N. Bicknell-Tassius and G. Landwehr, *J. Crystal Growth* 117 (1992) 660.
- [14] K. Nakagawa, K. Maeda and S. Takeuchi, *Appl. Phys. Lett.* 34 (1979) 574.
- [15] T. Taguchi and Y. Inuishi, *Jap. J. Appl. Phys.* 51 (1980) 4757.
- [16] S. Seto, to be published.



ELSEVIER

Journal of Crystal Growth 138 (1994) 352–356

JOURNAL OF  
**CRYSTAL  
GROWTH**

## p-Type ZnSe:N grown by molecular beam epitaxy: evidence of non-radiative recombination centers in moderately to heavily doped material

L.C. Calhoun, C.M. Rouleau, M.H. Jeon, R.M. Park \*

*Department of Materials Science and Engineering, University of Florida, Gainesville, Florida 32611, USA*

### Abstract

We present data in this paper which demonstrate that the luminescence efficiency of p-type ZnSe:N grown by molecular beam epitaxy using a remote RF plasma source is a strong function of doping concentration and that in moderately to heavily doped material (corresponding to  $N_A - N_D \geq 2 \times 10^{17} \text{ cm}^{-3}$ ) significant concentrations of non-radiative recombination centers strongly limit the luminescence efficiency of the material. Such data were obtained by performing real-time, in situ cathodoluminescence intensity measurements during epilayer growth for variously doped epilayers.

### 1. Introduction

Considerable success has been achieved recently with regard to growing p-type ZnSe epilayers by means of nitrogen doping during molecular beam epitaxy (MBE). The use of remote (to the substrate) "active nitrogen" plasma sources has made this success possible with various types of plasma source having been employed.

Initial success was achieved using RF plasma sources [1,2], while more recently comparable results have been reportedly obtained employing microwave [3] and electron cyclotron resonance (ECR) microwave [4] plasma sources as "active nitrogen" generators. It is interesting to note that in all three cases the maximum net acceptor

concentration,  $N_A - N_D$ , achievable in p-type ZnSe:N epilayers is in the  $(1-2) \times 10^{18} \text{ cm}^{-3}$  range [3–5].

With regard to using plasma sources as dopant sources, the particular species generated in the various types of plasma source is of significant interest. Optical emission spectroscopy (OES) analysis has been performed on each of the three types of plasma source mentioned above with a view to characterizing the "active nitrogen" plasmas in each case. For instance, Park [6] has presented a OES spectrum which is typical of the Oxford Applied Research Ltd., RF plasma source while Kawakami et al. [3] and Ohtsuka and Horie [4] have presented OES spectra which are representative of their microwave and ECR microwave plasmas, respectively. The various emission spectra reflect the level of excitation occurring in each type of source, the highest excitation level occurring in the ECR microwave source, followed by

\* Corresponding author.

the microwave source, followed by the RF plasma source. In the case of the ECR microwave and the microwave sources, the emission spectra seem to be dominated by transitions associated with the 2nd positive system of  $N_2$  ( $C^3\Pi_u \rightarrow B^3\Pi_g$ ) while the 1st positive system of  $N_2$  ( $B^3\Pi_g \rightarrow A^3\Sigma_u^+$ ) transitions dominate in the case of the RF plasma source in addition to significantly intense emission lines recently ascribed to various atomic nitrogen transitions in the near-IR regime [7]. The higher excitation level sources (ECR microwave and microwave) also exhibit transitions associated with the 1st negative system of  $N_2$  ( $B^2\Sigma_u^+ \rightarrow X^2\Sigma_g^+$ ) (more so in the case of the ECR microwave source), whereas transitions associated with nitrogen ions do not appear to be significant in the case of spectra recorded from RF plasma sources.

In each of the three types of plasma source, however, significant concentrations of atomic nitrogen appear to be present in either the ground state or in various excited states since positive first system of  $N_2$  transitions occur as a result of the recombination of ground state nitrogen atoms while second positive system of  $N_2$  transitions are a consequence of the recombination of ground state and excited state nitrogen atoms [8].

Given that the electrical characteristics, at least in terms of the maximum achievable net acceptor density,  $N_A - N_D$ , appear to be similar in the case of p-type ZnSe:N grown by the three types of plasma source, it is perhaps not unreasonable to conclude that the atomic nitrogen species are responsible for doping in all three cases and that the maximum net acceptor density achieved thus far represents a fundamental limit imposed by the material system itself. The upper limit of the net acceptor density would appear to be a consequence of strong self-compensation which occurs in heavily doped material. Chadi and Troullier [9], for instance, have suggested that N interstitials having a particular electronic configuration can act as shallow donors and could therefore compensate N acceptor type states, particularly in heavily doped material.

Although p-type ZnSe and related alloys doped with N by means of remote plasma sources (particularly RF sources) have been successfully em-

ployed as hole injector layers in diode laser devices, [10,11] the quantum efficiency (optical quality) of such material is low. In fact, as pointed out by Zheng et al. [12], the room temperature (or above) quantum efficiency of ZnSe in general is very low which they conclude is due to significant concentrations of deep-level non-radiative recombination centers present in the material despite the fact that the material can look good in terms of other measures (exciton linewidths, rocking curve linewidths, etc.).

In this paper we present data which demonstrate that the luminescence efficiency of p-type ZnSe:N is a strong function of doping concentration and that in moderately to heavily doped material ( $N_A - N_D \geq 10^{17} \text{ cm}^{-3}$ ) significant concentrations of non-radiative recombination centers strongly limit the luminescence efficiency of the material. Such data were obtained by performing real-time, in situ cathodoluminescence (CL) intensity measurements during epilayer growth for variously doped epilayers.

## 2. Experimental procedure

The experimental apparatus used in this investigation is shown in Fig. 1. As can be seen in the figure, the growth chamber was equipped with elemental Zn and Se effusion sources as well as a compound  $ZnCl_2$  effusion source which provided Cl for n-type doping [13]. In addition, an Oxford Applied Research Ltd., RF plasma source was employed to provide an atomic nitrogen flux for p-type doping [1].

As reported previously for the case of n-type doping [14], we have detected and quantified the integrated CL intensity (blue-green emission) which is observed during growth from the ZnSe sample surface by virtue of the electron beam normally employed for reflection high energy electron diffraction analysis impinging at a glancing angle of incidence. In this apparatus the CL emission is detected via a CCD video camera (CCD response range from 400 to 700 nm) whose output is displayed on a monitor and a Si wide-area photodiode is positioned over the imaged spot on the screen in order to quantify the inte-



grated CL intensity as a function of doping condition.

### 3. Results and discussion

Integrated CL intensity data recorded in situ during growth (at the growth temperature) have been collected as a function of doping density for both n-type (chlorine-doped) and p-type (nitrogen-doped) ZnSe/(100)GaAs epilayers. In both cases the CL data were obtained by growing under a fixed set of growth conditions other than the dopant source condition which was varied from sample to sample in order to vary the doping density.

In the case of the n-type material, post-growth room temperature Hall-effect measurements were performed on the samples to obtain free-electron concentrations while post-growth room temperature capacitance-voltage ( $C-V$ ) measurements

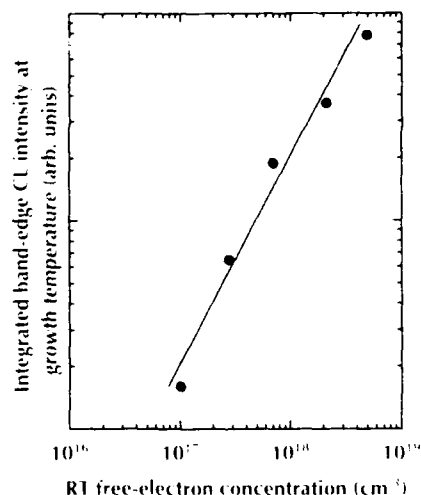


Fig. 2. Integrated band-edge cathodoluminescence intensity data recorded at the growth temperature plotted against the free-electron concentration measured at room temperature in n-type, chlorine-doped ZnSe epilayers.

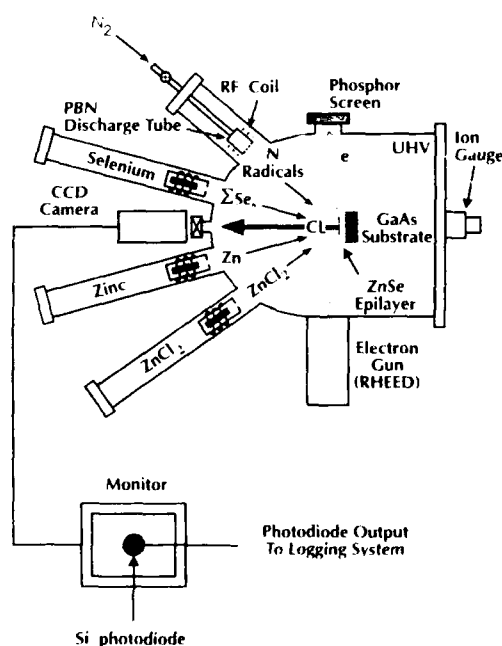


Fig. 3. Schematic drawing of ZnSe molecular beam epitaxy growth chamber showing n-type ( $\text{ZnCl}_2$  effusion cell) and p-type (RF plasma discharge) dopant sources as well as an in situ cathodoluminescence intensity measurement apparatus.

were made on the p-type samples in order to determine net acceptor concentrations.

As can be seen from the data shown in Fig. 2, a linear relationship was found in the case of n-type ZnSe between integrated CL intensity and free-carrier concentration over the carrier concentration range studied ( $10^{17}$  to  $5 \times 10^{18} \text{ cm}^{-3}$ ). Such data would imply that radiative recombination processes are dominant in the case of the chlorine-doped material over the indicated carrier concentration range while non-radiative recombination processes are insignificant in this case. The situation in the case of nitrogen-doped ZnSe, however, is markedly different. As can be seen from Fig. 3, the integrated CL intensity initially increases with increasing net acceptor concentration; however, for net acceptor concentrations above  $\sim 2 \times 10^{17} \text{ cm}^{-3}$ , the integrated CL intensity drops off dramatically with increasing net acceptor concentration. Such data would suggest that non-radiative recombination processes become more and more significant as the nitrogen doping level increases. It is postulated that the concentration of deep level non-radiative recombination centers increases with increasing nitrogen doping becoming the limiting factor in

terms of the luminescence efficiency at a doping level which corresponds to a net acceptor concentration around  $2 \times 10^{17} \text{ cm}^{-3}$ . As suggested by Talas and Allen [15], efficient non-radiative recombination channels could be provided in ZnSe due to the presence of Hall–Shockley–Read deep centers, these authors having studied the radiative efficiency of n-type ZnSe by examining blue luminescence decay times at room temperature.

Finally, Fig. 4 illustrates a model that we have devised in order to explain our p-type ZnSe:N data. The model suggests that at net acceptor densities less than  $\sim 2 \times 10^{17} \text{ cm}^{-3}$ , the integrated band-edge CL intensity is free-carrier concentration limited, i.e., radiative transitions are dominant, while at net acceptor densities greater than  $\sim 2 \times 10^{17} \text{ cm}^{-3}$ , the integrated band-edge CL intensity is quantum efficiency limited, which implies that non-radiative recombination centers assume significant concentrations in this range.

We conclude by suggesting that non-radiative deep levels require to be studied in heavily doped

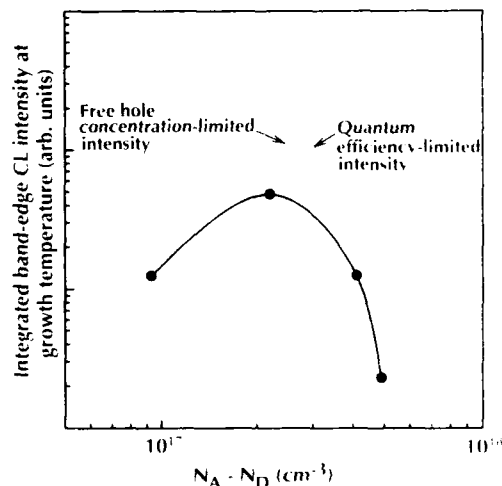


Fig. 4. Integrated band-edge cathodoluminescence intensity plotted against net acceptor concentration as measured in ZnSe:N epilayers by the capacitance–voltage technique. Also indicated are intensity limits postulated to be imposed by the free-hole concentration (in lightly doped material) and by the quantum efficiency of the material (for moderately to heavily doped ZnSe:N).

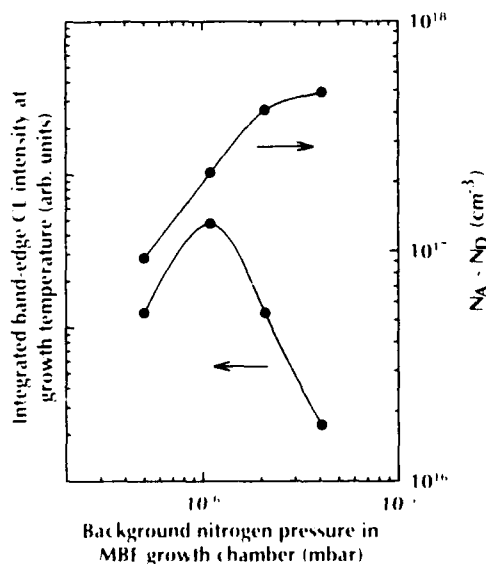


Fig. 5. Integrated band-edge cathodoluminescence intensity data and corresponding net acceptor concentration data obtained from p-type ZnSe:N epilayers plotted against the  $N_2$  partial pressure in the molecular beam epitaxy growth chamber during deposition.

ZnSe:N material intended for application in light-emitting devices and suggest that our real-time, in situ CL intensity measurement technique is a useful method of monitoring the impact of such centers.

#### 4. Acknowledgements

The authors wish to thank Dr. James DePuydt and Mr. Gregory Meis-Haugen of the 3M Co. (St. Paul, MN) for providing the C–V data. The research has been financially supported by the National Science Foundation (Grant No. DMR-9116880) and by the Advanced Research Projects Agency (University Research Initiative Grant No. N-00014-92-J-1895).

#### 5. References

- [1] R.M. Park, M.B. Trotter, C.M. Rouleau, J.M. DePuydt and M.A. Haase, *Appl. Phys. Lett.* 57 (1990) 2127.

- [2] K. Ohkawa, T. Karasawa and T. Mitsuyu, Jap. J. Appl. Phys. 30 (1991) L152.
- [3] Y. Kawakami, T. Ohnakado, M. Tsuka, S. Tokudera, Y. Ito, Sz. Fujita and Sg. Fujita, J. Vac. Sci. Technol., to be published.
- [4] T. Ohtsuka and K. Horie, Jap. J. Appl. Phys. 32 (1993) L233.
- [5] J. Qiu, J.M. DePuydt, H. Cheng and M.A. Haase, Appl. Phys. Lett. 59 (1991) 299.
- [6] R.M. Park, J. Vac. Sci. Technol. A 10 (1992) 701.
- [7] J.F. Schetzina, presented at Fall Workshop on Wide-Gap II-VI Materials for Lasers, Gainesville, FL, May 1993.
- [8] A.N. Wright and C.A. Winkler, Active Nitrogen (Academic Press, New York, 1968).
- [9] D.J. Chadi and N. Troullier, Physica B 185 (1993) 128.
- [10] M.A. Haase, J. Qiu, J.M. DePuydt and H. Cheng, Appl. Phys. Lett. 59 (1991) 1272.
- [11] H. Jeon, J. Ding, W. Patterson, A.V. Nurmikko, W. Xie, D.C. Grillo, M. Kobayashi and R.L. Gunshor, Appl. Phys. Lett. 59 (1991) 3619.
- [12] J. Zheng, J.W. Allen, D.E. Spence, W.E. Sleat and W. Sibbett, Appl. Phys. Lett. 62 (1993) 63.
- [13] K. Ohkawa, T. Mitsuyu and O. Yamazaki, J. Appl. Phys. 62 (1987) 3216.
- [14] C.M. Rouleau and R.M. Park, Appl. Phys. Lett. 60 (1992) 2723.
- [15] J.J.A. Talas and J.W. Allen, Semicond. Sci. Technol. 6 (1991) A138.



ELSEVIER

Journal of Crystal Growth 138 (1994) 357–361

JOURNAL OF  
**CRYSTAL  
GROWTH**

## Laser induced doping profiles in molecular beam epitaxy grown ZnSe doped with iodine

J.T. Mullins <sup>a,\*</sup>, G. Horsburgh <sup>a</sup>, J. Simpson <sup>a</sup>, P. Thompson <sup>a</sup>, M.R. Taghizadeh <sup>a</sup>,  
I. Hauksson <sup>a</sup>, S.Y. Wang <sup>a</sup>, K.A. Prior <sup>a</sup>, B.C. Cavenett <sup>a</sup>, G.M. Williams <sup>b</sup>,  
A.G. Cullis <sup>b</sup>

<sup>a</sup> Department of Physics, Heriot-Watt University, Edinburgh EH14 4AS, UK

<sup>b</sup> Defence Research Agency, St. Andrew's Road, Great Malvern, Worcestershire WR14 3PS, UK

### Abstract

An optical projection system has been developed which allows patterning of both layer thickness and donor concentration in epitaxial films of ZnSe during growth by molecular beam epitaxy. Doping features with a period as small as 40  $\mu\text{m}$  have been produced and it appears possible to reduce this by at least one order of magnitude. Such in-situ techniques may be valuable for the fabrication of more sophisticated devices than are currently being produced from the wide-gap II–VI compounds.

### 1. Introduction

ZnSe and related materials are currently of interest for the fabrication of optoelectronic devices operating in the blue/green region of the spectrum. The attainment of p-type doping in these materials has recently led to the development of blue/green laser diodes [1–3], optical modulators [4,5] and self-electro-optic devices (SEEDs) [6]. Improvements to these devices and the development of more sophisticated ones will require the spatial modulation of both layer thickness and dopant concentration. It would be advantageous if such modulation could be carried

out during growth, preferably by an optical technique, as this would considerably simplify device fabrication.

Previous studies have shown that, under above-band-gap illumination, the growth and doping of ZnSe by molecular beam epitaxy (MBE) are considerably modified by the generation and subsequent drift of electron–hole pairs and consequent shift of the Fermi energy at the growth surface. At high intensities (1–4 W cm<sup>−2</sup>), selenium may be preferentially desorbed from the growing surface leading to a reduction in growth rate [7,8] when the Se/Zn ratio at the growth surface falls below unity, while at lower intensities ( $\sim 200$  mW cm<sup>−2</sup>) local reductions exceeding one order of magnitude may be made in the donor concentration when iodine is used as a

\* Corresponding author.

dopant [9]. Potential exists, therefore, to spatially modulate both film thickness and carrier concentration during growth.

In this work, an optical system for the projection of patterns onto the growing layer in an MBE system is described and the photo-modulation of both layer thickness and donor concentration in ZnSe epitaxial layers is demonstrated.

## 2. Experimental procedure

Epitaxial layers of ZnSe were grown from elemental sources on  $n^+$  GaAs (100) substrates using a Vacuum Generators 288 MBE machine at substrate temperatures in the region of 280°C. The Se:Zn flux ratio (corrected for ion gauge sensitivity) during growth was approximately 1.5:1. Donor doping was achieved using iodine produced by an electrochemical iodine cell which has previously been described [10]. It was possible to illuminate the substrate surface during growth via a specially constructed double window comprising an outer vacuum window mounted in the source flange and an inner window heated to  $\approx 400^\circ\text{C}$  inside the growth chamber. By preventing deposition on any of the windows associated with the growth system, this arrangement eliminated the morphological problems often encountered in photo-modified growth resulting from scattering of the illumination and consequent variation in illumination intensity across the sample. In the present work, a Coherent Innova 1200

Kr ion laser operating at 350.7 nm was used as a source of stable, high intensity above band-gap radiation.

Fig. 1 shows the optical system used to project an optical grating onto the sample surface during growth. The laser beam passed through a diffraction grating (Damman grating [11]) followed by a cylindrical lens to form a first order diffraction pattern comprising 8 lines of equal intensity in the back focal plane of the cylindrical lens together with weaker higher order patterns either side (not shown). This plane could then be focussed onto the growing surface by the imaging lens. Approximately 80% of the laser light incident on the Damman grating was incorporated into the central first order pattern with each of the two second orders having  $\leq 10\%$ . This system allowed an image to be projected onto the growing surface with all optical components conveniently located external to the growth system. The distance from the imaging lens to the substrate was in the region of 1 metre. Final image size was adjustable by altering the relative positions of the three optical elements.

Cathodoluminescence studies were performed at 10 K using a Cambridge Stereoscan 150 Mk2 SEM equipped with a  $\text{LaB}_6$  source operated at 10 kV as is described in detail elsewhere [12].

## 3. Results and discussion

A photograph of the photoluminescence emission at room temperature from an iodine doped

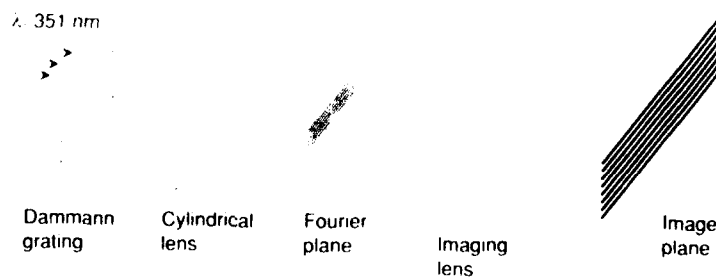


Fig. 1. Schematic diagram of the Fourier optics used to project an optical grating onto the substrate surface.

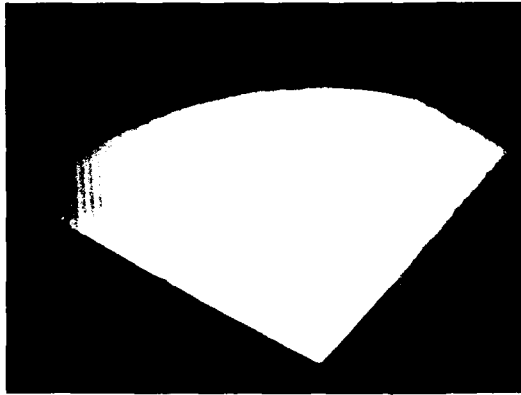


Fig. 2. Photograph of room temperature photoluminescence obtained from a layer of iodine doped ZnSe onto which an optical grating with a period of  $530\text{ }\mu\text{m}$  has been projected during growth. The donor concentration in the background (bright) is  $7 \times 10^{17}\text{ cm}^{-3}$ .

ZnSe layer grown using the patterning method described above is shown in Fig. 2. Close to the centre of the wafer is a clearly defined set of 8 dark lines with a period of  $532\text{ }\mu\text{m}$  corresponding to a negative image of the first order diffraction pattern produced by the Damman grating. At either side of this pattern are several sets of dark lines produced by the higher orders of diffraction. The dark lines correspond to areas in which the donor concentration has been reduced by the incident illumination and where, consequently, the donor bound excitonic emission is weaker. In the case of the first order grating the average illumination intensity in the (Gaussian) illuminated stripes was  $2\text{ W cm}^{-2}$  with a full width at half maximum (FWHM) of  $128\text{ }\mu\text{m}$ . The donor concentration in the (bright) background was  $7 \times 10^{17}\text{ cm}^{-3}$  as determined by capacitance–voltage profiling [13].

Fig. 3 shows a surface profile taken across the first order pattern obtained using a Dektak surface profiling system. In addition to the reduction in donor concentration, it is apparent that some growth rate reduction has also taken place leading to modulation of the sample surface. Troughs approximately  $200\text{ nm}$  deep replicating the Gaussian profile of the laser beam have been

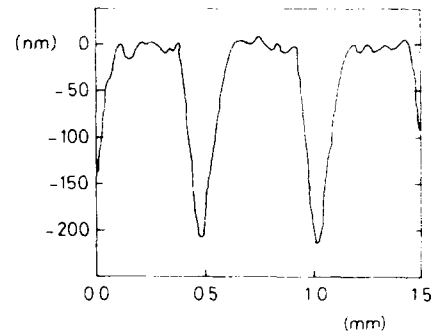


Fig. 3. Surface profile obtained from the layer shown in Fig. 2.

produced in a film  $0.92\text{ }\mu\text{m}$  thick. Profiling of the sample surface is much reduced in the second order patterns where the average intensity is  $\leq 10\%$  of that of the first order. In this case the troughs are reduced to a depth of  $\approx 40\text{ nm}$  corresponding to a maximum growth rate reduction of  $\approx 4\%$ .

A surface profile taken from a  $0.84\text{ }\mu\text{m}$  thick sample illuminated with the same pattern as previously, but with the period reduced to  $300\text{ }\mu\text{m}$  and an illumination intensity at FWHM of  $0.4\text{ W cm}^{-2}$  is shown in Fig. 4. In this case, modulation of the sample surface is reduced to  $\approx 30\text{ nm}$  or  $\approx 3\%$  of the growth rate. The micrograph in Fig. 5 is a cathodoluminescence image taken from part of this sample. As in the case of the photolumi-

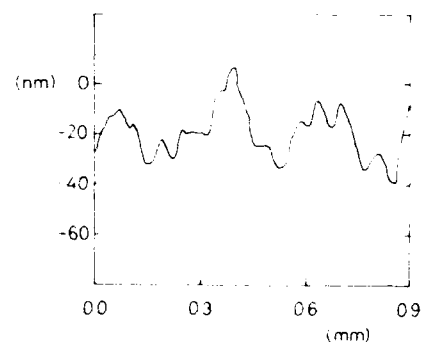


Fig. 4. Surface profile obtained from a layer of iodine doped ZnSe onto which an optical grating with a period of  $300\text{ }\mu\text{m}$  and an illumination intensity at FWHM of  $400\text{ mW cm}^{-2}$  had been projected during growth.

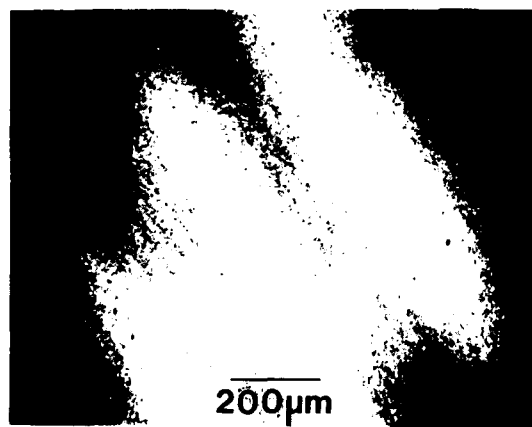


Fig. 5. Cathodoluminescence image obtained from the sample shown in Fig. 4. The donor concentration in the background (bright) is  $8 \times 10^{17} \text{ cm}^{-3}$ .

nesence image, the brighter regions correspond to areas where the donor concentration has not been reduced by illumination during growth. Three bright bands can be seen across the centre of the image with a period of approximately  $300 \mu\text{m}$  corresponding to the first order pattern. Superimposed on this, and visible in the darker regions, are series of lines with a period of one eighth of the first order pattern ( $\approx 40 \mu\text{m}$ ). These lines were unintentional and resulted from a slight mis-alignment of the optics. They do, however, illustrate the potential for producing fine structures with this system.

Optical microscopy of these samples showed that, notwithstanding the modulation of the layer thickness described above, the specular morphology of the non-illuminated areas was maintained in the illuminated regions indicating the effectiveness of the heated window.

The ultimate resolution of this technique may depend on three factors: (i) carrier diffusion, (ii) diffraction effects and (iii) machine vibration.

Carrier diffusion depends on the ambipolar diffusion coefficient,  $D$ , and the carrier lifetime,  $\tau$ , according to the relation  $x^2 = D\tau$  where  $x$  represents distance. Taking  $D = 2.5 \text{ cm}^2 \text{ s}^{-1}$  [14] and  $\tau = 250 \text{ ps}$  [14,15] for ZnSe gives a value of  $0.25 \mu\text{m}$ . Diffraction effects limit resolution to

the order of the wavelength of the light used, in this case  $350.7 \text{ nm}$ . The effects of machine vibration may be reduced to submicron levels as demonstrated by the use of electron beam writing in MBE [16]. There is therefore, in principle, no reason why resolution in the region of one micron should not be attainable.

#### 4. Conclusion

Photo-patterning of both layer thickness and donor concentration has been demonstrated in epitaxial films of ZnSe. The use of a projection system based on a Damman grating allows all optical components to be located external to the growth system and has enabled doping features with a period as small as  $\approx 40 \mu\text{m}$  to be realized. The lower limit on feature sizes is estimated to be in the region of  $1 \mu\text{m}$  and although this has not yet been reached, the present resolution is adequate for the current generation of ZnSe based devices. It would in principle be possible, for example, to define a ridge laser structure with reduced n-type doping outside of the ridge in order to provide gain as well as optical confinement. Such in-situ optical processing reduces the number of processing steps in device fabrication and also avoids the potential for damage likely in the fragile II-VI compounds if conventional techniques such as reactive ion etching or ion implantation are used.

#### 5. References

- [1] M.A. Haase, J. Qiu, J.M. DePuydt and H. Cheng, *Appl. Phys. Lett.* 59 (1992) 1272.
- [2] H. Jeon, J. Ding, W. Patterson, A.V. Nurmikko, W. Xie, D.C. Grillo, M. Kobayashi and R.L. Gunshor, *Appl. Phys. Lett.* 59 (1992) 3619.
- [3] S.Y. Wang, J. Simpson, H. Stewart, S.J.A. Adams, I. Hauksson, Y. Kawakami, M.R. Taghizadeh, K.A. Prior and B.C. Cavenett, *Physica B* 185 (1993) 508.
- [4] S.Y. Wang, Y. Kawakami, J. Simpson, H. Stewart, K.A. Prior and B.C. Cavenett, *Appl. Phys. Lett.* 62 (1993) 1715.
- [5] Y. Kawakami, S.Y. Wang, J. Simpson, I. Hauksson, S.J.A. Adams, H. Stewart, B.C. Cavenett and K.A. Prior, *Physica B* 185 (1993) 496.

- [6] S.Y. Wang, G. Horsburgh, P. Thompson, I. Hauksson, J.T. Mullins, K.A. Prior and B.C. Cavenett, *Appl. Phys. Lett.* 63 (1993) 857.
- [7] J. Simpson, S.J.A. Adams, J.M. Wallace, K.A. Prior and B.C. Cavenett, *Semicond. Sci. Technol.* 7 (1992) 460.
- [8] J. Simpson, S.Y. Wang, I. Hauksson, H. Stewart, S.J.A. Adams, K.A. Prior and B.C. Cavenett, *J. Crystal Growth* 127 (1993) 327.
- [9] J. Simpson, S.J.A. Adams, S.Y. Wang, J.M. Wallace, K.A. Prior and B.C. Cavenett, *J. Crystal Growth* 117 (1992) 134.
- [10] J. Simpson, J.M. Wallace, S.Y. Wang, H. Stewart, J.J. Hunter, S.J.A. Adams, K.A. Prior and B.C. Cavenett, *Semicond. Sci. Technol.* 7 (1992) 464.
- [11] For a general review of this and other types of diffractive optical elements, see M.R. Taghizadeh and J. Turunen, in: *Optical Computing and Processing* (Taylor and Francis, 1993).
- [12] G.M. Williams, A.G. Cullis, C.M. Sotomayor-Torres, S. Thomas, S.P. Beaumont, C.R. Stanley, D. Lootens and P. van Daele, in: *Microscopy of Semiconducting Materials 1991*, Inst. Phys. Conf. Ser. 117, Eds. A.G. Cullis and N.J. Long (Inst. Phys., Bristol, 1991) p. 695.
- [13] S.Y. Wang, J. Simpson, K.A. Prior and B.C. Cavenett, *J. Appl. Phys.* 72 (1992) 5311.
- [14] J.A. Bolger, A.K. Kar, B.S. Wherrett, K.A. Prior, J. Simpson, S.Y. Wang and B.C. Cavenett, *Appl. Phys. Lett.* 63 (1993) 571.
- [15] J.S. Massa, G.S. Buller, A.C. Walker, J. Simpson, K.A. Prior and B.C. Cavenett, *Appl. Phys. Lett.*, submitted.
- [16] G.A.C. Jones, private communication.





ELSEVIER

Journal of Crystal Growth 138 (1994) 362–366

CRYSTAL  
GROWTH

## Optical study of interdiffusion in CdTe and ZnSe based quantum wells

D. Tönnies <sup>a,\*</sup>, G. Bacher <sup>a</sup>, A. Forchel <sup>a</sup>, A. Waag <sup>b</sup>, Th. Litz <sup>b</sup>, D. Hommel <sup>b</sup>,  
Ch. Becker <sup>b</sup>, G. Landwehr <sup>b</sup>, M. Heuken <sup>c</sup>, M. Scholl <sup>c</sup>

<sup>a</sup> Technische Physik, Universität Würzburg, Am Hubland, D-97074 Würzburg, Germany

<sup>b</sup> Experimentelle Physik III, Universität Würzburg, Am Hubland, D-97074 Würzburg, Germany

<sup>c</sup> Institut für Halbleitertechnik-Lehrstuhl I, RWTH Aachen, Templergraben 55, D-52062 Aachen, Germany

### Abstract

The interdiffusion in single quantum well structures was studied for a variety of II–VI semiconductor materials based on CdTe and ZnSe. In particular we have investigated CdTe–CdMnTe, CdTe–CdMgTe,  $\text{Hg}_{1-x}\text{Cd}_x\text{Te}$ – $\text{Hg}_{1-x}\text{Cd}_x\text{Te}$  and ZnSe–CdZnSe structures in which an intermixing of column II elements can be induced as well as ZnSe–ZnSSe allowing an interdiffusion within the column VI sublattice. The diffusion was induced by rapid thermal annealing (RTA) for 1 min at different temperatures. The resulting blue shift of the characteristic emission spectrum was analyzed using photoluminescence spectroscopy. We observed a significant difference of the diffusion behavior between both groups of materials. While in all three CdTe based material systems an almost complete interdiffusion within the column II sublattice could be obtained at a high optical quality of the structures, both ZnSe based quantum wells show only remarkably small diffusion lengths. For all three CdTe based quantum wells we derived an activation energy of the interdiffusion process from a simple Fickian diffusion model applied to our measurements. We obtained a value of 2.8 eV for CdTe–CdMnTe and CdTe–CdMgTe and a value 2.1 eV for  $\text{Hg}_{1-x}\text{Cd}_x\text{Te}$ – $\text{Hg}_{1-x}\text{Cd}_x\text{Te}$ .

Due to the fundamental role of diffusion for the production of semiconductor devices, the study of diffusion in semiconductor crystals has been of large interest in the last years. Self-diffusion or impurity diffusion in III–V and II–VI bulk materials was studied, e.g. by secondary ion mass spectroscopy (SIMS), a technique that allows a direct scanning of the diffusion profile [1]. In recent years, diffusion has also been investigated in thin heterostructures which offer an

interesting source of concentration gradients. The interdiffusion of the materials in the well and barrier layers results in a blue shift of the emission spectrum [2]. The technological interest on this effect arises from the possibility to tune the wavelength of an optical emitter by simply annealing the device. On the other hand, it has been shown in III–V quantum wells that the selective implantation of ions in a semiconductor heterostructure offers the possibility to define a lateral confinement [3,4]. Up to now the investigation of diffusion in heterostructures has been restricted mainly to III–V materials. Only few

\* Corresponding author.

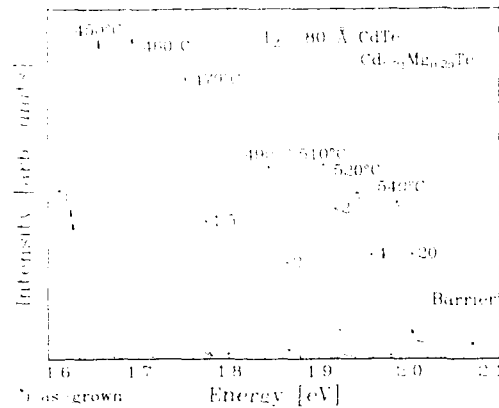


Fig. 1. PL spectra of the excitonic recombination of a 80 Å CdTe/Cd<sub>0.95</sub>Mg<sub>0.05</sub>Te quantum well before and after annealing for 1 min at temperatures between 450 and 550°C. The energy of the barrier is indicated by an arrow.

results have been reported on interdiffusion in II–VI heterostructures [5,6].

In this paper we report on a comparative investigation of diffusion in II–VI single quantum wells from five different material systems grown by molecular beam epitaxy (MBE) or metalorganic vapor phase epitaxy (MOVPE). Three of these, namely CdTe/CdMgTe, CdTe/CdMnTe and Hg<sub>0.95</sub>Cd<sub>0.05</sub>Te/Hg<sub>0.95</sub>Cd<sub>0.05</sub>Te, are based on CdTe while the other two, ZnSe/CdZnSe and ZnSe/ZnSSe, are based on ZnSe. In all three CdTe-based material systems and in ZnSe/CdZnSe, the interdiffusion takes place within the column II sublattice, while in ZnSe/ZnSSe the column VI elements are intermixing. We annealed single quantum well structures grown of

these materials and characterized the processed samples by photoluminescence (PL) spectroscopy. From the observed blue shifts we found a different diffusion behavior for CdTe and ZnSe-based materials. While CdTe-based materials show a blue shift up to the barrier energy, in ZnSe-based quantum wells no blue shift larger than a few meV could be induced.

In Table 1 an overview of the investigated samples is given. Listed for each material system are the growth technique, the growth temperature, the substrate material and the quantum well thickness. The interdiffusion was induced by rapid thermal annealing (RTA) at different temperatures with an annealing time chosen to be 1 min. During the annealing process, the samples were exposed to a continuous flux of N<sub>2</sub> to avoid surface oxidation and covered with a silicon wafer to reduce material evaporation. Due to the interdiffusion, the composition profile of the structures is altered in such a way that the bottom of the conduction band (top of the valence band) is shifted to higher (lower) energies resulting in a blue shift of the excitonic recombination. We used photoluminescence spectroscopy (PL) to characterize the annealed samples. The CdTe based structures were excited by the 514.5 nm line of an Ar<sup>+</sup> laser, while the 363 nm line was used to excite both ZnSe based systems. The photoluminescence signal was dispersed by a 0.3 m monochromator and detected by a CCD camera. For HgCdTe a cooled germanium detector was used.

Fig. 1 displays some photoluminescence spectra of the excitonic recombination of an 80 Å CdTe/CdMgTe quantum well annealed at differ-

Table 1

Structural properties of the single quantum wells investigated in this work; listed are the technique of epitaxial growth, the growth temperature, the substrate material and the quantum well thickness  $L_w$ .

Material	Growth technique	Growth temperature (°C)	Substrate	$L_w$ (Å)
CdTe/Cd <sub>0.95</sub> Mg <sub>0.05</sub> Te	MBE	230	CdZnTe	80
CdTe/Cd <sub>0.95</sub> Mn <sub>0.05</sub> Te	MBE	230	CdTe	40
Hg <sub>0.95</sub> Cd <sub>0.05</sub> Te/Hg <sub>0.95</sub> Cd <sub>0.05</sub> Te	MBE	180	CdZnTe	40
Cd <sub>0.95</sub> Zn <sub>0.05</sub> Se/ZnSe	MBE	300	GaAs	33
ZnSe/ZnS <sub>0.05</sub> Se <sub>0.95</sub>	MOVPE	480	GaAs	10

ent temperatures. The leftmost spectrum was taken from the as-grown structure. The other spectra are those of the annealed samples and exhibit the blue shift of the photoluminescence signal. For an annealing time of 1 min increasing the annealing temperatures from 450 to 540°C leads to an increasing blue shift of the photoluminescence spectra. For the highest annealing temperatures of 540°C the photoluminescence signal is blue-shifted almost to the energy of the barrier, i.e. nearly through the entire spectral region possible, indicating an almost complete intermixing of the well and barrier materials.

For quantum wells annealed at temperatures higher than 460°C, the halfwidth of the photoluminescence spectra increases from about 10 to 15 meV for CdTe/CdMgTe. This is probably due to a slightly inhomogeneous diffusion process leading to non-uniform shapes of the composition profile throughout the samples. Nevertheless the broadening of the photoluminescence signal is relatively small and indicates a good optical quality of the processed structures. In conjunction with the increase of the linewidth, the intensities of the PL signals decrease for the strongly intermixed quantum wells. We attribute this to the creation of defects during the diffusion process.

In Fig. 2, the corresponding blue shifts of the photoluminescence from the annealed structures are plotted versus the annealing temperature for all three CdTe-based materials. For CdTe/CdMgTe we observed energy shifts up to 360 meV. This value is larger than any interdiffusion induced energy gap change achieved in III–V materials so far. The proper temperature regions for 1 min annealing are roughly the same for CdTe/CdMnTe and CdTe/CdMgTe and lies between 400 and 540°C, while annealing temperatures between 280 and 330°C are sufficient to induce interdiffusion in Hg<sub>0.53</sub>Cd<sub>0.47</sub>Te/Hg<sub>0.20</sub>Cd<sub>0.80</sub>Te quantum wells. For all three materials the photoluminescence signal shifts close to the energy of the barrier. Thus, within all three CdTe-based materials, it is possible to intermix the well and barrier material almost completely without destroying the high quality of the epitaxy.

From the measured energy shifts we derived diffusion coefficients for each annealing tempera-

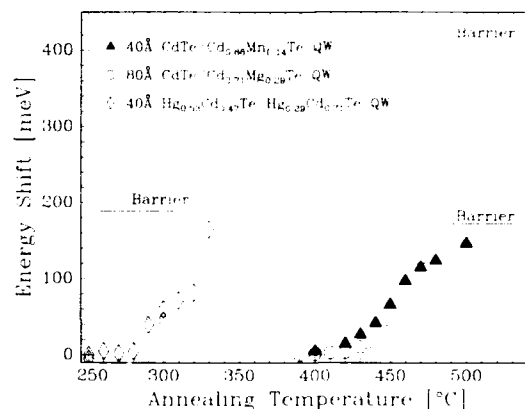


Fig. 2. Energy shifts of the PL signal of annealed Hg<sub>0.53</sub>Cd<sub>0.47</sub>Te/Hg<sub>0.20</sub>Cd<sub>0.80</sub>Te, CdTe/Cd<sub>0.51</sub>Mg<sub>0.49</sub>Te and CdTe/Cd<sub>0.86</sub>Mn<sub>0.14</sub>Te quantum well structures. The largest energy shifts of each material corresponds to the energy of the barrier in the as-grown samples.

ture. The profile of the interdiffused quantum well was determined from the composition profile depending on the diffusion length  $L_D$ . We solved the one-dimensional Schrödinger equation numerically [7] and obtained thereby a correlation between the measured blue shift and the diffusion length. Finally, the diffusion coefficient was calculated from  $D = L_D^2/\tau$ , where  $\tau$  is the annealing time. The results are displayed in Fig. 3. The diffusion coefficients  $D$  are plotted versus the reciprocal temperature  $1/kT$ . The approximately linear dependence of  $\ln D$  and  $1/kT$  allows one to model the temperature dependence of the diffusion coefficient by an Arrhenius law.

$$D(T) = D_0 \exp(-E_a/kT),$$

where  $E_a$  is the activation energy necessary for a single diffusion process of a particle within the crystal lattice. The activation energy can be derived from the slope of the linearly fitted curves. We obtained a value of 2.8 eV for both the CdTe/CdMnTe and the CdTe/CdMgTe quantum well and a value of 2.1 eV for Hg<sub>0.53</sub>Cd<sub>0.47</sub>Te/Hg<sub>0.20</sub>Cd<sub>0.80</sub>Te. In our calculations we neglected for simplicity the concentration dependence of the diffusion in HgCdTe, which is reported by several authors [6,8]. In consequence our value of

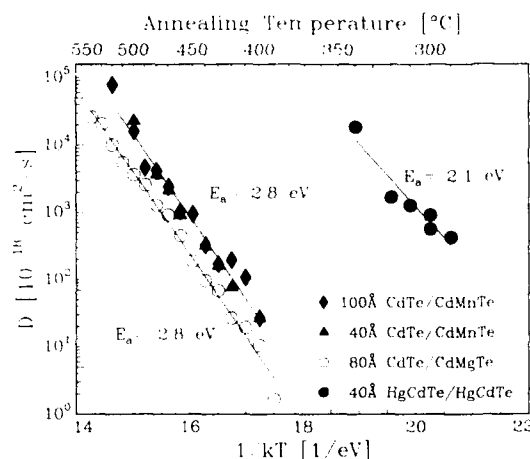


Fig. 3. Diffusion coefficients  $D$  versus the reciprocal temperature for CdTe/CdMnTe, CdTe/CdMgTe and  $\text{Hg}_{1-x}\text{Cd}_x\text{Te}/\text{Hg}_{1-x}\text{Cd}_x\text{Te}$ . The activation energies are estimated from the slope of the curves.

the activation energy in this material lies a little above those published in these works.

The investigation of the ZnSe-based material systems reveals a significantly different diffusion behavior. In Fig. 4, the PL spectrum of the as-grown 33 Å ZnSe/CdZnSe quantum well and of the same structure annealed at 600°C is displayed. The annealed sample exhibits an energy shift of 20 meV in conjunction with a decrease of

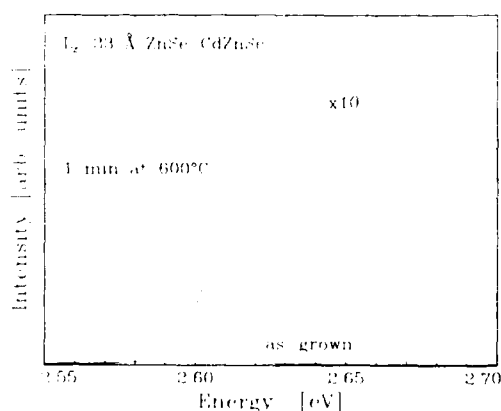


Fig. 4. PL spectra of the excitonic recombination of a 33 Å ZnSe/ $\text{Cd}_{0.20}\text{Zn}_{0.80}\text{Se}$  quantum well before and after annealing.

the PL intensity by more than one order of magnitude. Annealing at higher temperatures leads to no further energy shift but to a complete vanishing of the characteristic photoluminescence signal, although from the total confinement of the quantum well blue shifts up to 200 meV should be possible. The 10 Å ZnSe/ZnSSe samples were annealed at 580, 660 and 700°C, and reveal energy shifts smaller than 40 meV, which are lower than the band discontinuity of this quantum well structure of about 400 meV. A further increase of the annealing temperature quenches the PL intensity completely. For both material systems, a variation of the annealing time did not improve the quality of the annealed structures. This diffusion behavior is in strong contrast to that of CdTe based quantum wells, where a almost complete intermixing is possible without quenching the luminescence signal. The explanation of this effect is not clear yet. Although an explanation is probably difficult due to a lack of information on the crystal lattice, it is worth noting that CdTe, HgTe, MnTe and MgTe have noticeable larger lattice constants than the other materials (see Table 2), which might have an influence on the stability of these crystals against annealing.

Another interesting point are the temperature regions necessary to induce interdiffusion in the investigated quantum well structures. The smallest temperatures are necessary for  $\text{Hg}_{1-x}\text{Cd}_x\text{Te}/\text{Hg}_{1-x}\text{Cd}_x\text{Te}$  which show interdiffusion effects

Table 2

Properties of several II-VI semiconductor materials: listed are the lattice constant  $a$ , the Debye temperature  $\Theta_D$  at 0 K and the melting point  $T_m$

Material	$a$ (Å)	$\Theta_D$ at 0 K (K)	$T_m$ (°C)
HgTe	6.5 <sup>a</sup>	147 <sup>b</sup>	670 <sup>c</sup>
CdTe	6.5 <sup>a</sup>	150, 160 <sup>a</sup>	1092 <sup>a</sup>
MnTe	6.3 <sup>a</sup>		
MgTe	6.4 <sup>d</sup>		
CdSe	6.1 <sup>a</sup>	230, 315 <sup>b</sup>	1241 <sup>a</sup>
ZnSe	5.7 <sup>a</sup>	~ 270 <sup>b</sup>	1520 <sup>a</sup>
ZnS	5.4 <sup>a</sup>	334 <sup>b</sup>	1830 <sup>a</sup>

<sup>a</sup> Ref. [9].

<sup>b</sup> Ref. [10].

<sup>c</sup> Ref. [11].

<sup>d</sup> Ref. [12].

for temperatures smaller than 300°C. The proper temperature region for annealing CdTe/CdMgTe and CdTe/CdMnTe structures is roughly the same and lies within 390 and 540°C, while for ZnSe/CdZnSe as well as for ZnSe/ZnSSe, a temperature of about 600°C is necessary to obtain small blue shifts. It is interesting to compare the Debye temperature and the melting temperature of these materials, because both the temperature necessary for the activation of lattice vibrations and the destruction of the crystal lattice are expected to be correlated with the temperature necessary to induce interdiffusion. In Table 2, the Debye and melting temperatures are listed for a variety of semiconductor alloys. For HgTe, CdTe and ZnSe, the Debye temperature as well as the melting temperature are growing from HgTe to ZnSe and reveal therefore the same tendency as the characteristic interdiffusion temperatures of the material systems investigated in this paper.

In summary, we have investigated the diffusion in single quantum wells grown of five different II–VI semiconductor materials. We found that all three CdTe-based materials,  $\text{Hg}_{1-x}\text{Cd}_x\text{Te}$ /Hg<sub>1-x</sub>Cd<sub>x</sub>Te, CdTe/CdMnTe and CdTe/CdMgTe, offer the possibility to completely intermix the quantum well and barrier material without quenching the luminescence signal and as a consequence to shift the photoluminescence signal almost up to the energy of the barrier. This property makes these materials promising candidates for optical emitters with a wavelength that can be tuned by a thermal process. On the other hand, in ZnSe/CdZnSe and ZnSe/ZnSSe quantum wells, energy shifts of only a few meV were achieved without destroying the optical quality of the grown structures. Furthermore, the tempera-

ture necessary to obtain a significant diffusion for 1 min annealing is smallest for the  $\text{Hg}_{1-x}\text{Cd}_x\text{Te}$ /Hg<sub>1-x</sub>Cd<sub>x</sub>Te system and increases over CdTe/CdMg(Mn)Te to ZnSe/ZnCd(S)Se.

The work at Würzburg university was financially supported by the Bayerische Forschungsverbund.

## 1. References

- [1] D. Shaw, *J. Crystal Growth* 86 (1988) 778.
- [2] M.D. Camras, N. Holonyak, Jr., R.D. Burnham, W. Streifer, D.R. Scifres, T.L. Paoli and C. Linström, *J. Appl. Phys.* 54 (1983) 5637.
- [3] C. Vieu, M. Schneider, D. Mailly, R. Planel, H. Lanois, J.Y. Marzin and B. Descouts, *J. Appl. Phys.* 70 (1991) 1444.
- [4] H. Feier, A. Forchel, G. Hörcher, J. Hommel, S. Bayer, H. Rothfritz, G. Weimann and W. Schlapp, *J. Appl. Phys.* 67 (1990) 1805.
- [5] A. Hamoudi, E. Tigeon, K. Saminadayar, J. Cibert, L. S. Dang and S. Tatarenko, *Appl. Phys. Lett.* 60 (1992) 2797.
- [6] A. Tardot, A. Hamoudi, N. Magnea, P. Gentile and J.F. Pautrat, *Semicond. Sci. Technol.* 8 (1993) S276.
- [7] W.W. Lui and M. Fukuma, *J. Appl. Phys.* 60 (1986) 1555.
- [8] J.H.C. Hogg, A. Bairstow, G.W. Matthews, D. Shaw and J.D. Stedman, *Mater. Sci. Eng. B* 16 (1993) 195.
- [9] Landolt-Börnstein, New Series III/22a, Semiconductors: Intrinsic Properties of Group IV Elements and III–V, II–VI and I–VII Compounds, Ed. O. Madelung (Springer, Berlin, 1987).
- [10] Landolt-Börnstein, New Series III/17b, Semiconductors: Physics of II–VI and I–VII Compounds, Semimagnetic Semiconductors, Ed. O. Madelung (Springer, Berlin, 1982).
- [11] R.T. Delves and B. Lewis, *J. Phys. Chem. Solids* 24 (1963) 549.
- [12] A. Waag, H. Henke, S. Scholl, C.R. Becker and G. Landwehr, *J. Crystal Growth* 131 (1993) 607.

## Phase separation in $\text{ZnSe}_{1-x}\text{S}_x$ and $\text{Zn}_{1-y}\text{Mg}_y\text{Se}_{1-x}\text{S}_x$ layers grown by molecular beam epitaxy

G.C. Hua<sup>a,\*</sup>, N. Otsuka<sup>a</sup>, D.C. Grillo<sup>b</sup>, J. Han<sup>b</sup>, L. He<sup>b</sup>, R.L. Gunshor<sup>b</sup>

<sup>a</sup> School of Materials Engineering, Purdue University, West Lafayette, Indiana 47907, USA

<sup>b</sup> School of Electrical Engineering, Purdue University, West Lafayette, Indiana 47907, USA

### Abstract

The occurrence of phase separation in (100)  $\text{ZnSe}_{1-x}\text{S}_x$  and  $\text{Zn}_{1-y}\text{Mg}_y\text{Se}_{1-x}\text{S}_x$  layers grown by molecular beam epitaxy was found by transmission electron microscopy. The direction of the phase separation is [011], and the period of the composition modulation ranges from 300 to 500 Å. X-ray microanalysis of the two regions resulting from the phase separation showed one to be sulfur-rich and the other sulfur-deficient. The one-to-one correspondence of the wavy surface structure and the composition modulation suggests that the phase separation occurs via nonuniform incorporation of sulfur atoms into the wavy growth plane of the epilayer.

The employment of ternary  $\text{ZnSe}_{1-x}\text{S}_x$  and quaternary  $\text{Zn}_{1-y}\text{Mg}_y\text{Se}_{1-x}\text{S}_x$  phases has led to recent significant progress of blue-green diode lasers [1–3]. These alloy phases provide considerable flexibility for designing laser structures under the restriction of lattice matching to the GaAs substrate crystal. Room temperature laser operations under pulsed conditions (1  $\mu\text{s}$ ,  $10^{-3}$  duty) have been achieved for up to 1 h by using pseudomorphic structures in which ternary and quaternary layers serve as wave guiding and cladding layers, respectively [3].

During the course of the transmission electron microscope (TEM) analysis of laser structures grown by molecular beam epitaxy (MBE), we have found phase separation in a number of the ternary and quaternary layers. The phase separa-

tion occurred nearly along the [011] direction in the (100) epilayers. By X-ray microanalysis, the phase separation was found to be periodic changes of Se and S concentrations. Up to the present, phase separation has been observed in many III–V alloy epilayers [4]. To our knowledge, however, there are only few cases of phase separation in II–VI alloy epilayers [5]. The occurrence of phase separation may have significant implication to the development of laser structures based on these II–VI alloy phases. It is known to affect transport and optical properties [4]. Earlier studies on light emitting devices based on InGaAlP also suggest that phase separation may make the device more degradation resistant [6]. In this paper, we present TEM studies of phase separation in these II–VI alloy layers, including results of X-ray microanalysis.

The ternary and quaternary epilayers and laser structures containing alloy layers were grown

\* Corresponding author.

at temperatures ranging from 245 to 260°C on (100) GaAs by using a Perkin-Elmer 430 modular MBE system with elemental Zn, Se and Mg sources and a ZnS source. The total cation-to-anion flux ratio was adjusted to maintain a barely anion-stabilized growth surface, as evidenced by a diffuse  $(2 \times 1)$  surface reconstruction. Average compositions of quaternary epilayers were determined by using a Cameca SX50 electron microprobe. Average compositions of ternary layers in laser structures were estimated based on the flux conditions and X-ray rocking curve measurements. A JEM 2000EX transmission electron microscope and a JEM 2000 FX analytical electron microscope were used for examination of microstructures. Cross-sectional samples with two orthogonal  $\langle 011 \rangle$  directions and plan-view samples were prepared by ion milling. The convergent beam electron diffraction technique was employed in order to identify the  $[011]$  and  $[0\bar{1}\bar{1}]$  directions of cross-sectional samples [7].

A series of laser structures and alloy epilayers were examined by TEM observations of  $[011]$  and  $[0\bar{1}\bar{1}]$  cross-sectional samples. Among those layers, all quaternary epilayers with sulfur concentrations greater than  $x = 0.2$  exhibit strong phase separation. About one half of the  $\text{ZnSe}_{1-x}\text{S}_x$  layers with  $x \approx 0.07$  were found to have phase separation. In quaternary layers with sulfur contents close to  $x = 0.12$ , no clear image of phase separation was observed; some layers appear to exhibit very weak contrasts of phase separation.

Figs. 1a and 1b are  $\bar{2}00$  dark field images of  $[0\bar{1}\bar{1}]$  and  $[011]$  cross-sectional samples of a  $\text{Zn}_{1-x}\text{Mg}_x\text{Se}_{1-y}\text{S}_y$  epilayer. The average composition of this epilayer is  $x = 0.218$  and  $y = 0.075$ . The narrow bright band seen along the interface with the GaAs substrate is a thin ZnSe layer. Both images show many stacking faults originating at the interface region. They are believed to be caused by the lattice mismatch between the epilayer and the GaAs substrate. Ternary and quaternary layers in laser structures whose compositions were selected to give rise to close lattice matching to GaAs, however, were found to be nearly free from these defects [3]. In the image of the  $[0\bar{1}\bar{1}]$  cross-section, a periodic array of bright and dark bands parallel to the growth direction are seen from the bottom to the top of the quaternary epilayer. The period of this modulation is about 450 Å. In the image of the  $[011]$  cross-section, on the other hand, no such periodic modulation is observed, suggesting that the modulation is one-dimensional and parallel to the  $[011]$  direction. Fig. 2 is a  $020$  dark field image of a plan-view of the same quaternary epilayer. A highly regular periodic array of bright and dark bands is seen in the image. Directions of bands are nearly parallel to the  $[0\bar{1}\bar{1}]$  axis. Widths of bright and dark bands are not equal to each other; the former is about 80 Å and the latter 370 Å. Dark segments in the image are due to defects in the epilayer.

Fig. 3 is a bright field image of a  $[0\bar{1}\bar{1}]$  cross-

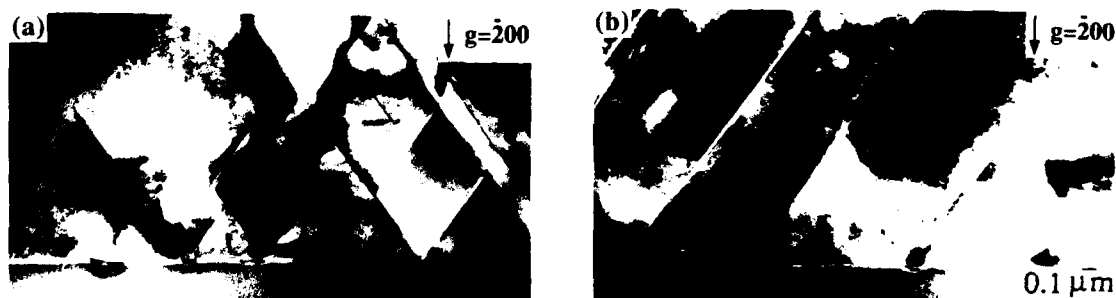


Fig. 1.  $\bar{2}00$  dark field images of (a) a  $[0\bar{1}\bar{1}]$  cross-section and (b) a  $[011]$  cross-section of a  $\text{Zn}_{1-x}\text{Mg}_x\text{Se}_{1-y}\text{S}_y$  ( $x = 0.218$  and  $y = 0.075$ ) epilayer.

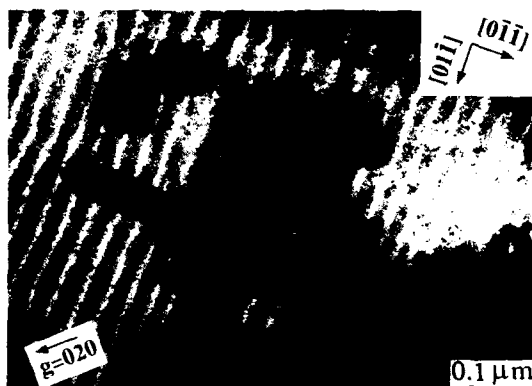


Fig. 2. 020 dark field image of a plan-view sample of a  $\text{Zn}_{1-x}\text{Mg}_x\text{Se}_{1-y}\text{S}_y$  ( $x = 0.218$  and  $y = 0.075$ ) epilayer.

section of a laser structure containing  $\text{ZnSe}_{1-x}\text{S}_x$  ( $x \approx 0.07$ ) layers. In the image, a periodic array of bright and dark bands due to phase separation is seen in the lower portion of the  $\text{ZnSe}_{1-x}\text{S}_x$  layer where Cl was doped as donors. In the upper portion of the  $\text{ZnSe}_{1-x}\text{S}_x$  layer where N was doped as acceptors, the contrast modulation due to phase separation is also seen, but its contrast is much weaker than that in the lower portion. The same trend, i.e., clearer images of phase separation in n-type layers than in p-type layers, was observed in all laser structures in which phase separation was found. The image of the phase separation was observed far more clearly in the quaternary layers with the sulfur concentrations greater than  $x = 0.2$  than in other layers, so that detailed analyses of phase separation were carried out by using these quaternary layers. The X-ray microanalysis of compositions in bright and dark bands was carried out on the plan-view sample shown in Fig. 2 by using a JEM 2000 FX analytical microscope. Concentrations of Se and S in each band were directly estimated by using the intensity ratio of the  $K\alpha$  radiation of Se and the K radiation of S, following the proportional relationship between the characteristic X-ray intensity and the concentration for thin specimens [8]. The average compositions of the epilayer was also used for the estimation. By this analysis, the sulfur concentrations in the bright and dark bands were found to be  $x \approx 0.13$  and  $x \approx 0.23$ , respec-

tively. The change of the Mg concentration and, hence, the change of the Zn concentration, was not detected because of the inability to observe an X-ray peak of Mg. The intensity of the X-ray radiation of Zn relative to those of Se and S did not exhibit any systematic change between the two bands.

Figs. 4a, 4b and 4c are dark field images taken from the same area of a  $[01\bar{1}]$  cross-sectional sample of the quaternary epilayer by using 200, 400 and 022 reflections, respectively. The change of the contrast of the periodic modulation is



Fig. 3. Bright field image of a  $[01\bar{1}]$  cross-section of a laser structure containing  $\text{ZnSe}_{1-x}\text{S}_x$  ( $x \approx 0.07$ ) layers.



consistent with the result of the X-ray microanalysis. The 200 dark field image, which is the most sensitive to the change of the composition within one sublattice of the zinc-blende type structure, exhibits the clearest image of the modulation. The 022 image also exhibits clear contrasts of the modulation, which is explained by the change of the spacing of (022) lattice planes due to the change of the sulfur concentration. The 400 image, on the other hand, does not show any signifi-

cant contrast of the modulation. The absence of the contrast in this image is attributed to the fact that the spacing of (*h*00) type lattice planes is not affected by this phase separation and the crystal structure of the 400 reflection is not sensitive to the composition change within one sublattice.

The results described above clearly indicate that phase separation can occur in  $\text{ZnSe}_{1-x}\text{S}_x$  and  $\text{Zn}_{1-y}\text{Mg}_y\text{Se}_{1-x}\text{S}_x$  epilayers grown by MBE. The X-ray microanalysis has shown that the phase

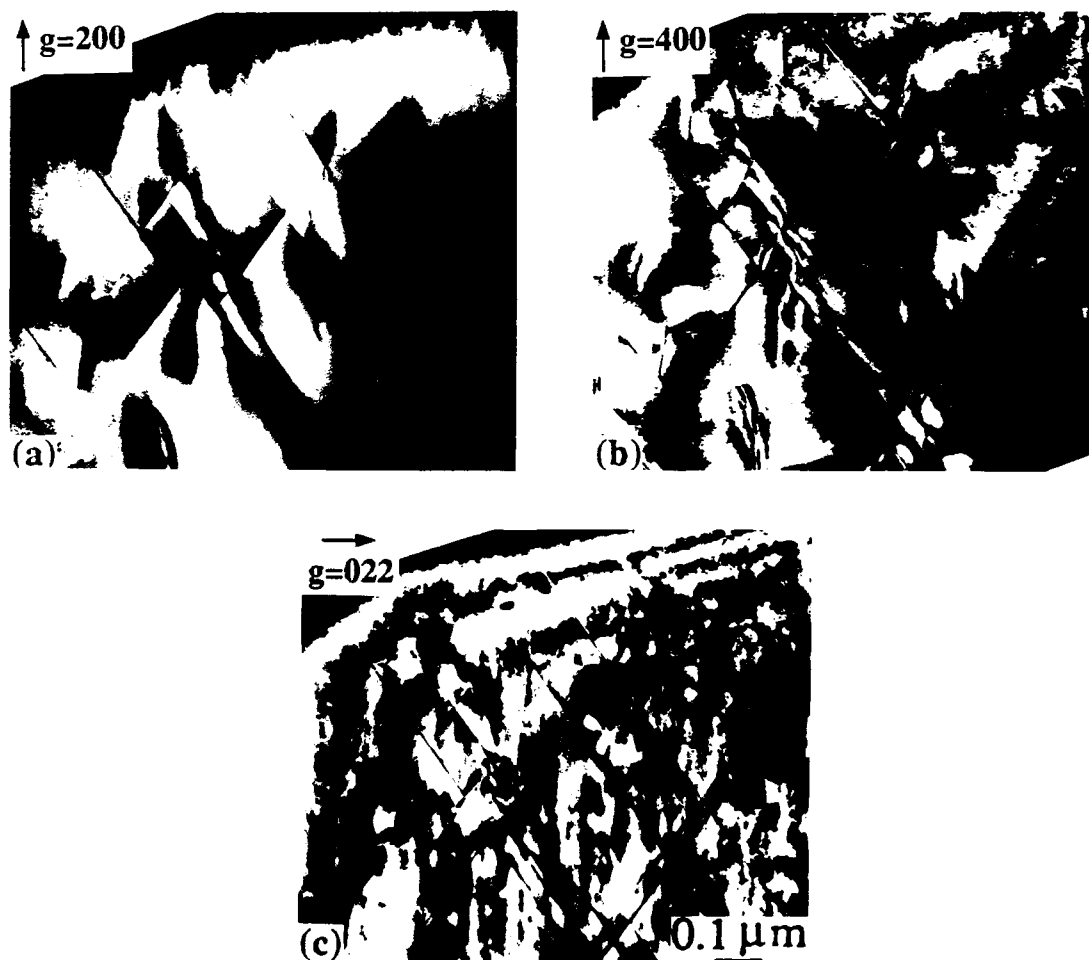


Fig. 4. Dark field images of a [011] cross-section of a  $\text{Zn}_{1-y}\text{Mg}_y\text{Se}_{1-x}\text{S}_x$  ( $x = 0.218$  and  $y = 0.075$ ) epilayer. Reflections used are (a) 200, (b) 400 and (c) 022.

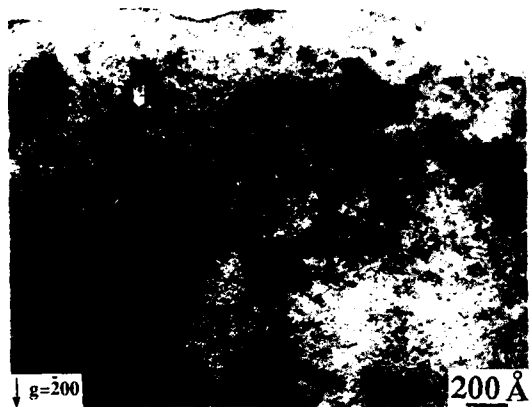


Fig. 5. Bright field image of a free surface region of a  $[01\bar{1}]$  cross-sectional sample of a  $\text{Zn}_{1-x}\text{Mg}_x\text{Se}_{1-y}\text{S}_y$  ( $x = 0.218$  and  $y = 0.075$ ) epilayer.

separation is described as the formation of S-rich and S-deficient bands. To date, there has been only one report on an experimental study of the phase stability of the  $\text{ZnSe}_{1-y}\text{S}_y$  system, which suggests that this alloy system is completely miscible at  $900^\circ\text{C}$  [9]. It is also interesting to note that, according to the delta lattice parameter (DLP) model [10], the  $\text{ZnSe}_{1-y}\text{S}_y$  system is expected to be completely miscible at the temperature used in the MBE growth of the ternary and quaternary layers. The present results, however, suggest strong possibility that these ternary and quaternary systems tend to become immiscible at the MBE growth temperature as the sulfur concentration increases.

There are some unusual features of phase separation in these alloy layers. Compared to compositional modulations resulting from phase separations in III–V alloy epilayers, the modulation in the present case is highly regular and its period is extremely large. Periods of compositional modulations in III–V alloy layers grown by MBE are typically several tens of ångströms, which are expected from surface diffusion lengths during the MBE growth of III–V alloy layers [11]. The very large periods of the modulation in the present case cannot be explained by surface dif-

fusion of atoms if one considers the growth temperature of these II–VI alloy layers. There is one observation which suggests a possible mechanism for the formation of the compositional modulation. TEM images of  $[01\bar{1}]$  cross-sectional samples of quaternary epilayers having phase separation show wavy surface structures of the epilayers. Fig. 5 is a bright field image showing such a wavy surface structure. As seen in Fig. 5, the period of the wavy surface structure exactly matches that of the compositional modulation. At each hill of the surface a sulfur-deficient band ends, and each valley of the surface matches a sulfur-rich band. Based on this observation, the following mechanism is suggested. Sulfur is a highly volatile species and, hence, is likely to attach only to step and kink sites during the MBE growth. The wavy surface structure, on the other hand, results in a periodic variation of the step density; the step density decreases at the hill and increases at the valley region. The wavy surface structure, therefore, may result in nonuniform incorporation of sulfur atoms and, hence, lead to the compositional modulation. It is unclear at present how such wavy surface structures have formed only in certain epilayers. Further studies are needed to clarify the origin of phase separation in these II–VI alloy layers.

This work has been supported by ARPA/ONR URI grant 218-25015, AFOSR grant F49620-92-J-0440 and NSF/MRG grant 8913706-DMR.

## 1. References

- [1] H. Okuyama, K. Nakano, T. Miyajima and K. Akimoto, *Jap. J. Appl. Phys.* 30 (1991) L1620.
- [2] J.M. Gaines, R.R. Drenten, K.W. Haberern, T. Marshall, P. Mensz and J. Petruzzello, *Appl. Phys. Lett.* 62 (1993) 2462.
- [3] D.C. Grillo, Y. Fan, J. Han, L. He, R.L. Gunshor, A. Salokatve, M. Hagerott, H. Jeon, A.V. Nurmikko, G.C. Hua and N. Otsuka, *Appl. Phys. Lett.* 63 (1993) 2723.
- [4] A. Zunger and S. Mahajan, Atomic ordering and phase separation in epitaxial III–V alloys, in: *Handbook on Semiconductors*, Vol. 3, 2nd ed. (Elsevier, Amsterdam, 1993).
- [5] A. Marbeuf, R. Druilhe, R. Triboulet and G. Patriarche, *J. Crystal Growth* 117 (1992) 10.

- [6] S. Mahajan, B.V. Dutt, H. Temkin, R.J. Cava and W.A. Bonner, *J. Crystal Growth* 68 (1984) 589.
- [7] J. Taftø and J.C.H. Spence, *J. Appl. Cryst.* 15 (1982) 60.
- [8] D.B. Williams, *Practical Analytical Electron Microscopy in Materials Science* (Verlag Chemie Intern., Deerfield, 1983).
- [9] S. Larach, R.E. Shreder and C.F. Stocker, *Phys. Rev.* 108 (1957) 587.
- [10] G.B. Stringfellow, *J. Phys. Chem. Solids* 34 (1973) 1749.
- [11] T.L. McDevitt, S. Mahajan, D.E. Laughlin, W.A. Bonner and V.G. Keramidas, *Phys. Rev. B* 45 (1992) 6614.

## In-situ monitoring by spectroscopic ellipsometry in ZnSe crystal growth by molecular beam epitaxy

Keishi Kato \*, Fujio Akinaga, Tsutomu Kamai, Mitsugu Wada

*Miyanodai Technical Development Center, Fuji Photo Film Co., 798 Miyanodai, Kaisai-machi, Ashigarakami-gun, Kanagawa 258, Japan*

### Abstract

We report the first in-situ monitoring by spectroscopic ellipsometry (SE) of the heteroepitaxial growth of ZnSe on GaAs by molecular beam epitaxy. In a series of experiments wherein ZnSe was grown on GaAs substrates or epilayers having various reconstructed GaAs surfaces, the trajectories of ( $\Psi$ ,  $\Delta$ ) and dielectric function spectra were measured and analyzed. It was found that the As-rich ( $4 \times 4$ ), the As-deficient ( $6 \times 4$ ) and the Ga-rich ( $4 \times 2$ ) reconstructed GaAs surfaces resulted in two-dimensional (layer-by-layer), pseudo-two-dimensional, and three-dimensional growth of ZnSe, respectively, and it was also found that the dielectric function of the as-grown ZnSe is quite different from that of the air-exposed ZnSe epilayer.

### 1. Introduction

In the development of II–VI semiconductor devices such as lasers, light emitting diodes (LEDs), and display devices, the development of high quality crystals is of potential importance. Many efforts have been made to achieve high quality crystals, where reflection high-energy electron diffraction (RHEED) has proven to be useful for in-situ monitoring the crystal growth by molecular beam epitaxy (MBE). Other ways of monitoring the crystal growth are optical techniques such as reflection difference spectroscopy (RDS) [1], surface photo-absorption (SPA) [2], spectroscopic ellipsometry (SE) [3] and so on, which have been applied to the growth of III–V

materials and have provided kinds of information different from those of RHEED. There have been few reports on the optical monitoring of the crystal growth of II–VI compounds [4,5]. In this paper, we report for the first time the results of in-situ monitoring by SE of the growth of ZnSe on GaAs substrates by MBE, exploring the capabilities of real-time monitoring of crystal growth by SE.

### 2. Experimental procedure

We used a Riber model 32P MBE system which has two growth chambers connected each to other by an ultrahigh vacuum pipeline. One growth chamber is used for the growth of GaAs epilayers on GaAs substrates. The other chamber, which has two special window ports provided

\* Corresponding author.

for optical access to the sample at an angle of approximately  $70^\circ$  for the in-situ SE measurements, is used for growth of II–VI materials and for the SE measurements. The SE measurements and the simulating calculations were performed using the commercial instrument (Jobin–Yvon phase modulated ellipsometer, UVISSEL) and its offered software, respectively. The measured ellipsometric parameters,  $\Psi$  and  $\Delta$ , are related to the equation,

$$\tan \Psi e^{i\Delta} = R_p/R_s,$$

where  $R_p$  and  $R_s$  are the complex reflection coefficients for light parallel and perpendicular to the plane of incidence, respectively. Our SE system was confirmed to be valid by the experimental result that the dielectric function spectrum of the as-grown GaAs epilayer grown on GaAs substrate was in excellent agreement with the “pseudodielectric function” of GaAs reported by Aspnes and Studna [6].

We used CrO-doped semi-insulating (100) GaAs substrates, which were degreased with methanol, acetone, and trichloroethane, etched in an 8:1:1 solution of  $H_2SO_4:H_2O_2:H_2O$ , rinsed in deionized water, and mounted on a molybdenum block with indium. ZnSe was grown either on GaAs substrates or on GaAs epilayers having various reconstructed GaAs surfaces at about  $300^\circ\text{C}$  under the condition of approximately unity II–VI beam equivalent pressure ratio. For the case of the growth of ZnSe on GaAs substrates having Ga-rich ( $4 \times 2$ ) and As-deficient ( $6 \times 4$ ) reconstructed surfaces, the GaAs substrates were heated in the absence of As flux in the II–VI chamber to above  $600^\circ\text{C}$  to remove surface native oxides of GaAs and to realize the desired reconstructed GaAs surfaces with monitoring the RHEED pattern. For the case of the growth of ZnSe on GaAs epilayers, the as-grown GaAs epilayers having As-rich  $c(4 \times 4)$  reconstructed surfaces were transferred to the II–VI chamber through the vacuum pipeline ( $< 3 \times 10^{-10}$  Torr) after the growth of the GaAs epilayer, and then heated to different temperatures:  $\sim 510$  or  $\sim 580^\circ\text{C}$  for realizing a ( $6 \times 4$ ) or a ( $4 \times 2$ ) reconstructed surface, respectively. For the growth of

ZnSe on  $c(4 \times 4)$  reconstructed GaAs, the as-transferred GaAs epilayer samples were used.

### 3. Results and discussions

#### 3.1. Dielectric function spectrum of ZnSe

Since there are few reports on the dielectric function of ZnSe [7,8], we measured the dielectric function spectrum or refractive indices of the as-grown ZnSe epilayer (about  $4.9 \mu\text{m}$  thick) grown on a GaAs epilayer, without removing the sample from the II–VI chamber to avoid oxidation. Also, for comparison, the same SE measurement was performed with the same sample after the sample was removed from the II–VI chamber and exposed to air for about one hour. The results are shown in Fig. 1, compared with the data of ZnSe bulk crystal reported by Adachi and Taguchi [7]. Although our measured spectra contain the interference effects below about 2.7 eV, they could be compared with the data obtained by Adachi and Taguchi in the higher energy

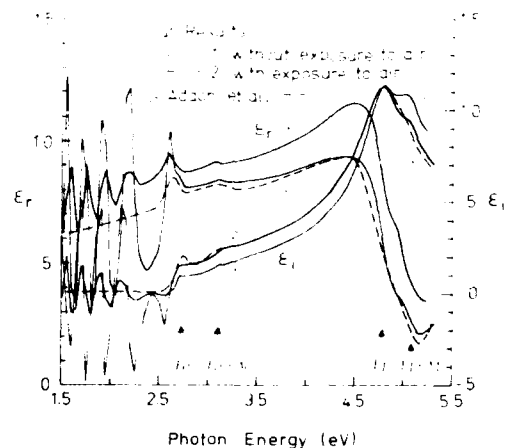


Fig. 1. Dielectric function spectra of ZnSe.  $\epsilon_1$  and  $\epsilon_2$  represent the real and imaginary parts of the dielectric constants, respectively. The two solid lines represent the measured spectra of the as-grown ZnSe epilayer at room temperature; one is measured in-situ without removing the sample from the chamber, and the other is measured ex-situ after the sample was removed from the chamber and exposed to air. The dashed line represents the data reported by Adachi and Taguchi [7].

spectral region ( $> 2.7$  eV), where the data are not affected by the interference effect because of the shorter penetration depth of light than the thickness of the ZnSe epilayer. As shown in Fig. 1, we found a remarkable difference between the data for the as-grown ZnSe epilayer and the air-exposed ZnSe epilayer sample, and the latter is in excellent agreement with the data reported by Adachi and Taguchi. These results strongly suggest that the ZnSe epilayer might be oxidized instantaneously when the sample is removed from the chamber and exposed to air. These results might be consistent with their experimental conditions, i.e., they were measured with the methanol-treated (110) ZnSe bulk crystal cleaved from the ZnSe ingot, which might be oxidized.

Considering that our result of the dielectric function of the as-grown ZnSe epilayer reveals the higher values of the real part of the dielectric constant, the clearer peaks corresponding to the several critical transitions ( $E_0$ ,  $E_0 + \Delta_0$ ,  $E_1$  and  $E_1 + \Delta_1$ ) shown in Fig. 1, and the well separation of  $E_1$  and  $E_1 + \Delta_1$ , our results of the as-grown epilayer would be the intrinsic values of ZnSe.

### 3.2. In-situ monitoring by SE in ZnSe growth on GaAs

In a series of experiments, wherein ZnSe was grown on GaAs substrates or GaAs epilayers having As-rich  $c(4 \times 4)$ , As-deficient  $(6 \times 4)$ , and Ga-rich  $(4 \times 2)$  reconstructed GaAs surfaces, the real-time trajectories of  $(\Psi, \Delta)$  were measured at 2.75 eV to monitor the growth of ZnSe on GaAs.

Fig. 2a shows the typical trajectory of  $(\Psi, \Delta)$  for the growth of ZnSe on an As-rich  $c(4 \times 4)$  reconstructed GaAs epilayer. In Fig. 2b,  $\Psi$  and  $\Delta$  at the early stage of growth are also plotted as a function of growth time. The trajectory shows a standard spiral (or oscillatory behavior) beginning and ending at the values of the underlying GaAs and deposited ZnSe, respectively. Assuming two-dimensional (layer-by-layer) growth of ZnSe and a constant growth rate, we can simulate the trajectory with using the three-phase model [9] involving the substrate, ZnSe epilayer, and ambient. As shown in Fig. 2, the simulated trajectory is nicely fitted to the experimental data. The growth rate determined from the simulation, 2.62

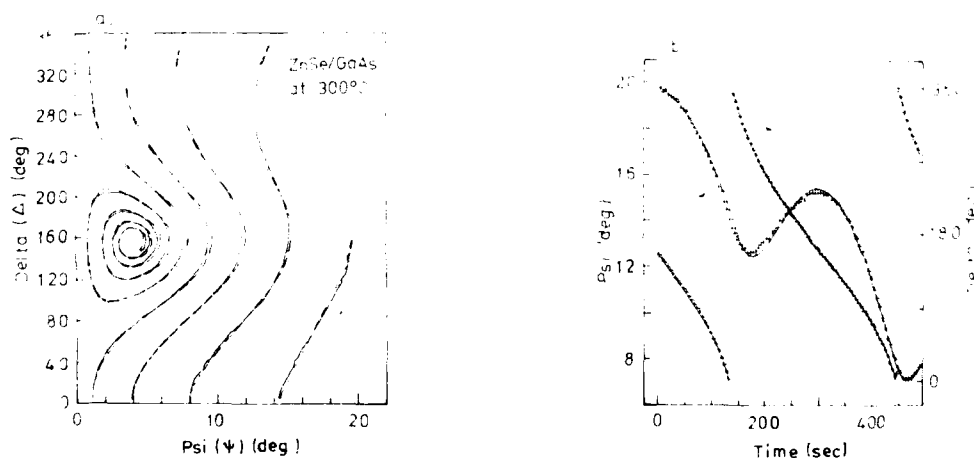


Fig. 2. (a) Real-time trajectory of  $(\Psi, \Delta)$  for the growth of ZnSe on an As-rich  $c(4 \times 4)$  reconstructed GaAs epilayer. The solid line represents the data measured at an interval of 5 s for about 45 min growth of ZnSe. The dashed line represents the simulated data with a growth rate of 2.62 Å/s. (b) Real-time trajectory of  $(\Psi, \Delta)$  plotted as a function of time for the growth of ZnSe on an As-rich  $c(4 \times 4)$  reconstructed GaAs epilayer. The symbols + represent the data measured at an interval of 5 s and the solid line represents the simulated trajectory with a growth rate of 2.62 Å/s.

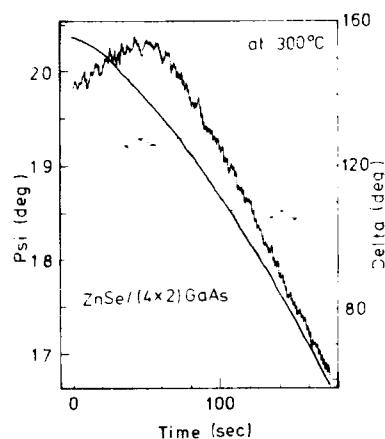


Fig. 3. Real-time trajectory of  $(\Psi, \Delta)$  for the growth of ZnSe on a Ga-rich  $(4 \times 2)$  reconstructed GaAs epilayer. The data were taken at intervals of 1 s.

$\text{\AA}/\text{s}$ , agrees very well with the growth rate determined by the film thickness measurement,  $2.6 \text{ \AA}/\text{s}$ .

Fig. 3 shows the trajectory of  $(\Psi, \Delta)$  for the growth of ZnSe on a Ga-rich  $(4 \times 2)$  reconstructed GaAs epilayer. As shown in Fig. 3, the

initial increase of  $\Psi$  is observed at the initial stage of ZnSe growth, independent of whether growth is on GaAs epilayer or on GaAs substrate. This is in contrast to the initial decrease of  $\Psi$ , which is observed for the case of ZnSe growth on a  $c(4 \times 4)$  reconstructed GaAs epilayer and is predicted for the two-dimensional growth of ZnSe on GaAs from the theoretical simulation, as described above.

To interpret the initial increase of  $\Psi$  qualitatively, we considered a crude model of three-dimensional inhomogeneous growth and applied the effective medium approximation (EMA) [10] to calculate the trajectory. In the EMA, the microscopically rough ZnSe surface, which might be caused from three-dimensional inhomogeneous growth in the early stage of ZnSe growth, is treated to be effectively equivalent to a homogeneous layer containing a certain amount of voids. Fig. 4b shows an example of the calculated trajectories with the EMA for the growth model including the step-functional decrease of the roughnesses with growth as shown in Fig. 4a, showing that the initial increase of  $\Psi$  is observed and that the magnitudes of the increase of  $\Psi$  become less with a decrease of the thickness of a three-dimen-

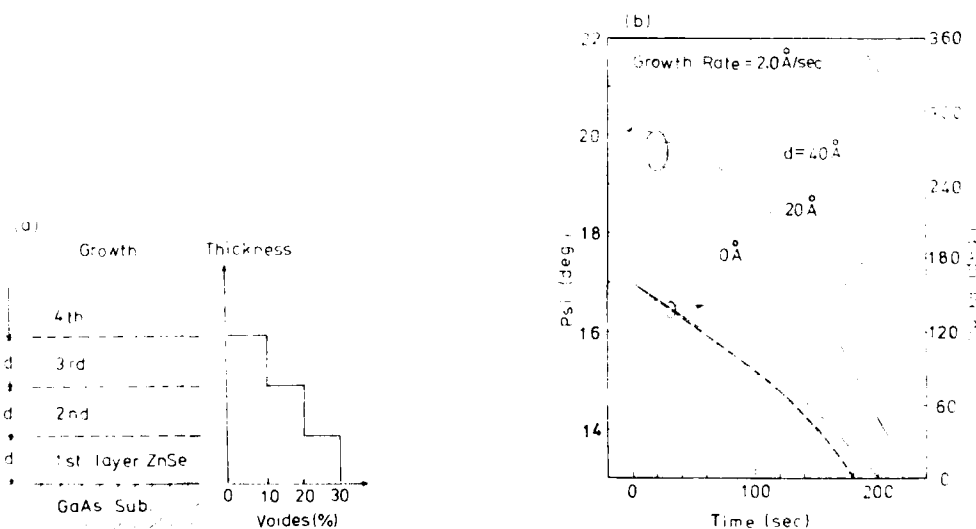


Fig. 4. (a) Crude model for three-dimensional growth. The model assumes that the microscopic roughness of the growth surface decreases step-functionally with an increase of the thickness of the growth layer. (b) Calculated trajectory of  $(\Psi, \Delta)$  for the model shown in (a).

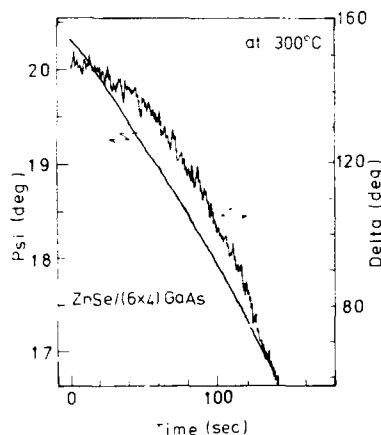


Fig. 5. Real-time trajectory of  $(\Psi, \Delta)$  for the growth of ZnSe on an As-deficient  $(6 \times 4)$  reconstructed GaAs epilayer. The data were taken at intervals of 1 s.

sionally grown layer. These qualitative results suggest that the initial increase of  $\Psi$  is characteristic for the three-dimensional growth. From these results, it can be concluded that three-dimensional growth occurs on Ga-rich  $(4 \times 2)$  reconstructed GaAs, consistent with the RHEED observations in the initial stage of growth of ZnSe reported by several authors [11].

Fig. 5 shows the trajectory of  $(\Psi, \Delta)$  for the case of the growth of ZnSe on an As-deficient  $(6 \times 4)$  reconstructed GaAs epilayer. The initial increase of  $\Psi$  is hard to be seen. However, it was found that the fitting of the simulated trajectories, with assuming layer-by-layer growth, to the experimental data is not as good as that obtained for the case of ZnSe growth on a  $c(4 \times 4)$  reconstructed GaAs. Similar results were obtained for the ZnSe growth on  $(6 \times 4)$  reconstructed GaAs substrates. These results indicate that three-dimensional growth occurs at the very initial stage of ZnSe growth, consistent with the RHEED observations by others [12].

As mentioned above, our results show that the initial growth modes in the growth of ZnSe on GaAs are not essentially dependent on whether the growth occurs on the substrates or on the epilayer, but are strongly dependent on the surface reconstructions of GaAs. These results might

be caused by the "stoichiometry-induced electrostatic effects" proposed by Farrell et al. [13].

### 3.4. Characterization of thin ZnSe epilayers grown on GaAs

In order to elucidate the effects of the initial growth modes on the quality of the ZnSe epilayer, thin ZnSe epilayers grown on an As-deficient  $(6 \times 4)$  and on a Ga-rich  $(4 \times 2)$  reconstructed GaAs substrate or epilayer were characterized by the measurements of the X-ray diffraction rocking curve. The thicknesses of the ZnSe epilayers were chosen to be all less than the critical thickness of the ZnSe on GaAs, about  $0.2 \mu\text{m}$  [14], because the X-ray diffraction data might be affected by the misfit dislocations caused in the crystal of above the critical thickness. Fig. 6 shows the results for the ZnSe epilayers grown on GaAs substrates. Similar results were obtained for the ZnSe epilayers grown on GaAs epilayers. The diffraction peaks of ZnSe in both samples are located at about  $800 \text{ arc sec}$  apart from that of GaAs, indicating that the ZnSe epilayers in both samples are coherently strained. However, it can also be seen that the ZnSe epilayer grown on a  $(6 \times 4)$  reconstructed GaAs shows a stronger and narrower X-ray diffraction pattern (FWHM of  $\sim 100 \text{ arc sec}$ ) than that of the ZnSe epilayer

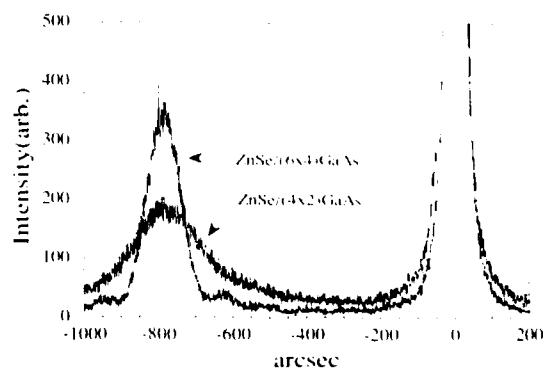


Fig. 6. X-ray rocking curves of thin ZnSe films grown on Ga-rich  $(4 \times 2)$ , and on As-deficient  $(6 \times 4)$  reconstructed GaAs substrates. The thicknesses of the former and the latter ZnSe epilayer, measured by SEM observation, are  $1440$  and  $840 \text{ \AA}$ , respectively.



on  $(4 \times 2)$  reconstructed GaAs, in spite of the fact that the thickness of the former ZnSe epilayer is less than that of the latter sample. This clearly suggests that the quality of the former ZnSe epilayers is higher than that of the latter sample, corresponding to the initial growth mode, i.e., two-dimensional growth in the former and three-dimensional growth in the latter, respectively. This might be demonstrated in further investigations by TEM or in other ways.

#### 4. Conclusions

In summary, we have first applied SE to the in-situ monitoring of the ZnSe growth on GaAs substrates or epilayers having various reconstructed GaAs surfaces. From these investigations, it was confirmed by the trajectories of  $(\Psi, \Delta)$  that the initial growth mode in the growth of ZnSe on GaAs is not essentially dependent on whether the substrate or the epilayer is used, but is strongly dependent on the reconstructed surface of GaAs, i.e., the GaAs substrate or epilayer reconstructed as As-rich  $(4 \times 4)$ , As-deficient  $(6 \times 4)$  and Ga-rich  $(4 \times 2)$  leads to two-dimensional, pseudo-two-dimensional and three-dimensional growth of ZnSe, respectively. We also found that the spectrum of the dielectric function or refractive indices of the as-grown ZnSe epilayer is quite different from that of the air-exposed ZnSe epilayer, suggesting the fast oxidation of

ZnSe. In addition, we showed that the SE is useful for the determination of the growth rates and thicknesses.

#### 5. References

- [1] D.E. Aspnes, J.P. Harbison, A.A. Studna and L. Florez, *Phys. Rev. Lett.* 59 (1987) 1687.
- [2] T. Makimoto, Y. Yamaguchi, N. Kobayashi and Y. Horikoshi, *Jap. J. Appl. Phys.* 29 (1990) L207.
- [3] D.E. Aspnes, W.E. Quinn and S. Gregory, *Appl. Phys. Lett.* 56 (1990) 2569.
- [4] Y. Demay, D. Arnoult, J.P. Gaillard and P. Medina, *J. Vac. Sci. Technol. A* 5 (1987) 139.
- [5] T. Okamoto and A. Yoshikawa, *Jap. J. Appl. Phys.* 30 (1991) L156.
- [6] D.E. Aspnes and A.A. Studna, *Phys. Rev. B* 27 (1983) 985.
- [7] S. Adachi and T. Taguchi, *Phys. Rev. B* 43 (1991) 9569.
- [8] Y.D. Kim, S.L. Cooper and M.V. Klein, *Appl. Phys. Lett.* 62 (1993) 2387.
- [9] R.M.A. Azzam and N.M. Bashara, *Ellipsometry and Polarized Light* (North-Holland, Amsterdam, 1977).
- [10] D.E. Aspnes, J.B. Theeten and P. Hottier, *Phys. Rev. B* 20 (1979) 3292.
- [11] M.C. Tamargo, J.L. de Miguel, D.M. Hwang and H.H. Farrell, *J. Vac. Sci. Technol. B* 6 (1988) 784.
- [12] J. Qiu, Q.D. Qian, R.L. Gunshor, M. Kobayashi, D.R. Menke, D. Li and N. Otsuka, *Appl. Phys. Lett.* 56 (1990) 1272.
- [13] H.H. Farrell, M.G. Tarmargo, J.L. de Miguel, F.S. Turco, D.M. Hwang and R.E. Nahory, *J. Appl. Phys.* 69 (1991) 7021.
- [14] K. Mohammed, D.A. Cammack, R. Dalby, P. Newbury, B.L. Greenberg, J. Petruzzello and R.N. Bhargava, *Appl. Phys. Lett.* 50 (1987) 37.

## Incorporation of nitrogen in ZnSe grown by metalorganic vapour phase epitaxy

A. Hoffmann <sup>\*a</sup>, R. Heitz <sup>a</sup>, B. Lummer <sup>a</sup>, Ch. Fricke <sup>a</sup>, V. Kutzer <sup>a</sup>, I. Broser <sup>a</sup>,  
W. Taudt <sup>b</sup>, G. Gleitsmann <sup>b</sup>, M. Heuken <sup>b</sup>

<sup>a</sup> Institut für Festkörperphysik, Technische Universität Berlin, Hardenbergstrasse 36, D-10623 Berlin, Germany

<sup>b</sup> Institut für Halbleitertechnik, RWTH Aachen, Templergraben 55, D-52056 Aachen, Germany

### Abstract

The incorporation processes and efficiencies of nitrogen doping for p-type conductivity in metalorganic vapour phase epitaxy (MOVPE) grown ZnSe/GaAs epilayers are investigated by means of time-integrated and time-resolved photoluminescence (PL) spectroscopy. Two nitrogen-doping methods are compared, plasma-enhanced doping during growth, and ion implantation of nitrogen with annealing after growth. Both types of doped layers exhibit the  $I_1^N$  transition from a neutral acceptor bound exciton complex ( $A_0^N$ , X), indicating an effective nitrogen embedding on selenium sites. With increasing nitrogen doping rates, a deeper bound exciton line  $I_1^N$  appears, lowering the intensity of the  $I_1^N$ . An observed reduction of the  $I_1^N$  and  $I_1^N$  lifetimes for higher nitrogen doping concentrations results from an enhanced overlap of the bound exciton wave functions with those of other impurity centres.

### 1. Introduction

The fabrication of p-conductive MOVPE ZnSe layers with high reproducibility would open up the exciting prospect of a variety of interesting applications. Low-resistive p-type material with high concentrations of free carriers has to date only been obtained in nitrogen-doped ZnSe grown by molecular beam epitaxy (MBE). Nitrogen concentrations of up to  $1 \times 10^{19} \text{ cm}^{-3}$  and free hole concentrations of up to  $7.7 \times 10^{17} \text{ cm}^{-3}$  have been reported [1]. The low-temperature photoluminescence spectra of such layers are dominated

by donor–acceptor pair (DAP) recombination with photon energies between 2.623 and 2.695 eV, depending on the growth conditions [2] and the nitrogen concentration [1]. In contrast, material grown by MOVPE suffers from a low activation of the incorporated nitrogen resulting in highly resistive layers as yet. The low activation of the incorporated nitrogen is due to self-compensation mechanisms which are controversially discussed in the literature [2–4]. In the present work we investigate the time-integrated and, for the first time, time-resolved photoluminescence of nitrogen-doped MOVPE ZnSe layers in the energy region of excitons and DAP recombination, yielding information on defects created during growth and doping, their interactions, and the efficiency of p-doping.

\* Corresponding author.

## 2. Experimental procedure

Two different doping procedures are compared, varying systematically the doping and preparation parameters in order to obtain high nitrogen concentrations and to control the incorporation process. Samples were grown on (100) GaAs substrates at temperatures between 380 and 550°C by plasma-enhanced low-pressure MOVPE using DIPSe (diisopropylselenide), DAsSe (diallylselenide) or DESe (diethylselenide), and DEZn (diethylzinc) as precursors. In-situ nitrogen doping is performed with a DC nitrogen plasma. Ex-situ nitrogen doping is carried out by ion implantation of nitrogen (dose  $1.5 \times 10^{13} \text{ cm}^{-2}$ , energy 40–240 keV) and subsequent annealing. SIMS measurements yield nitrogen concentrations around  $5 \times 10^{17} \text{ cm}^{-3}$ .

For the photoluminescence spectra, the ZnSe layers are excited above the band gap by the 364 nm line of an Ar-ion laser (Spectra). Time-resolved measurements are performed with a dye laser synchronously pumped by an actively mode-locked Nd:YAG laser (Coherent) with a frequency-tripling BBO crystal. The PL signal is analysed using the time correlated single-photon-counting technique and a micro-channel-plate photomultiplier tube. The transients are fitted by convolution of the apparatus response with two exponential functions, one for the luminescence rise ( $\tau_r$ ), and one for the luminescence decay ( $\tau_d$ ).

## 3. Experimental results

In Fig. 1, time-integrated PL spectra of differently nitrogen doped ZnSe epilayers in the energy range between 2.50 and 2.82 eV are compared with that of a DESe as-grown sample (a). Spectrum (b) in fig. 1 represents the emission behaviour of a DESe sample doped ex situ by ion-implantation with energies of 120 keV and subsequently annealed at 850°C for 30 s. In addition to the structures observed in the as-grown sample, a weak acceptor-bound exciton emission  $I_1^N$  at 2.790 eV (on the low energy shoulder of the  $I_2$ ) and a dominant  $I_1^c$  line are observed. Similar

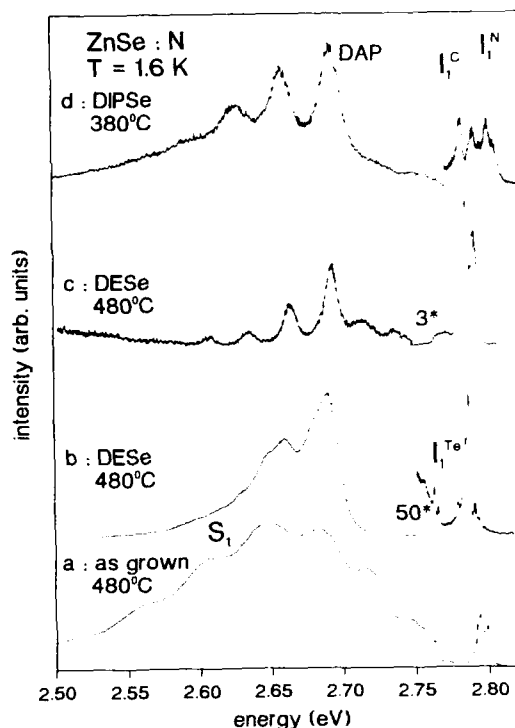


Fig. 1. Luminescence spectra at 1.6 K of differently nitrogen-doped ZnSe epilayers compared to an as-grown sample.

spectra are obtained from plasma-N-doped ZnSe using DESe (c) or DIPSe (d) as precursors. The existence of the  $I_1^N$  (recombination of the  $(A_{\text{N}}^0, X)$  complex) unambiguously evidences the incorporation of nitrogen on selenium sites in N-doped MOVPE-grown ZnSe layers. This is further confirmed by the energy position of the donor-acceptor pair recombination, yielding an ionization energy of the nitrogen acceptor of 110 meV. Nevertheless, the dominating  $I_1^c$  line grows with increasing nitrogen doping rate and indicates compensating defects. The origin of the  $I_1^c$  is debated in terms of a deeply bound exciton or a defect related centre to date [5]. We observe this transition in nitrogen-doped but not in undoped MOVPE samples, as the comparison of the spectrum in Fig. 1a with those in Figs. 1b, 1c or 1d clearly reveals.

Around 2.76 eV a doublet of sharp zero-phonon lines (ZPLs)  $I_1^c$  with strong longitudinal

optical (LO) phonon coupling appears in the spectra of Figs. 1a, 1b and 1d. The whole luminescence band is marked by  $S_1$ . In the as-grown sample (a) compared to (b) and (d), no DAP luminescence is to be seen. Using high purity precursors, the  $S_1$  can be diminished as is obvious from spectrum (c) of the DESe-grown sample. In Te-doped ZnSe epilayers, Dhese et al. [6] observed an  $S_1$  band in the same spectral region, which is assigned to recombinations of excitons bound at Te doublets on nearest neighbour anion sites. The periodic structure on the high-energy shoulder reflects the LO phonon energy in ZnSe (31.5 meV). The large FWHM is attributed to the large degree of electron–phonon coupling (insert of fig. 2). This is in agreement with the fact that the DIPSe, DEZn and DESe precursors are contaminated with Te, As, Zn, Sn and B [7]. The transients of this emission are found to be independent of the photon energy, giving a two-exponential decay with time constants of 11.1 and 55.1 ns for the  $I_1^{Te}$  doublet as well as for the  $S_1$  band (Fig. 2). A similar dynamical behaviour is known from the Cu-blue luminescence band in ZnS [8], which is attributed to a deeply Cu-bound exciton with two excited states.

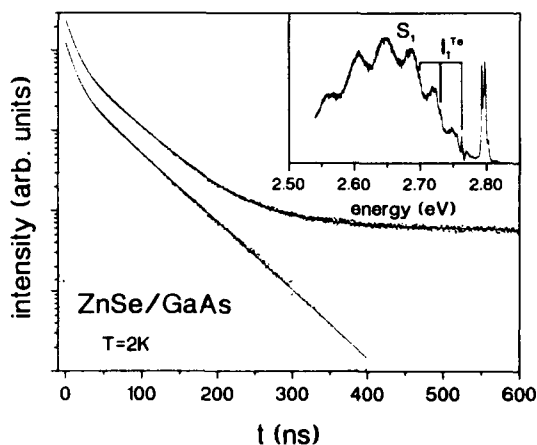


Fig. 2. Transients of the luminescence band  $S_1$  of MOVPE grown ZnSe using DESe as Se precursor and a growth temperature of 480°C. The lower transient is obtained by subtracting the long lived background from the DAP luminescence, clearly revealing a double exponential decay of  $S_1$ . The inset shows the pertaining luminescence spectrum.

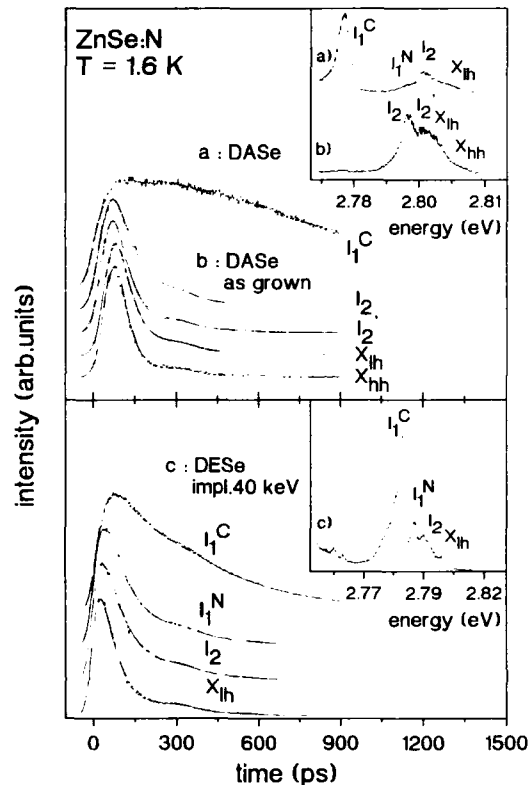


Fig. 3. Transients of different exciton emissions in MOVPE-grown and plasma-doped (a) or N-implanted (c) ZnSe samples compared to those of a DASE as-grown (b) sample.

Fig. 3b shows the transients of the free and bound excitons of the DASE as-grown sample compared to those of in-situ doped (Fig. 3a) and N-implanted (Fig. 3c) samples after interband excitation.

In the excitonic energy region, a typical as-grown spectrum exhibits the strain-split free exciton emissions  $X_{lh}$  and  $X_{hh}$  and the donor-bound exciton lines  $I_1$  and  $I_2$  (see the luminescence spectrum inset (b) in Fig. 3).

All rise ( $\tau_r$ ) and decay ( $\tau_d$ ) times are in the ps region (see Table 1). The decay times are found to increase with growing binding energy of the bound exciton complex. With increasing nitrogen concentration the decay times decrease, indicating the opening of competing nonradiative re-

Table 1

Rise  $\tau_r$  and decay  $\tau_d$  times (in ps) of free and different bound excitons in various ZnSe samples <sup>a</sup>

	MOVPE				MBE		Bulk	
	N-plasma		N-implanted		[12]		[11]	
	$\tau_r$	$\tau_d$	$\tau_r$	$\tau_d$	$\tau_r$	$\tau_d$	$\tau_r$	$\tau_d$
$X_{hh}$	–	35	–	–	20	100	–	–
$X_{lh}$	20	45	–	55	80	150	–	30
$X$	–	–	–	–	–	–	–	–
$I_2^{hh}$	20	50	–	–	110	140	–	–
$I_2^{lh}$	20	80	–	80	150	200	–	–
$I_1^s$	–	–	–	–	–	–	20	40
$I_1^{Li}$	–	–	–	–	–	–	50	280
$I_1^N$	–	–	–	–	–	–	50	350
$I_1^N$	–	–	–	–	120	300	–	–
$I_1^C$	20	90	5	90	–	–	–	–
$I_1^C$	20	900	20	260	–	–	–	–
$I_1^{deep}$	–	–	–	–	–	–	100	1020

<sup>a</sup>  $X_i$ , free excitons;  $I_2^s$ , donor bound excitons;  $I_1^s$ , acceptor bound excitons; lh and hh, strain split components.

combination channels. However, this effect is also observed for different growth conditions giving rise to different defect backgrounds. Detailed investigations show that ion implantation energies in the range of 40 keV lead to a dominant  $I_1^N$  line, whereas higher implantation energies favour the  $I_1^C$  emission. From the transients recorded after interband excitation (Fig. 3), it is obvious that there is a drastic reduction of the  $I_1^N$  and  $I_1^C$  lifetimes, while the lifetimes of the free excitons and the donor bound excitons remain nearly unchanged in comparison with the corresponding transitions in plasma doped samples (see Table 1). This behaviour becomes more pronounced with increasing implantation energy, indicating that defects created during the ion implantation process are responsible. The lifetime of the  $I_1^C$  line of 900 ps in plasma-doped ZnSe epilayers using DASE or DESe precursors corresponds well to that of the  $I_1^{deep}$  line in bulk material having a similar binding energy [9].

In Fig. 4 time-resolved investigations of the donor–acceptor pair (DAP) luminescence are presented. The inset of Fig. 4 shows the emission spectrum of a DIPSe plasma-doped ZnSe epilayer grown at 380°C compared with that of a

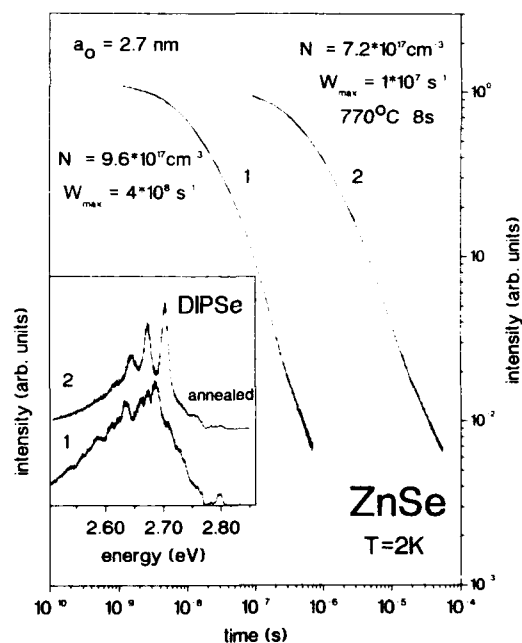


Fig. 4. Transients of the DAP luminescence in plasma-doped ZnSe epilayers grown with a DIPSe precursor at 380°C. Sample 1 has not been annealed, whereas sample 2 has been annealed for 8 s at 770°C. The inset shows the related DAP luminescence.

sample which was subsequently annealed for 8 s at 770°C. It is evident here that annealing leads to an increase of the DAP luminescence in comparison with the exciton emissions and  $S_1$  band. The decay of the DAP recombination yields information on doping concentration and on compensation mechanisms. Using the statistical model of Thomas and Hopfield [10], we determined an acceptor concentration of  $9.6 \times 10^{17} \text{ cm}^{-3}$  without and of  $7.2 \times 10^{17} \text{ cm}^{-3}$  after annealing. This indicates that this annealing temperature has a weak influence on the incorporation of shallow impurities in MOVPE-grown ZnSe epilayers. However, the decrease of  $W_{\text{max}}$ , which is a measure of the transition probability, demonstrates that the deep defect concentration is strongly reduced.

#### 4. Discussion

It is important to point out that both plasma doping and ion implantation lead to an efficient nitrogen doping of MOVPE-grown ZnSe layers. The occurrence of the  $I_1^N$  line, corresponding to the radiative recombination of an  $(A_N^0, X)$  complex, as well as the donor–acceptor pair recombination energy, indicate an incorporation of nitrogen atoms on selenium sites. These centres act as neutral acceptors and are required for p-type ZnSe. Nevertheless, all investigated nitrogen-doped MOVPE layers are highly resistive, indicating the simultaneous generation of compensating deep donors during the doping process. The dependence of the bound exciton lifetimes on the implantation energy confirms this interpretation.

A prominent feature of our nitrogen doped ZnSe epilayers is the  $I_1^C$  line, which is not present in undoped samples. A strong increase of the  $I_1^C$  intensity by two orders of magnitude takes place with increasing nitrogen doping rates, indicating a correlation between the  $I_1^C$  and nitrogen. However, we observe the same transition in undoped hot-wall epitaxy (HWE) grown ZnSe epilayers and bulk ZnSe crystals [11], too, but not in ultra-pure MBE samples [12]. Since the intensity of the  $I_1^C$  line depends more critically on growth parameters than on the various dopants, we assign this

line to a point-defect-related centre. Detailed investigations of undoped ZnSe samples clearly correlate the  $I_1^C$  intensity with an increasing Se/Zn ratio, supporting an interpretation as radiative recombination of an  $(A^0, X)$  complex formed at a deep acceptor based on a zinc vacancy. Thus, the dominating  $I_1^C$  line in nitrogen-doped MOVPE samples indicates the creation of zinc vacancies during nitrogen incorporation even in the case of in-situ plasma doping. Undoped MOVPE samples show no  $I_1^C$  line (Fig. 1a) indicating a sufficient quality of these layers. Nevertheless, the generation of deep acceptors does not prevent p-conductivity, which may be due to deep donors formed, e.g., by Te incorporation during growth using DEZn or DIPSe as precursors. Further progress in p-conductivity of MOVPE-grown ZnSe epilayers requires undoubtedly the reduction of the number of  $I_1^C$  related centres by the optimization of doping parameters and purified precursors. A further point is to diminish the growth temperature to 300°C, which is usual for MBE samples.

The lifetimes of the free and bound exciton complexes are sensitive to the defect concentration and thus give information on the defect concentration in the investigated layers. The formation of bound exciton complexes at shallow donors and acceptors is a major recombination channel for free excitons [9], limiting the free exciton lifetimes in doped crystals. For bound exciton complexes, both the screening of the electrostatic interaction at high doping concentrations [13] and the introduction of competing non-radiative recombination channels by energy transfer processes in the presence of deep centres lead to a reduction of their lifetimes. The longest excitonic lifetimes in ZnSe have been observed in ultra-pure MBE samples to date (see Table 1). Even in high purity bulk material, the free as well as the donor bound exciton lifetimes are strongly reduced, whereas the acceptor bound exciton lifetimes can be explained by the entirely radiative decay of the undisturbed complexes [11] with the model of Rashba and Gurgenshvili [14]. The comparatively short excitonic lifetimes observed for nitrogen-doped MOVPE samples result from a large concentration of disturbing defects. This

effect is especially pronounced for the  $I_1^N$  and the  $I_1^C$  complexes in nitrogen-implanted samples, indicating a large number of deep defects. The excitonic lifetimes become even shorter using higher implantation energies. Thus, it seems to be reasonable that zinc vacancies created during the implantation process form deep acceptors and are responsible for the large concentration of deep defects.

## 5. References

- [1] J. Qiu, J.M. DePuydt, H. Cheng and M.A. Haase, Appl. Phys. Lett. 59 (1991) 2993.
- [2] I.S. Hauksson, J. Simpson, S.Y. Wang, K.A. Prior and B.C. Cavenett, Appl. Phys. Lett. 61 (1992) 2208.
- [3] A. Ohki, Y. Kawaguchi, K. Ando and A. Katzui, Appl. Phys. Lett. 59 (1991) 671.
- [4] D.J. Chadi and K.J. Chang, Appl. Phys. Lett. 55 (1989) 575.
- [5] P.J. Dean and J.L. Merz, Phys. Rev. 178 (1969) 1310.
- [6] K.A. Dhese, J.E. Nicholls, P.J. Wright, B. Cockayne and J.J. Davies, J. Crystal Growth 126 (1993) 179.
- [7] Data Sheet, Morton International, USA.
- [8] A. Hoffmann, A. Franz, A. Ismail, F. Asch and I. Broser, Mater. Sci. Forum 38–41 (1992) (1989) 525.
- [9] R. Heitz, C. Fricke, A. Hoffmann and I. Broser, Mater. Sci. Forum 83–87 (1992) 1241.
- [10] D.G. Thomas, J.J. Hopfield and W.M. Augustyniak, Phys. Rev. 140 (1965) A 202.
- [11] G. Kudlek, U.W. Pohl, Ch. Fricke, R. Heitz, A. Hoffmann, J. Gutowski and I. Broser, Physica B 185 (1993) 325.
- [12] G. Kudlek, Ch. Fricke, N. Presser, R. Heitz, A. Hoffmann, J. Gutowski and I. Broser, in: Proc. 21st Int. Conf. on Physics of Semiconductors, Beijing, 1992 (World Scientific, Singapore, 1992) p. 1168.
- [13] Ch. Fricke, U. Neukirch, R. Heitz, A. Hoffmann and I. Broser, J. Crystal Growth 117 (1992) 783.
- [14] E.I. Rashba and G.E. Gurgenishvili, Sov. Phys.-Solid State 4 (1962) 759.



ELSEVIER

Journal of Crystal Growth 138 (1994) 385–390

JOURNAL OF  
**CRYSTAL  
GROWTH**

## Shallow impurity- and defect-related complexes in undoped ZnSe crystals

U.W. Pohl <sup>\*,a</sup>, G.H. Kudlek <sup>a</sup>, A. Klimakow <sup>b</sup>, A. Hoffmann <sup>a</sup><sup>a</sup> *Institut für Festkörperphysik, Technische Universität Berlin, Hardenbergstrasse 36, D-10623 Berlin, Germany*<sup>b</sup> *Institut für Optik und Spektroskopie, Humboldt-Universität Berlin, Invalidenstrasse 110, D-10115 Berlin, Germany*

### Abstract

The electronic structure of bound excitons involving native- as well as point-defects is investigated by optical spectroscopy using highly crystalline ZnSe samples grown by the Markov method. We demonstrate that the interactions of attendant single particles is responsible for the splitting of the ( $D^0$ , X) and ( $A^0$ , X) states. From these splittings the hole-hole interaction parameter  $\gamma$  and the cubic crystal-field parameter  $\beta$  for the Li bound exciton complex has been determined unambiguously for the first time. The  $I_1^d$  emission line shows a fine structure which is similar to the  $I_1^+$  exciton line.  $I_1^d$  is therefore assigned to an acceptor-bound exciton recombination with an associate formed by a zinc vacancy and an impurity donor combined acting as an acceptor.

### 1. Introduction

The increasing interest in growing high-quality ZnSe samples for opto-electronic device applications in the blue range of the visible spectrum raised a series of open questions about the responsible excitation channels [1] and the nature and behaviour of shallow impurities. In this context, a major problem is the strong self-compensation mechanism, avoiding effective p-type low-resistance conductivity. Up to now, only nitrogen seems to be a suitable candidate.

For the investigations of shallow donor and acceptor bound excitons and the interaction with point defects, we used ZnSe single crystals grown by the Markov vapour phase transport method [2]

at 1190°C with a thermal gradient of 10°C to the source material. Near-band-edge photoluminescence measurements at different temperatures, as well as excitation and reflection spectroscopy lead to detailed information on the electronic structure of the exciton complexes involved.

The emission spectrum obtained by band-to-band excitation, recorded in the exciton energy range, is shown in Fig. 1. Due to the high crystallinity of the used samples, pronounced donor-bound exciton lines  $I_2$  and a predominant acceptor-bound exciton recombination  $I_1^+$  could be resolved. The main interest is focussed on the nature of the  $I_1^d$  line (also denoted as  $I_1^{\text{deep}}$  or  $I_1^c$  by other authors) which up to now is controversially discussed in terms of either involved native acceptors or point-defect related centres. Due to the close relation of  $I_1^d$  to zinc vacancies and its appearance in doping studies of ZnSe epilayers,

\* Corresponding author.



the understanding of its origin is of great importance. From the LO coupling strength, a localization of the corresponding centre between that of donor–acceptor pairs (Q series) and that of shallow bound excitons ( $I_1$  and  $I_2$  lines) must be concluded (see Fig. 1). Since the  $I_1^d$  recombination centre interacts strongly with the weaker bound excitons, the precise understanding of the electronic structure of the involved shallow bound excitons is indispensable. Thus the shallow ( $D^0$ , X) and ( $A^0$ , X) complexes will be considered in more detail before referring to the nature of the  $I_1^d$  line.

## 2. Donor bound exciton complexes

The luminescence of ( $D^0$ , X) complexes shown in the insert of Fig. 1 is dominated by a strong  $I_{20}^{Al}$  line near 2.7977 eV exhibiting additional structures at the low energy side due to Ga and In donors. At the high energy side, several  $I_{2\alpha}$  lines ( $\alpha = a$  to  $e$ ) and a resonance at the free exciton transition can be recognized. The exact value of the free exciton transition at 2.8028 eV is obtained from reflection spectra. The  $I_{2\alpha}$  lines which have already been reported by Merz et al. [3], Dean et al. [4] and Isshiki et al. [5] have recently been explained by Kudlek et al. [6] in terms of radiating relaxation from excited states of the

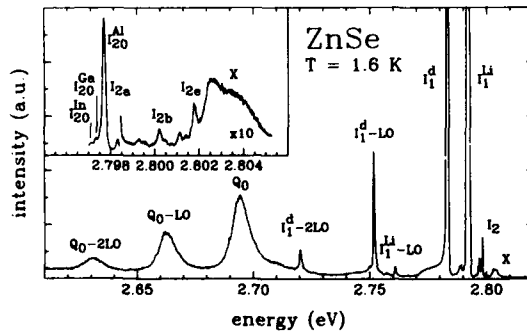


Fig. 1. Photoluminescence spectrum of a nominally undoped ZnSe bulk crystal in the near-band-edge region under band-to-band excitation. Insert: donor bound exciton luminescence and the free exciton recombination denoted X.

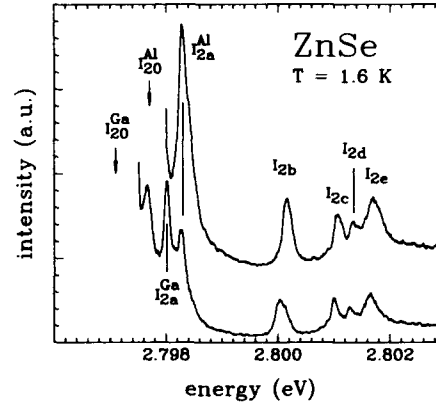


Fig. 2. Comparative photoluminescence excitation spectra of ( $D^0$ , X) complexes. Arrows indicate registration energies.

( $D^0$ , X) complexes. The  $I_{2\alpha}$  lines depicted in the insert of Fig. 1 are found to consist essentially of two superimposed series, one of which is connected to an Al donor and the other to Ga.

Narrow band registration of the  $I_{20}$  line due to a specific donor reveals the corresponding transitions in the excitation spectra (see Fig. 2). The observed energy differences  $E(I_{2\alpha}) - E(I_{20})$  can be described by a four-particle model regarding  $D^+$ ,  $e_D$  and the exciton particles  $e$  and  $h$  [7]. According to this model, the  $I_{2\alpha}$  resonances originate from excited states of the exciton hole classified by radial and angular quantum numbers  $n$  and  $l$ , respectively. The energy differences of the excited states  $E|n, l\rangle$  given in ref. [6] and the ( $D^0$ , X) ground state can be written

$$E|n, l\rangle - E|0, 0\rangle \sim -s^2 t^2 \frac{E_D}{\sigma} \times \left[ n + \frac{1}{2} + \left( \left( l + \frac{1}{2} \right)^2 + s t^2 \frac{a_c}{\sigma a_D} \right)^{1/2} \right]^{-2}, \quad (1)$$

with the specific donor Rydberg  $E_D$ , parameters  $s = 1.0136$  and  $t = 1.3370$  describing the Kratzer model potential of the hole,  $\sigma = m_e/m_h$  the ratio of the effective masses of electron and hole, and  $a_D/a_c$  the ratio of the donor electron radius and the Bohr radius, respectively. Using donor energies of  $E_D = 26$  meV and  $E_D = 27.7$  meV corre-

sponding to the Al and Ga donor ionization energies, the series  $E(I_{2a}) - E(I_{20})$  of both donors matches well the series  $E|n, l\rangle - E|0, 0\rangle$  computed without changing the other free parameters of  $\sigma = 0.26$  and  $a_D/a_c = 0.36$ . Lines  $I_{2a}$  to  $I_{2e}$  are thus assigned to the  $|n, l\rangle$  series of the states  $|0, 1\rangle$ ,  $|1, 0\rangle$ ,  $|1, 1\rangle$ ,  $|2, 0\rangle$  and  $|2, 1\rangle$ , respectively.

### 3. Acceptor bound exciton complexes

On the lower energy side of the donor bound excitons a dominant emission of an  $(A^0, X)$  complex is observed in samples of this kind (see Fig. 1). With the energy position of the donor–acceptor pairs  $Q_0$ , and the Al-donor Rydberg of 26 meV, an acceptor ionization energy of 114 meV was calculated. This value corresponds well with the reported Li Rydberg energy in ZnSe. In addition, the obtained transition energy matches the values reported from Li-doped samples [8]. The appearance of Li is quite reasonable due to the well-known incorporation of Li and Na in not intentionally doped ZnSe crystals, leading to dominant  $I_1^{\text{Li}}$  and  $I_1^{\text{Na}}$  lines.

While the term structure of Na-bound excitons is known [9], the structure of the  $(A^0_{\text{Li}}, X)$  complex is not yet clear. Bhargava [10] found a manifold structure in the  $I_1^{\text{Li}}$  energy regime. Exact energy positions, however, have not been given. In strained MBE-grown ZnSe/GaAs epilayers a double structure has been observed [11]. Taking into account the simultaneously acting influence of strain and the  $jj$  interaction, the authors discussed several possible parameter values for the hole-hole interaction and the cubic crystal field. To achieve a clear assignment, we used bulk ZnSe samples with highly resolved  $I_1$  lines. In this case the influence of strain can be neglected.

Fig. 3 shows the comparative luminescence spectra in the  $I_1^{\text{Li}}$  energy range for two different temperatures. The lower spectrum recorded at  $T = 1.6$  K contains three highly resolved transitions  $I_1$ ,  $I_{1a}$  and  $I_{1b}$  with 0.13 meV FWHM each.  $I_{1a}$  is shifted by 0.22 meV and  $I_{1b}$  by 0.37 meV to higher energy with respect to line  $I_1$ . The intensity ratio of the lines  $I_1$ ,  $I_{1a}$  and  $I_{1b}$  as determined

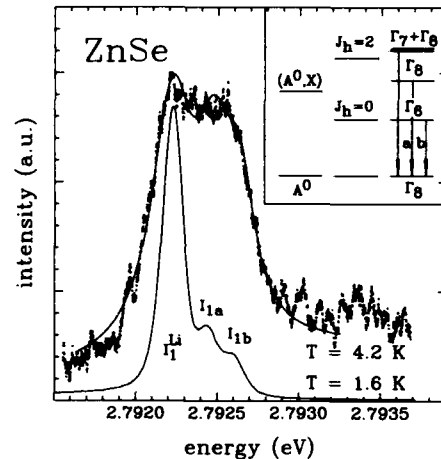


Fig. 3. Temperature-dependent emission of the  $(A^0_{\text{Li}}, X)$  exciton complex, showing three resolved subcomponents  $I_1$ ,  $I_{1a}$  and  $I_{1b}$ . The related term structure is given in the insert.

from a Lorentz profile analysis is 1:0.15:0.11. At a temperature of 4.2 K, a strong thermalization is observed, leading to a changed intensity ratio of roughly 1:0.93:0.82. Due to the strong correlation between these three lines, it is evident that all transitions belong to the same  $(A^0_{\text{Li}}, X)$  complex.

An explanation of  $I_1$ ,  $I_{1a}$  and  $I_{1b}$  can be given in terms of a fine-structure splitting of the  $(A^0, X)$  electronic ground state. The  $jj$  coupling of the two  $j = 3/2$  holes in this complex, one originating from the neutral acceptor  $A^0$  and the other from the free exciton, yields a total hole momentum of  $J_h = 0$  and  $J_h = 2$  (see insert of Fig. 3). These two states are separated by the hole-hole interaction  $\gamma$ . The additional coupling of the single electron leads to  $J = 1/2, 3/2$  and  $5/2$  states with  $\Gamma_6$ ,  $\Gamma_8$  and  $\Gamma_7 + \Gamma_8$  symmetry, respectively [12]. The  $\Gamma_8$  and  $\Gamma_7 + \Gamma_8$  degeneracy is lifted by the cubic crystal-field interaction  $\beta$ . Both the relative strength of the hole-hole interaction and the influence of the crystal field strongly depend on the used zincblende-structured host material, the incorporated chemical acceptor and the corresponding Rydberg energy [13–15].

The observed strong thermalization suggests a level sequence of increasing degeneracy  $\Gamma_6$ ,  $\Gamma_8$  and  $\Gamma_7 + \Gamma_8$  with increasing energy (see insert of

Fig. 3). From this ordering,  $\beta$  and  $\gamma$  can be determined according to

$$\beta = E(I_{1b}) - E(I_{1a}) = 0.14 \text{ meV}, \quad (2)$$

$$\gamma = E(I_{1a}) - E(I_1) + \frac{1}{5}\beta = 0.30 \text{ meV}. \quad (3)$$

Taking into account the intensity ratio and the separation energies at  $T = 4.2 \text{ K}$ , we calculate a oscillator strength ratio of 1:1.8:2.3 corresponding reasonably well to the theoretical ratio of 1:2:3.

In comparison with the  $(A_{\text{Na}}^0, X)$  complex [9], we observe an equal term sequence of the Li and Na acceptor exciton complexes in ZnSe. The influence of the cubic crystal-field  $\beta$  in both kinds of complexes is also comparable. Although in the Na-doped samples the splitting induced by  $\beta$  could not be resolved, it leads to a  $I_1'$  line being four times broader than the  $I_1$  line originating from the lowest state  $\Gamma_6$ . The  $jj$  coupling in the  $(A_{\text{Li}}^0, X)$  complex, however, is found to be much smaller.

#### 4. The $I_1^d$ emission centre

In contrast to the bound excitons described above, the nature of the  $I_1^d$  recombination centre has not been clarified up to now, due to reported different energy positions and various chemical impurities involved. The first interpretations in terms of an acceptor-bound exciton with copper acting as an acceptor are not in agreement with our investigations and magneto-optical results [16]. The authors observed a  $g$  value of 2 in accordance with a zinc vacancy with a free hole. The close correlation of the  $I_1^d$  centre to zinc vacancies  $V_{\text{Zn}}$  has been demonstrated by differently annealed ZnSe samples. In samples annealed in Zn atmosphere, a suppression of the  $I_1^d$  is observed, whereas on the other side the luminescence of ZnSe samples annealed in Se atmosphere is dominated by the strongly increasing  $I_1^d$  emission. These findings are supported by studies of the influence of the Zn-to-Se flux ratio in MBE-grown ZnSe epilayers [17] and CVD-grown polycrystalline ZnSe on the optical spectra [18]. Summarizing, the participation of  $V_{\text{Zn}}$  in the

$I_1^d$  centre without any connection to Cu must be concluded.

Zinc vacancies, however, are known to act as very deep and strongly localized defects with a double acceptor behaviour. The appearance as a more shallow single acceptor in the near-band-edge luminescence could be explained by the formation of an associate including a neighbored donor leading to an effective neutral acceptor. The participation of the donor induces a delocalization which can be clearly observed in the phonon coupling (see Fig. 1). The LO-phonon coupling of the  $I_1^d$  centre is significantly more pronounced than for the spatially localized shallow bound exciton complexes like  $(A_{\text{Li}}^0, X)$ , but still weaker than for the spatially extended donor-acceptor pairs. This intermediate localization can be expressed in terms of a Huang-Rhys factor which is calculated to be 0.2 for  $I_1^d$  compared to 0.01 for  $I_1^{\text{Li}}$  and 0.5 for  $Q_0$ .

To get additional information on the electronic structure of the  $I_1^d$  complex, we performed excitation spectroscopy in the energy range of the  $I_1^d$  transition recorded in the  $I_1^d$ -LO line (see

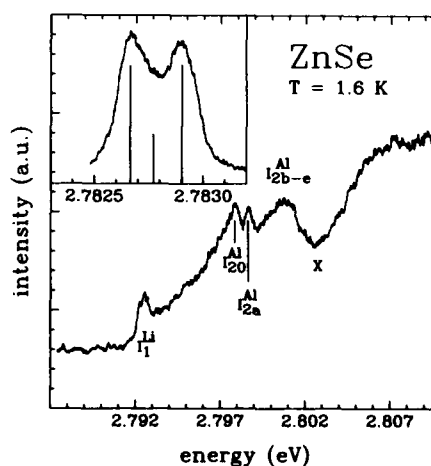


Fig. 4. Excitation spectrum of the  $I_1^d$  line in the excitonic energy range. To resolve the  $I_1^d$  fine structure the excitation spectrum recorded in the  $I_1^d$ -LO line is depicted in the insert: the bars denote energy positions and intensities of fitted Lorentz profiles.

insert of Fig. 4). In highly resolved spectra, a triplet line structure becomes evident, with energy positions at 2.78267, 2.78277 and 2.78290 eV. The intensity ratio fitted by three Lorentz profiles of 0.125 meV FWHM each is found to be 5:2:5, respectively. The energy distance between the two intensive components of 0.23 meV corresponds well to the value reported in ref. [19].

The triplet structure resembles the structure observed for the shallow  $(A^0, X)$  complexes, as described in the previous section. The oscillator strength ratio of the  $I_1^d$  subcomponents should be expected from an  $(A^0, X)$  complex under dominating crystal-field influence and weak  $jj$  coupling leading to a term sequence with the  $\Gamma_6$  state lying between the two levels of higher degeneracy. Similar to the  $(A_{Li}^0, X)$  and  $(A_{Na}^0, X)$  recombination lines, the oscillator strength ratio of the sum of the stronger subcomponents to the weaker one is 5:1.

As to the chemical nature of the  $I_1^d$  centre, the combination of a donor and a zinc vacancy  $V_{Zn}$  seems to be evident. The connection with shallow impurities can be seen in the excitation spectrum of the  $I_1^d$  line given in Fig. 4. The appearance of  $Li_{Zn}$  acceptors and  $Al_{Zn}$  donors is supposed to result from the spatial extension expressed by the intermediate localization of the  $I_1^d$  centre, as discussed above. While the connection of Al donors to  $V_{Zn}$  seems to be straightforward, an associate formed by  $V_{Zn}$  and  $Li_i$  ( $i$  = interstitial) is assumed to be more likely. The amphoteric behaviour of Li acting as a substitutional acceptor or an interstitial donor is well known [20]. Due to the strong tendency of Li to leave its substitutional Zn site and the considerably higher abundance of Li in the studied Markov samples, we assign the  $I_1^d$  centre to an  $(A^0, X)$  complex with a  $(V_{Zn}, Li_i)$  acceptor in these samples. The assignment should not exclude other donors to form a similar acting complex. As a consequence of the given assignment, the formation of an  $I_1^d$  centre in the Markov samples can be induced by a single  $Li_{Zn}$  leaving its substitutional site and thus creating a neighbored  $V_{Zn}$ . The participation of the amphoteric Li is of special interest due to a possible enhancement of the intrinsic self-compensation effect of ZnSe.

## 5. Conclusion

Due to the high crystalline quality of the studied ZnSe Markov-grown samples, sharp emission and excitation lines of Al, Ga, In and Li related shallow bound exciton complexes are observed. The electronic structure of the donor bound excitons is described by excited single hole states with quantum numbers  $n$  and  $l$ , changing only the donor Rydberg. The highly resolved fine structure of the  $(A_{Li}^0, X)$  complex is found to result from the  $jj$  splitting ( $\gamma = 0.3$  meV) and the influence of the cubic crystal field ( $\beta = 0.14$  meV).

Strong evidence is found for the  $I_1^d$ -related centre which exhibits an electronic fine structure comparable to the  $(A^0, X)$  complexes to be built by a  $(V_{Zn}, Li_i)$  associate acting as an acceptor. The instability of the Li acceptor against dissociation into a zinc vacancy ( $V_{Zn}$ ) and interstitial Li ( $Li_i$ ) leads to a self-compensation effect aggravating effective p-type doping.

## 6. References

- [1] N. Presser, Ch. Fricke, G. Kudlek, R. Heitz and I. Broser, *J. Crystal Growth* 138 (1994) 820.
- [2] E.V. Markov and A.A. Davydov, *Neorg. Mater.* 11 (1975) 1755.
- [3] J.L. Merz, H. Kukimoto, K. Nassau and J.W. Shiever, *Phys. Rev. B* 6 (1972) 545.
- [4] P.J. Dean, D.C. Herbert, C.J. Werkhoven, B.J. Fitzpatrick and R.N. Bhargava, *Phys. Rev. B* 23 (1981) 4888.
- [5] M. Isshiki, T. Kyotani, K. Masumoto, W. Uchida and S. Suto, *Phys. Rev. B* 36 (1987) 2568.
- [6] G.H. Kudlek, U.W. Pohl, Ch. Fricke, R. Heitz, A. Hoffmann, J. Gutowski and I. Broser, *Physica B* 185 (1993) 325. In this and in previous work,  $\sigma^{-1}$  has erroneously been replaced by  $\sigma$ .
- [7] J. Puls, F. Henneberger and J. Voigt, *Phys. Status Solidi (b)* 119 (1983) 291.
- [8] P.J. Dean, W. Stutius, G.F. Neumark, B.J. Fitzpatrick and R.N. Bhargava, *Phys. Rev. B* 27 (1983) 2419.
- [9] G.H. Kudlek, A. Hoffmann, R. Heitz, C. Fricke, J. Gutowski, G.F. Neumark and R.N. Bhargava, *J. Luminescence* 48&49 (1991) 138.
- [10] R.N. Bhargava, *J. Crystal Growth* 50 (1982) 15.
- [11] Y. Zhang, B.J. Skromme and H. Cheng, *Phys. Rev. B* 47 (1993) 2107.
- [12] B. Stebe and G. Munschy, *Solid State Commun.* 40 (1981) 663.
- [13] E. Molva and Le Si Dang, *Phys. Rev. B* 32 (1985) 1156.

- [14] W. Schairer, D. Bimberg, W. Kottler, K. Cho and M. Schmidt, *Phys. Rev. B* 13 (1976) 3452.
- [15] K.R. Elliot, G.C. Osbourn, D.L. Smith and T.C. McGill, *Phys. Rev. B* 17 (1978) 1808.
- [16] X.J. Jiang, T. Hisamune, Y. Nozue and T. Goto, *J. Phys. Soc. Japan* 52 (1983) 4008.
- [17] T. Taguchi and T. Yao, *J. Appl. Phys.* 56 (1984) 3002.
- [18] E. Krause, H. Hartmann, J. Menninger, A. Hoffmann, Ch. Fricke, R. Heitz, B. Lummer, V. Kutzer and I. Broser, *J. Crystal Growth* 138 (1994) 75.
- [19] P.J. Dean and J.L. Merz, *Phys. Rev.* 178 (1969) 1310.
- [20] T. Sasaki, T. Oguchi and H. Katayama-Yoshida, *Phys. Rev. B* 43 (1991) 9362.



ELSEVIER

Journal of Crystal Growth 138 (1994) 391–396

JOURNAL OF  
**CRYSTAL  
GROWTH**

## Blue-green light-emitting diodes with p-ZnSSe highly doped with nitrogen grown by metalorganic molecular beam epitaxy and molecular beam epitaxy

M. Migita\*, A. Taike, M. Momose, J. Gotoh

*Central Research Laboratory, Hitachi, Ltd., P.O. Box 2, Kokubunji, Tokyo 185, Japan*

### Abstract

The p-type doping of ZnSSe grown by MOMBE (metalorganic molecular beam epitaxy) and MBE (molecular beam epitaxy) has been comparatively studied. The p-type doping by using ammonia as a dopant source in MOMBE resulted in p-ZnSe with hole concentration of up to  $10^{17} \text{ cm}^{-3}$ . Perfect ohmic contact characteristics were achieved by MOMBE for Au/p-ZnSe:N with hole concentration of  $5.5 \times 10^{17} \text{ cm}^{-3}$ . On the other hand, p-type doping in MBE by using nitrogen plasma as a dopant resulted in p-ZnSe with net acceptor concentration of up to  $7.6 \times 10^{17} \text{ cm}^{-3}$ .  $I$ - $V$  characteristics with the lowest Schottky barriers were obtained for Au/p-ZnSe with net acceptor concentration of  $6.6 \times 10^{16}$  to  $7.6 \times 10^{17} \text{ cm}^{-3}$  for ZnSe:N and of  $2.8 \times 10^{16}$  to  $1.2 \times 10^{17} \text{ cm}^{-3}$  for  $\text{ZnS}_{1-x}\text{Se}_x$ :N ( $x = 0.03$ – $0.12$ ). The characteristics of ZnSe light emitting diodes with p-ZnSe grown by using ammonia in MOMBE are described. The characteristics of a ZnCdSe/ZnSSe laser diode with p-ZnSSe grown by using nitrogen plasma in MBE are discussed.

### 1. Introduction

Successful p-type doping of ZnSe, using nitrogen as a dopant, made it possible to demonstrate blue-green laser diodes [1–7]. At the present stage, laser oscillations have been attained only by MBE using nitrogen plasma as a dopant. However, it has not been elucidated whether MOVPE (metalorganic vapor phase epitaxy) and MOMBE can control p-type conductivity with high carrier concentration or not. Many efforts have been made to achieve it [9–11].

The obstacle remained the device quality of the laser diode. In order to achieve high-performance blue-green laser diodes, improvement of the electrical contacts of Au/p-ZnSe is an indispensable condition. There have been mainly two approaches to get ohmic contacts. One is to use a heavily doped narrow gap semiconductor grown on p-ZnSSe as a contact layer [8], and the other is to make the p-ZnSe low-resistive, which is caused by a leaky Schottky barrier [12]. In this paper, the electrical properties of p-type ZnSSe highly doped with nitrogen grown by MOMBE and of those grown by MBE are comparatively studied. It is demonstrated that the electrical contact characteristics of Au/p-ZnSe are extremely improved.

\* Corresponding author.

The characteristics of ZnCdSe/ZnSSe laser diodes are described.

## 2. Experimental procedure

The details of our MOMBE apparatus and the substrate preparation techniques have been reported previously [13,14]. Dimethylzinc (DMZ) and hydrogen selenide ( $\text{H}_2\text{Se}$ ) were used. As the dopant source, ammonia ( $\text{NH}_3$ ) was used. The MBE apparatus used in this study has two growth chambers. In the preparation of ZnCdSe/ZnSSe laser diodes, n-type layers were grown by MOMBE in one of the chambers, and then the substrates were transferred under vacuum (pressure below  $1 \times 10^{-10}$  Torr) to another chamber in which both p-type and active layers were grown by conventional MBE using nitrogen RF plasma as a dopant. Each growth chamber was evacuated to a background pressure below  $9 \times 10^{-11}$  Torr. Zn, Cd, Se, ZnS (6N grade), and ultra-pure  $\text{N}_2$  were used to grow p-type and undoped layers. DMZn, DMS, DMSe and  $\text{ZnCl}_2$  were used to grow the n-type layer. The Zn beam pressures were fixed at  $1 \times 10^{-6}$  Torr, and the Se, ZnS and Cd beam pressures were  $(1-3) \times 10^{-6}$ ,  $(2-9) \times 10^{-7}$  and  $(1-4) \times 10^{-7}$  Torr, respectively. The substrates were thermally etched at  $630^\circ\text{C}$  for 10 min under vacuum when monitoring the reflection high-energy electron diffraction (RHEED) reconstruction pattern of  $(2 \times 4)$ . The nitrogen plasma was produced by a Model MPD21 of Oxford Applied Research, UK. The nitrogen flow rate was controlled by a leak valve from  $3 \times 10^{-7}$  to  $4 \times 10^{-6}$  Torr. The nitrogen densities  $[\text{N}]$  in  $\text{ZnS}_x\text{Se}_{1-x}:\text{N}$  ( $x = 0-0.12$ ) were determined by monitoring the  $^{94}\text{SeN}^-$  by secondary ion mass spectrometry (SIMS) with 13 keV  $\text{Cs}^+$  as the primary beam. Integration of the  $^{94}\text{SeN}^-$  signal gave the nitrogen concentration in comparison with ZnSe:N standards implanted with  $^{14}\text{N}^+$  at concentrations of  $10^{17}$ ,  $10^{18}$  and  $10^{19} \text{ cm}^{-3}$ . The net acceptor concentration ( $N_a - N_d$ ) was determined by capacitance-voltage ( $C-V$ ) profiling. In these measurements, Au Schottky barrier diodes with a structure of Au/p-ZnSSe/p-GaAs/In of 300  $\mu\text{m}$  in diameter were used.

$N_a - N_d$  was estimated from the standard analysis of the slope of the  $C^{-2}$  versus voltage curve in the voltage range of  $-3$  to  $3$  V. The hole concentrations were determined by conventional Hall measurements. 7 mm square samples having 1.0 mm diameter contact pads in each of the four corners were used for the measurements. The current-voltage characteristics were measured by Semiconductor Parameter Analyser Model 4145B (Hewlett-Packard, USA). Photoluminescence (PL) spectra were measured under He-Cd laser excitation at a wavelength of 325 nm with a power density of less than  $100 \mu\text{W}/\text{cm}^2$ .

## 3. Characteristics of p-ZnSe:N grown by MOMBE

The electrical and photoluminescence properties of p-type ZnSe highly doped with nitrogen, grown by MOMBE, were reported previously [15]. In the present paper it is shown that the good electrical contacts for Au/p-type ZnSe highly doped with nitrogen were attained without thermal annealing. The p-ZnSe was a typically 1.0  $\mu\text{m}$  thick epilayer grown on a semi-insulating GaAs substrate at  $T_s$  of  $350-450^\circ\text{C}$ . Fig. 1 shows the typical current-voltage ( $I-V$ ) characteristics of Au/p-ZnSe for a ZnSe:N epilayer grown at  $350-450^\circ\text{C}$ , where the observed turn-on voltage is the reverse bias breakdown voltage. Fig. 1a shows the contact characteristics of the Au/p-ZnSe (sample MH-52) after Au deposition at room temperature (RT). Fig. 1b shows the characteristics after the application of 75 V/80  $\mu\text{s}$  pulses at 120 Hz at RT to the Au/p-ZnSe, and Fig. 1c shows the characteristics after the treatment of thermal annealing at a temperature in the range of  $200-350^\circ\text{C}$  for 5 min. In the order of Figs. 1a, 1b and 1c, it clearly appears that the Schottky barriers were reduced and the contact resistances were also improved. As shown in Fig. 1b, the application of the high voltage pulses can be effective to improve the contact of the Au/p-ZnSe. Perfect ohmic contact is achieved, as shown in Fig. 1c indicating a straight line through the origin. This result means that a hole can be injected into the ZnSe valence band through a

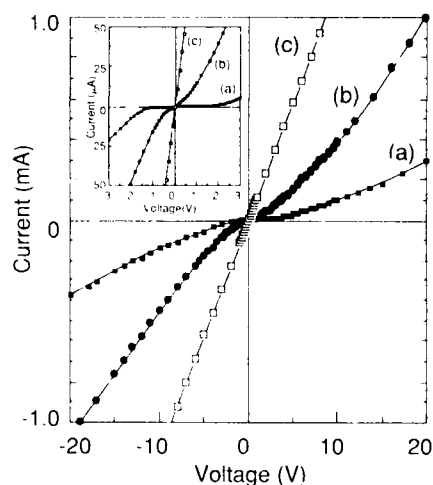


Fig. 1. Current-voltage characteristics of Au/p-ZnSe for sample MH-52 grown by MOMBE: (a) as-deposited Au, (b) followed by the application of 75 V/80  $\mu$ s pulses at 120 Hz for 1 min, and (c) after thermal annealing at 300°C for 5 min ( $p = 5.5 \times 10^{17} \text{ cm}^{-3}$  at RT).

Schottky barrier with a height of 1.25 eV [18] when low reverse bias-voltage is applied.

To study the crystal quality of the p-ZnSe grown by MOMBE, the photoluminescence (PL) spectra and X-ray diffraction were measured. The PL intensity of the p-ZnSe is too weak to be detected at RT, and there is no emission line in the band edge region even at 77 K. The full width at half maximum (FWHM) of the (400) diffraction was greater than 400 arc sec. These results suggest that the crystal quality of the p-ZnSe grown by MOMBE is lower, which is presumably useful in the improvement of the electrical contacts due to tunneling injection of holes into ZnSe through various defect states with less than 1.25 eV above the valence band.

Hall measurements were carried out for the p-type films with Au electrode annealed at less than 350°C for 5 min. The temperature dependent Hall measurements are shown in Fig. 2. The measured hole concentration as a function of temperature is governed by the theoretical expression:

$$\frac{p(p + N_a)}{N_a - N_d - p} = \frac{N_v}{g} \exp\left(-\frac{E_a}{kT}\right), \quad (1)$$

where  $p$  is the hole concentration,  $E_a$  is the acceptor ionization energy,  $N_v$  is the density of states of the valence band, with

$$N_v = 2(2m_v kT/h^2)^{3/2}.$$

$N_a$  is the acceptor concentration,  $N_d$  is the donor concentration,  $g$  is the degeneracy of the acceptor level,  $k$  is the Boltzmann constant, and  $T$  is the absolute temperature. The hole effective mass ( $m_v$ ) is  $0.79m_0$ , estimated from  $m_{lh} = 0.15m_0$  and  $m_{hh} = 0.75m_0$  [16].  $E_a$  values of 100 meV at  $N_a - N_d \sim (4-7) \times 10^{15} \text{ cm}^{-3}$  ( $p(\text{RT}) = 2.1 \times 10^{15} \text{ cm}^{-3}$ ) and of 90 meV at  $N_a - N_d \sim (2-4) \times 10^{16} \text{ cm}^{-3}$  ( $p(\text{RT}) = 5.0 \times 10^{16} \text{ cm}^{-3}$ ) have been obtained. As shown in the temperature dependent conductivity (Fig. 2b), the activation energy of p-type conductivity also appears to decrease with an increase in hole concentration (at RT). As the p-ZnSe with a hole concentration of  $5.5 \times 10^{17} \text{ cm}^{-3}$  contained a nitrogen concentration of around  $7 \times 10^{18} \text{ cm}^{-3}$  [14], the activation efficiency ( $p/[N]$ ) was estimated to be about 8%. The dependence of Hall mobility upon hole concentration of the p-ZnSe:N is shown in Fig. 3. The Hall mobility depends on the hole concentration, where the mobility decreased from 55 to 11  $\text{cm}^2/\text{V} \cdot \text{s}$  as the hole concentration increased from  $1.6 \times 10^{15}$  to  $5.5 \times 10^{17} \text{ cm}^{-3}$ .

Light emitting diodes with a structure of Au/p-ZnSe:N/n-ZnSe/n-GaAs/In were pre-

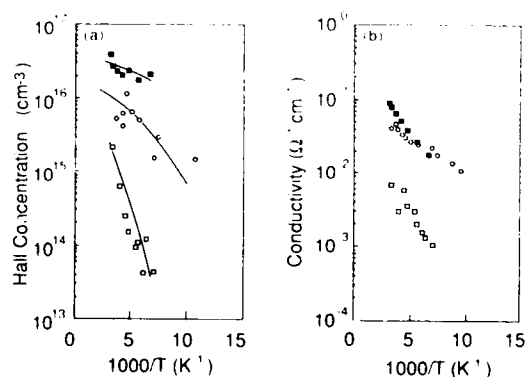


Fig. 2. Temperature dependent Hall measurements for ZnSe:N grown by MOMBE: (a) temperature dependencies of hole concentration and (b) temperature dependencies of conductivity.



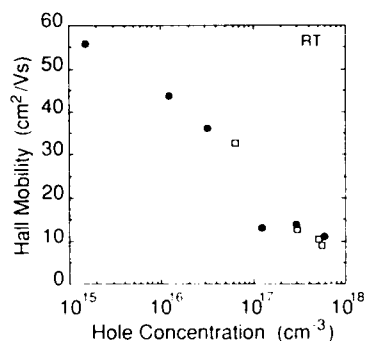


Fig. 3. Correlation between Hall mobility and hole concentration for p-type ZnSe:N grown by MOMBE (●) and MBE (□).

pared by MOMBE. In these devices, low resistive undoped ZnSe was used for the n-type layer. The net electron concentration of the n-ZnSe was estimated to be  $6 \times 10^{16} \text{ cm}^{-3}$ . Fig. 4 shows the emission characteristics by CW operation at 77 K. Current-voltage characteristics are also shown in the figure. The turn-on voltage is as low as 6 V. The emission spectrum was measured at a current of 6 mA at 13 V. The emissions observed at 459 nm (2.70 eV) and 475 nm (2.61 eV) can be assigned to those caused by the recombinations of free electron to acceptor hole (FA) [20] and DA pair, respectively.

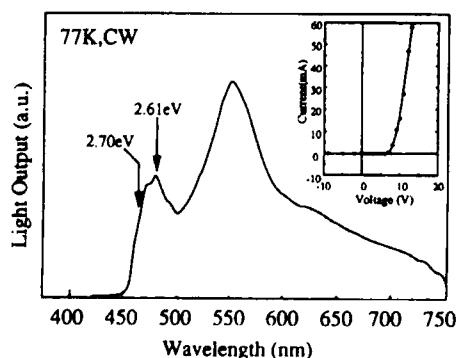


Fig. 4. Emission characteristics of the light-emitting diodes with a structure of Au/p-ZnSe:N/n-ZnSe/n-GaAs/In prepared by MOMBE.

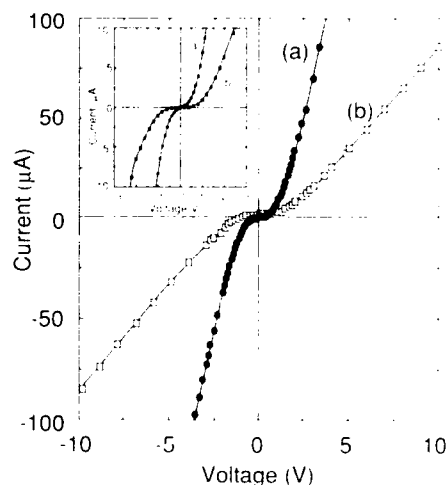


Fig. 5. Current-voltage characteristics of Au/p-ZnSe:N for sample 152 ( $p = 1.9 \times 10^{17} \text{ cm}^{-3}$  at RT) (a) and Au, p-ZnS<sub>0.04</sub>Se<sub>0.96</sub>:N for sample 150 ( $p = 2.8 \times 10^{16} \text{ cm}^{-3}$  at RT) (b) grown by MBE with using nitrogen plasma.

#### 4. Characteristics of p-ZnSSe:N grown by MBE and laser diodes

p-ZnSSe with a typically 2  $\mu\text{m}$  thick epilayer was grown by MBE at  $T_c = 250\text{--}450^\circ\text{C}$ . The RHEED pattern was streaky ( $2 \times 1$ ) for the ZnSSe:N grown at  $T_c$ , which is indicative of single crystal film growth. The FWHM of the (400) diffraction is almost independent of the amount of nitrogen incorporated, taking a constant value of 180–270 arc sec. In the PL spectra (at 77 K) of the p-ZnSe:N with nitrogen concentration higher than  $4.5 \times 10^{18} \text{ cm}^{-3}$ , the emissions at 458.5 nm (2.70 eV) assigned to the FA recombination are dominant.

Fig. 5 shows the typical current-voltage ( $I$ - $V$ ) characteristics of the Au/p-type films of the ZnSe:N with a net acceptor concentration ( $N_A - N_D$ ) of  $2.0 \times 10^{17}$  (sample 152) and ZnS<sub>0.04</sub>Se<sub>0.96</sub>:N with  $1.2 \times 10^{17} \text{ cm}^{-3}$  (sample 150), where no treatment for the contacts was performed after the gold deposition at RT. The characteristics of the contacts were not improved by the application of high voltage pulses or by any thermal annealing, which is different from the characteristics of the contacts for the p-ZnSe grown by

MOMBE described above. Petruzzello et al. have pointed out that the generation of point defects is accompanied by nitrogen doping, where nitrogen plasma was used as a doping source [21]. Qiu et al. have reported that the turn-on voltage of the Au/ZnSe contact can be decreased by an increase in the net acceptor concentration up to  $2 \times 10^{18} \text{ cm}^{-3}$ , which was accompanied by the degradation of crystal quality caused by reduction of  $T_s$  down to  $150^\circ\text{C}$  [12]. These results also suggest that the improvement of the contacts is presumably due to the tunneling injection of holes through the defect states with less than 1.25 eV above the valence band in highly doped p-ZnSSe.

To investigate the nitrogen incorporation in ZnSe as a function of substrate temperature under different nitrogen plasma fluxes (of  $3.2 \times 10^{-7}$  and  $4.5 \times 10^{-6} \text{ Torr}$ ), ZnSe:N films were grown with fixed RF power of 200 W, where  $T_s$  was varied from 250 to  $400^\circ\text{C}$ . Fig. 6 shows the net acceptor concentration as a function of the substrate temperature.  $N_a - N_d$  decreased slightly as  $T_s$  was increased, which indicates that the sticking coefficient of the effective nitrogen species increases with a decrease in  $T_s$ . The plasma flux dependence on  $N_a - N_d$  indicates that the lower plasma flux is effective to improve the p-type conductivity of ZnSe:N. In the next step, the doping conditions of the RF power were investigated under a fixed flux of nitrogen plasma of  $3.2 \times 10^{-7} \text{ Torr}$ . ZnSe:N films were grown at

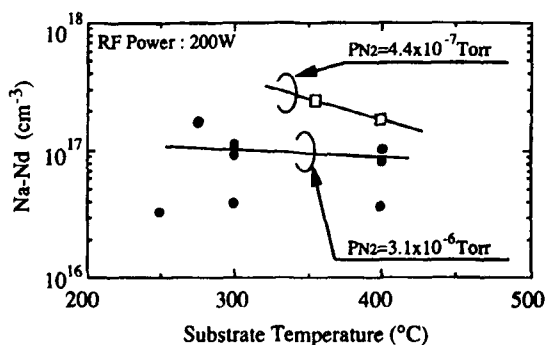


Fig. 6. Substrate temperature dependencies of net acceptor concentration for p-ZnSe:N grown under nitrogen plasma flux of  $3.2 \times 10^{-7} \text{ Torr}$  (■) and  $4.5 \times 10^{-6} \text{ Torr}$  (○) at RF power of 200 W.

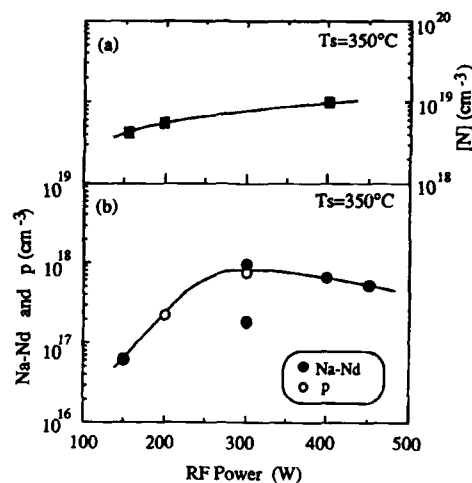


Fig. 7. RF power dependencies of nitrogen concentration (a), and net acceptor (○) and hole concentration (●) (b) for p-ZnSe:N grown at  $350^\circ\text{C}$ .

$T_s = 350^\circ\text{C}$ , where the RF power was varied from 150 to 450 W. Fig. 7a shows that the nitrogen concentration increased from  $3 \times 10^{18}$  to  $1 \times 10^{19} \text{ cm}^{-3}$  when the RF power was increased from 150 to 450 W. However, as shown in Fig. 7b, both the net acceptor concentration and the hole concentration increased as the power was increased up to 300 W, and then decreased as the power was increased to more than 300 W. The doping conditions have already been investigated under an RF power of less than 350 W [22]. In the results, the same tendency appeared slightly for the samples grown at a temperature of  $300^\circ\text{C}$ .

The maximum activation efficiency ( $N_a - N_d / [N]$ ) was achieved to be approximately 11% at nitrogen concentration of  $7 \times 10^{18} \text{ cm}^{-3}$ . This value at  $[N] = 7 \times 10^{18} \text{ cm}^{-3}$  is considerably larger than that reported previously [19]. Fig. 3 also shows the correlation between Hall mobility and hole concentration for the p-ZnSe as well as for p-ZnSSe grown by MBE. The mobility decreased from 32 to  $9 \text{ cm}^2/\text{V}\cdot\text{s}$  as the hole concentration increased from  $6 \times 10^{16}$  up to  $5.6 \times 10^{17} \text{ cm}^{-3}$ . These characteristics are almost the same as those for the p-ZnSe grown by MOMBE.

Laser diodes with a structure of p-ZnSe:N/p-ZnSSe:N/CdZnSe-ZnSe multi-quantum

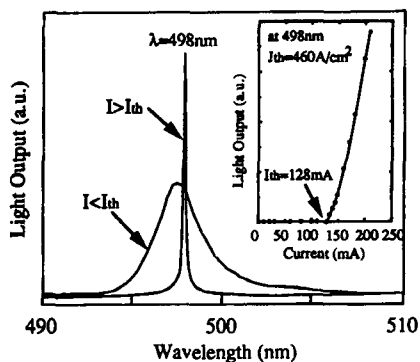


Fig. 8. Light-pulse characteristics of ZnCdSe/ZnSse laser diodes at 77 K (pulsed).

wells/n-ZnSe:Cl/n-ZnSse:Cl/n-GaAs(100)/In/Au were fabricated, where the p-type layers were made by using nitrogen plasma as a dopant in MBE. In these devices, the active layer is composed by  $\text{Cd}_{0.23}\text{Zn}_{0.77}\text{Se}(100 \text{ \AA})$ – $\text{ZnSe}(100 \text{ \AA})$  three quantum wells. The net hole concentrations measured by  $C$ – $V$  profiling are  $5 \times 10^{17} \text{ cm}^{-3}$  for p-ZnSe and  $2 \times 10^{17} \text{ cm}^{-3}$  for p-ZnSse. As shown in Fig. 8, the laser operation at a wavelength of 498 nm was observed when the pulsed voltage of more than 28 V was applied at 77 K. The current–light ( $I$ – $L$ ) characteristics of the laser diode are also shown in the figure. These devices with a typical threshold current density around  $460 \text{ A/cm}^2$  (threshold current  $I_{\text{th}} = 128 \text{ A}$ ) are operated with 300 ns pulses at 2 kHz repetition rates. In these devices, the end facets were uncoated.

## 5. Summary

The characteristics of p-type ZnSe heavily doped with nitrogen, grown by MOMBE, and those of p-ZnSse grown by MBE were comparatively studied. The p-type ZnSe with hole concentration of  $2 \times 10^{15}$  to  $5.5 \times 10^{17} \text{ cm}^{-3}$  was grown by MOMBE. Perfect ohmic contact characteristics were achieved for the Au/p-ZnSe of ZnSe:N grown by MOMBE. For the Au/p-ZnSse grown by MBE,  $I$ – $V$  characteristics with the lowest Schottky barriers were also obtained by using ZnSe:N with net acceptor concentrations of  $6.6 \times 10^{16}$  to  $7.6 \times 10^{17} \text{ cm}^{-3}$  and  $\text{ZnS}_{1-x}\text{Se}_x$ :N ( $x$

$= 0.03$ – $0.12$ ) with  $2.8 \times 10^{16}$  to  $1.2 \times 10^{17} \text{ cm}^{-3}$ , respectively. ZnCdSe/ZnSse laser diodes with a threshold current density of  $460 \text{ A/cm}^2$  at 77 K (pulsed) were fabricated.

## 6. References

- [1] M.A. Haase, J. Qiu, J.M. DePuydt and H. Cheng, Appl. Phys. Lett. 59 (1991) 1272.
- [2] H. Jeon, J. Ding, W. Patterson, A.V. Nurmikko, W. Xie, D.C. Grillo, M. Kobayashi and R.L. Gunshor, Appl. Phys. Lett. 59 (1991) 3619.
- [3] D.J. Olego, 1992 March Meeting American Physical Society, Indianapolis, IN, 1992.
- [4] S. Hayashi, A. Tsujima, S. Yoshii, K. Ohkawa and T. Mitsuyu, Jap. J. Appl. Phys. 31 (1992) L1478.
- [5] S.Y. Wang, I. Hauksson, J. Simpson, H. Stewart, S.J.A. Adams, J.M. Wallace, Y. Kawakami, K.A. Prior and B.C. Cavenett, Appl. Phys. Lett. 61 (1992) 506.
- [6] H. Okuyama, T. Miyajima, Y. Morinaga, F. Hiei, M. Ozawa and K. Akimoto, Electron. Lett. 28 (1992) 19.
- [7] Y. Kawaguchi, T. Ohno and T. Matsuoka, in: Extended Abstracts 1992 Int. Conf. on Solid State Devices and Materials, Tsukuba, 1992, p. 345.
- [8] Y. Fan, J. Han, L. He, J. Saraie, R.L. Gunshor, M. Hagerott, H. Jeon, A.V. Nurmikko, G.C. Hua and N. Otsuka, Appl. Phys. Lett. 61 (1992) 3160.
- [9] H. Kukimoto, J. Crystal Growth 101 (1990) 953.
- [10] K. Yanashima, K. Koyanagi, J. Hara, J. Yoshino and H. Kukimoto, J. Crystal Growth 124 (1992) 616.
- [11] S. Fujita, T. Asano, K. Maehara and S. Fujita, in: Abstracts Electronic Materials Conf., H7, 1993, A18.
- [12] J. Qiu, H. Cheng, J.M. DePuydt and M.A. Haase, J. Crystal Growth 127 (1993) 279.
- [13] A. Taïke, M. Migita and H. Yamamoto, Appl. Phys. Lett. 56 (1990) 1989.
- [14] M. Migita, A. Taïke and H. Yamamoto, J. Crystal Growth 101 (1990) 835.
- [15] M. Migita, A. Taïke and H. Yamamoto, J. Crystal Growth 111 (1991) 776.
- [16] G.E. Hite, D.T.F. Marple and B. Segall, Phys. Rev. 156 (1967) B850.
- [17] M. Migita, A. Taïke and H. Yamamoto, J. Appl. Phys. 68 (1990) 880.
- [18] F. Xu, M. Vos, J.H. Weaver and H. Cheng, Phys. Rev. B 38 (1988) 13418.
- [19] K. Ohkawa, A. Tsujimura, S. Hayashi, S. Yoshii and T. Mitsuyu, in: Extended Abstracts 1992 Int. Conf. on Solid State Devices and Materials, Tsukuba, 1992, p. 330.
- [20] K. Ohkawa, A. Ueno and T. Mitsuyu, J. Crystal Growth 117 (1992) 375.
- [21] J. Petruzello, J. Gaines, P. van der Sluis, D. Olego and C. Ponzoni, Appl. Phys. Lett. 62 (1993) 1496.
- [22] J. Qiu, J.M. DePuydt, H. Cheng and M.A. Haase, Appl. Phys. Lett. 59 (1991) 2992.



ELSEVIER

JOURNAL OF  
**CRYSTAL  
GROWTH**

Journal of Crystal Growth 138 (1994) 397–402

## Molecular beam epitaxy of ZnSe doped with nitrogen on vicinal (100)-oriented and (211)-oriented GaAs substrates

Ziqiang Zhu \*, Takashi Ebisutani, Kazuhisa Takebayashi, Kiyotake Tanaka,  
Takafumi Yao

*Department of Electrical Engineering, Hiroshima University, Higashi-Hiroshima 724, Japan*

### Abstract

This paper presents the growth and characterization of N-doped ZnSe grown on vicinal (100) and (211) GaAs substrates. The effects of the surface steps on the formation of deep donors are investigated by comparing PL properties and net-acceptor concentration of N-doped ZnSe epilayers grown on the vicinal surfaces with those grown on the exact (100) surface. It is shown that the use of the vicinal substrate suppresses the generation of deep donors and enhances the net acceptor concentration. The effects of the dangling bonds at Zn sites on the N-incorporation process are studied by comparing the net-acceptor concentration of N-doped ZnSe epilayers grown on the (211)A surface with that on the (211)B surface. It is found that the N incorporation is limited by the single dangling bond at the Zn sites.

### 1. Introduction

Low-resistivity p-type ZnSe has been achieved using a plasma source for nitrogen (N) doping during molecular beam epitaxy (MBE) [1,2]. This progress in p-type doping of ZnSe has led to the demonstration of a blue-green diode laser in ZnSe-based heterostructures [3,4]. The net acceptor concentration ( $N_A - N_D$ ) in p-type ZnSe increases monotonically with increasing concentration of incorporated nitrogen up to  $\sim 10^{18} \text{ cm}^{-3}$  [5,6], while it decreases when the N concentration exceeds  $\sim 5 \times 10^{18} \text{ cm}^{-3}$ . Under optimal conditions, a net acceptor concentration of up to  $1 \times 10^{18} \text{ cm}^{-3}$  in a p-type ZnSe epilayer with N concentration of  $5.2 \times 10^{18} \text{ cm}^{-3}$  was obtained

[5]. Typically, photoluminescence (PL) spectra of N-doped ZnSe with  $N_A - N_D < 1.0 \times 10^{17} \text{ cm}^{-3}$  show dominant emission between a shallow residual donor and an N-acceptor ( $D^0AP$ ) at about 2.693 eV, while the N-doped ZnSe epilayers with  $N_A - N_D > 1.0 \times 10^{17} \text{ cm}^{-3}$  exhibit dominant emission between a deep N-associated donor and an N-acceptor ( $D^dAP$ ) at about 2.681 eV [5,8]. PL spectra from the epilayers with  $N_A - N_D$  of  $1.0 \times 10^{17} \text{ cm}^{-3}$  show both the  $D^0AP$  and  $D^dAP$  emissions [7,8]. The ionization energy for the deep N-associated donor was determined as  $55 \pm 5$  meV from a recent optical study of N-doped ZnSe [8]. Therefore, one of the main causes of the limit on the maximum attainable net acceptor concentration is believed to be compensation related to the formation of the deep N-associated donor, which was proposed to be a complex of an N-acceptor and a defect [7,9].

\* Corresponding author.

The formation of defects in ZnSe during growth may depend on the surface structure, bond configuration, type of surface steps, and their density. The purpose of this study is to examine the effects of these parameters on the electrical and optical properties of N-doped ZnSe and on the N-incorporation. We have performed two types of experiments: comparison of growth on exact (100)-oriented GaAs with that on (100)-misoriented GaAs and comparison of N-doping of ZnSe grown on (211)A-oriented GaAs with that on (211)B. The use of the vicinal (100) surface allows us to study the effects of the surface steps and the step density, and the use of both the (211)A and (211)B orientations to investigate the effect of bond configuration. We have attempted to improve the crystal quality of N-doped ZnSe and then to suppress the generation of the deep N-associated donor by using the vicinal (100) surface, since two-dimensional growth is enhanced on a vicinal (100) surface. We will show that the use of the vicinal substrates suppresses the generation of the deep donor in heavily N-doped ZnSe and enhances the net acceptor concentration, and that the N-incorporation process depends strongly on the surface bonding nature.

## 2. Experimental procedure

The N-doped ZnSe films were grown on (100)- and (211)-oriented GaAs substrates by MBE. The active nitrogen flux produced by a microwave plasma source was injected into the MBE chamber through a quartz glass pipe. The flow rate of  $N_2$  was kept constant, such that the background pressure during growth was maintained at  $2 \times 10^{-6}$  Torr. The N concentration incorporated in the ZnSe films was controlled either by the changing microwave power in the range of 50–200 W or the growth rate of ZnSe. The beam pressure ratio of Zn to Se was varied from 0.5 to 3, and the substrate temperature was varied from 230 to 300°C. The growth rates were 0.7–1.0  $\mu\text{m/h}$  and the thicknesses of the films were about 2.8  $\mu\text{m}$ . For each growth run, the ZnSe:N samples to be compared were grown simultaneously on the substrates mounted side by side. The

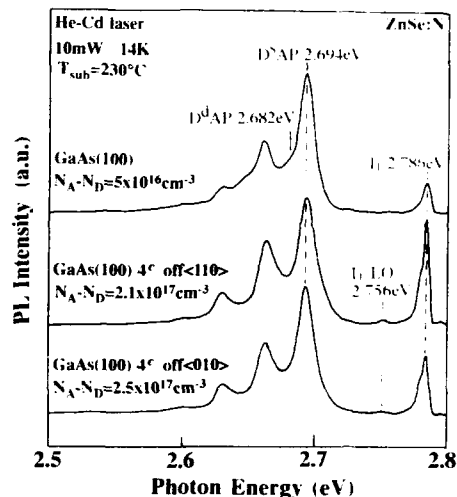


Fig. 1. PL spectra from the ZnSe:N epilayers grown on the exact (100) GaAs, and on (100) misoriented 4° off toward (110) and (010). The deep DAP emission was observed from the epilayer grown on the exact (100) GaAs, while it was not observed from the epilayers grown on the vicinal (100) GaAs.

epilayers were characterized by photoluminescence and capacitance–voltage ( $C$ – $V$ ) measurements. The PL spectra were measured using the 3250 Å line from a He–Cd laser of 10 mW as an excitation source at 14 K. The  $N_A - N_D$  value was determined by  $C$ – $V$  profiling using Au as a Schottky barrier metal.

## 3. Growth of ZnSe:N on vicinal (100)GaAs

### 3.1. Comparison of ZnSe:N grown on 4°-misoriented (100) with that on exact (100)

The electrical and PL properties of ZnSe:N grown on vicinal (100) GaAs have been compared with those on exact (100). Fig. 1 shows PL spectra from ZnSe:N epilayers grown simultaneously on the exact (100) GaAs, and (100) GaAs misoriented 4° off toward (110) and (010). The beam pressure ratio was unity and the substrate temperature was 230°C. No significant difference in growth rate between the epilayers grown on the exact and vicinal (100) GaAs has been found. The  $N_A - N_D$  values are measured to be  $5 \times 10^{16} \text{ cm}^{-3}$

for the epilayer grown on (100) GaAs,  $2.1 \times 10^{17} \text{ cm}^{-3}$  for the epilayer on (100) GaAs misoriented toward (110) and  $2.5 \times 10^{17} \text{ cm}^{-3}$  for the epilayer on (100) GaAs misoriented toward (010). The  $N_A - N_D$  values of the epilayers grown on vicinal surfaces are 4–5 times larger than that grown on the (100) GaAs. All the three samples show dominant DAP emissions at 2.694 eV. A small hump due to D<sup>d</sup>AP emission is observed at 2.682 eV for ZnSe:N grown on (100) GaAs, while it is not observed for ZnSe:N grown on vicinal substrates, which indicates reduction of the deep donors in ZnSe:N epilayers grown on vicinal surfaces. These facts indicate that the crystal quality of N-doped ZnSe is improved by using the vicinal surface, which results in the suppression of the formation of the deep donor and increases the  $N_A - N_D$  value. The strong emission at 2.786 eV is accompanied by phonon replica at 2.756 eV and can be attributed to a neutral acceptor-bound exciton ( $I_1$ ) [8].

The PL spectra from ZnSe:N samples with low N concentrations grown on exact and vicinal (100) GaAs exhibit dominant shallow DAP emissions at 2.692 eV, as shown in Fig. 2. The substrate temperature was 230°C and the beam pressure ratio of Zn to Se was 0.5. No deep DAP

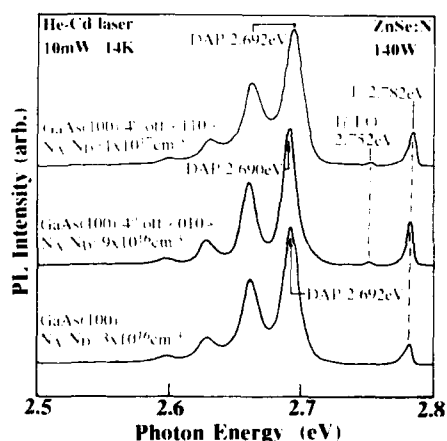


Fig. 2. PL spectra from the ZnSe:N epilayers with low N concentrations grown on the exact (100) GaAs, and on (100) GaAs misoriented 4° off toward (110) and (010). The PL spectra from the three samples show dominant shallow DAP emissions.

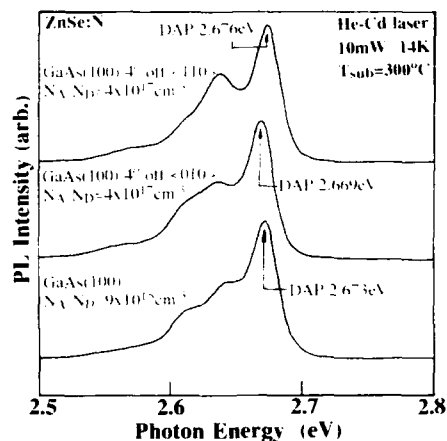


Fig. 3. PL spectra from the highly N-doped ZnSe epilayers grown on the exact (100) GaAs, and on (100) GaAs misoriented 4° off toward (110) and (010). The PL spectra from the three samples show dominant deep DAP emissions.

emission was observed. The  $N_A - N_D$  values obtained were  $(3-5) \times 10^{16} \text{ cm}^{-3}$  for the samples grown on exact (100) GaAs and  $(0.9-1) \times 10^{17} \text{ cm}^{-3}$  for the samples on vicinal (100) GaAs. This fact indicates that the use of vicinal (100) substrates reduces the defects in ZnSe and improves N activity, or enhances the N incorporation rate.

The highly N-doped ZnSe:N samples grown on exact and vicinal (100) GaAs show dominant deep DAP emissions at around 2.67 eV, as shown in Fig. 3. The  $N_A - N_D$  values obtained from the samples grown at substrate temperature of 250°C with the beam pressure ratio of Zn to Se being fixed at 0.5 were  $2 \times 10^{17} \text{ cm}^{-3}$  for exact (100) GaAs and  $4 \times 10^{17} \text{ cm}^{-3}$  for vicinal (100) GaAs. When the substrate temperature increased to 300°C, the  $N_A - N_D$  value decreased to  $9 \times 10^{15} \text{ cm}^{-3}$  for the sample on exact (100) GaAs, while it was not varied for the samples on vicinal (100) GaAs. Park et al. [10] have reported detailed substrate temperature dependence of the resistivity of ZnSe:N grown on exact (100) GaAs. The resistivity increased from 0.8 to 1.9  $\Omega \text{ cm}$  as the substrate temperature increased from 250 to 300°C. The increase in the resistivity of the ZnSe:N layer was explained to be due to compensation by generation of point defects at higher substrate temperature [10]. Therefore, the fact,

that the  $N_A - N_D$  did not vary with the substrate temperature in ZnSe:N grown on vicinal (100) GaAs indicates that the growth on the vicinal (100) GaAs really suppresses the generation of the defects.

The  $N_A - N_D$  values of the samples grown on (100) GaAs misoriented  $4^\circ$  off toward (110) and (010) are plotted against those on exact (100) GaAs in Fig. 4. The  $N_A - N_D$  values obtained from ZnSe:N grown on vicinal surfaces are at least twice of those on the exact (100) surface. It is clear that the net acceptor concentration is enhanced by using the vicinal (100) surfaces. No significant difference between the samples grown on (100) GaAs misoriented toward (110) and (010) is found.

### 3.2. Comparison of ZnSe:N grown on $2^\circ$ - and $4^\circ$ -misoriented (100) GaAs with those on exact (100) GaAs

Fig. 5 shows PL spectra from ZnSe:N epilayers grown simultaneously on exact (100) GaAs, and on (100) GaAs misoriented  $2^\circ$  and  $4^\circ$  off toward (110) at the substrate temperature of  $250^\circ\text{C}$  and with the beam pressure of unity. The  $N_A - N_D$  values are measured to be  $8 \times 10^{16} \text{ cm}^{-3}$  for the sample grown on (100) GaAs and  $9 \times 10^{16} \text{ cm}^{-3}$  for the samples on vicinal (100) GaAs. All the three samples show dominant D<sup>d</sup>AP emissions at 2.696 eV. The epilayers on vicinal (100)

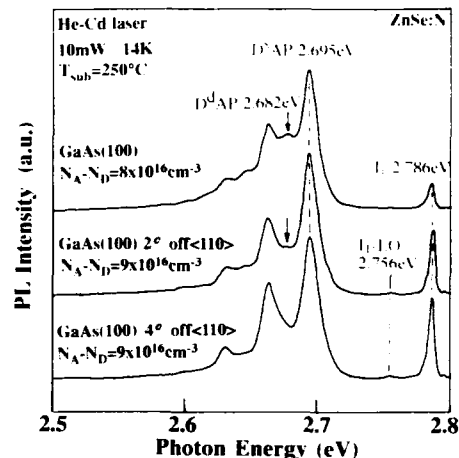


Fig. 5. PL spectra of ZnSe:N epilayers grown on the exact (100) GaAs, and on (100) GaAs misoriented  $2^\circ$  and  $4^\circ$  off toward (110).

GaAs show the emissions associated with neutral bound acceptor at 2.786 eV stronger than that from the epilayers on exact (100) GaAs. The D<sup>d</sup>AP emission at 2.682 eV appears distinctly in the spectrum from the epilayer on exact (100) GaAs, while it is reduced in the spectrum from the sample on  $2^\circ$ -misoriented (100) GaAs and disappears from the sample on  $4^\circ$ -misoriented (100) GaAs. These facts confirm that the growth of vicinal ZnSe:N suppresses the generation of the defects and deep donor.

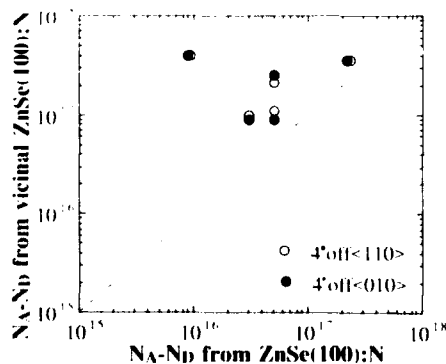


Fig. 4.  $N_A - N_D$  values of the samples grown on (100) GaAs misoriented  $4^\circ$  off toward (110) and (010) versus  $N_A - N_D$  values of the samples grown on exact (100) GaAs.

### 4. Growth of ZnSe:N on (211)GaAs

The N-incorporation process is dependent on the surface bonding nature. The polar (211) surface provides a tool for studying the incorporation process of impurities, since there are two kinds of dangling bonds (single and double dangling bonds) on the surface [11,12]. An ideally flat ZnSe (211) surface is schematically shown in Fig. 6. The N-acceptor sites are the ones with a single back-bond on the (211)A surface, whereas they are the ones with double back-bond on the (211)B surface. The density of N-acceptor sites, i.e., Se sublattice sites on the (211)A surface, is twice that on the (211)B surface. The incoming N atoms

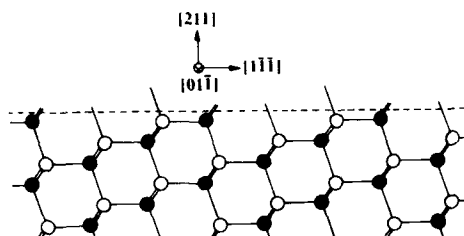


Fig. 6. Crystallographic model of ideal ZnSe (211) surface. On the (211)A surface, the white circles represent Zn atoms and the black ones Se atoms; on the (211)B surface, the arrangement is reversed.

would form bonds to Zn atoms with single dangling bond on the (211)A more easily than those with the double dangling bonds on the (211)B, since the double dangling bonds of Zn atoms would form dimers. Thus, it is expected that the N-incorporation rate into the (211)A surface is much larger than that into the (211)B surface.

Fig. 7 shows PL spectra from N-doped ZnSe epilayers grown simultaneously on (211)A and (211)B GaAs, where the beam pressure ratio of Zn to Se was 3 and the substrate temperature was 250°C. No significant difference in growth rate between the epilayers grown on (211)A and on (211)B GaAs has been found. The PL spectra from both samples show dominant shallow DAP emission at 2.690 eV and bound exciton emissions at deep acceptors ( $I_1^d$ ) at 2.782 eV. The  $N_A - N_D$  value of ZnSe:N grown on (211)A is

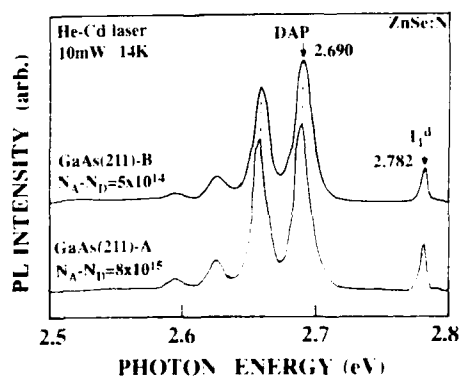


Fig. 7. PL spectra from the N-doped ZnSe epilayers grown on (211)A and (211)B GaAs.

estimated as  $8 \times 10^{15} \text{ cm}^{-3}$  for (211)A, which is 16 times larger than that on (211)B ( $5 \times 10^{14} \text{ cm}^{-3}$ ), indicating that the N-incorporation is limited by the number of single dangling bonds at Zn sites. The N concentrations in the epilayers have been estimated using secondary ion mass spectrometry (SIMS). The SIMS results indicate that the N concentrations in these particular samples are below the detection limit of SIMS ( $\sim 5 \times 10^{16} \text{ cm}^{-3}$ ).

## 5. Conclusion

We have investigated the effects of the surface steps on the generation of N-associated deep donors through a comparison of the PL properties and net-acceptor concentration of ZnSe:N epilayers grown on vicinal (100) surfaces with those grown on the exact (100) surface. It is shown that the use of the vicinal (100) substrate suppresses the generation of the defects in ZnSe:N, which results in the suppression of the formation of deep donors and enhances the net acceptor concentration. The effects of bonding natures at Zn sites on the N-incorporation process are studied by comparison of the net-acceptor concentration of ZnSe:N grown on the (211)A surface with that on the (211)B surface. It is found that the N-incorporation is limited by the single dangling bond at the Zn sites.

## 6. References

- [1] R.M. Park, M.B. Troffer, C.M. Rouleau, J.M. DePuydt and M.A. Haase, *Appl. Phys. Lett.* 57 (1990) 2127.
- [2] K. Ohkawa, T. Karasawa and T. Mitsuyu, *Jap. J. Appl. Phys.* 30 (1991) L152.
- [3] M.A. Haase, J. Qiu, J.M. DePuydt and H. Cheng, *Appl. Phys. Lett.* 59 (1991) 1272.
- [4] H. Jeon, J. Ding, W. Patterson, A.V. Nurmikko, W. Xie, D.C. Grillo, M. Kobayashi and R.L. Gunshor, *Appl. Phys. Lett.* 59 (1991) 3619.
- [5] J. Qiu, J.M. DePuydt, H. Cheng and M.A. Haase, *Appl. Phys. Lett.* 59 (1991) 2992.
- [6] T. Ohtsuka and K. Horie, *Jap. J. Appl. Phys.* 32 (1993) L233.
- [7] I.S. Hauksson, J. Simpson, S.Y. Wang, K.A. Prior and B.C. Cavenett, *Appl. Phys. Lett.* 61 (1992) 2208.



- [8] Z. Zhu, K. Takebayashi, K. Tanaka, T. Ebisutani, J. Kawamata and T. Yao, *Appl. Phys. Lett.*, to be published.
- [9] T. Yao, T. Matsumoto, S. Sasaki, C.K. Chung, Z. Zhu and F. Nishiyama, *J. Crystal Growth* 138 (1994) 290.
- [10] R.M. Park, M.B. Troffer, E. Yablonovitch and T.J. Gmitter, *Appl. Phys. Lett.* 59 (1991) 1896.
- [11] S. Subbanna, H. Kroemer and J.L. Merz, *J. Appl. Phys.* 59 (1986) 488.
- [12] P.N. Uppal, J.S. Ahearn and J.W. Little, *J. Vac. Sci. Technol. B* 6 (1988) 597.



ELSEVIER

Journal of Crystal Growth 138 (1994) 403–407

JOURNAL OF  
**CRYSTAL  
GROWTH**

## p-Type doping of ZnSe with a novel nitrogen exciter

Takashi Matsumoto \*, Tsuneo Inaba, Yasuo Yoda, Katsumi Egashira,  
Takamasa Kato, Tetsuya Akitsu

*Department of Electronic Engineering, Yamanashi University, Takeda 4, Kofu 400, Japan*

### Abstract

A novel nitrogen exciter for p-type doping of ZnSe has been developed. It is of a simple structure, easy to handle and to maintain, of a high reliability, and inexpensive. Emission spectra from excited nitrogen and doping efficiency are studied for different operating conditions of the exciter. Substrate temperature dependence of net acceptor concentrations are also examined. Net acceptor concentrations as high as  $8 \times 10^{17} \text{ cm}^{-3}$  are readily obtained.

### 1. Introduction

p-Type doping of low resistivity and high carrier concentration is one of the key technologies for device applications of ZnSe related wide gap II-VI compounds, such as laser diodes operating in the blue region of the spectrum [1]. Doping of nitrogen acceptors in high concentrations into ZnSe families grown by MBE has been succeeded by making use of RF-excited radical beam [2–4] or ECR-excited plasma of nitrogen [5]. However, the relation between exciting condition of nitrogen gas and doping characteristics has not yet been studied in detail. In this paper we describe a novel nitrogen exciter for p-type doping of ZnSe. The emission spectra from excited nitrogen are measured under different operating conditions of the exciter, such as electrode distance, RF power and gas pressure, and an optimum condition for p-type doping is determined. Net acceptor con-

centrations as high as  $8 \times 10^{17} \text{ cm}^{-3}$  are obtained.

### 2. Experiments

Layers of p-type ZnSe were grown in an MBE chamber equipped with a novel nitrogen exciter. Source materials are high-purity metallic zinc (6-nine S-1 grade of Osaka-Asahi Metal Co. and 7-nine grade of Dowa Mining Co.), high purity metallic selenium (6-nine super grade of Osaka-Asahi Metal Co.) and high purity nitrogen gas (S grade of Nippon Sanso Co.). Fig. 1 shows a schematic drawing of the nitrogen exciter (plasma cell) used in this study. A cell with 12 mm inner diameter and 70 mm long was made of fused quartz, and it was connected at the end of a 1/8 inch stainless pipe. The wall thickness of the cell was 1 mm. An aperture of 0.4–0.5 mm diameter was made at the center of the cell to effuse a beam of excited nitrogen. A pair of ring-shaped electrodes made of 1 mm diameter stainless wire were set around the cell on both sides of the

\* Corresponding author.

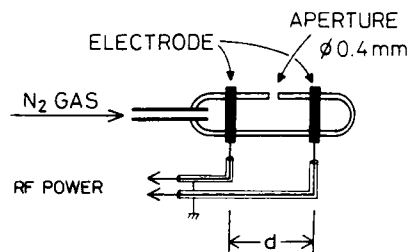


Fig. 1. Schematic drawing of the novel nitrogen exciter.

aperture, so that the distance between the two electrodes was easy to change. The nitrogen in the cell was excited by RF (2 MHz) power supplied through the electrodes by capacitive coupling. The nitrogen exciter was set in the growth chamber facing the substrate holder. The emission spectrum from the excited nitrogen was measured through a quartz window of the growth chamber with a focusing lens, an optical fiber, a 25 cm grating monochromator, a photomultiplier and a  $\mu$ -ampere meter.

ZnSe layers with a thickness of about 2  $\mu$ m were grown on p<sup>+</sup>-GaAs(100) substrates. The substrates were etched in a solution of 5H<sub>2</sub>SO<sub>4</sub> + H<sub>2</sub>O<sub>2</sub> + H<sub>2</sub>O and treated in (NH<sub>4</sub>)<sub>2</sub>S<sub>x</sub> solution just before setting in the growth chamber. Schottky contacts were made by evaporating Au onto the as-grown ZnSe surface. Net acceptor concentrations were estimated at room temperature by capacitance–voltage (C–V) measurements at 40 Hz and 1 MHz. ZnSe layers were characterized by PL measurements at 12 K.

### 3. Results and discussion

Emission spectra from the excited nitrogen are shown in Fig. 2 for a constant RF power of 50 W with different pressures and electrode distances. Emission lines in the ranges of 550–700 and 350–450 nm have been respectively assigned as the first and the second positive bands of N<sub>2</sub> molecules [6]. The lines indicated by solid circles have been assigned as due to N<sub>2</sub><sup>+</sup> ions. The emission spectra were found to change with N<sub>2</sub> gas flow rate (that is, the pressure in the cell and

the growth chamber), the distance between the two electrodes, and RF power. When the electrode distance  $d$  was 20 mm, the N<sub>2</sub><sup>+</sup> lines dominated the spectra and the lines due to excited N<sub>2</sub> molecules were very weak, as can be seen in Fig. 2c. When  $d$  was increased to 60 mm, the N<sub>2</sub><sup>+</sup> lines were reduced in intensity and the N<sub>2</sub> molecule lines became dominant, as shown in Figs. 2a and 2b. The difference between spectra 2a and 2b shows the effect of N<sub>2</sub> flow rate. When the N<sub>2</sub> flow rate was increased from 0.2 to 1 normal cubic centimeter per minute (NCCM), the intensity of the first positive band increased by a factor of 5, while that of the second positive band increased by a factor of 2. On the other hand, the N<sub>2</sub><sup>+</sup> lines reduced in intensity with increasing N<sub>2</sub> flow rate. The pressure in the cell for N<sub>2</sub> flow rate of 0.2 and 1.0 NCCM was estimated to be  $2.5 \times 10^{-2}$  and  $1.3 \times 10^{-1}$  Torr, respectively. An operating condition producing large intensity of the first positive band of the N<sub>2</sub> molecule is thought to be favorable for an efficient nitrogen doping, because nitrogen responsible for doping is active nitrogen of the N<sub>2</sub>(A<sup>3</sup> $\Sigma_u^+$ ) metastables, the lower state of the first positive transitions [6]. Therefore, we adopted a large electrode distance

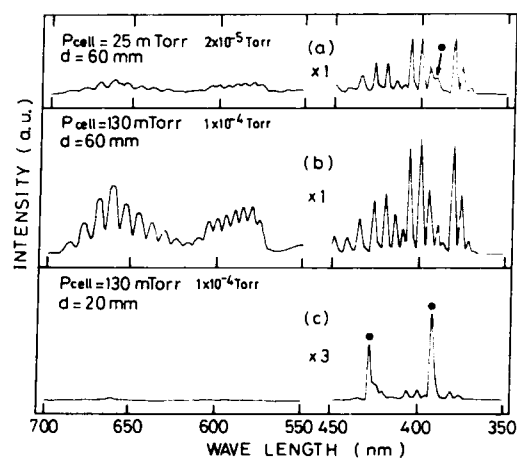


Fig. 2. Emission spectra from excited nitrogen under different operating conditions of the exciter: (a) electrode distance  $d = 60$  mm, N<sub>2</sub> flow rate  $N_{F_2} = 0.2$  NCCM, (b)  $d = 60$  mm,  $N_{F_2} = 1$  NCCM, and (c)  $d = 20$  mm,  $N_{F_2} = 1$  NCCM. RF power is 50 W for all.

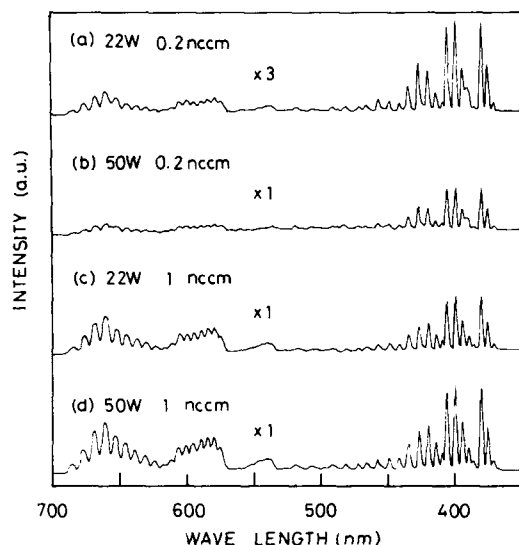


Fig. 3. RF power dependences of emission spectra from excited nitrogen for  $N_2$  gas flow rates of 0.2 and 1 NCCM. Electrode distance is 60 mm.

( $d = 60$  mm) and a high  $N_2$  flow rate ( $F_{N_2} = 0.7$ – $1$  NCCM) for the growth of p-type ZnSe layers. When the electrode distance was 20 mm, the  $N_2^+$  ion lines dominated the spectrum and the  $N_2$  molecule lines were very weak, even though the cell pressure was high.

Fig. 3 shows RF power dependences of the excited nitrogen spectra for a low cell pressure (Figs. 3a and 3b) and for a high cell pressure (Figs. 3c and 3d) with a electrode distance of 60 mm. The intensity ratio between the first and second positive bands of the  $N_2$  molecules was found to be almost independent of the RF power. The  $N_2^+$  lines increased in intensity more rapidly than the  $N_2$  lines with increasing RF power. The tendency of the increase of the  $N_2^+$  line intensities was observed distinctly for low cell pressures.

The effects of the nitrogen exciter on PL spectra of ZnSe layers are shown in Fig. 4. The sample shown in Fig. 4a was grown under undoped conditions, that is, nitrogen gas was not introduced into the growth chamber. Free and residual-donor-bound exciton lines dominate the spectrum. The sample in Fig. 4b was grown under conditions that nitrogen gas (0.75 NCCM) was

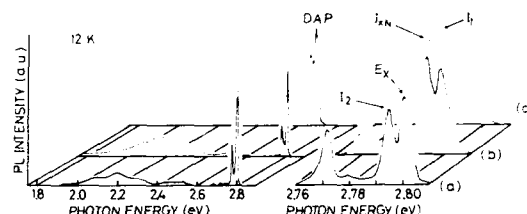


Fig. 4. PL spectra of ZnSe layers under different doping conditions. Substrate temperature is 267°C.

introduced in the growth chamber through the nitrogen exciter, but RF power was not applied. The PL spectrum was still dominated by the free and donor-bound exciton lines and nitrogen was not introduced into the layer. The sample in Fig. 4c was grown under the same conditions as Fig. 4b, but 50 W RF power was applied to the nitrogen exciter. The PL spectrum was dominated by a donor-acceptor pair band with a zero-phonon line at 2.690 eV. An emission line  $I_1$  due to acceptor-bound excitons at 2.786 eV was observed in the excitonic region of the spectrum. The sample in Fig. 4c had a net acceptor concentration of  $2 \times 10^{17} \text{ cm}^{-3}$ , while the samples in Figs. 4a and 4b were of high resistivities. These results indicate that the novel nitrogen exciter is effective for nitrogen doping into ZnSe.

Fig. 5 shows net acceptor concentrations in nitrogen doped ZnSe layers as a function of  $N_2$  gas flow rate for growth rates of 1 and 2  $\mu\text{m/h}$ . A series of samples of 2  $\mu\text{m/h}$  were grown with VI/II beam ratio of unity, while those of 1  $\mu\text{m/h}$  were grown with VI/II beam ratio of 0.6. When the  $N_2$  flow rate was lower than 0.2 NCCM, all grown layers were of high resistivities. With increasing  $N_2$  flow rate, the net acceptor concentration increased up to  $8 \times 10^{17} \text{ cm}^{-3}$ . The doped acceptor concentration was found to depend on growth rate and VI/II beam ratio. When the growth rate was decreased, the nitrogen beam intensity relative to Zn and Se source beams became higher and the introduced acceptor concentration became higher. When the VI/II beam ratio was low, nitrogen was easy to be introduced into Se site of ZnSe lattice.

Fig. 6 shows the substrate temperature dependence of the net acceptor concentrations. The

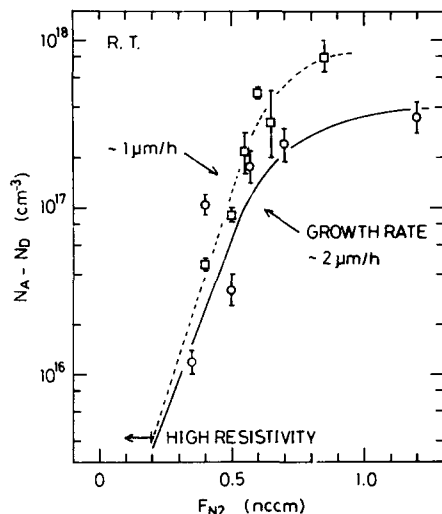


Fig. 5.  $N_2$  flow rate dependence of net acceptor concentrations in ZnSe layers for two different growth rates. Substrate temperature is 267°C, and RF power is 50 W.

intensities of Zn and Se beams were the same as those for the series with the growth rate of 2  $\mu\text{m/h}$  in Fig. 5. The growth rates were 1.9–2.2  $\mu\text{m/h}$ , being almost independent of growth temperature in this range. The  $N_2$  flow rate was 0.7 NCCM. Samples grown lower than 250°C were of high resistivities. However, the net acceptor con-

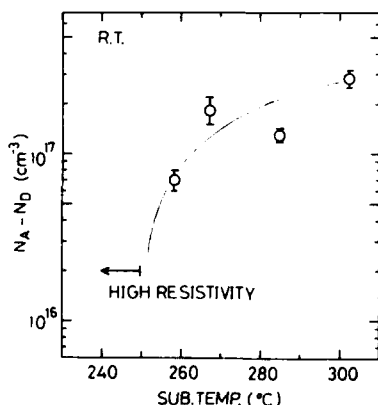


Fig. 6. Substrate temperature dependence of net acceptor concentrations in ZnSe layers.  $F_{N_2} = 0.7$  NCCM, RF power = 50 W, and growth rate = 1.9–2.2  $\mu\text{m/h}$ .

centration increased from  $7 \times 10^{16} \text{ cm}^{-3}$  to  $3 \times 10^{17} \text{ cm}^{-3}$  as the substrate temperature was increased from 258 to 302°C. The dependence is opposite to that expected from the temperature dependence of the sticking coefficient of the active nitrogen on ZnSe surface [4,7]. The PL spectra (donor–acceptor pair and acceptor-bound exciton emissions) were found to become stronger in intensity and sharper in line width when the substrate temperature became higher. The energy of the donor–acceptor pair band did not change, while the net acceptor concentration increased from  $7 \times 10^{16}$  to  $3 \times 10^{17} \text{ cm}^{-3}$ . The energies of donor–acceptor pair bands from the samples shown in Fig. 5, whose net acceptor concentrations were controlled by changing the  $N_2$  flow rate, were observed to become lower with increasing net acceptor concentration. Therefore, we have to ascribe the variations of net acceptor concentrations seen in Figs. 5 and 6 to different mechanisms. The X-ray diffraction peaks from the ZnSe layers in Fig. 6 were observed to increase in intensity and to become narrower with increasing substrate temperature. Therefore, the substrate temperature dependence of the net acceptor concentrations may be explained as follows: when  $T_{\text{sub}}$  becomes higher, the crystal quality of ZnSe becomes superior and the density of deep levels compensating the nitrogen acceptor levels becomes lower.

#### 4. Conclusions

We have developed a novel nitrogen exciter for p-type doping of ZnSe. It is of simple structure, easy to handle and to maintain, highly reliable, and inexpensive. The emission spectra from the excited nitrogen were measured and the operating conditions of the exciter favorable for an efficient nitrogen doping have been determined. That is, the electrode distance is 60 mm,  $N_2$  gas flow rate is 0.7–1.0 NCCM, and RF power is 50 W. With these conditions, the first and second positive band of the  $N_2$  molecules dominate the emission spectra. Net acceptor concentrations as high as  $8 \times 10^{17} \text{ cm}^{-3}$  were readily obtained by using the novel nitrogen exciter.

## 5. Acknowledgement

This work was partly supported by a Grant-in-Aid for Scientific Research on Priority Areas, New Functional Materials – Design, Preparation and Control from Ministry of Education, Science and Culture, Japan.

## 6. References

- [1] M.A. Haase, J. Qiu, J.M. DePuydt and H. Cheng, Appl. Phys. Letters 59 (1991) 1272.
- [2] K. Ohkawa, T. Karasawa and T. Mitsuyu, J. Crystal Growth 111 (1991) 797.
- [3] R.M. Park, M.B. Troffer, C.M. Rouleau, J.M. DePuydt and M.A. Haase, Appl. Phys. Letters 57 (1990) 2127.
- [4] J. Qiu, J.M. DePuydt, C. Cheng and M.A. Haase, Appl. Phys. Letters 59 (1991) 2992.
- [5] S. Ito, M. Ikeda and K. Akimoto, Japan. J. Appl. Phys. 31 (1992) L1316.
- [6] K. Ohkawa, A. Ueno, T. Mitsuyu, J. Crystal Growth 117 (1992) 375.
- [7] J. Qiu, H. Cheng, J.M. DePuydt and M.A. Haase, J. Crystal Growth 127 (1993) 279.



ELSEVIER

Journal of Crystal Growth 138 (1994) 408–411

JOURNAL OF  
**CRYSTAL  
GROWTH**

## Nitrogen doping into ZnSe by the catalysis of transition metal

Hideki Tojima <sup>a</sup>, Tamotsu Okamoto <sup>b</sup>, Akira Yamada <sup>a</sup>, Makoto Konagai <sup>\*b</sup>,  
Kiyoshi Takahashi <sup>a</sup>

<sup>a</sup> Department of Physical Electronics, Tokyo Institute of Technology, 2-12-1, O-okayama, Meguro-ku, Tokyo 152, Japan

<sup>b</sup> Department of Electrical and Electronic Engineering, Tokyo Institute of Technology, 2-12-1, O-okayama, Meguro-ku, Tokyo 152, Japan

### Abstract

The effect of the catalysis of transition metal such as tungsten (W) and iron (Fe) on nitrogen doping into ZnSe was investigated for the first time. In a hot W filament, the intensity of the donor–acceptor pair (DAP) emission in the N-doped ZnSe films using W filament at a temperature of 2000°C was stronger than that without heating of the W filament. In a hot Fe tube, neutral acceptor bound excitonic emission ( $I_1$ ) and DAP emission were observed in the N-doped ZnSe without heating of the Fe tube, while only DAP emission was observed with heated Fe tube at 300°C. From these results, it was found that nitrogen was effectively incorporated into ZnSe by the effect of heated transition metal.

### 1. Introduction

Nitrogen has been considered to be the most promising element as a p-type dopant for ZnSe, but the low sticking coefficient of  $N_2$  made it difficult to incorporate a large amount in ZnSe. Recently, it has been reported that MBE-grown low-resistivity p-type ZnSe was obtained with excited  $N_2$  by RF plasma [1–3]. In the plasma process, doping of nitrogen is achieved by active nitrogen. Recent developments in ZnSe-based optical devices greatly owe to p-type ZnSe prepared with a nitrogen RF plasma source [4–6].

It is well known that  $N_2$  dissociates on a heated transition metal such as tungsten (W), iron (Fe), and so on. Nornes and Donaldson have investi-

gated the interaction of nitrogen with a hot tungsten filament [7]. They reported that for the temperature of the W filament in the range of 2050 to 2300 K, the nitrogen dissociated on the hot W filament with an activation energy of 4.8 eV, which is half of the dissociation energy of nitrogen. In addition to the heated tungsten, it is well known that  $N_2$  dissociates on Fe at a temperature above 300°C. This process is widely used to produce  $NH_3$  from a  $H_2 + N_2$  gas mixture. In this paper, we propose the use of dissociative adsorption of  $N_2$  on transition metal (catalytic reaction) as a new nitrogen doping technique without using RF plasma.

### 2. Experimental procedure

The ZnSe films were grown on semi-insulating (100)GaAs by molecular beam epitaxy (MBE).

\* Corresponding author.

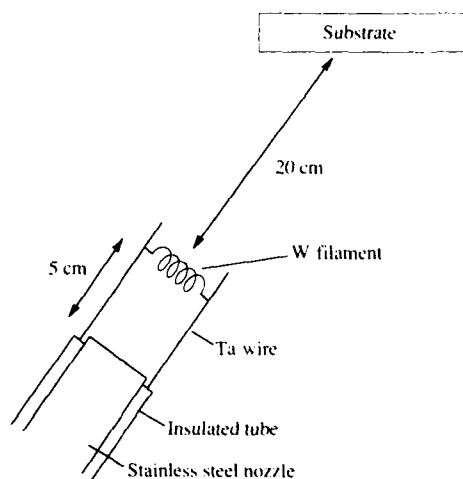


Fig. 1. Schematic diagram of the inlet nozzle of  $N_2$  gas with W filament.

using Zn and Se sources (6N purity). The dopant source is high purity 6N grade nitrogen gas. The flow rate of  $N_2$  gas, which was controlled by mass flow controller, was varied in the range of  $1 \times 10^{-5}$  to  $1 \times 10^{-4}$  Torr. The substrate temperature was  $320^\circ\text{C}$  and the beam flux ratio (VI/II ratio) was around 3. The growth rate of the film was about  $1 \mu\text{m/h}$ , and the film thickness was around  $4 \mu\text{m}$ . In these experiments, we investigated the catalytic effects of tungsten (W) and iron (Fe). Fig. 1 shows a schematic diagram of the inlet nozzles of  $N_2$  with W filament. The W filament (99.98% purity, 0.5 mm diameter and approximately 8 mm long) was attached to the outlet of the nozzle of  $N_2$ . The distance from the nozzle to the filament was about 5 cm, and the distance between the filament and the substrate was about 20 cm. The filament was heated at  $2000^\circ\text{C}$ , which was measured with a pyrometer. The Fe tube (6N purity) was approximately 8 mm in diameter and 10 cm long. The Fe tube was attached to a quartz tube to avoid heating the stainless steel nozzle, and the distance between Fe tube and substrate was about 20 cm. The tube was heated at  $300^\circ\text{C}$ . Those systems are very simple compared with RF plasma cell.

The photoluminescence (PL) spectra were measured at 4.2 K using a He–Cd laser (325 nm,

$8 \text{ mW/cm}^2$ ). The crystallinity was characterized by standard X-ray diffraction.

### 3. Results and discussion

First, we investigated the effect of the hot W filament for nitrogen doping into ZnSe. In the preliminary experiments, we confirmed that no difference of PL spectra and X-ray diffraction patterns of undoped ZnSe films with and without heating of the W filament was observed, which suggests that heating the W filament does not degrade the crystallinity of the ZnSe films. Fig. 2 shows PL spectra of N-doped ZnSe for  $N_2$  flow rate of  $1 \times 10^{-4}$  Torr with and without heating of the W filament. Detailed spectra in the excitonic and donor–acceptor pair (DAP) emission region are shown in the inset. These spectra show neutral acceptor bound excitonic emission ( $I_1$ ) at 2.794 eV and well-resolved DAP emission. Matsumoto et al. reported on nitrogen doping into ZnSe with thermally excited  $N_2$  by cracking cell with tantalum baffles, but the effect of the heated tantalum was not observed in PL spectra [8]. However, as indicated in Fig. 2, the intensity of

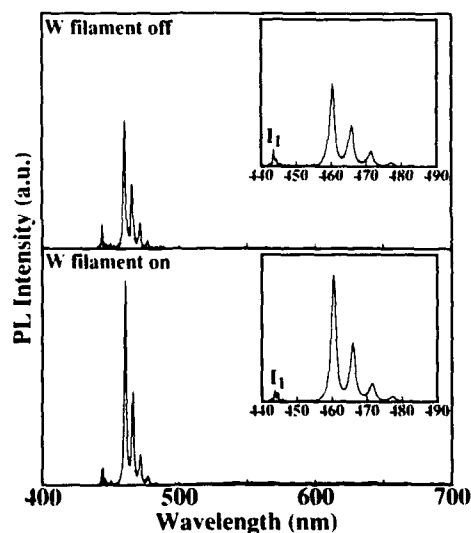


Fig. 2. Photoluminescence spectra of N-doped ZnSe with and without heating the W filament.



the donor–acceptor pair (DAP) emission in the N-doped ZnSe films using W filament at a temperature of 2000°C is stronger than that at room temperature. The deep level emission is very weak in both samples and no difference of X-ray diffraction patterns of N-doped ZnSe with and without heating of the W filament was observed. Furthermore, we investigated the dependence of the flow rate of  $N_2$ . Fig. 3 shows PL spectra of N-doped ZnSe films with and without heating of the W filament for various flow rates of  $N_2$ . With increasing nitrogen flow rate, the intensity of the DAP emission increases. This indicates that the concentration of nitrogen incorporated into ZnSe increases with increasing  $N_2$  flow rate. Besides, in any case, the intensity of DAP emission with W filament heating at 2000°C is stronger than that without heating. From these results, we consider that nitrogen is effectively incorporated into ZnSe by using high-temperature W filament. However, the energy of the zero-phonon DAP emission is 2.692 eV. This value is higher than that in the N-doped ZnSe grown by MBE with the excited  $N_2$  by RF plasma [1–3], and similar to that by MOVPE [9]. Qiu et al. reported that the zero-phonon DAP emission energy for the lightly doped ( $[N] < 6.0 \times 10^{17} \text{ cm}^{-3}$ ) ZnSe was 2.6975

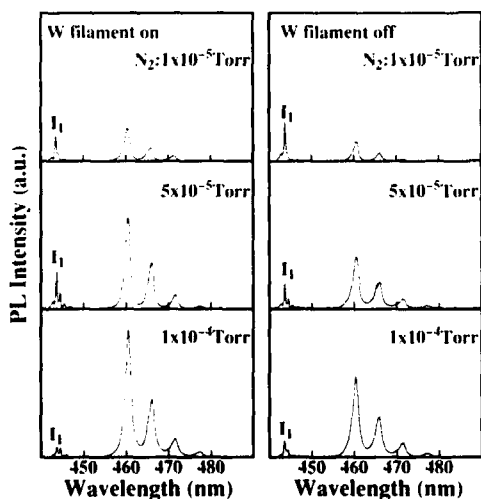


Fig. 3. Dependence of the PL spectra on the flow rate of  $N_2$  gas with and without heating the W filament.

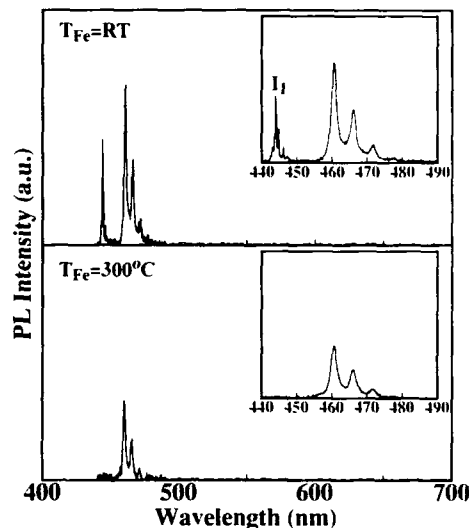


Fig. 4. Photoluminescence spectra of N-doped ZnSe with and without heating the Fe tube.

eV [3]. Therefore, it is considered that the concentration of the nitrogen in the obtained ZnSe films is low. We confirmed that all samples showed high resistivities.

In addition to the heated W filament, we investigated the effect of the heated Fe on nitrogen doping into ZnSe. Fig. 4 shows PL spectra of N-doped ZnSe films with and without heating of the Fe tube. Detailed spectra in the excitonic and DAP emission region are shown in the inset. Without heating of the Fe tube,  $I_1$  and well-resolved DAP emission are observed. On the other hand,  $I_1$  emission disappeared and only DAP emission is observed with the Fe tube heated at 300°C, although the intensity of DAP emission decreases. The deep-level emissions are not observed in both spectra. Furthermore, we confirmed that there was no difference of X-ray diffraction patterns of N-doped ZnSe with and without heating of the Fe tube. These results suggested that heating the Fe tube does not degrade the crystallinity of the ZnSe films. Referring to the results of Qiu et al.,  $I_1$  emission disappeared in the PL spectra of the highly doped ZnSe films [3]. Therefore, we concluded that nitrogen was effectively incorporated into ZnSe

by the effect of heated Fe tube as well as high temperature W filament. However, the zero-phonon DAP energy is 2.692 eV, which is similar to that for MOVPE, and we could not confirm the p-type conduction of the ZnSe film shown in Fig. 4. Further optimization of the catalytic cells is required.

#### 4. Conclusions

We investigated the effect of the catalysis of transition metal such as tungsten (W) and iron (Fe) on nitrogen doping into ZnSe for the first time. In a hot W filament, the donor-acceptor pair (DAP) emission in the N-doped ZnSe films using the W filament at the temperature of 2000°C was stronger than that without heating of the W filament. In a hot Fe tube,  $I_1$  and DAP emission were observed in the N-doped ZnSe without heating of the Fe tube, while only DAP emission was observed with heated Fe tube at 300°C. From these results, it was found that nitrogen was effectively incorporated into ZnSe by the effect of heated transition metal. However, we could not confirm the p-type conduction of the obtained ZnSe films.

#### 5. Acknowledgement

This work was supported by a Grand-in-Aid for Scientific Research on Priority Areas, New Functionality Materials-Design, Preparation and Culture, No. 04204014.

#### 6. References

- [1] K. Ohkawa, T. Karasawa and T. Mitsuyu, *J. Crystal Growth* 111 (1991) 797.
- [2] R.M. Park, M.B. Troffer, C.M. Rouleau, J.M. DePuydt and M.A. Haase, *Appl. Phys. Lett.* 57 (1990) 2127.
- [3] J. Qiu, J.M. DePuydt, H. Cheng and M.A. Haase, *Appl. Phys. Lett.* 59 (1991) 2992.
- [4] M.A. Haase, J. Qiu, J.M. DePuydt and H. Cheng, *Appl. Phys. Lett.* 59 (1991) 1272.
- [5] H. Jeon, J. Ding, W. Patterson, A.V. Nurmikko, W. Xie, D.C. Grillo, M. Kobayashi and R.L. Gunshor, *Appl. Phys. Lett.* 59 (1991) 3619.
- [6] K. Ohkawa, A. Ueno and T. Mitsuyu, *Jap. J. Appl. Phys.* 30 (1991) 3873.
- [7] S.B. Nornes and E.E. Donaldson, *J. Chem. Phys.* 44 (8) (1966) 2968.
- [8] S. Matsumoto, H. Tosaka, T. Yoshida, M. Kobayashi and A. Yoshikawa, *Jap. J. Appl. Phys.* 32 (1993) 731.
- [9] A. Yoshikawa, S. Muto, S. Yamaga and H. Kasai, *Jap. J. Appl. Phys.* 27 (1988) 922.



ELSEVIER

Journal of Crystal Growth 138 (1994) 412–417

JOURNAL OF **CRYSTAL  
GROWTH**

## Growth and doping of ZnTe and ZnSe epilayers with metalorganic vapour phase epitaxy

K. Wolf <sup>\*</sup>, H. Stanzl, A. Naumov, H.P. Wagner, W. Kuhn, B. Hahn, W. Gebhardt

*Institut für Festkörperphysik, Universität Regensburg, Universitätsstrasse 31, D-93040 Regensburg, Germany*

### Abstract

In this work we report on the growth and doping of ZnTe and ZnSe layers with metalorganic vapour phase epitaxy (MOVPE). Low resistive p-type ZnTe was grown by doping with arsenic and phosphorus. Acceptor concentrations of up to  $3.5 \times 10^{17} \text{ cm}^{-3}$  were achieved in the case of phosphorus-doped samples. For the first time nitrogen acceptors in ZnTe were investigated with photoluminescence at various temperatures and under resonant conditions. ZnSe layers were grown with DTBSe and DMZnTEN. The crystalline quality was investigated by high resolution X-ray diffraction. The halfwidths (150–500 arc sec) depend on the degree of relaxation and therefore on the layer thickness. Undoped ZnSe layers show at 2 K a strong recombination of free and bound excitons and a weak donor–acceptor pair luminescence.

### 1. Introduction

The commercial production of III/V light emitting diodes (LEDs) and laser structures by MOVPE has made this well controllable and high efficient process a preferable basic technology for optoelectronic devices. During the last years several groups have shown that this technique can also be adapted to grow epilayers of wide band gap II/VI semiconductors [1]. However, the problems of high p-type doping of ZnSe and n-type doping of ZnTe have not been solved. Therefore it seems to be necessary to develop new precursors in order to reduce the growth temperature and to avoid prereactions [2,3]. This search of new precursors should also be aimed at

reducing their toxicity and decreasing the environmental hazard. In the present work we use di-tertiarybutylselenide (DTBSe) and diisopropyltelluride (DiPTe) to grow ZnSe and ZnTe epilayers at a growth temperature of 340°C. Thus the growth of low-resistivity p-type ZnTe layers has been achieved by doping with P and As.

### 2. Experiments

All investigated epilayers were synthesized in our laboratory by atmospheric pressure metalorganic vapour phase epitaxy (MOVPE). An Aixtron AIX200 facility was used, equipped with a horizontal reactor. GaAs (001) served as substrate material. The substrates were prepared in a standard degrease, etched for 1 min in concentrated  $\text{H}_2\text{SO}_4$  and finally preheated for 15 min at

<sup>\*</sup> Corresponding author.

400°C prior to layer growth in the reactor. Dimethylzinc–triethylamine (DMZn–TEN), diisopropyltelluride (DiPTe) and di-tertiary-butylselenide (DTBSe) served as metalorganic precursors. The  $H_2$  carrier gas flow was set to 7 SLM, which results in a flow velocity of 5 cm/s. A flow of  $29 \mu\text{mol/min}$  of the zinc source gave a growth rate of  $1 \mu\text{m/h}$  at an input flow ratio of VI/II = 2 for ZnTe and VI/II = 3 for ZnSe at 340°C. For p-doping experiments we applied the compounds tertiary-butylamine (TBN), tertiary-butylphosphine (TBP) as well as tertiary-butylarsine (TBAs). The input flow of Zn, Te and Se were kept constant during doping experiments. The structural quality of the epitaxial layers was investigated with a high resolution X-ray diffractometer (HRXRD) and the thicknesses were determined from interference patterns and from ellipsometric measurements.

Strain-free ZnTe layers were prepared after removing the GaAs substrate by chemical polishing and successive chemical etching. Photoluminescence measurements were performed at 2 K in a liquid helium bath cryostat. In the temperature range 5–295 K a variable temperature cryostat was used. PL in the ZnTe and ZnSe layers was excited with the 458 nm line and the UV lines, respectively, of an argon-ion laser. The luminescence spectra were analysed with a 1 m double monochromator equipped with two gratings of 1800 lines per mm. The detector was a photomultiplier with a cooled GaAs cathode. For the ZnTe samples, a CW dye laser was operated with Coumarin 510 and pumped with the 458 nm line of a 20 W argon-ion laser which allows a continuous variation of the excitation wavelength selected by a birefringent filter. Resonant measurements on ZnSe layers were performed with Stilben 3 pumped by the UV lines of a 20 W argon ion laser.

Carrier concentrations were determined from temperature-dependent Hall measurements using the Van der Pauw configuration. The Hall equipment was equipped with a Keithley Hall package and a 1 T magnet. The samples were prepared with four contacts of  $500 \mu\text{m}$  diameter deposited at the corners of the samples. Antimony was used for electrical contacts on p-doped ZnTe samples.

### 3. Results for ZnTe

The near band gap PL of ZnTe layers shows a strong free-exciton peak split into a heavy- and a light-hole component ( $X_h$  and  $X_l$ ). This strain splitting is caused by a different thermal expansion of substrate and layer. The binding energy of the free exciton is 12.9 meV [4]. The donor bound exciton peak ( $I_2$ ) covers the  $X_l$  peak leaving the transitions unresolved. The  $I_1$  peak is related to excitons bound to neutral acceptors (Fig. 1). The donor and acceptor atoms were investigated with resonant luminescence measurements: two-electron transition (TET), two-hole transition (THT) and selective pair luminescence (SPL). The donors were identified as Ga [4] and the acceptors as As [4,5]. Therefore we suggest that donors and acceptors diffuse from the GaAs substrate into the ZnTe layer during growth. The intensity of the peak assigned with  $I_{1d}$ , which appears in undoped ZnTe/GaAs layers, depends on the

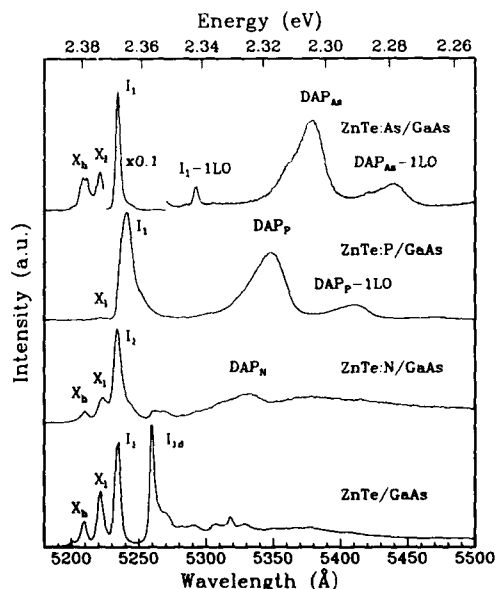


Fig. 1. Luminescence spectra of an undoped and N-, P- and As-doped ZnTe/GaAs layer (2 K).

growth conditions and has not been clearly identified until now.

In ZnTe/GaAs samples doped with As, P and N, a strong bound exciton luminescence  $I_1$  at approximately 2.370 eV is observed. Furthermore, these spectra show an additional strong donor–acceptor pair (DAP) luminescence at 2.305, 2.315 and 2.325 eV, respectively (fig. 1). The exact energetic positions depend on the distance  $r$  between donors and acceptors via the Coulomb energy term

$$E_{\text{DAP}} = E_{\text{gap}} - E_{\text{D}} - E_{\text{A}} + e^2/4\pi\epsilon_0\epsilon_{\text{Sr}}r.$$

Nitrogen acceptors in ZnTe were investigated by resonant and temperature dependent PL. The binding energy of the ground state was determined from the energetic difference between the bound and free exciton PL and the free-to-bound transition (eA), whose PL appears when the temperature is raised above 10 K. A binding energy of  $53 \pm 1$  meV for nitrogen acceptors is derived from various PL measurements (Fig. 2). Excited acceptor states were investigated by resonant photoluminescence methods, i.e., THT and SPL. The insert of Fig. 2 presents curves of luminescence intensity for different excitation energies. The spectra are plotted versus the energy difference of excitation and luminescence. The symbols of the acceptor states are those used by Baldereschi and Lipari [6]. The experiments were carried out on free-standing strain-free ZnTe layers in order to avoid strain-dependent effects. The corresponding binding energies derived from MOVPE-grown ZnTe layers are summarized in Tables 1 and 2. The results of resonant PL measurements for As and P acceptors were published elsewhere [4,7].

Temperature dependent PL measurements were also carried out for ZnTe:P. The binding energy of the ground state was found to be  $62 \pm 1$  meV (Fig. 3) and was determined in the same way as for ZnTe:N. The details of resonant PL measurements on ZnTe:P layers were published elsewhere [7]. In this paper, the ionization energy  $\Delta E_{\text{a}}$ , the donor concentration  $N_{\text{d}}$  and the acceptor concentration  $N_{\text{a}}$  of ZnTe:P layers were investigated by Hall measurements. The relevant parameters were derived from a fit of the experi-

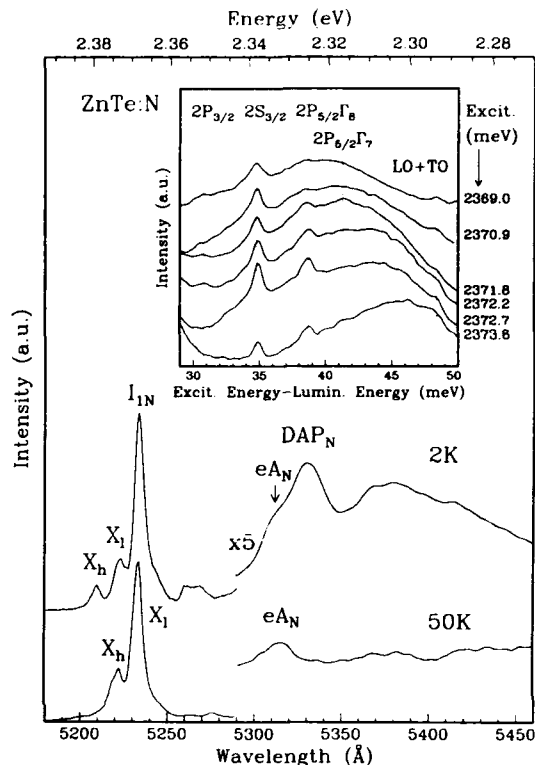


Fig. 2. Luminescence spectra of a N-doped ZnTe/GaAs layer at temperatures of 2 and of 50 K. Insert: Spectra of selective-pair luminescence and two-hole transitions of a strain free nitrogen doped layer. The spectra are plotted versus the difference of the excitation and luminescence energy.

mental data to a relation which is valid for a single monovalent impurity

$$\frac{N_{\text{v}}}{\beta} \exp\left(-\frac{\Delta E_{\text{a}}}{k_{\text{B}}T}\right) = \frac{p(p = N_{\text{d}})}{N_{\text{a}} - N_{\text{d}} - p}.$$

Table 1  
Binding energies of the ground state and of excited states for nitrogen acceptors in ZnTe

States of nitrogen	Energy (meV)
1S <sub>1/2</sub>	53.0
2P <sub>1/2</sub>	22.2
2S <sub>1/2</sub>	18.2
2P <sub>5/2</sub> (Γ <sub>8</sub> )	14.3
2P <sub>5/2</sub> (Γ <sub>7</sub> )	11.6

Table 2  
Binding energies of the ground state of various acceptors in ZnTe

Acceptor	Energy (meV)
N	53.0
P	62.0
As [1]	76.5

Other parameters used are  $m_h^* = 0.56$  [4] and the degeneracy factor  $\beta = 4$ . Fig. 3 shows the decrease of ionization energy with the third root of the donor concentration  $N_d$ . The ionization energy for ZnTe:P follows the rule [8]:

$$E_a(N_d) = 0.064 \text{ eV} - 4.8 \times 10^{-8} \text{ eV cm} \times N_d^{1/3}.$$

The value for  $N_d^{1/3} \rightarrow 0$  is in good agreement with results of the temperature-dependent luminescence measurements. The curves of temperature-dependent Hall mobilities  $\mu_{\text{Hall}}$  of ZnTe:P are shown in Fig. 4. At room temperature  $\mu_{\text{Hall}}$  is not influenced by the doping level and the scattering mechanism is dominated by polar optical phonon

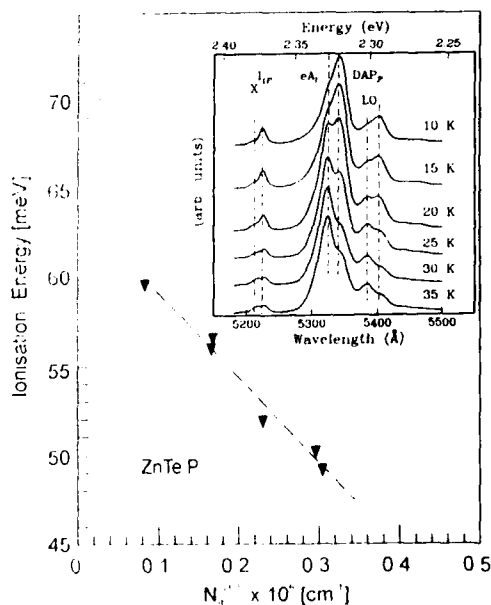


Fig. 3. Ionization energy of P-doped samples versus donor concentration  $N_d$ . Insert: Temperature-dependent luminescence of a P-doped ZnTe/GaAs sample prepared as a strain-free layer.

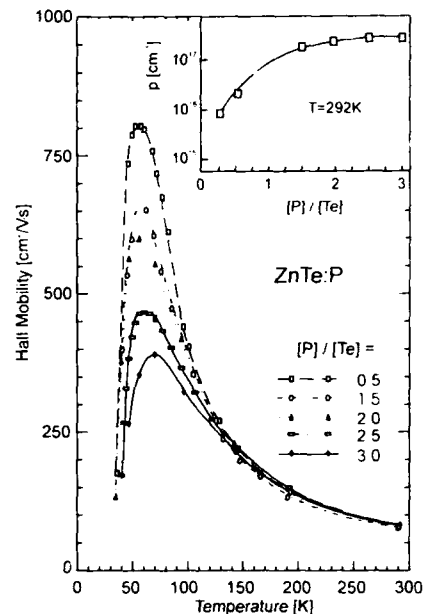


Fig. 4. Hall mobility of P-doped ZnTe samples doped at different input ratios  $[P]/[Te]$  versus temperature. Insert: Free hole concentration ( $N_p - N_d$ ) versus the input ratio  $[P]/[Te]$  ratio at room temperature.

scattering, whereas at low temperatures the Hall mobility is limited by scattering at ionized impurities. The insert of Fig. 4 shows the doping level at room temperature versus the  $[P]/[Te]$  ratio of the metalorganic compounds. At values  $[P]/[Te] \geq 3$ , saturation of solubility occurs. The compensation ratio  $N_d/N_a$  was typically 0.1.

As-doped samples show for  $[As]/[Te] > 0.25$  a specific resistivity  $\rho < 1.0 \Omega \text{ cm}$ . At ratios  $[N]/[Te] < 1$  for N doped samples, no change of the resistivity compared to undoped ZnTe ( $\rho > 10^5 \Omega \text{ cm}$ ) was observed.

#### 4. Results for ZnSe

DTBSe is a suitable precursor for the growth of ZnSe at temperatures below 400°C. An appropriate vapour pressure of the precursor appears in the range of  $283 < T < 323 \text{ K}$ :

$$\log(p[\text{Pa}]) = 16.56 - 4291/T.$$

Growth experiments were performed in the temperature range of 300 to 400°C. A growth rate of 1.0  $\mu\text{m/h}$  was obtained with a zinc input flow of 29  $\mu\text{mol/min}$  and a ratio  $[\text{Se}]/[\text{Zn}] = 3$ . For temperatures of  $320 < T < 380^\circ\text{C}$ , the growth rate remains constant (see Fig. 5a). The growth rate increases with the input flow ratio and remains constant with  $[\text{Se}]/[\text{Zn}] > 1$  (Fig. 5b).

Rocking curves were recorded for ZnSe layers of different thicknesses in order to investigate the crystalline quality and the relaxation processes of the samples. The lattice mismatch between GaAs and ZnSe is  $-0.27\%$ . It causes a strain in the layer which is relaxed by the nucleation of misfit dislocations during growth within a thickness of about 1  $\mu\text{m}$ . A small residual strain of  $+0.04\%$  is found for layers thicker than 2  $\mu\text{m}$ , which is due to different thermal expansions between sub-

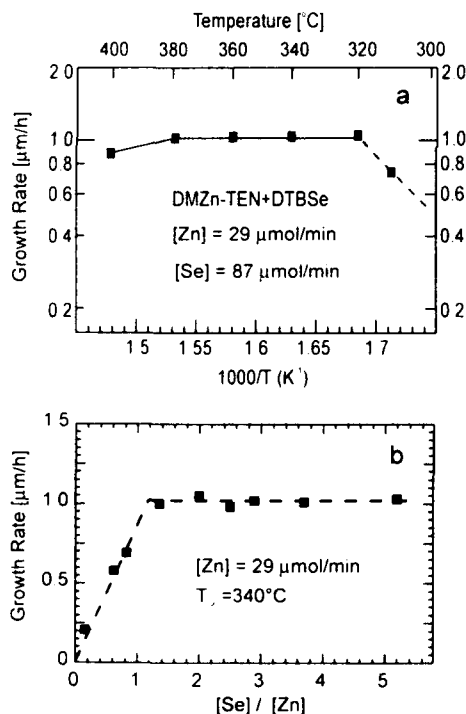


Fig. 5. Growth rate of ZnSe at different temperatures and VI/II flow. (a) Growth rate versus temperature. The ZnSe samples were grown at a flow of DMZn-TEN and DTBSe of 29 and 87  $\mu\text{mol/min}$ , respectively. (b) Growth rate of ZnSe versus input ratio  $[\text{Se}]/[\text{Zn}]$ .

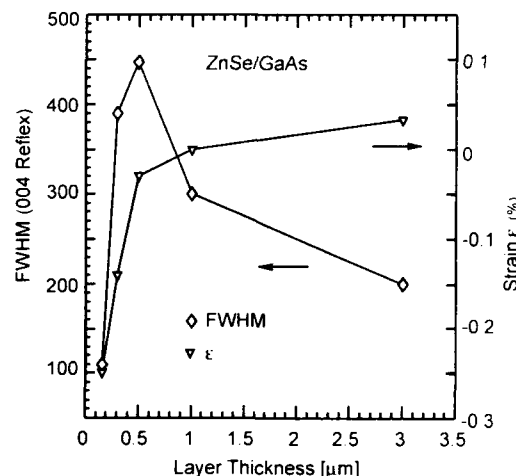


Fig. 6. FWHM values of rocking curves ( $\diamond$ ) and strain ( $\nabla$ ) of ZnSe/GaAs layers of various thicknesses.

strate and layer material. The halfwidth of the rocking curves depends on the density of dislocations and therefore on the degree of relaxation. Fig. 6 shows the full width at half maximum (FWHM) values of rocking curves and the strain as a function of the thickness for the growth conditions mentioned above.

A photoluminescence (PL) measurement of a 1  $\mu\text{m}$  ZnSe sample grown at  $340^\circ\text{C}$  with an input flow ratio of  $[\text{Se}]/[\text{Zn}] = 3$  is presented in Fig. 7. The spectra are dominated by a free (X; 2.800 eV) and strong donor bound exciton luminescence ( $I_2$ ; 2.795 eV). In the energy region between 2.75 and 2.65 eV, a weak PL of donor-acceptor pair (DAP) recombinations and their LO replicas are found. The signal at 2.6 eV corresponds to the well-known Y-line in ZnSe. The weak luminescence below 2.5 eV confirms the high quality of the sample. For a layer thickness of more than 1  $\mu\text{m}$ , also an acceptor bound exciton ( $I_1$ ; 2.792 eV) is observed. A respective peak is found at the same energy in arsenic doped samples. Obviously impurity atoms diffuse from the substrate into the layer, a process which is facilitated by misfit dislocations formed in ZnSe in order to relax the lattice mismatch between GaAs and ZnSe as mentioned above. Additionally to excitonic recombinations, LO replicas and

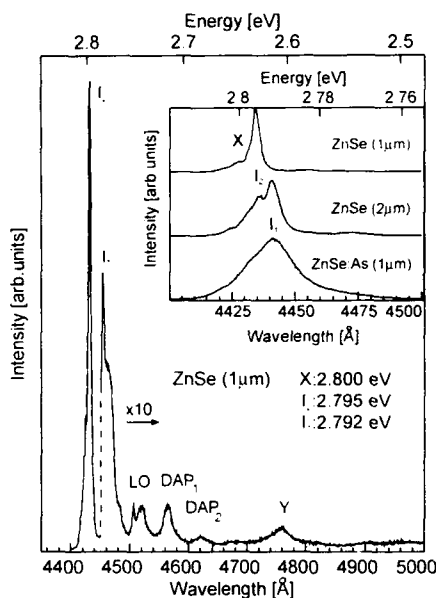


Fig. 7. Luminescence spectrum of a 1  $\mu\text{m}$  thick ZnSe/GaAs sample (2 K). Insert: PL of the excitonic region of an undoped 1  $\mu\text{m}$  and 2  $\mu\text{m}$  thick ZnSe/GaAs sample and of an As-doped layer.

the well-known Y-line, two emission bands at 2.715 and 2.685 eV were observed. Similar peaks were found in MBE grown ZnSe by Shibli et al. [9] and assigned as DAP recombinations. Therefore we suppose that As atoms, which diffuse from the substrate and a second acceptor, are incorporated in these undoped layers.

Donors were investigated with resonant PL measurements (TET). An energy difference of  $E_1 - E_2 = 19.5$  meV is observed (hydrogen model for donors). This value is in good agreement with investigations on chlorine donors in ZnSe as described in ref. [9]. We suggest that Cl donors are incorporated by one of the metalorganic sources.

## 5. Conclusion

MOVPE grown ZnTe layers were successfully doped with the acceptors N, P and As. The energies of the acceptor ground states were determined from temperature-dependent photoluminescence measurements. Excited acceptor

states were investigated with resonant PL methods. The determination of the ionization energy of phosphorus acceptors through temperature-dependent Hall measurements is in good agreement with the value of the PL measurement (62 meV). Using TBP as a dopant, a free hole concentration of  $3 \times 10^{17} \text{ cm}^{-3}$  can be achieved.

MOVPE ZnSe was grown with DTBSe and DMZnTEN. The growth rate was found to be 1  $\mu\text{m/h}$  in the temperature range of 320 to 380°C at an input flow ratio  $[\text{Se}]/[\text{Zn}] = 3$  at a flow of 29  $\mu\text{mol/min}$  of DMZnTEN. The FWHM values of rocking curves ( $< 500$  arc sec) depend on the degree of strain relaxation. In PL measurements, a strong free and donor bound excitonic recombination was observed. A very weak PL signal at energies smaller than 2.5 eV and the small halfwidth of rocking curves ((004) reflection) confirm the high quality of the samples.

## 6. Acknowledgement

This work was supported by the Bundesministerium für Forschung und Technologie (BMFT).

## 7. References

- [1] P.J. Wright, B. Cockayne, P.J. Parbrook, P.E. Olivier and A.C. Jones, *J. Crystal Growth* 108 (1991) 525.
- [2] H. Stanzl, K. Wolf, S. Bauer, A. Naumov and W. Gebhardt, *J. Electron. Mater.* 22 (1993) 501.
- [3] K. Nishimura, Y. Nagao and K. Sakai, *Jap. J. Appl. Phys.* 32 (1993) L 428.
- [4] H.P. Wagner, S. Lankes, K. Wolf, D. Lichtenberger, W. Kuhn, P. Link and W. Gebhardt, *J. Luminescence* 52 (1992) 41.
- [5] W. Kuhn, H.P. Wagner, H. Stanzl, K. Wolf, K. Wörle, S. Lankes, J. Betz, M. Würz, D. Lichtenberger, H. Leiderer, W. Gebhardt and R. Triboulet, *Semicond. Sci. Technol.* 6 (1991) A105.
- [6] A. Baldereschi and N.O. Lipari, *Phys. Rev. B* 9 (1974) 1525.
- [7] K. Wolf, M. Würz, H.P. Wagner, W. Kuhn, A. Naumov and W. Gebhardt, *J. Crystal Growth* 126 (1993) 643.
- [8] G.F. Neumark, *Phys. Rev. B* 5 (1972) 408.
- [9] S.M. Shibli, M.C. Tamargo, B.J. Skromme, S.A. Schwarz, C.L. Schwartz, R.E. Nahory and R.J. Martin, *J. Vac. Sci. Technol. B* 8 (1990) 187.
- [10] P. Blanconner, J.F. Hogrel, A.M. Jean-Louis and B. Sermage, *J. Appl. Phys* 52 (1981) 6895.





ELSEVIER

Journal of Crystal Growth 138 (1994) 418–424

JOURNAL OF  
**CRYSTAL  
GROWTH**

## Low temperature growth and plasma enhanced nitrogen doping of ZnSe by metalorganic vapour phase epitaxy

W. Taudt<sup>a</sup>, A. Schneider<sup>a</sup>, M. Heuken<sup>\*a</sup>, Ch. Fricke<sup>b</sup>, A. Hoffmann<sup>a</sup><sup>a</sup> Institut für Halbleitertechnik, RWTH Aachen, Templergraben 55, D-52056 Aachen, Germany<sup>b</sup> Institut für Festkörperphysik, Technische Universität Berlin, Hardenbergstrasse 36, D-10623 Berlin, Germany

### Abstract

The combination of diisopropylselenide (DIPSe) and diethylzinc (DEZn) was used to grow ZnSe by metalorganic vapour phase epitaxy (MOVPE). The results are compared with those obtained from samples grown with diethylselenide (DESe) and DEZn. Furthermore, we analysed the influence of plasma stimulation of DIPSe and DESe, as well as plasma enhanced nitrogen doping. Plasma stimulated growth with DESe at 480°C results in ZnSe which shows resolved free and bound excitons and negligible deep centre emissions in 11 K PL spectra. By using DIPSe without plasma stimulation, the kinetically controlled growth regime was found in the temperature range from 380 to 480°C. In PL only broad distributed emissions from 2.4 to 2.78 eV were observed, arising from impurities in the Se precursor. With plasma enhancement the diffusion controlled growth regime was extended down to 330°C. In the PL spectra, excitonic emissions were found beside the emission band (2.4–2.78 eV). Deep centre emission (2.0 eV) appeared only for  $T_D < 360^\circ\text{C}$ . Doping experiments were carried out by using plasma precracking of the Se precursor and simultaneously stimulating nitrogen dopant gas in a plasma. The donor–acceptor pair (DAP) emission of the doped layers increases for decreasing growth temperatures (440 to 360°C), if DIPSe and DEZn are used as precursors. Increasing the  $\text{N}_2$  flux causes an increasing nitrogen concentration. Samples grown in  $\text{N}_2$  carrier gas at 380°C show a maximum measured nitrogen concentration of  $1.7 \times 10^{18} \text{ cm}^{-3}$ . The layers were highly compensated, due to the impurities in the Se precursor and to additional hydrogen and carbon incorporation.

### 1. Introduction

For the production of optoelectronic devices, which work on the basis of ZnSe, the control of n- and p-type conductivity is necessary. Many attempts to grow p-type ZnSe failed [1]. p-type conducting ZnSe with a free carrier concentration above  $1 \times 10^{18} \text{ cm}^{-3}$  was demonstrated with molecular beam epitaxy (MBE) [2]. However, the physical mechanism of p-type conduction is not

clear yet. For the doping plasma activated nitrogen was used. It is difficult to use elements other than nitrogen for p-type doping, due to several reasons: One problem is the limited solubility of these elements in ZnSe [3]; another problem is the compensation. Lithium shows an amphoteric behaviour, since interstitial lithium acts as a donor and compensates the free holes generated by lithium on zinc sites [4]. The group V elements arsenic and phosphorus create deep centres. A theoretical model proposed by Chadi and Chang explains the compensation mechanism [5]. This theory predicts a reduced existence of deep centres with increasing electronegativity of the dop-

\* Corresponding author.

ing element. Therefore nitrogen is the most useful candidate to achieve p-type conduction. Until now, attempts to achieve p-type doping with other growth methods than MBE result in highly resistive samples or the carrier concentration was very low [6,7]. In MOVPE,  $\text{NH}_3$  was used as a doping gas for these attempts [6,7]. Due to the successful doping in MBE technology it should be useful to grow  $\text{ZnSe:N}$  at low temperatures and to use plasma stimulated nitrogen as well for doping in MOVPE to obtain highly conductive p-type  $\text{ZnSe}$ . The growth of  $\text{ZnSe}$  with the combination of  $\text{DEZn}$  and  $\text{DESe}$  requires a deposition temperature of at least  $480^\circ\text{C}$  [8]; therefore this combination does not seem to be useful for successful doping experiments. Because  $\text{DEZn}$  is decomposed at  $300^\circ\text{C}$  [9], we investigated the growth with and without plasma-cracked  $\text{DIPSe}$  and  $\text{DEZn}$ . The combination of diallylselenide and  $\text{DEZn}$ , investigated earlier [10,11] is not useful in reducing the growth temperature. For comparison we grew samples with the well known precursor combination  $\text{DESe}$  and  $\text{DEZn}$ .

## 2. Experimental procedure

The  $\text{ZnSe}$  layers were grown in a horizontal MOVPE reactor. The plasma precracking was carried out by a DC plasma source 10 cm in front of the susceptor as reported earlier [11]. As substrate we used (100) GaAs, which was  $2^\circ$  misoriented towards the nearest  $\langle 110 \rangle$  direction. The substrates were annealed for one minute at  $600^\circ\text{C}$  in a hydrogen atmosphere.  $\text{DEZn}$ ,  $\text{DESe}$  and  $\text{DIPSe}$ , which is contaminated with Zn, As, Sn, B, Sr and Te [12], were used as precursors. The vapour pressure of  $\text{DIPSe}$  ( $(\text{C}_3\text{H}_7)_2\text{Se}$ ) was measured and follows the expression:  $\log(p/\text{hPa}) = 8.56 - 2193.1 \text{ K}/T$ . Thus, at a bubbler temperature of  $17^\circ\text{C}$  the material yields a vapour pressure of 9.9 hPa, which is adequate for MOVPE. For the experiments, the Se partial pressure was set to 2.84 Pa and the VI/II ratio was varied from 0.2 to 12.3. We grew the layers using a total flux of 1.5 SLM of  $\text{H}_2$ . The total pressure was 100 hPa in the experiments without plasma enhancement and 20 hPa in experiments with plasma

precracking of the Se precursor. The plasma power was approximately 6 W. For the doping experiments, an additional nitrogen flux of 0.120 SLM was activated in a DC plasma with a power of 5.6 W. For comparison, layers were grown using  $\text{DESe}$  and  $\text{DEZn}$  under the same conditions. The epilayers were characterized by photoluminescence (PL) at 11 K, scanning electron-microscopy (SEM), Hall and SIMS measurements. SIMS measurements were carried out with 5.5 keV  $\text{O}_2^+$  and  $\text{Cs}^+$  primary ion beams. The detection limit was  $1 \times 10^{17}$  for nitrogen,  $4 \times 10^{17}$  for hydrogen and  $3 \times 10^{16}$  atoms  $\text{cm}^{-3}$  for carbon. A helium-cadmium laser (325 nm) and a 1 m monochromator with a GaAs photomultiplier were used for the PL measurements. The samples were irradiated with a low excitation power ( $0.01\text{--}0.5 \text{ W cm}^{-2}$ ).

## 3. Growth of $\text{ZnSe}$ without plasma

In Fig. 1, the dependence of  $\text{ZnSe}$  growth rate obtained with different Se precursors on reciprocal temperature is shown. At a total pressure of 100 hPa and a VI/II ratio of 2.1 ( $T_D = 480^\circ\text{C}$ ), we measure a growth rate of  $0.48 \mu\text{m/h}$  by using  $\text{DESe}$  and  $\text{DEZn}$  as precursors. Below a deposition temperature of  $480^\circ\text{C}$ , we found the kinetically controlled growth regime. Decreasing the

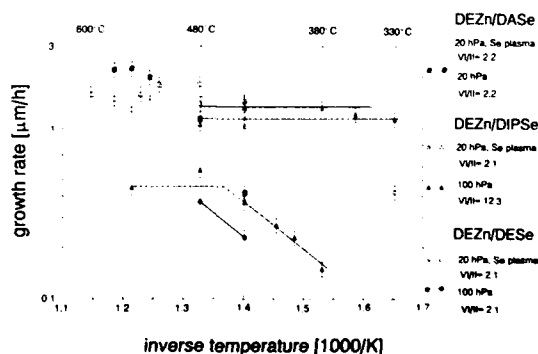


Fig. 1. Growth rate of  $\text{ZnSe}$  grown with different precursor combinations:  $\text{DESe}$ ,  $\text{DASE}$  (diallylselenide),  $\text{DIPSe}$  with  $\text{DEZn}$ . The filled symbols are results of growth without plasma enhancement and the open symbols are results of plasma enhanced growth.

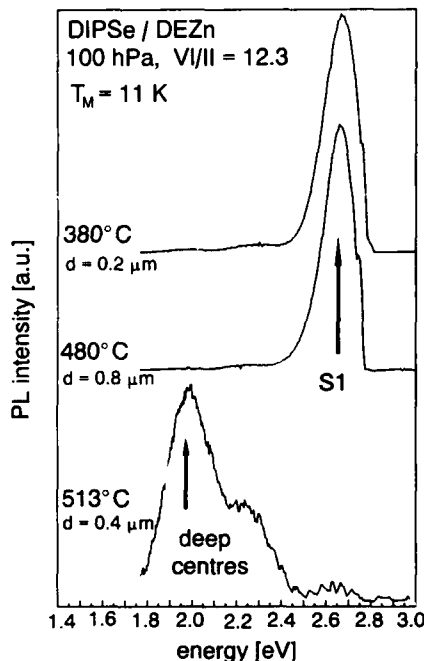


Fig. 2. 11 K PL spectra of layers grown with DIPSe and DEZn ( $P_D = 11$  hPa, VI/II = 12.3, without plasma enhancement) in dependence of growth temperature.

growth temperature below 480°C causes a reduction of the PL intensity. This indicates poor crystalline quality for samples grown below 480°C as shown earlier [8].

In growth rate experiments carried out with DIPSe and DEZn at a VI/II ratio of 12.3, we observed the kinetically controlled growth regime up to 480°C. At  $T_D = 380^\circ\text{C}$ , we found an extremely low growth rate of only  $0.2 \mu\text{m/h}$ . At temperatures higher than 480°C, the diffusion controlled growth regime was found. The growth rate was  $0.66 \mu\text{m/h}$ . The sample surface was mirror-like up to a growth temperature of 400°C. At higher growth temperatures the surface started to get rough. In SEM micrographs (magnification  $5000\times$ ), "pyramides" were observed on the surface. In Fig. 2, the 11 K PL spectra of ZnSe grown with DIPSe without plasma enhancement at different growth temperatures are shown. All PL spectra of samples grown below 500°C are

nearly identical. Only a broad emission band S1 in the energy interval from 2.4–2.78 eV was observed. We correlate this emission band to impurities in the Se precursor. An interpretation as donor–acceptor pair (DAP) luminescence seems to be incorrect, because from time-resolved measurements the decay of this emission is nonexponential in the ns range. We assume that this emission can be interpreted as an exciton bound to a deep centre [13]. Layers which were grown at temperatures higher than 500°C show dominating deep centre emissions at 1.95 and 2.25 eV. In all samples, no excitonic emissions were observed. At  $T_D = 480^\circ\text{C}$ , the variation of the VI/II ratio from 0.8 to 12.3 has no influence on the PL spectra. Below a VI/II ratio of 0.8, the PL spectra show deep luminescence at 1.74 eV. SIMS measurements show a carbon and hydrogen concentration below the detection limit of SIMS.

#### 4. Growth with plasma enhancement

The dependence of optical properties on growth temperature of ZnSe grown with plasma activated DESe is shown in Fig. 3. If DESe was used as the Se precursor together with plasma enhancement, the so-called copper green (2.25 eV) and self-activated centre emissions (2.0 eV) were reduced compared to non-plasma grown samples. At a growth temperature of 480°C, the samples show dominating resolved excitonic emissions in the PL spectra. The Y-peak at 2.6 eV which is attributed to lattice defects [14], is clearly visible and more enhanced in samples grown at 440°C. Phonon replica of the  $I_1^{\text{deep}}$  line (2.78 eV) can be detected. Deep centre emissions arise in the PL spectra of ZnSe grown below 440°C. This indicates a distorted lattice structure of ZnSe grown at temperatures below 480°C, although plasma precracking of DESe was used.

By using plasma precracking of the DIPSe precursor, the diffusion controlled growth regime is extended down to 330°C (see Fig. 1). The growth rate was  $1.66 \mu\text{m/h}$  with a VI/II ratio of 2.1 and at a total pressure of 20 hPa. The surfaces of the samples which were grown below 380°C were smooth in SEM micrographs. Macro-

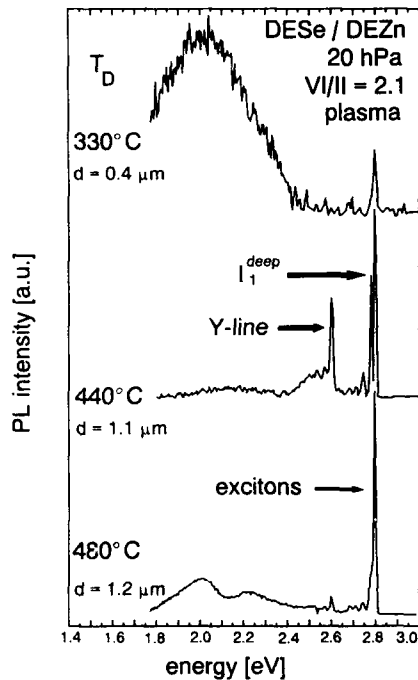


Fig. 3. PL spectra at 11 K of ZnSe samples grown with plasma precracking of DESe.

scopic defects on the surface were observed for epilayers which were grown at temperatures higher than 400°C. Below a deposition temperature of 360°C, deep centre emissions at 2.3 eV dominate in the PL spectra. In the PL spectra of layers grown at  $T_D$  higher than 360°C, the emission band S1 with a maximum at 2.65 eV due to the contaminations present in the Se precursor dominates the spectrum. Excitonic emissions of samples grown below 440°C can be resolved. The dominating emission band S1 is present even in samples grown with different VI/II ratios (0.8 to 12.3) and total pressures (20 hPa to 150 hPa). Samples grown with a VI/II ratio of 0.2 show only deep centre luminescence at 1.7 eV. SIMS measurements indicate that the hydrogen and carbon incorporation is below the detection limit of SIMS, comparable to the non-plasma grown samples.

### 5. Plasma enhanced nitrogen doping of ZnSe

Since free and donor bound excitons of ZnSe, grown with DESe and DEZn at a temperature of 480°C can be resolved, this growth temperature was first used for the doping experiments in spite of the high growth temperature. To increase the growth rate, the DESe was cracked with plasma. In Fig. 4, the PL spectra of ZnSe:N are shown. Fig. 4a shows the PL spectrum of ZnSe:N grown with DESe and DEZn with a VI/II ratio of 3.0. The nitrogen bound excitonic emission  $I_1^N$  at 2.79 eV cannot be resolved in the PL spectra, but the DAP emission at 2.7 eV and their phonon replica are observable. The DAP emission has the same energy position as the DAP emission in heavily nitrogen doped layers grown with MOVPE [7], but MBE grown p-type conducting samples show a DAP emission at 2.681 eV [15]. However, different strain magnitudes in the samples have to be taken into account due to different growth

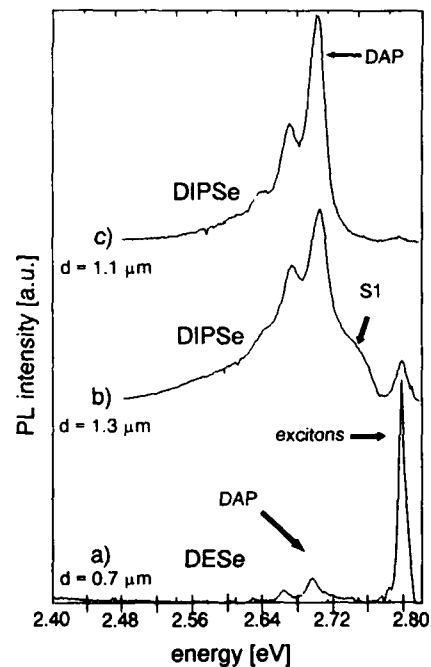


Fig. 4. PL spectra at 11 K of ZnSe:N grown with: (a) DESe, VI/II = 3.0,  $T_D$  = 480°C; (b) DIPSe, VI/II = 0.8,  $T_D$  = 380°C; (c) DIPSe, VI/II = 0.8,  $T_D$  = 360°C.

temperatures and layer thickness. Time resolved PL measurements carried out on samples grown with a VI/II ratio of 3.0 show nitrogen concentrations of  $1.5 \times 10^{17} \text{ cm}^{-3}$  [16]. With DIPSe as Se precursor, we reduced the growth temperature down to  $360^\circ\text{C}$  for the doping experiments, since at a growth temperature of  $480^\circ\text{C}$  and a VI/II ratio (DIPSe/DEZn) of 0.8 no DAP emission of the nitrogen was observed and the PL spectrum was not distinguishable from a PL spectrum of an undoped sample. The PL spectra of DIPSe grown samples doped with nitrogen are shown in Fig. 4b (VI/II ratio = 0.8,  $T_D = 380^\circ\text{C}$ ) and Fig. 4c (VI/II ratio = 0.8,  $T_D = 360^\circ\text{C}$ ). By decreasing the growth temperature to  $360^\circ\text{C}$ , the DAP emission of the nitrogen started to dominate the emission band S1 originating from the contamination of the DIPSe. This indicates an increased nitrogen incorporation in ZnSe with a reduced growth temperature. From time resolved PL measurements, a nitrogen concentration of  $4.5 \times 10^{17} \text{ cm}^{-3}$  (VI/II ratio = 0.8 at a growth temperature of  $380^\circ\text{C}$ ) was evaluated. Fig. 5 illustrates the DAP emission of samples grown with different nitrogen fluxes. The nitrogen incorporation can be estimated by the ratio of the intensity of the DAP emission to the intensity of the emission band S1. The shoulder on the high energy side of the DAP emission is clearly visible in Fig. 5. At a growth temperature of  $380^\circ\text{C}$  and a VI/II ratio of 0.8 we observed an increased nitrogen incorporation with an increased nitrogen flux as shown. A qualitative estimation is given by the ratio of DAP emission intensity to the excitonic emission intensity, which increases from 4.0 with a nitrogen flux of 34 ml/min to 5.7 at a nitrogen flux of 207 ml/min. All samples were semi-insulating in Hall measurements. To analyse the residual incorporation of extrinsic impurities originating from the growth process such as carbon and hydrogen and the amount of incorporated nitrogen, SIMS measurements were performed. In Fig. 6, a SIMS measurement of a ZnSe sample is shown. This ZnSe stack consists of several layers. The layers labelled (a) and (b) were grown with a VI/II ratio of 0.8 and were doped with plasma activated nitrogen. The layer (c) was grown totally in nitrogen, the hydrogen carrier gas was fully replaced

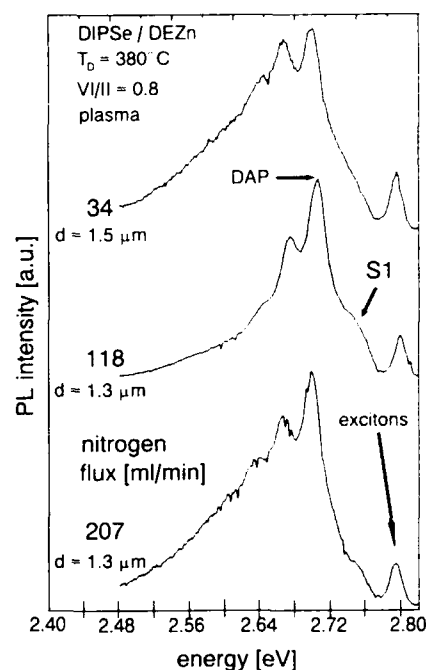


Fig. 5. PL spectra at 11 K of ZnSe:N grown with plasma cracked DIPSe and DEZn with different  $\text{N}_2$  doping gas fluxes.

by  $\text{N}_2$ , with the same VI/II ratio of 0.8. The other layers are undoped. The growth temperature was  $380^\circ\text{C}$ . In layers (a) and (c), the carbon content was approximately  $5 \times 10^{17} \text{ cm}^{-3}$  and the

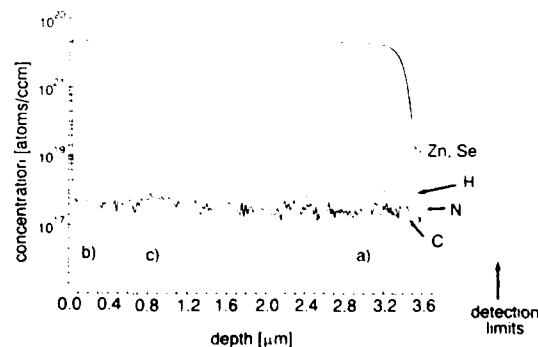


Fig. 6. SIMS measurement of a ZnSe stack: (a), (b)  $T_D = 380^\circ\text{C}$ , VI/II = 0.8,  $\text{H}_2$  as carrier gas,  $\text{N}_2$  as dopant gas; (c) like (a) and (b), but nitrogen as dopant and carrier gas.

hydrogen concentration was measured to  $1 \times 10^{18} \text{ cm}^{-3}$  for layer (a). In layer (c), we observed a hydrogen concentration of  $1 \times 10^{19} \text{ cm}^{-3}$ . This shows that the hydrogen originates from the precursors and not from the carrier gas. Time resolved measurements of nitrogen doped layers, grown with nitrogen instead of hydrogen as carrier gas, show a maximum nitrogen content of  $1 \times 10^{18} \text{ cm}^{-3}$ .

## 6. Discussion

By using plasma stimulated DESe and DEZn at  $480^\circ\text{C}$  the deep centre emission of ZnSe is reduced and free and bound excitons can be resolved. This shows that high quality ZnSe layers can be grown with the plasma MOVPE technique. Furthermore the growth rate is increased with plasma enhanced growth. For the investigated precursor combinations the diffusion controlled growth regime was extended to lower temperatures, for DIPSe/DEZn down to nearly  $330^\circ\text{C}$ , as shown in Fig. 1. Plasma enhanced growth results in a sufficiently high growth rate at a low deposition temperature. The emission due to the contamination of the DIPSe prevents the observation of other emissions (e.g., Y-peak, small intensity DAP and excitonic emissions) in DIPSe and DEZn grown samples. The main contamination seems to be tellurium. At a concentration above  $2 \times 10^{18} \text{ cm}^{-3}$ , this dopant causes exciton trapping and is responsible for the dominating S1 emission band [17], shown in Fig. 2. The absence of deep centre emissions proves that with DIPSe as Se precursor, the growth temperature for ZnSe can be reduced by  $100^\circ\text{C}$  in comparison to DESe as Se precursor. The nitrogen incorporation is achieved by plasma MOVPE and can be increased by growth temperature and nitrogen flux. A decrease of the VI/II ratio causes an increase of the nitrogen incorporation, since nitrogen is incorporated on Se lattice sites. Therefore we have three parameters to control the nitrogen incorporation. The choice of an extreme growth temperature ( $< 360^\circ\text{C}$ ,  $> 500^\circ\text{C}$ ; DIPSe) or an extremely low VI/II ratio leads to a deteriorated crystalline quality of the ZnSe:N layers. The

p-type conductivity of nitrogen doped ZnSe is totally compensated by the incorporation of carbon, hydrogen and the Te contamination, which originates from the precursor material. The hydrogen incorporation cannot be reduced by a simple substitution of the hydrogen carrier gas with nitrogen.

## 7. Conclusion

The optical properties of ZnSe can be improved by using plasma enhanced low pressure MOVPE. The diffusion limited growth regime can be extended to lower deposition temperatures. With DIPSe as Se precursor, a growth temperature of  $360^\circ\text{C}$  is suitable for the growth of ZnSe layers with well-resolved excitons in the PL spectra. Plasma activation of  $\text{N}_2$  as a dopant gas allows the incorporation of nitrogen up to a concentration of  $1.7 \times 10^{18} \text{ cm}^{-3}$ , but a parasitic incorporation of carbon and hydrogen occurs. The next steps in investigating p-type conducting ZnSe, grown by MOVPE, should be the avoidance of contaminations in the DIPSe source and the suppression of hydrogen and carbon incorporation into the layers.

## 8. Acknowledgements

We thank Prof. Dr. K. Heime for the fruitful discussions, R. Hövel for the vapour pressure measurements, AIXTRON GmbH for the technical assistance and Deutsche Forschungsgemeinschaft for the financial support of this work.

## 9. References

- [1] H. Kukimoto, J. Crystal Growth 101 (1990) 953.
- [2] J. Qiu, J.M. DePuydt, H. Cheng and M.A. Haase, Appl. Phys. Lett. 59 (1991) 2992.
- [3] C.G. Van de Walle, D.B. Laks, G.F. Neumark and S.T. Pantelides, Phys. Rev. B 47 (1993) 9425.
- [4] M.A. Haase, J.M. DePuydt, H. Cheng and J.E. Potts, Appl. Phys. Lett. 58 (1991) 1173.
- [5] D.J. Chadi and K.J. Chang, Appl. Phys. Lett. 55 (1989) 575.

- [6] N.R. Taskar, B.A. Khan, D.R. Dorman and K. Shahzad, *Appl. Phys. Lett.* 62 (1993) 270.
- [7] A. Ohki, N. Shibata, K. Ando and A. Katsui, *J. Crystal Growth* 93 (1988) 692.
- [8] M. Heuken, J. Söllner, F.E.G. Guimarães, K. Marquardt and K. Heime, *J. Crystal Growth* 117 (1992) 336.
- [9] G.B. Stringfellow, *Organometallic Vapour Phase Epitaxy: Theory and Practice* (Academic Press, San Diego, CA, 1989).
- [10] S. Patnaik, K.F. Jensen and K.P. Giapis, *J. Crystal Growth* 107 (1991) 390.
- [11] W. Taudt, J. Hermans, A. Schneider, J. Woitok, J. Geurts and M. Heuken, *Adv. Mater. Opt. Electron.*, in press.
- [12] Data Sheet, Morton International, USA.
- [13] A. Hoffmann, R. Heitz, B. Lummer, Ch. Fricke, V. Kutzer, I. Broser, W. Taudt, G. Gleitzmann and M. Heuken, *J. Crystal Growth* 138 (1994) 379.
- [14] J. Gutowski, N. Presser and G. Kudlek, *Phys. Status Solidi (a)* 120 (1990) 11.
- [15] R.M. Park, M.B. Troffer, C.M. Rouleau, J.M. DePuydt and M.A. Haase, *Appl. Phys. Lett.* 57 (1990) 2127.
- [16] Ch. Fricke, R. Heitz, B. Lummer, V. Kutzer, A. Hoffmann, I. Broser, W. Taudt and M. Heuken, *J. Crystal Growth* 138 (1994) 815.
- [17] K.A. Dhese, J.E. Nicholls, P.J. Wright, B. Cockayne and J.J. Davies, *J. Crystal Growth* 126 (1993) 179.

## Metalorganic molecular beam epitaxy doping of II–VI compound semiconductors

R.N. Bicknell-Tassius, W.M. Theis \*, Teresa Cole, Kelvin T. Higa,  
Thomas J. Groshens

*Research Department, Naval Air Warfare Center Weapons Division, China Lake, California 93555-6001, USA*

### Abstract

Site-selective metalorganic molecular beam epitaxy (MOMBE) is a new technique that shows much promise for the controlled substitutional doping of II–VI compound semiconductors. In the present work, initial results on the use of the site-selective doping are reported. The metalorganic compound  $[t\text{-BuZnAs}(t\text{-Bu})_2]_2$  which is employed in the present work is only one of a whole class of potential compounds in which a group II element is pre-bonded to a group V element. ZnSe epitaxial layers doped with this compound exhibit bright near edge luminescence that is dominated by acceptor-bound-exciton transitions. This indicates that the As contained in this designer dopant is incorporated on its proper substitution site.

### 1. Introduction

The limiting factor on devices using wide-gap II–VI materials has been in achieving methods of producing reliable and controllable doping of these compounds. An example has been the considerable difficulty in growing p-type ZnSe as well as producing doped materials with high carrier concentrations. Expected p-type dopants are the elements from groups I and V. The group III elements As and P have been investigated as potential p-type dopants with little success. The formation of acceptor states was inferred on the basis of photoluminescence results, although the sample remained highly resistive [1,2]. Li has been successfully employed to produce p-type ZnSe by

molecular beam epitaxy (MBE) and, in fact, light emitting diodes (LEDs) were successfully fabricated, although it diffuses too easily to be an ideal dopant [3–5]. Li is also hindered from being a useful dopant in that it tends to self-compensate at high concentrations by going onto interstitial sites [5].

The recent success in doping ZnSe p-type using a nitrogen atomic radical source has been a large step towards controlling the electrical properties of this material [6]. This success has led to the fabrication of the first laser diodes operating in the blue-green spectral region [7,8]. However difficulties still remain. At present, the highest p-type doping density remains in the low  $10^{18} \text{ cm}^{-3}$  range; furthermore the samples tend to be highly compensated ( $> 70\%$ ) and show a very small activation of the incorporated nitrogen [9]. Not only do there appear to be limits to the doping density that is achievable with nitrogen,

\* Corresponding author.



but the long term stability of the doping level has also been questioned [10].

In this paper a new and unique route to p-type doping of ZnSe is reported. Rather than using the traditional elemental sources such as N, As, P or Li, we employed a complex metalorganic molecule in which the potential acceptor is prebonded to a host atom. Previous published work on site-specific doping of II-VI compound semiconductors is limited to nitrogen doping of ZnSe grown by organometallic vapor phase epitaxy (OMVPE) [11,12].

## 2. Experimental details

The ZnSe epitaxial growth was carried out in an EPI MBE system. Connected to the II-VI system through a vacuum transfer system is a Perkin-Elmer 425B III-V MBE system. This combination allows the growth of II-VI epitaxial layers on a variety of virgin III-V buffer layers. Also connected to the II-VI MBE system is a gas handling cabinet that allows the precisely controlled introduction of various gases, high vapor pressure liquids or solids into the growth chamber. These can be injected through either conven-

tional gas injectors or an electron cyclotron resonance plasma (ECR) source. The system is also equipped with six solid sources, which include Zn, Se, Cd, Te and Mn, and a selenium cracker. In the present work, only high purity elemental Zn and Se in conventional low temperature cells were employed. The gas cabinet houses six conventional bubblers. One of these bubblers can be operated in a double-dilution mode and another can be used as a direct vapor injector. For the injection of the T-butyl (di-t-butyl) arsino zinc, the solid was placed in one of the conventional bubblers and the exit valve was opened after the temperature was stabilized at the operating temperature without the use of a carrier gas. A schematic diagram of the system is shown in Fig. 1. As can be seen in the figure, a combination of diffusion and cryo-pumping is employed. During standby periods and MBE growth the system is cryo-pumped. During MOMBE growth and doping, the system is pumped using a double liquid-nitrogen-trapped diffusion pump.

The ZnSe epilayers reported in this paper were grown at a substrate temperature of 260°C on thin GaAs epitaxial layers which were deposited in the III-V chamber before the substrate was transferred into the II-VI chamber. A

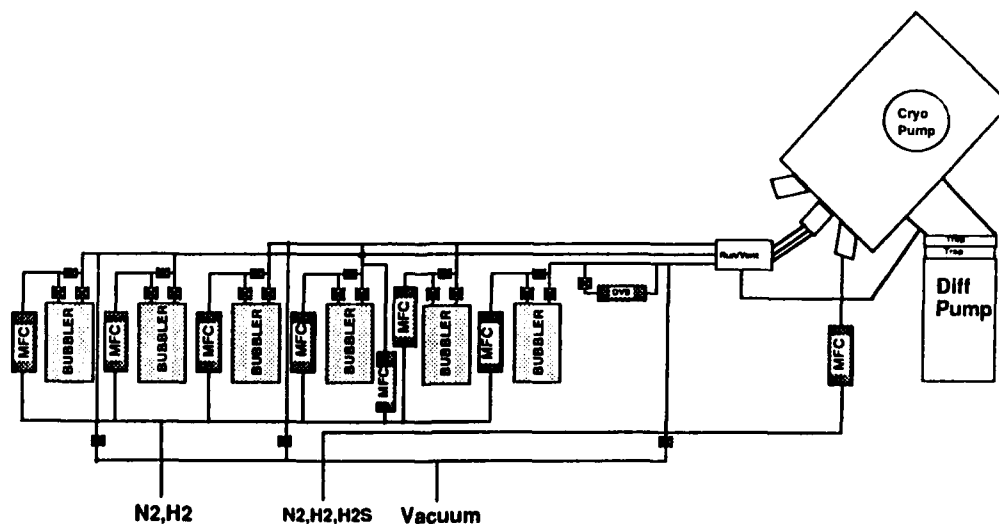


Fig. 1. Schematic diagram of the NAWCWPNS II-VI MOMBE system.

selenium-to-zinc beam pressure ratio of 2:1 was employed for all ZnSe epilayers reported here.

The optical properties of the epitaxial layers were investigated using low temperature photoluminescence (PL) at liquid helium temperatures. The PL signal was excited using a Spectra Physics Model 185 He–Cd laser. The luminescence was detected using a 1.25 m SPEX grating monochromator with a cooled GaAs photocathode photomultiplier and standard lock-in detection electronics.

The particular metalorganic compound that we have investigated in the present work is *T*-butyl (di-*t*-butyl) arsino zinc ( $[(t\text{-BuZnAs}(t\text{-Bu})_2)_2]$ ). The details of the synthesis and characterization of this particular compound have been reported earlier [13]. The structure of this compound is shown in Fig. 2. The novel aspect of this compound is that at its center are two Zn–As bonds. The existence of these Zn–As bonds in the precursor is hoped to enhance the site selectivity of the incorporation of the As at the growth front during the deposition process. The Zn portion of this compound is presumed to prefer incorporation on the Zn sublattice as opposed to the Se sublattice. The As will be forced to occupy the nearest neighbor Se site and thus be activated as a substitutional *p*-type dopant. This enhanced site selectivity should lead to a dramatic decrease in the density of anti-site and interstitial defects, and therefore a higher level of dopant activation. This

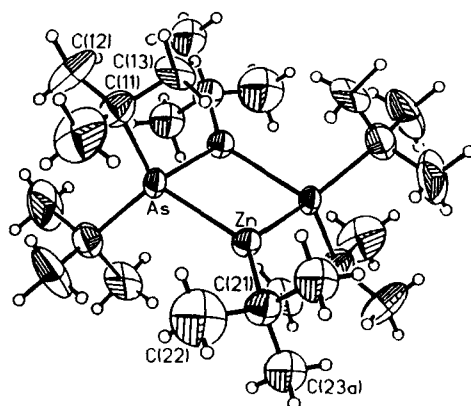


Fig. 2. Structure of  $[(t\text{-BuZnAs}(t\text{-Bu})_2)_2]$ .

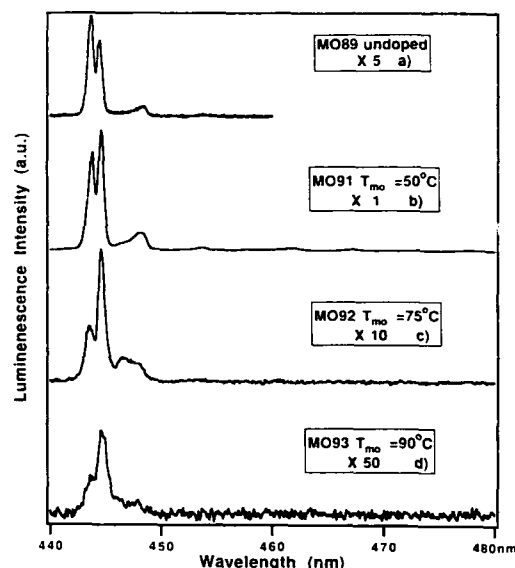


Fig. 3. Low-temperature photoluminescence spectra of  $[(t\text{-BuZnAs}(t\text{-Bu})_2)_2]$  doped ZnSe epitaxial layers grown using bubbler temperatures between 50 and 90°C.

reduction of point-defects should also lead to an improvement in device characteristics, since it is believed that point-defects contribute to the growth of dark-line defects causing a severe reduction in life-time of present generation blue-green laser diodes.

### 3. Results and discussion

In order to investigate the effectiveness of the site-selective doping technique a series of  $[(t\text{-BuZnAs}(t\text{-Bu})_2)_2]$  doped epitaxial layers was grown. All samples in this series were grown as nearly as possible using the same substrate temperature and fluxes. In this series the bubbler temperature was systematically varied between 50 and 90°C. The photoluminescence spectrum from this series of samples is shown in Fig. 3. The luminescence spectrum for undoped epitaxial ZnSe is shown in spectrum (a) for comparison. This spectrum is dominated by the free exciton line at 443.3 nm and an acceptor-bound-exciton line occurring at 444.4 nm. This sample exhibited

minimal deep level luminescence in the self-activated region of the spectrum.

Spectra (b) to (d) were grown using bubbler temperatures of 50, 75 and 90°C, respectively. The spectra for the sample grown using the lowest  $[t\text{-BuZnAs}(t\text{-Bu})_2]_2$  temperature of 50°C exhibits a strong increase in luminescence intensity. In fact, the luminescence intensity for this sample is about a factor of five more intense than the undoped sample. Accompanying the increase in the overall luminescence intensity is a shift of intensity from the free-exciton to acceptor-bound-exciton line. In previous work using  $[t\text{-BuZnAs}(t\text{-Bu})_2]_2$  as a p-type dopant in CdTe and ZnTe, p-type conductivity with hole concentrations in the mid  $10^{17} \text{ cm}^{-3}$  range were obtained when similar bubbler temperatures were employed. Details of this work will be published elsewhere.

As the bubbler temperature is increased further, a decrease in the overall intensity, and a further shift to acceptor-bound luminescence is observed. At a bubbler temperature of 90°C, the highest temperature investigated, the luminescence intensity has become relatively weak and significant deep level luminescence is observed. It should be noted, however, that the near-edge

luminescence is now completely dominated by the acceptor-bound exciton line. In Fig. 4 is plotted the peak-intensity ratio for this series of site-selectively doped ZnSe epilayers, demonstrating the strong increase in acceptor related luminescence.

These results indicate that the site-selective dopant  $[t\text{-BuZnAs}(t\text{-Bu})_2]_2$  can be successfully used to induce shallow acceptor sites in MBE grown ZnSe. At present efforts are underway to investigate both the amount of incorporated As and its electrical activation.

#### 4. Summary

In summary, we report for the first time the results of the MBE doping of ZnSe with a site-specific metalorganic precursor. Initial photoluminescence results indicate that significant amounts of acceptors have been introduced using this new technique. The T-butyl (di-t-butyl) arsino zinc precursor is only one of a large number of site specific dopants that need to be investigated. These designer dopants offer the potential of greatly reducing the introduction of point defects that are often associated with the incorporation of traditional acceptors in ZnSe. Once this is accomplished, higher dopant densities should be realized, with the associated improvements in related device properties.

#### 5. Acknowledgments

Two of the authors (W.M.T. and T.C.) wish to acknowledge support from Naval Air Warfare Center Weapons Division independent research funds. This research was also supported by the ONR/ASEE postdoctoral fellowship program.

#### 6. References

- [1] S.M. Shibli, M.C. Tamargo, B.J. Skromme, S.A. Schwartz, C.L. Schwartz, R.E. Nahory and R.J. Martin, J. Vac. Sci. Technol. B 8 (1990) 187.

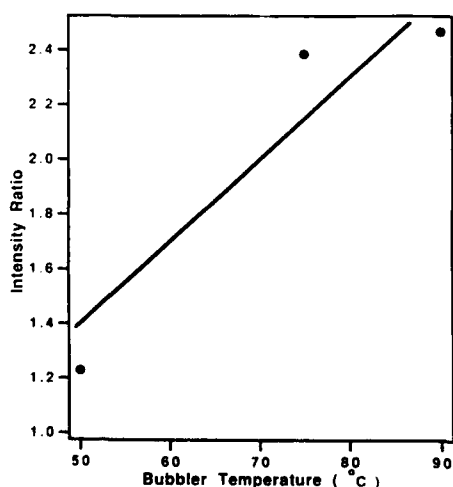


Fig. 4. Plotted is the ratio of the intensity of the light-hole to the acceptor bound exciton intensity in  $[t\text{-BuZnAs}(t\text{-Bu})_2]_2$  doped ZnSe epitaxial layers.

- [2] T. Yao and Y. Okada, *Jap. J. Appl. Phys.* 25 (1986) 821.
- [3] J.M. DePuydt, M.A. Haase, H. Cheng and J.E. Potts, *Appl. Phys. Lett.* 55 (1989) 1103.
- [4] J. Ren, K.A. Bowers, B. Sneed, D.L. Dreifus, J.W. Cook, Jr., J.F. Schetzina and R.M. Kolbas, *Appl. Phys. Lett.* 57 (1990) 1901.
- [5] M.A. Haase, H. Cheng, J.M. DePuydt and J.E. Potts, *J. Appl. Phys.* 67 (1990) 448.
- [6] R.M. Park, M.B. Troffer, C.M. Rouleau, J.M. DePuydt and M.A. Haase, *Appl. Phys. Lett.* 57 (1990) 2127.
- [7] M.A. Haase, J. Qiu, J.M. DePuydt and H. Cheng, *Appl. Phys. Lett.* 59 (1991) 1272.
- [8] H. Jeon, J. Ding, W. Xie, D.C. Grillo, W. Patterson, M. Kobayashi, R.L. Gunshor and A.V. Nurmikko, *Appl. Phys. Lett.* 59 (1991) 3691.
- [9] Z. Yang, K.A. Bowers, J. Ren, Y. Lansari, J.W. Cook, Jr. and J.F. Schetzina, *Appl. Phys. Lett.* 61 (1990) 2671.
- [10] J. Simpson, S.Y. Wang, H. Stewart, J. Wallace, S.J.A. Adams, I. Hauksson, K.A. Prior and B.C. Cavenett, *J. Electron. Mater.* 22 (1993) 431.
- [11] W.S. Rees, Jr., D.M. Green, T.J. Anderson and E. Bretschneider, in: *Proc. Wide Band Gap Semiconductor Symp.*, Boston, 1992 (Mater. Res. Soc., Pittsburgh, PA) p. 281.
- [12] W.S. Rees, Jr., D.M. Green, T.J. Anderson, E. Bretschneider, B. Pathangey, C. Park and J. Kim, *J. Electron. Mater.* 21 (1992) 361.
- [13] T.J. Groshens, K.T. Higa and R.J. Butcher, *J. Organometallic Chem.* 463 (1993) 97.



ELSEVIER

Journal of Crystal Growth 138 (1994) 430–436

JOURNAL OF  
**CRYSTAL  
GROWTH**

## Atomic nitrogen production in nitrogen-plasma sources used for the growth of ZnSe:N and related alloys by molecular-beam epitaxy

R.P. Vaudo, J.W. Cook, Jr., J.F. Schetzina \*

*Department of Physics, North Carolina State University, Raleigh, North Carolina 27695-8202, USA*

### Abstract

A high resolution study of the optical emission from nitrogen-plasmas produced by an Oxford Applied Research radio frequency plasma source is reported. Strong atomic emission lines in the near-infrared spectral region provide unequivocal evidence that the nitrogen-plasma source generates an appreciable flux of nitrogen atoms. Nitrogen atoms, rather than  $N_2$  molecules in the plasma, are the most likely nitrogen-plasma species responsible for the successful p-type doping of ZnSe:N and related alloys. Emission spectra from the radio frequency nitrogen-plasma source are compared with similar emission spectra obtained from an electron cyclotron resonance microwave nitrogen-plasma source.

### 1. Introduction

Nitrogen doping of ZnSe and related alloys has led to the demonstration of blue/green light emitting diodes [1–6] and laser diodes [7–11] by a number of research groups throughout the world. Most of these researchers employ an Oxford Applied Research [12] radio frequency (RF) plasma source during molecular-beam epitaxy (MBE) film growth to produce the p-type layers of the diode structures. Information about the nitrogen-plasma species responsible for the successful p-type doping, and the optimization of this desired species, is fundamentally important to the pursuit of higher p-type doping levels and improved performance of II–VI light emitting devices.

Other research groups have examined the emission from Oxford RF plasma sources to better understand the mechanisms involved in nitrogen doping. Ohkawa et al. attributed the p-type doping to “active” nitrogen in the plasma in the form of excited  $N_2$  molecules in the  $A^3\Sigma_u^+$  state, due to the long lifetime (2 s) of this metastable state [2]. Park argued that the presence of  $N_2$  molecules in the  $A^3\Sigma_u^+$  excited state implies that they were created by the recombination of two ground state N atoms within the plasma [13], although no spectroscopic evidence of N atoms in the optical emission spectrum was reported, nor were molecular excitations which might also be responsible for the observed  $A^3\Sigma_u^+$  excited molecular state addressed.

Here we report spectroscopic evidence that the nitrogen-plasma sources used for p-type doping of II–VI materials do, indeed, generate an

\* Corresponding author.

appreciable flux of N atoms. The optical emission from an Oxford Applied Research Model MPD21 RF plasma source was investigated over a range of plasma input powers and  $N_2$  gas flow rates. Source operating conditions which enhance atomic nitrogen production are discussed. An evaluation of an electron cyclotron resonance (ECR) microwave plasma source, as an alternative nitrogen source to the Oxford RF plasma source, is also presented.

## 2. Experimental details

Nitrogen-plasmas were produced using an Oxford Applied Research Model MPD21 RF plasma source which bolts directly onto an MBE chamber furnace port. The inductively-coupled 13.56 MHz input energy which generates the nitrogen-plasmas was varied from 200 to 500 W. A variable leak valve was used to carefully control the flow of high purity (5N5)  $N_2$  gas into the RF plasma source such that the MBE chamber pressure was varied from  $1.0 \times 10^{-6}$  to  $5.0 \times 10^{-5}$  Torr. These conditions provided a variety of stable nitrogen-plasmas to be analyzed.

Optical emission from the plasma source was monitored with an EG&G Princeton Applied Research Model 1235 monochromator, equipped with interchangeable 150 grooves/mm (low resolution) and 1200 grooves/mm (high resolution) gratings. The emission from the Oxford RF source was measured through a Kodial glass viewport. The dispersed nitrogen-plasma emission was detected with a Model 1455 intensified 700-pixel diode array detector (280–900 nm) and recorded by computer. The spectral response of the monochromator/detection system was determined using a calibrated 1000 W tungsten-halogen lamp operated at 8.30 Å. The measured spectral response curve was used to correct all of the nitrogen-plasma emission spectra obtained in this study.

## 3. Results and discussion

A representative optical emission spectrum from the Oxford MPD21 RF plasma source oper-

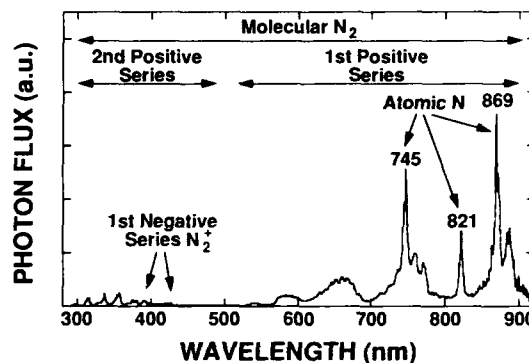


Fig. 1. Nitrogen-plasma emission spectrum from an Oxford Applied Research RF plasma source operated at an input power of 200 W and MBE chamber pressure of  $2 \times 10^{-6}$  Torr. The spectrum was obtained for the wavelength range 280–900 nm using the 150 grooves/mm grating. The emission spectrum is dominated by atomic nitrogen peaks in the near-IR. The spectrum also contains a number of molecular  $N_2$  and  $N_2^+$  emission bands throughout the spectral region investigated.

ated at 200 W and  $2 \times 10^{-6}$  Torr is shown in Fig. 1. A variety of nitrogen-plasma emission peaks span the measured spectral region, including emission from the first, positive and second-positive series transitions of the neutral  $N_2$  molecule, weak emission peaks of the first-negative series of the molecular  $N_2^+$  ion, and strong atomic lines in the near-infrared (IR) spectral region. The six multiple-peaked broad bands of emission which occur in the visible and near-IR spectral regions are associated with the first-positive series molecular transitions ( $B^3\Pi_g \rightarrow A^3\Sigma_u^+$  transitions) [14,15]. These bands are approximately centered at emission wavelengths of 540, 590, 655, 755, 820, and 880 nm. There are no resolvable peaks in the lowest wavelength band, but as the emission wavelength is increased, the separation between peaks increases and individual molecular transitions can be resolved. As a result, four peaks at 580, 585, 590 and 595 nm are evident within the molecular band centered at 590 nm. The peak at 662 nm is the strongest of the eight first-positive transition peaks visible between 632 and 687 nm. The three highest wavelength bands are dominated by atomic emission lines, but several molecular peaks are still recognizable. First-

positive molecular peaks at 716, 726, 737, 761, 773, and 787 nm are observed in the fourth band. The weak molecular band at 820 nm is nearly eclipsed by the atomic emission, but the highest wavelength molecular band includes observable peaks at 854 and 891 nm. All nineteen peaks detected correspond to the first-positive series transitions of the  $N_2$  molecule [14,15]. The largest bands of the much less intense second-positive molecular  $N_2$  system ( $C^3\Pi_u \rightarrow B^3\Pi_g$  transitions) [14,15] occur at 316, 337, 357, 380, 400 and 420 nm. Overall, the second-positive series of molecular transitions occur at wavelengths throughout the 300 to 500 nm region. The peaks at 391 and 428 nm are the most intense of the first-negative system of  $N_2^+$  ( $B^2\Sigma_u^+ \rightarrow X^2\Sigma_g^+$  transitions) [14,15]. Additional emission peaks of  $N_2^+$  were observed at 388, 417, 424, 428, 451, 455, 471, 501 and 508 nm.

Table 1  
Summary of observed atomic nitrogen emission lines

Atomic transition		Emission wavelength (nm)	
Transition array	Total angular momentum $J$	Accepted value [16–18]	This study
$3s^4P \rightarrow 3p^4S^\circ$	1/2–3/2	742.36	742.3
	3/2–3/2	744.23	744.2
	5/2–3/2	746.83	746.8
$3s^4P \rightarrow 3p^4P^\circ$	3/2–5/2	818.48	818.5
	1/2–3/2	818.80	818.8
	1/2–1/2	820.03	820.0
	3/2–3/2	821.07	821.0
	5/2–5/2	821.63	821.6
	3/2–1/2	822.31	822.3
	5/2–3/2	824.24	824.2
$3s^2P \rightarrow 3p^2P^\circ$	1/2–3/2	856.77	856.8
	1/2–1/2	859.40	859.4
	3/2–3/2	862.92	862.9
	3/2–1/2	865.59	865.5
$3s^4P \rightarrow 3p^4D^\circ$	5/2–7/2	868.03	868.0
	3/2–5/2	868.34	868.3
	1/2–3/2	868.62	868.6
	1/2–1/2	870.32	870.3
	3/2–3/2	871.17	871.2
	5/2–5/2	871.88	871.9
	3/2–1/2	872.89	872.8
	5/2–3/2	874.73	–

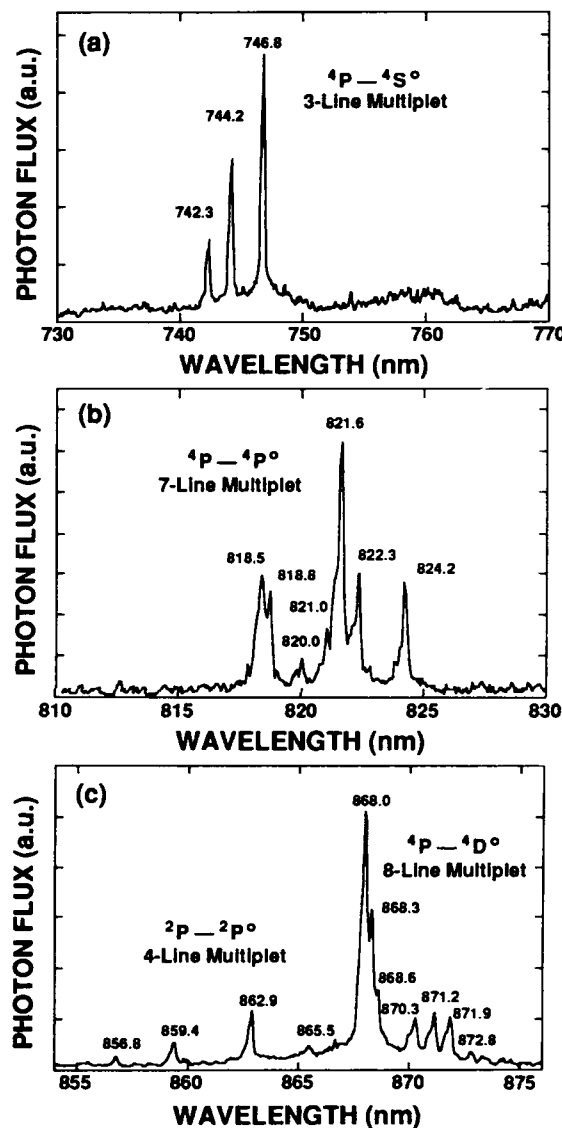


Fig. 2. High resolution spectra from the RF plasma source operated at an input power of 200 W and MBE chamber pressure of  $2 \times 10^{-6}$  Torr showing intense atomic nitrogen emission peaks within the (a) 730–770 nm, (b) 810–830 nm, and (c) 855–875 nm spectral regions.

The emission spectrum of Fig. 1 is dominated by the sharp atomic nitrogen emission peaks in the near-IR spectral region at 745, 821 and 869 nm. Confirmation of atomic nitrogen emission

was obtained by employing the high resolution grating (1200 grooves/mm). Fig. 2 shows high resolution spectra obtained from the MPD21 RF plasma source for the three near-IR spectral regions of interest. The high resolution spectra reveal that each of the atomic peaks we identified in Fig. 1 is actually composed of several lines, each corresponding to a different total electronic angular momentum transition. In Fig. 2a, the triplet of lines at 742.3, 744.2, and 746.8 nm is attributed to the  $3s^4P \rightarrow 3p^4S^o$  transitions of atomic nitrogen [16–18]. The three broad, low-intensity emission bands with bandheads at 738, 750, and 762 nm are due to transitions of the first-positive system of molecular  $N_2$  [14,15]. Fig. 2b shows a 7-line multiplet of peaks between 818.5 and 824.2 nm, which we attribute to the  $3s^4P \rightarrow 3p^4P^o$  transitions in atomic nitrogen [16–18]. Fig. 2c shows a total of eleven atomic nitrogen peaks at wavelengths ranging between 856.8 and 872.8 nm. The 4-line multiplet of peaks at 856.8, 859.4, 862.9, and 865.5 nm is due to the  $3s^2P \rightarrow 3p^2P^o$  transitions in atomic nitrogen [16–18]. The seven peaks between 868.0 and 872.8 nm are part of an 8-line multiplet of lines associated with the  $3s^4P \rightarrow 3p^4D^o$  transitions in atomic nitrogen [16–18].

Table 1 summarizes our findings with regard to the high resolution atomic nitrogen emission lines. The first column in the table lists selected atomic nitrogen transitions expressed by the usual spectroscopic symbols [16] for the final state and initial state, respectively. The second column gives the corresponding internal quantum numbers of the total electronic angular momentum  $J$  of each of the listed transitions. The third column enumerates reliable reference values [16–18] for the transition wavelengths in nanometers, followed by the fourth column of the observed transition wavelengths measured in the present spectroscopic study of the Oxford Applied Research Model MPD21 nitrogen-plasma source. Note that all of the twenty-one near-IR emission lines observed from the nitrogen-plasma generated within the MPD21 source are in excellent agreement with literature values of the atomic nitrogen transitions listed in the table [16–18]. These results unequivocally confirm that the Oxford MPD21

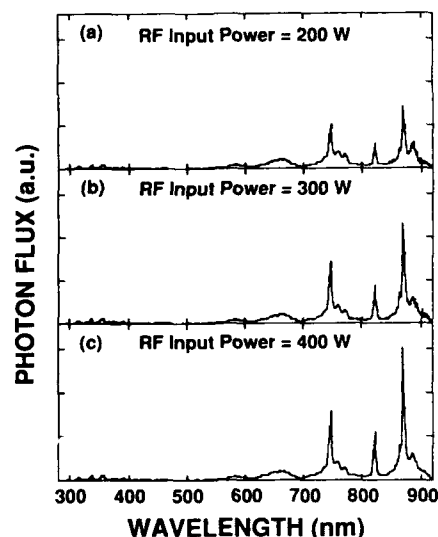


Fig. 3. Optical emission spectra from the RF plasma source operated at an MBE chamber pressure of  $5 \times 10^{-6}$  Torr and RF input power of (a) 200 W, (b) 300 W, and (c) 400 W. Note that as the input power increases, the atomic nitrogen peaks increase in intensity compared to the molecular nitrogen emission features.

RF plasma source produces an appreciable flux of neutral *nitrogen atoms*.

Nitrogen-plasma emission spectra were obtained for a range of RF input powers and  $N_2$  gas flow rates in order to determine operating parameters that would enhance atomic nitrogen generation relative to the molecular  $N_2$  plasma species. A series of emission scans recorded from the Oxford RF plasma source as the source input power is increased from 200 to 400 W is shown in Fig. 3. The MBE chamber pressure was held at  $2 \times 10^{-6}$  Torr. Each spectrum in Fig. 3 was normalized with respect to the molecular emission peak at 654 nm in order to illustrate the relative intensities of the atomic versus molecular nitrogen emission peaks. In general, as the input power to the nitrogen-plasma is increased, the intensity of each peak in the spectrum is increased, but the atomic nitrogen peaks grow more quickly than do the molecular bands. The relative intensity of the atomic nitrogen emission peaks at 745, 821, and 869 nm [16–18] steadily grow stronger as the input power is increased from 200 W in Fig. 3a to



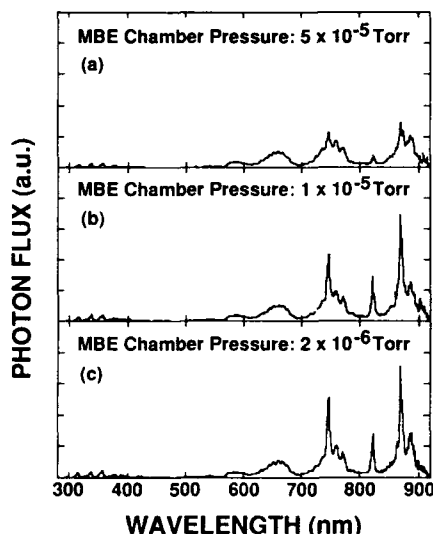


Fig. 4. Optical emission spectra from the RF plasma source operated at an RF input power of 200 W and MBE chamber pressure of (a)  $5 \times 10^{-5}$  Torr, (b)  $1 \times 10^{-5}$  Torr, and (c)  $2 \times 10^{-6}$  Torr. Note that lower  $N_2$  flow rates enhance the relative intensity of the atomic nitrogen peaks in the near-IR spectral region.

400 W in Fig. 3c. This trend suggests that larger input powers cause a larger fraction of the nitrogen molecules to dissociate and therefore produce relatively more nitrogen atoms.

Fig. 4 shows a sequence of emission spectra which illustrates the effects of changing the  $N_2$  gas flow rate. The input power was held constant at 200 W and, similar to the spectra of Fig. 3, the scans were normalized to the molecular emission peak centered at 654 nm. As the  $N_2$  gas flow rate decreases, the overall intensity of the emission is reduced. However, the atomic lines decrease at a slower rate than the molecular peaks. The sharp atomic nitrogen lines in the near-IR grow relative to the first-positive molecular bands from the highest input gas flow rate (MBE chamber pressure =  $5 \times 10^{-5}$  Torr) in Fig. 4a to the lowest (MBE chamber pressure =  $2 \times 10^{-6}$  Torr) in Fig. 4c. We believe that reducing the  $N_2$  gas flow, which reduces the pressure, decreases the probability that two atoms will collide within the plasma and recombine to form molecular  $N_2$ , hence favoring the net generation of atomic nitrogen.

Thus, low-pressure and high-power nitrogen-plasmas generate a higher percentage of nitrogen atoms.

#### 4. Conclusions

The results of this optical emission study clearly show that the Oxford Applied Research RF plasma source generates an appreciable flux of neutral nitrogen atoms. We believe that nitrogen atoms are the most likely nitrogen-plasma species responsible for the successful p-type doping of ZnSe:N and related alloy films to levels high enough to make blue/green laser diodes [7-11]. At an MBE chamber pressure of  $10^{-6}$  Torr, the mean free path of nitrogen atoms is greater than 50 m [19] – which is much larger than the source-to-substrate distance in typical MBE systems. Thus, nitrogen atoms from the plasma source impinge directly onto the film growth surface during MBE film growth and can be directly incorporated into the ZnSe crystal structure.

In contrast, very large fluxes of ground state  $N_2$  molecules used in earlier studies have produced very low doping levels in ZnSe [20] – which is to be expected because of the very large dissociation energy of  $N_2$  molecules in the ground state (9.9 eV) [21].  $N_2$  molecules in the  $A^3\Sigma_u^+$  excited state have also been proposed as another possible doping species, since  $N_2$  molecules in this metastable state remain excited for an average of 2 seconds [2] – sufficient time to travel to the growth surface. Theoretical calculations suggest that  $N_2$  molecules in the  $A^3\Sigma_u^+$  metastable state may also be able to adsorb to the ZnSe growth surface and subsequently dissociate [22]. However, 3.9 eV [21] of energy is still required to break the strong molecular bond of the  $A^3\Sigma_u^+$  metastable state. Since nitrogen atoms can incorporate directly into the lattice without expending the large amount of energy needed to dissociate the  $N_2$  molecules, we believe that nitrogen atoms are the plasma species that are in large part responsible for the p-type doping of ZnSe and related alloys.

At NCSU, we have also investigated the use of an ASTeX compact ECR microwave plasma

source [23] as an alternative nitrogen source to the Oxford RF plasma source for p-type doping of ZnSe-based materials. A high resolution study of the optical emission from the ECR plasma source [24] indicated that the nitrogen-plasmas generated by both the ASTeX ECR source and the Oxford RF source were very similar in many respects. As is shown for the RF plasma source studied in the present work, the ECR plasma source also generates a large flux of nitrogen atoms which is enhanced by higher source input powers and lower  $N_2$  gas flow rates [24]. However, the relative intensity of the atomic nitrogen versus molecular nitrogen emission peaks from both sources indicates that the Oxford RF plasma source produces a larger percentage of nitrogen atoms for a given set of operating conditions. Furthermore, using the ASTeX ECR source we were not able to successfully dope ZnSe or ZnSse films to  $10^{18} \text{ cm}^{-3}$  free hole concentrations at 300 K that were achieved with the Oxford RF plasma source [25]. These findings suggest that, because of the greater percentage of nitrogen atoms it is able to produce, the Oxford RF plasma source may be the preferred nitrogen source for p-type doping of ZnSe and related II–VI alloys.

However, direct correlation between the output of the nitrogen plasma sources described in this paper and the p-type doping of ZnSe:N will require additional electrical and optical film characterization experiments – which are beyond the intended scope of the present work. Such future studies are important, we believe, and should also include an investigation of the effects of MBE system parameters such as nitrogen source placement, source-to-substrate distance, system pumping type/speed, etc., on p-type doping levels of ZnSe:N and related alloys.

## 5. Acknowledgments

The authors wish to acknowledge stimulating discussions concerning the physics of nitrogen-plasmas with Dr. D. Dustin, Dr. J. Davis, and Dr. Margaret Mulbrandon at the Naval Research Laboratory in Washington, DC. This work was

supported by SDIO/ONR grant N00014-92-J-1756.

## 6. References

- [1] R.M. Park, M.B. Troffer, C.M. Rouleau, J.M. DePuydt and M.A. Haase, *Appl. Phys. Lett.* 57 (1990) 2127.
- [2] K. Ohkawa, T. Karasawa and T. Mitsuyu, *J. Crystal Growth* 117 (1992) 375.
- [3] W. Xie, D.C. Grillo, R.L. Gunshor, M. Kobayashi, G.C. Hua, N. Otsuka, H. Jeon, J. Ding and A.V. Nurmikko, *Appl. Phys. Lett.* 60 (1992) 463.
- [4] H. Jeon, J. Ding, A.V. Nurmikko, W. Xie, M. Kobayashi and R.L. Gunshor, *Appl. Phys. Lett.* 60 (1992) 892.
- [5] W. Xie, D.C. Grillo, R.L. Gunshor, M. Kobayashi, H. Jeon, J. Ding, A.V. Nurmikko, G.C. Hua and N. Otsuka, *Appl. Phys. Lett.* 60 (1992) 1999.
- [6] Z. Yu, J. Ren, Y. Lansari, B. Sneed, K.A. Bowers, C. Boney, D.B. Eason, R.P. Vaudo, K.J. Gossett, J.W. Cook, Jr. and J.F. Schetzina, *Jap. J. Appl. Phys.* 32 (1993) 663.
- [7] M.A. Haase, J. Qiu, J.M. DePuydt and H. Cheng, *Appl. Phys. Lett.* 59 (1991) 1272.
- [8] H. Jeon, J. Ding, W. Patterson, A.V. Nurmikko, W. Xie, D.C. Grillo, M. Kobayashi and R.L. Gunshor, *Appl. Phys. Lett.* 59 (1991) 3619.
- [9] H. Jeon, J. Ding, A.V. Nurmikko, W. Xie, D.C. Grillo, M. Kobayashi, R.L. Gunshor, G.C. Hua and N. Otsuka, *Appl. Phys. Lett.* 60 (1992) 2045.
- [10] Z. Yu, J. Ren, B. Sneed, K.A. Bowers, K.J. Gossett, C. Boney, Y. Lansari, J.W. Cook, Jr. and J.F. Schetzina, *Appl. Phys. Lett.* 61 (1992) 1266.
- [11] J.M. Gaines, R.R. Drenten, K.W. Haberern, T. Marshall, P. Mensz and J. Petruzzello, *Appl. Phys. Lett.* 62 (1993) 2462.
- [12] Oxford Applied Research, Crawley Mill, Witney, Oxfordshire OX8 5TJ, UK.
- [13] R.M. Park, *J. Vac. Sci. Technol. A* 10 (1992) 701.
- [14] R.W.B. Pearse and A.G. Gaydon, *The Identification of Molecular Spectra* (Wiley, New York, 1963) pp. 209–220.
- [15] A.N. Wright and C.A. Winkler, *Active Nitrogen* (Academic Press, New York, 1968).
- [16] A.R. Stringanow and N.S. Sventitskii, *Tables of Spectral Lines of Neutral and Ionized Atoms* (Plenum, New York, 1968) pp. 111–140b.
- [17] W.G. Richards and P.R. Scott, *Structure and Spectra of Atoms* (Wiley, New York, 1976) pp. 48–55.
- [18] CRC Handbook of Chemistry and Physics, 71st ed., Ed. D.R. Lide (CRC Press, Boca Raton, FL, 1990) pp. 10-66 to 10-68.
- [19] A.E. Barrington, *High Vacuum Engineering* (Prentice-Hall, Englewood Cliffs, NJ, 1963) p. 13.
- [20] R.M. Park, H.A. Mar and N.M. Salansky, *J. Appl. Phys.* 58 (1985) 1047.
- [21] K. Ohkawa, T. Karasawa and T. Mitsuyu, *J. Crystal Growth* 111 (1991) 795.

- [22] T. Nakao and T. Uenovama, *Jap. J. Appl. Phys.* 32 (1993) 660.
- [23] ASTeX Applied Science and Technology, 35 Cabot Road, Woburn, MA 01801, USA.
- [24] R.P. Vaudo, J.W. Cook, Jr. and J.F. Schetzina, in: *Proc. 13th North American Conf. on Molecular-Beam Epitaxy*, 1993 (*J. Vac. Sci. Technol. B*, to be published).
- [25] K.J. Gossett, Z. Yu, K.A. Bowers, J. Li, J. Ren, J.W. Cook, Jr. and J.F. Schetzina, 6th Int. Conf. on II–VI Compounds and Related Optoelectronic Materials, Newport, RI, September 1993.



ELSEVIER

Journal of Crystal Growth 138 (1994) 437–442

JOURNAL OF  
**CRYSTAL  
GROWTH**

## Halogen doping of II–VI semiconductors during molecular beam epitaxy

A. Waag <sup>\*,a</sup>, Th. Litz <sup>a</sup>, F. Fischer <sup>a</sup>, H. Heinke <sup>a</sup>, S. Scholl <sup>a</sup>, D. Hommel <sup>a</sup>,  
G. Landwehr <sup>a</sup>, G. Bilger <sup>b</sup>

<sup>a</sup> *Physikalisches Institut der Universität Würzburg, Am Hubland, D-97074 Würzburg, Germany*

<sup>b</sup> *Zentrum für Sonnenenergie und Wasserstoff-Forschung, D-70569 Stuttgart, Germany*

### Abstract

Results on the halogen doping of CdTe, (CdMn)Te as well as (CdMg)Te thin films and quantum well structures are reported. The structures were grown by molecular beam epitaxy. The samples have been investigated by Van der Pauw, photoconductivity, X-ray diffraction, XPS and SIMS measurements. ZnCl<sub>2</sub> and ZnBr<sub>2</sub> have been used as dopant sources. Free carrier concentrations at room temperature above  $10^{18} \text{ cm}^{-3}$  can easily be achieved for CdTe for a wide range of Cd/Te flux ratios and substrate temperatures. In the ternary alloys, the free carrier concentration decreases drastically with increasing  $x$ -values, despite a constant incorporation of the dopant species. In addition, persistent photoconductivity has been observed in n-type doped ternary thin films at low temperatures. The decrease of the free carrier concentration with  $x$ -value is common to other wide-gap ternary alloys, and the reason for it is discussed in the frame of DX-like deep donor impurities in ternary II–VI compounds. In first experiments on planar halogen doping of CdTe, a doping level of  $5 \times 10^{18} \text{ cm}^{-3}$  could be reached in the doped regions, the highest value ever reported for CdTe. A clear influence of dopant incorporation on the structural quality of CdTe thin films has been seen even for dopant concentrations of as low as  $10^{18} \text{ cm}^{-3}$ . The FWHM of the rocking curves decreased by a factor of 2 with increasing dopant incorporation. SIMS as well as XPS measurements demonstrate that the Cl/Zn and Br/Zn ratio in the doped films is 2/1, but no chemical shift corresponding to Zn–Cl or Zn–Br bonds could be detected. A model for the incorporation of the halogens is proposed on the basis of these results.

### 1. Introduction

The recent progress in II–VI device technology with the fabrication of blue-green ZnSe-based laser diodes [1] as well as HgCdTe infrared laser diodes [2] has been based on the successful electrical control of the epilayers. If one wants to

exploit the interesting properties of CdTe-based ternary alloys like (CdMn)Te, (CdZn)Te or (CdMg)Te in optoelectronic devices, one has to be able to dope the materials both n-type and p-type to high enough doping levels.

It has been demonstrated in the past that various donors in (CdZn)Te [3] as well as in (CdMn)Te [4] exhibit a deep-shallow metastability analogous to the DX center in AlGaAs [5]. In the binary base material CdTe, the DX-like center has been reported to be resonant with the

\* Corresponding author.

conduction band, and according to pressure-dependent resistivity measurements its energy level lies 50 and 260 meV above the conduction band edge for chlorine and bromine donors, respectively [6]. With pressure or with increasing band gap, the DX-like level is shifted into the band gap and therefore forms a deep donor. The DX-like centers are known to have repulsive barriers for both electron emission and electron capture, which is the reason for persistent photoconductivity at low temperatures. The existence of DX-like centers in the binaries GaAs and CdTe shows that the DX-like behavior is a characteristic of isolated donors.

It should be mentioned that the DX-like centers discussed here do not necessarily have the same microscopic structure as in the (AlGa)As system. The term "DX-like center" is used here because of the very similar behavior of the deep centers in ternary II–VI semiconductors and the DX centers in (AlGa)As.

In this contribution we report on the investigations of n-type doping of the ternary alloys (CdMn)Te and (CdMg)Te thin films during molecular beam epitaxy. Chlorine and bromine have been used as dopants. The thin films have been analyzed by X-ray diffraction, secondary ion mass spectroscopy (SIMS), Hall measurements as well as photoconductivity, both as a function of temperature.

## 2. Experimental procedure

The thin films have been grown onto (100) oriented CdTe or (CdZn)Te substrates. The substrates were chemomechanically polished using a bromine–methanol–ethyleneglycol solution. Before insertion into the molecular beam epitaxial (MBE) system, the substrates were etched with HCl and subsequently rinsed in deionized water. A heat treatment in vacuum at 350°C for 15 min in the presence of a Cd flux was used to clean the substrate surface. Before the growth of the doped layers, a CdTe buffer of 200 nm thickness was grown at a substrate temperature of 315°C. A CdTe compound source as well as elemental Mg and Cd sources were used.

For the doping,  $\text{ZnCl}_2$  and  $\text{ZnBr}_2$  have been evaporated from standard effusion cells. Free electron Hall concentration as well as Hall mobility of the n-doped layers were determined by applying the Van der Pauw method. A magnetic field of 0.3 T was employed for this. Photoconductivity was measured in a standard He-4 flow cryostat. Light from a red light emitting diode (LED) mounted in the cryostat was used for illumination. X-ray photoelectron spectroscopy (XPS) as well as SIMS measurements were performed on some of the bromine doped CdTe layers to get information on the amount of bromine and zinc incorporated. Positive SIMS for the elements Zn, Cd and Te and negative SIMS for Te and bromine were measured. For low concentrations of Zn, it cannot be evaluated from positive SIMS, as Zn has a low ionization probability and the ion from the isotope  $^{64}\text{Zn}^+$  interferes with the doubly charged  $^{128}\text{Te}^{++}$  isotope. A high resolution 5-crystal X-ray diffractometer has been used for the structural analysis.

## 3. Results and discussion

For the n-doping of the CdTe base material during molecular beam epitaxy, indium has been widely used, and free carrier concentrations in the low  $10^{18} \text{ cm}^{-3}$  range can be achieved [7,8]. For higher dopant incorporation, self-compensation occurs, decreasing the number of free carriers again. Therefore we have tested alternative dopants to possibly circumvent this problem: we have recently used halogens like chlorine and bromine for the n-type doping of CdTe [9,10]. Fig. 1 shows the free carrier concentration in CdTe thin films as a function of dopant source temperature. The higher the dopant source temperature, the higher the incorporation of the dopants. Results for both chlorine and bromine are shown. Again a limit for the free carrier concentration in the low  $10^{18} \text{ cm}^{-3}$  range occurs for both dopants, as is the case for indium doping.

In contrast to indium doping, the Cd/Te ratio offered during the MBE growth of halogen-doped CdTe layers has only a very small influence on

the free carrier concentration. This has been checked by growing samples under identical conditions. The only growth parameter varied was the Cd/Te ratio. In one case, a compound CdTe source was used only; in the other case an additional Cd flux was applied using an elemental Cd source. In both cases an efficient doping has been observed. In the case of indium, however, a high degree of compensation occurs if a CdTe compound source, which produces a stoichiometric flux, is used without additional Cd flux.

Another result demonstrates again that the doping via halogens does not critically depend on the growth parameters used. In Fig. 2 the free carrier concentration at room temperature is plotted as a function of substrate temperature. All other growth parameters like dopant and source fluxes have been kept constant. As can be seen from the figure, the free carrier concentration decreases by less than a factor of 10 if the substrate temperature is increased from 215 to 280°C. The decrease in free carrier concentration probably stems from a decreasing sticking coefficient of the dopant species. From photoluminescence studies, no indication of an increasing de-

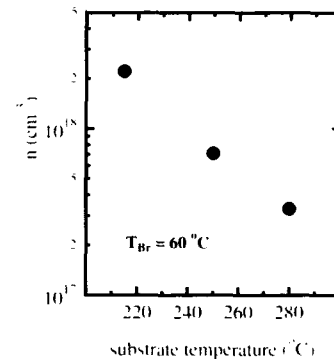


Fig. 2. Hall electron concentration at 300 K for CdTe:Br as a function of substrate temperature.

fect band, which would be a fingerprint of self-compensation, could be observed. As a result, a low substrate temperature is not necessary for the halogen doping of CdTe during MBE.

Because of the high vapor pressure of elemental halogens even at room temperature, we have used a Zn-halogen compound, which can be evaporated from standard effusion cells. ZnBr<sub>2</sub> and ZnCl<sub>2</sub> have been used for the doping experiments. It is known that for not too high temperatures, Zn-Hal<sub>2</sub> molecules sublime, where Hal = chlorine or bromine [11]. We have used the Zn-halogen instead of the Cd-halogen compound to get information on the Zn/halogen ratio incorporated into the CdTe films.

For this purpose, SIMS as well as XPS measurements have been performed. For highly doped CdTe, the concentration of both Zn and Br could be assessed by XPS. The SIMS data were then calibrated by the XPS data, to yield a quantitative estimate of both bromine and zinc concentrations as a function of bromine source temperature as measured by SIMS.

First of all, SIMS measurements show that the halogens are still incorporated, even if the free carrier concentration is decreasing for higher dopant cell temperature. This result clearly shows that the decrease in free carrier concentration for higher bromine incorporation is due to compensation. The same is certainly true for chlorine doping, but was not confirmed experimentally here.

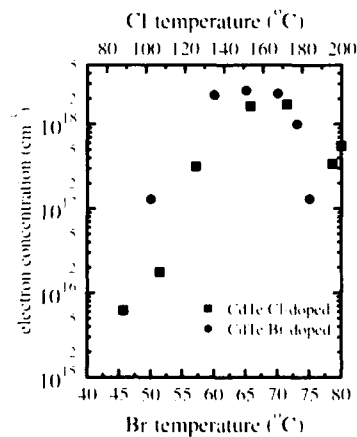


Fig. 1. Hall electron concentration at 300 K as a function of dopant source temperature for CdTe:Cl and CdTe:Br. In both cases the doping level cannot be increased to above some 10<sup>18</sup> cm<sup>-3</sup>. Two different temperature scales are used for better comparison of both dopant species. The source temperatures do not only depend on the dopant species, but also on the special design of the effusion cell used.

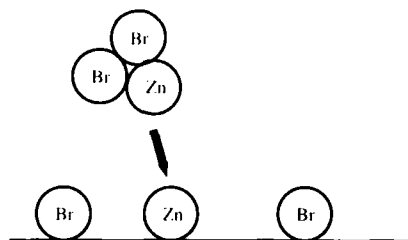


Fig. 3. Model for the incorporation of Zn-halogen molecules for the n-type doping of CdTe: molecules are impinging onto the surface, but the constituents are then incorporated separately, as has been shown by XPS.

For the highest doped sample, XPS experiments showed that the Zn/Br ratio in the CdTe layers is to a good approximation equal to 1/2, indicating that for each Zn atom two bromine atoms are incorporated. In addition the chemical shifts of the Zn  $2p^{3/2}$  photoelectron and the Zn  $L_{3/2}M_{45}M_{45}$  Auger energy levels were investigated. The binding energy of 1022 eV for the Zn  $2p^{3/2}$  photoelectron and kinetic energy of 987 eV for the Zn  $L_{3/2}M_{45}M_{45}$  Auger electrons is clearly related to Zn-Te and not to Zn-Br bondings, which are associated with energies of 1023 and 984.7 eV, respectively.

This demonstrates that the  $ZnBr_2$  molecule is not incorporated into the CdTe crystal as a whole, but is dissociated and the constituents are chemisorbed separately.

Therefore we propose the following model for the incorporation mechanism of halogen dopants by the Zn-halogen compound  $ZnBr_2$ , which is illustrated in Fig. 3: The molecular beam consists of  $ZnBr_2$  molecules, which are impinging onto the growth surface. There they are physisorbed. A dissociation followed by chemisorption is then believed to be the last step of the incorporation mechanism.

From the results given above it seems that the limit for the n-type doping of CdTe is an intrinsic property of the base material, and is not due to any dopant characteristic. Nevertheless, CdTe can be doped reproducibly up to the low  $10^{18} \text{ cm}^{-3}$  range, which is high enough for optoelectronic device applications. For contacts with very low

contact resistance, however, a higher doping level would be desirable.

Therefore, we have performed first planar doping experiments. As a result of the preliminary work, planar doping works at least as good as uniform doping concerning the effective free carrier concentration. In addition, the electron mobility of planar doped CdTe layers is higher compared to uniformly doped ones. Up to now we could not increase the maximum effective free carrier concentration to above  $3 \times 10^{18} \text{ cm}^{-3}$ .

The situation is quite different if one wants to dope ternary CdTe-based alloys like (CdMn)Te, (CdZn)Te or (CdMg)Te. In Fig. 4, the free carrier concentration at room temperature is plotted for (CdMn)Te and (CdMg)Te as a function of  $x$ -value. In this case bromine has been used as an n-type dopant, but similar results have been obtained for chlorine doping. As can be seen from Fig. 4, the free carrier concentration decreases drastically with increasing  $x$ -value. This is due to the fact that the shallow donors in CdTe become deep donors in the ternary alloys. A typical property of such donors is a deep-shallow metastability occurring at low temperatures. There exists a barrier between the shallow and the deep state of the donor, and below a certain critical temperature the shallow donors – which can be populated by illumination – cannot be transferred back

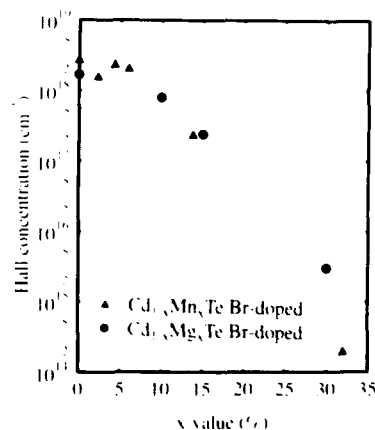


Fig. 4. Hall electron concentration at 300 K as a function of the  $x$ -value for (CdMn)Te:Br and (CdMg)Te:Br.

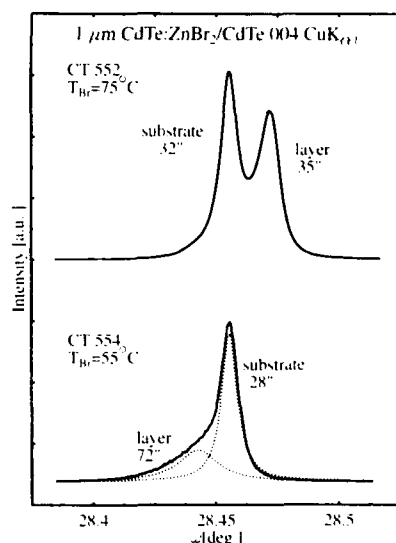


Fig. 5. Rocking curves of two CdTe:Br thin films. For highly doped layers, an improvement of the structural quality can be observed.

to the deep donors, leading to strong persistent photoconductivity effects.

A comparison with chlorine doping demonstrates that the occurrence of the deep donors is a property of the donor itself, and is due to the increasing band gap, which shifts the DX-like donor state into the band gap and converts the state lying resonant in the conduction band for CdTe to a deep donor in the ternary alloys. To circumvent this problem, one has to look for other dopant materials, which do not exhibit DX-like donor characteristics. Lattice mismatch or other properties of the ternary alloy obviously play a minor role for the occurrence of deep DX-like donor states.

A clear influence of dopant incorporation on the structural quality of the CdTe thin films has been seen. In Fig. 5, rocking curves of two CdTe films are compared: For sample CT552 the ZnBr<sub>2</sub> incorporation is approximately  $10^{18} \text{ cm}^{-3}$ , whereas sample CT554 has a ZnBr<sub>2</sub> incorporation, which is one order of magnitude smaller. For CT554 an unexpected difference between the lattice constants of substrate and layer is ob-

served, which is quite typical for the MBE growth of CdTe onto CdTe substrates. This usually goes along with an unusual strain state of the CdTe epitaxial layer, and is described in detail elsewhere [12]. If ZnBr<sub>2</sub> is incorporated into the CdTe film, the Zn substitutes a Cd atom, and the Br substitutes Te atoms. The covalent radii of both Zn and Br are smaller compared to the atoms they substitute. Therefore, the lattice constant decreases with increasing ZnBr<sub>2</sub> incorporation, which results in a clear separation of the substrate and layer peaks in Fig. 5. In addition, the FWHM of the layer peaks decreases, reflecting a better structural quality of the CdTe films compared to the undoped ones. A typical decrease of the FWHM of a factor of 2 for dopant incorporations above  $10^{18} \text{ cm}^{-3}$  has been observed for a large number of CdTe thin films.

Obviously, even a very small amount of Zn can stiffen the lattice, so that a better structural quality can be achieved. This effect is well known for the ternary alloy (CdZn)Te [13]. We suggest that this effect can be used to further increase the structural quality of CdTe thin films.

#### 4. Summary

We have investigated the doping of CdTe and CdTe-based ternary alloys by chlorine and bromine. For the uniform doping of CdTe, a limit of the free carrier concentration in the low  $10^{18} \text{ cm}^{-3}$  range exists. This is the case for the dopants indium, chlorine and bromine. Bromine has been found to be the dopant material which can be used for the widest range of growth parameters. Zn-halogen compounds have been found to be suitable for doping during MBE. A model for the incorporation mechanism has been proposed. Planar doped CdTe shows a higher mobility compared to uniformly doped CdTe with the same effective free carrier concentration.

For the doping of CdTe-based ternary alloys like (CdMn)Te and (CdMg)Te deep donors occur, leading to very low free carrier concentrations for higher  $x$ -values. The deep donors exhibit a DX-like behavior like persistent photoconductivity at low temperatures. This is a serious



restriction for the use of such ternary alloys in device applications.

### 5. Acknowledgements

We want to thank M. Bruder (AEG Heilbronn) for supplying us with CdTe source material, as well as P. Wolf and Th. Schuhmann for the substrate preparation. This project was supported by the Bundesminister für Forschung und Technologie and by the Deutsche Forschungsgemeinschaft.

### 6. References

- [1] M. Haase, J. Qiu, J. DePuydt and H. Cheng, *Appl. Phys. Lett.* 59 (1991) 1272.
- [2] M. Zandian, J.M. Arias, R. Zucca, R.V. Gil and S.H. Shin, *Appl. Phys. Lett.* 59 (1991) 1022.
- [3] B.C. Burkey, R.P. Koshla, J.R. Fischer and D.L. Losee, *J. Appl. Phys.* 47 (1976) 1095.
- [4] I. Terry, T. Penney, S. von Molnar and J.M. Rigotty, *Solid State Commun.*, to be published.
- [5] See, e.g., P.M. Mooney, *J. Appl. Phys.* 67 (1990) R1.
- [6] G.W. Iseler, J.A. Kafalas, A.J. Strauss, H.F. MacMillan and R.H. Bube, *Solid State Commun.* 10 (1972) 619; see also H.H. Woodbury, in: *Proc. Int. Conf. on Photoconductivity*, 1969, Ed. M. Pell (Pergamon, Oxford, 1969) p. 231.
- [7] A. Waag, T.A. Kuhn, S. Schmeusser, B. Schmied, M.M. Kraus, N. Kallis, W. Ossau, R.N. Bicknell-Tassius and G. Landwehr, *J. Crystal Growth* 117 (1992) 820.
- [8] F. Bassani, S. Tatarenko, K. Saminadayar, N. Magnea, R.T. Cox, A. Tardot and C. Grattapain, *J. Appl. Phys.* 72 (1992) 2927.
- [9] D. Hommel, A. Waag, S. Scholl and G. Landwehr, *Appl. Phys. Lett.* 61 (1992) 1546.
- [10] A. Waag, H. Heinke, S. Scholl, C.R. Becker and G. Landwehr, *J. Crystal Growth* 129 (1993) 243.
- [11] Gmelin, *Handbuch der Anorganischen Chemie*, Zn Ergänzungsband (Springer, Berlin, 1956).
- [12] H. Heinke, A. Waag, M.O. Möller, M.M. Regnet and G. Landwehr, *J. Crystal Growth* 135 (1994) 53.
- [13] S.B. Qadri, E.F. Skelton, A.W. Webb and J. Kennedy, *Physica* 139 (1986) 341.



ELSEVIER

Journal of Crystal Growth 138 (1994) 443–447

JOURNAL OF  
**CRYSTAL  
GROWTH**

## Nitrogen doping of molecular beam epitaxially grown CdTe with a radio-frequency plasma source

K.A. Dhese <sup>\*a</sup>, D.E. Ashenford <sup>b</sup>, J.E. Nicholls <sup>a</sup>, P. Devine <sup>b</sup>, B. Lunn <sup>b</sup>, C.G. Scott <sup>a</sup>,  
J. Jaroszyński <sup>b,1</sup>

<sup>a</sup> Department of Applied Physics, The University of Hull, Hull HU6 7RX, UK

<sup>b</sup> Department of Engineering Design and Manufacture, The University of Hull, Hull HU6 7RX, UK

### Abstract

We report on the use of an Oxford Applied Research MPD21 Atom/Radical RF source to dope CdTe layers with nitrogen (N). The layers were grown in a VG V80H MBE system, using CdTe as the source material. Photoluminescence (PL) measurements give evidence of N incorporation in our CdTe:N layers, as signified by an increase in intensity of the N acceptor bound exciton (ABE) line and the associated donor–acceptor pair (DAP) band, with increasing plasma RF power. The presence of N was confirmed using secondary ion mass spectrometry (SIMS). In addition, PL and SIMS results show the presence of significant levels of antimony (Sb) in the N-doped layers. The Sb acceptor depth was found to be 52 meV from observation of the associated free to bound transition. The unintentional presence of Sb is tentatively attributed to enhanced autodoping from the substrate, caused by the presence of N. Like the undoped layers, the N-doped samples are found to be n-type, but the carrier concentrations are  $< 10^{15} \text{ cm}^{-3}$ .

### 1. Introduction

Low resistivity p-type doping of II–VI compounds is a continuing goal of much research. In the case of epilayers of CdTe grown by MBE, reports of p-type doping are scarce. Sugiyama [1] investigated Cu, As and Sb doping, but found that only Cu led to p-type conduction with doping levels  $\sim 5 \times 10^{18} \text{ cm}^{-3}$ , whilst Sb doping was found to result in n-type layers. However, photoassisted MBE growth has led to p-type material

with hole concentrations of  $\sim 5 \times 10^{16} \text{ cm}^{-3}$  and  $\sim 6 \times 10^{18} \text{ cm}^{-3}$  using Sb [2] and As [3], respectively. Here we report on the optical and electrical properties of CdTe layers doped with nitrogen (N) using an RF plasma source. We present photoluminescence (PL) evidence of N incorporation as signified by an increase in intensity of an associated acceptor bound exciton (ABE) line and corresponding donor–acceptor pair (DAP) band with increasing plasma RF power. The presence of N was confirmed using secondary ion mass spectrometry (SIMS). In addition, PL and SIMS also indicated the presence of significant levels of Sb in the N-doped layers. The unintentional presence of Sb is tentatively attributed to enhanced autodoping from the substrate caused

\* Corresponding author.

<sup>1</sup> Permanent address: Institute of Physics, Polish Academy of Sciences, Warsaw, Poland.

by the presence of N species. In spite of the presence of Sb and N in these layers, preliminary electrical ( $C$ – $V$ ) measurements have indicated a lack of p-type activity.

## 2. Experimental procedure

The CdTe:N epilayers were grown in a VG Semicon V80H MBE system using a compound CdTe source and a nitrogen atom/radical beam source (Oxford Applied Research, MPD21), operated under various RF excitation powers. The samples were grown on InSb(001) substrates, prepared as previously described [4], at a rate of  $\approx 0.7 \mu\text{m/h}$  and at  $\approx 245^\circ\text{C}$ ; the structures were typically  $0.6 \mu\text{m}$  CdTe:N/ $0.1 \mu\text{m}$  CdTe/InSb.

Low temperature (1.8 K) photoluminescence (PL) was excited with the 514 nm  $\text{Ar}^+$  laser line at  $\sim 1 \text{ W cm}^{-2}$ .

## 3. Photoluminescence

Figs. 1 and 2 show the excitonic and DAP PL, respectively, for a series of CdTe layers. The spectrum of Fig. 1a (2a) was recorded from an undoped CdTe layer, whereas the spectra of Figs 1b to 1d (2b to 2d) were recorded from N-doped layers, doped at differing RF source powers. The sample of Fig. 1b (2b) was grown without an RF discharge, although the growing layer was exposed to a background N atmosphere from the source.

Fig. 2 shows a rise, with increasing RF power, in the relative intensity of DAP emission (and LO replicas) compared to the excitonic emission. For the sample grown with an RF power of 400 W (Fig. 2d), the excitonic region is heavily suppressed.

The undoped CdTe spectrum (Fig. 1a) shows the  $n = 1$  free exciton emission ( $X_n = 1$ ) at 1.5965 eV and the principal bound exciton lines,  $D^0_1X$  and  $A^0_1X$ , at 1.5933 and 1.5849 eV respectively. The  $D^0_1X$  possibly arises from diffusion of In from the substrate, whilst  $A^0_1X$  is attributed to deep acceptor bound excitons, possibly associated with cadmium vacancies [5]. With increasing RF

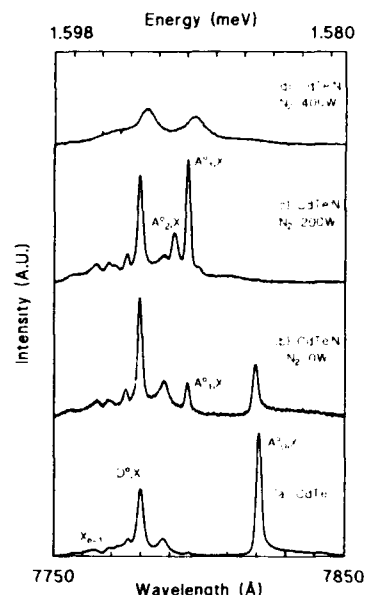


Fig. 1. Low temperature (1.8 K) PL spectra showing the excitonic region of CdTe (a) and doped CdTe:N (b to d) layers.

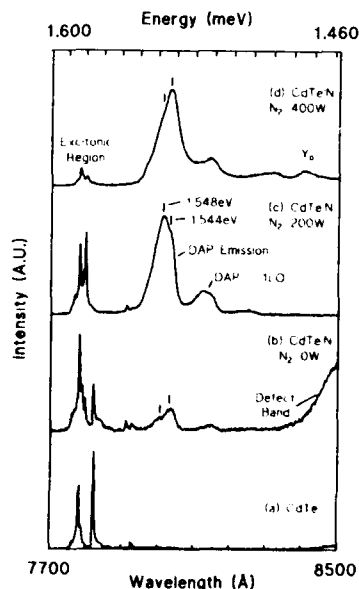


Fig. 2. Low temperature (1.8 K) PL spectra showing the DAP region of CdTe (a) and doped CdTe:N (b to d) layers.

power, a relative increase in an ABE line,  $A_1^0, X$ , at 1.5899 eV is observed along with a relative decrease in the  $A_D^0, X$  intensity. Fig. 1c shows this  $A_1^0, X$  line to be the dominant excitonic emission for growth with 200 W RF power. In the 400 W sample, the  $A_1^0, X$  and  $D^0, X$  are the only emissions resolved (Fig. 1d). We attribute the  $A_1^0, X$  acceptor line to N and associate its increase in relative intensity to the increase in N plasma RF power. The concomitant reduction in the  $A_D^0, X$  intensity is not understood at present.

Another acceptor line,  $A_2^0, X$  is observed at 1.5908 eV in the 200 W CdTe:N sample (Fig. 1c). An acceptor emission near this energy has previously been tentatively associated with Sb [6,7]. We found this acceptor line and an associated DAP band (see below) to be dominant in CdTe epilayers doped with an Sb source. In addition, SIMS measurements (below) for the sample of Fig. 3c (3d) show significant incorporation of Sb into this layer and we therefore associate, with some certainty, the  $A_2^0, X$  line at 1.5908 eV with Sb.

We attribute the DAP emissions observed at 1.548 eV and 1.544 eV (fig. 2) to Sb and N acceptors respectively. These assignments are consistent with the presence of their respective excitonic emissions and with the impurity depth of both acceptors, as discussed below.

In order to investigate the higher energy DAP emission further, low excitation intensity ( $0.005 \text{ W cm}^{-2}$ ) PL spectra were taken at different temperatures (Fig. 3). With increasing temperature, a high energy emission at 1.554 eV appears. This emission is attributed to a free to bound transition,  $e, A_2^0$ , associated with Sb acceptors. The binding energy of the acceptor is given by

$$E_A = E_g - E(e, A_2^0) + \frac{1}{2} k T_e,$$

where  $E_g$  is the CdTe band gap (1.606 eV at 2.0 K) and  $T_e$  is the equilibrium temperature of free electrons in the lattice, assumed to be close to the lattice temperature (1.8 K) because of the low excitation intensities used ( $0.005 \text{ W/cm}^{-2}$ ). This gives an acceptor depth of 52 meV for Sb, which compares with a value of 49 meV found in a similar way and attributed tentatively to Sb by Francou et al. [6]. Similar DAP studies on N

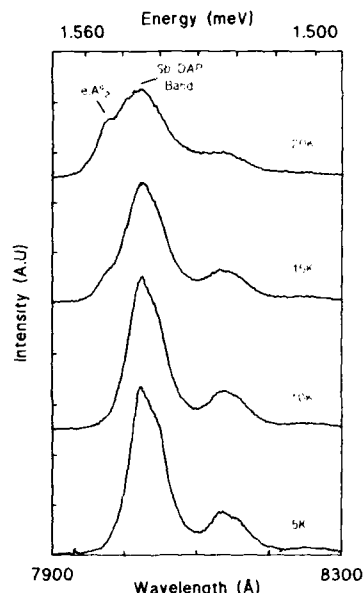


Fig. 3. Temperature dependence of the DAP emission at low excitation intensity ( $0.005 \text{ W cm}^{-2}$ ). The emergence of a free to bound emission ( $e, A_2^0$ ) associated with Sb acceptors is observed with increasing temperature.

implanted CdTe, by Molva et al. [8], found the N acceptor depth to be 56 meV.

#### 4. Secondary ion mass spectrometry

Secondary ion mass spectrometry (SIMS) measurements were performed using a 10 keV,  $0.1 \mu\text{A}$   $\text{Cs}^+$  ion beam, with negative ion detection,  $^{121}\text{Sb}$  for antimony and ( $^{130}\text{Te} + ^{14}\text{N}$ ) for nitrogen. The SIMS profiles were calibrated using CdTe layers implanted with N and Sb.

The SIMS profile for a CdTe:N epilayer doped at 200W RF power is shown in Fig. 4. Similar profiles were found for other layers grown with the plasma doping. For those samples grown without an RF discharge, Sb and N signals were not detected above background levels ( $\sim (1-3) \times 10^{17} \text{ cm}^{-3}$ ). Referring to Fig. 4, the N concentration over the initial  $\sim 1000 \text{ Å}$  CdTe layer grown without an RF discharge is low, but rises sharply at the point at which the RF discharge was switched on. However, this rise is accompa-

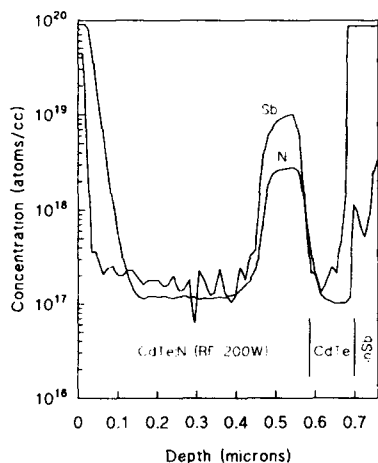


Fig. 4. SIMS profile for a doped CdTe:N epilayer. The apparent increase of N and Sb in the near surface region is believed to be an artefact of the SIMS measurement.

nied by a rise in the Sb signal. Later in the growth, both the N and Sb signals drop down to background levels almost simultaneously. We note that no evidence was found in our SIMS measurements to indicate the effects of any transient plasma state which might occur during switch on. The trends of Fig. 4 were confirmed by PL which, after etching away 2000 Å, showed a relative increase in the intensity of N and Sb DAP emissions compared to the excitonic emissions, and, in the excitonic region, a relative rise in both Sb and N ABEs.

Fig. 4 suggests that co-doping occurs in these layers, whereby N incorporates efficiently only in the presence of Sb. Evidence for the source of Sb comes from previous Raman studies which indicated the presence of an  $\text{In}_2\text{Te}_3$  and elemental Sb interface layer caused by a chemical reaction between the epilayer and substrate [9]. We suggest that the elemental Sb segregates on the surface of the growing layer throughout deposition, and is only incorporated significantly when the N plasma source is used. N-doping occurs until the surface layer of Sb becomes depleted, i.e. when the supply of Sb ends, the incorporation of N drops significantly. The integrated Sb dose in the sublayer region was  $\sim 10^{14} \text{ cm}^{-2}$  for all RF powers. This corresponds to the segregation

of approximately one quarter of a monolayer of Sb.

## 5. Electrical measurements

Owing to the high conductivity of the InSb substrate,  $C$ - $V$  measurements were employed to determine the nature and the concentration of free carriers in the epilayer. Layers grown without deliberate doping were found to be n-type with carrier densities up to  $4 \times 10^{15} \text{ cm}^{-3}$ . This is assumed to be due to diffusion of In from the substrate during growth and is therefore linked to the same donors responsible for the prominent  $\text{D}^0\text{X}$  PL emission. For all the N doped samples, the  $I$ - $V$  characteristics of the Schottky junctions (formed for the  $C$ - $V$  measurements) have indicated that the semiconductor retains an n-type character but, in each case, the free carrier concentration is so low that the depletion layer extends throughout the full width of the layer giving a voltage-independent capacitance set by the layer thickness. It follows that, for layers  $\sim 0.7 \mu\text{m}$  thick, the effective shallow donor concentration must be  $\leq 10^{15} \text{ cm}^{-3}$ . Thus, it is clear that the incorporation of nitrogen leads, at most, to a partial compensation of the residual In donors indicating that most of the N is electrically inactive. To explain this observation it is necessary to consider the sites on which the N is distributed and also the role played by both native point defects and extended defects. The latter are known to arise, particularly in the vicinity of the epilayer-substrate interface, from relaxation of strain resulting from the lattice mismatch at that interface. Such defects could provide a sink for dopants as has been previously discussed [10].

## 6. Conclusion

We have used PL and SIMS to confirm the presence of N in CdTe:N layers doped using an RF plasma source. In addition, the incorporation of Sb was also confirmed, and attributed to a co-doping process related to use of the N plasma source. An acceptor binding energy of 52 meV was obtained for Sb acceptors, determined from

observation of the associated free to bound transition. Electrical measurements found all doped layers to be n-type, with carrier concentrations  $< 10^{15} \text{ cm}^{-3}$ .

### 7. Acknowledgements

We wish to thank the Science and Engineering Research Council of the UK and the Procurement Executive, Ministry of Defence for financial support. One of us (J.J.) wishes to thank the Royal Society for a Postdoctoral Fellowship.

### 8. References

- [1] K. Sugiyama, *Thin Solid Films* 115 (1984) 97.
- [2] R.N. Bicknell, N.C. Giles, J.F. Schetzina and C. Hitzman, *J. Vac. Sci. Technol. A* 5 (1987) 3059.
- [3] R.L. Harper, Jr., S. Hwang, N.C. Giles, J.F. Schetzina, D.L. Dreifus and T.H. Myers, *Appl. Phys. Lett.* 54 (1989) 170.
- [4] G.M. Williams, A.G. Cullis, C.R. Whitehouse, D.E. Ashenford and B. Lunn, *Appl. Phys. Lett.* 55 (1989) 1303.
- [5] K. Zanio, in: *Semiconductors and Semimetals*, Vol. 13, Eds. R.K. Willardson and A.C. Beer (Academic Press, New York, 1978) pp. 139–163.
- [6] J.M. Francou, K. Saminadayar, J.L. Pautrat, J.P. Gailard, A. Million and C. Fontaine, *J. Crystal Growth* 72 (1985) 220.
- [7] Z.C. Feng, A. Mascarenhas and W.J. Choyke, *J. Luminescence* 35 (1986) 329.
- [8] E. Molva, K. Saminadayar, J.L. Pautrat and E. Ligeon, *Solid State Commun.* 48 (1983) 955.
- [9] D.R.T. Zahn, K.J. Mackay, R.H. Williams, H. Münder, J. Geurts and W. Richter, *Appl. Phys. Lett.* 50 (1987) 742.
- [10] D. Ashenford, P. Devine, J.H.C. Hogg, B. Lunn and C.G. Scott, *J. Phys. Condens. Matter* 3 (1991) 5245.

## Investigation of hydrogen, carbon and further impurities in the metalorganic vapour phase epitaxy of ZnSe with ditertiarybutylselenide and methylallylselenide

W.S. Kuhn <sup>a</sup>, R. Driad <sup>a</sup>, H. Stanzl <sup>b</sup>, A. Lusson <sup>a</sup>, K. Wolf <sup>b</sup>, B. Qu'Hen <sup>a</sup>, H. Sahin <sup>b</sup>,  
L. Svob <sup>a</sup>, C. Grattepain <sup>a</sup>, X. Quesada <sup>a</sup>, W. Gebhardt <sup>b</sup>, O. Gorochov <sup>\*,a</sup>

<sup>a</sup> Laboratoire de Physique des Solides de Bellevue, CNRS, 1 Place Aristide Briand, F-92195 Meudon, France

<sup>b</sup> Festkörperphysik, Institut für Physik II, Universität Regensburg, Universitätsstrasse 31, D-8400 Regensburg, Germany

### Abstract

The impurities in ZnSe layers grown by metalorganic vapour phase epitaxy (MOVPE) on (001) GaAs have been investigated by photoluminescence (PL) and secondary ion mass spectrometry (SIMS) measurements. The layers grown with the alkyl combination methylallylselenide/diethylzinc (MASE/DEZn) exhibit the incorporation of C and H detected by SIMS. The use of helium instead of the hydrogen carrier gas increases the incorporation of C and H. At very high concentrations ( $H \approx 10^{20} \text{ cm}^{-3}$ ) a new PL peak at 2.786 eV appeared. The mass spectroscopic investigation of the pyrolysis of MASE revealed a simple bound cleavage as the dominant mechanism which generates the intermediate species  $\text{SeCH}_3$ . The following extrinsic impurities were found in the layers: (1) Cu from the growth system (PL, SIMS); (2) halogen (Br and I) from the Se source (PL, synthesis, SIMS); (3) oxygen from the system or carrier gas (SIMS); (4) Te from former ZnTe growth (SIMS); (5) As and Ga from the substrate (SIMS). The layers grown with the alkyl combination ditertiarybutylselenide/dimethylzinc-triethylamine (DTBSe/DMZn-TEN) show weak contaminations by C and H as detected by SIMS. The mass-spectroscopic investigation of the pyrolysis of DTBSe revealed  $\text{H}_2\text{Se}$  and elemental Se as products from parallel mechanisms. The volatile alkyls isobutane and isobutene are found as reaction products. The role of the Zn alkyl as the source of the C and H incorporation is not yet clarified. The following extrinsic impurities were found in the layers: (1) Cu from the growth system (SIMS); (2) either Al or Cl as a donor (PL); (3) O from the system or carrier gas (SIMS); (4) S possibly from substrate preparation (SIMS); (5) As and Ga from the substrate (PL, SIMS). However, the layer purity is already sufficient for first doping experiments. With P doping, a hole concentration of  $10^{15} \text{ cm}^{-3}$  is achieved.

### 1. Introduction

Metalorganic vapour phase epitaxy (MOVPE) plays an important role in the growth of ZnSe as

well as other II–VI materials. The reports on successful p-type doping of ZnSe in MOVPE (e.g., ref. [1]; for a comprehensive study, see ref. [2]) open the way to a production of ZnSe-based optoelectronic devices by this well-established growth technique. The improvement of the material quality of the ZnSe layers is the main interest. Here, the chemistry of the metalorganics

\* Corresponding author.

greatly influences the growth kinetics and therefore the purity and crystallinity of the grown films. Especially, the incorporation of intrinsic impurities like hydrogen and carbon is greatly dependent on the detailed dissociation mechanisms and kinetics.

In the development of suitable selenium precursors, the lowering of the growth temperature and the replacement of the highly toxic, high vapour pressure  $\text{H}_2\text{Se}$  is a major challenge. Following the stability order of the radical hydrogen bond strength of hydrocarbons, one expects relatively low dissociation temperatures for butyl- or allyl-based metalorganics. In the case of tellurium alkyls, the decrease of thermal stability with an increasing number of hydrocarbon radicals directly attached to the central carbon atom bound to Te is well maintained [3].

Methylallylselenide (MASE) was first used by Giapis et al. [4] in combination with dimethylzinc (DMZn) to grow epitaxial ZnSe. Surprisingly, they needed relatively high growth temperatures ( $\approx 520^\circ\text{C}$ ) and found high concentrations of carbon ( $> 10^{18} \text{ cm}^{-3}$ ). A peak at 2.7920 eV in their PL spectra was first attributed to the C incorporation. New investigations support a strain shift of the light hole component of the ordinary neutral donor bound exciton peak ( $I_2^{\text{th}}$ ) [5].

In a preceding publication [6] we reported on initial growth results with ditertiarybutylselenide (DTBSe). In combination with the dimethylzinc-triethylamine adduct (DMZn-TEN) the growth of ZnSe layers at temperatures as low as  $330^\circ\text{C}$  was achieved. The layers showed good structural and optical properties. However, a residual chlorine contamination originating from the DTBSe synthesis was found.

Here, we present a more detailed investigation of the impurity incorporation in ZnSe layers grown with the alkyl combinations DTBSe/DMZn-TEN (Morton/Epichem) and MASE/DEZn (SMI/SMI). The layer impurities were identified with the help of low temperature photoluminescence (PL). Secondary ion mass spectrometry (SIMS) gave additional information. The reaction mechanisms of the alkyl pyrolysis was investigated by mass spectroscopy in an isother-

mal reactor. The discussion of the type and origin of the contamination concludes the paper.

## 2. Experimental details

All layers were grown on semi-insulating (100) GaAs substrates. The growth with MASE was performed in a experimental reactor cell with downward flow on a graphite susceptor placed in the centre of a cylindrical quartz tube. The standard parameters were as follows: total  $\text{H}_2$  flow 1 SLM (standard liter per minute),  $p_{\text{tot}} = 1 \text{ atm}$ ,  $p_{\text{MASE}} = 20 \text{ Pa}$  and  $p_{\text{DEZn}} = 10 \text{ Pa}$ . The growth with DTBSe and DASE was performed in a commercial horizontal flow reactor (Aixtron) with a SiC coated susceptor. The standard parameters were as follows: total  $\text{H}_2$  flow 7 SLM,  $p_{\text{tot}} = 1 \text{ atm}$ ,  $p_{\text{DTBSe}} = 30 \text{ Pa}$  and  $p_{\text{DMZn-TEN}} = 10 \text{ Pa}$ . The photoluminescence spectra of the layers grown with MASE were measured at 2 K with an excitation wavelength of 488 nm and a power of 10 mW focused on a small spot. The photoluminescence spectra of the layers grown with DTBSe were taken at 2 K using the UV lines of an argon ion laser for excitation. The luminescence was analysed with a 1 m double monochromator. The reaction mechanisms and the kinetics were measured in an isothermal reactor (quartz tube with a diameter of 10 mm and 28 cm length). The reaction products were sampled by a capillary tube behind the hot zone. The mass spectra were taken with a VG mass spectrometer ( $m/z$  1–400). An electron energy of 70 eV was chosen for the ionization. The SIMS spectra were taken with a Cameca IMS 4F system. The primary ion used was  $\text{Cs}^+$  with 14.5 keV.

## 3. Results with MASE

The structure and crystallinity of the samples grown with the alkyl combination MASE/DEZn can be briefly characterized as follows. Best results were achieved at growth temperatures around  $500^\circ\text{C}$  with an inlet partial pressure ratio VI/II  $\approx 2$ . Layers with thicknesses of  $\approx 4 \mu\text{m}$  have a weakly developed "orange peel" structure



with some surface particles ( $d < 5 \mu\text{m}$ ) indicating the start of gas phase nucleation. Double-crystal X-ray diffraction studies of the ZnSe layers grown on (100)GaAs reveal a decrease of the FWHM with the thickness for  $d > 0.5 \mu\text{m}$ . The layers reach favourable values of 150 arc sec at  $4.7 \mu\text{m}$  which are comparable with best results in the literature (e.g., ref. [7]).

**PL results:** Low temperature PL spectra (2 K) of the samples grown under various conditions with MASE/DEZn were recorded. In Fig. 1 the PL spectra of samples grown under  $\text{H}_2$  or He carrier gas are presented with a logarithmic intensity scale. We will first focus our discussion on the samples grown under  $\text{H}_2$ . The strain-split free excitons ( $E_1^h$  and  $E_1^l$ ) appear at the usual positions for ZnSe/GaAs grown in this temperature range. Additionally, all of the layers discussed in this section have thicknesses around  $4 \mu\text{m}$  and can be regarded as largely relaxed by dislocations at  $T_G$ . The  $I_1^h$  and  $I_1^l$  lines are due to a donor bound exciton ( $D^0, X$ ) which may be thermally strain split [8]. Few samples show a shoulder at  $I_1$  to lower energies or a weak peak.

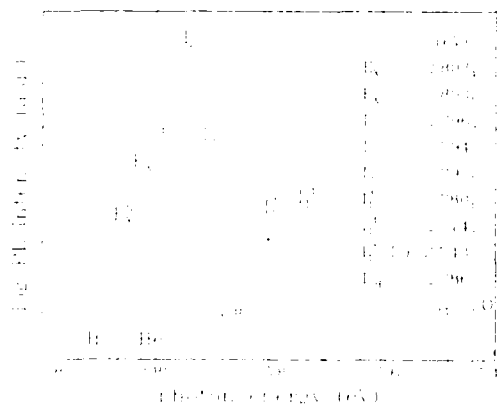


Fig. 1. PL spectra at 2 K of ZnSe/GaAs samples grown with MASE/DEZn at 520°C with  $V_{II}/II = 2$  and different carrier gases.  $H_1$ ,  $I_1^h$ ,  $I_1^l$  and  $I_2$  are due to a donor bound exciton.  $I_1^h$  is not apparent in this spectrum, but dominant under different growth conditions.  $I_1^l$  is not identified and masked by  $I_1^h$  in most spectra. He: A broad  $I_2$  peak from the donor contamination is observed. A new, even broader emission occurs at about 2.786 eV. It is not yet identified, but might be connected to the high levels of hydrogen and carbon incorporation found by SIMS measurements.

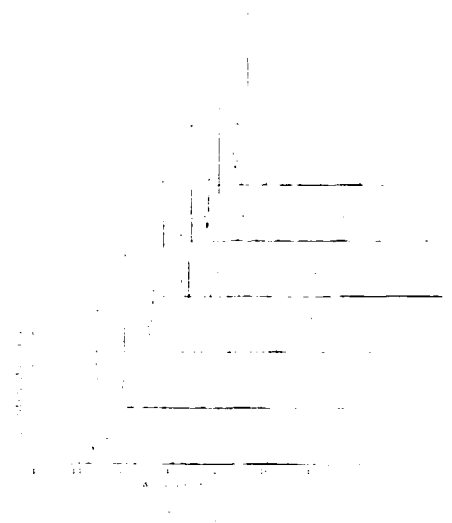


Fig. 2. PL spectra at 2 K for ZnSe/GaAs with  $d \approx 4 \mu\text{m}$  grown at different MASE partial pressures (15–50 Pa,  $p_{\text{DZn}} = 10 \text{ Pa}$ ) at 500°C. At high  $V_{II}/II$  values the halogen contamination of the MASE causes the dominance of  $I_1$ . The origin of the  $I_1^h$  peak may be a  $V_{\text{Zn}}$ -associated acceptor defect or it is an  $(\text{As}^0, \text{X})$  complex introduced by deep Cu acceptors.

In this example the position of this signal is found at 2.792(1) eV. A peak near this position may be interpreted as the recombination of excitons bound to ionized shallow donors ( $I_1^h$ ) [8]. An interpretation in terms of a strain-shifted  $I_1^h$  neutral donor bound exciton ([5]) seems less probable (three  $I_2$  peaks!). The peak  $I_1^h$  does not appear clearly in the spectra of Fig. 1, but is dominant in the spectra of certain samples. Its origin may be a  $V_{\text{Zn}}$ -associated acceptor defect or it is an  $(\text{As}^0, \text{X})$  complex introduced by deep Cu acceptors [8]. The peak  $I_1^l$  is not yet identified and is masked by  $I_1^h$  in most of the spectra.

In Fig. 2 the PL spectra of samples grown with MASE partial pressures from 15 to 50 Pa ( $p_{\text{DZn}} = 10 \text{ Pa}$ ) are shown. In all spectra weak free excitons and the  $Y_0$  line originating from dislocations are visible. Furthermore, phonon replicas from the  $Y_0$  and the  $I_1^l$  lines can be clearly observed.

A pronounced change of the dominant peak from the  $I_1^l$  line to  $I_1$  at higher  $V_{II}/II$  ratios is the

characteristic feature of this series of spectra. The question of the particular interface vapour pressures of the elements and their ratio which determines the stoichiometry of the growing crystal cannot be answered at this point. However, the disappearance of the  $I_1^d$  peak and the dominance of the  $I_2$  peak under Zn-poor conditions make an attribution of  $I_1^d$  to  $V_{Zn}$  less likely. Copper contamination, probably from the MOVPE system, must be assumed. At higher MASE partial pressures, contamination by a donor appears which we attribute to a halogen impurity in the precursor. The MASE was synthesized with the help of both iodine and bromine alkyls.

Furthermore, the so-called green copper DAP luminescence (2.252 eV) appears in the samples with the additional strong donor contamination. Self-activated luminescence appears at low and at high growth temperatures (450 and 550°C).

PL spectra were recorded from samples grown under standard conditions (500°C, VI/H = 2), but with He as a carrier gas. The layers showed a degraded inhomogeneous morphology and weak luminescence signals. In the PL spectrum of one sample, a broad emission at 2.786 eV appears (see Fig. 1: He,  $I^{(H)}$ ). The broad  $I_2$  peak originates probably again from the halogen contamination of the Se precursor. The emission at 2.786 eV is not yet identified. Regarding the SIMS results, one might ask whether the formation of a C–H complex is possible and likely at such high concentrations of hydrogen and carbon. A complex like C–H could give rise to a relative shallow donor or acceptor (e.g.  $C_{Zn}-H_{Zn}$  or  $C_{Se}-H_i$ ) and could well act as a center for exciton recombination.

**SIMS results:** Our SIMS spectra show clearly that the carbon incorporation is accompanied by hydrogen. Fig. 3 displays the absolute concentrations of hydrogen in ZnSe layers grown under either hydrogen or helium carrier gas. The high hydrogen concentration of  $10^{19} \text{ cm}^{-3}$  exceeds  $10^{20} \text{ cm}^{-3}$  under He carrier gas. Correspondingly, the carbon concentration is increased by one order of magnitude. This indicates a contribution of the  $H_2$  carrier gas to the decomposition and growth processes. In both samples, oxygen and arsenic were found as further impurities.

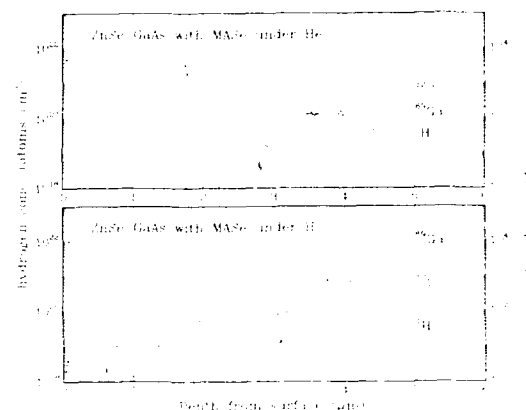
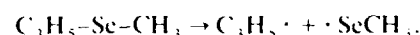


Fig. 3. SIMS spectra of two samples grown with MASE (DEZn) in  $H_2$  or He as the carrier gas (500°C, VI/H = 2). Observations: (1) The incorporation of C is accompanied by H. (2) The hydrogen level under  $H_2$  carrier gas is as high as  $10^{19} \text{ atoms/cm}^3$ . (3) The impurity level increases about one order of magnitude under He carrier gas. The curve of hydrogen is no more quantitative in the substrate region!

A sample grown at 550°C was investigated by mass scans for further impurities. Beneath the already discussed impurities, a weak contamination by Cu is found which confirms the PL results. Some tellurium was detected which stems presumably from former ZnTe growth experiments. The Se isotopes rendered a clear identification of Br difficult (overlap with SeH masses). No measurement of Cl was possible because of a contamination of the SIMS recipient. Finally, weak signals for I and Ga were found in the mass scans.

**Reaction mechanisms:** The thermal dissociation of MASE investigated by mass spectroscopy will be described in detail in a forthcoming paper. The dominant reaction mechanism was found as follows. The increase of the 1,5-hexadiene ( $C_6H_{10}$ ) concentration with the dissociation of MASE clearly indicates the recombination of two allyl radicals. The radicals are generated in a simple bond-break mechanism:



The carrier gas hydrogen reduces the contamination by carbon and hydrogen but does not eliminate it (SIMS). These results might be brought

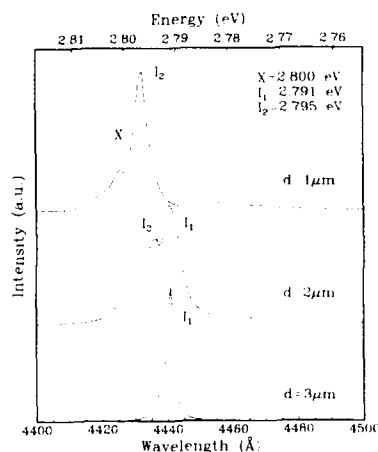


Fig. 4. PL spectra at 2 K of ZnSe/GaAs samples with different thicknesses grown with DTBSe at 340°C. The  $I_2$  donor contamination is masked by the  $I_1$  peak of an acceptor with increasing thickness. The donor may be either Al or Cl, whereas the acceptor stems from the outdiffusion of As from the substrate along the dislocations.

into context as follows. The radical  $\text{CH}_3\text{-Se}\cdot$  chemisorbs and leads to a partly incorporation of hydrogen and carbon. Possibly a C–H complex is generated after the release of  $\text{H}_2$ . Hydrogen carrier gas supports the formation of  $\text{CH}_4$  which is easily desorbed from the surface.

#### 4. Results with DTBSe

The structure and crystallinity of the samples grown with the alkyl combination DTBSe/DMZn-TEN can be briefly characterized as follows. Best results were achieved at growth temperatures around 330°C with VI/II = 3. Layers with  $\approx 1\ \mu\text{m}$  have a weakly developed "orange peel" structure. Double-crystal X-ray diffraction studies of the ZnSe layers grown on (100)GaAs reveal the expected decrease of the FWHM with the thickness for  $d > 0.5\ \mu\text{m}$ . Layers with a thickness of  $3\ \mu\text{m}$  show values of  $\text{FWHM} = 250\ \text{arc sec}$ .

**PL results:** In Fig. 4 the spectra of ZnSe/GaAs with three different thicknesses (1, 2 and  $3\ \mu\text{m}$ ) are shown (growth times: 1–3 h). The free exci-

tons are weakly developed in all three spectra. In the spectra of the  $1\ \mu\text{m}$  thick sample a donor bound exciton  $I_2$  ( $\text{D}^0, \text{X}$ ) at 2.795 eV is dominant. Even in a logarithmic presentation the  $I_2'$  or  $I_3$  are not visible. In resonant PL measurements we determined the 1s–2s energy difference of the donor states to be 19.5 meV. This value allows an attribution of the donor to either Cl or Al [9]. In the spectrum of the thicker sample ( $3\ \mu\text{m}$ ), the  $I_2$  peak has nearly vanished and an acceptor bound exciton  $I_1$  ( $\text{A}^0, \text{X}$ ) at 2.791 eV is dominant. This value is in good agreement with the recombination energy of the acceptor bound excitons in arsenic doped samples [9]. The sample with  $2\ \mu\text{m}$  thickness represents an intermediate case. The slight shifts ( $< 2\ \text{meV}$ ) of the  $I_1$  and  $I_2$  peaks in the spectra are due to the change of the relaxation with layer thickness.

This change from a donor to an acceptor impurity with the layer thickness can be explained as follows. A residual donor contamination is masked in thicker layers by the dislocation enhanced arsenic outdiffusion from GaAs. It should be noted, that GaAs substrates of identical stoichiometry were chosen for this experiments (see ref. [10]).

**SIMS results:** Preliminary measurements of samples grown at 340°C reveal weak concentrations of C and H which are constant throughout the layer depth (detection limits in the order of  $10^{17}$ – $10^{18}\ \text{cm}^{-3}$ ). Clear signals were detected for O, As and S, and weak signals were found for Ga and Cu. As already mentioned, no measurement of Cl was possible. No clear indications for Al and N (SeN) were found in the mass scans.

**Reaction mechanisms:** From the mass spectroscopic investigation we can draw the following conclusions. The thermal dissociation of DTBSe proceeds mainly via a two-step mechanism. In a first  $\beta$ -elimination tertiarybutylselenol is formed. It decomposes into equal parts by a second  $\beta$ -elimination or by a release of elemental Se. The generated alkyls isobutane and isobutene are volatile and are not suspected to lead to carbon incorporation. The dissociation temperature is found to be drastically reduced by the catalysis of a ZnSe surface. The observed pre-reactions of the butyl-based selenium alkyls with common Zn

alkyls can be completely eliminated by the use of the amine adduct DMZn-TEN. Investigations of this surface catalysis in conjunction with the copyrolysis of appropriate cation precursors are currently undertaken. These might reveal the origin of the C and H incorporation.

### 5. Conclusions

The two selenium alkyls DTBSe and MASE were investigated for their suitability in the growth of high purity ZnSe layers. The origins of most of the found impurities could be clarified.

With the alkyl combination MASE and DEZn, layers of ZnSe on GaAs with good morphology and structural quality have been grown. The PL at 2 K shows strong near-band-edge emissions. But the high growth temperature already indicates a problem in the dissociation of the MASE. Furthermore, high levels of carbon and hydrogen are found in the layers. The investigation of the reaction mechanisms reveals the simple bond breaking as the dominant pyrolysis mechanism. The intermediate species  $\text{SeCH}_3$  is obviously responsible for the incorporation of hydrogen and carbon detected by SIMS. Furthermore, a new peak  $\text{I}^{\text{CH}}$  at 2.786 eV appears in a layer with strong hydrogen ( $10^{20} \text{ cm}^{-3}$ ) and carbon contamination. The following extrinsic impurities were found in the layers: (1) Cu from the growth system (PL, SIMS); (2) halogen (Br and I) from the Se source (PL, synthesis, SIMS); (3) oxygen from the system or carrier gas (SIMS); (4) Te from former ZnTe growth (SIMS); (5) As and Ga from the substrate (SIMS). However, the intrinsic contamination by C and H and the high growth temperatures are obviously the most severe hindrances in the growth of ZnSe with MASE.

With the alkyl combination DTBSe and DMZn-TEN, the growth of ZnSe on GaAs at temperatures as low as  $320^\circ\text{C}$  is possible. The layers show a very good surface morphology and crystal structure [6]. In the thermal dissociation of DTBSe  $\beta$ -elimination mechanisms play an important role. No species known for carbon incorporation was observed, but in preliminary SIMS measurements contamination by C and H could be

detected. The investigation of the co-pyrolysis with appropriate Zn precursors might clarify the origin of this contamination. The following extrinsic impurities were found in the layers: (1) Cu from the growth system (SIMS); (2) either Al or Cl as a donor (PL); (3) O from the system or carrier gas (SIMS); (4) S possibly from substrate preparation by  $\text{H}_2\text{SO}_4$ ? (SIMS); (5) As and Ga from the substrate (PL, SIMS). However, the  $\text{I}_1$  peak from the  $(\text{A}_{\text{As}}^0, \text{X})$  emission can already mask the  $\text{I}_2$  peak from the  $(\text{D}_{\text{Cl}}^0, \text{X})$  emission. This indicates a relative weak residual donor contamination. On this basis a successful p-type doping of ZnSe in the MOVPE is possible. Initial doping experiments with phosphorus resulted in hole concentrations up to  $10^{15} \text{ cm}^{-3}$ . Details of these experiments will soon be published.

According to Skromme et al. [5], the incorporation of carbon in MOVPE ZnSe growth does not influence the optical properties of the material. Here, we have shown that the discussion has to be extended to the properties of C and H incorporated in MOVPE growth of ZnSe.

### 6. Acknowledgements

We thank Dr. Y. Marfaing, Dr U.W. Pohl and Dr. B.J. Skromme for helpful discussions.

### 7. References

- [1] T. Yasuda, I. Mitsuishi and H. Kukimoto, *Appl. Phys. Lett.* 52 (1988) 57.
- [2] H. Kukimoto, in: *Proc. 17th Int. Conf. on Defects in Semiconductors, Gmunden, Austria, July 1993*.
- [3] R. Korenstein, W.E. Hoke, P.I. Lemonias, K.T. Higa and D.C. Harris, *J. Appl. Phys.* 62 (1987) 4929.
- [4] K.P. Giapis, K.F. Jensen, J.E. Potts and S.J. Pachuta, *Appl. Phys. Lett.* 55 (1989) 463.
- [5] B.J. Skromme, W. Liu, K.F. Jensen and K.P. Giapis, *J. Crystal Growth* 138 (1994) 338.
- [6] W. Kuhn, A. Naumov, H. Stanzl, S. Bauer, K. Wolf, H.P. Wagner, W. Gebhardt, U.W. Pohl, A. Krost, W. Richter, U. Dümichen, K.H. Thiele, *J. Crystal Growth* 123 (1992) 605.
- [7] P.J. Wright, B. Cockayne, P.J. Parbrook, A.C. Jones, P. O'Brien and J.R. Walsh, *J. Crystal Growth* 104 (1990) 601.

- [8] J. Gutowski, N. Presser and G. Kudlek, *Phys. Status Solidi (a)* 120 (1990) 11.
- [9] K. Wolf, H. Stanzl, A. Naumov, H.P. Wagner, W. Kuhn, B. Hahn and W. Gebhardt, *J. Crystal Growth* 138 (1994) 412.
- [10] W. Kuhn, H.P. Wagner, H. Stanzl, K. Wolf, K. Woerle, S. Lankes, J. Betz, M. Woerz, D. Lichtenberger, H. Leiderer, W. Gebhardt and R. Triboulet, *Semicond. Sci. Technol.* 6 (1991) A105.



ELSEVIER

Journal of Crystal Growth 138 (1994) 455–463

JOURNAL OF  
**CRYSTAL  
GROWTH**

## Integrated heterostructure devices composed of II–VI materials with Hg-based contact layers

J. Ren <sup>a</sup>, D.B. Eason <sup>a</sup>, L.E. Churchill <sup>a</sup>, Z. Yu <sup>a</sup>, C. Boney <sup>a</sup>, J.W. Cook, Jr. <sup>a</sup>,  
J.F. Schetzina <sup>\*a</sup>, N.A. El-Masry <sup>b</sup>

<sup>a</sup> Department of Physics, North Carolina State University, Raleigh, North Carolina 27695-8202, USA

<sup>b</sup> Department of Materials Science and Engineering, North Carolina State University, Raleigh, North Carolina 27695-7907, USA

### Abstract

Integrated heterostructure devices (IHDs) composed of II–VI materials in epitaxial multilayered structures for light-emitting diode and laser diode applications are described. These IHDs combine a light emission multilayer structure with an abrupt or graded heterostructure which includes Hg-based materials for improved ohmic contact to the upper p-type layer of the light emitting structure.

### 1. Introduction

The problem of obtaining ohmic contacts for p-type ZnSe and related alloys is related to the deep valence band of ZnSe. As a consequence, all metals deposited onto p-type ZnSe, including Au and Pt, give rise to large energy barriers which impede the flow of holes across the metal–semiconductor interface. This is illustrated by the energy band diagram of Fig. 1a for a ZnSe/GaAs heterojunction. As shown in the figure, the conduction bands of these two semiconductors line up (to within  $\sim 0.1$  eV [1]) such that a valence band offset of  $\sim 1.4$  eV occurs. As a consequence, all metals, including Au and Pt, produce appreciable energy barriers ( $\geq 1.5$  eV) when they are deposited onto p-type ZnSe, as is illustrated by the energy band diagram of Fig. 1c

for a Au/ZnSe hetero-interface. Band diagrams for both n-on-p and p-on-n structures at zero bias are shown in Fig. 1b and Fig. 1d, respectively. Note the similarities in the two diagrams shown: both types of structures contain large energy barriers which limit hole transport.

The presence of large barriers is manifested by the need to apply very large voltages (10–20 V or more) to activate both n-on-p and p-on-n ZnSe-based light-emitting diodes (LEDs) and laser diodes (LDs). In the case of n-on-p structures, the forward-biased diode characteristics are dominated by tunneling at the reverse-biased ZnSe/GaAs interface, where a barrier  $\sim 1.4$  eV occurs as a consequence of the large valence band offset at the hetero-interface between these two materials, as is illustrated schematically in Fig. 2a. Similar tunneling, with the requisite large applied voltages, also occurs for p-on-n ZnSe-based diodes grown on n-type GaAs substrates. In this case the forward-biased characteristics of the diode are dominated by tunneling phenomena at

\* Corresponding author.

the reversed-biased metal semiconductor contact, as shown in Fig. 2b.

At North Carolina State University (NCSU), we have addressed the above fundamental issue in a novel way by employing an epitaxial layer of the semimetal HgSe to decrease the interfacial energy barrier (valence band offset) to about 0.6 eV [2,3]. This estimate is based on a "modified" common-anion rule for the mercury chalcogenides which assumes a valence band offset of  $\Delta E_v \sim 0.2 E_g$ , where  $E_g$  is the band gap of the corresponding wide band gap common-anion II–VI material (cadmium or zinc chalcogenide). Correspondingly, the conduction band offset is given by  $\Delta E_c \sim 0.8 E_g$ . This empirical "80%–20%" rule holds in the case of CdTe ( $E_g = 1.5$  eV) and HgTe for which a valence band offset  $\Delta E_v \sim 0.3$  eV has been measured [4]. It also holds approximately for ZnTe ( $E_g = 2.35$  eV) and HgTe for which  $\Delta E_v = 0.3$ –0.4 eV has been reported [4].

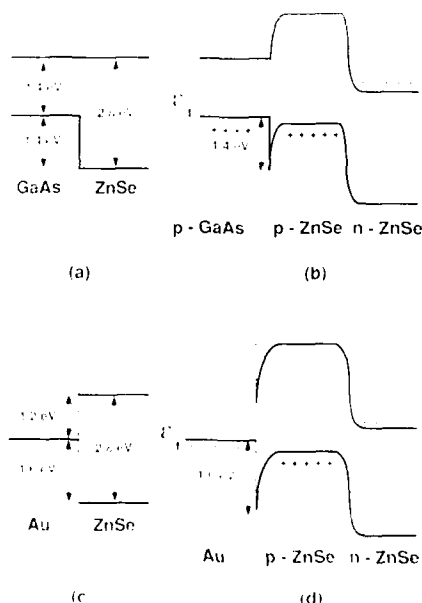


Fig. 1. Band diagrams for (a) GaAs/ZnSe heterojunction, (b) p-GaAs/p-ZnSe/n-ZnSe heterostructure at zero bias, (c) gold/ZnSe, and (d) gold/p-ZnSe/n-ZnSe heterostructure at zero bias. Energy band offsets are estimates obtained from a search of the literature.

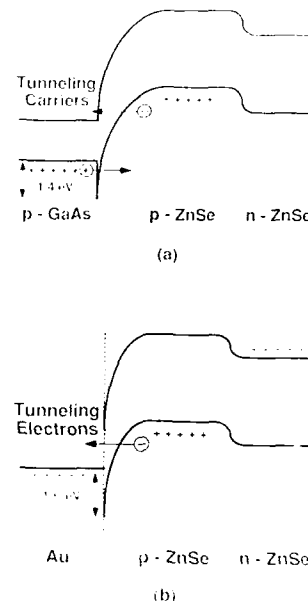


Fig. 2. Band diagrams for (a) n-on-p ZnSe diode on p-type GaAs and (b) p-on-n ZnSe diode with gold contact. Both diodes are forward biased.

The use of epitaxial HgSe has resulted in improved ohmic contacts for p-type ZnSe films and related diode structures [2,3,5]. Multilayered structures with intermediate or graded layers of  $\text{Hg}_{1-x}\text{Zn}_x\text{Se}$  or  $\text{ZnTe}_{1-x}\text{Se}_x$  have also been fabricated to further improve the electrical properties of II–VI light emitters. We refer to such structures as *integrated heterostructure devices (IHDs)* [5,6]. The term integrated heterostructure or integrated heterostructure device is here defined as a multilayered structure in which particular layers, or combination of layers, perform distinctly different functions. An example of an IHD is a semiconductor surface-emitting laser which contains (a) multilayers for optical mirrors, (b) an active light generation region which might consist of one or more additional layers or quantum wells, (c) p-type and n-type layers which supply the active light generation region with electron and holes under forward bias and (d) additional top layers for optically and electrically coupling the laser output to the outside world. These

various functions are integrated into a single epitaxial multilayered structure using sophisticated growth techniques such as molecular beam epitaxy (MBE) or metalorganic chemical vapor deposition (MOCVD). The p-on-n IHD structures being studied at NCSU consist of: (a) multilayers of II–VI compounds that form an optical-emission heterostructure, (b) abrupt or graded II–VI layers that serve as an electrical bridge to the p-type contact layers and (c) HgSe/metal contacts.

This paper discusses methods that have been developed at NCSU for the MBE growth of integrated heterostructure devices containing both narrow-band-gap and wide-band-gap II–VI materials. Device processing procedures are also discussed. Properties of light-emitting devices are described within the context of IHD design principles, including those of recently-fabricated high-brightness, high-efficiency blue and green LEDs [7]. The feasibility of using other II–VI semimetals such as HgTe, HgS, HgSSe, or HgSeTe as electrical contact layers in particular light-emitting and/or light-detecting IHD structures is also addressed.

## 2. Experimental details

Deposition of HgSe and other Hg-based compounds onto ZnSe-based p-on-n diode structures is carried out using two separate MBE chambers. Using the first MBE chamber, p-on-n diode structures are grown on (100) Si-doped n<sup>+</sup>-GaAs substrates. Film growth temperatures of 240–280°C are currently being employed. A variety of double-heterostructure light-emitting devices containing ZnSSe, ZnSe and ZnCdSe layers have been synthesized. All of the major constituents of the various layers of the heterostructures are grown using elemental Zn, Cd, Se and S. ZnCl<sub>2</sub> is used as a solid Cl source for growth of the n-type layers ( $n_0 \sim 1 \times 10^{18} \text{ cm}^{-3}$ ) of diode structures [8–10]. The p-type layers ( $p_0 \sim 1 \times 10^{18} \text{ cm}^{-3}$ ) are doped with N from an RF plasma source using N<sub>2</sub> gas [11,12].

Following deposition of the p-on-n heterostructure, the sample is transferred to a sec-

ond Hg-compatible MBE chamber where an epitaxial HgSe layer is deposited. At NCSU, we have developed a portable ultra-high-vacuum transfer device, equipped with a small ion pump, that allows us to extract a wafer from one MBE system and transfer it to a second MBE system. In this way, samples may be protected from oxidation during the transfer process. More recently, we have also employed a Se capping layer during sample transfer. In this case, the light-emitting heterostructure is cooled to room temperature under a Se flux in MBE chamber 1 to provide a Se capping layer on the surface. Following this, the wafer is transferred to the second Hg-compatible MBE chamber where the Se capping layer is desorbed by heating and an epitaxial layer of HgSe ( $\sim 100 \text{ Å}$  thick) is grown by MBE. Both procedures have proven to be satisfactory for the growth of epitaxial HgSe.

Optimum MBE growth conditions for HgSe thin films were determined based on the results of preliminary deposition experiments in which film growth parameters such as substrate temperature, Hg flux, Se flux and the Hg/Se flux ratio were systematically varied. The substrate temperature range investigated in these initial experiments was between 80 and 150°C. The Hg and Se beam equivalent pressures (BEPs) were varied in the range  $0.4 \times 10^{-4}$  to  $1.5 \times 10^{-4}$  Torr and  $0.6 \times 10^{-6}$  to  $1 \times 10^{-6}$  Torr, respectively. From these experiments, it was found that there was no appreciable condensation of HgSe for substrate temperatures above  $\sim 125^\circ\text{C}$ . In addition, at a substrate temperature of  $\sim 80^\circ\text{C}$  or less, the HgSe films exhibited poor structural quality and uniformly rough surfaces. In the range 80–125°C, for given Hg and Se BEPs, the growth rate was found to increase with decreasing temperature. It was also found that, at a given growth temperature, the Hg to Se BEP ratio has a definite effect on the growth rate. For instance, at a growth temperature of 100°C, and for Hg/Se BEP ratios between 90 and 130, the growth rate is controlled by the Se flux and increases when the Se BEP is increased. Below a Hg/Se BEP ratio of 90, on the other hand, film growth becomes Hg-flux-limited and the growth rate decreases even when a high Se flux is present at the substrate surface.



This behavior is a direct consequence of the well-documented [13,14] low sticking coefficient of Hg.

For Hg/Se BEP ratios higher than 130 (e.g., 130–180), a decrease of the growth rate was also observed. This may be due to a gas-phase beam interaction effect, which results in part of the Se flux being deflected by the high Hg atoms density and prevented from reaching the substrate surface. From a morphological and structural quality viewpoint, it was found that the best results were obtained for a BEP ratio in the range of 90–100, for a growth temperature of 100°C.

Based on the above results, in all subsequent HgSe growth experiments a substrate temperature of 100–110°C was used along with a Hg/Se BEP ratio of  $\sim 100$  (Hg and Se BEPs of  $\sim 1 \times 10^{-4}$  and  $\sim 1 \times 10^{-6}$  Torr, respectively). These conditions result in a film growth rate of  $\sim 1.1$  Å/s. Note that this growth rate is still quite low compared to that of HgTe grown under similar conditions. This may be related to the higher evaporation rate of the HgSe compound at low temperatures [5].

Transmission electron microscopy (TEM) studies of selected IHD structures were completed using a Hitachi-800 electron microscope operating at 200 kV. The samples were thinned at 77 K using argon-ion milling techniques. Both vertical-cross-section and planar TEM photomicrographs were used to assess the interfacial quality of the various layers of the integrated device structures and to estimate dislocation densities.

Mesa-type devices were prepared from selected IHD wafers using standard photolithographic and etching techniques to define mesa arrays. Mesa dimensions were  $500 \mu\text{m} \times 500 \mu\text{m}$ . Evaporated Au or In was used to form a metal contact to the top HgSe surface of each p-on-n mesa diode. Ohmic contact to the n-type layer was made at the back surface of the GaAs:Si substrate with In metal. During processing, the wafer was subjected to temperatures as high as 150°C with no obvious deleterious effects. After processing, a dicing saw was used to obtain individual diodes for electrical testing. The current–voltage ( $I$ – $V$ ) properties of the diodes were measured using a Tektronix model 370 curve tracer.

### 3. Results and discussion

#### 3.1. Transmission electron microscopy studies

Fig. 3 shows a vertical-cross-section TEM photograph of a representative IHD structure taken under two-beam conditions. This particular device is a blue-light-emitting diode based on a ZnSSe–ZnCdSSe double-heterostructure. As seen from the figure, the active region of the light emission heterostructure consists of five 100 Å ZnCdSSe quantum wells separated by four 150 Å ZnSSe barriers. Note that the active region of the

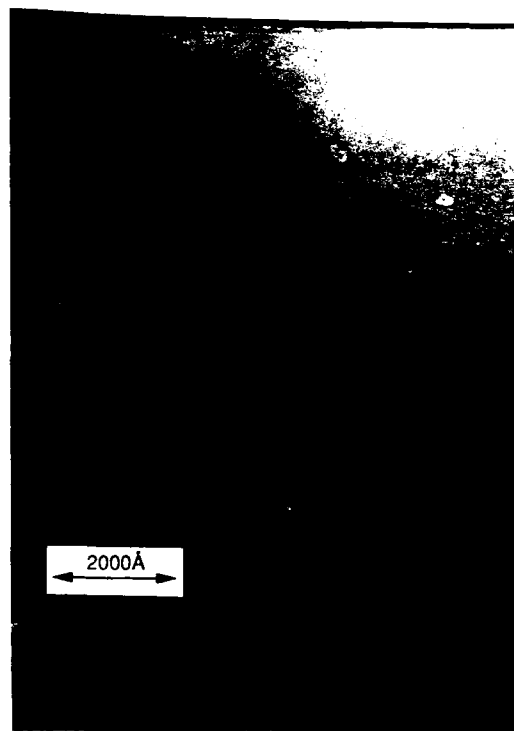


Fig. 3. Transmission electron micrograph of an integrated heterostructure device (IHD). The active region of the IHD consists of five 100 Å ZnCdSSe quantum wells which are at the bottom of the micrograph. The thin (100 Å) black highly-conducting layer at the top surface of the IHD is an epitaxial HgSe layer.

IHD is dislocation-free and exhibits exceptionally smooth and flat interfaces. The ZnSSe cladding layers above and below the active region of the device are also dislocation-free. Based on an analysis of many vertical-cross-section and planar TEM photographs of several similar devices, we estimate that the dislocation density is about  $10^5/\text{cm}^2$ , on average, from sample to sample.

At the top surface of the IHD shown in Fig. 3 is a dark and narrow ( $\sim 100 \text{ \AA}$ ) layer. This is the epitaxial HgSe layer at the top surface of the sample which is part of the ohmic contact portion of the integrated device structure. The epitaxial nature of the HgSe layer was confirmed by means of electron-diffraction and electron-channeling studies. The fact that the HgSe layer shown in Fig. 3 is very dark is a reflection of its very high electrical conductivity (carrier concentration  $\sim 10^{19} \text{ cm}^{-3}$ ; mobility  $\sim 10^4 \text{ cm}^2/\text{V} \cdot \text{s}$ ) which promotes lateral current spreading – a highly-desirable property for LED applications. In addition, because its thickness is only  $\sim 100 \text{ \AA}$ , the HgSe layer also serves as a semi-transparent (85–90%) electrode for surface-emitting LED applications.

### 3.2. Electrical characteristics of integrated heterostructure devices

The integrated heterostructure device concept produced a dramatic improvement in the observed electrical characteristics of ZnSe-based diode structures [2]. Fig. 4 shows an  $I$ - $V$  curve for one of the initial ( $500 \mu\text{m} \times 500 \mu\text{m}$  mesa) ZnSSe–ZnCdSe double-heterostructure diodes equipped with an epitaxial HgSe/gold contact, which was synthesized and processed at NCSU in July, 1991. This particular diode produced bright blue emission at 2.60 eV (476 nm) at room temperature. Note from the figure that the mesa diode device exhibits a turn-on voltage of about 2.8 V and passes 50 mA at 4.4 V at 300 K. This represented a substantial improvement compared with earlier devices prepared at NCSU [15–18] and elsewhere [19–24] that were equipped with metallic contacts.

To further reduce the  $\sim 0.6 \text{ eV}$  valence band offset between ZnSe and HgSe, multilayered structures with graded intermediate layers of

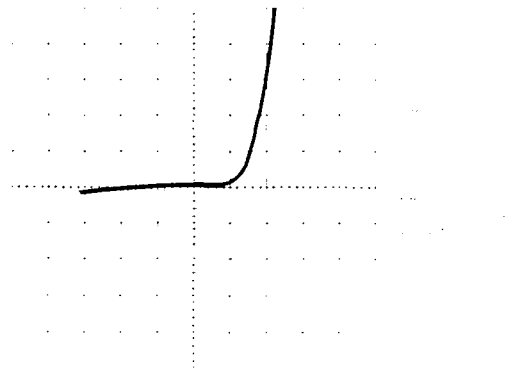


Fig. 4.  $I$ - $V$  characteristics for a p-on-n ZnSSe/ZnCdSe double-heterostructure light-emitting diode equipped with epitaxial HgSe/gold top contact.

$\text{Zn}_{1-x}\text{Hg}_x\text{Se}$  or  $\text{ZnTe}_{1-x}\text{Se}_x$  were investigated. The band gap versus lattice constant for these two ternary alloys is shown in Fig. 5. In this case, the idea is to dope the graded layer p-type to maintain the Fermi level close to its valence band edge as (in the case of  $\text{Zn}_{1-x}\text{Hg}_x\text{Se}$ ) the grading material changes from ZnSe to HgSe. By means of this grading/doping procedure the initial band offset can be eliminated, as has been shown for III–V materials [25], since the equilibrium Fermi energy must be constant throughout the heterostructure. For  $\text{ZnTe}_{1-x}\text{Se}_x$  grading layers, the grading should proceed from  $x = 1$  (ZnSe) to

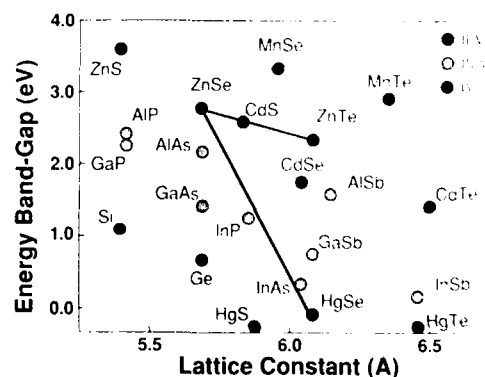


Fig. 5. Band gap versus lattice constant for selected semiconductors. The two solid lines shown in the figure refer to ZnHgSe and ZnTeSe ternary alloys, both of which are suitable materials for graded-layer contacts to p-type ZnSe.

about  $y \sim 0.4$ , since the valence band of  $\text{ZnTe}_{0.6}\text{Se}_{0.4}$  lines up with that of HgSe (assuming valence band of ZnTe is about 1.0 eV above that of ZnSe [26]).

At NCSU, IHDs with  $\text{Zn}_x\text{Hg}_{1-x}\text{Se}$  graded layers have been grown by MBE. However, the large difference in the optimum growth temperature of ZnSe ( $\sim 250^\circ\text{C}$ ) versus HgSe ( $\sim 100^\circ\text{C}$ ) required that both the Zn source temperature, which controls the Zn flux, and the substrate temperature be varied during growth of the  $\text{Zn}_x\text{Hg}_{1-x}\text{Se}$  grading layer. Thus, the MBE-growth procedure is a complex one and the results to date have only been marginally successful: while a slight improvement was noted in the  $I$ - $V$  curves of processed diode structures with  $\text{Zn}_x\text{Hg}_{1-x}\text{Se}$  grading layers from that of Fig. 4, reproducibility has proven to be a problem. As a consequence, we have recently instituted a new procedure – post-growth annealing – to grade the ZnSe–HgSe interface. In these experiments, an IHD sample with HgSe/gold surface layers is placed in an annealing oven. The sample is then annealed at a preselected time/temperature profile under flowing nitrogen gas to promote in-diffusion of Hg from the HgSe layer into the ZnSe layer, thus grading the heterointerface. (Annealing experiments of this type are routinely performed to control the electrical properties of HgCdTe infra-red detector diodes.) Initial results at NCSU have been encouraging: diode  $I$ - $V$  curves are consistently improved. However, optimum annealing parameters have not yet been determined. Work in this area is continuing at NCSU.

Improved diode  $I$ - $V$  properties were also observed for HgSe-based IHD structures having an intermediate graded layer of  $\text{ZnTe}_{1-y}\text{Se}_y$ , as we have previously reported [2]. In this case, a light-emitting structure was grown in MBE chamber 1 in the usual fashion. Following this, a  $\sim 100$  nm thick graded layer of nitrogen-doped  $\text{ZnTe}_{1-y}\text{Se}_y$  was grown at  $\sim 245^\circ\text{C}$ . The sample was then transferred to MBE chamber 2 where a 100 Å thick HgSe film was grown at  $\sim 100^\circ\text{C}$ . Processed diodes of this type show a smaller and sharper turn-on voltage (1.9 V) compared with that of Fig. 4a and produces 20 mA at 3.2–3.4 V.

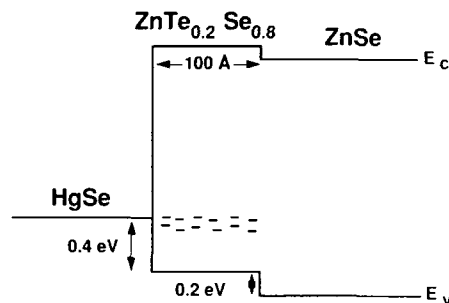


Fig. 6. Band diagram of improved ohmic contact for p-type ZnSe which employs two thin ( $\sim 100$  Å) layers of epitaxial HgSe/ $\text{ZnTe}_{0.2}\text{Se}_{0.8}$  as shown. The heavily-doped p-type  $\text{ZnTe}_{0.2}\text{Se}_{0.8}$  layer provides deep states for resonant-tunneling enhancement of the current flow.

Recently, we have modified the ohmic contact layers of II–VI integrated heterostructure devices. The new IHD structure, shown schematically in Fig. 6, involves MBE growth of a thin (100 Å)  $\text{ZnTe}_{0.2}\text{Se}_{0.8}$  layer between the ZnSe-based light-emitting heterostructure and the top epitaxial HgSe layer. The thin  $\text{ZnTe}_{0.2}\text{Se}_{0.8}$  layer is heavily doped p-type by means of nitrogen-plasma doping. This procedure creates deep states in the  $\text{ZnTe}_{0.2}\text{Se}_{0.8}$  layer which promote resonant tunneling of holes. The photomicrograph shown in Fig. 3 illustrates this new type of IHD structure. Upon careful inspection, a thin  $\sim 100$  Å layer can be seen at the top of the micrograph just under the black epitaxial surface layer of HgSe. This is the heavily-doped epitaxial  $\text{ZnTe}_{0.2}\text{Se}_{0.8}$  layer that provides deep states for resonant-tunneling enhancement of the current flow through the IHD structure. This, in turn, gives rise to improved  $I$ - $V$  characteristics of processed devices, as is illustrated in Fig. 7. Fig. 7a shows the  $I$ - $V$  curve for a blue-light-emitting diode that was processed from the IHD structure shown in Fig. 3. The device exhibits a turn-on voltage of 2.4 V and passes 25 mA at 3.2 V. These electrical characteristics compare favorably with those of a commercial SiC blue LED which are illustrated by the  $I$ - $V$  curve of Fig. 7b.

The characteristics of the blue-emitting device of Fig. 7a at high current levels are shown in Fig. 8. Note that the diode passes 500 mA of current

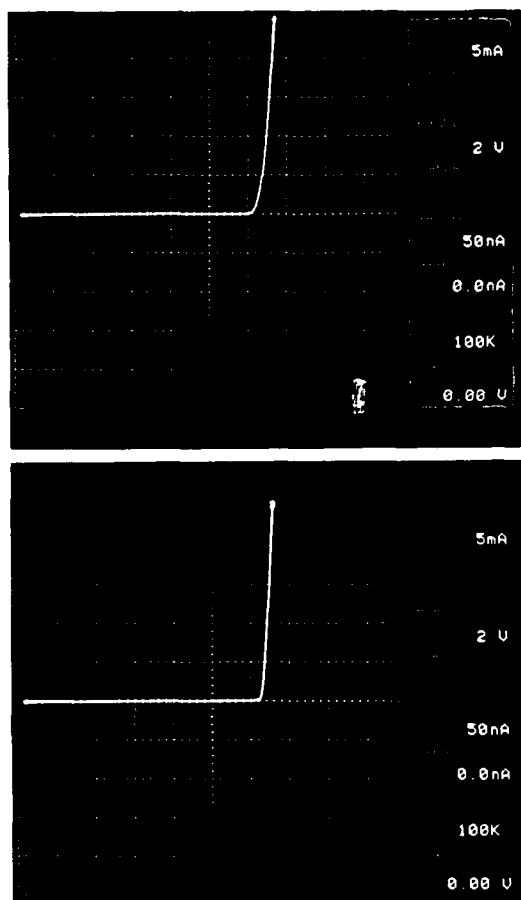


Fig. 7.  $I$ - $V$  curves for blue light-emitting diodes: (a) ZnSSe-ZnCdSSe double-heterostructure IHF; (b) commercial SiC p-n junction device.

at 4 V. This corresponds to a current density of  $200 \text{ A/cm}^2$  – comparable to current densities presently required for room temperature operation of II-VI laser diodes [27].

### 3.3. Use of other Hg-based semimetals for ohmic contact applications

The question arises: Can HgTe or cubic HgS be used to further improve the ohmic contact to p-type ZnSe and related alloys? Fig. 9 shows band offset diagrams which involve each of these semimetals. Fig. 9a shows the band diagram for a

CdTe/HgTe heterojunction showing a valence band offset of 0.3 eV, which has been determined by experiment [4]. Fig. 9b shows the band diagram for a ZnSe/HgSe heterojunction showing a valence band offset of 0.6 eV, while Fig. 9c shows a band diagram for a ZnS/HgS heterojunction showing a valence band offset of 0.8 eV. Band offsets shown in Figs. 9b and 9c are speculations based on the empirical “80%–20%” modified common-anion rule for II-VI materials which we have introduced [2]. Our results involving HgSe-based contacts to ZnSe provide experimental support that this modified common anion rule is at least approximately correct.

Referring to Fig. 9a, it might be argued that the absolute energy level of HgTe is substantially higher than HgSe. This is so because a corresponding modified *common cation* rule also seems to hold for II-VI materials such that the band gap difference between CdTe and ZnTe occurs mostly (80–90%) in the conduction band. Thus, the band offset for ZnTe/HgTe should be 400–500 meV, which implies that the absolute energy of HgTe lies approximately at the energy level of gold. As a consequence, HgTe should not provide an improved ohmic contact for p-type ZnSe. We have verified this fact at NCSU by depositing

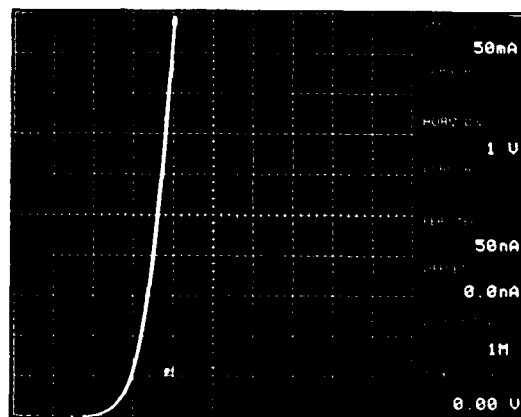


Fig. 8.  $I$ - $V$  characteristics of a ZnSSe-ZnCdSSe double-heterostructure IHF at high current levels. The IHF is a blue-light-emitting device ( $500 \mu\text{m} \times 500 \mu\text{m}$  mesa). At 4 V forward-bias the current flow is 500 mA, corresponding to a current density of  $200 \text{ A/cm}^2$ .

HgTe onto ZnSe-based diode structures by MBE. The  $I$ - $V$  characteristics of the p-on-n diodes with HgTe contacts are very similar to the  $I$ - $V$  characteristics of diodes equipped with deposited Au contacts – both types of samples display high turn-on voltages.

In contrast, cubic HgS would appear to be a very interesting ohmic contact material for p-type ZnSe. This is so because it is generally accepted that there is little or no conduction band offset between ZnSe and ZnS, as is illustrated by the band diagram shown in Fig. 10a. If this is the case, the absolute energy level of HgS should lie *below* the valence band of ZnSe by 0.2 eV, consistent with the band offsets shown in Figs. 9 and 10a. As a consequence, HgS should be an excel-

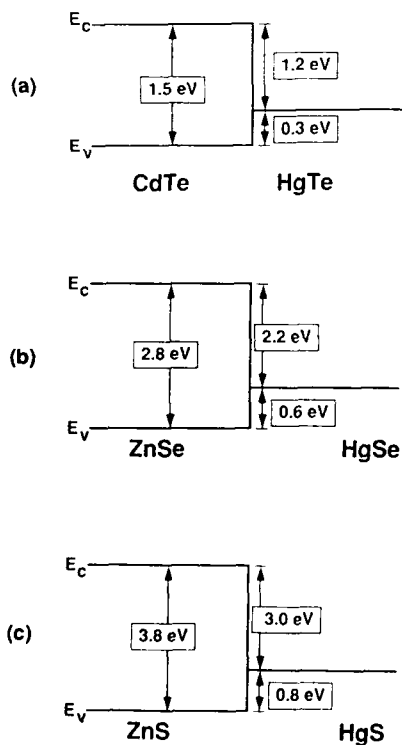


Fig. 9. Band diagrams for (a) CdTe/HgTe, (b) ZnSe/HgSe and (c) ZnS/HgS heterojunctions. Band offsets for (b) and (c) are speculations based on an empirical "80%–20%" modified common-anion rule for II–VI materials.

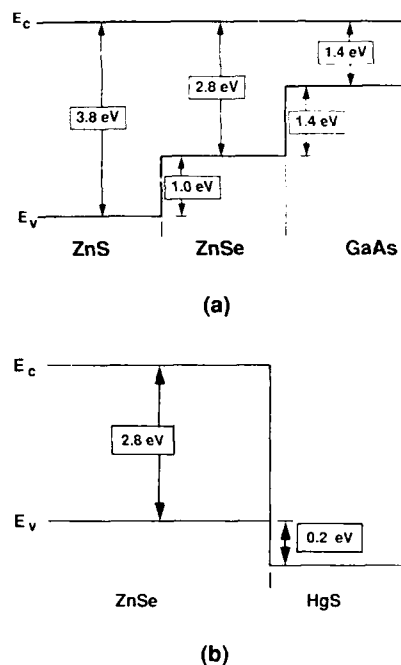


Fig. 10. Band diagrams for (a) ZnS/ZnSe/GaAs heterostructure and (b) ZnSe/HgS heterojunction. Band diagram (b) is a speculation consistent with the band offsets shown in Fig. 9 and in (a).

lent ohmic contact material for ZnSe-based p-on-n diode structures.

Based on the above speculative arguments, we have attempted to grow HgS layers on ZnSe-based diode structures by MBE. Our results so far have been discouraging. Depositions at 100°C using elemental Hg and S in varying flux ratios produced no deposits on clean ZnSe diode structures grown on GaAs substrates. Next, the ZnSe/GaAs substrate temperature was lowered to room temperature. Again, for a range of Hg and S flux ratios, no deposition of any kind occurred. Finally, by reducing the substrate temperature to –30°C, using a special substrate cooling stage, a dull black deposit formed on the ZnSe surface. The black deposit appeared to be stable at room temperature after the sample was removed from the MBE system. However, upon heating the sample above room temperature to about 50°C,

the black deposit completely vaporized leaving a specular ZnSe layer as the sample surface.

Additional MBE experiments were completed using elemental Zn, Hg and S in an effort to grow the ternary alloy  $\text{Zn}_{1-x}\text{Hg}_x\text{S}$ . These experiments also produced discouraging results. For growth at 100°C under a variety of favorable flux ratios, the deposited film was always transparent ZnS of poor structural quality. This was verified by differential reflectance measurements in the UV which determined the band gap to be that of ZnS. No Hg was incorporated in any of the layers grown at 100°C. Similar results were obtained upon lowering the substrate growth temperature to room temperature: no Hg was incorporated in any of the layers.

On the basis of the above preliminary film growth experiments, we have concluded that both HgS and  $\text{Zn}_{1-x}\text{Hg}_x\text{S}$  are difficult materials to grow by MBE. However, because of the potential importance of these materials for ohmic contact applications, work in this area will continue at NCSU. In addition, we recommend that other film growth techniques such as MOCVD and sputtering also be investigated.

#### 4. Acknowledgements

The authors wish to acknowledge the contributions of Y. Lansari and Z. Yang, who helped with the initial HgSe film growth and characterization experiments at NCSU. This work was supported by the ARPA/URI under grant N00014-92-J-1893, by ARPA grant DAAL03-91-G-0131, and by ONR grant N00014-92-J-1644.

#### 5. References

- [1] L. Kassel, H. Abad, J.W. Garland, P.M. Raccach, J.E. Potts, M.A. Haase and H. Cheng, *Appl. Phys. Lett.* 56 (1990) 42.
- [2] Y. Lansari, J. Ren, B. Sneed, K.A. Bowers, J.W. Cook, Jr. and J.F. Schetzina, *Appl. Phys. Lett.* 61 (1992) 2554.
- [3] Z. Yang, K.A. Bowers, J. Ren, Y. Lansari, J.W. Cook, Jr. and J.F. Schetzina, *Appl. Phys. Lett.* 61 (1992) 2671.
- [4] C. Hsu and J.P. Faurie, *J. Vac. Sci. Technol. B* 6 (1988) 772.
- [5] Y. Lansari, J.W. Cook, Jr. and J.F. Schetzina, *J. Electron. Mater.* 22 (1993) 809.
- [6] Y. Lansari, Z. Yu, J. Ren, C. Boney, J.W. Cook, Jr. and J.F. Schetzina, 1992 Materials Research Society Meeting, Boston, MA (Mater. Res. Soc. Symp. Proc., to be published).
- [7] D.B. Eason, Z. Yu, C. Boney, J. Ren, L.E. Churchill, J.W. Cook, Jr., J.F. Schetzina and N.A. El-Masry, *J. Crystal Growth* 138 (1994) 703.
- [8] K. Ohkawa, T. Mitsuyu and O. Yamazaki, *J. Appl. Phys.* 62 (1987) 3216.
- [9] H. Cheng, J. DePuydt, J. Potts and M. Haase, *J. Crystal Growth* 95 (1988) 512.
- [10] S. Hwang, J. Ren, K.A. Bowers, J.W. Cook, Jr. and J.F. Schetzina, *Mater. Res. Soc. Symp. Proc.* 161 (1990) 133.
- [11] R.M. Park, M.B. Troffer, C.M. Rouleau, J.M. DePuydt and M.A. Haase, *Appl. Phys. Lett.* 57 (1990) 2127.
- [12] K. Ohkawa, T. Karasawa and T. Mitsuyu, *J. Crystal Growth* 111 (1991) 797.
- [13] J.W. Cook, Jr., K.A. Harris and J.F. Schetzina, *Mater. Res. Soc. Symp. Proc.* 90 (1987) 419.
- [14] J.P. Faurie, A. Million, R. Boch and J.L. Tissot, *J. Vac. Sci. Tech. A* 1 (1983) 1593.
- [15] J. Ren, B. Sneed, K.A. Bowers, D.L. Dreifus, J.W. Cook, Jr. and J.F. Schetzina, *Appl. Phys. Lett.* 57 (1990) 1901.
- [16] J. Ren, K.A. Bowers, B. Sneed, F.F. Reed, J.W. Cook, Jr. and J.F. Schetzina, *J. Crystal Growth* 111 (1991) 829.
- [17] J. Ren, K.A. Bowers, R.P. Vaudo, J.W. Cook, Jr., J.F. Schetzina, J. Ding, H. Jeon and A.V. Nurmikko, *J. Crystal Growth* 117 (1992) 510.
- [18] J. Ren, K.A. Bowers, J.W. Cook, Jr. and J.F. Schetzina, *J. Vac. Sci. Technol. B* 10 (1992) 909.
- [19] R.M. Park, M.B. Troffer, E. Yablonovich and T.J. Gmitter, *Appl. Phys. Lett.* 59 (1991) 1896.
- [20] W. Xie, D.C. Grillo, R.L. Gunshor, M. Kobayashi, G.C. Hua, N. Otsuka, H. Jeon, J. Ding and A.V. Nurmikko, *Appl. Phys. Lett.* 60 (1992) 463.
- [21] H. Jeon, J. Ding, A.V. Nurmikko, W. Xie, M. Kobayashi and R.L. Gunshor, *Appl. Phys. Lett.* 60 (1992) 892.
- [22] W. Xie, D.C. Grillo, R.L. Gunshor, M. Kobayashi, H. Jeon, J. Ding, A.V. Nurmikko, G.C. Hua and N. Otsuka, *Appl. Phys. Lett.* 60 (1992) 1999.
- [23] H. Jeon, J. Ding, W. Patterson, A.V. Nurmikko, W. Xie, D.C. Grillo, M. Kobayashi and R.L. Gunshor, *Appl. Phys. Lett.* 59 (1991) 3619.
- [24] H. Jeon, J. Ding, A.V. Nurmikko, W. Xie, D.C. Grillo, M. Kobayashi, R.L. Gunshor, G.C. Hua and N. Otsuka, *Appl. Phys. Lett.* 60 (1992) 2045.
- [25] J.M. Woodall, J.L. Freeouf, G.D. Pettit, T. Jackson and P. Kirchner, *J. Vac. Sci. Technol.* 19 (1981) 626.
- [26] Y. Fan, J. Han, L. He, J. Saraie, R.L. Gunshor, M. Hagerott, H. Jeon, A.V. Nurmikko, G.C. Hua and N. Otsuka, *Appl. Phys. Lett.* 61 (1992) 3160.
- [27] J.M. Gaines, R.R. Drenten, K.W. Haberman, T. Marshall, P. Mensz and J. Petruzzello, *Appl. Phys. Lett.* 62 (1993) 2462.

## Ohmic contacts and transport properties in ZnSe-based heterostructures

J. Han <sup>\*a</sup>, Y. Fan <sup>a</sup>, M.D. Ringle <sup>a</sup>, L. He <sup>a</sup>, D.C. Grillo <sup>a</sup>, R.L. Gunshor <sup>a</sup>,  
G.C. Hua <sup>b</sup>, N. Otsuka <sup>b</sup>

<sup>a</sup> School of Electrical Engineering, Purdue University, West Lafayette, Indiana 47907, USA

<sup>b</sup> School of Materials Engineering, Purdue University, West Lafayette, Indiana 47907, USA

### Abstract

In this paper both horizontal and vertical transport properties of ZnSe based heterostructures were studied. Temperature-dependent Hall effect measurements were performed on nitrogen-doped ZnSe, ZnTe, Zn(S,Se) and (Zn,Mg)(S,Se) epilayers; acceptor concentration  $N_a$ , compensation donor concentration  $N_d$  and the activation energy  $E_a$  were derived by curve-fitting to the freeze-out behavior of the hole concentrations. Vertical transport study, through the use of an analytical computer simulation, suggested that the electron transport across the n-ZnSe/n-GaAs heterointerface is often hindered by the presence of a high density of interface states; both the employment of heavy doping near the interface and the modification of GaAs surface stoichiometry before the nucleation of ZnSe were found effective in reducing the device impedance.

### 1. Introduction

The demonstration of the first blue-green diode lasers [1,2] in the summer of 1991 sparked a renewed interest in the field of II–VI wide-gap compound semiconductors. Continuing advancement toward technological maturity, most notably the realization of stable continuous-wave laser operation at room temperature [3], demands still a greater appreciation of the fundamental issues such as the relationship between material quality and growth parameters, and the electrical transport properties, both from which the device behavior is derived. In the summer of 1992, with the

introduction of a Zn(Te,Se) pseudo-graded-layer between heavily p-doped ZnTe and p-ZnSe layers, we were able to address the problem of ohmic contacts to p-type ZnSe [4], a problem which became more crucial with the intensifying device research on wide bandgap II–VI materials. The effectiveness of this contact scheme was confirmed by the reduction of laser operating voltages (to as low as 7 V [5]) in our devices and also the capability for conducting stable Hall measurements on p-ZnSe from 320 to 77 K, where the latter experiments were not readily feasible with the conventional metal/p-ZnSe Schottky contacts.

In this paper we report the study of both horizontal and vertical transport properties of ZnSe-based structures. Results of the tempera-

<sup>\*</sup> Corresponding author.

ture-dependent Hall measurements on nitrogen-doped p-ZnSe [6] and p-ZnTe [7] are reviewed; emphasis will be given to the implications of the observed behavior relative to the acceptor activation energy of nitrogen in the ternary Zn(S,Se) and quaternary (Zn,Mg)(S,Se). While fully aware of the necessity for further improvement in contacting to, and doping of, p-type wide-gap II–VI semiconductors, we confine the study of vertical transport, specifically the current–voltage ( $I$ – $V$ ) characteristics, to an issue frequently overlooked by the II–VI community: the carrier transport across a II–VI/III–V heterovalent interface, in this case the ZnSe/GaAs interface.

## 2. Experimental procedure

A Perkin-Elmer 430 modular MBE system with separate II–VI and III–V growth chambers was employed; details of the growth conditions were described previously [8]. Also the design and growth of the Zn(Se,Te) pseudo graded contact to p-ZnSe was reported elsewhere [4]; the original configuration was adapted to contact p-(Zn,Mg)(S,Se) with the insertion of a p-Zn(S,Se) layer.

Transmission-line model (TLM) measurements were performed to characterize the metal/p-ZnTe/p-Zn(Se,Te) graded region/p-ZnSe contact. Fig. 1 shows a typical plot (of total resistance versus electrode spacing) from an (unannealed) Au/Pd/Zn(Se,Te) graded-region/p-ZnSe contact. A specific contact resistance of  $4 \times 10^{-4} \Omega \text{ cm}^2$  was derived from the plot using Berger's equation [9]. The reduction of specific contact resistance as compared to the Au/Zn(Se,Te) graded-region/p-ZnSe contact [4] was in qualitative agreement with the recent study of Pd contacts to p-ZnTe [10]. The material sheet resistivity, obtained from the slope of the plotted line, was  $4.6 \text{ k}\Omega/\square$  which is very close to the value ( $4.4 \text{ k}\Omega/\square$ ) derived from a separate Hall measurement. It is worth commenting that, given the slight deviation in the  $I$ – $V$  characteristics from a straight line near the origin as was observed for small contacts under high current level [4], the TLM resistance values were taken at a current

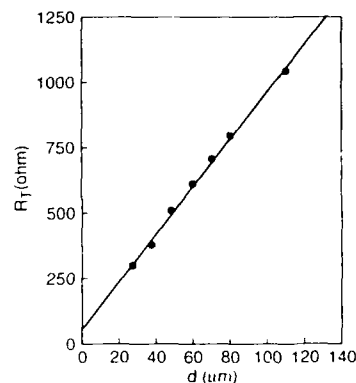


Fig. 1. The plot of measured total resistance vs the spacing between electrodes for a Au/Pd/p-ZnTe p-graded Zn(Te,Se)/p-ZnSe contact.

density of about  $250 \text{ A/cm}^2$ . The injection level was determined with a knowledge of the "effective contact area", a quantity which reflects the extent of current crowding near the edge of the electrodes and can be derived from the intersection of the data line to the abscissa [9]. The observed reduction of specific contact resistance by simply experimenting with different metallizations suggested that, at the current stage, the limiting factor of the graded contact scheme might lie at the metal/p-ZnTe interface.

A Van der Pauw configuration, with one electrode in each of the four corners of a square sample, was chosen for carrying out the Hall measurements. As was first pointed out by Van der Pauw [11], a deviation from the original assumption of point contacts can lead to erroneous results which are normally manifested by an *apparent* increase of carrier concentration and decrease of carrier mobility. An investigation was performed with the contact/sample size ratio varied from 5% to 18%; the measured free hole concentration (and mobility), from the same p-ZnSe epilayer, was increased (decreased) by 59% (27%). For the measurements employed throughout this study, the contact/sample size ratio was kept at around 3%. Despite the occurrence of carrier freeze-out and the corresponding increase of sample resistivity by more than three orders of magnitude as temperature was lowered from 295



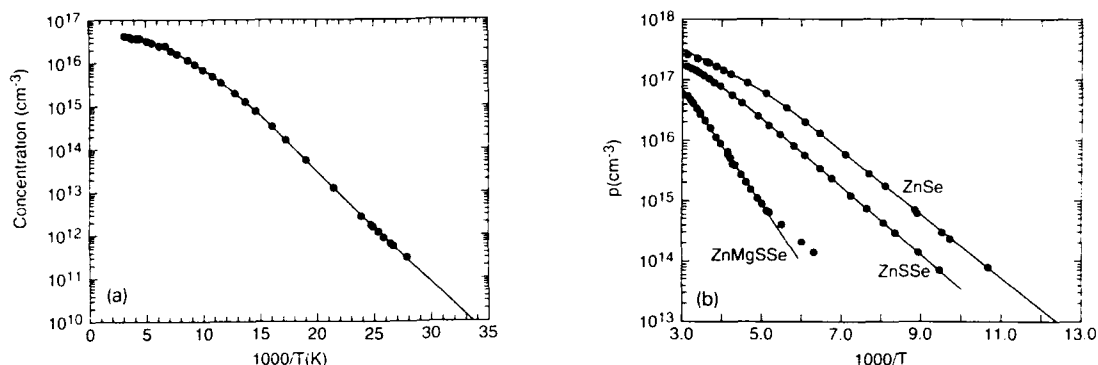


Fig. 2. (a) Temperature-dependent free hole concentration of nitrogen-doped ZnTe. (b) Measured free hole concentrations of nitrogen-doped ZnSe, ZnSSe, and ZnMgSSe. The difference in the activation energy is reflected by the different slopes of the freeze-out curves.

to 77 K, the  $I$ - $V$  linearity of the contacts was maintained [6].

### 3. Horizontal transport

Figs. 2a and 2b show the Arrhenius plot of measured free hole concentration as a function of  $1000/T$  for nitrogen doped ZnTe, ZnSe, Zn(S,Se) and (Zn,Mg)(S,Se). Least-squares curve fitting was carried out using the well-known equation

$$\frac{p(p + N_d)}{N_a - N_d - p} = \frac{N_v}{g \exp(-E_a/kT)},$$

which is essentially a rephrase of the charge-neutrality condition with non-degenerate carrier

statistics and the assumption of single acceptor level. Three fitting parameters, the total acceptor concentration  $N_a$ , the compensating donor concentration  $N_d$ , and the acceptor activation energy  $E_a$ , can be obtained from best curve-fitting. Given the uncertainty about the effective masses for the ternary and quaternary, the value of ZnSe was assumed throughout. The fitting parameters are summarized in Table 1.

In addition to the potential for application as a contacting material to p-ZnSe, nitrogen-doped ZnTe is also of scientific interest given the absence of any prior characterization of nitrogen acceptors in p-ZnTe. The activation energy of 46 meV at a doping level of mid- $10^{16}$  cm<sup>-3</sup>, which is perhaps the first report of nitrogen acceptor activation energy in ZnTe, is similar to the phospho-

Table 1  
Summary of temperature dependent Hall effect measurements

Sample	$p$ ( $\times 10^{17}$ cm <sup>-3</sup> )	$\mu_p$ (cm <sup>2</sup> /V·s)	$E_a$ (meV)	$N_a$ ( $\times 10^{17}$ cm <sup>-3</sup> )	$N_d$ ( $\times 10^{16}$ cm <sup>-3</sup> )	$N_d/N_a$
ZnTe	0.41 (295 K)	86.6 (295 K) 1302.0 (40 K)	46	0.49	0.75	0.15
ZnSe	2.20 (293 K)	34.3 (293 K) 147.1 (77 K)	92	9.54	10.1	0.11
ZnSSe	1.34 (293 K)	24.3 (293 K) 51.1 (106 K)	98	7.79	20.3	0.26
ZnMgSSe	0.35 (290 K)	11.6 (290 K) 14.4 (181 K)	177	16.3 <sup>a</sup>	16.4 <sup>a</sup>	0.10

<sup>a</sup> See text for explanation.

rus level in p-ZnTe (45 meV) [12]. Systematic Hall measurements on nitrogen-doped ZnSe epilayers with varying doping levels have been reported by the authors [6]; the linear dependence between the observed activation energies and the averaged ionized acceptor spacing, as well as the approximate consistency between the extrapolated activation energy at infinite dilution (114 meV) and the value (128 meV) from simple effective mass model, are consistent with the nitrogen acceptor behaving as a hydrogenic impurity in ZnSe.

We had previously reported that significantly higher free hole concentrations were obtained in ZnTe:N than ZnSe:N where both were grown under very similar growth conditions and with the same nitrogen flux [13]. The values of  $N_a$  for ZnSe and ZnTe were about  $9.5 \times 10^{17}$  and  $9 \times 10^{18} \text{ cm}^{-3}$  for particular samples from which we have recently obtained SIMS data. Of interest is that the measured N concentrations approximately tracked the acceptor concentrations at  $1 \times 10^{18} \text{ cm}^{-3}$  for ZnSe and  $8.8 \times 10^{18} \text{ cm}^{-3}$  for ZnTe. The implication of these measurements is that for the particular growth conditions and nitrogen plasma conditions, the limitation of p-doping level in ZnSe is not so much compensation limited as it is limited by the solubility of nitrogen acceptor [14].

In extending the study of horizontal transport into wider bandgap alloys such as  $\text{ZnS}_{0.08}\text{Se}_{0.92}$  and  $\text{Zn}_{0.93}\text{Mg}_{0.07}\text{S}_{0.14}\text{Se}_{0.86}$ , the differences in the temperature-dependence, i.e., the freeze-out behavior, become more noticeable as is revealed by the slopes of the lines in Fig. 2b. Given the lack of carrier (hole) saturation up to 320 K, the values of  $N_a$  and  $N_d$  for (Zn,Mg)(S,Se) may be somewhat higher than the real values. (The compensation ratio  $N_d/N_a$  is known, however.) Nevertheless, the activation energy of nitrogen in the (Zn,Mg)(S,Se) can be extracted from the linear region of the freeze-out curve to be 177 meV; this represents an increase of activation energy by about 80 meV in going from Zn(S,Se) to ZnMgSSe, a change which is not fully accounted for by the effective mass model assuming Vegard's law for most of the physical parameters. It is interesting to note that similar behavior, namely

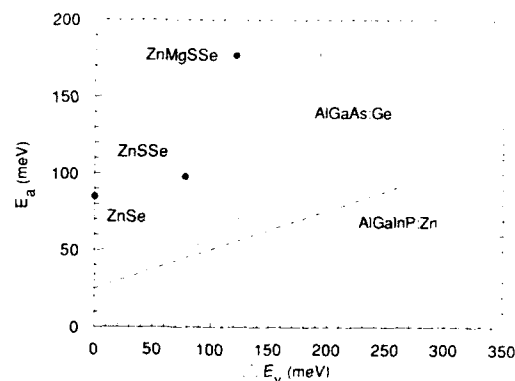


Fig. 3. Activation-energy versus valence band offset for Ge-doped AlGaAs [16], Zn-doped AlGaInP [15] (both in dashed lines), and N-doped ZnMgSSe (solid circles). Valence band edges of GaAs, GaInP, and ZnSe are used as reference points for the three material systems.

the rapid deepening of impurity levels toward wider-gap alloy compositions, has been observed in Zn-doped p-(Al,Ga)InP [15] and, more pronouncedly, in Ce-doped p-(Al,Ga)As [16]. The experimental data from the three material systems are compiled in Fig. 3 where the activation energies are plotted versus "valence band offset"; the valence band offsets were derived from alloy composition assuming conventional conduction/valence band offset ratios for the III-V compounds [17]. The valence band offset between ZnSe and ZnSSe was determined using Van de Walle's calculation [18] and an LCAO approach was chosen for the ZnMgSSe system [19]. Although the discrepancy between the observed  $E_a$  and the effective mass theory (which will be a very flat line on this scale) could well be due to the so-called "central cell correction" [20], further understanding of such corrections in mixed crystals is desirable to assert the physical origin of the observed behavior. Such a rapid increase of nitrogen activation energy in ZnMgSSe is worthy of concern given the implication of limited conductivity for the quaternary epilayers in the even bluer region.

As an additional elaboration on the freeze-out curve of the ZnMgSSe, one notices immediately a deviation of experimental data points from the

linear region when the temperature is below 160 K. Such phenomena could be attributed to the onset of impurity band conduction when the determination of free hole concentration from Hall coefficient, based on a single-band assumption, becomes ambiguous. Further examination on the above speculation using the conventional criterion, namely the comparison between the impurity Bohr radius and the average impurity spacing, revealed that the latter is still more than an order of magnitude larger than the former which makes the impurity-band model merely a remote possibility. An alternative explanation, which was provided in elucidating similar behavior in the Ge doping of AlGaAs [16], requires the presence of a second shallower acceptor level with a much lower concentration. The activation energy associated with this level can be determined from the slope of the  $\ln(pT^{-1.5})$  versus  $1/T$  plot to be about 88 meV.

#### 4. Vertical transport

The lack of high-quality conducting II–VI substrates has thus far constrained most of the ZnSe-based diode lasers and LEDs to closely lattice-matched GaAs substrates and/or epilayers. While the structural integrity was significantly advanced with the rigid control of alloy composition in achieving lattice compatibility, electrical transport across the n-ZnSe/n-GaAs heterovalent interfaces was presumed to play only a minor role in terms of the overall device  $I$ – $V$  characteristics. This seemingly plausible conjecture, based on the argument that the conduction band offset between ZnSe and GaAs is quite small [21], in fact overlooks the detrimental effect of carrier depletion near the heterovalent interface due to the presence of a high density of interface states.

Figs. 4a and 4b are the computer output of n-ZnSe/n-GaAs band diagrams with and without the presence of interface traps; the simulation program solves the Poisson and continuity equations using a drift-diffusion current model. Quantum mechanical tunneling and velocity saturation were not taken into account for the present ver-

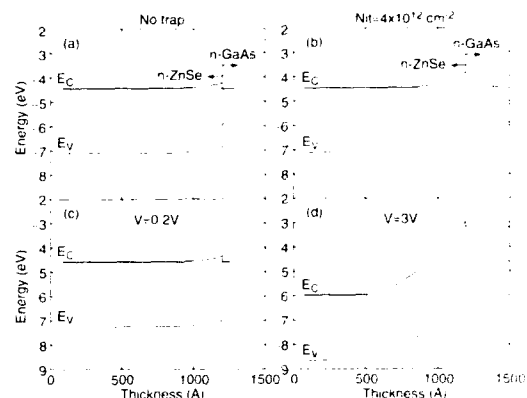


Fig. 4. Band diagrams of a ZnSe/GaAs heterointerface (i) under equilibrium without (a) and with (b) the presence of interface states, (ii) under high level injection without (c) and with (d) the presence of interface states. See text for details.

sion. Doping levels of ZnSe and GaAs were chosen to simulate the real device, a conduction band offset of 300 meV was used between ZnSe and GaAs, and an interface state density of  $4 \times 10^{12} \text{ cm}^{-2}$  was chosen from our previous studies of ZnSe/GaAs interfaces [22]. The extension of the depletion layer into p-ZnSe (in addition to the depletion region due to the band offset in Fig. 4a) is apparent in Fig. 4b. The hindrance to carrier transport is exacerbated under high level injection where, due to the sparseness of the carriers in the depletion region, a high electric field is essential to initiate an appreciable drift current component (Figs. 4c and 4d).

The width of the depletion region is intimately related to the doping concentration, and therefore can be reduced by employing of heavy doping near the ZnSe/GaAs interface. With the introduction of a 200 Å layer of n-ZnSe doped to  $2 \times 10^{18} \text{ cm}^{-3}$  (compared to the normal doping of  $5 \times 10^{17} \text{ cm}^{-3}$ ), we have indeed observed a reduction in the operating voltage of about 1.7 V at a current density of  $300 \text{ A/cm}^2$  from two typical (Zn,Mg)(S,Se) single quantum well lasers. In the context of a lasing threshold voltage as low as 7 V [5], such a reduction in terms of the device impedance is quite substantial. It is worth pointing out that the approach of using heavy doping is inevitably accompanied by a compromise in mate-

rial quality, which is particularly undesirable at the beginning of the epitaxial growth. To circumvent such a dilemma, an experiment based on our previous study [22] in controlling the stoichiometry of GaAs before the nucleation of ZnSe was performed. Two n-Zn(S,Se) epilayers of 1  $\mu\text{m}$  thick (samples A and B) were grown on thin layers of ZnSe, which were first nucleated on GaAs epilayers. The ZnSe layer of sample A, the reference sample, was nucleated on a c(4  $\times$  4) As-rich GaAs surface (this had been used for all of our laser structures). Doping levels of the ZnSe and Zn(S,Se) were  $2 \times 10^{18}$  and  $5 \times 10^{17}$   $\text{cm}^{-3}$ , respectively. On the other hand, the ZnSe of sample B was nucleated on the Ga-rich side of a (4  $\times$  6) GaAs surface [23], and a reduced level uniform doping of  $3 \times 10^{17}$   $\text{cm}^{-3}$  was employed throughout the II–VI layers; it was demonstrated by us that the nucleation of ZnSe on a Ga-rich GaAs surface could lead to a reduction of density of interface states by orders of magnitude compared to that nucleated on a As-rich GaAs surface. (A ZnSe layer of 500 Å with doping exceeding  $1 \times 10^{19}$   $\text{cm}^{-3}$  was grown as a top contacting layer for both samples.) The n-II–VI/n-GaAs structure studied here can be thought as one part of an actual laser device. Ti/Au was chosen to contact n-ZnSe [24], and a mesa etch was employed (etching down to the GaAs layer) to eliminate current spreading. It was shown that for an injection current density of 300 A/cm<sup>2</sup>, the operating voltage of sample B (1.7 V) is less than that of sample A (2.3 V) despite the fact that the doping was significantly lower in sample A.

## 5. Conclusions

Transport properties of ZnSe-based structures were characterized through the availability of the Zn(Te,Se) graded ohmic contact. The rapid increase of acceptor activation energy as a function of the bandgap of the ZnMgSSe indicated that the control and reduction of p-type conductivity might become an issue of primary concern as one tries to push the II–VI diode lasers into even shorter wavelength regime. We demonstrated the detrimental effect of interface states to the verti-

cal transport across the ZnSe/GaAs heterointerfaces. Two approaches were employed in addressing this problem: the use of a heavily doped ZnSe region near the interface to minimize the width of depletion region or alternatively, the control of GaAs stoichiometry prior to the nucleation of ZnSe to reduce the density of interface states.

## 6. Acknowledgments

The authors acknowledge the assistance from L.A. Kolodziejski at MIT and N.M. Johnson at Xerox for making the SIMS characterization available. We also acknowledge J.L. Gray in providing the simulation tools. This research is supported by ARPA/ONR URI grant 286-25043, AFOSR and Phillips Laboratory grant F49620-92-J-0440 and NSF/MRG grant 8913706-DMR, NSF grant 9202957-DMR and a gift from Hewlett Packard.

## 7. References

- [1] M.A. Haase, J. Qiu, J.M. DePuydt and H. Cheng, *Appl. Phys. Lett.* 59 (1991) 1273.
- [2] H. Jeon, J. Ding, W. Patterson, A.V. Nurmikko, W. Xie, D.C. Grillo, M. Kobayashi and R.L. Gunshor, *Appl. Phys. Lett.* 59 (1991) 3619.
- [3] N. Nakayama, S. Itoh, K. Nakano, H. Okuyama, M. Ozawa, A. Ishibashi, M. Ikeda and Y. Mori, *Electron. Letters* 29 (1993) 1488.
- [4] Y. Fan, J. Han, L. He, J. Saraie, R.L. Gunshor, M. Hagerott, H. Jeon, A.V. Nurmikko, G.C. Hua and N. Otsuka, *Appl. Phys. Lett.* 61 (1992) 3160.
- [5] A. Salokatve, H. Jeon, M. Hovinen, P. Kelkar, A.V. Nurmikko, D.C. Grillo, L. He, J. Han, Y. Fan, M. Ringle and R.L. Gunshor, 6th Int. Conf. on II–VI Compounds and Related Optoelectronic Materials, Newport, RI, Sept. 1993.
- [6] Y. Fan, J. Han, L. He, J. Saraie, R.L. Gunshor, M. Hagerott and A.V. Nurmikko, *Appl. Phys. Lett.* 63 (1993) 1812.
- [7] Y. Fan, J. Han, L. He, J. Saraie, R.L. Gunshor, M. Hagerott and A.V. Nurmikko, *J. Electron. Mater.*, in press.
- [8] W. Xie, D.C. Grillo, M. Kobayashi, R.L. Gunshor, G.C. Hua, N. Otsuka, H. Jeon, J. Ding and A.V. Nurmikko, *Appl. Phys. Lett.* 60 (1992) 463.
- [9] D.K. Schroder, *Semiconductor Material and Device Characterization* (Wiley, New York, 1990) p. 114.

- [10] M. Ozawa, F. Hiei, A. Ishibashi and K. Akimoto, *Electron. Lett.* 29 (1993) 503.
- [11] L.J. van der Pauw, *Philips Res. Rept.* 13 (1958) 1.
- [12] B.L. Crowder and W.N. Hammer, *Phys. Rev.* 150 (1966) 541.
- [13] J. Han, T.S. Starvinides, M. Kobayashi, R.L. Gunshor, M. Hagerott and A.V. Nurmikko, *Appl. Phys. Lett.* 62 (1993) 840.
- [14] D.B. Laks, C.G. Van de Walle, G.F. Neumark and S.T. Pantelides, *Appl. Phys. Lett.* 63 (1993) 1375.
- [15] M. Honda, M. Ikeda, Y. Mori, K. Kaneko and N. Watanabe, *Jap. J. Appl. Phys.* 24 (1985) L187.
- [16] A.W. Nelson and P.N. Robson, *J. Appl. Phys.* 54 (1983) 3965.
- [17] For AlGaAs, see H. Kroemer, *Surf. Sci.* 174 (1986) 299; For AlGaInP, see P.S. Zory, Jr., *Quantum Well Lasers* (Academic Press, San Diego, CA, 1993) p. 421.
- [18] C.G. Van de Walle, *Phys. Rev. B* 39 (1989) 1871.
- [19] H. Okuyama, Y. Morinaga and K. Akimoto, *J. Crystal Growth* 127 (1993) 335.
- [20] V. Swaminathan, J.L. Zilko, W.T. Tsang and W.R. Wagner, *J. Appl. Phys.* 53 (1982) 5163.
- [21] S.P. Kowalczyk, E.A. Kraut, J.R. Waldrop and R.W. Grant, *J. Vac. Sci. Technol.* 21 (1982) 482.
- [22] J. Qiu, Q.-D. Qian, R.L. Gunshor, M. Kobayashi, D.R. Menke, D. Li and N. Otsuka, *Appl. Phys. Lett.* 56 (1990) 1272.
- [23] Atomic layer epitaxy (ALE) was employed in the initial nucleation of ZnSe by alternative deposition of Se and Zn atoms while monitoring the recovery of RHEED intensity.
- [24] T. Miyajima, H. Okuyama and A. Akimoto, *Jap. J. Appl. Phys.* 31 (1992) L1743.

## The growth of HgSe by molecular beam epitaxy for ohmic contacts to p-ZnSe

S. Einfeldt \*, H. Heinke, M. Behringer, C.R. Becker, E. Kurtz, D. Hommel,  
G. Landwehr

*Physikalisches Institut der Universität Würzburg, Am Hubland, D-97074 Würzburg, Germany*

### Abstract

The structural properties of HgSe grown by molecular beam epitaxy (MBE) are investigated for different lattice mismatches to the substrate and various growth conditions. The growth rate is shown to depend strongly on the growth temperature above 100°C as well as on the Hg/Se flux ratio. It has been found that the crystalline perfection and the electrical properties are mainly determined by the layer thickness, especially for the growth on highly lattice mismatched substrates. Changes in the surface morphology are related to growth parameters. Differences between the electrical behavior of MBE-grown and bulk HgSe are discussed. The electrical properties of HgSe contacts on p-ZnSe are investigated as a function of different annealing procedures.

### 1. Introduction

The fabrication of low-resistance, ohmic contacts to p-ZnSe is still one of the major problems in the technology of blue and green light emitting devices based on ZnSe and related compounds. At present, gold is the most commonly used contact material which forms a Schottky contact with an offset of about 1.4 eV to the valence band of ZnSe. To obtain light emission, large voltages of 10–20 V are needed to break down the reverse biased Au/p-ZnSe junction in a forward biased diode device.

Recently Lansari et al. [1] produced nearly ohmic contacts to highly doped p-ZnSe by using HgSe. They observed smaller LED turn-on voltages of 2–3 V compared to that of gold as a

result of the lower valence band offset of 0.6–0.8 eV [2]. A p-type doped  $\text{Hg}_{1-x}\text{Zn}_x\text{Se}$  graded layer was predicted to further improve the diode properties [1,3].

The potential of HgSe as a contact to p-type ZnSe has lead to an increased interest in investigations of its MBE growth conditions. Until now very few publications concerning this matter have appeared in the literature [1,4]. In this article, characteristics of MBE growth of HgSe are presented and their influence on structural and electrical properties of the resulting epilayers are discussed.

### 2. Experimental details

Epitaxial growth was carried out in a Riber 2300 MBE system, equipped with a self-designed Hg effusion cell. The absolute Se flux was rou-

\* Corresponding author.

tinely calibrated by depositing Se on cold GaAs and Si substrates, assuming the Se sticking coefficient to be unity. HgSe was grown on (001) CdTe and (001) ZnTe substrates, which have a lattice mismatch of 6.1% and 0.27%, respectively. The substrates were chemo-mechanically polished with a solution of Br in methanol, degreased in standard solvents, etched with HCl, thermally cleaned in vacuum at 350°C (under Cd flux for the CdTe substrates) and overgrown with a homoepitaxial buffer layer. Nitrogen-doped, p-type ZnSe layers were grown on GaAs (001) substrates in a separate MBE growth chamber and transferred to the Hg chamber without breaking the ultrahigh vacuum (UHV).

The thickness of the HgSe epilayers on all samples was determined directly with a depth profiler by measuring the height of a step caused by a contact mask on the substrates. The electrical properties were determined using the Van der Pauw method for the Hall effect at 0.3 T. The data were analyzed with a one-charge carrier model. The crystalline quality of the epilayers was investigated by means of the (004) Bragg reflection in a high-resolution five-crystal X-ray diffractometer. Electrochemical  $C-I$  profiling was used to determine the carrier concentration in the ZnSe:N layers.

### 3. Results and discussion

The growth rate of HgSe depends strongly on the growth temperature, as shown in Fig. 1. This indicates a much higher desorption rate for HgSe than for HgTe whose growth rate remains nearly constant over the same temperature range [5]. The exponential fit indicated in Fig. 1 gives an activation energy for the desorption of only  $0.22 \pm 0.03$  eV. This value is lower than 0.51 and 0.52 eV, which are the congruent heats of sublimation for Hg(g) and Se<sub>8</sub>(g), respectively, in equilibrium with crystalline HgSe [6]. Heating HgSe in UHV shows that chemi-desorption is negligible for temperatures below 200°C. Therefore the observed decrease in the growth rate is related to the precursor state and not to the chemisorbed state. It should be mentioned that one is limited to

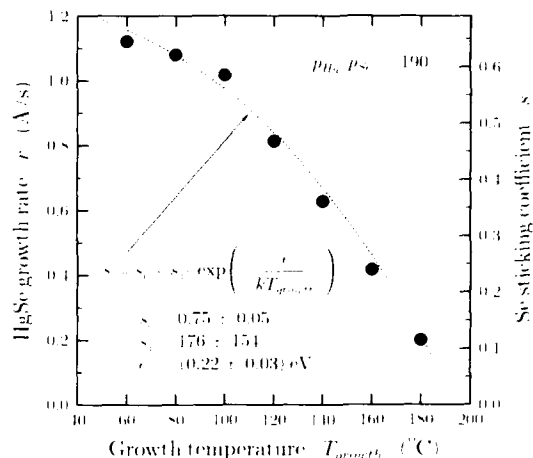


Fig. 1. The growth rate of HgSe and the Se sticking coefficient versus the growth temperature.

growth temperatures lower than 120°C for useful growth rates of HgSe.

In addition to its dependence on the growth temperature, the growth rate is also influenced by the Hg flux. Fig. 2 indicates the presence of distinctly different behavior of the growth rate for two ranges of Hg fluxes. The growth rate increases with increasing Hg/Se beam pressure

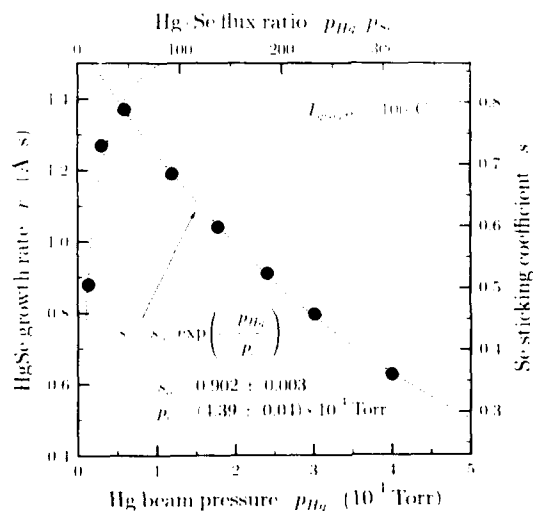


Fig. 2. The growth rate of HgSe and the Se sticking coefficient versus the Hg beam pressure and Hg/Se flux ratio.

ratio (in the following loosely referred to as flux ratio) as long as this ratio is lower than 50. This behavior is well known for the MBE growth of binary compounds AB (see, e.g., ref. [7]) and is indicative of growth under B-rich conditions, i.e. Se-rich conditions. This is the case in spite of the apparent excess of Hg, due to the extremely low Hg sticking coefficient. Polycrystalline growth occurs for Hg/Se flux ratios smaller than 20. For Hg/Se flux ratios higher than 50, the growth rate decreases exponentially, which might have several causes. A possible explanation is the prevention of the incorporation of Se into the crystal due to screening of the surface by a high surface concentration of Hg atoms in a physisorbed precursor state. Another mechanism could be the scattering of the  $\text{Se}_n$  ( $n = 6, 5, 7, \dots$ ) molecules by the high density of Hg atoms in the Hg beam. Recently, a similar but less obvious dependence on Hg flux was determined for the growth of HgTe by means of oscillations in the reflection of high-energy electron diffraction (RHEED) [5]. It is unclear at the present as to which mechanism (or combination of both) is responsible for the large decrease in HgSe growth rate.

The dependence of the growth rate on both the growth temperature and the Hg flux led us to study the structural properties of the HgSe layers as a function of their thickness in detail. Fig. 3 demonstrates that the crystalline quality of HgSe grown on highly lattice-mismatched CdTe depends strongly on the layer thickness. The best HgSe samples, i.e. thick layers, have rocking curves with a full width at half maximum (FWHM) down to 220 arc sec. The large dislocation density at the HgSe/CdTe interface becomes smaller with increasing thickness due to a healing process. The growth on nearly lattice-matched ZnTe provides partially strained layers which relax at a critical thickness  $d_c$  with subsequent generation of dislocations. This is clearly demonstrated by the maximum in Fig. 3 at  $d = 0.5 \mu\text{m}$ . Hence the critical thickness for HgSe on ZnTe must be smaller than  $0.5 \mu\text{m}$ , which is in fair agreement with the value of  $d_c = 0.25 \mu\text{m}$  obtained from the model of Matthews and Blakeslee [8]. Other models give values as small as 23 nm [9] or as large as  $2.4 \mu\text{m}$  [10].

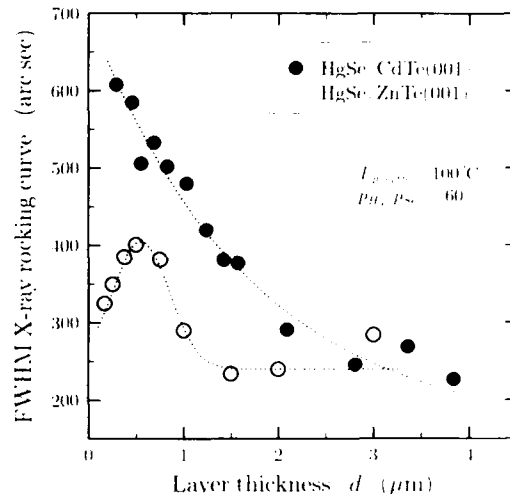


Fig. 3. Full width at half maximum (FWHM) of the (004) X-ray rocking curves versus the layer thickness of HgSe grown on CdTe and ZnTe.

The change of the crystalline quality with layer thickness is accompanied by a change in the electrical properties, as shown in Fig. 4 for the growth on CdTe. The mobility at 300 K is limited mainly by the crystal perfection which gets worse near the substrate interface. Moreover, the Hall data indicate that the higher dislocation density causes an increase in the carrier concentration.

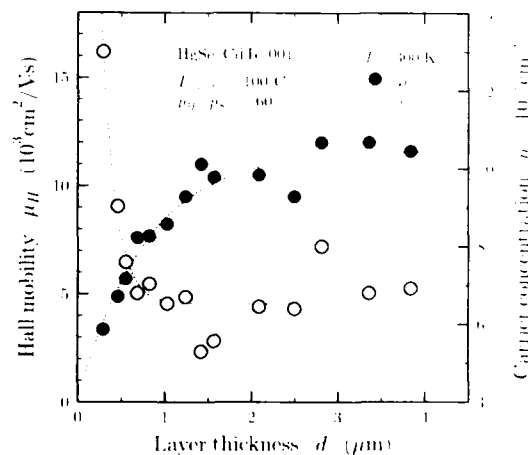


Fig. 4. Hall mobility and carrier concentration at 300 K versus layer thickness of HgSe grown on CdTe.



i.e. is related with the generation of donors. However, this is inconsistent with measurements of the interband absorption whose interpretation requires a nearly constant carrier concentration [11]. In the case of the MBE growth of HgSe on highly lattice-mismatched CdTe substrates, the dependence of the crystalline quality on the layer thickness is shown to be much stronger than its dependence on any growth parameter, i.e. growth temperature or Hg/Se flux ratio. Mobilities of the best, i.e. thick, epilayers range from  $12000 \text{ cm}^2/\text{V} \cdot \text{s}$  at 300 K to  $44000 \text{ cm}^2/\text{V} \cdot \text{s}$  at 20 K.

The surface of HgSe samples exhibits rectangular pyramidal hillocks similar to those observed on epitaxially grown (001) HgCdTe (see, e.g., ref. [12]). The density of these hillocks is  $6 \times 10^4$  to  $5 \times 10^5 \text{ cm}^{-2}$ . Furthermore, an additional "macroscopic" roughness was observed which depends on the growth parameters. Surface scans presented in Fig. 5 show a decrease in the roughness with decreasing growth temperature and increasing Hg/Se flux ratio. The surface roughening is possibly related to the Hg coverage of the growth

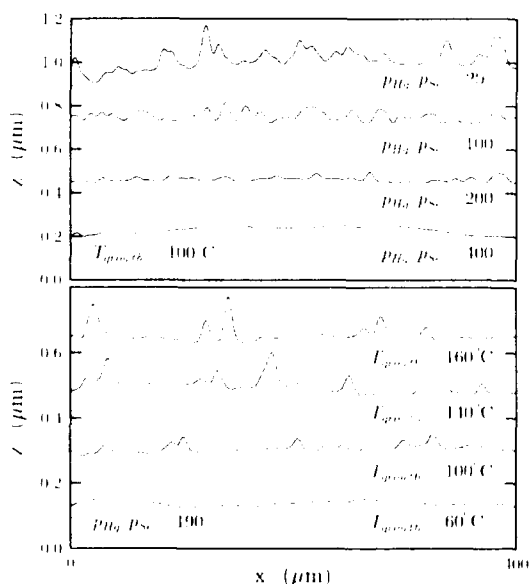


Fig. 5. Surface roughness of HgSe ( $d = 0.6 \mu\text{m}$ ) on CdTe for different growth temperatures and Hg/Se flux ratios.

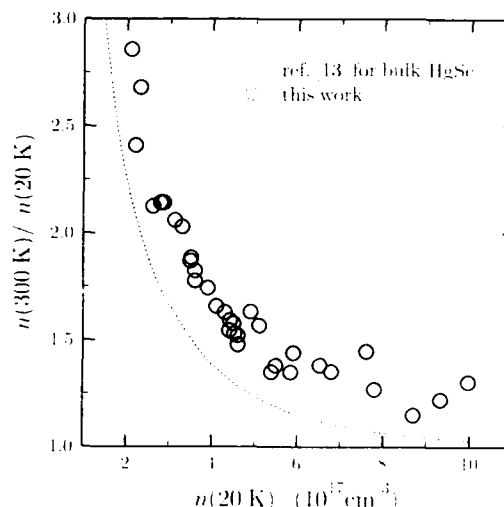


Fig. 6. Ratio of carrier concentrations at 300 and 20 K versus carrier concentration at 20 K.

surface, which decreases with higher temperatures and lower Hg fluxes.

Comparing the electrical data of our samples to bulk HgSe, we observe a stronger than expected decrease in the carrier concentration at lower temperatures, as shown in Fig. 6. The dashed line is the expected behavior, calculated using the method and parameters published for bulk HgSe [13]. Assuming that the band structure parameters are correct, the deviation for MBE grown HgSe can be explained by (1) postulating more than one type of charge carriers, (2) assuming a temperature dependence for the donor concentration, or (3) supposing different scattering mechanisms which would change the carrier concentration as calculated from the experimental Hall constant. At present none of these explanations could be shown to be the correct one.

In order to study the electrical properties of HgSe contacts on p-ZnSe, contact stripes ( $3.1 \text{ mm} \times 0.5 \text{ mm}$ ) of p-ZnSe ( $p = 4 \times 10^{17} \text{ cm}^{-3}$ ) with five equidistant mesas ( $0.1 \text{ mm} \times 0.5 \text{ mm}$ ) of HgSe(250 nm)/Ni(30 nm)/Au(220 nm) were fabricated using standard photolithographic, etching and lift-off techniques. Three- and four-point measurements provided the contact resistance and the resistivity of the p-ZnSe layer, respec-

tively. The samples were annealed in nitrogen atmosphere in order to produce a graded gap (HgSe–ZnSe) by Hg–Zn interdiffusion [14].  $I$ – $V$  curves measured between two HgSe contacts after annealing for different periods of time at 300°C are shown in Fig. 7. By extrapolating the linear part of the curve at high voltages to  $I = 0$ , typical voltage offsets of 1–2 V are obtained which are consistent with the values reported in ref. [1] for this hole concentration in p-ZnSe. Annealing the samples does not result in an ohmic behavior of the contacts, as has been shown for HgTe/p-CdTe contacts [15], but increases the total resistance as illustrated in Fig. 7. This is mainly due to an increase in the resistivity of the p-ZnSe layer during annealing, as determined by four-point measurements, see Fig. 8.  $C$ – $V$  measurements showed that the hole concentration in p-ZnSe decreased by annealing, but only in a 50 nm thick region near the surface by less than a factor of 4. Since this change in the hole concentration is too small to explain the increase in the resistivity, annealing seems to reduce the hole mobility. The physical background of this effect is not understood at present.

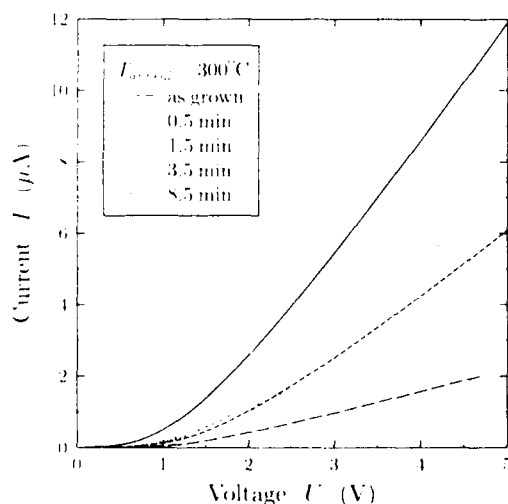


Fig. 7. Two-point measurements of current versus voltage for p-ZnSe with HgSe contacts after annealing at 300°C for different periods of time.

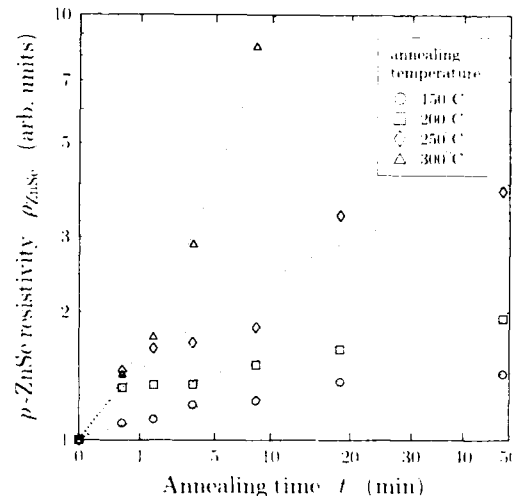


Fig. 8. Resistivity of a p-ZnSe layer determined by four-point measurements versus annealing time for different annealing temperatures.

The contact is not ohmic, as can be seen in the nonlinear  $I$ – $V$  curves of Fig. 7. However, the voltage drop across the contact as determined by three-point measurements was taken as a figure of merit for the contact. This value was reduced by 0.5 to 1.5 V upon annealing at temperatures up to 200°C. All experimental results lead to the conjecture that ohmic behavior of HgSe/p-ZnSe contacts cannot be obtained by annealing and that a graded gap between HgSe and p-ZnSe, which should display ohmic behavior, has to be grown by MBE.

#### 4. Conclusions

The influence of MBE growth parameters on the structural properties of HgSe was investigated. The growth rate was shown to depend on the growth temperature and the Hg/Se flux ratio. For the growth on highly lattice-mismatched substrates, the crystal perfection is determined mainly by the layer thickness and less by growth parameters. MBE-grown HgSe shows significant differences in electrical behavior compared to bulk HgSe. Electric contacts to p-ZnSe by means

of HgSe do not exhibit ohmic behavior after annealing, whereas the resistivity of annealed p-ZnSe increases significantly.

### 5. Acknowledgements

This work was supported by the Bundesministerium für Forschung und Technologie, Bonn, Germany. We would like to thank A. Schönteich for maintaining the MBE system, P. Wolf-Müller and T. Schuhmann for preparing the substrates and M. Koubek for fabricating the contacts.

### 6. References

- [1] Y. Lansari, J. Ren, B. Sneed, K.A. Bowers, J.W. Cook, Jr. and J.F. Schetzina, *Appl. Phys. Lett.* 61 (1992) 2554.
- [2] J.S. Best, J.O. McCaldin, T.C. McGill, C.A. Mead and J.B. Mooney, *Appl. Phys. Lett.* 29 (1976) 433.
- [3] Z. Yang and J.F. Schetzina, 1993 Electronic Materials Conf., Santa Barbara, CA, June 1993.
- [4] C.R. Becker, L. He, S. Einfeldt, Y.S. Wu, G. Léronde, H. Heinke, S. Oehling, R.N. Bicknell-Tassius and G. Landwehr, *J. Crystal Growth* 127 (1993) 331.
- [5] S. Oehling, Diploma Thesis, University of Würzburg (1993).
- [6] R.F. Brebrick, *J. Chem. Phys.* 43 (1965) 3846.
- [7] Th. Lit., Th. Behr, D. Hommel, A. Waag and G. Landwehr, *J. Appl. Phys.* 72 (1992) 3492.
- [8] J.W. Matthews and A.E. Blakeslee, *J. Crystal Growth* 27 (1974) 118.
- [9] J.H. Van der Merwe, *J. Appl. Phys.* 34 (1963) 123.
- [10] R. People and J.C. Bean, *Appl. Phys. Lett.* 47 (1985) 322.
- [11] S. Einfeldt, F. Goschenhofer, C.R. Becker and G. Landwehr, to be published.
- [12] A. Million, L. Di Cioccio, J.P. Gailliard and J. Piagnet, *J. Vac. Sci. Technol. A* 6 (1988) 2813.
- [13] S.L. Lehoczky, J.G. Broerman, D.A. Nelson and C.R. Whitsett, *Phys. Rev. B* 9 (1974) 1598.
- [14] V. Leute, H. Plate and H.M. Schmidtke, *Phys. Status Solidi (a)* 125 (1991) 217.
- [15] E. Janik and R. Triboulet, *J. Phys. D (Appl. Phys.)* 16 (1983) 2333.



ELSEVIER

Journal of Crystal Growth 138 (1994) 477–480

JOURNAL OF  
**CRYSTAL  
GROWTH**

## The hole diffusion length in epitaxial zinc selenide

Jiazhen Zheng, J.W. Allen \*

*Wolfson Institute of Luminescence, Department of Physics and Astronomy, University of St. Andrews, North Haugh,  
St. Andrews, Fife KY16 9SS, Scotland, UK*

### Abstract

Hole diffusion lengths were determined for two epitaxial n-type ZnSe layers by fitting the measured photoluminescence spectra to a theoretical expression which contains the measured absorption constants. The room temperature hole diffusion lengths are found to be 0.1 and 0.06  $\mu\text{m}$  for ZnSe with electron concentrations of  $1.6 \times 10^{17}$  and  $9.0 \times 10^{17} \text{ cm}^{-3}$ , respectively. These short diffusion lengths are attributed to a strong Hall–Shockley–Read recombination.

### 1. Introduction

Extensive studies have recently been carried out on the epitaxial growth and doping of ZnSe and related wide-band-gap II–VI compounds. As a result, room temperature blue ZnSe p–n junction light emitting diodes (LEDs) have been fabricated in experimental form and blue lasers containing ZnSe based quantum wells have been reported to work briefly at room temperature. At present, however, there are still many problems to be solved for further improvement of device performance. Other than the limit of maximum hole concentration attainable and the lack of very good ohmic contacts to p-type material, a major problem in ZnSe is that the radiative recombination efficiency of the blue emission at room tem-

perature under moderate excitation is low in samples which are currently available.

The minority carrier lifetime and diffusion length are of great importance for the performance of any minority-carrier solid-state device, since they govern the injection efficiency of the p–n junction and the radiative efficiency of the subsequent recombination. We have previously shown [1] that the decay time of the blue emission in metalorganic chemical vapour deposition (MOCVD) ZnSe epilayers is  $\sim 100$  ps, much shorter than that calculated for purely radiative transitions.

We report in this paper measurements of the hole diffusion length in n-type ZnSe samples which by present-day standards are good room temperature blue emitters. We used the method devised by Haynes and Nilsson [2] and used by them for Ge and subsequently used for GaAs by, for example, Hwang [3]. It is the reabsorption of the emitted radiation which enables us to determine the hole diffusion length from the measured optical absorption and photoluminescence.

\* Corresponding author.

## 2. Theory

Although the principles of the method employed are already known, we repeat here some salient points for completeness. In the photoluminescence measurements, the excitation light is absorbed near the sample surface within the absorption length of the light. The photo-produced minority carriers diffuse into the sample and recombine with the majority carriers within a depth determined by the diffusion length. The shape of the internal emission spectrum can be calculated from the measured absorption spectrum using detailed balance, as proposed by Van Roosbroeck and Shockley [4]. However, the external emission spectrum is modified by the reabsorption of radiative emission.

By taking into account the effect of reabsorption of emitted photons on the observed spectral response  $I(h\nu)$ , we can express the number of photons emerging from the crystal in unit time as

$$I(h\nu) d(h\nu) = A \int_0^{\infty} \Delta R e^{-\alpha(h\nu)x} dx, \quad (1)$$

where  $A$  is a proportional constant,  $\Delta R$  the net radiative recombination rate in the interval  $d(h\nu)$  and  $\alpha(h\nu)$  is the absorption constant of the radiative emission.

From the principle of detailed balance, Van Roosbroeck and Shockley [4] showed that the net radiative recombination rate, i.e. the difference between the total recombination rate and the thermal equilibrium value, for unit volume and an energy interval  $d(h\nu)$  is

$$\begin{aligned} \Delta R = & \left( \frac{1}{n_0} + \frac{1}{p_0} \right) \Delta p \frac{8\pi n_r^2}{h^3 c^2} (h\nu)^2 \alpha(h\nu) \\ & \times \exp\left(-\frac{h\nu}{kT}\right) d(h\nu), \end{aligned} \quad (2)$$

where  $n_r$  is the refractive index,  $n_0$  and  $p_0$  are the electron and hole concentrations in thermal equilibrium,  $\Delta p$  is the excess hole concentration and the other symbols have their usual meanings.

We assume that the electron-hole pair concentration created by the reabsorption of the radiative emission is small compared with that created by the external excitation. The concentra-

tion profile of the excess carriers near the surface is then determined by the minority carrier diffusion length  $L$ , the surface recombination velocity  $S$ , the diffusion constant  $D$ , and the absorption constant  $\alpha_0$  of the excitation light as follows

$$\begin{aligned} \Delta p(x) &= \frac{gL^2}{D} \frac{1}{1 - \alpha_0^2 L^2} \\ &\times \left[ \exp(-\alpha_0 x) - \frac{\alpha_0 + S/D}{L^{-1} + S/D} \exp\left(-\frac{x}{L}\right) \right], \end{aligned} \quad (3)$$

where  $x$  is the normal distance from the surface and  $g$  is the total generation rate of the electron-hole pairs by external excitation.

From Eqs. (1)–(3), the measured spectral response  $I(h\nu)$  is found to be

$$\begin{aligned} I(h\nu) = & A \left( \frac{1}{n_0} + \frac{1}{p_0} \right) \frac{8\pi n_r^2}{h^3 c^2} (h\nu)^2 \\ & \times \exp\left(-\frac{h\nu}{kT}\right) \frac{g}{D} \alpha(h\nu) \\ & \times \left[ \frac{S}{D} + \frac{1}{L} + \alpha_0 + \alpha(h\nu) \right] \\ & \times \left\{ \left( \frac{S}{D} + \frac{1}{L} \right) [\alpha_0 + \alpha(h\nu)] \left( \alpha_0 + \frac{1}{L} \right) \right. \\ & \left. \times \left[ \alpha(h\nu) + \frac{1}{L} \right] \right\}^{-1}. \end{aligned} \quad (4)$$

The quantities  $L$  and  $S/D$  can in principle be determined by fitting the measured  $I(h\nu)$  throughout the whole energy range to the right-hand side of Eq. (4) using the measured  $\alpha(h\nu)$ . The accuracy of this method depends on the uncertainty involved in the absorption measurements. Carrier trapping will not affect the result as this is a steady-state method.

## 3. Experiment

Epitaxial layers of ZnSe were grown on GaAs substrates at 280°C by MOCVD at UMIST.

Manchester. Carrier concentrations at room temperature were obtained from Hall effect measurements or capacitance–voltage characteristics. For photoluminescence measurements, a high-pressure mercury lamp with suitable filters was used as excitation light. The measured spectra were carefully corrected for the spectrometer and photomultiplier response.

The samples used in the absorption measurements were prepared in the following way. Some of the GaAs substrate was removed by mechanical grinding. Using a soft transparent wax, the sample was attached by the ZnSe face to a glass plate. The remaining GaAs was removed with a hydrogen peroxide–aqueous ammonia etch and the ZnSe was thinned using a bromine–methanol etch. Samples with thickness of 1.0 to 3.3  $\mu\text{m}$  were prepared in this way, where the layer thickness was determined from the interference fringes. A special sample holder containing holes with 500  $\mu\text{m}$  diameter in the centre of two parallel metal plates was used to block reflected light from reaching the detection system. The angle subtended by the sample at the monochromator entrance slit was kept small to minimize any photoluminescence being accepted. The absorption constants were calculated using a reflectivity of 0.2.

#### 4. Results and discussion

The photoluminescence spectra at room temperature for the two samples A and B are shown in Fig. 1. The room temperature electron concentration is  $1.6 \times 10^{17} \text{ cm}^{-3}$  for sample A and  $9.0 \times 10^{17} \text{ cm}^{-3}$  for sample B. As the doping increases, the half-width of the emission band becomes larger while the peak position remains the same until the doping exceeds  $2.0 \times 10^{18} \text{ cm}^{-3}$ . We have previously shown [5] that this blue emission is probably due to transitions between an electron on a donor and a free hole, although some contributions from band tailing states cannot be completely ruled out. This emission band spreads over an energy range where the absorption constant changes appreciably, and is thus suitable for use in determining the diffusion length.

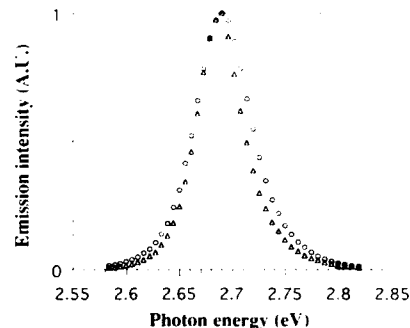


Fig. 1. The room temperature photoluminescence spectra of two n-type MOCVD ZnSe layers: ( $\Delta$ ) sample A and ( $\circ$ ) sample B. The two spectra are normalized to the same peak intensity.

Fig. 2 shows the absorption constant as a function of photon energy for samples A and B. Each absorption curve was obtained by two separate measurements on the same sample but of different thickness produced by bromine–methanol etching. The measured absorption constant is about  $4.7 \times 10^4 \text{ cm}^{-1}$  at a photon energy of 2.72 eV and increases slowly from 2.72 to 2.85 eV. This value is about a factor of 1.7 smaller than the absorption constant obtained by Adachi and Taguchi [6] on bulk ZnSe from spectroscopic ellipsometry, but is in close agreement with the value obtained by Peyghambarian et al. [7] on molecular beam epitaxial (MBE) ZnSe epilayers.

Using the measured absorption constants in Fig. 2, Eq. (4) was fitted to the measured emis-

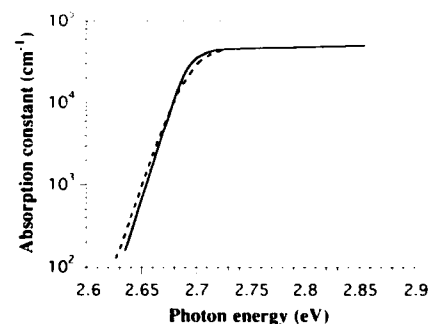


Fig. 2. The room temperature absorption constant for sample A (solid line) and sample B (broken line).

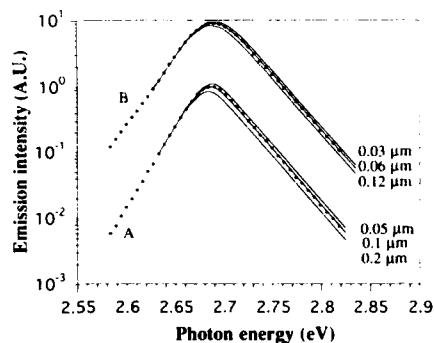


Fig. 3. Examples showing the best fit of the measured photoluminescence spectra to values calculated from Eq. (4) using three different diffusion lengths. The amplitudes for the two samples have been shifted for clarity.

sion spectra for each sample to determine  $L$  and  $S/D$ . The absorption constant  $\alpha_0$  at the excitation wavelength of 365 nm is chosen as  $9.0 \times 10^4 \text{ cm}^{-1}$ . This value is taken from the result of Adachi and Taguchi [6] and corrected for the difference factor of 1.7 between the two measurements. The fitting is not very sensitive to  $S/D$  as long as it is of the order of  $10^5 \text{ cm}^{-1}$ . Fig. 3 shows the fitting by choosing three different  $L$  values for each sample and a fixed value of  $2 \times 10^5 \text{ cm}^{-1}$  for  $S/D$ . The best fit gives the hole diffusion length of  $0.1 \text{ } \mu\text{m}$  for sample A and  $0.06 \text{ } \mu\text{m}$  for sample B. Our value of  $L$  is about a factor of three larger than that of bulk ZnSe with similar carrier concentration determined by Gautron and Lemasson [8] using a photoelectrochemical method.

The decay time  $\tau$  of the blue emission at room temperature has been measured previously for samples A and B to be 135 and 70 ps, respectively. From the measured  $L$  and  $\tau$ , the hole mobility  $\mu_p$  is calculated to be 30 and  $20 \text{ cm}^2$

$\text{V}^{-1} \text{ s}^{-1}$  for the two samples. These values are in the range of hole mobility reported [9] from electrical measurements of p-type ZnSe and they show the consistency of the decay time and diffusion length experiments.

## 5. Conclusion

The hole diffusion length at room temperature was determined for two MOCVD epitaxial ZnSe layers. The small hole diffusion length is consistent with our previous measurement of the short decay time of the blue emission and confirms that there is very strong recombination, implying that the concentration of Hall–Shockley–Read recombination centres is high. Thus improvement in ZnSe as a blue emitter requires control of the deep level recombination centres, as was the case in the early days of GaAs and InP.

## 6. References

- [1] Jiazhen Zheng, J.W. Allen, D.E. Spence, W.E. Sleat and W. Sibbett, *Appl. Phys. Lett.* 62 (1993) 63.
- [2] J.R. Haynes and N.G. Nilsson, Radiative recombination in Semiconductors, in: *Proc. 7th Int. Conf. on Physics of Semiconductors*, Paris, 1964 (Dunod, Paris) p. 27.
- [3] C.J. Hwang, *J. Appl. Phys.* 40 (1969) 3731.
- [4] W. van Roosbroeck and W. Shockley, *Phys. Rev.* 94 (1954) 1558.
- [5] Jiazhen Zheng and J.W. Allen, *J. Appl. Phys.* 67 (1990) 2060.
- [6] S. Adachi and T. Taguchi, *Phys. Rev. B* 43 (1991) 9569.
- [7] N. Peyghambarian, S.H. Park, S.W. Kock, A. Jeffery, J.E. Potts and H. Cheng, *Appl. Phys. Lett.* 52 (1988) 182.
- [8] J. Gautron and P. Lemasson, *J. Crystal Growth* 59 (1982) 332.
- [9] Z. Yang, K.A. Bowers, J. Ren, Y. Lansari, J.W. Cook, Jr. and J.F. Schetzina, *Appl. Phys. Lett.* 61 (1992) 2671.



ELSEVIER

Journal of Crystal Growth 138 (1994) 481–485

JOURNAL OF  
**CRYSTAL  
GROWTH**

## Mesoscopic phenomena in a dilute magnetic semiconductor $\text{Hg}_{1-x-y}\text{Cd}_y\text{Mn}_x\text{Te}$

G. Grabecki <sup>\*,a</sup>, T. Dietl <sup>a</sup>, W. Plesiewicz <sup>a</sup>, A. Lenard <sup>a</sup>, T. Skośkiewicz <sup>a</sup>,  
E. Kamińska <sup>b</sup>, A. Piotrowska <sup>b</sup>

<sup>a</sup> Institute of Physics, Polish Academy of Sciences, Al. Lotników 32 / 46, PL 02-668 Warszawa, Poland

<sup>b</sup> Institute of Electron Technology, Al. Lotników 32 / 46, PL 02-668 Warszawa, Poland

### Abstract

Microscopic four-contact probes to inversion layers adjacent to grain-boundaries of semimagnetic  $\text{HgCdMnTe}$  have been photolithographically patterned. Magnetoresistance measurements performed on these structures revealed aperiodic conductance fluctuations of the magnitude of the order of  $e^2/h$ . Analysis of both fluctuation amplitude and their mean period indicated that the studied system was in mesoscopic regime. Additionally, strongly nonlinear current–voltage characteristics were detected in the vicinity of the spin-glass freezing occurring at  $T = 100$  mK.

### 1. Introduction

It has recently been demonstrated that when the linear size of the conductor  $L$  becomes smaller than the phase breaking length  $L_\phi$ , quantum interference of scattered waves gives rise to random but reproducible fluctuations of the band conductance as a function of external parameters such as the magnetic field. Experimental studies [1], in agreement with theoretical predictions [2], show that in this mesoscopic regime the mean amplitude of the fluctuations is of the order of  $e^2/h$ , independent of material properties. Accordingly, the phenomenon is known under the name of universal conductance fluctuations

(UCF). At the same time, the fluctuation *pattern* turns out to be extremely sensitive to actual distribution of scattering potential in a given sample. Since in magnetic materials, because of spin fluctuations, scattering potential associated with localized spins varies in time, experimental studies of UCF and of related quantum phenomena in such systems may serve as a valuable tool for probing complex dynamics of disordered magnetic moments. In particular, one can study signatures of transition to the spin-glass phase [3].

We have undertaken millikelvin magnetotransport studies of microstructures with active layers containing diluted magnetic semiconductors in the form of IV–VI epilayers or II–VI bicrystals [4]. Previous transport studies of II–VI bicrystals, particularly of narrow-gap  $\text{Hg}_{1-x}\text{Mn}_x\text{Te}$  [5],  $\text{Hg}_{1-x-y}\text{Cd}_y\text{Mn}_x\text{Te}$  [6], and  $\text{Hg}_{1-x}\text{Cd}_x\text{Te}$  [7], showed that defects associated with the grain-

\* Corresponding author.



boundary plane had a donor character, and thus, in p-type bulk material, gave rise to the formation of an inversion layer with typical electron concentration  $n_s \approx 10^{12} \text{ cm}^{-2}$ . These electrons reside in a potential well of an average width 150 Å, occupy 3 to 4 electric subbands, and possess mobility as large as  $5 \times 10^4 \text{ cm}^2/\text{V} \cdot \text{s}$ , making observation of the low-field Shubnikov–de Haas oscillations and quantum Hall effect possible [6].

We discuss here a simple method suitable for examining mesoscopic properties of electrons accumulated in the grain-boundary plane, and we present the application of this method for search of spin-glass effects in  $\text{Hg}_{0.79}\text{Cd}_{0.19}\text{Mn}_{0.02}\text{Te}$ .

## 2. Samples and experimental methods

Ingots of  $\text{Hg}_{1-x}\text{Cd}_x\text{Mn}_y\text{Te}$  were grown by the solid-state recrystallization method with controlled mercury pressure, adjusted to give a high-resistance p-type material. The actual values of  $x$  and  $y$  were checked by means of electron microprobe, and found to be by about 0.5% smaller than the nominal values  $x = 0.02$  and  $y = 0.19$ . Optical transmission measurements pointed to an energy gap of about 0.18 eV at 4.2 K, a value consistent with the alloy composition. According to our AC magnetic susceptibility measurements, the spin-glass freezing occurs at  $T_f = 100 \text{ mK}$ , where inelastic and dephasing processes should be dominated by an electron coupling to Mn spins.

The ingots grown in the above way consist usually of several differently oriented single-crystalline grains of typical diameter 5–10 mm. The samples studied in the present work were prepared in the form of slabs about 0.5 mm thick, having the grain-boundary plane, i.e. the conducting layer, *perpendicular* to their surfaces. Our method of probing the conductance of a microregion is based upon the local character of the four-probe method [8]. Thus, the conducting layer was connected to the measuring circuit by four gold microcontacts, patterned by a standard 4  $\mu\text{m}$  photolithography and lift-off method, as shown in Fig. 1. Such contacts have linear current–voltage characteristics, which are tempera-



Fig. 1. Photograph of  $\text{HgCdMnTe}$  bicrystal sample with photolithographically patterned contacts. The distance between the probes is 15  $\mu\text{m}$ .

ture-independent below 10 K, and correspond to a resistance of 300 to 600  $\Omega$ . The four-terminal resistance of the studied samples is smaller, typically it amounts to 100  $\Omega$ . By placing the microcontacts in the single-crystalline region, we checked the absence of surface conductivity between the probes.

Our magnetotransport studies were carried out in a 20 mK dilution refrigerator equipped with a 9 T superconducting coil. Magnetoresistance measurements were performed by driving an AC current through either external or internal probes, and collecting the generated voltage in a phase-sensitive fashion by the two remaining probes. In order to measure the Hall effect, the current was driven between one external and one internal probe. Because of the extreme sensitivity of mesoscopic phenomena to external perturbations, careful shielding and filtering were employed. Moreover, neither measuring and nor data-acquisition equipment contained digital components.

### 3. Results and discussion

Fig. 2 shows magnetoresistance and Hall resistance in the regime of the quantum Hall effect for a mesoscopic sample prepared in the way described above, compared to results of the same measurements for a macroscopic Hall bar. The data are quite similar, except for irregular but perfectly reproducible resistance fluctuations visible in the case of the microstructure. The mean square root of the conductance fluctuations increases from  $0.25e^2/h$  for  $B < 1$  T to  $2.5e^2/h$  at  $B \approx 5$  T. At the same time, the width of the distribution characterizing fluctuation periods in-

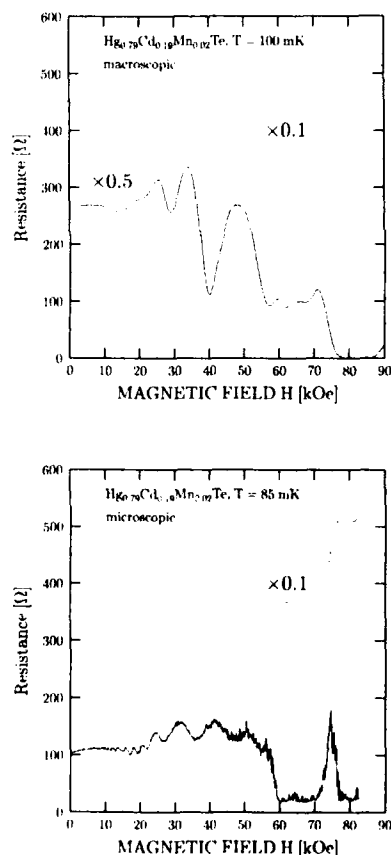


Fig. 2. Low-temperature magnetoresistance and Hall resistance for HgCdMnTe bicrystal with macro- and microcontacts.

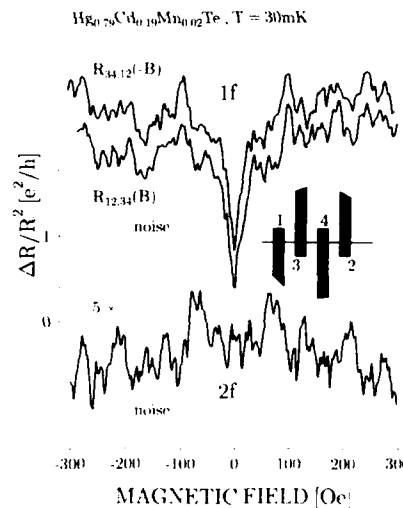


Fig. 3. Voltage changes (normalized to the current amplitude) as a function of the magnetic field measured in a four-microcontact arrangement at the fundamental and second harmonic of the excitation current (100 and 300 nA, respectively; sample resistance  $R = 100 \Omega$ ).

creases with the field. This indicates that the sizes of the regions enclosed by interfering electron wavefunctions shrink with the magnetic field. A similar effect was observed by Timp et al. [9] in quantum wires patterned from GaAs–AlGaAs heterostructures, and interpreted in terms of the magnetic-field-induced decrease of the width of the distribution of electron trajectories across the sample, an effect specific to the quantum Hall regime. However, in our case, we observed also the UCF amplitude to increase with the magnetic field, which remains unexplained.

Turning to the low-field region, we see in Fig. 3 that in addition to UCF, the data reveal a positive magnetoresistance. As already discussed elsewhere [4], such a weak-field magnetoresistance is caused by the influence of the vector potential on interference associated with self-intersecting trajectories. For a small value of the disorder involved ( $k_F l \approx 100$ , where  $k_F$  is the Fermi wavevector and  $l$  the mean free path for elastic scattering), the positive magnetoresistance implies that the dominant spin-dependent scat-

tering is caused by the spin-orbit coupling, as could be expected for a narrow-gap semiconductor [4]. On the other hand, spin-disorder scattering appears to be the main phase breaking mechanism. It leads to a saturation of the magnitude of the magnetoresistance below 600 mK, as well as to a saturation of the amplitude of the fluctuations below 200 mK, the temperature at which the phase breaking length  $L_\phi \approx 2.5 \mu\text{m}$  becomes shorter than the thermal length  $L_T = (\hbar D / k_B T)^{1/2}$ . This interpretation is further confirmed by the temperature decay of the UCF amplitude, which between 0.2 and 5 K can be described by the function  $T^{-0.55 \pm 0.10}$ .

In the case of the magnetoresistance, the dephasing effect of Mn spins is associated with noncommutation of spin rotations corresponding to electron motion in the opposite directions along the same self-intersecting paths [10]. In contrast, the apparent amplitude of the fluctuations is diminished by Mn spins if the average time between their flips  $\tau_f$  is shorter than the time constant of the resistance meter [11]. We conclude that for most Mn spins  $\tau_f \leq 1$  s, even in the spin-glass phase, as below  $T_f$  we found thermal and temporal stability of the fluctuation pattern. A relatively short time scale of the spin fluctuations explains also a surprising fulfilment of the modified Onsager symmetry relations  $R_{a,b}(B) = R_{a,b}(-B)$ , where a and b refer to the pair of current and voltage probes, respectively, as shown in Fig. 3.

In addition to the weak-localization magnetoresistance and universal conductance fluctuations discussed above, we found strongly nonlinear current-voltage characteristics, detected via the presence of a signal at the second harmonic of the frequency of the driving current. As shown in Fig. 3, this signal exhibits aperiodic fluctuations as a function of the magnetic field, but to a large extent is symmetric around  $B = 0$ , a property important when assessing the microscopic origin of second harmonic generation [12]. Similarly to the case of GaAs/AlGaAs microstructures [13], its magnitude shows first a square and then a linear dependence on the current, varied in our measurements from 30 nA to  $1 \mu\text{A}$ . A strongly non-ohmic behavior of mesoscopic con-

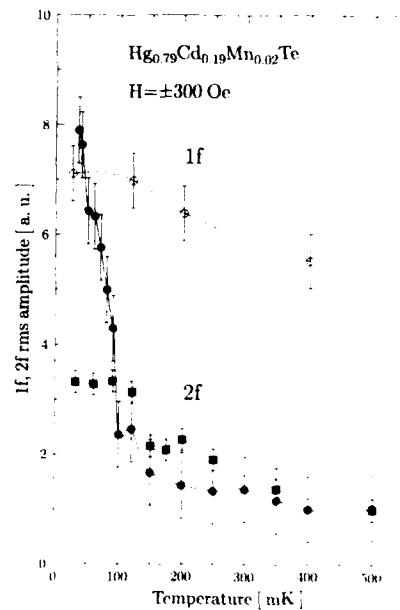


Fig. 4. Temperature dependence of the fluctuation amplitude at the second harmonic for two measurements separated by heating to 300 K (solid symbols). The open symbols show data at the fundamental frequency.

ductors may also be responsible for breakdown of the Onsager relations in some experiments [4,14]. Furthermore, in contrast to the signal at the fundamental frequency, the signal at the second harmonics changes strongly below 200 mK, as depicted in Fig. 4. In spite of some discrepancies between two measurements, perhaps because of perturbation effects of high frequency noise, it is tempting to speculate that the low-temperature increase of the signal is caused by the spin-glass freezing. In particular we take our data as an experimental indication for the dependence of the current-voltage characteristics upon the inelastic processes. This would open doors for quantitative studies of such processes, particularly in various magnetic phases.

#### 4. Acknowledgments

We are indebted to A. Mycielski and B. Witkowska for growing the crystals, and to S.

Washburn for valuable correspondence. This work was supported in part by KBN grant No. 2 0466 91 01.

## 5. References

- [1] S. Washburn and R. Webb, *Adv. Phys.* 35 (1986) 412;  
C.W.J. Beenakker and H. van Houten, *Solid State Phys.* 44 (1991) 1.
- [2] B.L. Al'tshuler and B.I. Skhlowskii, *Zh. Eksp. Teor. Fiz.* 91 (1986) 220;  
P.A. Lee, A.D. Stone and H. Fukuyama, *Phys. Rev. B* 35 (1987) 1039.
- [3] B.L. Al'tshuler and B.Z. Spivak, *Pis'ma Zh. Eksp. Teor. Fiz.* 42 (1985) 363;  
S. Feng, A.J. Bray, P. Lee and M.A. Moore, *Phys. Rev. B* 36 (1987) 5624;  
M. Cieplak, B. Bulka and T. Dietl, *Phys. Rev. B* 44 (1991) 12337.
- [4] G. Grabecki, J. Jaroszyński, A. Lenard, W. Plesiewicz, T. Skośkiewicz, T. Dietl, E. Kamińska, A. Piotrowska, G. Springholz and G. Bauer, in: *Proc. 21st Int. Conf. on the Physics of Semiconductors*, Beijing, 1992 (World Scientific, Singapore, 1992) p. 1407;
- T. Dietl, G. Grabecki and J. Jaroszyński, *Semicond. Sci. Technol.* 8 (1993) S141.
- [5] G. Grabecki, T. Dietl, P. Sobkowicz, J. Kossut and W. Zawadzki, *Appl. Phys. Lett.* 45 (1984) 1214.
- [6] T. Suski, P. Wiśniewski, L. Dmowski, G. Grabecki and T. Dietl, *J. Appl. Phys.* 65 (1989) 1203;  
G. Grabecki, A. Wittlin, T. Dietl, P.A.A. Teunissen, S.A.J. Wiegiers and J.A.A.J. Perenboom, *Semicond. Sci. Technol.* 8 (1993) S95.
- [7] W. Kraak, J. Kaldasch, P. Gille, Th. Shurig and R. Herrmann, *Superlattices Microstruct.* 9 (1991) 471.
- [8] L.J. van der Pauw, *Philips Res. Rept.* 13 (1958) 9.
- [9] G. Timp, A.M. Chang, P. Mankiewich, R. Behringer, J.E. Cunningham, T.Y. Chang and R.E. Howard, *Phys. Rev. Lett.* 59 (1987) 732.
- [10] See, e.g., G. Bergmann, *Phys. Rept.* 107 (1984) 1.
- [11] V.I. Fal'ko, *J. Phys. (Condens. Matter)* 4 (1992) 3943.
- [12] P.G.N. de Vegvar, *Phys. Rev. Lett.* 70 (1993) 837.
- [13] P.G.N. de Vegvar, G. Timp, P.M. Mankiewich, J.E. Cunningham, R. Behringer and R.E. Howard, *Phys. Rev. B* 38 (1988) 4326;  
see also S. Washburn and R.A. Webb, *Rept. Progr. Phys.* 55 (1992) 1311.
- [14] P.G.N. de Vegvar, L.P. Levy and T.A. Fulton, *Phys. Rev. Lett.* 66 (1991) 2380.



ELSEVIER

Journal of Crystal Growth 138 (1994) 486–492

JOURNAL OF **CRYSTAL  
GROWTH**

## A prediction of the electron mobility in medium gap HgCdTe and HgZnTe solid solutions

R. Granger <sup>\*</sup>, C.M. Pelletier

*Laboratoire de Physique des Solides, URA 786 au CNRS, INSA, BP 144, F-35043 Rennes Cedex, France*

### Abstract

Electron mobility in mercury cadmium telluride and mercury zinc telluride is computed by an iterative method. Polar optical scattering takes into account the Fröhlich interaction with the two vibration modes. Acoustic, alloy and charge centre scattering are also introduced. Calculated mobility values agree with known experimental results for  $\text{Hg}_{1-x}\text{Cd}_x\text{Te}$ , but are mostly predictive for  $\text{Hg}_{1-x}\text{Zn}_x\text{Te}$ .

### 1. Introduction

The electron mobility  $\mu$  has been measured and calculated extensively in  $\text{Hg}_{1-x}\text{Cd}_x\text{Te}$  (MCT  $x$ ) for  $x < 0.25$ , due to its importance for infrared detection, and also in the semimetal domain ( $x < 0.17$ ) [1]. More recently, experimental results on  $\mu$  in  $\text{Hg}_{1-x}\text{Zn}_x\text{Te}$  (MZT  $x$ ) have appeared [2], but there has been considerably less work devoted to these new solid solutions. Values of  $\mu$  in Hg-rich MCT and MZT have been calculated using iterative [3,4] or variational methods [5,6]. Calculations appear to be in good agreement with known experimental results, although a real comparison appears critical, as  $\mu$  is very sensitive not only to the actual density of defects which is discussed in refs. [4] and [6], but also to the composition homogeneity and its measurement precision [4]. However, the comparisons cited be-

fore show clearly that calculations where the non-elastic behaviour of scattering by optical phonon is considered can give actual values of the drift mobility when all the efficient scattering mechanisms which have to be taken into account are well characterized and the values of the necessary parameters precisely known: this situation is in fact verified exceptionally.

MZT appears as a promising material for photon emission in the near infrared [7], but also MCT in heterostructures [8]. The knowledge of transport properties of carriers in these medium gap semiconductors is of great importance for the modelling of device characteristics.

This paper presents results on  $\mu$  between 4 and 350 K on MCT  $x$  (for  $0.8 > x > 0.2$ ) and in MZT (for  $0.6 > x > 0.15$ ), using an iterative method to solve the Boltzmann equation and describing optical vibrations with a two-mode model. The parameters necessary to describe the most efficient scattering mechanisms are now known with enough precision in MCT to give

<sup>\*</sup> Corresponding author.

reliable results. In MZT the band structure is not so well known, but the evaluation of unknown constants is in fact based on the same assumptions used for MCT and appears generally realistic. The results of  $\mu$  are compared to the few experimental results which are known for MCT. The calculated values of  $\mu$  for MZT are purely predictive as no n-type MZT has been obtained for  $x > 0.2$ ; in these mixed crystals the p-type character of ZnTe seems to dominate already at low Zn content [9]. For low  $x$ , MCT and MZT of the same gap have mobility values which are very near [4,6]; this has led to the choice of composition values in both ternaries so that their gap was nearly the same. The presentation of  $\mu$  results is limited to the composition  $x = 0.8$  in MCT (and the composition of same gap in MZT). Only global results are given for the compositions studied and a detailed study of the different dispersion mechanisms is presented for MCT 0.5 where the alloy dispersion reaches its maximum.

## 2. Outline of the calculation and scattering parameters evaluation

The iterative method has been clearly described in several books to which the reader is referred [10,11]. The structure of the conduction band in these compounds is assumed to be spherical and is described with the usual three-band relation:

$$E'(E' + E_G)(E' + E_G + \Delta) = k^2 P^2 (E' + E_G + \frac{2}{3}\Delta), \quad (1)$$

where  $k$  is the electron wave vector,  $E' = E + \hbar^2 k^2 / 2m_0$ ,  $E$  being the electron state energy referred to the bottom of the conduction band,  $m_0$  is the free electron mass,  $E_G$  is the energy gap,  $\Delta$  the spin-orbit splitting energy and  $P$  the Kane matrix element.

In this study  $E_G$  is lower but comparable to  $\Delta$  which needs the use of the three-band model. The main variable of the calculation is  $E$ . From each  $E$  the corresponding  $k$  value is deduced from (1) by a numerical calculation starting from  $E = 0$ ; this calculation gives the  $k(E)$  relation with a precision better than  $10^{-6}$ ;  $E'$  is then deduced.

The coefficients of the corresponding wave function,

$$|k\rangle = ia_k |S\rangle \uparrow + \frac{b_k}{\sqrt{2}} |X + iY\rangle \downarrow + c_k |Z\rangle \uparrow,$$

are simply given by [12]:

$$a_k = kP(E' + E_G + \frac{2}{3}\Delta)D^{-1}, \quad b_k = \frac{1}{3}\sqrt{2}\Delta E'D^{-1},$$

$$c_k = E'(E' + E_G + \frac{2}{3}\Delta)D^{-1}, \quad (2)$$

where  $D$  is the normalizing factor so that  $a_k^2 + b_k^2 + c_k^2 = 1$ . The matrix element for the interaction of an electron with the different dispersive excitations can then be calculated using the expressions given in the text books like in ref. [11].

The iterative calculation takes into account the inelastic behaviour of the interaction with optical phonons, which is important at high temperatures. Moreover, in the mixed crystal considered two optical modes are present, one of HgTe type and the other of CdTe (or ZnTe) type. An electron interacts with the polarization field of these

Table 1

Optical  $\epsilon_z$  and static  $\epsilon_s$  dielectric constants, longitudinal  $\omega_L$  and transverse  $\omega_T$  frequencies of each of the optical modes in HgCdTe and HgZnTe for several composition values from refs. [15] and [16] for MCT and from ref. [17] for MZT

	$\epsilon_z$	$\epsilon_s$	$\omega_{TH}$ (cm <sup>-1</sup> )	$\omega_{LH}$ (cm <sup>-1</sup> )	$\omega_{TC}$ or $\omega_{TZ}$ (cm <sup>-1</sup> )	$\omega_{LC}$ or $\omega_{LZ}$ (cm <sup>-1</sup> )
MCT 0.300	11.6	16.4	121	136	149	157
MZT 0.197	12.6	18.4	123	139	171	182
MCT 0.400	11.0	15.6	123	135	147	159
MZT 0.272	11.8	17.4	125	140	171	187
MCT 0.500	10.2	14.5	124	134	146	161
MZT 0.348	11.0	16.4	127	140	172	191

modes of low wave vector, so that the Fröhlich interaction can be easily written [13,14]. The analytic expressions of the matrix element for the emission and absorption of each of the optical modes are written and more deeply discussed in ref. [4]. Their variation with composition, which is also given in ref. [4], shows that the interaction with the high-frequency mode (CdTe or ZnTe type) is enhanced when that for the low frequency one is weakened. The longitudinal and transverse frequency values for each mode and the optical ( $\epsilon_x$ ) and static ( $\epsilon_0$ ) dielectric constants have been taken from refs. [15] and [16] for MCT and from ref. [17] for MZT ternaries. Their values are given in Table 1.

The other interactions which are mainly elastic are added. The interaction with the acoustic modes remains comparatively weak; it leads to a decrease of  $\mu$  which is maximum near 80 K where it corresponds to less than 4% of the total  $\mu$ . Parameter values necessary for  $\mu$  calculation are interpolated between those of the end binaries, which are given in Table 2. We verify that taking the value of the deformation potential constant and equal to 4 eV does not alter the results.

The alloy scattering is treated in the virtual crystal approximation (VCA) which seems to describe well the mixed crystal behaviour of these ternaries, at least for MCT [19]. Moreover, it has the best of the simplicity, as the necessary parameters to describe this scattering are deduced from the offsets of the conduction band (for  $V$ ), the valence band (for  $W$ ) and the spin-orbit splitted

band (for  $\delta$ ) of the end binaries which have been experimentally measured. The expression for the corresponding relaxation time is the same as (26) of ref. [20] which is greatly simplified taking  $\delta = 0$ , as the spin-orbit splitting  $\Delta$  remains nearly the same in the three binaries, as seen in Table 2. The VCA probably does not apply so well to MZT, as the energy of the valence band extremum does not vary linearly with  $x$  [22] as it does in MCT [23]. The value of the potential well height used in the alloy scattering has been discussed by several authors in refs. [6] and [8] for MCT. Alloy scattering can be more generally described by the short range scattering with wells of which the depth and size modelize the actual clustering in the cation sublattice. However, the statistics in the clustering are not known and depend on sample growth. The reasonable assumption of a disordered lattice leads to the use of the VCA approximation [19].

The charged centre scattering is described in the Brooks-Herring approximation; it overestimates the scattering probability only in low concentration samples and at very low temperatures [21].

The energy gap variations with  $x$  and temperature  $T$  are taken from ref. [24] for MCT, for which the data rest on recent experimental results.  $E_G(x, T)$  for MZT taken from ref. [25] is less precise, but the errors on the data lead to small deviations on the corresponding composition.

The values of  $x$  given in the tables for MZT are chosen so that their  $E_G$  remains very nearly

Table 2  
Values of other parameters

	$a$ (Å)	$\Delta$ (eV)	$P$ (eV cm)	$\Theta$ (eV)	$\rho$ (g cm <sup>-3</sup> )	$C_L \times 10^{-10}$ (N m <sup>-2</sup> )	$\pi \times 10^{12}$ (Cb N <sup>-1</sup> )	$V \times 10^{-24}$ (eV cm <sup>-3</sup> )	$W \times 10^{-24}$ (eV cm <sup>-3</sup> )
HgTe	6.46	1.08	8.87	4	8	6.1	1.4		
CdTe	6.48	0.92	8.38	4	6.06	7.0	1.5		
ZnTe	6.10	0.91	8.74	3.5	5.72	8.4	0.9		
MCT								93	-23
MZT								143	-10

$a$  is lattice parameter,  $\Delta$  is spin-orbit splitting energy,  $P$  is Kane matrix element,  $\Theta$  is acoustical deformation potential,  $\rho$  is specific gravity,  $C_L$  is average longitudinal elastic constant and  $\pi$  is piezoelectric coupling constant. These parameters are linearly interpolated between the binary values. All values taken from refs. [3] and [16].  $V$  and  $W$  are the matrix element entering the alloy scattering expressions.

to that for MCT.  $\Delta$  is interpolated linearly with  $x$  between the end binary values. This interpolation scheme is applied for all parameters of which the value is only known for the binaries and is assumed constant in temperature. The effective mass  $m_d$  at the bottom of the conduction band is deduced from (1) for vanishing  $k$ ; for MCT with  $x$  near 0.2, its values are very comparable to those reported in the literature [16] and no second order corrections describing the interaction with remote bands have been applied. Before each  $\mu$  calculation,  $E_F$  is computed iteratively for each  $n$ ; values of  $m_d$  and  $E_F$  referred to the conduction band extremum are given for three temperatures in Table 3.

The electron concentration  $n$  runs from relatively low values ( $2.2 \times 10^{15} \text{ cm}^{-3}$ ) to high values ( $2 \times 10^{18} \text{ cm}^{-3}$ ) which are now obtained by doping. For a given  $n$ , several values of the charged centre concentration  $N_i$  have been used, as low concentration samples are usually compensated. No compensation is introduced for  $n = 2 \times 10^{18} \text{ cm}^{-3}$ ;  $n$  is fixed at low temperatures to the value given in the figures, but it is increased with  $T$  according to the intrinsic conduction band filling.

The electron kinetic energy  $E$  used as a variable in the iterative calculation runs from 0 to  $E_F + 10k_B T$ , where  $k_B$  is the Boltzmann constant. The range of  $E$  is extended to  $30k_B T$  if  $E_F$  is negative. The energy steps  $dE$  are smaller than  $k_B T/30$  and are chosen so that the energy of the two optical modes  $\hbar\omega_{1H}$  and  $\hbar\omega_{1C}$  (or  $\hbar\omega_{1Z}$  for MZT) remains very near to an integral multiple of  $dE$  with relative differences less than  $5 \times 10^{-3}$  [4]. The iterative calculations converge monotonically but not very rapidly, as often 7 iterations are needed to reach a 0.5% convergence.

### 3. Mobility in $\text{Hg}_{0.5}\text{Cd}_{0.5}\text{Te}$

The results for this ternary are presented as an example for the study of the contribution of the different scattering mechanisms; moreover, for this composition the alloy scattering is maximum.

Fig. 1 gives for three electron concentrations the mobility variations with  $T$  corresponding to the most efficient scattering mechanisms, except for the charged centre contribution. The polar optical scattering is complex due to the non-parabolicity of the band, the degeneracy of the distribution which varies with  $n$  and  $T$ , and the interaction with the two optical modes. As a consequence,  $\mu_{po}$  is higher for low  $n$  at low temperatures ( $T < 100 \text{ K}$ ), and does not vary monotonically with  $n$  at intermediate temperatures. However, it tends to values independent of  $n$  at high temperatures when the phonon bath goes towards the equipartition behaviour.

The alloy scattering importance is pointed out as it strongly limits the total mobility in a wide temperature range. This scattering increases with  $n$  and becomes independent of  $T$  as the Fermi energy becomes high (cf. Table 3). The 77 K value of  $\mu_{al}$  at low  $n$  agrees with that given by Berding et al. [26], who found also a stronger alloy scattering in MZT than in MCT. The acoustical scattering remains comparatively very weak and can be ignored in a first approximation, as seen in Fig. 1. The mobility  $\mu_c$  computed with

Table 3

Energy gap  $E_G$ , effective mass at the conduction band extremum  $m_d/m_0$ , Fermi energies  $E_{F1}$  for  $n = 2.2 \times 10^{15} \text{ cm}^{-3}$  and  $E_{F2}$  for  $n = 2 \times 10^{18} \text{ cm}^{-3}$  in  $\text{HgCdTe}$  and  $\text{HgZnTe}$  for different compositions and temperatures

	$T = 10 \text{ K}$				$T = 77 \text{ K}$				$T = 300 \text{ K}$			
	$E_G$ (meV)	$m_d/m_0$ $\times 10^3$	$E_{F1}$ (meV)	$E_{F2}$ (meV)	$E_G$ (meV)	$m_d/m_0$ $\times 10^3$	$E_{F1}$ (meV)	$E_{F2}$ (meV)	$E_G$ (meV)	$m_d/m_0$ $\times 10^3$	$E_{F1}$ (meV)	$E_{F2}$ (meV)
MCT 0.3	242	17	4	208	254	18	-8	203	301	22	-68	184
MZT 0.197	234	17	4	214	249	18	-7	209	297	21	-67	189
MCT 0.4	429	30	2	162	434	30	-13	160	457	32	-105	154
MZT 0.272	425	30	2	167	434	30	-13	160	454	32	-104	153
MCT 0.5	619	42	1	130	619	42	-16	130	619	42	-116	123
MZT 0.348	617	42	1	135	620	42	-16	130	632	43	-115	126



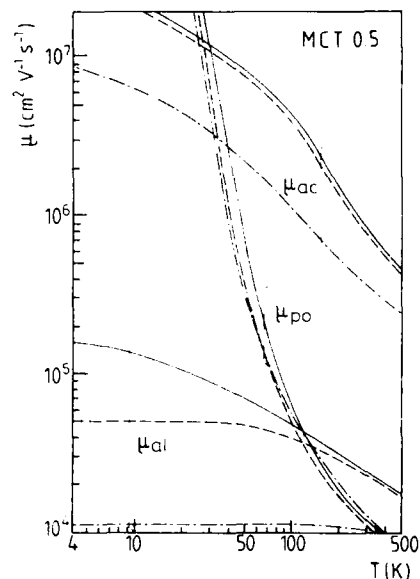


Fig. 1. Calculated mobility  $\mu$  versus temperature in MCT 0.5 limited by polar optical modes ( $\mu_{po}$ ), by acoustic phonons ( $\mu_{ac}$ ) and by alloy scattering ( $\mu_{al}$ ) for (—)  $n = 2.2 \times 10^{15} \text{ cm}^{-3}$ , (---)  $n = 6 \times 10^{16} \text{ cm}^{-3}$  and (· · ·)  $n = 2 \times 10^{18} \text{ cm}^{-3}$ .

the iterative method, taking into account the three interactions already cited, is plotted in Fig. 2 for MCT 0.5 and in Fig. 3 for MZT 0.348 with the same  $n$  values. The lower mobility in MZT is due to a stronger alloy scattering, although its corresponding  $x$  is lower than 0.5, but the alloy scattering potential in MZT is 1.5 times that in MCT (cf. Table 2).

The impurity scattering weakens considerably the mobility, as seen in Fig. 2 and Fig. 3, where  $\mu_i$  variations are plotted for several  $n$  and  $N_i$ .  $\mu_i(T)$  decreases monotonically with  $T$  for  $N_i = n$ . As  $N_i$  is increased above  $n$ ,  $\mu_i(T)$  becomes lower, and shows a maximum which shifts towards high temperatures with  $N_i$ . At high  $n$ ,  $E_i$  becomes greater than  $k_B T$  and  $\mu_i$  undergoes a weak variation with  $T$ . Some experimental results on bulk and epitaxial samples of MCT 0.5 are also given in Fig. 2. The experimental results for  $n = 2 \times 10^{18} \text{ cm}^{-3}$  agree with the calculated ones. In the case of the sample with  $n = 10^{16} \text{ cm}^{-3}$ ,  $N_i$  is not

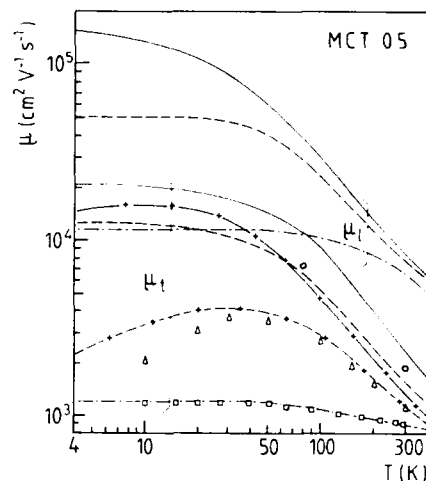


Fig. 2. Calculated mobility versus temperature in MCT 0.5:  $\mu$ , mobility limited by combined optical, acoustical and alloy scattering;  $\mu_i$ , total mobility after adding charged centre scattering with: (—)  $n = N_i = 2.2 \times 10^{15} \text{ cm}^{-3}$ , (---)  $n = N_i = 10^{16} \text{ cm}^{-3}$ , (· · ·)  $n = 2 \times 10^{18} \text{ cm}^{-3}$ , (— · —)  $n = 2.2 \times 10^{15} \text{ cm}^{-3}$ ,  $N_i = 5 \times 10^{15} \text{ cm}^{-3}$ , (· - · - ·)  $n = 10^{16} \text{ cm}^{-3}$ ,  $N_i = 5 \times 10^{16} \text{ cm}^{-3}$ . Experimental values: (○) bulk MCT 0.5, (Δ) epitaxial MCT 0.5,  $n = 10^{16} \text{ cm}^{-3}$ , (□) epitaxial MCT 0.5,  $n = 2 \times 10^{18} \text{ cm}^{-3}$ .

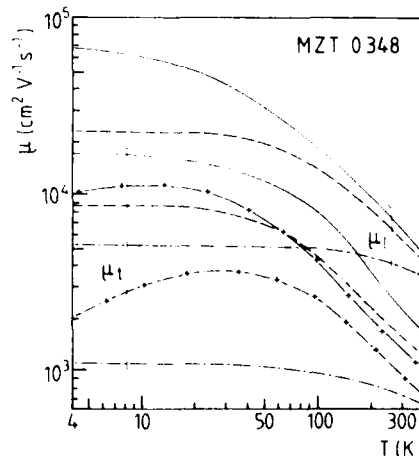


Fig. 3. Calculated total mobility versus temperature in MZT 0.348 with the same symbols as in Fig. 2.

known, but the impurity concentration is higher than  $5 \times 10^{16} \text{ cm}^{-3}$ .

#### 4. Mobility for medium composition MCT and MZT

The shapes of the  $\mu_i(T)$  curves for other compositions in MCT and MZT are the same as those given in Fig. 2 and Fig. 3, and the same as found for low  $x$  solid solutions [4,6]. The important and partly controllable parameter is the charged centre concentration  $N_i$  which must be as near as possible to  $n$ . To sum up the results on  $\mu_i$  variations with  $x$ , its computed values are plotted for the two remarkable temperatures of 77 and 300 K in Fig. 4 for MCT and Fig. 5 for MZT. The curves drawn correspond only to the case  $n = N_i$  and fix an upper limit of  $\mu_i$  which can be reached for an uncompensated material. The choice of  $n = 2.2 \times 10^{15} \text{ cm}^{-3}$  gives practically the maximum values of  $\mu_i$  corresponding to a non-degenerate electron gas. The rapid decrease of  $\mu_i$  at low  $x$  reflects mainly that of the effective mass which follows the increase in  $E_G$ . This decrease is less pronounced when  $n$  is in-

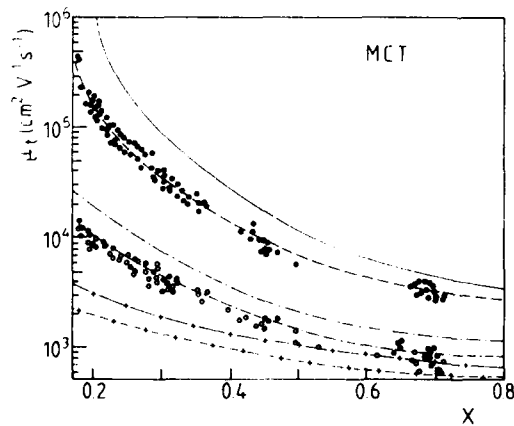


Fig. 4. Calculated mobility variations with composition  $x$  in MCT for  $n = N_i = 2.2 \times 10^{15} \text{ cm}^{-3}$  (—) at 77 K, (---) at 300 K for  $n = N_i = 10^{16} \text{ cm}^{-3}$ , (---) at 77 K, (---) at 300 K for  $n = N_i = 2 \times 10^{18} \text{ cm}^{-3}$  (— + —) at 77 K, (--- + ---) at 300 K; (●) Experimental values at 77 K; (○) experimental values at 300 K.

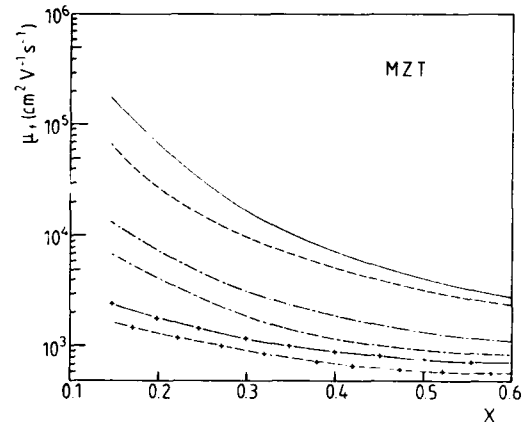


Fig. 5. Calculated total mobility variations with composition in MZT with the same symbols as in Fig. 4.

creased; for high  $n$  the conduction comes from electrons near  $E_F$  which is the highest for low effective masses corresponding to low  $x$  (cf. Table 3).

Experimental results are also shown in Fig. 4 for MCT. They have been obtained mainly on bulk crystals [16,27] for which the mobilities are among the highest known. But although these results agree with the  $\mu$  predictions, the problem of characterizing precisely a sample remains a real task, as it is necessary to know  $N_i$  on the one hand, and to evaluate precisely the scattering factor with all scattering mechanisms taken together on the other hand.

#### 5. Summary

Electron mobility has been computed for medium composition  $\text{Hg}_{1-x}\text{Cd}_x\text{Te}$  and  $\text{Hg}_{1-x}\text{Zn}_x\text{Te}$ . In MCT 0.5, alloy scattering which has been described in the virtual crystal approximation is large and increases strongly with the electronic concentration. Charged centre scattering is the most limiting scattering mechanism at low temperatures, even at low concentrations when optical phonons greatly control the mobility at high temperatures. The mobility computed for the case of uncompensated materials fixes the

upper limit which can be reached and which agrees with known experimental results.

## 6. Acknowledgements

The authors gratefully acknowledge Dr. T. Nguyen Duy for providing experimental results on bulk MCT, and Dr. N. Magnea and J.L. Pautrat for their results on MCT epitaxial layers. This work is partly supported by the ERO program under contract No. R and D E6563.E.E.01.

## 7. References

- [1] R.W. Miles, in: *Properties of Mercury Cadmium Telluride*, EMIS Data Review Series No. 3, Eds. J. Brice and P. Capper (INSPEC, New York, 1987) p. 109, and references therein.
- [2] R. Granger, A. Lasbley, S. Rolland, C.M. Pelletier and R. Triboulet, *J. Crystal Growth* 86 (1988) 682.
- [3] B.R. Nag, *Phys. Status Solidi (b)* 66 (1974) 719.
- [4] R. Granger and C.M. Pelletier, *J. Crystal Growth* 117 (1992) 203.
- [5] J.J. Dubowski, T. Dietl, W. Zymanska and R.R. Galazka, *J. Phys. Chem. Solids* 42 (1981) 351.
- [6] J.D. Patterson, W.A. Gobba and S.L. Lehoczky, *J. Mater. Res.* 7 (1992) 2211.
- [7] R. Triboulet, *J. Crystal Growth* 86 (1988) 79.
- [8] J.L. Pautrat, E. Monterrat, L. Ulmer, N. Magnea, H. Mariette, J. Bleuse and P.H. Jouneau, *J. Crystal Growth* 117 (1992) 454.
- [9] S. Rolland, private communication.
- [10] D.L. Rode, in: *Semiconductors and Semimetals*, Vol. 10, Eds. R.K. Willardson and A.C. Beer (Academic Press, New York, 1975) p. 1.
- [11] B.R. Nag, *Electron Transport in Compound Semiconductors* (Springer, Berlin, 1980).
- [12] H.J. Drouhin and J. Peretti, *Phys. Rev. B* 44 (1991) 7993.
- [13] L. Swierkowski, W. Zawadzki, Y. Guldner and C. Rigaux, *Solid State Commun.* 27 (1978) 245.
- [14] K.J. Nash, M.S. Skolnick and S.J. Bass, *Semicond. Sci. Technol.* 2 (1987) 329.
- [15] J. Baars and F. Sorger, *Solid State Commun.* 10 (1972) 875.
- [16] J. Brice and P. Capper, Eds., *Properties of Mercury Cadmium Telluride*, EMIS Data Reviews Series No. 3 (INSPEC, New York, 1987).
- [17] G. Lebastard, R. Granger, S. Rolland, Y. Marqueton and R. Triboulet, *J. Physique* 50 (1989) 3223.
- [18] W. Abdelhakim, J.D. Patterson and S.L. Lehoczky, *Mater. Lett.* 11 (1991) 47.
- [19] Qiang Dingrong, Tiang Wenguo, Shen Jie, Chu Junhao and Zheng Guozhen, *Solid State Commun.* 56 (1985) 813.
- [20] J. Kossut, *Phys. Status Solidi (b)* 86 (1978) 593.
- [21] J.R. Meyer and J.F. Bartoli, *J. Vac. Sci. Technol.* 21 (1982) 237.
- [22] A. Marbeuf, D. Ballutaud, R. Triboulet and Y. Marfaing, *J. Crystal Growth* 101 (1990) 608.
- [23] C. Hsu, Tran Minh Duc and J.P. Faurie, *J. Physique* 48 (1987) C5-307.
- [24] J.P. Laurenti, J. Camassel, A. Bouhemadou, B. Toulouse, R. Legros and A. Lusso, *J. Appl. Phys.* 67 (1990) 6454.
- [25] B. Toulouse, R. Granger, S. Rolland and R. Triboulet, *J. Physique* 48 (1987) 247.
- [26] M.A. Berding, S. Krishnamurthy, A. Sher and A.B. Chen, *J. Vac. Sci. Technol. A* 5 (1987) 3014.
- [27] The main part of the experimental results come from SAT, France; T. Nguyen Duy, private communication.



ELSEVIER

Journal of Crystal Growth 138 (1994) 493–498

JOURNAL OF **CRYSTAL  
GROWTH**

## Low temperature variable range hopping conductivity in doped CdTe crystals

N.V. Agrinskaya

*A.F. Ioffe Physico-Technical Institute, Politekhnikeskaya 26, St. Petersburg 194021, Russian Federation*

### Abstract

The temperature behavior of the conductivity and magnetoresistance of CdTe crystals doped by shallow donors (Cl) has been studied at temperatures of 0.4–100 K. The crossover from variable range hopping (VRH) over the states within Coulomb gap to VRH of the Mott type has been observed at some temperatures depending on the samples parameters (donor concentration and compensation degree). In addition, at low magnetic field a negative magnetoresistance due to interference phenomena in VRH has been observed, while at higher magnetic fields the system has exhibited positive magnetoresistance due to deformation of the centres' wave functions. A divergence of localization length and dielectric constant in the vicinity of metal–insulator transition is demonstrated.

Although Mott and Davis (MD) [1] and Shklovskii and Efros (SE) [2] predictions for variable range hopping conductivity (VRH) have appeared in the literature more than 15 years ago, some questions concerning electron transport in Anderson insulator in the vicinity of the metal–insulator transition (MIT) remain unanswered. Among them, one can point at the behavior of VRH conductivity at temperatures corresponding to crossover between MD and SE limits and at the effects of magnetic field and compensation degree.

In a previous paper [3] we have studied low-temperature VRH conductivity of highly doped compensated CdTe:Cl crystals in the temperature interval 1.7–100 K. In the course of temperature decrease, we have observed the crossover from MD to SE behavior. Soon afterwards, such a crossover has been reported for CdSe:In crystals in ref. [4]. Although the very observation of

the crossover seems to be of interest and evidences the theoretical prediction, the observation of both sorts of behavior for the same sample allows one to estimate important parameters like localization length and Fermi level density of states. Therefore more detailed investigation of the effects in question appears to be of importance.

To study VRH conductivity including the effects of magnetic field and compensation degree more profoundly, we have made measurements of the conductivity and magnetoresistance in a wide temperature interval of 0.4–300 K, thus covering a temperature variation of nearly three orders of magnitude.

The CdTe samples have been doped by shallow donor impurity in the melt. We have chosen 3 types of samples with an electron concentration  $n$  at 300 K close to  $10^{17} \text{ cm}^{-3}$  differing by the compensation degree; the latter appear to pro-

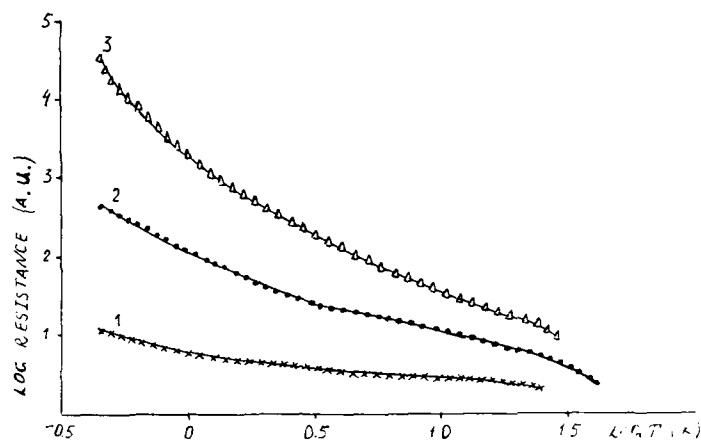


Fig. 1. Resistance versus temperature plotted on a double logarithmic scale for three insulating compensated n-type CdTe samples.

vide essentially different behavior of the low-temperature transport. Unfortunately we were not able to determine the net donor concentration directly. Thus we have evaluated the compensation degree and donor concentration  $N_D \sim (1.5-2) \times 10^{17} \text{ cm}^{-3}$  with the help of Hall coefficient and mobility measurements at temperatures higher than 20 K.

For uncompensated CdTe, the critical value of  $n$  corresponding to the Mott transition ( $n_{c0}^{1/3} a \sim 0.25$ ) is  $n_{c0} = 1.5 \times 10^{17} \text{ cm}^{-3}$ . For some degree

of compensation, Anderson localization may lead to formation of localized states, the  $n_c$  value increasing with an increase of  $K$  in [2]:

$$n_c \sim n_{c0}(1 - K)^{-2}. \quad (1)$$

Thus the samples with larger  $K$  are farther from the transition to metallic conduction.

As one can see from Fig. 1, the strongest changes of resistance with temperature  $R(T)$  (3–4 orders of magnitude) are observed for heavily compensated samples, while for weakly compen-

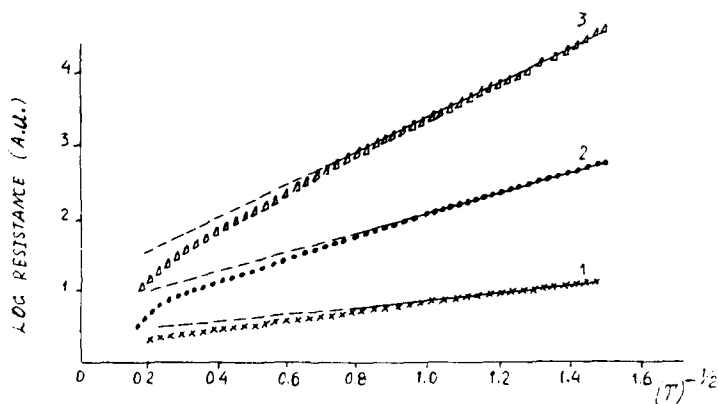
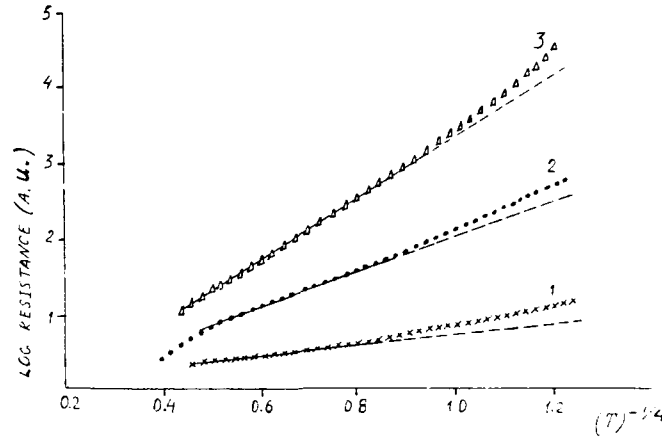


Fig. 2. Logarithm of the resistance on n-CdTe as a function of  $T^{-1/2}$ .

Fig. 3. Logarithm of the resistance of n-CdTe as a function of  $T^{-1/4}$ .

sated samples  $R(T)$  changes only by half of the order of magnitude. For all samples one can observe a transition from relatively weak dependence  $R(T)$  to a stronger dependence with decrease of temperature. It appears that one cannot describe the whole temperature behavior in question with the help of either MD or SE law:

$$R(T) \sim R_0 \exp(T_0/T)^{1/4}, \quad T_0 = \frac{18}{N(E_F)a^3}, \quad (2)$$

$$R(T) \sim R'_0 \exp(T_1/T)^{1/2}, \quad T_1 = \frac{2.8 e^2}{\kappa a}, \quad (3)$$

where  $a$  is the localization length,  $\kappa$  is the dielectric constant and  $N(E_F)$  is the Fermi level density of states (DOS). In particular, in Fig. 2 we show that at low temperatures  $\log R$  depends linearly on  $T^{-1/2}$ , which corresponds to Eq. (3),

while at higher temperatures deviations to lower resistances are pronounced. At the same time, at higher temperatures, one can fit the experimental curve by a linear dependence of  $\log R$  on  $T^{-1/4}$  (Eq. (2)); however, at the temperature decrease deviations to higher resistances are observed (Fig. 3). It is this sort of behavior that is expected for the crossover from MD to SE conductivities. For example, at temperatures lower than the crossover temperature  $T_c$  (SE region),  $\log R$  is a linear function of  $T^{-1/2}$ , while at  $T > T_c$  the trend toward  $\log R \propto T^{-1/4}$  has to be observed; in terms of coordinates  $x = T^{-1/2}$ , it has to be manifested as a transition from a linear behavior of  $\log R$  to a square root behavior which at small  $x$  (high temperature limit) corresponds to deviations to lower resistance values. Actually, the exact form of the curve in the crossover region should essentially depend as well on the relation between the pre-exponentials in Eqs. (2) and (3).

Table 1

Parameters of the samples studied measured and calculated in the way given in the text

Sample No	$n_{300K}$ ( $\text{cm}^{-3}$ )	$K$	$T_0$ (K)	$T_1$ (K)	$a$ ( $\text{\AA}$ )		$\kappa$ From $T_0, T_1$
					From NMR	From $T_0$	
1	$1.2 \times 10^{17}$	0.2	5.3	1.1	2000	1600	300
2	$9 \times 10^{16}$	0.4	354	5.6	400	380	235
3	$7.5 \times 10^{16}$	0.6	$6 \times 10^4$	33	80	125	150

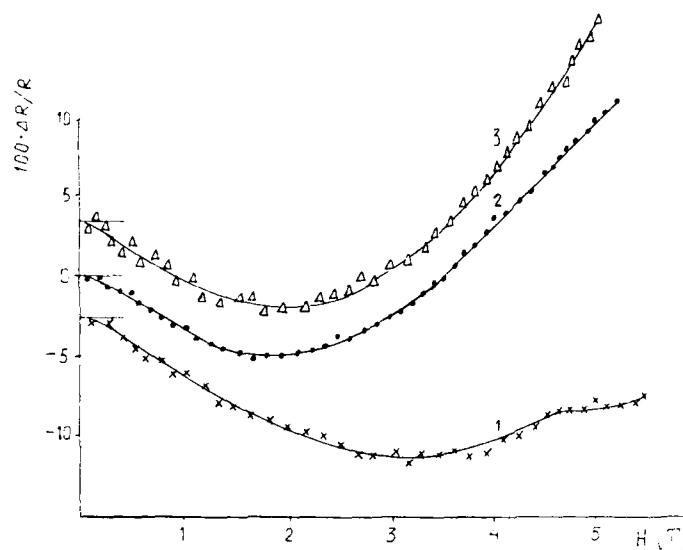


Fig. 4. Magnetoresistance of compensated n-CdTe versus magnetic field;  $T = 3$  K. For convenience, the zero point is shifted for samples 1 and 3.

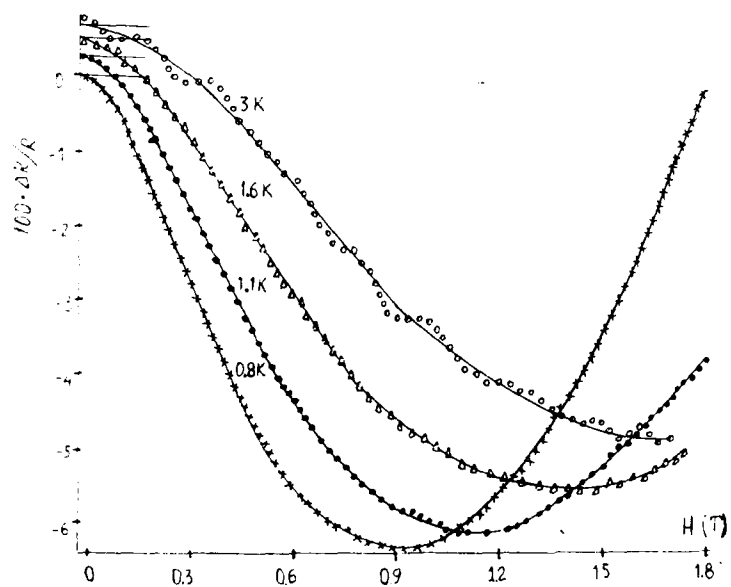


Fig. 5. Negative magnetoresistance of sample 2 versus magnetic field at different temperatures. For convenience, the zero point is shifted for different temperatures.

which are not expected to be equal because of a principal difference in DOS for the models in question. Note that this detail has not been taken into account by Aharony et al. [5] who have studied the crossover region. According to our experimental results, the pre-exponential  $R'_0$  is always larger than  $R_0$ , which is in agreement with theoretical calculations for different DOS [6]. It is in this case that the transition to MD type of VRH in scale  $T^{-1/2}$  has to be manifested as a deviation toward smaller resistance values, which is indeed observed.

Corresponding fitting procedures have led to estimates of  $T_0$  and  $T_1$  which are given in Table 1. The data obtained could give a possibility to estimate the important material parameters  $\kappa$ ,  $a$  and  $N(E_F)$  in two limiting cases: (1) For samples far away from MIT where  $\kappa = 10$  and  $a = 50$  Å and both are constant; in this case  $T_1 \sim 10^3$  K. (2) For samples close to MIT where  $\kappa$  and  $a$  diverge due to weakening of the carriers localization; in this case as was shown by Castner [7], the ratio of  $T_0$  and  $T_1$  should be constant:  $T_0/T_1 = 80$ . As one can see from Table 1, our samples rather correspond to the intermediate region, and thus it is necessary to have some additional experimental data to estimate one of the above mentioned parameters.

We have measured the magnetoresistance (MR) for our samples in magnetic fields of 0–6 T at different temperatures. One can see from Fig. 4 that the MR curves ( $\Delta R/R$  versus  $H$ ) are very different for different samples: in some samples negative MR (NMR) is observed together with positive one (PMR), and in sample 1 only NMR is observed. The values of the magnetic field  $H$  corresponding to minima of the MR curves are different for different samples and temperatures, which is apparently due to a difference in the localization lengths and hopping length ( $r$ ). If there were some general theory of MR in a variable range hopping, it would be possible to extract all the parameters of interest from the MR curves. However, until now a conventional theory has existed only for PMR, while there exist several models to explain NMR [8,9]. Let us consider the NMR region in Fig. 5 in detail. One clearly sees the transition from quadratic  $R(H)$

behavior to linear behavior for higher values of  $H$ . A value  $H = H_1$  corresponding to this transition decreases with a decrease in temperature, and at low temperatures only linear MR is observed. A similar feature has been observed in CdSe [10]. Such behavior has been predicted by theory [9,11] ascribing NMR to interference effects in VRH. A crossover from quadratic to linear behavior is expected for a magnetic field:

$$H_1 = \frac{\Phi_0}{r^{3/2}a^{1/2}} \exp(-r/a) \quad (4)$$

Here  $\Phi_0$  is a magnetic flux quantum. Localization lengths estimated with the help of Eq. (4) are given in Table 1. On the other hand, one can estimate the localization length with the help of Eq. (2) taking  $T_0$  from experimental curves  $R(T^{-1/4})$  and  $N(E_F) \sim N_D/\epsilon_1$ , where  $\epsilon_1$  is the activation energy for the high temperature region. The values of  $a$  obtained are given in Table 1; one clearly sees an agreement with the estimates based on NMR measurements.

Thus the data evidence a divergence of the parameters  $a$  and  $\kappa$  in the course of a decrease of compensation degree, which is related to an approach of MIT. In addition, an approach of MIT changes the character of the NMR behavior: far from MIT one has small NMR which is changed to a PMR, which corresponds to the fixed sign phase, while in the vicinity of MIT in sample 1 only NMR is observed for  $H = 0$ –6 T, which corresponds to the random sign phase [9]. In other words, a decrease of compensation degree leads to the sign phase transition predicted in ref. [9].

The temperature behavior of PMR and of the minima points was more complicated. This will be the subject of another publication.

Thus we have shown that in highly doped compensated CdTe crystals the possibility exists to observe the crossover from MD to SE VRH and interference effects in VRH, and to estimate some parameters characterizing the vicinity of our samples to metal–dielectric transition.

I am grateful to A.L. Balakai and D.V. Shamshur for the help in low temperature mea-



surements and to V.I. Kozub for valuable discussions.

### 1. References

- [1] N.F. Mott and E.A. Davis, *Electronic Processes in Non-Crystalline Materials* (Clarendon, Oxford 1971).
- [2] B.I. Shklovskii and A.L. Efros, *Electronic Properties of Doped Semiconductors* (Springer, Berlin, 1984).
- [3] N.V. Agrinskaya and A.N. Aleshin, *Soviet Phys.-Solid State* 31 (1989) 1996.
- [4] Y. Zhang, P. Dai, M. Levy and M.P. Sarachik, *Phys. Rev. Lett.* 64 (1990) 2687.
- [5] A. Aharony, Y. Zhang and M.P. Sarachik, *Phys. Rev. Lett.* 68 (1992) 3900.
- [6] R. Mansfield in: *Hopping Transport in Solids*, Eds. M. Pollak and B.I. Shklovskii (North-Holland, Amsterdam, 1991).
- [7] T.G. Castner, in: *Hopping Transport in Solids*, Eds. M. Pollak and B.I. Shklovskii (North-Holland, Amsterdam, 1991).
- [8] R.P. Khosia and J.R. Fisher, *Phys. Rev. B* 2 (1970) 4084.
- [9] B.I. Shklovskii and B.Z. Spivak, in: *Hopping Transport in Solids*, Eds. M. Pollak and B.I. Shklovskii (North-Holland, Amsterdam, 1991).
- [10] Y. Zhang, P. Dai and M.P. Sarachik, *Phys. Rev. B* 45 (1992) 9473.
- [11] W. Schirmacher, *Phys. Rev. B* 41 (1990) 2461.



ELSEVIER

Journal of Crystal Growth 138 (1994) 499–503

JOURNAL OF  
**CRYSTAL  
GROWTH**

## Ab initio calculation of electronic structure and structural properties of $\text{ZnSe}_x\text{Te}_{1-x}$

B. Freytag \*, U. Rössler

*Institut für Theoretische Physik, Universität Regensburg, D-93040 Regensburg, Germany*

### Abstract

The ternary mixed crystal system  $\text{ZnSe}_x\text{Te}_{1-x}$  has recently attracted renewed interest as basic material for the blue/green laser diode. We use norm-conserving pseudopotentials in connection with the local density and virtual crystal approximation for “ab-initio” calculations of the stable crystal structure and the lattice constant in dependence on the composition  $x$  of the system. Our results are in quantitative agreement with structural properties but we find a bowing in the bandgap much smaller than in the experimental data. To check the quality of our results, we use pseudopotentials which either consider the d-electrons of Zn in the core or treat them explicitly as valence electrons.

### 1. Introduction

In material science, ternary mixed crystal systems are frequently used for band structure engineering. Two prominent examples are II–VI semiconductors like  $\text{Zn}_x\text{Cd}_{1-x}\text{Te}$  [1,2] with energy gaps in the optical range and IV–VI materials like  $\text{Pb}_x\text{Sn}_{1-x}\text{Te}$  [3,4] with energy gap in the far-infrared spectral range. The major motivation behind current research in wide band gap II–VI semiconductors, in particular in the ternary system  $\text{ZnSe}_x\text{Te}_{1-x}$ , is to develop optoelectronic devices such as light emitting diodes (LEDs) or semiconductor lasers [5], within the blue/green region of the spectrum.

In this paper we report on total energy calculations in order to find the stable crystal structure, to determine structural and electronic properties of  $\text{ZnSe}_x\text{Te}_{1-x}$ .

The total energy as a ground state property of the many-particle system can be calculated by applying the concepts of density functional theory (DFT), which usually is evaluated in the local density approximation (LDA) [6,7]. For crystalline solids, pseudopotentials and plane-wave expansions of the wave functions have been used successfully to describe the fundamental properties of semiconductors of the zincblende or of the rocksalt family [8]. For reasons of convergence, special care must be taken in choosing pseudopotentials for atoms with d-electrons close to the valence s- and p-electrons [8]. We use smooth norm-conserving pseudopotentials [8,9] generated in a scheme proposed recently by Troullier and Martins [10]. The influence of the Zn 3d elec-

\* Corresponding author.

trons is taken into account by considering different pseudopotentials, which either incorporate the d-electrons in the core or take them into account explicitly as valence electrons. The mixed crystal aspects are considered within the virtual crystal approximation (VCA) by mixing the cation pseudopotentials according to the composition parameter  $x$ .

A brief outline of the method (DFT and LDA) for calculating the total energy of the crystal ground state is given in refs. [11,12]. In ref. [11] more computational details are given, e.g. the use of special points in performing sums in  $k$  space [13,14]. We used the Ceperley–Alder exchange-correlation potential as parametrized by Perdew and Zunger [15] and 19 special points in the irreducible wedge of the Brillouin zone.

In section 2 we discuss structural properties and compare our results with experimental data. In section 3 we show the electronic structure of the system  $\text{ZnSe}_x\text{Te}_{1-x}$ . One of the central points of this discussion is the bowing of the bandgap.

## 2. Structural properties

The system  $\text{ZnSe}_x\text{Te}_{1-x}$  has the zincblende structure as stable structure under normal conditions in the whole mixing range. The ground state of a solid is the equilibrium state for given thermodynamic conditions. We assume  $T = 0$  K and an infinite system without strain. In this case the equilibrium state is determined by minimizing the total energy  $\mathcal{E}$  with respect to crystal structure and lattice constant  $a$  or crystal volume  $V$ :

$$\mathcal{E} = T_0[n_0] + \int V_{\text{EXT}}(\mathbf{r}) n_0(\mathbf{r}) d^3\mathbf{r} + \int \frac{n_0(\mathbf{r}) n_0(\mathbf{r}')}{|\mathbf{r} - \mathbf{r}'|} d^3\mathbf{r} d^3\mathbf{r}' + E_{\text{XC}}[n_0] + E_{\text{EW}}, \quad (1)$$

where  $V_{\text{EXT}}$  is the external potential,  $E_{\text{XC}}$  the exchange-correlation potential, and  $E_{\text{EW}}$  the Ewald energy.

Convergence of the total energy with respect to the plane wave expansion depends on the

smoothness of the pseudopotential. While for the soft pseudopotential with the Zn d electrons in the core convergence [16] is achieved for a cutoff energy of 24 Ryd, it has to be 50 Ryd for the pseudopotential with explicit consideration of the d-electrons.

For the purpose of minimizing  $\mathcal{E}(V)$  the values of the total energy calculated at a fixed energy cutoff for different lattice constants have been fitted to Vinet's equation of state [17]. This function is a good empirical approximation of the dependence of the energy on volume and pressure,

$$\mathcal{E}(V) = -9B_0V_0 \exp \left\{ \gamma \left[ 1 - \left( \frac{V}{V_0} \right)^{1/3} \right] \right\} \times \left( \frac{1}{\gamma} + \frac{(V/V_0)^{1/3}}{\gamma} + \frac{1}{\gamma^2} \right), \quad (2)$$

with  $\gamma = \frac{2}{3}(B'_0 - 1)$ , and where  $B'_0$  is the derivative of the bulk modulus  $B_0$  with respect to the pressure.

Zincblende material under hydrostatic pressure normally undergoes a structural phase transition to rocksalt structure [18]. It is a well-known thermodynamic theorem that the phase transformation occurs, when the Gibbs free energy  $G = E_{\text{tot}} + pV - TS$  becomes equal between two phases. By applying this theorem to the zero temperature case considered here, the pressure induced phase transformation occurs along the common tangent line between the  $E_{\text{tot}}(V)$  curves of the two phases under consideration with the negative slope of the common tangent line being the transition pressure  $p_t$  [19].

The structural properties ( $a_0$ ,  $B_0$ ,  $B'_0$ ) derived with Vinet's equation of state obtained from a set of calculated data points are compared in Table 1 with the experimental values. For these calculations we use pseudopotentials, which either consider the d-electrons in the core or take the d-electrons explicitly into account as valence electrons (+d). In addition, we perform calculations in which the pseudopotential is corrected in the core in order to account for effects of d-electrons (nonlinear core correction or nlcc) [20]. For the

Table 1  
Equilibrium parameters of experiments and calculations ( $-d$ , nlcc and  $+d$ )

	$a_0$ (a.u.)	$B$	$p_{tr}$ (kbar)	$E_{gap}$ (eV)
ZnTe ( $-d$ )	10.67	770		3.00
ZnTe (nlcc)	11.34	571		2.45
ZnTe ( $+d$ )	11.58	501	78	0.78
ZnTe [30]	11.53	509	85	2.39
ZnSe ( $-d$ )	9.76	1102		3.30
ZnSe (nlcc)	10.48	753		2.23
ZnSe ( $+d$ )	10.93	605	98	0.58
ZnSe [30]	10.72	625	135	2.82

lattice constant we find good quantitative agreement with the experimental data for calculations which consider the d-electrons either explicitly ( $+d$ ) or as core correction (nlcc), while the ( $-d$ ) results are significantly smaller. The bulk modulus and the critical pressure for phase transitions are higher derivatives of the total energy and, therefore, more sensitive to the numerical accuracy. Nevertheless, the calculated results of the ( $+d$ ) version are in good agreement with the experimental data, while the (nlcc) and ( $-d$ ) versions deviate significantly. These results demonstrate that explicit consideration of d-electrons is essential for the calculation of the structural properties.

### 3. Electronic properties

In Figs. 2 and 3 we show the energy bands and the density of states of ZnTe and ZnSe obtained from a ( $+d$ ) version of pseudopotentials. The density of states has been calculated using the quadratic tetrahedron method [21,22]. In order to check the quality of the band structure we compare selected valence band energies with results calculated with the linearized APW method [23,24] and with experimental data (see Table 2 for ZnTe and Table 3 for ZnSe). In contrast to the pseudopotential method ( $+d$ , nlcc) the APW method is an all-electron calculation. Given the different exchange-correlation potentials used in these calculations – which can change the single particle energies by about 0.1 eV [23] – our

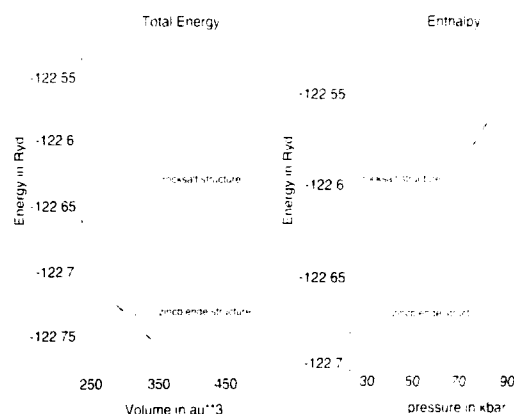


Fig. 1. (a) Total energy versus volume; (b) enthalpy versus the pressure.

pseudopotential calculations, which take d-electrons into account, reproduce the APW results. We find also good agreement with the experimental data except for the position of the d-electrons, which differ by about 2.5 eV. The values for the calculated band gaps (Table 1) show a decrease of  $E_{gap}$  by about 2 eV, when the d-electrons are taken explicitly into account. These results are consistent with those found earlier [24]

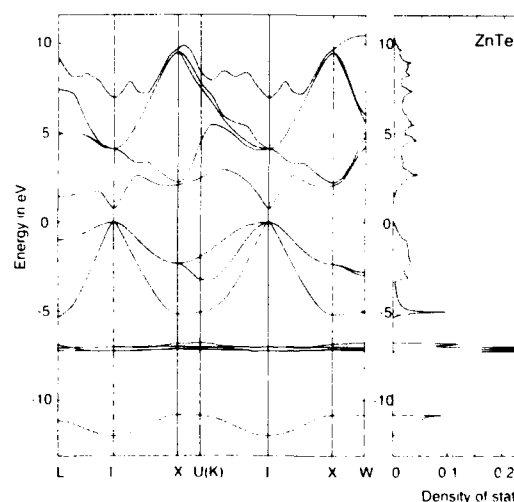


Fig. 2. Electronic bandstructure of ZnTe with the density of states ( $+d$ ).

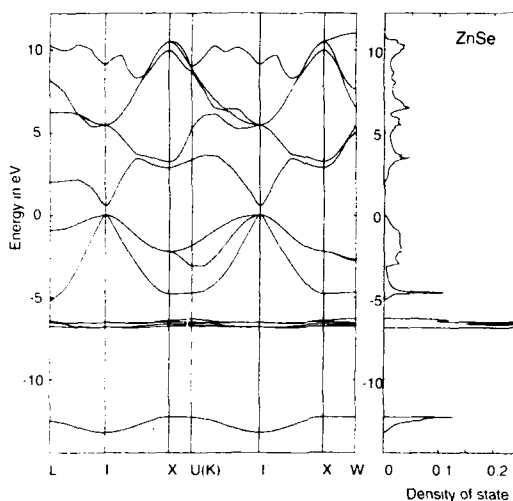


Fig. 3. Electronic bandstructure of ZnSe with the density of states (+d).

and can be ascribed to p-d repulsion, which shifts the p-valence band upwards.

For the mixed crystal system  $\text{ZnSe}_x\text{Te}_{1-x}$  we compare calculated values for the lattice constant (version +d or nlcc) with experimental data [23,24] (Fig. 4). As for ZnSe and ZnTe (Table 1) we find almost perfect agreement. The dependence of  $a_0$  on the composition parameter  $x$  is almost linear, as expected from Vegard's rule [25]. The small bowing is in accordance with a phenomenological model [26] and occurs in spite of using the virtual crystal approximation.

Table 2  
Experimental and theoretical results of bandstructure of ZnTe (energies in eV)

	Exp. [30]	LAPW [24]	(+d)	(nlcc)
$\Gamma_{1V}$	-13.0	-11.91	-11.99	-11.11
$\Gamma_{1sd}$	-9.8	-7.27	-7.24	
$\Gamma_{12d}$	-9.8	-7.05	-7.01	
$L_{1V}$	-12.0	-11.04	-11.14	-9.74
$L_{3V}$	-1.1	-0.92	-1.00	-0.90
$X_{1V}$		-10.73	-10.84	-9.20
$X_{3V}$	-5.5	-5.13	-5.19	-5.23
$L_{1V}$	-5.5	-5.27	-5.36	-5.31
$X_{3V}$	-2.4	-2.21	-2.34	-2.22

Table 3

Experimental and theoretical results of bandstructure of ZnSe (energies in eV)

	Exp. [30,23]	FLAPW [23]	(+d)	(nlcc)
$\Gamma_{1V}$	-15.2	-13.37	-13.19	-12.99
$\Gamma_{1sd}$	-8.9	-6.77	-6.81	
$\Gamma_{12d}$	-8.6	-6.41	-6.53	
$L_{1V}$	-13.1	-12.57	-12.49	-11.75
$L_{3V}$	-1.3	-0.91	-0.92	-0.85
$X_{1V}$	-12.5	-12.30	-12.25	-11.31
$X_{3V}$	-5.3	-4.89	-4.81	-5.08
$X_{5V}$	-2.1	-2.24	-2.23	-2.19

In view of applications in optoelectronic devices the energy gap of  $\text{ZnSe}_x\text{Te}_{1-x}$  has recently found much interest. Using photoluminescence, Rajakarunanayake et al. [27] and Ebina et al. [29] have determined the dependence of valence and conduction band edge on the composition parameter  $x$ . Besides a linear dependence of the valence band edge they find for the gap energy at 5 K the relation:

$$E_{\text{gap}}(x) = 2.82x + 2.39(1-x) - 1.23x(1-x) \quad \text{in eV.} \quad (3)$$

Except for the value of the bowing parameter  $\gamma$  (prefactor in front of  $x(1-x)$  in Eq. (3)), these results agree with those of ref. [28] (see Table 4). Our calculations give a linear dependence of the valence band edge on  $x$  and a bowing of the conduction band. A quantitative agreement be-

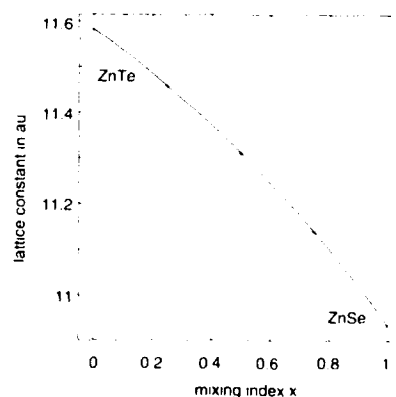


Fig. 4. Lattice constants of crystals versus mixing index  $x$ .

Table 4

Bowing of the bandgap; the bowing parameter  $\gamma$  is the prefactor in front of  $x(1-x)$  in Eq. (3)

	$E_{\text{gap}}$ (ZnTe) (eV)	$E_{\text{gap}}$ (ZnSe) (eV)	$\gamma$ bowing
Exp. [27,29]	2.39	2.82	-1.23
Exp. [28]	2.45	2.82	-1.57
(nlcc)	2.44	2.23	-0.5
(+d)	0.78	0.58	0.2

tween calculated and experimental values of the bowing parameter is not achieved.

In conclusion, we have performed ab-initio calculations for the structural and some electronic properties of  $\text{ZnSe}_x\text{Te}_{1-x}$  using pseudopotentials, which take into account the Zn 3d electrons with different accuracy ( $-d$ , nlcc and  $+d$ ). The structural properties (lattice constant, Vegard's rule, bulk modulus, critical pressure for structural transition) are in quantitative agreement with experimental data, if the Zn 3d electrons are taken explicitly into account ( $+d$  version). However, the energy gap and the bowing parameter of the band gap cannot be reproduced by this calculation. While the LDA is known to give too small values for the calculated gap energies, the VCA is likely to be responsible for the wrong value of the bowing parameter.

#### 4. Acknowledgments

We thank S. Baroni, A. Dal Corso and F.M. Mueller for the numerical support, and P. Pavone, G.H. Grosch, O. Schütt and K. Karch for useful discussions. This work has been performed with partial support from the Graduiertenkolleg "Komplexität in Festkörpern: Phononen, Elektronen und Strukturen" and from the Bayerische Forschungsförderung (FOROPTO).

#### 5. References

- [1] S.I. Radautsan, A.E. Tsurkan and O.G. Maksimova, Phys. Status Solidi 37 (1970) K9.
- [2] B. Gil and D.J. Dunstan, Semicond. Sci. Technol. 6 (1991) 428.
- [3] J.W. Wagner and R.K. Willardson, Trans. Met. Soc. AIME 242 (1968) 1968.
- [4] S. Gan and C. Chen, Semicond. Sci. Technol. 3 (1988) 1041.
- [5] M. Kobayashi, N. Minol, H. Katagiri, R. Kimura, M. Konagai and K. Takahashi, Appl. Phys. Lett. 48 (1986) 296.
- [6] R.M. Dreizler and E.K.U. Gross, Density Functional Theory – An Approach to the Quantum Many Body Problem (Springer, Berlin, 1990).
- [7] R.O. Jones and O. Gunnarsson, Rev. Mod. Phys. 61 (1989) 689.
- [8] G. Bachelet, D.R. Hamann and M. Schlüter, Phys. Rev. B 26 (1982) 4199.
- [9] D.R. Hamann, M. Schlüter and C. Chiang, Phys. Rev. Lett. 43 (1979) 1494.
- [10] N. Troullier and J.L. Martins, Phys. Rev. B 43 (1991) 1993.
- [11] B. Freytag, G. Grosch, U. Rössler, N.-J. Range and K. Karch, J. Chem. Phys. 99 (1993) 1111.
- [12] P. Giannozzi, S. de Gironcoli, P. Pavone and S. Baroni, Phys. Rev. B 43 (1991) 7231.
- [13] D.J. Chadi and M.L. Cohen, Phys. Rev. B 8 (1973) 5747.
- [14] H.J. Monkhorst and J.D. Pack, Phys. Rev. 13 (1976) 5188.
- [15] J. Perdew and A. Zunger, Phys. Rev. B 23 (1981) 5048.
- [16] G. Grosch, B. Freytag, K.-J. Range and U. Rössler, J. Quantum Chem., submitted.
- [17] P. Vinet, J.H. Rose, J. Ferrante and J.R. Smith, J. Phys. Cond. Matter 1 (1989) 1941.
- [18] S.B. Quadri, E.F. Skelton, A.W. Webb and J. Kennedy, Appl. Phys. Lett. 46 (1985) 257.
- [19] M.T. Yin and M.L. Cohen, Phys. Rev. B 24 (1982) 6121.
- [20] A. Dal Corso, S. Baroni, R. Resta and S. de Gironcoli, Phys. Rev. B 47 (1993) 3588.
- [21] M.S. Methfessel, M.H. Boon and F.M. Mueller, J. Phys. C 20 (1987) 1069.
- [22] G. Wiesenekker and E.J. Baerends, J. Phys. Cond. Matter (1991) 6721.
- [23] A. Continenza, S. Massida and A.J. Freeman, Phys. Rev. B 38 (1988) 12996.
- [24] S.-H. Wei and A. Zunger, Phys. Rev. B 37 (1987) 8958.
- [25] L. Vegard, Z. Physik 5 (1921) 17.
- [26] A. Prince, Alloy Phase Equilibria (Elsevier, Amsterdam, 1966).
- [27] Y. Rajakarunanyake, M.C. Phillips, J.O. McCaldin, D.R. Chow, D.A. Collins and T.C. McGill, SPIE Proc. 1285 (1990) 142.
- [28] M.J.S. Brasil, M.C. Tamargo, R.E. Nahory, H.L. Gilchrist and R.J. Martin, Appl. Phys. Lett. 59 (1991) 1206.
- [29] A. Ebina, M. Yamamoto and T. Takahashi, Phys. Rev. B 6 (1987) 3786.
- [30] Landolt-Börnstein, Numerical Data and Functional Relationship in Science and Technology, Vol. 17b, Ed. O. Madelung (Springer, Berlin, 1982).

## Photoionization of a deep centre in zinc selenide giving information about the conduction band structure

Jiazhen Zheng, J.W. Allen \*

*Wolfson Institute of Luminescence, Department of Physics and Astronomy, University of St. Andrews, North Haugh, St. Andrews, Fife KY16 9SS, Scotland, UK*

### Abstract

Thermal emission from a deep level to the conduction band in zinc selenide gives an apparent activation energy of 0.33 eV. The photoionization spectrum shows two thresholds, attributed to transitions from the level to the  $\Gamma$  and L valleys. An intervalley spacing of  $1.26 \pm 0.06$  eV is deduced.

### 1. Introduction

There are several reports of a variety of deep levels in the upper half of the band gap of zinc selenide grown by various methods. The measurements were made by DLTS or photocapacitance. It is found that the concentration is rather low, typically  $\sim 10^{14} \text{ cm}^{-3}$ . We have found a sample of ZnSe with one dominant level in the upper half of the gap, all other levels in this upper half having a concentration at least a factor of ten lower. We have been able to measure the photocapacitance spectrum over a wide energy range: this gives information about the centre producing the deep level and also about the structure of the conduction band. We have also made measurements of thermal emission of electrons from the level to the conduction band and of the capture of electrons at the level and hence have been able to relate the centre to centres reported in the literature.

### 2. Experimental methods and results

Zinc selenide was synthesized from the elements and a boule was grown by evaporation down a temperature gradient in a sealed evacuated silica tube. Aluminium was added to act as a donor. The material was made conducting by treatment in molten zinc. It may be significant that the boule was grown about twenty years ago, since we have evidence that some centres in ZnSe can change in concentration over a time-scale of years. It could be the age of the sample which results in its having only one dominant level in the upper half of the band gap. Schottky diodes were made with indium ohmic contacts and evaporated gold rectifying contacts.

Photoionization measurements were made by the transient technique. A forward bias was applied in order to fill the levels. A beam of monochromatic light then emptied the levels. During the emptying a reverse bias, typically 2V, was applied to minimize effects associated with the depletion layer edge. The change of capacitance as a function of time was monitored and

\* Corresponding author.

fitted to an exponential. It was found that over most of the transient a good fit could be obtained with a single exponential. The magnitude of the transient,  $\Delta C$ , is related to the dark capacitance  $C$ , the deep level concentration  $N_T$  and the uncompensated donor concentration  $N_D - N_A$  by

$$\frac{\Delta C}{C} = \frac{N_T}{2(N_D - N_A)} \quad (1)$$

when  $N_T \ll N_D - N_A$ , as is the case here. It was found that  $\Delta C$  is constant within experimental scatter over a photon energy range of 0.45–2.2 eV. Hence  $N_T$ , i.e. the concentration of deep levels being emptied, is constant over this energy range and one infers that only one energy level is involved. The shape of the transient is given by

$$\Delta C(t) = \Delta C(0) [1 - \exp(-t/\tau)], \quad (2)$$

where

$$\tau = \sigma_n^0 \phi, \quad (3)$$

with  $\sigma_n^0$  being the optical cross-section for the transition from the level to the conduction band and  $\phi$  the photon flux. The latter quantity was measured separately and hence  $\sigma_n^0$  was found. A spectrum at 55 K is shown in Fig. 1. Because it is difficult to make a precise measurement of the absolute value of  $\phi$  within the depletion region, the relative value of  $\sigma_n^0$  is shown in the figure. Measurements at 80 and 110 K gave almost identical results. Measurements could not be made at higher temperatures because thermal emission from the level becomes faster than optical emission.

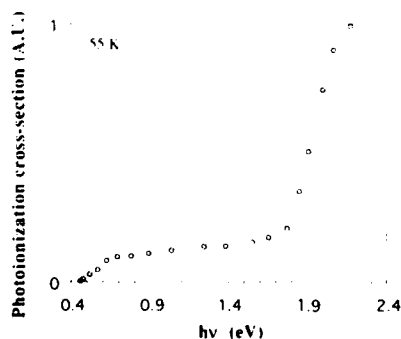


Fig. 1. The photoionization spectrum at 55 K for transitions from a level in ZnSe to the conduction band.

The spectrum of  $\sigma_n^0$  has two thresholds. By comparison with the pseudopotential calculations of Chelikowsky and Cohen [1], we attribute the first threshold to a transition from the level to the  $\Gamma$  valley and the second to transitions from the level to the L valleys. The energy separation of the thresholds,  $1.26 \pm 0.06$  eV, agrees within the experimental and calculational uncertainty with the calculated value for the  $\Gamma$ -L spacing of 1.20 eV. According to the calculation, the  $\Gamma$ -X spacing is 1.78 eV, beyond the range of our measurements. The upper limit of the range is imposed by the fact that, as in all ZnSe material which we have examined, there is a large concentration of levels at 0.7 eV above the valence band, i.e. 2.1 eV below the conduction band. Because transitions are seen with large amplitude out to the edge of the Brillouin zone, the centre must have a spread of its wavefunction in  $r$ -space which is substantially confined within one unit cell.

From the capacitance measurements the concentration of the level is estimated to be  $3 \times 10^{14} \text{ cm}^{-3}$ , much smaller than  $N_D - N_A$ , which is  $9 \times 10^{15} \text{ cm}^{-3}$ .

Thermal emission rates were determined by applying a forward bias to fill some of the centres and measuring the capacitance transient due to thermal emptying after the bias was removed. This is similar to a single-shot DLTS experiment. The temperature range was 118–150 K. Below 118 K the rate is too slow for accurate measurements; this is the range in which photoionization experiments are possible. Above 150 K the rate is too fast for our capacitance bridge. The thermal emission rate  $e_n^1$  was found by fitting the transient to an exponential.

There is a detailed balance relation between  $e_n^1$ , the capture cross-section  $\sigma$ , the thermal velocity  $v$ , the effective density of states  $N_c$  and the activation energy  $E$ :

$$e_n^1 = \sigma v N_c \exp(-E/kT). \quad (4)$$

For easy comparison of data, it is conventional to take  $\sigma$  and  $E$  as being independent of temperature. The combination  $v N_c$  gives a  $T^2$  dependence, so one makes an Arrhenius plot of the logarithm of  $e_n^1 T^2$  against  $T^{-1}$ . An apparent activation energy  $E$  is obtained from the slope



and an apparent cross-section from the absolute value. A much more detailed investigation is required if the actual values of the Gibbs free energy of activation and the actual cross-section averaged over the electron energy distribution are to be found. Using the simple analysis, the values obtained are  $E = 0.33 \pm 0.02$  eV and  $\sigma = 1.4 \times 10^{-14}$  cm<sup>2</sup>. Several authors have reported a level in ZnSe, measured by DLTS, with apparent activation energy, apparent cross-section and concentration similar to the values we find. Because of the difference in technique our results cover a different temperature range than the DLTS results. Fig. 2 shows the DLTS results for level B of Shirakawa and Kukimoto [2], level E<sub>2</sub> of Verity et al. [3], level E2 of Kosai [4] and level E<sub>1</sub> of Yoneda et al. [5] together with our own data. It is probable that all these levels are the same, with differences in the data being due to the electrical field in the depletion region which varies between different experiments.

Capture rates were measured by the technique of applying short forward bias pulses to fill some centres and deducing the concentration of centres which have been filled from the magnitude of the resultant change in capacitance. Without a detailed analysis of the effects of the edge of the space charge region, the values of the capture cross-section found by this method are not accurate but are adequate for comparison purposes. Fig. 3 shows the value of  $\sigma$  over the temperature range 77–110 K. There is a weak dependence on temperature.

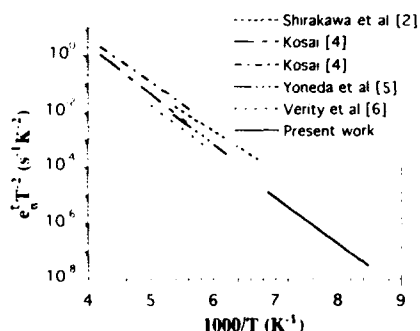


Fig. 2. Arrhenius plots of the emission rate of a level in ZnSe, as determined by various authors.

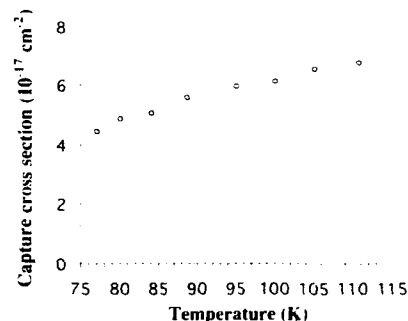


Fig. 3. The capture cross-section for electrons at a level in ZnSe as a function of temperature

There is a large difference between the apparent thermal energy 0.33 eV and the photoionization threshold 0.46 eV, and between the apparent cross-section  $1.4 \times 10^{-14}$  cm<sup>2</sup> and the measured value  $6 \times 10^{-17}$  cm<sup>2</sup>. Because, over the temperature range of measurement, the photoionization threshold energy and the capture cross-section do not vary strongly with temperature it is probable that the differences between apparent and actual values are largely due to electric field effects. Emission occurs in the high field of the depletion region but capture occurs at forward bias when the field is small, so Eq. (4) cannot be used to relate the experimentally measured quantities. Hu et al. [6] have observed strong electrical field effects for other centres in ZnSe. There have been suggestions in the literature that a photoionization threshold at 0.7 eV is associated with the level having an apparent thermal energy of 0.33 eV, implying a very strong lattice interaction. However, the 0.7 eV threshold was obtained by the initial-slope technique which picks out centres with large values of  $N_T \sigma_n^0$  rather than the centres with highest concentration, so this threshold is probably related to a different centre.

### 3. Conclusions

A sample of ZnSe has been found which has a single dominant level in the upper half of the band gap. Measurements of emission and capture rates show that the centre is probably the same as

one frequently observed in DLTS measurements. Differences between the values of the apparent activation energy and capture cross-section reported by different groups are attributed to electrical field effects. The photoionization spectrum has two thresholds, associated with transitions to different valleys in the conduction band. From the energy difference between the thresholds the  $\Gamma$ –L intervalley spacing is found to be  $1.26 \pm 0.06$  eV. This is the first time that direct experimental evidence for the intervalley spacing has been obtained for ZnSe.

#### 4. References

- [1] J.R. Chelikowsky and M.L. Cohen, *Phys. Rev. B* 14 (1976) 556.
- [2] Y. Shirakawa and H. Kukimoto, *J. Appl. Phys.* 51 (1980) 5859.
- [3] D. Verity, F.J. Bryant, J.J. Davies, J.E. Nicholls, C.G. Scott and D. Shaw, *J. Phys. C (Solid State Phys.)* 15 (1982) 5497.
- [4] K. Kosai, *J. Appl. Phys.* 53 (1982) 1018.
- [5] K. Yoneda, Y. Hishida and H. Ishii, *Appl. Phys. Lett.* 47 (1985) 702.
- [6] B. Hu, G. Karczewski, H. Luo, N. Samarth and J.K. Furdyna, *Phys. Rev. B* 47 (1993) 9641.



ELSEVIER

Journal of Crystal Growth 138 (1994) 508–512

JOURNAL OF  
**CRYSTAL  
GROWTH**

## Measurement of the $\text{MgSe}/\text{Cd}_{0.54}\text{Zn}_{0.46}\text{Se}$ valence band offset by X-ray photoelectron spectroscopy

M.W. Wang <sup>\*,a</sup>, J.F. Swenberg <sup>a</sup>, R.J. Miles <sup>a</sup>, M.C. Phillips <sup>a</sup>, E.T. Yu <sup>a,1</sup>,  
J.O. McCaldin <sup>a</sup>, R.W. Grant <sup>b</sup>, T.C. McGill <sup>a</sup>

<sup>a</sup> T.J. Watson, Sr., Laboratory of Applied Physics California Institute of Technology, Pasadena, California 91125, USA

<sup>b</sup> Rockwell International Science Center, Thousand Oaks, California 91360, USA

### Abstract

We have used X-ray photoelectron spectroscopy to measure the valence band offset for the  $\text{MgSe}/\text{Cd}_{0.54}\text{Zn}_{0.46}\text{Se}$  heterojunction grown by molecular beam epitaxy. Lattice matching and cubic zincblende growth were confirmed using X-ray diffraction and reflection high energy electron diffraction. By measuring core level to valence band maximum and core level to core level energy separations, we obtain a value of  $0.50 \pm 0.10$  eV for the valence band offset, with the valence band maximum of  $\text{MgSe}$  below that of  $\text{Cd}_{0.54}\text{Zn}_{0.46}\text{Se}$ . This value deviates from the common anion rule, as may be expected given the unoccupied cation d orbitals in  $\text{MgSe}$ . Application of our results to the design of current II–VI light emitters incorporating  $\text{Zn}_{1-x}\text{Mg}_x\text{S}_y\text{Se}_{1-y}$  and  $\text{Mg}_x\text{Cd}_{1-x}\text{Se}$  layers is discussed.

### 1. Introduction

The importance of Mg-based semiconductor compounds for II–VI wide bandgap light emitters has recently been demonstrated. In particular, the blue-green laser diodes (LDs) initially demonstrated by Haase et al. [1] are now fabricated with  $\text{Zn}_{1-x}\text{Mg}_x\text{S}_y\text{Se}_{1-y}$  cladding layers [2], resulting in the demonstration of the first blue LD [3] and the pulsed operation of pseudomorphic blue-green LDs up to temperatures as high as 394 K [4]. In addition, compositionally graded  $\text{Mg}_x$

$\text{Cd}_{1-x}\text{Se}$  used as an electron injector in the green light emitting diode (LED) design proposed by Phillips et al. [5] results in a device with nearly ideal current-voltage characteristics and favorable device lifetimes [6]. Finally, simulations show that  $\text{Mg}_x\text{Zn}_{1-x}\text{Te}$  layers can be used to shorten the wavelength of light emission in the graded electron injector devices [7].

To optimize the performance of these devices, an accurate measurement of the band offset between Mg-based semiconductors and other materials will be required. The importance of the valence band offset (VBO) to LED and LD design is considerable: the appropriate Mg concentrations needed in both the graded  $\text{Mg}_x\text{Cd}_{1-x}\text{Se}$  region and the  $\text{Zn}_{1-x}\text{Mg}_x\text{S}_y\text{Se}_{1-y}$  cladding layers are dependent on the respective VBOs, especially as the wavelength of light emission is extended

\* Corresponding author.

<sup>1</sup> Now at Department of Electrical and Computer Engineering, University of California at San Diego, La Jolla, California 92093, USA.

into the blue. Currently, the LD designs incorporating  $\text{Zn}_{1-x}\text{Mg}_x\text{S}_y\text{Se}_{1-y}$  layers assume a type I band lineup between  $\text{Zn}_{1-x}\text{Mg}_x\text{S}_y\text{Se}_{1-y}$  and  $\text{ZnS}_{1-z}\text{Se}_z$ , based on the common anion rule and experimental data in ref. [2] and on a semi-empirical tight binding method in ref. [9]. The devices using  $\text{Mg}_x\text{Cd}_{1-x}\text{Se}$  for a graded injector were also designed using the common anion rule.

The original common anion rule [8] was observed not to apply to the one cation, Al, then studied from the third row of the periodic table, so we should not expect it to necessarily apply to Mg, another third row cation. Similarly, Wei and Zunger [10] predict that the common anion rule applies only when the d orbitals of the cations on both sides of a heterojunction, e.g.  $\text{MgSe}/\text{Cd}_{0.54}\text{Zn}_{0.46}\text{Se}$ , interact with their respective valence bands in a comparable manner. Since the 3d orbitals in Mg are unoccupied, as in the case of Al, we might expect a deviation from the common anion rule similar to that observed in the AlAs/GaAs system.

In this paper we report the measurement of the  $\text{MgSe}/\text{Cd}_{0.54}\text{Zn}_{0.46}\text{Se}$  VBO by X-ray photoelectron spectroscopy (XPS). This system was chosen to avoid difficulties associated with measuring band offsets in lattice mismatched systems, and to test the validity of the common anion rule for Mg based compounds. Using our measured value for the  $\text{MgSe}/\text{Cd}_{0.54}\text{Zn}_{0.46}\text{Se}$  VBO, we can estimate the the  $\text{Zn}_{1-x}\text{Mg}_x\text{S}_y\text{Se}_{1-y}/\text{ZnS}_{1-z}\text{Se}_z$  and  $\text{Mg}_x\text{Cd}_{1-x}\text{Se}/\text{CdSe}$  VBOs by linear interpolation.

Section 2 of this paper describes the sample growth and the XPS experimental setup. Section 3 outlines the XPS data analysis. In section 4, we present and discuss our results, and we conclude with section 5.

## 2. Experiment

The structures studied here were grown in two Perkin-Elmer 430P molecular-beam epitaxy (MBE) systems, one devoted to III–V and the other to II–VI semiconductor growth. GaSb buffer layers were grown on GaSb (100) substrates to provide a smooth growth surface. After

the GaSb growth, the samples were transferred via an ultrahigh vacuum (UHV) transfer tube to the II–VI growth chamber. Thick ( $> 3000$  Å), relaxed  $\text{Cd}_{0.54}\text{Zn}_{0.46}\text{Se}$  layers, followed by the band offset structures, were grown at a substrate temperature of  $270^\circ\text{C}$  and a growth rate of approximately  $53$  Å/min. The  $\text{Cd}_{0.54}\text{Zn}_{0.46}\text{Se}$  composition was calibrated using XPS and X-ray diffraction. The measured  $\text{Cd}_{0.54}\text{Zn}_{0.46}\text{Se}$  lattice parameter was  $5.93$  Å, allowing us to neglect its small lattice mismatch (0.68%) to  $\text{MgSe}$  [2]. All layers were grown in the cubic zincblende structure as indicated by reflection high energy electron diffraction patterns.

Following the II–VI growth, the samples were transferred via an UHV transfer tube to a Perkin-Elmer Model 5500 analysis system with a monochromatic Al  $K\alpha$  X-ray source ( $h\nu = 1486.6$  eV). The base pressure in the XPS chamber was typically  $\sim 3 \times 10^{-10}$  Torr. Using measured XPS Au 4f core level peaks (HWHM =  $0.37$  eV), the instrumental resolution function of the system was modeled as a Voigt function with a Lorentzian fraction of 0.06, and a HWHM of  $0.28$  eV.

The core level to valence band maximum (VBM) energy separations were measured on two bulk  $\text{Cd}_{0.54}\text{Zn}_{0.46}\text{Se}$  and two bulk  $\text{MgSe}$  samples. The core level binding energy separations were measured on two thin ( $\sim 20$  Å)  $\text{Cd}_{0.54}\text{Zn}_{0.46}\text{Se}$  on  $\text{MgSe}$  samples, and one thin  $\text{MgSe}$  on  $\text{Cd}_{0.54}\text{Zn}_{0.46}\text{Se}$  sample. XPS energy separations measured on the same sample under identical conditions were typically reproducible to better than  $\pm 0.02$  eV. Commutativity of the band offset was confirmed, and all samples yielded energy separations that were reproducible to within experimental error.

## 3. XPS measurements and data analysis

To determine the  $\text{MgSe}/\text{Cd}_{0.54}\text{Zn}_{0.46}\text{Se}$  VBO using XPS we used the following relation:

$$\Delta E_{\text{VBM}} = (E_{\text{Zn } 3p_{3/2}} - E_{\text{CdZnSe}}^{\text{VBM}}) - (E_{\text{Mg } 2s} - E_{\text{MgSe}}^{\text{VBM}}) - (E_{\text{Zn } 3p_{3/2}} - E_{\text{Mg } 2s}), \quad (1)$$

where the three terms are XPS binding energy separations as measured on bulk  $\text{Cd}_{0.54}\text{Zn}_{0.46}\text{Se}$ , bulk  $\text{MgSe}$  and  $\text{Cd}_{0.54}\text{Zn}_{0.46}\text{Se}/\text{MgSe}$  or  $\text{MgSe}/\text{Cd}_{0.54}\text{Zn}_{0.46}\text{Se}$  heterojunctions respectively, as shown in Fig. 1. For  $\text{MgSe}$  the use of either the  $\text{Mg}2s$  or the  $\text{Mg}2p$  core level peaks in the analysis did not affect the results. For  $\text{Cd}_{0.54}\text{Zn}_{0.46}\text{Se}$ , the only resolvable core level peak is  $\text{Zn}3p$ , since  $\text{Se}$  is common to both sides of the junction and both the  $\text{Cd}4d$  and  $\text{Zn}3d$  peaks overlap with states from the valence band.

To determine the core level peak positions, we first performed an integrated background subtraction and then fit the peaks to Voigt functions, allowing the binding energy, HWHM, Lorentzian fraction and intensity to vary. In the case of the  $\text{MgSe}/\text{Cd}_{0.54}\text{Zn}_{0.46}\text{Se}$  heterojunction samples, the  $\text{Zn}3p_{3/2}$  and  $\text{Mg}2s$  core levels overlap, and it was necessary to constrain the peak shapes to those obtained from bulk  $\text{MgSe}$  and  $\text{Cd}_{0.54}\text{Zn}_{0.46}\text{Se}$  samples, so as to reduce the number of fit parameters. The resulting fit for the  $\text{Zn}3p_{3/2}$  and  $\text{Mg}2s$  core levels is shown in Fig. 2.

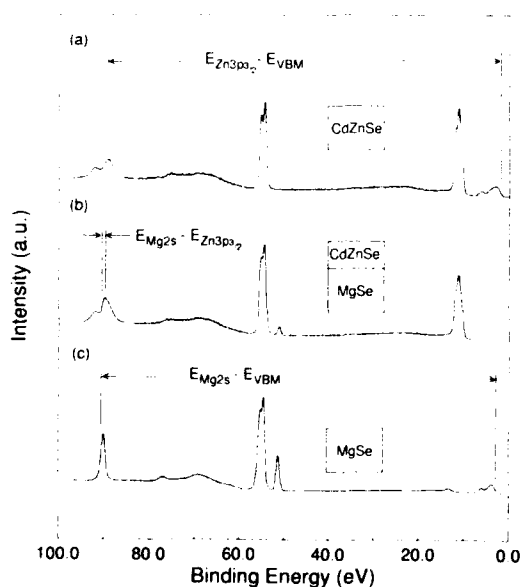


Fig. 1. XPS spectra for (a) bulk  $\text{Cd}_{0.54}\text{Zn}_{0.46}\text{Se}$ , (b) thin ( $\sim 20$  Å)  $\text{Cd}_{0.54}\text{Zn}_{0.46}\text{Se}$  on  $\text{MgSe}$ , and (c) bulk  $\text{MgSe}$ . Energy separations used in the band offset measurement are labeled.

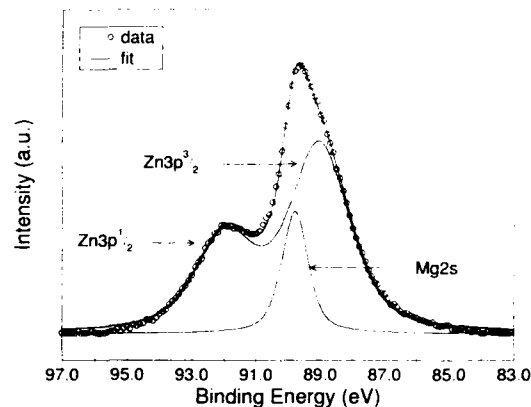


Fig. 2. Least squares fit of  $\text{Zn}3p_{3/2}$  and  $\text{Mg}2s$  core level peaks for 20 Å  $\text{MgSe}$  on  $\text{Cd}_{0.54}\text{Zn}_{0.46}\text{Se}$ . Four parameters (intensity and binding energy of each peak) were used in the fit.

To determine the VBM position, we followed the procedure outlined in ref. [11]. Briefly, this involves using a calculated band structure for each material to determine a theoretical valence band density of states (VB DOS). This VB DOS is then convolved with the instrumental resolution function. Finally, the instrumentally broadened theoretical VB DOS is fit to the experimental VB DOS to obtain the position of the VBM.

For  $\text{Cd}_{0.54}\text{Zn}_{0.46}\text{Se}$  the best fit for the VB DOS was obtained using the band structure of  $\text{ZnSe}$  calculated by the pseudopotential method [12], while allowing one additional energy scaling parameter to account for differences in the band structure of  $\text{ZnSe}$  versus  $\text{Cd}_{0.54}\text{Zn}_{0.46}\text{Se}$ . Spin-orbit interactions [13,14] and an electron effective mass parameter to incorporate the nonlocality of the pseudopotential [15] were included in the calculations. The critical point energies needed for the pseudopotential calculations, and parameters needed to determine the spin-orbit interactions were obtained from refs. [14] and [16,17] respectively.

For  $\text{MgSe}$  the empirical pseudopotential method could not be used since very little is known of its band structure. Instead, we calculated the  $\text{MgSe}$  band structure using the semiempirical linear combination of atomic orbitals method [18], including spin-orbit interactions

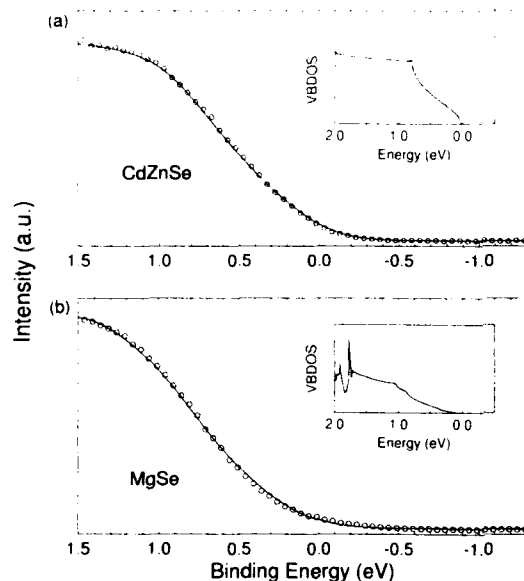


Fig. 3. Fit of experimental VBDOS ( $\circ$ ) and instrumentally broadened theoretical VBDOS (—) for (a)  $\text{Cd}_{0.54}\text{Zn}_{0.46}\text{Se}$ , and (b)  $\text{MgSe}$ . Insets show the theoretical VBDOS.

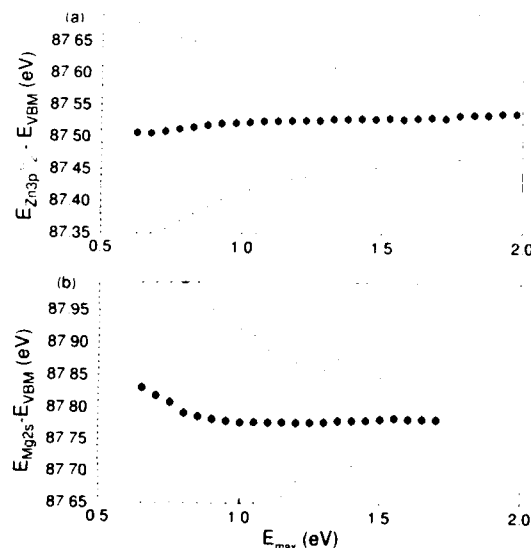


Fig. 4. Core level to VBM separation as function of the maximum binding energy of the fitting interval for (a)  $\text{Cd}_{0.54}\text{Zn}_{0.46}\text{Se}$ , and (b)  $\text{MgSe}$ . Low variance in the energy separations indicates accurate modeling of the experimental VBDOS.

[19], and allowing for the additional energy scaling parameter mentioned above.

Fig. 3 shows the fitted VBDOS for both  $\text{MgSe}$  and  $\text{Cd}_{0.54}\text{Zn}_{0.46}\text{Se}$ . The use of an energy scaling parameter required us to verify the validity of the calculated band structures. To do this we followed the procedure in ref. [11], and varied the VBM fit region as shown in Fig. 4. The small variation of the fitted VBM position as a function of fit region indicates that the VBDOS used accurately models the experimental VBDOS.

#### 4. Results and discussion

The average results from the XPS measurements are  $(E_{\text{Zn}3p_{3/2}} - E_{\text{VBM}(\text{CdZnSe})}) = 87.51 \pm 0.04$  eV,  $(E_{\text{Mg}2s} - E_{\text{VBM}(\text{MgSe})}) = 87.82 \pm 0.04$  eV, and  $(E_{\text{Zn}3p_{3/2}} - E_{\text{Mg}2s}) = 0.81 \pm 0.08$  eV. From Eq. (1) we obtain an average  $\text{MgSe}/\text{Cd}_{0.54}\text{Zn}_{0.46}\text{Se}$  VBO of  $0.50 \pm 0.10$  eV with the VBM of  $\text{MgSe}$  below that of  $\text{Cd}_{0.54}\text{Zn}_{0.46}\text{Se}$ . This deviates from the common anion rule in the same direction and with the same order of magnitude as the  $\text{AlAs}/\text{GaAs}$  system. Since both  $\text{Mg}$  and  $\text{Al}$  are third row elements in the periodic table and have unoccupied d orbitals, this supports the importance of including the repelling effects of cation d orbitals on the VBM in band offset predictions for common anion systems.

To apply the results of this band offset measurement to the design of current II–VI light emitters requires that we estimate the  $\text{Zn}_{1-x}\text{Mg}_x\text{S}_y\text{Se}_{1-y}/\text{ZnS}_{1-z}\text{Se}_z$  and  $\text{Mg}_x\text{Cd}_{1-x}\text{Se}/\text{CdSe}$  band offsets based on our new results. Using the  $\text{ZnSe}/\text{ZnS}$  band offset obtained from ref. [20], assuming a linear dependence of the band offset on composition, and neglecting strain effects, we estimate the  $\text{Zn}_{0.79}\text{Mg}_{0.21}\text{S}_{0.3}\text{Se}_{0.7}/\text{ZnS}_{0.06}\text{Se}_{0.94}$  VBO to be roughly 0.29 eV versus 0.19 eV obtained using the common anion rule. The corresponding conduction band offsets are 0.04 and 0.14 eV, respectively. These quantities are approximate; however, the qualitative trend indicates that the  $\text{Mg}$  and  $\text{S}$  concentrations in the  $\text{Zn}_{1-x}\text{Mg}_x\text{S}_y\text{Se}_{1-y}$  layers may need to be increased in the LD design for adequate electron confinement, especially if the wavelength of light

emission is extended further into the blue. Our results indicate that the Mg concentration in the  $\text{Mg}_x\text{Cd}_{1-x}\text{Se}$  layer for the graded electron injector device should also be increased for efficient carrier injection.

## 5. Conclusions

We have measured the VBO of the lattice matched  $\text{MgSe}/\text{Cd}_{0.54}\text{Zn}_{0.46}\text{Se}$  heterojunction using XPS. The measured VBO was  $0.50 \pm 0.10$  eV with the VBM of MgSe below that of  $\text{Cd}_{0.54}\text{Zn}_{0.46}\text{Se}$ . This value deviates significantly from the common anion rule, and supports the importance of cation d orbitals in VBOs for common anion heterojunctions. Our measured VBO indicates that the Mg and S concentrations in  $\text{Zn}_{1-x}\text{Mg}_x\text{S}_y\text{Se}_{1-y}$  cladding layers may need to be higher than previously thought for adequate electron carrier confinement, particularly as the emission wavelength is shortened. Also, the Mg concentration in  $\text{Mg}_i\text{Cd}_{1-i}\text{Se}$  grading layers needs to be increased for efficient electron injection in the graded electron injector devices.

## 6. Acknowledgment

This work was supported by the Advanced Research Projects Agency monitored under ONR Contract N00014-92-J-1845.

## 7. References

- [1] M.A. Haase, J. Qiu, J.M. DePuydt and H. Cheng, *Appl. Phys. Lett.* 59 (1991) 1272.
- [2] H. Okuyama, K. Nakano, T. Miyajima and K. Akimoto, *Jap. J. Appl. Phys.* 30 (1991) L1620.
- [3] H. Okuyama, T. Miyajima, Y. Morinaga, F. Hiei, M. Ozawa and K. Akimoto, *Electron. Lett.* 28 (1992) 1798.
- [4] J.M. Gaines, R.R. Drenten, K.W. Haberern, T. Marshall, P. Mensz and J. Petruzzello, *Appl. Phys. Lett.* 62 (1993) 2462.
- [5] M.C. Phillips, M.W. Wang, J.F. Swenberg, J.O. McCaldin and T.C. McGill, *Appl. Phys. Lett.* 61 (1992) 1962.
- [6] J.F. Swenberg, M.W. Wang, R.J. Miles, M.C. Phillips, A.T. Hunter, J.O. McCaldin and T.C. McGill, *J. Crystal Growth* 138 (1994) 692.
- [7] M.W. Wang, M.C. Phillips, J.F. Swenberg, E.T. Yu, J.O. McCaldin and T.C. McGill, *J. Appl. Phys.* 73 (1993) 4660.
- [8] J.O. McCaldin, T.C. McGill and C.A. Mead, *Phys. Rev. Lett.* 36 (1976) 56.
- [9] Y. Morinaga, H. Okuyama and K. Akimoto, *Jap. J. Appl. Phys.* 32 (1993) 678.
- [10] S. Wei and A. Zunger, *Phys. Rev. Lett.* 59 (1987) 144.
- [11] E.A. Kraut, R.W. Grant, J.R. Waldrop and S.P. Kowalczyk, *Phys. Rev. B* 28 (1983) 1965.
- [12] M.L. Cohen and T.K. Bergstresser, *Phys. Rev.* 141 (1966) 789.
- [13] L.R. Saravia and D. Brust, *Phys. Rev.* 176 (1968) 915.
- [14] J.R. Chelikowsky and M.L. Cohen, *Phys. Rev. B* 14 (1976) 556.
- [15] J. Chelikowsky, D.J. Chadi and M.L. Cohen, *Phys. Rev. B* 8 (1973) 2786.
- [16] F. Herman and S. Skillman, *Atomic Structure Calculations* (Prentice-Hall, Englewood Cliffs, NJ, 1963).
- [17] F. Herman, C.D. Kuglin, K.F. Cuff and R.L. Kortum, *Phys. Rev. Lett.* 11 (1963) 541.
- [18] W.A. Harrison, *J. Vac. Sci. Technol.* 14 (1977) 1016.
- [19] M.D. Jaffe and J. Singh, *Solid State Commun.* 62 (1987) 399.
- [20] K. Shahzad, D.J. Olego and C.G. Van de Walle, *Phys. Rev. B* 38 (1988) 1417.



ELSEVIER

Journal of Crystal Growth 138 (1994) 513–516

JOURNAL OF  
**CRYSTAL  
GROWTH**

## Superlattice effects on phonons in strained ZnTe–ZnSe structures

J. Frandon <sup>\*,a</sup>, M.A. Renucci <sup>a</sup>, N. Briot <sup>b</sup>, O. Briot <sup>b</sup>, R.L. Aulombard <sup>b</sup>

<sup>a</sup> *Laboratoire de Physique des Solides (URA 074 CNRS), Université P. Sabatier, 118 Route de Narbonne,  
F-31062 Toulouse Cedex, France*

<sup>b</sup> *Groupe d'Etudes des Semiconducteurs (URA 357 CNRS), USTL, Place Eugène Bataillon, F-34095 Montpellier Cedex, France*

### Abstract

Raman measurements are used to probe the built-in strain due to the large lattice mismatch in two short-period ZnSe–ZnTe superlattices. In the largest period structure, local information on confinement and strain effects in the different layers is deduced from the LO phonon frequencies. An estimate of the in-plane strain gives evidence of a partial relaxation of both layers; in this structure, folded acoustical phonons are clearly observed under resonant conditions. The Raman spectra of the shortest period superlattice are characterized by a unique structure assigned to an unusual propagative mode resulting from the overlap of the optical bands of the two constituents.

### 1. Introduction

The strain state of periodic artificial structures combining lattice-mismatched materials may play a major role in lattice dynamics, by governing the overlap of the longitudinal phonon dispersion curves of the two constituents and thus, the true nature (propagative or confined) of vibrational modes. In ZnTe–ZnSe superlattices, the large lattice mismatch (7.4%) is expected to generate an isotropic in-plane strain field, likely to induce an overlap of the strain-free optical bands of the two materials. Indeed, the zone centre phonon in ZnTe [1] is quasi-degenerate with its X zone edge counterpart in ZnSe [2], both mostly implying motions of the lightest zinc atoms.

Raman scattering, which has demonstrated its ability and sensitivity as a vibrational spectroscopy in superlattices studies [3], was used to probe phonons in short-period ZnSe–ZnTe superlattices. The structures were examined with various exciting wavelengths, in order both to take advantage of resonance effects and to achieve a depth profile of the samples.

### 2. Experimental procedure

Two short-period superlattices (ZnSe<sub>7</sub>–ZnTe<sub>14</sub> and ZnSe<sub>4</sub>–ZnTe<sub>7</sub>) were grown by metalorganic vapour phase epitaxy under an overall pressure of 400 Torr, at 300°C. ZnSe buffer layers, 200 nm thick, were deposited on (001) GaAs substrates, prior to the epitaxial growth of 80 alternating layers. Details on precursors and growth conditions have been given elsewhere [4,5].

\* Corresponding author.



The superlattice period was determined by double X-ray diffraction technique and the quality of interfaces checked by transmission electron microscopy (TEM) experiments. Reflectance and photoreflectance measurements carried out on the largest period sample ( $d = 6$  nm) at low temperature evidenced type II excitations at 2.52 and 2.65 eV, tentatively attributed to  $e_1$ - $hh_1$  ( $\Gamma$ ) and  $e_1$ - $hh_2$  ( $X_2$ ) transitions, respectively [4].

The Raman measurements were performed at room temperature, in an internal backscattering geometry along the [001] direction. The exciting radiation was provided by  $Ar^+$  and  $Kr^+$  ion lasers operating at different wavelengths. The scattered light was analysed with a T800 Coderg triple monochromator and detected by conventional photon counting electronics.

### 3. Raman results and discussion

Fig. 1 displays the unanalysed spectra recorded from the  $ZnSe_7$ - $ZnTe_{14}$  superlattice. The exciting energy was varied from above ( $\lambda_L = 457.9$  nm) to below ( $\lambda_L = 647.1$  nm) the band gap, as shown by the increase in intensity of the signal at  $292.5\text{ cm}^{-1}$  originating from the GaAs substrate.

Direct evidence of superlattice formation is given in the insert, where the first LA doublet, folded at the minizone centre by the new periodicity, merges at  $24.8\text{ cm}^{-1}$  for photons nearly resonant with the  $e_1$ - $hh_1$  ( $\Gamma$ ) transition. According to the layered elastic continuum model of Rytov [6], the doublet frequencies may be calculated from the LA dispersion curves of ZnTe and ZnSe [1,2]. For backscattering geometry with  $\lambda_L = 514.5$  nm, the upper component frequency is estimated to be  $21.7\text{ cm}^{-1}$ . The disagreement with experiment could result from strain-induced changes in elastic velocities or uncertainties in the value of the superlattice period.

The spectrum for  $\lambda_L = 457.9$  nm differs from the others in the optical frequency range, with the emergence of a complex structure peaking at  $252.5\text{ cm}^{-1}$ . In spite of strong absorption, the main peak comes from the ZnSe buffer layer, as evidenced by its frequency and its enhancement for outgoing photons in resonance with the ZnSe

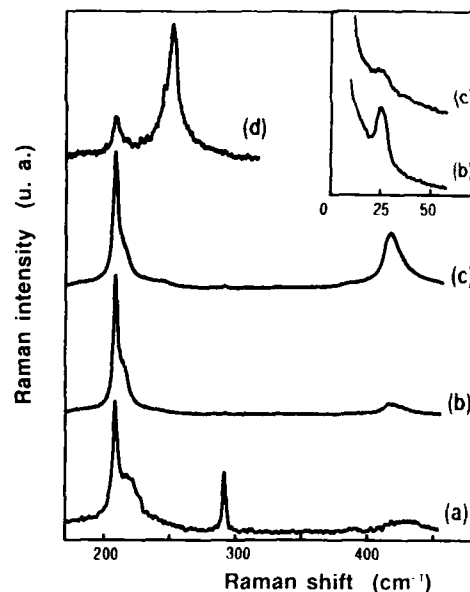


Fig. 1. Unanalysed Raman spectra of the  $ZnSe_7$ - $ZnTe_{14}$  superlattice recorded at room temperature, using the following laser wavelengths: (a)  $\lambda_L = 647.1$  nm; (b)  $\lambda_L = 514.5$  nm; (c)  $\lambda_L = 488.0$  nm; (d)  $\lambda_L = 457.9$  nm. Insert: low frequency side of the Raman spectra.

band gap at 2.67 eV. The weak and discrete lines observed on its low-frequency side are attributed to optical modes confined in the ZnSe layers, which can be described as standing waves, the frequency of which are given by the bulk dispersion relation  $\omega(q)$  for:

$$q_n = n\pi / (d_1 + \frac{1}{2}a_1), \quad (1)$$

where  $n$  is an integer,  $d_1$  the layer width and  $a_1$  the lattice parameter of bulk ZnSe [7]. The  $245.5\text{ cm}^{-1}$  line is identified as the  $n=2$  confined mode owing to its polarization selection rules (not discussed in the present paper). Its downwards shift  $\Delta\omega = -7\text{ cm}^{-1}$  with respect to the zone centre LO phonon of bulk ZnSe has two components, due respectively to confinement and strain effects:

$$\Delta\omega = \Delta\omega_{\text{confinement}} + \Delta\omega_{\text{strain}}. \quad (2)$$

From the LO phonon dispersion curves of ZnSe [2], we calculated  $\Delta\omega_{\text{confinement}} = -4\text{ cm}^{-1}$  for  $d_1 = 2$  nm and then  $\Delta\omega_{\text{strain}} = -3\text{ cm}^{-1}$ . Using

for the strain induced shift the equations and the data from Cerdeira et al. [8], we obtained the relation:

$$\Delta\omega_{\text{strain}} = -414\epsilon, \quad (3)$$

where  $\epsilon$  is the in-plane strain, from which a built-in tensile strain of 0.7% is deduced for the ZnSe layers.

All the spectra exhibit a sharp peak at  $208.5 \text{ cm}^{-1}$ , which gives further evidence of superlattice formation, owing to the resonant behaviour of this structure and of its overtone at  $417 \text{ cm}^{-1}$  when the energy of the outgoing photons is tuned on the  $e_1\text{-}hh_1$  ( $\Gamma$ ) excitation. The  $B_2$  symmetry (as determined by polarization measurements) and the frequency,  $2 \text{ cm}^{-1}$  higher than that of the zone centre LO phonon of ZnTe, suggest an  $n = 1$  confined mode in strained ZnTe layers. As the frequency shift due to confinement nearly balances the strain effect, a residual compressive strain of 0.9% is deduced from (1), using  $\Delta\omega_{\text{confinement}} = -1 \text{ cm}^{-1}$ , and

$$\Delta\omega_{\text{strain}} = -284\epsilon, \quad (4)$$

from ref. [8]. According to the Raman results, the  $\text{ZnSe}_7\text{-ZnTe}_{14}$  superlattice is thus partly relaxed.

Interface smudging associated to the admixture of lighter selenium atoms in ZnTe layers could be responsible for the structure observed around  $220 \text{ cm}^{-1}$ , the single mode frequency of  $\text{ZnSe}_x\text{-ZnTe}_{1-x}$  solid solutions for  $x \approx 0.2$  [9].

The Raman spectra from the  $\text{ZnSe}_4\text{-ZnTe}_7$  superlattice are somewhat different, as shown in Fig. 2. A broad band centred at  $217 \text{ cm}^{-1}$  constitutes the unique Raman signature of the superlattice, besides the signal from ZnSe showing up in resonant conditions and that from the GaAs substrate, both previously identified. The single mode appearance likely results from the overlap of the two LO phonon bands induced by strain, as discussed in the following. From relation (4), the  $20 \text{ cm}^{-1}$  upward shift of the ZnTe optical band, required for an overlap in the  $205\text{--}225 \text{ cm}^{-1}$  range, should be induced by an in-plane deformation close to the lattice mismatch for bulk constituents, as expected for pseudomorphic growth in relation to the buffer layer. This coherent growth is otherwise supported by the value of

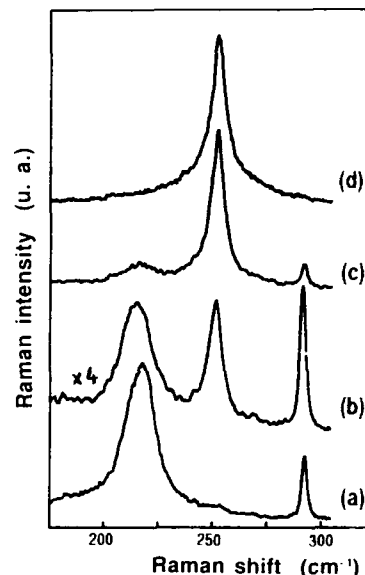


Fig. 2. Unanalysed Raman spectra of the  $\text{ZnSe}_4\text{-ZnTe}_7$  superlattice recorded at room temperature, using the following laser wavelengths: (a)  $\lambda_1 = 514.5 \text{ nm}$ ; (b)  $\lambda_1 = 472.7 \text{ nm}$ ; (c)  $\lambda_1 = 465.8 \text{ nm}$ ; (d)  $\lambda_1 = 457.9 \text{ nm}$ .

critical thickness of ZnTe layers on ZnSe [5]. According to this assumption, modes propagating throughout the superlattice are expected in the  $205\text{--}225 \text{ cm}^{-1}$  frequency range. As these folded modes are very close to each other, they form a continuum responsible for the observed band. On the other hand, the interpretation of this band in terms of alloying effects (due to interface smudging) only can be ruled out, in view of TEM observations.

#### 4. Conclusion

Raman measurements have evidenced different strain effects in short-period ZnTe–ZnSe superlattices, grown by MOVPE on ZnSe buffer layers. The first one (period 6 nm) has been proved to be close to a fully relaxed configuration. The strain field in the second one ( $d = 3.3 \text{ nm}$ ) is essentially localized in ZnTe layers, in accordance with a pseudomorphic growth in relation to the buffer.

### 5. Acknowledgements

This study was partly supported by the Commission of European Communities under an ESPRIT III Basic Research contract No. 6675, MTVLE.

### 6. References

- [1] N. Vagelatos, D. Wehe and J.S. King, *J. Chem. Phys.* 60 (1974) 3613.
- [2] B. Hennion, F. Moussa, G. Pepy and K. Kunc, *Phys. Lett. A* 36 (1971) 376.
- [3] J. Cui, H. Wang and F. Gan, *J. Appl. Phys.* 72 (1992) 1521.
- [4] N. Briot, T. Cloitre, O. Briot, B. Gil, D. Berto, C. Jouanin, R.L. Aulombard, J.P. Hirtz and A. Huber, *J. Electron. Mater.* 22 (1993) 537.
- [5] N. Briot, T. Cloitre, O. Briot, P. Boring, B.E. Ponga, B. Gil, R.L. Aulombard, M. Gailhanou, J.M. Salese and A.C. Jones, in: *Proc. Mater. Res. Soc., Spring Meeting Symp.*, San Francisco, 1993 (Mater. Res. Soc., Pittsburgh, PA, to be published).
- [6] S.M. Rytov, *Akust. Zh.* 2 (1956) 71 [*Sov. Phys.-Acoust.* 2 (1956) 68.]
- [7] B. Jusserand and M. Cardona, in: *Light Scattering in Solids V*, Eds. M. Cardona and G. Güntherodt (Springer, Berlin, 1989) p. 49.
- [8] F. Cerdeira, C.J. Buchenauer, F.H. Pollack and M. Cardona, *Phys. Rev. B* 5 (1972) 580.
- [9] S.I. Nakashima, T. Fukumoto and A. Mitsuishi, *J. Phys. Soc. Japan* 30 (1971) 1508.

## Interface morphology studies of liquid phase epitaxy grown HgCdTe films by atomic force microscopy

M. Azoulay, M.A. George, A. Burger \*, W.E. Collins, E. Silberman

*Center for Photonic Materials and Devices, Physics Department, Fisk University, Nashville, Tennessee 37208, U.S.A*

---

### Abstract

In this paper we report an investigation of the morphology of the interfaces of liquid phase epitaxy (LPE) grown HgCdTe thin films on CdTe and CdZnTe substrates by atomic force microscopy (AFM) on freshly cleaved (110) crystallographic planes. An empirical observation which may be linked to lattice mismatch was indicated by an angle between the cleavage steps of the substrate to those of the film. Te precipitates with size ranging from 5 nm to 20 nm were found to be most apparent near the interface.

---

### 1. Introduction

Epitaxially grown HgCdTe (MCT) thin films are often utilized in the manufacture of infrared detectors. The common methods of preparation of MCT thin films include molecular beam epitaxy (MBE), metalorganic chemical vapor deposition (MOCVD) and finally, the most-developed one, liquid phase epitaxy (LPE) [1]. However, even when using the LPE method, there are some difficulties in achieving high perfection and homogeneous MCT films. This is particularly due to interfacial defects which result from lattice mismatch between the substrate and the film. Film imperfections induced during growth consist of structural defects which propagate from the substrate into the film, and of the formation of Te precipitates [2]. The study of the interfacial defects in the cross-section of the film and the substrate is therefore essential and has been in-

deed investigated by various techniques. In the micrometer scale, optical microscopy has been employed to observe macro defects and precipitates [3]. Scanning electron microscopy (SEM) enabled the observation of misfit dislocations and etch pits in the submicrometer scale [4]. Recently, transmission electron microscopy (TEM) and high resolution TEM (HRTEM) have been utilized to study the interface and structural defects down to atomic resolution, revealing point defects, stacking faults, dislocations and twins [5]. However, both these techniques (TEM and HRTEM) require high vacuum conditions and face additional complications in sample preparation, particularly when low electrical conductors are considered. More recently, atomic force microscopy (AFM) has been employed as a very efficient tool for investigating the micromorphology of nanotwins in CdMnTe crystal [6], as well as single atomic layer cleavage steps in CdZnTe crystal [7]. In this article we present, for the first time, an AFM study on the micromorphology of interfaces between HgCdTe films on CdTe substrates (MCT/

---

\* Corresponding author.

CT) and HgCdTe films on CdZnTe substrates (MCT/CZT). The AFM measurements were carried out in the ambient, on freshly cleaved samples; they do not require any special sample preparation and are suitable for characterizing both conducting and insulating surfaces. The ability to image insulators is critical in the case of the MCT/substrate interface where MCT films, which have a low resistivity on the order of about  $10 \Omega \text{ cm}$ , are grown on CT or on CZT substrates which may have resistivities of  $10^7 \Omega \text{ cm}$  and higher.

## 2. Experimental procedure

The MCT films were grown by the conventional liquid phase epitaxy (LPE) method, from Te-rich solutions on (111) CdTe or  $\text{Cd}_{0.96}\text{Zn}_{0.04}\text{Te}$  substrates. The cross-sections of the film/substrate interfaces were established by cleaving the back side of the substrate along the (110) plane and parallel to the epitaxial growth direction, all the way through the MCT film. Optical microscope images of the interfaces between the film and the substrate did not show any defects or precipitates at this resolution.

The AFM studies were done using a Digital Instruments Nanoscope II equipped with piezoelectric tube scanners allowing imaging of cleaved crystals from atomic resolution up to  $130 \mu\text{m}$  maximal scans. The cantilevers were commercial nanoprobe made of gold coated silicon nitride. The force constant of the cantilevers used in this study was taken to be  $0.06 \text{ N/m}$ . This is the value specified by the manufacturers for this particular cantilever although the force constant can vary significantly due to the differences in the thickness of the silicon nitride wafers from which the cantilevers were made [8].

## 3. Discussion

Fig. 1a shows an image of the interface between an MCT film ( $\text{Hg}_{0.76}\text{Cd}_{0.24}\text{Te}$ ) and a CdTe substrate. The scanned area is about  $9 \mu\text{m} \times 9 \mu\text{m}$ . From the AFM images, it was observed that

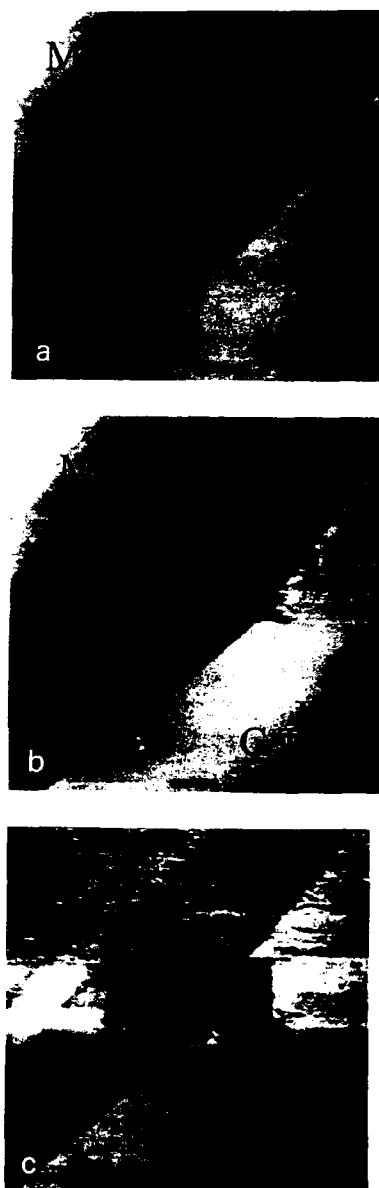


Fig. 1. AFM images on cleaved cross-section, illustrating the tip effect, (a) the image of the first scan, (b) image after scanning a smaller area and (c) image after rescanning the small regions shown in (b) at  $45^\circ\text{C}$  (marker represents  $1 \mu\text{m}$ ).

the film has been modified as a result of the AFM scanning, while the substrate did not have any apparent modification. The scanned area of

Fig. 1a was reimaged and the traces of the previous scans could be clearly visible in the subsequent scans. These traces are attributed to the interaction of the tip with the sample surface. Another image of the small area, shown in Fig. 1b, was obtained at a different scanning angle ( $45^\circ$ ) with respect to the first one. The result of this scan is shown in Fig. 1c, where the evidence of the shaped deformation in the film fits the scanning angles. Once again the substrate did not show any significant deformation, except in the region adjacent to the interface, from the substrate side. This sequence was completed by reimaging the largest area of Fig. 1a, where no

additional deformation to the film was apparent. In this case, the film deformation due to the  $3\ \mu\text{m} \times 3\ \mu\text{m}$  scan, seen in Fig. 1b, has been cleared away, showing a relatively smooth surface near the deformed region achieved by the interaction of the tip with the surface. The conclusion drawn from the series of images in Fig. 1 was that the difference in hardnesses of the film and the substrate required a calibration and adjustment of the force constant of the cantilever, in order to make it possible to analyze the interface with minimum damage to the film.

A force–distance plot provides the magnitude of the interacting forces between the sample and

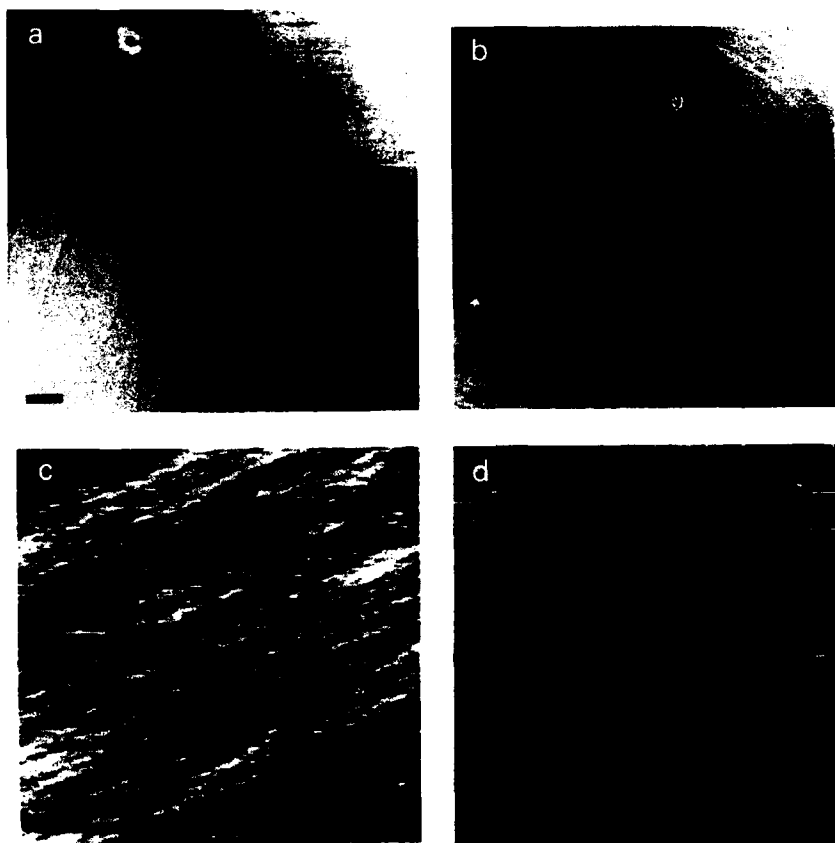


Fig. 2. A sequence of four AFM images on an MCT/CT cleaved cross-section, showing the micromorphology of (a) large area of the interface region, (b) small area of the interface region of higher resolution, (c) the film and (d) the substrate. The markers represent  $1\ \mu\text{m}$  in (a) and (b), and  $0.5\ \mu\text{m}$  in (c) and (d).

cantilever. If the spring constant (force constant)  $k$  of the cantilever is known, the applied force,  $F$ , can be determined. The calculated values of the forces for the film and the substrate were 11.1 and 17.16 nN in the case of MCT/CT, respectively, while for MCT/CZT the values were 13.18 and 17.78 nN, respectively. Zn is known to have the effect of lattice hardening in CdZnTe, increasing the crystal hardness as a function of the Zn content [9]; therefore it appears that the optimal applied force is related to the hardness of the material. Further, the MCT film, grown on the CZT substrate showed a slightly higher force, as compared to that of the MCT film grown on CT. Subsequent imaging required that the applied

forces be calibrated and optimized to image the interface region that would include both the substrate and the film in one image. Figs. 2a and 2b are AFM images of an MCT/CT interface, with no apparent tip effects, for a large area of  $13.6 \mu\text{m} \times 13.6 \mu\text{m}$  followed by a smaller area of  $3.8 \mu\text{m} \times 3.8 \mu\text{m}$ , respectively. In Fig. 2c the film itself is imaged, while in Fig. 2d only the substrate has been scanned. These imaged regions were of  $1.5 \mu\text{m} \times 1.5 \mu\text{m}$ .

As was mentioned earlier, the sample surface profile was performed after cleavage and the profile exhibited the cleavage steps which are clearly observed in Fig. 2a as the straight parallel

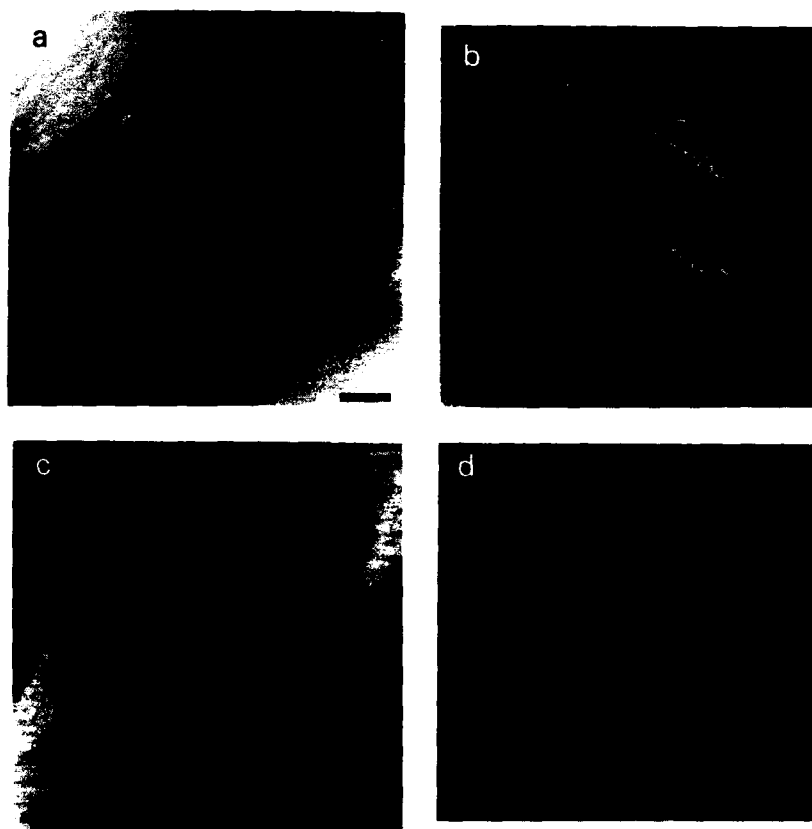


Fig. 3. A sequence of four AFM images on an MCT/CZT cleaved cross-section, showing the micromorphology of (a) large area of the interface region, (b) small area of the interface region with higher resolution, (c) the film and (d) the substrate. The markers represent  $1 \mu\text{m}$  in (a) and (b), and  $0.5 \mu\text{m}$  in (c) and (d).

lines in the substrate. These lines are propagating into the film at an apparent angle,  $\Theta$ , between the cleavage line of the substrate and the cleavage line of the film, designated in Fig. 2b. Another angle,  $\Phi$ , designated in Fig. 2a, was defined between the direction of the cleavage lines of the film and the epitaxial growth direction (perpendicular to the interface). As an empirical observation it appears that these angles,  $\Theta$  and  $\Phi$ , with values of  $25^\circ$  and  $8^\circ (\pm 1^\circ)$ , respectively, may be attributed to lattice mismatch between the film and substrate, which was calculated from the commonly applied expression:  $[a_0(\text{subst.}) - a_0(\text{MCT})]/[a_0(\text{subst.})]$ , and was found to have a value of about  $3 \times 10^{-3}$  for the CdTe substrate. It is evident that the film exhibits more cleavage steps, than the substrate. This is probably due to a high dislocation density near the interface, as a result of the misfit, which is known to occur in MCT/CT interfaces and has been observed by SEM [4].

The average surface roughnesses of the film and the substrate were calculated by utilizing a line-scan function on the images shown in Fig. 2c and Fig. 2d, employing procedures that have been reported recently [10], and found to be 0.32 and 0.17 nm, respectively, which fit the dimension of about one atomic layer.

Fig. 3 presents a sequence of images similar to that of Fig. 2; however, these images are for a MCT film ( $\text{Hg}_{0.79}\text{Cd}_{0.21}\text{Te}$ ), grown on a  $\text{Cd}_{0.96}\text{Zn}_{0.04}\text{Te}$  substrate rather than CdTe. A large area of  $9 \mu\text{m} \times 9 \mu\text{m}$  of the interface and a smaller scan of  $3.9 \mu\text{m} \times 3.9 \mu\text{m}$  with higher resolution are shown in Fig. 3a and Fig. 3b, respectively. In contrast to the MCT/CT system, the shapes of the cleavage steps on the film side are elongated triangles, initiated from the interface and widening towards the surface of the film, where the substrate exhibits fewer and smoother cleavage steps as compared to those of the CdTe. Fig. 3a and Fig. 3b show the images of the film and the substrate regions near the interface at a higher resolution than that of the images of Figs. 2c and 2d, indicating the presence of some Te precipitates [7] in the film, apparent as bright dots in Fig. 3c. The calculated average surface roughnesses of the MCT/CZT sample

Table 1

Summary of various parameters on the micromorphology of the films and the substrates

Film	$\Theta$ (deg)	$\Phi$ (deg)	Misfit	$R_a$ film (nm)	$R_a$ substrate (nm)
MCT/CT	25	8	$3.0 \times 10^{-3}$	0.32	0.17
MCT/CZT	30	3	$4.6 \times 10^{-4}$	0.21	0.15

were found to be slightly lower than those of MCT/CT, with values of 0.21 and 0.15 nm, due to a lower content of precipitates. The angles  $\Theta$  and  $\Phi$ , with values of  $3^\circ$  and  $30^\circ (\pm 1^\circ)$ , respectively, obtained on the MCT/CZT sample, differ significantly from those measured on the MCT/CT interface, apparently due to the lower lattice mismatch of  $4.6 \times 10^{-4}$ .

In summary, an empirical comparison between MCT/CT and MCT/CZT, is shown in Table 1 and may indicate a better crystalline quality of the MCT/CZT sample. AFM images have shown a sharp and smooth interface between the MCT films and substrates, where no apparent macro-defects could be observed with an optical microscope. This is in contrast to other reports [3,4], where relatively large precipitates were observed near the interface. However, Te precipitates of 15 nm in size have been observed by AFM in this study. Investigation of the interface micromorphology of MCT thin films grown on CT or CZT substrates by AFM has the advantage of obtaining the images at ambient without extensive sample preparation. To our knowledge, this is the first report of a film/substrate interface morphology study in II–VI compounds by AFM. Further studies are under way to achieve an increased resolution, down to the atomic level, by performing the AFM analysis under an inert gas atmosphere or in a liquid cell.

#### 4. Acknowledgement

The work was supported by NASA through the Fisk Center for Photonic Materials and Devices, Grant No. NAGW-2925.



## 5. References

- [1] R. Balcerak and L. Brown, *J. Vac. Sci. Technol.* B 10 (1992) 1353.
- [2] R.S. Rai, S. Mahajan, S. McDevitt and C.J. Johnson, *J. Vac. Sci. Technol.* B 9 (1992) 1892.
- [3] T. Maekawa, T. Saito, M. Yoshikawa and H. Takigawa, *Mater. Res. Soc. Symp. Proc.* 56 (1986) 109.
- [4] J.M. Arias, M. Zandian, S.H. Shin, W.V. McLevige, J.G. Pasko and R.E. DeWames, *J. Vac. Sci. Technol.* B 9 (1991) 1646.
- [5] G. Patriarche, R. Triboulet, Y. Marfaing and J. Castaing, *J. Crystal Growth* 129 (1993) 375.
- [6] M.A. George, M. Azoulay, W.E. Collins, A. Burger and E. Silberman, *J. Crystal Growth* 130 (1993) 313.
- [7] M. Azoulay, M.A. George, A. Burger, W.E. Collins and E. Silberman, *J. Vac. Sci. Technol.* B 11 (1993) 148.
- [8] J.P. Cleveland, S. Manne, D. Bocer and P.K. Hansma, *Rev. Sci. Instr.* 64 (1993) 403.
- [9] A. Sher, A.B. Chen and W.E. Spicer, *J. Vac. Sci. Technol.* A 3 (1985) 105.
- [10] M. Azoulay, M.A. George, Y. Biao, A. Burger and E. Silberman and D. Nason, *J. Vac. Sci. Technol.* B, in press.



ELSEVIER

JOURNAL OF **CRYSTAL  
GROWTH**

Journal of Crystal Growth 138 (1994) 523–528

## Investigation of crystal quality and surface morphology of ZnTe : N epilayers grown on ZnTe and GaSb substrates

R.J. Miles <sup>\*</sup>, J.F. Swenberg, M.W. Wang, M.C. Phillips, T.C. McGill

*T.J. Watson, Sr., Laboratory of Applied Physics, California Institute of Technology, Pasadena, California 91125, USA*

### Abstract

We investigate the crystal quality of ZnTe : N epilayers grown on ZnTe and GaSb substrates under various growth conditions using atomic force microscopy (AFM), transmission electron microscopy (TEM), and X-ray diffraction. Due to superior crystal quality, epilayers grown on GaSb substrates were of higher quality than those grown on ZnTe substrates. Hillocks, observed on the surfaces of ZnTe : N/ZnTe superlattice epilayers on ZnTe substrates, are the result of Te {111} fault planes emanating from the substrate and sets of Zn {111} twin planes originating at the superlattice interface. The number of dislocations at the GaSb substrate/buffer interface and corresponding ZnTe : N epilayer was significantly less than those grown on the ZnTe substrates.

### 1. Introduction

Recently, nitrogen doping has offered a partial solution to the doping and contact problems of ZnSe and ZnTe for the fabrication of II–VI blue light emitters [1–4]. However, to date there has been little progress on the understanding of the doping process or its affect on crystal growth and quality. It is the purpose of this paper to study the effect of nitrogen doping of ZnTe on crystal quality.

Crystal quality is especially importance for light emitting devices because defects and dislocations can act as potential nonradiative recombination centers and can also increase electrical resistivity, therefore significantly degrading device performance. Unfortunately, nitrogen, a substitutional acceptor in ZnTe, is likely to promote defect and

dislocation generation for several reasons. According to Chadi, the uncompensated neutral nitrogen atom can have either three-fold or four-fold coordination [5]. The more stable three-fold coordinated nitrogen results from a broken Zn bond, which can act as a source for dislocations. In addition, the tetrahedral bond formed in either state will be significantly shorter since the neutral nitrogen atom is about 42.5% smaller than the tellerium atom. This results in local strain fields that can also serve as nucleation sites for defects and dislocation formation. Finally, the change in cation/anion fluxes when nitrogen is introduced and its effect on the growth dynamics is a complex issue that needs to be understood and optimized to ensure stoichiometric growth. To gauge these effects, we have investigated the crystal quality and surface morphology of ZnTe : N epilayers grown on commercially-obtained ZnTe substrates and GaSb substrates using TEM, AFM, and X-ray diffraction. Electrical and photolumi-

<sup>\*</sup> Corresponding author.

nesence characterization will be presented elsewhere [6].

## 2. Substrate characterization

We have studied the effects of two different substrates, commercially-obtained ZnTe and GaSb, on the crystal quality of ZnTe:N epilayers. The ZnTe substrates [7], doped p-type with antimony to a resistivity of  $1.3 \Omega \text{ cm}$ , were grown using physical-vapor transport with a proprietary seeding process which seeds a single crystal across a 2 inch wafer. X-ray rocking curve full width half maximum (FWHM) for these substrates ranged from 54 to 100 arc sec. Further evidence of the substrate crystal quality was obtained by imaging the cleaved (110) plane using AFM. The surface showed several tilt boundaries which formed angles of  $11^\circ$ – $22^\circ$ , corresponding to an edge dislocation every 5–10 atomic planes. The GaSb substrates, silicon doped p-type to about  $10^{17} \text{ cm}^{-3}$ , were of higher crystal quality, with typical X-ray rocking curves FWHM of 15 arc sec. While GaSb is nearly lattice matched to ZnTe (0.15%), care must be taken to suppress interface reactions and substrate ion diffusion of Ga and Sb, which can act as dopants in ZnTe [8].

To prepare the substrate for epitaxial growth, surface oxides must be removed while minimizing surface roughness. For GaSb substrates, the surface oxides were removed by heating the substrate while under a sufficient Sb flux. ZnTe substrates, on the other hand, present a problem since the Zn and Te evaporate congruently at lower temperatures than ZnO. Thus the following steps were necessary to remove surface oxides prior to growth. First, a 2 min soak was performed sequentially with TCE, acetone, and methanol to remove organics from the surface. Then a 1 min 0.1% bromine/methanol etch was used to remove ionic contamination. The substrate was then annealed at  $460^\circ\text{C}$  in UHV to remove the tellurium oxides and finally sputtered with 3 keV Ar ions until Auger data indicated that the zinc oxides were removed.

We have performed a study of surface roughness of the ZnTe and GaSb substrates to investi-

Table 1  
Comparison of surface RMS and RMS standard deviation of ZnTe and GaSb substrates after processing

Sample description	RMS (nm)	SD (nm)	Comments
ZnTe, RCA clean	1.34	0.14	Wavy
ZnTe, etched	1.2	0.34	Small pits
ZnTe, sputtered	0.82	0.15	Grains
GaSb, HCl clean	1.1	0.07	Grains

gate correlations between roughness and growth quality. The results from two substrates are shown in Table 1. Nine images, acquired from different locations on the substrate, were used to calculate the average root mean square (RMS) and the RMS standard deviation of the image height data. The data were acquired with contact atomic force microscopy [9] with a silicon nitride tip and a contact force of 5 nN. The ZnTe substrates,

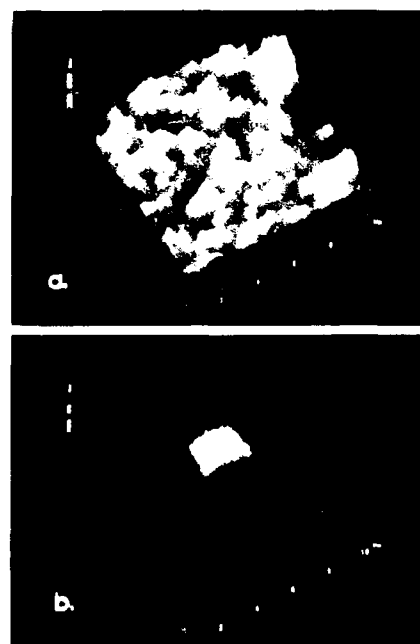


Fig. 1. (a)  $10 \mu\text{m} \times 10 \mu\text{m}$  AFM image of a continuous ZnTe:N epilayer grown on ZnTe substrate. Height range is 200 nm. (b) Image of ZnTe:N/ZnTe superlattice grown on same substrate.

which oxidize slowly, were analyzed immediately in air after each process step. GaSb substrates, which oxidize more rapidly, were cleaned with HCl and methanol and analyzed in a glovebox with less than one ppm oxygen.

From Table 1 we see that both substrates are quite similar in both roughness and morphology, after their final step of processing. The GaSb substrate was slightly smoother than the sputtered ZnTe substrate, yet both have small grains of less than 50 nm radius on the surface. The small grains on the ZnTe substrate are the result of sputtering damage. The grains on the GaSb substrate were most likely due to anisotropic oxide growth and their subsequent removal by HCl. Thus the variations in epitaxial quality grown on the subsequent layers are probably not due to variations in surface roughness, but may be due to other substrate properties such as inherent strain, residual impurities or oxides on the surface, etc.

### 3. Growth results: ZnTe substrate

For all growths, an undoped ZnTe buffer layer was grown followed by the nitrogen doped layer. The Zn:Te flux was adjusted during all growths to ensure slightly Zn-rich surface reconstruction. The radical nitrogen doping was produced by the discharge of an Oxford Applied Research RF (13.5 MHz) plasma source. The doping concentration was controlled by varying the nitrogen flow rate, which in turn was monitored by chamber pressure, for a fixed RF power. Doping levels were measured using standard Hall techniques. Two different approaches were used to obtain thick, conductive, nitrogen-doped epilayers: continuous doping during growth and delta doping between thicker undoped layers in a superlattice fashion. A comparison of these two approaches is illustrated in Fig. 1. Fig. 1a shows the surface of a sample grown with a 1.2  $\mu\text{m}$  thick buffer layer followed by a 1.8  $\mu\text{m}$  ZnTe:N doped to  $10^{19}$

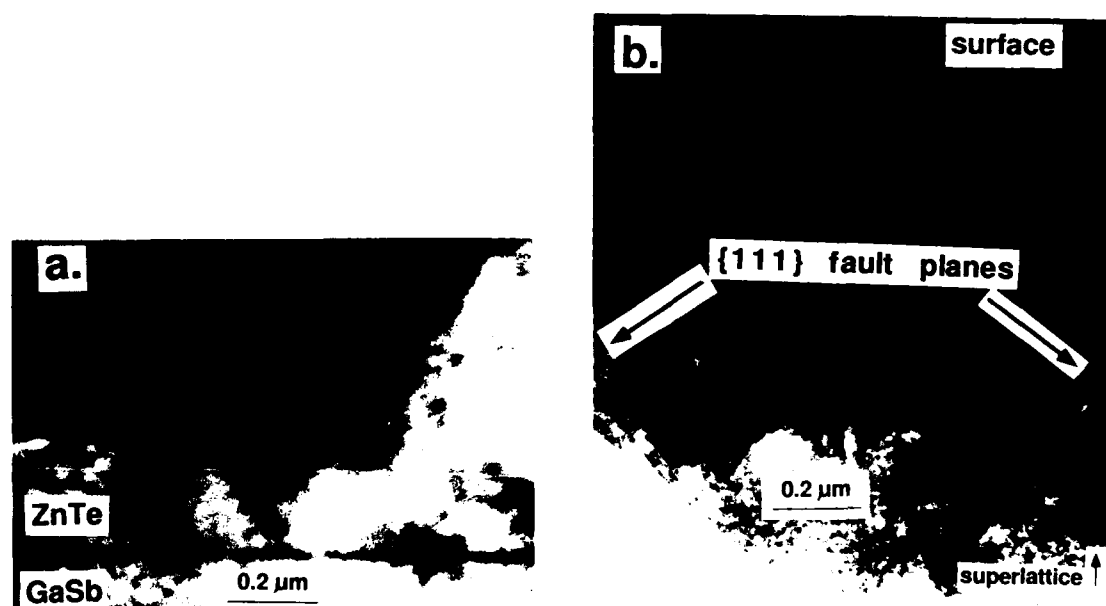


Fig. 2. (a) TEM cross-section ZnTe:N/ZnTe superlattice showing hillock originating from substrate/buffer interface. (b) Fault planes originating at superlattice/buffer interface with Zn {111} planes visible.

$\text{cm}^{-3}$ . The large RMS roughness of this surface, 18–19 nm, is caused by a high defect density on the order of  $10^8$  to  $10^7$  defects  $\text{cm}^{-2}$ . X-ray rocking curves show that the epilayer is fully relaxed from the substrate.

Fig. 1b shows the surface of a similar sample with a  $0.5 \mu\text{m}$  buffer layer grown followed by a 40 period superlattice of  $50 \text{ \AA}$  ZnTe:N and  $500 \text{ \AA}$  ZnTe. The mean doping of the superlattice region is about  $10^{18} \text{ cm}^{-3}$ . The surface RMS roughness has been reduced to about 4 nm with hillocks dispersed on the surface at a density of  $10^6 \text{ cm}^{-2}$ . The rocking curves again show that the epilayer is fully relaxed from the substrate. We have found

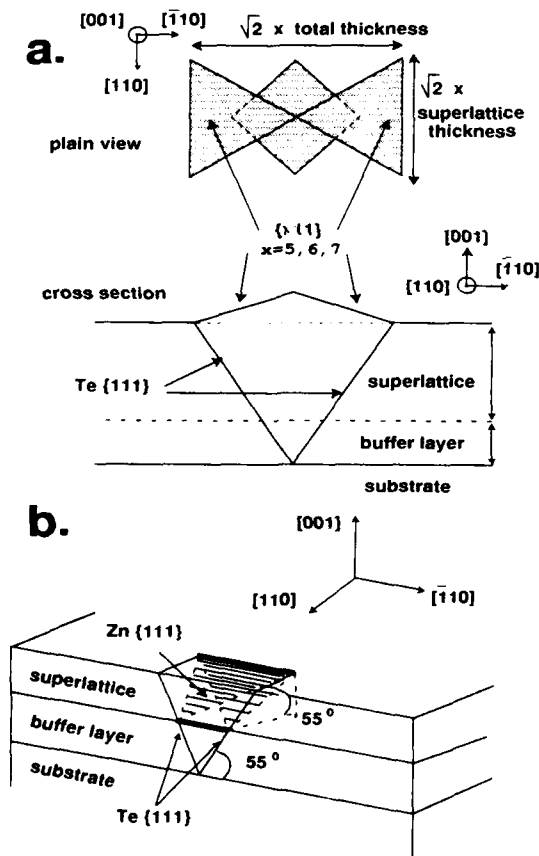


Fig. 3. Hillock model for ZnTe:N superlattice on ZnTe substrate.

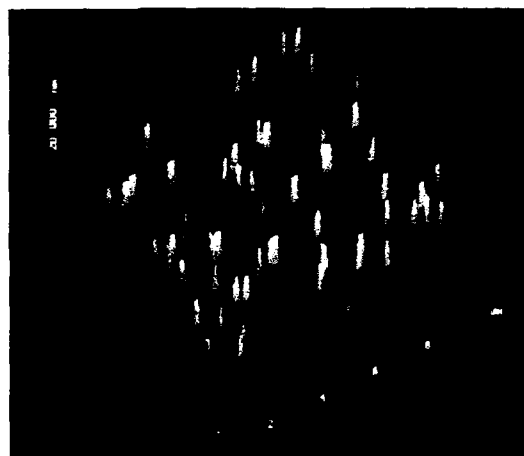


Fig. 4.  $10 \mu\text{m} \times 10 \mu\text{m}$  surface of ZnTe:N epilayer grown on GaSb substrate. Height range is 20 nm.

that the hillocks, in general, take the form of the one shown in Fig. 1b. From the cross-sectional TEM of a hillock shown in Fig. 2a, we see that the hillocks are bounded along the  $[\bar{1}10]$  base by  $\{111\}$  fault planes that start at the substrate/buffer interface. When the sample's  $(110)$  face is further milled and tilted in the  $[\bar{1}10]$  direction, additional  $\{111\}$  twinning planes became visible that emanated from the superlattice/buffer layer interface region, as shown in Fig. 2b. These sets of twin planes interact to form an amorphous core that provides the lift for the hillock peak.

The hillock model is presented in Figs. 3a and 3b. The different orientations were determined from the angles measured on the cross-sectional images, electron diffraction patterns of the different planes visible on these images, and dimensions measured using AFM images. The edges of these hillocks lie in the  $\langle 110 \rangle$  directions, which is just the intersection of the  $\{111\}$  fault planes with the  $(001)$  surface. The  $\{111\}$  fault planes originating at the substrate/buffer, as in Fig. 3a, interface define the  $[\bar{1}10]$  base of hillocks while the  $\{111\}$  fault planes originating at the superlattice/buffer interface define  $[110]$  base of hillocks, as in Fig. 3b. This is confirmed from the hillock's dimensions: the hillock in the  $[\bar{1}10]$  direction is  $\sqrt{2}$  times the thickness of the entire epilayer while in

the  $[110]$  direction the base is  $\sqrt{2}$  times the thickness of the superlattice layer. However, about 10% of the hillocks have a larger base in the  $[110]$  direction than predicted, with a few hillocks even forming symmetric pyramids. This indicates that some of the fault planes bounding the  $[110]$  base of the hillocks begin between the superlattice and substrate.

We have identified the  $\{111\}$  fault planes originating at the substrate to primarily be the Te  $\{111\}$  planes and the ones originating at the superlattice as primarily the Zn  $\{111\}$  planes through a selective etching technique. The technique involves etching the (001) surface in a solution of 20 ml, 10 ml, and 4 g of water, nitric acid, and potassium bichromate, respectively, and a trace of silver nitrate [10]. The nitric acid primarily attacks the zinc while  $(\text{Cr}_2\text{O}_7)^{-2}$ , a strong oxidizer, reacts with the tellurium to produce  $\text{TeO}_2$ , which is soluble in an acidic solution. The silver nitrate suppresses the zinc reaction so the tel-

lurium reaction proceeds more rapidly [11]. This causes a rectangular shaped pit to formed on the (001) surface with the short sides along the Te  $\{111\}$  planes and the long sides along the Zn  $\{111\}$  planes. Thus by noting the orientation of the etch pits with relation to hillock's orientation, we observed that the  $\{111\}$  planes emanating from the substrate interface are parallel to the Te planes as defined by the etch pits.

One possible reason why the Zn  $\{111\}$  twin planes preferentially form at the superlattice is because the nitrogen dopant forms a stable state with one broken Zn bond. This broken bond and the strain due to the short nitrogen radius acts to form dislocations along the Zn  $\{111\}$  planes. For the Te  $\{111\}$  fault planes, their origin is even more difficult to deduce since there is such a high concentration of defects near the substrate interface. Perhaps stoichiometry problems during initial growth could lead to local Te-rich conditions which are known to cause hillock formation [12].

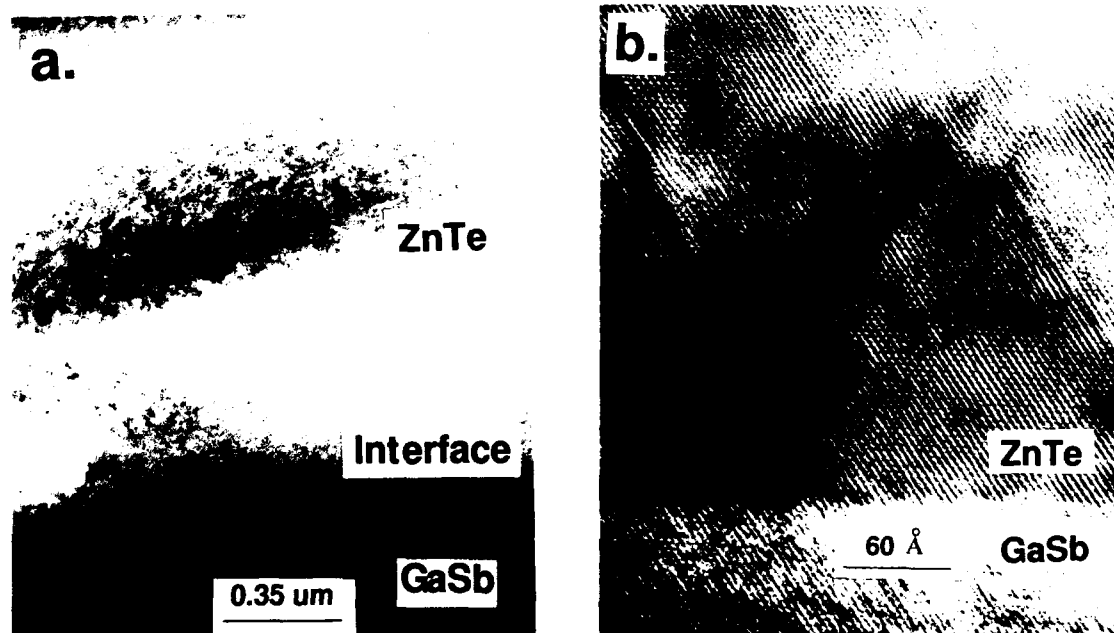


Fig. 5. (a) TEM cross-section of ZnTe:N epilayer grown on GaSb substrate. (b) HRTEM of ZnTe/GaSb interface.

#### 4. Growth results: GaSb substrate

After a 1400 Å buffer of GaSb was grown on the GaSb substrates, the sample was transferred to a II–VI MBE chamber through a UHV transfer tube where a buffer layer of ZnTe was then grown. The first several atomic layers were usually grown at lower substrate temperatures (270°C) than the rest of the growth (300°C) in order to reduce interface reactions and substrate ion diffusion.

The cross-sectional TEM of a sample with a ZnTe:N epilayer continuously doped to  $10^{19}$  cm<sup>-3</sup> in Fig. 4a shows a sharp reduction in dislocation density in this layer. The X-ray rocking curves now show that the epilayer is partially strained to the substrate. As seen from high resolution TEM of the GaSb/ZnTe interface in Fig. 4b, there is a visible region where interface reactions has occurred. Lomar and 60° dislocations at the interface along with loop dislocations are also visible. However, we do not observe their propagation through the doped epilayer nor do we see significant dislocation generation in the this layer. The surface morphology shown in Fig. 5 further illustrates the epilayer crystal quality. The RMS roughness of the surface has now been reduced to 1.7 nm without hillock formation. There does appear to be small precipitates on the surface with a maximum height of 10 nm. These are not the result of dislocations propagating in the epilayer as confirmed by TEM and may be substrate precipitates or Te pooling.

#### 5. Summary

In conclusion, we have found that substrate selection is critical to growing high quality pseudoeptaxial layers of ZnTe:N. Prepared ZnTe substrates, although similar in morphology and roughness to GaSb substrates, yields inferior epilayers of both continuously grown ZnTe:N and

ZnTe:N/ZnTe superlattices. Hillocks, on the ZnTe substrates with superlattice doping layers, are the result of Te {111} fault planes originating at the substrate interface and Zn {111} twin planes originating at the superlattice interface. The dislocation density in the epilayers grown on GaSb were reduced by a factor of 10–100 with no hillock growth but evidence of precipitates on the surface.

#### 6. Acknowledgments

Special thanks to Judy Garland for the TEM studies. This work was supported by the Advanced Research Projects Agency monitored under ONR contract N00014-92-J-1845.

#### 7. References

- [1] R.M. Park, M.B. Troffer, C.M. Rouleau, J.M. DePuydt and M.A. Haase, *Appl. Phys. Lett.* 57 (1990) 2127.
- [2] Y. Fan, J. Han, L. He, J. Saraie, R. Gunshor, M. Hagerott, H. Jeon, A. Nurmikko, G.C. Hua and N. Otsuka, *Appl. Phys. Lett.* 61 (1993) 3160.
- [3] M. Haase, J. Qiu, J. DePuydt and H. Cheng, *Appl. Phys. Lett.* 59 (1991) 1272.
- [4] M.C. Phillips, J.F. Swenberg, M.W. Wang, J.O. McCaldin and T.C. McGill, *Physica B* 185 (1993) 485.
- [5] D.J. Chadi, *Appl. Phys. Lett.* 59 (1991) 3589.
- [6] J.F. Swenberg, M.W. Wang, R.J. Miles, M.C. Phillips, A.T. Hunter, J.O. McCaldin and T.C. McGill, *J. Crystal Growth* 138 (1994) 692.
- [7] Eagle-Picher Research Laboratory, Miami, OK, USA.
- [8] Y. Rajakarunanyake, B.H. Cole, J.O. McCaldin, D.H. Chow, J.R. Soderstrom and T.C. McGill, *Appl. Phys. Lett.* 55 (1989) 1217.
- [9] Nanoscope III, Digital Instruments, Inc., Santa Barbara, CA, USA.
- [10] M. Inoue, I. Teramoto and S. Takayanagi, *J. Appl. Phys.* 33 (1962) 2578.
- [11] Y. Lu, R.K. Route, D. Elwell and R.S. Feigelson, *J. Vac. Sci. Technol. A* 3 (1985) 264.
- [12] R.D. Feldman, R.F. Austin, P.M. Bridenbaugh, A.M. Johnson, W.M. Simpson, B.A. Wilson and C.E. Bonner, *J. Appl. Phys.* 64 (1988) 1991.



ELSEVIER

Journal of Crystal Growth 138 (1994) 529–533

JOURNAL OF  
**CRYSTAL  
GROWTH**

## Comparison of CdTe, Cd<sub>0.9</sub>Zn<sub>0.1</sub>Te and CdTe<sub>0.9</sub>Se<sub>0.1</sub> crystals: application for $\gamma$ - and X-ray detectors

M. Fiederle <sup>\*,a</sup>, D. Ebling <sup>a</sup>, C. Eiche <sup>b</sup>, D.M. Hofmann <sup>c</sup>, M. Salk <sup>b</sup>, W. Stadler <sup>c</sup>,  
K.W. Benz <sup>a,b</sup>, B.K. Meyer <sup>c</sup>

<sup>a</sup> *Freiburger Materialforschungszentrum (FMF), Universität Freiburg, Stefan-Meier-Strasse 31a, D-79104 Freiburg, Germany*

<sup>b</sup> *Kristallographisches Institut, Universität Freiburg, D-79104 Freiburg, Germany*

<sup>c</sup> *Physikdepartment E 16, TU München, D-85747 Garching, Germany*

### Abstract

CdTe is one of the most encouraging semiconductor materials in the field of room temperature  $\gamma$ - and X-ray spectroscopy. To improve the detector properties, the ternary systems (Cd,Zn)Te and Cd(Te,Se), and CdTe were grown by vertical Bridgman technique. To achieve low noise detectors, the resistivity of all materials was increased by chlorine doping. The crystals were characterized by electrical (Hall measurements, photoinduced current transient spectroscopy) methods. The numbers of deep levels influencing the resistivity were reduced by introducing Se into the CdTe system. A common deep level close to the middle of the bandgap has been identified, responsible for the compensation effect in all three systems. In addition high resistivity and n-type conductivity were achieved in CdTeSe materials for the first time. Detectors were tested by irradiation with  $\alpha$  particles and low  $\gamma$ -rays. Best charge collection efficiency (CCE) of 91% was recorded for CdTe<sub>0.9</sub>Se<sub>0.1</sub> for both radiation types and smallest FWHM of about 10% at 60 keV.

### 1. Introduction

The use of semiconductor material as a radiation detector at room temperature requires a high resistivity to reduce noise by the low dark current, a high mobility–lifetime  $\mu\tau$  product and a high atomic weight to increase the energy absorption. In the literature [1–3], GaAs, CdTe and HgI<sub>2</sub> are described as semiconductors with good detector performance.

CdTe is the most frequently used semiconductor material presently used for room temperature  $\gamma$ - and X-ray detectors. It is suitable for low energy X-rays and for high  $\gamma$ -rays, for radiation monitoring in nuclear medicine, and in industrial fields [4,5]. The high resistivity is achieved by the compensation of shallow levels [6]. The compensation effects are produced by doping; the best combination of high resistivity and a very high  $\mu\tau$  product was obtained by chlorine doping [7].

Ternary crystals of Cd<sub>0.9</sub>Zn<sub>0.1</sub>Te and CdTe<sub>0.9</sub>Se<sub>0.1</sub> were grown by the vertical Bridgman technique to optimize the detector properties and to produce homogeneous material. The crystals were

\* Corresponding author.



chlorine doped to study the compensation mechanism and to achieve high-resistivity material. To compare the ternary systems with CdTe, it was grown under the same conditions. The electrical properties like resistivity and mobility were analyzed with Hall measurements. Compensation defects, scattering mechanisms and deep levels are identified by temperature-dependent Hall measurements and photoinduced current transient spectroscopy (PICTS). The mobility–lifetime product  $\mu\tau$  is based on the recorded  $\alpha$  spectra and expressed by the following relation [8]:

$$\eta = \frac{Q}{Q_\alpha} = \mu\tau \frac{E}{d} \left[ 1 - \exp\left(-\frac{d}{\mu\tau E}\right) \right], \quad (1)$$

where  $\eta$  is CCE,  $Q$  is detected charge,  $Q_\alpha$  is charge induced by  $\alpha$  particles,  $E$  is electrical field and  $d$  is detector thickness. The detector performance is investigated by  $\gamma$ -ray ( $^{57}\text{Co}$ , 122 keV and  $^{241}\text{Am}$ , 59.6 keV).

## 2. Crystal growth

All materials were grown according to the vertical Bridgman technique. The materials were synthesized from the elements Cd and Te (7N purity) and Zn or Se (6N purity), all from Nippon Mining. The material was doped with chlorine gas with a concentration of  $2 \times 10^{19} \text{ cm}^{-3}$  during the synthesis to obtain high-resistivity material. The synthesis and the crystal growth were performed in the same sealed quartz glass ampoule. The ampoule was initially heated up at a rate of

25°C/h up to 1120°C, and after a homogenization time of 6 h the ampoule was pulled at a rate of 2 mm/h (24 mm/day). Afterwards the ampoule was cooled down at a rate of 20°C/h.

## 3. Resistivity and mobility of charge carriers

The high resistivity, the mobility and the carrier concentration were determined by Hall measurements. Samples of the ternary crystals were selected to characterize different stages of the crystal growth. The results are listed in Table 1. Ohmic contacts were produced by evaporated metal layers of gold and indium and by chemical deposition of gold. A resistivity of about  $10^{10} \Omega \text{ cm}$  was obtained for  $\text{CdTe}_{0.9}\text{Se}_{0.1}$ . Comparing it with chlorine-doped CdTe, this represents an increase in resistivity of about one decade.

CdTe and  $\text{Cd}_{0.9}\text{Zn}_{0.1}\text{Te}$  showed p-type behavior with mobilities up to  $80 \text{ cm}^2/\text{V} \cdot \text{s}$  at 300 K. High resistivity and n-type conductivity were achieved in  $\text{CdTe}_{0.9}\text{Se}_{0.1}$  materials for the first time using chlorine doping. p-Type conductivity and the low mobility are typical for chlorine-doped CdTe.

Generally, the ternary crystals showed a higher homogeneity in the electrical properties compared to CdTe. The variation was less than 20% in the axial growth direction and less than 10% in radial direction, whereas the variation in CdTe was more than 25% and 20%, respectively.

To study the dependence of high resistivity on the doping process, correlated energy levels were

Table 1  
Electrical properties of CdTe,  $\text{Cd}_{0.9}\text{Zn}_{0.1}\text{Te}$  and  $\text{CdTe}_{0.9}\text{Se}_{0.1}$  from Hall measurements

Material	Carrier type	Stage of growth	Resistivity $\rho$ ( $\Omega \text{ cm}$ )	Mobility $\mu$ ( $\text{cm}^2/\text{V} \cdot \text{s}$ )	Carrier concentration ( $\text{cm}^{-3}$ )
CdTe	p-type		$1.0 \times 10^9$	80.0	$7.8 \times 10^7$
$\text{CdTe}_{0.9}\text{Se}_{0.1}$	n-type	Beginning	$6.0 \times 10^9$	470.0	$2.1 \times 10^6$
		Middle	$7.4 \times 10^9$	550.0	$1.5 \times 10^6$
		End	$5.2 \times 10^9$	390.0	$3.0 \times 10^6$
$\text{Cd}_{0.9}\text{Zn}_{0.1}\text{Te}$	p-type	Beginning	$3.8 \times 10^8$	62.0	$2.6 \times 10^8$
		Middle	$5.0 \times 10^8$	64.0	$2.0 \times 10^8$
		End	$5.6 \times 10^8$	64.0	$1.9 \times 10^8$

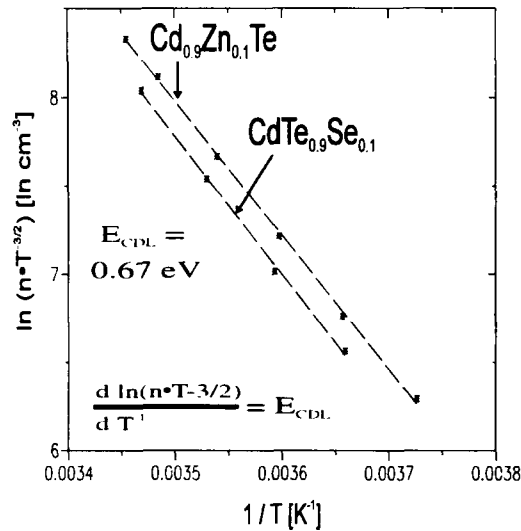


Fig. 1. Temperature dependent Hall measurements of  $\text{Cd}_{0.9}\text{Zn}_{0.1}\text{Te}$  and  $\text{CdTe}_{0.9}\text{Se}_{0.1}$ .

characterized. The compensation of the shallow levels is caused by a donor close to the middle of the bandgap. Following the principle of a three-level compensation proposed by Johnson et al. [9], the carrier concentration can be described as:

$$n = \frac{N_{\text{DD}} - (N_{\text{A}} - N_{\text{D}})}{N_{\text{A}} - N_{\text{D}}} N_{\text{C}} g \exp\left(-\frac{E_{\text{DD}}}{kT}\right), \quad (2)$$

where  $E_{\text{DD}}$  is the location of the deep donor measured from  $E_{\text{v}}$ ,  $N_{\text{DD}}$  is the concentration of

deep donor levels,  $N_{\text{A}}$  is the concentration of acceptor levels,  $N_{\text{D}}$  is the concentration of donor levels,  $N_{\text{C}}$  is the density of states of the conduction band and  $g$  presents the degeneracy factor.

$N_{\text{C}}$  is also temperature dependent with  $N_{\text{C}} \sim T^{3/2}$  [9]. Therefore, the energy level of the deep donor is calculated from the slope of a  $\ln(nT^{-3/2})$  versus  $1/T$  plot (Fig. 1). Temperature dependent measurements of  $\text{Cd}_{0.9}\text{Zn}_{0.1}\text{Te}$  and  $\text{CdTe}_{0.9}\text{Se}_{0.1}$  were carried out in a temperature range of 265 to 340 K.

It should be pointed out that the same energy level was measured for both materials. This common deep level ( $E_{\text{CDL}} = 0.67$  eV) proves to be a similar compensation defect in the ternary systems.

The temperature-dependent Hall measurements demonstrate that the charge carrier concentration is dominated by one deep level. Further experiments are necessary to investigate their influence on the detector properties.

#### 4. Characterization of deep levels

The energy level of the A-center [10] and further deep levels could be detected by PICTS (photoinduced current transient spectroscopy) measurements within a temperature range of 70 to 340 K. Fig. 2 shows the PICTS signal of CdTe,  $\text{Cd}_{0.9}\text{Zn}_{0.1}\text{Te}$  and  $\text{CdTe}_{0.9}\text{Se}_{0.1}$ . Corresponding

Table 2

Energy levels of CdTe,  $\text{Cd}_{0.9}\text{Zn}_{0.1}\text{Te}$  and  $\text{CdTe}_{0.9}\text{Se}_{0.1}$  calculated from PICTS measurements

Assignment	CdTe		$\text{Cd}_{0.9}\text{Zn}_{0.1}\text{Te}$		$\text{CdTe}_{0.9}\text{Se}_{0.1}$	
	Energy (eV)	Cross section ( $\text{cm}^2$ )	Energy (eV)	Cross section ( $\text{cm}^2$ )	Energy (eV)	Cross section ( $\text{cm}^2$ )
$\text{V}_{\text{Cd}}^{2-} - 2\text{Cl}_{\text{Te}}$	-0.06	$10^{-19}$	-0.07	$10^{-19}$	-0.06	$10^{-19}$
Zn related			+0.10	$10^{-18}$		
$\text{V}_{\text{Cd}}^{2-} \text{Cl}_{\text{Te}}^+$	+0.17	$10^{-16}$	+0.12	$10^{-18}$	+0.13	$10^{-18}$
Unknown <sup>a</sup>	+0.21	$10^{-14}$				
Unknown <sup>a</sup>	+0.23	$10^{-16}$			+0.23	$10^{-16}$
Au, Al	+0.28	$10^{-14}$				
$\text{Cd}_{\text{I}}$ , In, $\text{V}_{\text{Te}}$	+0.33	$10^{-15}$	+0.32	$10^{-13}$		
$\text{Cu}_{\text{Cd}}$			+0.37	$10^{-15}$		
$\text{V}_{\text{Cd}}$	+0.43	$10^{-14}$	+0.38	$10^{-9}$	+0.37	$10^{-14}$
$\text{Cd}_{\text{I}}^{2+}$	+0.54	$10^{-10}$	+0.54	$10^{-10}$		
Unknown <sup>a</sup>	+0.77	$10^{-9}$	+0.73	$10^{-11}$	+0.81	$10^{-11}$

<sup>a</sup> Unknown levels.

energy levels (Table 2) were calculated from the temperature dependent PICTS signal in an Arrhenius plot [11]. The identifications are taken by known deep levels of CdTe, published in Ref. [12].

All samples showed the same four levels:

- the A-center  $V_{Cd}^{2-}Cl_{Te}^{+}$  between 0.12 eV and 0.17 eV;
- the  $V_{Cd}^{2-} \cdot 2Cl_{Te}^{+}$  at  $-0.06$  eV;
- the cadmium vacancy at 0.43 eV;
- one level close to the middle of the bandgap at 0.77 eV.

Another level was detected in  $CdTe_{0.9}Se_{0.1}$ . However, in contrast to CdTe, additional impurities such as gold or indium could not be found and this indicates a much higher crystal quality and purity of the ternary material.

$Cd_{0.9}Zn_{0.1}Te$  shows a different type of behavior caused by additional deep levels: one zinc-related level at 0.31 eV and one cadmium interstitial at 0.41 eV.

The difference in the activation energies obtained using PICTS of 0.77 eV and by Hall measurements of 0.67 eV are to be explained by the different activation methods. PICTS measures a transient process emptying the conduction band, whereas the Hall effect requires a stationary current. Therefore, the compensation of defects in all three systems can be explained by one common deep level close to the middle of the

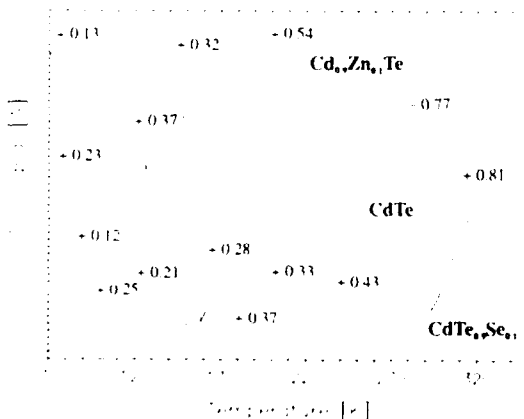


Fig. 2. PICTS spectra of CdTe,  $Cd_{0.9}Zn_{0.1}Te$  and  $CdTe_{0.9}Se_{0.1}$ . Energy levels are in eV.

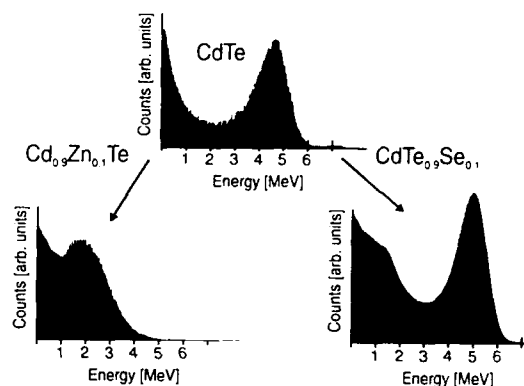


Fig. 3.  $\alpha$  spectra ( $^{241}Am$  5.6 MeV) of CdTe,  $Cd_{0.9}Zn_{0.1}Te$  and  $CdTe_{0.9}Se_{0.1}$ .

bandgap. Further identification of the common deep level has not been possible since both methods only describe the energy levels. Recent results show that it is probably not the cadmium vacancy, but another intrinsic defect, like  $Te_{Cd}$  [13].

## 5. $\mu\tau$ product and detector performance

The detector performances of all samples were tested using  $\alpha$ -radiation ( $^{241}Am$ ) and  $\gamma$ -radiation ( $^{241}Am$ ,  $^{57}Co$ ). The  $\alpha$  spectra are presented in Fig. 3. CdTe and  $CdTe_{0.9}Se_{0.1}$  show nearly the same charge collection efficiency (CCE) of about 85–91%. It could be increased by substituting Te with Se, whereas the substitution of Cd with Zn decreases the CCE to 35%. This is emphasized by the  $\mu\tau$  product calculated according to relation (1). The resulting values for the electrons are  $3.9 \times 10^{-4}$ ,  $4.2 \times 10^{-4}$  and  $2.5 \times 10^{-4}$   $cm^2/V$  for CdTe,  $CdTe_{0.9}Se_{0.1}$  and  $Cd_{0.9}Zn_{0.1}Te$  respectively.

Together with the results from electrical characterization, the good CCE of  $\alpha$  particles of  $CdTe_{0.9}Se_{0.1}$  were complemented by the detector performance for low  $\gamma$ -rays, where the same CCE of about 91% and a FWHM of about 10% were achieved. The spectra of  $^{241}Am$  (59.6 keV) are presented for CdTe and  $CdTe_{0.9}Se_{0.1}$  in Fig. 4. This means an increase of 6% compared to CdTe.

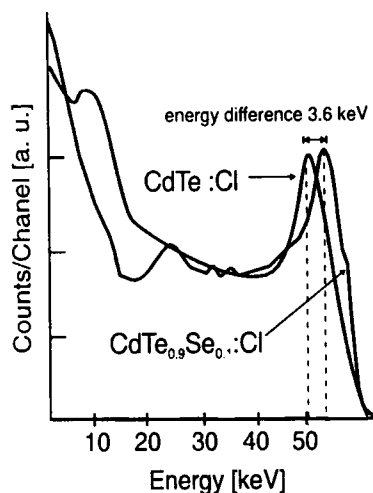


Fig. 4.  $\gamma$  spectra ( $^{241}\text{Am}$ , 59.6 keV) of CdTe (bias 300 V, thickness 1.54 mm) and  $\text{CdTe}_{0.9}\text{Se}_{0.1}$  (bias 150 V, thickness 1.34 mm). The CCEs were 85% (50.4 keV) and 91% (54.0 keV).

As was expected from the  $\alpha$  spectrum and the electrical properties, the  $\gamma$ -rays could not be detected using  $\text{Cd}_{0.9}\text{Zn}_{0.1}\text{Te}$ .

## 6. Conclusion

The detector performance of CdTe could be improved by the partial substitution of Te with Se. The same compensation defects were identified by different methods in the three materials. Although the presence of a common compensation mechanism is proposed,  $\text{Cd}_{0.9}\text{Zn}_{0.1}\text{Te}$  shows detectors with lower efficiencies compared to  $\text{Cd}(\text{Te},\text{Se})$ . Generally, the homogeneity of the electrical properties was increased in the ternary

systems. At the same time the number of deep levels was only reduced in  $\text{CdTe}_{0.9}\text{Se}_{0.1}$ . For the first time n-type conductivity and high resistivity  $\text{CdTe}_{0.9}\text{Se}_{0.1}$  was achieved for CdTeSe by chlorine doping.

It will be the aim of our future work to improve the ternary system  $\text{CdTe}_x\text{Se}_{1-x}$  in order to minimize the deep level concentration and to maximize the resistivity. The next step will be the identification of the common deep level and its correlation to a compensation mechanism.

## 7. References

- [1] K.W. Benz, R. Irsigler, J. Rosenzweig, K. Runge, F. Schäfer, J. Schneider and M. Webel, Nucl. Instr. Methods A 322 (1992) 493.
- [2] Rev. Physique Appl. 12 (1977) (Proc. 2nd Symp. on CdTe, Strasbourg, France, 1976).
- [3] C. Scharager, P. Siffert, A. Holtzer and M. Schieber, IEEE Trans. Nucl. Sci. NS-27 no. 1 (1980) 276.
- [4] Y. Eisen, Nucl. Instr. Methods A 322 (1992) 596.
- [5] C. Schreiber and J. Chambron, Nucl. Instr. Methods A 322 (1992) 604.
- [6] R.E. Kremer and W.B. Leigh, J. Crystal Growth 86 (1986) 490.
- [7] P. Moravec, M. Hage-Ali, L. Chibani and P. Siffert, Mater. Sci. Eng. B 16 (1993) 223.
- [8] R.O. Bell, Nucl. Instr. Methods 93 (1971) 341.
- [9] E.J. Johnson, J.A. Kafalas and R.W. Davies, J. Appl. Phys. 54 (1983) 204.
- [10] D.M. Hoffmann, P. Omling, H.G. Grimmeiss, B.K. Meyer, K.W. Benz and D. Sinerius, Phys. Rev. B 45 (1992) 6247.
- [11] C. Eiche, D. Maier, M. Schneider, D. Sinerius, J. Weese, K.W. Benz and J. Honerkamp, J. Phys. Cond. Matter 4 (1992) 6131.
- [12] W. Jantsch and G. Hendorfer, J. Crystal Growth 86 (1990) 404.
- [13] B.K. Meyer, D.M. Hofmann, W. Stadler, M. Salk, C. Eiche, M. Fiederle and K. W. Benz, in: Proc. Mater. Res. Soc. Meeting, San Francisco, April 1993, in press.



ELSEVIER

Journal of Crystal Growth 138 (1994) 534–537

JOURNAL OF  
**CRYSTAL  
GROWTH**

## The study of lattice strain and high-resolution transmission electron microscopy in ZnSe–ZnS strained-layer superlattices

Z.P. Guan <sup>a,\*</sup>, S.H. Song <sup>a</sup>, G.H. Fan <sup>a</sup>, X.W. Fan <sup>a</sup>, Y.G. Peng <sup>b</sup> and Y.K. Wu <sup>b</sup>

<sup>a</sup> Changchun Institute of Physics, Academia Sinica, Changchun 130021, People's Republic of China

<sup>b</sup> Institute of Metal Research, Academia Sinica, Shenyang 110015, People's Republic of China

### Abstract

The structural properties of ZnSe–ZnS strained-layer superlattices (SLSs) grown on GaAs (100) by atmospheric-pressure metalorganic chemical vapor deposition (AP-MOCVD) were studied using high-resolution transmission electron microscopy (HRTEM). The type and distribution of the defects in ZnSe–ZnS SLS are related to the surface quality of GaAs substrate, of the buffer layer and the thickness of each layer for ZnSe and ZnS in SLS. In this work we noticed that there are stacking faults (SFs), mismatch defects (MDs) and microtwins (MTs) in ZnSe<sub>1-x</sub>S<sub>x</sub> buffer layer at interfacial steps due to the GaAs surface not being smooth, and the dislocation can penetrate the ZnSe–ZnS SLS layer.

### 1. Introduction

In recent years there have been important developments in the p-type doping of ZnSe by atomic nitrogen using a radio frequency (RF) plasma technique [1], and device quality p–n junctions have been improved. So the study on the type and distribution of the defects in ZnSe and ZnSe–ZnS on GaAs is more significant. Matthews and Blakeslee made a detailed study of the theory and experiments on relief and formation of dislocations in superlattices [2,3]. Other authors investigated the different types of defects which react with each other, and their propagation factors [4,5]. Compared to the III–V compound superlattices, the defect density is higher

and has a poor surface in II–VI compound SLS. This is due to the higher mismatch in heteroepitaxy between GaAs substrate and ZnSe<sub>1-x</sub>S<sub>x</sub> buffer layer, buffer layer and SLS layer. Ponce et al. [6] have studied the defect structure of ZnSe epilayers and of their interface with the GaAs substrate in the <100> and <111> orientation using HRTEM. They observed that on GaAs (100) there was a large density of faulted loops and on GaAs (111) were microtwins and stacking faults parallel to the film–substrate interface. In this paper it is noticed that there are stacking faults (SFs), mismatch defects (MDs) and microtwins (MTs) at the interfacial steps of ZnSe<sub>1-x</sub>S<sub>x</sub> buffer layer due to the GaAs surface not being smooth, and enough dislocations can run through the SLS layer. In the ZnSe–ZnS SLS layer, the mismatch defects are mostly concentrated in the ZnS layer and they begin or end at the ZnSe/ZnS interface.

\* Corresponding author.

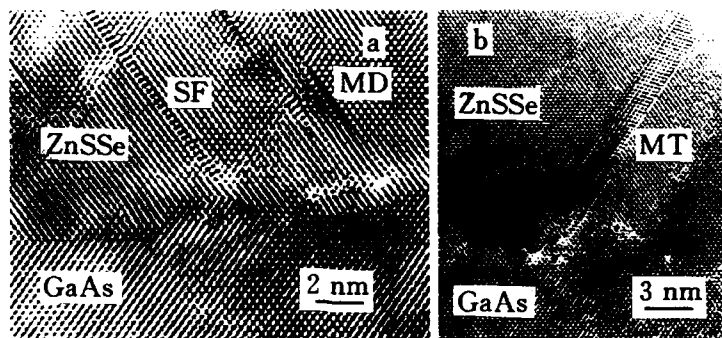


Fig. 1. Crystalline defects in interface of ZnSeS buffer layer and GaAs substrate.

## 2. Experimental procedure

The apparatus used for the growth of ZnSe–ZnS SLs was a horizontal atmospheric pressure reactor heated by an RF coil. The substrates were heated at about 600°C under a hydrogen flow a prior to growth, for elimination of the surface oxide layer. Then they were cooled to the desired growth temperature. Dimethylzinc (DMZ),  $\text{H}_2\text{Se}$  and  $\text{H}_2\text{S}$  were used as the source materials for Zn, Se and S, respectively. The substrate temperatures were varied between 280 and 500°C to optimize the growth condition. For  $\text{ZnSe}_{1-x}\text{S}_x$  ( $x < 0.3$ ) buffer layer, the growth temperatures were varied between 280 and 350°C, and for ZnS buffer layer, the growth temperature was 500°C. After the buffer layer was grown, the growth temperatures of ZnSe–ZnS SLs were about 400°C. The samples were thinned for electron transparency by mechanical thinning and argon-ion milling techniques. The thinned specimens were examined routinely by HRTEM using JEOL 2000EX II (point-to-point resolution, 0.21 nm,  $C_s = 0.7$  mm, 200 kV).

## 3. Results and discussion

### 3.1. TEM images between GaAs substrate and buffer layer

It is noticed that in ZnSeS buffer layer there are stacking faults (SFs), mismatch defects (MDs)

and microtwins (MTs) in interfacial steps due to the GaAs surface not being smooth. In Fig. 1a the arrow indicates the interfacial steps of the GaAs substrate, and the extrinsic stacking faults and surplus half-atomic surface of threading dislocations are also observed in this figure. Fig. 1b shows the microtwins which present a confounded arrangement at the interface. It can be considered that the nearby surface steps induce stacking faults and merge into a microtwin. Fig. 2 shows the procedure of interfacial steps inducing stacking faults. In the discontinuity at the surface of the GaAs interfacial step, the misfit atomic surface of ZnSeS cannot join together with that of the GaAs steps, so it appears as a surplus half-atomic surface and slide  $\frac{1}{2}\langle 112 \rangle$  stacking faults are formed. In a smooth GaAs substrate, the mismatch defects are also observed in the

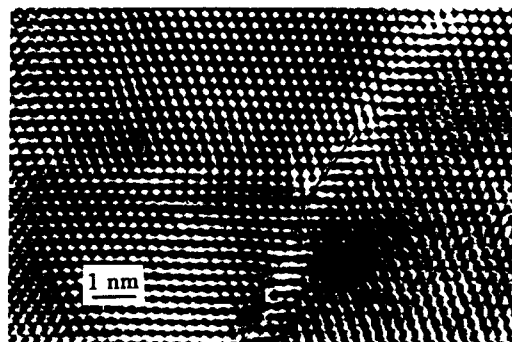


Fig. 2. GaAs substrate interface steps induce the faults.



Fig. 3. Misfit dislocation in ZnS buffer layer near the GaAs substrate.

large mismatch ZnS/GaAs interface, as seen in Fig. 3. From this figure the critical thickness  $h_c < 2$  nm was observed, which is in agreement with the calculated results [7]. Fig. 3 shows an interesting result: we do not know why a mismatch defect appears in a ZnS layer after 16 atomic layers for ZnS/GaAs structure.

### 3.2. TEM images of ZnSe-ZnS SLSs

As the substrate is not smooth, the SLS layer of ZnSe-ZnS is undulated near the buffer layer side until SLS layer thickness  $d > 500$  nm shown in Fig. 4. It leads to the disparity of optical



Fig. 4. Undulate superlattice film due to the GaAs substrate with surface steps.



Fig. 5. Mismatch defects in ZnS layer.

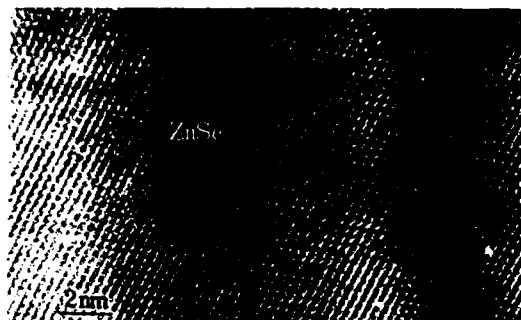


Fig. 6. Uniform interface of ZnSe–ZnS SLS.

properties for the ZnSe–ZnS SLS samples at different sites. Fig. 5 shows the mismatch defects almost concentrated in the ZnS layer; they begin or end at the ZnSe/ZnS interface. It is considered that the ZnS layer has a larger strain than the ZnSe layer in the ZnSe–ZnS/GaAs structure. This feature is favourable to obtain excitonic properties of ZnSe–ZnS SLS. In Fig. 6 it is observed that high-quality ZnSe–ZnS SLS structures without any mismatch defect and dislocation were also obtained. From TEM images, the interface images are indistinct. This means that there is interdiffusion between ZnSe and ZnS layers grown by AP-MOCVD.

#### 4. Conclusion

(1) The superlattice quality is intensely dependent on the substrate surface and buffer layer surface. The superlattices on a smooth buffer layer have a good quality and on a poor buffer layer they have more defects.

(2) The critical layer thickness of ZnS epilayer grown on smooth GaAs substrates ( $h_c < 2$  nm) is in agreement with the theory.

(3) The mismatch defects are found to be concentrated in the ZnS layers.

(4) In atmospheric pressure growth, on the interface of ZnSe and ZnS layers there exists some interdiffused layer that makes the interface lattice image vague and indistinct.

#### 5. Acknowledgements

This work was supported by the High Technology Program in China, and the Great National Natural Science Foundation of China. The Project was supported by the Laboratory of Excited State Processes, Changchun Institute of Physics, Chinese Academy of Sciences.

#### 6. References

- [1] R.M. Park, M.B. Trofer, C.M. Rouleau, J.M. DePuydt and M.A. Haase, *Appl. Phys. Lett.* 57 (1990) 2127.
- [2] J.W. Matthews and A.E. Blakeslee, *J. Crystal Growth* 27 (1974) 118.
- [3] J.W. Matthews and A.E. Blakeslee, *J. Crystal Growth* 29 (1975) 273.
- [4] D. Cherns, P.D. Greene, A. Hainsworth and A.R. Preston, in: *Microscopy of Semiconducting Materials 1987*, Inst. Phys. Conf. Ser. 87, Eds. A.G. Cullis and P.D. Augustus (Inst. Phys., Bristol, 1987) p. 83.
- [5] D.J. Eaglesham, D.M. Maher, H.L. Fraser, C.J. Humphreys and J.C. Bean, *Appl. Phys. Lett.* 54 (1989) 222.
- [6] F.A. Ponce, W. Stutius and J.G. Werthen, *Thin Solid Films* 104 (1983) 133.
- [7] R. People and J.C. Bean, *Appl. Phys. Lett.* 47 (1985) 322.





ELSEVIER

Journal of Crystal Growth 138 (1994) 538–544

JOURNAL OF  
**CRYSTAL  
GROWTH**

## Transmission electron microscopy investigations of II–VI/GaAs heterostructures

P.D. Brown <sup>\*a</sup>, Y.Y. Loginov <sup>b</sup>, J.T. Mullins <sup>c</sup>, K. Durose <sup>d</sup>, A.W. Brinkman <sup>d</sup>,  
C.J. Humphreys <sup>a</sup>

<sup>a</sup> Department of Materials Science and Metallurgy, University of Cambridge, Pembroke Street, Cambridge CB2 3QZ, UK

<sup>b</sup> Department of Physics, Krasnoyarsk State University, Svobodnii Pr., 660 062 Krasnoyarsk, Russian Federation

<sup>c</sup> Department of Physics, Heriot-Watt University, Edinburgh EH14 4AS, UK

<sup>d</sup> Department of Physics, University of Durham, South Road, Durham DH1 3LE, UK

### Abstract

Defect microstructures within heteroepitaxial layers may be categorized according to whether they arise due to problems at the epilayer/substrate interface, are introduced during growth itself or are due to some inherent materials problem. Examples taken from II–VI/GaAs systems showing interface reaction, lattice relaxation, banding due to compositional variations at the growth front and dimorphism are described.

### 1. Introduction

The eventual aim of any heteroepitaxial growth programme is to produce device quality material, but development is often hindered by microstructural defects, and hence there is a need to understand the nature of semiconductor heterostructure interfaces and multiple quantum wells, particularly with regard to threading and interfacial defects and interface chemistry. With regard to II–VI/GaAs heteroepitaxy, it is worth noting that II–VI compounds have low stacking fault energies and hence are highly susceptible to planar defect formation, as compared with III–V compounds, giving rise to a wide range of microstructures which need to be characterized in

order to identify effective measures for their reduction or elimination.

The reasons for defect introduction fit into three broad categories, irrespective of the mode of growth, i.e. (i) nucleation at epilayer/substrate interfaces due to problems arising from residual substrate surface damage, incomplete oxide desorption, or interfacial reaction/interdiffusion; (ii) processes occurring during growth which may be (a) inherent to the materials system such as twinning, ordering or dimorphism, or (b) due to lattice relaxation, growth front roughening, or alternatively may be related to problems such as source purity, or indeed the mode of growth; e.g. the interdiffused multilayer process (IMP) as compared with direct alloy growth (DAG) for ternary alloy deposition; (iii) problems post growth such as strain relaxation during cool down or post growth processing (such problems are common in SiGe technology, but will not be considered here).

\* Corresponding author.

The purpose of this paper is to make distinction between these different aspects of microstructural defect formation with regard to II–VI/GaAs heterostructures grown by metalorganic vapour phase epitaxy (MOVPE) and low pressure MOVPE, to illustrate the range of information which may be obtained using conventional and high resolution electron microscopy, and to emphasise some of the limiting problems for II–VI heteroepitaxy.

In this context it is instructive to briefly distinguish between large lattice mismatched and almost lattice matched epitaxy. During almost lattice matched epitaxy, for which the misfit is typically  $< 2\%$ , growth proceeds with the initial formation of a pseudomorphic layer which undergoes relaxation as it exceeds some critical thickness with the epilayer strain being accommodated by an array of interfacial dislocations. The source of these may be threading dislocations in the substrate or surface sources for example. It is noted that there is still much debate as to the source of defects within highly pure epilayers grown on almost defect free substrates [1], but II–VI/GaAs technology for the moment seems not to be short of defect sources. Large lattice mismatched systems ( $> 2\%$  misfit) are characterised by large epilayer threading dislocation

contents, and since predicted critical thicknesses are only of the order of 2–3 atomic layers, and depending on how the epilayer wets the substrate which in turn depends on surface energies, it becomes preferable to think in terms of 3D growth followed by island coalescence, leading to the formation of short misfit segments each terminated by 2 threading dislocations which in turn may interact and annihilate with other threading dislocations as they propagate through the epilayer.

## 2. Experimental procedure

Samples from the (Hg,Cd,Zn)Te system were grown by atmospheric pressure MOVPE using dimethyl-cadmium, dimethyl-zinc, diethyl-tellurium (at  $395^\circ\text{C}$ ) or di-isopropyl-tellurium (at  $325^\circ\text{C}$ ) and elemental mercury. (Hg,Zn)Te was deposited at  $395^\circ\text{C}$  onto (001)GaAs using the IMP [2], and also deposited at  $325^\circ\text{C}$  onto ZnTe buffer layers on (001) and  $\{111\}$ B oriented GaAs substrates. (Cd,Zn)Te was grown at  $\approx 400^\circ\text{C}$  by DAG. Samples from the (Cd,Zn)S system were grown by low pressure MOVPE using dimethyl-cadmium, dimethyl-zinc and  $\text{H}_2\text{S}$  as previously described [3]. During CdS || (Cd,Zn)S and

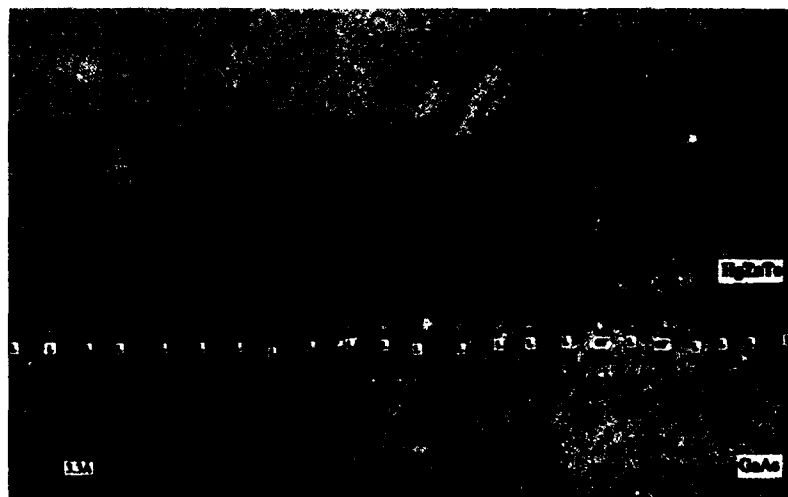


Fig. 1. High resolution micrograph of  $\text{Hg}_{0.1}\text{Zn}_{0.9}\text{Te}/(001)\text{GaAs}$  showing interface structure.

(Cd,Zn)S || ZnS superlattice growth, nominally  $\text{Cd}_{0.3}\text{Zn}_{0.7}\text{S}$  was initially deposited onto the GaAs substrate by DAG. The attraction of the CdS || (Cd,Zn)S system is that it may be lattice matched to GaAs, but the higher Cd content as compared with the (Cd,Zn)S || ZnS system is considered to be deleterious to the epilayer structural quality [4]. Samples were cross-sectioned using conventional techniques, with iodine reactive ion sputtering being used for the final stage of sample preparation, and examined using JEOL 4000FX, 4000EX II and 100CX electron microscopes.

### 3. Results and discussion

Each materials system may show more than one category of defect and so for ease of explanation, experimental results are considered on a material by material basis.

#### 3.1. (Hg,Zn)Te / (001)GaAs, (Hg,Zn)Te / ZnTe / (001)GaAs and (Hg,Zn)Te / ZnTe / $\{111\}$ B GaAs

Deposition of HgTe compounds directly onto GaAs substrates does not provide for a route for

infra-red device fabrication because of the problem of interfacial reaction [5] and Ga interdiffusion. The composition of the  $\text{Hg}_{0.3}\text{Zn}_{0.7}\text{Te}$  / (001)GaAs sample examined was estimated from diffraction and high resolution information, and it interesting to note that despite evident roughness over  $\approx 2$  unit cells the interface is delineated by a well defined dislocation array comprising primarily  $90^\circ$  (or Lomer (L) dislocations) with some  $60^\circ$  dislocations (Fig. 1). The origin of the moiré fringe contrast at features along the interface remains unclear but is possibly indicative of local tilts or rotations, or the presence of some phase with slightly different spacings which might suggest incomplete substrate desorption or interface reaction.

Buffer layers are commonly used for the control of epilayer orientation and additionally act as diffusion barriers.  $\text{Hg}_{0.8}\text{Zn}_{0.2}\text{Te}$  / ZnTe grown on (001)GaAs shown in Fig 2a, exhibits a high density of threading dislocations, as would be expected for such a highly lattice mismatched system, along with vertical sub-grain boundaries giving rise to the strong variations in epilayer contrast due to local variations from the Bragg position, and these observations are similar to features shown by CdTe grown on slightly misori-



Fig. 2. Conventional TEM images of  $\text{Hg}_{0.8}\text{Zn}_{0.2}\text{Te}$  / ZnTe on (a) (001) and (b)  $\{111\}$ B oriented GaAs showing threading dislocations and a twinned structure respectively.

ented (001)GaAs substrates [6]. In addition, there are epilayer dislocations parallel to the interface and these presumably arise as a consequence of the IMP used to deposit the (Hg,Zn)Te in this instance.

Conversely, for growth on a  $\{\bar{1}\bar{1}\bar{1}\}$ B GaAs substrate, the ZnTe buffer is found to contain a high density of twin lamellae lying parallel to the substrate (Fig. 2b), while the (Hg,Zn)Te epilayer contains double positioning twins. This type of defect microstructure is similar to that originally characterised for the (Hg,Cd)Te/ $\{\bar{1}\bar{1}\bar{1}\}$ B CdTe system [7]. The predisposition of ZnTe and CdTe to twin is an example of an inherent materials problem dominating microstructure, and  $\{111\}$  CdTe lamellae may form parallel to a variety of substrates [8]. In addition, the introduction of double positioning twins (particularly within Hg-rich tellurides on  $\{\bar{1}\bar{1}\bar{1}\}$ B substrates), leads to the formation of irregular lateral twin boundaries lying approximately perpendicular to the epilayer/substrate interface and, while being an interface nucleated feature, may still be regarded as being an inherent materials problem of the (Hg,Cd,Zn)Te system.

### 3.2. CdS||(Cd,Zn)S superlattices on (001)GaAs

Examination of CdS||(Cd,Zn)S and (Cd,Zn)S||ZnS superlattices on (001)GaAs substrates provides a more complex example of microstructural

defect formation [4]. The binary/ternary superlattice CdS||Cd<sub>0.3</sub>Zn<sub>0.7</sub>S (lattice matched to GaAs) is examined here and both inherent stacking disorders and interfacial problems are apparent. Figs. 3a and 3b show XTEM micrographs of such a superlattice on (001)GaAs taken from the near surface and interfacial regions respectively. Fig. 3a shows remanant floccular contrast indicative of the multilayer growth process (period  $\approx 40$  Å), but the layers closer to the interface which have been maintained at elevated temperature for longer have completely interdiffused (Fig. 3b). A very high density of planar defects emanate from this interface. Additionally, it is apparent that there is some amorphous phase at the interface (5 to 10 Å thick), and even though the epilayer is tailored to lattice match the substrate this can no longer be regarded as a lattice matched system. It is important to note that the (001) GaAs substrate has imposed an (001) oriented cubic lattice on the epilayer regardless of this interfacial layer, as compared with similar layers grown on  $\{\bar{1}\bar{1}\bar{1}\}$ B substrates which are  $\{\bar{1}\bar{1}\bar{1}\}$ B oriented, hexagonal and highly faulted [4]. The formation of this cubic phase of (Cd,Zn)S might be effected by local breaks in the amorphous phase leading to seeding of epilayer growth, or by registration of the overlying atoms with the substrate in which case the interfacial layer forms later by interdiffusion. There is no firm evidence for either mechanism as yet. The former mechanism would imply that

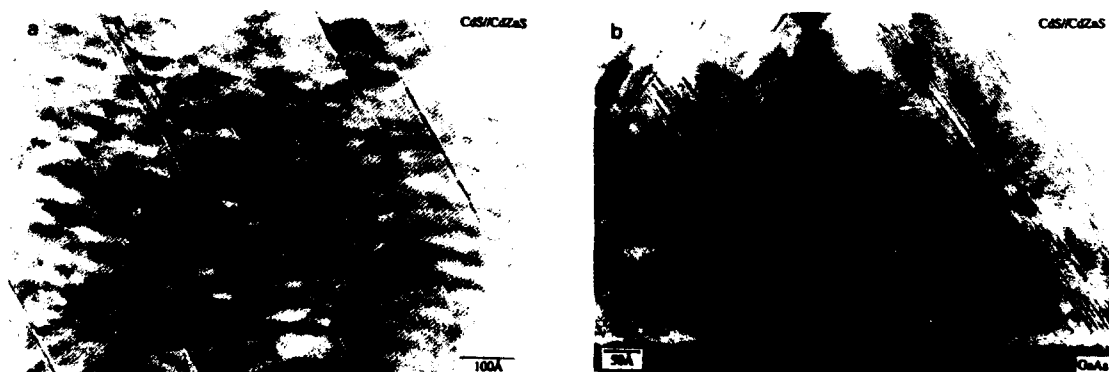


Fig. 3. High resolution micrographs of a CdS||Cd<sub>0.3</sub>Zn<sub>0.7</sub>S superlattice on (001)GaAs showing (a) remanant floccular contrast indicative of the multilayer deposition process (period  $\approx 40$  Å) and (b) inclined stacking disorder and amorphous interfacial phase.



Fig. 4. High resolution micrograph showing CdTe/(001)GaAs showing interfacial dislocation content and inclined stacking faults.

these are growth related stacking disorders, which form during lateral overgrowth on the amorphous interfacial layer, rather than being stress induced features (i.e. deformation related) and part of some relaxation accommodation process, and hence this microtwinning is still fundamentally an inherent materials problem.

The problem of interfacial phase formation is found for a variety of II–VI/III–V systems, with the formation of some  $\text{III}_2\text{–VI}_3$  compound, particularly with excess group VI overpressure [9,10]. However, Fig. 3b demonstrates that this may not be a simple, well defined crystallographic phase. In this instance the ternary layer was initially deposited with all three species being introduced simultaneously into the reactor, corresponding to conditions of excess group VI species. It is possible that initial deposition conditions under conditions of excess group II species before reverting to excess group VI conditions for improved growth might alleviate this problem.

### 3.3. CdTe/(001)GaAs

The (001)CdTe/(001)GaAs system which has a 14.6% lattice misfit is an case of lattice relaxation dominating epilayer defect microstructure. A well defined interface comprising  $90^\circ$  and  $60^\circ$  misfit dislocations, with the occasional presence of an inclined stacking fault (Fig. 4), the formation of which is considered to be related to local variation in the density of  $60^\circ$  dislocations and Lomer–Cottrell locks, the relative proportion of which leads to local CdTe misorientation which in turn introduces interfacial stresses which are relieved by stacking fault formation [11]. An extra  $60^\circ$  dislocation at the interface is associated with each stacking fault as would be expected, and it is

interesting to note that the  $90^\circ$  dislocations to the right of SFI are located one atomic plane above those to the left which is indicative of the presence of an interfacial step at the stacking fault nucleus. Conventional TEM images of the same structure, however, illustrate the high threading dislocation density above this interface [12]. The application of strained layer superlattices to reduce threading dislocation densities in such highly lattice mismatched systems has had limited success [13], with typical factors of 2–3 improvement having little impact on threading dislocation densities of the order of  $10^8\text{–}10^9\text{ cm}^{-2}$  (in view of device requirements which may be less than  $10^5\text{ cm}^{-2}$ ). Conversely, the growth of HgTe based compounds onto CdTe buffer layers grown on (001)GaAs is remarkably effective at filtering out



Fig. 5. Conventional TEM micrograph showing banding and faceting of the advancing growth front within  $\text{Cd}_{0.96}\text{Zn}_{0.04}\text{Te}/(001)\text{GaAs}$ .

threading dislocations [12], with glide of threading dislocations to provide misfit segments following the Matthews–Blakeslee mechanism. The plastic nature of the epilayer and the weak Hg–Te bond promote Hg cross-diffusion and combine to form a graded or vertically distributed interface.

### 3.4. (Cd,Zn)Te/(001)GaAs

The (Cd,Zn)Te/(001)GaAs system exhibits a distribution of threading dislocations similar to that of CdTe/(001)GaAs. But in low Zn content material grown by MOVPE there is also the problem of banding whereby striations within the growth front may be observed, as illustrated by the Cd<sub>0.96</sub>Zn<sub>0.04</sub>Te/GaAs sample shown in Fig. 5. This effect arises due to the non uniform supply of precursor species to the growth surface, indicative of either fluctuating substrate temperature or of too low a carrier gas flow rate through the Zn bubbler, leading to pulsing of the Zn alkyl into the reactor. The striations also reveal the faceting of the advancing growth front in this instance. This effect is related to growth temperature and occurs due to competition between developing {111} facets on the (001) growth surface and desorption, and as a consequence {411} or {511} facets may form, for example.

### 4. Conclusions

II–VI/GaAs heterostructures are found to exhibit a wide range of defect microstructures which may arise as a consequence of inadequate substrate preparation, interface reaction, or non-ideal growth conditions, or simply may be an inherent problem of the materials system itself. Examples of some of the factors controlling microstructural defect formation and distribution within II–VI/GaAs epilayers are described. (Hg,Zn)Te/ZnTe/{111}B GaAs is prone to lamellar twinning in the buffer layer, and double position twinning in the (Hg,Zn)Te as might be expected by comparison with (Hg,Cd)Te/CdTe/{111}B GaAs. (Cd,Zn)S based superlattices lattice matched to GaAs suffer from interfacial compound formation which may be responsible for the high den-

sity of planar defects in the epilayer. Dimorphism is controlled by substrate orientation and faulting is enhanced within Cd rich alloys or superlattices. In view of the instabilities and consequent introduction of stacking disorders, high mole fractions of cadmium are considered to be deleterious for II–VI heteroepitaxy. CdTe and (Cd,Zn)Te/(001)GaAs exhibit microstructures which are dominated by a half loop mechanism for relief of misfit strain. An example of compositional banding within Cd<sub>0.96</sub>Zn<sub>0.04</sub>Te/(001)GaAs due to faulty growth control is also given. Strict control over source purity and alkyl development to facilitate deposition at temperatures comparable to MBE are necessary steps for continued progress, and the challenge still remains for the II–VI community to accommodate or eradicate structural problems if reproducible, reliable emitter and detector device structures are to reach the commercial environment. The diversity of II–VI/GaAs heteroepitaxial systems ensures that the initial factors in the generation of microstructural defects in these films will be equally diverse.

### 5. Acknowledgements

With thanks to P.A. Clifton, H.A.I. Allak and M.Y. Simmons for provision of samples.

### 6. References

- [1] C.J. Humphreys, in: *Microscopy of Semiconducting Materials 1993*, Inst. Phys. Conf. Ser. 134, Eds. A.G. Cullis, A.E. Staton-Bevan and J.L. Hutchison (Inst. Phys., Bristol, 1993) p. 441.
- [2] J. Tunnicliffe, S.J.C. Irvine, O.D. Dosser and J.B. Mullin, *J. Crystal Growth* 68 (1984) 245.
- [3] Y. Kawakami, T. Taguchi and A. Hiraki, *J. Vac. Sci. Technol.* B5 (1987) 1171.
- [4] P.D. Brown, Y.Y. Loginov, K. Durose, J.T. Mullins, T. Taguchi, T. Burberry, S. Lawson-Jack and I. Jones, *J. Crystal Growth* 117 (1992) 536.
- [5] A.G. Cullis, N.G. Chew, S.J.C. Irvine and J. Giess, in: *Microscopy of Semiconducting Materials 1987*, Inst. Phys. Conf. Ser. 87, Eds. A.G. Cullis and P.D. Augustus (Inst. Phys., Bristol, 1987) p. 141.
- [6] T.T. Cheng, M. Aindow, I.P. Jones, J.E. Hails, D.J. Williams and M.G. Astles, in: *Evolution of Surface and*

- Thin Film Microstructure, Mater. Res. Soc. Symp. Proc., Vol. 280 (Mater. Res. Soc., Pittsburgh, PA, 1993).
- [7] J.E. Hails, G.J. Russell, P.D. Brown, A.W. Brinkman and J. Woods, *J. Crystal Growth* 86 (1988) 516.
- [8] P.D. Brown, J.E. Hails, G.J. Russell and J. Woods, *Appl. Phys. Lett.* 50 (1989) 1144.
- [9] R.L. Gunshor, M. Kobayashi, N. Otsuka and A.V. Nurmikko, *J. Crystal Growth* 115 (1991) 652.
- [10] M. Kolodziejczyk, Th. Filz, A. Krost, W. Richter and D.R.T. Zahn, *J. Crystal Growth* 117 (1992) 549.
- [11] J.E. Angelo, W.W. Gerberich, W.M. Stobbs, G. Bratina, L. Sorba and A. Franciosi, *Phil. Mag. Lett.* 67 (1993) 279.
- [12] K. Durose, A. Turnbull and P.D. Brown, *J. Mater. Sci. Eng. B* 16 (1993) 96.
- [13] A. Hobbs, O. Ueda, I. Sugiyama and H. Takigawa, *J. Crystal Growth* 117 (1992) 475.

## Scanning tunneling microscopy of CdSe single crystal cleaved and “real” surface

J. Vaitkus <sup>\*a</sup>, R. Baubinas <sup>a</sup>, V. Kazlauskienė <sup>a</sup>, D. Kuciauskas <sup>a</sup>, J. Miskinis <sup>a</sup>,  
U. Karlsson <sup>b</sup>, M. Hammar <sup>b</sup>, M. Göthelid <sup>b</sup>, M. Björqvist <sup>b</sup>, E. Lindberg <sup>b</sup>

<sup>a</sup> Department of Semiconductor Physics, Vilnius University, 2734 Vilnius, Lithuania

<sup>b</sup> Department of Materials Science, Royal Institute of Technology, Stockholm, Sweden

### Abstract

Ultrahigh vacuum-cleaved and as-grown surfaces of CdSe single crystals were investigated by scanning tunneling microscopy. The single crystals were grown by Reynolds–Green method. Striations and terrace-step structure have been found. The surface atomic geometry was found and investigated. The (11 $\bar{2}$ 0) face geometry (structure formed by elementary cell of  $0.75 \times 0.7 \text{ nm}^2$ ) as well as other type structures (e.g.,  $2.1 \times 0.75 \text{ nm}^2$  elementary cell) have been determined. The variations of the band gap at the surface have been found. The band values in the range 2.0–2.6 eV on a cleaved surface and 1.1–2.0 eV on an as-grown surface were measured and explained as being the influence of surface relaxation and gas adsorption.

### 1. Introduction

Study of the surface atomic geometry dependence on characteristic parameters of the bulk bonding and the surface reconstruction at cleavage faces or under influence of adsorbed (deposited) atoms has been a major topic in surface science for decades. The invention of the scanning tunneling microscope (STM) has made it possible to observe material structure on the atomic scale. These investigations have been mostly performed on silicon, gallium arsenide and related compounds, but STM is rarely used to

investigate more complicated compounds, II–VI type particularly. On the one hand, this is due to difficulties obtaining good surface quality and on the other hand rather great problems are caused by higher resistivity of materials. However, as II–VI compounds and particularly CdSe have interesting surface properties, as optical nonlinearities, sensitivity to different gases and especially complicated nature of initial growth of epitaxial layers, the attempt to study surface atomic geometries of CdSe single crystal has been performed in the present work.

As it is known, the (10 $\bar{1}$ 0) and (11 $\bar{2}$ 0) cleavage faces are usual for wurtzite-structure materials. Some fragmentary low energy electron diffraction data have been reported in the literature and some data about surface relaxation have been

\* Corresponding author.



obtained [1–4]. Also, striations, dislocation kinks and stacking faults are found by means of optical and high resolution electron microscopy [5,6].

Some attempts to study CdSe surface by means of the STM have been performed in [7], but as far as we know the present paper is the first presentation of the surface atomic geometry of this type of crystal. The CdS crystals have been investigated by injection luminescence with the STM, but atomic resolution has not been reached [8].

Different methods of CdSe crystal growth are known and they strongly influence the crystal quality. As it has been found earlier, investigating exciton spectra and Hall mobility, crystals of higher quality are those grown from the vapor phase [9]. Crystals grown by the Reynolds–Green method are of the bulk type; they can be easily cleaved and this is the reason for investigating them in this work. Preliminary results of measurements are presented in ref. [10]. Problems of the surface image analysis are concerned with the rather great noise, but quite evident surface patterns have been obtained for some sample areas.

## 2. Experiment

The experiment was performed in an ultrahigh vacuum system with a base pressure of approximately  $1 \times 10^{-10}$  Torr in which an Omicron STM had been incorporated. The STM images were acquired with electrochemically etched tungsten tips. The tip was controlled by imaging of the well-known Si(111)  $7 \times 7$  surface, which was also used for the STM calibration. The silver paste annealed at 150°C temperature was used as the ohmic type back-contact.

The investigated crystals have been grown by recrystallization at a temperature of 1413–1415 K, with the excess component controlled by the “cold” end of the ampoule (733 K), and cooled down up to room temperature during 20 h. The crystal under investigation has been preliminary notched by a wire saw and then cleaved with a knife in high vacuum. The main surface plain has been found to be (11 $\bar{2}$ 0) (Laue method has been used), but also striations that could contain a (10 $\bar{1}$ 0) face have been seen by the microscope.

The sample face therefore was terrace-like. The accuracy of adjustment of the tip on the surface spot was bad and it created problems identifying the surface face.

Surface images with different spatial resolution have been obtained and spectroscopic measurements have been performed. Fourier analysis and regular noise filtering have been applied to the experimental data. Two types of noise have been found: connected to the vibration spectrum in the equipment (a bit less than 50 Hz) and electrical circuit noise of 50 and 100 Hz. The resistivity of the crystal under investigation conditions was approximately 200  $\Omega$  cm.

Two types of surfaces have been investigated: (a) high vacuum cleaved and (b) “as-grown” crystal face.

## 3. Results and discussion

The main picture of a rather flat surface is shown in Fig. 1. The striations are seen very well. Clear evidence of the atomic scale resolution and of the noise are seen in different areas with different sharpness. As it has been found from the Fourier transform of the image, the periodic-



Fig. 1. Main STM image of the crystal surface.

ity of the lattice corresponds to the lattice constant, (characteristic periods) close to 0.7, 0.75, 0.4 and 0.3 nm. Also some larger periods, equal to about 1.0 nm (accuracy of all these values was up to 0.05) or more, were found. Large periods are supposed to be moiré patterns generated by the noise and the crystal structure, and some of them were easily evaluated. It is difficult to separate the moiré pattern and the influence of striation. Both can cause irregularity of pattern modulation. If the filtering of the image was performed at different areas of the image, similar patterns were obtained.

In the images in which we succeeded to clear up the best atomic geometry pictures, a distribution of atoms in rows directed perpendicular to the crystal  $c$ -axis has been found. Two images are

shown in Fig. 2. As the structure of the image is not seen very distinctly on the picture, small circles were drawn to clear up the atomic geometry (as it was seen on the computer screen). The distances between atoms and their positions correspond to the  $(11\bar{2}0)$  face of the crystal in some surface areas. In these places, atoms are at the edges of a rectangular with sides equal to 0.7 nm along the  $c$ -axis and 0.75 nm perpendicular to it (accuracy of values was 0.01 nm) with one atom shifted out of the rectangular center perpendicular to the  $c$ -axis. As it was found in the LEED experiments [1–4], reconstruction of the  $(11\bar{2}0)$  face was absent and this type of atomic geometry is demonstrated in Figs. 2a and 2b. Other atomic geometries were found in images too. The most typical of them have a distance equal to the triple

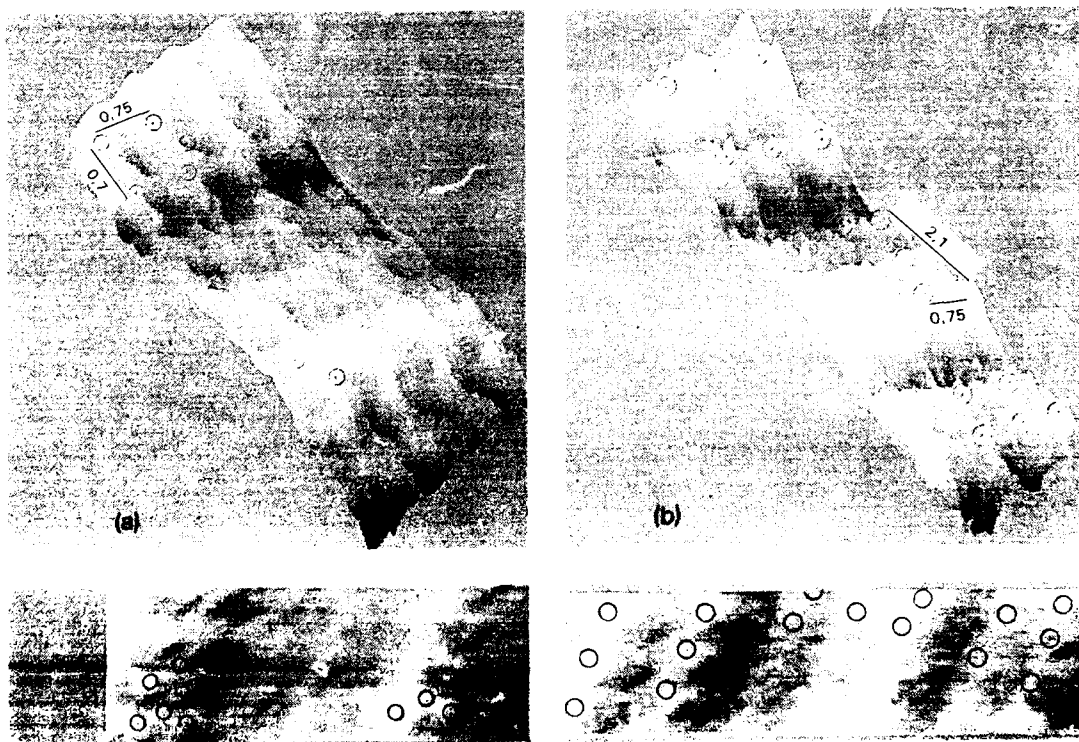


Fig. 2. High resolution STM images of the surface area. (a), (b) three-dimensional pictures; (c), (d) top view. The image length and width are equal to 6.4 nm  $\times$  2.7 nm and 8.7 nm  $\times$  2.4 nm in (a) and (b), respectively. The numbers shown on the pictures display the distance in nanometers.

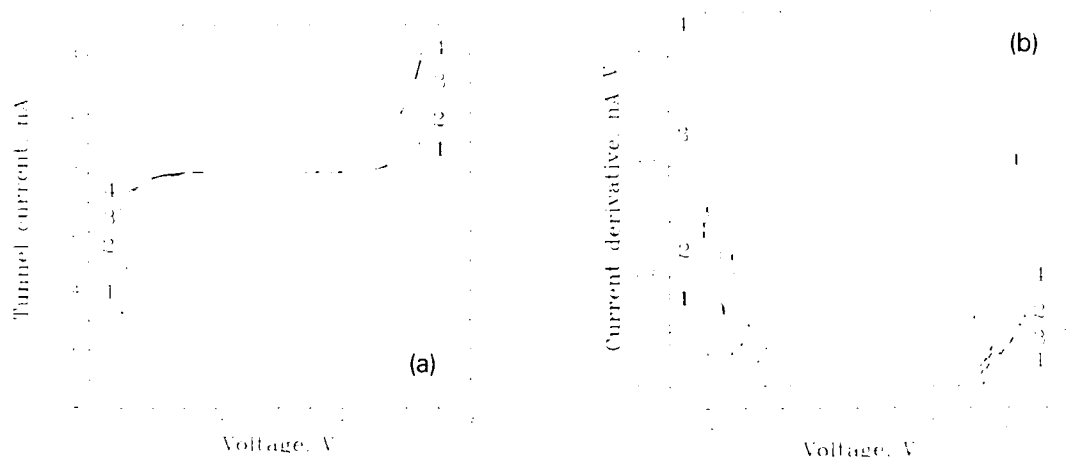


Fig. 3. Tunnel current (a) and its derivative (b) versus voltage of cleaved surface in different areas marked by numbers.

lattice constant. The terrace steps can be recognized in Fig. 2a, but it is necessary to perform more detailed investigations of cleaved surfaces to clear up the nature of the different atom geometries.

The images presented above were acquired probing empty crystal states. The resolution of filled states has been worse, but the atom geometry and terraces have been found to be similar to those in the previous case.

Spectroscopical measurements showed a larger band gap than in the crystal bulk (Fig. 3), with values in the range of 2.0–2.6 eV. This could be a result of two circumstances: (1) at a surface, a cation and an anion bonds are tilted outward and inward (due to surface relaxation, i.e. deformation, influence on effective band state density versus energy), respectively [4], and therefore the measured gap has to be larger than in an unrelaxed lattice; (2) the high resistivity of the crystal

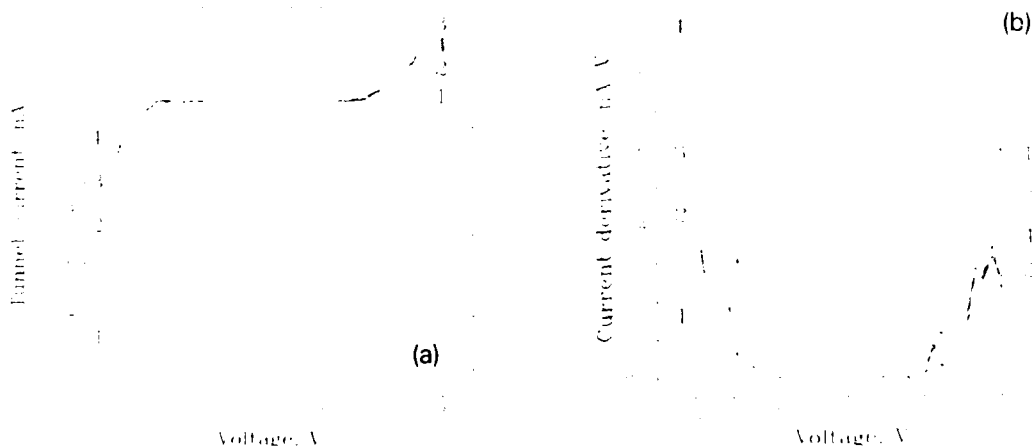


Fig. 4. Tunnel current (a) and its derivative (b) versus voltage of as-grown surface in different areas marked by numbers.

causes a potential drop in the crystal and if the tunneling current appears, it will increase the measured band gap value. The increase of sample illumination has changed the tunneling current, the potential drop was reduced, but we could not establish a decrease of the measured gap width. In any case, this dependence is necessary to investigate in details.

The noise in the as-grown crystal surface image was rather high, but after filtering of the image, rather irregular distribution of atom-like "spots" was found. Spectroscopical measurements showed that the current cut-off gap was narrower, and it changed from 1.1 to 2.0 eV (Fig. 4). This also demonstrates that the potential drop in the crystal is not dominant when the tunnel current is on. As it has been predicted, these results have shown that the surface has absorbed many atoms or molecules and that the surface density of states is large. The existence of the large surface state density was demonstrated earlier and these states have pinned the Fermi level to the surface [11].

#### 4. Conclusions

A CdSe single crystal surface with atomic resolution has been imaged for the first time. The step-wise surface (11 $\bar{2}$ 0) face has been analyzed, and the "ideal" (0.7 nm and 0.75 nm periodicity in the *c*-axis direction and perpendicular to it, respectively) and terrace-step atomic geometries have been found.

#### 5. Acknowledgements

One of the authors (J.V.) acknowledges Professor A. Flodström (Stockholm Royal Institute of Technology, Materials Science Department) for creating a possibility to work with the STM facilities. The Vilnius University part of this work was supported, in part, by a Soros Foundation Grant awarded by the American Physical Society.

#### 6. References

- [1] Y.R. Wang and C.B. Duke, *Phys. Rev. B* 37 (1988) 6417.
- [2] C.B. Duke, A. Paton, Y.R. Wang, K. Stiles and A. Kahn, *Surf. Sci.* 197 (1988) 11.
- [3] Lan Tian and Xu Fie-yue, *Acta Phys. Sinica* 39 (1990) 1082.
- [4] T.N. Horsky, G.R. Brandes, F.K. Canter, C.B. Duke, A. Paton, D.L. Lessor, A. Kahn, S.F. Horng, K. Stevens, K. Stiles and A.P. Mills, Jr., *Phys. Rev. B* 46 (1992) 7011.
- [5] J. Chikawa and T. Nakayama, *J. Appl. Phys.* 35 (1964) 2493.
- [6] R.W. Glaisher, M. Kuwabara, J.C.H. Spence and M.J. McKelvy, in: *Microscopy of Semiconducting Materials 1987*, Inst. Phys. Conf. Ser. 87, Eds. A.G. Cullis and P.D. Augustus (Inst. Phys., Bristol, 1987) section 5, p. 349.
- [7] Chong-yang Liu and Allen J. Bard, *Chem. Phys. Lett.* 174 (1990) 162.
- [8] R. Berndt and J.K. Gimzewski, *Phys. Rev. B* 45 (1992) 14095.
- [9] J. Vaitkus, M. Kurik and V. Manzhar, in: *Physical Problems of II–IV Compounds*, Vol. 1 (Vilnius University, Vilnius, 1972) p. 14.
- [10] J. Vaitkus, R. Baubinas, M. Hammar and A. Flodström, *Lith. Phys. J.* 32 (1992) 429.
- [11] I. Viscakas, A. Smilga, G. Juska, *Lith. Phys. J.* 8 (1968) 593.

## ZnTe fractional monolayers and dots in a CdTe matrix

N. Magnea

CEA / Département de Recherche Fondamentale sur la Matière Condensée, SP2M / PSC, 85X, F-38041 Grenoble Cédex, France

### Abstract

Coherent insertions of ZnTe submonolayers and dots in a CdTe matrix have been fabricated by molecular beam epitaxy. The realization of such ultra-small systems is conditioned by monitoring the two-dimensional growth on exactly (001) oriented substrates or vicinal surfaces. High resolution X-ray diffraction data show that the interfaces of the clusters are in perfect register with the surrounding material despite the 6.5% lattice mismatch between ZnTe and CdTe. Finite size effects are proposed to explain the partial relaxation of the strain of the ZnTe insertions. The short range isoelectronic potential introduces considerable perturbation in the electronic band structure of the superlattices. Light hole exciton trapping by ZnTe dots is experimentally observed. This effect is well described qualitatively by the envelope function model. As the lateral size of ZnTe islands can be made larger than the exciton Bohr radius by changing the growth conditions, discrete fluctuations of ZnTe thickness are observed. Disorder induced localization resulting from the breaking of the translational symmetry by the dots is proposed to explain the multiple excitonic lines observed in the optical spectra of superlattices incorporating fractional monolayers of ZnTe.

### 1. Introduction

The development of modern vapor phase epitaxy techniques allows one to engineer quantum devices and heterostructures on a subnanometer scale. Coherent insertion of monolayers or submonolayers of isoelectronic impurities is then possible in order to modify the band structure of electronic materials at a high level of accuracy. Numerous potential applications have been proposed for this technique in the field of semiconductor materials science:

(i) *Interfaces studies.* The inserted monolayers decorate the growing surface and strongly enhance the chemical (Hg in CdTe) or lattice mismatch (Zn in CdTe) contrast for X-ray diffraction (XRD) and transmission electron microscopy (TEM) studies of the interfacial roughness.

(ii) *Electronic properties.* The short range potential of the impurity sheets modifies the band structure by introducing carrier localization or scattering depending on the nature of the perturbation [1]. Ordered pseudo-alloy can be synthesized by introducing, for example, monolayers of ZnTe in CdTe. This could decrease the potential fluctuations if lateral thickness variations and interfacial roughness are mastered. The introduction of spatially localized perturbations can also be used to probe the electron or hole wavefunctions in a quantum well [2] and to study exciton localization or scattering.

(iii) *Low-dimensional systems.* If the lateral sizes of the islands are controlled, wires and dots can be fabricated by depositing fractional monolayers. Grown on flat surfaces, the island structures should be random with a distribution depending

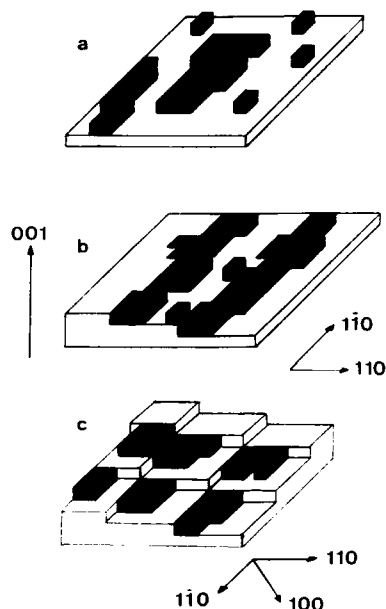


Fig. 1. Sketch of ZnTe islands (shadowed area) grown on various (001) surface and terrace configurations. (a) Nominal surface with random 2D islands. (b) Vicinal surface tilted towards (111) with one dominant step configuration and ZnTe wires running along (110). (c) Vicinal surface tilted towards (100) with steps running equally along (110) and (110). The ZnTe dots are formed by nucleation at the two step edges of the terraces.

on the growth conditions. Grown on vicinal surfaces with ordered kinks and terraces, a self-organized array of dots or wires could be formed, as shown in Fig. 1 [3].

The aim of this paper is to understand how to get, by molecular beam epitaxy, monolayers and submonolayers of the isoelectronic impurity Zn in a CdTe matrix. Knowledge of the parameters of a 2D growth (surface diffusion and mobility, growth interruptions, atomic exchange reaction on the surface, etc.) is essential for the control of interface morphology. Some of them are obtained from RHEED oscillations of the specular beam intensity on nominal and vicinal (001) surfaces of CdTe and ZnTe. The crystalline quality of the structure, as well as the total amount of Zn incorporated, are obtained from high resolution

X-rays diffraction data of strained superlattices incorporating 0.3 to 3 monolayers (ML) of ZnTe. The role of interdiffusion, roughness and strain field on compositional profile will be discussed. In particular, the partial relaxation of highly strained ZnTe microclusters or rough layers due to their finite size has been considered. The electronic properties of these superlattices are studied by different optical methods including photoluminescence, excitation spectroscopy, reflectivity and piezomodulated reflectance which identify light and heavy hole excitons. The exciton motion is shown to be strongly affected by the in-plane potential. The particular band structure of CdTe/ZnTe heterostructures makes this potential attractive for light holes, but repulsive for heavy holes and electrons. Light hole exciton localization by ZnTe dots of various sizes is observed.

## 2. Molecular beam epitaxy of ZnTe monolayers

The samples are grown by conventional MBE on CdTe and  $\text{Cd}_{0.97}\text{Zn}_{0.03}\text{Te}$  (001) substrates. They are either nominally (001) ( $\pm 0.2^\circ$ ) or mis-oriented by  $2^\circ$  ( $\pm 0.2^\circ$ ) towards [100]. For the vicinal surfaces, the terrace configuration resulting from the miscut angle would consist of two adjacent stair cases of steps along the  $[1\bar{1}0]$  and  $[110]$  directions (see Fig. 1c).

After degassing and surface stabilization under cation flux, RHEED oscillations are recorded on a short period (5 ML/5 ML) superlattice CdTe/CdZnTe. This calibration run is performed under experimental conditions identical to those used for the growth of the superlattices (SLs) with the ZnTe insertions. The ZnTe growth rate is given with 10% accuracy by the difference between the deposition rate of CdTe and CdZnTe. The thickness ratio of the CdTe and ZnTe layers is chosen such as to maintain the SL commensurate with the CdZnTe substrate, whose lattice parameter lies in between that of the two binaries [4]. The strain symmetrization which results from this choice allows growth of a thick (1  $\mu\text{m}$ ) superlattice with an average deformation close to zero avoiding the creation of extended defects.

The CdTe layers are grown under Cd excess and are followed by the deposition of monolayer or submonolayer of ZnTe. This is followed by a growth interruption, which cannot be performed under Cd or Zn excess because that would modify the total amount of Zn by the exchange reaction between Cd and Zn atoms [5]. A short growth interruption under vacuum is thus performed in order to allow surface rearrangement. For growth on nominal surfaces, one expects a random distribution of 2D islands (Fig. 1a) but on vicinal surfaces an ordered array of microclusters can be obtained by aggregation at step edges or kinks if mobility is high enough. Depending on the misorientation axis, wires should be obtained for a [110] rotation axis (Fig. 1b) or dots for a [100] direction (Fig. 1c).

To determine the condition for the growth to occur by step propagation, the surface diffusion length of Te atoms has been measured on vicinal surfaces by observing the temperature dependence of the disappearance of the RHEED oscillations [6]. The critical temperature ( $T_c$ ) corresponds to the transition from 2D nucleation on terraces (with RHEED oscillations) to step flow mode (no RHEED oscillations). Then one assumes that at  $T_s = T_c$ , the diffusion length ( $L_D$ ) will be equal to the terrace length (90 Å for a 2° miscut) with a lifetime  $\tau = N_s F^{-1}$ , where  $N_s$  is the surface site density and  $F$  the arrival rate of atoms per unit surface area [6]. Then the surface diffusion coefficient  $D_s = L_D^2 / \tau$  can be measured by varying the growth rate and the substrate temperature  $T_s$ . An example of such measurement of the disappearance of RHEED oscillations is shown in Fig. 2a for CdTe (001) misoriented toward (001) with a CdTe flux set at 0.75 ML/s. Fig. 2b shows the Arrhenius plot of  $D_s$  versus  $T_c$  for CdTe and ZnTe growth. Activation energies of  $1.6 \pm 0.3$  and  $2 \pm 0.3$  eV are obtained for CdTe and ZnTe surfaces, respectively. This difference reflects more or less the difference in the cohesive energy of the two materials. These data lead to a growth temperature of 330–340°C, for preferential nucleation at step edges, with a typical growth rate of 0.4 ML/s for CdTe and 0.1 ML/s for ZnTe.

At such a temperature, interdiffusion could be

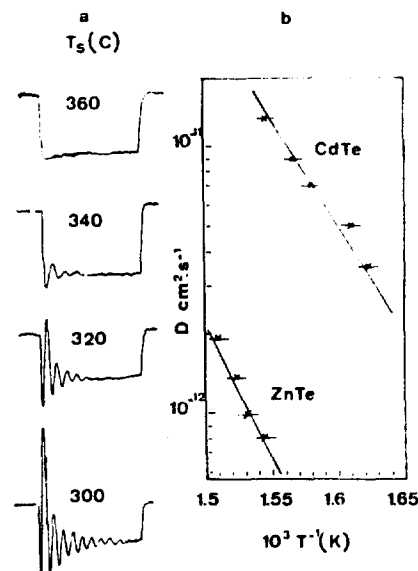


Fig. 2. (a) RHEED oscillations recorded at different substrate temperatures ( $T_s$ ) during the growth of CdTe on a (001) CdTe surface tilted 2° towards (100). (b) Arrhenius plot of the surface diffusion coefficient of Te atoms on CdTe and ZnTe surfaces, measured from the disappearance of the RHEED oscillations.

a severe limitation to the interface morphology. The interdiffusion coefficient of CdTe/CdZnTe interfaces has been measured as  $D = 114 \exp(-2.5 \text{ eV}/kT)$  [7]. At 330°C this gives an intrinsic coefficient for Zn diffusion of  $10^{-19} \text{ cm}^2/\text{s}$  which corresponds to an abruptness of  $\pm 1$  monolayer. The sharpness of the interface could be improved by using a higher miscut angle. The critical temperature would be lower, making the interdiffusion contribution negligible.

### 3. X-ray diffraction characterization

The structural parameters of the superlattices are deduced from X-ray diffraction (XRD) data which can be used to analyse layers having a thickness of 1 ML or less, provided the chemical or lattice constant contrast is high. Integral structural information is then obtained such as the total amount of Zn per inserted plane, the strain and the thickness of each layer and the state of coherence with the substrate.

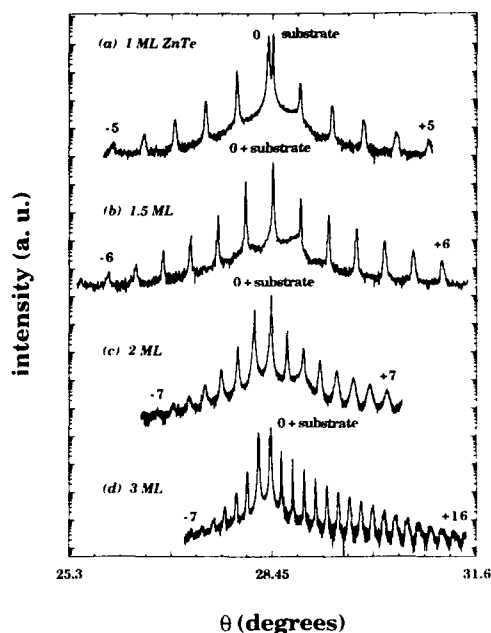


Fig. 3. (400) X-ray diffraction diagram of CdTe/ZnTe superlattices with different ZnTe layer thicknesses. The superlattice parameters are given in Table 1.

The diagrams are recorded in the  $\theta$ - $2\theta$  mode around the (004) reflection. Large angular scans are possible with a resolution of 10 arc sec and a dynamic range of  $10^4$ – $10^5$ . The XRD diagrams are simulated in the kinematical approximation.

Fig. 3 shows the diagrams obtained on CdTe/ZnTe superlattices with different ZnTe layer thicknesses. The parameters of these SLs are summarized in Table 1. The CdTe layer thicknesses have been adjusted to maintain coherence with the  $\text{Cd}_{0.97}\text{Zn}_{0.03}\text{Te}$  substrate. This is confirmed by the small splitting between the substrate peak and the zero-order peak of the SL (this peak gives the average lattice parameter of the SL along the growth direction). The equality of the two lattice constants ensures the absence of any lattice mismatch relaxation. The diagrams show highly resolved SL satellites with a small background coming from diffusion on structural imperfections. FWHMs varying from 20 to 30 arc sec for the first order peaks ( $n \leq 3, 4$ ), then increasing to 90–150 arc sec for higher orders

Table 1

Structural parameters of CdTe/ZnTe superlattices: the first two columns correspond to the nominal thickness of CdTe and ZnTe in number of monolayers, deduced from RHEED oscillations; the other three parameters are measured from X-ray diffraction.  $P$  is the period of the superlattice; all the samples are grown at 280°C, except sample Z 648 grown at 220°C and Z 682 grown at 300°C

	$N(\text{CdTe})$	$N(\text{ZnTe})$	$P$ (Å)	$N(\text{CdTe})$	$N(\text{ZnTe})$
Z 682	14	0.5	46.6	$13.8 \pm 0.5$	$0.4 \pm 0.05$
Z 587	27	1	90.7	$27 \pm 1$	$0.8 \pm 0.1$
Z 648	28	1	101	$30 \pm 1$	$0.63 \pm 0.05$
Z 671	35	1.5	117.7	$35 \pm 1$	$1.4 \pm 0.1$
Z 562	60	2	191.7	$58 \pm 1$	$1.7 \pm 0.1$

( $n = 6, 7$ ) are routinely obtained. In Fig. 4 we compare the experimental pattern with the computer simulation of a CdTe/ZnTe superlattice with nominal value of  $1 \pm 0.15$  ML of ZnTe as deduced from RHEED oscillations. As a result of the large mismatch between ZnTe and the CdZnTe substrate the zero-order peak position is

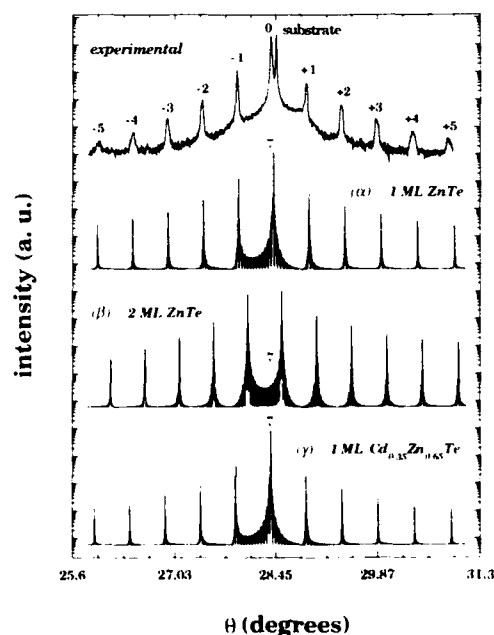


Fig. 4. Comparison of the experimental and calculated X-ray diffraction patterns of a 30 ML CdTe/1 ML ZnTe. The calculated diagrams are obtained for different Zn contents.



extremely sensitive to the total amount of Zn per period. While not clearly seen in Fig. 4 due to the too wide angular scan, the zero-order peak position cannot be fitted with the nominal value of 1 ML of ZnTe, but instead by taking  $0.65 \pm 0.05$  ML of ZnTe. In the calculation the fractional layers are represented by an integral monolayer of equivalent  $\text{Cd}_{1-x}\text{Zn}_x\text{Te}$  alloys. This assumption will be valid for a random distribution of islands with small lateral extension. For superlattices grown below 280°C where surface migration is limited, this approximation is probably correct. As shown in Table 1, the ZnTe insertion presents a deformation systematically 20–40% below that expected from elasticity theory for the amount of Zn measured from the RHEED oscillations.

While it is clear that measurement errors ( $\pm 10$ –15%) contribute to this difference, the experimental data seem to indicate a partial relaxation of the strain of the ZnTe islands or layers. Strain mapping along the growth direction obtained by analysing high resolution electron micrographs also shows a partial relaxation of ZnTe layers, which has been attributed to some Zn segregation [10]. While we cannot discard this interpretation, we must also consider the possibility of a reduction of the stress energy in strained systems of finite size, such as islands or rough layers [11]. Indeed, for an infinitely flat ZnTe layer, the biaxial stress imposed by the substrate lattice parallel to the interface results in a perfectly tetragonal distortion. However, if the source of strain is reduced to finite lateral extent by forming islands or by surface corrugation, first the strain field will propagate inside the surrounding matrix with a characteristic length comparable to the source dimension and, secondly, the ZnTe cluster deformation will be less than expected for a pure tetragonal distortion. Such an effect has been observed recently during the growth of InGaAs on GaAs [12]. In this particular case the relaxation takes place essentially at the free edges of the surface islands. When the microclusters are embedded in a matrix the relaxation is probably more isotropic.

Preliminary calculations made by taking ellipsoidal ZnTe clusters indicate that 25% of strain relaxation is expected for an ellipsoidal  $c/a$  ratio

close to 10 [13]. This means that 1 ML high islands extend laterally over 20–30 Å. Some of the optical data presented in the next section indicate also the presence of homogeneously distributed islands with a lateral size smaller than the exciton Bohr radius which is equal to 70 Å in CdTe bulk materials. In this scheme, the extra relaxation we observe for complete monolayers (it has also been observed for InGaAs/GaAs [12]) originates presumably from the surface roughness of the CdTe layers, which are not sufficiently smoothed at 280°C by the growth interruption, and also from the ZnTe growth mode which favors island formation.

#### 4. Investigation of quantum size effect and exciton localization by ZnTe dots

The CdTe/ $\text{Cd}_{1-x}\text{Zn}_x\text{Te}$  quantum structures exhibit a particular valence band alignment strongly dependent on the strain state of each constituent [14]. Light holes are generally confined in the barrier, which are in tensile strain, while heavy holes and electrons are localized in the CdTe wells (unstrained or in compression). Then one expects that ZnTe inserted in a CdTe matrix will act as an attractive potential for light holes, but repulsive for heavy holes and electrons (see the insert of Fig. 5b). A fundamental question is the actual nature of the potential which must be chosen to describe the ZnTe insertion correctly. The best approach is the atomistic model developed by Mäder and Baldereschi [15]. They used empirical tight binding (ETB) calculations adapted from those developed to treat iso-electronic impurity centres in bulk materials [16]. Another approach has been used to describe optical data for InAs in GaAs [17]. It uses the envelope function model (EFM) and, surprisingly, gives results for ground states comparable to ETB calculations. Possible explanations for the puzzling agreement despite the limitations of the EFM at the one monolayer scale is that the effective potential given by the overlap of the squared wavefunctions of the carriers and the short-range perturbation is generally small. Then the ground state wave function of the localized

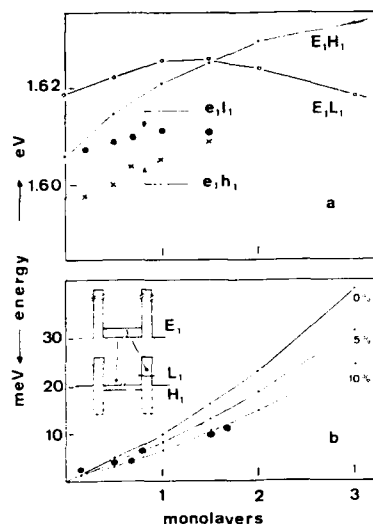


Fig. 5. Effect of the ZnTe layer thickness on (a) the calculated band gaps  $E_{1H_1}$  and  $E_{1L_1}$  and the experimental excitonic transitions,  $e_{1h_1}$  and  $e_{1l_1}$ , and (b) the calculated and experimental localization energies ( $E_{loc}^{1,1}$ ) of the light holes states. The superlattices are grown on  $Cd_{0.96}Zn_{0.04}Te$  substrates and the CdTe well thickness is 30 ML.

carriers can be represented by a hydrogenoid function  $a^{-1/2} e^{-az}$  and the ground state energy will not be sensitive to the shape of the potential as long as the spatial extension of the perturbation is much smaller than the carrier Bohr radius  $a$ .

In the following we will use the EFM by assuming a periodic sequence of square well potentials given by the band discontinuity of the constituents [18]. Then the barrier height for electrons, heavy hole and light hole are respectively 551, 112 and 228 meV, taking a chemical valence band offset of 5% and an  $a_c/a_v$  ratio equal to 2 ( $a_c$  and  $a_v$  are the hydrostatic deformation potentials of the conduction and valence band). Non-integer ZnTe layers are represented by a complete layer of the equivalent alloy. This "mean field" approximation is valid as long as excitons can average the potential fluctuations over distances comparable to their Bohr radius. The exciton binding energy  $E_{BX}$  is calculated within the EFM and shows very similar values for the heavy hole  $e_{1h_1}$  and light hole  $e_{1l_1}$  excitons, despite the

latter being "indirect" in the sense that electron and light hole are spatially separated [19]. However, the Coulomb interaction and the large probability of finding the light hole in the CdTe layers makes the  $e_{1l_1}$  transition quasi-direct.

Fig. 5a shows the variation of the  $E_{1H_1}$  and  $E_{1L_1}$  interband transitions (they differ from the  $e_{1h_1}$  and  $e_{1l_1}$  excitonic lines by the exciton binding energy) calculated for a SL containing 30 ML thick CdTe wells separated by ZnTe layers with thicknesses varying between 0 and 3 ML. The SL is coherently grown on a  $Cd_{0.96}Zn_{0.04}Te$  substrate which lifts valence band degeneracy of CdTe by an amount  $\delta HL \cong 12.0$  meV. The initial blue shift of the two transitions results from the progressive decoupling of the electron states when the effective barrier potential increases. Above 1 ML of ZnTe, the stabilization and then the red shift of the  $E_{1L_1}$  transitions result from the enhancement of the localization of light holes states by the ZnTe wells. The experimental values of the  $e_{1l_1}$  and  $e_{1h_1}$  exciton energies are also reported. They were obtained from the reflectivity spectra shown in Fig. 6. Piezomodulated reflectance was used to identify light and heavy hole excitons [20]. As predicted by the calculations, we clearly observe the decrease of the energy separation  $\delta(e_{1h_1}, e_{1l_1})$  between light and heavy hole exciton. A good fit of the absolute energy of the transitions is also obtained by taking exciton binding energies  $E_{BX}^{1,1} \cong E_{BX}^1 \cong 12$ –14 meV. Fig. 5b shows the plot of the calculated and experimental binding energies ( $E_{loc}^{1,1}$ ) of the light hole ground state as a function of Zn coverage.  $E_{loc}^{1,1}$  is measured from the top of the valence band of the barrier and is given by

$$E_{loc}^{1,1} = \delta(e_{1h_1}, e_{1l_1}) + \delta HL + \delta E_{BX}^{1,1} - H_1,$$

where  $H_1$  is the heavy hole confinement energy,  $\delta E_{BX}^{1,1}$  the difference between light and heavy hole exciton binding energy,  $\delta HL$  the heavy–light hole splitting in CdTe and  $\delta(e_{1l_1}, e_{1h_1})$  the energy separation between light and heavy excitonic transitions.  $E_{loc}^{1,1}$  depends on the chemical valence band offset  $\Delta V_{bv}$  and reasonable agreement between experiment and calculation is obtained for a ratio  $\Delta V_{bv}/\Delta E_g \cong 5$ –10%.

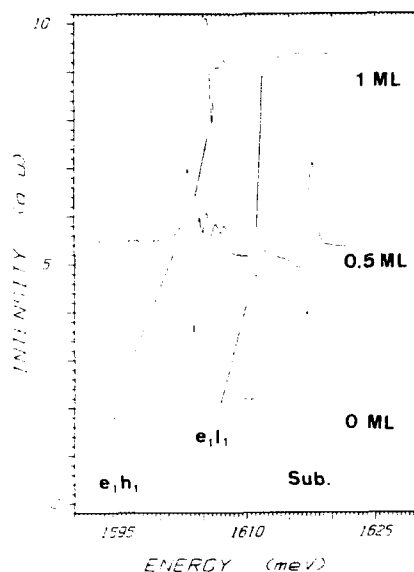


Fig. 6. 1.8 K reflectivity spectra obtained on CdTe layers with insertions of 0, 0.7 and 1 ML of ZnTe grown at 280°C on  $\text{Cd}_{0.9}\text{Zn}_{0.1}\text{Te}$  substrates. The undulations observed on the sample without ZnTe insertion are the results of the quantization of the free exciton motion along the growth axis. The whole "superlattice" (without internal barriers) acts as a single quantum well.

These experimental data show a monotonic variation of  $E_{\text{loc}}^{\text{LL}}$  for fractional monolayers with sharp ( $\leq 1$  meV) excitonic transitions  $e_1h_1$  and  $e_1l_1$ . This confirms the "mean field" approximation where the fluctuations are efficiently averaged. This means that for these superlattices which were grown below 280°C, the island size ( $L_s$ ) is smaller than the exciton Bohr radius ( $a_B$ ). In the opposite case ( $L_s \gg a_B$ ) one expects to observe multiple peaks with transition corresponding to the insertion of zero, 1 or possibly 2 ML.

Fig. 7 shows the reflectivity spectra obtained for samples grown on CdTe (001) vicinal surfaces at 340°C. As shown in section 2, this condition corresponds to a higher surface mobility of atoms and under these conditions an efficient coalescence of the ZnTe clusters is expected. Sample (a) incorporates sheets of ZnTe with a nominal thickness of 2 ML and for sample (b), 0.5 ML of ZnTe has been deposited in between 30 ML thick

CdTe layers. For sample (a), we observe three lines which fall close to the expected position of the  $e_1h_1$  excitons for 1, 2 and 3 ML of ZnTe. For the light hole exciton  $e_1l_1$ , which is very close to the CdTe substrate signal, only one line is detected. This is not surprising because, as shown in Fig. 6a, the  $e_1l_1$  line does not shift for ZnTe thickness varying between 1 and 2 ML. The observation of multiple peaks at positions corresponding to integral numbers of ZnTe monolayers is characteristic of a smooth interface with ZnTe islands larger than the exciton Bohr radius [21].

For sample (b) with 0.5 ML of ZnTe, a very different spectrum is obtained. The calculated positions of the  $e_1l_1$  and  $e_1h_1$  transition for 0, 0.5 and 1 ML ZnTe insertion are indicated. Contrary to sample (a), we observe several discrete lines which span the whole energy range expected for  $\pm 0.5$  ML fluctuations. This spectacular effect could result from a disorder-induced localization of carriers where the superlattice extended states

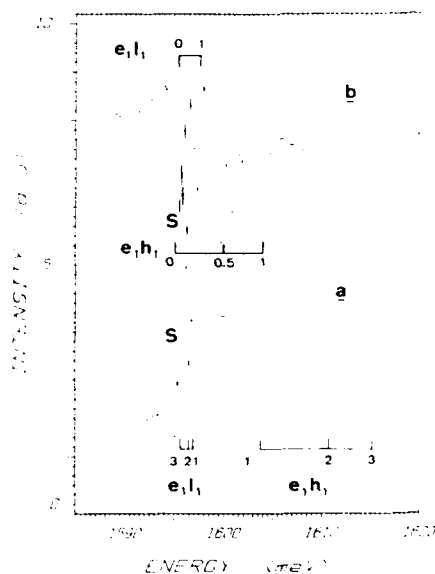


Fig. 7. 1.8 K reflectivity spectra obtained on CdTe layers with 0.5 and 2 ML ZnTe insertion grown at 340°C on CdTe vicinal surfaces. The expected positions of the light ( $e_1l_1$ ) and heavy ( $e_1h_1$ ) excitons for different thickness configurations of the ZnTe insertions are shown in the figure.

are replaced by spatially localized levels [22]. This leads to several recombination lines corresponding to different disorder configurations along the growth direction. The observation of this effect also requires large ZnTe islands resulting in a lateral modulation of the wavefunction. If we consider the case of electron states, in absence of disorder, the CdTe well states are strongly coupled through the 0.5 ML ZnTe barrier. A miniband is formed with a width  $\Delta \approx 30$  meV, and states are delocalized over the whole structure. However, the 1 ML high ZnTe islands are randomly distributed in the plane of the layers, which creates a disorder along the growth direction. As a first approximation, this disorder  $I$  corresponds to local fluctuations of 1 to 0 ML; thus  $I \approx 10$  meV (this is the difference in the electron confinement energy for CdTe wells of 30 ML and 60 ML). The electrons states are approximatively localized on a distance scale  $(\Delta/I)L_w \approx 2-3 L_w$ , where  $L_w$  is the CdTe thickness, and no extended states can exist. Similar effects are also expected for light hole states. On the contrary, for samples with a high density of small ZnTe islands (such as the samples grown at low temperature), the potential fluctuations are now very well averaged and then the disorder parameter  $I$  is small ( $\approx 1$  meV). Extended states can be formed and single transitions are observed for light and heavy excitons, respectively.

## 5. Conclusion

The conditions for fabricating ZnTe submonolayers and dots coherently inserted in a CdTe matrix by molecular beam epitaxy have been described. For temperatures close to the transition from growth by the formation of 2D clusters to growth by step advancement, ZnTe islands with lateral size comparable to the exciton Bohr radius are obtained ( $\approx 100$  Å). At lower temperature, the deposited ZnTe layer is distributed in small clusters (10–30 Å). In the latter case, all the types of fluctuations are averaged on the scale of the exciton wavefunction. X-ray diffraction studies shows that the Zn planes are well matched to the matrix, with sharp interfaces. Interdiffusion,

which can be an important limiting factor, does not seriously affect the morphology of CdTe/ZnTe interfaces. Partial strain relaxation of ZnTe dots due to finite size effects is proposed as an explanation of the discrepancy between the measurements of Zn content by X-rays data and RHEED oscillations.

The localization of light hole excitons by ZnTe dots and planes has been observed in various superlattice configurations. The ZnTe layers or submonolayers act as quantum wells for light holes and thus confirm the band alignment of the CdTe/ZnTe interface now widely accepted: a chemical valence band offset between 5% and 10% with type I alignment for electrons and heavy holes and type II for electrons and light holes. The exciton localization results first from the capture of the light hole by the short range potential of the dots, and then an electron is bound by the Coulomb field of the hole. The binding energy and the spatial extension of these excitons remain bulk-like, but the response of the system depends on the 2D nature of the isoelectronic potential. For pseudo-smooth interfaces we can define a mean potential with a strength proportional to the quantity of Zn. In this case the excitonic transitions vary continuously with the Zn content. When large size islands are created, the potential is laterally modulated over a distance comparable to the Bohr radius. The exciton energies are very sensitive to the interface structures, and discrete excitonic lines associated with the various configurations of the isoelectronic potential are observed.

These results demonstrate the interest of growing isoelectronic insertions. Valuable information on growth mechanisms, interfaces and exciton localization is obtained. Moreover, the absence of any interface and surface states makes this system extremely interesting for the study of ultra-small objects.

## 6. Acknowledgements

Special thanks are due to J. Allègre from the University of Montpellier for the piezoreflectance measurements, to A. Tardot and P. Blanc for

X-ray measurement and to P. Gentile for the MBE growth. J.L. Pautrat and R.T. Cox are acknowledged for critical reading of the manuscript.

## 7. References

- [1] T. Noda, J. Motohisa and H. Sakaki, *Superlattices Microstruct.* 13 (1993) 41.
- [2] J.M. Gérard and J.Y. Marzin, *Phys. Rev. Lett.* 62 (1989) 2172.
- [3] O. Brandt, L. Tapfer, K. Ploog, R. Biewolf, M. Hohenstein and F. Philip, *Phys. Rev. B* 44 (1991) 8043.
- [4] A. Ponchet, G. Lentz, H. Tuffigo, N. Magnea, H. Mariette and P. Gentile, *J. Appl. Phys.* 68 (1990) 6229.
- [5] S. Tatarenko, unpublished data.
- [6] J.H. Neave, P.J. Dobson, B.A. Joyce and J. Zhang, *Appl. Phys. Lett.* 47 (1985) 100.
- [7] N. Magnea, A. Tardot, H. Mariette and N. Pelekanos, *Mater. Sci. Eng. B* 16 (1993) 71.
- [8] A. Tardot, P. Gentile and N. Magnea, *Appl. Phys. Lett.* 20 (1993) 2548.
- [9] J. Singh and K.K. Bajaj, *Appl. Phys. Lett.* 47 (1985) 594.
- [10] P.H. Jouneau, G. Feuillet, H. Mariette and J. Cibert, *Appl. Phys. Lett.*, to be published.
- [11] S. Luryi and E. Suhir, *Appl. Phys. Lett.* 49 (1986) 140.
- [12] J. Massies and N. Grandjean, *Phys. Rev. Lett.*, to be published.
- [13] A. Bourret, private communication.
- [14] H. Tuffigo, N. Magnea, H. Mariette, A. Wasiela and Y. Merle d'Aubigné, *Phys. Rev. B* 43 (1991) 14629.
- [15] K.A. Mäder and A. Baldereschi, in: *Optics of Excitons in Confined Systems*, *Inst. Phys. Conf. Ser.* 123, Eds. A. D'Andrea and R. Del Sole (Inst. Phys., Bristol, 1991) pp. 341–344.
- [16] A. Baldereschi and J.J. Hopfield, *Phys. Rev. Lett.* 28 (1972) 171.
- [17] R. Cingolani, O. Brandt, L. Tapfer, G. Scamarcio, G.C. La Rocca and K. Ploog, *Phys. Rev. B* 42 (1990) 3209.
- [18] N. Pelekanos, Ph. Peyla, Le Si Dang and H. Mariette, *Phys. Rev. B* 48 (1993) 1517.
- [19] Ph. Peyla, Y. Merle d'Aubigné, A. Wasiela, R. Romestain, H. Mariette and M. Sturge, *Phys. Rev. B* 46 (1992) 1557.
- [20] J. Calatayud, J. Allègre, H. Mathieu, H. Mariette and N. Magnea, *Phys. Rev. B* 47 (1993) 9584.
- [21] B. Deveaud, J.Y. Emery, A. Chomette, B. Lambert and M. Baudet, *Appl. Phys. Lett.* 45 (1984) 1078.
- [22] A. Chomette, B. Deveaud, A. Regreny and G. Bastard, *Phys. Rev. Lett.* 57 (1986) 1464.



ELSEVIER

Journal of Crystal Growth 138 (1994) 559–563

JOURNAL OF  
**CRYSTAL  
GROWTH**

## Deep blue and UV photoluminescence from ZnS/CdS superlattices and quantum wells

G. Brunthaler <sup>a,\*</sup>, M. Lang <sup>b</sup>, A. Forstner <sup>a</sup>, C. Giftge <sup>c</sup>, D. Schikora <sup>c</sup>, S. Ferreira <sup>b</sup>,  
H. Sitter <sup>b</sup>, K. Lischka <sup>b</sup>

<sup>a</sup> Institut für Halbleiterphysik, Universität Linz, A-4040 Linz, Austria

<sup>b</sup> Forschungsinstitut für Optoelektronik, Universität Linz, A-4040 Linz, Austria

<sup>c</sup> Institut für Halbleiterphysik, TU Braunschweig, D-38106 Braunschweig, Germany

### Abstract

Ultrathin quantum wells (QWs) and short period superlattices (SLs) of ZnS/CdS were grown on (001) GaAs substrates by molecular beam epitaxy using elemental sources. The relaxation of the ZnS buffer and pseudomorphic growth of CdS QWs was investigated by reflection high-energy electron diffraction. The QW structures with 1 to 4 monolayers emit photoluminescence in the ultraviolet spectral region even at room temperature, whereas the SLs emit in the blue range. The SL structures were ascertained by the observation of satellites in X-ray diffraction spectra.

### 1. Introduction

Since the realization of the first blue-green diode lasers [1,2] in 1991 there has been a need for alternative and complementary II–VI materials for optoelectronic devices with band gaps in the blue and ultraviolet (UV) spectral region. Cubic ZnS has a room temperature band gap of 3.7 eV and is a promising material for optoelectronic applications in this spectral range [3]. Due to rapid advance in the growth of II–VI compounds in the recent years, it is now possible to fabricate ZnS/CdS quantum well (QW) [4,5] and superlattice (SL) [6,7] structures by molecular

beam epitaxy (MBE) and metalorganic chemical vapor deposition (MOCVD).

In this paper we report on the MBE growth of ZnS/CdS QWs and SLs with a thickness of the active layers of a few monolayers. The growth was monitored by reflection high-energy electron diffraction (RHEED) and a phase diagram for the surface reconstruction of ZnS was established. Photoluminescence (PL) measurements were performed at liquid helium temperatures and at room temperature and intense emission was detected at wavelength as short as 380 nm from a 2 monolayer CdS QW. The SL structures were in addition characterized by high resolution X-ray diffraction (HRXD) measurements which gives the average lattice constant and the exact period of the layers.

\* Corresponding author.

## 2. Experimental procedure

The epitaxial growth of all SL and QW structures was performed in an MBE system designed and constructed at University of Linz, especially for growth of high vapor pressure II–VI compounds. The MBE growth chamber is equipped with an extensive liquid  $N_2$  cryoshroud for efficiently freeze out of high vapor pressure materials such as sulfur.

The MBE growth was carried out using two standard low temperature effusion cells for elemental Zn and Cd. The Sulfur effusion cell consists of independently heated effusor and post-heating zones. The S cell is operated at about 110°C for effusor and at about 200°C for the post-heating zone, the sulfur beam equivalent pressure (BEP) was in the range of  $1$  to  $2 \times 10^{-6}$  nbar.

High purity elemental Cd (7N), Zn (6N) and S (5N) were used as MBE source materials. The heterostructures were grown on (001) GaAs  $2^\circ$  misoriented towards the next [110] direction. Each substrate was delivered epiready and degreased in trichloroethylene, acetone, methanol for 2 min at room temperature followed by a 2 min rinse in de-ionized water. The GaAs substrate was heated to about 650°C in the MBE chamber for appropriate time monitored by RHEED for oxide removal prior to film deposition. The surface reconstruction of the ZnS layers was in-situ monitored by the 35 kV RHEED system during growth and a surface phase diagram was established. It shows a  $(1 \times 2)$  reconstruction at lower substrate temperature  $T_{\text{sub}}$  and higher beam pressure ratio  $p_S/p_{Zn}$ , a region where no reconstruction was observed and at higher  $T_{\text{sub}}$  and lower  $p_S/p_{Zn}$  a  $c(2 \times 2)$  reconstruction was detected. The samples were grown at  $T_{\text{sub}} = 200$  to 230°C, in the region with no reconstruction observable, which is assigned to stoichiometric surface conditions [8]. In addition, at these temperatures the RHEED reflexes were streaky. At lower  $T_{\text{sub}}$  they showed arrow-head like shapes, indicating a faceting growth due to a reduced mobility of the surface atoms. The growth rate was about  $0.1 \mu\text{m/h}$ .

The MBE grown QW structures consist of a 1000 Å ZnS buffer on top of the GaAs substrate

followed by either single CdS wells or multi-QW structures containing several CdS wells separated by 330 Å of ZnS barriers from each other. The thickness of the wells was varied from nominal 1 to 6 ML of CdS. The structure is completed by a 330 Å ZnS cap layer. In order to get the desired layer thickness, the growth rate was determined from thickness measurements of layers with typically  $1 \mu\text{m}$  thickness and from the determination of the periodicity of SL samples characterized by X-ray measurements.

The SL structures were grown on (001) GaAs substrates and consist of  $(\text{ZnS})_m/(\text{CdS})_n$  layers with  $m$  and  $n$  the number of monolayers and  $(m/n) \times l = (2/2) \times 200$ ,  $(3/3) \times 65$ ,  $(4/2) \times 200$  and  $(9/4) \times 100$  for the different samples where  $l$  denotes the number of repetitions. Only the 3/3 SL was grown on a 9000 Å ZnS buffer layer, the other SL structures were grown directly on the substrate. The exact ratios of the superlattice periods were determined by HRXD investigations as will be described below.

## 3. Results and discussion

A QW structure which contained 1, 3 and 5 ML of CdS was investigated by RHEED measurements. After completion of each individual layer, the in-plane lattice constant was determined, the results are shown in Fig. 1. In order to reach a high accuracy, the RHEED pattern has

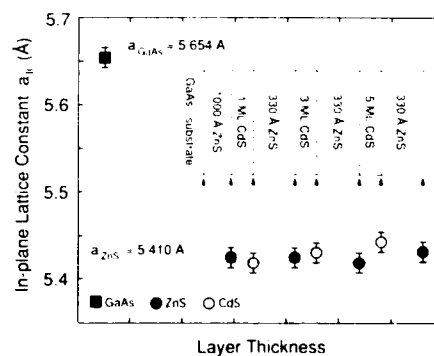


Fig. 1. The in-plane lattice constant, as determined by RHEED measurements, is shown for the completion of each layer as indicated in the inset. After 5 ML of CdS there is already a deviation from the ZnS lattice constant observable.

been photographed directly from the fluorescence screen. Then the pictures were converted to a photo-CD so that the patterns are accessible to a computer aided analysis. The distances between the RHEED reflexes were determined with a line-scanning program and give direct information about the in-plane lattice constant.

As indicated in Fig. 1, the lattice constant of the 1000 Å ZnS buffer layer on the GaAs substrate is fully relaxed to the bulk value of 5.410 Å. After 1 ML of CdS the RHEED analysis gives the same lattice constant. After an additional buffer layer of 330 Å ZnS the second CdS QW with 3 ML shows a lattice constant which seems to be slightly larger, but the change is below the accuracy of the determination. The situation is changed for the next layer sequence of 330 Å ZnS and 5 ML of CdS. On top of the ZnS buffer, the lattice constant is again that of bulk ZnS, but after deposition of 5 ML of CdS an increase of the inplane lattice constant of about 0.02 Å is observed. This is larger than the error bars indicated in Fig. 1. It seems that due to the large difference in the lattice constants of ZnS and CdS (7.5% lattice mismatch) already 5 ML of CdS exceed the critical thickness of pseudomorphic growth conditions. These results are in good agreement with the model of Van der Merwe and Jesser [9]. Similar results that show a partly relaxation of ZnSe and CdSe strained layers at about 4 ML have been obtained from HRXD analysis by Faschinger et al. for ZnSe/CdSe SL [10].

The ZnS/CdS QW samples with few monolayers (ML) of CdS were also investigated by PL measurements in order to evaluate their optical quality. The UV lines of an argon ion laser between 275 and 300 nm were used as excitation of the PL, the samples were mounted in a helium bath cryostat. Fig. 2a shows the 2 K spectrum of the sample which contains 1, 3 and 5 ML of CdS separated by 330 Å of ZnS barriers. The PL peak at 3.62 eV corresponding to 1 ML is weak, the 3 ML peak at 3.00 eV has a strong intensity and no emission from the 5 ML well was observed. We attribute the absence of the 5 ML emission to a poor crystalline quality of this well due to a partly lattice relaxation of the strained CdS layer which was deduced from the RHEED measurements.

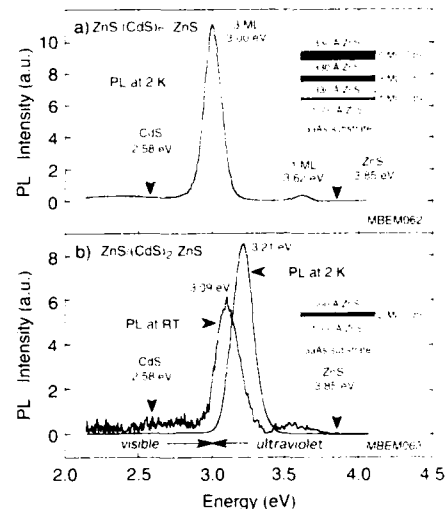


Fig. 2. Photoluminescence spectra of the multi QW structure with 1, 3 and 5 ML of CdS at 2 K (a) and a single QW sample with 2 ML of CdS at 2 K and room temperature (b). Schemes of the sample structures are shown as insets.

The assignment of the different peaks to the ML width as described above becomes clear if one compares the peak positions with the spectrum of another sample which contains a single 2 ML QW of CdS as shown in Fig. 2b. The maximum of the strong PL emission of the 2 ML structure occurs at an energy of 3.21 eV ( $\lambda = 386$  nm) at 4.2 K, the full width at half maximum is 160 meV. This emission is in the UV region of the optical spectrum. The PL emission was also observed at room temperature and is shown for comparison in Fig. 2b, too. The RT emission line is shifted to 3.09 eV and is broadened to 230 meV. The energetic position of the nominal 2, 3 and 4 ML CdS QW's was reproducible from sample to sample within 40 meV.

We calculated the carrier confinement energies of the ZnS/CdS QWs within the envelope wave function approach of a Kronig-Penney model. The calculated energies are compared with experimental energy positions at 4.2 K for different ML widths in Fig. 3. For the ZnS barrier the low temperature energy gap  $E_g$  was taken as 3.85 eV, the electron mass  $m_e = 0.34m_0$ , the heavy hole mass  $m_h = 0.5m_0$ . For the CdS well the



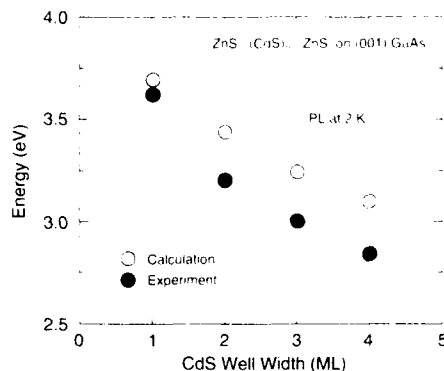


Fig. 3. Comparison of the experimental PL recombination energies with the calculated Kronig-Penney energies versus CdS well thickness in monolayers. The excitonic binding energy is not included in the calculated values.

corresponding values were  $E_g = 2.58$  eV,  $m_e = 0.14m_0$  and  $m_h = 0.5m_0$  [11]. The conduction band offset was taken as 0.75 of the bandgap difference which is a value usually assumed for heterostructures with common anions [3]. The experimental values for 1, 2 and 3 ML wells are taken as obtained from the measurements described above, the 4 ML value was taken from an additional sample which is not described in detail here.

As can be seen in Fig. 3, the calculated energies are higher than the measured ones. In the calculation, the excitonic binding energy is not included, which means that a value of 50 to 100 meV should be subtracted. In bulk ZnS the excitonic binding energy is 40 meV, in CdS the value is 28 meV [12,13]. In narrow QWs, the electron and hole wavefunction have some propagation into the barrier and the binding energy should be considered as a combined value of ZnS and CdS. In addition, there is a large confinement effect in narrow QWs, which increases the binding energy up to a factor of 4 compared to bulk values. Nevertheless, in our case the binding energy of the excitons can not account for the difference between calculated and measured recombination energies, because at 1 ML the difference is only about 40 meV whereas it increases up to about 250 meV for the 4 ML QW which is clearly larger than the excitonic binding energy.

We also varied the values of the conduction band offset and the effective masses for electrons and holes in the Kronig-Penney calculation, but within reasonable values no coincidence could be achieved. One reason for the difference may be due to strain induced changes of the band gap energies, which were not taken into account in our calculations [6].

The ZnS/CdS SL samples grown by MBE were investigated by HRXD. There clearly appear the peaks of (002) for GaAs substrate and zero-order diffraction with satellite reflections from the  $(\text{ZnS})_m/(\text{CdS})_n$  structure indicating the periodicity of the short period SL structure. The spacing  $d_0$  which means the average lattice constant of a unit cell of ZnS/CdS SL was calculated from the zero-order peak in the X-ray diffraction spectrum of each  $(\text{ZnS})_m/(\text{CdS})_n$  SL, assuming Vegard's law [14]. The experimental results of  $d_0$  are in good agreement with those predesigned. The well and barrier layer thickness were estimated from the  $n = \pm 1$  satellite peak around the zero-order peak. The spectra were simulated by a computer program [15] for the assumptions of freestanding, pseudomorphic and fully relaxed SL. The experimental value for the lattice constant is close to the simulated ones for a freestanding SL, but the value for fully relaxed layers is similar. However, the calculation for the pseudomorphic case, where all layer have the same in-plane lattice constant as the GaAs substrate, gives a clearly different value.

Fig. 4 shows the 2 K PL spectra of our  $(\text{ZnS})_3/(\text{CdS})_3$  and  $(\text{ZnS})_4/(\text{CdS})_2$  superlattice samples. The recombination energy of the 3/3 SL is 2.77 eV and has a width of 62 meV, the PL line of the 4/2 is at 2.82 eV and has a width of 80 meV. The smaller width of the 3/3 SL might be due to the additional buffer layer of 9000 Å ZnS which is absent in the 4/2 SL sample. The whole PL signal comes from the intense SL line, there is no luminescence at the band gap energy of ZnS or CdS. A Kronig-Penney calculation gives energies of 3.10 and 3.31 eV for the 3/3 and 4/2 SLs, respectively, which are 0.33 and 0.49 eV larger than the measured values. These large differences are not clear yet.

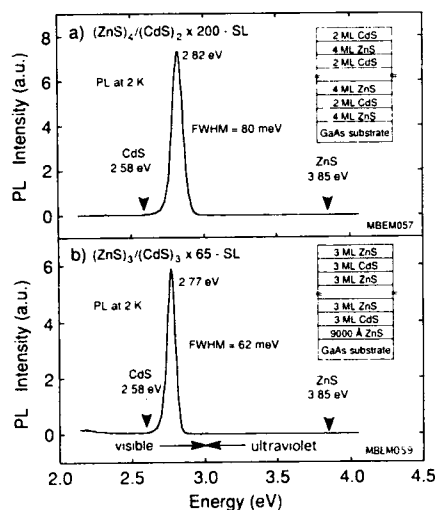


Fig. 4. Photoluminescence spectra of (a)  $(\text{ZnS})_4/(\text{CdS})_2 \times 200$  - SL and (b)  $(\text{ZnS})_3/(\text{CdS})_3 \times 65$  - SL superlattice structures at 2 K. The insets show the sample schemes.

#### 4. Conclusion

We have demonstrated that ZnS/CdS QWs with 1 to 4 monolayers of CdS give photoluminescence emission in the UV spectral region. The emission was observed at 2 K and at room temperature as well. By in-situ RHEED measurements, a relaxation of the in-plane lattice constant was observed for a QW thickness of only 5 ML. Superlattice structures showed photoluminescence in the blue spectral region, their lattice relaxation was investigated by HRXD and model calculations indicate that the structures are partly relaxed.

#### 5. Acknowledgments

This work is supported by the "Fonds zur Förderung der wissenschaftlichen Forschung",

P8833-TEC and P8358-PHY, and by the "Jubiläumsfonds der Österreichischen Nationalbank" No. 4442.

#### 6. References

- [1] M.A. Haase, J. Qiu, J.M. DePuydt and H. Cheng, Appl. Phys. Lett. 59 (1991) 1272.
- [2] H. Jeon, J. Ding, W. Patterson, A.V. Nurmikko, W. Xie, D.C. Grillo, M. Kobayashi and R.L. Gunshor, Appl. Phys. Lett. 59 (1991) 3619.
- [3] P.J. Parbrook and K.P. O'Donnell, in: II-VI Semiconductor Compounds, Ed. M. Jain (World Scientific, Singapore, to be published).
- [4] R.P. Vaudo, D.B. Eason, K.A. Bowers, K.J. Gossett, J.W. Cook, Jr. and J.F. Schetzina, J. Vac. Sci. Technol. B11 (1993) 875.
- [5] Z. Yu, J. Ren, Y. Lansari, B. Sneed, K.A. Bowers, C. Boney, D.B. Eason, R.P. Vaudo, K.J. Gossett, J.W. Cook, Jr. and J.F. Schetzina, Jap. J. Appl. Phys. 32 (1993) 663.
- [6] T. Taguchi, Y. Yamada, Y. Endoh, Y. Nozue, J.T. Mullins, T. Ohno, Y. Masumoto and S. Takeda, Superlattices Microstruct. 10 (1991) 207.
- [7] S. Ohta, S. Kobayashi, F. Kaneko and K. Kahiho, J. Crystal Growth 106 (1990) 166.
- [8] S.M. Newstead, R.A.A. Kubiak and E.H.C. Parker, J. Crystal Growth 81 (1987) 49.
- [9] J.H. van der Merwe and W.A. Jesser, J. Appl. Phys. 63 (1988) 1509.
- [10] W. Faschinger, P. Juza, A. Pesek and H. Sitter, in: Proc. 17th Int. Conf. on Defects in Semiconductors, Gmunden, Austria, 1993, Materials Science Forum (Trans Tech, Zürich, in press).
- [11] Landolt-Börnstein III, Vol. 17b, Ed. K.-H. Hellwege (Springer, Berlin, 1982).
- [12] T. Taguchi and Y. Endoh, Jap. J. Appl. Phys. 30 (1991) 952.
- [13] P.E. Lippens and M. Lannoo, Phys. Rev. B 39 (1989) 10935.
- [14] M.R. Khan, C.S.L. Chun, G.P. Felcher, M. Grimthditch, A. Kueny, C.M. Falco and I.K. Schuller, Phys. Rev. B 27 (1983) 7186.
- [15] A. Pesek, P. Kastler, L. Palmethofer, F. Hauzenberger, P. Juza, W. Faschinger and K. Lischka, J. Phys. D (Appl. Phys.) 26 (1993) A177.



ELSEVIER

Journal of Crystal Growth 138 (1994) 564–569

JOURNAL OF  
**CRYSTAL  
GROWTH**

## Optical confinement in ZnSe-based quantum well structure using impurity induced disordering

T. Yokogawa <sup>\*a,1</sup>, P.D. Floyd <sup>a</sup>, J.L. Merz <sup>a</sup>, H. Luo <sup>b</sup>, J.K. Furdyna <sup>b</sup>

<sup>a</sup> Department of Electrical and Computer Engineering, University of California at Santa Barbara, Santa Barbara, California 93106, USA

<sup>b</sup> Department of Physics, University of Notre Dame, Notre Dame, Indiana 46556, USA

### Abstract

We have investigated the phenomenon of layer disordering in CdZnSe/ZnSe strained layer superlattices (SLSs) by Ge diffusion and have fabricated CdZnSe/ZnSe optical waveguides using the Ge-induced disordering. Both the as-grown sample and the sample annealed without a Ge layer showed several orders of well-resolved double crystal X-ray satellite peaks due to SLS periodic structure. However, the satellite peaks completely disappeared in the Ge-diffused sample, indicating that the SLS structure was disordered by the Ge diffusion and not by the annealing process. PL measurements at 1.4 K of both the as-grown and the annealed samples without Ge diffusion show intense, sharp excitonic emission around 483 nm in CdZnSe/ZnSe SLS. After Ge diffusion, the PL peaks shift to higher energy confirming the layer disordering of the SLS. The blue shift due to disordering was also observed in the PL at room temperature (RT). The optical guided mode in the SLS guiding layer confined by the disordered alloy was confirmed. Lateral optical confinement in the stripe geometry laser was also confirmed by observing the RT stimulated emission produced by optical pumping.

### 1. Introduction

Wide bandgap II–VI materials such as ZnSe and CdZnSe have drawn much attention because of their application for blue laser diodes. The first blue-green laser diodes were reported by Haase et al. and Jeon et al. using a CdZnSe quantum well active layer [1,2], and the blue laser diode was also reported by Okuyama et al. using a ZnSe quantum well active layer [3]. The development of a variety of laser processing techniques

is one of the important issues for realizing room temperature, continuous-wave operation of ZnSe-based laser diodes. One such technique, impurity-induced disordering (IID) of semiconductor quantum well (QW) heterostructures, has proven to be extremely useful for patterning the refractive index and bandgap in the plane of the III–V QW layers [4–7]. The IID, particularly using Zn and Si diffusion, is now routinely used in the GaAs/AlGaAs system. Optical waveguides, heterostructure lasers and heterojunction bipolar transistors have been realized by IID. The disordering of ZnSe/ZnS strained layer superlattices (SLSs) has previously been demonstrated by Yokogawa et al. using N<sup>+</sup> or Li<sup>+</sup> ion implantation [8]. Ion implantation alone at room tempera-

\* Corresponding author.

<sup>1</sup> On leave from Matsushita Electric Industrial Co., Ltd., Osaka, Japan.

ture with light mass ions (e.g., N, Li, or Si) does not form a high quality, disordered alloy; the subsequent heating is needed to cause the annealing of implantation damage and the layer disordering. Impurity diffusion is also capable of enhancing the layer disordering, as clearly demonstrated in the III–V compounds. However, to date there are no reports of similar disordering in CdZnSe/ZnSe heterostructures by impurity diffusion. In this work, our objectives are to study the disordering phenomena in CdZnSe/ZnSe SLSs by Ge diffusion and the properties of optical waveguides in this system using Ge-induced disordering. This is a very important case because of the laser results cited above.

## 2. Experimental procedure

CdZnSe/ZnSe SLSs were grown by molecular beam epitaxy with elemental sources of Zn, Cd, and Se. The growth temperature was 250°C. The sample surface was monitored by reflection high-energy electron diffraction (RHEED) at 10 keV. The composition  $x$  of the  $\text{Cd}_x\text{Zn}_{1-x}\text{Se}$  alloy was determined by assuming a linear variation of the lattice constant with  $x$  (Vegard's law), and also confirmed by energy-dispersive X-ray fluorescence analysis. Details of the crystal growth were reported elsewhere [9]. The structure used for the disordering experiments, shown in Fig. 1, was grown on a (100) GaAs substrate and consisted of a ZnSe buffer layer (1.5  $\mu\text{m}$ ), a ten period superlattice of alternating 10 nm  $\text{Cd}_x\text{Zn}_{1-x}\text{Se}$  ( $x = 0.2$ ) and 20 nm ZnSe layers, and a ZnSe capping layer (0.1  $\mu\text{m}$ ) to prevent the degradation of crystalline quality of the SLS during Ge diffusion and annealing.

A 25 nm germanium layer was deposited on top of the structure, followed by a 60 nm  $\text{SiO}_2$  film. The Ge diffusion was carried out at 600°C for 4.5 h in a Se ambient atmosphere.

The samples for disordering experiments were studied using double crystal X-ray diffraction and photoluminescence (PL) measurement at both 1.4 K and room temperature. The X-ray rocking curves were obtained for symmetric (400) reflections using a  $\text{Cu K}\alpha_1$  line ( $\lambda = 0.15405$  nm). Be-

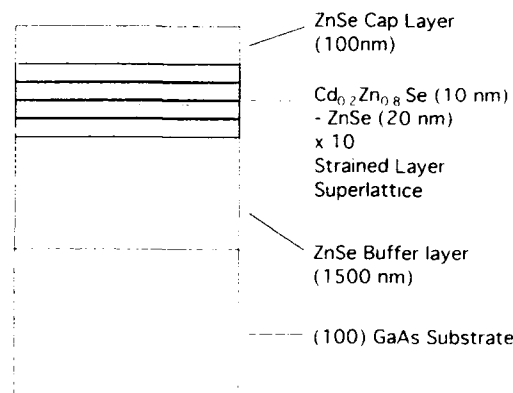


Fig. 1. The CdZnSe/ZnSe SLS structure used for the disordering experiments. The CdZnSe/ZnSe sample consisted of a ten period superlattice of alternating 10 nm  $\text{Cd}_x\text{Zn}_{1-x}\text{Se}$  ( $x = 0.2$ ) and 20 nm ZnSe layers.

fore the PL measurements, the  $\text{SiO}_2$  and Ge layers on the II–VI materials were chemically etched by HF and  $\text{CF}_4$  plasma, respectively. A He–Cd laser (325 nm) with an intensity of 5 mW and a  $\text{N}_2$  pulsed laser (337 nm, 3 ns and 30 Hz) was used as the excitation source of PL measurements. The optical waveguides were characterized at 632.8 nm wavelength by coupling the beam of a He–Ne laser through their cleaved edge and examining their cleaved output facet using a TV camera.

## 3. Results and discussion

### 3.1. Layer disordering of CdZnSe/ZnSe SLS

$\text{Cd}_x\text{Zn}_{1-x}\text{Se}/\text{ZnSe}$  interdiffusion was investigated by double crystal X-ray diffractometry. Fig. 2 shows the rocking curves (a) for the as-grown  $\text{Cd}_x\text{Zn}_{1-x}\text{Se}/\text{ZnSe}$  SLS (not annealed), (b) for the as-grown  $\text{Cd}_x\text{Zn}_{1-x}\text{Se}/\text{ZnSe}$  SLS (annealed), and (c) for the Ge-diffused SLS. Several orders of well-resolved satellite peaks are clearly observed in Figs. 2a and 2b, due to the periodic structure of the SLS. The angular separation of adjacent diffraction satellites, calculated for the 30 nm thick period of the superlattice [10,11], is 631.6 arc sec, which is in good agreement with the

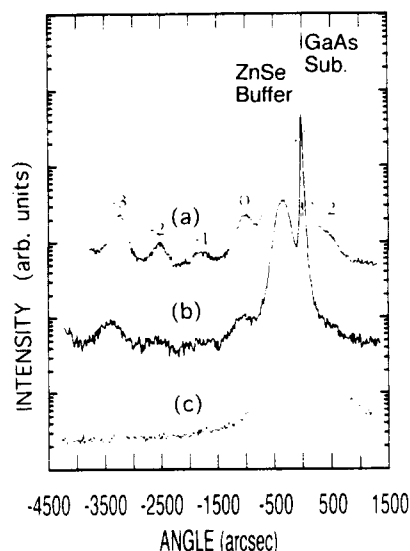


Fig. 2. X-ray rocking curves (a) for the as-grown  $\text{Cd}_{0.93}\text{Zn}_{0.07}\text{Se}/\text{ZnSe}$  SLS; (b) for the annealed SLS without the Ge-diffusion (600°C, 4.5 h), and (c) for the Ge-diffused SLS.

experimental result in Figs. 2a and 2b. However, the satellite peaks completely disappeared in the Ge-diffused SLS, as shown in Fig. 2c. This indicates that the SLS structure was disordered by the Ge diffusion.

PL measurements at 1.4 K were carried out in order to investigate the change of the effective energy gap with disordering. Fig. 3 shows PL spectra (a) from the as-grown  $\text{Cd}_{0.93}\text{Zn}_{0.07}\text{Se}/\text{ZnSe}$  SLS; (b) from the annealed SLS without the Ge-diffusion (600°C, 4.5 h); (c) from the Ge diffused top surface of the ZnSe capping layer on the SLS; and (d) from the Ge-diffused SLS in which the ZnSe capping layer was removed by a HCl etchant. PL measurements of both the as-grown and the annealed samples without Ge diffusion show intense, sharp excitonic emission around 483 nm. This indicates that the SLS structure is stable against the thermal annealing process. The PL spectrum shown in Fig. 3c is characterized by a dominant deep level, which is due to the high concentration of Ge impurities as well as surface degradation of the top ZnSe capping layer. However, when the ZnSe capping layer was

removed after the Ge diffusion, the PL again showed excitonic emission (E) and D–A pair emission with a phonon replica; the deep level emission intensity decreased significantly. The excitonic peak (E) was located at 451.4 nm (2.747 eV), which is about 6 meV below the band gap (450.4 nm; 2.753 eV) estimated in the completely disordered  $\text{Cd}_{0.93}\text{Zn}_{0.07}\text{Se}$  alloy with composition  $x = 0.067$ . This excitonic peak (E) position occurs at a much lower wavelength than the expected  $I_1^d$  line position of the pure ZnSe [12]. It is therefore thought that the excitonic line (E) of 451.4 nm is related to the band edge of the disordered  $\text{Cd}_{0.93}\text{Zn}_{0.07}\text{Se}$  alloy. These results therefore indicate that the observed large blue shift between the as-grown SLS and the Ge-diffused SLS is a result of layer disordering of the SLS.

The donor–acceptor (D–A) pair emission at 467.1 nm (2.65 eV), with its phonon replicas, might be related to the Ge impurity or its complex. Generally, the D–A pair emission of ZnSe is located at 2.697 eV. Thus, the observed D–A pair emission is also below the usual D–A pair emission peak of ZnSe, which shows that the bandgap of the Ge-diffused SLS is slightly smaller than the bandgap of pure ZnSe due to Cd incor-

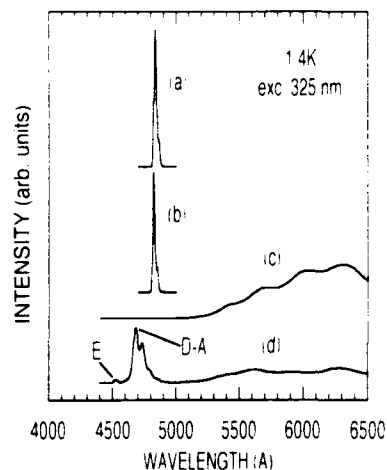


Fig. 3. PL spectra (a) from the as-grown  $\text{Cd}_{0.93}\text{Zn}_{0.07}\text{Se}/\text{ZnSe}$  SLS; (b) from the annealed SLS without Ge diffusion (600°C, 4.5 h); (c) from the Ge-diffused top surface of the ZnSe capping layer on the SLS; and (d) from the Ge-diffused SLS after the ZnSe capping layer was removed by etching in HCl.

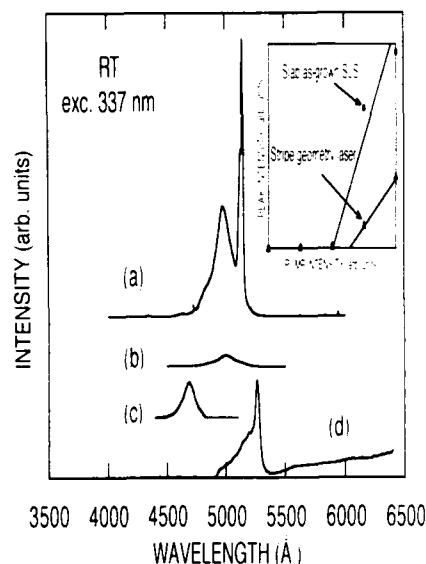


Fig. 4. PL spectra (a) from the edge facets of the slab as-grown CdZnSe/ZnSe SLS at high pump intensity above threshold, (b) from the edge facets of the slab as-grown SLS at low pump intensity below threshold, (c) from the Ge-diffused SLS, and (d) from the edge facets of the stripe geometry laser defined by IID at high pump intensity above threshold. The inset shows emission intensity as a function of pump intensity.

poration. The separation of the phonon replicas was about 30 meV, close to but slightly below the LO phonon energy of ZnSe (31.3 meV).

PL measurements at room temperature (RT) were carried out using a  $N_2$  pulsed laser as the excitation source in order to confirm the blue shift due to disordering and the optically-pumped laser oscillation. Fig. 4 shows PL spectra (a) from the edge facets of the slab as-grown CdZnSe/ZnSe SLS at high pump intensity above threshold, (b) from the edge facets of the slab as-grown SLS at low pump intensity below threshold, and (c) from the Ge-diffused SLS. The inset in Fig. 4 shows emission intensity as a function of pump intensity. PL measurement of the as-grown SLS at low pump intensity shows a broad emission around 500 nm, which is the spontaneous emission. At high pump intensity above threshold, a sharp peak appears at a wavelength of 514.8 nm (2.409 eV), as shown in Fig. 4a. A slight red shift

was observed, which may be due to a heating effect. This peak has a full width at half-maximum of 9 meV. The spectral narrowing and the steep rise of the emission indicate lasing. After the Ge diffusion, the large blue shift of the emission was observed, as shown in Fig. 4c. The emission peak in the Ge-diffused SLS was located at 469.2 nm (2.643 eV), which is in good agreement with the band gap estimated in the completely disordered  $Cd_{1-x}Zn_xSe$  alloy with composition  $x = 0.067$ .

### 3.2. Optical waveguides fabricated using layer disordering

CdZnSe/ZnSe optical waveguides were fabricated using the Ge-induced disordering in the superlattices. The layer structure used for the optical waveguide was grown on a (100) GaAs substrate and consisted of a ZnSe bottom layer (1.5  $\mu\text{m}$ ), a ten period superlattice of alternating 10 nm  $Cd_{1-x}Zn_xSe$  ( $x = 0.2$ ) and 20 nm ZnSe layers, and a ZnSe top layer (0.1  $\mu\text{m}$ ). In order to confirm the vertical confinement of the guided wave in the CdZnSe/ZnSe layer structure, the distribution of the guided field was calculated at a wavelength of both 633 nm and 515 nm. The refractive indexes used for  $Cd_{0.2}Zn_{0.8}Se$  and ZnSe were 2.940 and 2.580 at 633 nm and 3.086 and 2.710 at 515 nm, respectively. Fig. 5 shows the distribution of the guided field (TE polarization) calculated at the wavelength of (a) 633 nm and (b) 515 nm. These distributions indicate that the waveguide is single mode at both 633 nm and 515 nm. Laterally confined optical waveguides were formed by photolithography and IID. Fig. 6a shows the schematic diagram of the CdZnSe/ZnSe SLS optical waveguide fabricated by Ge-induced disordering. 20  $\mu\text{m}$  wide photoresist stripes were first formed on the material. Then, a 25 nm thick Ge film was deposited onto the wafer and diffusion windows were obtained through a lift-off process. Next, a 60 nm thick  $SiO_2$  film was deposited onto the samples and Ge diffusion was carried out at 600°C for 4.5 h.

The optical waveguides were characterized at 633 nm wavelength by coupling the beam of a He-Ne laser through their cleaved edge and ex-

aming the cleaved output facet using a vidicon camera. Fig. 6b shows the near-field distribution of the guided light. The optical confinement of the waveguide fabricated using disordering was confirmed although the waveguide exhibited multi-mode behavior. This result indicates that the superlattice in the guiding stripe is confined in the lateral direction by the disordered material, which has a larger band gap and smaller refractive index than the non-disordered material.

The stimulated emission produced by optical pumping was also investigated in the stripe geometry laser defined by IID. The structure of the stripe geometry laser defined by IID is the same structure as the waveguide shown in Fig. 6a. Fig. 4d shows a PL spectrum from the edge facets of the stripe geometry laser defined by IID at high pump intensity above threshold. A  $N_2$  pulsed laser was used as the excitation source. The inset

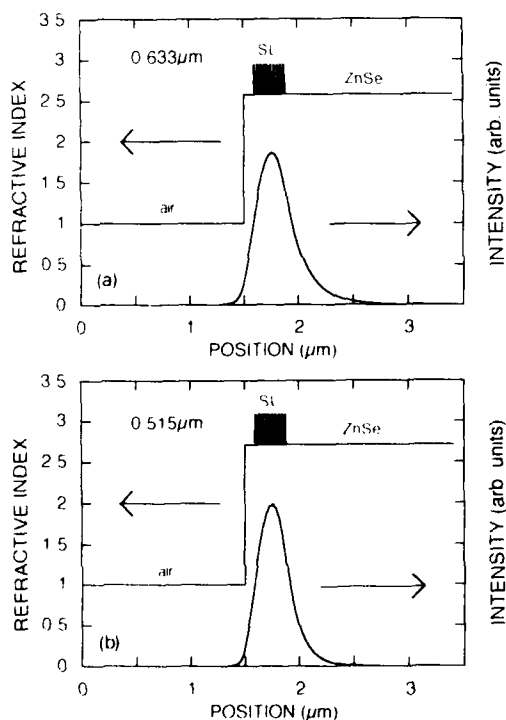


Fig. 5. Distribution of the guided field (TE polarization) calculated at wavelengths of (a) 633 nm and (b) 515 nm.

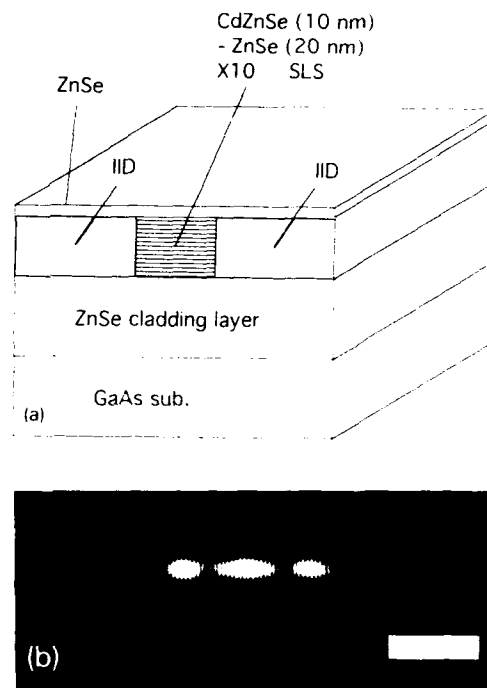


Fig. 6. (a) Schematic diagram of the CdZnSe/ZnSe SLS optical waveguide fabricated by Ge-induced disordering and (b) near-field distribution observed at the output facet for a 632.8 nm wavelength. Marker represents 10  $\mu\text{m}$ .

in Fig. 4 shows emission intensity as a function of pump intensity. The sharp narrowing and the steep rise of the emission were observed in the emission from the stripe geometry laser defined by IID. In the laterally confined structure with a cavity length of 300  $\mu\text{m}$ , lasing occurred at a wavelength of 526.4 nm at RT. Comparing with the slab as-grown CdZnSe/ZnSe SLS, a slight red shift was observed, which may be also due to a heating effect.

#### 4. Conclusion

We have demonstrated, for the first time, disordering of CdZnSe/ZnSe SLSs by Ge diffusion. As-grown samples showed several orders of well-resolved satellite peaks due to the SLS periodic structure. However, the satellite peaks completely

disappeared in Ge-diffused samples, indicating that the SLS structure became disordered by the Ge diffusion. Low-temperature PL measurements of both as-grown samples and samples annealed without Ge diffusion, show intense, sharp excitonic emission around 483 nm in CdZnSe/ZnSe SLSs, respectively. In Ge-diffused samples, however, we observed a large blue shift of the PL peak of the Ge diffused sample, indicating layer disordering of the SLS by the Ge diffusion. PL measurements at RT also show a large blue shift due to disordering. The guided mode in the superlattice guiding layer confined by the disordered alloy was confirmed and optically-pumped laser oscillation was obtained in the stripe geometry laser defined by IID.

### 5. Acknowledgments

We wish to thank T. Onuma of Matsushita Electric Ind. Co., Ltd., for continuous encouragement. This work effort was supported by ONR Grants N00014-89-J-1773 (UCSB) and N00014-90-J-1782 (Notre Dame). One of the authors (P.D.F.) was supported by a Graduate Mentorship Fellowship from UC Santa Barbara, and by

the NSF Science and Technology Center for Quantized Electronic Structures (QUEST).

### 6. References

- [1] M.A. Haase, J. Qiu, J.M. DePuydt and H. Cheng, *Appl. Phys. Lett.* 59 (1991) 1272.
- [2] H. Jeon, J. Ding, W. Patterson, A.V. Nurmikko, W. Xie, D.C. Grillo, M. Kobayashi and R.L. Gunshor, *Appl. Phys. Lett.* 59 (1991) 3619.
- [3] H. Okuyama, T. Miyajima, Y. Morinaga, F. Hiei, M. Ozawa and K. Akimoto, *Electron. Lett.* 28 (1992) 1798.
- [4] D.G. Deppe and N. Holonyak, Jr., *J. Appl. Phys.* 64 (1988) R93.
- [5] W.D. Laidig, N. Holonyak, Jr. and M.D. Camras, *Appl. Phys. Lett.* 38 (1981) 776.
- [6] W.X. Zou, K.K. Law, A.C. Gossard, E.L. Hu, L.A. Coldren and J.L. Merz, *Appl. Phys. Lett.* 57 (1990) 2534.
- [7] R.L. Thornton, W.J. Mosby and H.F. Chung, *IEEE Trans. Electron Devices* ED-36 (1989) 2156.
- [8] T. Yokogawa, T. Saitoh and T. Narusawa, *Appl. Phys. Lett.* 58 (1991) 53.
- [9] N. Samarth, H. Luo, J.K. Furdyna, R.G. Alonso, Y.R. Lee, A.K. Ramdas, S.B. Qadri and N. Otsuka, *Appl. Phys. Lett.* 56 (1990) 1163.
- [10] S.T. Picraux, B.L. Doyle and J.Y. Tsao, in: *Semiconductors and Semimetals*, Vol. 33, Ed. T.P. Pearsall (Academic Press, San Diego, CA, 1991) p. 187.
- [11] C.G. Van De Walle, *Phys. Rev. B* 39 (1989) 1871.
- [12] J.L. Merz, H. Kukimoto, H. Nassau and J.W. Shiever, *Phys. Rev. B* 6 (1972) 545.





ELSEVIER

Journal of Crystal Growth 138 (1994) 570-574

JOURNAL OF  
CRYSTAL  
GROWTH

## Ultraviolet lasing and excitonic gain in $\text{Cd}_{1-x}\text{Zn}_x\text{S}-\text{ZnS}$ strained-layer multiple quantum wells

Yoichi Yamada <sup>\*a</sup>, Yasuaki Masumoto <sup>a</sup>, Tsunemasa Taguchi <sup>b</sup>

<sup>a</sup> Institute of Physics, University of Tsukuba, Tsukuba, Ibaraki 305, Japan

<sup>b</sup> Department of Electrical Engineering, Faculty of Engineering, Osaka University, Suita, Osaka 565, Japan

### Abstract

Ultraviolet stimulated emission has been observed from  $\text{Cd}_{1-x}\text{Zn}_x\text{S}-\text{ZnS}$  strained-layer multiple quantum wells under both optical pumping at room temperature and pulsed current injection at 30 K. An exciton-related mechanism of optical gain formation was also studied on the basis of a partial phase-space-filling effect of excitons localized at the lower energy states of inhomogeneously broadened exciton resonance. It is proposed that the localization of excitons contributes to the formation of optical gain in wide-bandgap II-VI semiconductor quantum wells.

### 1. Introduction

The most exciting optoelectronic applications for wide-bandgap II-VI compound semiconductors are injection laser diodes and light-emitting diodes operating in short wavelength regions. Recent achievement of blue-green injection laser diodes based on  $\text{Cd}_{1-x}\text{Zn}_x\text{S}-\text{ZnS}$  quantum well (QW) structures embedded in a ZnSe p-n junction [1,2] has significantly triggered much interest in this research field of both basic physics and device applications. One of the physical interest is the laser action which is based on excitonic rather than electron-hole-plasma transitions. Excitons in the wide-bandgap II-VI compound semiconductors are characterized by a large binding energy and oscillator strength. As for ZnS, which has a large bandgap energy of

about 3.73 eV at room temperature, the binding energy of the exciton reaches to about 40 meV. This value is approximately one order of magnitude larger than that of GaAs, and is also comparable to the LO phonon energy ( $\hbar\omega_{\text{LO}} \sim 42$  meV). Therefore, it is expected that quasi-two-dimensional excitons in ZnS-based QWs, such as  $\text{Cd}_{1-x}\text{Zn}_x\text{S}-\text{ZnS}$  systems where excitons are formed into the ternary alloy  $\text{Cd}_{1-x}\text{Zn}_x\text{S}$  well layers, have very large binding energy due to the effect of quantum confinement and that the exciton binding energy exceeds the LO phonon energy. In fact, our calculations, which are based on the correlation between the well layer thickness and the Bohr radius of bulk excitons [3], give the binding energy as large as 66 meV in a  $\text{Cd}_{0.11}\text{Zn}_{0.89}\text{S}-\text{ZnS}$  QW with the well layer thickness of 4.1 nm. Such situation makes it possible to reduce the exciton-LO phonon coupling [4]. As a result, pronounced excitonic effects can be observed even at room temperature in spite of

\* Corresponding author.

the much stronger exciton–LO phonon coupling in the wide-bandgap II–VI materials compared to that in III–V materials.

This paper describes the first observation of ultraviolet stimulated emission taken from  $\text{Cd}_x\text{Zn}_{1-x}\text{S}$ –ZnS strained-layer multiple quantum wells (MQWs) under both optical pumping at room temperature and pulsed current injection at 30 K. It is also shown that an exciton-related mechanism of optical gain formation can well be explained by considering a partial phase-space-filling effect of localized excitons and population inversion of these localized excitons at the lower energy states of inhomogeneously broadened exciton resonance. Such gain formation due to exciton localization was previously reported by Majumder et al. as for disordered  $\text{CdS}_x\text{Se}_{1-x}$  systems [5].

## 2. MOCVD growth and laser structures

Cubic-structured  $\text{Cd}_x\text{Zn}_{1-x}\text{S}$ –ZnS MQWs were grown by a low-pressure metalorganic chemical vapor deposition (MOCVD) method with all gaseous sources [6,7]. For optical pumping experiments, the MQW layers were grown on semi-insulating (100)-oriented GaAs substrates, following the deposition of a 1.5  $\mu\text{m}$  thick ZnS buffer layer. The MQW structures consist of 50 periods of 4.1 nm thick  $\text{Cd}_x\text{Zn}_{1-x}\text{S}$  well layers separated by 8.1 nm thick ZnS barrier layers. For observation of stimulated emission, the samples were cleaved to approximately 1 mm long resonators with uncoated facets and were excited perpendicular to the MQW layer plane.

The laser diode (LD) structure was fabricated on (100)-oriented n<sup>+</sup>-GaAs substrates, following the deposition of a 2  $\mu\text{m}$  thick n-type ZnS layer doped with iodine. The active layer was a MQW structure consisting of 10 periods of 4.1 nm thick  $\text{Cd}_{0.31}\text{Zn}_{0.69}\text{S}$  well layers separated by 8.1 nm thick ZnS barrier layers. This MQW structure was embedded in a p–n junction made from ZnS layers doped with sodium acceptors and iodine donors. The carrier concentrations of sodium acceptors and iodine donors were estimated to be approximately  $1 \times 10^{16}$  and  $1 \times 10^{19} \text{ cm}^{-3}$  at room

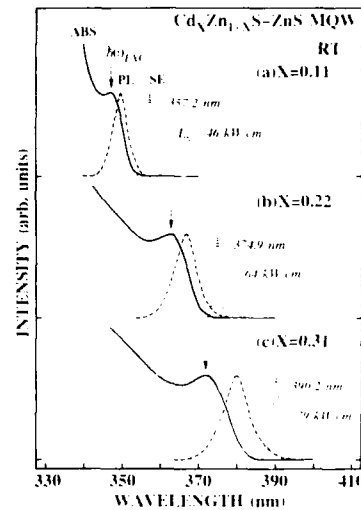


Fig. 1. Room-temperature ultraviolet stimulated emission spectra (SE, dotted lines) observed under resonant excitation of each excitonic absorption peak shown as the vertical arrow in  $\text{Cd}_x\text{Zn}_{1-x}\text{S}$ –ZnS MQWs: (a)  $x = 0.11$ ; (b)  $x = 0.22$ ; (c)  $x = 0.31$ . Absorption spectra (ABS, solid lines) and photoluminescence spectra (PL, dashed lines) from the front face of the sample are also shown.

temperature, respectively, both of which were confirmed by means of Hall measurement. Gain-guided lasers were fabricated using evaporated Au electrodes as the ohmic contact on the p-type ZnS:Na layer. Current confinement was achieved with 15  $\mu\text{m}$  wide stripes in a  $\text{SiO}_2$  insulator layer and 1 mm long cleaved resonator. A Au–Ge electrode was used as the ohmic contact on the n<sup>+</sup>-GaAs substrate.

## 3. Experimental results and discussion

Fig. 1 demonstrates room-temperature ultraviolet stimulated emission spectra (SE, dotted lines) taken from optically-pumped  $\text{Cd}_x\text{Zn}_{1-x}\text{S}$ –ZnS MQWs: (a)  $x = 0.11$ , (b)  $x = 0.22$ , and (c)  $x = 0.31$ . Absorption spectra (ABS, solid lines) and photoluminescence spectra (PL, dashed lines) observed from the front face of the sample are also shown in this figure. Each stimulated emission spectrum was observed under resonant excitation of the excitonic absorption peak shown as the

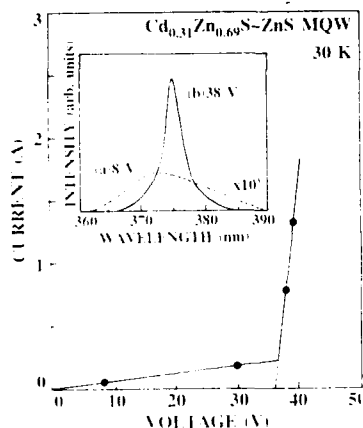


Fig. 2. Voltage-versus-current characteristics at 30 K for an injection diode based on a  $\text{Cd}_{0.31}\text{Zn}_{0.69}\text{S}$ -ZnS MQW. The inset shows the spontaneous emission ((a), dashed line) and stimulated emission ((b), solid line) spectra at 8 and 38 V, respectively.

vertical arrow by employing the second harmonic light of a dye laser pumped by a frequency-doubled  $Q$ -switched  $\text{Nd}^{3+}$ :YAG laser. The peak positions of each stimulated emission are located at (a) 357.2 nm, (b) 374.9 nm, and (c) 390.2 nm, and the threshold excitation power densities for each stimulated emission are estimated to be approximately (a) 46  $\text{kW}/\text{cm}^2$ , (b) 64  $\text{kW}/\text{cm}^2$ , and (c) 79  $\text{kW}/\text{cm}^2$ . It should particularly be noted that each peak position of the stimulated emission is located at lower energies compared to the absorption and photoluminescence peaks. The energy separation between the absorption and photoluminescence peaks is related to the Stokes shift which becomes large with increasing Cd composition  $x$ . This originates from localization of excitons towards the lower-energy states in the inhomogeneously broadened exciton resonance.

Fig. 2 shows the voltage-versus-current characteristics at 30 K for the laser diode structure mentioned above. The pulse width and the repetition rate were 300 ns and 4 Hz, respectively. The inset shows the spontaneous emission ((a), dashed line) and stimulated emission ((b), solid line) spectra. Spontaneous electroluminescence was obtained at about 372 nm at 8 V and its linewidth was estimated to be about 15 nm. From

the voltage-versus-current characteristics, the built-in voltage for causing stimulated emission was found to be about 36 V and the threshold current density was estimated to be about 1.5  $\text{kA}/\text{cm}^2$ . Above 36 V, the emission intensity became strong and the peak position moved towards the longer-wavelength side. The stimulated electroluminescence of linewidth less than 3 nm was clearly observed at the wavelength of 375 nm at 38 V. The present energy position is close to that of the stimulated emission observed at 10 K under optical pumping [8]. This result strongly demonstrates the possibility of lasing at ultraviolet wavelength [9].

It has already been shown by means of pump-and-probe experiments that excitons contribute to the formation of optical gain in the  $\text{Cd}_{0.31}\text{Zn}_{0.69}\text{S}$ -ZnS MQWs [8]. This is based on the observation of optical gain in the presence of the clear excitonic absorption peak, which is slightly bleached at the lower energy side. Excitonic gain and stimulated emission in wide-bandgap II-VI MQWs have firstly been reported by Ding et al. as for  $\text{Cd}_{0.31}\text{Zn}_{0.69}\text{Se}$ -ZnSe systems [10]. The exciton-related mechanism of optical gain formation was well explained by considering a partial phase-space-filling effect of excitons which were localized at the lower energy states of inhomogeneously broadened exciton resonance. This circumstance derives from the large enhancement in the exciton binding and its oscillator strength due to the effect of quantum confinement, so that quasi-two-dimensional excitons are stable against ionization by optical phonons up to room temperature. It was considered that these excitons were subjected to localization due to alloy composition fluctuations in ternary alloy well layers and interface fluctuations between well and barrier layers. Therefore, the excitons are localized at the lower energy states of the inhomogeneously broadened exciton resonance, and the partial phase-space-filling of these localized exciton states occurs. The localized exciton states are considered to be easily saturated because of the low density of states. As a result, the population of the localized exciton states can easily be inverted at the electron-hole pair (or exciton) densities below the onset to an electron-hole plasma [10,11].

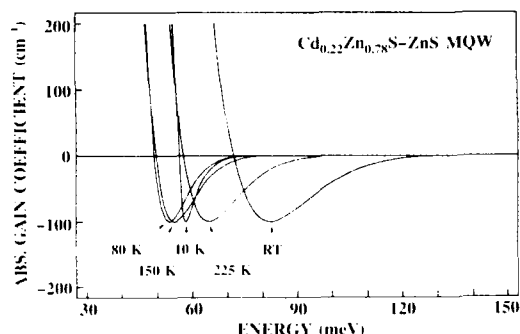


Fig. 3. Calculated results of optical gain spectra of a  $\text{Cd}_{0.22}\text{Zn}_{0.78}\text{S}$ -ZnS MQW as a function of temperature. In this figure, the horizontal axis indicates the photon energy measured from the center of the  $n=1$  heavy-hole inhomogeneously broadened exciton resonance.

Using the same procedure, optical gain spectra of  $\text{Cd}_x\text{Zn}_{1-x}\text{S}$ -ZnS MQWs were analyzed. Fig. 3 shows the calculated results for a  $\text{Cd}_{0.22}\text{Zn}_{0.78}\text{S}$ -ZnS MQW as a function of temperature. In this figure, the horizontal axis indicates the photon energy measured from the center of the inhomogeneously broadened  $n=1$  heavy-hole exciton resonance. With increasing temperature up to 80 K, the energy shift of the gain maximum with respect to the center of exciton resonance decreases. With further increasing temperature, this energy shift conversely increases. This aspect can be explained by considering both the temperature dependence of the distribution function of excitons and the homogeneous broadening due to the exciton-phonon interaction at higher temperature. Namely, the decrease in the energy shift up to 80 K can be explained only by the temperature-dependent slope around the chemical potential in the distribution function. Above 80 K, the increase in the homogeneous broadening due to the exciton-LO phonon interaction must be considered in addition to the above circumstance. Then, the energy shift increases with temperature above 80 K. These calculated energy shifts are summarized in Table 1 with the experimental results which are determined by the energy difference between the center of the  $n=1$  heavy-hole exciton resonance and the peak position of stimulated emission just above the threshold. The

electron-hole pair (or exciton) densities which are necessary for the threshold gain for stimulated emission ( $\sim 100 \text{ cm}^{-3}$ ) per quantum well are also summarized in Table 1. These values are also compared with the experimental results which are estimated from the threshold excitation power densities for stimulated emission. In this estimation, we used the exciton lifetime of 200 ps which was obtained from our separate time-resolved luminescence measurements. We note that the densities obtained both theoretically and experimentally are below the estimated value of electron-hole plasma phase transition ( $N_{\text{max}} \approx (\pi a_B^2)^{-1} = 6.1 \times 10^{12} \text{ cm}^{-2}$ ). It can be seen from this table that the calculated energy shifts of the gain maximum from the center of the exciton resonance are in good agreement with the experimental results. Moreover, the calculated results of the electron-hole pair (or exciton) densities show that the densities, which give threshold gain ( $\sim 100 \text{ cm}^{-3}$ ), increases with temperature. This tendency is consistent with the experimental results which are derived from the threshold excitation power densities for stimulated emission. In this way, it is understood that the localization of excitons occupying the lower-energy states of the inhomogeneously broadened exciton resonance contributes to the formation of optical gain in the  $\text{Cd}_x\text{Zn}_{1-x}\text{S}$ -ZnS MQWs. A more detailed discussion is shown elsewhere [12].

Table 1

Calculated energy shifts of the gain maximum ( $\sim 100 \text{ cm}^{-3}$ ) from the center of the exciton resonance and densities of excitons per quantum well as a function of temperature in a  $\text{Cd}_{0.22}\text{Zn}_{0.78}\text{S}$ -ZnS MQW; experimental energy shifts which were determined by the energy difference between the exciton resonance and the stimulated emission peaks, and experimental densities of excitons which were derived from the threshold excitation power densities for stimulated emission are also indicated

Temperature (K)	Energy shift (meV)		Density of excitons ( $\text{cm}^{-2}$ )	
	Calc.	Exp.	Calc.	Exp.
10	58	55	$1.1 \times 10^9$	$4.8 \times 10^{10}$
80	53	50	$4.6 \times 10^{10}$	$4.8 \times 10^{10}$
150	55	55	$3.8 \times 10^{11}$	$1.0 \times 10^{11}$
225	65	70	$1.2 \times 10^{12}$	$3.7 \times 10^{11}$
RT	82	95	$2.0 \times 10^{12}$	$7.2 \times 10^{11}$

#### 4. Conclusions

Ultraviolet stimulated emission has been observed from  $\text{Cd}_x\text{Zn}_{1-x}\text{S}-\text{ZnS}$  MQWs under both optical pumping at room temperature and pulsed injection mode at 30 K. In spite of a low acceptor concentration of ZnS doped with Na, the possibility of lasing at ultraviolet wavelength has been demonstrated in wide-bandgap II–VI quantum well structures. It was also proposed that the localization of excitons at the lower energy states of the inhomogeneously broadened exciton resonance, resulting from alloy fluctuations and interface fluctuations, is very important and contributes to the formation of optical gain in wide-bandgap II–VI quantum wells.

#### 5. References

- [1] M.A. Haase, J. Qiu, J.M. DePuydt and H. Cheng, *Appl. Phys. Lett.* 59 (1991) 1272.
- [2] H. Jeon, J. Ding, W. Patterson, A.V. Nurmikko, W. Xie, D.C. Grillo, M. Kobayashi and R.L. Gunshor, *Appl. Phys. Lett.* 59 (1991) 3619.
- [3] Y. Shinozuka and M. Matsuura, *Phys. Rev. B* 28 (1983) 4878; 29 (1984) 3717 (E).
- [4] N.T. Pelekanos, J. Ding, M. Hagerott, A.V. Nurmikko, H. Luo, N. Samarth and J.K. Furdyna, *Phys. Rev. B* 45 (1992) 6037.
- [5] F.A. Majumder, S. Shevel, V.G. Lyssenko, H.E. Swoboda and C. Klingshirn, *Z. Physik B* 66 (1987) 409.
- [6] T. Taguchi and Y. Endoh, *Jap. J. Appl. Phys.* 30 (1991) L952.
- [7] T. Taguchi, Y. Endoh and Y. Nozue, *Appl. Phys. Lett.* 59 (1991) 3434.
- [8] Y. Yamada, Y. Masumoto, J.T. Mullins and T. Taguchi, *Appl. Phys. Lett.* 61 (1992) 2190.
- [9] T. Taguchi, Ch. Onodera, Y. Yamada and Y. Masumoto, *Jap. J. Appl. Phys.* 32 (1993) L254.
- [10] J. Ding, H. Jeon, T. Ishihara, M. Hagerott, A.V. Nurmikko, H. Luo, N. Samarth and J. Furdyna, *Phys. Rev. Lett.* 69 (1992) 1707.
- [11] J. Ding, M. Hagerott, T. Ishihara, H. Jeon and A.V. Nurmikko, *Phys. Rev. B* 47 (1993) 10528.
- [12] Y. Yamada, Y. Masumoto and T. Taguchi, *Physica B* 191 (1993) 83.



ELSEVIER

Journal of Crystal Growth 138 (1994) 575–579

JOURNAL OF  
**CRYSTAL  
GROWTH**

## Exciton dynamics and high density effects in ZnSe/ZnMnSe quantum structures grown by molecular beam epitaxy

A. Schülzgen \*, F. Kreller, F. Henneberger, M. Lowisch, J. Puls

*Fachbereich Physik, Humboldt-Universität zu Berlin, Unter den Linden 6, D-10099 Berlin, Germany*

### Abstract

ZnSe well exciton features in ZnSe/ZnMnSe quantum structures grown by molecular beam epitaxy (MBE) are investigated using various spectroscopic techniques. Steady-state photoluminescence and excitation spectroscopy demonstrate an enhanced effective band offset due to tensile strain and a confinement induced shift of the excitonic resonances up to 100 meV. Progressive localization of excitons on the 10 ps time scale followed by rapid recombination within 100 ps is observed in time-resolved luminescence. Transient pump-probe measurements show clear nonlinear excitonic absorption under  $2 \mu\text{J}/\text{cm}^2$  excitation with a recovery on the same time scale as the radiative recombination.

### 1. Introduction

Wide-gap II–VI quantum well (QW) structures are attractive for electro-optical and photonic devices in the blue-green part of the visible spectrum. A specific element due to the large ionic component in the chemical bonding of wide-gap II–VI structures is the strong excitonic character so that absorptive as well as spontaneous and stimulated emission processes are likely to contain a substantial excitonic component up to device temperatures in these QW systems [1]. Well thickness and alloy fluctuations gives rise to exciton localization resulting in an inhomogeneous broadening of the exciton resonances accompanied by a Stokes shift between absorption and emission bands. Localization of excitons at potential fluctuations are, at least at lower tem-

peratures, related to the lasing process in such materials [2].

In the present paper we study ZnSe/ZnMnSe multiple quantum well (MQW) structures grown by MBE. This system provides type I heterostructures with binary wells excluding alloy fluctuations. In addition, deeper blue emission can be achieved in comparison with ZnCdSe/ZnSe mostly used for laser devices until now. Early work on ZnSe/ZnMnSe structures was done by the groups of Brown and Purdue [3]. The structures investigated in the present paper are grown on (001) GaAs substrates, on top of which a buffer layer of about  $1 \mu\text{m}$  is first deposited. Typically, a structure consists of 5 or 10 ZnSe quantum wells of the same thickness separated by about 100 nm wide ZnMnSe barrier layers. The well widths studied range from 1 to 10 nm. For a manganese composition of 18% to 28% a total band offset of 60 to 120 meV is expected for unstrained materials [4].

\* Corresponding author.

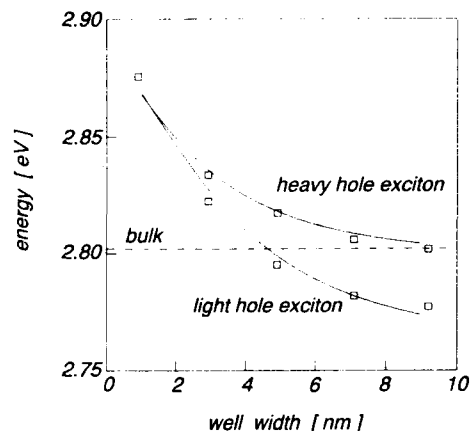


Fig. 1. Energetic positions of the ZnSe well lh and hh exciton resonances observed in PLE spectra of ZnSe/Zn<sub>0.75</sub>Mn<sub>0.25</sub>Se MQWs at 5 K: (□) experimental points; (—) calculation.

## 2. Optical characterization of well exciton states

Steady-state photoluminescence (PL) and photoluminescence excitation (PLE) experiments are used to characterize the excitonic states in the ZnSe wells. The low temperature PL spectra are dominated by a light hole (lh) exciton emission band accompanied by a more or less distinct low-energy structure. In the PLE spectra both the light and heavy hole (hh) exciton transitions are observed. The FWHM of the excitonic resonances is on the order of 5 to 10 meV and a Stokes shift between PL and PLE of 3 to 6 meV is found giving a first hint of exciton localization [5].

In Fig. 1 the energetic positions of the  $n = 1$  lh and hh exciton resonances taken from PLE spectra are plotted versus well width. The data reflect the interplay between strain and confinement. The well width in all MQW structures shown here is clearly smaller than both critical thickness and barrier width. So, the lattice misfit induced strain is entirely and coherently assimilated by the ZnSe quantum well and its magnitude can be assumed to be independent of the well width. The larger (001) lattice constant of ZnMnSe leads to a tensile in-plane strain of 0.5% to 1% for the present barrier manganese composition of 25%.

This strain results in a low-energy shift of the exciton resonances and a splitting of the lh and hh exciton states, where the lh exciton occurs energetically below the hh one. Therefore, the excitonic structures of the larger wells appear below the position of the ZnSe bulk exciton. Decreasing the well width the influence of the carrier confinement becomes increasingly important. The comparison between 9 and 1 nm well width gives a confinement induced high-energy shift of about 100 meV for the lh exciton resonance.

As can be seen in Fig. 1 a variational calculation taking into account both strain and excitonic effects yields reasonably good agreement with the experimental data for the well width dependence of the exciton energies. From the calculation we deduce that the 70 meV total band offset for the unstrained material taken from [4] is divided in 40 meV conduction and 30 meV valence band offset. These values are enlarged by the strain, so that the effective offset of about 120 and 80 meV for the lh and hh exciton, respectively, is considerably larger than predicted without strain. Additionally, we can deduce from our calculation that the exciton binding energy does not change dramatically in comparison with ZnSe bulk material. A maximum binding energy of 29 meV is found for 4.5 nm well width.

## 3. Time-resolved photoluminescence

For a time-resolved PL analysis a synchronously pumped tunable dye laser with a pulse duration of 2 ps is used for excitation. After passing a double monochromator in a subtractive arrangement yielding 0.6 meV spectral resolution the PL is recorded with a synchroscan streak camera. The overall time resolution of 10 ps is improved by data deconvolution using the instrumental response.

Fig. 2 shows the temporal evolution of the spontaneous emission spectrum in the vicinity of the lh exciton band from a ZnSe/Zn<sub>0.8</sub>Mn<sub>0.2</sub>Se MQW sample. The excitation is resonant to the hh exciton position observed in PLE. Since the picture is practically the same for excitation at hh

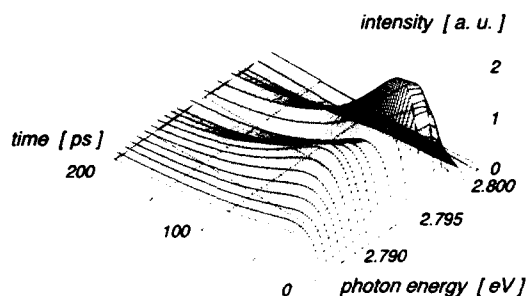


Fig. 2. Temporal development of the lh exciton luminescence of a  $\text{ZnSe}/\text{Zn}_{0.8}\text{Mn}_{0.2}\text{Se}$  structure consisting of 10 periods of 5 nm wells and 85 nm barriers at 5 K.

and lh exciton position as well as above the barrier bandgap energy we can conclude that the capture of the carriers by the wells and subsequent relaxation into the lh exciton state is completed within our time resolution. Right after excitation most of the emission is concentrated at the lh exciton position in absorption. During the first 10 to 15 ps the maximum of the PL spectrum shifts to lower energies and reaches the lh exciton peak of the time-integrated PL spectrum shown in Fig. 3. That is, the evolution of the Stokes shift found in steady-state experiments is resolved in

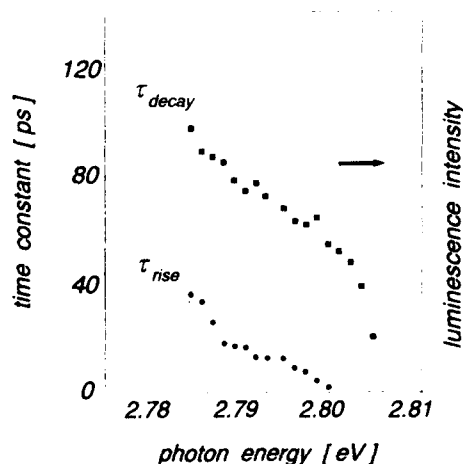


Fig. 3. PL rise and decay times versus detection energy deduced from Fig. 2 (left scale). For comparison the time-integrated PL spectrum is given (right scale).

time. The relation between exciton linewidth and energy shift is in agreement with previously published model calculations based on localization of excitons at interface potential fluctuations [5].

The time-integrated PL (see Fig. 3) shows in addition to the main lh exciton peak a structure on the low-energy side (L). The time-resolved measurements reveal that this structure occurs delayed with respect to the lh exciton emission. The redistribution from lh exciton to the L structure results in a growing contribution of the low-energy emission during the luminescence decay. After about 200 ps the emission at the L structure position becomes dominant. Fig. 3 shows that the described dynamic behaviour leads to an increase of the PL rise and decay times with decreasing photon energy obtained by fitting the decay curves within a double-exponential model. Since the recombination within approximately 100 ps is running on the same time scale as the spectral relaxation a noticeable number of excitons recombine before reaching the lowest energy states. Under CW excitation this results in a nonthermal distribution of excitons and a dominant lh exciton feature in the PL spectra.

Considering different features, various interpretations including bound excitons [6], biexcitons [7] and bound magnetic polarons [8] were given for the physical origin of the low energy PL structure. Taking into account the absence of any excitation intensity dependence of the shape of the PL spectra up to intensities of  $10 \text{ kW/cm}^2$  [9], an interpretation in terms of a bound as well as biexciton state seems to be improbable. Magnetic polaron formation caused by the semimagnetic barrier material and previously reported for  $\text{CdTe}/\text{CdMnTe}$  structures [10] is very unlikely too, because the L structure can be observed in CW PL up to 40 K, while magnetic polaron formation is known to appear only at very low temperatures. Although the physical origin of the state connected with the L structure cannot precisely determined from our experimental data its behaviour is similar to that of a self-trapped state. From the dynamics and the fact that neither in absorption nor in PLE a structure at the energetic position of the L peak is found, we conclude that the occurrence of this state re-



quires the presence of previously created excitons.

#### 4. Transient nonlinear absorption

To further detail the exciton dynamics transient pump-probe experiments are performed using amplified tunable 500 fs pulses for both exciting the sample as well as generating a probe continuum. The output pulses of a hybrid mode-locked dye laser are amplified in a four stage excimer laser pumped dye amplifier. The differential transmission signal (DTS) given by  $(T - T_0)/T_0$  is measured as a function of the delay between pump and probe pulse. To prepare the samples for transmission experiments, the GaAs substrates as well as the ZnSe buffer layers are removed using a selective wet etching process.

The DTS spectra of a 6.8 nm MQW sample are shown in Fig. 4, where the pump is resonant to the lh exciton. We observe a very fast unambiguously excitonic optical nonlinearity. The relative change in absorption  $\Delta\alpha/\alpha$  at the lh exciton position is considerably larger than that at the hh exciton position. The more effective bleaching of the lh exciton absorption should be explained in terms of a different amount of phase space filling [11] of lh and hh exciton states induced by the lh excitons generated. The recovery time of the nonlinear absorption of 150 ps is slightly higher than the PL decay times in Fig. 3. This can be attributed to the larger well width of the sample studied here. In addition to the induced transparency at the exciton positions, only a slight increase of absorption in the range between the excitons is observed. To account for the absorption bleaching in the carrier generation, we have measured that a portion of  $200 \text{ nJ/cm}^2$  from the pump pulse is absorbed by the sample, which gives a carrier density of  $10^{11} \text{ cm}^{-2}$  being clearly below the Mott density [11]. No indication for optical gain is found at this density.

Applying the method of stripe length variation with sub-ns dye laser excitation optical gain is observed at an excitation intensity of  $400 \text{ kW/cm}^2$  [9]. Gain up to  $100 \text{ cm}^{-1}$  is found about 20 meV energetically below the lh exciton resonance. The

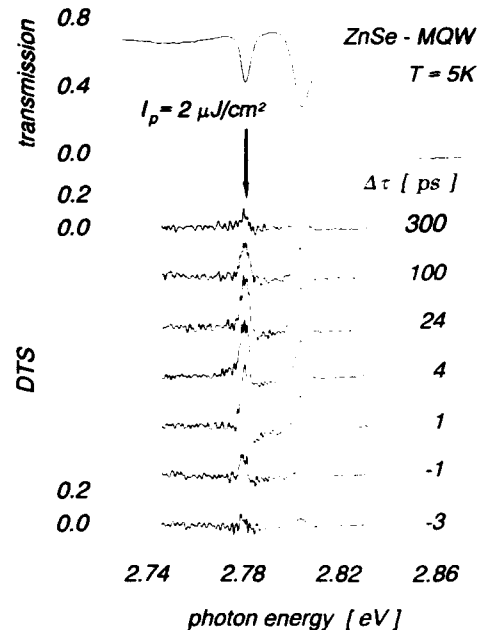


Fig. 4. DTS spectra of a ZnSe/ZnMnSe MQW structure of 6.8 nm well width measured at different pump-probe delays. For comparison the transmission spectrum is given in the upper part.

carrier density generated here is about one order of magnitude higher than that used for pump-probe experiments described above. This high density suggests an explanation of the gain in terms of a degenerated eh plasma.

In conclusion, the present study has demonstrated that the ZnSe/ZnMnSe system provides high-quality type-I quantum structures with distinct confinement effects. We have observed exciton localization on the 10 ps time scale and very rapid recombination within 100 ps. The spectrally sharp and fast excitonic nonlinear absorption found in transient pump-probe experiments make the ZnSe/ZnMnSe system interesting with respect to device applications.

#### 5. Acknowledgements

The authors thank N. Hoffmann, J. Griesche and K. Jacobs for cooperation in the MBE growth.

This work was partly supported by the Deutsche Forschungsgemeinschaft.

## 6. References

- [1] A.V. Nurmikko and R.L. Gunshor, in: *Optics of Semiconductor Nanostructures*, Eds. F. Henneberger, S. Schmitt-Rink and E.O. Göbel (Akademie Verlag, Berlin, 1993) ch. II.1, p. 231.
- [2] J. Ding, H. Jeon, T. Ishihara, M. Hagerott, A.V. Nurmikko, H. Luo, N. Samarth and J. Furdyna, *Phys. Rev. Lett.* 69 (1992) 1707.
- [3] L.A. Kolodziejski, R.L. Gunshor, N. Otsuka, S. Datta, W.M. Becker and A.V. Nurmikko, *IEEE J. Quantum Electron* QE-32 (1986) 1666.
- [4] R.L. Gunshor, L.A. Kolodziejski, N. Otsuka and S. Datta, *Surf. Sci.* 174 (1986) 522.
- [5] M. Wilkinson, Fang Yang, E.J. Austin and K.P. O'Donnell, *J. Phys. (Condens. Matter)* 4 (1992) 8863.
- [6] Y. Hefetz, J. Nakahara, A.V. Nurmikko, L.A. Kolodziejski, R.L. Gunshor and S. Datta, *Appl. Phys. Lett.* 47 (1985) 989.
- [7] Q. Fu, D. Lee, A. Mysyrowicz, A.V. Nurmikko, R.L. Gunshor and L.A. Kolodziejski, *Phys. Rev. B* 37 (1988) 8791.
- [8] R.B. Bylisma, J. Kossut, W.M. Becker, L.A. Kolodziejski, R.L. Gunshor and R. Frohne, *J. Appl. Phys.* 61 (1987) 3011.
- [9] F. Kreller, A. Schülzgen, F. Kreller, F. Henneberger, J. Puls and U. Streller, *Solid State Electron.*, to be published.
- [10] D.R. Yakovlev, W. Ossau, G. Landwehr, R.N. Bicknell-Tassius, A. Waag, S. Schmeusser and I.N. Uralsev, *Solid State Commun.* 82 (1992) 29.
- [11] S. Schmitt-Rink, D.S. Chemla and D.A.B. Miller, *Adv. Phys.* 38 (1989) 89.



ELSEVIER

Journal of Crystal Growth 138 (1994) 580-584

JOURNAL OF  
**CRYSTAL  
GROWTH**

## Confined and propagating phonons in atomic layer epitaxy grown $(\text{CdTe})_n(\text{ZnTe})_n$ superlattices

T. Fromherz <sup>a</sup>, Eunsoon Oh <sup>b</sup>, A.K. Ramdas <sup>b</sup>, E. Koppensteiner <sup>a</sup>, G. Bauer <sup>\*a</sup>,  
W. Faschinger <sup>a</sup>, H. Sitter <sup>c</sup>

<sup>a</sup> *Institut für Halbleiterphysik, Johannes Kepler Universität, A-4040 Linz, Austria*

<sup>b</sup> *Department of Physics, Purdue University, West Lafayette, Indiana 47907-1396, U.S.A*

<sup>c</sup> *Institut für Experimentalphysik, Johannes Kepler Universität, A-4040 Linz, Austria*

### Abstract

We report the occurrence of confined longitudinal and transverse optical phonons in  $(\text{CdTe})_n(\text{ZnTe})_n$  ( $2 \leq n \leq 5$ ) ultra-short-period superlattices as observed in their Raman and far-infrared reflectivity spectra. The dispersion curves of the optical phonons in CdTe and in ZnTe along [001], determined from the frequencies of the confined phonons, are in excellent agreement with neutron scattering data on the bulk compounds. For the  $n = 5$  superlattice sample, folded acoustic phonons have been observed.

### 1. Introduction

Due to recent progress in the growth of II-VI semiconductor heterostructures, superlattices (SLs) have become available with controlled composition and dimension down to a few monolayers of the constituent compounds. In the present paper we report the vibrational properties of highly strained ultrathin  $(\text{CdTe})_n(\text{ZnTe})_n$  SLs ( $n = 2, 3, 4$  and  $5$ ). Transverse optical (TO) and longitudinal optical (LO) phonon frequencies were measured using far-infrared reflectivity spectroscopy and Raman scattering, respectively. Since in the bulk CdTe and ZnTe neither the TO nor the LO phonon dispersion curves overlap, the phonons are confined to the respective superlattice layers. For the analysis of the data, it was

important to account for the biaxial compressive and tensile strains in the CdTe and ZnTe superlattice layers. Experimentally, these strains were determined by high resolution X-ray reciprocal space mapping.

### 2. Experimental results and discussion

The  $(\text{CdTe})_n(\text{ZnTe})_n$  superlattices were grown by atomic layer epitaxy (ALE) on 800 nm thick ZnTe buffer layers deposited on (001) GaAs substrates, with the total number of monolayers of each compound being kept constant (900 ML) in all the superlattices. The details of the sample growth are given in ref. [1]. In order to determine the TO phonon frequencies, far-infrared reflectivity measurements at nearly normal incidence with a spectral resolution of  $0.25 \text{ cm}^{-1}$  were performed at  $T = 10 \text{ K}$  using a Bruker IFS 113v

\* Corresponding author.

Fourier-transform spectrometer. Excitation lines from a  $\text{Kr}^+$  laser and from a dye laser with LC6500 (DCM) were used for measuring LO and folded acoustic phonons by Raman scattering under resonance conditions in the back-scattering geometry at  $T = 10$  K. The scattered light was analysed with a SPEX double and triple monochromator and detected with a photomultiplier and the associated photon counting system.

Fig. 1 shows the far-infrared reflectivity spectra of four short-period  $(\text{CdTe})_n(\text{ZnTe})_n$  superlattices ( $n = 2, 3, 4, 5$ ). In each spectrum three peaks appear. The most prominent among them at  $181 \text{ cm}^{-1}$  is due to the TO phonon of the ZnTe buffer. At the low-energy side of this peak a shoulder appears, which we attribute to the confined TO phonons in the ZnTe layers of the superlattices. The resonance frequencies of these phonons are clearly shifted to lower values with respect to the resonance frequencies of the corresponding phonons in the ZnTe buffer. The peak at about  $150 \text{ cm}^{-1}$  is ascribed to the confined TO phonons in the CdTe layers of the superlattices. The position of this peak systematically shifts to lower frequency values with increasing number of CdTe monolayers. Also shown in Fig. 1 are the results of a simulation of the reflectivity spectra using the standard phonon oscillator model for

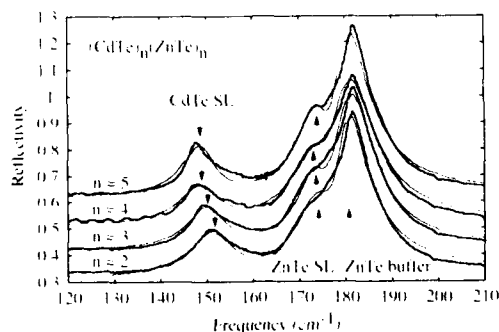


Fig. 1. Far-infrared reflectivity spectra of  $(\text{CdTe})_n(\text{ZnTe})_n$  superlattices at nearly normal incidence. The bold lines represent the experimental data at  $T = 10$  K, the thin lines are the result of a simulation using the standard dielectric model described in refs. [1,2]. The arrows mark the TO phonon frequencies obtained from the fit of the simulation to the experimental data. For clarity, the reflectivity curves for the  $n = 3, 4$  and  $5$  SLs are shifted vertically in steps of  $0.1$ .

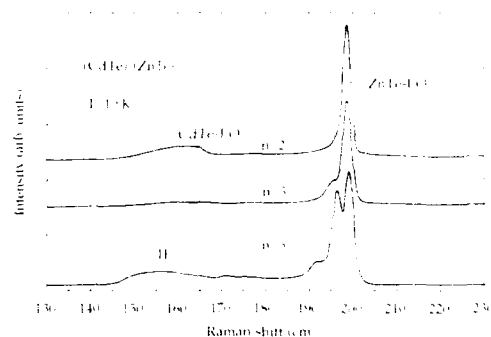


Fig. 2. Raman spectra for  $(\text{CdTe})_n(\text{ZnTe})_n$  superlattices for  $n = 2, 3$  and  $5$  measured at  $T = 10$  K in back-scattering geometry. The excitation wavelength was  $6309 \text{ \AA}$  for  $n = 2, 3$  and  $6471 \text{ \AA}$  for  $n = 5$ . The confined ZnTe LO and CdTe LO phonons are indicated in the figure. The peak around  $155 \text{ cm}^{-1}$  is attributed to an interface phonon.

the dielectric function described in detail in refs. [1,2]. By fitting the results of the simulation to the experimental data, we were able to determine the TO phonon frequencies with an accuracy of  $\pm 0.5 \text{ cm}^{-1}$ .

Fig. 2 shows the Raman spectra of the  $(\text{CdTe})_n(\text{ZnTe})_n$  superlattices. As the superlattice with  $n = 4$  was accidentally damaged after infrared reflectivity measurements, Raman measurements could only be performed for the superlattices with  $n = 2, 3, 5$ . The excitation wavelength was  $6309 \text{ \AA}$  ( $1.965 \text{ eV}$ ) for the  $n = 2$  and  $n = 3$  superlattices and  $6471 \text{ \AA}$  ( $1.916 \text{ eV}$ ) for the  $n = 5$  superlattice. The peaks around  $198 \text{ cm}^{-1}$  are attributed to confined LO phonons from the ZnTe layers and the weak signatures around  $163 \text{ cm}^{-1}$  for  $n = 2$  and  $3$  to the confined LO phonons from the CdTe layers. The broad peak at  $\sim 155 \text{ cm}^{-1}$  for  $n = 5$  is ascribed to the interface phonon (indicated by IF in the figure), whose frequency lies between those of the CdTe TO and LO phonons [3]. Even though the excitation energies used are very close to the quantum confined electronic transition energy in the CdTe well [4], the signatures from the ZnTe LO phonons are clearly observed. Following Menéndez et al. [5], the coupling of the excitation radiation to the ZnTe LO phonons under such resonance conditions involves the superlattice heavy-hole wave-

functions, which are only weakly localized in the CdTe layers. Under these resonance conditions, the wave vectors  $q_m$  (in units of  $2\pi/a$ ) are given by  $m/(n+1)$  with even integral values for  $m$  being allowed for confined CdTe LO phonons, whereas both even and odd  $m$  values characterize the confined ZnTe LO phonons. [2,5] The selection rules for the wavevectors of the confined TO phonons are given by the same equation with both even and odd  $m$  values being allowed [6].

It is well known that LO and TO phonon frequencies depend sensitively on the strain in a crystal. Therefore, to be able to distinguish between shifts of the phonon frequencies induced by strain and shifts due to the confinement of the phonons, it is crucial to know the strains in the superlattices. High resolution X-ray reciprocal space mapping was used to determine the strain distribution in the superlattice layers following the procedure outlined in ref. [7]. Fig. 3 shows the (004) and (115) reciprocal space maps of the  $n = 5$  superlattice. The contours of constant scattered intensity are shown for the ZnTe buffer and the SL reciprocal lattice points (RELPs) for (004) and (115) Bragg reflections of Cu  $K_{\alpha 1}$  radiation. In both maps, the SL satellites (SL - 1, SL 0, SL 1) lie along the [001] growth direction, apart from a slight tilt with respect to the ZnTe buffer. For a SL pseudomorphically grown on the ZnTe buffer, the SL satellites would appear on the broken line in the (115) map of Fig. 3. On the other hand, for a completely relaxed (free-standing) superlattice, the SL 0 RELP falls on a straight line connecting the origin of the reciprocal space with the (115) RELP of the completely relaxed

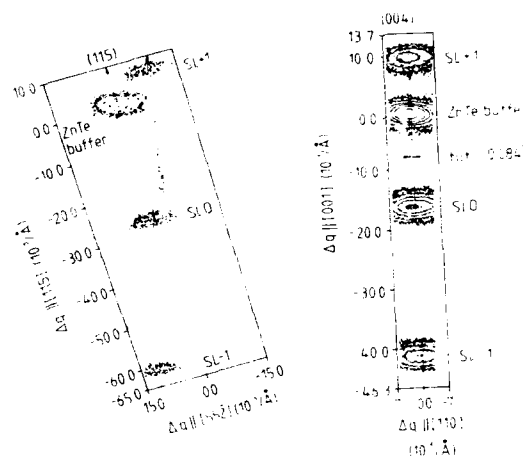


Fig. 3. Measured reciprocal space maps of the  $(\text{CdTe})_5(\text{ZnTe})_5$  SL. In the (004) map, the distance of the lines running parallel to (001) through the SL0 and the buffer RELP indicates a tilt of  $0.084^\circ$  of the lattice planes of the superlattice with respect to the lattice planes of the buffer. In the (115) map, the slight deviation of the maximum intensity of the SL0 RELP from the line running parallel to [115] through the buffer RELP and the origin of reciprocal space (000) is due to the residual in-plane strain of the superlattice ( $\bar{\epsilon}_{\parallel} = -0.27\%$ ). For a pseudomorphically grown SL, the SL0 RELP would appear on the broken line running through the buffer RELP parallel to the growth direction [001].

ZnTe buffer. Fig. 3 shows that in the (115) map the maximum intensity of the SL0 RELP deviates slightly from this line, indicating that the  $n = 5$  superlattice is not completely relaxed. The mean in-plane strain exerted on the SL by the ZnTe buffer is  $\bar{\epsilon}_{\parallel} = -0.27\%$ . Using the in-plane lattice constant determined by X-ray diffraction ( $a = 6.233 \text{ \AA}$ ) instead of the in-plane lattice constant

Table 1

Temperature- and strain-dependent values of the optical phonon frequencies in ZnTe and CdTe

	$\omega_{\text{TO}} (\text{cm}^{-1})$			$\omega_{\text{LO}} (\text{cm}^{-1})$		
	$T = 300 \text{ K}$	$T = 10 \text{ K}$	$\Delta\omega^{\text{strain}}$	$T = 300 \text{ K}$	$T = 10 \text{ K}$	$\Delta\omega^{\text{strain}}$
ZnTe	177 <sup>a</sup>	181 <sup>b</sup>	-4.5 <sup>b</sup>	206 <sup>a</sup>	209 <sup>c</sup>	-11.5 <sup>b</sup>
CdTe	141 <sup>d</sup>	144.7 <sup>c</sup>	+3 <sup>b</sup>	169 <sup>d</sup>	171 <sup>c</sup>	+12.2 <sup>b</sup>

<sup>a</sup> Ref. [10].

<sup>b</sup> Ref. [1].

<sup>c</sup> Ref. [5].

<sup>d</sup> Ref. [11].

<sup>e</sup> Ref. [12].

of the free standing configuration ( $a = 6.25 \text{ \AA}$ ), the strain induced frequency shift of the TO (LO) phonons calculated according to the equations given in ref. [1] is  $-3.9 \text{ cm}^{-1}$  ( $-10.1 \text{ cm}^{-1}$ ) for ZnTe and  $+3.2 \text{ cm}^{-1}$  ( $+13.2 \text{ cm}^{-1}$ ) for CdTe. These values differ from the respective ones calculated in our previous publications [1,2] (listed in Table 1), by about  $1 \text{ cm}^{-1}$ . Since no reciprocal space maps are available for the  $n = 2, 3, 4$  superlattices, in the following discussion we calculate the strain induced phonon frequency shifts for a free-standing superlattice, keeping in mind that the deviation of the actual strain from that assumed could introduce an error of about 10% from the calculated shifts of the phonon frequency. We emphasize that for the  $(\text{CdTe})_n$ ,  $(\text{ZnTe})_n$  short period SLs a linear chain model does not provide a reasonable description, neither of the confined LO nor of the confined TO modes. The bulk TO phonon dispersion curve along [001] direction is either nearly flat (ZnTe) or even the TO mode frequencies increase with increasing wavevector (CdTe). Such a behaviour is different from that observed in the GaAs/AlAs system.

In Fig. 4 the ZnTe and in Fig. 5 the CdTe TO and LO phonon dispersion curves obtained from the data in Figs. 1 and 2 are shown. Also shown are data from inelastic neutron scattering experiments performed on bulk ZnTe [8] (CdTe [9]) samples at  $T = 300 \text{ K}$ . The TO frequencies ob-

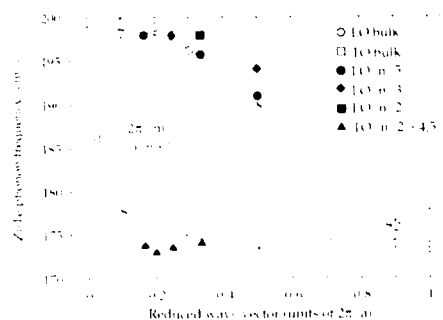


Fig. 4. Optical phonon frequencies for ZnTe. The full symbols are the results of the present work, the open symbols are results of neutron scattering experiments [8] shifted properly for the strain and the temperature (see Table 1). The lines through the open symbols serve as a guide to the eye.

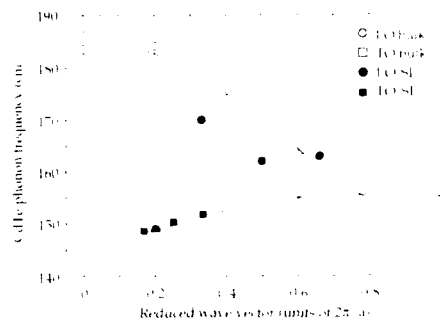


Fig. 5. Optical phonon frequencies for CdTe. The full circles and squares are from the present work, the open ones are from neutron scattering experiments [9] shifted properly for the strain and the temperature (see Table 1). The lines through the open symbols serve as a guide for the eye.

tained by neutron scattering have been shifted by  $-0.5 \text{ cm}^{-1}$  ( $+6.7 \text{ cm}^{-1}$ ), the LO frequencies by  $-8.5 \text{ cm}^{-1}$  ( $+14.2 \text{ cm}^{-1}$ ) accounting for both strain- (free standing) and temperature-induced shifts of the phonon frequencies. The detailed contributions of the temperature shift and the strain induced shift are listed in Table 1. Except for the CdTe LO phonons, which show very broad signatures in Fig. 2, the optically determined phonon frequencies are in excellent agreement with the neutron scattering data. Moreover, the phonon dispersions determined by optical methods are more accurate by a factor of about 4 than those obtained by neutron scattering.

In contrast to the optical phonons, acoustic phonons propagate through the entire superlattice since the acoustic dispersion curves overlap. The new periodicity in the growth direction reduces the extension of the Brillouin zone along this direction to  $-\pi/D < q \leq \pi/D$  where  $D$  is the SL period. As a consequence, the acoustic phonon branches are folded back, generating modes near the  $\Gamma$  point of the mini Brillouin zone, which can be detected as Raman shifts. For the  $(\text{CdTe})_5(\text{ZnTe})_5$  superlattice, folded longitudinal acoustic phonons are clearly resolved in the Raman spectrum (Fig. 6a) measured at room temperature with an excitation wavelength of  $6863 \text{ \AA}$ . The theoretical dispersion relation of the longitudinal acoustic phonons along the growth direction is given in ref. [2]. In this dispersion

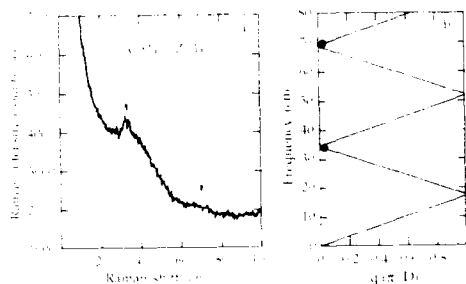


Fig. 6. (a) Folded acoustic phonons for  $(\text{CdTe})_5(\text{ZnTe})_5$  measured by Raman scattering with an excitation wavelength of 6863 Å at room temperature. (b) Dispersion curve for the longitudinal acoustic phonons along the superlattice axis.

relation, the only adjustable parameters are the thicknesses of the superlattice layers. In Fig. 6b the dispersion relation is plotted for  $d_{\text{ZnTe}} = 15.3$  Å and  $d_{\text{CdTe}} = 16.2$  Å. For these values of the layer thicknesses, which are in reasonable agreement with the values determined by X-ray diffraction ( $d_{\text{ZnTe}} = 14.9$  Å,  $d_{\text{CdTe}} = 17.0$  Å), the observed frequencies of the folded acoustic phonons are explained very well by the theory.

### 3. Summary

In the present study of  $(\text{CdTe})_n(\text{ZnTe})_n$  ultrathin superlattices, the LO phonons, directly observed in the Raman spectra, and the TO phonons, deduced from the analysis of the infrared reflectivity, have enabled the dispersion curves of CdTe and ZnTe optical phonons to be established for  $q$  values as large as approximately  $0.5 \times 2\pi/a$ . For a microscopic understanding, the influence of strain in the individual layers originating in the lattice mismatch between layers has clearly to be incorporated in the analysis. Experimentally, the most accurate information about the strain distribution within the superlattice is obtained from high resolution X-ray reciprocal space mapping. However, for the samples investigated the model of free-standing superlattices accounts for the strain in the superlattice satisfactorily.

### 4. Acknowledgments

The work in Linz is supported by the Fonds zur Förderung der wissenschaftlichen Forschung (P8446). The research at Purdue University is supported by the National Science Foundation, MRG (DMR-92-21590). We thank F. Hauzenberger for his help with the growth of the superlattices. Helpful discussions with Professor E. Molinari are gratefully acknowledged.

### 5. References

- [1] T. Fromherz, F. Hauzenberger, W. Faschinger, M. Helm, P. Juza, H. Sitter and G. Bauer, *Phys. Rev. B* 47 (1993) 1998.
- [2] Eunsoo Oh, A.V. Ramdas, T. Fromherz, W. Faschinger, G. Bauer and H. Sitter, *Phys. Rev. B* 48 (1993), to be published.
- [3] A.K. Sood, J. Menéndez, M. Cardona and K. Ploog, *Phys. Rev. Lett.* 54 (1985) 2115; A. Fasolino and E. Molinari, *Surface Sci.* 228 (1990) 112.
- [4] R.H. Miles, G.Y. Wu, M.D. Johnson, T.C. McGill, J.P. Faurie, and S. Sivananthan, *Appl. Phys. Lett.* 48 (1986) 1383.
- [5] J. Menéndez, A. Pinczuk, J.P. Valladares, R.D. Feldman and R.F. Austin, *Appl. Phys. Lett.* 50 (1987) 1101.
- [6] G. Scarmarcio, L. Tapfer, W. König, A. Fischer, K. Ploog, E. Molinari, S. Baroni, P. Giannozzi and S. de Gironcoli, *Phys. Rev. B* 43 (1991) 14754.
- [7] E. Koppensteiner, P. Hamberger, G. Bauer, A. Pesek, H. Kibbel, H. Presting and E. Kasper, *Appl. Phys. Lett.* 62 (1993) 1783.
- [8] N. Vagelatos, D. Wehe and J.S. King, *J. Chem. Phys.* 60 (1974) 3613; A. Dal Corso, S. Baroni, R. Resta and S. de Gironcoli, *Phys. Rev. B* 47 (1993) 3588.
- [9] J.M. Rowe, R.M. Nicklow, D.L. Price and K. Zanio, *Phys. Rev. B* 10 (1974) 671.
- [10] L. Ward, in: *Handbook of Optical Constants of Solids II*, Ed. E.D. Palik (Academic Press, New York, 1991) p. 746.
- [11] E.D. Palik, in: *Handbook of Optical Constants of Solids I*, Ed. E.D. Palik (Academic Press, New York, 1985) p. 411.
- [12] D.J. Olego, P.M. Raccach and J.P. Faurie, *Phys. Rev. B* 33 (1986) 3819; S. Perkowitz, L.S. Kim, Z.C. Feng and P. Becla, *Phys. Rev. B* 42 (1990) 1455; Eunsoo Oh, R.G. Alonso, I. Miotkowski and A.K. Ramdas, *Phys. Rev. B* 45 (1992) 10934.



ELSEVIER

Journal of Crystal Growth 138 (1994) 585–589

JOURNAL OF  
CRYSTAL  
GROWTH

## Temperature dependence of optical gain in CdTe/CdMnTe heterostructures

R. Legras <sup>a,\*</sup>, Le Si Dang <sup>a</sup>, C. Bodin <sup>a</sup>, J. Cibert <sup>a</sup>, F. Marcenat <sup>a</sup>, G. Feuillet <sup>b</sup>,  
J.L. Pautrat <sup>b</sup>, D. Herve <sup>c</sup>, E. Molva <sup>c</sup>

<sup>a</sup> Laboratoire de Spectrométrie Physique (URA 08, CNRS), Université J. Fourier, BP 87, F-38402 Saint-Martin-d'Hères Cedex, France

<sup>b</sup> CEA / Département de Recherche Fondamentale sur la Matière Condensée, SP2M / PSC, 85X, F-38041 Grenoble Cedex, France

<sup>c</sup> CEA / Technologies Avancées, LETI, 85 X, F-38041 Grenoble Cedex, France

### Abstract

CdTe/CdMnTe graded index separate confinement heterostructures have been used to produce visible laser emission under electronic or photo-pumping. The optical gain of the structures has been measured as a function of optical power and temperature. The maximum gain, about  $190\text{ cm}^{-1}$  for a structure containing two quantum wells, is easily attained under excitation of about  $6\text{ kW/cm}^2$  at 90 K. It decreases with increasing temperatures, displaying two distinct regimes: (i) in the low temperature regime (below 200–250 K), the gain decreases exponentially with a characteristic temperature  $T_0 = 110\text{ K}$ , and is interpreted as being due to the escape of holes from quantum wells and also to scattering of carriers by LO phonons; (ii) above 250 K, a faster decrease of gain takes place as a result of the thermal activation of carriers into the barriers.

### 1. Introduction

Since the first report of a blue-green ZnSe-based injection laser [1], which was made possible by the successful p-type doping of ZnSe, the main difficulty has been the problem of making an ohmic contact to a wide bandgap p-type semiconductor [2]. The microgun pumped semiconductor laser [3] has recently been proposed as an alternative solution which circumvents the difficulties of doping and making electrical contacts to the semiconductor material. In this device, arrays of microtip cathodes developed for flat panel dis-

plays, are used as cold cathode emitters. The electrons are subsequently accelerated by a moderate 10 kV voltage and focused onto the semiconductor optical cavity to produce electron-hole pairs within 100 to 500 nm below the surface. The semiconductor active region is a graded index separate confinement heterostructure (GRINSCH) which is designed to improve carrier collection into the quantum well (QW) and to avoid the surface recombination. In this work we report on a comparative optical study of various CdTe/CdMnTe GRINSCHs used in the microgun pumped laser. The net gain of these structures has been measured under optical pumping, at different excitation powers and different temperatures.

\* Corresponding author.



## 2. Experimental procedure

The net optical gain is measured by the variable stripe length method of Shaklee and Leheny [4]. The excitation stripe is formed by the frequency doubled beam of a *Q*-switched YAG–Nd laser. The width of the stripe is about 50  $\mu\text{m}$  and the length can be varied up to 1 mm. The pulse length is 250 ns and the repetition rate is 1 kHz. The power density in the stripe is 30  $\text{kW}/\text{cm}^2$ , which can be attenuated if necessary using neutral density filters. As the laser pulse duration is much longer than the radiative recombination time (1 ns or less) we can assume that the measurements are done under steady state conditions. The emitted light can be spectrally dispersed using a 1 m monochromator. The uncertainty on the gain values is estimated to be less than 10  $\text{cm}^{-1}$ .

The samples were grown by MBE on (001)  $\text{Cd}_{0.96}\text{Zn}_{0.04}\text{Te}$  substrates at 310°C under an excess cadmium flux. Sample characteristics are described in Table 1. The active region consists of 1 or 2 CdTe QWs located inside an asymmetric GRINSCH structure adapted for external pumping with a low energy (5 to 10 keV) electron beam. The composition gradient of the barriers, the high and low limits of which are indicated in Table 1, extends over approximately 600 nm on the surface side and 300 nm on the buffer side. This active part of the structure is coherently grown on top of a relaxed buffer layer (2  $\mu\text{m}$  of  $\text{Cd}_{0.75}\text{Mn}_{0.25}\text{Te}$  or  $\text{Cd}_{0.80}\text{Mn}_{0.20}\text{Te}$  depending on the sample). It has been carefully checked by cathodoluminescence imaging that the GRINSCH and QW regions are free of misfit interfacial dislocations for all samples described in this work.

Table 1  
Sample characteristics

Sample	Number of QWs	QW thickness (nm)	Mn gradient (%)	
			$x_{\text{min}}$	$x_{\text{max}}$
A	1	4.5	20	25
B	1	8.0	20	25
C	2	4.5	20	25
D	2	6.5	15	20

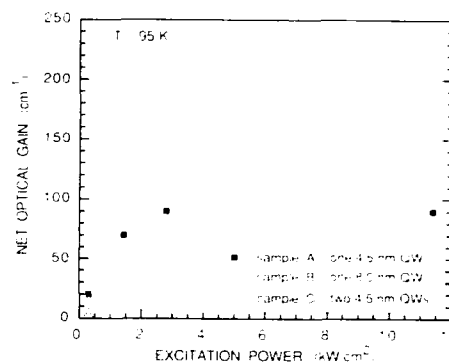


Fig. 1. Net gain (linear scale) measured in samples A, B and C at low temperature (95 K) as a function of the optical excitation density.

Note that the thickness of the QW region varies from 5 to 20 nm in our samples, much less than the lateral extension of the guided TE mode (500 nm). Therefore the optical confinement factor  $\Gamma$  is roughly the same and is of the order of a few percent in the various configurations.

## 3. Experimental results

The variation of the spectrally integrated optical gain with excitation power is presented in Fig. 1 for samples A, B and C, which were grown to check the role of the QW parameters (see Table 1). The lowest threshold is obtained for sample A which contains a single narrow QW. The gain increases with increasing excitation and reaches a maximum at 5  $\text{kW}/\text{cm}^2$  and above. However, the maximum gain is higher for the 2-QW (sample C) than for the 1-QW structures (samples A and B). These observations can be understood qualitatively on the basis of the density of states in the active region. At low temperatures and under low excitation power, the carriers are confined in the wells. A smaller density of states allows the population inversion condition to be reached faster. The narrow single well structure (sample A) must then give the higher gain at low power (e.g., 20  $\text{cm}^{-1}$  at 0.3  $\text{kW}/\text{cm}^2$ ), while the 2-QW structure (sample C) reaches the same inversion condition

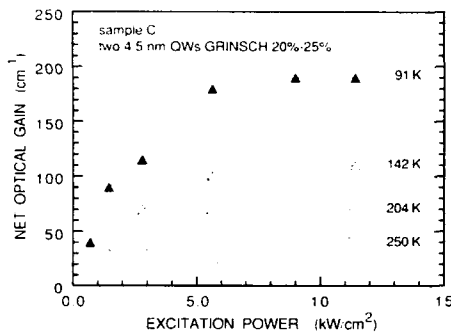


Fig. 2. Net gain (linear scale) measured in sample C at different temperatures as a function of the optical excitation density.

with twice as much power, and then gives twice more gain ( $40 \text{ cm}^{-1}$  at  $0.7 \text{ kW/cm}^2$ ).

At higher excitation densities, the gain increases with population inversion. It is expected to reach a maximum in a QW structure when the Fermi energy is well above the confined level, since the 2D density of states is constant with energy for a given subband. This is indeed the case for the 3 samples. Furthermore we observe that the maximum gain is independent of the well size, which is due to the fact that the 2D density of states is independent of the well thickness. For the 2-QW structure (sample C) it amounts to

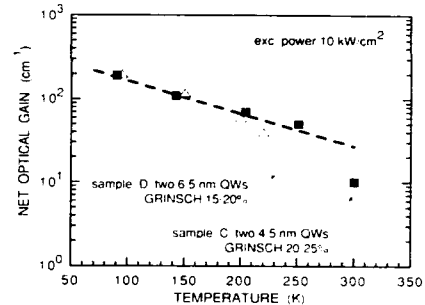


Fig. 3. Net gain (log scale) measured in samples C and D at high excitation density ( $10 \text{ kW/cm}^2$ ) as a function of the temperature.

about  $200 \text{ cm}^{-1}$ , which is twice the maximum gain (about  $100 \text{ cm}^{-1}$ ) in the 1-QW structures (samples A and B).

The power dependence of the gain at different temperatures is presented in Fig. 2 for sample C. As the temperature increases, the maximum gain is reached at higher powers. In order to get a better description of the temperature variation of the gain we have plotted in Fig. 3 the logarithm of gain (measured at  $10 \text{ kW/cm}^2$ ) versus the temperature for samples C and D. These two samples have been designed to present quite different distribution of density of states in QWs

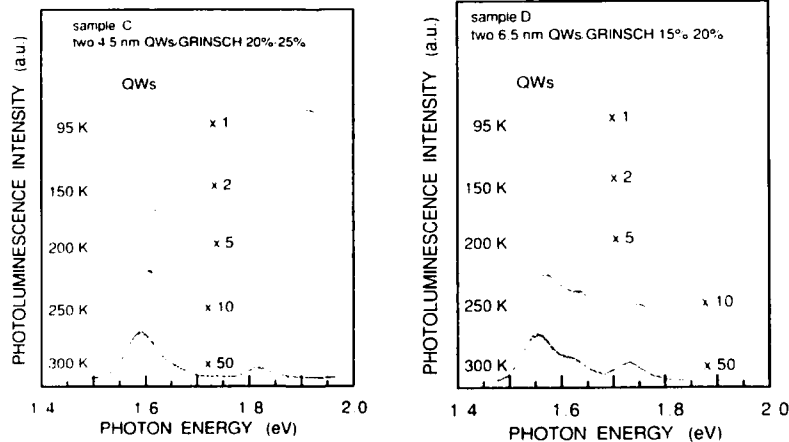


Fig. 4. Spontaneous emission (photoluminescence spectra from the sample surface) in samples C and D, at different temperatures. Samples are excited by a  $0.5 \text{ mm}$  long stripe at  $10 \text{ kW/cm}^2$ .

and barriers. Both have graded barrier layers of the same thickness with the same gradient (see Table 1). But sample C has deeper and narrower QWs, so that the ground states of electrons and holes are better decoupled from confined excited states and from the large density of states in the graded barriers. As shown in Fig. 3, the temperature dependence of the gain displays two distinct regimes. In the low temperature regime (under 200 K), the gain decreases exponentially with a characteristic temperature  $T_0 = 110$  K, in a similar way for the two samples. At higher temperature, a sharp drop of the gain is observed, above 200 K for sample D and 250 K for sample C.

Let us first discuss the high temperature regime. The faster decrease of the gain at temperatures above 200–250 K is ascribed to the thermal activation of carriers from the QWs to the graded barriers. Clear evidence of this effect is given by the temperature dependence of the spontaneous emission recorded from the sample surface under identical excitation conditions (see Fig. 4). At temperatures below 100 K, strong luminescence occurs from the barriers, indicating that carriers optically generated deep beyond the graded barrier layers are not collected into QWs. Transfer to QWs becomes better with increasing temperatures, so that the barrier luminescence decreases with respect to the QW luminescence. At still higher temperatures, one observes stronger luminescence from high energy tails of QWs as well as from the barrier: this thermalization takes place around 300 K in sample C, but around 250 K in sample D where excited levels are closer to the ground levels.

We have evaluated the balance between stimulated emission and absorption using a simple model assuming thermal equilibrium of carriers in QWs and barriers. Such a model has been used successfully to explain the better temperature behaviour of GRINSCH as compared to SCH in GaAs/GaAlAs single QW lasers [5]. In our case the fast decrease of gain above 250 K in sample D and above 300 K in sample C is reproduced very well by the model. The dominant mechanism is the very strong escape of holes into the barriers. Note that another detrimental effect of the enhancement of the carriers density in the barriers

might be an increase of the carrier losses due to defects in the alloy.

In the low temperature regime (under 200–250 K), the preceding calculations predict also a decrease of gain due to escape of carriers (especially holes) into the barriers, with a rate somewhat lower than what is observed. This may simply be due to the fact that thermal equilibrium is not realized in the low temperature regime as assumed in the model. However, it is interesting to note that similar  $T_0$  has been found for the temperature dependence of thresholds in other II–VI laser systems [6,7], in contrast to the higher values which are currently encountered in III–V materials. This suggests that the stronger coupling to LO phonon in II–VI materials may play a role, i.e. broadening of the density of states curve by LO phonon scattering. The temperature dependence of the exciton linewidth has been measured recently in similar structures [8]. It is shown that the broadening of the exciton line can be reduced considerably if the exciton binding energy is larger the LO energy of 20 meV. In such a favourable case, the exciton linewidth increases with temperature with an apparent  $T_0 \approx 150$  K, which should correspond to an upper limit for  $T_0$  associated to LO phonon scattering in II–VI materials.

#### 4. Conclusion

The gain in CdTe–CdMnTe GRINSCH QW adapted to electron pumping in a microtip semiconductor laser has been measured under optical pumping using the variable stripe length method. At low temperature (below 100 K), the population inversion is easily attained under a moderate excitation density, and the net gain reaches a maximum. The dependence of gain on the number of QWs (one or two) is easily understood qualitatively when taking into account the change in the density of states. A decrease in the maximum gain is observed when the temperature increases from 100 to 200–250 K: its rate ( $T_0 = 110$  K) is similar to the gain variation in other II–VI laser structures, as well as to the line broadening due to the rather high coupling to LO phonons.

At higher temperatures, a faster decrease of the gain is ascribed to thermal activation into excited and barrier states.

The room temperature gain of GRINSCH QW lasers can be improved with steeper gradients (hence smaller density of states, which is inversely proportional to the gradient, and better optical confinement), deeper QWs, and a larger number of QWs. However, it is desirable to keep the whole GRINSCH under the critical thickness for the onset of mismatch strain relaxation by misfit defects. This in turn puts a strong limitation on the usable structures in the CdTe–CdMnTe system (and even stronger in the ZnSe-based structures) as compared to the GaAs–GaAlAs case.

### 5. Acknowledgement

This work has been completed within the CEA-CNRS joint group “Microstructures de Semiconducteurs II–VI”.

### 6. References

- [1] M.A. Haase, J. Qiu, J.M. DePuydt and H. Cheng, *Appl. Phys. Lett.* 59 (1991) 1272.
- [2] C.T. Walker, J.M. DePuydt, M.A. Haase, J. Qiu and H. Cheng, in: *Proc. 7th Trieste ICTP–IUPAP Semiconductor Symposium on Wide Bandgap Semiconductors*, Ed. C.G. Van De Walle (North-Holland, Amsterdam 1993) p. 27.
- [3] E. Molva, R. Accomo, G. Labrunie, J. Cibert, C. Bodin, G. Feuillet and Le Si Dang, *Appl. Phys. Lett.* 62 (1993) 796.
- [4] K.L. Shaklee and R.F. Leheny, *Appl. Phys. Lett.* 18 (1971) 475.
- [5] J. Nagle, S. Hersee, M. Krakowski, T. Weil and C. Weisbuch, *Appl. Phys. Lett.* 49 (1986) 1325.
- [6] R.D. Feldman, T.D. Harris, J.E. Zucker, D. Lee, R.F. Austin and A.M. Johnson, *J. Electron. Mater.* 22 (1993) 479.
- [7] J.M. Gaines, R.R. Drenten, K.W. Haberern, T. Marshall, P. Mensz and J. Petruzzello, *Appl. Phys. Lett.* 62 (1993) 2462.
- [8] N.T. Pelekanos, H. Haas, N. Magnea, H. Mariette and A. Wasiela, *Appl. Phys. Lett.* 61 (1992) 3154.



ELSEVIER

Journal of Crystal Growth 138 (1994) 590–594

JOURNAL OF  
**CRYSTAL  
GROWTH**

## Photoluminescence of CdTe/ZnTe semiconductor wires and dots

C. Gourgon <sup>\*,a</sup>, B. Eriksson <sup>a</sup>, Le Si Dang <sup>a</sup>, H. Mariette <sup>a</sup>, C. Vieu <sup>b</sup>

<sup>a</sup> CEA-CNRS group "Microstructures de Semiconducteurs II-VI", Laboratoire de Spectrométrie Physique, Université J. Fourier, BP 87, F-38402 Grenoble, France

<sup>b</sup> Laboratoire de Microélectronique et de Microstructures, CNRS, 196 Avenue H. Ravaud, F-92225 Bagneux, France

### Abstract

Arrays of wires and dots have been fabricated by electron beam lithography and Ar<sup>+</sup> ion beam etching from CdTe/ZnTe quantum wells. The intrinsic exciton photoluminescence recombination (X line) is observed for wires (dots) as small as 100 nm (130 nm). In addition, photoluminescence intensity from excitons bound to localized centres (Y line) can be detected for the smallest wires (40 nm) and for the dots down to 100 nm. The emission intensity variation together with the polarization rate are also investigated as a function of the grating period.

### 1. Introduction

With the development of wide gap II–VI semiconductor heterostructures for optoelectronic applications and short visible wavelengths [1,2], it is important to investigate the optical properties of II–VI quantum wire and dot structures in order to evaluate the predicted attractive properties of such nanostructures (increase of the exciton oscillator strength, lower laser threshold). For II–VI nanostructures only wires and dots made of ZnSe compounds have been reported so far in the literature [3,4]. In this paper, we present the fabrication and the optical characterization of CdTe/ZnTe nanostructures processed by electron beam lithography and Ar<sup>+</sup> ion beam etching with lateral sizes down to 40 and 70 nm for the wires and dots, respectively. The total luminescence intensity in such nanostructures is compa-

table to the one obtained with the reference quantum well in the unetched part of the sample, but is dominated by the recombination of excitons localized on defects rather than by free exciton. Below 40 nm wire widths (100 nm dot widths), this extrinsic emission is completely quenched.

### 2. Experimental details

The CdTe/ZnTe (001) quantum wells were grown by molecular beam epitaxy on GaAs substrate, covered by a 2.7  $\mu\text{m}$  thick CdZnTe (16% Zn) buffer layer. The multiquantum well (MQW) structure contains 5 periods of QWs and barriers with thicknesses of 13 and 1.6 nm, respectively. Conventional electron beam nanolithography was used on a 150 nm thick polymethylmethacrylate resist layer to produce high density periodic patterns on the sample. The experimental conditions (exposure time, beam spot size) were optimized to obtain well-defined arrays of 40  $\mu\text{m} \times 40 \mu\text{m}$

\* Corresponding author.

of wires and dots. After deposition of a titanium layer of 50 nm, a lift-off process was used to produce metallic wires and dots. The transfer of this pattern to the underlying QWs was obtained by etching the sample through the Ti mask with a conventional  $\text{Ar}^+$  ion beam etching system. The nanostructures were observed using a high resolution scanning electron microscope (SEM). Fig. 1 shows such images attesting that the technological processes (lithography and etching) allow us to control lateral dimensions down to 40 nm for the wires and 70 nm for the dots. A close examination of SEM images shows that the typical inclination of the sidewalls was about  $10^\circ$ . Such patterns were reproduced with various lateral sizes (40 to 170 nm for the wires and 70 to 210 nm for the dots) for a given grating period (0.4  $\mu\text{m}$ ). Moreover, for a given wire width (80 nm), various arrays were made with different periods ranging from 0.4 to 2  $\mu\text{m}$ .

Optical spectroscopy (photoluminescence (PL), photoluminescence excitation) was performed at low temperature (1.8 K) with a mapping set-up

having a spatial resolution of 20  $\mu\text{m}$  (laser spot size). The sample was excited either above the band gap of the barrier with an Ar laser, or in resonance in the well using a dye laser with a typical power density of 500  $\text{W}/\text{cm}^2$ .

### 3. Optical results

Fig. 2 shows PL spectra of quantum wires with lateral sizes changing from 170 to 40 nm, together with a PL spectrum of quantum dots (210 nm size) and a 2D QW reference spectrum obtained on a large unetched area. This spectrum exhibits two lines: X line, corresponding to the  $e_1h_1$  intrinsic excitons in the CdTe–ZnTe QWs, and Y line, corresponding to the extrinsic excitons localized on residual defects (its energy, 4 meV below the X line, is compatible with a donor bound exciton [5,6]). Extrinsic luminescence at 1.57–1.58 eV is believed to be related to the extended defects [7]. The PL spectra of wide wires and dots, as compared to the 2D spectra, exhibit:

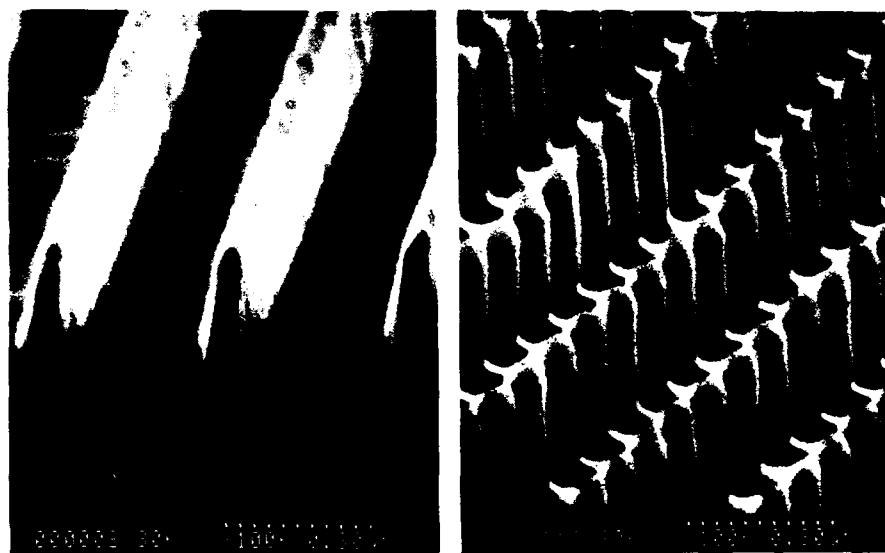


Fig. 1. SEM images of periodic quantum wires and dots etched into the CdTe/ZnTe heterostructures. The five QWs are located below the 100 nm CdZnTe cap layer. The sizes are 40 nm for the wires and 70 nm for the dots. (The scale is given by two successive points which correspond to 30 nm.)

- (i) a blue shift of both exciton lines towards higher energy ( $\approx 1.5$  meV for the wires and 3 meV for the dots);
- (ii) a vanishing of the extrinsic luminescence at 1.57–1.58 eV;
- (iii) a marked variation in the relative intensity of the intrinsic  $e_1h_1$  and extrinsic transitions (ratio  $X/Y$ ).

All the above PL features are similar to those observed on the PL spectra of samples implanted at 300 K with different ions (Zn, Ar, Cd) followed by a moderate annealing for which interdiffusion of CdTe/ZnTe strained QWs was observed [7]. In our case, the  $\text{Ar}^+$  ion beam etching creates both structural defects under the Ti mask by stragglings and a local annealing. This would induce an intermixing which gives rise to the blue shift observed for the exciton line. The vanishing of extrinsic luminescence at 1.57–1.58 eV is also a signature of some local annealing effect [7]. Finally, the increase of the Y line intensity can

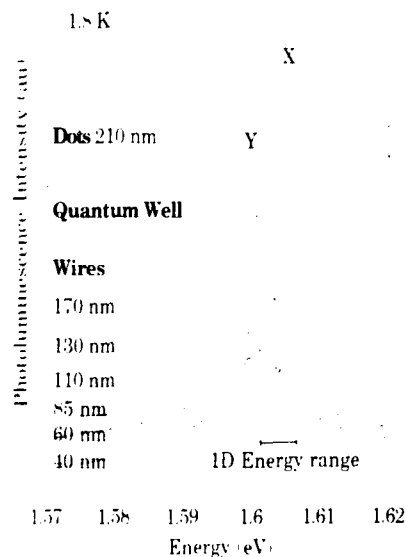


Fig. 2. Photoluminescence spectra of set of wires with various sizes (170 nm to 40 nm) together with a PL spectrum of quantum dots (210 nm) and of a reference 2D quantum well structure. The intensities of all the spectra are normalized to their maxima.

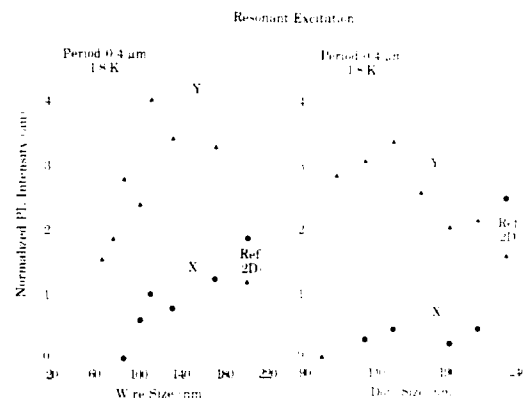


Fig. 3. Normalized PL intensities of the two exciton lines as a function of the lateral dimensions. The circles correspond to the intrinsic recombination (X line) and the triangles to extrinsic recombination (Y line). The dashed lines are only a guide to the eyes. The PL intensities observed for the reference 2D unetched part are also shown.

reveal a variation in the distribution of impurities or defects responsible for the extrinsic Y line during the ion beam etching.

For narrower wires and dots, the intrinsic X line disappears and only the Y line can be detected. This line broadens up to 10 meV for the smallest wire size (40 nm), and no significant blue shift due to lateral confinement is observed. (This broadening is also observed in photoluminescence excitation spectra.) In our case, the lateral confinement effect could be obscured by dispersion of lateral wire size in the MQW structure because of the inclined sidewalls. Taking wire sizes equal to  $40 \pm 15$  nm, one would expect a blue shift varying between 2 and 7 meV for an infinite lateral potential (this 1D energy range is reported in Fig. 2).

Fig. 3 shows the evolution of the X and Y exciton line intensities for both wires and dots as a function of their lateral sizes. These intensities are deduced after deconvoluting the PL spectra obtained under a resonant excitation, so that the carriers are created only in the CdTe QWs. Then the PL intensities are normalized to the wire (dot) surface. We would like to note that the PL results obtained for the 40 nm wires are not reported in this figure because they were ob-

tained on an array with a different period and with a different excitation power. In Fig. 3, the striking result is the increase of the Y line luminescence intensity for the wide nanostructures as compared to the one obtained for the reference 2D unetched part. The X and Y exciton line intensities drop by about one order of magnitude for the smallest patterns. The X line disappears for wire sizes lower than 100 nm and dot sizes lower than 130 nm: this difference between the two types of nanostructures could be due to the lateral surface damage which is expected to be more dominant for the dots.

Note that no overgrowth was realized to obtain these results, in contrast to the III–V nanostructures where the recovery of luminescence intensity was obtained by overgrowth on the etched patterns in order to reduce surface recombination [8]. The increase of the PL quantum efficiency in the wide nanostructure arrays is correlated with two experimental observations. First, in the implanted enhanced interdiffusion study mentioned above [7], an increase by a factor of 2

of the PL efficiency was observed between the 2D as-grown sample and the annealed one. Secondly, PL intensity from arrays of 80 nm wires is increased by a factor of 4 when the period is smaller than  $0.7 \mu\text{m}$ . This is reported in Fig. 4 where the PL intensity from 80 nm wires is plotted as a function of the wire period. A strong increase of the PL intensity is observed for periods between  $0.8$  and  $0.6 \mu\text{m}$ . Moreover, for these period values, the emission becomes strongly polarized along the wires for both excitation polarizations, parallel and perpendicular to the wires. It is to be noted that these thresholds for both the PL intensity and the polarization ratio appear for a period corresponding to the emission wavelength of the CdTe QWs. This strong polarization effect is not related to a lateral confinement effect, but is rather due to an electrodynamic effect such as an increase of the coupling between the emission light and the grating period of the wires. This polarization effect has to be calculated following the model presented in ref. [9].

Finally, as shown in Fig. 3, the free exciton

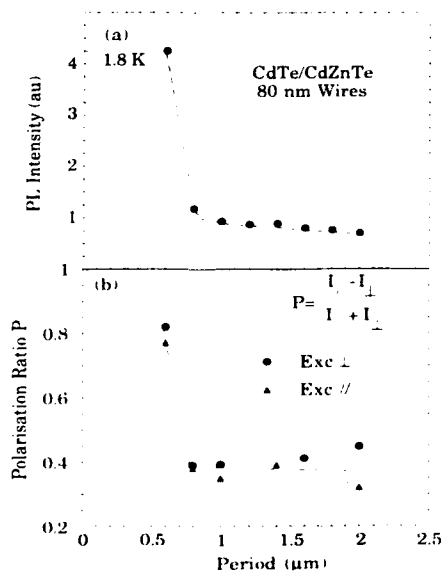


Fig. 4. Photoluminescence of 80 nm wires as a function of the array period. (a) PL intensity without any polarization. (b) Polarization ratio of the emission luminescence for excitation polarized parallel and perpendicular to the wires.



emission intensity (X line) vanishes always before the extrinsic one (Y line). This result can be due to the fact that free excitons can migrate to the wire (dot) sidewalls and recombine nonradiatively on surface defects. On the other hand, excitons trapping on localized centres such as impurities into the wires (dots) can favour the observation of radiative recombination (Y line) down to the smallest nanostructures sizes.

#### 4. Conclusion

Quantum wires and dots are fabricated from CdTe/ZnTe multiquantum wells grown by molecular beam epitaxy. High resolution electron beam lithography and  $\text{Ar}^+$  ion beam etching are used to define arrays of wires and dots with sizes down to 40 and 70 nm, respectively.

The PL spectra and the PL intensities of these nanostructures are studied as a function of their size. Without any overgrowth, the PL intrinsic exciton recombination (X line) is observed for wires (dots) as small as 100 nm (130 nm). In addition, PL intensity from extrinsic excitons bound to localized centres (Y line) can be detected for wires (down to 40 nm) and for dots (down to 100 nm). By studying the polarization dependence of the emitted light as a function of the grating period, we observed an electrodynamic polarization effect which modifies the emission properties of wire gratings.

#### 5. Acknowledgements

We are thankful to J. Cibert, K. Saminadayar and S. Tatarenko for providing the MBE growth samples.

#### 6. References

- [1] M.A. Haase, J. Qiu, J.M. DePuydt and H. Cheng, *Appl. Phys. Lett.* 59 (1991) 1272.
- [2] H. Jeon, J. Ding, W.R. Patterson, A.V. Nurmikko, W. Xie, D.C. Grillo, M. Kobayashi and R.L. Gunshor, *Appl. Phys. Lett.* 59 (1991) 3619.
- [3] W. Walecki, W.R. Patterson, A.V. Nurmikko, H. Luo, N. Samarth, J.K. Furdyna, M. Kobayashi, S. Durbin and R.L. Gunshor, *Appl. Phys. Lett.* 57 (1990) 2641.
- [4] M.A. Foad, A.P. Smart, M. Watt, C.M. Sotomayor Torres, W. Khun, P.H. Wagner, H. Leiderer, S. Bauer, C.D.W. Wilkinson, W. Gebhardt and M. Razeghi, in: *Proc. Int. Symp. on Nanostructures and Mesoscopic Systems*, Santa Fe, May 1991, Eds. W.P. Kirk and M.A. Reed (Academic Press, New York).
- [5] H. Mariette, F. Dal'bo, N. Magnea, G. Lentz and H. Tuffigo, *Phys. Rev. B* 38 (1988) 12443.
- [6] R.T. Cox, A. Mandray, S. Huant, F. Bassani, K. Saminadayar and S. Tatarenko, *Mater. Sci. Eng. B* 16 (1993) 83.
- [7] A. Hamoudi, J. Cibert, G. Feuillet, P.H. Jouneau, Le Si Dang, E. Ligeon, J.L. Pautrat, K. Saminadayar and S. Tatarenko, *J. Appl. Phys.* 74 (1993) 2524.
- [8] See, for example: A. Izrael, B. Sermage, J.Y. Marzin, A. Ougazzaden, R. Azoulay, J. Etrillard, V. Thierry-Mieg and L. Henry, *Appl. Phys. Lett.* 56 (1990) 830; P.D. Wang, C.M. Sotomayor Torres, H. Bessity, C. Weisbush and S.P. Beaumont, *Appl. Phys. Lett.* 61 (1992) 946; K. Pieger, CH. Gréus, J. Straka and A. Forchel, 7th EuroMBE, Bardonecchia, Italy, March 1993.
- [9] U. Bockelmann, *Europhysics Lett.* 16 (1991) 601.



ELSEVIER

Journal of Crystal Growth 138 (1994) 595–600

JOURNAL OF  
**CRYSTAL  
GROWTH**

## Exciton recombination in $\text{ZnSe}_x\text{Te}_{1-x}/\text{ZnTe}$ QWs and $\text{ZnSe}_x\text{Te}_{1-x}$ epilayers grown by metalorganic vapour phase epitaxy

A. Naumov <sup>\*,1</sup>, H. Stanzl, K. Wolf, A. Rosenauer, S. Lankes, W. Gebhardt*Institut für Festkörperphysik, Universität Regensburg, D-93040 Regensburg, Germany,*

### Abstract

We present the optical characterization of MOVPE grown  $\text{ZnSe}_x\text{Te}_{1-x}$  epilayers with  $0 < x < 0.35$  and  $\text{ZnSe}_x\text{Te}_{1-x}$  single quantum wells (SQWs) with  $L_z = 2.0\text{--}8.5$  nm. The structures were investigated using photoreflectance and photoluminescence spectroscopy. Transmission electron microscope analysis was used to determine quantum well thickness. The studied  $\text{ZnSe}_{0.3}\text{Te}_{0.7}$  SQWs show a bright emission band with a halfwidth  $\sim 10$  meV in the spectral region of 100–250 meV below the band gap of the corresponding mixed crystal. We suggest a type II bands alignment in  $\text{ZnSe}_x\text{Te}_{1-x}/\text{ZnTe}$  single quantum wells.

### 1. Introduction

The properties of semiconductor mixed crystals and quantum well structures of II–VI compounds attracted increasing interest because of the growing use of these materials in opto-electronic devices operating in the visible spectral region. In heterostructures with ZnSe, ZnTe and  $\text{ZnSe}_x\text{Te}_{1-x}$  materials the variation of the band gap at room temperature is possible from the blue to the yellow-red region. Molecular beam epitaxy (MBE) and metalorganic vapour phase epitaxy (MOVPE) growth of  $\text{ZnSe}_x\text{Te}_{1-x}$  epilayers in the whole concentration range was reported by different groups [1–3]. However, the most of experimental data on the optical proper-

ties of  $\text{ZnSe}_x\text{Te}_{1-x}$  epilayers are related to the composition close to ZnSe [2,3]. In this paper we present the evolution of the luminescence spectra in MOVPE grown  $\text{ZnSe}_x\text{Te}_{1-x}$  epilayers near ZnTe binary compound.

Experimental and theoretical studies of  $\text{ZnTe}_{1-x}\text{Se}_x/\text{ZnTe}$  strained layer superlattices [4] show that this system has a type II band alignment because of a large valence band offset ( $\sim 1$  eV) between ZnTe and ZnSe binary compounds. In the present work we show that in a strained layer  $\text{ZnSe}_x\text{Te}_{1-x}/\text{ZnTe}$  SQW, recombination has a type II behaviour when electrons are confined in the  $\text{ZnSe}_x\text{Te}_{1-x}$  QW and holes are in the ZnTe material.

### 2. Experimental procedure

The studied structures were grown in our laboratory by atmospheric pressure MOVPE at  $T =$

\* Corresponding author.

<sup>1</sup> Present address: Department of Physics and Astronomy, Dartmouth College, 6127 Wilder Laboratory, Hanover, New Hampshire 03755-3528, USA.

340°C with diisopropyltelluride (DIPTe) and diallylselenide (DASe) in combination with dimethylzinc–triethylamine (DMZn–TEN). (001) GaAs was used as a substrate for epilayers and QW structures. The growth rate was about 0.7  $\mu\text{m}/\text{h}$ . The composition rate  $x$  of the epilayers was measured by X-ray diffraction analysis and the monocrystalline quality was confirmed by transmission electron microscope (TEM) measurements. The growth of  $\text{ZnSe}_x\text{Te}_{1-x}$  QWs was performed with 10 min interruptions at the interfaces.

Photoluminescence (PL) spectra were measured at 2 K under the excitation with an Ar-ion laser line 458 nm (2.707 eV). PL spectra were detected at normal incidence using a 1 m double Jarrel–Ash spectrometer and a cooled GaAs photomultiplier.

A 1000 W halogen lamp and a 1/4 m monochromator were used for photoreflectance (PR) measurements to obtain a probe beam with a spectral halfwidth of 0.2 nm. A pump beam of a 336 nm line of a high pressure mercury lamp was focused at the sample placed in a helium bath cryostat. We used the sweeping photoreflectance technique described in ref. [5] to avoid the influence of the intense PL background. The luminescence and the reflected probe beam were detected in back-scattering configuration by a cooled bialkali photomultiplier.

{110} Cross-sectional samples were prepared for transmission electron microscope (TEM) investigation. The cleaved samples were glued together and cut into slices of 300  $\mu\text{m}$ . Then they were mechanically thinned to a thickness of about 25  $\mu\text{m}$ . Finally, the specimens were thinned to electron transparency during liquid nitrogen cooling by a two-gun  $\text{Ar}^+$  ion mill. TEM micrographs were obtained with a Philips CM30 microscope with a point resolution of the objective lens of 0.23 nm.

### 3. $\text{ZnSe}_x\text{Te}_{1-x}$ epilayers

The studied  $\text{ZnSe}_x\text{Te}_{1-x}$  epilayers show at  $T = 2\text{ K}$  a bright emission in the excitonic region which indicates to a high quality of the grown

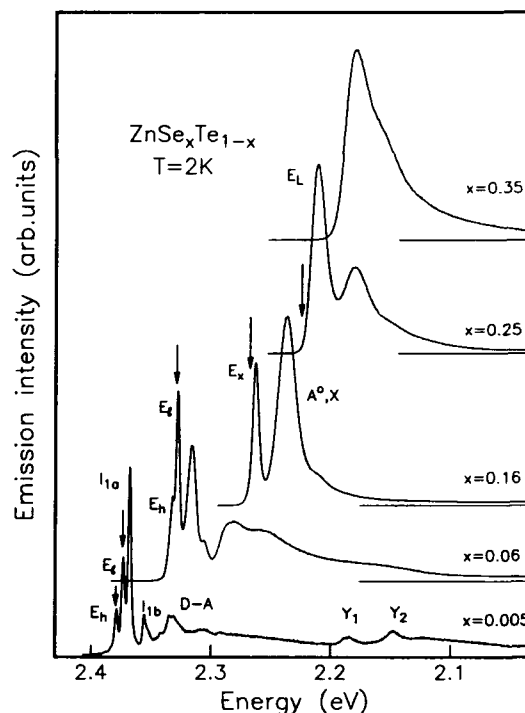


Fig. 1. PL spectra of  $\text{ZnSe}_x\text{Te}_{1-x}$  epilayers. Arrows mark the position of excitonic resonances obtained from photoreflectance measurements.

samples. Low temperature PL spectra of  $\text{ZnSe}_x\text{Te}_{1-x}$  are shown in Fig. 1. With the increase of the Se content in the layer the emission spectrum shifts to lower energies according to the band gap changes in  $\text{ZnSe}_x\text{Te}_{1-x}$  mixed crystals [1].

In the epilayers with low Se concentration ( $x < 0.1$ ), PL spectra are similar to those found in pure ZnTe layers grown by the same MOVPE technique [6]. The spectrum consists of free excitons line, split by thermal strain into heavy-hole ( $E_h$ ) and light-hole ( $E_l$ ) components, lines of excitons bound to neutral shallow acceptors  $I_{1a}$  and  $I_{1b}$ , and donor–acceptor (D–A) pair recombination band [6]. Two deep  $Y_1$  and  $Y_2$  bands in the sample with  $x = 0.005$  were assigned to the dislocation related transitions [7]. In the concentration region  $0.1 < x < 0.2$ , PL spectra contain two emission bands which were attributed to the

free exciton  $E_x$  and acceptor bound exciton ( $A^0$ , X) recombination [8]. In the region of compositions with  $x > 0.2$  for the best quality  $\text{ZnSe}_x\text{Te}_{1-x}$  epilayers, one emission band  $E_L$  and its 1LO phonon replica were observed. In the samples with higher concentration of residual impurities, 1LO phonon replica is overlapped by the ( $A^0$ , X) band.

The detailed study [8] of the spectral position, temperature dependence and the comparison with the spectra of the bulk  $\text{ZnSe}_x\text{Te}_{1-x}$  mixed crystals allowed us to attribute the  $E_L$  band to the radiative recombination of the excitons localized by compositional fluctuations of the mixed crystal [9]. This assignment is also supported by the essential increase of the whole PL intensity in  $\text{ZnSe}_x\text{Te}_{1-x}$  epilayers with the increase of composition  $x$ . It was shown in ref. [8] that in this concentration region there is a low energy shift of the peak position  $E_L$  band from the position of the excitonic resonance. The excitonic band edge

position was obtained from PL excitation spectra and from the temperature dependence of PL, since no distinguishable fine structure in the exciton reflection spectra has been observed for the compositions  $x > 0.1$ .

In this work we have used a photoreflectance technique to determine the position of excitonic resonance in the samples with a higher Se concentration. A pronounced excitonic structure in PR spectra was detected for the concentrations up to  $x = 0.25$ . At higher Se compositions, the broadening of the PR spectrum increases rapidly and smears out the excitonic fine structure. The exciton resonance positions obtained from the PR spectra are presented in Fig. 1. At low Se concentration, excitonic resonance is located near the maximum of free exciton emission  $E_x$ . For the sample with  $x = 0.25$ , the position of the excitonic resonance corresponds to the high energy edge of the PL band of localized excitons  $E_L$ . The concentration dependence of the exci-

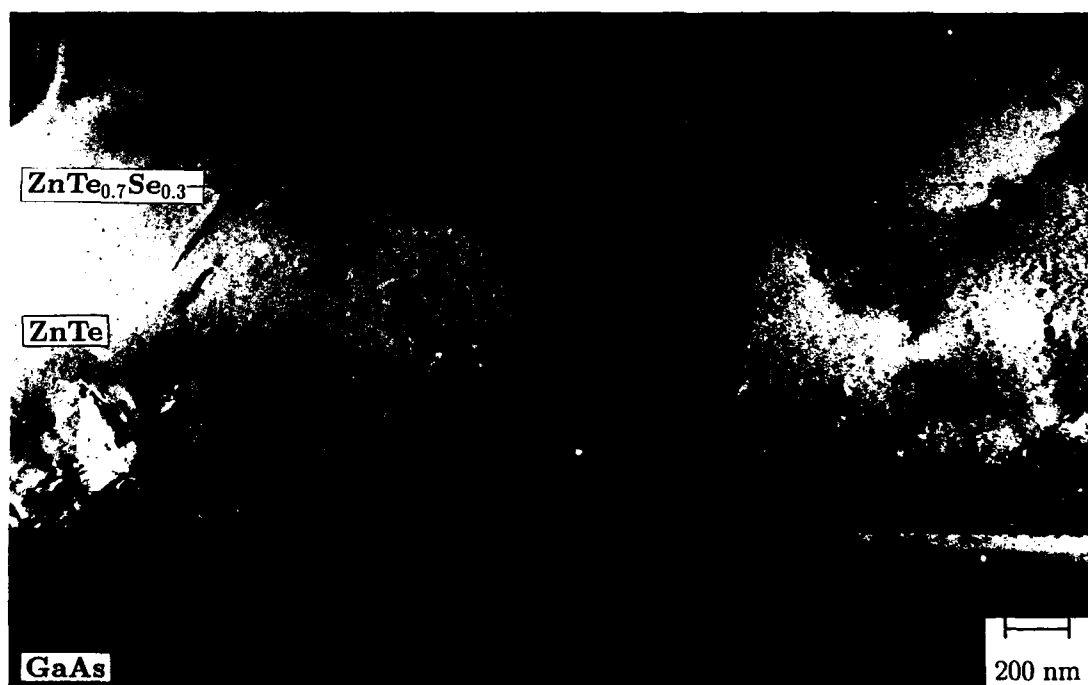


Fig. 2. Single beam bright field image of  $\text{ZnSe}_{0.3}\text{Te}_{0.7}$  SQW structure.

tonic band edge can be well fitted by a parabolic function

$$E_{\text{ex}}(x) = E_{\text{ex}}(0)(1-x) + E_{\text{ex}}(1)x - bx(1-x),$$

with a bowing parameter  $b = 1.35 \pm 0.1$  eV which is in agreement with  $b = 1.36$  eV obtained from temperature dependent of PL [8] and is smaller than the value  $b = 1.504$  eV determined from photoconductivity measurement [1].

#### 4. $\text{ZnSe}_x\text{Te}_{1-x}/\text{ZnTe}$ quantum wells

We have studied three samples with  $\text{ZnSe}_{0.3}\text{Te}_{0.7}$  QWs confined by ZnTe binary compound. Two samples contain single  $\text{ZnSe}_{0.3}\text{Te}_{0.7}$  QWs ( $L_z = 4.2$  nm and  $L_z = 6.3$  nm) with  $1.5 \mu\text{m}$  ZnTe buffer layer and  $0.5 \mu\text{m}$  ZnTe cap layer. The third sample contains three  $\text{ZnSe}_{0.3}\text{Te}_{0.7}$  QWs with thicknesses  $L_z = 2.1$ ,  $4.2$  and  $8.4$  nm separated by a  $0.5 \mu\text{m}$  ZnTe material.

Fig. 2 shows a single beam bright field image of the sample with  $4.2$  nm thick SQW. Since no dislocations can be found in the region of the quantum well, we assume that the QW layers are below the critical thickness for strain relaxation. The thicknesses of the investigated QWs were measured by high resolution transmission electron microscopy (HRTEM), facilitated by new digital analysis methods which will be described in detail elsewhere.

Since the quantum well lattice constant  $a_{\perp}^{\text{QW}}$  perpendicular to the interface plane differs from the lattice constant  $a_{\perp}^{\text{ZnTe}}$  of the embedding material, the thickness of the quantum well can be determined by the analysis of lattice spacing. For this purpose the HRTEM negatives are digitized with a CCD camera at a resolution of  $768 \times 512$  pixels. The digitized images are processed on a Silicon Graphics work station. The noise part of the Fourier transform which results from sample surface amorphization during the ion milling process, contamination during electron microscopy investigation, grains of the negative and noise of the CCD camera is detected automatically and reduced by Wiener filtering. After inverse Fourier transformation, the approximate atom position, can be found as local brightness maxima. Fitting

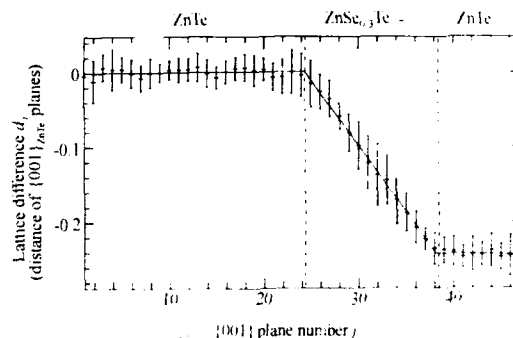


Fig. 3. Result of the digital analysis of lattice spacings in the structure with a  $\text{ZnSe}_{0.3}\text{Te}_{0.7}$  quantum well.

the parabolic curves to the intensities along straight lines which cross the brightness maxima enhances the accuracy of atom position determination to typically  $0.2$  pixel. The lattice basis vectors  $\mathbf{B}_{\langle 110 \rangle}$  and  $\mathbf{B}_{\langle 001 \rangle}$  are evaluated by averaging lattice spacings of the found atom positions in a region located safely in the ZnTe. The positions  $\mathbf{R}_{ij} = i\mathbf{B}_{\langle 110 \rangle} + j\mathbf{B}_{\langle 001 \rangle}$  form a reference lattice which can be compared to the determined atom positions  $\mathbf{P}_{ij}$ . The resulting difference vectors  $\mathbf{D}_{ij} = \mathbf{P}_{ij} - \mathbf{R}_{ij}$  are projected onto the  $\langle 001 \rangle$  direction, averaged over  $N$   $\{001\}$  planes and standardized to the  $\{001\}$  plane distance  $|\mathbf{B}_{\langle 001 \rangle}|$ , giving

$$d_j = \frac{1}{N} \sum_{i=1}^N \mathbf{D}_{ij} \frac{\mathbf{B}_{\langle 001 \rangle}}{|\mathbf{B}_{\langle 001 \rangle}|^2}.$$

The result of the analysis is shown in Fig. 3. Here the reference lattice was situated in the left part of the HRTEM image. In the region of the  $\text{ZnSe}_{0.3}\text{Te}_{0.7}$  quantum well, the smaller lattice constant  $a_{\perp}^{\text{QW}}$  causes decreasing values of the lattice difference  $d_j$  with increasing layer number  $j$  according to

$$d_j - d_{j-1} = (a_{\perp}^{\text{QW}} - a_{\perp}^{\text{ZnTe}}) / a_{\perp}^{\text{ZnTe}}.$$

Therefore, the  $14 \pm 2$  planes  $j = 25 \pm 1$  to  $j = 38 \pm 1$  in Fig. 3 belong to the  $\text{ZnSe}_{0.3}\text{Te}_{0.7}$  QW.

The studied  $\text{ZnSe}_{0.3}\text{Te}_{0.7}$  SQW structures show at low temperature a bright luminescence in yellow-red region. The PL spectrum of the sample with a single QW ( $L_z = 4.2$  nm) (Fig. 4b) contains emission of the pure ZnTe barrier and two bands

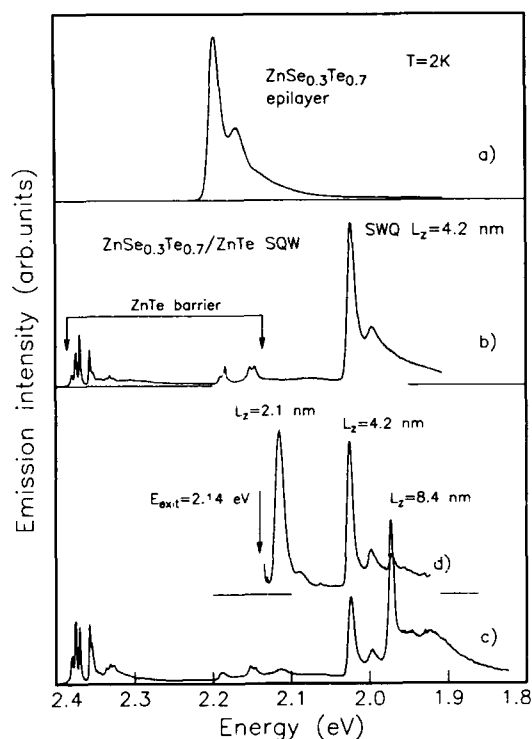


Fig. 4. Comparison of the PL spectra of  $\text{ZnSe}_{0.3}\text{Te}_{0.7}$  epilayer (a) and structures with  $\text{ZnSe}_{0.3}\text{Te}_{0.7}$  QWs (b,c,d). Spectrum (d) was detected from the sample with three  $\text{ZnSe}_{0.3}\text{Te}_{0.7}$  QWs under the excitation  $E_{\text{excit}}$  below the energy gap of ZnTe.

at about 200 meV below the band gap of the corresponding alloy (Fig. 4a). The main peak (2.022 eV) is attributed to the excitonic recombination in the QWs. The one at lower energies (1.996 eV) is probably related to the recombination involved residual impurities.

The spectral position of the QW PL band depends on the composition of the mixed crystal and on the QW thickness. The maximum of the PL band in the QW shifts to higher energies with a decrease of the QW thickness. In the sample with three QWs (Figs. 4c and 4d), the positions of the recombination bands are 1.972, 2.025 and 2.115 eV for  $L_z = 8.4$ , 4.2 and 2.1 nm, respectively. At the same time the halfwidth of the emission line increases monotonically from 7 to

12 meV. As it was mentioned above, the QWs are coherently strained and we assume that the blue shift of the PL bands is due to the confinement effect in QW.

The type of the band alignment in our system was determined using the concentration dependence of the band gap in  $\text{ZnSe}_{1-x}\text{Te}_x$  epilayers obtained from PR measurements. We used also the linear dependence of the valence band edge on the composition of the mixed crystal and a valence band offset of  $-0.9$  eV between ZnTe and ZnSe [4]. We found that the band alignment in  $\text{ZnSe}_{0.3}\text{Te}_{0.7}$  QW corresponds to the type II recombination when the electrons are quantized in a QW and the holes are situated in ZnTe. The depth of the QW in the conduction band of about 0.45 eV was derived for our system by fitting the positions of the PL peaks in the sample with three QWs using the theory for QWs with finite barriers.

## 5. Conclusions

We have studied the optical properties of  $\text{ZnSe}_{1-x}\text{Te}_x$  epilayers and SQWs. It was found that the mixed crystals with composition  $x < 0.1$  have the same recombination channels as binary ZnTe epilayers. The increase of Se composition leads to the essential broadening of all recombination lines. At the compositions  $x > 0.2$ , the PL spectrum is dominated by the recombination of excitons localized by the compositional disorder of the mixed crystal, which is a common property of II–VI mixed crystals with anion substitution [9].  $\text{ZnSe}_{1-x}\text{Te}_x$  SQW structures with ZnTe barriers show a type II band alignment when the electrons are confined in the  $\text{ZnSe}_{1-x}\text{Te}_x$  quantum well and the holes are in the ZnTe material.

## 6. References

- [1] M.J.S.P. Brasil, R.E. Nahory, E.S. Turzo-Sandorff, H.L. Gilchrist and R.J. Martin, *Appl. Phys. Lett.* 58 (1991) 2509.
- [2] K. Dhese, J.E. Nicholls, J. Gudwin, W.E. Hagston, J.J. Davies, M.P. Halsall, B. Cockayne and P.J. Wright, *J. Crystal Growth* 117 (1992) 91.

- [3] H. Oguri, K.S. Park, M. Isshiki and Y. Furukawa, *J. Crystal Growth* 117 (1992) 116.
- [4] Y. Rajakarunanyake, M.C. Phillips, J.O. McCaldin, D.H. Chow, D.A. Collins and T.C. McGill, *SPIE Proc.* 1285 (1990) 142.
- [5] H. Shen and M. Dutta, *Appl. Phys. Lett.* 57 (1990) 587.
- [6] H.P. Wagner, W. Kuhn and W. Gebhardt, *J. Crystal Growth* 101 (1990) 199; H.P. Wagner, S. Lankes, K. Wolf, D. Lichtenberger, W. Kuhn, P. Link and W. Gebhardt, *J. Luminescence* 52 (1992) 41.
- [7] A. Naumov, K. Wolf, T. Reisinger, H. Stanzl and W. Gebhardt, *J. Appl. Phys.* 73 (1993) 2581.
- [8] A. Naumov, H. Stanzl, K. Wolf, A. Rosenauer, S. Lankes and W. Gebhardt, *J. Appl. Phys.* 74 (1993) 6178.
- [9] S. Permogorov and A. Reznitsky, *J. Luminescence* 52 (1992) 201.



ELSEVIER

Journal of Crystal Growth 138 (1994) 601–606

JOURNAL OF  
**CRYSTAL  
GROWTH**

## Magneto-optical study of ZnSe/(Zn,Mn)Se and ZnSe/(Zn,Cd,Mn)Se quantum well structures and superlattices

W. Heimbrodt <sup>\*,a</sup>, O. Goede <sup>†,a</sup>, V. Weinhold <sup>a</sup>, M. Happ <sup>a</sup>, R. Knoch <sup>a</sup>, K. Hieke <sup>a</sup>, N. Hoffmann <sup>b</sup>, J. Griesche <sup>b</sup>, K. Jacobs <sup>b</sup>, F. Neugebauer <sup>c</sup>, D. Suisky <sup>c</sup>, J. Röseler <sup>c</sup>

<sup>a</sup> *Institut für Optik und Spektroskopie, Fachbereich Physik, Humboldt Universität zu Berlin, Invalidenstrasse 110, D-10115 Berlin, Germany*

<sup>b</sup> *MBE - Labor, Fachbereich Physik, Humboldt Universität zu Berlin, Invalidenstrasse 110, D-10115 Berlin, Germany*

<sup>c</sup> *Institut für Theoretische Physik, Fachbereich Physik, Humboldt Universität zu Berlin, Invalidenstrasse 110, D-10115 Berlin, Germany*

### Abstract

Quantum well structures with semimagnetic barriers, ZnSe/(Zn,Mn)Se, or semimagnetic wells, (Zn,Cd,Mn)Se/ZnSe, are studied by luminescence and reflection spectroscopy in an external magnetic field up to 7.5 T. A unique offset dependence on the manganese concentration and a type conversion of the ZnSe/(Zn,Mn)Se heterostructures due to the giant Zeeman splitting of the barriers are found. In the (Zn,Cd,Mn)Se/ZnSe structures, a strong reduced energy transfer from the exciton states to the Mn internal transition was found, which is further suppressed by an increasing magnetic field. Therefore (Zn,Cd,Mn)Se quantum wells can be proposed to be suitable and effective for tuneable blue-green laser devices in an external magnetic field. The field dependent energy splitting both of well and barrier excitons are significantly anisotropic with respect to the orientation of the magnetic field **B** parallel or perpendicular to the growth axis. This magneto-optical anisotropy can be explained by the mixing of the heavy and light hole states in the framework of a multi-band envelope-function approximation.

### 1. Introduction

ZnSe-based nanostructures are becoming more important as device applications, e.g. blue laser structures [1–3], begin to be realized. Using manganese-containing mixed crystals for preparing such nanostructures, semimagnetic quantum wells and superlattices can be formed, offering a wide tuning of the exciton energies in an external magnetic field. These exciton shifts are caused by

a giant Zeeman splitting due to a strong s,p–d exchange interaction between electron and hole band states and the localized Mn<sup>2+</sup> (3d<sup>5</sup>) electron states [4,5].

In the present paper luminescence and reflection measurements are reported of ZnSe/(Zn,Mn)Se single and multiple quantum wells and (Zn,Cd,Mn)Se/ZnSe single quantum well structures. The structures were deposited on 750 or 900 nm thick ZnSe buffer layers, respectively, which were grown on (100) oriented GaAs substrates in a DCA 350 MBE system equipped with effusion cells for Zn, Cd, Mn and Se. The optimum growth temperature has been found to be

\* Corresponding author.

† Deceased.



310°C. The growth process was monitored by means of RHEED. A  $(2 \times 1)$  and a  $c(2 \times 2)$  reconstruction were always seen. The growth was interrupted under Se-rich conditions of 3 min duration in order to smooth the interface between the individual layers [6].

The first magneto-optical investigations of ZnSe/(Zn,Mn)Se MQWs and superlattices were presented some years ago [7,8]. In section 2 of the present paper, results are discussed concerning the magnetic field induced change of the band alignment and type conversion of ZnSe/(Zn, Mn)Se heterostructures, due to the recently published unique offset dependence on the manganese concentration [9]. For comparison, (Zn,Cd,Mn)Se/ZnSe quantum well structures with semimagnetic wells were investigated (section 3). A significant anisotropy of the exciton splitting was found with respect to the orientation of the magnetic field parallel or perpendicular to the normal axis of all samples (section 4).

## 2. Type conversion in an external magnetic field

(Zn,Mn)Se exhibits a band gap dependence on the manganese concentration with a strong bowing for  $x_{\text{Mn}} < 0.1$  [10,11], leading to a unique offset dependence of the ZnSe/(Zn,Mn)Se heterostructures [9]. If the concentration is high enough ( $x_{\text{Mn}} > 0.2$ ) the samples exhibit, independent on the particular strain, a type I line-up where ZnSe acts as the quantum well and (Zn,Mn)Se as the barrier. For  $x_{\text{Mn}} < 0.1$ , type II heterostructures are formed. In Fig. 1 the energy position of the ZnSe well exciton emission is shown for a series of MQW samples with well widths in the range of 0.85 to 9.1 nm in an external magnetic field. The manganese concentration in the barriers is  $x_{\text{Mn}} \approx 0.25$ . (Zn,Mn)Se exhibits an increasing lattice constant with increasing manganese concentration. The resulting opposite strain in the wells and barriers leads to an opposite splitting of the respective valence band states. The upper valence band of the ZnSe wells has a light-hole character parallel to the superlattice axis and therefore the luminescence peaks have to be ascribed to the lh exciton state.

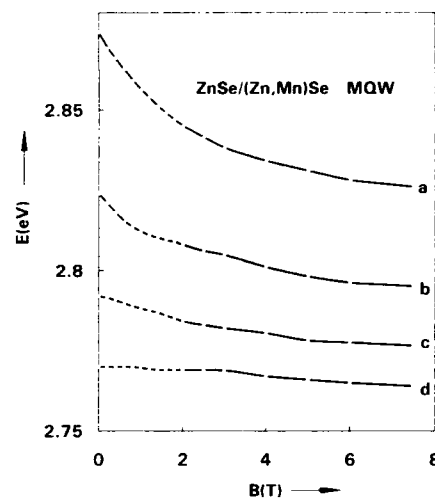


Fig. 1. Energy position of the well exciton luminescence of ZnSe/(Zn,Mn)Se MQW structures with various well widths in dependence on the external magnetic field.  $x_{\text{Mn}} = 0.25$ , barrier width  $L_b = 86$  nm, 10 wells. Well widths: (a)  $L_w = 0.85$  nm, (b) 2.85 nm, (c) 4.85 nm, (d) 9.1 nm.

A strong confinement effect for this series of samples was found, to be seen in Fig. 1 for zero field. With increasing magnetic field a shift of the exciton luminescence is observable, caused by the exchange interaction with the manganese d-states of that part of the well exciton wave function, which penetrates into the barrier. For the sample with  $L_w = 9.1$  nm nearly no shift is observable, but with a decreasing well width and therefore increasing confinement effect a stronger shift can be seen, due to the stronger delocalization of the exciton wave function.

In Fig. 2 the energy positions of the reflection spectra for ZnSe/(Zn,Mn)Se single quantum well structures are shown. The ZnSe wells had a constant thickness of about 5.1 nm, but different manganese concentrations. The thickness of the cladding layers ( $L_b = 500$  and 20 nm) made it possible to observe the well and barrier reflection signals, and therefore the Zeeman splittings of both hh exciton states are given in Fig. 2. The curves are measured in the Faraday configuration with the field parallel to the sample axis. With decreasing manganese concentration, the differences between the well and barrier exciton posi-

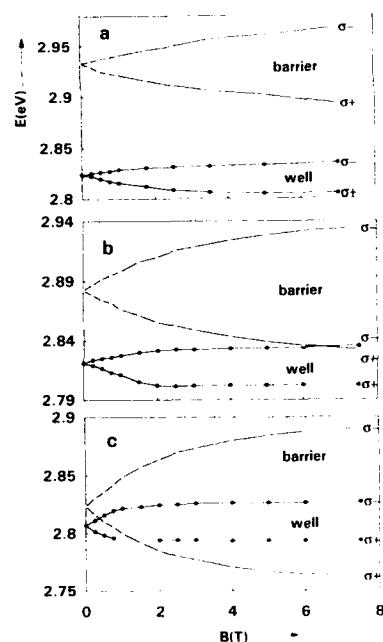


Fig. 2. Energy position of the heavy hole barrier (—) and well (●) exciton states in dependence on the external magnetic field measured by reflection spectroscopy for ZnSe/(Zn, Mn)Se SQW structures with various manganese concentrations in the barrier: (a)  $x_{\text{Mn}} = 0.28$ , (b)  $x_{\text{Mn}} = 0.21$ , (c)  $x_{\text{Mn}} = 0.12$ ; constant well width  $L_w = 5.1$  nm.

tions in zero field become smaller, as expected by the decreasing gap energy of the (Zn,Mn)Se barrier. A strong splitting between the  $\sigma^-$  and  $\sigma^+$  component is observable for the barrier hh states. The splitting is about 75 meV in Fig. 2a for a sample with  $x_{\text{Mn}} = 0.28$  in the barrier up to about 130 meV in Fig. 2c for  $x_{\text{Mn}} = 0.12$  at 7.5 T. This decrease of the Zeeman splitting with increasing manganese concentration is due to the increasing spin-glass behavior at 2 K, which reduces the amount of manganese ions which effectively take part in the exchange interaction process. A similar but weaker shift is observable for the well excitons. For the sample with  $x_{\text{Mn}} = 0.12$ , the lower energy  $\sigma^+$  branch of the hh barrier exciton intersects the  $\sigma^+$  well exciton state. This interesting behaviour is not known for CdTe/(Cd,Mn)Te quantum well structures and is caused by the band gap dependence of (Zn,Mn)Se. By two steps

the heterostructures change from a type I with ZnSe as the well into a type I line-up with (Zn,Mn)Se as the well for high magnetic fields: It is known from the offset determination published recently [9], the luminescence and reflection measurements with the observation of the expected plateau for a type I  $\rightarrow$  type II transition and especially the crossing of the  $\sigma$  and  $\sigma^+$  component (see section 4) that at first the barrier hh valence band edge crosses the well exciton state, yielding indirect excitons with the hole in the cladding layer and the electron in the former well. For higher field strengths, the conduction band edge also intersects the ZnSe electron state. Using the known exchange integrals for the conduction band  $N_0\alpha = 0.26$  eV and for the valence band  $N_0\beta = -1.31$  [12] of (Zn,Mn)Se, it is possible to calculate the shift of the valence and conduction band states separately, which gives a correspondence with all these experimental observations, using the zero field determined band offset.

### 3. Structures with semimagnetic quantum wells

For comparison, (Zn,Cd,Mn)Se/ZnSe quantum well structures with nonmagnetic ZnSe barriers, but semimagnetic quantum wells, were investigated. The Mn concentration of  $x_{\text{Mn}} = 0.085$  and Cd concentration of  $x_{\text{Cd}} = 0.25$  lead to a resulting band gap smaller than the ZnSe gap energy. Such semimagnetic quantum wells enable larger Zeeman splittings of the quantum well excitons in an external magnetic field, compared to nonmagnetic quantum wells with semimagnetic barriers. In Fig. 3 the Zeeman splitting is shown for samples with the same well composition but various well widths. The different well widths lead to different confinement effects, as can be seen in Fig. 3 for zero field. Contrary to ZnSe/(Zn,Mn)Se, we found for the smallest (Zn,Cd,Mn)Se well (Fig. 3a) a somewhat smaller Zeeman splitting compared to the wider wells (Figs. 3b and 3c). The increasing confinement effect leads to an increasing penetration of the exciton wavefunction into the ZnSe barrier, which now reduces the part of the wavefunction which really interacts with the Mn 3d states. Another differ-

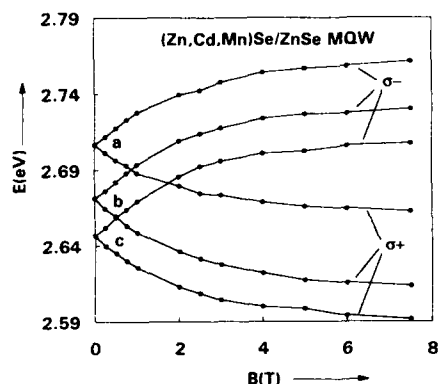


Fig. 3. Magnetic field dependence of the heavy hole exciton energies for (Zn,Cd,Mn)Se/ZnSe MQW structures with the same well composition ( $x_{\text{Mn}} = 0.085$ ,  $x_{\text{Cd}} = 0.25$ , 5 wells), but various well widths: (a)  $L_w = 4.5$  nm, (b) 8 nm, (c) 11 nm; barrier widths  $L_b = 22$  nm.

ence to ZnSe/(Zn,Mn)Se MQWs is that the typical asymmetric splitting of the well states now shows a stronger shift of the  $\sigma^-$  branch. The reason for this distinction is that the variation of the barrier height is caused in these samples by the splitting of the well bottom.

The most surprising result, however, was the observed strongly reduced energy transfer from the band exciton states to the internal manganese transitions which yield a strongly suppressed  ${}^4T_1 \rightarrow {}^6A_1$  manganese luminescence at about 2.1 eV compared to bulk semiconductors. Whereas in bulk (Zn,Cd,Mn)Se or (Zn,Mn)Se a most efficient energy transfer from the exciton and band states to the Mn 3d internal transitions occurs [5], in our semimagnetic quantum wells only a hardly detectable manganese luminescence was found. With increasing magnetic field the energy transfer is further suppressed, leading to a nearly vanishing Mn 3d luminescence. The reason for this unexpected result is not clear at the moment, because the energy transfer process from the band states to the internal manganese d-states in (II,Mn)VI semiconductors is still an open question, in spite of discussions for decades. Nevertheless, it should be connected with the increasing oscillator strength of the 1s exciton state in quantum wells and further increasing oscillator

strength with increasing magnetic field, e.g. due to the increasing barrier height for the  $\sigma^+$  component. In any case these experimental results make the (Zn,Cd,Mn)Se quaternary semiconductor an interesting material for magnetically tuneable quantum well lasers in the blue-green spectral region.

#### 4. Magneto-optical anisotropy

In Fig. 4 the Zeeman splitting of a ZnSe/(Zn,Mn)Se MQW structure is shown for the magnetic field directions parallel  $B \parallel z$  and perpendicular  $B \perp z$  to the growth axis of the sample. Although not all allowed and observable transitions for  $B \parallel z$  and for  $B \perp z$  could be clearly resolved in this sample by reflection spectroscopy, a magneto-optical anisotropy is found for both the well and the barrier states. As can be seen, strongly different splitting patterns are obtained for both field directions. For the barrier (Fig. 4a),

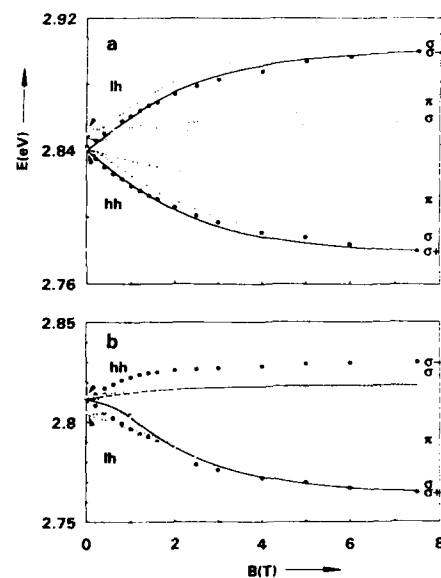


Fig. 4. Exciton energies as a function of the magnetic field  $B \parallel z$  (●, —) and  $B \perp z$  (○, ---) for the barrier (a) and wells (b) of a ZnSe/(Zn,Mn)Se MQW structure.  $L_w = 4.55$  nm,  $L_b = 75$  nm,  $x_{\text{Mn}} = 0.18$ , 10 wells; experimental points from reflection measurements; curves are calculated (see text).

the experimental peak energies with  $B \parallel z$  are shifted to lower energies compared to  $B \perp z$ . A similar behaviour was already reported for CdTe/(Cd,Mn)Te quantum well structures [13–16]. The lattice-misfit induced biaxial strain was shown to be the essential source of the magneto-optical anisotropy, leading to a strong mixing of the heavy and light hole states for the field perpendicular to the growth axis. This could be calculated in the framework of a multi-band envelope-function approximation, already successfully used for CdTe/(Cd,Mn)Te [17]. The calculated curves in Fig. 4a give good agreement with the experimental points, using only one scaling factor  $a_b(x_{Mn})$  for the effective manganese concentration. The reduction of the real Mn concentration is caused by an antiferromagnetic coupling of part of the Mn ions in the spin-glass phase. For the well states (Fig. 4b) no further fitting parameter is available. The calculations yield the right anisotropic behaviour for the well states and the right shift of the lower lying  $\sigma^+$  and corresponding  $\sigma$  levels, but the shift of the higher lying  $\sigma^-$  and  $\sigma$  levels is too small. The shift of the higher lying levels was found to be enhanced due to an enhanced paramagnetic behaviour of the Mn ions near the interface (decreasing antiferromagnetic coupling at the interface), which is the main region of interaction especially for the stronger localized  $\sigma^-$  well exciton lines.

For the well it is found that the  $\sigma^-$  component is shifted to higher energies than the corresponding  $\sigma$  component for  $B \perp z$ , which is just the opposite direction as found for the barrier. For the energetically lowest  $\sigma^+$  branch, which should normally lie above the lowest  $\sigma$  branch in the whole field range, an intersection of the  $\sigma$  branch is observable. This unusual behaviour is caused by the crossing of the (Zn,Mn)Se hh state with the hh state of ZnSe in this sample leading to a type I  $\rightarrow$  type II transition, as proved by our calculations. Due to the saturation of the s,p-d exchange interaction effect, the discussed second step (section 2) to a (Zn,Mn)Se well is not observable in this sample with 18% Mn.

It should be mentioned that sometimes for CdTe/(Cd,Mn)Te such anisotropic behaviour for the quantum wells in semimagnetic structures

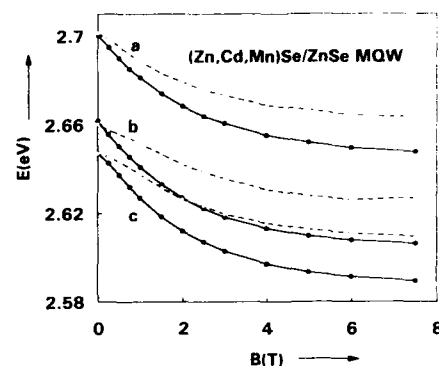


Fig. 5. Exciton luminescence of (Zn,Cd,Mn)Se/ZnSe MQW structures ( $x_{Mn} = 0.085$ ,  $x_{Cd} = 0.25$ , 5 wells) in dependence on the magnetic field direction  $B \parallel z$  (●, —) and  $B \perp z$  (○, ---). (a)  $L_w = 4.5$  nm, (b) 8 nm, (c) 11 nm; barrier widths  $L_b = 22$  nm.

was tentatively ascribed to a spin-pinning effect caused by the quasi-two-dimensional character of the well excitons [18]. The good agreement between theory and experiment, however, gives strong evidence of our explanation.

In Fig. 5 the luminescence of (Zn,Cd,Mn)Se/ZnSe quantum wells with different well widths is shown also for the two field directions parallel and perpendicular to the sample axis. In these structures the ZnSe barriers are practically unstrained; nevertheless the anisotropy for the well luminescence is observable. Now a pattern similar to that known for the CdTe/(Cd,Mn)Te heterostructures, with all branches for  $B \parallel z$  below the corresponding of  $B \perp z$  [16], was found, caused by the compressive strain in the wells.

## 5. Conclusions

The ZnSe/(Zn,Mn)Se quantum well structures show interesting new properties connected with the unique band gap dependence of (Zn,Mn)Se. Adjusting the right manganese concentration, type conversions as type I  $\rightarrow$  type II or type I  $\rightarrow$  type II  $\rightarrow$  type I are easily observable in an external magnetic field.

(Zn,Cd,Mn)Se/ZnSe is shown to be a suitable material for magnetic tuneable quantum well

lasers in the blue-green spectral range, due to a high quantum efficiency but a strong suppressed internal manganese luminescence.

It has been found that the magneto-optical anisotropy which is always present in the (II,Mn)VI nanostructures is due to the strong mixing of the hh and lh states for a magnetic field perpendicular to the sample axis.

## 6. References

- [1] A.V. Nurmikko and R.L. Gunshor, *Phys. Status Solidi (b)* 173 (1992) 291.
- [2] M.A. Haase, J. Qiu, J.M. DePuydt and H. Cheng, *Appl. Phys. Lett.* 59 (1991) 1272.
- [3] H. Jeon, J. Ding, W. Patterson, A.V. Nurmikko, W. Xie, D.C. Grillo, M. Kobayashi and R.L. Gunshor, *Appl. Phys. Lett.* 59 (1991) 3619.
- [4] J.K. Furdyna, *J. Appl. Phys.* 65 (1988) R29.
- [5] O. Goede and W. Heimbrodt, *Phys. Status Solidi (b)* 146 (1988) 11.
- [6] N. Hoffmann, J. Griesche, W. Heimbrodt, O. Goede and K. Jacobs, *J. Crystal Growth* 127 (1993) 347.
- [7] Y. Hefetz, W. Goltsos, D. Lee, A.V. Nurmikko, L.A. Kolodziejski and R.L. Gunshor, *Superlattices Microstruct.* 2 (1986) 455.
- [8] Y. Hefetz, J. Nakahara, A.V. Nurmikko, L.A. Kolodziejski, R.L. Gunshor and S. Datta, *Appl. Phys. Lett.* 47 (1985) 989.
- [9] W. Heimbrodt, O. Goede, V. Weinhold, K. Hieke, M. Happ, N. Hoffmann, J. Griesche and K. Jacobs, *Int. Conf on Luminescence*, Storrs, CT, 1993.
- [10] A. Twardowski, T. Dietl and M. Demianiuk, *Solid State Commun.* 48 (1983) 845.
- [11] L.A. Kolodziejski, R.L. Gunshor, R. Venkatasubramian, T.C. Bonsett, R. Frohne, S. Datta, N. Otsuka, R.B. Bylsma, W.M. Becker and A.V. Nurmikko, *J. Vac. Sci. Technol. B* 4 (1986) 583.
- [12] A. Twardowski, M. von Ortenberg, M. Demianiuk and R. Panthenet, *Solid State Commun.* 51 (1984) 849.
- [13] A.V. Nurmikko, X.C. Zhang, S.K. Chang, L.A. Kolodziejski, R.L. Gunshor and S. Datta, *Surf. Sci.* 170 (1986) 665.
- [14] L.L. Chang, *Superlattices Microstruct.* 6 (1989) 39.
- [15] O. Goede, W. Heimbrodt, Th. Köpp, H.-E. Gumlich, B. Lunn and D.E. Ashenford, *Phys. Status Solidi (b)* 166 (1991) 531.
- [16] O. Goede and W. Heimbrodt, *Festkörperprobleme (Adv. Solid State Phys.)* 32 (1992) 237.
- [17] F. Neugebauer, J. Röseler, D. Suisky, S. Rex, O. Goede, W. Heimbrodt and B. Lunn, in: *Proc. 21st Int. Conf on the Physics of Semiconductors*, Beijing, 1992, Vol. 1 (World Scientific, Singapore, 1992) p. 875.
- [18] E. Vornberger, W. Ossau, A. Waag, R.N. Bicknell-Tassius and G. Landwehr, in: *Proc. 21st Int. Conf. on the Physics of Semiconductors*, Beijing, 1992, Vol. 2 (World Scientific, Singapore, 1992) p. 1569.



ELSEVIER

Journal of Crystal Growth 138 (1994) 607–611

JOURNAL OF  
CRYSTAL  
GROWTH

## Electron-gas screening of the piezoelectric fields in indium-doped (211) CdTe/Cd<sub>1-x</sub>Zn<sub>x</sub>Te quantum wells

F. Bassani<sup>a,1</sup>, K. Kheng<sup>b</sup>, M. Mamor<sup>a</sup>, R.T. Cox<sup>b</sup>, N. Magnea<sup>b</sup>, K. Saminadayar<sup>b,\*</sup>, S. Tatarenko<sup>a</sup>

<sup>a</sup> Laboratoire de Spectrométrie Physique, CNRS Université Joseph Fourier, BP 87, F-38402 Saint-Martin-d'Hères, France

<sup>b</sup> Département de Recherche Fondamentale sur la Matière Condensée, SP2M/PSC, CENG, 17 Rue des Martyrs, F-38054 Grenoble Cedex 9, France

### Abstract

Indium donor doping of piezoelectric (211)B CdTe/Cd<sub>1-x</sub>Zn<sub>x</sub>Te multiple quantum wells by molecular beam epitaxy has been achieved. The effect of uniform doping of the Cd<sub>1-x</sub>Zn<sub>x</sub>Te barriers or delta-doping of the CdTe wells on the strain-induced piezoelectric fields in the wells was studied using low temperature luminescence spectroscopy. Doping in the barriers produces an electron-gas in the well which partially screens the piezoelectric field. Screening is also observed for structures delta-doped in the CdTe well, provided the indium plane is located so that the piezoelectric field separates the electrons from the donor cores.

### 1. Introduction

Epitaxial growth of compound semiconductors on polar orientations like (111) and (211) can yield remarkable new electronic and optical properties due to the strain-induced piezoelectric fields [1]. In CdTe/CdZnTe heterostructures coherently grown along (111) by molecular beam epitaxy (MBE), the strains resulting from lattice mismatch induce very large piezoelectric fields, which profoundly modify the electronic band structure [2]. However, while high quality growth on (111) is difficult to achieve, excellent results have been reported for MBE growth of II–VI materials on the (211)B face [3]. The major ad-

vantage of the (211) over the (111) orientation is that twin defects do not form on the (211) orientation, because the symmetry is broken: the (211) surface can be viewed as a (111) surface misoriented 19°47' toward (001). Thus, we have found that by growing CdTe/CdZnTe heterostructures on (211), one can study piezoelectric effects while retaining the high structural and optical quality usually associated only with the (100) orientation.

Controlled doping of such piezoelectric structures is of particular interest because one can study effects of free carriers on the built-in electric fields which may provide new possibilities for electro-optic modulation [4]. The following experiments will be presented in this paper: (i) indium doping of (211)B CdTe epilayers, (ii) uniform doping of the Cd<sub>1-x</sub>Zn<sub>x</sub>Te barriers and (iii) delta-doping of the CdTe wells of CdTe/Cd<sub>1-x</sub>Zn<sub>x</sub>Te ( $x < 10\%$ ) quantum wells (QWs). In the last two experiments, the screening of the

\* Corresponding author.

<sup>1</sup> Present address: CRMC<sup>2</sup>-CNRS, Campus de Luminy, Case 912, F-13288 Marseille Cedex 09, France.

strain-induced piezoelectric field by the electron-gas has been demonstrated.

## 2. Indium doping of (211) oriented CdTe layers

Up till now, studies of n-type doping of CdTe by MBE have mainly been done on the (001) surface. It is well-established that for this orientation essentially 100% activation is obtained in the  $10^{16}$ – $10^{18}$  cm $^{-3}$  range, at growth temperatures of 200–240°C, using photoassistance [5] or provided a cadmium overpressure is maintained during growth [6,7]. In the present work, the (211) CdTe:In layers were grown by MBE on (211)B CdZnTe (4% Zn) substrates. The growth is done at 240°C, using only CdTe and In cells, that is without excess Cd, contrarily to the case of (001) CdTe layers [7].

As compared to CdTe epilayers grown on tilted (111) substrates [8], transmission electron microscopy (TEM) at 200 and 400 keV shows that a 2  $\mu$ m thick (211) CdTe layer presents much better crystalline quality: in particular, the dislocation density of the (211) layer is much lower, probably because the high density of steps on the (211) surface inhibits the propagation of the dislocations into the epilayer [9].

The indium content ( $N_{\text{In}}$ ) and the carrier concentrations ( $n = N_{\text{D}} - N_{\text{A}}$ ) of the doped layers were obtained from secondary ion mass spectroscopy (SIMS), calibrated with an indium implanted layer, and from room temperature capacitance-voltage measurements, respectively. Comparison between results of these two techniques indicates that, for doping levels in the  $3 \times 10^{15}$ – $7 \times 10^{17}$  cm $^{-3}$  range, we obtain  $n = N_{\text{In}}$  within the total measurement precision of about 20%, i.e., an electrical activation efficiency close to 1. Transport properties of the doped layers were deduced from temperature dependent Hall-effect measurements. For a sample In-doped at  $n = 3 \times 10^{15}$  cm $^{-3}$  (which is the lowest doping level that can be achieved reproducibly because the minimum background acceptor concentration is  $N_{\text{A}} \approx 10^{15}$  cm $^{-3}$ ), the mobility attains a maximum value of 7300 cm $^2$ /V·s at 40 K. This is amongst the highest reported values for doped, and even for undoped [10] MBE grown (001) CdTe.

The photoluminescence (PL) spectra of the In-doped (211) CdTe layers are very similar to spectra obtained for In-doped (001) CdTe samples having the same doping level [7]. Up to  $n \approx 7 \times 10^{17}$  cm $^{-3}$  doping level, there is no or very little trace of the deep-centre emission at  $\approx 1.45$  eV which is generally attributed to compensation effects [11].

The growth conditions defined by doping (211)B CdTe have been used for the growth of “modulation-doped” Cd $_{1-x}$ Zn $_x$ Te/CdTe QWs. An additional ZnTe cell is used to obtain the Zn alloy composition. In these structures, indium doping is used to produce an electron-gas in the CdTe wells; thus a screening of the strain-induced piezoelectric field can be expected, as now described.

## 3. Uniform doping of the barriers in Cd $_{1-x}$ Zn $_x$ Te/CdTe ( $x = 8\%$ ) quantum wells

Two structures were grown on 2  $\mu$ m thick, strain-relaxed Cd $_{0.92}$ Zn $_{0.08}$ Te buffer layers, on (211)B Cd $_{0.96}$ Zn $_{0.04}$ Te substrates. Each structure consists of five CdTe wells (1, ..., 5) with thicknesses 20, 40, 80, 120 and 240 Å respectively, separated by 1500 Å thick CdZnTe barriers having the same composition as the buffer layer. As no RHEED (reflection high energy electron diffraction) oscillations are observed on (211) surfaces, the quantum well thicknesses were deduced from the CdTe growth rate (1.5 Å/s), calibrated from TEM micrographs of CdTe layers grown previously.

The energy of the luminescence peaks of the five wells are plotted as a function of the width  $L_{\text{w}}$  in Fig. 1. The sample labelled ZD 116 is undoped (curve a), while sample ZD 114 is uniformly doped in the barriers (“modulation doping”) with  $6 \times 10^{16}$  In cm $^{-3}$  (curve b), except in 50 Å spacer layers at each side of the CdTe wells to avoid diffusion of the indium into the CdTe wells.

The 0.46% mismatch between the lattice parameters of CdTe and the Cd $_{0.92}$ Zn $_{0.08}$ Te buffer induces very high strain in the CdTe layers, which produces a piezoelectric potential gradient across each well (diagram at top right in Fig. 1). The

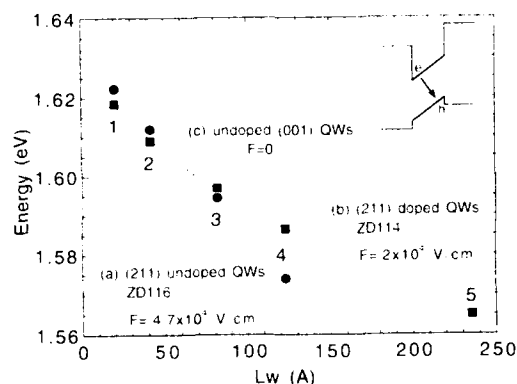


Fig. 1. Energy of the luminescence peak as a function of the quantum well-width  $L_w$ : (a) undoped (211)B QWs; (b) doped (211) QWs with uniformly indium doped barriers ( $n = 6 \times 10^{16} \text{ cm}^{-3}$ ); (c) calculated exciton energies for undoped (001) QWs.

electron-hole recombination luminescence peaks of the (211) QWs are then displaced to low energy (Figs. 1a and 1b) with respect to recombination energies for equivalent (001) QWs (Fig. 1c), that is non-piezoelectric QWs) [12]. In the limit of large well width  $L_w$ , the piezoelectric red-shift is approximately the potential change across the well width, that is  $F \times L_w$ , where  $F$  is the piezoelectric field [2]. For the undoped (211) QWs (curve a), the peaks lie on a straight line from which we determine  $F \approx 4.7 \times 10^4 \text{ V cm}^{-1}$ . Such a field completely separates the electron and the hole in the thickest well 5, completely quenching its luminescence [9].

In the modulation-doped (211) structure (Fig. 1b), for the thicker wells (3, 4 and 5) the luminescence peaks are shifted towards the theoretically calculated exciton energies for an equivalent (001) structure (Fig. 1c), luminescence peak 5 being readily detectable now. For the narrowest wells 1 and 2, any effect is of the order of the uncertainty in the structure parameters. For the broadest well 5, we deduce that the actual average field in the modulation-doped well is  $F \approx 2 \times 10^4 \text{ V cm}^{-1}$ ; thus compared to an undoped (211) QW, a screening factor of  $\approx 60\%$  has been obtained for this well. Such a reduction of the piezoelectric field separating electrons and holes explains why

the luminescence is now readily visible even for well 5 [9].

#### 4. Delta doping of the wells in $\text{Cd}_{1-x}\text{Zn}_x\text{Te}/\text{CdTe}$ ( $x = 6\%$ ) quantum wells

Another way to screen the strain-induced piezoelectric field can be the introduction of an electron-gas by doping right inside the wells. This is made possible using the delta-doping technique [7]. The piezoelectric field can ionize the donors in the well, producing an electron-gas which in turn screens the piezoelectric field. As seen in the conduction band diagram b in Fig. 3, this unique situation occurs when the indium plane is placed at the high potential side of the CdTe well. On the other hand, if the indium plane is located at the low potential side (diagram a in Fig. 3) the donor impurities stay neutral and no screening occurs.

We have made a comparative study of two delta-doped (211)  $\text{CdTe}/\text{Cd}_{0.94}\text{Zn}_{0.06}\text{Te}$  QW structures. An indium plane ( $2 \times 10^{11} \text{ In cm}^{-2}$ ) is placed at 3 monolayers ( $\approx 10 \text{ Å}$ ) from the barrier/well interface, either at the substrate side (ZD 147) or at the surface side (ZD 146). The barriers are undoped. The structures are grown on  $2 \mu\text{m}$  thick, strain-relaxed  $\text{Cd}_{0.94}\text{Zn}_{0.06}\text{Te}$  buffer layers, on (211)B  $\text{Cd}_{0.96}\text{Zn}_{0.04}\text{Te}$  substrates. Each structure consists again of five QWs (1, ..., 5). The thicknesses are 28, 56, 112, 168 and  $329 \text{ Å}$ , respectively (with the  $28 \text{ Å}$  well nearest the surface), separated by  $750 \text{ Å}$  thick CdZnTe barriers having the same composition as the buffer layer; thus only the wells are stressed.

We used SIMS profiling of the In, with profiling of the Zn atoms of the barriers as a reference, to check the position of the In in the CdTe wells, see Fig. 2. Since the depth resolution of this technique ( $\approx 50 \text{ Å}$ ) [7] is comparable to the widths of the narrowest wells, the off-centre position of the In plane can be detected for wells 4 and 5 only ( $L_w = 168$  and  $329 \text{ Å}$ ). An apparent broadening of the profiles is observed as we pass from the upper well 1 to the deepest well 5, representing the well-known decrease of the SIMS resolution in deep profiling. However, it can be seen



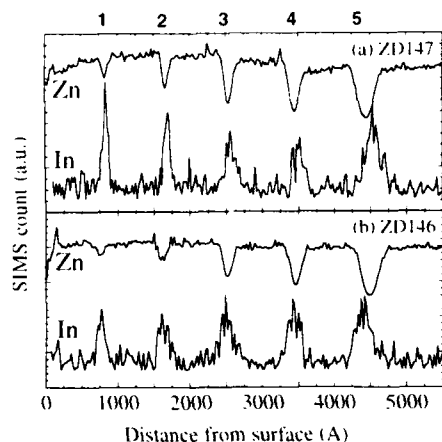


Fig. 2. SIMS (Xe: 1.6 keV) profiles for Zn and In in two (211)B structures, each consisting of five QWs. An indium plane is introduced at 3 monolayers ( $\approx 10$  Å) from each barrier (a) on the substrate side or (b) on the surface side of the QWs.

that the indium dopant plane is indeed localized at the substrate side of the wells for sample ZD 147 (curve a) and at the surface side for sample ZD 146 (curve b).

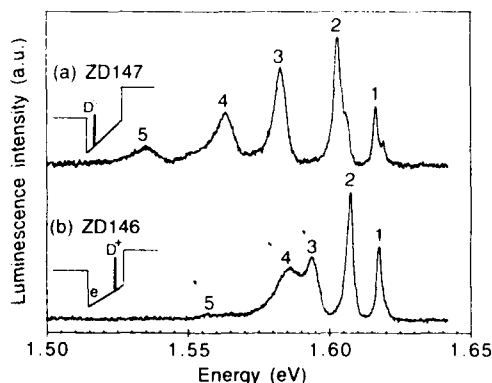


Fig. 3. 2 K photoluminescence spectra for two CdTe/Cd<sub>0.94</sub>Zn<sub>0.06</sub>Te structures grown at 240°C on 2 μm thick relaxed Cd<sub>0.94</sub>Zn<sub>0.06</sub>Te buffer layers (on (211)B Cd<sub>0.96</sub>Zn<sub>0.04</sub>Te substrates). Each structure consists of five CdTe wells (1,...,5, with thicknesses 28, 56, 112, 168 and 329 Å respectively), separated by 750 Å thick CdZnTe barriers. The QWs have an indium plane located at 3 monolayers ( $\approx 10$  Å) from each barrier, (a) on the substrate side or (b) on the surface side.

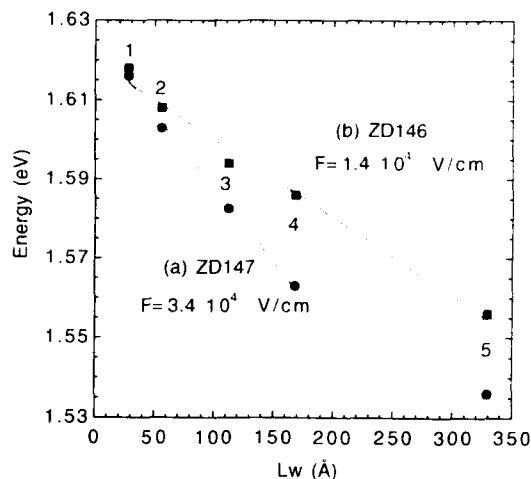


Fig. 4. Energy of the luminescence peaks of Fig. 3 as a function of the well-width  $L_w$ . The QWs have an indium plane located at 3 monolayers ( $\approx 10$  Å) from each barrier, (a) on the substrate side or (b) on the surface side. The lines have been drawn to estimate the effective electric field value  $F$  in the wells.

Fig. 3 shows 2 K PL spectra for these two structures. As compared to sample ZD 147 (spectrum a), a shift of the luminescence peaks toward higher energy is observed for wells 2, 3, 4 and 5 of sample ZD 146 (spectrum b). For the narrowest wells 1, since the In planes are located almost at the centre of the wells, there is no marked difference in the luminescence peak positions.

As in the preceding section, the screening phenomenon can be analysed using plots of the luminescence peak position as a function of the CdTe well width  $L_w$ . This is shown in Fig. 4. From the slope of the luminescence peak positions for wells 1 to 4 of sample ZD 147 (curve a), we deduce a piezoelectric field  $F \approx 3.4 \times 10^4$  V cm<sup>-1</sup>. In fact, if we take into account the difference in the Zn composition of the barriers ( $x = 6\%$  here instead of 8% for the undoped (211) QWs ZD 114 of section 3), this electric field value corresponds approximately to the value determined for the undoped (211)B QWs (Fig. 1). This shows that, when the indium plane is localized on the substrate side of the wells (see the conduction band diagram a in Fig. 3), there is no spatial separation of the electrons and the fixed donor cores (In<sub>Cd</sub><sup>+</sup>).

the absence of change in the strain-induced piezoelectric field of this doped (211) structure indicates that in such a configuration, i.e. donor impurities stays neutral.

The same treatment applied to structure ZD 146 (Fig. 4, curve b) yields  $F \approx 1.4 \times 10^4 \text{ V cm}^{-1}$  as an average effective field in the wells of this structure. Thus, as compared to an undoped (211) structure, a screening of the piezoelectric field is observed; the screening factor ( $\approx 60\%$ ) is quite comparable to that observed in the broader (211) wells with doped barriers (ZD 114 in section 3). It can be interpreted as a migration of the electrons toward the low potential side of the well, with the ionized donors  $\text{In}_{\text{Cd}}^+$  remaining fixed at the other side (see the conduction band diagram b in Fig. 3). This configuration of the charges induces a supplementary electric field which partially compensates the original strain-induced piezoelectric field.

Since, in the latter sample (conduction band diagram b in Fig. 3), the In plane is located in the surface side of the well, our results are coherently explained assuming that the strain-induced piezoelectric field is directed from the substrate toward the surface of the structure. More generally our experiment can be used as a method to determine the direction of the strain-induced piezoelectric field in (211) and (111) semiconductors. In particular, the result obtained here confirms that in this II–VI material the piezoelectric strain-coupling coefficient has opposite sign to that observed in GaAs/GaInAs.

## 5. Conclusion

Modulation doping of  $\text{CdTe}/\text{Cd}_{1-x}\text{Zn}_x\text{Te}$  ( $x = 6\text{--}8\%$ ) QWs on (211)B  $\text{Cd}_{0.96}\text{Zn}_{0.04}\text{Te}$  substrates has been achieved. Electronic screening in the modulation-doped QWs is detected as a reduction of the piezoelectric-induced shift of the luminescence peaks. Strong screening of the internal piezoelectric field has been demonstrated for QWs with uniformly doped barriers. Delta-doping of the wells of the QWs induces a screening of the piezoelectric field only when this field separates totally the electrons from the donor

cores, that is when the indium plane is located in the high potential side of the wells (the surface side for growth on (211)B). When the indium plane is placed at the substrate side, the donors stay neutral and no screening is observed.

## 6. Acknowledgement

Thanks are due to B. Blanchard (CEREM-CEA, Grenoble, France) for SIMS profile measurements.

## 7. References

- [1] D.L. Smith and C. Mailhot, *Rev. Mod. Phys.*, **62** (1990) 173.
- [2] J. Cibert, R. André, C. Deshayes, Le Si Dang, H. Okumura, S. Tatarenko, G. Feuillet, P.H. Jouneau, R. Mallard and K. Saminadayar, *J. Crystal Growth* **117** (1992) 421.
- [3] See, for example, J.M. Arias, M. Zandian, R. Zucca and R.E. DeWames, *Appl. Phys. Lett.* **58**, 2806 (1991); M.D. Lange, R. Sporken, K.K. Mahavadi and J.P. Faurie, *Appl. Phys. Lett.* **58** (1991) 1988, and references therein.
- [4] E.A. Caridi, T.Y. Chang, K.W. Goosen and L.F. Eastman, *Appl. Phys. Lett.* **56** (1990) 659.
- [5] Y.S. Wu, A. Waag and R.N. Bicknell-Tassius, *Appl. Phys. Lett.* **57** (1990) 1754, and references therein.
- [6] D.E. Ashenford, J.H. Hogg, D. Johnson, B. Lunn, C.G. Scott and D. Staudte, *J. Crystal Growth* **101** (1990) 157.
- [7] F. Bassani, S. Tatarenko, K. Saminadayar, J. Bleuse, N. Magnea and J.L. Pautrat, *Appl. Phys. Lett.* **58** (1991) 2651; F. Bassani, S. Tatarenko, K. Saminadayar, N. Magnea, R. Cox, A. Tardot and C. Grattapain, *J. Appl. Phys.* **72** (1992) 2927.
- [8] S. Tatarenko, F. Bassani, K. Saminadayar, R.T. Cox, P.H. Jouneau and N. Magnea, *J. Crystal Growth* **127** (1993) 318.
- [9] F. Bassani, S. Tatarenko, K. Zheng, P.H. Jouneau, K. Saminadayar, N. Magnea and R. Cox, *Appl. Phys. Lett.* **63** (1993) 2106.
- [10] S. Hwang, R.L. Harper, K.A. Harris, N.C. Giles, R.N. Bicknell, J.F. Schetzina, D.L. Dreifus and M. Kolbas, *J. Vac. Sci. Technol. B* **6** (1988) 777.
- [11] B.K. Meyer, W. Stadler, D.M. Hofmann, P. Omling, D. Sinerius and K.W. Benz, *J. Crystal Growth* **117** (1992) 656.
- [12] Note that as  $I_{\text{ex}} \rightarrow 0$ , the luminescence energy extrapolates, as it should, to the energy of an exciton in the CdZnTe barrier (point at  $I_{\text{ex}} = 0$  in Fig. 1, taken from the sample's reflectivity spectrum).



ELSEVIER

JOURNAL OF **CRYSTAL  
GROWTH**

Journal of Crystal Growth 138 (1994) 612–618

## Optical and X-ray analysis of $\text{ZnS}_x\text{Se}_{1-x}/\text{ZnSe}$ superlattices grown on GaAs by metalorganic vapour phase epitaxy

J. Hermans <sup>\*,a</sup>, J. Woitok <sup>a</sup>, W. Schiffrers <sup>a</sup>, J. Geurts <sup>a</sup>, A. Schneider <sup>b</sup>, M. Scholl <sup>b</sup>,  
J. Söllner <sup>b</sup>, M. Heuken <sup>b</sup>

<sup>a</sup> *I. Physikalisches Institut der RWTH Aachen, Aachen University of Technology, Sommerfeldstrasse 28, D-52056 Aachen, Germany*

<sup>b</sup> *Institut für Halbleitertechnik, RWTH Aachen, Templergraben 55, D-52056 Aachen, Germany*

### Abstract

X-ray diffractometry, Raman backscattering and photoluminescence were applied to characterize  $\text{ZnS}_x\text{Se}_{1-x}/\text{ZnSe}$  superlattices, grown on GaAs(100) by metalorganic vapour phase epitaxy (MOVPE). As sulphur precursor materials diethylsulphide (DES) and  $\text{H}_2\text{S}$  were compared. Furthermore, we investigated the influence of different kind of buffer layers, the effect of increasing the number of periods and the consequences of stabilization during growth interruptions. Superlattices with a high crystal quality and very regular periodicity were obtained for 120-period structures, grown with DES as precursor, without intentional buffer layer. They show very narrow folded acoustical phonons in the Raman spectrum and their X-ray diffraction pattern contains not only sharp satellite peaks, whose fine structure reveals monolayer fluctuations, but also fringes which are due to interference from the entire stack.

### 1. Introduction

The main motivation for ZnSe and  $\text{ZnS}_x\text{Se}_{1-x}$  epitaxial layers is their potential application in optoelectronic devices such as light emitting diodes (LEDs) and laser diodes in the blue to ultraviolet, since through the sulphur content their bandgap can be tuned in this range. Furthermore, for low S contents they are nearly lattice matched to GaAs. Besides  $\text{ZnS}_x\text{Se}_{1-x}$  epitaxial heterostructures, also  $\text{ZnS}_x\text{Se}_{1-x}/\text{ZnSe}$  superlattices are essential, especially for laser applications, due to their versatile tunability of the effective energy gap and because their carrier

confinement should reduce the threshold current. Recently, the development of pulsed room-temperature Cd-based quantum well lasers by molecular beam epitaxy (MBE) in the blue-green spectral region has been reported [1]. As an alternative to MBE, also MOVPE is applied for the epitaxial growth of  $\text{ZnSe}/\text{ZnS}_x\text{Se}_{1-x}$  superlattice structures. The optimization of these structures requires the exact knowledge of the crystalline quality, layer thicknesses, composition, interface sharpness and strain profile.

In this work we discuss the application of optical spectroscopy and X-ray diffractometry for the analysis of these properties. As optical spectroscopy methods we applied Raman spectroscopy and photoluminescence. In Raman spectroscopy we used the inelastic light scattering by

\* Corresponding author.

optical as well as acoustical phonons for the evaluation of the sulphur content, the lattice quality and the periodicity. Photoluminescence allows the determination of electronic energy levels in the superlattices. In X-ray diffraction the zero-order diffraction peak of the superlattice and its satellites reflect the structural quality, the average strain and the periodicity.

## 2. Experimental procedure

### 2.1. Sample growth

The  $\text{ZnS}_x\text{Se}_{1-x}/\text{ZnSe}$  strained-layer superlattice structures were grown on  $2^\circ$  misoriented (100) GaAs substrates by atmospheric-pressure MOVPE at  $480^\circ\text{C}$ , using  $\text{DEZn}$ ,  $\text{DESe}$ , and  $\text{H}_2\text{S}$  or  $\text{DES}$  as precursors. Further details are given in ref. [2]. Throughout this paper, the thicknesses of the  $\text{ZnSe}$  and  $\text{ZnS}_x\text{Se}_{1-x}$  layers are designated  $d_1$  and  $d_2$ , respectively. The periodicity  $d = d_1 + d_2$  was between 10 and 20 nm with up to 120 periods, while the nominal sulphur content  $x$  was varied between 0.10 and 0.15. In order to improve the layer quality by surface migration of the reactants, an interruption time  $t_p$  between the growth of the constituent layers was introduced, which was varied up to 20 s. For some samples we stabilized the freshly grown  $\text{ZnS}_x\text{Se}_{1-x}$  layers by sulphur and selenium precursor flow during these growth interruptions.

### 2.2. Analysis

The X-ray studies were carried out with a homemade double-crystal system with  $\text{Si}(004)$  first crystal and  $\text{Cu K}\alpha_1$  radiation. We used a X-ray beam size of  $0.08 \times 4 \text{ mm}^2$ . All measurements were performed in the  $\omega$ - $2\theta$  mode with a step width of  $0.001^\circ$  ( $3.6''$ ) in the vicinity of the (004) GaAs reflection. An aperture in front of the detector limited the acceptance angle range to  $1^\circ$ . For compensation of the substrate misorientation, the scattering vector was carefully aligned in the plane of diffraction. The miscut edge was adjusted perpendicular to the beam directions. Scans have been recorded for two settings with

$180^\circ$  difference in azimuthal angle around  $\langle 001 \rangle$  of the substrate to determine the offset angle and to check for the tilt of the SLs with respect to the substrate. The experimental diffraction curves were finally analyzed by applying the dynamical theory of X-ray diffraction [3] yielding the chemical composition as well as the thickness of the individual epilayers of the superlattice.

Photoluminescence measurements have been performed in the temperature region between 12 and 300 K, using a HeCd laser with an excitation wavelength of 325 nm. For this laser line the penetration depth in ZnSe is about 110 nm. The spectra were recorded with a Spex 1704 monochromator of 1 m focal length, equipped with a GaAs photomultiplier. The spectral resolution is better than  $0.03 \text{ nm}$ .

The Raman scattering measurements were performed in near-backscattering geometry with an argon ion laser as excitation light source. The laser power was kept below  $30 \text{ mW}$ , while the focus diameter was about  $60 \mu\text{m}$ . The Raman spectra were obtained by using a double monochromator (Spex 1403). In the acoustical-phonon region, spectra were recorded between 5 and  $20 \text{ cm}^{-1}$  at room temperature and at 80 K, using a GaAs photomultiplier for detection and the 465.8 and 458 nm laser lines for excitation. Especially the latter line leads to a resonant enhancement of the scattering efficiency. Also at 300 K, the samples were held in vacuum in order to suppress spurious low-frequency Raman lines from atmospheric  $\text{N}_2$  rotational transitions. The optical-mode region between 190 and  $350 \text{ cm}^{-1}$  was investigated at 80 K with the 476.5 nm laser line. Here we used a multichannel detector system (EG&G 1461). For all measurements the spectral accuracy is  $\pm 0.1 \text{ cm}^{-1}$  with an instrumental spectral peak width of about  $1 \text{ cm}^{-1}$ .

## 3. Results and discussion

For the optical region the lattice vibration frequencies of the superlattice and the underlying substrate are between  $200$  and  $350 \text{ cm}^{-1}$ . Fig. 1 shows typical Raman spectra of 120-period  $\text{ZnS}_{0.1}\text{Se}_{0.9}/\text{ZnSe}$  SLs grown with DES and  $\text{H}_2\text{S}$ .

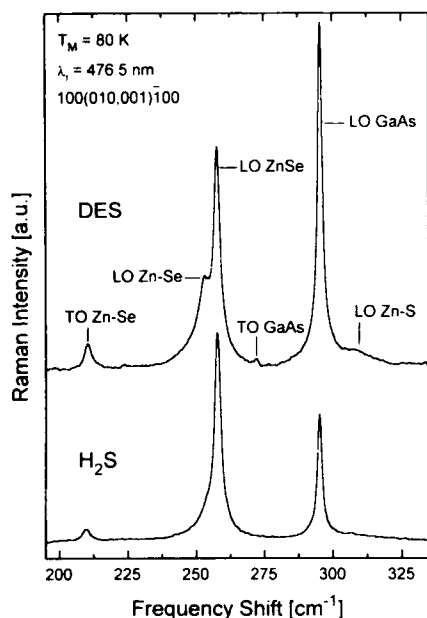


Fig. 1. Raman spectra of  $\text{ZnS}_{0.1}\text{Se}_{0.9}/\text{ZnSe}$  superlattices, consisting of 120 periods, grown with DES and  $\text{H}_2\text{S}$ , respectively, measured at 80 K in the optical phonon frequency region.

respectively and otherwise identical growth parameters. The polarization configuration in the Raman experiment was  $100(010, 001)\bar{1}00$ . In this configuration the deformation-potential scattering from LO phonons is allowed, while the TO phonon scattering is forbidden [4]. Besides the strong symmetry-allowed LO phonon from the GaAs substrate at  $296\text{ cm}^{-1}$  and the corresponding weak symmetry-forbidden TO phonon at  $272\text{ cm}^{-1}$ , we observe in the case of the DES-grown sample the LO phonon from the binary ZnSe at  $257.5\text{ cm}^{-1}$  and three vibration modes from the ternary ZnSSe: the Zn-Se LO, the Zn-S LO and Zn-Se TO vibration at  $252.8$ ,  $308.3$  and  $210.3\text{ cm}^{-1}$ , respectively. The occurrence of two LO peaks is typical for the two-mode behaviour of the  $\text{ZnS}_x\text{Se}_{1-x}$  mixed crystal [5]. The sharpness of the symmetry-allowed ZnSe LO phonon peak (full width at half maximum,  $\text{FWHM} \approx 2.5\text{ cm}^{-1}$ ) and the weakness of the symmetry-forbidden ZnSe TO peak reveal the good quality of the

layers. The broadening of the Zn-Se and Zn-S LO vibrational peaks of  $\text{ZnS}_x\text{Se}_{1-x}$  and the increased TO/LO ratio are inherent to the intrinsic alloy disorder in ternary layers. From the frequency shift of the ZnSe LO phonon ( $1.0\text{ cm}^{-1}$  with respect to bulk ZnSe) we conclude that the binary layers are biaxially compressive strained, which is consistent with pseudomorphic growth on the GaAs substrate, whose relative lattice constant difference to ZnSe is  $-0.27\%$  [6]. For the Zn-Se LO vibration of ZnSSe, there is a frequency shift due to the incorporated sulphur and an additional shift due to strain, which, of course, is correlated with the sulphur content. In order to separate these coupled effects quantitatively, we performed a selfconsistent calculation. Assuming pseudomorphic growth, we deduced a sulphur content of  $10\%$  for the ternary layers. For the  $\text{H}_2\text{S}$ -grown sample, the Raman spectrum shows a broadened, weak ternary Zn-Se mode at the low-frequency side of the binary LO ZnSe phonon and an increase of the TO/LO intensity ratio of the ternary peaks. This typical behaviour for  $\text{H}_2\text{S}$ -grown samples indicates an inferior quality with respect to the DES-grown samples.

For the study of the acoustical branches, the spectral region below  $40\text{ cm}^{-1}$  is of interest. In a superlattice, the bulk Brillouin zone is replaced by a smaller one because of the increased artificial periodicity along the growth direction [7]. As a result, the original acoustical phonon branch is folded, resulting in a series of eigenfrequencies in the low  $k$ -vector region, which are accessible to light scattering. Fig. 2 shows corresponding Raman spectra of DES-grown samples, taken for the polarization configuration  $100(010, 010)\bar{1}00$ . Besides a strong background, due to diffuse reflected laser light, two peaks are observed, which are assigned to the first-order longitudinal zone-folded doublet modes. From the observed folded-LA frequencies of the lower curve we evaluated the period thickness to  $9.8 \pm 0.5\text{ nm}$ . The peaks are sharp with a FWHM below  $2\text{ cm}^{-1}$ , which proves the well-defined periodicity, agreeing well with the X-ray results which are discussed below. For this superlattice the second-order peaks are forbidden due to the almost identical well and barrier thickness ( $d_1 = 4.7\text{ nm}$ ,  $d_2 = 4.8\text{ nm}$ , as

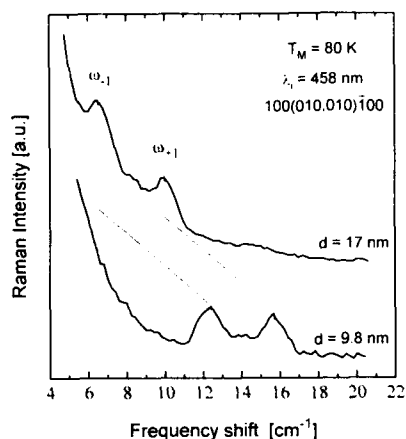


Fig. 2. Low-frequency Raman spectra for DES-grown  $\text{ZnS}_{0.1}\text{Se}_{0.9}/\text{ZnSe}$  superlattices with different periodicity lengths, showing folded acoustical phonon peaks.

derived from X-ray diffractometry results below). The upper curve shows the spectrum of a SL with a larger periodicity; we evaluated the period thickness to  $17 \pm 0.5$  nm. As can be seen from Fig. 2, the frequencies of the folded acoustical phonon (FAP) modes depend strongly on the superlattice periodicity  $d$ . For  $\text{H}_2\text{S}$ -grown samples, the folded acoustical phonons appear only very weakly, indicating a less homogeneous periodicity.

In order to suppress possible sulphur desorption from the ternary layers, which might occur during the growth interruptions,  $\text{ZnS}_x\text{Se}_{1-x}$ -to- $\text{ZnSe}$  interfaces were stabilized with  $\text{H}_2\text{S}$  and  $\text{DESe}$ . The Raman analysis of the stabilized samples shows a larger frequency shift of the ternary vibrations, from which a strong enhancement of the sulphur incorporation was deduced: we obtained 27%, while the nominal value was only 14%. The peak halfwidths of the LO modes in the optical region are larger as compared to the unstabilized samples. Furthermore, the stabilized superlattices show a weakening of the folded acoustical phonons, probably due to the formation of misfit dislocations caused by the large lattice mismatch between the SL stack and the substrate, as a result of the unintentional high sulphur content in the ternary layers. Therefore,

when stabilization is applied, the partial pressure of the S precursor during growth should be reduced appropriately.

In the investigation of the influence of different kind of buffers, optical and acoustical Raman spectra of a superlattice stack, grown on a  $1 \mu\text{m}$  thick  $\text{ZnS}_{0.1}\text{Se}_{0.9}$  buffer, show no significant improvement as compared to a sample without intentional buffer layer. For the same structure grown on a ZnSe buffer, the phonon halfwidths broaden and the intensity of the elastically scattered light increases, probably due to a relaxation of the superlattice, since the ZnSe buffer leads to an increased strain in the  $\text{ZnS}_x\text{Se}_{1-x}$  layers of the superlattice. Moreover, the ZnSe LO frequency in the buffer indicates that the buffer layer is not fully relaxed. Therefore it may contain a considerable concentration of dislocations.

In order to determine the influence of the stack thickness, we compared a rather thick superlattice (nominally  $5/5$  nm,  $120 \times$ ) with a thinner stack ( $2.5/2.5$  nm,  $120 \times$ ), both grown with the  $\text{H}_2\text{S}$  precursor and otherwise identical parameters. We observed folded acoustical phonons only for the thicker sample, which indicates that the upper layers have a better quality and periodicity than the underlying ones. However, for samples grown with DES, the folded acoustical phonons were observed already for a thin sample, thus confirming the superiority of this precursor material.

Confined optical ZnSe LO phonons and Zn–Se LO modes were not observed, probably because of a missing frequency gap between the binary and ternary phonon dispersion curves, due to the low sulphur content. For the LO Zn–S modes and the LO ZnSe phonons the frequency gap should be large enough to localize the modes in one type of layer, but, unfortunately, for the investigated sulphur content the LO Zn–S mode appears only as a weak peak, which, moreover, overlaps with the GaAs signal in the Raman spectrum.

Fig. 3 shows a typical X-ray diffraction profile, taken from the same optimized DES-grown 120-period superlattice which is shown in Fig. 1. Superlattice satellite peaks up to the fifth order are clearly observed. From this well-defined pattern

the period thickness  $d$  was calculated to be  $9.5 \pm 0.3$  nm, which is consistent the Raman-derived value of 9.8 nm. As can be seen in the zoomed inset of Fig. 3, even interference fringes due to the entire superlattice stack (pendellösung) are visible, giving a total thickness of the superlattice of  $1136.5 \pm 50$  nm which is in good agreement with 120 times the period thickness. The angular separation of the substrate and zero-order peak gives a mean lattice mismatch of  $-885 \pm 40$  ppm. The very narrow satellite peaks even for higher orders and the presence of interference fringes indicate the high quality of a well-defined modulated structure with smooth interfaces. A simulated curve based on a two-layer model is also shown in Fig. 3. A satisfactory fit to the experimental data, concerning peak positions as well as relative intensities was achieved assuming a perfect 120-period structure with abrupt interfaces and layer thicknesses of 4.7 nm for ZnSe and 4.8 nm for  $\text{ZnSe}_{1-x}\text{S}_x$ , while the sulphur content  $x$  was assumed to be 0.134. No improvement in the fit was obtained for a three-layer model including graded interfacial regions, since this only induces a weak modification of the X-ray diffraction pattern. This is in contrast to recent results on lattice-matched InGaAs/InP multiquantum well

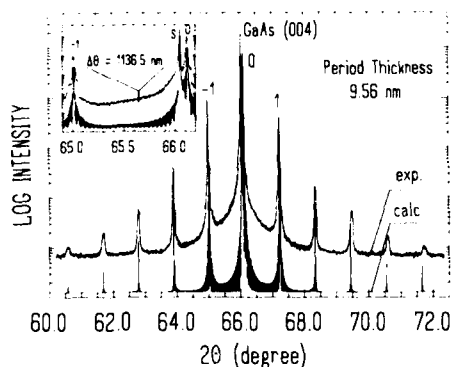


Fig. 3. (004) diffraction profile of a 120-period ZnSe/ZnSse superlattice. Upper curve: experimental result; lower curve: simulation (vertically shifted), using a two-layer model with 4.7 nm ZnSe and 4.8 nm  $\text{ZnSe}_{0.866}\text{S}_{0.134}$ . Inset: magnified picture of the region between the zero-order and  $(-1)$  satellite peaks.

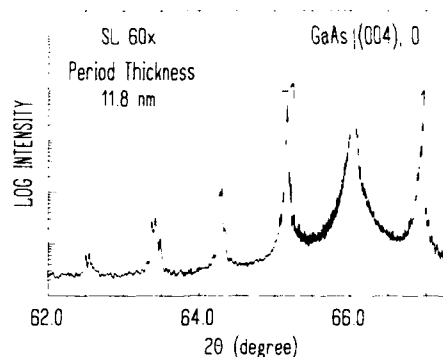


Fig. 4. Experimental (004) diffraction profile for a 60-period superlattice (high-angle satellites not shown).

structures, where reacted interface layers induce a strain which strongly influences the X-ray diffraction pattern [8]. We attribute this reduced sensitivity in the ZnSe/ZnSse system to the strain, which is already present in the individual layers, even if the mean strain in the entire stack is zero.

Samples grown with  $\text{H}_2\text{S}$  also show a large number of satellite peaks, but their width is often broadened with respect to the DES-grown series [2]. Additionally, they exhibit a progressively increasing width with the satellite order. This phenomenon is usually attributed to random variations in the period and composition. On the other hand, we were able to detect in some optimized DES-grown samples the presence of more than one superlattice. For instance, in the diffraction profile of Fig. 4, which shows a single narrow zero-order peak, the higher-order satellites are clearly splitted into separate sharp peaks whose difference in periodicity  $d$  is about 1 nm, corresponding to about 4 monolayers. Such a result rules out the possibility of random variations in layer thickness and/or composition. Besides these well-defined differences in periodicity, some superlattice structures showed well-defined compositional differences. These are revealed by a splitting of the zero-order peak [2].

For stabilized  $\text{ZnS}_x\text{Se}_{1-x}$ -to-ZnSe interfaces, the simulation of the X-ray diffraction pattern requires the assumption of an increased sulphur content in the barrier. This applies for both kind

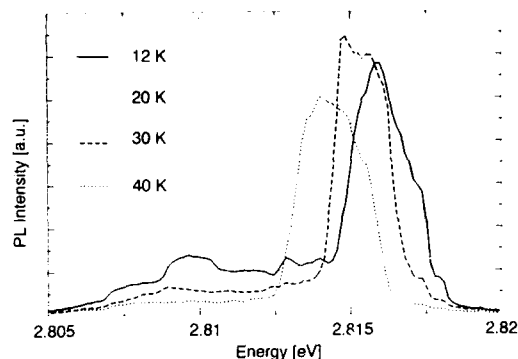


Fig. 5. Photoluminescence emission spectra in the near-band edge region of a 120-period superlattice for several sample temperatures between 12 and 40 K.

of sulphur precursors. For the samples grown on a ZnSe buffer layer, the structural quality decreases significantly, while for  $\text{ZnS}_{1-x}\text{Se}_x$  buffer layers no strong influence could be observed. However, the best structural quality so far was obtained without any intentional buffer. All these results are in accordance with the Raman results discussed before.

Fig. 5 shows photoluminescence spectra in the near-band-edge region of a DES-grown 120-period superlattice stack. The sample temperature was varied between 12 and 40 K. The dominant peak at about 2.815 eV is the free-exciton heavy-hole transition. The structure on the low-energy side is assigned to a bound exciton. Its weakness reveals the high sample quality. The free-exciton peak appears as a broad structure, which seems to be a superposition of several excitonic emission lines, probably due to small variations in thickness and/or composition, as also observed by X-ray diffractometry. While the temperature-induced energy shift of the spectrum reflects the  $T$ -dependence of the ZnSe gap energy, the changes in lineshape are attributed to a redistribution of the free carriers in the regions of the sample which have different composition and/or periodicity.

#### 4. Conclusions

In conclusion, we have shown from Raman scattering, X-ray diffractometry and photoluminescence that ZnSe/ZnSSe superlattices grown from diethylsulphide (DES) have better crystalline quality and a more regular periodicity than those grown from  $\text{H}_2\text{S}$ . For DES-grown samples, folded-acoustical-phonon peaks appear in the Raman spectrum. The presence of intense high-order satellite reflections in the X-ray diffraction scans confirms the high quality of the superlattices. The comparison with simulations, based on dynamical theory, implies that the interfaces are rather smooth and their periodicity is well defined. Moreover, interference fringes due to the entire stack are clearly observable. We were able to observe small variations in periodicity and composition as a result of changes in the growth conditions and to analyse the X-ray patterns with monolayer accuracy. Stabilization of the ZnSSe surfaces during growth interruptions results in a strongly enhanced sulphur content in the barriers. No improvement of the superlattice quality was achieved by growth on different kind of buffers. ZnSe buffers even lead to inferior quality, probably due to enhanced strain in the ZnSSe layers. Beneficial effects for the layer quality were achieved by increasing the number of periods, since the lower layers act as a buffer for the upper ones.

#### 5. Acknowledgement

The authors are indebted to Stiftung Volkswagenwerk for financial support. They also would like to thank Aixtron Semiconductor Technologies (Aachen) for their technical support.

#### 6. References

- [1] M. Haase, J. Qui, J. DePuydt and H. Cheng, Appl. Phys. Lett. 59 (1991) 1272.
- [2] J. Söllner, M. Scholl, A. Schneider, M. Heuken and J. Woitok, J. Crystal Growth 137 (1994) 35.



- [3] W.J. Bartels, J. Hornstra and D.J. Lobeck, *Acta Cryst. A* 42 (1986) 539.
- [4] J. Geurts, *Surf. Sci. Rept.* 18 (1993) 1.
- [5] O. Brafman, S. Mitra, I. Chang, G. Lengyel and E. Carnall, *Phys. Rev. Lett.* 19 (1967) 1120.
- [6] S. Ganesan, A. Maradudin and J. Oitmaa, *Ann. Phys.* 56 (1970) 556.
- [7] B. Jusserand and M. Cardona, in: *Topics in Applied Physics*, Vol. 66, *Light Scattering in Solids V*, Eds. M. Cardona and G. Güntherodt (Springer, Berlin, 1989).
- [8] J. Finders, M. Keuter, D. Gnoth, J. Geurts, J. Woitok, A. Kohl, R. Müller and K. Heime, *Mater. Sci. Eng. B* 21 (1993) 161.



ELSEVIER

Journal of Crystal Growth 138 (1994) 619–624

JOURNAL OF **CRYSTAL  
GROWTH**

## Characterization of alloy formation at the ZnSe/CdSe quantum-well interface by photoluminescence spectroscopy

Ziqiang Zhu \*, Hiroteru Yoshihara, Kazuhisa Takebayashi, Takafumi Yao

*Department of Electrical Engineering, Hiroshima University, Higashi-Hiroshima 724, Japan*

### Abstract

The interface of a binary single quantum-well (SQW) structure of ZnSe/CdSe, where CdSe of less than one monolayer is sandwiched between ZnSe layers (submonolayer SQW), is characterized by photoluminescence spectroscopy. The dependence of the energy, linewidth and intensity of excitonic emission from submonolayer SQWs on the well thickness of CdSe is extensively investigated. The characteristics of the excitonic emission are interpreted in terms of a heterostructure model in which 2 ML wide alloyed wells are taken into account. It is shown that the ZnCdSe alloy with layer thickness of about 2 ML forms at the interface in a ZnSe/CdSe quantum well heterostructure.

### 1. Introduction

Recently, blue-green laser diodes (LDs) and blue-light-emitting diodes (BLEDs) have been demonstrated using ZnSe-based heterostructures [1,2]. So far, the optically and electronically active region in the light-emitting devices has been mostly ZnCdSe/ZnSe or ZnCdSe/ZnSSe quantum wells [1–5]. One of the most important problems associated with the growth of quantum-well heterostructures (QWHs) is the structural disorder at the interfaces of heterostructures, which includes interface roughness and interfacial alloying. Such structural disorder has important effects on the performance of the devices [6].

The photoluminescence (PL) technique has been extensively used to characterize the inter-

face roughness of quantum well (QW) structures [7–11], since the free excitonic linewidth of the emission is closely correlated with the interface roughness [12]. The linewidth of the excitonic emission in QWs is mostly given by the probability distribution of lateral dimensions of islands and valleys at the interface, which produces potential fluctuation. The line broadening of excitonic emission spectra due to the interface roughness is enhanced as the QW layer thickness decreases, as was reported in the QWH structures of III–V compounds [13]. In the case of ZnS/ZnSe single quantum well (SQW) structure, a ZnSe quantum well thicker than 3 monolayers (ML) emitted a sharp excitonic emission with half-width of 15–30 meV, while a broad emission with half-width of 100 meV was observed from quantum wells thinner than 2 ML [14]. These experimental results suggested that the line broadening in very thin quantum wells of 1 and 2 ML is caused by fluctuations not only associated

\* Corresponding author.

with the quantum confinement effect along the growth direction, but also with the lateral quantum confinement effect in “quantum slabs” formed on islands and valleys at the interface. Most recently, we have fabricated ZnSe/(CdSe)<sub>n</sub>/ZnSe ( $n = 1\text{--}6$  ML) SQW structures by molecular beam epitaxy (MBE) and observed strong excitonic emission [15]. The energy of the excitonic emission increased with the decrease in well thickness, and the half-widths of the excitonic emissions were around 40 and 15 meV for quantum wells of 2–6 ML and 1 ML, respectively. It is obvious that in contrast to that from the ZnS/ZnSe SQW, the dependence of the linewidth on well thickness in ZnSe/CdSe SQWs cannot be interpreted in terms of potential fluctuation due to interface roughness. The observed decrease in linewidth is postulated to be due to alloy formation of ZnCdSe at the ZnSe/CdSe interface. The alloyed interface would result in an increase in entropy, which subsequently reduces the interface free energy in a strained SQW structure.

In the present study, a binary ZnSe/CdSe SQW, where CdSe of less than one monolayer is sandwiched between ZnSe layers (submonolayer SQW), is used to investigate the structural disorder at the interface of the ZnSe/CdSe heterostructure. Under optimal growth conditions, the ZnSe surface roughness along the growth direction is expected to be of one or two monolayers thickness. When CdSe of less than one monolayer is deposited on the ZnSe surface, three possible surface structures of CdSe submonolayer on the ZnSe arise: case I, formation of CdSe islands due to interface roughness; case II, formation of ZnCdSe alloy due to lateral interdiffusion of Zn and Cd atoms to reduce the interface free energy; case III, co-existence of the islands and alloy. In cases I and III, low-dimensional quantum effects due to the formation of islands in the submonolayer SQWs are expected. A line broadening of excitonic emission due to the distribution of island sizes should be observed, as was reported for ZnS/ZnSe SQW [14]. The submonolayer SQW structure is preferable to characterize the line broadening due to the hetero-interface compared to SQW structures with thicker

well thickness, since the excitonic spectrum is strongly enhanced in structures with thin wells.

This paper reports the characterization of alloy formation at the interface of a ZnSe/CdSe SQW by PL. We have studied extensively the dependence of the energy, linewidth and intensity of excitonic emission from submonolayer SQWs on the well thickness of CdSe. A heterostructure model in which 2 ML wide alloyed wells are taken into account is proposed to explain the characteristics of the excitonic emission.

## 2. Experimental procedure

The submonolayer SQWs of ZnSe/CdSe were fabricated as follows: A 2 mm thick ZnSe buffer layer was grown on a (100)GaAs substrate by MBE under optimal growth conditions. In which the ZnSe surface roughness along the growth direction is considered to be of one monolayer thickness. CdSe of less than one monolayer was deposited on the ZnSe surface and ZnSe of 0.1  $\mu\text{m}$  thickness was subsequently deposited to form a ZnSe/CdSe submonolayer SQW. The well thickness of CdSe was varied from 1/4 to 1 ML. The substrate temperature was kept at 280°C, and the Zn-, Se- and Cd-cell temperatures were fixed at 373, 170 and 190°C, respectively.

The well thickness of CdSe was controlled by the deposition time. Fig. 1 shows the X-ray diffraction (XRD) pattern observed from ZnSe/CdSe MQW with a period of 50. The

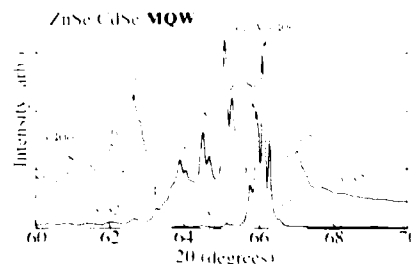


Fig. 1. X-ray diffraction pattern observed from ZnSe/CdSe MQW with a CdSe layer of 3 Å and a ZnSe layer of 163 Å. The period of the MQW is 50.

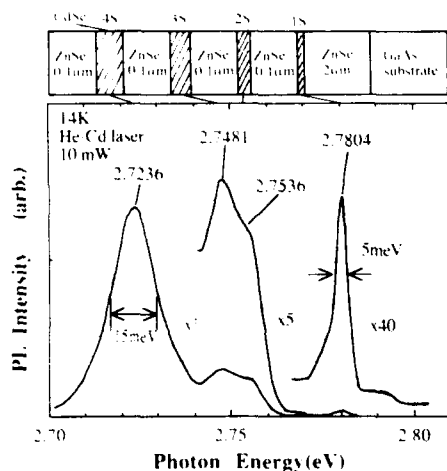


Fig. 2. Photoluminescence spectra from the sample with four ZnSe/CdSe submonolayer SQWs. A schematic drawing of the sample structure is shown in the upper part of the figure. The four peaks of excitonic emission associated with the four submonolayer SQWs are observed.

thicknesses are determined from the diffracted peak positions to be 3 Å for the CdSe layer and 163 Å for the ZnSe layer, which is in good agreement with the expected values. Thus, the deposition time for the growth of 1 ML CdSe is estimated to be 4 s. The thicknesses of CdSe submonolayers are assumed to be proportional to the deposition time. A 1 μm thick CdSe epilayer has been grown on a ZnSe epilayer. The CdSe epilayer was confirmed by XRD measurements to have the zincblende structure.

PL spectra were measured at 14 K using the 3250 Å line from a He–Cd laser as an excitation source.

### 3. Experimental results and discussion

Fig. 2 shows PL spectra from the sample consisting of four ZnSe/CdSe submonolayer SQWs. A schematic drawing of the sample structure is shown in the upper part of the figure. The deposition times for CdSe to form quantum wells were 1, 2, 3, and 4 s, which corresponds to 1/4, 1/2, 3/4, and 1 ML of CdSe, respectively. The thick-

ness of the ZnSe barrier layers was 0.1 μm, which is thick enough to separate the wells from each other. As shown in Fig. 2, the PL spectra show four dominant excitonic emissions from the four separated submonolayer SQWs, presumably due to radiative annihilation of free excitons. The emission energy increases with a decrease in CdSe layer thickness. The linewidth of the emission peak decreases from 15 to 5 meV as the CdSe layer decreases from 1 to 1/4 ML. It is obvious that this behavior cannot be understood in terms of the probability distribution of lateral dimensions of islands and valleys due to interface roughness. A weak and broad emission peak from the ZnSe layers appears at around 2.79 eV.

Fig. 3 shows the temperature dependence of the excitonic emission intensity from three ZnSe/CdSe SQWs with well thicknesses of 1, 1/2 and 1/4 ML. The peak energies of the excitonic emission coincide approximately with those from the sample with four submonolayer SQWs, as shown in Fig. 2. The activation energies are estimated to be 63, 28 and 16 meV for submonolayer SQWs of 1, 1/2 and 1/4 ML, respectively, which represents the activation energy for the transfer of electrons or holes from the well to the barrier region. The temperature dependence

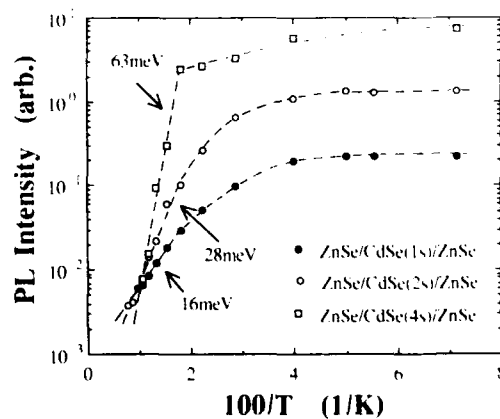


Fig. 3. Temperature dependence of intensity of excitonic emissions from three submonolayer SQWs with well thicknesses of 1, 1/2 and 1/4 ML. The activation energies are estimated to be 63, 28 and 16 meV for submonolayer SQWs of 1, 1/2 and 1/4 ML, respectively.

of the emission energy was compared with that of the free exciton energy obtained from ZnSe layers. The emission energies for the SQWs show the same temperature dependence as the free exciton energy for ZnSe, indicating the emission peaks of the SQWs due to free excitons.

#### 4. Comparison of model calculation with experiment PL results

The formation of ZnCdSe alloy at the interface due to lateral interdiffusion of Zn and Cd atoms is assumed in order to understand the above experimental PL results. Fig. 4 shows schematically a heterostructure model in which 2 ML wide alloyed wells are taken into account. When CdSe is deposited on a ZnSe surface with a surface roughness of 1 ML (Fig. 4a), there

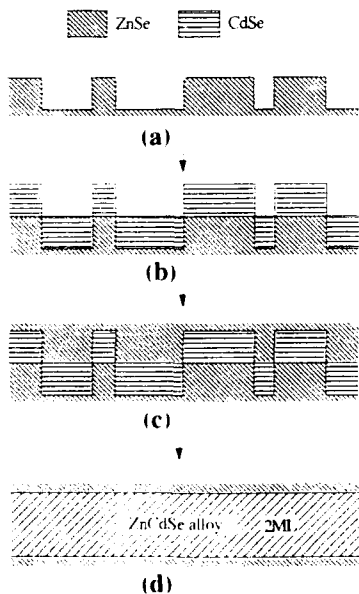


Fig. 4. Heterostructure model accounting for 2 ML wide alloyed wells. (a) ZnSe surface with roughness of 1 ML along the growth direction, (b) formation of CdSe islands and valleys with thicknesses of 1 ML after deposition of CdSe of less than 1 ML on ZnSe surface, (c) formation of SQW structure after deposition of ZnSe on CdSe, and (d) 2 ML wide alloyed well due to lateral interdiffusion of Zn and Cd.

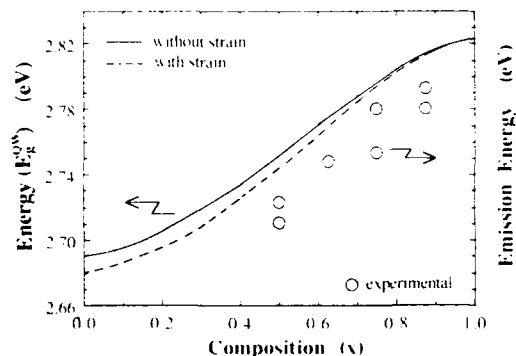


Fig. 5. Calculated dependence of  $E_{cl} - E_{hh1}$  on Zn composition ( $x$ ) for ZnSe/Zn<sub>x</sub>Cd<sub>1-x</sub>Se SQW with well thickness of 2 ML. Open circles represent the experimental data of excitonic emission energy.

would be formation of CdSe islands and valleys whose thicknesses are 1 ML (Fig. 4b). It is reasonable to assume that ZnCdSe alloying occurs within a 2 ML thickness in a submonolayer SQW structure. For simplicity, the well region of the submonolayer SQW is assumed to form a homogeneous Zn<sub>x</sub>Cd<sub>1-x</sub>Se alloy with thickness of 2 ML in the zincblende crystal lattice (Fig. 4d). The calculation of the transition energy between the ground states of the electron and the heavy hole confined to the SQW ( $E_g^{OW} = E_{e1} - E_{hh1}$ ) is based on a simple square well potential model. The numerical data such as effective masses, lattice constant, band-gap energy, etc. for the ZnCdSe compound are calculated by interpolation between relevant data of ZnSe and CdSe. The valance and conduction band offsets are determined on the basis of Harrison's linear combination of atomic orbital theory [16].

Fig. 5 shows the calculated dependence of  $E_g^{OW}$  on Zn composition ( $x$ ) for ZnSe/Zn<sub>x</sub>Cd<sub>1-x</sub>Se SQW with well thickness of 2 ML. The dashed and solid lines represent calculations with and without strain due to lattice mismatch. The experimental data are plotted where the Cd composition ( $1 - x$ ) is estimated by assuming that Cd is included to form a 2 ML thick ZnCdSe layer. As seen from the figure, the experimental results can be well explained by the calculated ones. The exciton binding energy is not included in the

calculation, which may be responsible for the difference in energy between the calculated and experimental results. The dependence of  $E_g^{OW}$  on the composition for ZnSe/ZnCdSe SQWs with well thicknesses of 1 and 3 ML was also calculated. The obtained  $E_g^{OW}$  values were much larger for the 1 ML and much smaller for the 3 ML well thickness than the experimental values.

The activation energies estimated from the temperature dependence of the emission intensity are considered to reflect the thermal activation process of electrons or holes from the well to the barrier layer and the dissociation process of excitons in the well. Fig. 6 shows the calculated dependence of the activation energies of electron and hole ( $\Delta E_{eff}^e$ ,  $\Delta E_{eff}^h$ ) on Zn composition ( $x$ ) for a ZnSe/Zn<sub>x</sub>Cd<sub>1-x</sub>Se SQW with well thickness of 2 ML, where the activation energy is the difference in energy between the ground state and the barrier, as is shown in the inset of the figure. Open circles represent the experimental data obtained from Fig. 3. The activation energy increases with the increase in Cd composition. The dissociation energy for an exciton in the well increases with an increase in activation energy, since the exciton binding energy is enhanced by the two-dimensional confinement effect. The experimental results are qualitatively explained by the calculations.

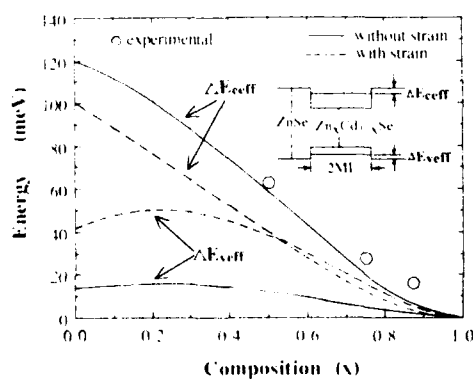


Fig. 6. Calculated dependence of activation energies of electron and hole ( $\Delta E_{eff}^e$ ,  $\Delta E_{eff}^h$ ) on Zn composition ( $x$ ) for ZnSe/Zn<sub>x</sub>Cd<sub>1-x</sub>Se SQW with well thickness of 2 ML. Open circles represent the experimental data of activation energy.

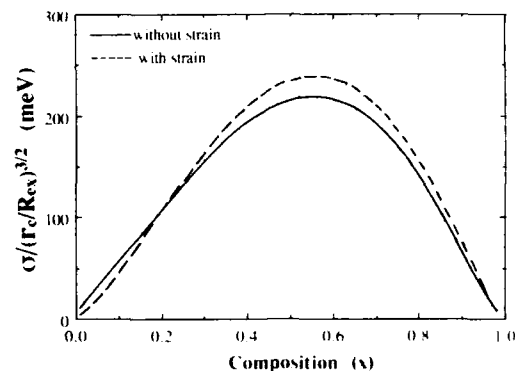


Fig. 7. Calculated linewidth of excitonic emission as a function of alloy composition for ZnSe/Zn<sub>x</sub>Cd<sub>1-x</sub>Se SQW with well thickness of 2 ML.  $\sigma$  is the linewidth,  $r_e$  the radius associated with the volume per cation ( $\sim 3$  Å), and  $R_{ex}$  the exciton radius of Zn<sub>x</sub>Cd<sub>1-x</sub>Se.

The linewidth of excitonic emission from a ZnSe/Zn<sub>x</sub>Cd<sub>1-x</sub>Se SQW with well thickness of 2 ML is discussed on the basis of the formalism developed by Singh and Bajaj [9], where the effect of the probability distribution of Zn or Cd concentration in the well layer is calculated. Fig. 7 shows the calculated linewidth of excitonic emission as a function of alloy composition for a ZnSe/Zn<sub>x</sub>Cd<sub>1-x</sub>Se SQW with well thickness of 2 ML. The linewidth is strongly dependent on the alloy composition. As the composition approaches ca. 0.5, the linewidth is rapidly broadened. Using the exciton radius ( $R_{ex}$ ) of ZnSe (28 Å) instead of that of Zn<sub>x</sub>Cd<sub>1-x</sub>Se, the linewidths are estimated as 10 and 4 meV for  $x = 0.5$  and  $0.875$ . These values are very close to the experimental data of 15 meV for  $x = 0.5$  and 5 meV for  $x = 0.875$ .

## 5. Conclusion

We have characterized the interfacial alloy formation in ZnSe/CdSe quantum well heterostructures by PL spectroscopy. The dependence of the energy, linewidth and intensity of excitonic emission from submonolayer SQWs on the well thickness of CdSe is extensively investigated. The characteristics of the excitonic emission are inter-

preted in terms of alloy formation at the interface. It is shown that a ZnCdSe alloy with layer thickness of about 2 ML forms at the interface in ZnSe/CdSe quantum well heterostructure.

## 6. References

- [1] M.A. Haase, J. Qiu, J.M. DePuydt and H. Cheng, *Appl. Phys. Lett.* 59 (1991) 1272.
- [2] H. Jeon, J. Ding, W. Patterson, A.V. Nurmikko, W. Xie, D.C. Grillo, M. Kobayashi and R.L. Gunshor, *Appl. Phys. Lett.* 59 (1991) 3619.
- [3] J. Ding, H. Jeon, A.V. Nurmikko, H. Luo, N. Samarth and J.K. Furdyna, *Appl. Phys. Lett.* 29 (1990) 2756.
- [4] J. Ren, K.A. Bowers, R.P. Vaudo, J.W. Cook and J.F. Schetzina, *J. Crystal Growth* 117 (1992) 510.
- [5] S. Hayashi, A. Tsujimura, S. Yoshii, K. Ohkawa and T. Mitsuyu, *Jap. J. Appl. Phys.* 31 (1992) L1478.
- [6] C.R. Leavens and R. Taylor, Eds., *Quantum Wells and Superlattices* (Plenum, New York, 1988).
- [7] D. Bimberg, J. Christen, T. Fukunaga, H. Nakashima, D.E. Mars and J.N. Miller, *J. Vac. Sci. Technol. B* 5 (1987) 1191.
- [8] R.C. Miller, D.A. Kleinman, W.A. Nordland, Jr. and A.C. Gossard, *Phys. Rev. B* 22 (1980) 863.
- [9] J. Singh and K.K. Bajaj, *J. Appl. Phys.* 57 (1985) 5433.
- [10] R.C. Miller and R. Bhat, *J. Appl. Phys.* 64 (1988) 3647.
- [11] M.A. Herman, D. Bimberg and J. Christen, *J. Appl. Phys.* 70 (1991) R1.
- [12] J. Singh, K.K. Bajaj and S. Chaudhuri, *Appl. Phys. Lett.* 44 (1984) 805.
- [13] D.F. Welch, G.W. Wicks and L.F. Eastman, *Appl. Phys. Lett.* 46 (1985) 991.
- [14] T. Yao, M. Fujimoto, S.K. Chang and H. Tanino, *J. Crystal Growth* 111 (1991) 823.
- [15] W. Shan, S.J. Hwang, J.M. Hays, J.J. Song, Z. Zhu and T. Yao, *J. Appl. Phys.* 74 (1993) 5699.
- [16] W.A. Harrison, *J. Vac. Sci. Technol.* 14 (1977) 1016.



ELSEVIER

Journal of Crystal Growth 138 (1994) 625–628

JOURNAL OF **CRYSTAL  
GROWTH**

## Light interference effect in optical bistability of multiple quantum well etalons

D.Z. Shen \*, X.W. Fan, B.J. Yang

*Changchun Institute of Physics, Academia Sinica, Changchun 130021, People's Republic of China*

### Abstract

The light interference effect in optical bistability of multiple quantum well (MQW) etalons has been studied by a simplified formula according to the light propagating theories in multiple layers medium. On the basis of the formula, the analyzed results show that the light interference effect in the MQW can directly affect the threshold of the optical bistability of the MQW etalons, particularly in the case of large periodic number and large reflectivity in interfaces between the well and barrier layers of the MQW etalons. The optical bistabilities in the CdZnSe–ZnSe and ZnSe–ZnTe MQW etalons have been measured and compared with the analyzed results; the experimental results further indicate that the large reflectivity in the interface between the well and barrier layers of the MQW will cause the threshold of the optical bistability in the MQW etalons to increase due to the light interference effect in the MQW etalons.

### 1. Introduction

Recently, optical bistability in MQW etalons has become an interesting research topic because of the possible application of the switching property in optical computer. Many studies on optical bistability in MQW etalons have been reported, in which the major interests are to reduce the threshold of optical bistability in MQW etalons by using optimal structure of the MQW and Fabry–Pérot (FP) cavity [1,2], but the light interference effect in the MQW is not considered. In this paper, we report the study of the light interference effect in MQW etalons, in which the light

interference effect in the MQW has been analyzed by a simplified formula. The research results indicate that the light interference effect in the MQW can directly affect the threshold of the analyzed bistability of the MQW etalons. On the basis of the analyzed results obtained here and the experimental results of optical bistabilities in the CdZnSe–ZnSe and ZnSe–ZnTe MQW etalons measured here, the influence of the light interference effect on the threshold of optical bistability in the CdZnSe–ZnSe MQW etalons is smaller than that in the ZnSe–ZnTe MQW etalons. The major reason for the difference is due to the smaller reflectivity in the interface between the well and barrier layers in the CdZnSe–ZnSe MQW etalons than that in the ZnSe–ZnTe MQW etalons.

\* Corresponding author.



## 2. Analysis

For an optical bistable device of a MQW etalon, when the direction of light propagation is perpendicular to the multilayers of the MQW etalon, the light wave is reflected on the interface between the well and barrier layers, and also on the front and back surfaces of the MQW etalons. In the general case, the difference of refractive indices of well and barrier layers is very small. Because of the very small reflectivity on the interface between the well and barrier layers in the MQW etalons, we only consider the first reflection of light on the interface and assume that the reflectivity of the front surface is equal to the reflectivity of back surface in the FP cavity. In this case, the transmission can be written in the form [3]:

$$T'_{\text{FP}} = \frac{F'(1-R)^2/4R}{1 + F' \sin^2 \delta / 2} (1 + 2\sqrt{RR_0} f_1), \quad (1)$$

where the finesse is

$$F' = 4R'_c / (1 - R'_c)^2, \quad (1a)$$

with

$$R'_c = R(1 - R_0)^{2n} e^{-\alpha L}, \quad (1b)$$

$$\delta = (4\pi/\lambda)(n_1 a_1 + n_2 a_2)n, \quad (1c)$$

$$R_0 = [(n_1 - n_2)/(n_1 + n_2)]^2. \quad (1d)$$

Here,  $n_1$  and  $n_2$  are the refractive indices of well and barrier layers, respectively,  $a_1$  and  $a_2$  are the widths of well and barrier layers, respectively,  $n$  and  $\alpha$  are the periodic number and average absorption coefficient of the MQW, respectively,  $\lambda$ ,  $L$  and  $R$  are the incident light wavelength, cavity length and reflectivity of the FP cavity, respectively, and  $f_1$  is the function of the parameters of the materials and structures in the MQW etalons [3]. In the general case,  $f_1$  is much smaller than one unless  $(4\pi/\lambda)(a_1 n_1 + a_2 n_2)$  is close to  $2\pi$ . Therefore,  $T'_{\text{FP}}$  becomes:

$$T'_{\text{FP}} = \frac{F'(1-R)^2/4R}{1 + F' \sin^2 \delta / 2} \quad (2)$$

Obviously, the form of Eq. (2) is the same as the expressive formula in the case of a uniform

medium; particularly in the case of  $R_0 = 0$ . Eq. (2) is identical with that in the case of uniform medium.

On the basis of the FP cavity's nonlinear theories, from Eq. (2), the finesse of the MQW etalons and the threshold of the optical bistability in the MQW etalons is not the same as that in a uniform medium; the threshold required for the optical bistability in a MQW etalons can be written as [3]:

$$I'_{\text{th}} = 2C'I_s, \quad (3)$$

where

$$C' = \frac{\alpha L(1 - R'_c)^2}{(1 - R)(1 + R'_c)(1 - T_0^{2n} e^{-\alpha L})}, \quad (3a)$$

with

$$R'_c = RT_0^{2n} e^{-\alpha L}, \quad (3b)$$

$$T_0 = 1 - R_0. \quad (3c)$$

Here  $I_s$  is the saturating absorption intensity of the MQW within a FP cavity. According to Eq. (3), the threshold  $I'_{\text{th}}$  increases with decreasing  $T_0^{2n}$  for any light absorption loss  $\alpha L$  and reflectivity  $R$  in the MQW etalons. Therefore, in order to get the lowest possible  $I'_{\text{th}}$ , we must increase the value of  $T_0^{2n}$ , i.e., use the smallest possible periodic number of MQW and smallest difference values of refractive indices between the well and barrier layers medium. Based on the above analysis, we can get results as follows: light interference effect in MQW etalons can directly affect the quality of FP cavity and the threshold of the optical bistability in the MQW etalons, and the effect depends on the periodic number and the reflectivity in the interface between the well and barrier layers in the MQW etalons.

## 3. Experimental results and discussion

ZnSe-based MQW is a kind of important material system; it has been used as the active layer in p-n junction blue-green lasers. Many studies on the ZnSe-based MQW have been reported, and the research results indicate that the ZnSe-based MQW has a strong room-temperature exci-

tonic effect, low nonlinear threshold and good waveguide character. In the MQW lasers, the FP cavity is parallel to the multilayers of the MQW, in which the emitting light needs to be limited in the multilayers so that the emission can propagate along the direction of the FP cavity. As an FP optical bistable device, the FP cavity is perpendicular to the multilayers of the MQW, in which the low threshold for the optical bistable device needs a small light interference effect in the MQW besides the strong room-temperature nonlinear effect according to the above-analyzed results. Because the CdZnSe–ZnSe MQW has smaller light reflectivity in the interface between the well and barrier layers than that in the ZnSe–ZnTe MQW, the influence on the threshold of the optical bistable device in the CdZnSe–ZnSe MQW etalons should be smaller than that in the ZnSe–ZnTe MQW etalons. Therefore, in order to study the influence of light interference effect on the MQW etalons for the threshold, CdZnSe–ZnSe and ZnSe–ZnTe MQW etalons are prepared and measured.

The two material systems within the FP cavities studied here are a Cd<sub>0.24</sub>Zn<sub>0.76</sub>Se–ZnSe MQW and a ZnSe–ZnTe MQW of total thicknesses of 0.75  $\mu\text{m}$  grown by metalorganic chemical vapor deposition on n-GaAs substrates, which consist of 50 periods of 5 nm Cd<sub>0.24</sub>Zn<sub>0.76</sub>Se (or ZnTe) wells and 10 nm ZnSe barriers. The GaAs substrates were removed by etching to allow making FP cavities; the FP cavities are prepared according to the method described in our earlier work [4].

In both optical bistable devices, the reflectivities of the interface between the well and barrier layers in the CdZnSe–ZnSe MQW and the ZnSe–ZnTe MQW are about  $1.6 \times 10^{-4}$  and  $8 \times 10^{-2}$ , respectively [5,6], and the reflectivities of the front and back surfaces in the both FP cavities are about 0.35 and 0.9, respectively.

On the basis of the measuring setup describe in our earlier work [7], the room-temperature optical bistabilities in CdZnSe–ZnSe and ZnSe–ZnTe MQW etalons are measured. Figs. 1a and 1b show the accumulated and normalized temporal shapes of incident and transmitted pulses in the CdZnSe–ZnSe and ZnSe–ZnTe MQW

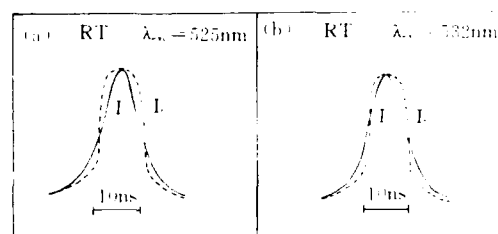


Fig. 1. Time dependence of averaged normalized incident (solid curve)  $I_0$  and transmitted (dashed curve)  $I_1$  pulses (a) in the CdZnSe–ZnSe MQW etalon and (b) in the ZnSe–ZnTe MQW etalon.

etalons, respectively. On the basis of the change of transmitted intensities as a function of incident intensities, the optical bistabilities in the CdZnSe–ZnSe and ZnSe–ZnTe MQW etalons are obtained as shown in Figs. 2a and 2b.

From Figs. 2a and 2b, we can see that the thresholds  $I_{th}$  in the CdZnSe–ZnSe and ZnSe–ZnTe MQW etalons are about 80 and 750  $\text{kW}/\text{cm}^2$ , respectively. The threshold of the optical bistability in the CdZnSe–ZnSe MQW etalons is about one order lower than that in the ZnSe–ZnTe MQW etalons. Because the nonlinear threshold in the CdZnSe–ZnSe found in experiments (not shown here) is close to that in ZnSe–ZnTe and the structure parameters of the FP cavities are the same in both optical bistable devices, the different thresholds in both optical bistable devices should be due to the different light reflectivities in the CdZnSe–ZnSe and ZnSe–ZnTe MQW etalons. This indicates that the experimental results agree with the analyzed

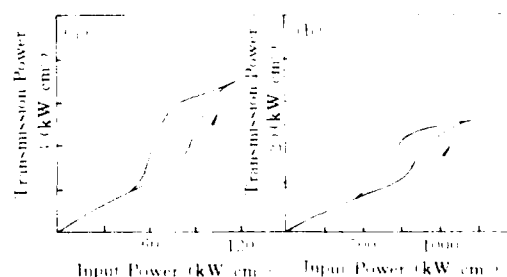


Fig. 2. The optical bistabilities (a) in the CdZnSe–ZnSe MQW etalon and (b) in the ZnSe–ZnTe MQW etalon.

results, i.e., the light interference effect in the MQW etalons can directly affect the threshold of the optical bistability in the MQW etalons. Therefore, in order to reduce the threshold of the optical bistability in the MQW etalons, it is necessary to consider the light interference effect in the MQW and use the material systems with smallest possible periodic number and reflectivity in the interface between the well and barrier layers in the MQW etalons.

#### 4. Conclusions

We have studied the light interference effect in the optical bistability of MQW etalons, in which the light interference effect can be described by a simplified formula. The research results indicate that the light interference effect in the MQW etalons can affect the quality of the FP cavity and the threshold of the optical bistability in the MQW etalons. Particularly in the case of large periodic number and large reflectivity on the interface between the well and barrier layers in the MQW etalons, the effect cannot be neglected. In order to get the lowest possible threshold of optical bistability in the MQW etalons, it is necessary to reduce the values of the periodic number and the reflectivity of the interface between the well and barrier layers in the MQW etalons. The experimental results of the optical bistabilities in the CdZnSe–ZnSe and ZnSe–ZnTe MQW etalons measured here further support the above analyzed results and indi-

cate that the optical bistable device in the CdZnSe–ZnSe MQW etalons is a better FP type optical bistable device because of the smaller light interference effect in the CdZnSe–ZnSe MQW etalons than that in the ZnSe–ZnTe MQW etalons.

#### 5. Acknowledgements

This work is supported by the “863” High Technology Research Program in China, the National Fundamental and Applied Research Project of China, the National Natural Science Foundation of China and the Project of the Laboratory of Excited State Processes of Changchun Institute of Physics of China.

#### 6. References

- [1] Z. Garmire, *IEEE J. Quantum Electron.* QE-25 (1989) 289.
- [2] H. Yokyama, *IEEE J. Quantum Electron.* QE-25 (1989) 1190.
- [3] D.Z. Shen, *Optical nonlinearities and optical bistability in ZnSe–ZnS MQW*, Chinese Doctor Thesis, Changchun Institute of Physics, Academia Sinica, Jilin, Changchun (1993).
- [4] D.Z. Shen, X.W. Fan, B.J. Yang and J.M. Sun, presented at Int. Conf. on Solid State Devices and Materials, Japan, 1993.
- [5] W.J. Walecki, A.V. Nurmikko, N. Samarth, H. Luo and J.K. Furdyna, *J. Opt. Soc. Am. B* 8 (1991) 1799.
- [6] D.T.F. Marple, *J. Appl. Phys.* 35 (1964) 539.
- [7] D.Z. Shen, X.W. Fan and G.H. Fan, *Nonlinear Opt.* 1 (1992) 319.



ELSEVIER

Journal of Crystal Growth 138 (1994) 629–632

JOURNAL OF  
**CRYSTAL  
GROWTH**

## Growth and optical bistability of $\text{Zn}_{0.78}\text{Cd}_{0.22}\text{Se}$ –ZnSe multiple quantum wells by metalorganic chemical vapor deposition

B.J. Yang, L.C. Chen, X.W. Fan \*, J.Y. Zhang, Z.H. Zheng, Y.M. Lu, Z.P. Guan,  
A.H. Yang, S.M. Wang

*Changchun Institute of Physics, Academia Sinica, Changchun 130021, People's Republic of China*

### Abstract

Room temperature (RT) excitonic optical bistability has been investigated in multiple quantum wells (MQWs) of (Zn, Cd) Se–ZnSe at blue-green wavelengths. The (Zn, Cd) Se–ZnSe MQWs with 50 periods were grown by atmospheric pressure MOCVD technique. Photoluminescence (PL) and transmission spectra of  $\text{Zn}_{0.78}\text{Cd}_{0.22}\text{Se}$ –ZnSe MQWs at RT were measured. Optical bistability (OB) of the MQWs at RT was obtained by an incident beam of 515 nm wavelength. The origin of the OB obtained here was attributed to the excitonic absorption.

### 1. Introduction

Optical bistability (OB) in II–VI wide band gap semiconductor strained layer superlattices (SLSs) and quantum wells (QWs) is of increasing interest for both basic and applied purposes [1–3]. For this reason, it is the most likely model system in studies concerning a future optical computer. Recently, rapid progress of ZnSe-based quantum well and superlattice systems has been ensued by molecular beam-epitaxy (MBE) [4], and metalorganic chemical vapor deposition (MOCVD) [5], leading to evident improvement in material quality. However, in ZnSe the exciton survey among absorption, reflection or luminescence is hard at room temperature. This is due to the fact that the exciton–LO phonon interaction is stronger than the exciton oscillator strength and leads to rapid dissociation of the exciton into free electron–hole

pair states with increasing temperature. In  $\text{Zn}_{1-x}\text{Cd}_x\text{Se}$ –ZnSe QWs with the addition of Cd component to form a ternary well, the exciton oscillator strength increases and binding energy can be made to exceed the LO phonon energy [7].  $\text{Zn}_{1-x}\text{Cd}_x\text{Se}$ –ZnSe QW material provides a strong exciton emission of which the wavelength can be varied in the blue-green-red region by adjusting the composition  $x$  or changing the ternary well width.

In this paper we report  $\text{Zn}_{1-x}\text{Cd}_x\text{Se}$ –ZnSe MQW growth on (100) GaAs substrate by atmospheric pressure MOCVD for the first time. The observation of the exciton absorption peak in  $\text{Zn}_{1-x}\text{Cd}_x\text{Se}$ –ZnSe MQWs, and optical bistability and mechanism in  $\text{Zn}_{0.78}\text{Cd}_{0.22}\text{Se}$ –ZnSe MQWs are studied.

### 2. Experimental procedure

Epitaxial growth of  $\text{Zn}_{1-x}\text{Cd}_x\text{Se}$ –ZnSe MQWs was performed by atmospheric pressure MOCVD

\* Corresponding author.

with a horizontal reactor. The GaAs substrates are n-type with orientation of (100) within  $\pm 0.5^\circ$  off towards (110). The sources used are dimethylzinc (DMZn), dimethylcadmium (DMCd) (Morton Co. Advanced Materials) and hydrogen selenide ( $\text{H}_2\text{Se}$ ) 10% in hydrogen. The substrates were degreased and etched in a  $\text{H}_2\text{SO}_4 : \text{H}_2\text{O}_2 : \text{H}_2\text{O} = 5 : 1 : 1$  solution at around  $50^\circ\text{C}$  for 1 min, rinsed in de-ionized water for 5 min, blow-dried, and then mounted onto the graphite susceptor. Before epitaxial growth the substrate was heated up to  $600^\circ\text{C}$  in Pd-diffusion  $\text{H}_2$  flow for 10 min to decompose the thin surface oxide layer on GaAs. Then a buffer layer of ZnSe of around  $1\ \mu\text{m}$  was grown at  $320^\circ\text{C}$ ; for multilayer growth, computer-controlled air-operated valves were performed to control separately binary and ternary compound growth.

$\text{Zn}_{1-x}\text{Cd}_x\text{Se}$ -ZnSe MQWs were assessed by observation of X-ray satellite peaks of (400) diffraction. PL measurements were carried out at 77 K and RT by the 337.1 nm line from a  $\text{N}_2$  laser as an excitation source in conjunction with a 44 W gating monochromator with a C31034 cooled photomultiplier. The optical bistability measurement apparatus has been described in detail elsewhere [1].

The excitation source was a dye laser pumped by the 337.1 nm line from a  $\text{N}_2$  laser. The dye laser pulse was 6 ns in duration with 0.5 mJ single pulse energy, and tuning range at 480–540 nm with a central wavelength of 515 nm. The time dependence of incident  $I_0$  and transmitted  $I_t$  pulses was measured by a model 4400 boxcar.

### 3. Results and discussion

It was found that the correlation between the gas phase and solid composition of co-cation ternary alloy ( $\text{Zn}_{1-x}\text{Cd}_x\text{Se}$ ) is unusually different from co-anion ternary alloy ( $\text{ZnSe}_{1-x}\text{S}_x$ ) [6]. The addition of Cd to ZnSe producing  $\text{Zn}_{1-x}\text{Cd}_x\text{Se}$  alloy ( $x < 0.5$ ) is much easier in comparison with the addition of S to ZnSe producing  $\text{ZnSe}_{1-x}\text{S}_x$  alloy. Fig. 1 shows the correlation between gas phase and solid composition of  $\text{Zn}_{1-x}\text{Cd}_x\text{Se}$  epilayer. One can see that there is no a one-to-one

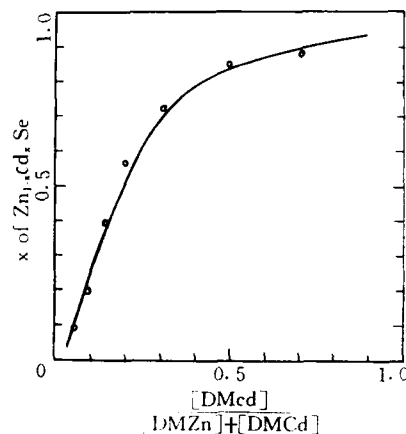


Fig. 1. Correlation between gas phase and solid composition of ZnCdSe ternary epilayer grown at  $320^\circ\text{C}$ .

correlation between the gas phase and the solid composition. The DMCd source seems to be more reactive to  $\text{H}_2\text{Se}$  than the DMZn source under the same growth conditions. The composition  $x$  in the ternary epilayer was determined from X-ray diffraction peak angles for (400) planes by Vegard's law.

For the well width measurement of  $\text{Zn}_{1-x}\text{Cd}_x\text{Se}$ -ZnSe MQWs, the period thickness of well plus barrier width can be measured by the separation between the satellite peaks of X-ray diffraction (400) rocking curve. Under MQW growth conditions, the simulation single layer well (ZnCdSe) and barrier (ZnSe) growth ratio were respectively obtained by the ratio of thickness to growth time, so that in practice the thickness of a period well and barrier can be controlled separately by growth time. The period well width calculated from X-ray diffraction is approximately corresponding to the well width of the growth experiment.

In comparison with Parbrook et al, at higher growth temperature the ZnSe-CdSe SL structure would deteriorate owing to the cation interdiffusion [7]. A growth temperature of  $320^\circ\text{C}$  was adopted in  $\text{Zn}_{1-x}\text{Cd}_x\text{Se}$ -ZnSe MQWs epitaxy.

PL spectra of ZnSe epilayer (a),  $\text{Zn}_{1-x}\text{Cd}_x\text{Se}$ ,  $x = 0.22$  ternary layer (b) and  $\text{Zn}_{0.78}\text{Cd}_{0.22}\text{Se}$ -ZnSe MQW layers (c,d) are shown in Fig. 2. The

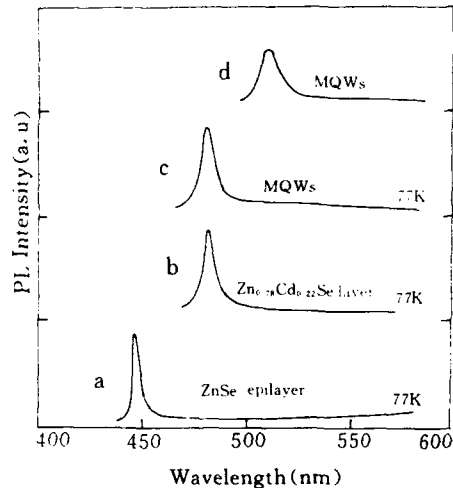


Fig. 2. PL spectra of ZnSe epilayer (a),  $\text{Zn}_{1-x}\text{Cd}_x\text{Se}$  epilayer (b) and  $\text{Zn}_{0.78}\text{Cd}_{0.22}\text{Se}$ -ZnSe MQWs at 77 K (c) and RT (d).

emission peaks of the MQWs are located around 480 nm (c) and 510 nm (d) at 77 K and RT, respectively. It is found that at 77 K the emission full width at half maximum (FWHM) of the  $\text{Zn}_{1-x}\text{Cd}_x\text{Se}$  layer is getting broadening with  $x$  value increasing, in contrast to the ZnSe epilayer (7 nm), while the FWHM of the ternary epilayer with  $x = 0.22$  (b) is 10 nm due to the Cd component. In  $\text{Zn}_{0.78}\text{Cd}_{0.22}\text{Se}$ -ZnSe MQWs, the 12 nm FWHM is broader than the ternary epilayer  $x = 0.22$  due to the another addition of well width fluctuation.

After the GaAs substrate of the MQW layer was removed by etching, the transmission spectra were measured by a W lamp as light source at 77 K and RT. Fig. 3 shows the transmission spectra of  $\text{Zn}_{0.78}\text{Cd}_{0.22}\text{Se}$ -ZnSe MQWs with narrow well ( $< 5$  nm) and wide well ( $> 10$  nm). From Fig. 3a it is found that in the narrow-well sample the transparency starts from 445 nm and with increasing wavelength an absorption appears at 480 nm at 77 K; from Fig. 3b it is found that the transparency starts from 460 nm and the absorption moves to 510 nm and broadens at RT. According to the description by Ding et al. [8], the absorption at 510 nm should be attributed to  $n = 1$  heavy hole exciton absorption, while in the wide-

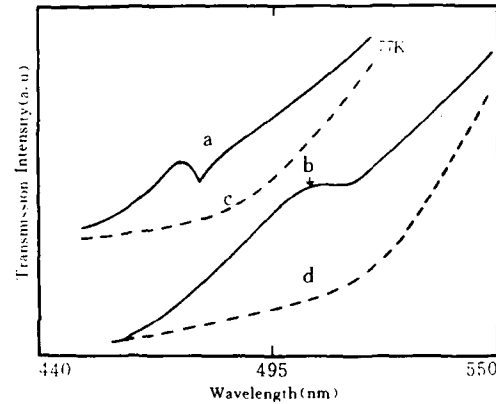


Fig. 3. Optical transmission spectra of  $\text{Zn}_{0.78}\text{Cd}_{0.22}\text{Se}$ -ZnSe MQWs with narrow wells and wide well at 77 K and RT.

well sample the transparency increases gradually with increasing wavelength without any absorption at both 77 K and RT, shown in Figs. 3c and 3d. This means that electronic confinement and quasi-2D exciton effect disappear in this case.

Fig. 4a shows the accumulated and normalized temporal shape of the incident  $I_0$  and transmitted  $I_t$  pulses during 515 nm wavelength as incident light. The experimental result from Fig. 4a shows that the incident  $I_0$  pulse with FWHM of 6 ns is compressed into transmitted  $I_t$  pulse with

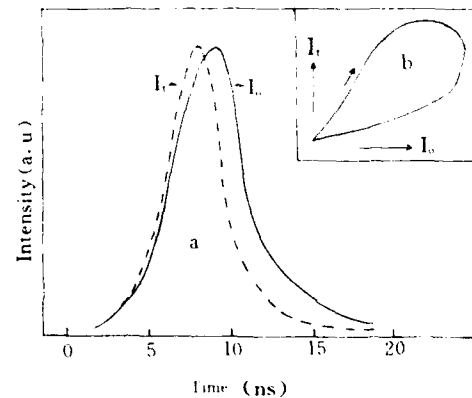


Fig. 4. (a) Time dependence of incident  $I_0$  (solid line) and transmitted  $I_t$  (dashed line) pulse of  $\text{Zn}_{0.78}\text{Cd}_{0.22}\text{Se}$ -ZnSe MQWs at room temperature. (b) Increasing absorption optical bistability hysteresis loop from (a).

FWHM of 4 ns. This indicates that the dependence of transmitted intensities  $I_t$  on incident intensities  $I_0$  is nonlinear. Fig. 4b gives the corresponding hysteresis loop  $I_t = f(I_0)$  and the direction of the hysteresis loop is clockwise. The optical bistability (OB) disappears if the incident wavelength is changed from 515 to 528 or 506 nm, respectively. Comparing the emission peak position around 510 nm at RT in Fig. 3b, it is reasonable to consider that the emission and absorption energy position at 510 nm at RT should have originated from the exciton.

Therefore, the optical bistability obtained using a wavelength of 515 nm as incident light in Fig. 4 should also be attributed to the excitonic absorption. It should be noted that by changing the wavelength of incident light from 515 to 528 or 506 nm, the OB of the sample disappears. This further established that the OB in Fig. 4 could be ascribed to the exciton absorption other than to a thermal effect.

In summary, we have reported the MOCVD growth and characterization of  $\text{Zn}_{1-x}\text{Cd}_x\text{Se}$ – $\text{ZnSe}$  MQWs and the observation of exciton absorption peak due to heavy hole. The optical bistability of  $\text{Zn}_{0.78}\text{Cd}_{0.22}\text{Se}$ – $\text{ZnSe}$  MQWs with ns response time at room temperature has been observed for the first time and is attributed to excitonic absorption.

#### 4. Acknowledgements

This work is supported by the “863” High Technology Research Program in China, The National Natural Science Foundation of China, The Laboratory of Excited State Process in Changchun Institute of Physics and the National Fundamental and Applied Research Projects of China.

#### 5. References

- [1] D.Z. Shen, X.W. Fan, G.H. Fan and J.Y. Zhang, *J. Luminescence* 48/49 (1991) 299.
- [2] D.Z. Shen, X.W. Fan, Z.S. Piao and G.H. Fan, *J. Crystal Growth* 117 (1992) 519.
- [3] Z.P. Guan, X.W. Fan, Y.M. Lu and B.J. Yang, *Superlattices Microstruct.* 13 (1993) 101.
- [4] M. Haase, J. Qin, J.M. DePuydt and H. Cheng, *Appl. Phys. Lett.* 59 (1991) 1272.
- [5] Y. Kawakami, T. Taguchi and A. Hiraki, *J. Crystal Growth* 89 (1988) 331.
- [6] P.J. Wright and B. Cockayne, *J. Crystal Growth* 59 (1982) 148.
- [7] P.J. Parbrook, P.J. Wright, B. Cockayne, A.G. Cullis, B. Henderson and K.P. O'Donnell, *J. Crystal Growth* 106 (1990) 503.
- [8] J. Ding, N. Pelekanos, A.V. Nurmikko, H. Luo, N. Samarth and J.K. Furdyna, *Appl. Phys. Lett.* 57 (1990) 2855.
- [9] H.X. Nguyen and R. Zimmermann, *Phys. Status Solidi (b)* 124 (1984) 191.

## Photoluminescence of ultrathin ZnSe–ZnTe superlattices

N. Takojima, F. Iida<sup>1</sup>, K. Imai<sup>\*</sup>, K. Kumazaki

*Department of Applied Electronics, Hokkaido Institute of Technology, Sapporo 006, Japan*

### Abstract

ZnSe–ZnTe superlattices were grown on GaAs (100) surfaces by molecular beam epitaxy without buffer layer. The thicknesses of ZnSe and ZnTe layers were varied from 5/4 to 9/4 monolayer (ML) and from 1/9 to 1 ML, respectively. The photoluminescence (PL) spectra due to isoelectronic traps of Te atoms and clusters are independent to the thickness of ZnSe layers. We can tune the photon energy of PL emission from about 2.65 to 2.35 eV under the thickness of ZnSe layers of 2 monolayers constant. The green emission was achieved at room temperature by the superstructure with blue band layers sandwiched by ZnTe of 1 ML.

### 1. Introduction

A design of the stacking structure of the ZnSe–ZnTe superlattice, that belongs to type II, is potential to make high emission efficiency and to tune the wavelength of emission light. Since the ZnSe–ZnTe system has a large lattice misfit of about 7.3%, the system is called a strained layer superlattice (SLS). The optical properties of this system have been studied by Raman scattering and photoluminescence (PL) [1]. We reported previously that the blue-light emission intensity of this superlattice system is several hundred times stronger than that of the  $I_2$  line of the simple ZnSe/GaAs(100) grown by molecular beam epitaxy (MBE) [2].

It is well known that Te in ZnSe acts as an isoelectronic trap [3] and that the emission efficiency of excitons captured at the traps is very high [4]. In the case of the mixed crystal  $\text{ZnSe}_{1-x}\text{Te}_x$ , the wavelength of PL emission due to this trap depends on the density  $x$  of Te in ZnSe. The emission light is blue (corresponding to  $S_1$  band in ref. [4]) for low Te density ( $\text{ZnSe}_{0.995}\text{Te}_{0.005}$ ) and green ( $S_2$ ) for high density ( $\text{ZnSe}_{0.95}\text{Te}_{0.05}$ ) alloys [5]. The control of Te content is important for application of this system to blue light optoelectronics devices. The origin of blue emission is due to the Te atom traps in ZnSe. On the other hand, the emission color is green when the Te atoms become clusters. Hence, the wavelength of emission light should have no dependence on the Te concentration essentially if we could grow a sample in which there exist solitary Te atoms or Te clusters. For instance, if the Te atom is put at a certain distance from the other Te atoms in the  $xy$  plane and if an isolation of Te atoms along the  $z$  growth direction is

<sup>\*</sup> Corresponding author.

<sup>1</sup> Present address: LSI Memory Division, NEC Corporation, Minamishimoto 3-chome, Sagami-hara 229, Japan.



secured, then the isoelectronic traps due to  $\text{Te}_i$  atoms are formed even if the distance between Te atoms is short along the  $z$  direction. It is expected that MBE is one of the suitable methods to grow such samples. The concentration of Te traps is controllable, which leads easily to application to devices. It is also interesting to grow a super-structure of the traps to increase the emission efficiency.

The aim of our study is to fabricate the blue light emission device that acts at room temperature by combining the high emission efficiency of isoelectronic traps with the large binding energy of excitons in superlattices. In this paper, we demonstrate PL spectra due to the traps in MBE-grown ZnSe–ZnTe superlattices. Then, it is demonstrated that the superlattice, which consists of multiple stacking of layers involving the traps and ZnTe of 1 monolayer (ML), emits green light at room temperature.

## 2. Experimental procedure

ZnSe–ZnTe SLSs were grown on GaAs (100) surfaces by MBE at a growth temperature of  $340^\circ\text{C}$ . The beam pressures of the source elements (6N super Zn, Se and Te) were 7, 7 and  $5 \times 10^{-8}$  Torr, respectively. The background pressure in the growth chamber was about  $8 \times 10^{-10}$  Torr during the growth. Under these growth conditions, the growth rates of the films were 1 ML per 4 s for ZnSe and 1 ML per 9 s for ZnTe. The thickness of each epilayer which constructs SLSs was controlled by the opening time of the shutter of Se and Te cells. Therefore, in this paper, the thickness under 1 ML of ZnTe means the content of Te atoms where the ZnTe layer should place. In other words, the thickness of the ZnTe layer expresses the concentration of Te at the interface between the ZnSe and ZnSe layers. The shutter of the Zn cell was opened through the growth. All the samples, except the next one, consisted of 300 cycles of ZnSe/ZnTe pairs.

The sample, whose structure consisted of 160 cycles of a fundamental layer, was grown to demonstrate a green PL signal at room temperature (RT). The fundamental layer consisted of 2

ML ZnSe/(1/9 ML ZnTe/2 ML ZnSe)<sub>2</sub>/1 ML ZnTe.

The samples employed in this study were grown layer by layer, which was confirmed by RHEED patterns monitored during the growth.

The PL spectra were measured by using a He–Cd laser of 4 mW as the excitation source in the temperature range of 10 K to RT.

## 3. Results and discussion

As stated above, it is predicted that the thickness of ZnSe in the superlattices gives no essential contribution to the PL spectra due to the traps. Fig. 1 shows the PL spectra as a function of the thickness of ZnSe. The thicknesses of ZnTe layers are 1/9 ML constant. These samples have almost similar peak energies and profiles of the emission spectra. The broad emission band around 2.64 eV is called the blue band. The steps in the high energy region correspond to phonon structures of free excitons. The full width at half maximum (FWHM) has a tendency to increase with decreasing thickness of ZnSe layer. The energy region of this increasing part corresponds to the green band which is shown in Fig. 2. This means that the Te atoms, which should act as the  $\text{Te}_i$  trap when the ZnSe layer is thick enough, make  $\text{Te}_n$  ( $n > 1$ ) traps together with the Te atoms in the next ZnTe layer through a kind of brakes (holes) of thin ZnSe layer.

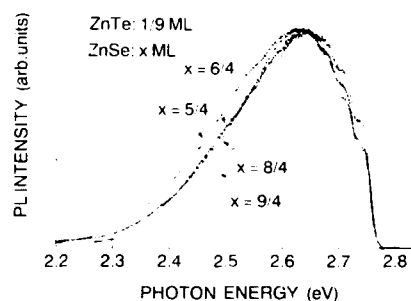


Fig. 1. PL spectra of 1/9 ML ZnTe samples with various ZnSe thicknesses at 10 K.

Fig. 2 shows the PL spectra of the samples that have a constant thickness of ZnTe of 2/9 ML. The broad band around 2.47 eV is called the green band. The blue band increases with increasing thickness of ZnSe layer. The reason of the increase of the blue band is that the Te atoms, which construct Te clusters through the brakes of ZnSe layers, are isolated from each other as the thickness of the ZnSe layer increases.

These facts mean that the emission profile is determined by the amount of Te in the respective portion where the ZnTe layer should be placed when the thickness of the ZnSe layers is over 2 ML. In other words, the emission spectra are independent of the thicknesses of the ZnSe layer when its thicknesses are over 2 ML, which is enough thickness without brake.

The spectra shown in Figs. 1 and 2 are quite similar to those of ZnSeTe mixed crystals [5] with 0.5 and 5 at% Te, respectively. In the mixed crystal with 0.5% Te, which indicates the blue band emission, the average distance between Te atoms is about 20 Å. The MBE grown sample which consists of, for example, 1/9 ML ZnTe and 2 ML ZnSe has a Te content of about 5%. In this sample the distance between Te atoms is about 12 Å along the growth plane. In the cases of green-band emitting mixed-crystal and epilayer, the distances are about 10 and 8 Å, respectively. Although the whole content of Te in the

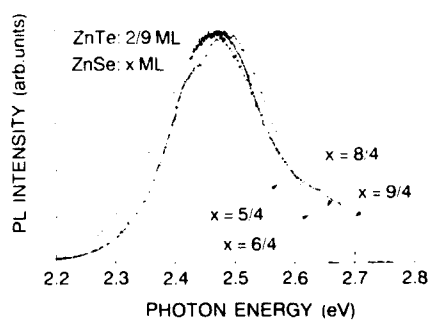


Fig. 2. PL spectra of 2/9 ML ZnTe samples with various ZnSe thicknesses at 10 K. As the thickness of the ZnSe layers increases, the blue band appears by the recovering of brakes in ZnSe layers.

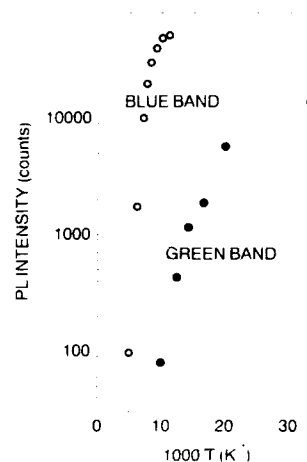


Fig. 3. Temperature dependence of the intensity of blue and green bands. The thermal binding energies for the blue and green bands are about 60 and 170 meV, respectively.

MBE grown samples is very high and the distance is short compared with the mixed crystal, the blue- and green-band emitting epilayers are grown by MBE with well distinction. This shows high controllability of MBE and also that we can fabricate quantum dots easily by MBE.

The temperature dependence of the intensity of blue and green bands indicates an activation type as shown in Fig. 3. As the temperature increases, the emission intensity of the blue band decays from 30 K with thermal binding energy of about 60 meV and that of the green band starts decaying from 100 K with a binding energy of 170 meV. In the temperature dependence of the blue band, a free-exciton-like peak at 2.78 eV and the green band appear with temperature increasing from 30 to 100 K. These situations are also quite similar to the case of  $\text{ZnSe}_{1-x}\text{Te}_x$  mixed crystals [5]; besides, the behavior is explained well by a configuration coordinate model [3–5]. We confirm that the blue and green bands originate from Te atom and Te cluster isoelectronic traps, respectively.

Since the emission profile depends only on the thickness of ZnTe, we can tune systematically the wavelength of emission light by control of the ZnTe thickness even under the constant ZnSe thickness. Fig. 4 shows the PL spectra as a func-

tion of ZnTe thickness under a constant ZnSe thickness of 2 ML. The sample of 1/9 ML ZnTe has the blue band with weak green band due to Te clusters constructed from locally concentrated Te atoms and/or through the brake of ZnSe layer. The sample of 2/9 ML ZnTe has the green band with weak blue band due to isolated Te atoms. The sample with 3/9 ML ZnTe indicates only green band emission. When the thickness of ZnTe is 5/9 ML, the spectrum consists of a green band and a broad peak at about 2.4 eV which is of the superlattice sample of 1 ML ZnTe. The peak energy of the sample with 1 ML ZnTe agrees with that of the ZnSe–ZnTe (17–3 Å) superlattice [6]. This means that, when the thickness of ZnTe is over 1 ML, the sample indicates optical properties of the superlattice with multi-quantum wells (MQWs). Thus we can tune easily the energy of emission light from about 2.7 to 1.8 eV [6] assorting the ultra-thin SLSs and MQWs grown by MBE.

In all cases of the superstructures, the emission intensity is quite high compared with that of  $I_2$  of the usual MBE-ZnSe. Considering the character of the ultra-thin SLSs as described above, we can grow a sample which indicates PL emission in the green-blue region at RT by special design for its structure. Fig. 5 shows the PL emission profile at RT. The structure of the SLS is illustrated in Fig. 5. The thermal binding energy of this emission band is about 250 meV. As

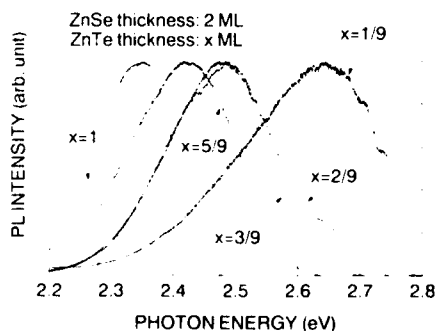


Fig. 4. PL spectra of 2 ML ZnSe samples with various ZnTe layer thicknesses at 10 K. The photon energy of the emission band is tuned systematically by changing the ZnTe thickness.

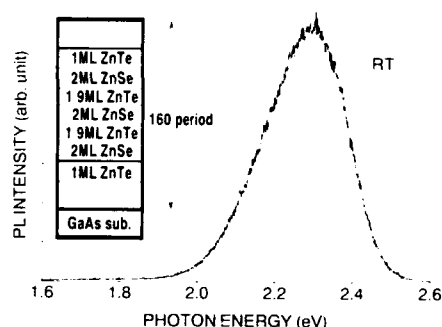


Fig. 5. PL spectra of the specially designed sample at RT. The sample consists of 160 periods of fundamental layer whose structure is (1 ML ZnTe)/(2 ML ZnSe)/(1/9 ML ZnTe)/(2 ML ZnSe)/(1/9 ML ZnTe)/(2 ML ZnSe), as drawn schematically. Te atoms are distributed in a 6 ML ZnSe layer sandwiched by 1 ML ZnTe layers.

shown in Fig. 5, the peak energy of the emission band at RT is about 2.3 eV. At low temperature (10 K), this peak energy is about 2.34 eV. This value agrees with that of a ZnSe–ZnTe (15–5 Å) superlattice [6] whose structure is interpreted as an SLS without the quantum dots of Te atoms. However, in the case of the superlattice, the thermal binding energy of the emission was about 160 meV and no emission structure could be detected above 250 K using our experimental system. It is considered that the special structure involving isoelectronic traps brings forth the emission at RT.

To conclude, it has been cleared that the thickness of the ZnTe layer determines the character of the PL emission in a ZnSe–ZnTe SLS system. PL of the samples with ZnTe of 1/9, 3/9 and 1 ML is mainly due to isoelectronic traps of Te atoms (peak at 2.64 eV: blue band), to those of Te clusters (2.48 eV: green band), and to the recombination of electron–hole pairs in the superlattice (2.36 eV), respectively, at 10 K. Our results with respect to temperature dependence of the emission due to the isoelectronic traps support the configuration coordinate model in refs. [3–5]. The PL spectrum of the sample with 2/9 ML ZnTe consists of a superposition of both types of the traps. The spectrum of the 5/9 sample agrees with the superposition of emissions due to Te cluster and to the superlattice. Thus,

we can achieve easily the control of the type of traps by MBE.

The emission efficiency increases in consequence of the design of SLS structure combined with the isoelectronic traps. We can see by the naked eye a bright green spot on the surface of the specially designed SLS sample at RT using a 4 mW He–Cd laser as the excitation source. Thus it is cleared that the emission efficiency of SLSs can be improved by a structural design.

#### 4. Acknowledgments

This work was partially supported by the Ogasawara Foundation for the Promotion of Science and Engineering, the Hokkaido Foundation for

Research and Development, the Hitachi Micro-computer System Foundation and the HIT Foundation.

#### 5. References

- [1] H. Ozaki, D. Suzuki, K. Imai and K. Kumazaki, *Phys. Status Solidi (a)* 133 (1992) 523.
- [2] F. Iida, K. Imai and K. Kumazaki, *J. Crystal Growth* 127 (1993) 356.
- [3] D. Lee, A. Mysyrowicz, A.V. Nurmikko and B.J. Fitzpatrick, *Phys. Rev. Lett.* 58 (1987) 1475.
- [4] T. Yao, M. Kato, J.J. Davies and H. Tanino, *J. Crystal Growth* 86 (1988) 552.
- [5] S.K. Chang, C.D. Lee, H.L. Park and C.H. Chung, *J. Crystal Growth* 117 (1992) 793.
- [6] H. Ozaki, K. Imai and K. Kumazaki, *J. Crystal Growth* 127 (1993) 361.



ELSEVIER

Journal of Crystal Growth 138 (1994) 638–642

JOURNAL OF  
**CRYSTAL  
GROWTH**

## Fabrication and optical characterization of wet chemically etched CdTe/CdMgTe wires

M. Illing <sup>\*,a</sup>, G. Bacher <sup>a</sup>, A. Forchel <sup>a</sup>, A. Waag <sup>b</sup>, T. Litz <sup>b</sup>, G. Landwehr <sup>b</sup>

<sup>a</sup> Technische Physik, Universität Würzburg, Am Hubland, D-97074 Würzburg, Germany

<sup>b</sup> Experimentelle Physik III, Universität Würzburg, Am Hubland, D-97074 Würzburg, Germany

### Abstract

We have fabricated optically active semiconductor wires based on CdTe/CdMgTe quantum well structures by electron beam lithography and wet chemical etching. Wire widths between 5 and 40 nm have been achieved. The wires have been characterized by photoluminescence spectroscopy. Down to about 300 nm, no significant decrease of the photoluminescence intensity is observed at 5 K. In narrower wires, free excitons can diffuse to the open wire surface and recombine nonradiatively thereby causing a reduction of the quantum efficiency. Increasing the temperature up to 100 K causes a larger diffusion length of free excitons which leads to a reduction of the quantum efficiency in small wires. Bound excitons, which cannot diffuse towards the wire surface, show significantly higher luminescence efficiency in narrow wires compared to free excitons.

The fabrication and investigation of nanostructures have been major topics of semiconductor physics in recent years. On the one hand, this research was stimulated by the prospect of microstructured devices, such as quantum wire lasers. On the other hand, quasi-one- and zero-dimensional structures have been developed in order to study the physical properties of low dimensional electronic systems. Most of the work so far has been done on III–V semiconductors. Several methods have been developed for these materials to produce nanostructures, including self-organized growth, growth in V-grooves and mask definition by lithography with subsequent dry or wet chemical etching step [1,2]. Of the latter, wet chemical etching has been shown to

yield less fabrication induced defects as compared to dry etching. This leads to a better luminescence efficiency in small structures [3].

In recent years epitaxial growth techniques have been increasingly applied to II–VI materials. This has resulted in new II–VI based optoelectronic applications, especially the blue-green laser based on ZnSe and ZnTe [4–6]. However, at the present time there are only few reports on the fabrication of nanostructures on II–VI semiconductors, all of which, to our knowledge, have been produced by dry etching techniques [7,8].

In this paper we report about the fabrication of wire structures by wet chemical etching. The wires reported here are based on CdTe/CdMgTe heterostructures, a novel wide-gap material system, which covers the whole visible range (from 1.6 to 3.2 eV gap energy) [9]. To process this material we chose a wet etching technique to

\* Corresponding author.

avoid the formation of an optically inactive surface layer (dead layer). The wires produced have a geometrical width down to 40 nm as determined from SEM micrographs. Optically active wires down to 60 nm have been investigated by photoluminescence spectroscopy. Exciton diffusion to the sidewalls and nonradiative recombination at surface states is found to determine the luminescence efficiency in small wires. This is confirmed by the comparison of the wire width dependence of bound and free exciton luminescence and by temperature dependent investigations of free exciton quantum efficiency. For the wire patterning a MBE-grown CdTe/CdMgTe quantum well structure, grown on a CdZnTe substrate at a growth temperature of 230°C is used. The CdTe wells have a well width between 2.5 and 8 nm and are embedded in  $\text{Cd}_{1-x}\text{Mg}_x\text{Te}$  barriers ( $x = 0.25\text{--}0.5$ ). The cap layer thickness was between 20 and 50 nm.

After a cleaning procedure in organic solvents, the samples are baked for 2 h at 200°C to ensure a homogeneous sample surface. The samples then were spin-coated with negative resist (SAL 601). The patterns have been defined using a scanning electron microscope connected to a pattern generator. After a 1 min post-exposure bake the resist is developed in MF 322 developer.

The patterns are transferred into the semiconductor material using a bromine–ethyleneglycol solution. At a ratio of 2:1000 this etchant has an etch rate of 90 nm/min. The etchant has been chosen because of its reproducible etch rate, independence of the etch rate from the Mg content of the sample, and the relatively smooth surfaces it produces. Typical etch depths are in the range of 70 to 150 nm. A typical pattern consists of wire arrays each 100  $\mu\text{m}$  by 100  $\mu\text{m}$  wide. Within an array the wire width is constant. Wire widths between 5  $\mu\text{m}$  and 40 nm have been realized. The area filling factor, i.e. the ratio of the area covered by wires to the total area of the array, was held constant at 1/8.

Fig. 1 shows an SEM micrograph of a wire of 40 nm geometrical width. The optically active quantum well is located 20 nm below the top of the structures. The wire is well defined and displays the typical isotropic etch profile of the

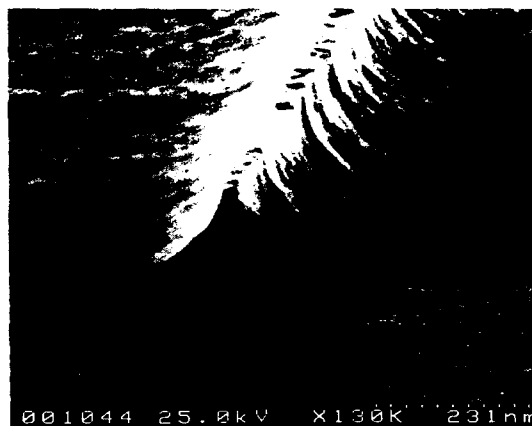


Fig. 1. SEM micrograph of a CdTe/CdMgTe wire, with  $L_w \approx 40$  nm. The wire has been produced using electron lithography and subsequent wet etch process.

bromine etch. This isotropic etch characteristic also leads to considerable underetching of the mask. For example, the 40 nm wires have been produced with a mask width of 100 nm. From the SEM micrograph the wire width fluctuation due to the roughness of the substrate is estimated to be 5 to 10 nm.

To analyze the optical properties of the wires, we performed photoluminescence measurements. As excitation light source we used the 514.5 and 363 nm lines of an argon ion laser, depending on the barrier height of the investigated sample. Low excitation density ( $< 5 \text{ W/cm}^2$ ) was used to avoid a saturation of defects. The photoluminescence signal was dispersed by a 0.3 m monochromator and detected by a CCD camera. The experiments were performed in a variable temperature dewar between 5 and 100 K.

Fig. 2 shows typical spectra of CdTe/Cd<sub>0.6</sub>Mg<sub>0.4</sub>Te wires for different wire widths. The topmost spectrum is from a 100  $\mu\text{m}$  wide reference mesa structure. Due to the small quantum well width of 3 nm the line width of the as-grown layer is about 21 meV. Clear luminescence signals can be observed for wires as small as 60 nm. For each wire array the geometrical wire width has been determined from SEM micrographs and is indicated in the figure. Even for narrow wires the

emission shows no considerable change in line shape and line width as compared to the reference spectrum.

In the inset of Fig. 2 the integrated luminescence intensity is plotted versus the geometrical wire width. The intensity is corrected with the area filling factor and normalized to the mesa structures. For wire widths greater than about 300 nm, no significant change in luminescence efficiency compared to a 2D reference is observed. Further decreasing the wire width causes a strong reduction of luminescence intensity up to 3 orders of magnitude. This can be explained by nonradiative recombination of excitons at the open surface of the wires. The actual rate of nonradiative recombination is determined by two

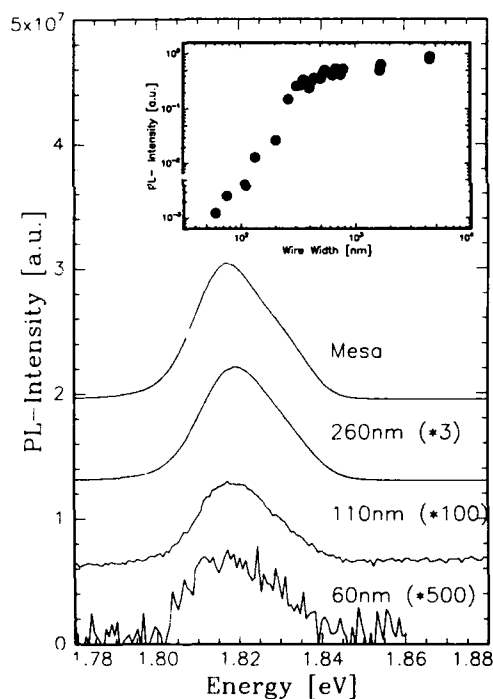


Fig. 2. Luminescence spectra from CdTe/CdMgTe wires in comparison to the emission spectra of a mesa structure. The corresponding wire widths are indicated in the figure. The inset shows the luminescence intensity versus wire width. Nonradiative recombination at open wire surfaces leads to a quenching of the emission intensity up to 3 orders of magnitude for 60 nm wires.

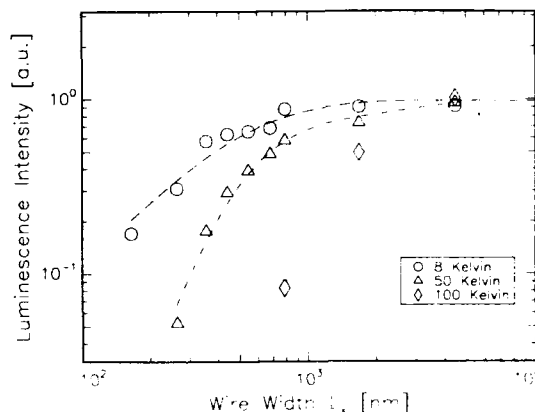


Fig. 3. Wire width dependence of the luminescence efficiency at various temperatures. The lines are guides to the eyes.

factors. The first is the surface recombination velocity, which is basically determined by the material system and the etch process used [10]. The second factor is the ability of excitons to reach the wire surface, i.e. the exciton diffusion length. A reduced diffusion length enables less excitons to reach the surface, thus increasing the quantum efficiency in narrow wires. We can estimate the diffusion length from the onset of the drop in the luminescence intensity shown in the inset of Fig. 2. In the sample presented here the diffusion length is of the order of 150 nm, corresponding to half the geometrical wire width.

To confirm this idea, we have varied the exciton diffusion length by increasing the temperature. In Fig. 3 the wire width dependence of the luminescence intensity is shown for temperatures of  $T = 8, 50$  and  $100$  K. For all temperatures, a reduction of the quantum efficiency is observed in narrow wires. However, while the photoluminescence intensity at 8 K remains nearly constant down to a wire width of 300 nm, the quenching of the PL intensity at 100 K starts at wire widths of about 2000 nm. This can be explained by the increased diffusion length at high temperatures which enables excitons to reach the wire surface even in wide wires. From the discussion above we can estimate the diffusion length at 50 K to be of the order of 400 nm. At 100 K the diffusion length amounts to about 1000 nm.

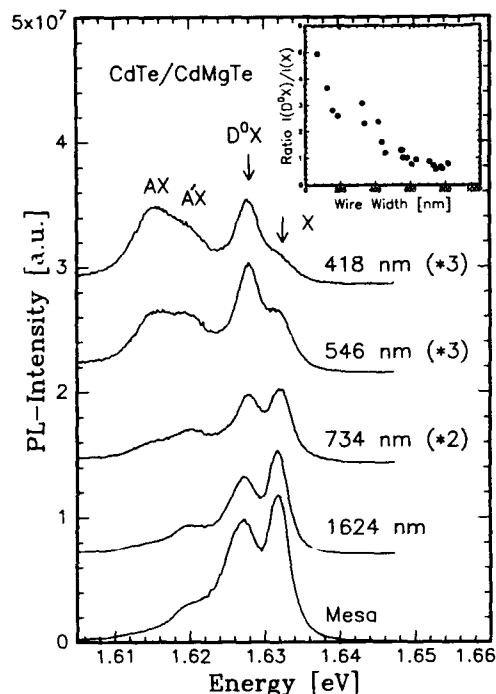


Fig. 4 Spectra of different CdTe/CdMgTe quantum well wires consisting of a free exciton (X), donor bound exciton ( $D^0X$ ) and two different acceptor related (AX,  $A'X$ ) excitons. The inset shows the ratio of donor bound exciton luminescence intensity to free exciton luminescence intensity versus wire width.

In addition to the case of the free exciton discussed above, we have studied the wire width dependence of the quantum efficiency for the extreme case of bound excitons where diffusion should be suppressed. To verify this assumption we patterned a quantum well sample ( $L_z = 8$  nm) that featured a system of four different emission lines. The spectra from this sample are shown in Fig. 4 for different wire widths in comparison to the emission of a mesa reference. Temperature and excitation density dependent measurements let us identify the high energy line as free excitonic emission (X) while the others are most likely related to a donor ( $D^0X$ ) and to acceptor bound excitons (AX,  $A'X$ ). The difference in behavior between free and bound excitons in wires is most easily seen when comparing the free

exciton peak with the donor bound exciton peak (indicated by arrows in the figure). For the mesa reference, the free exciton emission dominates the PL spectrum. This changes when the wire width is reduced. While the free exciton luminescence is quenched strongly, the bound exciton luminescence decreases only slightly with decreasing wire width and becomes the dominant part of the emission spectrum for wire widths below 600 nm.

The inset in Fig. 4 shows the ratio of intensities of the donor-bound exciton and the free exciton for wire widths between 1000 and 100 nm. We observe an increase of the ratio from about 0.7 to 5 when reducing the wire width from 1000 to 100 nm. This behavior can be understood qualitatively by considering the influence of the exciton diffusion length on quantum efficiency. At small wire widths, free excitons can diffuse toward the surface and recombine nonradiatively. In contrast, bound excitons cannot move freely to the sidewalls of the wire. Therefore the nonradiative recombination at the wire surface should be suppressed and the emission intensity is not expected to be reduced significantly with decreasing wire width. The small variation of the bound exciton intensity observed in our experiments is due to the fact that one exciton type must be regarded as part of a system of four interacting exciton states. Bound excitons can be thermally excited into free exciton states. Thus the thermal equilibrium between both types of excitons causes a quenching even for bound excitons when reducing the wire width.

In summary, we have fabricated optically active wires starting from CdTe/CdMgTe quantum wells by electron beam lithography and subsequent wet etching step. We obtained wires from 5  $\mu\text{m}$  down to 40 nm in lateral size. Luminescence signals could be observed for wires as small as 60 nm. The lineshape of the emission spectrum remains constant even for narrow wires revealing no structural damage induced by the fabrication process. The luminescence intensity is reduced by 3 orders of magnitude when the wire width is reduced down to 60 nm. The comparison of the wire width dependence of the luminescence for different temperatures as well as a comparison of



the quantum efficiency for free and bound excitons indicates that ambipolar diffusion to the wire surface and nonradiative recombination at the lateral surface is the dominant factor for the quenching of luminescence intensity with decreasing wire width.

The financial support of this work by the Bayerische Forschungsförderung is gratefully acknowledged.

## 1. References

- [1] M. Walther, E. Kapon, J. Christen, D.M. Hwang and R. Bhat, *Appl. Phys. Lett.* 60 (1992) 521.
- [2] M. Notomi, M. Naganuma, T. Nishida, T. Tamamura, H. Iwamura, S. Nojima and M. Okamoto, *Appl. Phys. Lett.* 61 (1992) 1199.
- [3] B. Jacobs, H. Zull, A. Forchel, I. Gyuro, P. Speier, E. Zielinski and P. Röntgen, *Microelectron. Eng.* 21 (1993) 401.
- [4] M. Haase, J. Oim, J.M. DePuydt and H. Cheng, *Appl. Phys. Lett.* 59 (1991) 1272.
- [5] H. Jeon, J. Ding, W. Patterson, A. Nurmikko, W. Xie, D. Grillo, M. Kobayashi and R.L. Gunshor, *Appl. Phys. Lett.* 60 (1992) 2045.
- [6] T. Ishihara, G. Brunthaler, W. Walecki, M. Hegerott, A.V. Nurmikko, N. Samarth, H. Luo and J. Furdyna, *Appl. Phys. Lett.* 60 (1992) 2460.
- [7] W. Walecki, W.T. Patterson, A.V. Nurmikko, H. Luo, N. Samarth, J.K. Furdyna, M. Kobayashi, S. Durbin and R.L. Gunshor, *Appl. Phys. Lett.* 57 (1990) 2641.
- [8] M.A. Foad, A.P. Smart, M. Watt, C.M. Soromayor, Torres, W. Kuhn, H.P. Wagner, H. Leiderer, S. Bauer, C.D.W. Wilkinson, W. Gebhardt and M. Razeghi, *Surf. Sci.* 267 (1992) 223.
- [9] A. Waag, T. Fischer, Th. Litz, B. Kuhn-Henrich, U. Zehnder, W. Ossau, W. Spahn, H. Henke and G. Landwehr, *J. Crystal Growth* 138 (1994) 155.
- [10] B. Maile, A. Forchel, R. Germann and D. Grützmacher, *Appl. Phys. Lett.* 54 (1989) 1552.

## Structural characteristics and higher-order zone-folded phonon modes in ZnSe–ZnS strained-layer superlattices

Aishi Yamamoto \*, Yoshihiko Kanemitsu, Yasuaki Masumoto

*Institute of Physics, University of Tsukuba, Tsukuba, Ibaraki 305, Japan*

---

### Abstract

We have observed higher-order (up to the 5th order) zone-folded phonon modes in ZnSe–ZnS strained-layer superlattices by means of Raman scattering spectroscopy. The structural characterizations of both the fluctuation of the periodicity and the roughness of the interface were obtained from the images of the transmission electron microscopy. The Raman spectrum of the zone-folded modes is well explained by the theoretical calculation which takes account of the two structural characteristics. Furthermore, we found that the strain does not play a dominant role in the Raman spectrum of the zone-folded modes.

---

Raman spectroscopy is a very useful tool to study lattice dynamics in semiconductor low-dimensional structures as well as bulk semiconductors. In the case of superlattices, new behavior of phonons such as zone-folding of acoustic phonons and confinement of optical phonons, has been studied extensively [1]. The Raman signal is sensitive to the periodicity, the roughness of the interface and the stress. Most of the II–VI semiconductor superlattices have a biaxial stress at the heterojunction interface due to the lattice mismatch. For example, stress-induced peak shifts of optical phonons were observed in strained-layer superlattices (SLSs) [2]. The spectra of zone-folded acoustic phonons were broad and up to the third order modes were observed [3]. One speculates that the lattice mismatch makes it

difficult to establish high-quality epitaxial layers and to observe zone-folded modes.

The stress comes from two types of lattice mismatch, which exists between SLSs and a substrate, and between the alternate layers in the SLSs. In order to reduce the stress between SLSs and the substrate, we have used ZnSe–ZnS SLSs whose average lattice constant [4] is equal to that of a GaAs substrate. As a result, we were able to observe up to the 5th order doublet phonon modes. The structural characterization of both the fluctuation of the periodicity and the roughness of the interface was obtained from the images of the transmission electron microscopy (TEM). A model calculation based on the transmission electron microscopy (TEM) data reproduced well the zone-folded spectrum. It was found that the Raman spectrum reflects dominantly both the periodicity of the superlattices and the roughness of the interface rather than the stress.

---

\* Corresponding author.

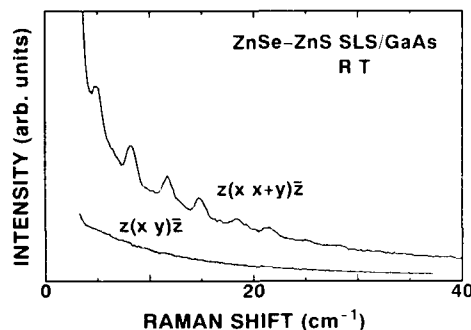


Fig. 1. Polarization dependence of Raman spectra of zone-folded modes. All the zone-folded modes are allowed only in  $z(x, x)\bar{z}$  configuration, where  $x$  and  $y$  denote the polarization of the incident and scattered light ( $x \parallel \langle 100 \rangle$ ,  $y \parallel \langle 010 \rangle$ ).

The sample used in this work was ZnSe-ZnS SLSs grown by metalorganic molecular beam epitaxy (MOMBE) on a (100) GaAs substrate [4]. The designed thicknesses of ZnSe and ZnS layers were 200 and 10 Å, respectively. The average lattice constant of the SLSs was equal to the GaAs substrate in order to reduce the stress between the SLSs and the substrate. Raman scattering experiments were performed at room temperature with the 4579 Å line of an Ar ion laser in a quasi-backscattering configuration. Raman spectra were obtained by a double monochromator (Spex 1403) with a photomultiplier.

Fig. 1 shows the polarization dependence of the Raman spectra. The sample was kept in vacuum to avoid scattering from the air. Several peaks were observed assigned to be the zone-folded longitudinal acoustic (LA) modes. Fig. 1 shows that all the zone-folded modes are allowed in  $z(x, x)\bar{z}$  configuration and are forbidden in  $z(x, y)\bar{z}$  configuration, where  $x$  and  $y$  denote the polarization of the incident and scattered light ( $x \parallel \langle 100 \rangle$ ,  $y \parallel \langle 010 \rangle$ ). However, theoretical group analysis predicts that the lower energy mode of the doublet is allowed only in  $z(x, x)\bar{z}$  configuration, whereas the higher energy mode is allowed only in  $z(x, y)\bar{z}$  configuration. The same results were obtained in GaAs-GaAlAs superlattices [5]. Jusserand et al. [5] attributed the breaking of the selection rules to the fact that the non-zone-center phonons display other symmetry.

Fig. 2a shows the spectrum where the background was subtracted from the spectrum of Fig. 1. The background has probably originated from Rayleigh scattering and single particle excitations [6]. Fig. 2a shows zone-folded doublet modes up to the 5th order.

In the continuum limit, a phonon dispersion is given by the conventional Rytov model [7]. It is written by

$$\cos(qd) = \cos\left(\frac{\omega d_1}{v_1}\right) \cos\left(\frac{\omega d_2}{v_2}\right) - \frac{1 + \kappa^2}{2\kappa} \times \sin\left(\frac{\omega d_1}{v_1}\right) \sin\left(\frac{\omega d_2}{v_2}\right), \quad (1)$$

where  $\omega$  and  $q$  are the phonon frequency and the superlattice wavevector,  $v_1$  and  $v_2$  the sound velocities of ZnSe and ZnS,  $d_1$  and  $d_2$  the thicknesses of the two constituting layers and  $d$  the period of the SLSs defined by  $d = d_1 + d_2$ . The coefficient  $\kappa$  is defined by  $\kappa = v_1 \rho_1 / v_2 \rho_2$ , where  $\rho_1$  and  $\rho_2$  are the ZnSe and ZnS densities, respectively. The inset of Fig. 2a shows the phonon dispersion calculated by using Eq. (1). We have used the values  $v_1 = 4.054 \times 10^5$  cm/s and  $\rho_1 =$

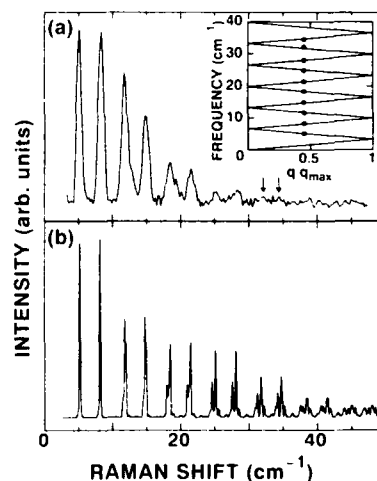


Fig. 2. Observed (a) and calculated (b) Raman spectra of zone-folded modes. The arrows show the peak positions of the fifth-order folded modes. Inset is phonon dispersion using conventional Rytov model, where  $q_{\max}$  is the zone-edge wavevector  $\pi/d$  and  $d$  is the superlattice period.

5.266 g/cm<sup>3</sup> for ZnSe, and  $v_2 = 5.047 \times 10^5$  cm/s and  $\rho_2 = 4.086$  g/cm<sup>3</sup> for ZnS [8]. The solid circles in the inset are observed peak frequencies of the zone-folded modes. When the thicknesses  $d_1$  and  $d_2$  are designed values, 200 and 10 Å, the calculated peak energies do not agree well with the observed ones. The period,  $d$ , was estimated to be 205 Å from the X-ray diffraction experiment [4], although the constituting layer thicknesses,  $d_1$  and  $d_2$ , were not obtained exactly. Therefore, we fixed  $d$  to be 205 Å, and varied  $d_1$  and  $d_2$  to fit all of the observed frequencies of the zone-folded modes. The fitted values of  $d_1$  and  $d_2$  were 198 and 7 Å, respectively. These values were used to calculate the dispersion shown in the inset of Fig. 2a. The calculation fits the experimental data satisfactorily.

So far, zone-folded modes were observed in ZnTe–ZnSe [3,9] and InAs–AlAs [10] SLs. It was suggested that the observed peak energies of the folded modes do not completely agree with the calculated ones. This discrepancy was believed to have originated from the strain between the alternate layers. Recio et al. [10] considered the effect of the strain on the sound velocities deduced from the stress-induced peak shifts of LO-Raman modes and Grüneisen constants. We tried to include the stress effect on the sound velocities using their method. However, all the estimated peak energies were larger than the observed ones by  $\sim 0.2$  cm<sup>-1</sup>. The calculation does not fit the experimental data better than the stress-free calculation. Furthermore, it was found that the changing of the thicknesses by a few ångströms induces the peak shift of the folded modes more than the stress.

Fig. 3a shows high-resolution TEM image of our sample. We also took a low-resolution TEM image which shows good periodicity of the each layer [11]. However, a large fluctuation exists near the interface, as shown in Fig. 2a. Fig. 2b shows the histogram of the lattice points of ZnS. We obtained each data point in the histogram by counting the lattice points of ZnS along the straight arrays of lattice points parallel to the interface plane. The full width at half maximum (FWHM) of the histogram is about 4 layers and it is a little larger than the fitted value for the

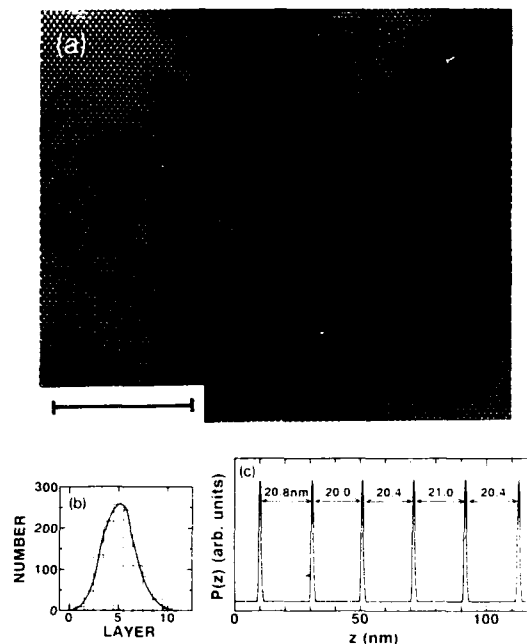


Fig. 3. (a) High-resolution TEM image of ZnSe–ZnS SLs. (b) Histogram of the lattice points of ZnS. We obtained each data point in the histogram by counting the lattice points of ZnS along the straight arrays of lattice points parallel to the interface plane. The solid line is a guide to the eye. (c) Photoelastic coefficient  $P(z)$  deduced from the TEM images. The intervals between the peak points are shown in the figure, showing the fluctuation of the periodicity. Marker in (a) represents 10 nm.

thickness of the ZnS layer, 7 Å. The position at the center of the ZnS layers fluctuated. Therefore the FWHM of the histogram is larger than the thickness of the ZnS layer.

The intensity of Raman scattering from the folded LA modes can be calculated theoretically by a photoelastic model, where the superlattices have bulk photoelastic coefficients  $P_1$  and  $P_2$  [12]. The photoelastic model has been used previously to predict the intensity of the folded modes [13] and to characterize the periodicity and the roughness of the interface [14] in GaAs–GaAlAs superlattices. According to this model, the modulation of photoelastic coefficient,  $P(z)$ , along the growth direction  $z$  reflects the modulation in the

structure of the SLs. The  $m$ th order folded modes at  $\omega_m = |2m\pi/d \pm q|v_{\text{SL}}$  has intensity

$$I_m \propto \omega_m(n_m + 1)|Q_m|^2, \quad (2)$$

where  $n_m$  is the Bose factor,  $v_{\text{SL}}$  is sound velocity of superlattices defined through  $d/v_{\text{SL}} = d_1/v_1 + d_2/v_2$ , and  $Q_m$  is the  $m$ th order Fourier component of  $P(z)$ . It is noted that we do not need the absolute values of  $P_1$  and  $P_2$ , but need only the lineshape of  $P(z)$  in order to calculate the intensity of Raman spectrum.

When  $P(z)$  is assumed to be a square-wave function, in an ideal case, the higher order Fourier component  $Q_m$  decreases very slowly. This means that the higher order  $I_m$  decreases very slowly. Since the square-wave assumption cannot reproduce our spectrum at all, we took account of the fluctuation of the periodicity and the interface roughness using the TEM data. The roughness of the interface was directly deduced from the distribution of ZnS layers as shown in Fig. 3b. The fluctuation of the periodicity was deduced from two-dimensional densitometric data of the low-resolution TEM image. Thus the profile of  $P(z)$  was obtained by taking account of the fluctuation of the periodicity and the roughness of the interface. Fig. 3c shows the obtained profile of  $P(z)$ . The intervals between the peaks, i.e., the fluctuation of the periodicity, are shown in Fig. 3c. By using Eq. (2), the Raman spectrum of zone-folded modes was calculated, as shown in Fig. 2b. The Raman spectrum reproduces the experimental data in the following two essential points: the higher order modes becomes wider and more than 6th order modes reduce their height obviously. In this calculation, we have assumed that the roughness of all layer interfaces is the same. If the roughness of all layer interfaces is taken into account, the intensity of the higher order zone-folded modes decreases more and the model calculation reproduces the Raman spectrum more precisely.

In conclusion, we have observed higher order (up to the 5th order) zone-folded phonon modes in ZnSe–ZnS strained-layer superlattices by means of Raman scattering. We were able to reproduce our zone-folded spectrum using TEM data and a photoelastic model. The agreement

between our calculation and the measurement shows that the Raman spectrum reflects dominantly the periodicity of the superlattices and the roughness of the interface.

The authors would like to thank Hitachi Research Lab. for providing TEM images, and Mr. K. Nagao of Fuji Photo Film Co., Ltd., for acquiring two-dimensional densitometric data. Part of this work was done at the Cryogenic Center, University of Tsukuba. One of the authors (A.Y.) acknowledges the support from the Japan Society for the Promotion of Science and the Scientific Research Grant-in-Aid from the Ministry of Education, Science and Culture of Japan.

## 1. References

- [1] See, for example, M. Cardona and G. Güntherodt, Eds., *Light Scattering in Solids V*, Topics in Applied Physics, Vol. 66 (Springer, Berlin, 1989).
- [2] A. Yamamoto, Y. Yamada and Y. Masumoto, *Appl. Phys. Lett.* 58 (1991) 2135.
- [3] J. Cui, H. Wang and F. Gan, *J. Crystal Growth* 117 (1992) 505.
- [4] H. Oniyama, S. Yamaga and A. Yoshikawa, *Jap. J. Appl. Phys.* 28 (1989) L2137.
- [5] B. Jusserand, D. Paquet, A. Regreny and J. Kervarec, *Solid State Commun.* 48 (1983) 499.
- [6] M.V. Klein, in: *Light Scattering in Solids*, Topics in Applied Physics, Vol. 8, Ed. M. Cardona (Springer, Berlin, 1975) p.148.
- [7] S.M. Rytov, *Akust. Zh.* 2 (1956) 71 [*Soviet Phys.-Acoust.* 2 (1956) 68].
- [8] Landolt-Börnstein, *Numerical Data and Functional Relationships in Science and Technology*, Vol. 17b (Semiconductors – Physics of II–VI and I–VII Compounds, Semimagnetic Semiconductors), Eds. O. Madelung, M. Schulz and H. Weiss (Springer, Berlin, 1982) p. 145.
- [9] Y.H. Wu, H. Yang, A. Ishida, H. Fujiyasu, S. Nakashima and K. Tahara, *Appl. Phys. Lett.* 54 (1989) 239.
- [10] M. Recio, G. Armelles, A. Ruiz, A. Mazuelas and F. Briones, *Appl. Phys. Lett.* 54 (1989) 804.
- [11] A. Yamamoto, Y. Kanemitsu, Y. Masumoto, S. Yamaga and A. Yoshikawa, *Appl. Phys. Lett.* 61 (1992) 1700.
- [12] C. Colvard, T.A. Gant, M.V. Klein, R. Merlin, R. Fischer, H. Morkoç and A.C. Gossard, *Phys. Rev. B* 31 (1985) 2080.
- [13] M.V. Klein, C. Colvard, R. Fischer and U. Morkoç, *J. Physique Colloq.* 45 (1984) C5-131.
- [14] S.K. Hark, B.A. Weinstein and R.D. Burnham, *J. Appl. Phys.* 62 (1987) 1112.



ELSEVIER

Journal of Crystal Growth 138 (1994) 647–651

JOURNAL OF **CRYSTAL  
GROWTH**

## A ZnSe/ZnCdSe quantum well symmetric self-electro-optic effect device operating in the blue-green region

S.Y. Wang <sup>\*</sup>, P. Thompson, G. Horsburgh, J.T. Mullins, I. Hauksson, K.A. Prior,  
B.C. Cavenett

*Department of Physics, Heriot-Watt University, Edinburgh EH14 4AS, UK*

### Abstract

In this paper, we report the first observation of a II–VI symmetric self-electro-optic device (SEED) operating as an optical switch at a wavelength of 488 nm at room temperature. Quantum confined Stark effect modulators based on ZnSe/ZnCdSe p–i–n structures were fabricated by molecular beam epitaxy and used in the symmetric mode where one modulator was used to bias a second modulator which showed bistable transmission characteristics with a contrast ratio of 1.5:1 between the high and low transmission states.

### 1. Introduction

A new generation of II–VI semiconductor devices, both lasers [1–4] and modulators [5], are being developed for use in visible opto-electronic systems. The important role of such structures can be found in optical switching processes using the self-electro-optic effect device, or SEED. Whilst such devices are already firmly established in III–V materials, until recently they had not been demonstrated for the blue-green spectral region. Following work previously published on the development of the diode SEED (D-SEED) [6] we now demonstrate the SEED in its symmetric form (S-SEED).

Multiple quantum well (MQW) p–i–n structures were grown by molecular beam epitaxy

(MBE) and used the quantum confined Stark effect (QCSE) to change the absorption across the junction region with applied bias. The inherently strong excitonic nature of this structure, resulting from quantum well confinement (i.e. a binding energy greater than  $kT$  at room temperature), provides a contrast similar to that of III–V devices.

SEED structures use the large changes in absorption [7], produced by the internal electric field when the device is reverse biased, as a basis for bistable optical switching. Two transmission states are seen when the device is activated by an optical control signal, or via electronic circuits built into each pixel in more complicated devices. The S-SEED combines two of the p–i–n modulator structures in a series configuration, thus removing the requirement for a resistive load found in simpler devices. For further reference, Miller

<sup>\*</sup> Corresponding author.

[8] has reviewed the SEED structure and its operation in detail.

Optical bistability (caused by thermal effects [9,10]) has been known in bulk ZnSe for some time, but only the recent advent of p-doping has allowed fabrication of p-i-n optoelectronic devices.

## 2. Experiment

The SEED device is based on a quantum confined Stark effect modulator structure. Grown by MBE in a VG288 growth kit it consists of an  $n^+$ -GaAs substrate, a  $0.4 \mu\text{m}$   $n^+$ -ZnSe layer, an undoped buffer layer ( $0.24 \mu\text{m}$ ),  $30 \text{ Cd}_{0.2}\text{Zn}_{0.8}\text{Se}$  quantum wells  $40 \text{ \AA}$  wide with  $60 \text{ \AA}$  ZnSe barriers, a second undoped buffer layer ( $250 \text{ \AA}$ ) and a  $0.8 \mu\text{m}$  p-ZnSe layer. Iodine was used for the n-doping and nitrogen, from an Oxford Applied Research RF plasma source, was used for the p-doping. In order to apply electric fields perpendicular to the quantum-well layers, an indium ohmic contact was made to the GaAs substrate and In-Ga was used for the top p-ZnSe layer. Finally an optical window, approximately  $0.5 \text{ mm}$  in diameter, was chemically etched in the substrate to form the device which was approximately  $1.2 \text{ mm} \times 3 \text{ mm}$  in size and is shown schematically in Fig. 1.

The In-Ga contact to the p-ZnSe is not ohmic, but forms a Schottky junction in series with the p-i-n diode. Since the polarities of the two diodes are opposite, the majority of the voltage is

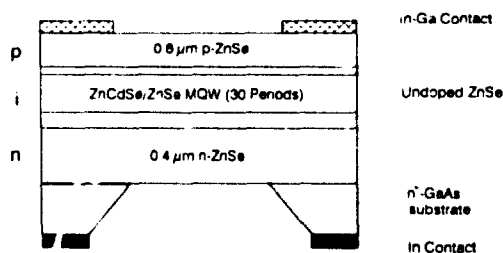


Fig. 1. Schematic structure of the ZnCdSe/ZnSe multiple quantum well p-i-n diode, with an In-Ga contact on the p-ZnSe layer, an In contact on the GaAs substrate and the etched window.

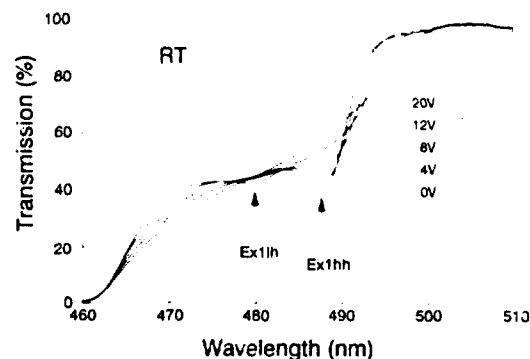


Fig. 2. Room temperature transmission of the ZnCdSe/ZnSe multiple quantum well p-i-n diode versus reverse bias voltages as indicated. The curves were normalized to 100% transmission at wavelength below the QW absorption peak.

dropped across the p-i-n diode when it is reverse biased. Moreover, the voltage drop across the Schottky junction will remain approximately constant and was estimated from the measurement of the open circuit voltage of the device to be approximately  $1.6 \text{ V}$ . The leakage current of the device was typically less than  $50 \text{ nA}$  at  $-20 \text{ V}$  reverse bias.

## 3. Results and discussion

The optical transmission and photo-current spectra were measured using a tungsten white light source and a monochromator with  $0.5 \text{ nm}$  resolution. Fig. 2 shows the room temperature transmission of the p-i-n diode as a function of applied reverse bias. The transmission spectra are normalized to 100% at a wavelength below the absorption edge of the quantum well. We can see from the figure that there is a strong excitonic absorption peak for the  $n = 1$  heavy hole exciton (Ex1hh). This ionizes rapidly with increased reverse base, resulting in a change in transmission from about 40% to 60% when the reverse bias changes from 0 to  $20 \text{ V}$ . The  $n = 1$  light hole exciton (Ex1lh) is also observed at zero bias. The transmission cutoff at wavelengths shorter than  $460 \text{ nm}$  is due to the absorption of ZnSe bandgap.

As an increasing reverse bias is applied to the p-i-n diode, the exciton shows a clear “red shift” with the exciton peaks remaining resolvable up to approximately 12 V. Above this value, the exciton peaks finally broaden and quench due to the strength of the internal electric field. The absorption coefficient, calculated from Fig. 2 with respect to well thickness (not the combined thickness of barrier and well), of the Ex1hh exciton is as high as  $7.8 \times 10^4 \text{ cm}^{-1}$  at zero bias and decreases to  $4.6 \times 10^4 \text{ cm}^{-1}$  at the same wavelength with a 20 V reverse bias at room temperature. The half-width at half maximum (HWHM) linewidth of the Ex1hh absorption on the low energy side at zero bias is about 16 meV which is smaller than the shift of the exciton peak under the electric field.

The linewidth of the exciton is significantly larger than that of III-V semiconductors due to the stronger exciton-LO-phonon interaction of II-VI materials (HWHM  $\approx 4 \text{ meV}$  in AlGaAs/GaAs). Further, in contrast with III-V materials, the change of absorption due to the exciton peak shift is less important than its quenching. From theory, wider wells would result in a larger excitonic peak shift, however, the reduced confinement of the exciton in such a structure would also result in a smaller excitonic absorption strength. Therefore, for an electro-optic device using the OCSE, where large absorption changes are desired, such trade-offs must be considered in the design of the structure. In fact, the magnitude of the electroabsorption is already larger than the best III-V semiconductor and it follows that wider exciton peaks would reduce any sensitivity to wavelength and temperature changes.

In order to use the p-i-n device in the SEED configuration, it is necessary to measure the photo-current response curve, which gives the change in photo-current with applied voltage at a fixed wavelength. The solid lines in Fig. 3 show the photo-current response curves for different light intensities at 488 nm, i.e. the wavelength which corresponds to the Ex1hh absorption at zero volts. We note that the maximum photo-current occurs at about 4 V reverse bias and then decreases monotonically as the voltage increases up to 20 V. In forward bias the photo-current

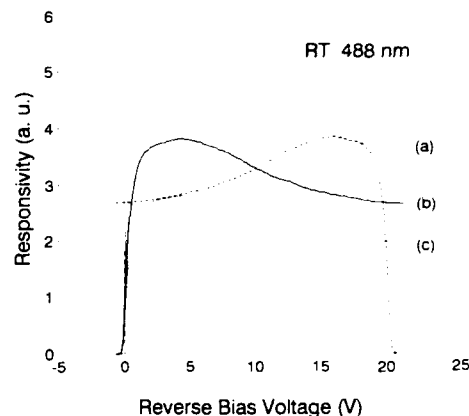


Fig. 3. The solid lines show photo-current response curves as a function of illumination intensity for the p-i-n junction with reverse bias at a wavelength of 488 nm, which corresponds to the peak position of the Ex1hh at zero volts shown in Fig. 2. The dotted line gives the load-line from the voltage power supply with a reverse-biased p-i-n diode under constant illumination.

decreases rapidly with the cut-off at 0.7 V due to the potential barrier caused by the Schottky contact at the p-layer, discussed above, compensating the built-in potential of the p-i-n diode.

The photo-current spectra are similar to the absorption curves, which suggests that although absorption at the exciton peak initially creates excitons, these are ionized into free electrons and holes via thermionic emission from the quantum wells.

To operate a modulator structure such as a symmetric SEED optical switch, two reverse biased p-i-n diodes are placed in series together, one acting as the “load” for the other. Fig. 4 shows the optical arrangement and the interconnection of the p-i-n diodes with the voltage supply. The 488 nm line from a CW Ar<sup>+</sup> laser was used as the light source, with constant optical power ( $P_{in}$ ) supplied to diode 1 by means of a beam splitter inserted in the laser path. The second diode received a triangular ramped input ( $P_m$ ) produced by an acousto-optic modulator placed in the secondary path formed by the beam splitter. The optical power output ( $P_{out}$ ) is the transmitted power from p-i-n diode 2, with the



bias current controlled by a change in the light intensity of the illumination on diode 1 by using a neutral density filter.

The dotted curve in Fig. 3 gives the load-line for the supply with a reverse-bias across diode 1. This diode can be considered as a voltage controlled constant current source. If there is no light on diode 2, no current flows and all of the bias voltage appears across this modulator, creating a high electric field across the quantum wells. Therefore, the device is in a high transmission state as the absorption is at a minimum. As the optical input power is slowly increased, the photo-current also increases but the voltage drop on diode 2 remains, approximately, unchanged due to the constant current bias. When the photo-current generated by diode 2 is comparable (see curve (a) in Fig. 3) with or larger than the bias current provided by diode 1, positive feedback occurs, leading to the majority of the voltage being dropped across diode 1. This then leaves diode 2 in a low transmission state as the absorption is now at a maximum. Once this low transmission state is reached, the input power can be decreased whilst still retaining the high absorp-

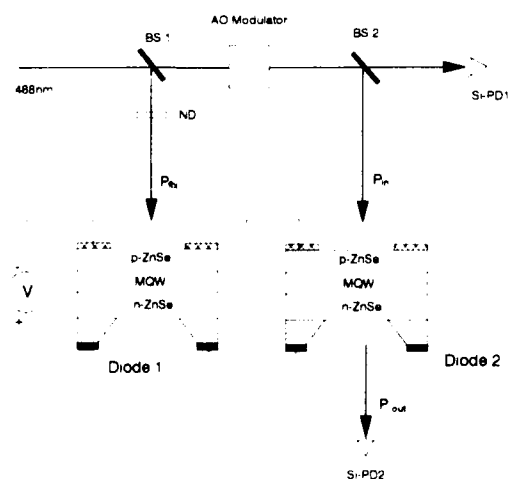


Fig. 4. Optical arrangement used to characterize the S-SEED and the electrical interconnections of the two p-n diodes to form the D-SEED configuration. BS 1 and BS 2 are beam splitters, ND is a neutral density filter and Si-PD1 and Si-PD2 are silicon photo diodes.

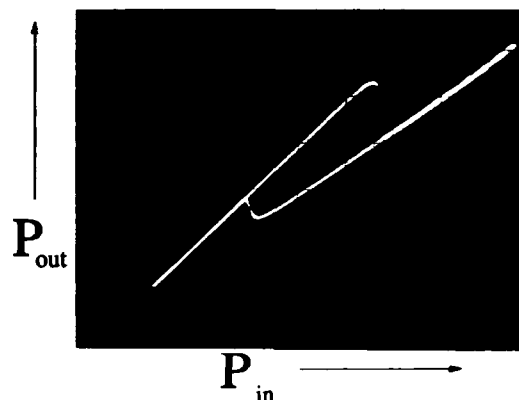


Fig. 5. Optical input-output characteristic for the S-SEED configuration, showing optical bistability. This characteristic is taken with a  $20 \mu\text{A}$  bias current and  $20 \text{ V}$  supply voltage. The input ( $P_{\text{in}}$ ) and output ( $P_{\text{out}}$ ) optical powers correspond to approximately 40 and  $12 \mu\text{W/div}$ , respectively.

tion state until a lower critical "switch-up" input power is reached (see curve (c) in Fig. 3). At this point, the positive feedback operates in reverse, and the device switches back to a high transmission state. Therefore, between these two powers, the device is bistable and can operate in a either a high or low transmission.

The optically bistable input-output characteristic for the S-SEED is shown in Fig. 5, where the input and output intensities of the laser are approximately 40 and  $12 \mu\text{W/div}$ , respectively, with a bias current and voltage of  $20 \mu\text{A}$  and  $20 \text{ V}$ . The contrast ratio of the high and low states in this device is about 1.5:1, which could be improved by increasing the number of quantum wells. In the cases of the S-SEED and the D-SEED, we are able to observe bistability at  $7 \text{ V}$ , whereas it can be seen from the response curve (Fig. 3) that if a resistive load was used, a bias voltage of about  $35 \text{ V}$  would be necessary. As expected, the switch power ratio of the S-SEED is greatly improved compared with the D-SEED configuration.

Because of the large RC constant caused by the large area and the resistive p-ZnSe layer in this device, the switching times of the device are relatively slow compared with the fully integrated III-V devices. By improving the design and de-

vice fabrication, the II-VI semiconductor devices should be able to work faster than III-V due to the shorter free carrier life time.

#### 4. Conclusion

In summary, we report the first observation of electronic optical bistability in the blue-green region using a II-VI ZnSe/ZnCdSe quantum confined Stark effect modulator structure in the form of an S-SEED device. With optimized structures in II-VI semiconductors QCSE devices would form suitable components for information processing in the UV to infrared spectral region. In addition, the shorter wavelength of operation of these devices results in a reduced diffraction limited pixel size by a factor of  $\sim 2$  over AlGaAs/GaAs structures and correspondingly reduced energy requirements for switching.

#### 5. Acknowledgements

We are grateful to SERC and VG Semicon for continued support.

#### 6. References

- [1] M.A. Haase, J. Qiu, J.M. DePuydt and H. Cheng, *Appl. Phys. Lett.* 59 (1991) 1272.
- [2] H. Jeon, J. Ding, A.V. Nurmikko, W. Xie, D.C. Grillo, M. Kobayashi, R.L. Gunshor, G.C. Hua and N. Otsuka, *Appl. Phys. Lett.* 60 (1992) 2045.
- [3] K. Ohkawa, A. Tsejamura, S. Hayshi, S. Yoshii and T. Mitsuyu, *Physica B* 185 (1992) 112.
- [4] S.Y. Wang, J. Simpson, H. Stewart, S.J.A. Adams, I. Hauksson, Y. Kawakami, M.R. Taghizadeh, K.A. Prior and B.C. Cavenett, *Physica B* 185 (1992) 508.
- [5] S.Y. Wang, Y. Kawakami, J. Simpson, K.A. Prior and B.C. Cavenett, *Appl. Phys. Lett.* 62 (1992) 1715.
- [6] S.Y. Wang, G. Horsburgh, P. Thompson, I. Hauksson, J.T. Mullins, K.A. Prior and B.C. Cavenett, *Appl. Phys. Lett.* 63 (1993) 875.
- [7] D.A.B. Miller, D.S. Chemla, T.C. Damen, A.C. Gossard, W. Wiegmann, T.H. Wood and C.A. Bumis, *Appl. Phys. Lett.* 45 (1984) 13.
- [8] D.A.B. Miller, *Opt. Quantum Electron.* 22 (1990) S61.
- [9] S.D. Smith, J.G.H. Mathew, M.R. Taghizadeh, A.C. Walker, B.S. Wherrett and A. Hendry, *Opt. Commun.* 51 (1984) 357.
- [10] M.R. Taghizadeh, I. Janossy and S.D. Smith, *Appl. Phys. Lett.* 46 (1985) 331.



ELSEVIER

Journal of Crystal Growth 138 (1994) 652–655

JOURNAL OF  
**CRYSTAL  
GROWTH**

## Polar magneto-optic Kerr effect in (Cd,Mn)Te/CdTe superlattices

B. Buda, M. Dahl \*, N. von Truchsess, A. Waag

*Physikalisches Institut, Universität Würzburg, Am Hubland, D-97074 Würzburg, Germany*

### Abstract

The polar magneto-optic Kerr effect is used to investigate (Cd,Mn)Te/CdTe superlattices. It is demonstrated that the magneto-optic Kerr effect provides a nondestructive technique to study excitons. An oscillator model is applied to analyze the data, and the Zeeman splitting and the magnetic field dependence of the oscillator strength for a 60 Å period superlattice is given as an example.

### 1. Introduction

Quantum well (QW) and superlattice (SL) structures based on II–VI semiconductors have gained increased interest due to their potential for application in optoelectronics in the visible-light region. There is also a variety of reasons to study fundamental physics of II–VI based QWs and SLs. One particular aspect making II–VI based QWs and SLs an attractive material system to study is the possibility of including diluted-magnetic semiconductors (DMSs) into the structures. In DMSs a fraction of group II ions is replaced by magnetic ions and the strong sp–d exchange interaction leads to a variety of phenomena. A discussion of the exchange-induced optical properties of DMS based SLs can be found in ref. [1] and references therein.

One of the most prominent effects is the giant Faraday rotation. In bulk DMSs it is used rou-

tinely to study the band structure and excitonic properties or as an optical method to determine the magnetization [2,3]. Recently Kohl et al. [4,5] demonstrated the possibility of detecting Faraday rotation from (Cd,Mn)Te/CdTe multiquantum wells (MQWs). To perform Faraday experiments in SLs and QWs, substrates have to be transparent or removed by etching. In the following we will demonstrate that the polar magneto-optic Kerr effect (MOKE) – observation of the magnetic circular birefringence and dichroism in reflection geometry – is more suitable for routine-type experiments in SLs.

### 2. Experimental details

The samples used in this investigation are SLs of (Cd,Mn)Te/CdTe grown on CdTe substrates by molecular beam epitaxy. The SLs are embedded between a buffer layer (6000 Å) and a cap layer (1000 Å) of (Cd,Mn)Te.

The setup used to measure the derivative of the Kerr rotation  $\Delta\theta_K/\Delta B$  is similar to the one

\* Corresponding author.

used in ref. [5]. The fundamental difference is that we observe the reflected light and therefore do not need any special sample preparation. Linearly polarized light from a tunable laser is reflected (at near normal incidence) from the sample and split into two orthogonal components by a polarizing beamsplitter. Typical power densities for the experiments were as low as approximately  $1 \text{ W/cm}^2$ . The sample is placed into an optical split-coil magnet cryostat ( $B \leq 7 \text{ T}$ ); an additional small coil allows one to apply modulation fields ( $B_{\text{mod}} \leq 5 \text{ mT}$ ,  $f_{\text{mod}} \leq 1 \text{ kHz}$ ). Both fields are directed parallel to the propagation direction of the light, which coincides with the growth axis of the samples. The two orthogonally polarized light beams are detected by a pair of Si diodes. Sum and difference of the photocurrents are generated by analog amplifiers. The beamsplitter is set to a position where the two beams are of equal intensity outside the resonance.

An analysis of the experiment shows that the ratio of the difference signal detected by a lock-in amplifier at the modulation frequency ( $I_{\Delta}^{\text{AC}}$ ) and the DC sum signal ( $I_{\Sigma}^{\text{DC}}$ ) is independent of the apparatus characteristics and depends only on intrinsic properties of the sample:

$$S = \frac{I_{\Delta}^{\text{AC}}}{I_{\Sigma}^{\text{DC}}} = 2 \frac{\text{Im}[d(r_{+}^{*} r_{-})/dB]}{|r_{+}|^2 + |r_{-}|^2}, \quad (1)$$

where  $r_{\pm}$  denotes the amplitude reflection coefficient  $r_{\pm} = \rho_{\pm} e^{i\theta_{\pm}} = E_{\pm}^r/E_{\pm}^i$  for right (+) and left (-) circular polarization. This expression simplifies for zero background field to:

$$S = \frac{I_{\Delta}^{\text{AC}}}{I_{\Sigma}^{\text{DC}}} = 2 \frac{d\theta_K}{dB} \Big|_{B=0} B_{\text{mod}}, \quad (2)$$

where  $\theta_K = \theta_{+} - \theta_{-}$  is the Kerr angle. In a finite background field and under resonance conditions where the difference between  $\rho_{+}$  and  $\rho_{-}$  is not negligible, Eq. (1) has to be used for data analysis.

### 3. Experimental results

A typical spectrum for field-modulated MOKE is shown in Fig. 1 together with photolumines-

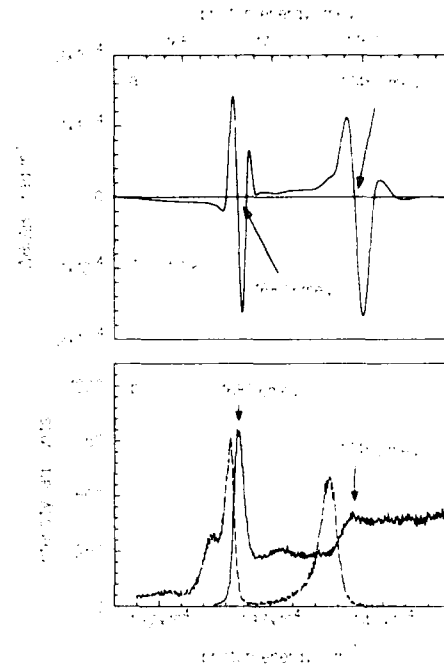


Fig. 1. (a) Differential polar magneto-optic Kerr rotation for a  $\text{Cd}_{0.9}\text{Mn}_{0.1}\text{Te/CdTe}$  superlattice ( $L_{\text{K}} = L_{\text{w}} = 20 \text{ \AA}$ ). (b) Photoluminescence (dashed line) and photoluminescence-excitation (solid line) spectra of the same sample.

cence (PL) and photoluminescence-excitation (PLE) spectra of the same sample. PL and PLE spectra of similar samples have been investigated in detail before [1]; therefore we will give only a brief discussion of these data. The PL spectrum (Fig. 1b) shows two lines: a double structure at  $E = 1676 \text{ meV}$  related to SL excitons and a line at  $E = 1731 \text{ meV}$  corresponding to the luminescence from the (Cd,Mn)Te buffer layer. The comparison with the PLE data reveals a pronounced redshift of the buffer-layer PL which is due to magnetic polaron formation; the PL line from the SL excitons also shows a redshift. This energy difference can be explained by exciton localization due to fluctuations of the well width, small contributions due to two-dimensional magnetic polaron formation are possible. The low energy line is likely to be associated with an exciton bound to an acceptor.

A comparison of the field modulated MOKE and the PLE data clearly reveals that the structures in the MOKE data are related to the free excitons in the SL as well as in the buffer material. The zero crossing of the MOKE structure coincides within the experimental error with the peak position in the PLE spectra. This was confirmed for all the samples investigated and therefore provides a simple way to determine the free exciton energy from the spectra.

#### 4. Numerical data analysis

To extract more information from the MOKE data, it is necessary to model the data using Eq. (1). This requires calculating the amplitude reflection coefficients  $r_{\perp}$  for the multilayer structures. This task is simplified by recently published theoretical investigations of magneto-optics in multilayer structures [6]. These authors formulate the problem in terms of a  $4 \times 4$  transfer matrix for each layer depending only on the dielectric function of the layer material and the layer thickness. Any structure can be described by the product of the corresponding matrices. Imposing proper boundary conditions on the resulting transfer matrix defines reflection coefficients as ratio of two elements of the transfer matrix. Assuming that the contribution from the heavy-hole exciton (11h) is dominating the dielectric function we used a single-oscillator model of the following form for each material:

$$\epsilon_{\perp}(B) = \epsilon_{\infty} + \frac{\epsilon_{\infty} \omega_{\perp 1}^2(B)}{\omega_{\perp 1}^2(B) - \omega^2 - \frac{1}{2}i\Gamma^*(B)}, \quad (3)$$

where  $\omega_{\perp 1}(B)$  is the resonance frequency corresponding to the 11h,  $\omega_{\perp 1}$  is the longitudinal-transverse splitting which is directly proportional to the oscillator strength, and  $\Gamma^*(B)$  is a phenomenological damping constant [7].

To calculate the field modulated MOKE, we have to make assumptions on the field dependence of the parameters in (3). We use a Taylor expansion at the background field  $B_b$

$$\omega_{\perp 1}(B) = \omega_{\perp 1}(B)|_{B_b} + \left. \frac{d\omega_{\perp 1}(B)}{dB} \right|_{B_b} B_{\text{mod}} + \dots, \quad (4)$$

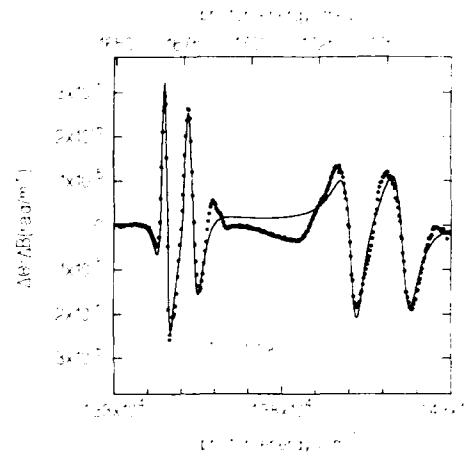


Fig. 2. Differential magneto-optical Kerr rotation for a  $\text{Cd}_{0.9}\text{Mn}_{0.1}\text{Te}/\text{CdTe}$  superlattice ( $L_s = L_b = 30$  Å) in a background field of  $B = 0.5$  T. Solid line is calculated.

Since the lock-in signal is taken at the first harmonic of the modulation frequency, only the linear term in (4) contributes to the signal. As the Zeeman splitting is "giant" in DMS we neglect contributions of  $\omega_{\perp 1}$  and  $\Gamma^*$ , i. e. assuming:

$$\frac{d\omega_{\perp 1}}{dB} \gg \frac{d\omega_{\perp 1}}{dB} \approx \frac{d\Gamma^*}{dB} \approx 0. \quad (5)$$

Using the transfer-matrix formalism and a dielectric function of the form (3) for each material, we can calculate the modulated MOKE spectra. Treating  $\omega_{\perp 1}$ ,  $\omega_{\perp 1}$ ,  $\Gamma^*$ , and  $d\omega_{\perp 1}/dB$  as fitting parameters, we get a reasonably good fit to the main structures of the data. An example is shown in Fig. 2 for a  $(\text{Cd,Mn})\text{Te}/\text{CdTe}$  superlattice in a background field of  $B = 0.5$  T. It has to be pointed out here that the lineshape of the spectra is strongly influenced by the values of the background dielectric constant  $\epsilon_{\infty}$  for the  $(\text{Cd,Mn})\text{Te}$ . This high sensitivity can be understood as an effect of multiple reflections between the surface and the substrate. The calculated spectra deviate significantly from the experiment on the high energy side of the 11h structure where a sharp peak is not reproduced. We expect the light-hole exciton contribution which is not included in our model to be in this range. The deviation is also significant in the region between the 11h struc-

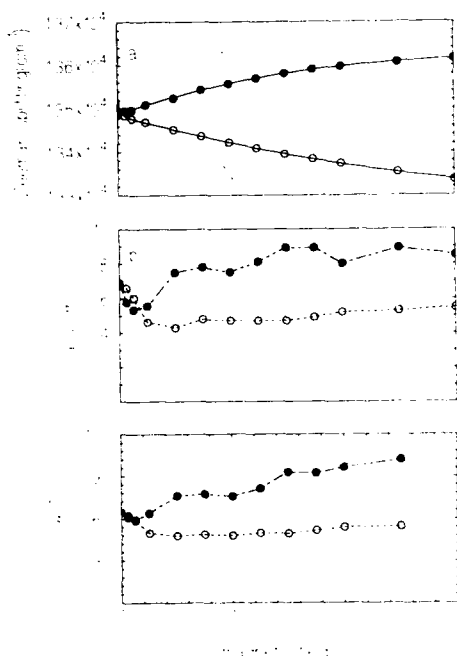


Fig. 3. Zeeman splitting (a), longitudinal-transverse splitting (b) and damping (c) for a  $L_n = L_w = 30$  Å superlattice of  $\text{Cd}_{0.7}\text{Mn}_{0.3}\text{Te}/\text{CdTe}$ . The solid lines in (a) are Brillouin functions. The dashed lines in (b) and (c) are guides to the eye.

ture and the barrier structure. Here we believe that the neglect of the real band structure of the superlattice is responsible for the deviation. A dielectric function taking into account not only the excitonic contributions but also the full mini- and subband structure would be necessary.

Fig. 3 comprises the results of an analysis for the SL exciton in background fields up to  $B = 3$  T. The Zeeman splitting of the  $^1\text{h}$  (fig. 3a) fits excellently to Brillouin functions (solid lines) [1] with values of the parameter  $T_0 = 1.2$  K for the upper  $\sigma_+$  component and  $T_0 = 3.6$  K for the lower  $\sigma_-$  component. This asymmetry may be explained by the different probabilities for the two spin states to be found in the barrier, combined with the assumption that  $T_0$  is decreased at the boundary of the  $(\text{Cd,Mn})\text{Te}$  layers. Further investigations of this subject are under way.

The  $\omega_{\text{LT}}$  values, i.e. the oscillator strength,

show a monotonic behaviour and no pronounced evidence for a change of the band alignment of the  $\sigma_-$  component. This is in agreement with the results reported in ref. [7] for a similar structure. The increase of the oscillator strength with  $B$  for the  $\sigma_-$  component reflects the gain in two-dimensionality as the confinement potential increases.

## 5. Conclusion

We demonstrated that the polar MOKE is a sensitive tool to study DMS based SLs. Comparison of MOKE and PLE shows that an evaluation of the zero crossings of the signal gives a good approximation of the exciton energies. Phenomenological description of the dielectric function in terms of a single-oscillator model reproduces the main structures of the data well; however, a dielectric function based on a band-structure calculation may be necessary for a complete description of the data.

## 6. Acknowledgement

We express our gratitude to Prof. Dr. G. Schaack for his interest and support.

## 7. References

- [1] G. Peter, E. Deleporte, G. Bastard, J.M. Berron, C. Delalande, B. Gil, J.M. Hong and L.L. Chang, *J. Luminescence* 52 (1992) 147.
- [2] D.U. Bartholomew, J.K. Furdyna and A.K. Ramchar, *Phys. Rev. B* 34 (1986) 6943.
- [3] B. Leclercq, C. Rigaux, A. Mycielski and M. Menant, *Phys. Rev. B* 47 (1993) 6169.
- [4] M. Kohl, M.R. Freeman, J.M. Hong and D.D. Awschalom, *Phys. Rev. B* 43 (1990) 2431.
- [5] M. Kohl and D.D. Awschalom, *J. Appl. Phys.* 70 (1991) 6377.
- [6] S. Visnovsky, *Mater. Res. Soc. Symp. Proc.* 232 (1991) 325.
- [7] E.L. Ivchenko, A.V. Kavokin, V.P. Kochereshko, G.R. Posina, I. N. Ural'tsev, D.R. Yakovlev, R.N. Bicknell-Lassus, A. Waag and G. Landwehr, *Phys. Rev. B* 46 (1992) 7713.



ELSEVIER

Journal of Crystal Growth 138 (1994) 656–660

JOURNAL OF  
**CRYSTAL  
GROWTH**

## Spin-flip Raman scattering by electrons bound to donors in CdTe/Cd<sub>1-x</sub>Mn<sub>x</sub>Te multiple quantum well structures as a function of barrier composition

D. Wolverson <sup>\*,a</sup>, J.J. Davies <sup>a</sup>, S.V. Railson <sup>a</sup>, M.P. Halsall <sup>a,1</sup>, D.E. Ashenford <sup>b</sup>,  
B. Lunn <sup>b</sup>

<sup>a</sup> *a School of Physics, University of East Anglia, Norwich NR4 7TJ, UK*

<sup>b</sup> *Department of Engineering Design and Manufacture, University of Hull, Hull HU6 7RX, UK*

### Abstract

Experimental and theoretical studies of the exchange-enhanced spin-flip Raman scattering from electrons bound to donors in a series of CdTe/Cd<sub>1-x</sub>Mn<sub>x</sub>Te multiple quantum well structures have been carried out. In this series, the CdTe well width has been kept constant and the barrier Mn concentration has been varied from 1% to 12%. In some samples two spin-flip Raman signals are observed, attributed to electrons located in the quantum wells, but bound to donors located either in the quantum wells or in the barriers adjacent to the wells. This work provides a new test of a model developed previously for these two signals; the results suggest that the conduction band offset in CdTe/Cd<sub>1-x</sub>Mn<sub>x</sub>Te heterostructures is not a function of Mn concentration at low concentrations.

### 1. Introduction

Dilute magnetic semiconductors (DMSs; for instance, Cd<sub>1-x</sub>Mn<sub>x</sub>Te) show a dependence of the bandgap on the applied magnetic field, owing to the strong spin-exchange coupling of the carriers with the magnetic ions [1]. When the barriers of multiple quantum well (MQW) structures are formed from DMS material, the barrier bandgap becomes an adjustable quantity. We have previously exploited this effect in CdTe/Cd<sub>1-x</sub>Mn<sub>x</sub>Te MQWs containing donor ions, using spin-flip Ra-

man (SFR) spectroscopy [2] to study how the Coulomb fields of donor impurities affect electrons confined in the wells [3,4]. The Raman shifts correspond to the Zeeman splitting of the electron states in the magnetic field, enhanced by the exchange field due to the manganese ions by an amount determined by the penetration of the electronic wavefunction into the magnetic barrier region. Thus, the Raman shifts observed in SFR give a probe of any effects which modify the electron wavefunction.

In a uniformly-doped n-type MQW structure, the electrons will consist of two types. First, there will be those bound at the donors in the wells, and, secondly, there will be those which originated from the donors in the barriers, but which are now trapped in the well region. Since the

\* Corresponding author.

<sup>1</sup> Present address: Laboratoire de Spectrométrie Physique, Université Joseph Fourier de Grenoble, BP 87, F-38402 Saint-Martin-d'Hères Cedex, France.

degree of penetration of the two types of electron into the barriers will be different, the Zeeman splitting of the two types, and thus their SFR Raman shifts, will also differ. We have shown previously that the two distinct series of SFR signals that we observe in a set of CdTe/Cd<sub>0.93</sub>Mn<sub>0.07</sub>Te multiple quantum well structures of different well widths can be interpreted as being due to these two types of electron state [3]. Here, we discuss the extension of that study to samples of constant well width but varying Mn concentration.

## 2. Experimental details

CdTe/Cd<sub>1-x</sub>Mn<sub>x</sub>Te multiple quantum wells (MQWs) with well and barrier widths of 50 and 150 Å, respectively, were grown on 1000 Å buffer layers of CdTe on (001) InSb substrates by molecular beam epitaxy, with barrier manganese concentrations of  $x = 0.01, 0.02, 0.03, 0.07$ , and  $0.12$ . The growth technique is described elsewhere and typically yields n-type material with net neutral donor concentrations of order  $10^{14} \text{ cm}^{-3}$  [5]. Raman scattering experiments were conducted at 1.5 K in the backscattering geometry; magnetic fields from zero to 6 T were applied in the plane of the sample. A Ti-sapphire laser was used as the excitation source and the scattered light was analysed with a triple monochromator and CCD detector. Resonance profiles of the SFR signals were obtained using an automated scanning technique described elsewhere [6].

## 3. Results and discussion

Fig. 1 shows SFR spectra for three samples, at the magnetic fields and temperatures indicated. The experimental data have been fitted via a least-squares routine, and the fits are indicated on the figure by solid lines; the photoluminescence (PL) background was approximated by a straight line of appropriate gradient. For the  $x = 0.07$  sample (Fig. 1b), the experimental spectrum consists of two clearly-resolved Gaussian bands (at 38 and 51  $\text{cm}^{-1}$  at saturation) which we label

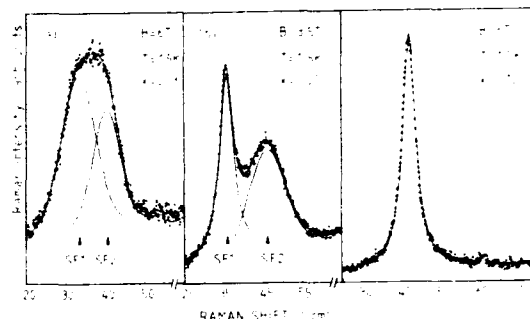


Fig. 1. Spin-flip Raman spectra of three MQW structures of well width 50 Å and barrier Mn concentrations ( $x$ ) as indicated. (+) Experimental data; (—) fits to the data, and the individual components of each fit.

SF1 and SF2. For the  $x = 0.03$  sample (Fig. 1a), two unresolved Gaussian components (at 33 and 40  $\text{cm}^{-1}$ ) can be identified on fitting the data. These spectra agree with our previous work, and we interpret the two components of the spectra as being due to electrons in the quantum wells bound to donors located in the wells (SF1) or bound to donors located in the barriers (SF2).

The Raman signals were identified with spin-flip processes as follows. In our experimental geometry, the selection rule for SFR of  $\Delta m_j = \pm 1$  implies that signals will only be detected when the linear excitation and detection polarizations are mutually perpendicular. Also, SFR signals show a modified Brillouin function-like dependence on magnetic field which identifies them as magnetic excitations [2]. Polarization and magnetic field dependences confirmed the origin of the Raman signals discussed here.

Applying the model developed earlier, we can calculate the spin-flip energy of a donor-bound electron for different donor positions in the present structures. Details of the calculation are presented elsewhere [3]. We use a variational approach and assume a donor electron envelope function consisting of a product of the one-dimensional finite potential well envelope wavefunction and a three-dimensional hydrogen-like state; the variational parameter characterises the deviation from the spherical shape of the three-dimen-



sional bulk donor wavefunction. The variational energy is calculated using the Hamiltonian for a hydrogen-like donor in a square well potential [7]. In order to calculate spin-flip energies, a particular value of the conduction band offset  $\Delta_c$  in zero magnetic field is assumed. When the field is applied, the offset becomes  $(\Delta_c - E_{st}/2)$  or  $(\Delta_c + E_{st}/2)$ , according to the direction of the electron spin, where  $E_{st}$  is the conduction band Zeeman splitting. The electron energies are calculated for each of these two offset values, and their difference gives the Zeeman splitting of the donor-bound electron, which is the spin-flip Raman energy observed. The parameters of the calculation are given in ref. [3]. The value of the conduction band offset  $\Delta_c$  was treated as a free parameter previously; a value of  $60 \pm 5$  meV was deduced for the heterostructure with  $x = 0.07$  [3]. It is possible that this quantity varies with Mn concentration, since other work on samples with higher Mn concentrations suggests a larger value [8,9]. The calculation also requires a knowledge of the barrier Zeeman splitting, and thus the effective Mn concentration,  $\bar{x}$ . This is less than the actual Mn concentration,  $x$ , due to the spin-pairing of neighbouring Mn ions, and therefore varies with  $x$  (increasing with  $x$  until  $x \approx 0.05$  and then decreasing as the likelihood of Mn pairing increases). The exact dependence of  $\bar{x}$  on  $x$  is not known and several experimentally determined relationships have been published [10–12] which differ principally for  $x > 0.10$ .

The calculation can now be applied to our experimental results. Since a uniform distribution of donors throughout the sample gives rise to only two main contributions to the Raman spectrum, calculating the Raman shift for a donor placed centrally in the well gives an approximation to the SF1 signal, whilst when the donor is placed in the barrier and within a few lattice constants of the well, we obtain an estimate for the Raman shift of SF2. Fig. 2 shows the calculated Raman shifts of the SF1 and SF2 signals for donors at the well centre and at  $10 \text{ \AA}$  into the barrier as a function of the barrier Mn concentration; a fixed ratio of  $\Delta_c/\Delta E_g = 0.54$  was used, where  $\Delta E_g$  is the band gap energy difference at 1.5 K.

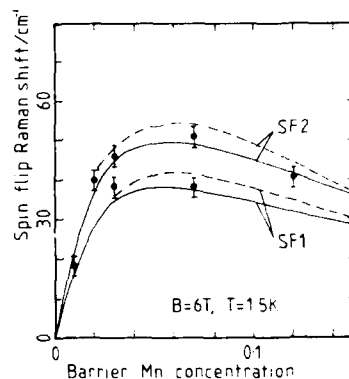


Fig. 2. Dependence of the saturation spin flip Raman shift on barrier Mn concentration. (—) Calculated dependence of SF1 and SF2 Raman shift with effective Mn concentration according to ref. [12]; (---) calculations for SF1 and SF2 with effective Mn concentration according to ref. [11]; (●) experimental data.

The experimental values are also indicated on Fig. 2 and it is clear that for the  $x = 0.03$  and  $x = 0.07$  samples, the agreement between calculation and experiment is good. In view of the uncertainty in the form of  $\bar{x}(x)$ , we performed two sets of calculations taking different estimates for  $\bar{x}(x)$ , from refs. [10] and [11] (the dashed curves) and [12] (the solid curves). The data of refs. [10] and [11] give the best agreement with our SFR data for these MQWs and for an  $x = 0.07$  epitaxial layer.

For the  $x = 0.01$  and  $0.02$  samples, our model suggests that SF1 and SF2 bands will not be sufficiently separated in energy to be experimentally resolved. In both cases only one SFR band is observed, with Raman shifts in reasonable agreement with our predictions.

However, the experimental results for the  $x = 0.12$  sample (Fig. 1c) are not as expected. The spectrum can be fitted with a single Lorentzian curve, centred at about  $42 \text{ cm}^{-1}$ ; two Gaussian bands centred at the same Raman shift can reproduce its lineshape, but within our model for SFR in these structures, SF1 and SF2 bands cannot occur at identical positions, so that a different explanation for the lineshape and Ra-

man shift must be sought. The observed Raman shift is higher than expected for SF1 signals, and it is necessary to confirm that this signal is associated with the quantum wells of the structure. We therefore studied the dependence of the SFR signal intensity on excitation photon energy; Fig. 3a shows a set of SFR spectra taken for laser wavelengths in the range 7415 to 7505 Å, stepping the laser in 2 Å steps. The SFR signal shows clear resonances in this energy range, which are shown, by comparison with the quantum well PL spectrum (Fig. 3b), to correspond to the quantum well transitions.

Several explanations for the observed Raman shift can be proposed: firstly, interdiffusion of Mn into the quantum wells would increase the spin-flip shift, since the overlap of the electronic wavefunction with the predominantly unpaired interdiffused Mn ions would be significant. Sec-

ondly, an unexpectedly high level of doping could result in an electron concentration in the well sufficient to decrease the effective potential of the well, and thereby increase the penetration of the carriers into the barrier. Changes in the band offset ratio with Mn concentration could explain our results, but as noted above it appears that if any dependence on  $x$  exists, published work suggests an increase with  $x$ , leading to *stronger* electron confinement in the well and therefore *smaller* SFR shifts.

A final explanation is that the reduced probability of spin-pairing for Mn ions situated close to the barrier–well interface results in a locally enhanced value of the paramagnetic Mn concentration,  $\bar{x}$ , compared to that determined in bulk samples [13]. Since the well electron wavefunction probes specifically the part of the barrier close to the interface, it would be particularly sensitive to this effect and the spin-flip Raman shift would be correspondingly increased. Indeed, SFR studies of further MQW structures with  $0.1 < x < 0.2$  would be valuable in investigating the question of Mn magnetization near an interface.

#### 4. Summary

We have reported the observation of two distinct electron SFR spectra in  $\text{CdTe}/\text{Cd}_{1-x}\text{Mn}_x\text{Te}$  multiple quantum well samples of different barrier concentrations. The spectra of four samples are accounted for by the existence of a uniform low level of donors throughout the well and barrier regions. A fifth sample gives an anomalous result for which two explanations have been considered; this result illustrates the sensitivity of the SFR technique to sample quality and doping levels. A variational model has been applied, and its predictions for the former two samples are consistent with the observed trend in the spin-flip energies with barrier concentration if the zero-field conduction band offset is taken to be  $0.54\Delta E_g$ . This work therefore provides further evidence for a constant value of the band offset ratio in  $\text{Cd}_{1-x}\text{Mn}_x\text{Te}$  at low  $x$  values.

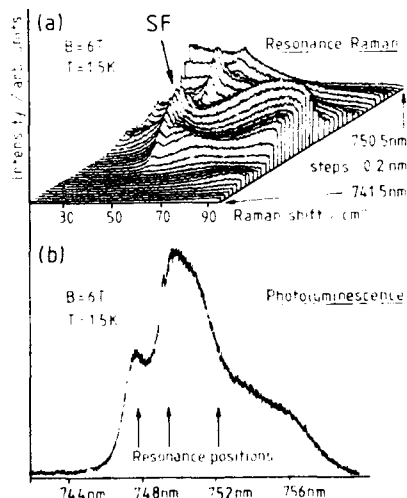


Fig. 3. (a) Resonance Raman and (b) photoluminescence (PL) spectra of the MQW with barrier Mn concentration of  $x = 0.12$ . In (a), the range of each spectrum is at a fixed Raman shift from the laser energy, which decreases from front to back of the figure. The band (labelled SF) which remains at a constant position in each spectrum is the spin flip signal of interest here; other bands are due to PL. In (b), the wavelengths at which the SF signal is strongest are marked with arrows.

## 5. Acknowledgement

The support of this work by the Science and Engineering Research Council of Great Britain is gratefully acknowledged.

## 6. References

- [1] For reviews of DMSs, see:  
J.K. Furdyna, *J. Appl. Phys.* 64 (1989) R29;  
O. Goede and W. Heimbrodt, *Phys. Status Solidi (b)* 146 (1988) 9.
- [2] For a review of Raman scattering in DMSs, see:  
A.K. Ramdas and S. Rodriguez, in: *Semiconductors and Semimetals*, Vol. 25, Eds. R.K. Willardson and A.C. Beer (Academic Press, Boston, MA, 1988) p. 345.
- [3] M.P. Halsall, P.J. Boyce, D. Wolverson, J.J. Davies, D.E. Ashenford and B. Lunn, *Solid State Commun.* 83 (1992) 85.
- [4] S.V. Railson, D. Wolverson, J.J. Davies, D.E. Ashenford and B. Lunn, *Superlattices Microstruct.* 13 (1993) 487.
- [5] A. Wasiela, Y. Merle D'Aubigné, J.E. Nicholls, D.E. Ashenford and B. Lunn, *Solid State Commun.* 76 (1990) 263.
- [6] D. Wolverson and S.V. Railson, *Measurement Sci. Technol.* 4 (1993) 1080.
- [7] G. Bastard, *Wave Mechanics Applied to Semiconductor Heterostructures* (Editions de Physique, Les Ulis, 1988) ch. 9.
- [8] S.K. Chang, A.V. Nurmikko, J.W. Wu, L.A. Kolodziejski and R.L. Gunshor, *Phys. Rev. B* 37 (1988) 991.
- [9] N. Pelekanos, Q. Fu, J. Ding, W. Walecki, A.V. Nurmikko, S.M. Durbin, J. Han, M. Kobayashi and R.L. Gunshor, *Phys. Rev. B* 41 (1990) 9966.
- [10] M. Hirsch, PhD Dissertation, Julius-Maximilians-Universität, Würzburg (1992).
- [11] J.A. Gaj, C. Bodin-Deshayes, P. Peyla, J. Cibert, G. Feuillet, Y. Merle d'Aubigné, R. Romestain and A. Wasiela, in: *Proc. Int. Conf. on the Physics of Semiconductors*, Beijing, 1992 (World Scientific, Singapore).
- [12] Y. Shapira, S. Foner, D.H. Ridgley, K. Dwight and A. Wold, *Phys. Rev. B* 30 (1984) 4021.
- [13] R. Meyer, M. Hirsch, G. Schaack, A. Waag and R.N. Bicknell-Tassius, *Superlattices Microstruct.* 9 (1991) 165.



ELSEVIER

Journal of Crystal Growth 138 (1994) 661–666

JOURNAL OF  
**CRYSTAL  
GROWTH**

## Optical studies of quantum wells induced by magnetic fields in $\text{Cd}_{1-x}\text{Mn}_x\text{Te}/\text{Cd}_{1-y}\text{Zn}_y\text{Te}$ epitaxial structures

J.J. Davies <sup>a,\*</sup>, R.T. Cox <sup>b</sup>, G. Feuillet <sup>b</sup><sup>a</sup> *The School of Physics, The University of East Anglia, Norwich NR4 7TJ, UK*<sup>b</sup> *Laboratoire de Physique des Semiconducteurs, DRFMC / SP2M, Centre d'Etudes Nucléaires de Grenoble, BP 85 X,  
F-38041 Grenoble Cedex, France*

### Abstract

$\text{Cd}_{1-y}\text{Zn}_y\text{Te}/\text{Cd}_{1-x}\text{Mn}_x\text{Te}/\text{Cd}_{1-y}\text{Zn}_y\text{Te}$  structures have been grown by MBE, the values of  $x$  and  $y$  being chosen such that the excitonic bandgaps of the layers are approximately equal. Reflectivity measurements show that application of a magnetic field changes the bandgap of the dilute magnetic layer and switches on and deepens  $\text{Cd}_{1-x}\text{Mn}_x\text{Te}$  potential wells that did not exist in zero-field. As the wells deepen, the intensity of the quantum well photoluminescence increases from zero at a well-defined threshold exciton energy. Excitons cannot transfer from the  $\text{Cd}_{1-y}\text{Zn}_y\text{Te}$  barriers to the  $\text{Cd}_{1-x}\text{Mn}_x\text{Te}$  well unless the well is at least 5 meV deep.

### 1. Introduction

In dilute magnetic semiconductors such as  $\text{Cd}_{1-x}\text{Mn}_x\text{Te}$  the magnetic properties of the electrons and holes can be enhanced by up to two orders of magnitude by the exchange interaction with the magnetic ions [1]. As a result, the bandgap for a given spin state can be altered by several tenths of an electron volt by the application of a magnetic field at low temperature. When such materials are incorporated into heterostructures, one can take advantage of this to change the depths of the potential wells during the course of an experiment. The present report concerns a study of this type carried out on thin  $\text{Cd}_{1-x}\text{Mn}_x\text{Te}$  layers sandwiched between layers of  $\text{Cd}_{1-y}\text{Zn}_y\text{Te}$ , the values of  $x$  and  $y$  being chosen so that the

zero-field bandgaps of the two materials are approximately equal. In this way, structures were produced in which wells in the  $\text{Cd}_{1-x}\text{Mn}_x\text{Te}$  could be “switched on” and their depth controlled from zero by application of the magnetic field. In comparison with previous work on field-induced “spin superlattices” such as  $\text{ZnSe}/\text{Zn}_{1-x}\text{Fe}_x\text{Se}$  and  $\text{ZnSe}/\text{Zn}_{1-x}\text{Mn}_x\text{Se}$  [2,3], our use here of *two* alloy materials gives greater flexibility. Our aim was to study the way in which optical properties such as excitonic oscillator strength, excitonic capture and subsequent emission intensity are related to the depth of a quantum well.

### 2. The structures

The layers were grown by molecular beam epitaxy in a Riber 32P system at 280°C on sub-

\* Corresponding author.

strates of (100)  $\text{Cd}_{0.885}\text{Zn}_{0.115}\text{Te}$ . The specimens are very simple, in each case consisting of only a single layer of  $\text{Cd}_{1-x}\text{Mn}_x\text{Te}$  (of thickness 200 Å) with 1000 Å of  $\text{Cd}_{1-y}\text{Zn}_y\text{Te}$  on each side, the value  $y$  of the zinc concentration being matched as closely as possible to that of the substrate (0.115). Four specimens were studied, with manganese concentrations  $x$  of 0.029 (S1), 0.038 (S2), 0.050 (S3) and 0.056 (S4), as determined from the reflectivity spectra (see section 3). The thickness of the  $\text{Cd}_{1-x}\text{Mn}_x\text{Te}$  layer is below the critical value for relaxation, so that it is strained to the substrate lattice, with a heavy-hole/light-hole energy splitting of about 35 meV (depending on  $x$ ), the heavy-hole bandgap being the smaller.

### 3. The optical spectra

The excitonic transitions were studied by reflectivity and photoluminescence (PL) spectroscopy mainly in the Faraday configuration, with the magnetic field normal to the layer planes. In Fig. 1 we show the dependence of the reflectivity signals on magnetic field for the four specimens with different manganese concentrations. The signals whose positions depend strongly on field (solid lines) are due to the  $\text{Cd}_{1-x}\text{Mn}_x\text{Te}$  layers, whilst those due to the  $\text{Cd}_{1-y}\text{Zn}_y\text{Te}$  layers (broken lines) are only slightly affected by the field. The large shifts in the  $\text{Cd}_{1-x}\text{Mn}_x\text{Te}$  line positions are due to the exchange interactions of the electrons and holes with the manganese ions and the Brillouin-like behaviour reflects the paramagnetic behaviour of the manganese magnetization. The lowest energy feature for each specimen in Fig. 1 is due to the  $\text{Cd}_{1-x}\text{Mn}_x\text{Te}$   $m_j = -3/2$  heavy hole,  $m_s = -1/2$  excitonic transition and its position gives the manganese concentration  $x$ . A noticeable feature of the reflectivity signals from the  $\text{Cd}_{1-x}\text{Mn}_x\text{Te}$  layers is that they are sharp when the spin states are such (filled data points in Fig. 1) that the  $\text{Cd}_{1-x}\text{Mn}_x\text{Te}$  exciton bandgap is less than that of the adjoining  $\text{Cd}_{1-y}\text{Zn}_y\text{Te}$ , but are broadened (open data points) when the converse is the case. In the latter case the broadening is attributed to the  $\text{Cd}_{1-x}\text{Mn}_x\text{Te}$  exciton states being in resonance

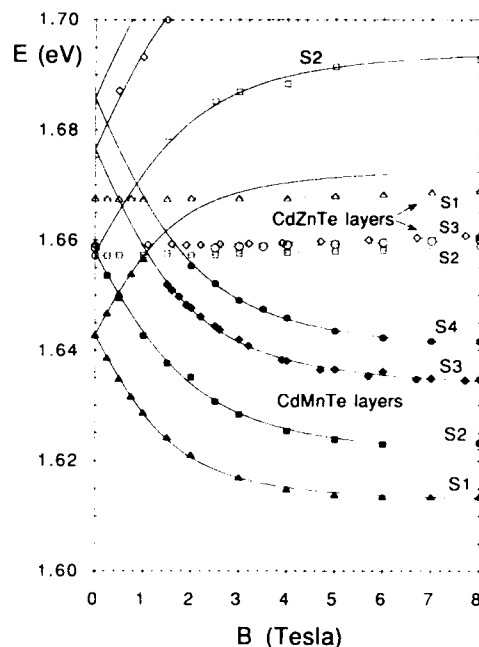


Fig. 1. Magnetic field dependence of exciton energies for  $\text{Cd}_{1-x}\text{Mn}_x\text{Te}/\text{Cd}_{1-y}\text{Zn}_y\text{Te}$  samples S1, ..., S4, from reflectivity spectra. Excitons associated with  $\text{Cd}_{1-y}\text{Zn}_y\text{Te}$  epilayers (broken lines) shift only slightly with field (the signals for sample S1 lie higher than those for S2, S3, S4 because S1 has accidentally high Zn content). Brillouin curves (solid lines) have been fitted to the positions of excitons associated with the  $\text{Cd}_{1-x}\text{Mn}_x\text{Te}$  layers (confinement energies and diamagnetic shifts are neglected). The black data points on the lower,  $\sigma^+$  polarized branch (and points from 0 to 1 T on the upper,  $\sigma^-$  polarized branch for sample S1) correspond to narrow resonance features in the reflectivity. The white data points on the upper branches represent very broad reflectivity features.

with the electron-hole continuum of the  $\text{Cd}_{1-y}\text{Zn}_y\text{Te}$ .

It can be seen that for specimens S3 and S4 in Fig. 1, the zero-field excitonic bandgaps of the  $\text{Cd}_{1-x}\text{Mn}_x\text{Te}$  layers are greater than that of the  $\text{Cd}_{1-y}\text{Zn}_y\text{Te}$ ; for S1 the converse is the case. In zero-field, it is therefore only in S1 ( $x = 0.029$ ) that the  $\text{Cd}_{1-x}\text{Mn}_x\text{Te}$  layer forms a potential well for excitons. In contrast, creation of an exciton well in S3 and S4 requires (at 2 K) fields of 1.0 and 1.7 T, respectively. Specimen S2 is an interesting special case in which the zero-field excitonic bandgaps are very nearly equal.

Photoluminescence spectra were recorded under excitation from the visible lines of an argon-ion laser. The excitation penetrates the epitaxial layers and, in all cases, PL signals were observed from the substrate (free, donor-bound and acceptor-bound excitons) and from the  $\text{Cd}_{1-x}\text{Mn}_x\text{Te}$ . The most striking feature of the excitonic photoluminescence spectra is that, for the three specimens of highest manganese concentration, the intensity of the emission from the  $\text{Cd}_{1-x}\text{Mn}_x\text{Te}$  depends very strongly on the magnetic field (see, e.g., Fig. 2) and, above a certain threshold field, strengthens markedly as the depth of the well is increased. Close inspection shows that the threshold field is *not* the field required to make the  $\text{Cd}_{1-x}\text{Mn}_x\text{Te}$  exciton energy equal to that of the  $\text{Cd}_{1-x}\text{Zn}_x\text{Te}$ , but is slightly larger.

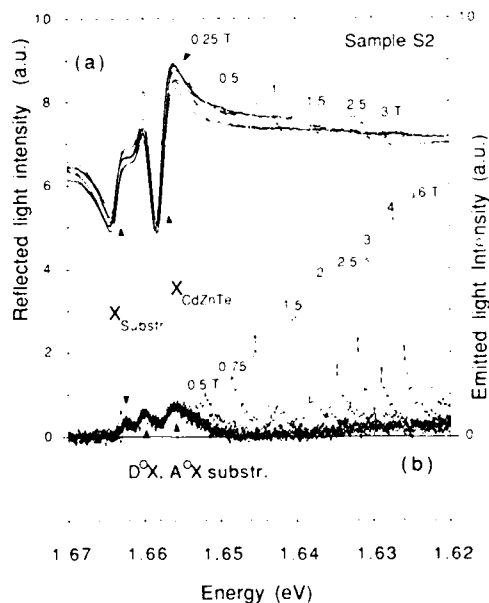


Fig. 2. (a) Reflectivity spectra (unpolarized, left scale, where a.u. indicates arbitrary units) and (b) luminescence spectra (in  $\sigma^+$  polarization, right scale, again in arbitrary units) for  $\text{Cd}_{1-x}\text{Mn}_x\text{Te}/\text{Cd}_{1-x}\text{Zn}_x\text{Te}$  sample S2 at field values from 0.25 to 6 T. For this sample, the  $\text{Cd}_{1-x}\text{Zn}_x\text{Te}$  and  $\text{Cd}_{1-x}\text{Mn}_x\text{Te}$  exciton energies almost coincide in zero-field. The well-defined  $\text{Cd}_{1-x}\text{Mn}_x\text{Te}$  reflectivity-resonance demonstrates the abrupt "switching-on" of an excitonic quantum well by the magnetic field. By contrast, the well's luminescence develops more progressively.

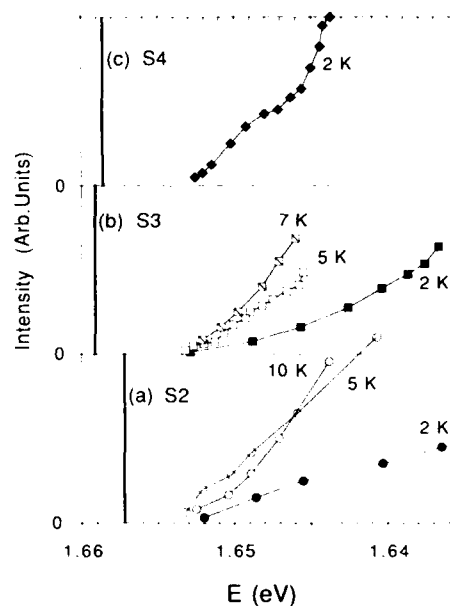


Fig. 3. Amplitudes of luminescence intensity peaks from the confined  $\text{Cd}_{1-x}\text{Mn}_x\text{Te}$  layers at various values of magnetic field and temperature, plotted against their energy positions. The relation between the vertical scales for samples S2, S3, S4 is arbitrary but for a given sample the scale is the same for the different temperatures. The thick vertical bars at 1.6572, 1.6591 and 1.6586 eV mark the (zero-field) energy of an exciton in the  $\text{Cd}_{1-x}\text{Zn}_x\text{Te}$  barriers (cf. Fig. 1).

We have also measured the photoluminescence intensity at different temperatures. As the temperature is increased, higher fields are required to produce a given polarization of the  $\text{Mn}^{2+}$  spin system and hence to produce a given change in the excitonic bandgap of the  $\text{Cd}_{1-x}\text{Mn}_x\text{Te}$  layer. The threshold fields for the onset of photoluminescence are therefore greater. However, when the intensity data are plotted as a function of the  $\text{Cd}_{1-x}\text{Mn}_x\text{Te}$  exciton energy (which depends on both field and temperature), the threshold *energies* for the onset of the photoluminescence at different temperatures are found to be the same to within experimental error (see Fig. 3a).

For the specimens S3 and S4 with higher manganese concentrations, the threshold *fields* for the appearance of the photoluminescence are

greater because larger fields are now required to induce the potential wells, but, again, the threshold energies are found to be independent of temperature (Figs. 3b and 3c). Moreover, they are found to be approximately the same (1.653 eV) for all three specimens S2, S3 and S4.

We conclude that, irrespective of the temperature and irrespective of the manganese concentration, the  $\text{Cd}_{1-x}\text{Mn}_x\text{Te}$  exciton bandgap has to be adjusted to lie beneath a single threshold value before the  $\text{Cd}_{1-x}\text{Mn}_x\text{Te}$  exciton photoluminescence can be observed. A particularly important result is that this threshold energy does *not* coincide with the excitonic bandgap of the  $\text{Cd}_{1-x}\text{Zn}_x\text{Te}$  layers, but lies about 5 meV lower.

For specimen S1, in which the  $\text{Cd}_{1-x}\text{Mn}_x\text{Te}$  layer has  $x = 0.029$ , the PL intensity is found not to be a strong function of the magnetic field and can be observed even in zero-field. This is as expected, since now the exciton well depth is already about 25 meV before the field is applied.

Finally, when the magnetic field is applied in the *plane* of the epitaxial layers (Voigt configuration) for specimen S2, we again observe that the excitonic photoluminescence appears only below the threshold energy of 1.653 eV. For this arrangement, the field-induced shift of the energy of the  $\text{Cd}_{1-x}\text{Mn}_x\text{Te}$  excitonic transitions is much smaller than when the field is normal to the planes (because the magnetic energy of the strain-split hole states is anisotropic [4]). For specimens S3 and S4 the excitonic transition energies now lie above 1.653 eV at all field values and we see no  $\text{Cd}_{1-x}\text{Mn}_x\text{Te}$ -related photoluminescence.

#### 4. Discussion

The maximum depth of the conduction and valence band quantum wells is small in these samples (particularly for S2, S3 and S4, as shown in Fig. 4). Also, the width of the  $\text{Cd}_{1-x}\text{Mn}_x\text{Te}$  layers was deliberately chosen to be quite large (200 Å), about three times the exciton Bohr radius (70 Å in CdTe). In this situation, excitonic energies and oscillator strengths are best described in terms of "centre of mass quantization"

[5]. The individual values of the conduction and valence band offsets do not appear in this description: in particular, it is inappropriate to attempt to decide whether an exciton is spatially direct ("type I") or indirect ("type II"). The exciton, of mass  $M^* = m_c^* + m_h^*$ , is confined in the simple potential well formed by the difference between the bandgaps of the  $\text{Cd}_{1-x}\text{Mn}_x\text{Te}$  and  $\text{Cd}_{1-x}\text{Zn}_x\text{Te}$  layers or, more precisely, by the difference between their exciton energies. The observed reflectivity spectra, particularly the immediate development of a sharp, quantum-well associated reflectivity feature when the magnetic field pulls the exciton energy in the  $\text{Cd}_{1-x}\text{Mn}_x\text{Te}$  layer below that of the exciton in the confining  $\text{Cd}_{1-x}\text{Zn}_x\text{Te}$  layers (e.g., Fig. 2a), are as expected from this description.

We must nevertheless consider the possibility that the threshold for luminescence is associated not with the exciton bandgap but with critical values of either the conduction or valence bands. In Fig. 4 we show the band energies of  $\text{Cd}_{1-x}\text{Mn}_x\text{Te}$  as a function of  $x$ , the layer being assumed to be strained to the  $\text{Cd}_{0.888}\text{Zn}_{0.112}\text{Te}$  substrate. In calculating these energies we have followed the procedure of Peyla et al. [6] and have used the most recent estimates of the conduction band to valence band offset ratios (0.6 and 1.0 for nominally unstrained  $\text{Cd}_{1-x}\text{Mn}_x\text{Te}/\text{CdTe}$  [7,8] and  $\text{Cd}_{1-x}\text{Zn}_x\text{Te}/\text{CdTe}$  [6], respectively). We also show the effect of saturating the manganese magnetization by applying a high magnetic field normal to the layer plane. For all four specimens the  $\text{Cd}_{1-x}\text{Mn}_x\text{Te}$  forms a potential barrier for holes in zero-field and, for the appropriate hole orientation, this barrier can be changed into a well. We can, however, discount the possibility that the threshold energy for luminescence is associated with critical values of the valence band offset (for example, the value at which the valence band well is switched on), since the threshold value of 1.653 eV (specimen S2) is independent of field direction whilst the energies of the hole states are not. It is also clear that the threshold is not associated with a critical value of the conduction band offset, since, whilst for S4 ( $x = 0.056$ ) the  $\text{Cd}_{1-x}\text{Mn}_x\text{Te}$  forms a (very slight) electron barrier in zero-field, for S3 ( $x = 0.050$ )

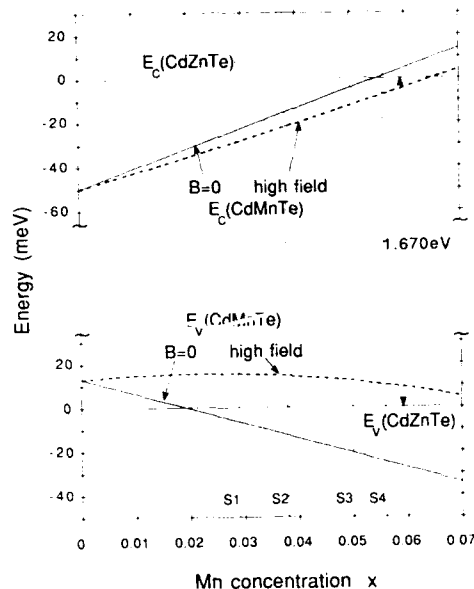


Fig. 4. Energies  $E_C$  and  $E_V$  of the conduction and valence band edges for  $\text{Cd}_{1-x}\text{Mn}_x\text{Te}$  alloys plotted against manganese content  $x$ , compared with  $E_C$  and  $E_V$  for unstrained  $\text{Cd}_{1-x}\text{Zn}_x\text{Te}$  alloy of zinc content 11.5%. The  $\text{Cd}_{1-x}\text{Mn}_x\text{Te}$  is strained to the  $\text{Cd}_{1-x}\text{Zn}_x\text{Te}$  lattice parameter. Energies are based on best literature estimates of band offset ratios and strain effects in the  $\text{CdTe}/\text{Cd}_{1-x}\text{Zn}_x\text{Te}$  and  $\text{CdTe}/\text{Cd}_{1-x}\text{Mn}_x\text{Te}$  systems. The dotted curves represent the band edges for  $\text{Cd}_{1-x}\text{Mn}_x\text{Te}$  with  $\text{Mn}^{2+}$  spin polarization saturated.

and S2 ( $x = 0.038$ ) the electron well already exists (it is 15 meV deep for S2). It is also evident that to require a critical value of the conduction band offset would not lead to the same value for the excitonic threshold energy in all three specimens.

Thus it is the exciton energies that are the relevant quantities. One might at first sight expect the onset of the photoluminescence to occur as soon as the  $\text{Cd}_{1-x}\text{Mn}_x\text{Te}$  exciton bandgap is made smaller than that of the  $\text{Cd}_{1-x}\text{Zn}_x\text{Te}$ . Instead, a threshold energy of about 5 meV appears to be necessary before the excitation can transfer into the  $\text{Cd}_{1-x}\text{Mn}_x\text{Te}$  layer. One possibility is that this energy is associated with the exciton spin system, since the energies of the excitonic spin states in the  $\text{Cd}_{1-x}\text{Zn}_x\text{Te}$  and in  $\text{Cd}_{1-x}\text{Mn}_x\text{Te}$  in a magnetic field are arranged in the opposite

order, so that both the electron and the hole in an exciton in the lowest spin state in the  $\text{Cd}_{1-x}\text{Zn}_x\text{Te}$  have to undergo spin flips on entering the  $\text{Cd}_{1-x}\text{Mn}_x\text{Te}$  well. We can, however, discount this possibility since it would not lead to a sample and field independent energy threshold. The possibility that transfer of an exciton from the  $\text{Cd}_{1-x}\text{Zn}_x\text{Te}$  to the  $\text{Cd}_{1-x}\text{Mn}_x\text{Te}$  must be accompanied by the creation of an optical phonon [9] can also be eliminated since the optical phonon energies are about 20 meV, well in excess of 5 meV.

It may be significant that 5 meV is of the order of the 1s–2s energy difference (8 meV) for an exciton in these materials. Possibly exciton transfer into the well can be assisted by passage via the 2s state and improves progressively as higher excited states (3s, ...) and then the electron–hole continuum of the  $\text{Cd}_{1-x}\text{Mn}_x\text{Te}$  drop below the  $\text{Cd}_{1-x}\text{Zn}_x\text{Te}$  exciton energy.

## 5. Conclusions

By making use of the magnetic tunability of the bandgap in a dilute magnetic semiconductor, we have demonstrated clearly the switching on of a sharp excitonic reflectivity feature and of photoluminescence by the creation of a previously non-existent potential well. We have shown that it is the exciton potential well, rather than the wells seen individually by the electrons and holes, that is the relevant quantity. The experimental data show that the emission occurs only when the depth of the exciton well in  $\text{Cd}_{1-x}\text{Mn}_x\text{Te}$  exceeds about 5 meV, this threshold value being independent of temperature over the range studied (2 to 10 K) and independent of magnetic field. It appears that excitons in the barrier layers cannot transfer into the  $\text{Cd}_{1-x}\text{Mn}_x\text{Te}$  wells unless the exciton state in the well lies about 5 meV below the barrier level.

## 6. Acknowledgements

We are grateful to the Ministère de la Recherche et de la Technologie for a scholarship



to J.J. Davies whilst carrying out this work at Grenoble. We thank Dr. P.J. Boyce for doing the experiment in the Voigt configuration.

## 7. References

- [1] For reviews of dilute magnetic semiconductors, see e.g.: J.K. Furdyna, *J. Appl. Phys.* 64 (1989) R29; O. Goede and W. Heimbrod, *Phys. Status Solidi (b)* 146 (1988) 9.
- [2] W.C. Chou, A. Petrou, J. Warnock and B.T. Jonker, *Phys. Rev. Lett.* 67 (1991) 3820.
- [3] N. Dai, H. Lou, F.C. Zhang, N. Samarth, M. Dobrowolska and J.K. Furdyna, *Phys. Rev. Lett.* 67 (1991) 3824.
- [4] P. Peyla, A. Wasiela, Y. Merle d'Aubigné, D.E. Ashenford and B. Lunn, *Phys. Rev. B* 47 (1993) 3783.
- [5] H. Tuffigo, R.T. Cox, N. Magnea, Y. Merle d'Aubigné and A. Million, *Phys. Rev. B* 37 (1988) 4310; H. Tuffigo, R.T. Cox, G. Lentz, N. Magnea and H. Mariette, *J. Crystal Growth* 101 (1990) 778.
- [6] P. Peyla, Y. Merle d'Aubigné, A. Wasiela, R. Romestain, H. Mariette, M.D. Sturge, N. Magnea and H. Tuffigo, *Phys. Rev. B* 46 (1992) 1557.
- [7] M.P. Halsall, D. Wolverson, J.J. Davies, D.E. Ashenford and B. Lunn, *Solid State Commun.* 86 (1993) 15.
- [8] A. Wasiela, Y. Merle d'Aubigné, J.E. Nicholls, D.E. Ashenford and B. Lunn, *Solid State Commun.* 75 (1990) 263.
- [9] J.A. Brum and G. Bastard, *Phys. Rev. B* 33 (1986) 1420.



ELSEVIER

Journal of Crystal Growth 138 (1994) 667–676

JOURNAL OF  
**CRYSTAL  
GROWTH**

## Room temperature II–VI lasers with 2.5 mA threshold

J.M. DePuydt <sup>\*</sup>, M.A. Haase, S. Guha, J. Qiu, H. Cheng, B.J. Wu, G.E. Höfler,  
G. Meis-Haugen, M.S. Hagedorn, P.F. Baude

*3M Company, 201-1N-35 3M Center, St. Paul, Minnesota 55144, USA*

### Abstract

Buried-ridge II–VI laser diodes operating at 511 nm at room temperature were fabricated from separate-confinement heterostructures. The layers consisted of a pseudomorphic CdZnSe quantum well and lattice-matched ZnSSe light-guiding and MgZnSSe cladding layers. Stripe gain-guide lasers fabricated from similar wafers exhibited threshold current densities as low as 630 A/cm<sup>2</sup> and threshold voltages less than 9 V. The buried-ridge devices operated in single lateral and transverse modes under pulsed excitation at room temperature. Threshold currents as low as 2.5 mA and 50% duty cycles at room temperature were demonstrated with these structures. A conventional model for the threshold currents was used in an initial attempt to fit the thresholds as functions of cavity length and temperature (100–325 K); excitonic mechanisms were not included. The electron lifetime in the light-guiding layer was the only adjustable parameter in the model. Good agreement between measurement and theory was obtained with the electron lifetime taken as 42 ps; this value also agrees well with independent lifetime measurements. All reports of II–VI diode lasers to date indicate very short device lifetimes at room temperature. Electroluminescence topography and TEM studies were carried out on both LEDs and stripe lasers in order to gain insight to the failure mechanisms and to study their evolution. Two types of dark line defects (along the  $\langle 100 \rangle$  and  $\langle 110 \rangle$  directions) and patches with extremely large densities ( $10^{10}$  cm<sup>-2</sup>) of a dislocation network consisting of elongated dislocation segments were observed in degraded devices. This work represents the first detailed study of II–VI device failure and indicates that the rapid failure is due to the formation of dark defects at the high current densities required for lasing.

### 1. Buried-ridge devices

Our goal is to develop short-wavelength lasers suitable for a variety of applications including optical data storage where low threshold currents and single lateral-mode operation are required. While the development of wide band gap II–VI materials has attracted much attention since the first demonstration of blue-green injection lasers [1], little advanced device design has been re-

ported. Guided by the success of buried-ridge or buried-heterostructure technology in III–V laser diodes [2,3], we report the first II–VI buried-ridge laser diodes operating in the blue-green ( $\lambda = 511$  nm).

The epitaxial layers (Fig. 1) used for these devices were grown by molecular beam epitaxy on (100) GaAs substrates. This separate-confinement structure contains nominally lattice-matched MgZnSSe cladding and ZnSSe guiding layers and a single strained, pseudomorphic CdZnSe quantum well; this structure was first described by Gaines et al. [4]. The cladding layers are each 0.8

<sup>\*</sup> Corresponding author.

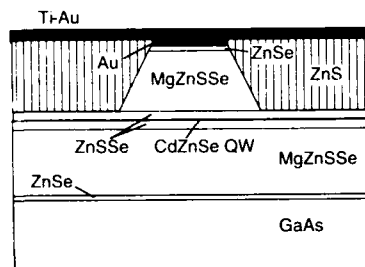


Fig. 1. Schematic diagram of a buried-ridge separate confinement laser diode.

$\mu\text{m}$  thick, with the lower and upper layers doped to  $10^{17} \text{ cm}^{-3}$  with Cl and N from an RF plasma source [5], respectively. The band gap of the cladding layers is 2.85 eV; the composition is estimated to be  $\text{Mg}_{0.1}\text{Zn}_{0.9}\text{S}_{0.15}\text{Se}_{0.85}$ . The  $\text{ZnS}_{0.07}\text{Se}_{0.93}$  guiding layers are each  $0.125 \mu\text{m}$  thick, are doped at the same levels as their adjacent cladding layers, and have a 2.72 eV band gap. The quantum well is grown at a temperature of  $150^\circ\text{C}$  by "alternating beam epitaxy (ABE)" [6] and consists of three periods of  $(\text{CdSe})_1(\text{ZnSe})_2$ , thus the total well thickness is approximately  $25 \text{ \AA}$  and the effective composition is  $\text{Cd}_{0.33}\text{Zn}_{0.67}\text{Se}$ . Thin ( $< 0.1 \mu\text{m}$ ) heavily doped ZnSe layers are included at the top and bottom of the II-VI stack for electrical contact. The p<sup>+</sup>-ZnSe contact layer is grown at  $150^\circ\text{C}$ , and is doped to  $N_A - N_D = 10^{18} \text{ cm}^{-3}$ .

To characterize the material,  $20 \mu\text{m}$  wide gain-guided lasers were fabricated, using high-reflectivity (90%) facet coatings. The lowest room temperature pulsed threshold current density was  $630 \text{ A/cm}^2$  and the voltage at threshold was slightly less than 9 V. The unacceptably high operating voltage is due to a poor electrical contact to the p-ZnSe [7]. The emission wavelength at room temperature is  $511 \text{ nm}$ .

Fabrication of the buried-ridge devices begins with evaporation of a  $0.25 \mu\text{m}$  Au layer over the p<sup>+</sup>-ZnSe layer. Photoresist is used to define a ridge, typically  $2$  or  $3 \mu\text{m}$  wide and  $\text{Xe}^+$  ion beam etching is used to etch through the Au and the upper MgZnSSe cladding layer. The degree of lateral optical confinement in these laser diodes depends mainly on the etch depth. Since the

etching does not extend into the active layer of the device, edge recombination is expected to be negligible. After etching, the sample is immediately transferred through air to an evaporator in which ZnS is deposited from a thermal source containing crystalline ZnS. The etched sample is not intentionally heated during the ZnS deposition. The thickness of the deposited ZnS is chosen to exactly fill the areas where the semiconductor has been etched away. The deposited ZnS is polycrystalline, and appears to grow in a columnar structure. The ZnS deposited on top of the remaining photoresist on the ridge is removed in a subsequent lift-off process, leaving a nearly planar surface as shown in Fig. 1. The final step involves evaporating Ti-Au over the original Au on the ridge and over the evaporated ZnS.

The buried-ridge lasers were studied under pulsed current injection at room temperature. For the data discussed here, the pulse width was  $300 \text{ ns}$  and the duty factor was  $0.01\%$ , although duty factors up to  $50\%$  have been obtained. Fig. 2 shows the light intensity from one facet as a function of injected current and applied voltage. This device is  $2 \mu\text{m}$  wide at the quantum well and  $1.5 \mu\text{m}$  wide at the top electrode. It was cleaved to a length of  $180 \mu\text{m}$  and both facets were coated to provide reflectivities of  $90\%$ . The resulting threshold current is  $2.5 \text{ mA}$ , which is nearly a factor of 20 lower than the room-temper-

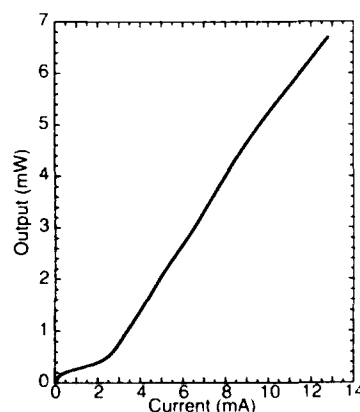


Fig. 2. The  $I$ - $I$  from a buried-ridge device. The threshold current is  $2.5 \text{ mA}$ .

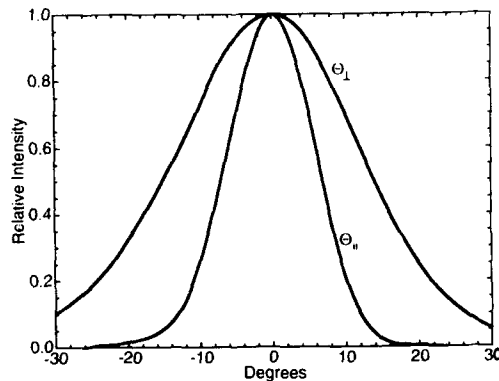


Fig. 3. The far-field pattern from a buried-ridge laser. The FWHMs are 29° and 13°.

ature threshold current of any previously reported II–VI laser diode [8]. The corresponding threshold current density of 700 A/cm<sup>2</sup> is slightly larger than that for the gain-guided devices. Presumably the increase is due to added optical loss caused by scattering from the ridge sidewalls. The single-facet differential quantum efficiency of 25% exhibited by the device of Fig. 2 allows us to estimate the modal cavity losses to be 6 cm<sup>−1</sup>. This value equals the sum of scattering and free-carrier losses.

Fig. 3 shows the measured far-field pattern from a device with a ridge width of 2 μm at the quantum well. The large divergence (FWHM = 29°) in the direction normal to the junction plane is indicative of the strong optical confinement provided by the MgZnSSe cladding layers, as reported by Gaines et al. [4]. The gaussian-like profile in the direction parallel to the junction plane (FWHM = 13°) indicates that the device is operating in a single lateral mode and that the lateral confinement is also quite strong. An analysis of the waveguide indicates that the FWHM of the near-field optical mode is 0.32 μm × 1.2 μm. This optical beam is expected to be suitable for applications requiring a diffraction-limited spot.

Although the high operating voltage of these devices is obviously undesirable, the most serious concern is the rapid degradation that they exhibit. Heat-transfer calculations indicate that even with junction-up mounting these devices should

operate cw at room temperature. This is supported experimentally by observations of laser operation during pulses as long as 50 μs, which is longer than the time required for the junction to reach thermal steady-state. Unfortunately, at the current densities required for cw operation the internal quantum efficiency of these materials rapidly degrades. The fast degradation is discussed later in this paper.

## 2. Modeling

Next we describe a rudimentary model that predicts the dependence of the threshold current density on cavity length and temperature. The physics is identical to that of III–V quantum well lasers – particularly those using strained GaInAs wells. This work extends earlier efforts [9–11] by including strain, the separate-confinement design, leakage current due to carrier drift and diffusion, and non-radiative recombination in the quantum well.

Our model first calculates the temperature-dependent gain of the optical mode as a function of the two-dimensional carrier density ( $n = p$ ) in the quantum well. From  $n$  we can calculate the threshold current density which includes: (1) radiative recombination in the quantum well, (2) recombination in the guiding layers, and (3) recombination in the cladding layers (which is negligible). The available gain is calculated using [10]

$$g = g_{\text{sat}} (f(-E_{\text{Fn}}) + f(-E_{\text{Fp}}) - 1), \quad (1)$$

$$g_{\text{sat}} = Nq^2 \langle r \rangle^2 m_r h\nu / \hbar \epsilon_0 c \bar{n} W_m, \quad (2)$$

$$\langle r \rangle^2 = \frac{\hbar^2 (E_g + \Delta)}{4h\nu (E_g + \frac{2}{3}\Delta)} \left( \frac{1}{m_c} - \frac{1}{m_v} \right), \quad (3)$$

$$m_r = (1/m_c + 1/m_{\text{hh}})^{-1}, \quad (4)$$

$$f(E) = 1 / (1 + e^{E/kT}), \quad (5)$$

$$E_{\text{Fn}} = kT \ln \left[ \exp \left( \frac{n}{\rho_c kT} \right) - 1 \right], \quad (6a)$$

$$E_{\text{Fp}} = kT \ln \left[ \exp \left( \frac{p}{\rho_h kT} \right) - 1 \right]. \quad (6b)$$

Here  $E_{Fn}$  and  $E_{Fp}$  are the Fermi energies in the well relative to the first bound state,  $N$  is the number of quantum wells,  $W_m$  is the width of the optical mode,  $\Delta$  is the spin-orbit splitting,  $\bar{n}$  is the refractive index of the quantum well and  $\rho_c$  and  $\rho_h$  are two-dimensional densities of states. These equations allow us to directly calculate  $g(n)$  and they are simplified by the fact that in the thin, highly strained CdZnSe well, there is only one confined band for the electrons and one for the holes. The wells are intentionally grown thin to keep them pseudomorphic; the resulting strain shifts the light hole band out of the well. The strain also affects the in-plane hole effective mass,  $m_{h||}$ , within the quantum well [12]. Band mixing is neglected since the other bands reside at much higher energies. Intraband relaxation broadening is also neglected, as is often done in III-V lasers, despite the fact that electron-phonon coupling is stronger in II-VI materials.

The radiative recombination within the quantum well may be calculated using the spontaneous spectral emission rate:

$$r_{sp}(E) = r_c E f \left( \frac{m_r}{m_c} (E - E_g) - E_{Fn} \right) \times f \left( \frac{m_r}{m_{h||}} (E - E_g) - E_{Fp} \right), \quad (7)$$

$$r_c = 2q^2 \bar{n} \langle r \rangle^2 m_r (h\nu)^2 / \epsilon_0 \hbar^6 \pi^2 c^3. \quad (8)$$

The current due to radiative recombination in the well is

$$J_{sp} = qN \int_{h\nu}^{\infty} r_{sp}(E) dE. \quad (9)$$

Dark recombination in the well may be described by a carrier lifetime;

$$J_d = qNn/\tau_w. \quad (10)$$

The calculation of the leakage current into the guiding and cladding layers includes both drift and diffusion and takes into account the separate confinement design [13]. It is worth noting that the leakage current due to holes is much smaller than that due to electrons because of lower mobilities, higher n-type conductivity and Fermi energies lying closer to the band edge.

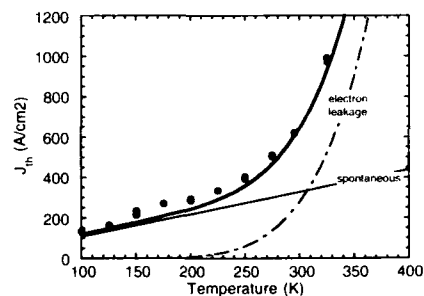


Fig. 4. The measured and calculated threshold current densities for a separate confinement laser. The major components of the current, due to spontaneous recombination and leakage, are also shown.

To compare the model with experimental data, the threshold current was measured for several blue-green laser diodes as a function of temperature. The devices are separate confinement laser diodes described earlier in this paper. Fig. 4 shows the measured and calculated threshold current densities for similar devices, from 80 to 320 K. The measurements are taken with 500 ns pulses and a 0.01% duty factor to minimize heating effects. Both facets are coated to provide 90% reflectivities. The model provides an good description of the observed threshold current densities over the entire temperature range. The only adjusted parameter is the minority electron lifetime outside of the quantum well,  $\tau_n$ . The value used in Fig. 4, 42 ps, is close to that recently measured (35 ps) in p-type ZnSe [14]. The only unknown parameter is the carrier lifetime for dark recombination in the well, but for these calculations, it is believed to be sufficiently long (5 ns) and thus can be neglected.

One useful result of these calculations is the breakdown of the threshold current into individual components, as shown in Fig. 4. These data clearly show that electron leakage across the quantum well makes a significant contribution to the total leakage current at temperatures near and above room temperature. By varying the parameters, we learned that the electron leakage current strongly depends on both  $\tau_n$  and the difference between the laser photon energy and

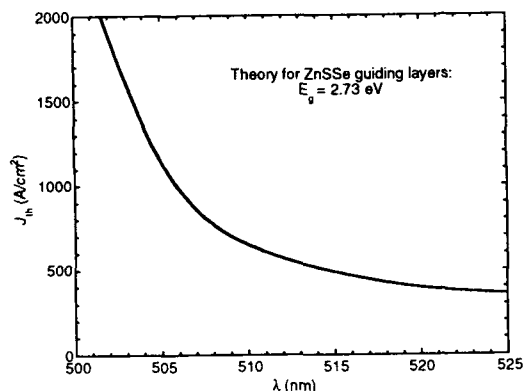


Fig. 5. The threshold current density calculated as a function of emission wavelength (quantum well depth) for fixed minority carrier lifetime.

the band gap of the guiding (barrier) layers. Fig. 5 illustrates the latter dependency.

As a further test of the model, we measured the threshold current density in several diodes cleaved to various cavity lengths. For this experiment, the facets were not coated ( $r_1, r_2 = 0.21$ ). Fig. 6 shows the relationship between the total gain (loss) and the current density at threshold. The total modal gain required at threshold for these devices is given by

$$g = \alpha_0 + (1/2L) \ln(1/r_1 r_2), \quad (11)$$

where  $r_1$  and  $r_2$  are the facet reflectivities, and  $L$  is the cavity length. The internal optical loss in the waveguide  $\alpha_0$  is deduced from differential

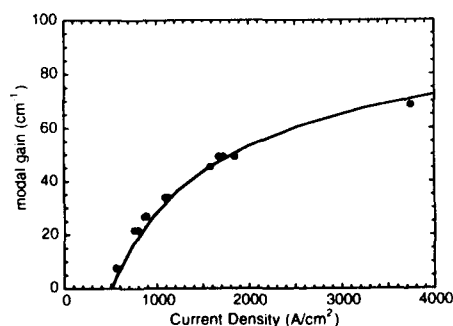


Fig. 6. The measured and calculated threshold as a function of injected current density.

quantum efficiency measurements. The agreement between the model and the data is remarkable, considering that there are *no* adjustable parameters (other than  $\tau_n$  which was established above).

This model seems to accurately predict the behavior of the threshold current density in CdZnSe quantum well devices without invoking excitonic recombination mechanisms. Exciton-related stimulated emission, however, has been clearly identified at low temperatures with resonant optical pumping and it has been speculated that such mechanisms also play a role at room temperature [15]. While the success of our non-excitonic model certainly does not prove that excitons are absent at room temperature, it does suggest that their effects may be more subtle than first anticipated. Exciton-related gain will be included in future models.

### 3. Device degradation

While there have been several papers over the past two years that deal with the demonstration of II-VI compound blue or blue-green light emitting devices, there has been no work that seriously addresses the issue of degradation of these devices. Understanding and eliminating degradation mechanisms is, however, critical since they control device lifetimes: a major problem with II-VI light emitters today. For example, in our laboratory, blue-green lasers last only for a few minutes to an hour at room temperature while light emitting diodes (LEDs) last from several minutes to a few days. Here we report the first detailed study of the degradation of II-VI blue-green light emitters. Through studies on light emitting diodes and gain guided stripe lasers tested at room temperature, we show that the degradation is related to crystal defects that originate from pre-existing defects and propagate throughout the active region, acting as non-radiative recombination centers.

The results described here are from a quantum well laser structure grown by MBE in the following sequence: GaAs(100) substrate/ $n^+$ -ZnSe buffer (500 Å)/ $n$ -ZnSSe (1.85  $\mu\text{m}$ )/

CdZnSe quantum well/p-ZnSSe (1.85  $\mu\text{m}$ )/p<sup>+</sup>-ZnSe (0.25  $\mu\text{m}$ ). The ZnSSe was lattice-matched to GaAs. The quantum well was grown at 150°C by ABE and consists of 4 periods of (CdSe)<sub>1</sub>(ZnSe)<sub>2</sub>, resulting in a mean Cd composition of 0.33. Light emitting diodes were fabricated by depositing a 250  $\mu\text{m}$  diameter, 90 Å thick gold dot that is surrounded by a 0.1  $\mu\text{m}$  thick Ti-Au contact ring. Degradation studies were carried out on these LEDs by electroluminescence (EL) microscopy and plan view transmission electron microscopy (TEM). Gain guided stripe lasers with 100 Å thick and 20  $\mu\text{m}$  wide transparent gold electrodes were also fabricated and studied by EL microscopy. Electroluminescence imaging is done by passing the light exiting from the top surface of the LED or stripe laser through an optical microscope system allowing the degradation progress to be studied during device operation. Specimens for plan view TEM observation were made from the degraded LEDs by a combination of chemical etching and ion milling to produce electron transparent regions containing the quantum well. TEM studies were carried out in a JEOL 200CX microscope at 200 kV.

Figs. 7a to 7e are video still frame EL images showing successive stages of degradation of an LED. The current density during the test was progressively increased from 10 to 130 A/cm<sup>2</sup>. Fig. 7a, taken a few seconds after turn-on, shows the pre-existing defects in the structure; these defects exhibit dark contrast since they act as non-radiative recombination centers. The long, dark lines lie along the [011] direction and are misfit dislocations lying in the quantum well/ZnSSe interface. The faint dark spots (indicated by the arrow) are crystal defects that cut across the quantum well. At the first stage of degradation (Fig. 7b), the faint spots become darker, implying enhanced local non-radiative recombination. In the second stage (Fig. 7c) these defects emit dark line defects (DLDs) along <001> directions, similar to observations made for GaAs/AlGaAs lasers [16,17]. In the third stage (Fig. 7d) the DLDs break up into elongated dark patches and the dark spots also enlarge individually into such patches. Clusters of dark patches

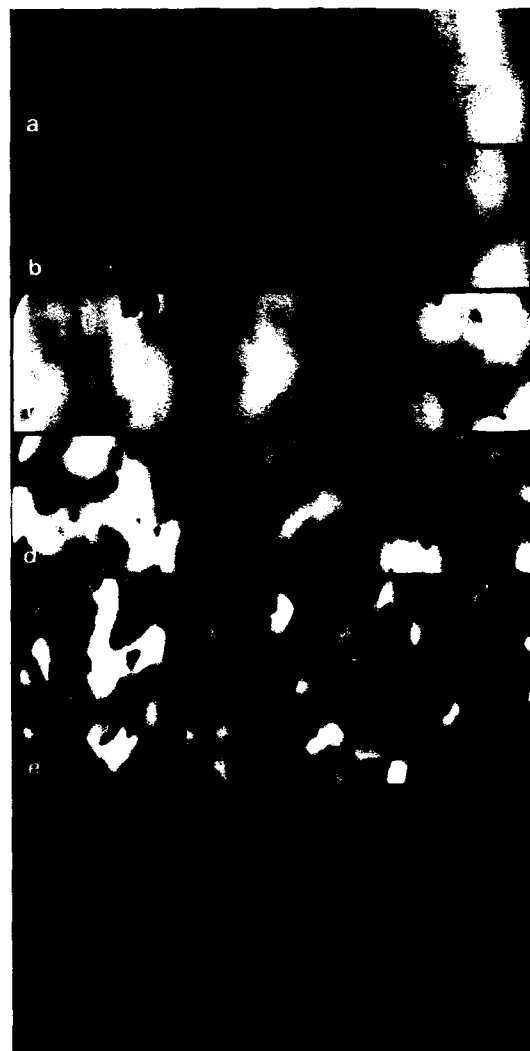


Fig. 7. EL micrographs showing the various stages of degradation of a light emitting diode.

now define regions of very poor luminescence on the LED. In the final stage of degradation (Fig. 7e), these dark patches cover the entire LED and appear to assume geometric shapes bounded by <011> directions and straight lines making fixed angles with <011>.

Electroluminescence studies carried out on gain guided stripe lasers at 1500 A/cm<sup>2</sup> current

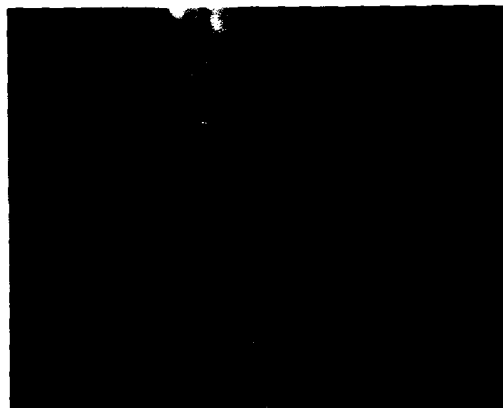


Fig. 8. EL micrograph of the surface of a diode laser.

densities and 0.08% duty cycle also showed similar degradation features. Fig. 8 shows a still frame taken at the third stage of degradation. The edge of the stripe is along a  $\langle 011 \rangle$  direction. Misfit dislocations,  $\langle 001 \rangle$  DLDs and dark patches are all clearly visible. We note that since the laser facets were uncoated no lasing occurred during the tests.

Plan view TEM studies on the as-grown sample show that the defect structure consists of V-shaped stacking faults that originate at the substrate–epilayer interface and rise up to the epilayer surface. At the quantum well/ZnSSe interface these stacking faults act as sources for misfit dislocations that are ejected along  $\langle 011 \rangle$  direction [18]. The stacking fault density measured by TEM is  $4 \times 10^5 \text{ cm}^{-2}$ . This is in reasonable agreement with the dark spot density of  $7 \times 10^5 \text{ cm}^{-2}$  found in Fig. 7c. This suggests that the initial degradation originates from the vicinity of the stacking faults. The density of these faults varies from sample to sample even when the nucleation of ZnSe is two-dimensional and reasons for their origin is not clear at the present time.

After the EL studies, a specimen for plan-view TEM was made of the LED tested in Fig. 7. Degraded regions directly under the Au contact pad as well as adjacent regions not under the Au pad (therefore not degraded) were studied for

comparison. Fig. 9 is a plan view micrograph showing the defect structure in the non-degraded part of the specimen. As mentioned earlier, the stacking faults (indicated by arrow 1) rise to the quantum well and form the misfit dislocations (arrows marked 2). No other defects could be seen in this region. We now turn to the degraded region of the sample. Figs. 10 and 11 are plan view, bright field micrographs (excited with orthogonal  $\langle 022 \rangle$  reflections, respectively) showing a degraded area representative of the final stages of degradation. In addition to the stacking faults (which shows vanishing contrast in Fig. 11 due to the diffraction conditions) and misfit dislocations, patches of regions containing large numbers of small defects (arrows marked 1) can be seen. They appear to be a network of small dislocations with elongated segments having local densities  $> 10^{10} \text{ cm}^{-2}$  and contribute to the device degradation. Henceforth they will be referred to as degradation defects. These patches are the dark features observed in Fig. 7c and appear dark in the EL micrographs since the degradation defects



Fig. 9. Plan-view bright field TEM micrograph of a non-degraded layer. Arrows 1 and 2 indicate a stacking fault and misfit dislocation, respectively.



contained in them act as non-radiative recombination centers. Since the EL images are formed with light emitted from the quantum well, the appearance of the dark patches in the image indicates that the degradation defects reside within the quantum well. This conclusion is supported by observation of electron stereomicrographs. The degradation defects themselves are aligned along both the  $\langle 011 \rangle$  directions contained in the  $(100)$  interface plane as can be seen in the bright field micrographs of Figs. 10 and 11. The micrographs also show that only one set of degra-

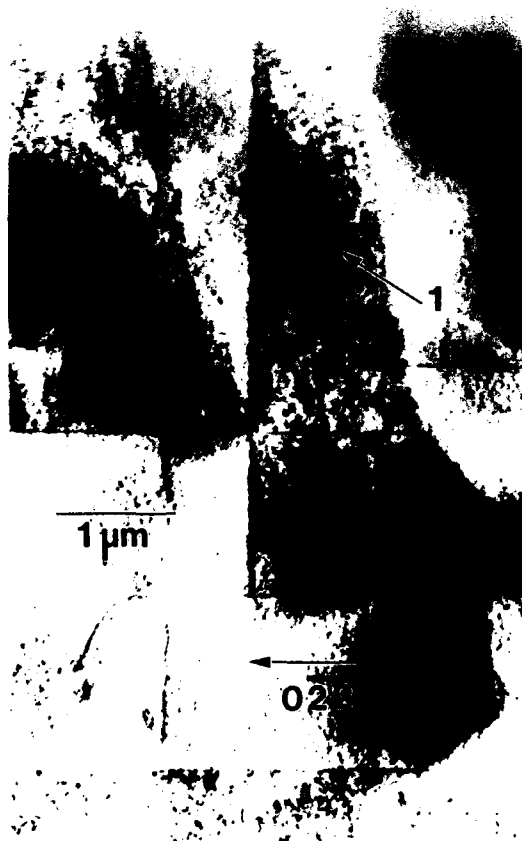


Fig. 10. Plan-view TEM micrograph (two-beam condition  $02\bar{2}$ ) from a degraded region. Only one set of degradation defects (marked 1) are visible.



Fig. 11. Plan-view TEM micrograph (two beam condition  $02\bar{2}$ ) from the same degraded region shown in Fig. 10. The excited reflection is orthogonal to the case in Fig. 10 and consequently the visible degradation defects (marked 1) are perpendicular to those in Fig. 10. The stacking fault shows vanishing contrast.

dation defects are observed in each image, with the set of defects with their lengths perpendicular to the excited  $\langle 022 \rangle$  reflection being absent. When the  $\langle 040 \rangle$  reflections are excited on the other hand, both set of defects are observed. Assuming that the Burgers vectors are of the usual  $b = \frac{1}{2}a \langle 110 \rangle$  type, this would indicate that the Burgers vectors of these defects lie in the interface plane in a direction along the lengths of the defects. We note that this is different from the Burgers vectors of degradation induced dislocation networks in GaAs/AlGaAs lasers which make an angle of

45° to the interface plane. TEM studies indicate that these degradation defects appear to originate from both isolated misfit dislocation segments as well as from the vicinity of stacking faults with misfit dislocations propagating from them.

As can be seen from both the EL and the TEM images, the patches formed by the degradation defects are bounded by well defined directions; some of which are  $\langle 011 \rangle$ . The TEM studies show that these directions arise since the patches are often bounded on one or more sides by misfit dislocations – a consequence of the interaction between the stress fields of the misfit dislocations and the degradation defects. As may also be seen from the TEM micrographs, the degradation defects also appear to end abruptly along directions other than  $\langle 011 \rangle$  where no restraining line defect is observed; this behavior is not understood at the present time.

We now turn to the consequence of defect formation in lasers. The studies above clearly show that the degradation of the devices is related to the propagation of crystal defects. Formation of such defects reduces the light emission from the device. The reduction of quantum efficiency drives up the current density needed to reach threshold. With the larger injected current comes even more rapid propagation of defects. This run-away process eventually leads to such large current densities that the contacts fail. The observation of cw lasing, therefore, is primarily inhibited by the rapid formation and propagation of degradation defects. We note that although the use of a separate confinements lattice matched structures will reduce threshold current densities, as demonstrated recently using Zn-MgSSe clad layers, methods for reducing pre-existing defects are necessary for long-lived cw laser operation.

#### 4. Conclusion

In conclusion, very low-threshold buried-ridge laser diodes have been fabricated for the first time in II–VI semiconductors. These devices emit at 511 nm at room temperature under pulsed

current injection, and operate in a single lateral mode. The fabrication process is thought to be manufacturable and results in a planar surface, suitable for die bonding. We have shown that the threshold current density of CdZnSe quantum well laser diodes can be accurately predicted with techniques previously developed for III–V laser diodes. At room temperature, electron leakage current can be an important component of the total threshold current. We have examined the structural aspects of II–VI blue-green light emitter degradation by fabricating LEDs and stripe lasers from quantum well laser structures. Degradation appears to occur initially by the formation of new crystal defects from the vicinity of pre-existing ones such as stacking faults. These defects propagate along  $\langle 010 \rangle$  directions and their evolution finally results in the formation of patches of regions spread out across the device and consisting of high densities of small dislocations that lie in the quantum well. These defects act as non-radiative recombination centers that reduce the light emission of the device.

#### 5. Acknowledgements

We gratefully acknowledge valuable discussions with Professor Peter Zory and preprint information from our colleagues at North American Philips.

#### 6. References

- [1] M.A. Haase, J. Qiu, J.M. DePuydt and H. Cheng, *Appl. Phys. Lett.* 59 (1991) 1272.
- [2] T. Tsukada, *J. Appl. Phys.* 45 (1974) 4899.
- [3] T.R. Chen, B. Zhao, Y.H. Zhuang, A. Yariv, J.E. Ungar and S. Oh, *Appl. Phys. Lett.* 60 (1992) 1782.
- [4] J.M. Gaines, R.R. Drenten, K.W. Haberern, T. Marshall, P. Mensz and J. Petrozzello, *Appl. Phys. Lett.* 62 (1993) 2462.
- [5] R.M. Park, M.B. Troffer, C.M. Rouleau, J.M. DePuydt and M.A. Haase, *Appl. Phys. Lett.* 57 (1990) 2127.
- [6] J. Qiu, H. Cheng, J.M. DePuydt and M.A. Haase, *J. Crystal Growth* 127 (1993) 279.
- [7] J.M. DePuydt, M.A. Haase, H. Cheng and J.E. Potts, *Appl. Phys. Lett.* 55 (1989) 1103.
- [8] N. Nakayama, S. Itoh, T. Ohata, K. Nakano, H. Okuyama,

- M. Ozawa, A. Ishibashi and K. Akimota, *Electron. Lett.* 29 (1993) 766.
- [9] R.L. Aggarwal, J.J. Zayhowski and B. Lax, *Appl. Phys. Lett.* 62 (1993) 2899.
- [10] D. Ann, T.K. Yoo and H.Y. Lee, *Appl. Phys. Lett.* 59 (1991) 2669.
- [11] M. Kuramoto, T.C. Chong, A. Kikuchi and K. Kishino, *Electron. Lett.*, submitted.
- [12] E. Yablonovitch and E.O. Kane, *IEEE J. Lightwave Technol.* LT-4 (1986) 504; LT-4 (1986) 961.
- [13] D.P. Bour, D.W. Treat, R.L. Thornton, R.S. Geels and D.F. Welch, *IEEE J. Quantum Electron.* QE-29 (1993) 1337.
- [14] J.A. Bolger, A.K. Kar, B.S. Wherett, K.A. Prior, I. Simpson, S.Y. Wang and B.C. Cavenett, *Appl. Phys. Lett.* 63 (1993) 571.
- [15] H. Jeon, J. Ding, A.V. Nurmikko, H. Luo, N. Samarth and J. Furdyna, *Appl. Phys. Lett.* 59 (1991) 1293.
- [16] P. Petroff and R.L. Hartman, *Appl. Phys. Lett.* 23 (1973) 469.
- [17] P.W. Hutchinson and P.S. Dobson, *Phil. Mag.* 32 (1975) 745.
- [18] S. Guha, J.M. DePuydt, J. Qiu, G. Hofler, B.J. Wu, M.A. Haase and H. Cheng, unpublished.

## Advances in blue laser diodes

Akira Ishibashi \*, Yoshifumi Mori

*Sony Corporation Research Center, 174 Fujitsuka-cho, Hodogaya-ku, Yokohama 240, Japan*

### Abstract

We have demonstrated the feasibility of ZnMgSSe as cladding layers for blue and blue-green laser diodes. The ZnMgSSe, fully lattice-matched to GaAs substrates, suppresses carrier overflow with its large energy-gap having type I heterostructure with Zn(S)Se. This has led to a successful demonstration of room temperature pulsed operation of a blue laser diode with a wavelength of 498.5 nm and room temperature CW operation of a 523.5 nm blue-green laser diode with a threshold current of 45 mA, based on a ZnCdSe/ZnSe/ZnMgSSe SCH structure.

### 1. Introduction

II–VI wide gap semiconductor laser diodes (LDs) have been a focus of attention, since Haase et al. reported the first semiconductor blue-green laser diode based on ZnCdSe/Zn(S)Se [1]. The ZnCdSe/Zn(S)Se system has intrinsic problems caused by a small energy-gap difference between the ZnCdSe active layer and the Zn(S)Se cladding layer. This makes operation at a high temperature or at a short wavelength difficult due to insufficient confinement of injected carriers. For shorter wavelength laser diodes, i.e., for LDs with an active layer made of ZnSe or ZnCdSe with less Cd mole fraction, use of conventional II–VI materials such as ZnSe, ZnS, ZnTe, and CdS only is not sufficient to fulfill the requirement of carrier confinement. For example, ZnSTe, which was supposed to have a wider energy gap than

ZnSe, has in reality an energy gap narrower than ZnSe due to heavy band-bowing, while ZnCdS, another candidate for such a cladding layer, indeed has a wide energy gap but forms a type II heterostructure with ZnSe. Thus these two materials are not suitable for the cladding layers of wide gap II–VI semiconductor LDs with a wavelength of less than  $\sim 520$  nm. We have found that ZnMgSSe, with an energy gap tunable up to as high as  $\sim 4.5$  eV [2], fully lattice-matched to GaAs (001) substrates, forms a type I heterostructure with ZnSe. Using ZnMgSSe as cladding layers for wide gap II–VI LDs, we already have demonstrated 77 K continuous wave (CW) operation of ZnSe/ZnMgSSe multi-quantum well (MQW) LD with wavelength of 447 nm [3]. Since then, we have optimized the LD structure improving the contacts [4,5] to p-ZnSe. Quite recently, we have succeeded in room temperature (RT) pulsed operation of a blue LD with a wavelength of 498.5 nm [6], and RT CW operation of a 523 nm blue-green LD for the first time [7].

\* Corresponding author.

## 2. ZnMgSSe alloy and its feasibility as a cladding layer

In seeking a wide energy-gap material that is lattice-matched to GaAs, ZnSSe serves as a good starting material. ZnS has an energy gap of 3.80 eV (at 77 K) with a lattice constant of 5.41 Å. Needed is a column II element that bonds with S or Se to form a wide-gap II-VI compound with a lattice constant larger than 5.66 Å, the lattice constant of GaAs. Then the column II element is to be mixed with ZnSSe to form a quaternary alloy. The reason we look for a column II element is as follows. For a compound semiconductor, its conduction band is made mainly from s-orbitals of the cation (the column II element in the present case), and its valence band from p-orbitals of the anion (the column VI element). Since S in ZnSSe modulates only the valence band with respect to that of ZnSe, it is the column II element that can modulate the conduction band with respect to Zn(S)Se for confining electrons in an active layer.

Generally, compound semiconductors consisting of elements sitting in upper rows of the Periodic Table have a wide energy gap, because the outermost orbitals of the upper row elements have a wide spacing in energy. Thus, keeping in mind that both Zn and Se are in the fourth row of the Periodic Table, we postulate that the column II element needed to make the energy gap wider will be in between the first and the third rows (Postulate a). On the other hand, atomic radii, in general, become longer as the row number increases in the Periodic Table (Tendency 1), because the number of orbitals around the nucleus increases for elements in lower rows. In each row of the Periodic Table, the atomic radius becomes longer as the column number decreases (Tendency 2), since the positive charge of the nucleus is less for small column-number elements in that row. In this context, the column II element needed to make the lattice constant larger will be a small column-number element in the fifth row or lower of the Periodic Table (Postulate b). Since Postulate b contradicts Postulate a sharply, it seems impossible to have such a column II element that enables both a large

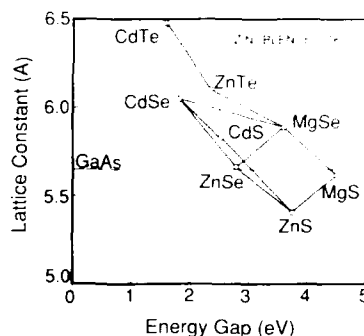


Fig. 1. Energy gap versus lattice constant for wide gap II-VI semiconductors including ZnMgSSe.

lattice constant and a wide energy gap concurrently. However, because Tendency 2 becomes stronger for upper rows, there occurs a dramatic reversal in Tendency 1, i.e., upper-row elements do have longer covalent radii than lower-row ones for specific pairs of elements [8]. For column Ib, Ag in the fifth row has a larger covalent radius than Au in the sixth row. For column II materials, i.e., the current focus of attention, Mg, in the third row, has a larger tetrahedral covalent radius than Zn in the fourth row. Note that for the third and the fourth rows the column III elements, Al and Ga, are on the verge of the reversal, i.e., they have the same tetrahedral covalent radius, which leads to the well-known fact that AlAs and GaAs have an identical lattice constant, a fact that makes a wide-range of heterostructure physics blossom in the AlAs/GaAs system. Exploiting the reversal for the column II elements, we finally have proved that Mg in Zn(S)Se makes the energy gap wider and the lattice constant longer than Zn(S)Se, as desired. In the lattice-constant-energy-gap plane (Fig. 1), MgSe (in zinc-blende structure) and ZnS are located at roughly symmetrical positions with respect to ZnSe and GaAs. Incorporating Mg into ZnSSe allows us to cover a wide range of energy from 2.78 to ~4.5 eV (at 77 K), remaining fully lattice-matched to GaAs, as we can see in Fig. 1. Further, from the common anion/cation rule, the ZnSe/ZnMgSSe system is shown to have a type I heterostructure [2]. Although MgS and MgSe nat-

usually have the rock-salt structure, we have found that ZnMgSSe grown on GaAs has the zinc blende structure. In addition, from a reflection-spectrum measurement [9], we have found that ZnMgSSe has a refractive index smaller than that of ZnSe, as shown in Fig. 2. Those two facts indicate that both photons and carriers can be well confined in the ZnSe/ZnMgSSe double-heterostructure (DH). Encouraged by that, we tried photo-pumped lasing experiments using undoped Zn(S)Se/ZnMgSSe DH structures. We have succeeded in photo-pumped lasing at temperatures up to 500 K [10]. This proves our prediction that the ZnMgSSe forms a type I heterostructure with ZnSe and has a refractive index smaller than that of ZnSe. It also suggests that ZnMgSSe has good thermal stability. For current-injected laser operation, we need both n-type and p-type doping. Using  $\text{ZnCl}_2$  we can dope ZnMgSSe with an electron concentration up to  $3 \times 10^{18} \text{ cm}^{-3}$ . Using a nitrogen plasma excited by electron cyclotron resonance (ECR) [11], we are able to dope ZnMgSSe with a hole concentration up to  $\sim 1 \times 10^{17} \text{ cm}^{-3}$  (for  $E_g \sim 2.95 \text{ eV}$  at 77 K), while maintaining a high epitaxial quality [3]. Then we grew a blue-light-emitting ZnSe/ZnMgSSe MQW LD, and succeeded in 77 K CW operation of the blue LD with threshold current

density of  $225 \text{ A/cm}^2$  at a wavelength of 447 nm [3]. Thus we believe the feasibility of ZnMgSSe for the cladding layer of blue LDs has been well proven.

### 3. Improvement of p-contacts to p-ZnSe

Reported threshold voltages of blue-green LDs are still too high for room temperature (RT) operation. We must suppress parasitic heating, which is caused mainly by a poor ohmic contact to p-ZnSe. We need a lower resistance ohmic contact to p-type ZnSe. Our effort to obtain a good contact to the p-ZnSe that is to follow the p-ZnMgSSe cladding layer is two-fold.

#### 3.1 Au / Pt / Pd multi-layered metal to p-ZnTe

HgSe was found to form ohmic contacts to p-type ZnSe by reducing the metal-semiconductor interfacial energy barrier [12]. ZnTe is another candidate for a hole injection layer for p-contacts among II-VI compounds. ZnTe is promising, because it can be doped with a p-concentration above  $10^{19} \text{ cm}^{-3}$  in marked contrast to ZnSe which can only be doped as high as  $\sim 10^{18} \text{ cm}^{-3}$ . The use of p-ZnTe with other II-VI semi-

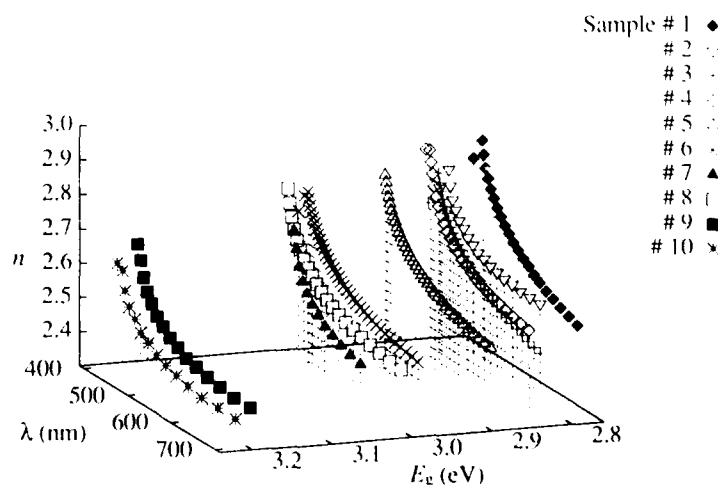


Fig. 2. Dependence of the refractive index on the energy gap and the wavelength for the Zn(Mg)SSe system: (1) ZnSe; (2), (3) ZnSSe; (6)-(10) ZnMgSSe.

conductors such as ZnSe and recently improved p-type doping techniques [11,13,14] makes fabrication of high performance devices possible. Although p-type ZnTe is becoming increasingly important, ohmic contacts to this material have not been studied much. The most commonly used ohmic contacts to p-ZnTe are Au and Ag [15]. However, the specific contact resistance of these metals is not low enough for practical use. Since the work functions of Pt and Au are large (5.65 and 5.1 eV, respectively) [16], these two metals are expected to form a good ohmic contact to p-type ZnTe. A thin layer of a reactive transition metal such as Pd or Ni will also be helpful, because reactions between the metal layer and the surface of the semiconductor are expected. Thus, we have tried Au/Pt/Pd ohmic contacts to p-doped ZnTe grown on a (001) GaAs substrate by MBE. The p-type doping is achieved with a nitrogen plasma excited by ECR. The contact metals are evaporated successively in an electron beam evaporator. The dependence of the specific contact resistance on the Pd layer thickness is shown in Fig. 3. The samples are annealed at 200°C. The specific contact resistance has its minimum at the Pd thickness of 5–10 nm, for which the specific contact resistance is as low as  $5 \times 10^{-6} \Omega \text{ cm}^2$  [4]. This value of the specific contact resistance is two orders of magnitude lower than that of Au or Au/Pt contacts to p-ZnTe. Thus

we have obtained a good ohmic contact metal to p-ZnTe.

### 3.2. ZnTe/ZnSe resonant tunneling MQW

The remaining problem is what to put between the p-ZnTe and the p-ZnSe. One candidate is a ZnTe/ZnSe pseudo-graded layer, which has shown to be feasible [17]. In this case, however, the superlattice is more a substitute for a graded ZnSeTe ternary alloy whose energy gap is difficult to design due to large band-bowing than a structure to bear current through resonant tunneling mechanism. Focussing on the latter strategy, we propose a ZnTe/ZnSe multi-quantum well (MQW) structure whose resonating subbands make possible a quasi-ohmic contact to p-type ZnSe.

In designing the resonant tunneling MQW structure for holes, the key parameter is the valence band offset. According to theories, the valence-band offsets span a wide range of 0.3 through 1.1 eV [18]. The prediction of the linear combination of atomic orbitals (LCAO) theory is 1.08 eV for a ZnTe/ZnSe heterojunction [19], while from the common anion rules, the valence band offset is estimated to be about 0.50 eV. To clarify the valence band offset experimentally, we have grown on a (100) GaAs substrate a ZnTe/ZnSe QW structure having 0.3, 1, 2, 4, and 8 nm wide ZnTe wells isolated by 50 nm thick ZnSe barriers. Fig. 4 shows a spectrum of the photoluminescence (PL) at 4.2 K from the QW structure. We have observed PL from the wells, although we could not identify the PL peak from the 0.3 nm thick well. The inset shows the experimental result together with calculated values for different valence-band offsets. The calculated result is derived assuming a type II heterointerface between ZnTe and ZnSe, and assuming that the origin of PL emission is due to transitions of free electrons to the lowest hole subband in the valence band. Based on the lattice-mismatch between ZnTe and ZnSe, the energy shift due to the strain is assumed to be 177 meV, independent of the well-width for simplicity. We have used the hole mass of  $0.60 m_0$  both for ZnSe and for ZnTe, where  $m_0$  is the electron mass in

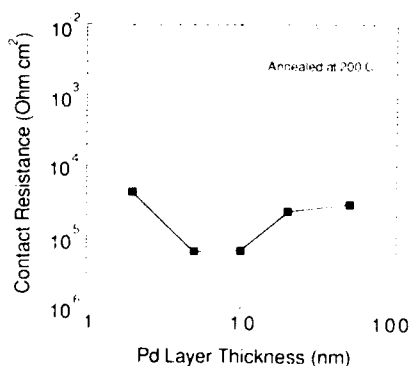


Fig. 3. Specific contact resistance of the Au/Pt/Pd multi-layered metal contact to p-ZnTe as a function of Pd layer thickness. Annealed at 200°C.

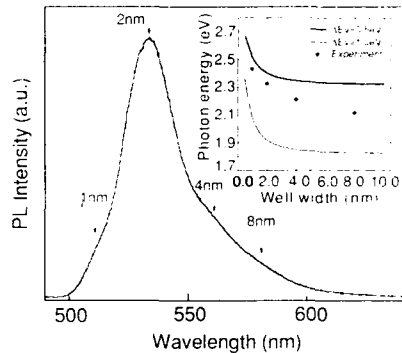


Fig. 4. Photoluminescence spectrum from ZnTe/ZnSe quantum wells at 4.2 K. The inset shows the PL energy as function of well width. The thin line is for the net  $\Delta E_v$  of 0.5 eV and the thick line for the net  $\Delta E_v$  of 1.0 eV. The solid circles show the experimental result.

vacuum. The net valence band offset is estimated to be about 0.5 eV for the ZnTe/ZnSe heterostructure [5], because of the better agreement between experiment and calculation for the net valence-band offset of 0.5 eV than for that of 1.0 eV. The discrepancy seen for the wide wells can be ascribed to the fact that we have assumed a constant strain-induced energy-shift where the strain distribution should be considered.

Valence band discontinuity being obtained, we now design the structure. First, the total thickness of the MQW is set to be roughly equal to the ZnSe depletion-layer thickness that we would have for an abrupt ZnSe/ZnTe single heterointerface. Then p-ZnTe/ZnSe quantum wells are employed whose widths are so designed that the lowest hole-subbands align in energy, cancelling the parabolic potential due to the depletion, allowing holes to tunnel resonantly from the top p-ZnTe into the p-ZnSe. As shown in Fig. 5a, the resonant tunneling MQW consists of 0.3, 0.4, 0.5,

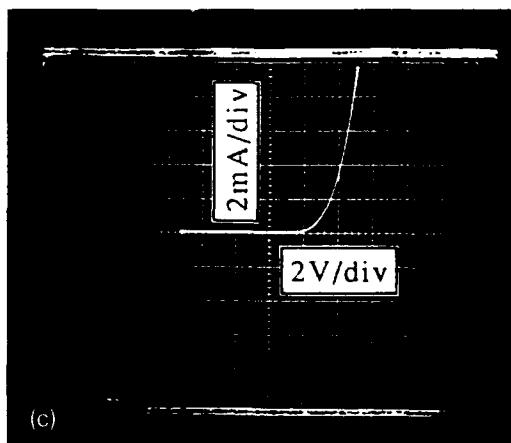
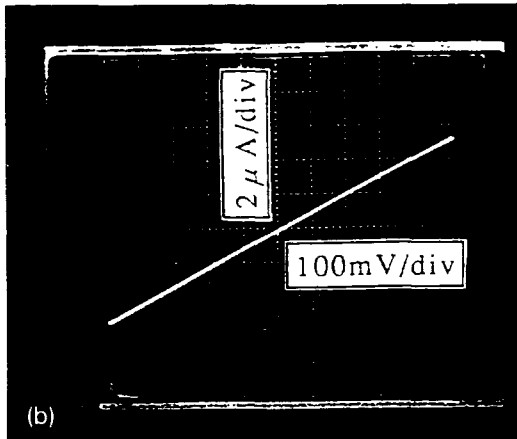
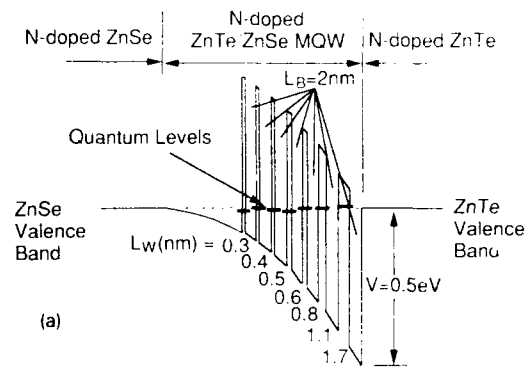


Fig. 5. (a) Schematic valence-band structure of the ZnTe/ZnSe resonant tunneling MQW. Seven thick short lines denote the lowest hole subband for each well.  $L_w$  is the well (ZnTe) width and  $L_b$  the barrier (ZnSe) thickness. (b)  $I$ - $V$  characteristics between two resonant tunneling MQW p-contacts. (c)  $I$ - $V$  characteristics of a ZnSe-based diode having the resonant tunneling MQW p-contact.



0.6, 0.8, 1.1, and 1.7 nm thick ZnTe wells sandwiched between 2 nm thick barriers of ZnSe, the last of which is followed by the top p-ZnTe layer. Energy levels calculated for the quantum wells are also shown. As shown in Fig. 5b, the p-contact shows ohmic characteristics, and the specific contact resistance obtained is as low as  $5.0 \times 10^{-2} \Omega \text{ cm}^2$  [4]. The measured resistance consists of the contact resistance for the p-metal/p-ZnTe interface and that for the ZnTe/ZnSe MQW. The measured value is mainly due to the MQW, because the specific contact resistance is orders of magnitudes smaller for the metal/p-ZnTe interface as discussed in section 3.1. The resistance can be lowered by optimizing the MQW structure to make the hole-transmission probability as high as possible. An example of improvements brought by the resonant tunneling ZnTe/ZnSe MQW is shown in Fig. 5c as well as in the I-V characteristics discussed in section 4. Note that the applied voltage is  $\sim 5$  V for the current of  $\sim 10$  mA, to which the threshold current, we believe, will eventually be reduced as discussed in section 5. Optimization of the resonant MQW, especially for applied net voltages of order  $\sim 1$  V, will lead to further reduction in the operation voltage of the blue LDs.

#### 4. Room temperature pulsed operation of a blue laser diode

Since a good, if not very good, p-contact from the p-electrode to the p-cladding layer has been thus achieved, we then optimize a blue-light emitting LD using a ZnCdSe/ZnSe/ZnMgSSe separate-confinement heterostructure (SCH). We add a small amount of Cd to the active layer to obtain a sufficient energy-gap difference but still to remain in the blue region of wavelength. The energy gap has to be more than  $\sim 0.35$  eV to prevent electrons from overflowing into the p-cladding layer. The schematic structure of the LD is shown in Fig. 6. The epitaxial layers for the laser diodes are grown on Si-doped GaAs(100) substrates by molecular beam epitaxy (MBE) at a substrate temperature of 280 °C. The epitaxial layers consist of (i) an n-ZnMgSSe cladding layer

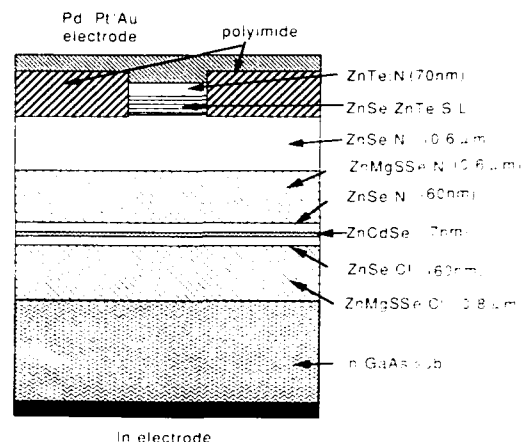


Fig. 6. Schematic structure of the ZnCdSe/ZnSe/ZnMgSSe SCH laser.

( $N_D - N_A = 8 \times 10^{17} \text{ cm}^{-3}$ ), (ii) an n-ZnSe optical guiding layer ( $N_A - N_D = 8 \times 10^{17} \text{ cm}^{-3}$ ), (iii) a  $\text{Cd}_{0.12}\text{Zn}_{0.88}\text{Se}$  single quantum well active layer, (iv) a p-ZnSe optical guiding layer ( $N_A - N_D = 5 \times 10^{17} \text{ cm}^{-3}$ ), (v) a p-ZnMgSSe cladding layer ( $N_A - N_D = 2 \times 10^{17} \text{ cm}^{-3}$ ), (vi) a p-ZnSe layer ( $N_A - N_D = 5 \times 10^{17} \text{ cm}^{-3}$ ), (vii) a p-ZnSe/p-ZnTe MQW, and (viii) a p-ZnTe contact layer ( $p = 3 \times 10^{18} \text{ cm}^{-3}$ ), where  $N_A - N_D$  ( $N_D - N_A$ ) is the net acceptor (donor) concentration measured by C-V technique, and  $p$  the hole concentration obtained from Hall measurements. The energies of the band edge emission of ZnCdSe and ZnMgSSe at 77 K are 2.62 and 2.96 eV, respectively. The energy gap difference between the active and the cladding layers is estimated to be 340 meV. The LD has a 10  $\mu\text{m}$  wide stripe and a 1 mm long cavity.

Mounting the LD with the p-side down on a heat sink, we have obtained pulsed laser operation of the ZnCdSe/ZnSe/ZnMgSSe SCH lasers at room temperature with uncoated facets [4]. The relationship of the light output power to the current is shown in Fig. 7. The pulse width and the repetition rate are 400 ns and 250 Hz, respectively. The laser diode operates at a duty cycle as high as  $10^{-3}$  at 295 K. We have been able to obtain a peak output-power of 130 mW from each facet at 300 K. The slope efficiency is 0.25

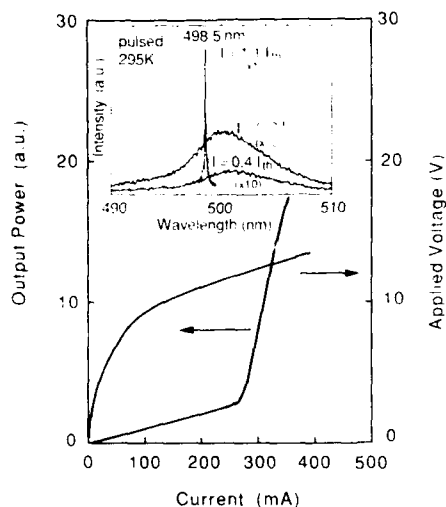


Fig. 7.  $L-I$  and  $V-I$  characteristics under pulsed operation at RT. The inset shows emission spectra of the laser diode under pulsed operation with different injection levels at RT.

W/A per facet at 295 K. The threshold current  $I_{th}$  is 280 mA, which corresponds to a threshold current density  $J_{th}$  of 2.8 kA/cm<sup>2</sup>. A relatively small voltage of  $\sim 12$  V is applied across the diode at the threshold current  $I_{th}$ , which shows that our resonant tunneling MQW p-contact works well. The emission spectrum at room temperature is shown in the inset of Fig. 7. The lasing wavelength is 498.5 nm, which is the shortest for RT laser operation thus far reported. The LD has a lifetime of several hours under the operating conditions. We attribute the short wavelength lasing to the use of the wide gap ZnMgSSe cladding layers that confine carriers more efficiently than the conventional ZnSSe cladding layers.

##### 5. Room temperature CW operation of a blue-green LD

For CW operation [7], we have made the energy gap difference between the active layer and the cladding layers larger than the case of section 4. We also have employed facet coating to reduce mirror loss. Since the internal loss  $\alpha$  of our LDs

is found to be small, i.e., 2–4 cm<sup>-1</sup> [20], highly reflective (HR) facet-coating can drastically reduce the threshold current density. Except for a lower Cd content in the active layer and the absence of the ZnTe/ZnSe MQW at the p-contact, the LD structure is essentially the same as the one shown in Fig. 6. The epitaxial layers consist of an n-ZnMgSSe cladding layer ( $N_D - N_A = 5 \times 10^{17}$  cm<sup>-3</sup>,  $d = 1.5$   $\mu$ m), an n-ZnSe optical guiding layer ( $N_D - N_A = 5 \times 10^{17}$  cm<sup>-3</sup>,  $d = 80$  nm), a Zn<sub>0.81</sub>Cd<sub>0.19</sub>Se quantum well (9 nm), a p-ZnSe optical guiding layer ( $N_A - N_D = 5 \times 10^{17}$  cm<sup>-3</sup>,  $d = 80$  nm), a p-ZnMgSSe cladding layer ( $N_A - N_D = 2 \times 10^{17}$  cm<sup>-3</sup>,  $d = 0.8$   $\mu$ m), a p-ZnSSe layer ( $N_A - N_D = 8 \times 10^{17}$  cm<sup>-3</sup>,  $d = 0.8$   $\mu$ m), and a p-ZnSe contact layer ( $N_A - N_D = 8 \times 10^{17}$  cm<sup>-3</sup>,  $d = 45$  nm), where  $N_A - N_D$  ( $N_D - N_A$ ) is again the net acceptor (donor) concentration and  $d$  is the layer thickness. The designed band-gap energies of the ZnCdSe and the ZnMgSSe are 2.54 and 2.94 eV at 77 K, respectively, and the energy-gap difference is thus 400 meV, which is set larger than that of the blue LD in section 4 in order to suppress the electron overflow across the active layer under the CW operation. The p-ZnSe top contact layer is chemically etched off leaving a 5  $\mu$ m wide mesa stripe. An insulating layer is deposited on the exposed p-ZnSSe layer to reduce the current path. Pd/Pt/Au multi-layered metal [4] is then evaporated onto the p-ZnSe as a p-electrode. Indium metal serves as an n-electrode to the n-GaAs substrate. The wafer is cleaved into 640  $\mu$ m wide bars, whose facets are then HR-coated. The reflectivities are 70% for the front facet and 95% for the rear. The strips are then cleaved into 400  $\mu$ m wide pellets and each pellet is mounted with the p-side down onto a copper heat sink.

The emission spectrum taken at RT (296 K) is shown in Fig. 8. Stimulated emission is observed at wavelengths of 521.6 nm under pulsed operation and 523.5 nm under continuous operation. The inset of Fig. 8 shows the light-output versus injection-current ( $L-I$ ) characteristics of the laser diode at RT (296 K) measured under continuous and pulsed-current conditions. For  $L-I$  measurements under continuous operation, the injection current is increased from zero to 100 mA at a

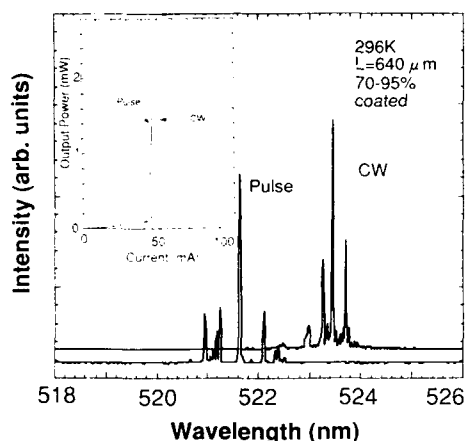


Fig. 8. Emission spectra under pulsed and continuous operation at RT. The inset shows  $L-I$  characteristics under pulsed and continuous current operation at RT.

rate of 500 mA/s. The pulsed  $L-I$  curve is measured with a pulse width of 2  $\mu$ s and a repetition rate of 1 ms. The threshold current ( $I_{th}$ ) under continuous operation is 45 mA corresponding to a threshold current density of 1.4 kA/cm<sup>2</sup>, while that under pulsed operation is 42 mA corresponding to a threshold current density of 1.3 kA/cm<sup>2</sup>. The small difference in the threshold current densities for CW and pulsed operation is ascribed to the fact that the SCH LD has a high characteristic temperature ( $T_0$ ) of 216 K because of the large energy-gap difference between the active and the cladding layers. Slope efficiencies under pulsed and continuous operation are 0.34 and 0.31 W/A, respectively [7]. These characteristics are comparable to conventional III-V materials-based LDs for optical pick-ups. The voltage at the lasing threshold is about 17 V, because we did not use ZnTe/ZnSe MQW at the p-contact. The LD has a lifetime of  $\sim 1$  s. We believe that we will be able to realize RT CW operation of blue LDs by merging the two efforts, i.e., by aiming at a short wavelength and a low operating voltage as shown in section 3, and by pursuing a low threshold current as discussed in this section. A high p-doping concentration in a wide gap ZnMgSSe is essential.

## 6. Conclusion

We have demonstrated the feasibility of ZnMgSSe as cladding layers for blue and blue-green laser diodes. The ZnMgSSe, suppressing carrier overflow with its large energy-gap and forming type I heterostructure with Zn(S)Se, enables us to have II-VI semiconductor blue lasers fully lattice-matched to GaAs substrates. The ZnMgSSe/Zn(S)Se system is of potential interest to make the II-VI wide-gap semiconductor physics blossom just in the same way as AlAs/GaAs system does the III-V heterostructure physics. We have introduced, as well as the Au/Pt/Pd multi-layered metal to p-ZnTe, the ZnTe/ZnSe resonant tunneling multi-quantum well (MQW) through which the holes flow via a resonant tunneling mechanism so that quasi-ohmic characteristics can be obtained at the p-contact. We have succeeded at room temperature both in pulsed operation of a blue laser diode with a wavelength of 498.5 nm and in CW operation of a blue-green laser diode with a wavelength of 523.5 nm and a threshold current of 45 mA. We believe that we will be able to achieve room temperature CW operation of a blue LD by lowering both the threshold voltage and the threshold current, optimizing the LD structure in terms of the energy difference between the active/cladding layers and the hole tunneling/avalanche efficiency through the ZnTe/ZnSe MQW.

## 7. Acknowledgements

We would like to thank Director Watanabe for continuous encouragement and are grateful to the II-VI Group of Sony Corporation Research Center for fruitful discussions.

## 8. References

- [1] M.A. Haase, J. Qiu, J.M. DePuydt and H. Cheng, Appl. Phys. Lett. 59 (1991) 1272.
- [2] H. Okuyama, K. Nakano, T. Miyajima and K. Akimoto, Jap. J. Appl. Phys. 30 (1991) L1620; J. Crystal Growth 117 (1992) 139.

- [3] H. Okuyama, T. Miyajima, Y. Morinaga, F. Hiei, M. Ozawa and K. Akimoto, *Electron. Lett.* 28, (1992) 1798.
- [4] M. Ozawa, F. Hiei, A. Ishibashi and K. Akimoto, *Electron. Lett.* 29 (1993) 503.
- [5] F. Hiei, M. Ikeda, M. Ozawa, T. Miyajima, A. Ishibashi and K. Akimoto, *Electron. Lett.* 29 (1993) 878.
- [6] S. Itoh, H. Okuyama, S. Matsumoto, N. Nakayama, T. Ohata, T. Miyajima, A. Ishibashi and K. Akimoto, *Electron. Lett.* 29 (1993) 766.
- [7] N. Nakayama, S. Itoh, T. Ohata, K. Nakano, H. Okuyama, M. Ozawa, A. Ishibashi, M. Ikeda and Y. Mori, *Electron. Lett.* 29 (1993) 1488.
- [8] L. Pauling, *The Nature of the Chemical Bond* (Cornell Univ. Press, Ithaca, NY, 1960) p. 246.
- [9] M. Ukita, H. Okuyama, M. Ozawa, A. Ishibashi, K. Akimoto and Y. Mori, *Appl. Phys. Lett.* 63 (1993) 2082.
- [10] H. Okuyama, Y. Morinaga and K. Akimoto, *J. Crystal Growth* 127 (1993) 335.
- [11] S. Ito, M. Ikeda and K. Akimoto, *Jap. J. Appl. Phys.* 31 (1992) L1316.
- [12] Y. Lansari, J. Ren, B. Sneed, K.A. Bowers, J.W. Cook, Jr. and J.F. Schetzina, *Appl. Phys. Lett.* 61 (1992) 2554.
- [13] R.M. Park, M.B. Troffer, C.M. Rouleau, J.M. DePuydt and M.A. Haase, *Appl. Phys. Lett.* 57 (1990) 2127.
- [14] K. Ohkawa, T. Karasawa and T. Mitsuyu, *Jap. J. Appl. Phys.* 30 (1991) L152.
- [15] P.A. Tupenevich, V.K. Kononenko and A.K. Lyakhovich, *Instr. Exptl. Tech.* 17 (1974) 1509.
- [16] H.B. Michaelson, *J. Appl. Phys.* 48 (1977) 729.
- [17] Y. Fan, J. Han, L. He, J. Saraie, R.L. Gunshor, M. Hagerott, H. Jeon, V. Nurmikko, G.C. Hua and N. Otsuka, *Appl. Phys. Lett.* 61 (1992) 3160.
- [18] M. Averous, D. Bertho, D. Boiron, P. Boring, T. Cloitre, C. Jouanin, P. Lefebvre and B. Ponga, *Semicond. Sci. Technol.* 6 (1991) A1.
- [19] W.A. Harrison, *J. Vac. Sci. Technol.* 14 (1977) 1016.
- [20] M. Ukita, Y. Morinaga, H. Okuyama, K. Nakano, T. Ohata, A. Ishibashi and K. Akimoto, unpublished.



ELSEVIER

Journal of Crystal Growth 138 (1994) 686–691

JOURNAL OF  
**CRYSTAL  
GROWTH**

## Improvement in lasing characteristics of II–VI blue-green lasers using quaternary and ternary alloys to produce pseudomorphic heterostructures

J. Petruzzello \*, R. Drenten, J.M. Gaines

*Philips Laboratories, 345 Scarborough Road, Briarcliff Manor, New York 10510, USA*

### Abstract

Pseudomorphic heterostructures with increased electrical and optical confinement were used to improve II–VI blue-green laser operating characteristics. These lasers employ  $\text{Zn}_{1-x}\text{Mg}_x\text{S}_y\text{Se}_{1-y}$  alloys for the cladding layers,  $\text{ZnS}_y\text{Se}_{1-y}$  for the waveguiding layers and  $\text{Zn}_{1-x}\text{Cd}_x\text{Se}$  quantum wells for the active layer. The defect density through the active layer in such a heterostructure was found to range from  $\leq 4 \times 10^6$  to  $6 \times 10^8 \text{ cm}^{-2}$ . The density found in the active layer is directly related to the growth of the quaternary alloy which is often accompanied by a high density of stacking faults and threading dislocations. By comparing lasers with varying defect densities a direct correlation between the threshold current density and the structural quality has been observed. The lasers with the lowest defect density have threshold current densities of  $400 \text{ A/cm}^2$  (without facet coating) which are the lowest reported for II–VI devices and comparable to state-of-the-art III–V devices.

### 1. Introduction

The lasing characteristics of II–VI blue-green lasers are significantly improved by using  $\text{Zn}_{1-x}\text{Mg}_x\text{S}_y\text{Se}_{1-y}$  and  $\text{ZnS}_y\text{Se}_{1-y}$  and ZnSe for the cladding and waveguiding layers, respectively. The improvements are realized because of the increased electrical and optical confinement, due to the increased band offsets, and the higher structural quality resulting from the pseudomorphic growth of the entire laser heterostructure (all of the layers are nearly Lattice-matched except the quantum well active layer). The lowest room temperature threshold current density,  $320 \text{ A/cm}^2$

(with facet coatings), highest operating temperature, 394 K, and highest room temperature peak power, 0.5 W/facet, reported to date have been accomplished with these lasers [1]. Brief room temperature CW operation has also been achieved with a similar structure by Nakayama et al. [2]. Their structure has  $\text{Zn}_{1-x}\text{Mg}_x\text{S}_y\text{Se}_{1-y}$  cladding layers and ZnSe guiding layers. Although these significant strides have been taken, research efforts are still required to improve the electrical and structural characteristics of the materials to produce stable long lived laser devices for commercial applications. This report will discuss the evolution and current status of the structural properties of the epitaxial layers in the II–VI blue-green lasers and their correlation with the laser operating characteristics. The structural

\* Corresponding author.

properties of the heterostructures were investigated by transmission electron microscopy (TEM). The defect density through the active layer in pseudomorphic heterostructures was observed to range between  $\leq 4 \times 10^6$  and  $6 \times 10^8 \text{ cm}^{-2}$  for different growths with stacking faults and threading dislocations making up the majority of the defects. The lasers with the lowest defect density gave the best operating characteristics, while those with higher defect densities gave correspondingly worse results. Therefore obtaining reproducible low defect density heterostructures is of great importance to the development of these devices.

## 2. Experimental procedure

The laser structures were grown with a Varian Gen II MBE chamber using source materials of Zn, Se, Cd, Mg, ZnS (S source), ZnCl (n dopant) and  $\text{N}_2$  (p dopant). All growths were performed on GaAs (001) substrates. The layer combinations and thicknesses of the SCH laser samples studied are shown in the schematic drawing of Fig. 1. The nominal S and Mg fractions in the quaternary cladding layers are between 0.08 and 0.12, as

estimated by X-ray fluorescence. The guiding layers in the first sample (Fig. 1a) are made of ZnSe, while those in the second sample (Fig. 1b) are made of  $\text{ZnS}_x\text{Se}_{1-x}$  (with  $y = 0.06$ , about lattice matched to GaAs). The active layer in all the samples is a  $\text{Zn}_{1-x}\text{Cd}_x\text{Se}$  quantum well with  $x = 0.2$ . Gain-guided lasers of  $50 \mu\text{m}$  stripe width and 1 mm length were fabricated using a patterned polyimide layer as an electrical insulator and Au as a contact. In was used as the contact to the GaAs substrate. These lasers were operated with 100 ns pulses at a frequency of 1 kHz. The typical measured operating voltage was 12 V for a device at room temperature. Room temperature threshold current densities as low as  $320 \text{ A/cm}^2$  have been obtained with facet coating. (Henceforth, current densities will be quoted for devices without facet coatings.) The structural characteristics of the epitaxial layers were investigated with TEM. All of the electron micrographs were taken with a Philips EM430 operating at 300 kV.

## 3. Results and discussion

The first demonstrated blue-green lasers were separate confinement heterostructures (SCHs) [3]

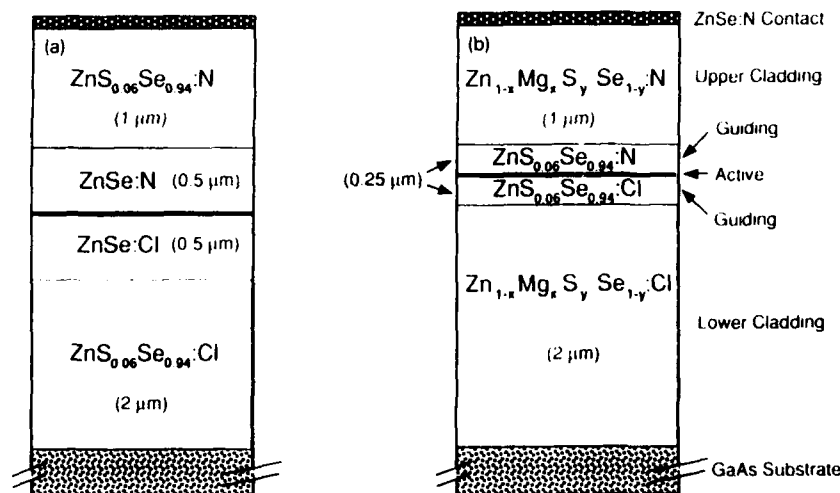


Fig. 1. Schematic drawing of the SCH lasers with (a) ZnSe guiding and  $\text{ZnS}_x\text{Se}_{1-x}$  cladding layers and (b) a completely pseudomorphic structure using  $\text{ZnS}_x\text{Se}_{1-x}$  guiding and  $\text{Zn}_{1-x}\text{Mg}_x\text{S}_y\text{Se}_{1-y}$  cladding layers.

as the one depicted in Fig. 1a. The cladding layers were  $\text{ZnS}_y\text{Se}_{1-y}$  with  $y = 0.06$ , the lattice matching composition to the GaAs substrate. The ZnSe optical guiding layer, however, possessed a lattice mismatch of 0.27% to the substrate. Since the guiding layer thickness was greater than the critical thickness (1500 Å) for relaxation by introduction of misfit dislocations, a high density of misfit and threading dislocations existed in this region of the structure. Typical densities of threading dislocations through the active region for this structure range from  $10^8$  to  $10^9 \text{ cm}^{-2}$  [4].

The micrograph in Fig. 2 shows a cross-sectional TEM image of the threading and misfit dislocations in such a device structure. This dislocation density is unacceptable for practical devices. Densities of  $< 10^4 \text{ cm}^{-2}$  are needed to produce dislocation free devices with dimensions of 500 by  $10 \mu\text{m}$ .

To reduce the density of dislocations in SCH lasers, the entire structure should be grown pseudomorphically (no relaxation by misfit dislocations, i.e. nearly lattice-matched) to the GaAs substrate. As mentioned previously, this can be

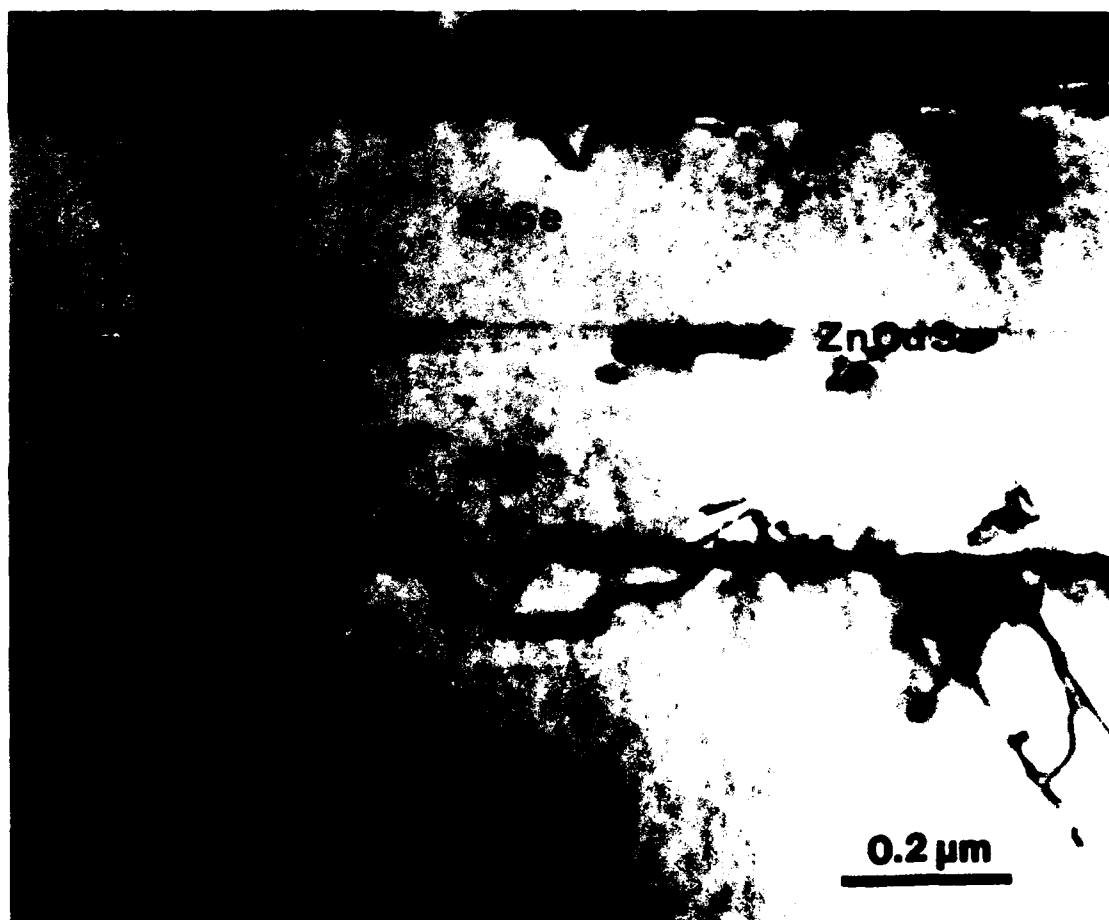


Fig. 2. Cross-sectional bright field TEM micrograph of the laser in Fig. 1a showing misfit and threading dislocations in the active region. Threading dislocation density through the  $\text{Zn}_{1-y}\text{Cd}_y\text{Se}$  quantum well is about  $10^9 \text{ cm}^{-2}$ .

accomplished by a structure such as the one shown in Fig. 1b. The active layer and adjacent region of a quaternary/ternary SCH are shown in the cross sectional TEM micrograph of Fig. 3a. There were no threading dislocations or stacking faults found to intersect the active layer in the 50  $\mu\text{m}$  length of cross section examined which corresponds to a density of  $\leq 4 \times 10^6 \text{ cm}^{-2}$ , assuming an average thickness of 0.5  $\mu\text{m}$  for the sample. This density is low enough to make the use of TEM impractical and the development of a reliable technique, such as defect etches used in III–V materials, is necessary to know if the density is below the  $10^4 \text{ cm}^{-2}$  level needed for long-lived stable lasers.

The growth of the quaternary material can be



Fig. 3. Bright-field micrographs of the active region of the SCH laser using pseudomorphic quaternary and ternary layers with (a) low defect density ( $< 4 \times 10^6 \text{ cm}^{-2}$ ) and (b) high defect density ( $6 \times 10^8 \text{ cm}^{-2}$ ).

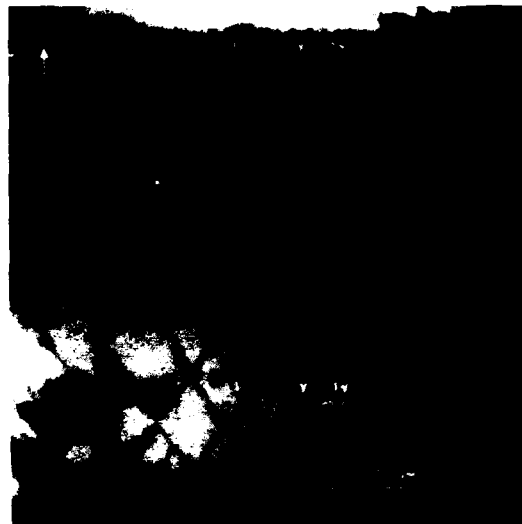


Fig. 4. Bright-field micrograph of the entire quaternary/ternary SCH laser structure with the high defect density showing the stacking faults starting at the GaAs substrate interface.

accompanied by defects such as stacking faults and threading dislocations. Consequently in some laser structures, densities of stacking faults and threading dislocations ranging up to  $6 \times 10^8 \text{ cm}^{-2}$  have been observed, as shown in Fig. 3b. The stacking faults appear as straight dark lines in the image, starting at the GaAs substrate–lower cladding layer interface, as seen in Fig. 4. The faults are present throughout the entire structure with a slight decrease in density towards the surface. The density of defects intersecting the active layer is about  $6 \times 10^8 \text{ cm}^{-2}$ , which is similar to the density in the lattice-mismatched structures described previously.

At present the cause of the stacking faults is not understood. The source of the faults that start at the GaAs substrate–lower cladding layer interface is probably provided by the pregrowth surface of the substrate and/or the initial stages of epilayer nucleation. Fig. 5 is a TEM micrograph of the GaAs substrate–lower cladding layer interface in cross section, where the sample has been tilted about  $30^\circ$  about an axis in the inter-



face plane which is perpendicular to the electron beam. This allows the observation of the interface plane (between the dotted lines in Fig. 5). There is a dark dislocation loop-like contrast in the interface plane that appears to be associated with the stacking fault-interface intersection. Further analysis of these loops is needed to characterize their nature, which may give some insight into the formation mechanism of the stacking faults.

The effect of the defects, stacking faults and threading dislocations on the threshold current densities of laser devices was found to be significant. The threshold current densities,  $J_{th}$  of three SCH quaternary lasers with varying defect densities are compared in the plot of Fig. 6. The three lasers are identical, except for the defect content and a slight variation in Cd composition in the active region (about 2% absolute based on PL emission wavelength). The threshold current density is increased by a factor of four between the low and high defect density lasers at room temperature. The threshold current density found for the lowest defect density laser is comparable to state-of-the-art III-V devices.[5] Apart from the

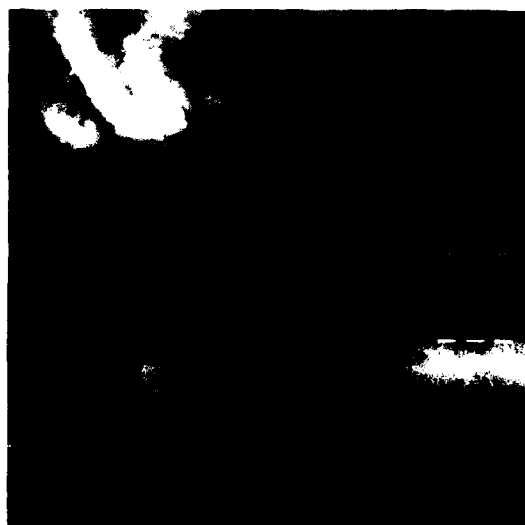


Fig. 5. Tilted bright-field view of the GaAs substrate-quaternary interface showing the dislocation loop contrast at the base of the stacking faults.



Fig. 6. Plot of threshold current density,  $J_{th}$  as a function of temperature for three quaternary/ternary SCH laser structures with varying defect densities.

threshold current density differences, the  $T_0$  values were also found to be influenced negatively by a high dislocation density.  $T_0$  is defined as the inverse slope,  $(d \ln J_{th}/dT)^{-1}$ , of the  $J_{th}$  versus  $T$  curve. The increase in threshold current density with increasing defect density is explained by the defects acting as non-radiative recombination centers. This reduces the fraction of injected carriers that recombine radiatively in the active layer and hence increases the threshold current density.

In addition to the effects on the lasing characteristics, the defects are a source of degradation and failure of devices. The process of dislocation motion and propagation from pre-existing defects under optical [6] and injection [7] stimulation in III-V lasers has been well documented. This process has been directly related to the failure of devices. Guha et al. [8] have observed similar degradation in electroluminescence measurements on II-VI lasers. Dark lines appear in the device along crystallographic directions ([100] and [110]), which increase in density and grow with time until failure. Investigation of these degraded devices by TEM found high densities of small dislocation loops around pre-existing misfit dislocations and stacking faults that correlated well with the density of dark lines in the electroluminescence measurements.

#### 4. Conclusions

The performance of II–VI blue-green lasers can be significantly improved when pseudomorphic heterostructures are produced by using  $\text{Zn}_x\text{Mg}_{1-x}\text{S}_y\text{Se}_{1-y}$  as the cladding layers. The quaternary-containing laser structures can be grown with a dramatic decrease in defect density compared to lattice mismatched structures. The laser with the lowest defect density has produced threshold current densities which are comparable to state-of-the-art III–V devices. The quaternary material, however, is susceptible to high densities of stacking faults and threading dislocations. The density of these defects has a direct effect on the threshold current of lasers.

#### 5. Acknowledgements

The authors would like to thank S. Flamholtz, K. Haberern, S. Herko, T. Marshall, P. Mensz, D.

Olego and C. Ponzoni for all the work and helpful discussions.

#### 6. References

- [1] J.M. Gaines, R.R. Drenten, K.W. Haberern, T. Marshall, P. Mensz and J. Petruzzello, *Appl. Phys. Lett.* 62 (1993) 2462.
- [2] N. Nakayama, S. Itoh, T. Ohata, K. Nakano, H. Okuyama, M. Ozawa, A. Ishibashi, M. Ikeda and Y. Mori, *Electron. Lett.* 29 (1993) 1488.
- [3] M.A. Haase, J. Qiu, J.M. DePuydt and H. Cheng, *Appl. Phys. Lett.* 59 (1991) 1272.
- [4] J. Petruzzello, J. Gaines and P. van der Sluis, *J. Appl. Phys.*, submitted.
- [5] C.J. van der Poel, H.P.M.M. Ambrosius, R.W.M. Linders, N.J. Kiewit and J. Rijpers, *J. Crystal Growth* 124 (1992) 300.
- [6] P. Petroff, W.D. Johnson and R.L. Hartman, *Appl. Phys. Lett.* 25 (1974) 226.
- [7] L.C. Kimerling, P. Petroff and H.J. Leamy, *Appl. Phys. Lett.* 28 (1976) 297.
- [8] S. Guha, private communication.

## Advances in the development of graded injector visible light emitters

J.F. Swenberg <sup>\*,a</sup>, M.W. Wang <sup>a</sup>, R.J. Miles <sup>a</sup>, M.C. Phillips <sup>a</sup>, A.T. Hunter <sup>b</sup>,  
J.O. McCaldin <sup>a</sup>, T.C. McGill <sup>a</sup>

<sup>a</sup> T.J. Watson, Sr., Laboratory of Applied Physics, California Institute of Technology, Pasadena, California 91125, USA

<sup>b</sup> Hughes Research Laboratories, Malibu, California 90265, USA

### Abstract

Novel visible light emitters with low turn-on voltages and efficient room temperature operation have been demonstrated in the n-CdSe/p-ZnTe heterojunction separated by a graded Mg<sub>0.5</sub>Cd<sub>0.5</sub>Se injecting region. The successful p-type doping of ZnTe up to  $1 \times 10^{20} \text{ cm}^{-3}$  using a nitrogen plasma source has allowed using higher quality GaSb substrates and growing of p-ZnTe epilayers. Diodes with ideality factors of 1.8 are realized with turn-on voltages near that of the bandgap of ZnTe. This deviation from an ideality of 1 may be due to using too small a peak Mg concentration in the Mg<sub>0.5</sub>Cd<sub>0.5</sub>Se layer resulting in a barrier for electron injection and increasing recombination at the interface.

### 1. Introduction

The wide bandgap II–VI semiconductors have seen a tremendous advance as candidates for optoelectronic devices since the announcement of blue-green laser diodes and light emitting diodes (LEDs) based on ZnSe [1]. This success has largely been achieved by using a nitrogen plasma source as a p-type dopant during growth by molecular beam epitaxy (MBE) of ZnSe [2–4]. Unfortunately this progress has been frustrated by the problems of obtaining layers of p-ZnSe and p-ZnSSe with doping levels well above  $2 \times 10^{18} \text{ cm}^{-3}$ , which is necessary for making device-quality ohmic contacts, and the question of stability

and device lifetime [5]. Prior to these difficulties, we proposed an alternative device structure based on the only closely lattice matched p–n heterojunction pair among the II–VI binaries, namely CdSe/ZnTe [6]. Ohmic contacting problems are avoided since this heterojunction pair uses the doping types which tend to occur naturally in these materials. This “graded injector” LED operates by using a graded Mg<sub>0.5</sub>Cd<sub>0.5</sub>Se junction between the n-CdSe and p-ZnTe to allow efficient minority carrier injection into the wider bandgap material to take place. Early devices had been limited by the lack of a suitable p-type dopant source for MBE grown ZnTe. Thus, the early device had to be grown on poor quality p-ZnTe substrates, and we had to rely on the p-typeness of the substrate with only a thin buffer layer for device operation. Recently, heavy p-type doping of MBE ZnTe, with doping levels ap-

\* Corresponding author.

proaching  $1 \times 10^{19} \text{ cm}^{-3}$  have been reported using a nitrogen plasma source [7]. We used this same technique to grow low resistivity p-ZnTe. We have examined the graded injector LED with epilayers of ZnTe:N grown on GaSb substrates.

## 2. p-Doping of ZnTe

Epilayers of nitrogen doped ZnTe were grown in a Perkin-Elmer 430P MBE system on (100) ZnTe substrates to study the electrical characteristics of ZnTe:N using procedures and growth conditions similar to those previously reported [7,8]. Nitrogen doping was achieved by using an Oxford Applied Research RF plasma source, with a  $21 \times 0.3 \text{ mm}$  aperture, operated at 125 W. The nitrogen flow rate was controlled with a precision leak valve which was set for these experiments to yield a chamber pressure in the range  $6 \times 10^{-7}$  to  $1 \times 10^{-6}$  Torr. The nitrogen doped layers were each grown to approximately  $2 \text{ }\mu\text{m}$  after the growth of roughly  $1 \text{ }\mu\text{m}$  of undoped ZnTe. Doped layers of ZnTe:N grown under these conditions were extremely conductive with resistivities of  $10^{-3} \text{ }\Omega \text{ cm}$ . We were unable to significantly reduce the nitrogen beam flux, while maintaining a plasma, for the given nitrogen source aperture. Therefore, to reduce the average doping concentration, we modulated the doping in a superlattice-type fashion by repeatedly growing periods of undoped ZnTe followed by doped ZnTe:N. Fig. 1 shows the results of Hall measurements of three different epilayers all grown to roughly the same thickness: one continuously doped ZnTe:N, and two modulated doped layers with periods of  $500 \text{ }\text{\AA}/50 \text{ }\text{\AA}$  and  $500 \text{ }\text{\AA}/25 \text{ }\text{\AA}$  for the ZnTe/ZnTe:N. The lack of any temperature dependence is characteristic of degenerately doped material. The modulated doping effectively reduces the average carrier concentration and increases the resistivities of the epilayers by up to 2 orders of magnitude to levels more appropriate for LEDs, and improves the luminescence efficiencies of the epilayers, as evidenced in the room temperature photoluminescence (PL) intensities. This modulated doping technique was incorporated to fabricate graded injector LEDs.

## 3. Light emitting devices

Light emitting devices based on the graded injector design [6] have been grown on both (100) GaSb substrates and (100) p-ZnTe substrates incorporating a modulated nitrogen doped ZnTe layer. Devices grown on GaSb showed significantly better electrical and optical properties than those grown on the ZnTe, so we concentrated on those with GaSb substrates. A GaSb buffer layer, approximately  $3000 \text{ }\text{\AA}$  thick, was first grown in a separate III-V growth chamber under conditions previously reported [8]. The sample was then transferred via an ultra-high vacuum tube to the II-VI chamber. The growth of the device structure then proceeded at a growth temperature of  $300^\circ\text{C}$ . An initial  $3500 \text{ }\text{\AA}$  undoped buffer layer of ZnTe was grown followed by a region of modulated nitrogen doped ZnTe. This doped layer was 40 periods of  $15 \text{ }\text{\AA}$  ZnTe:N/ $250 \text{ }\text{\AA}$  ZnTe. Next, the graded  $\text{Mg}_{1-x}\text{Cd}_x\text{Se}$  and  $\text{CdSe:Al}$  layers were grown with estimated thickness of 300 and  $250 \text{ }\text{\AA}$ , respectively. The peak Mg concentration was measured by X-ray photoelectron spectroscopy of bulk layers of  $\text{Mg}_{1-x}\text{Cd}_x\text{Se}$  to be

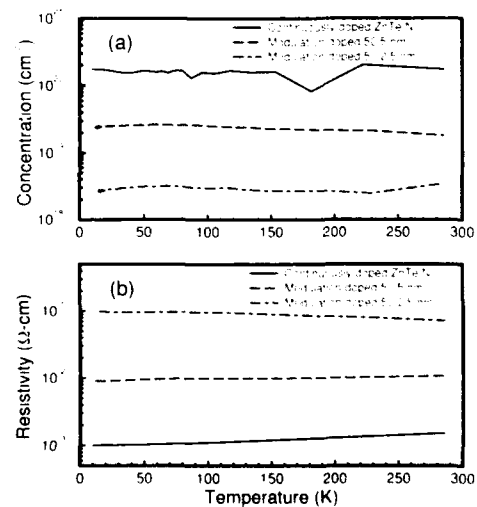


Fig. 1. Hall data as a function of temperature for (a) carrier concentration and (b) resistivity of nitrogen doped epilayers. The modulated doped period thicknesses are given as undoped/doped.

$x = 0.6$ . The Mg grading was obtained by shutting off the power to the Mg cell. The Mg flux transient, monitored by a residual gas analyzer, was used to set the CdSe growth rate to achieve the desired grading thickness. The band diagram of an idealized LED structure is shown in Fig. 2a. In this case we have assumed the common anion rule for the valence band edge of the  $\text{Mg}_x\text{Cd}_{1-x}\text{Se}$  and CdSe layers, and continuous grading of the conduction band edge. Device simulations show that the exact shape of the grading is not important to device operation. But as we will show, the conduction band edge alignment is crucial to optimal performance.

Diode mesas were lithographically defined with areas of  $1.8 \times 10^{-4} \text{ cm}^2$ . Electrical isolation was formed with a 0.5% bromine:ethylene glycol wet etch 4000 Å into the p-ZnTe layer, well beyond the p-n junction. Lateral ohmic contacts to the p-ZnTe and top contacts to the CdSe:Al were made with evaporated Au/Ge and standard lift-off procedures. The devices were then wire bonded and electrically and optically characterized.

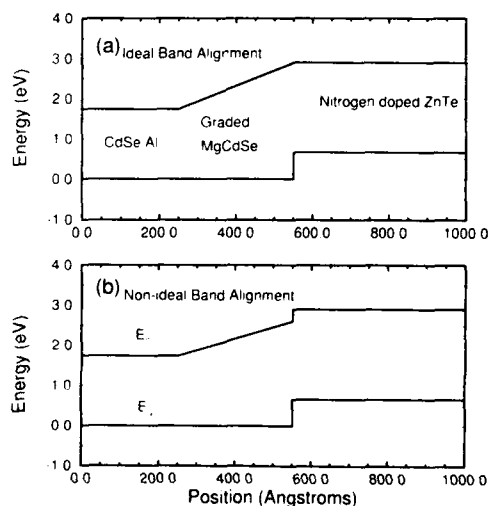


Fig. 2. (a) Flatband diagram of an ideal graded injection device with a continuous conduction band. (b) Flatband diagram for a 300 meV discontinuity in the conduction band grading.

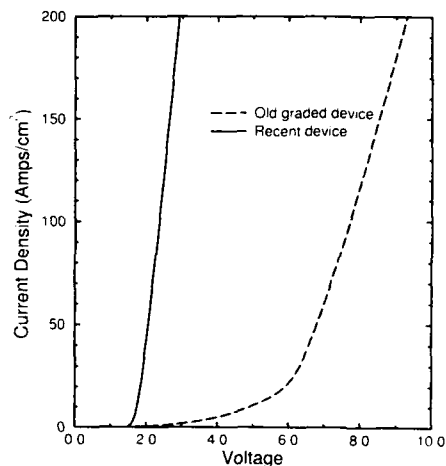


Fig. 3. Room temperature electrical characteristics of the recent graded device compared to the earlier reported device.

The room temperature electrical characteristics of the present device and the LED first demonstrated [6] are shown in Fig. 3. We see that many of the earlier device's shortcomings have been eliminated by being able to grow doped layers of p-ZnTe. The high series resistance of the earlier device was due to the ZnTe substrate, and the high turn-on voltage was probably due to charging of traps in the thin undoped ZnTe epilayer. The present devices turn on at roughly the bandgap of ZnTe. Since we have a thin  $1 \mu\text{m}$  layer of roughly  $0.1 \Omega \text{ cm}$  p-ZnTe and have lateral contacts, most of the  $25 \Omega$  series resistance in the present device is due to the current spreading through the thin epilayer and not from the contact or junction region. This has been substantiated by the linear dependence of the resistance as a function of contact to contact separation on the p-ZnTe epilayer.

To better understand the current injection mechanisms in the LED, we plot the current density on a log scale as seen in Fig. 4. From this we can extract the ideality factor ( $n$ ) for the diode. We measure an ideality of  $n = 1.8$ , indicating predominantly a recombination current rather than a diffusion current. Also plotted with the experimental data are results from device simulations based on the drift-diffusion transport equa-

tions [9]. The lower curve is calculated from the “ideal” case corresponding to the band diagram shown in Fig. 2a with a continuous grading of the conduction band. Not surprisingly, the ideality for this case is  $n = 1$ . When we model the device as per the “non-ideal structure” shown in Fig. 2b with a discontinuous junction we obtain the other calculated curve in Fig. 4. Here the conduction band of the  $\text{Mg}_x\text{Cd}_{1-x}\text{Se}$  grades to 300 meV below ZnTe. This leaves a barrier blocking electron injection, and the resulting carrier accumulation leads to increased recombination at the  $\text{Mg}_x\text{Cd}_{1-x}\text{Se}/\text{ZnTe}$  interface. This offers a better approximation to the experimental data consistent with the ideality factor. It would appear that in our device we have undershot the conduction band of ZnTe and hence have a barrier that holds carriers for recombination, thereby reducing the injection efficiency. With our present device, we only have an estimate for the Mg concentration in the junction and a large discrepancy in the value of the bandgap of MgSe ranging from 3.6 to 5.6 eV [10,11]. So it is very unlikely that we are grading the conduction band precisely from CdSe to ZnTe. In addition, preliminary band offset measurements for MgSe suggest that the common anion rule does not apply and that the

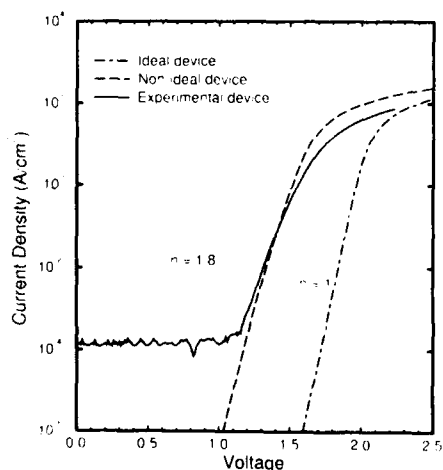


Fig. 4. Experimental  $J-V$  compared to various device simulation parameters. The ideal device corresponds to the structure in Fig. 2a and the non-ideal device is depicted in Fig. 2b.

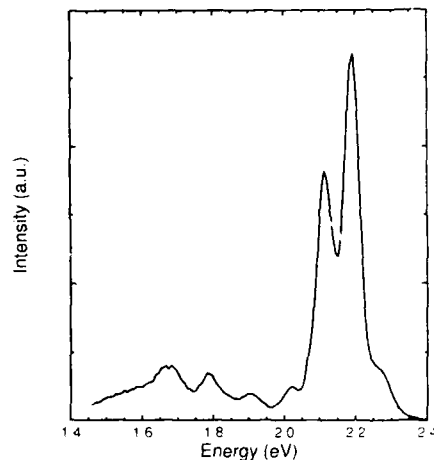


Fig. 5. Room temperature electroluminescence spectrum operated at 20 mA and 2.7 V.

valence band of  $\text{Mg}_x\text{Cd}_{1-x}\text{Se}$  would be lower than that of CdSe [12]. Since the conduction band alignment is crucial, the peak Mg concentrations may have to be increased to widen the bandgap.

In spite of the reduced injection efficiency, this device turns on, as exhibited by the onset of room temperature electroluminescence (EL), at about 1.95 V. So we are obtaining electron injection with carriers thermalizing over any potential barrier at the junction interface. One noticeable problem with the present devices is the degenerate doping levels of the ZnTe:N. As seen in the EL in Fig. 5 as well as PL, the high doping levels lead to the formation of deep recombination centers not observable in undoped ZnTe epilayers and lower doped ZnTe:N [7]. We therefore expect this problem to be corrected by adjusting our nitrogen source to reduce the beam flux. Development of other p-type doping sources employing As or Sb could also result in a solution of this problem and could result in doping more appropriate for visible light emitters. The two near gap emission peaks about 60 and 135 meV smaller than the band gap of bulk ZnTe are also attributed to the nitrogen impurity. The high energy peak is similar to that previously observed in ZnTe:N [7].

#### 4. Summary

In conclusion, we have used modulated doped ZnTe:N to fabricate graded injecting LEDs on GaSb with greatly improved electrical characteristics. Device simulations coupled with our revised estimates for the band offsets suggest that the current devices have a barrier between the conduction band edge of the  $\text{Mg}_{1-x}\text{Cd}_x\text{Se}$  layer and the ZnTe. This barrier acts to accumulate electrons resulting in reduced injection efficiency and diode characteristics that have ideality factors differing from one but less than two.

However, in spite of the non-ideal character of the current devices, we observe electron injection and a low turn-on voltage for light emission at room temperature.

#### 5. Acknowledgements

This work was supported by the Advanced Research Projects Agency monitored under ONR contract N00014-92-J-1845.

#### 6. References

- [1] M.A. Haase, J. Qiu, J.M. DePuydt and H. Cheng, *Appl. Phys. Lett.* 59 (1991) 1272.
- [2] K. Ohkawa, T. Mitsuyu and O. Yamazaki, *J. Crystal Growth* 86 (1988) 329.
- [3] R.M. Park, M.B. Troffer, C.M. Rouleau, J.M. DePuydt and M.A. Haase, *Appl. Phys. Lett.* 57 (1990) 2127.
- [4] K. Ohkawa, T. Karasawa and T. Mitsuyu, *J. Crystal Growth* 111 (1991) 797.
- [5] J. Qiu, H. Cheng, J.M. DePuydt and M.A. Haase, *J. Crystal Growth* 127 (1993) 279.
- [6] M.C. Phillips, M.W. Wang, J.F. Swenberg, J.O. McCaldin and T.C. McGill, *Appl. Phys. Lett.* 61 (1992) 1962.
- [7] J. Han, T.S. Stavrinides, M. Dobayashi, R.L. Gunshor, M.M. Hagerott, M.M. Hagerott and A.V. Nurmikko, *Appl. Phys. Lett.* 62 (1993) 840.
- [8] Y. Rajakarunanyake, B.H. Cole, J.O. McCaldin, D.H. Chow, J.R. Söderström, T.C. McGill and C.M. Jones, *Appl. Phys. Lett.* 55 (1989) 1217.
- [9] M.W. Wang, M.C. Phillips, J.F. Swenberg, E.T. Yu, J.O. McCaldin and T.C. McGill, *J. Appl. Phys.* 73 (1993) 4660.
- [10] H. Okuyama, K. Nakano, T. Miyajima and K. Akimoto, *Jap. J. Appl. Phys.* 30 (1991) L1620.
- [11] W.H. Strehlow and E.L. Cook, *J. Phys. Chem. Ref. Data* 2 (1973) 163.
- [12] M.W. Wang, J.F. Swenberg, R.J. Miles, M.C. Phillips, E.T. Yu, J.O. McCaldin, R.W. Grant and T.C. McGill, *J. Crystal Growth* 138 (1994) 508.



ELSEVIER

Journal of Crystal Growth 138 (1994) 697–702

JOURNAL OF  
**CRYSTAL  
GROWTH**

## Electrical and optical modeling of II–VI semiconductor diode lasers

P.M. Mensz

*Philips Laboratories, Briarcliff Manor, New York 10510, USA*

### Abstract

The electrical and optical operation of  $\text{ZnCd}_{1-x}\text{Se}_{1-y}/\text{ZnSe}/\text{ZnS}_y\text{Se}_{1-y}$  and  $\text{Zn}_{1-z}\text{Cd}_z\text{Se}/\text{ZnS}_y\text{Se}_{1-y}/\text{Zn}_{1-z}\text{Mg}_z\text{S}_y\text{Se}_{1-y}$  quantum-well blue-green injection lasers were studied by numerical simulation. The physical model in this study is based on the self-consistent solution of Poisson's equation, the current continuity equations, including the thermionic emission theory for carrier transport across heterojunctions, the photon rate equation and the scalar wave equation. The optical gain of strained quantum well lasers was calculated using  $k \cdot p$  theory based on the inter-band electron–hole pair recombination. Good agreement was obtained between the experimental and the calculated  $\text{Zn}_{1-z}\text{Cd}_z\text{Se}/\text{ZnS}_y\text{Se}_{1-y}/\text{Zn}_{1-z}\text{Mg}_z\text{S}_y\text{Se}_{1-y}$  laser characteristics, over a wide temperature range of 85 to 394 K, without including excitonic effects.

### 1. Introduction

Following the first successful implementation of  $\text{ZnCd}_{1-x}\text{Se}_{1-y}/\text{ZnSe}/\text{ZnS}_y\text{Se}_{1-y}$  [1] strained quantum well (QW) injection lasers in the blue-green emission range, several groups calculated optical gain for these new devices [2–4]. Similarly to the III–V lasers, the gain calculations of II–VI semiconductor lasers were based on the theory of stimulated emission of free electron–hole plasma with momentum conserving transitions between electric subbands in strained quantum wells. The band structure and the electron and hole wave functions were obtained from  $k \cdot p$  method applied to strained QW [5].

Recently it was suggested by Ding et al. [6,7] that the optical gain in  $\text{Zn}_{1-z}\text{Cd}_z\text{Se}$  QW lasers, particularly at low temperatures, may arise from a recombination via localized excitonic states.

They found that the energy of lasing photons corresponds to the low energy tail of the exciton luminescence spectrum. Moreover, from the optical pump experiments, it was established that stimulated emission is observed when the incident beam energy was in resonance with the exciton absorption [6,7]. However, to conclude that the gain in a blue-green injection laser comes from the identical excitonic recombination mechanism as demonstrated in optically pumped lasers would be a large simplification. The usual argument is that, created by photons, an electron–hole pair, of nearly same momentum, can form an excitonic bound state much easier than electrons and holes externally injected into the QW from the barrier region with completely different energy and momentum. Here we present the results of the calculated laser output characteristics, such as light emission power versus current ( $I$ – $I$ ).



which were obtained using the conventional theory of free electron–hole recombination. Comparison of these results with experimental data, would test a significance of the possible excitonic gain enhancement in the blue-green injection lasers.

## 2. Physical model

In this work a complete simulation of some blue-green injection lasers,  $\text{ZnCd}_x\text{Se}_{1-x}/\text{ZnSe}/\text{ZnS}_y\text{Se}_{1-y}$  (structure I) and  $\text{Zn}_{1-x}\text{Cd}_x\text{Se}/\text{ZnS}_y\text{Se}_{1-y}/\text{Zn}_{1-z}\text{Mg}_z\text{S}_u\text{Se}_{1-u}$  (structure II) [1,8], was performed using conventional electron–hole plasma theory for the optical gain in strained quantum well lasers [9] and classical one-dimensional transport in semiconductor heterostructures [10,11]. The physical model is based on the self-consistent solution of the Poisson's equation, the current continuity equations, including the thermionic emission theory for carrier transport across heterojunctions [11], the photon rate equation [12] and the scalar wave equation for the optical field [13]. The band structure of the strained  $\text{Zn}_{0.8}\text{Cd}_{0.2}\text{Se}/\text{ZnS}_{0.06}\text{Se}_{0.94}$  QW was calculated using  $k \cdot p$  theory following the work of ref. [5]. The biaxial compressive strain and quantum confinement in  $\text{Zn}_{0.8}\text{Cd}_{0.2}\text{Se}/\text{ZnS}_{0.06}\text{Se}_{0.94}$  quantum wells of 65 Å thickness separate the ground subbands of light and heavy holes by

more than 80 meV. This simplifies the band calculations considerably, as one can neglect the heavy and light hole mixing in momentum space, and use a parabolic approximation for the hole subbands. The band-gap energy for the new quaternary  $\text{Zn}_{1-x}\text{Mg}_x\text{S}_y\text{Se}_{1-y}$  ( $x \approx 0.08$ – $0.10$  and  $y \approx 0.10$ – $0.12$ ) was established from photoluminescence measurements, and band offsets in the  $\text{Zn}_{1-x}\text{Mg}_x\text{S}_y\text{Se}_{1-y}/\text{Zn}_{0.06}\text{Se}_{0.94}$  heterojunction were assumed based on the common anion and cation rule (70 meV and 40 meV of the conduction and valence band offset, respectively).

## 3. Results

### 3.1. Electrical and optical confinement

At first, I compare the optical and electrical confinement of the laser structures:  $\text{ZnCd}_x\text{Se}_{1-x}/\text{ZnSe}/\text{ZnS}_y\text{Se}_{1-y}$  (structure I) with  $\text{Zn}_{1-x}\text{Cd}_x\text{Se}/\text{ZnS}_y\text{Se}_{1-y}/\text{Zn}_{1-z}\text{Mg}_z\text{S}_u\text{Se}_{1-u}$  (structure II). The layer structure of both lasers is shown in Fig. 1.

The expected improvement in the optical confinement of structure II arises from a higher refractive index step between the cladding and guiding layers. The numerical values of refractive indexes at the wavelength 505 nm for  $\text{Zn}_{1-x}\text{Mg}_x\text{S}_y\text{Se}_{1-y}$ ,  $\text{ZnS}_{0.06}\text{Se}_{0.94}$ , and  $\text{ZnSe}$  were 2.640, 2.724, and 2.750, respectively. They were deter-

Table 1  
The most significant parameters used in the calculation

	$\text{Zn}_{0.8}\text{Cd}_{0.2}\text{Se}$	$\text{ZnS}_{0.06}\text{Se}_{0.94}$	$\text{Zn}_{1-x}\text{Mg}_x\text{S}_y\text{Se}_{1-y}$
Bandgap at 300 K (eV)	2.41	2.71	2.84
Bandgap renormalization coefficient ( $10^{-4}$ eV m)	2.8	2.8	2.8
Electron mass, $m_e/m_0$	0.16	0.17	0.18
{100} heavy hole mass, $m_h/m_0$	0.54	0.54	0.61
{111} heavy hole mass, $m_h/m_0$	1.18	1.21	1.42
Light hole mass, $m_h/m_0$	0.14	0.15	0.18
Acceptor ionization energy (meV)	110	110	110
Lattice constant (Å)	5.7505	5.6537	5.6537
Refractive index at 505 nm	2.875	2.724	2.640
Hydrostatic deformation potential (eV)	−5.04	—	—
Shear deformation potential (eV)	−1.12	—	—
Elastic constant $C_{11}$ ( $10^{10}$ N/m <sup>2</sup> )	7.94	—	—
Elastic constant $C_{12}$ ( $10^{10}$ N/m <sup>2</sup> )	4.91	—	—

mined experimentally by us using the m-line measurement method describe in ref. [14]. The refractive index of 2.875 was estimated for  $\text{Zn}_{0.8}\text{Cd}_{0.2}\text{Se}$ . The presence of the, 65 Å wide, QW has no significant influence on the optical field distribution. The calculated optical field distribution across the structure of both lasers (near field pattern) resulted in the confinement factor in the central  $\text{Zn}_{0.8}\text{Cd}_{0.2}\text{Se}$  active region of  $\Gamma = 0.0182$  for structure II versus  $\Gamma = 0.0132$  for structure I. The calculated value of the FWHM far field pattern  $32.5^\circ$  for structure II agrees very well with  $33^\circ$ – $34^\circ$  measured experimentally. The corresponding value of FWHP for structure I was only  $21^\circ$ , which also agrees with the experiments.

Another advantage of structure II over structure I arises from the higher conduction and valence band offsets at the heterojunction of the cladding and the guiding layers, which reduces minority carrier leakage, shown in the Fig. 2. In addition, approximately 40 meV higher valence band offset of  $\text{Zn}_{0.8}\text{Cd}_{0.2}\text{Se}/\text{ZnS}_{0.06}\text{Se}_{0.94}$ , as

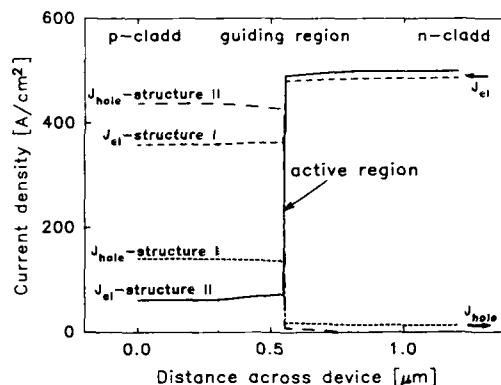


Fig. 2. The electron current (from right to left) and hole current (from left to right) at the total current density of  $j_{th} = 500 \text{ A/cm}^2$  and room temperature. Here electron current (solid lines) and hole current (long dash line) for structure II are compared with corresponding electron (medium dash line) and hole current (short dash line) for structure I. The leakage current density was reduced by nearly a factor of 6 for electrons, and by factor of 90 for holes at that current density in structure II compare to structure I.

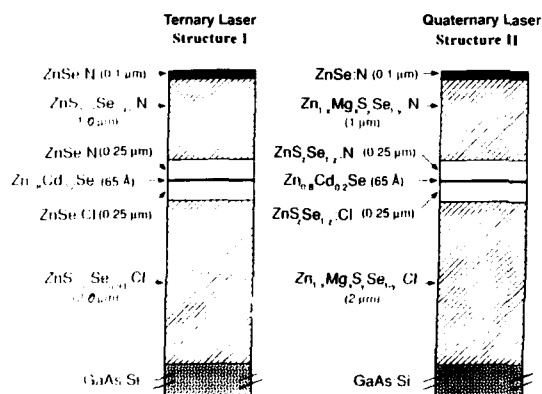


Fig. 1. Layer structure of lasers analyzed in this work. In ternary laser structure I, the cladding and guiding layers are formed by  $\text{ZnS}_{0.06}\text{Se}_{0.94}$  and  $\text{ZnSe}$ , whereas in quaternary laser structure II they are formed by  $\text{Zn}_{1-x}\text{Mg}_x\text{S}_y\text{Se}_{1-y}$  and  $\text{ZnS}_{0.06}\text{Se}_{0.94}$ . In both cases, the nitrogen acceptor concentration in the p-type cladding and guiding layers was  $1.5 \times 10^{17}$  and  $3.0 \times 10^{17} \text{ cm}^{-3}$ , respectively. The chlorine donor concentration in the n-type cladding and guiding layers was  $2 \times 10^{17} \text{ cm}^{-3}$ . The undoped  $\text{Zn}_{0.8}\text{Cd}_{0.2}\text{Se}$  QW forms the active region in both laser structures.

compared to  $\text{Zn}_{0.8}\text{Cd}_{0.2}\text{Se}/\text{ZnSe}$ , improves quantum confinement of holes into  $\text{Zn}_{1-x}\text{Cd}_x\text{Se}$  QW, and reduces hole leakage into the barrier region (see Fig. 2). Finally, structure II can be grown pseudomorphically with GaAs substrate, whereas in structure I the guiding  $\text{ZnSe}$  layer is partially relaxed. By replacing  $\text{ZnS}_{0.06}\text{Se}_{0.94}$  with  $\text{Zn}_{1-x}\text{Mg}_x\text{S}_y\text{Se}_{1-y}$  cladding layers, the calculated leakage current from the guiding region was reduced by nearly a factor of 6 for electrons, and by a factor of 90 for holes at room temperature, at the total current density  $j = 500 \text{ A/cm}^2$ . In case of structure I only 30% of the electrons recombine with holes in the active region and the remaining 70% would contribute as minority carrier leakage likely causing significant device heating (see Fig. 2).

The net result of these improvements is that structure II could lase at room temperature, at  $j = 500 \text{ A/cm}^2$  (for  $50 \times 1000 \mu\text{m}^2$  stripe and no facet coatings), whereas structure I, based on the calculations, requires more than  $4000 \text{ A/cm}^2$  (not including the the heating effects caused by the large electron leakage current).

### 3.2. Freeze-out of holes

The simulation showed that due to the high resistivity of the  $p\text{-Zn}_{1-x}\text{Mg}_x\text{S}_y\text{Se}_{1-y}$  cladding layer, and the freeze-out of free holes below temperature of  $T = 200$  K, more than a 100 V applied to the device would be necessary in order to pass any considerable amount of current, which is inconsistent with experimental results. At room temperature this effect was less severe; nevertheless, the calculations showed an addition of 2 V drop across the  $p\text{-Zn}_{1-x}\text{Mg}_x\text{S}_y\text{Se}_{1-y}$  layer, which was needed to assure the carrier injection for the laser operation. To circumvent this problem, the Frenkel–Poole effect [15], which accounts for the lowering of the ionization energy of impurities or localized defects in an electric field, has been incorporated into our model of electrical transport. As a result, the laser threshold current density of the order of  $100 \text{ A/cm}^2$  could be reached at a few volts of the external bias (not taking into account the voltage drop across the contacts), even at the lowest examined temperature,  $T = 85$  K. Fig. 3 shows the energy band diagram of structure II under forward bias at 85 K, which indicates still a significant voltage drop developed across p-cladding layer. This results clearly suggest that the electrical transport in p-type  $\text{Zn}_{1-x}\text{Mg}_x\text{S}_y\text{Se}_{1-y}$  cladding layer of structure II type diode lasers is not completely diffusive and field ionization of acceptors, particularly below room temperature, is essential for hole injection into the active region of laser diode. Higher doping level of p-type  $\text{Zn}_{1-x}\text{Mg}_x\text{S}_y\text{Se}_{1-y}$  is needed to circumvent this problem.

### 3.3. Gain calculations

A proper model for the line broadening is essential for the gain calculations. At low currents, when the material gain is negative, the Lorentzian line broadening function was used. However, near and above the transparency condition, the assumption of energy independent broadening characterized by the Lorentzian line function is not correct [16,17]. In this case, Landsberg energy dependent line broadening [17] has been incorporated. The Landsberg model proved

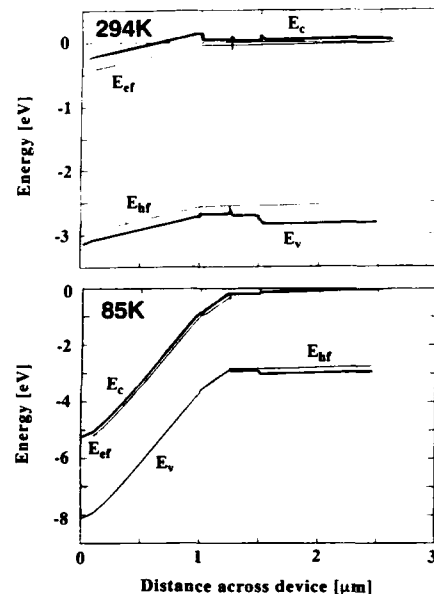


Fig. 3. The band diagrams of structure II at forward bias at  $T = 85$  K. Approximately 5 V voltage drop across  $p\text{-Zn}_{1-x}\text{Mg}_x\text{S}_y\text{Se}_{1-y}$  (on the left) reduces to about 0.4 V at  $T = 295$  K, at an external bias of  $j = 500 \text{ A/cm}^2$ . The Frenkel–Poole correction to the acceptor ionization energy was included in the electrical transport, in order to obtain this graph. The field ionization of acceptor levels in p-cladding layers of II–VI blue green lasers is an important factor even at room temperature.

to be successful in reproducing the gain spectra in multi QW III–V lasers [18]. Similar spectra for the II–VI lasers have not been reported yet.

The peak of the modal gain as a function of current is shown in Fig. 4 for different temperatures and a constant carrier scattering time  $\tau = 25$  fs, which was used to fit the experimental data. Here the peak gain is plotted as a function of the injection (not a recombination) current density of the diode laser, which is only possible to accomplish when both optical and electrical laser simulation are completed. In this calculation a constant  $7 \text{ cm}^{-1}$  background loss of the optical mode was assumed [19]. The free carrier absorption was calculated in the simulation directly, as a local loss proportional to the carrier density with proportionality coefficient of  $2 \times 10^{-17} \text{ cm}^2$ . The lasing threshold is reached at a net modal gain peak

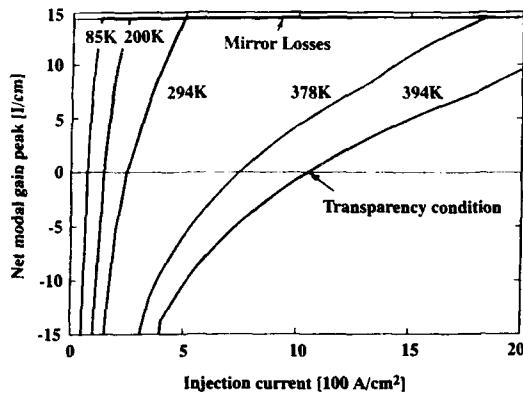


Fig. 4. The calculated peak of the modal gain of structure II for 1 mm long stripe with uncoated facets [8] for different temperatures. Mode losses of  $7 \text{ cm}^{-1}$ , and mirror losses of  $14.5 \text{ cm}^{-1}$  were used in the calculations. A constant, temperature independent carrier scattering time  $\tau = 25 \text{ fs}$  was assumed.

of  $g_{\text{max}} = 14.5 \text{ cm}^{-1}$ , as indicated in Fig. 4, which is a value of the mirror losses for 1 mm cavity length for the facet reflectivity  $R = 0.234$  (no facet coatings). The transparency currents corresponding to  $g_{\text{max}} = 0$  can be found from the plot in Fig. 4, and they vary from 75 and 252 to  $1050 \text{ A/cm}^2$  for  $T = 85, 294$ , and  $394 \text{ K}$ , respectively.

### 3.4. Laser output characteristics.

Fig. 5 presents the calculated threshold current density and the external differential quantum efficiency obtained from the full electrical and optical simulation of the 1 mm long  $\text{Zn}_{1-x}\text{Cd}_x\text{Se}/\text{ZnS}_y\text{Se}_{1-y}/\text{Zn}_{1-z}\text{Mg}_z\text{S}_u\text{Se}_{1-u}$  laser structure II, as reported in ref. [8]. These results are compared with the previously reported experimental results [8]. A constant carrier scattering time of  $\tau = 25 \text{ fs}$  was assumed in these calculations for the temperature range of 85 to  $394 \text{ K}$ . This value is in the range of expected relaxation times,  $\tau = 18 \text{ fs}$  at  $T = 295 \text{ K}$  and  $\tau = 38 \text{ fs}$  at  $T = 85 \text{ K}$ , determined from the FWHM of the photoluminescence and electroluminescence spectra below the lasing threshold. The results calculated for these experimentally determined relaxation times were also included in Fig. 5. The calculated values of the threshold current density are in good agreement with experiments, particularly at room and higher temperatures. At low temperatures the calculated threshold is slightly lower than experimentally determined. The agreement of the calculated external efficiency with the experiment is also quite good, considering the 10–20% of the estimated error in the experimental data presented in Fig. 5.

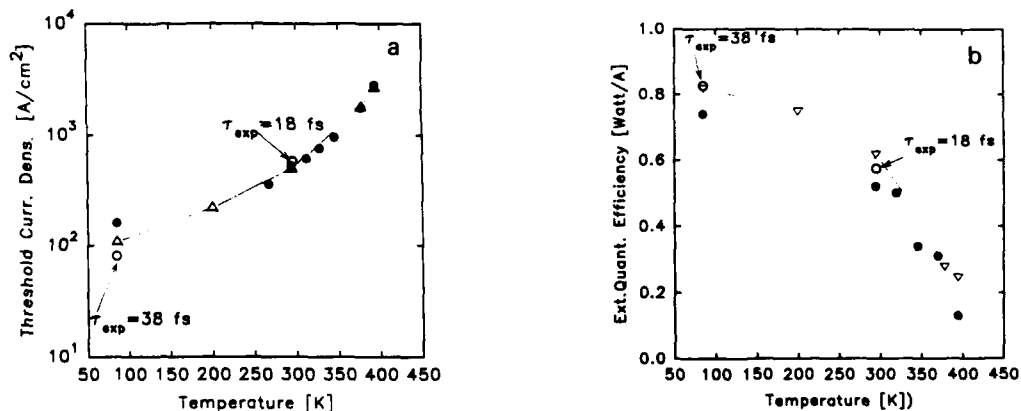


Fig. 5. Calculated threshold current density (a) and external quantum efficiency (b) obtained from the full electrical and optical simulation of the 1 mm long  $\text{Zn}_{1-x}\text{Cd}_x\text{Se}/\text{ZnS}_y\text{Se}_{1-y}/\text{Zn}_{1-z}\text{Mg}_z\text{S}_u\text{Se}_{1-u}$  laser structure without facet coatings. The open triangles guided by a dotted line are calculated results with assumed constant relaxation time  $\tau = 25 \text{ fs}$  for all temperatures. The results of calculations using the experimentally determined relaxation times of  $\tau = 18 \text{ fs}$  at  $T = 295 \text{ K}$  and  $\tau = 38 \text{ fs}$  at  $T = 85 \text{ K}$  are shown by the open circles. The solid circles are experimental data from ref. [8].

#### 4. Conclusion

QW blue-green injection lasers were studied by finding self-consistent numerical solution of the electrical and optical problem in the geometry of a semiconductor diode laser. As a result, the optical and electrical confinement in these lasers was calculated. Evidence of the important role of the field ionization in blue-green II–VI lasers, due to the low doping and high ionization energy in the p-cladding layer, was demonstrated. Finally, the output  $L$ – $I$  characteristics were calculated in a broad temperature range, based on the free electron–hole band-to-band recombination gain model, without including excitonic effects. Good quantitative agreement of the calculated threshold current density and quantum efficiency with experimental data has been achieved, using  $\tau = 25$  fs as a fitting parameter from  $T = 85$  K to  $T = 394$  K. Similar agreement was achieved, without fitting procedure, using an experimentally determined  $\tau$ , obtained from the FWHM of the luminescence spectra. This agreement suggests that the blue-green laser  $L$ – $I$  characteristics are not significantly affected by a possible enhancement in optical gain due to the electron–hole recombination via an excitonic state.

#### 5. Acknowledgments

The author would like to express his gratitude to S. Lee for the software support and important assistance which made this work possible, and to R. Drenten and M. Krijn for stimulating discussions on number of occasions. R. Drenten and J. Petruzzello are acknowledged for the optical measurements, which provided the experimental base for these calculations, and M. Krijn for calculations of effective masses for II–VI materials.

#### 6. References

- [1] M.A. Haase, J. Qiu, J.M. DePuydt, H. Luo, N. Samarath and J.K. Furdyna, *Appl. Phys. Lett.* 59 (1991) 1273.
- [2] D. Ahn, T.-K. Yoo and H.Y. Lee, *Appl. Phys. Lett.* 59 (1991) 2669.
- [3] I. Suemune, K. Nakanishi, Y. Fujii, M. Fujimoto and M. Yamanishi, *J. Crystal Growth* 117 (1992) 1068.
- [4] R.L. Aggarwal, J.J. Zayhowski and B. Lax, *Appl. Phys. Lett.* 62 (1993) 2889.
- [5] S.L. Chuang, *Phys. Rev. B* 43 (1991) 9649.
- [6] J. Ding, H. Jeon, T. Ishihara, M. Hagerott, A.V. Nurmikko, H. Luo, M. Samarth and J. Furdyna, *Phys. Rev. Lett.* 69 (1992) 1707.
- [7] J. Ding, M. Hagerott, T. Ishihara, H. Jeon and A.V. Nurmikko, *Phys. Rev. B* 47 (1993) 10528, 3161, 1992.
- [8] J. Gaines, R. Drenten, K.W. Haberern, T. Marshall, P.M. Mensz and J. Petruzzello, *Appl. Phys. Lett.* 62 (1993) 2462 (the data for the facet coated lasers are unpublished).
- [9] For example: S.W. Corzine, R.H. Yan and L.A. Coldren, in: *Quantum Well Lasers*, Ed. P.S. Zory, Jr. (Academic Press, New York, 1993) ch. 1.
- [10] M.S. Lundstrom and R.J. Schuelke, *IEEE Trans. Electron Devices* ED-30 (1983) 1151.
- [11] M. Grupen, K. Hess and G.H. Song, in: *Simulation of Semiconductor Devices and Processing*, Vol. 4, Eds. W. Fichtner and D. Aemmer (Hartung-Gorre, Konstanz, 1991) p. 303.
- [12] G.P. Agrawal and N.K. Dutta, *Longitudinal Semiconductor Lasers* (Van Nostrand-Reinhold, New York, 1986).
- [13] D.P. Wilt and Y. Yariv, *IEEE J. Quantum Electron.* QE-17 (1981) 1941.
- [14] R. Ulrich and R. Torge, *Appl. Opt.* 12 (1973) 2901.
- [15] For example: J.J. O'Dwyer, *The Theory of Electrical Conduction and Breakdown in Solid Dielectrics* (Clarendon, Oxford, 1973) p. 136.
- [16] For example: M. Asada, in: *Quantum Well Lasers*, Ed. P.S. Zory, Jr. (Academic Press, New York, 1993) ch. 2.
- [17] P.T. Landsberg, *Phys. Status Solidi* 15 (1966) 623; P.T. Landsberg and D.J. Robins, *Solid State Electron.* 28 (1985) 137.
- [18] E. Zielinski, H. Schweizer, S. Hausser, R. Stuber, M.H. Pilkuhn and G. Weimann, *IEEE J. Quantum Electron.* QE-23 (1987) 967; E. Zielinski, F. Keppler, S. Hausser, M.H. Pilkuhn, R. Sauer and W.T. Tsang, *IEEE J. Quantum Electron.* QE-25 (1989) 1407.
- [19] R. Drenten, private communication; see also: C.T. Walker, J.M. DePuydt, M.A. Haase, J. Qiu and H. Cheng, *Physica B* 185 (1993) 27.



ELSEVIER

Journal of Crystal Growth 138 (1994) 703–708

JOURNAL OF  
**CRYSTAL  
GROWTH**

## Quaternary II–VI alloys for blue and green light emitting diode applications

D.B. Eason <sup>a</sup>, Z. Yu <sup>a</sup>, C. Boney <sup>a</sup>, J. Ren <sup>a</sup>, L.E. Churchill <sup>a</sup>, J.W. Cook, Jr. <sup>a</sup>,  
J.F. Schetzina <sup>\*a</sup>, N.A. El-Masry

<sup>a</sup> Department of Physics, North Carolina State University, Raleigh, North Carolina 27695-8202, USA

<sup>b</sup> Department of Materials Science and Engineering, North Carolina State University, Raleigh, North Carolina 27695-7907, USA

### Abstract

Blue and green light emitting diodes (LEDs) based on ZnSSe double-heterostructures were grown on (100) GaAs substrates by molecular beam epitaxy. The quaternary alloys ZnCdSSe and ZnSSeTe were used as active layer regions in the blue light emitting and green light emitting structures, respectively. The green LEDs produce 238  $\mu$ W of light at room temperature when operating at 10 mA (3.8 V) and exhibit an external efficiency of 0.62%. At 20 mA, the devices produce 428  $\mu$ W of green light. The blue LEDs produce 213  $\mu$ W of light when operating at 10 mA and exhibit an external efficiency of 0.57% at room temperature. At 20 mA, the devices produce 370  $\mu$ W of blue light.

### 1. Introduction

During the past two years there has been important progress in the development of blue/green light emitters based on wide band gap II–VI semiconductor heterostructures. In particular, successful p-type nitrogen-plasma-doping of ZnSe and related II–VI semiconductor alloys [1,2] has led to a number of demonstrations of blue/green light emitting diodes (LEDs) [3–7] and laser diodes (LDs) [8–11].

The first laser diode structures were grown on GaAs substrates by molecular beam epitaxy (MBE) and consisted of cladding layers of lattice-matched ZnSSe coupled with a light-guiding layer of ZnSe in which was located single or multiple quantum well(s) of ZnCdSe. In the sum-

mer of 1992, however, scientists at Sony Laboratories announced [12] the successful demonstration of a blue laser diode in which the quaternary alloy ZnMgSSe [13–16], lattice-matched to GaAs, was used as barrier layers in a double-heterostructure with ZnSe serving as the active layer material. Subsequently, researchers at Philips Laboratory [17] reported improved blue/green laser diode properties by employing a pseudomorphic laser structure based on quaternary ZnMgSSe cladding layers, optical confinement layers of ZnSSe, and an active light emitting region consisting of a single ZnCdSe quantum well.

At NCSU, we are investigating the use of the quaternary alloys ZnCdSSe and ZnSSeTe as active layer materials for blue and green light emitting diode (LED) applications, respectively. These quaternary alloys, like ZnMgSSe, can be closely lattice-matched to GaAs substrates – in contrast to the corresponding ternary alloys ZnCdSe and

\* Corresponding author.

ZnTeSe. As a consequence, double-heterostructures appropriate for LED applications can be grown by combining one of these quaternary alloys along with cladding layers of  $\text{ZnS}_{0.06}\text{Se}_{0.94}$  which are also lattice-matched to GaAs.

## 2. Experimental details

Blue and green LED structures which employ ZnCdSSe or ZnSSeTe layers, respectively, as the active regions of DH devices were grown by MBE at 240–280°C. GaAs substrates with pre-deposited GaAs buffer layers [18] were employed to provide a smooth surface for II–VI film growth, thereby reducing dislocation densities in LED structures to about  $10^5 \text{ cm}^{-2}$ . The DHs were prepared so that the active region consisted of either five 100 Å ZnCdSSe quantum wells (blue LEDs) or a single 1000 Å ZnSSeTe quantum well (green LEDs). The concentration of Te or Cd in the respective quaternary alloy was varied between 5% and 20% in order to change the output wavelength of the LEDs. The cladding layers of the p-on-n DHs consisted of 1 µm of p-type N-doped  $\text{ZnS}_{0.06}\text{Se}_{0.94}$  and 2 µm of n-type Cl-doped  $\text{ZnS}_{0.06}\text{Se}_{0.94}$ , respectively. The n-type doping was achieved using a solid-source dopant,  $\text{ZnCl}_2$  (5N) [1,2,22]. The p-type doping was achieved using an Oxford Applied Research MPD21 radio frequency (RF) plasma source containing flowing  $\text{N}_2$  gas [22–24]. During the MBE growth sequence, the Zn, S, and Se source shutters were always open, such as to maintain a close lattice match to GaAs for growth of the  $\text{ZnS}_{0.06}\text{Se}_{0.94}$  cladding layers. The Te or Cd shutter was opened only during growth of the ZnSSeTe or ZnCdSSe active region layers. Thus, the active regions of the devices are not lattice-matched to GaAs. Rather, they are pseudomorphically strained, as was determined from subsequent transmission electron microscopy studies. A schematic diagram of each of these structures is shown in Fig. 1.

In order to make ohmic contact to each of the p-on-n heterostructures, a thin ( $\sim 100 \text{ Å}$ ) layer of nitrogen-doped  $\text{ZnTe}_{0.2}\text{Se}_{0.8}$  was deposited by MBE after growth of the top p-type  $\text{ZnS}_{0.06}\text{Se}_{0.94}$

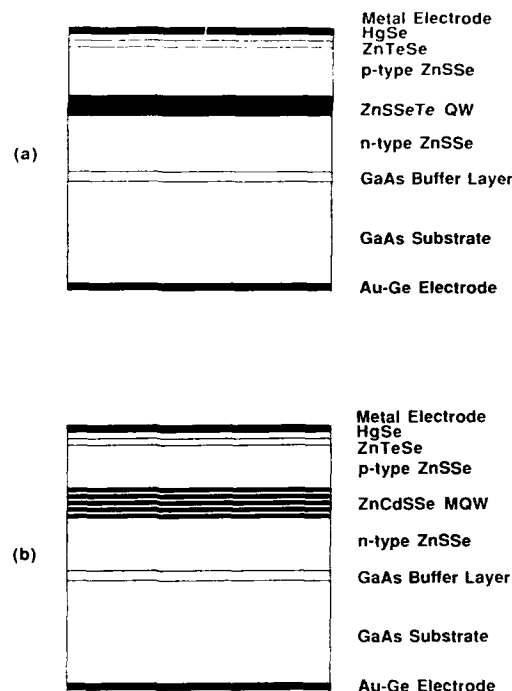


Fig. 1. Schematic diagrams of (a) ZnSSeTe-based green LED structure and (b) ZnCdSSe-based blue LED structure.

layer. The heterostructure was then cooled to room temperature under a Se flux to provide a Se cap layer on the surface. Following this, the wafer was transferred to a second Hg-compatible MBE chamber where the Se cap layer was desorbed by heating and an epitaxial layer of HgSe ( $\sim 100 \text{ Å}$  thick) was grown by MBE [23]. In this way, a multilayered structure which combines a light emission heterostructure with epitaxial layers for p-type ohmic contacts was synthesized. We refer to such epitaxial structures as *integrated heterostructure devices* (IHDs) [24].

Transmission electron microscopy (TEM) studies of samples from selected wafers were completed using a Hitachi-800 electron microscope operating at 200 kV. The samples were thinned at 77 K using argon-ion milling techniques. Many vertical-cross-section and planar TEM photomicrographs were used to assess the interfacial quality of the various layers of the integrated

device structures and to estimate dislocation densities.

Mesa-type LEDs were prepared from selected wafers using standard photolithographic and etching techniques to define mesa arrays. Mesa dimensions ranged from  $300\text{ }\mu\text{m} \times 300\text{ }\mu\text{m}$  to  $500\text{ }\mu\text{m} \times 500\text{ }\mu\text{m}$ . Evaporated Au or In was used to form a metal contact to the top HgSe surface of each p-on-n mesa diode. Ohmic contact to the n-type layer was made at the back surface of the GaAs:Si substrate with Au–Ge or In metal.

Individual LED mesas were set on a header structure with the n-type GaAs substrate bonded to the header with silver epoxy. Electrical contact was made to the top of the mesa using gold wire bonds. The header structure was encapsulated in a clear epoxy dome, 5 mm in diameter, to make an industry-standard T-1 $\frac{3}{4}$  lamp. LED efficiency measurements were performed at room temperature under direct current (DC) conditions with the T-1 $\frac{3}{4}$  LED lamp placed in a calibrated integrating sphere in order to accurately measure its total optical power output in  $\mu\text{W}$ .

### 3. Results and discussion

Fig. 2 shows a vertical-cross-section TEM photograph of a representative green LED structure taken under two-beam conditions. The ZnSSeTe active region, which is pseudomorphically strained, is dislocation free and exhibits smooth interfaces. The ZnSSe cladding layers above and below the active region of the device are also dislocation free. Based on an analysis of many vertical-cross-section and planar TEM photographs of several similar devices, we estimate that the dislocation density is about  $10^5\text{ cm}^{-2}$ , on average, from sample to sample.

At the top surface of the green LED structure shown in Fig. 2 is a dark and narrow ( $\sim 100\text{ }\text{\AA}$ ) layer. This is the epitaxial HgSe layer which is part of the ohmic contact portion of the integrated heterostructure device. The epitaxial nature of the HgSe layer was confirmed by means of electron diffraction studies.

Both the blue-emitting and green-emitting LEDs display *spectacular optical properties*. This

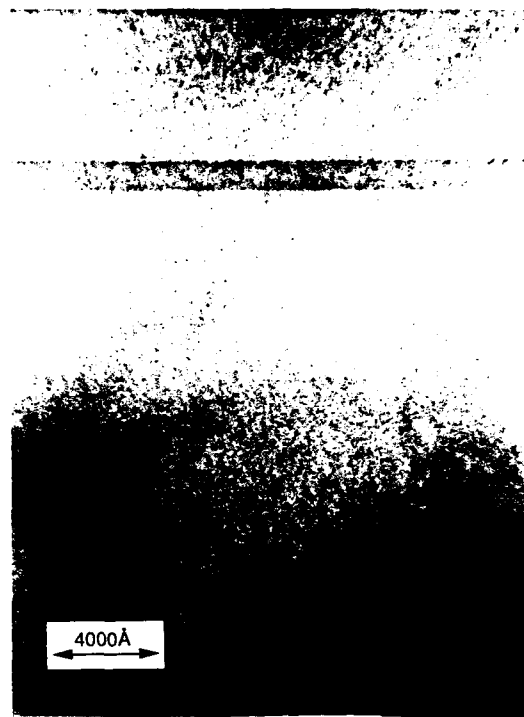


Fig. 2. Vertical-cross-section transmission electron micrograph of green LED structure. The ZnSSeTe quantum well is visible and exhibits smooth interfaces. No dislocations are present in this micrograph, although dislocation densities are estimated to be about  $10^5\text{ cm}^{-2}$  throughout the epitaxial layers.

is illustrated by the light emission spectrum of one of the ZnSSeTe-based green LEDs shown in Fig. 3. Note that the green LED produces  $238\text{ }\mu\text{W}$  of light at room temperature when operating at 10 mA (3.8 V). This corresponds to an external efficiency (power efficiency) of 0.62% at 300 K. The spectrum peaks at 506 nm, but the emission peak has a relatively-broad asymmetric shape, due to the nature of Te which acts as an isoelectronic hole trap [25–28] in the ZnSSeTe alloy, that tails off at larger wavelengths. This makes the light output appear as a deep emerald-green to the eye. The optical power output of the green LED as a function of operating current is shown in Fig. 4. It is seen that the device produces  $428\text{ }\mu\text{W}$  at 20 mA drive current (4.04 V), corresponding to an external efficiency (power efficiency) of



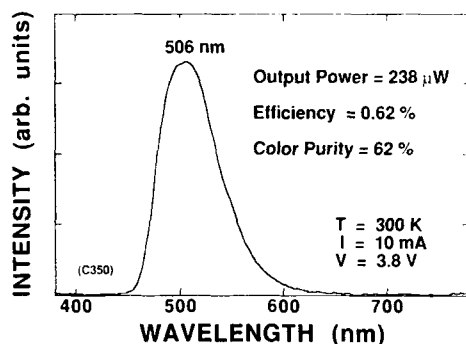


Fig. 3. Light output characteristics at 300 K for ZnSSeTe-based green LED.

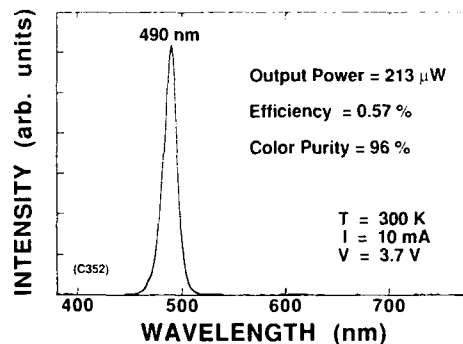


Fig. 5. Light output characteristics at 300 K for ZnCdSSe-based blue LED.

0.53%. By varying the Te content of the ZnSSeTe active layer, we have produced LEDs of similar optical quality with outputs peaking in the green spectral region between 502 and 514 nm.

The light emission spectrum of a representative ZnCdSSe-based blue LED is shown in Fig. 5. In this case, the light emission is sharply peaked at 490 nm. The emission peak has a full width at half-maximum (FWHM) of only 16 nm. The device produces 213  $\mu\text{W}$  of blue light at room temperature when operating at 10 mA (3.7 V), corresponding to a 300 K external power efficiency of 0.57%. When operated at 20 mA, the blue LED produces 370  $\mu\text{W}$  of light. By varying the Cd content of the ZnCdSSe active layer

quantum wells, we have fabricated and tested high-brightness blue LEDs with peak emission at 300 K ranging from 482 to 490 nm.

To put the above results in proper perspective, commercial blue LEDs made from SiC have efficiencies of 0.02–0.03% and produce 12–18  $\mu\text{W}$  of light at 20 mA [29]. Commercial green LEDs made from GaP, which operate at 555 nm (yellow-green), exhibit external efficiencies of  $\sim 0.1\%$  [30] and produce light outputs of 60–70  $\mu\text{W}$  when operated at 20 mA. Thus, the present results are important since they show, for the first time, that II–VI semiconductor heterostructures can produce both blue and green light emission at room temperature that is much brighter and more efficient than present day commercial blue/green LEDs.

The spectacular light emitting properties of the blue and green LEDs described herein stem from the fact that the II–VI materials employed are “direct” band gap semiconductors, which are inherently better light emitters than the “indirect” band gap materials SiC and GaP. However, the present devices exhibit much higher efficiencies and light outputs than previously-reported LEDs based on similar II–VI heterostructures. This is attributed to the fact that the present structures, which employ active layers comprised of the quaternary alloys ZnSSeTe or ZnCdSSe, are more closely lattice-matched to GaAs. This, along with optimization of MBE growth procedures, has led to the successful elimination of

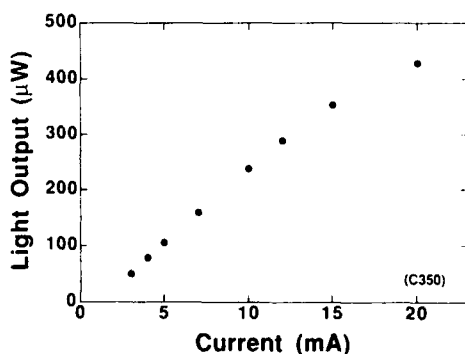


Fig. 4. Light output power versus applied dc current for ZnSSeTe-based green LED. At 20 mA, the applied voltage is 4.04 V.

unwanted non-radiative centers in the active layer regions of the devices.

At the present time, both the blue ZnCdSSe-based and green ZnSSeTe-based LEDs have useful lifetimes of only a few hundred hours: Our best encapsulated devices exhibit light outputs of 60–65% of their initial light outputs after operating at 10 mA (4 A/cm<sup>2</sup>) for 250 h. This limited lifetime is attributed to the relatively high dislocation density ( $\sim 10^5$  cm<sup>-2</sup>) in the devices. Device degradation studies show that the light degradation process involves the generation of dark-line-defects which increase in number and size with time – similar to the dark-line-defect degradation which occurs in GaAs-based and GaP-based LED structures when they contain comparable dislocation densities [31].

At North Carolina State University, we have seen II–VI heterostructure LED lifetimes increase from several minutes, to several hours, to several hundreds of hours as the device dislocation density has been reduced from  $10^7$  cm<sup>-2</sup>, to  $10^6$  cm<sup>-2</sup>, to  $10^5$  cm<sup>-2</sup> over the past two years. It would seem, based on this limited data base, that dislocation density reduction to less than  $10^4$  cm<sup>-2</sup> may be required for LED lifetimes to reach 10,000 h. This is the last major hurdle – however formidable it may prove to be – that must be addressed before the high-brightness, high-efficiency integrated heterostructure devices that we have described are ready for commercialization.

#### 4. Acknowledgments

The authors wish to thank J.C. Edmond of CREE Research for help with device packaging and testing. J. Matthews provided assistance with MBE system maintenance; K.A. Bowers and B. Sneed contributed to device processing. This work was supported by the US Advanced Research Projects Agency (ARPA) under grant DAAL03-91-G-0131, by ARPA/URI grant N00014-92-J-1893 which is administered by the Office of Naval Research (ONR), and by ONR grant N00014-92-J-1644.

#### 5. References

- [1] R.M. Park, M.B. Troffer, C.M. Rouleau, J.M. DePuydt and M.A. Haase, *Appl. Phys. Lett.* 57 (1990) 2127.
- [2] K. Ohkawa, T. Karasawa and T. Mitsuyu, *J. Crystal Growth* 111 (1991) 797.
- [3] W. Xie, D.C. Grillo, R.L. Gunshor, M. Kobayashi, G.C. Hua, N. Otsuka, H. Jeon, J. Ding and A.V. Nurmikko, *Appl. Phys. Lett.* 60 (1992) 463.
- [4] H. Jeon, J. Ding, A.V. Nurmikko, W. Xie, M. Kobayashi and R.L. Gunshor, *Appl. Phys. Lett.* 60 (1992) 892.
- [5] W. Xie, D.C. Grillo, R.L. Gunshor, M. Kobayashi, H. Jeon, J. Ding, A.V. Nurmikko, G.C. Hua and N. Otsuka, *Appl. Phys. Lett.* 60 (1992) 1999.
- [6] J. Ren, K.A. Bowers, J.W. Cook, Jr. and J.F. Schetzina, *J. Vac. Sci. Technol. B* 10 (1992) 909.
- [7] Y. Lansari, J. Ren, B. Sneed, K.A. Bowers, J.W. Cook, Jr. and J.F. Schetzina, *Appl. Phys. Lett.* 61 (1992) 2554.
- [8] M.A. Haase, J. Qiu, J.M. DePuydt and H. Cheng, *Appl. Phys. Lett.* 59 (1991) 1272.
- [9] H. Jeon, J. Ding, W. Patterson, A.V. Nurmikko, W. Xie, D.C. Grillo, M. Kobayashi and R.L. Gunshor, *Appl. Phys. Lett.* 59 (1991) 3619.
- [10] S.Y. Wang, I. Kauksson, J. Simpson, H. Stewart, S.J.A. Adams, J.M. Wallace, Y. Kawakami, K.A. Prior and B.C. Cavenett, *Appl. Phys. Lett.* 61 (1992) 506.
- [11] Z. Yu, J. Ren, B. Sneed, K.A. Bowers, K.J. Gossett, C. Boney, Y. Lansari, J.W. Cook, Jr., J.F. Schetzina, G.C. Hua and N. Otsuka, *Appl. Phys. Lett.* 61 (1992) 1266.
- [12] Reported on page B8 in the July 23, 1992, issue of *The Wall Street Journal* (New York, NY, 1992).
- [13] H. Okuyama, K. Nakano, T. Miyajima and K. Akimoto, *Jap. J. Appl. Phys.* 30 (1991) L1620.
- [14] H. Okuyama, F. Hiei and K. Akimoto, *Jap. J. Appl. Phys.* 31 (1992) L340.
- [15] H. Okuyama, Y. Morinaga and K. Akimoto, *J. Crystal Growth* 127 (1993) 335.
- [16] Y. Morinaga, H. Okuyama and K. Akimoto, *Jap. J. Appl. Phys.* 32 (1993) 678.
- [17] J.M. Gaines, R.R. Drenten, K.W. Habernern, T. Marshall, P. Mensz and J. Petruzzello, *Appl. Phys. Lett.* 62 (1993) 2462.
- [18] J. Ren, D.B. Eason, Y. Lansari, Z. Yu, K.A. Bowers, C. Boney, B. Sneed, J.W. Cook, Jr., J.F. Schetzina, M.W. Koch and J.F. Schetzina, *J. Vac. Sci. Technol. B* 11 (1993) 955.
- [19] K. Ohkawa, T. Mitsuyu and O. Yamazaki, *J. Appl. Phys.* 62 (1987) 3216.
- [20] H. Cheng, J. DePuydt, J. Potts and M. Haase, *J. Crystal Growth* 95 (1988) 512.
- [21] S. Hwang, J. Ren, K.A. Bowers, J.W. Cook, Jr. and J.F. Schetzina, *Mater. Res. Soc. Symp. Proc.* 161 (1990) 133.
- [22] Z. Yang, K.A. Bowers, J. Ren, Y. Lansari, J.W. Cook, Jr. and J.F. Schetzina, *Appl. Phys. Lett.* 61 (1992) 2671.
- [23] Y. Lansari, J.W. Cook, Jr. and J.F. Schetzina, *J. Electron. Mater.* 22 (1993) 809.

- [24] J. Ren, Y. Lansari, Z. Yu, J.W. Cook, Jr. and J.F. Schetzina, *J. Electron. Mater.* 22 (1993) 973.
- [25] D. Lee, A. Mysyrowicz, A.V. Nurmikko and B.J. Fitzpatrick, *Phys. Rev. Lett.* 58 (1987) 1475.
- [26] J.J. Davies, *Semicond. Sci. Technol.* 3 (1988) 219.
- [27] Q. Fu, D. Lee, A.V. Nurmikko, L.A. Kolodziejski and R.L. Gunshor, *Phys. Rev. B* 39 (1989) 3173.
- [28] J. Ren, K.A. Bowers, R.P. Vaudo, J.W. Cook, Jr., J.F. Schetzina, J. Ding, H. Jeon and A.V. Nurmikko, *J. Crystal Growth* 117 (1992) 510.
- [29] J.C. Edmond, H. Kong and C.H. Carter, Jr., *Physica B* 185 (1993) 453.
- [30] M.G. Craford, *Circuits and Devices* (Sept. 1992) 24.
- [31] C.L. Sipfel, in: *Semiconductors and Semimetals*, Vol. 22, Part C, Eds. R.K. Willardson and A.C. Beer, Vol. Ed. W.T. Tsang (Academic Press, New York, 1985) ch. 6.



ELSEVIER

Journal of Crystal Growth 138 (1994) 709–713

JOURNAL OF  
**CRYSTAL  
GROWTH**

## Optical modulators using quantum confined Stark effect in ZnSe based multiple quantum well structures

F. Jain <sup>\*a</sup>, W. Huang <sup>a</sup>, R. LaComb <sup>a</sup>, C. Chung <sup>b</sup>, G. Drake <sup>c</sup>

<sup>a</sup> Department of Electrical and Systems Engineering, University of Connecticut, Storrs, Connecticut 06269-3157, USA

<sup>b</sup> Trinity College, Hartford, Connecticut 06106, USA

<sup>c</sup> United Technologies Photonics, Bloomfield, Connecticut 06002, USA

### Abstract

Optical modulator structures employing quantum confined Stark effect tuning in ZnSe based material systems are described. Computations are presented to illustrate the feasibility of designing transmission and reflection mode Fabry–Perot modulators using ZnCdSe–ZnSSe (or ZnCdSe–ZnMgSSe) MQW cavities. Changes in the excitonic absorption coefficient (e.g., 3–5 nm shift in peak) and index of refraction ( $\sim 2\%$ ), in the presence of an externally applied perpendicular electric field  $E_{\perp}$  ( $10^4$ – $10^5$  V/cm), are calculated and used to obtain variations in transmittance (contrast ratio). Both matched and asymmetric Fabry–Perot structures realized on ZnSe and GaAs substrates are discussed. In contrast to the AlGaAs–GaAs system, the excitonic binding energies in the ZnCdSe–ZnSSe system are found to be significantly higher. The variations in excitonic wavefunction  $|\phi_{ex}|^2$  are, therefore, significantly different. However, the contrast ratios are not as good as for the AlGaAs–GaAs system due to poor dielectric mirror reflectivities.

### 1. Introduction

The successful p-doping [1] of ZnSe and subsequent announcement of blue-green lasers [2] have stimulated interest in ZnSe based integrated optical systems including lasers, modulators, waveguides, and detectors. Tunable multiple quantum well (MQW) optical modulators employing the quantum confined Stark effect (QCSE) have been investigated extensively [3–6] in III–V material systems during the past 5 years. We have presented preliminary field-dependent exciton bind-

ing energy calculations showing the feasibility of ZnSe based MQW modulators [7]. The experimental fabrication of ZnCdSe–ZnSSe based Stark effect modulators has recently been reported by Wang et al. [8].

This paper reports computations of absorption coefficient  $\alpha$ , index of reflection  $n$ , and associated changes in these parameters due to an external electrical field in ZnCdSe–ZnSSe and/or ZnCdSe–ZnMgSSe MQWs. Unlike GaAs–AlGaAs systems, the binding energy and its variation as a function of  $E_{\perp}$  are significantly larger in the ZnCdSe–ZnSSe system. Various modulator structures using standard p–i–n formats and MQWs configured as Fabry–Perot cavities are

\* Corresponding author.

proposed. Modulators operating in both reflection and transmission modes realized on GaAs as well as ZnSe substrates are discussed. In the case of reflection mode devices using GaAs substrates, no substrate etching is required.

## 2. Field dependent changes in the absorption coefficient and index of refraction

The imaginary part of the dielectric constant  $\epsilon_i(h\omega)$ , involving excitonic transitions in MQW layers is given by [3,9]

$$\epsilon_i = (C/L) \left| \int \psi_e(x) \psi_h(x) dx \right|^2 F(\hbar\omega_{ex} - \hbar\omega), \quad (1)$$

$$C = [2\pi e^2 / \epsilon_0 m_0^2 \omega^2] |M_b|^2 |\phi_{ex}(0)|^2, \quad (2)$$

where  $\phi_{ex}(x)$  is the exciton wave function,  $\hbar\omega_{ex}$  is the exciton energy,  $F$  is the Gaussian line shape function,  $\psi_e$  and  $\psi_h$  are electron and hole wavefunctions, respectively,  $L$  is the width of quantum well,  $\epsilon_0$  is the permittivity of free space,  $m_0$  is the electron rest mass, and  $M_b$  is the Bloch matrix element [9]. Using the Kramers–Kronig relation, we can express the real part  $\epsilon_r(h\omega)$  as

$$\epsilon_r(h\omega) = 1 + \frac{2}{\pi} P \int_0^\infty \frac{\omega' \epsilon_i(\omega') d\omega'}{\omega'^2 - \omega^2}, \quad (3)$$

where  $P$  is the Cauchy principal integral. The complex index of refraction  $n_c (= n - i\kappa)$  is related to the complex dielectric constant. Thus,  $n$  and  $\kappa$  can be evaluated from  $\epsilon_r$  and  $\epsilon_i$ .  $\kappa$  is related to the absorption coefficient by

$$\alpha(h\omega) = 4\pi\kappa/\lambda_0. \quad (4)$$

The application of an electrical field  $E_z$ , perpendicular to the plane of MQW layers, results in

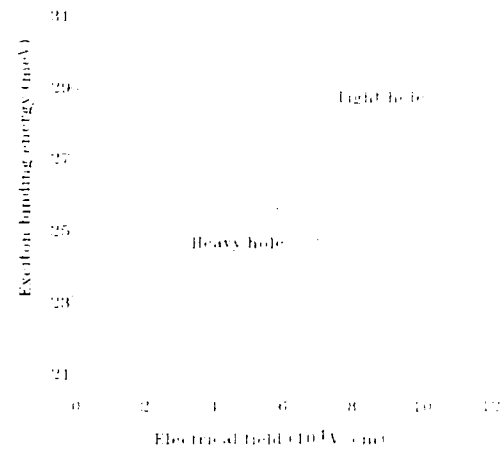


Fig. 1. Exciton binding energy as a function of  $E_z$  for ZnCdSe–ZnSSe QW.

the modification of the electron wavefunctions  $\psi_e$ , the hole wavefunctions  $\psi_h$ , and the exciton wavefunctions. These lead to changes in the exciton binding energies as well as the oscillator strength

$$|\phi_{ex}(0)|^2 \left| \int \psi_e(x) \psi_h(x) dx \right|^2,$$

and the line shape function  $F$ . The computed exciton binding energies as a function of  $E_z$  for the ZnCdSe–ZnSSe quantum well structure are shown in Fig. 1. The parameters used in the calculation are listed in Table 1. The oscillator strength dependence on exciton binding energy is shown in Fig. 2. As the applied field increases, the exciton binding energies and the oscillator strength decrease because of the increasing separation between the electron and hole in the well region. The resulting changes in  $\alpha$  and  $n$  are

Table 1  
Parameters used in the exciton binding energy calculations

Layers	$x$	Quantum well width ( $\text{\AA}$ )	Dielectric constant	Electron effective mass	Light hole effective mass	Heavy hole effective mass
Zn <sub>1-x</sub> Cd <sub>x</sub> Se	0.2	80	7.67	$0.16m_0$	$0.14m_0$	$0.54m_0$
ZnS <sub>1-x</sub> Se <sub>x</sub>	0.06	80	7.42	$0.17m_0$	$0.15m_0$	$0.54m_0$
ZnSe			7.56			
ZnMgSSe			6.97			

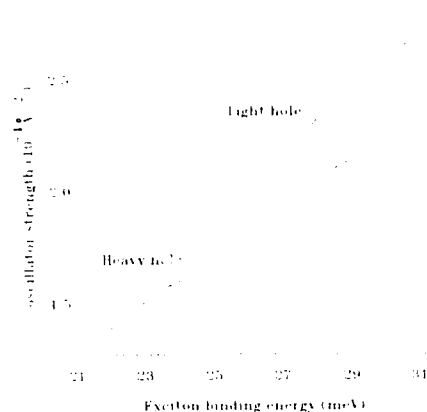


Fig. 2. Oscillator strength versus exciton binding energy for ZnCdSe-ZnSSe QW.

shown in Figs. 3 and 4, respectively. The peak value of the absorption coefficient at zero field turns out to be  $9000 \text{ cm}^{-1}$ , which is in good agreement with the experiment [8]. The changes in  $\alpha$  and  $n$  are comparable to those obtained in III-V Stark effect devices [3–6]. These changes can be utilized to obtain optical modulation depending on the nature of device application.

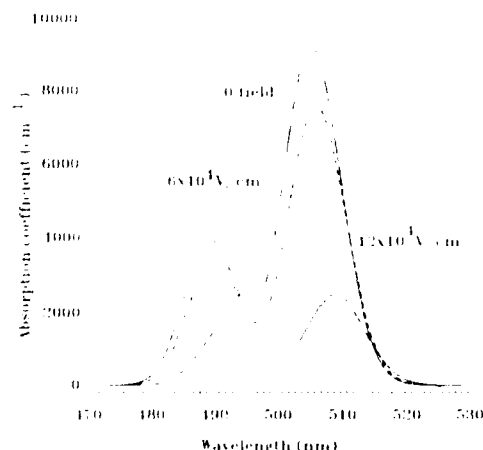


Fig. 3. Absorption coefficient as a function of electric field  $E$  and wavelength for the structure in Fig. 5.

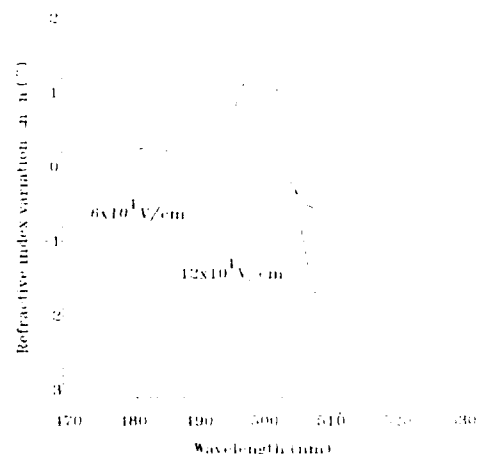


Fig. 4.  $\Delta n/n$  as a function of operating wavelength for the structure in Fig. 5.

### 3. Proposed optical modulator structures

Modulators using Stark effect induced variations in  $\alpha$ ,  $n$ , and birefringence have been designed in variety of configurations [5]. When a high contrast ratio is desired, Fabry-Perot (FP) structures, utilizing the MQW cavity, are generally employed. They are classified into two broad categories: (a) photorefractive and (b) photoabsorptive. A degree of photorefractive has also been observed in InGaAs-GaAs asymmetric FP modulators primarily using the photoabsorptive phenomenon in the presence of an external optical pump [4].

Fig. 5 illustrates a Fabry-Perot modulator having ZnSe/ZnSSe dielectric mirrors with 20 and 23.5 periods for top and bottom mirrors, respectively. The MQW cavity consists of 75 periods of ZnCdSe-ZnSSe multiple quantum wells. The computed transmittance through the structure including the ZnSe substrate is shown in Fig. 6. The transmittance is calculated using the transfer matrix approach. The  $\lambda/4$  stack dimensions are used at the desired operating wavelength (505 nm). The MQW index is computed using barrier and well dimensions of 80 Å. The index of refraction is assumed to be constant for different wavelength in the preliminary computations. Changes in the index of the cavity under the applied

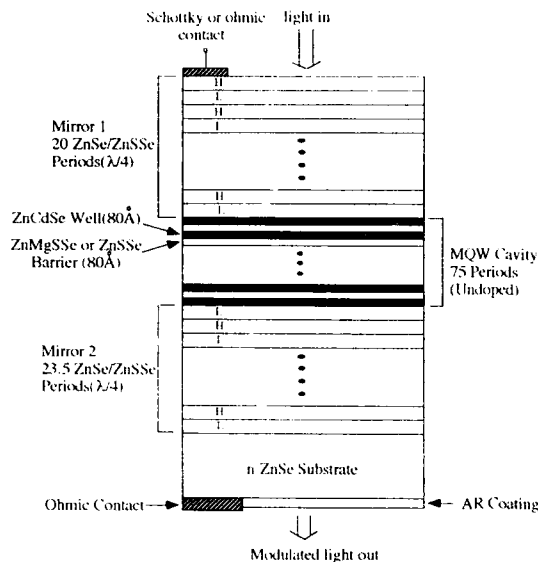


Fig. 5. Fabry-Perot modulator structure consists of ZnCdSe-ZnSSe MQW cavity sandwiched between ZnSe-ZnSSe (or ZnSe-ZnMgSSe)  $\lambda/4$  dielectric mirrors.

electrical field  $E_z$  are taken from the computed data of Fig. 4. The mirrors are assumed to have  $\alpha = 1 \text{ cm}^{-1}$ . The transmittance variation is rather smaller compared with the InGaAs-GaAs MQW devices [4,6]. This is attributed to the small  $\Delta n$  difference between layers, which results in poor reflectivity of the dielectric mirrors.

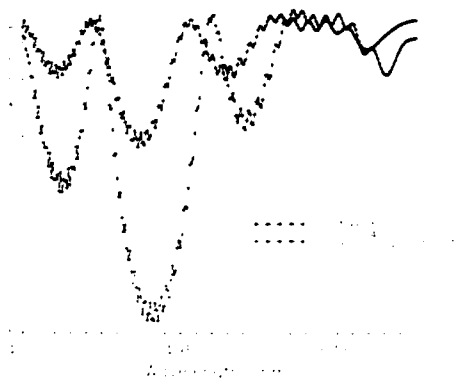


Fig. 6. Transmittance of the Fig. 5 Fabry-Perot cavity consisting of a MQW using ZnSSe as barrier with a  $\Delta n = 0.02$  (as presented in Fig. 3).

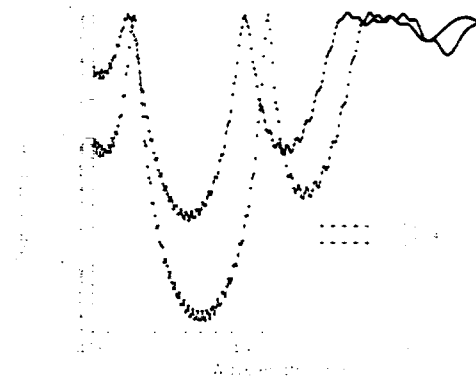


Fig. 7. Transmittance of the Fig. 5 Fabry-Perot cavity consisting of ZnSe-ZnMgSSe mirrors and MQWs using ZnSSe as barrier.

Use of the lattice matched ZnMgSSe  $10 \lambda/4$  layers in place of ZnSSe layers for the dielectric mirror yields improved transmittance. Fig. 7 shows a plot of transmittance using ZnSe/ZnMgSSe mirrors. The contrast ratio is improved by 15 times higher than using the ZnSe/ZnSSe dielectric mirror. In addition, the use of ZnMgSSe is expected to yield enhanced carrier/excitonic con-

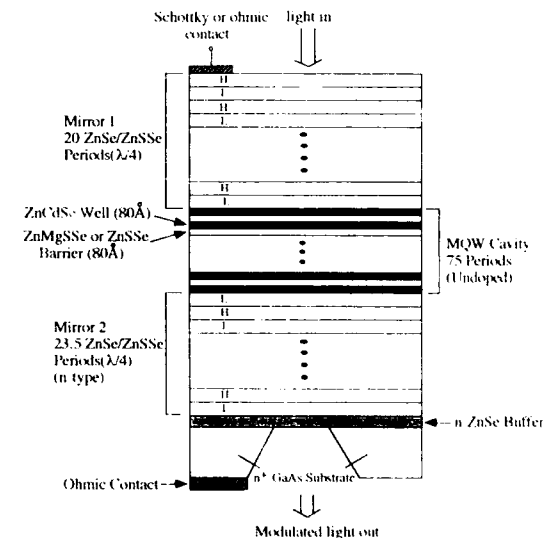


Fig. 8. Fabry-Perot modulator on GaAs substrate (transmission mode).

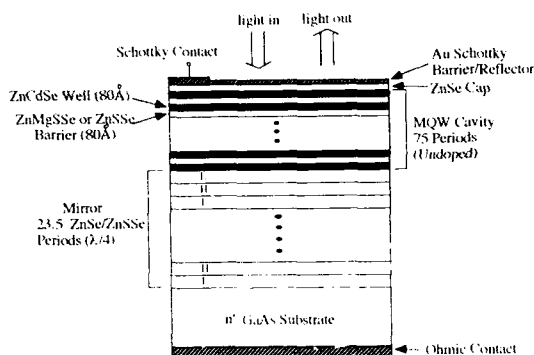


Fig. 9. Reflection mode asymmetric Fabry-Perot modulator on GaAs substrate.

finement and resultant optical parameters in the MQW cavity.

Figs. 8 and 9 show cross-sectional schematic drawings of Fabry-Perot modulators using GaAs substrates in matched/symmetric and asymmetric configurations. The device of Fig. 8 is a transmission mode, electrically addressed device. Fig. 9, by contrast, represents a reflection mode device. An external optical pump can be used here, in a manner similar to III-V modulators [4], in place of electrical biasing. The devices grown on GaAs substrates are believed to be of immediate importance due to the unavailability of suitable ZnSe substrates.

#### 4. Conclusions

The exciton binding energy and its variation due to an external  $E_z$  field are, in general, significantly higher in ZnSe based MQWs than obtained in the AlGaAs-GaAs or InGaAs-GaAs systems. The variation in optical parameters including  $\alpha$  (3–5 nm shift in peak) and  $n$  ( $\sim 2\%$ ) by the application of an external electric field ( $\sim 10^4$ – $10^5$  V/cm) are comparable to III-V devices, and are adequate to design efficient modulators and spatial light modulators. However, improvement in the reflectivity of the  $\lambda/4$  dielectric mirrors is needed to enhance the contrast ratio of

the modulator. The feasibility of both reflection and transmission mode devices, realized on GaAs and ZnSe substrates, is demonstrated. Progress in fabricating room temperature blue-green lasers [12] requires the investigation of modulators, waveguides, and other devices in order to develop optical integrated circuits operating at shorter wavelengths.

#### 5. Acknowledgements

This work is in part supported by a Connecticut Department of Economic Development grant. The authors gratefully acknowledge the IBM Corporation for providing the RISC workstations (under the SUR contract) which were used to carry out the computations.

#### 6. References

- [1] R. Park, M.B. Troffler, C.M. Rouleau, J.M. DePuydt and M.A. Haase, *Appl. Phys. Lett.* 57 (1990) 2127.
- [2] M.A. Haase, H. Cheung, D.K. Misemer, T.A. Strand and J.M. DePuydt, *Appl. Phys. Lett.* 59 (1991) 2127.
- [3] D.A.B. Miller, D.S. Chemla, T.C. Daman, A.C. Gossard, W. Wiegmann, T.H. Wood and C.A. Burrus, *Phys. Rev. B* 32 (1985) 1043.
- [4] R. Jin, G. Khitrova, H.M. Gibbs, C. Lowry and N. Peyghambarian, *Appl. Phys. Lett.* 59 (1991) 3261.
- [5] F. Jain, K. Battacharjee and T.W. Grudkowski, in: *Proc. 1991 Ultrasonic Symp.*, Lake Buena Vista, FL, December 1991, pp. 529.
- [6] S. Cheung, F. Jain, R. Sacks, D. Cullen, G. Ball and T. Grudkowski, *Appl. Phys. Lett.* 63 (1993) 296.
- [7] W. Huang, F. Jain, C. Cheung and G. Drake, in: *Proc. Connecticut Microelectronic and Optoelectronic Symp.*, SNET, New Haven, CT, March 1993.
- [8] S.Y. Wang, Y. Kawakami, J. Simpson, H. Stewart, K.A. Prior and B.C. Cavenett, *Appl. Phys. Lett.* 62 (1993) 1715.
- [9] Y. Kan, H. Nagai, M. Yamanishi and I. Suemune, *IEEE J. Quantum Electron.* QE-23 (1987) 2167.
- [10] H. Okuyama, K. Nakano, T. Miyajima and K. Akimoto, *Jap. J. Appl. Phys.* 30 (1991) L1620.
- [11] Y.S. Park and B.K. Shin, in: *Recent Advances in Injection Luminescence in Electroluminescence*, Ed. J. Pankove (Springer, Berlin, 1977).
- [12] A. Ishibashi and Y. Mori, *J. Crystal Growth* 138 (1994) 677.





ELSEVIER

Journal of Crystal Growth 138 (1994) 714–718

JOURNAL OF  
**CRYSTAL  
GROWTH**

## Quantitative study of mechanism responsible for high operating voltage in II–VI laser diodes

I. Suemune

*Research Institute for Electronic Science, Hokkaido University, Sapporo 060, Japan*

### Abstract

Current–voltage ( $I$ – $V$ ) characteristics of II–VI laser diodes were calculated considering thermionic emission and tunneling processes at metal/p-ZnSe contacts. The physical parameter dependence of the tunneling current, which dominates the  $I$ – $V$  characteristics in high voltage regions, especially the dependence on the barrier height and the acceptor concentration, is quantitatively clarified. The relation between the measured low ohmic contact resistance and the high diode voltage for laser operations is discussed.  $I$ – $V$  characteristics of ZnSSe p–n diodes grown by metalorganic vapor-phase epitaxy were studied with the present model and the mechanism of the low-voltage operation observed was examined.

### 1. Introduction

Recently, blue/green laser diodes have been realized [1] following the successful p-type doping of the wide-gap II–VI semiconductor, ZnSe, by nitrogen radical doping during molecular-beam epitaxy (MBE) [2,3]. Room temperature operation has also been reported by several groups [4–7]. One of the key issues is ohmic contacts to p-type ZnSe and related alloys. The use of semimetal HgSe [8] or ZnTe/ZnSe graded band gap layers [9] has been proposed and the reduction of the ohmic contact resistance reported. Diode voltages for laser operations were reduced in these trials, but voltages exceeding 10 V were still necessary [9].

The mechanism responsible for the high diode voltage has been studied, and a tunneling process through the barrier at the metal/p-ZnSe was proposed by Ren et al. [10]. This idea was further

developed considering the depletion layer at the Schottky contact [11]. In this model, the expansion of the depletion layer from the metal/p-ZnSe interface and the dependence of the electric field on the acceptor concentration was taken into account. Thermionic emission as well as the tunneling current flowing across the interface was taken into account, as shown schematically in Fig. 1. These two currents satisfy the continuity of the current flowing through the p–n junction. Physical parameters such as the barrier height,  $\phi_B$ , were estimated by fitting the theoretical model to the measured current–voltage ( $I$ – $V$ ) characteristics, and the inclusion of the thermionic emission was effective in producing an accurate fit [11].

Fig. 2 shows one example of the fitting [11] of the theoretical model to the  $I$ – $V$  characteristics measured for a blue/green laser diode [1]. The calculated  $I$ – $V$  characteristics show that the voltage was mainly applied to the p–n junction in the

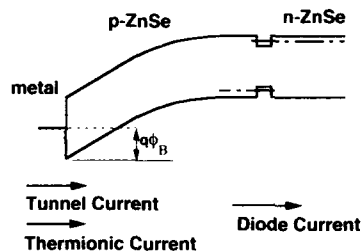


Fig. 1. Schematic band diagram for the current flow through metal/p-ZnSe contact under forward bias of the p-n junction.

low voltage region ( $< 1.5$  V). For the moderate bias (1.5–4 V), the current was limited by thermionic emission and the voltage was induced in the depletion layer near the metal/p-ZnSe contact. The corresponding increase of the electric field in the depletion layer enhanced the tunneling current in the higher voltage region ( $> 4$  V). The dashed line in Fig. 2 was calculated without considering the thermionic emission.

In this paper, the dependence of the  $I$ - $V$  characteristics on physical parameters is quantitatively discussed based on the above theoretical modeling. In particular, the tunneling process which dominates the  $I$ - $V$  characteristics in the high voltage region is critically dependent on the barrier height and the acceptor concentration in p-ZnSe. The conditions necessary for the realization of low-voltage laser operations will be discussed. It has been reported that the ohmic con-

tact resistance was low, but that the diode voltage for laser operations was still above 10 V [7,9]. The relation of these apparently contradictory measurements will be discussed. Finally,  $I$ - $V$  characteristics of diodes grown by metalorganic vapor-phase epitaxy (MOVPE) will be discussed from the viewpoint of the present theoretical model.

## 2. Parameter dependence of $I$ - $V$ characteristics

In the fit shown in Fig. 2, the acceptor concentration in the p-ZnSe layer was taken as  $1 \times 10^{18} \text{ cm}^{-3}$  [1] and the barrier height was estimated to be 0.61 V [11]. This estimated barrier height of 0.61 V was much lower than the Schottky barrier height of 1.3 V for Au/p-ZnSe. In the following, the dependence of the  $I$ - $V$  characteristics on the barrier height will be discussed.

Details of the analytical procedure will be given elsewhere [11], and mainly numerical results are discussed in this work. The  $I$ - $V$  characteristics were calculated for several barrier heights at the metal/p-ZnSe contact, as shown in Fig. 3. The dashed line is the p-n junction voltage, which does not depend on the barrier height. The acceptor concentration in the p-ZnSe layer was assumed to be  $1 \times 10^{18} \text{ cm}^{-3}$ , which is the highest net acceptor concentration obtained with MBE up to now. A variation of the barrier height by 0.1 V results in a variation of the current by more than one order of magnitude. A barrier height

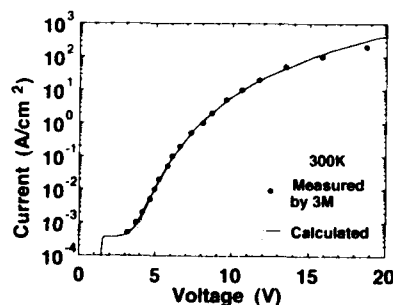


Fig. 2. Theoretical fit to the measured  $I$ - $V$  characteristics for a blue/green laser diode [1] shown by closed circles. The dashed line was calculated without considering the thermionic emission current flow over the barrier.

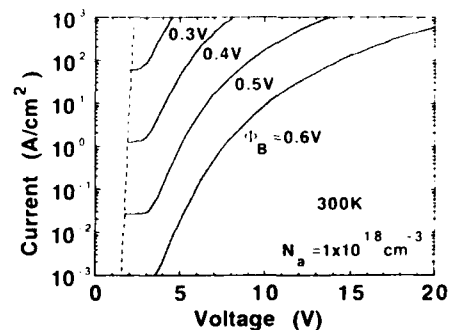


Fig. 3. Barrier height dependence of diode  $I$ - $V$  characteristics calculated for an acceptor concentration of  $1 \times 10^{18} \text{ cm}^{-3}$ . Dashed line is the p-n junction voltage.

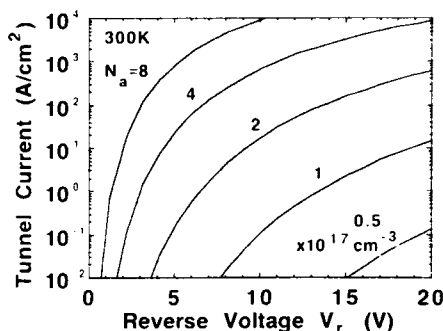


Fig. 4. Acceptor concentration dependence of tunneling current flowing through a metal/p-ZnSe interface calculated for a barrier height of 0.35 V.

greater than 0.6 V results in a very low current flow. Therefore, the assumption of a Schottky barrier height of 1.3 V results in the extremely low current flow and is not a realistic value to fit the measured  $I$ - $V$  characteristics.

The reason why the estimated barrier height was low is not clear at present. One possibility is the Schottky effect which reduces the effective barrier height with an image potential. The lowering of the barrier height was estimated to be 0.12 V for a reverse bias of 10 V. This does not explain the measured barrier height; however, the position of the maximum barrier height is separated from the Au/p-ZnSe interface by only  $\sim 7$  Å. Therefore it is probable that the barrier height for the tunneling is influenced by the slight interface mixing after thermal annealing. The result shown in Fig. 3 indicates that the diode voltage for a current density of 1 kA/cm², which will be high enough for laser operation at room temperature with an adequate structural design, will be reduced below 5 V when the barrier height is reduced to 0.3 V.

The tunneling current, which dominates the  $I$ - $V$  characteristics in Fig. 3 in the high voltage region, is also sensitively dependent on the acceptor concentration in p-ZnSe. It has been calculated for several acceptor concentrations, as shown in Fig. 4. The barrier height in this case was assumed to be 0.35 V. A doubling of the acceptor concentration results in more than one order of magnitude change in the  $I$ - $V$  character-

istics. Therefore, a reproducible high acceptor concentration is necessary for reproducibly good  $I$ - $V$  characteristics in laser diodes.

It is well known that tunneling probabilities do not depend on temperature. Therefore, the tunneling current shows a temperature dependence smaller than those of the usual thermal processes. The tunneling current density at 77 and 300 K showed a change of about 10 times. This variation arises from the temperature dependence of the energy distribution of carriers in the metal.

### 3. Relation between ohmic contact resistance and diode operation voltage

It has been reported that even when the measured ohmic contact resistance was low, the diode voltage for laser operations was still above 10 V [7,9]. The relation of these apparently contradictory phenomena will be discussed in the following. The diode voltage for laser operations is dominated by the tunneling current, as discussed in the previous section. On the other hand, for the current flow across the metal/p-ZnSe for low bias, which will be the usual case for the measurements of the ohmic contact resistance, thermionic emission will dominate, as indicated in Figs. 2 and 3.

For the schematic representation of the measurement of the series resistance through two surface contacts shown in Fig. 5, the thermionic emission current density flowing over the barrier is given by

$$J_{th} = AT^2 \exp(-q\phi_B/kT) \times [1 - \exp(-qV_r/kT)], \quad (1)$$

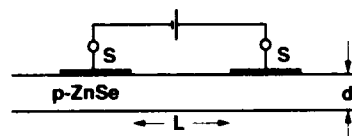


Fig. 5. Schematic representation of the measurement of ohmic contact resistance.

where  $A$  is the Richardson constant given by  $120(m^*/m_0) A/cm^2$ . The current flow in Fig. 5 will be limited by the surface contact under reverse bias. For a moderate reverse bias of  $V_r < kT/q$ , the ohmic contact resistance is given by the differential resistance derived from Eq. (1) as

$$r_{th} = (k/qAT) \exp(q\phi_B/kT) (\Omega \text{ cm}^2). \quad (2)$$

Therefore the ohmic contact resistance for a given temperature is determined solely by the barrier height.

Using a hole effective mass of 0.6 for p-ZnSe, the ohmic contact resistance at room temperature is  $\sim 6 \times 10^{-4} \Omega \text{ cm}^2$  for a barrier height of 0.3 V. For a surface contact area of  $50 \mu\text{m} \times 100 \mu\text{m}$ , the series resistance at the contact is  $r_{th}/S \approx 12 \Omega$ . The sheet resistance of p-ZnSe for a hole concentration of  $p = 2 \times 10^{17} \text{ cm}^{-3}$ , mobility of  $\mu = 10 \text{ cm}^2/\text{V} \cdot \text{s}$ , and film thickness of  $d = 2 \mu\text{m}$  will be given as  $\rho/d = 1/qp\mu d \approx 16 \text{ k}\Omega$ . Then, for  $L = 100 \mu\text{m}$ , this results in a series resistance of  $16 \text{ k}\Omega$ . When a bias voltage of 10 V is applied for the measurement, the series connection of the above electrical resistances in the circuit of Fig. 6 will result in 8 mV induced at the surface contact. This reverse bias at the surface contact satisfies the above condition of  $V_r < kT/q$ .

It will be clear from the above discussion that the main current flow mechanism is different between the laser diode operation and the measurement of the ohmic contact resistance. The former is dominated by the tunneling current,

while the latter is dominated by the thermionic emission current. This different current flow mechanism will show the apparent inconsistency between the low ohmic contact resistivity and the high diode operating voltage.

#### 4. Study of $I$ - $V$ characteristics measured on diodes grown by MOVPE

In this section,  $I$ - $V$  characteristics of diodes recently grown by MOVPE will be discussed from the viewpoint of the present theoretical model. Two ZnSe/ZnSSe heterostructures were studied. One is an n-i-i heterostructure diode where the upper ZnSSe cladding layer was left undoped [12], and the other is a p-i-n heterostructure where the upper  $\text{ZnS}_{0.09}\text{Se}_{0.91}$  cladding layer was doped p-type with nitrogen incorporation [13]. An Au electrode was used in both heterostructures.

The  $I$ - $V$  characteristics measured for the n-i-i heterostructure with pulsed operation are shown by the closed circles in Fig. 6. A reasonable fit assuming a tunneling current was not possible in this case, and the low bias range was fitted by considering only thermionic emission. The barrier height was estimated to be 0.37 V from the fitting. The increase above the solid line is taken to be the contribution of the electron current flowing over the active layer. This interpretation is consistent with the optical properties observed for this diode [12].

The  $I$ - $V$  characteristics measured on the p-i-n heterostructure are shown by the closed circles in Fig. 7. The  $I$ - $V$  characteristics below a voltage of 6 V were fitted reasonably well with the barrier height of 0.37 V and a net acceptor concentration of  $8 \times 10^{17} \text{ cm}^{-3}$ . The current flow for the higher bias was much lower than this fitting curve. This deviation may be due to a reduction of the net acceptor concentration from the metal/semiconductor interface toward the p-n junction. The curves calculated assuming reduced net acceptor concentrations shown in Fig. 7 give a reasonable interpretation. There are two possible explanations for this phenomenon. The heterostructure was grown at  $560^\circ\text{C}$  by MOVPE, and

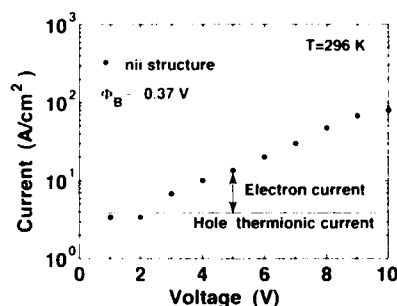


Fig. 6.  $I$ - $V$  characteristics (●) measured on an i-i-n diode grown by MOVPE and theoretical fit considering thermionic emission (—).

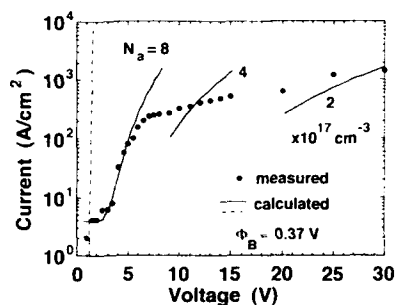


Fig. 7.  $I$ - $V$  characteristics (●) measured for a p-i-n diode grown by MOVPE and theoretical fit considering tunneling current and thermionic emission (—). For a reasonable fit at higher bias, a reduced net acceptor concentration toward the p-n junction was assumed.

diffusion of iodine from the lower n-type cladding layer into the upper-grown layers has been suggested [12,13]. This depth-dependent compensation may be one possibility. The other is the possible desorption of hydrogen from the grown surface during the cooling. This may recover some nitrogen acceptors near the surface.

In both cases, the barrier height at the Au/ZnSse contact was estimated to be 0.37 V, which is lower than the barrier height of 0.61 V estimated for the diode laser [1]. This result is consistent with the much improved  $I$ - $V$  characteristics in the p-n diodes grown by MOVPE compared with laser diodes grown by MBE [12,13]. This also suggests that the barrier height is dependent on the growth methods and growth conditions. Therefore lowering of the barrier height may be possible by adjusting these conditions.

## 5. Conclusion

Dependence of the II-VI diode  $I$ - $V$  characteristics on physical parameters was studied using a recently developed theoretical model. For the reduction of the diode voltage at high currents, a reduction of the metal/semiconductor barrier height below 0.3 V and net acceptor concentrations above  $1 \times 10^{18} \text{ cm}^{-3}$  will be necessary. It has been shown that a lower barrier height was possible in heterostructure diodes grown by

MOVPE. This shows that the barrier height is not a fixed parameter but can be adjusted by, for example, the selection of growth method. The relation between the measurement of ohmic contact resistance and the diode voltage for laser operations was discussed. It was shown that the current flow mechanism is different between the two cases and that this resulted in apparently inconsistent characteristics.

## 6. Acknowledgments

This work was supported in part by a Grant-in-Aid for Scientific Research from the Ministry of Education, Science and Culture, No. 04402032.

## 7. References

- [1] M.A. Haase, J. Qiu, J.M. DePuydt and H. Cheng, *Appl. Phys. Lett.* 59 (1991) 1272.
- [2] K. Ohkawa, T. Karasawa and T. Mitsuyu, *Jap. J. Appl. Phys.* 30 (1991) L152.
- [3] R.M. Park, M.B. Troffer, C.M. Rouleau, J.M. DePuydt and M.A. Haase, *Appl. Phys. Lett.* 57 (1990) 2127.
- [4] C.T. Walker, J.M. DePuydt, M.A. Haase, J. Qiu and H. Cheng, 7th Trieste Semiconductor Symp., Trieste, 1992, paper We-am-1.
- [5] A.V. Nurmikko, R.L. Gunshor, N. Otsuka and M. Kobayashi, in: *Extended Abstracts 1992 Int. Conf. on Solid State Devices and Materials*, Tsukuba, 1992, p. 342.
- [6] J.M. Gaines, R.R. Drenten, K.W. Habernern, T. Marshall, P. Mensz and J. Petruzzello, *Appl. Phys. Lett.* 62 (1993) 2462.
- [7] S. Itoh, N. Nakayama, H. Okuyama, T. Ohata, M. Ozawa, K. Nakano, A. Ishibashi, M. Ikeda, K. Akimoto and Y. Mori, in: *Extended Abstracts 1993 Int. Conf. on Solid State Devices and Materials*, Chiba, 1992, p. 53.
- [8] Y. Lansari, J. Ren, B. Sneed, K.A. Bowers, J.W. Cook and J.F. Schetzina, *Appl. Phys. Lett.* 61 (1992) 2554.
- [9] Y. Fan, J. Han, L. He, J. Saraie, R.L. Gunshor, M. Hagerott, H. Jeon, A.V. Nurmikko, G.C. Hua and N. Otsuka, *Appl. Phys. Lett.* 61 (1992) 3160.
- [10] J. Ren, K.A. Bowers, R.P. Vaudo, J.W. Cook, J.F. Schetzina, J. Ding, H. Jeon and A.V. Nurmikko, *J. Crystal Growth* 117 (1992) 510.
- [11] I. Suemune, *Appl. Phys. Lett.* 63 (1993) 2612.
- [12] Y. Fujii, I. Suemune, K. Okamoto, M. Fujimoto and K. Okamura, in: *Extended Abstracts 1993 Int. Conf. on Solid State Devices and Materials*, Chiba, 1992, p. 65.
- [13] I. Suemune, Y. Fujii and M. Fujimoto, *J. Crystal Growth* 138 (1994) 750.

## Gain and dynamics in ZnSe-based quantum wells

J. Ding <sup>\*a</sup>, M. Hagerott <sup>a</sup>, P. Kelkar <sup>a</sup>, A.V. Nurmikko <sup>a</sup>, D.C. Grillo <sup>b</sup>, Li He <sup>b</sup>,  
J. Han <sup>b</sup>, R.L. Gunshor <sup>b</sup>

<sup>a</sup> Division of Engineering and Department of Physics, Brown University, Providence, Rhode Island 01912, USA

<sup>b</sup> School of Electrical Engineering, Purdue University, West Lafayette, Indiana 47907, USA

### Abstract

Gain spectroscopy and population dynamics are investigated in ZnCdSe/ZnSSe/ZnMgSSe separate confinement heterostructure (SCH) diode lasers. Both steady state and time-resolved methods are applied to characterize the dense electron–hole pair gas in the ZnCdSe active quantum well (QW) region from 77 K to room temperature. Effects due to the carrier interaction with optical phonons and electron–hole Coulomb effects are discussed. A direct measurement of the carrier lifetime at pair densities under typical laser conditions has also been obtained.

### 1. Introduction

Good progress is being made with the blue-green diode lasers, where several groups have recently focused on the ZnCdSe/ZnSSe/ZnMgSSe separate confinement heterostructure (SCH) diode lasers [1]. For example, ridge waveguide devices which also incorporate Zn(Se,Te) graded gap ohmic contacts have been realized in the authors' group for CW operation at voltages approaching 4 V at room temperature [1]. A consequence of extended device lifetime (especially under low duty cycle pulsed conditions) is that issues of gain and electron–hole pair population dynamics can now be studied spectroscopically. Such information will be important in the continuing efforts to optimize the optical and electronic designs of the diode lasers. In this paper we present recent results in which the gain

spectra of a SCH diode laser has been determined by a technique which correlates spontaneous emission (through the top of a device) with its stimulated output (through the cleaved facets). In general, gain characterization in the wide gap II–VI diode lasers has so far been very sparse, limited mainly to extraction of the gain coefficient from the threshold current density and without any spectroscopic insight. By applying ultrashort pulse excitation from an external laser source, we have also measured the electron–hole pair lifetime in the SCH structure over a wide range of temperatures.

### 2. Background: gain spectroscopy in optically pumped structures

One of the “optical precursors” to the blue/green diode laser demonstration was the recognition that the (Zn,Cd)Se/ZnSe quantum well (QW) was an effective type I system, with useful

<sup>\*</sup> Corresponding author.

quasi-2D electronic properties [2]. Beyond the demonstration of an optically pumped, pulsed room temperature laser operation [3], this QW was also the subject of a range of spectroscopic studies, including the gain spectroscopy at cryogenic temperatures (typically  $T = 77$  K) in structures which did not incorporate a pn-junction. In this section we wish to highlight some of the principal conclusions of these earlier results in the authors' group, before returning to the diode lasers themselves.

In the low temperature work we raised the basic question about the presence of an exciton component in the stimulated emission in the ZnSe-based QWs. As shown elsewhere, the unusual condition in the ZnSe-based QWs is that the exciton binding energy can be made large enough so that the LO-phonon induced dissociation process into the free e-h pair continuum is much weakened. This circumstance, which is not found in the bulk (or, e.g., in GaAs QWs), allows the excitons to be present in principle not only in absorption, but also in emission beyond liquid helium temperatures. Direct evidence for the presence of "excitonic gain" in the (Zn,Cd)Se MQW structures was obtained by using ultrafast time-resolved spectroscopic methods [4,5]. In these pump-probe experiments (with both beams traveling through the structure perpendicular to layer planes), a form of photomodulation spectroscopy is performed so that the probe pulses measure the optical constants near the  $n = 1$  HH exciton, following the intense short pulse excitation at time  $t = 0$ . Fig. 1 shows the results of one such experiment at  $T = 77$  K for a structure housing six (Zn,Cd)Se QWs, each of 30 Å thickness. The gain/absorption spectrum measured by the probe 10 ps after the resonant excitation by the pump is displayed, as well as the absorption in the absence of excitation (establishing the exciton resonance profile for reference). Note that while most of the exciton resonance is maintained (as an absorptive entity), large reduction of absorption as well as actual presence of gain is realized on the low-energy tail of the resonance. In a sample with cleaved end facets, laser emission ensues at a photon energy consistent with the position of maximum gain. The experimental ac-

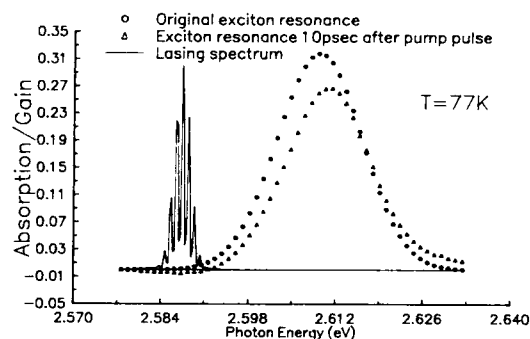


Fig. 1. Gain/absorption spectra of a (Zn,Cd)Se/ZnSe MQW sample, obtained in the transient pump-probe experiment at  $T = 77$  K. The open circles show the  $n = 1$  HH exciton absorption in the absence of the pump, while closed triangles show the optical properties of the photoexcited QW at 10 ps following the pump pulse. The laser emission spectrum obtained in a separate optical pumping experiment on a cleaved sample is also shown, coinciding spectrally to the presence of gain at around  $h\nu \approx 2.588$  eV.

curacy is such that the actual measurement of the gain coefficient ( $g \approx 1500 \text{ cm}^{-1}$  at  $h\nu = 2.588$  eV) is possible. The details of observed dynamical behavior can be understood on the basis of broadening of the exciton absorption line by exciton-exciton collisions, followed by the exciton population energy relaxation to the low energy tail, where gain develops. Both from the standpoint of the typical electron-hole pair densities at laser threshold ( $\sim 5 \times 10^{11} \text{ cm}^{-2}$  at 77 K) and from the experimental observation of the remaining presence of (a partially saturated) exciton resonance in pump-probe experiments, we deduced that a free electron-hole plasma is clearly not present at cryogenic temperatures (e.g. at  $T = 77$  K), and appears to play a much diminished role even at higher temperature conditions.

These experimental results beg the question as to the importance of Coulomb interactions between the carriers in the new blue/green diode lasers, under room temperature conditions. In the decades-old standard model, where gain and stimulated emission are retrieved from a degenerate free-electron-hole plasma (EHP), the allowance for the many-body electron/hole Coulomb interactions (exchange and correlation) can be made to first order by simply renormaliz-

ing the bandgap according to a density dependence (which is also a function of the dimensionality of the system). In the new II–VI QW lasers, given the clear evidence of excitonic component at cryogenic temperatures, a fundamental question exists about the relationship between the pairwise Coulomb correlations and the two-component Fermi liquid; that is, how and under what conditions does a transition from one to the other take place.

Another issue of practical consequence on gain characteristics which draws from the polar nature of ZnSe-based II–VI semiconductors is the very strong coupling of electron–hole pairs with the longitudinal optical (LO) phonons via the Fröhlich interaction. Major consequences of this for a room temperature light emitter are: (a) broadening of optical linewidths and (b) decrease in the carrier mobility, especially for holes. A measure of the former can be obtained from the linewidth of the exciton resonance in a ZnCdSe/ZnSe QW as a function of temperature [6]. Beyond cryogenic elevated temperatures, the Fröhlich interaction (scattering of the electron–hole pair by the phonons) manifests itself by a pronounced increase in the exciton absorption linewidth. Such a broadening would similarly “smear” the ideal 2D density of states edge in the gain spectrum of a ZnCdSe QW laser regardless of the detailed model used (exciton or EHP). We note that this effect is 6–8 times larger than in GaAs lasers (based on the ratio of the known Fröhlich constants). Elsewhere, in p-ZnSe, mobility measurements have recently yielded values on the order of  $\mu \approx 35\text{--}39 \text{ cm}^2/\text{V}\cdot\text{s}$  at  $T = 300 \text{ K}$  [7] and lower [8]. Such low values (even if containing extrinsic scattering contributions) indicate the severity of the polar mode (LO-phonon) scattering for holes through the prism of a transport experiment. (In unstrained bulk material, of course, the dominant hole state is the heavy mass one corresponding to the  $J = 3/2$  state at  $k = 0$ .)

A pedagogical schematic illustration of the impact of the interaction between LO-phonons and e–h pairs on the gain of a QW laser is shown in Fig. 2, in which the calculated gain spectra (the zero in the horizontal axis corresponds to the band gap) in a simple electron–hole plasma

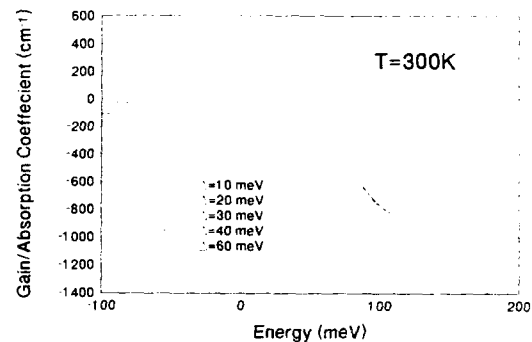


Fig. 2. Gain in a ZnCdSe/ZnSSe QW, calculated in an ideal 2D electron–hole system in the one-electron model at  $T = 300 \text{ K}$ , showing the effects of scattering (characterized by a broadening parameter  $\Delta$  in units of meV).

(EHP) model is shown for a (Zn,Cd)Se/Zn(S,Se) case at room temperature. Only the  $n = 1$  levels in the conduction band and HH valence band are considered. In this calculation, we use the following values for the in-plane effective masses:  $m_c = 0.147m_0$  and  $m_{\text{HH}} = 0.33m_0$ . The scattering is included by convolving the product of the density of states and the Fermi distribution by a Lorentzian lineshape function with linewidth parameter  $\Delta$ . In general, the choice of this lineshape function depends on the physical model of the scattering for the carriers [9]; in particular for the very large broadening which may occur in the II–VI lasers, the validity of the usual adiabatic approximations have to be re-examined. The assumed e–h pair density in a  $L_w = 100 \text{ Å}$  well has been taken as  $n_e = 3 \times 10^{12} \text{ cm}^{-2}$ , a value which is in the range of typical experimental conditions. In this example, note how the sharp 2D density-of-states edge is quickly eliminated and the peak gain is suppressed. At the same time, for moderate broadening, gain becomes available below the 2D bandgap. For this injection density, no gain is available when  $\Delta$  exceeds a value of about 30 meV.

### 3. Experimental results: gain spectroscopy of SCH diode lasers

The ZnCdSe/ZnSSe/ZnMgSSe separate confinement heterostructure diode laser structures



were grown by molecular beam epitaxy in a two chamber machine, on n-GaAs buffer layers and substrates. The active ZnCdSe QW layer(s), of 75 Å thickness, were sandwiched between p- and n-type layers of ZnSSe of approximately 1000 Å in thickness, respectively. The outer p- and n-type cladding layers of ZnMgSSe were approximately 1 μm thick. To facilitate an ohmic contact, a graded gap ZnSeTe ohmic contact layer [10] was grown atop the p-ZnMgSSe. Details of the growth can be found in ref. [11]. Gain guided devices with 20 μm wide stripes were fabricated with indium tin oxide (ITO) top transparent electrodes [12]. Spectroscopy was performed by recording the spontaneous emission through the top electrode and the stimulated (or spontaneous) emission through the cleaved end facets, as shown schematically in Fig. 3a, which also shows the layered heterostructure. Fig. 3b shows an example of the top emission spectra of a device for different levels of current injection at room temperature. The active region of this particular device was composed of three quantum wells. The well thickness was  $L_w = 75$  Å and the separating ZnSSe barriers were  $L_b = 100$  Å thick. The room temperature pulsed threshold current for the laser devices ranged from 280 to 400 mA depending on the lengths. The typical threshold current density was about  $I_{th} \approx 1.4$  kA/cm<sup>2</sup>, i.e. approximately 470 A/cm<sup>2</sup> per QW.

The correlation between spontaneous emission (top emission) and edge-stimulated emission spectra was first employed by Henry et al. to derive actual gain spectra for a GaAs double heterostructure laser [13]. It has been subsequently used to construct detailed gain spectra for GaAs QW diode lasers as well [14]. The formulation is independent of the details of the gain mechanism or the nature of the electronic states that participate in the radiative process, and draws from the fundamental connection between gain and absorption by detailed balance arguments. This leads to the following explicit relationship between the gain spectrum  $g(E)$  and experimental spontaneous emission spectrum  $S(E)$ , where the separation between the quasi-Fermi levels,  $\Delta E_F$ , is also experimentally obtained from the spontaneous emission spectrum

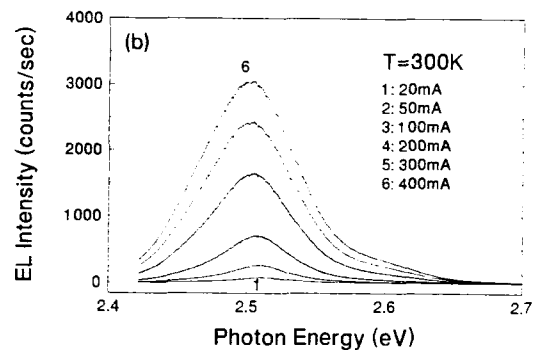
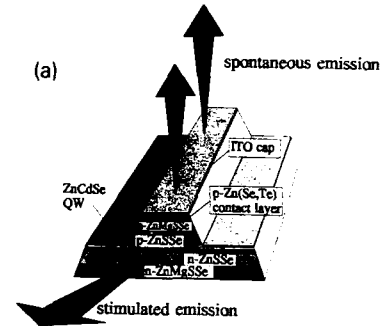


Fig. 3. (a) Experimental geometry for the gain spectroscopy in the ZnCdSe/ZnSSe/ZnMgSSe SCH QW diode laser structures. (b) The spontaneous emission spectra at  $T = 300$  K, obtained through the transparent top electrode at different levels of current injection.

at threshold conditions and the known position of laser emission:

$$g(E, \Delta E_F) = C \frac{S(E)}{E^2} \left[ 1 - \exp\left(-\frac{E - \Delta E_F}{kT}\right) \right].$$

In this expression,  $C$  includes fundamental constants and experimental amplitude calibration factors. By following such an approach, and with input provided directly from our experiments, Fig. 4 shows the results for the gain spectrum of a typical SCH QW diode laser at  $T = 77$  K and at room temperature, for different levels of current injection. While spectral lineshapes can be reliably obtained by the technique, quantitative calibration of the vertical axis is difficult. Hence we

have found it more reliable to obtain such calibration from the cavity length dependence of the threshold current. The peak modal gain coefficient at threshold condition for this particular device is determined to be  $48 \text{ cm}^{-1}$ . On the low energy side (e.g. for  $\hbar\omega < 2.47 \text{ eV}$  at  $T = 300 \text{ K}$ ), the value of gain is substantially larger than the original absorption, indicative of the impact of the large homogeneous broadening in our system. We comment on these features below. A larger spectral window of gain/absorption spectra at room temperature is shown in Fig. 5, where the unambiguous presence of both the  $n = 1$  HH and LH exciton resonances is quite evident at photon energies of  $\hbar\omega = 2.52 \text{ eV}$  and  $2.625 \text{ eV}$ , respectively, when the injection current is low. The identification of the LH state is made clear by analyzing the polarization of the edge emission at

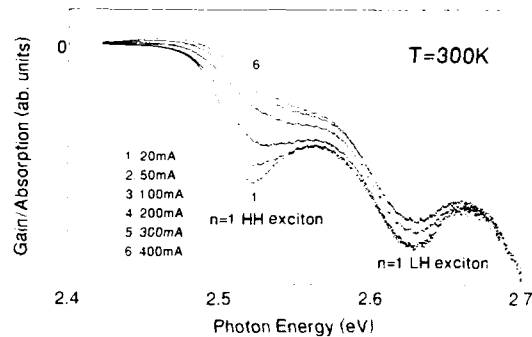


Fig. 5. A wider spectral view of the gain/absorption spectrum of a SCH device, showing the effects of injection on the HH and LH exciton states from below to above the laser threshold.

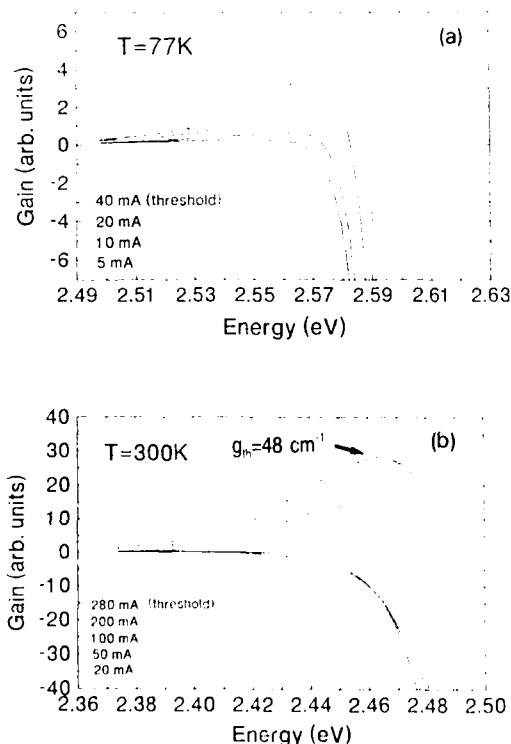


Fig. 4. Gain spectra obtained for a SCH QW diode laser at  $T = 77 \text{ K}$  and  $300 \text{ K}$  for different levels of current injection.

around  $2.62 \text{ eV}$ . (The uniaxial strain in the ZnCdSe QW (in our pseudomorphic structures) splits the HH and LH bands such that the in-plane mass for the HH state is relatively light ( $m_{\parallel} \approx 0.33m_0$ ), while that for the LH state is heavier ( $m_{\parallel} \approx 0.5m_0$ ). Precise mass values require taking into account the mixing between the HH and LH states which occurs away from  $k = 0$ .)

Another important and useful experimental parameter in the new blue/green laser diodes which has not been directly measured so far is the electron-hole pair lifetime. This quantity is required, for example, to calculate the pair density in the QW for a given injection level in modeling of the laser and its gain quantitatively. We have performed time-resolved photoluminescence experiments in the same SCH diode laser structures, where ultrashort (picosecond) pulses from a tunable dye laser have been used as the source of excitation. The photon energy of this excitation was carefully controlled to coincide with the absorption edge of the ZnSSe ternary, hence mimicking the carrier injection under actual diode laser operating conditions. A wide range of excitation conditions have been studied in order to distinguish between radiative and nonradiative contributions to the decay of the transient luminescence. For example, sufficient levels of excitation were required for these SCH structures in order to saturate defect and impu-

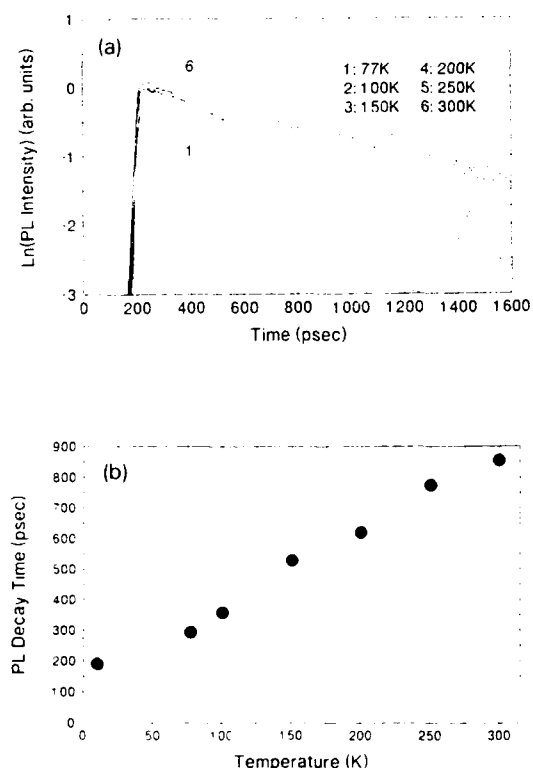


Fig. 6. (a) Photoluminescence intensity (natural log scale) as a function of time for several temperatures, measured at the QW emission wavelength. (b) Summary of lifetime measurements from  $T = 10$  K to room temperature.

rity related traps. A relatively high excitation level is also necessary in an unbiased device in order to shunt the built-in depletion field at the QW position, which otherwise interferes with the lifetime measurements (by separating the electron-hole pairs and hence acting like a fast photodetector). Fig. 6a shows an example of the actual experimental data of transient luminescence signals from  $T = 77$  K to 300 K (on semilogarithmic scale), under optical excitation at a level which is equivalent to a current injection of 200 mA (below laser threshold). A single exponential decay is dominant. Fig. 6b summarizes a portion of our lifetime measurements, displaying the decay time constant as a function of temperature from  $T = 10$  K to room temperature.

#### 4. Discussion

The experimentally derived gain and absorption spectra in Figs. 4 and 5 provide a heretoforth largely unavailable glimpse at the operation of the SCH diode laser. The gain spectra of Fig. 4 at room temperature show a striking, nearly exponential tail. There are at least three contributions to the low energy tail: (i) Alloy potential fluctuations, which add an inhomogeneous contribution of approximately 6–7 meV for the Cd composition in our structures ( $x \sim 0.15$ ) (in good agreement with the experimentally observed low-temperature exciton absorption linewidth). (ii) the Fröhlich interaction which is a major contributor to homogeneous linewidth broadening of optical resonances in the ZnSe-based QWs at room temperature. This effect can add on the order of 20–50 meV to the linewidth (depending on the details of the QW configuration, e.g. in terms of the particular hole states that are involved). (iii) The many body interaction (scattering) in the many particle electron-hole gas, either direct or intermediated by phonons, makes another contribution at higher carrier densities. (Under typical laser diode conditions, e-h pair densities are not yet high enough to significantly screen the Fröhlich interaction.)

While leaving the more detailed analysis of the gain spectral lineshape elsewhere, we note that the result in Fig. 4 contains dominant contributions from processes (ii) and (iii). The contribution from the equilibrium LO-phonon population has been already referred to, including its prior experimental approximate quantification [6]. The importance of carrier-carrier interaction and carrier-nonequilibrium phonon interaction (phonons emitted by the carriers during their energy relaxation processes) can be directly seen in the linewidth of the spontaneous emission spectrum in the bottom panel of Fig. 3, which increases substantially at higher injection levels. The role of the carrier-carrier scattering can be addressed in two limits as Coulomb interactions in terms of a pairwise contribution (exciton-like bound states) or that in a many-body Fermi liquid, respectively. The former was already shown to be important in stimulated emission at cryogenic temperatures in

the optical pumping experiments on ZnCdSe QWs in Fig. 1. At room temperature under high injection conditions, the distinction between the two limits is much more difficult to detail theoretically and experimentally, and may in fact be to some extent unrecognizable in practice. However, the fact that electron–hole Coulomb effects remain important in our diode lasers is strongly suggested by the data in Fig. 5. At low levels of injection, the HH and LH exciton resonances are initially clearly visible. Increase in the injection level seems to nearly saturate the HH exciton resonance, while gain appears on the low-energy side of the HH exciton spectrum. Under these conditions, where the exciton resonance merges (or begins to) into the EHP, the pairwise correlations seems to remain strong, in a many-body analog to the continuum states of a single exciton.

Further evidence on the impact of the e–h Coulomb interactions on the interband matrix elements is obtained directly by the electron–hole lifetime measurements. Other evidence not shown here strongly supports the conclusion that the lifetime data in Fig. 6 is measured in the *radiative* limit for the ZnCdSe QWs. This is consistent with the roughly linear temperature dependence, expected from both a one-electron theory for radiative recombination (no Coulomb effects) and for excitons. However, when calculating the radiative lifetime  $\tau_{\text{rad}}$  from the one-electron model [15] for the material parameters of ZnSe (in the effective mass approximation), we obtain, e.g., at room temperature a value for  $\tau_{\text{rad}} \geq 5$  ns. This is much longer than the experimentally observed value. This discrepancy can be readily bridged when adding Coulomb effects that enhance the oscillator strength, here under conditions at which the present ZnCdSe QW diode lasers operate.

## 5. Conclusion

We have demonstrated how the new ZnCdSe/ZnSSe/ZnMgSSe SCH diode lasers can be studied at room temperature in terms of their optical spectra near the  $n = 1$  QW state. Gain spectral lineshapes have been derived that show the pro-

nounced effects of contributions by optical phonon scattering and electron–hole interaction. These effects suppress the maximum gain predicted from simple theory, yet provide gain in the low-energy region of the spectrum where optical attenuation by the uninverted portion of the optical volume is reduced. Radiative lifetime data also demonstrate the presence of this interaction, which cannot be ignored on fundamental grounds in the II–VI QW emitters. The appreciation of these effects may be of increasingly practical value as novel diode laser designs are pursued.

## 6. Acknowledgement

Research supported by the ARPA/URI, NSF, and AFOSR.

## 7. References

- [1] J.M. DePuydt et al., *J. Crystal Growth* 138 (1994) 667; A. Ishibashi and Y. Mori, *J. Crystal Growth* 138 (1994) 677; J. Petruzello, R. Drenten and J.M. Gaines, *J. Crystal Growth* 138 (1994) 686. For the low voltage operation, note also: A. Salokatve, H. Jeon, J. Ding, M. Hovinen, A.V. Nurmikko, D.C. Grillo, Li He, J. Han, Y. Fan, M. Ringle and R.L. Gunshor, *Electron. Lett.* 29 (1993) 2192.
- [2] J. Ding, N. Pelekanos, A.V. Nurmikko, H. Luo, N. Samarth and J. Furdyna, *Appl. Phys. Lett.* 57 (1990) 2885.
- [3] H. Jeon, J. Ding, A.V. Nurmikko, H. Luo, N. Samarth, J. Furdyna, W. Bonner and R. Nahory, *Appl. Phys. Lett.* 57 (1990) 2413.
- [4] J. Ding, H. Jeon, T. Ishihara, H. Luo, N. Samarth and J. Furdyna, *Surf. Sci.* 259 (1992) 616; J. Ding, H. Jeon, T. Ishihara, H. Luo, N. Samarth and J. Furdyna, *Phys. Rev. Lett.* 60 (1992) 1707.
- [5] J. Ding, T. Ishihara, M. Hagerott, H. Jeon, H. Luo, N. Samarth and J. Furdyna, *Phys. Rev. B* 47 (1993) 10528.
- [6] N.T. Pelekanos, J. Ding, M. Hagerott, A.V. Nurmikko, H. Luo, N. Samarth and J. Furdyna, *Phys. Rev. B* 45 (1992) 6037.
- [7] See, e.g., C.T. Walker, J. DePuydt, M.A. Haase, J. Qiu and H. Cheng, *Physica B* 185 (1993) 27; Y. Fan, J. Han, J. Saraie, R.L. Gunshor, M. Hagerott and A.V. Nurmikko, *Appl. Phys. Lett.* 63 (1993) 1812.
- [8] Z. Yang, K.A. Bowers, J. Ren, Y. Lansari, J.W. Cook, Jr. and J.F. Schetzina, *Appl. Phys. Lett.* 61 (1993) 2671.

- [9] See, e.g., M. Asada, Intraband relaxation effect on optical spectra, in: *Quantum Well Lasers*, Ed. P. Zory (Academic Press, San Diego, CA, 1993) pp. 97–130.
- [10] Y. Fan, J. Han, L. He, J. Saraie, R.L. Gunshor, M. Hagerott, H. Jeon, A.V. Nurmikko, G.C. Hua and N. Otsuka, *Appl. Phys. Lett.* 61 (1992) 3160.
- [11] D.C. Grillo, Y. Fan, J. Han, H. Li, R.L. Gunshor, M. Hagerott, H. Jeon, A. Salokatve, G. Hua and N. Otsuka, *Appl. Phys. Lett.* 63 (1993) 2723.
- [12] M. Hagerott, H. Jeon, J. Ding, A.V. Nurmikko, W. Xie, D.C. Grillo, M. Kobayashi and R.L. Gunshor, *Appl. Phys. Lett.* 60 (1992) 2825.
- [13] C.H. Henry, R.A. Logan and F.R. Merritt, *J. Appl. Phys.* 51 (1980) 3042.
- [14] M.P. Kesler and C. Harder, *Appl. Phys. Lett.* 57 (1990) 123; P. Blood, A.I. Kucharska, J.P. Jacobs and K. Griffiths, *J. Appl. Phys.* 70 (1991) 1144.
- [15] See, e.g., G. Lasher and F. Stern, *Phys. Rev.* 133 (1964) A553.



ELSEVIER

Journal of Crystal Growth 138 (1994) 727-736

JOURNAL OF  
**CRYSTAL  
GROWTH**

## Comparison of GaN- and ZnSe-based materials for light emitters

Takashi Matsuoka \*, Akira Ohki, Tetsuichiro Ohno, Yoshihiro Kawaguchi

*NTT Opto-electronics Laboratories 3-1, Morinosato Wakamiya, Atsugi-Shi, Kanagawa Pref. 243-01, Japan*

### Abstract

Recent progress in research on GaN- and ZnSe-related materials is remarkable. Based on these results, this paper compares the characteristics of GaN- and ZnSe-based materials from the viewpoint of achieving reliable light emitting devices, in particular laser diodes (LDs) based on experience gained in the development of LDs such as the InGaAsP/InP and GaAs/AlGaAs LDs widely used at present. The relationship between lattice constant and bandgap energy, the dispersion of refractive indices, the equilibrium vapor pressure of elements over materials, and self-diffusion coefficients can be compared. The current status of both materials is reviewed with respect to light emitters. The transport devices are also described, briefly. Finally, future prospects are discussed.

### 1. Introduction

Research on GaN- and ZnSe-related materials has greatly progressed during the last few years, coming out of a long dark tunnel. In ZnSe, control of the conduction type, which is the most difficult problem, has been achieved by molecular beam epitaxy (MBE). In 1991, a ZnCdSe/ZnSe quantum well laser diode (LD) successfully demonstrated pulsed operation at room temperature [1]. At present, many researchers are striving to achieve reliable and stable CW operation of blue and blue-green lasers. Meanwhile, high-quality GaN has been grown by metalorganic vapor phase epitaxy (MOVPE) [2,3] and its conduction type has been successfully controlled. Single crystals of InN and InGaN have also been grown [4]. A GaN/AlGaIn double-heterostructure (DH) has

shown optically pumped lasing in the UV region at room temperature. High efficiency InGaIn/GaN DH structure light emitting diodes have been also obtained.

In this paper, at first the characteristics of GaN- and ZnSe-based materials from the viewpoint of achieving reliable light emitting devices are compared, in particular LDs based on experience gained in the development of LDs such as the InGaAsP/InP and GaAs/AlGaAs LDs widely used at present. The relationship between lattice constant and bandgap energy, the dispersion of refractive indices, the equilibrium vapor pressure of elements over materials, self-diffusion coefficients can be compared. In contrast, band discontinuity, optical gain and absorption coefficient cannot be easily discussed because there are few clear data. For the reliability of light emitting devices, dislocation behavior and surface recombination velocity are important with respect to dark line defects and catastrophic optical damage

\* Corresponding author.

at facets, respectively, but they have not been studied. Next, the application of these wide-gap materials for transport devices are reviewed briefly. Finally, the future prospects of these materials for light emitters are discussed.

## 2. Requirements of materials for light emitters

To realize high-performance light emitters, in particular laser diodes, the following characteristics are required for materials [5]. Naturally, the crystal quality is the most important thing. This is because the purity and dislocation density affect conduction-type control, radiative recombination and device lifetime. Next, for high performance light emitters, DH structure is indispensable. To ensure carrier confinement in the active region, the discontinuity between active and cladding layers in the valence and conduction bands must be more than 200 meV. Moreover, for optical confinement, the difference of refractive indices has

to be greater than 10%. Regarding device fabrication, tough electrodes with a low built-in voltage are needed. Cleaved mirror facets are better, but of course, an etched mirror would also do.

## 3. Comparison of GaN- and ZnSe-based materials

At the beginning of comparison of GaN- and ZnSe-based materials, the properties of ZnSe and GaN, and the technologies used for them are shown in Table 1. Here, GaN with a wurtzite structure is discussed. As substrates for GaN and ZnSe growth, the (0001) plane of sapphire and the (001) plane of GaAs are usually used, respectively. Sapphire does not have a wurtzite structure, but it is similar to GaN. The lattice mismatch between GaN and (0001) plane of sapphire is 13.8%. This is much larger than the mismatch between ZnSe and GaAs. However, introducing AlN and GaN buffer layers [2,3], good quality

Table 1  
Properties and present technology of ZnSe and GaN

Item	ZnSe	GaN
Melting point (°C)	1520	1700
Thermal conductivity (W/K·cm)	0.19	1.3
Substrate	GaAs	(0001) sapphire
Lattice mismatch <sup>a</sup> ( $a_{\text{epi}} - a_{\text{sub}})/a_{\text{sub}}$ (%)	3	13.8
Thermal expansion coefficient ( $\alpha_{\text{epi}} - \alpha_{\text{sub}})/\alpha_{\text{sub}}$ (%)	13.7	-25.5 (a-axis)
Growth method	MBE, MOVPE	MOVPE
Etch pit density (cm <sup>-2</sup> )	10 <sup>4</sup> - 10 <sup>7</sup>	Undefined
X-ray rocking curve width (arc sec)	~ 20	~ 100
Acceptor (300 K)		
Dopant	N	Mg (LEEBI <sup>b</sup> )
Concentration (cm <sup>-3</sup> )	1 × 10 <sup>18</sup>	3 × 10 <sup>18</sup>
Mobility (cm <sup>2</sup> /V·s)	10-20	15
Donor (300 K)		
Dopant	Cl	Si
Concentration (cm <sup>-3</sup> )	10 <sup>19</sup>	10 <sup>19</sup>
Mobility (cm <sup>2</sup> /V·s)	~ 200	~ 200
Electrode		
p-Type	Schottky (Au)	Ohmic (Al)
n-Type	Ohmic (In)	Ohmic (Au)
Cleavability of crystal	Yes	No

<sup>a</sup> Lattice constant along c-axis.

<sup>b</sup> LEEBI: low-energy electron-beam irradiation.

films can be grown, and a typical X-ray rocking curve width of 100 arc sec has been achieved.

The p-type dopant for GaN is magnesium. It is activated by low-energy electron-beam irradiation at an acceleration voltage of 15 kV [6]. Thermal activation is also possible [7].

Regarding electrodes, the ohmic contacts for both p- and n-type GaN can be easily formed using aluminum and gold, respectively. Meanwhile, for ZnSe, p-type electrode formation is difficult. There have been some attempts, but they are not sufficient for LDs which need low voltage and high current density.

Further comparison items besides Table 1 are discussed below.

### 3.1. Relationship between lattice constant and bandgap energy

The relationship between lattice constant and bandgap energy is a basic consideration for device fabrication. The relationship between the bandgap energy and lattice constant of various materials is shown in Fig. 1. The bandgap energy of the InGaAlN system ranges from 2 to 6.2 eV. This corresponds to a wavelength of 200 to 600 nm, i.e., from ultraviolet to red. From this figure, in order to form a DH structure under lattice-matching conditions which are desirable, the InGaAlN system seems to have an advantage over

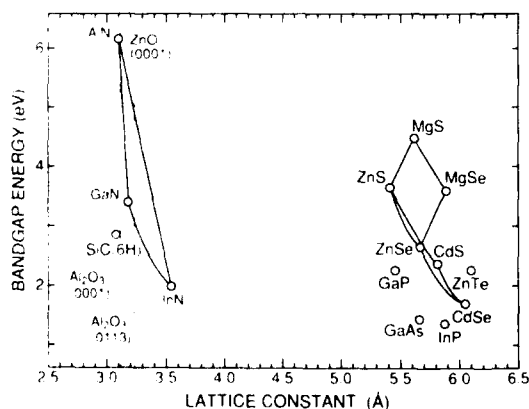


Fig. 1. Relationship between bandgap energy and lattice constant.

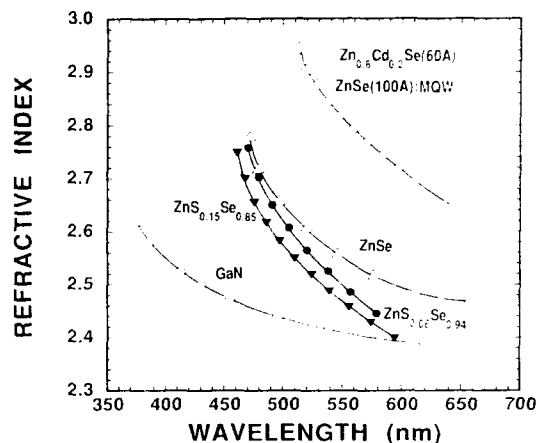


Fig. 2. Dispersion of refractive indices. GaN data from ref. [9].

II-VI systems. Regarding growth, the most important things are to obtain heteroepitaxial growth and lattice-matching between the substrate and the film. Unfortunately, there is no substrate for homoeptitaxial growth yet. In this figure, some candidate materials for substrates are also shown, by open circles for II-VI systems and by dotted lines for InGaAlN systems.

### 3.2. Dispersion of refractive indices

For the design of light emitters, the refractive index, in particular its dispersion near the band edge, is very important. But this dispersion near the band edge is generally unknown. The dispersion of refractive indices is shown in Fig. 2. ZnSe, ZnSSe, and ZnCdSe/ZnSe multi-quantum wells (MQWs) were grown on GaAs substrates. The peak wavelength in photoluminescence of ZnCdSe/ZnSe MQWs was 520 nm. These data were measured using the interference in the reflectivity [8]. Detailed data will be reported elsewhere. For GaN, the dispersion measured by Ejder [9] is plotted. A steep increase of refractive indices for all the films can be observed near their bandgaps. The dispersion for GaN is noticed to be a little softer than for the ZnCdSSe system, as shown in this figure. The difference in refractive index of ZnSe and MQWs is greater than 10%, which is just what is required.



### 3.3. Equilibrium vapor pressure of groups V and VI over II-VI and III-V materials

The equilibrium vapor pressure of elements over compounds must be checked to obtain good crystal growth and stable crystals. The equilibrium vapor pressure of V and VI elements over compounds is shown in Fig. 3 [5,10]. For comparison, the pressure of group V elements over GaAs and InP is also shown. This pressure corresponds to a partial pressure of group V and VI elements dissolved in group II and III melts, and in equilibrium with the solid phase. This pressure affects MOVPE growth more severely than MBE because the growth in MOVPE occurs much closer to thermal equilibrium. For instance, the nitrogen pressure of InN is the highest among these binary materials. Therefore InN growth requires a very high nitrogen pressure. This pressure also shows the stability of materials under high temperature. This figure suggests that the InGaAlN system, except for InN, is more stable under high temperature than II-VI materials.

### 3.4. Self-diffusion coefficient

The last item for comparison is self-diffusion. This seems to be related to defects, such as dislocations and deep states. The self-diffusion

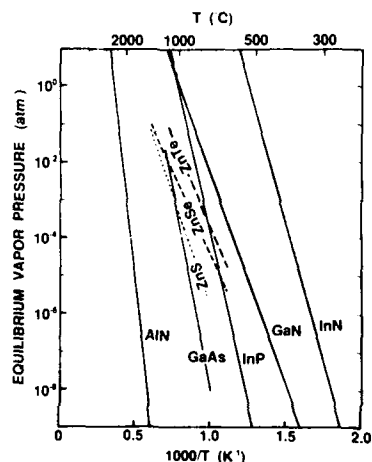


Fig. 3. Equilibrium vapor pressure of group III and VI elements over II-VI and III-V materials, after refs. [5] and [10].

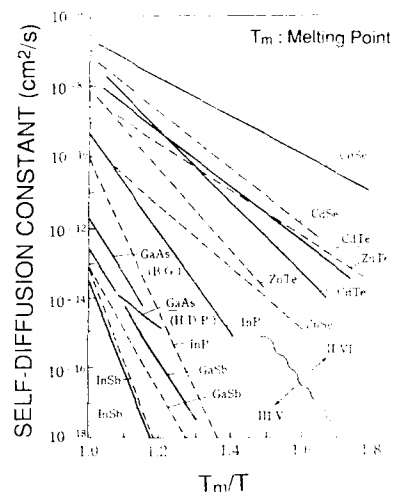


Fig. 4. Self-diffusion coefficient, after ref. [11].

coefficient is important for the stable operation of a device with a layer structure. The self-diffusion coefficient versus the reciprocal reduced temperature,  $T_m$  over  $T$ , is shown in Fig. 4 [11]. Here,  $T_m$  is the melting point. It is instructive to compare the self-diffusion coefficients of III-V and II-VI materials. These coefficients for II-VI compounds can be found to be about 3 orders of magnitude higher than those for the III-V materials. This may account for the pronounced compensation effects in II-VI materials, which result from the formation of defect-impurity complexes.

For the InGaAlN system, the data are not clear. However, judging from the equilibrium vapor pressure, the self-diffusion coefficients are probably similar to those of other III-V materials. Therefore, defect generation and other types of degradation may be less severe than in II-VI systems.

## 4. Current status of GaN- and ZnSe-based materials

In this section, the current status of growth, doping, and light emitters is reviewed. Finally, some transport devices are also reviewed.

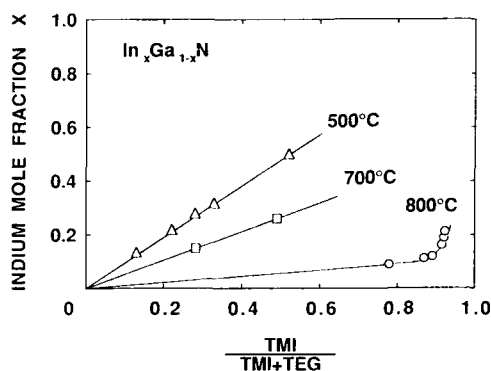


Fig. 5. Composition control of InGaIn, after ref. [12].

#### 4.1. InGaIn system for light emitters

##### 4.1.1. Composition control of InGaIn

One important issue is composition control, so at first let us describe the composition control of the ternary crystal InGaIn [12]. The growth method was MOVPE, and the source gases were trimethylindium (TMI), triethylgallium (TEG), and ammonia. The carrier and bubbling gases were nitrogen. The flow rate ratio of ammonia to the group III sources was generally between 2000 and 20000. The growth temperature was from 500 to 800°C. The reactor pressure was a constant 76 Torr. To obtain a high-quality crystal, the sapphire substrates were first annealed at 1150°C in ammonia to nitride the surface. Fig. 5 shows the relationship between the indium mole fraction of InGaIn and the flow rate ratio of indium to the sum of the group III sources. The data are for the growth of a mirror-smooth single crystal on a sapphire substrate at temperatures of 500, 700 and 800°C. The indium mole fraction was estimated from the lattice constant determined by X-ray diffraction measurements, using the assumption that they have a linear relationship. The first thing to notice is that the incorporation of indium drops as the temperature rises. This is probably because the vapor pressure of indium is higher than that of gallium. Another thing is that, at a temperature of 800°C, indium incorporation rises steeply when the flow rate ratio goes above 0.9. In InGaIn grown at a temperature of 800°C,

the observed photoluminescence showed that the band-to-band emission shifted toward a longer wavelength as the indium mole fraction was increased [13].

In single-crystal GaInN, composition control is possible up to an aluminum mole fraction of 0.4 [14].

##### 4.1.2. Lattice-matching growth

In the growth of the InGaIn system, a (0001) plane sapphire substrate is most commonly used. As shown in Table 1, 13.8% of lattice-mismatching between this substrate and GaN exists. As shown in Fig. 1, the lattice constant of the (0113) plane sapphire comes near that of GaN and this new plane, (0113), would seem to be more suitable. Actually, a GaN film grown on this substrate without a buffer layer had been reported to show good crystal quality [12]. The (0001) plane of ZnO actually falls within the InGaIn triangle, and would be even better for DH structures for optical devices. Therefore the lattice-matching growth on a ZnO substrate had been attempted. Since single crystals of ZnO are not commercially available, bulk ZnO single crystal was grown and this substrate was made in our laboratory. Fig. 6 shows the X-ray diffraction spectrum of InGaIn with an indium content of 22% on a ZnO substrate. Only one peak for the InGaIn corresponding to the (0002) plane was observed [12]. The difference in the diffraction

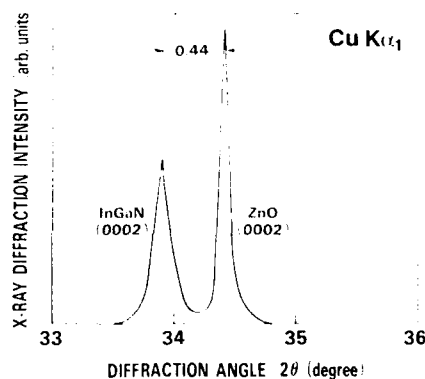


Fig. 6. Lattice-matching growth of InGaIn on ZnO substrate, after ref. [12].

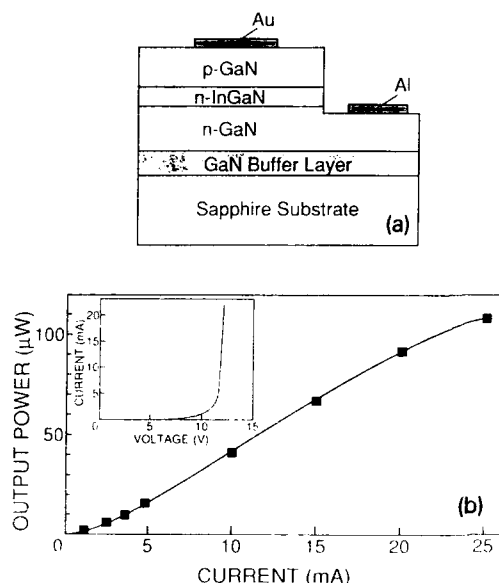


Fig. 7. InGaN/GaN DH LED: (a) structure and (b) characteristics, after ref. [15].

angle of the film and the substrate was  $0.44^\circ$ . This coincides with the difference in the lattice-constant oriented along the  $c$ -axis between ZnO and InGaN, so there is in-plane lattice-matching between InGaN and ZnO.

However, the width of the X-ray rocking curve is larger than that of state-of-the-art III-V materials like GaAs. The reason for this is thought to be that the crystal quality of the ZnO was not very good. In addition, neither the surface treatment of the ZnO nor the growth conditions for InGaN have been optimized yet.

#### 4.1.3. InGaN / GaN DH LED

Fig. 7 shows the structure of an InGaN/GaN DH LED and the output power-current characteristics [15]. n-GaN and n-InGaN were Si-doped, and p-GaN was Mg-doped. The n-InGaN film was 20 nm thick, and had an indium mole fraction of 20%. The GaN was grown at a temperature of  $1000^\circ\text{C}$ , and the InGaN at  $800^\circ\text{C}$ . The emission was blue with a peak wavelength of 440 nm.

#### 4.1.4. Stimulated emission by optically pumping

Fig. 8 shows the device structure used for the demonstration of stimulated emission by optical pumping and the emission spectra [16]. The device had a  $3.5\ \mu\text{m}$  thick n-type GaN layer grown on an AlN buffer layer on a sapphire substrate. The stripe width was about 2 mm. Pumping was performed by a nitrogen laser with a peak power of 250 kW. The threshold pumping power for stimulated emission was  $0.7\ \text{MW}/\text{cm}^2$  at room temperature.

#### 4.1.5. Reactive fast atom beam etching

As shown in Table 1, GaN films and sapphire substrates cannot be cleaved to form the cavity mirrors of laser diodes. Therefore it is desirable to form an etched mirror. GaN is etched with phosphoric acid at a temperature of more than  $150^\circ\text{C}$ . This etchant is unique among the usually used chemicals. However, this etchant was not suitable for the etched mirror, because the etched profile was not perpendicular to the top surface

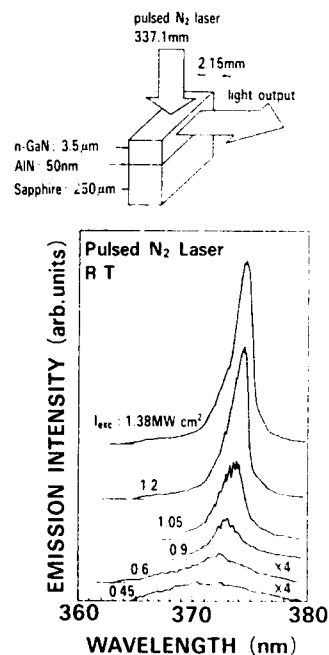


Fig. 8. Stimulated emission from GaN by optically pumping, after ref. [16].



Fig. 9. Reactive fast atom beam etching of GaN.

of the film. On the other hand, in fabrication of GaAs LSIs and optoelectronic devices, dry etching has succeeded. Reactive etching using chlorine-containing gas is one promising method [17-19]. Successful etching of GaN is introduced below [20].

The method used was reactive fast atom beam etching (R-FABE) [19]. The chlorine gas pressure during etching was  $5 \times 10^{-4}$  Torr. The acceleration voltage was about 1.5 kV. The substrate was heated up to 130°C. The etching rate was 100 nm. Here, a hard-baked photoresist was used for the etching masks. After etching, these photoresist masks were removed by oxygen plasma. Fig. 9 shows a bird's eye view of an etched GaN film grown on a sapphire substrate. The rather smooth surface perpendicular to the top surface can be observed.

One problem with using a high kinetic energy is that it can damage the samples, but there is no damage at all with this method because of high etching rate. This has been confirmed using GaAs laser diodes. Therefore, R-FABE can make it possible to form etched mirror facets for lasers. Moreover, the etching rates of sapphire and photoresist are less than one tenth of the rate of GaN. This suggests that the R-FABE technique has good potential for selective etching of epitaxial films. GaN islands on a sapphire substrate can be fabricated easily using this technique.

#### 4.2. II-VI materials

##### *Increase of acceptor concentration using tilted substrate*

In order to stable operation in a laser diode, the doping method must provide both high doping concentration and stable doping. As one way to achieve this, using a tilted substrate has been proposed [21]. Fig. 10 shows the dependence of the acceptor concentration on the tilt angle of GaAs substrates. To supply acceptors, nitrogen was doped using RF plasma cell [22]. Then, the concentration was measured by the double Schottky  $C-V$  method. The solid circles are for substrates tilted in the  $\langle 111 \rangle A$  direction, and the open circles are for  $\langle 111 \rangle B$ . Films were grown simultaneously on all the substrates tilted in the same direction. The data for the nominal (100) substrates show how much the concentration varied from run to run. However, the important point is that, regardless of the direction of tilt, the net acceptor concentration on tilted substrates is twice as large as for (100) substrates. The exception to this is (111) substrates, which had a high resistivity.

From secondary ion mass spectrometry measurements, a higher acceptor concentration on tilted substrates was concluded, due to better nitrogen incorporation.

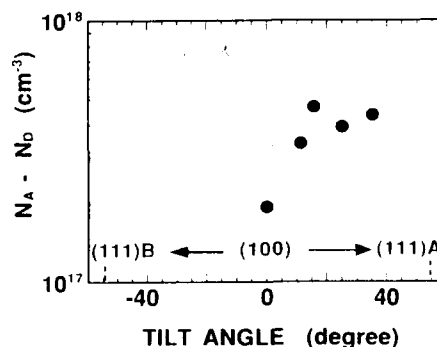


Fig. 10. Dependence of acceptor concentration on tilt angle of substrate, after ref. [21]. The solid circles are for substrates tilted in the  $\langle 111 \rangle A$  direction and the open circles are for  $\langle 111 \rangle B$ .

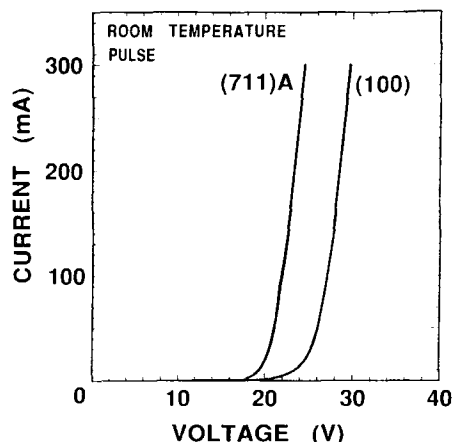


Fig. 11. Current-voltage characteristics, after ref. [21].

The effect of the higher acceptor concentration on laser diode characteristics was investigated. The LDs fabricated had a separate-confinement heterostructure with a ZnCdSe/ZnSe MQW active layer [23]. The cavity length was 900  $\mu\text{m}$  and both facets had a reflectivity of 90%. Fig. 11 shows the current-voltage characteristics under pulsed operation at room temperature. Notice that the turn-on voltage of the LD on the (711)A substrate is 5 V lower than for the (100) substrate. This is due to the higher acceptor concentration of the p-ZnSe cap layer. Typical characteristics of LDs on (711)A substrates under pulsed operation are shown in Fig. 12. The operating temperature ranged from  $-68$  to  $25^\circ\text{C}$ . The threshold current was 3.1 A at  $25^\circ\text{C}$ , and the wavelength was 501 nm.

#### 4.3. Transport devices

So far, optical devices have been described. In this section, the potential of wide-gap semiconductors for transport devices is discussed.

##### 4.3.1. GaN metal-semiconductor field-effect transistor

A metal-semiconductor field-effect transistor (MESFET) fabricated with GaN grown on a sapphire substrate is shown in Fig. 13 [24]. The large bandgap, ability to form heterojunctions, and in-

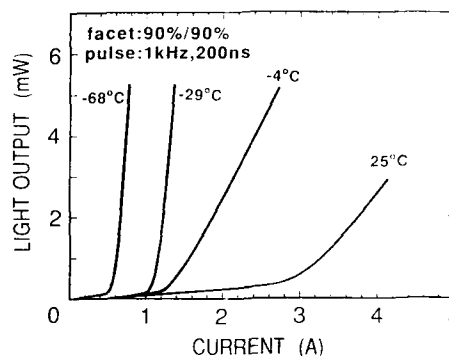


Fig. 12. Typical characteristics of LDs on (711)A substrates, after ref. [21].

ulating nature of AlN make AlGaIn an ideal material system for high-performance MESFETs. Another advantage is that it enables high-temperature operation, since these materials are stable at high temperatures, as mentioned in section 3. The insulator was AlN. The n-GaN was 1  $\mu\text{m}$  thick and had a carrier concentration of  $1 \times 10^{17} \text{ cm}^{-3}$ . The ohmic contacts were made of titanium. As a basic characteristic of a transistor, the dependence of the current-voltage characteristics between the source and the drain ( $I_{\text{ds}} - V_{\text{ds}}$ )

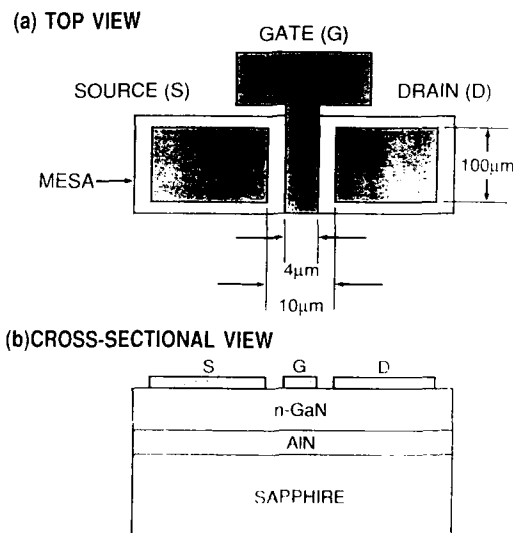


Fig. 13. GaN MESFET structure: (a) top view and (b) cross-sectional view, after ref. [24].

on the bias between the source and the gate ( $V_{gs}$ ) is shown in Fig. 14. At a gate voltage of  $-12$  V, the channel was completely depleted, and at a gate bias of  $-1$  V, the transconductance was estimated to be  $23$  mS/mm. The breakdown field between source and drain was  $10^{15}$  V/cm.

#### 4.3.2. Enhancement of electron mobility in GaN / GaAlN heterostructure

Just as for a GaAs/AlGaAs heterojunction, the electron mobility in a AlGaN/GaN heterojunction is also enhanced. Fig. 14 shows the dependence of the mobility on temperature for an AlGaN/GaN heterojunction compared with that for GaN [25]. At room temperature, the value for AlGaN/GaN was around  $620$  cm<sup>2</sup>/V·s, but it was only 56 for the bulk GaN. This enhancement may make it possible to fabricate high-performance electronic devices that can operate at high temperatures.

#### 4.3.3. ZnSe / GaAs HBT

A schematic drawing of a ZnSe/GaAs heterostructure bipolar transistor (HBT) and the common base characteristics are shown in Fig. 15 [26]. The use of a wide-gap emitter increases the design flexibility with regard to the base and emitter doping. The substrate, collector and base were GaAs, and n-type ZnSe was used for the wide-gap emitter. From Fig. 15b, the common base characteristics can be found to be fine.

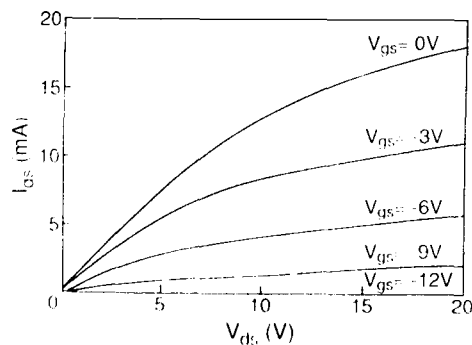
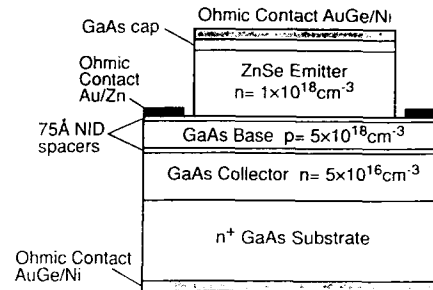
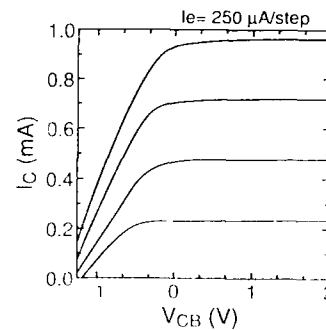


Fig. 14. Enhancement of electron mobility in GaN/GaAlN heterostructure, after ref. [25].



(a) SCHEMATIC DIAGRAM



(b) COMMON BASE CHARACTERISTICS

Fig. 15. ZnSe/GaAs HBT, after ref. [26]: (a) schematic drawing of a ZnSe/GaAs HBT and (b) common base characteristics.

## 5. Future prospects

One goal is a laser diode made of a II–VI wide-gap semiconductor with stable CW operation at room temperature. Based on the experience with III–V laser diode development, there are several important issues that need to be resolved. It is necessary to lower the turn-on voltage, develop good ohmic contact, and analyze the simulated emission mechanism. To obtain a long lifetime, it is required to understand the dislocation behavior as it relates to dark line defects. To avoid catastrophic optical damage at the facet, measurement and suppression of the surface recombination velocity must be performed. In the InGaAlN system, one of the most important things is to improve the crystal quality, and the acceptor concentration also has to be increased. It is expected that a good substrate for lattice-

matched growth will appear for both types of materials.

Although there is still a lot of work to be done, the prospects look bright. In the not too distant future, blue and green lasers made with II-VI semiconductors, and violet and ultraviolet lasers made with InGaAlN, should enjoy wide use.

## 6. Acknowledgments

The authors would like to thank Drs. Y. Imamura, K. Sugii and H. Iwamura for giving them the chance to perform this work and for their encouragement throughout this work.

## 7. References

- [1] M.A. Haase, J. Qiu, J.M. DePuydt and H. Cheng, *Appl. Phys. Lett.* 59 (1991) 1272.
- [2] H. Amano, N. Sawaki and I. Akasaki, *Appl. Phys. Lett.* 48 (1986) 353.
- [3] S. Nakamura, *Jap. J. Appl. Phys.* 30 (1991) L1705.
- [4] T. Matsuoka, H. Tanaka, T. Sasaki and A. Katsui, in: *Proc. 16th Intern. Symp. on GaAs and Related Compounds*, Karuizawa, 1989, *Inst. Phys. Conf. Ser.* 106, Eds. T. Ikoma and H. Watanabe (Inst. Phys., Bristol, 1990) p. 141.
- [5] T. Matsuoka, T. Sasaki and A. Katsui, *Optoelectron. Devices Technol. (OP-DET)* 5 (1990) 53.
- [6] H. Amano, M. Kito, K. Hiramatsu and I. Akasaki, *Jap. J. Appl. Phys.* 28 (1989) L2112.
- [7] S. Nakamura, T. Mukai, M. Senoh and N. Iwasa, *Jap. J. Appl. Phys.* 31 (1992) L139.
- [8] Y. Suzuki and H. Okamoto, *J. Electron. Mater.* 12 (1983) 397.
- [9] E. Ejder, *Phys. Status Solidi (a)* 6 (1971) 445.
- [10] H. Hartmann, R. Mach and B. Selle, in: *Current Topics in Materials Science*, Vol. 9, Ed. E. Kaldis (North-Holland, Amsterdam, 1982) pp. 1-414, see p. 12.
- [11] R.N. Bhargava, *Optoelectron. Devices Technol. (OP-DET)* 7 (1992) 19.
- [12] T. Matsuoka, N. Yoshimoto, T. Sasaki and A. Katsui, *J. Electron. Mater.* 21 (1992) 157.
- [13] N. Yoshimoto, T. Matsuoka, T. Sasaki and A. Katsui, *Appl. Phys. Lett.* 59 (1991) 2251.
- [14] Y. Koide, H. Itoh, M.R.H. Kahn, K. Hiramatsu, N. Sawaki and I. Akasaki, *J. Appl. Phys.* 61 (1987) 4540.
- [15] S. Nakamura, M. Senoh and T. Mukai, *Appl. Phys. Lett.* 62 (1993) 2391; S. Nakamura, M. Senoh and T. Mukai, *Jap. J. Appl. Phys. Lett.* 32 (1993) L8.
- [16] H. Amano, T. Asahi and I. Akasaki, *Jap. J. Appl. Phys.* 29 (1990) L205.
- [17] E.L. Hu and R.E. Howard, *J. Vac. Sci. Technol. B* 2 (1984) 85.
- [18] K. Asakawa and S. Sugita, *Jap. J. Appl. Phys.* 22 (1983) L653.
- [19] F. Shimokawa, H. Tanaka, Y. Uenishi and R. Sawada, *J. Appl. Phys.* 66 (1989) 2613.
- [20] H. Tanaka, F. Shimokawa, T. Sasaki and T. Matsuoka, *Optoelectron. Devices Technol. (OP-DET)* 6 (1991) 150.
- [21] T. Ohno, Y. Kawaguchi, A. Ohki and T. Matsuoka, in: *Extended Abstracts 1993 Int. Conf. on Solid State Devices*, Tsukuba, 1993, *Late News* p. 976.
- [22] K. Ohkawa and T. Mitsuyu, *J. Appl. Phys.* 70 (1991) 439.
- [23] Y. Kawaguchi, T. Matsuoka, T. Ohno and A. Ohki, in: *Extended Abstracts 1992 Int. Conf. on Solid State Devices*, Tsukuba, 1992, p. 345.
- [24] M. Asif Kahn, J.M. Hove, J.N. Kuznia and D.T. Olson, *Appl. Phys. Lett.* 62 (1993) 1786.
- [25] M. Asif Kahn, J.N. Kuznia, A.R. Bhattarai and D.T. Olson, *Appl. Phys. Lett.* 58 (1991) 2408.
- [26] A. Glaeser, R. Naholy and M. Tamargo, *Device Research Conf.*, Boulder, CO, 1991, paper VIA-7.



ELSEVIER

Journal of Crystal Growth 138 (1994) 737–744

JOURNAL OF **CRYSTAL  
GROWTH**

## Photo-assisted metalorganic vapor-phase epitaxy for nitrogen doping and fabrication of blue-green light emitting devices of ZnSe-based semiconductors

Shizuo Fujita \*, Takeharu Asano, Kensaku Maehara, Tsuyoshi Tojyo, Shigeo Fujita

*Department of Electrical Engineering, Kyoto University, Kyoto 606-01, Japan*

### Abstract

Photo-assisted metalorganic vapor-phase epitaxy was proposed as a promising technique for acceptor doping in ZnSe-based semiconductors. The growth was carried out using diethylzinc and dimethylselenide as source precursors, and tertiarybutylamine as a dopant material. Photoluminescence, electrical properties of Schottky diodes, and electroluminescence of junction diodes supported p-type behavior of the ZnSe:N layers. As an example, net acceptor concentration was estimated as  $2 \times 10^{17} \text{ cm}^{-3}$  for the ZnSe:N layer with nitrogen atomic concentration of  $5 \times 10^{17} \text{ cm}^{-3}$ . However, it was also pointed out that the doping characteristics were seriously affected by purity of source precursors, and this problem should be overcome, together with optimization of doping conditions, in order to achieve higher acceptor concentrations without heavy compensation.

### 1. Introduction

Metalorganic vapor-phase epitaxy (MOVPE) possesses a promising potential such as the possibility of selective area growth and precise flow rate control of source precursors, which are desirable for fabrication of novel and high performance optoelectronic devices including lasers. However, for II–VI semiconductors, in contrast to molecular beam epitaxy (MBE) where p-type doping with nitrogen [1,2] and p–n junction lasers [3] have successfully been achieved, MOVPE has not met technological breakthrough for reliable and low resistive p-type doping as well as opto-

electronic device applications. Worldwide efforts and interests are now focused on p-type doping in MOVPE.

The highest hole concentration in MOVPE was reported by Yasuda et al. [4] as  $9 \times 10^{17} \text{ cm}^{-3}$  by doping with lithium and nitrogen, which led to p–n junction blue electroluminescent diodes. However, problems of lithium diffusion seem to remain and to be overcome [5]. On the other hand, simply doping with nitrogen using  $\text{NH}_3$  as a dopant source, previous work resulted in hole concentrations of only  $10^{14}$ – $10^{15} \text{ cm}^{-3}$  for as-grown layers [6,7] or net acceptor concentrations of up to  $3 \times 10^{16} \text{ cm}^{-3}$  for rapid thermal annealed layers [8].

For the acceptor doping, as well as for fabrication of well-defined quantum wells (QWs), we

\* Corresponding author.



expect that photo-assisted MOVPE using alkyl-precursors both for group-II and group-VI elements is a promising technique, because it simultaneously offers low temperature growth, little gas-phase reaction, and possibility of effective impurity doping. In this paper, the state-of-the-art in nitrogen doping using photo-assisted MOVPE is described; electroluminescence (EL) from homo- and double-heterojunction diodes suggests the high potential of this technique for acceptor doping.

## 2. Photo-assisted MOVPE

It is now commonly recognized that low temperature growth is one of the most important requirements for high quality II–VI semiconductor epilayers, well-defined multilayered structures with abrupt interfaces, and high doping concentrations. Using hydrides such as  $H_2Se$  as group-VI precursors in MOVPE together with dialkyl-compounds of group-II elements, the growth can be carried out at a temperature of as low as 300–350°C [9]. However, this source combination easily causes premature reaction in the gas phase and results in predeposition on the chamber wall as well as rough surface morphology, leading to wavy interfaces [10].

The problem of premature reaction can be minimized by using dialkyl-chalcogens such as dimethylselenide (DMSe) for group-VI sources [11]. Successful growth of highly planar epilayers compared to those grown with hydrides, and photo-pumped lasing of multiple quantum wells (MQWs) were demonstrated [12]. However, the high growth temperature, e.g., 450–500°C, is against the effective doping, high quality epilayers with low defect density, and abrupt interfaces.

In order to overcome the high temperature necessary for the growth using alkyl-chalcogens, we have developed photo-assisted growth techniques [13,14]. Different from the photo-irradiation effects during the growth of III–V compounds and Si-related semiconductors, (i) the growth rate is markedly increased by above band gap irradiation, by which direct absorption by source materials cannot be expected [13–15], and

(ii) the irradiation intensity can be as low as less than 100 mW/cm<sup>2</sup> [13–16]. As a plausible mechanism for the growth with irradiation, we proposed photocatalytic reactions where the carriers generated by irradiation enhance the alkyl elimination from precursors (probably alkyl-zinc [17,18]) chemisorbed at the growth surface [14]. Using this novel technique, low temperature (300–400°C) growth [13–16] and high (dc or) doping efficiency [14,16,19] have been demonstrated.

We recognize that the photo-irradiation is also effective for acceptor doping, because (i) low growth temperature incorporates more acceptor impurities, (ii) reduction of compensating defects and activation of acceptor impurities under photo-irradiation are theoretically predicted [20,21], and (iii) photocatalytic reaction can enhance the decomposition of a dopant precursor if it contains alkyls. From these points of view, photo-assisted MOVPE is expected to be a promising technique for fabrication of well-defined QWs and for conductivity control.

The epitaxial growth was carried out in a vertical reactor at a reactor pressure of 200 Torr. The source precursors for ZnSe growth were diethyl-zinc (DEZn) and dimethylselenide (DMSe), whose flow rates were typically 9.4 and 72  $\mu\text{mol/min}$ , respectively. As the doping source for nitrogen, we chose tertiarybutylamine (t-BNH<sub>3</sub>), because it is thermally decomposed at lower temperature compared to NH<sub>3</sub> and tertiarybutyl-base may be decomposed by photocatalytic reactions. A recent report shows a net acceptor concentration of  $(1\text{--}2) \times 10^{16} \text{ cm}^{-3}$  using this doping source [22]. The substrates were (100)-oriented GaAs wafers. X-ray diffraction and surface morphology were not dependent on the flow rate of t-BNH<sub>3</sub> up to 180  $\mu\text{mol/min}$ .

## 3. Photoluminescence

### 3.1. Variation of spectrum with nitrogen doping

A typical example of variation of photoluminescence (PL) spectrum with nitrogen doping, measured at 4.2 K under excitation by a He–Cd

laser, is shown in Fig. 1. Here, the growth temperature was 350°C, the irradiation intensity was 45 mW/cm<sup>2</sup>, and the ZnSe layer thickness was about 1 μm. No appreciable deep emissions were observed at the wavelength region longer than that shown in Fig. 1, i.e., from 500 to 700 nm.

Non-doped ZnSe exhibits both free excitonic emission ( $E_x$ ) and donor-bound excitonic emission ( $I_x$ ). Intensity ratio between these two peaks, i.e.  $I_x/E_x$ , reflects concentration of residual donor impurities. Judging from the fact that the intensity of  $I_x$  is lower than that of  $E_x$ , we may recognize that the non-doped ZnSe possesses high purity suitable for acceptor doping. Detailed discussions on residual impurities and their effects on doping will be given later. It should also be noted that the layers have high electrical resistance.

For nitrogen-doped ZnSe grown by MBE, it is commonly understood that (i) for lightly-doped layers, the PL is dominated by both acceptor-bound excitonic emission ( $I_x^*$ ) and donor-acceptor pair (DAP) emission with zero phonon line (ZPL) at around 460 nm (shallow DAP), and (ii)

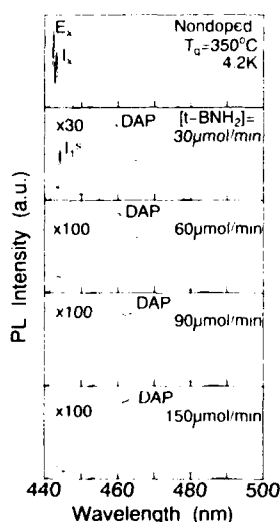


Fig. 1. 4.2 K PL spectra from non-doped and nitrogen-doped ZnSe layers grown at 350°C.

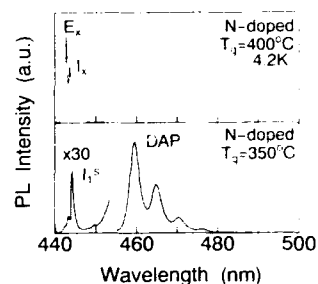


Fig. 2. 4.2 K PL spectra from ZnSe:N layers grown at different substrate temperatures. Flow rate of t-BNH<sub>3</sub> was 30 μmol/min.

for heavily-doped layers, it is totally dominated by DAP with ZPL at around 463 nm (deep DAP) [23,24].

According to these criteria, we can see in Fig. 1 for nitrogen-doped layers that (i) for [t-BNH<sub>3</sub>] = 30 or 60 μmol/min, the acceptor concentration is relatively low, because of the clear appearance of the deep DAP, (ii) a ZPL of the deep DAP exists at 459.4 nm (2.699 eV) for [t-BNH<sub>3</sub>] = 30 μmol/min and at 460.0 nm (2.696 eV) for [t-BNH<sub>3</sub>] = 60 μmol/min; the shift of a ZPL to longer wavelength with increase of acceptor (nitrogen) concentration coincides with the observation in MBE-grown ZnSe:N [23], and (iii) for [t-BNH<sub>3</sub>] = 90 or 150 μmol/min, the DAP region is characterized as overlapping of deep and shallow DAP bands. These results support the sufficient incorporation of nitrogen in ZnSe layers, at a flow rate of t-BNH<sub>3</sub> as high as 90 or 150 μmol/min.

Fig. 2 shows the comparison of PL spectra for the ZnSe layers grown at different substrate temperatures, under the same flow rate of [t-BNH<sub>3</sub>] = 30 μmol/min. Clear DAP emission, shown at the substrate temperature of 350°C, is hardly observed at 400°C. This drastic change with the substrate temperature suggests that low temperature growth, which becomes possible by photo-irradiation, is important for effective nitrogen doping, probably due to more sticking of nitrogen at lower temperature.

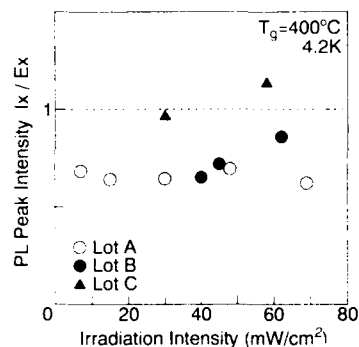


Fig. 3. PL intensity ratio  $I_x/E_x$  against irradiation intensity for non-doped ZnSe grown using different lots of DMSe.

### 3.2. Problems of precursor purity

A few years ago, non-doped ZnSe grown by photo-assisted MOVPE exhibited strong donor-bound excitonic emission ( $I_x$ ) in PL and n-type conductivity with electron concentration of around  $10^{16} \text{ cm}^{-3}$  [13,16], especially in those grown at higher irradiation intensity [16]. This phenomenon has seriously obstructed the effective acceptor doping, due to compensation by the donors. The origin of these donors was supposed to be residual impurities in source precursors, probably chlorine in alkyl-zinc [25]. Then, the purity of precursors commercially available seems to have been gradually improved, and recently the layers grown without intentional doping successfully show strong free excitonic emissions in PL as Fig. 1. However, we will show later that

there still remain purity problems which seriously affect the impurity doping; further efforts should be continued and this may be the key factor for MOVPE to compete with or be superior to MBE in fabrication of practical optoelectronic devices.

Fig. 3 demonstrates the intensity ratio of  $I_x$  to  $E_x$  in PL of non-doped ZnSe grown with a different lot of DMSe. This experiment was carried out at a substrate temperature of 400°C. Using lot C,  $I_x$  appears strong with respect to  $E_x$  and its intensity increases with the irradiation intensity. For lot B, the intensity of  $I_x$  is weaker compared to lot C, but it also tends to increase with the irradiation intensity. On the other hand, for lot A, the intensity of  $I_x$  is the lowest and is not changed with the irradiation intensity. These results suggest that the purity is the best for lot A and the worst for lot C among the sources used here.

When we grow nitrogen-doped ZnSe epilayers with either lot A or lot B, the variation of PL spectra for different irradiation intensity is shown in Fig. 4. Here, the flow rate of  $\text{t-BNH}_3$  was 90  $\mu\text{mol/min}$ . For lot B (Fig. 4b), the higher irradiation intensity, 80  $\text{mW/cm}^2$ , results in strong  $I_x$  line rather than DAP emission. Nevertheless, more incorporation of acceptors for higher irradiation intensity is expected for lot A (Fig. 4a), judging from the broader shape of the DAP bands. This drastic difference originates from the different purity of source precursors (DMSe in this experiment). Precise chemical analysis on residual impurities and detailed investigation on variation of the PL spectra with growth conditions, which

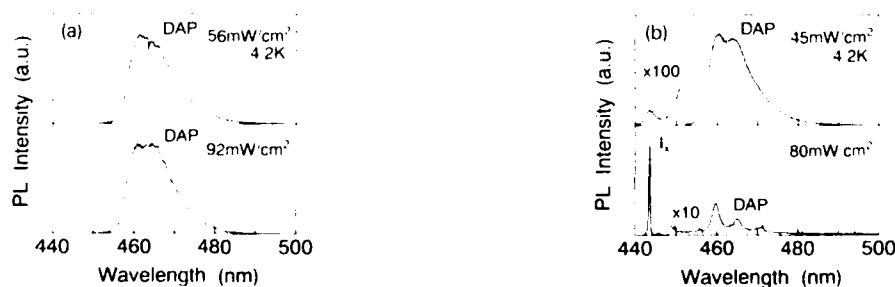


Fig. 4. Variation of 4.2 K PL spectra from ZnSe:N layers grown at different irradiation intensity using (a) DMSe lot A and (b) DMSe lot B. Flow rate of  $\text{t-BNH}_3$  was 90  $\mu\text{mol/min}$ .

have not been conducted in the present study, will elucidate the origin which affect the epilayer quality and the effective acceptor doping. Anyhow, it can be concluded that the doping characteristics of the present epilayers grown by MOVPE are seriously influenced by the purity of source precursors, and that the future improvements of doping behavior are indebted to the purer precursors available.

#### 4. Electrical properties

The electrical properties of ZnSe:N layers were characterized by current–voltage and capacitance–voltage characteristics of Schottky diodes grown on p<sup>+</sup>-GaAs substrates with front–back contact configuration. The thickness of the ZnSe:N layers was 1  $\mu\text{m}$ , and the Schottky contacts to the ZnSe:N layers were fabricated by evaporating gold (Au) dots with 1 mm in diameter.

Variation of current–voltage ( $I$ – $V$ ) characteristics with flow rate of t-BNH<sub>2</sub> is shown in Fig. 5. Negative voltage applied to the Au electrode corresponds to the forward bias if the ZnSe:N layer behaves as p-type. Resistance and turn-on voltage in negative voltage polarity have markedly

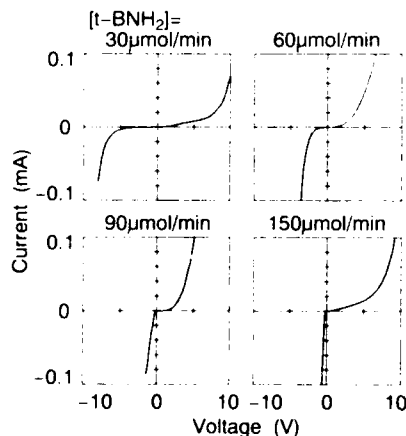


Fig. 5. Current–voltage characteristics of Au/ZnSe:N/p<sup>+</sup>-GaAs Schottky diodes whose ZnSe:N layers were grown at different flow rates of t-BNH<sub>2</sub>.

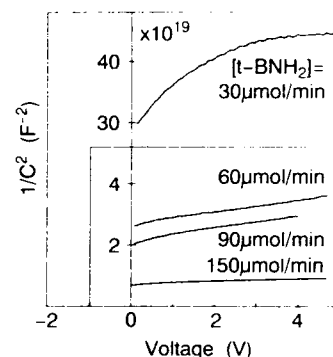


Fig. 6.  $1/(\text{capacitance})^2$ -voltage characteristics of Au/ZnSe:N/p<sup>+</sup>-GaAs Schottky diodes whose ZnSe:N layers were grown at different flow rates of t-BNH<sub>2</sub>.

decreased with increasing flow rate of t-BNH<sub>2</sub>; these phenomena are characterized by p-type conduction of ZnSe:N layers. It should be noted that the turn-on voltage for the sample grown with [t-BNH<sub>2</sub>] = 90 or 150  $\mu\text{mol/min}$  seems to be too small (0.5–1 V) compared to what we can expect from the ideal band diagram including the potential barriers at the Au/p-ZnSe and p-ZnSe/p<sup>+</sup>-GaAs junctions. However, this phenomenon seems to be supported by the recent experimental result which suggests a lower potential barrier at a contact to a p-type layer when it is grown by MOVPE compared to MBE [22].

Fig. 6 shows the  $1/(\text{capacitance})^2$ -voltage ( $1/C^2$ - $V$ ) characteristics. The measurement frequency is 1 MHz. Decrease of the  $1/C^2$  values and of the slopes of the  $1/C^2$ - $V$  curves with increasing flow rate of t-BNH<sub>2</sub> suggests higher impurity concentrations. Together with the variation of PL spectra shown in Fig. 1 and of the  $I$ – $V$  characteristics shown in Fig. 5, it seems reasonable to assume an increase of net acceptor concentration  $N_a - N_d$  for higher flow rate of t-BNH<sub>2</sub>.

It should be noted that, in the present front–back contact configuration, the measured capacitance  $C$  is expressed by the series connection of depletion layer capacitance at the Au/ZnSe:N Schottky junction ( $C_{\text{SB}}$ ) and that at the ZnSe:N/p<sup>+</sup>-GaAs heterojunction ( $C_{\text{HJ}}$ ), i.e.,  $C = (1/C_{\text{SB}} + 1/C_{\text{HJ}})^{-1}$ . Therefore,  $C$  is always

smaller than  $C_{SB}$ . However, if the relation  $C_{SB} \ll C_{IJ}$  becomes valid,  $C_{SB}$  can be approximated by  $C$ , from which one can characterize the net acceptor concentration.

When the measurement was carried out at lower frequency,  $C_{IJ}$  increased due to lateral spreading of the depletion layer at the heterojunction, and the measured capacitance increased and approached  $C_{SB}$ . It is claimed, therefore, that accurate values of net acceptor concentration can be obtained at relatively low measurement frequency, e.g., 2–10 kHz [26].

Another technique to increase  $C_{IJ}$  compared to  $C_{SB}$  is to measure the capacitance at larger (reverse) bias voltage. At positive bias applied to the Au electrode, the heterojunction and the Schottky barrier are forward- and reverse-biased, respectively, for a p-type ZnSe layer; hence with increasing the bias voltage sufficiently, the relationship  $C_{SB} \ll C_{IJ}$  is satisfied and  $C$  approaches  $C_{SB}$ . In the present sample, reliable capacitance measurements at low frequency were difficult due to relatively large leakage current in the Schottky diodes, as shown in Fig. 5. Therefore, using the 1 MHz  $1/C^2$ - $V$  characteristics, the net acceptor concentration was estimated from their slopes at relatively large bias voltage, e.g., 4 V, according to the conventional equation. This consideration can minimize the errors caused by series connection of  $C_{IJ}$ .

For  $[t\text{-BNH}_2] = 90 \mu\text{mol/min}$ , the net acceptor concentration was estimated from the above procedure to be  $2 \times 10^{17} \text{ cm}^{-3}$ . Secondary ion

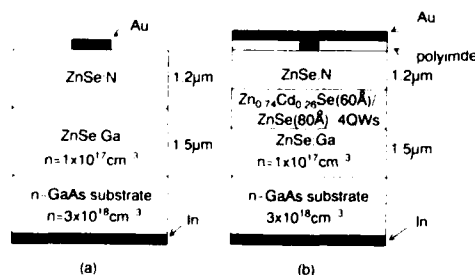


Fig. 7. EL diode structures: (a) planar geometry homo-junction diode with Au electrode of 1 mm diameter and (b) cleaved geometry double hetero-junction diodes with the stripe-shaped Au electrode of  $1 \text{ mm} \times 20 \mu\text{m}$ .

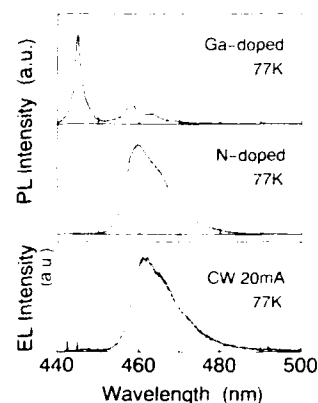


Fig. 8. 77 K EL spectrum from the homo-junction diode shown in Fig. 7a together with 77 K PL spectra from ZnSe:N and ZnSe:Ga layers.

mass spectrometry (SIMS) for this sample had exhibited nitrogen concentration of  $5 \times 10^{17} \text{ cm}^{-3}$ , which is in reasonable correlation to the net acceptor concentration calculated.

For other samples, since the SIMS data are not available, it seems better not to discuss the net acceptor concentration, due to remaining problems in electrical measurements. The reliability of the present result and the highest net acceptor concentration will be discussed in the future with SIMS data and/or reliable low-frequency  $C$ - $V$  characteristics.

## 5. Electroluminescence

In order to investigate the performance of the ZnSe:N layers, EL from the diode structures shown in Fig. 7 is investigated. Here, the ZnSe:N layer was grown with  $[t\text{-BNH}_2] = 90 \mu\text{mol/min}$  and the electron concentration in the ZnSe:Ga layers was  $1 \times 10^{17} \text{ cm}^{-3}$ .

The ZnSe homo-junction diode, shown in Fig. 7a, exhibited the 77 K EL spectrum as shown in Fig. 8. Here, 77 K PL spectra of ZnSe:N and ZnSe:Ga layers are shown simultaneously. The EL peak wavelength (460 nm) is nearly equal to the PL peak wavelength from the ZnSe:N layer (probably free-to-acceptor emission) rather than

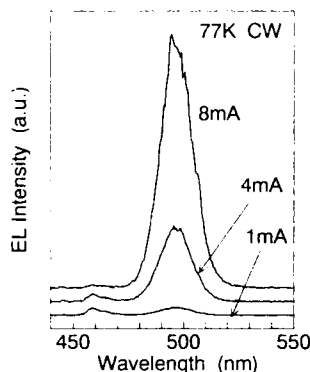


Fig. 9. 77 K EL spectra from the double hetero-junction diode shown in Fig. 7b.

that from the ZnSe:Ga layer (444 nm, free-to-donor emission). This result is well attributed to the electron injection from the ZnSe:Ga layer to the ZnSe:N layer, and to the recombination with holes in the ZnSe:N layer, i.e., the ZnSe:N layer behaves as p-type.

For the ZnCdSe/ZnSe MQW double hetero-junction diode shown in Fig. 7b, the 77 K EL spectra are shown in Fig. 9. The emission at 496 nm is attributed to the QW, and it increases remarkably with current. Strong blue-green emission was observed by the naked eye under normal room lighting conditions at an applied DC voltage of about 10 V.

One may argue the possibility that the EL of a homo-junction diode, shown in Fig. 7a, originates from the Au/ZnSe:N Schottky contact break-

down. However, we do not believe this because a similar peak should appear in Fig. 8 if the Schottky breakdown were the dominant reason for EL. Therefore, the EL observed in this study is well attributed to carrier injection at p–n junctions.

One of the MQW diodes, whose QW structure was slightly different from that of Fig. 7b, showed very low (4 V at 77 K and 3 V at RT) turn-on voltage, as shown in Fig. 10a. This result might be because this sample happens to possess a surface condition different from other samples, but we cannot understand the reason at present. Extremely strong EL, whose spectra are shown in Fig. 10b, was observed for this sample. The origin of the narrow emission line at 10 mA is not understood so far, because of the short lifetime, but it might be characterized by symptoms of stimulated emission. If this assumption is true, however, considering the low current compared to MBE-grown lasers, the emission occurs from a limited area under the stripe-shaped electrode where the current flow is concentrated.

## 6. Summary

Photo-assisted MOVPE is found to be a promising technique for acceptor doping in ZnSe, due to more incorporation of nitrogen at low temperature growth, highly non-equilibrium conditions during the growth, and enhanced decomposition of  $t\text{-BNH}_3$ . The net acceptor concentration was estimated to be  $2 \times 10^{17} \text{ cm}^{-3}$  for the

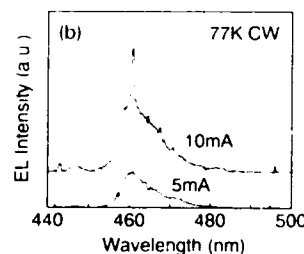
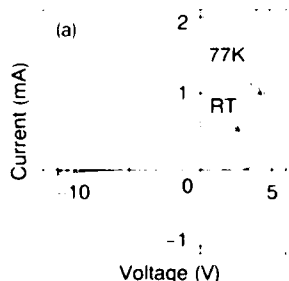


Fig. 10. (a) Current-voltage characteristics and (b) EL spectra at 77 K for one of the MQW diodes, which exhibited the lowest turn-on voltage in forward-bias.

sample with nitrogen atomic concentration of  $5 \times 10^{17} \text{ cm}^{-3}$ . However, the DAP band in PL appeared as a broad peak, in contrast to MBE-grown epilayers with similar nitrogen concentration, where a ZPL at 463 nm is followed by clearly separated phonon replicas. This suggests more compensation in ZnSe:N layers grown by MOVPE compared to MBE. For achieving higher concentration of acceptors in MOVPE without heavy compensation, the use of more purified precursors as well as the optimization of doping conditions are necessary in future studies.

### 7. Acknowledgements

This work was supported in part by a Grant-in-Aid on Priority-Area Research on "Photo-Excited Process" from the Ministry of Education, Science and Culture, Japan.

### 8. References

- [1] R.M. Park, M.B. Troffer, C.M. Rouleau, J.M. DePuydt and M.A. Haase, *Appl. Phys. Lett.* 57 (1990) 2127.
- [2] K. Ohkawa, T. Karasawa and T. Mitsuyu, *Jap. J. Appl. Phys.* 30 (1991) L152.
- [3] M.A. Haase, J. Qiu, J.M. DePuydt and H. Cheng, *Appl. Phys. Lett.* 59 (1991) 1272.
- [4] T. Yasuda, I. Mitsuishi and H. Kukimoto, *Appl. Phys. Lett.* 52 (1988) 57.
- [5] Y. Yamada, I. Kidoguchi, T. Taguchi and A. Hiraki, *Jap. J. Appl. Phys.* 28 (1989) L837.
- [6] A. Ohki, N. Shibata and S. Zembutsu, *Jap. J. Appl. Phys.* 27 (1988) L909.
- [7] I. Suemune, K. Yamada, H. Masato, T. Kanda, Y. Kan and M. Yamanishi, *Jap. J. Appl. Phys.* 27 (1988) L2195.
- [8] N.R. Taskar, B.A. Khan, D.R. Dorman and K. Shahzad, *Appl. Phys. Lett.* 62 (1993) 270.
- [9] W. Stutius, *Appl. Phys. Lett.* 33 (1978) 656.
- [10] P.J. Parbrook, P.J. Wright, B. Cockayne, A.G. Cullis, B. Henderson and K.P. O'Donnell, *J. Crystal Growth* 106 (1990) 503.
- [11] H. Mitsuhashi, I. Mitsuishi and H. Kukimoto, *J. Crystal Growth* 77 (1986) 219.
- [12] P.J. Parbrook, A. Kamata and T. Uemoto, *Jap. J. Appl. Phys.* 32 (1993) 669.
- [13] Sz. Fujita, A. Tanabe, T. Sakamoto, M. Isemura and Sz. Fujita, *Jap. J. Appl. Phys.* 26 (1987) L2000.
- [14] Sz. Fujita and Sz. Fujita, *J. Crystal Growth* 117 (1992) 67, and references therein.
- [15] A. Yoshikawa, T. Okamoto, T. Fujimoto, K. Onoue, S. Yamaga and H. Kasai, *Jap. J. Appl. Phys.* 29 (1990) L225.
- [16] T. Yasuda, Y. Koyama, J. Wakitani, J. Yoshino and H. Kukimoto, *Jap. J. Appl. Phys.* 28 (1989) L1628.
- [17] Sz. Fujita, S. Hirata and Sz. Fujita, *Jap. J. Appl. Phys.* 30 (1991) L507.
- [18] Sz. Fujita, S. Hirata and Sz. Fujita, *J. Crystal Growth* 115 (1991) 269.
- [19] Sz. Fujita, A. Tanabe, T. Kinoshita and Sz. Fujita, *J. Crystal Growth* 101 (1990) 48.
- [20] M. Ichimura, T. Wada, Sz. Fujita and Sz. Fujita, *Jap. J. Appl. Phys.* 30 (1991) 3475.
- [21] M. Ichimura, T. Wada, Sz. Fujita and Sz. Fujita, *J. Crystal Growth* 117 (1992) 689.
- [22] Y. Fujii, I. Suemune, K. Okamoto, M. Fujimoto and K. Okamura, in: *Extended Abstracts 1993 Int. Conf. on Solid State Devices and Materials*, Makuhari, 1993 (Business Center for Academic Societies Japan, Tokyo, 1993) p. 65.
- [23] J. Qiu, J.M. DePuydt, H. Cheng and M.A. Haase, *Appl. Phys. Lett.* 59 (1991) 2992.
- [24] I.S. Hauksson, J. Simpson, S.Y. Wang, K.A. Prior and B.C. Cavenett, *Appl. Phys. Lett.* 61 (1992) 2208.
- [25] H. Kukimoto, *J. Crystal Growth* 101 (1990) 953.
- [26] T. Marshall and D.A. Cammack, *J. Appl. Phys.* 69 (1991) 4149.

## Helium gas mixing in nitrogen plasma for the control of the acceptor concentration in p-ZnSe

M. Kobayashi \*, H. Tosaka, T. Nagatake, T. Yoshida, A. Yoshikawa

*Department of Electrical and Electronics Engineering, Chiba University, 1-33 Yayoi-cho, Inage-ku, Chiba 263, Japan*

### Abstract

Nitrogen and helium mixed gas plasma was used to control the acceptor concentration of p-ZnSe and p-ZnSSe. Using the mixed gas, the acceptor concentration of p-ZnSe can be controlled from  $6 \times 10^{16}$  to  $7 \times 10^{17} \text{ cm}^{-3}$ , whereas the acceptor concentration of p-ZnSSe can be controlled from  $4 \times 10^{16}$  to  $4 \times 10^{17} \text{ cm}^{-3}$ . Doping characteristics such as the acceptor concentration and the PL properties depend on the gas mixing ratio and the RF power. p-Layers grown with this technique were used for blue-green laser diode structures. Lasing was observed at 77 K under pulsed operation.

### 1. Introduction

Recently, high net acceptor concentration p-ZnSe layers were grown using plasma excited nitrogen with an RF plasma source [1–5]. At the present stage, however, the maximum doping concentrations of those p-ZnSe:N layers are not high enough for practical device applications; formation of the better ohmic contact, reduction of the contact resistance, and reduction of the series resistance of the device can be achieved by using higher carrier concentration p-ZnSe layers. The widely used RF plasma cell for the p-doping of ZnSe has a serious disadvantage in the formation of the plasma and the control of the beam intensity. The formation of the plasma (generation of the plasma excited nitrogen beam) requires cer-

tain ranges of the gas pressure and the RF power; dopant beam intensity cannot be tuned in a wide dynamic range. In order to circumvent this problem, nitrogen gas was mixed with helium gas in the plasma cell so that the plasma could be formed in the cell regardless of the nitrogen gas pressure in the cell; plasma-excited nitrogen gas intensity would be controlled in a much wider range by mixing the nitrogen gas with an additional gas. Another expected advantage of the gas mixing is that the nitrogen plasma characteristics could be changed by the gas mixing and effective nitrogen species for the doping could be increased. The He gas mixing technique was also used in the variety of film growth processes such as sputtering and plasma CVD in order to increase the useful species in the plasma and to improve the growth process [6–8]. In this paper, the gas mixing technique was also applied to grow laser diode structures.

\* Corresponding author.



## 2. Experiments

ZnSe and ZnSSe films were grown on  $p^+$ -GaAs (100) substrates in a conventional MBE system using Zn, Se, and ZnS sources. The beam flux intensity ratio was adjusted to maintain a slightly ( $2 \times 1$ ) Se-stabilized surface in the RHEED pattern during the growth. The growth temperature was about 240°C and the film thickness of all the samples was about 2  $\mu\text{m}$ . The mole fraction of S in the ZnSSe layer was adjusted to form the lattice matched layer on the GaAs substrate (about 6%).  $\text{N}_2$  and He were introduced into the plasma cell separately, hence the flow rate of these gases could be controlled independently. The RF power used for this experiment was between 150 and 350 W. In this study, the partial pressure of  $\text{N}_2$  ( $P_{\text{N}_2}$ ) was maintained at  $9.0 \times 10^{-7}$  Torr and the partial pressure of He ( $P_{\text{He}}$ ) was varied from 0 to  $2.7 \times 10^{-6}$  Torr. The electrical and optical properties of the grown films were measured by  $C$ - $V$  and PL method, respectively.

## 3. Results and discussion

### 3.1. $p$ -ZnSe and $p$ -ZnSSe

Fig. 1 shows  $N_a - N_d$  of the ZnSe layers as a function of the He partial pressure.  $N_a - N_d$  of

the film doped only with nitrogen gas was typically  $3 \times 10^{17} \text{ cm}^{-3}$  under the growth conditions used for this study;  $N_a - N_d$  was about  $1 \times 10^{17} \text{ cm}^{-3}$  when the RF power was 350 W. As shown in Fig. 1a, the net acceptor concentration was gradually decreased to the range of  $10^{16} \text{ cm}^{-3}$  by adding the He gas up to  $2.7 \times 10^{-6}$  Torr when the RF power was 150 or 220 W. On the other hand, when the RF power was about 300 or 350 W, the acceptor concentration was increased until  $P_{\text{He}}$  reached about  $1 \times 10^{-6}$  Torr. The highest  $N_a - N_d$  value was  $7 \times 10^{17} \text{ cm}^{-3}$ , and further increase of the  $P_{\text{He}}$  resulted in a decrease of the acceptor concentration.

Fig. 2 shows low temperature PL spectra of samples grown using (a) only  $\text{N}_2$  and (b) a mixture of  $\text{N}_2$  and He with an RF power of 220 W. The spectrum obtained from the sample doped using only  $\text{N}_2$  was dominated by rather strong DAP emissions (at 2.682 eV). On the other hand, the sample doped using the mixture of  $\text{N}_2$  and He showed a strong  $I_1$  line; two sets of DAP emissions were observed at 2.697 and 2.681 eV, respectively. The intensities of the  $I_1$  emission and the DAP emission at 2.697 eV increased, and the DAP emission intensity at 2.681 eV decreased with increasing  $P_{\text{He}}$ . The same tendency was observed from the sample doped using an RF power of 150 W. It is reasonable to assign that the nitrogen concentration in the ZnSe layer was

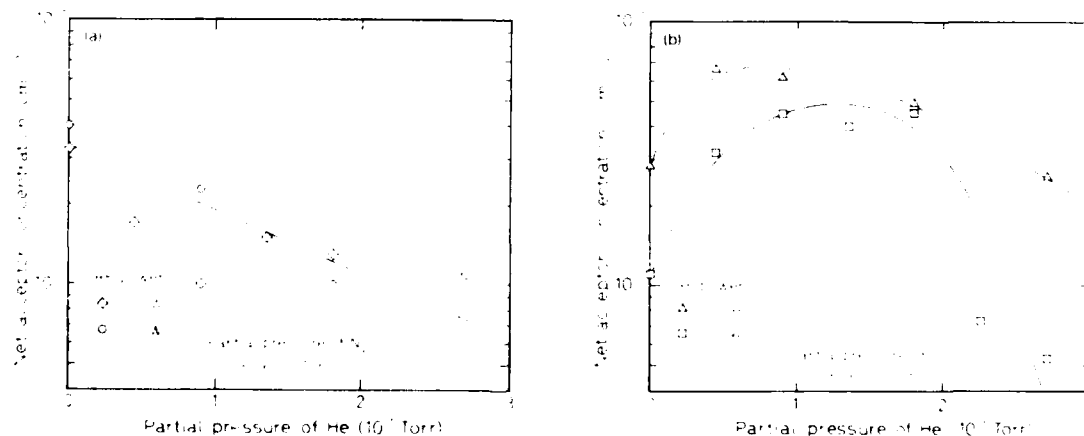


Fig. 1. Net acceptor concentration of ZnSe as a function of partial pressure of He. Partial pressure of  $\text{N}_2$  was  $9 \times 10^{-7}$  Torr, and RF power was (a) 150 and 220 W, and (b) 300 and 350 W. The frequency used for the measurement was 1 MHz.

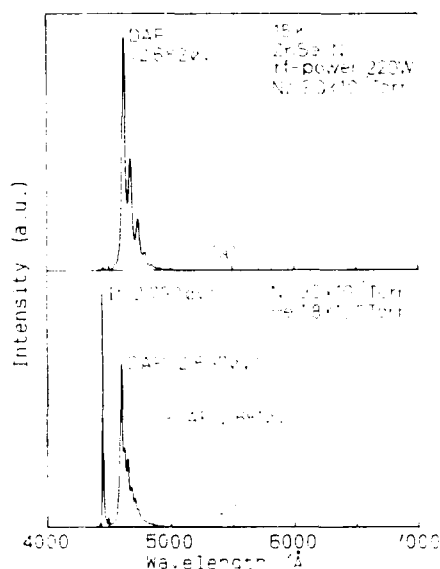


Fig. 2. PL spectra of samples (a) doped with only  $N_2$ , (b) doped with  $N_2$  and He mixture ( $P_{He}$  was  $1.8 \times 10^{-6}$  Torr). The RF power was 220 W. PL spectra were measured using a He–Cd laser (325 nm, about 0.3 W/cm<sup>2</sup>) as an excitation source.

reduced [4] as He was added (when the RF power was 150 or 220 W). By contrast, as shown in Fig. 3, the PL spectra showed no significant variation although  $P_{He}$  was increased when the RF power was 300 W (or 350 W). The DAP emission and well-resolved phonon replicas peaking at 2.684 eV dominated the spectrum. (The origin of the slight shift to the lower energy side with increasing  $P_{He}$  is now under study.) Compared to the PL results obtained from samples doped using RF powers of 150 and 220 W, the nitrogen concentration in the ZnSe layer would not be affected significantly by the increase of  $P_{He}$  when the RF power was 300 or 350 W; the variation of  $N_a - N_d$  may not have originated mainly from the nitrogen concentration in the film. Due to the relatively small variation of  $N_a - N_d$  (between  $3 \times 10^{17}$  and  $7 \times 10^{17}$  cm<sup>-3</sup> when the RF power was 300 W), SIMS measurement did not show a clear indication of the relationship between the nitrogen concentration and  $N_a - N_d$ .

This technique was also useful in growing p-

ZnSse layers. The acceptor concentration of p-ZnSe and p-ZnSse was compared and summarized in Fig. 4 as a function of the partial pressure of He: the RF power used for the experiments was 300 and 350 W. The acceptor concentrations of the p-ZnSse layers have a slightly lower value compared to those of p-ZnSe layers, yet the acceptor concentrations of the p-ZnSse layers could be similarly tuned by the gas mixing technique.

The enhancement and reduction of the acceptor concentration as well as the variation of the PL spectra should be related to the variety and the density of the species in the plasma. In order to study the origin of the enhancement and reduction of the acceptor concentration, plasma discharge emission spectra were measured. Preliminary observation suggests that the varieties of the species in the plasma were not significantly affected by the He gas mixing or by the RF power used for this study, even though the densities of the species were slightly affected by the He gas mixing [9].

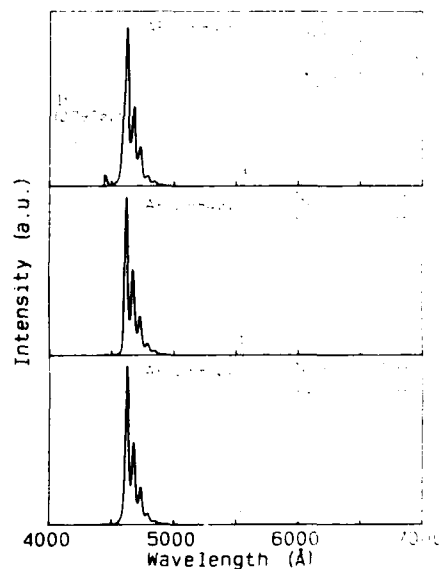


Fig. 3. PL spectra of samples (a) doped with only  $N_2$ , (b) doped with  $N_2$  and He mixture ( $P_{He}$  was  $9.0 \times 10^{-6}$  Torr), and (c) doped with  $N_2$  and He mixture ( $P_{He}$  was  $2.7 \times 10^{-5}$  Torr). The RF power was 300 W.

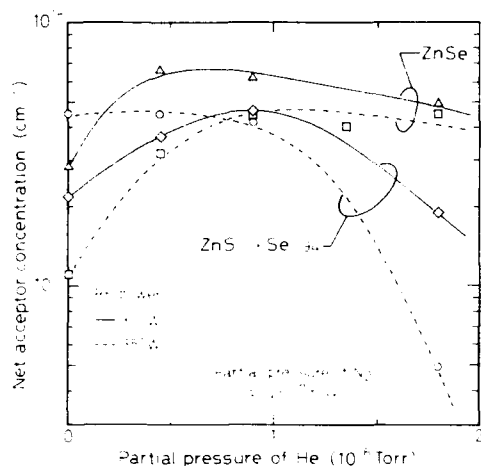


Fig. 4. Net acceptor concentration of ZnSe and ZnS<sub>0.8</sub>Se<sub>0.2</sub> as a function of  $P_{\text{He}}$ . The RF power used for the experiment was 300 and 350 W.

### 3.2. Laser diode structures

Blue-green laser diode structures whose p-layers were doped using this technique were fabricated. Fig. 5 shows the schematic structure of the laser diode. Laser devices were fabricated by preparing about 800  $\mu\text{m}$  long cleaved resonator structures with a 25  $\mu\text{m}$  wide Au stripe electrode. Neither facets have high-reflectivity coating layers. As shown in Fig. 6, the lasing emission was observed at 77 K under the pulse operation, and the lasing wavelength was 482 nm. The threshold

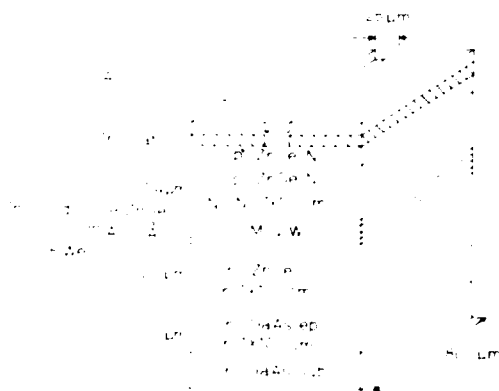


Fig. 5. Schematic structure of the laser diode.

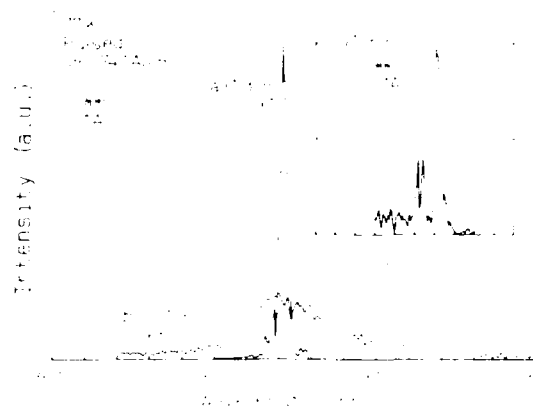


Fig. 6. Electroluminescence from the sample with various current levels: (a)  $J = 1.3J_{\text{th}}$  and (b)  $J = 0.7J_{\text{th}}$ . (c) The spectrum was taken with a high resolution power (0.1  $\text{\AA}$ ) at a current level of  $J = 1.3J_{\text{th}}$ .

current density was about 720  $\text{A}/\text{cm}^2$  and the driving voltage was about 40 V. As shown in the inset of the figure, fine structures were observed by improving the resolution power of the scan.

### 4. Conclusions

The He gas mixing is a useful technique to control the acceptor concentration in the nitrogen doped p-ZnSe and p-ZnS<sub>0.8</sub>Se<sub>0.2</sub> layers. The acceptor concentration has been tuned between  $6 \times 10^{16}$  and  $7 \times 10^{17} \text{ cm}^{-3}$  for ZnSe, and tuned between  $4 \times 10^{16}$  and  $4 \times 10^{17} \text{ cm}^{-3}$  for ZnS<sub>0.8</sub>Se<sub>0.2</sub>. The doping characteristics were affected by the gas mixture ratio and the RF power. The p-layer grown using this technique was applied for the laser diode structure.

### 5. Acknowledgments

This work was partly supported by a Grant-in-Aid for Scientific Research on Priority Areas, New Functionality Materials – Design, Preparation and Control, from the Ministry of Education, Science and Culture, and partly supported by a Research Promotion Fund in the field of Interna-

tional Telecommunications. The authors wish to express their gratitude to New Japan Radio Co., Ltd., for their cooperation in the use of the equipment.

## 6. References

- [1] R.M. Park, M.B. Troffer, C.M. Roulea, J.M. DePuydt and M.A. Haase, *Appl. Phys. Lett.* 57 (1990) 2127.
- [2] K. Ohkawa, T. Karasawa and T. Mitsuyu, *Jap. J. Appl. Phys.* 30 (1991) L152.
- [3] M. Haase, J. Qiu, J. DePuydt and H. Cheng, *Appl. Phys. Lett.* 59 (1991) 1272.
- [4] J. Qiu, J.M. DePuydt, H. Cheng and M.A. Haase, *Appl. Phys. Lett.* 59 (1991) 1896.
- [5] H. Jeon, J. Ding, W. Patterson, A.V. Nurmikko, W. Nie, D.C. Grillo, M. Kobayashi, R.L. Gunshor, G.C. Hua and N. Otsuka, *Appl. Phys. Lett.* 59 (1991) 3619.
- [6] D.V. Tsu, G.N. Parsons and G. Lucovsky, *J. Vac. Sci. Technol. A* 6 (1988) 1849.
- [7] T. Fujii, K. Morofuji, T. Koyanagi, R. Oi and K. Matsubara, in: *Proc. 9th Symp. on Plasma Processing*, 1992, p.71.
- [8] A.A. Bright, J. Batey and E. Tierney, *Appl. Phys. Lett.* 58 (1991) 619.
- [9] H. Tosaka, T. Nagatake, T. Yoshida, M. Kobayashi and A. Yoshikawa, *Jap. J. Appl. Phys.* 32 (1993) L1722.



ELSEVIER

Journal of Crystal Growth 138 (1994) 750–754

JOURNAL OF  
**CRYSTAL  
GROWTH**

## Improvement of electrical and optical properties of ZnSSe p–n heterostructure diodes with optimization in metalorganic vapor phase epitaxy

I. Suemune <sup>\*,1</sup>, Y. Fujii, M. Fujimoto

*Faculty of Engineering, Hiroshima University, 1-4-1 Kagamiyama, Higashihiroshima 724, Japan*

### Abstract

p-Type ZnSSe films were grown with nitrogen doping in atmospheric-pressure metalorganic vapor-phase epitaxy at the growth temperature of 560°C. ZnSe/ZnSSe p–n heterostructure diodes thus prepared showed better voltage–current characteristics than those reported with laser diodes prepared with molecular-beam epitaxy. With improvement of the growth process, blue luminescence was observed with current injection of 20 mA and the operating voltage of 2 V.

### 1. Introduction

In comparison to the successful p-type doping with nitrogen (N) radical doping in molecular-beam epitaxy (MBE) [1,2], it has been difficult to have reproducible p-type conductivities in nitrogen-doped ZnSe grown by metalorganic vapor-phase epitaxy (MOVPE) [3,4]. Recent studies suggested that N can be doped up to  $10^{20} \text{ cm}^{-3}$  [5], but the depth profile of the doped N was almost completely overlapped by the profile of hydrogen (H) [6]. These results suggested the neutralization of the doped N acceptors with N–H bondings.

ZnSe films are usually grown in the temperature range of 250–350°C in both MBE and MOVPE. To avoid the problem of the N–H bondings in MOVPE, epitaxial growth at higher growth temperature to dissociate the N–H bondings may be one of the solutions to this difficulty. Formerly, a problem in n-type doping at higher growth temperature was studied, and electron concentrations greater than  $1 \times 10^{18} \text{ cm}^{-3}$  were observed for a growth temperature above 500°C in atmospheric-pressure MOVPE [7].

In this paper, p-type ZnSe was grown with N doping in MOVPE at a growth temperature above 500°C. ZnSe/ZnSSe heterostructure p–n diodes were fabricated, and electrical and optical properties were studied. With improvement of the diode properties based on the examination of the problems found through the studies, blue luminescence was observed with low-voltage operations.

<sup>\*</sup> Corresponding author.

<sup>1</sup> Presently at Research Institute for Electronic Science, Hokkaido University, Sapporo 060, Japan.

## 2. N doping and properties of p–n diodes

Growth of ZnSe and ZnSSe was performed at a temperature of 560°C by atmospheric-pressure horizontal-type MOVPE on (001) GaAs substrates. The precursors and the respective flow rates were 0.45, 2.5, and 2.4  $\mu\text{mol}/\text{min}$  for diethylzinc (DEZn), diethylselenide (DESe), and diethylsulfide (DES) for the growth of  $\text{ZnS}_{0.06}\text{Se}_{0.94}$ . The flow rate of DES depended on the S mole fraction of ZnSSe. The growth rate of ZnSe at 560°C was  $\sim 1 \mu\text{m}/\text{h}$ . In the present growth system, GaAs substrates were heated with infrared lamps and the unintentional increase of the visible light irradiation at the higher growth temperature enhanced the growth rate [8]. Iodine was doped in n-type layers by supplying ethyl iodide (EtI).

Details of the N doping properties will be reported elsewhere [9], but the main points will be briefly described below. Nitrogen was doped in p-type layers by supplying tert-butylamine (tBA). tBA was introduced to the growing surface through a quartz tube separate from that for the other precursors with pure  $\text{N}_2$  as a carrier gas. tBA was thermally cracked with a furnace during the transport into the quartz reactor. Thermal cracking of tBA was necessary to increase the donor–acceptor (DA) pair emission that is the usually-accepted indication of N incorporation. There was an optimum temperature range for the cracking of tBA and the increase of the DA pair emission was maximum in the temperature range of 700–800°C.

Fig. 1 shows the schematic structure of a ZnSe/ZnSSe heterostructure diode. The active layer consists of a multiple quantum well (MQW)

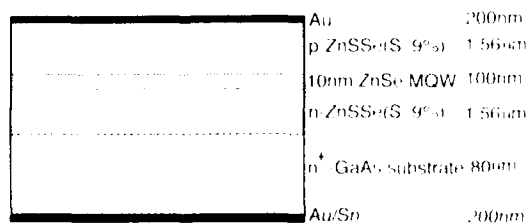


Fig. 1. Schematic structure of ZnSe/ZnSSe p–n diode structure.

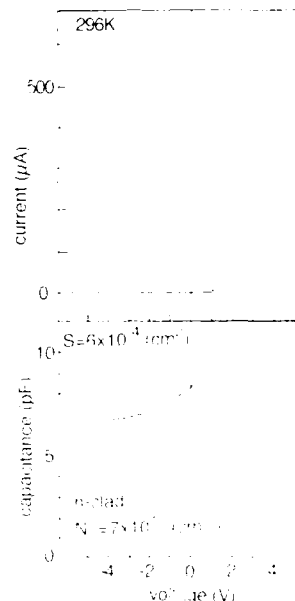


Fig. 2.  $I$ – $V$  and  $C$ – $V$  characteristics measured on the p–n diode.

with five 10 nm thick ZnSe wells and 10 nm thick  $\text{ZnS}_{0.06}\text{Se}_{0.94}$  barriers. The lower n-type cladding layer was 1.56  $\mu\text{m}$  thick  $\text{ZnS}_{0.06}\text{Se}_{0.94}$  where iodine was doped with the EtI flow rate of 1.4  $\mu\text{mol}/\text{min}$ . The net donor concentration of the doped film was  $7 \times 10^{17} \text{ cm}^{-3}$ . The upper p-type cladding layer was also 1.56  $\mu\text{m}$  thick  $\text{ZnS}_{0.06}\text{Se}_{0.94}$ , where N was doped with a tBA flow rate of 130  $\mu\text{mol}/\text{min}$  and with a cracking temperature of 800°C. A 100  $\mu\text{m}$  wide Au stripe electrode was formed on the p- $\text{ZnS}_{0.06}\text{Se}_{0.94}$  surface and the sample was annealed at 200°C for 40 min to improve the ohmic contact.

Fig. 2 shows the voltage–current ( $I$ – $V$ ) and capacitance–voltage ( $C$ – $V$ ) characteristics measured on the heterostructure diode shown in Fig. 1 at room temperature. The apparent built-up voltage seen in the  $I$ – $V$  characteristic changes with the vertical scale for the current. The variation of the measured diode capacitance with the bias shows that the upper cladding layer has p-type conductivity and the width of the depletion layer at the p–n junction changes with the bias voltage. The net acceptor concentration,  $N_A$ ,

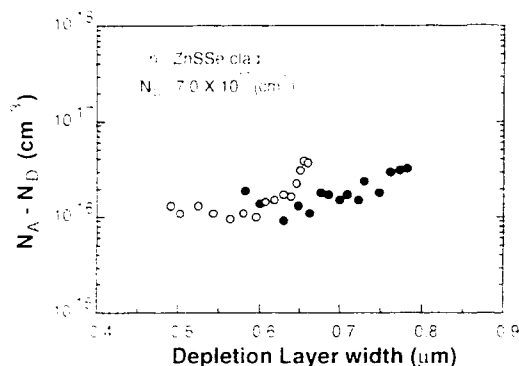


Fig. 3. Estimated net acceptor concentration in N-doped ZnSSe layer.

$-N_D$  was estimated from the measured  $C$ - $V$  characteristics assuming the uniform donor concentration in the lower n-cladding layer, and the results are shown in Fig. 3. The open and closed circles show the results for two samples. The net acceptor concentrations estimated near the p-n junction using a donor concentration of  $7 \times 10^{17} \text{ cm}^{-3}$  in the n-cladding layer was on the order of  $10^{16} \text{ cm}^{-3}$ . The depletion layer under this condition expands mainly toward the p-type layer. The tendency of the increase of the net acceptor concentration with the expansion of the depletion layer will be discussed in the next section.

The  $V$ - $I$  characteristic measured at room temperature with a pulsed operation to cover the higher current range is shown in Fig. 4 by closed circles. The pulse duration of the current was 50 ns and the repetition was 1 kHz. The open circles are the reproduction of the  $V$ - $I$  characteristic measured on the blue-green laser diode reported by 3M [10]. The drastic improvement of the  $V$ - $I$  characteristic in the present diode grown by MOVPE is clear. The physical origin of this relative improvement will be discussed elsewhere [11], but this comparison shows the possibility to realize low-voltage operations for blue lasers with MOVPE, especially toward the reliable continuous-wave laser operations.

### 3. Improvement of diode properties

#### 3.1. Unintentional incorporation of iodine into p-type layers

In our previous work on a heterostructure similar to that shown in Fig. 1 where the upper cladding layer was left undoped, diffusion or segregation of iodine from the lower n-type cladding layer into the upper-grown layers by about  $0.1 \mu\text{m}$  was indicated [12]. This gives the possibility for the p-type layer near the p-n junction to be compensated by the incorporation of iodine during the growth. To minimize this problem, a modulation-doped  $\text{ZnSe}(5 \text{ nm})/\text{ZnS}_{0.18}\text{Se}_{0.82}(5 \text{ nm})$  superlattice structure was used in the lower cladding layer. The iodine was doped only in the ZnSe layers to a concentration of  $7 \times 10^{17} \text{ cm}^{-3}$  and the  $\text{ZnS}_{0.18}\text{Se}_{0.82}$  layers were left undoped, and a total thickness of the superlattice of about  $1.5 \mu\text{m}$  was grown. The other growth conditions for the active and p-cladding layers remained essentially the same.

The net acceptor concentrations estimated from the  $C$ - $V$  measurements are shown in Fig. 5 with the squares. The open and closed squares are the results for two samples. The donor concentration averaged in the superlattice was used

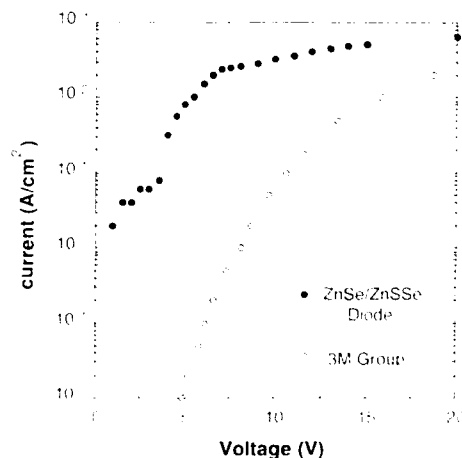


Fig. 4. Comparison of the measured  $V$ - $I$  characteristic with that of the diode laser reported from 3M.

in this estimation. The circles are the reproduction of the results shown in Fig. 3. Since the donor concentration in the n-type layer near the p–n junction may not be uniform, as indicated by the above discussion, the estimated values for the net acceptor concentration may have some uncertainty. However, the decrease of the depletion layer width near zero bias up to 0.1–0.2  $\mu\text{m}$  was observed in the present structure compared to the previous structure shown by the circles. Since depletion layer widths generally decrease for higher impurity concentrations, this indicates that the effective acceptor concentration in the p-type ZnSSe layer near the p–n junction was increased in the present structure by reducing the compensation effect with the iodine incorporation.

The variation of the net acceptor concentrations seen in both types of diodes shown in Fig. 5 was observed in the series of measurements. There is a possibility from the above discussion that the compensation due to the iodine incorporation in the p-type layer near the p–n junction resulted in the spatial distribution of the estimated net acceptor concentration.

Fig. 6 shows a comparison of the  $V$ – $I$  characteristics measured in the two types of diodes. The closed circles show the characteristic measured on the present structure where the modulation-doped superlattice structure was used for the

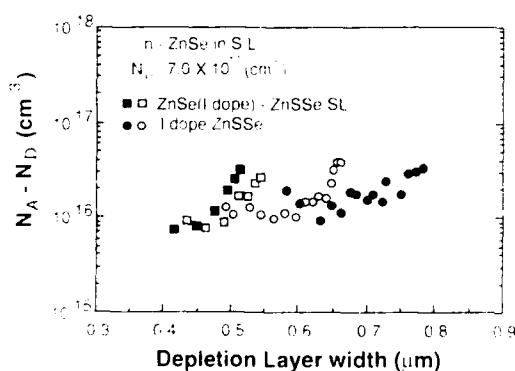


Fig. 5. Comparison of net acceptor concentrations estimated on two kinds of diodes with different n-cladding layers, where iodine (I) was doped in ZnSe layers in the ZnSe/ZnSSe superlattice structure (squares) and the uniformly doped ZnSSe layer (circles).

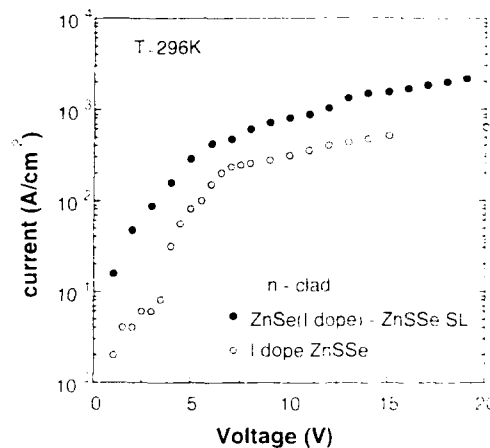


Fig. 6. Comparison of  $V$ – $I$  characteristics measured on two kinds of diodes with different n-cladding layers, where I was doped in ZnSe layers in the ZnSe/ZnSSe superlattice structure (closed circles) and the uniformly-doped ZnSSe layer (open circles).

n-cladding layer. The open circles are the ones measured on the diode with the uniformly-doped n-ZnSSe cladding layer. The low-voltage operation was clearly observed in the present structure. Since the overall current flow in II–VI diodes is limited by the tunneling process through the Schottky contact on the surface [11,13], the observed improvement with the modification of the n-cladding layer is slightly surprising. However, this may indicate that the incorporation of the iodine in the upper-grown layers is mainly due to the segregation during the growth. The improvement of the  $V$ – $I$  characteristic shown in Fig. 6 is consistent with the reduction of the depletion layer shown in Fig. 5, considering the suppression of the iodine segregation by the modulation-doped ZnSe/ZnSSe superlattice in place of the uniformly-doped ZnSSe for the n-cladding layer.

### 3.2. Purging time for the growth of p-type layers

In the present work of p-type doping, thermal cracking of tBA was necessary. Since radical species formed with the thermal cracking will have a short lifetime, the distance for the transport should be as small as possible. No valves



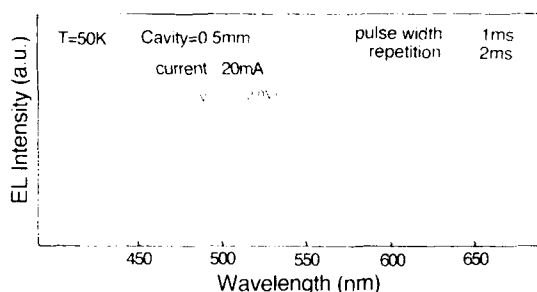


Fig. 7. Luminescence measured with current injection of 20 mA with diode voltage of 2 V.

were used in the transport line after the thermal cracking. In the growth of the diodes, however, there arises a problem when the furnace should be heated. Heating the furnace during the growth of the lower layers may change the growth conditions. In the early stage, a purging time up to 30 min was inserted between the growth of the active layer and the p-type cladding layer to stabilize the temperature of the furnace, but this seriously deteriorated the luminescence properties of the diodes. Therefore the purging time was minimized to 2–3 min by initiating the heating during the growth of the active layer.

Fig. 7 shows the luminescence observed from a cleaved facet of the diode thus prepared. The cavity length of the diode was 0.5 mm. The blue luminescence was observed at 50 K. The blue luminescence was also observed at room temperature, but the luminescence intensity was reduced to  $\sim 1/60$ . It is noted that the diode operating voltage was only 2 V for the current injection of 20 mA, or  $40 \text{ A/cm}^2$ . This low-voltage operation reflects the improvement of the  $V$ – $I$  characteristics discussed above.

#### 4. Conclusion

p-Type ZnSSe films were grown with N doping by thermal cracking of tBA in MOVPE at the higher growth temperature of  $560^\circ\text{C}$ . The  $V$ – $I$  characteristics measured on the ZnSe/ZnSSe p–n diodes showed much lower-voltage operation than

those of laser diodes prepared with MBE. A problem found in this work was the segregation of iodine doped in the lower n-cladding layer. This was reduced by introducing the modulation-doped superlattice structure in the n-cladding layer, and blue luminescence was observed with the current injection of 20 mA and with the low operating voltage of 2 V.

#### 5. Acknowledgements

The authors wish to thank Professor M. Yamanishi for valuable discussions. They wish to thank Trichemical Co. for supplying the metalorganic precursors. This work was supported in part by a Grant-in-Aid for Scientific Research from the Ministry of Education, Science and Culture, No. 04402032.

#### 6. References

- [1] K. Ohkawa, T. Karasawa and T. Mitsuyu, *J. Crystal Growth* 111 (1991) 797.
- [2] R.M. Park, M.B. Troffer, C.M. Rouleau, J.M. DePuydt and M.A. Haase, *Appl. Phys. Lett.* 57 (1990) 2127.
- [3] A. Ohki, N. Shibata and S. Zembutsu, *Jap. J. Appl. Phys.* 27 (1988) L909.
- [4] I. Suemune, K. Yamada, H. Masato, T. Kanda, Y. Kan and M. Yamanishi, *Jap. J. Appl. Phys.* 27 (1988) L2195.
- [5] S. Tohno, S. Zembutsu and A. Katsui, in: *Extended Abstracts 38th Spring Meeting, 1991 Japan Society of Applied Physics*, No. 1, p. 258 (in Japanese).
- [6] A. Kamata, H. Fujita and H. Mitsuhashi, in: *Extended Abstracts 53rd Autumn Meeting, 1992 Japan Society of Applied Physics*, No. 1, p. 226 (in Japanese).
- [7] M. Fujimoto, I. Suemune, H. Osaka and Y. Fujii, *Jap. J. Appl. Phys.* 32 (1993) L524.
- [8] Sz. Fujita and Sg. Fujita, *J. Crystal Growth* 117 (1992) 67.
- [9] M. Fujimoto, I. Suemune and Y. Fujii, unpublished.
- [10] M.A. Haase, J. Qiu, J.M. DePuydt and H. Cheng, *Appl. Phys. Lett.* 59 (1991) 1272.
- [11] I. Suemune, *J. Crystal Growth* 138 (1994) 714.
- [12] Y. Fujii, I. Suemune and M. Fujimoto, 1993 Int. Conf. on Solid State Devices and Materials, Makuhari, Japan, 1993.
- [13] J. Ren, K.A. Bowers, R.P. Vaudo, J.W. Cook, J.F. Schetzina, J. Ding, H. Jeon and A.V. Nurmikko, *J. Crystal Growth* 117 (1992) 510.



ELSEVIER

Journal of Crystal Growth 138 (1994) 755–758

JOURNAL OF  
**CRYSTAL  
GROWTH**

## Metalorganic vapor phase epitaxy growth of p-type ZnSSe and its application for blue-green lasers

K. Yanashima <sup>\*</sup>, D. Yamasaki, S. Watabe, K. Hara, J. Yoshino, H. Kukimoto

*Imaging Science and Engineering Laboratory, Tokyo Institute of Technology, 4259 Nagatsuda, Midori-ku, Yokohama 227, Japan*

### Abstract

p-Type doping of ZnSSe layers lattice-matched to GaAs substrates are investigated by metalorganic vapor phase epitaxy (MOVPE) growth, where dimethylzinc, dimethylselenide, and diethylsulfide (DES) or dimethylsulfide (DMS) are used as the host sources and dimethylaminolithium as the acceptor dopant. Low-temperature photoluminescence and capacitance measurements show that acceptor impurities, nitrogen and/or lithium, are effectively doped in ZnSSe layers grown by using DMS as the sulfur source, while they are hardly doped in the layers grown by using DES. Stimulated emission in the blue to green spectral region are observed at 77 K from MOVPE-grown structures of separate confinement heterostructure single quantum well (SCH-SQW), ZnSSe/ZnSe/ZnCdSe/ZnSe/ZnSSe/GaAs, under optical excitation, and evidence of stimulated emission by current injection in a pulsed mode was observed.

### 1. Introduction

There has been increasing interest in ZnSe and related alloys of ZnCdSe, ZnSSe and ZnMgSSe since blue-green lasers based on these materials grown by molecular beam epitaxy (MBE) were demonstrated by several research groups [1–4]. We pay attention to a growth technique of metalorganic vapor phase epitaxy (MOVPE) for fabricating blue-green lasers for two reasons. One is that MOVPE is more suitable than MBE in principle for growing the materials which involve volatile elements such as phosphorus and sulfur. The other is that MOVPE has a mass-production capability. A significant

progress has already been made in the MOVPE growth of n-type ZnSe and related alloys, and a main issue remaining yet to study is a reproducible MOVPE growth of p-type layers. We have taken an approach to the solution of this issue by growing at relatively high temperatures and by using an acceptor dopant which may not produce hydrogen upon decomposition, in order to overcome a problem of hydrogen passivation of acceptors. We have already reported that p-type ZnSe layers with a carrier concentration of mid  $10^{16} \text{ cm}^{-3}$  can be grown by MOVPE at 470–600°C using dimethylaminolithium (DMNLI) as the acceptor dopant [5].

In this paper we report a successful MOVPE growth of the p-type ZnSSe layer lattice matched to GaAs which is an important component of ZnSe-based lasers, using the dopant of DMNLI

<sup>\*</sup> Corresponding author.

as was previously used [5], but using dimethylsulfide instead of diethylsulfide as an appropriate sulfur source. We also demonstrate the fabrication of separate confinement heterostructure single quantum well (SCH-SQW), ZnSSe/ZnSe/ZnCdSe/ZnSe/ZnSSe/GaAs, based on the p-type control of ZnSSe layers.

## 2. Growth and characterization of p-type ZnSSe

The growth was carried out in an atmospheric pressure MOVPE system consisting of a cold wall horizontal reactor. Dimethylzinc (DMZn), dimethylselenide (DMSe), and diethylsulfide (DES) or dimethylsulfide (DMS) were used as source materials. The flow rates of DMZn and DMSe were 2.5 and 12  $\mu\text{mol}/\text{min}$ , respectively. The sulfur content of about 7% in ZnSSe for lattice-matching to GaAs was controlled by a typical flow rate of about 15  $\mu\text{mol}/\text{min}$  for DES or about 50  $\mu\text{mol}/\text{min}$  for DMS. GaAs substrates were chemically etched for 1 min in a  $1\text{NH}_4\text{OH}:1\text{H}_2\text{O}_2:10\text{H}_2\text{O}$  solution [6], followed by surface treatment in a  $(\text{NH}_4)_2\text{S}_x$  solution, and then they were immediately loaded to the reactor. The typical growth rate at a growth temperature of 470°C was about 0.8  $\mu\text{m}/\text{h}$ . Layer thickness was typically about 2  $\mu\text{m}$ .

The low-temperature photoluminescence spectra for the layers grown using DES as the sulfur source were dominated by the free exciton emission line, located at 2.83–2.84 eV near the band edge of ZnSSe, no matter whether or not they were doped with DMNLI. This indicates that acceptors were not effectively introduced in layers probably owing to a prereaction taking place between DES and DMNLI. The undoped layer grown using DMS as a sulfur source showed a dominant free exciton line, labeled FE, as shown in fig. 1a. However, the doped layers grown using DMS as a sulfur source showed acceptor-bound exciton emission lines, labeled  $\text{A}^0\text{X}$ , located at 10 meV below the free exciton line as shown in Figs. 1b and 1c, indicating that nitrogen and/or lithium are introduced in these layers. It is also noted from the photoluminescence spectra that the bound exciton line shifts slightly toward lower

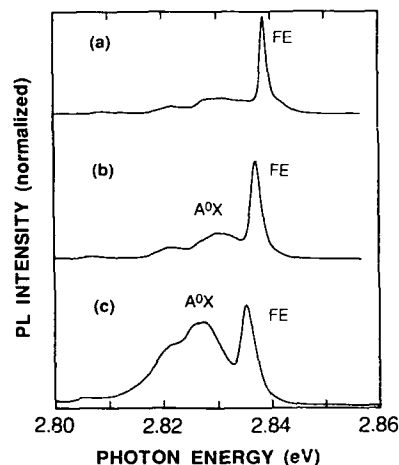


Fig. 1. Photoluminescence spectra at 33 K for (a) an undoped layer, and (b) and (c) doped ZnSSe layers grown at 470°C using DMS as sulfur source. Doping of layers (b) and (c) were performed at hydrogen flow rates of 200 and 500 SCCM, respectively, passing through a DMNLI container kept at 95°C.

energies with increasing doping level. The behavior could be ascribed to a slight decrease of sulfur content in ZnSSe due to a prereaction between DMS and DMNLI although it would be much weaker, if any, than between DES and DMNLI. Capacitance measurements for Schottky barriers made on the sample of Fig. 1c have shown a hole concentration of mid  $10^{16} \text{ cm}^{-3}$ .

## 3. Application for visible lasers

Before applying the p-ZnSSe layer for lasers, we fabricated undoped SCH-SQW samples on GaAs substrates to investigate the quality of all constituting layers in terms of crystallinity and heterointerfaces. A 1  $\mu\text{m}$  thick  $\text{ZnS}_{0.07}\text{Se}_{0.93}$  layer was first grown on the (100) GaAs substrate, followed by a 200 nm thick ZnSe layer, 10 nm thick  $\text{Zn}_{1-x}\text{Cd}_x\text{Se}$  layer ( $x = 0.1-0.2$ ), 200 nm thick ZnSe layer, and finally a 1  $\mu\text{m}$  thick  $\text{ZnS}_{0.07}\text{Se}_{0.93}$  layer. The samples used for photoluminescence measurements had a 600  $\mu\text{m}$  long Fabry-Perot cavity consisted of two parallel cleaved surfaces.

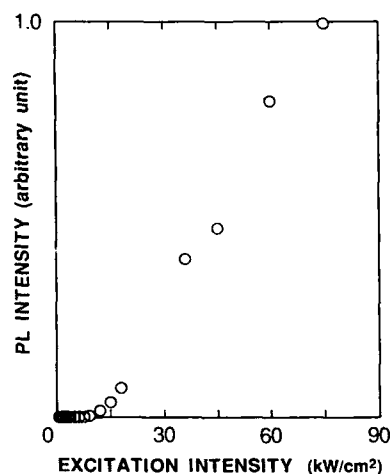


Fig. 2. The relation between light output at 77 K from a single facet of an SCH-SQW and the excitation power of the pulsed 355 nm light from a Nd:YAG laser. The Cd content in the SQW layer was 17%.

With excitation at 77 K by the 355 nm third harmonic pulsed light from a Nd:YAG laser operating at 10 Hz with a pulse width of 20 ns, the structures showed emission in the blue-to-green spectral region depending on the Cd content  $x$  of the  $\text{Zn}_{1-x}\text{Cd}_x\text{Se}$  quantum well layers in the structure. Fig. 2 shows an example of the relation between light output from a single facet as a function of excitation intensity. Emission intensity increases superlinearly with excitation intensity above a threshold power density of about  $18 \text{ kW/cm}^2$ . Fig. 3 shows emission spectra observed under different excitation levels of the same sample as in Fig. 2. Above a threshold excitation level, a spectral narrowing takes place with a spectral linewidth of about 0.7 nm which may be limited by the resolution of the present measurement system. The observed luminescence behavior can be attributed to the stimulated light emission, indicating that the SCH-SQW structure can be successfully fabricated by MOVPE.

Based on the undoped SCH-SQW structure for optical pumping experiments, we have tried fabricating SCH-SQW injection lasers with structure as schematically shown in Fig. 4. The structure consists of a 800 nm thick  $\text{n-ZnS}_{0.07}\text{Se}_{0.93}$  layer grown on the n-type (100) GaAs substrate

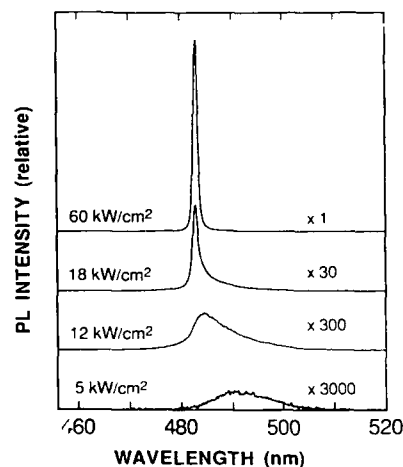


Fig. 3. Photoluminescence spectra at 77 K of an SCH-SQW sample excited by the 355 nm pulsed light (width of 20 ns and repetition rate of 10 Hz) from a Nd:YAG laser.

(Si-doped,  $n = 1 \times 10^{18} \text{ cm}^{-3}$ ), a 200 nm thick n-ZnSe layer, a 10 nm thick undoped  $\text{Zn}_{1-x}\text{Cd}_x\text{Se}$  ( $x = 0.1-0.2$ ) single quantum-well layer, a 200 nm thick p-ZnSe layer, a 500 nm thick p-ZnS<sub>0.07</sub>Se<sub>0.93</sub> layer, and a 12.5 nm thick p-ZnSe contact layer. The p- and n-type layers of the structure were grown using DMNLI and ethyl iodide ( $\text{C}_2\text{H}_5\text{I}$ ) as acceptor and donor dopants, respectively. Carrier concentrations in these p- and n-type layers were estimated to be around  $10^{16} \text{ cm}^{-3}$  from the capacitance measurements of epitaxial layers separately grown under the same growth conditions.

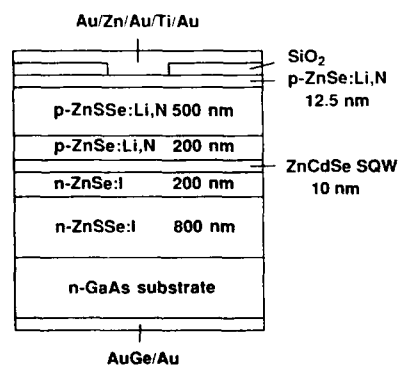


Fig. 4. Schematic structure of an SCH-SQW light emitter. The Cd content in the SQW layer was about 11%.

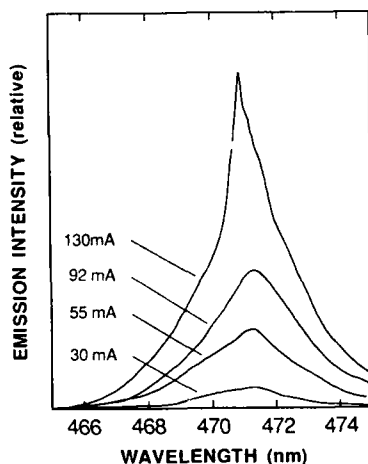


Fig. 5. Emission spectra at 77 K from an SCH-SQW light emitter under different pulsed current levels.

For making ohmic contacts, Au/Zn/Au/Ti/Au and AuGe/Au were evaporated on the top of the p-ZnSe layer and on the back of the n-GaAs substrate, respectively, followed by annealing at 350°C in a nitrogen atmosphere for 210 s. The 15  $\mu\text{m}$  wide stripe pattern was made by forming a  $\text{SiO}_2$  layer on the top surface. The diode wafer was cleaved into bars with a cavity length of about 600  $\mu\text{m}$ .

Blue to green light emission was observed from samples at 77 K depending on the cadmium content  $x$  in the  $\text{Zn}_{1-x}\text{Cd}_x\text{Se}$  quantum wells under pulsed current injection with a pulse width of 5  $\mu\text{s}$  and at a repetition rate of 2 kHz. Photoluminescence spectra from a single facet of an SCH-SQW sample at different current levels are shown in Fig. 5. We can clearly see evidence of spectral narrowing under a voltage of 8 V and at a current of 130 mA. Unfortunately, an operation above this current level led to the sample degradation. The threshold voltage of 8 V is surprisingly low compared with the reported values for the devices of similar structure grown by MBE. This may be due to the special nature of MOVPE-grown p-type ZnSe surfaces and/or an effect of the electrode material used in this study.

Further study is necessary to substantiate the observed behavior and to move forward the fabri-

cation of blue lasers of better performance by MOVPE. The important issues to further investigate would include an achievement of much higher carrier concentration in both p- and n-type layers used in the structure as well as a fabrication of better ohmic contacts on p-layers.

#### 4. Summary

p-Type ZnSSe layers, lattice-matched to GaAs substrates, were successfully grown at 470°C by MOVPE using DMZn, DMSe, DMS and DMNLi. Undoped SCH-SQW structures grown by MOVPE showed stimulated emission of blue to green light at 77 K under optical excitation by the Nd:YAG third harmonic pulsed light. The SCH-SQW injection laser structures were also fabricated by MOVPE based on the results of p-type doping of ZnSSe layers lattice-matched to GaAs. Evidence of stimulated emission in the blue spectral region was observed at 77 K under pulsed current injection.

#### 5. Acknowledgements

The authors thank Mr. H. Fujiwara for help in photoluminescence measurements using a Nd:YAG laser. They also thank all members of Professor Iga's laboratory at the Tokyo Institute of Technology for processing of laser structures.

#### 6. References

- [1] J. Qiu, J.M. DePuydt, H. Cheng and M.A. Haase, *Appl. Phys. Lett.* 59 (1991) 2992.
- [2] M.A. Haase, J. Qiu, J.M. DePuydt and H. Cheng, *Appl. Phys. Lett.* 59 (1991) 1272.
- [3] K. Ohkawa, T. Karasawa and T. Mitsuyu, *J. Crystal Growth* 111 (1991) 797.
- [4] H. Jeon, J. Ding, W. Pattern and A.V. Nurmikko, *Appl. Phys. Lett.* 59 (1991) 3619.
- [5] K. Yanashima, K. Koyanagi, K. Hara, J. Yoshino and H. Kukimoto, *J. Crystal Growth* 124 (1992) 616.
- [6] J. Gotoh, H. Fujiwara, H. Shirai, J. Hanna and I. Shimizu, *J. Crystal Growth* 117 (1992) 85.



ELSEVIER

Journal of Crystal Growth 138 (1994) 759–763

JOURNAL OF  
**CRYSTAL  
GROWTH**

## Photoluminescence excitation spectroscopy of the lasing transition in ZnSe–(Zn,Cd)Se quantum wells

Y. Kawakami<sup>1</sup>, I. Hauksson, J. Simpson, H. Stewart, I. Galbraith, K.A. Prior,  
B.C. Cavenett \*

*Department of Physics, Heriot Watt University, Edinburgh EH14 4AS, UK*

### Abstract

Photoluminescence excitation spectroscopy of the lasing transition in II–VI laser structures allows direct observation of the absorption edge during laser operation. We have investigated a set of  $\text{Zn}_{0.8}\text{Cd}_{0.2}\text{Se}/\text{ZnSe}$  multiple quantum well structures with well widths ranging from 30 to 120 Å and the photoluminescence at low excitation levels consistently shows the  $n = 1$  heavy hole exciton transition, while above threshold the lasing peak is observed to be red-shifted with a localization energy which is always much greater than the Stokes shift due to inhomogeneities. Excitonic absorption features can be observed up to the highest excitation energies and the localization energy for all well widths remains around 30 meV suggesting that the optical gain above lasing threshold involves exciton–LO phonon emission.

### 1. Introduction

An important objective at present is the development of II–VI laser diodes which operate in a continuous wave mode at room temperature and understanding the lasing mechanism in these lasers is essential for the optimum design of laser structures. Current II–VI quantum well laser diode devices operate at room temperature in a pulsed mode with very short lifetimes [1]. In III–V semiconductors, recombination from the electron–hole plasma is the dominant lasing process and so only band-to-band transitions are generally included in gain spectra calculations.

However, in a compound such as ZnSe, the Mott density is  $\sim 6 \times 10^{18} \text{ cm}^{-3}$ , two orders of magnitude larger than for GaAs, and so excitons may play an important role in the lasing mechanism. This has been seen in other bulk II–VI materials [2].

In this paper we examine the recombination processes in undoped ZnSe–(Zn,Cd)Se multiple quantum well structures by optically pumping the lasing transition in structures with different well widths. The strongly excitonic character of the absorption during lasing can be investigated using photoluminescence excitation spectroscopy (PLE) where the intensity of the lasing transition is monitored as a function of the excitation wavelength. The results show that even above the lasing threshold the PLE spectra display a strong excitonic character.

\* Corresponding author.

<sup>1</sup> Permanent address: Department of Electrical Engineering, University of Kyoto, Kyoto 606-01, Japan.

Historically, exciton-related lasing mechanisms have been studied for bulk II–VI crystals at low temperature. Guillaume et al. [3] attributed the optical gain in CdS excited by an electron beam at 10 K to three exciton-related processes namely (1) a low gain process owing to the annihilation of a free exciton with the emission of a photon and a LO phonon ( $E_x$ -LO phonon process), (2) a medium gain process of exciton–exciton inelastic scattering, (3) a high gain process involving exciton–electron scattering. More recently, Newbury et al. [4] concluded that the exciton–exciton inelastic collision is the dominant stimulated emission process at 6 K in an optically pumped ZnSe epilayer. Exciton-related lasing processes have been investigated in multiple quantum well (MQW) structures such as (Zn,Cd)Se–ZnSe [5–9], ZnSe–Zn(S,Se) [10], (Zn,Cd)Se–Zn(S,Se) [11] and (Zn,Cd)S–ZnS [12].

## 2. Experimental procedure

The (Zn,Cd)Se–ZnSe MQW layers were grown in a VG Semicon molecular beam epitaxy system using conventional Knudsen cell sources of zinc, cadmium and selenium on semi-insulating (Cr-doped) (100) GaAs substrates at a temperature of 280°C. Details of growth techniques have been published previously [13].

The MQW structures consist of a ZnSe buffer layer (1.0  $\mu\text{m}$ ), 15 cycles of  $\text{Zn}_{0.80}\text{Cd}_{0.20}\text{Se}$  wells and ZnSe barriers and a ZnSe cap layer (0.20  $\mu\text{m}$ ) and in these experiments, a series of samples with different well widths of 15, 30, and 120 Å, and a constant barrier width of 80 Å were investigated. Given an exciton Bohr radius ( $a_B$ ) of 35 Å in bulk  $\text{Zn}_{0.80}\text{Cd}_{0.20}\text{Se}$ , these well widths cover the range of  $0.43a_B$  to  $3.4a_B$ . Thus we span the transition from quasi-two-dimensional to bulk excitonic character.

The samples were cleaved to approximately 500  $\mu\text{m}$  and mounted on a copper cryostat holder. An Xe–Cl excimer laser (Lambda Physik LPX-100) pumped tunable dye laser (Lambda Physik FL2001) with dyes of Coumarin 120 and Coumarin 47 was used for the photopumping to cover the spectral range of 440 to 476 nm. The pulse dura-

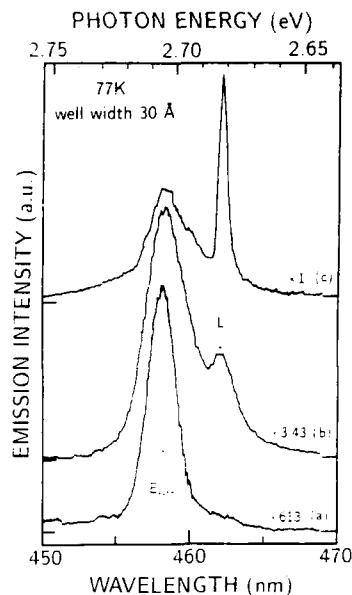


Fig. 1. Emission spectra taken from the cleaved edge of the MQW sample ( $L_w = 30$  Å) under pulsed photo (2.7365 eV) excitation of: (a) 0.063  $\text{kW}/\text{cm}^2$ , (b) 6.3  $\text{kW}/\text{cm}^2$  and (c) 20.0  $\text{kW}/\text{cm}^2$ .

tion of the pump laser is 5 ns, which is much longer than the recombination time in the materials, so that the excitation was quasi-CW. The pump intensity was controlled using neutral density filters and was focused onto the sample surface using a cylindrical lens. The pulsed emission signal with a repetition rate of 15 Hz from the cleaved edge of the sample was focused into a Spex 0.6 m single grating monochromator using collection optics and was averaged using a boxcar integrator.

## 3. Experimental results

Fig. 1, curve (a), shows the pulsed emission at 77 K from the cleaved edge as a function of the excitation power obtained from a ZnSe/ $\text{Zn}_{0.80}\text{Cd}_{0.20}\text{Se}$  multiple quantum well structure with well width of 30 Å pumped at 2.7365 eV. At higher excitation intensities, the stimulated emission is observed at 2.6818 eV (curves (b) and (c))

whereas the Ex 1hh exciton emission is at 2.7132 eV. Thus there is a large red shift. Note that the emission peak of the heavy hole exciton does not shift with increasing excitation intensity and is still observable above the lasing threshold. Reflectivity and CW absorption measurements were used to determine the Stokes shift of the exciton emission from the exciton absorption energy. The intensity of the lasing transition as a function of excitation wavelength is shown in Fig. 2 for pump intensities increasing from (a) to (e), as indicated, where the data in (a) correspond to the threshold condition ( $1.0I_{th}$ ). Both the light hole, Ex 1lh, and heavy hole, Ex 1hh, excitation transitions are observed and the spectrum is similar to the low power CW absorption. With increasing intensity the exciton peaks become less distinct and there is a small shift to higher energy. The net shift is the result of several effects, namely the exciton

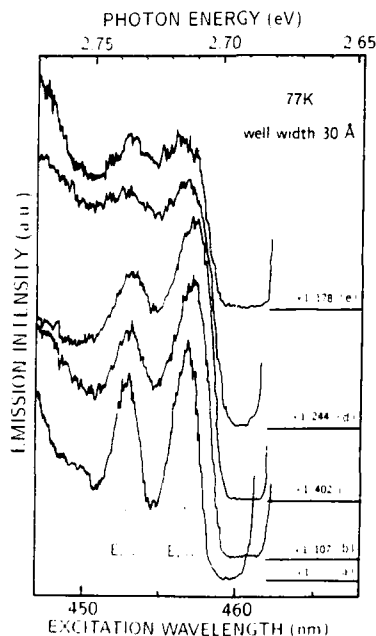


Fig. 2. Lasing peak intensity taken from the MQW ( $L_w = 30$  Å) as a function of excitation wavelength under excitation intensity of (a)  $1.0I_{th}$ , (b)  $2.5I_{th}$ , (c)  $5.0I_{th}$ , (d)  $7.9I_{th}$  and (e)  $11.2I_{th}$  respectively. In this case,  $I_{th}$  is the threshold intensity under resonant excitation of the  $E_{v1hh}$  line.

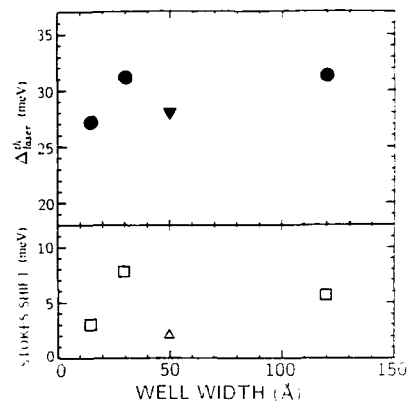


Fig. 3. Stokes shift of the CW PL (□) and the  $F_{laser}^{th}$  value (●) as a function of well width. Data obtained from a  $Zn_{0.85}Cd_{0.15}Se-ZnS_{0.08}Se_{0.92}$  MQW ( $L_w = 50$  Å) are also shown (Δ) [8].

band filling (a blue shift), a reduction of the exciton binding energy due to the exciton-self-screening (a blue-shift) and the renormalization of the bandgap (a red-shift). This shift we designate the localization energy at threshold,  $\Delta E_{laser}^{th}$ , and is defined as the energy difference between the Ex 1hh peak in the PLE and the lasing line. For the 30 Å sample,  $\Delta E_{laser}^{th}$  is 27.1 meV.

Similar results have been obtained for  $ZnSe/Zn_{0.80}Cd_{0.20}Se$  structures with 15 and 120 Å quantum well widths. Stimulated emission is observed at 2.7411 eV for the 15 Å wells and 2.6021 eV for the 120 Å wells. For the 15 Å wells, the PLE spectra show the excitation transitions into the light and heavy hole excitons, as well as into the ZnSe barrier/cladding layers. The red shift,  $\Delta E_{laser}^{th}$ , for this sample is 31.4 meV. For the 120 Å wells the Ex 1hh peak at 2.6336 eV is much broader and weaker than observed in the other sample and disappears if the excitation intensity is raised above  $1.5I_{th}$ . The Ex 1lh is not observed and  $\Delta E_{laser}^{th}$  is 31.5 meV.

Fig. 3 summarizes the data for the Stokes shift and the red shift  $\Delta E_{laser}^{th}$  for the three samples reported in this paper together with data from a previous study of a  $Zn_{0.85}Cd_{0.15}Se/ZnS_{0.08}Se_{0.92}$  quantum well laser structure (well width of 5 nm) [9].



#### 4. Discussion

The  $\Delta E_{\text{laser}}^{\text{th}}$  values of these samples are much larger than the Stokes shifts. The values are close to both the LO-phonon energy ( $E_{\text{LO}}$ ) of 31 meV and the exciton binding energy  $E_{\text{b}} \approx 35$  meV and so two processes may be responsible for the lasing. One is the LO-phonon assisted recombination of excitons and the other is the exciton–exciton scattering process.

Parametric lasing processes such as these have been previously considered in bulk II–VI materials [2,13,14]. The stimulated emission is viewed as a scattering event in the polariton picture from the exciton-like branch to the photons-like branch.

The exciton–exciton scattering process involves two excitons, e.g. on the  $n = 1$  exciton-like polariton branch. The Coulomb interaction between them may scatter one onto the photon-like branch and the other onto a higher-lying, exciton-like polariton branch. In either case  $E_{\text{laser}}^{\text{th}}$  should be proportional to  $E_{\text{b}}$  and should follow the well width dependence of  $E_{\text{laser}}^{\text{th}}$ . Fig. 4 shows the exciton binding energy of  $n = 1$  heavy hole exciton ( $E_{\text{b}}$ ) in the ZnSe–Zn<sub>0.80</sub>Cd<sub>0.20</sub>Se–ZnSe quantum well as a function of  $L_{\text{w}}$  calculated using a two-parameter variational approach. In

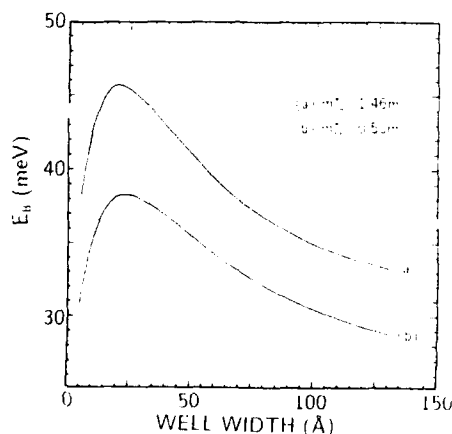


Fig. 4. Calculated binding energy of excitons confined in a Zn<sub>0.80</sub>Cd<sub>0.20</sub>Se QW as a function of well width, assuming that the in-plane effective mass of the heavy-hole in Zn<sub>0.80</sub>Cd<sub>0.20</sub>Se is (a)  $1.46m_0$  and (b)  $0.50m_0$ .

this analysis, the conduction and heavy hole band discontinuities ( $\Delta E_{\text{c}}$ ,  $\Delta E_{\text{v, hh}}$ ) are assumed to be  $\Delta E_{\text{c}} = 168$  meV and  $\Delta E_{\text{v, hh}} = 66$  meV, respectively, and the calculation has been done for two different in-plane heavy hole masses: (a)  $m_{\text{hh}||} = 1.46m_0$  and (b)  $m_{\text{hh}||} = 0.50m_0$ . As far as we are aware, there are, to date, no comprehensive measurements of the valence subband dispersion in these materials. However, the actual in-plane mass would be between the two. For example, the  $E_{\text{b}}$  value at  $L_{\text{w}} = 15$  Å is estimated to be in the range between 37 and 45 meV, which is substantially larger than the observed  $\Delta E_{\text{laser}}^{\text{th}}$  value (27.1 meV). More significantly, if exciton–exciton scattering were dominant, the value of  $\Delta E_{\text{laser}}^{\text{th}}$  should follow the strong well width dependence of the binding energy. In fact, Fig. 3 shows that the  $\Delta E_{\text{laser}}^{\text{th}}$  data lie between 27.1 and 31.5 meV, and do not show any distinct dependence on the well width.

Purely from an energy consideration, the results are consistent with the lasing mechanism at threshold being LO-phonon mediated rather than being due to exciton–exciton scattering. LO-phonon scattering from the exciton-like branch to the photon-like branch of the polariton is accompanied by the emission of one LO-phonon with the light emission occurring one LO-phonon energy beneath the exciton energy. No well width dependence of  $E_{\text{laser}}^{\text{th}}$  is expected with this mechanism and the laser threshold should show a very distinct behaviour with temperature [14]. Below  $\sim 70$  K the threshold for lasing should remain constant, but rise exponentially thereafter. The exponential rise is due to the emergence of a population of thermally excited phonons, which contribute to a phonon-assisted absorption, thus making lasing more difficult to achieve. To confirm this we have followed the lasing threshold as a function of temperature and show the results in Fig. 5. Clearly we see the expected sharp rise in threshold above  $\sim 70$  K indicative of the exciton–LO phonon process.

The Stokes shifts are in the range between 3.0 and 7.7 meV, which is substantially smaller than the  $E_{\text{laser}}^{\text{th}}$ . Therefore, it is expected that the localisation of excitons by alloy disorder and/or the fluctuation of the well width is not directly re-

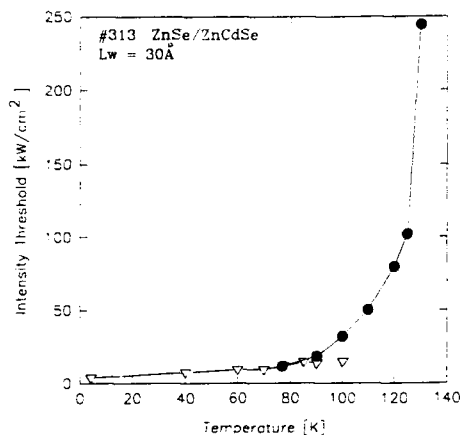


Fig. 5. Laser intensity threshold ( $\text{kW cm}^{-2}$ ) as a function of temperature for the 30 Å sample.

lated to the lasing mechanism in the series of samples investigated here. This is in contrast to recent work [6–8] in which it was argued that the lasing mechanism arose from an inhomogeneously broadened facet emission which was very different from the luminescence of the Ex1hh observed normal to the laser [16]. The difference is due to the presence of a large apparent Stokes shift in their samples which they attributed to re-absorption. In our samples the facet and normal emissions are the same and the stimulated emission does *not* emerge from the peak of the facet luminescence but at some 30 meV lower energy. We have also repeated our measurements on different cavity lengths and obtained the same  $E_{\text{laser}}^{\text{th}}$  values and so reabsorption effects can be neglected. Thus we believe the LO-phonon mechanism is responsible for the lasing at threshold in our samples.

#### 4. Conclusions

PLE spectra of the stimulated emission in the ZnSe–Zn<sub>0.80</sub>Cd<sub>0.20</sub>Se MQWs with a series of different well widths have been investigated at 77 K with the series of different well widths. It has been shown that the  $E_{\text{laser}}^{\text{th}}$  value is substantially larger than the Stokes shift of the CW PL and equal to the LO-phonon energy. Furthermore it

is independent of the well width. Even under lasing conditions, excitonic peaks are clearly seen in the PLE spectra confirming the importance of excitonic transitions in the lasing process. We conclude that exciton-LO phonon scattering is the dominant process for the optical gain in the range from  $I = I_{\text{th}}$  to  $7I_{\text{th}}$ .

#### 5. Acknowledgements

The authors are grateful to SERC, The Royal Society and VG Semicon Ltd. for support of this research. Yoichi Kawakami would like to express his sincere thanks to Professor S. Fujita for valuable discussions.

#### 6. References

- [1] M.A. Haase, J. Qiu, J.M. DePuydt and H. Cheng, in: Proc. 18th Int. Symp. on GaAs and Related Compounds, Seattle, WA, 1991, Inst. Phys. Conf. Ser. 120, Ed. G.B. Stringfellow (Inst. Phys., Bristol, 1992) p. 9.
- [2] S.W. Koch, H. Haug, G. Schmieder, W. Bohnert and C. Klingshirn, Phys. Status Solidi (b) 89 (1978) 431.
- [3] C.B. Guillaume, J.M. Deveber and F. Salvan, Phys. Rev. 177 (1969) 567.
- [4] P.R. Newbury, K. Shazard and D.A. Cammack, Appl. Phys. Lett. 58 (1991) 1065.
- [5] H. Jeon, J. Ding, A.V. Nurmikko, H. Luo, N. Samarth and J.K. Furdyna, Appl. Phys. Lett. 59 (1991) 1293.
- [6] J. Ding, H. Jeon, T. Ishihara, A.V. Nurmikko, H. Luo, N. Samarth and J. Furdyna, Surf. Sci. 267 (1992) 616.
- [7] J. Ding, H. Jeon, T. Ishihara, M. Hagerott, A.V. Nurmikko, H. Luo, N. Samarth and J. Furdyna, Phys. Rev. Lett. 69 (1992) 1707.
- [8] J. Ding, M. Hagerott, T. Ishihara, H. Jeon and A.V. Nurmikko, Phys. Rev. B 47 (1993) 10528.
- [9] Y. Kawakami, I. Hauksson, H. Stewart, J. Simpson, I. Galbraith, K.A. Prior and B.C. Cavenett, Phys. Rev. 48 (1993) 11994.
- [10] Y. Kuroda, I. Suemune, Y. Fujii and M. Fujimoto, Appl. Phys. Lett. 61 (1992) 1182.
- [11] Y. Kawakami, B.C. Cavenett, K. Ichino, S. Fujita and S. Fujita, Jap. J. Appl. Phys. 32 (1993) L730.
- [12] Y. Yamada, Y. Masumoto, J.T. Mullins and T. Taguchi, Appl. Phys. Lett. 61 (1992) 2190.
- [13] K.A. Prior, J.M. Wallace, J.T. Hunter, S.J. Adam, M.S. Haines, M. Saoudi and B.C. Cavenett, J. Crystal Growth 101 (1990) 176.
- [14] H. Haug, J. Appl. Phys. 33 (1968) 4687.
- [15] H. Haug and S. Koch, Phys. Status Solidi (b) 82 (1977) 531.
- [16] J. Ding, private communication.



ELSEVIER

Journal of Crystal Growth 138 (1994) 764–767

JOURNAL OF  
**CRYSTAL  
GROWTH**

## Dependence of device characteristics on quantum well thickness in ZnSe/ZnCdSe multi-quantum well blue-green laser diodes

Y. Tomomura <sup>\*</sup>, S. Hirata, T. Okumura, M. Kitagawa <sup>1</sup>, A. Suzuki, H. Takiguchi

*Central Research Laboratories, Corporate Research and Development Group, Sharp Corporation, 2613-1 Ichinomoto, Tenri, Nara 632, Japan*

### Abstract

ZnSe/Zn<sub>0.85</sub>Cd<sub>0.15</sub>Se multi-quantum well (MQW) diode structures with different well thicknesses ( $L_w$ ) in the range of 6–13 nm were fabricated, and device characteristics of the diodes were studied in terms of crystalline quality of the MQW layers. In order to investigate the relationship between the device characteristics and the crystalline quality of the MQW layers, the intensity of spontaneous emission from MQW diode structures was measured. The emission intensity increased with increasing  $L_w$  and showed a maximum value at  $L_w = 10$  nm, followed by rather rapid reduction of the emission intensity at  $L_w > 10$  nm. This decrease of emission intensity is suggested to be due to the lattice relaxation caused by dislocation formation at the interface taking account of critical thickness of the MQW structure. The lasing characteristics of ZnSe/ZnCdSe MQW blue-green laser diodes are also described.

### 1. Introduction

Recently, the ZnSe/ZnCdSe quantum well structure has attracted great interest in the area of blue-green laser diodes. The first laser operation has been achieved using a ZnSe/ZnCdSe single-quantum well (SQW) separate confinement heterostructure (SCH) laser diode [1]. Since then, several groups have reported on device characteristics of ZnSe/ZnCdSe QW structures,

not only using ZnSSe cladding layers [2], but also using ZnMgSSe cladding layers [3]. These QW structures have strain at the hetero-interface, and the relation between the device characteristics and the crystalline quality is not clear.

In this paper, we will describe the characteristics of ZnSe/ZnCdSe QW devices in terms of crystalline quality of the QW layers. In order to investigate the relation between the device characteristics and the crystalline quality of the QW layers, the intensity of spontaneous emission of several devices with different well thickness was measured. Dependence of the intensity on quantum well thickness is discussed taking account the critical thickness of ZnCdSe well layers in ZnSe barrier layers.

<sup>\*</sup> Corresponding author.

<sup>1</sup> Present address: Department of Electrical and Electronic Engineering, Tottori University, Koyama, Tottori 680, Japan.

The lasing characteristics of ZnSe/ZnCdSe MQW laser diodes operated at 77 K (pulsed) will also be described.

## 2. Experimental procedure

The device structure shown in Fig. 1 was grown by molecular beam epitaxy in an ULVAC SLD-260 system. Epitaxial layers were grown on Si-doped n-GaAs (100) substrates at a growth temperature of 300°C. Elemental Zn, Cd, and Se were used as source materials. ZnCl<sub>2</sub> and N excited by RF plasma were used for n- and p-type dopants, respectively. The diode structure consists of an n-ZnSe:N cladding layer ( $n = 5 \times 10^{17} \text{ cm}^{-3}$ ,  $d = 2.0 \text{ } \mu\text{m}$ ), a ZnSe/ZnCdSe MQW active layer and a p-ZnSe:N cladding layer ( $N_a^- - N_d^+ = 5 \times 10^{17} \text{ cm}^{-3}$ ,  $d = 1.0 \text{ } \mu\text{m}$ ). The MQW layer was composed of six wells of Zn<sub>0.85</sub>Cd<sub>0.15</sub>Se. Well thickness ( $L_w$ ) was varied from 6 to 13 nm and barrier thickness was fixed at 10 nm. To reduce the operation voltage of the devices, an n<sup>+</sup>-ZnSe:Cl buffer layer ( $n = 1 \times 10^{18} \text{ cm}^{-3}$ ,  $d = 0.1 \text{ } \mu\text{m}$ ) and a p<sup>+</sup>-ZnSe:N/p<sup>+</sup>-ZnTe:N graded contacting layer [4] were adopted.

Both LEDs and gain-guided LDs were fabricated.  $500 \times 500 \text{ } \mu\text{m}^2$  size LED chips were made by evaporating Au electrode (200  $\mu\text{m}$  in diameter, 15 nm in thickness) on top of the diode structure. The chips were mounted on the stem (TO-18). The gain-guided laser was fabricated by making 20  $\mu\text{m}$  wide stripe with Al<sub>2</sub>O<sub>3</sub> insulating

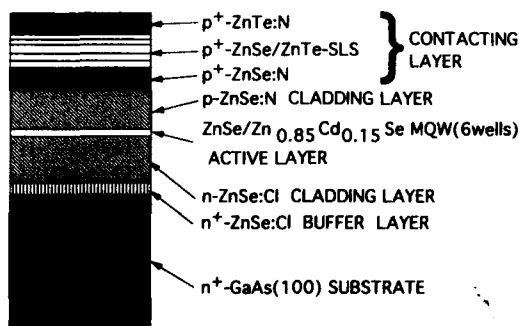


Fig. 1. Layer structure of ZnSe/ZnCdSe MQW diode.

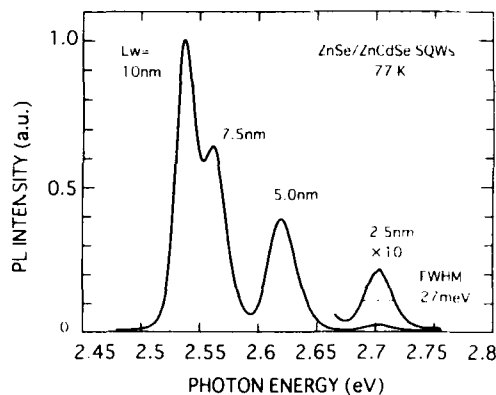


Fig. 2. PL spectrum of ZnSe/ZnCdSe SQWs at 77 K.

layer. Au–Cr electrodes were evaporated onto both p- and n-side.

## 3. Results and discussion

First, to confirm the interfacial quality of ZnSe/ZnCdSe quantum well structure, photoluminescence (PL) spectra of single quantum wells (SQWs) were measured at 77 K using He–Cd laser (325 nm). Fig. 2 shows PL spectrum of a multilayer structure which consisted of four single-quantum well layers with different  $L_w$  of 2.5, 5.0, 7.5 and 10.0 nm, separated from one another by 20 nm thick barrier layers. Sharp peaks from all wells were clearly observed. From the fact that the FWHMs of the peaks are rather large [5] and that the integrated intensity of the peak from the well with  $L_w = 2.5 \text{ nm}$  is smaller than those of other peaks, it is implied that a roughness of a few monolayers exists at the ZnSe/ZnCdSe hetero-interface. From these results it is confirmed that quantum wells with  $L_w$  larger than 5 nm were successfully fabricated.

Fig. 3 shows the dependence of emission intensity of the diode structure on well thickness. The emission intensity was measured from the LED devices at RT under CW operation with injection currents of 5 and 10 mA. The emission intensity increased with increasing  $L_w$  in the range of  $L_w = 6\text{--}10 \text{ nm}$ . This increase is thought

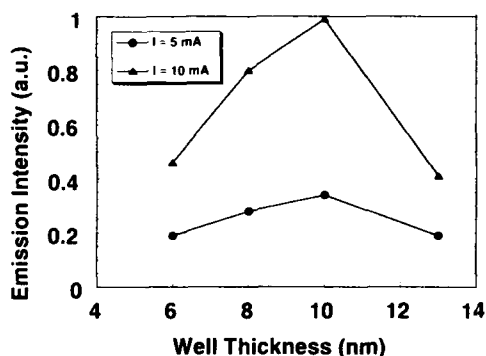


Fig. 3. Dependence of emission intensity of ZnSe/ZnCdSe MQW LED on well thickness ( $L_w$ ).

to be due to the decrease of influence of interfacial roughness. The emission intensity decreases with an increase of  $L_w$  in the range of 10–13 nm. This decrease of the emission intensity seems to be due to the lattice relaxation caused by dislocation formation. In order to confirm this hypothesis, the critical thickness of ZnSe/ZnCdSe was calculated. The calculation was based on the model proposed for the SiGe/Ge system [6,7]. Fig. 4 shows the calculated critical thicknesses of ZnCdSe well layers in the relaxed ZnSe barrier layers with different well numbers ( $N_w$ ) of 1, 3, and 6. For the calculation of the critical thickness, the Poisson ratio is assumed to be 0.2 by fitting the calculated value for a ZnSe layer on

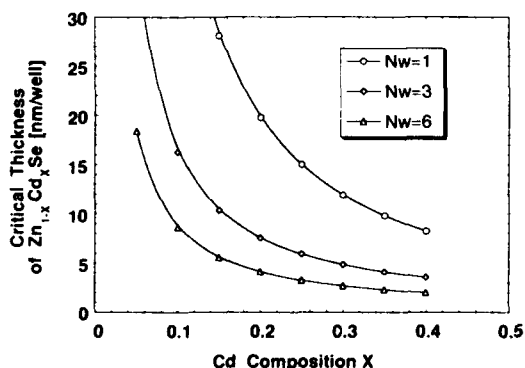


Fig. 4. Calculated critical thickness of ZnCdSe well layer in relaxed ZnSe barrier layers. (Thickness of ZnSe barrier layer is 10 nm.)

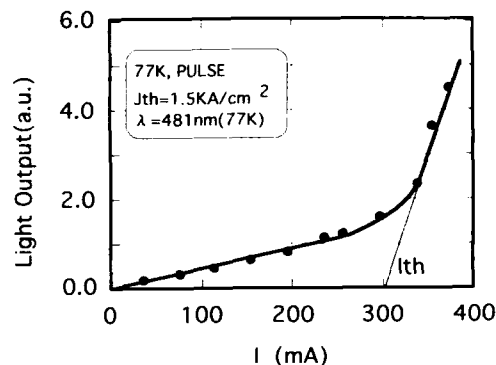


Fig. 5. Optical output characteristics of ZnSe/ZnCdSe MQW blue-green laser diode at 77 K (pulsed).

GaAs substrate with its experimental value. As shown in Fig. 4, the critical thickness for ZnSe/ $\text{Zn}_{0.85}\text{Cd}_{0.15}\text{Se}$  with  $N_w = 6$  is about 6 nm. Therefore the decrease of emission intensity in the range of  $L_w > 10$  nm in Fig. 3 is thought to be due to the creation of a nonradiative center caused by lattice relaxation through formation of dislocations.

Based on these results, a ZnSe/ZnCdSe MQW blue-green LD was fabricated with the smallest well thickness (6 nm). Fig. 5 shows the typical optical output characteristics of the laser diode operated at 77 K (pulsed). Laser operation was successfully obtained. Lasing wavelength was 481 nm and threshold current was 300 mA (threshold current density was  $1500 \text{ A/cm}^2$ ). The relatively high threshold current density [8] may be due to small optical confinement and large carrier spread in the  $p^+-\text{ZnTe:N}$  layer.

#### 4. Summary

ZnSe/ZnCdSe quantum well structures with different well thicknesses of 6 to 13 nm were fabricated. The intensity of spontaneous emission of the diode structures was measured at RT. The emission decreased for well thickness larger than 10 nm. Comparing this result with the calculated critical thickness of the system, it is suggested that the decrease of emission intensity is due to

the formation of a nonradiative center caused by lattice relaxation through dislocation formation.

A ZnSe/ZnCdSe MQW blue-green LD with well thickness of 6 nm showed laser action at 77 K with lasing wavelength of 481 nm.

### 5. Acknowledgments

The authors would like to thank I. Fujimoto, M. Aramoto and N. Hashizume for helpful discussions and continuous encouragement.

### 6. References

- [1] M.A. Haase, J. Qiu, M. DePuydt and H. Cheng, Appl. Phys. Lett. 59 (1991) 1272.
- [2] H. Jeon, J. Ding, W. Patterson, A.V. Nurmikko, W. Xie, D.C. Grillo, M. Kobayashi and R.L. Gunshor, Appl. Phys. Lett. 59 (1991) 3619.
- [3] S. Itoh, H. Okuyama, S. Matsumoto, N. Nakayama, T. Ohata, T. Miyajima, A. Ishibashi and K. Akimoto, Electron. Lett. 29 (1993) 766.
- [4] Y. Fan, J. Han, L. He, J. Saraie, R.L. Gunshor, M. Hagerott, H. Jeon, A.V. Nurmikko, G.C. Hua and N. Otsuka, J. Appl. Phys. 61 (1992) 3160.
- [5] Y. Kawaguchi, T. Ohno and T. Matsuoka, in: Extended Abstracts 1992 Int. Conf. on Solid State Devices and Materials, Tsukuba, 1992, p. 345.
- [6] D.C. Houghton, D.D. Perovic, J.-M. Baribeau and G.C. Weatherly, J. Appl. Phys. 67 (1990) 1850.
- [7] P.J. Parbrook, B. Henderson, K.P. O'Donnell, P.J. Wright and B. Cockayne, J. Crystal Growth 117 (1992) 492.
- [8] S.Y. Wang, J. Simpson, H. Stewart, S.J.A. Adams, I. Hauksson, Y. Kawakami, M.R. Taghizadeh, K.A. Prior and B.C. Cavenett, 7th Trieste Semiconductor Symp., Trieste, 1992, paper LN-4.



ELSEVIER

Journal of Crystal Growth 138 (1994) 768–775

JOURNAL OF **CRYSTAL  
GROWTH**

## InGaAlP visible light laser diodes and light-emitting diodes

Kazuhiko Itaya <sup>\*,1</sup>, Hideto Sugawara, Gen-ichi Hatakoshi

*Toshiba Research and Development Center, 1 Komukai Toshiba-cho, Saiwai-ku, Kawasaki 210, Japan*

### Abstract

In this paper, we review and discuss the critical problems involved in the research and development of InGaAlP visible light devices along with some of our achievements. High p-doping of a cladding layer, and a multi-quantum-barrier structure improved the temperature characteristics of InGaAlP laser diodes. These techniques have made it possible to realize a high temperature CW operation above 70°C at the wavelength of 633 nm. New structure InGaAlP light-emitting diodes (LEDs) which employ an off-angle substrate and a Bragg reflector have improved both quantum efficiency and light extraction efficiency. Candela-class, high-brightness LEDs have been achieved for operation in the orange to green color region.

### 1. Introduction

Quaternary InGaAlP alloys have been extensively investigated for optical device applications in the visible-light region. InGaAlP alloys can be lattice-matched to GaAs, and provide a direct transition type band-gap energy from red to green [1]. InGaAlP visible-light laser diodes oscillating in the 0.6  $\mu\text{m}$  wavelength range have attracted much interest as light sources for optical information processing systems, such as high-density optical disk systems and bar-code reader systems. Room-temperature continuous-wave (CW) operation of InGaAlP lasers was first achieved in 1985 [2–4] for InGaP/InGaAlP double-hetero (DH) structure grown by metalorganic chemical vapor deposition (MOCVD). However, the wavelength

of these lasers was relatively long (670–690 nm), compared with He–Ne gas laser (633 nm), and the maximum operation temperature was limited to a temperature as low as 50°C. The development of shorter-wavelength InGaAlP laser diodes, oscillating below 670 nm, has been continued for the use in high-density optical disk applications and the realization of a small-size light source of relevant emission wavelength for the substitution of conventional He–Ne gas lasers [5–16]. These approaches also made it possible to realize the high-power operation of InGaAlP laser diodes [17–23].

InGaAlP light-emitting diodes (LEDs) are also attractive because of their numerous potential applications, such as outdoor displays and automobile indicators. In LED applications, the conventional current-spreading structure consisting of a low-resistive and thick transparent layer is indispensable for efficient light extraction, since it effectively spreads the current flow [24]. Employment of the current spreading layer of

<sup>\*</sup> Corresponding author.

<sup>1</sup> Current address: Department of Electrical and Computer Engineering, University of California, Santa Barbara, California 93106, USA.

GaAlAs or GaP resulted in a candela-class high-brightness operation from orange to yellow [25–27]; however, the efficiency of green LEDs still remained low.

In this paper, we review and discuss the critical problems involved in the research and development of InGaAlP visible light devices along with some of our achievements. First, InGaAlP laser diodes are described. Discussions will be focused on the improvement of temperature characteristics towards the aim of the production of the 633 nm laser diode. Next, the design of InGaAlP LEDs grown by MOCVD is discussed, which is indispensable for realization of high-efficiency operation in the green region. This will be focused on a new structure which is well matched to the MOCVD growth technique.

These results and discussions are considered to be useful for research and development of ZnSe blue-green devices.

## 2. Experimental procedure

The epitaxial layers used in this study were grown by low-pressure MOCVD. The growth temperature was 730°C. Trimethylindium (TMI), trimethylgallium (TMG), trimethylaluminum (TMA),  $\text{AsH}_3$  and  $\text{PH}_3$  were used as source materials. The doping sources were dimethylzinc (DMZ) and  $\text{SiH}_4$  for the p- and n-type layers, respectively. The GaAs substrates used were (100), and cut 15° off the (100) plane toward the [011] direction (off-angle substrate). Ridge waveguide structure was employed in the investigation of laser diodes [28,29]. A GaAlAs current spreading layer was employed for the LED structure investigated in this study.

## 3. InGaAlP laser diodes

### 3.1. What limited the performance of InGaAlP laser diodes?

One of the problems in realizing a short-wavelength InGaAlP laser diodes was that it was difficult to obtain high-temperature operation. The

maximum operation temperature decreased with decreasing wavelength. For practical use of short-wavelength InGaAlP lasers, improvement of the temperature characteristics is indispensable. The deterioration of the temperature characteristics in the short-wavelength region is considered to originate from an increase in the electron overflow caused by a small band-gap energy difference between the active layer and the p-type cladding layer. In this section, we describe the effect of the following methods, high p-doping [7,8] and the multi-quantum-barrier (MQB) structure [11–13], on the reduction of the electron overflow in InGaAlP lasers.

### 3.2. Improvements of temperature characteristics

Fig. 1 shows the schematic energy band diagram of an InGaAlP laser. The conduction band discontinuity in the heterojunction is relatively small [30]. Even when high Al content cladding layers are employed, the maximum operation temperatures are limited to low temperatures

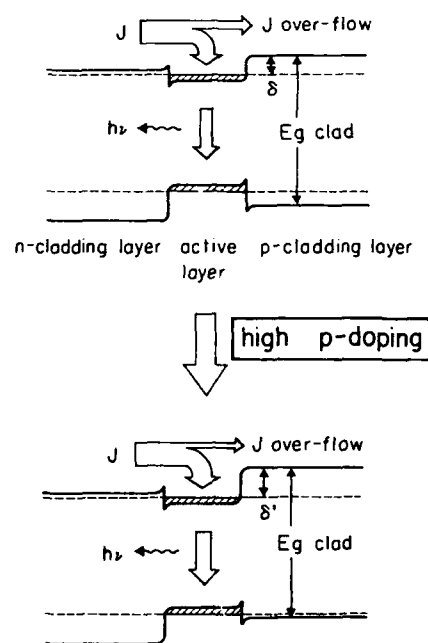


Fig. 1. Schematic energy band diagram of an InGaAlP laser.



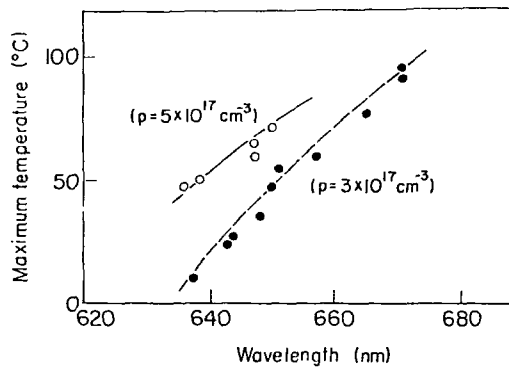


Fig. 2. Acceptor concentration dependence of the maximum temperature for CW operation against oscillation wavelength.

when shortening the wavelength. This is because the electron overflow into the cladding layer from the active layer increases, and also because the threshold current is increased.

When the p-cladding layer is highly doped, the Fermi level in the valence band side moves towards the valence band. The hetero-barrier between the active layer and p-cladding layer in the conduction band effectively increases and thus the electron overflow is reduced. Fig. 2 shows the acceptor concentration dependence of the maximum temperature for CW operation against oscillation wavelength. The maximum operation temperature was drastically improved over a wide wavelength range by high p-doping. By using the highly doped p-type cladding layer, the maximum operation temperature was increased to 70°C for a laser with an oscillation wavelength of 650 nm.

Next, the use of the quantum effect, MQB, on the improvement of the temperature characteristics is described. Fig. 3 shows a schematic band structure of the laser with an MQB. Interwell interference of the electron levels can be obtained by incorporating a series of the wells and barriers in the p-cladding layer [31]. It raises the electron conduction level.

Fig. 4 shows the temperature dependence of the threshold current of InGaAlP lasers with and without an MQB [13]. The wavelength was 634 nm. Reduction of threshold current was clearly confirmed. Also, the characteristic temperature,

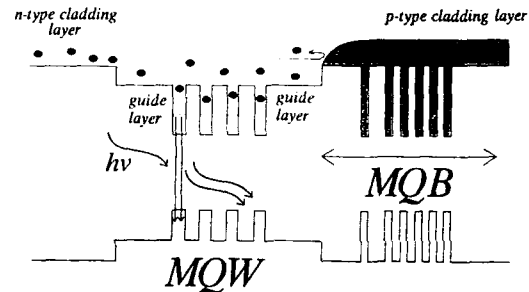


Fig. 3. Schematic band structure of the laser with an MQB.

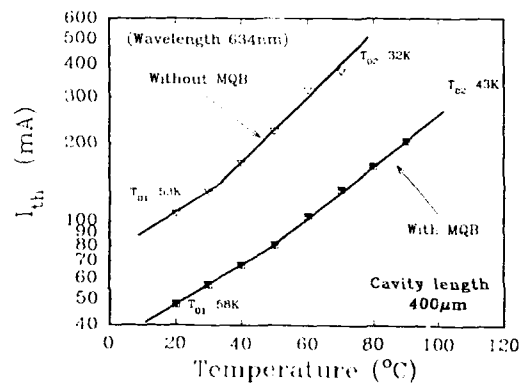


Fig. 4. Temperature dependence of the threshold current of InGaAlP lasers with and without MQB. The wavelength was 634 nm.

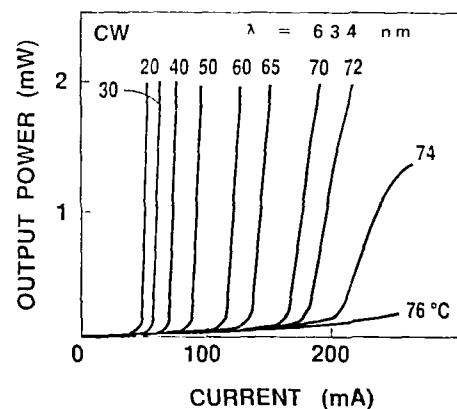


Fig. 5. Temperature dependence of  $I$ - $L$  characteristic of InGaAlP laser with MQB structure.

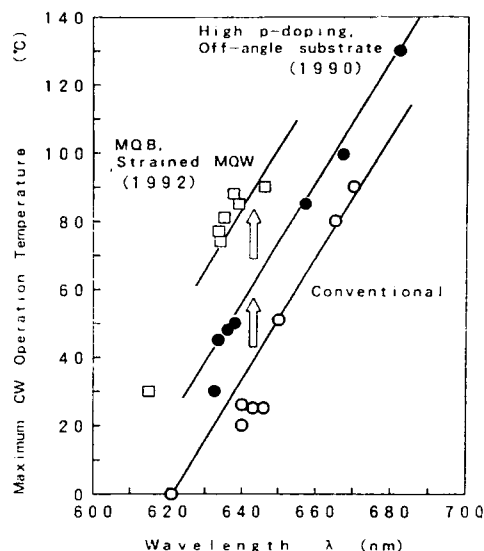


Fig. 6. Relation between reported CW wavelength and maximum operation temperature.

$T_0$  was increased by introducing the MQB. Fig. 5 shows the temperature dependence of the  $I$ - $L$  characteristics of the MQB laser [13]. The CW threshold current was 49 mA. Maximum operation temperature of over 70°C was realized at the wavelength of 634 nm.

Fig. 6 shows the relation between reported CW wavelength and maximum operation temperature. High p-doping and the MQB have drastically improved the temperature characteristics. These improvements in the maximum operation temperature have made it possible to replace the He-Ne gas laser with InGaAlP laser diodes. Recently, we have realized over  $1 \times 10^{18} \text{ cm}^{-3}$  doping in InAlP using Zn as the dopant [32]. Also, much effort has been expended towards the research on strained MQW active layers of InGaAlP lasers [14–16]. Due to these techniques, further improvements of maximum operation temperature of InGaAlP lasers can be expected.

### 3.3. Reliability of InGaAlP lasers

We have found several degradation modes in the reliability tests of InGaAlP lasers [20,21,33,34].

A facet degradation, due to the oxidation of a laser facet, occurred in the InGaAlP lasers [33]. Other degradation modes, related to the operation current density [34], or the optical density in the active layer [20], were also confirmed through numerous results of reliability tests. Facet coatings, and improvements of the device design and MOCVD growth techniques resulted in the realization of a highly reliable operation of InGaAlP lasers [20,21,33,34]. A stable operation was confirmed for the lasers oscillating in the 630 nm band [13,16]. High reliability was also realized in high-power operation of InGaAlP lasers [20,21,23].

### 3.4. Comparison with ZnSe blue-green lasers

The threshold current density of the first CW operation of InGaAlP lasers was several times  $10^3 \text{ A cm}^{-2}$ . It was reduced to  $1 \times 10^3 \text{ A cm}^{-2}$  at the first production of the InGaAlP lasers due to the optimization of the DH structure. Further reduction has been realized by an employment of the strained MQW structure. In the case of ZnSe blue-green lasers, a relatively low threshold current density as  $1 \times 10^3 \text{ A cm}^{-2}$  was already realized, which shows that ZnSe material systems are promising as semiconductor laser materials. Results and discussions described in this paper are considered to be useful for the research and development of ZnSe blue-green lasers.

## 4. InGaAlP LEDs

### 4.1. What limited the efficiency of InGaAlP LEDs?

The employment of a current spreading layer of GaAlAs or GaP resulted in candle-class LEDs from orange to yellow [25–27]. However, it has been difficult to obtain high-efficiency InGaAlP LEDs in the green region. The values of external quantum efficiency below 590 nm were lower than the values estimated from theoretical calculation, considering band structure of InGaAlP alloys [26]. This is because a high Al composition in the InGaAlP emission layer is required to shorten the emission wavelength, and this in-

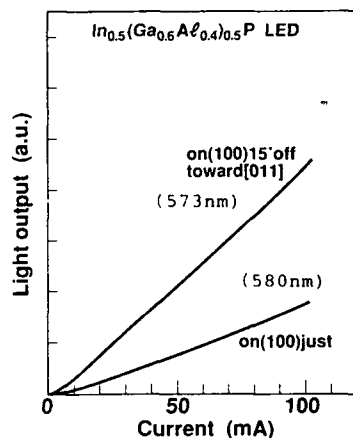


Fig. 7. Dependence of  $I$ - $L$  characteristics of InGaAlP LEDs on substrate type.

creases the generation of nonradiative recombination centers through the contamination of Al with residual oxygen [26]. On the other hand, the GaAs substrate absorbs a large part of emission light. This has also reduced the light extraction efficiency.

In this section we describe the approach to the realization of high brightness InGaAlP green LEDs, by employment of the MOCVD growth on the off-angle substrate and a newly designed Bragg reflector.

#### 4.2. Improvement of quantum efficiency by off-angle substrate

Fig. 7 shows the dependence of  $I$ - $L$  characteristics on substrate type. The efficiency of LEDs grown on off-angle substrates was three times larger than that of LED grown on (100) just substrates. The emission wavelength was also shortened for the LED grown on an off-angle substrate by disordering. Fig. 8 shows the dependence of the DLTS signals in undoped InGaAlP layers on 15° off and just substrates [35]. A, B, and C peaks were clearly observed in the layer grown on the (100) substrate. On the other hand, B and C deep-level peaks were drastically reduced in the layer grown on the off-angle substrate. Fig. 9 shows the dependence of the oxygen

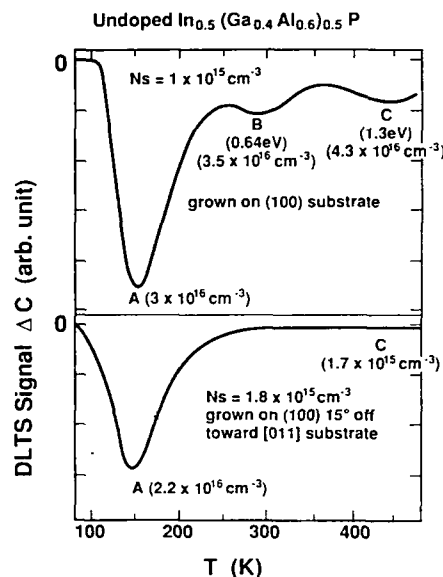


Fig. 8. Dependence of DLTS signals in undoped InGaAlP layers on 15° off and (100) substrates.

concentration in undoped InGaAlP layers on substrate type, by SIMS measurement [35]. The oxygen was clearly detected in these layers. This is because InGaAlP alloys contain Al which is very reactive. The oxygen concentration was re-

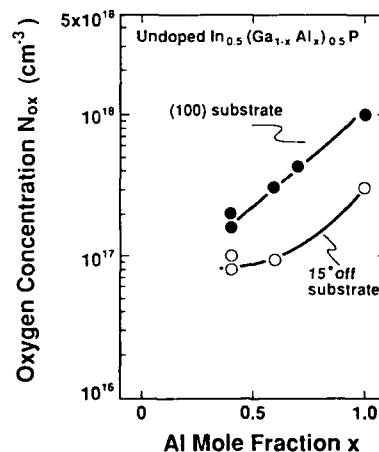


Fig. 9. Dependence of oxygen concentration in undoped InGaAlP layers on substrate type, measured by SIMS.

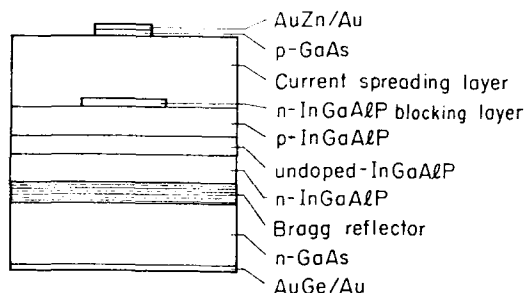


Fig. 10. Schematic structure for green InGaAlP LED.

duced by the employment of an off-angle substrate. Comparing to the previous results, as shown in Fig. 8, it seems that the occurrence of deep levels is closely related to the incorporated oxygen. It is considered that the off-angle substrate reduces the oxygen concentration in InGaAlP alloys; thus, non-radiative recombination centers related to B and C deep levels are also reduced, which improves the emission efficiency.

#### 4.3. New structure for InGaAlP LED with multi-layers

Fig. 10 shows the schematic structure for a green InGaAlP LED [36]. In this structure, the current injected from the p-side spreads through the current-spreading layer and does not flow through the undesired region under the electrode, because of a blocking layer. This structure also employs a newly designed Bragg reflector, to reduce absorption by the GaAs substrate [37]. The use of a Bragg reflector is a promising way to resolve such a problem. Wide-band and high reflectivity characteristics are required in the design for the Bragg reflector. To realize such characteristics, we employed a new type of reflector consisting of stacked layers of InAlP/GaAs.

Fig. 11 shows the calculation results for the dependence of the reflectivity on the number of layer pairs [37]. It was found that the large refractive index difference between InAlP and GaAs can be utilized to construct a high-reflectivity structure in spite of the absorption loss in GaAs. High reflectivity was obtained for a relatively

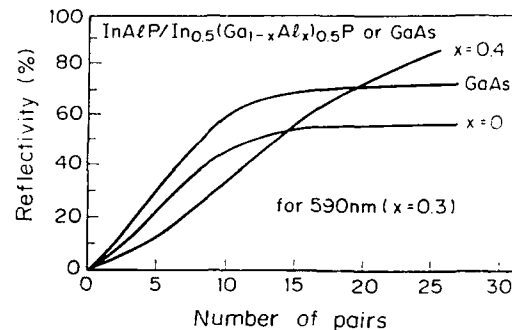


Fig. 11. Calculation results for the dependence of the reflectivity on the number of layer pairs.

small number of pairs, which also leads to a wide band spectrum. Fig. 12 shows the spectra for the InAlP/GaAs Bragg reflector and the InAlP/InGaAlP Bragg reflector. The number of pairs in each Bragg reflector was 10 and 20, respectively. The band width of the reflection spectrum for the InAlP/GaAs Bragg reflector was about three times larger than that for the InAlP/InGaAlP Bragg reflector. A reflectivity of 70% was also measured, which is sufficient for improving LED efficiencies.

Fig. 13 shows the external quantum efficiency for InGaAlP LEDs. The use of an off-angle substrate provided the improvement of quantum efficiency and shortened the wavelength. Further improvement was obtained by using the new

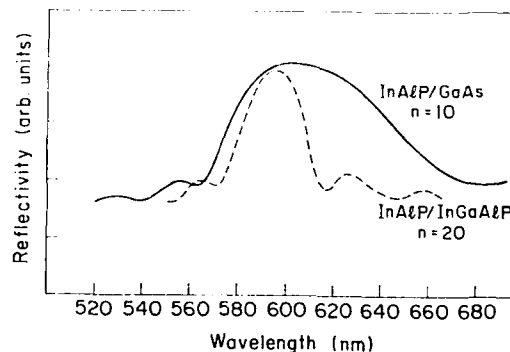


Fig. 12. Comparison of reflective spectra for the InAlP/GaAs Bragg reflector and the InAlP/InGaAlP Bragg reflector.

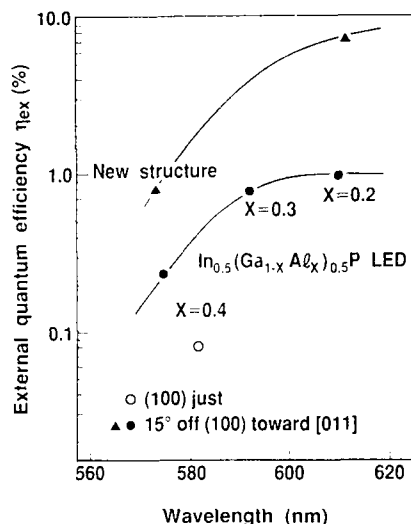


Fig. 13. External quantum efficiency for InGaAlP LEDs.

structure with blocking layer and a wide-band Bragg reflector. A candela-class green LED, operating at 573 nm, was realized, and a nearly 10% high efficiency LED was also realized for orange light.

## 5. Summary

Recent progress in the InGaAlP visible light devices has been described. The high p-doping of a cladding layer and an MQB structure have improved the temperature characteristics of InGaAlP laser diodes in terms of the reduction of the electron overflow. These improvements have made it possible to realize a high-temperature CW operation above 70°C at a wavelength of 633 nm.

New-structure InGaAlP light-emitting diodes (LEDs) which employ an off-angle substrate and Bragg reflector have improved both quantum efficiency and light-extraction efficiency. Candela-class, high-brightness LEDs have been achieved for the orange to green color region.

These results show that InGaAlP visible light devices have been commercially available in a variety of applications.

## 6. Acknowledgements

The authors would like to thank J. Rennie, M. Suzuki, M. Ishikawa, M. Watanabe, H. Okuda, M. Okajima, H. Nozaki and Y. Idei for discussions and technical support. They also would like to thank M. Azuma and Y. Uematsu for their encouragement throughout this research.

## 7. References

- [1] H.C. Casey, Jr. and M.B. Panish, *Heterostructure Lasers*, Part B (Academic Press, New York, 1978) p. 3.
- [2] M. Ishikawa, Y. Ohba, H. Sugawara, M. Yamamoto and T. Nakanishi, *Appl. Phys. Lett.* 48 (1986) 207.
- [3] K. Kobayashi, S. Kawata, A. Gomyo, I. Hino and T. Suzuki, *Electron Lett.* 21 (1985) 931.
- [4] M. Ikeda, Y. Mori, H. Sato, K. Kaneko and N. Watanabe, *Appl. Phys. Lett.* 47 (1985) 1027.
- [5] S. Kawata, K. Kobayashi, A. Gomyo, I. Hino and T. Suzuki, *Electron Lett.* 21 (1985) 1162.
- [6] S. Kawata, H. Fujii, K. Kobayashi, A. Gomyo, I. Hino and T. Suzuki, *Electron Lett.* 23 (1987) 1327.
- [7] K. Itaya, M. Ishikawa and Y. Uematsu, *Electron Lett.* 26 (1990) 839.
- [8] G. Hatakoshi, K. Itaya, M. Ishikawa, M. Okajima and Y. Uematsu, *IEEE J. Quantum Electron.* QE-27 (1991) 1476.
- [9] H. Hamada, M. Shono, S. Honda, R. Hiroshima, K. Yodoshiki and T. Yamaguchi, *IEEE J. Quantum Electron.* QE-27 (1991) 1483.
- [10] A. Valster, C.T.H.F. Liedenbaum, J.M.M. van der Heijden, M.N. Finke, A.L.G. Severens and M.J.B. Boermans, in: *Tech. Dig., 12th IEEE Int. Semiconductor Laser Conf.*, Davos, 1990, paper C1.
- [11] K. Kishino, A. Kikuchi, Y. Kaneko and I. Nomura, *Appl. Phys. Lett.* 58 (1991) 1822.
- [12] J. Rennie, M. Okajima, M. Watanabe and G. Hatakoshi, *Electron Lett.* 28 (1992) 150.
- [13] J. Rennie, M. Okajima, M. Watanabe and G. Hatakoshi, *IEEE J. Quantum Electron.* QE-29 (1993) 1857.
- [14] A. Valster, C.J. van der Poel, M.N. Finke and M.J.B. Boermans, *Electron Lett.* 28 (1992) 144.
- [15] C.J. Chang-Hasnain, R. Bhat and M.A. Koza, *Electron Lett.* 27 (1991) 1553.
- [16] M. Watanabe, J. Rennie, M. Okajima and G. Hatakoshi, *Appl. Phys. Lett.* 63 (1993) 1486.
- [17] K. Itaya, Y. Watanabe, M. Ishikawa, G. Hatakoshi and Y. Uematsu, *Appl. Phys. Lett.* 56 (1990) 1718.
- [18] K. Itaya, M. Ishikawa, G. Hatakoshi and Y. Uematsu, *IEEE J. Quantum Electron.* QE-27 (1991) 1496.
- [19] K. Nitta, K. Itaya, Y. Nishikawa, M. Ishikawa, M. Okajima and G. Hatakoshi, *Electron Lett.* 27 (1991) 1660.
- [20] K. Itaya, M. Ishikawa, K. Nitta, M. Okajima and G. Hatakoshi, *Jap. J. Appl. Phys.* 30 (1991) L590.

- [21] K. Nitta, M. Okajima, Y. Nishikawa, K. Itaya and G. Hatakoshi, *Electron. Lett.* 28 (1992) 1069.
- [22] Y. Ueno, K. Endo, H. Fujii, K. Kobayashi, K. Hara and T. Yuasa, *Electron. Lett.* 26 (1990) 1726.
- [23] Y. Ueno, H. Fujii, H. Sawano and K. Endo, *Electron. Lett.* 28 (1992) 860.
- [24] C.J. Nuese, J.J. Toetjen, J.J. Gannon and H.F. Gassenberger, *J. Electrochem. Soc.* 116 (1969) 248.
- [25] H. Sugawara, M. Ishikawa and G. Hatakoshi, *Appl. Phys. Lett.* 58 (1991) 1010.
- [26] H. Sugawara, K. Itaya, M. Ishikawa and G. Hatakoshi, *Jap. J. Appl. Phys.* 31 (1992) 2446.
- [27] K.H. Huang, J.G. Yu, C.P. Cuo, R.M. Fletcher, T.D. Osentowski, L.J. Stinson, M.J. Craford and A.S.H. Liao, *Appl. Phys. Lett.* 61 (1992) 1045.
- [28] M. Ishikawa, Y. Ohba, Y. Watanabe, H. Sugawara, M. Yamamoto and G. Hatakoshi, *Trans. IECE Japan* E69 (1986) 382.
- [29] K. Itaya, M. Ishikawa, Y. Watanabe, K. Nitta, G. Hatakoshi and Y. Uematsu, *Jap. J. Appl. Phys.* 27 (1989) 2414.
- [30] M.O. Watanabe and Y. Ohba, *Appl. Phys. Lett.* 50 (1987) 906.
- [31] K. Iga, H. Uenohara and F. Koyama, *Electron Lett.* 22 (1986) 1008.
- [32] M. Suzuki, K. Itaya and M. Okajima, *Jap. J. Appl. Phys.* 33 (1994) 749.
- [33] K. Itaya, M. Ishikawa, H. Okuda, Y. Watanabe, K. Nitta, H. Shiozawa and Y. Uematsu, *Appl. Phys. Lett.* 53 (1988) 1363.
- [34] M. Ishikawa, H. Okuda, K. Itaya, H. Shiozawa and Y. Uematsu, *Jap. J. Appl. Phys.* 28 (1989) 1615.
- [35] M. Suzuki, K. Itaya, Y. Nishikawa, H. Sugawara and M. Okajima, *J. Crystal Growth* 133 (1993) 303.
- [36] H. Sugawara, K. Itaya, H. Nozaki and G. Hatakoshi, *Appl. Phys. Lett.* 61 (1992) 1775.
- [37] H. Sugawara, K. Itaya and G. Hatakoshi, *J. Appl. Phys.* 74 (1993) 3189.



ELSEVIER

Journal of Crystal Growth 138 (1994) 776–785

JOURNAL OF **CRYSTAL  
GROWTH**

## Recent progress in III–V quantum optoelectronic devices

C. Weisbuch

*Laboratoire de Physique de la Matière Condensée, Ecole Polytechnique, F-91120 Palaiseau, France*

### Abstract

Three generations of quantum optoelectronic devices are described. Although the field of many successes, the subject is still progressing at an undiminished pace. A number of the effects so far illustrated in III–V materials could be implemented with II–VI materials.

### 1. Introduction

We are witnessing a major revolution in the performance of optical and optoelectronic devices [1], based on the ever-increasing number of new device concepts allowed by the more and more refined implementations of heterostructure materials (Table 1). After a “zeroth” generation using heterostructures in absence of quantum effects which gave the room-temperature double-heterostructure (DH) laser, a *first generation* of quantum heterostructures occurred in the late seventies when the new growth methods of molecular beam epitaxy (MBE) and metalorganic chemical vapor deposition (MOCVD) allowed depositing ultrathin semiconductor layers with precision down to the atomic layer. In such a case, the carrier motion is quantized in one direction across the layer, and carriers experience a two-dimensional motion along the layer, one degree of freedom being “frozen”. The “first-order” effects associated with such two-dimensional structures give their performance to some very important devices as the quantum well laser.

The *second generation* of quantum heterostructures started in the early eighties and is

based on “subtler” effects of layered materials, such as increased light–matter interaction, improved electro- and non-linear-optical effects, bandgap engineering, strain effects, etc. The devices relying on these effects are electro-optical and non-linear optical modulators, IR detectors, etc.

The *third generation* of quantum heterostructures, started in the late eighties, aims at exploiting completely new (and better?) properties of heterostructure materials when *material structuring at the nanometer level occurs in two or three directions*. They stem from the realization that the usual broad optical features in solids arise from the existence of a continuum of states for both electrons and photons, which allow transitions for all energies and polarizations. Electron state quantization can be one way to reduce the continuum of transitions to discrete ones, in an increasing way when quantizing motion in 1 direction (quantum wells QWs), 2 directions (quantum well wires QWWs) and 3 directions (quantum boxes QBs). Photon mode quantization in an optical cavity is another one, which seems much more promising due to the additional advantages brought along by the light emission into

Table 1

The various concepts implemented through hetero-structures, yielding improved performance

Physical effect	Property impacted
Energy band discontinuities	Carrier localization and concentration
Index of refraction difference	Optical wave concentrated
Diminished density of states	Reduced transparency current lower non-linear threshold
Square density-of-states in 2D QW	Larger differential gain
Excitons at room temperature	Stronger light-matter coupling
Giant matrix element	Stronger light-matter coupling
Quantum-confined Stark effect	Stronger electro-optical coefficient
Phase-space filling	Stronger electro-optical coefficient
Sharp density of states (1D, 0D)	Improved, sharper gain curve
Photon mode control	Controlled spontaneous emission into single optical mode
Enhanced resonant cavity field intensity	Coherent light-matter coupling

one or several optical modes only, and by the increased light-matter coupling due to the electric-field enhancement occurring in resonant cavities. Effects similar to those obtained from optical microcavities are also accessible by the use of photonic band gap (PBG) materials.

## 2. The first generation device: the quantum well laser

The “obvious” property of an ultrathin semiconductor layer is the size quantization of electron motion occurring in one direction. Therefore, one degree of freedom is frozen when compared to the three-dimensional nature of electron motion in classical DH lasers. How does this translate into better lasing properties? Let us first recall that the gain versus current curve has two components: a number of carriers is required to reach carrier inversion. This number is called the transparency carrier density and it defines the transparency current: below transparency, an optical wave is absorbed rather than amplified. Above it, additional carriers of the second component create optical gain. The net gain per carrier for that current component above the transparency current only depends on the optical transition strength, proportional to the optical matrix element, and can be shown to be independent of layer size and even of carrier quantization in 1, 2 or 3 directions (QWs, QWWs and QBs,

respectively). Therefore, in first approximation, diminishing layer thickness mainly diminishes the transparency density which is proportional to the number of states and therefore varies linearly with  $L$  reaching the quantum well limit (QWL) when only one transverse electron state exists within the well (Fig. 1).

The QWL is actually better than just that: the two-dimensional nature of electron motion changes the spectral shape of the density of states, and hence of the optical gain. We mentioned earlier that each inverted e-h pair yields the same gain independent of dimensionality. However, depending on dimensionality, the gain is more and more spectrally concentrated (Fig. 1) (and even more so as it decreases toward 0D, see below). Therefore, carriers are more “efficient” in QWs as only the maximum gain value is determining laser threshold. This leads to the strong curvature of the QW laser gain curve (Fig. 1, bottom right), which translates into high differential gain, leading to many improved features such as higher-frequency operation, narrower linewidth, lower frequency chirping [1].

The very thin QW active layer, however, has an adverse effect on the waveguiding of the optical mode: the optical confinement factor  $\Gamma$  describing the overlap of the laser mode with the active layer decreases as  $L^{-2}$  when the active layer thickness is below 1000 Å. Therefore, several schemes have been implemented by to retain acceptable values for  $\Gamma$ , either by the use of



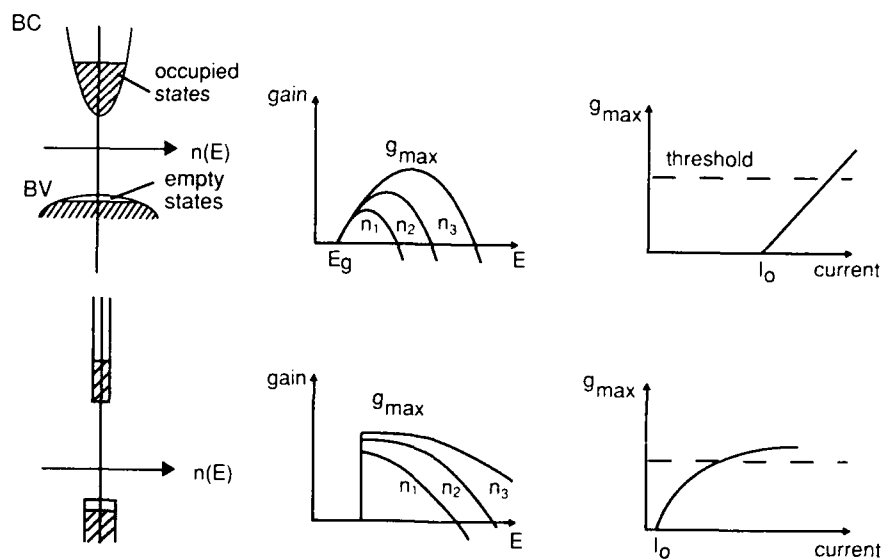


Fig. 1. Schematic drawing of the gain formation in 3D bulk DH active material (top) and in a 2D QW material (bottom). Due to the smaller density of states in 2D the transparency current  $I_0$  is diminished. Due to the square density of states, a given number of injected carriers is more efficient to create gain in the 2D QW (center), which translates into a steeper gain-current curve (right).

multiple quantum wells (MQWs) or by the use of separate confinement heterostructures (SCHs) (Fig. 2). Of course, these various structures have

different operational properties: as is clear from Fig. 2, MQW lasers should have a better temperature coefficient  $T_0$ , as the structure allows fewer

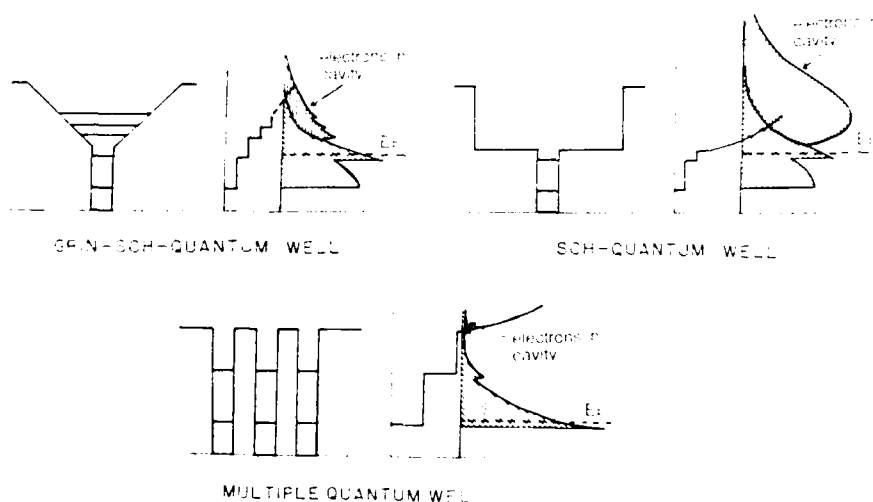


Fig. 2. Schematic drawings of several QW laser structures and associated energy levels and occupied electron states under carrier injection.

hot electrons in the thermal tail of the distribution function. Conversely, its threshold current is not optimum as the transparency current is increased  $n$ -fold as compared to the single QW laser if the structure has  $n$  QWs.

The recent progress in this field is still impressive: whereas strain effects were considered detrimental in terms of reliability, they have recently been shown to significantly improve the performance, due to the valence band modifications which they provide [2]. Another recent concept is the electron reflector barrier, in which a multiple layer stack of GaAs/GaAlAs is used as an electron-wave mirror, exactly similar to the quarter-wave stacks used in DBR multilayer mirrors [3]. The bound states occurring in an electron "cavity" between two such mirrors, in a structure exactly mimicking the Fabry–Perot optical interferometer, have been evidenced by Capasso et al. [4].

### 3. The second device generation: subtle effects of layered heterostructures

#### 3.1. The increased light–matter interaction

As we mentioned already, the strength of the light–matter interaction per optical transition is determined by the optical matrix element. Usually, in interband transitions (i.e. between valence and conduction bands) the spreading out of transitions over the energy bands leads to weak and energy-broadened optical features such as absorption. The two-dimensional quantization occurring in quantum wells changes such a behavior in two instances, due to *exciton* effects in *interband transitions* [5] or to the giant matrix element occurring in *intersubband transitions* [6] (Fig. 3).

As is well known, the Coulomb interaction between photoexcited electrons and holes in *interband transitions* produces a well-defined optical resonance somewhat below the semiconductor bandgap (by the effective semiconductor Rydberg energy  $R^*$ ) and concentrates optical strength at that energy.

Whereas excitons also exist in bulk semiconductors, their binding energy  $R^*$  is much smaller than the room-temperature thermal energy  $kT$

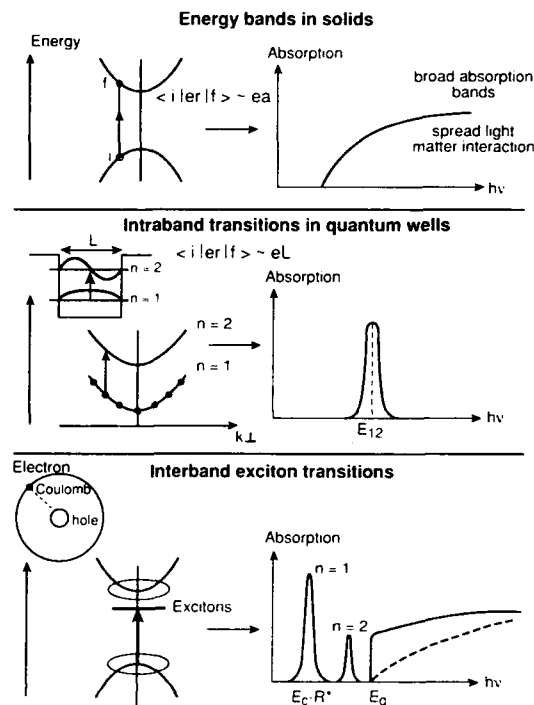


Fig. 3. Comparison of absorption transitions in bulk material (top), in intersubband transitions in QWs (center), and in QW exciton interband transitions (bottom).

(where  $k$  is the Boltzmann constant) and they are therefore so easily dissociated that no exciton effects are to be observed at room temperature in any semiconductor material. In QWs, due to the concentration of the electron and hole wavefunctions in the QW, the Rydberg energy is increased (up to four times for perfectly squeezed two-dimensional excitons) and exciton effects can easily be observed for those optical phenomena which rely on *unrelaxed optical excitation* such as absorption or dispersion [5]. For those phenomena which rely on *relaxed excitations*, such as luminescence and laser action, the binding energy even in QWs is still too small to prevent exciton dissociation at a room temperature. Notwithstanding this limitation for *relaxed interband transitions*, exciton effects give QWs their superior electrooptical and non-linear-optical properties, as those are based on *virtual, unrelaxed excitations*.

For intersubband transitions occurring between the QW quantized levels, either in the conduction band or the valence band, two effects increase the optical interaction. First, the optical matrix element is largely increased: the QW acts as an electric dipole moment of size  $L$  (QW thickness), whereas atoms and ordinary solids yield dipoles of the order  $a$  (atom size). Second, as the energy dispersion of the quantum states for the two-dimensional motion is the same, all transitions occur at the same energy for all electrons, independent of their kinetic energy (see Fig. 3 for the difference with usual interband transition). Therefore, due to these two effects, QWs can act as good radiation detectors in the IR spectrum although the number of QW electrons that can detect photons (limited to  $\approx 10^{19} \text{ cm}^{-3}$  for metallurgical reasons) is much smaller than that of valence electrons ( $\approx 10^{23} \text{ cm}^{-3}$ ) in interband bulk detectors like mercury cadmium telluride (MCT).

The performance of the IR QW detectors is indeed very promising [6] compared to that of MCT-based devices, and offers the prospect of much better mastered technology. It should be kept in mind at this point that a major limitation in performance of such detectors is due to the very short lifetime of excited states in QWs: electrons can always relax between intersubband levels by emitting LO phonons in  $\approx 10^{-12} \text{ s}$ , whereas for interband detectors like MCT the lifetime in the conduction band is very long (in the  $10^{-6} \text{ s}$  range), as phonon emission cannot occur across the forbidden gap. This translates into a background-limited infrared performance (BLIP) temperature of 60–70 K.

### 3.2. Electro-optical and non-linear-optical effects

Interband electro-optical effects in QWs are much stronger than in any other material, due to the increased light-matter interaction brought along by the exciton effects described above and by the increased sensitivity of QW energy levels to applied electric fields, described first by Miller as a quantum confined Stark effect (QCSE). It can easily be seen from Fig. 4 that application of an electric field across a QW drastically changes

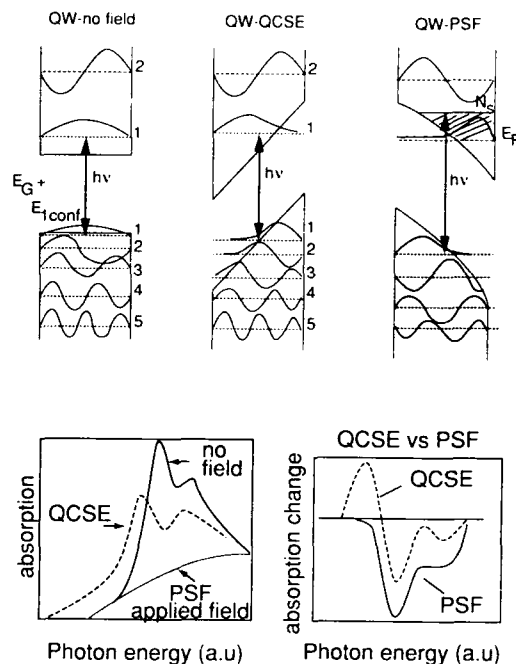


Fig. 4. Electro-optical effects in quantum wells. Top, energy levels and wavefunctions: from left to right: transitions with no applied field; transitions with applied electric field in the absence of carriers (quantum confined Stark effect, QCSE); transitions with carrier bandfilling (so-called phase-space filling PSF). Bottom, from left to right: absorption curves for QCSE and PSF conditions, and comparison of the absorption changes for QCSE and PSF (from D.A.B. Miller and H. Sakaki).

its energy levels. However, due to the squeezing of the electron and hole wavefunctions against the QW interfaces, the electron-hole optical interaction remains very strong even at high electric fields, at variance with the smoothing out of absorption peaks in bulk materials.

From the strength of the electro-optical effects in QWs it has been possible to operate two-dimensional arrays of QW light-absorption modulators. Under such conditions, however, the contrast ratio between the on-off beams is quite low, limited below 10. By using a reflectivity geometry, with Fabry-Perot (FP) cavity effects obtained by placing the electro-active QWs between dielectric mirrors, several authors were able to drastically

improve the contrast ratio: it suffices to use asymmetric FP modulators (AFPMs) such that the overall reflectance of the structure is zero (by having the reflectance of the first mirror exactly balancing the QW absorption and the reflectance of the second mirror) at zero applied electric field and destroying that balance under applied electric field. Contrast ratios above 100 were obtained [7].

Another type of electro-optical effect is also obtained by injecting carriers in QWs (Fig. 4): under such conditions bleaching of the exciton absorption by phase-space filling (PSF) is obtained for quite low carrier densities, in the few  $10^{11} \text{ cm}^{-2}$  range, due to the two-dimensional nature of the QWs. This electro-optical effect based on absorption bleaching is being implemented in a number of planar waveguide modulators due to its low insertion loss and low drive-voltage capability [8].

Non-linear optical performance of QWs is also superior to that of other materials. Here again the performance is based on the strong light-matter coupling brought along by the interband exciton effects or by the giant intersubband ma-

trix element and the bleaching of that coupling at low injected densities due to the small 2D density-of-states in QWs. The performance is well evidenced by the fact that low-power CW lasers can be used to perform frequency doubling or degenerate four-wave mixing (DFWM) experiments.

Another hybrid scheme to obtain non-linear effects is to use at the same time the photoconductive and the electro-optical properties of QWs. Under proper bias, a bistable behavior can be obtained in the so-called self-electro-optic device (SEED). Many implementations of SEEDs have been proposed. Optical "integrated" circuits with up to 2048 devices have been fabricated [9].

#### 4. The third-generation sharp optical features: confined electrons and/or photons?

##### 4.1. Quantum wires and quantum boxes

Capitalizing on the many improvements brought along by the one-dimensional quantization of layered semiconductors heterostructures

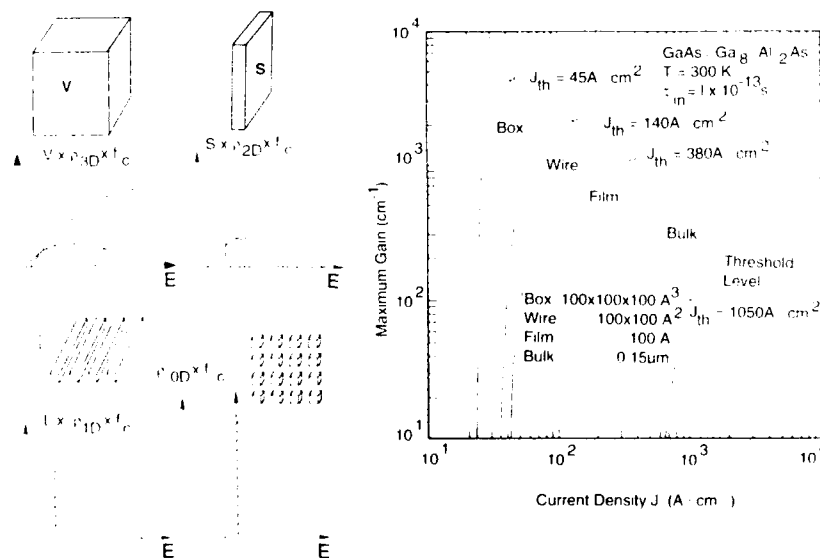


Fig. 5. Comparison of gain formation in bulk, QW, quantum wire (QWW) and quantum box (QB) materials, and corresponding gain-current curves (from M. Asada, Y. Miyamoto and Y. Suematsu, IEEE J. Quantum Electron QE-22 (1986) 1915).

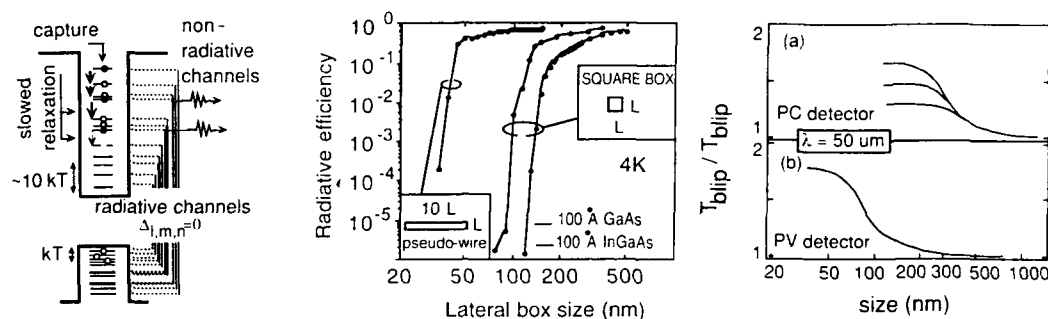


Fig. 6. Impact of the phonon relaxation bottleneck on quantum wire and quantum box luminescence quantum efficiency (center, after H. Benisty [10]) and on BLIP temperature of infrared intersubband QW detectors (right, H. Benisty and C. Weisbuch, unpublished).

just described, further improvements of optical properties were predicted for structures with more fully quantized states in two or three dimensions in quantum-well wires (QWWs) or quantum boxes (QBs) [1]. In particular, fully quantized motion of electrons in all three dimensions should yield sharp isolated optical transitions, which should lead to well-improved maximum gain under excitation conditions similar to 3D, 2D or 1D (Fig. 5). Although many realizations of 1D QWWs or 0D QBs have been reported in the past few years, most of them re-

ported worse, or at most as good properties as 2D QWs, at strong variance with the universal improvement brought along by QWs when compared to three-dimensional heterostructures [1]. We have recently shown [10] that beyond the surface and material damage brought along by the 2D and 3D manufacturing processes of 1D QWWs and 0D QBs, some intrinsic mechanism should be responsible for such a universal behavior, independent of the many fabrication schemes used. We actually found that whereas optical properties are predicted to improve with decreas-

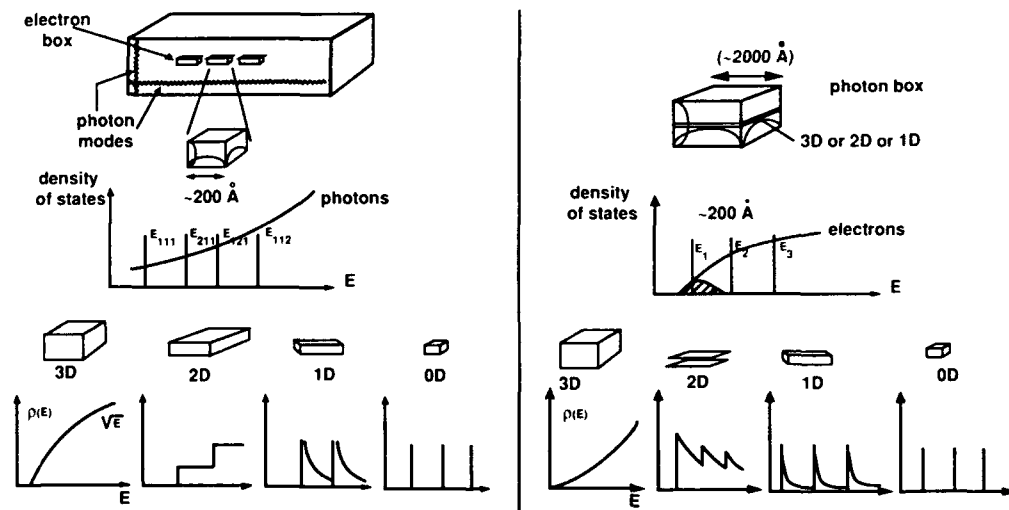


Fig. 7. Schematic drawings of the matching between electronic states and photonic states for electron quantization (left) or photon mode quantization (right).

ing dimensionality thanks to the sharper optical transitions, there is conversely a price to pay for such a fuller quantization, i.e. reduced carrier energy relaxation rates. It is then simulated that energetically-injected electrons and holes in QWWs, and above all in QBs, most often remain in orthogonal quantum states, therefore forbidding radiative recombination in interband transitions (Fig. 6). Several improved relaxation schemes have recently been proposed to bypass this relaxation bottleneck such as resonant LO phonon relaxation in specially-designed QBs [11] or electron–electron Auger collisions [12]. On the other hand, the relaxation bottleneck is full of promises for intraband-based devices [13] such as infrared detectors, which as mentioned at the end of section 3.1, are most often limited in performance due to the fast inter-level transition rate brought along by LO and LA phonon emission (Fig. 6).

#### 4.2. Photon mode quantization in optical microcavities

A new way to obtain sharp optical features in solids has recently been opened thanks to the photon quantization in microcavities [14]. The basic principle is easy to grasp: Electrons and holes in energy bands can usually recombine at the various energies allowed by carrier populations energy and momentum conservation (“verti-

cal” transitions), because there exist under the usual conditions a continuum of photon states which induce spontaneous emission through the so-called vacuum-field fluctuations (Fig. 7). If we consider that the active material is placed in an optical cavity where only a single photon mode has a spectral overlap with the emission band, radiative recombination can only take place in that photon mode. The emitted light has the spectral characteristics of the photon mode, i.e., can be extremely narrow as determined by the photon lifetime in the cavity. The fate of all electron–hole pairs not matching the energy and momentum of the mode photon is to either recombine non-radiatively or, in “good” samples, to reach the photon-matched states by momentum and energy relaxation before non-radiative recombination takes place. Like for electron states, the photon mode quantization can be achieved in 2D, 1D or 0D using planar cavities, cylindrical cavities or closed cavities respectively (Fig. 7). Similar control of spontaneous emission can be obtained from the recently-developed concept of photonic band gap (PBG) materials [15]: such materials have a periodically modulated dielectric constant, as provided by the use of a 3D periodic heterostructure. The exclusion of unwanted photon modes is provided by the multiple reflections occurring in the periodic structure, analogous to the opening of a bandgap in the electronic energy levels in periodic solids. Of course, one requires

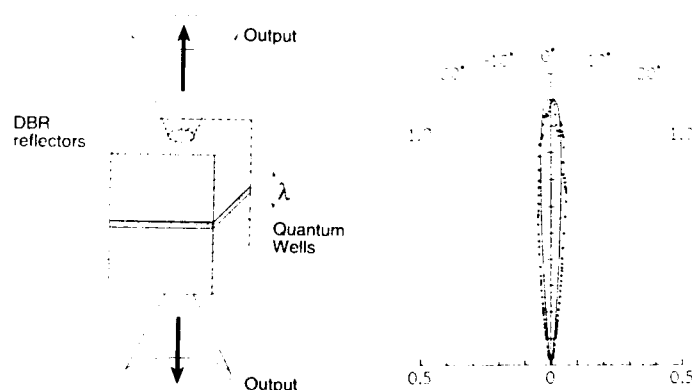


Fig. 8. Schematic drawings of a quantum microcavity (left) and its angular spontaneous emission diagram (Björk et al. [14]).

within the photonic bandgap an allowed mode which would let light escape from the crystal. This is provided by breaking the exact translation invariance of the perfect photonic crystal by a “photon impurity”, i.e. localizing an optical mode by a photonic crystal defect [15]. We have recently shown the two approaches of microcavities and photonic bandgap materials to be equivalent, the microcavity representing an optimal impurity in a PBG material [16].

Semiconductor microcavity structures have very simple 1D implementations: one uses planar Fabry–Perot (FP) microcavities where the mirrors are multi-quarter wave stacks distributed Bragg reflectors (DBRs) (Fig. 8). The usual multi-pass interference description of the FP resonator shows that the resonant photon mode, for which all reflected waves in the cavity are in phase, has an intensity increased by a factor  $4/(1-R)$ , where  $R$  is the DBR mirror reflectivity [14]. Conversely, those non-resonant photon modes are suppressed by a factor  $\approx 1-R$ . The cavity acts as if it concentrated the electric field from all non-resonant modes into the resonant mode. The net effect is therefore that the spontaneous lifetime has hardly changed, as long as efficient relaxation towards the photon-coupled electron–hole state prevents a too-strong hole burning phenomenon.

Many predictions of the impact of microcavity effects have been verified. One of the most promising device-wise is the concentration of the spontaneously emitted light in the narrow angle of the cavity mode (Fig. 8), of the order of  $(1-R)/\pi$  inside the microcavity material. This opens the way to high efficiency LEDs with fiber-matched emission angles instead of the approximately Lambertian emission of cavityless structures. It should be remarked that this effect, directly due to the photon mode quantization, yields a major improvement when compared with the quantum box electron quantization where the electric dipole of electron–hole pairs or excitons radiates in all directions. It should also lead to the “thresholdless” laser [14] as the emission process will continuously switch from spontaneous to stimulated in the same single photon mode while increasing exciting power.

The spectral narrowing of LED emission due to the cavity resonance is also very useful: it reduces the dispersion in high-data rate transmission. An improvement of  $\approx 3$  was recently observed by Hunt [17] in the maximum distance–frequency product.

Recently, we have evidenced the resonant interaction of the microcavity photon mode with the QW excitons, which gives rise to the vacuum-field Rabi oscillation of the excitons [18]. Rabi oscillations can be seen as a coupled-oscillator process, by which resonantly coupled electronic and photon oscillators periodically exchange energy. In a classical coupled oscillator description, the overall system response yields two split modes corresponding to the normal modes of the system. In an atomic transition language, one considers the system as undergoing a coherent evolution with a photon being absorbed by an atom, which subsequently emits a photon with the same energy and wavevector  $k$ , that photon being reabsorbed, and so on. This observation, recently extended to room temperature, shows that the association of quantum wells and microcavities yields an optical “hybrid” material which exhibits a strong optical coupling, i.e. the *coherent interaction of light and matter*. This might well be the “ultimate” optical material.

## 5. Conclusions

As can be seen, the field of optical heterostructures has already provided many important devices, and will continue to do so in the future [19]. The exciting feature of this field is that breakthrough concepts are appearing at an undiminished pace, to the contrary! We hope to have conveyed some of the excitement experienced by the researchers in this field in this short overview.

## 6. Acknowledgements

I would like to thank my various coworkers on various aspects of the work described here: H. Benisty, C. Sotomayor-Torres, Y. Arakawa, M.

Nishioka, A. Ishikawa, R. Stanley, R. Houdre, U. Oesterle and M. Illegems.

## 7. References

- [1] In order to keep this reference list to a reasonable size, we refer the reader to our recent book where many of the concepts developed here are detailed and where an extensive list of references is supplied. We only add here specially important or recent references.  
C. Weisbuch and B. Vinter, *Quantum Semiconductor Structures: Physics and Applications* (Academic Press, Boston, MA, 1991).
- [2] See, e.g., M. Nido, K. Naniwae, J. Shimizu, S. Murata and A. Suzuki, *IEEE J. Quantum Electron.* QE-29 (1993) 885, and references therein.
- [3] T. Takagi, F. Koyama and K. Iga, *IEEE J. Quantum Electron.* QE-27 (1991) 1511.
- [4] F. Capasso, C. Sirtori, J. Faist, D. Sivco, S.N. Chu and A. Cho, *Nature* 258 (1992) 565.
- [5] D.S. Chemla and D.A.B. Miller, *J. Opt. Soc. Am. B* 2 (1985) 1155.
- [6] E. Rosencher, B. Vinter and B. Levine, Eds., *Intersubband Transitions in Quantum Wells*, NATO ASI Series B Physics, Vol. 288 (Plenum, New York, 1992).
- [7] See, e.g., G.D. Boyd and G. Livescu, *Opt. Quantum Electron.* 24 (1991) 5147.
- [8] J.E. Zucker, T.Y. Chang, M. Wegener, N. Sauer, K.L. Jones and D.S. Chemla, *IEEE Phot. Technol. Lett.* PTL-2 (1990) 29.
- [9] See, e.g., D.A.B. Miller, *Opt. Quantum Electron.* 22 (1990) S61, and references therein.
- [10] H. Benisty, C.-M. Sotomayor-Torres and C. Weisbuch, *Phys. Rev. B* 44 (1991) 10945.
- [11] T. Inoshita and H. Sakaki, *Phys. Rev. B* 46 (1992) 7260.
- [12] U. Böckelmann and T. Egeler, *Phys. Rev. B* 46 (1992) 15574.
- [13] H. Benisty and C. Weisbuch, to be published.
- [14] See, e.g., G. Björk, Y. Yamamoto, S. Machida and K. Igeta, *Phys. Rev. A* 44 (1991) 669;  
T. Baba, T. Hamano and R. Koyama, *IEEE J. Quantum Electron.* QE-27 (1991) 1347;  
H. Yokoyama, *Science* 256 (1992) 66.
- [15] See, e.g., E. Yablonovitch, *J. Opt. Soc. Am. B* 10 (1993) 283, and the following papers of that special issue on Photonic Bandgap Materials.
- [16] R. Stanley, R. Houdre, U. Oesterle, M. Illegems and C. Weisbuch, *Phys. Rev. A* 48 (1993) 2246.
- [17] N.E.J. Hunt, E.F. Schubert, R.F. Kopf, D.L. Sivco, A.Y. Cho and G.J. Zydzik, *Appl. Phys. Lett.* 63 (1993) 2600.
- [18] C. Weisbuch, M. Nishioka, A. Ishikawa and Y. Arakawa, *Phys. Rev. Lett.* 69 (1992) 3314.
- [19] See also Proc. NATO Advanced Study Institute on Confined Electrons and Photons: New Physics and Applications, Erice, 1993 NATO ASI Series B, Eds. C. Weisbuch and E. Burstein (Plenum, New York, 1994).





ELSEVIER

Journal of Crystal Growth 138 (1994) 786–790

JOURNAL OF  
**CRYSTAL  
GROWTH**

## Stimulated emission of II–VI epitaxial layers

C. Klingshirn <sup>\*a</sup>, H. Kalt <sup>a</sup>, M. Umlauff <sup>a</sup>, W. Petri <sup>a</sup>, F.A. Majumder <sup>a</sup>,  
S.V. Bogdanov <sup>a</sup>, W. Langhein <sup>a</sup>, M. Grün <sup>a</sup>, M. Hetterich <sup>a</sup>, K.P. Geyzers <sup>b</sup>,  
M. Heuke <sup>b</sup>, A. Naumov <sup>c</sup>, H. Stanzl <sup>c</sup>, W. Gebhardt <sup>c</sup>

<sup>a</sup> Fachbereich Physik, Universität Kaiserslautern, D-67663 Kaiserslautern, Germany

<sup>b</sup> Institut für Halbleitertechnik der RWTH, D-52062 Aachen, Germany

<sup>c</sup> Institut für Physik II der Universität, D-93053 Regensburg, Germany

### Abstract

After a short review of the typical gain processes in II–VI semiconductors, we present examples for various compounds considering rather thick epilayers and superlattices. The observed gain processes include inelastic scattering processes, biexcitons and plasma formation.

### 1. Introduction

In the seventies and eighties we saw already a phase of intense work towards the understanding of gain processes in II–VI semiconductors. The failure at that time to grow efficient p–n junctions caused a shift of the interest to other topics [1]. The recent success based on advanced growth and doping techniques like molecular beam epitaxy (MBE) and metalorganic chemical vapour deposition (MOCVD) [2] brought the interest back to the above-mentioned field. While commercial laser diodes for the (infra-) red range based on GaAs or InP rely essential on the recombination in a degenerate three- or two-dimensional electron–hole plasma (EHP) as gain mechanism [3], it became rather early clear, that excitonic processes contribute in addition in the case of wide gap II–VI [4] (and III–V) materials

due to the dependence of the effective density of states or of the Mott density on material parameters like the dielectric constant and the effective masses [1]. In the following we shall shortly review the gain processes, present the investigated samples, some of their properties and the observed gain spectra. We finish with a short conclusion and outlook.

### 2. Gain processes

The main gain process in semiconductors have been compiled already several times (see, e.g., refs. [1,4–7] and references therein). We can be therefore rather short here.

At low temperatures, there are extrinsic processes like the recombination of an exciton bound to a defect under emission of an acoustic phonon or under scattering with a free carrier or exciton [6]. These processes contribute to the so-called M-band. Furthermore there can be gain due to

\* Corresponding author.

free-to-bound transitions or due to population inversion in the tail of exciton states, localized by disorder occurring, e.g. in alloys or at interfaces (well width fluctuations) [4,8]. In the intermediate density regime there are a large number of intrinsic processes depending on temperature, material parameters and excitation conditions which generally resemble a four level system and show gain. Examples are the decay of biexcitons (including both incoherent processes contributing to the M-band and coherent antiStokes raman scattering (CARS)-like ones) [6,7], the decay of an exciton under emission of one (or more) LO phonons [6,9], or inelastic scattering processes in which one exciton (or electron–hole pair) decays radiatively, however transferring part of its energy to another exciton, which is excited to a state with  $n_B = 2, 3, \dots, \infty$ , resulting in the so-called  $P_{n_B}$  bands, or to a free carrier [6]. These so-called exciton–exciton and exciton–electron (or hole) scattering processes can survive also when the excitons are increasingly ionized either thermally or by increasing excitation density in the transition to an electron–hole plasma. In the case of a degenerate EHP such processes are also known as “Fermi sea shake-up” [10]. The exciton-carrier scattering shifts with increasing temperature faster to the red than the band-gap does [1,6]. At the highest excitation intensities, an EHP is reached in all semiconductors. In the case of a degenerate EHP, i.e. when the chemical potential  $\mu$  of the electron–hole pair system is situated above the reduced band gap  $E_g'$ , one has population inversion between the bands and gain due to direct band-to-band recombination between  $\mu$  and  $E_g'$  [6]. The gain can extend to energies below  $E_g'$  due to final state damping [6], Fermi sea shake-up [10] or the emission of plasmons and/or phonons [6,10]. Some of the last mentioned processes may result in gain also in a non-degenerate EHP.

### 3. Investigated samples and experimental techniques

We investigate partly epilayers with thicknesses above  $0.1 \mu\text{m}$  for which quantization ef-

fects are negligible, partly superlattices (SLs) or multiple quantum well (MQW) structures with well width  $l_z$  comparable to the excitonic Bohr radius. The hexagonal CdS and CdSe epilayers and the CdS/CdSe superlattices have been grown on GaAs (111) substrates in Kaiserslautern by hot-wall epitaxy. Details about the growth process are given in ref. [11]. The ZnTe epilayers have been grown on GaAs (100) in Regensburg by MOCVD [12] and the ZnSe epilayers and ZnSe/ZnS<sub>0.1</sub>Se<sub>0.9</sub> SL in Aachen also by MOCVD [13]. In some cases the layers have been glued on a sapphire chip and the substrate has been removed by selective etching.

The linear transmission, reflection and luminescence spectra have been recorded by standard techniques using a He flow cryostat, a spectrometer and an optical multichannel analyser for detection. For high excitation, the samples have been illuminated either by 7 ns pulses from a tunable dye laser pumped by a nitrogen laser or by 80 ps pulses from a quenched cavity dye laser pumped by an excimer laser. In the latter case the emission was temporally dispersed by a streak camera. Gain spectra have been obtained from the emission spectra under variation of the excitation stripe length [14] and care has been taken to avoid gain saturation. The product of gain and layer thickness is usually so low that pump-and-probe measurements through the sample are not applicable for gain measurements.

### 4. Results for thick epilayers

The gain processes at low temperatures show a rather consistent picture in various samples. The gain is mainly due to inelastic exciton–exciton scattering with contributions of the ex-LO process. At the highest pump powers close to the damage threshold EHP features appear. Gain spectra have been published for the above-mentioned ZnTe [15] and CdSe layers [16]. They agree with luminescence spectra under high excitation [17,18]. We give here in Fig. 1 an example for a  $0.5 \mu\text{m}$  wide ZnSe layer grown on GaAs between ZnS<sub>0.1</sub>Se<sub>0.9</sub> buffer and cap layers of 2 and  $0.5 \mu\text{m}$ , respectively. We see in the absorp-

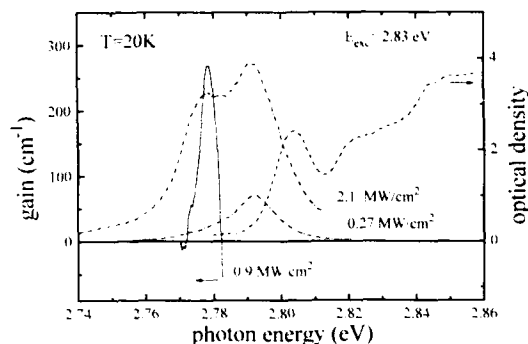


Fig. 1. The absorption spectrum (---), luminescence spectra for two different excitation intensities (---) and a gain spectrum (—) for a ZnSe epilayer grown between  $\text{ZnS}_{0.1}\text{Se}_{0.9}$  cladding layers on GaAs.

tion spectrum the broadened  $\Gamma_5$   $n_B = 1$  exciton centred around 2.803 eV, the continuum transitions starting above 2.82 eV and the absorption of buffer and cap layers beyond 2.84 eV. The luminescence observed in a backward scattering configuration shows at  $I_{\text{exc}} = 0.27 \text{ MW/cm}^2$  an M-band like structure [6,17] to which an emission from excitons bound to defects and/or to interface disorder may contribute, apart from the effects mentioned in section 2. At higher excitation an additional structure appears around 2.78 eV, which dominates the in-plane emission spectra due to stimulation. The optical gain is concentrated in this band and reaches values up to  $250 \text{ cm}^{-1}$ . From its spectral position and its similarity with CdSe or ZnTe [15–17] we attribute it to inelastic exciton–exciton scattering.

## 5. Results for superlattices

We continue with a SL consisting nominally of 120 periods of 6 nm ZnSe and 11 nm  $\text{ZnS}_{0.1}\text{Se}_{0.9}$ . In Fig. 2a, its linear optical properties are summarized. When the sample is still on the GaAs substrate, it shows strong Fabry–Pérot modes in reflection (upper trace) in the transparent part of the spectrum and in reflection a main resonance of the  $n_B = 1$   $\Gamma_5^1$  exciton in ZnSe at 2.815 eV. After removal of the substrate, this resonance is only slightly shifted (lower trace). In addition, the

absorption spectrum can be measured. It shows several structures: a weak shoulder at 2.809 eV, a first main peak at 2.815 eV another one at 2.825 eV, a weaker one at 2.831 eV and a step-like feature above 2.84 eV. The interpretation of these data is rather complex due to some uncertainties in well and barrier widths and compositions, and in the combined effects of strain (including the unknown thermal behaviour of the adhesive), quantization and enhancement of the exciton binding energy. An interpretation of the shoulder at 2.809 eV as  $n_B = 1$  lh exciton [19] is for the present system rather unlikely due to the presumably compressive strain. In this case the hh exciton should be lower [19–21]. So we attribute the shoulder to some defect transitions or well-width fluctuations. The absorption and reflection signals at 2.815 eV correspond then to the  $n_B = 1$  hh exciton. For the higher peaks we put forward two alternate assignments: (i) 2.825 eV,  $n_B = 1$  lh exciton; 2.831 eV,  $n_B = 2$  hh exciton; around 2.84

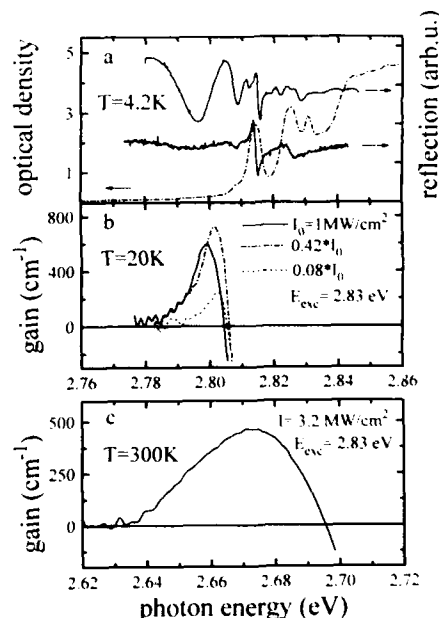


Fig. 2. Optical properties of a ZnSe/ $\text{ZnS}_{0.1}\text{Se}_{0.9}$  SL: (a) reflection spectra before and after removal of the GaAs substrate (—) and absorption spectrum (---); (b) Gain spectra at low lattice temperature for various values of the excitation intensity; (c) Gain spectrum at room temperature.

eV, onset of the exciton continuum of the wells and of the barrier absorption. In this case the binding energy of the exciton would be enhanced from the bulk value of 20 meV to about 25 meV. (ii) Splitting of hh and lh excitons below the observed width of the resonances of about 5 meV. Then we would have 2.825 eV,  $n_B = 1$  exciton of barriers, 2.831 eV,  $n_B = 2$  exciton of wells and at 2.84 eV, the onset of the continuum for wells and barriers. Further work is in progress to distinguish between (i) and (ii). The low temperature gain spectra start rather close to the exciton resonance. Therefore we can exclude ex-ex scattering for both above assignments. The spectral position coincides rather with the M-band, so in principle all processes contributing to this feature (see above or ref. [6]) have to be considered and in addition localized tail states caused by well width fluctuations. The rather high peak values of the gain lead us to favour the latter interpretation or the biexciton decay process [21]. The binding energy of the biexciton would then be in the range of 5 meV roughly compatible with the enhanced exciton binding energy.

Around 80 K the gain process changes evidently. The gain spectrum is getting broader and shifts more strongly with temperature as can be seen from the slopes given in Fig. 3a. The laser threshold increases (Fig. 3b). At 300 K it reaches a FWHM of 40 meV.

These features are strong hints for an inelastic scattering process between free carriers and excitons [20] or holes and electrons in an EHP. A simple guess with the generation rate and a lifetime of 200 ps indicates, that the EHP could be just at the onset of degeneracy at RT with  $n_p$  of several  $10^{18} \text{ cm}^{-3}$ .

As a last example, we show in Fig. 4 time resolved emission spectra of a hexagonal type-II CdS/CdSe SL grown on GaAs (111). The shift of the emission with time is connected with the screening of internal piezo-fields by the free carriers and is treated in more detail in ref. [22]. Here we concentrate on the strong peak around 1.8 eV which appears with a threshold character for the highest excitation energies only and which decays almost synchronously with the excitation

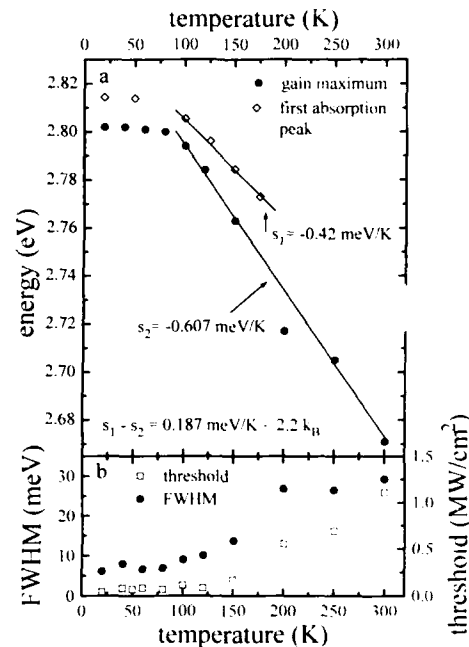


Fig. 3. The temperature dependence of the exciton energy (—○—) and of the gain maximum just beyond threshold (—●—) (a) and the temperature dependence of the FWHM of the gain spectrum (—●—) and the excitation intensity at threshold (—□—) (b).

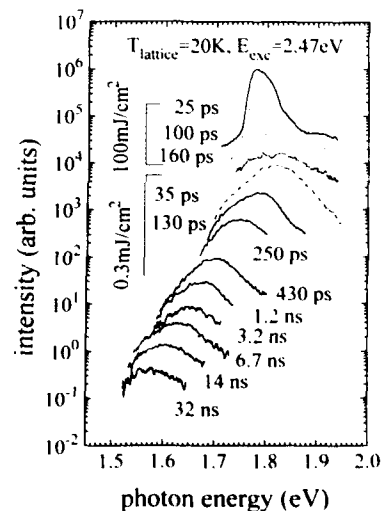


Fig. 4. Time resolved emission spectra after ps excitation of 30 periods of 6 nm CdSe and 6 nm CdS on GaAs (111) for two different pump powers.

pulse. These features confirm that this emission is of stimulated origin. A detailed analysis [22] of the (mini-) band structure in this SL shows that the stimulated emission is due to the transition from the second quantized electron level to the first quantized hole level due to the stronger overlap integral. The first quantized hole level is with increasing excitation populated first, but the optical transition matrix element is too small to overcome the losses. Since the parity selection rule  $\Delta n_z = 0$  is relaxed by the internal piezofields, the transitions between the second electron and the first hole subband are allowed and get indeed a higher oscillator strength than the fundamental transition [22]. The densities at which these states start to be populated are in the  $10^{13} \text{ cm}^{-2}$  range and thus beyond the 2d Mott density. This means, that we have here an example of plasma gain in a II–VI SL.

## 6. Conclusion and outlook

We have seen that the gain processes for several II–VI epilayers and SL follow the trends known from bulk materials. In the future we can expect the optimization of these processes towards application (i.e., room temperature lasing in a forward biased p–n junction) and a quantitative analysis and understanding of, e.g., the scattering processes, the band alignment and renormalization.

## 7. Acknowledgement

This work has been supported by the Deutsche Forschungsgemeinschaft.

## 8. References

- [1] C. Klingshirn, *Advan. Mater. Opt. Electron.* 2 (1993), in press.
- [2] See, e.g., M.A. Haase, J. Qiu, J.M. DePuydt and H. Cheng, *Appl. Phys. Lett.* 59 (1991) 1272; H. Jeon, J. Ding, W. Patterson, A.V. Nurmikko, W. Xie, D.C. Grillo, M. Kobayashi and R.L. Gunshor, *Appl. Phys. Lett.* 59 (1991) 3619; or the contributions to this conference and references therein.
- [3] S.M. Sze, *Physics of Semiconductor Devices*, 2nd ed. (Wiley, New York, 1981); 3rd ed. (Wiley, New York, 1991); K.J. Ebeling, *Integrierte Optoelektronik*, 2nd ed. (Springer, Berlin, 1992).
- [4] A.V. Nurmikko and R.L. Gunshor, *Phys. Status Solidi (b)* 173 (1992) 291.
- [5] H. Kalt, J.H. Collet, Le Si Dang, J. Cibert, S.D. Baranovskii, R. Saleh, M. Umlauff, K.P. Geysers, M. Heuken and C. Klingshirn, *Physica B* 191 (1993) 90.
- [6] C. Klingshirn and H. Haug, *Phys. Rept.* 70 (1981) 315.
- [7] B. Hönerlage, R. Lévy, J.B. Grun, C. Klingshirn and K. Bohnert, *Phys. Rept.* 124 (1985) 161.
- [8] F.A. Majumder, S. Shevel, V.G. Lyssenko, H.-E. Swohoda and C. Klingshirn, *Z. Physik B* 66 (1987) 409.
- [9] K. Wüstel, and C. Klingshirn, *Opt. Commun.* 32 (1980) 269.
- [10] M.S. Skolnick et al., in: *Proc. 21st Int. Conf. on Physics of Semiconductors* (World Scientific, Singapore, 1982) p. 41, and references therein.
- [11] M. Grün, M. Hetterich, C. Klingshirn, A. Rosenauer, J. Zweck and W. Gebhardt, *J. Crystal Growth* 138 (1994) 150.
- [12] W. Gebhardt, *Mater. Sci. Eng. B* 11 (1992) 1.
- [13] J. Söllner, M. Scholl, A. Schneider, M. Heuken and J. Woitok, *J. Crystal Growth* 138 (1994) 35.
- [14] K.L. Shaklee, R.E. Nahory and R.F. Leheny, *J. Luminescence* 7 (1973) 284.
- [15] F.A. Majumder, H. Kalt, C. Klingshirn, A. Naumov, H. Stanzl and W. Gebhardt, in: *Proc. ICL '93, J. Luminescence*, to be published.
- [16] S.V. Bogdanov, M. Grün, H. Kalt and C. Klingshirn, *Solid State Commun.* 86 (1993) 273.
- [17] J. Gutowski, *Semicond. Sci. Technol.* 6 (1991) A51.
- [18] C. Klingshirn, *J. Crystal Growth* 117 (1992) 753.
- [19] H.P. Wagner, S. Laukes, K. Wolf, W. Kuhn, P. Link and W. Gebhardt, *J. Crystal Growth* 117 303 (1992); G. Kudlek, N. Presser, U.W. Pohl, J. Gutowski, J. Lilja, E. Kuusisto, K. Imai, M. Pessa, K. Hingerl and H. Sitter, *J. Crystal Growth* 117 (1992) 309.
- [20] M. Dabbicco, M. Treppe, R. Cingolani, G. Scamarcio, M. Ferrara and I. Suemune, *Semicond. Sci. Technol.* 7 (1992) 681.
- [21] Y. Kuroda, I. Suemune, M. Fujimoto, Y. Fujii, N. Otsuka and Y. Nakamura, *J. Appl. Phys.* 72 (1992) 3029.
- [22] W. Langbein, H. Kalt, M. Hetterich, M. Grün and C. Klingshirn, *J. Crystal Growth* 138 (1994) 191.



ELSEVIER

Journal of Crystal Growth 138 (1994) 791–795

JOURNAL OF  
**CRYSTAL  
GROWTH**

## Dephasing of excitons in a CdTe/Cd<sub>0.86</sub>Mn<sub>0.14</sub>Te multiple quantum well

R. Hellmann <sup>a,\*</sup>, M. Koch <sup>a</sup>, J. Feldmann <sup>a</sup>, S.T. Cundiff <sup>a</sup>, E.O. Göbel <sup>a</sup>,  
D.R. Yakovlev <sup>b</sup>, A. Waag <sup>b</sup>, G. Landwehr <sup>b</sup>

<sup>a</sup> Fachbereich Physik und Wissenschaftliches Zentrum für Materialwissenschaften, Philipps-Universität, D-35032 Marburg, Germany

<sup>b</sup> Physikalisches Institut, Universität Würzburg, D-97074 Würzburg, Germany

### Abstract

The dephasing of heavy- and light-hole excitons in CdTe/Cd<sub>0.86</sub>Mn<sub>0.14</sub>Te multiple quantum wells is investigated by means of subpicosecond transient four-wave mixing. We find dephasing times on the order of 2 ps, corresponding to a homogeneous linewidth of 0.65 meV, for the free heavy-hole exciton at 5 K and moderate exciton density. Density and temperature dependent measurements of the homogeneous linewidth allow the determination of the interaction strength for exciton–exciton and exciton–phonon scattering as well as of the residual contribution due to extrinsic scattering processes. Simultaneous excitation of heavy- and light-hole excitons leads to the appearance of quantum beats, allowing the determination of the light-hole dephasing time. We find that the light hole dephases 4–5 times faster than the heavy-hole exciton. This faster dephasing of the light-hole exciton is attributed to a resonant coupling between the 1s light-hole and the 2s heavy-hole exciton state. The results are compared to published data for GaAs/Al<sub>1-x</sub>Ga<sub>x</sub>As quantum wells.

### 1. Introduction

Recently various time-resolved optical techniques, including time-resolved photoluminescence (TRPL), pump and probe, or transient four-wave mixing (TFWM), have been employed to study the dynamics of excitons in II–VI semiconductor bulk materials [1] and heterostructures [2,3]. Among these, TFWM allows direct measuring of the exciton dephasing time  $T_2$ , and thus determining the homogeneous linewidth,  $\Gamma_{\text{hom}} = \hbar/\pi T_2$ . Due to its dependence on scattering processes, the dephasing time and hence the homo-

geneous linewidth of optical, in particular exciton, transitions is a very sensitive measure of the extrinsic and intrinsic properties of the materials and structures. For example, amongst the different scattering processes contributing to the dephasing, defect-, impurity-, alloy- and interface-scattering are extrinsic processes, which often depend on growth conditions, while quasi-particle interactions, like exciton–exciton and exciton–phonon scattering, are intrinsic. Thus, a detailed investigation of these processes and a comparison of the optical properties of quantum wells (QWs) based on wide gap II–VI semiconductors with III–V QWs are also of great importance for the further development and improvement of optoelectronic devices based on II–VI materials.

\* Corresponding author.

Here we report on subpicosecond TFWM studies of scattering processes contributing to the optical dephasing of heavy-hole and light-hole excitons in a semimagnetic  $\text{CdTe}/\text{Cd}_{0.86}\text{Mn}_{0.14}\text{Te}$  multiple quantum well (MQW).

## 2. Experimental details

The  $\text{CdTe}/\text{Cd}_{0.86}\text{Mn}_{0.14}\text{Te}$  MQW was grown by molecular beam epitaxy on (100)-oriented CdTe substrate after a  $0.2\text{ }\mu\text{m}$  CdTe buffer layer [4]. The MQW consists of 50 periods of 8.5 nm thick CdTe wells and 9.5 nm thick  $\text{Cd}_{0.86}\text{Mn}_{0.14}\text{Te}$  barriers. A tunable mode locked Ti-sapphire laser was used as an excitation source for the TFWM experiments. This laser produces a train of 110 fs pulses (spectral width 22 meV) at a repetition rate of 76 MHz. The  $T_2$  times were measured in the two-pulse self-diffraction TFWM configuration in the reflection geometry [5], allowing FWM experiments on structures with opaque substrates. The nonlinear signal was detected time integrated by a photomultiplier as a function of the time delay between the two incident pulses. For inhomogeneously broadened transitions, the exponential decay of the TFWM signal  $\tau_{\text{TFWM}}$  is related to the dephasing time by  $T_2 = 4\tau_{\text{TFWM}}$  [6]. For the TRPL experiments, excitation was provided by a synchronously pumped mode-locked Pyridin 2 dye laser with pulse duration of 7 ps. A synchroscan streak camera with a time resolution of 25 ps was used for detection. The sample was kept in a temperature variable helium flow cryostat, allowing temperature dependent measurements.

## 3. Results and discussion

The photoluminescence excitation spectrum (PLE) of the sample is shown in Fig. 1. The resonances of the 1s heavy- and light-hole excitons (hh and lh) can be observed at 1.620 eV (hh) and 1.633 eV (lh). This corresponds to a lh–hh splitting of 13 meV. The linewidth is 4.3 meV for the hh and 5.0 meV for the lh. The broadening is

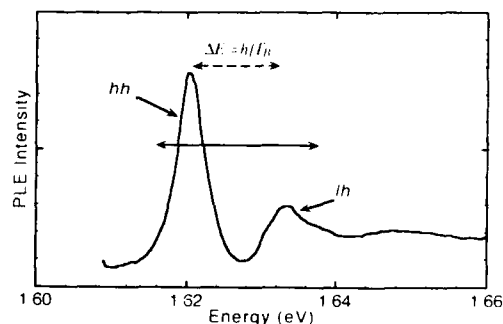


Fig. 1. Photoluminescence excitation spectrum at  $T = 1.6\text{ K}$ . The horizontal solid arrow indicates the spectral full width at half maximum of the laser pulses used in the TFWM experiments. The dashed line corresponds to the energy splitting determined from the observed beat period.

attributed to well-width fluctuations on the order of three monolayers.

Fig. 2 shows the transient behaviour of the luminescence detected from the free 1s heavy-hole exciton recombination under nonresonant excitation, i.e. excited above the 1s heavy-hole exciton resonance. The TRPL signal can be well fitted with an exponential decay constant of 205 ps, a typical value for II–VI semiconductor QWs [2,7].

TFWM traces measured at 4.2 and 45 K and an exciton density of  $10^{12}\text{ cm}^{-2}$  are shown in Fig. 3. In order to excite only the hh exciton transition, the laser was tuned well below the hh resonance. The decay times of the TFWM signals, obtained by an exponential fit to the data, corre-

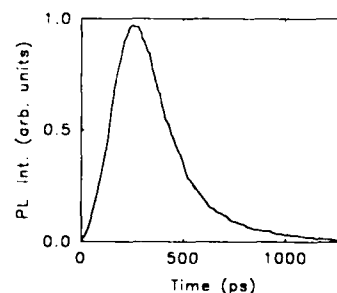


Fig. 2. TRPL of the heavy-hole exciton at 5 K as measured under nonresonant excitation, i.e. excited above the 1s heavy-hole exciton energy.

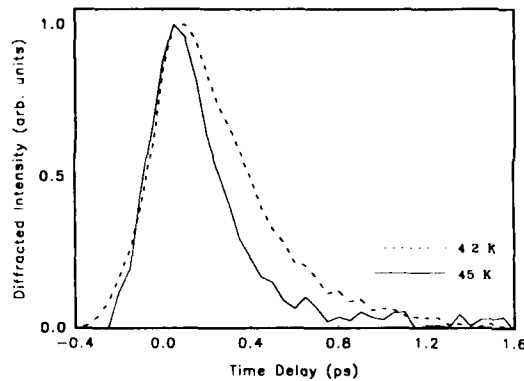


Fig. 3. TFWM signal as a function of the delay time between the two exciting laser pulses at  $T = 4.2$  and  $45$  K.

spond to dephasing times  $T_2$  of 1.38 and 840 fs, respectively. These dephasing times are much shorter than the observed exciton recombination time of 205 ps. Thus, we can conclude that the recombination process does not contribute to the dephasing and that the  $T_2$  times are determined solely by scattering processes, which will be discussed in detail in the following.

Temperature dependent TFWM measurements between 4.2 and 45 K reveal a linear increase of the homogeneous linewidth from 0.95 to 1.54 meV, as shown in Fig. 4. The linear increase implies that acoustic phonon scattering

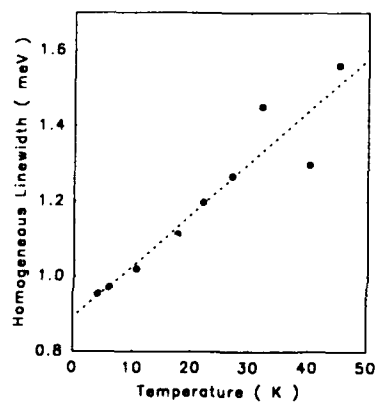


Fig. 4. Homogeneous linewidth as a function of temperature. The dashed line represents a linear regression, which yields the coupling strength for exciton-acoustic phonon scattering.

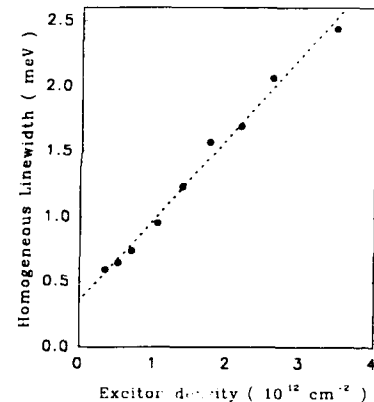


Fig. 5. Homogeneous linewidth as a function of exciton density. The dashed line is the result of a linear regression, which yields the parameter for exciton-exciton interaction.

is the dominant temperature dependent dephasing mechanism below 45 K [8]. The slope of the linear increase is a measure of the exciton-acoustic phonon coupling strength  $\gamma_{ph}$ , whereas the intercept  $\Gamma_{hom}(T=0)$  accounts for temperature independent processes such as exciton-exciton interaction and scattering by defects, impurities, interface roughness and alloy fluctuations [9,10]. A linear regression to our data yields  $\gamma_{ph} = 13.7$   $\mu\text{eV/K}$  and an intercept of 0.89 meV. The value for  $\gamma_{ph}$  is a factor of three larger than the one reported for a 13.5 nm GaAs/AlGaAs QW [9]. Thus, we conclude that exciton-acoustic phonon scattering is weaker in GaAs/AlGaAs as compared to CdTe/CdMnTe QWs.

As mentioned above,  $\Gamma_{hom}(T=0)$  involves a contribution due to exciton-exciton scattering. We have determined this contribution by measuring the density dependence of  $\Gamma_{hom}$  at 4.2 K in the range between  $3.4 \times 10^{11}$  and  $5.5 \times 10^{12} \text{ cm}^{-2}$ . The obtained values are plotted in Fig. 5.  $\Gamma_{hom}$  increases linearly with exciton density from 0.6 meV to 2.4 meV in this range. This linear increase is attributed to exciton-exciton scattering and can be described by [11]:

$$\Gamma_{hom}(n_x) = \Gamma_{hom}(n_x = 0) + \gamma_{xx} a_B^2 E_B n_x. \quad (1)$$

Here  $a_B$  is the exciton Bohr radius (4.5 nm in our particular structure) and  $E_B$  the exciton binding



energy (20 meV in our case).  $\gamma_{xx}$  is a dimensionless parameter and gives a measure of the exciton–exciton interaction strength.  $I_{\text{hom}}(n_x = 0)$  is the density independent contribution to the homogeneous linewidth and includes all residual interactions of the excitons with acoustic phonons, impurities, interfaces and alloy fluctuations. Fitting Eq. (1) to our data yields an exciton–exciton interaction strength of 0.16 and a density independent contribution of 0.35 meV at 4.2 K. The value of  $\gamma_{xx}$  is nearly one order of magnitude smaller than the one reported by Honold et al. for a 12 nm GaAs QW [12]. Since the differences in exciton parameters ( $a_B$ ,  $E_B$ ) are already taken into account in Eq. (1), we expect  $\gamma_{xx}$  to be similar in different materials. Slight differences can be partly attributed to the different screening of the Coulomb potentials between excitons, i.e. due to the different dielectric constants of both the well and the barrier materials. In addition,  $\gamma_{xx}$  will also be modified by localization (for localized excitons a smaller  $\gamma_{xx}$  is expected). However, assuming localization is in contradiction to the temperature dependent TFWM results, since the observed linear temperature dependence is consistent with the interaction between *free* excitons and single acoustic phonons [10]. This, however, was also found in another II–VI QW system (CdZnTe/ZnTe) by Stanley [13]. Nevertheless, this point is not yet fully understood and further work is definitely needed.

Since we have measured both the interaction strength for exciton–acoustic phonon and exciton–exciton scattering, we are now able to determine the contribution to  $I_{\text{hom}}$  due to the residual extrinsic scattering processes, e.g. alloy, interface and impurity scattering, which often depend on growth conditions. Hence  $I(T = 0; n_x = 0)$  might be considered as a measure for the structural quality of the sample. By extrapolating the data to zero temperature and zero density we find  $I_{\text{hom}}(T = 0; n_x = 0) = 0.28$  meV, which is a factor of 2.5 larger than the value reported for GaAs QWs [9]. Spin scattering between the exciton spin and the spin of the manganese ions in the semi-magnetic barrier may contribute to  $I(T = 0; n_x = 0)$ ; however, further careful study is required to investigate the role of this spin-spin interaction.

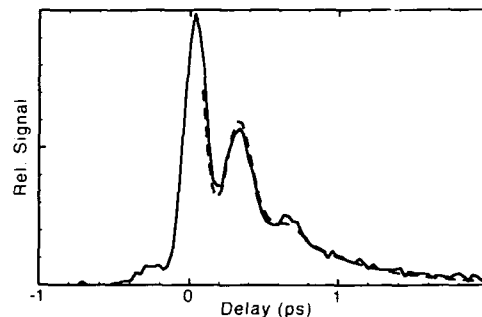


Fig. 6. TFWM signal (solid line) detected under simultaneous excitation of the heavy- and light-hole excitons. The dashed line is a fit to the data, which provides the energy splitting and the dephasing times of the two transitions involved in the beat phenomena.

The primary contribution to this difference is probably due to the different structural quality.

For the TFWM experiments described above, the exciting laser was tuned well below the hh resonance in order to excite only the hh exciton. Tuning the laser center frequency (spectral width 22 meV) to higher energies between the hh and lh resonance, both transitions are excited simultaneously. This results in the appearance of a periodic modulation in the TFWM signal, as shown in Fig. 6 (solid line), which is attributed to quantum beats between the 1s hh and 1s lh [14]. By analyzing the temporal dependence of the TFWM signal, both the energy splitting  $\Delta E = h/T_B$  ( $T_B$  is the beat period) between the respective transitions and their dephasing times can be obtained. A fit to the observed data is shown in Fig. 6 by the dashed line and yields an energy splitting of 12 meV, in reasonable agreement with the splitting in the PLE [15]. The dephasing times for the hh and lh excitons are found to be  $1.90 \pm 0.05$  ps for the hh and  $0.4 \pm 0.1$  ps for the lh, i.e. the lh exciton dephases approximately 4–5 times faster than the hh exciton. This shorter dephasing time of the lh exciton is attributed to scattering between the excitonic 1s lh state and the nearly degenerate 2s hh exciton state.

#### 4. Summary

In summary, we have performed transient four-wave-mixing experiments to study the scattering processes contributing to the dephasing of heavy- and light-hole excitons in CdTe/Cd<sub>0.86</sub>Mn<sub>0.14</sub>Te multiple quantum wells. We find dephasing times for the heavy-hole excitons on the order of 2 ps, corresponding to a homogeneous linewidth of 0.65 meV at 5 K and moderate exciton density. Comparison with exciton lifetimes demonstrates that the dephasing of the heavy-hole excitons is solely determined by scattering and not affected by recombination. Temperature and density dependent measurements of the homogeneous linewidth of the heavy-hole excitons allow the extraction of the interaction strength for exciton–acoustic phonon and exciton–exciton scattering, as well as the contribution due to residual scattering processes. In comparison with GaAs QWs we found a stronger exciton–acoustic phonon coupling and a weaker exciton–exciton interaction. The contribution to the homogeneous linewidth due to the residual, extrinsic scattering processes is slightly larger than in GaAs. Quantum beat spectroscopy enabled us to determine the dephasing time of the light-hole exciton, which has been found to be 4–5 times shorter than the heavy-hole exciton dephasing time. This faster dephasing is attributed to scattering between the 1s light-hole exciton state and the 2s heavy-hole state.

#### 5. Acknowledgements

The work at the University of Marburg has been supported through the Leibniz Förderpreis of the Deutsche Forschungsgemeinschaft. The work at the University of Würzburg was sup-

ported by the Bundesministerium für Forschung und Technologie, Bonn.

#### 6. References

- [1] See, e.g., H. Schwab, C. Dörnfeld, E.O. Göbel, J.M. Hvam, C. Klingshirn, J. Kuhl, V.G. Lysenko, S.A. Majumder, G. Noll, J. Nunnenkamp, K.H. Pankte, R. Renner, A. Reznitsky, U. Siegner, H.E. Swoboda and Ch. Weber, *Phys. Status Solidi (b)* 172 (1992) 479, and references therein.
- [2] R. Stanley, J. Hegarty, R. Fischer, J. Feldmann, E.O. Göbel, R.D. Feldman and R.F. Austin, *Phys. Rev. Lett.* 67 (1991) 128.
- [3] P.C. Becker, D. Lee, A.M. Johnson, A.G. Prosser, R.D. Feldman, R.F. Austin and R.E. Behringer, *Phys. Rev. Lett.* 68 (1992) 1878.
- [4] A. Waag, S. Schmeusser, R.N. Bicknell-Tassius, D.R. Yakovlev, W. Ossau, G. Landwehr and I.N. Uraltsev, *Appl. Phys. Lett.* 59 (1991) 2995.
- [5] A. Honold, L. Schultheis, J. Kuhl and C.W. Tu, *Appl. Phys. Lett.* 52 (1988) 2105.
- [6] T. Yajima and Y. Taira, *J. Phys. Soc. Japan* 47 (1980) 160.
- [7] A. Pohlmann, R. Hellmann, E.O. Göbel, D.R. Yakovlev, W. Ossau, A. Waag, R.N. Bicknell-Tassius and G. Landwehr, *Appl. Phys. Lett.* 61 (1992) 2929.
- [8] J. Lee, E.S. Koteles and M.O. Vasseell, *Phys. Rev. B* 33 (1986) 5512.
- [9] J. Kuhl, A. Honold, L. Schultheis and C.W. Tu, in: *Festkörperprobleme/Advances in Solid State Physics*, Vol. 29, Ed. U. Rössler (Vieweg, Braunschweig, 1989) p. 157.
- [10] T. Takagahara, *Phys. Rev. B* 32 (1985) 7013.
- [11] G. Manzke, K. Henneberger and V. May, *Phys. Status Solidi (b)* 130 (1987) 233.
- [12] A. Honold, L. Schultheis, J. Kuhl and C.W. Tu, *Phys. Rev. B* 40 (1989) 6442.
- [13] R. Stanley, PhD Thesis, Trinity College, University of Dublin, Dublin (1991).
- [14] K. Leo, T.C. Damen, J. Shah, E.O. Göbel and K. Köhler, *Appl. Phys. Lett.* 57 (1990) 19.
- [15] For the details of the fit procedure, see: M. Koch, R. Hellmann, S.T. Cundiff, J. Feldmann, E.O. Göbel, D.R. Yakovlev, A. Waag and G. Landwehr, *Solid State Commun.* 88 (1993) 521.



ELSEVIER

Journal of Crystal Growth 138 (1994) 796–799

JOURNAL OF  
CRYSTAL  
GROWTH

## Two-photon spectroscopy in ZnSe/ZnS quantum wells

Fujio Minami <sup>\*,a</sup>, Kouji Yoshida <sup>b</sup>, Kuon Inoue <sup>b</sup>, Hiroshi Fujiyasu <sup>c</sup><sup>a</sup> Department of Applied Physics, Tokyo Institute of Technology, Meguro-ku, Tokyo 152, Japan<sup>b</sup> Research Institute for Electronic Science, Hokkaido University, Sapporo 060, Japan<sup>c</sup> Department of Electronics, Faculty of Engineering, Shizuoka University, Hamamatsu 432, Japan

### Abstract

We have studied the electronic structure of strained-layer ZnSe/ZnS superlattices by using two kinds of two-photon spectroscopy: two-photon absorption spectroscopy and resonant second-harmonic generation. The exciton binding energy is found to exhibit a blue shift as compared to the bulk value due to the exciton confinement effect. Based on the observed subband energies, we derive a conduction-band offset of  $\sim 70$  meV and a valence-band offset of  $\sim 800$  meV.

### 1. Introduction

Wide band gap II–VI semiconductor heterostructures are becoming more and more important as prospects for utilizing these materials in a variety of optoelectric device applications. In particular, ZnSe-based heterostructures are potentially useful for such devices as blue-emitting diodes and blue injection lasers. As compared to the case of GaAs-based quantum-well structures, however, less background knowledge is available for this structure. In this paper, we apply two-photon spectroscopy, i.e., two-photon absorption (TPA) spectroscopy [1,2] and resonant second-harmonic generation (SHG) [1,3], to the study of electronic structure of ZnSe/ZnS strained-layer superlattices (SLSs). The TPA and resonant SHG provide detailed information about the fundamental electronic structure of the superlattices, which cannot be obtained by means of linear

spectroscopic techniques. We determine the energy of the 1S–2P splittings of heavy-hole (hh) and light-hole (lh) excitons, exciton binding energies, and conduction- and valence-band offsets in the ZnSe/ZnS superlattices.

### 2. Theoretical background

The TPA in bulk ZnSe has been shown to result predominantly from transition terms which are described in the framework of a two-band model [1]. In this model, allowed two-photon transitions occur to final P-exciton states via discrete S-exciton states as intermediates. The lowest-energy final state is then the 2P exciton. In ZnSe/ZnS superlattices, one must distinguish between  $E \parallel z$  and  $E \perp z$  polarization configurations because of the different selection rules [2]. For  $E \perp z$ , the situation is not so different from the bulk case. The onset of TPA occurs when twice the incident photon energy,  $2\hbar\omega$ , is equal to the hh1–cl band edge. We use hereinafter the

\* Corresponding author.

notation hhi-cj and lhi-cj for the optical transitions, where hh (lh) refers to the heavy (light) hole, and i (j) is the hole (electron) subband. Including the exciton effect, the lowest-energy state reached is the 2P state of the hh1-c1 excitons as in the bulk case. For  $E \parallel z$ , the TPA spectra differ greatly from those of the bulk crystal, reflecting subband quantization. The onset of two-photon transition occurs at the lh2-c1 or lh1-c2 transition, which is higher in energy than the hh1-c1 transition. (The hh2-c1 transition is forbidden because for  $E \parallel z$  the interband transition is not allowed between heavy-hole and conduction bands.)

The forbidden SHG signal is found to be enhanced drastically when twice the incident photon energy is resonant with the excitation energy of a 2P exciton in semiconductors [3,4]. The polarization selection rules of the resonant SHG is the same as those for the TPA. Further, resonant behavior of the SHG signal can be also observed at the 1S exciton energy [3,4]. From the resonant SHG data alone, therefore, we can obtain information on the 1S and 2P exciton states.

In ZnSe/ZnS SLS grown on a [001]-oriented substrate, the strain tensors  $\epsilon_{ij}$  corresponding to ZnSe or ZnS layers, are given by  $\epsilon_{xx} = \epsilon_{yy} = (a_{\parallel} - a_0)/a_0$ ,  $\epsilon_{zz} = -2\epsilon_{xx}C_{12}/C_{11}$ ,  $\epsilon_{xy} = \epsilon_{yz} = \epsilon_{zx} = 0$  [5,6], where  $a_{\parallel}$  is the in-plane lattice constant of the superlattice,  $a_0$  is the lattice constant of bulk ZnSe or ZnS, and  $C_{ij}$  are the elastic stiffness constants. Due to the in-plane biaxial strain, the fourfold  $\Gamma_8$  valence band splits into two doubly degenerate bands, i.e., hh ( $J_z = \pm 3/2$ ) and lh ( $J_z = \pm 1/2$ ) bands. As a function of the biaxial strain  $\epsilon_{xx}$ , the energy separations between the conduction and valence bands are given by [5,6]

$$\Delta E_{hh} = [2a(1 - C_{12}/C_{11}) - b(1 + 2C_{12}/C_{11})]\epsilon_{xx}, \quad (1)$$

$$\Delta E_{lh} = [2a(1 - C_{12}/C_{11}) + b(1 + 2C_{12}/C_{11})]\epsilon_{xx}, \quad (2)$$

where  $a$  and  $b$  refer, respectively, to the hydrostatic and shear deformation potentials appropriate to tetragonal distortion. In addition to the strain-induced renormalization of the energy

bands, electron and hole confinement also causes the transition energies to move higher energies. The confinement energies are calculated by using the modified Kronig-Penney model [7].

### 3. Experimental procedure

The ZnSe/ZnS superlattices studied here were grown on a (001) GaAs substrate without buffer layers by hot wall epitaxy (HWE). The experimental data were obtained from two samples: an SLS consisting of 1200 periods of 20 Å ZnSe and 18 Å ZnS layers, and an SLS composed of 1100 periods of 15 Å ZnSe and 40 Å ZnS. The actual structural configuration of the sample has been assessed by high-resolution double crystal X-ray diffraction. The incident laser beam was propagated normal to the epitaxial growth direction,  $z$ , so that either the  $E \parallel z$  or  $E \perp z$  polarization configuration was possible [3]. The samples were directly immersed into liquid helium pumped to 2 K. The excitation source was a home-made Ti:sapphire laser pumped by a CW Q-switched, intracavity frequency-doubled Nd:YAG laser operating at 6 kHz. The Ti:sapphire laser had a tuning range from 700 to 1000 nm, a pulse duration of 30 ns and an average output power of  $\sim 100$  mW. The tuning accuracy of the Ti:sapphire laser was about 1 Å, corresponding to  $\sim 0.3$  meV uncertainty in the energy determination of  $2\hbar\omega$ . The TPA signals were monitored via the luminescence from 1S free excitons (two-photon excitation spectroscopy). The luminescence and scattered light were dispersed with a monochromator and detected by a gated optical-multichannel detector. The spectral resolution of the present measurement is mainly limited by the linewidth of the tunable Ti:sapphire laser.

### 4. Results and discussion

In Fig. 1, we show the TPA spectra obtained from 20 Å ZnSe/18 Å ZnS sample. For experimental points indicated by open circles, the polarization vector of the laser beam is chosen parallel to  $z$ . The filled circles are obtained for

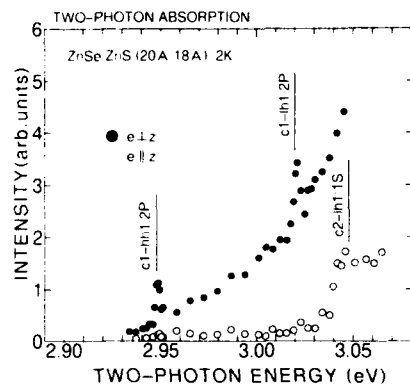


Fig. 1. Two-photon absorption spectra of the 20 Å ZnSe/18 Å ZnS superlattice for the  $E \perp z$  (●) and  $E \parallel z$  (○) configurations.

$E \perp z$ . In the  $E \perp z$  configuration, the TPA process involves final 2P excited states for the hh1-cl and lh1-cl excitonic transitions. For  $E \parallel z$ , the TPA enhancement is observed around  $2\hbar\omega = 3.05$  eV, which has a resemblance to the one-photon exciton absorption feature. Taking into account the polarization selection-rules and the small conduction-band offset between ZnSe and ZnS [6,10], this feature can be assigned to the transition between the lh1 and the conduction-band continuum states. At higher energies, we can find other two peaks: 1S c1-hh2 peak at 3.175 eV and 2P c2-hh2 peak at 3.249 eV.

Variation of the SHG intensity with  $2\hbar\omega$ , i.e., the excitation spectrum for SHG, is shown in Fig. 2. No correction due to reabsorption of the signal was made for simplicity. For  $E \perp z$ , four peaks exist strikingly in the energy region concerned. The second and fourth lowest peaks in the excitation spectrum can be easily identified as appearing as a result of resonance with the 2P excitons. The first and third peaks at 2.917 and 2.985 eV, which have a corresponding feature in the one-photon absorption spectrum, are attributable to 1S hh1-cl and lh1-cl free exciton transitions, respectively.

From the measured energy splitting between the 1S and 2P excitons, we can estimate the exciton binding energy. The binding energies are found to be  $38 \pm 2$  and  $44 \pm 2$  meV respectively

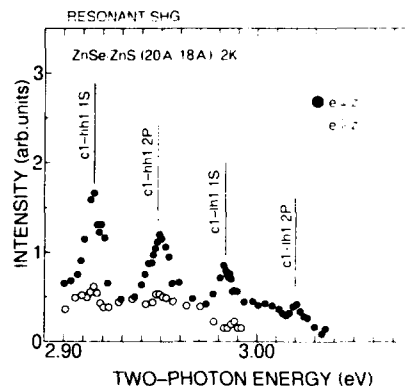


Fig. 2. SHG intensities from the 20 Å ZnSe/18 Å ZnS superlattice as a function of  $2\hbar\omega$  for  $x(yy, unp)z$  (●) and  $x(zz, unp)z$  (○) configurations.

for the hh and lh excitons. There is a significant increase in the binding energy in our sample, as compared to that in bulk ZnSe ( $\sim 20$  meV). This increase will be caused by the exciton confinement effect. An appreciable difference in the binding-energy between the hh and lh excitons can be detected, as the effective mass theory predicted [8,9].

Similar results have been obtained in the case of the 15 Å ZnSe/40 Å ZnS SLS. The TPA

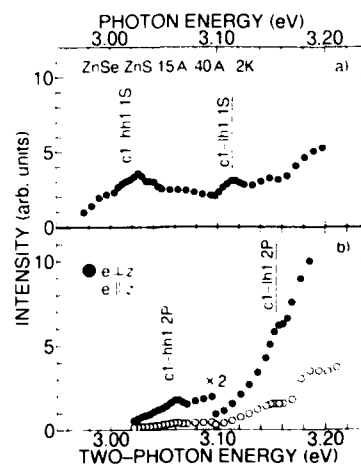


Fig. 3. (a) One-photon photoluminescence excitation spectrum of the 15 Å ZnSe/40 Å ZnS superlattice. (b) Two-photon absorption spectra of the 15 Å ZnSe/40 Å ZnS superlattice for the  $E \perp z$  (●) and  $E \parallel z$  (○) configurations.

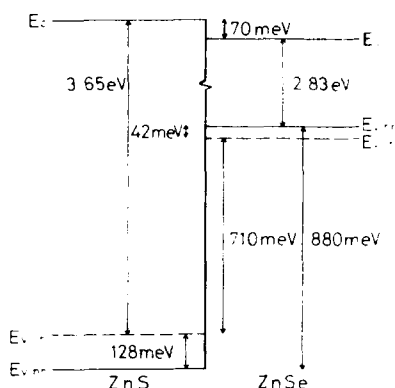


Fig. 4. Band lineups of the 20 Å ZnSe/18 Å ZnS strained-layer superlattice. The heavy- and light-hole valence bands are represented by solid and dashed lines, respectively.

spectra for this SLS are presented in Fig. 3. The two broader peaks in the  $E \perp z$  spectrum come from the 2P hh1-cl and lh1-cl excitonic transitions. The TPA enhancement around  $2\hbar\omega = 3.18$  eV in the  $E \parallel z$  spectrum is due to the transition between the lh1 and the conduction band continuum states. The resonant SHG signal could not be observed clearly in this sample because of smaller ZnSe volume and larger inhomogeneous broadening. Instead of the SHG data, the one-photon excitation spectrum is shown in the figure. Two 1S exciton peaks can be observed in the one-photon spectrum. It is found from these data that the binding energies are  $45 \pm 2$  and  $51 \pm 2$  meV.

A careful comparison between the observed subband splittings and those from the Kronig-Penney calculations using the lattice constant  $a_{||}$  as an adjusting parameter reveals the band line-ups in the superlattice. The line-ups for the 20 Å ZnSe/18 Å ZnS SLS we propose are illustrated in Fig. 4. The conduction-band offset is estimated to be  $\sim 70$  meV. The strain-induced splitting between the hh and lh bands becomes  $\sim 42$  meV in the ZnSe layers. It is thus found that one-third of the hh-lh splitting ( $\sim 70$  meV) is attributable to quantum confinement effects. The discontinuities in the hh and lh bands at the interface are  $880 \pm 10$  and  $710 \pm 10$  meV, respectively. The

discontinuity in the center of gravity of the hh and lh bands is  $\sim 795$  meV. The in-plane lattice constant  $a_{||}$  is  $\sim 5.62$  Å and  $\epsilon_{||}$  is calculated to be  $\sim 0.8\%$ , which agrees approximately with the value of 1% estimated from Raman scattering. The lattice constant  $a_{||}$  is larger than that ( $\sim 5.51$  Å) predicted in the case of a free-standing superlattice [5,6]. This means that the  $a_{||}$  is still affected by the substrate even in thick samples. As for the 15 Å ZnSe/40 Å ZnS SLS,  $\epsilon_{||}$  is calculated to be  $\sim 1\%$  and the strain-induced splitting between the hh and lh bands becomes  $\sim 52$  meV in the ZnSe layers.

## 5. Concluding remarks

We have shown that two-photon absorption spectroscopy and resonant SHG can yield crucial information on electronic structures of ZnSe/ZnS strained-layer superlattices. These methods have improved the accuracy in determination of exciton binding energy and band offsets in the strained-layer superlattices. It should be interesting to apply this method for other strained-layer superlattices, such as CdS/ZnS superlattices.

## 6. References

- [1] H. Mahr, in: Quantum Electronics, Vol. I, Eds. H. Rabin and C.L. Tang (Academic Press, New York, 1975) p. 285.
- [2] K. Tai, A. Mysyrowicz, R.J. Fischer, R.E. Slusher and A.Y. Cho, Phys. Rev. Lett. 62 (1989) 1784.
- [3] F. Minami, K. Inoue, Y. Kato, K. Yoshida and K. Era, Phys. Rev. Lett. 67 (1991) 3708.
- [4] K. Yoshida, F. Minami, K. Inoue and H. Fujiyasu, in: Proc. 21st Int. Conf. on Physics of Semiconductors (World Scientific, Singapore, 1992) p. 811.
- [5] C.G. Van de Walle, Phys. Rev. B 39 (1989) 1871.
- [6] K. Shahzad, D.J. Olego, C.G. Van de Walle and D.A. Cammack, J. Luminescence 46 (1990) 109.
- [7] G. Bastard, Phys. Rev. B 24 (1981) 5693.
- [8] R.L. Greene, Phys. Rev. B 29 (1984) 1807.
- [9] M. Matsuura and Y. Shinozuka, J. Phys. Soc. Japan 53 (1984) 3138.
- [10] Y. Yamada, Y. Masumoto, T. Taguchi and K. Takemura, Phys. Rev. B 44 (1991) 1801.



ELSEVIER

Journal of Crystal Growth 138 (1994) 800–804

JOURNAL OF  
**CRYSTAL  
GROWTH**

## Nonlinear quantum beat spectroscopy of bound biexcitons in II–VI semiconductors

J. Erland <sup>\*</sup>, B.S. Razbirin <sup>1</sup>, V.G. Lyssenko <sup>2</sup>, K.-H. Pantke, J.M. Hvam <sup>3</sup>

*Fysisk Institut, Odense Universitet, Campusvej 55, DK-5230 Odense M, Denmark*

### Abstract

With the technique of nonlinear quantum beat spectroscopy (NQBS), based on time-integrated, spectrally resolved four-wave mixing, the nonlinearities of biexcitons localized at neutral acceptor sites in CdSe are investigated. The NQBS offers the possibility to distinguish between quantum beats from a three-level system and polarization interference from independent two-level systems. The localized biexciton states are discussed in analogy with excited states of holes in neutral donor complexes.

### 1. Introduction

Nonlinear quantum beat spectroscopy (NQBS) has in recent years turned out to be an important, ultrafast technique applicable to semiconducting compounds and structures. Close-lying excitonic transitions have been investigated using lasers with pulse lengths in the picosecond or subpicosecond regime, which is shorter than the dephasing times  $T_2$  of the excited states. Particularly are studied beat phenomena in GaAs multiple quantum wells [1–3], but also in bulk semi-

conductors [4,5]. This field of ultrafast laser spectroscopy has recently been reviewed by Pantke and Hvam [6].

Our NQBS is based on four-wave mixing (FWM) in which a laser beam of ultrafast pulses is split into two beams with wavevectors  $k_1$  and  $k_2$ . The nonlinear FWM signal is detected, time-integrated, in the background-free direction  $2k_2 - k_1$ , as a function of the delay  $\tau$  between the pulses in the two beams. The correlation trace will appear either as a free polarization decay or as a photon echo with intensity  $I_{\text{FWM}}(\tau) \propto I(0) e^{-c\gamma\tau}$  depending on whether the transition is homogeneously ( $c = 2$ ) or inhomogeneously ( $c = 4$ ) broadened, respectively, where  $\gamma = 1/T_2$  [7]. If nearly degenerate multilevel systems are simultaneously and coherently excited by the same ultra-short laser pulse, the correlation trace may additionally be modulated by the difference frequency  $\Delta\omega$  between the levels [1–3,5], i.e. as

$$I_{\text{FWM}}(\tau) = I_{\text{ave}}(\tau) [1 + I_m(\tau) \cos(\Delta\omega\tau + \phi)], \quad (1)$$

<sup>\*</sup> Corresponding author.

<sup>1</sup> Permanent address: A.F. Ioffe Physical-Technical Institute, Politekhnicheskaya 26, 194921 St. Petersburg, Russian Federation.

<sup>2</sup> Permanent address: Institute of Microelectronics Technology and Superpure Materials, Chernogolovka, Moscow District 142432, Russian Federation.

<sup>3</sup> Present address: Mikroelektronik Centret, Technical University of Denmark, DK-2800 Lyngby, Denmark.

where the decays of the average intensity  $I_{\text{ave}}(\tau)$  and of the modulation amplitude  $I_m(\tau)$  are governed by the dephasing rates  $\gamma_i$  of the individual transitions. The phase of the modulation is specified by  $\phi$ .

Two methods have been described to distinguish whether or not the underlying microscopic systems are coupled. Koch et al. [8] *time-resolve* the FWM signal by cross correlation with a third, delayed laser beam and observe the modulation in real time for different delays between the two incident beams. In the  $(t, \tau)$  domain they distinguish between polarization interferences (PI) and quantum beats (QB) by identifying signal trajectories at  $(t - 2\tau)$  and  $(t - \tau)$ , respectively. Alternatively, our group [9] *spectrally-resolve* the FWM signal with a spectrometer. By this method, the distinction is made in the  $(\omega, \tau)$  domain analysing the modulation amplitude  $I_m$  and phase  $\phi$ , as a function of the detected frequency around one of the resonances. As we shall see in the following, the most distinct signature is a phase shift of  $\pi$  passing through a resonance, in the case of polarization interferences, which is absent in the case of quantum beats.

In a highly excited semiconductor, biexcitons may form, and possibly bind to impurity centres to form multi-exciton complexes. Such complexes were first observed in indirect-gap semiconductors, e.g. silicon [10,11], germanium [12] and silicon carbide [13]. Later, observations in the direct-gap semiconductors GaAs [14], CdTe [15] and, recently, CdS [16] followed.

Using the NQBS technique, we study the presence of localized biexciton states  $A^0M$  associated with neutral acceptor sites  $A^0$  in the II–VI semiconductor CdSe. Together with the one-exciton states  $A^0X$ , the  $A^0M$  states form a cascaded three-level system in which the intermediate state  $A^0X$  is shared by the ground state to exciton ( $A^0 - A^0X$ ) transition and the exciton to biexciton ( $A^0X - A^0M$ ) transition.

The observed quantum beats are distinguished from beats arising from polarization interference between different impurity bound excitons, which could be detected as well. To see the difference between the cascaded three-level system and the independent two-level systems, we find the spec-

tral dependence of the FWM signal by solving the Bloch equations and calculating the third order nonlinear polarization  $P^{(3)}(t, \tau)$  [7,17,18]. The spectrally resolved signal  $P^{(3)}(\omega, \tau)$  is then the Fourier transform of  $P^{(3)}(t, \tau)$ .

## 2. Theory for polarization interference and quantum beat

Denoting the complex transition frequencies  $\Omega_{j0} = \omega_j - \omega_0 - i\gamma_j$  ( $j = 1, 2$ ) for two independent two-level systems, and assuming Fourier limited pulses having a spectral width, which is much smaller than  $\omega_1$  and  $\omega_2$  and much larger than  $|\omega_2 - \omega_1|$ , the third order nonlinear polarization is expressed by [18]

$$P_{\text{PI}}^{(3)}(\omega, \tau) = \frac{R_1 e^{i\Omega_{10}\tau}}{\Omega_{10} - \omega} + \frac{R_2 e^{i\Omega_{20}\tau}}{\Omega_{20} - \omega} \quad (2)$$

where  $R_i = 2N_i M_i^4$  with dipole moment  $M_i$ .  $N_i$  is a function of the incident fields, the spectral overlap with resonance  $i$ , and the concentration of two-level centres of type  $i$ . The nonlinear signal is proportional to the absolute square of the polarization in Eq. (2), yielding an expression as in Eq. (1). The beat signal involves the cross-product in Eq. (2), i.e. both resonance denominators, giving rise to the phase shift of  $\pi$  and the minimum of  $I_m$  in resonance. No signal is present for negative delay,  $\tau < 0$ , i.e. when pulse #1 arrives before pulse #2.

Similarly, for a cascaded three-level system, considering positive delay  $\tau > 0$ , the third order nonlinear polarization is expressed by [18]

$$P_{\text{QB}}^{(3)}(\omega, \tau) = \frac{R_1 e^{i\Omega_{10}\tau} + Q_{12} e^{i\Omega_{20}\tau}}{\Omega_{10} - \omega} - \frac{R_2 e^{i\Omega_{20}\tau} + Q_{21} e^{i\Omega_{10}\tau}}{\Omega_{20} - \omega} \quad (3)$$

with  $Q_{ij} = N_i M_i^2 M_j^2$ . Squaring Eq. (3), we find a nonlinear signal, again on the form of Eq. (1), where no phase shift and only a slight change of  $I_m$  is found when  $\omega$  moves through the resonance. A signal is also present for negative delay



( $\tau < 0$ ) which, however, does not show any modulations [18].

### 3. Experimental setup and technique

We use pulses generated by a mode-locked argon-ion laser pumping synchronously a tunable dye laser (DCM) with a repetition rate of 82 MHz and a pulse coherence time of less than 500 fs [5]. The experiments are performed at 2 K.

In the experiments, we spectrally resolve the nonlinear signal from the region below the lowest free exciton ( $A_{n=1}$  at 1.8251 eV). In this region, we find the  $A^0X$  impurity complex ( $I_1$  with binding energy 8.3 meV) and the neutral donor complex  $D^0X$  ( $I_2$  with binding energy 3.4 meV). Recording the nonlinear signal for zero delay ( $\tau = 0$ ) as shown in Fig. 1, the resonance enhancement around the  $I_1$  and  $I_2$  resonances is evident. The exciting laser was centred near the  $I_1$  complex (see Fig. 1). Around the  $I_2$  complex, two lines, denoted  $I_1^M$  (at 1.8212 eV) and  $I_1^M$  (at 1.8223 eV), are present in addition. These lines are very difficult to observe in other experiments, e.g. in a luminescence experiment (see Fig. 1). After band-to-band excitation, the lines appeared only at high excitation as weak shoulders on the

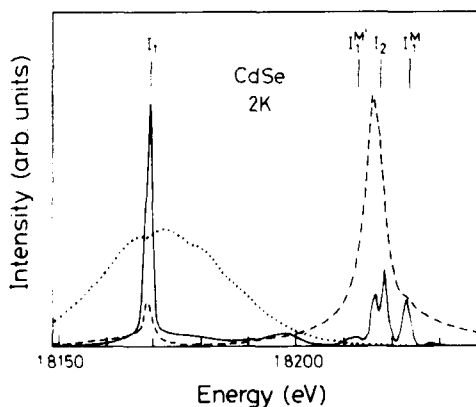


Fig. 1. Luminescence after band-to-band excitation (dashed curve), the nonlinear signal from a FWM process (solid curve) for zero delay  $\tau = 0$ , and the excitation profile for the nonlinear signal (dotted curve).

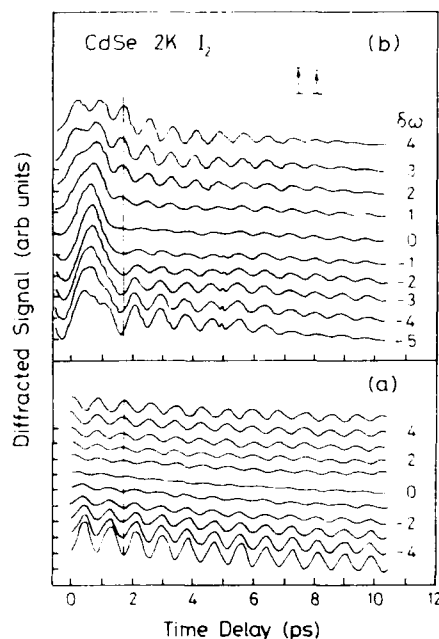


Fig. 2. Polarization interferences detected near the  $I_2$  resonance: (a) calculation after Eq. (2) with  $\hbar\Delta\omega = 4.8$  meV,  $\gamma_1 = 0$ ,  $\hbar\gamma_2 = 0.03$  meV, and  $R_1/R_2 = 1.6$ , and (b) experiment. The different frequency components are separated by  $\delta\omega = \hbar(\omega - \omega_1)/0.08$  meV.

high and low energy side of the  $I_2$  luminescence peak, respectively.

We will show in the following that the lines  $I_1^M$  and  $I_1^M$  are associated with biexciton states localized at neutral acceptor sites by observing the modulated nonlinear signal near the  $I_2$  complex, as a function of time delay  $\tau$ .

### 4. The exciton–biexciton system

In CdSe, beats between different impurity bound excitons have earlier been identified [5]. An example is shown in Fig. 2b from a sample with pronounced  $I_1$ – $I_2$  beats. A phase shift of nearly  $\pi$  and a minimum in  $I_m$  are observed around the  $I_2$  line, as compared with theory in Fig. 2a, giving evidence of polarization interference. To study the lines  $I_1^M$  and  $I_1^M$ , a sample with very short dephasing time of the  $I_2$  excitons

was selected. In this case the nonlinear signal showed only a few beats. At the  $I_1^M$  and  $I_1^M$  lines, however, pronounced oscillations could be observed. The  $I_1^M$  line has a modulation period of  $T(I_1^M) = 750$  fs (see Fig. 3b) corresponding to the  $I_1-I_1^M$  splitting of 5.4 meV, whereas the  $I_1^M$  line has a modulation period of  $T(I_1^M) = 950$  fs (see Fig. 3c) corresponding to the  $I_1-I_1^M$  splitting of 4.3 meV. At both lines, no phase shift and only a slight change of modulation amplitude are observed, suggesting that the beating states belong to the same quantum system, as calculated in Fig. 3a.

Additional experiments were performed to give further evidence of the localized biexciton. In direct two-photon excitation, as sketched in Fig.

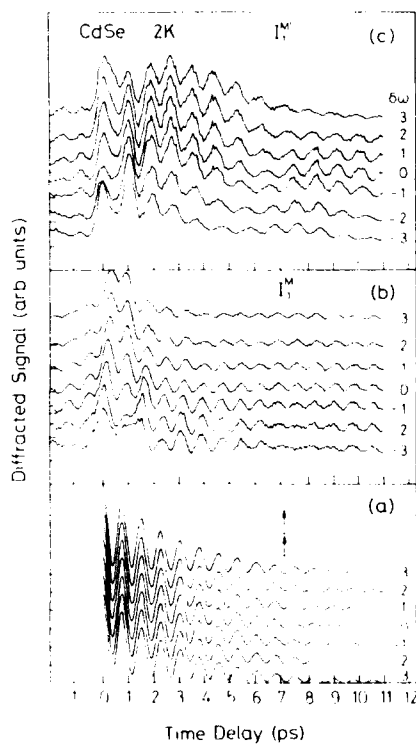


Fig. 3. Quantum beats detected in the  $I_1^M$  and  $I_1^M$  lines: (a) calculation after Eq. (3) with  $\hbar\Delta\omega = 5.4$  meV,  $\hbar\gamma_1 = \hbar\gamma_2 = 0.11$  meV, (b) experiment detected in  $I_1^M$  and (c) experiment detected in  $I_1^M$ . The different frequency components are separated by  $\delta\omega = \hbar(\omega - \omega_{\text{RES}})/0.06$  meV,  $\omega_{\text{RES}} = \omega_{I_1^M}$ ,  $\omega_{I_1^M}$ .

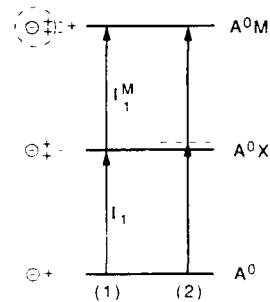


Fig. 4. Level scheme for the bound exciton-biexciton system with (1) the excitation via the exciton and (2) the direct two-photon excitation via a virtual state. On the left are shown the electronic configurations.

4, i.e. with photon energy  $\hbar\omega_{\text{TPA}} = \frac{1}{2}(E_{I_1} + E_{I_1^M})$ , the  $I_1^M$  line is detected in luminescence. The spectral width of the laser was, for this experiment, reduced to 0.3 meV by introducing an etalon in the laser cavity. The two-photon absorption to the  $I_1^M$  state was evident, as the luminescence intensity was strongly dependent on small shifts of the laser around  $\omega_{\text{TPA}}$ . This experiment demonstrated clearly the biexciton nature of the  $I_1^M$  line. Similarly for the  $I_1^M$  line.

In the following, we discuss the structure of the biexciton complex in analogy with the excited states of holes in neutral donors. For the  $A^0M$  complex, the immobile negatively charged impurity centre with the two surrounding holes (dashed circle, Fig. 4) can be thought of as an immobile positively charged centre. The overall complex is thus analogous to an exciton bound at a neutral donor ( $D^0X$ ) with the difference that only two holes can be in the 1S ground state, due to the Pauli exclusion principle. The third hole must therefore be in an excited state. The existence of excited state holes for a  $D^0X$  complex was demonstrated theoretically for hexagonal II-VI semiconductors and experimentally in CdS by Puls et al. [19]. The excitation of the  $A^0M$  complex follows the optical transitions

$$A^0X + \hbar\omega \rightarrow A^0M \quad \text{or} \quad 2\hbar\omega \rightarrow A^0M, \quad (4)$$

which show the transitions from an excited neutral acceptor  $A^0X$  to the biexciton  $A^0M$  and the two-photon transition to the biexciton  $A^0M$ . Cal-

culating the energy of the corresponding photon  $\hbar\omega$ , it is noticed that the annihilation of one of the excitons in the complex releases an energy

$$\hbar\omega = E_g - R - E_b + \Delta E, \quad (5)$$

where  $E_g$  is the band gap,  $R$  is the exciton Rydberg,  $E_b$  is the binding energy of an exciton bound to a neutral donor type centre, and  $\Delta E$  is the energy difference between the 2P (or 3D) and 1S states of the hole. These considerations show that the emission line from  $I_1^M$  ( $I_1^{M'}$ ) is found close to the  $I_2$  line. As no excited states of an exciton  $A^0X$  are possible [19], the two lines  $I_1^{M'}$  and  $I_1^M$  are thus attributed to two different states of the excited hole, split by 1.1 meV.

## 5. Conclusion

In this paper we have applied the technique of nonlinear quantum beat spectroscopy to study biexcitons localized at neutral acceptor sites in CdSe. The biexciton forms together with one exciton at the same neutral acceptor site a three-level system. In such a system no phase shift of the spectrally resolved nonlinear signal is found when the detected frequency is scanned through the resonance, as predicted by theory. Making an analogy with excited holes of neutral donor complexes, the energy of the biexciton complexes is expected to be close to the  $I_2$ , as found experimentally.

## 6. Acknowledgements

The work was supported by the Danish Natural Science Research Council. The authors are indebted to I. Balslev for valuable discussions.

## 7. References

- [1] E.O. Göbel, K. Leo, T.C. Damen, J. Shah, S. Schmitt-Rink, W. Schäfer, J.F. Müller and K. Köhler, *Phys. Rev. Lett.* 64 (1990) 1801.
- [2] D.J. Lovering, R.T. Phillips, G.J. Denton and G.W. Smith, *Phys. Rev. Lett.* 68 (1992) 1880.
- [3] K.-H. Pantke, D. Oberhauser, V.G. Lyssenko, J.M. Hvam and G. Weimann, *Phys. Rev. B* 47 (1993) 2413.
- [4] H. Stolz, V. Langer, E. Schreiber, S. Permogorov and W. von der Osten, *Phys. Rev. Lett.* 67 (1991) 679.
- [5] K.-H. Pantke, V.G. Lyssenko, B.S. Razbirin, J. Erland and J.M. Hvam, in: *Proc. 21st Int. Conf. on the Physics of Semiconductors*, Beijing, 1992, Eds. P. Jiang and H.-Z. Zheng (World Scientific, Singapore, 1992) p. 129.
- [6] K.-H. Pantke and J.M. Hvam, *Int. J. Mod. Phys. B* 7 (1993).
- [7] C. Dörfeld and J.M. Hvam, *IEEE J. Quantum Electron.* QE-25 (1989) 904.
- [8] M. Koch, J. Feldmann, G. von Plessen, E.O. Göbel, P. Thomas and K. Köhler, *Phys. Rev. Lett.* 69 (1993) 3631.
- [9] V.G. Lyssenko, J. Erland, I. Balslev, K.-H. Pantke, B.S. Razbirin and J.M. Hvam, *Phys. Rev. B* 48 (1993) 5720.
- [10] Ya.E. Pokrovskii, *Phys. Status Solidi (a)* 11 (1972) 385.
- [11] R. Sauer, *Phys. Rev. Lett.* 31 (1973) 576.
- [12] R.W. Martin, *Solid State Commun.* 14 (1974) 369.
- [13] P.J. Dean, D.C. Herbert, D. Bimberg and W.J. Choyke, *Phys. Rev. Lett.* 37 (1976) 1635.
- [14] R.J. Almassy, D.C. Reynolds, C.W. Litton, K.K. Bajaj and G.L. McCoy, *Solid State Commun.* 31 (1979) 365.
- [15] A.V. Malyavkin, *Solid State Commun.* 39 (1981) 1315.
- [16] B.S. Razbirin and D.K. Nelson, *JETP Lett.* 56 (1992) 291.
- [17] T. Yajima and Y. Iaira, *J. Phys. Soc. Japan* 47 (1979) 1620.
- [18] J. Erland and I. Balslev, *Phys. Rev. A* 48 (1993) R1765.
- [19] J. Puls, F. Henneberger and J. Voigt, *Phys. Status Solidi (b)* 119 (1983) 291.



ELSEVIER

Journal of Crystal Growth 138 (1994) 805–808

JOURNAL OF  
**CRYSTAL  
GROWTH**

## Free induction decay and quantum beat of excitons in ZnSe

T. Saiki <sup>a,a,b</sup>, K. Takeuchi <sup>a</sup>, K. Ema <sup>a</sup>, M. Kuwata-Gonokami <sup>a</sup>,  
K. Ohkawa <sup>c</sup>, T. Mitsuyu <sup>c</sup>

<sup>a</sup> Department of Applied Physics, Faculty of Engineering, The University of Tokyo, Hongo, Bunkyo-ku, Tokyo 113, Japan

<sup>b</sup> Kanagawa Academy of Science and Technology, Sakado, Takatsu-ku, Kawasaki, Kanagawa 213, Japan

<sup>c</sup> Central Research Laboratories, Matsushita Electric Company, Ltd., Morinouchi-shi, Osaka 570, Japan

### Abstract

We study coherent transient phenomena of excitons using femtosecond time-resolved four-wave mixing (TR-FWM) in two types of high quality thin films of ZnSe: one is a homo-epitaxial film (1.2  $\mu\text{m}$  thickness) and the other is a very thin (50 nm) hetero-epitaxial film on GaAs substrate. Free induction decay (FID) behavior of the third-order polarization is clearly observed. We obtained the same values of exciton dephasing time from the temporal measurements, the decay time of FID, and the frequency domain measurements, analyses of reflection spectra. This implies that the excitons in ZnSe films are homogeneous. In the thin film sample, we observe a beat signal in time-integrated and time-resolved FWM. Based on the perturbational calculation, we conclude that the beat originates from the quantum interference of heavy- and light-hole excitons.

### 1. Introduction

The development of tunable short pulse lasers enables us to study the coherent transient phenomena, such as free induction decay (FID), photon echo (PE) [1] and quantum beats (QB) [2–4], in semiconductors where the induced polarization decays much faster than in atoms. These phenomena have so far been studied extensively in GaAs quantum wells. Although the growth technique of GaAs epitaxial layers has been well established, the strict control of inhomogeneous broadening of excitons is still difficult. This is because the binding energy of excitons in GaAs quantum well is so small that the small imperfection of the structures such as well width fluctua-

tion causes the significant effect on the optical responses of excitons. Thus we often encounter the sample dependent phenomena even qualitatively. On the other hand, the epitaxial growth technique of wide gap II–VI semiconductors has been remarkably improved. In wide gap II–VI semiconductors, the excitons are very stable and the resonant effects of excitons can be clearly observed. We observed a very large nonlinear phase shift at the exciton resonance in ZnSe films [5], which is then applied to the demonstration of all optical serial to parallel conversion up to sub-Tbit/s [6].

In this paper, we report the coherent transient nonlinear responses of excitons in high quality ZnSe films using high repetition rate tunable sub-picosecond pulses. We measure temporal responses of the third-order polarization in four-wave mixing. We use two types of thin film sam-

\* Corresponding author.

ples, one is the homo-epitaxial ZnSe film, where we observe the FID behavior of excitons. The other is the very thin film grown on GaAs substrate, where we observed the QB signal of heavy- and light-hole excitons. Based on these results, we discuss the intrinsic nature of the excitonic third-order nonlinearity.

## 2. Experiments

High quality ZnSe thin films samples are grown by molecular beam epitaxy method. One is a homo-epitaxial ZnSe film of 1.2  $\mu\text{m}$  thickness grown on ZnSe substrate (sample I) [7]. The other is a ZnSe film with thickness of 50 nm grown on GaAs substrate (sample II) [8]. In sample II, the valence band splits into a heavy- and a light-hole bands caused by the biaxial strain. In Fig. 1, we show the reflection spectra. A heavy- and a light-hole exciton are clearly observed in sample II (Fig. 1b). Sample I is free from any strain and we observe a single exciton band, as shown in Fig. 1a. We use the second harmonics of a CW passively mode-locked Ti:sapphire laser (Coherent Mira-900). This laser generates high-repetition rate pulses suitable for the detection of weak signals. The pulse duration is 100 fs and the spectral width is 13 meV. We use the spatially parametric type two-pulse degenerate four-wave-mixing configuration as shown in Fig. 2. The

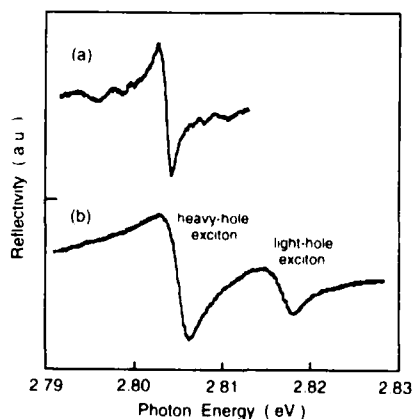


Fig. 1. Reflection spectra of sample I (a) and of sample II (b).

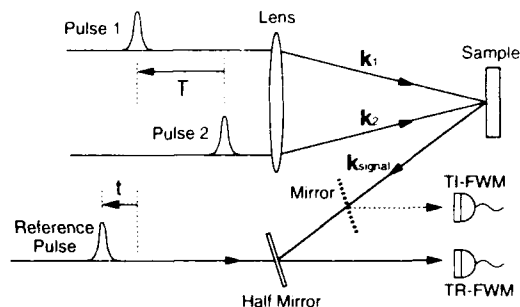


Fig. 2. Schematic drawing of the experimental configuration of TR-FWM and TI-FWM in reflection geometry.

sample is excited by two pulses with wave vectors  $k_1$  and  $k_2$ . They are set to be co-polarized. The interval between two pulses,  $T$ , is positive when pulse 1 follows pulse 2. The third-order nonlinear signal in the direction  $2k_1 - k_2$  is detected in a reflection-type geometry [9]. We measure the temporal responses of the signal using the field correlation method. We denote this as time-resolved four-wave-mixing (TR-FWM) signal which is a function of the reference delay time,  $t$ . The temporal resolution is determined by the pulse width, about 150 fs. We define the time zero,  $t = 0$ , as the time when pulse 1 reaches the sample. All the experiments are performed at 10 K. The excitation density is estimated as  $2 \times 10^{15} \text{ cm}^{-3}$ . In this excitation density region, the intensity of the FWM signal shows a third-order power dependence of the input pulses.

## 3. Results and discussion

### 3.1. Sample I: observation of free induction decay of exciton

Fig. 3 shows TR-FWM signals of sample I as a function of reference delay  $t$  at excitation delay  $T = 0$  ps and 1 ps. The signals appear at the time when pulse 1 reaches the sample and the signals decay exponentially. The decay times are independent of the excitation delay  $T$ .

We performed a third-order perturbational calculation based on the elementary excitation picture which we have recently applied to the

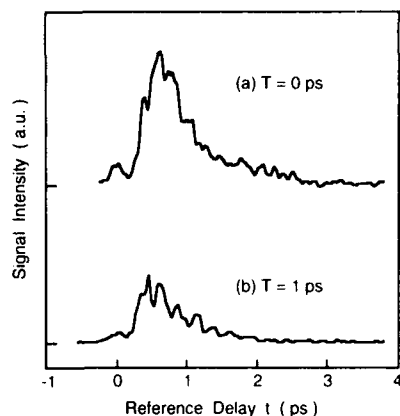


Fig. 3. TR-FWM signals of sample I at excitation delay,  $T = 0$  ps (a) and at  $T = 1$  ps (b).

four-wave-mixing signals in a GaAs quantum well. For the inhomogeneously broadened system, the TR-FWM signal behaves like a photon echo. The signal profile is Gaussian and its peak position depends on  $T$ . For the homogeneously broadened system, on the contrary, the signal behaves as free induction decay. The signal peaks at  $t = 0$  (on the arrival of pulse 1) and decays with the dephasing time of  $T_2$ . Our observations of Fig. 3 coincide with the latter case. According to this model, the decay time of the TR-FWM signal gives us the  $T_2$  of the excitons as 1.3 ps. This is in good agreement with the homogeneous line width ( $= \hbar/2\pi T_2$ ) estimated from the reflection spectrum in Fig. 1a. Such coincidence of the estimations of dephasing times obtained from both temporal and spectral domain measurements implies that our exciton system is truly homogeneous. Our observation clarifies that the intrinsic exciton system shows a free induction decay in the low excitation regime. Such behavior is consistent with the many body theory with semiconductor Bloch equations [10].

### 3.2. Sample II; observation of quantum beat of heavy- and light-hole excitons

The coherent excitation of two nearly degenerate transitions in a three-level system (Fig. 4a) creates a quantum-mechanical beating signal

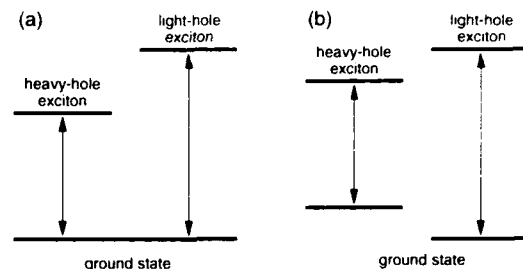


Fig. 4. Energy level diagrams of quantum beat regime (a) and classical beat regime (b).

(QB). On the other hand, if we have two independent two-level systems (Fig. 4b) and we excite them simultaneously, the polarization interference of two oscillators causes the beating signal. We call the latter phenomenon a “classical beat” (CB). In an excitonic system, the distinction between QB and CB is not a simple problem because of the complexity due to the many body nature of the system and the inhomogeneity of the samples. It has already been reported that it is possible to distinguish them from the measurements of TR-FWM signals as a function of  $T$  and  $t$  [3].

Fig. 5a shows the  $T$ -dependent time integrated (TI-FWM) signal of sample II. The beat period is 350 fs, which corresponds to an energy splitting of 12 meV. This is in good agreement with the splitting energy of heavy- and light-hole excitons, as shown in Fig. 1b. In TI-FWM, the modulation

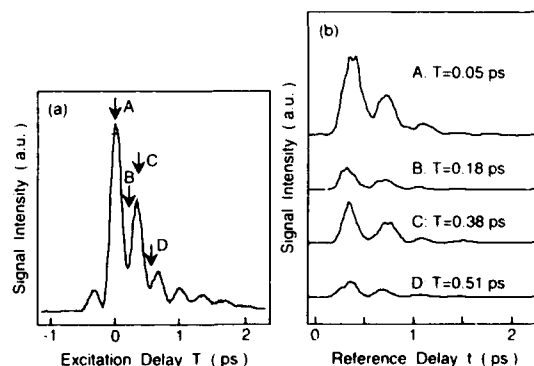


Fig. 5. TI-FWM signal of sample II (a) and TR-FWM signals at various excitation delays,  $T$  (b).

depth is the most important measure to distinguish the two types of beats. Third-order perturbational calculation predicts the 100% modulation depth for QB under the condition of equal spectral weights of heavy-hole exciton and light-hole exciton. In the case of CB, however, the modulation depth is 14% at the maximum within the possible range of  $T_2$  from the reflection spectrum, which is  $0.9 < \hbar/2\pi T_2 < 1.7$  meV [11]. In Fig. 5a, we observe a modulation depth of more than 60%, which is much larger than the limit obtained from the CB regime.

Fig. 5b shows the results of TR-FWM at various excitation delay  $T$  (indicated by the arrow in Fig. 5a). As the case depicted in Fig. 3, we again observe the free-induction-decay type responses. The signals start at  $t = 0$  and the profiles are independent of  $T$ . The perturbational calculation of TR-FWM predicts that there is a qualitative difference between the two regimes. In the QB regime, the signal is promptly emitted when pulse 1 arrives, and the peak position is independent of  $T$ . In the CB regime, on the contrary, the rise and the peak time of the signals vary with  $T$  [3]. Our observations coincide with the behavior expected for QB. Thus, we conclude that the excitons in our thin film sample are also free from the inhomogeneous broadening effect, and the observed beating in Figs. 5a and 5b are the results of the quantum interferences of heavy- and light-hole excitons in ZnSe.

#### 4. Conclusion

We demonstrate the time-resolved FWM signal in high quality ZnSe films by using stable femtosecond optical pulses. FID behavior of the third-order polarization is clearly observed. We also observe the beat signal in time-integrated and time-resolved FWM. By perturbational calculation with the three-level system and two independent two-level systems, we conclude that the

origin of the beat is the quantum interference of heavy- and light-hole excitons, not the classical polarization interference. Our results assure that the excitons in ZnSe films have no inhomogeneity. Thus the ZnSe excitons are suitable for a rigorous comparison between experiments and theories especially to prove the various many body phenomena predicted by the theory, such as intrinsic photon echo [10].

#### 5. Acknowledgments

The authors are grateful to Professor E. Hanamura for enlightening discussions. This work is supported by a Grant-in-Aid for General Scientific Research and a Grant-in-Aid for Developmental Scientific Research from the Ministry of Education, Science and Culture, Japan.

#### 6. References

- [1] S.T. Cundiff and D.G. Steel, *IEEE J. Quantum Electron.* QE-28 (1992) 2423.
- [2] K. Leo, E.O. Göbel, T.C. Damen, J. Shah, S. Schmitt-Rink, W. Schäfer, J.F. Müller, K. Köhler and P. Ganser, *Phys. Rev. B* 44 (1991) 5726.
- [3] M. Koch, J. Feldmann, G. von Plessen, E.O. Göbel, P. Thomas and K. Köhler, *Phys. Rev. Lett.* 69 (1992) 3631.
- [4] B.F. Feuerbacher, J. Kuhl, R. Eccleston and K. Ploog, *Solid State Commun.* 74 (1990) 1279.
- [5] T. Saiki, K. Takeuchi, M. Kuwata-Gonokami, K. Ohkawa and T. Mitsuyu, *Appl. Phys. Lett.* 60 (1992) 192.
- [6] K. Ema, M. Kuwata-Gonokami and F. Shimizu, *Appl. Phys. Lett.* 59 (1991) 2799.
- [7] K. Ohkawa, T. Karasawa and T. Mitsuyu, *J. Vac. Sci. Technol. B* 9 (1991) 1934.
- [8] K. Ohkawa, T. Mitsuyu and O. Yamazaki, *Phys. Rev. B* 38 (1988) 12465.
- [9] T. Saiki, K. Takeuchi, M. Kuwata-Gonokami, T. Mitsuyu and K. Ohkawa, *J. Crystal Growth* 117 (1992) 802.
- [10] M. Lindberg, R. Binder and S.W. Koch, *Phys. Rev. A* 45 (1992) 1865.
- [11] K. Takeuchi, T. Saiki and M. Kuwata-Gonokami, 18th Int. Quantum Electronics Conf., Vienna, 1992.



ELSEVIER

Journal of Crystal Growth 138 (1994) 809–814

JOURNAL OF  
**CRYSTAL  
GROWTH**

## Degenerate four-wave mixing at bound excitons in II–VI semiconductors

I. Broser, B. Lummer, R. Heitz \*, A. Hoffmann

*Institut für Festkörperphysik, Technische Universität Berlin, Hardenbergstrasse 36, D-10623 Berlin, Germany*

### Abstract

The coherent and incoherent dynamics of bound exciton complexes in CdS are investigated by means of degenerate four-wave mixing and differential transmission spectroscopy. We observe dephasing times  $T_2$  up to 800 ps for the ( $A^0$ , X) complex and up to 150 ps for the forbidden  $A_F$  exciton. The dephasing times  $T_2$  are found to be generally shorter than expected from the energy relaxation times  $T_1$ . Pure dephasing processes not connected with exciton or phonon scattering are found and discussed in view of impurity interactions and nuclear spin-flip processes.

### 1. Introduction

The first step in the relaxation of an excited electronic system like bound excitons in semiconductors is the loss of coherence due to dephasing processes. Thus, the study of dephasing processes yields information on basic interactions at the investigated system. Most dephasing processes in semiconductors take place on a fs or ps time scale and are connected either with a continuum of electronic states or with the scattering of quasi-particles [1]. These processes are expected to depend on the degree of localization of the investigated system. However, the influence of the localization on dephasing processes is still an open question [2].

Energy relaxation processes of free and bound excitons in wide band-gap II–VI semiconductors are intensively studied by means of time resolved photoluminescence [3–5]. However, only little and

contradictory information on the coherent dynamics is available yet. On the one hand, using transient four-wave mixing, dephasing times  $T_2$  of several hundred ps could be determined only for the neutral acceptor bound exciton ( $A^0$ , X) in CdSe [6] and CdS [7]. On the other hand, a dephasing time of 300 ps has been found for the ionized donor bound exciton ( $D^+$ , X) in CdS [8] by means of quantum beat spectroscopy, whereas no quantum beats have been observed for the deeper bound exciton complexes. Detailed knowledge of the coherent dynamics of bound excitons in single crystals would help to understand the basic dephasing processes of localized systems in semiconductors.

In the present paper we investigate nonlinear effects and dephasing processes of excitonic states in CdS by means of degenerate four-wave mixing (DFWM). The dephasing times are found to be too short to result exclusively from energy relaxation, indicating pure dephasing processes. Phonon and exciton scattering are intensively investigated in ref. [7] and can be excluded under

\* Corresponding author.



suitable experimental conditions. Here, possible dephasing processes of excitonic complexes due to impurity interactions and nuclear spin-flip processes are discussed.

## 2. Experimental procedure

The samples used for the measurements are high-quality platelets of CdS with thicknesses between 10 and 20  $\mu\text{m}$ . The samples are selected for excellent surfaces and appropriate  $I_1$  absorption.

The excitation source for the DFWM experiments is a dye laser synchronously pumped by a mode-locked and frequency-tripled Nd:YAG laser providing pulses of about 3 ps duration. Using Coumarin 102, the dye laser is tunable between 460 and 510 nm with an energy resolution of 250  $\mu\text{eV}$ . The laser beam is split into two beams with one chopped at 1.5 kHz. Neutral glass filters are used to adjust the laser power. Changes in the probe beam transmission as well as the first order diffracted signal are detected using photo-diodes allowing the simultaneous recording of the differential transmission spectra (DTS) and the DFWM signal, respectively.

## 3. Experimental results

Fig. 1 gives representative absorption and emission spectra of the investigated CdS platelets in the near band gap region which are typical for high quality CdS samples [9]. In the polarization,  $E \perp c$  transitions involving A excitons are allowed. Two different neutral acceptor bound exciton complexes produce an  $I_1$  doublet around 2.5357 eV with an energy splitting of 190  $\mu\text{eV}$ . Around 2.546 eV, several  $I_2$  transitions corresponding to excitons bound at different neutral donors are observed. These absorptions are situated on a tail of the A exciton absorption but dominate the luminescence spectrum. In the polarization  $E \parallel c$  instead of the strong A exciton absorption the forbidden ( $A_F$ ) and the longitudinal ( $A_L$ ) A exciton are clearly resolved in absorption as well as in emission. B excitons bound at a

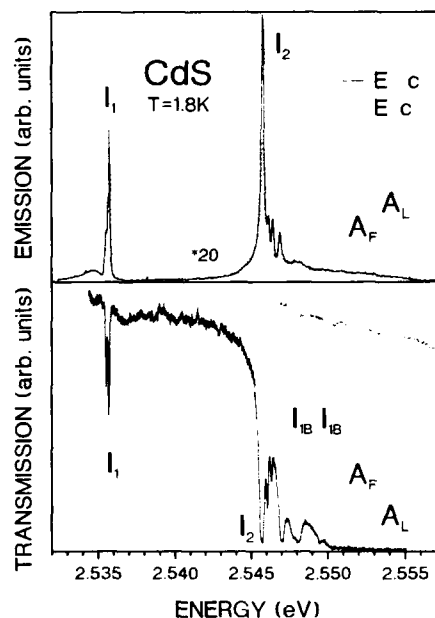


Fig. 1. Polarized absorption and emission spectra of CdS at  $T = 1.8$  K.

neutral acceptor ( $I_{1B}$ ,  $I'_{1B}$ ) are observed in absorption only. However, the interpretation of weak emission lines in the same spectral region in terms of ionized donor bound exciton complexes is not clearly established to date.

CdS exhibits strong nonlinearities in the near band-gap region correlated with excitonic processes. Fig. 2 shows the energy dependence of the DTS as well as of the DFWM signals for fixed delays  $\tau$  between the two incoming pulses of 10 ps (dotted traces) and 60 ps (full traces) recorded with the pulse polarizations perpendicular to the crystal  $c$ -axis. Strong signals are observed at the bound exciton resonances. Both  $I_1$  and  $I_2$  show saturation leading to a long-living induced transmission. Nevertheless, all fine structures are situated on a broad induced absorption band following the tail of the A exciton absorption (see Fig. 1), probably connected with excited state absorption of free excitons. The induced absorption in the energy region between  $I_1$  and  $I_2$  disappears very fast. Strong DFWM signals occur for the different bound exciton complexes ( $I_1$ ,  $I_2$ ) and

additional weak signals are observed for the  $I_3$  and on the low energy side of the  $I_2$  resonance. The strong absorption starting at the  $I_2$  resonance influences the DFWM signal, leading to a small energy shift between the DTS and the DFWM signals of  $I_2$ . DFWM signals of the  $A_F$  and the  $A_L$  exciton are observed using light pulses polarized parallel to the crystal  $c$ -axis (not shown in Fig. 2). It should be noted that the separate investigation of the different bound exciton transition becomes possible using a narrow bandwidth laser system as done in this study.

Comparing the spectra taken at delays  $\tau$  of 10 and 60 ps, it is apparent that only the  $I_1$  bound exciton complex has a dephasing time longer than a few 10 ps. Corresponding spectra for the polarization  $E \parallel c$  show a resolvable dephasing process for the forbidden  $A_F$  exciton too. Fig. 3 depicts transients of the DFWM signal for the  $I_1$ , the  $I_2$ ,

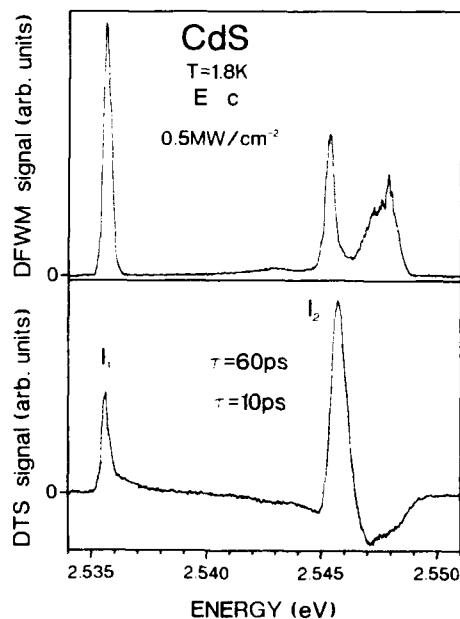


Fig. 2. Differential transmission (DTS) and degenerate four-wave mixing (DFWM) signals in dependence on the excitation energy in the band-gap region of CdS at  $T = 1.8$  K and two different delays  $\tau$  between the two incoming pulses. The exciting light pulses are polarized perpendicularly with respect to the crystal  $c$ -axis.

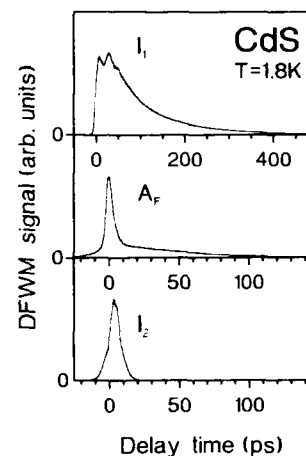


Fig. 3. Transients of the DFWM signals observed for the  $(A^0, X)$  ( $I_1$ ) and the  $(D^0, X)$  ( $I_2$ ) bound exciton complexes ( $E \perp c$ ) and the  $A_F$  exciton in CdS ( $E \parallel c$ ) at  $T = 1.8$  K. Notice the changed time scale for  $I_1$ .

and the  $A_F$  resonances recorded at an excitation density of  $0.5 \text{ MW cm}^{-2}$  giving a reasonable signal-to-noise ratio. Only for the  $I_1$  complex and for the forbidden  $A_F$  exciton does the signal extend noticeably beyond the autocorrelation function of the exciting laser pulses, indicating extremely fast dephasing processes for most of the excitonic states. Time-resolved investigations of the photon echo of  $I_1$  prove the inhomogeneous broadening of the  $I_1$  resonance [7]. For an inhomogeneously broadened two-level system, the DFWM signal decays with  $I \propto \exp(-4t/T_2)$ . However, the time-integrated photon echo signal of the  $I_1$  resonance is non-exponential (Fig. 3). Photon echo experiments in dependence of the excitation density [7] demonstrate that the *fast early part* results from interactions with a time-dependent bath, probably free excitons, and that the exponential part at longer delays gives the dephasing time of the investigated system. We determine dephasing times  $T_2$  between 550 and 800 ps for the  $(A^0, X)$  complex depending on the investigated crystal. The DFWM signal observed for the  $A_F$  exciton resonance shows a fast part following the autocorrelation of the exciting laser pulses and a slower exponential decay yielding

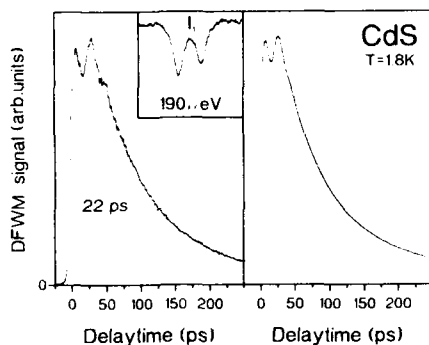


Fig. 4. Experimental (left side) and calculated (right side) DFWM signals of the  $(A^0, X)$  bound exciton complex in CdS showing polarization interference. The inset gives a high resolution absorption spectra showing the two involved  $I_1$  absorptions.

dephasing times  $T_2$  between 100 and 150 ps depending on the investigated sample. DFWM excitation spectra show that the *fast component* is not resonant with the  $A_F$  exciton.

On the left-hand side, Fig. 4 shows enlarged the modulation in the early part of the time integrated photon echo signal observed for the  $(A^0, X)$  resonance. Such modulation can either result from quantum beats or from polarization interference [10]. The beating has been observed for a sample showing two clearly resolved  $I_1$  resonances, as is obvious from the high resolution absorption spectrum depicted in the insert. The beat period of 22 ps corresponds well to the energy difference between the two  $I_1$  resonances of 190  $\mu\text{eV}$ . These beats are absent in crystals showing only a single or two poorly resolved  $I_1$  resonances, proving that the beats result from polarization interference caused by the simultaneous excitation of two independent  $(A^0, X)$  complexes. Recently, polarization interference between the  $(A^0, X)$  and the  $(D^0, X)$  complexes in CdSe has been reported [11]. On the right-hand side, Fig. 4 shows the beating of the time-integrated photon echo signal calculated for a system consisting of two inhomogeneously broadened oscillators. Using the energy splitting and the FWHMs determined from the absorption spectrum, good agreement with the experimental

results is obtained. The fast decay of the beating results from the inhomogeneous broadening of the two oscillators.

#### 4. Discussion

For some systems a significant influence of exciton localization on dephasing processes has been found [2]. For these systems the dominating factor is the reduction of relaxation channels with increasing localization. Thus, it can be expected that excitons localized at a single impurity forming atomic-like electronic systems show no comparable fast dephasing processes. Indeed, recent quantum beat [8] and DFWM [6,7] experiments as well as the present results show dephasing times of some hundred ps for bound exciton complexes in the wide band gap II–VI semiconductors. Without pure dephasing processes only energy relaxation contributes to the dephasing time  $T_2$ , then given by  $T_2 = 2T_1$ . In this paper,  $T_2$  times are determined for bound exciton complexes which are always shorter than expected from pure energy relaxation processes. For example, the dephasing time  $T_2$  of the  $(A^0, X)$  complex of about 700 ps is considerably shorter than expected from the energy relaxation time  $T_1$  of 980 ps measured by time resolved photoluminescence spectroscopy. This discrepancy is even more pronounced for the  $(D^0, X)$  complex. DFWM experiments in dependence on sample temperature and excitation density show a strong interaction with resonant acoustical phonons and free excitons [6,7]. However, at low temperature and moderate excitation density, both processes do not contribute any longer to the dephasing. Thus, there is evidence for an additional dephasing process of bound exciton complexes.

Excluding exciton and phonon scattering, pure dephasing processes of bound exciton complexes could be due either to impurity interactions or to nuclear spin-flip processes of the surrounding host ions. Time-resolved photoluminescence measurements show that higher impurity concentrations can alter even the energy relaxation times [12] and, e.g., the dephasing of excited Cr ions in  $\text{Al}_2\text{O}_3$  results from nuclear spin-flip processes of

neighbouring ions [13]. It is obvious that the interaction of a bound exciton complex with other impurities as well as with surrounding spins depends critically on its localization. With increasing extension of its wave function, the bound exciton probes larger areas of the crystal leading to a faster dephasing. This is in good agreement with our experimental results. Only the impurity interaction depends on the defect concentration, making the dephasing time  $T_2$  dependent on the investigated crystal. Our experiments show only a small variation of the dephasing time of the  $(A^0, X)$  complex in CdS, caused either by slightly different impurity concentrations or by the different chemical nature of the neutral acceptor. It has to be noted that we expect the investigated crystals to be very similar, since they are grown using the same equipment and selected for a suitable  $I_1$  absorption. Thus, no unambiguous distinction between the two dephasing processes is possible at this point.

It is interesting to compare the results of linear quantum beat [8] and DFWM experiments yielding apparently contradictory results in the case of bound exciton complexes in CdS. Quantum beat experiments, in principle, do not probe the "optical" coherence between the ground and excited states of a system, but the "quantum" coherence between two nearby excited states, which means that additional relaxation processes between the two excited states would decrease the measured dephasing time. Further on, a magnetic field is used to generate and tune the two excited states. The magnetic field alters the electronic states and can directly influence dephasing processes [13]. Thus, DFWM experiments give more reliable results, since they work in each two-level system showing absorption. This means that a short DFWM signal proves a short dephasing time, whereas a missing quantum beat signal can have different reasons.

Our DFWM experiments indicate extremely short dephasing times for the  $(D^0, X)$  as well as for the weaker bound exciton complexes. In contrast, the quantum beat experiments give a dephasing time of 300 ps for the weakly bound  $(D^0, X)$  complex [8]. This indicates either a much lower impurity concentration or an influence of

the magnetic field on the dephasing process by stabilization of the nuclear spins. In both cases, the  $(D^0, X)$  and the  $(A^0, X)$  complexes should possess even longer dephasing times. However, no quantum beat signals have been observed for the neutral donor or acceptor bound exciton complexes. The lack of a quantum beat signal can have many different reasons, especially considering the complicated level structure of bound exciton complexes formed at neutral donors or acceptors.

Completely different is the situation in the case of the forbidden  $A_f$  exciton, showing a comparatively long dephasing time between 100 and 150 ps. In general, generating free excitons, exciton–exciton collisions lead to a dephasing on a fs time scale [1]. However, the forbidden exciton has only a small dipole moment, and thus experiences a weaker interaction with other electronic excitations.

## 5. Conclusion

DFWM spectroscopy is an appropriate technique to study coherent processes in the near band-gap region of semiconductors. The presented experimental results demonstrate dephasing times  $T_2$  of several hundred ps for the acceptor bound exciton  $(A^0, X)$  complex in CdS, which are still too short to be limited by energy relaxation processes. Neither phonon nor exciton scattering contributes to the dephasing process under the experimental conditions used in this work [7]. However, impurity interactions or nuclear spin-flip processes in the surroundings could explain the dependence of the dephasing rate on the localization of the bound exciton complex. Additionally, for the forbidden  $A_f$  exciton, dephasing times longer than 100 ps are observed.

## 6. Acknowledgments

The authors are indebted to J.M. Wagner for performing the calculations. This work is partly supported by the Deutsche Forschungsgemeinschaft.

## 7. References

- [1] P.C. Becker, H.L. Fragnito, C.H. Brito Cruz, R.L. Fork, J.E. Cunningham, J.E. Henry and C.V. Shank, *Phys. Rev. Lett.* 61 (1988) 1647.
- [2] G. Noll, U. Siegner, S.G. Shevel and E.O. Göbel, *Phys. Rev. Lett.* 64 (1990) 792.
- [3] P. Wiesner and U. Heim, *Phys. Rev. B* 11 (1975) 3071.
- [4] F. Minami and K. Era, *Solid State Commun.* 53 (1985) 187.
- [5] R. Heitz, C. Fricke, A. Hoffmann and I. Broser, *Mater. Sci. Forum* 83–87 (1992) 1241.
- [6] H. Schwab, V.G. Lyssenko and J.M. Hvam, *Phys. Rev. B* 44 (1991) 3999.
- [7] R. Heitz, B. Lummer, A. Hoffmann and I. Broser, *J. Luminescence*, in press.
- [8] H. Stolz, V. Langer, E. Schreiber, S. Permogorov and W. von der Osten, *Phys. Rev. Lett.* 67 (1991) 679.
- [9] D.G. Thomas and J.J. Hopfield, *Phys. Rev.* 128 (1962) 2135.
- [10] M. Koch, J. Feldmann, G. von Plessen, E.O. Göbel, P. Thomas and K. Köhler, *Phys. Rev. Lett.* 69 (1992) 3631.
- [11] K.-H. Pandke, V.G. Lyssenko, B.S. Razbirin, J. Erland and J.M. Hvam, in: *Proc. 21st Int. Conf. on Physics of Semiconductors*, Beijing, 1992, Eds. K. Huang and L.L. Chang (World Scientific, Singapore, 1993) p. 129.
- [12] Ch. Fricke, U. Neukirch, R. Heitz, A. Hoffmann and I. Broser, *J. Crystal Growth* 117 (1992) 783.
- [13] I.D. Abella, N.A. Kurnit and S.R. Hartmann, *Phys. Rev.* 141 (1966) 391.



ELSEVIER

Journal of Crystal Growth 138 (1994) 815–819

JOURNAL OF **CRYSTAL  
GROWTH**

## Time-resolved donor–acceptor pair recombination luminescence in highly n- and p-doped II–VI semiconductors

Ch. Fricke <sup>a</sup>, R. Heitz <sup>a</sup>, B. Lummer <sup>a</sup>, V. Kutzer <sup>a</sup>, A. Hoffmann <sup>\*a</sup>, I. Broser <sup>a</sup>,  
W. Taudt <sup>b</sup>, M. Heuken <sup>b</sup>

<sup>a</sup> *Institut für Festkörperphysik, TU Berlin, Hardenbergstrasse 36, D-10623 Berlin, Germany*

<sup>b</sup> *Institut für Halbleiterphysik, RWTH Aachen, Templergraben 55, D-52056 Aachen, Germany*

### Abstract

Time resolved luminescence measurements of the donor–acceptor pair (DAP) luminescence of n-doped CdS:In bulk crystals, undoped bulk ZnSe crystals grown with various VI/II ratios, and p-doped ZnSe:N epilayers in the near band gap region are presented. The decay of the donor–acceptor pair recombination luminescence is investigated for dopant concentrations below the Mott density. A discussion on the basis of a statistical theory by Thomas and Hopfield for DAP recombination yields, by knowledge of the Bohr radii of the impurities, the number of electronically active impurity centres. The reliability of this method to determine impurity concentrations is discussed.

### 1. Introduction

Wide band gap II–VI materials became of extreme interest since the reliable fabrication of highly p-doped epitaxial structures has been realized recently. Based on these materials new prospects are opened for technical applications like short-wavelength lasers [1] and detectors. However, one important problem is the exact knowledge of impurity doping levels, which is required for p- or n-doped II–VI compounds. One fairly easy access is given by time-resolved measurements of the DAP luminescence, being strongly dependent on the doping concentration. Thomas et al. [2] performed time-integrated and time-resolved measurements, showing a reduction

of the decay time with increasing doping concentration, and explained the development in a statistical approach by the reduction of the mean distance between donor and acceptor ions. In the present paper, the dynamics of the DAP luminescence of n-doped CdS:In, undoped bulk ZnSe grown with a large variety of VI/II ratios and p-doped ZnSe:N epilayers are presented. Time resolved measurements of DAP luminescence are introduced as a standard technique to determine the impurity concentration in II–VI semiconductors (bulk material as well as epilayers) for a wide range of concentrations below the Mott density.

### 2. Experimental technique

The investigated CdS crystals are grown by the Frerichs–Warminsky method from the gaseous

\* Corresponding author.

phase [3]. The indium doping was achieved either during growth or subsequent by indiffusion. The ZnSe bulk material is grown by low pressure chemical vapour deposition (CVD) at  $T = 675^\circ\text{C}$  using various VI/II ratios. The ZnSe epilayers are grown by metalorganic vapour phase epitaxy (MOVPE) with  $\text{DeZn}$  and  $\text{DeSe}$  as precursors at a temperature of  $480^\circ\text{C}$ . The doping is carried out during growth by a nitrogen plasma. For the luminescence measurements the crystals are immersed in liquid He at 2 K. A synchronously pumped dye laser with 3 ps pulse duration and 1.9 MHz repetition rate excites the samples with an average output power of 100 mW, reduced by neutral glass filters for low excitation densities. Time resolved luminescence measurements are performed with a subtractive grating monochromator and a micro-channel-plate photo-multiplier tube (MCP-PMT) using time correlated single photon counting.

### 3. Experimental results

In all three systems –  $\text{CdS}:\text{In}$ ,  $\text{ZnSe}$  and  $\text{ZnSe}:\text{N}$  – free excitons, bound exciton complexes and a luminescence band, several 10 meV below the band gap with strong phonon replica, are observed at liquid-helium temperatures. The broad band is attributed to donor–acceptor pair recombination [4]. Each donor–acceptor pair has a distinct separation  $r$  and a radiative recombination energy  $E = E(r)$ . We assume therefore exponential recombination kinetics for a single donor–acceptor pair. The superposition of a large number of exponential decays from each pair leads to the observed luminescence band. A theoretical treatment to determine the impurity concentration of the radiative dynamics is by far more reliable than line shape analyses, since in the latter case too many parameters are involved. The influence of doping on the DAP recombination dynamics is studied by time resolved measurements.

Using effective-mass theory to calculate the recombination probability  $W(r)$  for a single donor–acceptor pair, where one of the impurities has a significantly larger  $a_0$  ( $a_0$ : Bohr radius)

than the other, one gets:

$$W(r) = W_{\max} \exp(2r/a_0) \quad (1)$$

Eq. (1) is only valid for hydrogen-like pairs of reasonably large separation, i.e.,  $r \gg a_0$  [2]. Due to the fact that only the Bohr radius of the weaker bound impurity atom is used to deduce Eq. (1), the following calculations are valid with the same Bohr radius  $a_0$  for both acceptor or donor excess.

Admitting donors or acceptors in excess, one gets for the intensity of light  $I$  emitted at time  $t$  [2]:

$$I(t) = \left\{ 4\pi N \int_0^\infty W(r) \exp[-W(r)t] r^2 dr \right\} \times \left\{ \exp \left[ 4\pi N \int_0^\infty \{ \exp[-W(r)t] - 1 \} r^2 dr \right] \right\}. \quad (2)$$

$N$  is the concentration of the majority constituent which should be of the order of the carrier concentration derived in Hall measurements at  $T = 300$  K.

Fig. 1 shows time integrated luminescence spectra at liquid helium temperature of  $\text{CdS}$  crystals doped with indium at concentrations ( $N_{\text{In}}$ ) between  $10^{17}$  and  $5 \times 10^{18} \text{ cm}^{-3}$ . The lowest spectrum in the inset of Fig. 1 exhibits in the near-band-gap region the DAP recombination luminescence. The energy position of the  $1_2$  line at 2.5460 eV corresponds to a bound exciton complex formed at a substitutional indium impurity on cadmium site [5]. The energy position of the DAP luminescence confirms the incorporation of indium as a donor. The green luminescence becomes broader and the recombination dynamics faster (main part of Fig. 1) with increasing indium concentration. A good agreement between theoretical calculations using Eq. (2) and experimental transients could be established (Fig. 1). The fitting of the experimental data with  $a_0 = 2.4$  nm and  $W_{\max} = (3 \pm 2) \times 10^8 \text{ s}^{-1}$  using Eq. (2) gives the concentration of donors  $N$  in the  $\text{CdS}:\text{In}$  samples (see Table 1).

The inset of Fig. 2 depicts time integrated measurements of the DAP recombination lumi-

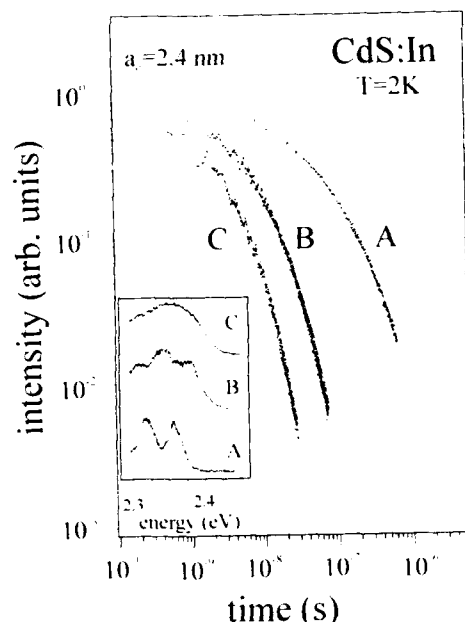


Fig. 1. Transients of the DAP luminescence of CdS with various  $N_{\text{In}}$  at low excitation densities ( $I_{\text{exc}} = 10 \text{ kW cm}^{-2}$ ). Points represent experimental data and full lines give theoretical fits using Eq. (2). In concentrations and results are given in Table 1. The corresponding luminescence is given in the inset.

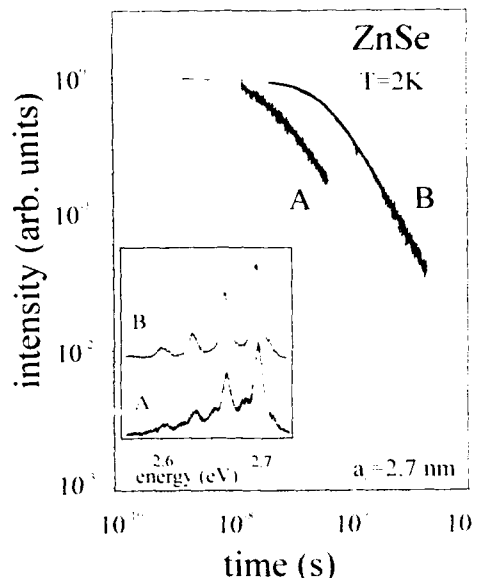


Fig. 2. Transients of the DAP luminescence of CVD-grown bulk ZnSe grown with two VI/II ratios, (A) 0.6 and (B) 0.3, during growth at low excitation densities ( $I_{\text{exc}} = 10 \text{ kW cm}^{-2}$ ). Points represent experimental data and full lines give theoretical fits using Eq. (2). Results are given in Table 1. The corresponding luminescence is given in the inset.

nescence at  $T = 2 \text{ K}$  of bulk ZnSe crystals grown by CVD for two VI/II partial pressure ratios below one (0.6 and 0.3). The main part of Fig. 2

Table 1

Fitted values according to Eq. (2) for CdS:In, ZnSe and ZnSe:N (see Figs. 1, 2 and 3);  $N_{\text{doping}}$  gives the concentration deduced from growth conditions, and  $N$  and  $W_{\text{max}}$  give the fitted concentration and transition constant using Eq. (2), respectively

		$N_{\text{doping}}$ ( $\text{cm}^{-3}$ )	$N$ ( $\text{cm}^{-3}$ )	Impurity	$W_{\text{max}}$ ( $\text{s}^{-1}$ )
CdS:In	A	$1 \times 10^{17}$	$3.0 \times 10^{17}$	Donor	$(3+2) \times 10^8$
	B	$1 \times 10^{18}$	$1.2 \times 10^{18}$	Donor	$(3+2) \times 10^8$
	C	$5 \times 10^{18}$	$3.5 \times 10^{18}$	Donor	$(3+2) \times 10^8$
ZnSe (bulk)	A		$2.1 \times 10^{17}$	..	$8 \times 10^6$
	B		$6.4 \times 10^{17}$	..	$1 \times 10^8$
ZnSe (epilayer)	A		$1.5 \times 10^{17}$	..	$8 \times 10^7$
	B		$4.5 \times 10^{17}$	..	$5 \times 10^8$
	C		$1.7 \times 10^{18}$	..	$3 \times 10^9$

shows the corresponding transients taken at the maximum of the luminescence intensity. The used values of  $W_{\text{max}}$ ,  $a_0$  and  $N$  are given in Table 1. The DAP luminescence showing clearly pronounced phonon replica (curve A) decays slower than that of curve B. The VI/II ratio of the latter ones is closer to one than that of the first ones.

The results of time-resolved luminescence measurements of MOVPE grown ZnSe epilayers doped in situ with nitrogen are presented in Fig. 3. The inset shows time-integrated spectra of crystals (curve A) grown with a VI/II ratio of 3.0 and a plasma power of 5.5 W as well as with a ratio of 0.8 for two plasma powers (curve B: 5.9 W; curves C: 6.5 W). The corresponding transients taken at the maximum of the DAP luminescence are given in the main part of the figure. We observe with decreasing VI/II ratio a decrease of the luminescence lifetime. The fitted



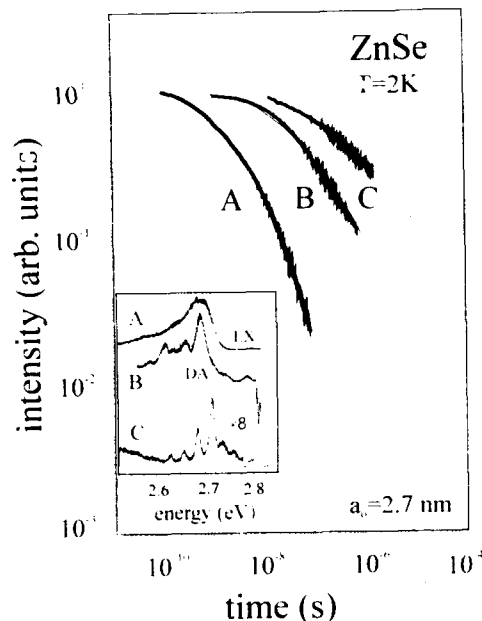


Fig. 3. Transients of the DAP luminescence of MOVPE-grown ZnSe doped with nitrogen at low excitation densities ( $I_{\text{exc}} = 10 \text{ kW cm}^{-2}$ ) for various VI/II ratios and nitrogen plasma powers: (A) VI/II = 3.0,  $P_{\text{plasma}} = 5.5 \text{ W}$ ; (B) VI/II = 0.8,  $P_{\text{plasma}} = 5.9 \text{ W}$ ; (C) VI/II = 0.3,  $P_{\text{plasma}} = 6.5 \text{ W}$ . Points represent experimental data and full lines give theoretical fits using Eq. (2). Results are given in Table 1. The corresponding luminescence is given in the inset.

values of  $W_{\text{max}}$  and  $N$  using Eq. (2) are given in Table 1.

#### 4. Discussion

The DAP luminescence in a semiconductor offers a unique spectroscopic access to the concentration of impurities. It is the only luminescence whose dynamics depend critically on the impurity concentration. Nevertheless, interactions with deep impurities affect the dynamics, making it complicated to obtain reliable information in a straightforward manner, as will be discussed for the three examples given above.

Under ideal conditions, i.e. the crystal contains only effective-mass-like donors and acceptors in a statistical manner, the statistical approach of

Thomas and Hopfield (Eqs. (1) and (2)) is expected to be valid and an analysis of the DAP luminescence decay yields the concentration of the dominating dopant. This situation is given to a good extent for the CdS:In samples. With increasing indium concentration, the decay becomes faster. However, all transients can be fitted with one  $W_{\text{max}}$ , as expected from the theory (see Table 1). The obtained doping concentrations are in good agreement with the estimated indium concentration and  $N_A - N_D$  values determined by electrical methods. It should be noted that the fit of the DAP transients gives the total acceptor or donor concentration and not only the uncompensated part. Thus, a combination of time-resolved and electrical data yields the majority constituent ( $N_A$  or  $N_D$ ), its concentration, and information on the compensation.

The situation becomes more difficult if non-effective mass type defects are involved. Especially, deep defects can alter the transition probability of a DAP due to competing nonradiative recombination channels. For example, efficient excitation of 4f ions over DAPs has been attributed to a "three-centre Auger" process [6]. In this case  $W_{\text{max}}$  should increase with the deep defect concentration and  $N$  represents only an upper limit for the majority constituent ( $N_A$  or  $N_D$ ). This behaviour is obvious for the CVD ZnSe samples. Both samples have been grown under the same conditions except of different VI/II ratios. The VI/II ratios critically determines the concentration of deep native defects generated during growth at 675°C. The DAP luminescence of the crystal grown with a VI/II ratio of 0.3 decays considerably faster than that of the sample with VI/II = 0.6, indicating a much higher defect concentration. However, the analysis using Eqs. (1) and (2) shows a large increase of  $W_{\text{max}}$  and only a small increase in  $N$ , see Table 1. At a VI/II ratio of 0.3, much more deeper native defects are generated, leading to an enhanced DAP recombination probability. Obviously,  $W_{\text{max}}$  is a sensitive sensor for deep defects.

The example of the MOVPE grown samples is the most complicated one. Nitrogen doping of ZnSe leads to p-conductivity in high quality MBE ZnSe epilayers. However, MOVPE-grown ZnSe

layers will suffer from the high impurity content of the available precursors, as is obvious from the high impurity concentrations determined for sample B. Upon N-doping the defect concentration increases. The simultaneous increase of the transition probability  $W$  indicates that N-doping produces not only shallow acceptors, but also deep defects. This is affirmed by electrical measurements showing that all MOVPE grown ZnSe layers are semi-insulating. Nevertheless, at high concentrations of shallow impurities energy transfer processes among DAPs can be important, too [7].

### 5. Conclusion

The analysis of the time behaviour of the DAP luminescence yields a fast and reliable access to impurity concentration and compensation in semiconductors. Under "ideal" conditions (deep defects can be neglected), an accuracy of about 30% can be obtained. Especially helpful is a comparison with electrical data giving the majority constituent ( $N_A$  or  $N_D$ ) and the degree of compensation. In the presence of deep defects, information on the defect density can be obtained too, but a reliable determination of the shallow defect concentration becomes difficult. In gen-

eral, it should be noted that the analysis of the DAP dynamics gives reliable concentrations in either p- or n-conducting samples but only qualitative arguments in case of dominating deep defects, i.e. semi-insulating samples.

### 6. Acknowledgements

The authors wish to thank Dr. R. Broser and E. Krause for supplying the crystals. This work was partly supported by the Deutsche Forschungsgemeinschaft and the Siemens AG.

### 7. References

- [1] J.M. DePuydt, M.A. Haase, H. Cheng and J.E. Potts, *Appl. Phys. Lett.* 55 (1989) 1103.
- [2] D.G. Thomas, J.J. Hopfield and W.M. Augustyniak, *Phys. Rev.* 140 (1965) A202.
- [3] I. Broser and R. Broser-Warminsky, Deutsches Patentamt, Patentschrift No. 814 193 (1950).
- [4] K. Colbow and K. Yuen, *Can. J. Phys.* 50 (1972) 1518.
- [5] K. Nassau, C.H. Henry and J.W. Shrieffer, in: *Proc. 10th Int. Conf. on Physics of Semiconductors*, Cambridge, MA, 1970, p. 629.
- [6] K. Swiatek, A. Suchoki and M. Godlewski, *Appl. Phys. Lett.* 75 (1990) 40.
- [7] G.-J. Yi and G.F. Neumark, *J. Luminescence* 52 (1992) 243.



ELSEVIER

Journal of Crystal Growth 138 (1994) 820–825

JOURNAL OF  
**CRYSTAL  
GROWTH**

## Energy transfer processes via the interface of ZnSe/GaAs epilayers

N. Presser, Ch. Fricke, G. Kudlek, R. Heitz, A. Hoffmann\*, I. Broser

*Institut für Festkörperphysik, Technische Universität Berlin, Hardenbergstrasse 36, D-10623 Berlin, Germany*

### Abstract

In the present paper, energy transfer processes via the interface of molecular beam epitaxy (MBE) grown ZnSe/GaAs epilayers are investigated by means of time-resolved photoluminescence spectroscopy. High excitation experiments show that an electron-hole plasma exists in free-standing ZnSe layers only. By comparing the time-resolved luminescence properties of ZnSe/GaAs heterostructures and of free-standing ZnSe layers, we demonstrate which kind of energy transfer mechanism is predominant in heterostructures: At low excitation densities energy is transferred by re-absorption of the ZnSe luminescence. At higher excitation densities, an ambipolar carrier diffusion via the ZnSe/GaAs interface is the dominating process.

### 1. Introduction

In the past decade, ZnSe epilayers have been the object of intense research in view of possible application to optoelectronics. The improvement in growing pure crystalline ZnSe by epitaxial growth methods, especially by molecular beam epitaxy (MBE), recently culminated in the first registered blue laser activity in a ZnSe-based device [1]. However, the responsible process for this lasing is still not well understood. Therefore, it is necessary to study the nonlinear optical processes in such epilayers, and especially, to understand the influence of the substrate on these nonlinearities.

Time-integrated photoluminescence of ZnSe/GaAs heterostructures under low CW excitation densities ( $I_{\text{exc}} < 5 \text{ mW/cm}^2$ ) has been thoroughly

investigated [2,3]. In the excitonic regime the luminescence depicts split exciton recombination lines,  $X_{\text{hh}}$  and  $X_{\text{hh}}$ , and split bound exciton emission lines,  $I_2$  and  $I_2'$ . This splitting of the excitonic features is correlated with the splitting of the upper  $I_8$  valence band of ZnSe, because of the strain induced by the lattice mismatch (0.27% at room temperature) and the different thermal expansion coefficients of layer and substrate [2]. Time-resolved luminescence of free excitons in the investigated heterostructures yields decay times of 100 ps for the  $X_{\text{hh}}$  exciton and 150 ps for the  $X_{\text{hh}}$  exciton [3]. The photoluminescence of the ZnSe/GaAs heterostructures under high-density excitation of a ns pulse laser shows two strong bands, which are called  $P_2$  and  $P_2'$ . They have been assigned to exciton-exciton collision processes [4,5]. In contrast to the heterostructures, the photoluminescence of highly excited free-standing ZnSe layers (obtained after a specially developed etching procedure of the GaAs sub-

\* Corresponding author.

strate) depicts an additional N band on the low energy side of the P bands, which has been interpreted as the recombination of electron–hole pairs in an electron–hole plasma (EHP) [6]. This means the carrier density seems to be higher in layers without substrate and points out that energy transfer processes are present in the ZnSe/GaAs heterostructures.

In this paper we investigate the kind of energy transfer processes from the ZnSe layer into the GaAs substrate in ZnSe/GaAs heterostructures. We first compare the luminescence dynamics of ZnSe/GaAs heterostructures to those of free-standing ZnSe layers under low and high excitation densities with ps time-resolution. Afterwards, we investigate the dynamics of the GaAs substrate luminescence upon excitation of the ZnSe epilayer to distinguish between the different possible energy transfer mechanisms via the interface of the ZnSe/GaAs heterostructure.

## 2. Experimental setup

All ZnSe samples were nominally undoped single-crystal MBE layers with thicknesses of 1 to 2  $\mu\text{m}$ . The growth conditions on (100) undoped GaAs substrates have been described in an earlier publication [7]. In order to have free-standing ZnSe layers, we used a chemical etching procedure of the GaAs substrate, described in ref. [4]. The samples were immersed in liquid He at 1.8 K. In time-resolved luminescence experiments, a dye-laser synchronously pumped by an actively mode-locked frequency-tripled Nd:YAG laser with 3 ps pulse duration and 3.8 MHz repetition rate excited the samples. The luminescence transients were detected through a time-compensated double monochromator by means of time-correlated single photon counting using a multi-channel-plate photomultiplier. The ps laser system yields excitation densities up to 350  $\text{MW}/\text{cm}^2$  in the used configuration. The luminescence transients were fitted by convolution of the apparatus response to the exciting 3 ps laser pulse with a sum of two exponential functions. This sum describes the investigated transition and has the rise time  $\tau_{\text{rise}}$  and the decay time  $\tau_{\text{decay}}$  of the transi-

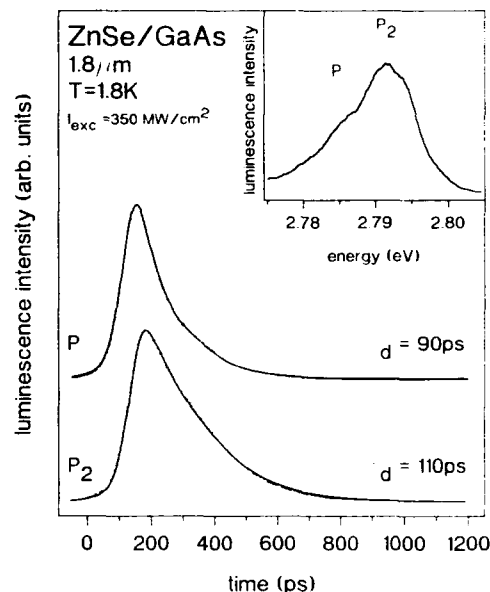


Fig. 1. Luminescence transients of the  $P_2$  and  $P_1$  bands in the emission of ZnSe/GaAs heterostructures in the excitonic regime under high band-to-band excitation densities ( $E_{\text{exc}} = 2.83$  eV and  $I_{\text{exc}} = 350$   $\text{MW}/\text{cm}^2$ ) with a ps laser system described in the text. The insert shows the corresponding time-integrated luminescence for the same experimental conditions.

tion as fitting parameters. This convolution technique allows a time resolution better than 10 ps.

## 3. Time-resolved results

### 3.1. ZnSe/GaAs heterostructures

For a laser energy above the ZnSe band gap and at high ps excitation densities ( $> 300$   $\text{MW}/\text{cm}^2$ ), the time-integrated luminescence of ZnSe/GaAs heterostructures shows two strong bands on the low energy side of the excitonic regime which are called  $P_2$  and  $P_1$  (see insert of Fig. 1). They have been attributed to exciton–exciton collision processes, where one exciton is scattered in an upper excitonic polariton branch ( $n = 2, \dots, \infty$ ), while the other exciton is scattered in the lower photonic branch under energy and momentum conservation and is then detected as

a photon leaving the crystal [8]. Considering the conservation laws, the photon detected at the energy position of the  $P_2$  band stems from an exciton, which originates from the neighbourhood of the bottleneck, because its collision partner has been scattered in the  $n = 2$  polariton branch. In the case of the photon detected at the energy position of  $P_x$ , it has a lower energy than the photon of the  $P_2$  band, and therefore originates from an exciton which is more distant from the bottleneck. It is already known that polaritons which are in the vicinity of the bottleneck of the polariton dispersion curve have a relatively longer life time [9]. The decay time of the  $P_2$  band ( $= 110$  ps) is found to be greater than that of the  $P_x$  band ( $= 90$  ps) (Fig. 1). This underlines the correlation of the polariton dispersion with the decay times of the P bands, and supports the interpretation of these bands in terms of excitonic collision processes.

### 3.2. Free-standing ZnSe epilayers

By removing the GaAs substrate, a relaxation of the strain in the free-standing ZnSe layer is observed. Therefore, the luminescence and absorption spectra of such layers depict only one degenerate free exciton and one bound exciton feature. Time-resolved measurements show that the lifetime of the free exciton in those free-standing ZnSe layers ( $= 200$  ps) is much longer than that in a ZnSe/GaAs heterostructure. This means that the strain in the heterostructure together with the interface defects and dislocations actually reduce the lifetime of free excitons.

The luminescence transient of the  $P_2$  band depicted in Fig. 2 has a decay of 170 ps. The decay of the  $P_x$  band has been measured at the same sample and amounts to 110 ps. In both cases, we see that the luminescence of the P bands behaves similarly to the free exciton luminescence having longer decay times in free-standing ZnSe layers than those in ZnSe/GaAs heterostructures. This is again consistent with the interpretation of the high-density P bands as exciton–exciton collision processes.

The time integrated luminescence spectrum of free-standing ZnSe layers shows an additional N

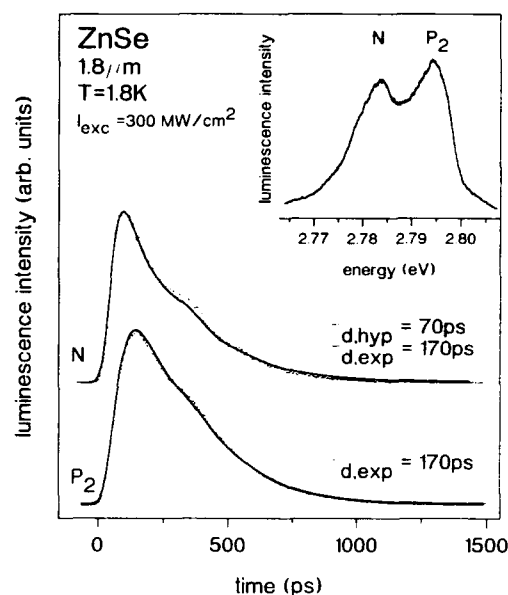


Fig. 2. Luminescence transients of the N and  $P_2$  band in the emission of highly excited free-standing ZnSe layers for the same laser energy as in Fig. 1 and with  $I_{\text{exc}} = 350 \text{ MW/cm}^2$ . The insert depicts the corresponding time integrated luminescence.

band for excitation densities above  $300 \text{ MW/cm}^2$  (see insert in Fig. 2), which has been interpreted in terms of electron–hole plasma recombination [6]. As the N band superimposes the  $P_2$  band, the theoretical fit of the N transient contains an exponential part of about 50% decaying with the corresponding  $\tau_{\text{d,exp}} = 170$  ps. The remaining experimental transient of the N luminescence band (Fig. 2) can only be fitted by a hyperbolic decay function ( $\tau_{\text{d,hyp}} = 70$  ps) with deconvolution of the luminescence transient, which actually corresponds to an EHP luminescence decay process [10]. At even higher excitation densities we register that the transient of the N band shows a very fast decay time of about 10 ps, which indicates the beginning of stimulated emission processes.

### 3.3. Energy transfer processes in ZnSe/GaAs epilayers

The fact that an EHP can be built up only in a free-standing ZnSe layer and not in a ZnSe/GaAs

heterostructure demonstrates that the carrier density is limited in a ZnSe/GaAs heterostructure. To show that ambipolar carrier diffusion actually takes place via the interface, we use the GaAs luminescence as a detector to investigate the excitation mechanism. When a band-to-band excitation of the ZnSe layer of a ZnSe/GaAs heterostructure is applied, we observe the luminescence of both ZnSe and GaAs, which means that an excitation of the GaAs substrate is present. For the used excitation energy, the laser light is strongly absorbed in the first  $0.1 \mu\text{m}$  of the ZnSe layer ( $\alpha \approx 10^5 \text{ cm}^{-1}$  [11]), and cannot be the source of the excitation in the GaAs substrate.

Actually we have to consider two main types of excitation mechanisms in order to explain the observed excitation of the GaAs substrate (see Fig. 3):

(1) Excitation by light transfer: the emitted ZnSe luminescence light is absorbed in the GaAs substrate and creates electron–hole pairs, which then recombine. In this case the GaAs luminescence transient has to be fitted by convolution of the corresponding ZnSe luminescence transient with a two-exponential function (describing the investigated transition in GaAs).

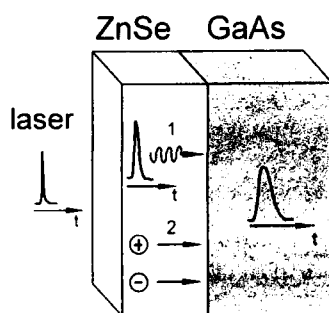


Fig. 3. Schematic presentation of the different kinds of excitation of the GaAs substrate. The laser excites the ZnSe layer with an energy greater than the band gap and is completely absorbed. In process (1), the ZnSe layer emits blue light with its proper dynamics, which transfers into the GaAs substrate, where it causes an excitation of the substrate. In process (2), the photogenerated carriers at the surface of the ZnSe layer diffuse into the GaAs substrate and cause there an excitation. The time-resolved GaAs luminescence allow us to determine which excitation process is predominant.

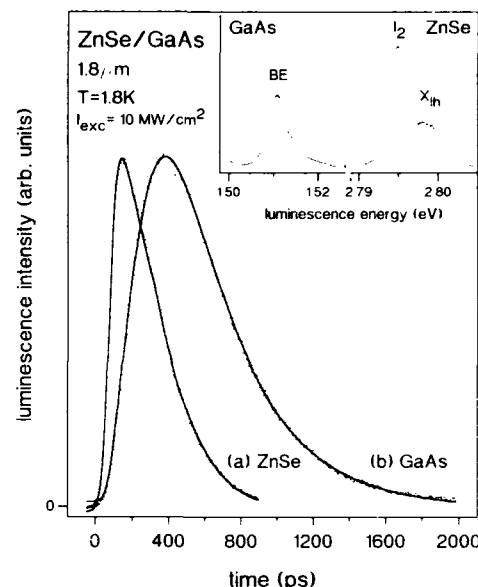


Fig. 4. Luminescence transients of the blue emission of the ZnSe layer and the red emission of the GaAs substrate in the excitonic regime under band-to-band excitation with  $I_{\text{exc}} = 10 \text{ MW/cm}^2$ . The insert shows both types of time-integrated luminescence detected simultaneously. The full curves are the fits obtained from convolution techniques described in the text.

(2) Excitation by free carriers, which diffuse ambipolarly from the ZnSe layer into the GaAs substrate: this process is favoured by the specific band offset structure of the heterostructure of type I [12]. There, we expect that this type of excitation starts delayed at a time given by the ambipolar diffusion of the photogenerated carriers through the  $1\text{--}2 \mu\text{m}$  ZnSe layers. In this case the GaAs transient has to be fitted by convolution of the sum of two exponential functions with given rise and decay times with the apparatus response and taking into account the occurring delay time.

The insert of Fig. 4 shows the time integrated luminescence spectra in the excitonic ranges of the ZnSe layer and of the GaAs substrate under low excitation densities of the layer ( $E_{\text{exc}} = 2.83 \text{ eV}$  and  $I_{\text{exc}} = 10 \text{ MW/cm}^2$ ). The simultaneous detection of both types of luminescence is possible under the same experimental conditions, be-

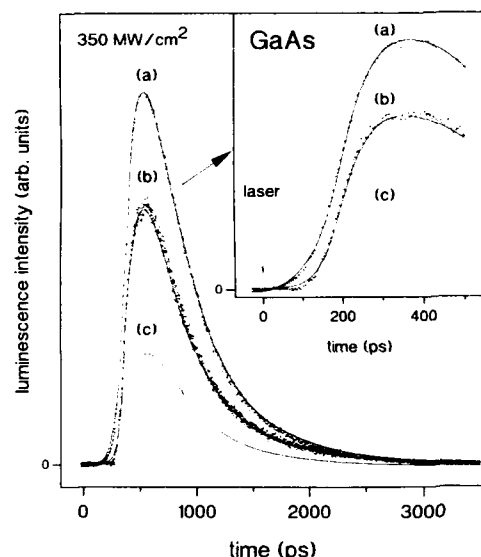


Fig. 5. (a) Luminescence transient of the emission of the GaAs substrate detected by band-to-band excitation of the ZnSe layer in a heterostructure at high excitation densities ( $I_{\text{exc}} = 350 \text{ MW/cm}^2$ ). (c) calculated GaAs luminescence transient if light transfer is assumed as the excitation process and amounts to 30%. (b) calculated transient if the excitation takes place through carrier diffusion and amounts to 70%.

cause the red luminescence of the GaAs substrate passes undisturbed through the ZnSe layer. Fig. 4 depicts the corresponding transients of the bound exciton luminescence maxima of ZnSe (a) and of GaAs (b). The predominant luminescence of ZnSe ( $I_2$ ) decays within 150 ps. The bound-exciton luminescence transient of GaAs can be fitted very good by convolution of the recorded  $I_2$  transient (and not the apparatus response of the laser pulse) with a two-exponential function ( $\tau_{\text{rise}} < 90 \text{ ps}$  and  $\tau_{\text{decay}} = 350 \text{ ps}$ ). This indicates that here the light transfer is the only responsible excitation mechanism of the GaAs substrate.

For excitation densities above  $300 \text{ MW/cm}^2$ , the excitation mechanism of the GaAs obviously changes: The recorded transients of the GaAs luminescence cannot be fitted if we assume only light transfer between layer and substrate. In Fig. 5 we show the transient of the GaAs luminescence in the excitonic range at its energetic maxi-

mum (a). In order to fit properly the GaAs transient we have to consider two components:

The first one is depicted by curve (c) and represents the part of the light transfer (about 30%), which is obtained by convolution of the corresponding ZnSe luminescence transient with a two-exponential function ( $\tau_{\text{rise}} < 80 \text{ ps}$  and  $\tau_{\text{decay}} = 560 \text{ ps}$ ).

The second part is depicted by curve (b) and represents the part of the carrier diffusion (about 70%). This part results from convolution of the apparatus response to a delta-like excitation (e.g. the 3 ps laser pulse) with a two-exponential function with the same rise and decay times ( $\tau_{\text{rise}} < 80 \text{ ps}$  and  $\tau_{\text{decay}} = 560 \text{ ps}$ ). However, we have to consider an additional delay time of about 160 ps for the fit (b) in order to reach a fit of the GaAs luminescence transient (a), as the sum of curve (b) and curve (c). This delay time can be understood as the time needed for the carriers to reach the substrate. With a thickness of about  $2 \mu\text{m}$  and a registered delay time of 160 ps, we obtain a diffusion velocity of  $1.2 \times 10^9 \text{ cm s}^{-1}$  corresponding to results obtained in CdS bulk crystals [13]. With these results, we prove that at high excitation densities, the ambipolar carrier diffusion via the interface plays an increasing role, in addition to the light transfer.

In this paper, we demonstrate that above a certain high excitation density ( $> 300 \text{ MW/cm}^2$ ), carrier diffusion via the interface of ZnSe/GaAs heterostructure becomes important, which represents an energy loss in the ZnSe layer. In this context, it explains why an EHP cannot be built up in those heterostructures. However, if we consider that the decay time of the EHP ( $= 100 \text{ ps}$ ) is shorter than the diffusion time of the carriers through the ZnSe layer ( $= 160 \text{ ps}$ ), it should be possible to see plasma luminescence also in the ZnSe/GaAs heterostructure. As this is not the case, we take into account additional mechanisms which prevent the carrier density from increasing. As greater decay times of the P bands are measured in the free-standing ZnSe layer, this shows that the strain situation in ZnSe/GaAs heterostructure actually reduces the decay times, which represents also a competing process reducing the carrier density.

#### 4. References

- [1] M.A. Haase, J. Qiu, J.M. DePuydt and H. Cheng, *Appl. Phys. Lett.* 59 (1991) 1272.
- [2] K. Shahzad, *Phys. Rev. B* 38 (1988) 8309.
- [3] G. Kudlek, Ch. Fricke, N. Presser, R. Heitz, A. Hoffmann, J. Gutowski and I. Broser, in: *Proc. 21st Intern. Conf. on the Physics of Semiconductors*, Beijing, 1992.
- [4] N. Presser, G. Kudlek, J. Gutowski, S. Durbin, D. Menke, M. Kobayashi and R.L. Gunshor, *Phys. Status Solidi (b)* 159 (1990) 443.
- [5] P. Newbury, K. Shahzad and D.A. Cammack, *Appl. Phys. Lett.* 58 (1991) 1065.
- [6] N. Presser, G. Kudlek and J. Gutowski, *J. Luminescence* 53 (1992) 435.
- [7] G. Kudlek, N. Presser, J. Gutowski, S.M. Durbin, D.R. Menke, M. Kobayashi and R.L. Gunshor, *J. Crystal Growth* 101 (1990) 667.
- [8] C. Benoît à la Guillaume, J.M. Debever and F. Salvan, *Phys. Rev.* 177 (1969) 567.
- [9] P. Wiesner and U. Heim, *Phys. Rev. B* 11 (1975) 3071.
- [10] J. Gutowski and A. Hoffmann, *Adv. Mater. Opt. Electron.* 2 (1993).
- [11] F.A. Majumder, H.-E. Swoboda, K. Kempf and C. Klingshirn, *Phys. Rev. B* 32 (1988) 2407.
- [12] L. Kassel, H. Abad, J.W. Garland, P.M. Raccach, J.E. Potts, M.A. Haase and H. Cheng, *Appl. Phys. Lett.* 56 (1990) 42.
- [13] C.E. Bleil and I. Broser, *J. Phys. Chem. Solids* 25 (1964) 11.



## Polarization dependent dephasing measurements in $\text{Cd}_x\text{Zn}_{1-x}\text{Te}/\text{ZnTe}$ multiple quantum well structures

J.P. Doran <sup>a,\*</sup>, R.P. Stanley <sup>b</sup>, J. Hegarty <sup>a</sup>, R.D. Feldman <sup>c</sup>, R.F. Austin <sup>c</sup>

<sup>a</sup> Department of Pure and Applied Physics, Trinity College Dublin, Dublin 2, Ireland

<sup>b</sup> Institut de Micro- et Optoélectronique, Ecole Polytechnique Fédérale de Lausanne, CH-1015 Lausanne, Switzerland

<sup>c</sup> AT&T Bell Laboratories, Holmdel, New Jersey 07733, USA

### Abstract

Polarization dependent dephasing measurements are performed in inhomogeneously broadened  $\text{Cd}_x\text{Zn}_{1-x}\text{Te}/\text{ZnTe}$  multiple quantum wells at low and high exciton densities. At low temperature and density the self-diffracted signal when the beams are cross-polarized is much weaker than, and decays much faster than, the signal obtained when the beams are co-polarized. At high densities the signal strengths become the same. A model is proposed to explain the results. We find that the dynamics of a small subset of excitons which are created in a spatially bunched manner can be probed by cross polarizing the beams.

Exciton dynamics in quantum wells have been examined extensively over the last decade [1,2]. Four-wave mixing is a powerful tool for this work and has been applied in a wide variety of ways, to measure many different aspects of exciton dynamics such as recombination times [3], diffusion times [4], dephasing times [5,6], and spin related phenomena [7]. Many of the systems studied are partly disordered due to imperfect interfaces and alloying, and in such systems localization effects become important. While a growth in the understanding of exciton dynamics in such disordered systems has taken place, much of this work has been on III–V materials and comparison with II–VI and other materials should be useful. Studies have been carried out on the dependence of the four-wave mixing signal on pump beam polar-

izations [8]. It has been observed that the nature of the response is fundamentally different for the situations where the polarizations of the beams are co- or cross-linearly polarized. In this paper we describe self-diffraction experiments performed under various laser beam polarization conditions on excitons in  $\text{Cd}_x\text{Zn}_{1-x}\text{Te}/\text{ZnTe}$  quantum wells, at low and high exciton densities. Using this technique, new aspects of the exciton dynamics can be exposed. In particular we find that, for low exciton densities and low temperatures, the magnitude and the decay time of the self-diffracted signal are much smaller for perpendicularly polarized beams than for parallel beams. Similar effects have been observed in other semiconductor systems [8] although they are not observed in other types of inhomogeneously broadened systems, such as doped glasses. A model is proposed which explains the observed behaviour.

\* Corresponding author.

The samples used in this work contain fifteen periods of 50 Å thick  $\text{Cd}_{1-x}\text{Zn}_x\text{Te}$  strained wells, separated by 100 Å ZnTe barriers grown on a GaAs substrate with a 2 μm ZnTe buffer layer for strain relief. The excitons in these wells are inhomogeneously broadened to a linewidth ( $\Gamma_i$ ) of 10 meV full width at half maximum due to fluctuations in the thickness of the well and to the alloy nature of the wells. In comparison, the homogeneous linewidth ( $\Gamma_h$ ) at  $T = 4.2$  K at an exciton density in each well of  $5 \times 10^9$  excitons/cm<sup>2</sup> is 70 μeV and the laser linewidth ( $\Gamma_L$ ) is  $\approx 1$  meV. This situation is shown schematically in Fig. 1. The inhomogeneity of the transition is central to the effects we observe. Also shown in Fig. 1 are the quantum numbers associated with the conduction and valence band states involved in exciton transitions in an ideal semiconductor. The optically active exciton states are denoted by  $|+1\rangle = |+\frac{3}{2}, -\frac{1}{2}\rangle$  and  $| -1\rangle = |-\frac{3}{2}, +\frac{1}{2}\rangle$ . Some authors have claimed that these states are mixed by disorder induced effects in the crystal [8].

The experiments are performed using  $\approx 4$  ps dye laser pulses and are carried out in a He bath cryostat at temperatures between 4 K and 50 K.

As in the normal self-diffraction geometry the laser beam is split in two, one beam delayed with

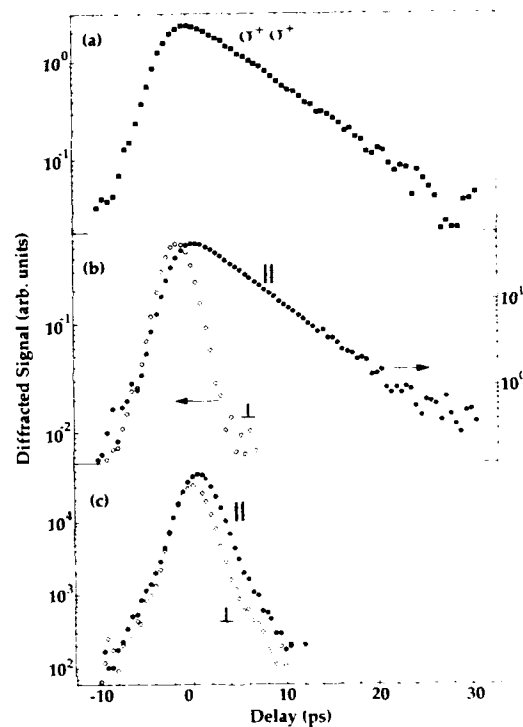


Fig. 2. Decay of the diffracted intensity for: (a) co-circularly polarized beams; (b) co-linearly (●) and cross-linearly (○) polarized beams at low exciton density ( $5 \times 10^9$  excitons/cm<sup>2</sup>); (c) same as (b) except the exciton density is high ( $2.5 \times 10^{11}$  excitons/cm<sup>2</sup>).

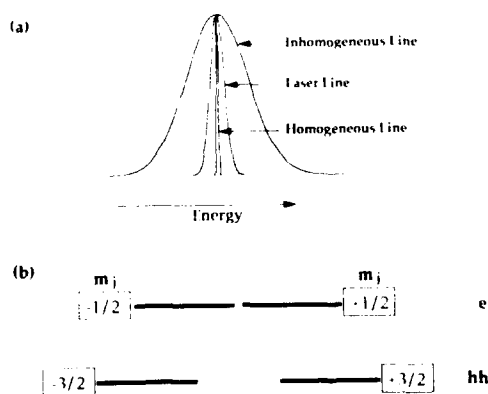


Fig. 1. (a) Schematic representation of the relative magnitudes of the various linewidths. (b) Energy level scheme for an ideal semiconductor:  $|+1\rangle$  and  $| -1\rangle$  excitons are made up from these electron and hole states.

respect to the other, and the beams recombined on the sample. The first pulse imparts its coherence to the excitons it creates. A grating will result only if this exciton polarization has not lost its coherence on arrival of the second pulse. By varying the delay between the two pulses and monitoring the strength of the diffracted signal, the coherence time of the excitons can be measured.

The exciton peak in this sample at 4.2 K is at 2.1 eV and the laser is tuned 2 meV below the peak for the dephasing measurements described below. Previous measurements have shown that the dephasing time of the excitons does not vary rapidly across the inhomogeneous profile in these samples [5]. Fig. 2a shows the diffracted signal

versus delay between the pulses for the case of co-circularly polarized beams ( $\sigma^+$ ,  $\sigma^+$ ). The decay time of this signal is 5.3 ps which translates, assuming inhomogeneous broadening, to a dephasing time of 21.2 ps. When the two beams are circularly polarized in the opposite sense ( $\sigma^+$ ,  $\sigma^-$ ) then no diffracted signal is observed from our sample. This indicates that there is not any coherent mixing between the spin states in these materials. If the states were mixed due to, e.g., disorder in the system, or biexcitons, then using oppositely circularly polarized beams should result in the formation of a grating and thus in a diffracted signal.

Fig. 2b shows the result for parallel and perpendicular linearly polarized beams at low exciton densities ( $\approx 5 \times 10^9$  excitons/cm<sup>2</sup>). For the parallel case, the signal again decays with a time constant similar to the co-circularly polarized case. However when the beams are cross-polarized the decay becomes faster than our system resolution,  $< 2$  ps. Also, the signal strength in this case is  $\approx 10^2$  weaker than in the parallel case. These results leave two questions to be answered: (1) Why does the observed decay time of the self-diffracted signal depend on the relative linear polarizations of the two beams? and (2) Why does the strength of the signal depend on the relative polarizations?

In addressing these questions, it is useful to look first at what happens when the exciton density is increased. Fig. 2c shows the results for linearly parallel and perpendicular polarizations at a much higher exciton density of  $2.5 \times 10^{11}$  excitons/cm<sup>2</sup>. The strengths of the two signals are now very similar and the time decay in both cases is less than the system resolution. The reduction of the decay time in the parallel case is due to exciton–exciton collisions which become the main dephasing mechanism when the exciton density is increased to these levels [9].

The explanation of the results lies in the relative magnitudes of the homogeneous, inhomogeneous, and laser linewidths (see Fig. 1) and the nature of the exciton nonlinearities. Without describing in detail the nature of excitonic nonlinearities in semiconductors [10], we can divide the exciton nonlinearity into two broad classes: (1)

resonant nonlinearities, of strength  $R$ , which are due to excitons with the same energy, spin, and spatial position (this type of nonlinearity is often referred to as phase space blocking); (2) non-resonant nonlinearities, of strength  $NR$ , which occur when some of the above characteristics are not the same, e.g. if the excitons have different spin or different energy. Coulomb screening, band gap renormalization and exciton induced dephasing (EID) are all examples of this latter class.

The four-wave mixing signal at a given energy will depend on the relative strengths of these different types of nonlinearities. The exciton states  $|+1\rangle$  and  $|-1\rangle$  are coupled to the ground state by circularly polarized photons and  $\sigma^+$  and  $\sigma^-$ . The linearly polarized photons are made up from combinations of circularly polarized photon states. Photons polarized along, say, the  $y$ -axis can be described as  $\sigma^+ + \sigma^-$ , while photons polarized along the  $x$ -axis are described by  $\sigma^+ - \sigma^-$  ( $x$ - and  $y$ -axis are both in the plane of the well). For parallel polarized beams the  $|+1\rangle$  and  $|-1\rangle$  gratings are overlapped spatially while for perpendicularly polarized beams the gratings are spatially out of phase (see Fig. 3). The diffraction of  $\sigma^+$  light from a  $\sigma^+ \sigma^-$  grating is due to the nonresonant nonlinearities described above and thus has strength  $NR$ . Diffraction of  $\sigma^+$  light from a  $\sigma^+ \sigma^+$  grating has both resonant and nonresonant components and thus has strength  $R + NR$ . The reverse is true for  $\sigma^-$  light.

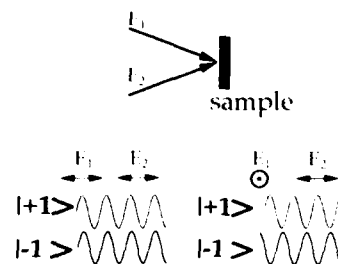


Fig. 3. Upper part shows self-diffraction experimental set-up.  $E_1$  and  $E_2$  are the electric field vectors of the beams. When  $E_1 \parallel E_2$  (bottom left) the gratings for the  $|+1\rangle$  and  $|-1\rangle$  transitions are in-phase spatially while for  $E_1 \perp E_2$  (bottom right) they are out-of-phase spatially.

For parallel polarized beams, because the gratings are in phase, the resulting signal strength is the sum of the above contributions:

$$\text{parallel signal} = R + 2 NR. \quad (1)$$

For perpendicular beams, the gratings are out of phase and the total diffracted strength is the difference of the two:

$$\text{perpendicular signal} = R + NR - NR = R. \quad (2)$$

The ratio of the parallel to perpendicular signals can therefore be seen to depend on the relative importance of the terms  $R$  and  $NR$ .

At low temperatures and low exciton densities the homogeneous linewidth of the excitons is less than the laser linewidth. In this case most of the nonlinear interaction is non-resonant and so  $NR > R$ . This explains why the signal in the cross-polarized case is much less than in the co-polarized case. The decay of the signal in the co-polarized case reflects dephasing due to a combination of acoustic phonon scattering and scattering off the disorder in the system. The signal observed in the cross-polarized case has a different decay and reflects the different dynamics of a subset of the exciton population. The signal in this case is due to excitons created very close together in space, which scatter off each other very quickly. The short decay time of the signal in this case illustrates that the homogeneous linewidth of these particular excitons is comparable to, or greater than, the laser linewidth. The implied existence of inhomogeneous and homogeneous resonances at the same energy is a result of the disorder in the system and non-uniform creation of excitons spatially. The creation of excitons in small spatial subgroups leads to rapid EID which broadens the linewidth of such excitons such that all groups overlap in energy (within the laser linewidth). In this way the response of exciton groups is homogeneous in nature. On the other hand spatially separated excitons have no EID so that inhomogeneous broadening dominates.

When the exciton density is increased, as shown earlier, the magnitude of the two signals become closer together. At high densities the scattering is due to exciton–exciton scattering and becomes very rapid [9]. The homogeneous linewidth of the

excitons broadens and becomes similar to the laser linewidth. In this case the dominant signal is due to the  $R$  component of the nonlinearity and so, in terms of our model, it becomes clear why the difference in the parallel and perpendicular signal strengths is reduced. It should be noted that at high intensities EID saturates in purely homogeneously broadened transitions [11]; however, at such intensities the dephasing rate is already high.

It can be seen that all excitons are not created equal. The response of a set of excitons that are created in a bunched manner in certain regions of the crystal is masked by the response of the far greater number of excitons which are spatially separated. This minority of excitons can only be probed by performing dephasing measurements with cross-polarized beams.

Cundiff and Steel [8] have performed extensive polarization dependent measurements on GaAs/AlGaAs quantum well samples where they have time resolved the diffracted signal in a three-beam experiment. With parallel polarized beams they see an emission delayed with respect to the second pulse: this is a photon echo and is the expected response from an inhomogeneously broadened system. When they perpendicularly polarize the beams, the emission becomes prompt. This is a free polarization decay and is the signature of a homogeneously broadened transition. The dephasing times measured in the two cases and the relative magnitudes of the signals behave in a manner similar to what we have observed in  $\text{Cd}_{1-x}\text{Zn}_x\text{Te}/\text{ZnTe}$ . They interpret their result of the co-existence of homogeneously and inhomogeneously broadened resonances at the same energy as evidence for the existence of localized and delocalized excitons at the same energy, a result which was not expected. They also invoke a model of spin mixing of the exciton states due to biexcitons to explain their results.

We note that our model is simpler: we do not resort to biexcitonic effects. While we also imply the co-existence of homogeneously and inhomogeneously broadened resonances at the same energy, we do not interpret this result in terms of the localization and delocalization of the excitons.

In summary, we have studied the polarization dependence of the self-diffracted signal from excitons in  $\text{Cd}_x\text{Zn}_{1-x}\text{Te}/\text{ZnTe}$  quantum wells. The magnitude and decay time of the signal was found to depend on the relative polarization of the beams in a manner that depends on the exciton density in the wells. We propose a straightforward model for explaining these results which relies on the different types of nonlinearities that the excitons experience and on the relative magnitude of the laser linewidth and the homogeneous linewidth of the excitons. In terms of this model we find that the dynamics of a small subset of excitons that are created in spatially bunched regions can be observed by cross-polarizing the beams.

## 1. References

- [1] T. Takagahara, *J. Luminescence* 44 (1989) 347;  
M.D. Webb, S.T. Cundiff and D.G. Steel, *Phys. Rev. B* 43 (1991) 12658.
- [2] L. Schultheis, J. Kuhl, A. Honold and C.W. Tu, *Phys. Rev. Lett.* 57 (1986) 1797.
- [3] A. Harwitt, M.B. Ritter, J.M. Hong, D.D. Awschalom and L.L. Chang, *Appl. Phys. Lett.* 55 (1989) 1783.
- [4] J. Hegarty and M.D. Sturge, *J. Opt. Soc. Am. B* 2 (1985) 1143.
- [5] R.P. Stanley, J. Hegarty, R. Fischer, J. Feldmann, E.O. Göbel, R.D. Feldman and R.F. Austin, *Phys. Rev. Lett.* 67 (1991) 128.
- [6] G. Noll, U. Siegner, S.G. Sheval and E.O. Göbel, *Phys. Rev. Lett.* 64 (1990) 792.
- [7] S. Bar-Ad and J. Bar-Joseph, *Phys. Rev. Lett.* 68 (1992) 349;  
T.C. Damen, K. Leo, J. Shah and J.E. Cunningham, *Appl. Phys. Lett.* 58 (1991) 1902.
- [8] S.T. Cundiff and D.G. Steel, *IEEE J. Quantum Electron.* QE-28 (1992) 2423;  
M.D. Webb, S.T. Cundiff and D.C. Steel, *Phys. Rev. Lett.* 66 (1991) 934.
- [9] L. Schultheis, J. Kuhl, A. Honold and C.W. Tu, *Phys. Rev. Lett.* 57 (1986) 1635.
- [10] S. Scmitt-Rink, D.S. Chemla and D.A.B. Miller, *Adv. Phys.* 38 (1989) 89.
- [11] H. Wang, K. Ferrio, D. Steel, Y.Z. Hu, R. Binder and S.W. Koch, *Phys. Rev. Lett.* 71 (1993) 1261.

## Exciton transfer dynamics in CdTe/(Cd,Zn)Te asymmetric double quantum well structures

S. Haacke <sup>\*,a</sup>, N.T. Pelekanos <sup>b,c</sup>, H. Mariette <sup>b</sup>, A.P. Heberle <sup>c</sup>, W.W. Rühle <sup>c</sup>,  
M. Zigone <sup>a</sup>

<sup>a</sup> High Magnetic Field Laboratory, MPIF-CNRS, BP 166, F-38042 Grenoble Cédex, France

<sup>b</sup> CEA-CNRS Joint Group "Microstructures de Semiconducteurs II-VI", BP 85, F-38042 Grenoble Cédex, France

<sup>c</sup> Max-Planck-Institut für Festkörperforschung, Heisenbergstrasse 1, D-70506 Stuttgart, Germany

### Abstract

Time-resolved photoluminescence measurements on CdTe/(Cd,Zn)Te asymmetric double quantum wells (AD-QWs) with electron and hole confinement potentials of some tens of meV are reported. The carrier transfer from the narrow into the wide well is evidenced by photoluminescence decay times of the narrow well as short as a few picoseconds. The observed tunneling times depend strongly upon the barrier and well widths of the investigated samples which determine the relative position of spatial direct and cross exciton transitions. Very efficient tunneling is found in ADQWs in which the transfer of spatial direct excitons under emission of LO phonons is possible. In any case, one has to consider excitonic rather than single particle electron or hole states in order to explain the observed behaviour of the tunneling times.

### 1. Introduction

Asymmetric double quantum wells (ADQWs) consisting of a narrow and a wide quantum well separated by a single barrier are well suited systems for the investigation of tunneling in semiconductor heterostructures. Photoluminescence experiments with picosecond time resolution allow the study of the carrier transfer dynamics via tunneling by an analysis of the decay and rise behaviour of the emitting narrow well (NW) and the collecting wide well (WW), respectively.

The sub-millimeter radiation emitted by an electron wave-packet coherently oscillating be-

tween two resonantly coupled QWs is a direct manifestation of tunneling which has recently been detected [1]. Further applications of ADQWs are tuneable lasers [2] or optical absorbers with ultra-fast recovery times [3]. The knowledge of minority-carrier tunneling times is also of importance for the operation of perpendicular transport devices (e.g. light emitting tunnel diodes) [4].

GaAs/(Al,Ga)As is the most widely studied material system in which resonant and non-resonant tunneling of electrons and holes has been observed [5]. From a more fundamental point of view, resonant electron tunneling has been demonstrated to occur via excitonic states, i.e. that the tunneling process can be understood as a transfer from a direct NW exciton into a "cross"

\* Corresponding author.

exciton made up of the WW electron and the NW heavy hole [6],[7]. Indeed, in ADQWs with strong carrier confinement such as GaAs/(Al,Ga)As [8] or CdTe/(Cd,Mn)Te [9] holes are believed to tunnel much slower than electrons due to the different effective masses. Tunneling of excitons as an entity has not been reported yet.

In the low-confinement system CdTe/(Cd,Zn)Te the valence band discontinuity equals the exciton binding energy for a Zn concentration  $x \leq 0.18$ . This has led to the picture of an additional hole confinement through Coulomb attraction by an electron [10]. In the same respect the observation of the excitonic centre-of-mass wavevector rather than of single particle states [11] emphasize the importance of excitonic binding. Furthermore, heavy holes are expected to have tunneling times similar to electrons since the heavier effective mass is almost compensated by the much lower valence-band discontinuity. Let us finally recall that due to strain effects, the light-hole  $I_h$  band-edge is split-off in the CdTe QW from the heavy hole band-edge by  $\approx 50$  meV leading to a type-II confinement of light hole in the (Cd,Zn)Te barrier [12]. Mixing of hole states should therefore not be important for tunneling.

## 2. Samples and experimental details

The ADQWs investigated here are grown by MBE on a (100) Cd<sub>0.96</sub>Zn<sub>0.04</sub>Te substrate. A Cd<sub>1-x</sub>Zn<sub>x</sub>Te buffer layer of 2  $\mu$ m thickness determines the lattice constant of the strained ADQW. The latter consists of a narrow CdTe layer of thickness  $L_N$ , a Cd<sub>1-x</sub>Zn<sub>x</sub>Te barrier with thickness  $L_B$  and, finally a wide CdTe QW ( $L_W$ ). The Zn concentration  $x$  ranges between 0.13 and 0.18 depending on the growth run. The intentionally undoped structures are capped by a thin CdTe layer ( $\leq 100$  nm). The samples are labelled  $L_N/L_B/L_W$  hereafter, the actual thicknesses (determined by RHEED oscillations) being compiled in Table 1. The band-diagram accounting for strain effects and the confinement levels are displayed in Fig. 1.

For the time-resolved photoluminescence (TRPL) measurements, the samples were excited by the 5 ps pulses of a synchronously pumped Styryl 8 dye laser or by a mode-locked Ti:sapphire laser. The excitation density estimated to be below  $10^{10}$  cm<sup>-2</sup> per pulse was low enough to avoid space charge effects. The PL was dispersed in a 0.32 m monochromator (resolution 5 Å) and

Table 1

List of quantum well ( $L_N$ ,  $L_W$ ) and barrier ( $L_B$ ) thicknesses, characteristic times of PL decay ( $\tau_W$ ,  $\tau$ ) and tunneling ( $\tau_I$ ); the energy differences between the calculated electron levels in both wells ( $e_N - e_W$ ), between the observed direct exciton transitions ( $X(N) - X(W)$ ) and between the direct NW and cross exciton ( $X(N) - X'(e_W, hh_N)$ ) are reported

$L_N$ (Å)	$L_B$ (Å)	$L_W$ (Å)	$\tau_W$ (ps)	$\tau$ (ps)	$\tau_I$ (ps)	$e_N - e_W$ (meV)	$X(N) - X(W)$ (meV)	$X(N) - X'(e_W, hh_N)$ (meV)
"Fast" samples								
41	48	70	176	< 7	< 7	21.3	25.9	8.8
34	117	76	108	12.5	14	24.0	32.2	9.7
40	109	74	157	18	21	16.3	19.1	1.2
42	138	74	158	55	88	19.5	24.2	2.2
37	518	67	164	138	2200	21.3	26.5	
"Slow" samples								
44	75	64	166	32	41	12.5	15.9	0.1
49	110	78	118	45	65	13.7	18.2	1.2
72	110	160	94	102	330	16.7	16.4	1.1

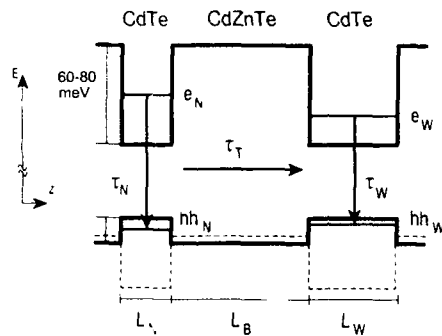


Fig. 1. Band diagram of the ADQW structures in growth direction  $z$  representing the electron and heavy hole confinement energies  $e_N$ ,  $e_W$ ,  $hh_N$ , and  $hh_W$  and the thicknesses of the CdTe quantum wells  $L_N$ ,  $L_W$  and (Cd,Zn)Te barrier  $L_B$ . Characteristic times are the tunneling time  $\tau_T$  and the excitonic lifetimes  $\tau_N$  and  $\tau_W$  in narrow and wide well, respectively. The dashed line is the light-hole valence band potential showing type-II confinement.

detected by a two-dimensional synchroscan streak camera with an S20 cathode. The limit of the measured PL decay time was 7 ps. The sample temperature was varied between 10 and 70 K in a cold-finger cryostat.

### 3. Experimental results

In the following, we will focus on low-temperature TRPL results since the steady-state properties of the investigated ADQWs are described in a previous paper [13]. Complementary data are presented here obtained on new ADQWs for which the well widths have been changed, keeping the barrier thickness constant at roughly  $L_B = 110$  Å. The carrier transfer from the NW into the WW is exhibited by the NW photolumines-

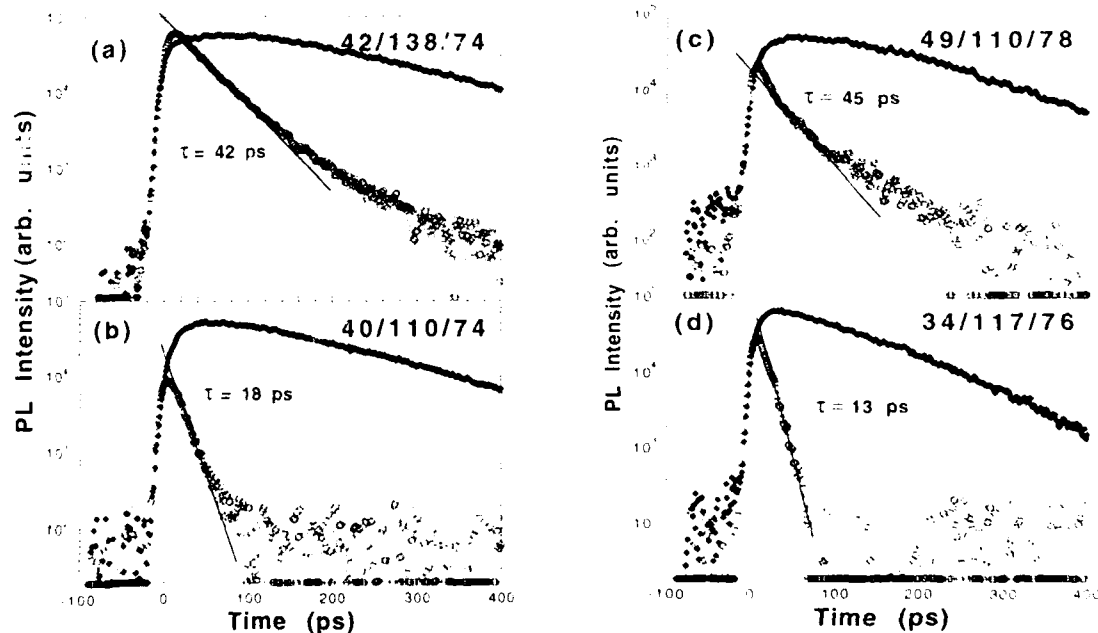


Fig. 2. Decay behaviour at  $T = 10$  K of NW (○) and WW (■) photoluminescence in a semi-log plot for various samples:  $L_N/L_B/L_W$  (in Å). The increase of the NW decay time  $\tau$  with increasing barrier thickness  $L_B$  (a + b) and with increasing barrier height (larger NW width  $L_N$ , c + d) is demonstrated. See discussion of tunneling times in the text.



cence decay times  $\tau$  (Fig. 2) which are much shorter than the ones observed in single CdTe QWs (see below). In addition, the WW decay deviates clearly from a straight exponential law demonstrating the arrival of carriers at early times ( $t \leq 200$  ps). Figs. 2a and 2b display the NW and WW PL responses at  $T = 10$  K for the 40/109/74 and the 42/138/74 structures when excited in resonance with the lowest NW exciton transition  $X(e_{\lambda}, hh_{\lambda})$ . The NW decay times  $\tau$  are 18 and 42 ps, respectively, whereas the WW decay times  $\tau_w$  are the same for both structures (see Table 1). The effect of an increasing barrier width is, as expected, to increase the NW decay time from 7 to 138 ps for barrier widths ranging between 50 and 520 Å. It is worth noticing that  $\tau$  does not depend on the laser excitation energy neither on the sample temperature for  $T \leq 40$  K [13].

The short NW decay times have to be compared to the PL decay time  $\tau_{SQW}$  of a single CdTe/Cd<sub>0.8</sub>-Zn<sub>0.1</sub>Te QW grown in a separate reference sample that we measured to be  $\tau_{SQW} = 147$  ps. The NW PL decay rate is a sum of the tunneling rate  $\tau_1^{-1}$  and the NW excitonic recombination rate  $1/\tau_{\lambda}$  according to  $\tau^{-1} = \tau_{\lambda}^{-1} + \tau_1^{-1}$ . Assuming  $\tau_{\lambda}$  to be equal to the SQW decay time  $\tau_{SQW}$  allows us to calculate the tunneling times  $\tau_1$  which are compiled in Table 1.

The effect of changing the narrow well width  $L_{\lambda}$  is shown in Figs. 2c and 2d by a comparison of the 34/117/76 and the 49/110/78 ADQWs. The slower PL decay observed for the second structure with the wider NW is consistent with the larger difference  $V - e_{\lambda}$ , between the electron confinement level  $e_{\lambda}$  and the height of the conduction band barrier  $V$ . The same argument holds if the heavy hole level  $hh_{\lambda}$  is considered. The sample 72/110/160 confirms this trend qualitatively with a quite long tunneling time of 330 ps. Nevertheless, we will show in the following that the relative distance between *excitonic* states rather than between *single particle* states is the relevant parameter governing the tunneling times of comparable structures.

In the limit of weak delocalization of the electron wavefunctions, i.e. large barrier widths, the electronic tunneling times  $\tau_1$  depend exponentially on the ratio of the barrier width  $L_B$  and the

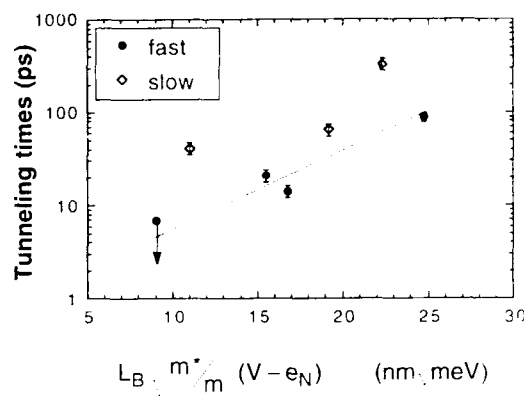


Fig. 3. Tunneling times  $\tau_1$  of the investigated ADQWs as a function of the ratio of barrier thickness  $L_B$  and barrier penetration depth  $\lambda$  in a semi-log plot. The "fast" samples (closed circles) can be connected by a straight line (guide to the eye). Above the straight line the "slow" structures are situated with longer tunneling times but comparable sample parameters.

barrier penetration length  $\lambda$

$$\tau_1 = b \exp\left(a \frac{L_B}{\lambda}\right) = b \exp\left(a \frac{L_B}{h} 2m^*(V - e_{\lambda})\right), \quad (1)$$

where  $m^*$  is the effective electron mass in CdTe [14],  $b$  is a prefactor depending on the difference  $\epsilon$  between NW and WW states ( $\epsilon = e_{\lambda} - e_w$ ) when calculated without coupling and on a level broadening  $\Gamma$  characterizing the intrawell relaxation (e.g. for phonon emission):

$$b = h(4\epsilon^2 + \Gamma^2)/2\Gamma E_n^2, \quad (2)$$

where the energy  $E_n$  depends slightly on the form of the electronic wavefunctions [14]. Here,  $b$  is minimum in a resonance ( $\epsilon = 0$ ). A proportionality factor  $a$  is introduced in the exponent [15].

Fig. 3 displays the dependence of the observed  $\tau_1$  [16] on

$$G = L_B \left( \frac{m^*}{m_0} \right) (V - e_{\lambda}),$$

$m_0$  being the free electron mass. One can actually

distinguish between two sets of samples: the “fast” structures following a straight line as predicted by Eq. (1) with roughly the same value of  $b$  (closed circles) and the “slow” structures (open triangles) having longer tunneling times than their “fast” partners with comparable values of  $G$ . It is surprising to note that the “slow” samples have a small difference  $\epsilon = e_N - e_W$  which should lead to short tunneling times if the transfer mechanism and thus  $I$  were the same for the “slow” and the “fast” structures (Eq. (2)). It appears then that different transfer mechanisms are determining the tunneling process leading to different values of  $b$  for both subsets of samples. We will figure out different carrier transfer mechanisms that can increase the tunneling rate in the “fast” structures and which are absent, i.e. energetically forbidden, in the “slow” structures.

First of all, we can rule out the importance of free carrier states (electrons and holes) for the tunneling mechanism. Indeed, those states are never in resonance in all the structures investigated. Moreover, in some “fast” ADQWs the difference between the calculated electron confinement levels  $e_N - e_W$  is smaller (Table 1) than the optical phonon energy  $\hbar\omega_{LO}$  in CdTe (21.2 meV) so that non-resonant electron transfer assisted by LO phonon emission does not explain the difference between “fast” and “slow”. The difference between heavy hole confinement levels  $hh_N - hh_W$  amounts only to 4–8 meV implying that resonances with LO phonons are not important for heavy holes. On the other hand, due to the strong excitonic binding energies in comparison to the confinement potentials one should not neglect the importance of the electron–hole correlation during the tunneling process.

We will therefore consider two charge transfer mechanisms implying excitonic states which are depicted in Fig. 4. The first process “direct-cross” (DC) is the transfer of an electron bound in a direct NW exciton  $X(e_N, hh_N)$  towards a cross exciton state  $X'(e_W, hh_N)$  (Fig. 4a). This transfer has been demonstrated to be very efficient even in GaAs/(Al,Ga)As double QWs where confinement is much stronger than in the system investigated here [17,18]. It has been identified to be the relevant mechanism for resonant electron

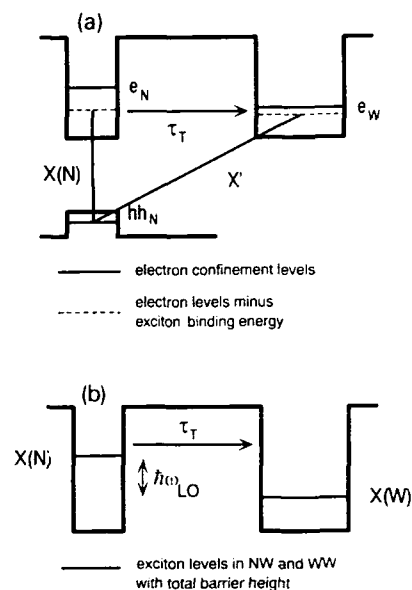


Fig. 4. Schematic representation of the tunneling processes. (a) Process DC: electrons tunnel via excitonic states: the transfer from the direct NW exciton  $X$  into the cross exciton  $X'$ . (b) Process DD: the tunneling of the direct NW exciton into the direct WW exciton by emission of an LO phonon can be represented as a single particle tunneling through a barrier with a total height equal to the conduction plus valence band offset.

tunneling in GaAs/(Al,Ga)As ADQWs [6,7]. On the other hand, tunneling can also involve the exciton as a whole, i.e. in form of a transfer from the spatial direct NW exciton into the direct WW exciton (process DD) by emission of an LO phonon (Fig. 4b).

Considering the first process DC, the cross exciton  $X'(e_W, hh_N)$  is not observed in the CW spectra and the binding energies of the cross excitons are therefore calculated by a variational approach with an excitonic trial wavefunction following Leavitt and Little [19]. The actual valence band offset (VBO) of this heterostructure system is still a matter of discussion [10]. We have chosen a zero chemical offset and the hydrostatic deformation potential for the valence band  $a_v$  to one third [20] of the bulk value  $a = 3.81$  eV [21].

The supplementary confinement of heavy holes by the electronic Coulomb potential is not taken into account. The direct NW and WW exciton transition energies calculated with this model agree with the observed values within  $\pm 2$  meV.

If the difference  $\Delta' = X(e_N, hh_N) - X'(e_W, hh_N) > 0$ , the DC process is possible and could even lead to a resonant electron transfer if  $\Delta' \approx 0$  thus explaining fast tunneling times. Indeed,  $\Delta'$  is positive for the "fast" structures but also for some "slow" structures. The DC process might be present in the majority of the studied samples but does not explain the different tunneling behaviour in the two sets of samples. On the other hand, one should realize that  $\Delta'$  can change by  $\pm 2$  meV depending on the VBO assumed for the calculations. It is therefore impossible to reliably discriminate the ADQWs in which the DC process is energetically allowed or forbidden. Applying an external electric field would help to directly observe the cross exciton transition energy.

For the second process (DD), the energy difference between both NW and WW direct excitons  $\Delta = X(e_N, hh_N) - X(e_W, hh_W)$  is directly accessible since it has been determined quite accurately by steady-state PL excitation spectra (Table 1). We notice that for all "slow" ADQWs  $\Delta$  is smaller than the LO phonon energy of CdTe, so that the DD process is energetically forbidden. On the other hand,  $\Delta - \hbar\omega_{LO}$  is positive for almost all the "fast" structures. One can therefore conclude that the transfer of direct excitons by emission of LO phonons is effective in the "fast" samples and accelerates the tunneling process in these structures with respect to the "slow" ADQWs.

We would like to stress that there might be still other coupling mechanisms between NW and WW (scattering of the NW exciton into WW continuum states, exciton transfer without LO phonon emission). Consider as an example the sample 49/110/78 with a tunneling time of 65 ps. Tunneling is relatively efficient although both the DD and the DC process are energetically forbidden. The use of external electric or magnetic fields should provide further insight concerning the relative importance of the different charge transfer processes.

#### 4. Summary

We have presented tunneling times measured by picosecond photoluminescence on a large set of CdTe/(Cd,Zn)Te ADQWs varying over three orders of magnitude as a function of the barrier thickness. The investigated structures are divided into a "fast" and a "slow" subset which can be distinguished by the presence of relevant transfer mechanisms. In fact, the energy structure of the "fast" samples allows a direct transfer of excitons from the NW to the WW under emission of optical phonons in contrast to the "slow" structures. It is difficult to assess the importance of electron tunneling as a transfer from the direct NW exciton to the cross exciton  $X'(e_W, hh_N)$  since the binding energy of the latter is not known with sufficient accuracy. Nevertheless, one has to emphasize that the observed behaviour of the tunneling times can only be explained by scattering between excitons and not between single particle electron or hole states.

#### 5. Acknowledgements

The authors would like to acknowledge H. Tuffigo-Ulmer and N. Magnea for providing results of energy and wavefunction calculations and for collaboration during the sample growth. They also thank K. Rother and H. Klann for the technical assistance during the TRPL measurements. S.H. thanks the Deutscher Akademischer Austauschdienst (HSPH/AUFE) for financial support.

#### 6. References

- [1] H.G. Roskos, M.C. Nuss, J. Shah, K. Leo, D.A.B. Miller, A.M. Fox, S. Schmitt-Rink and K. Köhler, *Phys. Rev. Lett.* **68** (1992) 2216.
- [2] S. Ikeda, A. Shimizu and T. Hara, *Appl. Phys. Lett.* **55** (1989) 1155.
- [3] A. Takeuchi, S. Muto, T. Inata and T. Fuji, *Appl. Phys. Lett.* **58** (1991) 1670.
- [4] C. Van Hoot, E. Goovaerts and G. Borghs, *Phys. Rev. B* **46** (1992) 6982.

- [5] See for instance: K. Leo, J. Shah, E.O. Göbel, J.P. Gordon and S. Schmitt-Rink, *Semicond. Sci. Technol.* 7 (1992) B394, and references therein.
- [6] A.P. Heberle, W.W. Rühle, M.G.W. Alexander and K. Köhler, *Semicond. Sci. Technol.* 7 (1992) B421.
- [7] R. Ferreira, P. Rolland, Ph. Roussignol, C. Delalande, A. Vinattieri, L. Carraresi, M. Colocci, N. Roy, B. Sermage, J.F. Palmier and B. Etienne, *Phys. Rev. B* 45 (1992) 11782.
- [8] Ph. Roussignol, A. Vinattieri, L. Carraresi, M. Colocci and A. Fasolino, *Phys. Rev. B* 44 (1991) 8873.
- [9] O. Goede, W. Heimbrodt, K. Hieke, H.-E. Gumlich, Th. Pier, B. Lunn, D.E. Ashenford, S. Jackson and J.E. Nicholls, *Superlattices Microstruct.* 12 (1992) 363.
- [10] Y. Merle d'Aubigné, Le Si Dang, A. Wasiela, N. Magnea, F. d'Albo and A. Million, *J. Physique* 48 (1987) C5-363; H. Tuffigo, R.T. Cox, N. Magnea, Y. Merle d'Aubigné and A. Million, *Phys. Rev. B* 37 (1988) 4310.
- [11] H. Tuffigo, N. Magnea, H. Mariette, A. Wasiela and Y. Merle d'Aubigné, *Phys. Rev. B* 43 (1991) 14629.
- [12] H. Mariette, F. Dal'Bo, N. Magnea, G. Lentz and H. Tuffigo, *Phys. Rev. B* 38 (1988) 12443.
- [13] S. Haacke, N.T. Pelekanos, H. Mariette, M. Zigone, A.P. Heberle and W.W. Rühle, *Phys. Rev. B* 47 (1993) 16643.
- [14] S.A. Gurvitz, I. Bar-Joseph and B. Deveaud, *Phys. Rev. B* 43 (1991) 14703.
- [15] In the original work of Gurvitz et al.,  $a$  has a value of  $a = 2$  in good agreement with experimental results [14]. But recent studies on resonant electron tunneling revealed a value of  $a = 1$  for a large number of samples and resonances [6]. Nevertheless, for the qualitative discussion presented here concerning the origin of the tunneling transfer the value of  $a$  is not of importance.
- [16] The sample 37/518/67 is not represented in Fig. 3 since due to the small difference of  $\tau$  and  $\tau_{\text{QW}}$  the absolute uncertainty for this sample is  $\pm 800$  ps. Anyway, the QWs can be considered as decoupled in this structures since the excitonic recombination prevails over tunneling ( $\tau_{\text{QW}} \ll \tau_1$ ).
- [17] S. Charbonneau, M.L.W. Thewalt, F.S. Koteles and B. Elman, *Phys. Rev. B* 38 (1988) 6287.
- [18] A.M. Fox, D.A.B. Miller, G. Livescu, J.E. Cunningham, J.E. Henry and W.Y. Jan, *Phys. Rev. B* 42 (1990) 1841.
- [19] R.P. Leavitt and J.W. Little, *Phys. Rev. B* 42 (1990) 11774.
- [20] D.L. Camphausen, G.A.N. Connel and W. Paul, *Phys. Rev. Lett.* 26 (1971) 184.
- [21] M. Zigone, H. Roux-Buisson, H. Tuffigo, N. Magnea and H. Mariette, *Semicond. Sci. Technol.* 6 (1991) 454.



ELSEVIER

Journal of Crystal Growth 138 (1994) 838–841

JOURNAL OF  
**CRYSTAL  
GROWTH**

## Excitonic emission in ZnCdSe–ZnSe multiple quantum wells

J.-Y. Zhang \*, X.W. Fan, B.J. Yang, Z.P. Guan, Y.M. Lu, D.Z. Shen

*Changchun Institute of Physics, Academia Sinica, Changchun 130021, People's Republic of China*

### Abstract

Zn<sub>1-x</sub>Cd<sub>x</sub>Se–ZnSe multiple quantum wells (MQWs) are grown on GaAs (100) substrate by MOCVD. Their photoluminescence (PL) is studied at temperatures between 77 and 300 K. We have observed five emission bands in Zn<sub>0.68</sub>Cd<sub>0.32</sub>Se–ZnSe MQWs under the 457.9 nm line of an Ar ion laser excitation at 77 K for the first time. Three of these bands are attributed to different exciton emission: the  $n = 1$  heavy-hole (HH) exciton transition, the  $n = 1$  light-hole (LH) exciton transition and the  $n = 1$  HH exciton transition with the emission of two LO phonons. The two exciton emission bands  $P_2$  and  $P_3$  of  $n = 1$  HH and  $n = 1$  HH with two LO phonons emission can be observed up to 230 K.

### 1. Introduction

Wide band gap II–VI strained layer superlattices (SLSs) and quantum well (QW) structures are of interest for their superior luminescence and non-linear optical properties [1–3]. One of the optical characteristics of these SLSs or QW systems is their efficient photon emission property, which is an important factor in II–VI semiconductor-based visible short-wavelength laser diodes. Since the demonstration of blue-green injection laser operation by Haase et al. [1], its electronic and optical properties are widely discussed in Zn<sub>1-x</sub>Cd<sub>x</sub>Se–ZnSe QW materials, especially for excitonic properties. The nonlinear excitonic absorption and thermal stability have been also studied [2]. We have reported the excitonic optical bistability in ZnCdSe–ZnSe MQWs at 77 K [4]. In this paper, the PL of Zn<sub>0.68</sub>Cd<sub>0.32</sub>

Se–ZnSe MQWs grown by atmospheric pressure metalorganic chemical deposition (AP-MOCVD) is studied at different temperature and five emission bands are observed at 77 K by using Ar ion laser excitation for the first time. Three of these bands are attributed to the different exciton emission.

### 2. Experimental procedure

The Zn<sub>0.68</sub>Cd<sub>0.32</sub>Se–ZnSe MQWs structure in this study is formed on (100) GaAs substrates by MOCVD. Dimethylzinc, dimethylcadmium and H<sub>2</sub>Se are used as the source materials. Each sample is composed of fifty Zn<sub>0.68</sub>Cd<sub>0.32</sub>Se quantum wells of thicknesses  $L_w = 10$  nm, separated by the ZnSe barrier layer with  $L_b = 10$  nm. The ZnSe and ZnCdSe layer are grown at 320°C. A 1  $\mu$ m thick buffer layer of ZnSe is grown directly on a GaAs substrate. The spectral distribution of the luminescence is measured by using a 44 W

\* Corresponding author.

grating monochromator with a C31034 cooled photomultiplier and a JY-T 800 Raman spectra equipment. PL is excited by the 337.1 nm line from a  $N_2$  laser and the 457.9 nm line from an Ar ion laser.

### 3. Experimental results and discussion

Fig. 1 shows a typical X-ray diffraction pattern from  $Zn_{0.68}Cd_{0.32}Se$ -ZnSe MQWs with 50 periods on a GaAs (100) substrate with a ZnSe (1  $\mu m$ ) buffer layer, measured by conventional diffraction using Cu  $K\alpha$  lines. It clearly shows the satellite peaks with a good quality MQWs structure. The lattice mismatch between the  $Zn_{1-x}Cd_xSe$  and the ZnSe is 1.6% for  $x = 0.32$ . The critical thicknesses of  $Zn_{1-x}Cd_xSe$  with  $x = 0.32$  on the ZnSe layers are estimated to be 23 nm by People's formula [5]. Fig. 2 shows the PL spectra of the  $Zn_{0.68}Cd_{0.32}Se$ -ZnSe MQW sample at different excitation densities by the 337.1 nm line of a  $N_2$  laser at 77 K. The PL spectra exhibit two peaks. The higher energy peak is located at 475 nm (2.610 eV) and the lower energy peak is located at 510 nm (2.451 eV). When the excitation density ( $I_0$ ) is 3 MW/cm<sup>2</sup>, the emission

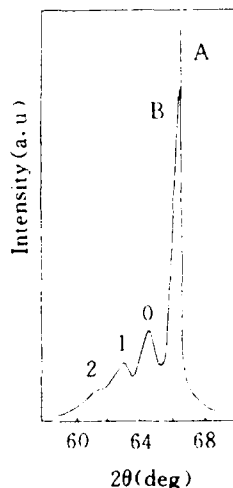


Fig. 1. X-ray diffraction pattern of  $Zn_{0.68}Cd_{0.32}Se$ -ZnSe (50 periods) MQWs on GaAs substrate.

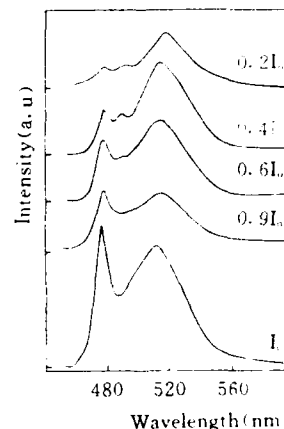


Fig. 2. PL spectra in  $Zn_{0.68}Cd_{0.32}Se$ -ZnSe MQW excited by the 337.1 nm line of a  $N_2$  laser at 77 K under different excitation intensities.

intensity of the high energy band is stronger than that of the low energy band. With decreasing excitation density, the high energy band becomes weak and the low energy band becomes strong. When the excitation intensity is  $0.4 I_0$ , the low energy band emission is dominant and both the high energy and the low energy band shift to the low energy. The low energy peak position moves towards the low energy about 20 meV at  $0.4 I_0$ . The PL spectra of  $Zn_{0.68}Cd_{0.32}Se$ -ZnSe MQWs at temperatures between 77 and 300 K under the 457.9 nm line of Ar ion laser excitation are shown in Fig. 3. Some fine structures are observed at 77 K in Fig. 3. The high energy band at 479.4 nm corresponds to the high energy band in Fig. 2. In the low energy region there are four emission bands, namely  $P_1$  (515.0 nm),  $P_2$  (530.5 nm),  $P_3$  (543.0 nm), and  $P_4$  (570.0 nm). The emission intensity of band  $P_2$  is about six times stronger than that of the high energy band in the temperature region of 77–85 K. With an increase of temperature to 124 K, the high energy band disappears and band  $P_1$  maintains only a small shoulder on the high energy side of band  $P_2$ . In addition, the luminescence in Fig. 3 mainly consists of bands  $P_2$  and  $P_3$  at 124 K because band  $P_4$  also disappears. With a further increase of the temperature to 175 K, the emission intensity of band  $P_2$

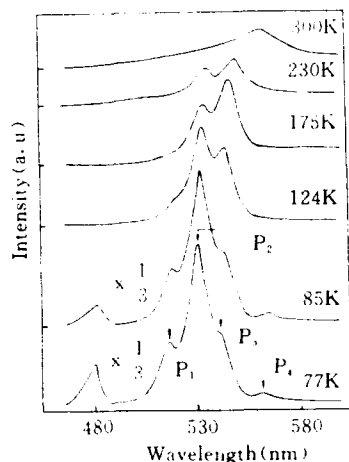


Fig. 3. PL spectra in  $\text{Zn}_{0.68}\text{Cd}_{0.32}\text{Se-ZnSe}$  MQWs at 77–300 K by the 457.9 nm line of  $\text{Ar}^{+}$  laser excitation.

has clearly decreased and that of band  $P_3$  becomes strong. Both band  $P_2$  and band  $P_3$  can be observed up to 230 K. Then band  $P_1$  disappears with an increase of the temperature and band  $P_2$  can be measured at 300 K. Here we are interested in the origin of the above emission bands. In II–VI wide band gap quantum wells, the enhancement of exciton binding energy and the large oscillator strength make it possible to observe these effects at room temperature (RT). Usually, the absorption and luminescence characteristics observed at RT in  $\text{ZnCdSe-ZnSe}$  MQWs are thought to be due mainly to the  $n=1$  HH exciton recombination [6–11]. In our case, band  $P_2$  (530 nm) in Fig. 3 at 77 K might be considered to be the  $n=1$  HH exciton recombination, according to its emission characteristics. In order to describe this conjecture, the absorption spectra in the  $\text{Zn}_{0.68}\text{Cd}_{0.32}\text{Se-ZnSe}$  MQW at 77 K (a) are measured, as shown in Fig. 4. Two well-defined structures (labeled LH and HH) are observed and they are located at 513 and 526 nm. These are attributed to the light and heavy hole exciton ground states ( $n=1$ ) in the quasi-two-dimensional system [9]. The separation of the  $n=1$  LH and the  $n=1$  HH exciton is approximately 78 meV. Curve (b) in Fig. 4 is the emission spectrum for the above MQWs at 77 K. From Fig. 5 it is

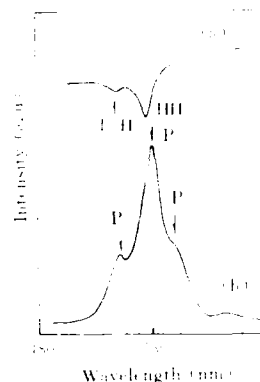


Fig. 4. Absorption (a) and emission (b) spectra in  $\text{Zn}_{0.68}\text{Cd}_{0.32}\text{Se-ZnSe}$  MQWs at 77 K.

found that band  $P_2$  is located at the low energy side (530 nm) of the absorption peak (526 nm) and the peak energy is found to shift to the lower energy side (red-shift) from the HH exciton ground quantum level. The amount of the red-shift is about 24 meV; however, it exhibited a marked size effect. So band  $P_2$  is attributed to the  $n=1$  HH exciton emission. According to ref. [2], the calculation predicts a LH uniaxial strain splitting of 75 meV so that the LH state corresponds to a weakly type-II quantum well. From Fig. 3 and Fig. 4, the energy difference between bands  $P_2$  and  $P_1$  is 70–78 meV and band  $P_1$  (515 nm) is located at the low energy side of the

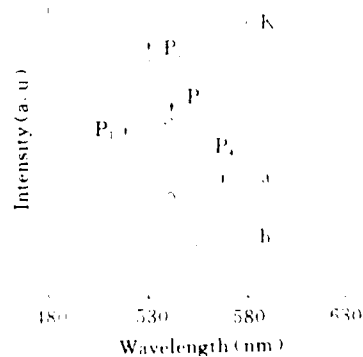


Fig. 5. PL spectra in  $\text{Zn}_{0.68}\text{Cd}_{0.32}\text{Se-ZnSe}$  MQWs with different excitation wavelength: (a) 457.9 nm line; (b) 488.0 nm line.

absorption peak L-H (513 nm). As mentioned above, it is reasonable to think that band  $P_1$  is ascribed to the  $n = 1$  LH exciton emission. It should be noticed that the weaker LH confinement is in agreement with the disappearance of band  $P_1$  with increasing temperature in Fig. 3. The energy difference between bands  $P_2$  and  $P_3$  is 58 meV from Fig. 3. This value corresponds to the energy of the 2 LO phonon in ZnSe, where the 2 LO phonon energy is 60 meV [2]. So it is possible to think that band  $P_3$  is attributed to the  $n = 1$  HH exciton recombination with 2 LO phonons. If this explanation is correct, the energy difference between bands  $P_2$  and  $P_3$  should not be changed with excitation wavelengths. Fig. 5 shows PL spectra of  $\text{Zn}_{0.68}\text{Cd}_{0.32}\text{Se-ZnSe}$  MQWs at 90 K by using the 457.9 and the 488.0 nm line of an Ar ion laser. From Fig. 5, the peak positions of bands of  $P_2$  and  $P_3$  are the same under two excitation wavelengths. This result further proves that band  $P_3$  is the  $n = 1$  HH exciton recombination with the emission of two LO phonons. The origin of the additional high energy band located at 475 nm and band  $P_4$  have not been clear to us up to now.

In summary, we have observed five emission bands in  $\text{Zn}_{0.68}\text{Cd}_{0.32}\text{Se-ZnSe}$  MQWs at 77 K for the first time. The origin of these bands is discussed. Three of these bands are attributed to the  $n = 1$  HH exciton transition, the  $n = 1$  LH exciton transition and the  $n = 1$  HH exciton recombination with the emission of two LO phonons, respectively.

#### 4. Acknowledgements

This work is supported by the "863" High Technology Research Program in China, the National Natural Science Foundation of China, the Laboratory of Excited State Process in Changchun Institute of Physics of Chinese Academy of Sciences, and the National Fundamental and Applied Research Projects of China.

#### 5. References

- [1] M.A. Haase, J. Qiu, J.M. DePuydt and H. Cheng, *Appl. Phys. Lett.* 59 (1991) 1272.
- [2] J. Ding, N. Pelekanos and A.V. Nurmikko, *Appl. Phys. Lett.* 57 (1990) 2885.
- [3] J. Ding, H. Jeon and A.V. Nurmikko, *Appl. Phys. Lett.* 57 (1990) 2756.
- [4] B.J. Yang, S.H. Song, J.Y. Zhang, T.C. Chen, Z.H. Zheng, Y.M. Lu and X.W. Fan, *Chinese J. Luminescence* 14 (3) (1993) 180.
- [5] R. People, *Appl. Phys. Lett.* 47 (1985) 322.
- [6] T. Taguchi, Y. Endoh, T. Ohno and Y. Nozue, *J. Luminescence* 52 (1992) 123.
- [7] A.V. Nurmikko and R.L. Gunshor, *J. Luminescence* 52 (1992) 89.
- [8] H.J. Lozykowski and V.K. Shastri, *J. Luminescence* 48& 49 (1991) 740.
- [9] K. Ando, A. Ohki and S. Zembutsu, *Jap. J. Appl. Phys.* 31 (1992) 11362.
- [10] H.J. Lozykowski and V.K. Shastri, *J. Appl. Phys.* 69 (1991) 3235.
- [11] S. Hayashi, A. Tsujimura and S. Yoshii, *J. Appl. Phys.* 73 (1992) 11478.





ELSEVIER

Journal of Crystal Growth 138 (1994) 842–848

CRYSTAL  
GROWTH

## Nonlinear transmission dynamics of $\text{ZnS}_x\text{Se}_{1-x}/\text{ZnSe}$ and $\text{ZnS}_x\text{Se}_{1-x}/\text{ZnS}_y\text{Se}_{1-y}$ ( $x > y$ ) waveguide structures

M. Nägele<sup>a</sup>, W. Ebeling<sup>a</sup>, J. Gutowski<sup>\*a</sup>, K.P. Geyzers<sup>b</sup>, M. Heuken<sup>b</sup>

<sup>a</sup> Institut für Experimentelle Physik, Universität Bremen, P.O. Box 330440, D-28334 Bremen, Germany

<sup>b</sup> Institut für Halbleitertechnik, RWTH Aachen, Sommerfeldstrasse, D-52056 Aachen, Germany

### Abstract

We investigate the nonlinear transmission properties of  $\text{ZnS}_x\text{Se}_{1-x}/\text{ZnSe}$  and  $\text{ZnS}_x\text{Se}_{1-x}/\text{ZnS}_y\text{Se}_{1-y}$  ( $x > y$ ) waveguides grown by MOVPE. All waveguides were designed as three-layer waveguides with either a  $\text{ZnS}_x\text{Se}_{1-x}$  or a ZnSe layer as guiding layer. The light-guiding structures are examined using a time-resolved ns-pulse pump-and-probe technique, with the probe beam propagating through the waveguide and the pump laser being focused onto the cap layer of the waveguide. We observe induced absorption and transmission of the sample close to the absorption edge under pump light irradiation. This can be understood in terms of free carrier absorption, many-body effects and heating of the sample. The waveguides with ZnSe as guiding layer show interference patterns in the transmission spectra with unusually large spacing between the maxima for energies 30 meV below the absorption edge. This feature is understood as beating between two guided modes of the waveguide and can be observed at room temperature. The creation of free carriers in the waveguide can suppress these patterns. For lower carrier densities a blue shift of the interference fringes is observed.

### 1. Introduction

Besides the creation of a laser active layer in a laser structure based on  $\text{ZnS}_x\text{Se}_{1-x}/\text{ZnSe}$ , the design of the waveguiding properties of such a structure is also a key issue. The waveguide selects the transverse modes of the laser structure and the polarization of the emitted light. Proper design of the layered system can also increase reflectivity of the end facets of the waveguide and hence lower the threshold for laser operation [1]. In addition to this, waveguides play an important

role for the design of blue-light modulators for integrated optics. Several modulators based on ZnSe have been reported [2,3], to make use of the linear electro-optic effect, which can lead to a change of refractive index as large as  $\Delta n = 0.0008$  [3], or of the quantum-confined Stark effect in  $\text{ZnCdSe}/\text{ZnSe}$  [4].

We report on nonlinear transmission changes close to the absorption edge of a waveguide based on ZnSSe being induced by the creation of free carriers in the cap or the guiding layer. Our experiments were conducted by a time resolved pump-and-probe technique using a ns dye laser system. The pump pulses provided a high density of carriers (up to  $10^{17} \text{ cm}^{-3}$ ), which is known to

\* Corresponding author.

create a change in the absorption of the light propagating through the waveguide with the energy in the excitonic range [5]. A density of carriers of  $\Delta N \approx 2 \times 10^{16} \text{ cm}^{-3}$  induces a change in the refractive index in the order of  $\Delta n \approx -0.003$  near the band edge, being larger than reported in previous work [6].

## 2. Experimental set-up

The  $\text{ZnS}_x\text{Se}_{1-x}/\text{ZnSe}$  and  $\text{ZnS}_x\text{Se}_{1-x}/\text{ZnS}_y\text{Se}_{1-y}$  ( $x > y$ ) waveguides were grown by MOVPE on GaAs substrates. The structures were not intentionally doped and have a background doping of less than  $10^{16} \text{ cm}^{-3}$ . For details of growth see references [8,9]. The samples were cleaved to a size of approximately  $1 \times 3 \text{ mm}$ . The sample composition and dimensions are listed in Table 1.

The experiments were performed using two synchronously excimer laser pumped dye lasers (pulse duration 12 ns). One laser pumped the waveguide structures with a narrow (25  $\mu\text{eV}$  energy width) laser pulse. The second laser provided an intense broad band luminescence of the dye. This light was used to probe the transmission through the waveguides. Both laser pulses were sent via optical fibers to obtain a variable time delay between them. The delay time was always measured with respect to the onset of the pump pulse. The pump beam was focused onto the cap layer of the layer structures achieving an intensity of more than  $200 \text{ kW/cm}^2$ .

The transmitted probe beam was spectrally resolved by a SPEX 1704 double grating monochromator and detected by a bialkali photo-

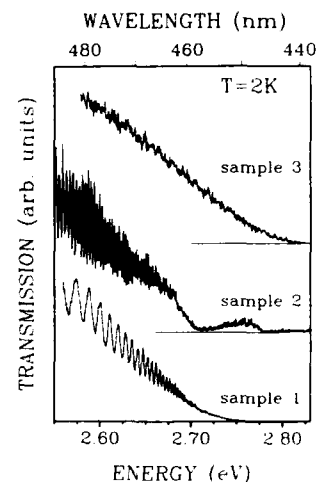


Fig. 1. Unpolarized transmission spectra of the investigated samples with no pump light excitation at a temperature of 2 K.

multiplier tube or an EG&G 1455 optical multi-channel analyser (OMA). With the OMA detector being optically triggered by the pump laser pulse, the transmission was recorded with 5 ns time resolution in a spectral range of 7 nm. The luminescence of the sample that was generated by the pump light was measured separately with the probe light off and subtracted from the transmission spectra.

## 3. Experimental results and discussion

Transmission spectra without additional pump light on the samples are shown in Fig. 1. A remarkable feature are the beatings in the spectra of samples 1 and 2 being discussed later in this paper. Sample 3 has a  $\text{ZnS}_x\text{Se}_{1-x}$  layer as guiding layer, hence it is transmitting light for higher energies than samples 1 and 2. The decrease of transmission of sample 2 around 2.71 eV can be understood as absorption of light due to impurities. First, we will discuss experimental results obtained close to the absorption edge of the waveguides in dependence of the excitation wavelength. The second part of this paper will address the beating patterns and the induced

Table 1  
Nominal composition and thickness of the investigated  $\text{ZnS}_x\text{Se}_{1-x}/\text{ZnS}_y\text{Se}_{1-y}$  waveguides; all samples were grown by MOVPE on GaAs substrates

	Sample 1		Sample 2		Sample 3	
	x (%)	d (nm)	x (%)	d (nm)	x (%)	d (nm)
Cap layer	4.5	500	11	500	22	500
Guiding layer	0	500	0	500	14	500
Buffer layer	4.5	2000	11	2000	22	2000

changes of the refractive index due to the excitation.

### 3.1. Transmission changes close to the absorption edge

Excitation of the structure with wavelengths above the excitonic resonance of the cap layer will lead to an increase of transmission through the waveguide in the spectral range between 2.70 and 2.775 eV. This effect is large at liquid helium temperature, it becomes smaller for increasing temperatures and vanishes at 250 K. In such cases the differential transmission signal (DTS) defined as  $(T - T_0)/T_0$  is measured, where  $T$  is the transmission of the sample with pumping and  $T_0$  without pumping. For sample 2, the probe wavelength was chosen 448 nm (2.76 eV) and the excitation wavelength was 408 nm (3.05 eV), which is well above the band gap of the cap layer. A purely exponential decay of the DTS was found with a time constant of 25 ns. This relates our observation to optical transitions involving impurities, which are known to have time constants of a couple of 10 ns in ZnSe at moderate doping levels [10].

The DTS of samples 2 and 3 is shown as a function of pump intensity in Fig. 2, saturating for pump intensities beyond 100 kW/cm<sup>2</sup>. Sample 1 exhibits a very weak induced transmission

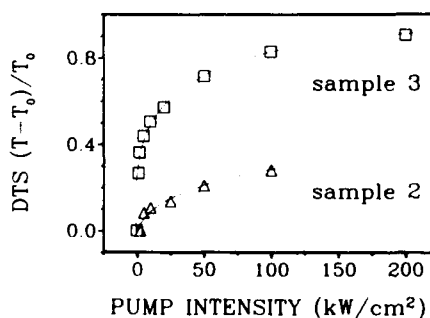


Fig. 2. Differential transmission signal DTS,  $(T - T_0)/T_0$ , for sample 2 and sample 3 in dependence of the excitation intensity at a temperature of 2 K. The excitation wavelength was 405 nm (3.06 eV). The DTS was measured at 448 nm (2.766 eV) for sample 2 and at 441 nm (2.810 eV) for sample 3.

and was not included in the figure. The wavelengths characteristics, the time constants, and this saturation behaviour indicate that the phenomenon is to be interpreted in terms of bleaching of acceptor–conduction band transitions, being well known to occur in other II–VI materials like CdS [11,12]. Acceptors are built in by self-compensation in all n-type II–VI materials and are most probably vacancy–donor centres (with the vacancy acting as double acceptor), if not provided by contaminations of material sources.

The strength of the DTS signals is a criterion for the impurity concentration in the samples. The enhanced impurity contents of sample 2 compared to sample 1 is also confirmed by time-resolved analysis of their stimulated emission under intense pump light excitation. It decays much faster in the first than in the second sample, if a 1.5 ps pulse is applied [13]. Sample 3 exhibiting the largest DTS and thus the highest impurity concentration was grown from H<sub>2</sub>S instead of diethylsulfide (DES) which was used for samples 1 and 2. This source may have provided a larger number of contaminations in the cap layer. As will be discussed below, the electric field distribution inside the waveguide shows a large field strength even inside the cap layer. This makes the transmission of light through the waveguide very sensitive to losses inside this layer.

In contrast to the behaviour of the probe transmission described above, an induced absorption of the guided light is observed for pump energies below the excitonic resonances of the cap layer. For such a case, the DTS of sample 1 in the energy range below 2.790 eV is shown in Fig. 3 as a function of probe delay with respect to the pump pulse. The pump energy of 2.82 eV was just in the ZnSe guiding-layer band edge, the excitation density was chosen to be 100 kW/cm<sup>2</sup>. In this case, the transmission spectra exhibit a complicated time evolution.

First, a pronounced increase of transmission is observed in the spectral region between 2.77 and 2.79 eV even after correction of the detector signal for the luminescence of the sample caused by the pump light. This peak is not explicitly shown in Fig. 3, but indicated by the blank area in the left upper corner caused through the cut-off

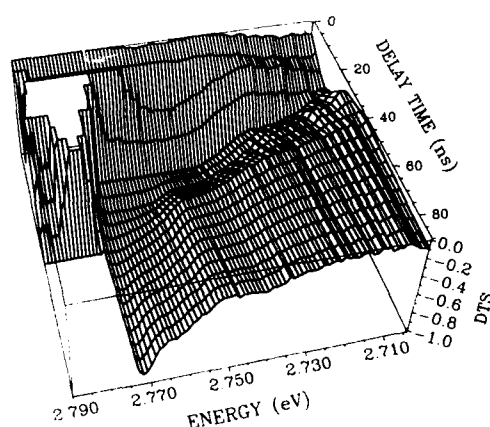


Fig. 3. Differential transmission spectra DTS,  $(T - T_0)/T_0$ , of sample 1 for delay time between 0 and 90 ns at a temperature of 2 K. The excitation wavelength was 439.5 nm (2.82 eV) with an intensity of  $100 \text{ kW/cm}^2$ .

of positive DTS values. It appears for delay times between 2 and 22 ns and shows a narrowing for increasing delay after correction of the detector signal for the luminescence of the sample caused by the pump light. The development of the transmission increase in time is closely related to the shape of the pump pulse (for the latter, see Fig. 4). Since it is known that samples 1 and 2 show stimulated emission in a strip-length pump geometry [14], it is plausible to interpret the positive

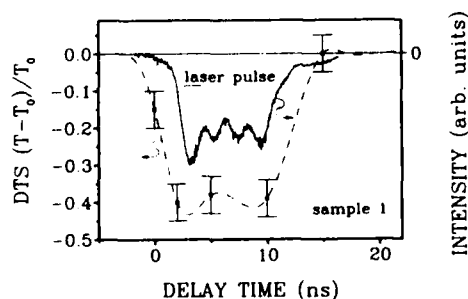


Fig. 4. Differential transmission signal DTS,  $(T - T_0)/T_0$ , for sample 1 at a wavelength of 635.5 nm (1.95 eV) in dependence of the delay time at a temperature of 2 K (dashed curve). The excitation wavelength was 439.5 nm (2.82 eV) with an intensity of  $100 \text{ kW/cm}^2$ . The shape of the pump laser pulse is also shown (solid line).

DTS signal in this energy and time window as an amplification of the probe light by stimulated recombination. The free-carrier lifetime is known to be as short as a few 100 ps in these ZnSe systems, even being shortened by stimulated emission effects [7]. Thus, it is understandable that the effect immediately follows the time evolution of the ns pump pulse.

The same is valid for a fast induced absorption effect on the low-energy side of stimulated emission, i.e., below 2.75 eV. This absorption effect can be observed even at 635 nm where its development in time is shown in Fig. 4. It is strongly correlated with the shape of the pump pulse which is explicitly depicted as full line. The magnitude of this absorption effect goes as a roughly quadratic law with the detection wavelength, in accordance with experimental measurements and predictions by Broser et al. [15] concerning the absorption of light by free carriers. The applied pump intensity of  $100 \text{ kW/cm}^2$  is estimated to create a carrier density of  $10^{17} \text{ cm}^{-3}$ . The free-carrier cross section calculated according to Seeger [16] yields a change of the absorption coefficient in a semiconductor in the order of 0.1 to  $3 \text{ cm}^{-1}$  if a carrier density as given above is created. We determine the experimental change of the absorption coefficient as  $0.2 \text{ cm}^{-1}$  at 490 nm, which compares well with the theoretical calculations.

On a longer delay time scale, the free carrier absorption vanishes in favour of an intense induced absorption just on the low-energy edge of the stimulated emission peak. This feature lasts considerably longer than the pump pulse, but is restricted to 2.71 to 2.77 eV and shows a high-energy shift with time until it disappears. For longer delay times, this effect is probably due to simple heating of the sample by the intense light absorption and correlates in time with a red shift of the interference patterns described later. The lack of transmission of light in the spectral region where the amplification took place and the high-energy shift of the DTS edge for longer delays (more than 100 ns) can be attributed to a temperature related shift of the band gap. We estimated the temperature increase due to the pump light absorption to amount to 10–30 K at a helium bath

temperature of 2 K, taking the given pump intensity and the specific heat of ZnSe [17].

As a conclusion it has to be mentioned that bleaching of impurity-band transitions is only observed when directly exciting band-to-band transitions in the cap layer. It is completely overwhelmed by other effects when pumping into the guiding layer's band only. For band-to-band excitation into the cap the light is mostly absorbed there and carriers are hardly created in the guiding region. However, efficient migration of the carriers from the cap into the guiding layer increases the bleaching effect of the impurity-related transitions in the cap layer by suppression of recombination into the acceptor centres. So, due to light propagation in the guiding as well as in the cap layer, in this case integral probe transmission in the sample increases since the carrier densities in the guiding layer remain moderate. This changes in case of direct excitation of carriers in the guiding region. Now, strong free-carrier absorption and sample heating exceed any effect of impurity bleaching, yielding induced absorption in total, apart from stimulation just in the band edge.

### 3.2. Transmission changes below the absorption edge

The transmission spectra of samples 1 and 2 show a beating for energies below the absorption edge at 2 K as well as at room temperature. These features possessing an oscillation period of 2 nm can not be explained as a conventional Fabry–Perot oscillation between the end facets of the waveguide which should show a 0.03 nm wide spacing between the maxima at 490 nm for a 3 mm long waveguide with a refractive index of 2.8. The interference fringes depend on the polarization of the light. A probe beam with a polarization parallel to the layered structure (TE wave) will produce narrower fringes than the perpendicular polarization (TM wave). The TM wave undergoes twice as much attenuation as the TE wave.

If we assume a conventional Fabry–Perot resonator as source of the observed beatings, we can calculate a distance of 43  $\mu\text{m}$  between the mir-

rors (wavelength 490 nm,  $n = 2.8$  for ZnSe). Given this distance, we conclude that neither the length nor the width of the samples can explain the beatings. The propagation of light through a waveguide can be described as a zig-zag wave, being reflected at the interfaces between the different layers. The propagation constants of such a wave and the field distribution in the waveguide can be computed by a matrix formalism [18], in case of detailed knowledge of the refractive index  $n(\lambda)$  of the different layers. We adapted the theoretical description of Adachi [19], because it relates the refractive index  $n$  to material parameters, like the fundamental band gap  $E_g$  at the  $\Gamma$  point and  $E_1$  at the L point. The refractive index for the ternary compounds is estimated by a linear approximation [2] of the shifts of  $E_g$  and  $E_1$  and calculated with the model of Adachi. All other parameters of the model were left constant. The computations show, that a waveguide like sample 1 does support two guided modes for TE and TM polarized light, respectively. The field distributions of the modes do not reach the GaAs with a significant field strength, hence no GaAs related losses can be expected. The dispersion relation and the field distribution are nearly the same for both polarizations.

An interference between two guided modes of the waveguide cannot be observed if a large aperture (e.g. a microscope lens) is used, since the modes of a waveguide are orthogonal, i.e. the integral of the two field distributions  $E_1$  and  $E_2$  of the modes over the whole end facet is zero. However, we used lenses with 150 mm focal length and a diameter of 6 cm, which is equivalent to perform the integrate over a smaller area. Theoretical calculations of this lens system show a significant beating of the two guided modes, with a spacing between the maxima that is similar to the observed one.

A reflection measurement of sample 1 indicates a total thickness of the structure of 3.45  $\mu\text{m}$ . This is 15% larger than the intended total thickness of the structure; hence we increased the nominal thickness of each layer by 15%. A good fit to the spectrum was found for a sulphur concentration of 0.9% in the cap and 4.5% in the buffer layer at 300 K. This strongly asymmetric

sulphur concentration in the buffer and cap layer disagrees with the results of SIMS measurements, that were conducted on different samples grown at the RWTH Aachen. The concentration of sulphur was found to be symmetric for the measured waveguides. Hence, our description of the refractive indices of the ternary compounds may not be valid and we have to include not only the shifts of the band gaps  $E_0$  and  $E_1$ , but also the changes of the other model parameters, i.e. excitonic line width and oscillator strength [20]. The calculated sulphur concentrations should be translated into the refractive indices of the different layers, which has to be higher in the cap layer compared to the buffer layer.

The stronger attenuation of the TM polarized light is well known from the literature and can be attributed to different loss mechanisms of the TM wave compared to the TE wave [21,22]. They also have smaller reflection coefficients at the end facets [1].

The time evolution of the beating pattern under the influence of pump light is shown in Fig. 5. We observed a blue-shift of the modes for short delay times between the pump-and-probe pulse at 2 K, being as large as 0.3 nm for a probe wavelength of 468 nm and an excitation density of 20 kW/cm<sup>2</sup>. This blue-shift disappeared as soon as the pump pulse was over, which suggests again a free-carrier related effect. Within our model the induced change of the refractive index was estimated to decrease by  $\Delta n = -0.003$ , which

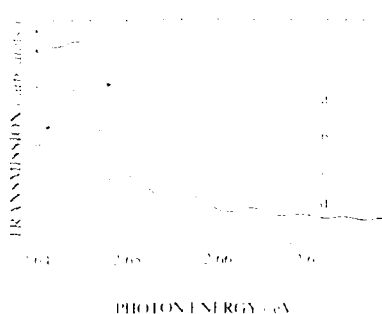


Fig. 5. Transmission spectra of sample 1 in dependence of the wavelength for different pump excitation intensities and delays: (a) no excitation; (b) 20 kW/cm<sup>2</sup>, 6 ns delay; (c) 200 kW/cm<sup>2</sup>, 6 ns delay; (d) 200 kW/cm<sup>2</sup>, 47 ns delay.

gives a nonlinear refractive cross section  $\sigma_n = \Delta n/\Delta N$  of  $1.5 \cdot 10^{-19}$  cm<sup>3</sup>. This value is one order of magnitude larger than previously reported results [6,23]. The beatings were suppressed for excitation densities above 20 kW/cm<sup>2</sup> (at 2 K and room temperature). This might be attributed to scattering of light at free carriers. For longer delay times (above 20 ns), we did observe a red-shift persistent for more than 100 ns. This relates the red-shift to the temperature shift of the band gap, as was already described earlier in this paper.

#### 4. Acknowledgement

The authors would like to acknowledge the financial support of the Volkswagenstiftung, Germany.

#### 5. References

- [1] T. Ikegami, IEEE J. Quantum Electron., QE-8 (1972) 470.
- [2] M.H. Jupina, E.M. Garmire, N. Shibata and S. Zembutsu, IEEE J. Quantum Electron., QE-28 (1992) 663.
- [3] M.A. Haase, H. Cheng, D.K. Misemer, E.A. Strand and J.M. DePuydt, Appl. Phys. Lett., 59 (1991) 3228.
- [4] S.Y. Wang, Y. Kawakami, J. Simpson, H. Stewart, K.A. Prior and B.C. Cavenett, Appl. Phys. Lett., 62 (1993) 1715.
- [5] N. Peyghambarian, S.H. Park, S.W. Koch, A. Jettely, J.I. Potts and H. Cheng, Appl. Phys. Lett., 52 (1988) 182.
- [6] J.A. Bolger, I. Galbraith, A.K. Kar, J. Simpson, S.Y. Wang, K.A. Prior, B.C. Cavenett and B.S. Wherrett, Appl. Phys. Lett., 63 (1993) 709.
- [7] J.A. Bolger, A.K. Kar, B.S. Wherrett, K.A. Prior, J. Simpson, S.Y. Wang and B.C. Cavenett, Appl. Phys. Lett., 63 (1993) 571.
- [8] M. Heuken, K.P. Geizers, F.E.G. Guimarães, J. Sollner, A. Schneider and K. Heyme, J. Crystal Growth, 124 (1992) 633.
- [9] M. Heuken, J. Sollner, K.P. Geizers, F.E.G. Guimarães and A. Schneider, Adv. Mater. Opt. Electron., in press.
- [10] P. Bäume, F. Kubacki and J. Gutowski, J. Crystal Growth, 138 (1994) 266.
- [11] R. Schmolke, F. Schöll, and J. Gutowski, J. Crystal Growth, 117 (1992) 650.
- [12] R. Schmolke, F. Schöll, M. Nägele and J. Gutowski, J. Crystal Growth, 138 (1994) 213.
- [13] U. Neukirch, private communication.

- [14] M. Nägele, D. Weckendrup, U. Neukirch, J. Gutowski, K.P. Geyzers and M. Heuken, *Adv. Mater. Opt. Electron.*, in press.
- [15] I. Broser, R. Broser and E. Birkicht, *J. Crystal Growth* 101 (1990) 497.
- [16] K. Seeger, *Semiconductor Physics* (Springer, Berlin, 1991) pp. 306 ff.
- [17] U. Roessler, in: *Landolt-Börnstein III/22a*, Ed. O. Madelung (Springer, Berlin, 1987) p. 177.
- [18] H. Kogelnik, in: *Guided-Wave Optoelectronics*, Ed. T. Tamir (Springer, Berlin, 1990) p.7.
- [19] S. Adachi, *Phys. Rev. B* 43 (1991) 9569.
- [20] P.R. Newbury, K. Shahzad, J. Petruzello and D.A. Cammack, *J. Appl. Phys.* 66 (1989) 4950.
- [21] T. Yokogawa, M. Ogura and T. Kajiwara, *Appl. Phys. Lett.* 52 (1988) 120.
- [22] A.B. Buckman, *J. Opt. Soc. Am.* 72 (1982) 688.
- [23] W. Ji, J.R. Milward, A.K. Kar, B.S. Wherrett and C.R. Pidgeon, *J. Opt. Soc. Am. B* 7 (1990) 868.



ELSEVIER

Journal of Crystal Growth 138 (1994) 849–855

JOURNAL OF  
**CRYSTAL  
GROWTH**

## Exciton relaxation dynamics in ultrathin CdSe/ZnSe single quantum wells

U. Neukirch <sup>\*a</sup>, D. Weckendrup <sup>a</sup>, W. Faschinger <sup>b</sup>, P. Juza <sup>b</sup>, H. Sitter <sup>b</sup>

<sup>a</sup> Institut für Experimentelle Physik, Universität Bremen, P.O. Box 330 440, D-28334 Bremen, Germany

<sup>b</sup> Institut für Experimentalphysik, Universität Linz, A-4040 Linz, Austria

### Abstract

Ultrathin CdSe/ZnSe single quantum wells grown by self-limiting monolayer epitaxy are investigated by means of time integrated as well as picosecond time-resolved luminescence spectroscopy. Well thicknesses are 1, 2 and 3 monolayers of CdSe. All samples exhibit a bright excitonic luminescence which shows, for an SQW of one monolayer thickness, a blue shift of 850 meV with respect to bulk CdSe. The transient behavior of the luminescence varies depending on energy of detection. At high energies, the decay is very fast and nonexponential. At the low-energy side of the luminescence band, a slower, simply exponential decay is observed. A model of excitons relaxing in a random potential is set up to describe and discuss the experimental data. Under resonant excitation into higher well states, several phonon replica of recombining, resonantly excited excitons occur.

### 1. Introduction

Recently, the interest on the field of wide band-gap II–VI semiconductors has been concentrated more and more on materials whose optical transitions are in the blue-green spectral region. Additionally, application or at least applicability in optoelectronic devices plays a major role [1].

At a first glance, the mid-band-gap CdSe/ZnSe system which is the subject of this investigation does not fit these trends. However, when looking at the properties of the samples, we found an outstanding quality which enabled us to drive the well width to its natural limit of one monolayer thickness. Besides the fundamental interest in dynamical properties of excitons in ultrathin quantum wells, this small width pushes optical transitions of the system into the blue-green spectral region, due to the large electronic confine-

ment [2]. Thus, our work deals with a system which is, on the one hand, of interest for basic research, due to its extreme geometry, and is, on the other hand, possibly suited for optoelectronic applications, due to its large exciton energy, long exciton lifetime and bright luminescence.

### 2. Experimental setup

All investigated single-crystalline CdSe/ZnSe single quantum wells were grown by a modified molecular beam epitaxy process called self-limiting monolayer epitaxy (SME) [3]. Samples consisting of a single quantum well, as well as structures containing a series of uncoupled wells of different thicknesses, were investigated. Intended thicknesses were one, two and three monolayers (ML), respectively.

The transient behavior of the well luminescence was measured by time-correlated single-

\* Corresponding author.



photon counting. For excitation of the samples, the frequency-doubled light of a mode-locked titanium-sapphire laser running at 4 or 82 MHz repetition rate is used. The pulse duration amounts to 1.5 ps with energies up to 4 nJ/pulse. After being dispersed by a subtractive double-monochromator of 320 mm focal length, the luminescence photons are detected by a microchannel-plate photomultiplier tube (MCP-PMT). Part of the laser light is used to illuminate a photodiode for triggering. The system response (including electronics) to the short laser pulse itself reveals a FWHM of about 50 ps. Usual time-integrated luminescence spectra can be obtained by counting all of the detection pulses from the MCP-PMT while tuning the monochromator. Detection is performed in a direction rectangular to the exciting beam with the sample slightly tilted off 45° to avoid direct reflection of the laser beam into the monochromator.

The excitation intensities were kept below a time-integrated power of 1 mW. For band-to-band excitation of ZnSe with an absorption coefficient of  $10^4 \text{ cm}^{-1}$  and a radius of the excitation spot of 0.15 mm, this corresponds to a density of excited carriers just after the exciting pulse of about  $10^{15} \text{ cm}^{-3}$ .

All optical investigations were performed in superfluid helium at  $T = 1.6 \text{ K}$ .

### 3. Experimental results

At low temperatures the samples exhibit bright excitonic luminescence for excitation into band states of the ZnSe barrier as well as for resonant excitation into the CdSe wells. Fig. 1 shows the time-integrated luminescence of a sample containing three quantum wells with thicknesses of 1, 2, and 3 ML, respectively. For this spectrum the sample was excited at 3.20 eV, i.e., into band states of the ZnSe barrier. Each quantum well emits a single distinct luminescence band, which becomes evident when comparing the characteristic luminescence of samples that each contain one single quantum well only (of 1, 2, or 3 ML thickness, respectively). Whereas the intensity ratio between the 1 ML and 2 ML bands scatters around one, depending on the actual location of

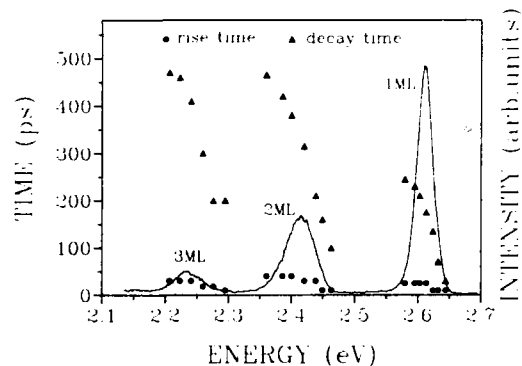


Fig. 1. Time-integrated luminescence spectrum of a CdSe/ZnSe structure containing a 1 ML, 2 ML, and 3 ML SQWs. Additionally, rise times and decay times are given at different energies of detection.

the laser spot on the sample surface, the intensity of the 3 ML emission is smaller than the others in any case. This is probably caused by misfit dislocations which degrade the layer quality for increasing well width when the critical thickness is exceeded ( $4 \pm 1 \text{ ML}$  [2]). The halfwidth of the luminescence bands increases with increasing well width.

Table 1 shows the energy positions, halfwidths and relative energy shifts (with respect to the energy of free excitons in hexagonal bulk CdSe) of the luminescence bands for different samples. Although the CdSe layers in our samples are assumed to grow in cubic modification, the comparison is made with hexagonal CdSe since data for cubic bulk CdSe are lacking. However, theoretical evaluations as well as measurements on thin cubic CdSe films yield values of the band

Table 1

Luminescence data of two different CdSe/ZnSe SQW samples under investigation; the blue shift refers to the exciton energy of 1.826 eV in wurtzite bulk CdSe; SQW 1 ML denotes a sample containing just 1 ML CdSe, SQW 123 one containing non-coupled 1 ML, 2 ML, and 3 ML CdSe layers

Sample	Luminescence peak energy (eV)			FWHM (meV)	Blue shift (meV)
	1 ML	2 ML	3 ML		
SQW 1 ML	2.678	—	—	24.5	850
SQW 123	2.611	—	—	29.7	790
SQW 123	—	2.415	—	54.4	590
SQW 123	—	—	2.238	56.0	410

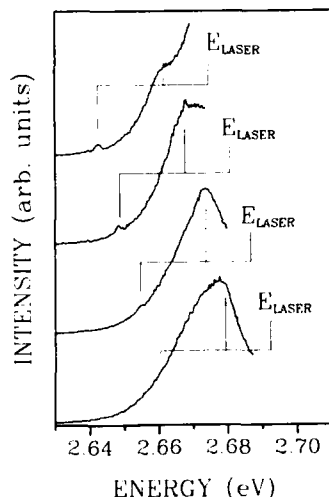


Fig. 2. Time-integrated luminescence spectra for a 1 ML well for different excitation energies. Besides the energy of the exciting laser,  $E_{\text{laser}}$ , two energy positions are marked where sharp spectral features occur. These labels are 13 and 32 meV below  $E_{\text{laser}}$ .

gap,  $E_{\text{G,cub}}$ , of cubic CdSe close to those of the hexagonal modification,  $E_{\text{G,hex}}$  [4,5]. As a result, the blue shift of the excitonic emission amounts up to 850 meV for a 1 ML sample.

When exciting the samples at energies below the ZnSe exciton but above the quantum well luminescence, sharp structures superimposed on the broad excitonic emission band are seen. This is shown in Fig. 2 for a 1 ML sample. When the laser energy is tuned, these small peaks also shift in energy, keeping a constant energy separation of 13 and 32 meV with respect to the energy of excitation.

As can be seen from the data added in Fig. 1, the decay times  $\tau_d$  of the luminescence bands vary between 30 and 470 ps, increasing monotonically with the wavelength of detection for each emission band. At the maxima of the different luminescence bands,  $\tau_d$  increases with increasing well width. The data given here are results of fitting the transients with an exponential rise ( $\tau_r$ ) and an exponential decay ( $\tau_d$ ). For comparison with experimental data, the theoretical curves are convoluted with the system response to the ultra-short laser pulse itself. Doing so we obtain satisfy-

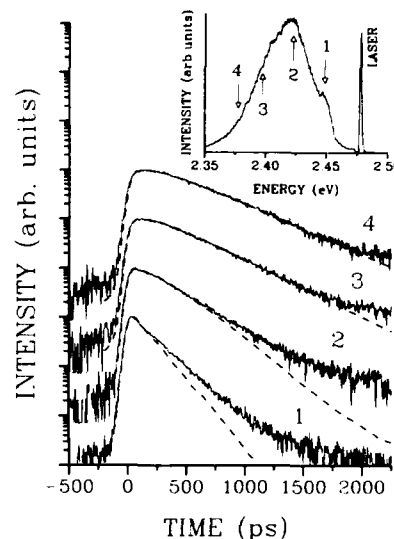


Fig. 3. Transient luminescence behavior of a 2 ML SQW (solid lines) at four different energy positions, indicated in the inset, which shows the time-integrated luminescence. Dashed curves are fits to the experimental data. The energy of excitation amounts to 2.478 eV.

ing fits on the low-energy side of the emission bands only. This is shown for a 2 ML sample in Fig. 3. Obviously, the exponential decay observed at the low-energy side of the luminescence band changes smoothly to a complicated nonexponential one at the high-energy side.

When exciting the samples below the barrier

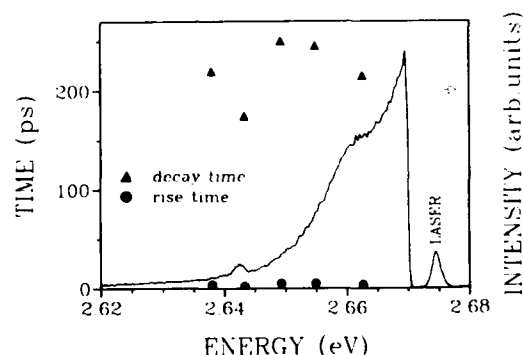


Fig. 4. Luminescence spectrum of the resonantly excited 1 ML SQW together with fitted rise times and decay times ( $E_{\text{laser}} = 2.642$  eV).

exciton, the temporal behavior changes. The rise times become considerably shorter. This is observed not only for detection on the low-energy side, but also on the high-energy side of the luminescence band. The large  $\tau_d$  values at lower energies remain almost unchanged. There is one exception from this behavior concerning the additional sharp structures superimposed to the emission band in case of resonant excitation of the wells. The transients at these energies show a fast initial decay which is attributed to the decay of the sharp lines. Fig. 4 shows a luminescence spectrum together with fitted  $\tau_d$  for a fixed excitation energy. Notice the distinct drop of decay time when measuring on top of the sharp structure.

#### 4. Discussion

Interpretation of the time-integrated spectra allows a rough estimate of the well width fluctuation in our samples from the ratio between the blue shift of the excitonic emission (with respect to bulk CdSe) and its FWHM. This gives a very small value of less than 0.1 ML well width fluctuations for a 1 ML sample. Inside a two-dimensional potential relief, defined by the spatial distribution of well widths, excitons relax in energy by migration. Thus, energy relaxation is expected to reduce the population of exciton states at higher energies, leading to a complicated shape of the luminescence as well as to complicated transient behavior. This situation is directly related to alloy disorder in ternary semiconductors. To change the well width in a CdSe/ZnSe system means, especially for the ultrathin wells as are discussed here, to substitute a Zn atom by a Cd atom at the interface of the well. This is exactly the same as to increase the Cd content in a  $\text{Zn}_{1-x}\text{Cd}_x\text{Se}$  alloy. Having this in mind, consider that it is known from cation-substituted ternary II–VI alloys that, due to the small ratio of electron mass to hole mass  $m_e/m_h$ , exciton localization is weak compared to anion-substituted systems like  $\text{CdS}_x\text{Se}_{1-x}$  [6]. However, reduction of the dimensionality of the system to 2D should increase localization.

If the recombination time  $\tau_0$  of excitons is assumed to be independent of energy, at least in the small energy interval defined by level variation caused by well width fluctuations, the observed changes of the decay times  $\tau_d$  when tuning the energy of detection over the exciton luminescence band (see Fig. 1) are clearly due to the characteristics of energy relaxation. This is put up in a simple model described below.

##### 4.1. Model considerations

Phonon-assisted tunneling is discussed as a mechanism for energy relaxation in localized exciton systems (see refs. [6–8]). In our measurements, the experimental findings are similar to those reported for  $\text{CdS}_x\text{Se}_{1-x}$  [8]: the luminescence at high energies decays, at first, very fast but the decay slows down more and more at later times (see Fig. 3). Our interpretation of this behavior is that some excitons cannot relax in energy. The model separates the number of excitons at a given energy into two groups. Excitons belonging to the first group are able to relax in energy by spatial migration into areas of wider well widths, while the others are assumed to be captured in local minima of the localizing potential. All of them are able to recombine radiatively or nonradiatively. The concept is as follows:

- Well width fluctuations cause a random 2D potential for the excitons.

- The spatially integrated density of states (DOS) for 2D excitons in a quantum well of varying width is a Heavyside-function with a smoothed edge which depends on the actual distribution of potential energy. If a very fast relaxation of kinetic energy is assumed, only states at  $k = 0$  are considerably occupied. The DOS for  $k = 0$  is proportional to the energy distribution of excitonic ground states in the potential relief. It is called  $g(E)$  and is chosen to be a Gaussian distribution around a mean value  $E_x$  having a width of  $W_x$ :

$$g(E) \sim e^{-(E_x - E)^2 / W_x^2}. \quad (1)$$

- The population of excitons at a given energy is  $N(E) = N_{\text{RR}}(E) + N_{\text{R}}(E)$ , with  $N_{\text{RR}}(E)$  excitons being able both to relax and to recombine, and  $N_{\text{R}}(E)$  excitons resting in a local minimum and waiting for recombination with time constant  $\tau_0$ .

– According to this, the rate of loss at  $E_{\text{init}}$  for  $N_R$  is given by recombination only. The rate equation for  $N_R$  is (terms which increase the population are abbreviated as *gain* and are given below)

$$\frac{dN_R(E_{\text{init}})}{dt} = -\frac{N_R(E_{\text{init}})}{\tau_0} + \text{gain.} \quad (2)$$

The relaxation probability for an exciton at energy  $E_{\text{init}}$  into a state  $E_{\text{final}}$  is proportional to the density of states  $g(E_{\text{final}})$ . Therefore, a second term has to be added to the recombination loss for  $N_{RR}$ . This yields

$$\begin{aligned} \frac{dN_{RR}(E_{\text{init}})}{dt} &= -\frac{N_{RR}(E_{\text{init}})}{\tau_0} - WN_{RR}(E_{\text{init}}) \int_{-\infty}^{E_{\text{init}}} g(E) dE \\ &\quad + \text{gain.} \end{aligned} \quad (3)$$

Setting the constant fit parameter  $W$  independent of  $E$  neglects the influence of the exciton-phonon coupling on the transition probability [7,8]. Then, the last term in Eq. (3) can be simplified by introduction of an effective, energy-dependent time constant  $\tau_1(E_{\text{init}})$ :

$$\begin{aligned} \frac{dN_{RR}(E_{\text{init}})}{dt} &= -\frac{N_{RR}(E_{\text{init}})}{\tau_0} - \frac{N_{RR}(E_{\text{init}})}{\tau_1(E_{\text{init}})} \\ &\quad + \text{gain.} \end{aligned} \quad (4)$$

– Corresponding to this, gain of population at a final state  $E_{\text{final}}$  is given by a fraction of the relaxation losses at higher energies. This fraction is given by the density of states  $g(E_{\text{final}})$  of the state under consideration divided by the integrated density of states for all possible final states with  $E < E_{\text{init}}$ :

$$\begin{aligned} \frac{d(N_R(E_{\text{final}}) + N_{RR}(E_{\text{final}}))}{dt} &= -\text{loss} + \int_{E_{\text{final}}}^{\infty} \frac{N_{RR}(E)}{\tau_1(E)} \frac{g(E_{\text{final}})}{\int_{-\infty}^E g(\bar{E}) d\bar{E}} dE. \end{aligned} \quad (5)$$

The gained population (Eq. (5)) at a given  $E$  is distributed among  $N_{RR}(E)$  and  $N_R(E)$  by a Fermi function called  $M(E)$  which depends on energy,

is centered at  $E_M$  (the mobility edge), and has a width  $W_M$ :

$$M(E) = (e^{(E-E_M)/W_M} + 1)^{-1}. \quad (6)$$

At a given energy  $E$ , an exciton relaxing from higher energies is added to  $N_R(E)$  with probability  $M(E)$ , and to  $N_{RR}(E)$  with probability  $1 - M(E)$ . Thus,  $M(E)$  defines a mobility edge with adjustable width  $W_M$ . At high energies  $M(E)$  is zero (all excitons are mobile) and at low energies  $M(E)$  is unity (all excitons are localized).

– At time  $t = 0$  the ultrashort laser pulse excites a sharp population of excitons at  $E_{\text{laser}}$  only.

This model was computed by iteration for discrete energy levels and discrete times to fit the experimental data. Fig. 5 shows the result of fitting a set of three transients and the luminescence band using the same set of fit parameter values for width and energy of the mobility edge and of the exciton DOS, transition probability  $W$ , and recombination time  $\tau_0$ . The reasonably good fit of the time-integrated luminescence given by the mean value of population at each energy over the entire time window (Fig. 5a), as well as of the transients (Fig. 5b) underscores the true value of the model used. The slow down of the decay for later times at high energies (here 2.6906 eV) is well reproduced (in this example even too strong). However, fitting the extremely fast rise of the transients even at low energies by assuming a high relaxation probability makes the fits at higher energies much faster in rise and decay than experimental data. Therefore, the model gives too fast behavior at high energies and too slow behavior at low energies. To explain the fast onset of luminescence at lower energies excitons can be assumed to be created in a non- $k$ -conserving process in areas of wider well width having large kinetic energy, being followed by very fast relaxation to optically active states at  $k \approx 0$ . Or, exciton recombination under phonon emission which contributes to the luminescence at lower energies leading to a fast component in the transient (see section 4.2). However, the luminescence of the particular sample in Fig. 5 does not show resolved phonon replica. Thus, phonon coupling is not very strong. Both mechanisms were not included in the model in order to keep the number of unknown parameters small.

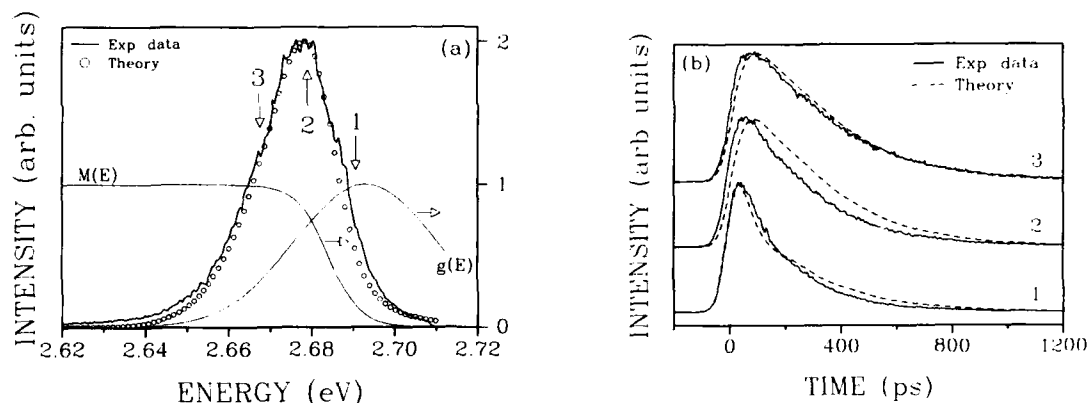


Fig. 5. Experimental data of a 1 ML SQW in comparison with fitted results of the model: (b) experimental (solid lines) and theoretical (dashed lines) transients taken at three different energies of detection, see (a); (a) experimental (solid line) and theoretical (open circles) time-integrated luminescence spectrum of the sample. DOS of excitons  $g(E)$  (dotted line), and mobility edge  $M(E)$  (dashed lines). Labels (1), (2), and (3) refer to the energy positions where the transients shown in (b) are taken.  $E_{\text{laser}}$  amounts to 2.712 eV.

#### 4.2. Exciton-phonon coupling

Let us now consider the sharp features superimposed on the broad luminescence band in case of resonant excitation (see Fig. 2). The line at lower energies, which is spectrally better resolved, occurs 32 meV apart from the excitation energy  $E_{\text{laser}}$ . This energy amounts to that of LO phonons,  $E_{\text{LO,ZnSe}}$ , in bulk ZnSe [4]. Here, different explanations are possible. First, part of the exciting photons may directly create a ZnSe LO phonon and a quantum-well exciton at the energy  $E_{\text{laser}} - E_{\text{LO,ZnSe}}$ , leading to an enhanced exciton population and, thus, enhanced luminescence intensity. Secondly, relaxation of resonantly excited excitons by LO phonon emission subsequent to the exciting pulse is possible. In both cases, the transient decay behavior of the luminescence at a fixed energy should be independent of the occurrence of a phonon replica at that energy. From time resolved measurements this was concluded to be the case in  $\text{Cd}_x\text{Zn}_{1-x}\text{Te}/\text{ZnTe}$  quantum wells by Stanley et al. [9], in  $\text{CdTe}/\text{ZnTe}$  quantum wells by Kalt et al. [10], and in  $\text{Cd}_x\text{Zn}_{1-x}\text{Se}/\text{ZnSe}$  quantum wells by ourselves [11]. In contrast to this, in  $\text{CdSe}/\text{ZnSe}$  the transient behavior depends on the excitation energy showing a faster decay if  $E_{\text{laser}} = E_{\text{detect}} + E_{\text{LO,ZnSe}}$ .

According to this, at fixed  $E_{\text{laser}}$  the decay slows down if  $E_{\text{detect}}$  is slightly detuned from the sharp replica line (see Fig. 4). From this we conclude that the line is a 1 LO phonon replica of recombining excitons resonantly excited at  $E_{\text{laser}}$ . Here, the phonons are emitted at the time the excitons recombine radiatively. Therefore, the transient behavior of the luminescence on a replica is composed of the transient behavior of the exciton population at  $E_{\text{laser}}$  (fast, 1 LO replica luminescence) and at  $E_{\text{detect}}$  (slower, phonon-free luminescence).

The second line observed 13 meV below  $E_{\text{laser}}$  is rather hard to detect in time-resolved measurements, because it is broader than the phonon replica discussed above and is placed on a much larger background of broad excitonic emission (see Fig. 2). Its energy separation of 13 meV does not equal any known phonon in bulk CdSe or ZnSe. It might be a phonon replica caused by a phonon mode of the CdSe layer, but this cannot be unambiguously decided at this stage.

#### 4.3. Exciton lifetime versus well width

As can be seen from Fig. 1,  $\tau_d$  decreases monotonically with decreasing well width. The reason for this is the growing overlap between the

electron and the hole wavefunctions for decreasing well width. This behavior is expected theoretically and also observed experimentally in 2D quantum wells [12,13]. For very small well widths, the wave function of the electron with its smaller mass extends considerably into the barrier material, resulting in  $\tau_d$  to increase again. This was observed in a III–V semiconductor [14]. Due to their smaller exciton Bohr radii, it is questionable whether this effect occurs in II–VI semiconductors. In the CdSe/ZnSe samples under investigation, an increase of  $\tau_d$  is not observed even for smallest widths.

The difference between the decay times of the 2 ML and the 3 ML wells is remarkably small. We attribute this to the minor quality of the 3 ML well which seems to be near the critical thickness of the CdSe/ZnSe system. In this case, competing non-radiative recombination channels reduce the effective lifetime of excitons. This is also confirmed by the weak luminescence intensity of the 3 ML well.

## 5. Conclusions

In conclusion, we want to recall three important results. First, from comparison between experimental data and the theoretical model presented here, it becomes clear that in CdSe/ZnSe QWs part of the excitons in a random potential remain localized even at high energies. Thus, the system has to be described by at least two relaxation probabilities at a given energy  $E$ . This conclusion seems to be valid also for ternary bulk II–VI semiconductors like  $\text{CdS}_{1-x}\text{Se}_x$  [8]. Secondly, we have shown that our SME-grown CdSe/ZnSe SQWs exhibit very unusual properties which are, in our opinion, very promising for future application as active layers in optoelectronic devices. Those are the large blue shift and brightness of the excitonic emission, the small well width fluctuations and the relatively long lifetime of excitons (up to 250 ps in localized states of 1 ML samples) compared to the life-

times measured in  $\text{Zn}_{1-x}\text{Cd}_x\text{Se/ZnSe}$  [11] or  $\text{Zn}_{1-x}\text{Cd}_x\text{Te/ZnTe}$  QWs [9]. Further, we observed ZnSe LO phonon replica of radiatively recombining excitons, a behavior which differs from that in systems like CdTe/ZnTe or  $\text{Zn}_{1-x}\text{Cd}_x\text{Se/ZnSe}$  quantum wells, where the occurrence of similar lines is attributed to exciton relaxation by LO phonon emission.

## 6. Acknowledgement

The authors would like to thank Prof. Dr. J. Gutowski for helpful discussions.

## 7. References

- [1] See, e.g., invited papers of 6th Int. Conf. on II–VI Compounds and Related Optoelectronic Materials, Newport, RI, 1993 [J. Crystal Growth 138 (1994)].
- [2] H. Zajicek, P. Juza, E. Abramof, O. Pankratov, H. Sitter, M. Helm, G. Brunthaler and W. Faschinger, Appl. Phys. Lett. 62 (1993) 717.
- [3] W. Faschinger, P. Juza, S. Ferreira, H. Zajicek, A. Pesek, H. Sitter and K. Lischka, Thin Solid Films 225 (1993) 270.
- [4] Landolt–Börnstein, New Series, Vol. 17, Subvolume b, Eds. O. Madelung, M. Schulz and H. Weiss (Springer, Berlin, 1982).
- [5] N. Samarth, H. Luo, J.K. Furdyna, S.B. Qadri, Y.R. Lee, A.K. Ramdas, and N. Otsuka, Appl. Phys. Lett. 54 (1989) 2680.
- [6] S. Permogorov and A. Reznitzky, J. Luminescence 52 (1992) 202.
- [7] E. Cohen and M. Sturge, Phys. Rev. B 25 (1982) 3828.
- [8] C. Gourdon and P. Lavallard, Phys. Status Solidi (b) 153 (1989) 641.
- [9] R.P. Stanley, J. Hegarty, R. Fischer, J. Feldmann, E.O. Göbel, R.D. Feldman and R.F. Austin, Phys. Rev. Lett. 67 (1991) 128.
- [10] H. Kalt, J. Collet, S.D. Baranovskii, R. Saleh, P. Thomas, L.S. Dang and J. Cibert, Phys. Rev. B 45 (1992) 4253.
- [11] U. Neukirch, D. Weckendrup, J. Gutowski, D. Hommel and G. Landwehr, J. Crystal Growth 138 (1994) 861.
- [12] E.O. Göbel, J. Kuhl and R. Höger, J. Luminescence 30 (1985) 541.
- [13] J. Cui, H.-L. Wang, F.-X. Gan, X.-G. Huang, Z.-G. Cai, Q.-X. Li and Z.-X. Yu, Appl. Phys. Lett. 61 (1992) 1540.
- [14] U. Cebulla, G. Bacher, A. Forchel, G. Mayer and W.T. Tsang, Phys. Rev. B 39 (1989) 6257.



ELSEVIER

Journal of Crystal Growth 138 (1994) 856–860

JOURNAL OF **CRYSTAL  
GROWTH**

## Many body effects in transient luminescence spectra of a homogeneous electron–hole plasma in CdTe/CdMnTe quantum wells

G. Bacher <sup>\*,a</sup>, F. Daiminger <sup>a</sup>, A. Forchel <sup>a</sup>, A. Waag <sup>b</sup>, Th. Litz <sup>b</sup>, G. Landwehr <sup>b</sup>

<sup>a</sup> Technische Physik, Universität Würzburg, Am Hubland, D-97074 Würzburg, Germany

<sup>b</sup> Experimentelle Physik III, Universität Würzburg, Am Hubland, D-97074 Würzburg, Germany

### Abstract

Using time resolved photoluminescence spectroscopy, we have investigated many body effects and the dynamics of a high density electron–hole plasma in strained CdTe/CdMnTe quantum wells. Great care has been taken to achieve a spatially homogeneous plasma by mesa etching of single quantum well structures. Our experimental data show strong band filling effects up to the barrier energy due to the Pauli principle within a few tenths of ps. A lineshape analysis yields plasma densities up to  $2 \times 10^{12} \text{ cm}^{-2}$  and carrier temperatures up to 335 K (bath temperature 2 K). A band gap renormalization of the emission spectrum up to around 23 meV as compared to a low excitation reference spectrum is observed. The reduction of the carrier density due to recombination causes an increase of the emission intensity at the 1e–1hh exciton transition, indicating an enhancement of the oscillator strength below the Mott density.

As semiconductor laser structures operate at high carrier densities, many body effects as well as the dynamics of the electron–hole plasma have become of great interest during the last years. A lot of experimental and theoretical work has been done especially for III–V quantum well heterostructures due to the application of these systems for optoelectronic devices [1–4]. Typical many body effects like band filling due to the Pauli principle or band gap renormalization due to exchange correlation effects were quantitatively analyzed by a lineshape fit of photolumi-

nescence spectra of the spatially homogeneous electron–hole plasma [3]. Recently, new optoelectronic device prospects on the base of II–VI heterostructures have caused intense investigations mainly in the wide gap ZnSe system [5]. On the other hand, II–VI compounds on the base of CdTe, as for example CdTe/CdMgTe [6] are able to cover the whole visible spectral range. In CdTe/CdMgTe as well as CdTe/CdMnTe heterostructures, stimulated emission was reported recently [7,8], indicating the potential of these systems for optoelectronic applications. However, not only from the viewpoint of applications, but also due to the basic physics, the study of many body effects and the dynamics of the high density electron–hole plasma in II–VI heterostructures

\* Corresponding author.

is of great interest. One point of interest is the role of excitonic effects in wide gap II–VI heterostructures even at high excitation densities [5,9,10].

In this paper we present time-resolved optical studies on a high density electron–hole plasma in CdTe/CdMnTe quantum wells. A spatially homogeneous plasma was achieved using single quantum well mesa structures with lateral extensions smaller than the laser beam diameter used for excitation. Band filling up to the barrier energy occurs within a few tenths of ps. Many body effects cause a strong red shift due to band gap renormalization. A quantitative description of the high density plasma emission spectra was performed using a lineshape analysis. If the carrier density is reduced below the Mott density by recombination, an increase of the spectrally resolved emission intensity at the 1e–1hh exciton transition indicates an enhancement of the oscillator strength.

The single quantum well structures were grown by molecular beam epitaxy at a growth temperature of 230°C on a (100) oriented CdTe substrate. The CdTe layer was embedded between a 200 nm CdMnTe buffer layer and a 30 nm CdMnTe cap layer. A Mn content of about 12% was chosen for the barrier layers. Mesa structures with an extension of  $50\text{ }\mu\text{m} \times 50\text{ }\mu\text{m}$  were obtained by electron beam lithography and wet chemical etching using a  $\text{Br}_2$  in ethylene glycol solution. The electron–hole plasma was excited by a mode-locked, compressed and frequency doubled Nd–YAG laser. The pulse width was about 3 ps and taking into account the repetition rate of 82 MHz, a maximum peak intensity of about  $3\text{ MW}/\text{cm}^2$  could be achieved. The transient luminescence spectra were dispersed by a 0.3 m monochromator and detected by a streak camera with S1 photocathode. The overall time resolution of the setup is about 15 ps. All experiments are performed at a bath temperature of 2 K.

In Fig. 1 we have plotted the transient photoluminescence (PL) spectra of a 5 nm CdTe/CdMnTe quantum well. Several interesting features can be seen directly in the PL spectra. At short delay times, the emission is dominated by the barrier signal. Due to an efficient capture,

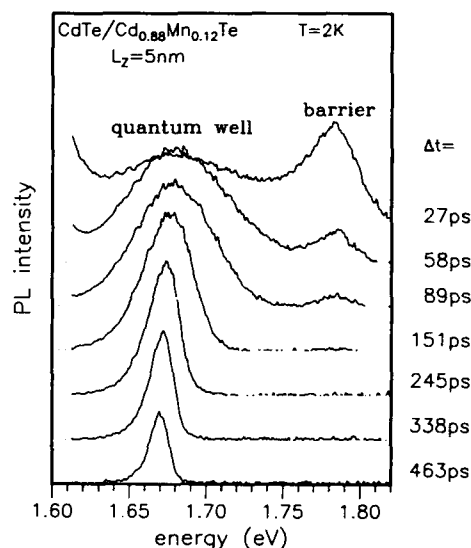


Fig. 1. Transient PL spectra of a 5 nm CdTe/CdMnTe quantum well structure. The peak excitation density was about  $3.2\text{ MW}/\text{cm}^2$ . The spectra are not normalized, but vertically shifted for clarity. The PL signal at around 1.6 eV originates from the substrate and can be observed at short delay times for high excitation densities.

the intensity of the barrier emission decays within a few tenths of ps, causing a high density electron–hole plasma in the quantum well. The broadening of the spectra due to band filling as well as a red shift of the low energy tail of the luminescence line due to exchange correlation effects is clearly demonstrated. With increasing time a narrowing of the PL spectrum is observed, caused on the one hand by an efficient cooling of the hot carrier system and on the other hand by a reduction of the plasma density due to recombination. In this structure there is only one subband in the conduction band and the light hole subband edge is strongly shifted to higher energy due to strain effects. Thus, only one emission peak of the quantum well luminescence, related to the 1e–1hh transition, can be observed.

Due to the Pauli principle, the intensity of the low energy tail of the emission spectrum saturates for high plasma densities. Further increasing the excitation power results in a broadening of the luminescence line. As can be seen in Fig. 1 the



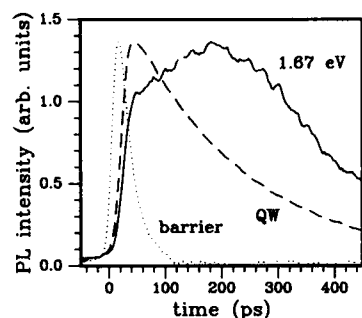


Fig. 2. PL intensity as a function of time for the integrated barrier signal (dotted line), the spectrally integrated quantum well signal (dashed line) and the spectrally resolved PL signal at 1.67 eV, corresponding to the energy of the low excitation 1e–1hh exciton transition (solid line).

states of the quantum well can be completely filled up to the barrier energy. This is a consequence of the discontinuity distribution between the conduction and the valence band  $\Delta Q_C/\Delta Q_V = 70/30$  [11] and the ratio of the electron and the heavy hole in plane masses of about 1/1.5 as calculated from the Luttinger–Kohn parameters [12]. Energy and momentum conservation results in an almost equal band filling of the potential wells in the conduction and the valence band. This is completely different as compared for example to the InGaAs/InP system, where a maximum broadening of the emission spectrum of only 1/3 of the total discontinuity between the quantum well and the barrier can be observed. In this system the discontinuity distribution is about  $\Delta Q_C/\Delta Q_V = 35/65$  resulting in a maximum linewidth of the plasma luminescence spectrum corresponding to the depth of the potential well in the conduction band.

The influence of excitonic effects even at high carrier densities is demonstrated in Fig. 2. The PL intensity as a function of time is compared for the integrated barrier signal (dotted line), the spectrally integrated quantum well luminescence (dashed line) and the spectrally resolved signal at  $E = 1.67$  eV, corresponding to the energy of the low excitation 1e–1hh exciton transition (solid line). The lifetime of the integrated quantum well signal is found to be about 210 ps. The carrier collection from the barrier occurs within 25 ps,

controlling the decay of the barrier signal as well as the onset of the integrated quantum well emission.

Regarding the dynamics at  $E = 1.67$  eV (solid line), we also observe at first a fast onset due to carrier collection. However, an additional delayed increase is found within a few hundreds of ps after the collection process from the barrier states. This effect was observed in all CdTe/CdMnTe structures under investigation. We attribute this to the formation of excitons if the plasma density is reduced below the Mott transition due to recombination. The associated enhancement of the oscillator strength causes an increase of the spectrally resolved PL intensity at  $E = 1.67$  eV. This is in contrast to experiments in III–V quantum well structures as, e.g., reported by Daiminger et al. [13] or Deveaud et al. [14], where a PL intensity independent of time at the low energy tail of the plasma emission was observed during more than 1 ns after the carrier collection process. Plasma recombination in this high density region mainly causes a narrowing of the spectrum, leaving the PL intensity of the energetically lowest 1e–1hh transition unchanged. In II–VI heterostructures, however, the excitonic enhancement of the oscillator strength is expected to be especially pronounced due to the large excitonic binding energies in these systems causing the observed increase of the PL intensity due to the formation of excitons.

To obtain quantitative values for the density and the temperature of the electron–hole plasma and the band gap renormalization, we have performed a lineshape analysis based on the model of Tränkle et al. [1]. We used parabolic bands characterized by the in-plane masses as calculated from the Luttinger–Kohn parameters and constant matrix elements. A broadening due to intervalley relaxation after the method of Landsberg [15] is included. In Fig. 3 we have compared the experimental data (dots) as obtained from time-resolved photoluminescence measurements with calculated spectra (solid lines). The high energy tail of the spectra is determined by the carrier temperature, whereas the spectral linewidth is mainly given by the density of the electron–hole plasma. An excellent agreement be-

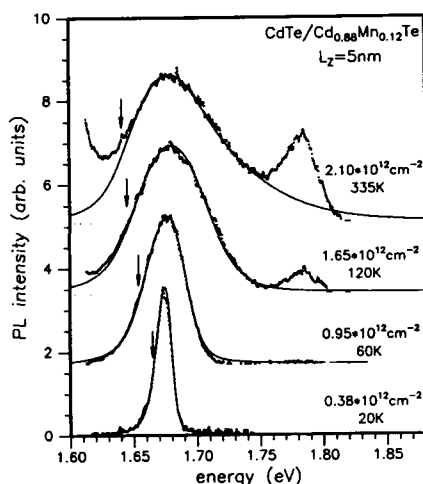


Fig. 3. Typical high excitation spectra of a 5 nm CdTe/CdMnTe quantum well as obtained from experiments (dots) and from a lineshape analysis (solid lines) as described in the text. The experimental data corresponds to transient PL spectra at  $\Delta t = 42, 73, 151$  and  $463$  ps (from top to bottom), respectively. The arrows indicate the red shift of the band gap due to many body effects.

tween the experimental data and the theoretical spectrum is obtained, yielding densities up to  $2 \times 10^{12} \text{ cm}^{-2}$  and temperatures between 20 and 335 K.

In a high density electron–hole plasma, exchange correlation effects cause a red shift of the characteristic emission line due to band gap renormalization. This is indicated by the arrows in Fig. 3. From the low energy tail of the spectra, we obtain a red shift of about 23 meV for a carrier density of  $2 \times 10^{12} \text{ cm}^{-2}$  as compared to the low excitation spectrum. As the band gap renormalization is commonly related to the band edge of the transition between the first subbands of the conduction and the valence band, the observed red shift corresponds to a band gap renormalization of 43 meV, taking into account an exciton binding energy of about 20 meV [16]. This value is in good agreement with experimental data of different III–V quantum well heterostructures as reported for example by Kulakovskii et al. [3] and Lach et al. [17], indicating the fundamental relevance of exchange correla-

tion effects for the fundamental band gap of different semiconductor materials.

In summary we have studied many body effects and the dynamics of a high density spatially homogeneous electron–hole plasma in CdTe/CdMnTe quantum wells using time resolved photoluminescence spectroscopy. The transient emission spectra were analyzed quantitatively by a lineshape analysis. Carrier densities up to  $2 \times 10^{12} \text{ cm}^{-2}$  and plasma temperatures up to 335 K were obtained, causing band filling up to the barrier energy within a few tenths of ps. Exchange correlation effects lead to a band gap renormalization up to 43 meV. If the carrier density is reduced below the Mott density by recombination, a delayed increase of the intensity at the 1e–1hh exciton transition indicates an enhancement of the oscillator strength due to exciton formation.

We are grateful to M. Illing for the preparation of the mesa structures. The financial support of the Bayerische Forschungsförderung is gratefully acknowledged.

## 1. References

- [1] G. Tränkle, H. Leier, H. Haug, C. Ell and G. Weimann, Phys. Rev. Lett. 58 (1987) 419.
- [2] S. Schmitt-Rink, D.S. Chemla and D.A.B. Miller, Adv. Phys. 38 (1989) 89.
- [3] V.D. Kulakovskii, E. Lach, A. Forchel and D. Grützmacher, Phys. Rev. B 40 (1989) 8087.
- [4] R. Cingolani, H. Kalt and K. Ploog, Phys. Rev. B 42 (1990) 7655.
- [5] A.V. Nurmikko and R.L. Gunshor, J. Luminescence 52 (1992) 89.
- [6] A. Waag, H. Heinke, S. Scholl, C.R. Becker and G. Landwehr, J. Crystal Growth 131 (1993) 607.
- [7] G. Bacher, A. Forchel, A. Waag and G. Landwehr, to be published.
- [8] J. Cibert, C. Bodin-Deshayes, G. Feuillet, P.H. Joneau, Le Si Dang and E. Molva, Mater. Sci. Eng. B 16 (1993) 279.
- [9] C. Klingshirn, J. Crystal Growth 117 (1992) 753.
- [10] Y. Masumoto, B. Fluegel, K. Meissner, S.W. Koch, R. Binder, A. Paul and N. Peyghambarian, J. Crystal Growth 117 (1992) 732.
- [11] B. Kuhn-Heinrich, W. Ossau, M. Popp, E. Bangert, A. Waag and G. Landwehr, in: Proc. 21st Int. Conf. on Physics of Semiconductors, ICPS-21, Beijing, 1992 (World Scientific, Singapore, 1992) p. 923.
- [12] Landolt-Börnstein, New Series III/22a Semiconductors: Intrinsic Properties of Group IV Elements and III–V.

- II–VI and I–VII Compounds, Ed. O. Madelung (Springer, Berlin, 1987).
- [13] F. Daiminger, B. Neppert, A. Forchel and J. Straka, *Phys. Status Solidi (b)* 173 (1992) 397.
- [14] B. Deveaud, F. Clérot, A. Regreny and K. Fujiwara, *Superlattices Microstruct.* 8 (1990) 85.
- [15] P.T. Landsberg, *Phys. Status Solidi* 15 (1966) 623.
- [16] Calculated using a variational approach according to J.A. Brum and G. Bastard, *J. Phys. C (Solid State Phys.)* 18 (1985) L789.
- [17] E. Lach, A. Forchel, D.A. Broido, T.L. Reinecke, G. Weimann and W. Schlapp, *Phys. Rev. B* 42 (1990) 5395.



ELSEVIER

Journal of Crystal Growth 138 (1994) 861–867

JOURNAL OF  
**CRYSTAL  
GROWTH**

## Dynamical properties of excitons in $\text{Zn}_{1-x}\text{Cd}_x\text{Se}/\text{ZnSe}$ quantum wells and $\text{Zn}_{1-x}\text{Cd}_x\text{Se}$ epilayers grown by molecular beam epitaxy

U. Neukirch<sup>a</sup>, D. Weckendrup<sup>a</sup>, J. Gutowski<sup>\*a</sup>, D. Hommel<sup>b</sup>, G. Landwehr<sup>b</sup>

<sup>a</sup> Institut für Experimentelle Physik, Universität Bremen, P.O. Box 330 440, D-28334 Bremen, Germany

<sup>b</sup> Physikalisches Institut, Universität Würzburg, Am Hubland, D-97074 Würzburg, Germany

### Abstract

$\text{Zn}_{1-x}\text{Cd}_x\text{Se}/\text{ZnSe}$  single quantum wells (SQWs) and  $\text{Zn}_{1-x}\text{Cd}_x\text{Se}/\text{GaAs}$  epilayers grown by molecular beam epitaxy are investigated by picosecond time-resolved luminescence spectroscopy as well as by time integrated luminescence, reflection, and transmission spectroscopy. The well thicknesses of the SQW samples are 3.3 and 5 nm, and the Cd contents amount to 0.09, 0.18, and 0.20, respectively. Whereas the epilayer luminescence is dominated by free-exciton emission, the SQW luminescence exhibits free and bound-exciton bands of comparable intensity. The decay times of the luminescence are shorter than 140 ps in any case. When tuning the energy of detection,  $E_{\text{det}}$  over the free-exciton band, the decay time decreases for increasing energy. This is also known from other localizing ternary systems like  $\text{Cd}_{1-x}\text{S}_x\text{Se}$  or  $\text{CdSe}/\text{ZnSe}$ . In contrast to those systems, the transient behavior of the luminescence in the  $\text{Zn}_{1-x}\text{Cd}_x\text{Se}$  samples exhibits a simple exponential rise and decay even at high  $E_{\text{det}}$ . This is probably caused by the short length scale of the localizing potential. At high excitation densities emission from recombining biexcitons is observed in the SQWs.

### 1. Introduction

The first II–VI laser diodes presented in 1991 contained ternary  $\text{Zn}_{1-x}\text{Cd}_x\text{Se}$  as material for the active layer [1,2]. Thus,  $\text{Zn}_{1-x}\text{Cd}_x\text{Se}$  belongs to the few II–VI semiconductors used in an optoelectronic device up to now. In spite of that success, little is known for this material about localization, relaxation and recombination dynamics of excitons which dominate the optical properties over a wide range of carrier densities and, in case of quantum wells, a wide range of temperatures [3]. In this paper a detailed investi-

gation on the dynamical properties of excitonic luminescence in  $\text{Zn}_{1-x}\text{Cd}_x\text{Se}/\text{ZnSe}$  single quantum wells and  $\text{Zn}_{1-x}\text{Cd}_x\text{Se}$  epilayers is presented.

### 2. Experimental setup

All investigated samples were grown by molecular beam epitaxy (MBE) in a 3-chamber Riber 2300 system using elemental source materials Zn, Cd, and Se. All structures and epilayers were grown on semi-insulating (100)GaAs substrates.  $\text{Zn}_{1-x}\text{Cd}_x\text{Se}/\text{ZnSe}$  single quantum wells (SQWs) of 3.3 nm thickness and epilayers were grown with a Se:Zn beam pressure ratio of 2:1 and

\* Corresponding author.

cadmium contents of  $x = 0.09$  and  $0.20$ , respectively. Recently, a new growth chamber for GaAs has been interconnected to the three II–VI chambers. This allows a careful oxygen desorption under As overpressure and the growth of GaAs buffer layers. SQW samples with thicknesses of 3.3 or 5 nm and a Cd content of  $x = 0.18$  were deposited on such buffer layers. Here, the thicknesses of the whole structures were chosen to be 150 nm in order not to exceed the critical thickness for ZnSe growth on GaAs and, thus, to avoid generation of misfit dislocations in the well region. The thicknesses of the  $\text{Zn}_{1-x}\text{Cd}_x\text{Se}/\text{GaAs}$  epilayers amount to 1  $\mu\text{m}$ .

The optical investigations were performed in superfluid helium at  $T = 1.6$  K.

### 2.1. Time-resolved luminescence spectroscopy

The transient behavior of the luminescence was measured by time-correlated single photon counting. For excitation of the samples, the frequency-doubled light of a mode-locked titanium-sapphire laser running at 4 or 82 MHz repetition rate is used. The pulse duration amounts to 1.5 ps with energies up to 4 nJ/pulse. After being dispersed by a subtractive double-monochromator of 320 mm focal length, the luminescence photons are detected by a microchannel-plate photomultiplier tube (MCP-PMT). Part of the laser light is used to illuminate a photodiode for triggering. The system response (including electronics) to the short laser pulse itself reveals a FWHM of about 50 ps. Detection is performed in a direction rectangular to the exciting beam with the sample slightly tilted off  $45^\circ$  to avoid direct reflection of the laser beam into the monochromator.

### 2.2. Time-integrated spectroscopy

The usual time-integrated luminescence spectra are obtained with the setup described in section 2.1 by counting all of the detection pulses from the MCP-PMT while tuning the monochromator.

Excitation spectroscopy is performed by use of an excimer-pumped dye laser (10 ns pulses) for

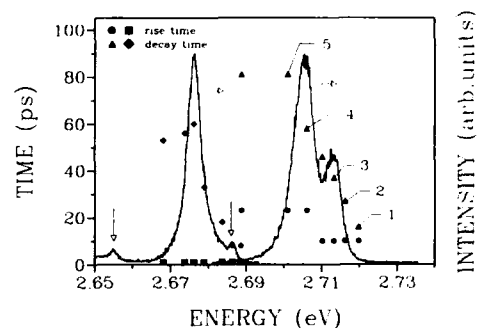


Fig. 1. Luminescence spectra of a  $\text{Zn}_{0.91}\text{Cd}_{0.09}\text{Se}$  epilayer (left band,  $E_{\text{laser}} = 2.719$  eV) and a  $\text{Zn}_{0.91}\text{Cd}_{0.09}\text{Se}/\text{ZnSe}$  SQW ( $E_{\text{laser}} = 2.739$  eV). For structures marked by arrows, see text. Additionally, fitted rise times and decay times are given for different energies. Labels 1 to 5 refer to the transients given in Fig. 3.

excitation and a 0.85 m double monochromator equipped with a photomultiplier for detection. In reflection spectroscopy a halogen lamp is used for excitation. For transmission spectroscopy a piece of one SQW sample was released from the GaAs substrate by grinding followed by selective etching.

### 3. Experimental results

All samples under investigation exhibit bright excitonic luminescence which is, in case of the epilayers, dominated by a single line (see Fig. 1). By comparison with reflection spectra, this emission is proven to be recombination radiation of free excitons (FEs). Its full width at half maximum (FWHM) amounts to 4.5 and 5.0 meV for  $x = 0.09$  and  $0.20$ , respectively. The ternary system  $\text{Zn}_{1-x}\text{Cd}_x\text{Se}$  under investigation is expected to localize excitons in a random potential which is caused by composition fluctuations in epilayers and, in addition to this, by well width fluctuations in the SQWs (see, e.g., the review [4]). This should be kept in mind when the term “free excitons” is used for simplicity in the following as a distinction to impurity-bound excitons.

In contrast to the bulk ternary layers, the luminescence of the SQWs is composed of two

overlapping lines exhibiting comparable intensity. From reflection spectroscopy it is found that the line at higher energies belongs to recombination radiation of free well excitons for all SQW samples. This was also confirmed by absorption spectroscopy performed on a substrate-free piece of a SQW sample [5]. The energy separation of the maxima of these two lines scatters between 8 and 11 meV for different samples. Their intensity ratio  $R = I_{FE}/I_L$  ( $I_{FE}$  = intensity of free exciton line and  $I_L$  = intensity of low-energy line) depends on the energy of excitation as well as on the excitation intensity. Fig. 2 shows sets of luminescence spectra taken at different excitation intensities for two SQW samples. The luminescence spectra are normalized with respect to the actual excitation intensity. Obviously, the dependence of the intensity ratio  $R$  on excitation intensity is opposite. While for the 5 nm well the free-exciton luminescence gains relatively in intensity (Fig. 2a), this is valid for the low-energy line of the 3.3 nm well (Fig. 2b).

The epilayer luminescence (Fig. 1) exhibits two additional small and sharp lines besides the exciton band at 2.654 and 2.686 eV, respectively. When the energy of the exciting laser is tuned, these lines also shift. Their distances to the energy of excitation remain constant and amount to 32 and 64 meV, respectively. Similar spectral features are also observed for the SQW samples.

Time-resolved spectroscopy yields a very fast transient behavior of the dominant luminescence bands possessing decay times shorter than 130 ps at any energy in any sample. The data are presented for a  $\text{Zn}_{0.91}\text{Cd}_{0.09}\text{Se}$  SQW and the corresponding epilayer in Fig. 1 (left-hand axis). The time values  $\tau_r$  and  $\tau_d$  given in the figure are results of fitting an exponential rise and decay (see Eq. (1)) to the experimental transients:

$$I(t) \sim (\tau_r - \tau_d)^{-1} [\exp(-t/\tau_r) - \exp(-t/\tau_d)]. \quad (1)$$

For comparison with experimental data, the computed curves were convoluted with the system's response (FWHM  $\approx 50$  ps) to the ultrashort laser pulse; this procedure gives an accuracy for the fitted rise and decay times of about  $\pm 5$  ps. For decreasing energy of detection, the rise times  $\tau_r$  and decay times  $\tau_d$  increase in all samples. The computed transients fit the experimental data quite well for more than two decades of dynamic range of the luminescence decay (Fig. 3). This is true for any energy of detection for the SQWs as well as for the epilayers. Table 1 shows  $\tau_d$  at the maximum of the excitonic luminescence band of the epilayers as well as at the two lines of the SQW samples. Due to the spectral overlap of the FE and the low-energy band in the SQWs, it is hard to derive a decay time of the latter in its maximum. Instead, the lowest-energy decay time

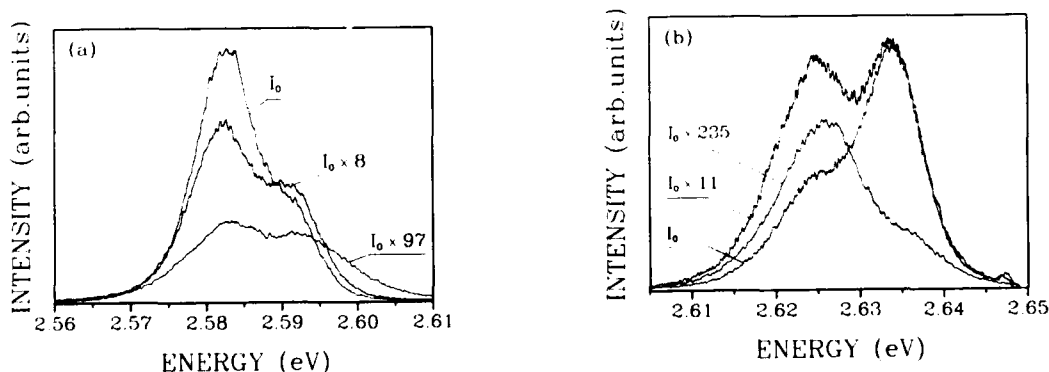


Fig. 2. Luminescence spectra of a 5 nm (a) and a 3.3 nm (b)  $\text{Zn}_{0.82}\text{Cd}_{0.18}\text{Se}$  SQW for different excitation intensities  $I_{exc}$ . The spectra are normalized to  $I_{exc}$ .  $I_0$  amounts to: (a)  $1.6 \text{ nJ cm}^{-2}$  per pulse; (b)  $1.0 \text{ nJ cm}^{-2}$  per pulse.

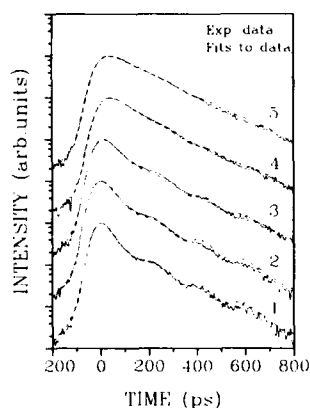


Fig. 3. Transient behavior of the luminescence of a  $\text{Zn}_{0.91}\text{Cd}_{0.09}\text{Se}/\text{ZnSe}$  SQW of 3.3 nm thickness taken at five different energies of detection (solid lines) in comparison to fitted curves (dashed lines). Labels 1 to 5 refer to the energy positions given in Fig. 1.

is given where overlap by the FE band is negligible. Obviously, the decay of free exciton luminescence in quantum wells is faster than that in the corresponding ternary “bulk” material.

Concerning the small peaks superimposed on the luminescence band under “resonant” excitation, no change of the transient behavior is observed at a fixed energy  $E_{\text{det}}$  if such a peak is tuned from another energy position onto  $E_{\text{det}}$ . Fig. 4 shows the luminescence spectrum of a  $\text{Zn}_{0.80}\text{Cd}_{0.20}\text{Se}/\text{ZnSe}$  SQW of 3.3 nm well width for resonant excitation whose energy was chosen to have one of the additional peaks just on top on the FE band. The decay times (triangles) added to the figure increase monotonically for decreasing energy of detection. Especially, the decay of

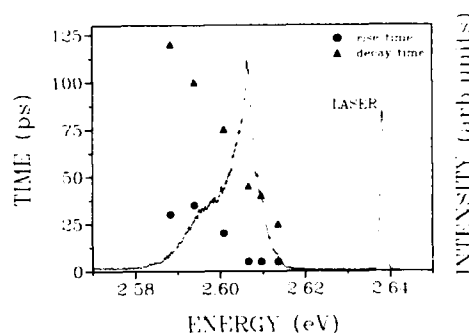


Fig. 4. Luminescence spectrum of a  $\text{Zn}_{0.80}\text{Cd}_{0.20}\text{Se}/\text{ZnSe}$  SQW of 3.3 nm thickness under resonant excitation into well states. A sharp feature occurs 32 meV below the energy of excitation. Additionally, the rise and decay times of the transients are given at different energies of detection.

the structure at 2.607 eV fits into the general trend.

#### 4. Discussion

The luminescence of the  $\text{Zn}_{1-x}\text{Cd}_x\text{Se}$  epilayers exhibits dominant emission of recombining free excitons. From their energy  $E_X$ , the cadmium content  $x$  can be computed. To do so we use the composition-dependent band gap  $E_G(x)$  calculated in ref. [6] which is in agreement with experimental data [7]. The exciton binding energy  $E_B(\text{FE})$  was linearly interpolated between the values for CdSe (15 meV) and ZnSe (20 meV) [8]. This yields cadmium contents of  $x = 0.09$ , 0.18, and 0.20, respectively.

The missing of bound exciton (BE) lines in the epilayer luminescence spectra, being quite unusual for  $\text{Zn}_{1-x}\text{Cd}_x\text{Se}$  systems (see refs. [4,7,9]), points to binding of free excitons to donors and acceptors to be less probable in these samples, indicating their good quality. In contrast to this, a second line occurs at the low-energy side of the free exciton emission in our SQW samples, being attributed to  $(\text{D}^0, \text{X})$  complexes of donor-bound excitons (compare ref. [6]). As expected for such a case, the intensity ratio  $R = I_{\text{FE}}/I_1$  decreases for increasing excitation intensity in the 5 nm sample (Fig. 2a), due to saturation of the number

Table 1  
Decay times (in ps) of the luminescence bands of free-exciton and bound-exciton emission in epilayer and SQW samples (well width 3.3 nm)

Composition	Epilayer: free exciton	QW	
		Free exciton	Second line
$\text{Zn}_{0.91}\text{Cd}_{0.09}\text{Se}$	60	37	81
$\text{Zn}_{0.82}\text{Cd}_{0.18}\text{Se}$	—	70	140
$\text{Zn}_{0.80}\text{Cd}_{0.20}\text{Se}$	65	60	130

of donor sites available for binding of free excitons. In excitation spectra, the free-exciton absorption occurs as a strong resonance of the BE emission. The binding energy derived from the energy separation to the FE band (8–11 meV) is well within the expected range for  $(D^0, X)$  systems. Bound-exciton binding energies in QW systems roughly obey a kind of Haynes rule, i.e. [10–12]

$$E_{B,L_z}(D^0, X) = f_H(L_z) E_D(L_z), \quad (2)$$

where  $f_H$  is the Haynes factor only weakly depending on the well width  $L_z$  and  $E_D(L_z)$  the donor ionization energy strongly increasing for  $L_z$  approaching and falling below the 3D donor radius. Thus, an increase of  $E_B(D^0, X)$  by a factor of 2–2.5 when compared to values in the bulk [13] is well understandable in the SQWs whose  $L_z$  values are close to the donor Bohr radii. Thus, BE emission in the SQWs, despite their absence in the epilayers (which are grown under identical conditions), may be caused by the increase of binding energy  $E_B(D^0, X)$  in QWs which enhances the capture cross section for FE. In addition to this, the creation of intrinsic defects at the interfaces of the wells may increase the density of donors in QWs.

As was explained in section 3 (Fig. 2b), the low-energy line gains more intensity than the free-exciton emission in the 3.3 nm SQW for increasing excitation intensity. The latter behavior was already measured without interpretation in bulk  $Zn_{0.21}Cd_{0.79}Se$  [9]. As the spectra of Fig. 2 are normalized to the excitation intensity, curves 1 and 2 clearly show that the intensity of the low-energy line increases superlinearly, while that of the free exciton increases linearly. From this, we suppose the occurrence of a high-excitation process which emits light in the same energy region as do the recombining  $(D^0, X)$  complexes. This interpretation becomes quite reasonable if the low-intensity luminescence spectra are directly compared. At low densities, the 3.3 nm SQW exhibits a weak  $(D^0, X)$  emission compared to the FE band, while the opposite situation is valid for the 5 nm SQW. Thus, free-exciton high-density effects are likely to occur for the first, but

may be suppressed for the second wider SQW by efficient exciton capture at donor centres. Since the energy separation of the high-density band with respect to the FE emission is too small to be explained by exciton–exciton collision (where  $dE \geq \frac{3}{4}E_B(FE)$ , the free-exciton binding energy), it is most probably due to biexciton formation in the SQW. Such superlinear biexciton-related bands have been found in ZnSe/ZnMnSe QWs [14]. The biexciton binding energy is not known for  $Zn_{1-x}Cd_xSe$  alloys, but amounts to 1.1–3.5 meV in ZnSe [15] and 0.8–1.2 meV in CdSe [16], so that roughly  $2 \pm 1$  meV have to be expected in  $Zn_{0.80}Cd_{0.20}Se$  bulk. A giant increase of the biexciton binding energy under quantum confinement has been reported for the ZnSe/ZnMnSe system [14] and confirmed by theoretical calculations in low-dimensional systems [17,11,18]. Since the biexciton wavefunction is spread much wider than the exciton Bohr radius, the biexciton/exciton binding energy ratio is increased by a factor of 3 to 4 in the 2D limit [14,17,11]. When, additionally taking the increase of the free-exciton binding energy in the 2D case into account, an increase of the biexciton binding energy by a factor of 5 to 10 compared to the 3D case as found in III–V materials at respective  $L_z/a_B$  ratios [17] is reasonable and thus also to be expected in the systems described here.

The overall decay time range of up to 130 ps is in rough agreement with results from spontaneous emission of a  $Zn_{0.82}Cd_{0.18}Se/ZnSe$  SQW [23] and of a  $Zn_{0.86}Cd_{0.14}Se/ZnSe$  superlattice [22] yielding 300 and 100 ps, respectively, obtained from rough estimations of spectrally not resolved decay data. Especially with regard to the rather short decay times when being compared with those in CdSe/ZnSe QWs [21], we definitely do not rule out competing nonradiative relaxation channels for free excitons in all presented cases.

The increase of the decay time  $\tau_d$  for decreasing energy of detection  $E_{det}$  found inside the free-exciton band for epilayers as well as for the SQW samples (Fig. 1) is characteristic for localized-exciton systems (see, e.g., refs. [19,20,4]). Having this aspect in mind, the transient behavior which is perfectly described by an exponential decay at any energy  $E_{det}$  is, on a first glance,



somewhat irritating for those transients taken on the FE emission (Fig. 1 and Fig. 3, curves 1 to 3). As is found in other localized II–VI systems like  $\text{CdS}_x\text{Se}_{1-x}$  bulk material [20,19] or  $\text{CdSe}/\text{ZnSe}$  SQWs [21], transients taken at the high-energy side of the exciton luminescence band behave in a complicated nonexponential manner. In ref. [21] we supposed that this complicated transient behavior is caused by different relaxation probabilities for excitons at a given energy  $E$ , due to the characteristics of the localizing potential which forces some excitons to remain localized in a local minimum since deeper adjoining minima are lacking. However, if the length scale of the fluctuations in potential energy is of the order of the exciton Bohr radius or even smaller, this idea does not work. Then, the relaxation probability depends on energy only, and the decay should behave exponentially, as is the case in our ternary samples.

Concerning bound excitons in ternary alloys, a purely exponential decay is expected, at least if it is dominated by radiative recombination, since relaxation effects in the random potential are suppressed by efficient localization of the excitons at the impurities. Such an exponential behavior was measured in  $\text{Zn}_{1-x}\text{Cd}_x\text{Te}$  [24], thus being in full agreement with our finding for all detection energies in the BE band regime. The BE band is broadened due to the fact that the BE binding energy should be roughly independent of local fluctuations so that the band shape resembles that of the FE. Because of missing relaxation, increasing decay time might not be expected for decreasing detection energy in the BE band regime; however, the true BE  $\tau_d$  values cannot be determined here due to the strong overlap of the BE and FE emission. Intentionally doped QW samples with dominating BE emission would be required for such a study. The step-like increase of rise time when shifting the detection from the FE onto the BE band indicates the time necessary to bind an FE to an impurity in the system.

The sharp spectral features superimposed on the exciton luminescence under resonant excitation are spaced by 32 meV from the energy of the exciting laser  $E_{\text{laser}}$  (see Figs. 1 and 2). This

energy amounts to that of a  $\text{ZnSe}$  bulk LO phonon. However, due to the small  $x$  values in our  $\text{Zn}_{1-x}\text{Cd}_x\text{Se}$  samples, it is hard to decide whether the phonons represent a  $\text{Zn}_{1-x}\text{Cd}_x\text{Se}$  mode or a  $\text{ZnSe}$  mode. Since the occurrence of these luminescence structures does not change the transient behavior at a given energy of detection (with respect to the nonresonant behavior), they are attributed to an enhanced exciton population. This enhancement is caused either by LO phonon assisted relaxation of excitons resonantly excited at  $E_{\text{laser}}$  or by direct excitation of LO phonons and excitons at  $E_{\text{laser}} - E_{\text{LO}}$  by the exciting photons. The first process is suggested to occur in  $\text{Cd}_x\text{Zn}_{1-x}\text{Te}/\text{ZnTe}$  quantum wells [25] as well as in  $\text{CdTe}/\text{ZnTe}$  quantum wells [26]. Both processes are leading to the same transient decay behavior, and thus, both or at least one of them is obviously responsible for the observed behavior in our samples. In contrast to this, in  $\text{CdSe}/\text{ZnSe}$  SQWs the sharp peaks are found to be phonon replicas of recombining hot excitons resonantly excited at  $E_{\text{laser}}$  [21]. Thus, the interesting question arises which material and structure parameters govern the dominance of one of these mechanisms in a given QW structure.

## 5. Conclusions

In conclusion, this investigation yielded optical properties of  $\text{Zn}_{1-x}\text{Cd}_x\text{Se}/\text{ZnSe}$  QWs which are of interest not only for basic research, but also for application in optoelectronic devices. First, binding of free excitons to donors is more likely in SQWs than in ternary epilayers. This may be caused by the increased binding energy  $E_B(D^0, X)$  of 8–11 meV and/or by increased generation of donor centres at the  $\text{Zn}_{1-x}\text{Cd}_x\text{Se}/\text{ZnSe}$  interface during growth. Secondly, at high excitation densities in SQW samples emission from recombining biexcitons occurs whose binding energy is found to exceed the 3D value by a factor of about 5 caused by quantum confinement. The unusually simple exponential transient behavior of the free exciton luminescence is probably caused by the short length scale of composition fluctuations or

by strongly competing nonradiative relaxation channels in  $\text{Zn}_{1-x}\text{Cd}_x\text{Se}$ .

## 6. Acknowledgements

The authors would like to thank Mr. K. Wundke for preparing the free standing SQW layer and Mr. F. Kubacki for measuring the excitation spectra. The assistance of Mrs. P. Wolf and Mr. T. Schumann in MBE substrate preparation is gratefully acknowledged.

## 7. References

- [1] M.A. Haase, J. Qiu, J.M. DePuydt and H. Cheng, *Appl. Phys. Lett.* 59 (1991) 1272.
- [2] H. Jeon, J. Ding, W. Patterson, A.V. Nurmikko, W. Xie, D.C. Grillo, M. Kobayashi and R.L. Gunshor, *Appl. Phys. Lett.* 59 (1991) 3619.
- [3] J. Ding, N. Pelekanos, A.V. Nurmikko, H. Luo, N. Samarth and J.K. Furdyna, *Appl. Phys. Lett.* 57 (1990) 2885.
- [4] S. Permogorov and A. Reznitzky, *J. Luminescence* 52 (1992) 202.
- [5] K. Wundke, D. Weckendrup, U. Neukirch and J. Gutowski, to be published.
- [6] H.J. Lozykowski and V.K. Shastri, *J. Appl. Phys.* 69 (1991) 3235.
- [7] N. Samarth, H. Luo, J.K. Furdyna, R.G. Alonso, Y.R. Lee, A.K. Ramdas, S.B. Qadri and N. Otsuka, *Appl. Phys. Lett.* 56 (1990) 1163.
- [8] Landolt-Börnstein, New Series, Vol. 17, Subvolume b, Eds. O. Madelung, M. Schulz and H. Weiss (Springer, Berlin, 1982) p. 319.
- [9] A.S. Nasibov, L.G. Suslina, D.L. Fedorov, Y.V. Korostelin, P.V. Shapkin and L.S. Markov, *Soviet Phys.-Solid State* 31 (1989) 1691.
- [10] R.C. Miller, A.C. Gossard, W.T. Tang and O. Munteanu, *Solid State Commun.* 43 (1982) 519.
- [11] D.A. Kleinman, *Phys. Rev. B* 28 (1983) 871.
- [12] W.T. Masselink, Y. Chang and H. Morkoç, *Phys. Rev. B* 32 (1985) 5190.
- [13] J. Gutowski, N. Presser and G. Kudlek, *Phys. Status Solidi (a)* 120 (1990) 11.
- [14] Q. Fu, D. Lee, A. Mysyrowicz, A.V. Nurmikko, R.L. Gunshor and L.A. Kolodziejski, *Phys. Rev. B* 37 (1988) 8791.
- [15] O. Akimoto and E. Hanamura, *Solid State Commun.* 10 (1972) 253;  
W.T. Huang, *Phys. Status Solidi (b)* 60 (1973) 309;  
Y. Nozue, M. Itoh and K. Cho, *J. Phys. Soc. Japan* 50 (1981) 889.
- [16] J. Gutowski and I. Broser, *J. Phys. C* 20 (1987) 3771.
- [17] R.C. Miller, D.A. Kleinman, A.C. Gossard and O. Munteanu, *Phys. Rev. B* 25 (1982) 6545.
- [18] L. Banyai, I. Galbraith, C. Ell and H. Haug, *Phys. Rev. B* 36 (1987) 6099.
- [19] C. Gourdon and P. Lavallard, *Phys. Status Solidi (b)* 153 (1989) 641.
- [20] H. Schwab, C. Dörnfeld, E.O. Göbel, J.M. Hvam, C. Klingshirn, J. Kuhl, V.G. Lyssenko, F.A. Majumder, G. Noll, J. Nunnenkamp, K.H. Pantke, C. Renner, A. Reznitsky, U. Siegner, H.E. Swoboda and Ch. Weber, *Phys. Status Solidi (b)* 172 (1992) 479.
- [21] U. Neukirch, D. Weckendrup, W. Faschinger, P. Juza and H. Sitter, *J. Crystal Growth* 138 (1994) 849.
- [22] H. Jeon, J. Ding, A.V. Nurmikko, H. Luo, N. Samarth, J.K. Furdyna, W.A. Bonner and R.E. Nahory, *Appl. Phys. Lett.* 57 (1990) 2413.
- [23] J. Ding, H. Jeon, A.V. Nurmikko, H. Luo, N. Samarth and J.K. Furdyna, *Appl. Phys. Lett.* 57 (1990) 2756.
- [24] S.S. Yom, S. Perkowitz, P.M. Amirtharaj and J.J. Kennedy, *Solid State Commun.* 65 (1988) 1055.
- [25] R.P. Stanley, J. Hegarty, R. Fischer, J. Feldmann, E.O. Göbel, R.D. Feldman and R.F. Austin, *Phys. Rev. Lett.* 67 (1991) 128.
- [26] H. Kalt, J. Collet, S.D. Baranovskii, R. Saleh, P. Thomas, L.S. Dang and J. Cibert, *Phys. Rev. B* 45 (1992) 4253.



ELSEVIER

Journal of Crystal Growth 138 (1994) 868–872

JOURNAL OF  
**CRYSTAL  
GROWTH**

## Photo-induced screening of the excitonic interaction in ZnSe–ZnTe type II strained-layer superlattices

B. Gil \*, T. Cloitre, N. Briot, O. Briot, P. Boring, R.L. Aulombard

*Groupe d'Etudes des Semiconducteurs, Université de Montpellier II, Place Eugène Bataillon, Case Courrier 074, F-34095 Montpellier Cedex 5, France*

### Abstract

We report the observation of nonlinear optical properties of ZnSe–ZnTe superlattices under photo-injected carriers, at pumped liquid helium temperature. Identification of several transitions measured by transmission on samples grown by metalorganic vapour phase epitaxy and etched away from the GaAs substrate is made in the context of the envelope function approach. This reveals that the conduction to valence band line-ups are type II in these samples. This situation is invoked in order to interpret the efficiency of the exciton screening.

### 1. Introduction

During the last two decades, semiconductor physics has developed towards studies of low-dimensional systems made possible to synthesize due to the advent of modern growth techniques such as molecular beam epitaxy (MBE) or metalorganic vapour phase epitaxy (MOVPE). The possibility to conceive new devices downstream of the fundamental studies has not been ignored however, and the influence of free carriers on the optical properties of low-dimensional systems has been in particular the subject of many investigations. The physics of II–VI compounds has not yet undergone the investigations devoted to the III–V compounds, for which numerous applications are expected, and has long seemed prone to

remain embryonic. The recent achievement of p-type doping of ZnSe by MBE, followed by the realisation of II–VI based blue-light emitters [1–4] renewed the interest for these compounds. On the other hand, combining binary or ternary II–VI compounds may lead to superlattices exhibiting type II fundamental band gaps wider than the red band gap obtained when using GaAs–AlAs based quantum structures. Such superlattices may also present efficient non-linear optical behaviour (optical bistability was recently observed in ZnSe–ZnTe superlattices grown on  $\text{CaF}_2$  substrates [5]). This gives strong potentialities to such superlattices in the area of wide gap semiconductors.

In this communication we show that the cancellation of excitonic effects by photo-injected carriers can be easily produced in ZnSe–ZnTe superlattices. This combination is interesting since it has a type II band alignment in real space [6,7]. The image charge effects correlated to differ-

\* Corresponding author.

ences in dielectric constants of ZnSe and ZnTe plays an important role in the localization of electrons and holes at the interfaces. Moreover, strong confinements of electrons and holes by large band offsets lead to important values of Rydberg energies [8]. Thus important energy-shifts of some 20 meV are *a priori* expected to be measured when exciton screening is produced in such superlattices.

## 2. Experimental methods and results

We have first grown short-period ZnSe–ZnTe superlattices by MOVPE on (100) GaAs substrates after either a ZnSe or ZnTe relaxed buffer layer was deposited. Details on growth apparatus and growth conditions have been reported elsewhere [9,10]. The periods and thicknesses of the individual layers were obtained from X-ray diffraction measurements. Collection of X-ray data obtained for a series of samples with similar designs (80 repeats of a  $\sim 4$  nm building block each consisting of a 1 to 5 monolayers thick ZnSe barrier and a 10 to 20 monolayers thick ZnTe well) leads us to conclude that such superlattices are free-standing whatever the buffer is (ZnSe or ZnTe). For such structures grown onto a ZnSe buffer a complete relaxation occurs in the first superlattice periods, whilst in case of superlattices deposited onto a ZnTe buffer, the relaxation is distributed over a large number of periods, leading to a free-standing state only near the superlattice surface [10].

We have performed optical transmission measurements at superfluid liquid helium temperature in order to reveal several radiative transitions. For this purpose, we have grown a 80-period superlattice on a  $5\text{ }\mu\text{m}$  thick ZnTe buffer layer, each period being constituted of a  $7.9\text{ }\text{\AA}$  thick ZnSe layer and a  $32.7\text{ }\text{\AA}$  thick ZnTe layer. The substrate was removed by chemical etching using a 7% aqueous solution of NaOCl. This experiment summarised in Fig. 1 reveals the broad plateau-shaped absorption characteristics of two-dimensional semiconductors. The shape of the absorption in type I and type II superlattices has been investigated by Voisin et al. [11]. Deconvo-

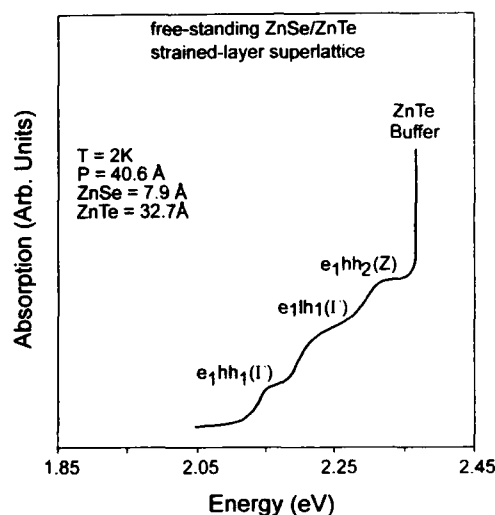


Fig. 1. 2 K absorption spectrum of a ZnSe–ZnTe free standing superlattice.

lution of the spectrum in order to extract the contribution of the superlattice to the absorption from the contribution of the Urbach tail of the ZnTe buffer is difficult since the buffer layer is thick ( $5\text{ }\mu\text{m}$ ) compared to the superlattice (325 nm). This currently prevents us from determining the absolute value of the absorption coefficients for the different plateaux with an accuracy better than 25%. The measured absorption coefficient is  $3 \times 10^4\text{ cm}^{-1}$ . This value is to be compared to those obtained for other II–VI superlattices grown by MBE like CdSe–(Zn, Mn)Te type II superlattices ( $3.7 \times 10^4\text{ cm}^{-1}$ ) [12] or ZnSe–(Zn, Cd)Se type I superlattices ( $10^5\text{ cm}^{-1}$ ) [13]. Knowledge of the absorption coefficient is important in order to establish the relationship between the photo-induced carrier densities and the photo-excitation power density. An identification of the observed transitions is offered in Fig. 1. This identification is based on calculation of the electronic structure of superlattice using a multi-band description of the envelope function formalism and a strain-free value of 1200 meV for the valence band offset. We note that the observation of zone centre transitions as well as transition associated with the miniband dispersion can be reported. The envelope functions calculated for

the first electron, light-hole and heavy-hole subbands are reported in Fig. 2. Data corresponding to the second heavy-hole states are also given in order to point out that the overlap between envelope functions of  $e_1(z)$  and  $hh_2(z)$  states is not zero, making the  $e_1hh_2(z)$  saddle point transition observable. Observation of sharp peak at the resonance energies is not reported. This we attribute to a broadening of the exciton resonance related to fluctuations of the thickness of both ZnSe and ZnTe layers. We note particularly that, due to the very small ZnSe layer thickness (7.9 Å), one could expect an important variation of the confinement energy of the electron for a single monolayer fluctuation of the ZnSe thickness.

We now discuss the influence of the injection density on the photoluminescence. Fig. 3 displays the evolution of the photoluminescence band of the superlattice when the intensity of the 488 nm

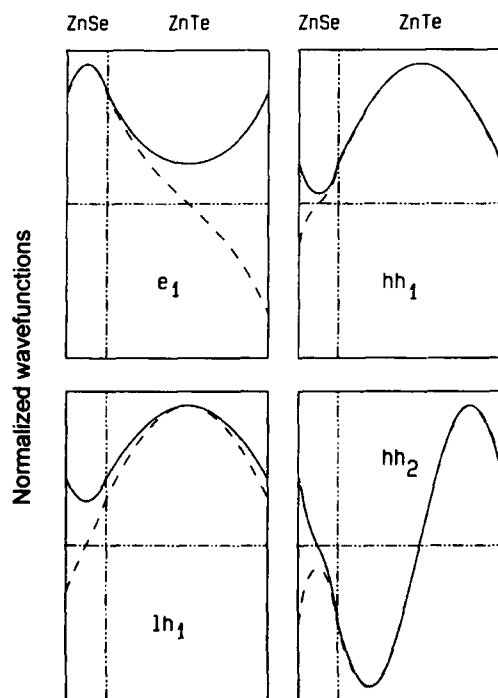


Fig. 2. Envelope functions for the first relevant states. Full (dashed) lines are for the calculation at zone centre (Z mini-zone edge).

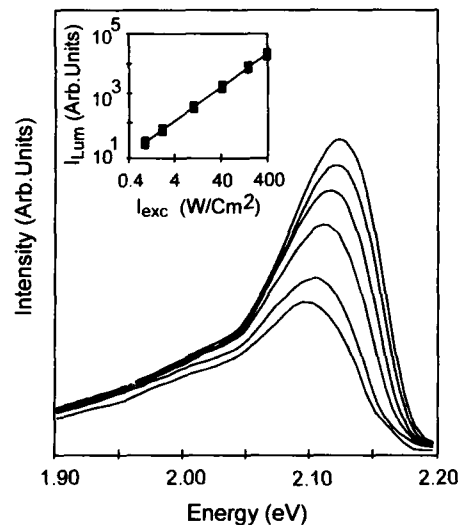


Fig. 3. Evolution of the normalized photoluminescence with pump power. The pump power increases from bottom to top. Inserted is the logarithm plot of the integrated intensity against the photo-excitation power density.

line of an argon ion laser was scaled over three decades. The highest power density estimated from the experimental conditions was 400 W/cm<sup>2</sup>. The integrated intensity of the photoluminescence follows a linear power law of the excitation (see insert of Fig. 3). We note that even under high excitation condition, we do not observe any significant broadening of the photoluminescence band, whose energy position saturates at around 25 meV above the value measured under low excitation condition. The magnitude of the blue-shift first depends linearly upon injection density, but saturates at higher pump intensities as observed with GaAs-(Ga, Al)As microstructures of various thicknesses under moderate injection densities [14]. Let us now briefly review the state of the art for the GaAs-(Ga, Al)As combination. For type I microstructures, for which both electrons and holes are confined in the same layer (GaAs), the blue-shift observed under low excitation conditions was interpreted in terms of the existence of an exciton gas rather than an electron-hole plasma [14]. For sufficiently large injection densities, a gain region appears below the absorption edge of the semi-

conductor, due to recombination in a photoexcited plasma [15]. The situation is somewhat different for type II GaAs–AlAs microstructures for which the spatial separation of electron and holes in real and reciprocal spaces creates a space charge potential [16]. We note particularly that no experimental observation of optical gain has been reported for this system to our knowledge.

In our experiment, the line shape of the photoluminescence is almost independent of the photo-carrier density. Thus, the saturation of the photoluminescence energy is not related to the creation of a dense electron–hole plasma and the subsequent onset of band gap renormalisation effects, which, if any, would have strongly broadened the photoluminescence and modify its line-shape. Since the photoluminescence energy peak falls in the low energy tail of the first structure observed in the transmission spectrum, this emission could be related to carriers trapped on structural defects. In order to determine the areal density of such defects, we have performed a study using ETOCAPS (etching technique on chemically angle polished samples) [17–19] at “Laboratoire Central Jet Recherches Thomson–CSF”. This experiment revealed an areal structural defect density of  $10^6 \text{ cm}^{-2}$ . Next, we have correlated the photo-excitation power density with the induced photocarrier density. Most of the incident photons ( $\lambda = 488 \text{ nm}$ ) are absorbed in the superlattice (the absorption coefficient exceeds  $10^5 \text{ cm}^{-1}$  for this radiation). In the simplest approach, where diffusion and surface recombination are neglected, the injection rate is given by

$$dn/dt = (1 - R)I_0\alpha e^{-\alpha z} - n/\tau = 0, \quad (1)$$

$$n = (1 - R)I_0\alpha\tau \int_{\text{superlattice}} e^{-\alpha z} dz, \quad (2)$$

where  $I_0$  represents the incident areal pump density, and  $\alpha$  and  $R$  are the absorption and reflectivity coefficients, respectively. Thus, at  $400 \text{ W/cm}^2$ , a plasma density of some  $10^{12} \text{ cm}^{-2}$  is generated if the radiative lifetime  $\tau$  is some 1 ns, a value reasonable for type II superlattices.

In calculating the induced-electric field effects correlated to the presence of free carriers in the superlattice, we need to obtain the wave functions for various photocarrier densities, and then, to evaluate the modification of the image charge effect (a value of 3 meV is obtained from the zero charge calculation). We have computed the electronic structure of the sample as a function of the areal carrier density, in the simplest possible approach, by self-consistently solving Poisson's and Schrödinger's equations. In view of subbands separations in the valence band, and the low temperature of the experiment, we limited the phase space filling to the first heavy-hole state. This required to solve local equations of the kind:

$$\left[ \frac{-\hbar^2}{8\pi^2} \frac{\partial}{\partial z} \frac{1}{m_c(z)} \frac{\partial}{\partial z} + V_c(z) - qz\phi - E_c \right] \times \chi_c(z) = 0, \quad (3)$$

with

$$\begin{aligned} &\phi(z + \Delta z) - \phi(z) \\ &= \sigma \int_z^{z+\Delta z} \frac{\chi_c(\xi)^2 - \chi_{hh}(\xi)^2}{\epsilon(\xi)} d\xi. \end{aligned} \quad (4)$$

In these equations, as usual,  $\chi_c$  represents the envelope functions,  $V_c$  the potential line-ups and  $m_c$  the  $z$ -dependent carrier confining masses (with  $c = e$  or  $hh$  for the electron and heavy hole, respectively). The integral  $\Phi$  is calculated for various areal carrier densities  $\sigma$ , and  $\epsilon(z)$  is the dielectric constant.  $\Phi$  is nothing else than the local polarization field photo-induced between  $z$  and  $z + \Delta z$ . From symmetry arguments (we only fill one electron and one heavy-hole band), it is obvious that  $\Phi$  vanishes at the middle of both ZnTe and ZnSe layers. Fig. 4 illustrates the blue-shift obtained from this calculation. We obtain a linear dependence, whilst the experimental observation is non-linear. Moreover, because of the strong confining potentials, the envelope functions are not significantly altered and the image charge effect calculated using Eq. (8b) of ref. [8] remains sensibly constant whatever  $\sigma$  is. At this stage we interpret the observed blue shift in terms of screening of the exciton by photo-induced electron–hole pairs. The effect is found to

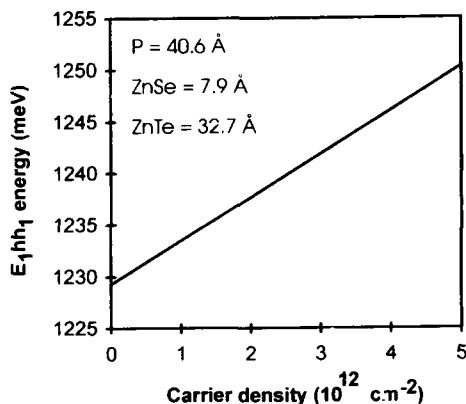


Fig. 4. Blue shift of the electron-to-heavy-hole transition energy as a function of carrier density.

be rather efficient comparing to the situation in III–V compounds.

### 3. Conclusion

We have performed optical transmission measurements on ZnSe–ZnTe superlattices and evidenced for the first time a nonlinear blue-shift of the photoluminescence with the photo-excitation power density. From theoretical modelling, we deduced that such superlattices are type II with a large valence band offset of 1200 meV. The absorption coefficient estimated from the absorption spectrum is around  $3 \times 10^4 \text{ cm}^{-1}$ . We also deduced that the observed blue-shift of the photoluminescence peak is related to the screening of the exciton by the electric field resulting from the spatial separation of the photo-induced free carriers in the type II superlattice.

### 4. Acknowledgements

We are grateful to Dr. A.M. Huber from "Laboratoire Central de Recherches Thomson-CSF" for ETOCAPS measurements. This work was supported by the Commission of the European Community (CEC) under an Esprit III Basic

Research contract No. 6675 – MTVLE. The "Groupe d'Etudes des Semiconducteurs" is an "Unité de Recherches Associée au CNRS No. 357".

### 5. References

- [1] M.A. Haase, J. Qiu, J.M. DePuydt and H. Cheng, *Appl. Phys. Lett.* 59 (1991) 1272.
- [2] H. Jeon, J. Ding, A.V. Nurmikko, H. Luon, N. Samarth and J. Furdyna, *Appl. Phys. Lett.* 59 (1991) 1293.
- [3] H. Jeon, J. Ding, A.V. Nurmikko, W. Xie, M. Kobayashi and R.L. Gunshor, *Appl. Phys. Lett.* 60 (1992) 892.
- [4] S.Y. Wang, I. Hauksson, J. Simpson, H. Stewart, S.J.A. Adams, Y. Kawakami, K.A. Prior and B.C. Cavenett, *Appl. Phys. Lett.* 61 (1992) 506.
- [5] D.Z. Shen, X.W. Fan, Z.S. Piao and G.H. Fan, *J. Crystal Growth* 117 (1992) 519.
- [6] Y. Rajakarunayake, R.H. Miles, G.Y. Wu and T.C. McGill, *Phys. Rev. B* 37 (1988) 10 212.
- [7] J.J. Davies, *Semicond. Sci. Technol.* 3 (1989) 219.
- [8] X.L. Liu, Y. Rajakarunayake and T.C. McGill, *J. Crystal Growth* 117 (1992) 742.
- [9] N. Briot, T. Cloitre, O. Briot, B. Gil, D. Bertho, C. Jouanin, R.L. Aulombard, J.P. Hirtz and A. Huber, *J. Electron. Mater.* 22 (1993) 537.
- [10] N. Briot, T. Cloitre, O. Briot, P. Boring, B.E. Ponga, B. Gil, R.L. Aulombard, M. Gailhanou, J.M. Sallese and A.C. Jones, in: *Mater. Res. Soc. Symp. Proc.* 308 (1993) 461.
- [11] P. Voisin, G. Bastard and M. Voos, *Phys. Rev. B* 29 (1984) 935.
- [12] F.C. Zhang, H. Luo, N. Dai, N. Samarth, M. Dobrowolska and J.K. Furdyna, *Phys. Rev. B* 47 (1993) 3806.
- [13] J. Ding, N. Pelekanos, A.V. Nurmikko, H. Luo, N. Samarth and J.K. Furdyna, *Appl. Phys. Lett.* 57 (1990) 2885.
- [14] D. Hulin, A. Mysyrowicz, A. Antonetti, A. Migus, W.T. Masselink, H. Morkoç, H.M. Gibbs and N. Peyghambarian, *Phys. Rev. B* 33 (1986) 4389.
- [15] S. Schmitt-Rink, D.S. Chemla and D.A.B. Miller, *Phys. Rev. B* 32 (1985) 6601.
- [16] I. Galbraith, P. Dawson and C.T. Foxon, *Phys. Rev. B* 45 (1992) 13 499.
- [17] A.M. Huber, C. Grattapain and P. Collot, in: *Proc. 5th Int. Conf. on Defects in Semiconductors*, 1989, Ed. K. Sumino (North-Holland, Amsterdam) p. 1523.
- [18] A.M. Huber and C. Grattapain, *Mater. Sci. Forum* 38–41 (1989) 1345.
- [19] A.M. Huber, in: *Proc. 1st Int. Conf. on Epitaxial Crystal Growth*, Budapest, 1991, *Crystal Properties and Preparation* 32–34, Ed. D. Lendvay (Trans Tech, Aedermannsdorf, 1991) p. 358.



ELSEVIER

Journal of Crystal Growth 138 (1994) 873–876

JOURNAL OF **CRYSTAL  
GROWTH**

## Exciton and Raman processes of ZnS under tunable picosecond light pulse excitations

H. Uchiki \*, H. Kinto, T. Moriyama, S. Hata, N. Tsuboi, J. Wang, S. Iida

*Nagaoka University of Technology, Kamitomioka 1603-1, Nagaoka 940-21, Japan*

### Abstract

The decay time of excitons bound to neutral acceptors ( $I_1$  line) appearing in low temperature ZnS films on GaAs (100) substrates grown by vapor phase epitaxy was measured for the first time with the use of a streak camera. The measured decay time of  $\sim 190$  ps agreed with a value calculated by the giant oscillator strength model. Under tunable (3.7–3.9 eV) picosecond light pulse excitations, resonant enhancements of Raman scattering intensities were seen for LO-, 2LO-, 3LO-, TO- and 2TO-phonon lines. The dependence of 2LO-phonon Raman line intensity on excitation photon energy showed resonance enhancements with free and bound exciton states.

### 1. Introduction

ZnS is a wide-band-gap II–VI semiconductor and a promising material for blue-light emitting optical devices. Successful p-type doping has been reported [1,2], but the physics of impurity behavior are now under investigation. Bound exciton emissions ( $I_1$  and  $I_2$  emissions from neutral acceptor- and neutral donor-bound excitons, respectively) were reported to appear in epitaxial ZnS films on GaAs substrates [3–5]. Studies of decay kinetics of the bound exciton emissions will give important information on the characterization of the bound excitons and impurities. However, the decay kinetics of the bound excitons in ZnS has not been studied extensively. (For bulk ZnSe, see ref. [6].)

In exciton emission region spectra, some sharp lines were reported to appear by excitation of a 325 nm (3.815 eV) line from a He–Cd laser [2]. These lines were reported to be Raman scattering lines resonantly enhanced with the free exciton state [7]. One can examine the behavior of resonance enhancements of these Raman scattering intensities by the use of a tunable light source, and consider the main contribution process to the scattering. For the second order (2LO-phonon) Raman scattering in CdS, the successive two-phonon scattering process was reported to be a dominant process [8]. However, there is no report on the scattering process of 2LO-phonon lines in ZnS.

This paper reports the decay kinetics of the neutral acceptor bound excitons in picosecond time scale for epitaxial ZnS films on (100) GaAs substrates grown by vapor phase epitaxy and resonant enhancement behavior of Raman intensi-

\* Corresponding author.



ties by the use of a tunable (3.7–3.9 eV) picosecond light source. Measured values of the decay time of the bound exciton emission are analyzed with the giant oscillator strength model. Discussion is made for the enhancement behavior observed for the 2LO-phonon scattering process.

## 2. Experimental procedure

Measurement was done for two ZnS films (No. 190 and V73) of p-type conduction grown on (100) GaAs substrates by vapor phase epitaxy [2]. The samples cooled at 14 K in a cryostat were excited by the second harmonics (3.7–3.9 eV,  $\sim 100 \mu\text{W}$ ) of picosecond light pulses from a CW mode-locked and cavity-dumped (at 4 MHz repetition rate) DCM dye laser which was synchronously pumped by the second harmonics of a CW mode-locked Nd:YAG laser. Time-integrated intensities of the bound exciton emission and Raman scattered radiation were measured with a combination of a 30 cm double monochromator and a cooled photomultiplier followed by a photon counter. The combination of a single polychromator and a synchronously-scanning streak camera (effective resolution of 80 ps) with a cooled CCD area sensor was used to measure the intensities of the emission and scattered radiation as functions of wavelength and time in a single measurement. Temporal behavior of the bound exciton emission and the scattered radiation, which was used to separate the emission and scattering processes, was observed by the use of the double monochromator and a microchannel plate photomultiplier followed by a time-correlated single-photon counting system (effective resolution of 100 ps).

## 3. Results and discussion

### 3.1. Decay times of the bound exciton emissions

Fig. 1 shows the time-integrated exciton region spectra in sample No. 190 at 16 K under excitation by the tunable light at several photon energies. The emission at 3.781 eV denoted as  $I_1$  was

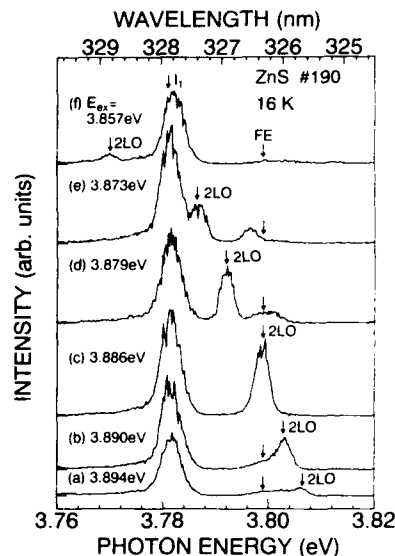


Fig. 1. Enhancement of the 2LO Raman scattering line resonant with the free exciton ( $I_1$ ) and the bound exciton ( $I_1$ ) in VPE ZnS at 16 K.  $E_{ex}$  denotes the exciting photon energy.

considered to be due to annihilation of excitons bound to neutral acceptors. The free exciton emission was not observed in sample No. 190. The free exciton energy ( $E_x$ ) was determined to be 3.799 eV at 14 K from a reflectance anomaly. A line denoted as 2LO is a Raman line scattered by two LO-phonons. Fig. 2 shows the temporal behavior of the 2LO-phonon Raman scattering intensity and that of the  $I_1$  emission intensity under the above band-gap excitation at 3.887 eV which was obtained with the use of the streak camera. The Raman intensity was synchronized with the exciting light pulse, whereas the  $I_1$  emission grew up until about 30 ps after the exciting light pulse. This time would correspond to the formation time of bound excitons and/or the trapping time of free excitons by acceptors. The decay times of the  $I_1$  emission in samples No. 190 and V73 were estimated to be 190 and 196 ps, respectively. A calculation of the decay time for a bound exciton can be done by the giant oscillator strength model given by Henry and Nassau [9]. Taking  $m_e$  (electron effective mass)  $\approx 0.30m_0$ ,  $m_h$  (hole effective mass)  $= 0.42m_0$ ,  $f_A$  (oscillator

strength of free exciton per molecule) =  $4.3 \times 10^{-3}$  [10],  $\lambda$  (wavelength of transition in cm) =  $327.9 \times 10^{-7}$ ,  $E_B$  (binding energy) = 17 meV,  $\Omega_{\text{mol}}$  (volume of one ZnS molecule) =  $39.6 \text{ \AA}^3$ , and  $n$  (refractive index) = 2.4, the decay time

$$\tau = 4.50 \lambda^2 \Omega_{\text{mol}} [2(m_e + m_h) E_B]^{3/2} / 8\pi \hbar^3 n f_x$$

was calculated to be 161 ps, which compares reasonably well with the experimentally observed values.

### 3.2. Resonant enhancement of Raman intensities and scattering processes

As is seen in Fig. 1, the 2LO-phonon Raman line intensity was resonantly enhanced when excitation photon energy  $E_{\text{ex}}$  became  $E_x + 2E_{\text{LO}}$  (= 3.886 eV) or  $E_{\text{BE}} + 2E_{\text{LO}}$  (= 3.869 eV). The enhancement in the latter case is seen better at  $E_{\text{ex}} - E_x = 70 \text{ meV}$  in Fig. 3. Similar resonant enhancement was observed for other lines of LO, TO, LO + TO, and 3LO-phonons with excitation

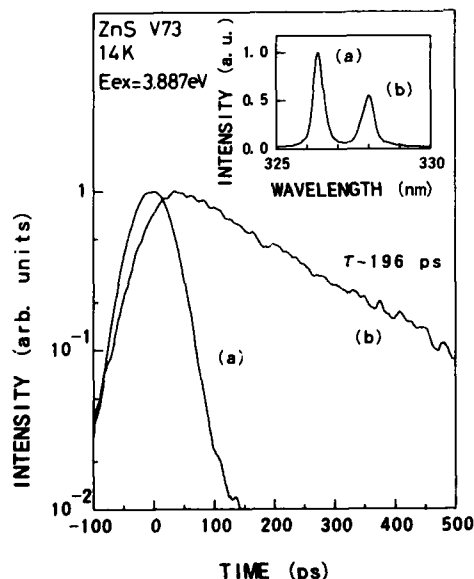


Fig. 2. Temporal behavior of (a) 2LO Raman scattering intensity and (b) bound exciton ( $I_1$ ) emission under the resonant exciting condition ( $E_{\text{ex}} = E_x + 2E_{\text{LO}}$ ) in ZnS (V73) at 14 K excited by 3.887 eV light. The decay time of the  $I_1$  emission intensity is 196 ps. The inset shows a time-integrated spectrum.

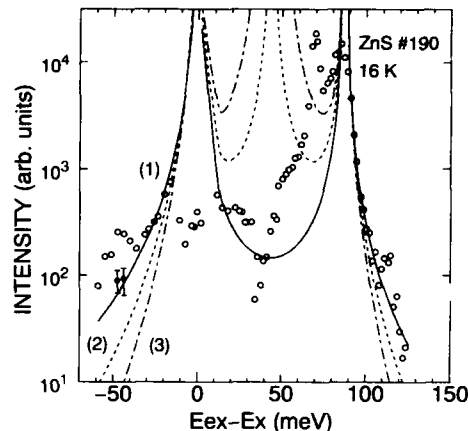


Fig. 3. 2LO Raman intensity in ZnS (No. 190) as a function of exciting light frequency. Theoretical curves of the 2LO Raman intensity are shown for three processes of (1) simultaneous two-phonon scattering, (2) successive two-phonon scattering and (3) two consecutive first-order one-phonon scattering.

at  $E_{\text{ex}} \sim E_x + pE_{\text{LO}} + qE_{\text{TO}}$  or at  $E_{\text{ex}} \sim E_{\text{BE}} + pE_{\text{LO}} + qE_{\text{TO}}$ , where  $p$  and  $q$  are integers. To clarify the Raman scattering process of 2LO-phonons, we measured excitation photon energy dependence of the time-integrated intensity of the 2LO Raman line. The result is shown in Fig. 3 by open circles as a function of  $E_{\text{ex}} - E_x$ , where  $E_{\text{ex}}$  is the excitation photon energy. When  $E_{\text{ex}} - E_x \sim -46 \text{ meV}$ , some background luminescence having a longer decay time of about 300 ps was observed. Using the time-correlated single-photon counting system combined with the double monochromator, this background luminescence could be subtracted from the measured intensity data. The closed circles in Fig. 3 show the data corrected by the above procedure. The data near  $E_{\text{ex}} - E_x = -17 \text{ meV}$  are considered to contain contribution of  $I_1$ -2LO luminescence.

For the 2LO-phonon Raman line, three scattering processes are known [11]: (1) simultaneous two-phonon scattering, (2) successive two-phonon scattering and (3) two consecutive first-order one-phonon scattering. The enhancement behavior in Fig. 3 seems to be explained as the process (1), since the intensity variation was fitted to the  $(E_x + 2E_{\text{LO}} - E_{\text{ex}})^{-2}(E_x - E_{\text{ex}})^{-2}$  relation with the free exciton resonance. In the case of CdS the successive two-phonon scattering process was re-

ported to be the dominant process [8]. However, in our data when the excitation photon energy was located between  $E_{ex} - E_x = -17$  meV (the bound exciton energy) and  $E_{ex} - E_x = 0$  (the free exciton energy), the Raman scattering intensity had decreased. This suggests that the effect of the bound excitons should be added in the fitting procedure. In order to identify the dominant Raman scattering process of ZnS, comparison with samples showing no  $I_1$  emission is thought to be necessary. Measurements with samples showing  $I_2$  (donor bound exciton) emission are also desirable.

#### 4. References

- [1] S. Iida, T. Yatabe and H. Kinto, Jap. J. Appl. Phys. 28 (1989) L535.
- [2] S. Iida, T. Yatabe, H. Kinto and M. Shinohara, J. Crystal Growth 101 (1990) 141.
- [3] Y. Kawakami, T. Taguchi and A. Hiraki, J. Crystal Growth 89 (1988) 331.
- [4] J. Gutowski, I. Broser and G. Kudlek, Phys. Rev. B 39 (1989) 3670.
- [5] H. Kinto, M. Yagi, K. Tanigashira, T. Yamada, H. Uchiki and S. Iida, J. Crystal Growth 117 (1992) 348.
- [6] G.H. Kudlek, U.W. Pohl, Ch. Fricke, R. Heitz, A. Hoffmann, J. Gutowski and I. Broser, Physica B 185 (1993) 325.
- [7] H. Kanie, M. Nagano and M. Aoki, Jap. J. Appl. Phys. 30 (1991) 1360.
- [8] Y. Oka and T. Kushida, J. Phys. Soc. Japan 33 (1972) 1372.
- [9] C.H. Henry and K. Nassau, Phys. Rev. B1 (1970) 1628.
- [10] B. Segall and D.T.F. Marple, in: Physics and Chemistry of II-VI Compounds, Eds. M. Aven and J.S. Prener (North-Holland, Amsterdam, 1967) p. 337.
- [11] A.K. Ganguly and J.L. Birman, Phys. Rev. 162 (1967) 806.



ELSEVIER

Journal of Crystal Growth 138 (1994) 877–883

JOURNAL OF **CRYSTAL  
GROWTH**

## Antiferromagnetic spin ordering and interlayer magnetic correlations in MnTe/CdTe superlattices

T.M. Giebultowicz <sup>\*a,d</sup>, W. Faschinger <sup>b</sup>, V. Nunez <sup>c,d</sup>, P. Klosowski <sup>c,d</sup>, G. Bauer <sup>b</sup>,  
H. Sitter <sup>b</sup>, J.K. Furdyna <sup>a</sup>

<sup>a</sup> University of Notre Dame, Notre Dame, Indiana 46556, USA

<sup>b</sup> Institut für Experimentalphysik, Universität Linz, A-4040 Linz, Austria

<sup>c</sup> University of Maryland, College Park, Maryland 20742, USA

<sup>d</sup> National Institute of Standards and Technology, Gaithersburg, Maryland 20899-0001, USA

### Abstract

Results of neutron scattering studies on MnTe/CdTe superlattices with ultrathin non-magnetic CdTe “barriers” are presented and compared with data from earlier studies on MnSe/ZnSe, MnTe/ZnTe, and MnSe/ZnTe multilayers with thick non-magnetic spacers. The experiments revealed two qualitatively new effects – namely, (i) the existence of pronounced interlayer magnetic correlations in the case of the CdTe thickness corresponding to two single monolayers and (ii) the coexistence of two magnetic phases that never occurred simultaneously in the previously studied systems.

### 1. Introduction

We report the first results of neutron diffraction studies of spin ordering phenomena in MnTe/CdTe superlattices. This system belongs to the family of artificial multilayered structures composed from zinc-blende (ZB) II–VI semiconducting compounds and Mn chalcogenides using the techniques of molecular beam epitaxy (MBE) or atomic layer epitaxy (ALE). Other known examples of binary systems from this group are MnSe/ZnSe, MnTe/ZnTe, or MnSe/ZnTe superlattices.

The Mn–VI/II–VI multilayers are highly interesting magnetic systems for several reasons.

One of these is that in such artificial structures – due to the epitaxial growth conditions and to “sandwiching” between layers of ZB II–VI materials – the Mn–VI constituent is also enforced to grow in the ZB phase. It should be noted that these tetrahedral crystallographic modifications of MnSe and MnTe cannot be obtained by any of the known bulk growth techniques. In contrast to the naturally existing crystals (of the NaCl, and of the NiAs structure, respectively) which belong to common antiferromagnetic (AF) classes, the ZB forms offer unique practical realizations of one of the most intriguing AF systems – namely, an FCC Heisenberg spin lattice with dominant nearest-neighbor (NN) AF interactions. Such a lattice is naturally “frustrated” (i.e., all AF bonds cannot be simultaneously satisfied), and one of the important consequences of this fact is a strong

\* Corresponding author.

degeneracy of the magnetic ground state. This degeneracy can be lifted by weak symmetry-breaking perturbations, either intrinsic or externally induced – e.g., by magnetic dilution, dipole–dipole or Dzyaloshinski–Moriya anisotropic terms in the spin–spin interaction Hamiltonian, or by external strains. As has been theoretically predicted [1], such circumstances may stabilize some of the degenerate ground state configurations, and thus produce a rich variety of collinear and non-collinear AF structures. However, the limited availability of naturally existing NN FCC antiferromagnets has resulted in relatively little experimental work in this field.

The emergence of the MBE-grown ZB forms of MnSe and MnTe opens new opportunities for such studies – especially, for investigating the strain-induced effects. It should be noted that the MnSe and MnTe layers stabilized in the SL structures are invariably strained due to the relatively large (2–4%) lattice mismatch between the constituent materials. As shown by X-ray and neutron diffraction measurements, the lattice parameters match up in the multilayer plane ( $xy$ ) to establish one “common” period, while in the perpendicular direction ( $z$ ) they accordingly contract or elongate to diminish the change in the material volume (Fig. 1). In other words, both lattices experience a *tetragonal distortion*, with the  $c/a$  ratio being  $> 1$  for one of them, and  $< 1$

Table 1

Undistorted lattice parameters of the constituent materials, and typically observed  $c/a$  values in the strained Mn–VI layers in previously studied [2–4] MBE-grown Mn–VI/Zn–VI superlattice systems with relatively thick non-magnetic layers, and in MnTe/CdTe multilayers prepared by the combined MBE/ALE technique investigated in the present work

Layer materials	Undistorted lattice parameters (Å)		$c/a$ for the Mn–VI lattice
	Mn–VI material	II–VI material	
MnSe/ZnSe	5.90	5.67	$\sim 1.05$
MnTe/ZnTe	6.34	6.10	$\sim 1.06$
MnSe/ZnTe	5.90	6.10	$\sim 0.94$
MnTe/CdTe	6.34	6.49	$\sim 0.98$ – $0.99$

for the other. Hence – as is illustrated by Table 1 – by taking various material combinations, one can obtain magnetic layers with two different distortion types. As shown by previous neutron diffraction studies on Zn-based forms (MnSe/ZnSe, MnTe/ZnTe, and MnSe/ZnTe [2–4]), the strain indeed has a profound influence on spin ordering phenomena and phase transition behavior in the frustrated Mn–VI layers. One noteworthy finding of those studies was that a *tensile* strain (which is the case in MnSe/ZnTe superlattices) produces a transition to a new incommensurate helical AF phase which has not yet been observed in any other FCC antiferromagnet [2].

The MnTe/CdTe superlattices discussed in the present work offer another example of a system with tensile strain in the magnetic layers. However, an interesting novel aspect of these multilayers is that here the magnitude of the strain may be considerably lower than in the previously investigated MnSe/ZnTe structures. All the Mn–VI/Zn–VI specimens for neutron diffraction studies have been grown by MBE, and the stability of the growth process in this method can be ensured only if the thickness of the Zn–VI “spacers” is larger than that of the Mn–VI layers. Hence, the distortion of the Mn–VI lattice is stronger than for the Zn–VI lattice.

The MnTe/CdTe specimens have been prepared using a combined method which utilizes the technique of ALE for the growth of CdTe layers. As has been demonstrated by the Linz

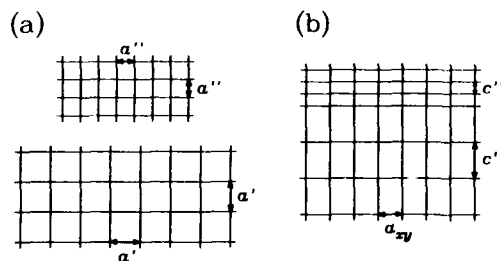


Fig. 1. A scheme illustrating lattice distortion effects in a binary superlattice consisting of two materials with different lattice periods. Plot (a): unstrained materials with lattice parameters  $a' > a''$ . Plot (b): a bilayer with a “common” lattice period  $a'' < a_{xy} < a'$  in the layer plane ( $xy$ ), and appropriately changed periodicities ( $c' > a'$ ,  $c'' < a''$ ) in the growth direction ( $z$ ).

group [5–9], this modification allows the preparation of good-quality superlattices with extremely thin (2–3 monolayers) CdTe spacers, and much thicker MnTe layers (even up to 10 monolayers). Due to the changed thickness proportions, the distortion of the AF lattice is decidedly weaker than in the previously studied case of MnSe/ZnTe (see Table 1), thus allowing the investigation of the onset of incommensurate helical effects. An additional highly interesting aspect of such specimens is – in contrast to the situation in the systems with MBE-grown Zn–VI layers – that the non-magnetic layer thickness becomes comparable with the range of the Mn–Mn AF exchange. This leads to observable magnetic inter-layer coupling effects which have never been seen in any of the Mn–VI/Zn–VI systems [2–4].

In section 2 of this paper we briefly recapitulate the results of previous neutron studies of Mn–VI layered systems with various strain types. In section 3 we describe the technique of preparation of MnTe/CdTe multilayers in greater detail, and present the results of first neutron diffraction experiments on such specimens. In section 4 we summarize and discuss the results.

## 2. Studies of Mn–VI/Zn–VI multilayers and MnTe single crystal films

**Unstrained lattice: MnTe films.** In contrast to the situation in multilayered forms, MBE-grown MnTe single crystal films are essentially strain-free due to their relatively large ( $\sim 1 \mu\text{m}$ ) thickness. Such films provide therefore “standards” with which to compare the results from the strained layers. Low-temperature diffraction data from the films reveal the formation of the expected Type III AF structure (AFM-III) with an  $(a, a, 2a)$  unit cell. The cubic symmetry dictates three possible domain configurations (Fig. 2), and all of them are indeed seen [3] in the films. The temperature dependence of the magnetic peak intensity indicates a *first-order* AF phase transition which is in agreement with the predictions of the renormalization group theory for AFM-III systems [10].

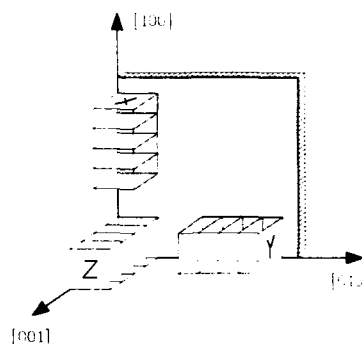


Fig. 2. Three possible AFM-III domain configuration in an epitaxial layer grown on a (001) substrate. While in a bulk crystal these three states are equivalent, in an epitaxial layer the magnetic energy for the “Z” configuration may be different from that for the “X” and “Y” configurations due to strain-induced anisotropy in the exchange interactions.

**Strained layers with  $c/a > 1$ : MnSe/ZnSe and MnTe/ZnTe superlattices.** The experiments [3,4] show that MnSe and MnTe layers exhibit the same spin structure which is seen in unstrained MnTe films, but now only a *single* AFM-III domain state is populated – namely, the one with the magnetic unit cell doubling direction parallel to the SL axis (the “Z” configuration in Fig. 2). This preference is clearly a manifestation of strain effects: the lattice distortion leads to slight changes in the Mn–Mn distances, thus introducing an anisotropy in the NN exchange coupling. Consequently, the magnetic energies of different domain states are no longer equivalent. In fact, the observed configuration is the one that minimizes the energy in the case of  $c/a > 1$ . Another conspicuous strain-induced effect is that the AF transition in the superlattices is of the *second* order. As follows from renormalization group theoretical considerations, the underlying factor in the first-order phase transition is the *cubic symmetry*, so that lowering of this symmetry should result in a shift to a second-order transition [11]. Because of the lack of appropriate AFM-III systems which could be subjected to significant strains, that theory prediction could not be experimentally verified before the emergence of the epitaxial Mn–VI forms.

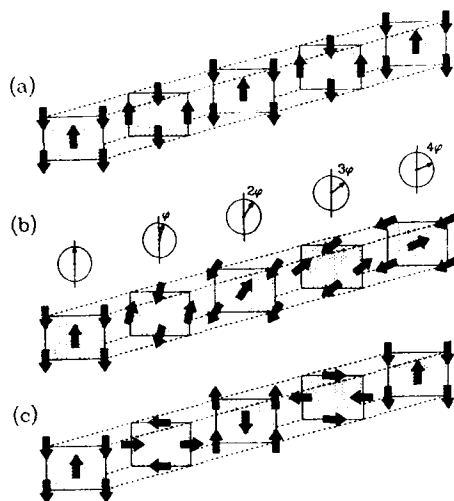


Fig. 3. Helical spin ordering in tetragonally distorted MnSe or MnTe layers in MnSe/ZnTe or MnTe/CdTe superlattices (b). For  $\varphi = 0$  (a), this arrangement is equivalent to collinear Type I AF (AFM-I) order, and for  $\varphi = 90^\circ$  (c), it is equivalent to the canted (Keffer) modification of the AFM-III ordering. The orientation of the spin planes (shaded contours) with respect to the multilayer plane corresponds to the "X" or "Y" situations in Fig. 2.

*Strained layers with  $c/a < 1$ : MnSe/ZnTe superlattices.* This type of distortion appears to have the most dramatic influence on the spin order in the magnetic layers. Diffraction experiments [2] show that in such superlattices the AFM-III structure occurring in unstrained systems as well as in those with  $c/a > 1$  becomes replaced by an entirely new *incommensurate* helical AF ordering never before seen in any FCC antiferromagnet (Fig. 3). The helical period  $\Lambda$  observed in different samples varied from  $2.9a$  to  $3.45a$  (where  $a$  is the in-plane lattice parameter). The formation of such a helix in a frustrated FCC lattice can be explained by applying a mean-field approach [3] which leads to the following equation for the angle  $\varphi$  describing the spin rotation in consecutive AF planes:

$$\varphi = \arccos(\Delta J_{NN}/2J_{NNN}), \quad (1)$$

with the helix pitch being related to  $\varphi$  as:

$$\Lambda = \pi a / \varphi, \quad (2)$$

where  $J_{NNN}$  is the next-nearest neighbor exchange parameter, and  $\Delta J_{NN}$  is the strain-induced anisotropy in the NN exchange. Assuming that  $J_{NN}$  depends primarily on the ion-ion distance, and that only the linear term in this dependence is essential for small lattice distortions, one obtains that  $\Delta J_{NN}$  is approximately proportional to a "distortion parameter" defined as  $\gamma = 1 - c/a$ . It should be noted that the value of  $c/a$  for the MnSe lattice in this specific SL system is not fixed, but can be varied within certain limits by changing the MnSe:ZnTe thickness ratio. As follows from the above – and which has been indeed confirmed by our experiments – one can actually *control* the helix pitch in the layers.

### 3. Sample preparation and neutron diffraction measurements

The CdTe/MnTe superlattices were grown by a combination of atomic layer epitaxy (ALE) for the CdTe and mass spectrometer controlled MBE for the MnTe. The ALE method is based on the fact that the Cd–Te bond is much stronger than the Cd–Cd or the Te–Te bond. If Cd and Te are deposited alternately, only the atoms, which can form Cd–Te bonds, will stick, whereas the surplus atoms are re-evaporated. In the ideal case this leads to the formation of exactly one CdTe monolayer within one so-called reaction cycle, independent of the amount of deposited material. In fact such monolayer growth has been achieved for CdTe [5], but it turns out that for superlattices it is more efficient to work at higher substrate temperature where only 0.5 monolayers per reaction cycle are formed [6]. The actual growth conditions were a substrate temperature of  $310^\circ\text{C}$  and a reaction cycle time of 4 s. Since the Mn–Mn bond is stable at this temperature, ALE cannot be applied to the growth of MnTe. In order to achieve comparable accuracy, we used a quadrupole mass spectrometer (QMS) situated near the substrate to monitor the Mn flux in situ. The QMS signal was fed into a computer, and the averaged and background-corrected values served as a feedback for the Mn shutter opening time. The combination of these two growth techniques

allowed a precise tailoring of superlattices with very short period [7–9].

Neutron studies were performed at the 20 MW Research Reactor at the National Institute of Standards and Technology on a triple axis spectrometer with a (002) pyrolytic graphite (PG) monochromator and analyzer fixed for elastic scattering, and a PG filter in the incident beam. An incident energy of 13.7 or 14.8 meV with 40 arc min collimation throughout was used for most of the experiments. The samples were placed in a variable-temperature He cryostat, and were oriented with either the [001] direction (the growth axis), or the [100] in-plane axis perpendicular to the scattering plane. Those two sample orientations enabled the observation of different families of magnetic reflections. The experiments have been performed for four samples with the following CdTe:MnTe thickness proportions (in monolayers): 2:7, 2:10, 4:9, and 6:10. The number of bilayers in each sample was 100.

Search for magnetic reflections at low temperature has revealed peaks corresponding to an incommensurate helical AF phase of the same kind as previously observed in MnSe/ZnTe superlattices. However, the helical modulation period appeared to be much shorter than in those specimens, which is consistent with the weaker strain in the magnetic layers. In particular, for the three latter specimens the observed values of  $\Lambda$  are  $2.05a$ ,  $2.07a$ , and  $2.15a$ , respectively. The increase of  $\Lambda$  reflects the gradual increase of the lattice strain in the Mn layers due to the growing CdTe thickness (it should be kept in mind that the zero-strain  $\Lambda$  value is  $2a$ , since the normally occurring AFM-III structure can be looked at as a special case of a spin helix with the pitch exactly equal to two lattice periods).

Surprisingly, in one of the investigated samples (with 2 CdTe monolayers) the measurements have revealed – in addition to peaks corresponding to the helical phase – also the presence of maxima characteristic for the AFM-III domain arrangements occurring in strained layers in the case of  $c/a > 1$  (i.e., that seen in MnSe/ZnSe and MnTe/ZnTe superlattices [3,4]). The peak intensity indicated approximately equal populations of the two phases. A simultaneous occurrence of the

two phases cannot be understood on the grounds of the simple mean field model used for the interpretation of the data from Mn-VI/Zn-VI systems [2–4]. However, as pointed out below, such a behavior can be explained by applying a more sophisticated theoretical approach [12].

Another striking difference between the results of observations for the Mn-VI/Zn-VI systems and for MnTe/CdTe multilayers with ultrathin non-magnetic layers was the width of the magnetic peaks in  $Q$ -space diffraction scans parallel to the growth direction. For all former specimens those peaks were strongly broadened – the widths,  $\Delta Q$ , clearly corresponding to the thickness of a *single magnetic layer* for a given sample,  $D_M$ , transformed from real space to  $Q$ -space ( $\Delta Q = 2\pi/D_M$ ). This behavior clearly indicates the absence of any correlation between spin ordering in individual magnetic layers, and is consistent with the large thickness of the non-magnetic spacers which effectively isolate the magnetic layers from one another. In contrast, the magnetic peaks seen in MnTe/CdTe superlattices with 2 CdTe monolayers are only slightly broader than the instrumental resolution width (Fig. 4). Such a width indicates a coherence between the spin orientation in individual layers, with the range of these correlations corresponding to at least 10 bilayer thicknesses (computer simulation of a diffraction pattern from a  $(\text{MnTe})_7-(\text{CdTe})_2$  multilayer with such a range of interlayer magnetic correlations is shown in Fig. 5).

#### 4. Summary and discussion

In conclusion, neutron diffraction experiments on MnTe/CdTe superlattices with ALE-grown ultrathin non-magnetic barriers reveal at least two qualitatively new effects not previously seen in any Mn-VI/II-VI multilayered systems. The first of these is magnetic interlayer coupling through the non-magnetic barriers. This effect is clearly evidenced by the observed narrowing of the magnetic reflections. A totally convincing proof for that would be, of course, the observation of superlattice satellite peaks of those reflec-



tions. However, it should be noted that the observation of satellite maxima for samples in which the thickness of the magnetic layers is much larger than the CdTe spacer thickness is not a trivial task. In such a situation, as is illustrated in Fig. 5, the intensity of the satellites is very strongly suppressed by the bilayer structure factor (for definition, see, e.g., ref. [3]) which has  $|F_{BL}|^2 = 0$  minima not far from the positions where the first-order satellites occur. Hence, their intensity becomes very small. The detection of the satellites would require a radical improvement of the signal/background ratio in our measurements –

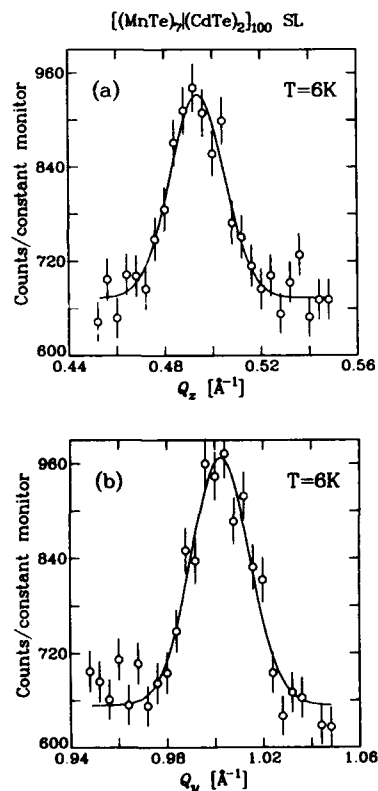


Fig. 4. Diffraction scans through a magnetic reflection from a  $[(\text{MnTe})_7/(\text{CdTe})_2]_{100}$  superlattice sample in two perpendicular directions in  $Q$ -space: parallel to the  $[001]$  growth axis (a), and parallel to the  $[010]$  in-plane axis (b). In both cases the peaks show essentially no broadening effects; the absence of broadening in the  $[001]$  direction indicates the existence of pronounced interlayer magnetic correlations in the system.

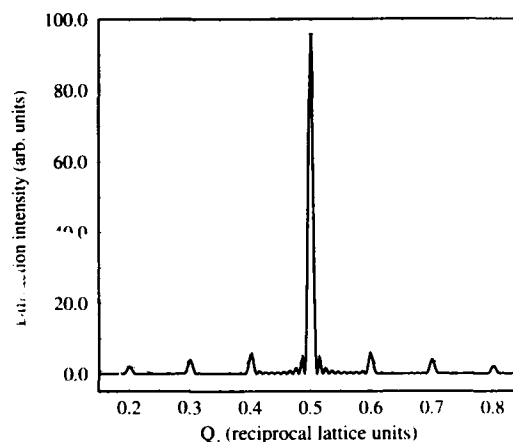


Fig. 5. Computer simulation of a magnetic diffraction pattern from a  $(\text{MnTe})_7/(\text{CdTe})_2$  superlattice with 10 correlated magnetic layers (thick curve). The thin curve is the square of the structure factor for a single bilayer "unit cell",  $|F_{BL}|^2$ , which is the "envelope function" describing the intensity of the satellite peak group (see, e.g., ref. [3]).

either through the preparation of much larger samples than currently used ( $\sim 0.3\text{--}1\text{ cm}^2$ ), or by using a cryostat with special windows – and such experiments are planned. Detailed studies of interlayer coupling effects – especially, systematic investigation of their dependence of the CdTe layer thickness – may give us new insight into the nature of weak long-range magnetic exchange interactions in diluted magnetic semiconductors based on II–VI compound. So far, relatively little is known about interactions ranging beyond the second-nearest magnetic neighbor in these compounds.

Second, the experiments reveal that in certain circumstances the normal AFM-III phase may coexist with the helical phase, even though the MnTe layers exhibit a distortion with  $c/a < 1$ . As noted, this fact can not be understood on the grounds of a simple mean field approach, from which it follows that the boundary between the two phases is located exactly at  $c/a = 1$ . However, the problem has been recently treated theoretically by Cohen and Newman [12] using a more sophisticated Landau–Ginzburg formalism. As shown by their study, the phase boundary in

question may actually be slightly shifted toward  $c/a < 1$  values. Simultaneous occurrence of the two phases might therefore be explained by assuming that the magnitude of the strain in the sample is close to the critical value, and strain fluctuations, which are invariably present in epitaxial systems, may locally “flip” the magnetic state from one phase to another.

A general conclusion one can draw from Cohen and Newman’s work is that experimental data from the region of weak strains are of considerable importance for theoretical understanding of distorted frustrated lattices. The fact that MnTe/CdTe superlattices make it possible to examine this region is certainly a great advantage of this system. However, testing of theoretical models would require more thorough studies of the parameters of the helical spin structure versus strain. The amount of data collected so far in our experiments is not yet sufficient for this purpose. The results from samples with different CdTe thicknesses clearly indicate that the helix pitch increases with increasing strain in the MnTe layers, but such a behavior is in qualitative agreement with both of the aforementioned models.

## 5. Acknowledgments

The work of the Linz group was supported by the FWF Project No. 8446, and the neutron scat-

tering research carried out in the USA was supported by NSF Grant DMR 9121353.

## 6. References

- [1] See, e.g., C.L. Henley, *J. Appl. Phys.* 61 (1987) 3962, and references therein.
- [2] T.M. Giebultowicz, N. Samarth, H. Luo, P. Klosowski, J.K. Furdyna and J.J. Rhyne, *Phys. Rev. B* 46 (1992), 12076.
- [3] T.M. Giebultowicz, P. Klosowski, N. Samarth, H. Luo, J.K. Furdyna and J.J. Rhyne, *Phys. Rev. B* 48 (1993) 12817.
- [4] N. Samarth, P. Klosowski, H. Luo, T.M. Giebultowicz, J.K. Furdyna, B. Larson and N. Otsuka, *Phys. Rev. B* 44 (1991) 4701.
- [5] W. Faschinger and H. Sitter, *J. Crystal Growth* 99 (1990) 566.
- [6] F. Hauzenberger, W. Faschinger, P. Juza, A. Pesek, K. Lischka and H. Sitter, *Thin Solid Films* 225 (1993) 265.
- [7] W. Faschinger, F. Hauzenberger, P. Juza, H. Sitter, A. Pesek, H. Zajicek and K. Lischka, *Mater. Sci. Eng. B* 16 (1993) 79.
- [8] E. Abramof, W. Faschinger, H. Sitter and A. Pesek, *J. Crystal Growth* 135 (1994) 447.
- [9] E. Abramof, W. Faschinger, H. Sitter and A. Pesek, *Appl. Phys. Lett.*, submitted.
- [10] D. Mukamel and S. Krinsky, *Phys. Rev. B* 13 (1976) 5078; P. Bak and D. Mukamel, *Phys. Rev. B* 13 (1976) 5086; P. Bak, S. Krinsky and D. Mukamel, *Phys. Rev. Lett.* 36 (1976) 52.
- [11] M. Kerszberg and D. Mukamel, *Phys. Rev. B* 23 (1981) 3953.
- [12] R. Cohen and K. Newman, *Phys. Rev. B* 46 (1992) 14282.



ELSEVIER

Journal of Crystal Growth 138 (1994) 884–888

JOURNAL OF **CRYSTAL  
GROWTH**

## Photoluminescence in a ZnSe/(Zn,Mn)Se heterostructure: magnetic-field induced transition from light to heavy excitons

E. Deleporte <sup>\*,a</sup>, T. Lebihen <sup>a</sup>, P. Roussignol <sup>a</sup>, B. Ohnesorge <sup>a</sup>, C. Delalande <sup>a</sup>,  
S. Guha <sup>b,1</sup>, H. Munekata <sup>b</sup>

<sup>a</sup> Laboratoire de Physique de la Matière Condensée, Ecole Normale Supérieure, 24 Rue Lhomond, F-75005 Paris, France

<sup>b</sup> IBM Research Division, Thomas J. Watson Research Center, P.O. Box 218, Yorktown Heights, New York 10598, USA

### Abstract

Magneto-excitation spectroscopy experiments are performed up to 5.5 T at low temperature (4.2 K) in a ZnSe/Zn<sub>0.73</sub>Mn<sub>0.27</sub>Se double quantum well structure. The experimental results are compared to calculations of the excitonic transitions, taking into account the strain effects, the giant Zeeman effect in the (Zn,Mn)Se layers, the diamagnetic shift of the exciton. We show that a magnetic-field induced transition in the nature of the fundamental excitonic state (from light to heavy hole exciton) occurs for a certain critical magnetic field.

Among the various II–VI compounds, the ZnSe based materials require a particular attention because of their blue emission. As a matter of fact, the first blue laser emission has been obtained with ZnSe based compounds [1]. The ZnSe/(Zn,Mn)Se semimagnetic heterostructures are of particular interest because of their great magneto-optical properties, due to the exchange interaction between the spin of the carriers and the spin of the paramagnetic Mn<sup>2+</sup> ions located in (Zn,Mn)Se layers [2]. The so-called giant Zeeman effect can lead to the formation of a spin superlattice structure in which the carriers can be separated and spatially localized according to their spin [3,4]. We show here that it is possible to tune the nature of the fundamental optical

transition from a light hole exciton to a heavy hole exciton by changing the magnetic field. Photoluminescence and excitation spectroscopy under a magnetic field have been performed on two different ZnSe/Zn<sub>0.73</sub>Mn<sub>0.27</sub>Se quantum wells, and the comparison between the experimental results and the calculation of the excitonic transitions has allowed us to underline this effect.

The heterostructure has been grown by molecular beam epitaxy along the (100) axis and consists in two ZnSe quantum wells whose thicknesses are 53 and 106 Å, respectively, separated by a 350 Å thick Zn<sub>0.73</sub>Mn<sub>0.27</sub>Se layer. The double quantum well is grown on a 1200 Å Zn<sub>0.73</sub>Mn<sub>0.27</sub>Se layer deposited on a 9700 Å thick ZnSe buffer layer. The cap layer consists in a 350 Å Zn<sub>0.73</sub>Mn<sub>0.27</sub>Se layer. The substrate is GaAs.

The photoluminescence spectrum of the heterostructure, shown in Fig. 1, has been performed at zero magnetic field, at low temperature (4.2 K) with the 363 nm line of an Ar<sup>+</sup> laser. Two lines

\* Corresponding author.

<sup>1</sup> Present address: 3M Company, 3M Center, St. Paul, Minnesota 55144-100, USA.

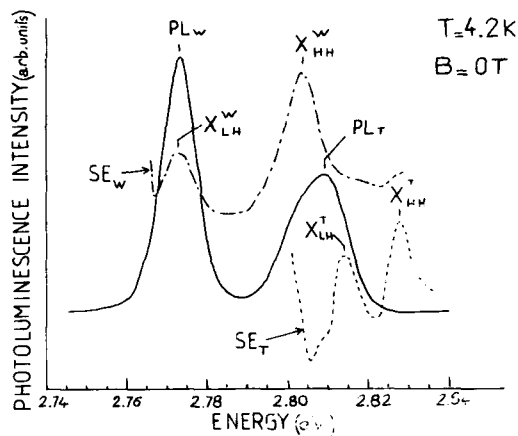


Fig. 1. Photoluminescence (full line) and excitation spectroscopy  $SE_W$  and  $SE_T$  of the two quantum wells at zero magnetic field and at low temperature (4.2 K).  $SE_W$  (dash-dotted line) is the excitation spectroscopy of the 106 Å wide well performed at  $E_{det} = 2.764$  eV and  $SE_T$  (dashed line) is the excitation spectroscopy of the 53 Å thin well performed at  $E_{det} = 2.792$  eV.

are observed: the 2.773 eV one, called  $PL_W$ , corresponds to the luminescence of the wide (106 Å thick) well, the 2.808 eV one, called  $PL_T$ , corresponds to the luminescence of the thin (53 Å thick) well. The excitation spectroscopy of the two photoluminescence lines is shown in Fig. 1:  $SE_W$  performed at the detection energy  $E_{det} = 2.764$  eV and  $SE_T$  performed at  $E_{det} = 2.792$  eV. As excitation source between 4500 and 4200 Å, we have used the second harmonics of a picosecond CW mode-locked Ti-Sa laser. The photoluminescence signal was analyzed by a double Jobin-Yvon  $f = 25$  cm monochromator, and detected by standard photon counting techniques. First, we can remark that the small Stokes shifts (6 meV for the thin well and 2 meV for the wide well) between the photoluminescence lines and the first line of their excitation spectra are not high, indicating the good quality of the sample. Secondly, comparing the two excitation spectra  $SE_W$  and  $SE_T$ , we can conclude that the two wells are not coupled. Thus these wells will be treated in this paper like single quantum wells.

From the comparison between the experiments and the calculation of the excitonic transi-

tions [5], we have interpreted the different lines of the excitation spectra and determined the band structure of the heterostructure (see ref. [6] for more details). In particular, this comparison has allowed an estimation of the strain effects, which are very strong in this heterostructure. It has been found that the 1200 Å  $Zn_{0.73}Mn_{0.27}Se$  layer is partially relaxed on ZnSe buffer layer; the (Zn,Mn)Se barrier layers are compressed. The residual strain in the barrier:  $\epsilon_{bar} = [a - a^0(x)]/a$ , where  $a$  is the mean parameter in the strained layer, and  $a^0(x)$  is the strain-free lattice constant of  $Zn_{1-x}Mn_xSe$  is found  $\epsilon_{bar} = -5.5 \times 10^{-3}$ . To know the strain state of the ZnSe layers, we assume an elastic accommodation of the lattice parameter of the two ZnSe wells with the barrier one. Moreover, from the energy difference between the heavy and light hole excitons, we have evaluated the percentage of the strain-free band gap difference which is in the valence band, called the relative valence band offset:  $q_v^0 = 10\%$ . The resulting band structure is represented in Fig. 2. This heterostructure has a quite unusual configuration: the fundamental optical transitions of the two wells:  $X_{LH}^W$  and  $X_{LH}^T$  are type-I (electrons

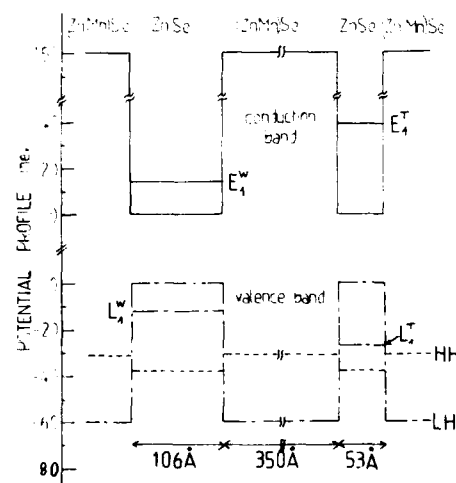


Fig. 2. Calculated potential profile along the growth axis of the heterostructure taking into account the strain effects on the structure band. The relative valence band offset is taken  $q_v^0 = 10\%$ , the strain in (Zn,Mn)Se layers is taken  $\epsilon_{bar} = -5.5 \times 10^{-3}$ .

and light holes are localized in the same layers) light hole excitons; the first excited transitions,  $X_{HH}^W$  and  $X_{HH}^T$ , are type-II (electrons and heavy holes are localized in adjacent layers) heavy hole excitons. The type-II excitons can be seen very clearly in the excitation spectra: they are in fact interface excitons [7], and have an oscillator strength which can be comparable to the oscillator strength of type-I excitons.

Magneto-excitation spectroscopy experiments have been performed at liquid helium temperature (4.2 K) with the same laser system and with a superconducting magnet up to 5.5 T, in the Faraday configuration. The laser ingoing and the photoluminescence outgoing lights were collected by a multi-fiber-optic guide. Fig. 3 shows the behavior of the excitation spectra of the thin well (Fig. 3a) and wide well (Fig. 3b) photoluminescence lines for several values of the magnetic field.

For the thin well, when the magnetic field increases up to 1 T, the  $X_{LH}^T$  line energy does not change, the  $X_{HH}^W$  line splits into two components  $X_{HH}^T(\sigma^+)$  and  $X_{HH}^T(\sigma^-)$ . This splitting is due to the giant Zeeman effect existing in the semimagnetic material (Zn,Mn)Se, originating from the strong exchange interaction between the spin of

the  $Mn^{2+}$  ions and the spin of the carriers. Following the sign of the exchange interaction versus the carriers spin in the conduction and valence band [2], the component  $X_{HH}^T(\sigma^+)$  (respectively  $X_{HH}^T(\sigma^-)$ ) at lower (respectively higher) energy corresponds to the  $-1/2$  (respectively  $+1/2$ ) z-component spin of the electrons ( $z$  is the growth axis of the heterostructure and the axis of the magnetic field) and the  $-3/2$  (respectively  $+3/2$ ) z-component spin of the heavy holes. The splitting of the  $X_{LH}^T$  line can not be observed here. It is much smaller than the splitting of  $X_{HH}^T$  for two reasons: first the exchange interaction is three times smaller for the light holes than for the heavy holes; secondly, the heavy holes are localized in the semimagnetic layers and are more sensitive to the exchange interaction than the light holes which are localized in non-semimagnetic layers. At 2 and 3.5 T, the  $X_{HH}^T(\sigma^-)$  line is clearly seen, but because of the width of the lines, the  $X_{LH}^T$  and  $X_{HH}^T(\sigma^+)$  lines can not be distinguished and appear in a broad line. Above 4.5 T, these two lines can be resolved. In Fig. 4, we have reported the energy position of the lines with their full width at half-maximum versus the magnetic field.

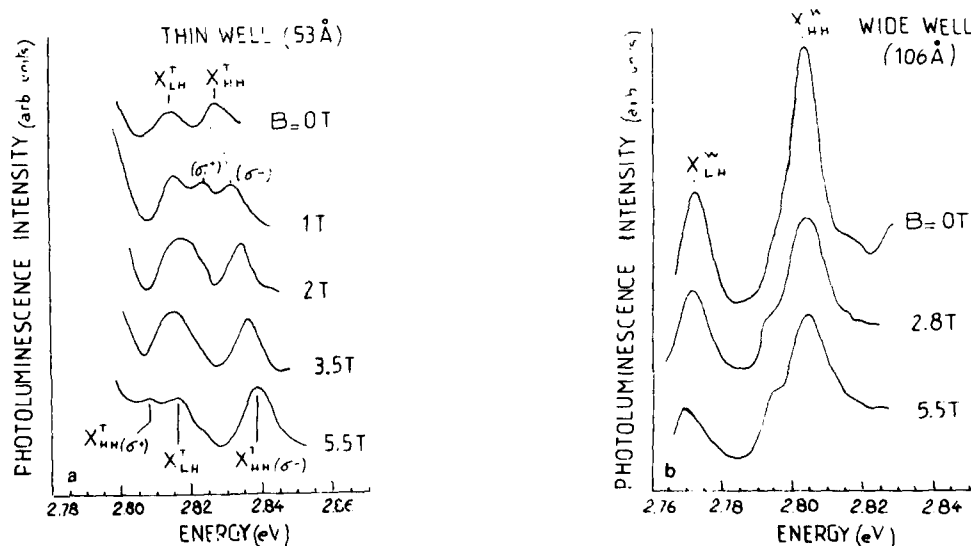


Fig. 3. Evolution of the excitation spectra of the 53 Å thin well, (a)  $E_{det} = 2.795$  eV, and of the 106 Å wide well, (b)  $E_{det} = -2.764$  eV, for different magnetic fields, at low temperature (4.2 K).

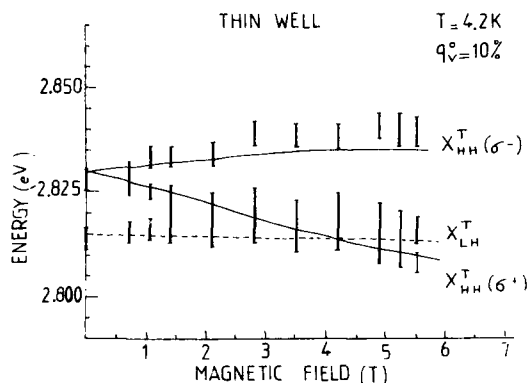


Fig. 4. Energy position of the different lines observed in the excitation spectrum of the 53 Å thin well and their full width at half-maximum (vertical segments) versus the magnetic field. The lines show the calculated excitonic heavy hole (solid line) and light hole (dashed line) transitions.

Fig. 3b shows the behavior of the excitation spectrum of the wide well versus the magnetic field. The splitting of the  $X_{HH}^W$  line can be observed, and it is clearly seen that the  $X_{LH}^W$  line does not change at all, at least up to 5.5 T.

In Fig. 4, the calculated energies of the excitonic transitions of the thin well versus the magnetic field are reported. The calculation which takes into account the strain effects, the coulombic effects, the exchange interaction and the diamagnetic shift of the excitons, is performed in the parabolic approximation, and is valid for a type-I and a type-II structure [5]. The relative valence band offset is taken as 10%. According to this calculation, the excitation spectrum above 4.5 T can be easily interpreted: the fundamental optical transition is the  $X_{HH}^T(\sigma^+)$  heavy hole exciton and the first excited transition is the  $X_{LH}^T$  light hole exciton. Fig. 4 shows clearly the crossing between the  $X_{LH}^T$  and  $X_{HH}^T(\sigma^+)$  transitions, and so the existence of a critical magnetic field  $B_0$  for which a transition in the nature of the fundamental state occurs: for  $B < B_0$ , the fundamental optical transition is a type-I light hole exciton, for  $B > B_0$ , the fundamental optical transition is a type-II heavy hole exciton. The precise value of  $B_0$  depends on the value of the relative valence band offset, so a measurement of  $B_0$  could provide information on  $q_v^0$ . In spite of the limited resolu-

tion due to the width of the lines, we can note a good agreement between the experiment and the calculation for  $q_v^0 = 10\%$ .

The excitation spectra of the wide well versus the magnetic field do not show the same behavior as the excitation spectra of the thin well. In fact, such a transition is expected at a higher critical magnetic field for the wide well (about 8 T). The critical magnetic field depends on the thickness of the well. This property can be understood by analyzing the valence band schematized in Fig. 2. When the well thickness increases, the energy difference between the light and heavy hole transitions at zero magnetic field increases. This property is due to the decrease of the confinement energy of the light hole, and to the fact that the interface exciton binding energy of the type-II heavy hole exciton is smaller for a wide well than for a thin well (the recovering between the electronic and heavy hole wavefunctions being smaller for a wide well than for a thin well). The energy difference between the light and heavy excitons at zero magnetic field increasing, the value of the critical magnetic field, for which the crossing between  $X_{LH}^T$  and  $X_{HH}^T(\sigma^+)$  occurs, increases.

In summary, magneto-excitation spectroscopy experiments up to 5.5 T, performed on a 53 Å thin quantum well and compared to calculations of the excitonic transitions, have allowed us to demonstrate the existence of a magnetic field induced transition in the nature of the excitonic fundamental transitions for a certain critical magnetic field. Below this field, the fundamental excitonic state is a light hole exciton, above this field, it is a heavy hole exciton. The value of this critical magnetic field depends on the thickness of the well and on the relative valence band offset  $q_v^0$ . Our results seem to be coherent with the value  $q_v^0 = 10\%$ . To confirm our results, we plan to perform magneto-excitation spectroscopy of the 106 Å wide well at higher magnetic field in order to observe this transition.

## 1. References

- [1] M. Haase, J. Qiu, J. De Puydt and H. Cheng, Appl. Phys. Lett. 59 (1991) 1272.

- [2] A. Twardowski, T. Dietl and N. Demianiuk, *Solid State Commun.* 48 (1983) 845.
- [3] Y. Hefetz, J. Nakahara, A.V. Nurmikko, L.A. Kolodziejski, R.L. Gunshor and S. Datta, *Appl. Phys. Lett.* 47 (1985) 989.
- [4] B.T. Jonker, X. Liu, W.C. Chou, A. Petrou, J. Warnock, J.J. Krebs and G.A. Prinz, *J. Appl. Phys.* 69 (1991) 6097.
- [5] G. Peter, E. Deleporte, G. Bastard, J.M. Berroir, C. Delalande, B. Gil, J.M. Hong and L.L. Chang, *J. Luminescence* 52 (1992) 147.
- [6] T. Lebihen, E. Deleporte, M. Voos, S. Guha and H. Munekata, in: *Proc. 3rd Int. Conf. on Optics of Excitons in Confined Systems*, Montpellier, 1993 (*J. Physique*, to be published).
- [7] E. Deleporte, J.M. Berroir, C. Delalande, N. Magnea, H. Mariette, J. Allègre and J. Calatayud, *Phys. Rev. B* 45 (1992) 6305.



ELSEVIER

Journal of Crystal Growth 138 (1994) 889–894

JOURNAL OF **CRYSTAL  
GROWTH**

## Magnetic field dependence of the exciton transfer in semimagnetic double quantum well structures

Th. Pier <sup>\*,a</sup>, K. Hieke <sup>b</sup>, B. Henninger <sup>a</sup>, W. Heimbrodt <sup>b</sup>, O. Goede <sup>b,†</sup>,  
H.-E. Gumlich <sup>a</sup>, J.E. Nicholls <sup>c</sup>, M. O'Neill <sup>c</sup>, S.J. Weston <sup>c</sup>, B. Lunn <sup>d</sup>

<sup>a</sup> Institut für Festkörperphysik, Technische Universität Berlin, Hardenbergstrasse 36, D-10623 Berlin, Germany

<sup>b</sup> Institut für Optik und Spektroskopie, Humboldt Universität, Unter den Linden 6, D-10099 Berlin, Germany

<sup>c</sup> Department of Applied Physics, University of Hull, Cottingham Road, Hull HU6 7RX, UK

<sup>d</sup> Department of Engineering Design and Manufacture, University of Hull, Cottingham Road, Hull HU6 7RX, UK

### Abstract

The energy transfer between the wells of asymmetric CdTe/Cd<sub>1-x</sub>Mn<sub>x</sub>Te double quantum well structures was investigated by both CW and time-resolved optical measurements. The barrier heights were tuned by an external magnetic field. Furthermore, in samples with a wide semimagnetic well magnetic fields caused resonances and level crossings of the electron and hole energies. This was observed in the magnetic field dependence of the CW luminescence and luminescence excitation intensities of the respective transitions. The luminescence decay was measured using selective ps excitation. In the case of a field induced resonance we got a strong decrease of the decay time constant as a function of the magnetic field. A kinetic model for the exciton transfer is given taking into account the independent tunnelling of electrons and holes and the exciton lifetimes in both wells. A set of rate equations describe the time dependent carrier densities in the quantum wells. The solutions are given for CW and ps excitation.

### 1. Introduction

The magnetic properties of CdTe/Cd<sub>1-x</sub>Mn<sub>x</sub>Te asymmetric double quantum well (DQW) structures allow one to study the exciton transfer as a function of the barrier height tuned by an external magnetic field. The field-induced changes of the coupling strength influences the energy transfer between the two wells. In the case that the wide well consists of Cd<sub>1-x</sub>Mn<sub>x</sub>Te too, even the band edge energy of this semimagnetic

well can be tuned by the magnetic field. This can lead to resonances between energy levels in wide and narrow wells. If such a resonance occurs, a drastic increase of the exciton transfer probability can be expected. To study these resonances, either CW and time-resolved spectroscopy can be used.

In this paper we studied asymmetric CdTe/Cd<sub>1-x</sub>Mn<sub>x</sub>Te DQW structures with  $x \leq 0.25$  grown by MBE on (100) InSb substrates at a temperature of 240°C and a growth rate of 0.7  $\mu\text{m/h}$ .

Our set of samples consist of structures with non-magnetic wells and barrier widths ranging

\* Corresponding author.

† Deceased.



from 25 to 200 Å. The well widths are 40 and 80 Å for the wide and narrow wells, respectively. In samples with a semimagnetic wide well, the amount of Mn in that well was about 4%.

The CW luminescence and luminescence excitation measurements were carried out using an Ar<sup>+</sup> laser pumped dye-laser system. The samples were cooled in an Oxford magnet cryostat which allowed one to apply fields up to 10 T.

For the time-resolved spectroscopy, the sample was excited with a ps dye laser synchronously pumped by a mode-locked Ar<sup>+</sup> laser. The dye laser pulse has a halfwidth of 6 ps at a repetition rate of 800 kHz. The luminescence signal was detected by a microchannelplate photomultiplier, which fed its signal to the analysing electronic system on the base of time-correlated single-photon counting. With this setup we were able to get a time resolution of about 40 ps.

## 2. CW measurements

### 2.1. Energies

The samples were chosen for the CW measurements to cover a wide range from non-coupled to strongly coupled wells. For a barrier width of 100 Å, we found strongly coupled and nearly decoupled wells when the Mn concentration in the barriers was 8.5% and 29.5%, respectively. To characterize the optical transitions in our DQW samples, we show in Fig. 1 the photoluminescence (PL) and photoluminescence excitation (PLE) spectra ( $T = 1.8$  K) of the latter sample. The PLE spectra were recorded monitoring the emission from the bound excitons in either well. The excitonic emission is mainly due to donor bound excitons ( $D^0X$ ), as can be concluded from their energetic position, compared with the free excitons observed in reflectivity and PLE, and from their behaviour in an external magnetic field. In the PLE spectrum of the narrow well (NW) emission we find distinct resonances which belong to the free heavy hole (hh) and light hole (lh) excitons localized in the narrow well. In contrary, in the wide well (WW) PLE spectrum there are five resonances observable which are at-

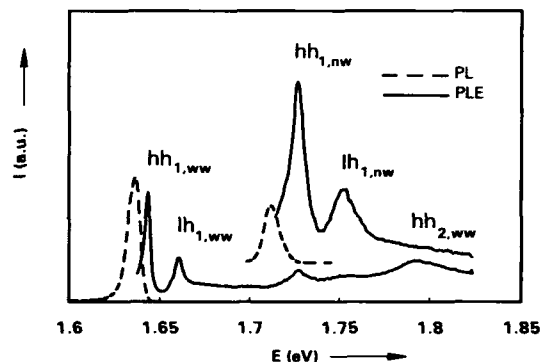


Fig. 1. PL spectrum (---) and PLE spectra (—) of a DQW structure with  $L_B = 100$  Å and  $x_{Mn} = 29.5\%$  ( $T = 1.8$  K).

tributed to the free hh and lh transitions in both wells. In more detail, the two lowest energy transitions are the  $n = 1$  hh and lh excitons localized in the ww, whereas the highest energy peak belongs to the  $n = 2$  hh exciton of the same well. With less intensity we can observe the  $n = 1$  hh and lh excitons of the NW. The difference in the PLE peak heights indicates that the two wells are nearly decoupled. In fact, for somewhat thicker barriers (150 Å) but even lower Mn concentrations (18.5%), the two wells were already proved to be completely decoupled (see ref. [1]). The energetic positions of the free exciton transitions can be calculated using a two-well model in envelope-function approximation [1], taking into account the strain-induced valence band splitting. The excitonic binding energies are estimated using a fractional dimension model (see ref. [2]). The valence band offset in our calculations was supposed to be 20% of the total offset in accordance with ref. [3]. In an external magnetic field up to 10 T, the Mn ions in the barriers cause a wide tuning of the band gap energy due to the so-called "giant Zeeman effect" [4]. In our case the band gap energy of the CdMnTe barriers can vary by about  $\pm 50$  meV between the  $\sigma^+$  and  $\sigma^-$  components. According to this effect, we observe a splitting of the WW and NW exciton states which can be well reproduced in our calculations using the measured barrier energy splitting (see Fig. 2). As our measurements were done in Fara-

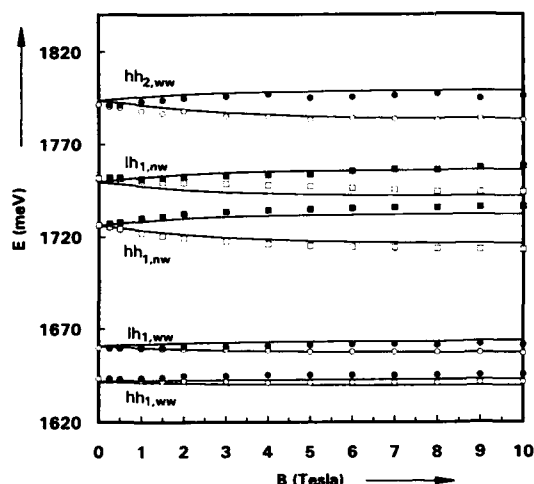


Fig. 2. Measured PLE peak energies (excitons localized in WW: (○)  $\sigma^+$  and (●)  $\sigma^-$ ; excitons localized in NW: (□)  $\sigma^+$  and (■)  $\sigma^-$ ), and calculated exciton energies (—) of the sample from Fig. 1 as a function of the magnetic field.

day configuration, no band mixing has to be taken into account.

## 2.2. Transfer

The exciton transfer through the potential barrier can be described as tunneling of electrons and holes, although in more sophisticated computations it can be considered as intersubband relaxation between states localized in neighbouring wells [5]. However, in our case the barrier width and height dependence of the transfer can be satisfactorily explained using the formula

$$\frac{1}{T} = \frac{\sqrt{2E/m}}{2L_w} P, \quad (1)$$

where

$$P = \frac{16E(V-E)}{V^2} \exp\left(-\frac{\sqrt{8m}}{\hbar} \alpha\right)$$

is the tunneling probability and  $\alpha = L_B \sqrt{V-E}$  the coupling parameter ( $T$  is the transfer time of the considered carriers,  $E$  and  $V$  are the subband energy and potential, respectively,  $m$  denotes the effective mass,  $L_w$  is the well width and  $L_B$  is the

width of the barrier). To connect the estimated transfer times with the measured intensities in CW excitation experiments, we solved a system of four coupled differential equations for the densities of spatial direct and indirect excitons in both wells [6]. The spatially indirect excitons had to be included as intermediate states to take into account the different tunneling times of electrons and holes. The solution for stationary excitation above the bandgap is given approximately by:

$$\frac{I_{NW}}{I_{WW}} \approx \left(1 + 2 \frac{T_e^{-1} + T_h^{-1}}{\tau_{NW}^{-1}}\right)^{-1}, \quad (2)$$

where  $I_{NW}$  and  $I_{WW}$  are the PL intensities from NW and WW, respectively,  $T_e$  and  $T_h$  denote the electron and hole transfer times, respectively, and  $\tau_{NW}$  is the exciton recombination time in NW. Formula (2) shows that the ratio of the PL intensities of both wells depends mainly on the ratio of the NW exciton recombination time and the shortest of either electron or hole transfer time. As in general the electron transfer times are faster by about two orders of magnitude than the heavy hole transfer times, we expect to observe PL emission from the NW only if the barrier is thick enough to find the electron transfer time being comparable with the excitonic recombination time. This recombination time was measured in the ps excitation experiments (see below). In our calculations we found good agreement with the data for a series of samples (see ref. [1]). It was established that over the hole range of realized barrier parameters, the ratio of the PL intensities was dependent only on the coupling parameter  $\alpha$  which describes the effective barrier width and height for electrons. In contrast, in an external magnetic field, the valence and conduction band edges of the barriers decrease for the  $\sigma^+$  component leading to a faster carrier transfer. As in CdMnTe about 80% of the total energy shift is taking place in the valence band [7], the heavy hole transfer times can decrease by several orders of magnitude depending on the sample parameters. For an illustration, see Fig. 3. The PL intensity ratio for three samples with same barrier widths (100 Å) but different Mn concentrations are plotted versus the magnetic field. For

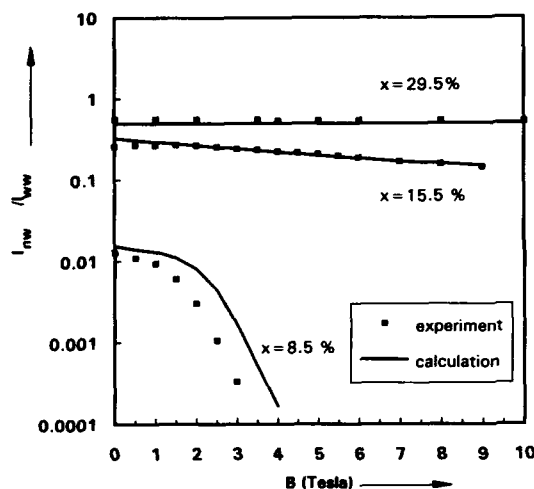


Fig. 3. PL intensity ratio  $I_{NW}/I_{WW}$  for three samples with the same barrier widths (100 Å) and Mn concentrations of 29.5%, 15.5% and 8.5% versus the magnetic field.

the highest Mn concentration (29.5%), no change in the intensity ratio could be observed, because in this case the hh and electron transfer times even for higher fields are still much longer than the recombination time. On the other hand, for the lowest Mn concentration (8.5%), the NW PL intensity is decreasing rapidly. The reason for this is that the relative shift of the valence band edge in a magnetic field is larger for lower Mn concentrations because of the decreased antiferromagnetic coupling. Some authors even discuss a type I–type II transition for comparable Mn concentrations [8]. Although we could not find any hint for a type II potential lineup, we can assume the barrier height for the hh to become very small. Consequently, the hh can even become faster than the electrons tunneling through the barrier and will determine the NW PL intensity for sufficiently high magnetic fields. The solid lines in Fig. 3 represent the calculations done with our kinetic model and agree well with the experimental results.

### 2.3. Semimagnetic well

Another type of DQW structure was designed with a semimagnetic wide well to study the exci-

ton level resonances in magnetic fields (see refs. [9,10]). Fig. 4 shows the PL energies of a sample with 14% Mn content in barriers and 4% in the wide well and 60 Å barrier thickness versus the magnetic field. Because of the Mn content in the wide well, the WW emission band occurs at higher energy than the NW one. Both the WW and NW spatial direct exciton emission are observable in spite of the fact that the inner barrier is only 60 Å thick. However, at zero magnetic field the WW emission is very weak and increases with increasing magnetic field. The exact dependence of the PL intensities on the magnetic field in this case is not yet fully understood and an explanation requires to extend the kinetic model introduced above. At 2.7 T we observed very clearly a crossing of the excitonic energies. This indicates that energy resonance of the hh or electron states must have occurred at a somewhat lower magnetic field. For comparison, we calculated the free carrier energies in the framework of our two-well model. In this model we found an anti-crossing of the hh states at 1.8 T. If we consider the different binding energies in both wells, the exciton energy resonance would occur at about 2.6 T, which is in good agreement with our exper-

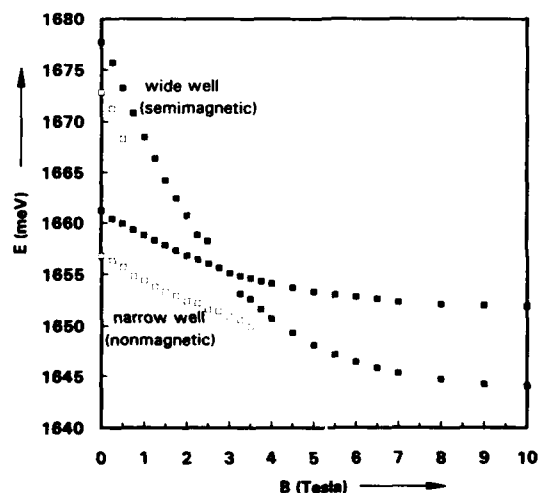


Fig. 4. PL peak energies (■) versus magnetic field for a DQW sample with semimagnetic wide well (Mn content in barriers 14%, in the wide well 4%) and 60 Å barrier thickness (□: bound exciton luminescence).

iments. The anticrossing nature of the resonance cannot be established experimentally as the PL linewidth is much larger than the minimum energy spacing between the two states. In spite of the hh anticrossing, we do not expect any spatial indirect exciton emission, because the barrier thickness of 60 Å is comparable with the normal exciton Bohr radius in CdTe and would probably not allow any indirect recombination. Furthermore, the ground electron state is spread over both wells according to our calculations and therefore in both wells direct excitons could be formed.

### 3. Picosecond measurements

The time-resolved experiments were made by detecting the luminescence decay of the respective radiative transitions. From choosing different excitation energies applying to transitions in WW and NW, we can get luminescence light with and without exciton transfer through the barrier. For both cases the luminescence decay curves can be fitted in good approximation by single exponential functions. The exponential decay constants without energy transfer which we attribute to the exciton recombination time were found to be around 120 ps for all samples, a typical value for CdMnTe quantum wells [11].

The energy transfer which determines the respective PL decay is influenced by the barrier width and the barrier height. For barrier widths of about 25 Å, we got decay times in the order of the exciton recombination time, and for samples with barrier widths of 100 Å, the decay time is about 300 ps due to a slower tunneling process.

The barrier height is given by the concentration of Mn, but depends also on the magnetic field which additionally influences the energy levels in a semimagnetic well. This influence can lead to the resonances as described above.

Fig. 5 shows a comparison of the exponential decay times as a function of the magnetic field for a sample with a nonmagnetic wide well (a, ●) and a sample with a semimagnetic wide well (b, ■) at sample temperatures of 4.2 K. The magnetic field was applied in Faraday configura-

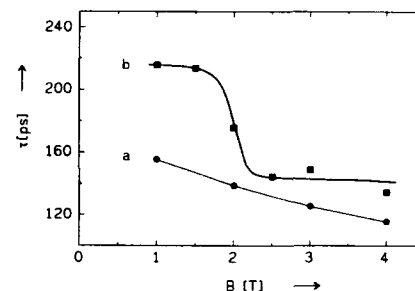


Fig. 5. PL decay constants  $\tau$  as a function of the magnetic field  $B$  for (a) transfer NW  $hh\sigma^+ \rightarrow WW hh\sigma^+$  between nonmagnetic wells,  $L_B = 100$  Å and (b) transfer WW  $hh\sigma^+$  (semimagnetic)  $\rightarrow$  NW  $hh\sigma^+$  (nonmagnetic),  $L_B = 60$  Å (the lines are guides to the eye).

tion. In curve (a) we pumped into the NW and observed the luminescence of the WW. The sample has a barrier width of 100 Å and a Mn concentration of 29.5%. The decay time shows only a slight decrease from 160 ps at 1.0 T down to 120 ps at 4.0 T due to the decreasing barrier height with increasing field. Curve (b) represents the luminescence decay constants of the NW pumped via the semimagnetic wide well of the sample described in part (c). For this case a strong decrease of the decay constant  $\tau$  is observable between 1.5 and 2.5 T.  $\tau$  reaches its lowest value of 150 ps at 2.5 T and stays then more or less constant. This is in good agreement with the results obtained from the CW measurements and the theoretical calculations which found the resonance of the hh states at 1.8 T, which means clearly before the exciton resonance at about 2.7 T occurs. This yields further evidence that the hole tunneling is the limiting process for the energy transfer.

### 4. References

- [1] O. Goede, W. Heimbrodt, K. Hieke, H.-E. Gumlich, Th. Pier, B. Lunn, D.E. Ashenford, S. Jackson and J.E. Nicholls, *Superlattices Microstruct.* 12 (1992) 363.
- [2] H. Mathieu, P. Lefebvre and P. Christol, *J. Appl. Phys.* 72 (1992) 300.
- [3] B. Kuhn, W. Ossau, A. Waag, R.N. Bicknell-Tassius and G. Landwehr, *J. Crystal Growth* 117 (1992) 871.
- [4] O. Goede and W. Heimbrodt, *Phys. Status Solidi (b)* 146 (1988) 11.

- [5] U. Rössler, private communication.
- [6] K. Hieke, W. Heimbrod et al., to be published.
- [7] J.A. Gaj, R. Planel and G. Fishman, *Solid State Commun.* 29 (1979) 435.
- [8] A. Wasiela, P. Peyla, Y. Merle d'Aubigné, J.E. Nicholls, D.E. Ashenford and B. Lunn, *Semicond. Sci. Technol.* 7 (1992) 571.
- [9] I. Lawrence, G. Feuillet, H. Tuffigo, C. Bodin, J. Cibert, P. Peyla and A. Wasiela, *Mater. Sci. Eng. B* 16 (1993) 234.
- [10] S.J. Weston, J.E. Nicholls, M. O'Neill, T. Stirner, P. Harrison, W.E. Hagston, J.H.C. Hogg, B. Lunn, D.E. Ashenford and K. Hieke, in: *Proc. 3rd Int. Conf. on Optics of Excitons in Confined Systems*, Montpellier, 1993 (*J. Physique*, to be published).
- [11] A. Pohlmann, R. Hellmann, E.O. Göbel, D.R. Yakovlev, W. Ossau, R.N. Bicknell-Tassius and G. Landwehr, *Appl. Phys. Lett.* 61 (1992) 2929.



ELSEVIER

Journal of Crystal Growth 138 (1994) 895–899

JOURNAL OF  
**CRYSTAL  
GROWTH**

## Orbital exchange in diluted magnetic semiconductors

A.K. Bhattacharjee

*Laboratoire de Physique des Solides, associé au CNRS, Université Paris-Sud, F-91405 Orsay, France*

### Abstract

An effective Hamiltonian for the hybridization-induced hole-ion interaction, reported previously, is used to calculate the valence-band Zeeman splitting in cubic V-, Cr-, Ni- and Cu-based diluted magnetic semiconductors (DMS). The orbital coupling terms predicted for these systems lead to drastic modifications of the band splitting expected from the usual spin-exchange model. In V-based DMS we obtain a highly asymmetric splitting. But, in the case of Cr static Jahn–Teller distortion tends to quench the orbital effects, in agreement with experiment in  $\text{Zn}_{1-x}\text{Cr}_x\text{Se}$ . For Ni-based DMS a sign reversal of the  $m = \pm \frac{1}{2}$  subbands is predicted. The splitting vanishes in Cu-based DMS.

### 1. Introduction

Semimagnetic or diluted magnetic semiconductors (DMS) are typically solid solutions of II–VI compounds:  $\text{A}_{1-x}^{\text{II}}\text{M}_x\text{B}^{\text{VI}}$ , where  $\text{A}^{\text{II}} = \text{Cd}, \text{Zn}, \text{Hg}$ ,  $\text{B}^{\text{VI}} = \text{Te}, \text{Se}, \text{S}$  and  $\text{M}$  is a transition metal. Mn-based DMS have been investigated most extensively. The Fe- and Co-based ones have been synthesized and studied more recently. The spectacular magneto-optical properties of the Mn-based DMS were early interpreted in terms of the Kondo-like exchange Hamiltonian of the form  $-J_s \cdot S$ , for the coupling between the band electron spin  $s$  and the  $\text{Mn}^{2+}$  ion spin  $S$ , with the Hund rule value  $S = \frac{5}{2}$ . The same Hamiltonian is used for describing transport properties and bound magnetic polarons. A mean-field analysis of combined magneto-reflectivity and magnetization measurements yields accurate values of the exchange parameter in wide-gap DMS [1]. Generally speaking, the exchange parameter for the conduction band minimum  $N_0\alpha$  is positive (ferromagnetic) and of order 0.2 eV, whereas that for

the valence band maximum  $N_0\beta$  is negative (antiferromagnetic) and of order 1.0 eV. We [2] have accounted for these features in the following manner. The relatively small  $N_0\alpha$  corresponds to the ordinary exchange integral of the Coulomb potential between a conduction band electron and the Mn d electrons. On the other hand,  $N_0\beta$  is dominated by the effective exchange arising from the hybridization between the valence band states and the localized d orbitals. The Schrieffer–Wolff transformation [3] was used to quantitatively relate  $N_0\beta$  to the Anderson hybridization parameter and the energy of the d level below the valence band maximum. These ideas have been further developed by Larson et al. [4]. The Schrieffer–Wolff formula is valid for the S-state ion  $\text{Mn}^{2+}$ . For other transition-metal ions  $L \neq 0$  and orbital coupling terms were also expected [5]. Blinowski et al. [6] studied the cases of  $\text{Cr}^{2+}$  and  $\text{Fe}^{2+}$ .

Recently we deduced [7] an effective hole-ion coupling Hamiltonian for the general case of  $3d^n$  configuration in tetrahedral symmetry, by using

group-theoretical methods. As the valence band at  $\Gamma$  belongs to the irreducible representation  $t_2$  no coupling is obtained for  $n = 1$  ( $\text{Sc}^{2+}$ ) or 2 ( $\text{Ti}^{2+}$ ) because the hybridizing  $t_2$  subshell of the ion is empty. For  $n = 5$  ( $\text{Mn}^{2+}$ ), 6 ( $\text{Fe}^{2+}$ ) and 7 ( $\text{Co}^{2+}$ ) with half-filled  $t_2$  subshell, the coupling reduces to the usual spin-exchange Kondo form, in agreement with experiments [8]. However, the Schrieffer–Wolff formula is modified by a normalization factor  $(2S)^{-1}$  which mostly accounts for the observed increase of  $|N_0\beta|$  from Mn to Fe to Co in a given host. On the other hand, for  $n = 3$  ( $\text{V}^{2+}$ ), 4 ( $\text{Cr}^{2+}$ ), 8 ( $\text{Ni}^{2+}$ ) and 9 ( $\text{Cu}^{2+}$ ), in addition to the spin–spin coupling, we obtained terms involving the orbital degrees of freedom. In the present work the complete effective Hamiltonian is used to calculate the valence band Zeeman splitting in V-, Cr-, Ni- and Cu-based diluted magnetic semiconductors. A comparison of the results with those of the simple spin-exchange model in each case reveals the importance of the orbital exchange terms. We summarize the theoretical model in section 2. The results are presented and discussed case by case in section 3. We also discuss the experimental study of  $\text{Zn}_{1-x}\text{Cr}_x\text{Se}$  [9], the only one reported so far in this family of DMS.

## 2. Theoretical model

The transition-metal ion ( $3d^n$ ) is treated in the intermediate crystal-field coupling scheme. The Hund rule ground term ( $L, S$ ) is split in the tetrahedral crystal field leading to the ground multiplet ( $i, S$ ), where  $i$  is an irreducible representation of  $T_d$ . In the cases  $n = 3, 4, 8$  and  $9$ ,  $i$  is triply degenerate (either  $T_1$  or  $T_2$ ) and the hole-ion effective interaction Hamiltonian is given by [7]

$$\begin{aligned} H_n^{\text{eff}} &= I_n \left\{ \gamma_1 \alpha(A_1, 1) s \cdot S \right. \\ &+ \frac{1}{2} \left[ \gamma_0 \alpha(T_1, 0) + 3\gamma_1 \alpha(T_1, 1) s \cdot S \right] I \cdot I \\ &+ \frac{1}{6} \left[ \gamma_0 \alpha(E, 0) + 3\gamma_1 \alpha(E, 1) s \cdot S \right] \end{aligned}$$

$$\begin{aligned} &\times \left[ (3I_z^2 - 2)(3I_x^2 - 2) + 3(I_x^2 - I_y^2)(I_x^2 - I_y^2) \right] \\ &+ \frac{1}{2} \left[ \gamma_0 \alpha(T_2, 0) + 3\gamma_1 \alpha(T_2, 1) s \cdot S \right] \\ &\times \left[ (I_x I_y + I_y I_x)(I_x I_y + I_y I_x) \right. \\ &+ (I_y I_z + I_z I_y)(I_y I_z + I_z I_y) \\ &\left. + (I_z I_x + I_x I_z)(I_z I_x + I_x I_z) \right] \}. \quad (1) \end{aligned}$$

Here  $I$  ( $I = 1$ ) and  $s$  ( $s = \frac{1}{2}$ ) correspond to the p-like valence band states at  $\Gamma$ . The pseudo-angular-momentum operators  $I$  in the subspace  $i$  are represented by the usual  $I = 1$  angular momentum matrices. In this subspace, the ionic orbital angular momentum  $L = rI$ , with  $r = -1$  for  $L = 2$  ( $\text{Cr}^{2+}$ ,  $\text{Cu}^{2+}$ ) and  $r = -3/2$  for  $L = 3$  ( $\text{V}^{2+}$ ,  $\text{Ni}^{2+}$ ). Note that the tetrahedrally invariant form of  $H_n^{\text{eff}}$  is completely general; only the coupling coefficients depend on the mechanism. They were deduced from the Anderson model for single-electron p–d hybridization (mixing) by using the irreducible tensor method.  $\gamma_0$ ,  $\gamma_1$  and  $\alpha(\Delta, \Sigma)$  are given in ref. [7]:

$$I_n = \frac{16V_{pd}^2}{N_0} \left( \frac{1}{E_v - \epsilon_d} + \frac{1}{\epsilon_d + U_{\text{eff}} - E_v} \right), \quad (2)$$

where  $N_0$  is the number of primitive cells per unit volume and  $V_{pd}$  the real-space hopping amplitude from the transition metal d orbital to a neighbouring anion p orbital. The energy denominator of the first term in Eq. (2) corresponds to the virtual emission of an electron from the ionic  $t_2$  subshell to the valence band. The second term corresponds to the inverse virtual process.

In order to calculate the contribution of  $H_n^{\text{eff}}$  to the valence-band Zeeman splitting in the mean-field approximation, we first evaluate the expectation values of the band operators in the states  $|jm\rangle$ . In a zinc-blende DMS, the  $\Gamma_8$  valence band ( $j = \frac{3}{2}$ ) splits into four components with energies

$$\begin{aligned} E_m &= N_0 x I_n \left\{ \frac{1}{3} m \left[ \gamma_1 \alpha(A_1, 1) \langle S_z \rangle \right. \right. \\ &+ \gamma_0 \alpha(T_1, 0) \langle I_z \rangle \left. \right] \\ &+ \frac{1}{2} \gamma_1 \alpha(T_1, 1) \left[ \left( \frac{3}{8} - \frac{1}{6} m^2 \right) \right. \\ &\left. \left. \times (\langle S_x I_x \rangle + \langle S_y I_y \rangle) + \left( \frac{1}{3} m^2 - \frac{1}{4} \right) \langle S_z I_z \rangle \right] \right\} \end{aligned}$$

$$\begin{aligned}
& + \frac{1}{6} \gamma_0 \alpha(E, 0) (m^2 - \frac{5}{4}) \langle 3I_z^2 - 2 \rangle \\
& + \frac{1}{2} \gamma_1 \alpha(E, 1) (m^3 - \frac{23}{12} m) \langle S_z (3I_z^2 - 2) \rangle \\
& - \frac{1}{2} \gamma_1 \alpha(T_2, 1) (m^3 - \frac{9}{4} m) [\langle S_x (I_z I_x \\
& + I_x I_z) \rangle + \langle S_y (I_y I_z + I_z I_y) \rangle] \} \quad (3)
\end{aligned}$$

for magnetic field along a cube axis ( $z$ ). On the other hand, the spin-exchange model gives

$$E_m^{(0)} = \frac{N_0 x I_n}{3S} m \langle S_z \rangle. \quad (4)$$

The expectation values of the ionic operators have to be calculated in the eigenstates of the Zeeman Hamiltonian including the spin-orbit interaction and then thermally averaged. The spin-orbit interaction splits the ground multiplet [10]. The Zeeman Hamiltonian mixes the spin-orbit eigenstates. We solve the  $3(2S+1)$ -dimensional eigenvalue problem in order to calculate the thermal averages.

For magnetic field along a trigonal direction, the quantization axis is  $\zeta \parallel \langle 111 \rangle$ . A new set of orthogonal axes ( $\xi$ ,  $\eta$  and  $\zeta$ ) is used to rewrite  $H_n^{\text{eff}}$  and to calculate the averages.

### 3. Results and discussion

#### 3.1. V-based DMS

Spin-orbit interaction splits the ground multiplet  $^4T_1$  of  $V^{2+}$  into four levels:  $\Gamma_8$ ,  $\Gamma_7$ ,  $\Gamma_8$  and  $\Gamma_6$  with energies  $-9\lambda/4 - (1305\lambda^2/64\Delta)$ ,  $-9\lambda/4 - (225\lambda^2/64\Delta)$ ,  $3\lambda/2 - (45\lambda^2/4\Delta)$  and  $15\lambda/4 - (225\lambda^2/64\Delta)$ , respectively [10]. Here  $\lambda$  is the spin-orbit coupling constant and  $\Delta$  is the crystal-field splitting. After adding the Zeeman Hamiltonian, we have a  $12 \times 12$  eigenvalue problem. However, for  $B \parallel \langle 100 \rangle$ , the Hamiltonian matrix reduces into four  $3 \times 3$  blocks. For  $B \parallel \langle 111 \rangle$  we have two  $2 \times 2$  blocks and two  $4 \times 4$  blocks. Exact diagonalization is carried out numerically and the valence subband energies calculated. The parameters used are  $\lambda = 50 \text{ cm}^{-1}$  and  $\Delta = 3600 \text{ cm}^{-1}$  suitable for the CdTe host crystal [11].

Fig. 1 shows the dimensionless subband energies  $E_m/(N_0 x I_3)$  versus magnetic field  $B$  (in tesla)

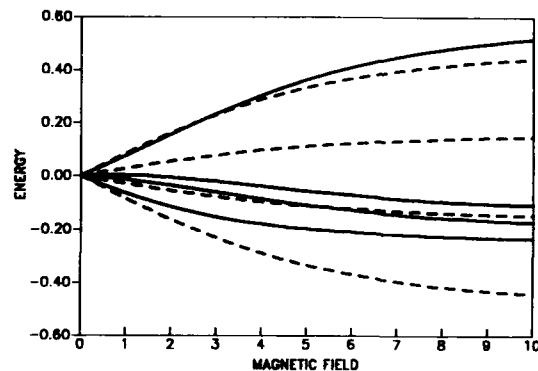


Fig. 1. Theoretical valence-band splitting in a V-based DMS at  $T = 2 \text{ K}$  for  $B \parallel \langle 100 \rangle$ . Subband energies  $E_m/(N_0 x I_3)$  are plotted against  $B$  (in tesla). The solid curves correspond to the full effective Hamiltonian and the dashed ones to the spin-exchange model. In both series the subbands  $m = \frac{3}{2}, \frac{1}{2}, -\frac{1}{2}$  and  $-\frac{3}{2}$  are in order of increasing energy, with  $m = \frac{3}{2}$  at the bottom.

along a cube axis at  $T = 2 \text{ K}$ . The solid curves obtained from Eq. (3) correspond to the full effective Hamiltonian. The dashed curves result from the spin-exchange model Eq. (4). In each series the subbands  $m = \frac{3}{2}, \frac{1}{2}, -\frac{1}{2}$  and  $-\frac{3}{2}$  are in order of increasing energy, with  $m = \frac{3}{2}$  at the bottom. It can be seen that the orbital coupling terms lead to qualitatively new results. A remarkable feature is the large asymmetry of the band splitting with respect to the zero-field energy. At 10 T, the energy of the  $m = -\frac{3}{2}$  subband is  $+0.52$ , while that of  $m = +\frac{3}{2}$  is  $-0.23$ . In magneto-optical experiments, one would expect a corresponding asymmetry between the  $\sigma_+$  and  $\sigma_-$  components with respect to the zero-field exciton line.

Fig. 2 shows the band splitting in magnetic field along a trigonal axis. Comparison between Figs. 1 and 2 reveals strong anisotropy. Note that the splitting asymmetry is reduced for  $B \parallel \langle 111 \rangle$ . Fig. 3 presents the average magnetic moment per  $V^{2+}$  ion (in  $\mu_B$ ) versus  $B$ . Here the solid curve is for  $B \parallel \langle 100 \rangle$  and the dashed one for  $B \parallel \langle 111 \rangle$ . Notice the significant anisotropy of magnetization.

The effects of the orbital coupling terms, illustrated above, would be drastically attenuated in case of strong Jahn-Teller distortion. (Evidence



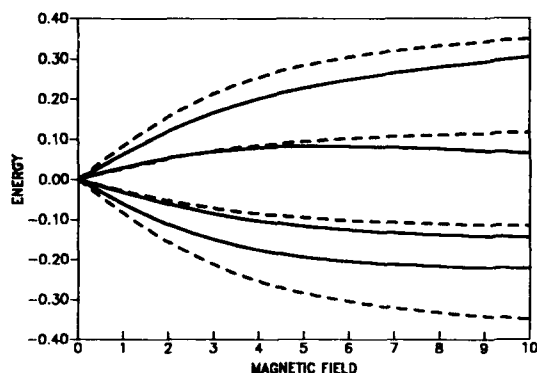


Fig. 2. Theoretical valence-band splitting in a V-based DMS at  $T = 2$  K for  $B \parallel \langle 111 \rangle$ . See the caption of Fig. 1 for further description.

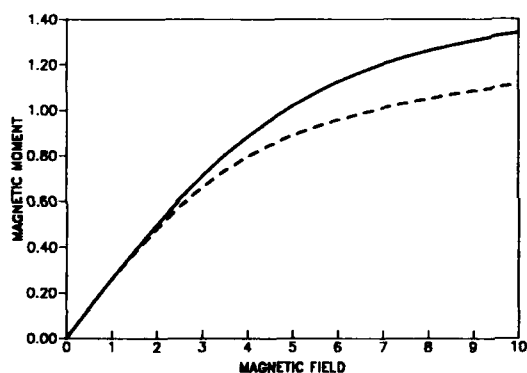


Fig. 3. Theoretical magnetization curves for a V-based DMS at  $T = 2$  K. Magnetic moment per  $V^{2+}$  ion (in  $\mu_B$ ) is shown against  $B$  (in tesla). The solid curve is for  $B \parallel \langle 100 \rangle$  and the dashed one for  $B \parallel \langle 111 \rangle$ .

for a trigonal distortion was reported in  $ZnS:V$  [12].) On the other hand, the orbital effects are expected to be most important in wurtzite-structure DMS. Preliminary calculations suggest that the Zeeman splitting of the A band in  $Cd_{1-x}V_xSe$  is smaller than that of the B band, in contrast with the spin-exchange model.

### 3.2. Cr-based DMS

Cr as impurity in cubic II-VI compounds has been systematically investigated [13]. In all cases, the  $Cr^{2+}$  ion shows a strong static Jahn-Teller distortion along a tetragonal axis. The ground

orbital triplet  $T_2$  splits into a singlet ground state and a doublet excited state separated by  $\sim 1500$   $cm^{-1}$ . The spin-orbit coupling lifts the spin degeneracy in the second order. At low temperatures, the orbital part of the ground state remains mostly  $|T_2, 0\rangle$ . Thus, for  $B$  parallel to the distortion axis, we obtain from Eq. (3) the subband energy per ion

$$\epsilon_m^{\parallel} = \frac{I_4}{6} \left[ \left( m^2 - \frac{5}{4} \right) (1 + m \langle S_{\parallel} \rangle) \right]. \quad (5a)$$

For  $B$  along a cube axis perpendicular to the distortion, we find

$$\epsilon_m^{\perp} = \frac{I_4}{6} \left[ -\frac{1}{2} \left( m^2 - \frac{5}{4} \right) - \frac{1}{2} \left( m^2 - \frac{13}{4} \right) m \langle S_{\perp} \rangle \right]. \quad (5b)$$

As the distortion axes for different ions are randomly oriented, for  $B \parallel \langle 100 \rangle$ , the subband energies are

$$E_m = \frac{N_0 x I_4}{9} \left[ m \langle S_{\perp} \rangle + \frac{1}{2} \left( m^2 - \frac{5}{4} \right) m (\langle S_{\parallel} \rangle - \langle S_{\perp} \rangle) \right]. \quad (6)$$

Thus the band splitting is qualitatively similar to that in the spin-exchange model. However, the second term increases the splitting between  $-\frac{3}{2}$  and  $+\frac{3}{2}$ , and decreases that between  $-\frac{1}{2}$  and  $+\frac{1}{2}$ . But this correction decreases with increasing field and vanishes at saturation.

An experimental study has been reported [9] in  $Zn_{1-x}Cr_xSe$  with  $x$  rather small (maximum  $x = 0.0045$ ). The magnetorefectance data indeed fit in with the spin-exchange model. But the most striking feature is the sign reversal of the valence-band splitting: the  $m = \frac{3}{2}$  subband lies above  $m = -\frac{3}{2}$ . This implies a ferromagnetic effective exchange, in contrast with the cases of Mn-, Fe- or Co-based DMS. On the other hand, the magnitude of the exchange parameter is of order 1 eV, much too large for the direct exchange mechanism. A tempting interpretation is to assume a negative  $I_4$  value. This would, however, mean that the Cr d level ( $\epsilon_d$ ) lies above the valence band edge ( $E_v$ ), implying an unstable  $3d^4$  configuration. The presence of a hole should then lead to real transition into the  $Cr^{3+}$  state. Apparently, the time delay for such a process is

sufficiently long and the effective hole-ion interaction Hamiltonian with  $n = 4$  can be used phenomenologically for analyzing the Zeeman splitting of the exciton line. Of course, photoemission experiments should be performed in order to check the energy level scheme.

### 3.3. Ni-based DMS

The spin-orbit interaction splits the ground multiplet  $^3T_1$  of  $Ni^{2+}$  into four levels. The ground state is a singlet. The first excited level lies  $G = -3\lambda/2 - 15(\lambda^2/4\Delta)$  above. With  $\Delta = 4200$  and  $\lambda = -300$ , we estimate  $G = 370 \text{ cm}^{-1}$ . The field-induced mixing can be treated as a perturbation and the low-temperature operator averages calculated analytically. We obtain

$$E_m = \frac{N_0 x I_8}{20} (m^2 - \frac{5}{3}) m \langle S_z \rangle. \quad (7)$$

Thus, orbital coupling leads to a sign reversal for the  $m = \pm \frac{1}{2}$  subbands. Unfortunately, it would be hard to detect experimentally, because  $\langle S_z \rangle$  is rather small:  $\langle S_z \rangle = -\frac{14}{3} \mu_B B / G \approx -0.06$  at 10 T. The estimated low-temperature magnetization of such Van Vleck paramagnets is also small; the magnetic moment per ion is given by  $3.5 \langle S_z \rangle \mu_B$ .

### 3.4. Cu-based DMS

The ground multiplet of  $Cu^{2+}$  is  $^2T_2$ . The spin-orbit coupling splits it into a doublet ( $\Gamma_7$ ) ground state and a quartet ( $\Gamma_8$ ) excited level separated by  $G = -\frac{3}{2}\lambda - (3\lambda^2/2\Delta)$ . Assuming  $\Delta = 5500$  and  $\lambda = -800$ , we estimate  $G \approx 1000 \text{ cm}^{-1}$ . We can therefore neglect the  $\Gamma_8$  level and calculate the operator averages analytically. We find

$$E_m = 0. \quad (8)$$

This indeed represents a drastic contradiction with the spin-exchange model that predicts an overall splitting of  $(N_0 x I_9)/3$  at saturation.

### 4. Concluding remarks

We have calculated the valence-band Zeeman splitting in cubic V-, Cr-, Ni- and Cu-based DMS

with an effective hole-ion interaction Hamiltonian reported previously. The coupling terms involving the orbital degrees of freedom lead to drastic modifications of the band splitting expected from the simple spin-exchange model. In V-based DMS large magneto-optical asymmetry is predicted. In the case of Cr, static Jahn-Teller distortion tends to quench the orbital effects, in agreement with experimental data in  $Zn_{1-x}Cr_xSe$ . But the observed sign reversal of the band splitting suggests a negative  $I_4$  value, implying that the Cr d level in ZnSe lies above the valence band. On the other hand, in Ni-based DMS the orbital coupling terms lead to a sign reversal of the  $m = \pm \frac{1}{2}$  subbands. However, the spin-orbit coupling is so large that the magnetization and band splittings are expected to be rather small in these Van Vleck paramagnets. In Cu-based DMS the total effective Hamiltonian predicts a vanishing valence-band splitting in complete contradiction with the spin-exchange model. Our results would hopefully encourage experimental studies of new DMS systems, in particular, those based on V and Cu.

### 5. References

- [1] J.A. Gaj, R. Planel and G. Fishman, *Solid State Commun.* 29 (1979) 435.
- [2] A.K. Bhattacharjee, G. Fishman and B. Coqblin, *Physica B* 117 & 118 (1983) 449.
- [3] J.R. Schrieffer and P.A. Wolff, *Phys. Rev.* 149 (1966) 491.
- [4] B.E. Larson, K.C. Hass, H. Ehrenreich and A.E. Carlson, *Phys. Rev. B* 37 (1988) 4137.
- [5] L.L. Hirst, *Adv. Phys.* 27 (1978) 231.
- [6] J. Blinowski, P. Kacman and H. Przybylinska, *Solid State Commun.* 79 (1991) 1021.
- [7] A.K. Bhattacharjee, *Phys. Rev. B* 46 (1992) 5266.
- [8] F. Hamdani, J.P. Lascaray, D. Coquillat, A.K. Bhattacharjee, M. Nawrocki and Z. Golacki, *Phys. Rev. B* 45 (1992) 13298.
- [9] W. Mac, Nguyen The Khoi, A. Twardowski, J.A. Gaj and M. Demianiuk, *Acta Phys. Pol. A* 82 (1992) 902.
- [10] M. Villeret, S. Rodriguez and E. Kartheuser, *Phys. Rev. B* 41 (1990) 10028.
- [11] P.A. Slodowy and J.M. Baranowski, *Phys. Status Solidi (b)* 49 (1972) 499.
- [12] J. Schneider, B. Dischler and A. Räuber, *Solid State Commun.* 5 (1967) 603.
- [13] J.T. Vallin and G.D. Watkins, *Phys. Rev. B* 9 (1974) 2051.

## Magnetic properties of $\text{Cd}_{1-x}\text{Mn}_x\text{Te}$ grown by molecular beam epitaxy

M. Sawicki <sup>a,1</sup>, M.A. Brummell <sup>\*,a</sup>, P.A.J. de Groot <sup>a</sup>, G.J. Tomka <sup>a</sup>,  
D.E. Ashenford <sup>b</sup>, B. Lunn <sup>b</sup>

<sup>a</sup> Department of Physics, University of Southampton, Highfield, Southampton SO9 5NH, UK

<sup>b</sup> Department of Engineering Design and Manufacture, University of Hull, Hull HU6 7RX, UK

### Abstract

Temperature dependent magnetization measurements have been performed on both thick  $\text{Cd}_{1-x}\text{Mn}_x\text{Te}$  layers and a  $\text{CdTe}/\text{Cd}_{1-x}\text{Mn}_x\text{Te}$  superlattice grown by molecular beam epitaxy (MBE). The general behaviour of the thick layers is similar to bulk-grown material, with a spin-glass state being formed at low temperatures, but the magnitude of the high-temperature susceptibilities differs significantly. This may be due to structural differences in the material grown by different methods. The layer with the highest Mn fraction of  $x = 0.70$  shows antiferromagnetic behaviour with a Néel temperature of 48 K. The superlattice structure containing 100 Å thick layers of  $\text{Cd}_{0.55}\text{Mn}_{0.45}\text{Te}$  also showed a spin-glass transition, but had an enhanced paramagnetic contribution to the susceptibility at low temperatures. This could be caused by the reduction in dimensionality or by an interface effect.

The magnetic properties of bulk dilute magnetic semiconductors such as  $\text{Cd}_{1-x}\text{Mn}_x\text{Te}$  have been extensively studied in recent years. For Mn fractions  $x$  between 0.2 and 0.6 this material condenses into a spin-glass phase below a critical temperature  $T_f(x)$  [1], although the precise nature of this state has been the subject of some discussion [2,3]. For  $x > 0.6$  it has been suggested that the ordering is antiferromagnetic [1], but experiments are hampered by the formation of mixed structural phases in bulk-grown material for  $x > 0.7$ . Investigations of the magnetic behaviour of low-dimensional  $\text{CdMnTe}$  are less nu-

merous. Theory predicts a critical dimensionality of between two and three for the spin-glass state [4], so this would be expected to vanish as the thickness of a  $\text{CdMnTe}$  layer is reduced. This disappearance was observed by Awschalom et al. [5,6] in a series of  $\text{CdMnTe}/\text{CdTe}$  superlattices with  $\text{CdMnTe}$  layer thicknesses between 80 and 20 Å. They also found thermal hysteresis in the thinnest layers, which is not fully understood.

In this paper we report measurements of the magnetization as a function of temperature in  $\text{CdMnTe}$  structures grown by MBE. The behaviour of thick layers ( $\sim 2 \mu\text{m}$ ) is qualitatively similar to that of bulk-grown samples, but quantitative differences are observed which may reflect structural differences in the material grown by the two methods. Significantly different results are obtained from a  $\text{CdMnTe}/\text{CdTe}$  superlattice

\* Corresponding author.

<sup>1</sup> Present and permanent address: Institute of Physics, Polish Academy of Sciences, 02-668 Warsaw, Poland.

containing 100 Å CdMnTe layers, which may be due to interface effects or a consequence of the reduced dimensionality.

The samples studied were grown by MBE on InSb (100) substrates at the University of Hull [7]. The magnetization was measured in a DC SQUID magnetometer: the normal measuring field was 0.1 T, although no significant dependence of the susceptibility upon magnetic field was observed up to 1.0 T. The Mn concentrations  $x$  were deduced from both high resolution double-crystal X-ray diffraction rocking curves, and dynamical simulation [8] and from Raman measurements of the CdTe-like and MnTe-like longitudinal optic phonon frequencies [9]: the former technique also gives the layer thicknesses in the superlattice sample.

Typical results for a thick layer are shown in Fig. 1, which plots the magnetization  $M$  as a function of temperature for a 2  $\mu\text{m}$  thick sample of  $\text{Cd}_{0.72}\text{Mn}_{0.28}\text{Te}$ . The  $M(T)$  curve shows a cusp at a temperature of 4 K, below which the magnetization depends upon whether the sample was cooled in zero magnetic field (ZFC) or with the measuring field already applied (FC). This be-

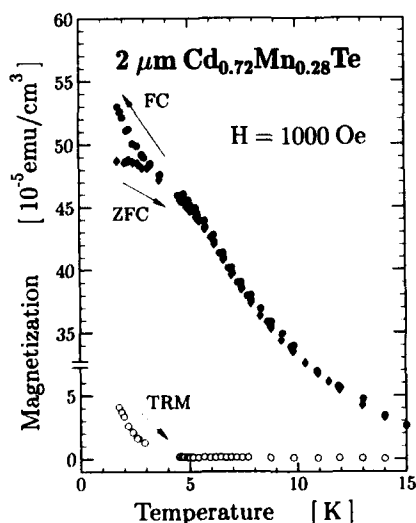


Fig. 1. The magnetization of the thick layer with  $x = 0.28$ , showing the divergence of the field-cooled (FC) and zero-field-cooled (ZFC) data and the thermoremanent magnetization (TRM) below 4 K, indicative of the spin-glass state.

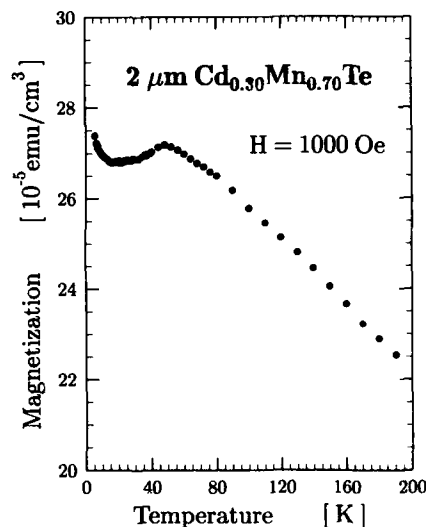


Fig. 2. The magnetization of the thick layer with  $x = 0.70$ . There is no difference between FC and ZFC data and no TRM, suggesting antiferromagnetic ordering. The cusp in the magnetization gives a Néel temperature of 48 K.

haviour is characteristic of the spin-glass formation in bulk-grown CdMnTe [1,10] and the point of divergence of the FC and ZFC curves is normally taken as the freezing temperature  $T_f$ . With our use of a DC SQUID we were also able to measure the thermoremanent magnetization (TRM) produced when the sample is cooled in field and the field then removed [10,11], and we feel that the vanishing of the TRM provides the most accurate indication of  $T_f$ .

This behaviour characteristic of a spin-glass phase was seen in thick layers with  $x = 0.28$  and  $x = 0.53$ , the values of  $T_f$  deduced being 4 K and 22 K respectively. These are similar to the transition temperatures found in bulk-grown material [1,10,11]. However, a thick layer with  $x = 0.70$  gave rather different results, as shown in Fig. 2. There is a cusp in the magnetization at a temperature of 48 K, below which the temperature dependence is weak, with no difference between FC and ZFC data, and there is no TRM. We interpret this as due to antiferromagnetic ordering, as observed previously by Galazka et al. [1]. The Néel temperature of 48 K is the highest value

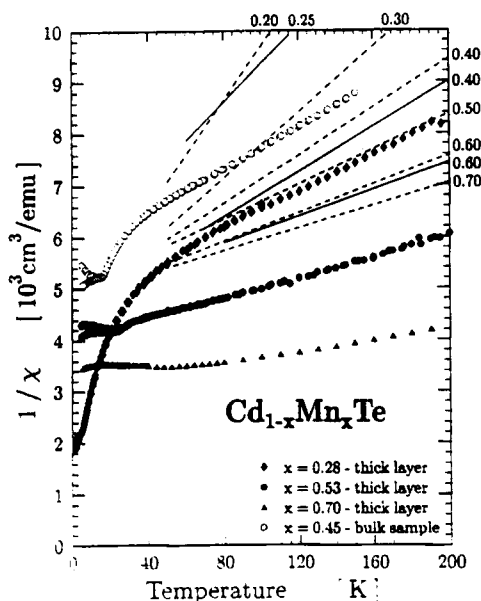


Fig. 3. The inverse susceptibility of the three thick layer samples, plus a bulk sample for comparison. The solid and dashed lines show the bulk data of refs. [10] and [12], respectively. Although the MBE samples have high temperature susceptibilities of Curie-Weiss form, as seen in the bulk, the actual magnitudes are significantly higher.

from magnetization studies that we are aware of, and this may reflect the ability of MBE to grow pure cubic material following the substrate structure at Mn concentrations where bulk growth produces mixed structural phases.

At temperatures well above  $T_f$  bulk-grown CdMnTe behaves paramagnetically, with a susceptibility  $\chi$  of the Curie-Weiss form  $\chi = C(x)/[T + \theta(x)]$ , where  $\theta(x)$  is the Curie-Weiss temperature [10,12]. Thus a plot of  $\chi^{-1}$  against  $T$  gives a straight line whose gradient and intercept reflect  $C(x)$  and  $\theta(x)$ , respectively. Our data from the MBE-grown thick layers follow this form, as shown in Fig. 3, but the values of  $C(x)$  and  $\theta(x)$  differ significantly from those seen in bulk-grown material. The results from refs. [10] and [12] are shown by solid and dashed lines, respectively, and it can be seen that the MBE samples have considerably higher susceptibilities than bulk-grown material of the same composition. The values of  $C(x)$  are of order 50% greater in the MBE samples, while  $\theta(x)$  is 270 K and 340 K for the  $x = 0.28$  and  $x = 0.53$  layers, respectively, compared with values of 140 K and 320 K expected from ref. [12]. Fig. 3 also shows measurements made in our equipment on a bulk-grown

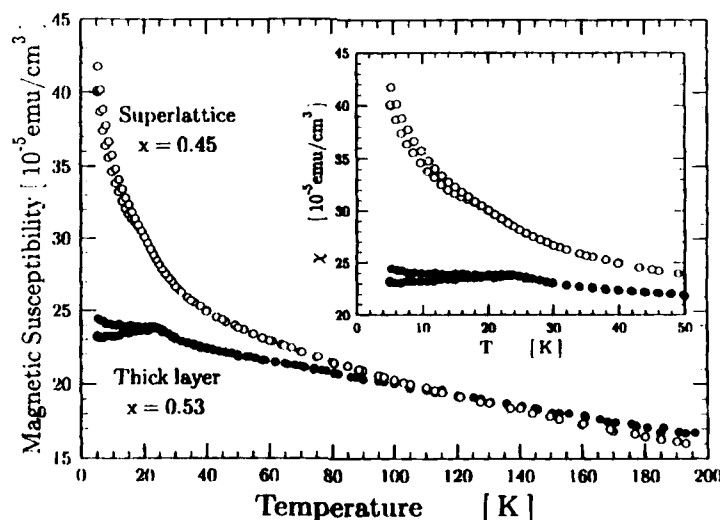


Fig. 4. A comparison of the susceptibilities of a thick layer and of 100 Å layers in a superlattice. Although both show spin-glass behaviour at low temperatures, there is an additional paramagnetic contribution to the susceptibility of the superlattice layers.

sample with  $x = 0.45$ , which provides a test for systematic errors. This sample gives a somewhat lower susceptibility than the data of refs. [10] and [12], in contrast to the MBE layers, with  $\theta(x) = 280$  K as compared with the value of 260 K expected from ref. [12]. The cause of this difference between bulk- and MBE-grown samples is unclear at present, but one possibility is that the distribution of Mn ions on the cation sites is nonrandom in either or both types of material. This would alter the number of clusters of Mn ions interacting antiferromagnetically, and thus change the susceptibility. It has been suggested previously that the Mn distribution in bulk-grown CdMnTe is nonrandom [1,16], although this may be due to the limitations of the theoretical models used [11]. Alternatively, the MBE-grown CdMnTe may have an ordered distribution of Cd and Mn ions of the form found in various III–V alloys when grown by MBE.

Fig. 4 compares the susceptibility of the  $2\text{ }\mu\text{m}$  thick layer of  $\text{Cd}_{0.47}\text{Mn}_{0.53}\text{Te}$  described above with that of  $100\text{ }\text{\AA}$  thick layers of  $\text{Cd}_{0.55}\text{Mn}_{0.45}\text{Te}$  in a superlattice structure. The superlattice contained 200 CdMnTe layers separated by 50  $\text{\AA}$  layers of CdTe, and the Mn fraction in the CdMnTe layers was confirmed by both X-ray diffraction and Raman scattering studies with the strain in the structure taken into account [8,9]. The superlattice shows the behaviour characteristic of a spin-glass, with a difference between the FC and ZFC data and the appearance of TRM below the transition temperature of  $T_f = 19$  K. This freezing temperature for  $x = 0.45$  is consistent with the values seen in the thick layers and in bulk-grown material. However, the superlattice sample shows a greatly enhanced paramagnetic component to the susceptibility at low temperatures. This difference between the two samples is more than 10 times greater than can be accounted for by the small difference in their Mn concentrations.

One possible explanation of this enhanced paramagnetism would be that the CdTe layers in the superlattice actually contain a small fraction of Mn arising from Mn diffusion during growth. In fact, the data can be fitted very well if it is assumed that the CdTe layers contain a Mn frac-

tion of  $x \sim 0.03$ , and thus contribute an additional paramagnetic magnetization. However, there is evidence from other sources that such interdiffusion has not occurred in this sample. The Raman studies [9] give an upper limit of  $x = 0.02$  for the Mn content of the CdTe layers, while the energy of the free exciton photoluminescence from the quantum wells could not be consistent with  $x > 0.01$  in the wells and reasonable assumptions about the band offsets and exciton binding energy. Most convincing, however, is the shift of the free exciton emission in magnetic field, which implies a Mn content in the wells of  $x < 0.001$  [13]. These optical measurements sample only the uppermost  $\sim 0.1\text{ }\mu\text{m}$  of the superlattice, whereas the magnetization results reflect the full  $3\text{ }\mu\text{m}$  thickness of the structure, so the enhanced paramagnetism could arise from greater interdiffusion at the bottom of the superlattice, which is held at elevated temperatures for a longer time in the growth process. This was shown not to be a serious factor by etching away a section of the substrate and comparing the photoluminescence from the top and bottom of the superlattice [13]. The peak emission energy from the bottom of the structure was  $\sim 3\text{ meV}$  higher, which corresponds to a Mn fraction in the wells only 0.002 greater.

We thus believe that the enhanced paramagnetism that we observe in the superlattice is not due to interdiffusion, but is either a consequence of the reduced dimensionality or an effect of the CdTe–CdMnTe interfaces. We observed no dependence of the susceptibilities measured upon whether the magnetic field was applied parallel or perpendicular to the layers: the observation of such a difference would have strongly suggested that the reduced dimensionality was responsible. The layer thickness of  $100\text{ }\text{\AA}$  is considerably greater than the value of  $40\text{ }\text{\AA}$  where Awschalom et al. [5,6] saw the onset of dimensional crossover in CdMnTe layers of rather lower Mn content. Given the short-range nature of the interaction between Mn ions, we feel that the additional paramagnetism is more likely to arise from an interface effect. The Mn ions near a CdTe–CdMnTe interface will have fewer magnetic neighbours in an anisotropic distribution, and

may therefore be less likely to form antiferromagnetic clusters than Mn ions in the bulk of a layer. This idea is supported by spin-flip Raman measurements on the same sample [14], which show an energy shift of Brillouin function form in a magnetic field, implying that the electron states in the quantum wells are coupled to paramagnetic ions. The Mn concentrations in the CdTe necessary to explain these shifts are 0.01–0.02, whereas the photoluminescence data give  $x < 0.001$  in the wells [13]. The CdMnTe layers are in the spin-glass phase at the measurement temperature of 1.5 K, and so should not give rise to energy shifts of paramagnetic resonance form. Furthermore, since the signals are detected through the electron states in the CdTe quantum wells, they should only be sensitive to the regions of the CdMnTe layers very close to the interfaces. Thus these results not only confirm the presence of additional paramagnetic ions in the superlattice, they also provide support for the hypothesis that these are located at or near the CdTe–CdMnTe interfaces.

We wish to thank T. Dietl for useful discussions, and acknowledge financial support from

the Science and Engineering Research Council, UK.

## 1. References

- [1] R.R. Galazka, S. Nagata and P.H. Keesom, *Phys. Rev. B* 22 (1980) 3344.
- [2] M. Escorne and A. Mauger, *Phys. Rev. B* 25 (1982) 4674.
- [3] J.K. Furdyna and N. Samarth, *J. Appl. Phys.* 61 (1987) 3526.
- [4] K. Binder and A.P. Young, *Rev. Mod. Phys.* 58 (1986) 801.
- [5] D.D. Awschalom, J.M. Hong, L.L. Chang and G. Grinstein, *Phys. Rev. Lett.* 59 (1987) 1733.
- [6] J.M. Hong, D.D. Awschalom, L.L. Chang and A. Segmüller, *J. Appl. Phys.* 63 (1988) 3285.
- [7] B. Lunn and J.J. Davies, *Semicond. Sci. Technol.* 5 (1990) 1155.
- [8] J.H.C. Hogg, J.E. Nicholls, S.R. Jackson, W.E. Hagston, D.E. Ashenford, B. Lunn and S. Alli, *Mater. Sci. Eng. B* 16 (1993) 60.
- [9] S.V. Railson, D. Wolverson and J.J. Davies, private communication.
- [10] S.B. Oseroff, *Phys. Rev. B* 25 (1982) 6584.
- [11] S.B. Oseroff and F.G. Gandra, *J. Appl. Phys.* 57 (1985) 3421.
- [12] J. Spalek, A. Lewicki, Z. Tarnawski, J.K. Furdyna, R.R. Galazka and Z. Obuszko, *Phys. Rev. B* 33 (1986) 3407.
- [13] K. Dhese and J.E. Nicholls, private communication.
- [14] P.J. Boyce, D. Wolverson and J.J. Davies, private communication.



ELSEVIER

Journal of Crystal Growth 138 (1994) 905–909

JOURNAL OF  
**CRYSTAL  
GROWTH**

# The influence of exchange interaction on the composition dependence of interband transitions in $\text{Zn}_{1-x}\text{Mn}_x\text{Se}$

Ch. Jung <sup>a,b</sup>, H.-Ch. Mertins <sup>a</sup>, S. Katholy <sup>a</sup>, H.-E. Gumlich <sup>a</sup>

<sup>a</sup> Institut für Festkörperphysik, Technische Universität Berlin, Hardenbergstrasse 36, D-10623 Berlin, Germany

<sup>b</sup> BESSY GmbH, Lentzeallee 100, D-14195 Berlin, Germany

## Abstract

We report on synchrotron radiation reflectance spectroscopy experiments on the interband transitions of  $\text{Zn}_{1-x}\text{Mn}_x\text{Se}$  for concentrations  $0 \leq x \leq 0.4$  within the energy range from 2 to 15 eV at a temperature of 30 K. By use of Kramers–Kronig transformation, the dielectric function was calculated, the imaginary part of which was analysed. In addition to the well-known anomalous concentration dependence of the band gap, the same anomaly is found for the critical point transitions  $E_1$  and  $E_1 + \Delta_1$  and for the Zn 3d core level transitions. For all other critical point transitions we find a linear concentration dependence. The anomalous behaviour is discussed by means of sp–d exchange interaction, assuming that this interaction influences mainly s-like conduction states but that the influence vanishes for mainly p-like conduction states.

## 1. Introduction

$\text{Zn}_{1-x}\text{Mn}_x\text{Se}$  belongs to the family of diluted magnetic semiconductors (DMSs) in which transition metal atoms substitute for the group II elements. The magnetic moments introduced by the transition metal atoms lead to several interesting optical and magneto optical properties [1], one of them being the variation of critical point energies. It has been shown that the Mn-based wide gap materials do not show a common concentration dependence. The band gap varies linearly with manganese concentration  $x$  for  $\text{Cd}_{1-x}\text{Mn}_x\text{Te}$  and  $\text{Zn}_{1-x}\text{Mn}_x\text{S}$  [2,3], but in  $\text{Zn}_{1-x}\text{Mn}_x\text{Te}$  and  $\text{Zn}_{1-x}\text{Mn}_x\text{Se}$  an anomalous concentration dependence is found [4,5]. For  $\text{Zn}_{1-x}\text{Mn}_x\text{Se}$  the

band gap first decreases up to a manganese concentration of  $x = 0.03$  and then increases with further increasing amount of manganese.

The band gap  $E_g$  variation of DMS due to various interactions such as transition metal concentration, temperature and exchange interaction can be described if they are taken as energy corrections to the band gap energy  $E_0$  of the pure ( $x = 0$ ), unperturbed crystal at zero temperature [4,5]:

$$E_g(x, T) = E_0 + E_x + E_T + E_{ex}, \quad (1)$$

where  $E_x$ ,  $E_T$  and  $E_{ex}$  denote the energy corrections due to composition, temperature and exchange interaction, respectively. In a first order approximation, the composition-derived energy correction term  $E_x$  can be assumed to vary linearly with concentration  $x$ . For the temperature dependence, the description presented by Varshni

\* Corresponding author.



can be applied [6]. A possible deviation  $\Delta E(x)$  of the concentration dependence of the experimental band gap values from a linear behaviour now can be ascribed to the influence of exchange interaction. If the temperature is kept constant,  $\Delta E(x)$  and thus the term  $E_{ex}$  can be expressed as follows:

$$\Delta E(x) = E_{ex}(x) = E_g(x) - (d + c), \quad (2)$$

with  $c = E_0 - aT^2/(T + \Theta)$  representing the correction due to the given temperature [6].

The influence of magnetic interaction can be calculated directly if second order perturbation theory is applied to the Hamiltonian describing the coupling of band electrons with localized Mn spins. The calculation delivers the following equation:

$$E_{ex} = -b\chi(x, T)T, \quad (3)$$

where  $b$  contains the unit cell volume and the exchange parameters, and  $\chi(x, T)$  is the susceptibility (for a detailed presentation, see Bylsma et al. [5]). The considerations presented above for the fundamental transition  $E_g$  were applied also for the analysis of the concentration dependence of higher energy critical points and Zn 3d core level transitions.

## 2. Experimental procedure

The high-resolution reflectance spectroscopy experiments were carried out at the 3m-NIM 1 beamline of the synchrotron radiation storage ring BESSY in Berlin. Crystals were grown at our institute using a modified Bridgman technique, and the manganese content was checked by microprobe analysis. From the bulk crystals, samples were prepared by cleaving under ambient conditions. The samples were then mounted in an Oxford Instruments CF 1100 cryostat, allowing experiments in the temperature range of 25 K up to room temperature. From the reflectance data, the dielectric function was calculated via Kramers–Kronig transformation, and the imaginary part of the dielectric function was subjected to a lineshape analysis (for detailed information, see ref. [7]).

## 3. Results and discussion

For the pure ZnSe ( $x = 0$ ), the imaginary part of the dielectric function shows well-pronounced structures due to interband and Zn 3d core level transitions. Especially for the interband transition region up to 10 eV, the structures are well known, and the assignment is supported by detailed theoretical work [8] (see Fig. 1 and Table 1). The results of the line shape analysis are summarized in Table 1. For the interband transitions, best fit results were achieved using two-dimensional critical point line shape and corresponding excitonic line.

To confirm our data, we first analysed the concentration dependence of the band gap. The anomalous behaviour of  $E_g$  is clearly shown in Fig. 2. The result is in excellent agreement with the data reported by Bylsma et al. [5]. From the experimental band gap data, we extrapolated the band gap energy of hypothetical zincblende MnSe ( $x = 1$ ) (see Table 1) and calculated the term

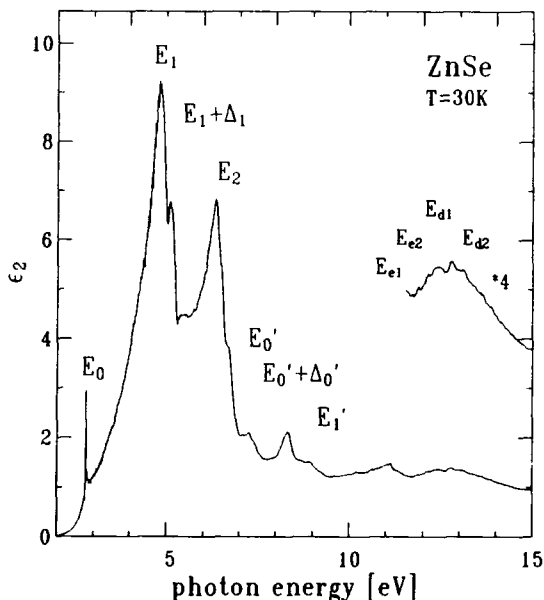


Fig. 1. Imaginary part of the dielectric function of ZnSe at  $T = 30$  K. The critical points are labeled according to ref. [8]. For the energy range of Zn 3d transitions the scale is enlarged.

$\Delta E(x)$  (see Eq. (2)). The resulting data are shown in Fig. 3. A comparison with susceptibility data of Bylsma et al. recorded at  $T = 8$  K [5] shows a linear relation as predicted by Eq. (3) (see Fig. 3).

For the critical point transitions  $E_1$  and  $E_1 + \Delta_1$  located at the L-point of the Brillouin zone, an interesting behaviour is observed. The concentration dependences show the same anomaly as the fundamental transition, but their shape is reversed: the critical point energies first increase with increasing amount of manganese up to a maximum at about  $x = 0.03$ , and then decrease with further increasing Mn concentration (see Fig. 2). The spin-orbit splitting  $\Delta_1$  remains con-

stant over the whole concentration range. As for  $E_g$ , the exchange-interaction-derived contribution  $\Delta E(x)$  of  $E_1$  and  $E_1 + \Delta_1$  is proportional to the susceptibility (see Fig. 3).

The structures in the energy range of 5.5 to 10 eV can be followed up to a manganese concentration of  $\approx 0.2$ . The broad structure peaking at 6.4 eV is a convolution of four critical point transitions which are located in the volume of the Brillouin zone ( $E_{21}$ ), along the  $\Delta$ -line ( $E_{22}$  and  $E_{23}$ ), and near the X-point [8]. The line shape analysis delivers a linear concentration dependence for the critical points  $E_{21}$  to  $E_{24}$ . The same result is found for the critical points  $E'_0$ ,  $E'_0 + \Delta'_0$ ,

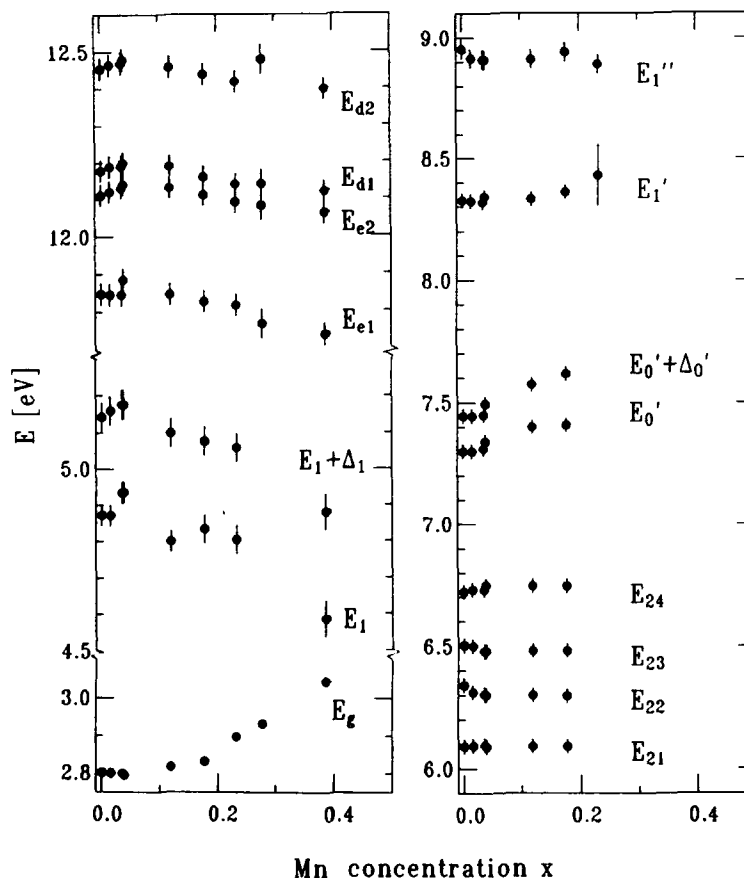


Fig. 2. Concentration dependence of the critical point energies determined by line shape analysis. Left: critical points showing an anomalous concentration dependence (see also Table 1); right: critical points varying linearly with  $x$ . Solid lines are drawn to guide the eye.

Table 1

Critical point energies of pure ZnSe; the theoretical data are from Chelikowsky and Cohen [8]; for transitions with an anomalous concentration dependence the extrapolated energies of hypothetical zincblende MnSe are given

Structure	Critical point energy (eV)		
	ZnSe ( $x = 0$ )	Theory	MnSe ( $x = 1$ )
$E_g$	2.80		3.39
$E_1$	4.88	4.79	3.90
$E_1 + \Delta_1$	5.13	5.06	4.20
$E_{21}$	6.13		
$E_{22}$	6.34		
$E_{23}$	6.54	6.50	
$E_{24}$	6.72	6.71	
$E'_0$	7.30	7.22	
$E'_0 + \Delta'_0$	7.45	7.47	
$E'_1$	8.33	8.39	
$E''_1$	8.95	8.86	
$E_{c1}$	11.85		11.50
$E_{c2}$	12.11		11.82
$E_{d1}$	12.18		11.87
$E_{d2}$	12.45		12.17

$E'_1$  and  $E''_1$ .  $E'_0$  and  $E'_0 + \Delta'_0$  are assigned to transitions from the valence band maximum into higher conduction band states  $\Gamma_7$  and  $\Gamma_8$ . The conduction band spin-orbit splitting  $\Delta'_0$  at the

$\Gamma$ -point increases with increasing amount of manganese. The transitions associated to the critical points  $E'_1$  and  $E''_1$  are located at the L-point and along  $\Lambda$  [8]. The concentration dependence of the above structures is shown in Fig. 3.

The structures near 12 eV are due to the excitation of Zn 3d core level excitons and transitions from 3d core levels into the CB minimum at the  $\Gamma$ -point [7]. The interpretation of the experimental data is based on a model presented for ZnS [9]. Due to crystal field and spin-orbit interaction, the Zn d states at the  $\Gamma$ -point are split into three states:  $\Gamma_8$ ,  $\Gamma_7$  and  $\Gamma_6$ . The ordering and the energy separation of the states is strongly influenced by p-d repulsion [10]. In ZnSe, the energy separation between the upper  $\Gamma_8$  and  $\Gamma_7$  is rather small and thus impossible to be resolved experimentally. We therefore find only two core exciton lines  $E_{c1}$  and  $E_{c2}$  at 11.85 and 12.11 eV, respectively (for ZnS three core exciton lines were observed [9]). The associated core level to conduction band transitions  $E_{d1}$  and  $E_{d2}$  are at 12.18 and 12.45 eV, respectively, giving an exciton binding energy of 335 meV. The analysis of the concentration dependence of the Zn 3d core level transitions delivers the same anomalous behaviour as found for  $E_1$  and  $E_1 + \Delta_1$ . The magnetic exchange correction  $\Delta E(x)$  of the core level transitions is shown in Fig. 3, also being proportional to  $\chi(x)$ .

The influence of the sp-d exchange interaction on the different critical point and core level transitions can be discussed in the light of the wave function character of the corresponding final CB states. Band structure calculations [10,11] yield the CB wave function character at the different points of the BZ. Near the CB minimum ( $\Gamma_6$ ) they show pure s-character. For  $k \neq 0$ , mixing of s, p and d states occurs and the following distributions are found [10,11]: near the L-point 75% s-, 15% p- and 10% d-character, and near the X-point 26% s-, 43% p- and 31% d-character. The higher CB states ( $\Gamma_{7,8}$ ,  $L_{4,5}$ ) are built of 75% p- and 25% d-character, but no s-character. The initial valence states of the interband transitions are built by p-like wave functions.

All transitions into final states with predominantly s-character, i.e.  $E_g$ ,  $E_1$ ,  $E_1 + \Delta_1$ , and the

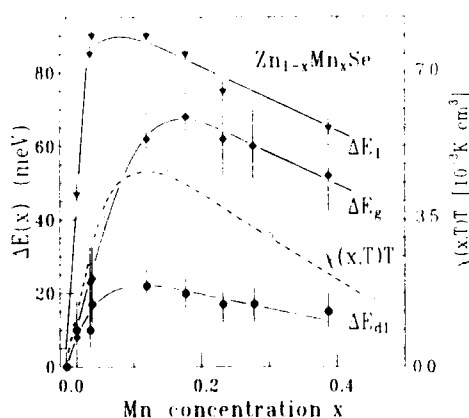


Fig. 3. Energy corrections  $\Delta E(x)$  for  $E_g$ ,  $E_1$  and  $E_{d1}$ . The data are proportional to the susceptibility data of Bylsma et al. [5], also shown for comparison. Lines are drawn as guides to the eye.

Zn core level excitations, are influenced by the exchange correlation. In contrast to this, transitions into final states with predominantly p-character are not influenced by the exchange interaction and thus depend linearly on the  $x$ . The symmetry of the wave function of the excited electron seems to play a dominant role for the mechanism of coupling between the CB electron and the localized Mn spins. The Mn 3d states and the p- and d-like final state wave functions are described by the same symmetry. Thus the symmetry of the wave functions should be considered to calculate the influence of exchange interaction at different points of the Brillouin zone for a better insight into the mechanism of coupling between band electrons and Mn spins.

### 5. Conclusions

We have presented a systematic study on the concentration dependence of the critical point and Zn 3d core level transitions of  $\text{Zn}_{1-x}\text{Mn}_x\text{Se}$ . The sp-d exchange interaction between band electrons and localized Mn spins influences the critical point transitions. The strength of the interaction depends on the symmetry of the final state wave functions: if the final state is predominantly of p-character, the influence of exchange interaction is weak and the critical point energies vary linearly with  $x$ ; for mainly s-like final states, exchange interaction leads to an anomalous con-

centration dependence as observed for the first time for the fundamental transition.

### 6. Acknowledgments

We would like to acknowledge Dr. Krost's and H. Broschat's work of growing and Dr. F. Galbert's expert analysis of the crystals. This project was supported by the Bundesminister für Forschung und Technologie.

### 7. References

- [1] J.K. Furdyna and J. Kossut, in: *Semiconductors and Semimetals*, Vol. 25 (Academic Press, San Diego, CA, 1988).
- [2] R. Bückner, H.-E. Gumlich and M. Krause, *J. Phys. C* 18 (1985) 661.
- [3] K. Mayrhofer, K. Hochberger and W. Gebhardt, *J. Phys. C* 21 (1988) 4393.
- [4] H.-Ch. Mertins, Ch. Jung and H.-E. Gumlich, *Semicond. Sci. Technol.* 8 (1993) 1634.
- [5] R.B. Bylsma, W.M. Becker, J. Kossut, U. Debska and D. Yoder-Short, *Phys. Rev. B* 33 (1986) 8207.
- [6] Y.P. Varshni, *Physica* 34 (1967) 149.
- [7] Ch. Jung, H.-E. Gumlich, A. Knack and H.-C. Mertins, *J. Crystal Growth* 101 (1990) 926.
- [8] J.R. Chelikowsky and M.L. Cohen, *Phys. Rev. B* 14 (1976) 556.
- [9] Ch. Jung, H.-Ch. Mertins and H.-E. Gumlich, *J. Crystal Growth* 138 (1994) 1066.
- [10] S.-H. Wei and A. Zunger, *Phys. Rev. B* 37 (1988) 8958.
- [11] R.M. Wentzcovitch, S.L. Richardson and M.L. Cohen, *Phys. Lett. A* 114 (1986) 203.



ELSEVIER

Journal of Crystal Growth 138 (1994) 910–912

JOURNAL OF **CRYSTAL  
GROWTH**

## Magnetic or nonmagnetic behavior of isolated scandium ions in II–VI compounds

D. Schumann <sup>a</sup>, H.-E. Mahnke <sup>\*a</sup>, B. Spellmeyer <sup>a</sup>, G. Sulzer <sup>a</sup>, H. Waldmann <sup>a</sup>,  
W.-D. Zeitz <sup>a</sup>, U.W. Pohl <sup>b</sup>, H.-E. Gumlich <sup>b</sup>

<sup>a</sup> *Bereich Schwerionenphysik, Hahn-Meitner-Institut Berlin GmbH, Glienicker Strasse 100, D-14109 Berlin, Germany*

<sup>b</sup> *Institut für Festkörperphysik, TU Berlin, Hardenbergstrasse 36, D-10623 Berlin, Germany*

### Abstract

The local magnetic behavior of recoil-implanted isolated Sc ions has been studied in II–VI and other semiconducting compounds. In all cases nonmagnetic configurations were observed consistent with an empty d-shell of the Sc ion. Additionally a different influence of nearby defects on the Sc probe ion was observed in the various types of compound semiconductors.

### 1. Introduction

Transition-element impurities greatly influence the electrical and optical properties of semiconductors. They occur in different electronic configurations and charge states. Depending on the position of their energy levels within the band gap relative to the Fermi level, such impurities can act as deep traps for electrons and holes. Therefore the determination of the electronic states, the charge state as well as the configuration, and their dynamics under equilibrium and non-equilibrium conditions is of great importance for the understanding of the role of the impurity atoms in such isolated states in semiconducting materials.

The magnetic behavior directly reflects the configuration of the outer electrons, which results

from the interplay of inter- and intra-atomic correlations in the solid. Therefore the local magnetism of isolated transition-metal ions in semiconductors can be used to investigate and identify their electronic states.

Complementary to electron paramagnetic resonance (EPR), we study the magnetic behavior of transition element ions in semiconductors via the hyperfine interaction at the nucleus using the nuclear method of perturbed angular distribution (PAD) after recoil implantation. In the case of Fe and Ni ions in ZnS and ZnTe, at least two different electronic configurations attributed to different charge states were observed. The occurrence of the presumably  $1^+$  state of Fe (and Ni) was interpreted as resulting from electron capture during the slowing-down of the ions in the recoil-implantation process [1].

In this context, the behavior of the elements at the beginning (scandium) and the end (copper) of the transition element series is of interest. For

\* Corresponding author.

these elements the distinction of different charge states might be easier than for elements in the middle of the series. For the  $3^+$  state in scandium and the  $1^+$  state in copper, nonmagnetic configurations should dominate, since configurations with a completely empty or filled d-shell, respectively, should be favored, while for the  $2^+$  state for d-like electrons a magnetic behavior is expected. In contrast to EPR, both magnetic and nonmagnetic states are easily detected and investigated with a nuclear method. In this contribution, we report on studies of scandium in II-VI and other semiconducting compounds for which information has been rather scarce so far. If electron capture processes occur as discussed for Fe and Ni ions [1] then, in the case of Sc, they may be detected via the observation of magnetic configurations well distinguished from nonmagnetic configurations. In fact, the occurrence of  $2^+$  Sc ions in ZnS at low temperature has been shown by EPR spectroscopy after optical excitations [2,3].

## 2. Experiment

In the experiments reported here we have studied the magnetic behavior of Sc ions in various II-VI compounds as well as in a few III-V semiconductors via the hyperfine interaction at the nucleus using the PAD method after recoil implantation. As probe nucleus we used the isomeric state of  $^{43}\text{Sc}$  ( $I = 19/2$ ,  $T_{1/2} = 473$  ns, nuclear  $g$ -factor  $g = 0.3286$ ) in an applied external field of 1.6 T. The nuclei were produced in a nuclear reaction using a pulsed heavy ion beam from the accelerator VICKSI at the Hahn-Meitner-Institut. The reaction used was  $^{12}\text{C}(^{36}\text{Ar}, \alpha p)^{43}\text{Sc}$  with a  $^{36}\text{Ar}$ -ion beam of 136 MeV energy. Due to the transferred kinetic energy from the nuclear reaction, the ions recoil out of the target foil, a 2.3 mg/cm<sup>2</sup> thick carbon foil, and are implanted deeply into the sample (up to a few  $\mu\text{m}$ ) mounted directly behind the reaction foil. The nuclear process, in addition, produces the alignment of the nuclear spins, resulting in anisotropically emitted  $\gamma$ -radiation. The hyperfine interaction, observed as the variation in time of the anisotropic angular distribution, is mea-

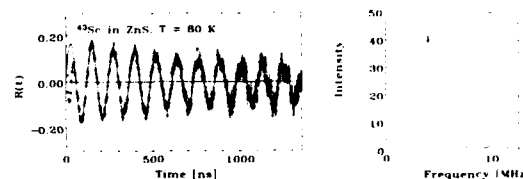


Fig. 1. PAD modulation spectrum and corresponding Fourier transform of the  $19/2$  isomer in  $^{43}\text{Sc}$  implanted into ZnS at 80 K with an externally applied magnetic field of 1.6 T.

sured in situ and immediately after the isomeric state is populated and implanted into the samples.

The samples (zinc chalcogenide samples: single crystalline platelets grown using the Bridgman method; InP: Zn and Sn doped material from MCP Electronic Materials Ltd.; InSb: Cd-doped, and Si: Sb-doped, both from Wacker Chemie) were attached to the cold tip of a He continuous-flow cryostat allowing temperatures between 20 and 400 K. The external magnetic field of 1.6 T was applied perpendicular to the ion beam direction in a conventional magnet setup.

An example of the observed modulation spectra is presented in Fig. 1 for Sc in ZnS, where the modulation is shown as time spectrum and its Fourier transform as frequency spectrum.

From modulation spectra like the one shown, the following information can be extracted:

- (i) *The modulation frequency*: Deviations from the pure Larmor frequency in the external magnetic field indicate paramagnetic contributions either from neighboring ions or from the own electronic magnetic moment in which case the temperature dependence may be Curie-like, i.e. inverse proportional to the temperature.
- (ii) *The amplitude of the modulation*: This is a measure for the fraction of probe atoms in a specific configuration. The maximum amplitude is given by the nuclear parameters, it is experimentally measured typically in a metallic host in which the probe atoms occupy substitutional sites with negligible defect concentration nearby.
- (iii) *The damping of the modulation*: Defects in the neighborhood of the probe atom can result in deviations from the crystal symmetry and yield quadrupole interactions superimposed to the

magnetic interaction. The damping constant is a measure for the mean quadrupole coupling constant resulting from different unresolved nearby defects.

In the II–VI compounds ZnO, ZnS, ZnSe, ZnTe, and CdTe as well as in the III–V semiconductors InP, InSb and in silicon, the recoil-implanted isolated scandium ion exhibits a nonmagnetic configuration in the temperature range from 77 to 300 K. The frequency of the modulation observed in all these cases equals the Larmor frequency in the external magnetic field within the limits of accuracy. Only one unique fraction of scandium ions was observed which amounted to almost all recoil-implanted scandium ions. However, differences were found in the damping of the modulation in the different compounds.

Although the damping is not such a characteristic quantity as the frequency, certain trends were found independent of the model with which the damping is described. The damping is weaker in the II–VI compounds as compared with the III–V compounds and the elemental semiconductor Si. For both types of compound semiconductors, it seems to correlate with the lattice constants: compounds with larger lattice constants show smaller damping.

### 3. Discussion

The most simple explanation for the diamagnetic behavior of nearly all the recoil-implanted Sc ions is that the Sc ions adopt the  $3^+$  charge state with an empty d-shell which corresponds to their regular chemical valency. This would imply either that an electron capture process as argued for Fe and Ni does not occur for Sc in the systems studied, or that the captured electron does not occupy a magnetic d-like state. This is not in contradiction to the earlier EPR experiments [2,3] by which the  $2^+$  state was detected after optical excitation: in our experiment the population has to occur at the end of the slowing-down process of the recoiling ion or within nanoseconds thereafter.

From the observed damping of the modulations, additional information can be extracted. Since no magnetic configurations are being involved, paramagnetic relaxation caused by spin fluctuations can be ruled out as the damping mechanism. The dipole–dipole interactions with adjacent nuclear spins are much too small to explain the measured damping of the modulation. However, the observed correlation with the lattice constant implies that we rather have to assume an additional electric quadrupole interaction superimposed to the interaction with the external magnetic field. The electric field gradients yielding the quadrupole interaction result from deviations from the cubic symmetry in the vicinity of the Sc probe ion due to defects produced in the slowing-down process. The variation of the electric field gradient with  $r^{-3}$  in general explains easily the observed correlation of the damping of the modulation with the lattice constant within one class of compounds. The damping is not very characteristic of a specific type of defect, but rather the result of various defect configurations and orientations. Although nearby defects, leading to impurity–defect pairs, e.g. the A-center with the trivalent In impurity [4], yield large well-defined quadrupole interactions, their formation probability under non-equilibrium conditions is very small compared to defects further away from the probe atom.

Finally, we want to point out that the generally smaller damping strength in the II–VI compounds reflects the higher stability against defect formation as compared to III–V compounds and silicon.

### 4. References

- [1] H. Waldmann, H.-E. Mahnke, B. Spellmeyer, G. Sulzer, W.-D. Zeitz, H. Hoffmann, H.-E. Gumlich and U. Pohl, *J. Crystal Growth* 117 (1992) 715.
- [2] A.O. Barksdale and T.L. Estle, *Phys. Lett. A* 42 (1973) 426.
- [3] I. Broser and M. Schulz, *J. Phys. C (Solid State Phys.)* 7 (1974) L147.
- [4] T. Wichert, T. Krings and H. Wolf, *Physica B* 185 (1993) 297.



ELSEVIER

Journal of Crystal Growth 138 (1994) 913–916

JOURNAL OF  
**CRYSTAL  
GROWTH**

## Nature of the absorption bands in $\text{Zn}_{1-x}\text{Co}_x\text{S}$

L. Martinez <sup>\*,a</sup>, S.A. Lopez-Rivera <sup>a</sup>, W. Giritat <sup>b</sup>, F. Medina <sup>c</sup><sup>a</sup> Laboratorio de Física Aplicada, Departamento De Física Universidad de los Andes, Zona Postal 5101, Mérida, Venezuela<sup>b</sup> Instituto Venezolano de Investigaciones Científicas, Apartado 1827 Caracas, Venezuela<sup>c</sup> Physics Department, Florida Atlantic University, Boca Raton, Florida 33431, USA

### Abstract

To study the nature of the absorption bands in  $\text{Zn}_{1-x}\text{Co}_x\text{S}$  single crystals, optical absorption measurements were made on samples with cobalt composition  $x = 0.03$  and  $0.05$  as a function of temperature in the wavelength region between 400 and 3000 nm. Each spectrum showed three well-defined absorption bands below the fundamental absorption gap, corresponding to transitions from the fundamental  $^4\text{A}_2(^4\text{F})$  ground state to the  $^4\text{T}_1(^4\text{F})$ ,  $^4\text{T}_2(^4\text{F})$  and  $^4\text{T}_1(\text{P})$  excited states. Besides these main bands, the infrared region has a series of small peaks. In the visible region, just below the onset of the band edge, there is a well-defined structure related to electronic transitions from the 3d shell of the cobalt ion.

### 1. Introduction

The optical properties of diluted magnetic semiconductors (DMSs) have received much attention in the past few years. Most of the research done was concentrated on manganese-based II–VI compounds [1–4]. Lately, good single crystals have been prepared with different transition elements such as  $\text{Zn}_{1-x}\text{Co}_x\text{S}$  [5], where the divalent cobalt ion randomly replaces the divalent zinc ion. In this work an optical absorption study is presented for two different concentrations, 0.03 and 0.05. This study was carried out at different temperatures in the visible and near-infrared regions. Besides the three main absorption bands due to the presence of the transition element and a fine structure in the high-energy

region of the  $^4\text{T}_2(\text{F})$  band, there are two smaller bands in the visible region of the spectrum. The spectra shown here have better resolution than previously published data [6,7].

### 2. Experimental procedure and results

The samples used in this work were prepared by chemical transport with nominal cobalt concentrations of  $x = 0.03$  and  $0.05$ . Details of the growth procedure are given elsewhere [5]. The absorption spectra were taken on samples lapped to the appropriate thickness for wavelengths between 400 and 3000 nm and temperatures between 50 and 300 K, using a Cary 17 spectrometer and an Air Products Closed Cycle system. At wavelengths below 600 nm, the absorption spectra for the two samples show essentially the same features as can be seen in Fig. 1, while in the visible region the band localized at 474 nm (2.612

\* Corresponding author.



eV) is absent for the sample with 5% cobalt concentration, as can be seen in Fig. 2b.

### 3. Discussion

In the past, the absorption spectra of  $\text{Co}^{2+}$  ion in ZnS have been interpreted considering crystal field theory, the Racah parameter, and spin-orbit coupling [6]. A free  $\text{Co}^{2+}$  ion has  $3d^7$  configuration and  $^4F$ ,  $^4P$ ,  $^2G$ ,  $^2H^2P$ ,  $^2D_m$ , and  $^2F$  energy levels. When the cobalt ion is placed in the tetrahedral crystal field of ZnS, the  $^4F$  level splits in a  $^4A_2(F)$  singlet ground state and in two higher lying orbital triplets  $^4T_2(F)$  and  $^4T_1(F)$  [5,6]. When the spin-orbit interaction is taken into account, the levels are split further, as shown in Fig. 3. The energy position of the different levels of the cobalt ion within the ZnS crystal have been calculated by Fazzio et al. [8].

The three main bands are identified as the internal transitions due to the cobalt ion from the

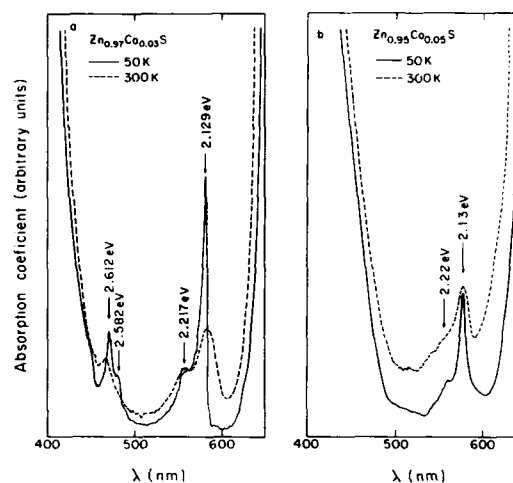


Fig. 2. Visible portion of the spectra of  $\text{Zn}_{1-x}\text{Co}_x\text{S}$  single crystal for (a)  $x = 0.03$  and (b)  $x = 0.05$ . For clarity only data for two different temperatures are shown.

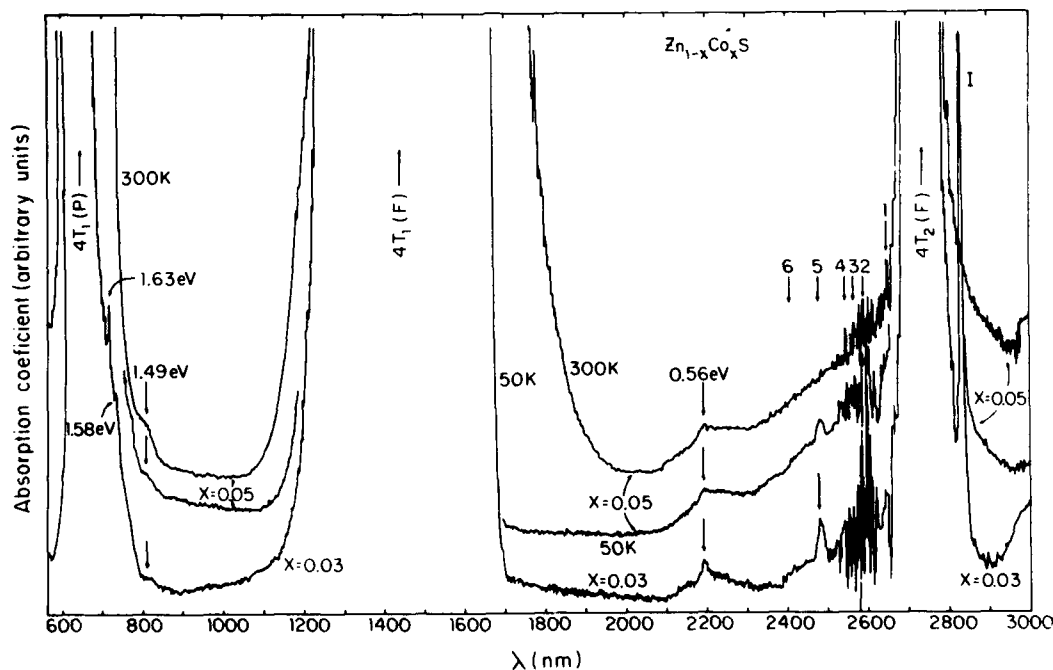


Fig. 1. Absorption spectra of  $\text{Zn}_{1-x}\text{Co}_x\text{S}$  single crystals for  $x = 0.03$  and  $x = 0.05$ . The spectrum for  $x = 0.05$  at  $T = 50$  K is only partially shown. Each spectrum has been displaced vertically for clarity.

ground state to the excited states, as shown in Fig. 1. This identification agrees with other experimental and theoretical results [6,8]. Furthermore, this is supported by the fact that the positions of the bands are temperature- and concentration-independent [4]. In the following, each band will be discussed.

### 3.1. ${}^4T_2(F)$ band

The absorption band from the ground state  ${}^4A_2(F)$  to the first excited state  ${}^4T_2(F)$  is centered around 0.457 eV with a half-width that goes from 0.180 eV for  $x = 0.03$  to 0.260 eV for  $x = 0.05$ . On the high-energy side of this band there are a series of lines; the position and identification of the main lines are given in Table 1. The assignment of these lines was made following the arguments given in refs. [6,9] and with the aid of Fig. 3. Table 1 also includes the narrow and intense line (label I) observed on the low-energy side of this band, and is attributed to a zero phonon line (ZPL) as in ref. [9]. The identification of the remaining lines of the structure is in progress.

### 3.2. ${}^4T_1(F)$ band

The absorption band originating from the  ${}^4A_2(F)$  to the  ${}^4T_1$  excited state is centered at 0.827 eV having a half-width that goes from 0.25

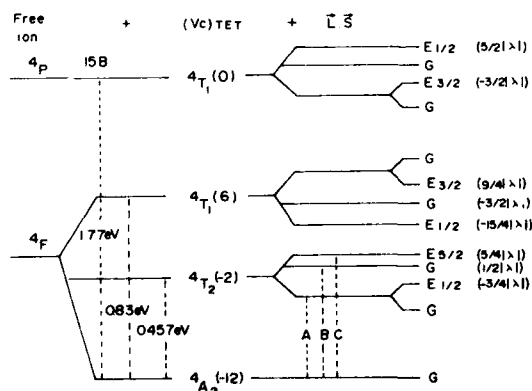


Fig. 3. Energy level diagram for  $\text{Co}^{2+}$  ion in a tetrahedral crystal field (after ref. [6]). The lines A, B and C indicate transitions in the infrared region.

Table 1

Energy position of the structure observed on the wings of the  ${}^4A_2(F) \rightarrow {}^4T_2(F)$  absorption band of  $\text{Co}^{2+}$ ; see Fig. 2 for identification of the A, B and C transitions

No.	Energy (ev)	Assignment
1	0.4380	A
1	0.4670	B
2	0.4760	TO(x)
3	0.4810	LO(x)
4	0.4860	C
5	0.4930 <sup>a</sup>	TO(x) + TA(x) <sup>b</sup>
6	0.5170	2TO(x)
7	0.5220	TO(x) + LO(x) <sup>c</sup>

<sup>a</sup> Seen below 100 K.

<sup>b</sup> TA(x) = 90  $\text{cm}^{-1}$  [9].

<sup>c</sup> Absent for  $x = 0.05$ .

eV for  $x = 0.03$  and 50 K to 0.46 eV for the higher concentration of  $x = 0.05$  at RT. This band does not present any appreciable structure as in the case of more diluted samples [6,9]. The two samples studied gave a similar band.

### 3.3. ${}^4T_1(P)$ band

This band corresponds to a transition from the ground state  ${}^4A_2(F)$  to the first excited state  ${}^4T_1(P)$ , and is centered around 1.77 eV. Its half-width, as in the previous cases, depends on temperature and concentration going from 0.25 eV for  $x = 0.03$  at 58 K to 0.41 eV for  $x = 0.05$  at RT. The structure observed on the low-energy side of this band may be attributed [6,8] to transitions from the ground state to doublet states as follows: the small peak at 1.49 eV to the  ${}^2E$ , the shoulder at 1.58 eV to the  ${}^2T_1$  and the line at 1.63 eV to the  ${}^2A_1$  state. The first two peaks are only observed at low temperatures and for the lower concentration.

### 3.4. Visible band

The visible region of the spectra is shown in Fig. 3 for the two concentrations under study at two different temperatures. This part of the spectra shows two bands of interest. The first band has one sharp peak located at 2.129 eV and a weak shoulder at 2.217 eV. The intensity and the

line width of this band decrease and become broader as the temperature and the concentration  $x$  increase. The first line has been attributed by Dreyhsig et al. [7] to a transition from the ground state to a  $^2T_1$  or a  $^2T_2$ , or a mixture of both. Following Noras et al., this structure may be attributed to a ZPL and its phonon replica [10]. The second band is only observed for the sample with 0.03 cobalt concentration and shows a small shoulder at 2.582 eV and a sharp line at 2.612 eV. This structure is located in the rising tail of the fundamental absorption band edge and has been observed and identified previously [7,10].

Using straight extrapolation in Figs. 2a and 2b, it is easy to see that the absorption edge value shifts towards lower energy as the cobalt concentration increases. This shift is the reason for not seeing the lines at high energy in the sample with  $x = 0.05$  cobalt concentration.

Finally, it is worth mentioning that the half-width increase of each absorption band as the temperature increases may be due to the perturbations introduced by the vibrational lattice effect.

## 5. Conclusions

In the present work, the positions of the  $3d^7$  internal transitions due to the cobalt ion in the DMS  $Zn_{1-x}Co_xS$  were obtained with good resolution for all the bands. The phonon-related fine structures on the low-energy side of the spectra

were obtained for both concentrations even at room temperature. The two samples show essentially the same features, except for the band located in the tail of the fundamental absorption edge, which is present only for the sample with 0.03 cobalt concentration.

## 6. Acknowledgment

This work has been done with the financial aid of CDCHT of the University of Los Andes.

## 7. References

- [1] W. Giriat and J.K. Furdyna, in: *Semiconductors and Semimetals*, Vol. 25 Eds. J.K. Furdyna and J. Kossut (Academic Press, Boston, MA, 1998) ch. 1, p.1.
- [2] M. Jain and J.L. Robins, in: *Diluted Magnetic Semiconductors*, Ed. M. Jain (World Scientific, Singapore, 1991) ch.1, p.1.
- [3] C. Benecke and H.E. Gumlich, in ref. [2], ch. 3, p.85.
- [4] L. Martinez, L.R. Gonzalez and W. Giriat, *Phys. Status Solidi (b)* 180 (1993) 267.
- [5] T.M. Glebultowicz, P. Klosowski, J.J. Rhyne, T.J. Udovic, F.K. Furdyna and W. Giriat, *Phys. Rev. B* 41 (1990) 504.
- [6] H.A. Wakliem, *J. Chem. Phys.* 36 (1961) 2117.
- [7] J. Dreyhsig, K. Klein, H.E. Gumlich and J.W. Allen, *Solid State Commun.* 85 (1993) 19.
- [8] A. Fazzio, M.J. Caldas and A. Zunger, *Phys. Rev. B* 30 (1984) 3440.
- [9] P. Koidl, O.F. Schirmer and U. Kaufmann, *Phys. Rev. B* 8 (1973) 4926.
- [10] J.M. Noras, H.R. Szawelska and J.W. Allen, *J. Phys. C (Solid State Phys.)* 14 (1981) 3255.



ELSEVIER

JOURNAL OF **CRYSTAL  
GROWTH**

Journal of Crystal Growth 138 (1994) 917–923

## Electron beam induced current assessment of doped and diffused junctions in epitaxial $\text{Cd}_x\text{Hg}_{1-x}\text{Te}$

M.P. Hastings <sup>\*a</sup>, C.D. Maxey <sup>a</sup>, B.E. Matthews <sup>a</sup>, N.E. Metcalfe <sup>a</sup>, P. Capper <sup>a</sup>,  
C.L. Jones <sup>a</sup>, I.G. Gale <sup>b</sup>

<sup>a</sup> GEC-Marconi Infra-Red Ltd., P.O. Box 217, Millbrook Industrial Est., Southampton, SO9 7QG, UK

<sup>b</sup> Philips Research Laboratories, Redhill, Surrey, RH1 5HA, UK

### Abstract

Electron beam induced current (EBIC) measurements have been applied to shallow-angle bevelled sections through  $\text{Cd}_x\text{Hg}_{1-x}\text{Te}$  (CMT) epitaxial layers containing p-n junctions. Samples studied include (a) fully doped homo- and heterostructures grown by metalorganic vapour phase epitaxy (MOVPE) and (b) vacancy-doped CMT layers grown by MOVPE or liquid-phase epitaxy (LPE) where the junction has been formed by ion-beam milling or Hg in-diffusion from a surface oxide layer. The bevelled sections were formed by chemical etching and profiles of the bevel surfaces were measured to enable accurate junction positions to be obtained. For grown junctions, chemical dopant profiles determined by secondary-ion mass spectrometry (SIMS) and the position of the electrical junction, from Hall and strip depth profiling, agree with the position of the electrical junction revealed by EBIC studies. For junctions formed in MOVPE samples by Hg in-diffusion from a surface oxide, EBIC reveals contrast consistent with interspersed p and n regions. These observations can be explained by uneven Hg diffusion including fast diffusion down defects producing n-type channels within a p-type matrix. This effect was not observed in MOVPE samples with doped or ion beam milled junctions or LPE samples with diffused junctions, highlighting the difference between the microstructure of MOVPE and LPE CMT. EBIC assessment can provide an indication of the likely performance of test devices.

### 1. Introduction

$\text{Cd}_x\text{Hg}_{1-x}\text{Te}$  photovoltaic devices can be made using a variety of junction formation techniques. Broadly, these techniques fall into the categories of Hg-diffusion [1–4], impurity-diffusion [5], doping [6–8] or ion implantation methods [9–11]. The Te-rich liquid phase epitaxy (LPE) CMT growth procedure used in this laboratory [12]

precludes doping with the acceptors As or Sb. Hg in-diffusion is used most commonly for junction formation in LPE material [1,3]. In contrast, metalorganic vapour phase epitaxy (MOVPE) has been used to prepare extrinsically doped structures with well-controlled, sharp dopant junctions. Both donor and acceptor doping can be achieved readily during MOVPE growth [7,13,14]. Assessment of homo- or heterojunction structures requires reliable techniques for the measurement of electrical properties. Electrical junction positions can be determined by Hall/strip techniques or, for doped grown junctions, sec-

\* Corresponding author.

ondary ion mass spectrometry (SIMS) can provide dopant profiles, which should agree with the electrical junction position [15]. The electron beam induced current (EBIC) imaging technique in the scanning electron microscope (SEM) can be used to observe charge depletion regions and electrically active defects in semiconductor materials. EBIC allows p–n junctions to be easily located and imaged and is useful as an aid to device characterisation.

EBIC has been widely applied to silicon and other semiconductor materials [16–18]. In comparison, relatively few EBIC studies of CMT material and device structures have been published [19–23]. Recently, we reported the application of EBIC to shallow-angle bevelled sections through doped MOVPE CMT layered structures [15]. In the work reported here, this method was used to characterize electrical behaviour in doped MOVPE layers and to study junctions formed by Hg in-diffusion in LPE and MOVPE material. Interesting aspects of the EBIC assessment technique applied to a number of samples are highlighted and discussed.

## 2. Experiment

Doped homo- and heterostructures of CMT were grown in a horizontal, atmospheric pressure MOVPE reactor at 360°C using the interdiffused multilayer process [24]. The layers were given an open tube 200°C isothermal Hg anneal to eliminate metal vacancies. LPE layers were grown at 500°C from a Te-rich solution using a horizontal sliding-boat system. Samples were annealed after growth to vacancy concentrations in the range 4 to  $6 \times 10^{16} \text{ cm}^{-3}$ .

On-substrate samples were obtained by cleaving pieces of the appropriate size from an LPE or MOVPE slice. Monolithic (i.e. off-substrate) samples were prepared by waxing the sample, CMT surface down, onto a clean sapphire carrier and removing the substrate using a selective etch. Monoliths (thickness 8–11  $\mu\text{m}$ ) were defined in the CMT layer, etched out and mounted individually onto sapphire carriers for handling convenience.

For vacancy-doped samples, in-diffusion of Hg is employed for type-conversion of CMT by reduction of Hg vacancies, using one of two means. In the first case, CMT samples were ion beam milled using a neutralized argon ion beam with junction depth determined by the milling time and the p-type carrier concentration (vacancy concentration). The second approach, developed by Jenner and Blackman [3], involves the formation of an anodic oxide on the CMT surface which acts as a source of free Hg during a subsequent heat treatment. Samples were anodized, and then heated in air at 180°C, in order to type-convert the CMT surface to a depth of  $\sim 5 \mu\text{m}$ . The anneal time required for conversion to this depth is dependent on the vacancy concentration. Finally, the anodic oxide was removed by etching in a weak HBr solution.

Bevelled sections in small samples of CMT (e.g.,  $4 \times 10 \text{ mm}$ ) were prepared using a technique based on work by Huber and Grattapain [25]. The method, in which low angle bevels were formed by controlled immersion in an etchant, has been described previously [15]. Where required, profiles of chemically etched bevels were measured using a profilometer. Bevelled samples were contacted and mounted on an EBIC sample holder (see ref. [15]), before loading onto a cryogenically cooled (77 K) stage, located in a JEOL SEM specimen chamber. In most cases, a 25 keV incident electron beam was used with the minimum current necessary to observe a good EBIC signal. The junction position with respect to the indium contacts was obtained by overlaying the EBIC line scan image on a SEM picture of the surface. From this, the lateral distance of the junction along the bevel from the intersection of the CMT/CdTe interface with the bevelled surface can be determined and given the bevel slope, the vertical distance of the electrical junction from the CMT/CdTe interface can be obtained.

For some on-substrate samples, the EBIC measurement of junction position was compared with the results of electrical profiling and, for doped grown junctions, with the results of chemical profiling. Electrical profiles were obtained from differential analysis of successive 77 K Hall measurements on etch-thinned samples. Chemi-

cal dopant profiles were measured by SIMS using a 12 keV oxygen primary ion beam for arsenic (via the  $\text{AsO}^+$  species, detection limit  $\sim 10^{15}$  atoms  $\text{cm}^{-3}$ ) and an argon primary ion beam was used for the iodine profile (via the  $\text{I}^-$  species). The dopant junction position can be deduced from the sharp change in dopant concentrations.

### 3. Results

#### 3.1. Interpretation of the EBIC signal and determination of junction position

Electron/hole pairs are generated by the incident electron beam and are separated and collected by the electric field of a p-n junction (or Schottky barrier) within a range determined by the minority carrier diffusion properties. EBIC contrast occurs where there is variation in the generation or recombination of electron/hole pairs within diffusion range of the junction. The application of EBIC to a bevelled section provides a direct means of viewing the p-n junction and electrically active defects within the layer. However, as a result of the sample geometry, careful interpretation of the EBIC signal is necessary.

When the electron beam impinges on the bevel surface, excess carriers are generated in a characteristic "tear-drop" shaped generation region below the surface. The shape, size, penetration depth and the distribution of carriers associated with the "generation volume" will be functions of the material and the incident electron beam energy. A representation of the generation volume and variation of carrier density with depth is shown in Fig. 1. An EBIC signal is obtained when excess carriers arrive at the depletion layer and are collected at the junction. Below the junction, an EBIC signal can arise only from long lateral diffusion, which will depend upon the characteristic diffusion length of the material. Further up the bevel, carriers begin to diffuse to the depletion layer giving an EBIC signal and eventually the generation volume overlaps directly with the depletion layer. The maximum signal will arise when the overlap is such that the maximum num-

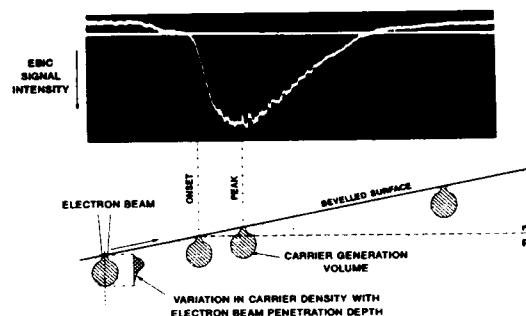


Fig. 1. EBIC line scan signal from bevel section through doped MOVPE-grown  $p-n^+$  heterostructure VG 239, related to the carrier generation volume at various points along the bevel section. The shaded regions represent the generation volume and the variation in carrier density with electron beam penetration depth.

ber of carriers are collected at the junction. Beyond the junction, the signal decays slowly as the overlap of the generation volume with the depletion layer decreases. After direct overlap has ceased, an EBIC signal may continue as a result of vertical carrier diffusion. If diffusion lengths are short, the EBIC signal will be relatively narrow and result almost completely from direct overlap. A typical EBIC signal observed in a  $p-n^+$  heterojunction (low arsenic, low  $x$ ; high iodine, high  $x$ ), sample VG 239, is shown in Fig. 1. The junction position corresponds to the point at which the slope of the signal increases sharply due to the onset of direct overlap of the carrier generation volume with the depletion layer.

#### 3.2. Doped junctions

The EBIC image of a bevelled  $pp^-n^+$  heterostructure (high arsenic, high  $x$ ; low arsenic, low  $x$ ; high iodine, low  $x$ ), sample VG 244, is shown as a photomontage in Fig. 2. The  $p-n^+$  junction is revealed clearly and a weak signal from the  $pp^-$  junction can also be seen. The EBIC signal from the latter occurs where a change in carrier concentration and a change in  $x$  coincide. In other cases, a change in  $x$  or in p-type carrier concentration alone has not given rise to an EBIC signal. Scratches from handling damage

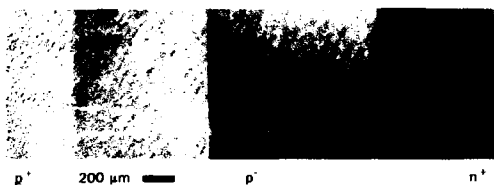


Fig. 2. EBIC picture from bevel section through doped MOVPE-grown  $p^+ p^- n^+$  heterostructure VG 244, showing faint signal from the  $p^+ p^-$  junction (electron beam energy 25 keV).

are often electrically active and one is evident in the lower central part of the EBIC picture.

Junction positions determined from the EBIC study of four doped MOVPE layered structures are compared with Hall/stripe results and SIMS chemical dopant profiles [7] in Table 1. The EBIC results and SIMS dopant profiles show good agreement, within error limits of the techniques. In most cases, the Hall/stripe results indicate shallower junctions than those of the other methods. In junction depth studies, the resolution of the Hall/stripe method depends on the thicknesses of etched portions removed in successive stripping steps. The narrowest EBIC signal observed was for a sample VG 732, implying short diffusion lengths. From the signal width and the measured bevel slope, the penetration depth of a 25 keV electron beam was calculated to be  $\leq 1.3 \mu\text{m}$ , less than reported in the literature [16].

Fig. 3 shows the EBIC signal from a fully doped  $pn$  heterojunction, sample VG 735. A single EBIC line scan is shown superimposed on this

image. At onset, the EBIC signal rises sharply, corresponding to the actual junction position on the bevel surface. The EBIC signal tails off rather more slowly, a function of both bevel/junction geometry and longer diffusion length on the  $n$ -type side of the junction. The dark region in the EBIC tail corresponds to an electrically active scratch, which was also visible on the SEM image. A slight change in slope of the EBIC signal occurs in the tail region and this corresponds to a change in the iodine dopant level, seen in the SIMS depth profile.

### 3.3. Diffused junctions

In general, EBIC images of the diffused junctions, such as those described below, show a less distinct signal onset than for the doped junctions described above. Figs. 4a and 4b show the EBIC signals from monoliths ( $\sim 10 \mu\text{m}$  thick) of LPE and MOVPE CMT (samples LZ 1295 and VG 683) with junctions formed via Hg in-diffusion from an anodic oxide on the surface. For sample LZ 1295 (Fig. 4a), the junction has a slightly

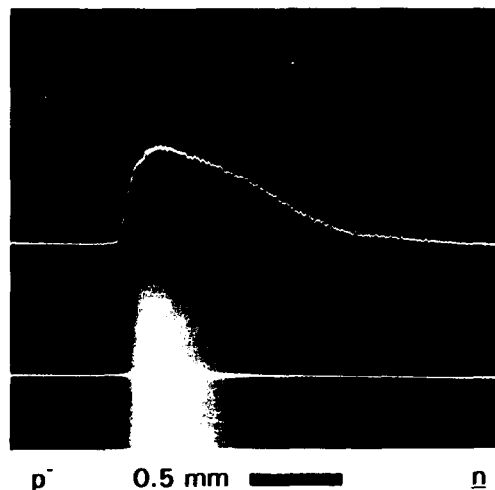


Fig. 3. EBIC picture from bevel section through doped MOVPE-grown  $pn$  heterojunction VG 735, with EBIC single line scan superimposed (15 keV). Note that the sample is connected to EBIC amplifier with opposite polarity compared to sample in previous figure.

Table 1  
Comparison of junction positions,  $x_j$  (distance from buffer layer,  $\mu\text{m}$ ) in doped MOVPE layered structures

Sample	Junction type	Hall/stripe ( $\pm 0.5$ )	SIMS ( $\pm 0.4$ )	EBIC ( $\pm 0.4$ )
VG 244	$p^+ p^-$	5.2	5.7 ( $\pm 0.7$ )	5.6
	$p^- n^+$	11.4	11.9	12.3
VG 734	$p^- n^+$	8.7	8.6	8.5
VG 735	$pn$	8.0	8.4	8.3
VG 737	$p^- n$	14.0	14.4	14.5

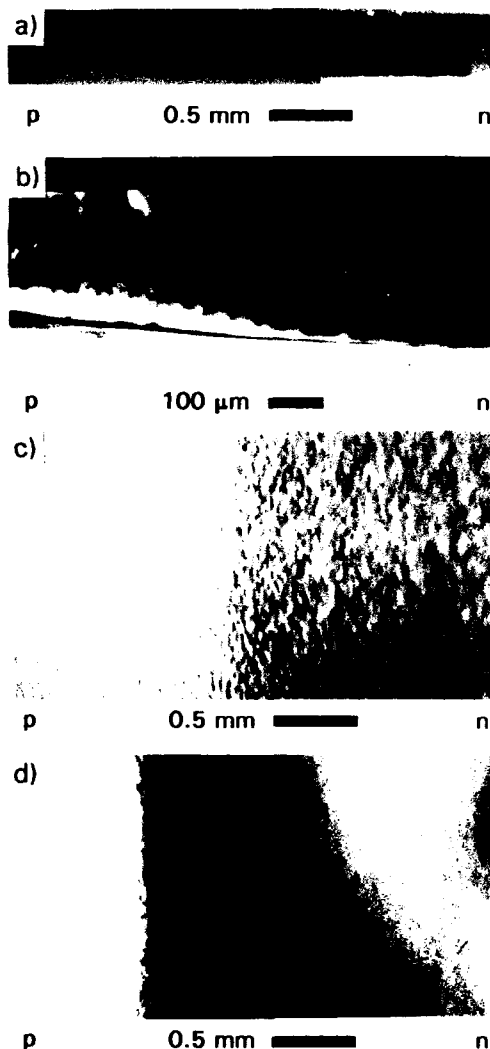


Fig. 4. EBIC pictures from bevel sections through samples with diffused pn junctions: (a) monolith of LPE CMT with junction formed by Hg in-diffusion from anodic oxide (25 keV); (b) monolith of MOVPE CMT with junction formed by Hg in-diffusion from anodic oxide (30 keV); (c) on-substrate MOVPE CMT layer with junction formed by Hg in-diffusion from anodic oxide (25 keV); (d) on-substrate MOVPE CMT layer with junction formed by ion beam milling (30 keV).

ragged appearance at the leading edge, probably as a result of uneven in-diffusion of the Hg. The curved junction shape is a result of the junction "plane" intersecting the rounded surface of the bevel etched monolith. Diffusion length in the n-type region of this layer appears to be relatively long. The EBIC image of sample VG 683 reveals a narrow junction signal with additional EBIC contrast either side of the junction. This mottled, highly contrasting EBIC structure arises from electrically active features, probably consisting of interspersed p and n regions over the entire sample surface. This result is typical of MOVPE monolith samples in which a p-n junction has been formed by in-diffusion of Hg from an anodic oxide. Fig. 4c shows the EBIC image from an on-substrate MOVPE sample VG 736. A similar EBIC signal to that in Fig. 4b can be seen, but with reduced contrast. This effect was not observed for MOVPE samples with grown junctions or for diffused junctions in LPE CMT. These observations are consistent with highly uneven Hg diffusion from the anodic oxide in MOVPE samples, possibly including fast diffusion down defects to give a ragged p-n junction and n-type channels within the p-type matrix. This indicates a difference in microstructure for MOVPE and LPE CMT.

For the on-substrate MOVPE sample VG 761, shown in Fig. 4d, the junction was formed by ion beam milling. EBIC signal onset is slightly ragged but the junction signal is relatively intense. The less mottled appearance of this sample may imply that the diffusion process associated with the ion beam mill, at relatively low temperature, has a different mechanism from that of Hg in-diffusion at 180°C.

### 3.4. Correlation with device results

A qualitative correlation of EBIC signals obtained from bevelled samples with diode results from test arrays has been attempted. Doped MOVPE layers have been fabricated into mesa diode test structures and for undoped MOVPE or LPE layers with diffused junctions, loop-hole [26] or planar geometry test arrays have been prepared. The  $I$ - $R$ - $V$  characteristics of these



arrays were measured at 77 K. Doped MOVPE sample VG 244 and LPE sample LZ 1295 with a diffused junction both showed strong EBIC signals with a sharp signal onset and good diode characteristics. In other cases, no EBIC signal or a faint EBIC signal correlated with very poor diode characteristics. Usually, a strong EBIC signal is an indicator of good diode performance.

#### 4. Conclusions

Shallow-angle bevelled sections through CMT epitaxial layers containing p-n junctions have been studied using the EBIC technique. Electrical contacting to the bevelled structures is relatively straightforward compared to a cleaved section and good EBIC signals have been recorded for doped and diffused junction samples investigated in this study. In the case of doped on-substrate samples, the position of the EBIC signal has been used to measure junction positions and results agree well with dopant and electrical junctions determined by SIMS dopant profiling and Hall/stripe measurements. In general, changes in either *x* or p-type carrier concentration alone do not give rise to an EBIC signal, but if both occur concurrently, EBIC contrast can be observed. A change in carrier concentration due to variation in dopant levels was detected in the EBIC signal for one sample. Defects, including handling defects such as scratches, are often revealed in EBIC images. EBIC imaging of diffused junctions shows a less distinct signal onset than for doped grown junctions. For junctions formed in MOVPE samples by Hg in-diffusion from a surface oxide, EBIC reveals a strongly contrasting background signal along the surface of the bevelled sample, probably caused by interspersed p and n regions. These observations are consistent with uneven Hg diffusion, including fast diffusion down defects producing n-type channels within a p-type matrix. This effect was not observed for MOVPE samples with doped or ion beam milled junctions or for LPE samples with diffused junctions, highlighting a difference between the microstructure of MOVPE and LPE CMT. In many cases, a

qualitative correlation can be made between EBIC signals and diode performance.

#### 5. Acknowledgements

The authors would like to thank P. Mackett and E.S. O'Keefe for the supply of MOVPE and LPE layers respectively. This work was carried out with the support of the Procurement Executive, Ministry of Defence, sponsored by DRA (Malvern).

#### 6. References

- [1] M.V. Blackman, D.E. Charlton, M.D. Jenner, D.R. Purdy, J.T.M. Wotherspoon, C.T. Elliott and A.M. White, *Electron. Lett.* 23 (1987) 978.
- [2] I.M. Baker and R.A. Ballingall, *SPIE Proc.* 510 (1985) 210.
- [3] M.D. Jenner and M.V. Blackman, *US Patent Spec.* 4,318,217 (1992).
- [4] D.T. Dutton, E. O'Keefe, P. Capper, C.L. Jones, S. Mugford and C. Ard, *Semicond. Sci. Technol.* 8 (1993) S266.
- [5] J. Wong and R.J. Roedel, *J. Vac. Sci. Technol. A* 9 (1991) 2258.
- [6] P. Capper, *J. Vac. Sci. Technol.* 9 (1991) 1667.
- [7] C.D. Maxey, I.G. Gale, J.B. Clegg and P.A.C. Whiffin, *Semicond. Sci. Technol.* 8 (1993) S183.
- [8] M. Boukerche, P.S. Wijewarnasuriya, S. Sivanathan, I.K. Sou, Y.J. Kim, K.K. Mahavadi and J.P. Faurie, *J. Vac. Sci. Technol. A* 6 (1988) 2830.
- [9] L.O. Bubulac and C.R. Viswanathan, *J. Crystal Growth* 123 (1992) 555.
- [10] L.O. Bubulac, S.J. Irvine, E.R. Gertner, J. Bajaj, W.P. Lin and R. Zucca, *Semicond. Sci. Technol.* 8 (1993) S270.
- [11] G.L. Destefanis, *J. Crystal Growth* 86 (1988) 700.
- [12] P. Capper, J.E. Harris, E. O'Keefe, C.L. Jones, C.K. Ard, P. Mackett and D. Dutton, *Mater. Sci. Eng. B* 16 (1993) 29.
- [13] C.D. Maxey, P. Capper, P.A.C. Whiffin, B.C. Easton, I.G. Gale, J.B. Clegg, A. Harker and C.L. Jones, *J. Crystal Growth* 101 (1990) 300.
- [14] C.D. Maxey, P.A.C. Whiffin and B.C. Easton, *Semicond. Sci. Technol.* 6 (1991) C26.
- [15] I.G. Gale, J.B. Clegg, S. Mugford, C.D. Maxey, S. Barton, P. Capper, M. Hastings and C.L. Jones, *Semicond. Sci. Technol.* 8 (1993) S281.
- [16] D.B. Holt and D.C. Joy, *SEM Microcharacterization of Semiconductors* (Academic Press, New York, 1989), pp. 241-338.

- [17] W.H. Hackett, Jr., J. Appl. Phys. 43 (1972) 1649.
- [18] C. Donolato, Optik 52 (1978) 19.
- [19] T.M. Moore and H.F. Schaaake, J. Vac. Sci. Technol. A 1 (1983) 1666.
- [20] J.H. Tregilgas, J. Vac. Sci. Technol. 21 (1982) 208.
- [21] S.L. Price, Proc. IEDM 84 (1984) 560.
- [22] M. Lanir, A.H.B. Vanderwyck and C.C. Wang, J. Appl. Phys. 49 (1978) 6182.
- [23] C.F. Byrne and P. Knowles, GEC J. Res. 6 (1988) 129.
- [24] J. Tunnicliffe, S.J.C. Irvine, O.D. Dosser and J.B. Mullin, J. Crystal Growth 66 (1984) 245.
- [25] A.M. Huber and C. Grattapain, in: Proc. 15th Int. Conf. on Defects in Semiconductors (Transtech, Aedermannsdorf, 1988) p. 1345.
- [26] I.M. Baker, G.J. Crimes, M.D. Jenner, J.E. Parsons, R.A. Ballingall and C.T. Elliott, in: Proc. 4th Int. Conf. on Advanced Infrared Detectors and Systems (IEE, London, 1990) p. 78.



ELSEVIER

Journal of Crystal Growth 138 (1994) 924–933

JOURNAL OF **CRYSTAL  
GROWTH**

## Characterization of intrinsic and impurity deep levels in ZnSe and ZnO crystals by nonlinear spectroscopy

V. Gavryushin <sup>\*,a</sup>, G. Račiukaitis <sup>a</sup>, D. Juodžbalis <sup>b</sup>, A. Kazlauskas <sup>a</sup>,  
V. Kubertavičius <sup>a</sup>

<sup>a</sup> Nonlinear Spectroscopy Laboratory, Department of Semiconductor Physics, Vilnius University, Naugarduko 24, 2006 Vilnius, Lithuania

<sup>b</sup> Institute of Physics, Gostauto 12, 2060 Vilnius, Lithuania

### Abstract

Laser induced absorption and photoluminescence are used for the investigation of band states and deep levels (DLs) in ZnSe and ZnO bulk crystals. Interband two-photon and two-step absorption processes, both via DLs as intermediate (virtual and real, correspondingly) states, take place and give information about the main parameters of the DLs. The effects are investigated depending on doping and thermal treatment which change the contamination of native defects. The results illustrate the great possibilities of nonlinear spectroscopy methods in condensed matter science and especially in local defect study.

### 1. Introduction

Nonlinear spectroscopy of semiconductors based on the induced absorption, as a rule, are determined by the competition of different two-quantum phenomena:

- (i) Among them, two-photon absorption (TPA) spectroscopy has been strongly confirmed as a procedure developed for the study of the fundamental properties of crystals [1,2], such as band and exciton structure.
- (ii) The presence of defects in real crystals disrupts the translational symmetry of the lattice, causing changes in the near-band-edge region of TPA [3]. In this case TPA, as a symmetry forbid-

den and a low probability process, has two advantages: the possibility to approach close to the fundamental edge of bulk crystals, and, secondly, the tendency to reveal defect-perturbed band states where the symmetry forbiddenness is lost.

(iii) In real crystals, an additional channel of interband "impurity" TPA (ITPA) appears, with participation of deep levels (DLs) of defects or impurities in the forbidden gap (as virtual intermediate states of TPA event) [4].

(iv) Part of the local defects which are in resonance with the exciting radiation, which changes their population, give rise to non-coherent two-step absorption (TSA) [5,6] via such deep levels as real intermediate states.

(v) If we change the excitation-modulation conditions in such a way that laser radiation leads to two-photon excitation of the crystal, the induced

\* Corresponding author.

absorption by nonequilibrium free carriers appears [7]. In this case, shallow traps of carriers and deep centers of rapid capture undergo nonequilibrium overcharging, which leads to a

photoinduced change of the impurity absorption and TSA [8].

In this paper, we hope to confirm experimentally that concomitant incoherent phenomena

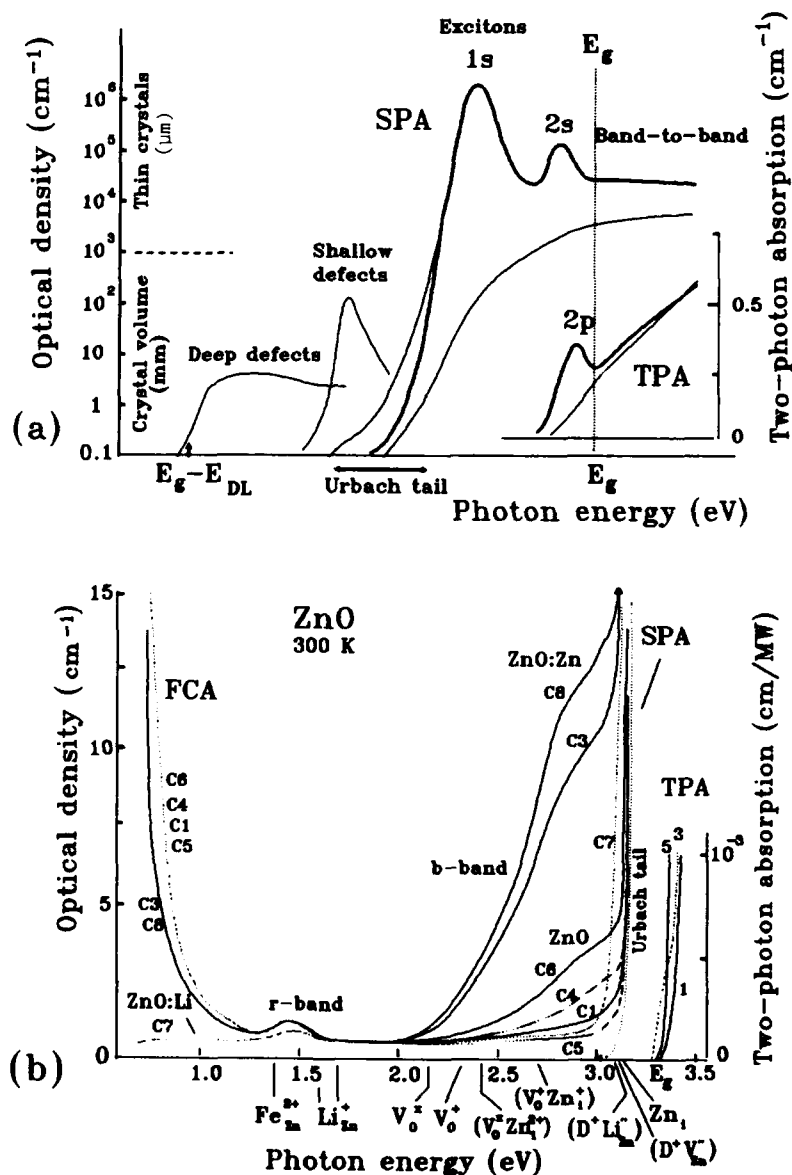


Fig. 1. Comparison of the common features of single- and two-photon absorption spectra. (a) Scheme of typical spectra components. (b) Free carrier (left part) and impurity (right part) absorption spectra of ZnO crystal samples (300 K) of different thermal treatments (Table 2). Urbach tail and two-photon absorption edges are shown for some crystals.

with participation of local defects give a lot of information for the studies and metrology of these states [3–9].

## 2. Two-photon-defectoscopy of band-gap edge

The near-edge region of energy-band states in crystals has an exceptional influence on practical optoelectronic devices and it is also the most sensitive to crystal structure defects. Therefore, there is every reason to seek new ways of revealing distortions of the density-of-states function around the interband absorption edge of real crystals. In Fig. 1, we compare schematically the common features of traditional single- and two-photon spectroscopies and illustrate this by the corresponding spectra of ZnO.

The investigation of the fundamental edge of a single-photon absorption (SPA) in bulk crystals is complicated by an extra-strong excitonic and “band-to-band” absorption ( $\alpha > 10^5 \text{ cm}^{-1}$ ) and by the influence of shallow defects. The exponential “Urbach tails” are typical for SPA in crystals. These have no adequate theory and cannot give first-hand information on the bands.

In contrast, the transparency region of crystals is used in TPA spectroscopy. In this range, the light-induced TPA losses are low ( $\alpha < 1 \text{ cm}^{-1}$ ) and are essentially of a bulk nature. These are the reasons for the specific nature of TPA: (i) It is possible to avoid the influence of surface and of surface defects. (ii) TPA is practically not influenced by shallow defects and impurity states and neither by exponential “Urbach tails”. The reason is that all of them are out of sensitivity of TPA measurements. (iii) As a rule, the ground 1s exciton states do not participate in TPA because of the symmetry forbiddance [1,2]. Therefore, TPA spectroscopy of bulk crystals may be regarded as an alternative to single-photon spectroscopy on thin samples [10,11]. (iv) We consider “off-allowed” by symmetry TPA which makes it possible to approach very close the fundamental edge of bulk crystals, but also helps to reveal defect-perturbed band states for which the selection rules for symmetry, parity and momentum are alleviated by local fluctuations of band states. These features illustrated by Fig. 2c suggest novel

applications of “band-gap-edge TPA defectoscopy” [3].

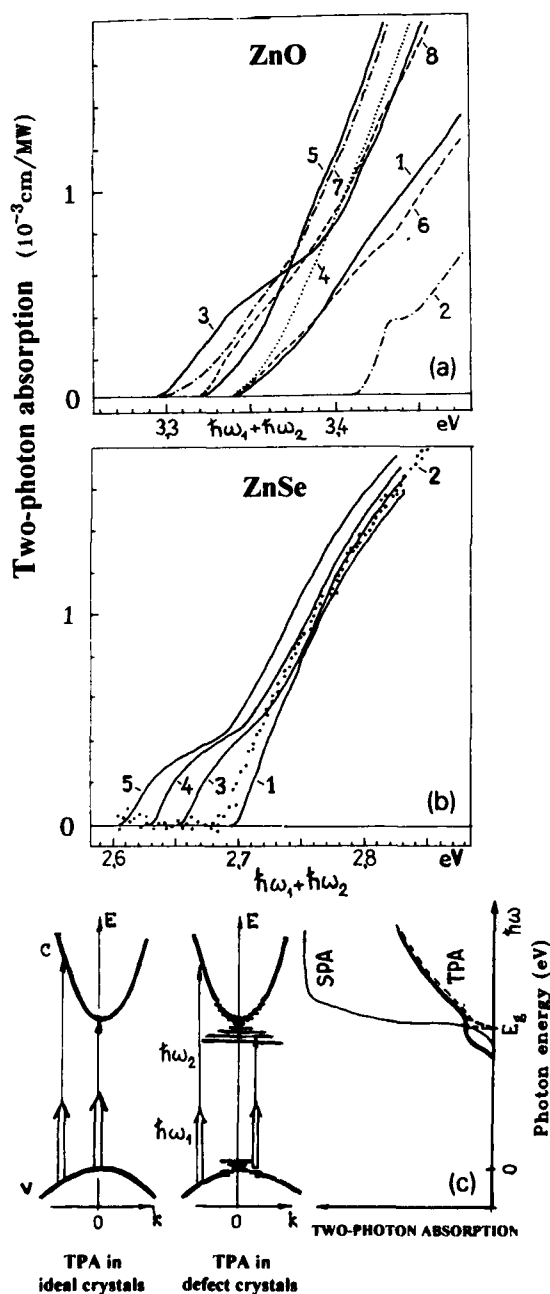
*Experimental evidence.* We investigated two-photon spectra in wide-gap II–VI semiconductors subjected to various heat treatments that affect the stoichiometry and the content of the point defects. Fig. 2 shows the long-wavelength parts of the TPA spectra of ZnO and ZnSe samples of various quality: initial, and the same but annealed under an overpressure of their components and diffusion-doped. The TPA edge was localized at much shorter wavelengths (more than 150 meV beyond the Urbach edge; see, for example, Fig. 1b), in close agreement with the band-gap  $E_g$  (300 K).

In these zinc compounds, “saturated” by an excess of the interstitial defects of  $\text{Zn}_i$  type ( $\text{ZnO}:\text{Zn}$ ,  $\text{ZnSe}:\text{Zn}$ ) and also by  $\text{Li}_i$ -type ( $\text{ZnO}:\text{Li}$ ) [12–14], spectral distortions were exhibited in the form of the long-wavelength shifts or the shoulders up to 50 meV in the case of ZnO and up to 90 meV for ZnSe. These take place only in the near-band-edge region.

Zn-excess in ZnO could be reduced by means of the annealing under oxygen overpressure. Such treatments had practically no effect on the original sample, but once performed, they lead to the reduction of the shoulders (curves 4 and 6 in Fig. 2a). Annealing in Zn-vapour or in a self-vapour in an evacuated ampoule increases off-stoichiometry and is reflected in the spectral changes. The spectra of strongly isovalently doped  $\text{ZnSe}:\text{Te}$  ( $\text{Te} \sim 1\%$ , curve 2 in Fig. 2b) differed slightly from the initial sample, in contrast to the  $\text{ZnO}:\text{Li}$  case (curve 7 in Fig. 2a). This is in agreement with the hypothesis of Te incorporation only in substitutial form of  $\text{Te}_{\text{Se}}$  [6]. The most perturbed by interstitial defect incorporation are the states near to the band extreme with a small momentum. This reflects the loss of a long-range order of crystal translational symmetry and has a statistically spatial inhomogeneous nature.

## 3. Enhancement of coherent nonlinear losses by deep levels

Deep levels can influence nonlinear optical phenomena by their participation as additional



virtual intermediate states [4,15]. The specifics of strong spatial localization of DL states leads, for example, to the possibility of nonresonance character of such “impurity TPA” (ITPA) via DLs, without the conservation of momentum in these stages. This is displayed in an increase of nonlinear losses over the whole spectrum of interband TPA, weakly distorting its spectral form. The resonance character of ITPA (with conservation of momentum) is determined by interference effects of the oscillator strengths of the whole spatially distributed ensemble of deep levels [4].

**Nonresonant ITPA.** In Fig. 3a, the TPA spectra for pure ZnO crystal are given, which agree with the theory of TPA to the p-exciton continuum (curve 1), and also for doped ZnO:Li with a concentration of  $\sim 10^{17} \text{ cm}^{-3}$  of  $\text{Li}_{\text{Zn}}$  acceptors with  $E_{\text{VA}} = 1.2 \text{ eV}$ . The theoretical spectrum of interband ITPA [4] (curve 2) agrees with the experimental spectrum for ZnO:Li. The components of ITPA spectra are shown for the transitions “with conservation of wave vector” (curve 4) and for the case of virtual scattering of wave-vector in a DL state (curve 5) because of its indeterminacy in the local state. It must be mentioned that only the component with “ $k$ -conservation” can have resonant features. The contribution of ITPA component “without  $k$ -conservation” under resonance conditions obtains a threshold form specific for the two-step absorption via deep levels.

**Resonant ITPA.** Two-photon and two-step absorption via local states are mutually connected in the conditions of the intermediate resonance between quanta and local states. The incoming into resonance conditions leads to the increase of electron lifetimes in local intermediate states,

Fig. 2. Long-wavelength parts of two-photon spectra of ZnO (a) and ZnSe (b) undoped (original, curves 1) samples and of different heat treatment prehistory samples (ZnO in Table 2). For ZnSe: (2) ZnSe:Te (1%); (3) annealed in Se vapour; (4) annealed in Zn (ZnSe:Zn); (5) self-vapour annealed. (c) Model, explaining the difference between single- and two-photon edge spectrum formation in defect crystals.

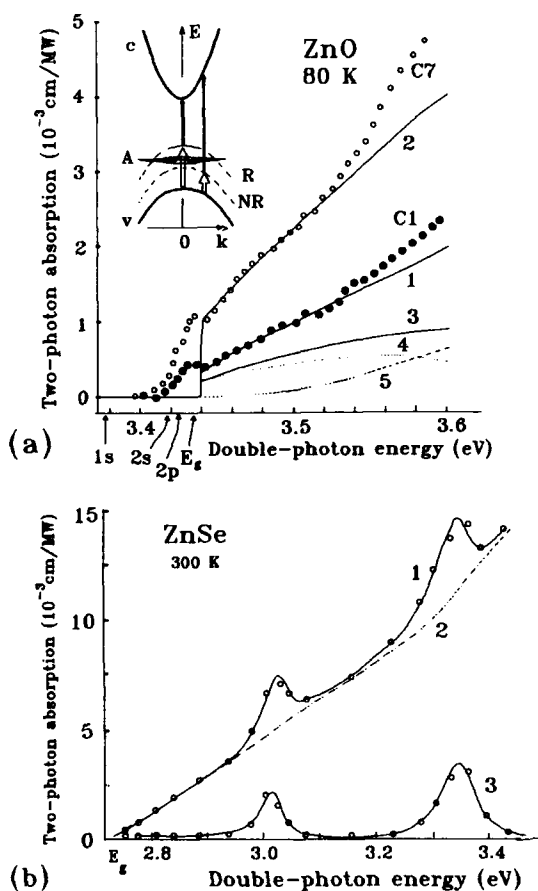


Fig. 3. Influence of two-photon absorption via deep levels on the nonlinear spectrum formation. (a) Nonresonant TPA spectra for pure crystals ZnO (C1) and for the same but diffusionally doped ZnO:Li (C7). Theoretical curves: (1) intrinsic TPA into p-exciton continuum; (2) summary spectrum of TPA and ITPA; summary contribution of "impurity" TPA with "k-conservation" (4) and without one (5). (b) Resonant evidence of two-photon absorption via deep levels in ZnSe crystals (curve 1). Intrinsic TPA (2) and the resolved impurity TPA (3) parts of spectra are also presented. Curves are calculated according to Eq. (2).

starting from disappearingly small for coherent TPA and finishing by terminate lifetimes of real states of noncoherent TSA. So, the coherence of the process is lost with the appearance of its dependence on occupation of the "real" intermediate states. Such connection between TPA and

TSA may be introduced by a damping parameter of intermediate states:

$$\Gamma = \frac{1}{2}(\tau_T^{-1} + \tau_L^{-1} + W_{vA} + W_{Ac}), \quad (1)$$

which includes the probabilities  $W$  of optical changes of the centre population additionally to transversal ( $k$ ) and longitudinal ( $E$ ) relaxation times. Therefore, the resonant ITPA can be dependent on the modulation intensity, seen in damping and saturation of spectral resonances. Thus, on separate ZnSe crystals, on the background of intrinsic interband TPA spectra we have seen two intensity-dependent resonances (Fig. 3b) described satisfactorily by ITPA theory [4,16]:

$$\beta_r(\omega) \sim \sum_i \frac{C_i \Gamma_i}{\left(E_{vA_i} - \hbar\omega_L + \frac{\mu}{m_v^*} \Delta\right)^2 + \Gamma_i^2}, \quad (2)$$

where  $\Delta = \hbar\omega + \hbar\omega_L - E_g$ ,  $\mu^{-1} = m_v^{-1} + m_c^{-1}$ , and  $C_i$  is a quantity slightly changeable in a resonance region and proportional to a squared concentration of centres  $C_i \sim N_i^2$ . Summation is through the number of different nature levels. Results of Fig. 3b correspond to (2) if  $E_{vA_1} = 1.06$  eV,  $E_{vA_2} = 1.12$  eV and  $\Gamma_1 = 20$  meV,  $\Gamma_2 = 30$  meV. It should be noted that the spectral resolution in determination of the energy of DL states is increased as a result of the difference in effective masses of the bands  $m_v^* > m_c^*$ . Besides this, unlike in ITPA, the defect states in the linear optics generally cannot have the resonant spectral peculiarities under their optical overcharge conditions.

#### 4. Deep level nonlinear spectroscopy (DLNS)

DLNS is a method [5,6,9] of investigation of nonequilibrium processes of optically modulated impurity absorption up to the saturation by means of so-called direct and/or indirect laser modulation of quasistationary two-step absorption (LM TSA) via deep levels. It permits one, firstly, to separate the spectral contributions of DLs which are different in nature, even in the case of their complete energy overlap; secondly, to determine

the basic set of phenomenological parameters, the composition of DLs, and also, in some cases, to determine directly the role of these defects in

formation of the luminescence properties of crystals [8,9].

On account of short duration and high inten-

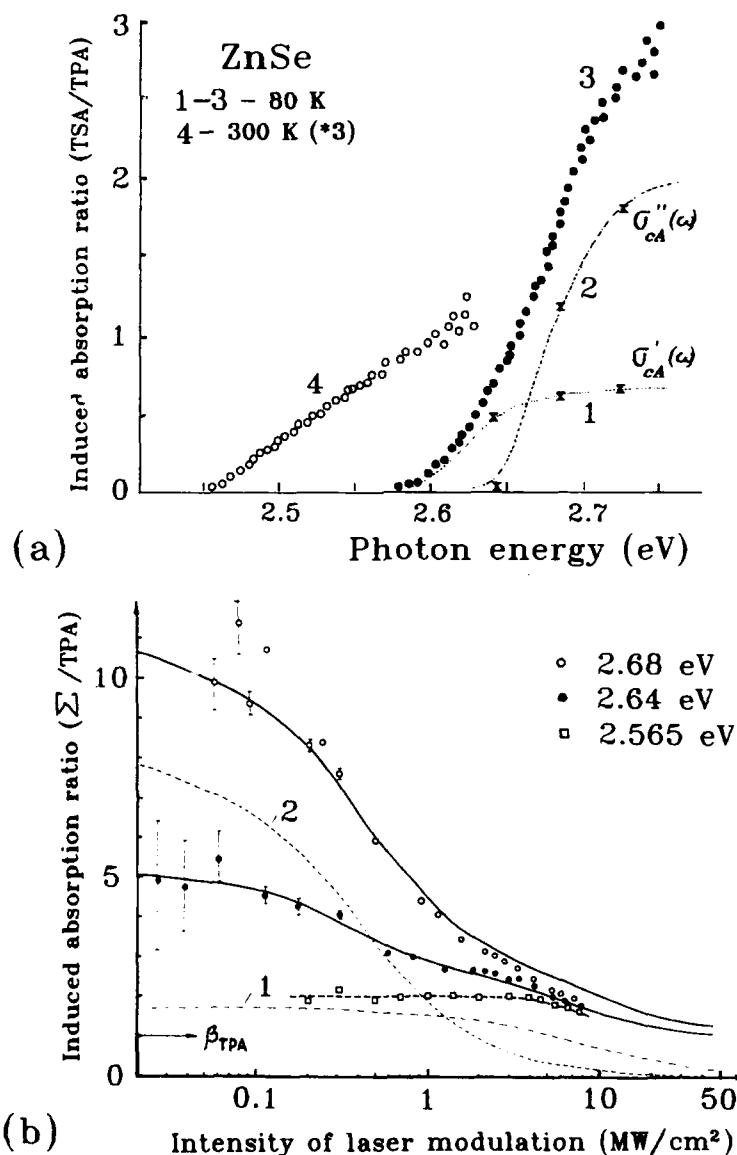


Fig. 4. Separation of spectral contributions (curves 1a and 2a) of LM TSA caused by two deep centres in ZnSe crystals mutually unresolved in spectra (curve 3a), (a) Spectra and their separation to the components (curves 3 and 4). (b) Intensity dependences of induced absorption for different probe quanta and their theoretical components (curves 1 and 2) caused by two deep levels differing in photon capture cross-sections.



sity of laser modulation, the DL depletion by laser quanta is the main process during the laser illumination. According to this, the induced absorption dependence on the intensity of modulating illumination ( $\Delta\alpha(I_f)$ ) has a saturating character determined only by the value of a cross-section of the photon capture  $\sigma(\omega_L)$ . This allows us to determine the parameter directly. Furthermore, the separation of spectral contributions of the centres of different nature is possible, even at close activation energies. The latter is illustrated by experimental results in Fig. 4.

As a result, we can determine in DLNS the main set of parameters associated with deep centres: (i) Energetic position in a band-gap ( $E_{VA}$  and  $E_{AC}$ ; study of Franck–Condon losses). (ii) Values and spectra of cross-sections of both photoionization and photoneutralization, i.e. the photo-activities of DL. (iii) Coefficients of carrier capture, i.e. electroactivity of DL. (iv) Lifetimes of carriers localized in DLs. (v) Quasi-stationary occupation of DLs just before the modulation. (vi) Concentration of the centres.

**Deep level metrology in ZnSe.** The annealing of compound crystals under overpressure of their component vapours strongly influences the crystal properties, as a consequence of the stoichiometry, and the defect content changes during the treatment. This way of a post-growth rearrangement of defect ensemble is a standard for the attempts to identify their nature. Fig. 5 shows the spectra of probe light absorption changes.

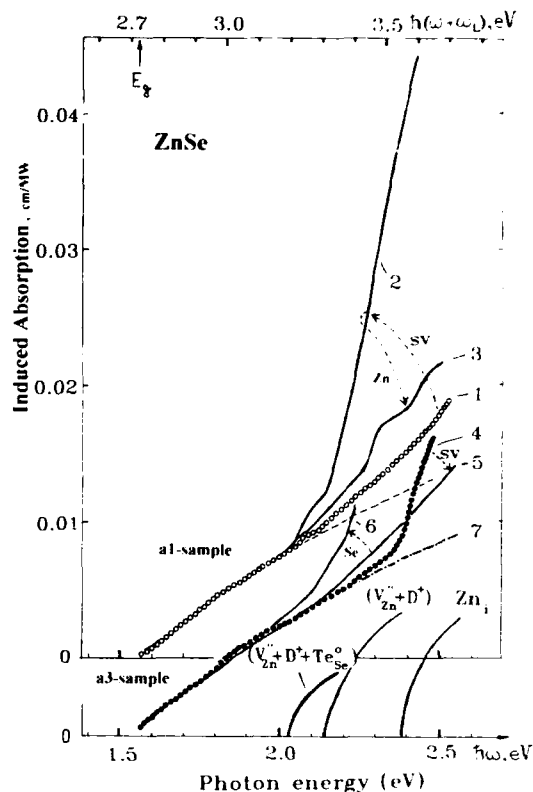


Fig. 5. Induced absorption spectra changes caused by different annealing of two ZnSe samples: (1, 4) original samples a1 and a3; (2, 5) annealed in self vapours (SV) at 550°C for 12 h; (3, 6) additionally annealed in Zn (3) and Se (6) vapours; (7) theoretical spectrum of two-photon absorption by p-exciton continuum

Table 1  
Parameters of deep levels in ZnSe and ZnSe:Te crystals

Nature of centres	$E_{VA}, E_{VD}^a$ (eV)	$E_{AC}, E_{AD}^b$ (eV)	$\sigma_{VA}(\omega_1), \sigma_{VD}(\omega_1)^c$ (cm <sup>2</sup> )	$\sigma_{AC}(\omega), \sigma_{AD}(\omega)^d$ (cm <sup>2</sup> )	Largest concentration (cm <sup>-3</sup> )	Corresponding luminescence band (eV)
Centres included $Fe_{Zn}^{3+}$	1.05	1.77	$10^{-16}$	$2 \times 10^{-16}$	$2 \times 10^{15}$	—
A-centre ( $D^+ + v_{Zn}''$ )	0.62	2.15	$2 \times 10^{-17}$	$4 \times 10^{-17}$	$5 \times 10^{16}$	~ 2.05
M-centre ( $D^+ + V_{Zn}'' + Te_{Se}^0$ )	0.72	2.05	$6 \times 10^{-17}$	$3.5 \times 10^{-16}$	$7 \times 10^{16}$	~ 1.95
Associated with $Te_{Se}$	0.82	2.31	$10^{-17}$	$5 \times 10^{-17}$	$5 \times 10^{16}$	—
Interstitial donor $Zn_i$	0.44	2.38	$5 \times 10^{-18}$	$10^{-17}$	$2 \times 10^{17}$	—
Centre of fast hole capture	1.45	2.59	$2 \times 10^{-16}$	—	—	~ 1.28

<sup>a</sup> Photoionization energy.

<sup>b</sup> Photoneutralization energy.

<sup>c</sup> Photoionization cross-section.

<sup>d</sup> Photoneutralization cross-section.

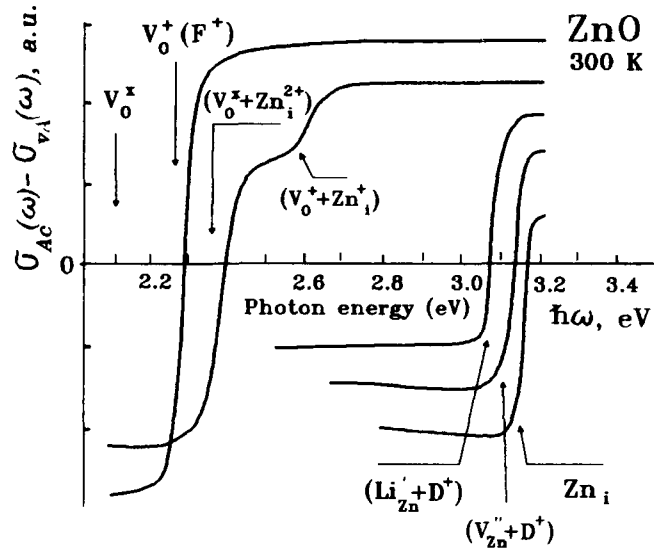


Fig. 6. Spectral components of LM TSA from different deep levels influencing the formation of induced absorption spectra in ZnO crystals (Table 2).

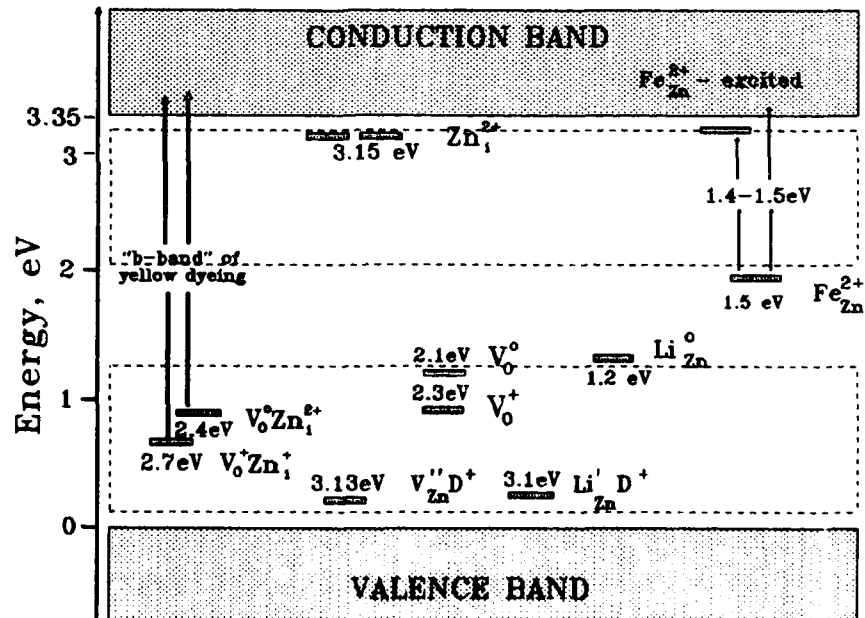


Fig. 7. Defect states in ZnO crystals investigated and identified by means of deep level nonlinear spectroscopy.

induced by laser radiation, for a number of the different prehistory samples of two ZnSe crystals. The long-wave part of the spectra is determined mainly by interband two-photon absorption. Curve 7 shows the theoretical spectra for TPA by p-exciton continuum. On this background we see the "game" of three DL bands with the thresholds at 2.03, 2.15 and 2.38 eV.

After annealing under the self-vapour, a significant enhancement of two overlapping bands is seen in the spectrum of crystal a1 (curve 2). Such a spectrum of crystal a3 (curve 5) becomes the same as that of the original sample a1 (curve 1). A renewed heating in Zn vapour (curve 3) decreases the two bands, and the treatment in Se (curve 6) makes them stronger. The band at 2.38 eV in the original crystal a3 (curve 4), on the contrary, is removed after the self-vapour (SV) annealing. These results of Fig. 5 allow one to suppose that the 2.38 eV band is evidently caused by superstoichiometric zinc, and exactly in interstitial  $Zn_i$  form. In this case, selenium vacancies are not involved, since the vacuum annealing gives the opposite result, similar to that for heating in Se, but not in Zn. The 2.03 and 2.15 eV

bands are somehow related to the loss of Zn from the crystal during annealing, i.e. to the formation of  $V_{Zn}$ , since they are reversibly enhancing and weakening under treatments in Se and in Zn vapours, respectively. The 2.03 eV band is less sensitive to annealing than the 2.15 band, although their behaviour is similar. The measured concentration of "2.2 eV centres" correlates with SA luminescence intensity (self-activated), and their binding energy is in good agreement with that for the SA centre ( $V_{Zn} + D$ ) [12,17].

Identical technological treatments are employed in DLNS experiments on isovalently doped ZnSe:Te crystals [6]. The parameters of deep levels, characteristic for ZnSe and ZnSe:Te crystals, determined in this work, are presented in Table 1.

*Deep level metrology in ZnO.* Spectral dependencies of  $\{\sigma_{cA}(\omega) - \sigma_{vA}(\omega)\}$  type for LM TSA components for the observed DLs, summarized for all ZnO samples, are given in Fig. 6. The results of DLNS study of deep defects, identified also by their reaction on different thermal annealings of ZnO and of diffusionally doped ZnO:Li crystals, are summarized in Fig. 7 and in

Table 2  
Parameters of deep levels in ZnO crystals

	Defect				
	$V_O$	$(V_O + Zn_i)$	$(D^+ + V_{Zn}^+)$	$Zn_i$	$(D^+ + Li_{Zn}^+)$
Photoionization cross-section, $\sigma_{vA}(\omega_L), \sigma_{cD}(\omega_L)$ (cm <sup>2</sup> )	$1.5 \times 10^{-18}$	$6 \times 10^{-17}$	$10^{-18}$	$5 \times 10^{-18}$	$0.5 \times 10^{-17}$
Neutralization cross-section, $\sigma_{cA}(\omega), \sigma_{vD}(\omega)$ (cm <sup>2</sup> )	$3.5 \times 10^{-18}$	$10^{-16}$	$2 \times 10^{-18}$	$7 \times 10^{-18}$	$1.5 \times 10^{-17}$
Photoionization energy, $E_{cA}, E_{vD}$ (eV)	2.3	2.4, 2.7	~ 3.13	~ 3.15	~ 3.10
Annealing	Defect concentration (cm <sup>-3</sup> )				
C1 Initial sample	$2 \times 10^{16}$	$3 \times 10^{15}$	~ $10^{18}$	×	-
C4 O <sub>2</sub> , 830°C, 25 h	$5 \times 10^{16}$	$7 \times 10^{15}$	~ $3 \times 10^{18}$	×	-
C6 O <sub>2</sub> , 440°C, 25 h	$7 \times 10^{16}$	$1.5 \times 10^{16}$	~ $10^{18}$	×	-
C5 Vacuum, 1100°C, 25 h	$1.6 \times 10^{16}$	$1.5 \times 10^{15}$	~ $10^{18}$	~ $10^{17}$	-
C8 Self-vapour, 605°C, 25 h	$6 \times 10^{17}$	$7.5 \times 10^{16}$	×	$7 \times 10^{17}$	-
C3 Zn, 600°C, 25 h	$3.5 \times 10^{17}$	$5.5 \times 10^{16}$	×	$8 \times 10^{17}$	-
C7 Li <sub>2</sub> CO <sub>3</sub> , 830°C, 102 h	$2.5 \times 10^{16}$	$10^{15}$	×	~ $10^{18}$	$5 \times 10^{17}$

Note: × absence in spectra; - low concentration ( $< 10^{15}$ ).

Table 2. Their optical density spectra are presented in Fig. 1b. The regimes of annealing and the determined parameters of deep levels and their content in the samples of different prehistory are presented in Table 2.

#### 4. Conclusions

The possibilities of so-called DLNS or “deep level nonlinear spectroscopy” based on the phenomena of laser modulation (up to saturation) of the occupation of the states of deep local defects are used for the investigation of the ones in ZnSe and ZnO crystals. The effects are studied depending on doping and post-growth thermal treatment which rearranged the ensemble of point defects. The characteristics of DLs and their relation to radiating properties of the crystals are determined from the analysis of photo-induced absorption and luminescence data.

Deep levels as additional intermediate states of two-photon absorption significantly change the probability and spectral response of the process depending on energetic position and concentration of DL. Resonant and non-resonant processes are investigated in technologically different crystals of ZnSe and ZnO.

Changes in the band edge density of states caused by a fluctuating potential of defect distribution in the crystals are for the first time directly detected by means of interband two-photon spectroscopy.

#### 5. Acknowledgment

This work was partially supported by a Meyer Foundation Grant awarded by the American Physical Society.

#### 6. References

- [1] D. Fröhlich, *Festkörperprobleme* 10 (1970) 227.
- [2] B. Honerlage, R. Levy, J.B. Grun, C. Klingshirn and K. Bohnert, *Phys. Rept.* 124 (1985) 161.
- [3] R. Baltramiejūnas and V. Gavryushin, *J. Crystal Growth* 101 (1990) 699.
- [4] R. Baltramiejūnas, V. Gavryushin, G. Račiukaitis et al., *Phys. Status Solidi (b)* 151 (1989) 721.
- [5] R. Baltramiejūnas, R. Baubinas, J. Vaitkus et al., *Sov. Phys.-Solid State* 27 (1985) 227.
- [6] R. Baltramiejūnas, V. Ryzhikov, G. Račiukaitis et al., *Physica B* 185 (1993) 245.
- [7] R. Baltramiejūnas, J. Vaitkus and V. Gavryushin, *Sov. Phys.-JETP* 60 (1984) 43.
- [8] R. Baltramiejūnas, V. Gavryushin, V. Kubertavičius and G. Račiukaitis, *Physica B* 185 (1993) 336.
- [9] V. Gavryushin, R. Baltramiejūnas, G. Račiukaitis et al., *Sov. J. Appl. Spectrosc.* 51 (1989) 503.
- [10] A.P. Roth, J.B. Webb and D.F. Williams, *Phys. Rev. B* 25 (1982) 7836.
- [11] E.G. Batev, Yu.A. Pusep and M.P. Sinyukov, *Sov. Phys.-Solid State* 27 (1985) 708.
- [12] T. Marshall, *Physica B* 185 (1993) 433.
- [13] D.J. Chadi and N. Troullier, *Physica B* 185 (1993) 128.
- [14] H.L. Cotal and B.G. Markey, *Physica B* 185 (1993) 103.
- [15] I.P. Areshev, *Fiz. Tverd. Tela* 11 (1976) 962.
- [16] R. Baltramiejūnas, J. Vaitkus and V. Gavryushin, *Sov. Phys.-Solid State* 18 (1976) 1723.
- [17] G.D. Watkins, in: *Defects and Radiation Effects in Semiconductors*, Eds. N.B. Urii and J.W. Corbett (Inst. Phys., Bristol, 1977) p. 95.



ELSEVIER

JOURNAL OF **CRYSTAL  
GROWTH**

Journal of Crystal Growth 138 (1994) 934–939

## Angle resolved X-ray photoelectron spectroscopy of the surface of $\text{Hg}_{0.85}\text{Zn}_{0.15}\text{Te}$ and after passivation processes

A. Quemerais <sup>a</sup>, K.H. Khelladi <sup>b</sup>, D. Lemoine <sup>b</sup>, R. Granger <sup>\*b</sup>, R. Triboulet <sup>c</sup>

<sup>a</sup> Laboratoire de Spectroscopie du Solide et d'Electronique Quantique, URA 1202 CNRS, Université de Rennes, F-35042 Rennes Cedex, France

<sup>b</sup> Laboratoire de Physique des Solides, URA 786 CNRS, INSA, F-35043 Rennes Cedex, France

<sup>c</sup> Laboratoire de Physique des Solides de Bellevue, UPR 1332 CNRS, F-92195 Meudon Cedex, France

### Abstract

First results on the characterization of  $\text{Hg}_{0.85}\text{Zn}_{0.15}\text{Te}$  surfaces are given. They show that the stoichiometry just under the surface can be kept after several chemical processes. The modulations due to diffraction of the outgoing photoelectrons indicate that the lattice is not damaged. All the surface processes studied leave a layer containing mainly carbon, but also oxygen which cannot come from an atmospheric contamination.

### 1. Introduction

The surface of  $\text{Hg}_{1-x}\text{Cd}_x\text{Te}$  (MCT  $x$ ) has been extensively studied as it is of crucial importance in the fabrication of infrared devices [1]. The low binding energy in MCT results in a change of stoichiometry near the surface and damage of the lattice if great care is not taken during surface treatments.  $\text{Hg}_{1-x}\text{Zn}_x\text{Te}$  (MZT  $x$ ) appears as an alternative material to MCT because of its higher bond strength [2,3], which leads also to a lower segregation of mercury near the surfaces [4]. The study of MCT surfaces has been only performed on  $\langle 111 \rangle$  surfaces, this orientation is preferred for epitaxial growth as twins which may appear are perpendicular to this direction. However, for the  $\langle 100 \rangle$  direction the interpretation of the angle

resolved X-ray photoelectron spectroscopy (ARXPS) patterns are simpler and clearer than in other crystallographic directions. Reliable information about the crystal lattice of MZT 0.15 under its surface is reported using ARXPS. The different surface preparations before ARXPS study are presented in the first section and the experimental conditions necessary to monitor the ARXPS spectra are then recalled. Analysis of the chemical composition near the surface after the different treatments is given in section 4. The photodiffraction features are then discussed in section 5.

### 2. MZT growth and surface treatments

MZT ingots with  $x$  near 0.15 are grown by the travelling heater method. Details and a discussion on the growth process are given in ref. [5].

\* Corresponding author.

The ARXPS results presented here have been obtained on one of the samples with (100) orientation and 2 cm<sup>2</sup> of surface. It has been cut in an ingot which appeared almost a single crystal. However, a subsequent careful analysis revealed that the sample is constituted of a great number of crystallites of which the size is broadly distributed around the mean value of 1 mm; they are separated by subgrain boundaries. The deviation in crystallographic orientation between neighbouring grains remains generally small ( $\approx 20$  arc min), but the whole of these orientations is spread on a 2.5° cone. The sample surface is first mechanically polished with 15  $\mu\text{m}$  silicon-carbide grains and finished with 0.3  $\mu\text{m}$  alumina grains. Its composition has been checked with a microprobe [6] on 15 points of its surface: the mean value of  $x$  is 0.144 with a variation of  $\pm 0.015$ .

The sample is chemomechanically polished with a 2% bromine in methanol solution before each new treatment, to remove a 10  $\mu\text{m}$  layer. The sample has been first submitted to a stoichiometric annealing at 400°C in a closed silica ampoule with Hg at 380°C in order to remove precipitated tellurium and to decrease the vacancy concentration. After this annealing the hole concentration is  $1.2 \times 10^{17} \text{ cm}^{-3}$  [7]. Before the ARXPS analysis, three different types of surface treatment have been applied which are:

(I) The sample is dipped into a solution of

bromine, methanol and ethylene glycol (5%, 15%, 80%) for 1 min, rinsed with methanol and dried with nitrogen gas. This treatment is similar to the process used to polish MCT samples.

(IIa) After step (I), an oxide layer is grown by electrochemistry in a solution of 0.1M KOH in ethylene glycol and deionized water (90%, 10%). The current density is kept constant at 300  $\mu\text{A cm}^{-2}$  during the whole growth process until the voltage between the sample and a standard calomel electrode reaches 30 V where the growth is stopped [8]. The oxide layer, with thickness slightly larger than 100 nm, is immediately removed with a 1M solution of lactic acid. The sample is then rinsed with pure water and dried under a nitrogen flow.

(IIb) The process is the same as (IIa), but after the chemical removal of the anodic oxide layer, the sample is rinsed in methanol and dried under nitrogen.

(III) After step (I), the sample is put in a solution of deionized water which is saturated with KCN. It is then rinsed with water and dried. When the sample is taken out of the KCN solution, its surfaces become unwettable and appear stable in air as checked by ARXPS. This process (step (III)) has already been proposed to obtain near stoichiometric surfaces on Cd-rich MCT, the KCN solution dissolving all the tellurium-related oxides of the top layers [9].

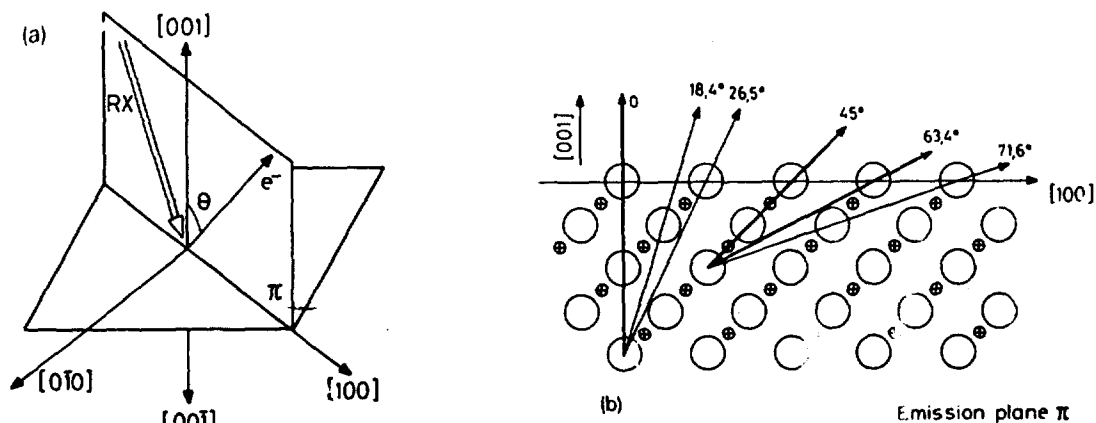


Fig. 1. (a) Overview of the photoelectron monitoring referred to sample crystallographic axis. (b) Atomic arrangement of the sphalerite structure in the probing plane  $\pi$  of (a).

All three processes are entirely performed in a closed box under a nitrogen atmosphere, and the sample is placed in a bag which is sealed in this box. This bag, used to carry the sample, is open inside the preparation lock of the XPS apparatus which is filled with nitrogen. The lock is then evacuated and the sample transferred to the analysis chamber with a sliding rod. This procedure avoids, *a priori*, a contamination by atmospheric species.

### 3. XPS apparatus and analysis details

The photoemission spectroscopy setup is placed in a UHV chamber ( $10^{-10}$  Torr). Its X-ray source is a twin Al/Mg anode tube; however, the Mg  $K\alpha$  peak (1254 eV) is used in this study. The photoelectron analyser is a VSWMA 100, its acceptance angle is  $3^\circ$  and its energy resolution 0.7 eV for a 10 eV pass energy.

The intensity of the photoemission from the core levels Hg4f, Te4d, Zn2p<sub>3/2</sub>, C1s and O1s is monitored as a function of the polar angle  $\theta$  between the electron escape direction and the normal to the sample which is a (001) axis of its lattice, as shown in Fig. 1a. The sample is rotated around the (010) crystallographic axis so that the analysis is performed in the plane  $\pi$ . The periodic array of atoms belonging to the two sublattices in this plane  $\pi$  is drawn in Fig. 1b. The direct wave (part of the non-scattered wave) of the outgoing electron emitted by an atom interferes with the same wave elastically scattered by the neighbouring atoms. So, for the kinetic energies of the analysed photoelectrons, the diffusion amplitudes are peaked in the forward directions where the atomic densities in the lattice are the highest; these directions have been drawn in Fig. 1b. The amplitude of the modulations in the photoelectron intensity depends on the deviations of the atomic positions near the surface as compared to those of a perfect lattice; they are a test of the lattice defects created by surface treatments.

For  $\theta = 0$ , a complete scan in photoelectron energy is monitored. It gives a first chemical analysis of the possible species found near the

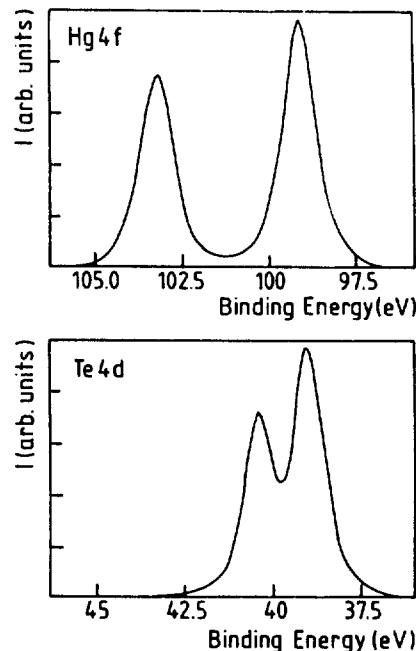


Fig. 2. Intensity profiles of Hg4f and Te4d core levels after processes (II) and (III) described in the text.

surface. ARXPS has been studied only on surfaces with no detectable species other than the crystal constituents, carbon and oxygen. The sample is rotated by steps of  $2.5^\circ$ , and scans of the electron intensity versus the energy are monitored around the characteristic energies of the core levels already cited.

As the mean free path of the photoemitted electrons varies with their kinetic energy, the emissions from core levels Hg4f and Te4d, of which the energies are close, have been chosen so that the Hg/Te ratios are directly comparable. The intensity profiles are obtained by subtraction of the background contribution using the method of Shirley [10]; they allow one to separate clearly the different types of chemical binding for each element studied. Fig. 2 displays the Hg4f and Te4d energy profiles after processes (II) and (III) for which they are the same. No chemical shift corresponding to a bonding of Hg and Te with other atomic species (particularly oxygen) is observed, showing that Hg and Te are not bound to oxygen. Each profile is integrated numerically

in energy and divided by the corresponding ionization cross section to give the normalized intensity.

The level  $\text{Zn } 2p_{3/2}$ , excited by the  $\text{Mg K}\alpha$  radiation, has a cross section greater than the  $\text{Zn } 3p$ ; nevertheless the corresponding electron current remains comparatively small and in an energy domain where the background contribution increases steeply. The signal/noise ratio of the  $\text{Zn } 2p_{3/2}$  profiles is lower than for the other levels and the results are less precise. The mean free path of the  $\text{Zn } 2p_{3/2}$  electrons is shorter due to their lower kinetic energy; this difference is simply taken into account in the calculation of the normalized intensities, although the depth tested by these photoelectrons is lower than for Hg and Te.

#### 4. Results and discussion

After process (I), the surface is deeply oxidized with mainly  $\text{TeO}_2$  and has an excess of Te. It is depleted of Hg but not of Zn. The lack of Hg can be explained by the loss of  $\text{HgO}$  in the UHV chamber as it is volatile. Oxygen is highly present as bound in oxides, but it remains also in the top layer with carbon and bromine which cannot be completely removed by the several rinsing steps. These results appear non-reproducible when repeating process (I) and must be considered as only qualitative; they are of the same type as found in MCT [11].

After processes (IIa) and (IIb), Br, N and K are not detectable. On the other hand, O and particularly C remain as seen in Fig. 3, showing the polar spectra for these elements and the constituents after process (IIb). The profile in energy of Te and Hg does not show any detectable contribution coming from one of their respective oxidized forms (cf. Fig. 2). Moreover, the amplitude of the normalized intensity corresponding to O remains almost constant of  $\theta$  (cf. Fig. 3). C is in larger abundance at the surface than O, as seen in Fig. 3; it is difficult to assess the exact mean thickness of this top layer, but we can fix an upper limit for its value of 10 to 15 Å if it is considered homogeneous. Beyond a thick-

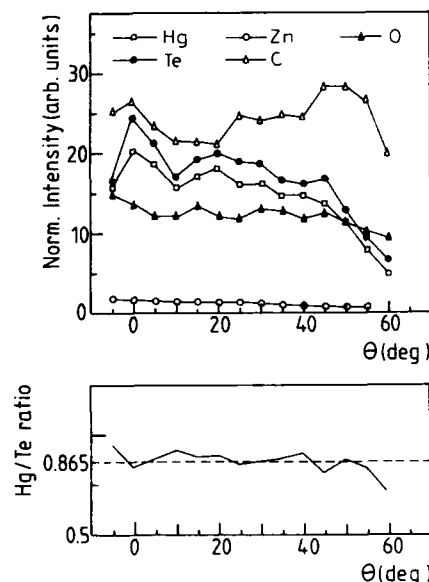


Fig. 3. Normalized intensities and Hg/Te ratio versus polar escape angle  $\theta$  after process (IIb).

ness of 20 Å and for a disordered top layer, the modulations due to the diffraction of the photoelectrons disappear [12]. We will see in the following that the thickness of this top layer appears rather homogeneous on the sample. We have not been able to remove this layer, which originates from the chemical processes themselves, as the sample has been continuously maintained under a nitrogen atmosphere during all the processes. Profile analysis of C shows a very small content of carbonates for processes (IIa) and (IIb); for process (IIa) almost all the carbon corresponds to an aliphatic form, when for process (IIb) about half of the carbon is in an aliphatic binding; the remainder belongs to an alcohol form.

Fig. 4 shows the Hg and Te normalized intensity variations with  $\theta$  after process (IIa). It shows interference modulations (as in Fig. 3) with extrema at polar angles shown in Fig. 1b which are characteristic of a slight damage of the lattice in the first atomic layers under the surface. The ratio of the height of the peak at  $\theta = 0^\circ$  for Te to its minimum near  $\theta = 10^\circ$  is about 3/2. This value can be compared to that obtained on (100)



GaAs epitaxial layers which are considered as a reference, where this ratio is 2/1 [13]. In the case of MZT, the ratio is actually reduced due to the spread of  $2.5^\circ$  found in the (010) axis of the crystallites in the sample; the relative decrease of this ratio has been estimated to be of 20%. Fig. 4 shows also that the modulation in the intensity of Te is clearly seen near  $\theta = 45^\circ$ , but that of Hg has almost disappeared. The smaller amplitude for Te is an effect of the carbon top layer; in return the loss of modulation for Hg corresponds to a perturbed cation sublattice under the top layer.

The mean intensity variations of Te, Hg and Zn are the same; this is evidenced in Fig. 3 and Fig. 4 for the Hg/Te evolution with  $\theta$ . The Hg/Te ratio after process (III) is larger than the value obtained after process (IIa), where it is very near the stoichiometric value after process (IIb).

The values of the relative fractions of Te, Hg, Zn have been put in the usual compositional triangle [1,11], the corresponding points are scattered in a circle of radius 0.03 centred on the mean fraction value. This mean value corresponds to  $\text{Hg}_{0.88}\text{Zn}_{0.09}\text{Te}_{1.00}$  for process (IIb) and

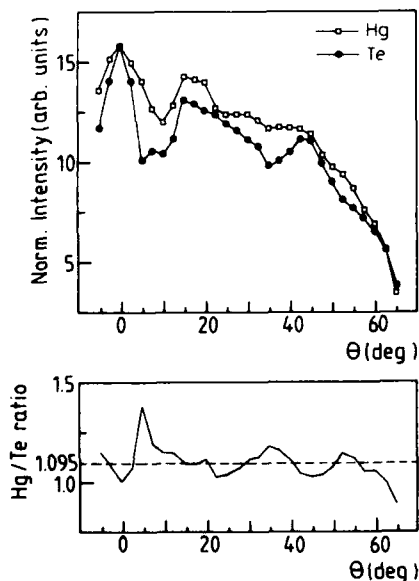


Fig. 4. Normalized intensities and Hg/Te ratio versus polar escape angle  $\theta$  after process (IIa).

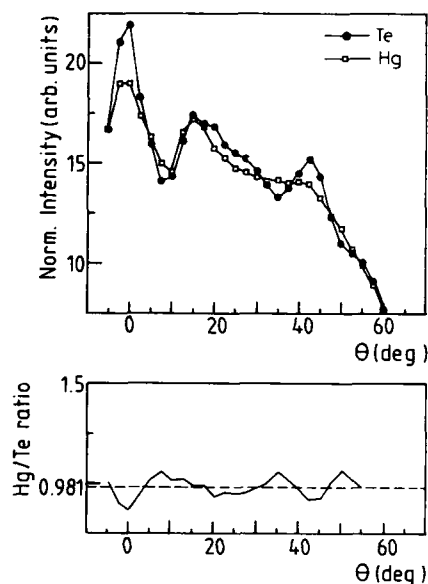


Fig. 5. Normalized intensities and Hg/Te ratio versus polar escape angle  $\theta$  after process (III).

to  $\text{Hg}_{1.08}\text{Zn}_{0.08}\text{Te}_{1.00}$  for process (IIa). The small variations of these values with  $\theta$  correspond to a constant composition lattice under the carbon layer and must be that of the bulk. The difference between the fractional values and the composition of the sample actually remains small and may be attributed mostly to the top most layer in which the mean free path of a photoelectron emitted by Zn is shorter, leading to a smaller normalized intensity. The difference in Hg/Te ratio between processes (IIa) and (IIb) is also attributed to the effect of the top layer.

After process (III), Br, N and K cannot be detected at the surface but the contamination with C and O is as high as with processes (II). An example of normalized intensity curves is presented in Fig. 5 which gives also the Hg/Te ratio as a function of  $\theta$ . The profiles of intensity of Hg and Te are like those given in Fig. 2 and show no oxidation of the constituents. Fig. 5 shows that intensity modulations are of amplitude comparable to those found after processes (II); they are related to a low damage of the crystal under a top layer of carbon. The relative fractions of Te, Hg

and Zn with  $\theta$  have been drawn in the composition triangle; the points remain inside a circle of radius 0.03, whose mean value corresponds to  $\text{Hg}_{0.98}\text{Zn}_{0.08}\text{Te}_{1.00}$ . These small variations correspond here also to a constant composition crystal, which must be that of the bulk under a relatively homogeneous top layer of about 10 to 15 Å.

The mean Hg/Te ratio is the highest after process (IIa) for which the modulations appear a little broadened (cf. Fig. 4a). In return this ratio is lower for processes (IIb) and (III) and the modulation slightly pronounced. This may be explained by a crystal terminated mainly by Hg atoms which are more displaced than the Te atoms after process (IIa). In the case of processes (IIb) and (III), the crystal will be terminated mainly by Te atoms which are less displaced. This explanation would be consistent with the unwetability behaviour of the surface after process (III). However, the carbon top layer is not sufficiently characterized to assess its physicochemical properties. There is little difference between the compositions of this layer after processes (IIa) and (III) when the sample surface is wettable after the first process (IIa) and unwettable after the second (III).

The difference between atomic fractions deduced from ARXPS results and the composition of the sample are attributed to the effect of the upper layer coming from chemical processes themselves.

## 5. Conclusion

First results on the study of the surface of  $\text{HgZnTe}$  are given. We show that process (III), where the oxidized layer present at the sample surface after the usual bromine-methanol treatment is removed in a KCN solution, keeps the stoichiometry of the crystal very near the surface. Moreover, the lattice is slightly damaged, but the crystal is covered with a top layer containing mainly carbon and some oxygen; its depth is about 10 Å and appears homogeneous. The same quality of the near-surface layer is obtained with processes (II) where an anodic oxide layer is

removed by an acid. The difference in the relative fractions of the constituents must be attributed to the effect of the top layer and gives a limit in the composition precision which can be reached by the method used.

A comparison with  $\text{HgCdTe}$  remains difficult, the intensity modulations appear stronger than those found on  $\text{HgCdTe}$  surfaces [1], but the crystallographic orientations of the samples are not the same. The stoichiometry near the surface is conserved in  $\text{HgZnTe}$  after a simple chemical process, which is consistent with the higher stability of its lattice [2,4]; however, the simple process we used should be tested also on Hg-rich  $\text{HgCdTe}$ .

## 6. Acknowledgements

Professor G. Jezequel is acknowledged for encouraging this study, and C. Pobla and J.C. Chabreyron for sample preparations. This work is partly supported by La Direction des Recherches et Etudes Techniques (France) under contract 92-036.

## 7. References

- [1] M. Seelmann-Eggebert, G. Carey, V. Krishnamurthy and C.R. Helms, *J. Vac. Sci. Technol. B* 10 (1992) 1297, and references therein.
- [2] R. Triboulet, *J. Crystal Growth* 86 (1988) 79.
- [3] D. Bagot, R. Granger and S. Rolland, *Phys. Status Solidi (b)* 177 (1993) 295.
- [4] M.A. Berding, A. Sher, A.B. Chen and R. Patrick, *Semicond. Sci. Technol.* 5 (1990) S86.
- [5] R. Triboulet, A. Lasbley, B. Toulouse and R. Granger, *J. Crystal Growth* 79 (1986) 695.
- [6] West Microprobe Facility, Ifremer, Brest, France.
- [7] S. Rolland, A. Lasbley, A. Seyni, R. Granger and R. Triboulet, *Rev. Physique Appl.* 24 (1989) 795.
- [8] K.H. Khelladi, D. Lemoine, S. Rolland, R. Granger and R. Triboulet, *Semicond. Sci. Technol.* 8 (1993) 56.
- [9] R. Tenne, R. Brenner and R. Triboulet, *J. Vac. Sci. Technol. A* 7 (1989) 2570.
- [10] D.A. Shirley, *Phys. Rev. B* 5 (1972) 4709.
- [11] M. Seelmann-Eggebert and H. Richter, *J. Vac. Sci. Technol. A* 6 (1988) 2699.
- [12] A. Quémérais, private communication.
- [13] A. Quémérais, G. Jezequel, B. Lepine D. Sebilléau and I. Pollini, to be published.

## Ultrafast diffusion of Hg in $\text{Hg}_{1-x}\text{Cd}_x\text{Te}$ ( $x \approx 0.21$ )

E. Belas <sup>\*,a</sup>, P. Höschl <sup>a</sup>, R. Grill <sup>a</sup>, J. Franc <sup>a</sup>, P. Moravec <sup>a</sup>, K. Lischka <sup>b</sup>, H. Sitter <sup>b</sup>,  
A. Toth <sup>c</sup>

<sup>a</sup> Institute of Physics, Charles University, Ke Karlovu 5, CZ-121 16 Prague 2, Czech Republic

<sup>b</sup> Research Institute for Optoelectronics, Johannes Kepler University, Altenbergerstrasse 69, Linz, Austria

<sup>c</sup> Research Institute for Technical Physics, Hungarian Academy of Sciences, Pf. 76, Budapest, Hungary

### Abstract

The shape and position of the p–n junction created by ion beam milling was studied using a scanning electron microscope. The shape of the p–n junction demonstrates the diffusion-like character of the p–n conversion process. A model for the explanation of the conversion based on the assumption of an extremely low Hg interstitial migration energy is proposed. A comparison with radiotracer self-diffusion is reported.

### 1. Introduction

Most as-grown single crystals  $\text{Hg}_{1-x}\text{Cd}_x\text{Te}$  are p-type due to Hg vacancies. This material can usually be converted to n-type by annealing at low temperature ( $\approx 300^\circ\text{C}$ ) in an Hg overpressure [1–4] or by ion-beam milling (IM) [5–9]. Large discrepancy between mercury diffusion coefficient deduced from annealing experiments and IM exists [9] and it is not completely explained yet. Tracer diffusion profiles of Hg usually contain two branches (slow and fast) with diffusion coefficients at  $\sim 400^\circ\text{C}$  in the range of ( $D \approx 10^{-10}$ – $10^{-9}$   $\text{cm}^2/\text{s}$ ) [10–13]. However IM experiments can be explained only by much faster diffusion ( $D \approx 10^{-6}$   $\text{cm}^2/\text{s}$ ) at temperatures  $\sim 50^\circ\text{C}$ .

In our paper the explanation of this discrepancy between both coefficients based on the assumption of an extremely low interstitial migration energy is given.

### 2. Experiment

The bulk  $\text{Hg}_{1-x}\text{Cd}_x\text{Te}$  single crystals with  $x \approx 0.21$  were produced by the modified Bridgman method with a floating source. As-grown crystals were p-type. Their hole concentration was in the range  $10^{16}$ – $10^{17}$   $\text{cm}^{-3}$  and the mobility varied between 250 and 700  $\text{cm}^2/\text{V} \cdot \text{s}$  at 77 K. A VEECO ion beam etching system was used with optimal etching parameters: energy of neutralized argon ions 750 eV and current density 600  $\mu\text{A}/\text{cm}^2$ . A part of the surface of some samples was coated with a photoresist mask to shield it from the ion beam. The samples are mounted on a water-cooled copper holder by a heat-conducting grease. The sample temperature was obtained during the IM process by a thermal sensor (pyramids from Wood's metal) and did not exceed  $70^\circ\text{C}$ . Similar results were reported in ref. [7].

Secondary electron (SE) and electron beam induced current (EBIC) observations were used to determine the shape and position of the p–n

\* Corresponding author.

junction after IM. The typical scanning electron microscope (SEM) parameters were 25 keV, 10 nA beam current and a magnification between 60 and 300. The samples were investigated with the e-beam perpendicular to the cleaved cross section and the temperature of the samples was 75–100 K. Indium was used to provide good ohmic contact between material and bonding Au leads.

### 3. Results

Fig. 1 shows a mixed mode SEM micrograph (both EBIC and SE images together) of cleaved cross section of a sample which was prepared by IM (750 eV, 600  $\mu\text{A}/\text{cm}^2$ , 25 min). Before milling one half of the sample was covered by a photoresist mask. It can be seen that the distance of the p–n junction from the milled surface is uniform in the whole sample and the thickness of the n-type layer reaches approximately 170  $\mu\text{m}$ . In addition, the n-type region extends deep under the photoresist mask (the white solid line on the surface of the sample marks the position of the photoresist mask).

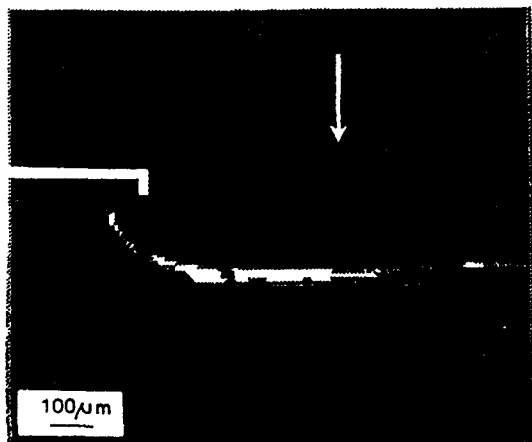


Fig. 1. A mixed EBIC–SE micrograph of the cross section of sample 49-13-E6. The white solid line marks the position of the photoresist mask which shielded a part of the sample from ion milling; arrow indicates direction of incident argon ions.

### 4. Theory and discussion of diffusion

A great difference between Hg diffusion coefficients deduced from IM and annealing experiments is the reason why the ordinary diffusion mechanisms of n-type layer creation are abandoned and other (nonstandard) diffusion mechanisms are looked for – see ref. [7]. The theory proposed here removes this apparent discrepancy of diffusion coefficients and proves that the ordinary diffusion mechanism can explain both the observed phenomena.

#### 4.1. Diffusion model of ion milling

During IM the mercury interstitials ( $\text{Hg}_i$ ) are liberated near the surface. Then the region close to the bombarded surface of the sample is supersaturated by them and the concentration of  $\text{Hg}_i$  significantly exceeds their thermal equilibrium concentration in this region.  $\text{Hg}_i$  diffuse either into the bulk or out from the sample. Consequently, by a recombination with  $\text{Hg}_i$  the concentration of Hg vacancies decreases significantly and residual uncompensated donors convert the region into n-type. After finishing of IM, the  $\text{Hg}_i$  recombine fast and their concentration returns to the thermal equilibrium one. The diffusion of other components (Cd, Te) as well as sputtering of the surface during IM are neglected here.

The model suggested here starts from the assumption that diffusion of Hg is driven by a combined interstitial–vacancy mechanism. The sample is homogeneous with plain surface at coordinate  $y = 0$ . The coupled one-dimensional equations of diffusion for the  $\text{Hg}_i$  and Hg vacancy diffusion read:

$$\frac{\partial c_i}{\partial t} = D_i \frac{\partial^2 c_i}{\partial y^2} - R c_i c_v + S \delta(y), \quad (1)$$

$$\frac{\partial c_v}{\partial t} = D_v \frac{\partial^2 c_v}{\partial y^2} - R c_i c_v, \quad (2)$$

where  $c_i \equiv c_i(y, t)$ ,  $c_v \equiv c_v(y, t)$ , and  $D_i$  and  $D_v$  are concentrations of interstitials and vacancies and diffusion coefficients, respectively.  $S$  is the source of the interstitials located on the surface.

A thermal creation of vacancies at the surface and interstitial–vacancy pairs in the bulk is very weak at low temperature and is left out here.  $\delta(y)$  is the Dirac function.  $R$  represents the interstitial–vacancy recombination constant [14]:

$$R = 4\pi(D_i + D_v)e^2/\epsilon k_B T, \quad (3)$$

where  $e$ ,  $\epsilon$ ,  $k_B$  and  $T$  are the electron charge, the dielectric constant, the Boltzmann constant and the temperature, respectively. In view of the fact that the p–n structure is long-time stable at room temperature,  $D_v$  can be set zero.

Generally,  $S$  describes also a loss of  $\text{Hg}_i$  diffusing out from the sample. Thus  $S$  is divided formally into two parts  $S = S_1 - S_2 c_i(0, t)$ , where the second term describes the above-mentioned case.

The concentration of vacancies has decreased significantly in the converted n-type region. Thus the recombination term in Eq. (1) can be neglected there and diffusion of Hg is driven by the diffusion coefficient  $D_i$ .

Eqs. (1) and (2) were solved numerically for initial conditions and model parameters  $c_i(y, 0) = 0$ ,  $c_v(y, 0) = 10^{16} \text{ cm}^{-3}$ ,  $D_i = 10^{-6} \text{ cm}^2/\text{s}$ ,  $D_v = 0$ ,  $T = 320 \text{ K}$ ,  $S_1 = 10^{11} \text{ cm}^{-2}/\text{s}$  and  $S_2 = 5 \times 10^{-5} \text{ cm}/\text{s}$ . At time  $t = 1500 \text{ s}$ , the source  $S_1$  was switched off ( $S_1(t > 1500 \text{ s}) = 0$ ). The resulting  $c_i(y, t)$  is shown in Fig. 2. Starting IM at  $t = 0$ ,  $c_i$  increases,  $\text{Hg}_i$  diffuse into the bulk and recom-

bine with Hg vacancies, and consequently the n-type region is created. After switching off the source  $\text{Hg}_i$  recombine at the p–n junction and on the surface and their concentration decreases quickly.

#### 4.2. Tracer self-diffusion

The model of annealing describes diffusion in a crystal at chemical equilibrium, i.e. uniform chemical and native defect composition (self-diffusion). This regime is invariably studied using radiotracers, therefore involving a net isotopic flux. Similarly as in the case of IM, the isotopic flux is described by the coupled one-dimensional equations of diffusion for the Hg radiotracers in the interstitial and lattice sites:

$$\begin{aligned} \frac{\partial c_i}{\partial t} = & D_i \frac{\partial^2 c_i}{\partial y^2} + R \left( K_F \frac{c_L}{c_{\text{Hg}}} - c_i c_v \right) \\ & + S_1 P_{\text{Hg}} \left( 1 - \frac{c_i c_v}{K_F} \right) \delta(y). \end{aligned} \quad (4)$$

$$\begin{aligned} \frac{\partial c_L}{\partial t} = & D_L \frac{c_v}{c_{\text{Hg}}} \frac{\partial^2 c_L}{\partial y^2} - R \left( K_F \frac{c_L}{c_{\text{Hg}}} - c_i c_v \right) \\ & + S_L c_v P_{\text{Hg}} \left( 1 - \frac{c_L}{c_{\text{Hg}}} \right) \delta(y). \end{aligned} \quad (5)$$

Here  $c_i$ ,  $c_L$ ,  $c_{\text{Hg}}$ ,  $K_F$  and  $P_{\text{Hg}}$  are radiotracer interstitial and lattice sites concentrations, the total Hg lattice sites concentration, the Frenkel constant and the Hg pressure, respectively. The last terms with  $\delta$ -function describe transport of radiotracers through the surface.  $S_1$  and  $S_L$  are pressure-independent model parameters. Note that due to chemical equilibrium,  $c_v \propto P_{\text{Hg}}^{-1}$ , but is independent of  $y$  and  $t$ .

Eqs. (4) and (5) can be simplified if we realize that the generation–recombination terms (proportional to  $R$ ) exceed by several orders of magnitude those with time and space derivatives. This means that  $c_i$  and  $c_L$  are locally near the equilibrium [15] where

$$c_i = K_F c_L / c_{\text{Hg}} c_v. \quad (6)$$

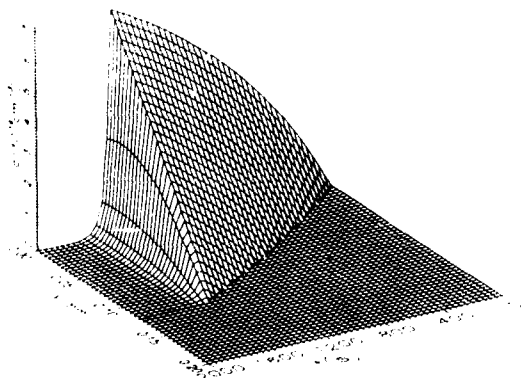


Fig. 2. The example of  $c_i(y, t)$  calculated for model parameters given in the text. The surface with source is at  $y = 0$ . The dashed line shows the position of the p–n junction.

Summing (4) and (5) and substituting (6), the equation for total radiotracer diffusion is obtained in the form

$$\frac{\partial c_T}{\partial t} = D_{\text{Hg}}^* \frac{\partial^2 c_T}{\partial y^2} + S_T \left( 1 - \frac{c_T}{c_{\text{Hg}}} \right) \delta(y), \quad (7)$$

where  $c_T$  is total radiotracer concentration  $c_T = c_I + c_L$ ,

$$S_T = (S_I + S_L c_v) P_{\text{Hg}}, \quad (8)$$

and  $D_{\text{Hg}}^*$  is Hg self-diffusion coefficient,

$$D_{\text{Hg}}^* = (D_I K_F + D_v c_v^2) / (c_{\text{Hg}} c_v + K_F). \quad (9)$$

Assuming  $c_{\text{Hg}} c_v \gg K_F$ , Eq. (9) can be rewritten in a more visual form:

$$D_{\text{Hg}}^* = (D_I c_{\text{IT}} + D_v c_v) / c_{\text{Hg}}, \quad (10)$$

where  $c_{\text{IT}}$  is total  $\text{Hg}_I$  concentration.

The dependence of  $D_{\text{Hg}}^*$  on  $P_{\text{Hg}}$  agrees with the form obtained experimentally in ref. [11]. At low  $P_{\text{Hg}}$ ,  $c_v$  is high. Then the diffusion occurs by the vacancy mechanism, given by the second term in numerator of (10) and  $D_{\text{Hg}}^*$  is proportional to  $P_{\text{Hg}}^{-1}$ . At high  $P_{\text{Hg}}$ ,  $c_v$  is low, the diffusion occurs by the interstitial mechanism given by the first term in numerator of (10) and  $D_{\text{Hg}}^*$  is proportional to  $P_{\text{Hg}}$ .

From this expression, a qualitative estimate of the relation between  $D_{\text{Hg}}^*$  and  $D_I$  during annealing experiments can be done. The exact equilibrium concentration of  $\text{Hg}_I$  is not known. Theoretical calculation of Berding and co-workers [16] yields  $c_{\text{IT}}/c_{\text{Hg}} \sim 10^{-13}$  at 500°C and  $\sim 10^{-14}$  at 300°C. This results in a huge difference between  $D_I$  and  $D_{\text{Hg}}^*$ . Although the theoretical calculation of  $c_{\text{IT}}$  may be questionable, it is evident, that in any case  $D_I$  exceeds  $D_{\text{Hg}}^*$  by many orders of magnitude.

Generally, the temperature dependence of  $D_I$  is mostly described by the Arrhenius exponential where  $\text{Hg}_I$  migration activation energy defines its slope. Deducing from ref. [16], this energy is very low ( $< 0.2$  eV). This means that by decreasing the temperature to room ones,  $D_I$  will not be significantly changed in comparison with high-temperature values.

## 5. Conclusion

The shape and position of the p–n junction created by ion beam milling was studied using scanning electron microscopy. The shape of the p–n junction demonstrates the diffusion-like character of the p–n conversion process. The estimates explain that the great value of the diffusion constant of mercury interstitials  $D_I$  observed during ion beam milling experiments is not in contradiction with standard values of radiotracer mercury self-diffusion constant  $D_{\text{Hg}}^*$  established from equilibrium annealing experiments.

This work was supported in part by the Hungarian National Scientific Research Fund under contract No. OTKA T7615.

## 6. References

- [1] E. Bartlett, P. Capper, J.E. Harris and M.J.T. Quelch, *J. Crystal Growth* 49 (1980) 600.
- [2] A.J. Syllaos and M.J. Williams, *J. Vac. Sci. Technol.* 21 (1982) 201.
- [3] C.L. Jones, M.J.T. Quelch, P. Capper and J.J. Gosney, *J. Appl. Phys.* 53 (1982) 9080.
- [4] H.F. Shaake, J.H. Tregilgas, A.J. Lewis and P.M. Everett, *J. Vac. Sci. Technol. A* 1 (1983) 1625.
- [5] J.M.T. Wotherspoon, UK Patent GB 2,095,898 (1981).
- [6] M.V. Blackman, D.E. Charlton, M.D. Jenner, D.R. Purdy, J.M.T. Wotherspoon, C.T. Elliott and A.M. White, *Electron. Lett.* 23 (1987) 978.
- [7] G. Bahir and E. Finkman, *J. Vac. Sci. Technol. A* 7 (1989) 348.
- [8] V.I. Ivanov-Omskii, K.E. Mironov and K.D. Mynbajev, *Sov. Phys.-Semicond.* 24 (1990) 1379.
- [9] E. Belas, P. Höschl, R. Grill, J. Franc, P. Moravec, K. Lischka, H. Sitter and A. Toth, *Semicond. Sci. Technol.* 8 (1993) 1695.
- [10] M. Brown and A.F.W. Willoughby, *J. Crystal Growth* 59 (1982) 27.
- [11] D.A. Stevenson and M.F.S. Tang, *J. Vac. Sci. Technol. B* 9 (1991) 1615.
- [12] N.M. Archer, H.D. Palfrey and A.F.W. Willoughby, *J. Crystal Growth* 117 (1992) 177.
- [13] D. Shaw, *Semicond. Sci. Technol.* 7 (1992) 1230.
- [14] F.A. Kröger, *The Chemistry of Imperfect Crystals*, Vol. 3 (North-Holland, Amsterdam, 1974) p. 2.
- [15] V.V. Bogobojaschii, A.I. Elizarov, V.I. Ivanov-Omskii, V.R. Petrenko and V.A. Petryakov, *Fiz. Tekh. Poluprovodn.* 19 (1985) 819.
- [16] A. Sher, M.A. Berding, M. van Schilgaarde and An-Ban Chen, *Semicond. Sci. Technol.* 6 (1991) C59.



ELSEVIER

Journal of Crystal Growth 138 (1994) 944–949

JOURNAL OF  
**CRYSTAL  
GROWTH**

## Indium doped $\text{Hg}_{0.7}\text{Cd}_{0.3}\text{Te}$ /undoped $\text{Hg}_{0.8}\text{Cd}_{0.2}\text{Te}$ /CdTe heterojunction grown by Te-rich liquid phase epitaxy

S.W. Moon <sup>a</sup>, S.H. Suh <sup>\*,a</sup>, C.S. Choi <sup>b</sup>

<sup>a</sup> Division of Electronics and Information Technology, Korea Institute of Science and Technology, P.O. Box 131, Cheongryang, Seoul, South Korea

<sup>b</sup> Department of Metallurgical Engineering, Yonsei University, Seoul 120-749, South Korea

### Abstract

Firstly, we have studied the indium doping concentration dependence of the electrical properties of  $\text{Hg}_{0.7}\text{Cd}_{0.3}\text{Te}$  monolayers grown by liquid phase epitaxy (LPE). Below the indium concentration of  $1 \times 10^{18} \text{ cm}^{-3}$ , nearly 100% of indium was electrically active. Indium-doped  $\text{Hg}_{0.7}\text{Cd}_{0.3}\text{Te}$ /undoped  $\text{Hg}_{0.8}\text{Cd}_{0.2}\text{Te}$ /CdTe heterojunction was grown in a double bin graphite boat, using a slider LPE technique. After the growth, Hg-annealing was performed. An n-type  $\text{Hg}_{0.8}\text{Cd}_{0.2}\text{Te}$  layer was formed just beneath the  $\text{Hg}_{0.7}\text{Cd}_{0.3}\text{Te}$  cap layer by Hg-diffusion. The  $\text{Hg}_{0.8}\text{Cd}_{0.2}\text{Te}$  p–n homojunction formed thereby would have no misfit defects.

### 1. Introduction

Mercury cadmium telluride (HgCdTe) is the most important semiconducting material for the fabrication of infrared photon detectors and imaging arrays [1–3]. However, the low junction impedance and high leakage current have been the major challenges for HgCdTe photodiodes to be used for the detection of 8–12  $\mu\text{m}$  infrared. Heterojunctions (wide bandgap on narrow bandgap HgCdTe) have been considered as a way of increasing the performance of HgCdTe photodiodes by many authors [4–6].

In the frontside illumination mode, photon absorption takes place near the surface of the HgCdTe layer. Therefore, the recombination of

photo-carriers at the interface between the insulating layer and HgCdTe reduces the quantum efficiency. If a wide bandgap HgCdTe film is deposited onto the narrow bandgap HgCdTe, absorption of the desired radiation (longer wavelengths) will occur mainly in the narrow bandgap photoabsorbing layer. Here, the wide bandgap HgCdTe acts as a spectral filter for the incident radiation [7]. Therefore, this kind of heterojunction is expected to reduce the surface recombination and background photon flux.

Most of the HgCdTe p–n heterojunctions grown by LPE (liquid phase epitaxy) have undergone a two-step process of growing sequentially p- and n-type layers with using Te-rich and Hg-rich solutions [8,9]. Recently, p- $\text{Hg}_{0.75}\text{Cd}_{0.25}\text{Te}$ /p- $\text{Hg}_{0.78}\text{Cd}_{0.22}\text{Te}$ /CdTe grown by using only a Te-rich slider LPE process was reported by Yasumura et al. [10]. In this study, we have grown n- $\text{Hg}_{0.7}\text{Cd}_{0.3}\text{Te}$ /p- $\text{Hg}_{0.8}\text{Cd}_{0.2}\text{Te}$ /CdTe hetero-

\* Corresponding author.

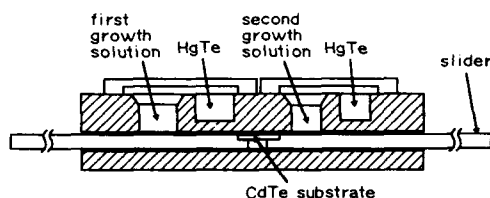


Fig. 1. Schematic diagram of a double-bin slider boat for LPE growth of HgCdTe DLHJs.

junctions by indium doping in a double-bin graphite boat, using a Te-rich slider type LPE. The characteristics of the heterojunction will be discussed.

## 2. Experimental procedure

HgCdTe layers were grown on CdTe (111)A substrates ( $12 \times 12 \text{ mm}^2$ ) by LPE technique, using a double-bin graphite slider boat (Fig. 1) under purified hydrogen flow at atmospheric pressure. Mercury vapor loss from the growth solutions was precisely controlled in a specially designed boat. The mercury overpressure created by a HgTe source next to each melt bin was used to compensate for the mercury loss from each growth solution [11]. The weight gain of each growth solution measured at the growth start temperature was used to determine the optimum growth temperature, with using the Maudes equations [12]. The compositions of the growth solutions and the growth temperatures used are listed in Table 1.

For the growth of n-type  $\text{Hg}_{0.7}\text{Cd}_{0.3}\text{Te}$  layers, indium was doped in the growth solution. Te ingots containing 0.01% indium were used for the synthesis of growth solutions. Indium concentra-

tions ( $\text{atoms}/\text{cm}^3$ ) in the growth solutions were measured by AA (atomic absorption analysis). SIMS (secondary ion mass spectrometry) was used to determine the indium concentrations in the HgCdTe epi-layers, using  $\text{O}_2^+$  ions as a primary ion beam. The segregation coefficient of indium ( $K$ ) was calculated from the AA and SIMS data.

For the double layer heterojunction (DLHJ), the composition of the base layer was determined by a Fourier transform infrared spectrometer (FTIR), using a relationship by Finkman and Schacham [13]. A wavelength dispersive spectrometer (WDS) was used to determine the composition of the cap layer and the composition grading width.

Hg-annealing was carried out in a sealed quartz ampoule. Annealing was done at  $250^\circ\text{C}$  for several hours, with the samples kept  $5^\circ\text{C}$  warmer than the Hg reservoir to prevent condensing of mercury on the sample. Differential Hall measurement was used to determine the junction depth ( $x_j$ ) and the electrical properties [14].

## 3. Results and discussion

### 3.1. Indium-doped $\text{Hg}_{0.7}\text{Cd}_{0.3}\text{Te}$

An undoped HgCdTe layer grown using a Te-rich solution is usually of p-type conductivity with a high hole concentration due to Hg vacancies which act as doubly ionized acceptors [15]. Hg-annealing at  $200$ – $250^\circ\text{C}$  reduces the Hg vacancy concentration in HgCdTe, the conduction types being determined by residual impurities [16]. To obtain an n-type conductivity accurately, intentional donor-doping is needed. The most widely used n-type dopant for HgCdTe is indium [17]. Firstly, we have determined the segregation coefficient of indium in our Te-rich LPE process. The indium concentration in the growth solution was  $2.7 \times 10^{18} \text{ cm}^{-3}$  and that in the epi-layer was  $7.5 \times 10^{18} \text{ cm}^{-3}$ , resulting in a segregation coefficient ( $K$ ) of 2.8.

We have studied the indium-doping concentration dependence of the electrical properties of LPE grown  $\text{Hg}_{0.7}\text{Cd}_{0.3}\text{Te}$  monolayers.  $\text{Hg}_{0.7}$

Table 1  
The composition of the growth solutions and the growth temperatures for HgCdTe double layer heterojunctions

Composition of solution	Growth temperature ( $^\circ\text{C}$ )
$\text{Hg}_{0.8}\text{Cd}_{0.2}\text{Te}$ Hg:Cd:Te = 0.150:0.007:0.843	475.1–465.9
$\text{Hg}_{0.7}\text{Cd}_{0.3}\text{Te}$ Hg:Cd:Te = 0.114:0.009:0.877	465.9–465.1



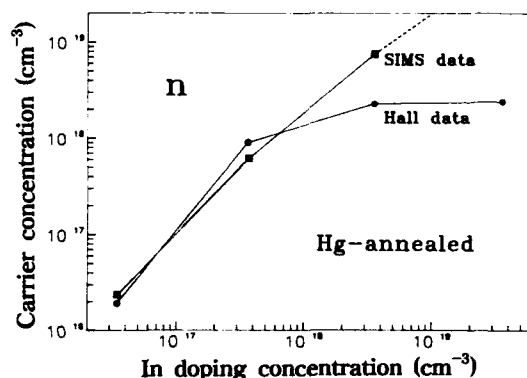


Fig. 2. Carrier concentrations measured at 77 K ( $\text{cm}^{-3}$ ) for In-doped  $\text{Hg}_{0.7}\text{Cd}_{0.3}\text{Te}$  monolayers versus concentrations of indium in the layers measured by SIMS ( $\text{cm}^{-3}$ ) after the Hg-annealing at  $250^\circ\text{C}$  for 35 h.

$\text{Cd}_{0.3}\text{Te}$  layers were grown using the growth solutions doped with different concentrations of indium. These layers were Hg-annealed at  $250^\circ\text{C}$  for 35 h to remove the Hg vacancies and activate the indium. Fig. 2 shows the carrier concentrations measured at 77 K versus the concentrations of indium in the layers. Below the doping of  $1 \times 10^{18} \text{ cm}^{-3}$ , In-doping is well controlled. In other words, nearly 100% of indium was electrically active. The carrier concentration levels off at  $2 \times 10^{18} \text{ cm}^{-3}$ . This is probably because the solubility limit is reached as the indium concentration approaches  $2 \times 10^{18} \text{ cm}^{-3}$ . A similar result has been reported from MOVPE materials [16]. Our result supports the idea that above the solubility limit, most of the indium atoms remain as electrically inactive In complexes, like  $\text{In}_2\text{Te}_3$ , with only a small fraction of indium in Hg lattice sites playing the role of active donors [18].

### 3.2. As-grown double layer heterojunction

For the growth of DLHJ, an undoped  $\text{Hg}_{0.8}\text{Cd}_{0.2}\text{Te}$  base layer was grown first on the CdTe substrate, using a Te-rich solution. Subsequently, a  $\text{Hg}_{0.7}\text{Cd}_{0.3}\text{Te}$  cap layer doped with indium of  $5 \times 10^{16} \text{ cm}^{-3}$  was grown onto the base  $\text{Hg}_{0.8}\text{Cd}_{0.2}\text{Te}$  layer. DLHJs were free of melts left on the surface and looked like mirrors. Terrace structures were observed, due to small misorien-

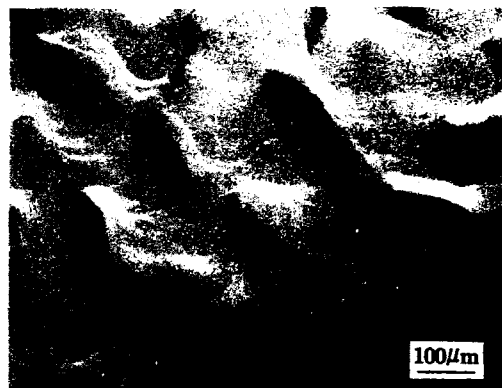


Fig. 3. Surface morphology of HgCdTe DLHJ grown by LPE on CdTe (111)A substrate.

tations of the substrates from the exact (111) orientation (Fig. 3).

Fig. 4 shows the room temperature FTIR transmission spectra for a DLHJ. From the FTIR spectra, the composition  $x$  of the base layer ( $\text{Hg}_{1-x}\text{Cd}_x\text{Te}$ ) was measured to be 0.205. Since the composition of the cap layer could not be measured by FTIR due to absorption of infrared by the base layer of the lower energy band gap, it was measured by WDS. The cadmium composition measured across the cleaved surface is shown in Fig. 5. The cap layer composition  $x$  was 0.3 and the composition grading width was thinner than  $0.5 \mu\text{m}$ . The entire layer thickness and the

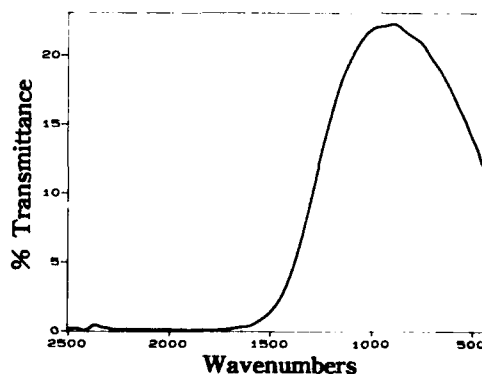


Fig. 4. Room temperature FTIR transmission spectra for DLHJ.

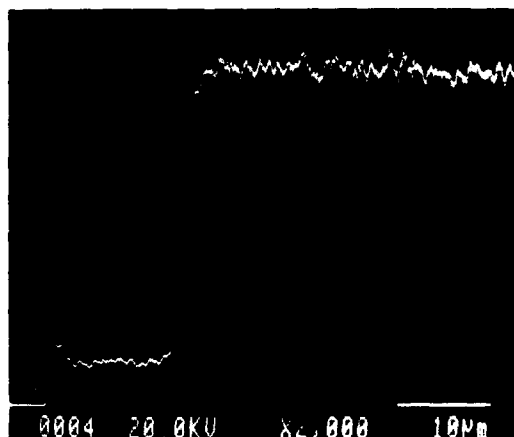


Fig. 5. Cadmium compositional profile of HgCdTe DLHJ measured across epitaxial layers on cleaved surface.

cap layer thickness were 15 and 1.8  $\mu\text{m}$ , respectively.

Fig. 6 shows the SIMS depth profile data of the indium concentration in an as-grown DLHJ which has the cap layer doped with indium of  $5 \times 10^{16} \text{ cm}^{-3}$ . We can see that an indium concentration of  $9 \times 10^{15} \text{ cm}^{-3}$  exists throughout the undoped base layer. Indium diffusion from the indium-doped growth solution bin to the undoped growth solution during the LPE growth might be the major cause of this result.

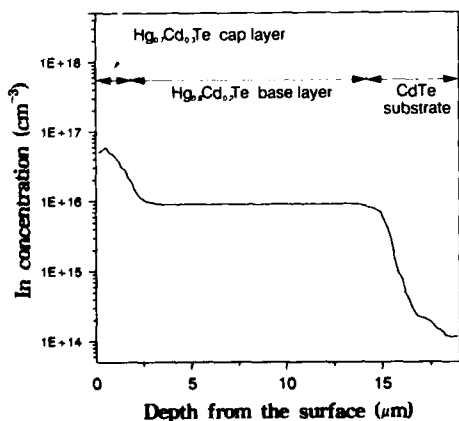


Fig. 6. SIMS depth profile of indium concentration in as-grown DLHJ.

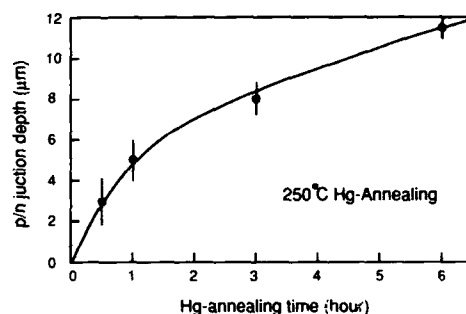


Fig. 7. The p-n junction depth as a function of Hg-annealing time at 250°C for the DLHJ having a cap layer doped with indium of  $5 \times 10^{16} \text{ cm}^{-3}$ .

### 3.3. Hg-annealed double layer heterojunction

Misfit dislocations are usually observed at the HgCdTe heterojunction interface, due to the lattice mismatch [19]. Misfit dislocations are believed to act as recombination centers in photodetectors. Therefore, it is desirable to position the p-n junction in the base  $\text{Hg}_{0.8}\text{Cd}_{0.2}\text{Te}$  layer in which no misfit dislocations exist.

In this study we tried to position the p-n junction within the  $\text{Hg}_{0.8}\text{Cd}_{0.2}\text{Te}$  base layer, using a low temperature Hg-annealing at 250°C. The diffused mercury lowers the density of the Hg vacancies below that of the indium concentrations, converting the top part of the base layer as well as the cap layer to n-type. The carrier concentrations of n-type layers are determined by the indium concentration in the HgCdTe layers. The thickness of the n-type  $\text{Hg}_{0.8}\text{Cd}_{0.2}\text{Te}$  layer can be controlled by the Hg-annealing time.

To place the p-n junction at a desired depth in the base layer, we have done some diffusion experiments. Fig. 7 shows the p-n junction depth as a function of Hg-annealing time at 250°C for a DLHJ with the cap layer containing indium of  $5 \times 10^{16} \text{ cm}^{-3}$ . Junction depths have been measured by differential Hall measurements. From Fig. 7, we could obtain the two unknown parameters, i.e., constant value  $A$  and the activation energy  $E_a$ , in the diffusion equation of

$$x_j^2 N_a / \text{time} = A \exp(-E_a / kT),$$

where  $k$  is Boltzmann's constant and  $T$  is the

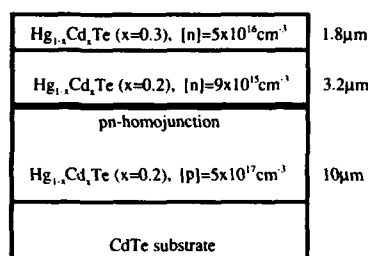


Fig. 8. Schematic drawing of the cross section after Hg-annealing at 250°C for 1 h.

annealing temperature in kelvin,  $x_j$  is the junction depth and  $N_a$  is the initial vacancy concentrations [20].  $E_g$  and  $A$  were determined as 0.47 eV and  $7.5 \times 10^{22} \text{ cm}^{-1} \text{ s}^{-1}$ , respectively.

From these experiments, we could show that the p-n junction was located 5  $\mu\text{m}$  down from the surface after Hg-annealing for 1 h. Fig. 8 depicts a schematic drawing of the cross section for this case. This DLHJ consists of three different layers. The first layer is the n-type  $\text{Hg}_{0.7}\text{Cd}_{0.3}\text{Te}$  with 1.8  $\mu\text{m}$  thick. The second layer is n-type  $\text{Hg}_{0.8}\text{Cd}_{0.2}\text{Te}$  with a carrier concentration of  $9 \times 10^{15} \text{ cm}^{-3}$  and its thickness is 3.2  $\mu\text{m}$ , which were confirmed by SIMS and differential Hall measurement. The formation of this second layer is the result of the Hg-diffusion. The third layer, which is 10  $\mu\text{m}$  thick, shows p-type conductivity with carrier concentration of  $5 \times 10^{17} \text{ cm}^{-3}$  due to the as-grown Hg vacancies. Therefore, a p-n junction was formed between n-type  $\text{Hg}_{0.8}\text{Cd}_{0.2}\text{Te}$  and p-type  $\text{Hg}_{0.8}\text{Cd}_{0.2}\text{Te}$ . The  $\text{Hg}_{0.8}\text{Cd}_{0.2}\text{Te}$  p-n homojunction formed thereby would have no misfit defects and no band discontinuity.

Since this  $\text{Hg}_{0.8}\text{Cd}_{0.2}\text{Te}$  p-n homojunction also has the wide band gap cap layer of  $\text{Hg}_{0.7}\text{Cd}_{0.3}\text{Te}$  on top of it, a LWIR photodiode with good detectivity is expected from this structure if other device processing details such as passivation are optimized later on.

#### 4. Summary

We have demonstrated the growth of In-doped  $\text{Hg}_{0.7}\text{Cd}_{0.3}\text{Te}$ /undoped  $\text{Hg}_{0.8}\text{Cd}_{0.2}\text{Te}$ /CdTe het-

erojunctions, using a Te-rich slider LPE techniques. The cap layer thickness was 1.8  $\mu\text{m}$  and the composition grading width was thinner than 0.5  $\mu\text{m}$ .

A p-n homojunction was formed within the  $\text{Hg}_{0.8}\text{Cd}_{0.2}\text{Te}$  base layer by Hg-annealing at 250°C for 1 h. In conjunction with the wide band gap cap layer of  $\text{Hg}_{0.7}\text{Cd}_{0.3}\text{Te}$ , this  $\text{Hg}_{0.8}\text{Cd}_{0.2}\text{Te}$  p-n homojunction having no misfit defects and no band discontinuity is expected to bring forth a LWIR photodiode with good detectivity.

#### 5. Acknowledgements

The authors would like to thank H. Jung and K. Kim of KAIST for helpful discussions. They also thank Dr. H.G. Kim, Dr. J.M. Kim and Dr. S.B. Lee of ADD for their encouragement. This work was sponsored by the Agency for Defence Developments in Korea. This support is greatly appreciated.

#### 6. References

- [1] S.H. Shin, A.H.B. Vanderwyck, J.C. Kim and D.T. Cheung, *Appl. Phys. Lett.* 37 (1980) 402.
- [2] M. Chu and C.C. Wang, *J. Appl. Phys.* 51 (1980) 2255.
- [3] D.E. Charlton, *J. Crystal Growth* 59 (1982) 98.
- [4] M.W. Goodwin, M.A. Kinch and R.J. Koestner, *J. Vac. Sci. Technol. A* 8 (1990) 1226.
- [5] Tse Tung, M.H. Kalisher, A.P. Stevens and P.E. Herning, *Mater. Res. Soc. Symp. Proc.* 90 (1986) 321.
- [6] P.R. Bratt, *J. Vac. Sci. Technol. A* 1 (1983) 1687.
- [7] M.A. Herman and M. Pessa, *J. Appl. Phys.* 57 (1985) 2671.
- [8] C.C. Wang, *J. Vac. Sci. Technol. B* 9 (1991) 1740.
- [9] G.N. Pults, P.W. Norton, E. Eric Krueger and M.B. Reine, *J. Vac. Sci. Technol. B* 9 (1991) 1724.
- [10] K. Yasumura, T. Murakami, M. Suita, H. Takada, K. Takahashi and M. Nunoshita, *J. Crystal Growth* 117 (1992) 20.
- [11] S.H. Suh, S.W. Moon, J.S. Kim, S.W. Lim, N.J. Kwak, H.K. Kim and J.M. Kim, *J. Crystal Growth* 121 (1992) 417.
- [12] J. Sanz-Maudes, J. Sangrador and T. Rodriguez, *J. Crystal Growth* 102 (1990) 1065.
- [13] E. Finkman and S.E. Schacham, *J. Appl. Phys.* 56 (1984) 2896.
- [14] P. Koppel and K. Owens, *J. Appl. Phys.* 67 (1990) 6886.

- [15] H.R. Vydyanath, J. Electrochem. Soc. 128 (1981) 2609.
- [16] J.S. Gough, M.R. Houlton, S.J.C. Irvine, N. Shaw, M.L. Young and M.G. Astles, J. Vac. Sci. Technol. B 9 (1991) 1687.
- [17] M.H. Kalisher, J. Crystal Growth 70 (1984) 365.
- [18] H.R. Vydyanath, J. Electrochem. Soc. 128 (1981) 2619.
- [19] H. Takigawa, M. Yoshikawa and T. Maekawa, J. Crystal Growth 86 (1988) 446.
- [20] C.L. Jones, M.J.T. Quelch, P. Capper and J.J. Gosney, J. Appl. Phys. 53 (1982) 9080.



ELSEVIER

Journal of Crystal Growth 138 (1994) 950–955

JOURNAL OF  
CRYSTAL  
GROWTH

## Hg<sub>0.8</sub>Cd<sub>0.2</sub>Te grown by liquid phase epitaxy using Cd<sub>0.94</sub>Zn<sub>0.06</sub>Te buffer layer

N.J. Kwak <sup>a</sup>, I.H. Choi <sup>a</sup>, S.W. Lim <sup>b</sup>, S.H. Suh <sup>\*b</sup><sup>a</sup> Department of Materials Science and Engineering, Korea University, Seoul 136-701, South Korea<sup>b</sup> Division of Electronics and Information Technology, Korea Institute of Science and Technology, P.O. Box 131, Cheongryang, Seoul, South Korea

### Abstract

Buffered structures of Hg<sub>0.8</sub>Cd<sub>0.2</sub>Te/Cd<sub>0.94</sub>Zn<sub>0.06</sub>Te/Cd<sub>0.97</sub>Zn<sub>0.03</sub>Te were grown by a slider LPE technique and their material properties were compared with those of Hg<sub>0.8</sub>Cd<sub>0.2</sub>Te/Cd<sub>0.97</sub>Zn<sub>0.03</sub>Te structures which have no buffer layer. Photoluminescence spectroscopy (PL) was used to determine the compositions of the buffer layers and the substrates and analyse the impurities in the buffer layers. Auger electron spectroscopy (AES) was used to analyse impurities. Either sodium or lithium related donor–acceptor pair (DAP) peaks were observed in the substrate, but not in the Cd<sub>0.94</sub>Zn<sub>0.06</sub>Te buffer layer. AES analysis revealed that the substrate contained some impurities such as Si, Al, O, K, Fe, and Mg. In the Cd<sub>0.94</sub>Zn<sub>0.06</sub>Te buffer layer, the above impurities were not detected. The distribution of dislocations in the epi-layers were analysed by defect etching as well as double crystal X-ray diffraction. For the buffered structure, most misfit etch-pits were located just above the interface between the Hg<sub>0.8</sub>Cd<sub>0.2</sub>Te and Cd<sub>0.94</sub>Zn<sub>0.06</sub>Te buffer, and their density was much lower than that in the unbuffered structure, in which etch-pits were distributed rather broadly in the epi-layer. Electrical properties of the Hg<sub>0.8</sub>Cd<sub>0.2</sub>Te epi-layers, which were Hg-annealed at 250°C, were analysed by Hall measurement at 77 K. The buffered structure showed the carrier concentrations of  $7 \times 10^{13}$  to  $1 \times 10^{14}$  cm<sup>-3</sup> and Hall mobilities of 2 to  $5 \times 10^5$  cm<sup>2</sup>/V · s.

### 1. Introduction

Hg<sub>1-x</sub>Cd<sub>x</sub>Te is the most widely used material for infrared (IR) detectors. The energy band gap of Hg<sub>1-x</sub>Cd<sub>x</sub>Te varies with the mole fraction of CdTe (*x*). Hg<sub>0.8</sub>Cd<sub>0.2</sub>Te has the energy band gap of 0.1 eV, therefore being exclusively used for detecting infrared of 8–12 μm.

Liquid phase epitaxy (LPE) has become a major manufacturing process of Hg<sub>1-x</sub>Cd<sub>x</sub>Te for the last decade. Hg<sub>1-x</sub>Cd<sub>x</sub>Te materials grown by LPE have both uniform composition and excellent

electrical properties. CdZnTe and CdTe have been used as substrates for LPE growth of Hg<sub>1-x</sub>Cd<sub>x</sub>Te. The electrical property of a Hg<sub>1-x</sub>Cd<sub>x</sub>Te epi-layer depends largely on the impurity concentration and crystalline defects of the substrate [1]. Hg<sub>1-x</sub>Cd<sub>x</sub>Te epi-layers can be contaminated by impurities in the substrate [2]. Not only dislocations in the substrate but also misfit dislocations created at the interface propagate into the epi-layers, deteriorating the electrical properties.

In this paper we have tried to improve the electrical properties of LPE-grown Hg<sub>0.8</sub>Cd<sub>0.2</sub>Te by inserting a buffer layer Cd<sub>0.94</sub>Zn<sub>0.06</sub>Te between the Hg<sub>0.8</sub>Cd<sub>0.2</sub>Te epi-layer and the Cd<sub>0.97</sub>

\* Corresponding author.

$\text{Zn}_{0.03}\text{Te}$  substrate. Electrical and defect-related properties of the buffered structures were compared to those of the unbuffered structures of  $\text{Hg}_{0.8}\text{Cd}_{0.2}\text{Te}/\text{Cd}_{0.97}\text{Zn}_{0.03}\text{Te}$ .

## 2. Experimental procedure

LPE growths of  $\text{Hg}_{0.8}\text{Cd}_{0.2}\text{Te}$  epi-layers and  $\text{Cd}_{0.94}\text{Zn}_{0.06}\text{Te}$  buffer layers were carried out, using an open tube slider system [3]. The solution compositions and temperature ranges used for the growths are given in Table 1.  $\text{Cd}_{0.97}\text{Zn}_{0.03}\text{Te}$  with (111)A orientation and of the size  $12 \times 12 \text{ mm}^2$  were used as substrates.

After a  $\text{Cd}_{0.94}\text{Zn}_{0.06}\text{Te}$  buffer layer was grown, it was taken out of the boat and etched. A  $\text{Hg}_{0.8}\text{Cd}_{0.2}\text{Te}$  epi-layer of  $25 \mu\text{m}$  thickness was grown on top of it. Isothermal Hg-annealing at  $250^\circ\text{C}$  for 40 hr was performed to convert the as-grown p-type  $\text{Hg}_{0.8}\text{Cd}_{0.2}\text{Te}$  to n-type.

LPE grown epi-layers were characterized as follows. PL spectra were obtained at 12 K both for the substrate and buffer layers. Ar ion laser was used as an excitation source. The spectral resolution was  $1 \text{ \AA}$ . Impurities on the surface of the substrate and buffer layers were analysed by Auger electron spectroscopy (AES). Just before the analysis, the surface of the substrate and buffer layers were sputtered by  $\text{Ar}^+$  ions. Compositions of the  $\text{Hg}_{0.8}\text{Cd}_{0.2}\text{Te}$  layers were determined from the cut-on wavelengths on the IR transmittance curves. Hall effect measurements were performed on Hg-annealed specimens at 77 K to obtain electrical properties.

The distributions of dislocations in the  $\text{Hg}_{0.8}\text{Cd}_{0.2}\text{Te}$  epi-layer, the buffer layer, and the substrate were studied by defect etching of both

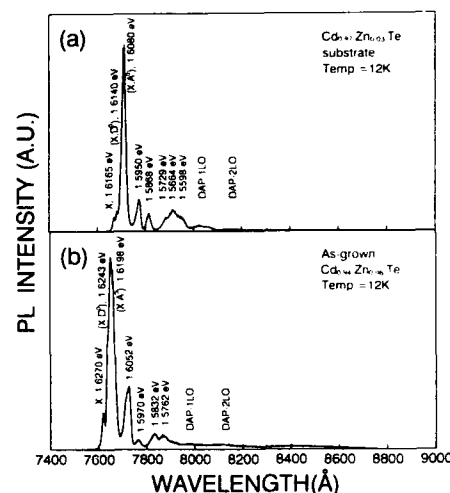


Fig. 1. PL spectrum of (a) the  $\text{Cd}_{0.97}\text{Zn}_{0.03}\text{Te}$  substrate and (b) the  $\text{Cd}_{0.94}\text{Zn}_{0.06}\text{Te}$  buffer layer.

(111)A as-grown and (110) cleaved surfaces, using Polisar II [4], Nakagawa [5], and a new etchant [6], respectively. The crystallinity was evaluated using a double crystal X-ray diffractometry (DCX). InSb was used as the first crystal. Full widths at half maximum (FWHM) of double crystal rocking curves (DCRC) were obtained at different depths of the specimen by repeated etching and measuring.

## 3. Results and discussion

### 3.1. PL characteristic of $\text{Cd}_{0.94}\text{Zn}_{0.06}\text{Te}$ buffer layers

Figs. 1a and 1b show PL spectra obtained from a substrate and a buffer layer, respectively. The peak position of free exciton (X) was used to determine the ZnTe mole fraction in both buffer layers and substrates [7]. The ZnTe mole fraction of the buffer layer determined from the PL spectrum was about 0.060. This value matches very well with the result of wavelength dispersive spectrometry (WDS) analysis (about 0.061). The experimental error in the WDS measurement of ZnTe was  $\pm 0.1 \text{ at\%}$ .

Table 1  
Solution compositions and temperature ranges for LPE growth of  $\text{Cd}_{0.94}\text{Zn}_{0.06}\text{Te}$  and  $\text{Hg}_{0.8}\text{Cd}_{0.2}\text{Te}$  epi-layers

	Solution composition (mole fraction)	Growth temperature range ( $^\circ\text{C}$ )
$\text{Cd}_{0.94}\text{Zn}_{0.06}\text{Te}$	$\text{Cd}_{0.0206}\text{Zn}_{0.0008}\text{Te}_{0.9783}$	513–493
$\text{Hg}_{0.8}\text{Cd}_{0.2}\text{Te}$	$\text{Hg}_{0.1598}\text{Cd}_{0.0080}\text{Te}_{0.8322}$	478–468

Table 2  
Electrical properties of Hg-annealed  $\text{Hg}_{1-x}\text{Cd}_x\text{Te}$  at 77 K

Sample No.	Composition, $x$	Carrier concentration ( $\text{cm}^{-3}$ )	Hall mobility ( $\text{cm}^2/\text{V} \cdot \text{s}$ )	Type	Remark
1	0.205	$1.2 \times 10^{14}$	$4.1 \times 10^5$	n	Buffered structure
2	0.210	$7.0 \times 10^{13}$	$3.3 \times 10^5$	n	Buffered structure
3	0.205	$9.8 \times 10^{13}$	$2.4 \times 10^5$	n	Buffered structure
4	0.206	$1.0 \times 10^{14}$	$5.8 \times 10^5$	n	Buffered structure
5	0.203	$1.5 \times 10^{15}$	$1.2 \times 10^4$	n	Unbuffered structure
6	0.204	$2.0 \times 10^{14}$	$8.3 \times 10^4$	n	Unbuffered structure

The PL spectrum of the substrate has free exciton (X) and bound exciton ((X,  $A^0$ ), (X,  $D^0$ )) peaks. The peaks at 1.5950 and 1.5868 eV are LO-phonon replica peaks of X and (X,  $A^0$ ), respectively [8]. The peaks at 1.5729, 1.5664 and 1.5598 eV are thought to be donor–acceptor pair (DAP) peaks [9–14]. The peak at 1.5664 eV seems to be due to nitrogen (N) and the one at 1.5598 eV to either sodium (Na) or lithium (Li) impurities [9]. The origin of the peak at 1.5729 eV could be some other acceptor impurity.

The PL spectrum of the LPE grown  $\text{Cd}_{0.94}\text{Zn}_{0.06}\text{Te}$  buffer layer is somewhat different from the one of the substrate. Firstly, the ratio of X to (X,  $A^0$ ) emission peak heights is larger than that of the substrate. Cooper et al. [15] used the ratio

of X to (X,  $A^0$ ) as a measure of crystal quality in CdTe. The ratio was 0.19 for the buffer layer, compared to 0.077 for the substrate. The higher X/(X,  $A^0$ ) ratio for the buffer layer is thought due to reduction of impurities in the buffer layer. Secondly, in the buffer layer, the DAP peak, which was considered to be related to Na or Li impurities, disappeared. The buffer layer seems to have effectively blocked Na or Li impurities. Reduction of impurities in the buffer layer is shown also by AES analysis (see next section).

### 3.2. Electrical properties of $\text{Hg}_{0.8}\text{Cd}_{0.2}\text{Te}$

Table 2 shows the results of Hall effect measurements at 77 K for 250°C Hg-annealed speci-

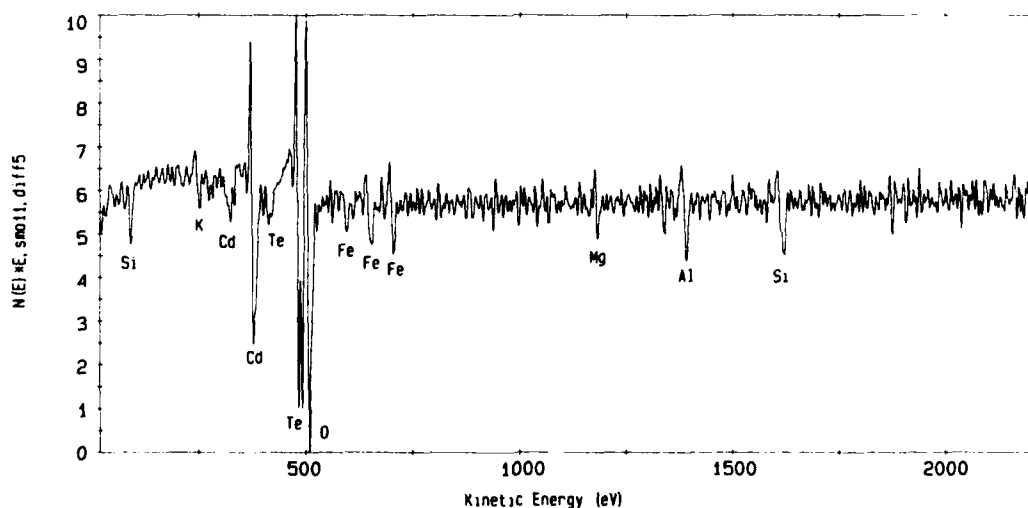


Fig. 2. Auger spectrum of the surface of  $\text{Cd}_{0.97}\text{Zn}_{0.03}\text{Te}$  substrate.

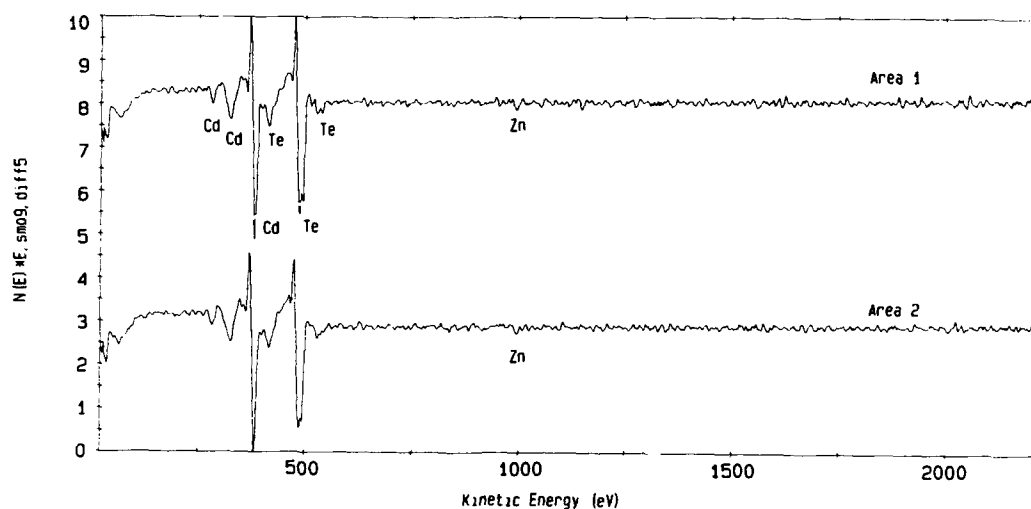


Fig. 3. Auger spectrum of the surface of  $\text{Cd}_{0.94}\text{Zn}_{0.06}\text{Te}$  buffer layer.

mens. The buffered structures have excellent electrical properties: carrier concentrations of  $7.0 \times 10^{13}$  to  $1.2 \times 10^{14} \text{ cm}^{-3}$  and Hall mobilities of  $2.4$  to  $5 \times 10^5 \text{ cm}^2/\text{V} \cdot \text{s}$ . Our result is one of the best ever reported, comparable to those of Astles et al. [16] and Pelliciani et al. [17]. From the Hall effect measurements, we conclude that the concentration of residual impurities in the buffered epi-layer is much smaller than that in the unbuffered layer.

Impurities in substrate and buffer layer were analysed by AES. Fig. 2 shows the AES spectrum of the surface of the substrate. Some granular defects were observed on the surface. Si, Al, O, K, Fe, and Mg elements are found in the granular-type defects. These impurities might have been introduced into the substrate during either crystal growing or wafering process [18,19]. Fig. 3 shows the result of AES analysis of the buffer layer. No granular defects have been found in the buffer

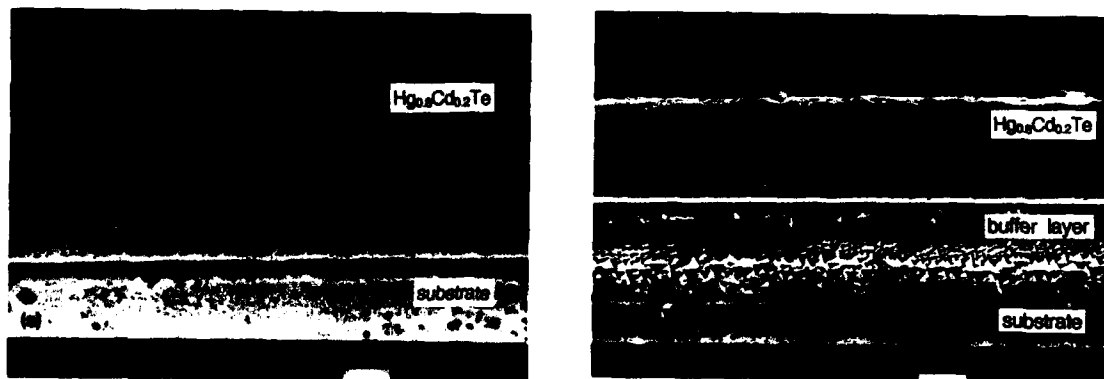


Fig. 4. SEM micrographs of the cross sections of  $\text{Hg}_{0.8}\text{Cd}_{0.2}\text{Te}$  layers which were defect etched: (a)  $\text{Hg}_{0.8}\text{Cd}_{0.2}\text{Te}/\text{Cd}_{0.97}\text{Zn}_{0.03}\text{Te}$  unbuffered structure; (b)  $\text{Hg}_{0.8}\text{Cd}_{0.2}\text{Te}/\text{Cd}_{0.94}\text{Zn}_{0.06}\text{Te}/\text{Cd}_{0.97}\text{Zn}_{0.03}\text{Te}$  buffered structure.



layer. The surface of the buffer layer does not contain the impurity elements which were observed in the substrate.

These AES analyses as well as the PL results described in the former section show that the  $\text{Cd}_{0.94}\text{Zn}_{0.06}\text{Te}$  buffer layer improves the electrical properties of  $\text{Hg}_{0.8}\text{Cd}_{0.2}\text{Te}$  epi-layer by blocking outdiffusion of impurities from the substrate.

### 3.3. Crystallinity of $\text{Hg}_{0.8}\text{Cd}_{0.2}\text{Te}$

Figs. 4a and 4b show the distribution of etch-pits on the  $(\bar{1}10)$  cleaved planes of the buffered and unbuffered structures, respectively. These etch-pits correspond to misfit dislocations caused by the lattice mismatch between the epi-layer and the buffer layer or the substrate. For the buffered structures, most etch-pits are located just above the interface between the  $\text{Hg}_{0.8}\text{Cd}_{0.2}\text{Te}$  epi-layer and the  $\text{Cd}_{0.94}\text{Zn}_{0.06}\text{Te}$  buffer, and their density is much lower than that in the unbuffered structure, in which etch-pits are distributed rather broadly in the epi-layer.

The etch-pit distribution was observed on the surface planes, i.e.,  $(111)\text{A}$  of the substrate, the buffer layer, and the  $\text{Hg}_{0.8}\text{Cd}_{0.2}\text{Te}$  epi-layer, respectively. The etch-pit density of the buffer layer ( $\approx 1.8 \times 10^5 \text{ cm}^{-2}$ ) is about 5 times higher than that of the substrate ( $\approx 3.4 \times 10^4 \text{ cm}^{-2}$ ). The  $\text{Hg}_{0.8}\text{Cd}_{0.2}\text{Te}$  layer shows a slightly lower etch-pit density ( $\approx 7.7 \times 10^4 \text{ cm}^{-2}$ ) than the buffer layer.

A series of double crystal rocking curves (DCRC) were obtained at different depths for a buffered structure and the results are shown in Fig. 5. We can see from the relative positions of the rocking curves of the layers that the lattice constants of  $\text{Hg}_{0.8}\text{Cd}_{0.2}\text{Te}$  epi-layer ( $a_e$ ),  $\text{Cd}_{0.94}\text{Zn}_{0.06}\text{Te}$  buffer layer ( $a_b$ ) and substrate ( $a_s$ ) have the following order in magnitude:  $a_s > a_e > a_b$ . We can also see in the figure that the lattice mismatch between the  $\text{Hg}_{0.8}\text{Cd}_{0.2}\text{Te}$  and the buffer layer is larger than that between the  $\text{Hg}_{0.8}\text{Cd}_{0.2}\text{Te}$  epi-layer and the substrate. The ZnTe mole fraction of the buffer layer was calculated from the DCRC peak spacing between the  $\text{HgCdTe}$  epi-layer and the buffer layer. The calculated ZnTe mole fraction (about 0.063) agrees with the results of PL and WDS analysis (see

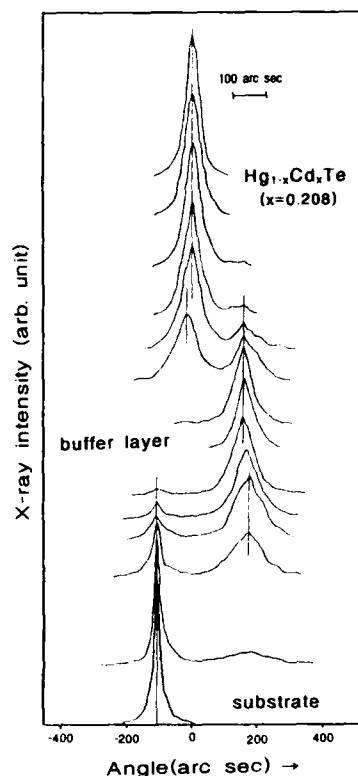


Fig. 5. Double crystal X-ray rocking curve profiles of a  $\text{Hg}_{0.8}\text{Cd}_{0.2}\text{Te}/\text{Cd}_{0.94}\text{Zn}_{0.06}\text{Te}/\text{Cd}_{0.97}\text{Zn}_{0.03}\text{Te}$  buffered structure obtained after sequential etching.

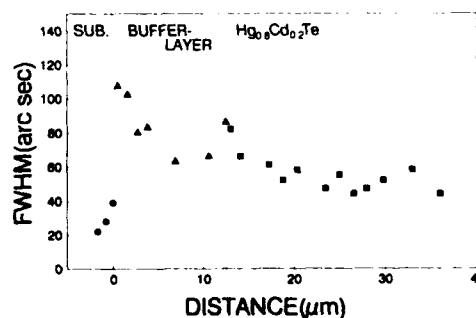


Fig. 6. Depth profiles of FWHM (full widths at half maximum) of double crystal X-ray rocking curve in a  $\text{Hg}_{0.8}\text{Cd}_{0.2}\text{Te}/\text{Cd}_{0.94}\text{Zn}_{0.06}\text{Te}/\text{Cd}_{0.97}\text{Zn}_{0.03}\text{Te}$  buffered structure.

section 3.1). Fig. 6 shows the variation of the FWHM of the DCRC with depth. Here, “distance” means the layer thickness after each etching. There is an abrupt increase of the FWHM in the buffer layer because of the large lattice mismatch. Then, the FWHM continues to decrease up to the surface, except at the HgCdTe/buffer layer interface where there is a slight increase. These results of DCRC are exactly matched to the etch-pit observations on the (111)A surface.

The DCRC results indicate that the sign of  $\Delta a$ , which is the difference in lattice parameter between the HgCdTe epi-layer and the buffer layer (or the substrate), is a critical parameter for the distribution and density of misfit dislocations. The negative value of  $\Delta a$ , which is the case for our buffered structure, seems to be more effective in reducing misfit dislocations than either the exact lattice match or the positive value of  $\Delta a$ , which is our unbuffered case. However, this reasoning should be confirmed by comparing the present results with those obtained from buffered structures of positive  $\Delta a$ .

#### 4. References

- [1] A. Sher, A. Tsigelman, E. Weiss and N. Mainzer, *J. Vac. Sci. Technol. A* 8 (1990) 1093.
- [2] M.G. Astles, H. Hill, G. Blackmore, S. Courtney and N. Shaw, *J. Crystal Growth* 91 (1988) 1.
- [3] S.H. Suh, S.W. Moon, J.S. Kim, S.W. Lim, N.J. Kwak, H.K. Kim and J.M. Kim, *J. Crystal Growth* 121 (1992) 417.
- [4] P.F. Fewster, S. Cole, F.W. Willoughby and M. Brown, *J. Appl. Phys.* 52 (1981) 4568.
- [5] K. Nakagawa, K. Meada and S. Takeuchi, *Appl. Phys. Lett.* 34 (1979) 574.
- [6] J.S. Chen, United States Patent No. 4,897,152.
- [7] D.J. Olego, J.P. Faurie, S. Sivananthan and P.M. Raccach, *Appl. Phys. Lett.* 47 (1985) 1172.
- [8] K. Zanio, in: *Semiconductors and Semimetals*, Vol. 13, Eds. R.K. Willardson and A.C. Beer (Academic Press, New York, 1978) ch. 2, p. 101.
- [9] Z.C. Feng, M.J. Bevan, W.J. Choyke and S.V. Krishnaswamy, *J. Appl. Phys.* 64 (1988) 2595.
- [10] F.P. Doty, J.F. Butler, J.F. Schetzina and K.A. Bowers, *J. Vac. Sci. Technol. B* 10 (1992) 1418.
- [11] J.M. Francou, K. Saminaday, J.L. Pautrat, J.P. Gaillard, A. Million and C. Fontaine, *J. Crystal Growth* 72 (1985) 220.
- [12] J.M. Wrobel, J.J. Dubowski and P. Belca, *J. Vac. Sci. Technol. A* 7 (1989) 338.
- [13] N.C. Giles-Taylor, R.N. Bicknell, D.K. Blanks, T.H. Myers and J.F. Schetzina, *J. Vac. Sci. Technol. A* 3 (1985) 76.
- [14] E. Molva, J.L. Pautrat, K. Saminadayar, G. Milchberg and N. Magnea, *Phys. Rev. B* 30 (1984) 3344.
- [15] D.E. Cooper, J. Bajaj and P.R. Newman, *J. Crystal Growth* 86 (1988) 544.
- [16] M.G. Astles, N. Shaw, G. Blackmore and R.S. Hall, *J. Crystal Growth* 117 (1992) 213.
- [17] B. Pellicciari, G.L. Destéfani and L. Di Cioccio, *J. Vac. Sci. Technol. A* 7 (1989) 314.
- [18] B.E. Dean, C.J. Johnson and F.J. Kramer, *J. Crystal Growth* 106 (1990) 47.
- [19] P. Rudolph, M. Mühlberg, M. Neubert, T. Boeck, P. Möck, L. Parthier, K. Jacobs and E. Kropp, *J. Crystal Growth* 118 (1992) 204.



ELSEVIER

Journal of Crystal Growth 138 (1994) 956–963

JOURNAL OF  
**CRYSTAL  
GROWTH**

## Bridgman growth of $\text{Hg}_{1-x}\text{Cd}_x\text{Te}$ from melt of constant composition

P. Höschl \*, R. Grill, J. Svoboda, P. Hlíděk, P. Moravec, J. Franc and E. Belas

*Institute of Physics, Charles University, Ke Karlovu 5, CZ-121 16 Prague 2, Czech Republic*

### Abstract

A modified Bridgman method is applied for the growth of semiconducting alloys  $\text{Hg}_{1-x}\text{Cd}_x\text{Te}$  from the melt. The large separation between the liquidus and solidus lines in the  $T$ - $x$  phase diagram and further non-planar melt/crystal interface shape cause significant axial and radial gradients in the composition. In order to reduce these difficulties, the proposed method – Bridgman growth from melt of constant composition (BGCC) – is based on a demand to simply ensure a melt of constant composition near the melt/crystal interface during growth. The missing CdTe is transported to the phase boundary by diffusion from a suitable source – for example floating solid CdTe. A model of diffusion of CdTe in the liquidus was verified by a fast cooling of the melt above the growing crystal and its composition analysis. In this way the equilibrium segregation coefficient and solute diffusion coefficient of CdTe were determined. As-grown crystals were p-type Hg-vacancy-doped. By an annealing near-Hg-saturated condition or in a Hg bath, and also by ion beam milling, the n-type material can be prepared. Electrical, optical and photoelectrical properties are briefly discussed.

### 1. Introduction

The pseudo-binary alloy material  $\text{Hg}_{1-x}\text{Cd}_x\text{Te}$  (MCT) has recently received a great deal of attention due to its utility both as a semiconductor and as a photoconductor. The forbidden energy gap is dependent on the mole fraction of CdTe  $x$ , ranging from a wide-gap semiconductor for  $x = 1$  to a zero-gap semiconductor for  $x = 0.16$ . These materials are widely used in photoconductive and photovoltaic devices. They are also a centre of interest in modelling of the dynamics of growth. High sensitivity of semiconducting properties on

the composition uniformity requires very careful processing of MCT.

The bulk material grown by directional solidification methods is still in widespread use for infrared detectors, despite rapid progress in the various epitaxial growth techniques [1]. The vertical Bridgman growth of crystals was one of the first used for MCT. In the classical Bridgman growth (CBG), the material  $\text{Hg}_{1-x}\text{Cd}_x\text{Te}$  in a sealed silica ampoule is initially heated above the liquidus temperature for given  $x$  and the temperature is then slowly lowered with translation rate  $v$  through a temperature gradient  $G$  below the solidus temperature. From the wide separation of the liquidus and solidus curves in the  $T$ - $x$  phase diagram, it is apparent that the original simple CBG gives a low yield of material with suitable  $x$

\* Corresponding author.

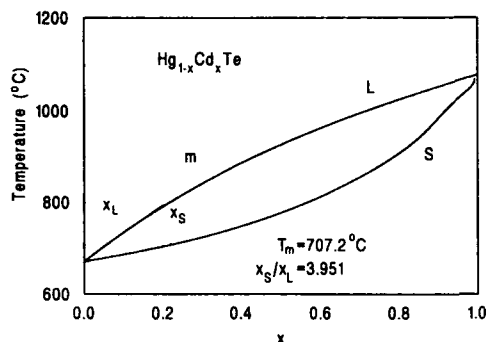


Fig. 1. Pseudobinary HgTe-CdTe  $T$ - $x$  phase diagram ( $m$  is the slope of the liquidus curve at  $x = x_L$ ).

values [2]. Moreover, the combination of the difference in thermal conductivities between melt and crystal and the thick silica ampoule leads to a highly curved melt/crystal interface  $I_{mc}$ . The curvature  $I_{mc}$  has been identified as a major factor causing the radial nonuniformity. A number of solutions of this problem were attempted: solid state recrystallization (SSR) [3], slush-growth (SG) [4,5], accelerated crucible rotation technique (ACRT) [6] and fast Bridgman growth (FBG)

[7,8]. Comparing these methods from the point of view of their technical burdensomeness and a yield of material with suitable purity and radial homogeneity, it is evident that each of them has together with priorities also some imperfections. Some of them, SSR, SG, CBG and ACRT, are successfully used in production. Extensive experimental studies of the FBG method contributed to understanding of temperature and solute fields in the melt [8,9].

The method proposed by us – the Bridgman growth from melt of constant composition (BGCC) – is based on a demand to ensure melt of constant composition  $x_L$  above the crystal during growth.

## 2. Theoretical model – thermodynamic consideration

In further considerations we shall concentrate on the preparation of  $\text{Hg}_{1-x}\text{Cd}_x\text{Te}$  crystals with  $x = 0.22$ . The same advancement can be applied to arbitrary composition. The way out is the phase diagram  $T$ - $x$  depicted in Fig. 1. The curves of liquidus (L) and solidus (S) were determined with

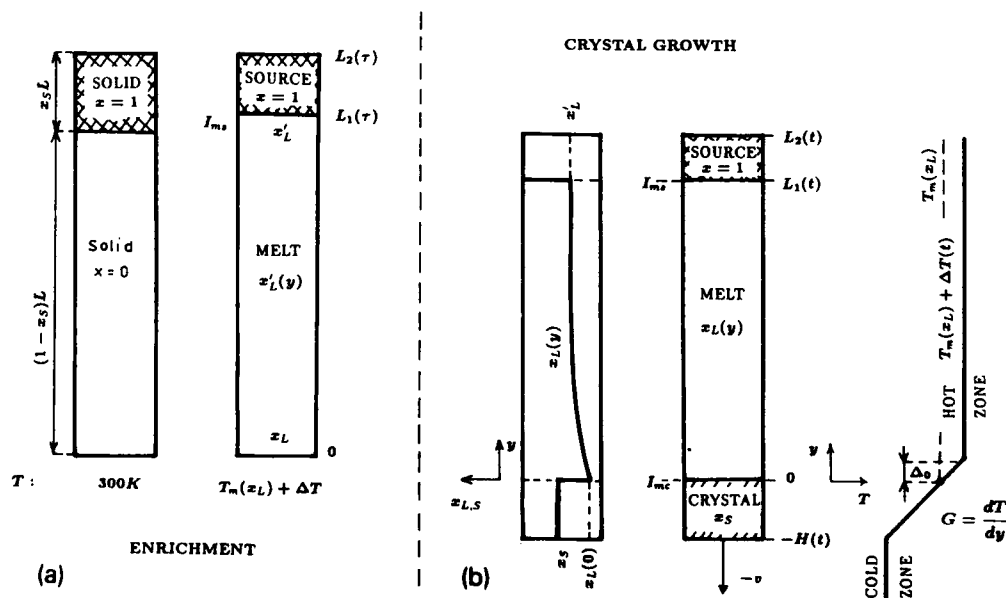


Fig. 2. Schematic representation of one-dimensional model of (a) enrichment of melt and (b) crystal growth.

the help of analytical relations (1) and (2), derived in ref. [10] for the melting point  $T_m$  in dependence on the composition of liquidus  $x_L$  and the equilibrium segregation coefficient  $k$  in dependence on  $x_L$ , which agrees well with experimental data [11]:

$$T_m(^{\circ}\text{C}) = \sum_{i=0}^3 a_i x_L^i, \quad (1)$$

$$k = \sum_{i=0}^5 b_i x_L^i, \quad x_S = k x_L, \quad (2)$$

where the coefficients have values  $\{a_i\} = \{670.94, 671.46, -375.07, 110.54\}$  and  $\{b_i\} = \{4.726, -15.935, 39.335, -59.151, 46.752, -14.743\}$ . At temperature  $T = 707.2^{\circ}\text{C}$ , the corresponding values are  $x_S = 0.22$ ,  $x_L = 0.0557$  and  $k = 3.95$ . The model of two-component melt (HgTe and CdTe) is used [12,13].

The principle of our BGCC method, evident from Fig. 2b, is based on the fact that the crystal grows for most of the time from the melt with composition  $x_L = x_S/k$  which corresponds to a relevant temperature  $T_m(x_L)$ , as is evident from Fig. 1. The missing CdTe is during the whole process of growth transported to the phase boundary  $I_{mc}$  by diffusion from a suitable source.

### 2.1. Enrichment of melt

As we can see from Fig. 2a, an ampoule of a whole length  $L$  completely filled in the bottom part with a column of HgTe with length  $(1 - x_S)L$  and in the upper part with a column of CdTe source with length  $x_S L$  is placed in a hot-zone Bridgman furnace with temperature  $T_m(x'_L) = T_m(x_L) + \Delta T$ . The melting temperature  $T_m(x_L) = 707.2^{\circ}\text{C}$  corresponds to the crystal composition which we want to produce ( $x_S = 0.22$ ), and  $\Delta T > 0$  is the temperature difference ensuring the demanded flux of CdTe by diffusion to the phase boundary  $I_{mc}$  during crystal growth. The value of  $\Delta T$  will be determined in the next section.

The HgTe melt is gradually enriched by CdTe from the solid source of CdTe by diffusion described by the Fick's second law:

$$\frac{\partial x'_L(y, t)}{\partial t} = D_L \frac{\partial^2 x'_L(y, t)}{\partial y^2}, \quad 0 \leq y \leq L_1, \quad (3)$$

where  $D_L$  is the solute diffusion coefficient of CdTe in the melt ( $D_L \approx 5 \times 10^{-5} \text{ cm}^2/\text{s}$  [8]),  $y$  is the distance from the bottom of the ampoule into the melt and  $x'_L(y, t)$  is the mole fraction of CdTe at the place  $y$  and in the time  $t$ . In the time  $t = 0$ ,  $x'_L(y, 0) = 0$ . The boundary condition defines zero flux of CdTe at the bottom of the ampoule:

$$J_{\text{CdTe}} \Big|_{y=0} = -D_L \frac{\partial x'_L(y, t)}{\partial y} \Big|_{y=0} = 0. \quad (4)$$

The situation at the phase boundary melt/source  $I_{ms}$  is described by the condition

$$x'_L(y, t) \Big|_{y=L_1} = x'_L, \quad t > 0, \quad (5)$$

where  $x'_L$  is determined by relation (1) for temperature  $T_m(x'_L) = T_m(x_L) + \Delta T$ . It is true that a thin layer of (HgCd)Te with composition  $x'_S = x'_L k(x'_L)$  is created on the CdTe source. However, diffusion of Hg in solid CdTe passes with a diffusion coefficient at least two orders of magnitude lower than diffusion of CdTe in the melt and therefore making the balance of lengths and composition, the thickness of this layer can be neglected.

The solution of differential equation (3) fulfilling the above conditions, supposing that the length of the column of liquid does not change too much, is of the shape

$$x'_L(y, t) = x'_L \left[ 1 - \frac{4}{\pi} \sum_{k=0}^{\infty} \frac{1}{2k+1} \times \exp \left( - \frac{(2k+1)^2 \pi^2}{4L_1^2} D_L t \right) \times \cos \left( \frac{(2k+1)\pi}{2L_1} y \right) \right]. \quad (6)$$

For times  $t > 4.5 \times 10^{-2} L_1^2 / D_L$ , it is sufficient to calculate only the first term of the series (the error is 1%). Under this condition we can simply determine the time  $\tau$ , at which the composition of the melt at the bottom of the ampoule  $x'_L(0, \tau)$  corresponds to the composition  $x_L$  from which the crystal of composition  $x_S$  should grow. From the relation  $x'_L(0, \tau) = x_L$ :

$$\tau \approx \frac{4L_1^2}{\pi^2 D_L} \ln \left( \frac{4}{\pi} \frac{x'_L}{x'_L - x_L} \right). \quad (7)$$

At this time we can determine from the balance of CdTe content in the ampoule the length of melt  $L_1(\tau)$ :

$$[L - L_1(\tau)] + Q'_{\text{CdTe}} = x_S L, \quad (8)$$

where  $Q'_{\text{CdTe}}$  is the CdTe content in the melt at time  $\tau$ :

$$\begin{aligned} Q'_{\text{CdTe}} &= \int_0^{L_1(\tau)} x'_L(y, \tau) dy \\ &\approx x'_L L_1(\tau) \left( 1 - \frac{2}{\pi} \frac{x'_L - x_L}{x'_L} \right). \end{aligned} \quad (9)$$

For  $L_1(\tau)$ , it is valid that

$$L_1(\tau) = \frac{1 - x_S}{1 - x'_L \left( 1 - \frac{2}{\pi} \frac{x'_L - x_L}{x'_L} \right)} L. \quad (10)$$

For  $L = 10$  cm and  $\Delta T = 18^\circ\text{C}$ ,  $x'_L = 0.084$ ,  $L_1(\tau) = 8.3$  cm and  $\tau = 8$  days. Therefore, during this time, the length of the liquid does practically not change  $L_1(\tau) - L_1(0) = 0.5$  cm.

## 2.2. Crystal growth

In further considerations on crystal growth in the arrangement depicted in Fig. 2b, we shall suppose that:

- (a) the solute transport in the melt is controlled by diffusion;
- (b) the one-dimensional approximation is valid and the interfaces  $I_{\text{mc}}$  and  $I_{\text{ms}}$  are flat;
- (c) the enrichment of melt with CdTe passed for a period  $\tau$  determined from relation (7) and the ampoule was subsequently shifted to the temperature gradient  $G = dT/dy$  in such a way that the bottom of the ampoule is located in the place with temperature  $T = T_m(x_L)$ .

If, in the time  $t = 0$ , melt with composition  $x_L$  at the bottom of the ampoule is lowered with translation rate  $v$ , then a crystal with composition  $x_S = kx_L$  starts to grow at the bottom of the ampoule in the initial stage. If we demand the crystal composition to stabilize at value  $x_S$  during the growth (which means that in any time the crystal will grow in the place with temperature

$T_m(x_L)$ ), the flux of CdTe  $J_{\text{CdTe}}$  driven by diffusion to the phase boundary  $I_{\text{mc}}$  from phase boundary  $I_{\text{ms}}$  must be constant in any time and the sum of CdTe fluxes at the interface  $I_{\text{mc}}$  must be zero. This demand is described in relation (11).

The flux  $J_{\text{CdTe}}$  of CdTe species is related to the concentration gradient of the species and to the motion of melt relative to the interface by Fick's first law:

$$J_{\text{CdTe}} = -D_L \frac{\partial x_L(y)}{\partial y} - vx_L(y) = -vx_S, \quad (11)$$

where  $x_L(y)$  is the mole fraction of CdTe in the melt and  $y$  is the distance measured from the interface  $I_{\text{mc}}$  into the liquid,  $0 \leq y \leq L_1$ . A coordinate system moves with interface  $I_{\text{mc}}$  where its beginning is situated. The demanded condition for phase interface  $I_{\text{mc}}$  reads

$$x_L(y)|_{y=0} = x_L = x_S/k. \quad (12)$$

The solution of differential equation (11) then has the form

$$\begin{aligned} x_L(y) &= x_S \left[ 1 - \frac{k-1}{k} \exp\left(-\frac{vy}{D_L}\right) \right] \\ &\approx x_L \left[ 1 + (k-1) \frac{v}{D_L} y \right]. \end{aligned} \quad (13)$$

The second part of relation (13) is valid under condition  $L_1 \ll D_L/v$ .

Together with gradual increase of crystal length  $H(t)$  with rate  $v$  when  $H(t) = vt$ , the length of the column of the melt above the crystal,  $L_1 = L_1(t)$ , decreases but with different speed  $v_S = dL_1(t)/dt$ . In the phase  $y = L_1(t)$ , where in the time  $t$  the phase boundary melt/source  $I_{\text{ms}}$  is situated, the composition of melt  $x'_L(t)$  must be determined by relation (13),  $x'_L(t) = x_L(L_1)$ , if relations (11) and (12) are to be fulfilled all the time. This means that the value  $x'_L(t)$  must gradually decrease with time to copy the diffusion profile in the melt determined by (13) for given  $D_L$  and  $k$ . This can be reached by a decrease of temperature of the upper zone, where CdTe (source) is located in the way to fulfil

$$T_m(x'_L) = T_m(x_L) + \Delta T(t). \quad (14)$$

The length of the melt  $L_1(t)$  can be determined from the balance of lengths and the balance of CdTe content in the ampoule:

$$H(t) + L_2(t) = L, \quad (15)$$

$$H(t)x_S + Q_{\text{CdTe}} + [L_2(t) - L_1(t)] = x_S L. \quad (16)$$

The value of the mole fraction of CdTe in the melt  $Q_{\text{CdTe}}$  is given by

$$Q_{\text{CdTe}} = \int_0^{L_1(t)} x_L(y) dy = x_S L_1(t) + (x_S - x_L) \frac{D_L}{v} \left[ \exp\left(-\frac{vL_1(t)}{D_L}\right) - 1 \right]. \quad (17)$$

For  $L_1(t)$  we obtain

$$L_1(t) = (1 - x_S)(L - vt) + Q_{\text{CdTe}} \approx \frac{1 - x_S}{1 - x_L} (L - vt). \quad (18)$$

The second part of relation (18) is valid under the condition  $L_1 \ll D_L/v$ . The exact value  $L_1(t)$  can be determined by numerical solution of the set of Eqs. (18) and (17). The value  $x'_L(t) = x_L(L_1)$ , determined with the help of relation (13), allows us together with (1) to fix at time  $t$ ,  $T_m(x'_L) = T_m(x_L) + \Delta T(t)$ . In approximation  $L_1 \ll D_L/v$  and for not very high  $x'_L(t) < 0.1$ , relation (19) is valid and  $\Delta T(t)$  can be determined with the help of (20):

$$x'_L(t) \approx x_L(0) \left[ 1 + \frac{x_S - x_L(0)}{x_L(0)} \frac{1 - x_S}{1 - x_L(0)} \times \frac{v}{D_L} (L - vt) \right], \quad (19)$$

$$\Delta T(t) \approx a_1 \frac{(x_S - x_L)(1 - x_S)}{1 - x_L} \frac{v}{D_L} (L - vt) \times \left[ 1 + \frac{a_2 x_L}{a_1} \left( 2 + \frac{x_S - x_L}{1 - x_L} \times \frac{v}{D_L} (L - vt) \right) \right]. \quad (20)$$

Relation (20) in first approximation shows that if the crystal of constant composition  $x_S$  should grow with rate  $v$ , it is necessary to linearly decrease the temperature of the hot zone from the beginning of growth from the value  $T_m(x_L) + \Delta T(0)$  to the value  $T_m(x'_L)$ . Due to the fact that the starting value  $\Delta T(0) \sim v$ , it is necessary to use small rates, so that the temperature difference between the source and the crystal is not too high. For  $L = 10$  cm,  $v = 1.16 \times 10^{-6}$  cm/s,  $D_L = 5.5 \times 10^{-5}$  cm<sup>2</sup>/s,  $x_S = 0.22$  and  $x_L = 0.0557$ , we obtain  $L_1(0) = 8.3$  cm,  $Q_{\text{CdTe}} = 3.06$  mol. fr. cm,  $x'_L = 0.084$  and  $\Delta T(0) = 18^\circ\text{C}$ .

In fact, the situation is not so simple because the heat transfer is far from the one-dimensional case near the interface  $I_{mc}$ . The difference in thermal conductivity between the melt and the crystal forces the heat of solidification to flow from the melt into the silica ampoule and leads to radial temperature gradients near  $I_{mc}$  [10,12]. The consequence is the concavely curved interface  $I_{mc}$  [13] and thermally driven convection near  $I_{mc}$ , which was not taken into account.

### 3. Experimental procedure

The principle of the method used for preparation of crystals of composition  $x_S \approx 0.22$  is evident from the model described in the preceding section.

The starting binary materials HgTe and CdTe are prepared by reacting the elements (purity 6N) in a sealed evacuated silica ampoule. The ampoule outer/inner diameter is 20/14 mm for HgTe and 19/13 for CdTe, and the total length of the ampoule is  $L \leq 10$  cm. After synthesis, the ampoule with HgTe is carefully opened and an ingot of CdTe with dimensions corresponding the situation in Fig. 2a is placed above HgTe. The ampoule prepared in this way is put on a silica pedestal into the hot zone of the Bridgman growth furnace with temperature  $T_m(x'_L) = T_m(x_L) + \Delta T(0)$ , where it is left for 3–7 days. The ampoule is then lowered to the temperature gradient with rate  $v$ .

The most difficult step is to realize experimentally the demanded composition of liquid  $x_L$  at

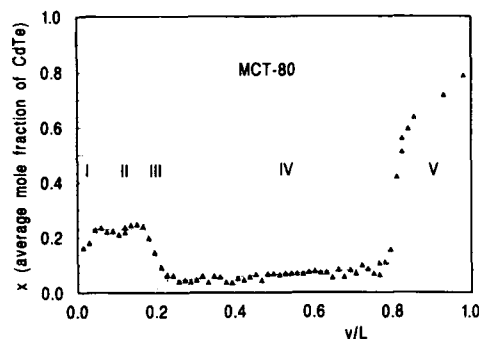


Fig. 3. Axial distribution of the average composition in the ingot which is quenched to room temperature during growth.

the bottom of the ampoule in the moment when the bottom of the ampoule is located at temperature  $T_m(x_L)$ . If the melt is too enriched in initial state, a crystal with composition higher than  $x_S$  starts to grow and the composition equilibrates on the demanded value  $x_S$  only after some time (see Fig. 4). On the contrary, if the crystal starts to grow with time, when the composition on the bottom of the ampoule has not reached the value  $x_L$ , the composition at the beginning of the crystal is lower than  $x_S$  (see Fig. 3). From the point of view of controlling the process of enrichment, the most advantageous method seems to be to move first the ampoule with rate  $v_c \approx \Delta_0/\tau$  until temperature  $T = T_m(x_L)$  at the bottom of the ampoule is reached, and then start moving with rate  $v$ .

The value  $\Delta T$ , which depends on the growth rate, is determined from (20). The furnace is constructed with two zones, with thermal isolation between the hot and the cold zone. The temperature of the cold zone was 520°C. The temperature gradient  $G$  in the place with temperature  $T_m(x_L) = 707.2^\circ\text{C}$  was  $G \approx 10^\circ\text{C}/\text{cm}$ . The temperature during enrichment of the melt and crystal growth is measured and checked by two thermocouples situated at the top and at the bottom of the ampoule. The low temperature gradient is chosen such that the influence of the curved phase interface on radial composition is not too substantial.

It is necessary to choose such a growth rate  $v$  for the given temperature gradient  $G$  to eliminate constitutional supercooling. For the maximum rate  $v_{\max}$  that can be used it is [14]

$$v_{\max} = \frac{GD_L}{mx_S} \frac{k-1}{k}, \quad (21)$$

where  $m = dT_m(x_L)/dx_L = 630 \text{ K/mol-fraction}$  at  $707.2^\circ\text{C}$ ; in our case we have chosen  $v = 1.16 \times 10^{-6} \text{ cm/s} \approx v_{\max}/2$ . For this rate we can determine also the value  $\Delta T(0)$  determining the increased temperature of the upper zone at the beginning of growth,  $\Delta T(0) \approx 18^\circ\text{C}$ . Together with the beginning of lowering of the ampoule with rate  $v$ , the temperature of the hot zone is decreased linearly to fulfil  $\Delta T(t) = 0$  in the time  $t = L/v$ . The rate of decrease of the temperature of the hot zone is optimized based on experimental results. A sublinear temporal dependence of the temperature is found to be convenient, especially at the end of the crystal growth.

For a better understanding of processes occurring during crystal growth in the region of phase interface and in the melt, one experiment is interrupted during the growth and the whole ampoule is quickly cooled to room temperature. The solidified ingot is cut perpendicularly to the growth axis into plates with thickness 500  $\mu\text{m}$ . The average  $x$  values are calculated from the measured mass densities and values of the lattice constant [15]. The concentration profile obtained along the ingot axes is evident from Fig. 3 and several regions can be seen in it. Region (I) represents the initial stage of crystal growth, when the concentration increases relatively quickly to the value  $x_S$  (the enrichment of melt was insufficient). Region (II) represents the crystal grown in the period before the ampoule was quickly cooled to room temperature, with composition  $x_S \approx 0.22$ . The decrease of  $x$  values in region (III) is probably caused by a convex meniscus creating the melt/crystal interface  $I_{mc}$ , the depth of the meniscus being about 3.5 mm. Region (IV) is the region, where the crystal was in a liquid state before rapid cooling and where the value roughly linearly increases to region (V), where CdTe with a surface enriched by HgTe is located. A moder-



ate increase of  $x$  in region (V) is probably caused by a concave shape of the melt/source phase boundary  $I_{ms}$ . Fitting the concentration profile  $x(y)$  in region (IV) with the help of (13), a segregation coefficient on the phase boundary  $I_{mc}$ ,  $k = 5.9$  and the effective solute diffusion coefficient of CdTe in the melt at  $\approx 715^\circ\text{C}$ ,  $D_L = 10^{-5} \text{ cm}^2/\text{s}$  were determined, see solid line in Fig. 3. The last value is in relatively good agreement with the value found out by Szofran et al. [8]. The segregation coefficient found by us is about  $1.5 \times$  higher than its value determined with the help of relation (2).

#### 4. Material characterization

The as-grown crystals were in most cases composed from one single-crystal grain. The course of axial composition determined from the mass density measurements is evident from Fig. 4. Fig. 5 shows the radially symmetrical distribution of the composition  $x$  across a typical wafer cut from a single crystal. The  $x$  values have been measured by EPMA at Humboldt University Berlin. Axial homogeneity  $\Delta x = \pm 0.02$  and radial homogeneity  $\Delta x = \pm 0.005$  were typical values. Higher composition is apparent at the periphery of the wafer due to non-flat interface  $I_{mc}$ .

The single crystals are p-type Hg-vacancy-doped with hole concentration at 77 K of  $3 \times 10^{15}$

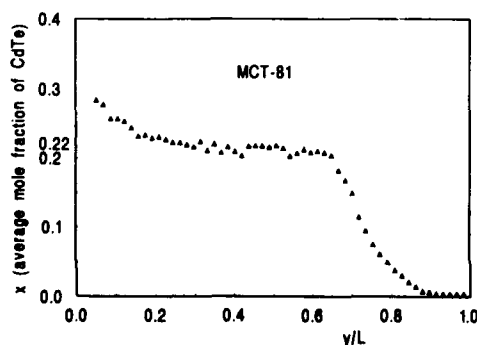


Fig. 4. Axial profile of the average composition along the quenched ingot.

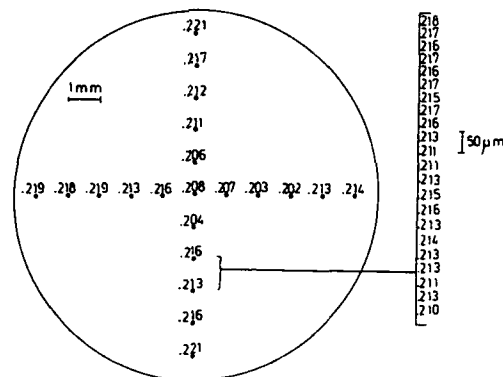


Fig. 5. Radial distribution of the composition across a wafer.

to  $5 \times 10^{16} \text{ cm}^{-3}$  and mobility of holes at 30 K ranging from 600 to  $1100 \text{ cm}^2/\text{V} \cdot \text{s}$ . According to a former model [16], a simultaneous analysis of the Hall coefficient and electrical conductivity yields ionization energies of 5 meV and  $0.5 E_g$  for Hg vacancies and 10 meV for residual acceptors, respectively.

Investigation of the absorption edge in samples cut from the BGCC crystals is presented in ref. [17], where the very high slope of absorption edge ( $S(10 \text{ K}) \approx 10^3 \text{ eV}^{-1}$ ) is discussed.

The quality of our crystals prepared by BGCC for photovoltaic applications was found to be comparable to that prepared by THM method.  $n^+/p$  photodiodes were prepared by implanting boron ions with an energy of 50 keV and dose of  $2 \times 10^{14} \text{ cm}^{-2}$ . At  $T = 80 \text{ K}$  and field of view (FOV) =  $60^\circ$ , background limited detectivity of photodiodes with a cut-off wavelength of  $\lambda_{\text{CU}} = 10.7 \mu\text{m}$  was achieved [18].

#### 5. Discussion

The method of the crystal preparation described above does not require synthesizing a ternary system  $\text{Hg}_{1-x}\text{Cd}_x\text{Te}$ , but only its binary components HgTe and CdTe. The whole technological process is relatively safe and modest. The transport processes ensuring the constant flow of CdTe to the melt/crystal phase boundary are

optimized by the variation of translation rate and by the magnitude of concentration gradient. The low temperature gradient ensures stabilized crystal growth and also contributes to relatively small bending of the melt/crystal interface and a subsequent good radial homogeneity of the crystal. The axial homogeneity is satisfactory between  $1/2$  and  $2/3$  of the length of the crystal. Regarding the prevention of the constituent supercooling, the low temperature gradient claims a low translation rate, so that the crystal growth takes a time of 2 to 3 months. This disadvantage is compensated by a sufficient segregation of impurities within the growth. The crystals fulfil the strict requirements, e.g. for detector grade material, even when not very high-pure source elements (6N) are used. Considering that the as-grown vacancy-doped p-type material can be converted to low-carrier-concentration n-type material by two-temperature annealing or by ion-beam milling [19,20], a low concentration of residual donors and acceptors is expected.

At present the best results for the Bridgman growth have been reached by the ACRT method developed in the Philips Laboratory (UK) [11]. Similar results were obtained by THM [21,22]. The electrical, optical and photoelectrical properties of our BGCC-prepared samples seem to be comparable.

## 6. Acknowledgements

The authors wish to thank Ms. Věra Poláková, Mr. Alan Brehovszký and Mr. Miloš Černý for their technical assistance in experimental work.

## 7. References

- [1] P. Capper, *Progr. Crystal Growth Characterization* 19 (1989) 259.
- [2] B.E. Bartlett, P. Capper, J.E. Harris and M.J.T. Quelch, *J. Crystal Growth* 47 (1979) 341.
- [3] P.W. Kruse, *Appl. Opt.* 4 (1965) 687.
- [4] T.C. Harman, *J. Electron. Mater.* 2 (1972) 230.
- [5] G. Fiorito, G. Gasparrini and D. Passoni, *J. Electrochem. Soc.* 125 (1978) 315.
- [6] P. Capper, J.J.G. Gosney and C.L. Jones, *J. Crystal Growth* 10 (1984) 356.
- [7] G. Dittmar, *Kristall Tech.* 13 (1978) 639.
- [8] F.R. Szofran, D. Chandra, J.C. Wang, E.K. Cothran and S.L. Lehoczky, *J. Crystal Growth* 47 (1979) 343.
- [9] F.R. Szofran and S.L. Lehoczky, *J. Crystal Growth* 70 (1984) 349.
- [10] D.H. Kim and R.A. Brown, *J. Crystal Growth* 114 (1991) 411.
- [11] J.C. Brice, P. Capper and C.L. Jones, *J. Crystal Growth* 75 (1986) 395.
- [12] D.H. Kim and R.A. Brown, *J. Crystal Growth* 96 (1989) 609.
- [13] R.J. Naumann and S.L. Lehoczky, *J. Crystal Growth* 61 (1983) 707.
- [14] J.C. Brice, *The Growth of Crystals from Liquids* (North-Holland, Amsterdam, 1973) p. 163.
- [15] J.C. Wooley and B. Ray, *J. Phys. Chem. Solids* 13 (1960) 151.
- [16] P. Höschl, P. Moravec, V. Prosser, V. Szöcs and R. Grill, *Phys. Status Solidi (b)* 145 (1988) 637.
- [17] K. Kučera, P. Hlíděk, P. Höschl, V. Koubele and M. Zvára, *Solid State Commun.* 78 (1991) 173.
- [18] H. Bittner, P. Höschl and B. Schubert, *Crystal. Res. Technol.* 26 (1991) 667.
- [19] E. Belas, P. Höschl, P. Moravec and J. Franc, *European Mater. Res. Soc. Symp. Proc.* 25 (1992) 81.
- [20] E. Belas, P. Höschl, R. Grill, J. Franc, P. Moravec, K. Lischka, H. Sitter and A. Toth, *Semicond. Sci. Technol.* 8 (1993) 1695.
- [21] R. Triboulet, T. Nguyen Duy and A. Durand, *J. Vac. Sci. Technol. A* 3 (1985) 95.
- [22] P. Gille, F.M. Kiessling and M. Burkert, *J. Crystal Growth* 114 (1991) 77.



ELSEVIER

Journal of Crystal Growth 138 (1994) 964–969

JOURNAL OF **CRYSTAL  
GROWTH**

## HgTe and $\text{Hg}_{1-x}\text{Cd}_x\text{Te}$ vapor phase epitaxial growth under controlled Hg pressure

H. Kuwabara <sup>\*a</sup>, H. Tatsuoka <sup>a</sup>, Y. Nakanishi <sup>b</sup>, A. Ichida <sup>c</sup>, H. Fujiyasu <sup>c</sup>,  
M. Nakayama <sup>d</sup>, T. Yamanari <sup>e</sup>

<sup>a</sup> College of Engineering, Shizuoka University, 3-5-1, Johoku, Hamamatsu 432, Japan

<sup>b</sup> Research Inst. of Electronics, Shizuoka University, 3-5-1, Johoku, Hamamatsu 432, Japan

<sup>c</sup> Faculty of Engineering, Shizuoka University, 3-5-1, Johoku, Hamamatsu 432, Japan

<sup>d</sup> Hamamatsu Photonics, 325-6, Sunayama-chou, Hamamatsu 432, Japan

<sup>e</sup> Fuji Seiki Inc., 1220-12 Suyama, Susono 410-12, Japan

### Abstract

We tried to make the epitaxial growth of HgTe and  $\text{Hg}_{1-x}\text{Cd}_x\text{Te}$  films on CdTe substrates from the vapor phase under controlled mercury pressure in a sealed reaction chamber. As a reaction chamber, a horizontal quartz tube with 3 cm diameter and 30 cm length was used. The temperature ranges of substrate and HgTe source were 200–250 and 300–350°C, respectively. The mercury pressure employed was 0.1–10 Torr. HgTe and  $\text{Hg}_{1-x}\text{Cd}_x\text{Te}$  were successfully grown. A growth rate of 1–4 Å/s was obtained for HgTe film, but the rate depends severely on source and substrate temperatures and Hg pressure.

### 1. Introduction

Because of the potential use of  $\text{Hg}_{1-x}\text{Cd}_x\text{Te}$  and other Hg-based materials in infrared detector device applications, the growth of such materials has attracted much attention. Vapor phase epitaxial growth techniques such as molecular beam epitaxy (MBE) [1,2] and metalorganic chemical vapor phase deposition (MOCVD) [3,4] enables low temperature growth of these materials. In those systems, however, a fairly large amount of mercury is wasted because of low

sticking or condensation coefficients for mercury [5,6]. On the contrary, in liquid phase epitaxy a rather high growth temperature (typically 550°C) is required, although the mercury loss during the growth is negligible [7]. It would be useful to realize a low temperature and low mercury consumption growth technique for HgTe and Hg-based alloy materials.

In this paper, a vapor phase epitaxial growth system designed for growing HgTe and  $\text{Hg}_{1-x}\text{Cd}_x\text{Te}$  under controlled mercury pressure is presented. The system has been used successfully to grow HgTe and  $\text{Hg}_{1-x}\text{Cd}_x\text{Te}$  films. Results on crystallinity assessments and structural characterization studies of grown films are also presented.

\* Corresponding author.

## 2. Experimental procedure

Fig. 1 shows a schematic diagram of the proposed HgTe and  $\text{Hg}_{1-x}\text{Cd}_x\text{Te}$  film growing system. As a reaction chamber, a horizontal quartz tube with 3 cm diameter and 30 cm length was used. One end of the tube was sealed and the other end was welded to a stainless steel conflat flange. A Hg reservoir, made by Pyrex glass, was also welded to a stainless steel flange which was connected to the reaction chamber through a high vacuum valve. This reaction chamber system was connected to an evacuation system through a valve and could be evacuated to  $1 \times 10^{-7}$  Torr. During the growth, the reaction chamber was isolated from the evacuation system and the Hg pressure was controlled by the temperature of the reservoir. After the growth, the excess Hg was withdrawn back to the reservoir by cooling.

HgTe and  $\text{Hg}_{1-x}\text{Cd}_x\text{Te}$  were grown on CdTe(100) and CdTe(111) substrates prepared on GaAs(100) by hot-wall epitaxy [8]. The CdTe substrates were etched with 1% bromine–methanol immediately before loading into the reaction chamber. Polycrystalline HgTe and cadmium (99.9995%) were used as tellurium and cadmium sources, respectively.

Assessment of crystallinity of the grown films were carried out by X-ray diffraction observation, reflection high-energy electron diffraction (RHEED), and electrical measurements. Compositional profiles of the grown crystals in growth

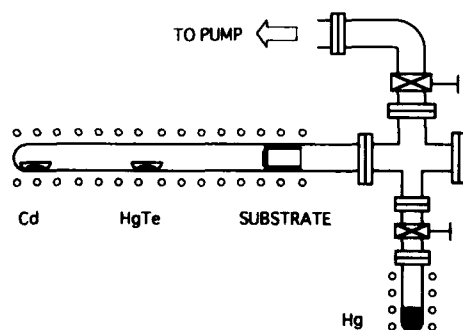


Fig. 1. Schematic diagram of HgTe and  $\text{Hg}_{1-x}\text{Cd}_x\text{Te}$  growth system.

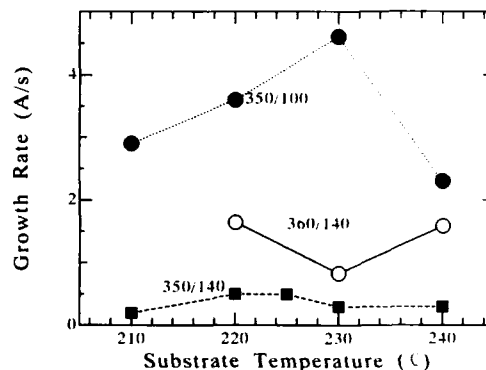


Fig. 2. Growth rate of HgTe on CdTe(100). Numbers represent temperatures of HgTe and Hg source ( $T_{\text{HgTe}}/T_{\text{Hg}}$ ).

direction were examined by Auger electron spectroscopy (AES).

## 3. Results and discussion

### 3.1. HgTe growth

The Hg reservoir was maintained at a temperature in the range 80–180°C, which corresponds to Hg vapor pressures of about 0.1–10 Torr. Substrates were preheated at 160°C for 30 min in the pressure of  $2 \times 10^{-7}$  Torr, and HgTe films were grown at a substrate temperature of 210–240°C.

The HgTe film could be grown epitaxially on both CdTe(100) and CdTe(111) substrates. In Fig. 2, growth rates of HgTe films on CdTe(100) are plotted as a function of substrate temperature ( $T_s$ ), in which the parameters are HgTe source temperature ( $T_{\text{HgTe}}$ ) and Hg temperature ( $T_{\text{Hg}}$ ). The growth rate of HgTe depends critically on the temperatures of substrate, source HgTe and Hg. At a high Hg temperature (140°C), the growth rate is almost constant for a substrate temperature of 210–240°C. On the contrary, for low Hg temperature the rate goes to a maximum value with increasing substrate temperature and then decreases with a further increase of the substrate temperature. At a given substrate temperature,

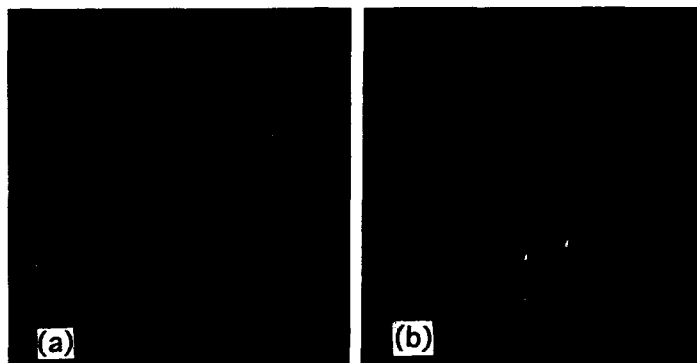


Fig. 3. RHEED patterns of HgTe films on CdTe(100) (a) and CdTe(111) (b).

the growth rate increases with decreasing Hg temperature, i.e. Hg pressure, and also increases with HgTe source temperature. These facts are understood as follows: Te atoms or molecules are supplied to the substrate surface through diffusion in Hg pressure, which is controlled by Hg temperature. The contribution of Hg atoms from the source HgTe to the Hg pressure and hence to its impinging rate on the substrate is considered to be small. Thus the growth rates are expected to increase with Te supply rate as long as sufficient Hg is supplied to the substrate surface at a given substrate temperature. This is evident in Fig. 2. The decrease of growth rate at higher temperature for the uppermost case in the figure is considered to be due to the decrease of the sticking coefficient of Hg at high temperature.

RHEED patterns of HgTe films grown on CdTe(100) and CdTe(111) substrates are shown in Fig. 3. As is seen in the figure, a single crystalline HgTe film is obtained epitaxially both on the CdTe(100) and the CdTe(111) substrate. The epitaxial orientation is (100), [001]HgTe || (100), [001]CdTe for CdTe(100). Streaks and Kikuchi lines in the pattern indicate that the HgTe films are of high quality. For the CdTe(111) substrate, two orientations  $[2\bar{1}\bar{1}]$ HgTe ||  $[011]$ CdTe and  $[\bar{2}11]$ HgTe ||  $[0\bar{1}1]$ CdTe are possible, and twins or micro-twins are often observed.

Fig. 4 shows the substrate temperature dependence of the FWHM of X-ray rocking curves

from the (400) Cu  $K\alpha_1$  diffraction line of HgTe(100)/CdTe(100) films. Generally, the value of the FWHM is smaller for the films prepared with faster growth rate. For a Hg temperature of 100°C, the FWHM becomes small for a substrate temperature of around 230°C. This indicates that there is an optimum substrate temperature for given HgTe and Hg source temperature. For a higher Hg temperature (140°C), the HgTe source temperature of 360°C is not sufficient for good film growth. Indeed we have found that when the Hg temperature is very high (180°C), a HgTe source temperature higher than 400°C was re-

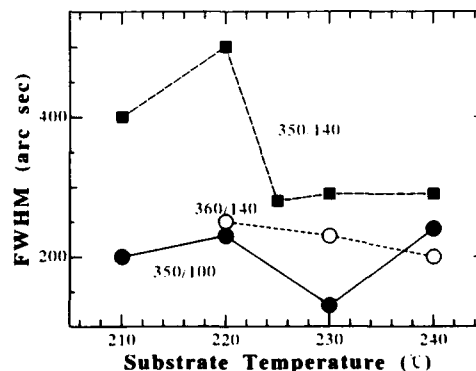


Fig. 4. Substrate temperature dependence of FWHM of X-ray rocking curve from (400) of Cu  $K\alpha_1$  diffraction lines of HgTe(100)/CdTe(100).

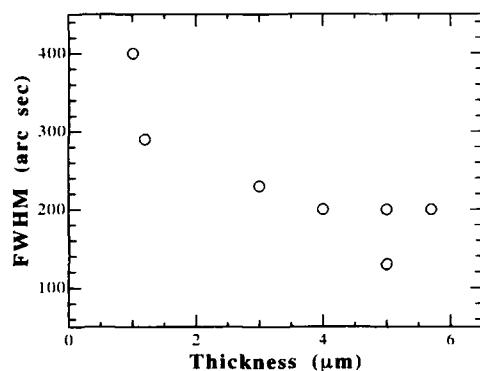


Fig. 5. Thickness dependence of FWHM.

quired to obtain an appropriate growth rate and hence good quality films.

The FWHM of HgTe(100)/CdTe(100) film decreased with increasing film thickness and became almost constant for films thicker than about 2  $\mu\text{m}$ . This is shown in Fig. 5. As often seen in heteroepitaxial growth [9], the initial decrease of FWHM may be considered to be due to the initial diminution of dislocations originating at the HgTe/CdTe interface caused by surface defects on the substrate and/or the lattice-mismatch between HgTe and CdTe.

Fig. 6 shows a typical AES sputter profile through the HgTe/CdTe interface. It is difficult to evaluate the precise composition of the HgTe

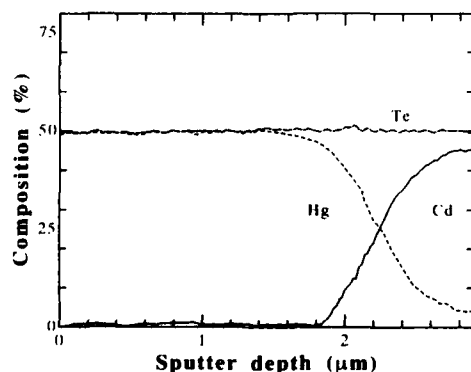


Fig. 6. Typical AES sputter profile through HgTe/CdTe interface.

Table 1  
Properties of HgTe films (n-type)

Sample No.	Substrate	$n$ ( $\text{cm}^{-3}$ )	$\mu$ ( $\text{cm}^2 \text{V}^{-1} \text{s}^{-1}$ )	FWHM (HgTe) (arc min)
46	CdTe(100)	$4.2 \times 10^{17}$	$1 \times 10^4$	4.5 (400)
101	CdTe(111)	$5.5 \times 10^{17}$	$3 \times 10^4$	3.3 (333)

films because of preferential sputtering of Hg [10]. The profile is corrected with the appropriate Auger sensitivity factors. The vertical axis represents the composition of the constituent atoms and the horizontal axis represents the distance from the surface of the film toward the interface. HgTe has been known to evaporate incongruently [11] and the composition of the HgTe source must be changed during the growth run. However, as is clear from the figure, the compositional profile of the grown layer is very flat. Hence it can be concluded that this growth system is very effective for growing HgTe films at rather low temperatures.

In Table 1, results of Hall measurements at room temperature are shown for HgTe(100)/CdTe(100) and HgTe(111)/CdTe(111) films. Carrier concentration and Hall mobility are almost the same for both films and are  $(4-6) \times 10^{17} \text{ cm}^{-3}$  and  $(1-3) \times 10^4 \text{ cm}^2 \text{V}^{-1} \text{s}^{-1}$ , respectively. These values compare well with those obtained for films grown by MBE [12].

From the above considerations, thick HgTe layers ( $> 2 \mu\text{m}$ ) grown under the appropriate conditions are thought to be of good quality.

### 3.2. $\text{Hg}_{1-x}\text{Cd}_x\text{Te}$ growth

For the growth of  $\text{Hg}_{1-x}\text{Cd}_x\text{Te}$ , Cd is loaded into the reaction tube separately from the source HgTe, as shown in Fig. 1. The Cd source was heated at a temperature between 270 and 330°C, depending on the temperatures of HgTe source, Hg reservoir and substrate.

Fig. 7 shows X-ray diffraction patterns of 1.3  $\mu\text{m}$  thick  $\text{Hg}_{1-x}\text{Cd}_x\text{Te}(100)/\text{CdTe}(100)$  and 5  $\mu\text{m}$  thick  $\text{Hg}_{1-x}\text{Cd}_x\text{Te}(111)/\text{CdTe}(111)$ . The temperatures of Cd, HgTe source, Hg and substrate during the growth are 280, 350, 230 and

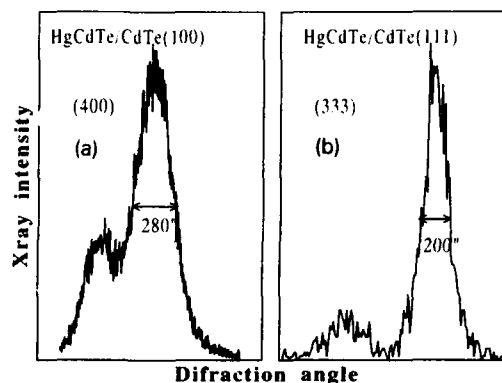


Fig. 7. X-ray diffraction patterns of  $\text{Hg}_{1-x}\text{Cd}_x\text{Te}(100)$  on  $\text{CdTe}(100)$  (a) and  $\text{Hg}_{1-x}\text{Cd}_x\text{Te}(111)$  on  $\text{CdTe}(111)\text{B}$  (b).

100°C for  $\text{Hg}_{1-x}\text{Cd}_x\text{Te}(100)$ , and 320, 380, 250 and 140°C for  $\text{Hg}_{1-x}\text{Cd}_x\text{Te}(111)$ , respectively. In each pattern, the dominant peak corresponds to the film and the other one to the substrate. It can be seen from the figure that  $\text{Hg}_{1-x}\text{Cd}_x\text{Te}$  grows epitaxially on both  $\text{CdTe}(100)$  and  $\text{CdTe}(111)$ . This was also confirmed in RHEED observation of the film. The values of FWHM are 280 and 200 arc sec for  $\text{Hg}_{1-x}\text{Cd}_x\text{Te}(100)$  and  $\text{Hg}_{1-x}\text{Cd}_x\text{Te}(111)$ , respectively, and larger than those of the corresponding substrates, especially for  $\text{Hg}_{1-x}\text{Cd}_x\text{Te}(100)$ . Fluctuation of the composition,  $X$ , in the film probably may be one of the reasons for broadening of FWHM.

Fig. 8 shows the relationship between composition  $X$  and Cd temperature when the temperatures of substrate, HgTe source and Hg are main-

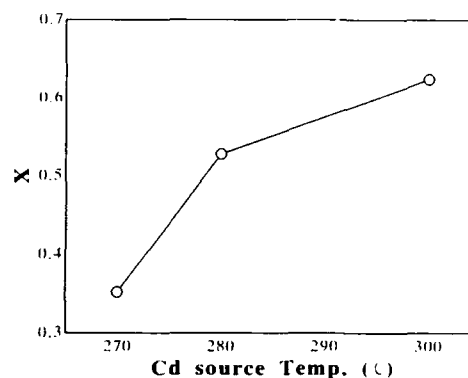


Fig. 8. Relationship between Cd temperature and composition  $X$ .  $T_s$ ,  $T_{\text{HgTe}}$  and  $T_{\text{Hg}}$  were maintained at 220, 350 and 100°C, respectively.

tained at 220, 350 and 100°C, respectively. The values of  $X$  are roughly estimated by AES measurements.  $X$  increases evidently with increasing Cd temperature, suggesting the controllability of Cd fraction in the  $\text{Hg}_{1-x}\text{Cd}_x\text{Te}$  alloy.

Fig. 9 shows depth profiles of composition in the  $\text{Hg}_{1-x}\text{Cd}_x\text{Te}$  films grown at temperature  $T_{\text{Hg}} = 100^\circ\text{C}$  (a) and  $80^\circ\text{C}$  (b). For the film grown at  $T_{\text{Hg}} = 100^\circ\text{C}$ , the composition in the layer is almost constant. For  $T_{\text{Hg}} = 80^\circ\text{C}$ , however, the composition in the layer changes greatly during the growth, although the substrate and source HgTe temperature are maintained constant. This means that the concentration ratio of Hg and Cd on the substrate surface changes during the growth. The reason for this is not clear at this

Table 2  
Properties of  $\text{Hg}_{1-x}\text{Cd}_x\text{Te}$  films (n-type)

Sample No.	Substrate	$n$ ( $\text{cm}^{-3}$ )	$\mu$ ( $\text{cm}^2 \text{V}^{-1} \text{s}^{-1}$ )	FWHM ( $\text{Hg}_{1-x}\text{Cd}_x\text{Te}$ ) (arc min)	$X$
66	$\text{CdTe}(100)$	$9.5 \times 10^{17}$	$1 \times 10^4$	10.5 (400)	0.02
111	$\text{CdTe}(100)$	$2 \times 10^{17}$	$4 \times 10^4$	10 (400)	0.6
208	$\text{CdTe}(100)$	$1 \times 10^{18}$	$3 \times 10^3$	3.7 (400)	0.1
107	$\text{CdTe}(111)$	$1.0 \times 10^{17}$	$1 \times 10^4$	3.3 (333)	0.4
110	$\text{CdTe}(111)$	$1.3 \times 10^{17}$	$2 \times 10^4$	6.7 (333)	0.8

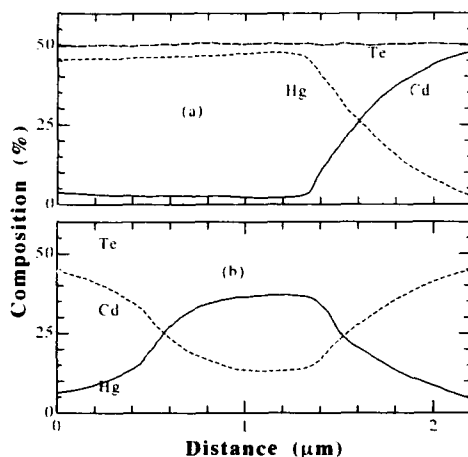


Fig. 9. Depth profile of composition in  $\text{Hg}_{1-x}\text{Cd}_x\text{Te}$  films grown at  $T_{11g} = 100^\circ\text{C}$  (a) and  $80^\circ\text{C}$  (b).

time. Depletion of source or sources and change in the temperature profile of the furnace are not recognized. The only reason that can be thought of is movement of the source such as  $\text{HgTe}$  during the growth run, resulting from a change of effective source temperature. This will be one of the problems in the future.

Table 2 shows the results of Hall measurements at room temperature for several  $\text{Hg}_{1-x}\text{Cd}_x\text{Te}$  films on as-grown  $\text{CdTe}(100)$  and  $\text{CdTe}(111)$  films with FWHM and composition  $X$ . Carrier concentration and Hall mobilities obtained range from  $1 \times 10^{17}$  to  $1 \times 10^{18}$  and from  $3 \times 10^3$  to  $4 \times 10^4$ , respectively. The values are comparable to those obtained for an as-grown MBE sample [13].

From the above results, the proposed growth system is considered to be effective for growing  $\text{Hg}_{1-x}\text{Cd}_x\text{Te}$  and controlling composition.

#### 4. Conclusion

We presented a simple vapor phase growth system under controlled mercury pressure for  $\text{HgTe}$  and  $\text{Hg}_{1-x}\text{Cd}_x\text{Te}$ . With this system,  $\text{HgTe}$  and  $\text{Hg}_{1-x}\text{Cd}_x\text{Te}$  films were successfully grown on both  $\text{CdTe}(100)$  and  $\text{CdTe}(111)$ . The grown  $\text{HgTe}$  films were compositionally homogeneous in growth direction and showed good electrical quality.  $\text{Hg}_{1-x}\text{Cd}_x\text{Te}$  were grown epitaxially on both  $\text{CdTe}(100)$  and  $\text{CdTe}(111)$  substrate. Composition  $X$  was shown to be controlled by Cd source temperature. Film growth under Hg pressure was shown to be effective for  $\text{HgTe}$  and Hg-based materials.

#### 5. References

- [1] J.P. Faurie, A. Million and J. Piagnet, *J. Crystal Growth* 59 (1982) 10.
- [2] P.P. Chow and D. Johnson, *J. Vac. Sci. Technol. A* 3 (1985) 67.
- [3] J.B. Mullin and S.J.C. Irvine, *J. Phys. D (Appl. Phys.)* 14 (1981) L149.
- [4] S.J.C. Irvine, J. Tunnicliffe and J.B. Mullin, *J. Crystal Growth* 65 (1983) 479.
- [5] R.F.C. Farrow, *J. Vac. Sci. Technol. A* 3 (1985) 67.
- [6] J.P. Faurie, M. Boukerche, J. Reno, S. Sivananthan and C. Hsu, *J. Vac. Sci. Technol. A* 3 (1985) 55.
- [7] J.L. Schmit, R.J. Hager and R.A. Wood, *J. Crystal Growth* 56 (1982) 485.
- [8] H. Tatsuoka, H. Kuwabara, H. Fujiyasu and Y. Nakamishi, *J. Appl. Phys.* 68 (1990) 4592.
- [9] H. Tatsuoka, H. Kuwabara, H. Fujiyasu and Y. Nakamishi, *J. Crystal Growth* 117 (1992) 554.
- [10] C.M. Stahle, C.R. Helms and A. Simmons, *J. Vac. Sci. Technol. B* 5 (1987) 1092.
- [11] A. Lopez-Otero, *Thin Solid Films* 49 (1978) 3.
- [12] K.A. Harris, S. Hwang, D.K. Blanks, J.W. Cook, Jr. and J.F. Schetzina, *J. Vac. Sci. Technol. A* 4 (1966) 2061.
- [13] J.M. Arias, S.H. Shin, J.T. Cheung and J.S. Chen, *J. Vac. Sci. Technol. A* 5 (1987) 3133.





ELSEVIER

Journal of Crystal Growth 138 (1994) 970–975

JOURNAL OF **CRYSTAL  
GROWTH**

## Doped zinc sulfide nanocrystals precipitated within a poly(ethylene oxide) matrix – processing and optical characteristics

D. Gallagher <sup>\*</sup>, W.E. Heady, J.M. Racz, R.N. Bhargava <sup>†</sup>

*Philips Laboratories, Philips Electronics North America Corporation, 345 Scarborough Road, Briarcliff Manor, New York 10510, USA*

### Abstract

Zinc sulfide nanocrystals doped with a manganese activator element were precipitated within a poly(ethylene oxide) polymer matrix to study the effects of size and quantum confinement on the luminescent properties of ZnS:Mn. Ultraviolet absorption demonstrates the increased bandgap due to quantum confinement. Photoluminescence measurements show the characteristic  $\text{Mn}^{2+}$  emission from within the ZnS host crystal and photoluminescent excitation measurements show a change in excitation which is indicative of the increased bandgap. These characteristics are shown to change with growth of the particles. The growth rate of the ZnS particles is contrasted with the growth rate of CdS by calculating the molecular diffusivity for diffusion controlled growth in each case.

### 1. Introduction

Nanometer-sized and quantum-confined semiconductor particles doped with an activator element have optical properties which differ from those of an identical bulk material, and from the quantum-confined host material alone [1,2]. The dopant element, a luminescence activator, emits light as a result of electron–hole transitions within the bandgap of the host crystal, and thus the emission is affected by the change in bandgap and e–h localization produced by quantum confinement. The crystalline synthesis technique of Bianconi et al. [3] creates matrix bound semicon-

ductor crystallites like zinc sulfide, which in their early stages of growth reveal quantum confinement effects [4]. This matrix-mediated growth technique was modified to make manganese and terbium-doped zinc sulfide particles which demonstrate quantum confinement effects as deduced from the luminescent properties of both the host crystal and the dopant. The synthesis of this material, its properties, and how the molecular level environment and growth kinetics affect the properties will be discussed in this paper.

When the radius of a semiconductor crystallite is comparable to the excitonic Bohr radius ( $\sim 50$  Å in ZnS), the electronic properties change [5]. For instance, a blue shift was observed in the bandgap (increased  $E_g$ ) for quantum-sized ZnS particles in solution by Henglein in 1984 [6]. Since then, most of the II–VI, some III–V, and

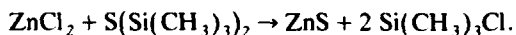
<sup>\*</sup> Corresponding author.

<sup>†</sup> Present address: Nanocrystals Technology, P.O. Box 820, Briarcliff Manor, New York 10510, USA.

group IV semiconductors, when prepared as quantum-sized particles, demonstrate quantum size effects in their physical properties. Besides the size, another requirement is that particles must remain isolated from one another; if allowed to aggregate, the material will exhibit bulk properties despite the small size of the particles.

Bulk manganese-doped zinc sulfide has a yellow luminescence which results from the d–d transition of the Mn, involving the 4T<sub>1</sub>–6A<sub>1</sub> levels, and its emission peaks at about 2.12 eV (585 nm). The photoluminescent excitation (PLE) wavelength of this emission was measured to be 3.65 eV (340 nm) which is close to the bandgap of ZnS (3.66 eV) [1]. In quantum confined ZnS:Mn particles, this excitation energy is seen to increase with the increase in bandgap (i.e. a blue shift) [1]. The radiative recombination lifetime of this transition in bulk material is about 1.7 ms. In the quantum-confined ZnS:Mn we have shown that the recombination lifetime shortens dramatically to approximately 4 ns and the efficiency of this luminescence is comparable to that measured in bulk ZnS:Mn (18%) [2].

The matrix-mediated growth technique is particularly appropriate for making quantum-confined doped semiconductors for two reasons: (1) crystallites form on the matrix, and grow by intermolecular diffusion through the matrix, thus isolation of the particles is assured once growth conditions are removed, and (2) the chemistry lends itself to doping with a metal salt of the activator element. The process is to dissolve poly(ethylene oxide) polymer (PEO) in water with the desired metal salts which bind to the polymer, this material is dried and placed in a nonsolubilizing solution (typically a hydrocarbon) with the sulfur donating reactant, hexamethyldisilthian ( $\text{S}(\text{Si}(\text{CH}_3)_3)_2$ ). The reaction to form ZnS in the PEO matrix is:



With time, ZnS molecules diffuse and heterogeneously nucleate stable particles which then grow by continued molecular additions or aggregation of discrete particles.

There are also two drawbacks to this approach: (1) the final concentration of doped semi-

conductor particles in the matrix is low and (2) particles of greater complexity are limited by the chemistry. Other polymer matrix based synthesis routes are less attractive because either the matrix will not bind the particles or reactions are too selective to allow incorporation of the dopant.

The application of this process to make a luminescent quantum-confined material, and the incorporation of an activator element into the semiconductor phase is unique. To manipulate the optical properties of an activator element by the quantum confinement of its host is an important new area for materials research.

## 2. Experimental procedure

A solution was prepared as follows: 0.09 gram  $\text{ZnCl}_2$  and 0.01 g  $\text{MnCl}_2$  (weighed in a nitrogen glovebox) were dissolved into 30 ml distilled and deionized water to which 1.35 g 200,000 MW polyethylene oxide polymer (PEO) was added. This was then stirred for 2 h to dissolve the PEO. The translucency of the PEO matrix can be improved by lowering the initial pH, and thus avoiding polymer crystallization. The solution was cast onto 4 × 6 inch plate glass sheets and dried under flowing nitrogen for 4 h before being peeled. Complete drying of the coupons is essential to improving the rate of particle forming. After further drying on the reverse side, the PEO matrix was cut into 0.5 square inch coupons and put into 40 ml vials filled with a cyclohexane and hexamethyldisilthian solution; this reactive solution consists of 100 ml  $\text{C}_6\text{H}_{12}$  cyclohexane with 0.40 ml  $\text{S}(\text{Si}(\text{CH}_3)_3)_2$  hexamethyldisilthian. Growth experiments were done by removing the coupons from the reactive solution at various times, drying under nitrogen, and evaluating the properties. Samples are stable for up to 8 months, but some variation in optical characteristics were seen after 1 year in samples prepared with high concentrations of reactants.

Ultraviolet absorption measurements were made by direct transmission on a Perkin-Elmer 330 UV-VIS spectrophotometer. The photoluminescent (PL) emission and photoluminescent excitation (PLE) spectra of  $\text{Mn}^{2+}$  ion in bulk pow-

ders and the nanocrystalline ZnS within the PEO matrix were measured at room temperature using Spex-Fluorolog 1680, 0.22 m double grating spectrometer. The excitation source was a xenon lamp and the PL data were taken with exciting wavelength of 300 nm. All spectra were corrected for source intensity variation with the Spex DM1B spectroscopy laboratory coordinator system.

### 3. Results and discussion

Ultraviolet spectroscopy of the PEO/ZnS:Mn coupons show that the ZnS bandgap is greatly increased in the initial precipitates. Fig. 1 shows the ultraviolet absorption for a time series of ZnS:Mn precipitates in PEO. The peak in the UV absorption is indicative of the bandgap of the semiconductor ZnS particle. The curves demonstrate that the bandgap of the material shifts towards higher wavelengths as the particles grow. The initial absorption peak is at 261 nm after five days, which is blue shifted from that expected for bulk ZnS, 340.6 nm, by about 78 nm. Based on the calculations of Rossetti et al. [7], this indicates a size of approximately 27 Å. After 35 days, the absorption peak is at 277 nm and particles are estimated to be about 36 Å in size. The UV

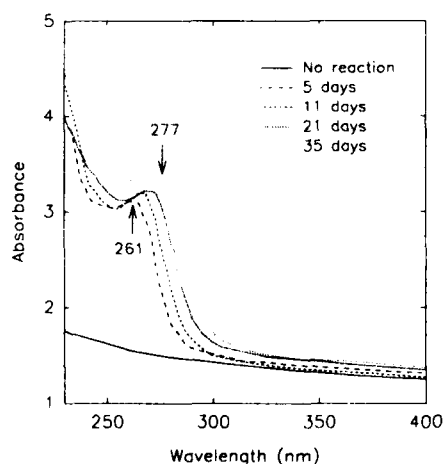


Fig. 1. UV absorption of ZnS:Mn/PEO nanocomposites and the change in absorption with time.

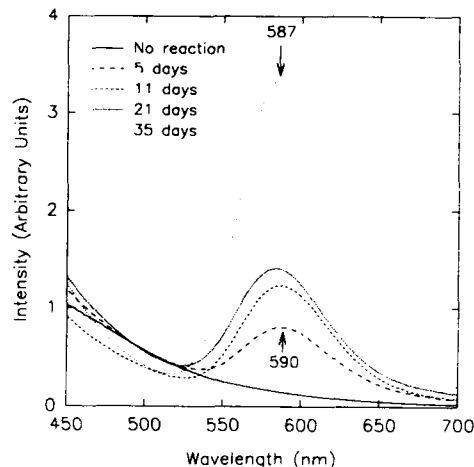


Fig. 2. Photoluminescent emission of ZnS:Mn nanocomposites, excitation energy 300 nm.

spectrum revealed a red shift and shape change characteristic of particle growth, yet remained blue shifted (shorter wavelengths) with respect to a bulk material and are still quantum sized.

Photoluminescence measurements demonstrate the effects of doping the ZnS with Mn. The light emission of the ZnS:Mn/PEO nanocomposite show the characteristic orange emission of Mn in a ZnS host (585 nm). This photoluminescent emission is shown in Fig. 2. Bulk ZnS:Mn powder has its emission centered at 585 nm, while the emission varies from 590 nm for short growth times to 587 nm at longer growth times. This spectrum is evidence that the activator has been incorporated into the ZnS particles, otherwise efficient emission at these wavelengths would be impossible. This change in PL with time, and therefore as a function of particle growth, is characterized by an intensity increase, most likely from the increased number of particles in the matrix, and a slight change in peak position and a narrowing. The shift in peak position with growth is thought to be a result of e-h localization in the quantum-confined particles lifting the degeneracy of the 4T1 and 6A1 levels and thereby shifting the transition to lower energy levels [8]. The narrowing is perhaps attributable to changes in the size distribution, to be discussed below.

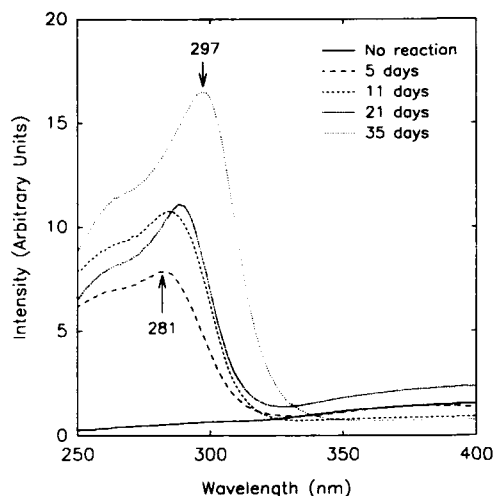


Fig. 3. Photoluminescent excitation of ZnS:Mn/PEO nanocomposites, emission energy was selected based on the maximum emission value of the individual sample (590 to 587 nm).

The unique character of this material becomes more apparent in the excitation spectra for the Mn emission, which is shown in Fig. 3. In bulk ZnS:Mn, the PLE has its maximum at 332 nm. This excitation wavelength is close to the bandgap of bulk ZnS (340 nm). The Mn excitation in the smallest of the quantum-sized ZnS particles has its maximum intensity at a wavelength of 281 nm (4.41 eV), in which UV absorption indicated a bandgap of 261 nm. In spite of the variation between the two values, it is clear that the changes in the excitation energy of the  $\text{Mn}^{2+}$  transition is due to the increased band gap of the quantum confined ZnS host, while the Mn transition remains at about 585 nm in bulk and quantum size ZnS samples. The difference in the excitation spectra of the two materials results from the change in the ZnS band gap. With the growth of particles, the peak becomes sharper, more intense, and shifts to 297 nm (4.17 eV) as in the UV absorption. This material displays a significant shift in its excitation spectra with no accompanying shift in the emission peak location and is indicative of the quantum confinement of the matrix bound particles.

The evolution of the optical characteristics in Figs. 2 and 3 also gives us information about the growth of the particles and indirectly about the chemical interaction of the precipitate and the matrix. PEO is known to bind monovalent, divalent and trivalent cations [9] and it is likely that the zinc chloride, and after reaction the zinc sulfide molecules, bond with the negatively charged ether oxygens of the PEO by either electrostatic attraction or by the partial sharing of a lone pair of electrons – thereby forming a coordinate bond [10]. The strength of this attraction will dictate the growth rate of the ZnS particles.

From the PLE data in Fig. 3, we can study the diffusion controlled growth of the ZnS particles which follows the initial heterogeneous nucleation. By treating the matrix as a solution and assuming that growth occurs under steady state conditions, and that the concentration is not depleted significantly by nucleation, it is possible to calculate a diffusivity for ZnS molecules in the PEO. From the ZnS growth shown above, there is a shift in bandgap from 4.41 to 4.17 eV over 30 days, from theoretical calculations [7] this indicates particle growth from approximately 27 to 36 Å, giving a growth rate ( $dR/dt$ ) of 0.0125 Å/h. The molar volume of ZnS,  $V$ , is 23.83 cm<sup>3</sup>/mol and the equilibrium concentration  $C_x^B$  of ZnS molecules (assuming complete conversion of  $\text{ZnCl}_2$ ) is  $6.25 \times 10^{-9}$  mol/cm<sup>3</sup>. The steady state diffusion controlled growth of a single component can be described with the simplified equation [11]:

$$\frac{dR}{dt} = \frac{VC_x^B D_{\text{ZnS}}}{R}$$

For the samples described above,  $D_{\text{ZnS}}$  is 2.3 Å<sup>2</sup>/h.

This diffusivity will vary with the attraction of the cation to the PEO. In the binding of monovalent cations to PEO, the binding constant decreases with increased atomic number [12]. The same is expected to hold true for divalent cations like Zn and Cd. PLE measurements of the band to band excitation for undoped CdS precipitated in PEO is presented in Fig. 4. The growth of CdS was observed to be much faster than the ZnS,

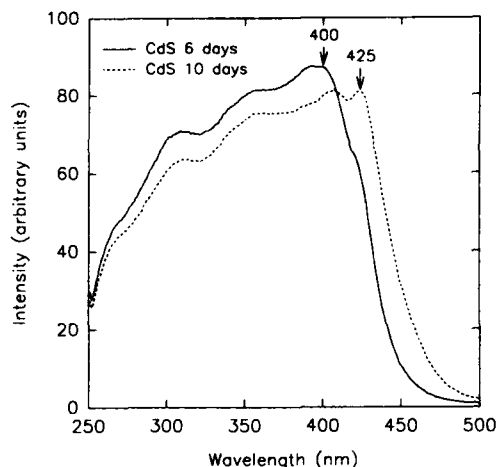


Fig. 4. Photoluminescent excitation of CdS/PEO nanocomposite, measured at 80 K. Emission energy was 650 nm for the 6 day sample and 680 nm for the 10 day sample.

and  $E_g$  varies from 3.1 to 2.92 eV, an increase in size from 39 to 50 Å [13], in only 4 days. For the values of  $V$  ( $29.97 \text{ cm}^3/\text{mol}$ ) and  $C_\infty^B$  ( $5.33 \times 10^{-7} \text{ mol/mm}^3$ ) of these samples, the  $D_{\text{CdS}}$  is  $279.7 \text{ Å}^2/\text{h}$ , a 123-fold increase from the ZnS. This difference in diffusivity cannot be entirely attributed to differences in electrostatic attraction between the molecules and the PEO matrix. Differences in conformation of the solute molecules to the binding sites on the PEO, and the effect of the solute molecules on the structure and crystallinity of the matrix, may also contribute to the enhanced growth rate of the CdS in PEO.

By viewing this technique as heterogeneous precipitation followed by diffusion controlled growth, it is possible to better characterize the evolution of the quantum confinement related properties. The precipitates are isolated throughout the matrix, rather than clustered, and as the particles grow the width of the distribution will narrow [11] as is usual with diffusion controlled growth, producing sharper and more intense spectral characteristics. Eventually the particles will become large enough for interparticle attraction forces to dominate and clusters will form. Besides changing the chemistry, the eventual size distribution can be effected by changes in solute

concentration, matrix density, and temperature. There is also an effect from the choice of organic solvent in the reactive solution, because of differences in the solvation of the solute molecules will alter the binding to the matrix. For example, the decrease in binding energy from toluene in this work is apt to be less than that for tetrahydrofuran.

#### 4. Conclusions

The precipitation of semiconductors within a polymer matrix is attractive for both its simplicity and the uniform size distribution of discrete particles created. We have presented an example where a dopant was incorporated simultaneously in a nanosize particle. This material shows the characteristic emission associated with the dopant and characteristic effects of quantum confinement, including increased bandgap and shortening of the radiative recombination lifetime. Further development of this technique will require the development of techniques to extract particles while retaining quantum confinement. This should be possible by the use of surfactants in solvents for the PEO matrix. The possible future applications of this type of material include sensor materials and optical switches.

#### 5. References

- [1] R.N. Bhargava, D. Gallagher and T. Welker, *J. Luminescence*, in press.
- [2] R.N. Bhargava, D. Gallagher, X. Hong and A.V. Nurmikko, *Phys. Rev. Lett.*, submitted.
- [3] P.A. Bianconi, J. Lin and A.R. Strzelecki, *Nature* 349 (1991) 315.
- [4] P.A. Bianconi, Penn State University, private communication; CdS crystals were seen to be quantum-sized by UV measurements.
- [5] L.E. Brus, *Nanostructured Mater.* 1 (1992) 71; Y. Wang and N. Herron, *J. Phys. Chem.* 95 (1991) 525, and references contained within.
- [6] H. Weller, U. Koch, M. Gutierrez and A. Henglein, *Ber. Bunsenges. Physik. Chem.* 88 (1984) 649.
- [7] R. Rossetti, R. Hull, J.M. Gibson and L.E. Brus, *J. Chem. Phys.* 1 (1985) 552. Bandgap values corrected for differences between low temperature (calculation) and room temperature values.

- [8] W. Busse, H.E. Gumlich, B. Meissner and D. Theis, *J. Luminescence* 12/13 (1976) 693.
- [9] G.C. Farrington and R.G. Linford, in: *Polymer Electrolyte Reviews - 2* (Elsevier, Amsterdam, 1989).
- [10] H. Yang and G.C. Farrington, *J. Electrochem. Soc.* 139 (1992) 1646.
- [11] J.A. Dirksen and T.A. Ring, *Chem. Eng. Sci.* 46 (1991) 2389.
- [12] R. Sartori, L. Sepulveda, F. Quina, E. Lissi and E. Abuin, *Macromolecules* 23 (1990) 3878.
- [13] M.L. Steigerwald and L.E. Brus, *Ann. Rev. Mater. Sci.* 19 (1989) 471. Bandgap values corrected for differences between low temperature (calculation) and room temperature values.



ELSEVIER

Journal of Crystal Growth 138 (1994) 976–980

JOURNAL OF **CRYSTAL  
GROWTH**

## Electric field induced absorption modulation of CdS quantum dots in an organic matrix

U. Woggon <sup>\*,a</sup>, S.V. Bogdanov <sup>b</sup>, O. Wind <sup>a</sup>, V. Sperling <sup>a</sup>

<sup>a</sup> Fachbereich Physik, Universität Kaiserslautern, E.-Schrödinger-Strasse, D-67663 Kaiserslautern, Germany

<sup>b</sup> Institute of Microelectronics, Academy of Sciences, Chernogolovka 142432, Russian Federation

### Abstract

CdS quantum dots under weak confinement conditions embedded in a polyvinyl alcohol (PVA) polymer film have been studied in the presence of an external electrical field at different densities of photoexcited carriers. Applying an external electric field strength of  $5 \times 10^4$  V/cm, the observed absorption change  $\Delta\alpha/\alpha$  in this material is  $\approx 7\%$ . At high laser excitation the electric field separates the laser excited carriers and the change in absorption is attributed to a compensation of the many-particle interaction by the external electrical field. A restoring of the oscillator strength is observed and explained by screening effects of the polarization fields in the interface region due to the photogenerated electron–hole pairs.

### 1. Introduction

At present, intensive research work is going on concerning the electrooptic properties of II–VI quantum dots embedded in glass comprising detailed line shape analysis of the electric field induced absorption change [1–6]. These investigations show relatively small changes in  $\alpha$ , with values far below 1% and often only visible in modulation spectroscopy and at field strengths of  $\geq 10^5$  V/cm. An essential problem arises from the low filling factor ( $\leq 10^{-2}$ ) resulting in a flat absorption edge in the linear spectra, from the strong inhomogeneous broadening by the size distribution, and from the technological problem in the realization of electric contacts. For the above reasons, it seems interesting to investigate

quantum dots in organic matrices instead of glasses, allowing us a better control of the development and growth of the quantum dots. The promising nonlinear optical properties of CdS in a polymer film environment have already been demonstrated in refs. [7–9]. Some first results of electro-optic experiments have been published for CdS and CdSe embedded in an acrylonitril–styrene copolymer (AS) and in polymethylmethacrylate (PMMA) [10,11].

The main topic of our contribution is the investigation of the electro-optic changes of the absorption spectra of CdS quantum dots embedded in PVA. The action of the electric field will be discussed in connection with different levels of optical excitation, i.e. at different optically induced charged carrier concentrations. Special attention has been paid to hints on interface-induced internal polarization fields similar to those produced by the lattice mismatch at the interface in strained-layered, two-dimensional superlat-

\* Corresponding author.

tices. In these structures a large electro-optic response has been found for piezoelectrically generated polarization fields, modulated by external electrical fields or high densities of laser excited carriers [12–14].

## 2. Sample characterization

With regard to the electric field experiments, one has to find samples which meet the following requirements: (i) well-defined sizes and thus good knowledge of the confinement regime, e.g. for the clarification of the influence of Coulomb interaction between electron and hole on the electro-optic properties, (ii) a sharp absorption edge or a narrow absorption peak for the optimum modulation of the contrast, (iii) a volume fraction of the semiconductor quantum dots in the range of 1% to 10% to decrease the layer thickness down to some tens of microns ensuring a high electrical field at moderate voltages and a reasonable absorption coefficient, and (iv) no (or low) electrical conductivity, realized by an insulating matrix and by keeping an upper limit for the volume fraction of semiconductor dots to prevent a mutual contact or percolation. Polyvinyl alcohol (PVA) has been proved to be a good stabilizer for quantum dots of the narrow gap semiconductor PbS [15] and is also well suited for the incorporation of CdS.

The films were prepared by the procedure described in detail in ref. [16]. After drying, a water free CdS/PVA film of a dimension of  $\sim 10 \text{ cm}^2$  and a thickness of 50 to 75  $\mu\text{m}$  was obtained showing a clear yellow colour. For the contacts, a symmetric coplanar electrode configuration was used (see ref. [17]) by evaporating metal films at both sides of the sample leaving a free slit in the centre of about 100  $\mu\text{m}$  width for light transmission and detection. In the following the electric field strength is given in terms of the *external* electrical field because the knowledge of depolarization factors is rather poor. At room temperature, a value of the electrical conductivity  $\kappa = 6 \times 10^{-8} \text{ S/cm} = 6 \times 10^{-12} \text{ m}/(\Omega \text{ mm}^2)$  was obtained, which is approximately the value of the pure PVA polymer.

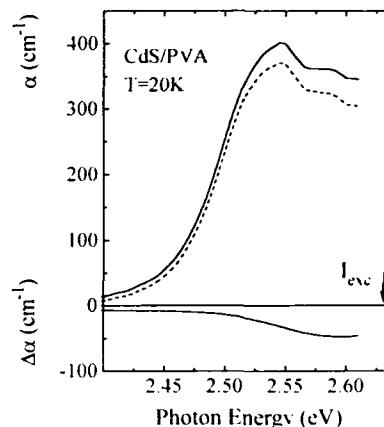


Fig. 1. Linear absorption spectrum (solid curves), spectrum of the change in optical density  $-\Delta\alpha$ , and the bleached absorption (dashed curves) of CdS quantum dots embedded in PVA (thickness of the sample  $d = 75 \mu\text{m}$ ,  $T = 20 \text{ K}$ , laser excitation energy at 2.63 eV and  $2 \text{ MW/cm}^2$ ).

For the characterization of the material, an analysis of the linear and nonlinear absorption and the luminescence has been carried out and described in ref. [16]. High-resolution electron microscopy gives an estimation of the radii of  $\approx 20 \text{ nm}$  ( $\approx 7a_B$ ). These radii correspond to the weak confinement regime. The confinement induced high energy shift expected in the linear absorption spectrum is only in the order of some meV. Accordingly, the linear absorption spectrum in Fig. 1 is still similar to that of bulk CdS. A steep rise of the absorption of over  $300 \text{ cm}^{-1}$  in an energy interval of only 50 meV can be seen for the CdS/PVA film. Evidently, the sharp onset of the absorption has been achieved which is necessary for an application in electric field experiments. The steepness of the absorption edge is essentially preserved up to room temperature. Furthermore, a volume fraction of the semiconductor material in the host as large as 1% to 3% can be determined from the absorption coefficient. The sizes of quantum dots realized in the CdS/PVA film are rather large, so that the properties will be close to the bulk properties and let expect a great influence of excitonic effects.

The measurements of the nonlinear absorption of Fig. 1 were performed using a pump-and-probe



set-up consisting of excimer-laser-pumped dye lasers. The narrow-band pump laser was tuned to an excitation energy of 2.63 eV. The experiment shows a broad absorption bleaching over the whole spectral range of the ground state absorption peak. This behaviour can be explained in analogy to the bulk mechanisms causing the optical nonlinearity. In bulk CdS, the excitonic absorption vanishes with increasing carrier density due to the Mott transition and formation of a dense electron-hole plasma (see, e.g., refs. [18,19]). Screening of the Coulomb interaction and gap shrinkage appear connected with band filling effects. In contrast to the bulk, in the large CdS quantum dots investigated here, no induced absorption has been found either at low or at room temperature. A strong line broadening of the linear absorption of the ground state could mask this feature; however, more important for the explanation of the nonlinear absorption spectra is the change in the interaction mechanisms within the many-particle system occurring due to the weak confinement. The higher exciton binding energy in lower dimensional systems and the minor importance of screening effects due to the restricted mobility of the electron-hole pairs [20] should result in more pronounced exciton-exciton interaction effects.

### 3. Electric field effects at different excitation densities

The spectrum obtained in electroabsorption at low light excitation and presented in Fig. 2 shows a distinctly larger change in the absorption coefficient compared to those reported for CdS in glasses [1-6]. This can be easily explained by the higher filling factor and by an optimum contact configuration resulting in a homogeneous field and giving an efficient potential drop over the microcrystal.

The description by a three-line feature, as known from the increase of damping of an isolated Lorentzian resonance, fails, obviously, due to the presence of two or more near neighbouring and strongly broadened states and their superposition. The excitonic effects are not destroyed by

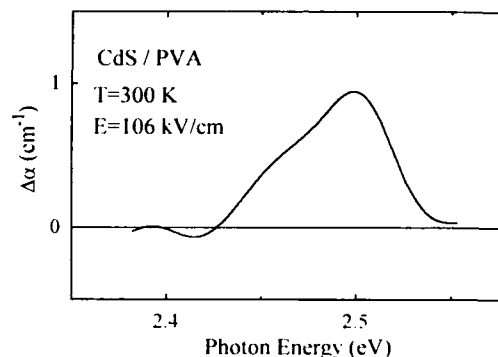


Fig. 2. Electric field induced change of the absorption coefficient  $\Delta\alpha$  at low light excitation, room temperature and an electric field strength of  $E = 106$  kV/cm.

the electrical field even for an electric field strength larger than the ionizing field strength of the bulk semiconductor of  $\approx 10^4$  V/cm in CdS [21]. The field ionization is suppressed because the exciton feels the surrounding potential barrier. As already proposed in refs. [1-5,10], the result of Fig. 2 is discussed in terms of the quantum-confined Stark effect; however, with a typical behaviour more similar to bulk CdS, i.e. more pronounced broadening and a smaller red shift.

In Fig. 3 the difference in absorption with and without an electrical field of  $E = 50$  kV/cm has been measured in the presence of a photoexcited

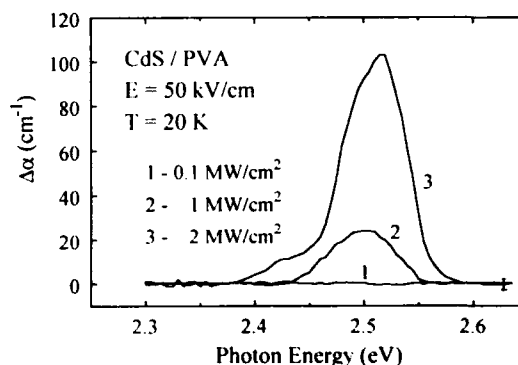


Fig. 3. Change of the absorption coefficient  $\Delta\alpha$  of the CdS/PVA film with an applied electric field of 50 kV/cm and increasing excitation at 2.63 eV (measured at  $T = 20$  K): (1) 100 kW/cm<sup>2</sup>; (2) 1 MW/cm<sup>2</sup>; (3) 2 MW/cm<sup>2</sup>.

dense carrier system. Because of the use of the broad band continuum of a pulsed dye laser to measure the corresponding reference absorption spectra, a lower experimental accuracy has to be taken into account compared to the experiments at low light intensity.  $\Delta\alpha$  has been calculated with the *nonlinear absorption* as the reference spectrum at zero electrical field strength.

Starting with an excitation intensity of  $100 \text{ kW/cm}^2$ , where the absorption is bleached by only some  $\text{cm}^{-1}$ , the action of an external electric field on the nonlinear absorption is small and within the experimental error (spectrum (1)). However, a pronounced effect can be detected at excitation intensities of  $1 \text{ MW/cm}^2$ . The corresponding nonlinear spectrum shows an absorption bleaching of about  $20 \text{ cm}^{-1}$ . Thus, the applied electric field compensates nearly completely the high-density effects induced by the laser excitation (spectrum (2)). Exciting the CdS quantum dots with an intensity of  $2 \text{ MW/cm}^2$ , the change in absorption obtained is even larger than the bleaching at the same intensity without field (spectrum (3)).

We explain our results as follows: The electrical field acts on a high-density particle system generated by the laser excitation. The most simple excited state consists of a four-particle system and it is obvious that already this state is more sensitive with respect to the ionizing effect of the external electrical field destroying the excited states. The electrical field then separates the excited carriers and cancels the many-particle interaction in the microcrystal, the bleaching is reduced, and a positive change in  $\alpha$  is obtained. On the other hand, the optically excited electrons and holes, which are separated and driven by the external field near the interfaces, create a depolarization field. There the charged carrier cloud screens the internal fields and potential fluctuations produced by the interface. Consequently, a restoring of the oscillator strength is evidently connected with an increase of the absorption peak.

To further clarify the situation, the absorption spectra (Fig. 4) are shown at three different conditions: spectrum (1) is the linear spectrum without field and excitation, (2) is the spectrum for

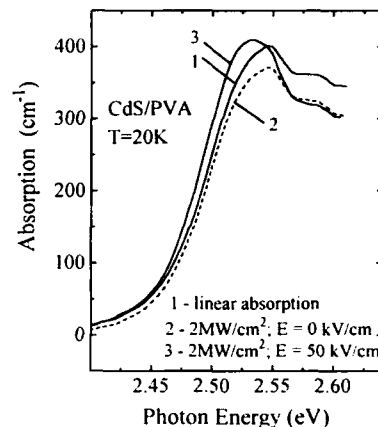


Fig. 4. Absorption spectra of the CdS/PVA film without electric field and at low excitation densities (1), without electric field but under laser excitation of  $2 \text{ MW/cm}^2$  (2), with electric field of  $50 \text{ kV/cm}$  and laser excitation of  $2 \text{ MW/cm}^2$  (3).

high excitation intensity of  $2 \text{ MW/cm}^2$  resulting in a bleaching of the absorption without electrical field. When an electrical field is switched on, the nonlinear bleaching effect declines in strength for the reasons given above and the linear absorption spectrum is gradually restored. Moreover, at the highest excitation the action of the electrical field results in a larger absorption maximum and in a slight decrease of the linewidth (3). The experimental data in Figs. 3 and 4 show the modulation of  $\alpha$  by controlling the efficiency of the many-particle interaction by the external electrical field.

#### 4. Conclusion

When CdS quantum dots are grown in a polymer film environment (PVA), the observed change in the absorption under the action of an electrical field is large compared to quantum dots in glasses. This is partly attributed to the higher filling factor and to the optimum contact configuration resulting in a homogeneous field penetration and in an efficient potential drop over the quantum dot. In addition, the weak confinement increases the ionization field strength of the exciton giving an excitonic absorption also at higher electrical

fields. In the nonlinear optical behaviour, the weak quantum confinement yields in a reduction of screening effects and thus influences the spectral shape and the saturation intensity of the bleaching. The polymer environment gives an intrinsic potential field near the interface which can be modulated by (i) high carrier concentrations or (ii) extrinsic field strengths. Such a mechanism for modulating the absorption spectrum by combining CdS quantum dots and a polymer has not been reported up to now.

### 5. Acknowledgements

The authors are grateful to C. Klingshirn (Kaiserslautern) and A.I. Efros (München) for stimulating discussions, P. Chatziagorastou and H.P. Fritz (München) for the support in preparing the samples, and H. Pier and K.H. Schlaad (Kaiserslautern) for the preparation of contacts. This work has been supported by the "Deutsche Forschungsgemeinschaft", the "Materialforschungsschwerpunkt des Landes Rheinland-Pfalz" at the University Kaiserslautern and the "Fonds der chemischen Industrie Deutschlands". One of the authors (S.B.) thanks the DAAD for a grant to stay in Kaiserslautern.

### 6. References

- [1] F. Hache, D. Ricard and C. Flytzanis, *Appl. Phys. Lett.* 55 (1989) 1504.
- [2] A.I. Ekimov, A.I. Efros, T.V. Shubina and A.P. Skvortsov, *J. Luminescence* 46 (1990) 97.
- [3] H. Rossmann, A. Schülzgen, F. Henneberger and M. Müller, *Phys. Status Solidi (b)* 159 (1990) 287.
- [4] D. Cotter, H.P. Girdlestone and K. Moulding, *Appl. Phys. Lett.* 58 (1991) 1455.
- [5] S. Nomura and T. Kobayashi, *Phys. Rev. B* 45 (1992) 1305.
- [6] V. Esch, B. Fluegel, G. Khitrova, H.M. Gibbs, Xu Jiajin, K. Kang, S.W. Koch, L.C. Liu, S.H. Risbud and N. Peyghambarian, *Phys. Rev. B* 42 (1990) 7450.
- [7] K. Misawa, H. Yao, T. Hayashi and T. Kobayashi, *J. Chem. Phys.* 94 (1991) 4131.
- [8] L.E. Brus, *Appl. Phys. A* 53 (1991) 465.
- [9] Y. Wang, N. Herron, W. Mahler and A. Suna, *J. Opt. Soc. Am. B* 6 (1989) 808.
- [10] T. Sekikawa, H. Yao, T. Hayashi and T. Kobayashi, *Solid State Commun.* 83 (1992) 969.
- [11] V.L. Colvin and A.P. Alivisatos, *J. Chem. Phys.* 97 (1992) 730.
- [12] D.L. Smith and C. Mailhot, *Rev. Mod. Phys.* 62 (1990) 173.
- [13] M.P. Halsall, J.E. Nicholls, J.J. Davies, B. Cockayne and P.J. Wright, *J. Appl. Phys.* 71 (1992) 907.
- [14] C. Klingshirn, H. Kalt, M. Umlauff, W. Petri, F.A. Majmder, S.V. Bogdanov, W. Langbein, M. Grün, M. Hetterich, K.P. Geyzers, M. Heuken, A. Naumov, H. Stanzl and W. Gebhardt, *J. Crystal Growth* 138 (1994) 786.
- [15] A. Henglein, *Chem. Rev.* 89 (1989) 1861.
- [16] U. Woggon, S.V. Bogdanov, O. Wind, K.-H. Schlaad, H. Pier, C. Klingshirn, P. Chatziagorastou and H.P. Fritz, *Phys. Rev. B*, in press.
- [17] M. Cardona, *Modulation spectroscopy*, in: *Solid State Physics*, Vol. 11, Eds. F. Seitz, D. Turnbull and H. Ehrenreich (Academic Press, New York, 1969).
- [18] R. Zimmermann, in: *Many Particle Theory of Highly Excited Semiconductors*, Teubner Texte zur Physik 18, Ed. W. Ebeling (Teubner, Leipzig, 1987).
- [19] H. Haug and S. Schmitt-Rink, *Progr. Quantum Electron.* 9 (1984) 3.
- [20] S. Schmitt-Rink, D.S. Chemla and D.A.B. Miller, *Phys. Rev. B* 32 (1985) 6601.
- [21] J.D. Dow and D. Redfield, *Phys. Rev. B* 1 (1970) 3358.



ELSEVIER

Journal of Crystal Growth 138 (1994) 981–987

JOURNAL OF **CRYSTAL  
GROWTH**

## Photoluminescence study of $\text{HgTe-Hg}_{0.9}\text{Cd}_{0.1}\text{Te}$ superlattice.

J.R. Meyer <sup>\*a</sup>, A.R. Reisinger <sup>b</sup>, K.A. Harris <sup>b</sup>, R.W. Yanka <sup>b</sup>, L.M. Mohnkern <sup>b</sup>,  
L.R. Ram-Mohan <sup>c</sup>

<sup>a</sup> Code 5613, Naval Research Laboratory, Washington, DC 20375, USA

<sup>b</sup> Martin Marietta Electronics Laboratory, Syracuse, New York 13221, USA

<sup>c</sup> Worcester Polytechnic Institute, Worcester, Massachusetts 01609, USA

### Abstract

Infrared photoluminescence (PL) measurements have been performed on 17 [211]-oriented superlattices with energy gaps spanning the range 110–495 meV. The spectra for 7 different samples display double peaks, which are attributed to monolayer fluctuations in the average thickness of the quantum wells. The peak splittings vary systematically with PL energy gap ( $E_p$ ), and are accurately reproduced by orientation-dependent band structure calculations if the magnitude of the fluctuations is taken to be 1.5 monolayers. These data confirm that the low-temperature [211] growth produces islands with monolayer average smoothness over lateral dimensions of at least 500–1000 Å. Results are compared with earlier determinations of the interface roughness correlation length from magneto-transport measurements. In agreement with theoretical predictions, the decrease of  $dE_p/dT$  with increasing  $E_p$  is as rapid as that in the  $\text{Hg}_{1-x}\text{Cd}_x\text{Te}$  alloy.

This work reports a comprehensive experimental and theoretical investigation of infrared photoluminescence (IRPL) in  $\text{HgTe-CdTe}$  superlattices. By correlating results for a large number of samples with a broad range of layer thicknesses and energy gaps, we are able to probe the fundamental nature of the IRPL. We focus in particular on the first observation of multiple PL peaks due to monolayer (ML) fluctuations of the quantum well thickness. These are indicative of exceptional growth quality, since they imply the existence of large lateral islands over which the average layer thickness is smooth to within 1 ML. In only two previous studies of  $\text{HgTe-CdTe}$  and  $\text{Hg}_{1-x}\text{Cd}_x\text{Te-CdTe}$  superlattices have multiple

peaks been reported near the band edge [1,2], and in both cases the energy splittings were far too large to be associated with ML fluctuations (they agreed with calculated energy differences between the heavy and light valence bands). While an earlier report of PL data from one of the present samples attributed the second peak to bound-exciton transitions [3], we now believe that interpretation to be incorrect.

The  $\text{HgTe-Hg}_{1-x}\text{Cd}_x\text{Te}$  superlattices were deposited directly onto [211]B  $\text{CdTe}$  substrates by photo-assisted molecular beam epitaxy (PAMBE) [3–5]. The growth temperature was 170°C, and barrier compositions  $x$  were  $\approx 0.9$  due to a continuous Hg overpressure. Table 1 lists the well and barrier thicknesses ( $d_w$  and  $d_b$ ) for 17 different superlattices, as determined from a correlation of the growth rate, the total thickness, and

\* Corresponding author.

comparison of the PL energy gap to theory [6]. Transmission electron microscopy (TEM) measurements on some of the superlattices [3–5] indicated sharp interfaces with no significant interdiffusion, and that the thickness was essentially uniform from front to back over as many as 400 periods. While the dislocation densities were too low to be accurately determined by TEM, chemical defect etching indicated densities in the range  $10^3$ – $10^4$  cm $^{-2}$  [4]. These are the lowest reported to date for MBE-grown Hg-based superlattices, and are among the best for Hg-based films grown by any technique. Double crystal X-ray rocking curves displaying satellite peaks provide further evidence for the periodicity and high structural quality [4].

IRPL measurements employing excitation by a CW Nd:YAG laser were carried out at Martin Marietta, in a system which has been described elsewhere [7]. All 17 of the investigated samples emitted photoluminescence, which is not surprising since recombination lifetimes for a number of these superlattices were in the 100 ns to 20  $\mu$ s range [3–8]. Table 1 summarizes the experimental PL peak energies ( $E_p$ ) and full widths at half maximum (FWHM) for all samples, as well as

Table 1

Well and barrier thicknesses, photoluminescence peak energy, full width at half maximum, and double-peak energy separation for 17 [211]-oriented HgTe–Hg $_{0.10}$ Cd $_{0.90}$ Te superlattices

Growth No.	$d_w$ (Å)	$d_B$ (Å)	$E_p$ (77 K) (meV)	FWHM (77 K) (meV)	$\Delta E$ (meV)
617	37	50	159	16	–
619	45	47	110	28	–
632	36	39	133	25	14
637	15	65	495	26	60
650	41	41	122	45	–
741	22	60	325	27	37
749	35	31	145	37	–
751	35	38	161	17	–
764	40	30	117	21	–
788	19	24	320	19	55
790	37	28	127	37	–
832	16	35	429	19	50
833	15	41	470	45	–
840	24	41	275	40	–
862	22	24	262	28	31
866	36	34	150	38	–
881	33	53	188	30	18

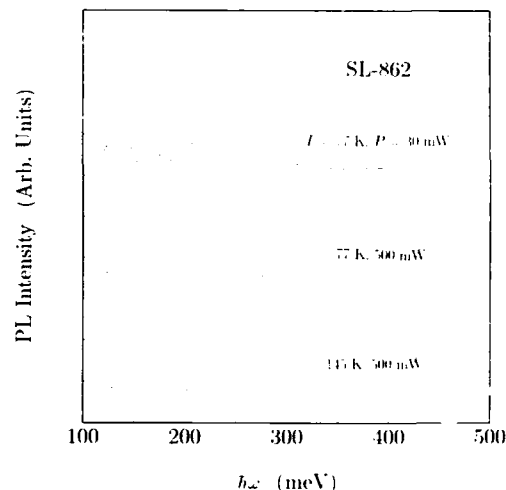


Fig. 1. Experimental PL spectra showing the double peak for SL-862 at 77 K (for two pump powers), and at 145 K.

double-peak energy splittings ( $\Delta E$ ) for those 7 which displayed clearly-resolvable multiple peaks. While the other 10 superlattices exhibited only a single peak, in several cases that feature contained a shoulder or other substructure suggesting that the PL in fact consisted of poorly-resolved multiple contributions. Double peaks were observed in both n- and p-doped samples, as well as in undoped superlattices.

Typical IRPL spectra displaying the double peaks are illustrated in Fig. 1 for SL-862. Data are shown at 77 and 145 K for the maximum pump power ( $P$ ) of 500 mW and at 77 K for a much lower  $P$  (30 mW). The two peaks separated by 30 meV are seen to have similar line shapes and FWHM (28 meV). Note that whereas the lower-energy peak is more intense at the lower temperature and pump power, the higher-energy peak becomes dominant once the temperature is increased to 145 K.

We carried out detailed theoretical modeling of the PL line shapes in order to determine whether some aspect of the band structure could account for the presence of prominent double peaks with the observed properties. It is well known that the complicated free carrier dispersion relations in HgTe–CdTe superlattices lead

to multiple peaks in both the magneto-transmission spectra (e.g., double hole cyclotron resonance) [9] and the “mobility spectra” from the conductivity tensor (e.g., due to “mass broadening” and the extremely nonparabolic hole mass) [10]. However, our calculations demonstrate that these phenomena have a relatively weak effect on the PL line shape. Whereas the magneto-optical and magneto-transport data are quite sensitive to variations in the electron and hole masses individually, the density of states which governs the photoluminescence depends only on the reduced electron–hole mass ( $m_r^{-1} \equiv m_n^{-1} + m_p^{-1}$ ). Thus even a very strong variation in the hole mass shifts  $m_r$  and the PL intensity by less than a factor of 2. While the model based on non-fluctuating layer thicknesses sometimes produces a shoulder due to contributions from different regions of the miniband or a very weak second feature due to transitions involving the light hole band, we find that those mechanisms fail completely to account for the energy splittings, intensity ratios, and layer-thickness dependences of the observed multiple peaks.

It has recently been shown that in the case of GaAs–Al<sub>x</sub>Ga<sub>1-x</sub>As heterostructures, monolayer fluctuations in the quantum well thickness can lead to well-resolved multiple peaks in the excitonic PL [11–13]. The observation of double peaks in the present spectra (e.g., Fig. 1) may similarly be attributed to the coexistence of extended islands having a given average  $d_w$  with other islands whose average thickness differs by approximately 1 ML. This model accounts for the near equality of the observed FWHM for the two peaks, as well as for the temperature shift of the intensity ratio. While the lower-energy PL line dominates at low temperatures because the electron and hole wavefunctions are localized in the islands with thicker quantum wells, the higher-energy line gains intensity with increasing temperature as carriers are thermally excited into the islands with thinner  $d_w$ .

The strongest evidence for this interpretation is that it accurately accounts for both the magnitude and the energy-gap dependence of the splitting energy. The filled circles in Fig. 2 plot the experimental variation of  $\Delta E$  with  $E_p$  (higher-

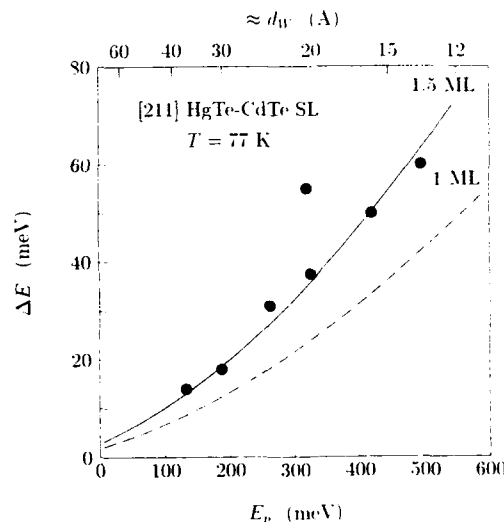


Fig. 2. Double-peak splitting versus PL energy gap (higher-energy peak). The curves are based on theoretical analyses, assuming well-width fluctuations of 1 monolayer (1.32 Å, dashed curve) and 1.5 monolayers (1.85 Å, solid curve). The barrier thickness in the calculation is 30 Å, for which the top scale gives the well thickness corresponding to the energy gap in the bottom scale.

energy line) for the 7 superlattices displaying double peaks. Apart from one anomalous point, the dependence is seen to be quite systematic. Using an 8-band transfer-matrix algorithm ( $k \cdot p$ ) which explicitly accounts for the growth orientation [6], we have calculated the expected shift of  $E_p$  resulting from a 1 ML fluctuation [14] of  $d_w$  (assuming  $d_B = 30$  Å) in a [211] HgTe–Hg<sub>0.1</sub>Cd<sub>0.9</sub>Te superlattice. The result is given by the dashed curve in Fig. 2. We find that to lowest order, this calculation without adjustable parameters accounts quite well for both the magnitude and the layer-thickness dependence of the observed  $\Delta E$ . Furthermore, the solid curve indicates that if the fluctuation magnitude is taken to be 1.5 ML, the data are reproduced almost exactly. It should be noted that the multiple-peak splittings reported for GaAs–Al<sub>x</sub>Ga<sub>1-x</sub>As heterostructures typically corresponded to 0.6–1.2 ML rather than precisely 1 ML [11,12,15].

The experimental observation of monolayer thickness fluctuations in the PL data is indicative

of high growth quality, since it implies that the islands over which the average quantum well thickness maintains monolayer smoothness must be quite large. Neighboring islands contribute separately to the photoluminescence only if their diameter is larger than the electron and hole wavefunctions. Comparison with estimates for either the exciton diameter or the de Broglie wavelengths yields that the island size in the present structures must exceed 500–1000 Å [16]. However, it should be emphasized that the interfaces are known to remain microrough on the atomic scale, i.e., the implied “smoothness” pertains only to a constant *average* layer thickness within a given island [11,12,15,17].

These conclusions from our PL data should be considered in the context of earlier magnetotransport determinations of  $\Lambda$ , the interface roughness correlation length (whose interpretation is roughly equivalent to that of the island diameter discussed here) [18,19]. By fitting a phenomenological model for interface roughness scattering to experimental electron mobilities in HgTe–CdTe superlattices with thin quantum wells,  $\Lambda \approx 300$  Å was obtained for a series of [100]-oriented (PAMBE) samples [10,20] and  $\Lambda \approx 200$  Å for a series of [211]-oriented (non-photo-assisted growth) superlattices [6]. The discussion of the previous paragraph implies that these  $\Lambda$  are somewhat smaller than the minimum required for the observation of multiple PL peaks, and in fact such features due to ML thickness fluctuations have never been observed in materials fabricated under the growth conditions employed in refs. [6] and [10].

Further information about the nature of the islands is provided by scanning  $E_p$  as a function of lateral position. For SL-862, spectra were obtained at a grid of 41 different locations on the surface of the  $2 \times 2$  cm<sup>2</sup> wafer. Although the relative intensities varied from point to point, double peaks were observed at most positions, and both energies shifted smoothly and in tandem with translation of either in-plane coordinate. Data acquired for coarser grids on several of the other samples similarly indicated gradual shifts of the peak energies with location on the surface. Since abrupt rather than gradual varia-

tions should have been obtained if the net layer thicknesses change only in sudden jumps as one moves from island to island, these observations imply that the discrete steps of  $\approx 1.5$  ML occur at only one of the two interfaces of each quantum well [12], i.e., either HgTe-on-CdTe or CdTe-on-HgTe but not both. Recent reflection high energy electron diffraction (RHEED) data by Myers et al. [21] indicate that for [211] growth it is the HgTe-on-CdTe interface which is smoother. One also expects that a lateral variation in the flux rate should lead to transition regions in which islands with three different layer thicknesses coexist in relatively close proximity. Spectra for SL-637 confirm that while either one or two PL peaks are observed at most positions on the wafer, a third peak occasionally emerges as the surface is scanned. The three FWHM are comparable ( $\approx 30$  meV), and the two energy splittings separating the peaks are nearly equal ( $\Delta E \approx 60$  meV). Additional conclusions concerning the [211] growth kinetics are discussed in a separate work [7].

Having identified the origin of the multiple peaks in the spectra for some of the samples, we now consider in more detail the implications of the PL results for all 17 superlattices. We begin by noting that the 77 K values of the FWHM from Table 1 show little apparent correlation with  $E_p$  or layer thickness. The spectra as a function of  $T$  (down to 10 K in some cases) generally yielded a zero-temperature extrapolation FWHM<sub>0</sub> in the range 9–18 meV. These are somewhat narrower than previous low-temperature values of 18–110 meV [1,2,22–25], and the FWHM of 10 meV obtained earlier [3] for SL-632 at 4.5 K is, to our knowledge, the narrowest ever reported for a Hg-based superlattice. The non-thermal contribution to the observed linewidth is probably due primarily to broadening of the conduction and valence extrema by potential fluctuations [24,26]. One obvious source of these fluctuations is the presence of monolayer roughness (on a lateral scale smaller than the exciton diameter and de Broglie wavelength) at one of the two interfaces for each quantum well (as mentioned earlier, the RHEED results imply that it is the CdTe-on-HgTe interface which is rougher [21]).

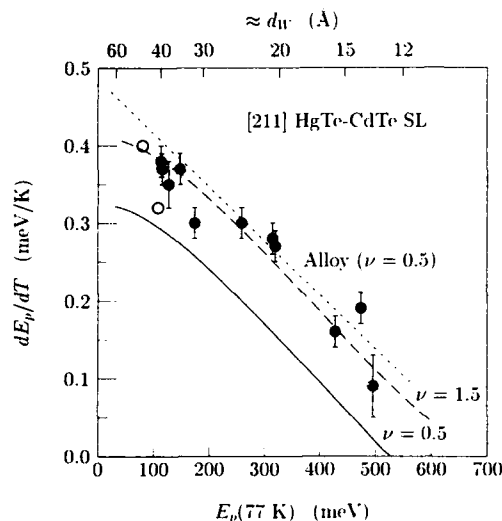


Fig. 3. Experimental (circles) and theoretical temperature coefficients for the superlattice PL energy gap versus peak energy at 77 K, where the theory employed  $d_B = 30$  Å and  $\nu$  as indicated on the curves. The filled circles are from the present work, while the open circles are from the previous study of Baukus et al. [22,23]. Also shown as the dotted curve is the analogous dependence for the  $\text{Hg}_{1-x}\text{Cd}_x\text{Te}$  alloy [27]. All results represent an average over the temperature range 77–300 K.

Broadening is also expected due to fluctuations in the alloy composition of the barrier layers. The band structure calculations indicate that fluctuations on the order of  $\Delta x_B \approx \pm 0.05$  would account for a significant fraction of the observed  $\text{FWHM}_0$ .

We next consider the related issue of how  $E_p$  and the energy gap  $E_g$  vary with temperature. It is well known that  $dE_g/dT$  is positive for HgTe and negative for CdTe, with a cross-over at  $x \approx 0.5$ . In lowest order, one may expect the superlattice to mimic HgTe, since the baseline for the confinement-induced energy levels is  $E_g(T)$  in the quantum well material. However, a more detailed calculation indicates that when  $d_w$  is very thin, the net temperature coefficient in the superlattice becomes quite sensitive to  $dE_g/dT$  in the barrier layers. This is evident from both experimental and theoretical results for  $dE_p/dT$  in Fig. 3, which illustrates that the decrease of the temperature coefficient with increasing en-

ergy gap is just as rapid in the superlattice as it is in the  $\text{Hg}_{1-x}\text{Cd}_x\text{Te}$  alloy [27] (dotted curve). The data are taken from spectra at  $T$  between 77 and 300 K for 11 of the present samples (filled circles), along with two superlattices studied previously by Baukus et al. [22,23] (open circles). Theoretical dependences were obtained using temperature-dependent [211] energy gaps from the transfer-matrix algorithm, where we have employed the relation

$$E_p(T) = E_g(T) + \nu k_B T. \quad (1)$$

The solid curve in the figure represents  $\nu = 1/2$ , which is appropriate for momentum-conserving band-to-band transitions when non-thermal broadening mechanisms are ignored. Since the calculation employs no adjustable parameters, the agreement with experiment should be considered relatively good.

However, the dashed curve in Fig. 3 indicates that theory and experiment come into much better agreement over the entire range of energy gaps if  $\nu = 0.5$  is replaced by  $\nu \approx 1.5$ . Many previous studies of temperature-dependent PL in Hg-based superlattices and alloys have similarly found that  $dE_p/dT$  is equivalent to  $dE_g/dT + \nu k_B$ , with  $E_g(T)$  determined independently, only when  $1 < \nu < 6$  is employed [22–24,28–33]. This finding is often interpreted [28–31] as implying that momentum is not conserved in the radiative transitions, since theory then yields  $\nu = 2$  [29]. However, that interpretation is inconsistent with other aspects of the data, particularly the magnitude of  $\nu_{\text{FWHM}}$ , the temperature coefficient of the FWHM. Ravid and Zussman have pointed out that while  $\nu_{\text{FWHM}} \approx 1.8$  is expected for momentum-conserving processes, a much larger value of  $\nu_{\text{FWHM}} \approx 3.4$  is predicted for non- $k$ -conservation [34]. Our spectra yield  $1.1 < \nu_{\text{FWHM}} < 1.8$ , which is far too small to be explained within the non-conservation-of-momentum hypothesis, and nearly all previous PL data at higher temperatures similarly imply  $\nu_{\text{FWHM}} \ll 3.4$  [22–24,31,33]. It should be noted that Hunter and McGill limited their original discussion of the possible importance of this mechanism in  $\text{Hg}_{1-x}\text{Cd}_x\text{Te}$  to the low temperature regime ( $T \leq 30$  K), for which an electron-hole droplet like model was invoked [29]. The earlier



theory of Lasher and Stern for non- $k$ -conserving transitions in GaAs was similarly restricted to low temperatures, since it was based on processes involving localized states in the tails of the bands [35]. Those authors specifically argued that momentum should be conserved at higher temperatures, since most of the carriers then occupy non-localized states well above the band extrema. Previous attributions of  $\nu > 0.5$  at  $T \geq 77$  K to non-conservation of momentum therefore seem physically unreasonable. A more likely interpretation is that the observed value of  $\nu$  results from a broadening of the density of states by potential fluctuations [24]. At lower temperatures, for which the electrons and holes preferentially occupy states in the tails of the fluctuations, PL can occur at energies below the average band gap. However, as  $k_B T$  approaches the magnitude of the fluctuations the PL energy becomes more representative of the average  $E_g$ , hence  $E_p$  displays an anomalously large temperature shift between the two regions. To account for the discrepancy between theory (with  $\nu = 0.5$ ) and experiment in Fig. 3, the additional energy shift between 77 and 300 K must be approximately 15–20 meV, i.e., of the same order as the non-thermal broadening of the PL line.

While our data show no positive evidence for exciton or shallow-impurity contributions to the PL, one cannot rule out that those processes contribute since the predicted binding energies are much smaller than the observed FWHM [2,24]. It can, however, be concluded that deep acceptors play no significant role in the PL for our superlattices.

In summary, we have experimentally and theoretically investigated the photoluminescence properties of HgTe–CdTe superlattices with a broad range of energy gaps. A sizable fraction of the samples display double PL peaks due to monolayer fluctuations in the quantum well thickness. The systematic variation of peak splitting with energy gap is reproduced by [211] band structure calculations if the thickness fluctuations are taken to have units of 1.5 ML. These results confirm that the superlattice growth quality achievable by PAMBE is quite high, and that at least one interface for each quantum well has

monolayer average smoothness over island dimensions exceeding 500 Å. Data for  $dE_p/dT$  as a function of  $E_p$  have been compared with the theoretical temperature shift of the energy gap. The relatively modest discrepancy has been attributed to the influence of potential fluctuations rather than to non-conservation of momentum as proposed in several previous works.

We are grateful for discussions with C.A. Hoffman, B.V. Shanabrook, N. Otsuka, T.H. Myers, and N.C. Giles, and thank Quantum Semiconductor Algorithms for the use of superlattice band structure software. This research was supported by the Air Force Wright Laboratory Materials Directorate.

## 1. References

- [1] T.H. Myers, R.W. Yanka, K.A. Harris, A.R. Reisinger, J. Han, S. Hwang, Z. Yang, N.C. Giles, J.W. Cook, Jr., J.F. Schetzina, R.W. Green and S. McDevitt, *J. Vac. Sci. Technol. A* 7 (1989) 300.
- [2] E. Monterrat, L. Ulmer, R. Mallard, N. Magnea, J.L. Pautrat and H. Mariette, *J. Appl. Phys.* 71 (1992) 1774.
- [3] K.A. Harris, R.W. Yanka, L.M. Mohnkern, A.R. Reisinger, T.H. Myers, Z. Yang, Z. Yu, S. Hwang and J.F. Schetzina, *J. Vac. Sci. Technol. B* 10 (1992) 1574.
- [4] K.A. Harris, T.H. Myers, R.W. Yanka, L.M. Mohnkern and N. Otsuka, *J. Vac. Sci. Technol. B* 9 (1991) 1752.
- [5] R.W. Yanka, K.A. Harris, L.M. Mohnkern, A.R. Reisinger and T.H. Myers, *J. Electron. Mater.* 22 (1993) 1107.
- [6] C.A. Hoffman, J.R. Meyer, R.J. Wagner, F.J. Bartoli, X. Chu, J.P. Faurie, L.R. Ram-Mohan and H. Xie, *J. Vac. Sci. Technol. A* 8 (1990) 1219.
- [7] J.R. Meyer, A.R. Reisinger, K.A. Harris, R.W. Yanka and L.M. Mohnkern, *Appl. Phys. Lett.*, submitted.
- [8] A.R. Reisinger, K.A. Harris, T.H. Myers, R.W. Yanka, L.M. Mohnkern and C.A. Hoffman, *Appl. Phys. Lett.* 61 (1992) 699.
- [9] J.R. Meyer, C.A. Hoffman, R.J. Wagner and F.J. Bartoli, *Phys. Rev. B* 43 (1991) 14715.
- [10] C.A. Hoffman, J.R. Meyer, F.J. Bartoli, J.W. Han, J.W. Cook, Jr., J.F. Schetzina and J.N. Schulman, *Phys. Rev. B* 39 (1989) 5208.
- [11] C.A. Warwick, W.Y. Jan, A. Ourmazd and T.D. Harris, *Appl. Phys. Lett.* 56 (1990) 2666.
- [12] D. Gammon, B.V. Shanabrook and D.S. Katzer, *Appl. Phys. Lett.* 57 (1990) 2710.
- [13] C. Parks, A.K. Ramdas, M.R. Melloch and L.R. Ram-Mohan, *Phys. Rev. B* 48 (1993) 5413.

- [14] Monolayer planes along the [211] axis are more closely spaced ( $1 \text{ ML} \rightarrow a/2\sqrt{6} \approx 1.32 \text{ \AA}$ ) but contain fewer atoms than those along the [100] axis. There are 6 monolayers per unit cell.
- [15] C.A. Warwick and R.F. Kopf, Appl. Phys. Lett. 60 (1992) 386.
- [16] We expect the island dimensions to be elongated, since atomic diffusions along the two in-plane axes are inequivalent in [211] growth.
- [17] Y. Kim, A. Ourmazd, M. Bode and R.D. Feldman, Phys. Rev. Lett. 63 (1989) 636.
- [18] J.R. Meyer, D.J. Arnold, C.A. Hoffman and F.J. Bartoli, Appl. Phys. Lett. 58 (1991) 2523.
- [19] J.R. Meyer, D.J. Arnold, C.A. Hoffman, F.J. Bartoli and L.R. Ram-Mohan, Phys. Rev. B 46 (1992) 4139.
- [20] Although ref. [19] derived  $A = 80 \text{ \AA}$  for the [211] sample, that result was invalidly based on use of the [100] monolayer thickness for both orientations.
- [21] T.H. Myers, R.G. Benz II, B.K. Wagner and C.J. Summers, private communication.
- [22] J.P. Baukus, A.T. Hunter, O.J. Marsh, C.E. Jones, G.Y. Wu, S.R. Hetzler, T.C. McGill and J.P. Faurie, J. Vac. Sci. Technol. A 4 (1986) 2110.
- [23] J.P. Baukus, A.T. Hunter, J.N. Schulman and J.P. Faurie, J. Appl. Phys. 64 (1988) 283.
- [24] C.L. Cesar, M.N. Islam, R.D. Feldman, R. Spitzer, R.F. Austin, A.E. DiGiovanni, J. Shah and J. Orenstein, Appl. Phys. Lett. 54 (1989) 745.
- [25] M.M. Kraus, M.M. Regnet, C.R. Becker, R.N. Bicknell-Tassius and G. Landwehr, J. Appl. Phys. 71 (1992) 5610.
- [26] E. Monterrat, L. Ulmer, N. Magnea, H. Mariette, J.L. Pautrat, K. Kheng and F. Fuchs, J. Appl. Phys. 71 (1992) 1774.
- [27] M.H. Weiler, in: Semiconductors and Semimetals, Vol. 16, Eds. R.K. Willardson and A.C. Beer (Academic Press, New York, 18981) p. 119.
- [28] D. Schikora, J.W. Tomm, K. Rakkenus and M. Pesa, Phys. Status Solidi (a) 118 (1990) K123.
- [29] A.T. Hunter and T.C. McGill, J. Appl. Phys. 52 (1981) 5779.
- [30] P. Gille, K.H. Herrmann, N. Puhlmann, M. Schenk, J.W. Tomm and L. Werner, J. Crystal Growth 86 (1988) 593.
- [31] A. Ravid and A. Zussman, J. Appl. Phys. 67 (1990) 4260.
- [32] F. Fuchs and P. Koidl, Semicond. Sci. Technol. 6 (1991) C71.
- [33] P. Bochut, G. Destefanis, J.P. Chamonal, A. Million, B. Pellicciari and J. Piagnet, J. Vac. Sci. Technol. B 9 (1991) 1794.
- [34] A. Ravid and A. Zussman, J. Appl. Phys. 73 (1993) 3979.
- [35] G. Lasher and F. Stern, Phys. Rev. A 133 (1973) 553.



ELSEVIER

Journal of Crystal Growth 138 (1994) 988–992

JOURNAL OF **CRYSTAL  
GROWTH**

## CdS quantum dots in the weak confinement

U. Woggon \*, M. Saleh, A. Uhrig, M. Portuné, C. Klingshirn

*FB Physik, Universität Kaiserslautern, E.-Schrödinger-Strasse, D-67663 Kaiserslautern, Germany*

### Abstract

By means of linear and nonlinear spectroscopy, the energy states and linewidths were investigated for CdS quantum dots under weak confinement grown in the coalescent or normal growth process. The homogeneous line broadening measured by differential absorption spectroscopy and non-degenerate four-wave mixing is strongly influenced by the interface properties and is considerably larger than reported for bulk CdS. This difference has been attributed to a dephasing process introduced by interface polarizations. The direct electron-hole pair recombination is characterized by a sharp luminescence peak 20 meV below the absorption band. The Huang-Rhys parameters have been estimated from both the luminescent Stokes shift and the linewidth, and good agreement has been achieved.

To characterize the quantum confinement of zero-dimensional structures (quantum dots, QDs), the analysis generally starts with the determination of energy states and linewidths derived from the absorption spectra. Because of the rather smooth structures in the linear absorption of quantum dots, nonlinear optical methods have been successfully applied as a useful tool to resolve the electronic levels [1–10]. Concerning II–VI quantum dots, the studies were mostly concentrated on the strong confinement with radii smaller than the Bohr radius, but a lack of information exists with respect to the weak confinement, where the properties of the quantum dots should converge to the corresponding solid state material.

In this paper we report on CdS QDs in the weak confinement range ( $R \approx 7\text{--}9$  nm corre-

sponding to  $2.5 a_B$  to  $3.5 a_B$ , where  $a_B = 2.6$  nm) adjusted by special heat treatments. Besides the known influence of the growth process on the inhomogeneous line broadening, it has been found that likewise the homogeneous linewidth  $\Gamma$  can no longer be considered as independent of the growth process.  $\Gamma$  can be modified, e.g. by changing the polar coupling constant due to interface polarizations or charge localizations. For the CdS QDs investigated, the energy states have been identified by differential absorption spectroscopy (DAS) and the linewidths  $\Gamma$  have been estimated. The value of  $\Gamma$  obtained from the analysis of the hole-burning has been compared with results obtained by luminescence experiments and nondegenerate four-wave mixing (NDFWM).

The experiments have been carried out at three representative samples. They were grown using the same matrix composition of 56% SiO<sub>2</sub>, 8% B<sub>2</sub>O<sub>3</sub>, 24% K<sub>2</sub>O, 3% CaO and 9% BaO. The

\* Corresponding author.

first sample has been obtained from a diffusion controlled process near nucleation, carried out at the low temperature of 600°C over 60 h (labelled in the following as 600°C/60 h). The second sample is grown at high temperature to promote directly the coalescence avoiding the normal growth stage (labelled 700°C/8 d). Whereas for this 700°C/8 d sample a preceding preannealing step has been performed at 560°C over some days, the third sample is grown without this nucleation phase (labelled 700°C/7 d/no nucleation). For sample 600°C/60 h, the sizes of the quantum dots have been carefully determined by small-angle X-ray scattering to be  $R = 7.5$  nm with an average deviation of 20%. For the samples grown at 700°C, a somewhat larger average radius around 9 nm can be estimated from the absorption onset at lower energies, compared to the sample 600°C/60 h.

Fig. 1 shows the linear and nonlinear absorption spectra of the CdS quantum dots arising from the different growth stages. The differences in the linear absorption spectra of the three samples are essentially confined to the different scale in  $\alpha d$  caused by the different realized volume fractions of the semiconductor material. In con-

trast to small CdSe QDs, no sharp peaks but two pronounced steps characterize the spectral behaviour of the linear spectra. The observed changes in absorption in the bleached spectra (dashed lines) are concentrated in the spectral region of these steps. The nonlinear absorption ( $\Delta\alpha d$ ) has been measured by nanosecond pump-and-probe spectroscopy with different energies of the pump laser ranging from 2.6 to 2.75 eV. To compare the absorption changes of the different samples in Fig. 1, the pump intensity has been normalized to excite nearly equal carrier densities. A fitting procedure based on the superposition of multiple Lorentzian curves has been carried out, keeping in mind that this gives only a first approximation. The obtained information can be summarized in the following items:

(i) The first absorption maximum related to the electron-hole pair ground state has been found at 2.64 eV for sample 600°C/60 h and at 2.61 eV for the 700°C samples. Compared to the lowest bulk exciton energy (2.55 eV) and to the radii of the quantum dots, the high-energy shift experimentally observed is larger than expected from the confinement. This is a clear hint at the presence of additional potentials besides the con-

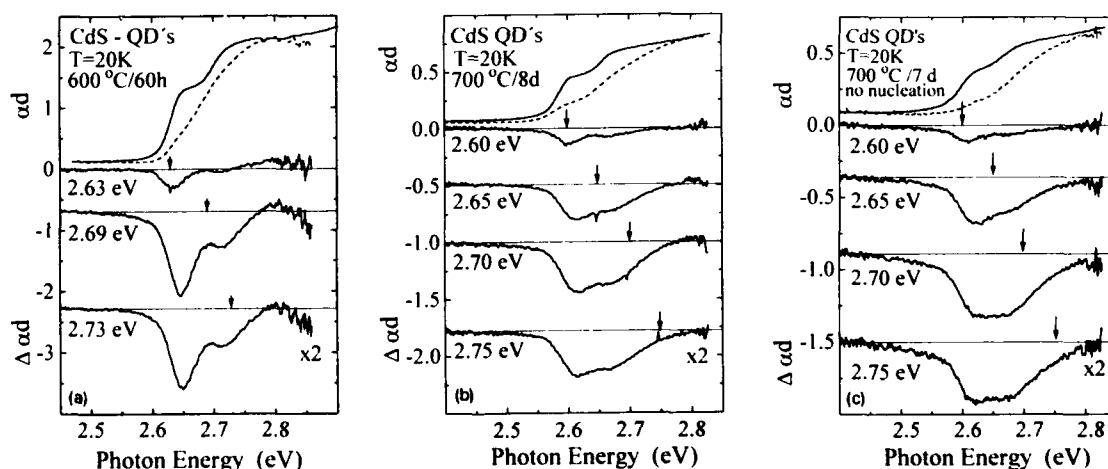


Fig. 1. Linear and differential absorption spectra of the CdS quantum dots measured at  $T = 20$  K and at excitation intensities normalized to excite approximately the same carrier density: (a) 600°C/60 h,  $I_{\text{exc}} = 200$  kW/cm<sup>2</sup>; (b) 700°C/8 d,  $I_{\text{exc}} = 2$  MW/cm<sup>2</sup>; (c) 700°C/7 d/no nucleation,  $I_{\text{exc}} = 2$  MW/cm<sup>2</sup>. The pump energy is indicated by arrows. The dashed line shows the bleached absorption spectrum for the pump energy being resonantly to the second peak at 2.7 eV, respectively.

fining barrier, e.g. strain or intrinsic polarizations, at the interface.

(ii) A second transition can be resolved in the  $\Delta\alpha$  spectra, in particular for sample 600°C/60 h. The energy position has been determined to be 2.71 eV for sample 600°C/60 h (difference with the first peak is 70 meV) and 2.675 eV for the other two samples (65 meV difference). The energy distance between the first and the second peak is very similar to the A–C valence band splitting of bulk CdS and shows a small tendency to increase with decreasing size. The two lowest peaks were therefore attributed to the electron–hole pair states with the lowest hole states arising from the upper and the spin–orbit split-off valence band.

(iii) The width of the bleaching spectrum is strongly dependent on the growth procedure. For discussing tendencies, an estimation of the homogeneous linewidth can be made assuming the dominance of a single Lorentzian resonance for each peak. The full width at half of the maximum (FWHM) is then for the first peak in the DAS of sample 600°C/60 h approximately 35 meV, and 54 meV and 58 meV for samples 700°C/8 days and 700°C/7 days, respectively. The differences in the linewidth of the bleaching spectra of Figs. 1a–1c were also preserved with decreasing pump intensity, so that power broadening gives always the same (small) contribution.

Apparently, the different growth processes introduced different interface configurations, thereby giving rise to a change in the scattering mechanisms. Because of the weak confinement range, the energy shift of the resonances is small compared to their homogeneous linewidth, and the homogeneous and inhomogeneous broadening are of the same order of magnitude. Changing the pump energy, the bleaching spectrum is spectrally constant and does not shift with the laser excitation.

(iv) For all samples the second peak has a larger line broadening than the first peak. This behaviour is typical for scattering processes from excited states to the ground state. Obviously, an effective relaxation to the ground state takes place, also demonstrated by the ratios of the intensities of the two peaks (sample 600°C/60 h).

Exciting with pump energies resonant to the high-energy peak, a distinct bleaching at lower energies has been observed. This is in contrast to the result obtained for very small CdSe QDs in the strong confinement [10], where the ratio of the intensities of the bleaching signal from the two lowest electron–hole pair transitions is opposite and relaxation seems to be suppressed.

(v) The absolute value of  $\Delta\alpha$  is significantly larger for sample 600°C/60 h. For the matrix composition considered, the diffusion controlled growth process near nucleation, carried out at low temperatures, resulted in approximately one order of magnitude smaller saturation intensities and higher nonlinear optical response compared to a high-temperature heat treatment.

(vi) Compared to the narrow linewidth in the DAS obtained for small CdSe QDs [11], the lowest limit for the optimum growth procedure of sample 600°C/60 h is still considerably large. Reasons could be the remaining power broadening, the excitation of more than one resonance or stronger strain-induced broadening.

If the linewidth is mainly determined by the polar electron–hole pair/phonon coupling, correspondence should be obtained between the results from the DAS and the coupling parameter derived from the Stokes shift of the luminescence with respect to the absorption of the corresponding electron–hole pair transition. One problem which gives difficulties in the determination of this Stokes shift arises from the contributions of red-shifted luminescence caused by trap states. The luminescence of the selected samples has been measured at different excitation conditions and is shown in Fig. 2. The dashed lines show the luminescence spectra of the 600°C/60 h and the 700°C/7 days samples excited with a mercury lamp in the UV region. At this low intensity a broad, low-energetically shifted luminescence can be seen accompanied for sample 700°C/7 days by a second band around 1.7 eV, which has not been found for sample 600°C/60 h. The solid lines show the luminescence under high excitation using a dye laser tuned resonantly to 2.7 eV. The luminescence spectra at different excitation intensities show saturable and nonsaturable parts which allow to attribute the recombination pro-

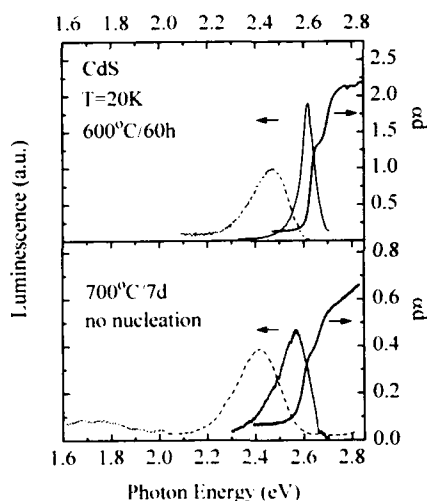


Fig. 2. Luminescence spectra measured at different excitation conditions: (—) excited with low intensity with the mercury lamp in the UV region, (---) excited with high intensity with the dye laser tuned to 2.7 eV. For comparison the linear absorption spectra are shown, too.

cesses to impurities and direct electron-hole pair recombination. In sample 600°C/60 h, the trap density is small and its luminescence saturates with increasing intensity. At higher excitation, the influence of the traps is suppressed and can only be seen in the low-energy tail of the luminescence band. The direct electron-hole pair recombination is characterized by a sharp luminescence band 20 meV below the absorption. On the other hand, in the samples grown at 700°C, the trap luminescence cannot be saturated and determines the linewidth of the luminescence peak further on. A similar situation has been found for small CdSe quantum dots [12].

Calculating for sample 600°C/60 h the Huang-Rhys parameter  $S$  from the luminescent Stokes shift  $\Delta_{\text{Stokes}} = 20$  meV and from the linewidth  $\Delta_{\text{FWHM}} = 35$  meV, we get  $S = 0.285$  and  $S = 0.25$ , respectively ( $\hbar\omega_{\text{LO}} = 35$  meV for CdS).

Finally, NDFWM as a further nonlinear optical method has been applied to measure the homogeneous line broadening (for experimental details, see ref. [13]). For the measurement of the

diffraction efficiency, two tunable dye lasers have been used. The beam of laser 1 was fixed in energy and the diffracted signal has been measured during the stepwise scanning of laser 2. From the dependence of the diffraction efficiency on the detuning the dephasing time – and by this the homogeneous linewidth – can be determined (see ref. [14]). Fig. 3 shows the result at low excitation intensity of 500 kW/cm<sup>2</sup>. In the present stage of application of NDFWM to quantum dots, the two-level model is the best-developed description of the quantum-confined states and therefore used for the fitting procedure of the experimental results. From this analysis, a dephasing time  $T_2 \sim 200$  fs has been determined which gives for the homogeneous linewidth  $\Gamma$  an approximately twice smaller value than obtained from DAS. This finding will be the subject of further investigation.

In conclusion, for the presented matrix composition, a low temperature growth process results in an effective nonlinear optical response with large signals in the differential absorption spectrum. For CdS QDs of average radius of 7.5 nm, the two lowest transitions have been resolved at 2.64 and 2.71 eV. The homogeneous broadening is strongly influenced by the interface properties and is considerably larger than that reported for bulk CdS or small CdSe QDs in the strong confinement range. Band-edge related luminescence has been observed and good agreement could be

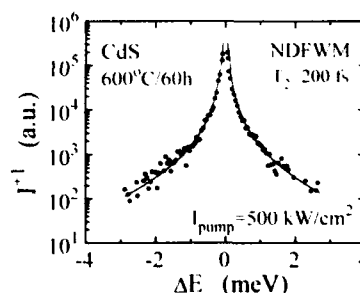


Fig. 3. Intensity of the first diffracted order of a nondegenerate four-wave-mixing experiment using two dye-lasers and obtained by tuning the frequency of one of the dye-lasers through the resonance, whereas the second is fixed to the resonance frequency.

achieved for the Huang-Rhys factor determined both from luminescent Stokes shift and from the linewidth.

The authors are grateful to A.L. Efros (München) and to B. Hönerlage (Strasbourg) for stimulating discussions, and to M. Müller (Jena) for the support in preparing the samples and providing the data about the sizes and the size distribution. This work has been supported by the "Deutsche Forschungsgemeinschaft", the "Materialforschungsschwerpunkt des Landes Rheinland-Pfalz" at the University Kaiserslautern.

# 1. References

- [1] A.P. Alivisatos, A.L. Harris, N.J. Levinos, M.L. Steigerwald and L.E. Brus, *J. Chem. Phys.* 89 (1988) 4001.
- [2] P. Roussignol, D. Ricard, C. Flytzanis and N. Neuroth, *Phys. Rev. Lett.* 62 (1989) 312.
- [3] V. Esch, K. Kang, B. Fluegel, Y.Z. Hu, G. Khitrova, L.C. Liu and L.C. Risbud, *J. Nonlin. Opt. Phys.* 1 (1992) 25.
- [4] S. Nomura and T. Kobayashi, *Phys. Rev. B* 45 (1992) 1305.
- [5] A.I. Ekimov, F. Hache, M.C. Schanne-Klein, D. Ricard, C. Flytzanis, I.A. Kudryavtsev, T.V. Yazeva, A.V. Rodina and A.L. Efros, *J. Opt. Soc. Am. B* 10 (1993) 106.
- [6] Ch. Spiegelberg, F. Henneberger and J. Puls, *Superlattices Microstruct.* 9 (1991) 487.
- [7] K.I. Kang, B.P. McGinnis, Sandalphon, Y.Z. Hu, S.W. Koch, N. Peyghambarian, A. Mysyrowicz, L.C. Liu and S.H. Risbud, *Phys. Rev. B* 45 (1992) 3465.
- [8] K. Misawa, H. Yao, T. Hayashi and T. Kobayashi, *J. Chem. Phys.* 94 (1991) 4131.
- [9] A. Uhrig, L. Banyai, Y.Z. Hu, S.W. Koch, C. Klingshirn and N. Neuroth, *Z. Physik B* 81 (1990) 385.
- [10] U. Woggon, S. Gaponenko, A. Uhrig, W. Langbein and C. Klingshirn, *Adv. Mater. Opt. Electron.*, in press.
- [11] U. Woggon, S. Gaponenko, W. Langbein, A. Uhrig and C. Klingshirn, *Phys. Rev. B* 47 (1993) 3684.
- [12] O. Wind, H. Kalt, U. Woggon and C. Klingshirn, *Adv. Mater. Opt. Electron.*, in press.
- [13] A. Uhrig, U. Woggon, M. Portuné, V. Sperling and C. Klingshirn, in: *Proc. NATO Workshop on Coherent Optical Interaction in Semiconductors*, Cambridge, UK, 1993, to be published.
- [14] T. Yajima and H. Souma, *Phys. Rev. A* 17 (1978) 309, 324.



ELSEVIER

Journal of Crystal Growth 138 (1994) 993–997

JOURNAL OF **CRYSTAL  
GROWTH**

## CdS quantum dots in colloids and polymer matrices: electronic structure and photochemical properties

V.S. Gurin \*, M.V. Artemyev

*Physico-Chemical Problems Research Institute, Belarussian State University, Minsk 220080, Belarus*

### Abstract

We have studied the optical properties and electronic structures of quantum-confined CdS particles (Q-particles, quantum dots) prepared as CdS colloids in different solvents, CdS particles embedded in polymer matrices and vacuum evaporated island films of CdS. Due to the quantum-confined effect, the optical spectra of these systems exhibit the explicit blue shift of fundamental interband absorption and the appearance of well-pronounced exciton peaks at room temperature. The electronic structure of CdS quantum dots was examined by X-ray photoelectron spectroscopy and semi-empirical quantum-chemical calculations were performed. Both XRS data and results of calculations reveal the clear difference in valence band density of states for CdS Q-particles with respect to bulk CdS. Semiconductor-like electronic structure, especially for d-band, appears for CdS clusters containing more than 100 atoms. We also compare the relative stability of CdS clusters of different structure. Additionally, we studied the photochemical properties of CdS Q-particles and observed the effect of spectral hole burning in the absorption spectra of CdS colloids in 2-propanol during UV laser irradiation. This phenomenon results probably from selective photo-oxidation of CdS Q-particles, whose exciton absorption bands are close to irradiation wavelength.

### 1. Introduction

Various systems, containing CdS Q-particles, like color optical glasses, colloids and polymer matrices with such particles, are now popular objects to study the optical properties of quantum confined semiconductor particles. A number of quantum size effects have been observed for CdS particles: size-dependent variation of absorption and luminescence spectra [1–6], transient induced absorption, hole burning and related non-linear effects [7–11]. Also, selective size-dependent photochemistry of semiconductor quantum

dots opens new possibilities in realization of various photochemical processes [12,13].

Interpretation of optical properties of direct-gap semiconductor Q-particles is based on description of excitonic states in the effective mass approximation (EMA) [1,14]. Such interpretation explains quantitatively the main experimental data. However, the electronic structure of quantum dots with diameter less than 10 nm cannot be represented as a simple extrapolation of bulk material band structure, especially for excited states [15–17]. Likewise, there are certain problems to determine experimentally the electronic structure of quantum dots because of their polydispersity in real systems. In this work we used some experimental methods like electron mi-

\* Corresponding author.



croscopy (EM), X-ray diffraction analysis (XRD), optical spectroscopy and X-ray photoelectron spectroscopy (XPS), and carried out quantum-chemical calculations to obtain more information about electronic structure of CdS Q-particles.

## 2. Properties of CdS Q-particles in different systems

We prepared CdS Q-particles as:

- (1) colloids in water, 2-propanol, acetonitrile;
- (2) particles in poly(vinyl alcohol) PVA films;
- (3) CdS thin island films on optical quartz.

Colloids of CdS Q-particles were prepared by chemical reaction in solution between  $\text{Cd}^{2+}$  and  $\text{H}_2\text{S}$  or  $\text{Na}_2\text{S}$  in the presence of PVA as a stabilizer.

The PVA films, containing CdS Q-particles, were prepared by evaporation of solvents at  $20^\circ\text{C}$  from the above-mentioned colloidal solutions at optical quartz support until solid PVA film with good optical quality was formed. CdS island films were obtained by thermal high-vacuum evaporation of CdS powder on optical quartz glass. The thickness of the CdS films was 3–10 nm.

Fig. 1 shows absorption spectra in the UV-visible region of PVA films with CdS quantum dots obtained both from water and from acetonitrile-based colloidal solutions and vacuum evaporated CdS film of 3 nm thickness. The existence of exciton absorption bands is observed at all these absorption spectra. We have found also a

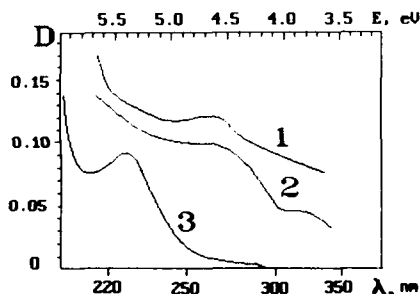


Fig. 1. Absorption spectra of CdS Q-particles in PVA films prepared from aqueous (1) and acetonitrile (2) colloids, and vacuum evaporated CdS films of 3 nm thickness (3).

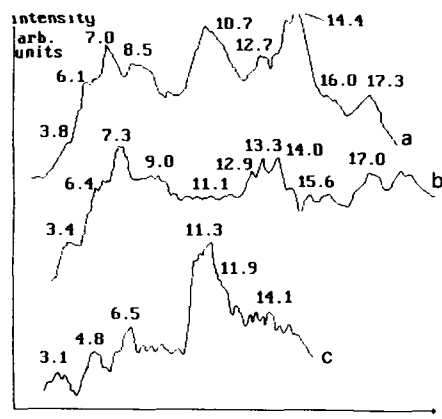


Fig. 2. XPS data for valence band of CdS Q-particles in PVA matrix prepared from aqueous (a) and acetonitrile (b) colloids, and in island evaporated film of 3 nm thickness (c).

variable high-energy shift of the exciton bands with respect to the absorption edge of bulk CdS (2.58 eV). This is clear evidence of the quantum-confined effect in CdS particles. Our results conform quantitatively with data of preceding studies [1–6,12,13].

According to XRD data, CdS Q-particles embedded in PVA films have sphalerite crystal lattice. The average particle diameter has been estimated to be about 2–3 nm, from the analysis of XRD line broadening. The mean diameter of CdS Q-particles in the vacuum evaporated film has been determined to be about 50 nm, from EM investigation. Thus, to explain the quantum-confinement effect in the absorption spectra of the CdS evaporated film in Fig. 1, the existence of 1D quantization in thin planar CdS islands should be proposed.

Optical spectroscopy gives information about energy levels of highest occupied molecular orbital (HOMO or top of valence band (VB)) and lowest unoccupied molecular orbital (LUMO) if the semiconductor quantum dots are considered to be molecular clusters. Other VB levels affect weakly the energy of optical transitions. Such levels can be very significant for other properties of semiconductor particles when electrons from the VB would be excited. We studied the VB structure by means of XPS (Fig. 2). There is an

explicit difference in XPS data for three different kinds of CdS Q-particles. The photoemission threshold is located at  $\sim 6$  eV for colloidal particles and at  $\sim 10$  eV for evaporated films (in the last case there is also some peak in the 4.5–6 eV region), while the photoemission peaks for bulk CdS lie at about 2 and 11 eV [20]. It should be noticed that we obtained a more dramatic size-dependent shift of photoemission spectrum than in ref. [21] for 6.8 nm CdS particles. Within the EMA approach, this shift can be conditioned by quantum-confinement of electrons in quantum dots. According to molecular orbital approach, the downward shift can be explained as bond formation from lower s-orbitals of Cd and p-orbitals of S (see the following section).

### 3. Quantum-chemical calculations of electronic structure of CdS clusters

The quantum-chemical approach principally allows one to determine the various properties of molecules and clusters. Quantum dots can be considered as large clusters with definite structures, and computational troubles are simplified when semi-empirical methods are used [22,23]. In the present work we consider the theoretical model of particles that have the same sizes as in the experiment. We used the extended Hückel method in the Wolfsberg–Helmholz parametrization with charge self-consistence [23] (constant  $K$  was fitted according to thermodynamic data).

We calculated a number of model clusters (Table 1) of different size, being the fragments of sphalerite and wurtzite lattices (point groups  $T_d$

Table 1

Relative stability of different clusters  $(\text{CdS})_n$  estimated from total electron energies <sup>a</sup>; the Cd–S distance is assumed to be equal to 0.229 nm (as in the bulk sphalerite lattice)

Cluster	Symmetry group	$E_{\text{total}}/n$ (eV)
$\text{Cd}_6\text{S}_8^{4-} + \text{Cd}_8\text{S}_6^{4+}$	$O_h$	272.04
$\text{Cd}_6\text{S}_9^{6-} + \text{Cd}_8\text{S}_9^{6+}$	$O_h$	271.69
$\text{Cd}_8\text{S}_8$	$D_{4h}$	273.76
$\text{Cd}_4\text{S}_6^{4-} + \text{Cd}_6\text{S}_4^{4+}$	$T_d$	272.43
$\text{Cd}_4\text{S}_{10}^{12-} + \text{Cd}_{10}\text{S}_4^{12+}$	$T_d$	270.05
$\text{Cd}_{12}\text{S}_{14}^{4-} + \text{Cd}_{14}\text{S}_{12}^{4+}$	$O_h$	270.56
$\text{Cd}_{14}\text{S}_{16}^{4-} + \text{Cd}_{16}\text{S}_{14}^{4+}$	$T_d$	272.55
$\text{Cd}_{54}\text{S}_{63}$	$O_h$	269.50
$\text{Cd}_{54}\text{S}_{18}^{18-} + \text{Cd}_{63}\text{S}_{54}^{18+}$	$O_h$	268.44
$\text{Cd}_{17}\text{S}_{10}^{14-} + \text{Cd}_{10}\text{S}_{17}^{14+}$	$C_{3v}$	271.82

<sup>a</sup> In the case of a different number of Cd and S atoms in clusters, for adequate comparison of  $E_{\text{total}}$  we take the unbounded pairs of clusters with the same structure  $\text{Cd}_x\text{S}_y + \text{Cd}_y\text{S}_x$ .

and  $C_{3v}$ , respectively) and other symmetrical configurations ( $D_{4h}$ ,  $O_h$ ). Most of the structures we took into consideration were stable clusters with binding energies per Cd–S bond of more than 1 eV. The general result of our calculations is the appearance of bulk-like band structure already in 10–20 atomic clusters (Fig. 3). For the d-band, this tendency is most explicit. Near-located energy levels are merged into a quasicontinuum, and the energy gap ( $\Delta$ ) between HOMO and LUMO (which is shown by the arrow in the schemes) contracts with increasing cluster size. The schemes of energy levels in Fig. 3a reflect clear variations of electronic structures of CdS clusters with different number of atoms.

The data which we obtained can be used to predict the optical properties of the clusters and

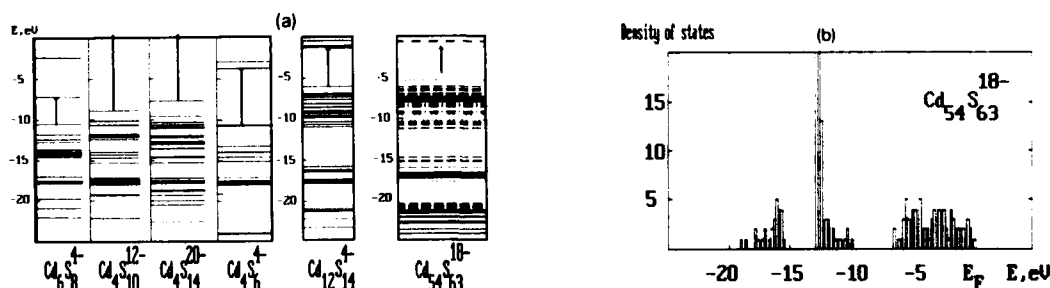


Fig. 3. (a) Schemes of energy levels for various  $\text{Cd}_x\text{S}_y$  clusters obtained from quantum-chemical calculations. (b) Calculated density of states for  $\text{Cd}_{54}\text{S}_{63}^{18-}$  cluster.

correlate with known values of optical transitions energies of  $(\text{CdS})_x$  clusters [2–4,12]. For example, the near-edge maximum in the absorption spectrum is specific for many semiconductor clusters (it is interpreted as an excitonic-like transition in EMA) and corresponds to HOMO–LUMO transition. For  $\text{Cd}_{54}\text{S}_{63}^{18-}$ ,  $\Delta = 3.15$  eV, and for  $\text{Cd}_{12}\text{S}_{14}^{4-}$ ,  $\Delta = 4.75$  eV, which is in agreement with the observed location of the  $(\text{CdS})_x$  absorption band.

We compared the calculated values of  $\Delta$  for CdS clusters of different structure and the energy of excitonic resonances in absorption spectra of various CdS Q-particles (Fig. 1). For selected clusters of  $O_h$  symmetry, exactly  $\text{Cd}_{54}\text{S}_{63}^{18-}$ ,  $\text{Cd}_{63}\text{S}_{54}^{18+}$  and  $\text{Cd}_{54}\text{S}_{54}$ , the  $\Delta$  value of  $\text{Cd}_{54}\text{S}_{63}^{18-}$  corresponds well to the energy of the excitonic resonances in Fig. 1. Hence, CdS Q-particles are probably the clusters of such a structure where excess sulphur comes from solution during the synthesis and stabilizes the cluster. The XPS spectroscopy data on the VB energy of  $(\text{CdS})_x$  1–2 nm particles immobilized in polymer film coincide qualitatively with the calculated data for a  $\text{Cd}_{54}\text{S}_{63}^{18-}$  cluster (this cluster is a cube with sides of 0.916 nm). Fig. 3b shows the formation of three bands of states in the energy spectrum of this cluster. The position of the bands is in agreement with the energy of the experimental peaks. This is the evidence of general adequacy of the calculation, especially if the non-monodispersity of CdS Q-particles in experimental samples is taken into account.

It should be noticed that according to calculations all of the above CdS clusters have a variety of geometrical configurations or isomeric structures with approximately the same diameter and energy, and each isomer could give specific peaks in the absorption spectra.

#### 4. Photochemical properties of CdS quantum dots

Photochemistry of CdS, PbS and other semiconductor Q-particles was studied frequently [26–28]. Optical excitation of CdS colloids in different solvents results in photo-oxidation of the CdS phase up to the number of soluble  $(\text{SO}_4^{2-})$

and insoluble (S) products [26]. Thus, CdS particles undergo photostimulated etching and degradation, and we observe a uniform decay of CdS fundamental absorption. However, in the case of real CdS Q-particles obtained in experiment, the absorption spectra of the Q-particles consist of superposition of excitonic resonances of all particles, which shift to the high-energy region when the particle diameter decreases. Irradiation of Q-particles with certain size distribution by monochromatic laser light results in photo-oxidation of particles whose excitonic resonances are close to the irradiation wavelength. Selective photochemical degradation of such particles gives rise to hole burning in the absorption spectra at the irradiation wavelength.

We observed the hole burning in absorption spectra of CdS Q-particles in 2-propanol during UV-irradiation by pulsed  $\text{N}_2$  laser ( $\lambda = 337.1$  nm, pulse energy was 3  $\mu\text{J}$  of 9 ns duration, and repetition frequency was 100 Hz). Colloids with CdS Q-particles were prepared by mixing of  $2 \times 10^{-4}$  M cadmium acetate and  $\text{Na}_2\text{S}$  both in 2-propanol containing 0.1% polyvinylpyrrolidone

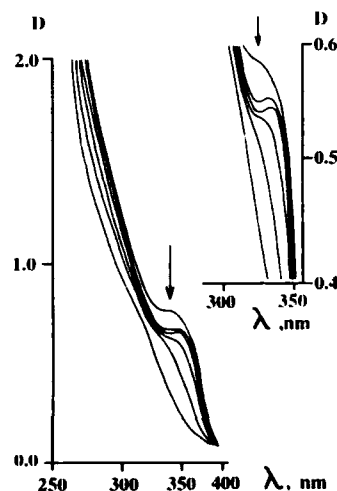


Fig. 4. Optical density  $D$  versus wavelength  $\lambda$  of CdS Q-particles in 2-propanol before (upper curve) and after (lower curves)  $\text{N}_2$ -laser irradiation of various duration. Irradiation time increases from upper to lower curves with 30 min steps. Excitation wavelength is indicated by arrow. Insert: part of spectra around irradiation wavelength with higher resolution.

— PVPR (MW 20,000) as a stabilizer. The mean diameter of the CdS particles has been estimated to be about 2 nm from the position of the exciton absorption band at the energy scale.

Fig. 4 shows the absorption spectra of CdS Q-particles in 2-propanol before and after laser irradiation. After the first 60 min of laser illumination, a well-pronounced dip appears at the irradiation wavelength, and further prolonged illumination transforms the hole burning effect into complete disappearance of the exciton band. This hole burning process is irreversible.

Because the absorption spectra of CdS Q-particles consist of a series of bands related to various excitonic transitions  $E_{1s,1s}$ ,  $E_{1p,1p}$ , etc. [29], selective degradation of Q-particles could give a number of holes in the absorption spectra at the corresponding transitions location. Indeed, we can see an additional strongly broadened dip around  $\lambda = 270$  nm (Fig. 4). The dip at  $\lambda = 337$  nm corresponds to the  $E_{1s,1s}$  transition, and the high energy dip can be associated with the  $E_{1p,1p}$  transition.

### 5. Acknowledgements

The authors thank Professor V.V. Sviridov for reading the manuscript and for helpful suggestions, E.A. Tiavlovskaya for assistance in the XPS study and N.B. Barkovsky for supply of the quantum-chemical calculation program. The work is performed under support of the Fundamental Research Foundation of Belarus.

### 6. References

- [1] L.E. Brus, *J. Chem. Phys.* 80 (1985) 4403.
- [2] R. Rossatti, R. Hull, J.M. Gibson and L.E. Brus, *J. Chem. Phys.* 82 (1985) 552.
- [3] Y. Wang, *Acc. Chem. Res.* 24 (1991) 133.
- [4] Y. Wang and N. Herron, *J. Phys. Chem.* 95 (1991) 525.
- [5] M.L. Steigerwald and L.E. Brus, *Ann. Rev. Mater. Sci.* 19 (1989) 471.
- [6] A. Eychmüller, A. Hässelbarth, L. Katsikas and H. Weller, *Ber. Bunsenges. Physik. Chem.* 95 (1991) 79.
- [7] F. Hennenberger, U. Woggon, J. Puls and Ch. Spiekerberg, *Appl. Phys. B* 46 (1988) 19.
- [8] L. Brus, *Appl. Phys. A* 53 (1991) 465.
- [9] E.F. Hilinski, P.A. Lucas and Y. Wang, *J. Chem. Phys.* 89 (1988) 3435.
- [10] Y. Wang, A. Suna and J. McHugh, *J. Chem. Phys.* 92 (1990) 6927.
- [11] C. Klingshirn, *Semicond. Sci. Technol.* 5 (1990) 957.
- [12] A. Henglein, *J. Chim. Physique* 84 (1987) 1043.
- [13] R.D. Stramel, T. Nakamura and J.H. Thomas, *J. Chem. Soc. Faraday Trans.* 84 (1988) 1287.
- [14] A.L. Efros and A.L. Efros, *Fiz. Tekh. Poluprovodn.* 16 (1982) 1209.
- [15] M.V. Rama Krishna and R.A. Friesner, *J. Chem. Phys.* 95 (1991) 8309.
- [16] P.E. Lippens and M. Lannoo, *Phys. Rev. B* 39 (1989) 10935.
- [17] L.E. Brus, *J. Chim.* 11 (1987) 123.
- [18] M. Möller, *Synth. Metals* 41/43 (1991) 1159.
- [19] I.A. Akimov, I.Y. Denisiyuk and A.M. Meshkov, *Opt. Spectrosc.* 72 (1992) 1026.
- [20] L. Ley, R.A. Pollak, R.R. McFeely et al., *Phys. Rev. B* 9 (1974) 600.
- [21] J.G. Tobin, V.L. Colvin and M.P. Alivisatos, *J. Vac. Sci. Technol. A* 9 (1991) 852.
- [22] R.C. Baetzold, *Advan. Catal.* 25 (1976) 1.
- [23] A.B. Kovrikov, N.B. Barkovsky, A.M. Ludchik et al., *Spatial Symmetry and Optimization of Molecular Spectra Calculations* (BGU, Minsk, 1983) (in Russian).
- [24] Y. Nosaka, K. Yamaguchi, H. Miyama and H. Hayashi, *Chem. Lett.* 4 (1988) 605.
- [25] N. Herron, Y. Wang and H. Eckert, *J. Am. Chem. Soc.* 112 (1990) 1326.
- [26] A. Henglein, A. Fojtic and H. Weller, *Ber. Bunsenges. Physik. Chem.* 91 (1987) 441.
- [27] M.T. Nenadović, M.I. Comor, V. Vasić and O.I. Mičić, *J. Phys. Chem.* 94 (1990) 6390.
- [28] S. Gallardo, M. Gutierrez, A. Henglein and A. Janata, *Ber. Bunsenges. Physik. Chem.* 93 (1989) 1080.
- [29] N. Peyghambarian, B. Fluegel, D. Hulin et al., *IEEE J. Quantum Electron.* QE-25 (1989) 2516.



ELSEVIER

Journal of Crystal Growth 138 (1994) 998–1003

JOURNAL OF **CRYSTAL  
GROWTH**

## Absorption properties of CdS nanocrystals in glasses; evidence of both weak and strong confinement regimes

J. Allègre <sup>a</sup>, G. Arnaud <sup>a</sup>, H. Mathieu <sup>a</sup>, P. Lefebvre <sup>\*,a</sup>, W. Granier <sup>b</sup>, L. Boudes <sup>b</sup>

<sup>a</sup> *Groupe d'Etudes des Semiconducteurs, CNRS, Université Montpellier II, cc 074, F-34095 Montpellier Cedex 5, France*

<sup>b</sup> *Laboratoire de Physico-chimie des Matériaux Solides, CNRS, Université Montpellier II, cc 003, F-34095 Montpellier Cedex 5, France*

### Abstract

Experimental evidence of both weak and strong confinement regimes is reported on CdS nanocrystals embedded in glass matrix. Classic methods for nanocrystallite preparation meet a principal difficulty, the polydispersion in size of crystallites due to several difficulties such as coalescence and decomposition of particles with time and high temperatures. In this work, we used a new route to elaborate CdS-doped sodium borosilicate glass from gel formed in an aqueous medium. Our vitreous matrix is fully and swiftly densified at relatively low temperature, providing us with CdS nanocrystallites yielding fine band-edge structure and small size dispersion. Low temperature absorption spectra have been interpreted in terms of excitons and electron–hole confinements, taking account of both a Lorentzian broadening of the energy states inside each nanocrystal and a Gaussian size-distribution. It has been shown that, for very small crystallites, the strong blue-shift of the absorption edge due to the quantum size effects, is partially compensated by a red-shift associated to the size distribution.

### 1. Introduction

Non-linear optical phenomena are at the origin of ultra-fast optical functions such as optical switching and bistability, or highly non-linear waveguides, etc. Generally, semiconductors are favourable media for observing non-linearities, particularly when structured into quantum-well layers or quantum wires, where quantum-confinement effects enhance those properties [1]. Even further in the field of low-dimensional systems, semiconductor nanocrystallites constitute interesting quantum dots or boxes in which a pre-

sumed stronger confinement operates along the three dimensions of space when the crystal size is of the order of the exciton Bohr radius. Of course, the use of such crystallites for improving semiconductor lasers or the performance of absorbing or emitting devices at a precise wavelength implies a perfect control of the size of the grown quantum boxes.

Classical methods for nanocrystallite preparation (colloidal suspensions, insertion in porous zeolites, inclusion in glass prepared by conventional melting processes, etc.) usually meet the main difficulty, i.e. the dispersion in size of the crystallites. This dispersion originates from several mechanisms such as coalescence and decomposition of particles with time and high temperatures.

\* Corresponding author.

Recently, a sol-gel process was applied to synthesize nano-particles in a glass of porous silica, at low temperature, with quite a sharp size distribution [2]. However, in this case, obtaining well-stabilized nanocrystals seems to necessitate a full and fast densification of the gel into glass at low temperature [3,4].

In this paper, we describe a new route to elaborate  $\text{Na}_2\text{O} \cdot \text{B}_2\text{O}_3 \cdot \text{SiO}_2$  glass doped with CdS semiconductor crystallites, from a gel formed in aqueous medium. Our vitreous matrix is fully and swiftly densified at relatively low temperature. A quantitative analysis of optical absorption spectra is proposed.

## 2. Preparation of sodium borosilicate glass doped by CdS nanocrystallites

The sodium borosilicate gel is synthesized in aqueous solution by mixing sodium metasilicate  $\text{Na}_2\text{SiO}_3$  and boric acid  $\text{H}_3\text{BO}_3$ , in molar ratio 1:2. This solution is stirred and heated at 60–80°C. After a few minutes, a slight blur appears and a stiff gel is formed in 30 min.

The gel is dried at 100°C during 12 h. The major part of the solvation water is thus evaporated, and a monolithic and transparent gel is obtained. Polycondensation water due to a combination of hydroxyl groups is eliminated between 100 and 400°C. The gel then loses 18% in weight and its density becomes very low ( $1.5 \text{ g/cm}^3$ ). At this stage, the texture of the material is that of a juxtaposition of opened pores of more than  $100 \mu\text{m}$  in diameter. When heated between 400 and 600°C, this texture collapses: the pores close and fuse together to become a fritted and smooth material. The fusion arises at 732°C. Quenching the liquid at room temperature gives a transparent glass of composition  $\text{Na}_2\text{O} \cdot \text{B}_2\text{O}_3 \cdot \text{SiO}_2$ .

The chosen cadmium precursor ( $3\text{CdSO}_4 \cdot 8\text{H}_2\text{O}$ ) is first dissolved in distilled water. Then  $\text{H}_3\text{BO}_3$  is added and the result is stirred so as to obtain a clear solution. Then  $\text{Na}_2\text{SiO}_3 \cdot \text{H}_2\text{O}$  is introduced to initiate the gelation.

The evolution of the texture between 400°C and the fission point prevents the oxidation of cadmium sulphide and permits two sulfuration methods, which are sketched in Fig. 1. The first one consists in the sulfuration of  $\text{Cd}^{2+}$  by expo-

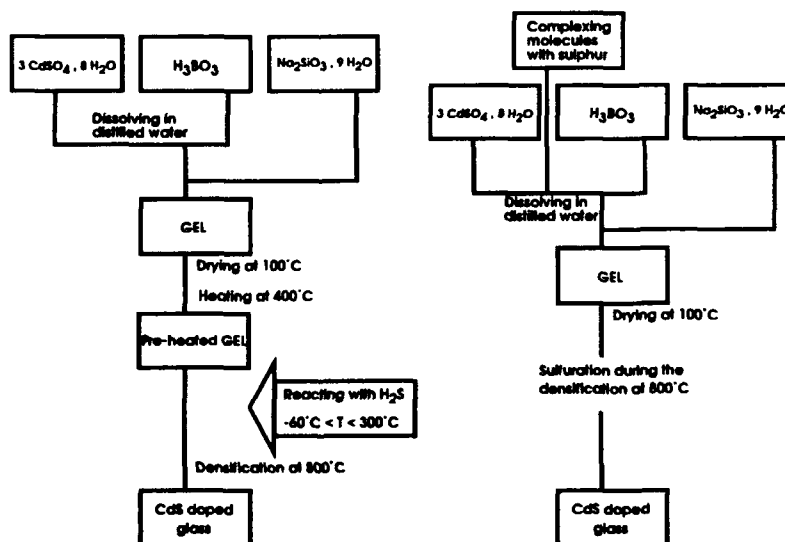


Fig. 1. Illustration of two different synthesis processes of sodium borosilicate glasses doped with CdS crystallites.

sure of the pre-heated gel to  $\text{H}_2\text{S}$  gas. In this case, the sulfuration can be performed at different temperatures, and especially at the liquefaction temperature of  $\text{H}_2\text{S}$  ( $-61^\circ\text{C}$ ). The second method consists in an in-situ sulfuration of  $\text{Cd}^{2+}$  by using the complexing power of some organic and inorganic molecules containing sulphur with a free electron doublet and oxidation step lower than 6 (for instance 5 sulfosalicylic acid of ammonium thiocyanate). The complexing molecules are dissolved in the starting cadmium solution. The sulfuration of  $\text{Cd}^{2+}$  then takes place during the gel degradation, at temperatures varying between 300 and  $500^\circ\text{C}$ , depending on the chosen complexing molecules.

### 3. Spectroscopic data

Fig. 2 displays four typical optical density spectra for samples containing nanocrystallites with various average diameters. From the top to the bottom of the figure, the spectra evolve from a shape quite similar to that for bulk CdS to a much smoother one, shifted towards high energies. This evolution is evidence of an increasing degree of quantum confinement. Such results can be compared to model calculations, so as to extract quantitative data about the crystallite sizes.

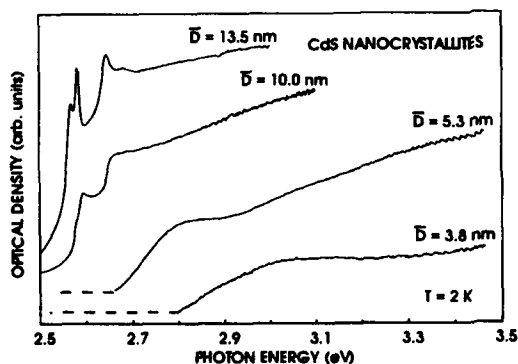


Fig. 2. Typical absorption spectra of glasses doped with CdS crystallites of various average sizes. The shift to higher energies of the absorption onset reveals the quantum confinement of carriers. Assuming a Gaussian distribution of crystal diameters, the typical width  $\sigma$  never exceeds 1 nm.

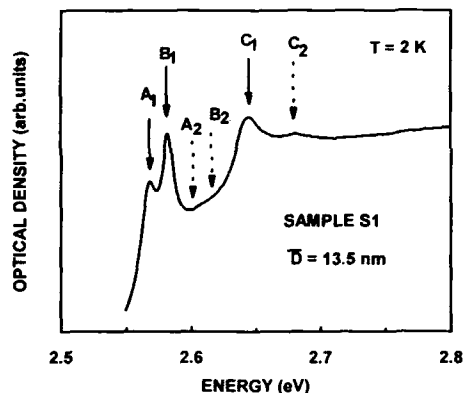


Fig. 3. Absorption spectrum of sample S1. Arrows indicate the energies of the main excitonic peaks. Solid lines indicate ground states and dashed lines indicate first excited states, calculated for this sample.

The simplest model used to calculate the quantum confinement in nanocrystallites consists in regarding the crystallites as spherical particles with an infinitely high potential wall surrounding the sphere. Theoretical investigations have been done, using the standard effective mass approximation by Efros and Efros [5], Brus [6] and Kayanuma [7] and in the tight-binding framework by Lippens and Lannoo [8].

The absorption spectrum of sample S1, containing rather large crystals, is displayed in Fig. 3. Clearly we observe three main absorption lines labelled A1, B1 and C1 which correspond to the excitons associated with the three valence subbands in the hexagonal CdS crystal. As a result of the quantum confinement, these peaks are shifted to higher energy by an amount of about 14 meV. In this sample, corresponding to the weak confinement regime, only the centre-of-mass motion of the exciton is quantized and the blue-shifts of the exciton levels are governed by the total mass of the exciton. The transition energies are given by [5]:

$$E_n^j = E_g^j - E_{ex} + n^2 \frac{2\hbar^2 \pi^2}{MD^2}, \quad (1)$$

where  $E_g^j$  is the energy of the band-to-band transition ( $j = A, B, C$ ),  $E_{ex}$  is the binding energy of the bulk exciton,  $M = m_e + m_h$  is the total mass

of the exciton,  $D$  is the crystallite diameter and  $n$  the quantum number of both the electron and the hole subband. By using Eq. (1), we have calculated the energies of the first quantum-confined states, taking the following material parameters for CdS: excitonic energy gaps  $E_{\text{gx}}^j = E_g^j - E_{\text{ex}} = 2553, 2568$  and  $2632$  meV [9] for  $j = \text{A, B and C}$ , respectively; exciton binding energy  $E_{\text{ex}} = 29$  meV [10]; electron effective mass  $m_e = 0.2m_0$  [9]; hole effective mass  $m_h = 0.5m_0$  [8]. The full and dashed arrows in Fig. 3 correspond to the ground ( $n = 1$ ) and first excited ( $n = 2$ ) states, respectively, for crystallites with an average diameter  $\bar{D} = 135$  Å.

In this range of crystallite size, the energy shift associated to a size variation is typically  $\Delta E \approx 3$  meV for  $\Delta D = 10$  Å for the ground state energy. Consequently, the peak broadening resulting from the size distribution is very small and the halfwidth at half maximum for the main structures almost corresponds to the only intrinsic broadening  $\Gamma$  specific of the chemical and crystallographic qualities of the crystallites. We get  $\Gamma \approx 8$  meV which we shall keep for all samples. Indeed, the best-fitting calculations described below have shown that the intrinsic broadening parameter should not be much larger than this value. In particular, a larger  $\Gamma$  value forbids describing correctly some details such as peaks and dips in the absorption spectrum (see Fig. 4).

Now let us consider the absorption spectra for samples containing rather small crystallites. In that case, for infinitely high potential walls, and in the absence of Coulomb interaction, the corresponding Schrödinger equation may be analytically solved and the kinetic energy eigenvalues of the electron–hole pair written as [7]:

$$E_c = \frac{2\hbar^2}{m_e} \left( \frac{\alpha_{n_e l_e}}{D} \right)^2 + \frac{2\hbar^2}{m_h} \left( \frac{\alpha_{n_h l_h}}{D} \right)^2, \quad (2)$$

where  $\alpha_{nl}$  is the  $n$ th root of the  $l$ th order spherical Bessel function. It is usual to refer to the  $(n, l)$  eigenstates as 1S, 1P, ..., 2S, etc. When the Coulomb interaction is included, the problem can no longer be solved analytically and one has to use numerical or approximate methods. Brus [6]

has calculated the excitonic energy in a first order perturbation model, as the mean value of the Coulomb interaction over the sphere. For the first excited states this gives  $E_{\text{ex}} \approx 3.6 e^2/\epsilon D$  where  $\epsilon = 5.7\epsilon_0$  [6] is the dielectric constant of CdS. On account of the selection rules,  $\Delta n = 0$  and  $\Delta l = 0$ , the energies of the dipole-allowed transitions may be written as:

$$E_{nl}^j = E_g^j + \frac{2\hbar^2 \alpha_{nl}^2}{\mu D^2} - \frac{3.6e^2}{\epsilon D}, \quad (3)$$

where  $\mu = (1/m_e + 1/m_h)^{-1}$  is the reduced effective mass of the electron–hole pair.

Let us now consider the process of interband absorption of light. We have to take account of the orbital degeneracy of each energy level and of the broadening due to the finite lifetime of excitons. The latter is a homogeneous broadening associated with crystalline and chemical defects characteristic of a given crystallite. This may be described by using a Lorentzian broadening function  $\Gamma \pi^{-1}(E^2 + \Gamma^2)^{-1}$ , where  $\Gamma$  is the halfwidth at half maximum of the Lorentzian. The associated lifetime is  $\hbar/2\Gamma$ . Then, the absorption coefficient for a crystallite of diameter  $D$  can be expressed as [5]:

$$\bar{\alpha}_D(\hbar\omega) = \frac{A}{\pi\sqrt{2\pi}} \times \sum_{j,n,l} (2l+1) \frac{\Gamma}{(\hbar\omega - E_{nl}^j)^2 + \Gamma^2}, \quad (4)$$

where  $A$  is a constant proportional to the square of the matrix element of the dipole moment between Bloch functions. At low temperature, the absorption spectrum of a single crystallite consists in a series of Lorentzian peaks centred around electron–hole pair energies  $E_{nl}^j$ .

Now, the experimental exciton peaks are broadened by the statistical distribution of sizes: crystallites with different diameters yield absorption structures at the different energies corresponding to their excitonic transitions. The size dispersion gives rise to a series of broad maxima of the absorption coefficient with the profiles and



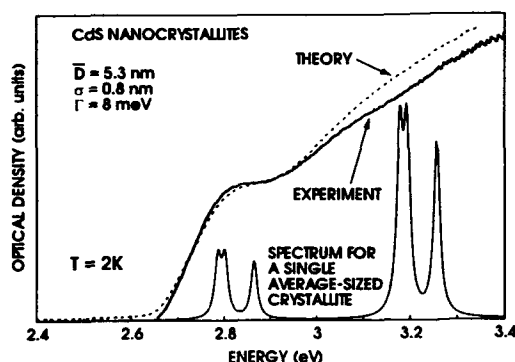


Fig. 4. Comparison between the measured and calculated absorption spectra for sample S3. The parameters for the best fitting are indicated. At the bottom of the figure lies the calculated spectrum of a crystallite having exactly the average diameter  $\bar{D}$ . Note the role played by the first excited states, whose larger degeneracy allows a larger contribution to the absorption.

positions given by the size distribution function,  $P(D)$ . The resulting absorption coefficient is:

$$\bar{\alpha}(\hbar\omega) = \frac{1}{\bar{D}^3} \int_0^{+\infty} D^3 \bar{\alpha}_D(\hbar\omega) P(D) dD. \quad (5)$$

In the following, we postulate that the size dispersion is normally distributed with a central value  $\bar{D}$  and variance  $\sigma^2$ . In other words, the size distribution function is assumed to be a Gaussian function given by:

$$P(D) = \frac{1}{\sigma\sqrt{2\pi}} e^{-(D-\bar{D})^2/2\sigma^2}. \quad (6)$$

Consequently, for small crystal sizes, the absorption coefficient depends on the average diameter  $\bar{D}$ , on the width  $\sigma$  of the size distribution, and on the quality of the material through the  $\Gamma$  parameter. Now should be noted that a quantitative fit to experimental data is very difficult and somewhat unrealistic because one needs to introduce several arbitrary parameters to describe both the real thickness of the active medium and the scattering of light by a crowd of differently sized crystallites embedded in the dielectric matrix. As a result, we shall merely compare the shapes of the experimental and calculated absorbance spectra.

Fig. 4 shows a comparison between the experimental (full lines) and calculated (dashed lines) absorbances for sample S3. The dotted lines show the calculated absorption coefficient of the individual crystallites (Eq. (4)) with exactly the diameter  $\bar{D}$ . The best agreement between experiments and calculations is obtained with  $\bar{D} = 53 \text{ \AA}$ : the positions of the absorption onset, of the first peak and the shape of the spectrum at higher energy, are indeed reproduced with this value within an accuracy of  $\sim \pm 4 \text{ \AA}$ . For smaller crystallites, the quality of the fitting is the same and the accuracy is comparable. As a result of the size dispersion, the macroscopic spectrum (dashed lines) clearly exhibits a broadening and a red-shift with regard to the individual absorption structures (dotted lines). Indeed, the macroscopic absorption is dominated by the contributions of the larger particles within the distribution since the optical density is scaled by the particle volume. We remark that the red-shift of the absorption onset may be as large as  $\sim 100 \text{ meV}$ , while  $\sigma$  hardly exceeds the lattice parameter of the crystal. This is due to the large sensitivity of the energy to the diameter, in this range of crystal sizes.

#### 4. Conclusion

Quantum size effects have been observed on the fundamental optical band-gap of CdS nanocrystallites embedded in sodium borosilicate glasses. Two confinement regimes can be distinguished. First, a weak blue-shift of the gap is obtained for rather large crystallites, and the motion of the centre-of-mass of the exciton can be considered as quantized as a whole. Second, a strong blue-shift of the absorption onset is measured when the average crystal diameter is small. Then the Coulomb interaction between the electron and the hole is enhanced, and another model is applied for calculating the blue-shift of the gap. For small crystal sizes, we have modelled the absorption spectrum, taking account of the size dispersion of the crystallites. A best fit to experimental data allows one to conclude in favour of a good and constant quality of crystals  $\Gamma = 8 \text{ meV}$  and of rather a sharp size dispersion ( $\sigma = 8 \text{ \AA}$ ).

These results testify to the efficiency of our growth technique, which is full of promise.

## 5. References

- [1] E. Rosencher, P. Bois, J. Nagle and S. Delaitre, *Electron. Lett.* 25 (1989) 1063.
- [2] M. Nogami, S. Suzuki and K. Nagasaka, *J. Am. Ceram. Soc.* 75 (1992) 220, and references therein.
- [3] N. Nogami and K. Nagasaka, *J. Non-Crystalline Solids* 147 (1992) 231.
- [4] T. Takada, T. Yano, A. Yasumori, M. Yamane and J.D. Mackenzie, *J. Non-Crystalline Solids* 147 (1992) 631.
- [5] A.I. Efros and A.L. Efros, *Soviet Phys. Semicond.* 16 (1982) 772.
- [6] L.E. Brus, *J. Chem. Phys.* 80 (1984) 4403.
- [7] Y. Kayanuma, *Solid State Commun.* 59 (1986) 405.
- [8] P.E. Lippens and M. Lannoo, *Phys. Rev. B* 39 (1989) 10935.
- [9] J.J. Hopfield and D.G. Thomas, *Phys. Rev.* 122 (1961) 35; D.G. Thomas and J.J. Hopfield, *Phys. Rev.* 116 (1959) 573.
- [10] R. Zimmermann and M. Hartmann, *J. Crystal Growth* 101 (1990) 341.



ELSEVIER

Journal of Crystal Growth 138 (1994) 1004–1009

JOURNAL OF **CRYSTAL  
GROWTH**

## Carrier dynamics in CdSe quantum dots embedded in glass

J. Puls, V. Jungnickel \*, F. Henneberger, A. Schülzgen

*Fachbereich Physik, Humboldt-Universität zu Berlin, D-10099 Berlin, Germany*

### Abstract

The relaxation and recombination of carriers excited by ultrashort optical pulses are studied on specially prepared II–VI quantum dots in a silicate-type host. Photoluminescence with ps resolution allows to observe the emission from the confined, intrinsic energy levels of the dots under non- and size-selective excitation, respectively. A comparison with data of transient non-linear absorption reveals that the relaxation pathway of electron and holes may be substantially different and depends strongly on the dot size.

### 1. Introduction

In a quantum dot the translational symmetry of the former bulk material is completely removed by confining the carriers in all three dimensions. As a result, a ladder of discrete energy levels is formed. The related change of the optical properties is the subject of various predictions that quantum dots might be very useful in device applications. Some of those ideas were recently summarized by Brus [1]. The present study is aimed to the carrier dynamics in very small ( $< 3$  nm) wide-gap II–IV quantum dots embedded in a glass matrix. These dynamics are of fundamental physical interest, but also of practical importance as it controls the switching transients of possible devices.

### 2. Samples

The CdSe quantum dots used in the present study are grown in a boro-silicate glass by the conventional heat treatment method. Generally, the growth process establishes a size distribution. Small-angle X-ray data yield a Gaussian-like shape with a typical standard deviation of 20% to 30%. Here we concentrate on samples of a mean particle radius  $\langle R \rangle$  which is clearly smaller than the bulk exciton radius (5 nm). Thus, Coulomb effects are of less importance and the confined single-particle energies are dominant in the total electron–hole pair energy (strong confinement regime). The absorption spectra of the samples exhibit an isolated ground-state feature followed by less pronounced structures on the high-energy side. The quantum size effect is clearly evidenced from the high-energy shift of the ground state with decreasing average dot radius. For the 1.4 nm sample this shift is – measured relative to the bulk energy gap of CdSe – as large as 1 eV (cf.

\* Corresponding author.

Fig. 3). The total broadening of the transitions is formed from homogeneous and inhomogeneous contributions to an approximately equal extent, as seen from quasi-stationary hole-burning data [2]. A quantitative estimate of the data obtained from a sample with  $\langle R \rangle = 2.0$  nm yields a FWHM figure of 60 to 80 meV for the homogeneous width of the e–h pair ground state at room temperature and a decrease down to about 25 meV at 1.8 K [3]. No essential change of these values is found for the average radius range from 1.6 to 2.8 nm. The homogeneous width at room temperature is consistent with the dephasing time of a few 10 fs found in non-degenerate four-wave mixing measurements on the same samples. We believe that scattering at defect states, the existence of which is clearly exposed by the luminescence spectrum (see below), is the underlying process. Further evidence for this assumption comes from the fact that the homogeneous width can be influenced by long-term optical excitation [4].

In addition to the homogeneous width, the hole-burning data reveal a substructure of the energy spectrum which is not exhibited by the inhomogeneously broadened sample absorption. The data demonstrate at least the existence of three states. A quantitative analysis [2] accounting for also the 430 meV split-off band shows that the three hole states identified experimentally are s–d mixtures of total angular momentum 3/2 (first and second state) and 1/2 (third state), respectively. An independent study [5] based on luminescence has led to the same conclusion.

## 2. Time-resolved photoluminescence

Under CW and ns excitation, the photoluminescence of quantum dots in glass is usually dominated by (nonexponentially) slow and spectrally broad components, which are strongly low-energy shifted with respect to the absorption edge [3]. This is commonly assigned to the participation of various defects which localize the carriers prior to recombination. To study the “intrinsic” emission of the quantum dots from the confined energy levels, the measurements are done on the ps time

scale. Pulses of 2.5 ps duration from a tunable dye laser synchronously pumped by the third harmonic of an Antares mode-locked YLF laser are used to excite the samples. Sample heating is suppressed by acousto-optical modulation of the 76 MHz dye laser output yielding pulse trains of typically 300  $\mu$ s duration with 1 s apart. The luminescence is detected with a synchroscan streak camera with an overall time resolution of 10 ps. The energy density per pulse was lowered down to about 100 nJ/cm<sup>2</sup> to avoid saturation effects as well as photo-structural changes.

### 2.1. Non-selective excitation

Fig. 1 presents data for excitation markedly above the absorption edge. In this situation the quantum dot system is practically homogeneously excited across its size distribution since several of the inhomogeneously broadened transitions (see above) interfere spectrally at the pump photon energy. Wavelength selection of the photoluminescence is achieved with interference filters with a spectral resolution matched to the homogeneous line-width at low temperatures. In the decay curves drawn in the lower section of Fig. 1, a fast component superimposed to a background is clearly manifested. The background (as well as the finite luminescence intensity at negative times) is caused by the repetitive excitation within the pulse train and, therefore, a direct measure of the contribution from slow parts. On the other hand, the rise of the curves around zero allows one to construct the emission spectrum right after excitation, as depicted in the upper section of Fig. 1. The broad band extends down to the energy range of deep traps, the emission of which is primarily seen under CW conditions [3].

The occurrence of the fast emission component with ps life-time in Fig. 1 is restricted to the direct vicinity of the absorption edge. The life-time, however, is strongly photon-energy dependent. Fig. 2 summarizes the 1/e times deduced from the decay curves for the 2.0 nm sample and three others of different average radius. Observation at a given photon energy samples predominantly the emission from quantum dots of a certain size. This is confirmed by the fact that the

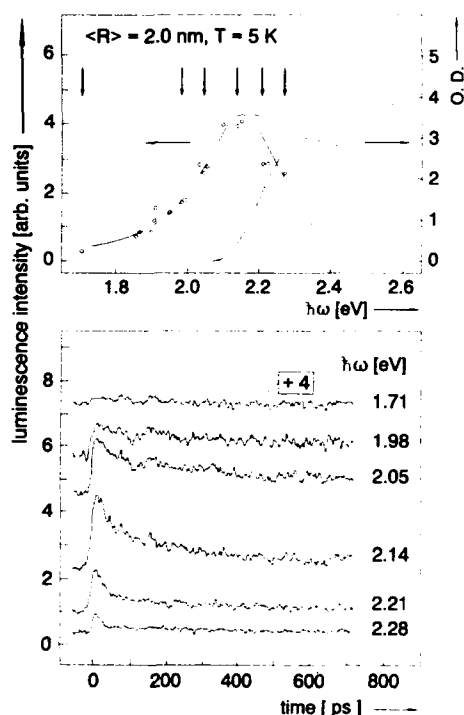


Fig. 1. Lower part: Luminescence decay curves at selected photon energies for a sample with an average dot radius of 2.0 nm at  $T = 5$  K. Upper part: Luminescence intensity versus photon energy 10 ps after the maximum of the excitation pulse derived from the rise of the decay curves around zero. The data (circles) are corrected for reabsorption. The line is used to guide the eye. For comparison the absorption spectrum is figured on the right-hand side. Arrows mark the photon energies where the decay curves below are taken.

life-times found at a given photon energy are practically the same for all samples in Fig. 2, although the average radii are different and the linear absorption peaks of the 2.8 and 1.6 nm samples are shifted by 450 meV relative to each other. Therefore, the more than one-order-of-magnitude increase of the life-time in Fig. 2 is directly related to the size of the emitting dot.

## 2.2. Size-selective excitation

Fig. 3 summarizes the time-resolved photoluminescence obtained from a sample with  $\langle R \rangle =$

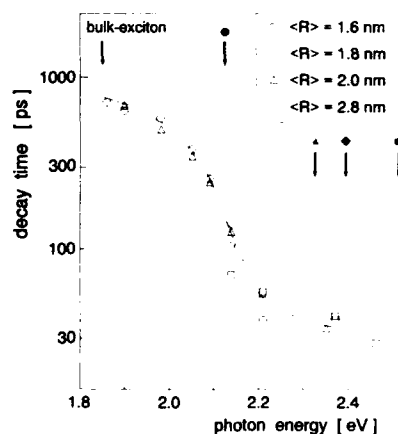


Fig. 2. Life-times ( $1/e$ ) of the direct emission versus photon energy deduced from decay curves measured at 5 K on four samples of different average dot radius. The line is used to guide the eye. Dashed symbols mark the position of the absorption maximum for each of the samples investigated.

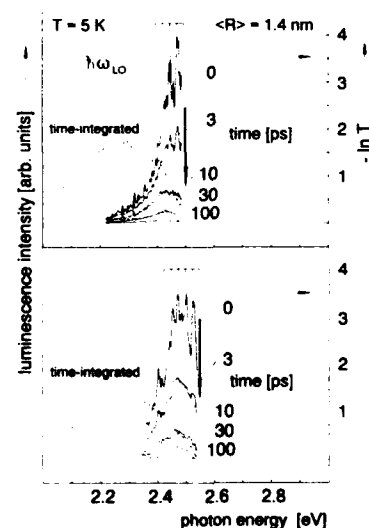


Fig. 3. Time-resolved luminescence spectra for a sample with  $\langle R \rangle = 1.4$  nm using size-selective excitation at a photon energy  $\hbar\omega_{exc} = 2.50$  eV (upper part) and 2.55 eV (lower part), respectively. The time integrated luminescence spectra and the linear absorption are shown for comparison, respectively. The spectral spacing corresponding to the LO phonon energy is indicated.

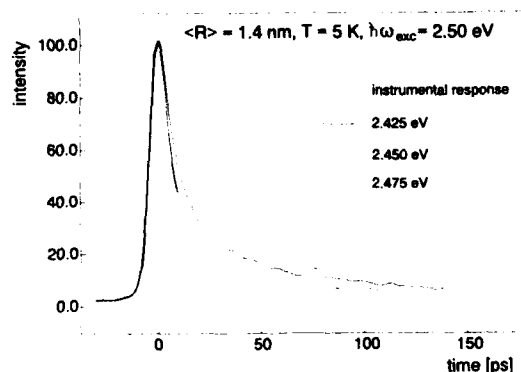


Fig. 4. Luminescence decays (normalized) taken at the energetic positions of the 1, 2 and 3 LO phonon replica in the upper part of Fig. 3. For comparison the instrumental response is given.

1.4 nm for two different photon energies of the exciting ps pulses at the low-energy wing of the ground-state absorption. Thereby, a very sharp distribution of dots is excited, which is determined by the relation between the homogeneous width of the ground-state transition and the tail of the overall size distribution in the sample. The luminescence obtained here is spectrally decomposed by a double monochromator in a subtractive mode, yielding a resolution better than 5 meV. The decay curves measured at successive photon energies by the streak camera are used to construct the time resolved spectra taking into account the instrumental response by standard deconvolution technique. Clear vibronic structures due to coupling to the  $200\text{ cm}^{-1}$  LO phonon mode of CdSe appear during the very first picoseconds. Decay curves measured just at the energetic positions of the LO phonon replica (cf. the upper section of Fig. 3) are given in Fig. 4 in comparison with the instrumental response. The finite decay time clearly seen rules out a dominant contribution of Raman processes in the time resolved spectra. In contrast to the situation in Fig. 1, the decay curves are independent of photon energy, and confirm the size-selection of excitation.

### 3. Transient hole-burning

Transient nonlinear absorption measurements were performed with tunable sub-ps pulses from a hybrid mode-locked dye laser pumped again by the third harmonic of the YLF laser. Single pulse selection and amplification are done in a four-stage dye amplifier pumped by an excimer laser. The resulting 500 fs pulses of some hundred  $\mu\text{J}$  were used to excite the sample and to generate a probe continuum. Care was taken to minimize chirp effects of the probe. The result for a sample with 2.0 nm average radius is presented in Fig. 5. The differential transmission signal is defined by  $\text{DTS} = (T - T_0)/T_0$ , where  $T$  and  $T_0$  are the sample transmission with and without pump, respectively. The spectrum exhibits a remarkable dynamical evolution with increasing pump-probe delay. A bleaching feature develops at first in the direct vicinity of the pump and, then, a second more pronounced one occurs in the range of the linear peak. During the first few ps the maximum

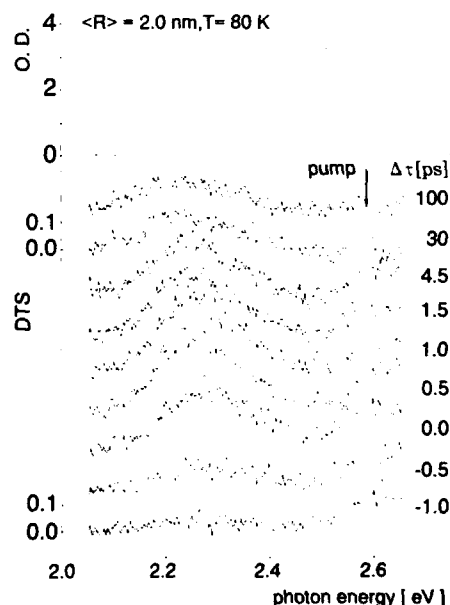


Fig. 5. DTS spectra of a 2.0 nm average radius sample at different pump-probe delays. The pump energy density is  $200\text{ }\mu\text{J}/\text{cm}^2$ . The corresponding linear absorption spectrum is shown in the upper part.

of the latter shifts to lower energies. Simultaneously, a weak, but clearly present induced absorption feature evolves on the high-energy side. About one half of the bleaching at the linear peak recovers to  $1/e$  within 30 ps. At the low-energy side somewhat slower recovery is found, in agreement with the results given in Fig. 2. At delays larger 100 ps a permanent, spectrally broad absorption bleach persists which survives up to 1  $\mu$ s as shown in an independent measurement on a larger time scale [3].

### 5. Discussion

The 800 ps decay constant on the low-energy side in Fig. 2 is on the order of the radiative life-time expected for CdSe quantum dots in the strong confinement regime. Since this value is practically size-independent, the much shorter life-times on the high-energy side have to be attributed to a non-radiative process that becomes increasingly important with decreasing dot size. Coherent effects [6] are ruled out in view of the much shorter dephasing times found in non-degenerate four-wave mixing experiments on the same samples. We assign the short life-times to the trapping of carriers at surface and defect states that give rise to the slow and low-energy shifted part of the luminescence. It is clear from cross section arguments that the trapping rate will increase considerably in small dots. We note that the data collected in Fig. 2 were acquired on samples grown under different conditions which exhibit different defect emission, but are practically equal with regard to the “band-to-band” recombination. Thus, the dramatic increase of the non-radiative rate below a radius of 3 nm is obviously a general quantum dot feature.

Under size selective excitation, vibronic structures show up in the luminescence spectra which are similar to those obtained in ref. [7] on surface passivated CdSe quantum dots in an organic host using ns-pulse and CW excitation. However, on the present dots in a glassy host, those structures are only seen during the first ps after excitation in a hot luminescence regime. This very fast disappearing indicates that at least one of the photoexcited carriers is scattered from its initial state

on a 1 ps time scale. Similar conclusions can be drawn indirectly from the results of non-selective excited photoluminescence in the upper part of Fig. 1. Emission found in the region of the deep traps immediately after the excitation pulse proves that corresponding fast capture times occur. Times of about 1 ps are obviously sufficient to transform an electronic energy in excess on the order of 1 eV to the vibrational system. This fact intimates a quasi-continuous density-of-state tail in the “forbidden gap” with a separation of the involved energy levels smaller or on the order of the LO-phonon energy, so that enough states are available for the carrier scattering. We note that a 1.5 nm CdSe dot consists of about 500 atoms from which about  $1/3$  are on the surface. Those atoms give rise to the same number of states in the “forbidden gap”, either as dangling bonds or through the association of host atoms. The existence of those states is thus an intrinsic feature of the energy spectrum for a quantum dot. In the present samples with a glassy host, the energy distribution of such states seems to be rather broad compared with surface passivated dots in organic solution.

The strong coupling of carriers to surface and defect states, especially in dots with  $R$  smaller than 2.0 nm, suggests a rather low quantum yield. Recent calorimetric absorption measurements on a sample with  $\langle R \rangle = 1.4$  nm, however, have shown that only about one half of the absorbed photons is converted into heat [8]. The other part is re-emitted at lower energies so that the total radiative yield is on the order of some 10%. Apparently, this is a consequence of the confinement which, in contrast to the bulk, prevents spatial separation of the electron and hole so that the optical rate remains large, even when the carriers are localized at “defect” states.

The vibronic structures are not seen in quasi-stationary hole-burning experiments using ns-pulse excitation [2,3]. This has to be related to a partially relaxed state of electron-hole pairs, which is tested on such a time scale. In the transient DTS experiment depicted in Fig. 5 the excitation is markedly above the linear peak, so that initially higher quantum dot levels are populated. The signal in the first few ps reveals relax-

ation of the carriers down to the ground state. Probably, hole relaxation across the s–d sublevels is mostly seen. The induced absorption structure is similar to that observed in ref. [9], where it was assigned to Coulomb effects in the two-particle spectrum. As our dots are smaller, those effects are less pronounced. The long-living and broad absorption bleach is unambiguously related to the electron, as this carrier blocks the absorption regardless of the hole state involved in the optical transition. Otherwise, the bleaching would be located in a relatively narrow range at the ground state peak.

## 6. Conclusions

The use of ultrashort optical excitation has enabled us to study the direct and unrelaxed photoluminescence from electrons and holes in a quantum dot surrounded by glass. Under size-selective excitation, we demonstrate for the first time the existence of vibronic structures which are otherwise hidden by slow processes. The carrier life-time is a function of the dot size and below a radius of 3 nm, a dramatic increase of the nonradiative capture rate sets in. Nonlinear absorption data suggest that the hole leaves the “band-edge” resonant states on a 1 ps time scale, while the electron survives there for a much longer time.

## 7. Acknowledgements

The authors are much indebted to A.I. Ekimov (St. Petersburg) and M. Müller (Jena) for providing the samples. This work was partly supported by the Deutsche Forschungsgemeinschaft.

## 8. References

- [1] L.E. Brus, *Appl. Phys. A* 53 (1991) 465.
- [2] F. Henneberger and J. Puls, in: *Optics of Semiconductor Nanostructures*, Eds. F. Henneberger, S. Schmitt-Rink and E.O. Göbel (Akademie-Verlag, Berlin, 1993) p. 497.
- [3] F. Henneberger, J. Puls, A. Schülzgen, V. Jungnickel and Ch. Spiegelberg, *Adv. Solid State Phys.* 32 (1992) 279.
- [4] A. Uhrig, A. Wörner, W. Langbein, U. Woggon, S. Gaponenko, M. Saleh, O. Wind, H. Kalt and C. Kling-shirn, in: *Proc. 21st Int. conf. on Physics of Semiconductors*, Beijing, 1992, Eds. P. Jiang and H.-Z. Zheng (World Scientific, Singapore, 1992) p. 1379.
- [5] A.I. Ekimov, F. Hache, M.C. Schanne-Klein, D. Ricard, C. Flytzanis, I.A. Kudryavtsev, T.V. Yazeva, A.V. Rodina and A.L. Efros, *J. Opt. Soc. Am. B* 10 (1993) 100.
- [6] K. Misawa, H. Yao, T. Hayashi and T. Kobayashi, *J. Crystal Growth* 117 (1992) 617.
- [7] M.G. Bawendi, P.J. Carroll, W.L. Wilson and L.E. Brus, *J. Chem. Phys.* 96 (1992) 946.
- [8] V. Jungnickel, L. Podlowski, J. Puls, A. Hoffmann, I. Broser and F. Henneberger, to be published.
- [9] Y.Z. Hu, S.W. Koch, M. Lindberg and N. Peyghambarian, *Phys. Status Solidi (b)* 159 (1990) 249.





ELSEVIER

Journal of Crystal Growth 138 (1994) 1010–1016

JOURNAL OF **CRYSTAL  
GROWTH**

## SrS–ZnS electroluminescence materials

Hiroshi Kobayashi

*Department of Electrical and Electronic Engineering, Tottori University, Koyama, Tottori 680, Japan*

### Abstract

SrS–ZnS multilayered thin films are proposed as novel thin film electroluminescent (EL) phosphors. Recent advances in the development of  $(\text{SrS}:\text{Ce}/\text{ZnS})_n$  multilayered thin film EL devices are summarized. Growth of  $(\text{SrS}/\text{ZnS})_n$  multilayered thin films by using the hot wall technique, which enables us to grow ZnS and SrS thin films at the same substrate temperature and then to prepare  $(\text{SrS}/\text{ZnS})_n$  thin films having a large number of ZnS and SrS films, is discussed. Features and problems of ZnS and SrS thin film EL phosphors are also discussed.

### 1. Introduction

Thin film electroluminescent (EL) display panels having Mn-doped ZnS (IIb–VIb compound) phosphors have been developed and have entered into the marketplace. The EL matrix display panels with a variety of sizes and resolutions are now commercially available. SrS (IIa–VIb compound) thin films are also promising host materials to produce color thin film EL devices [1,2]. By using rare-earth ions as luminescent centers, these materials show color electroluminescence. With these thin film EL phosphors, however, there are several problems. For rare-earth-doped ZnS thin films, low solubility of rare-earth ions in the ZnS host lattice has to be considered. In the case of SrS thin films, chemical instability due to its hygroscopic nature becomes problem. To solve these problems, many color EL research programs are being continued mainly to find and to develop promising EL materials and luminescent centers. This approach of dealing with only EL

materials appears to be confronted by many difficult problems. One of alternative approaches is to deal with the thin-film phosphor structure in addition to materials. One of the possible ideas is the introduction of phosphor films having multilayered structure [3]. As this kind of phosphor, we have proposed  $(\text{SrS}/\text{ZnS})_n$  multilayered thin films as a new thin film EL phosphor material [4,5]. By using such structures, one can expect such  $(\text{SrS}/\text{ZnS})_n$  multilayered thin film ELs to show superior electrical and optical characteristics when compared to individual ZnS and SrS thin films.

Here, we summarize briefly the features and problems of ZnS and SrS thin film EL phosphors. Then, we review the recent progress of the  $(\text{SrS}:\text{Ce}/\text{ZnS})_n$  multilayered thin film EL devices [4–7]. Growth of  $(\text{SrS}/\text{ZnS})_n$  multilayered thin films by using hot wall technique are also discussed [8]. This method enables us to grow  $(\text{SrS}:\text{Ce}/\text{ZnS})_n$  multilayered thin films having a large number of ZnS and SrS films.

## 2. ZnS and SrS thin film EL

### 2.1. ZnS and SrS host materials

Phosphor materials to be used for thin film EL panels must be doped with luminescence centers. In addition, to excite the luminescence centers by hot electrons created by an electric field, it must be possible to apply a very high electric field over 1 MV/cm to the thin film. To satisfy these requirements, semiconductors with fairly wide gap of 3.5–4.5 eV, such as wide gap II–VI compounds, must be used as host materials. One such material is ZnS and other is SrS.

Suitable luminescent centers for these host materials are different from each other; for instance,  $\text{Mn}^{2+}$  ions for ZnS and  $\text{Ce}^{3+}$  ions for SrS hosts. This results from the difference in energy band structure of these host materials and in type of luminescent centers. The band structures of these materials are shown in Figs. 1a and 1b, respectively. ZnS has a direct band gap structure [9]. The conduction band minimum at the  $\Gamma$  point, where it is s-like, comes from the 4s wave-function of Zn atoms. The valence band maximum at the  $\Gamma$  point, where it is p-like, comes from the 3p wave-function of S atoms. The occupied Zn  $3d^{10}$  level is located at about 7–8 eV below the valence band maximum. When Mn atoms are doped in the ZnS lattice, the Mn  $3d^5$  level, which is the ground state of d–d transitions, lies about 3–5 eV below the valence band maximum [10]. Therefore, the  $3d^5$  electron configuration in  $\text{Mn}^{2+}$  ions

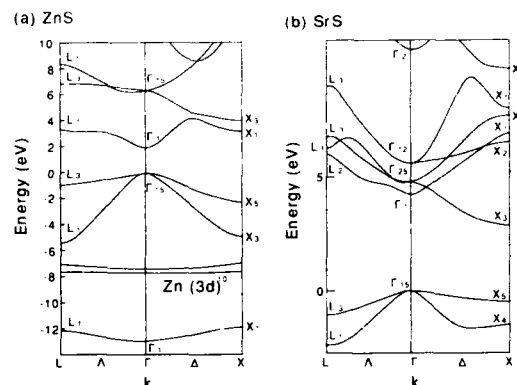


Fig. 1. Energy band structure of (a) ZnS and (b) SrS.

is well localized and then isolated from the band electrons. This may be one reason why the  $3d^5$  electrons of the  $\text{Mn}^{2+}$  centers are mainly excited by direct impact excitation.

Contrary to the case of ZnS, SrS has an indirect band structure. The conduction band minimum at the X point comes from the wave-function of unoccupied 4d wave-function of the Sr atoms [11]. It is therefore d-like. The valence band maximum at the  $\Gamma$  point comes from the 3p wave-function of S atoms, same as in ZnS. When  $\text{Ce}^{3+}$  centers are doped in the SrS lattice, the 4f ground state level lies in the forbidden gap and 5d excited state lies fairly close to the conduction band minimum at the X point. Therefore, it is expected that the 5d excited state of the  $\text{Ce}^{3+}$

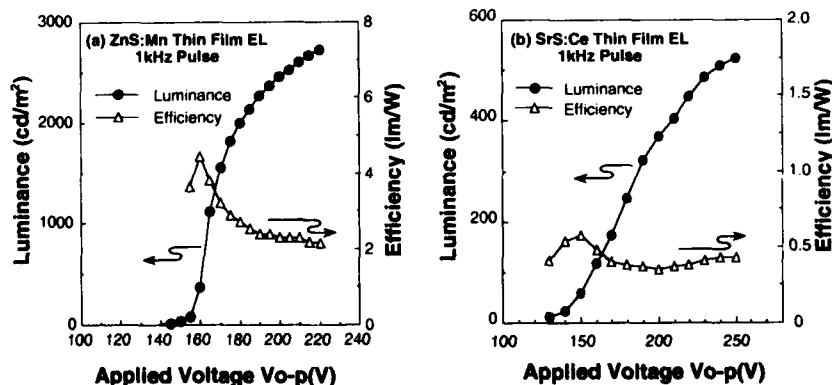


Fig. 2. Typical luminance-voltage and efficiency-voltage characteristics of (a) ZnS:Mn and (b) SrS:Ce thin film EL devices.

centers will interact well with conduction electrons and the  $\text{Ce}^{3+}$  ions are ionized by the electric field [12].

## 2.2. EL devices with ZnS:Mn and SrS:Ce thin films

Typical luminance–voltage and efficiency–voltage characteristics of ZnS:Mn and SrS:Ce thin film EL devices under a 1 kHz drive are shown in Figs. 2a and 2b, respectively. The devices have a conventional double insulating structure consisting of a glass substrate, an indium tin oxide (ITO) transparent electrode, a first dielectric layer, a phosphor layer, a second insulating layer and Al rear electrodes. The typical thickness of the ZnS:Mn phosphor film is 600 nm and that of the SrS:Ce film is 1000–1300 nm. The luminance rises steeply at voltages above the threshold and the saturated luminance level reaches 2500  $\text{cd/m}^2$  for ZnS:Mn and 500  $\text{cd/m}^2$  for SrS:Ce. It is noted that the threshold voltages for both devices are almost the same, although the thickness of the SrS:Ce films is twice that of the ZnS:Mn films. In other words, the average electric field of 0.8 MV/cm for the SrS:Ce films is one-half of 1.6 MV/cm for the ZnS:Mn films [13]. The lower electric field observed for SrS:Ce devices results from band bending due to space charge caused by ionization of  $\text{Ce}^{3+}$  luminescent centers [13,14].

## 3. (SrS:Ce/ZnS)<sub>n</sub> multilayered EL

### 3.1. Multilayered EL structure

The concept of an electroluminescent multilayer device is illustrated in Fig. 3 [3]. Each layer is classified depending on its function such as electron acceleration layer, light emission layer, barrier layer, carrier confinement layer, etc. Many varieties of combination can be considered [3]. Sometimes, we can not separate the layer's function clearly, for instance, one layer serves as acceleration and electroluminescent layer at the same time.

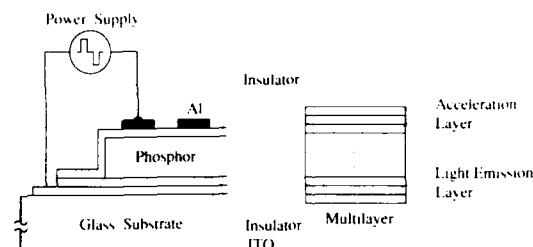


Fig. 3. Schematic structure of multilayered thin film EL device.

### 3.2. (SrS:Ce/ZnS)<sub>n</sub> multilayered EL phosphors

To prepare the (SrS:Ce/ZnS)<sub>n</sub> multilayered thin film EL devices, we have used two different methods, namely reactive evaporation and electron-beam evaporation [4,5]. In the first case, the evaporation is based on Knudsen sources, where ZnS is evaporated from the compound and SrS:Ce from pure elements. In the latter case, a mixed SrS:Ce,K target is used. The preparation conditions have been adjusted in order to obtain highly adherent, high quality films. In the case of reactive evaporation, the optimum substrate temperatures for the deposition of ZnS and SrS:Ce have been found to be 200 and 600–650°C, respectively [4]. In the case of electron-beam evaporation, the optimum substrate temperature has been found to be the same as for reactive evaporation [2].

The scanning electron microscope (SEM) image of the cross sections of the multilayered films prepared by reactive evaporation technique are shown in Fig. 4 [7]. The SEM image clearly shows the grained structures of a 9 multilayered thin film phosphor. The overall thickness is 1.5  $\mu\text{m}$ . Due to the perfectly separated films, it is obvious that no intermixing between the ZnS and SrS:Ce occurs, which is somewhat surprising because of the high temperature processing of the SrS films. Furthermore, the SEM images of the multilayered phosphors exhibit perfect adhesion between the single layers within the SrS:Ce/ZnS stack.

Fig. 5 shows high resolution X-ray diffraction (XRD) patterns of ZnS (Fig. 5a), SrS (Fig. 5b) and (SrS/ZnS)<sub>9</sub> (Fig. 5c) multilayered thin films



Fig. 4. SEM image of the cross section of the  $(\text{SrS}/\text{ZnS})_9$  multilayered film prepared by reactive evaporation technique.

deposited by electron-beam evaporation (full line) and by reactive evaporation (broken line) [4]. The ZnS films are oriented in the (0001) direction of the hexagonal structure or in the (111) direction of the zincblende structure, whereas SrS exhibits

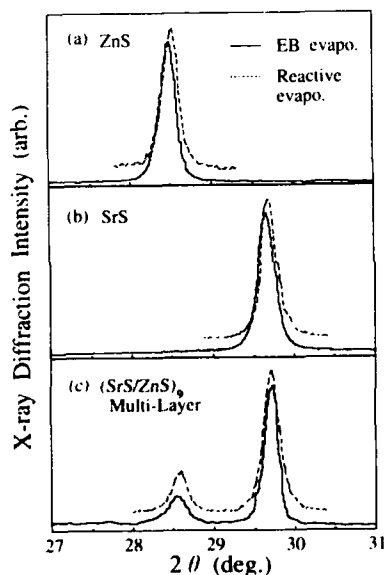


Fig. 5. High resolution X-ray diffraction patterns of (a) ZnS, (b) SrS and (c)  $(\text{SrS}/\text{ZnS})_9$  multilayered thin films deposited by electron beam evaporation (full lines) and by reactive evaporation (broken lines) methods.

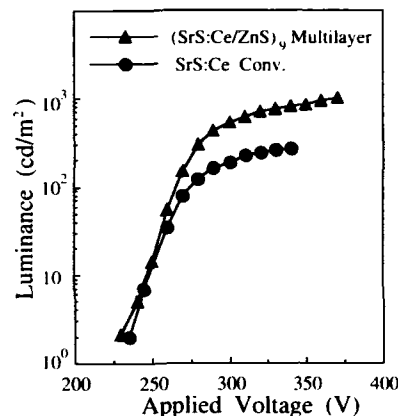


Fig. 6. Luminance-applied voltage characteristic of  $(\text{SrS:Ce}/\text{ZnS})_9$  multilayered thin film EL device.  $L$ - $V$  characteristics of a conventional SrS:Ce thin film EL device are also shown, for comparison.

a strong (200) texture in the rock-salt structure. As shown in Fig. 5c, both diffraction lines originating from the SrS and the ZnS are observed. This indicates that nonintermixed  $(\text{SrS}/\text{ZnS})_n$  multilayered phosphor films were prepared, as expected from the SEM image in Fig. 4. However, a slight shift of the ZnS peak towards the SrS peak is observed, indicating a strained growth of ZnS on SrS. The evaluation of the FWHM of the XRD peaks reveals the good crystallinity of all films. The same tendency in the structural feature of the multilayered thin films for both preparation techniques has been observed.

### 3.3. Luminance-applied voltage characteristics of multilayered thin film EL

Typical luminance versus applied voltage ( $L$ - $V$ ) characteristics are shown in Fig. 6 [4]. The conventional structure of the ZnS/SrS:Ce/ZnS thin film EL device is contrasted with the  $(\text{SrS:Ce}/\text{ZnS})_9$  multilayered thin film EL device prepared by reactive evaporation. As expected, the introduction of  $(\text{SrS:Ce}/\text{ZnS})_n$  multilayered phosphors in thin film EL devices leads to a significant increase of luminance and efficiency. The maximum luminance of  $1100 \text{ cd/m}^2$  at 1 kHz is higher for the multilayered structure than for

the conventional device ( $300 \text{ cd/m}^2$ ). The overall increase in luminance of the 9 multilayer device compared with the conventional one is about 3 times. The threshold voltage of about 250 V for the multilayered TFEL device is lower than for the conventional thin film EL device, although the multilayered phosphor has larger thickness. Probably, the reasons are related to the primary electron generation from the SrS/ZnS hetero-interfacial states.

#### 4. Hot wall technique for $(\text{SrS}/\text{ZnS})_n$ multilayered thin film growth

##### 4.1. Hot wall deposition technique

To obtain  $(\text{SrS}/\text{ZnS})_n$  multilayered thin films with larger layer number and with good quality, it is beneficial if the SrS and ZnS thin films are grown at the same substrate temperature. As mentioned in section 3.2, in the case of reactive evaporation and electron beam evaporation, ZnS thin films are usually grown at a relatively low substrate temperature of 200–300°C. Contrary to this, the optimum substrate temperature during SrS thin film deposition is higher (500°C). This results in difficulty in growing  $(\text{SrS}/\text{ZnS})_n$  multilayered thin films. To grow  $(\text{SrS}/\text{ZnS})_n$  multilayered thin films at the same substrate temperature, we have tried to use the hot wall deposition technique, and studied the thin film growth of ZnS and SrS thin films at the wide substrate temperature range of 300–600°C.

The hot wall deposition equipment used in this experiment has two hot wall cells for ZnS and for SrS thin film growth [8]. ZnS thin films were grown by using a ZnS powder source, which was resistively heated to 700–850°C. To increase the deposition rate, sulfur vapor was also introduced into the ZnS cell. SrS thin films were grown through the chemical reaction of Sr and S vapor. Sr vapor was supplied from the Sr metal source resistively heated to 580–650°C. Controlled S vapor was supplied to the Sr cell.  $(\text{SrS}/\text{ZnS})_n$  multilayered thin films were grown by the sequential deposition of the SrS and ZnS films. To achieve

the sequential deposition, the substrate was exposed alternatively to ZnS cell and SrS cell.

##### 4.2. Growth of ZnS and SrS thin films

Fig. 7 shows the dependence of the deposition rate of ZnS and SrS films on the substrate temperature  $T_{\text{sub}}$  [8]. The temperature of the ZnS powder source  $T_{\text{ZnS}}$  was 800 and 850°C. The deposition rate of the ZnS films decreased rapidly with an increase of the substrate temperature, and became less than  $1 \text{ Å/s}$  at  $T_{\text{sub}} > 400^\circ\text{C}$ , even when  $T_{\text{ZnS}}$  was increased to 850°C. It is reported that to grow SrS thin films having a good crystallinity, substrate temperatures over 400°C have to be used [2]. Therefore, to deposit ZnS and SrS films at the same temperature, ZnS films should be deposited at least at 400°C. To increase the deposition rate of the ZnS thin films, we have tried to introduce S vapor during ZnS deposition. In other words, we increased the S/Zn ratio during deposition to reduce the re-evaporation of Zn from the surface of the ZnS thin films. As a result, we have found that the deposition rate of the ZnS films was remarkably increased by supplying S vapor, as shown in Fig. 7.

Fig. 7 also shows the dependence of the deposition rate of SrS thin films on the substrate

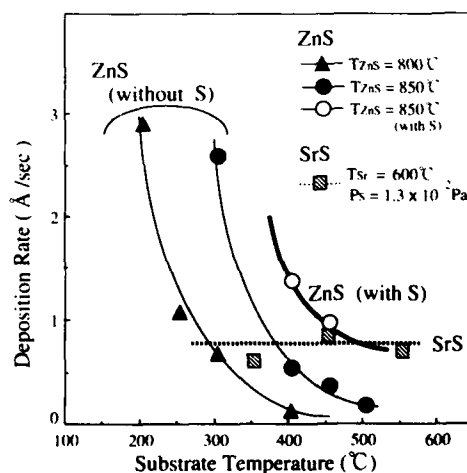


Fig. 7. Dependence of the deposition rate of ZnS and SrS thin films on the substrate temperature.

temperature. Since Sr metal has higher vapor pressure, the deposition rate increases remarkably at  $T_{\text{Sr}} > 600^\circ\text{C}$ . Therefore, we used  $T_{\text{Sr}}$  of  $580\text{--}600^\circ\text{C}$  to control the Sr vapor pressure. On the other hand, the deposition rate of SrS films depends slightly on the S vapor pressure. As shown in Fig. 7, a deposition rate of  $1 \text{ \AA/s}$  for SrS films can be achieved in the substrate temperature range of  $350\text{--}550^\circ\text{C}$  under the deposition conditions of  $T_{\text{Sr}} = 600^\circ\text{C}$  and sulfur pressure of  $1.3 \times 10^{-2} \text{ Pa}$ .

These results imply that a proper deposition rate of the order of  $1 \text{ \AA/s}$  was obtained for both ZnS and SrS thin films at the same substrate temperature region of  $400\text{--}500^\circ\text{C}$ . As a result, it became possible to deposit ZnS and SrS films sequentially at the same substrate temperature.

#### 4.3. Growth of $(\text{SrS}/\text{ZnS})_n$ multilayered thin films

Fig. 8 shows the XRD patterns of  $(\text{SrS}/\text{ZnS})_n$  multilayered films having 11 and 51 layers. The total thickness is  $1 \mu\text{m}$ . The overall thicknesses of SrS and ZnS are almost the same (about  $500 \text{ nm}$ ). For comparison, the XRD patterns of SrS and ZnS films are shown in Figs. 8b and 8c. Since the diffraction peaks due to ZnS and SrS lattices are observed for multilayered thin films, ZnS and SrS layers were grown successfully even for 51 thin film layers, in which each SrS and ZnS layer was only  $20 \text{ nm}$  thick. The ZnS layers were strongly oriented to  $\langle 111 \rangle$  for both multilayered thin films. This result is the same as in the case of the electron beam evaporated and reactive evaporated  $(\text{SrS}/\text{ZnS})_n$  multilayered thin films mentioned in section 3.2. On the contrary, for SrS films, the (200) peak became weak and the (111) and (220) peaks became rather strong. This indicates that the orientation of the SrS thin films in the multilayered films is strongly affected by the ZnS interface. Since both the (111) surface of ZnS and that of SrS are polar, but the SrS (200) surface is electrically neutral, SrS films with  $\langle 111 \rangle$  orientation tend to grow on ZnS (111) surface. However, the growth kinetics of  $(\text{SrS}/\text{ZnS})_n$  multilayered thin films by different growth technique are not yet well understood.

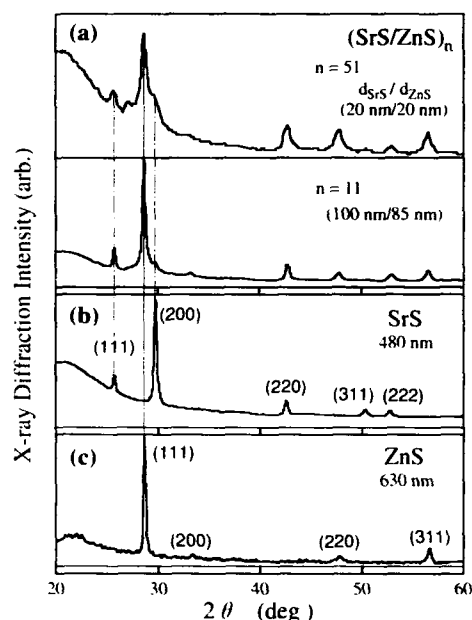


Fig. 8. (a) X-ray diffraction patterns of  $(\text{SrS}/\text{ZnS})_n$  multilayered thin films with 11 and 51 layers, which were grown by using hot wall deposition technique. XRD patterns of (b) SrS and (c) ZnS thin films are shown for comparison.

#### 4.4. EL characteristics

Thin film EL devices having hot wall grown  $(\text{SrS}:\text{Ce}/\text{ZnS})_n$  multilayered phosphors were prepared. The device showed a greenish-blue EL emission. A luminance of  $10 \text{ cd/m}^2$  at  $1 \text{ kHz}$  was obtained. This value is lower than those for the multilayered EL devices prepared by electron beam and reactive evaporation techniques, because the Ce concentration and other device parameters have not been optimized yet.

#### 5. Summary

We have summarized the recent experimental results for  $(\text{SrS}:\text{Ce}/\text{ZnS})_n$  multilayered thin film EL devices prepared by reactive evaporation and electron beam evaporation techniques. The EL characteristics, such as luminance and efficiency, of  $(\text{SrS}:\text{Ce}/\text{ZnS})_n$  multilayered thin film EL de-

vices are improved two to three times compared with conventional SrS:Ce thin film EL devices. Growth of  $(\text{SrS}/\text{ZnS})_n$  multilayered thin films by using hot wall technique has been studied. This deposition method enables us to grow ZnS and SrS thin films at the same substrate temperature and then enables us to prepare  $(\text{SrS}/\text{ZnS})_n$  thin films having large layer number. The potential of multilayered thin film EL devices is promising. The development, however, is still in its early stages and further research is required to develop appropriate thin film growth techniques and to understand the EL mechanism of the multilayered thin film EL devices.

## 6. Acknowledgments

The author gratefully acknowledges valuable discussions with Professor S. Tanaka of the Tottori University and Dr. R. Mauch of the Heinrich Hertz Institute. Part of this work has been carried out in collaboration with the group at the University of Stuttgart and with the Heinrich Hertz Institute. He also acknowledges contributions to this work from colleagues and many students at the Tottori University. This work was supported in part by a Grant-in-Aid for Scientific Research on Priority Areas, New Functionality Materials – Design, Preparation and Control, from the Ministry of Education, Science and Culture.

## 7. References

- [1] H. Kobayashi and S. Tanaka, in: Proc. 5th Intern. Workshop on Electroluminescence, Helsinki, Acta Polytech. Scand., Appl. Phys. Ser. No. 170 (1990) p. 69.
- [2] S. Tanaka, *J. Crystal Growth* 101 (1990) 958.
- [3] H. Kobayashi, in: Proc. 6th Intern. Workshop on Electroluminescence, El Paso, 1992, p. 179.
- [4] K.O. Velthaus, R.H. Mauch, H.W. Schock, S. Tanaka, K. Yamada, K. Ohmi and H. Kobayashi, in: Proc. 6th Intern. Workshop on Electroluminescence, El Paso, 1992, p. 187.
- [5] R.H. Mauch, K.O. Velthaus, H.W. Schock, S. Tanaka and H. Kobayashi, in: 1992 SID Intern. Symp. Digest Tech. Papers, 1992, p. 178.
- [6] R.H. Mauch, K.O. Velthaus, B. Huttli and H.W. Schock, in: 1993 SID Intern. Symp. Digest Tech. Papers, 1993, p. 769.
- [7] K.O. Velthaus, R.H. Mauch and H.W. Schock, *Adv. Mater. Opt. Electron.* 2 (1993).
- [8] K. Ohmi, Y. Yamano, S.-T. Lee, T. Ueda, S. Tanaka and H. Kobayashi, *J. Crystal Growth* 138 (1994) 1061.
- [9] J.E. Bernard and A. Zunger, *Phys. Rev. B* 36 (1987) 3199.
- [10] T. Taguchi, in: Proc. 4th Intern. Workshop on Electroluminescence, Tottori, Springer Proceedings in Physics 38 (Springer, Heidelberg, 1989) p. 93.
- [11] A. Hasegawa and A. Yanase, *J. Phys. C (Solid State Phys.)* 13 (1980) 1995.
- [12] H. Yoshiyama, S.H. Sohn, S. Tanaka and H. Kobayashi, in: Proc. 4th Intern. Workshop on Electroluminescence, Tottori, Springer Proceedings in Physics 38 (Springer, Heidelberg, 1989) p. 48.
- [13] K. Ohmi, S. Tanaka, Y. Yamano, K. Fujimoto and H. Kobayashi, in: Proc. 12th Intern. Display Research Conf., Hiroshima, 1992, p. 725.
- [14] S. Tanaka, K. Ohmi, K. Fujimoto, H. Kobayashi, T. Nire, A. Matsuno and A. Miyakoshi, in: Proc. 13th Intern. Display Research Conf., Strasbourg, 1993, p. 237.



ELSEVIER

Journal of Crystal Growth 138 (1994) 1017–1022

JOURNAL OF  
**CRYSTAL  
GROWTH**

## Trailing edge phenomena in $\text{SrS}:\text{CeCl}_3$ thin film electroluminescent devices

U. Troppenz \*, B. Hüttl, K.O. Velthaus, R.H. Mauch

*Heinrich-Hertz-Institut für Nachrichtentechnik Berlin GmbH, AG Elektrolumineszenz, Hausvogteiplatz 5-7, D-10117 Berlin, Germany*

### Abstract

$\text{SrS}:\text{CeCl}_3$  based thin film electroluminescent devices in conventional and multilayer structures have been investigated by means of time and voltage dependent photoluminescence (PL) measurements after laser excitation of the  $\text{Ce}^{3+}$  ions. It turned out that a significant photo-induced transferred charge as well as photo-induced electroluminescence (PEL) occurs at voltage levels far below the actual EL threshold, mainly in the trailing edge of the voltage pulse. Furthermore, a reduction of the PL intensity by increasing the applied voltage is observed. At EL threshold voltage, the PL intensity is as low as 65–75% of the zero voltage value. These observations are independent of the device structure. The PEL can be described as a partial regain of the quenched PL, being more pronounced in the multilayer case due to a higher mean electric field strength in the  $\text{SrS}:\text{CeCl}_3$  layers. To explain the experimental findings, a quenching caused by weakly accelerated electrons is proposed.

### 1. Introduction

Since rare-earth activated alkaline-earth sulfides (AESs) have been introduced as promising phosphor materials in AC-driven thin film electroluminescence (AC-TFEL), a contradictory discussion about the involved excitation mechanisms is in progress [1–3]. In particular, the understanding of the so-called trailing edge (TE) emission of such devices which occurs when the voltage pulse is switched off is important, because it is usually not observed in  $\text{ZnS}:\text{Mn}$  TFEL devices. Furthermore, it is not decided whether the TE emission is inherent in AES phosphors or only caused by

imperfections originating from the incorporation of rare-earth ions. Hence, the clarification of the nature of the TE emission will give important hints for a further optimization of AES based TFEL.

The reported experimental findings for  $\text{SrS}:\text{Ce}$  and  $\text{CaS}:\text{Eu}$  are as follows: It seems to be proven that the TE emission is related to the recombination of electrons via luminescent centres which have been ionized during the high field period of the voltage pulse. The ionization is caused by a mechanism called field-quenching or field-delocalization [1,2,4]. An experimental indication of this model is given by the appearance of a photo-induced transferred charge after photoluminescence (PL) excitation in an electric field [5,6]. The field-quenching mechanism is explained by sev-

\* Corresponding author.



eral authors [7,8] as field-stimulated tunnelling of electrons from the excited 5d level of  $\text{Ce}^{3+}$  and  $\text{Eu}^{2+}$  into the conduction band, assuming that the 5d level is located in the forbidden gap of the host, 1 eV or less below the conduction band edge.

It is believed that the TE emission compensates to some extent the luminescence losses during the electroluminescence (EL) process in the leading edge. However, if the quenching of the luminescence in the leading edge (LE) is a prerequisite for the TE emission, it is not clear whether the trailing edge emission is beneficial or should be avoided for improving the device efficiency. On the other hand, if the mechanism generating TE emission is efficient and can be enhanced, as for instance the multilayer approach indicates, one should make use of it. It was found that the luminance and efficiency of multilayer devices is two- to threefold compared to conventional devices [9,10].

In order to evaluate the mechanisms involved, field and time dependent PL measurements have been carried out on  $\text{SrS}:\text{CeCl}_3$  EL devices in conventional and multilayer structure.

## 2. Device fabrication

$\text{SrS}:\text{CeCl}_3$  EL devices with various phosphor layer structures were prepared by means of reactive evaporation as previously reported [11]. Two types of devices have been investigated, conventional devices with a  $\approx 1 \mu\text{m}$  thick  $\text{SrS}:\text{CeCl}_3$  film embedded between two ZnS layers and 9 multilayer devices having 9 alternating ZnS and  $\text{SrS}:\text{CeCl}_3$  films as active layers. In either case, ZnS is forming the interface to the insulators. In the multilayer devices, the thickness of each  $\text{SrS}:\text{CeCl}_3$  single layer was around 200 nm. All samples were fabricated with the same combination of insulating films using  $\text{Si}_3\text{N}_4$  as bottom and  $\text{Si}_3\text{N}_4/\text{Ta}_2\text{O}_5$  as top insulator. The doping of the SrS films was provided by  $\text{CeCl}_3$  coevaporation and adjusted to a concentration of about 0.5 at% Ce in all samples. The ZnS layers remained undoped.

## 3. Measurements

The PL excitation in the range of 400–480 nm was done by means of a nitrogen-laser-pumped dye laser with 1  $\mu\text{J}$  pulse energy and 500 ps pulse width. A digital oscilloscope was used to acquire the time resolved behaviour of EL and PL, which has been measured with a fast photomultiplier. For the low temperature measurements, a refrigerator cryostat was used which could provide temperatures as low as 15 K.

### 3.1. Photo-induced trailing edge emission

The photo-excitation of  $\text{SrS}:\text{Ce}$  TFEL devices at wavelengths fitting the  $\text{Ce}^{3+}$  absorption band results in a voltage dependent photo-current or photo-induced transferred charge [5,6]. It turns out that the same excitation spectrum as for the blue-green 5d–4f luminescent transition of  $\text{Ce}^{3+}$  is observed, supporting the assumption that some excited  $\text{Ce}^{3+}$  centres are ionized in high electric fields. Looking in more detail on the response of  $\text{SrS}:\text{CeCl}_3$  devices after laser excitation not only a transferred charge, but also a photo-induced EL (PEL) is observed even at voltages much lower than the EL threshold voltage  $U_{\text{th}}$  (Fig. 1). As stated above for the photo-transferred charge  $Q_{\text{ph}}$ , the excitation spectrum of the PEL coincides with the  $\text{Ce}^{3+}$  excitation spectrum indicating related mechanisms.

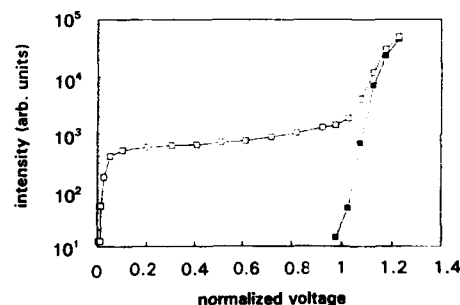


Fig. 1. Typical intensity versus voltage characteristics of  $\text{SrS}:\text{CeCl}_3$  based TFEL devices with (□) and without (■) laser excitation (voltage is normalized to the EL threshold  $U_{\text{th}}$ ).

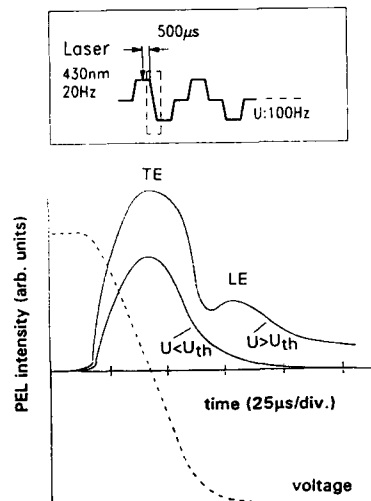


Fig. 2. Time resolved PEL response at voltages above and below the EL threshold (TE: trailing edge; LE: leading edge emission).

As shown in the inset of Fig. 2, the laser excitation with a frequency of 20 Hz was adjusted to the pulse dwell of the 100 Hz driving pulse. Fig. 2 shows an example of the time resolved PEL at driving voltages below as well as above the threshold  $U_{th}$ . The latter was determined by the difference between “dark” EL and photo-EL. To avoid any misinterpreting of leading and trailing edge PEL processes, a specially designed voltage shape with a steady decrease after the laser excitation was applied. As exhibited in Fig. 3, where the integrated luminescence response is dis-

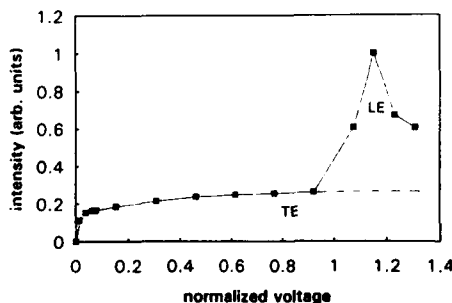


Fig. 3. Integrated PEL intensity versus applied voltage (voltage is normalized to  $U_{th}$ ).

played, a remarkable PEL is observed already at voltage levels of only  $0.01U_{th}$ . A further increase of voltage results in a soft increase of PEL before it peaks just above the EL threshold. An evaluation of the PEL response indicates that below EL threshold, only a PEL in the trailing edge is found. An increase of voltage above  $U_{th}$  leads mainly to an additional leading edge response. These features were found in conventional as well as in multilayer structures. However, in the latter case the additional response in the leading edge is more pronounced. These findings are in contrast to experiments carried out on ZnS:Mn devices under UV irradiation, which exhibit the well-known EL mechanism above and below threshold voltage [12].

### 3.2. Photoluminescence in high electric fields

In order to elucidate the mechanisms responsible for the photo-induced transferred charge and the PEL, the integral PL intensity and the photoluminescence decay time  $\tau$  of the  $Ce^{3+}$  emission were measured under EL driving conditions. The decay time  $\tau$  has been determined by fitting the

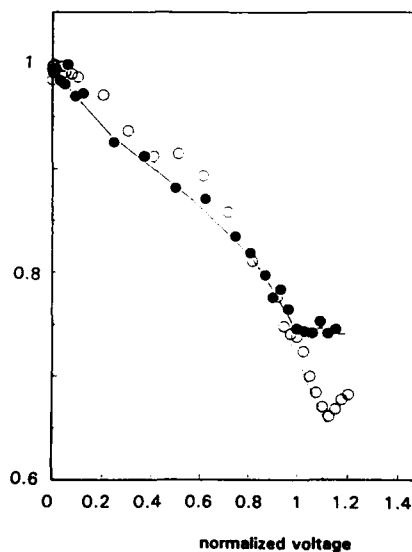


Fig. 4. Normalized PL response versus applied voltage of conventional (●) and multilayer (○) devices.

exponential PL decay curve over 2 orders of magnitude. As a common feature, it can be seen from Fig. 4 that the decrease of the PL follows continuously the increase of the applied voltage. The PL intensity at EL threshold remains at about 65–75% of the value at zero voltage ( $PL_0$ ). In Fig. 5 the voltage dependences of  $\tau/\tau_0$  ( $\tau_0$ : decay time without applied voltage) and of  $PL/PL_0$  are displayed. Since  $\tau_0$  varies from 22 to 25 ns for the different samples, indicating a more or less disturbed incorporation of the luminescent centres, the decrease of  $\tau/\tau_0$  under applied voltage is almost independent of  $\tau_0$  and only about 8–10% at  $U_{th}$ . Hence, the contribution of the field-reduced 5d–4f decay time to the decrease of the PL intensity seems to be negligible. To evaluate the influence of thermal activation, these measurements were also carried out at a temperature of 15 K. As shown in Fig. 5, an even weaker decrease of the decay time versus applied voltage in the low temperature case is found, whereas at  $U_{th}$  the PL intensity is reduced to approximately the same level as found in the room temperature measurement. A modification of  $\tau_0$  and  $PL_0$  with temperature was not observed.

Summarizing this section, the more pronounced drop of  $PL/PL_0$  compared to  $\tau/\tau_0$  can be explained by considering a quenching process which is much faster than the time resolution of 1 ns of the measuring setup. In addition, the  $Ce^{3+}$  decay time  $\tau$  is affected by temperature, whereas the quenching process represented by  $PL/PL_0$  is almost temperature independent.

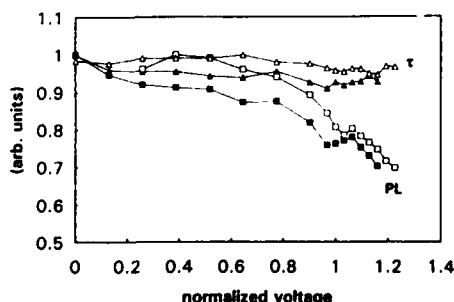


Fig. 5. Normalized PL intensity and decay time versus normalized voltage measured at room temperature (filled symbols) and 15 K (open symbols).

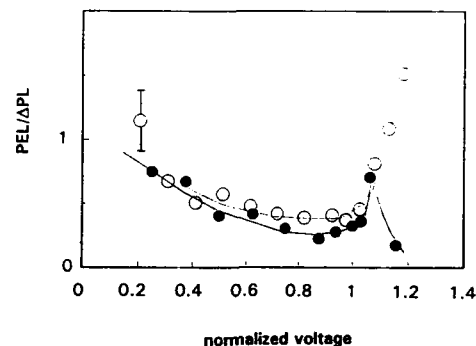


Fig. 6. PEL regain related to PL loss  $\Delta PL$  versus applied voltage of conventional ( $\bullet$ ) and multilayer ( $\circ$ ) devices (voltage is normalized to  $U_{th}$ ).

No significant differences between multilayer and conventional devices have been observed so far; however, it is known from EL data that the multilayer devices are more luminant and more efficient than the conventional ones. Therefore, to obtain a further parameter for the comparison of the two types of devices, the ratios of the photo-induced electroluminescence (PEL) to the PL losses ( $\Delta PL$ ) for the various device structures have been calculated.  $PEL/\Delta PL$  can be seen as a measure for the regain of losses occurring in either PL or EL during the time period when a high electric field is applied.

Fig. 6 shows the behaviour of  $PEL/\Delta PL$  versus applied voltage for a conventional and for a multilayer device. In the low field region,  $PEL/\Delta PL$  is about 1, reduced to 0.6–0.4 just before the threshold voltage for both types. However, a further increase of the applied voltage leads to a distinct behaviour of the different structures. Whereas in the conventional case  $PEL/\Delta PL$  increases slightly, followed by a drop even below the threshold level, a significant increase of  $PEL/\Delta PL$  in the multilayer case is observed, mainly due to a gain in the PEL leading edge (see Fig. 3).

#### 4. Discussion

It turned out that the photo-induced transferred charge  $Q_{ph}$  as well as the photo-induced

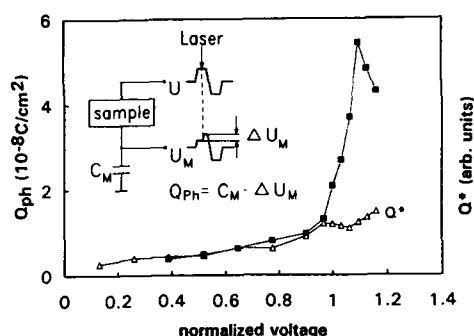


Fig. 7. Measured (■) and estimated (△) photo-induced transferred charge versus normalized voltage.

TE emission observed in SrS:Ce based TFEL devices are accompanied by a decrease of photoluminescence intensity with increasing voltage. Therefore, clear evidence is given that the bases for the efficient TE emission in PL and EL are ionized luminescent centres. Furthermore, the trailing edge emission can be seen as a regain of losses caused by the ionization process.

The regain below EL threshold is comparable for conventional and multilayer devices and is caused by a PEL emission in the trailing edge. In contrast, by increasing the voltage above threshold, the regain is more pronounced in the multilayer case. This occurs not in the trailing edge but in the subsequent leading edge (Fig. 3), accompanied by an increase of photo-induced transferred charge, as shown in Fig. 7. Also shown in Fig. 7 is the expected charge  $Q^*$  which can be deduced from the PL losses. The relative measure of  $Q^*$  was calculated according to the formula  $Q^* \sim \Delta I_{v,0} + I_{v,0}(\tau_0 - \tau)/\tau_0$ . Herein,  $I_{v,0}$  represents the number of excited luminescent centres evaluated from the time-resolved PL at time  $t = 0$  and measured at the respective voltage levels.  $\Delta I_{v,0} = I_{0,0} - I_{v,0}$  includes the fast quenching mechanism as discussed above. Comparing the voltage dependence of  $Q^*$  with  $Q_{ph}$ , a significant difference above  $U_{th}$  is observed. This can be attributed to a multiplication of initial carriers which originate from luminescent centres or from interface states, resulting in an even stronger

quenching as seen in the dip of the PL in Fig. 4 around  $U_{th}$ . Hence, the proposed multiplication is not caused by a band-to-band ionization process, but by an electron transition from  $Ce^{3+}$  into the conduction band. Further hints for this mode are found if the decrease of  $\tau$  and PL intensity with increasing voltage is taken into account. Such behaviour can hardly be described by Frenkel-Poole emission or tunnelling through a barrier, where both follow exponentially the electric field. It should be noted that the electric field in the SrS:CeCl<sub>3</sub> layer changes from 0.01 to about 1 MV/cm.

Again focussing on the different device structures, the more pronounced loss of PL associated with a larger gain of photo-induced transferred charge is observed in the multilayer case. This can be attributed to a higher mean electric field strength in the emitting layer, which is caused by the thinner SrS:CeCl<sub>3</sub> (200 nm) compared to the conventional device (1  $\mu$ m). This has also been observed in ref. [13], where conventional devices with different SrS:Ce thicknesses have been compared in EL. It was shown that the thinner the SrS:Ce, the higher the mean electric field strength. Hence, the higher electric field in the multilayer case results in the observed higher reduction of PL intensity, the higher photo-induced transferred charge as well as the enhanced regain.

In conclusion, the ionization of excited  $Ce^{3+}$  luminescent centres has been identified as a prerequisite for trailing edge. It has been shown that the gain in luminance and efficiency in multilayer devices is only partially due to an increased trailing edge response, because the additional emission in the subsequent leading edge contributes significantly to the overall emission. The quenching of the excited  $Ce^{3+}$  centres by impact of electrons is considered to be the responsible mechanism. The multilayer approach gives rise to achieving a higher mean electric field strength in the light emitting SrS:CeCl<sub>3</sub> layers. Therefore, further investigations on AES based TFEL devices should focus on both, optimized incorporation of the luminescent centres including the question of codoping as well as device structures which allow high electric fields in the AES films.

### 5. Acknowledgement

This work has been supported by the Bundesministerium für Forschung und Technologie under contract 01 BK 202/7.

### 6. References

- [1] R.S. Crandall, *Appl. Phys. Lett.* 50 (1987) 641.
- [2] R.S. Crandall, *Appl. Phys. Lett.* 50 (1987) 551.
- [3] G.O. Müller, R. Mach, B. Selle and H. Ohnishi, *J. Crystal Growth* 101 (1990) 999.
- [4] S. Tanaka, *J. Luminescence* 40&41 (1988) 20.
- [5] S. Tanaka, H. Yoshiyama, J. Nishiura, S. Ohshio, H. Kawakami, N. Nakamura and H. Kobayashi, in: *Springer Proceedings in Physics*, Vol. 38, Eds. S. Shionoya and H. Kobayashi (Springer, Berlin, 1989) p. 56.
- [6] G.O. Müller and R. Mach, *Adv. Mater. Opt. Electron.*, in press.
- [7] H. Yoshiyama, S.H. Sohn, S. Tanaka and H. Kobayashi, in: *Springer Proceedings in Physics*, Vol. 38, Eds. S. Shionoya and H. Kobayashi (Springer, Berlin, 1989) p. 48.
- [8] M. Ando, in: *Proc. 6th Workshop on Electroluminescence*, Eds. V.P. Singh and J.C. McClure (Cinco Puntos, El Paso, 1992) p. 85.
- [9] R.H. Mauch, K.O. Velthaus, H.W. Schock, S. Tanaka and H. Kobayashi, in: *1992 SID Int. Symp., Digest of Technical Papers*, SID, Boston, MA, 1992, p. 178.
- [10] K.O. Velthaus, R.H. Mauch and H.W. Schock, *Adv. Mater. Opt. Electron.*, in press.
- [11] K.O. Velthaus, R.H. Mauch, H.W. Schock, S. Tanaka, K. Yamada, K. Ohmi and H. Kobayashi, in: *Proc. 6th Workshop on Electroluminescence*, Eds. V.P. Singh and J.C. McClure (Cinco Puntos, El Paso, 1992) p. 187.
- [12] G.O. Müller and R. Mach, *Phys. Status Solidi (a)* 77 (1983) K179.
- [13] S. Tanaka, K. Ohmi, K. Fujimoto, H. Kobayashi, T. Nire, A. Matsuno and A. Miyakoshi, in: *Eurodisplay 1993, SID and Le Club Visu*, Strasbourg, 1993, p. 237.



ELSEVIER

Journal of Crystal Growth 138 (1994) 1023–1027

JOURNAL OF  
**CRYSTAL  
GROWTH**

## Space charge and excitation efficiency in ZnS thin film electroluminescent devices

A. Zeinert <sup>\*,a,b</sup>, P. Benalloul <sup>b</sup>, J. Benoit <sup>b</sup>, C. Barthou <sup>b</sup>, H.-E. Gumlich <sup>a</sup>

<sup>a</sup> *Institut für Festkörperphysik PN 4-1, Technische Universität Berlin, Hardenbergstrasse 36, D-10623 Berlin, Germany*

<sup>b</sup> *Laboratoire d'Acoustique et d'Optique de la Matière Condensée, Université Pierre et Marie Curie, Tour 13, 5e Etage, Case 86, 4 Place Jussieu, F-75252 Paris Cedex 05, France*

### Abstract

Measurements under continuous UV illumination permit one to investigate the influence of a bulk space charge on the excitation efficiency  $\eta_{\text{exc}}$  in ZnS thin film electroluminescent devices. Depending on the irradiation intensity, the addition of UV reduces or even erases the space charge which is responsible for the inhomogeneous excitation efficiency. When the space charge is reduced,  $\eta_{\text{exc}}$  is higher in the region near the anodic insulator–semiconductor interface. In another experiment, neodymium doped ZnS samples are used to determine the variation of the space charge during the charge transfer. Under our driving conditions, the space charge increases during the charge transport in the steady state regime.

### 1. Introduction

Alternating-current-driven thin-film electroluminescence devices (ACTFELDs) have been extensively investigated in the last decade. However, some important questions are still open. In particular it is necessary, in order to develop reliable full colour displays, to elucidate the problems related to the charge carrier transport and the field distribution in the semiconductor.

It has been shown in ref. [1] that the well-known decrease of the efficiency of ZnS:Mn ACTFELD at high excitation levels is partly due to a strong decrease of the excitation efficiency  $\eta_{\text{exc}}$  (ratio of the number of excited luminescent

centres to the transferred charge) with increasing transferred charge. Among different hypotheses, it has been suggested that the decrease of  $\eta_{\text{exc}}$  stems from a space charge in the ZnS layer [1]. By using probe layer devices, where only selected parts of the ZnS layer are doped, it has been observed that  $\eta_{\text{exc}}$  is nonuniform [2]. As the excitation efficiency is related to the electric field, the field must be nonuniform, too. This result is a strong indication for the presence of bulk space charge.

In this work we present two methods which provide further insight into the role of the space charge in ACTFELDs. (1) By illuminating the device with UV, one can erase the space charge and verify if  $\eta_{\text{exc}}$  becomes independent of the position in the ZnS layer. (2) The doping of the probe layer with a luminescent centre providing a fast emission allows one to investigate the excita-

\* Corresponding author.

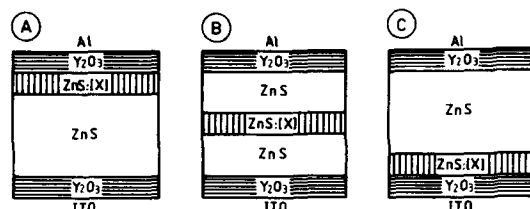


Fig. 1. Schematic structure of probe layer samples. [X] designates either Mn,  $\text{TbF}_3$  or  $\text{NdF}_3$ . The doped layer thickness is about one fifth to one sixth of the total semiconductor thickness.

tion efficiency and the behaviour of the space charge during the charge transfer.

## 2. Samples

All the samples have the metal–insulator–semiconductor–insulator–metal (MISIM) structure. The semiconductor was grown by electron beam evaporation and the doping was realized by thermal co-evaporation in order to ensure uniformity of the dopant. Depending on the sample, the doped layer is located in a different part of the ZnS layer: either near the insulator–semiconductor (IS) interface or in the middle of the ZnS layer (Fig. 1). The thickness of the doped ZnS layer was about a fifth of the unintentionally doped ZnS layer. For a series of samples, the doped layers were deposited in the same process, ensuring thereby that all have the same dopant content and equal luminescent properties. The dopant is either Mn or  $\text{TbF}_3$  (section 3.1) or  $\text{NdF}_3$  (section 3.2).

## 3. Results and discussion

### 3.1. UV illumination

After a charge transfer for a given electric pulse, there is a polarization  $P$  in the ZnS layer caused by the stored charge in the insulator–ZnS interfaces and by some residual bulk space charge. When UV is added, the UV-generated charge carriers can drift under the polarization field and

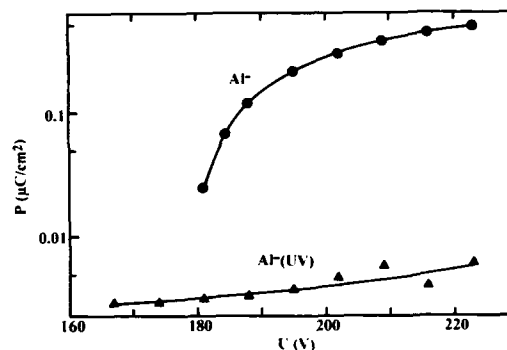


Fig. 2. Internal residual polarization  $P$  of the ZnS layer versus applied voltage  $U$ . "Al<sup>-</sup>" indicates that the polarization is determined just before the aluminium electrode is negatively biased. (●) Without UV illumination; (▲) under UV illumination.

recombine with the opposite charged centres. As a consequence,  $P$ , and thereby the residual space charge, are suppressed. This is depicted in Fig. 2 (UV illumination came from a mercury lamp with a filter system providing UV between 340 and 400 nm). This process is very efficient at low frequencies (some Hz) of the electric excitation (as the recombination takes time), and at high levels of transferred charge because of the strong residual polarization field. By varying the irradiation intensity, one can choose the degree of space charge erasing in the semiconductor.

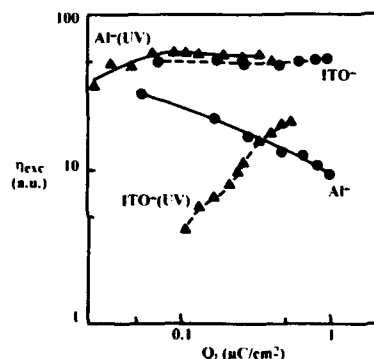


Fig. 3. Excitation efficiency  $\eta_{\text{exc}}$  versus transferred charge  $Q_t$ . "Al<sup>-</sup>" or "ITO<sup>-</sup>" designates the negatively biased electrode. Sample of type C (see Fig. 1). (●) Without UV illumination; (▲) under UV illumination.

Fig. 3 depicts some typical curves of  $\eta_{\text{exc}}$  for an excitation pulse length of 2  $\mu\text{s}$ . Here, the probe layer is adjacent to the ITO/IS interface (structure C, Fig. 1). When the electron injection comes from the IS interface opposite to the probe layer ( $\text{Al}^-$ ),  $\eta_{\text{exc}}$  is lower than for the other polarity and decreases with increasing charge. The results are analogous for structure A, irrespective of the used dopant (Mn or Tb). These are the main results of ref. [2].

The key point is: how behaves the excitation efficiency when the space charge is suppressed? When UV is added, the excitation efficiency for  $\text{Al}^-$  becomes higher and there is no decrease. This confirms the influence of the space charge on the excitation efficiency. When ITO $^-$  is negatively biased, the situation is somewhat more complex. At low voltage level, there is almost no electron injection from the IS interfaces and the charge carriers created by UV in the bulk are predominant. As most of these carriers are generated "behind" the probe layer, they cannot excite the centres therein. As a consequence,  $\eta_{\text{exc}}$  is very low and increases the more the electrons injected at the IS interface contribute to the transferred charge. At high level,  $\eta_{\text{exc}}$  does not reach the value obtained without UV. This may be explained by the suppression of the space charge which can diminish the field near the cathode. One observes at the same time a difference between  $\text{Al}^-$  and ITO $^-$  under UV at high excitation level. We suggest that this is due to the less good crystallinity of the first grown ZnS on the ITO side which results in a somewhat lower excitation efficiency compared to  $\text{Al}^-$  under the same conditions as already observed in ref. [2]. This would explain why for the structure A,  $\eta_{\text{exc}}$  is slightly higher under UV when  $\text{Al}^-$  compared to  $\eta_{\text{exc}}$  for ITO $^-$  under UV.

### 3.2. Nd emission

The measurements presented in the previous section as well as those presented in refs. [1,2] permit one to investigate the excitation efficiency at different parts of the semiconductor layer, but it is still integrated over the time of charge transfer. Therefore, the second series of experiences

were dedicated to the time behaviour of the space charge during the charge transfer. For this purpose, we realized probe layer samples with a dopant providing a sufficient fast emission that follows very closely the charge transfer. The transit time of one electron in an ACTFELD at high fields (about 1 MV/cm) for a 1  $\mu\text{m}$  thick ZnS layer lies in the order of some picoseconds. However, due to the electron emission mechanism (which is generally assumed to be the tunnel effect [3]), the time of the real conduction current is of the order of microseconds. Thus, one is looking for an emission with a decay time below 1  $\mu\text{s}$ . The red emission due to the  $^4\text{G}_{5/2} \rightarrow ^4\text{I}_{9/2}$  transition of  $\text{Nd}^{3+}$  satisfies this requirement. For a concentration of about 1 mol%, its decay time  $\tau_e$  is about 300 ns, as revealed from our cathodoluminescence measurements. As shown in former experiments, direct impact excitation prevails in Nd-doped ZnS [4], so that the short decay time allows one to measure an instantaneous efficiency by taking at each time the ratio of the Nd luminescence to the conduction current.

Fig. 4 shows a typical result for a sample (structure A). The conduction current density  $J$  was determined using the bridge method that permits one to compensate the displacement current [5].  $J(t)$  is virtually independent of the polarity. For the sake of legibility,  $J$  is only repre-

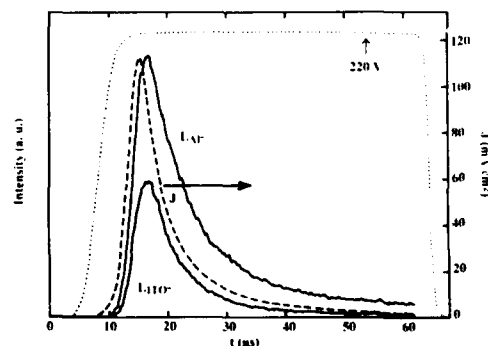


Fig. 4. Luminescence  $L$  at 600 nm and conduction current density  $J$  versus time  $t$ . The indices " $\text{Al}^-$ " or ITO $^-$ " designate the negatively biased electrode. Applied pulse form is shown by dotted line. Sample of type A (see Fig. 1).



sented for one polarity ( $\text{Al}^-$ ). The total transferred charge during the applied pulse of  $50 \mu\text{s}$  length is around  $1 \mu\text{C}/\text{cm}^2$ . This corresponds to a high level where existence of strong space charge is expected.

The  $\text{Nd}^{3+}$  luminescence at  $600 \text{ nm}$  is compared for the two polarities: For structure A, the luminescence  $L$  is all the time higher when  $\text{Al}^-$  compared to  $\text{ITO}^-$  (Fig. 4). This asymmetry is in keeping with the results in Mn or Tb doped samples revealing that the field at the cathode is higher than near the anode. One can observe a delay of  $1 \mu\text{s}$  between the maxima of  $J$  and  $L$  which has to be explained in order to determine the exact behaviour of

$$\eta_{\text{exc}}^{(\text{Al}^-)}(t) = \left( \frac{L(t)}{J(t)} \right)^{(\text{Al}^-)},$$

$$\eta_{\text{exc}}^{(\text{ITO}^-)}(t) = \left( \frac{L(t)}{J(t)} \right)^{(\text{ITO}^-)}.$$

Nevertheless, the ratio of the two instantaneous efficiencies can be expressed as  $R = \eta_{\text{exc}}^{(\text{Al}^-)}(t) / \eta_{\text{exc}}^{(\text{ITO}^-)}(t)$ .

Fig. 5 shows  $R$  for the structure A. At the beginning of the charge transfer, the efficiency is about two times higher for  $\text{Al}^-$ . This polarity dependence of the efficiency reflects the presence of a residual space charge before the charge

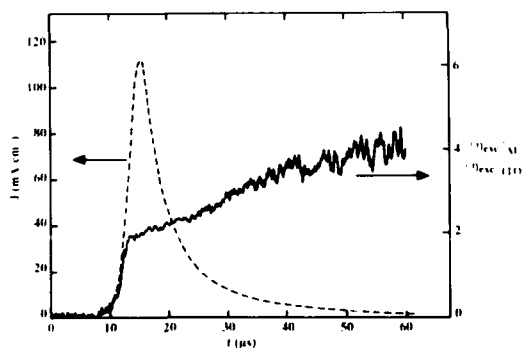


Fig. 5. Ratio of the instantaneous excitation efficiencies  $\eta_{\text{exc}}^{(\text{Al}^-)}(t)$  and  $\eta_{\text{exc}}^{(\text{ITO}^-)}(t)$  versus time  $t$ . Sample of type A (see Fig. 1).

transfer in agreement with ref. [2] and the results under UV illumination.

There is an important additional result which concerns the dynamic behaviour of the space charge:  $R$  increases during the charge transport by a factor 2. This indicates that in the steady state regime and under our driving conditions (6 Hz, pulse width of  $50 \mu\text{s}$ ), the space charge builds up during the pulse. Note in this context that experiments on integrally doped  $\text{ZnS:Mn}$  devices, where the instantaneous excitation efficiency was determined by deconvolution of the Mn luminescence response, show that  $\eta_{\text{exc}}$  decreases during the charge transfer [6]. This also suggests that the space charge increases during the charge transfer in these devices. The exact picture of the space charge dynamics, however, may depend on the characteristics of the grown layer and the driving conditions.

#### 4. Conclusions

Measurements under UV illumination prove the influence of space charge on the excitation efficiency in ZnS thin film electroluminescent devices. When the space charge is suppressed by the UV irradiation, the excitation efficiency is almost uniform across the semiconductor layer at high excitation levels. Nd doped ZnS samples can be used to determine the variation of the space charge during the charge transfer. In the steady state regime, there is a residual space charge which results in a non uniform excitation efficiency from the beginning of charge transport. The non uniformity of the excitation efficiency increases with higher transferred charge, indicating that the space charge increases during charge transfer.

#### 5. Acknowledgement

The "Laboratoire d'Acoustique et d'Optique de la Matière Condensée" is an "Unité associée au CNRS".

## 6. References

- [1] A. Zeinert, P. Benalloul, J. Benoit, C. Barthou, J. Dreyhsig and H.-E. Gumlich, *J. Appl. Phys.* 71 (1992) 2855.
- [2] J. Benoit, C. Barthou and P. Benalloul, *J. Appl. Phys.* 73 (1993) 1435.
- [3] D.H. Smith, *J. Luminescence*, 23 (1981) 209.
- [4] H. Kobayashi, S. Tanaka, H. Sasakura and Y. Hamakawa, *Jap. J. Appl. Phys.* 13 (1974) 1110.
- [5] Y.S. Chen and D.C. Krupka, *J. Appl. Phys.* 43 (1972) 4089.
- [6] D. Corlaian, P. De Visschere, K. Neyts and J. Van den Bossche, in: *Eurodisplay '93 Conf. Proc.*, 1993, p. 491.



ELSEVIER

Journal of Crystal Growth 138 (1994) 1028–1033

JOURNAL OF  
**CRYSTAL  
GROWTH**

## Mn-3d derived partial density of states at the interface of epitaxially grown zinc-blende MnTe on CdTe(100)

P.R. Bressler \*, H.-E. Gumlich

*Institut für Festkörperphysik, PN4-1, Technische Universität Berlin, Hardenbergstrasse 36, D-10623 Berlin, Germany*

### Abstract

Zinc-blende MnTe films (0 to 10 monolayers (ML)) were grown by molecular beam epitaxy (MBE) on CdTe(100). Angle-resolved photoelectron spectroscopy (ARPES) and resonantly enhanced photoelectron spectroscopy (RPES) were performed. The Mn-3d derived partial density of states (Mn-3d PDOS) was determined for the first time. By analysis of the Fano-like Mn 3p–3d resonance near  $h\nu = 50$  eV, three contributions to the Mn-3d PDOS were derived (denoted M, at 3.6 eV binding energy (BE), V, at 1.9 eV BE and S, near 7.5 eV BE). The Fano  $q$ -parameters obtained agree with the prediction that V relates basically to charge transferred states of Mn-3d<sup>5</sup> L character and S represents predominantly Mn-3d<sup>4</sup> satellite emission. The relative branching ratios for the latter two features to the first (V/M and S/M) grow monotonically as a function of thin MnTe coverage exceeding bulk  $\text{Cd}_{1-x}\text{Mn}_x\text{Te}$  values for thicker films. This behavior is possibly due to strain and distortion of the tetrahedral symmetry at the interface and due to the phase transition to NiAs structure.

### 1. Introduction

It is well established that MnTe in zinc-blende structure can be stabilized by means of epitaxial growth on related II–VI substrates [1–3]. Thus the entire concentration range of Mn in  $\text{II}_{1-x}\text{Mn}_x\text{VI}$  compounds (e.g.,  $\text{Cd}_{1-x}\text{Mn}_x\text{Te}$ ) can be investigated experimentally. In particular, the exchange interaction between Mn-3d spin and the valence or conduction band electrons, the actual electronic structure and the degree of p–d hybridization have been subject of several investigations on bulk  $\text{II}_{1-x}\text{Mn}_x\text{VI}$  compounds [4]. By

means of resonant enhancement of the Mn-3d emission at the Mn-3p threshold in resonant photoelectron spectroscopy (RPES), the Mn-3d derived partial density of states (PDOS) has been studied in  $\text{HgMnVI}$  [5],  $\text{CdMnVI}$  [6–8] and  $\text{ZnMnVI}$  [9,10]. These experimental investigations have been previously limited to the range of Mn concentration available in bulk samples (e.g.,  $0 < x < 0.77$  for zinc-blende  $\text{Cd}_{1-x}\text{Mn}_x\text{Te}$ ), whereas most theoretical work has focussed on binary Mn chalcogenides [11–13]. In this paper we present the first photoemission study of the electronic structure of epitaxially grown MnTe on CdTe(100) using synchrotron radiation. The Mn-3d derived partial density of states in zinc-blende MnTe is determined by utilizing the well-known Mn 3p–3d resonance near 50 eV excitation energy.

\* Corresponding author.

## 2. Experimental procedure

Thin CdTe and MnTe films were grown by molecular beam epitaxy (MBE) and characterized by Auger electron spectroscopy (AES) and reflection high-energy electron diffraction (RHEED). Angular-resolved ultra-violet photoelectron spectroscopy (ARUPS) and (angular-resolved) resonant photoelectron spectroscopy (RPES) were performed in situ. Epitaxial growth, characterization and PE experiments were performed in situ in a three-chamber system. The work reported here was carried out at the Berlin synchrotron radiation source BESSY using a toroid grating monochromator (TGM) beamline. The photon energy ranged from 10 to 140 eV. Energy distribution curves (EDCs) of the emitted photoelectrons were detected with a commercial hemispherical energy analyzer. The overall resolution was  $\sim 200$  meV at 70 eV photon energy. Working pressure in the PE chamber was  $< 8 \times 10^{-10}$  mbar and  $< 5 \times 10^{-9}$  mbar in the growth chamber. General details concerning the experimental set-up and our photoemission (PE) experiment have already been described and can be found in ref. [14].

CdTe buffer layers were grown on commercial InSb(100) substrates. Coverages ranged from 50 to 150 monolayers (InSb(100): 1 ML =  $4.76 \times 10^{14}$  particles/cm<sup>2</sup>) for use in turn as substrate surfaces for monolayer growth of MnTe in zincblende (ZB) structure. CdTe was deposited from two elemental effusion cells (Cd: 4.5N and Te: 5N material) and from a single CdTe effusion cell (4.5N). Typical elemental cell temperatures were 220°C for Cd and 280°C for Te. Binary-cell temperatures ranged around 310°C. Typical growth rates were 0.3 to 3 ML/min.

Enhanced Auger intensity ratios of In (404 eV) and Te (483 eV) to Cd (376 eV) indicated the formation of In<sub>2</sub>Te<sub>3</sub> at the interface with depletion of Cd in the first few monolayers at  $T_{\text{sub}} > 210^\circ\text{C}$ . To avoid this, samples were grown at  $T_{\text{sub}} = 170\text{--}190^\circ\text{C}$ . RHEED patterns along three azimuths ( $\langle 001 \rangle$ ,  $\langle 011 \rangle$  and  $\langle 0\bar{1}1 \rangle$ ) of InSb(100), CdTe buffer layers and MnTe films (up to 10 ML) indicated good two-dimensional surface quality.  $(8 \times 2)$  and  $(4 \times 2)$  surface reconstructions

of the InSb(100) substrates were detected.  $(4 \times 2)$  and  $(2 \times 1)$  surface reconstructions of CdTe(100) were observed. Below  $T_{\text{sub}} = 140^\circ\text{C}$ , RHEED patterns became spotty.  $(2 \times 1)$  surface reconstruction is found throughout deposition of MnTe. No other specific changes of the RHEED pattern were detected during MnTe deposition.

Deposition of MnTe (0 to 10 ML) occurred in situ at  $T_{\text{sub}} \approx 180^\circ\text{C}$ . Elemental sources and a MnTe compound cell were used. Typical temperatures for the Mn source were  $\sim 800^\circ\text{C}$ . MnTe cell temperatures were  $\sim 720^\circ\text{C}$ . MnTe growth rates were  $\sim 0.5$  ML/min. The source power was controlled between 30 and 40 W for the Mn source. The Mn flux rate was monitored with a cross-beam quadrupole mass spectrometer. Depositions were calibrated by relating coverages to flux rates with AES data and with reflectivity spectroscopy (RS) data from our thick films.

MnTe coverages were also checked by comparing the Cd-4d core level attenuation in ARUPS as a function of coverage with published results by Wall et al. [8] (Mn on CdTe(110)) and Niles et al. [15] (MnTe/CdTe(110)). This way independently determined inelastic mean free paths were extracted assuming a simple exponential attenuation versus film coverage [16]. Fig. 1 shows a combined plot of MnTe films grown on CdTe(100) (our data) and MnTe films grown on CdTe(110)

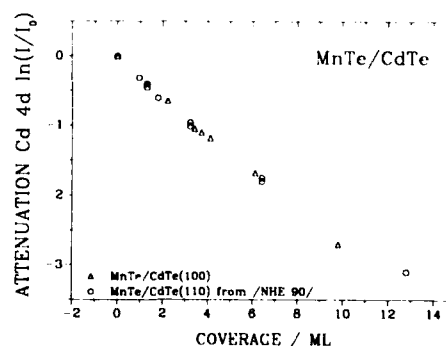


Fig. 1. Logarithmic plot of the attenuation of Cd-4d core level emission at 70 eV photon energy versus deposition of MnTe. Data from this work, obtained via deposition time and by extrapolation from growth rates of thick films measured by RS, fit on the same line as data from ref. [15] (MnTe/CdTe(110)).

(data from ref. [15]). The logarithmic plot of PE intensity and the nominal MnTe coverage are found to be linear with the evaporation time.

### 3. Mn-3d derived density of states

The total yield of the Mn 3p–3d threshold excitation as detected by measuring the sample current versus excitation energy is presented in Fig. 2. The signal current was scaled to the monochromator output (determined by the photocurrent from the Au exit mirror of the beam line). The Te-4d core level absorption is seen at 41.1 eV ( $4d_{5/2}$  edge) and at 42.7 eV ( $4d_{3/2}$  edge). This is 0.2 eV lower than in  $\text{Cd}_{1-x}\text{Mn}_x\text{Te}$ . Mn-3d derived absorption features are predominant between 45 and 60 eV. They arise from resonantly enhanced Mn-3d emission. The Fano-like resonance is due to the interference between the direct Mn-3d emission (channel 1) and Mn 3p  $\rightarrow$  3d transitions followed by autoionization which lead to the same final state (channel 2):

Channel 1:  $\text{Mn}: 3p^6 3d^5 + h\nu \rightarrow 3p^6 3d^4 + e^-$ , continuous excitation.

Channel 2:  $\text{Mn}: 3p^6 3d^5 + h\nu \rightarrow 3p^5 3d^6 \rightarrow 3p^6 3d^4 + e^-$ , discrete excitation.

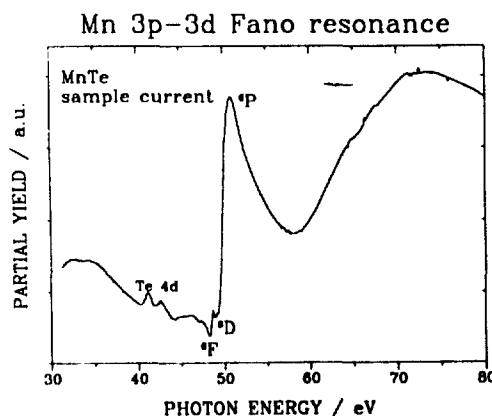


Fig. 2. Total photoemission yield of 6.1 ML MnTe/CdTe(100) as a function of photon energy. Te-4d threshold is double-peaked at 41.1(1) eV and 42.7(1) eV. The predominant Mn 3p–3d resonance ( $^6\text{P}$  multiplet) is at 50.5 eV. Preceding features are denoted to weaker  $^6\text{D}$  and  $^6\text{F}$  multiplets (dipole forbidden transitions). (Step below 50 eV is assigned to  $^6\text{D}$ .  $^6\text{F}$  should hardly be visible in the plot.)

The different structures in Fig. 2 are from different multiplets of the final  $3p^5 3d^6$  configuration ( $^6\text{D}$ ,  $^4\text{F}$  and  $^6\text{P}$ ). The prominent absorption band near 50 eV is due to transition from the  $3p^6 3d^5$  ( $^6\text{S}$ ) ground state into the  $3p^5 3d^6$  ( $^6\text{P}$ ) excited state. The  $^6\text{P}$  multiplet is the only dipole-allowed transition from the  $^6\text{S}$  ground state in L–S coupling. The asymmetric line shape and width are governed by the quantum-mechanical interference with the degenerate continuum transition from the ground state into the  $3p^6 3d^4 \epsilon f$  state [17], [18]. The small resonance on the low energy edge of the  $^6\text{P}$  resonance is assigned to the  $^6\text{D}$  and  $^6\text{F}$  members of the  $3p^5 3d^6$  multiplet [18].

The Fano-like enhancement can be used to separate the Mn-3d related portion of the valence band emission [5–10]. The Fano profile [17,18] of the photoelectron intensity  $I(E)$  can be written as:

$$I(E) = I_{\text{NR}}(E) + I_0(E)(q + \epsilon)^2 / (\epsilon^2 + 1). \quad (1)$$

$I_{\text{NR}}(E)$  represents the non-resonant background emission.  $I_0(E)$  is the Mn-3d emission in absence of autoionization and  $\epsilon$  is the rescaled energy,  $\epsilon = (E - E_0)/\Gamma$ , with  $E_0$  being the resonance energy and  $\Gamma$  the width of the resonance. The Fano  $q$ -parameter is determined by the strength of the interference between the particular final states. A set of EDCs taken in the range of resonance excitation for 6.1 ML MnTe/CdTe(100) is shown in Fig. 3. Clearly, three features appear to enhance drastically above ca. 50 eV: at 7.5 eV, at 3.7 eV and near 1.5 eV  $\Delta E$ . The Mn  $M_{2,3}M_{4,5}M_{4,5}$  Auger peak found in metallic Mn [19] and in MnP [20] is not detected in our spectra. This supports the assumption that the predominant decay channel of the ( $^6\text{P}$ ) Mn 3p–3d core excitation is by autoionization (direct recombination) rather than by Auger decay [7].

A difference curve (“on” resonance minus “off” resonance) for 2.2 ML MnTe is presented in fig. 4. The spectra were normalized to the monochromator output and corrected for secondary electrons. The normalized EDCs taken at off resonance (MnTe:  $\hbar\omega = 47.3$  eV) were subtracted from the EDCs recorded on resonance

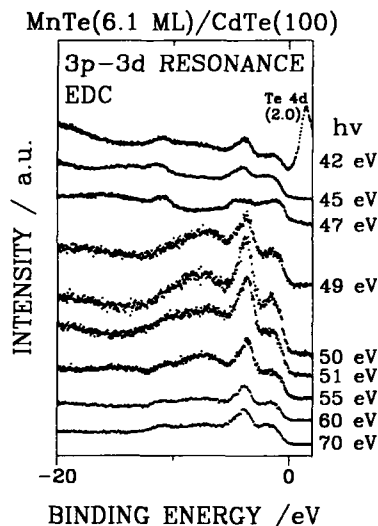


Fig. 3. Set of EDCs of 6.1 ML MnTe on CdTe(100) in the photon energy range of the Mn 3p-3d excitation. Te-4d emission excited by second order light of the monochromator is seen in the upmost spectrum (42 eV) at the valence band maximum.

(MnTe:  $\hbar\omega = 50.4$  eV). Due to the nature of the Fano resonance, only Mn-3d electrons contribute to the resonance [7,18]. The difference curve thus

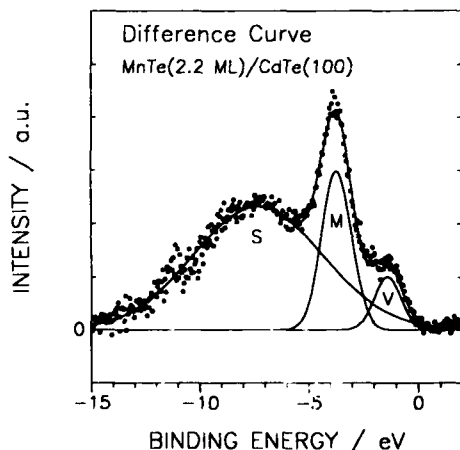


Fig. 4. Selected Mn-3d derived photoelectron spectrum for 2.2 ML MnTe/CdTe(100) (data points). The fitted curve (top solid line) contains three Gaussians for the three major structures M, S and V (underlying solid curves).

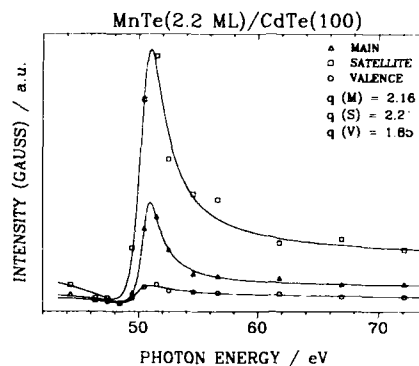


Fig. 5. Constant initial state-like spectra of S, M and V emission of 2.2 ML MnTe/CdTe(100). Data points were obtained by evaluating the area underneath the Gaussian fits to the three structures. The solid lines are Fano profile fits. The corresponding Fano  $q$ -parameters are inserted in the plot.

represents the Mn-3d derived photoemission spectrum. The spectrum itself contains the partial density of Mn-3d states in the valence region and emission from the p-d charged transferred states as well as Mn-3d<sup>4</sup> satellite emission. In accordance to the configuration interaction model [21] for a MnTe<sub>4</sub><sup>0-</sup> cluster [7] the three structures are related to emission of Mn-3d<sup>4</sup> satellites (S) and Mn-3d<sup>5</sup> L (ligand hole) emission resulting from charge transfer (V and M). All three structures consist of final states of both <sup>5</sup>T<sub>2</sub> and <sup>5</sup>E symmetry; however, M contains predominantly <sup>5</sup>E symmetry, and V and S contain predominantly <sup>5</sup>T<sub>2</sub> final state emission. The curve features have been reproduced in Fig. 4 using three Gaussians (solid lines).

The resonance behavior of the three features S, M and V is investigated by subtracting the "off"-resonance curve from all other spectra after normalization. The area of the curves is determined and fitted by a Fano resonance (Eq. (1)). The fit results (solid lines) for 2.2 ML MnTe/CdTe(100) are presented in Fig. 5. The corresponding Fano  $q$ -parameters of the individual curves have been inserted. One trend observed is that the  $q$ -parameter of V is lower than that of the other structures due to the stronger contribution from p-d charge transfer states in V

[7,11–14]. This indicates a stronger degree of p–d hybridization and delocalization of the final states involved. The values agree fairly well with results from bulk ternary  $\text{Cd}_{1-x}\text{Mn}_x\text{Te}$  [6].

In Fig. 6 the difference curves (“on” resonance minus “off” resonance) of several MnTe films are plotted versus binding energy. The relative intensities of features S and V normalized to M should reflect the degree of p–d hybridization: S/M should decrease and V/M should increase with stronger p–d hybridization. The relative branching ratios of the individual curves were compiled by fitting the spectra to three Gaussians, as described for the 2.2 ML film. These branching ratios are plotted in Fig. 7 as a function of MnTe coverage. The original difference curves were obtained by subtraction, as described above, after the data had been normalized to photon flux and a secondary background had been subtracted. Other methods had been tested (e.g., normalizing data to total valence band emission after second-

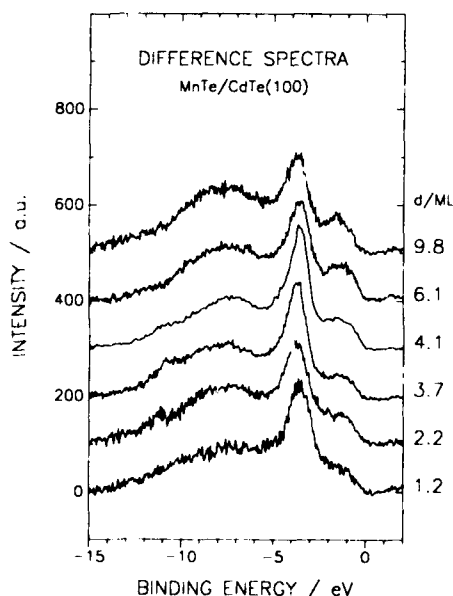


Fig. 6. Set of Mn-3d derived valence band photoemission spectra (difference spectrum: normalized “on” resonance EDC minus “off” resonance EDC) for six different MnTe/CdTe(100) heterostructures.

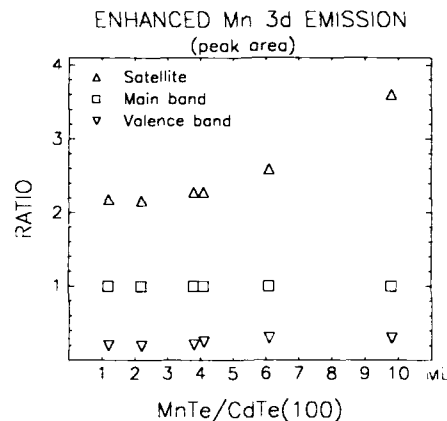


Fig. 7. Plot of the emission ratio (Gaussian areas) of M, S and V normalized to the main structure M as a function of MnTe coverage.

aries correction). The same trend (increase of the branching ratios) as in Fig. 7 was always found.

An interpretation of this finding cannot follow the p–d hybridization argumentation [6–10] because both S/M and V/M appear to increase with MnTe coverage. Principally, this indicates an increase in emission of  $^5T_2$  final state symmetry with respect to  $^5E$  final states onsetting near 6 ML. Below 6 ML MnTe coverage, the branching ratios agree with values obtained from bulk samples. This behavior differs significantly from the continuous increase of the branching ratios up to bulk values found in MnSe/ZnSe(100) [14]. The lattice mismatch of the two systems is of opposite sign:  $\Delta a(\text{MnSe/ZnSe}(100)) \approx +4.5\%$  and  $\Delta a(\text{MnTe/CdTe}(100)) \approx -4.0\%$ . This will give rise to different strain induced effects on the charge transfer mechanisms in the different films. A possible explanation for the step-like variation is an initiating phase transition from ZB to NiAs structure below 10 ML. Previously, the transition has been reported to occur near 12 ML under similar growth conditions in the MnTe/CdTe(110) system [15].

#### 4. Acknowledgements

We are very grateful to H.U. Middelmann for important and fruitful discussions on RPES and

our data. We further acknowledge the valuable assistance of T. Hannappel and H.C. Mertins during beamtime. This work was partially financed by the Bundesminister für Forschung und Technologie (BMFT), Bonn, Germany under contract No. 05414 CB17.

## 5. References

- [1] L.A. Kolodziejski, R.L. Gunshor, N. Otsuka, B.P. Gu, Y. Hefetz and A.V. Nurmikko, *Appl. Phys. Lett.* 48 (1986) 1482.
- [2] R.L. Gunshor, A.V. Nurmikko, L.A. Kolodziejski, M. Kobayashi and N. Otsuka, *J. Crystal Growth* 101 (1990) 14.
- [3] M. Kobayashi, R.L. Gunshor and L.A. Kolodziejski, in: *Wide Gap II–VI Compounds for Optoelectronic Applications*, Ed. H.E. Ruda (Chapman and Hall, London, 1992) p. 124.
- [4] J.K. Furdyna, *J. Appl. Phys.* 64 (1988) R29.  
O. Goede and W. Heimboldt, *Phys. Status Solidi (b)* 146 (1988) 11.
- [5]  $\text{Hg}_{1-x}\text{Mn}_x\text{Se}$ : A. Franciosi, C. Caprile and R. Reifemberger, *Phys. Rev. B* 31 (1985) 8061.
- [6] M. Taniguchi, A. Fujimori, M. Fujisawa, T. Mori, I. Souma and Y. Oka, *Solid State Commun.* 62 (1987) 431.
- [7] L. Ley, M. Taniguchi, J. Ghijsen, R.L. Johnson and A. Fujimori, *Phys. Rev. B* 35 (1987) 2839.
- [8] A. Wall, A. Raisanen, G. Haugstad, L. Vanzetti and A. Franciosi, *Phys. Rev. B* 44 (1991) 8185.
- [9] R. Weidemann, H.E. Gumlich, M. Kupsch, H.U. Middelman and U. Becker, *Phys. Rev. B* 45 (1992) 1172.
- [10]  $\text{Zn}_{1-x}\text{Mn}_x\text{Te}$  and a comparison with  $\text{Cd}_{1-x}\text{Mn}_x\text{Te}$ : M. Taniguchi, K. Soda, I. Souma and Y. Oka, *Phys. Rev. B* 46 (1992) 15789.
- [11] K.C. Hass and H. Ehrenreich, *Acta Phys. Polon. A* 73 (1988) 933.
- [12] B.E. Larson, K.C. Hass, H. Ehrenreich and A.E. Carlson, *Phys. Rev. B* 37 (1988) 4137.
- [13] S.H. Wei and A. Zunger, *Phys. Rev. B* 35 (1987) 2340.
- [14] P.R. Bressler, T. Klöpper and H.-E. Gumlich, *J. Vac. Sci. Technol. B* 11 (1993) 1621.
- [15] D.W. Niles, H. Höchst and M.A. Engelhardt, *J. Electron Spectrosc. Related Phenom.* 52 (1990) 139.
- [16] J. Kolaczkiwicz and E. Bauer, *Surf. Sci.* 144 (1984) 495.  
M.P. Seah and W.A. Dench, *Surf. Interf. Anal.* 1 (1979) 1.
- [17] U. Fano, *Phys. Rev.* 124 (1961) 1866.
- [18] L.C. Davis, *J. Appl. Phys.* 59 (1986) R29.
- [19] H. Kato, T. Ishii, S. Masuda, Y. Harada, T. Miyano, T. Komeda, M. Onchi and Y. Sakisaka, *Phys. Rev. B* 32 (1985) 1992.
- [20] A. Naito, A. Kakizaki, T. Komatsubara, H. Sugawara, I. Nagakura and T. Ishii, *J. Phys. Soc. Japan* 54 (1985) 416.
- [21] A. Fujimori and F. Minami, *Phys. Rev. B* 30 (1984) 957.





ELSEVIER

Journal of Crystal Growth 138 (1994) 1034–1039

JOURNAL OF **CRYSTAL  
GROWTH**

## Peculiarities of transport properties in semiconductors with resonant impurities: HgSe:Fe versus PbTe:Cr

E. Grodzicka, W. Dobrowolski, J. Kossut <sup>\*</sup>, T. Story, B. Witkowska

*Institute of Physics, Polish Academy of Sciences, Al. Lotników 32 / 46, 02-668 Warsaw, Poland*

### Abstract

We compare the transport properties of two semiconducting systems containing resonant donors, HgSe:Fe and PbTe:Cr, with concentrations of dopants corresponding to the Fermi level being stabilized at the resonant state. It is known that under such conditions, at a low temperature, there arises a spatial correlation of electric charges localized on donor centers. The occurrence of the correlation is driven by the inter-donor Coulomb repulsive interaction. In the case of HgSe:Fe, the correlation leads to a sizable enhancement of the conduction electron mobility. In the case of PbTe:Cr, high values of the dielectric constant limit the temperature region in which the correlation is expected to occur, to temperatures below approximately 3.5 K. Therefore, no direct observation of the mobility enhancement was possible. On the other hand, a lack of a strong suppression of the mobility by the resonant scattering mechanism can be taken as an indirect indication that the positions of charged donor centers are correlated to such an extent that formation of the Coulomb gap (due to inter-donor Coulomb repulsive interaction) causes the resonant scattering to be very inefficient.

### 1. Introduction

There are several cases of donor impurity states whose energies are known to be resonant with the conduction band states. In II–VI semiconductors, for example in HgSe and related materials ( $\text{Hg}_{1-x}\text{Zn}_x\text{Se}$ ,  $\text{Hg}_{1-x}\text{Mn}_x\text{Se}$ ,  $\text{HgS}_x\text{Se}_{1-x}$ , etc.), such a state is given rise to by an iron substitutional impurity [1,2]. In materials containing resonant donors, the position of the Fermi level can be stabilized (or trapped) at the resonant level position provided that the concentration of the resonant impurities is high enough. In such a situation, only part of the Fe donors are

ionized (and therefore charged); thus the system of donors is sometimes referred to as possessing a mixed valence character.

Under the condition of the Fermi level being pinned to the resonant donor level, one may expect that the conduction electron mobility would be additionally reduced because of the onset of an additional and efficient scattering mechanism – the resonant scattering. Contrary to these expectations, some of the HgSe:Fe samples in the mixed valence regime were found to be characterized by surprisingly high values of the electron mobility [3,4]. As suggested by Mycielski [5], this effect is to be associated with a spatial correlation of impurity charges, which can arise at low temperatures in a system of impurities incompletely filled with electrons, driven by

<sup>\*</sup> Corresponding author.

inter-donor Coulomb repulsive interactions. This interpretation (with some quantitative modifications) is now widely accepted (see refs. [6–8]).

Another example of a resonant donor state which can pin the Fermi level is the case of DX centers in GaAs under hydrostatic pressure [6]. Also in the case of the latter material, a reduction of the scattering rate of conduction electrons by charged impurities was observed and attributed to spatial correlations within the systems of the scattering centers.

In the case of IV–VI semiconducting compounds, the resonant nature of impurity states is even more common than in other semiconductor systems. There are several well-evidenced cases of resonant acceptors as well as resonant donors [9,10]. PbTe, even when doped with nonresonant impurities, often displays high values of electronic mobility at low temperatures (since charged impurity scattering is strongly suppressed due to very high values of the dielectric constant in this material [11]). It is interesting to see if it is possible to combine this feature with mobility enhancement related to the spatial correlation mechanism.

## 2. Experimental procedure

We have prepared PbTe samples, doped with chromium, by the Bridgman method and investigated Hall effect and resistivity at temperatures ranging from 3.5 to 300 K. We studied both as-grown and annealed samples. Doping with Cr leads at first to an increase of the electron concentration in the conduction band (see Fig. 1). At very small concentrations of Cr, the as-grown samples turn out to be p-type; it is possible to convert them into n-type by isothermal annealing process in Pb vapor, which reduces the number of Pb vacancies that act as compensating acceptors. For concentrations of Cr ions introduced into the crystals that exceed approximately  $1.3 \times 10^{19} \text{ cm}^{-3}$  (which corresponds to molar fraction  $x^* = 0.0009$ ), a saturation of the  $n$  versus  $x$  curve is observed. This is evidence of the Fermi level pinning. Annealing of the samples with  $x > x^*$  does not lead to any changes of the conduction

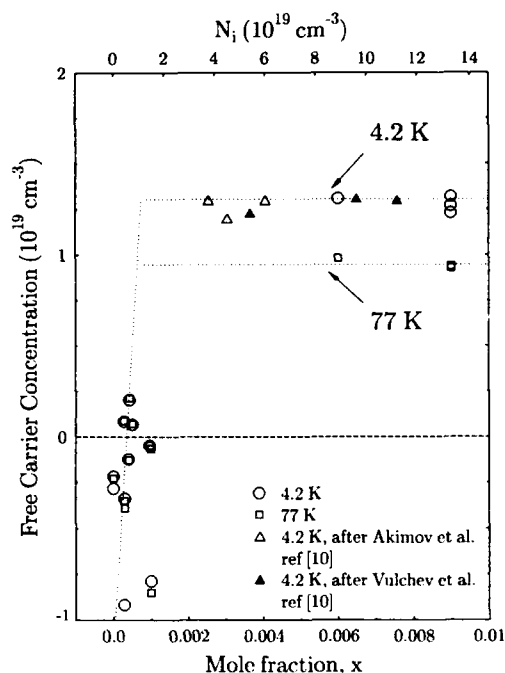


Fig. 1. Conduction electron concentration in PbTe doped with Cr as a function of Cr molar fraction for two temperatures. The lines are only a guide to the eye.

electron concentrations. It shifts, however, the Fermi level across the resonant impurity density of states. Also, it improves greatly the mobility. The increase of the mobility upon annealing is sometimes by a factor of about 4 (see Fig. 3). From the value of the conduction electron concentration at the saturation, it is possible to estimate the value of the energy of the resonant Cr state that equals 100 or 70 meV (see ref. [12] for more details), depending on the band structure parameters of PbTe used in the calculation. Below  $x^*$  all Cr ions are ionized and possess  $\text{Cr}^{+3}$  configuration, while in the saturation region part of them exist in a neutral (with respect to the host lattice)  $\text{Cr}^{+2}$  state. This is in agreement with magnetic susceptibility [13] and EPR [14] measurements carried out on this compound.

The conduction electron concentration displays an interesting temperature dependence. Fig. 2 shows an example of  $n$  versus  $T$  curves for samples from various regions of Cr contents. In

the  $x = 0.009$  sample (with the Fermi level trapped by the resonant Cr state), a decrease of  $n$  with an increase in  $T$  is mostly related to a downward temperature shift of the impurity level. In the sample with  $x = 0.00042$ , all Cr ions are in  $\text{Cr}^{+3}$  state. After an initial slight increase of  $n$  with  $T$  (attributed to the presence of the defect states in the gap), a decrease of the concentration with temperature is observed. This is due to trapping of thermally excited electrons by the large density of available Cr resonant states. The sample with the smallest number of Cr ions, shown in Fig. 2, displays a dependence that is typical for PbTe crystals [15]. The trends in  $n$  versus  $T$  dependence resemble those seen earlier in HgSe:Fe in various regimes of iron doping [3].

The mobility of our PbTe:Cr samples (especially after annealing) shows very high values characteristic of PbTe crystals, where the dielectric constant ( $\epsilon \approx 1300$ , see ref. [16]) screens out the charged impurity Coulomb potentials that normally limit the mobility in semiconductors at

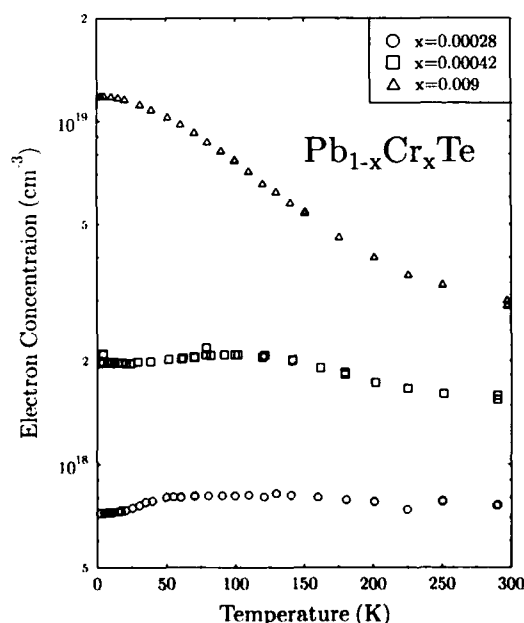


Fig. 2. Conduction electron concentration as a function of temperature in three PbTe samples with different Cr contents.

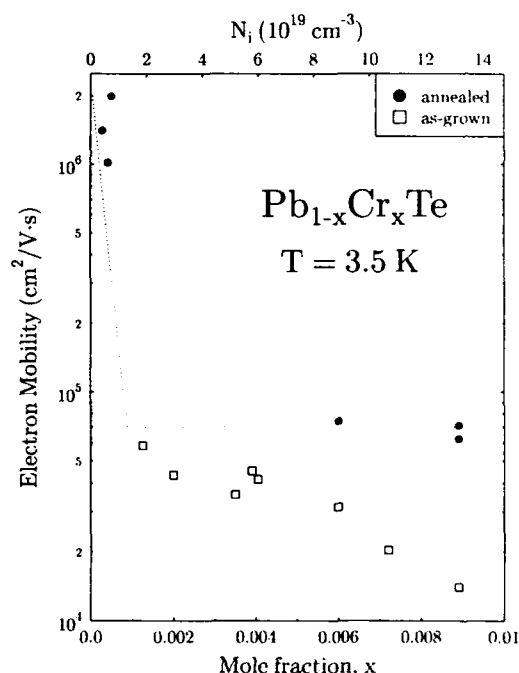


Fig. 3. Electron mobility in PbTe:Cr measured at 3.5 K. The lines show the mobility displayed by best PbTe samples doped with nonresonant donors taken from refs. [11,17].

low temperatures. The highest mobility value observed in our samples was  $2 \times 10^6 \text{ cm}^2/\text{V}\cdot\text{s}$ . This was seen in the sample which was only very slightly doped with Cr—cf. Fig. 3. Samples in the mixed valence regime (i.e., with concentrations of Cr greater than  $1.3 \times 10^{19} \text{ cm}^{-3}$ ) have lower mobilities; however, they correspond to the best mobilities observed in the heavily doped PbTe [17]—see Fig. 3. The good mobility of a heavily doped PbTe:Cr material is also evident from the magnetotransport studies by Akimov and co-workers [10], where the Shubnikov–De Haas oscillations were characterized by small Dingle temperatures.

### 3. Analysis

Having in mind the high value of the dielectric constant of PbTe, we could expect the mobility enhancement to become visible only in the lowest

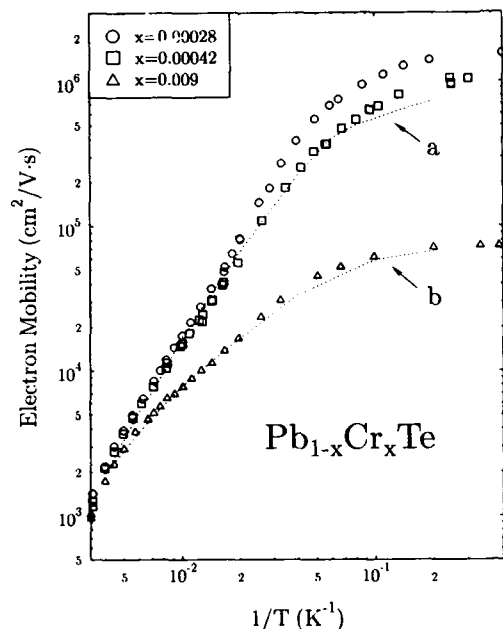


Fig. 4. Electron mobility as a function of inverse temperature in three PbTe:Cr samples. Broken lines show the mobility measured in PbTe doped with nonresonant donors by Allgeier and Scanlon [17] in samples with: (a)  $n = 3.3 \times 10^{18} \text{ cm}^{-3}$  and (b)  $n = 9.48 \times 10^{18} \text{ cm}^{-3}$ .

temperature studied by us. An estimate of the characteristic temperature of the onset of the correlation within the short range correlation model [6,7] gives  $T^* = E_c/k_B = 3.5 \text{ K}$ , where  $E_c$  is the energy gain (per charged impurity) due to the spatial correlation of impurity charges. For comparison, the value of  $T^*$  in HgSe:Fe is about 70 K. In the latter system the enhanced values of the mobility are clearly observable at temperatures as high as  $2T^*$ . In the present case of PbTe:Cr, it is impossible to find unambiguously any characteristic features of the enhanced mobility (e.g., strong temperature variation of the mobility in the region where the correlation forms, i.e., below  $\sim 2T^*$ ) down to the lowest temperatures studied. This is clearly seen in Fig. 4, where the weak temperature dependence of the mobility observed in our samples, in the lowest temperature region, is similar to that seen in PbTe samples containing the same concentration of

conduction electrons due to nonresonant dopants. Obviously, to completely exclude the possibility of existence of mobility enhancement in PbTe:Cr, our investigation needs to be extended to even lower temperatures, i.e., well below  $T^*$ .

On the other hand, the high values of the mobility in our samples from the mixed valence regime indicate also that there is little (if any) contribution from the resonant scattering. This scattering was reported to be observable in the case of other resonant acceptors in PbTe [18]. The relaxation time for this scattering mechanism can be expressed by (assuming that there is only one characteristic energy of the resonant donor state  $\epsilon_i$ )

$$\frac{1}{\tau_r} = \frac{\rho_i(\epsilon) \Gamma}{\rho_b(\epsilon) \hbar}, \quad (1)$$

where  $\rho_b$  stands for the density of states in the conduction band and

$$\rho_i = \frac{N_i}{2\pi} \frac{\Gamma}{\frac{1}{4}\Gamma^2 + (\epsilon - \epsilon_i)^2} \quad (2)$$

is the resonant impurity density of states,  $N_i$  is the total concentration of the impurities,  $\Gamma$  is the width of the resonant level due to hybridization (not to be confused with the spread of the impurity energy  $\epsilon_i$  values due to the spatial Coulomb potential fluctuations). For strong degeneracy of the electron gas one has to calculate the above expression for the relaxation time at the Fermi level  $\epsilon_F$ . We estimated the mobility limited by the resonant scattering (assuming for simplicity a spherical and parabolic conduction band) taking  $\Gamma \approx 1 \text{ meV}$ , the value consistent with extremely narrow line width of the EPR signal [14]. The position of the Fermi energy within the broadened density of impurity states was estimated from the ratio, known for each sample, of the Cr impurity centers filled with electrons to the total number of Cr impurity centers:

$$\frac{N_f}{N_i} = 1 - \frac{n}{N_i} = \frac{\int_0^{\epsilon_F} \sqrt{\epsilon} \frac{1}{\frac{1}{4}\Gamma^2 + (\epsilon - \epsilon_i)^2} d\epsilon}{\int_0^{\infty} \sqrt{\epsilon} \frac{1}{\frac{1}{4}\Gamma^2 + (\epsilon - \epsilon_i)^2} d\epsilon}. \quad (3)$$

The resulting value of the mobility for, e.g., the sample with  $N_i = 1 \times 10^{20} \text{ cm}^{-3}$  (and having  $n = 1.3 \times 10^{19} \text{ cm}^{-3}$  electrons in the conduction band) turns out to be  $\mu_r = 126 \text{ cm}^2/\text{V} \cdot \text{s}$ . This value is completely incompatible with the high mobility values experimentally observed in this sample. We suggest, therefore, that – similarly to the case of HgSe:Fe – there is a mechanism that very efficiently suppresses the resonant scattering. The formation of the Coulomb gap in the impurity density of states in the situation of incomplete filling of these states by electrons [19] can provide such a mechanism. When the inter-donor Coulomb interactions are taken into account, the impurity system cannot be characterized by a single value of the energy  $\epsilon_i$ . One has to introduce a distribution of this energy  $\rho(\epsilon_i)$  and integrate Eq. (1) with this distribution over possible energies  $\epsilon_i$ . The formation of the Coulomb gap means the appearance of a strong depletion in this distribution at exactly the Fermi level. This, in turn, reduces the value of the resonant scattering.

Let us stress that the existence of the Coulomb gap is just another manifestation of a spatial correlation that exists in the impurity center system, due to inter-donor Coulomb interactions, since there is a one-to-one correspondence between the spatial arrangement of the charged impurities and the energetics of such a system.

#### 4. Conclusions

Our study of PbTe doped with resonant Cr donors does not reveal any enhancement of the mobility due to the spatial correlation of impurity charges down to temperatures as low as 3.5 K. This is in contrast to the case of HgSe doped with resonant Fe donors. However, the spatial correlation in PbTe:Cr can not be entirely excluded since the mobility observed in the samples studied is relatively high without any observable influence of the resonant scattering. We associate this with the formation of the Coulomb gap in the impurity one-electron density of states.

#### 5. Acknowledgments

The work was supported in part by Committee for Scientific Research under Grant 20483/91/01.

#### 6. References

- [1] W. Dobrowolski, K. Dybko, C. Skierbiszewski, T. Suski, E. Litwin-Staszewska, S. Miotkowska, J. Kossut and A. Mycielski, in: *Proc. 19th Int. Conf. on the Physics of Semiconductors*, Warsaw, 1988, Ed. W. Zawadzki (Institute of Physics, Polish Academy of Sciences, Warsaw, 1988) p. 1247.
- [2] A. Mycielski, P. Dzwonkowski, B. Kowalski, B.A. Orlowski, M. Dobrowolska, M. Arciszewska, W. Dobrowolski and J.M. Baranowski, *J. Phys. C* 19 (1986) 3605.
- [3] F. Pool, J. Kossut, R. Reifenger and U. Debska, *Phys. Rev. B* 35 (1987) 3900.
- [4] W. Dobrowolski, K. Dybko, A. Mycielski, J. Mycielski, J. Wróbel, S. Piechota, M. Palczewska, H. Szymczak and Z. Wilamowski in: *Proc. 18th Int. Conf. on the Physics of Semiconductors*, Stockholm, 1986, Ed. O. Engström (World Scientific, Singapore, 1987), p. 1743.
- [5] J. Mycielski, *Solid State Commun.* 60 (1986) 165.
- [6] J. Kossut, Z. Wilamowski, T. Dietl and K. Świątek, in: *Proc. 20th Int. Conf. on The Physics of Semiconductors*, Thessaloniki, 1990, Eds. E.M. Anastassakis and J.D. Joannopoulos (World Scientific, Singapore, 1990) p. 613.
- [7] J. Kossut, W. Dobrowolski, Z. Wilamowski, T. Dietl and K. Świątek, *Semicond. Sci. Technol.* 5 (1990) S260.
- [8] I.G. Kuleev, I.I. Lyapilin and I.M. Tsidi'kovskii, *Zh. Eksp. Teor. Fiz.* 102 (1992) 1652 (*Sov. Phys.-JETP* 75 (1992) 893); I.M. Tsidi'kovskii, I.G. Kuleev and I.I. Lyapilin, *Zh. Eksp. Teor. Fiz.* 102 (1992) 326 (*Sov. Phys. JETP* 75 (1992) 172).
- [9] See, e.g., S.D. Darchuk, L.A. Korovina and F.F. Sizov, *Fiz. Tekh. Poluprov.* 26 (1992) 845; V.I. Kaidanov and S.A. Nemov, *Fiz. Tekh. Poluprov.* 15 (1981) 542.
- [10] M. Ratuszek and M.J. Ratuszek, *J. Phys. Chem. Solids* 46 (1985) 837; B.A. Akimov, P.V. Verteletskii, V.P. Zlomanov, L.I. Ryabova, O.I. Tananaeva and N.A. Shirokova, *Fiz. Tekh. Poluprov.* 23 (1989) 244 (*Sov. Phys.-Semicond.* 23 (1989) 151); L.M. Kashirskaya, L.I. Ryabova, O.I. Tananaeva and N.A. Shirokova, *Fiz. Tekh. Poluprov.* 24 (1990) 1349 (*Sov. Phys.-Semicond.* 24 (1990) 848); V.D. Vulchev and L.D. Borisova, *Phys. Status Solidi (a)* 99 (1987) K53.
- [11] L. Palmethofer, K.H. Gresslehner, L. Ratschbacher and A. Lopez-Otero, in: *Lecture Notes in Physics*, Vol. 152 (Springer, Berlin, 1982) p. 391.

- [12] E. Grodzicka, W. Dobrowolski, J. Kossut, T. Story and B. Witkowska, *Acta Phys. Pol. A*, in print.
- [13] T. Story, E. Grodzicka, B. Witkowska, J. Górecka and W. Dobrowolski, *Acta Phys. Pol. A* 82 (1992) 879.
- [14] T. Story, Z. Wilamowski, E. Grodzicka, B. Witkowska and W. Dobrowolski, *Acta Phys. Pol. A*, in press.
- [15] K. Lischka, *Appl. Phys. A* 29 (1982) 177.
- [16] G. Nimtz and B. Schlicht, in: *Narrow Gap Semiconductors*, Springer Tracts in Modern Physics, Vol. 98, Ed. G. Höhler (Springer, Berlin, 1985) p. 1.
- [17] R.S. Allgeier and W.W. Scanlon, *Phys. Rev.* 111 (1958) 1029.
- [18] V.I. Kaidanov, S.I. Nemov and Yu. I. Ravich, *Fiz. Tekh. Poluprov.* 26 (1992) 201.
- [19] A.L. Efros and B.I. Shklovskii, in: *Electron–Electron Interactions in Disordered Systems*, Eds. A.L. Efros and M. Pollak (Elsevier, Amsterdam, 1985) p. 409.



ELSEVIER

Journal of Crystal Growth 138 (1994) 1040–1045

JOURNAL OF  
**CRYSTAL  
GROWTH**

## The thermodynamics of indium–vacancy pairs in $\text{Hg}_{0.79}\text{Cd}_{0.21}\text{Te}$

Wm.C. Hughes <sup>\*</sup>, J.C. Austin, M.L. Swanson

*Department of Physics and Astronomy, University of North Carolina at Chapel Hill, Chapel Hill, North Carolina 27599-3255, U.S.A*

### Abstract

We have measured the thermodynamic properties of In–V<sub>Hg</sub> pairs in the infrared material  $\text{Hg}_{0.79}\text{Cd}_{0.21}\text{Te}$  by using the method of perturbed angular correlation (PAC). PAC allows the determination of the absolute fraction of indium atoms in particular defects. Previous measurements have characterized the In–V pairs with hyperfine interaction frequencies of 83 and 92 MHz. These defects were observed in materials which were quenched from  $> 350^\circ\text{C}$  to retain a large number of metal vacancies. After subsequent low temperature ( $60 < T_A < 110^\circ\text{C}$ ) anneals, the fraction of indium atoms that had trapped vacancies increased because of the migration of metal vacancies. By measuring the rate of increase at different temperatures, we determined the vacancy migration energy to be  $E_m = 0.45 \pm 0.04$  eV. Anneals at slightly higher temperatures dissociated the In–V pairs. From the decrease in the In–V pair fraction with temperature, the In–V pair binding energy was found to be  $E_b = 0.44 \pm 0.15$  eV.

### 1. Introduction

The compound semiconductor alloy  $\text{Hg}_{1-x}\text{Cd}_x\text{Te}$  has been used for many years in the production of infrared photodiodes and focal plane arrays. The narrow energy gap of the  $x = 0.21$  and  $x = 0.3$  materials makes them useful for the 9 and 5  $\mu\text{m}$  atmospheric windows of interest for many applications. However, the weakness of the Hg–Te bond makes the material particularly susceptible to mercury vacancy defects. These vacancies act as acceptors and are present in all as-grown  $\text{Hg}_{1-x}\text{Cd}_x\text{Te}$ ; therefore, it is important to understand their interaction with other dopants.

The interaction of vacancies with dopants has not been well examined. The most common type

of donor dopant in  $\text{Hg}_{1-x}\text{Cd}_x\text{Te}$  is indium. Since indium has a valence of +3, it acts as a donor when substituting for metal atoms. However, in many cases the amount of indium present exceeds the conduction electron concentration of  $\text{Hg}_{1-x}\text{Cd}_x\text{Te}$ . Two mechanisms have been proposed for this compensation of indium. Indium may form  $\text{In}_2\text{Te}_3$  [1,2], or indium could directly pair with compensating vacancies [3–5].

We have recently published results using the technique of perturbed angular correlation which show that indium does in fact pair with vacancies [6]. When there is an exceptionally large number of vacancies present, such as in samples quenched to room temperature from above  $350^\circ\text{C}$ , In–V pairs were observed to be stable at room temperature. These In–V pairs were identified by the observation of two hyperfine interaction frequencies, 83 and 92 MHz. The fraction of indium atoms participating in these In–V pairs increased during subsequent annealing in the 60 to  $110^\circ\text{C}$

<sup>\*</sup> Corresponding author.

range. This fraction likewise increased with increasing quenching temperatures above 350°C. The pairs were removed by annealing at temperatures between 110 and 350°C. By understanding the annealing processes which govern these behaviors, we may determine the migration energy of vacancies and the binding energy of the In–V pairs.

## 2. Experimental method

The method used in this research is that of perturbed angular correlation (PAC). PAC essentially measures the precession of nuclear spins in an electric field gradient (EFG). This precession is measured by observing the angular distribution between consecutive gamma rays emitted from the probe nucleus. In this study, the probe  $^{111}\text{In}$  was used. This isotope decays by electron capture to an excited state of  $^{111}\text{Cd}$ . This in turn decays by emission of two gamma rays. The first of these decays populates an  $I = 5/2$  state. This state may interact with local EFGs, perturbing the angular distribution of the second radiation which takes the nucleus to its final, stable state.

Typically, the angular correlation between the two gamma rays is measured using four NaI detectors at right angles. Spectra of counts versus time for detection of the first gamma at a particular detector and the second at another detector are measured using a standard slow-fast coincidence technique. Eight such spectra are measured for four combinations of detectors at 180° to each other and four combinations at 90°. These spectra are then divided in an appropriate ratio to give what is known as  $R(t)$ . This  $R(t)$  spectrum can be thought of as the time dependence of the angular anisotropy between the two radiations. If a number of the indium probe nuclei are in sites where they experience definite non-zero EFGs, the  $R(t)$  will show a regular modulation corresponding to the precession of the nuclear spins. The frequency of this modulation is directly proportional to the strength of the EFG and can be used to label particular defect sites. Since the EFG is proportional to  $r^{-3}$ , this is most sensitive to neighboring point defects such as

vacancies within a few lattice spacings. In addition, the hyperfine splitting of the  $I = 5/2$  state causes the presence of three frequencies in the  $R(t)$  spectrum. The relative amplitudes and positions of these frequencies can be used to determine the asymmetry of the EFG and provide more detail on the structure of the defect. Finally, since the unperturbed anisotropy of the radiations from the  $^{111}\text{Cd}$  nucleus is known, the absolute fraction of indium atoms in defect sites may be measured by fitting the  $R(t)$  spectrum to a formula derived from theory. For a more detailed explanation of the PAC technique, the reader is encouraged to consult review articles in the literature [7, 8].

In this work, we have used undoped, bulk samples of  $\text{Hg}_{0.79}\text{Cd}_{0.21}\text{Te}$  supplied by Texas Instruments. These samples were grown by solid state recrystallization. The samples were cleaned by dipping in 0.5% bromine/methanol solution and rinsing with methanol and sealed in cleaned quartz ampoules at a pressure  $< 10^{-5}$  Torr with a small amount ( $\approx 10^{12}$  molecules) of  $^{111}\text{InCl}_3$ . The sealed ampoules were then annealed in a tube furnace at 350°C for 6 h or more to diffuse the indium into the sample to depths of several microns. PAC spectra were taken at room temperature with the samples sealed in the ampoules to avoid any exposure to air. All subsequent anneals were also performed in these ampoules.

## 3. Annealing experiments

### 3.1. Vacancy migration

It was observed that the fraction of indium atoms participating in In–V complexes was increased by annealing at temperatures near 100°C. This increase was attributed to the migration of frozen in vacancies and their subsequent trapping at indium atoms. That is, there is enough thermal energy for the free vacancies to become mobile, but not enough to separate trapped vacancies from the indium donors to which they are bound. Therefore, if a vacancy comes close to an indium atom before being trapped elsewhere or destroyed, it will be trapped and remain there. A



vacancy can also be created or annihilated at sinks such as dislocations or surfaces. These processes can be described by the following reactions (where C represents the In–V complex):



The first of these, Eq. (1), represents the creation/annihilation of In–V pairs. The second, Eq. (2), represents the destruction/creation of vacancies at extended defects or surfaces. The rate constants,  $K_1$ ,  $K_2$ ,  $K_3$ , and  $K_4$ , have an exponential dependence on  $T^{-1}$ :

$$K_n = K_{n0} \exp(-E_n/kT),$$

where  $E_n$  is the activation energy of the process.

Using these reactions, we may state the rate equations:

$$d[C]/dt = K_1[\text{In}][V] - K_2[C], \quad (3)$$

$$d[V]/dt = -K_1[\text{In}][V] + K_2[C] - K_3[V] + K_4, \quad (4)$$

where the square brackets represent the site fraction of the particular defect or atom. Near 100°C it is obvious from the experimental data that the reaction in Eq. (1) proceeds in a forward direction. This means that the rate equation for this reaction, Eq. (3), can be approximated by

$$d[C]/dt = K_1[\text{In}][V]. \quad (5)$$

We can further simplify the problem by realizing that the number of indium atoms is much smaller than the number of vacancies. Therefore, the dominant mechanism for the destruction of vacancies is trapping at other sinks and not at indium atoms. Furthermore, the concentration of vacancies is much greater than the equilibrium concentration, so that the destruction/creation reaction may be assumed to proceed entirely in the direction of vacancy destruction. Based on these assumptions, we may simplify Eq. (4):

$$d[V]/dt = -K_3[V]. \quad (6)$$

This equation is easily solved for [V]. When the solution for [V] is substituted into Eq. (5), that

equation is also easily solved:

$$d[C]/dt = K_1[\text{In}][V_0] e^{-K_3 t}, \quad (7)$$

$$\ln \left( \frac{[\text{In}_{\text{tot}}] - [C(t)]}{[\text{In}_{\text{tot}}] - [C(0)]} \right) = - \frac{K_1[V_0]}{K_3} (q - e^{-K_3 t}). \quad (8)$$

Since the fraction obtained by PAC is the ratio of In–V concentration to the total indium concentration,

$$f = [C]/[\text{In}_{\text{tot}}], \quad (9)$$

then we can solve Eq. (8) for this fraction as a function of time:

$$f(t) = 1 - [1 - f(0)] \times \exp \left[ - \frac{K_1[V_0]}{K_3} (1 - e^{-K_3 t}) \right]. \quad (10)$$

To measure the time-dependence of the In–V fraction, a series of isothermal annealing experiments were performed by annealing samples of  $\text{Hg}_{0.79}\text{Cd}_{0.21}\text{Te}$  for various lengths of time at temperatures between 60 and 110°C after the samples had been quenched from 350°C. Between each anneal, PAC spectra were taken to determine the In–V fraction (Fig. 1). These fractions were then plotted versus time as shown in Fig. 2. The data in Fig. 2 were then fitted using Eq. (10) to determine the values of  $K_3$  as a function of temperature. Note that  $K_1/K_3$  should be independent of  $T$  since both processes involve the thermally activated migration of vacancies. From an Arrhenius plot of  $K_3$  versus  $T^{-1}$  (Fig. 3), the energy of the process was determined. The process described by  $K_3$  is the migration of vacancies to indium traps, and therefore this energy is simply the migration energy of metal vacancies. This migration energy was determined by this method to be  $0.45 \pm 0.04$  eV.

### 3.2. In–V pair binding

In a similar manner, the binding energy of the In–V pair could be determined. A simple analysis based on the law of mass action is not possible since the vacancy concentration depends on temperature. Therefore, we determined this binding

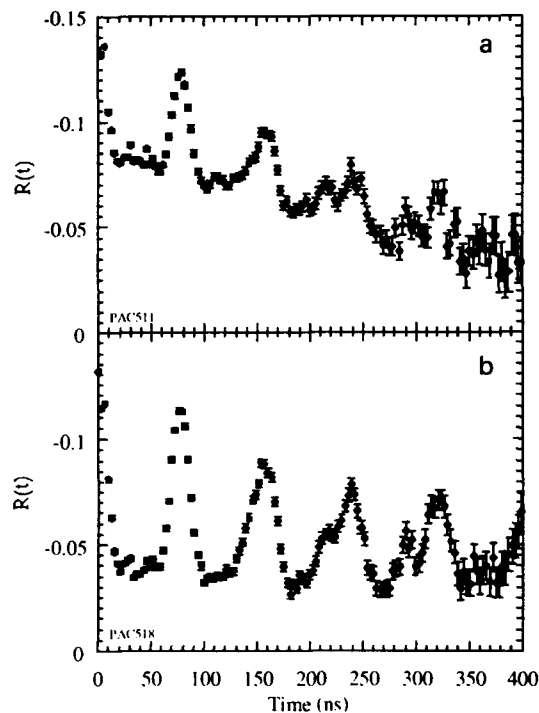


Fig. 1. PAC spectrum for  $^{111}\text{In}$ -doped  $\text{Hg}_{0.79}\text{Cd}_{0.21}\text{Te}$ . The modulation is due to In–V complexes which are identified by two frequencies: 83 and 92 MHz: (a) room temperature spectrum of a sample quenched from  $350^\circ\text{C}$  (b) increase in the amplitude of the frequencies after the sample is annealed at  $85^\circ\text{C}$  for 8 h.

energy by observing the break-up of the In–V pairs during annealing above  $100^\circ\text{C}$ . The PAC spectra were taken at room temperature as usual.

The In–V concentration in quenched samples is higher than equilibrium because of the excess of vacancies frozen in. As seen above, these vacancies can be trapped in In–V pairs which are stable at room temperature. However, at temperatures slightly higher than room temperature these complexes are no longer stable. When the complexes break apart, the vacancies are likely to migrate to sinks until the equilibrium concentration of vacancies is reached. In this temperature range, the reaction in Eq. (1) runs right to left

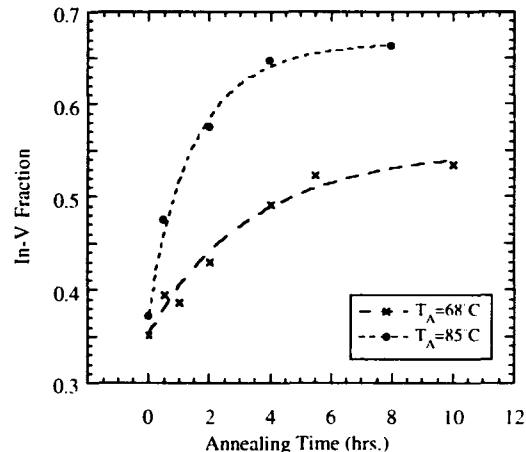


Fig. 2. Typical annealing curves showing the formation of In–V complexes. Shown are the fractions of indium atoms paired with vacancies as a function of annealing time for anneals at  $68$  and  $85^\circ\text{C}$ . The dashed lines represent least squares fits of each set of data to Eq. (10).

and the corresponding rate equation, Eq. (3), may be simplified to

$$d[C]/dt = -K_2[C], \quad (11)$$

which is easily solved for  $[C]$  and therefore for  $f$ :

$$f(t) = f(0) e^{-K_2 t}. \quad (12)$$

To measure  $K_2$ , a sample of  $\text{Hg}_{0.79}\text{Cd}_{0.21}\text{Te}$  was annealed at  $350^\circ\text{C}$ , quenched, and annealed

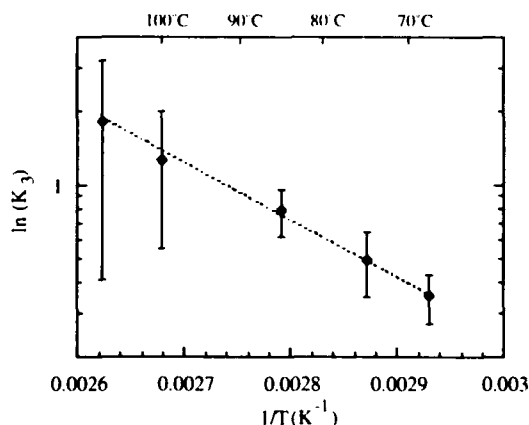


Fig. 3. Arrhenius plot of the logarithm of the reaction rate constant  $K_3$  versus  $T^{-1}$ .

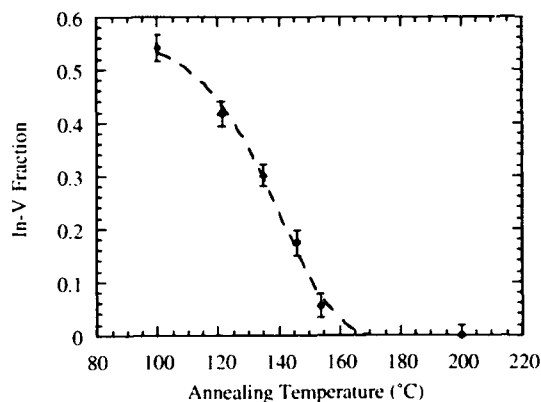


Fig. 4. In-V fraction versus annealing temperature in the range of temperatures where In-V pair dissociation dominates.

at 100°C for 12 h in order to create a large number of In-V pairs. Then the sample was isochronally annealed at temperatures between 100 and 200°C with PAC spectra taken between each anneal. The results of these spectra are plotted in Fig. 4. This temperature dependence may be modeled using Eq. (12):

$$f(T) = f(0) \exp[-K_{20} e^{-E_2/kT} t_A], \quad (13)$$

where  $t_A$  is the annealing time (2 h). The fit of the data using this equation is shown by the dotted line in Fig. 3. The value of  $E_2$  determined from this fit is 0.89 eV. This energy represents not only the energy needed to liberate the vacancy from the indium, but also the energy needed for the vacancy to move away from the indium. Therefore, the energy is the sum of the vacancy migration and In-V binding. Using the migration energy determined above, the In-V binding energy is found to be  $E_b = E_2 - E_1 = 0.44 \pm 0.15$  eV. The only previous measurement of this energy, 0.34 eV, was published by a group in Leningrad (St. Petersburg) in 1979 [9].

#### 4. Conclusions

The measurements of the thermodynamic properties of defect complexes such as the In-V

pair studied here serve several purposes. They help to define parameters which can be used for comparison with theoretical models. They may also help to understand the diffusion properties of certain defects. Finally they may help us discover mechanisms of compensation of dopants in materials used for devices.

The first quantity measured here, the vacancy migration energy, is closely related to the self-diffusion of mercury atoms in  $\text{Hg}_{0.79}\text{Cd}_{0.21}\text{Te}$ . This has been observed several times to be a two-component diffusion process [10, 11]. However, all previous measurements were performed at higher temperatures than those in the current study. The lowest temperature measurements reported energies of 0.15 and 0.35 eV. The other studies report energies over a wide range from 0.3 to 0.61 eV. Also reported are higher energy processes with energies between 1.5 and 2.4 eV. If we assume that these higher energies are related to other diffusion mechanisms, then the value reported here, 0.35 eV, falls within the range of 0.15 to 0.61 eV of the other measurements.

The second energy, the In-V pair binding energy, has only been reported once [9]. Though it is not clear how the result was obtained, it was reported that this binding energy was 0.34 eV. This is slightly less than the migration energy of 0.44 eV which we report here.

We have shown that PAC may be used as a technique to characterize the thermodynamics of In-V interactions in  $\text{Hg}_{0.79}\text{Cd}_{0.21}\text{Te}$  and some properties of the vacancies alone. This characterization includes the migration energy of vacancies as well as the In-V pair binding energy. We note that these measurements are done using an extremely small concentration of indium (so that we are working in the infinite dilution approximation), and furthermore, that the analysis is independent of the indium concentration in contrast to analysis by other methods.

#### 5. Acknowledgement

This work was supported by a grant from the US Army Research Office.

## 6. References

- [1] H.R. Vydyanath, *J. Electrochem. Soc.* 128 (1981) 2619.
- [2] M. Boukerche, P.S. Wijewarnasuriya, S. Sivananthan, I.K. Sou, Y.J. Kim, K.K. Mahavadi and J.P. Faurie, *J. Vac. Sci. Technol. A* 6 (1988) 2830.
- [3] Qian Dingrong, Tang Wenguo, Shen Jie, Chu Junhao and Zheng Guozhen, *Solid State Commun.* 56 (1985) 813.
- [4] V.I. Ivanov-Omskii, K.E. Mironov, K.D. Mynbaev and V.V. Bogoboyashchii, *Soviet Phys.-Semicond.* 25 (1991) 857.
- [5] G.N. Pain and T. McAllister, *Semicond. Sci. Technol.* 7 (1992) 231.
- [6] W.C. Hughes, J.C. Austin and M.L. Swanson, *Appl. Phys. Lett.* 59 (1991) 938.
- [7] Gary L. Catchen, *J. Mater. Educ.* 12 (1990) 253.
- [8] Th. Wichert and E. Recknagel, in: *Microscopic Methods in Metals, Topics in Current Physics*, Vol. 40, Ed. U. Gonser (Springer, Berlin, 1986) p. 317.
- [9] F.A. Zaitov, A.V. Gorshkov and G.M. Shalyapina, *Soviet Phys.-Solid State* 21 (1979) 112.
- [10] A.V. Gorshkov, F.A. Zaitov, G.M. Shalyapina and S.B. Shagin, *Soviet Phys.-Solid State* 25 (1983) 1532.
- [11] Mei-Fan Sung Tang and D.A. Stevenson, *J. Vac. Sci. Technol. A* 7 (1989) 544.



ELSEVIER

Journal of Crystal Growth 138 (1994) 1046–1050

JOURNAL OF **CRYSTAL  
GROWTH**

## Electroluminescence spectra of rare-earth-doped $\text{ZnS}_{1-x}\text{Se}_x$ thin films

Noboru Miura \*, Kiyoshi Ogawa, Shuko Kobayashi, Hironaga Matsumoto,  
Ryotaro Nakano

*Department of Electronics & Communication, School of Science & Technology, Meiji University, 1-1-1 Higashi-Mita, Tama-ku,  
Kawasaki 214, Japan*

### Abstract

Electroluminescence has been measured for  $\text{ZnS}_{1-x}\text{Se}_x$  thin films doped with rare-earth ions. As  $x$  increases the band-gap energy of the host decreases. The emission levels of trivalent rare-earth ions are not observed when the band-gap energy is narrower than the excitation levels. This is because of the energy transfer between the host and the emission center.

### 1. Introduction

Thin-film electroluminescent (EL) devices have been actively investigated. In these devices, II–VI compounds are generally used as the host material. Although many experiments have been performed, the excitation mechanism of the emission center is not yet clear at present. In a previous study, we examined the excitation process by measuring the transient behavior of host and  $\text{Tb}^{3+}$  emission for  $\text{ZnS}:\text{TbF}_x$  EL device [1] and using rare-earth-doped  $\text{Zn}_{1-x}\text{Cd}_x\text{S}$  EL devices [2], and reported that energy transfer participates in the excitation of thin-film EL devices. This work is an extended study of the excitation process. The EL behavior was measured for  $\text{ZnS}_{1-x}\text{Se}_x$  thin-film EL devices with various

band-gap energies ( $E_g$ ). Based on these experiments, we discuss the energy transfer process in the EL devices.

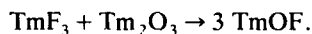
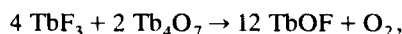
### 2. Experimental procedure

#### 2.1. Sample preparation

Conventional double-insulating EL devices were used in this experiment. The devices were fabricated on glass substrates (Asahi Glass: AN) coated with indium tin oxide (ITO). As an emission layer,  $\text{Tb}^{3+}$ - or  $\text{Tm}^{3+}$ -doped  $\text{ZnS}_{1-x}\text{Se}_x$  ( $0 \leq x \leq 1$ ) thin films (550 nm thick) were prepared by electron-beam evaporation at a substrate temperature of 150°C, with subsequent annealing at 400°C for 1 h in vacuum. As the evaporation source for the emitting layer, ZnS and ZnSe powders were mixed with TbOF or TmOF pow-

\* Corresponding author.

der, pressed into pellets and sequentially fired for 1 h at 1000°C in Ar atmosphere. As the starting materials for TbOF and TmOF powder, oxide and fluoride compounds were mixed and baked at 1200°C for 2 h in Ar atmosphere to undergo the reactions below:



The concentrations of TbOF and TmOF were 0.45 and 1 mol%, respectively, in the starting materials. In this paper, the value of  $X$ , which indicates the composition of the  $\text{ZnS}_{1-X}\text{Se}_X$  host, is described as the atomic ratio between S and Se in the starting materials. The emission layer was sandwiched between 450 nm thick  $\text{Y}_2\text{O}_3$  insulating layers. An aluminum electrode was placed on a second insulating layer to complete the EL device.  $\text{ZnS}_{1-X}\text{Se}_X$  films were also directly deposited on the quartz glass substrates as samples

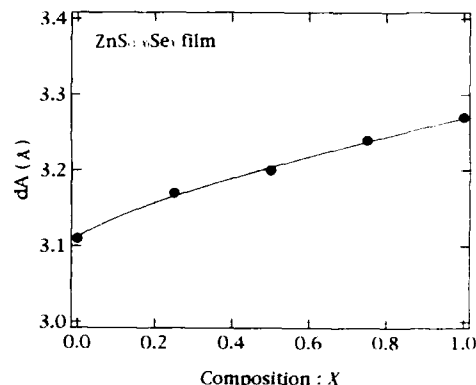


Fig. 1. Interplanar spacing ( $dA$ ) as a function of host composition for  $\text{ZnS}_{1-X}\text{Se}_X$  thin films.

for the measurement of the X-ray diffraction pattern, photoabsorption spectra and PL, in order to avoid confusing signals from other films in the device.

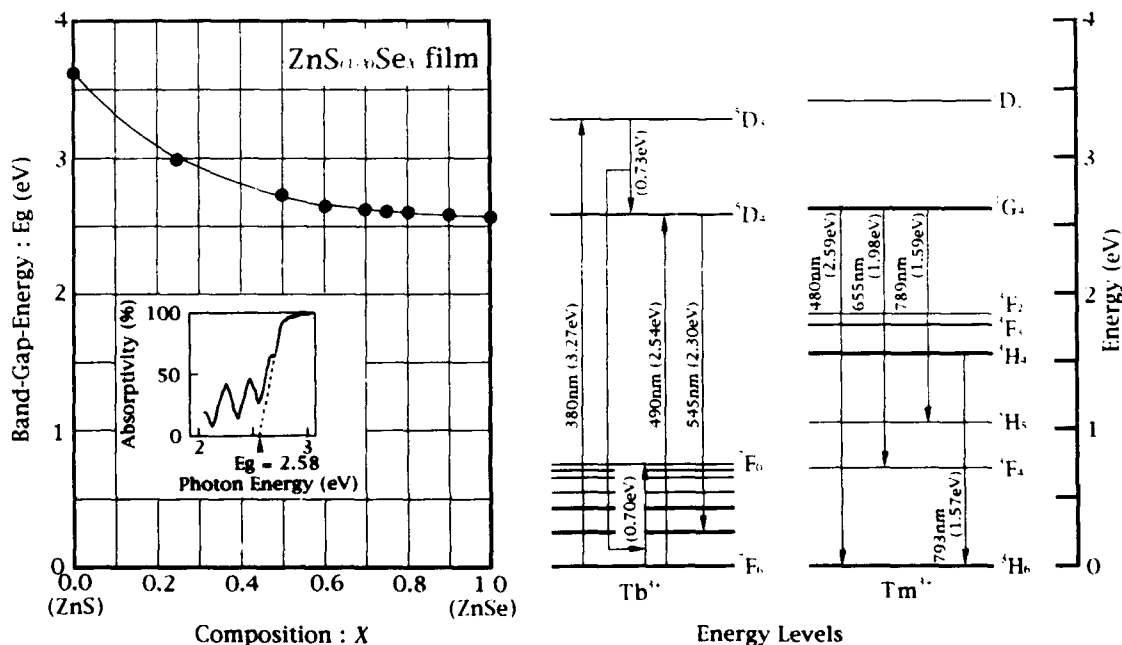


Fig. 2.  $X$  value dependence of the band-gap energy ( $E_g$ ) for  $\text{ZnS}_{1-X}\text{Se}_X$  thin-films. The energy levels of  $\text{Tb}^{3+}$  and  $\text{Tm}^{3+}$  ion are also shown. The photoabsorption spectrum of the  $\text{ZnS}_{0.2}\text{Se}_{0.8}$  film is shown in the inset.

## 2.2. Measurement system

For the measurement of the photoabsorption spectra, the samples were irradiated by light from a 300 W Xe lamp combined with a monochromator. The transmitted light was detected by a thermopile. The output of the thermopile was fed to a lock-in amplifier and the data were calibrated with the intensity of the irradiated light sensitivity and with the transmissivity of the quartz glass substrate.

The emission spectra were taken by a system comprising a photomultiplier (Hamamatsu Photonics R-928), monochromator (Jobin-Yvon H-20 visible) with a resolution of 1 nm, electrometer (Advantest TR8651) and X-Y recorder. The spectral sensitivity of the detection system and transmissivity in the EL devices were not calibrated. The EL devices were driven by pulse voltage of alternating polarities with 40  $\mu$ s pulse width and 50 Hz. For PL, a He-Cd laser (Kimmon: CD302R, 20 mW) with a wavelength of 325 nm (3.82 eV) was used as the excitation light source. All measurements were performed at room temperature.

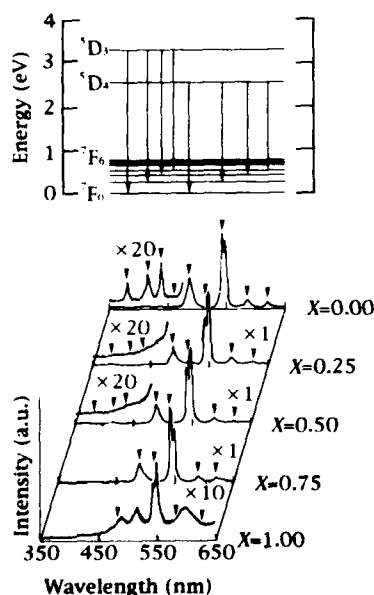


Fig. 3. EL spectra for  $\text{ZnS}_{1-x}\text{Se}_x:\text{TbOF}$  thin films.

## 3. Experimental results

### 3.1. Crystalline properties

Fig. 1 shows the  $X$  value dependence of the interplanar spacing ( $dA$ ). With increasing  $X$ ,  $dA$  shifted from 3.11 (ZnS) to 3.27 (ZnSe).

The  $X$  value dependence of the  $E_g$  for the  $\text{ZnS}_{1-x}\text{Se}_x$  thin films is shown in Fig. 2. The energy levels of  $\text{Tb}^{3+}$  and  $\text{Tm}^{3+}$  ions are also shown.  $E_g$  is defined by the slope of the photoabsorption spectra, as shown in the inset in Fig. 2. With an increase of  $X$ ,  $E_g$  decreased from 3.6 eV (ZnS) to 2.56 eV (ZnSe) in our films. A similar result was reported for mixed crystals [3]. The band-gap energies are about 2.96, 2.72, 2.64, 2.62, 2.60, 2.58, and 2.57 eV when the values for  $X$  are 0.25, 0.50, 0.60, 0.70, 0.75, 0.80 and 0.90, respectively.

### 3.2. EL spectra for $\text{ZnS}_{1-x}\text{Se}_x:\text{TbOF}$

The EL spectra for the  $\text{ZnS}_{1-x}\text{Se}_x:\text{TbOF}$  device are shown in Fig. 3. When  $X = 0$  (ZnS:TbOF;  $E_g = 3.6$  eV), the EL spectrum consists of strong emission peaks at 490, 545, 590 and 625 nm and weak emission peaks at 380, 420, 440 and 460 nm, due to both  $^5D_4 \rightarrow ^7F_J$  and  $^5D_3 \rightarrow ^7F_J$  ( $J = 3, 4, 5$  and 6) transitions, respectively. For  $X \geq 0.25$ , the emission arising from the  $^5D_3$  level is not observed. On the other hand, the emission corresponding to the transition of  $^5D_4 \rightarrow ^7F_J$  ( $J = 3, 4, 5$  and 6) is observed, independent of the composition ( $X$ ).

### 3.3. EL spectra for $\text{ZnS}_{1-x}\text{Se}_x:\text{TmOF}$

The EL spectra for the  $\text{ZnS}_{1-x}\text{Se}_x:\text{TmOF}$  devices are shown in Fig. 4. When  $X = 0$  (ZnS:TmOF;  $E_g = 3.6$  eV), the EL spectrum consists of two main peaks at 480 nm (2.59 eV) and 793 nm (1.57 eV), and a weak peak at 655 nm (1.50 eV). The 480 and 655 nm emissions are assigned to the transitions from the same level of  $^1G_4$  to two terminal levels of  $^3H_6$  and  $^3F_4$ , respectively. The 793 nm emission is due to the transition of  $^3H_4 \rightarrow ^3H_6$ . With an increase of  $X$ , the 480 and 655 nm emissions become weak and

ultimately disappear. On the other hand, the 793 nm emission is observed, independent of the value of  $X$ .

### 3.4. PL spectra for $\text{ZnS}_{1-X}\text{Se}_X:\text{TmOF}$

Fig. 5 shows the PL spectra for the  $\text{ZnS}_{1-X}\text{Se}_X:\text{TmOF}$  films. The PL spectra show the same behavior as in the case of EL. In the case of  $X=0$ , the spectra are composed of the emissions from the two emission levels of  $^1\text{G}_4$  and  $^3\text{H}_4$ . As  $X$  increases, the emission from the  $^1\text{G}_4$  level is not observed. The 793 nm emission due to the  $^3\text{H}_4 \rightarrow ^3\text{H}_6$  transition is observed in all samples. In PL, the broad-band emission is observed.

## 4. Discussion

The EL emission has been measured for  $\text{ZnS}_{1-X}\text{Se}_X$  thin films doped with rare-earth ions.

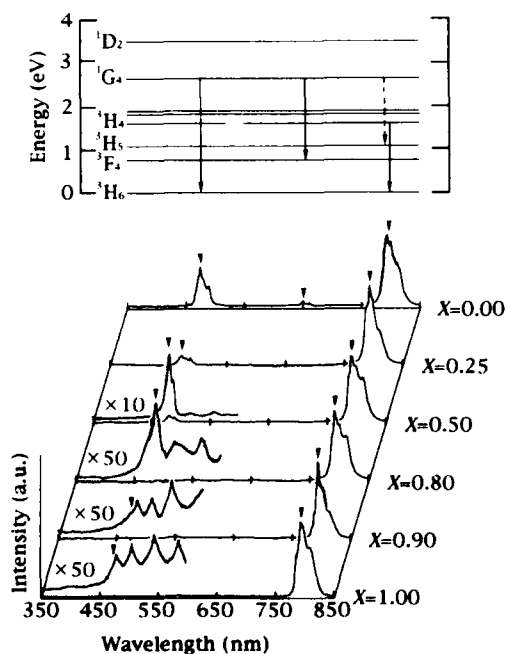


Fig. 4. EL spectra for  $\text{ZnS}_{1-X}\text{Se}_X:\text{TmOF}$  thin films.

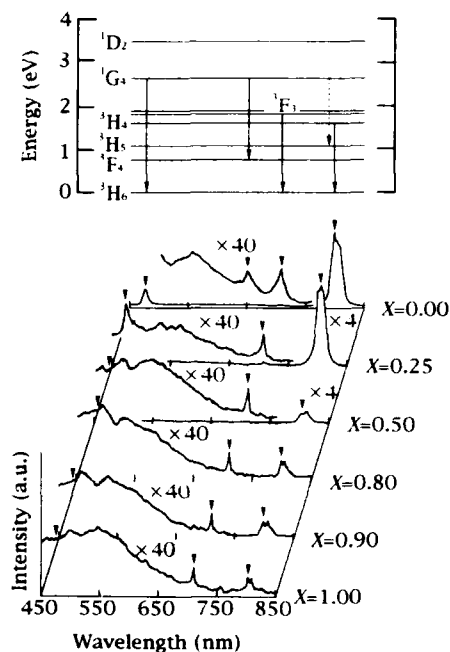


Fig. 5. PL spectra for  $\text{Zn}_{1-X}\text{Cd}_X\text{S}:\text{TmOF}$  thin films.

In these devices, emissions from levels higher than  $E_g$  of the host are not observed, and the composition of those spectra changes with the host composition ( $X$ ). Similar behavior was also observed in rare-earth-doped  $\text{Zn}_{1-X}\text{Cd}_X\text{S}$  thin-film EL devices [2]. Two causes of the changes of the spectra are considered. One is the case where levels higher than the host are not excited. In this case, it is suggested that the emission center is excited via energy transfer by way of recombination in the host, and hence the levels higher than  $E_g$  cannot be excited [2]. The other cause involves the direct impact excitation model of hot electrons which are accelerated in a high electric field, in which the emission levels are higher than that of the band-gap of the host. In this case, emission is not observed from levels higher than  $E_g$ , although the levels are pumped. If this phenomenon occurs, we believe that the energy transfer from the rare-earth center to the host (back-energy transfer), which is reported not only in rare-earth-doped III-V semiconductors such as InP [4], but also in II-VI compounds [5,6].



takes place. To clarify the energy transfer process, further experiment is required.

### 5. Conclusions

The EL spectra for rare-earth-doped  $\text{ZnS}_{1-X}\text{Se}_X$  thin films were measured. As  $X$  increased,  $E_g$  of the host decreased, and emission from levels higher than  $E_g$  disappears. This is because of the energy transfer between the 4f electron of the trivalent rare-earth ions and the host.

### 6. Acknowledgments

The authors would like to thank Kenichiro Takahei of the NTT Basic Research Laboratories for invaluable discussions. Thanks are also ex-

tended to Toshifumi Suda of Meiji University for his support. This work was supported in part by a Grant-in-Aid for General Scientific Research from The Ministry of Education, Science and Culture, Japan.

### 7. References

- [1] N. Miura, H. Matsumoto and R. Nakano, *Jap. J. Appl. Phys.* 31 (1992) 288.
- [2] N. Miura, T. Sasaki, H. Matsumoto and R. Nakano, *Jap. J. Appl. Phys.* 31 (1992) 295.
- [3] Y.S. Park and B.K. Shin, in: *Electroluminescence. Topics in Applied Physics*, Vol. 17, Ed. J.I. Pankove (Springer, Berlin, 1977) p. 133.
- [4] K. Takahei, A. Taguchi, H. Nakagome, K. Uwai and P.S. Whitney, *J. Appl. Phys.* 66 (1989) 4941.
- [5] H. Zimmermann and R. Boyn, *Phys. Status Solidi (b)* 135 (1986) 379.
- [6] R. Boyn, *Phys. Status Solidi (b)* 148 (1988) 11.



ELSEVIER

Journal of Crystal Growth 138 (1994) 1051–1054

JOURNAL OF **CRYSTAL  
GROWTH**

## Formation and optical properties of homogeneous solid solutions of $\text{Ca}_{1-x}\text{Sr}_x\text{S}:\text{Ce}$

B.W. Arterton, J.W. Brightwell, B. Ray, I.V.F. Viney \*

*Divisions of Applied Physics and Chemical Sciences, Coventry University, Priory Street, Coventry CV1 5FB, UK*

### Abstract

Samples of  $\text{Ca}_{1-x}\text{Sr}_x\text{S}:0.001\text{ Ce}$  were prepared by reduction of mixed sulphates with  $\text{H}_2/\text{H}_2\text{S}$  at elevated temperatures. In the absence of a flux, only at  $1200^\circ\text{C}$  for long reaction times did near complete solid solution occur. However, addition of LiF flux to samples prepared at  $1100^\circ\text{C}$  did yield homogeneous single phase mixed sulphides but of poor crystallinity. Photoluminescence excitation and emission spectra were determined for these solid solutions at 295 and 77 K. Peak emission wavelengths at 77 K ranged from 500 nm for  $\text{CaS}:\text{Ce}$  to 478 nm for  $\text{SrS}:\text{Ce}$ . The wavelength shift reflects the sensitivity of the 5d state of the  $\text{Ce}^{3+}$  ion to the strength of the crystal field.

### 1. Introduction

Alkaline-earth sulphides doped with rare-earth ions offer the possibility of multicolour electroluminescent and cathodoluminescent devices. Fine tuning of the emission colour can be achieved by, for example, varying the composition of a solid solution of calcium and strontium sulphides as the host lattice.

Solid solutions between calcium and strontium sulphides were originally investigated by Rumpf and Travnicek [1] who observed large apparent deviations from Vegard's law which they could not satisfactorily explain. Primak, Kaufman and Ward [2] demonstrated that complete solid solution of the two sulphides results from fluxing with

LiF, with the resultant material obeying Vegard's law very closely. Okamoto and Kato [3] used a sulphurizing flux to produce  $(\text{CaSr})\text{S}$  phosphors whose lattice constant increased linearly with mole fraction of SrS.

The work reported here is an extension of previous studies by Brightwell et al. [4] and Bickerton et al. [5] on the photoluminescence of  $\text{Ca}_{1-x}\text{Sr}_x\text{S}$  and focuses on the behaviour of cerium as the emitting centre.

### 2. Experimental procedure

#### 2.1. Sample preparation and characterization

Calcium and strontium nitrates in the chosen proportion were dissolved in deionized water at  $80^\circ\text{C}$  and a "mixed" sulphate precipitated by the

\* Corresponding author.

addition of a 10% stoichiometric excess of  $(\text{NH}_4)_2\text{SO}_4$  solution. The resultant precipitate was then digested for a range of times at 60 or 90°C before filtration and washing with cold deionized water. The Ce dopant was added to the sulphates as a dilute solution of ammonium sulphatocerate(IV) to provide a dopant level of 0.001 moles Ce per mole of sulphide. Alternatively, the cerium was added, as nitrate, to the solution before coprecipitation of the sulphates. The mixed sulphates were dried in an air oven and the product finely ground. A few samples had 1.5 mol% LiF added at this stage.

Reduction to the sulphide was carried out in a tube furnace with flowing  $\text{H}_2$  at temperatures of 1000, 1100 and 1200°C for times ranging from 1 to 4 h. A small amount of  $\text{H}_2\text{S}$  was added to the gas flow to eliminate any oxide formation.

X-ray analysis of the final product was carried out using a Philips diffractometer (PW1730/1710) using  $\text{Cu K}\alpha$  radiation. Scanning electron micrographs of the samples were taken using a Philips 505 SEM at a magnification of 2500.

## 2.2. Optical measurements

Optical measurements were with a Perkin-Elmer LS50 fluorescence spectrometer which permitted excitation and emission spectra to be determined at 77 and 295 K. The procedure adopted in measurement was to produce an emission spectrum by exciting at 254 nm. An excitation spectrum was then obtained with the spectrometer set at the emission wavelength of the major peak observed in the initial emission spectrum. A second emission spectrum was then produced for each sample using the optimum exciting wavelength, between 430 and 460 nm, for the emission peak associated with the cerium centre.

## 3. Results

With the exception of the samples prepared using LiF flux, all of the mixed sulphides were to some extent two phased, these phases were calcium sulphide at close to the ideal lattice parame-

ter and the calcium–strontium sulphide solid solution. In contrast, addition of LiF resulted in complete solid solution at 1100°C within 1 h; however, for this material the X-ray diffraction traces were much less sharp. The distinct differences observed in particle morphology are illustrated in Fig. 1 for  $\text{CaS}:\text{Ce}$ ,  $\text{Ca}_{0.5}\text{Sr}_{0.5}\text{S}:\text{Ce}$  and  $\text{SrS}:\text{Ce}$ .

The PL excitation and emission spectra consisted of main and minor peaks similar to those of  $\text{CaS}:\text{Ce}$  at 77 K shown in Fig. 2. The excitation spectrum consists of two main bands with peaks at 250 and 455 nm for  $\text{CaS}:\text{Ce}$ , and 255 and 431 nm for  $\text{SrS}:\text{Ce}$ . The two emission bands occur at 500 and 570 nm in  $\text{CaS}:\text{Ce}$  and 478 and 534 nm in  $\text{SrS}:\text{Ce}$  respectively. The main peak emission wavelength was observed to shift to shorter wavelengths with increasing strontium content,  $x$ , at both 77 and 295 K; Fig. 3 illustrates that behaviour at 77 K for samples excited by 254 nm wavelength radiation. In Fig. 3 the peak wavelength ( $\lambda_{\text{max}}$ ) is plotted as a function of the lattice constant,  $a_0$ , with the present work compared to the results of Okamoto and Kato [3] and Kasano et al. [6]. Also shown are the “optical absorption edge” values of Lehmann [7].

At 295 K, the peak emission intensity varied with composition showing a maximum value at intermediate compositions. At 77 K, the peak emission intensity decreases with increasing strontium content. The emission intensity levels are significantly greater at 77 K particularly at calcium rich compositions.

## 4. Discussion

The co-precipitation of the sulphates did not produce a single phased product but a mixture of the separate sulphates. Increased digestion times served only to increase the particle size and hence to inhibit the formation of a solid solution of the sulphides on sintering. The scanning electron micrographs show that the reaction with  $\text{H}_2/\text{H}_2\text{S}$  produced separate sulphides with a particle size and shape reflecting that of the sulphates. Only at 1200°C and for long reaction times did near complete solid solution occur.

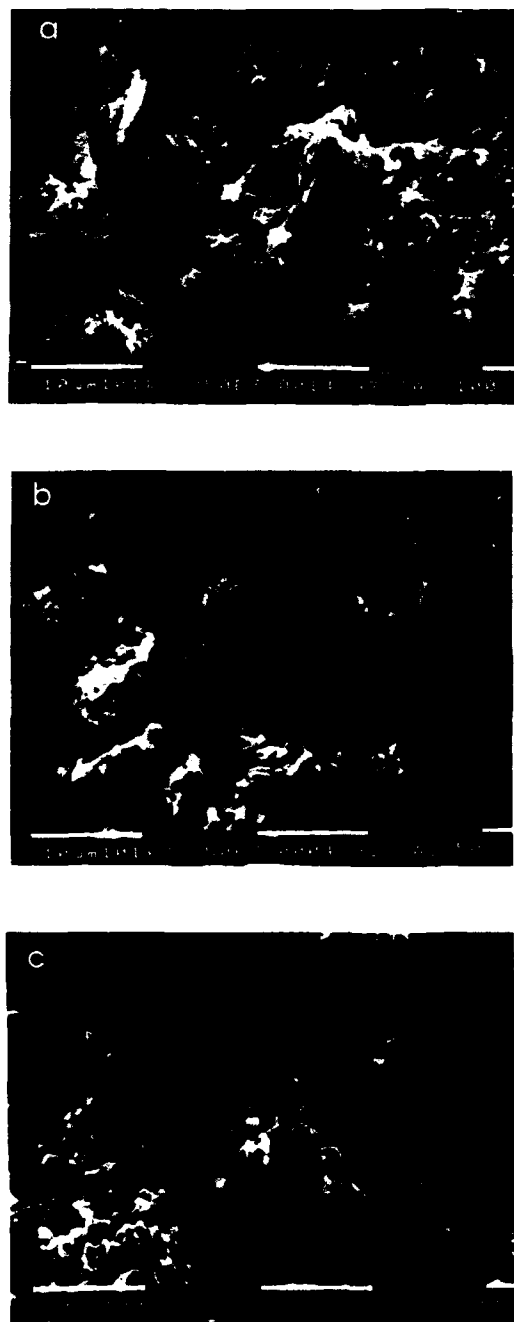


Fig. 1. Scanning electron micrographs of  $\text{Ca}_{1-x}\text{Sr}_x\text{S}:\text{Ce}$  powder phosphors for (a)  $x = 0$ , (b)  $x = 0.5$  and (c)  $x = 1$ .

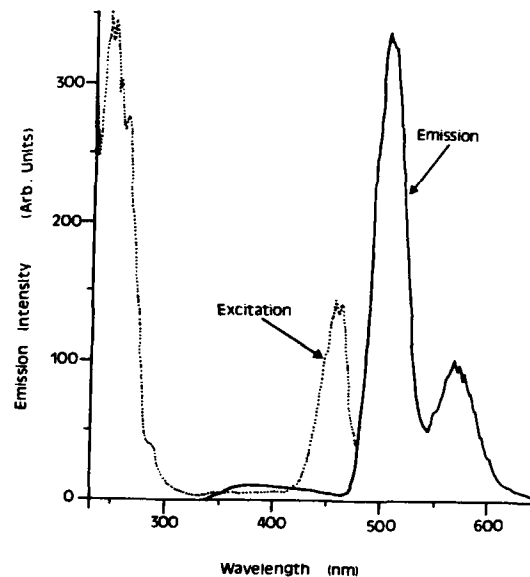


Fig. 2. PL excitation and emission spectra for  $\text{CaS}:0.001 \text{ Ce}$  at 77 K.

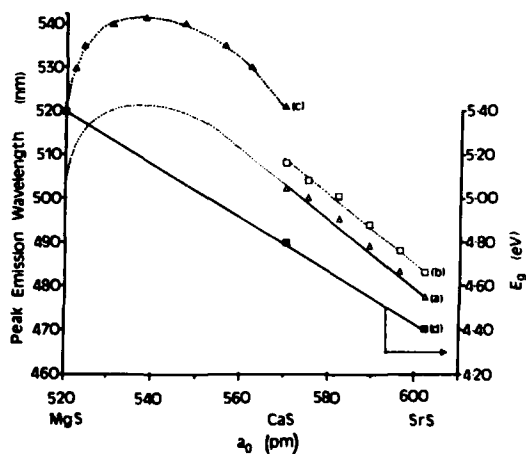


Fig. 3. Peak fluorescent emission wavelength as a function of lattice constant,  $a_0$ . (a) this work, at 77 K excited by 254 nm wavelength radiation; (b) Okamoto and Kato [3], cathodoluminescence; (c) Kasano et al. [6], cathodoluminescence; (d) Optical absorption edge energy values for  $\text{MgS}$ ,  $\text{CaS}$ ,  $\text{SrS}$  from Lehmann [7].

The addition of 1.5 mol% LiF to samples prepared at 1100°C did, however, yield single phase material but the distinctly less sharp nature of the X-ray diffraction traces gives rise to doubts about the homogeneity of the products.

The photoluminescence results can be explained using a model proposed by Yamashita et al. [8]. The two overlapping emission bands correspond to transitions from the  $5d(^2T_{2g})$  excited state of the  $Ce^{3+}$  ion to the  $4f(^2F_{7/2})$  and  $4f(^2F_{5/2})$  states. The saddle between these two emission peaks becomes deeper as the temperature drops from 295 to 77 K due to suppression of lattice vibrations. In the excitation spectrum, the peak at about 440 nm arises from the  $4f(^2F_{5/2})$  to  $5d(^2T_{2g})$  ground to excited state transition. The crystal field splitting of the 5d state will be smaller for the larger SrS lattice. The blue shift in peak emission wavelength results from the increase in energy of the  $5d(^2T_{2g})$  to  $4f(^2F_{5/2})$  transition. The variation of peak wavelength,  $\lambda_{max}$ , with composition of solid solution across the MgS–CaS–SrS system, shown in Fig. 3, has been rationalized, particularly for the MgS–CaS system, in terms of local stresses around dopant ions [6]. These stresses are of two types: (I) due to difference in ionic radii of host lattice and dopant cation and (II) due to difference in radii of the two host lattice cations. Although changes in fluorescence intensity with composition may be explained by invoking type II stresses, it is difficult

to see why these type II stresses should have such a striking effect in the MgS–CaS system, yet a negligible effect in the CaS–SrS system. It seems possible that the reduction in the value of  $\lambda_{max}$  as the composition changes from  $Mg_{0.65}Ca_{0.35}S$  to MgS has its origin elsewhere and perhaps from a change in energy band structure.

The general displacements between plots a, b and c in Fig. 3 have their origin in different preparative techniques of the samples, different dopant levels and different stimulation processes.

The apparent monotonic variation of “optical absorption edge” with lattice constant,  $a_0$ , d in Fig. 3, is in striking contrast with the variation of peak emission wavelength for the three sulphides.

## 5. References

- [1] E. Rumpf and M. Travnicek, *Ann. Physik* 4 (1930) 725.
- [2] W. Primak, H. Kaufman and R. Ward, *J. Am. Chem. Soc.* 70 (1948) 2043.
- [3] F. Okamoto and K. Kato, *J. Electrochem. Soc.* 130 (1983) 432.
- [4] J.W. Brightwell, B. Ray and C.N. Buckley, *J. Crystal Growth* 59 (1982) 210.
- [5] J.C. Bickerton, I.V.F. Viney and B. Ray, *J. Crystal Growth* 72 (1985) 290.
- [6] H. Kasano, K. Megumi and H. Yamamoto, *J. Electrochem. Soc.* 131 (1984) 1953.
- [7] W. Lehmann, *J. Electrochem. Soc.* 117 (1970) 1389.
- [8] N. Yamashita, Y. Michitsui and S. Asano, *J. Electrochem. Soc.* 134 (1987) 2932.



ELSEVIER

Journal of Crystal Growth 138 (1994) 1055–1060

JOURNAL OF **CRYSTAL  
GROWTH**

## Electrical and optical stimulation of luminescence in $\text{Ca}_{1-x}\text{Cd}_x\text{S}$

I.V.F. Viney \*, B.W. Arterton, B. Ray, J.W. Brightwell

*Divisions of Applied Physics and Chemical Sciences, Coventry University, Priory Street, Coventry CV1 5FB, UK*

### Abstract

Mixtures of CaS and CdS treated at 1020°C for 2 h in a nitrogen atmosphere with an excess sulphur pressure have resulted in solid solutions,  $\text{Ca}_{1-x}\text{Cd}_x\text{S}$  up to  $x = 0.41$ . Fluorescence emission studies have indicated massively enhanced broad band emission spectra for  $x$  between 0.01 and 0.10 at both 77 and 300 K. Electroluminescence studies of copper-coated powder-based samples under AC excitation conditions at  $x = 0.05$  have indicated significant emission intensities broadly aligned spectrally with those from photo-stimulation at the same composition. Further investigations are being directed at optimization of composition, particle size, layer thickness and excitation conditions for enhanced electroluminescence emission intensities.

### 1. Background

The earlier reports [1–6] of extensive solid solutions in the  $\text{Ca}_{1-x}\text{Cd}_x\text{S}$  system for  $x$  up to 0.55 and broad band fluorescence emission characteristics of compositions with  $x$  between 0.01 and 0.10 have prompted this particular study. The solid solutions have the sodium chloride structure of calcium sulphide with the lattice parameter having a linear dependence on composition over the range of solid solubility [3,6]. The temperature of preparation has a significant influence on the limit of solid solubility with Lehmann [2] observing it to be  $x = 0.55$  at 1200°C and Viney et al. [6]  $x = 0.40$  at 1025°C; this variation is not unexpected although the magnitude of change

with temperature is surprisingly large. Susa et al. [3] reported a linear dependence of lattice parameter across the whole composition range when the sodium chloride structure was quenched in from elevated pressures for larger  $x$  values.

This study is centred on a well-established method for the preparation of samples to confirm the reported fluorescence emission spectral behaviour in  $\text{Ca}_{1-x}\text{Cd}_x\text{S}$  over the range  $x = 0$  to 0.41 [6], but then focuses in on the composition  $\text{Ca}_{0.95}\text{Cd}_{0.05}\text{S}$ . At this composition enhanced optically stimulated broad band fluorescence emission occurs at both 77 and 300 K. Particulate samples of  $\text{Ca}_{0.95}\text{Cd}_{0.05}\text{S}$  have been treated to permit AC electroluminescence to be observed and comparisons of the emission spectra observed made with those for the same samples subjected to optical stimulation. The crystal quality of samples across the full solid solubility range in  $\text{Ca}_{1-x}\text{Cd}_x\text{S}$  has been investigated also to assess

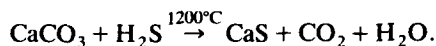
\* Corresponding author.

whether there is any correlation between crystal quality and luminescence emitting performance.

## 2. Experimental methods

### 2.1. Sample preparation

The calcium sulphide starting material was prepared from high purity calcium carbonate using a metathesis reaction with hydrogen sulphide at 1200°C:



The CaS was mixed intimately under dry argon with CdS (5N purity) and 5 mg of elemental sulphur was added to provide a sulphurising atmosphere during heating. The mixture was loaded into a closed end silica tube of 10 mm diameter which in turn was capped by a similar tube of larger diameter. The capped tube arrangement was loaded into a 40 mm diameter furnace tube plugged with glass wool through which a silica delivery tube introduced a supply of inert gas to retain an overpressure during heating, see Fig. 1.

Samples were heated from room temperature to 1020°C in a nitrogen atmosphere, held at 1020°C for 2 h, then removed from the furnace and cooled rapidly to room temperature whilst still in nitrogen.

Electroluminescent powder samples were prepared by coating with copper from a solution of copper(II) chloride dihydrate giving about 1 mol% copper dissolved in methanol. The powder was heated under reflux for 15 min, then filtered and

washed with methanol before drying at 100°C. The dried and coated powders were sieved through a 45 µm mesh and loaded into capped quartz tubes, heated in a nitrogen atmosphere at 850°C for 30 min and then cooled to room temperature.

### 2.2. Optical measurements

Luminescence spectra were determined with a Perkin-Elmer LS50 fluorescence spectrometer permitting measurements at both 77 and 295 K. A detailed excitation spectrum for each emission peak was obtained and the optimum exciting wavelengths were identified to obtain the maximum emission intensities for each peak.

### 2.3. Electroluminescence measurements

Electroluminescence measurements were made using a demountable test cell in which a deformable particulate/dielectric mixture was sandwiched between central metal and conducting glass transparent electrodes separated by 125 µm. The particulate  $\text{Ca}_{0.95}\text{Cd}_{0.05}\text{S}$  was mixed with castor oil in the ratio of 2:1 by weight to provide a spreadable and deformable mixture. The exciting AC field was derived from a voltage-frequency signal generator operating in the ranges 0–550 V and 0.4–10 kHz. The electroluminescence emission spectrum was measured with a Rofin-Sinar optical spectrum analyser.

### 2.4. X-ray diffraction measurements

A Philips PW1730/1710 X-ray diffractometer was used to assess the phase purity, lattice parameter and crystal quality. The methods of determining phase purity and lattice parameter from X-ray diffractometry data are well established. Crystal quality measurements use the same data and the assessment criterion applied to define quality is the level of resolution of the  $K\alpha_1$ – $K\alpha_2$  X-ray diffraction peaks close to  $2\theta = 80^\circ$ . The ratio of the minimum height,  $b$ , between the  $K\alpha_1$  and  $K\alpha_2$  peaks to the  $K\alpha_1$  peak height,  $a$ , was the particular measure taken with low  $b/a$  ratios marking high crystal quality.

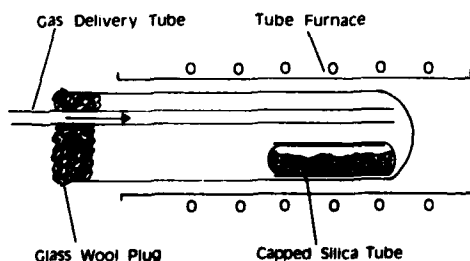


Fig. 1. Experimental arrangement for the preparation of  $\text{Ca}_{1-x}\text{Cd}_x\text{S}$  solid solutions.

### 2.5. Atomic absorption spectrophotometric measurements

A Varian AA475 atomic absorption spectrophotometer was used to analyse for the cadmium content in the samples. It demonstrated that cadmium loss occurred from  $\text{Ca}_{1-x}\text{Cd}_x\text{S}$  samples with  $x > 0.1$ . In combination with X-ray diffractometry measurements, it permitted the proportion of cadmium incorporated in the single phase solid solution to be calculated.

## 3. Results

### 3.1. Structural and crystal quality

It was observed that solid solutions of  $\text{Ca}_{1-x}\text{Cd}_x\text{S}$  occurred for  $x$  up to 0.41 having the sodium chloride crystal structure at a preparation temperature of 1020°C in a sulphur-rich ambient. For  $x = 0.31$  and 0.41 there was evidence of a second phase being present, having the wurtzite structure of CdS, and increasing in level with increasing  $x$ . The lattice parameter values conformed with those observed in earlier reports [5,6].

Whilst the crystal quality measure is crude, it did indicate a decline in quality from  $x = 0$  to a minimum at  $x = 0.10$ , followed by a progressive increase up to the solid solubility limit at  $x = 0.41$ . Fig. 2 illustrates the dependence of the crystal quality parameter  $b/a$  on composition in  $\text{Ca}_{1-x}\text{Cd}_x\text{S}$ .

### 3.2. Optically stimulated excitation and fluorescence emission spectra

#### 3.2.1. Excitation spectra

Excitation spectra at 295 K for the blue-green fluorescence emission in the undoped  $\text{Ca}_{1-x}\text{Cd}_x\text{S}$  at  $x$  between 0 and 0.22 exhibited a steep rise from short wavelengths to peaks between 290 and 340 nm. As the cadmium concentration is increased, the excitation spectrum becomes broader with the intensity at 300 nm never falling below 80% of the peak value for  $x = 0.01, 0.05, 0.10$  and 0.22.

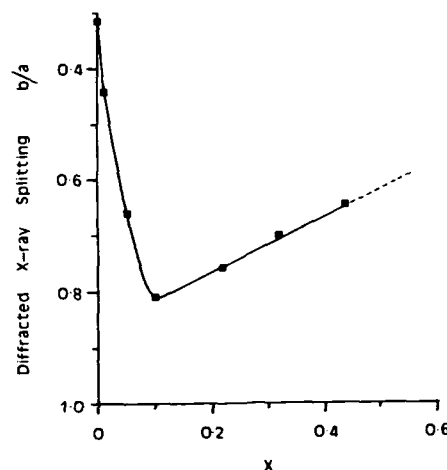


Fig. 2. Crystal quality parameter  $b/a$  as a function of composition in  $\text{Ca}_{1-x}\text{Cd}_x\text{S}$ .

At 77 K, all samples exhibited substantial fluorescence emission and excitation spectra were obtained for the peak emission wavelength in each sample. For  $x = 0.01$  and in particular  $x = 0.05$ , well-defined sharp excitation peaks are seen at 285 nm with secondary peaks at 310 nm of about 80% of intensity of the principal peak. At higher values of  $x$ , once again as at room temperature, broadening of the excitation spectra occurs. Fig. 3 indicates the nature of the excitation spectral characteristics for  $x = 0, 0.01, 0.05$  and 0.10.

#### 3.2.2. Fluorescence emission spectra

At 295 K,  $\text{Ca}_{1-x}\text{Cd}_x\text{S}$  solid solutions excited by 300 nm wavelength radiation exhibited intense fluorescent emission spectra for  $x = 0.01, 0.05$  and 0.10. There was a progressive shift in the peak emitting wavelength with values of 405, 423, 439 and 460 nm for  $x = 0.01, 0.05, 0.10$  and 0.22 respectively. The fluorescence emission characteristics of the copper-coated  $\text{Ca}_{0.95}\text{Cd}_{0.05}\text{S}$  sample were also investigated at 295 K using 300 nm wavelength exciting radiation; the emission intensity was reduced by 70% and the emission peak shifted from 423 to 520 nm.

At 77 K, fluorescence emission spectra for all samples were excited by 300 nm wavelength and



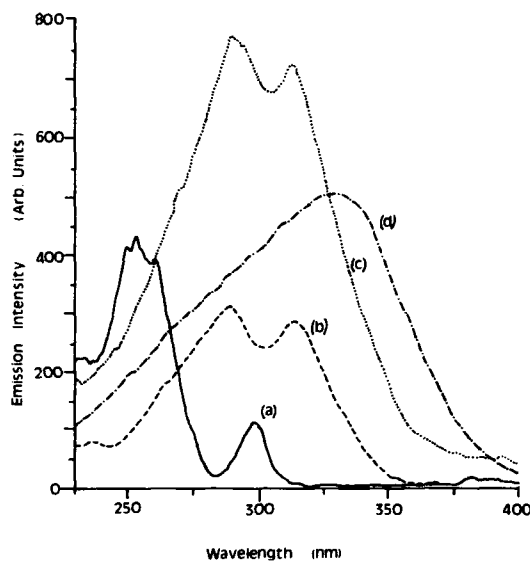


Fig. 3. Excitation spectra at 77 K for the principal blue-green emission peak in  $\text{Ca}_{1-x}\text{Cd}_x\text{S}$  with (a)  $x = 0$ , (b)  $x = 0.01$ , (c)  $x = 0.05$  and (d)  $x = 0.10$ .

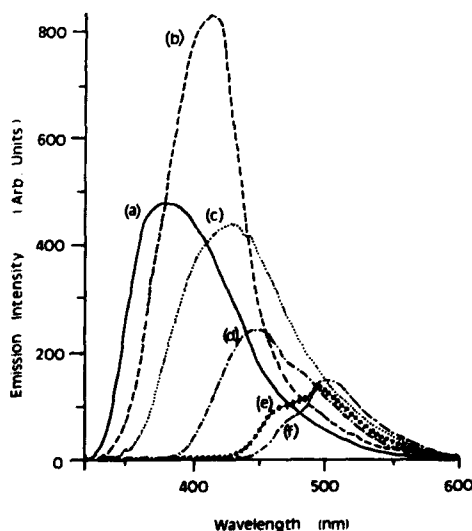


Fig. 4. Fluorescence emission spectra at 77 K excited by 300 nm wavelength radiation in  $\text{Ca}_{1-x}\text{Cd}_x\text{S}$  with (a)  $x = 0.01$ , (b)  $x = 0.05$ , (c)  $x = 0.10$ ,  $x = 0.22$  and (e)  $x = 0.41$ .

Fig. 4 illustrates the characteristic emission for  $x = 0.01, 0.05, 0.10, 0.22$  and  $0.41$ . The fluorescent emission is particularly intense for  $x = 0.01, 0.05$  and  $0.10$  with that at  $x = 0.05$  being the most intense. The emission peaks were also sharper at liquid nitrogen temperatures and, for  $x = 0.31$  and  $0.40$ , there was also evidence of emission from the second phase based on the CdS phase present.

### 3.3. Electroluminescence

#### 3.3.1. Brightness versus voltage and frequency

The electroluminescence brightness as a function of voltage in the copper-coated  $\text{Ca}_{0.95}\text{Cd}_{0.05}\text{S}$  samples exhibited the familiar  $B = A \exp(-a/V^{1/2})$  relationship over the frequency range 0.4 to 10 kHz at voltages between 250 and 550 V. The brightness dependence on frequency was substantially sub-linear in the frequency range investigated.

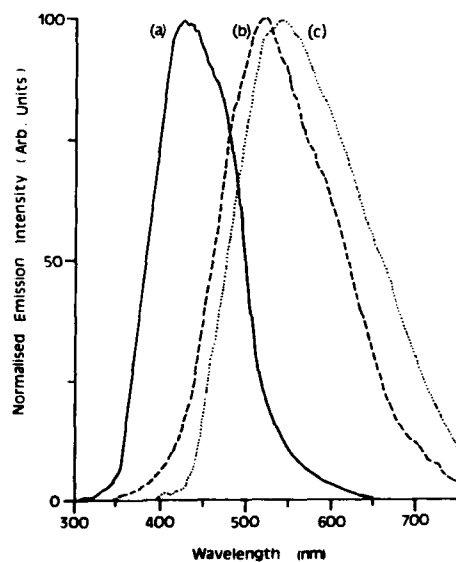


Fig. 5. Normalized fluorescence emission spectra at 295 K of  $\text{Ca}_{0.95}\text{Cd}_{0.05}\text{S}$  for: (a) optical stimulation at 300 nm of an undoped sample, (b) optical stimulation at 300 nm of a copper coated sample and (c) electrical stimulation at 550 V and 10 kHz of a copper coated sample.

### 3.3.2. Spectral distribution of the electrically excited fluorescence emission

Copper-coated  $\text{Ca}_{0.95}\text{Cd}_{0.05}\text{S}$  electrically stimulated at 550 V and 10 kHz had a spectral emission peak at 540 nm with an emission profile very similar to that of optically-stimulated material of the same composition. Fig. 5 compares the fluorescence emission spectra at room temperature of  $\text{Ca}_{0.95}\text{Cd}_{0.05}\text{S}$  (a) undoped and optically stimulated at 300 nm, (b) copper-coated and optically stimulated at 300 nm, and (c) copper-coated and electrically stimulated at 550 V and 10 kHz.

## 4. Discussion

The excitation and fluorescence emission studies at 77 and 295 K have served to extend and confirm earlier observations [5,6] of the broad band emission spectra excited by radiation in the spectral region 290 to 310 nm. The peak emission wavelength shifts from the blue to longer wavelengths as  $x$  is increased from 0.01 to 0.41 in undoped  $\text{Ca}_{1-x}\text{Cd}_x\text{S}$ . At 77 K the emission peaks are better resolved and of greater intensity and for  $x = 0.01$  and 0.05 the peak is blue shifted by 20 nm relative to that at 300 K. The samples, in which the  $\text{Ca}_{1-x}\text{Cd}_x\text{S}$  coexisted with a second phase based on wurtzite-structured CdS, had fluorescence emission spectra characteristics of both component phases with CdS fluorescence being significant particularly at  $x = 0.41$ .

The coating of  $\text{Ca}_{0.95}\text{Cd}_{0.05}\text{S}$  with copper, in order to allow its study under electrical stimulation, resulted in a substantial shift in the fluorescence emission peak wavelength from 423 to 520 nm. The explanation for this is centred around the incorporation of the copper into the  $\text{Ca}_{0.95}\text{Cd}_{0.05}\text{S}$  lattice as emitting centres instead of the defect states found as emitting centres in untreated CaS and  $\text{Ca}_{1-x}\text{Cd}_x\text{S}$ . The absorption process for the exciting radiation could be either directly by the host lattice or the copper centre itself but whichever was the case, still giving rise to longer wavelength emission associated with the copper centre. The unincorporated copper residing on the surface of phosphor particles had the general affect of attenuating the transmission of

the exciting and emitted radiation. The intensity of the overall fluorescence emission peak in the copper-coated sample is 70% of that from the undoped  $\text{Ca}_{0.95}\text{Cd}_{0.05}\text{S}$  sample.

The electroluminescence observations are believed to be the first reported on the  $\text{Ca}_{1-x}\text{Cd}_x\text{S}$  system. They are evidence of the realization of the potential predicted for the system first by Lehmann [2] following his extensive studies on cathodoluminescence and subsequently by Ray et al. [4] from parallel photo-stimulated fluorescence studies. The brightnesses obtained for the copper-coated  $\text{Ca}_{0.95}\text{Cd}_{0.05}\text{S}$  samples were for a non-optimal arrangement and were estimated to be up to  $3 \text{ cd m}^{-2}$  for the active emission area. The 125  $\mu\text{m}$  gap cell structure used in the investigations will have resulted in effectively six particle layers, given the average phosphor particle size of 20  $\mu\text{m}$ , within which emission can be generated and substantial scattering/absorption loss can occur. Smaller particle sizes, fewer particle layers and optimization of the suspending dielectric media will all contribute to increasing the electroluminescence intensity and the effective electric field applied to excite the active layer. Clearly thin film AC EL structures offer further potential for development, as does tuning to the optimal composition and level of copper-coating required.

Comparison of the optically-stimulated fluorescence and electroluminescence emission spectra in the copper-coated  $\text{Ca}_{0.95}\text{Cd}_{0.05}\text{S}$  samples with peak emission intensities at 520 and 540 nm suggests a relatively good match of emission characteristics for the different excitation mechanisms. The enhanced level of infrared emission in the electroluminescence emission spectrum could be linked to electrical power dissipation raising the local temperature. Optimization of the EL test cell structure and component constituents will contribute to reducing such power dissipated losses.

The structural studies were undertaken to assess whether crystal quality had an influence on the electroluminescence characteristics of the particulate phosphors. Insufficient focus has yet been given to the key compositions in the range  $x = 0.01$  to 0.09 to assess whether there is any

intrinsic relationship between quality and the capacity to accommodate emitting centres. However, the initial results with the poorest crystal quality being observed in  $\text{Ca}_{0.90}\text{Cd}_{0.10}\text{S}$  do not point to it being a key factor in obtaining strong electroluminescence. Nevertheless, future studies will continue to involve crystal quality as part of the standard characterization of  $\text{Ca}_{1-x}\text{Cd}_x\text{S}$  phosphors for test under AC EL excitation.

Particular focuses of further study in the laboratory are (i) compositions adjacent to  $\text{Ca}_{0.95}\text{Cd}_{0.05}\text{S}$  particularly between  $x = 0.01$  and  $0.09$ , (ii) optimizing the level of copper deposition on and incorporation in the phosphor, (iii) adapting the preparative processes to produce smaller particle sizes of the electroluminescent  $\text{Ca}_{1-x}\text{Cd}_x\text{S}$

powders, (iv) incorporation of other emitting centres, and (v) working with much thinner electroluminescent test structures.

#### 4. References

- [1] W. Lehmann, *J. Electrochem. Soc.* 117 (1970) 1389.
- [2] W. Lehmann, *J. Luminescence* 5 (1972) 87.
- [3] K. Sasa, T. Kobayashi and S. Taguchi, *J. Solid State Chem.* 33 (1980) 197.
- [4] B. Ray, J.W. Brightwell, D. Allsop and A.G.J. Green, *J. Crystal Growth* 86 (1988) 644.
- [5] I.V.F. Viney, A.G.J. Green, J.W. Brightwell and B. Ray, *J. Luminescence* 48/49 (1991) 593.
- [6] I.V.F. Viney, B. Ray, J.W. Brightwell and B.W. Arterton, *J. Crystal Growth* 117 (1992) 806.



ELSEVIER

Journal of Crystal Growth 138 (1994) 1061–1065

JOURNAL OF **CRYSTAL  
GROWTH**

## Growth and characterization of SrS/ZnS multilayered electroluminescent thin films grown by hot wall technique

Koutoku Ohmi \*, Yoshihiko Yamano, Sang Tae Lee, Takehiro Ueda, Shosaku Tanaka, Hiroshi Kobayashi

*Department of Electrical and Electronic Engineering, Tottori University, Koyama, Tottori 680, Japan*

### Abstract

The growth of thin films of ZnS and SrS by the hot-wall evaporation technique has been investigated. By supplying additional sulfur (S) vapor, the deposition rate of ZnS was increased, allowing ZnS films to be grown at substrate temperatures over 400°C. SrS thin films were grown through the chemical reaction of Sr and S vapor with the substrate temperature in the region of 350–500°C. SrS/ZnS multilayered thin films were grown by the sequential deposition of the SrS and ZnS films. The (SrS/ZnS)<sub>51</sub> multilayered thin film showed X-ray diffraction lines from both ZnS and SrS layers, even when the thickness of each SrS and ZnS layer is 20 nm. The electroluminescent devices with SrS:Ce/ZnS multilayered thin films showed a greenish blue EL emission.

### 1. Introduction

ZnS and SrS thin films are promising host materials to produce thin film electroluminescent (EL) devices [1,2]. Recently, it has been reported that SrS:Ce/ZnS multilayered thin film EL devices showed higher luminance and efficiency than conventional SrS:Ce thin film EL devices [3–5]. To prepare SrS/ZnS multilayered thin films, reactive evaporation and electron beam evaporation methods have been employed. In these methods, the optimum substrate temperature for ZnS and SrS thin film growth is different [3]. ZnS thin films are usually grown at relatively low substrate temperature of 200–300°C. On the other hand, the substrate temperature during SrS thin

film deposition is high (500–600°C) [2,3]. This causes the difficulties in growing SrS/ZnS multilayered thin films.

It has been reported that a hot wall deposition method is widely applied to the thin film growth of II–VI compounds, such as PbTe [6], CdTe [7,8], ZnSe and ZnS [9], etc., and these superlattices [10]. In the hot wall deposition method, the vapor pressure near the substrate is relatively high compared with the reactive evaporation and electron beam evaporation methods. Therefore, it is expected that one can grow SrS and ZnS thin films in a wide substrate temperature range.

In this paper, we report on the growth and the characteristics of SrS/ZnS thin films grown by the hot wall deposition. The SrS/ZnS multilayered thin films were successfully grown at the same substrate temperature. Multilayered thin film EL devices prepared by hot wall deposition are also reported.

\* Corresponding author.

## 2. Experimental procedure

Fig. 1 shows a schematic diagram of the hot wall deposition equipment. There are two walls for ZnS and SrS thin film growth. The distance between a wall and the glass substrate is about 15 mm. ZnS thin films were grown using a ZnS powder source resistively heated to 700–850°C. Sulfur (S) vapor was introduced to the ZnS wall to increase the deposition rate of ZnS at high substrate temperatures. S vapor was supplied from a S furnace placed on the outside of the growth chamber. The S vapor pressure in the S furnace was controlled by a temperature of 200–300°C, which corresponds to an equilibrium sulfur vapor pressure of 700–10000 Pa. The sulfur vapor pressure was reduced to 0.01–0.1 Pa by a bellows valve. SrS thin films were grown through the chemical reaction of Sr and S vapor. Sr vapor was produced from a Sr metal source resistively heated to 580–650°C. Controlled S vapor at a pressure of  $(0.8\text{--}2) \times 10^{-2}$  Pa was supplied to the Sr wall in the way described above. The thin film growth was carried out at several substrate temperatures in the range of 200–550°C. SrS/ZnS multilayered thin films were grown by the se-

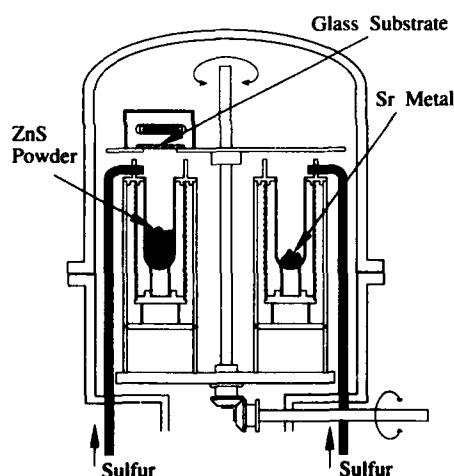


Fig. 1. Schematic diagram of hot wall equipment.

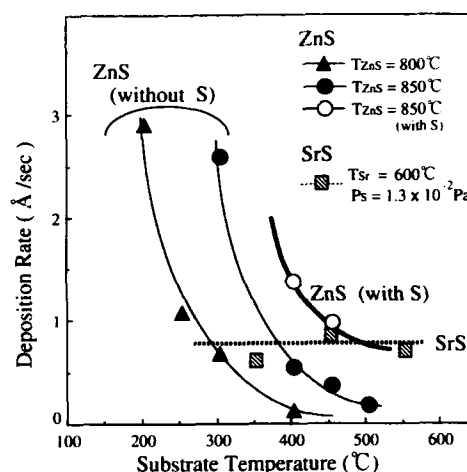


Fig. 2. Dependence of deposition rate of ZnS and SrS thin films on substrate temperature.

quential deposition of the SrS and ZnS films by moving the glass substrate.

## 3. Results and discussion

### 3.1. Growth of ZnS and SrS thin films

Fig. 2 shows the dependence of the deposition rate of the ZnS and SrS thin films on the substrate temperature. The deposition rate of the ZnS films decreases rapidly with an increase of the substrate temperature and is less than 1 Å/s over 400°C, even at a ZnS cell temperature of 850°C. It is reported that, to grow SrS thin films with a good crystallinity, substrate temperatures over 400°C have to be used [2]. Therefore, to deposit ZnS and SrS films at the same substrate temperature, ZnS films should be deposited at 400°C or above. To increase the deposition rate of ZnS thin films, we introduced S vapor during ZnS growth. We have found that the deposition rate of ZnS film was increased remarkably by the introduction of S vapor, as shown in Fig. 2. This may be caused by the following facts. For the growth of ZnS thin film, since the sticking coefficient of S is low at a growth temperature over 400°C, Zn atoms were re-evaporated easily from

the surface of the ZnS thin film. Therefore, supplying S vapor suppresses the re-evaporation of Zn atoms, and results in an increase of the ZnS deposition rate. In contrast, the deposition rate of the SrS films is almost constant in the range of 350–550°C. In the case of the growth of SrS thin films, Sr atoms hardly re-evaporate. Therefore, it is thought that the growth rate of SrS thin films does not depend on the substrate temperature and mainly depends on the supplying rate of Sr vapor.

As a result, by introducing S vapor into the ZnS cell, it becomes possible to deposit ZnS and SrS films sequentially at the same substrate temperature of 400–500°C.

### 3.2. Growth of SrS / ZnS multilayered thin films

Fig. 3a shows the X-ray diffraction (XRD) patterns of  $(\text{SrS}/\text{ZnS})_n$  multilayered thin films having numbers of layers ( $n$ ) from 3 to 51; here  $n$  denotes the total number of SrS and ZnS layers. The total film thickness is about 1  $\mu\text{m}$ . The overall thickness of SrS and ZnS is almost the same (about 500 nm) for each multilayered film. In other words, the SrS and ZnS thickness for one layer ( $d_{\text{SrS}}$ ,  $d_{\text{ZnS}}$ ) decreases with increase of  $n$ . For comparison, XRD patterns of SrS and ZnS thin films are shown in Figs. 3b and 3c, respectively. These films were deposited on quartz glass substrates at the same substrate temperature of 450°C.

First, we discuss the growth characteristics of ZnS and SrS thin films. Fig. 3c shows the result of the ZnS thin film grown by supplying ZnS and S vapor, simultaneously. The thin film has a zincblende structure and is strongly oriented in the (111) plane. By introducing S vapor, the deposition rate increased 2–3 times, as mentioned in section 3.1. It is known that the crystallinity usually becomes poor with increasing deposition rate. However, it is probable that by introducing S vapor, the crystallinity is improved, because the value of full width at half maximum (FWHM) of 0.23° for ZnS film grown by supplying S vapor is narrower than that of 0.29° for ZnS grown by supplying only ZnS vapor. As shown in Fig. 3b, the SrS film has a rocksalt structure and is strongly

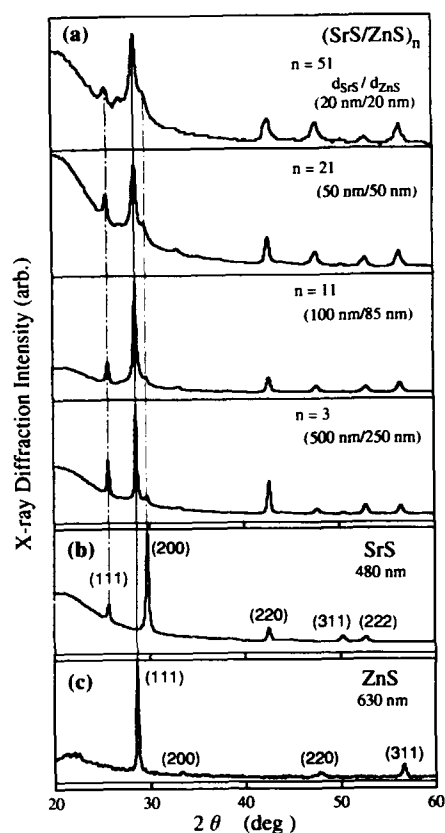


Fig. 3. X-ray diffraction patterns (XRD) of (a)  $(\text{SrS}/\text{ZnS})_n$  multilayered thin films with  $n = 3, 11, 21, 51$ ; (b) and (c) show XRD patterns for SrS and ZnS thin films, respectively.

oriented to the (200) plane. The SrS thin films deposited at a substrate temperature of 350–550°C have almost the same X-ray diffraction pattern as in Fig. 3b. This suggests that SrS films with good crystallinity can be obtained at relatively low substrate temperature by the hot wall technique.

The  $(\text{SrS}/\text{ZnS})_n$  multilayered thin films show XRD peaks due to both ZnS and SrS lattices, as shown in Fig. 3a. Even for 51 multilayered thin films, in which each SrS and ZnS layer is only 20 nm thick, it is obvious that ZnS and SrS layers exist and that the interdiffusion between ZnS and SrS films hardly takes place even at a high substrate temperature of 450°C. The ZnS layers in

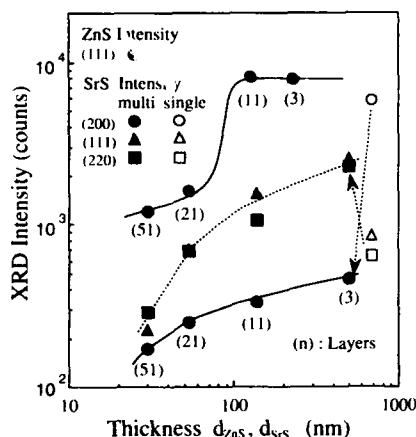


Fig. 4. Dependence of X-ray diffraction (XRD) intensity from ZnS and SrS layers on each thickness ( $d_{\text{ZnS}}$ ,  $d_{\text{SrS}}$ ). Overall thickness of multilayer was kept at  $1 \mu\text{m}$  ( $d_{\text{ZnS}} \times n_{\text{ZnS}}$  (500 nm) +  $d_{\text{SrS}} \times n_{\text{SrS}}$  (500 nm)). XRD intensities of 500 nm thick SrS film for (200) ( $\circ$ ), (111) ( $\Delta$ ) and (220) ( $\square$ ) planes are also plotted.

the  $(\text{SrS}/\text{ZnS})_n$  multilayered thin films are strongly oriented in the  $\langle 111 \rangle$  direction. The orientation axis of ZnS thin films in the multilayered film is the same as for the single ZnS thin film. The dependence of XRD intensity of the (111) peak due to ZnS lattice on the thickness of each ZnS layer ( $d_{\text{ZnS}}$ ) is plotted in Fig. 4. The intensity of the ZnS (111) peak decreases rapidly at a thickness of about 100 nm. This is caused by an increase of the dead layer near the interface between the SrS and ZnS layers. Since the lattice constant of SrS is  $6.019 \text{ \AA}$  and that of ZnS is  $5.409 \text{ \AA}$ , the lattice mismatch is very large (10%). Therefore, it is supposed that epitaxial growth of SrS on ZnS or ZnS on SrS hardly occurs and that ZnS films with poor crystallinity are grown in a thickness of 100–200 nm, as reported for ZnS thin films grown on a glass substrate [11].

The orientation of the SrS thin films in the multilayered thin films changes drastically compared with the SrS single film, as shown in Fig. 3a. The dependence of XRD intensity of the (200), (111), and (220) peaks due to SrS lattices on the thickness of each SrS layer ( $d_{\text{SrS}}$ ) are plotted in Fig. 4. For comparison, XRD intensi-

ties of a 500 nm thick SrS film are also plotted. The (200) peak of the SrS layers in the  $(\text{SrS}/\text{ZnS})_3$  film is much weaker than that of SrS thin films, although both SrS thicknesses are almost the same. On the other hand, the (111) and (220) peaks of the  $(\text{SrS}/\text{ZnS})_3$  film are stronger. These results indicate that the orientation of the SrS thin films in the multilayered films is strongly affected by the ZnS interface. This may be caused by the following. The (111) surface of the ZnS zincblende structure has only Zn or S atoms. For SrS lattice, the (200) and (220) surfaces are the surfaces with both Sr and S atoms. On the contrary, the (111) surface is Sr or S surface. Therefore, the SrS thin films deposited on the  $\langle 111 \rangle$  oriented ZnS surface tend to grow in the  $\langle 111 \rangle$  direction rather than the  $\langle 100 \rangle$  or  $\langle 110 \rangle$  direction. It is reported that the orientation of SrS thin films of SrS/ZnS multilayered thin films grown by reactive evaporation method is the same as that of single SrS thin films [3–5]. However, the difference in growth kinetics between the hot wall and the reactive evaporation methods is not yet well understood. The intensities of the (200), (111) and (220) peaks decrease with a decrease of  $d_{\text{SrS}}$ . This is caused by the increase of the dead layer, the same as in the case of the ZnS (111) intensity.

### 3.3. SrS:Ce/ZnS multilayered thin film electroluminescent devices

Electroluminescent devices with  $(\text{SrS}:\text{Ce}/\text{ZnS})_n$  multilayered thin films ( $n = 3\text{--}11$ ) were prepared by using the hot wall deposition method. The Ce luminescent centers were doped by using a  $\text{CeCl}_3$  hot wall cell heated at  $600^\circ\text{C}$ . The devices have a conventional double insulating structure. The devices showed a broad greenish-blue EL emission peaking at 490 nm under 1 kHz drive. This broad EL emission ranging from 430 to 650 nm is due to the 5d–4f transition of  $\text{Ce}^{3+}$  luminescent centers. The luminance–applied voltage ( $L$ – $V$ ) characteristics of a  $(\text{SrS}:\text{Ce}/\text{ZnS})_{11}$  multilayered thin film EL device are shown in Fig. 5. The luminance rises steeply at 180 V. The obtained luminance value was still quite low compared with the luminance level of

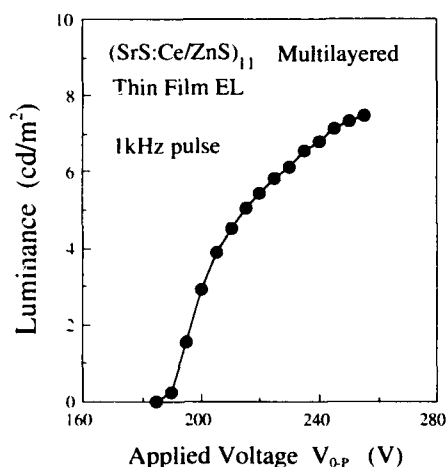


Fig. 5. Luminance–applied voltage characteristics of hot wall grown  $(\text{SrS:Ce/ZnS})_{11}$  multilayered thin film EL device.

500–1000  $\text{cd/m}^2$  for the multilayered EL devices prepared by electron beam and reactive evaporation methods [3–5]. To improve the luminance levels, the growth conditions, such as substrate temperature, Ce concentration, and ZnS and SrS thickness, have to be optimized.

#### 4. Summary

We have demonstrated the growth of SrS/ZnS multilayered thin films by the hot wall technique at the same substrate temperature during deposition of both ZnS and SrS layers. By supplying additional S vapor during ZnS deposition, the deposition rate of ZnS was increased, allowing ZnS films to be grown at high substrate temperature over 400°C. SrS thin films of good quality were grown by the chemical reaction of Sr and S vapor at substrate temperatures between 350 and 500°C. SrS/ZnS multilayered thin films were grown by the sequential deposition of the SrS and

ZnS films. EL devices with hot wall grown SrS:Ce/ZnS multilayered thin films showed a greenish blue EL emission.

#### 5. Acknowledgements

The authors gratefully acknowledge Professor Hiroshi Fujiyasu of the Shizuoka University for technical advice on hot wall equipment. They also thank Professor Hiroshi Saito of the Okayama University of Science for the X-ray diffraction measurements. This work was supported in part by a Grant-in-Aid for Scientific Research on Priority Areas, New Functionality Materials – Design, Preparation and Control, from the Ministry of Education, Science and Culture.

#### 6. References

- [1] H. Kobayashi and S. Tanaka, in: Proc. 5th Intern. Workshop on Electroluminescence, Helsinki, 1990, Acta Polytech. Scand., Appl. Phys. Ser. No. 170 (1990) 69.
- [2] S. Tanaka, J. Crystal Growth 101 (1990) 958.
- [3] R.H. Mauch, K.O. Velthaus, H.W. Schock, S. Tanaka and H. Kobayashi, in: 1992 SID Intern. Symp. Digest Tech. Papers, Boston, MA, 1992, p. 178.
- [4] R.H. Mauch, K.O. Velthaus, B. Hüttel and H.W. Schock, in: 1993 SID Intern. Symp. Digest Tech. Papers, Seattle, WA, 1993, p. 769.
- [5] K.O. Velthaus, R.H. Mauch and H.W. Schock, Adv. Mater. Opt. Electron. 2 (1993), in press.
- [6] A. Lopez-Otero, J. Appl. Phys. 48 (1977) 446.
- [7] J. Humenberger and H. Sitter, J. Crystal Growth 72 (1985) 80.
- [8] R. Korenstein and B. MacLeod, J. Crystal Growth 86 (1988) 382.
- [9] Y. Takeuchi, Y. Okuno, T. Nakamura, K. Ishino, A. Ishida and H. Fujiyasu, Jap. J. Appl. Phys. 31 (1992) 1391.
- [10] S. Mohammadnejad, K. Matsushita, T. Izutsu, A. Ishida and H. Fujiyasu, Jap. J. Appl. Phys. 31 (1992) 3951.
- [11] H. Venghaus, D. Theis, H. Oppolzer and S. Schild, J. Appl. Phys. 53 (1982) 4146.





ELSEVIER

Journal of Crystal Growth 138 (1994) 1066–1070

JOURNAL OF  
**CRYSTAL  
GROWTH**

## The influence of crystal structure on the Zn 3d states in $\text{Zn}_{1-x}\text{Mn}_x\text{S}$

Ch. Jung <sup>a,b</sup>, H.-Ch. Mertins <sup>a</sup>, H.-E. Gumlich <sup>a</sup>

<sup>a</sup> Institut für Festkörperphysik, Technische Universität Berlin, Hardenbergstrasse 36, D-10623 Berlin, Germany

<sup>b</sup> BESSY GmbH, Lentzeallee 100, D-14195 Berlin, Germany

### Abstract

High resolution reflectance spectroscopy experiments were performed to study the Zn 3d states of  $\text{Zn}_{1-x}\text{Mn}_x\text{S}$  over the whole concentration range ( $0 \leq x \leq 0.56$ ). For zincblende-type samples ( $x < 0.05$ ), we observe the excitation of three core level excitons reflecting the threefold split Zn 3d states at the  $\Gamma$ -point. The splitting of the  $\Gamma_8$  state due to spin-orbit interaction is  $\Delta_{\text{so}} = 251$  meV. For the core exciton binding energy, a value of 517 meV is determined. For wurtzite-type samples ( $x > 0.05$ ), the core exciton derived structures are broadened, reflecting the tenfold splitting of the 3d states under  $C_{6v}$  symmetry.

### 1. Introduction

The electronic structure of II–VI semiconductors is distinguished from that of III–V compounds by having a cation d-band inside the main valence band. Among other effects, the band gap, the spin-orbit splitting at the valence band maximum and the valence band offsets between semiconductors are thus influenced by the metal d-bands [1]. In contrast to this, the cation d-electrons are treated as part of the chemically inert atomic core in the interpretation of photoemission data [2,3] and in most calculations (see the publications cited in ref. [1]).

In this paper we examine the influence of crystal structure on the metal d-electrons of  $\text{Zn}_{1-x}\text{Mn}_x\text{S}$ . The semimagnetic semiconductor  $\text{Zn}_{1-x}\text{Mn}_x\text{S}$  is an excellent candidate for these

investigations because (i) the crystal structure changes from zincblende to wurtzite for manganese concentrations in the range from  $x = 0.05$  to  $x = 0.1$ , depending on the technique applied for growing the crystals [4], and (ii) its band gap varies linearly with  $x$ , independent of the crystal structure [5].

### 2. Experimental procedure

The high-resolution reflectance spectroscopy experiments were carried out at the 2m-SEYA beamline of the synchrotron radiation storage ring BESSY in Berlin. Crystals were grown at our institute using a modified Bridgman technique, and the manganese content was checked by microprobe analysis. From the bulk crystals, samples were prepared by cleaving under ambient conditions. The samples were then mounted in an Oxford Instruments CF 1100 cryostat.

\* Corresponding author.

experiments in the temperature range of 25 K up to room temperature. From the reflectance data, the dielectric function was calculated via Kramers–Kronig transformation, and the imaginary part of the dielectric function was subjected to a lineshape analysis (for detailed information, see ref. [6]).

### 3. Results and discussion

An important result of the location of the cation d-bands inside the main valence band of II–VI compounds is that the d states are influenced also by crystal field interaction, whereas they can be treated as core-like states for III–V semiconductors [1]. Thus, when calculating the electronic structure especially for the cation d-bands, the crystal structure and the symmetry representations have to be taken into account, and for ZnS only a few band structure calculations are available where the metal d-atoms were not treated as core-like atoms [1,7].

Since we were interested in the analysis of Zn 3d derived transitions, we calculated the expected splitting of the d states for both crystal structures under study. Our calculations were restricted to the centre of the Brillouin zone, because only for this symmetry point can zincblende and wurtzite structure be compared directly.

Zincblende structure has a tetrahedral point group ( $T_d$ ). Because of the missing inversion symmetry, zincblende-type semiconductors exhibit a mixing of central-atom d states and ligand-atom p states [1]. If only crystal field interaction is considered we find two Zn 3d states at the  $\Gamma$ -point. Applying Bethe's notation the irreducible representations  $\Gamma_3$  (twofold degenerate) and  $\Gamma_5$  (threefold degenerate) result (according to Bouckaert's notation  $\Gamma_{12}$  and  $\Gamma_{15}$ , as presented in the work of Wei and Zunger [1] and Eckelt [7]). Under the influence of spin–orbit interaction, the  $\Gamma_3$  state is not affected and transforms into a  $\Gamma_8$  representation, whereas the  $\Gamma_5$  state splits into one  $\Gamma_7$  and one  $\Gamma_8$  representation. For this spin–orbit splitting, Eckelt calculated a value of 300 meV [8]. Taking into account the number of two atoms per unit cell, the above result reflects

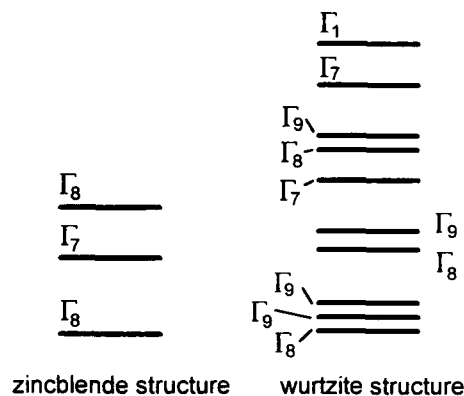


Fig. 1. Resulting Zn 3d-electronic states at the  $\Gamma$ -point of the Brillouin zone for zincblende (left) and wurtzite structure (right). In the calculation, crystal field and spin–orbit splitting are included.

the number of 10 d-electrons. The resulting electronic states at the  $\Gamma$ -point are shown in Fig. 1.

For wurtzite structure the situation is more complicated. At the centre of the Brillouin zone the symmetry representation is  $C_{6v}$  and is thus reduced with respect to zincblende. Furthermore, for the hcp lattice the unit cell contains four atoms, and we expect 20 d-electrons at the  $\Gamma$ -point. Due to the reduced symmetry we find already six d states if spin–orbit interaction is neglected: two non-degenerate  $\Gamma_1$  and  $\Gamma_4$  states and four twofold degenerate  $\Gamma_5$  and  $\Gamma_6$  states. If spin–orbit interaction is considered, the degeneracy is cancelled out, and we get ten non-degenerate states (the irreducible representations are shown in Fig. 1).

The result of our reflectance spectroscopy experiments is shown in Fig. 2 for pure ZnS (i.e.,  $x = 0$ ) in zincblende structure. The first structure in this figure peaking at 11.5 eV is due to an interband transition located along the  $\Sigma$ -direction in the Brillouin zone [9]. The sharp structures around 12 eV are subject to our investigations. They originate in the excitation of Zn 3d core level excitons. Two distinct peaks are clearly resolved, and a third structure appears as a low energy shoulder of the first peak.

From a lineshape analysis we achieve an excellent fit of the experimental  $\epsilon_2$  data if three

Lorentzians are used. The resulting energies are 11.896, 12.045 and 12.296 eV, respectively. We ascribe the observed lines to the excitation of core level excitons of the Zn 3d states  $\Gamma_8$ ,  $\Gamma_7$  and  $\Gamma_8$  at the  $\Gamma$ -point (see bottom of Fig. 2 and also Fig. 1). From the excitation energies of the  $\Gamma_7$  and  $\Gamma_8$  core excitons at 12.045 and 12.296 eV, respectively, the spin-orbit splitting  $\Delta_{so}$  can be calculated. The resulting value is  $\Delta_{so} = 251$  meV. This triplet of core exciton structures observed for ZnS can be clearly followed for  $\text{Zn}_{1-x}\text{Mn}_x\text{S}$  up to a manganese concentration of  $x = 0.037$ , being the highest amount of manganese for which our samples are in the zincblende structure. Both the core exciton energies and the spin-orbit splitting remain constant within this concentration range.

The core level exciton derived structures are followed by core level conduction band transitions at the  $\Gamma$ -point, dominated by the peak in the  $\epsilon_2$  spectrum at 12.554 eV which is correlated to the  $\Gamma_7$  core exciton at 12.045 eV. The peak at 12.820 eV correlates to the  $\Gamma_8$  core exciton at 12.296 eV, the spin-orbit splitting calculated from

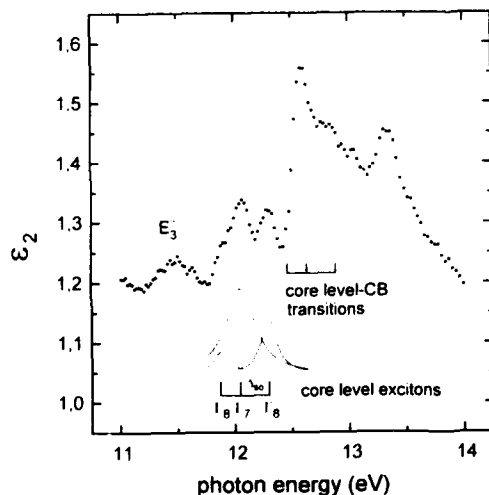


Fig. 2. Top: Imaginary part of the dielectric function of zincblende-type ZnS in the energy range of the cation 3d transitions; bottom: result of the line shape analysis for the core exciton lines. The energy levels and the spin-orbit splitting are shown, and the range of transitions into the conduction band minimum is indicated.

Table 1

Experimentally determined binding energies and spin-orbit splitting of the cation 3d states of ZnS (the data of Eckelt [7,8] are from calculations)

Reference	Binding energy (eV)	$\Delta_{so}$ (meV)
Vesely and Langer [11]	8.97	560
	9.53	
Ley et al. [2]	9.03	-
	9.03	
This work	8.60	251
	8.78	
	9.03	
Eckelt [7,8]	7.0	300

these two transitions is identical with the value derived from the respective core exciton lines. The structure corresponding to the uppermost  $\Gamma_8$  core excitation at 11.896 eV is hidden at the onset of the peak at 12.554 eV.

From the difference in energy between the direct conduction band transitions and the core exciton lines, the exciton binding energy can be calculated. We achieve a value of 517 meV in agreement with "first principles" calculations reported by Chacham et al. [10]. If also the band gap energy is known, the binding energy of the cation d states can be obtained: 8.60 eV for  $\Gamma_8$ , 8.78 eV for  $\Gamma_7$  and 9.03 eV for  $\Gamma_8$  (see Table 1 and references therein).

Transitions from the cation d states into the conduction band minimum at the  $\Gamma$ -point are well separated from transitions at other points of high symmetry inside the Brillouin zone because of (i) the high energy separation between the conduction band minima at the  $\Gamma$ - and the L-point of at least 1.5 eV (the L-point minimum being the second lowest conduction band minimum) [7] and (ii) a dispersion of the d-bands being one order of magnitude smaller than that of the lowest conduction band [1]. We therefore ascribe the structure peaking at 13.3 eV in the  $\epsilon_2$  spectrum of Fig. 2 to the onset of transitions at the L-point.

In contrast to the energy range of transitions at the  $\Gamma$ -point, where pronounced structures are observed, no fine structure can be resolved for energies above 13 eV. One reason is given by the fact that at the L-point the symmetry is lower

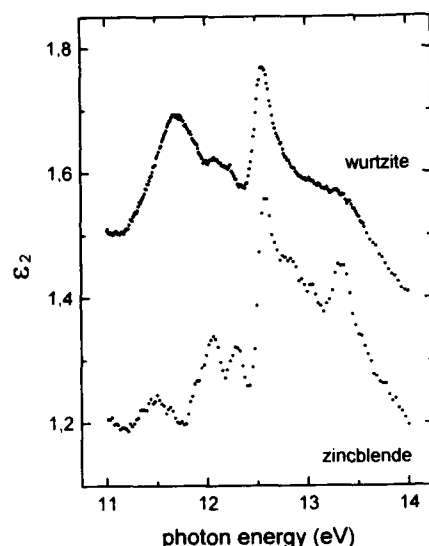


Fig. 3. Imaginary part of the dielectric function of  $\text{Zn}_{1-x}\text{Mn}_x\text{S}$ . Lower curve:  $x = 0$ , zincblende structure; upper curve:  $x = 0.07$ , wurtzite structure.

than at the centre of the Brillouin zone. Thus five d states result, spread over a wider energy range than the electronic states at the  $\Gamma$ -point. Nearly the same electronic structure is found for the X-point, the conduction band minima at L and X being only separated by a few tenths of an electron volt [7]. The structures derived by transitions from d states into the conduction band minima at L and X thus partly overlap, and the resulting  $\epsilon_2$  spectrum is almost unstructured.

As mentioned earlier, the spectral shape presented in Fig. 2 can be followed as long as the  $\text{Zn}_{1-x}\text{Mn}_x\text{S}$  samples have the zincblende structure. For manganese concentrations above  $x = 0.05$  the samples have the wurtzite structure. For a  $\text{Zn}_{1-x}\text{Mn}_x\text{S}$  sample with a manganese content of  $x = 0.07$ , the  $\epsilon_2$  spectrum is shown in Fig. 3. From a comparison with the spectrum of pure ZnS given at the bottom of Fig. 3 it can be seen that the onset of conduction band transitions at the  $\Gamma$ -point is almost not affected by the change in crystal structure, due to the very small variation of the band gap with increasing manganese concentration [5].

A significant change is found in the core level exciton structures within the energy range between 11 and 12.5 eV. For wurtzite type samples we now observe only two broad and intense structures, replacing the interband transition peak  $E_3''$  and the core level exciton peaks found for zincblende structure. These spectral features can be followed up to the highest available manganese concentration of  $x = 0.563$ . As discussed in the first part of this section, this change is due to the difference in the electronic structure of the Zn 3d states at the  $\Gamma$ -point of the two crystal structures under study. Since we now have ten electronic d states rather than three for the zincblende structure (see Fig. 1), the experimental  $\epsilon_2$  data reflect the changes in the electronic structure. Due to the high amount of electronic states involved and the fact that eight of them result from the spin-orbit interaction, a line shape analysis could not deliver reliable results.

#### 4. Conclusions

The excitation of Zn 3d core level excitons in zincblende-type  $\text{Zn}_{1-x}\text{Mn}_x\text{S}$  could be used to reveal the electronic structure of the cation d states at the centre of the Brillouin zone. The theoretically predicted splitting into three electronic states and accordingly the spin-orbit splitting could be confirmed by the experimental data and a detailed line shape analysis. At the same time it could be shown that the cation d states of II–VI compounds are influenced by the crystal field. Due to the change in the crystal structure at a manganese concentration of  $x \approx 0.05$ , the distinct core level exciton peaks found for zincblende-type samples are replaced by two broad and unstructured lines.

#### 5. Acknowledgments

We gratefully acknowledge Dr. A. Krost and H.-J. Broszat for growing samples covering the whole concentration range available. Dr. F. Gilbert performed expert microprobe analysis to determine the manganese concentration of our sam-

ple to a high accuracy. The work was supported by the Bundesminister für Forschung und Technologie under grant No. 05314 CI.

## 6. References

- [1] S.-H. Wei and A. Zunger, *Phys. Rev. B* 37 (1988) 8958.
- [2] L. Ley, R.A. Pollack, F.R. McFeely, S.P. Kowalczyk and D.A. Shirley, *Phys. Rev. B* 9 (1974) 600.
- [3] N.J. Shevchik, J. Tejada, M. Cardona and D.W. Langer, *Phys. Status Solidi (b)* 59 (1973) 87.
- [4] A. Pajczkowska, *Progr. Crystal Growth Characterization* 1 (1978) 289.
- [5] K. Mayrhofer, K. Hochberger and W. Gebhardt, *J. Phys. C* 21 (1988) 4393.
- [6] Ch. Jung, H.-E. Gumlich, A. Knack and H.-C. Mertins, *J. Crystal Growth* 101 (1990) 926.
- [7] P. Eckelt, *Phys. Status Solidi* 29 (1967) 307.
- [8] P. Eckelt, *Solid State Commun.* 6 (1968) 489.
- [9] J.P. Walter and M.L. Cohen, *Phys. Rev.* 183 (1969) 763.
- [10] H. Chacham, J.L.A. Alves, M.L. De Sequeira and J.R. Leite, *J. Phys. Chem. Solids* 49 (1988) 969.
- [11] C.J. Vesely and D.W. Langer, *Phys. Rev. B* 4 (1971) 451.

## Late News

# The nitrogen–hydrogen complex in ZnSe

J.A. Wolk<sup>a</sup>, J.W. Ager III<sup>a</sup>, K.J. Duxstad<sup>a,b</sup>, W. Walukiewicz<sup>a</sup>, E.E. Haller<sup>a,b</sup>,  
N.R. Taskar<sup>c</sup>, D.R. Dorman<sup>c</sup>, D.J. Olega<sup>c</sup>

<sup>a</sup> Lawrence Berkeley Laboratory, Berkeley, California 94720, USA

<sup>b</sup> University of California, Berkeley, California 94720, USA

<sup>c</sup> Philips Laboratories, Briarcliff Manor, New York 10510, USA

Recent progress in p-type doping of ZnSe has been achieved by using the MBE growth technique with nitrogen free-radicals as a source for the acceptor doping [1]. The concentrations of electrically active N acceptors as high as  $10^{18} \text{ cm}^{-3}$  have been reported. Attempts to reproduce these results with the MOVPE growth technique have not been successful so far. It has been suggested that a major impediment to achieving large free hole concentrations using MOVPE is the passivation of N acceptors by H. The possible sources of H contamination in the growth process include  $\text{NH}_3$  used as a N source,  $\text{H}_2$  as a carrier gas and H as a decomposition product of the Zn and Se precursor molecules.

In this late-news paper we present the first spectroscopic evidence for the presence of N–H complexes in MOVPE-grown ZnSe [2]. The ZnSe layers were grown by photo-assisted MOVPE on (100) semi-insulating substrates using dimethyl-zinc and dimethyl-selenium as precursors. The growth temperature was  $350^\circ\text{C}$  and the layers were  $2.3$  to  $3 \mu\text{m}$  thick. The layers were doped with N using  $\text{NH}_3$  in a flow modulation epitaxy. The capacitance–voltage measurements have shown the concentration of electrically active acceptors to be less than  $10^{15} \text{ cm}^{-3}$ , although the total concentration of N atoms determined from SIMS measurements exceeded  $10^{18} \text{ cm}^{-3}$ . Fourier transform infrared absorption spectra were taken at 9 K and at room temperature. Room tempera-

ture Raman scattering experiments were performed in a pseudo-backscattering geometry using an ion argon laser.

The results of the infrared absorption measurements at 9 K are shown in Fig. 1. Two peaks, one at  $3194 \text{ cm}^{-1}$  and one at  $783 \text{ cm}^{-1}$ , were clearly observed in the spectrum. Since these peaks have only been observed in N-doped MOVPE grown ZnSe and have not been detected in an undoped reference sample, we assign them

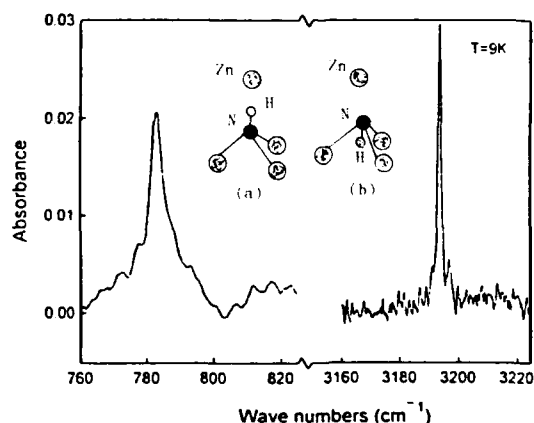


Fig. 1. Infrared absorption lines in N-doped ZnSe containing H. The H stretch vibration mode ( $3194 \text{ cm}^{-1}$ ) and the H wag mode ( $783 \text{ cm}^{-1}$ ) are shown. Two configurations shown as inserts in (a) and (b) are fully compatible with the IR and Raman spectroscopy data.

to local vibrational modes of the N–H complex. The high energy peak at  $3194\text{ cm}^{-1}$  corresponds to the stretching and the low energy peak at  $783\text{ cm}^{-1}$  corresponds to the wagging mode of the complex. The energy of the stretching mode is 8% lower than the energy of N–H vibrations in the  $\text{NH}_3$  molecule at  $3444\text{ cm}^{-1}$ . This is consistent with the empirical rule stating that the LVM frequency is several percent lower for a bond in the crystal lattice than it is for the same bond in a free molecule. An analysis of the polarized Ra-

man spectroscopy results has shown that the N–H complex has  $C_{3v}$  symmetry. Therefore, as is shown in the insert of Fig. 1, the H atom can be bonded to the N atom in a bonding or antibonding direction. In analogy with C–H complexes in GaAs, the bonding position of the H atoms is a more likely configuration for the N–H complex.

[1] R.M. Park et al., *Appl. Phys. Lett.* 57 (1990) 2127.

[2] J.A. Wolk et al., *Appl. Phys. Lett.*, to be published.

# Late News

## The influence of nitrogen on the p-conductivity in ZnSe epilayers grown by molecular beam epitaxy

A. Hoffmann <sup>a</sup>, B. Lummer <sup>a</sup>, L. Eckey <sup>a</sup>, V. Kutzer <sup>a</sup>, Ch. Fricke <sup>a</sup>, R. Heitz <sup>a</sup>,  
I. Broser <sup>a</sup>, E. Kurtz <sup>b</sup>, B. Jobst <sup>b</sup>, D. Hommel <sup>b</sup>

<sup>a</sup> Institut für Festkörperphysik, Technische Universität Berlin, Hardenbergstrasse 36, D-10623 Berlin, Germany

<sup>b</sup> Physikalisches Institut, Universität Würzburg, Am Hubland, D-97074 Würzburg, Germany

The relation between the incorporation of nitrogen into ZnSe/GaAs epilayers grown by molecular beam epitaxy (MBE) and the resulting p-conductivity is not fully understood to date. Native point defect reactions are believed to strongly interfere with the control of carrier type and conductivity. Our MBE samples were grown on p-type (100) GaAs:Zn substrates in a 4-chamber system using elemental sources for Zn and Se with a Se/Zn flux ratio of 2:1. N was incorporated during growth using a plasma source. Varying the substrate parameters we are able to produce p-type or n-type conductivity. We present time-integrated and time-resolved photoluminescence (PL) measurements yielding new information on the incorporation mechanisms of N into p-type ZnSe epilayers.

Spectra of n-type and weakly p-type samples exhibit bound exciton (BE) and donor–acceptor pair (DAP) luminescence (cf. Fig. 1). From their energies the BE emissions are attributed to the decay of excitons bound to a Ga donor ( $I_2$ ), a N acceptor ( $I_1^N$ ), and to a complex of a Zn vacancy and interstitial Ga ( $I_1^C$ ), evidencing interdiffusion of Ga and incorporation of N on Se sites. This is supported by the fact that samples grown at higher temperatures tend to be n-type. The DAP luminescences around 2.70 eV are consistent with a N acceptor level between 100 and 110 MeV. With higher N concentrations and  $N_A - N_D \geq 1 \times 10^{17}$

$\text{cm}^{-3}$ , instead of BE and DAP luminescences a new broad band appears around 2.63 eV. However, time-resolved PL proves the DAP character

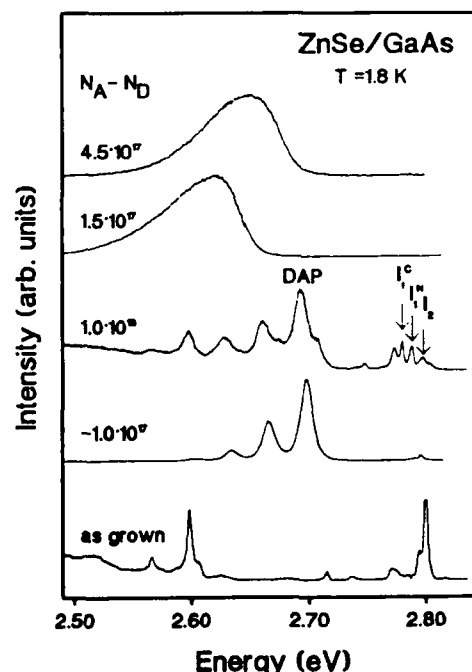


Fig. 1. Luminescence of N-doped ZnSe/GaAs in the band edge region.



of this band. From this we estimate a N-associated donor level at 50 meV. The acceptor concentrations, determined by means of time-resolved PL (for the method, see ref. [1]), are in reasonable agreement with  $N_A - N_D$  values from  $C-V$  profiling measurements (given in Fig. 1). A further increase of the N-concentration results in a blue shift of this broad band, a behaviour known from highly n-doped CdS [1] and explained by screening of shallow impurity levels.

The growth temperature is an important parameter for p- or n-conductivity of ZnSe grown in a N plasma, since it is related to the incorporation of native defects. RHEED studies in the growth regime showed a clear  $(2 \times 1)$  reconstruction for p-samples, indicating a surface rich of Se, whereas n-samples exhibited a  $(2 \times 2)$  reconstruction typical for a surface rich of Zn.

[1] Ch. Fricke et al., J. Crystal Growth 138 (1994) 815.



ELSEVIER

Journal of Crystal Growth 138 (1994) 1075

JOURNAL OF **CRYSTAL  
GROWTH**

### Late News

## SrS single crystals grown by physical vapor transport

R. Helbing, R.S. Feigelson

*Center for Materials Research, Stanford University, Stanford, California 94205, USA*

Alkaline earth sulfides have recently been found to have interesting luminescent properties for applications in thin film electroluminescence devices. Strontium sulfide doped with rare earth ions is one of the most promising of these materials for blue or white emitting displays. However, little is known about the basic material properties of the IIa–VI semiconductors, one of the reasons being the difficulty to grow single crystals of these materials. Thus, we have investigated the crystal growth and characterization of SrS. In preliminary experiments using the laser heated pedestal growth (LHPG) technique, the high evaporation rate of the SrS prevented the formation of a stable molten zone. However, the re-condensed material in the system was found to be pure, stoichiometric SrS and, therefore, vapor phase transport appeared a more promising approach. Using the physical vapor transport (PVT) technique, we have been able to grow SrS crystals about 1 cm in diameter and 1 cm in length containing only a few grains. Crystals were grown in a single zone, high temperature graphite furnace in a graphite ampoule at 1650°C and  $10^{-4}$  Torr. The as-grown crystals were slightly colored. Electron microprobe, XPS and X-ray diffraction

showed no deviation from stoichiometry, within the limits of detection. The photoluminescence spectra of as-grown SrS crystals showed a broad band emission centered at around 630 nm, its excitation peak being at 290 nm – in close agreement with the band gap energy of about 4.3 eV. Upon annealing in a sulfur and selenium atmosphere, respectively, the crystals turned completely black. After heat-treating of these crystals at elevated temperature, the original color of the as-grown crystals returned. However, annealing of as-grown crystals in an argon atmosphere at 2000°C in an arc image furnace resulted in colorless crystals. The coloration of the as-grown crystals may result from carbon incorporation during growth. The PVT-grown crystals were remarkably stable with respect to an ambient air atmosphere. After several months open storage, no signs of degradation were observed, polished surfaces stayed mirror-like. Only after heat-treating of as-grown crystals in air for 16 h at 600°C, a thin, oxygen-containing surface layer was found. Compared to as-grown material, photoluminescence measurements of these crystals revealed an additional emission as well as excitation peak at 480 and 315 nm, respectively.



ELSEVIER

Journal of Crystal Growth 138 (1994) 1076

JOURNAL OF **CRYSTAL  
GROWTH**

### Late News

## Studies of blue-green laser structures with asymmetric and pseudomorphic ZnSe wave guides

D. Hommel<sup>a</sup>, E. Kurtz<sup>a</sup>, T. Behr<sup>a</sup>, A. Jakobs<sup>a</sup>, B. Jobst<sup>a</sup>, S. Scholl<sup>a</sup>, K. Schüll<sup>a</sup>,  
V. Beyersdorfer<sup>a</sup>, G. Landwehr<sup>a</sup>, H. Cerva<sup>b</sup>

<sup>a</sup> *Physikalisches Institut, Universität Würzburg, D-97074 Würzburg, Germany*

<sup>b</sup> *Siemens AG, Otto-Hahn-Ring 6, D-81739 München, Germany*

The laser structures were grown in the 3M configuration with  $\text{Cd}_x\text{Zn}_{1-x}\text{Se}$  quantum well, ZnSe wave guide and  $\text{ZnS}_{0.06}\text{Se}_{0.94}$  cladding layers lattice matched to the n-type GaAs:Si substrate. Au-Ge contacts were applied to the GaAs backside and 30  $\mu\text{m}$  Au stripes to the top of the p-ZnSSe:N layer.

Based on confinement calculations for a 10 nm thick CdZnSe well, an asymmetric wave guide with 320 nm ZnSe below and 160 nm above the quantum well was chosen to ensure that the ZnSe layer is at least partially relaxed before the active region is grown.

Laser emission was studied using pulses with a length between 100 and 400 ns and a repetition rate up to 10 kHz, usually at 77 K. For a cavity length of 1.3 mm the longitudinal mode spacing was 0.32 Å. Single mode operation has been observed as well. The threshold current density was about 570 A/cm<sup>2</sup> and the power output per uncoated facet more than 50 mW. The lifetime exceeded 3 h at 77 K, while lasing was observed up to 250 K.

Carrier densities as measured by C-V profiling will be discussed as well as structural properties determined by high resolution X-ray diffraction reciprocal space mapping.

A novel approach to prevent the formation of misfit dislocations within the active layer of such laser structures without using quaternary compounds is the growth of strained ZnSe wave guides. The thickness of the ZnSe at both sides of the quantum well was chosen as 70 nm in order to be below the critical thickness of 150 nm for ZnSe on GaAs. TEM studies of such quantum well and laser structures confirm the excellent crystalline quality. The active region of such laser structures is free of misfit dislocations. The optical confinement factor is 1.8%, a value still above the one calculated for structures with partially relaxed wave guides.

Lasing of such a structure has been observed recently.



ELSEVIER

Journal of Crystal Growth 138 (1994) 1077

JOURNAL OF **CRYSTAL  
GROWTH**

### Late News

## Ridge waveguide, separate confinement green-blue heterostructure lasers

A. Salokatve <sup>a</sup>, H. Jeon <sup>a</sup>, M. Hovinen <sup>a</sup>, P. Kelkar <sup>a</sup>, A.V. Nurmikko <sup>a</sup>, D.C. Grillo <sup>b</sup>,  
Li He <sup>b</sup>, J. Han <sup>b</sup>, Y. Fan <sup>b</sup>, R.L. Gunshor <sup>b</sup>

<sup>a</sup> Division of Engineering and Department of Physics, Brown University, Providence, Rhode Island 02912, USA

<sup>b</sup> School of Electrical Engineering, Purdue University, West Lafayette, Indiana 47907, USA

We report on the room temperature performance of ZnCdSe/ZnSSe/ZnMgSSe separate confinement (SCH) diode lasers which also incorporate Zn(Se,Te) graded gap ohmic contacts. A heavily doped p-ZnTe forms the top layer for metal (Pd) contact. The pseudomorphic heterostructures have been fabricated into ridge waveguides by a self-aligned contact process, with a typical mesa width in the 5–6  $\mu\text{m}$  range. Specific dry etch and other processing methods are necessary due to the chemical differences between ZnSe and ZnTe. Room temperature laser operation at voltages as low as 7 V have been obtained for 500  $\mu\text{m}$  long devices with uncoated facets, with single transverse mode output, and with differential quantum efficiency at approximately 20–25% per facet. Both single and multiple quantum well structures have been employed, with threshold current density in the range of 1.2–1.5  $\text{kA}/\text{cm}^2$  for the former, and about 600  $\text{A}/\text{cm}^2$  per quantum well for the latter. Pulsed high-duty cycle operation up to several tens of percent has been verified in heatsunk devices.

At the high, quasi-CW duty cycle level of operation, the device lifetime is reduced to seconds. The slope efficiency deteriorates quickly and we frequently observe in the temporal output distinct

but random pulsations as the devices degrade. The laser pulsations can occur on a timescale of a microsecond or less and appear to be directly connected to defect formation and propagation in the active layers. By employing transparent electrode material, we have also used optical microscopy to visualize the formation of defects in real time during the degrading of the laser devices, by spatially imaging the spontaneous emission along the stripe electrode atop the active region. Clear evidence is seen of the coalescing of defected microareas into macroscopic regions which leads to an accelerated reduction in the optical emission from the device, impairing of the vertical transport, and to a subsequent catastrophic failure. Eventually, large dark areas within the stripe, with regular geometrical features along principal crystallographic planes, show nearly total quenching of optical activity. These spatially resolved observations are similar to those recently reported by the group at 3M in the LED regime in a study which also included transmission electron microscope analysis of the dislocation-derived defect microstructure.

Research supported by the ARPA, NSF, and AFOSR.



ELSEVIER

Journal of Crystal Growth 138 (1994) 1078

JOURNAL OF **CRYSTAL  
GROWTH**

## Late News

## Reduction of the Au/p-ZnSe(100) Schottky barrier height using a thin Se interlayer

W. Chen <sup>a</sup>, J. Gaines <sup>b</sup>, C. Ponzoni <sup>b</sup>, D. Olego <sup>b</sup>, P.S. Mangat <sup>c</sup>, P. Soukiasian <sup>d</sup>,  
A. Kahn <sup>a</sup><sup>a</sup> Department of Electrical Engineering, Princeton University, Princeton, New Jersey 08544, USA<sup>b</sup> Philips Laboratories, Briarcliff Manor, New York 10510, USA<sup>c</sup> Department of Physica, Northern Illinois University, DeKalb, Illinois 60115-2854, USA<sup>d</sup> CEA, Centre d'Etudes de Saclay, F-91191 Gif-sur-Yvette Cedex, France

We present a study of the formation of Schottky barriers (SBs) between Au and p-ZnSe(100) using high-resolution synchrotron-radiation photoemission spectroscopy (PES). PES is a powerful technique in that it provides information on interface chemical reaction, intermixing, growth mode of the metal layer and intermediate values of the barrier during the interface formation. Au/p-ZnSe(100) is an important test-case interface. Theoretically, high work function metals like Au should produce low barriers for holes on p-ZnSe. Low barrier, or ohmic, contacts are crucial for further developments of II-VI-based light emitting devices.

p-Type ZnSe(100), nitrogen-doped with a free carrier concentration of  $\sim 5 \times 10^{17} \text{ cm}^{-3}$ , was grown by molecular beam epitaxy on p-GaAs(100) substrates. The thickness of the ZnSe layers was 5000 Å. These samples were capped in the growth chamber with a thick Se layer for protection during transfer to the photoemission system, and then decapped in ultra-high vacuum to obtain clean ZnSe(100) surfaces. Depending on the annealing temperature, Se-rich (1 × 1), (2 × 1) and Zn-rich c(2 × 2) reconstructed surfaces were obtained. The deposition of Au was done by evaporation from a W filament.

The measurement of SB heights by PES relies on the determination of the Fermi level ( $E_F$ ) position relative to the valence band maximum (VBM) on the clean surface, and of the shift of the semiconductor core levels as a function of metal deposition. Using this technique, we found  $E_F$  to be initially at 1.1 eV above the VBM (1.1 eV downward band bending) and to assume a final position at 1.13 eV above VBM for thick Au overlayers. The 1.13 eV hole barrier is consistent with previously reported PES results [1]. The analysis of the core level spectra shows that Au grows in a layer-by-layer mode, and that no significant chemical reaction nor intermixing takes place at room temperature.

A substantial modification of this barrier was obtained by leaving a thin interlayer (2–3 monolayers) of Se between Au and the ZnSe surface. The initial  $E_F$  position was  $\sim 0.1$  eV closer to the VBM than that of the clean surface, and the final Au SB height was 0.88 eV,  $\sim 0.25$  eV lower than that obtained without the thin Se layer. This result will be discussed in terms of the large electronegativity and work function of Se.

[1] M. Vos et al., Phys. Rev. B 39 (1989) 10744.



ELSEVIER

Journal of Crystal Growth 138 (1994) 1079–1080

JOURNAL OF **CRYSTAL  
GROWTH**

## Late News

# Growth of MgTe and $\text{Zn}_{1-x}\text{Mg}_x\text{Te}$ thin films by metalorganic vapour phase epitaxy

B. Qu'Hen, X. Quesada, W.S. Kuhn, J.E. Bourée, L. Svob, A. Lusson, O. Gorochov

*Laboratoire de Physique des Solides de Bellerue, CNRS, 1 Place Aristide Briand, F-92195 Meudon, France*

One of the main challenges in the field of light emitting semiconductor laser diodes is the shift of the wavelengths in the blue and the UV range [1]. This can be achieved by alloying binary material as ZnTe with more ionic group II elements as, for example, Mg.

Here we report for the first time on metalorganic vapour phase epitaxial (MOVPE) growth of the large band gap semiconductor MgTe and the variable band gap ternary alloy  $\text{Zn}_{1-x}\text{Mg}_x\text{Te}$ . We chose the precursors diisopropyltellurium (DIPTe), diethylzinc (DEZn) and bis-methylcyclopentadienylmagnesium ( $\text{MCP}_2\text{Mg}$ ). All layers were grown on semi-insulating (100) GaAs substrates in an experimental reactor cell with down-flow on a graphite susceptor placed in the centre of a cylindrical vertical tube. The growth parameters were: total  $\text{H}_2$  flow = 1 SLM,  $p_{\text{tot}} = 1$  atm and  $T_g = 350^\circ\text{C}$ .

Bulk MgTe is a known but not well studied material (very hygroscopic) with wurtzite type structure and a direct band gap of the order of 3.5 eV [2]. The MgTe layers were found to be polycrystalline. These films were very quickly degraded by hydration even if they were covered by a ZnTe film.  $\text{Zn}_{1-x}\text{Mg}_x\text{Te}$  epitaxial layers were grown with a Mg concentration of  $0 < x < 0.6$ . In this range of composition they appeared stable in air. Up to 50% Mg concentration, the phase is essentially a zincblende structure and beyond this value both structures seem to coexist [2]. The crystalline quality of the layers of

$\text{Zn}_{1-x}\text{Mg}_x\text{Te}$  alloys was comparable with that of ZnTe grown on (100) GaAs substrates (e.g.,  $\text{Zn}_{0.83}\text{Mg}_{0.17}\text{Te}$ : 1.5  $\mu\text{m}$ , X-ray (004) FWHM  $\sim 700$  arc sec). Quantitative analysis of sample composition has been performed with SEM-EDX. A ZnTe thin film and a well characterized bulk  $\text{Zn}_{0.74}\text{Mg}_{0.26}\text{Te}$  alloy have been used as a reference. The composition of the layer versus the inlet partial pressure ratio of the alkyls  $p_{\text{Mg}}/(p_{\text{Mg}} + p_{\text{Zn}})$  is presented in Fig. 1. One observes an overproportional incorporation of the Mg in the layers. It is not yet clear whether this behaviour stems from the low thermal stability of the  $\text{MCP}_2\text{Mg}$  compared to DEZn, or whether the thermodynamics of the solid solution influences the composition.

Photoluminescence measurements exhibit a deep emission in the green region. It is located about 210 meV below the band gap edge lumi-

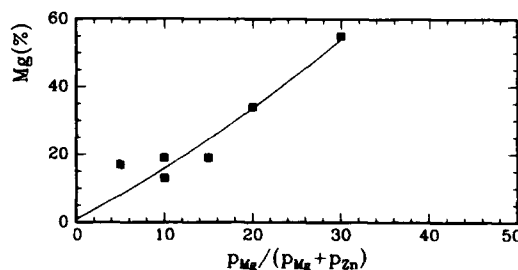


Fig. 1. Composition of layers as a function of the inlet partial pressure ratio of the alkyls,  $p_{\text{Mg}}/(p_{\text{Mg}} + p_{\text{Zn}})$ .

nescence reported in ref. [3].

The feasibility of growing cubic  $\text{Zn}_{1-x}\text{Mg}_x\text{Te}$  by MOVPE has been demonstrated. The usual optimization of the growth parameters (temperature, inlet partial pressure, purity, growth rate) should result in better optical quality of the material. However, an easy control of the composition is possible with the selected precursors.

The authors would like to thank Dr. J. Chevallier for suggesting this investigation.

- [1] R.N. Bhargava, J. Crystal Growth 117 (1992) 894.
- [2] S.G. Parker, A.R. Reinberg, J.E. Pinnel and W.C. Holton, J. Electrochem. Soc. Solid State Sci. 118 (1971) 979.
- [3] K. Somogyi, J. Chevallier, J.F. Rommeluere, J. Marine and B. Schaub, IEEE Trans. Electron Devices ED-26 (1985) 165.



ELSEVIER

Journal of Crystal Growth 138 (1994) 1081–1096

JOURNAL OF **CRYSTAL  
GROWTH**

## Author index

- Abounadi, A., see Bouchara 138 (1994) 121  
 Achtziger, N., see Rüb 138 (1994) 285  
 Affrossman, S., see Fisher 138 (1994) 86  
 Ager III, J.W., see Wolk 138 (1994) 1071  
 Agrinskaya, N.V., Low temperature variable range hopping conductivity in doped CdTe crystals 138 (1994) 493  
 Akinaga, F., see Kato 138 (1994) 373  
 Akita, N., see Suzuki 138 (1994) 199  
 Akitsu, T., see Matsumoto 138 (1994) 403  
 Akram, S. and I. Bhat, Organometallic vapor phase epitaxial growth of p-type ZnSe using phenylhydrazine as the dopant source 138 (1994) 105  
 Akram, S., see Bhat 138 (1994) 127  
 Allègre, J., G. Arnaud, H. Mathieu, P. Lefebvre, W. Granier and L. Boudes, Absorption properties of CdS nanocrystals in glasses: evidence of both weak and strong confinement regimes 138 (1994) 998  
 Allen, J.W., see Zheng 138 (1994) 477  
 Allen, J.W., see Zheng 138 (1994) 504  
 Ammann, N., see Gleitsmann 138 (1994) 324  
 Aoudia, A., see Rzepka 138 (1994) 244  
 Araki, H., see Kanie 138 (1994) 145  
 Arnaud, G., see Allègre 138 (1994) 998  
 Artemyev, M.V., see Gurin 138 (1994) 993  
 Arterton, B.W., J.W. Brightwell, B. Ray and I.V.F. Viney, Formation and optical properties of homogeneous solid solutions of  $\text{Ca}_{1-x}\text{Sr}_x\text{S}:\text{Ce}$  138 (1994) 1051  
 Arterton, B.W., see Viney 138 (1994) 1055  
 Asano, T., see Fujita 138 (1994) 737  
 Ashenford, D.E., see Dhese 138 (1994) 443  
 Ashenford, D.E., see Wolverson 138 (1994) 656  
 Ashenford, D.E., see Sawicki 138 (1994) 900  
 Astles, M.G., see Fisher 138 (1994) 86  
 Aulombard, R.L., see Bouchara 138 (1994) 121  
 Aulombard, R.L., see Frandon 138 (1994) 513  
 Aulombard, R.L., see Gil 138 (1994) 868  
 Austin, J.C., see Hughes 138 (1994) 1040  
 Austin, J.C., see Doran 138 (1994) 826  
 Averous, M., see Bouchara 138 (1994) 121  
 Azoulay, M., see Biao 138 (1994) 219  
 Azoulay, M., M.A. George, A. Burger, W.E. Collins and E. Silberman, Interface morphology studies of liquid phase epitaxy grown HgCdTe films by atomic force microscopy 138 (1994) 517  
 Bacher, G., see Tönnies 138 (1994) 362  
 Bacher, G., see Illing 138 (1994) 638  
 Bacher, G., F. Daiminger, A. Forchel, A. Waag, Th. Litz and G. Landwehr, Many body effects in transient luminescence spectra of a homogeneous electron-hole plasma in CdTe/CdMnTe quantum wells 138 (1994) 856  
 Bailly, F., see Cohen-Solal 138 (1994) 68  
 Barbé, M., see Cohen-Solal 138 (1994) 68  
 Barthou, C., see Zeinert 138 (1994) 1023  
 Bassani, F., K. Kheng, M. Mamor, R.T. Cox, N. Magnea, K. Saminadayar and S. Tatarenko, Electron-gas screening of the piezoelectric fields in indium-doped (211) CdTe/ $\text{Cd}_{1-x}\text{Zn}_x\text{Te}$  quantum wells 138 (1994) 607  
 Baubinas, R., see Vaitkus 138 (1994) 545  
 Baude, P.F., see DePuydt 138 (1994) 667  
 Bauer, G., see Fromherz 138 (1994) 580  
 Bauer, G., see Giebulowicz 138 (1994) 877  
 Bäume, P., F. Kubacki and J. Gutowski, Characterization of impurities in II–VI semiconductors by time-resolved line-shape analysis of donor-acceptor pair spectra 138 (1994) 266  
 Becker, C.R., see Schikora 138 (1994) 8  
 Becker, C.R., see Einfeldt 138 (1994) 471  
 Becker, Ch., see Tönnies 138 (1994) 362  
 Becla, P., see Ji 138 (1994) 187  
 Becla, P., see Feng 138 (1994) 239  
 Behr, T., see Ruppert 138 (1994) 48  
 Behr, T., see Hommel 138 (1994) 331  
 Behr, T., see Hommel 138 (1994) 1076  
 Behringer, M., see Einfeldt 138 (1994) 471  
 Belas, E., P. Höschl, R. Grill, J. Franc, P. Moravec, K. Lischka, H. Sitter and A. Toth, Ultrafast diffusion of Hg in  $\text{Hg}_{1-x}\text{Cd}_x\text{Te}$  ( $x = 0.21$ ) 138 (1994) 940



- Belas, E., see Höschl 138 (1994) 956  
 Benalloul, P., see Zeinert 138 (1994) 1023  
 Benoit, J., see Zeinert 138 (1994) 1023  
 Benz, K.W., see Salk 138 (1994) 161  
 Benz, K.W., see Fiederle 138 (1994) 529  
 Berlouis, L.E.A., see Fisher 138 (1994) 86  
 Beyersdorfer, V., see Hommel 138 (1994) 331  
 Beyersdorfer, V., see Hommel 138 (1994) 1076  
 Bhargava, R.N., see Gallagher 138 (1994) 970  
 Bhat, I., see Wang 138 (1994) 43  
 Bhat, I., see Akram 138 (1994) 105  
 Bhat, I. and S. Akram, Atomic layer epitax-  
 ial growth studies of ZnSe using dimeth-  
 ylzinc and hydrogen selenide 138 (1994) 127  
 Bhattacharjee, A.K., Orbital exchange in di-  
 luted magnetic semiconductors 138 (1994) 895  
 Biao, Y., M. Azoulay, M.A. George, A.  
 Burger, W.E. Collins, E. Silberman, C.-H.  
 Su, M.E. Volz, F.R. Szofran and D.C.  
 Gillies, Photoluminescence of vapor and  
 solution grown ZnTe single crystals 138 (1994) 219  
 Bicknell-Tassius, R.N., W.M. Theis, T. Cole,  
 K.T. Higa and T.J. Groshens, Metalor-  
 ganic molecular beam epitaxy doping of  
 II-VI compound semiconductors 138 (1994) 425  
 Bilger, G., see Hommel 138 (1994) 331  
 Bilger, G., see Waag 138 (1994) 437  
 Björqvist, M., see Vaitkus 138 (1994) 545  
 Bodin, C., see Legras 138 (1994) 585  
 Bogdanov, S.V., see Klingshirn 138 (1994) 786  
 Bogdanov, S.V., see Woggon 138 (1994) 976  
 Boney, C., see Ren 138 (1994) 455  
 Boney, C., see Eason 138 (1994) 703  
 Boring, P., see Gil 138 (1994) 868  
 Bouchara, D., A. Abounadi, M. Di Blasio,  
 N. Briot, T. Cloitre, O. Briot, B. Gil, J.  
 Calas, M. Averous and R.L. Aulombard,  
 Contamination effects from tellurium in  
 ZnS-ZnSe superlattices 138 (1994) 121  
 Boude's, L., see Allègre 138 (1994) 998  
 Bourée, J.E., see Qu'Hen 138 (1994) 1079  
 Bremond, G., see Rzepka 138 (1994) 244  
 Bressler, P.R. and H.-E. Gumlich, Mn-3d  
 derived partial density of states at the  
 interface of epitaxially grown zinc-blende  
 MnTe on CdTe(100) 138 (1994) 1028  
 Brightwell, J.W., see Arterton 138 (1994) 1051  
 Brightwell, J.W., see Viney 138 (1994) 1055  
 Brinkman, A.W., see Jones 138 (1994) 274  
 Brinkman, A.W., see Brown 138 (1994) 538  
 Briot, N., see Bouchara 138 (1994) 121  
 Briot, N., see Frandon 138 (1994) 513  
 Briot, N., see Gil 138 (1994) 868  
 Briot, O., see Bouchara 138 (1994) 121  
 Briot, O., see Frandon 138 (1994) 513  
 Briot, O., see Gil 138 (1994) 868  
 Broser, I., see Krause 138 (1994) 75  
 Broser, I., see Hoffmann 138 (1994) 379  
 Broser, I., B. Lummer, R. Heitz and A.  
 Hoffmann, Degenerate four-wave mixing  
 at bound excitons in II-VI semiconduc-  
 tors 138 (1994) 809  
 Broser, I., see Fricke 138 (1994) 815  
 Broser, I., see Presser 138 (1994) 820  
 Broser, I., see Hoffmann 138 (1994) 1073  
 Brown, P.D., Y.Y. Loginov, J.T. Mullins,  
 K. Durose, A.W. Brinkman and C.J.  
 Humphreys, Transmission electron mi-  
 croscopy investigations of II-VI/GaAs  
 heterostructures 138 (1994) 538  
 Brummell, M.A., see Sawicki 138 (1994) 900  
 Brunthaler, G., see Lang 138 (1994) 81  
 Brunthaler, G., M. Lang, A. Forstner, C.  
 Gifftge, D. Schikora, S. Ferreira, H. Sitter  
 and K. Lischka, Deep blue and UV pho-  
 toluminescence from ZnS/CdS superlat-  
 tices and quantum wells 138 (1994) 559  
 Buda, B., M. Dahl, N. von Truchsess and A.  
 Waag, Polar magneto-optic Kerr effect in  
 (Cd,Mn)Te/CdTe superlattices 138 (1994) 652  
 Burger, A., see Biao 138 (1994) 219  
 Burger, A., see Azoulay 138 (1994) 517  
 Busch, M.C., see Rzepka 138 (1994) 244  
 Calas, J., see Bouchara 138 (1994) 121  
 Calhoun, L.C., C.M. Rouleau, M.H. Jeon  
 and R.M. Park, p-Type ZnSe:N grown  
 by molecular beam epitaxy: evidence of  
 non-radiative recombination centers in  
 moderately to heavily doped material 138 (1994) 352  
 Capper, P., see Hastings 138 (1994) 917  
 Cavenett, B.C., see Prior 138 (1994) 94  
 Cavenett, B.C., see Mullins 138 (1994) 357  
 Cavenett, B.C., see Wang 138 (1994) 647  
 Cavenett, B.C., see Kawakami 138 (1994) 759  
 Cerva, H., see Hommel 138 (1994) 1076  
 Chadi, D.J., Acceptor and donor states of  
 impurities in wide band gap II-VI semi-  
 conductors 138 (1994) 295  
 Chang, S.K., see Lee 138 (1994) 136  
 Chen, L.C., see Yang 138 (1994) 629  
 Chen, W., J. Gaines, C. Ponzoni, D. Olego,  
 P.S. Mangat, P. Soukiasian and A.  
 Kahn, Reduction of the Au/p-ZnSe(100)  
 Schottky barrier height using a thin Se  
 interlayer 138 (1994) 1078  
 Cheng, H., see Zhang 138 (1994) 310  
 Cheng, H., see DePuydt 138 (1994) 667  
 Cherkaoui, K., see Rzepka 138 (1994) 244  
 Choi, C.S., see Moon 138 (1994) 944  
 Choi, I.H., see Kwak 138 (1994) 950  
 Chung, C., see Jain 138 (1994) 709  
 Chung, C.H., see Hwang 138 (1994) 131  
 Chung, C.H., see Lee 138 (1994) 136

- Chung, C.K., see Yao 138 (1994) 290  
 Chung, I.H., see Hwang 138 (1994) 131  
 Churchill, L.E., see Ren 138 (1994) 455  
 Churchill, L.E., see Eason 138 (1994) 703  
 Cihert, J., see Legras 138 (1994) 585  
 Clark, J.C., see Jones 138 (1994) 274  
 Cloitre, T., see Bouchara 138 (1994) 121  
 Cloitre, T., see Gil 138 (1994) 868  
 Cockayne, B., see Dhese 138 (1994) 140  
 Cohen-Solal, G., F. Bailly and M. Barbé,  
 Critical thickness in heteroepitaxial  
 growth of zinc-blende semiconductor  
 compounds 138 (1994) 68  
 Cole, T., see Bicknell-Tassius 138 (1994) 425  
 Collins, W.E., see Biao 138 (1994) 219  
 Collins, W.E., see Azoulay 138 (1994) 517  
 Cook, Jr., J.W., see Vaudo 138 (1994) 430  
 Cook, Jr., J.W., see Ren 138 (1994) 455  
 Cook, Jr., J.W., see Eason 138 (1994) 703  
 Coronado, C.A., see Lu 138 (1994) 1  
 Cox, R.T., see Bassani 138 (1994) 607  
 Cox, R.T., see Davies 138 (1994) 661  
 Cullis, A.G., see Mullins 138 (1994) 357  
 Cundiff, S.T., see Hellmann 138 (1994) 791  
 Cuniot, M., see Rzepka 138 (1994) 244
- Dahl, M., see Buda 138 (1994) 652  
 Daiminger, F., see Bacher 138 (1994) 856  
 Dairaku, S., see Suzuki 138 (1994) 199  
 Dang, L.S., see Legras 138 (1994) 585  
 Dang, L.S., see Gourgon 138 (1994) 590  
 Davies, J.J., see Dhese 138 (1994) 140  
 Davies, J.J., see Wolverson 138 (1994) 656  
 Davies, J.J., R.T. Cox and G. Feuillet, Opti-  
 cal studies of quantum wells induced  
 by magnetic fields in  $\text{Cd}_{1-x}\text{Mn}_x\text{Te}/$   
 $\text{Cd}_{1-x}\text{Zn}_x\text{Te}$  epitaxial structures 138 (1994) 661  
 De Groot, P.A.J., see Sawicki 138 (1994) 900  
 Delalande, C., see Deleporte 138 (1994) 884  
 Deleporte, E., T. Lebihen, P. Roussignol, B.  
 Ohnesorge, C. Delalande, S. Guha and  
 H. Munkata, Photoluminescence in a  
 $\text{ZnSe}/(\text{Zn,Mn})\text{Se}$  heterostructure: mag-  
 netic-field induced transition from light  
 to heavy excitons 138 (1994) 884  
 DePuydt, J.M., M.A. Haase, S. Guha, J. Qiu,  
 H. Cheng, B.J. Wu, G.E. Höfler, G.  
 Meis-Haugen, M.S. Hagedorn and P.F.  
 Baude, Room temperature II-VI lasers  
 with 2.5 mA threshold 138 (1994) 667  
 Devine, P., see Dhese 138 (1994) 443  
 Dhese, K.A., J.E. Nicholls, W.E. Hagston,  
 P.J. Wright, B. Cockayne and J.J. Davies,  
 The metalorganic chemical vapour depo-  
 sition and photoluminescence of tel-  
 lurium-doped  $\text{ZnS}/\text{CdS}:\text{Te}$  strained  
 layer superlattices 138 (1994) 140
- Dhese, K.A., D.E. Ashenford, J.E. Nicholls,  
 P. Devine, B. Lunn, C.G. Scott and J.  
 Jaroszyński, Nitrogen doping of molecu-  
 lar beam epitaxially grown CdTe with a  
 radio-frequency plasma source 138 (1994) 443  
 Di Blasio, M., see Bouchara 138 (1994) 121  
 Didier, G., see El Mokri 138 (1994) 168  
 Dietl, T., see Grabecki 138 (1994) 481  
 Ding, J., M. Hagerott, P. Kelkar, A.V. Nur-  
 mikko, D.C. Grillo, L. He, J. Han and  
 R.L. Gunshor, Gain and dynamics in  
 $\text{ZnSe}$ -based quantum wells 138 (1994) 719  
 Diskett, D.J., see Fisher 138 (1994) 86  
 Dobrowolski, W., see Grodzicka 138 (1994) 1034  
 Doran, J.P., R.P. Stanley, J. Hegarty, R.D.  
 Feldman and R.F. Austin, Polarization  
 dependent dephasing measurements in  
 $\text{Cd}_{1-x}\text{Zn}_x\text{Te}/\text{ZnTe}$  multiple quantum  
 well structures 138 (1994) 826  
 Dorman, D.R., see Wolk 138 (1994) 1071  
 Drake, G., see Jain 138 (1994) 709  
 Drenten, R., see Petruzzello 138 (1994) 686  
 Driad, R., see Kuhn 138 (1994) 448  
 Durose, R., see Brown 138 (1994) 538  
 Duxstad, K.J., see Wolk 138 (1994) 1071
- Eason, D.B., see Ren 138 (1994) 455  
 Eason, D.B., Z. Yu, C. Boney, J. Ren, L.E.  
 Churchill, J.W. Cook, Jr., J.F. Schetzina  
 and N.A. El-Masry, Quaternary II-VI  
 alloys for blue and green light emitting  
 diode applications 138 (1994) 703  
 Ebeling, W., see Nägele 138 (1994) 842  
 Ebisutani, T., see Zhu 138 (1994) 397  
 Ebling, D., see Fiederle 138 (1994) 529  
 Eckey, L., see Hoffmann 138 (1994) 1073  
 Egorov, A.V., see Salk 138 (1994) 161  
 Egashira, K., see Matsumoto 138 (1994) 403  
 Eiche, C., see Fiederle 138 (1994) 529  
 Einfeldt, S., see Schikora 138 (1994) 8  
 Einfeldt, S., H. Heinke, M. Behringer, C.R.  
 Becker, E. Kurtz, D. Hommel and G.  
 Landwehr, The growth of  $\text{HgSe}$  by  
 molecular beam epitaxy for ohmic con-  
 tacts to p-ZnSe 138 (1994) 471  
 El-Masry, N.A., see Ren 138 (1994) 455  
 El-Masry, N.A., see Eason 138 (1994) 703  
 El-Mokri, A., R. Triboulet, A. Lusson, A.  
 Tromson-Carli and G. Didier, Growth of  
 large, high purity, low cost, uniform  
 $\text{CdZnTe}$  crystals by the "cold travelling  
 heater method" 138 (1994) 168  
 Ema, K., see Saiki 138 (1994) 805  
 Eriksson, B., see Gourgon 138 (1994) 590  
 Erland, J., B.S. Razbirin, V.G. Lyssenko,  
 K.-H. Pantke and J.M. Hvam, Nonlinear  
 quantum beat spectroscopy of bound  
 biexcitons in II-VI semiconductors 138 (1994) 800

- Fan, G.H., see Guan 138 (1994) 534  
 Fan, X., see Li 138 (1994) 231  
 Fan, X.W., see Guan 138 (1994) 534  
 Fan, X.W., see Shen 138 (1994) 625  
 Fan, X.W., see Yang 138 (1994) 629  
 Fan, X.W., see Zhang 138 (1994) 838  
 Fan, Y., see Han 138 (1994) 464  
 Fan, Y., see Salokatve 138 (1994) 1077  
 Faschinger, W., see Fromherz 138 (1994) 580  
 Faschinger, W., see Neukirch 138 (1994) 849  
 Faschinger, W., see Giebultowicz 138 (1994) 877  
 Feigelson, R.S., see Helbing 138 (1994) 1075  
 Feldmann, J., see Hellmann 138 (1994) 791  
 Feldman, R.D., see Doran 138 (1994) 826  
 Feng, Y.P., see Feng 138 (1994) 239  
 Feng, Z.C., see Ji 138 (1994) 187  
 Feng, Z.C., P. Becla, L.S. Kim, S. Perkowitz, Y.P. Feng, H.C. Poon, K.P. Williams and G.D. Pitt, Raman, infrared, photoluminescence and theoretical studies of the II–VI–VI ternary CdSeTe 138 (1994) 239  
 Ferreira, S., see Brunthaler 138 (1994) 559  
 Feuillet, G., see Legras 138 (1994) 585  
 Feuillet, G., see Davies 138 (1994) 661  
 Fiederle, M., see Salk 138 (1994) 161  
 Fiederle, M., D. Ebling, C. Eiche, D.M. Hofmann, M. Salk, W. Stadler, K.W. Benz and B.K. Meyer, Comparison of CdTe,  $\text{Cd}_{0.9}\text{Zn}_{0.1}\text{Te}$  and  $\text{CdTe}_{0.9}\text{Se}_{0.1}$  crystals: application for  $\gamma$ - and X-ray detectors 138 (1994) 529  
 Fischer, F., see Waag 138 (1994) 155  
 Fischer, F., see Waag 138 (1994) 437  
 Fisher, J.M., L.E.A. Berlouis, L.J.M. Sawers, S.M. MacDonald, S. Affrossman, D.J. Diskett and M.G. Astles, Growth and characterization of electrodeposited films of cadmium telluride on silicon 138 (1994) 86  
 Fisher, P.A., see Lu 138 (1994) 1  
 Floyd, P.D., see Yokogawa 138 (1994) 564  
 Forchel, A., see Tönnies 138 (1994) 362  
 Forchel, A., see Illing 138 (1994) 638  
 Forchel, A., see Bacher 138 (1994) 856  
 Forchel, A., see Lang 138 (1994) 81  
 Forstner, A., see Brunthaler 138 (1994) 559  
 Franc, J., see Belas 138 (1994) 940  
 Franc, J., see Höschl 138 (1994) 956  
 Frandon, J., M.A. Renucci, N. Briot, O. Briot and R.L. Aulombard, Superlattice effects on phonons in strained ZnTe–ZnSe structures 138 (1994) 513  
 Freytag, B. and U. Rössler, Ab initio calculation of electronic structure and structural properties of  $\text{ZnSe}_{1-x}\text{Te}_x$  138 (1994) 499  
 Fricke, Ch., see Krause 138 (1994) 75  
 Fricke, Ch., see Hoffmann 138 (1994) 379  
 Fricke, Ch., see Taudt 138 (1994) 418  
 Fricke, Ch., R. Heitz, B. Lummer, V. Kutzer, A. Hoffmann, I. Broser, W. Taudt and M. Heuken, Time-resolved donor–acceptor pair recombination luminescence in highly n- and p-doped II–VI semiconductors 138 (1994) 815  
 Fricke, Ch., see Presser 138 (1994) 820  
 Fricke, Ch., see Hoffmann 138 (1994) 1073  
 Fromherz, T., E. Oh, A.K. Ramdas, E. Koppensteiner, G. Bauer, W. Faschinger and H. Sitter, Confined and propagating phonons in atomic layer epitaxy grown  $(\text{CdTe})_n(\text{ZnTe})_n$  superlattices 138 (1994) 580  
 Fuchs, F., see Tomm 138 (1994) 175  
 Fujii, Y., see Suemune 138 (1994) 750  
 Fujimoto, M., see Suemune 138 (1994) 750  
 Fujita, Sg., see Ichino 138 (1994) 28  
 Fujita, Sg., see Fujita 138 (1994) 737  
 Fujita, Sz., see Ichino 138 (1994) 28  
 Fujita, Sz., T. Asano, K. Maehara, T. Tojyo and Sg. Fujita, Photo-assisted metalorganic vapor-phase epitaxy for nitrogen doping and fabrication of blue-green light emitting devices of ZnSe-based semiconductors 138 (1994) 737  
 Fujiyasu, H., see Minami 138 (1994) 796  
 Fujiyasu, H., see Kuwabara 138 (1994) 964  
 Furdyna, J.K., see Yokogawa 138 (1994) 564  
 Furdyna, J.K., see Giebultowicz 138 (1994) 877  
 Gaines, J.M., see Petruzzello 138 (1994) 686  
 Gaines, J.M., see Chen 138 (1994) 1078  
 Galbraith, I., see Kawakami 138 (1994) 759  
 Gale, I.G., see Hastings 138 (1994) 917  
 Gallagher, D., W.E. Heady, J.M. Racz and R.N. Bhargava, Doped zinc sulfide nanocrystals precipitated within a poly(ethylene oxide) matrix – processing and optical characteristics 138 (1994) 970  
 Gavryushin, V., G. Račiukaitis, D. Juodžbalis, A. Kazlauskas and V. Kubertavičius, Characterization of intrinsic and impurity deep levels in ZnSe and ZnO crystals by nonlinear spectroscopy 138 (1994) 924  
 Gebhardt, W., see Grün 138 (1994) 150  
 Gebhardt, W., see Wolf 138 (1994) 412  
 Gebhardt, W., see Kuhn 138 (1994) 448  
 Gebhardt, W., see Naumov 138 (1994) 595  
 Gebhardt, W., see Klingshirm 138 (1994) 786  
 George, M.A., see Biao 138 (1994) 219  
 George, M.A., see Azoulay 138 (1994) 517  
 Geurts, J., see Gleitsmann 138 (1994) 324  
 Geurts, J., see Hermans 138 (1994) 612  
 Geyzers, K.P., see Klingshirm 138 (1994) 786  
 Geyzers, K.P., see Nägele 138 (1994) 842  
 Giapis, K.P., see Skromme 138 (1994) 338

- Giebultowicz, T.M., W. Faschinger, V. Nunez, P. Klosowski, G. Bauer, H. Sitter and J.K. Furdyna, Antiferromagnetic spin ordering and interlayer magnetic correlations in MnTe/CdTe superlattices 138 (1994) 877
- Giftge, C., see Schikora 138 (1994) 8
- Giftge, C., see Lang 138 (1994) 81
- Giftge, C., see Brunthaler 138 (1994) 559
- Gil, B., see Bouchara 138 (1994) 121
- Gil, B., T. Cloitre, N. Briot, O. Briot, P. Boring and R.L. Aulombard, Photo-induced screening of the excitonic interaction in ZnSe-ZnTe type II strained-layer superlattices 138 (1994) 868
- Gillies, D.C., see Biao 138 (1994) 219
- Giriati, W., see Martinez 138 (1994) 913
- Gleitsmann, G., N. Ammann, J. Hermans, A. Schneider, J. Geurts, P. Karduck and M. Heuken, Comparison between gallium-implanted layers of ZnSe and ZnS<sub>1-x</sub>Se<sub>x</sub> by optical, electrical and electron beam characterization methods 138 (1994) 324
- Gleitsmann, G., see Hoffmann 138 (1994) 379
- Göbel, E.O., see Hellmann 138 (1994) 791
- Goede, O., see Heimbrodt 138 (1994) 601
- Goede, O., see Pier 138 (1994) 889
- Goncharova, E.V., see Jakobson 138 (1994) 225
- Gorochoy, O., see Kuhn 138 (1994) 448
- Gorochoy, O., see Qu'Hen 138 (1994) 1079
- Göthelid, M., see Vaitkus 138 (1994) 545
- Gotoh, J., see Migita 138 (1994) 391
- Gourgou, C., B. Eriksson, L.S. Dang, H. Mariette and C. Vieu, Photoluminescence of CdTe/ZnTe semiconductor wires and dots 138 (1994) 590
- Grabecki, G., T. Dietl, W. Plesiewicz, A. Lenard, T. Skośkiewicz, E. Kamińska and A. Piotrowska, Mesoscopic phenomena in a dilute magnetic semiconductor Hg<sub>1-x-y</sub>Cd<sub>y</sub>Mn<sub>x</sub>Te 138 (1994) 481
- Granger, R. and C.M. Pelletier, A prediction of the electron mobility in medium gap HgCdTe and HgZnTe solid solutions 138 (1994) 486
- Granger, R., see Quemerais 138 (1994) 934
- Granier, W., see Allègre 138 (1994) 998
- Grant, R.W., see Wang 138 (1994) 508
- Grattepain, C., see Kuhn 138 (1994) 448
- Gravey, P., see Rzepka 138 (1994) 244
- Griesche, J., N. Hoffmann and K. Jacobs, Surface engineering during molecular beam epitaxial growth of wide-gap II-VI structures 138 (1994) 55
- Griesche, J., N. Hoffmann and K. Jacobs, On the mechanism of reflection high-energy electron diffraction oscillations studied by phase-locked epitaxy of ZnSe 138 (1994) 59
- Griesche, J., see Heimbrodt 138 (1994) 601
- Grill, R., see Belas 138 (1994) 940
- Grill, R., see Höschl 138 (1994) 956
- Grillo, D.C., see Hua 138 (1994) 367
- Grillo, D.C., see Han 138 (1994) 464
- Grillo, D.C., see Ding 138 (1994) 719
- Grillo, D.C., see Salokatve 138 (1994) 1077
- Grodzicka, E., W. Dobrowolski, J. Kossut, T. Story and B. Witkowska, Peculiarities of transport properties in semiconductors with resonant impurities: HgSe:Fe versus PbTe:Cr 138 (1994) 1034
- Grosheims, T.J., see Bicknell-Tassius 138 (1994) 425
- Grün, M., M. Hetterich, C. Klingshirn, A. Rosenauer, J. Zweck and W. Gebhardt, Strain relief and growth modes in wurzite type epitaxial layers of CdSe and CdS and in CdSe/CdS superlattices 138 (1994) 150
- Grün, M., see Langbein 138 (1994) 191
- Grün, M., see Klingshirn 138 (1994) 786
- Guan, Z.P., S.H. Song, G.H. Fan, X.W. Fan, Y.G. Peng and Y.K. Wu, The study of lattice strain and high-resolution transmission electron 138 (1994) 534
- Guan, Z.P., see Yang 138 (1994) 629
- Guan, Z.P., see Zhang 138 (1994) 838
- Guha, S., see DePuydt 138 (1994) 667
- Guha, S., see Deleporte 138 (1994) 884
- Gumlich, H.-E., see Pier 138 (1994) 889
- Gumlich, H.-E., see Jung 138 (1994) 905
- Gumlich, H.-E., see Schumann 138 (1994) 910
- Gumlich, H.-E., see Zeinert 138 (1994) 1023
- Gumlich, H.-E., see Bressler 138 (1994) 1028
- Gumlich, H.-E., see Jung 138 (1994) 1066
- Gunshor, R.L., see Hua 138 (1994) 367
- Gunshor, R.L., see Han 138 (1994) 464
- Gunshor, R.L., see Ding 138 (1994) 719
- Gunshor, R.L., see Salokatve 138 (1994) 1077
- Gurin, V.S. and M.V. Artemyev, CdS quantum dots in colloids and polymer matrices: electronic structure and photochemical properties 138 (1994) 993
- Gutowski, J., see Schmolke 138 (1994) 213
- Gutowski, J., see Bäume 138 (1994) 266
- Gutowski, J., see Nägele 138 (1994) 842
- Gutowski, J., see Neukirch 138 (1994) 861
- Haacke, S., N.T. Pelekanos, H. Mariette, A.P. Heberle, W.W. Rühle and M. Zigone, Exciton transfer dynamics in CdTe/(Cd,Zn)Te asymmetric double quantum well structures 138 (1994) 831
- Haase, M.A., see DePuydt 138 (1994) 667
- Hage-Ali, M., see Rzepka 138 (1994) 244
- Hagedorn, M.S., see DePuydt 138 (1994) 667
- Hagerott, M., see Ding 138 (1994) 719
- Hagston, W.E., see Dhese 138 (1994) 140
- Hahn, B., see Wolf 138 (1994) 412

- Haller, E.E., see Wolk 138 (1994) 1071  
Halsall, M.P., see Wolverson 138 (1994) 656  
Hammar, M., see Vaitkus 138 (1994) 545  
Han, J., see Hua 138 (1994) 367  
Han, J., Y. Fan, M.D. Ringle, L. He, D.C. Grillo, R.L. Gunshor, G.C. Hua and N. Otsuka, Ohmic contacts and transport properties in ZnSe-based heterostructures 138 (1994) 464  
Han, J., see Ding 138 (1994) 719  
Han, J., see Salokatve 138 (1994) 1077  
Happ, M., see Heimbrodt 138 (1994) 601  
Hara, K., see Yanashima 138 (1994) 755  
Harris, K.A., see Meyer 138 (1994) 981  
Hartmann, H., see Krause 138 (1994) 75  
Hartmann, H. and D. Siche, ZnSe single crystal growth by the method of dissociative sublimation 138 (1994) 260  
Hastings, M.P., C.D. Maxey, B.E. Matthews, N.E. Metcalfe, P. Capper, C.L. Jones and I.G. Gale, Electron beam induced current assessment of doped and diffused junctions in epitaxial  $\text{Cd}_x\text{Hg}_{1-x}\text{Te}$  138 (1994) 917  
Hata, S., see Uchiki 138 (1994) 873  
Hatakoshi, G., see Itaya 138 (1994) 768  
Hauksson, I., see Prior 138 (1994) 94  
Hauksson, I., see Mullins 138 (1994) 357  
Hauksson, I., see Wang 138 (1994) 647  
Hauksson, I., see Kawakami 138 (1994) 759  
Hausleitner, H., see Schikora 138 (1994) 8  
Hayashi, M., see Inoue 138 (1994) 182  
He, L., see Hua 138 (1994) 367  
He, L., see Han 138 (1994) 464  
He, L., see Ding 138 (1994) 719  
He, L., see Salokatve 138 (1994) 1077  
Heady, W.E., see Gallagher 138 (1994) 970  
Heberle, A.P., see Haacke 138 (1994) 831  
Hegarty, J., see Doran 138 (1994) 826  
Heimbrodt, W., O. Goede, V. Weinhold, M. Happ, R. Knoch, K. Hieke, N. Hoffmann, J. Griesche, K. Jacobs, F. Neugebauer, D. Suisky and J. Röseler, Magneto-optical study of ZnSe/(Zn,Mn)Se and ZnSe/(Zn,Cd,Mn)Se quantum well structures and superlattices 138 (1994) 601  
Heimbrodt, W., see Pier 138 (1994) 889  
Heinke, H., see Ruppert 138 (1994) 48  
Heinke, H., see Waag 138 (1994) 155  
Heinke, H., see Waag 138 (1994) 437  
Heinke, H., see Einfeldt 138 (1994) 471  
Heitz, R., see Krause 138 (1994) 75  
Heitz, R., see Hoffmann 138 (1994) 379  
Heitz, R., see Broser 138 (1994) 809  
Heitz, R., see Fricke 138 (1994) 815  
Heitz, R., see Presser 138 (1994) 820  
Heitz, R., see Hoffmann 138 (1994) 1073  
Helbing, R. and R.S. Feigelson, SrS single crystals grown by physical vapor transport 138 (1994) 1075  
Hellmann, R., M. Koch, J. Feldmann, S.T. Cundiff, E.O. Göbel, D.R. Yakovlev, A. Waag and G. Landwehr, Dephasing excitons in a  $\text{CdTe}/\text{Cd}_{0.86}\text{Mn}_{0.14}\text{Te}$  multiple quantum well 138 (1994) 791  
Henneberger, F., see Schützgen 138 (1994) 575  
Henneberger, F., see Puls 138 (1994) 1004  
Henninger, B., see Pier 138 (1994) 889  
Hermans, J., see Gleitsmann 138 (1994) 324  
Hermans, J., J. Woitok, W. Schiffrs, J. Geurts, A. Schneider, M. Scholl, J. Söllner and M. Heuken, Optical and X-ray analysis of  $\text{ZnS}_x\text{Se}_{1-x}/\text{ZnSe}$  superlattices grown on GaAs by metalorganic vapour phase epitaxy 138 (1994) 612  
Herrmann, K.H., see Tomm 138 (1994) 175  
Herve, D., see Legras 138 (1994) 585  
Hetterich, M., see Grün 138 (1994) 150  
Hetterich, M., see Langbein 138 (1994) 191  
Hetterich, M., see Klingshirn 138 (1994) 786  
Heuken, M., see Söllner 138 (1994) 35  
Heuken, M., see Gleitsmann 138 (1994) 324  
Heuken, M., see Tönnies 138 (1994) 362  
Heuken, M., see Hoffmann 138 (1994) 379  
Heuken, M., see Taudt 138 (1994) 418  
Heuken, M., see Hermans 138 (1994) 612  
Heuken, M., see Klingshirn 138 (1994) 786  
Heuken, M., see Fricke 138 (1994) 815  
Heuken, M., see Nägele 138 (1994) 842  
Hieke, K., see Heimbrodt 138 (1994) 601  
Hieke, K., see Pier 138 (1994) 889  
Higa, K.T., see Bicknell-Tassius 138 (1994) 425  
Hirata, S., see Tomomura 138 (1994) 764  
Hlídek, P., see Höschl 138 (1994) 956  
Ho, E., see Lu 138 (1994) 1  
Hoerstel, W., see Tomm 138 (1994) 175  
Hoffmann, A., see Krause 138 (1994) 75  
Hoffmann, A., R. Heitz, B. Lummer, Ch. Fricke, V. Kutzer, I. Broser, W. Taudt, G. Gleitsmann and M. Heuken, Incorporation of nitrogen in ZnSe grown by metalorganic vapour phase epitaxy 138 (1994) 379  
Hoffmann, A., see Pohl 138 (1994) 385  
Hoffmann, A., see Taudt 138 (1994) 418  
Hoffmann, A., see Broser 138 (1994) 809  
Hoffmann, A., see Fricke 138 (1994) 815  
Hoffmann, A., see Presser 138 (1994) 820  
Hoffmann, A., B. Lummer, L. Eckey, V. Kutzer, Ch. Fricke, R. Heitz, I. Broser, E. Kurtz, B. Jobst and D. Hommel, The influence of nitrogen on the p-conductivity in ZnSe epilayers grown by molecular beam epitaxy 138 (1994) 1073

- Hoffmann, N., see Griesche 138 (1994) 55  
 Hoffmann, N., see Griesche 138 (1994) 59  
 Hoffmann, N., see Heimbrodt 138 (1994) 601  
 Höfler, G.E., see DePuydt 138 (1994) 667  
 Hofmann, D.M., see Fiederle 138 (1994) 529  
 Holy, V., see Lang 138 (1994) 81  
 Hommel, D., see Ruppert 138 (1994) 48  
 Hommel, D., B. Jobst, T. Behr, G. Bilger, V. Beyersdorfer, E. Kurtz and G. Landwehr, Correlation between electrical and structural properties of chlorine doped ZnSe epilayers grown by molecular beam epitaxy 138 (1994) 331  
 Hommel, D., see Tönnies 138 (1994) 362  
 Hommel, D., see Waag 138 (1994) 437  
 Hommel, D., see Einfeldt 138 (1994) 471  
 Hommel, D., see Neukirch 138 (1994) 861  
 Hommel, D., see Hoffmann 138 (1994) 1073  
 Hommel, D., E. Kurtz, T. Behr, A. Jakobs, B. Jobst, S. Scholl, K. Schüll, V. Beyersdorfer, G. Landwehr and H. Cerva, Studies of blue-green laser structures with asymmetric and pseudomorphic ZnSe wave guides 138 (1994) 1076  
 Horsburgh, G., see Prior 138 (1994) 94  
 Horsburgh, G., see Mullins 138 (1994) 357  
 Horsburgh, G., see Wang 138 (1994) 647  
 Höschl, P., see Belas 138 (1994) 940  
 Höschl, P., R. Grill, J. Svoboda, P. Hlídek, P. Moravec, J. Franc and E. Belas, Bridgman growth of  $\text{Hg}_{1-x}\text{Cd}_x\text{Te}$  from melt of constant composition 138 (1994) 956  
 House, J.L., see Lu 138 (1994) 1  
 Hovinen, M., see Salokatve 138 (1994) 1077  
 Hua, G.C., N. Otsuka, D.C. Grillo, J. Han, L. He and R.L. Gunshor, Phase separation in  $\text{ZnSe}_{1-x}\text{S}_x$  and  $\text{Zn}_{1-x}\text{Mg}_x\text{Se}_{1-x}\text{S}_x$  layers grown by molecular beam epitaxy 138 (1994) 367  
 Hua, G.C., see Han 138 (1994) 464  
 Huang, W., see Jain 138 (1994) 709  
 Hughes, Wm.C., J.C. Austin and M.L. Swanson, The thermodynamics of indium-vacancy pairs in  $\text{Hg}_{0.79}\text{Cd}_{0.21}\text{Te}$  138 (1994) 1040  
 Humenberger, J., see Lang 138 (1994) 81  
 Humphreys, C.J., see Brown 138 (1994) 538  
 Hunter, A.T., see Swenberg 138 (1994) 692  
 Hüttl, B., see Troppenz 138 (1994) 1017  
 Hvam, J.M., see Erland 138 (1994) 800  
 Hwang, J.-S., B.J. Koo, I.H. Chung, H.L. Park and C.H. Chung, Growth of CdTe/CdZnTe strained-layer single quantum wells by modified hot-wall epitaxy method and their properties 138 (1994) 131  
 Ichida, A., see Kuwabara 138 (1994) 964  
 Ichikawa, S., N. Matsumura, K. Yamawaki, K. Senga and J. Saraie, Migration enhancement on ZnSe surface in photoassisted molecular beam epitaxy and long duration time of the effects 138 (1994) 14  
 Ichino, K., T. Onishi, Y. Kawakami, Sz. Fujita and Sg. Fujita, Growth of ZnS and ZnCdSSe alloys on GaP using an elemental sulfur source by molecular beam epitaxy 138 (1994) 28  
 Iida, F., see Takojima 138 (1994) 633  
 Iida, S., see Uchiki 138 (1994) 873  
 Illing, M., G. Bacher, A. Forchel, A. Waag, T. Litz and G. Landwehr, Fabrication and optical characterization of wet chemically etched CdTe/CdMgTe wires 138 (1994) 638  
 Imai, K., see Takojima 138 (1994) 633  
 Inaba, T., see Matsumoto 138 (1994) 403  
 Inagaki, K., see Suzuki 138 (1994) 199  
 Inoue, K., T. Kuroda, F. Minami, K. Yoshida, M. Hayashi, Study of electronic structure in strained ZnSe/GaAs thin films by nonlinear optical and Brewster-angle reflection spectroscopies 138 (1994) 182  
 Inoue, K., see Minami 138 (1994) 796  
 Ishibashi, A. and Y. Mori, Advances in blue laser diodes 138 (1994) 677  
 Ishizaka, K., see Kanie 138 (1994) 145  
 Itaya, K., H. Sugawara and G. Hatakoshi, InGaAlP visible light laser diodes and light-emitting diodes 138 (1994) 768  
 Iwashita, T., see Matsumoto 138 (1994) 63  
 Jacobs, K., see Griesche 138 (1994) 55  
 Jacobs, K., see Griesche 138 (1994) 59  
 Jacobs, K., see Rudolph 138 (1994) 249  
 Jacobs, K., see Heimbrodt 138 (1994) 601  
 Jain, F., W. Huang, R. LaComb, C. Chung and G. Drake, Optical modulators using quantum confined Stark effect in ZnSe based multiple quantum well structures 138 (1994) 709  
 Jakobs, A., see Hommel 138 (1994) 1076  
 Jakobson, M.A., V.D. Kagan, R.P. Seisyan and E.V. Goncharova, Optical properties of "pure" CdS and metal-insulator-semiconductor structures on CdS at electrical operation 138 (1994) 225  
 Jaroszyński, J., see Dhese 138 (1994) 443  
 Jensen, J.E., see Rajavel 138 (1994) 19  
 Jensen, K.F., see Skromme 138 (1994) 338  
 Jeon, M.H., see Calhoun 138 (1994) 352  
 Jeon, M.H., see Salokatve 138 (1994) 1077  
 Ji, W., A.K. Kukaswadia, Z.C. Feng, S.H. Tang and P. Becla, Nonlinear refraction and optical limiting in bulk ZnTe crystal 138 (1994) 187  
 Jobst, B., see Hommel 138 (1994) 331  
 Jobst, B., see Hoffmann 138 (1994) 1073

- Jobst, B., see Hommel 138 (1994) 1076
- Jones, E.D., J.C. Clark, J.B. Mullin and A.W. Brinkman, Studies on the diffusion of zinc in cadmium telluride at 800°C 138 (1994) 274
- Jones, E.D., J. Malzbender, J.B. Mullin and N. Shaw, Incorporation of iodine into CdTe by diffusion 138 (1994) 279
- Jones, C.L., see Hastings 138 (1994) 917
- Jung, Ch., H.-Ch. Mertins, S. Katholy and H.-E. Gumlich, The influence of exchange interaction on the composition dependence of interband transitions in  $\text{Zn}_{1-x}\text{Mn}_x\text{Se}$  138 (1994) 905
- Jung, Ch., H.-Ch. Mertins and H.-E. Gumlich, The influence of crystal structure on the Zn 3d states in  $\text{Zn}_{1-x}\text{Mn}_x\text{S}$  138 (1994) 1066
- Jungnickel, V., see Puls 138 (1994) 1004
- Juodžbalis, D., see Gavryushin 138 (1994) 924
- Juza, P., see Neukirch 138 (1994) 849
- Kagan, V.D., see Jakobson 138 (1994) 225
- Kahn, A., see Chen 138 (1994) 1078
- Kalt, H., see Langbein 138 (1994) 191
- Kalt, H., see Klingshirn 138 (1994) 786
- Kamai, T., see Kato 138 (1994) 373
- Kamińska, E., see Grabecki 138 (1994) 481
- Kanemitsu, Y., see Yamamoto 138 (1994) 643
- Kanie, H., H. Araki, K. Ishizaka, H. Ohta and S. Murakami, Epitaxial growth of ZnS on GaP by molecular beam deposition 138 (1994) 145
- Karduck, P., see Gleitsmann 138 (1994) 324
- Karlsson, U., see Vaitkus 138 (1994) 545
- Katholy, S., see Jung 138 (1994) 905
- Kato, T., see Matsumoto 138 (1994) 63
- Kato, K., F. Akinaga, T. Kamai and M. Wada, In-situ monitoring by spectroscopic ellipsometry in ZnSe crystal growth by molecular beam epitaxy 138 (1994) 373
- Kato, T., see Matsumoto 138 (1994) 403
- Kawaguchi, Y., see Matsuoka 138 (1994) 727
- Kawakami, Y., see Ichino 138 (1994) 28
- Kawakami, Y., I. Hauksson, J. Simpson, H. Stewart, I. Galbraith, K.A. Prior and B.C. Cavenett, Photoluminescence excitation spectroscopy of the lasing transition in ZnSe-(Zn,Cd)Se quantum wells 138 (1994) 759
- Kazlauskas, A., see Ullrich 138 (1994) 234
- Kazlauskas, A., see Gavryushin 138 (1994) 924
- Kazlauskienė, V., see Vaitkus 138 (1994) 545
- Kelkar, P., see Ding 138 (1994) 719
- Kelkar, P., see Salokatve 138 (1994) 1077
- Khelladi, K.H., see Quemerais 138 (1994) 934
- Kheng, K., see Bassani 138 (1994) 607
- Kim, B.K., see Lee 138 (1994) 136
- Kim, J.W., see Lee 138 (1994) 136
- Kim, L.S., see Feng 138 (1994) 239
- Kinto, H., see Uchiki 138 (1994) 873
- Kitagawa, M., see Tomomura 138 (1994) 764
- Kissel, H., see Tomm 138 (1994) 175
- Klimakow, A., see Pohl 138 (1994) 385
- Klingshirn, C., see Grün 138 (1994) 150
- Klingshirn, C., see Langbein 138 (1994) 191
- Klingshirn, C., H. Kalt, M. Umlauff, W. Petri, F.A. Majumder, S.V. Bogdanov, W. Langbein, M. Grün, M. Hetterich, K.P. Geyzers, M. Heuken, A. Naumov, H. Stanzl and W. Gebhardt, Stimulated emission of II-VI epitaxial layers 138 (1994) 786
- Klingshirn, C., see Woggon 138 (1994) 988
- Klosowski, P., see Giehlutowicz 138 (1994) 877
- Kobayashi, H., SrS-ZnS electroluminescence materials 138 (1994) 1010
- Kobayashi, H., see Ohmi 138 (1994) 1061
- Kobayashi, M., H. Tosaka, T. Nagatake, T. Yoshida and A. Yoshikawa, Helium gas mixing in nitrogen plasma for the control of the acceptor concentration in p-ZnSe 138 (1994) 745
- Kobayashi, S., see Miura 138 (1994) 1046
- Kobayashi, T., see Ullrich 138 (1994) 234
- Koch, M., see Hellmann 138 (1994) 791
- Koebel, J.M., see Rzepka 138 (1994) 244
- Kolodziejski, L.A., see Lu 138 (1994) 1
- Konagai, M., see Okamoto 138 (1994) 204
- Konagai, M., see Tojima 138 (1994) 408
- Koo, B.J., see Hwang 138 (1994) 131
- Koppensteiner, E., see Fromherz 138 (1994) 580
- Kossut, J., see Grodzicka 138 (1994) 1034
- Knoch, R., see Heimbrodt 138 (1994) 601
- Krause, E., H. Hartmann, J. Menninger, A. Hoffmann, Ch. Fricke, R. Heitz, B. Lummer, V. Kutzer and I. Broser, Influence of growth non-stoichiometry on optical properties of doped and non-doped ZnSe grown by chemical vapour deposition 138 (1994) 75
- Kreller, F., see Schülzgen 138 (1994) 575
- Kubacki, F., see Bäume 138 (1994) 266
- Kubertavičius, V., see Gavryushin 138 (1994) 924
- Kuciauskas, D., see Vaitkus 138 (1994) 545
- Kudlek, G.H., see Pohl 138 (1994) 385
- Kudlek, G.H., see Presser 138 (1994) 820
- Kuhn, W., see Wolf 138 (1994) 412
- Kuhn, W.S., R. Driad, H. Stanzl, A. Lusson, K. Wolf, B. Qu'Hen, H. Sahin, L. Svob, C. Grattapain, X. Quesada, W. Gebhardt and O. Gorochoy, Investigation of hydrogen, carbon and further impurities in the metalorganic vapour phase epitaxy of ZnSe with ditertiarybutylselenide and methylallylselenide 138 (1994) 448
- Kuhn, W.S., see Qu'Hen 138 (1994) 1079
- Kuhn-Heinrich, B., see Waag 138 (1994) 155
- Kukaswadia, A.K., see Ji 138 (1994) 187
- Kukimoto, H., see Yanashima 138 (1994) 755

- Kumazaki, K., see Takojima 138 (1994) 633  
 Kuroda, T., see Inoue 138 (1994) 182  
 Kurtz, E., see Hommel 138 (1994) 331  
 Kurtz, E., see Einfeldt 138 (1994) 471  
 Kurtz, E., see Hoffmann 138 (1994) 1073  
 Kurtz, E., see Hommel 138 (1994) 1076  
 Kutzer, V., see Krause 138 (1994) 75  
 Kutzer, V., see Hoffmann 138 (1994) 379  
 Kutzer, V., see Fricke 138 (1994) 815  
 Kutzer, V., see Hoffmann 138 (1994) 1073  
 Kuwabara, H., H. Tatsuoka, Y. Nakanishi, A. Ichida, H. Fujiyasu, M. Nakayama and T. Yamanari, HgTe and  $\text{Hg}_{1-x}\text{Cd}_x\text{Te}$  vapor phase epitaxial growth under controlled Hg pressure 138 (1994) 964  
 Kuwata-Gonokami, M., see Saiki 138 (1994) 805  
 Kwak, N.J., I.H. Choi, S.W. Lim and S.H. Suh,  $\text{Hg}_{0.8}\text{Cd}_{0.2}\text{Te}$  grown by liquid phase epitaxy using  $\text{Cd}_{0.94}\text{Zn}_{0.06}\text{Te}$  buffer layer 138 (1994) 950  
 LaComb, R., see Jain 138 (1994) 709  
 Landwehr, G., see Schikora 138 (1994) 8  
 Landwehr, G., see Ruppert 138 (1994) 48  
 Landwehr, G., see Waag 138 (1994) 155  
 Landwehr, G., see Hommel 138 (1994) 331  
 Landwehr, G., see Tönnies 138 (1994) 362  
 Landwehr, G., see Waag 138 (1994) 437  
 Landwehr, G., see Einfeldt 138 (1994) 471  
 Landwehr, G., see Illing 138 (1994) 638  
 Landwehr, G., see Hellmann 138 (1994) 791  
 Landwehr, G., see Bacher 138 (1994) 856  
 Landwehr, G., see Neukirch 138 (1994) 861  
 Landwehr, G., see Hommel 138 (1994) 1076  
 Lang, M., D. Schikora, T. Widmer, C. Gifftge, A. Forstner, V. Holy, J. Humenberger, K. Lischka, G. Brunthaler, H. Sitter and M. von Ortenberg, Structural properties of perfect ZnTe epilayers on (001) GaAs substrates 138 (1994) 81  
 Lang, M., see Brunthaler 138 (1994) 559  
 Langhein, W., H. Kalt, M. Hetterich, M. Grün and C. Klingshirn, Influence of the screening of piezo-fields on the carrier dynamics in CdS/CdSe superlattices 138 (1994) 191  
 Langhein, W., see Klingshirn 138 (1994) 786  
 Lankes, S., see Naumov 138 (1994) 595  
 Lebihen, T., see Deleporte 138 (1994) 884  
 Lee, C.D., B.K. Kim, J.W. Kim, H.L. Park, C.H. Chung, S.K. Chang, J.I. Lee and S.K. Noh, Thickness dependent properties of ZnSe on (100) GaAs grown by atomic layer epitaxy 138 (1994) 136  
 Lee, J.I., see Lee 138 (1994) 136  
 Lee, S.T., see Ohmi 138 (1994) 1061  
 Lefebvre, P., see Allègre 138 (1994) 998  
 Legras, R., L.S. Dang, C. Bodin, J. Cibert, F. Marcenat, G. Feuillet, J.L. Pautrat, D. Herve and E. Molva, Temperature dependence of optical gain in CdTe/CdMnTe heterostructures 138 (1994) 585  
 Lemoine, D., see Quemerais 138 (1994) 934  
 Lenard, A., see Grabecki 138 (1994) 481  
 Li, M.M., see Strachan 138 (1994) 318  
 Li, Z., G. Xiong, Z. Zhao and X. Fan, Measurement of optical nonlinear susceptibility of CdS single crystal using a single beam 138 (1994) 231  
 Lim, S.W., see Kwak 138 (1994) 950  
 Lindberg, E., see Vaitkus 138 (1994) 545  
 Lindstaedt, M., see Tomm 138 (1994) 175  
 Lischka, K., see Schikora 138 (1994) 8  
 Lischka, K., see Lang 138 (1994) 81  
 Lischka, K., see Brunthaler 138 (1994) 559  
 Lischka, K., see Belas 138 (1994) 940  
 Litz, T., see Waag 138 (1994) 155  
 Litz, T., see Tönnies 138 (1994) 362  
 Litz, T., see Waag 138 (1994) 437  
 Litz, T., see Illing 138 (1994) 638  
 Litz, T., see Bacher 138 (1994) 856  
 Liu, W., see Zhang 138 (1994) 310  
 Liu, W., see Skromme 138 (1994) 338  
 Loginov, Y.Y., see Brown 138 (1994) 538  
 Lopez-Rivera, S.A., see Martinez 138 (1994) 913  
 Lowisch, M., see Schülzgen 138 (1994) 575  
 Lu, K., J.L. House, P.A. Fisher, C.A. Coronado, E. Ho, G.S. Petrich and L.A. Kolodziejski, (In,Ga)P buffer layers for ZnSe-based visible emitters 138 (1994) 1  
 Lu, Y.M., see Yang 138 (1994) 629  
 Lu, Y.M., see Zhang 138 (1994) 838  
 Lübke, K., see Schikora 138 (1994) 8  
 Lummer, B., see Krause 138 (1994) 75  
 Lummer, B., see Hoffmann 138 (1994) 379  
 Lummer, B., see Broser 138 (1994) 809  
 Lummer, B., see Fricke 138 (1994) 815  
 Lummer, B., see Hoffmann 138 (1994) 1073  
 Lunn, B., see Dhese 138 (1994) 443  
 Lunn, B., see Wolverson 138 (1994) 656  
 Lunn, B., see Pier 138 (1994) 889  
 Lunn, B., see Sawicki 138 (1994) 900  
 Luo, H., see Yokogawa 138 (1994) 564  
 Lusson, A., see El Mokri 138 (1994) 168  
 Lusson, A., see Rzepka 138 (1994) 244  
 Lusson, A., see Kuhn 138 (1994) 448  
 Lusson, A., see Qu'Hen 138 (1994) 1079  
 Lyssenko, V.G., see Erland 138 (1994) 800  
 MacDonald, S.M., see Fisher 138 (1994) 86  
 Maehara, K., see Fujita 138 (1994) 737  
 Magnea, N., ZnTe fractional monolayers and dots in a CdTe matrix 138 (1994) 550  
 Magnea, N., see Bassani 138 (1994) 607  
 Mahnke, H.-E., see Schumann 138 (1994) 910  
 Majumder, F.A., see Klingshirn 138 (1994) 786



- Malzbender, J., see Jones 138 (1994) 279
- Mamor, M., see Bassani 138 (1994) 607
- Mangat, P.S., see Chen 138 (1994) 1078
- Marcenat, F., see Legras 138 (1994) 585
- Marfaing, Y., see Rzepka 138 (1994) 244
- Marfaing, Y., Limits of acceptor impurity doping in wide band gap II-VI semiconductors 138 (1994) 305
- Mariette, H., see Gourgon 138 (1994) 590
- Mariette, H., see Haacke 138 (1994) 831
- Marrakchi, G., see Rzepka 138 (1994) 244
- Martinez, L., S.A. Lopez-Rivera, W. Girit and F. Medina, Nature of the absorption bands in  $\text{Zn}_{1-x}\text{Co}_x\text{S}$  138 (1994) 913
- Masumoto, Y., see Yamada 138 (1994) 570
- Masumoto, Y., see Yamamoto 138 (1994) 643
- Mathieu, H., see Allègre 138 (1994) 998
- Matioukhin, D.G., see Salk 138 (1994) 161
- Matsumoto, H., see Miura 138 (1994) 1046
- Matsumoto, T., T. Iwashita, K. Sasamoto and T. Kato, Atomic layer epitaxy of CdSe/ZnSe short period superlattices 138 (1994) 63
- Matsumoto, T., see Yao 138 (1994) 290
- Matsumoto, T., T. Inaba, Y. Yoda, K. Egashira, T. Kato and T. Akitsu, p-Type doping of ZnSe with a novel nitrogen exciter 138 (1994) 403
- Matsumura, N., see Ichikawa 138 (1994) 14
- Matsuoka, T., A. Ohki, T. Ohno and Y. Kawaguchi, Comparison of GaN- and ZnSe-based materials for light emitters 138 (1994) 727
- Matsuura, K., see Seto 138 (1994) 346
- Matthews, B.E., see Hastings 138 (1994) 917
- Mauch, R.H., see Troppenz 138 (1994) 1017
- Maxey, C.D., see Hastings 138 (1994) 917
- Mayer, H., U. Rössler, S. Permogorov, H. Stolz, H. Vogelsang and W. von der Osten, Resonant Brillouin scattering in biaxially strained ZnSe 138 (1994) 195
- McCaldin, J.O., see Wang 138 (1994) 508
- McCaldin, J.O., see Swenberg 138 (1994) 692
- McGill, T.C., see Wang 138 (1994) 508
- McGill, T.C., see Miles 138 (1994) 523
- McGill, T.C., see Swenberg 138 (1994) 692
- Medina, F., see Martinez 138 (1994) 913
- Meier, J., see Rüb 138 (1994) 285
- Meis-Haugen, G., see DePuydt 138 (1994) 667
- Menninger, J., see Krause 138 (1994) 75
- Mensz, P.M., Electrical and optical modeling of II-VI semiconductor diode lasers 138 (1994) 697
- Mertins, H.-Ch., see Jung 138 (1994) 905
- Mertins, H.-Ch., see Jung 138 (1994) 1066
- Merz, J.L., see Yokogawa 138 (1994) 564
- Metcalfe, N.E., see Hastings 138 (1994) 917
- Meyer, B.K., see Fiederle 138 (1994) 529
- Meyer, J.R., A.R. Reisinger, K.A. Harris, R.W. Yanka, L.M. Mohnkern and L.R. Ram-Mohan, Photoluminescence study of HgTe-Hg<sub>0.9</sub>Cd<sub>0.1</sub>Te superlattices 138 (1994) 981
- Migita, M., A. Taike, M. Momose and J. Gotoh, Blue-green light-emitting diodes with p-ZnSSe highly doped with nitrogen grown by metalorganic molecular beam epitaxy and molecular beam epitaxy 138 (1994) 391
- Miles, R.J., see Wang 138 (1994) 508
- Miles, R.J., J.F. Swenberg, M.W. Wang, M.C. Phillips and T.C. McGill, Investigation of crystal quality and surface morphology of ZnTe:N epilayers grown on ZnTe and GaSb substrates 138 (1994) 523
- Miles, R.J., see Swenberg 138 (1994) 692
- Minami, F., see Inoue 138 (1994) 182
- Minami, F., K. Yoshida, K. Inoue and H. Fujiyasu, Two-photon spectroscopy in ZnSe/ZnS quantum wells 138 (1994) 796
- Miskinis, J., see Vaitkus 138 (1994) 545
- Mitsuyu, T., see Saiki 138 (1994) 805
- Miura, N., K. Ogawa, S. Kobayashi, H. Matsumoto and R. Nakano, Electroluminescence spectra of rare-earth-doped Zn S<sub>1-x</sub>Se<sub>x</sub> thin films 138 (1994) 1046
- Molva, E., see Legras 138 (1994) 585
- Mohnkern, L.M., see Meyer 138 (1994) 981
- Moine, O., see Rzepka 138 (1994) 244
- Moisan, J.Y., see Rzepka 138 (1994) 244
- Momose, M., see Migita 138 (1994) 391
- Moon, S.W., S.H. Suh and C.S. Choi, Indium doped Hg<sub>0.7</sub>Cd<sub>0.3</sub>Te/undoped Hg<sub>0.8</sub>Cd<sub>0.2</sub>Te/CdTe heterojunction grown by Te-rich liquid phase epitaxy 138 (1994) 944
- Moravec, P., see Belas 138 (1994) 940
- Moravec, P., see Höschl 138 (1994) 956
- Mori, Y., see Ishibashi 138 (1994) 677
- Moriyama, T., see Uchiki 138 (1994) 873
- Mullin, J.B., see Jones 138 (1994) 274
- Mullin, J.B., see Jones 138 (1994) 279
- Mullins, J.T., see Prior 138 (1994) 94
- Mullins, J.T., G. Horsburgh, J. Simpson, P. Thompson, M.R. Taghizadeh, I. Hauks-son, S.Y. Wang, K.A. Prior, B.C. Cavenett, G.M. Williams and A.G. Cullis, Laser induced doping profiles in molecular beam epitaxy grown ZnSe doped with iodine 138 (1994) 357
- Mullins, J.T., see Brown 138 (1994) 538
- Mullins, J.T., see Wang 138 (1994) 647
- Munekata, H., see Deleporte 138 (1994) 884
- Murakami, S., see Kanie 138 (1994) 145
- Muranoi, T., S. Onizawa and M. Sasaki, Iodine doping in ZnSe films grown by vapor phase epitaxy 138 (1994) 255
- Murdin, B., see Prior 138 (1994) 94

- Nagao, Y., see Nishimura 138 (1994) 114  
 Nagatake, T., see Kobayashi 138 (1994) 745  
 Nägele, M., see Schmolke 138 (1994) 213  
 Nägele, M., W. Ebeling, J. Gutowski, K.P. Geyzers and M. Heuken, Nonlinear transmission dynamics of  $\text{ZnS}_x\text{Se}_{1-x}/\text{ZnSe}$  and  $\text{ZnS}_x\text{Se}_{1-x}/\text{ZnS}_y\text{Se}_{1-y}$  ( $x > y$ ) waveguide structures 138 (1994) 842  
 Nakanishi, Y., see Kuwabara 138 (1994) 964  
 Nakano, R., see Miura 138 (1994) 1046  
 Nakao, T., see Uenoyama 138 (1994) 301  
 Nakayama, M., see Kuwabara 138 (1994) 964  
 Naumov, A., see Wolf 138 (1994) 412  
 Naumov, A., H. Stanzl, K. Wolf, A. Rosenauer, S. Lankes and W. Gebhardt, Exciton recombination in  $\text{ZnSe}_x\text{Te}_{1-x}/\text{ZnTe}$  QWs and  $\text{ZnSe}_x\text{Te}_{1-x}$  epilayers grown by metalorganic vapour phase epitaxy 138 (1994) 595  
 Naumov, A., see Klingshirm 138 (1994) 786  
 Neugebauer, F., see Heimbrodt 138 (1994) 601  
 Neukirch, U., D. Weckendrup, W. Faschinger, P. Juza and H. Sitter, Exciton relaxation dynamics in ultrathin  $\text{CdSe}/\text{ZnSe}$  single quantum wells 138 (1994) 849  
 Neukirch, U., D. Weckendrup, J. Gutowski, D. Hommel and G. Landwehr, Dynamical properties of excitons in  $\text{Zn}_{1-x}\text{Cd}_x\text{Se}/\text{ZnSe}$  quantum wells and  $\text{Zn}_{1-x}\text{Cd}_x\text{Se}$  epilayers grown by molecular beam epitaxy 138 (1994) 861  
 Neumark, G.F., see Radomsky 138 (1994) 99  
 Neumark, G.F., see Yi 138 (1994) 208  
 Nicholls, J.E., see Dhese 138 (1994) 140  
 Nicholls, J.E., see Dhese 138 (1994) 443  
 Nicholls, J.E., see Pier 138 (1994) 889  
 Nishihata, A., see Suzuki 138 (1994) 199  
 Nishimura, K., Y. Nagao and K. Sakai, Low pressure growth and nitrogen doping in metalorganic vapor phase epitaxy of  $\text{ZnSe}$  138 (1994) 114  
 Nishiyama, F., see Yao 138 (1994) 290  
 Noh, S.K., see Lee 138 (1994) 136  
 Nunez, V., see Giebultowicz 138 (1994) 877  
 Nurmikko, A.V., see Ding 138 (1994) 719  
 Nurmikko, A.V., see Salokatve 138 (1994) 1077  
 Ogawa, K., see Miura 138 (1994) 1046  
 Oh, E., see Fromherz 138 (1994) 580  
 Ohishi, M., see Yoneta 138 (1994) 110  
 Ohkawa, K., see Saiki 138 (1994) 805  
 Ohki, A., see Matsuoka 138 (1994) 727  
 Ohmi, K., Y. Yamano, S.T. Lee, T. Ueda, S. Tanaka and H. Kobayashi, Growth and characterization of  $\text{SrS}/\text{ZnS}$  multilayered electroluminescent thin films grown by hot wall technique 138 (1994) 1061  
 Ohnesorge, B., see Deleporte 138 (1994) 884  
 Ohno, T., see Matsuoka 138 (1994) 727  
 Ohta, H., see Kanie 138 (1994) 145  
 Okamoto, T., A. Yamada, M. Konagai and K. Takahashi, Polarized photoluminescence in vacancy-ordered  $\text{Ga}_2\text{Se}_3$  138 (1994) 204  
 Okamoto, T., see Tojima 138 (1994) 408  
 Okumura, T., see Tomomura 138 (1994) 764  
 Olego, D.J., see Wolk 138 (1994) 1071  
 Olego, D.J., see Chen 138 (1994) 1078  
 O'Neill, M., see Pier 138 (1994) 889  
 Onishi, T., see Ichino 138 (1994) 28  
 Onizawa, S., see Muranoi 138 (1994) 255  
 Ortenberg, M. von, see Schikora 138 (1994) 8  
 Ortenberg, M. von, see Lang 138 (1994) 81  
 Ossau, W., see Waag 138 (1994) 155  
 Osten, W. von der, see Mayer 138 (1994) 195  
 Otsuka, N., see Hua 138 (1994) 367  
 Otsuka, N., see Han 138 (1994) 464  
 Pantke, K.-H., see Erland 138 (1994) 800  
 Park, H.L., see Hwang 138 (1994) 131  
 Park, H.L., see Lee 138 (1994) 136  
 Park, R.M., see Calhoun 138 (1994) 352  
 Pautrat, J.L., see Legras 138 (1994) 585  
 Pelekanos, N.T., see Haacke 138 (1994) 831  
 Pelletier, C.M., see Granger 138 (1994) 486  
 Peng, Y.G., see Guan 138 (1994) 534  
 Perkowitz, S., see Feng 138 (1994) 239  
 Permogorov, S., see Mayer 138 (1994) 195  
 Petri, W., see Klingshirm 138 (1994) 786  
 Petrich, G.S., see Lu 138 (1994) 1  
 Petruzzello, J., R. Drenten and J.M. Gaines, Improvement in lasing characteristics of II–VI blue-green lasers using quaternary and ternary alloys to produce pseudomorphic heterostructures 138 (1994) 686  
 Pier, Th., K. Hieke, B. Henninger, W. Heimbrodt, O. Goede, H.-E. Gumlich, J.E. Nicholls, M. O'Neill, S.J. Weston and B. Lunn, Magnetic field dependence of the exciton transfer in semimagnetic double quantum well structures 138 (1994) 889  
 Phillips, M.C., see Wang 138 (1994) 508  
 Phillips, M.C., see Miles 138 (1994) 523  
 Phillips, M.C., see Swenberg 138 (1994) 692  
 Pidgeon, C.R., see Prior 138 (1994) 94  
 Piotrowska, A., see Grabecki 138 (1994) 481  
 Pitt, G.D., see Feng 138 (1994) 239  
 Plesiewicz, W., see Grabecki 138 (1994) 481  
 Pohl, U.W., G.H. Kudlek, A. Klimakow and A. Hoffmann, Shallow impurity- and defect-related complexes in undoped  $\text{ZnSe}$  crystals 138 (1994) 385  
 Pohl, U.W., see Schumann 138 (1994) 910  
 Ponzoni, C., see Chen 138 (1994) 1078  
 Poon, H.C., see Feng 138 (1994) 239  
 Portuné, M., see Woggon 138 (1994) 988

- Presser, N., Ch. Fricke, G. Kudlek, R. Heitz, A. Hoffmann and I. Broser, Energy transfer processes via the interface of ZnSe/GaAs epilayers 138 (1994) 820
- Prior, K.A., B. Murdin, C.R. Pidgeon, S.Y. Wang, I. Hauksson, J.T. Mullins, G. Horsburgh and B.C. Cavenett, Compensation processes in molecular beam epitaxially grown zinc selenide doped with nitrogen 138 (1994) 94
- Prior, K.A., see Mullins 138 (1994) 357
- Prior, K.A., see Wang 138 (1994) 647
- Prior, K.A., see Kawakami 138 (1994) 759
- Puls, J., see Schülzgen 138 (1994) 575
- Puls, J., V. Jungnickel, F. Henneberger and A. Schülzgen, Carrier dynamics in CdS quantum dots embedded in glass 138 (1994) 1004
- Qiu, J., see DePuydt 138 (1994) 667
- Quemerais, A., K.H. Khelladi, D. Lemoine, R. Granger and R. Triboulet, Angle resolved X-ray photoelectron spectroscopy of the surface of  $\text{Hg}_{0.85}\text{Zn}_{0.15}\text{Te}$  and after passivation processes 138 (1994) 934
- Quesada, X., see Kuhn 138 (1994) 448
- Quesada, X., see Qu'Hen 138 (1994) 1079
- Qu'Hen, B., see Kuhn 138 (1994) 448
- Qu'Hen, B., X. Quesada, W.S. Kuhn, J.E. Bourée, L. Svob, A. Lusson and O. Gorochov, Growth of  $\text{MgTe}$  and  $\text{Zn}_{1-x}\text{Mg}_x\text{Te}$  thin films by metalorganic vapour phase epitaxy 138 (1994) 1079
- Račiukaitis, G., see Gavryushin 138 (1994) 924
- Racz, J.M., see Gallagher 138 (1994) 970
- Radomsky, L., G.-J. Yi and G.F. Neumark, Observation of preferential donor-acceptor pairing in ZnSe:Na 138 (1994) 99
- Radomsky, L., see Yi 138 (1994) 208
- Railson, S.V., see Wolverson 138 (1994) 656
- Rajavel, D., J.J. Zinck and J.E. Jensen, Metalorganic molecular beam epitaxial growth kinetics and doping studies of (001) ZnSe 138 (1994) 19
- Ramda, A.K., see Fromherz 138 (1994) 580
- Ram-Mohan, L.R., see Meyer 138 (1994) 981
- Ray, B., see Arterton 138 (1994) 1051
- Ray, B., see Viney 138 (1994) 1055
- Razbirin, B.S., see Erland 138 (1994) 86a
- Reisinger, A.R., see Meyer 138 (1994) 981
- Reislöhner, U., see Rüb 138 (1994) 285
- Ren, J., D.B. Eason, L.E. Churchill, Z. Yu, C. Boney, J.W. Cook, Jr., J.F. Schetzina and N.A. El-Masry, Integrated heterostructure devices composed of II-VI materials with Hg-based contact layers 138 (1994) 455
- Ren, J., see Eason 138 (1994) 703
- Renucci, M.A., see Frandon 138 (1994) 513
- Rinas, U., see Rudolph 138 (1994) 249
- Ringle, M.D., see Han 138 (1994) 464
- Röseler, J., see Heimbrodt 138 (1994) 601
- Rosenauer, A., see Grün 138 (1994) 150
- Rosenauer, A., see Naumov 138 (1994) 595
- Rössler, U., see Mayer 138 (1994) 195
- Rössler, U., see Freytag 138 (1994) 499
- Rouleau, C.M., see Calhoun 138 (1994) 352
- Roussignol, P., see Deleporte 138 (1994) 884
- Rüb, M., N. Achtziger, J. Meier, U. Reislöhner, P. Rudolph, M. Wienecke and W. Witthuhn, Complex formation in In- and Ag/Cu-doped CdTe 138 (1994) 285
- Rudolph, P., U. Rinas and K. Jacobs, Systematic steps towards exactly stoichiometric and uncompensated CdTe Bridgman crystals 138 (1994) 249
- Rudolph, P., see Rüb 138 (1994) 285
- Rühle, W.W., see Haacke 138 (1994) 831
- Ruppert, P., D. Hommel, T. Behr, H. Heinke, A. Waag and G. Landwehr, Molecular beam epitaxial growth mechanism of ZnSe epilayers on (100) GaAs as determined by reflection high-energy electron diffraction, transmission electron microscopy and X-ray diffraction 138 (1994) 48
- Rzepka, E., A. Aoudia, M. Cuniot, A. Lusson, Y. Marfaing, R. Triboulet, G. Brémond, G. Marrakchi, K. Cherkaoui, M.C. Busch, J.M. Koebel, M. Hage-Ali, P. Siffert, J.Y. Moisan, P. Gravey, N. Wolffer and O. Moine, Optical and thermal spectroscopy of vanadium-doped CdTe and related photorefractive effect 138 (1994) 244
- Sahin, H., see Kuhn 138 (1994) 448
- Saiki, T., K. Takeuchi, K. Ema, M. Kuwata-Gonokami, K. Ohkawa and T. Mitsuyu, Free induction decay and quantum beat of excitons in ZnSe 138 (1994) 805
- Saito, H., see Yoneta 138 (1994) 110
- Sakai, K., see Nishimura 138 (1994) 114
- Saleh, M., see Woggon 138 (1994) 988
- Salk, M., M. Fiederle, K.W. Benz, A.S. Senchenkov, A.V. Egorov and D.G. Matiukhin, CdTe and  $\text{CdTe}_{0.9}\text{Se}_{0.1}$  crystals grown by the travelling heater method using a rotating magnetic field 138 (1994) 161
- Salk, M., see Fiederle 138 (1994) 529
- Salokatve, A., H. Jeon, M. Hovinen, P. Kelkar, A.V. Nurmikko, D.C. Grillo, L. He, J. Han, Y. Fan and R.L. Gunshor, Ridge waveguide, separate confinement green-blue heterostructure lasers 138 (1994) 1077
- Saminadayar, K., see Bassani 138 (1994) 607

- Saraie, J., see Ichikawa 138 (1994) 14
- Sasaki, M., see Muranoi 138 (1994) 255
- Sasaki, S., see Yao 138 (1994) 290
- Sasamoto, K., see Matsumoto 138 (1994) 63
- Sawers, L.J.M., see Fisher 138 (1994) 86
- Sawicki, M., M.A. Brummell, P.A.J. de Groot, G.J. Tomka, D.E. Ashenford and B. Lunn, Magnetic properties of  $\text{Cd}_{1-x}\text{Mn}_x\text{Te}$  grown by molecular beam epitaxy 138 (1994) 900
- Schetzina, J.F., see Vaudo 138 (1994) 430
- Schetzina, J.F., see Ren 138 (1994) 455
- Schetzina, J.F., see Eason 138 (1994) 703
- Schiffers, W., see Hermans 138 (1994) 612
- Schikora, D., H. Hausleitner, S. Einfeldt, C.R. Becker, Th. Widmer, C. Giftge, K. Lübke, K. Lischka, M. von Ortenberg and G. Landwehr, Epitaxial overgrowth of II-VI compounds on patterned substrates 138 (1994) 8
- Schikora, D., see Lang 138 (1994) 81
- Schikora, D., see Brunthaler 138 (1994) 559
- Schneider, A., see Söllner 138 (1994) 35
- Schneider, A., see Gleitsmann 138 (1994) 324
- Schneider, A., see Taudt 138 (1994) 418
- Schneider, A., see Hermans 138 (1994) 612
- Schmolke, R., E. Schöll, M. Nägele and J. Gutowski, Nonlinear optical switching fronts in CdS 138 (1994) 213
- Schöll, E., see Schmolke 138 (1994) 213
- Scholl, M., see Söllner 138 (1994) 35
- Scholl, M., see Tönnies 138 (1994) 362
- Scholl, M., see Hermans 138 (1994) 612
- Scholl, M., see Waag 138 (1994) 437
- Scholl, S., see Hommel 138 (1994) 1076
- Schüll, K., see Hommel 138 (1994) 1076
- Schülzgen, A., F. Kreller, F. Henneberger, M. Lowisch and J. Puls, Exciton dynamics and high density effects in  $\text{ZnSe}/\text{ZnMnSe}$  quantum structures grown by molecular beam epitaxy 138 (1994) 575
- Schülzgen, A., see Puls 138 (1994) 1004
- Schumann, D., H.-E. Mähne, B. Spellmeyer, G. Sulzer, H. Waldmann, W.-D. Zeitz, U.W. Pohl and H.-E. Gumlich, Magnetic or nonmagnetic behavior of isolated scandium ions in II-VI compounds 138 (1994) 910
- Scott, C.G., see Dhese 138 (1994) 443
- Seisyan, R.P., see Jakobson 138 (1994) 225
- Senchenkov, A.S., see Salk 138 (1994) 161
- Senga, K., see Ichikawa 138 (1994) 14
- Seto, S., A. Tanaka, F. Takeda and K. Matsumura, Defect-induced emission band in CdTe 138 (1994) 346
- Shaw, N., see Jones 138 (1994) 279
- Shen, D.Z., X.W. Fan and B.J. Yang, Light interference effect in optical bistability of multiple quantum well etalons 138 (1994) 625
- Shen, D.Z., see Zhang 138 (1994) 838
- Shibli, S.M., see Zhang 138 (1994) 310
- Siche, D., see Hartmann 138 (1994) 260
- Siffert, P., see Rzepka 138 (1994) 244
- Silberman, E., see Biao 138 (1994) 219
- Silberman, E., see Azoulay 138 (1994) 517
- Simpson, I., see Kawakami 138 (1994) 759
- Simpson, J., see Mullins 138 (1994) 357
- Sitter, H., see Lang 138 (1994) 81
- Sitter, H., see Brunthaler 138 (1994) 559
- Sitter, H., see Fromherz 138 (1994) 580
- Sitter, H., see Neukirch 138 (1994) 849
- Sitter, H., see Giebultowicz 138 (1994) 877
- Sitter, H., see Belas 138 (1994) 940
- Skośkiewicz, T., see Grabecki 138 (1994) 481
- Skromme, B.J., see Zhang 138 (1994) 310
- Skromme, B.J., W. Liu, K.F. Jensen and K.P. Giapis, Effects of C incorporation on the luminescence properties of ZnSe grown by metalorganic chemical vapor deposition 138 (1994) 338
- Söllner, J., M. Scholl, A. Schneider, M. Heuken and J. Woitok, Optimization of strained short-period  $\text{ZnSSe}/\text{ZnSe}$  superlattices grown by metalorganic vapour phase epitaxy 138 (1994) 35
- Söllner, J., see Hermans 138 (1994) 612
- Song, S.H., see Guan 138 (1994) 534
- Soukiasian, P., see Chen 138 (1994) 1078
- Spahn, W., see Waag 138 (1994) 155
- Spellmeyer, B., see Schumann 138 (1994) 910
- Sperling, V., see Woggon 138 (1994) 976
- Stadler, W., see Fiederle 138 (1994) 529
- Stanley, R.P., see Doran 138 (1994) 826
- Stanzl, H., see Wolf 138 (1994) 412
- Stanzl, H., see Kuhn 138 (1994) 448
- Stanzl, H., see Naumov 138 (1994) 595
- Stanzl, H., see Klingshirn 138 (1994) 786
- Stewart, H., see Kawakami 138 (1994) 759
- Stolz, H., see Mayer 138 (1994) 195
- Story, T., see Grodzicka 138 (1994) 1034
- Strachan, D.J., M.M. Li, M.C. Tamargo and B.A. Weinstein, Acceptor state instabilities in ZnSe under hydrostatic pressure 138 (1994) 318
- Su, C.-H., see Biao 138 (1994) 219
- Suemune, I., Quantitative study of mechanism responsible for high operating voltage in II-VI laser diodes 138 (1994) 714
- Suemune, I., Y. Fujii and M. Fujimoto, Improvement of electrical and optical properties of  $\text{ZnSSe}$  p-n heterostructure diodes with optimization in metalorganic vapor phase epitaxy 138 (1994) 750
- Sugawara, H., see Itaya 138 (1994) 768
- Suh, S.H., see Moon 138 (1994) 944
- Suh, S.H., see Kwak 138 (1994) 950
- Suisky, D., see Heimbrodt 138 (1994) 601

- Sulzer, G., see Schumann 138 (1994) 910  
 Suzuki, A., see Tomomura 138 (1994) 764  
 Suzuki, K., N. Akita, K. Inagaki, A. Nishihata, N. Takojima and S. Dairaku, Alloy broadening in photoluminescence spectra of  $\text{Cd}_{1-x}\text{Zn}_x\text{Te}$  crystals grown from Te solution 138 (1994) 199  
 Suzuki, M., see Uenoyama 138 (1994) 301  
 Svob, L., see Kuhn 138 (1994) 448  
 Svob, L., see Qu'Hen 138 (1994) 1079  
 Svoboda, J., see Höschl 138 (1994) 956  
 Swanson, M.L., see Hughes 138 (1994) 1040  
 Swenberg, J.F., see Wang 138 (1994) 508  
 Swenberg, J.F., see Miles 138 (1994) 523  
 Swenberg, J.F., M.W. Wang, R.J. Miles, M.C. Phillips, A.T. Hunter, J.O. McCaldin and T.C. McGill, Advances in the development of graded injector visible light emitters 138 (1994) 692  
 Szofran, F.R., see Biao 138 (1994) 219  
 Taghizadeh, M.R., see Mullins 138 (1994) 357  
 Taguchi, T., see Yamada 138 (1994) 570  
 Taïke, A., see Migita 138 (1994) 391  
 Takahashi, K., see Okamoto 138 (1994) 204  
 Takahashi, K., see Tojima 138 (1994) 408  
 Takebayashi, K., see Zhu 138 (1994) 397  
 Takebayashi, K., see Zhu 138 (1994) 619  
 Takeda, F., see Seto 138 (1994) 346  
 Takeuchi, K., see Saiki 138 (1994) 805  
 Takiguchi, H., see Tomomura 138 (1994) 764  
 Takojima, N., see Suzuki 138 (1994) 199  
 Takojima, N., F. Iida, K. Imai and K. Kumazaki, Photoluminescence of ultrathin  $\text{ZnSe-ZnTe}$  superlattices 138 (1994) 633  
 Tamargo, M.C., see Zhang 138 (1994) 310  
 Tamargo, M.C., see Strachan 138 (1994) 318  
 Tanaka, A., see Seto 138 (1994) 346  
 Tanaka, K., see Zhu 138 (1994) 397  
 Tanaka, S., see Ohmi 138 (1994) 1061  
 Tang, S.H., see Ji 138 (1994) 187  
 Taskar, N.T., see Wolk 138 (1994) 1071  
 Tatarenko, S., see Bassani 138 (1994) 607  
 Tatsuoka, H., see Kuwabara 138 (1994) 964  
 Taudt, W., see Hoffmann 138 (1994) 379  
 Taudt, W., A. Schneider, M. Heuken, Ch. Fricke and A. Hoffmann, Low temperature growth and plasma enhanced nitrogen doping of  $\text{ZnSe}$  by metalorganic vapour phase epitaxy 138 (1994) 418  
 Taudt, W., see Fricke 138 (1994) 815  
 Theis, W.M., see Bicknell-Tassius 138 (1994) 425  
 Thompson, P., see Mullins 138 (1994) 357  
 Thompson, P., see Wang 138 (1994) 647  
 Tojima, H., T. Okamoto, A. Yamada, M. Konagai and K. Takahashi, Nitrogen doping into  $\text{ZnSe}$  by the catalysis of transition metal 138 (1994) 408  
 Tojyo, T., see Fujita 138 (1994) 737  
 Tomka, G.J., see Sawicki 138 (1994) 900  
 Tomm, J.W., K.H. Herrmann, W. Hoerstel, M. Lindstaedt, H. Kissel and F. Fuchs, On the nature of the excitonic luminescence in narrow-gap  $\text{Hg}_{1-x}\text{Cd}_x\text{Te}$  ( $x \approx 0.3$ ) 138 (1994) 175  
 Tomomura, Y., S. Hirata, T. Okumura, M. Kitagawa, A. Suzuki and H. Takiguchi, Dependence of device characteristics on quantum well thickness in  $\text{ZnSe/ZnCdSe}$  multi-quantum well blue-green laser diodes 138 (1994) 764  
 Tönnies, D., G. Bacher, A. Forchel, A. Waag, Th. Litz, D. Hommel, Ch. Becker, G. Landwehr, M. Heuken and M. Scholl, Optical study of interdiffusion in  $\text{CdTe}$  and  $\text{ZnSe}$  based quantum wells 138 (1994) 362  
 Tosaka, H., see Kobayashi 138 (1994) 745  
 Toth, A., see Belas 138 (1994) 940  
 Triboulet, R., see El Mokri 138 (1994) 168  
 Triboulet, R., see Rzepka 138 (1994) 244  
 Triboulet, R., see Quemerais 138 (1994) 934  
 Tromson-Carli, A., see El Mokri 138 (1994) 168  
 Troppenz, U., B. Hüttel, K.O. Velthaus and R.H. Mauch, Trailing edge phenomena in  $\text{SrS:CeCl}_3$  thin film electroluminescent devices 138 (1994) 1017  
 Truchsess, N. von, see Buda 138 (1994) 652  
 Tsuboi, N., see Uchiki 138 (1994) 873  
 Uchiki, H., H. Kinto, T. Moriyama, S. Hata, N. Tsuboi, J. Wang and S. Iida, Exciton and Raman processes of  $\text{ZnS}$  under tunable picosecond light pulse excitations 138 (1994) 873  
 Ueda, T., see Ohmi 138 (1994) 1061  
 Uenoyama, T., T. Nakao and M. Suzuki, Interaction between  $\text{N}_2$  and stabilized  $\text{ZnSe}$  surface 138 (1994) 301  
 Uhrig, A., see Woggon 138 (1994) 988  
 Ullrich, B., A. Kazlauskas, S. Zerlauth and T. Kobayashi, First realization of bistable light emitting devices 138 (1994) 234  
 Umlauff, M., see Klingshirn 138 (1994) 786  
 Vaitkus, J., R. Baubinas, V. Kazlauskienė, D. Kuciauskas, J. Miskinis, U. Karlsson, M. Hammar, M. Göthelid, M. Björqvist and E. Lindberg, Scanning tunneling microscopy of  $\text{CdSe}$  single crystal cleaved and "real" surface 138 (1994) 545  
 Vaudo, R.P., J.W. Cook, Jr. and J.F. Schetzina, Atomic nitrogen production in nitrogen-plasma sources used for the growth of  $\text{ZnSe:N}$  and related alloys by molecular-beam epitaxy 138 (1994) 430  
 Velthaus, K.O., see Troppenz 138 (1994) 1017

- Vieu, C., see Gourgon 138 (1994) 590  
 Viney, I.V.F., see Arterton 138 (1994) 1051  
 Viney, I.V.F., B.W. Arterton, B. Ray and J.W. Brightwell, Electrical and optical stimulation of luminescence in  $\text{Ca}_{1-x}\text{Cd}_x\text{S}$  138 (1994) 1055  
 Vogelsang, H., see Mayer 138 (1994) 195  
 Volz, M.E., see Biao 138 (1994) 219  
 Von der Osten, W., see Mayer 138 (1994) 195  
 Von Ortenberg, M., see Schikora 138 (1994) 8  
 Von Ortenberg, M., see Lang 138 (1994) 81  
 Von Truchsess, N., see Buda 138 (1994) 652  
  
 Waag, A., see Ruppert 138 (1994) 48  
 Waag, A., F. Fischer, Th. Litz, B. Kuhn-Heinrich, U. Zehnder, W. Ossau, W. Spahn, H. Heinke and G. Landwehr, Wide gap  $\text{Cd}_{1-x}\text{Mg}_x\text{Te}$ : molecular beam epitaxial growth and characterization 138 (1994) 155  
 Waag, A., see Tönnies 138 (1994) 362  
 Waag, A., Th. Litz, F. Fischer, H. Heinke, S. Scholl, D. Hommel, G. Landwehr and G. Bilger, Halogen doping of II-VI semiconductors during molecular beam epitaxy 138 (1994) 437  
 Waag, A., see Illing 138 (1994) 638  
 Waag, A., see Buda 138 (1994) 652  
 Waag, A., see Hellmann 138 (1994) 791  
 Waag, A., see Bacher 138 (1994) 856  
 Wada, M., see Kato 138 (1994) 373  
 Wagner, H.P., see Wolf 138 (1994) 412  
 Waldmann, H., see Schumann 138 (1994) 910  
 Walukiewicz, W., see Wolk 138 (1994) 1071  
 Wang, J., see Uchiki 138 (1994) 873  
 Wang, M.W., J.F. Swenberg, R.J. Miles, M.C. Phillips, E.T. Yu, J.O. McCaldin, R.W. Grant and T.C. McGill, Measurement of the  $\text{MgSe}/\text{Cd}_{0.54}\text{Zn}_{0.46}\text{Se}$  valence band offset by X-ray photoelectron spectroscopy 138 (1994) 508  
 Wang, M.W., see Miles 138 (1994) 523  
 Wang, M.W., see Swenberg 138 (1994) 692  
 Wang, S.M., see Yang 138 (1994) 629  
 Wang, S.Y., see Prior 138 (1994) 94  
 Wang, S.Y., see Mullins 138 (1994) 357  
 Wang, S.Y., P. Thompson, G. Horsburgh, J.T. Mullins, I. Hauksson, K.A. Prior and B.C. Cavenett, A  $\text{ZnSe}/\text{ZnCdSe}$  quantum well symmetric self-electro-optic effect device operating in the blue-green region 138 (1994) 647  
 Wang, W.-S. and I. Bhat, Use of germanium interfacial layer for the hetero-epitaxial growth of  $\text{CdTe}$  on Si substrates 138 (1994) 43  
 Watabe, S., see Yanashima 138 (1994) 755  
 Weckendrup, D., see Neukirch 138 (1994) 849  
 Weckendrup, D., see Neukirch 138 (1994) 861  
  
 Weinhold, V., see Heimbrodt 138 (1994) 601  
 Weinstein, B.A., see Strachan 138 (1994) 318  
 Weisbuch, Recent progress in III-V quantum optoelectronic devices 138 (1994) 776  
 Weston, S.J., see Pier 138 (1994) 889  
 Widmer, T., see Schikora 138 (1994) 8  
 Widmer, T., see Lang 138 (1994) 81  
 Wienecke, M., see Rüb 138 (1994) 285  
 Williams, G.M., see Mullins 138 (1994) 357  
 Williams, K.P., see Feng 138 (1994) 239  
 Wind, O., see Woggon 138 (1994) 976  
 Witkowska, B., see Grodzicka 138 (1994) 1034  
 Witthuhn, W., see Rüb 138 (1994) 285  
 Woggon, U., S.V. Bogdanov, O. Wind and V. Sperling, Electric field induced absorption modulation of  $\text{CdS}$  quantum dots in an organic matrix 138 (1994) 976  
 Woggon, U., M. Saleh, A. Uhrig, M. Portuné and C. Klingshirn,  $\text{CdS}$  quantum dots in the weak confinement 138 (1994) 988  
 Woitok, J., see Söllner 138 (1994) 35  
 Woitok, J., see Hermans 138 (1994) 612  
 Wolf, K., H. Stanzl, A. Naumov, H.P. Wagner, W. Kuhn, B. Hahn and W. Gebhardt, Growth and doping of  $\text{ZnTe}$  and  $\text{ZnSe}$  epilayers with metalorganic vapour phase epitaxy 138 (1994) 412  
 Wolf, K., see Kuhn 138 (1994) 448  
 Wolf, K., see Naumov 138 (1994) 595  
 Wolffer, N., see Rzepka 138 (1994) 244  
 Wolk, J.A., J.W. Ager III, K.J. Duxstad, W. Walukiewicz, E.E. Haller, N.R. Taskar, D.R. Dorman and D.J. Olego, The nitrogen-hydrogen complex in  $\text{ZnSe}$  138 (1994) 1071  
 Wolverson, D., J.J. Davies, S.V. Railson, M.P. Halsall, D.E. Ashenford and B. Lunn, Spin-flip Raman scattering by electrons bound to donors in  $\text{CdTe}/\text{Cd}_{1-x}\text{Mn}_x\text{Te}$  multiple quantum well structures as a function of barrier composition 138 (1994) 656  
 Wright, P.J., see Dhese 138 (1994) 140  
 Wu, B.J., see DePuydt 138 (1994) 667  
 Wu, Y.K., see Guan 138 (1994) 534  
  
 Xiong, G., see Li 138 (1994) 231  
  
 Yakovlev, D.R., see Hellmann 138 (1994) 791  
 Yamada, A., see Okamoto 138 (1994) 204  
 Yamada, A., see Tojima 138 (1994) 408  
 Yamada, Y., Y. Masumoto and T. Taguchi, Ultraviolet lasing and excitonic gain in  $\text{Cd}_{1-x}\text{Zn}_x\text{S}-\text{ZnS}$  strained-layer multiple quantum wells 138 (1994) 570  
 Yamamoto, A., Y. Kanemitsu and Y. Masumoto, Structural characteristics and higher-order zone-folded phonon modes in  $\text{ZnSe}-\text{ZnS}$  strained-layer superlattices 138 (1994) 643

- Yamanari, T., see Kuwabara 138 (1994) 964  
 Yamano, Y., see Ohmi 138 (1994) 1061  
 Yamasaki, D., see Yanashima 138 (1994) 755  
 Yamawaki, K., see Ichikawa 138 (1994) 14  
 Yanashima, K., D. Yamasaki, S. Watabe, K. Hara, J. Yoshino and H. Kukimoto, Metalorganic vapor phase epitaxy growth of p-type ZnSSe and its application for blue-green lasers 138 (1994) 755  
 Yang, A.H., see Yang 138 (1994) 629  
 Yang, B.J., see Shen 138 (1994) 625  
 Yang, B.J., L.C. Chen, X.W. Fan, J.Y. Zhang, Z.H. Zheng, Y.M. Lu, Z.P. Guan, A.H. Yang and S.M. Wang, Growth and optical bistability of  $\text{Zn}_{0.78}\text{Cd}_{0.22}\text{Se}$ -ZnSe multiple quantum wells by metalorganic chemical vapor deposition 138 (1994) 629  
 Yang, B.J., see Zhang 138 (1994) 838  
 Yanka, R.W., see Meyer 138 (1994) 981  
 Yao, T., T. Matsumoto, S. Sasaki, C.K. Chung, Z. Zhu and F. Nishiyama, Lattice location of N atoms in heavily N-doped ZnSe studied with ion beam analysis and its implication on deep level defects 138 (1994) 290  
 Yao, T., see Zhu 138 (1994) 397  
 Yao, T., see Zhu 138 (1994) 619  
 Yi, G.-J., see Radomsky 138 (1994) 99  
 Yi, G.-J., L. Radomsky and G.F. Neumark, Temperature dependence of luminescence in ZnSe and role of excitation transfer 138 (1994) 208  
 Yoda, Y., see Matsumoto 138 (1994) 403  
 Yokogawa, T., P.D. Floyd, J.L. Merz, H. Luo and J.K. Furdyna, Optical confinement in ZnSe-based quantum well structure using impurity induced disordering 138 (1994) 564  
 Yoneta, M., H. Saito and M. Ohishi, Auto-doping of Ga in ZnSe/GaAs layers grown at low temperatures by post-heated molecular beam epitaxy 138 (1994) 110  
 Yoshida, K., see Inoue 138 (1994) 182  
 Yoshida, K., see Minami 138 (1994) 796  
 Yoshida, T., see Kobayashi 138 (1994) 745  
 Yoshihara, H., see Zhu 138 (1994) 619  
 Yoshikawa, A., see Kobayashi 138 (1994) 745  
 Yoshino, J., see Yanashima 138 (1994) 755  
 Yu, E.T., see Wang 138 (1994) 508  
 Yu, Z., see Ren 138 (1994) 455  
 Yu, Z., see Eason 138 (1994) 703  
 Zehnder, U., see Waag 138 (1994) 155  
 Zeinert, A., P. Benalloul, J. Benoit, C. Barthou and H.-E. Gumlich, Space charge and excitation efficiency in ZnS thin film electroluminescent devices 138 (1994) 1023  
 Zeitz, W.-D., see Schumann 138 (1994) 910  
 Zerlauth, S., see Ullrich 138 (1994) 234  
 Zhang, J.Y., see Yang 138 (1994) 629  
 Zhang, J.Y., X.W. Fan, B.J. Yang, Z.P. Guan, Y.M. Lu and D.Z. Shen, Excitonic emission in ZnCdSe-ZnSe multiple quantum wells 138 (1994) 838  
 Zhang, Y., W. Liu, B.J. Skromme, H. Cheng, S.M. Shibli and M.C. Tamargo, Systematic investigation of shallow acceptor levels in ZnSe 138 (1994) 310  
 Zhao, Z., see Li 138 (1994) 231  
 Zheng, J. and J.W. Allen, The hole diffusion length in epitaxial zinc selenide 138 (1994) 477  
 Zheng, J. and J.W. Allen, Photoionization of a deep centre in zinc selenide giving information about the conduction band structure 138 (1994) 504  
 Zheng, Z.H., see Yang 138 (1994) 629  
 Zhu, Z., see Yao 138 (1994) 290  
 Zhu, Z., T. Ebisutani, K. Takebayashi, K. Tanaka and T. Yao, Molecular beam epitaxy of ZnSe doped with nitrogen on vicinal (100)-oriented and (211)-oriented GaAs substrates 138 (1994) 397  
 Zhu, Z., H. Yoshihara, K. Takebayashi and T. Yao, Characterization of alloy formation at the ZnSe/CdSe quantum-well interface by photoluminescence spectroscopy 138 (1994) 619  
 Zigone, M., see Haacke 138 (1994) 831  
 Zinck, J.J., see Rajavel 138 (1994) 19  
 Zweck, J., see Grün 138 (1994) 150



ELSEVIER

Journal of Crystal Growth 138 (1994) 1097–1099

JOURNAL OF **CRYSTAL  
GROWTH**

## Subject index

### Aluminum

- gallium arsenide 727

### Apparatus

- for doping
- - of zinc selenide 403
- for thin film growth
- - by molecular beam epitaxy
- - - laser induced doping in zinc selenide 357

### Cadmium

- magnesium selenide 692
- magnesium telluride 155, 437, 638
- manganese telluride 437, 585, 652, 656, 661, 791, 856, 900
- mercury telluride 175, 486, 517, 917, 940, 944, 950, 956, 964, 981, 1040
- selenide 63, 150, 191, 545, 601, 619, 800, 849, 1004
- selenide telluride 239
- sulphide 150, 191, 213, 225, 231, 234, 559, 809, 976, 988, 993, 998
- telluride 8, 43, 86, 131, 161, 168, 244, 249, 274, 279, 285, 346, 437, 443, 493, 529, 578, 550, 580, 585, 590, 638, 652, 656, 791, 831, 856, 877, 900
- telluride selenide 161, 529, 607
- zinc selenide 1076
- zinc telluride 131, 168, 199, 244, 455, 529, 538, 607, 661, 826, 831, 950

### Calcium

- cadmium sulphide 1055
- strontium sulphide 1051

### Characterization

- of cadmium sulphide 809, 815
- of zinc selenide 805, 815
- optical properties
- - of cadmium sulphide 225, 231
- - of zinc telluride 187
- resonant Brillouin scattering
- - in zinc selenide 195
- spectroscopy
- - of cadmium telluride 244
- - of cadmium zinc telluride 244
- theoretical calculations of properties
- - - of II–VI ion implanted compounds 910
- - - of zinc manganese selenide 905
- - - of zinc selenium telluride 499

### Computer simulation

- of floating zone growth 161
- of heteroepitaxial growth 68
- of particle photochemical degradation 993
- of II–VI diode lasers, modeling of 697
- of vacancy concentrations 94

### Convection 161, 168

### Device characterization

- diodes 367, 391, 455, 727, 917, 940, 1078
  - electroluminescent materials 1010, 1017, 1023, 1061
  - electronic materials 99, 161, 175, 199, 208, 266, 285, 305, 331, 367, 391, 471, 477, 481, 486, 493, 504, 523, 607, 873, 924, 1034, 1046, 1051, 1055
  - heterojunction 1, 391, 455, 464, 508, 538, 601, 607, 643, 692, 727, 944
  - lasers 35, 63, 75, 105, 121, 131, 136, 140, 208, 219, 255, 367, 385, 391, 397, 418, 448, 464, 559, 564, 570, 585, 633, 667, 677, 686, 697, 714, 719, 737, 745, 750, 755, 759, 764, 768, 1076, 1077
  - light emitting diodes 692, 703, 768
  - modulators 709
  - optical 234
  - optoelectronic materials 204, 239, 338, 612, 800, 805, 1073
  - quantum dots 976, 988, 998, 1004
  - quantum wells 131, 155, 182, 191, 362, 391, 559, 564, 570, 575, 585, 590, 595, 601, 607, 619, 625, 629, 656, 661, 709, 719, 745, 759, 776, 791, 796, 826, 831, 838, 849, 856, 861, 884, 889, 1076
  - quantum wires 638
  - wave guides 843, 1076
  - theory 709, 714
- ### Diffusional control
- in solution crystal growth 970
  - in II–VI based semiconductors 362
  - of doping 140, 324
  - of elements into cadmium telluride 274, 279, 285
  - of interstitial vacancy 940
  - of vacancies 94
- ### Diodes, see Device characterization

Electronic materials, see Device characterization

Epitaxy, see Thin film growth

### Etching

- chemical 638, 934



- electron beam lithography 590, 638, 856
- ion beam 940
- photolithographic 8, 481

## Gallium

- arsenide 727
- indium aluminum phosphide 768
- indium arsenide phosphide 727
- selenide 43

## Germanium 43

## Gold 1078

Heterojunction, see Device characterization  
Hydrodynamics, see Convection

## Indium

- gallium phosphide 1

## Kinetics

- of complex formation 285
- of energy transfer 889
- of excitons 291
- of growth 8, 14, 19, 48, 367, 471, 970
- of nucleation 373
- of optical switching 213
- of pair defects 1040

Lasers, see Device characterization

## Lasers, crystals for

- cadmium sulphide 231
- II-VI compounds 786
- zinc cobalt sulphide 913

## Lead

- telluride 1034

Light emitting diodes, see Device characterization

## Magnesium

- selenide 295, 508
- telluride 295, 877, 1079

## Manganese

- selenide 601
- telluride 1028

## Melt growth technique

- by Bridgman-Stockbarger method
- - of cadmium selenium telluride 239, 529
- - of cadmium telluride 249, 529
- - of cadmium zinc telluride 529
- - of mercury cadmium telluride 956
- - of zinc manganese sulphide 1066
- by traveling heater method
- - of cadmium telluride 161, 168, 346
- - of cadmium telluride selenide 161
- - of cadmium zinc telluride 168
- - of mercury cadmium telluride 175
- - of zinc telluride 219

## Mercury

- cadmium telluride 175, 486, 517, 917, 940, 944, 950, 956, 964, 981, 1040
- cadmium manganese telluride 481
- selenide 471, 1034
- telluride 8, 964, 981
- zinc telluride 538, 934

## Microgravity, growth under

- of cadmium telluride 161
- of cadmium telluride selenide 161

## Morphological stability

- of zinc telluride 523

## Nucleation

- of cadmium sulphide 993
- of zinc selenide 1

## Numbers

- Prandtl 168
- Rayleigh 168

Optoelectronic materials, see Device characterization

## Phase diagrams

- of cadmium-tellurium 249

## Precursor

- for II-VI compounds 425

## Solid growth technique

- by recrystallization
- - of cadmium telluride 168
- - of cadmium zinc telluride 168

## Solution growth technique

- by chemical reaction
- - of cadmium sulphide 993
- by electrochemical deposition
- - of cadmium telluride 86
- by flux method
- - of cadmium zinc telluride 199
- - of calcium strontium sulphide 1051
- by gel method
- - of cadmium sulphide 998
- by low temperature method
- - of zinc sulphide 970

## Strontium

- sulphide 1010, 1017, 1061, 1075

## Superlattices, multilayers

- of III-V compounds 776
- of II-VI compounds 35, 63, 121, 140, 150, 182, 191, 513, 534, 550, 559, 564, 580, 590, 601, 612, 633, 643, 647, 652, 656, 661, 750, 776, 786, 796, 826, 868, 877, 884, 889, 900, 981, 1028

## Surface structure

- of cadmium selenide 545
- of mercury cadmium telluride 517
- of mercury zinc telluride 934
- of zinc selenide 55, 59

## Thin film growth, epitaxy

- by atomic layer epitaxy
  - of cadmium selenide 63
  - of zinc selenide 63, 136
- by hot wall epitaxy
  - of cadmium selenide 150, 191
  - of cadmium sulphide 150, 191
  - of cadmium telluride 131
  - of cadmium zinc telluride 131
  - of strontium sulphide 1010, 1061
  - of zinc sulphide 1010, 1061
  - of zinc telluride 81
- by liquid phase epitaxy
  - of cadmium zinc telluride 950
  - of mercury cadmium telluride 517, 944, 950
- by metalorganic molecular beam epitaxy
  - of zinc selenide 19, 391, 425
  - of zinc sulphoselenide 391
- by molecular beam epitaxy
  - of cadmium magnesium selenide 692
  - of cadmium magnesium telluride 155, 437
  - of cadmium manganese telluride 437, 652, 661, 856
  - of cadmium selenide 601, 619
  - of cadmium sulphide 559
  - of cadmium telluride 8, 437, 443, 550, 590, 607, 652, 856
  - of cadmium zinc telluride 607, 661
  - of gallium selenide 204
  - of indium gallium phosphide 1
  - of magnesium selenide 508
  - of manganese selenide 601
  - of manganese telluride 1028
  - of mercury selenide 471
  - of mercury telluride 8
  - of zinc cadmium selenide 391, 455, 564, 647, 686, 745, 861
  - of zinc cadmium sulphoselenide 28, 703
  - of zinc magnesium sulphoselenide 367, 686
  - of zinc selenide 1, 14, 48, 55, 59, 94, 110, 182, 266, 290, 331, 352, 357, 373, 391, 397, 403, 408, 455, 464, 564, 601, 619, 633, 647, 745, 861, 1073
  - of zinc sulphide 28, 145, 559
  - of zinc sulphoselenide 28, 182, 331, 367, 391, 455, 686, 745
  - of zinc sulphoselenide telluride 703
  - of zinc telluride 8, 81, 523, 550, 590, 633, 692
- by molecular beam epitaxy, through plasma source
  - of zinc selenide 430
- by vapor phase epitaxy
  - through chemical vapor deposition
    - of zinc selenide 75
  - through evaporation and condensation
    - of mercury cadmium telluride 964
    - of mercury telluride 964
    - of zinc selenide 255
  - through metalorganic chemical vapor deposition
    - of cadmium mercury telluride 917

- of cadmium sulphide 140
  - of cadmium telluride 43, 538
  - of cadmium zinc sulphide 538, 570
  - of cadmium zinc telluride 538
  - of gallium indium aluminum phosphide 768
  - of germanium 43
  - of mercury zinc telluride 538
  - of zinc cadmium selenide 629
  - of zinc selenide 35, 105, 114, 121, 127, 182, 208, 266, 324, 338, 379, 412, 448, 513, 534, 595, 612, 629, 750
  - of zinc selenide telluride 595
  - of zinc sulphide 121, 140, 418, 534, 578
  - of zinc sulphoselenide 35
  - of zinc telluride 412, 513, 538
  - through metalorganic chemical deposition, photo-assisted
    - of zinc cadmium selenide 737
    - of zinc selenide 737, 1071
  - theory of 68
- Two-six (II–VI) compounds
- doping and impurities in 290, 310, 318, 324, 338, 352, 357, 379, 385, 391, 397, 403, 408, 418, 425, 437, 443, 448, 607, 737, 745, 750
  - theory 295, 301, 305, 820, 895

## Vapor growth technique

- by evaporation and condensation
  - of strontium sulphide 1075
  - of zinc selenide 260
  - of zinc telluride 219

## Zinc

- cadmium selenide 391, 508, 564, 625, 629, 647, 667, 677, 686, 709, 714, 719, 745, 759, 764, 838, 861, 1077
- cadmium sulphide 538, 570
- cadmium sulphoselenide 28, 391, 703
- cobalt sulphide 913
- magnesium sulphoselenide 367, 667, 677, 686, 709, 719, 1077
- magnesium sulphoselenide telluride 1079
- manganese selenide 575, 905, 1066
- oxide 924
- selenide 1, 14, 19, 35, 48, 55, 59, 63, 75, 94, 99, 105, 110, 114, 127, 136, 195, 255, 260, 290, 295, 301, 305, 310, 318, 324, 331, 338, 352, 357, 373, 379, 385, 391, 397, 403, 408, 412, 425, 430, 448, 455, 464, 477, 504, 534, 564, 575, 595, 601, 619, 625, 629, 633, 643, 647, 677, 714, 727, 745, 750, 759, 764, 796, 805, 820, 838, 849, 861, 868, 924, 1071, 1073, 1076, 1078
- selenide telluride 595
- sulphide 28, 140, 145, 418, 534, 559, 570, 643, 796, 873, 970, 1010, 1023, 1061
- sulphoselenide 28, 35, 324, 331, 367, 455, 667, 686, 709, 714, 719, 745, 750, 755, 1046, 1076, 1077
- sulphoselenide telluride 703
- telluride 8, 81, 187, 219, 295, 412, 523, 538, 550, 580, 590, 633, 692, 826, 868